

# Encyclopedia of Nanoscience and Nanotechnology

Volume 4 Number 1 2004

- [▶ view](#) Hydrogen and Oxygen Interaction with Carbon Nanotubes 1  
*George E. Froudakis*
- [▶ view](#) Hydrogen Storage by Carbon Nanotubes 13  
*R. G. Ding; J. J. Finnerty; Z. H. Zhu; Z. F. Yan; G. Q. Lu*
- [▶ view](#) Hydrogenated Nanocrystalline Silicons 35  
*K. Shimakawa*
- [▶ view](#) Impurity States and Atomic Systems Confined in Nanostructures 43  
*R. Riera; R. Betancourt-Riera; J. L. Marín; R. Rosas*
- [▶ view](#) Inherently Conducting Polymer Nanostructures 113  
*Gordon G. Wallace; Peter C. Innis; Leon A. P. Kane-Maguire*
- [▶ view](#) Inorganic Nanomaterials from Molecular Templates 131  
*Sanjay Mathur; Hao Shen*
- [▶ view](#) *In-situ* Microscopy of Nanoparticles 193  
*Mark Yeadon*
- [▶ view](#) *In-situ* Nanomeasurements of Individual Carbon Nanotubes 205  
*Zhong Lin Wang*
- [▶ view](#) Integrated Passive Components 215  
*Richard Ulrich*
- [▶ view](#) Interatomic Potential Models for Nanostructures 231  
*H. Rafii-Tabar; G. A. Mansoori*
- [▶ view](#) Interfacial Defects in Nanostructures 249  
*I. A. Ovid'ko*
- [▶ view](#) Interfacial Effects in Nanocrystalline Materials 267  
*K. T. Aust; G. Hibbard; G. Palumbo*
- [▶ view](#) Ion Implanted Nanostructures 283  
*Karen J. Kirkby; Roger P. Webb*
- [▶ view](#) Ion Sputtering on Metal Surfaces 295  
*C. Boragno; F. Buatier de Mongeot; U. Valbusa*
- [▶ view](#) Ionic Conduction in Nanostructured Materials 309  
*Philippe Knauth*

<a href="#">▶ view</a> Kelvin Probe Technique for Nanotechnology <i>G. Koley; M. G. Spencer</i>	<a href="#">327</a>
<a href="#">▶ view</a> Kinesin and Nanoactuators <i>Konrad J. Böhm; Eberhard Unger</i>	<a href="#">345</a>
<a href="#">▶ view</a> Kinetics in Nanostructured Materials <i>V. V. Skorokhod; I. V. Uvarova; A. V. Ragulya</i>	<a href="#">359</a>
<a href="#">▶ view</a> Kondo Effect in Quantum Dots <i>H. Matsumura; R. Ugajin</i>	<a href="#">379</a>
<a href="#">▶ view</a> Laser-Scanning Probe Microscope Assisted Nanofabrication <i>Piero Morales</i>	<a href="#">389</a>
<a href="#">▶ view</a> Laser Fusion Target Nanomaterials <i>Keiji Nagai; Takayoshi Norimatsu; Yasukazu Izawa; Tatsuhiko Yamanaka</i>	<a href="#">407</a>
<a href="#">▶ view</a> Laser Induced Surface Nanostructuring <i>Yuji Kawakami; Eiichi Ozawa; Isamu Miyamoto</i>	<a href="#">421</a>
<a href="#">▶ view</a> Layer-by-Layer and Langmuir-Blodgett Films from Nanoparticles and Complexes <i>Marysilvia Ferreira; Valtencir Zucolotto; Marystela Ferreira; Osvaldo N. Oliveira Jr.; Karen Wohnrath</i>	<a href="#">441</a>
<a href="#">▶ view</a> Layer-by-Layer Nanoarchitectonics <i>Katsuhiko Ariga</i>	<a href="#">467</a>
<a href="#">▶ view</a> Lead Sulfide Nanoparticles <i>Jochen Fick; Alessandro Martucci</i>	<a href="#">481</a>
<a href="#">▶ view</a> Light-Harvesting Nanostructures <i>Teodor Silviu Balaban</i>	<a href="#">505</a>
<a href="#">▶ view</a> Light Scattering of Semiconducting Nanoparticles <i>G. Irmer; J. Monecke; P. Verma</i>	<a href="#">561</a>
<a href="#">▶ view</a> Localization and Interactions in Magnetic Nanostructures <i>F. G. Aliev; V. K. Dugaev; J. Barnaś</i>	<a href="#">587</a>
<a href="#">▶ view</a> Low-Dimensional Nanocrystals <i>Shu-Hong Yu; Jian Yang; Yi-Tai Qian</i>	<a href="#">607</a>
<a href="#">▶ view</a> Low-Frequency Noise in Nanomaterials and Nanostructures <i>Mihai N. Mihaila</i>	<a href="#">649</a>
<a href="#">▶ view</a> Low-Temperature Scanning Tunneling Microscopy <i>Wolf-Dieter Schneider</i>	<a href="#">667</a>
<a href="#">▶ view</a> Luminescence of Semiconductor Nanoparticles <i>Wei Chen; Alan G. Joly; Shaopeng Wang</i>	<a href="#">689</a>



<a href="#">▶ view</a>	Luminescent Organic-Inorganic Nanohybrids <i>R. A. Sá Ferreira; L. D. Carlos; V. de Zea Bermudez</i>	<u>719</u>
<a href="#">▶ view</a>	Macroscopically Aligned Carbon Nanotubes <i>Pascale Launois; Philippe Poulin</i>	<u>763</u>
<a href="#">▶ view</a>	Magnesium-Nickel Nanocrystalline and Amorphous Alloys for Batteries <i>H. K. Liu</i>	<u>775</u>
<a href="#">▶ view</a>	Magnetic Field Effects in Nanostructures <i>R. Riera; J. L. Marín; H. León; R. Rosas</i>	<u>791</u>
<a href="#">▶ view</a>	Magnetic Semiconductor Nanostructures <i>Wolfram Heimbrodt; Peter J. Klar</i>	<u>835</u>
<a href="#">▶ view</a>	Magnetism in Nanoclusters <i>C. Binns</i>	<u>899</u>
<a href="#">▶ view</a>	Magnetism in Rare Earth/Transition Metal Multilayers <i>V. O. Vas'kovskiy; A. V. Svalov; G. V. Kurlyandskaya</i>	<u>925</u>
<a href="#">▶ view</a>	Magnetoimpedance in Nanocrystalline Alloys <i>B. Hernando; P. Gorria; M. L. Sánchez; V. M. Prida; G. V. Kurlyandskaya</i>	<u>949</u>

---

Copyright © 2004 American Scientific Publishers

# Hydrogen and Oxygen Interaction with Carbon Nanotubes

George E. Froudakis

*University of Crete, Heraklio, Crete, Greece*

## CONTENTS

1. Introduction
  2. A Brief Experimental Overview
  3. The Need for Theoretical Modeling
  4. *Ab Initio* Approaches in Large Systems
  5. Hydrogen Interaction with Carbon Nanotubes
  6. Oxygen Interaction with Carbon Nanotubes
  7. Conclusions
- Glossary  
References

## 1. INTRODUCTION

Since the discovery of carbon nanotubes a lot of experimental and theoretical work has appeared investigating and analyzing their structural and electronic properties [1–3]. Especially single walled carbon nanotubes (SWNTs) were proposed both as microcavities for storage [4–9] and as ideal molecular wires for microelectronic applications [10]. Furthermore the functionalization of the SWNT surface was found to affect both their storage capacity [9] and their electronic properties [10–12].

Hydrogen has been recognized as an ideal energy carrier but has not been used yet to a large extent. One of the major problems is the difficulty of efficient storage. In the beginning metal alloys were tested for storage tanks but even though they have sufficient storage capacity, they are expensive and heavy for commercial production focused on mobile applications. In the recent years, carbon based materials attracted attention due to the discovery of novel carbon nanomaterials like fullerenes, nanofibers, and nanotubes [1–3]. Especially SWNTs, which have diameters of typically a few nanometers, have been suggested as suitable materials for gas storage [4]. Since pores of molecular dimensions can adsorb large quantities of gases, hydrogen can condense to high density inside narrow SWNTs even at room temperature [5]. The high hydrogen uptake of these

materials suggests that they can be used as hydrogen-storage materials for fuel-cell electric vehicles [6–8].

Recently it was experimentally proved that the electronic and transport properties of SWNTs are extremely sensitive to their exposure to gas molecules [10–12]. Especially oxygen attracted a lot of interest due to the importance of its interaction with SWNTs both in their synthesis by purification and their functionalization for controlling their electronic properties. Considering that all previous experimental studies of SWNTs have used samples exposed to air, the results of these measurements must be carefully reevaluated.

## 2. A BRIEF EXPERIMENTAL OVERVIEW

A lot of recent experiments are trying to investigate the hydrogen storage in SWNTs. First, in 1997, Dillon et al. reported that SWNTs could store hydrogen [4]. Using temperature-programmed desorption spectroscopy they showed that hydrogen would condense inside SWNTs under conditions that do not induce adsorption within a standard mesoporous activated carbon.

Two years later Liu et al. found out that this storage can take place in room temperature [5]. They used SWNTs of 1.85 nm diameter, synthesized by a semicontinuous hydrogen arc discharge method, and found a storage capacity of 4.2 wt% at room temperature and under modestly high pressure; 78.3% of the adsorbed hydrogen can be released under ambient pressure and room temperature.

The same year Chen et al. reported that alkali-doped carbon nanotubes possess high hydrogen uptake [9]. They investigated lithium and potassium doped carbon nanotubes and found hydrogen absorption of 14 to 20 wt% between 400 °C and room temperature. These values are higher than those of metal hydride and cryoadsorption systems. The stored hydrogen could be released at higher temperatures and the sorption–adsorption cycle can be repeated with minor loss of the storage capacity.

After that a lot of experimental work has been performed trying to investigate the hydrogen adsorption in SWNTs and to improve the storage capacity of the tubes by doping them

[13–20]. Nevertheless the experiments on hydrogen storage in nanotube samples have been controversial as reported by the recent review of Ding et al. [8].

Concerning the electronic properties of the nanotubes, Collins et al. reported that they are extremely sensitive to the chemical environment [10]. The exposure to atmospheric air or oxygen dramatically influences the nanotubes' electrical resistance, thermoelectric power, and density of states, as determined by transport measurements and scanning tunneling microscopy [10]. The most interesting observation of Collins et al. is that these electronic parameters can be reversibly tuned by a surprisingly small concentration of adsorbed gases.

### 3. THE NEED FOR THEORETICAL MODELING

On the other hand, until recently, there was no sufficient theoretical explanation of gas adsorption in SWNTs but only guesses about this procedure. This affected badly both the understanding of the nature of these materials and the improvement of their storage capacity that ended up in a random procedure. The need for theoretical modeling was crucial because even though the experiments can inform us *what* is happening, only theory allows us to find out *why* it is happening and what will happen in similar conditions.

Concerning the gas adsorption in carbon nanotubes, the theoretical calculations can be extremely useful for understanding the elementary steps of the adsorption procedure and give an insight into the phenomenon.

### 4. AB INITIO APPROACHES IN LARGE SYSTEMS

One of the major headaches in computational material science is how accurate theoretical techniques can be applied in large systems. By “accurate theoretical techniques” we mean quantum chemistry methods, called *ab initio*, due to the fact that they do not enforce any parameters to the system but solve the Schrödinger equations from first principles. The greater advantage of the *ab initio* methods is that they can provide structural, electronic, and dynamic properties of the calculating system in high accuracy. On the other hand the computational cost increases dramatically with the number of the electrons in the system.

The problem that arises in polyatomic systems is how to compromise the relatively large size of the system and an accurate *ab initio* method without ending up with a prohibitively large calculation. There are three possible solutions to this dilemma of treating large systems with *ab initio* methods: (a) the periodic density functional theory model, (b) the mixed quantum mechanics/molecular mechanics model, and (c) the cluster model.

#### 4.1. Periodic Density Functional Theory Model

The periodic density functional theory (DFT) model is schematically presented in Figure 1a for a (4,4) SWNT. A part of the system (central part of the tube presented

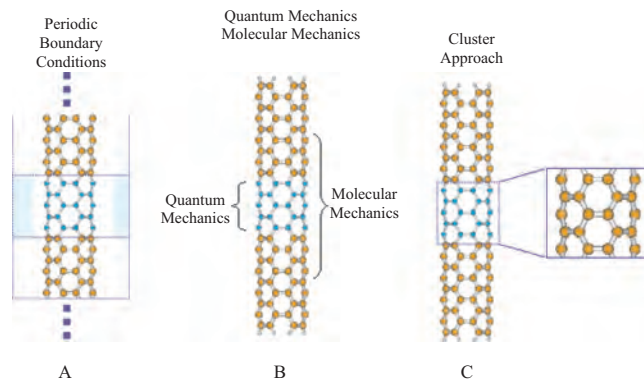


**Figure 1.** Three possible models for treating large systems with *ab initio* methods. (A) Periodic DFT model simulating a (4,4) SWNT. A part of the system (blue colored carbon atoms) is separated and treated as unit cell for a periodic building of the system. (B) The QM/MM model simulating a (4,4) SWNT. The total 200-atom tube was separated in three cylindrical parts. The inner one was treated with DFT (40 blue color carbon atoms) while the two outer parts with molecular mechanics (brown color carbon atoms). The dangling bonds at the ends of the tube were saturated with hydrogen atoms. (C) The *cluster* model. A part of the system is separated and treated as individual cluster.

with blue color carbon atoms) is separated and treated as a unit cell. This unit cell is periodically repeated in the space (for the tube in one dimension only) building an infinite system. Implementation of periodic boundaries conditions to the equations solves the mathematical part of the problem. The advantage of this approach is that the total system is treated with *ab initio* techniques. The disadvantage is that local interactions and defects studied in the unit cell are automatically repeated periodically. In this way local properties become periodic. An example of the use of this approach is presented in Section 5.3.1.

#### 4.2. Quantum Mechanics/Molecular Mechanics Mixed Model

The mixed quantum mechanics/molecular mechanics (QM/MM) model is schematically presented in Figure 1b. The basic idea of this method is that the system is divided in two parts: one is treated by *ab initio* methods and the other by molecular mechanics. The bordering of the two parts is arranged by introducing link atoms. More details for this model can be found in [21].

For the (4,4) SWNT presented in Figure 1b, the total 200-atom tube was separated in three cylindrical parts. The inner one was treated with DFT (40 blue color carbon atoms) and the two outer parts with molecular mechanics (brown color carbon atoms). The dangling bonds at the ends of the tube were saturated with hydrogen atoms.

The advantage of the QM/MM model is that no periodic constraints are introduced to the systems. The disadvantage is that only a relatively small part of the system is treated quantum mechanically while the rest is used for constraining the boundaries. This method is suitable for studying local properties. An example of the implementation of the QM/MM approach in SWNTs is presented in Section 5.3.2.

### 4.3. The Cluster Model

In the *cluster* model (Fig. 1c) a part of the system is separated and treated as an individual cluster. Extra attention has to be given to the dangling bonds that are generated at the braking areas. These dangling bonds have to be saturated properly with the addition of extra atoms (for example hydrogens). In this way the boundary instabilities that arise from QM/MM and the periodicity problems introduced by periodic DFT can be eliminated. The drawback of this method is that only a relatively small part of the system can be used. An example using the cluster model approximation is presented in Section 6.1.

It is clearly shown that no one of all these three techniques gives a perfect and unique solution to the problem. All show advantages and disadvantages and the decision as to which one we should choose have to be made according to the problem we face each time.

## 5. HYDROGEN INTERACTION WITH CARBON NANOTUBES

The theoretical simulations in this field can be generally classified in two categories according to the theoretical approximation that they are based on. The first group employs Monte Carlo and molecular mechanics *classical* algorithms in order to investigate the physisorption of hydrogen in SWNTs while the second uses *ab initio* or semiempirical *quantum* techniques for studying mainly the chemisorption of atomic hydrogen in SWNTs. A review of theoretical calculation of hydrogen storage in carbon-based materials can be found in [22].

### 5.1. Hydrogen Physisorption in Carbon Nanotubes

First Darkrim and Levesque in late 1998 using a Lennard-Jones potential performed a grand canonical Monte Carlo simulation of hydrogen storage in a cell of SWNTs and investigated the influence of the tube diameter on the storage capacity [23]. They found that adsorption decreased as the SWNT diameter increased due to the fact that a large part of the volume inside or outside the tube is out of the attractive force range of the solid-gas interaction. They also note the dependence of their results on the intermolecular potential used for the hydrogen-carbon interaction. This is the major disadvantage of classical simulations and points to the need for *ab initio* calculations in the field.

In 1999 Johnson and co-workers using the Silvera-Goldman potential for the H<sub>2</sub>-H<sub>2</sub> interaction and the Crowell-Brown potential the H<sub>2</sub>-tube interaction studied hydrogen adsorption in neutral [24] and positively and negatively charged [25] SWNTs. Their results show that idealized graphitic nanofibers (slit pores) give significantly better performance for hydrogen storage than SWNT arrays. They also underline the importance of the packing geometry of the SWNTs in the storage capacity. In addition, a 0.1 e/C charging of the nanotubes increased the adsorption up to 30%.

In the year 2000 Williams and Eklund simulated H<sub>2</sub> physisorption in finite-diameter carbon nanotube ropes

using grand canonical Monte Carlo [26]. Their simulation clearly shows that small diameter ropes are preferable for hydrogen storage. They also point out an essential difference between models and experiments that has to do with the ideal and “atomically clean” surface of the tubes in the simulation.

The great advantage of these classical approaches, except for the luxury to take into account large systems, is the temperature dependence of the simulations. On the other hand they are parameter dependent and cannot provide an insight into the chemical bond as the *ab initio* methods do.

### 5.2. Quantum Approaches

In 2001 the *quantum picture* was introduced to the molecular dynamic study of hydrogen in SWNTs either by quantum molecular dynamics algorithms [27] or by minimal *ab initio* calculations in parts of classical-optimized tube geometries [28]. In the first case, Cheng et al. using the Vienna *ab initio* simulation package performed a quantum mechanical molecular dynamics simulation of H<sub>2</sub> absorption in a trigonal two-dimensional lattice of armchair (9,9) SWNTs [27]. The potential energy surface near the equilibrium point was found to be relatively flat and significant changes of the lattice constants (>0.5 Å) resulted in only small changes in the lattice energy (<1 kcal/mol). Cheng et al. also investigated the site selectivity during the adsorption, since arrays of SWNTs with open ends may accommodate hydrogen inside the tube (endohedral adsorption) or inside the pores formed by different tubes (exohedral adsorption). According to their thermodynamical studies, the exohedral adsorption was found to be energetically more favorable [27].

On the other hand Ma et al. first used a many body Tersoff-Brenner potential to simulate low energy collision of atomic H on the sidewall of an armchair (5,5) SWNT [28]. On top of this they performed minimal HF/STO-3G *ab initio* calculations to some selected snapshots of the molecular dynamics simulations. The interesting part of their work is the sorting of the collision results with respect to the hydrogen energy. Their results indicate that if the hydrogen energy is in the range of 1–3 eV the H will be adsorbed in the tube sidewall while with a energy between 4 and 14 eV the H has large possibility to rebound off the wall. With energy in the interval of 16–25 eV the H has a high probability of penetrating into the tube and being trapped inside forming hydrogen molecules and gradually condensing to become liquid hydrogen inside the tube. Finally with an energy range from 20 to 30 eV the H atom can enter the tube from one side and escape from the other or break a C–C bond [28].

Since only quantum chemistry calculations can give insight into the hydrogen interaction with SWNTs, Dubot and Cenedese used semiempirical AM1 simulations to give binding sites, energetics, and orbital pictures of lithium and molecular hydrogen adsorption in SWNTs [29]. They found that Li can adsorb inside and outside a zigzag tube and the most stable site is above the center of a tube hexagon. After the Li adsorption, molecular hydrogen can be bound to the Li atom with a binding energy of 0.5 eV. Their AM1 calculation showed also that molecular hydrogen is repelled from the tube wall if the tube is not doped [29].

In 1999 Jeloica and Sidis used DFT to investigate hydrogen adsorption on a graphitic cluster model [30], but only in 2000 did first principle calculations of the hydrogen adsorption in SWNTs appear in the literature [31–35].

The main reason that *ab initio* calculations in SWNTs appear lately is the system size. In order to take into account a large enough model of SWNT you need approximately 200 atoms. The problem that arises in such an attempt is how to compromise the large size of the system and an accurate *ab initio* method without ending up in a prohibitively large calculation.

As analyzed in Section 4, there are three different ways to overcome this dilemma. Two of them were used in this specific problem. The first uses the periodicity of the SWNTs and combines an *ab initio* method with periodic boundary conditions [31, 32]. The second uses a two level quantum mechanics/molecular mechanics (QM/MM) approach [21, 33–35]. In the latter the tube is divided into two different parts treated with different methods. The advantage of the first is that the total system is treated with *ab initio* techniques while the obvious disadvantage is that an external periodicity is forced to the system. For the QM/MM model there is no periodic constrain. The disadvantage is that only a relatively small part of the system is treated quantum mechanically while the rest is used for constraining the boundaries. In addition, both approaches have the disadvantage of excluding temperature from the calculations.

### 5.3. Atomic Hydrogen Interaction with Carbon Nanotubes

#### 5.3.1. Application of Periodic DFT Model

The hydrogen chemisorption in SWNTs was studied with both quantum chemistry models that we described earlier. Lee and Lee first employed the periodic DFT approach for studying chemisorption site of atomic hydrogen outside and inside of a (5,5) and a (10,10) SWNT [31]. They used supercells of eight layers along the tube axis and their results are presented in Figure 2. Their periodic-DFT calculations showed two hydrogen chemisorption sites in SWNTs. Both are *top* positions, inside (Fig. 2b) and outside (Fig. 2d) the tube walls. They predict also that hydrogen molecules can exist in the empty space inside the nanotube. The maximum storage capacity is mainly determined by the steric interaction between the H<sub>2</sub> molecules and between the H<sub>2</sub> and the tube wall. As a result the capacity increases linearly with the tube diameter. Excessive hydrogen storage will result in large repulsion energies and eventually break down the tube wall [31].

#### 5.3.2. Application of QM/MM Mixed Model

The QM/MM mixed model has been employed for studying the hydrogen interaction with SWNTs by Bauschlicher [33, 34] and Froudakis [35]. In this approach the total system is divided in two different sections: the inner part that is treated with an accurate quantum chemistry method and the outer part where a molecular mechanics force field is employed (Fig. 1b). This two-level approach combines the high accuracy of the *ab initio* treatment of the inner part of the tube in which the interaction with hydrogens will take

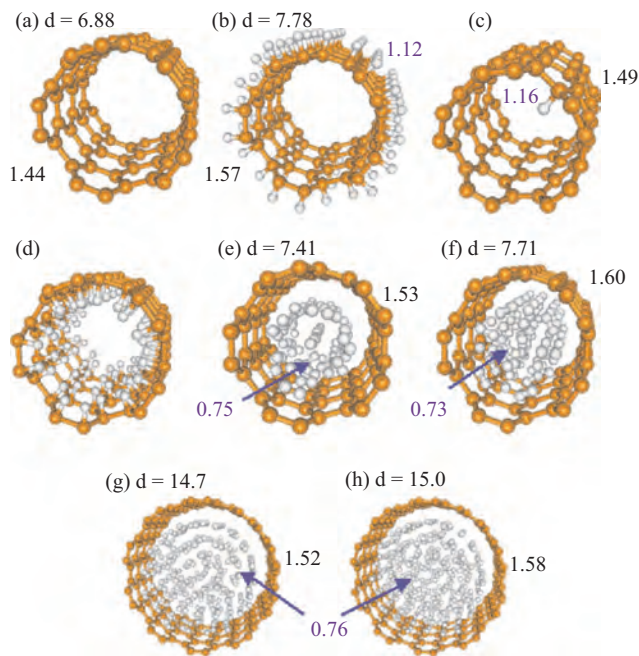


**Figure 2.** The calculations of Lee and Lee [31] for the chemical adsorption of H in SWNTs: (a) (5,5) SWNT before storage; (b) hydrogens adsorbed at the exterior of the tube wall; (c) adsorption of a single hydrogen atom at the interior of the wall; (d) initial and (e) fully relaxed geometry of (d); (f) molecular hydrogen inside the (5,5) SWNT; (g) H<sub>2</sub> inside (10,0) SWNT with an analogy of two H per one C atom and with 2.4 H/C (f). Bond lengths are in Å.

place, with the relaxation accuracy that the large size of the tube guarantees.

Bauschlicher used an (10,0) carbon nanotube for studying the hydrogen and fluorine binding to its wall [33] and for examining the maximum coverage of the tube wall [34]. The entire model used 200 carbon atoms while the *ab initio* section includes 24 carbon atoms. The ONIOM two level method of Dapprich and co-workers [21] was used for this purpose as it is implemented in the Gaussian 98 program package [36]. The higher level was treated with DFT and the lower level with MM. More specifically the B3LYP hybrid functional together with the 4-31G basis set was employed for the QM part and the universal force field (UFF) for the MM part. The preferable sites for the chemisorption of one, two, and four hydrogen atoms in the tube walls are reported together with the binding energies [33].

In [35] we applied the QM/MM approach in a 200-atom (4,4) SWNT, treating up to 64 carbons and 32 hydrogens with the higher level of theory (Fig. 1b). The small diameter of the tube together with the large number of atoms considered allow the higher level model to include a cylindrical part of the tube. This is very critical for investigating changes of the shape of the tube during the adsorption procedure.

In Figure 1b, we can see the two-level ONIOM [21] model that was used in [35]. The B3LYP functional was employed for inner part of the tube, as in [33, 34]. Nevertheless a larger set of double- $\zeta$  basis was employed (6-31G\*) that includes polarization functions. The two outer cylindrical parts were treated with the UFF while the dangling bonds at the ends of the tube were saturated with hydrogen atoms.



All the computations were performed with the Gaussian 98 program package [36].

These studies [33–35] mainly try to answer two questions: The first concerns the coverage of SWNTs by hydrogen atoms and the second deals with the difficulty of putting hydrogen atoms inside the tube. From the work of Bauschlicher [33] and Froudakis [35] it is clear that the hydrogen atoms that approach the SWNT will be bound to the tube walls in neighboring C atoms for minimizing the loss of C–C  $\pi$  bonds. But there are many different ways of doing this: One is to follow a zigzag line parallel to the tube axis while another is to follow an armchair ring vertical to the tube axis. First principle calculations [35] showed that the second procedure is energetically more favorable as has also been found experimentally for similar systems [13].

Furthermore it is interesting to see the effect of the two different hydrogen chemisorption patterns mentioned before on the shape of the tube walls. In Figure 3 we can see the optimized structures with 64 C and 16 H atoms in the QM region from [35]. The C atoms that hydrogens are bonded to pass from the  $sp^2$  to  $sp^3$  hybridization. This affects drastically the bond lengths and the size of the tube hexagons. The C–C bond length increases from 1.43 to 1.59 Å while the diameter of the hexagons goes from 2.84 to 3.15 Å if four hydrogen atoms are attached to this hexagon (Fig. 3b). These cause a strain that leads to tube deformation.

In the case of the line orientation of the hydrogens the shape of the tube changes from cyclic to elliptic (Fig. 3a). The 5.4 Å diameter of the tube without hydrogen split to

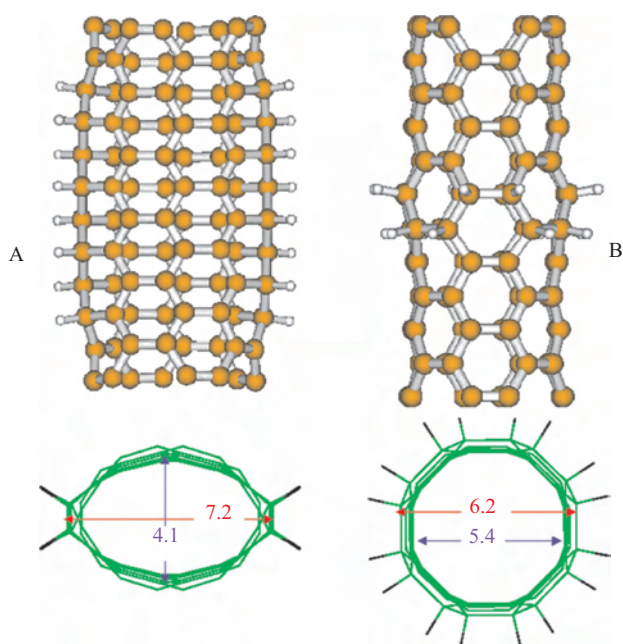


**Figure 3.** Optimized geometries from [35] showing 16 hydrogen atoms bonded in the tube in the two different ways: (A) following two zigzag lines parallel to the tube axis and (B) following an “armchair” ring vertical to the tube axis. In the lower part of the figure we see the tube toward its axis and we report the changing of its diameter in angstroms. Modified from [35], G. E. Froudakis, *Nano Lett.* 1, 179 (2001). © 2001, American Chemical Society.

a small 4.1 Å and large 7.2 Å diameter of an ellipsis. In the case of the ring orientation we see an enlargement of the tube diameter from 5.4 to 6.2 Å but keeping the cyclic shape (Fig. 3b). The second orientation is more favorable because the strain can be relaxed with the enlargement of one ring that does not affect the whole tube, while in the first case, an axial enlargement of the tube cannot take place only in one zigzag C line. This effect results in an energy difference of 2.6 eV between these two orientations. It is worth mentioning that in the line format we have no change in the volume of the tube while in the ring one, we have a 30% enlargement of the volume.

Since the hydrogens “prefer” to form rings around the tube the next question that arise is how close can those rings be? For answering this question in [35] we performed calculations with two different zigzag ring orientations (48 carbons and 32 hydrogens in the QM region). In the first, the rings were separated and in the second they were close together as can be seen in Figure 4a (middle and right upper part, respectively). After optimizing the geometries the separated configuration showed a repeated increasing and decreasing of the tube diameter of almost 1 Å. On the other hand, when the rings were closed together, the tube diameter was increased in the first ring by 1 Å and decreased to the normal value at the last ring. The total energy of the “ring by ring” configuration was favored energetically from the “all rings together” configuration by 17 eV.

This energy difference can be explained from the nature of the hybridization of the carbon atoms. During hydrogen addition the carbon atoms pass from  $sp^2$  to  $sp^3$  hybridization and a three-dimensional (3D) bond orientation is preferable. This 3D orientation can be obtained by the continued changing of the tube diameter in the “ring by ring”

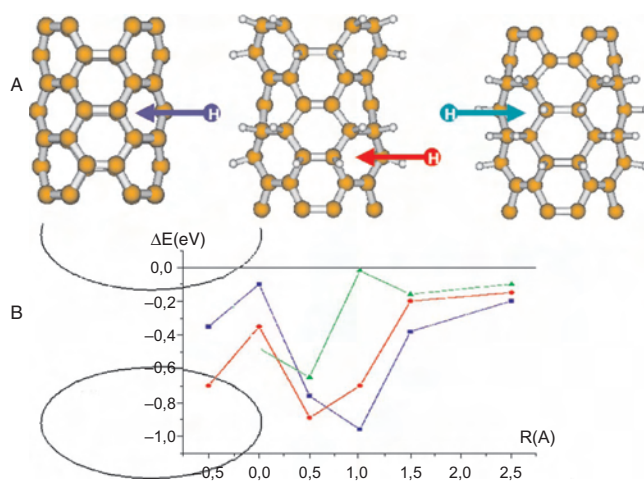


**Figure 4.** (A) Optimized geometries [35] of 32 hydrogen atoms bonded in the tube in the two different ways: “ring by ring” configuration (in the middle) and “all rings together” configuration (at the right part) as analyzed in the text. The geometry of the tube without hydrogens is also plotted for comparison (left part). (B) Potential curves during the hydrogen approach to the three different carbon nanotubes shown in (A) (SWNT with no hydrogen atoms to its walls: blue line; SWNT with walls half filled with hydrogens: red line; and SWNT with walls full with hydrogen: green line). Modified from [35], G. E. Froudakis, *Nano Lett.* 1, 531 (2001). © 2001, American Chemical Society.

configuration. In this case the tube wall is not flat toward the tube axis but shows a zigzag shape (Fig. 4a, middle). In the case of the “all rings together” configuration the tube wall is changing shape only in the beginning and at the end, while in between it stays flat (Fig. 4a, right). The flat wall shape that was favorable when carbon atoms had  $sp^2$  hybridization is not favored after the hydrogen adsorption because carbon atoms changed hybridization to  $sp^3$ . Extending this configuration to an infinite atom tube will end up to 50% coverage since one C-zigzag ring has hydrogens and the next does not, periodically. This procedure will cause a 15% enlargement of the tube volume (half of the rings gain 30% in volume).

Bauschlicher in [34] reported also 50% hydrogen coverage in a (10,0) SWNT. He tested with the ONIOM approach a lot of random and prefixed bonding configurations of hydrogen in the tube walls. The “pairs of lines” configuration is presented in Figure 5 and found to be energetically more favorable. This result is not in disagreement with that previously mentioned for a (4,4) SWNT by Froudakis [35] since the (10,0) tube is significantly larger than the (4,4), and the curvature was found to play an important role in the adsorption procedure to SWNTs [37–39]. Furthermore Froudakis has not calculated a “pair of lines” configuration in the (4,4) SWNT.

The second question we tried to answer in [35] is what happens after the adsorption of hydrogens to the tube walls. Is it easier to fill up the tube with hydrogens? In

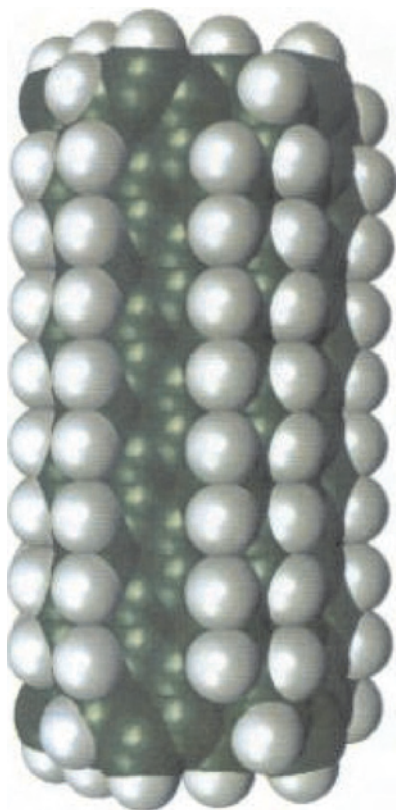


**Figure 5.** The most stable configuration of 50% hydrogen coverage in a (10,0) SWNT calculated by Bauschlicher. Modified from [34], C. W. Bauschlicher, Jr., *Nano Lett.* 1, 223 (2001). © 2001, American Chemical Society.

Figure 4b we report the potential curves when atomic hydrogen approaches the center of three tube-wall hexagons which differ only in the adsorption rate. The first has no hydrogen, the second is half filled with hydrogen, and the third is full of hydrogen. Analyzing these potential curves we see two competing forces in the approaching procedure. In one hand it is clear that the more hydrogen we have in the C hexagon, the larger the hexagon is and the easier the outgoing H passes. This can be easily observed by lowering the barrier at the tube wall as the number of hydrogens in the hexagon increases. On the other hand, the hydrogen in the hexagon is screening the attraction of the carbon atom to the external hydrogen. This screening, in the case of a fully hydrogenated hexagon, inserts a barrier in the outgoing hydrogen at a distance of 1 Å from the tube wall (where the bonded hydrogens are actually located). As a result, the energetically favorable H approach is when the tube wall is half filled with hydrogens. This happens because in the first part of the approach there is no barrier caused by steric repulsion of the bonded hydrogens, while in the entrance of the tube wall the barrier is smaller by almost 0.3 eV than the case of the bare tube.

Comparing the QM/MM results of Froudakis [35] with those of Seifert et al. [32] and Kudin et al. [40] obtained with periodic boundary condition models, we find an agreement concerning the stoichiometry (C: 2 ligand: 1) and the deformation of the tube that take place during the adsorption. Nevertheless there is a disagreement about the ligand orientation around the tube wall that could be a consequence of the different approach used (QM/MM versus periodic box) and/or from the different ligand (H versus F) and/or from the different tube examined (4,4 versus 10,10 that have almost double diameter).

#### 5.4. Molecular Hydrogen Interaction with Doped Carbon Nanotubes

After 1999 when Chen et al. [9] reported that alkali-doped carbon nanotubes possess high hydrogen uptake a lot of experimental work has been performed trying to investigate the hydrogen adsorption in SWNTs and to improve the storage capacity of the tubes by doping them [15]. On the other hand, there was no sufficient theoretical explanation of this phenomenon.

All the theoretical calculations reported so far can be divided in two categories. Either they are empirical [23–29] or they are based on first principle methods but deal only with atomic hydrogen [30–35]. The first category cannot give an understanding of the elementary steps in the adsorption process. Since these methods are not *ab initio* but based on parameters, they cannot provide insight into the chemical bond. The first principle methods can, but they deal only with atomic hydrogen while the most important interaction for the storage, which is the molecular hydrogen interaction with SWNTs, remains untouched. The reason *ab initio* studies of the  $H_2$  interaction with SWNTs do not exist is obvious. The interaction is weak and the system is large.

In [41] we tried to investigate the nature of the  $H_2$  adsorption in alkali-doped SWNTs and to compare it with the adsorption in pure SWNTs. Only in this way it is possible to answer why alkali doped carbon nanotubes have high  $H_2$

uptake. In order to compromise the large size of the system together with an accurate *ab initio* method without ending up in a prohibitively large calculation we applied the QM/MM mixed model as described earlier (Section 4.2) in a closed (5,5) SWNT with 150 carbon atoms. K atoms dope the tube in a  $2 \times 2$  pattern as suggested by Gao et al. [42]. In this pattern the K atoms were placed on “hollow” positions above the center of the C hexagons of the tube in such a way that if one hexagon has potassium, all the neighboring ones do not (Fig. 6). A geometry optimization confirmed that these positions were optimum for our model, too. Twenty-four carbon atoms together with two potassium atoms and all the  $H_2$  molecules that were interacting with these two K atoms were kept in the QM region, while the rest of the atoms were treated by MM.

The first case considered (Fig. 6, left) was a doped tube where a single  $H_2$  molecule was interacting with each K atom. After the geometry was optimized, the binding energy of the  $H_2$  to the K was 3.4 Kcal/mol/ $H_2$ . The distance of the K atom from the center of the  $C_6$  hexagon of the tube was 3.0 Å while the distance of the closer H of the  $H_2$  molecule from the K was 3.0 Å, too. In the next case (Fig. 6, middle) two hydrogen molecules were interacting with each K and finally three (Fig. 6, right). The binding energies were 2.5 and 1.8 kcal/mol/ $H_2$  respectively. The  $H_2$  distance from the K was found to be 3.3 and 3.5 Å while the K–tube distance remained the same (3.0 Å).

From these results is clearly showed that at least three hydrogen molecules can bound each K atom of a doped tube even though the binding energy is consistently decreasing with the number of ligands. The two questions that immediately arise are: How many  $H_2$  can be accommodated to each alkali of the doped tube? And why do the doped tubes have larger hydrogen uptake that the pure carbon nanotubes?

For answering the first question we also calculated in [41] the case where five  $H_2$  molecules were attached at each K of the doped tube. The binding energy was 1.1 kcal/mol/ $H_2$ . Then the binding energy per hydrogen molecule was plotted with respect to the number of the  $H_2$  molecules. As can be seen from Figure 7 the binding energy decays exponentially. This result has to be considered together with the

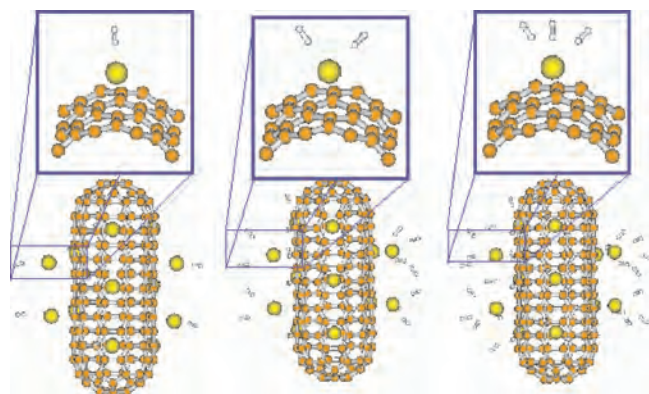


**Figure 6.** Three of the alkali metal doped (5,5) SWNTs used by Froudakis [41] to study the interaction with molecular hydrogen. The first has one  $H_2$  per K, the second two, and the third three. A magnified part of all pictures is also presented.

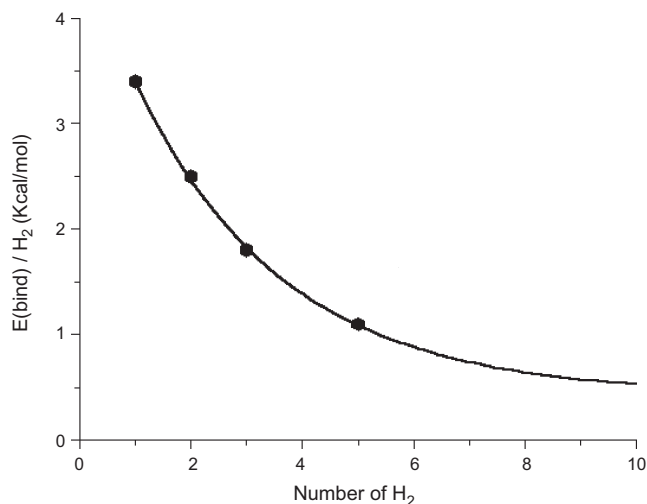


**Figure 7.** Binding energy per hydrogen molecule with respect to the number of the  $H_2$  molecules. The hexagons represent the calculated values where the line was fitted. Modified from [41], G. E. Froudakis, *Nano Lett.* 1, 531 (2001). © 2001, American Chemical Society.

geometrical constrains (i.e., the space around the K atoms has a maximum number of  $H_2$  molecules that can be introduced without having steric interactions). From this graph we can estimate the amount of  $H_2$  molecules that can be attached to a doped tube according to the temperature that plays the role of the energetic cutoff.

For the second question (why the doped tubes have a larger hydrogen uptake) we have to understand the nature of the  $H_2$  interaction with the pure carbon and the alkali-doped nanotubes. In the case of the doped tube there is a charge transfer from the alkali metal to the tube. This charge was calculated by Mulliken population analysis to be 0.6  $|e|$  for the K doped tube [41]. The positively charged K atoms polarize the  $H_2$  molecules. Even though there is no charge transfer from the  $H_2$  to the K the charge induced dipole interaction gives the character of the bonding (Fig. 8). In the case of the pure tube, where the  $H_2$  interaction was calculated for comparison, there is neither charge transfer nor polarization of the  $H_2$  molecule and this results in an extremely weak interaction, under the accuracy of our theoretical level.

Comparing these results [41] with previous work for atomic hydrogen we can see *physisorption* of the molecular hydrogen to doped or undoped SWNTs while for the atomic hydrogen we have *chemisorption*. There is in agreement of our QM/MM results [41] and the semiempirical results of Dubot and Cenedese [29] indicating that the alkali metal is responsible for the adsorption of molecular hydrogen to doped tubes. Nevertheless they predict an adsorption energy of 11.5 kcal/mol [29], while we found 3.4 kcal/mol [41]. The fact that we use K while they use Li for doping the tube does not explain this large difference, which is probably due to the empirical nature of their calculations [29]. In addition, the explanation that the alkali metal act as a catalytic active center for the  $H_2$  dissociative adsorption proposed by Chen et al. [9] does not seem very possible since the alkali metal– $H_2$  interaction is too weak to cause a  $H_2$  dissociation.



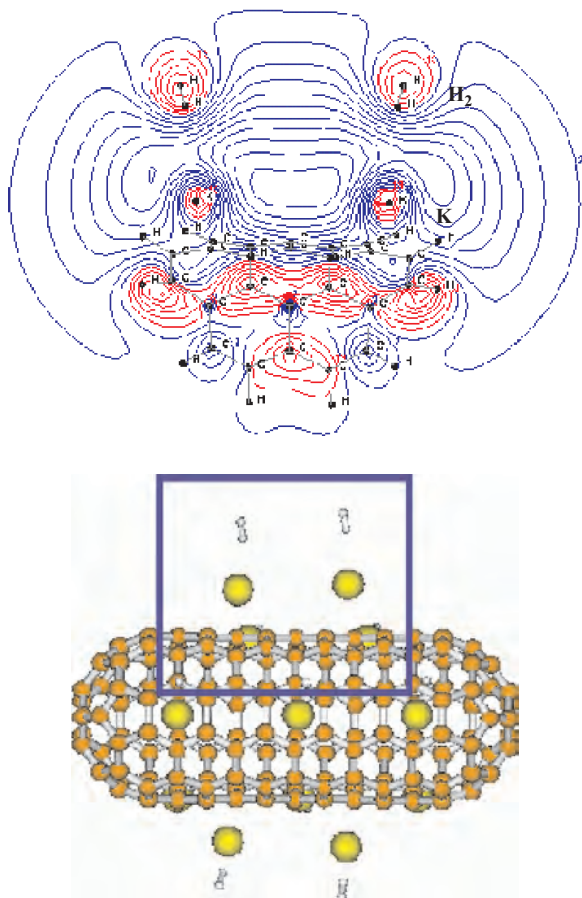


**Figure 8.** Constant amplitude contours presenting the highest occupied molecular orbital of the (5,5) K-doped SWNT with one H<sub>2</sub> per K atom. The plotted area is also marked on the entire tube. Modified from [41], G. E. Froudakis, *Nano Lett.* 1, 531 (2001). © 2001, American Chemical Society.

## 6. OXYGEN INTERACTION WITH CARBON NANOTUBES

Despite the importance of oxygen adsorption on SWNTs the theoretical work existing in the literature about this interaction is controversial and can be briefly summarized in the next few paragraphs.

Jhi et al. combining pseudopotentials together with local density approximation (LDA) and local spin density approximation studied the oxygenation of an (8,0) SWNT [43]. They found that O<sub>2</sub> binds to a bridge position between to carbon atoms of the tube with adsorption energy of 0.25 eV and a distance of 2.7 Å. Nevertheless the O–O distance was kept frozen.

Zhu et al. performed tight binding (TB) DFT calculations to study the adsorption and desorption of an oxygen molecule to the edges of a (5,5) and a (9,0) SWNT [44]. They found that an O<sub>2</sub> molecule arriving at the tube wall edges will not adsorb on the wall but instead will glide into the edges with a binding energy of 4.61 eV [44, 45].

Sorescu et al. using pseudopotential DFT studied the adsorption of oxygen atom and molecules on an (8,0) SWNT [46]. The atomic O performed epoxide-like structures with adsorption energy up to 44 kcal/mol, while the molecular O<sub>2</sub>

is predicted to weakly physisorb (0.9 kcal/mol) to the SWNT surface. It is also found to perform unstable chemisorbed species 10.2 kcal/mol above the reactants [46].

Park et al. using the pseudopotential LDA method investigated atomic and molecular oxygen adsorption in the fullerene type caps of a (5,5) SWNT [47]. They observed epoxide-type bridge positions for the atomic oxygen with binding energies of 6.6 to 6.7 eV and square-type four-center geometries for the binding of the O<sub>2</sub> molecule with binding energies of 1.66 to 3.02 eV [47].

Even though all the references presented [43–47] use methods based on similar approaches like pseudopotential or TB, a big *variety* of binding energies is reported, as is also pointed out by Park et al. [47]. On top of this the question whether the molecular oxygen reacts exothermically with carbon nanotubes remains unanswered.

### 6.1. Application of the Cluster Model

In order to answer this question we performed a fully *ab initio* study of the atomic and the molecular oxygen adsorption to a carbon nanotube [48]. We use the DFT method in the *cluster* approximation. A large enough part of an armchair (4,4) SWNT containing 56 carbon atoms is separated and treated as an individual system. The dangling bonds at the end of the tube are saturated by hydrogen atoms (Fig. 1c).

The RI-DFT as implemented in the TURBOMOLE program package in combination with an auxiliary basis set was used for studying the atomic and molecular hydrogen interaction with the 56-atom SWNT [49]. The efficiency and the computational speed of the methodology we use made the geometry optimization of a C<sub>56</sub>H<sub>16</sub>O<sub>2</sub> system possible in a Linux personal computer.

### 6.2. Atomic Oxygen Interaction with Carbon Nanotubes

In the beginning we investigated the atomic oxygen adsorption on SWNTs [48]. As can be seen in Figure 9 there are only two stable positions. These positions are epoxide-like with the oxygen bridging two neighboring carbon atoms of the tube. All other possibilities of the O sitting on top of a single carbon atom or in the center of a C hexagon are unstable and relax to the bridge positions after geometry optimization. The binding energy for the 9a isomer is

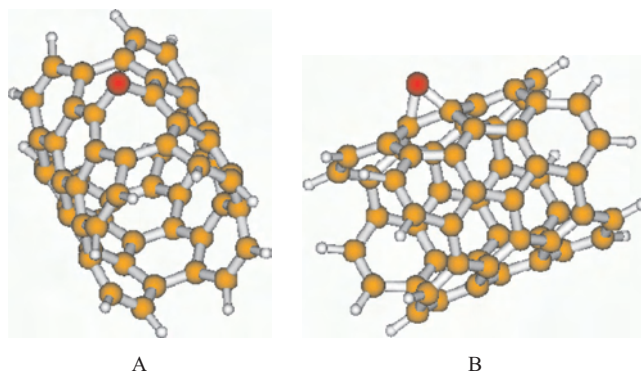


**Figure 9.** The two stable isomers of the atomic oxygen chemisorption in a (4,4) SWNT forming epoxides. In the first (A) the C–C bond opens.

94.6 kcal/mol while that for the 9b is 62.6 kcal/mol. From the binding energies it is clearly shown that both additions are exothermic and the high energy gain indicates a chemisorption procedure.

Comparing these two different bridge positions of the atomic oxygen on carbon nanotubes we observe an energy difference of 33.8 kcal/mol. In order to explain the stabilization of bridge 9a over bridge 9b we have to look closer at the geometric features of the two isomers. In the 9a isomer the oxygen atom is actually breaking the C–C bond (2.062 Å) while the O–C bond is 1.397 Å. In the 9b case the C–C bond opens slightly, 1.522 from 1.415 Å of a bare tube, and the O–C bond is 1.450 Å. In both cases in the chemisorption procedure we have the addition of one C–O bond to each of two neighboring  $sp^2$ -hybridized carbon atoms of the tube. This leads to overcoordinated C atoms that either have to pass to  $sp^3$  hybridization or to break one bond. In the 9a isomer the breaking of the C–C bond is geometrically possible and energetically favorable. The cyclical shaped tube turned locally to an oval-shaped distorted one, and this allowed the C atoms that are connected to the O to keep the  $sp^2$  hybridization (Fig. 9a). The O is coming to the same plane with both the hexagonal rings that it is connected and the angle of these two hexagonal rings with respect to the oxygen is  $95^\circ$ .

In the bridge 9b isomer distortion of the tube parallel to the tube axis is not possible and that is why the C atoms change to unfavorable  $sp^3$  hybridization with weaker bonds (Fig. 9b). Thus the isomer 9b is energetically higher from the 9a by 33.8 kcal/mol. The same interesting phenomenon was observed also in the case of H adsorption in SWNTs (Section 5.3.2).

### 6.3. Molecular Oxygen Interaction with Carbon Nanotubes

Since the oxygen in the atmosphere appears in molecular form, it is of great importance to examine the molecular oxygen adsorption to carbon nanotubes and to analyze the nature of this procedure [48]. Using our *ab initio* method we perform geometry optimization of all the possible adducts of  $O_2$  molecules and (4,4) SWNTs. We tried both parallel and vertical orientations of the  $O_2$  molecule to the tube axis. Two different pathways of oxygen approach were tested (one oxygen atom attaching the tube walls; both oxygen atoms attaching the tube walls). Finally all these were combined with binding positions on *top* of a carbon atom, in the *hollow* position of C hexagons, and *bridging* C–C bonds.

After the geometries were optimized we found two stable adducts presented in Figure 10. In both of these local minima the oxygen molecule is *bridging* C–C bonds—the two different kinds of bonds that exist in the tube—making square rings. In the first case the bridged C–C bond is vertical to the tube axis (Fig. 10a) and in the second it is semiparallel (Fig. 10b). All other possibilities of  $O_2$  approaching the tube walls were either unstable or after the geometry optimization end up in the bridge positions (Fig. 10a or b).

In the first bridge isomer the C–C bond opens from 1.40 to 1.68 Å, the O–O is 1.51 Å, and the two C–O are 1.45 Å while in the second case the C–C bond opens from 1.41 to 1.55 Å, the O–O is 1.51 Å, and the two C–O are 1.48 Å.

In the second isomer the formed square ring is not totally planar but slightly twisted (dihedral angle  $19^\circ$ ). The binding energies of these two species are +13 and +18 kcal/mol respectively and the addition is endothermic in both cases. The electron density of the bonding area of isomer 10a is presented in Figure 10c.

From our fully optimized calculations, without any symmetry constraints, it is clear that both bridge adducts are local minima. Nevertheless for the discussion of the binding energy we have to take into account the electronic configuration of the reactants together with the one of the product cluster (SWNT +  $O_2$ ). Since for both adducts (bridge 1 & 2) the ground state configuration is singlet, we consider first the singlet reaction.

For bridge 1 (9a) the addition  $^1\text{SWNT} + ^1O_2 \rightarrow ^1(\text{SWNT} + O_2)$  is exothermic by 25 kcal/mol. Despite this the ground state of the  $O_2$  is triplet. The analogous triplet addition  $^1\text{SWNT} + ^3O_2 \rightarrow ^3(\text{SWNT} + O_2)$  is endothermic by 29 kcal/mol. These two energy curves are separated from the complicated multidimensional energy hypersurface of the system and presented in Figure 11 (solid lines). Since they are of different symmetry they can cross each other (diabatic curves) and some more reaction possibilities arise. This also explains the controversial results existing in the literature.

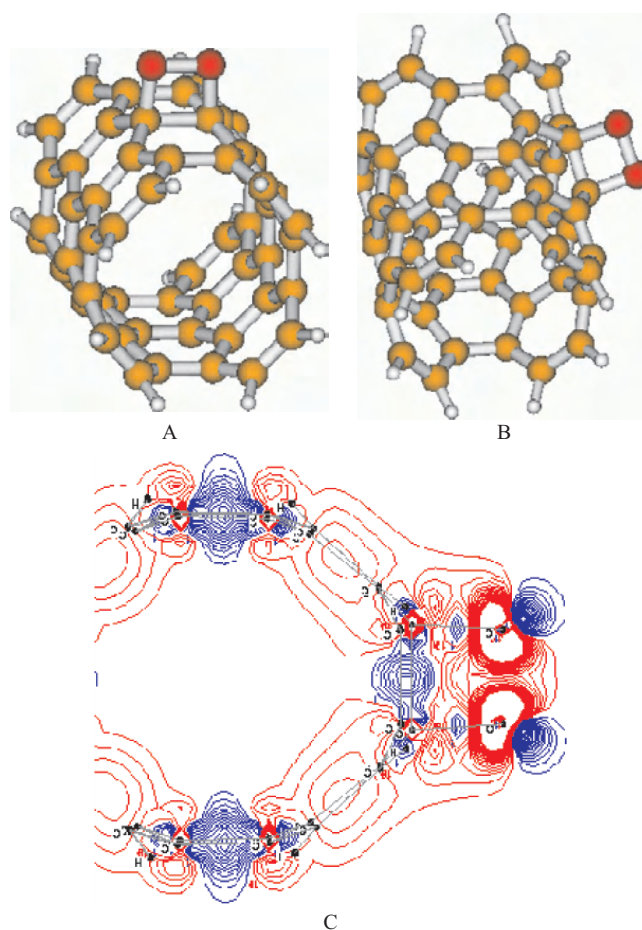


**Figure 10.** The two stable isomers of the molecular oxygen adsorption in a (4,4) SWNT forming orthogonal rings. The electron density of the bonding area of isomer 10a is presented in (C).

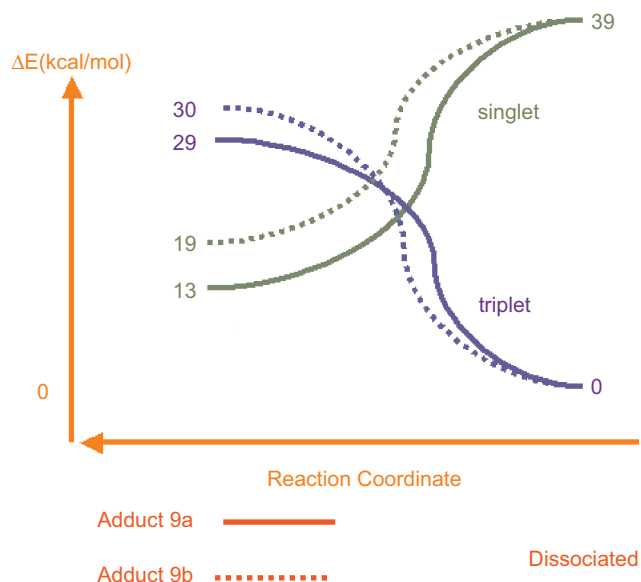


**Figure 11.** Four energy curves separated from the complicated multidimensional energy hypersurface of the (4,4) SWNT when  $O_2$  is approaching from the left side of the diagram. Solid lines end up in the adduct 9a with dashed lines for 9b. Blue lines represent triplet states and green lines singlet states.

The curve connecting the two ground states starts from the separate  $^1SWNT$  and  $^3O_2$ , presents a barrier where the total symmetry changes to singlet (crossing point), and falls down to the adduct  $^1(SWNT + O_2)$ . This barrier is approximately 15 kcal/mol.

According to this figure there are two different possibilities for  $O_2$  adsorption to the SWNT: In the first the  $O_2$  is excited to its singlet electronic configuration and then it automatically reacts exothermically with the tube. In the second case we start with  $O_2$  in its triplet ground state and energy of  $\sim 15$  kcal/mol has to be offered to the system in order to overpass the energy barrier and react with the tube.

For the bridge 2 (9b) adsorption a picture completely analogous to bridge 1 (9a) exists and is presented in Figure 11 (dashed lines). The only difference is the relative energy values. Finally, since all these cases (singlet and triplet, bridge 1 and 2) are coexisting, a combination of all these four energy curves is needed in order to have the complete adsorption picture (Fig. 11).

In real—and not ideal—systems, when the tubes possess defects and the temperature is not absolute zero—as in quantum mechanical calculations—the triplet  $O_2$  adsorption is possible. The barrier is relatively small and the defects of the tube can lower it even more. Also the temperature “movements” can help the procedure.

## 7. CONCLUSIONS

In this chapter we review the existing theoretical literature of hydrogen and oxygen interaction to single walled carbon nanotubes. The importance of theoretical simulations for understanding the adsorption procedure and for improving the storage capacity of these nanomaterials is underlined. We report three different approaches to treating large

systems with *ab initio* methods the periodic DFT, the mixed QM/MM model, and the *cluster* model. For all advantages and disadvantages are presented.

Specifically for the hydrogen adsorption, it is showed that both periodic DFT and mixed QM/MM models can successfully be employed in the SWNT and provide a solution to the problem of making accurate calculations in large systems like nanotubes. The results of Bauschlicher [34] and Froudakis [35] demonstrate that atomic hydrogen will bind to the tube walls and not enter in the tube interior. This binding can take place either in pairs of lines toward the tube axis, as the first suggests, or in zigzag rings around the tube walls, supported by the second. This will result in a change of the tube shape during the hydrogen adsorption and an enlargement of the tube volume [35]. Both found 50% to be the maximum coverage of the tube walls. After the tube walls are half filled with hydrogen, the energetically more favorable procedure of hydrogen insertion in the tube is obtained [35].

Since the storage capacity is mostly obtained by molecular hydrogen, Froudakis [41] tried to answer why alkali-doped carbon nanotubes possess high hydrogen uptake as put forward by Chen et al. in 1999 [9]. His results demonstrate a charge transfer from the alkali metal to the tube that polarizes the  $H_2$  molecule. This charge induced dipole interaction characterizes the  $H_2$  physisorption on alkali metal doped tubes and is responsible for the higher hydrogen uptake of the doped tubes.

As a general remark for hydrogen we can report that in the last couple of years the theoretical modeling of the hydrogen storage in carbon nanotubes has obtained only its first goal (i.e., to give an understanding of what it is going on in the laboratory experiments by explaining the elementary parts of the adsorption procedure). The second and most important goal, which is still to come, is to predict how the storage capacity of carbon nanotubes can be improved and reach a sufficient level for commercial use in fuel-cell electric vehicles.

As far the oxygen adsorption in carbon nanotubes is concerned we showed that atomic oxygen exothermically reacts with the tube walls performing epoxides. For molecular oxygen the picture is not so clear. Both singlet and triplet states have to be taken into account. These configuration states have to be combined with the two different isomers found, resulting a complicated potential energy hypersurface (PES). This complicated PES characterizes the oxygen adsorption to carbon nanotubes and is also responsible for the controversy existing in the literature.

According to our results there are two different possibilities for the atmospheric oxygen adsorption to carbon nanotubes: In the first the  $O_2$  is excited to its singlet electronic configuration and then it automatically reacts exothermically with the tube. In the second case we start with  $O_2$  in its triplet ground state and an energy of  $\sim 15$  kcal/mol has to be offered to the system in order to overpass the energy barrier and react with the tube. The latter pathway can be supported by the existence of defects in the tube and temperature in the environment.

Considering this theoretical result together with the experimental observation that the electronic and transport properties of carbon nanotubes are extremely sensitive to



their exposure to gas molecules [10–12], we can draw the conclusion that the results of all previous experimental studies of SWNTs must be carefully reevaluated, since all measurements have used samples exposed to air.

## GLOSSARY

**Ab initio methods** Theoretical quantum chemistry techniques that solve the Schrödinger equation for the electrons of a molecular system. They are very accurate since they do not enforce any parameters to the system but on the other hand they are computationally very heavy.

**Atomic cluster** A collection of atoms that form a unique system stabilized by interatomic forces.

**Carbon nanotubes** Rolls of graphitic sheets that come in a variety of forms and shapes. They can be zigzag, armchair, or chiral because of the different ways that the graphitic sheet can be rolled. They are valuable for nanoelectronics and as storage devices.

**Chemisorption** An adsorption in which the adsorbed system is stabilized by strong chemical bonds.

**Monte Carlo method** A statistical mechanics empirical method for obtaining optimal conformations of molecular systems. The trial movements of the atoms are performed randomly and for this reason the method took its name from the famous casino.

**Physisorption** An adsorption in which the adsorbed system is stabilized by weak interactions.

**Single walled carbon nanotube** A carbon nanotube that consists of only one graphitic sheet. If the tube has more than one cylindrical shell it is called a multi walled nanotube.

## REFERENCES

- H. W. Kroto, J. R. Heath, S. C. O'Brian, R. F. Curl, and R. E. Smalley, *Nature* 318, 162 (1985).
- S. Iijima, *Nature* 354, 56 (1991).
- S. Iijima and T. Ichihashi, *Nature* 363, 603 (1993).
- A. C. Dillon, K. M. Jones, T. A. Bekkedahl, C. H. Kiang, D. S. Bethune, and M. J. Heben, *Nature* 386, 377 (1997).
- C. Liu, Y. Y. Fan, M. Liu, H. T. Cong, H. M. Cheng, and M. S. Dresselhaus, *Science* 286, 1127 (1999).
- A. C. Dillon and M. J. Heben, *Appl. Phys. A* 72, 133 (2001).
- U. Bunger and W. Zittel, *Appl. Phys. A* 72, 147 (2001).
- R. G. Ding, G. Q. Lu, Z. F. Yan, and M. A. Wilson, *J. Nanosci. Nanotech.* 1, 7 (2001).
- P. Chen, X. Wu, J. Lin, and K. L. Tan, *Science* 285, 91 (1999).
- P. G. Collins, K. Bradley, M. Ishigami, and A. Zettl, *Science* 287, 1801 (2000).
- K. Bradley, S. H. Jhi, P. G. Collins, J. Hone, M. L. Cohen, S. G. Louie, and A. Zettl, *Phys. Rev. Lett.* 85, 4361 (2000).
- G. U. Sumanasekera, C. K. W. Adu, S. Fang, and P. C. Eklund, *Phys. Rev. Lett.* 85, 1096 (2000).
- K. F. Kelly, I. W. Chiang, E. T. Mickelson, R. H. Hauge, J. L. Margrave, X. Wang, G. E. Scuseria, C. Radloff, and N. J. Halas, *Chem. Phys. Lett.* 313, 445 (1999).
- Y. Ye, C. C. Ahn, C. Witham, B. Fultz, J. Liu, A. G. Rinzler, D. Colbert, K. A. Smith, and R. E. Smalley, *Appl. Phys. Lett.* 74, 2307 (1999).
- R. T. Yang, *Carbon* 38, 623 (2000).
- H. W. Zhu, *J. Mater. Sci. Lett.* 19, 1237 (2000).
- A. Kuznetsova, D. B. Mawhinney, V. Naumenko, J. T. Yates, Jr., J. Liu, and R. E. Smalley, *Chem. Phys. Lett.* 321, 292 (2000).
- C. M. Brown, T. Yildirim, D. A. Neumann, M. J. Heben, T. Genett, A. C. Dillon, J. L. Alleman, and J. E. Fischer, *Chem. Phys. Lett.* 329, 311 (2000).
- M. Hirscher, M. Becher, M. Haluska, U. Dettlaff-Weglikowska, A. Quintel, G. S. Duesberg, Y.-M. Choi, P. Downes, M. Hulman, S. Roth, I. Stepanek, and P. Bernier, *Appl. Phys. A* 72, 129 (2001).
- A. Cao, H. Zhu, X. Zhang, X. Li, D. Ruan, C. Xu, B. Wei, J. Liang, and D. Wu, *Chem. Phys. Lett.* 342, 510 (2001).
- S. Dapprich, I. Komaromi, K. S. Byun, K. Morokuma, and M. J. Frisch, *J. Mol. Structure* 461, 1 (1999).
- G. E. Froudakis, *J. Phys.: Condens. Matter* 14, 453 (2002).
- F. Darkrim and D. J. Levesque, *Chem. Phys.* 109, 4981 (1998).
- Q. Wang and J. K. Johnson, *J. Chem. Phys.* 110, 577 (1999).
- V. V. Simonyan, P. Diep, and J. K. Johnson, *J. Chem. Phys.* 111, 9778 (1999).
- K. A. Williams and P. C. Eklund, *Chem. Phys. Lett.* 320, 352 (2000).
- H. Cheng, G. P. Pez, and A. C. Cooper, *J. Am. Chem. Soc.* 123, 5845 (2001).
- Y. Ma, Y. Xia, M. Zhao, R. Wang, and L. Mei, *Phys. Rev. B* 63, 115422 (2001).
- P. Dubot and P. Cenedese, *Phys. Rev. B* 63, 241402 (2001).
- L. Jeloica and V. Sidis, *Chem. Phys. Lett.* 300, 157 (1999).
- S. M. Lee and Y. H. Lee, *Appl. Phys. Lett.* 76, 2877 (2000).
- G. Seifert, T. Kohler, and T. Frauenheim, *Appl. Phys. Lett.* 77, 1313 (2000).
- C. W. Bauschlicher, Jr., *Chem. Phys. Lett.* 322, 237 (2000).
- C. W. Bauschlicher, Jr., *Nano Lett.* 1, 223 (2001).
- G. E. Froudakis, *Nano Lett.* 1, 179 (2001).
- M. J. Frisch, G. W. Trucks, H. B. Schlegel, G. E. Scuseria, M. A. Robb, J. R. Cheeseman, V. G. Zakrzewski, J. A. Montgomery, Jr., R. E. Stratmann, J. C. Burant, S. Dapprich, J. M. Millam, A. D. Daniels, K. N. Kudin, M. C. Strain, O. Farkas, J. Tomasi, V. Barone, M. Cossi, R. Cammi, B. Mennucci, C. Pomelli, C. Adamo, S. Clifford, J. Ochterski, G. A. Petersson, P. Y. Ayala, Q. Cui, K. Morokuma, D. K. Malick, A. D. Rabuck, K. Raghavachari, J. B. Foresman, J. Cioslowski, J. V. Ortiz, A. G. Baboul, B. B. Stefanov, G. Liu, A. Liashenko, P. Piskorz, I. Komaromi, R. Gomperts, R. L. Martin, D. J. Fox, T. Keith, M. A. Al-Laham, C. Y. Peng, A. Nanayakkara, C. Gonzalez, M. Challacombe, P. M. W. Gill, B. Johnson, W. Chen, M. W. Wong, J. L. Andres, C. Gonzalez, M. Head-Gordon, E. S. Replogle, and J. A. Pople, Gaussian 98, Revision A.7. Gaussian, Inc., Pittsburgh, PA, 1998.
- M. Menon, A. Andriotis, and G. Froudakis, *Chem. Phys. Lett.* 320, 425 (2000).
- A. Andriotis, M. Menon, and G. Froudakis, *Appl. Phys. Lett.* 76, 3890 (2000).
- A. Andriotis, M. Menon, and G. Froudakis, *Phys. Rev. Lett.* 85, 3193 (2000).
- K. N. Kudin, H. F. Bettingen, and G. E. Scuseria, *Phys. Rev. B* 63, 45413 (2001).
- G. E. Froudakis, *Nano Lett.* 1, 531 (2001).
- G. Gao, T. Cagin, and A. Goddard III, *Phys. Rev. Lett.* 80, 5556 (1998).
- S. H. Jhi, S. G. Louie, and M. L. Cohen, *Phys. Rev. Lett.* 85, 1710 (2000).
- X. Y. Zhu, S. M. Lee, Y. H. Lee, and T. Frauenheim, *Phys. Rev. Lett.* 85, 2757 (2000).
- C. Kim, Y. S. Choi, S. M. Lee, J. T. Park, B. Kim, and Y. H. Lee, *J. Am. Chem. Soc.* 124, 9906 (2002).
- D. C. Sorescu, K. D. Jordan, and P. Avouris, *J. Phys. Chem. B* 105, 11227 (2001).
- N. Park, S. Han, and J. Ihm, *Phys. Rev. B* 64, 125401 (2001).
- G. E. Froudakis, M. Schnell, M. Muhlhauser, S. D. Peyerimhoff, A. Andriotis, M. Menon, and R. M. Sheetz, *Phys. Rev. B* 68, 115435 (2003).
- Turbomole, R. Ahlrichs, and M. Armin, in "METECC-95" (E. Clementi and G. Corongiu, Eds.).



# Hydrogen Storage by Carbon Nanotubes

R. G. Ding

*University of Queensland, Brisbane, Australia; and  
University of Petroleum, Dongying, Shandong, People's Republic of China*

J. J. Finnerty

*School of Engineering, University of Queensland, Brisbane, Australia*

Z. H. Zhu

*Curtin University of Technology, Perth, Western Australia, Australia*

Z. F. Yan

*University of Petroleum, Dongying, Shandong, People's Republic of China*

G. Q. Lu

*University of Queensland, Brisbane, Australia*

## CONTENTS

1. Introduction
  2. Experimental Studies of Hydrogen Storage by Carbon Nanotubes (CNTs)
  3. Theoretical Calculations of Hydrogen Storage by Carbon Nanotubes
  4. Interaction Between Hydrogen and CNTs
  5. Future Perspectives
- Glossary  
References

## 1. INTRODUCTION

There has been an ever-increasing interest in sustainable and renewable energy technology due to environmental and climate change pressures. The search for such technologies

has intensified in the last decade, mainly due to the debate of climate change and the Kyoto protocol. The public and legislative demand for more renewable or sustainable energy supplies has been driving the push for the so-called "hydrogen economy." Such an economy is one where hydrogen is used for energy storage, distribution, and utilization. Fuel cell technology has emerged as a forerunner of the clean energy race. The promises of fuel cells utilizing hydrogen as the fuel are tantalizing; they have the potential to simultaneously double the energy efficiency of cars while significantly reducing air pollution and greenhouse gas emissions. If the predictions are true, over the next few decades, we will see a shift away from the current fossil-fuel-based economy toward a cleaner hydrogen future.

Hydrogen's physical and chemical properties make it a good low-polluting energy carrier. However, several technological problems must be overcome before we can realize the full hydrogen economy. These relate to how hydrogen will be generated in an efficient and low-polluting manner, and how it will be transported, distributed, and stored. Once

both of these questions are answered in an economical way, the hydrogen economy will be in place. Here, we look at recent work on the use of carbon nanotubes for the storage of hydrogen.

### 1.1. Hydrogen Storage Technologies

Although many advances in hydrogen production and utilization technologies have been made, hydrogen storage technologies must be significantly advanced if a hydrogen-based energy system, particularly in the transportation sector, is to be established [1]. Hydrogen can be made available on board vehicles in several ways: compression, as a liquid, metal hydrides, chemical storage, or gas-on-solid adsorption. Although each method possesses desirable characteristics, currently no approach satisfies all of the efficiency, size, weight, cost, and safety requirements for transportation or utility use.

Liquid hydrogen storage systems lose up to 1% a day by boiling and up to 30% during filling, as well as requiring good (bulky) insulation to keep the hydrogen at 20 K.

Daimler Chrysler's Nectar II utilizes compressed hydrogen gas, and suffers from permeability of the tank housing and high energy input to achieve pressurization. The associated safety risks from hydrogen continually being released currently make both of these approaches impractical. Storage in a solid-state matrix, as a metal hydride for instance, has a safety advantage, and is the current method for storage above room temperatures and below 2–4 MPa. The disadvantages of a metal hydride system are a hydrogen storage capacity of at most 7 wt% (the ratio of stored hydrogen weight to the system weight) and typically 2 wt% [2] and a large desorption energy, making it less than ideal for automotive applications [3].

Physical adsorption of hydrogen onto an adsorbent has the advantage of a low desorption energy, but currently very low storage capacities. In contrast to the chemisorption in metal hydrides, the adsorbent adsorbs hydrogen molecules by physical, van der Waals type forces. This generally requires cryoadsorption, where the adsorbent is cooled to very low temperatures, to store large amounts of hydrogen. Hydrogen adsorption studies on highly porous amorphous carbon at 123 K showed that they had a capacity of 0.05 wt% of carbon at 2 MPa [4]. Recent parametric modeling of adsorption storage on activated carbons has shown that a passive adsorbent system could approach the U.S. Department of Energy (DOE) goals at low temperatures ( $\sim 77$  K) by improving the bulk density and specific surface area of the adsorbent [5]. Although not as severe as liquid hydrogen, cryoadsorption suffers as an economic proposition because of the need to maintain such a low temperature [6, 7].

### 1.2. Novel Carbon Adsorbents

The discovery of the third carbon allotrope Buckminsterfullerene ( $C_{60}$ ) in 1985 by Kroto et al. initiated a novel, round, and curved carbon nanocosmos [8]. Subsequently,

the mass production of  $C_{60}$  and the family of fullerenes became available [9]. It was in this light that the discovery of carbon nanotubes received instant recognition. Carbon nanotubes (CNTs) were discovered accidentally in 1991 by Iijima [10], while looking for new carbon structures in the deposit formed on graphite cathode surfaces during the electric arc discharge that is commonly employed to produce fullerene soot. They were identified as fullerene tubes consisting of multiple shells in which many tubes were in a coaxial, concentric arrangement. The scanning electron microscopy (SEM) and transmission electron microscopy (TEM) images of multiwalled carbon nanotubes (MWNTs) synthesized by the catalytic chemical vapor deposition method are shown in Figure 1. Each layer is composed of a cylindrical graphene sheet, with an interlayer spacing of 0.34 nm, which is slightly larger than the 0.336 nm spacing found between sheets of graphite [11]. In retrospect, hollow carbon tubules were observed in the 1970s as forming the core of carbon fibers in a certain process, although the broad implications were not clearly realized at the time.

In 1993, Iijima's group and Bethune and his colleagues independently found that the use of transition-metal

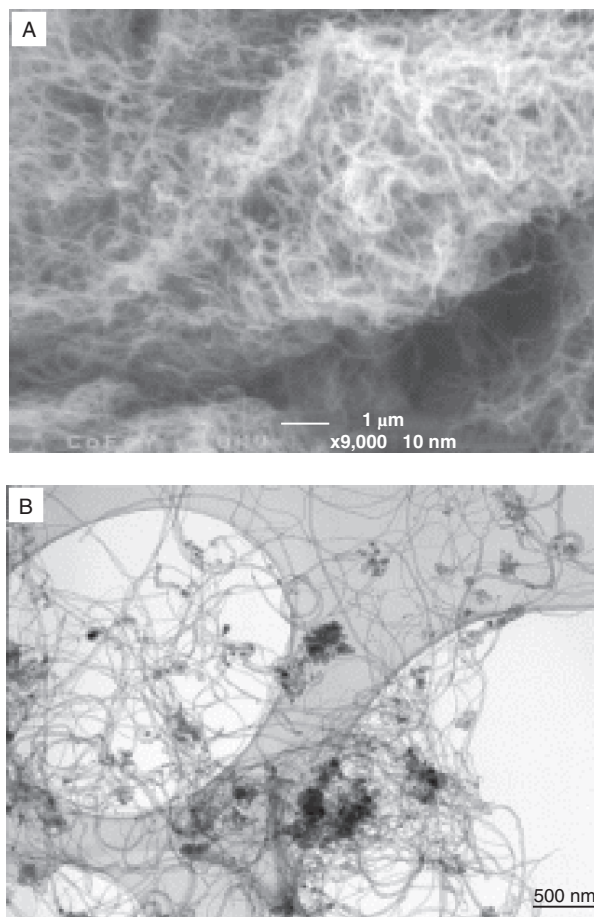


**Figure 1.** SEM image (A) and TEM image (B) images of MWNTs obtained by the catalytic pyrolysis of  $C_2H_2$  at 700 °C in a flow of  $H_2$ . Images are from [57], R. G. Ding et al., unpublished work (2003).

catalysts led to nanotubes with only one single shell [12, 13]. Due to their simple and well-defined structure, such single-wall nanotubes (SWNTs) serve as model systems, both for theoretical calculations and for key experiments. Carbon nanotubes are cylindrical molecules with a diameter as little as 1 nm and a length up to many micrometers. The high-resolution TEM images of typical SWNTs and MWNTs are shown in Figure 2. They have unique structural, mechanical, and electrical properties that make them attractive systems for fundamental scientific studies, as well as for a broad range of applications.

The unique properties of carbon nanotubes hold the promise for applications such as catalysis and energy storage. The theoretical description of capillarity in carbon nanotubes by Pederson and Broughton [14] suggested that gaseous species such as hydrogen might be drawn into the capillaries of carbon nanotubes.

There have been some reviews of experimental and theoretical investigations of hydrogen storage in carbonaceous materials available in the literature [1, 3, 15–18]. The field of hydrogen storage on CNTs is undergoing rapid progress. Here, we attempt to provide a comprehensive and critical review of this topic at the time of writing. Both experimental and theoretical calculation studies are included, along with an outline of current challenges in the field.

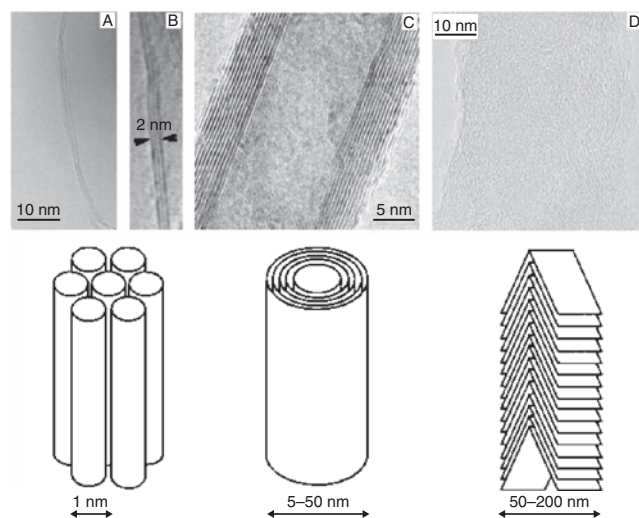


**Figure 2.** High-resolution transmission electron microscopy images of typical SWNT (A), (B), MWNT (C), and a carbon nanofiber (CNF) of the herringbone-type morphology (D) and corresponding schematic structures. Two individual SWNT tubes with a diameter of  $\sim 1$  nm are shown in (A), and an SWNT bundle consisting of two tubes with an outer diameter of  $\sim 2$  nm is shown in (B). Open MWNT tip is shown in panel (C). The separation between the closely spaced fringes in the MWNT is 0.34 nm, close to the spacing between graphite planes. Every layer in the image correspond to the edges of each cylinder in the nanotube assembly. Images are from [57], R. G. Ding et al., unpublished work (2003).

## 2. EXPERIMENTAL STUDIES OF HYDROGEN STORAGE BY CARBON NANOTUBES (CNTs)

Of the problems to be solved for the utilization of hydrogen energy, how to store hydrogen easily and inexpensively, has been given high priority. A vehicle powered by a fuel cell would currently require  $\sim 3.1$  kg of hydrogen for a 500 km range. This amount of hydrogen stored in the weight and volume of a typical petrol tank (50 L) requires system densities approaching 6.5 wt% or  $63 \text{ kg H}_2/\text{m}^3$  [19]. Therefore, the U.S. Department of Energy Hydrogen Plan has set this as the standard for providing a commercially significant reversible hydrogen storage technology [7]. No storage technology is currently capable of meeting these goals [17]. Meeting this target requires major advances in storage density, and the energy required for storage without compromising safety and cost. Most of these issues would be resolved by a lightweight material capable of reversibly storing and releasing hydrogen in a modest range of near-ambient temperatures and pressures. Novel lightweight carbon nanotubes were seen to be an ideal candidate as it was assumed that hydrogen molecules could be physisorbed both inside the tubes and in the interstitial pore spaces between the tubes.

A large number of hydrogen adsorption experiments have been conducted to measure the storage capacity of carbon nanotubes. At the same time, many researchers have calculated the adsorption performance of the carbon nanotubes by means of various models and theories. Here, we first summarize the recent experimental and theoretical results, then briefly discuss the interaction between hydrogen and carbon nanotubes for elucidating the hydrogen adsorption nature within carbon nanotubes. Currently, there are two major methods of hydrogen storage in carbon nanotubes being studied: gaseous storage and electrochemical storage.

The three main methods for the preparation of carbon nanotubes are electric arc discharge, chemical vapor deposition, and laser ablation. All of these methods rely on creating highly energetic carbon clusters that condense to form carbon materials such as fullerenes and nanotubes. Recent advances have been to use metals as condensation catalysts that template and promote certain types of materials. The prepared nanotubes can then be purified and/or treated in some manner to open the nanotube ends. It is interesting to note that high-capacity room-temperature adsorption was first demonstrated for arc-generated SWNTs, and not laser-produced nanotubes. This may be attributed to a much smaller number of ends or defects in the laser produced tubes and/or an enhancement in their stability toward opening procedures or cutting [1]. Significant research has been undertaken to improve synthesis methods, and to more accurately characterize the unique mechanical and chemical properties of carbon nanotubes. A discussion of these topics is outside the scope of this chapter, but the reader can be directed to a wealth of related literature [20–25].



## 2.1. Hydrogen Storage Measurement Techniques

The main methods used for determining the hydrogen storage capacity are temperature-programmed desorption (TPD), volumetric analysis, thermogravimetric analysis (TGA), and the electrochemical method.

The temperature-programmed desorption method consists of using a mass spectrometer to measure the hydrogen desorbed from a carbon sample during controlled heating [26]. Thermal desorption spectroscopy is highly sensitive, allowing the study of samples with masses below 1 mg. The sensitivity can be even improved by using deuterium-loaded samples, and avoiding any disturbing background from water or other hydrogen-containing adsorbates [27]. For calibration, the hydrogen desorption of a well-known metal hydride or an alloy of known hydrogen content has to be measured [28]. The activation energy of desorption can be directly measured from the temperature at which hydrogen appears in the spectrometer. As different adsorption mechanisms and sites will have different activation energies, each peak in the thermogram will indicate a different site or mechanism. It will be shown that carbon adsorbents have a desorption peak around 130 K, and nanotubes can have one (at  $\sim 300$  K) or more additional peaks. The amount of hydrogen desorbed requires integration of the signal, and may have significant errors [26]. In volumetric analysis, the adsorption of hydrogen is measured by a pressure change in a fixed volume, with pressure variations attributed to adsorption or desorption. A complication with this technique is the presence of thermal effects during the filling of the sample cell. Hydrogen has an appreciable temperature-dependent compressibility that needs to be taken into account as the temperature changes due to compressing the gas during filling and the exothermic adsorption. Unless this problem is specifically addressed, the change in pressure caused by temperature fluctuations will cause overestimation of the amount of hydrogen adsorbed [18]. The calibration should be done by measuring a well-known metal hydride.

The thermogravimetric analysis method consists of measuring the weight of a sample as the temperature is varied under constant pressure. The technique is well known, with the difficulty being the sensitivity of the instrumentation on the relatively small sample sizes used in these studies. The gravimetric analysis is capable of measuring very low sample masses of about 10 mg in specially designed devices, but it is a nonselective analysis. The high specific surface area of carbon nanotubes increases the possibility of the adsorption of residual gases. Therefore, the apparatus has to be extremely clean, and high-purity hydrogen has to be used.

Hydrogen can be incorporated into the sample due to the electrochemical technique. To prepare the carbon-containing working electrode, the carbon material has to be mixed with conductive powder, for example, nickel or gold and compacted [29–31]. The counterelectrode is, for example, metallic nickel. Both electrodes are placed in a KOH solution which provides the hydrogen atoms, and they are separated by a polymer separator. During the charging process, water dissociates at the negative working electrode, and atomic hydrogen may intercalate into the carbon material. The following discharge process results in the recombining of water. By maintaining a constant current, the voltage

is measured across the two electrodes during the charging and discharging. The amount of desorbed hydrogen is determined by measuring the electric charge in a galvanostatic setup.

A comprehensive study which involved a broad range of carbon materials was conducted recently by Tibbetts et al. [32], whose experimental results cast serious doubts on many claims so far for room-temperature hydrogen sorption in carbon materials larger than 1 wt%. The authors analyzed the possible pitfalls in the gaseous hydrogen adsorption process using volumetric techniques [32], and proposed techniques to handle all of those problems [33]. The chief areas where hydrogen adsorption experiments may be in error are as follows.

The first is that leaks can be difficult to distinguish from hydrogen storage. Hydrogen molecules disappear from a pressurized reservoir. If hydrogen molecules leak from a system of volume  $V$  at a nearly constant rate  $L = dP/dt$  over the period of the experiment  $t$ , an observer could incorrectly attribute the pressure decrease to a wt% hydrogen stored in a sample of mass  $m$  proportional to  $VL/m$ . For small sample masses, the consequences of this can be particularly treacherous.

A second source of error is that, in a high-pressure experiment, pressure changes arising from ambient temperature variations can be mistakenly interpreted as substantial sorption. At 10 MPa and 300 K, the pressure change with temperature is 33.3 kPa/K. If this were interpreted as sorption by a 1 g sample in a 1 L volume, the result would be 2.6 wt% per degree temperature drop. Most reports in the literature have samples smaller than 1 g.

A more significant, but less obvious source of temperature variation stems from the thermodynamic principle that a chamber being pressurized experiences a temperature rise. The enthalpy of high-pressure gas is higher than that of low-pressure gas, and so the flux of high-enthalpy molecules from a high-pressure chamber to a low-pressure chamber raises the temperature of the gas in the low-pressure chamber. This temperature is not easily measured if the temperature sensor is not in good thermal contact to the gas or if the walls of the chamber have a large heat capacity. For an ideal gas adiabatic ally bled into an evacuated chamber, the temperature rise is  $(C_p/C_v - 1)I_{\text{initial}}$ , corresponding to a 41% increase in absolute temperature for hydrogen [34]. The authors believed that many high-pressure adsorption experimental results should be carefully corrected to exclude the pressure drop brought by return to thermal equilibrium after pressurization. Figure 3 shows the effect of thermal equilibrium after pressurization on the pressure change in the sample chamber [32].

It is worth noting that the metal hydride research community has devised experimental techniques to handle all of these problems [33]. First, to avoid spurious readings from gas cooling to ambient, use two calibrated volumes connected by a valve, one an initially pressurized reservoir and the other containing the sample. Then determine the precise equilibrium temperatures and pressures of both volumes before and after opening the connecting valve. Second, to unambiguously establish that there are no leaks, measure not only the gas adsorbed, but also the gas desorbed from

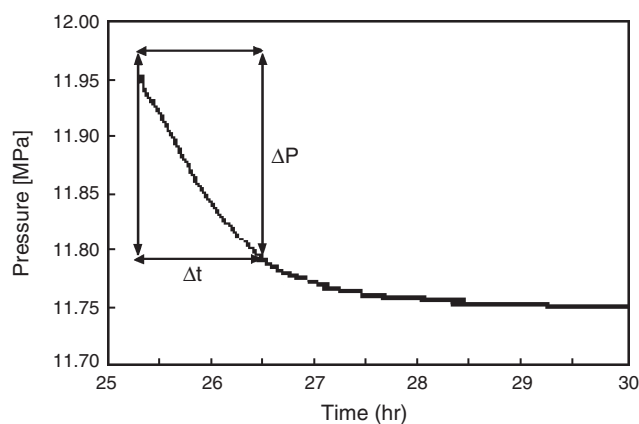


**Figure 3.** Hydrogen pressure versus time for a 307 mL chamber containing no sample. This shows pressurization to 11.97 MPa from vacuum at 25.3 h and the subsequent pressure decrease. Reprinted with permission from [32], G. G. Tibbetts et al., *Carbon* 39, 2291 (2001). © 2001, Elsevier Science.

the sample. Third, present a complete pressure composition isotherm that precisely defines the pressure and composition at which the hydrogen-adsorbent bond is formed and decomposes. A complete pressure composition isotherm would show an interesting change in curvature with pressure that would be very useful in classifying the sorption, and lending credibility to the research [32].

## 2.2. Gaseous Hydrogen Storage in CNTs

A summary of gaseous hydrogen storage in undoped and doped carbon nanotubes from the literature is given in Table 1.

Dillon et al. [26] were the first to publish experimental data on hydrogen adsorption in nanotubes, and measured exactly the desorption of hydrogen of nonpurified SWNT samples (containing additional cobalt catalyst and amorphous carbon). Using TPD, the authors found that the hydrogen desorbed from both the nanotubes and activated carbon samples at about the same temperature ( $\sim 133$  K). However, a second peak appeared at higher temperature for SWNTs ( $\sim 290$  K), indicating that there were additional adsorption sites in SWNTs. They proposed that these sites were when hydrogen molecules had access to the nanotube cores. The authors did not see this high-temperature site in either activated carbon or in arc-generated soot produced without a catalyst. The SWNT constituent of the sample appeared to be especially effective for hydrogen adsorption, and an activation energy for hydrogen desorption was found to be  $19.6 \text{ kJ} \cdot \text{mol}^{-1}$  (approximately five times that of planar graphite). In 2000, Heben's group performed inelastic neutron scattering on this material, and showed that hydrogen is physisorbed [35], but the authors made no statement about the total amount.

The hydrogen storage capacity was estimated to range between 5 and 10 wt% [26]. This figure was derived from the measured hydrogen desorption of 0.01 wt% and an SWNT content estimated at 0.2 wt%. Furthermore, it was assumed

that only the SWNTs in the sample contributed to the hydrogen adsorption, so the analysis required a large correction for 99.8 wt% of material that was assumed inert. However, hydrogen adsorption in high-porosity carbon (AX-21 carbon) is as high as 5.3 wt% at a temperature of 77 K and a hydrogen pressure of 1 MPa [36].

In a more recent paper, Dillon et al. [37] presented an oxidative technique to open the nanotubes: the degassing of the samples in vacuum to 970 K, and an oxidizing in water in the 325–975 K temperature range. They measured the adsorption of hydrogen in such treated samples by their TPD method, and found a noticeable enhancement (up to a factor of 3 in the most favorable case) of the characteristic desorption peak between 250 and 300 K. They attributed this improvement of the adsorption capacity to the opening and filling of the nanotubes. Taking into account that their carbon soot samples containing only 0.05% of nanotubes can adsorb  $\sim 0.005\%$  weight of hydrogen, Dillon and his colleagues believed that the pure adsorbed hydrogen was therefore  $\sim 10$  wt%. These authors have further developed a cutting method to produce samples with a high concentration of short SWNTs with open ends that are accessible to the entry of hydrogen molecules. With these better characterized nanotube samples, they were able to achieve a more accurate determination of hydrogen adsorption, which they estimated to be at  $\sim 3.5$ – $4.5$  wt% hydrogen at room temperature and 0.07 MPa hydrogen pressure [38]. By opening and recapping the nanotubes, they concluded that most of the hydrogen is stored within the capillary, rather than in the interstitial spaces between the SWNT.

Ye et al. [39] were motivated to perform measurements on SWNT material of high purity because the previous measurements were made on dilute SWNTs which required a large correction for material that was assumed inert. Ye et al. were the first to report hydrogen-adsorption investigations on purified [40] laser-generated [41] SWNTs. They undertook their experimental measurements of hydrogen adsorption on high-purity “cut SWNTs.” To cut the SWNT material and disrupt the tightly packed rope structure found in highly crystalline pristine SWNTs, a small quantity of material was sonicated in dimethylformamide, and then extracted from the solvent by vacuum filtration. TEM revealed that this treatment broadens the diameter distribution of the SWNT ropes, and also increases the number of SWNT terminations within ropes (hence the SWNTs are said to be “cut”). These differences were not evident in the X-ray diffraction patterns of the material before and after the treatment, perhaps indicating that the average rope diameter was largely unchanged.

The adsorption of hydrogen was measured by the volumetric method without correction for thermal effects. The highest gravimetric hydrogen storage capacity achieved in SWNT material treated in this manner was 8.25 wt% (an H/C atomic ratio of 1.0), at a temperature of 80 K and pressure of  $\sim 7$  MPa. At a pressure of  $\sim 4$  MPa, a sudden increase in the adsorption capacities of the SWNT samples was reported; the authors suspected that a structural phase transition was responsible for this effect. In their method, the ropes were split into individual tubes, thereby increasing the surface area available for physisorption. In their conclusion, the authors [39] advanced that the ability of SWNT

**Table 1.** Summary of the reported gaseous hydrogen storage capacity in carbon nanotubes and carbon nanofibers.

Sample	Purity (%)	$T$ (K)	$P$ (MPa)	wt% $H_2$	Ref.
SWNT	assumed 100	133	0.04	5–10	[26]
SWNT	high	ambient	0.067	3.5–4.5	[38]
SWNT	~50	300	10.1	4.2	[42]
Aligned SWNT	purified	ambient	11	4	[46]
SWNT	purified	77–300	8	1–1.5	[47]
SWNT	high	80	~7	8.25	[39]
MWNT	purified	~300–700	ambient	0.25	[48]
SWNT	purified	ambient	4.8	1.2	[49]
SWNT-TiAl <sub>0.1</sub> V <sub>0.04</sub>	sonicated >98	ambient	0.067	6.5	[50]
SWNT-Ti-6Al-4V	purified	ambient	0.08	1.47	[53]
SWNT-Fe	purified	ambient	0.08	<0.005	[53]
Ball-milled SWNT in Ar	<50	ambient	0.08	<0.1	[58]
Ball-milled SWNT in D <sub>2</sub>	<50	ambient	0.9	1.0	[58]
CNT	purified	298–773	0.1	0.4	[58]
Doped CNT	—	—	—	0.5–1.0	[67]
Li-CNT	purified	473–673	0.1	20	[64]
K-CNT	purified	<313	0.1	14	[64]
Li-CNT (wet H <sub>2</sub> )	purified	473–673	0.1	12	[65]
Li-CNT (dry H <sub>2</sub> )	purified	473–673	0.1	2.5	[65]
K-CNT (wet H <sub>2</sub> )	purified	<313	0.1	21	[65]
K-CNT (dry H <sub>2</sub> )	purified	<313	0.1	1.8	[65]
Li-CNT	10–40	473–663	0.1	0.7–4.2	[66]
SWNT	80–90	273	0.04	7	[50]
SWNT	(90 vol%)	298	—	0.63	[90]
MWNT	unpurified	298	—	0.05	[90]
MWNT	unpurified	293	6.5	2.0	[57]
CNT	—	ambient	ambient	0.5	[59]
SWNT	purified	77	0.2	6	[60]
Aligned MWNT	high	298	10	3.0	[61]
Aligned MWNT	high	290	10	2.4	[62]
Random MWNT	high	298	10	0.68	[61]
MWNT	high, untreated	300	1.0	5–7	[63]
MWNT	high, acid treated	300	1.0	13.8	[63]
MWNT	high	300	7.0	0.7–0.8	[150]
SWNT	unpurified	295	0.1	0.93	[149]
SWNT	unpurified	77	0.1	2.37	[149]
MER MWNT	10–15%	298	3.6	0.03	[32]
Rice SWNT	high	298	3.6	0.05	[32]
CNT	—	298	11.35	11.26	[83]
GNF (herringbone)	—	298	11.35	67.55	[83]
GNF (platelet)	—	298	11.35	53.68	[83]
GNF	—	77–300	0.8–1.8	0.08	[84]
CNF	—	300	12	6.5	[86]
GNF	—	300	10.5	0.7	[87]
CNF	—	293	10	1	[88]
CNF	—	298	12	1.4	[89]
Ball-milled GNF in D <sub>2</sub>	—	ambient	0.9	0.5	[58]
GNF	—	300	11	<0.1	[28]
VGCF	—	298	3.6	<0.1	[32]
CNF	—	300	12.5	1.6	[91]
herringbone GNF	purified	77–300	1.5	1–1.8	[92]
GNF	—	300	12	10	[93]
GNF	—	300	12	10	[94]
CNF	—	77	12	12.38	[95]
CNF	—	300	11	5.7	[45]

Note: — represents data unavailable.

material to adsorb and desorb hydrogen over a narrower range of pressure may be used in storage systems without wide pressure excursions.

High hydrogen-storage capacities on a total sample weight basis were subsequently demonstrated on SWNTs with a large mean diameter of about 1.8 nm produced at high yield by a semicontinuous arc-discharge method [42]. In this study, a sulfur promoter (FeS) was added, and H<sub>2</sub> rather than He was used as the buffer gas, and the electrodes made an oblique angle in the synthesis process which were a little different from the traditional arc method [43]. They treated their samples (containing ~50% SWNTs) by soaking in hydrochloric acid and heating to high temperature (770 K) under vacuum. Their adsorption measurement technique consisted of monitoring the pressure change of hydrogen versus time in a constant-volume cell containing the nanotubes sample; when equilibrium is achieved, the pressure decrease corresponds to the amount of hydrogen adsorbed. The results at room temperature and 10.1 MPa were 2, 2.5, and 4.2 wt% for nontreated, partially treated, and entirely treated samples, respectively (Fig. 4). The relatively high hydrogen storage capacity was attributed to the large mean tube diameter of about 1.85 nm, which they ascribed to the addition of a sulfur-containing growth promoter [44, 45]. About 78.3% of the adsorbed hydrogen (3.3 wt%) could be released under ambient pressure at room temperature, while the release of the residual stored hydrogen (0.9 wt%) required heating of the sample.

The same group examined the storage capacity of single-walled carbon nanotubes pressed into tablets and heat treated under argon flow at 1473 K for 2 h. They obtained a storage capacity of 4 wt% at room temperature and 11 MPa [46]. About 70% of the adsorbed hydrogen was released under ambient pressure. However, these high storage capacities could not be confirmed by other groups using the same measuring method. Tibbetts et al. [32] found storage capacities of below 0.05 wt% for different nanotubes at

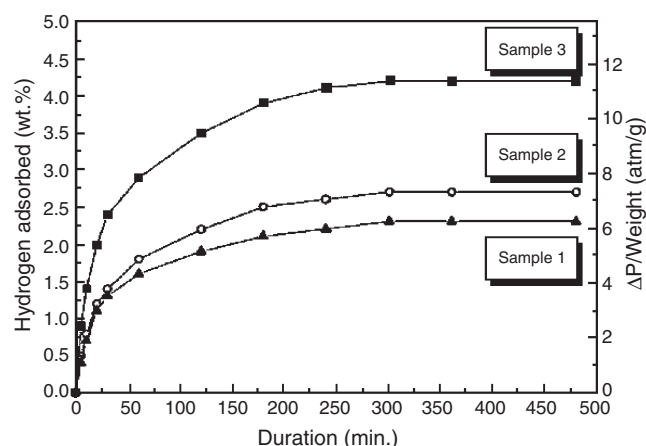


**Figure 4.** Amount of H<sub>2</sub> in wt% for SWNT samples, and the pressure change versus the adsorption time. Sample 1 was used as synthesized. Sample 2 was soaked in 37% HCl acid for 48 h, rinsed with deionized water, and dried at 423 K. Sample 3 was pretreated in the same way as sample 2, then vacuum heat treated for 2 h. Reprinted with permission from [42], C. Liu et al., *Science* 286, 1127 (1999). © 1999, American Association for the Advancement of Science.

11 MPa and room temperature. Chen et al. examined different purified and nonpurified SWNTs with the volumetric method at 77 K and room temperature, applying hydrogen pressures up to 8 MPa. The measurements gave no indication that carbon nanotubes exceed the storage capacity of activated carbon. At room temperature, the hydrogen uptake was below 1 wt%, and at 77 K about 1.5 wt% [47].

Wu et al. [48] probed the hydrogen-adsorption properties of multiwall nanotubes synthesized by the catalytic decomposition of CO and CH<sub>4</sub> on powdered La<sub>2</sub>O<sub>3</sub> catalysts. The CO-generated tubes consisted of concentric cylinders, while the CH<sub>4</sub>-produced tubes contained graphite layers that were tilted with respect to the tube axis, forming cones. In both cases, the catalyst was removed by stirring in dilute nitric acid. The purified nanotubes were then annealed to 1370 K in vacuum in order to increase crystallinity. The TGA analysis in flowing hydrogen showed that CO-generated CNTs adsorbed a small quantity of hydrogen (0.25 wt%) when the sample was cooled from 470 K to room temperature.

With a tapered element oscillating mass analyzer, Smith et al. [49] measured SWNTs from Tubes@Rice at room temperature and pressures up to 4.8 MPa. The highest storage capacity of 1.2 wt% at 4.8 MPa was obtained for purified SWNTs after an oxidation under a stream of CO<sub>2</sub> at about 900 K. The activation of the SWNT samples by mild oxidation in CO<sub>2</sub>, followed by heat treatment in an inert atmosphere, increases the hydrogen adsorption capacity of the SWNT samples by about a factor of 3 at 4.8 MPa.

A newly developed high-energy ultrasonic cutting procedure which incorporates a TiAl<sub>0.1</sub>V<sub>0.04</sub> alloy has been applied to purified, laser-generated SWNT materials, allowing high-capacity hydrogen adsorption at ambient conditions [50]. The degassed samples underwent a brief room-temperature H<sub>2</sub> exposure at 0.07 MPa, and the H<sub>2</sub> TPD spectrum is characterized by two separate desorption signals peaked at ~375 and 600 K, indicating at least two different types of sites for hydrogen adsorption. The hydrogen adsorption capacity, as measured by calibrated TPD, was ~6.5 wt% on a total sample weight basis after sonication in 4 M HNO<sub>3</sub> for 16 h at 50 W · cm<sup>-2</sup> and degassing to 825 K. This sample was found to contain ~15 wt% alloy of composition TiAl<sub>0.1</sub>V<sub>0.04</sub> due to decomposition of the ultrasonic probe. The pure TiAl<sub>0.1</sub>V<sub>0.04</sub> samples generated using the same method exhibited X-ray patterns consistent with the alloy found in the SWNT samples and only ~2.5 wt% hydrogen adsorption. Assuming that the alloy in the SWNT sample behaves like the pure alloy sample, the hydrogen uptake on the SWNT fraction is ~7.2 wt%. Samples with higher alloy contents had reduced overall hydrogen capacities, but the value of ~7 wt% on the SWNT fraction was relatively constant. The presence of the alloy might, in fact, stimulate hydrogen adsorption and desorption. Several control experiments have shown that the observed uptake is not solely due to the presence of the alloy, and there are some experimental indications of partial electron transfer being responsible for the stability of the hydrogen [50]. Unfortunately, the high storage capacity of about 6.5 wt% could not be confirmed by volumetric measurements performed by the same group, which give a value of 2.3–2.8 wt% [51]. In the DOE report of year 2001, Heben's group declared that, unfortunately, they cannot reproduce the high hydrogen storage capacities using

SWNTs generated with a new laser [52]. The hydrogen storage capacities of these new SWNTs range from 2 to 4 wt%.

Recently, Hirscher et al. [53] investigated the influence of sonication on the hydrogen storage capacity of SWNTs. The samples were sonicated in 5 M  $\text{HNO}_3$  for various periods of time using an ultrasonic probe of the alloy Ti-6Al-4V or stainless steel. The sonication treatment introduces particles of the Ti alloy or Fe into the samples, and the hydrogen storage capacity increases with the sonication time. After heating in high vacuum up to 900 K, the maximum value of overall hydrogen storage at room temperature was found to be 1.47 wt% in an SWNT-alloy composite, with a sharp comparison to the value below 0.005 wt% in the SWNT-Fe composite. Directly after the sonication treatment, the samples show no hydrogen uptake at room temperature, whereas after heating in high vacuum up to 900 K, hydrogen storage at room temperature is observed. This is the well-known activation procedure of titanium removing the natural oxide layer under vacuum and in the temperature range from 700 to 900 K [54]. Afterwards, titanium readily takes up hydrogen at room temperature. With increasing sonication time, the hydrogen storage capacity increases, as well as the titanium content in the carbon samples. After hydrogen loading, X-ray diffraction measurements yield clear evidence of the formation of titanium hydride (see Fig. 5). If the total amount of hydrogen is ascribed to the fraction of Ti-alloy particles in the SWNTs, the maximum content in the alloy will be 3.3 wt%, which is below the maximum storage capacity of this Ti alloy and titanium itself. Encouraged by these findings, the authors concluded that all of the hydrogen uptake could be ascribed to the Ti-alloy particles [53].

Heben suggests that nanotubes in some of the samples are being “activated” in some way by the alloy particles so that they adsorb more hydrogen than they would in the absence of the metal [55]. The alloy, he believes, may assist hydrogen uptake by a catalytic effect in which the titanium dissociates the  $\text{H}_2$  or via thermal effects, where the exothermic reaction of hydrogen with the titanium could locally create

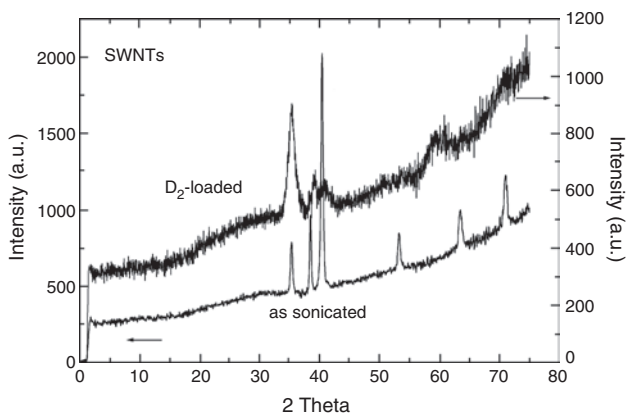


**Figure 5.** X-ray diffraction spectra (Cu  $K_\alpha$  radiation) of SWNTs sonicated in 5 M  $\text{HNO}_3$  for 16 h using a Ti-alloy horn. The as-sonicated material shows the diffraction peaks of titanium. After deuterium loading (0.08 MPa  $\text{D}_2$  at room temperature for 15 min) these maxima vanish, and the diffraction peaks of titanium deuteride appear. Reprinted with permission from [53], M. Hirscher et al., *Appl. Phys. A* 72, 129 (2001). © 2001, Springer-Verlag.

thermal disturbances to the tube that might aid in the addition of the hydrogen. A mechanism that is midway between physisorption and chemisorption is favored because much of the stored hydrogen desorbs at higher temperatures than is typically found for physisorption. The mechanism could involve fractional electron charge transfer between hydrogen molecules and the nanotube, with the hydrogen molecule remaining intact [55].

Another strategy that might help crack the hydrogen-storage mystery is to “decouple” the nanotube-cutting process from the alloy-introduction step. With this in mind, Heben’s group found ways to cut nanotubes without sonication using a controlled dry cutting method that nondestructively cuts the SWNTs without incorporating a metal alloy in the latest DOE report of 2002 [56]. It is regrettable that the details of this process have not been revealed yet. In order to establish the degree of control achieved, they used Raman spectroscopy to monitor the degree of cutting caused by the new method. They found that, when identical conditions are employed to presumably achieve similar degrees of cutting, the ratio of the Raman  $D$  band, which is correlated to the number of defects (i.e., ends), to the  $G$  band of the nanotubes increases by a fixed amount.

The hydrogen storage capacities of samples obtained by this cutting method were evaluated with temperature-programmed desorption. Hydrogen exposures were at room temperature and 0.07 MPa for several minutes, and the samples were then cooled in the presence of the gas. The TPD spectra of both uncut and cut samples contain a hydrogen desorption peak at  $\sim 138$  K, which can be attributed to the normal physisorbed hydrogen which is seen for activated carbons. The spectrum of the cut sample additionally shows a hydrogen desorption peak at  $\sim 338$  K, revealing the presence of hydrogen that is stabilized at ambient temperatures. The hydrogen desorption peaks occur at the different temperature ranges for the sonicated samples which incorporate metal hydride alloy and “dry-cut samples” without metal species. Obviously, the hydrogen adsorption mechanism is strongly influenced by the incorporation of the metal hydride species. Unfortunately, the hydrogen storage capacity was not clearly provided, although the “dry-cut” samples were evaluated with temperature-programmed desorption and volumetric techniques. It was estimated that this new cutting process avoided metal impurities, and resulted in storage capacities below 1 wt% [56]. However, they claimed that the values scattered, and were hard to reproduce. Optimization of the process and the subsequent incorporation of catalytic metallic species will be explored in the future to determine if high-temperature, high-storage capacity materials may be prepared in a reproducible manner [56].

Ding et al. [57] tested CVD-grown MWNTs using the volumetric measurement method with corrections for thermal effects. The MWNTs were prepared by acetylene decomposition, and pressed into pellets without further treatment. These pellets were degassed at 673 K for 6 h to remove the moisture and other absorbed contaminants. The ambient temperature was carefully monitored to correct the pressure changes arising from the temperature variation. At the same time, the sample chamber temperature was also recorded. The gravimetric hydrogen storage capacity



found was 2.0 wt% at room temperature and a pressure of  $\sim 6.5$  MPa.

Hirscher et al. [58] also conducted the hydrogen storage on ball-milled graphite, graphite nanofibers, and SWNTs which were ball milled under Ar or D<sub>2</sub> atmosphere in order to modify the microstructure. A very low reversible hydrogen uptake for the SWNTs milled under argon was observed. However, they found 0.3, 0.5, and 1.0 wt% hydrogen uptake on graphite, graphite nanofibers, and SWNTs, respectively, and reversible hydrogen storage only for SWNTs. During high-energy ball milling under hydrogen pressure, the microstructure of carbon nanotubes is severely damaged by mechanical impact, and furthermore, dangling carbon bonds may be formed which can react with the surrounding hydrogen atmosphere. It is suggested that opening or cutting of the tubes and ropes is essential.

The hydrogen uptake of carbon nanotubes in the low-pressure range up to ambient pressure was measured by Adu et al. [59] with a thermogravimetric analyzer. The storage capacity at ambient temperature is nearly constant, and about 0.5 wt%. However, Pradhan et al. [60] obtained a hydrogen storage capacity of up to 6 wt% at 0.2 MPa with processed bundles of SWNTs utilizing the same measuring method.

Zhu et al. [61] tested the bundles of well-aligned multiwalled carbon nanotubes, and found that the hydrogen storage capacity is over 3 wt% under 290 K and  $\sim 10$  MPa pressure. However, they obtained a value of 0.68 wt% for the random material at the same pressure. The same group obtained a similar value of 2.4 wt% under similar conditions for the aligned MWNT samples [62]. Unfortunately, the masses used for the volumetric measurement have been far below 1 g (about 100 mg). Even more startling were the claims of Chen and his co-workers [63], who reported that certain aligned carbon nanotubes can store hydrogen at levels exceeding 5–7 wt% at room temperature under a pressure of 1 MPa. Aligned carbon nanotubes with diameters of 50–100 nm were grown on a stainless-steel wafer by plasma-assisted hot-filament chemical vapor deposition. The mass of the examined carbon material was less than 1 mg, and the weight of the substrate about 60–70 mg. They measured the mass decrease of loaded nanotubes together with the substrate by heating up to 600 K. In this study, quadruple mass spectroscopy and thermogravimetric analysis were employed to probe the hydrogen storage capacity. However, a reference measurement of the substrate is missing. After the pretreatments of heating the samples to 570 K and removing the catalyst tips, the hydrogen storage capacity can be increased up to 13.8 wt% and the pressure required for storage decreased. However, the community still awaits confirmation of these experimental results by workers in other research groups.

### 2.3. Gaseous Hydrogen Storage in Doped CNTs

All the above H<sub>2</sub>-uptake systems require high pressure or subambient temperatures, or both. Recently, Chen and co-workers [64] reported high hydrogen adsorption in alkali-metal-doped carbon nanotubes at ambient pressure and slightly elevated temperatures. The carbon nanotubes used

in this work were synthesized by catalytic decomposition of methane. Doping of the carbon nanotubes was carried out by means of solid-state reactions with Li- or K-containing compounds such as carbonates and nitrates. The extent of hydrogen uptake was determined by TGA and confirmed by TPD. The authors reported dramatic enhancement of hydrogen storage in the alkali-doped systems, with the best results found in the case of Li-CNTs (20 wt% gravimetric storage). The remarkable storage improvement in Li-CNTs (Fig. 6) relative to the virtually negligible (0.4 wt%) storage in undoped nanotubes was attributed by them to adsorption by means of metal hydride interaction.

Using *in-situ* FTIR spectroscopy, the authors correlated an increase in intensity of the characteristic lithium hydride vibration at  $\sim 1420$  cm<sup>-1</sup> with increased hydrogen adsorption in the temperature range of 473–673 K. A new infrared band, which the authors attributed to C–H stretching vibration, appeared in the spectral region of  $\sim 2600$ – $3400$  cm<sup>-1</sup>. This feature was observed to disappear upon thorough desorption of hydrogen. The authors suggested that an explanation for the remarkable boost in storage capacity may require dissociation of H<sub>2</sub>, catalyzed by the intercalated alkali metal in the carbon nanotubes. The special open-ended, layered structure of the nanotubes are also helpful to improve the adsorption performance of hydrogen.

However, Yang [65] thought that the above measurement results for the hydrogen adsorption should be corrected. The grade of hydrogen used in the work of Chen et al. was not reported, but a purity 99.99% was noted [64]. Therefore, special care should be taken to eliminate possible moisture contamination. In addition, special caution needs to be taken in using TGA for measuring adsorption or reaction kinetics. Upon a change in temperature or gas composition/flow rate, the accompanying change caused by changes in buoyancy and friction forces from the gas flow is usually of the same order of magnitude as the signal that is being measured (i.e., the actual weight change). Hence, rigorous calibration must be done for all changes.

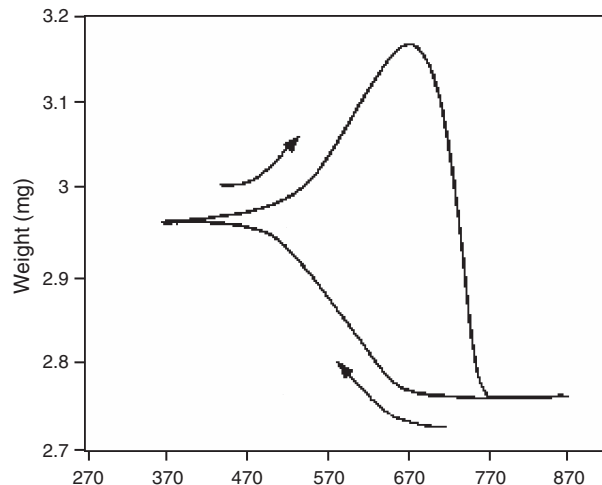


**Figure 6.** TGA profile of reversible H<sub>2</sub> sorption-desorption cycle on Li-doped CNT. The sample was cooled to 300 K, and then heated again to 873 K. Reprinted with permission from [64], P. Chen et al., *Science* 285, 91 (1999). © 1999, American Association for the Advancement of Science.

Yang prepared alkali-doped carbon nanotubes according to the method prescribed in the work of Chen et al. [64]. Nevertheless, ultrahigh-purity hydrogen (99.999%, with moisture trap) was used to conduct the adsorption measurements on Li-doped SWNT (Fig. 7). The results of hydrogen adsorption with added water (2.3 vol%) was also obtained to compare with the results of dry hydrogen adsorption (Fig. 8). Furthermore, calibration runs were made under the same conditions to calibrate the weight gains/losses [65]. The similar qualitative features of the result of Chen et al. [64] were reproduced over Li/nanotubes; however, the total weight differential was only 2.5%, rather than 20% reported by Chen et al. The essential qualitative feature of the TGA profile was still maintained with moisture addition, and the total weight differential in wet  $H_2$  was substantially greater, at 12%, compared to 2.5% in dry  $H_2$ . The weight gains reached 1.8 and 21% over K/nanotubes in dry or wet  $H_2$ , respectively, compared to 14% reported by Chen et al.

Yang also reported the IR spectrum of LiOH (with one hydrate), and a striking similarity existed between this spectrum and that of Chen et al. This shows that the alkali hydroxide and additional hydrates may form. The weight gains by forming hydroxides (plus hydrates) agreed well with the total weight gains reported by Chen et al. Although Chen et al. did not find the emergence of water in the desorption product using TPD, the work of Yang showed that the TGA measurements strongly depended on the concentration and rate of supply of moisture.

Pinkerton et al. [66] made further investigations on doped CNTs. The results indicate that, on Li-doped CNTs, neither hydrogen nor carbon is required to generate the qualified

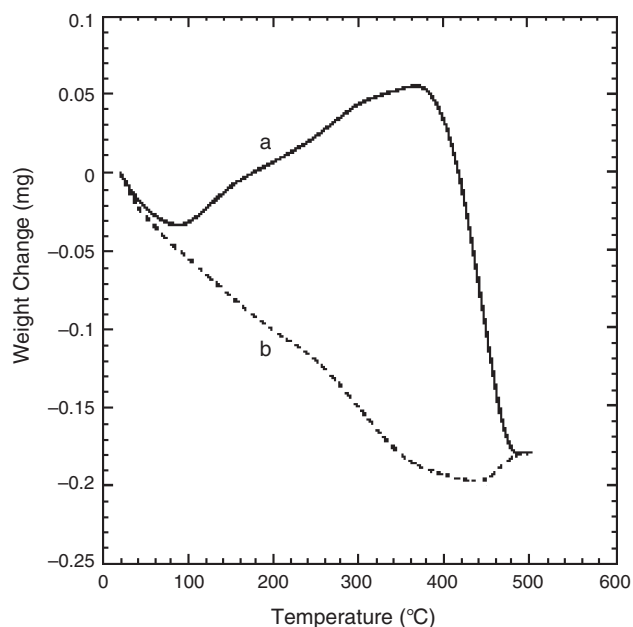


**Figure 7.** TGA profile of Li-doped carbon nanotubes in 0.1 MPa dry  $H_2$ . (a) Increasing temperature from 20 to 500 °C at 5 °C/min. (b) Cooling at slower rates. The total weight of Li/C was 10 mg. Ultrahigh purity  $H_2$  (>99.999%) with additional  $H_2O$  trap used. Reprinted with permission from [65], R. T. Yang, *Carbon* 38, 623 (2000). © 2000, Elsevier Science.

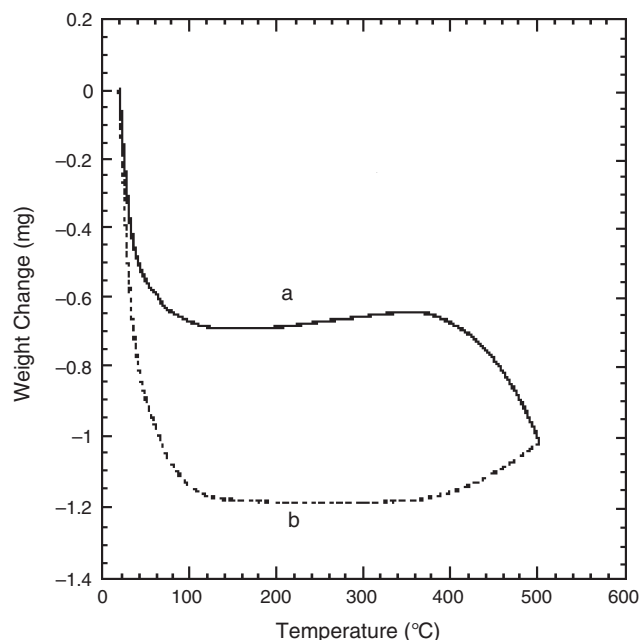


**Figure 8.** TGA profile of Li-doped carbon nanotubes in 0.1 MPa wet  $H_2$ . (a) Increasing temperature from 20 to 500 °C at 5 °C/min. (b) Cooling at slower rates. The total weight of Li/C was 10 mg. 2.3% (vol.) water vapor was added in  $H_2$ . Reprinted with permission from [65], R. T. Yang, *Carbon* 38, 623 (2000). © 2000, Elsevier Science.

TGA cycling features, which are strikingly similar to those reported by Chen [64] and Yang [65]. This result is obtained for Li-containing samples measured in Ar without  $H_2$  and in LiOH samples measured in either  $H_2$  or Ar. To elucidate the species responsible for weight cycling, additional gases ( $N_2$ ,  $O_2$ ,  $H_2O$ , or air) are deliberately introduced into the TGA furnace (Fig. 9). Adding 0.5 sccm of dry air to the TGA gas stream has spectacular effects on the cycling features, and the magnitude grows as the  $O_2$  concentration increases with continued exposure. The amplification derives from the catalytic reaction between  $H_2$  and  $O_2$  under the specific conditions with the Pt pan as a catalyst. Therefore, these cycling features arise from atmospheric impurities in the TGA which finally react with Li or K to form LiOH or KOH. The authors conclude that the cycling species responsible for the weight changes is, in fact,  $H_2O$ , in agreement with Yang [65]. The  $H_2$  storage results vary from 0.72 to 4.2 wt%, depending on the initial weight and scan rate under 46%  $H_2$  in Ar on Li-doped CNTs.

Zidan and Rao [67] believed that the introduction of nanoparticles (dopants) to the nanotubes can enhance hydrogen bonding at the edge and inside the tubes, allowing for hydrogen storage to occur. The success of making doped carbon nanotubes with transition metals and alloys can allow for a weak covalent bond similar to cases of a dihydrogen bond that is not restricted to a pure physisorption or chemisorption bond [68, 69]. Controlling the type and size of tubes and dopant is expected to tune the product for hydrogen sorption to occur at a desired temperature and pressure. Preliminary results showed an indication of 0.5–1% by weight hydrogen uptake and release from samples. A thermogravimetric system capable of operating at a wide

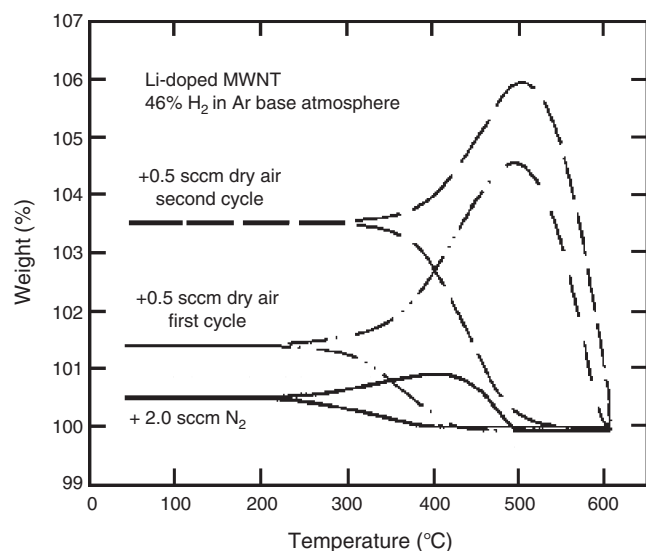


**Figure 9.** Temperature cycling characteristics of Li-doped multiwall nanotubes in an  $H_2/Ar$  gas mixture with dry air added to the input gas stream. The solid curve shows the cycling behavior in  $H_2/Ar$  with additional  $N_2$ ; the  $N_2$  by itself has essentially no effect on the cycling characteristic compared with that in  $H_2/Ar$  alone. The first cycle (dash-dot curve) and second cycle (dashed curve) after introducing 0.5 sccm of dry air to the input gas trace the evolution of greatly enhanced cycling magnitude. Reprinted with permission from [66], F. E. Pinkerton et al., *J. Phys. Chem. B* 104, 9460 (2000). © 2000, American Chemical Society.

range of temperatures was used to measure the hydrogen uptake and release. Unfortunately, no samples and experimental details were revealed in this study [67].

#### 2.4. Electrochemical Hydrogen Storage

Table 2 summarizes reported experimental results thus far achieved for electrochemical hydrogen storage in carbon nanotubes. The electrochemical hydrogen storage capacity

**Table 2.** Summary of the reported electrochemical  $H_2$  storage capacity in carbon nanotubes.

Sample	Purity (%)	Charge capacity (mA · h/g)	Max. wt% $H_2$	Ref.
SWNT	unpurified	110	0.40	[30]
MWNT	(10–40%)	100	0.37	[30]
SWNT	unpurified	550	2.0	[31]
SWNT	—	160	0.57	[29]
MWNT	—	200	0.74	[73]
SWNT	80	800	2.9	[74]
SWNT	—	360	0.9	[75]
SWNT	90	440	1.6	[76]
Li-CNT	—	160	0.59	[76]
Li-SWNT	—	640	2.4	[76]
SWNT rope	—	503	1.84	[78]
SWNT	95	316	1.2	[77]
MWNT	95	1157	4.1	[79]
SWNT	purified	1200	4.35	[80]
Li-SWNT	—	1080	3.9	[81]

Note: — represents data unavailable.

of SWNTs was measured by Nutzenadel et al. [30] using carbon nanotube samples from worldwide research groups or companies. In each case, 20 mg of SWNTs were finely ground, mixed with 80 mg of Au powder (which serves as a compacting additive, and does not participate in the electrochemical reaction), and pressed at a pressure of 500 MPa to form a pellet. The SWNT/Au pellet served as the negative electrode, and an Ni plate was used to form the counterelectrode. Experiments were conducted in a half cell, using a solution of 6 M KOH as the electrolyte; potentials were referred to an  $Hg/HgO/OH^-$  reference electrode. The hydrogen weight density was deduced from the amount of discharged current. The obtained hydrogen storage capacity was  $\sim 0.40$  wt%. Nevertheless, the effect of chemical posttreatment and/or metallic impurities on the absorptive capacity of the SWNT samples was not quantified in this work. MWNT samples exhibited a similar hydrogen storage capacity of 0.37 wt%. The same group presented further investigations on a variety of carbon nanotubes [31, 70]. The storage densities range from 0.04 up to 2 wt%, and correlate with the specific surface area of the sample [71]. Nijkamp et al. [72] also observed a similar correlation in low-temperature volumetric measurements on high-surface-area carbon materials.

Lee et al. [29] conducted electrochemical charge-discharge cycling experiments recently. CNT-based composite electrodes were fabricated by mixing and grinding first with conductive Ni powders (99.8%) for 50 min, and later with the organic binder of polytetrafluoroethylene (PTFE) for 20 min with a mixing composition ratio of CNT:Ni:PTFE = 40:50:10. The pellet was made by pressing the mixture into a mold of 10 mm diameter at 200 MPa. This pellet was inserted into Ni metal mesh, and used for a working electrode. The counterelectrode Ni was separated by a polymer separator. The charge-discharge cycles were carried out in a solution of 6 M KOH solution. An  $Ag/AgCl$  standard electrode was used as a reference electrode in this measurement. A charge/discharge capacity of 160 mA · h/g was demonstrated, which corresponds to a gravimetric capacity of  $\sim 0.57$  wt%.

Qin et al. [73] investigated the electrochemical properties of an MWNT-Ni electrode. The MWNT-Ni electrode was found to have a high discharge capacity of 200 mA · h/g ( $\sim 0.7$  wt%) and a long charge/discharge cycle life. Recently, electrodes made of purified and open SWNTs behaved like metal hydride electrodes in Ni-MH batteries, showing high electrochemical reversible charging capacity up to 800 mA · h/g corresponding to a hydrogen storage capacity of 2.9 wt% [74]. Most recently, Züttel et al. [75] studied the electrochemical hydrogen storage capacity of a series of CNTs, and found the highest value of capacity up to 0.9 wt%.

Kibria et al. [76] investigated the electrochemical hydrogen storage behaviors of undoped and alkaline-metal-doped CNTs produced by various preparation techniques. Laser-ablation-grown CNTs produce the highest hydrogen storage capacity of 1.6 wt%. The alkali metal-doped CNTs showed higher hydrogen storage capacities than undoped CNTs. Although the hydrogen storage capacities of Li-doped CVD and AD (arc discharge)-grown CNTs were six times higher than that of undoped CNTs, it is only 0.6 wt%.



For Li-doped LA grown CNTs, the hydrogen storage capacity reached 2.4 wt%. The high hydrogen storage capacity of alkali metal-doped CNTs seems to originate from increasing the hydrogen adsorption sites of CNTs due to introducing the doped metals in nanotube bundles, and separating the tubes, but not from their chemical effects. Purified SWNTs with a large mean diameter of approximately 1.85 nm, which were synthesized by a semicontinuous hydrogen arc-discharge method [42], were also used for electrochemical hydrogen adsorption experiments [77]. After high-temperature treatment, a reproducible maximum discharge capacity of 316 mA · h/g, corresponding to 1.2 wt% hydrogen storage, was achieved at 298 K under normal pressure. After 100 charge/discharge cycles, >81% of the maximal capacity was maintained.

Dai et al. [78] further measured the electrochemical charge/discharge hydrogen capacity of macroscopically long ropes (up to 100 mm in length) of well-aligned SWNTs (60–70 wt% purity) with a larger mean diameter of about 1.72 nm. A discharge capacity of 503 mA · h/g, corresponding to 1.84 wt% hydrogen, was achieved reproducibly at ambient temperature under normal atmosphere. A much higher charge capacity of 1157 mA · h/g, corresponding to 4.1 wt% hydrogen, was obtained using electrodes made up of MWNTs [79].

Reversible insertion of lithium into purified single-wall carbon nanotubes was achieved electrochemically [80]. Carbon nanotubes exhibited reversible capacities of approximately 460 mA · h/g and very high irreversible capacities of 1200 mA · h/g, corresponding to 4.35 wt% hydrogen, which the authors ascribe to the large specific surface area (350 m<sup>2</sup>/g). *In-situ* X-ray diffraction revealed an irreversible loss of crystallinity, suggesting that doping disrupts the intertube binding, analogous to exfoliation in layer hosts. In another study, lithium-inserted carbon nanotubes exhibited reversible capacities approximately 780 mA · h/g and very high irreversible capacities of 1080 mA · h/g, corresponding to 3.9 wt% hydrogen [81].

Pekker et al. [82] performed the hydrogen storage experiments with carbon nanotubes and graphite via a dissolved metal reduction method in liquid ammonia. Dried ammonia was condensed to the carbon material which had been mixed with lithium under an inert atmosphere. The suspension was stirred for 1 h at about 220 K, and then ammonia was evaporated by heating to room temperature. After a second condensation, methanol was added to the sample. The sample was heated again to room temperature to evaporate NH<sub>3</sub>, and then it was washed and dried. With thermoanalytical and electron-microscopic studies, the authors could show that the applied hydrogenation method gives rise to the formation of strongly bound derivatives. Desorption of hydrogen takes place at around 770 K, and the content was 1.7 and 0.7 wt% for graphite and carbon nanotubes, respectively.

Generally speaking, the electrochemical loading of carbon nanostructures shows no spectacular high storage capacity. Furthermore, the uptake seems to be proportional to the specific surface area of the carbon material, and therefore comparable to activated carbon [28].

## 2.5. Hydrogen Storage in Carbon Nanofibers

Carbon nanotubes are not the only carbon structures which are able to retain hydrogen in their framework; graphite nanofibers also exhibit hydrogen adsorption potential. The hydrogen storage experimental results for graphite nanofibers are also listed in Table 1. Rodriguez's group prepared various graphite nanofibers, and conducted hydrogen adsorption experiments using the produced nanofibers [83]. These graphite nanofibers consist of catalytically produced graphene sheets that are oriented to form various fibrous structures. The orientation of the sheets in the fibers can be controlled by the choice of catalyst. Hydrogen gas applied at 11.35 MPa was absorbed at room temperature (298 K). The hydrogen storage capacity was found to be, for CNTs, 11.26 wt%, for herringbone carbon fibers 67.55 wt%, for platelet fibers 53.68 wt%, and finally, for graphite 4.52 wt%. Unfortunately, this surprising hydrogen adsorption capacity has not been confirmed to date, neither experimentally nor theoretically [18]. Attempts by other researchers to reproduce these high-hydrogen storage densities have failed, and typically, results of only 0.08 wt% have been achieved [84]. The extraordinarily high results were later suggested to be influenced by the presence of water vapor, which expanded the spacing between the graphite layers (typically ~3.4 Å) to accept multiple layers of hydrogen [85]. Browning et al. [86] synthesized carbon nanofibers at 870 K by passing ethylene over a series of Fe–N–Cu catalysts. They obtained a hydrogen storage capacity in their sample at room temperature and 12 MPa of 4.18 and 6.54 wt% with a postproduction treatment. Poirier et al. [87] tested the hydrogen storage performance of carbon nanofibers, as well as intercalated and exfoliated carbon materials. At room temperature, carbon nanofibers adsorb 0.7 wt% at a hydrogen pressure of 10.5 MPa, which is comparable to activated carbon. However, the hydrogen coverage per unit surface area is found to be substantially larger on carbon nanostructures than on activated carbon. de la Casa-Lillo et al. [88] found that the highest values of hydrogen adsorption in activated carbons or activated carbon fibers was close to 1 wt% at 10 MPa and room temperature. Hwang et al. [89] reported that the carbon nanofibers from methane decomposition using an Ni–MgO catalyst exhibited a hydrogen adsorption capacity up to 1.4 wt% after heat treatment at 1470 K in N<sub>2</sub> atmosphere. Hirscher et al. [28] also performed volumetric measurements at 11 MPa and 300 K using GNFs prepared by catalytic vapor deposition, and observed a hydrogen uptake lower than 0.1 wt%. Nevertheless, the ball-milled graphite fiber reached up to 0.5 wt% hydrogen adsorption capacity at 0.9 MPa and room temperature using the TDS technique [58]. Tibbetts et al. [32] studied the sorption of hydrogen very carefully by nine different carbon materials at pressures up to 11 MPa and temperatures from 193 to 773 K. The largest sorption observed is less than 0.1 wt% hydrogen at room temperature and 3.5 MPa. Ritschel et al. [90] observed a storage capacity of 1273 K Ar-treated GNF less than 0.2 wt% at room temperature and 4.5 MPa.

Using the thermogravimetric analysis, Ströbel et al. [91] measured the hydrogen adsorption of carbon nanofibers and activated carbon at high pressure. At a pressure of 12.5 MPa

and room temperature, they observed a maximum weight increase corresponding to a hydrogen uptake of 1.6 wt% in activated carbon and of 1.2 wt% for the fibrous material. Harutyunyan et al. [92] obtained consistent results on purified tubular-formed and herringbone-type GNFs. They found 1.8 wt% at 77 K and about 1 wt% at room temperature under 1.5 MPa hydrogen pressure.

However, encouraging results have been reported by Gupta and Srivastava [93, 94], who achieved hydrogen adsorption capacities of  $\sim 10$  and  $\sim 15$  wt% for graphite nanofibers grown by thermal cracking. The GNFs were activated by heating 1 h at 420 K under  $10^{-7}$  MPa in a steel reactor. After 15–16 h, hydrogen absorption started, and the hydrogen uptake saturated at pressures higher than 9 MPa. More recently, Fan et al. reported a 10–13 wt % hydrogen adsorption capacity using vapor-grown carbon fibers [95]. In a further research paper [45], the same group reduced the storage capacity of carbon fibers by a factor of 2. As with carbon nanotubes, a large degree of variation in the results exists, and further verification is required.

The rather scattered experimental results published on hydrogen storage measurements of carbon nanofibers also listed in Table 1. The figures in the table show that the large discrepancies between claims of high hydrogen storage capacities and almost no storage at all exist up to the present day. The experimental data range from 67.55 down to 0.08 wt%.

### 3. THEORETICAL CALCULATIONS OF HYDROGEN STORAGE BY CARBON NANOTUBES

Theoretical models allow the study of ideal systems, and are useful tools for investigating complex systems. Models have been made of the physical adsorption of molecular hydrogen on carbon nanotubes, as well as chemical adsorption of both atomic and molecular hydrogen. These studies have investigated hydrogen binding sites on the carbon framework and adsorption isotherms and density profiles. Theoretical investigations can be extremely useful in developing an understanding of the elementary steps in the adsorption process, as well as in predicting an upper limit on the hydrogen storage capacity.

The theoretical calculations are generally classified into two groups according to how they treat time within their theoretical model. Statistical mechanics and molecular dynamics include time, and are used for looking at molecules in motion. Quantum mechanics (electronic structure methods) and molecular mechanics are time independent, and can perform accurate energy calculations on snapshots of the molecular system.

#### 3.1. Statistical Mechanics (Monte Carlo) Methods

Most grand canonical Monte Carlo (GCMC) studies on hydrogen adsorption in carbon nanotubes have used a 12:6 Lennard–Jones [96–98] potential to model the classical molecular interactions. The study of hydrogen adsorption

is complicated by a significant contribution from quantum effects [99, 100]. Darkrim and co-workers [99, 101] state that Chakravarty et al. [102] found that, for molecular hydrogen clusters at temperatures above 20 K, a full path-integral formalism was unnecessary, and the less computation-intensive Feynman–Hibbs [103] perturbative approach to modeling quantum effects seemed sufficient. Darkrim found that, for simulations of hydrogen adsorption on nanotubes, the Feynman–Hibbs-based corrections accounted for a 5% difference at room temperature and about 15–25% at 77 K. This clearly demonstrates that, while an uncorrected Lennard–Jones potential can be used successfully for qualitative work at room temperature and above, quantitative work requires treatment of the quantum effects. Another complicating factor now often included is a treatment of the quadrupole and dipole interactions [104, 105], and which were mandatory for the studies of charged systems [106]. A summary of the methods and some parameters can be found in Table 3.

All of the simulations reported so far have made two assumptions. First, they base their calculations on semiempirical potentials taken from work on planar graphite systems. Second, they assume that the same potentials can be used for both endohedral and exohedral adsorption. It is therefore reasonable to be skeptical of the quantitative accuracy of these studies until these two assumptions are shown to be reasonable enough to give good quantitative results.

#### 3.2. Electronic Structure Method Studies

One approach to eliminate the two assumptions made for the statistical mechanic studies (*vide supra*) is to use electronic structure methods. These methods may also treat quantum effects and electron correlation directly or indirectly, and can lead to highly accurate results ( $\pm 4$  kJ  $\cdot$  mol $^{-1}$ ) [107]. The major difficulty of these methods is the computational effort required, with the more accurate methods scaling catastrophically with model size [e.g.,  $O(N^{5-7})$ ]. Additionally, processes involving hydrogen particularly require the more accurate methods to be used, due to the problem of basis-set incompleteness [108]. However, these methods are ideal for studies of process mechanisms and thermodynamics. This makes these studies complementary to the statistical mechanics studies, as they can be used to refine the statistical mechanic models and parameters.

Recent advances in electronic structure methods have allowed larger systems to be studied more accurately than before. The development of several methods that use periodic boundary conditions has been very advantageous for indefinite systems such as graphite, crystals, and nanotubes. The pseudopotential plane-wave method [109] or the self-consistent charge-density-functional-based tight-binding method (SCC–DFTB) [110] are the main methods used to study nanotubes. These methods use either a local density approximation (LDA) [111] or a generalized gradient approximation (GGA) [112]. The GGA is generally more accurate than the LDA, but it has been criticized for overestimating repulsive interactions in systems characterized by weak bonding forces. Another new development

**Table 3.** Summary of Monte Carlo simulation methods and parameters.

Move, insert, delete prob.	Pot. type	C–C ( $\sigma/\text{nm}$ )	H <sub>2</sub> –H <sub>2</sub> ( $\sigma/\text{nm}$ )	( $\epsilon/\text{K}$ )	C–H <sub>2</sub> ( $\sigma/\text{nm}$ )	( $\epsilon/\text{K}$ )	Chem. pot.	Temp.	Quant. inc.	Polar. inc.	Ref.
1, 1, 1	L–J <sup>a</sup>	0.34	0.2958	36.7	3.179	32.056	–2.7	293	Yes, F–H <sup>b</sup>	Yes	[101]
1, 1, 1	L–J <sup>a</sup>		0.297	33.3	3.179 (sic?)	30.5			No	No	[121]
0.1, 0.45, 0.45	S–G <sup>c</sup> , C–B <sup>d</sup>								Yes, P–I <sup>e</sup>		[100]
0.4, 0.3, 0.3	S–G <sup>c</sup> , D–J <sup>f</sup>										[106]
	L–J <sup>a</sup>		0.296	41.5	0.318	34.1			No	No	[151]
	S–G <sup>c</sup> type		0.297	42.8					No	No	[118]
0.5, 0.25, 0.25	L–J <sup>a</sup>	0.335	0.296	36.7					No	No	[152]

<sup>a</sup> Lennard–Jones potential [96–98].

<sup>b</sup> Feynman–Hibbs perturbative approach [103].

<sup>c</sup> Silvera–Goldman potential [153], which includes three-body terms.

<sup>d</sup> Crowell–Brown potential [154]; accounts for polarizability of carbon atoms [100].

<sup>e</sup> Path-integral method of Feynman [155].

<sup>f</sup> Diep–Johnson anisotropic force field [156].

Note: Primary sources for interaction potentials: W. A. Steele, “The Interaction of Gases with solid Surface.” Pergamon, Oxford, U.K., 1974 (used by Yin et al. [151]); T. Kihara, “Intermolecular Forces.” Wiley, New York, 1978 (used by Yin et al. [151]).

is the ONIOM [113] method that allows simple molecular mechanics methods to be combined with more accurate quantum mechanics. These new methods are allowing ever more accurate studies to be performed on carbon nanotube systems.

### 3.3. Binding Sites for Molecular Hydrogen Physisorption on Graphitic Materials

Molecular hydrogen physisorption can occur at a number of sites on graphitic systems. These include on top of atoms, bonds, and the center of the carbon hexagons. One density functional theory study [114] used a local density approximation (LDA), and they found that the most stable configuration for hydrogen molecules was above the center of a hexagon, although the preference for this position was small, indicating that the barriers for classical diffusion would be small. Dubot and Cenedese [115] used semiempirical AM1 simulations to model Li-doped SWNTs, and found that Li adsorbed inside and outside the tube, with the most stable site also being the center of a hexagon. More recently, both static and dynamic calculations were conducted by Arelano et al. [116] to investigate the interaction of molecular and atomic hydrogen with single-wall carbon nanotubes. An *ab initio* FGI96MD code [117] was selected, in which the DFT was used to compute the electron density and the total energy of the system, and LDA to account for exchange and correlation effects. Molecular physisorption inside and outside the nanotube walls was predicted to be the more stable state of those systems, with the binding energies for physisorption of the hydrogen molecule outside the nanotube in the range 4–7 kJ · mol<sup>–1</sup>. From their GCMC study of nanotube bundles, Williams and Eklund [118] showed that the geometry of the site affected the average adsorption potential experienced by the hydrogen molecule. They found that the three endohedral sites they studied had a larger potential than sites inside the nanotube. The largest

potential was for endohedral sites in the internal channels (11 kJ · mol<sup>–1</sup>), followed by the grooves (9 kJ · mol<sup>–1</sup>) and surfaces (6 kJ · mol<sup>–1</sup>) on the outer surface of the bundle, with the sites inside the tube being only (5 kJ · mol<sup>–1</sup>). This means that physical adsorption and desorption of molecular hydrogen from nanotubes are low-energy processes, as many experimental studies have shown. A recent study of the interaction of molecular hydrogen with planar graphite clusters by Okamoto and Miyamoto [119] confirmed that the LDA interaction energy curve was in very good agreement with the results of *ab initio* second-order Møller–Plesset (MP2) calculations.

### 3.4. Hydrogen Density Profile

Lee et al. [29, 120] used SCC–DFTB calculations, and found that hydrogen molecules existed in a number of concentric layers inside the nanotubes. At room temperature, statistical mechanics studies that reported the density profile about the carbon nanotube exhibited a single dense monolayer of hydrogen molecules close to the nanotube wall [100, 101, 106, 121, 122]. This monolayer was present both inside and outside the tube. After this monolayer the density rapidly reduced to the equivalent of a bulk phase at the same compression, indicating that the thermal vibration energy overcomes the ordering enthalpy for the second and subsequent monolayers. Statistical mechanics studies show that at 77 K, the lower thermal vibration energy of the hydrogen molecules did allow a second [99] dense monolayer shell to form, with a density intermediate between the first monolayer and the bulk phase.

Adding charge to the carbon nanotube increased the interaction with hydrogen molecules, and also induced a second monolayer shell at room temperature [106]. The authors of this study suggest that such a charged system could be created by either metal intercalation or by electrostatic charging. Dubot and Cenedese [115] used semiempirical

AM1 simulations to study molecular hydrogen adsorption in Li-doped SWNTs. The molecular hydrogen bound to the Li atom with a binding energy of  $43 \text{ kJ} \cdot \text{mol}^{-1}$ , and was repelled from the tube wall if the tube was not doped. Froudakis [123] used the ONIOM method to investigate the nature of the hydrogen adsorption in K-doped SWNTs, and to compare it with the adsorption in pure SWNTs. The calculations showed that the charge transfer from the alkali metal to the tube polarizes the hydrogen molecule, and this charge-induced dipole interaction is responsible for higher hydrogen uptake in the doped tubes. This may explain why the hydrogen uptake is improved by the doping of catalysts used in making the carbon nanotube.

All of these monolayers appear to have an average thickness of  $\sim 3.5 \text{ \AA}$ . This agrees nicely with the SCC-DFTB calculations of Tada et al. [124], who found that there was an energy threshold to entering the nanotube that was dependent on the tube diameter, with the barrier reducing to ambient energy levels only when the diameter was above  $6 \text{ \AA}$ . The density of the external monolayer is higher than for the same monolayer on an ideal graphite sheet, and the density of the internal monolayer is higher again [121].

### 3.4.1. Implications of the Density Profile

The increased adsorption of ideal carbon nanotubes appears to be based on the presence of the dense monolayer. These monolayers are dependent on the surface area, which scales with the number of carbons. Alternately, the bulk phase is dependent on the interstitial spaces and nanotube internal volume. These areas are dependent on the square of the number of atoms. This means that a graph of either nanotube size or nanotube packing separation against system density over bulk density will have a maximum. Therefore, when compared with a simple nonadsorbent system, the carbon nanotubes will have configurations of maximum benefit. For systems for which a single monolayer is predicted, this maximum occurs when one monolayer is adsorbed on the nanotube surfaces (radius  $\sim 1.2 \text{ nm}$ , tube separation  $\sim 0.7 \text{ nm}$ ) [101]. No one has quantified the maximum for charged or low-temperature systems where two monolayers may exist, but intuitively, it would be expected to be at an additional multiple of  $3.5 \text{ \AA}$ , a radius of  $\sim 1.55$  or  $\sim 1.9 \text{ nm}$  and a separation of  $\sim 1.05$  or  $\sim 1.4 \text{ nm}$ . Countering any "ideal" configuration is the random distribution of diameter and nanotube arrangement in experimental systems. A recent theoretical study [125] on randomly generated bundles predicted adsorption isotherms that appeared insensitive to the details of the geometry.

### 3.5. Isotope Separation Using Carbon Nanotubes

The separation of atomic isotopes is an energy-intensive and time-consuming process. A recent paper by Challa et al. [126] modeled that separation of the isotopes of hydrogen using a GCMC method including quantum treatment via a path-integral method. They calculated selectivities of 10,000 for  $\text{T}_2/\text{H}_2$  and 1000 for  $\text{D}_2/\text{H}_2$  at low temperature and pressure ( $20 \text{ K}; 10^{-4} \text{ Pa}$ ), which reduced to, respectively, 6 and 5 at  $77 \text{ K}$  and  $1300 \text{ Pa}$ . These results indicate that

carbon nanotubes have great potential for use in isotope separation.

### 3.6. Nanotube Properties

The chemical reactivity of nanotubes has been analyzed by comparing unstrained and strained systems. One group [127] used first principle calculations to look at atomic hydrogen adsorption on a tube that had been elastically squashed to form an elliptic tube. They found a large ( $\sim 100 \text{ kJ} \cdot \text{mol}^{-1}$ ) difference in the binding energy between the regions of high and low curvature in the ellipse. Another group [128] analyzed, using an empirical method, the reactivity at areas of high curvature caused by twisting or bending the nanotubes. They also found that sites of higher curvature have higher binding energies ( $\sim 155 \text{ kJ} \cdot \text{mol}^{-1}$ ) for atomic hydrogen. They also presented some preliminary experimental evidence that nanotubes can preferentially react at strained sites. The finding that the reactivity of carbon nanotubes is modifiable by physical distortion of the tube structure makes carbon nanotubes quite different from planar graphitic materials where increased reactivity occurs only at defect sites.

### 3.7. Chemical Adsorption on Carbon Nanotubes

No chemical adsorption was observed in studies using statistical mechanic methods on systems with molecular hydrogen at ambient energy levels. Only the studies with atomic hydrogen discussed below had reactions leading to chemisorption of the hydrogen. None of those systems modeled carbon nanotubes at conditions proposed for hydrogen storage nor proposed a mechanism for release of the chemisorbed hydrogen. However, it is well known that certain metal catalysts promote the formation of atomic hydrogen, and some of these metals are being combined with carbon nanotubes.

Using density functional theory, Jeloica and Sidis [129] calculated the interaction between atomic hydrogen and a graphite surface. A coronene-like model of the (0001) graphite surface is considered. Two adsorption regions separated by a barrier were found: a physisorption region around  $3 \text{ \AA}$  from the surface, and a chemisorption region around  $1.5 \text{ \AA}$ . The former is site independent, and compatible with a high mobility of the hydrogen atoms parallel to the surface. The latter is located exclusively on top of a carbon atom, which was consistent again with earlier studies using the semiempirical method [130–133], and more details can be found from our recent review [134]. Yang and Yang [135] focused on the adsorption of H atoms on three faces of graphite: (0001) basal plane, (1010) zigzag edge, and (1121) armchair edge. The relative energies of adsorption (or C–H bond energies) follow the order zigzag edge > armchair edge > basal-plane edge. They also found that adsorption on the basal plane sites is exothermic and stable. On the edge sites, the C–H bond energy decreases by nearly  $125 \text{ kJ} \cdot \text{mol}^{-1}$  when two H atoms are adsorbed on the same site. On the basal plane, the C–H bond energy decreases from  $190 \text{ kJ} \cdot \text{mol}^{-1}$  when two H are adsorbed on alternating sites to  $110 \text{ kJ} \cdot \text{mol}^{-1}$  when they are adsorbed on two adjacent sites.

Lee et al. [29, 120] used an SCC–DFTB method, and identified two chemisorption sites for atomic hydrogen on SWNTs: similarly to graphite, the carbon atom top sites at the exterior and the interior of the tube wall. Gülseren and co-workers [127, 136] and Tada et al. [124] found that the binding energy depends sensitively on the curvature of the nanotubes, either zigzag or armchair, and was proportional to the inverse of the radius. They found that the  $sp^3$  rehybridization of a single carbon atom from  $sp^2$  was always exothermic, provided the new bonding orbital was exohedral, and predicted that no chemisorption could occur inside the nanotube. However, Tada et al. reported repulsive interactions between hydrogen and a planar graphite layer that are not in agreement with the results of Arellano et al. [114]; the discrepancy between the results of the two calculations may be due to the different treatments (GGA by Tada et al. and LDA by Arellano et al.), with GGA known to overestimate repulsive interactions. Gülseren and co-workers [127, 136] also found that the  $C_nH_n$  nanotubes formed were direct band insulators with a gap of 1.5–2.0 eV at the G point of the electronic band structure, in contrast to pure nanotubes which are metallic or semiconductors.

Bauschlicher [137] used a (10,0) carbon nanotube for studying the hydrogen and fluorine binding using the ONIOM method (B3LYP/4-31G:UFF). The addition of two or four hydrogen atoms (from molecular hydrogen) to a (10,0) tube is computed to be endothermic. As a comparison, fluorine atoms appear to favor bonding next to existing fluorine atoms, and the adsorption is quite exothermic. The reason may be that the  $H_2$  bonding energy (460  $\text{kJ} \cdot \text{mol}^{-1}$  at B3LYP level) is larger than  $F_2$  bonding energy (140  $\text{kJ} \cdot \text{mol}^{-1}$ ). In another study, Bauschlicher [138] examined the maximum coverage of the tube wall, finding that the average C–H bond energy for the more stable 50% coverage is 240  $\text{kJ} \cdot \text{mol}^{-1}$ , which is higher than that of 100% coverage (160  $\text{kJ} \cdot \text{mol}^{-1}$ ). This indicates that it is very difficult to achieve 100% coverage on a (10,0) tube. The favorable 50% coverage corresponds to about 4% by weight storage of hydrogen.

Froudakis [139] applied the ONIOM approach to a 200-atom (4,4) SWNT, treating up to 64 carbons and 32 hydrogens with the higher level of theory. The small diameter of the tube together with the large number of atoms considered allow the higher level model to include a cylindrical part of the tube. The calculations showed that hydrogen atoms bond to the tube walls, and do not enter the tube interior. This binding takes places in zigzag rings around the tube walls, and not in lines toward the tube axis, changing the tube shape and causing an enlargement of the tube volume by 15%. After the tube walls are half filled with hydrogens, the energetically more favorable procedure of hydrogen insertion in the tube is obtained.

These results for hydrogen chemisorption on the exterior wall of SWNT are in fair agreement with that on the basal plane of graphite. The values of 110  $\text{kJ} \cdot \text{mol}^{-1}$  from Yang and Yang [135] and 160–240  $\text{kJ} \cdot \text{mol}^{-1}$  from Bauschlicher [138] agree well with 96  $\text{kJ} \cdot \text{mol}^{-1}$  from experimental desorption of hydrogen from MWNT. However, more studies, both experimental and theoretical, need to be made to eliminate the remaining differences. Furthermore, these large energy barriers somewhat preclude hydrogen

chemisorption as a useful storage method at ambient temperatures.

### 3.8. Hydrogen Storage Inside Closed SWNT

In another series of studies [140, 141], hydrogen atoms were used to bombard the wall of a model nanotube in a molecular dynamics study. They found that atoms with kinetic energy in the range 90–360  $\text{kJ} \cdot \text{mol}^{-1}$  were chemically adsorbed on the surface. Atoms with energy higher than this but lower than 1.3  $\text{MJ} \cdot \text{mol}^{-1}$  bounced off the tube. Atoms with energy higher than 1.3  $\text{MJ} \cdot \text{mol}^{-1}$  began to pass through the tube wall; some did this without damaging the wall, some would remain in the tube while others passed out the other side, and some entered and damaged the wall. The study also showed that any damage was “healed” within a short time (1–3 ps). The studies proposed that carbon nanotubes could be used as molecular-sized containers for hydrogen, or deuterium and tritium, particularly where very high densities are required.

Lee et al. [142] addressed the issue of a possible mechanism for the insertion of hydrogen molecules into the nanotubes using an SCC–DFTB method. According to their hypothesis, a hydrogen atom bonded to a carbon atom in an arch-type geometry could push the carbon atoms down, and then flip into the C–C midbond. The C–C bond recovers after the H atom flips into the internal space. Once the first atoms has flipped in, the nearest neighbor top site atoms can flip more easily because of the lower activation barrier, leading to a continuous flip-in process. Then the zigzag flip-in process, that is, the continuous flip-in process in the second nearest neighbor top site, ultimately results in the formation of zigzag geometry. A kick-in mechanism was proposed to explain hydrogen insertion in the nanotubes. Repeating the kick-in process eventually leads to the formation of molecular hydrogen inside the tubes. The storage mechanism is completed by a similar hydrogen extraction mechanism with a low energy barrier. Similarly to Gülseren and co-workers [127, 136] mentioned earlier, the calculations revealed that C–H bond formation changes the electronic structures of metallic carbon nanotubes to semiconductors during the electronic chemical storage process. This suggests that doping or adding conductive materials to the nanotube electrode was required in the electrochemical storage experiments.

## 4. INTERACTION BETWEEN HYDROGEN AND CNTS

Current theoretical studies of simple physical adsorption on pure carbon nanotubes predict a maximum of 14 wt% under low temperature and ideal conditions. The real adsorption process is likely to be more complicated, and the theoretical simulations have the potential for further refinement. In particular, as more quantitative and microscopically in-depth experimental results become available, the model parameters and assumptions will become more realistic.

Only some of the experimental results agree well with the theoretical calculations. It is not difficult to understand this because experiments are performed on real-world

materials, whereas calculations are based on idealized models. The carbon nanotubes made from various preparation methods under varied conditions will have different structural features. It is also probable that the carbon nanotubes are synthesized with defects or damaged, disordered, and functionalized during purification and cutting treatments. Molecular simulations which consider the effects of packing disorder, diameter polydispersity, functionalization, and nanotube wall effects are currently underway [143].

Little is known of the effects of nanotube stereochemistry on hydrogen uptake. SWNTs may, in the future, be prepared in bulk quantities with a variety of diameters and stereochemistries, depending on the nature of the rolling process of the graphitic sheet. Zigzag, armchair, and chiral nanotubes have been identified by Raman spectroscopy [144], but methods of forming them in pure high yield have not been discovered. The structure of the nanotube affects its properties, including conductance, density, and lattice structure, and possibly hydrogen adsorption. For example, an SWNT is metallic if the value ( $m - n$ ) is divisible by 3. Consequently, when tubes are formed with random values of  $m$  and  $n$ , we would expect that two-thirds of nanotubes would be semiconducting, and the other third metallic. Raman studies at multiple wavelengths which enable the differentiation between semiconducting and metallic nanotubes may enable an answer which is better suited for hydrogen adsorption [145]. If a preference is determined, the aim of current preparative carbon nanotube research should be directed to producing specific metallic or semiconducting nanotubes. Recently, diameter tuning of SWNTs has been reported through variation in laser pulse power [146]. This advance is important in furthering progress toward the DOE goals since there is theoretical and experimental evidence that the diameter of SWNTs can affect the capacity, thermodynamics, and kinetics of hydrogen storage. In addition to controlling nanotube size distributions, Heben's group also learned how to detangle and order nanotubes on a large scale [147]. This capability may eventually be important for achieving high packing densities, and therefore high volumetric hydrogen storage densities.

There is considerable debate over the issue of how SWNTs interact with hydrogen in the scientific community [50]. Is it a purely physical or chemical interaction or is it perhaps somewhere in between? It is important to obtain a deeper understanding of this process so that accurate theoretical models and predictions may be developed. Factors such as tube diameter and chirality may need to be targeted for synthesis, and so that their interaction with storage capacity and performance characteristics can be understood and optimized. In a previous study, Dillon et al. [26] showed that hydrogen is not dissociated when adsorbed on arc-generated SWNTs, even though the binding energy is  $19.62 \text{ kJ} \cdot \text{mol}^{-1}$ . Recently, they used TPD and FTIR techniques to show that hydrogen is nondissociatively adsorbed on laser-generated nanotubes [50]. They found that the interaction between hydrogen and SWNTs was midway between conventional van der Waals adsorption and chemical bond formation. Both infrared and Raman investigations on hydrogen-charged high-capacity purified samples of SWNTs are presently underway in an effort to better understand the nature of the carbon-hydrogen interaction.

None of the experiments has so far addressed the local structure of the binding sites, further complicating comparisons with theoretical predictions. Binding energies of physisorbed hydrogen can be obtained by thermal analysis, but these do not provide atomic-scale geometric information about the binding sites. Furthermore, experimental binding energies are generally much larger than values calculated for the idealized structure. Inelastic scattering of thermal neutrons, a spectroscopic technique that is sensitive to the local environment in which the hydrogen molecules are trapped, is now being used to probe the nature of the hydrogen adsorption site in carbon nanotubes [148]. A proof-of-principle experiment was recently published, and Figure 10 shows the temperature dependence of the neutron energy-loss spectra from this work. In principle, one should be able to determine how much hydrogen is trapped in multiple sites of different symmetry. Furthermore, the temperature dependence of the energy-loss peaks associated with different sites is a direct measure of the binding energy, a quantity that can be directly compared with theory. The shift in peak position and the decrease in intensity with temperature signify physisorption on a tube surface, with a binding energy slightly larger than would be obtained on a flat graphite surface. This experiment demonstrates that rotational spectroscopy using thermal neutrons provides important microscopic information about hydrogen-binding sites in nanotubes, although the experimental conditions are of no practical interest (0.6 g as-grown SWNTs, 25 K, 11 MPa).

As shown in Table 1, there is a large range of published values for reversible hydrogen storage in carbon nanotubes. One reason for this range may be insufficient characterization of the carbon nanotubes as mixtures of opened and unopened, single-walled and multiwalled, various diameter and helicities have been tested together with other unknown carbonaceous species. Another reason may be insufficient rigor in making hydrogen adsorption measurements on samples on the order of several milligrams where minute parasitic effects can easily and erroneously be attributed to

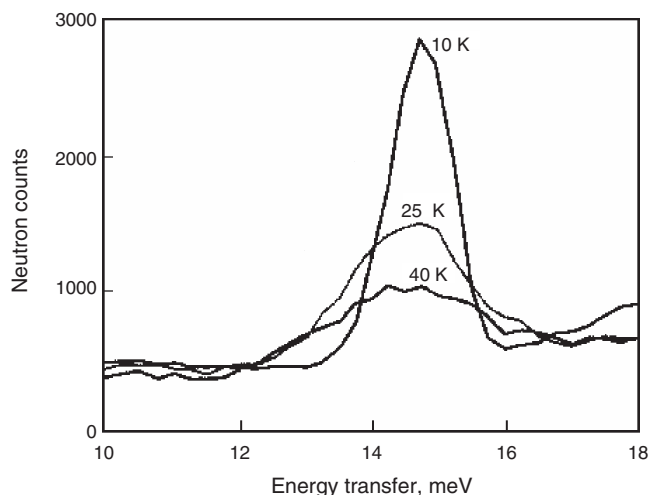


**Figure 10.** Neutron energy-loss spectra of raw SWNT material loaded with hydrogen at low temperature and high pressure show a peak resulting from excitation of quantized molecular rotation levels of physisorbed hydrogen. Reprinted with permission from [16], J. E. Fischer, *Chem. Innov.* 30, 21 (2000). © 2000, American Chemical Society.

hydrogen uptake. This means that we should be interpreting currently described experiments with care. Nevertheless, these results do give some indications that reaching the DOE target for hydrogen storage may be achievable, and they must be regarded as an intermediate step within an advanced learning process.

## 5. FUTURE PERSPECTIVES

Research reports aimed at optimizing the carbon nanotubes for hydrogen storage appear frequently in the literature. The current reliable values for hydrogen uptake in carbon nanostructures [3, 32] need to be greatly increased to meet the DOE target. The feasibility of a viable carbon-nanostructure-based storage medium for hydrogen remains undetermined from the results reviewed here, with the current state of the art not providing a solution. This field of study is complicated by the publication of inaccurate storage capacities. It has been shown that it is easy to make large errors in determining hydrogen storage capacities. In this quickly moving field, it becomes critical for every experimental result to be confirmed and corroborated by other groups, to avoid the continued dissemination of unreliable results. In this regard, we would like to advocate that systematic studies of the complementary measurement methods should be carried out, and standard procedures for measuring the  $H_2$  uptake within the limitations of each method should be established. International conferences and workshops on gas adsorption measurement in carbon nanotubes should be called to discuss this challenging topic.

The computational chemistry studies provide a useful model of hydrogen physisorption on carbon nanotubes. At room temperature, a single dense monolayer of molecular hydrogen forms on the inside and outside of the tube. Due to the geometry of the system, this implies that a limiting arrangement for maximum storage exists. A second monolayer, less dense than the first, can form at low temperature and when the nanotubes are charged. This will further increase the storage capacity, but will also have a limiting geometric arrangement. This second charge-induced monolayer may be one explanation for the enhanced storage in nanotubes with intercalated metals. Alternately, a mechanism that involves the hydrogen molecule dissociating on a metal catalyst followed by atomic hydrogen moving across the tube surface before adsorption is proposed. However, it remains to be shown experimentally or theoretically that these metals can directly promote hydrogen chemisorption and, more importantly for hydrogen storage, whether such a process is reversible.

The temperature and pressure requirements for molecular hydrogen adsorption and desorption, and the kinetics for charging and discharging are also expected to be a function of nanotube diameter and aspect ratio, and still need to be addressed. More work needs to be done to refine these theoretical models, and to develop a model compatible with the requirements of the DOE Hydrogen Plan. Highly accurate experimental results could provide more realistic modeling parameters for the theoretical simulations of hydrogen storage.

It may be a combination of experimental and theoretical efforts that will lead to a full understanding of the adsorption process, so that the uptake can be rationally optimized to commercially attractive levels. It is scientifically interesting and challenging to continue research on the sophisticated experimental techniques and interactions of hydrogen with different and well-characterized carbon nanostructures. On the basis of a thorough understanding of the hydrogen adsorption in carbon nanotubes, fine adjustments and optimization of the production conditions can be conducted to obtain carbon nanotubes with specific structures which facilitate the hydrogen storage in carbon nanotubes. After optimization is complete, it will be necessary to scale up the synthetic and purification techniques that generate the ideal adsorbent nanotubes. These issues represent significant technological and theoretical challenges in the years to come.

## GLOSSARY

***Ab initio* method** Method solely based on the laws of quantum mechanics—the first principles referred to the name *ab initio*—and on the values of a small number of physical constants.

**AM1 simulations** Semiempirical electronic structure method. The full name is Austin Model 1, similar to MNDO (modified intermediate neglect of differential overlap), based upon NDDO (neglect of diatomic differential overlap).

**Buckminsterfullerene** Broad term covering the variety of buckyballs and carbon nanotube structures. Named after the architect Buckminster Fuller, who is famous for the geodesic dome, which buckyballs resemble.

**Capillarity** General term for phenomena observed in liquids due to intermolecular attraction at the liquid boundary, for example, the rise or depression of liquids in narrow tubes, the formation of films, drops, bubbles, and so on.

**Compressed hydrogen storage** Hydrogen storage pressure (typically some 20 MPa).

**Density functional theory** In parallel to the development of *ab initio* theory, it was theorized that all molecular properties could be described as a function of the electron density (Hohenberg and Kohn, 1964). Density function theory is a theoretical approach to describe the electron density by using mathematical functions, called functionals.

**Electronic structure method** Uses the laws of quantum mechanics rather than classical physics as the basis for their computation. Quantum mechanics states that the energy and other related properties of a molecule may be obtained by solving the Schrödinger equation ( $H\psi = E\psi$ , where  $H$  is the Hamiltonian operator,  $E$  is the energy of the particle, and  $\psi$  is the wavefunction). There are now three major classes of electronic structure methods: semiempirical method, *ab initio* method, and density functional method.

**Fuel cell** Electrochemical device that continuously converts the chemical energy of a fuel to electrical energy.

**Hydrogen economy** Such an economy is one where hydrogen is used for energy storage, distribution, and utilization.



**Inelastic neutron scattering (INS)** Process of scattering neutrons from a specimen, accompanied by a change in energy of the neutron. Neutron beams for INS may be produced by nuclear reactors or by spallation reactions induced by accelerating charged particles into an appropriate target. After moderation, a monochromatic neutron beam can be extracted either using crystal monochromators or via time-of-flight methods.

**Lennard–Jones potential** Mathematical form of the potential-energy curve that describes the interaction of molecules, which stems from the work of the English chemist J.E. Lennard–Jones.

**Metal hydride storage** Storage of hydrogen by use of a metal alloy. The hydrogen is soaked into the alloy like into a sponge, and fills the spaces in the crystal lattice of the alloy. The storage is filled, applying a modest overpressure, and is usually operated in the temperature range of 20–80 °C.

**Molecular dynamics** Simulation of the time-dependent behavior of a molecular system, such as vibrational motion or Brownian motion. It requires a way to compute the energy of the system, most often using a molecular mechanics calculation. This energy expression is used to compute the forces on the atom for any given geometry.

**Molecular mechanics method** Uses the laws of classical physics to predict the structures and properties of molecules.

**Møller–Plesset (MP) calculation** This was theorized that the electron correlation was a perturbation of the wavefunction, and so the MP perturbation theory could be applied to the HF (Hartree–Fock) wavefunction to include the electron correlation. As more perturbations are made to the system, more electron correlation is included; these methods are denoted as MP2, MP3, and MP4.

**Monte Carlo methods** There are many types of calculations that are referred to as Monte Carlo calculations. All Monte Carlo methods are built around some sort of a random sampling, which is simulated with a random-number-generating algorithm. In computational chemistry, a Monte Carlo simulation is usually one in which the location, orientation, and perhaps geometry of a molecule or collection of molecules are chosen according to a statistical distribution.

**MWNT** Multiwalled carbon nanotube.

**ONIOM approach** The full name is “our own *n*-layered integrated molecule orbital and molecular mechanics” developed by Svensson et al. at Emory University, USA, in 1996. This method allows the accuracy of quantum mechanics and the large molecule capability of molecular mechanics methods to be combined. The method works by dividing a molecular system into successively smaller domains that can each be treated at increasingly sophisticated theory levels.

**Semiempirical method** Uses parameters derived from experimental data to simplify the computation. It solves an approximate form of the Schrödinger equation that depends on having appropriate parameters available for the type of chemical system under investigation.

**Statistical mechanics methods** Statistical mechanics is the mathematical means to calculate the thermodynamic properties of bulk materials from a molecular description of the materials. Statistical mechanics computations are often

tacked onto the end of *ab initio* vibrational frequency calculations for gas-phase properties at low pressure. For condensed-phase properties, often molecular dynamics or Monte Carlo calculations are necessary in order to obtain statistical data.

**SWNT** Single-walled carbon nanotube.

## REFERENCES

1. A. C. Dillon and M. J. Heben, *Appl. Phys. A* 72, 133 (2001).
2. H. W. Pohl, Ed., “Hydrogen and Other Alternative Fuels for Air and Ground Transportation.” Wiley, 1995.
3. K. Atkinson, S. Roth, M. Hirscher, and W. Grunwald, *Fuel Cells Bull.* 38, 9 (2001).
4. J. Jagiello, T. J. Bandosz, K. Putyera, and J. A. Schwarz, *J. Chem. Soc., Faraday Trans.* 91, 2929 (1995).
5. P. Bénard and R. Chahine, *Int. J. Hydrogen Energy* 26, 849 (2001).
6. K. A. G. Amankwah, J. S. Noh, and J. A. Schwarz, *Int. J. Hydrogen Energy* 14, 437 (1989).
7. S. Hynek, W. Fuller, and J. Bentley, *Int. J. Hydrogen Energy* 22, 601 (1997).
8. H. W. Kroto, J. R. Heath, S. C. O. Brien, R. F. Curl, and R. E. Smalley, *Nature* 318, 162 (1985).
9. W. Kratschmer, L. D. Lamb, K. Fostiropoulos, and D. R. Huffman, *Nature* 347, 354 (1990).
10. S. Iijima, *Nature* 354, 56 (1991).
11. J. Cook, J. Sloan, and M. L. H. Green, *Chem. Ind.* 600 (1996).
12. S. Iijima and T. Ichihashi, *Nature* 363, 603 (1993).
13. D. S. Bethune, C. H. Kiang, M. S. de Vries, G. Gorman, R. Savoy, J. Vazquez, and R. Beyers, *Nature* 363, 605 (1993).
14. M. R. Pederson and J. Q. Broughton, *Phys. Rev. Lett.* 69, 2689 (1992).
15. V. Meregalli and M. Parrinello, *Appl. Phys. A, Mater. Sci. Processing* 72, 143 (2001).
16. J. E. Fischer, *Chem. Innov.* 30, 21 (2000).
17. M. S. Dresselhaus, K. A. Williams, and P. C. Eklund, *MRS Bull.* 24, 45 (1999).
18. F. L. Darkrim, P. Malbrunot, and G. P. Tartaglia, *Int. J. Hydrogen Energy* 27, 193 (2002).
19. M. DeLuchi, “Hydrogen Fuel-Cell Vehicles.” Davis, 1992.
20. M. S. Dresselhaus, G. Dresselhaus, and P. C. Eklund, “The Science of Fullerenes and Carbon Nanotubes.” Academic, 1996.
21. M. S. Dresselhaus, G. Dresselhaus, and P. Avouris, “Carbon Nanotubes: Synthesis, Structure, Properties, and Applications,” p. 464. Springer-Verlag, New York, 2001.
22. T. W. Ebbesen, Ed., “Carbon Nanotubes, Preparation and Properties.” CRC Press, 1997.
23. P. J. F. Harris, “Carbon Nanotubes and Related Structure: New Materials for the Twenty-First Century.” Cambridge University Press, 1999.
24. R. Saito, G. Dresselhaus, and M. S. Dresselhaus, “Physical Properties of Carbon Nanotubes.” Imperial College Press, 1998.
25. H. S. Nalwa, Ed., “Handbook of Nanostructured Materials and Nanotechnology, Vol. 1: Synthesis and Processing.” Academic, 2000.
26. A. C. Dillon, K. M. Jones, T. A. Bekkedahl, C. H. Kiang, D. S. Bethune, and M. J. Heben, *Nature* 386, 377 (1997).
27. N. Mommer, M. Hirscher, F. Cuevas, and H. Kronmüller, *J. Alloys Comp.* 266, 255 (1998).
28. M. Hirscher and M. Becher, *J. Nanosci. Nanotech.* (2003).
29. S. M. Lee, K. S. Park, Y. C. Choi, Y. S. Park, J. M. Bok, D. J. Bae, K. S. Nahm, Y. G. Choi, S. C. Yu, N. G. Kim, T. Frauenheim, and Y. H. Lee, *Synth. Met.* 113, 209 (2000).
30. C. Nutzenadel, A. Zuttel, D. Chartouni, and L. Schlapbach, *Electrochem. Solid-State Lett.* 2, 30 (1999).



31. A. Zuttel, C. Nutzenadel, P. Sudan, P. Mauron, C. Emmenegger, S. Rentsch, L. Schlapbach, A. Weidenkaff, and T. Kiyobayashi, *J. Alloys Comp.* 330–332, 676 (2002).
32. G. G. Tibbetts, G. P. Meisner, and C. H. Olk, *Carbon* 39, 2291 (2001).
33. G. Sandrock, *J. Alloys Comp.* 293–295, 877 (1999).
34. M. M. Abbott and H. C. Van Ness, Eds., “Schaum’s Outline of Theory and Problems of Thermodynamics,” 2nd ed. McGraw-Hill, 1989.
35. C. M. Brown, T. Yildirim, D. A. Neumann, M. J. Heben, T. Gennett, A. C. Dillon, and A. J. L., J. E. Fischer, *Chem. Phys. Lett.* 329, 311 (2000).
36. R. Chahine and T. K. Bose, *Int. J. Hydrogen Energy* 19, 161 (1994).
37. A. C. Dillon, T. A. Bekkedahl, K. M. Jones, and M. J. Heben, *Fullerenes* 3, 716 (1999).
38. A. C. Dillon, T. Gennett, J. L. Alleman, K. M. Jones, P. A. Parilla, and M. J. Heben. “Proceedings of 1999 U.S. DOE, Hydrogen Program Review,” 1999.
39. Y. Ye, C. C. Ahn, C. Witham, B. Fultz, J. Liu, A. G. Rinzler, D. Colbert, K. A. Smith, and R. E. Smalley, *Appl. Phys. Lett.* 74, 2307 (1999).
40. A. G. Rinzler, J. Liu, H. Dai, P. Nikolaev, C. B. Huffman, F. J. Rodriguez-Macias, P. J. Boul, A. H. Lu, D. Heymann, D. T. Colbert, R. S. Lee, J. E. Fischer, A. M. Rao, P. C. Eklund, and R. E. Smalley, *Appl. Phys. A* A67, 29 (1998).
41. A. Thess, R. Lee, P. Nikolaev, H. J. Dai, P. Petit, J. Robert, C. Xu, Y. Lee, S. Kim, A. G. Rinzler, D. Colbert, G. Scuse-ria, D. Tomanek, J. Fischer, and R. E. Smalley, *Science* 273, 483 (1996).
42. C. Liu, Y. Y. Fan, M. Liu, H. T. Cong, H. M. Cheng, and M. S. Dresselhaus, *Science* 286, 1127 (1999).
43. C. Journet, W. K. Maser, P. Bernier, A. Loiseau, M. Lamy de la Chapells, S. Lefrant, P. Deniard, R. Lee, and J. E. Fischer, *Nature* 388, 756 (1997).
44. H. M. Cheng, F. Li, X. Sun, S. D. M. Brown, M. A. Pimenta, A. Marucci, G. Dresselhaus, and M. S. Dresselhaus, *Chem. Phys. Lett.* 289, 602 (1998).
45. H. M. Cheng, C. Liu, Y. Y. Fan, F. Li, G. Su, H. T. Cong, L. L. He, and M. Liu, *Z. Metallkd.* 91, 306 (2000).
46. C. Liu, Q. H. Yang, Y. Tong, H. T. Cong, and H. M. Cheng, *Appl. Phys. Lett.* 80, 2389 (2002).
47. X. Chen, U. Dettlaff-Weglikowska, M. Haluska, M. Hulman, S. Roth, M. Hirscher, and M. Becher, *Mater. Res. Soc. Symp. Proc.* 706, 295 (2002).
48. X. B. Wu, P. Chen, J. Lin, and K. L. Tan, *Int. J. Hydrogen Energy* 25, 261 (1999).
49. M. R. Smith, E. W. Bittner, W. Shi, J. K. Johnson, and B. C. Bock-rath, *J. Phys. Chem.* (2003).
50. A. C. Dillon, T. Gennett, J. L. Alleman, K. M. Jones, P. A. Parilla, and M. J. Heben. “Proceedings of 2000 U.S. DOE, Hydrogen Program Review,” 2000.
51. P. A. Parilla, A. C. Dillon, T. Gennett, J. L. Alleman, K. M. Jones, and M. J. Heben, *Mater. Res. Soc. Symp. Proc.* 633, A 14.36.1 (2001).
52. A. C. Dillon, K. E. H. Gilbert, J. L. Alleman, T. Gennett, K. M. Jones, P. A. Parilla, and M. J. Heben, “Proceedings of the 2001 Hydrogen Program Review,” 2001.
53. M. Hirscher, M. Becher, M. Haluska, U. Dettlaff-Weglikowska, A. Quintel, G. S. Duesberg, Y. M. Choi, P. Downes, M. Hulman, S. Roth, I. Stepanek, and P. Bernier, *Appl. Phys. A* 72, 129 (2001).
54. A. Ding, IEA/DOE/SNL, On-line hydride database, <http://hyd-park.ca.sandia.gov>, 2000.
55. R. Dagani, *Chem. Eng. News* 2, 25 (2002).
56. A. C. Dillon, K. E. H. Gilbert, P. A. Parilla, J. L. Alleman, G. L. Hornyak, K. M. Jones, and M. J. Heben, “Proceedings of 2002 U.S. DOE, Hydrogen Program Review,” 2002.
57. R. G. Ding, G. Q. Lu, and Z. F. Yan, unpublished result (2003).
58. M. Hirscher, M. Becher, M. Haluska, A. Quintel, V. Skakalova, Y. M. Choi, U. Dettlaff-Weglikowska, S. Roth, I. Stepanek, P. Bernier, A. Leonhardt, and J. Fink, *J. Alloys Comp.* 330–332, 654 (2002).
59. C. K. W. Adu, G. U. Sumanasekera, B. K. Pradhan, H. E. Romero, and P. C. Eklund, *Chem. Phys. Lett.* 337, 31 (2001).
60. B. K. Pradhan, A. Harutyunyan, D. Stojkovic, P. Zhang, M. W. Cole, V. Crespi, H. Goto, J. Fujiwara, and P. C. Eklund, *Mater. Res. Soc. Symp. Proc.* 706, 331 (2002).
61. H. Zhu, A. Cao, X. Li, C. Xu, Z. Mao, D. Ruan, J. Liang, and D. Wu, *Appl. Surf. Sci.* 178, 50 (2001).
62. A. Cao, H. Zhu, X. Zhang, X. Li, D. Ruan, C. Xu, B. Wei, J. Liang, and D. Wu, *Chem. Phys. Lett.* 342, 510 (2001).
63. Y. Chen, D. T. Shaw, X. D. Bai, E. G. Wang, C. Lund, W. M. Lu, and D. D. L. Chung, *Appl. Phys. Lett.* 78, 2128 (2001).
64. P. Chen, X. Wu, J. Lin, and K. L. Tan, *Science* 285, 91 (1999).
65. R. T. Yang, *Carbon* 38, 623 (2000).
66. F. E. Pinkerton, B. G. Wicke, C. H. Olk, G. G. Tibbetts, G. P. Meisner, M. S. Meyer, and J. F. Herbst, *J. Phys. Chem. B* 104, 9460 (2000).
67. R. Zidan and A. M. Rao, “Proceedings of the 2002 U.S. DOE, Hydrogen Program Review,” 2002.
68. G. J. Kubas, R. R. Ryan, B. I. Swanson, P. J. Vergamini, and J. Wasserman, *J. Am. Chem. Soc.* 106, 451 (1984).
69. G. J. Kubas, *Acc. Chem. Res.* 21, 120 (1988).
70. A. Zuttel, P. Sudan, P. Mauron, C. Emmenegger, T. Kiyobayashi, and L. Schlapbach, “6th International Symposium on Electrochemical/Chemical Reactivity of Amorphous and Nanocrystalline Materials,” Mount-Tremblant (Quebec) Canada, 2001.
71. L. Schlapbach and A. Zuttel, *Nature* 414, 353 (2001).
72. M. G. Nijkamp, J. E. M. J. Raaymakers, A. J. van Dillen, and K. P. de Jong, *Appl. Phys. A* 72, 619 (2001).
73. X. Qin, X. P. Gao, H. Liu, H. T. Yuan, D. Y. Yan, W. L. Gong, and D. Y. Song, *Electrochem. Solid-State Lett.* 3, 532 (2000).
74. N. Rajalakshmi, K. S. Dhathathreyan, A. Govindaraj, and B. C. Satishkumar, *Electrochim. Acta* 45, 4511 (2000).
75. A. Zuttel, P. Sudan, P. Mauron, T. Kiyobayashi, C. Emmenegger, and L. Schlapbach, *Int. J. Hydrogen Energy* 27, 203 (2002).
76. A. K. M. F. Kibria, Y. H. Mo, and K. S. Park, *Int. J. Hydrogen Energy* 26, 823 (2001).
77. G. P. Dai, M. Liu, D. M. Chen, P. X. Hou, T. Yu, and H. M. Cheng, *Electrochem. Solid-State Lett.* 5, E13 (2002).
78. G. Dai, C. Liu, M. Liu, M. Wang, and H. Cheng, *Nano Lett.* 2, 503 (2002).
79. G. P. Dai, “Electrochemical Hydrogen Storage in Carbon Nanotubes,” Institute of Metal Research, Chinese Academy of Sciences, Shenyang, 2002.
80. A. S. Claye, J. E. Fischer, C. B. Huffman, A. G. Rinzler, and R. E. Smalley, *J. Electrochem. Soc.* 147, 2845 (2000).
81. E. Frackowiak and F. Beguin, *Carbon* 40, 1775 (2002).
82. S. Pekker, J. P. Salvetat, E. Jakab, J. M. Bonard, and L. Forro, *J. Phys. Chem. B* 105, 7938 (2001).
83. A. Chambers, C. Park, R. T. K. Baker, and N. M. Rodriguez, *J. Phys. Chem. B* 102, 4253 (1998).
84. C. C. Ahn, Y. Ye, B. V. Ratnakumar, C. Whitlam, R. C. Bowman, and B. Fultz, *Appl. Phys. Lett.* 73, 3378 (1998).
85. C. Park, P. E. Anderson, A. Chambers, C. D. Tan, R. Hidalgo, and N. M. Rodriguez, *J. Phys. Chem. B* 103, 10572 (1999).
86. D. J. Browning, M. L. Gerrard, J. B. Laakeman, I. M. Mellor, R. J. Mortimer, and M. C. Turpin, “13th World Hydrogen Energy Conference,” International Hydrogen Association, Beijing, P.R. China, 2000.
87. E. Poirier, R. Chahine, and T. K. Bose, *Int. J. Hydrogen Energy* 26, 831 (2001).
88. M. A. de la Casa-Lillo, F. L. Darkrim, D. Cazorla-Amoros, and A. Linares-Solano, *J. Phys. Chem. B* 106, 10930 (2002).

89. J. Y. Hwang, S. H. Lee, K. S. Sim, and J. W. Kim, *Synth. Metals* 126, 81 (2002).
90. M. Ritschel, M. Uhlemann, O. Gutfleisch, A. Leonhardt, A. Graff, C. Taschner, and J. Fink, *Appl. Phys. Lett.* 80, 2985 (2002).
91. R. Ströbel, L. Jorissen, T. Schliermann, V. Trapp, W. Schutz, K. Bohmhammel, G. Wolf, and J. Garche, *J. Power Sources* 84, 221 (1999).
92. A. R. Harutyunyan, B. K. Pradhan, T. Tokune, J. Fujiwara, and P. C. Eklund, "Proceedings of the 25th International Conference on Carbon, CARBON '01," American Carbon Society, Lexington, KY, 2001.
93. B. K. Gupta and O. N. Srivastava, *Int. J. Hydrogen Energy* 25, 825 (2000).
94. B. K. Gupta and O. N. Srivastava, *Int. J. Hydrogen Energy* 26, 857 (2001).
95. Y. Y. Fan, B. Liao, M. Liu, Y. L. Wei, M. Q. Liu, and H. M. Cheng, *Carbon* 37, 1649 (1999).
96. T. J. Mays, in "Fundamentals of Adsorption" (M. D. LeVan, Ed.), p. 603. Kluwer Academic, Boston, MA, 1996.
97. M. P. Allen and D. J. Tildesley, "Computer Simulation of Liquids." Clarendon, 1987.
98. N. G. Parsonage and D. Nicholson, "Computer Simulation and the Statistical Mechanics of Adsorption." Academic Press, San Diego, 1982.
99. F. Darkrim and D. Levesque, *J. Phys. Chem. B* 104, 6773 (2000).
100. Q. Wang and J. K. Johnson, *J. Chem. Phys.* 110, 577 (1999).
101. F. Darkrim and D. Levesque, *J. Chem. Phys.* 109, 4981 (1998).
102. G. Charkravarty, M. C. Gordillo, and D. M. Ceperley, *J. Chem. Phys.* 109, 2123 (1998).
103. R. P. Feynman, "Statistical Mechanics." McGraw Benjamin, 1992.
104. D. Marx and P. Nielaba, *Phys. Rev. A* 45, 8968 (1994).
105. D. Marx, O. Optiz, P. Nielaba, and K. Binder, *Phys. Rev. Lett.* 101, 2908 (1993).
106. V. V. Simonyan, P. Diep, and J. K. Johnson, *J. Chem. Phys.* 111, 9778 (1999).
107. J. B. Foresman and A. E. Frisch, "Exploring Chemistry with Electronic Structure Methods," 2nd ed. Gaussian, 1993.
108. M. J. Frisch, J. E. Del Bene, J. S. Binkley, and H. F. Schaefer, III, *J. Chem. Phys.* 84, 2279 (1986).
109. M. C. Payne, M. P. Teter, D. C. Allen, T. A. Arias, and J. D. Joannopoulos, *Rev. Modern Phys.* 64, 1045 (1992).
110. M. Elstner, D. Prezag, G. Jungnickel, J. Elsner, M. Haugk, T. Frauenheim, S. Suhai, and G. Geifert, *Phys. Rev. B* 58, 7260 (1998).
111. J. P. Perdew and Y. Wang, *Phys. Rev. B* 46, 6671 (1992).
112. A. D. Becke, *J. Chem. Phys.* 88, 2547 (1988).
113. S. Dapprich, I. Komáromi, K. S. Byun, K. Morokuma, and M. J. Frisch, *Theochem* 461-462, 1 (1999).
114. J. S. Arellano, L. M. Molina, A. Rubio, and J. A. Alonso, *J. Chem. Phys.* 112, 8114 (2000).
115. P. Dubot and P. Cenedese, *Phys. Rev. B: Cond. Matter Mater. Phys.* 63, 241402/1 (2001).
116. J. S. Arellano, L. M. Molina, A. Rubio, M. J. Lopez, and J. A. Alonso, *J. Chem. Phys.* 117, 2281 (2002).
117. B. Bockstedte, A. Kley, J. Neugebauer, and M. Scheffler, *Comp. Phys. Commun.* 107, 187 (1997).
118. K. A. Williams and P. C. Eklund, *Chem. Phys. Lett.* 320, 352 (2000).
119. Y. Okamoto and Y. Miyamoto, *J. Phys. Chem. B* 105, 3470 (2001).
120. S. M. Lee and Y. H. Lee, *Appl. Phys. Lett.* 76, 2877 (2000).
121. M. Rzepka, P. Lamp, and M. A. de la Casa-Lillo, *J. Phys. Chem. B* 102, 10894 (1998).
122. C. Gu, G. H. Gao, Y. X. Yu, and Z. Q. Mao, *Int. J. Hydrogen Energy* 26, 691 (2001).
123. G. E. Froudakis, *Nano Lett.* 1, 531 (2001).
124. K. Tada, S. Furuya, and K. Watanabe, *Phys. Rev. B: Cond. Matter Mater. Phys.* 63, 155405/1 (2001).
125. M. R. Smith, Jr., E. W. Bittner, W. Shi, J. K. Johnson, and B. Bockrath (2003).
126. S. R. Challa, D. S. Sholl, and J. K. Johnson, *J. Chem. Phys.* 116, 814 (2002).
127. O. Gülseren, T. Yildirim, and S. Ciraci, *Phys. Rev. Lett.* 87, 116802 (2001).
128. D. Srivastava, D. W. Brenner, J. D. Schall, K. D. Ausman, M. Yu, and R. S. Ruoff, *J. Phys. Chem. B* 103, 4330 (1999).
129. L. Jeloica and V. Sidis, *Chem. Phys. Lett.* 300, 157 (1999).
130. A. J. Bennett, B. McCarroll, and R. P. Messmer, *Surf. Sci.* 24, 191 (1971).
131. R. P. Messmer and A. J. Bennett, *Phys. Rev. B* 6, 633 (1972).
132. R. Caballol, J. Igual, F. Illas, and J. Rubio, *Surf. Sci.* 149, 621 (1985).
133. V. Barone, F. Lejl, and C. Minichino, *Surf. Sci.* 189, 185 (1987).
134. Z. H. Zhu, G. Q. Lu, J. Finnerty, and R. T. Yang, *Carbon* (2002).
135. F. H. Yang and R. T. Yang, *Carbon* 40, 437 (2002).
136. T. Yildirim, O. Gulseren, and S. Ciraci, *Phys. Rev. B: Cond. Matter Mater. Phys.* 64, 075404/1 (2001).
137. C. W. Bauschlicher, Jr., *Chem. Phys. Lett.* 332, 237 (2000).
138. C. W. Bauschlicher, Jr., *Nano Lett.* 1, 223 (2001).
139. G. E. Froudakis, *Nano Lett.* 1, 179 (2001).
140. Y. Ma, Y. Xia, M. Zhao, R. Wang, and L. Mei, *Phys. Rev. B: Cond. Matter Mater. Phys.* 63, 115422/1 (2001).
141. Y. Ma, Y. Xia, M. Zhao, and M. Ying, *Phys. Rev. B: Cond. Matter Mater. Phys.* 65, 155430/1 (2002).
142. S. M. Lee, K. H. An, Y. H. Lee, G. Seifert, and T. Frauenheim, *J. Am. Chem. Soc.* 123, 5059 (2001).
143. V. V. Simonyan and J. K. Johnson, *J. Alloys Comp.* 330-332, 659 (2002).
144. H. Kuzmany, B. Burgler, A. Thess, and R. E. Smalley, *Carbon* 36, 709 (1998).
145. S. D. M. Brown, P. Corio, A. Marucci, M. S. Dresselhaus, M. A. Pimenta, and K. Kneipp, *Phys. Rev. B: Cond. Matter Mater. Phys.* 61, R5137 (2000).
146. A. C. Dillon, P. A. Parilla, J. L. Alleman, J. D. Perkins, and M. J. Heben, *Chem. Phys. Lett.* 316, 13 (2000).
147. T. Gennett, A. C. Dillon, J. L. Alleman, F. S. Hassoon, K. M. Jones, and M. J. Heben, *Chem. Mater.* 12, 599 (2000).
148. C. M. Brown, T. Yildirim, D. A. Neumann, M. J. Heben, T. Gennett, A. C. Dillon, J. L. Alleman, and J. E. Fischer, *Chem. Phys. Lett.* 329, 311 (2000).
149. N. Nishimiya, H. Ishigaki, H. Takikawa, M. Ikeda, Y. Hibi, T. Sakakibara, A. Matsumoto, and K. Tsutsumi, *J. Alloys Comp.* 339, 275 (2002).
150. A. Badzian, T. Badzian, and E. Breval et al., *Thin Solid Films* 78, 2128 (2001).
151. Y. F. Yin, T. Mays, and B. McEnaney, *Langmuir* 16, 10521 (2000).
152. C. Gu, G.-H. Gao, Y.-X. Yu, and Z.-Q. Mao, *Int. J. Hydrogen Energy* 26, 691 (2001).
153. I. F. Silvera and V. V. Goldman, *J. Chem. Phys.* 69, 4209 (1978).
154. A. D. Crowell and J. S. Brown, *Surf. Sci.* 123, 296 (1982)
155. R. P. Feynman and A. R. Hibbs, "Quantum Mechanics and Path Integrals." 1965, McGraw-Hill, 1965.
156. P. Diep and J. K. Johnson, *J. Chem. Phys.* 112, 4465 (2000).
157. J. Liu, A. G. Rinzler, H. Dai, J. H. Hafner, R. K. Bradley, P. J. Boul, A. Lu, T. Iverson, K. Shelimov, C. B. Huffman, F. Rodriguez-Macias, Y.-S. Shon, T. R. Lee, D. T. Colbert, and R. E. Smalley, *Science* 280, 1253 (1998).



# Hydrogenated Nanocrystalline Silicons

K. Shimakawa

*Gifu University, Gifu, Japan*

## CONTENTS

1. Introduction
  2. Preparation of Hydrogenated Nanocrystalline Silicon
  3. Spectroscopic Characterization
  4. Electronic and Optical Properties
  5. Applications
  6. Conclusions
- Glossary  
References

## 1. INTRODUCTION

Hydrogenated nanocrystalline silicon (nc-Si:H) or microcrystalline Si ( $\mu$ c-Si:H) films appear as a promising material for thin-film devices such as solar cells, thin-film transistors, and sensors, since the electron mobility of nc-Si:H is much improved compared to that of hydrogenated amorphous silicon films (a-Si:H). Understanding the electronic transport and optical properties of nc-Si:H is very important for improving such device properties. As schematically shown in Figure 1, structure of nc-Si:H is very complex and is characterized by “crystalline grain clusters” (region A) which consist of crystalline grains from nano-size to  $\sim 20$  nm, and it is surrounded by “disorder zones” (region B) [1, 2]. Region A forms columnar clusters of much larger dimensions extending perpendicular to the substrate. Although the influences of the grain size and crystalline volume fraction on the electronic transport have been discussed, the details of their quantitative natures are still not clear [1–8].

To understand the physical properties in such complex materials, a percolation approach may be useful. A percolation path for electronic transport in nc-Si:H films has been suggested [3]. In fact, three-dimensional conductance network calculations (computer simulations) for the conductivity,  $\sigma$ , and Hall mobility,  $\mu_H$ , show an existence of critical threshold of such percolation path [9]. It is suggested that an effective medium approximation (EMA) [10] is useful for explaining the quantitative transport and optical properties in inhomogeneous systems [11]. In the present chapter,

current understanding of electronic and optical properties of nc-Si:H films is briefly reviewed along the idea of EMA in which random mixture of particles (region A and B) is assumed for simplicity [11].

Nonactivated behavior of electronic transport (temperature-dependent dc conductivity), on the other hand, is one of the important and unsolved problems, which can be related to complicated structure of nc-Si:H films. In some cases, the dc conductivity seems to be proportional to  $\exp(-B/T^{1/2})$  [12, 13]. Reasons for these behaviors have been discussed in terms of hopping conductivity in a traditional manner [12, 13]. In this chapter, the non-activated behavior can be, alternatively, explained in terms of thermionic emissions of electrons over random barriers between crystalline clusters [14].

## 2. PREPARATION OF HYDROGENATED NANOCRYSTALLINE SILICON

Low-temperature fabrication process can be required for thin-film transistors and photovoltaic cells with inexpensive substrates. The following preparation techniques have been used to achieve it: (i) plasma-enhanced chemical vapor deposition (PECVD) of silane ( $\text{SiH}_4$ ) gas diluted in  $\text{H}_2$  gas, (ii) thermocatalytic or hot-wire assisted chemical vapor deposition (HWCVD) of  $\text{SiH}_4$  gas diluted in  $\text{H}_2$  gas, and (iii) pulsed laser crystallization (PLC) of amorphous silicon films. These techniques are summarized below.

### 2.1. Plasma-Enhanced CVD

This method has been well established in depositing hydrogenated amorphous silicon films (a-Si:H) and hence we only modify the deposition conditions to prepare nanocrystalline silicon (nc-Si:H) [1–5]. The structural compositions of nc-Si:H vary by changing the deposition conditions, that is, the silane to hydrogen ratio and the plasma excitation frequency. Unlike a-Si:H deposition, decrease of the silane to hydrogen gas ratio (less than 2% in gas ratio) is required to increase volume fraction of crystalline. It should be noted that the material prepared by PECVD is a phase mixture of amorphous and crystalline regions. The substrate

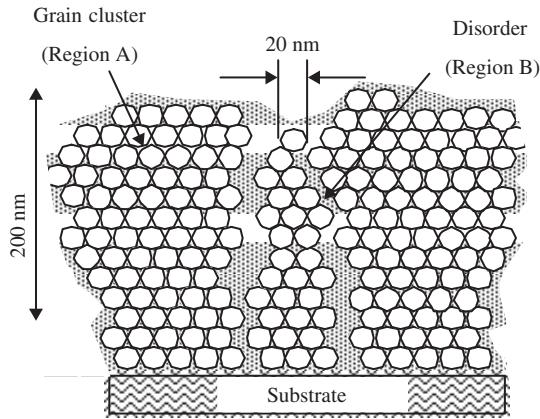


**Figure 1.** Schematic illustration of a structure of  $\mu\text{c-Si:H}$ . Region A is a crystalline grain cluster and region B is a disordered zone which surrounds region A.

temperature is taken to be around  $200\text{ }^\circ\text{C}$ . Higher plasma excitation frequency up to  $100\text{ MHz}$  leads to a simultaneous increase of the deposition rate (commercially very important and is  $\sim 0.1\text{ nm/s}$ ) [15, 16], the crystalline volume fraction ( $\sim 80\%$ ), and the average grain size ( $\sim 30\text{ nm}$ ) [15]. It is known that atomic hydrogen (H) plays an important role for nucleation of crystallization, although the reason for this is not clear.

## 2.2. Hot-Wire Assisted CVD

Hot filament, such as tungsten (W) or tantalum (Ta) filament, assists catalytic decomposition of a silane and hydrogen gas mixture in this technique [17–19]. A wide range of deposition parameters is adjustable for the deposition. The most important parameter for this technique to produce nc-Si:H is the silane to hydrogen gas ratio (less than  $\sim 3\%$  in gas ratio). A filament diameter, for example, is  $250\text{ }\mu\text{m}$  and substrates are placed in the cm range from the filament whose temperature is kept around  $1600\text{ }^\circ\text{C}$ . Substrate temperature is around  $200\text{ }^\circ\text{C}$ . Much higher deposition rate in this technique than PECVD has been reported and it approaches  $\sim 3\text{ nm/s}$  depending on deposition conditions. Although overall qualitative electronic properties of HWCVD nc-Si:H are similar to those of PECVD nc-Si:H, the mobility-lifetime product, for example, is smaller in HWCVD samples than PECVD ones. This can be attributed to larger number of defects in HWCVD nc-Si:H films.

## 2.3. Pulsed Laser Crystallization

Crystallization of amorphous silicon films occurs at a liquid-solid phase induced by pulsed excimer laser heating (see, e.g., [20]). To reach the melting threshold, the laser energy,  $160\text{ mJ/cm}^2$  for example, is required for the pulse width around  $30\text{ ns}$ . This required energy is very small, since the region heated by irradiation is limited to near surface. A rapid crystallization with low processing temperature is achieved by this method and the grain size around  $100\text{ nm}$  is obtained. Uniformity and reproducibility in crystallization may still be a problem.

## 3. SPECTROSCOPIC CHARACTERIZATION

As the optical transmission properties (optical absorption below and above bandgap) will be discussed in the next section, we concentrate here on only the structure-related spectroscopies. As already stated, nanocrystallines prepared by PECVD and HWCVD have complex structures. Combined data of X-ray diffraction (XRD), Raman spectroscopy (RS), and transmission electron microscopy (TEM) can be useful to analyze the structure of nanosilicon [4]. Raman spectroscopy and XRD are used to estimate crystalline volume fraction, in which the intensity ratio of the different signal contributions is calculated from a deconvolution of the spectra. A popular method to estimate the grain size is the application of the Scherrer formula on XRD peaks.

It is noted that RS and XRD are not sensitive for low crystalline volume fraction  $X_c$  ( $10\text{--}20\%$ ) and are not sensitive to the spatial distribution of crystallites (or amorphous phase), although TEM imaging still reveals isolated grains in amorphous tissue for low  $X_c$ . TEM imaging in cross section is important to know the spatial inhomogeneity. It is noted also that the crystalline volume fraction  $X_c$  estimated from Raman spectroscopy is always smaller than that estimated from XRD [4]. In spite of this difficulty of exact determination of  $X_c$ , RS or XRD is an easy technique and hence these techniques are often used as a measure of crystalline volume fraction.

The other spectroscopic methods, such as electron spin resonance (ESR) study, produce information on defect structure [7, 8, 21]. The ESR signals at  $g$ -values,  $2.0052 \pm 0.004$ ,  $2.0043 \pm 0.002$ ,  $1.996 < g < 1.998$  (depending on doping and temperature), and  $2.1$ , have been found in nanocrystalline silicon films and each can be attributed to Si dangling bonds ( $2.0052$ ), dangling bonds in oxygen-rich regions ( $2.0043$ ), electrons in conduction band, conduction band tails or donor states ( $1.996\text{--}1.998$ ) which is called the conduction electron (CE) resonance, and acceptor states ( $2.1$ ). The spin densities of  $g = 2.0052$  and  $2.0043$  resonances remain around  $10^{16}\text{ cm}^{-3}$  for undoped and doped samples, while the spin density of  $g = 1.996\text{--}1.998$  increases with P-doping up to around  $10^{18}\text{ cm}^{-3}$ . The CE resonance increases with the dc conductivity, which will be discussed also in Section 4, and the density of CE is reported to be almost the same as that of the donor density.

The number of Si dangling bonds ( $g = 2.0052$ ) is smaller compared with polycrystalline Si, which may be due to an excellent hydrogen passivation during the PECVD process. The majority of Si dangling bonds are expected to locate at the boundaries between crystalline column and disordered (amorphous) region.

## 4. ELECTRONIC AND OPTICAL PROPERTIES

In this section, we concentrate on the electronic and optical properties of nanocrystalline Si prepared by the PECVD method. Since particular interest has been paid to the electronic and optical properties of these films, the thermal and mechanical properties have not been discussed so far. As the

deposition temperature is around 200 °C, the physical properties should be stable below this temperature. Si is classified into a “hard” material and thus nanocrystalline Si should also be expected as a mechanically tough material.

### 4.1. Effective Medium Approximation

We briefly introduce the effective medium approximation (EMA) before proceeding with the discussion. The EMA predicts the total network conductance  $\sigma_m$  for composite materials in  $D$  dimensions:

$$\left\langle \frac{\sigma - \sigma_m}{\sigma + (D - 1)\sigma_m} \right\rangle = 0 \tag{1}$$

where  $\sigma$  is a random variable of conductivity. Assuming that a random mixture of particles of *two* different conductivities, for example, a volume fraction,  $C$ , has conductivity of  $\sigma_0$ , and the remainder has conductivity of  $\sigma_1$ , substantially less than  $\sigma_0$ , simple analytical expressions of dc conductivity and Hall mobility as a function of  $C$  have been derived (see the pioneering works by Kirkpatrick [10] and Cohen and Jortner [22]). EMA has been also extended to calculate the ac conductivity in which case  $\sigma$  in Eq. (1) becomes a complex admittance ( $\sigma^* = \sigma_1 + i\sigma_2$ ) [23]. As the dielectric constant,  $\varepsilon^* = \varepsilon_1 - i\varepsilon_2 = \sigma_2/\omega - i\sigma_1/\omega$ , is closely related to  $\sigma^*$ , optical absorption coefficient  $\alpha(\omega)$  can be calculated using  $\alpha(\omega) = 4\pi\sigma(\omega)/cn$ , where  $c$  is the light speed and  $n$  the refractive index [11].

### 4.2. Application of EMA to the Experimental Data

Solid circles in Figure 2 show the dc conductivity at room temperature as a function of crystalline volume fraction,  $X_c$ , for a series of undoped  $\mu c$ -Si:H films [3]. Note that theoretical prediction of such a dependence for complicated systems is a very hard task. Shimakawa [11] has applied the

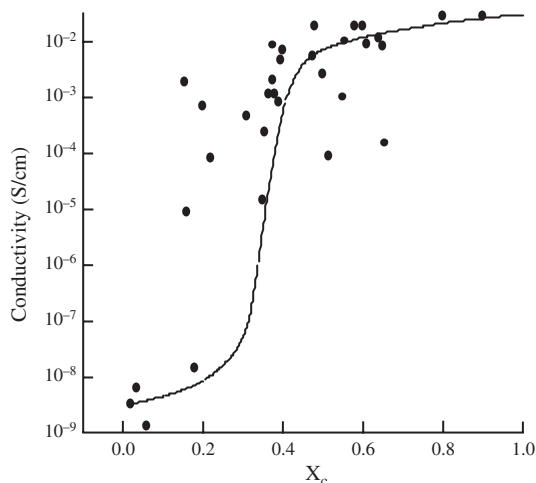


**Figure 2.** Room-temperature conductivity as a function of crystalline volume fraction for a series of undoped nc-Si:H. Reprinted with permission from [11], K. Shimakawa, *J. Non-Cryst. Solids* 266–269, 223 (2000). © 2000, Elsevier Science.

EMA to the experimental data and the result of the EMA is shown by the solid line, where  $\sigma_1 = 3 \times 10^{-9}$  ( $X_c = 0$ ) and  $\sigma_0 = 3 \times 10^{-2}$  S cm<sup>-1</sup> ( $X_c = 1$ ) were used in  $D = 3$ . The experimental data do not fit the solid line very closely, which may be attributed to the varying grain sizes. In other words, the system we treated cannot be an ideal case for EMA. Following the solid line, however, the percolation threshold appears at  $X_c = 0.33$ , which agrees very well with the computer simulation ( $X_c = 0.32$ ) [9].

Solid circles in Figure 3 show the room temperature Hall mobility in undoped  $\mu c$ -Si:H as a function of volume fraction of crystalline Si [24]. Shimakawa [11] has tried to apply the Cohen and Jortner approach (EMA) [22] and the solid line shows the calculated result with  $\mu_1 = 0.2$  ( $X_c = 0$ ) and  $\mu_0 = 2$  cm<sup>2</sup> V<sup>-1</sup> s<sup>-1</sup> ( $X_c = 1$ ). Note, however, that  $\mu_1 = 0.2$  cm<sup>2</sup> V<sup>-1</sup> s<sup>-1</sup> used here is not the true Hall mobility of the amorphous state ( $X_c = 0$ ), because the well-known anomaly of the Hall effect observed in hydrogenated amorphous silicon (a-Si:H) interferes with obtaining a proper value of Hall coefficient [25]. The fitting of the calculation to the experimental data is reasonably good and the percolation threshold is shown to exist at  $X_c = 0.33$  [11]. The small Hall mobility ( $\sim 2$  cm<sup>2</sup> V<sup>-1</sup> s<sup>-1</sup>) even at  $X_c = 1.0$  is about three orders of magnitude smaller than that for single-crystalline Si [26]. This can be attributed to the complicated structure of  $\mu c$ -Si:H. As already shown in Figure 1, the grain boundaries (between region A) dominate the transport properties and hence the mobility of  $\mu c$ -Si:H films is reduced significantly. This means that crystalline Si wears “grain boundary” and hence the mobility for a crystalline itself is still small.

Next, we argue the size effect of crystallite on the Hall mobility. In earlier works [3, 5, 26], the Hall mobility with the same  $X_c$  has been suggested to increase *linearly* with crystallite size  $\delta$  and has been explained by the *grain-boundary trapping* model (electronic transport is dominated by thermionic emission over a potential barrier). In commercial viewpoint, this may be very hopeful, since higher-mobility materials can be easily realized by bigger size of

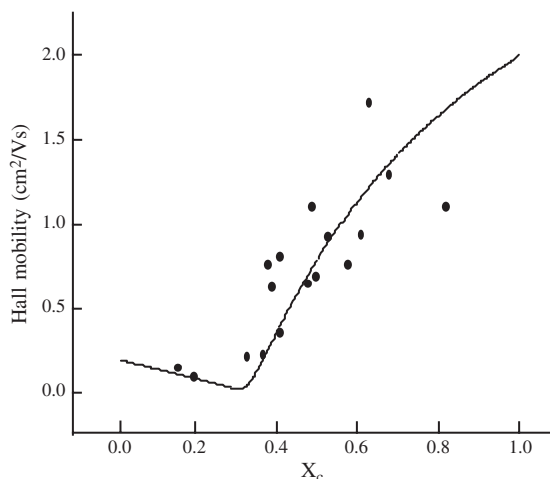


**Figure 3.** Room-temperature Hall mobility as a function of crystalline volume fraction in undoped nc-Si:H. Reprinted with permission from [11], K. Shimakawa, *J. Non-Cryst. Solids* 266–269, 223 (2000). © 2000, Elsevier Science.

crystallites. Unfortunately, however, as shown in Figure 4, a series of experimental data of the Hall mobility is shown to depend on the crystallite size as  $\delta^\gamma$  with  $\gamma \approx 0.3$  [11]. This *sublinear* dependence of  $\mu_H$  has been explained by the following way [11]: At the same  $X_c$ , the area of a disordered zone (DZ) (and hence the number of localized states in region B) can be regarded to be proportional to the surface to volume ratio  $R_{SV}$ . Since  $\mu_H$  is expected to be inversely proportional to the area of DZs, we get  $\mu_H \propto R_{SV}^{-1}$ . As  $R_{SV}$  is proportional to  $\delta^\alpha/\delta^\beta$ , where  $\alpha = 2.0$  and  $\beta = 3.0$  in Euclid space dimension and  $\alpha < 2$  and  $\beta < 3.0$  in fractal space, the relation of  $\mu_H \propto \delta^\gamma$  gives  $\gamma = \beta - \alpha$ .

In Euclid space dimension, we get  $\gamma = 1$ . This can be also easily understood by the following way. Imagine a cubic length  $\delta = L$  in Euclid space. The total surface area for this cubic is  $6L^2$ . When it is divided into eight parts, that is,  $\delta = L/2$ , the total surface area is  $12L^2$ . The total surface area (grain boundary) is thus expected to be inversely proportional to  $\delta$ , when the volume is kept the same  $L^3$ . However, if we consider  $\alpha$  and  $\beta$  in the fractal dimensions, one gets the sublinear dependence. In fact, the fractal dimensions of  $\beta \approx 1.9$  and  $\alpha \approx 1.6$  are predicted from a computer simulation for metallic clusters growing in thin films [27], which gives  $\mu_H \propto \delta^{0.3}$ .

Next, the *excess* optical absorption in fundamental absorption region is discussed. A larger optical absorption coefficient for nc-Si:H than for crystalline silicon (c-Si) from the infrared to the blue region has been reported [5, 28, 29]. This is an advantage for using solar cells, because many more photons can be absorbed in the films. An example of this difference is shown in Figure 5. Three solid lines are the experimental data for a-Si:H, nc-Si:H, and c-Si. Why such an excess optical absorption is observed in  $\mu c$ -Si:H is still a matter of debate. Although a scattering of light is suggested to be an origin of the enhanced optical absorption [29], Shimakawa [11] took the EMA, in an alternative way, to explain the excess absorption. The results obtained from EMA for  $X_c = 0.8$  and  $D = 3$  are shown by open circles. The frequency (energy)-independent refractive index,  $n_0 = 3.9$  for c-Si and  $n_1 = 3.2$  for a-Si:H which can be given as the root of real part of optical dielectric constant, are used in the

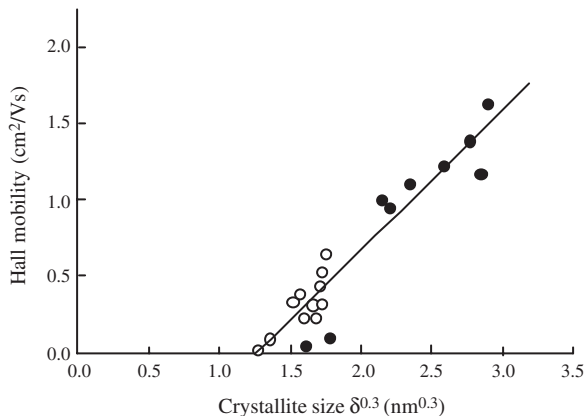


**Figure 4.** Hall mobility at room temperature as a function of grain size. Reprinted with permission from [11], K. Shimakawa, *J. Non-Cryst. Solids* 266–269, 223 (2000). © 2000, Elsevier Science.

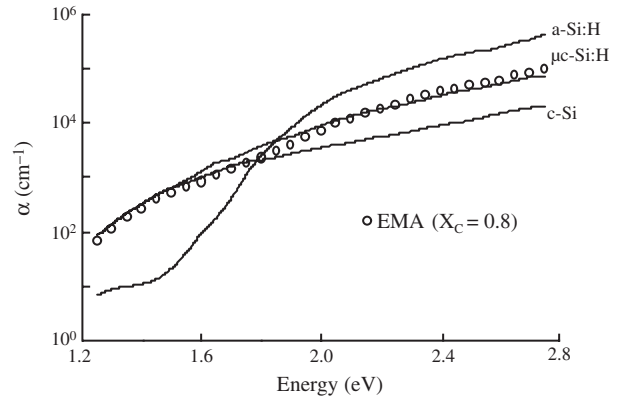


**Figure 5.** Comparison of the optical absorption coefficient of a-Si:H, nc-Si:H, and c-Si. The EMA results are given by solid circles. Reprinted with permission from [11], K. Shimakawa, *J. Non-Cryst. Solids* 266–269, 223 (2000). © 2000, Elsevier Science.

calculation. The calculated results agree very well with the experimental data, except at energy of around 1.7 eV. This suggests that a mean field constructed by mixture of amorphous and crystalline states dominates the optical absorption in nc-Si:H. The multiple light scattering seems to be not so important in this energy range.

### 4.3. Transport Mechanism

We understand in the preceding section that the EMA is useful to understand the *macroscopic* electronic and optical properties of composite materials, in particular the dependence of crystalline volume fraction of physical properties of nc-Si:H. In this section, we discuss the *microscopic* electronic transport mechanisms of nc-Si:H. For example, the mechanism of dc conductivity is very unclear.

Data shown in Figure 6 exhibit the temperature dependence of dc conductivity for n-type nc-Si:H films [6]. These cannot be fitted to the conventional relation  $\sigma_{dc} = \sigma_0 \exp(-\Delta E/kT)$  with a single activation energy at higher

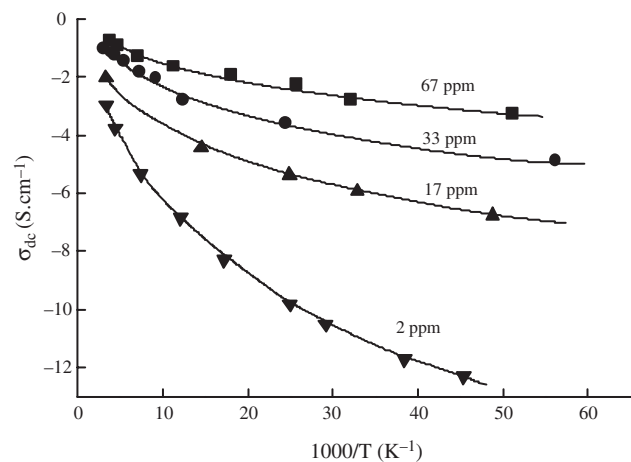


**Figure 6.** Band diagram near the conduction band. A percolation threshold for electronic transport by thermionic emission process is represented by the dashed line. The Fermi level is given by the dash-dotted line.



temperatures. Above 20 K, Finger and co-workers [6] have suggested that conduction occurs across potential barrier  $\phi$  ( $=\Delta E$ ) between different crystalline regions and a barrier energy distribution leads to a curvature of  $\ln \sigma_{dc}$  versus  $1/T$ . They further suggested that the transport takes place across higher barriers at higher temperatures and lower barriers at lower temperatures [8].

More quantitative discussion of the transport mechanism is given as follows by Shimakawa [14]. At relatively high temperatures, the dc conductivity due to thermionic emission of electrons over a potential barrier between crystalline grain clusters is expected to occur and can be given as

$$\sigma_{dc} = AT^2 eW \exp(-\phi/kT)/kT \quad (2)$$

where  $A$  is the Richardson constant,  $W$  the barrier width, and  $\phi$  the barrier height measured from the Fermi level [30]. Figure 7 shows the band diagram representing this situation. The barrier height may be randomly distributed and hence the electronic transport can be dominated by the percolation level  $E_{pc}$  (dashed line).  $\phi$  defined here should therefore correspond to  $E_{pc} - E_F$ . Note that Eq. (2) is based on one-dimensional array of potential barriers and therefore, strictly speaking, Eq. (2) cannot be applied to the present materials, since we should consider three-dimensionally distributed potential barriers. This point will be discussed in a future publication.

Here the nonactivated behavior suggests that  $\phi$  ( $=E_{pc} - E_F$ ) decreases with decreasing temperature, which can be attributed to the temperature-dependent ionization of donors (upward shift of the Fermi level). From this temperature-dependent conductivity, temperature variation of  $E_{pc} - E_F$  can be deduced. The temperature dependence of  $E_{pc} - E_F$  should include the temperature dependence of bandgap in the discussed temperature range, that is,  $\gamma T$ , where  $\gamma$  is the coefficient of temperature variation in bandgap and is taken to be  $4 \times 10^{-4}$  eV/K [31]. The net temperature variation of  $E_{pc} - E_F$  ( $=\phi(T) - \gamma T$ ) is given in Figure 8. From the pre-exponential term in Eq. (2), the barrier width  $W$  is also estimated. It is of interest that  $W = (2-4) \times 10^{-6}$  cm is estimated for *all* the samples. This value seems to be a reasonable value.

A linear temperature dependence of the value of  $E_{pc} - E_F$ , at relatively high temperatures, suggests that the donors are essentially all ionized (“exhaustion” or “saturation” regime) [31]. In this regime,  $E_{pc} - E_F$  is given as follows:

$$E_{pc} - E_F = kT \ln \frac{N_c}{N_d} \quad (3)$$

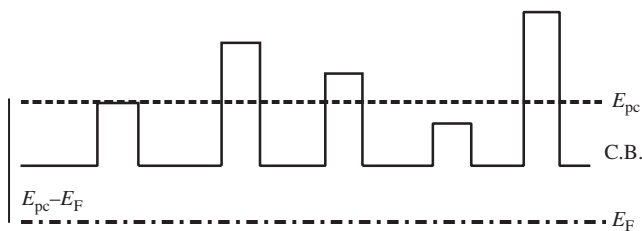


**Figure 7.** Temperature variation of  $\sigma_{dc}$  at relatively high temperatures as a function of doping levels.

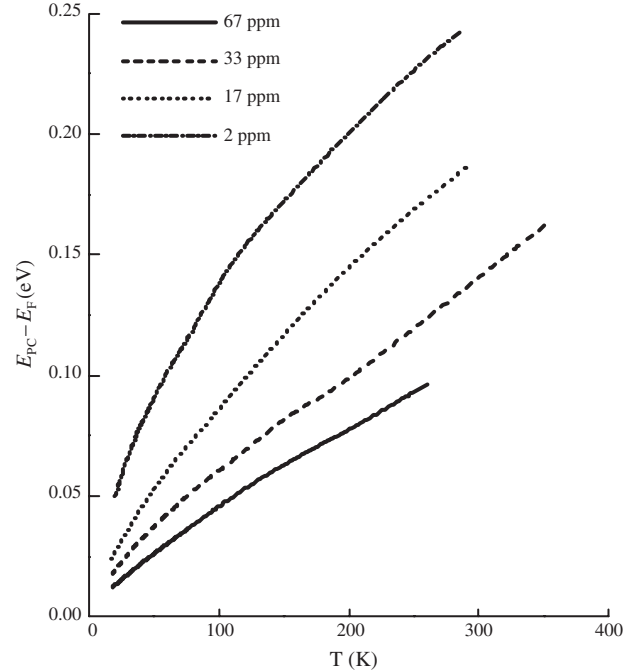


**Figure 8.** Temperature variation of the magnitude of  $E_{pc} - E_F$ .

where  $N_c$  (effective density of conduction band) is taken to be  $5 \times 10^{19}$   $\text{cm}^{-3}$ , and  $N_d$  is the donor concentration. From Eq. (3), the estimated values of  $N_d$  are plotted as a function of doping gas ratio, which are shown in Figure 9.  $N_d$  is almost linearly dependent on the doping gas ratio and this relationship deduced here is nearly the same as those obtained from the SIMS and the other measurements such as ESR by Finger et al. [8].

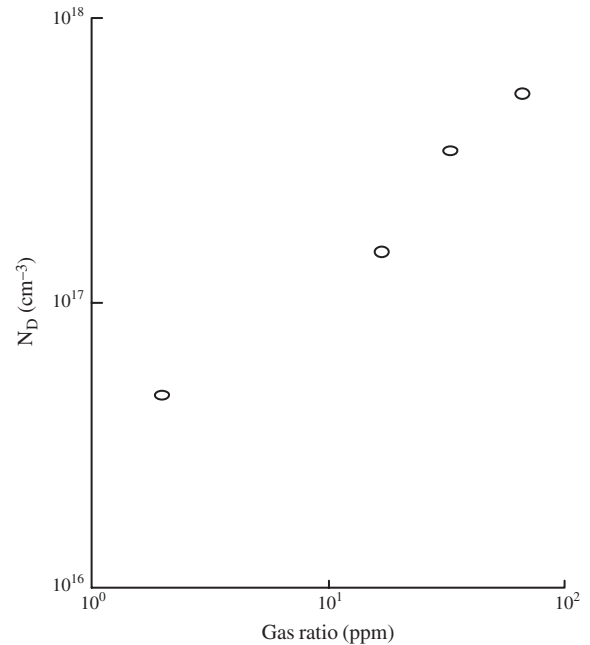


**Figure 9.** Estimated correlation between the donor concentration and doping gas ratio.

Finally, we should discuss the other transport mechanisms which have been proposed so far. The temperature-dependent dc conductivity below room temperature, on one hand, has been represented by the following expression in undoped and doped  $\mu\text{c-Si:H}$  films:

$$\sigma_{\text{dc}} = \sigma_0 \exp\left[-\left(\frac{T_0}{T}\right)^x\right] \quad (4)$$

where  $T_0$  is a constant and  $x = \frac{1}{2}$  [12, 13]. This type behavior can be understood either by *variable-range* hopping in the Coulomb gap [32] or by *nearest-neighbor* hopping between granular (conducting) islands [33]. Ram et al. [13] suggest that the unrealistically large Coulomb gap is estimated from the parameter  $T_0$  and hopping of electrons between granular islands dominates the transport. It should be noted that the pre-factor  $\sigma_0$  in Eq. (4) has a serious problem: It is well known that there is the discrepancy, by many orders of magnitude, between experimental and theoretical values of the constant  $\sigma_0$  [34]. This means that the experimentally observed conductivity cannot be replicated by Eq. (4) quantitatively. To the present author's view, therefore, a careful treatment using the concept of variable-range hopping may be required for reaching proper conclusion.

The model of thermionic emission over potential barriers cannot be applied to the carrier transport at lower temperatures below 20 K. Instead, nearest-neighbor hopping of electrons between donor sites has been suggested, in which carriers move *through* potential barriers (hopping sites also exist in barrier regions). Hopping of carriers is a special issue and hence the details of hopping conductivity at lower temperatures are discussed elsewhere [14].

There are also many interesting features of these inhomogeneous materials, for example, the growth mechanisms and related ac transport [2] and the photoconductivity [19]. A general behavior of photoconductivity in nc-Si:H is very similar to that found in a-Si:H [19]. A recent work of ac and dc photoconductivities in a-Si:H [35, 36], in which "inhomogeneity" is taken into consideration, may be useful to understand the photoconductivity in the present materials as well. These were not discussed in the present brief review.

## 5. APPLICATIONS

Nanocrystalline Si (nc-Si:H) thin films prepared by PECVD or HWCVD are a candidate for electronic and photovoltaic applications such as thin-film transistors (TFTs) (see, e.g., [37]) and solar cells. Nanocrystalline Si solar cells are more stable than a-Si:H-based solar cells [38, 39], since nc-Si:H is relatively free from light-induced degradation. Taking p-i-n structure, the open circuit voltage  $V_{\text{oc}}$  is achieved to be 600 meV and the efficiency is approaching 10% [40, 41].

The applications of TFTs in large-area flat panel displays are very attractive using Si thin films. TFTs based on hydrogenated amorphous silicon films (a-Si:H) have been used in massive produced displays and sensor arrays. Although the mobility (TFT mobility) of a-Si:H TFTs is low ( $\sim 1 \text{ cm}^2 \text{ V}^{-1} \text{ s}^{-1}$ ), they are suitable as the pixel switches in active matrix liquid crystal displays. This is due to a capability of

fabrication with low cost and large area ( $> 15 \text{ in}$ ), with high yield and very uniform performance. To get high-resolution displays, larger electron mobility should be required in the pixel TFTs. The major drawbacks for a-Si:H-based TFTs are (i) low electron mobility and (ii) low stability: the threshold voltage  $V_{\text{th}}$  shifts with successive switching. The TFT mobility using nc-Si:H is reaching  $\sim 20 \text{ cm}^2 \text{ V}^{-1} \text{ s}^{-1}$  and higher stability is reported. Note that the TFT mobility in polycrystalline Si by pulsed laser crystallization (PLC) is reported to be  $\sim 600 \text{ cm}^2 \text{ V}^{-1} \text{ s}^{-1}$  [20]. The challenge to get higher mobility and higher stability in nc-Si:H films is continuing.

## 6. CONCLUSIONS

The study of hydrogenated nanocrystalline Si (nc-Si:H) is advancing day by day, since nc-Si:H films are regarded as promising materials for commercially accepted large-area solar cells and thin-film transistors. The nc-Si:H films take very complex structures consisting of disordered (amorphous) and ordered (crystalline) forms. The quantitative explanation of the electronic and optical properties of nc-Si:H, therefore, is very hard.

A current understanding of nc-Si:H films has been briefly reviewed in the present chapter, including preparation methods and spectroscopic characterization. It was shown that an effective medium approximation was useful to explain the electronic transport and optical properties in nano- or microcrystalline Si films, which strongly depend on the volume fraction of crystallite. The present chapter also made clear the following unknown properties of these complicated materials: (i) The Hall mobility is sublinearly proportional to the crystallite size, which can be attributed to a fractal nature of the microcrystalline system. (ii) The nonactivated temperature variation of dc conductivity at relatively high temperatures is well explained in terms of the band transport across the potential barriers (percolation-limited thermionic emission process). Hopping transport may dominate only at lower temperatures.

All results predicted here may help further understanding and development of nano-, micro-, and polycrystalline materials.

## GLOSSARY

**EMA** Effective medium approximation, one of the percolation approximations which are useful to calculate the electrical and optical properties in condensed matters.

**Variable-range hopping** One of the hopping mode of electron hopping between localized states, which has been proposed by Mott.

## REFERENCES

1. F. Finger, J. Muller, C. Malten, and H. Wagner, *Philos. Mag.* B 77, 805 (1998).
2. A. Fejfar, T. Mates, C. Koch, B. Rezek, V. Svrcek, P. Fojtik, H. Stuchlikova, J. Stuchlik, and J. Kocka, MRS Spring Meeting, 2001, p. 1.

3. G. Willeke, in "Amorphous and Microcrystalline Semiconductor Devices" (J. Kanicki, Ed.), Vol. 1, p. 55. Artech House, Norwood, 1992.
4. F. Finger, R. Carius, P. Hapke, L. Houben, M. Luysberg, and M. Tzolov, in "Future Directions in Thin Film Science and Technology" (J. M. Marshall, N. Kirov, A. Vavrek, and J. M. Maud, Eds.), p. 1. World Scientific, Singapore, 1996.
5. R. Carius, F. Finger, M. Luysberg, P. Hapke, and U. Backhausen, in "Future Directions in Thin Film Science and Technology" (J. M. Marshall, N. Kirov, A. Vavrek, and J. M. Maud, Eds.), p. 11. World Scientific, Singapore, 1996.
6. R. Carius, J. Muller, F. Finger, N. Harder, and P. Hapke, in "Thin Film Materials and Devices—Developments in Science and Technology" (J. M. Marshall, N. Kirov, A. Vavrek, and J. M. Maud, Eds.), p. 157. World Scientific, Singapore, 1999.
7. J. Muller, F. Finger, R. Carius, and H. Wagner, *Phys. Rev. B* 60, 11666 (1999).
8. F. Finger, J. Muller, C. Malten, R. Carius, and H. Wagner, *J. Non-Cryst. Solids* 266–269, 511 (2000).
9. H. Overhof and M. Otte, in "Future Directions in Thin Film Science and Technology" (J. M. Marshall, N. Kirov, A. Vavrek, and J. M. Maud, Eds.), p. 23. World Scientific, Singapore, 1996.
10. S. Kirkpatrick, *Rev. Mod. Phys.* 45, 574 (1973).
11. K. Shimakawa, *J. Non-Cryst. Solids* 266–269, 223 (2000); "Proceedings of the 11th International School on Condensed Matter Physics," 2000, p. 1.
12. M. Taguchi, Y. Tsutsumi, R. N. Bahatt, and S. Wagner, *J. Non-Cryst. Solids* 198–200, 899 (1996).
13. S. K. Ram, S. Kumar, R. Vanderhagen, and P. Rocca i Cabarrocas, *J. Non-Cryst. Solids* 299–302, 411 (2002).
14. K. Shimakawa, *Mater. Sci.* (to be published).
15. F. Finger, P. Hapke, M. Luysberg, R. Carius, H. Wagner, and M. Scheib, *Appl. Phys. Lett.* 65, 2588 (1994).
16. M. Kondo, M. Hukawa, L. Guo, and A. Matsuda, *J. Non-Cryst. Solids* 266–269, 84 (2000).
17. H. Weismann, A. K. Ghosh, T. McMahon, and M. Strongin, *J. Appl. Phys.* 50, 3752 (1979).
18. H. Matsumura, *Jpn. J. Appl. Phys.* 25, L949 (1986).
19. R. Bruggemann, W. Bronner, A. Hierzenberger, M. B. Schubert, and I. Zrinscak, in "Thin Film Materials and Devices—Developments in Science and Technology" (J. M. Marshall, N. Kirov, A. Vavrek, and J. M. Maud, Eds.), p. 1. World Scientific, Singapore, 1999.
20. T. Sameshima, *J. Non-Cryst. Solids* 227–230, 1196 (1998).
21. M. Kondo, S. Yamasaki, and A. Matsuda, *J. Non-Cryst. Solids* 266–269, 544 (2000).
22. M. H. Cohen and J. Jortner, *Phys. Rev. Lett.* 30, 696 (1973); *ibid.* 30, 699 (1973).
23. B. E. Springett, *Phys. Rev. Lett.* 31, 1463 (1973).
24. A. Matsuda, *J. Non-Cryst. Solids* 59&60, 767 (1983).
25. R. A. Street, "Hydrogenated Amorphous Silicon," p. 224. Cambridge Univ. Press, 1991.
26. J. Y. W. Seto, *J. Appl. Phys.* 46, 5247 (1975).
27. H. P. Peters, *Z. Physik. B* 34, 399 (1979).
28. N. Beck, J. Meier, J. Fric, Z. Remes, A. Poruba, R. Fluckiger, J. Pohl, A. Shah, and M. Vanecek, *J. Non-Cryst. Solids* 198–200, 903 (1996).
29. M. Vanecek, A. Poruba, Z. Remes, N. Beck, and M. Nesladek, *J. Non-Cryst. Solids* 227–230, 967 (1998).
30. S. M. Sze, "Physics of Semiconductor Devices." Wiley, New York, 1969.
31. N. B. Hannay, "Semiconductors." Reinhold, New York, 1959.
32. B. I. Shklovskii and A. L. Efros, "Electronic Properties of Doped Semiconductors." Springer, Berlin, 1984.
33. B. Abeles, P. Sheng, M. D. Coutts, and Y. Arie, *Adv. Phys.* 24, 407 (1975).
34. K. Shimakawa and K. Miyake, *Phys. Rev. Lett.* 61, 994 (1988).
35. K. Shimakawa and A. Ganjoo, *Phys. Rev. B* 65, 165213 (2002).
36. K. Shimakawa, *Philos. Mag. Lett.* 82, 635 (2002).
37. R. E. I. Schropp, B. Stannovski, and J. K. Path, *J. Non-Cryst. Solids* 299–302, 1304 (2002).
38. J. Meier, P. Torres, R. Platz, S. Dubail, U. Kroll, J. A. Anna Selvan, N. Pellaton Vaucher, Ch. Hof, D. Fisher, H. Keppner, A. Shah, K. D. Ufert, P. Giannoules, and J. Koehler, *Mat. Res. Soc. Symp. Proc.* 420, 3 (1996).
39. K. Yamamoto, M. Yoshimi, Y. Tawada, Y. Okamoto, and A. Nakajima, *J. Non-Cryst. Solids* 266–269, 1082 (2000).
40. S. Klein, J. Wolf, F. Finger, R. Carius, H. Wagner, and M. Stutzmann, *Jpn. J. Appl. Phys.* 41, L10 (2002).
41. S. Klein, F. Finger, R. Carius, B. Rech, L. Houben, and M. Stutzmann, *Mat. Res. Soc. Symp. Proc.* 715, A26.2 (2002).



# Impurity States and Atomic Systems Confined in Nanostructures

R. Riera, R. Betancourt-Riera, J. L. Marín

*Universidad de Sonora, Hermosillo, Sonora, México*

R. Rosas

*Universidad de Sonora, Hermosillo, Sonora, México*

## CONTENTS

1. Introduction
  2. Methods of Synthesis and Fabrication of Nanostructured Materials
  3. Physical Effects of Impurity States and Atomic Systems Confined in Semiconductor Nanostructures
  4. Nonconventional and Atomic Idealized Confined Systems in Nanostructures
  5. Mechanism of Terahertz Lasing in SiGe/Si Quantum Wells
- Glossary  
References

## 1. INTRODUCTION

The real confined systems, also called low-dimensional systems or nanostructures, are any three-dimensional quantum systems in which the carriers are free to move in only two, one, or even zero dimensions.

In nanostructured semiconductors the concept of quasi-particles is related to electrons, holes, and excitons; the characteristic length that defines the confinement degree is the effective Bohr radius of excitons,  $a_B^*$ . This magnitude may be considerably larger than lattice constant,  $a_L$ . Therefore, it is possible to create a mesoscopic structure which is, in one, two, or three dimensions, comparable to or even lesser than  $a_B^*$  but still larger than  $a_L$ . In these structures the elementary excitations will experience quantum confinement, resulting in a finite motion along the confinement axis and an infinite motion in other directions. This way, one deals with the so-called nanostructured systems or, in a broad accepted classification, the quasi-two-dimensional systems (single heterostructures, quantum wells, multiple quantum wells, and

superlattices), quasi-one-dimensional systems (quantum well wires), and quasi-zero-dimensional systems (quantum dots, crystallites, and quantum boxes).

The confinement degree of quasi-particles is related to the magnitudes  $a_B^*$  and the quantum confinement size  $d$  (or  $r_0$ ); two regimes can be readily distinguished: the weak confinement regime and the strong confinement regime. The weak confinement regime corresponds to the case when the nanostructure confinement size [ $d$  (or  $r_0$ )] is smaller but still a few times larger than  $a_B^*$ . The mathematical condition is  $a_B^* \ll d$  (or  $r_0$ ). In this case, the electron and hole are correlated; the exciton can be envisioned as a quasi-particle moving around inside the nanostructure with only little energy increment due to confinement. In this case, the infinite potential well model (within the single band effective mass approximation) gives a reasonable description of the experimentally observed shift in the exciton ground state energy.

The strong confinement regime corresponds to the condition  $a_B^* \gg d$  (or  $r_0$ ). In this case the confinement effect dominates over the Coulomb potential, and the electron and hole should be viewed as individual particles predominantly in their respective single particle ground states with only little spatial correlation between them. In this regime the exciton in the nanostructure “feels” the boundary effects strongly, and the inclusion of a finite height for the confining potential barrier has become an important requirement in order to account for recent experiments on the optical properties of small nanostructures.

In general the nanostructures are fabricated using two different materials A and B, considering that A and B are semiconductors with bandgaps  $\varepsilon_g^A$  and  $\varepsilon_g^B$ , respectively. In the nanostructure growth process, one of the materials is deposited over the other one and a potential barrier is formed in the interface due to the difference of bandgaps. According to the gap positions and values, three types of

nanostructures can be obtained which we will identify as type I, II, and III nanostructures (see Fig. 1).

In the type I nanostructures, B material is a barrier for both the valence and conduction electrons, which are localized within the same A material. Examples of type I nanostructures are GaAs–Ga(Al)As,  $\text{Ga}_{0.47}\text{Al}_{0.53}\text{As}$ –InP, GaSb–AlSb, etc.

In the type II nanostructures (also called staggered nanostructures) one material acts as a well for conduction electrons but as a barrier for valence electrons. Examples of the type II nanostructures are InP– $\text{Al}_{0.53}\text{In}_{0.48}\text{As}$  where the electrons are mostly in the InP material and the holes in  $\text{Al}_{0.53}\text{In}_{0.47}\text{As}$ , and InAs–GaSb where the electrons are mostly in the InAs semiconductor and the holes are mostly in the GaSb semiconductor. In type II nanostructures, we deal with interface excitons where the interacting particles are spatially separated, a situation which is reminiscent of that of the bound impurity states created by impurities placed in the barriers of the quantum structures.

The general importance of the confined systems and nanostructured materials has been widely suggested to be a key process in the future of nanotechnology and of interest in diverse fields including magnetics, pharmaceuticals, aerospace, nanoelectronics, optoelectronics, etc.

Several methods for obtaining the confined systems exist, namely, the reduction of some spatial directions to quantum scale, by the application of any kind of fields or by limiting the borders in the synthesis of the materials.

Several forms of classifying the confined systems exist; the most universal considers the number of directions where the particle could move freely. For example, quasi-two-dimensional systems (Q2D) have two directions for the free movement of the carriers and one confined spatial direction (see Fig. 2). The Q1D system has only one direction for free movement and two directions of confined movement where the carriers are compelled to move in a reduced space of quantum scale (see Fig. 3). The Q0D systems have no directions for free movement; the three spatial directions are confined (see Fig. 4). The energy spectrum in the spatial direction of confinement is always discrete if the particle remains totally confined and discrete and continuous if the particle remains partially confined.

Recently, a great number of experimental type articles have been published which are related to the impurity states and atomic systems confined in different types of nanostructures; we will mention some of them. Cheong and Jeong [1] studied the GaAs/AlGaAs quantum wells

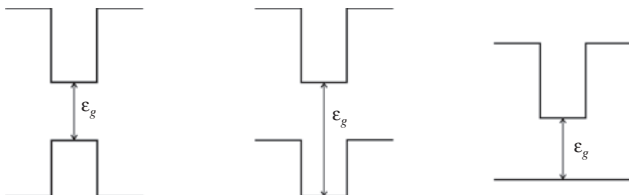


**Figure 1.** Types of semiconductor nanostructures. (a) Type I; (b) type II; (c) type III. Reprinted with permission from [205], J. L. Marín et al., in “Handbook of Advanced Electronic and Photonic Materials and Devices” (H. S. Nalwa, Ed.). Academic Press, San Diego, 2001. © 2001, Academic Press.

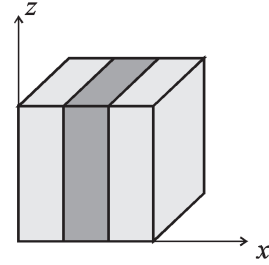


**Figure 2.** Quasi-two-dimensional system (single square quantum well).

using reflectance-based optically detected resonance spectroscopy. This technique consists of monitoring changes in the strength of the  $e_1h_1$  excitonic reflectance feature induced by the far-infrared laser beam. A reflectance signal is modulated when the far-infrared photon energy matches the energy difference between two electronic states of the system under study. The more conventional optically detected resonance spectroscopy with which the interband photoluminescence intensity is monitored will be referred to as photoluminescence based optically detected resonance [2–6]. By comparing photoluminescence optically detected resonance and reflectance-based optically detected resonance results from the same samples it was established that reflectance-based optically detected resonance was sensitive to both neutral and negatively charged donors. In this work they proved the utility of this new technique, reflectance-based optically detected resonance, for investigating the electronic states of neutral and negatively charged donors in several GaAs/AlGaAs multiple-quantum-well samples. The high sensitivity of reflectance-based optically detected resonance reveals new internal donor transitions of negatively charged donors. These results were agreed with theoretical calculations [6, 7].

Zhu and Xu [8] presented advances in nanoscopic probing techniques that have led to the development of direct spatial and spectroscopic methodologies, which have revealed a wealth of information about single quantum dots. These techniques, combined with the favorable properties of naturally formed quantum dots, have allowed one to

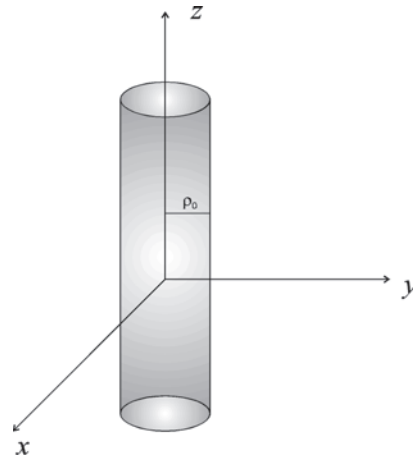


**Figure 3.** Quasi-one-dimensional system (cylindrical quantum well wire).



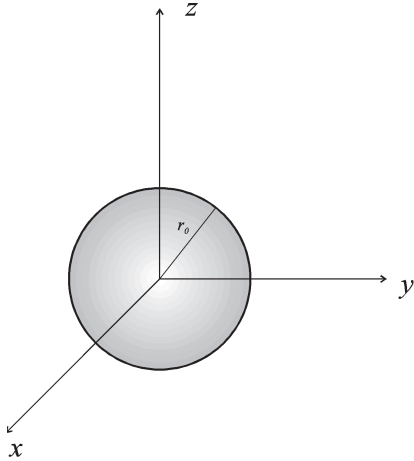


Figure 4. Quasi-zero-dimensional system (spherical quantum dot).

treat a single exciton confined to a quantum dot as a single solid state quantum absorber in analogy to atomic and molecular systems. Direct measurements on these systems, including absorption and coherent nonlinear spectroscopy, have revealed dipole moments and dynamic time scales of the individual excitations. Combined with microscopy, these probes have revealed global properties of the quantum dot system.

Zhao et al. [9] experimentally and theoretically studied the electronic structures of acceptors confined at the center of  $\text{In}_x\text{Ga}_{1-x}\text{As}/\text{Al}_{0.3}\text{Ga}_{0.7}\text{As}$  quantum wells. The aim of this investigation was to explore the effects of biaxial deformation potential on acceptors confined in quantum well structures. Satellite peaks related to  $2S$  and  $2P$  of the confined acceptors were observed in selective photoluminescence spectra. The deduced energy separations between the acceptor heavy-hole-like ground state and different excited states were compared with the theoretical calculated results. The impurity states were calculated using a four-band effective mass theory, in which the valence band mixing as well as the mismatch of the band parameters and the dielectric constants between well and barrier materials were taken into account. An excellent agreement between experimental and theoretical data was found.

In [10] coherent transport in Si metal–oxide–semiconductor field-effect transistors with nominal gate lengths 50–100 nm and various widths at very low temperature were investigated. Independent of the geometry, localized states appear when  $G \cong e^2/h$  and transport is dominated by resonant tunneling through a single quantum dot formed by an impurity potential. They found that the typical size of the relevant impurity quantum dot is comparable to the channel length and that the periodicity of the observed Coulomb blockade oscillations is roughly inversely proportional to the channel length. The spectrum of resonance and the nonlinear  $I$ – $V$  curves allowed them to measure the charging energy and the mean level energy spacing for electrons in the localized state. Furthermore, they found that in the dielectric regime the variance  $\text{var}(\ln g)$  of the logarithmic conductance  $\ln g$  is proportional to its average value  $\langle \ln g \rangle$ , consistent with one-electron scaling models.

On the other hand, there are many theoretical works carried out on the impurity states and atomic systems confined in the nanostructures. We will mention some of them. Thus, in [11] the effect of a spatially dependent effective mass in a finite  $\text{GaAs}/\text{Al}_x\text{Ga}_{1-x}\text{As}$  parabolic quantum well with a magnetic field on hydrogenic impurity ground state ( $1S$ ) binding energies and lowly excited state ( $2p_{\pm}$ -like) was calculated, respectively, as a function of well width and magnetic field and impurity position by using the one-dimensional method. They compared their results with square quantum wells and without the effect of spatially dependent effective mass result. The physical meaning of the square wavefunction was discussed.

Hsieh and Chuu [12] studied the binding energy of the ground state of a hydrogenic impurity located at the center of a multilayered quantum wire within of the effective mass approximation. The multilayered quantum wire consisted of a core wire (GaAs) coated by cylindrical shell ( $\text{Ga}_{1-x}\text{Al}_x\text{As}$ ) and then embedded in the bulk ( $\text{Ga}_{1-x}\text{Al}_x\text{As}$ ). The calculation was performed, by using a trial wavefunction. To make a comparison, the ground and excited state ( $1s$ ,  $2p$ , and  $3d$  states) binding energies of a hydrogenic impurity located at the center of a single-layered quantum wire were also calculated. It was found for small wire radius that the ground state binding energy of the hydrogenic impurity located at the center of a multilayered quantum wire behaves very differently from that of a single-layered quantum wire.

Hsieh [13] calculated the ground state binding energy of the hydrogenic impurity located at the center and off center of a multilayered quantum wire in a constant magnetic field applied parallel to the wire axis by using the effective mass approximation. His system was constructed as a core wire made of GaAs surrounded by a cylindrical shell of  $\text{Al}_x\text{Ga}_{1-x}\text{As}$  and then embedded in the bulk of  $\text{Al}_y\text{Ga}_{1-y}\text{As}$ . A variational trial wavefunction was proposed. It was found for a small wire radius that the ground state binding energy of a hydrogenic impurity located at the center of a multilayered quantum wire behaves very differently from that of a single-layered quantum wire. The calculation showed that the binding energy depends on the potential profiles, potential barrier height, impurity position, shell thickness, magnetic field, and the difference between the Al concentration contained in the shell and bulk regions. His trial function was also able to reproduce the binding energies of a hydrogenic impurity located at the center of a single-layered quantum wire; a good agreement with the previous results was obtained.

In [14] the ground state energies of several interacting electrons confined in a parabolic dot in two dimensions were obtained by using hyperspherical coordinates and high order perturbation theory. The effect of a perpendicular magnetic field is to change the ground state discontinuously in orbital angular momentum  $L$ . The preferred values of  $L$  for the ground state and the associated electronic structures were studied in detail. It was found that the effective interaction between two electrons moving in different cyclic orbits is a short-range attraction matched a long-range repulsive tail. Because of this, electrons tend to fill adjacent cyclic orbits and form bunches in the ground states. The effects of an impurity ion were also considered.

Chen et al. [15] employed a simple approximation treatment, which combines the spirit of the variational principle and the perturbation approach to study the confined phonon effect on the binding energy of a hydrogenic impurity located inside a quantum well. The electron bulk longitudinal optical phonon and the electron surface phonon interactions were both taken into account in their calculation. The image charge effects may be significant if there is a large dielectric discontinuity between the well and the surrounding medium. However, since the purpose of this work is to concentrate on the confined phonon effects on the impurity binding energies, the image effects were not taken into account in their calculation.

Sali et al. [16] reported a calculation of the photoionization cross-section describing the excitation of a shallow bound electron from the hydrogenic donor impurity ground state to three of the conduction subbands  $n_x$ ,  $n_y$ , and  $n_z$  corresponding, respectively, to the  $x$ ,  $y$ , and  $z$  directions of the dot in the case of an infinite well model. The photoionization cross-section associated with a hydrogenic shallow donor impurity was calculated as a function of the excitation energy  $\hbar\omega$  in a GaAs quantum dot for several values of the dimensions of the dot and for an on-center donor impurity and off-center donor impurities.

Reyes-Gómez et al. [17] extended the fractional-dimensional space approach to study exciton and shallow-donor states in symmetric-coupled GaAs/Ga<sub>1-x</sub>Al<sub>x</sub>As multiple quantum wells. In this scheme, the real anisotropic “exciton (or shallow donor) plus multiple quantum well” semiconductor system is mapped, for each exciton (or donor) state, into an effective fractional-dimensional isotropic environment, and the fractional dimension is essentially related to the anisotropy of the actual semiconductor system. Moreover, the fractional-dimensional space approach was extended to include magnetic-field effects in the study of shallow-impurity states in GaAs/Ga<sub>1-x</sub>Al<sub>x</sub>As quantum wells and superlattices. In their study, the magnetic field was applied along the growth direction of the semiconductor heterostructure and introduced an additional degree of confinement and anisotropy besides the one imposed by the heterostructure barrier potential. The fractional dimension was then related to the anisotropy introduced both by the heterostructure barrier potential and magnetic field. Calculations within the fractional-dimensional space scheme were performed for the binding energies of 1s-like heavy-hole direct exciton and shallow-donor states in symmetric-coupled semiconductor quantum wells, and for shallow-impurity states in semiconductor quantum wells and superlattices under growth-direction applied magnetic fields. Fractional-dimensional theoretical results were shown to be in good agreement with previous variational theoretical calculations and available experimental measurements.

Reference [18] presented that interelectron interactions and correlations in quantum dots can lead to spontaneous symmetry breaking of the self-consistent mean field, resulting in the formation of Wigner molecules. With the use of spin-and-space unrestricted Hartree–Fock calculations, such symmetry breaking was discussed for field-free conditions, as well as under the influence of an external magnetic field. Using as paradigms impurity-doped (as well as the limiting case of clean) two-electron quantum dots (which are

analogous to heliumlike atoms), it was shown that the interplay between the interelectron repulsion and the electronic zero-point kinetic energy leads, for a broad range of impurity parameters, to the formation of a singlet ground state electron molecule, reminiscent of the molecular picture of doubly excited helium. A comparative analysis of the conditional probability distributions for the spin-and-space unrestricted Hartree–Fock and exact solutions for the ground state of two interacting electrons in a clean parabolic quantum dot revealed that both of them describe the formation of an electron molecule with similar characteristics. The self-consistent field associated with the triplet excited state of the two-electron quantum dot (clean as well as impurity doped) exhibits a symmetry breaking of Jahn–Teller type, similar to that underlying formation of nonspherical open-shell nuclei and metal clusters. Furthermore, they showed that impurity and/or magnetic field effects can be used to achieve controlled manipulation of the formation and pinning of the discrete orientations of the Wigner molecules. Impurity effects were further illustrated for the case of a quantum dot with more than two electrons.

In [19] Buonocore et al. presented the results of their theoretical studies on the influence of hydrogenic impurities on the electron localization in a deformed quantum wire. Although their primary interest was on porous silicon, it must be said that the calculation methods they illustrated are very general and can be applied to all those situations where the effects of the nanostructure geometry cannot be neglected.

Kayanuma [20] showed that the eigenvalue problem for bound states of hydrogenic donors located at the edge of a semiconductor surface could also be solved exactly for arbitrary values of the edge angle. Considering a neutral donor located at the edge of a crystal surface, which is formed by an intersection of two flat surfaces, he chose the edge line as the  $z$  axis. The two surfaces were assumed to be given by  $y = \pm \tan(\phi_0/2)x$ , with  $\phi_0$  the angle between edges. For  $0 < \phi_0 < \pi$ , the crystal surface has a wedgelike shape, but for  $\pi < \phi_0 < 2\pi$ , it has a notch. The polar coordinates  $(r, \theta, \varphi)$  of the electron were defined in the usual way. It was assumed that the electron is completely confined in the region  $-\phi_0/2 \leq \phi \leq \phi_0/2$ . Throughout his work, he adopted the effective mass approximation. The attractive potential due to the positive ion core was given by  $V(r) = -e^2/\kappa r$ , in which  $\kappa$  is the dielectric constant of the crystal. The penetration of the wavefunction outside the crystal and the effect of the image potential were both neglected. All these effects should be taken into account as a refinement of the model in actual analyses of experimental data [21]. Levine’s model of the surface donor [22] was included in his model as a special case.

Kandemir and Cetin [23] studied the dependence of low-lying energy levels of impurity magnetopolaron subjected to a 3D parabolic potential on both magnetic field and spatial confinement length. To achieve this, they restricted to the case of bulk longitudinal optical (LO) phonons and introduced a trial wavefunction taken to be the direct product of an electronic part and a part of coherent phonons. They were also concerned with the study of the effects due to the electron–LO–phonon interaction, quantum confinement, and magnetic field on the cyclotron masses associated with

the transitions between the ground and first-excited states of an electron bound to a hydrogenic impurity in a 3D parabolic potential. They found an analytical expression for the impurity magnetopolaron energy that allows them to perform a systematical analysis of the effects of both magnetic field and spatial confinement on the binding energies of impurity magnetopolaron in quantum dots, quantum well wires, and quantum wells. They established a unified treatment that allows them to make comparisons between the results of binding energies of impurity magnetopolarons in these three systems.

Schlottmann [24] studied an Anderson impurity placed at the center of a nanosized metallic sphere. The main difference with the standard mixed-valence problem is that the energy spectrum of the host is now discrete. Similar to the Kondo impurity [25], the problem could be mapped onto the Bethe ansatz solution of the Anderson model [26, 27]. The model and the Bethe ansatz equations diagonalizing were solve numerically for the ground state and the lowest energy charge and spin excitations. The energies of the states increase monotonically with the  $f$ -level energy. For an even number of electrons in the system (in  $s$  states and localized at the impurity), the impurity in the ground state is spin compensated into a spin singlet via the Kondo effect. The specific heat and the susceptibility are exponentially activated at low  $T$  due to the discreteness of the energy spectrum, with the gaps given by the lowest energy charge and spin excitations. The model also represented a quantum dot as a side branch to a short quantum wire.

Yen [28] theoretically studied resonant states of shallow donor arbitrarily lying in a two-dimensional quantum well structure based on the multisubband model. The density-of-states spectra of the resonant states were obtained using the resolvent operator technique. For illustration, he calculated the binding energy, the density of state spectrum width, and the resonance energy shift of the  $2p_0$  state in a quantum well as a function of the impurity position. Considerable coupling was found. It caused a capture or escape time as short as  $\approx 0.1$  ps.

Apalkov and Chakraborty [29] considered a system of an incompressible quantum Hall liquid in close proximity to a parabolic quantum dot containing a few electrons. They observed a significant influence of the interacting electrons in the dot on the excitation spectrum of the incompressible state in the electron plane. Their calculated charge density indicates that, unlike the case of an impurity, interacting electrons in the dot seem to confine the fractionally charge excitations in the incompressible liquid.

Yang and Hsu [30] calculated the binding energy of the ground state of hydrogenic impurity seated at the center of quantum well GaAs/Ga<sub>1-x</sub>Al<sub>x</sub>As with the inclusion of the effect due to the image charges (excluding the self-energy image potential). For a given depth of the quantum well, they found that the absolute value of the image potential energy without the metallic mirror is equal to that with a fixed metallic mirror while a certain width of the quantum well is met. Hence, it was proposed that the binding energy of the shallow impurity ground state in the quantum well with and without the metallic mirror could be separately measured by the variation of the width of quantum well. The contribution of the image potential energy to the binding

energy of the shallow impurity ground state could then be deduced.

Essaoudi et al. [31] discussed the stability of an exciton bound to an ionized donor impurity in a GaAs/Ga<sub>1-x</sub>Al<sub>x</sub>As semiconductor quantum well subjected to an external magnetic field for different values of the impurity location. The binding energy was calculated in the effective mass approximation by means of variational method. At zero magnetic field, the complex becomes unstable when the impurity is far away from the center of the well. When the magnetic field increases, the stability holds in all cases for an impurity located at the center of the well.

Brandi et al. [32] treated the interaction of light with a spherical GaAs/AlGaAs quantum dot within a dressed-band approach. The Kane band structure scheme was used to model the GaAs bulk semiconductor and the interaction with the laser field is treated through the renormalization of the semiconductor energy gap and conduction/valence effective masses. This approach, valid far from resonances, was used to investigate the light shifts induced in the electronic and shallow on-center donor states in semiconductor quantum dots, which were shown to be quite considerable. This model calculation could be extended to include magnetic-field effects, and it was suggested that the strong localization of the electronic and impurity states due to the quantum dot and enhanced by laser confinement could prove useful for manipulation of electronic and donor states in some proposed solid-state-based quantum computers.

Stébé et al. [33] concentrated their study on the  $(D^+, X)$  complex resulting from the binding of an exciton  $X$  to an ionized hydrogenic donor impurity  $D^+$ . Its possible existence was predicted in 1958 by Lampert [34]. Its stability and binding in 3D semiconductors was the subject of several theoretical studies within the effective-mass approximation as a function of the electron to hole effective mass ratio  $\sigma = m_e/m_h$ . As a result, it appeared [35] that the  $(D^+, X)$  complex is stable if  $\sigma \leq \sigma_c = 0.454$ . It was expected that due to the quantum confinement, the  $(D^+, X)$  complex will be more stable in quantum wells than in 3D semiconductors. There are few measurements available [36–40] on an exciton bound to ionized donors in quantum wells. From the theoretical point of view, variational determinations of the ground state energies [41, 42] have first proven that the  $(D^+, X)$  complex with the impurity located at the center of the well is stable in GaAs/Ga<sub>1-x</sub>Al<sub>x</sub>As quantum wells with  $x = 0.15$  and  $x = 0.30$ .

## 2. METHODS OF SYNTHESIS AND FABRICATION OF NANOSTRUCTURED MATERIALS

There is increasing interest in producing structures of nanometer size for use in device fabrication and proof of physics laws in nanometer sized structures. This is a growing field and nowadays is very important for investigating new techniques for nanometer device fabrication.

The most used materials for production of nanostructured materials are, in first place, semiconductors and metals and, in second place, dielectrics, magnetic, and superconductor compounds. They are also manufactured using organic materials, polymers, biomaterials, etc.

Nowadays there are so many methods of synthesis and production of nanostructured materials, in a laboratory scale, but the most important are those where high quality quantum nanostructures are achieved. These methods produce materials that have one atomic layer precision, with abrupt grown interfaces with one monolayer roughness and with great control for purity and doped impurities.

In addition to this technology, in order to guarantee the high quality of the nanostructured materials, the investigation laboratories need to count on several characterization techniques *in-situ*. Independently of the dimensionality of the grown nanostructures, the most used and known techniques for the production or fabrication of the different kinds of nanostructured materials are molecular beam epitaxy (MBE), metal organic chemical vapor deposition (MOCVD), and lithography, also known as nanolithography.

## 2.1. Molecular Beam Epitaxy

MBE is a method by means of which a semiconductor, such as GaAs, is grown in an ultrahigh vacuum environment by supplying molecular and/or atomic beams of Ga, As, and other constituents onto a cleaned crystalline substrate [43–51]. Because one can prepare semiconductor films of high quality by MBE with a precision in thickness of one atomic layer or better, it is now widely used in all nanostructured materials. MBE is one of the best methods for the preparation of a very flat surface of one semiconductor on which another semiconductor of an arbitrary thickness can be deposited. This feature allows one to control the composition profile and thereby to implement an artificial potential  $V(z)$  as a function of position  $z$  along the direction of stacking. A number of studies have shown, however, that interfaces of GaAs–AlAs (or AlGaAs) grown by MBE are generally abrupt but have a roughness  $\Delta$  of one monolayer,  $a = 2.83 \text{ \AA}$ . Hence it is very important to clarify the origin and nature of such roughness and to establish a method for controlling the atomic structure of interfaces. In addition, one should note that the atomic structure of an interface is usually a frozen image of the freshly grown surface and therefore provides valuable information on the microscopic process of epitaxial growth. On the other hand, the high purity of the low-dimensional system obtained by MBE indicates that the mobility is dominated mainly by scattering by phonons. The advantages of epitaxial growth by MBE, with respect to other methods or technologies, are multiple techniques *in-situ* that permit an absolute control of the ground parameters of the grown structure, such as size, high purity, abruptness and flatness of interface and impurities in doped heterostructures, and the ultrahigh vacuum environment that it possesses.

## 2.2. Metal Organic Chemical Vapor Deposition

The MOCVD method is the most useful and conventional process for fabricating thin layer semiconductor heterostructures. In general MOCVD has a reaction chamber that is basically dependent upon the heating system, which fits for long growth run. It is possible to use a radio frequency

induction coil as an alternative heater; there is a possibility of dissociation of gases, which produces radicals due to a plasma discharge in reduced pressures, and then it is necessary to employ a large-scaled electric power supply in connection with a precise electric circuit. However, in the case of synthesis of the II–VI compound semiconductors, it should be pointed out that there are several problems concerning the difficulty in precisely controlling the II/VI mole ratio because of the high dissociation pressure of VI elements and also the premature reaction taking place in the vapor phase prior to epitaxial deposition on a substrate. In order to avoid such problems, Yamada [52] has used new metal organic sources diluted in a He gas, namely, dimethylzinc (DMZn) with a concentration of 1.06% in a He gas, for the growth of cubic-structured  $\text{Cd}_x\text{Zn}_{1-x}\text{S}$ –ZnS strained-layer multiple quantum wells [53–55]. A mixture of 10%  $\text{H}_2\text{S}$  in a  $\text{H}_2$  gas was used as the sulfur source. Its MOCVD apparatus consists of a main reaction chamber and a sample exchange supplemental chamber with a transfer tube. A special feature is that they employ a halogen lamp capable of heating substrates up to 600 °C by infrared radiation. Two chambers are constructed for all VI materials and each inner wall is coated with TiN films, to avoid accidental impurity contamination. In order to control the gas flow ratio of II/VI, a personal computer connected to a relay box linked to an interface which was capable of switching both the piezovalves of the MFC (mass flow controller) and air valves on or off is used. Then, all of gas sources flowed directly into the MFCs, so that the bubbling system by a carrier gas was unnecessary for the metal organic (DMZn and DMCD) gas flow as well as the  $\text{H}_2\text{S}$  gas flow [56, 57]. Therefore, the process using the low-pressure MOCVD system with all gaseous sources has proven to be advantageous for precise control of II/VI mole ratio as well as lower temperature growth (350 °C) of the II–VI compound heterostructures.

## 2.3. Lithography

It is instructive to consider the conventional but advanced forms of lithography as practiced today. As it has developed for the semiconductor industry, lithography is the creation of a pattern in a resist layer, usually an organic polymer film, on a substrate material. A latent image, consisting of a chemical change in the resist, is created, by exposing the desired area with some form of radiation. The pattern is developed by selectively removing either the exposed areas of resist (for a positive resist) or the unexposed areas (for a negative resist). These processes are shown schematically in Figure 5. The development of a polymeric resist is usually done with a solvent that brings out the pattern based on the solubility difference created by exposure.

### 2.3.1. Overview of Lithography

Electrons, ions, and photons can all be used for exposure in the lithography process. Because of intrinsic scattering mechanisms, in no case can the energy provided by the exposing radiation be confined to arbitrarily small volumes. First, the radiation or particle beam cannot be confined arbitrarily because of diffraction, Coulomb repulsion

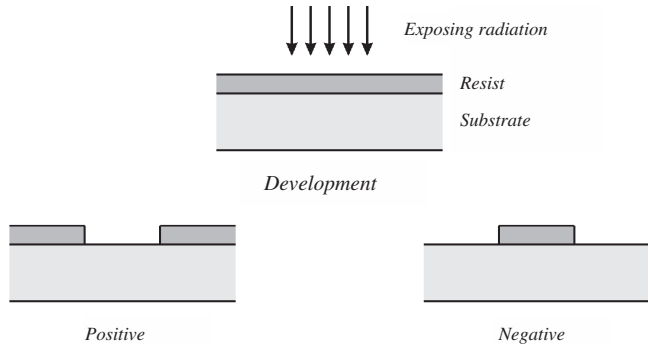


**Figure 5.** Schematic diagram of the basic lithographic steps of resist exposure and development.

among particles, optical limitations, or other effects. Second, the energy incident on a resist layer spreads in the film, because of intrinsic scattering mechanisms in the solid.

The figures of merit for a resist/developer system include: the sensitivity to the exposure dose dependence of the resist response, the resolution dictating the minimum feature size, and the suitability of the resist for pattern transfer. While the sensitivity and contrast of a system are vital in determining the speed and process latitude, it is the resolution and pattern transfer utility that are most important to research level nanostructure fabrication.

Inorganic resist materials exist and have been applied in the high resolution of the field. Related processes include vapor or plasma developments that operate on difference in gas phase or plasma reactivity rather than liquid development based on solubility differences. Self-developing resists are of some importance in the high resolution of the area. For these materials the exposing radiation volatilizes the resist, creating a pattern in the resist without a development step. By this method, structures on the order of unit cell dimensions were made some years ago [58].

### 2.3.2. Photon Lithography

The use of photons for high resolution of the lithographic exposure is a broad field that includes most of the lithography in use today. This is the technique most widely used by the semiconductor industry and illustrates the general technique of lithography. It can be taken to include X-ray lithography and deep and near-ultraviolet photolithography. Only the shortest wavelengths are directly relevant to high resolution of the fabrication. The projection and proximity printing processes to be described are analogous to processes that could be used at nanometer dimensions for parallel printing with electrons or ions.

In projection lithography a mask containing the desired pattern is demagnified by an optical system and projected on the resist layer. This is desirable since there is no damaging contact between the mask and wafer, and the fabrication of the mask is not so critical since it is demagnified. The resolution is limited, however, by diffraction and the quality of the optics. The diffraction limit for the minimum resolvable grating period is usually taken as the Rayleigh criterion for the overlap of the diffraction peaks, which is approximately

$$\text{minimum line resolvable spacing} \approx \frac{\lambda}{\text{NA}} \quad (1)$$

where  $\lambda$  is the wavelength and NA is the numerical aperture of the optical system, which is of the order of one. The shortest wavelength to be used with conventional optics is about 193 nm from an excimer laser source. The use of wavelengths much shorter than this is limited by absorption in optical materials. While the technology constantly improves, with better optics, improved contrast enhanced resists, and sources of shorter wavelength, the limit of far-field diffraction is a fundamental one that prevents its use for feature sizes smaller than the wavelength of light. Photolithography is essentially ruled out for fabrication at dimensions below 100 nm.

Projection systems employing X-rays would reduce diffraction effects, but the problem of fabricating optics to use in the X-ray region remains. Work in this area is advancing, with the development of multilayer mirrors and X-ray mask technology.

Proximity printing allows the 1:1 replication of a mask pattern. The effects of near field diffraction can be arbitrarily reduced by decreasing the distance between mask and substrate. Qualitatively, the minimum linewidth is

$$d \approx \sqrt{\lambda s} \quad (2)$$

where  $s$  is the separation between mask and substrate.

Proximity printing can be done effectively by X-ray exposure where the shorter wavelengths, of the order of 1 nm, allow much greater mask-substrate separation. With short wavelength X-rays, diffraction can effectively be ignored for attainable gaps of the order of a few micrometers. However, the exposure of polymeric resist by X-rays takes place primarily through the generation of photoelectrons, which then expose the resist by the same mechanisms as an electron beam. The range of the photoelectrons in the resist will limit the resolution. Since the photoelectrons can have energies up to that of the X-rays, their range can be greater than 100 nm for the shorter wavelength X-rays. We can see qualitatively that there is a trade-off between diffraction and the range of photoelectrons in limiting the resolution. Perhaps the most significant problem with X-ray printing is the creation of a durable and stable mask of high contrast. All materials absorb X-rays, so the transparent area of the mask must be very thin or nonexistent. An absorbing metal, such as gold supported on a thin film such as  $\text{SiN}_4$ , is one type of mask. Some of the smallest features replicated by X-rays were 17.5 nm in extent, fabricated by using edge-evaporated metal as a mask. Some other high-resolution process is necessary to generate the mask features; in most cases this means electron beam lithography.

### 2.3.3. Electron Beam Lithography

This technique has now developed substantially and has been used extensively for the generation of photolithographic masks. Schemes for electron beam 1:1 printing similar to those using X-rays or ions have been explored but generally not for the creation of nanostructures. Because of the ready availability of small electron sources and the high



quality of electron optics, electron beams can be focused to dimensions less than 1 nm and scanned with great accuracy.

In scanned electron beam lithography, a small electron source is imaged on the substrate through a series of electromagnetic lenses in an electron-optic column. The beam can be rapidly scanned over the sample to trace out any desired pattern. In the normal exposure of organic polymer resist, the electron beam causes the breaking of bonds or induces additional chemical bonds to be formed. This results in different molecular sizes in the exposed versus the unexposed areas, and this can be translated into differences in solubility in an appropriate developer.

The problem with electron beams is to confine the deposition of energy to a small area in the resist. There are several scattering processes in the material that lead to the deposition of energy at distances remote from the initial impact point of the electron. This leads to the well-known proximity and resolution limiting affects.

The scattering effect of longest range is the backscattering of electrons, resulting in large-angle scattering with energies near that of the incident electron. The range of these backscattering electrons can be many micrometers for typical electron beam energies. This range has been determined to have a dependence power law, proportional to (Energy)<sup>1.7</sup>, over a wide electron energy range. This presents the greatest problems for energies where the electron range is comparable to the feature spacing [59].

Because of small-angle scattering events, forward scattering tends to spread the incident beam passing through the resist. The scattering angles decrease with electron energy, and the spread of the beam is obviously more important for thicker resist layers.

With electron beams it is possible to expose such small areas that the molecular size of the resist can become significant. This can be of the order of 10 nm for large organic molecules. The grain size of a polycrystalline layer to be patterned can also become larger than the size of the desired features. Clearly there are many new materials considerations to be addressed at nanometer dimensions. Another consideration important for the ultrasmall size range is the time it takes to write a pattern by a scanning serial process. This time is inversely related to the size of the pixel. The smaller the electron beam size, the lower the current available for exposure and the longer the exposure time. The resists of highest resolution also require higher exposures. Fortunately the areas involved in exposures for devices are small. The time for writing is insignificant for experimental devices where only a few objects are being written, and the benefits and success of scanned electron beam lithography have been great.

A recently studied alternative approach to scanned electron beam lithography is to use technology related to the scanning tunneling microscope to scan a low energy electron beam in close proximity to the surface. The use of low energy beams allows only thin conducting layers to be modified by the electron beam. There are exciting possibilities for manipulating individual atoms, as demonstrated by IBM researchers. For dimensions larger than this, the flexibility and capabilities of scanned beams as opposed to scanned sources are, as yet, more significant for fabricating devices for research.

### 2.3.4. Ion Beam Lithography

The use of ion beams is diverse, with a great range of ion species and energies. Both collimated beams of large area and scanned focused beams have been applied. The interaction of the ion beam with a solid can be to expose resist, which is most appropriate for high energy and low mass ions. It is also possible to etch away material, to change the chemistry by implantation, to deposit films selectively, or to induce structural changes within a selected area [60].

For ion lithographic printing, the effects of diffraction are negligible, because of the extremely small de Broglie wavelengths. Masks of high contrast are a challenge to fabricate, since the ions are absorbed in all solids. The use of ion channeling masks consisting of absorbers on oriented single crystals and of shadow masks supported by grids has been demonstrated. These masks are usually defined by electron beam lithography. Considerations of ion scattering in solids are similar to those for electrons but are less severe.

Scanned focused beams can be used to draw patterns of any desired shape. The limits of the size of the ion source and the quality of focusing optics have been the factors limiting focused beam resolution. The quality of ion optics is poor compared to light optics and aberrations have limited the size of the spot. Advances with liquid metal field emitters have been significant in producing bright ion sources. Scanned focused systems with liquid metal sources have been demonstrated with beam diameters as small as about 20 nm.

In the exposure of resist by scanned ion beams there is no proximity effect of the type seen for electron beams, and energy is transferred very efficiently to the resist. By appropriate choices of resist processes, it is possible to expose thin imaging layers very efficiently without ion damage to the substrate. Resist features as small as 20 nm have been demonstrated by exposure using focused systems with liquid metal ion sources. Direct ion milling with scanned focused beam or chemically assisted ion milling processes can be used to etch materials directly with impressive resolution approaching the size of the beam. However, the rates achieved limit this approach to removal of small volumes of material.

By implantation-enhanced disordering within selected areas, lateral quantum structures have been created in GaAs–AlGaAs heterostructures. These techniques allow for lateral modulation of the composition and the bandgap, without exposing surfaces.

## 2.4. Envelope Function Approximation

In this section we shall deal with the determination of eigenstates in the low-dimensional systems. The emphasis will be focused on a simple description of these eigenstates.

First, we shall present the assumptions used to derive the envelope function scheme. The reader will perceive that when the  $\vec{k}$  wavevector of carrier is zero, the algebra is relatively easy. Let see, in general way, what the method fundamentals are. The description is based on the dispersion relations of the host materials.

Remember that the electronic state in the periodic field is described by a Bloch function,

$$\phi_{\vec{k}n}(\vec{r}) = \exp(i\vec{k} \cdot \vec{r})u_{\vec{k}n}(\vec{r}) \quad (3)$$

which is periodic in the “ $\vec{k}$ ” space,

$$\phi_{\vec{k}n}(\vec{r}) = \phi_{\vec{k}+\vec{g},n}(\vec{r}) \quad (4)$$

where  $\vec{g}$  is a reciprocal lattice vector and  $n$  is the band number. Therefore, this function can be expressed as in a Fourier series in the reciprocal space,

$$\phi_{\vec{k}n}(\vec{r}) = \frac{1}{\sqrt{N}} \sum_{\vec{l}} a_n(\vec{r}, \vec{l}) \exp(i\vec{k} \cdot \vec{l}) \quad (5)$$

where  $\vec{l}$  is a direct lattice vector. The coefficients of this expansion,

$$a_n(\vec{r}, \vec{l}) = \frac{1}{\sqrt{N}} \sum_{\vec{k}} \phi_{\vec{k}n}(\vec{r}) \exp(-i\vec{k} \cdot \vec{l}) \quad (6)$$

are denominated the Wannier functions, They can also be written as

$$a_n(\vec{r}, \vec{l}) = \frac{1}{\sqrt{N}} \sum_{\vec{k}} u_{\vec{k}n}(\vec{r}) \exp[i\vec{k} \cdot (\vec{r} - \vec{l})] \quad (7)$$

Remember that  $N$  is the number of possible values of  $\vec{k}$  for the  $n$ th band in the first Brillouin zone.

One can appreciate that the Wannier functions do not depend on the  $\vec{k}$  wavevector, possessing also the following properties:

1. There are as many Wannier functions as points in the direct lattice and therefore as values of  $\vec{k}$  in the first Brillouin zone.  
Indeed, in Eq. (5) there are as many terms [and consequently many values of  $a_n(\vec{r}, \vec{l})$ ] as different values of  $\vec{l}$  (actually  $N$ ).
2. The Wannier functions are located at the proximity of each  $\vec{l}$  node of the direct lattice.
3. The Wannier functions obey also that

$$a_n(\vec{r}, \vec{l}) = a_n(\vec{r} - \vec{l}) \quad (8)$$

which is almost evident if we take into account the periodicity of  $u_{\vec{k}n}(\vec{r})$  in Eq. (7).

4. The Wannier functions satisfy the relation

$$a_n(\vec{r} - \vec{s}, \vec{l}) = a_n(\vec{r}, \vec{l} + \vec{s}) \quad (9)$$

which is obtained immediately from Eq. (8).

5. The Wannier functions are orthonormalized:

$$\int a_n^*(\vec{r}, \vec{l}') a_n(\vec{r}, \vec{l}) d\vec{r} = \delta_{nn'} \delta_{\vec{l}'\vec{l}} \quad (10)$$

That is,

$$\begin{aligned} \int a_n^*(\vec{r}, \vec{l}') a_n(\vec{r}, \vec{l}) d\vec{r} &= \frac{1}{N} \sum_{\vec{k}'} \sum_{\vec{k}} \exp[-i(\vec{k} \cdot \vec{l} - \vec{k}' \cdot \vec{l}')] \\ &\quad \times \int \phi_{\vec{k}',n'}^*(\vec{r}) \phi_{\vec{k}n}(\vec{r}) d\vec{r} \\ &= \frac{1}{N} \delta_{nn'} \sum_{\vec{k}} \exp[-i\vec{k} \cdot (\vec{l} - \vec{l}')] \\ &= \delta_{nn'} \delta_{\vec{l}'\vec{l}} \end{aligned} \quad (11)$$

### 2.4.1. Effective Hamiltonian

We will now look for the solution of the nonstationary Schrödinger equation for one electron in the crystal, under an external potential; that is,

$$\{\widehat{H} + \widehat{U}\} \psi(\vec{r}, t) = i\hbar \frac{\partial \psi(\vec{r}, t)}{\partial t} \quad (12)$$

where  $\widehat{H}$  is the Hamiltonian of the electron in the periodic field of crystal and  $\widehat{U}$  is the perturbation potential associated with the external field.

Let us look for a solution of the form

$$\psi(\vec{r}, t) = \sum_n \sum_{\vec{l}} f_n(\vec{l}, t) a_n(\vec{r}, \vec{l}) \quad (13)$$

where  $f_n(\vec{l}, t)$  is denominated envelope function of the  $n$ th band. Notice that the solution involves all the bands.

Substituting the Eq. (13) in (12), after multiplying by  $a_n^*(\vec{r} - \vec{l}')$  and integrating, we get

$$\begin{aligned} \sum_n \sum_{\vec{l}} \int a_n^*(\vec{r} - \vec{l}') [\widehat{H} + \widehat{U}] a_n(\vec{r} - \vec{l}) f_n(\vec{l}, t) d\vec{r} \\ = i\hbar \sum_n \sum_{\vec{l}} \frac{\partial f_n(\vec{l}, t)}{\partial t} \int a_n^*(\vec{r} - \vec{l}') a_n(\vec{r} - \vec{l}) d\vec{r} \end{aligned} \quad (14)$$

Considering the normalization condition of the Wannier functions and making the sum in the right side of the equation we get

$$\sum_n \sum_{\vec{l}} f_n(\vec{l}, t) \int a_n^*(\vec{r} - \vec{l}') [\widehat{H} + \widehat{U}] a_n(\vec{r} - \vec{l}) d\vec{r} = i\hbar \frac{\partial f_n(\vec{l}', t)}{\partial t} \quad (15)$$

Remembering that for the nonperturbed electron

$$\widehat{H} \phi_{\vec{k}n}(\vec{r}) = \varepsilon_n(\vec{k}) \phi_{\vec{k}n}(\vec{r}) \quad (16)$$

we apply the  $\widehat{H}$  operator to the Wannier functions [Eq. (6)] and taking into account Eq. (5) we get

$$\begin{aligned} \widehat{H} a_n(\vec{r} - \vec{l}) &= \frac{1}{\sqrt{N}} \sum_{\vec{k}} \varepsilon_n(\vec{k}) \phi_{\vec{k}n}(\vec{r}) \exp(-i\vec{k} \cdot \vec{l}) \\ &= \frac{1}{N} \sum_{\vec{k}} \varepsilon_n(\vec{k}) \exp(-i\vec{k} \cdot \vec{l}) \\ &\quad \times \sum_{\vec{l}'} a_n(\vec{r} - \vec{l}') \exp(i\vec{k} \cdot \vec{l}') \end{aligned}$$

$$\begin{aligned}
&= \frac{1}{N} \sum_{\vec{l}} a_n(\vec{r} - \vec{l}) \sum_{\vec{k}} \varepsilon_n(\vec{k}) \exp[i\vec{k} \cdot (\vec{l} - \vec{l}')] \\
&= \sum_{\vec{l}} \varepsilon_{n, \vec{l} - \vec{l}'} a_n(\vec{r} - \vec{l}') \quad (17)
\end{aligned}$$

where we have introduced

$$\varepsilon_{n, \vec{l} - \vec{l}'} = \frac{1}{N} \sum_{\vec{k}} \varepsilon_n(\vec{k}) \exp[-\vec{k} \cdot (\vec{l} - \vec{l}')] \quad (18)$$

that is, the Fourier transform of the energy in the  $\vec{k}$  space that shows the overlap integral of  $\hat{H}$  between two Wannier functions in  $\vec{l}$  and  $\vec{l}'$  for the same band. That is,

$$\begin{aligned}
\int a_n^*(\vec{r} - \vec{l}') \hat{H} a_n(\vec{r} - \vec{l}) d\vec{r} &= \sum_{\vec{l}} \varepsilon_{n, \vec{l} - \vec{l}'} \int a_n^*(\vec{r} - \vec{l}') a_n(\vec{r} - \vec{l}) d\vec{r} \\
&= \sum_{\vec{l}} \varepsilon_{n, \vec{l} - \vec{l}'} \delta_{nn'} \delta_{\vec{l}\vec{l}'} = \varepsilon_{n, \vec{l} - \vec{l}'} \delta_{nn'} \quad (19)
\end{aligned}$$

Substituting (19) in (15), we obtain

$$\sum_n \sum_{\vec{l}} \{ \delta_{nn'} \varepsilon_{n, \vec{l} - \vec{l}'} + U_{nn'}(\vec{l}, \vec{l}') \} f_n(\vec{l}, t) = i\hbar \frac{\partial f_{n'}(\vec{l}', t)}{\partial t} \quad (20)$$

where

$$U_{nn'}(\vec{l}, \vec{l}') = \int a_n^*(\vec{r} - \vec{l}') \hat{U} a_n(\vec{r} - \vec{l}) d\vec{r} \quad (21)$$

is the matrix element of the perturbation potential.

Considering that the Fourier series for energy, in the  $\vec{k}$  space, is

$$\varepsilon_n(\vec{k}) = \sum_{\vec{l}} \varepsilon_{n\vec{l}} \exp(i\vec{k} \cdot \vec{l}) \quad (22)$$

where the  $\varepsilon_{n\vec{l}}$  coefficients are given by Eq. (18), and considering that

$$\vec{k} \rightarrow -i\nabla \quad (23)$$

we can get the following product:

$$\varepsilon_n(\vec{k}) f(\vec{r}) = \sum_{\vec{l}} \varepsilon_{n\vec{l}} \exp[i(-i\nabla) \cdot \vec{l}] f(\vec{r}) = \sum_{\vec{l}} \varepsilon_{n\vec{l}} \exp(\vec{l} \cdot \nabla) f(\vec{r}) \quad (24)$$

But

$$\exp(\vec{l} \cdot \nabla) = 1 + \vec{l} \cdot \nabla + \frac{1}{2} (\vec{l} \cdot \nabla)^2 \quad (25)$$

Then

$$\begin{aligned}
\varepsilon_n(-i\nabla) f(\vec{r}) &= \sum_{\vec{l}} \varepsilon_{n\vec{l}} \left\{ f(\vec{r}) + \vec{l} \cdot \nabla f(\vec{r}) + \frac{1}{2} \vec{l}^2 \nabla^2 f(\vec{r}) + \dots \right\} \\
&= \sum_{\vec{l}} \varepsilon_{n\vec{l}} f(\vec{r} + \vec{l}) \quad (26)
\end{aligned}$$

where we have taken into account that the term in curls is the Taylor series for the function  $f(\vec{r} + \vec{l})$ .

Using Eq. (26), we can get

$$\begin{aligned}
\sum_{\vec{l}} \varepsilon_{n', \vec{l} - \vec{l}'} f_{n'}(\vec{l}, t) &= \sum_{\vec{l}} \varepsilon_{n', \vec{l} - \vec{l}'} f_{n'}(\vec{l}' + \vec{l} - \vec{l}', t) \\
&= \varepsilon_{n'}(-i\nabla) f_{n'}(\vec{r}, t) |_{\vec{r}=\vec{l}'} \quad (27)
\end{aligned}$$

Then, we can write Eq. (20) as follows:

$$\begin{aligned}
&\left[ \varepsilon_{n'}(-i\nabla) f_{n'}(\vec{r}, t) - i\hbar \frac{\partial f_{n'}(\vec{r}, t)}{\partial t} \right]_{\vec{r}=\vec{l}'} \\
&+ \sum_{n'} \sum_{\vec{l}} U_{nn'}(\vec{l}, \vec{l}') f_n(\vec{l}, t) = 0 \quad (28)
\end{aligned}$$

This is the expression for the envelope function, also called the Schrödinger equation in the Wannier representation.

Suppose that the electron moves in only one band. This means that the external potential is weak enough in order to not induce interband transitions; therefore

$$U_{nn'}(\vec{l}, \vec{l}') = \delta_{nn'} U_{nn}(\vec{l}, \vec{l}') \quad (29)$$

We will also consider that the potential varies slowly with the position; that is,

$$a_L \frac{\Delta U}{U} \ll 1 \quad (30)$$

$a_L$  being the lattice constant. Then,

$$U_{nn}(\vec{l}, \vec{l}') = U(\vec{r}, t) \delta_{\vec{l}\vec{l}'} \quad (31)$$

where we have taken into account Eqs. (10) and (21).

Introducing

$$U_{nn}(\vec{l}, \vec{l}') = U(\vec{r}, t) |_{\vec{r}=\vec{l}'} \quad (32)$$

and substituting Eqs. (29) and (31) in Eq. (28) we obtain

$$\left[ \varepsilon_n(-i\nabla) + U(\vec{r}, t) - i\hbar \frac{\partial}{\partial t} \right] f_n(\vec{r}, t) = 0 \quad (33)$$

where it is clear that  $\vec{r} = \vec{l}'$ .  $f_n(\vec{r}, t)$  is formally tried as a continuous function that varies slowly with the position around  $\vec{l}'$  [according to Eq. (30)].

Indeed, let us compare Eq. (13) with Eq. (5) [considering Eq. (8)].

If a weak external field, which varies slowly in distances of the order of lattice constant, is applied, the electron wavefunction in a determined band is expressed as [according to Eq. (13)]

$$\phi_{\vec{k}n}(\vec{r}, t) = \sum_{\vec{l}} a_n(\vec{r} - \vec{l}) f_n(\vec{l}, t) \quad (34)$$

where  $f_n(\vec{l}, t)$  is defined from (33). We have considered that the following relation must be satisfied:

$$f_n(\vec{r}, t) |_{\vec{r}=\vec{l}} = f(\vec{l}, t) \quad (35)$$

and where we formally have passed from the discrete variable  $l$  to the continuous one  $\vec{r}$ , which is acceptable if  $f_n(\vec{l}, t)$  varies slowly in distances of the order of the lattice constant, around the  $\vec{l}$  node.

In absence of external field [ $U(\vec{r}, t) = 0$ ], we simply obtain

$$f_n^0(\vec{l}, t) = \exp\left[i\left(\vec{k} \cdot \vec{l} - \frac{\varepsilon(\vec{k})}{\hbar} t\right)\right] \quad (36)$$

which, if is substituted in Eq. (34), leads to the equation of the stationary states.

Notice that instead of the original Eq. (12), now we have a Schrödinger equation for the envelope function, in which the  $\widehat{H} + \widehat{U}$  Hamiltonian has been substituted by the effective Hamiltonian

$$\widehat{H}_{ef} = \varepsilon_n(-i\nabla) + \widehat{U} \quad (37)$$

that, as one can appreciate, depends on the dispersion relation  $\varepsilon_n(\vec{k})$ .

Thus, the envelope function can be understood like the effective wavefunction for the electron in the crystal.

Fortunately, in most of physical phenomena occurring in semiconductors and metals, the participating electrons are those situated in the bottom or the top of the bands (this is, in their extremes). For these electrons it is convenient to introduce the effective mass and the effective Hamiltonian, which can be written as follows:

$$\widehat{H}_{ef} = -\left[\frac{\hbar^2}{m_{nx}^*} \frac{\partial^2}{\partial x^2} + \frac{\hbar^2}{m_{ny}^*} \frac{\partial^2}{\partial y^2} + \frac{\hbar^2}{m_{nz}^*} \frac{\partial^2}{\partial z^2}\right] + \widehat{U} \quad (38)$$

In the isotropic crystal case, the effective masses are equal in any direction and Eq. (38) is rewritten as

$$\widehat{H}_{ef} = -\frac{\hbar^2 \nabla^2}{2m_n^*} + \widehat{U} \quad (39)$$

where  $m_n^*$  is the effective mass of the  $n$  band.

In this case we say that the band is parabolic since the dispersion relation is given by

$$\varepsilon_n(\vec{k}) = \frac{\hbar^2 k^2}{2m_n^*} \quad (40)$$

which is, besides, isotropic.

So for a constant potential (in the time) one can write the effective Schrödinger equation for a stationary state as

$$\left\{ -\frac{\hbar^2}{2} \left[ \frac{1}{m_{nx}^*} \frac{\partial^2}{\partial x^2} + \frac{1}{m_{ny}^*} \frac{\partial^2}{\partial y^2} + \frac{1}{m_{nz}^*} \frac{\partial^2}{\partial z^2} \right] + \widehat{U}(\vec{r}) \right\} f_n(\vec{r}) = \varepsilon f_n(\vec{r}) \quad (41)$$

which is widely used.

This method is known as the effective mass approximation.

## 2.5. Envelope Function Description of Quasi-Particle States for Nanostructured Systems

The envelope function model is particularly adequate to study quasi-particle properties of low-dimensional semiconductor structures. This is a dynamic method for the determination of energy bands of particles in solid state physics, and the nanostructures are considered dynamic systems since they are always under the action of either a barrier potential or interface potential. The envelope function scheme and the effective mass approximation were clearly discussed, for first time, by Bastard [61, 62].

In order to obtain the nanostructure energy states, in the envelope function scheme, our problem will be to find the boundary conditions which the slowly varying part of the nanostructure wavefunctions must fulfill at the heterointerfaces.

Other approaches to the nanostructure eigenenergies have been proposed which are more microscopic in essence than the envelope function description. The tight-binding model is nowadays successfully used for nanostructures of any size, although it may have difficulties in handling self-consistent calculations, which arise when charges are present in the nanostructures. Another microscopic approach is the pseudo-potential formalism, which is very successful for the bulk materials. The advantage of these microscopic approaches is their capacity to handle any nanostructure energy levels (i.e. those close to or far from the  $\Gamma$  edge). This occurs because these models reproduce the whole bulk dispersion relations. The envelope function approximation has no such generality. Basically, it is restricted to the vicinity of the high-symmetry points in the host's Brillouin zone ( $\Gamma, X, L$ ). However, we feel that it is invaluable due to its simplicity and versatility. It often leads to analytical results and leaves the user with the feeling that he can trace back, in a relatively transparent way, the physical origin of the numerical results. Besides, most of the nanostructures energy levels relevant to actual devices are relatively close to a high symmetry point in the host's Brillouin zone.

In the following we shall assume that A and B materials constituting the nanostructure are perfectly lattice matched and they crystallize with the same crystallographic structure. In order to apply the envelope function model two key assumptions are made:

- (1) Inside each material the wavefunction is expanded on the Wannier functions (with  $\vec{l} = 0$ ) of the edges under consideration

$$\psi(\vec{r}) = \sum_n f_n^A(\vec{r}) u_{n, \vec{k}_0}^A(\vec{r}) \quad (42)$$

if  $\vec{r}$  corresponds to an A material, and

$$\psi(\vec{r}) = \sum_n f_n^B(\vec{r}) u_{n, \vec{k}_0}^B(\vec{r}) \quad (43)$$

if  $\vec{r}$  corresponds to a B material, where  $\vec{k}_0$  is the point in the Brillouin zone around which the nanostructure states are built. The summation over  $n$  runs over as many edges as are included in the analysis.

- (2) The periodic parts of the Bloch functions are assumed to be the same in each kind of material, which constitutes the nanostructure

$$u_{n,\vec{k}_0}^A(\vec{r}) \equiv u_{n,\vec{k}_0}^B(\vec{r}) \quad (44)$$

Thus our nanostructure wavefunction will be written as

$$\psi(\vec{r}) = \sum_n f_n^{A,B}(\vec{r}) u_{n,\vec{k}_0}(r) \quad (45)$$

and our objective will be to determine  $f_n^{A,B}(\vec{r})$ . The envelope function  $f_n^{A,B}(\vec{r})$  depends of the kind of low-dimensional system.

### 2.5.1. Quasi-Two-Dimensional System

The quasi-two-dimensional systems are formed by multiple heterostructures such as quantum wells, multiple quantum wells, and superlattices. The envelope function in this case is

$$f_n^{A,B}(\vec{r}_\perp, z) = \frac{1}{\sqrt{S}} \exp(i\vec{k}_\perp \cdot \vec{r}_\perp) \chi_n^{A,B}(z) \quad (46)$$

where  $S$  is the sample area and  $\vec{k}_\perp = (k_x, k_y)$  is a two-dimensional wavevector which is the same in the A and B layers in order to preserve translational invariance in plane  $(x, y)$ .

Although  $\vec{k}_\perp$  could theoretically span the whole in-plane section of the host's Brillouin zone, it is in practice seldom larger than  $\approx 1/10$  of its size.

We shall also assume that for all  $n$ ,  $\chi_n^{A,B}(z)$  varies slowly at the scale of the host's unit cell. Thus the heterostructure wavefunction  $\psi(\vec{r})$  is a sum of the products of rapidly varying functions.

The heterostructure Hamiltonian can be written in the form

$$\hat{H} = \frac{\hat{p}_x^2}{2m_x^*} + \frac{\hat{p}_y^2}{2m_y^*} + \frac{\hat{p}_z^2}{2m_z^*} + V_A(\vec{r})Y_A + V_B(\vec{r})Y_B \quad (47)$$

where  $Y_A(Y_B)$  are step functions which are unity if  $\vec{r}$  corresponds to an A layer (to a B layer) and  $V_A(V_B)$  is the potential in the A(B) layer.

The envelope function in the  $z$  direction,  $\chi_n(z)$ , of an A/B layer is the solution of the Schrödinger equation

$$\left\{ -\frac{\hbar^2}{2m_{nz}^*} \frac{d^2}{dz^2} + V_n(z) \right\} \chi_n(z) = \varepsilon_n \chi_n(z) \quad (48)$$

where  $V_n(z)$  is the heterostructure potential determined by the band discontinuity:  $m_{nz}^* \equiv m_n^*(z) = m_{n,A}^*(m_{n,B}^*)$  and  $V_n(z) = 0$  in the A(B) layer.

Let us see the general case of a superlattice. In a given A/B superlattice there is a new periodicity along the growth direction  $z$ . The SL period  $d$  (sum of the layer thickness of the A and B layers,  $d_A + d_B$ ) is longer than the lattice constants of the constituents, so that a new mini-Brillouin zone is formed in the wavevector range of  $-\pi/d \leq k_z \leq \pi/d$ . The mini-Brillouin zone formation results in generation of miniband structures in the conduction and valence bands.

We consider the miniband structures of the  $\Gamma_6$  conduction band and the  $\Gamma_8$  valence band (heavy hole,  $|J, M_J\rangle = |3/2, \pm 3/2\rangle$  and light hole,  $|3/2, \pm 1/2\rangle$ ). The total wavefunction in each layer can be written in the form

$$\psi_{\vec{k}}^{A,B}(r) = \sum_n f_{n,\vec{k}}^{A,B}(\vec{r}) u_{n,\vec{k}=0}(\vec{r}) \quad (49)$$

where we can use the following form of the envelope function:

$$F_{n,\vec{k}}^{A,B}(\vec{r}) = \exp(ik_{n,x}^{A,B}x) \exp(ik_{n,y}^{A,B}y) f_{n,\vec{q}}^{A,B}(z) \quad (50)$$

Then  $f_{n,\vec{q}}^{A,B}(z)$  is the envelope function determined by the SL potential and the effective masses, and  $\vec{q}$  is the SL wavevector parallel to  $z$ . The periodicity of the SL results in the Bloch theorem for the envelope function:

$$f_{n,\vec{q}}^{A,B}(z + md) = \exp(imqd) f_{n,\vec{q}}^{A,B}(z) \quad (51)$$

where  $m$  is integer.

The envelope function of an A/B SL is the solution of the Schrödinger equation

$$\left\{ -\frac{\hbar^2}{2m_n^*(z)} \frac{d^2}{dz^2} + V_n(z) \right\} f_{n,\vec{q}}(z) = \varepsilon_n f_{n,\vec{q}}(z) \quad (52)$$

where  $V_n(z) = 0(\Delta\varepsilon_n)$  in the A(B) layer. For convenience we will omit the band index  $n$  in the following treatment. The form of the envelope function can be written as

$$f_{\vec{q}}(z) = \begin{cases} f_{\vec{q}}^A(z) = \alpha_{\vec{q}}^A \exp(ik_A z) + \beta_{\vec{q}}^A \\ \quad \times \exp(-ik_A z) & \text{in the A layer} \\ f_{\vec{q}}^B(z) = \alpha_{\vec{q}}^B \exp(ik_B z) + \beta_{\vec{q}}^B \\ \quad \times \exp(-ik_B z) & \text{in the B layer} \end{cases} \quad (53)$$

$$k_A = \sqrt{2m_A^* \varepsilon / \hbar} \quad k_B = \sqrt{2m_B^* (\varepsilon - \Delta\varepsilon) / \hbar} \quad (54)$$

Considering the continuity of the probability density,  $|f_{\vec{q}}(z)|^2$ , for a stationary state, we obtain the following boundary condition of the envelope function at the A/B interface for  $(z_A - z_B) \rightarrow 0$ :

$$\begin{aligned} f_{\vec{q}}^A(z_A) &= f_{\vec{q}}^B(z_B) \quad \text{and} \\ \frac{1}{m_A^*} \frac{df_{\vec{q}}^A(z_A)}{dz} &= \frac{1}{m_B^*} \frac{df_{\vec{q}}^B(z_B)}{dz} \end{aligned} \quad (55)$$

Finally, the miniband dispersion relation, which is similar to the well known Kronig-Penney relation, is given by

$$\begin{aligned} \cos(qd) &= \cos(k_A d_A) \cos(k_B d_B) \\ &- \frac{1}{2} \left( \frac{k_A m_B^*}{k_B m_A^*} + \frac{k_B m_A^*}{k_A m_B^*} \right) \sin(k_A d_A) \sin(k_B d_B) \end{aligned} \quad (56)$$

This equation has been widely used to calculate the miniband energies.

Figure 6 shows (a) the potential structure and the envelope function profiles of the electron and heavy hole in a



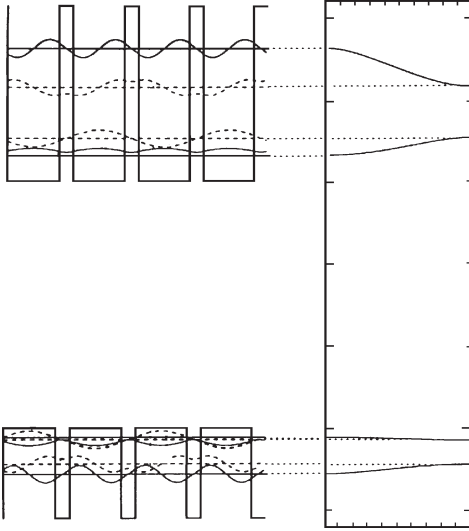


**Figure 6.** Potential structure and the envelope function profiles in superlattice. Reprinted with permission from [205], J. L. Marín et al., in “Handbook of Advanced Electronic and Photonic Materials and Devices” (H. S. Nalwa, Ed.). Academic Press, San Diego, 2001. © 2001, Academic Press.

GaAs(3.2 nm)/AlAs(0.9 nm) SL and (b) the dispersion relations of the electron and heavy hole minibands, calculated using Eq. (56). In Figure 6a, the solid and dashed lines indicate the envelope functions at the mini-Brillouin-zone center ( $q = 0$ ,  $\Gamma$  point) and the mini-Brillouin-zone edge ( $q = \pi/d$ ,  $\pi$  point), respectively. In this calculation, the following effective-mass parameters are used [63]:  $m_e^* = 0.0665m_0$ ,  $m_{hh}^* = 0.34m_0$ , and  $m_{lh}^* = 0.117m_0$  for the electron, heavy hole, and light hole GaAs, and  $m_e^* = 0.15m_0$ ,  $m_{hh}^* = 0.4m_0$ , and  $m_{lh}^* = 0.18m_0$  for AlAs, where  $m_0$  is the free-electron mass. The miniband dispersions are tailored by changing the layer thickness, potential height, and effective masses, which are structural parameters in crystal growth. Figure 7 shows the  $n = 1$  and  $n = 2$  electron miniband of the energies at  $\Gamma$  and  $\pi$  points in a GaAs(3.2 nm)/AlAs( $d_B$  nm) SL as a function of the AlAs layer thickness. This figure exhibits a typical example of the miniband tailoring. The miniband width increases with the decrease of the AlAs (barrier) thickness, which results from the increase of the coupling strength of wavefunctions because of the increase of the tunneling probability. In the case of the disappearance of the miniband width, the electronic state corresponds to a quasi-two-dimensional state in an isolated quantum well (QW).

The  $z$  dependence of the effective mass means, in principle, that it is different in different layers but in general may vary even in a given medium if no abrupt interfaces are considered. Then, the kinetic energy term in Eq. (52) should be substituted by the more general Ben Daniel and Duke [64] hermitian form

$$-\frac{\hbar^2}{2} \frac{\partial}{\partial z} \frac{1}{m^*(z)} \frac{\partial}{\partial z} \quad (57)$$

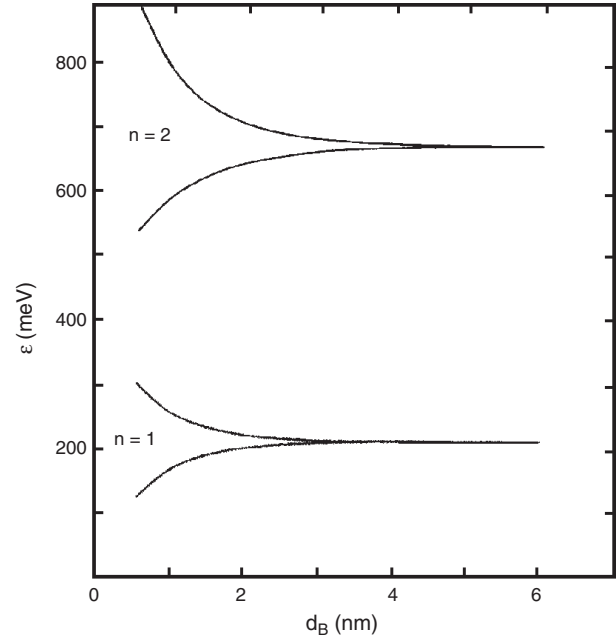


**Figure 7.** Electron miniband energies at  $\Gamma$  and  $\pi$  points in a superlattice. Reprinted with permission from [205], J. L. Marín et al., in “Handbook of Advanced Electronic and Photonic Materials and Devices” (H. S. Nalwa, Ed.). Academic Press, San Diego, 2001. © 2001, Academic Press.

Finally, Eq. (52) for the envelope function can be generalized as

$$\left\{ -\frac{\hbar^2}{2} \frac{\partial}{\partial z} \frac{1}{m^*(z)} \frac{\partial}{\partial z} + V(z) \right\} \chi(z) = \varepsilon \chi(z) \quad (58)$$

### 2.5.2. Quasi-One-Dimensional System

Let us consider a quasi-one-dimensional system with finite length and width formed by A and B materials; in general, the wavefunction can be written as

$$\psi(\vec{r}) = \sum_n f_n^{A,B}(\vec{r}) u_{n,\vec{k}_0}(r) \quad (59)$$

We will also consider that the quasi-one-dimensional system is a quantum well wire of rectangular or circular cross-section, where the  $z$  direction coincides with the free direction of the carrier motion; that is, the confinement direction is in the cross section.

The envelope function for both cases can be written as

$$f_n^{A,B}(\vec{r}) = \exp(ik_z z) \chi_n^{A,B}(\vec{r}_\perp) \quad (60)$$

where  $\chi_n^{A,B}(\vec{r}_\perp)$  depends on the cross section symmetry,

$$\chi_n^{A,B}(\vec{r}_\perp) = \begin{cases} X_{n,l}^{A,B}(x) Y_{n,m}^{A,B}(y) & \text{rectangular quantum} \\ & \text{well wire} \\ \exp(il\theta) R_{n,l}^{A,B}(r) & \text{circular quantum} \\ & \text{well wire} \end{cases} \quad (61)$$

where  $l, m$  are integer numbers and  $(r, \theta, z)$  are the cylindrical coordinates. For convenience we will omit the band index  $n$  in the following treatment.

The differential equations for the envelope functions are now

$$\begin{cases} -\frac{\hbar^2}{2m^*(x)} \frac{d^2}{dx^2} + V_b^{A,B}(x) \} X_l^{A,B}(x) = \varepsilon_l X_l^{A,B}(x) \\ -\frac{\hbar^2}{2m^*(y)} \frac{d^2}{dy^2} + V_b^{A,B}(y) \} Y_m^{A,B}(y) = \varepsilon_m Y_m^{A,B}(y) \end{cases} \quad (62)$$

for rectangular symmetry. In this case the barrier potential is

$$V_b^{A,B}(\vec{r}) = \begin{cases} V_b^{A,B}(x) = \begin{cases} 0 & \text{for } 0 < x < a \\ \infty & \text{for } a < x \end{cases} \\ V_b^{A,B}(y) = \begin{cases} 0 & \text{for } 0 < y < b \\ \infty & \text{for } b < y \end{cases} \\ V_b^{A,B}(z) = 0 & \text{for } -L < z < L \end{cases} \quad (63)$$

The rectangular quantum well wire behavior is, according to the  $x$ ,  $y$  directions, as two isolated single quantum wells under the action of an infinite barrier potential, where the boundary conditions are simply  $X_l^{A,B}(a) = 0$  and  $Y_m^{A,B}(b) = 0$ . With this requirement the eigenfunctions are

$$\begin{aligned} X_l^{A,B}(x) &= \sqrt{\frac{2}{a}} \sin \frac{l\pi}{a} x \\ Y_m^{A,B}(y) &= \sqrt{\frac{2}{b}} \sin \frac{m\pi}{b} y \quad l, m = 1, 2, 3, \dots \end{aligned} \quad (64)$$

The energy levels for the  $n$ th band are

$$\varepsilon_{l,m} = \frac{\pi^2 \hbar^2}{2m_A^* a^2} l^2 + \frac{\pi^2 \hbar^2}{2m_B^* b^2} m^2 \quad (65)$$

For circular symmetry the differential equation for the envelope function is

$$\frac{d^2 R_l^{A,B}}{d\rho^2} + \frac{1}{\rho} \frac{dR_l^{A,B}}{d\rho} \pm \left(1 \mp \frac{l^2}{\rho^2}\right) R_l^{A,B} = 0 \quad (66)$$

where

$$\rho = \alpha^{A,B} r \quad \alpha^A = \sqrt{\frac{2m_A^*(r)\varepsilon_l}{\hbar^2}} \quad \alpha^B = \sqrt{\frac{2m_B^*(V_0 - \varepsilon_l)}{\hbar^2}} \quad (67)$$

The upper signs in Eq. (66) correspond to material A (we are considering that the potential  $V_b^A$  is zero) and the lower signs correspond to material B, where the interface potential is  $V_b^B = V_0$ . Equation (66) is the Bessel differential equation (+, -) and modified Bessel differential equation (-, +) respectively.

Integrating Eq. (66) for each material we obtain the Bessel function of the first kind,  $J_l(\alpha^A r)$ , and the modified Bessel function,  $K_l(\alpha^B r)$ , respectively; these functions and their derivatives must satisfy the continuity requirement for  $R_l$  in the  $r = r_0$  interface, where  $r_0$  is confinement circular section radius. That is,

$$\begin{aligned} aJ_l(\alpha^A r_0) &= bK_l(\alpha^B r_0) \quad \text{and} \\ \frac{a}{m_A^*} J_l'(\alpha^A r_0) &= \frac{b}{m_B^*} K_l'(\alpha^B r_0) \end{aligned} \quad (68)$$

where  $a$ ,  $b$  are constants which are determined using the normalization condition for the wavefunction  $\psi(\vec{r})$ . Then we can calculate the energy levels for each  $n$  band solving the following transcendental equation;

$$\frac{J_l'(\alpha^A r_0)}{m_A^* J_l(\alpha^A r_0)} = \frac{K_l'(\alpha^B r_0)}{m_B^* K_l(\alpha^B r_0)} \quad (69)$$

### 2.5.3. Quasi-Zero-Dimensional System

In this case the electron is totally or partially confined in the three spatial directions and since there is no direction for the free movement, the total energy does not depend on any of reciprocal space  $\vec{k}$  wavevector components. Nor can we define, in a mathematical sense, the effective mass as a function of  $\vec{k}$ . However, since the electron still is under the action of the crystalline field, we can use the concept of effective mass as the change of its properties, as well as the effective mass scheme.

Therefore, if we continue with the final result obtained from the envelope function method or the effective mass approximation, the wavefunction can be written as

$$\psi(\vec{r}) = \sum_n f_n^{A,B}(\vec{r}) u_{n,\vec{k}_0}(\vec{r}) \quad (70)$$

where we are assuming that the quasi-zero-dimensional system is a spherical quantum dot formed by two materials A and B, where the potential  $V_0$  is given by

$$V_b^{A,B}(r) = \begin{cases} 0 & 0 \leq r \leq r_0 \quad (\text{A material}) \\ V_0 & r > r_0 \quad (\text{B material}) \end{cases} \quad (71)$$

Taking into account the problem symmetry, it is reasonable to consider the spherical coordinates ( $r$ ,  $\theta$ ,  $\varphi$ ). In these coordinates the Hamiltonian can be written as

$$\hat{H} = -\frac{\hbar^2}{2m_{A,B}^*} \left\{ \frac{\partial^2}{\partial r^2} + \frac{2}{r} \frac{\partial}{\partial r} - \frac{\hat{L}^2}{r^2 \hbar^2} \right\} + V_b^{A,B}(r) \quad (72)$$

where the  $\hat{L}^2$  operator is

$$\hat{L}^2 = \frac{1}{\sin \theta} \left[ \frac{\partial}{\partial \theta} \left( \sin \theta \frac{\partial}{\partial \theta} \right) + \frac{1}{\sin^2 \theta} \frac{\partial^2}{\partial \varphi^2} \right] \quad (73)$$

In this case, the envelope function  $f_n^{A,B}(\vec{r})$  is expressed as a product of functions of  $r$ ,  $\theta$ , and  $\varphi$ ,

$$f_n^{A,B}(\vec{r}) = f_n^{A,B}(r) Y_{l,m}(\theta, \varphi) \quad (74)$$

where  $Y_{l,m}(\theta, \varphi)$  are the spherical harmonics, and  $f_n^{A,B}(r)$  are the new envelope functions that fulfill with the equations

$$\frac{d^2 f_{n,l}^{A,B}}{d\rho^2} + \frac{1}{\rho} \frac{df_{n,l}^{A,B}}{d\rho} \pm \left(1 \mp \frac{l(l+1)}{\rho^2}\right) f_{n,l}^{A,B} = 0 \quad (75)$$

where the new variable  $\rho$  is defined as

$$\begin{aligned} \rho &= \alpha^{A,B} r \quad \alpha^A = \sqrt{\frac{2m_A^*(r)\varepsilon_{n,l}}{\hbar^2}} \\ \alpha^B &= \sqrt{\frac{2m_B^*(V_0 - \varepsilon_{n,l})}{\hbar^2}} \end{aligned} \quad (76)$$

For convenience we will omit the band index  $n$  in the following treatment.

The upper signs correspond to the interior region of quantum dot and lower signs correspond to the exterior. The solutions of these equations are the envelope functions in A and B materials and can be written as

$$f^{A,B}(\vec{r}) = \begin{cases} f_l^A(\rho)Y_{l,m}(\theta, \varphi) = aj_l(\alpha^A r)Y_{l,m}(\theta, \varphi) \\ f_l^B(\rho)Y_{l,m}(\theta, \varphi) = bk_l(\alpha^B r)Y_{l,m}(\theta, \varphi) \end{cases} \quad (77)$$

where  $j_l(\alpha^A r)$  is the spherical Bessel function of the first kind,  $k_l(\alpha^B r)$  is the modified spherical Bessel function of the third kind, and  $a, b$  are constants which are determined with the normalization condition of the wavefunction. The new boundary condition in the  $r = r_0$  interface of quantum dot can be expressed as

$$\begin{aligned} aj_l(\alpha^A r_0) &= bk_l(\alpha^B r_0) \quad \text{and} \\ \frac{a}{m_A^*} j_l'(\alpha^A r_0) &= \frac{b}{m_B^*} k_l'(\alpha^B r_0) \end{aligned} \quad (78)$$

Then, the eigenstates are determined solving the following transcendental equation:

$$\frac{j_l'(\alpha^A r_0)}{m_A^* j_l(\alpha^A r_0)} = \frac{k_l'(\alpha^B r_0)}{m_B^* k_l(\alpha^B r_0)} \quad (79)$$

The energy states  $\varepsilon_{n,l,m}$  of the system are characterized by three quantum numbers, namely, the principal number  $n$ , the orbital number  $l$ , and the magnetic number  $m$ . The orbital quantum number determines the angular momentum value  $\hat{L}$ :

$$\hat{L}^2 = \hbar^2 l(l+1) \quad l = 0, 1, 2, 3 \dots \quad (80)$$

The magnetic quantum number determines the  $\hat{L}_z$  component parallel to the  $z$  axis:

$$\hat{L}_z = \hbar m \quad m = 0, \pm 1, \pm 2, \dots, \pm l \quad (81)$$

Every state with a certain  $l$  value is  $(2l+1)$  degenerate according to  $2l+1$  values of  $m$ . The states corresponding to different  $l$  values are usually denoted as  $s, d, f,$  and  $g$  states and so forth in alphabetical order. For example, states with zero angular momentum ( $l=0$ ) are referred to as  $s$  states, those with  $l=1$  are denoted as  $p$  states, and so on. The parity of states corresponds to the parity of the  $l$  value, because the radial function is not sensitive to inversion ( $r$  remains the same after inversion) and spherical function after inversion transforms as follows:

$$Y_{l,m}(\theta, \varphi) \rightarrow (-1)^l Y_{l,m}(\theta, \varphi) \quad (82)$$

The specific values of energy are determined by the  $V_b^{A,B}(\vec{r})$  function. Consider a simple case corresponding to one spherically symmetric potential well with an infinite barrier; that is,

$$V_b^{A,B}(\vec{r}) = \begin{cases} 0 & \text{for } 0 \leq r \leq r_0 \\ \infty & \text{for } r > r_0 \end{cases} \quad (83)$$

In this case energy values are expressed as

$$\varepsilon_{n,l} = \frac{\hbar^2 X_{n,l}^2}{2m_A^* r_0^2} \quad (84)$$

where  $X_{n,l}$  are roots of the spherical Bessel functions with  $n$  being the number of the root and  $l$  being the order of the function.

This formulation can be adapted to the case of a rectangular quantum box where the envelope function can be written as

$$f_{n,x}^{A,B}(\vec{r}) = X_n^{A,B}(x)Y_n^{A,B}(y)Z_n^{A,B}(z) \quad (85)$$

and thus we obtain three equations in order to calculate the  $X, Y,$  and  $Z$  new envelope functions for each direction,

$$\begin{aligned} \left\{ -\frac{\hbar^2}{2m_{A,B}^*(x)} \frac{d^2 X_n^{A,B}(x)}{dx^2} + V_b^{A,B}(x) \right\} X_n^{A,B}(x) \\ = \varepsilon_{n,x} X_n^{A,B}(x) \end{aligned} \quad (86)$$

$$\begin{aligned} \left\{ -\frac{\hbar^2}{2m_{A,B}^*(y)} \frac{d^2 Y_n^{A,B}(y)}{dy^2} + V_b^{A,B}(y) \right\} Y_n^{A,B}(y) \\ = \varepsilon_{n,y} Y_n^{A,B}(y) \end{aligned} \quad (87)$$

$$\begin{aligned} \left\{ -\frac{\hbar^2}{2m_{A,B}^*(z)} \frac{d^2 Z_n^{A,B}(z)}{dz^2} + V_b^{A,B}(z) \right\} Z_n^{A,B}(z) \\ = \varepsilon_{n,z} Z_n^{A,B}(z) \end{aligned} \quad (88)$$

which represent three uncoupled equations corresponding to three isolated single quantum wells. If we consider that the dimensions of the rectangular quantum box are  $a, b,$  and  $c,$  according to  $x, y,$  and  $z$  directions, respectively, then, taking into account the infinite barrier potential between A and B materials, we obtain the solutions

$$\begin{aligned} X_l^A(x) &= \sqrt{\frac{2}{a}} \sin \frac{l\pi}{a} x & Y_m^A(y) &= \sqrt{\frac{2}{b}} \sin \frac{m\pi}{b} y \\ Z_p^A(z) &= \sqrt{\frac{2}{c}} \sin \frac{p\pi}{c} z \end{aligned} \quad (89)$$

where  $l, m,$  and  $p$  are quantum numbers taking positive nonzero integers.

In this case energy values are expressed as follows:

$$\varepsilon_{l,m,p} = \frac{\pi^2 \hbar^2}{2m_A^*(x)a^2} l^2 + \frac{\pi^2 \hbar^2}{2m_A^*(y)b^2} m^2 + \frac{\pi^2 \hbar^2}{2m_A^*(z)c^2} p^2 \quad (90)$$

The theory of the quasi-particle states used previously to study the nanostructures is suitable for quasi-particles like electrons and holes; however, in order to be used for the excitons we need to make some modifications.

## 2.6. Idealized Confined Systems when Symmetry of the Confinement Region Does Not Have Regular Form and the Schrödinger Equation is Nonseparable

When the Schrödinger equation for a given quantum system is nonseparable in nature, then some approximation techniques must be used to study its solution. In a similar situation for a confined quantum system, the variational method might constitute an economical and physically appealing approach. It has been shown that the variational method is useful for studying this class of systems when their symmetries are compatible with those of the confining boundaries.

We will only consider the application of the variational method in the case of a symmetric quantum system confined by impenetrable potentials, as a simple example of a more general situation.

### 2.6.1. General Description of the Method

For the moment, let us assume that, for a given system, the time-independent Schrödinger equation can be written as

$$\hat{H}\psi_n = E_n\psi_n \quad (91)$$

where  $\hat{H} = -(1/2)\nabla^2 + V(q)$  is the associated Hamiltonian for this system,  $\{q\}$  is the set of coordinates on which  $V$  depends, and  $\hbar = m = 1$ .

An approximate solution of Eq. (91) may be obtained by replacing  $\psi_n$  by a trial wavefunction  $\chi_n$ , which possesses a similar behavior at the “origin” as well as asymptotically at infinity. An estimate of the energy of the system is then obtained by minimizing the functional

$$\int \chi_n^* \hat{H} \chi_n d\tau \quad (92)$$

with the additional restriction that

$$\varepsilon_n = \min \int \chi_n^* \hat{H} \chi_n d\tau = \delta_{n,n'} \quad (93)$$

As is shown in any quantum mechanics textbook, one can find that

$$\varepsilon_n = \min \int \chi_n^* \hat{H} \chi_n d\tau \geq E_n \quad (94)$$

That is, a poor guess of  $\chi_n$  leads to a poor estimate of  $\varepsilon_n$ , which means that we have not properly included our qualitative knowledge of the system under study.

In practical calculations, the functions  $\chi_n$  depend upon the coordinates, say  $\{q_1, q_2, \dots, q_s\}$ , and on a set of unknown parameters  $\{\alpha_1, \alpha_2, \dots, \alpha_k\}$  such that  $\varepsilon_n = \varepsilon_n\{\alpha_1, \alpha_2, \dots, \alpha_k\}$ . In order to determine the set  $\{\alpha_k\}$  one must solve the system of equations

$$\frac{\partial \varepsilon_n}{\partial \alpha_i} = 0 \quad i = 1, 2, \dots, k \quad (95)$$

from which  $\varepsilon_n$  can be readily obtained. In doing this we have  $\varepsilon_n$  and  $\chi_n$  as an approximate energy and wavefunction for the state  $n$ , respectively.

Let us assume a quantum system confined within a domain  $D$ , for which the Hamiltonian can be written as

$$\hat{H} = \hat{H}_0 + V(q) \quad (96)$$

where  $\hat{H}_0$  is the Hamiltonian for the free system, and

$$V(q) = \begin{cases} +\infty & q \notin D \\ 0 & q \in D \end{cases} \quad (97)$$

is the confining potential.

The solution of Eq. (96) must satisfy

$$\psi(q) = 0 \quad q \in \partial D \quad (98)$$

where  $\partial D$  is the boundary of  $D$ .

In order to use the variational method, we must construct a trial wavefunction that satisfies the boundary condition imposed by Eq. (98). This function can be defined as

$$\chi(q) = g(q)\psi_0(q, \alpha) \quad (99)$$

where  $\psi_0(q, \alpha)$  has a structure similar to the solution of the Schrödinger equation for  $\hat{H}_0$ , but the good quantum number(s) that define the energy of the free system is (are) replaced by a parameter (or a set of parameters)  $\alpha$ , because the confining conditions impose new quantization rules.

The function  $g(q)$  must satisfy the boundary condition given by Eq. (98). This technique can be used when the symmetry of the confining potential is compatible with the symmetry of the system under study.

When the latter is not the case, the form of the trial wavefunction given by Eq. (99) must be slightly changed since the symmetry is broken by the confinement potential. However, in spite of the lack of compatibility between both symmetries, the system and confinement domain often are related through a coordinate transformation of the form

$$q = q(q') \quad (100)$$

where  $q'$  are the coordinates of the center of symmetry of  $D$  and  $q$  are the coordinates of the center of symmetry of the system.

Even in the aforementioned case, it is still possible to construct the trial wavefunction as in Eq. (99), except that the coordinates  $q$  of the system under study must be written in terms of the coordinates  $q'$  of  $D$  using the rule given in Eq. (100). Under such conditions the trial wavefunction for this asymmetry situation can be written as

$$\chi(q(q')) = g(q(q'))\psi_0(q(q'), \alpha) \quad (101)$$

Once the latter has been done, the energy functional can be constructed and minimized with respect to  $\alpha$ , as usual.

### 3. PHYSICAL EFFECTS OF IMPURITY STATES AND ATOMIC SYSTEMS CONFINED IN SEMICONDUCTOR NANOSTRUCTURES

In contrast to bulk materials, the nanostructures are characterized by a lack of translational invariance along the confinement direction. Thus, the impurity binding energy explicitly depends on the precise location of the impurity. It is important to know where the impurity atom is placed in the nanostructure, and the binding energy of the donor state associated with impurity atom will depend on whether the impurity atom sits at the center or the axis of the nanostructure.

The second important feature of Coulombic problems in nanostructures is the variation of the impurity binding energy with the characteristic dimension of the well. When the nanostructure confinement dimension (confinement size) decreases, the impurity binding energy increases, as long as the penetration of the unperturbed nanostructure wavefunction in the barrier remains small. This may seem surprising at first sight since we intuitively associate extra kinetic energy with the localization of a particle in a finite region of space. Moreover, it is actually true that the energy of the ground bound state of the impurity increases as the confinement size decreases, when it is measured from some fixed reference. However, the onset of the impurity continuum, which (for donors) coincides with the energy of the nanostructure bound state, also moves up with decreasing confinement size. The binding energy finally increases since, in the bound impurity states, the carrier is kept near the attractive center by nanostructure walls and thus experiences a larger potential energy than in the absence of a nanostructure. On the other hand the onset of the impurity continuum does not benefit from any extra potential energy gain, as the continuum states are hardly affected by the Coulombic potential.

When the Schrödinger equation for a given quantum system is nonseparable in nature, then some approximation techniques must be used to study its solution. In a similar situation for a confined quantum system, the variational method might constitute an economical and physically appealing approach [65]. It has been shown [66] that the variational method is useful for studying this class of systems when their symmetries are compatible with that of the confining boundaries. In general, in the problems related to impurity and atoms confined in the different nanostructures, these considerations are fulfilled.

#### 3.1. Hydrogenic Impurity in Quasi-Two-Dimensional Systems

In Figure 8, we sketched the shape of the impurity wavefunction, keeping the in-plane distance between the carrier and the attractive center  $\rho$  ( $\rho = \sqrt{x^2 + y^2}$ ) equal to zero. Several quantum well thicknesses (upper part of Fig. 8) and several impurity positions in a thick well (lower part of Fig. 8) have been considered. For thick wells ( $L \gg a_B^*$ ) the on-center impurity wavefunction resembles that of the bulk 1s states. On the other hand, the on-edge impurity

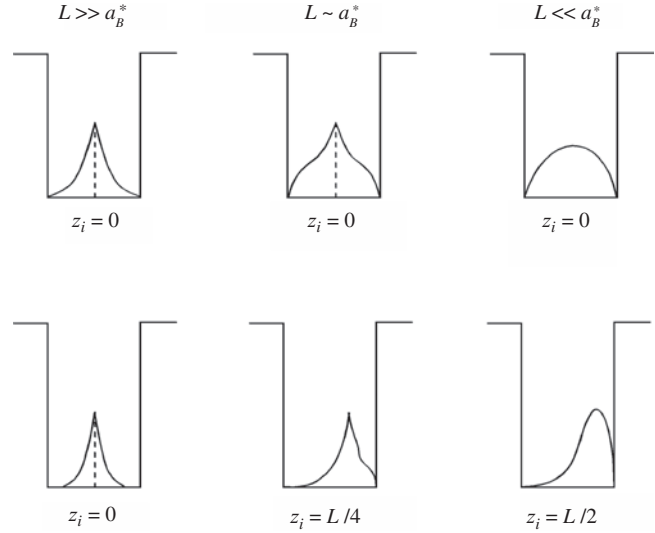


**Figure 8.** Evolution of the shape of the impurity wave function in a quantum well of decreasing well thickness for an on-center impurity (upper part) and with the impurity position in a thick well (lower part).

wavefunction approaches the shape of a  $2p_z$  wavefunction if  $(L/a_B^*) \gg 1$ . This is because the barrier potential forces the impurity wavefunction to almost vanish at  $z = \pm L/2$ . If  $L/a_B^* \ll 1$  and if the barrier height is very large, the electron  $z$  motion becomes forced by the quantum well potential. Thus, along the  $z$  axis the impurity wavefunction looks like the ground state wavefunction of the well  $\chi_1(z)$ .

#### 3.1.1. Approximate Solutions of the Hydrogenic Impurity Problem

In all that follows we will consider donorlike impurities unless otherwise specified. The conduction bands of both host materials of the quantum well are assumed to be isotropic and parabolic in  $k$ . We neglect the effective mass jumps at the interfaces as well as the differences in the relative dielectric constants of the two host materials. The impurity envelope functions are the solutions of the effective Hamiltonian

$$\hat{H} = \hat{H}_0 + V_I = \frac{\hat{p}_z^2}{2m_e^*} + \frac{\hat{p}_x^2 + \hat{p}_y^2}{2m_e^*} + V_0 Y\left(z^2 - \frac{L^2}{4}\right) - \frac{e^2}{\kappa \sqrt{\rho^2 + (z - z_i)^2}} \quad (102)$$

where  $V_0$  is the barrier height and  $Y(x)$  is the step function [ $Y(x) = 1$  if  $x > 0$ ;  $Y(x) = 0$  if  $x < 0$ ]. The impurity position along the growth axis is  $z_i$ . The  $(x, y)$  origin is at the impurity site because all the impurity positions are equivalent in the layer plane;  $\vec{\rho}$  is the projection of the electron position vector in the layer plane [ $\rho(x, y)$ ].

In the absence of the impurity the eigenstates of  $\hat{H}_0$  are separable in  $(x, y)$  and  $z$ ,

$$\hat{H}_0 |v, \vec{k}_\perp\rangle = \left( \varepsilon_v + \frac{\hbar^2 k_\perp^2}{2m_e^*} \right) |v, \vec{k}_\perp\rangle \quad (103)$$



where  $\nu$  labels the quantum well eigenstates (energy  $\varepsilon_\nu$ ), that is, the quantum well bound ( $\varepsilon_\nu < V_0$ ) and unbound states ( $\varepsilon_\nu > V_0$ ) and  $\vec{k}_\perp = (k_x, k_y)$ . Since the  $|\nu, \vec{k}_\perp\rangle$  basis is complete we may always expand the impurity wavefunction  $\psi_{\text{loc}}$  in the form

$$|\psi_{\text{loc}}\rangle = \sum_{\nu, \vec{k}_\perp} c(\nu, \vec{k}_\perp) |\nu, \vec{k}_\perp\rangle \quad (104)$$

The Coulombic potential couples a given subband  $\nu$ , as well as a given vector  $\vec{k}_\perp$  with all others. The intersubband coupling (especially the one with the subbands of the quantum well continuum) is difficult to handle. In a quasi-two-dimensional situation we would like to set  $c(\nu, \vec{k}_\perp) \equiv c_{\nu_0}(\vec{k}_\perp) \delta_{\nu, \nu_0}$ , that is, to neglect intersubband coupling [67, 68]. This procedure is convenient as the impurity wavefunction displays a separable form:

$$\langle \vec{r} | \psi_{\text{loc}} \rangle = \chi_{\nu_0}(z) \varphi(\vec{\rho}) \quad (105)$$

The wavefunction  $\varphi(\vec{\rho})$  is the solution of the two-dimensional Schrödinger equation

$$\left[ \frac{\hat{p}_x^2 + \hat{p}_y^2}{2m_e^*} + V_{\text{eff}}(\rho) \right] \varphi(\vec{\rho}) = (\varepsilon - \varepsilon_{\nu_0}) \varphi(\vec{\rho}) \quad (106)$$

where  $V_{\text{eff}}$  is the effective in-plane Coulombic potential,

$$V_{\text{eff}}(\rho) = \frac{-e^2}{\kappa} \int_{-\infty}^{+\infty} dz \chi_{\nu_0}^2(z) \frac{1}{\sqrt{\rho^2 + (z - z_i)^2}} \quad (107)$$

which is  $\nu_0$  and  $z_i$  dependent. A solution of Eq. (106) can be sought variationally, the simplest choice for the ground state being the nodeless one-parameter trial wavefunction

$$\varphi_0(\rho) = \frac{1}{\lambda} \sqrt{\frac{2}{\pi}} \exp(-\rho/\lambda) \quad (108)$$

where  $\lambda$  is the variational parameter. The bound state energy is obtained through the minimization of the function

$$\begin{aligned} \varepsilon_{\nu_0}(z_i, \lambda) &= \frac{\hbar^2}{2m_e^* \lambda^2} - \frac{2e^2}{\kappa \lambda} \int_0^\infty x e^{-x} \\ &\times \int_{-\infty}^{+\infty} \frac{dz \chi_{\nu_0}^2(z)}{\sqrt{x^2 + \frac{4}{\lambda^2} (z - z_i)^2}} dx + \varepsilon_{\nu_0} \end{aligned} \quad (109)$$

and the binding energy is

$$\varepsilon_{b\nu_0}(z_i) = \varepsilon_{\nu_0} - \text{Min}_\lambda \varepsilon_{\nu_0}(z_i, \lambda) \quad (110)$$

One should be aware that the decoupling procedure [Eqs. (105)–(110)] runs into difficulties in the limits  $L \rightarrow \infty$  and  $L \rightarrow 0$ . In the former case the energy difference  $\varepsilon_{\nu_0+1} - \varepsilon_{\nu_0}$  becomes very small and many subbands become admixed by the Coulombic potential. Clearly, for infinite  $L$  one cannot describe the bulk  $1s$  hydrogenic bound state by a separable wavefunction. In the latter case ( $L \rightarrow 0$ ) one finds similar problems due to the energy proximity between the ground quantum well subband  $\varepsilon_1$  and the top of the well  $V_0$ . Consequently  $\chi_1(z)$  leaks more and more heavily in the

barrier. At  $L = 0$  the only sensible result is to find a  $1s$  bulk hydrogenic wavefunction corresponding to the barrier-acting material (in this model the latter has a binding energy equal to  $R_y^*$ ). Once again this state cannot have a wavefunction like that of Eq. (105). If  $V_0$  is infinite the result at  $L = 0$  is qualitatively different. The quantum well only has bound levels whose energy separation increases like  $L^{-2}$  when  $L$  decreases. The smaller the well thickness, the better the separable wavefunction becomes. At  $L = 0$ , one obtains a true two-dimensional hydrogenic problem whose binding energy is  $4R_y^*$  whereas  $\lambda = a_B^*/2$ .

To circumvent the previous difficulties and obtain the exact limits at  $L = 0$  and  $L = \infty$  for any  $V_0$  one may use [69–71]

$$\psi_{\text{loc}}(\vec{r}) = N \chi_1(z) \exp\left[-\frac{1}{\lambda} \sqrt{\rho^2 + (z - z_i)^2}\right] \quad (111)$$

where  $N$  is a normalization constant,  $\lambda$  is the variational parameter, and attention is focused on the ground bound state attached to the ground quantum well subband  $\varepsilon_1$ . Calculations are less simple than with the separable wavefunction [Eq. (105)]. Comparing the binding energy deduced from Eqs. (105)–(111) one finds, for infinite  $V_0$ , that the separable wavefunction gives almost the same results as the nonseparable wavefunction if  $L/a_B^* \leq 3$ . This is the range where for most materials the quantum size effects are important.

Other variational calculations have been proposed [72, 73]. For example, instead of using a nonlinear variational parameter one uses a finite basis set of fixed wavefunctions (often Gaussian ones) in which  $\hat{H}$  is numerically diagonalized. The numerical results obtained by using a single nonlinear variational parameter compare favorably with these very accurate treatments.

### 3.1.2. Results for the Ground Impurity State Attached to the Ground Subband

Figures 9 to 11 give a sample of some calculated results for the ground impurity state attached to the ground subband. Two parameters control the binding energy:

- (i) Thickness dependence of the impurity binding energy: the dimensionless ratio  $L/a_B^*$  indicates the amount of two-dimensionality of the impurity state. If  $L/a_B^* \geq 3$  or  $L/a_B^* \leq 0.2$  and  $V_0 \approx 3$  eV in GaAs–Ga<sub>1-x</sub>Al<sub>x</sub>As the problem is almost three-dimensional. This is either because the subbands are too close ( $L/a_B^* \geq 3$ ) or because the quantum well continuum is too close ( $L/a_B^* \leq 0.2$ ). The on-center donor binding energy increases from  $R_y^*(L \rightarrow \infty)$  to reach a maximum ( $L/a_B^* \leq 1$ ) whose exact  $L$  location and amplitude depend on  $V_b$ . Finally it decreases to the value  $R_y^*$  at  $L = 0$  [72, 73]. If  $V_0$  is infinite, the maximum is only reached at  $L = 0$  and has a value of  $4R_y^*$  [69].
- (ii) Position dependence of the impurity binding energy: the impurity binding energy monotonically decreases when the impurity location  $z_i$  moves from the center to the edge of the well and finally deep into the

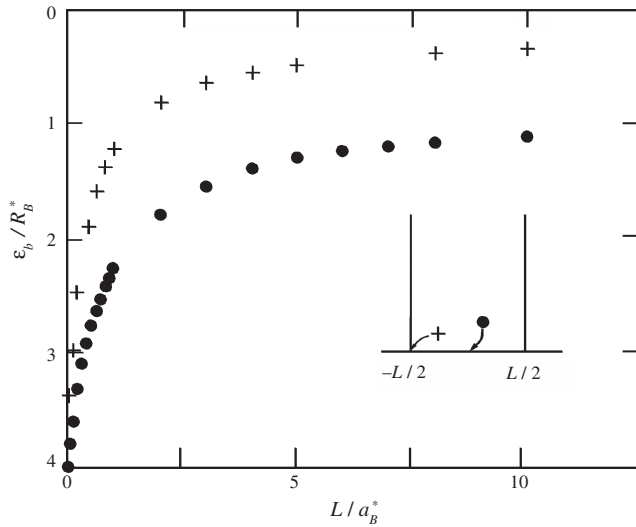


**Figure 9.** Calculated dependence of the on-edge (crosses) and on-center (circles) hydrogenic donor binding energy versus the well thickness  $L$  in a quantum well with an infinite barrier height. Reprinted with permission from [205], J. L. Marín et al., in “Handbook of Advanced Electronic and Photonic Materials and Devices” (H. S. Nalwa, Ed.). Academic Press, San Diego, 2001. © 2001, Academic Press.

barrier. In Figure 12, it is shown that this decrease is rather slow for  $z_i > L/2$ ; for instance, a donor placed 150 Å away from a GaAs–Ga<sub>0.7As</sub>Al<sub>0.3</sub>As quantum well ( $L = 94.8$  Å) still binds a state by  $\approx 0.5R_y^*$  which is  $\approx 2.5$  meV [70].

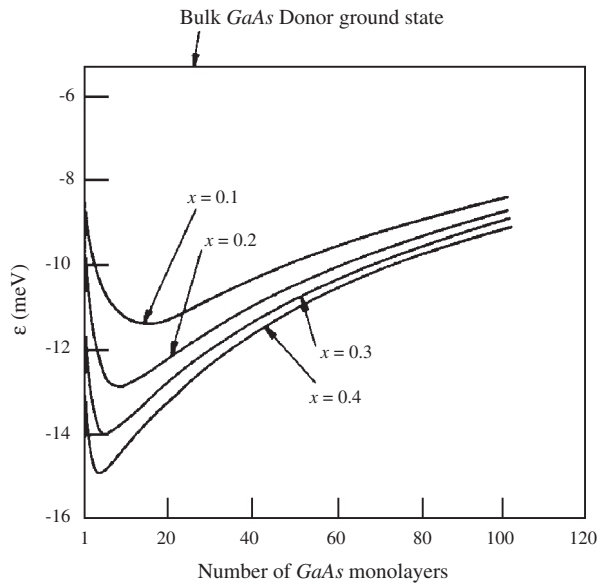


**Figure 10.** Dependence of on-center hydrogenic donor binding energy in GaAs–Ga<sub>1-x</sub>Al<sub>x</sub>As quantum wells versus the GaAs slab thickness  $L$ .  $V_b(x) = 0.85 [\varepsilon_g(\text{Ga}_{1-x}\text{Al}_x\text{As}) - \varepsilon_g(\text{GaAs})]$ . One monolayer is 2.83 Å thick. Reprinted with permission from [205], J. L. Marín et al., in “Handbook of Advanced Electronic and Photonic Materials and Devices” (H. S. Nalwa, Ed.). Academic Press, San Diego, 2001. © 2001, Academic Press.

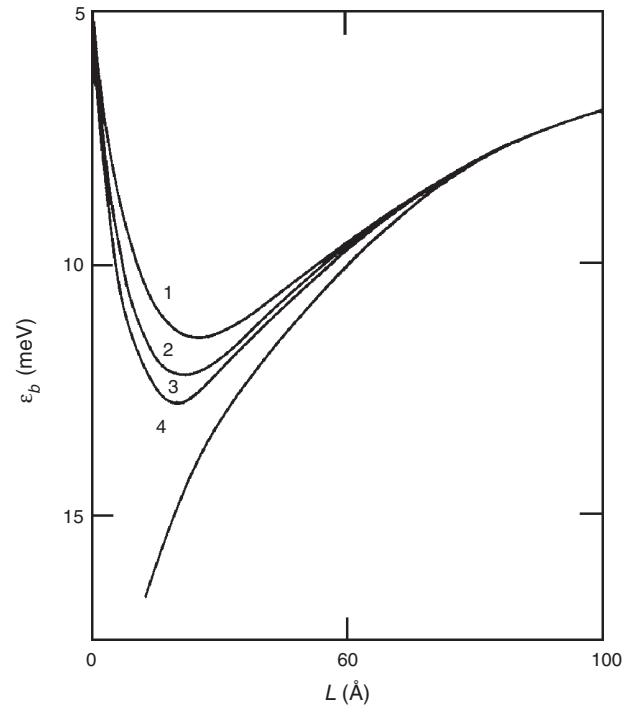


**Figure 11.** Dependence of the on-edge hydrogenic donor binding energy in GaAs–Ga<sub>1-x</sub>Al<sub>x</sub>As quantum wells versus the GaAs slab thickness  $L$ .  $m_e^* = 0.067m_0$ .  $\kappa = 13.1$ .  $V_0 = 212$  meV (curve 1); 318 meV (curve 2); 424 meV (curve 3); and infinite (curve 4). Reprinted with permission from [205], J. L. Marín et al., in “Handbook of Advanced Electronic and Photonic Materials and Devices” (H. S. Nalwa, Ed.). Academic Press, San Diego, 2001. © 2001, Academic Press.

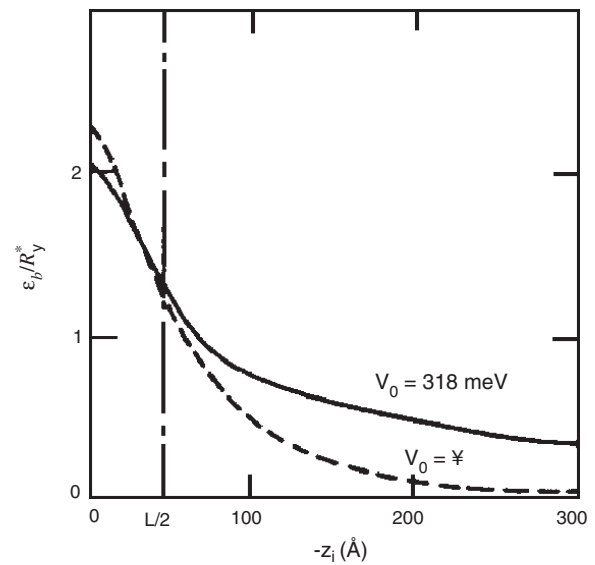


**Figure 12.** Dependence of the hydrogenic donor binding energy in a quantum well versus the impurity position  $z_i$  (a) in the case of a finite barrier well ( $V_0 = 318$  meV) and (b) in the case of an infinite barrier well [69]. There is an interface at  $-z_i = L/2$ .  $L = a_B^* = 94.8$  Å. Reprinted with permission from [205], J. L. Marín et al., in “Handbook of Advanced Electronic and Photonic Materials and Devices” (H. S. Nalwa, Ed.). Academic Press, San Diego, 2001. © 2001, Academic Press.

### 3.1.3. Excited Subbands: Continuum

The procedure followed for the bound state attached to the  $\varepsilon_1$  subband can be generalized for excited subbands  $\varepsilon_2, \varepsilon_3, \dots$  as well as for the quantum well continuum.

However, it becomes rapidly cumbersome since a correct variational procedure for excited states requires the trial wavefunctions to be orthogonal to all the states of lower energies. For separable wavefunctions [Eq. (105)] this requirement is automatically fulfilled and one may safely minimize  $\varepsilon_{\nu_0}(z_i, \lambda)$  to obtain a lower bound of  $\varepsilon_{b\nu_0}(z_i)$ . The new feature associated with the bound states attached to excited subbands is their finite lifetime. This is due to their degeneracy with the two-dimensional continua of the lower lying subbands. This effect, however, is not very large [67, 68] since it arises from the intersubband coupling, which is induced by the Coulombic potential: if the decoupling procedure is valid the lifetime of the quasi-bound state calculated with Eq. (105) should be long.

For impurities located in the barriers (an important practical topic with regard to the modulation-doping technique), we have seen that they weakly bind a state below the  $\varepsilon_1$  edge. There exists (at least) a second quasi-discrete level attached to the barrier edge (i.e., with energy  $\approx V_0 - R_y^*$ ). This state is reminiscent of the hydrogenic ground state of the bulk barrier. Due to the presence of the quantum well slab it becomes a resonant state since it interferes with the two-dimensional continua of the quantum well subbands  $\nu(\varepsilon_\nu < V_0)$ . Its lifetime  $\tau$  can be calculated using the expression

$$\frac{\hbar}{2\tau} = \frac{2\pi}{\hbar} \sum_{\nu, \vec{k}_\perp} \left| \left\langle \tilde{\varphi}(\vec{r}, z_i) \left| \frac{-e^2}{\kappa\sqrt{\rho^2 + (z - z_i)^2}} \right| \nu \vec{k}_\perp \right\rangle \right|^2 \times \delta \left( V_0 - R_y^* - \varepsilon_\nu - \frac{\hbar^2 k_\perp^2}{2m_e^*} \right) \quad (112)$$

where  $\tilde{\varphi}$  is the  $1s$  bulk hydrogenic wavefunction of the barrier. If the distance  $d$  separating the impurity from the quantum well edge is much larger than  $a_B^*$ , Eq. (112) simplifies to

$$\frac{\hbar}{2\tau} \approx 16R_y^* \sum_\nu P_\nu \left( \frac{R_y^*}{V_0 - \varepsilon_\nu} \right)^{3/2} \exp \left( -\frac{2d}{a_B^*} \sqrt{\frac{V_0 - \varepsilon_\nu}{R_y^*}} \right) \quad (113)$$

where  $P_\nu$  is the total integrated probability of finding the carrier in the  $\nu$ th state (energy  $\varepsilon_\nu$ ) in any of the two barriers of the quantum well. One sees from Eq. (113) that the lifetime  $\tau$  is strongly dominated by the escape processes to the excited subband  $\varepsilon_\nu$  whose energy is nearest to  $V_0 - R_y^*$ . As an example let us take a GaAs–GaAlAs quantum well with thickness  $L = 50 \text{ \AA}$ ,  $V_0 = 0.2 \text{ eV}$  and assume that  $d = 3a_B^*$  (i.e.,  $d \approx 300 \text{ \AA}$ ). We then get  $\tau \approx 3 \times 10^{-6} \text{ s}$ . The quasi-bound state can thus be considered, to a reasonable approximation, as stationary ( $\hbar/\tau \approx 4 \times 10^{-8} R_y^*$ ).

### 3.1.4. Excited Impurity Levels Attached to the Subband

The Schrödinger equation [Eq. (102)] has several bound states below  $\varepsilon_1$ ; their binding energies have been calculated by several groups [72, 73]. The calculated energy

difference between the on-center donor ground state (quasi  $1s$ ) and the excited states (quasi  $2p_x, 2p_y$ ) agrees with the far-infrared absorption and magnetoabsorption data [74]. On-edge donor levels have also been investigated.

### 3.1.5. Acceptor Levels in a Quantum Well

The problem of acceptor levels in semiconductor quantum wells is much more intricate than the equivalent donor problem. This is due to the degenerate nature of the valence bands in cubic semiconductors. In quantum wells this degeneracy is lifted (light and heavy holes have different confinement energies).

However, the energy separation between the heavy and light hole subbands is seldom comparable to the bulk acceptor binding energies. Thus many subbands are coupled by the combined actions of the Coulombic potential and the quantum well confining barrier potential. No simple decoupling procedures appear manageable.

Masselink et al. [75] used variational calculations to estimate the binding energy of the acceptor level due to carbon (a well-known residual impurity in MBE grown GaAs layers). Their results, shown in Figure 13, agree remarkably with the experiments of Miller et al. [76]. One notices in Figure 13 the same trends versus quantum well thickness as displayed by Coulombic donors (Figs. 10 and 11). The binding energy first increases when  $L$  decreases (increasing

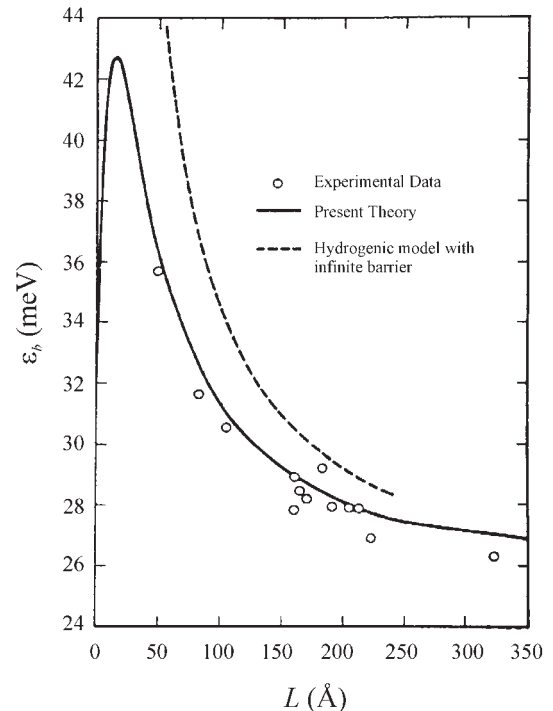


**Figure 13.** Dependence of the on-center carbon binding energy versus well width in GaAs–Ga<sub>1-x</sub>Al<sub>x</sub>As quantum wells.  $V_b(x) = 0.15 [\varepsilon_g(\text{Ga}_{1-x}\text{Al}_x\text{As}) - \varepsilon_g(\text{GaAs})]$  is the assumed hole confining barrier height. The open circles are the experimental values obtained by Miller et al. [76]. Reprinted with permission from [205], J. L. Marin et al., in “Handbook of Advanced Electronic and Photonic Materials and Devices” (H. S. Nalwa, Ed.). Academic Press, San Diego, 2001. © 2001, Academic Press.

tendency to two-dimensional behavior), then saturates, and finally drops to the value of the acceptor binding energy of the bulk barrier. Finally, it should be noted that the relative increase in binding is smaller for acceptors than for donors. This is because the bulk acceptor Bohr radius is much smaller than that of the bulk donor.

### 3.2. Hydrogenic Impurities within Asymmetric and Symmetric Quantum Well Wires

In this section the energy of the ground and first excited states, the binding energy, and oscillator strengths for hydrogenic impurities confined within a cylindrical quantum well wire with a finite-height potential well are studied variationally as a function of the wire radius and of the relative position of the nucleus within the quantum well wire for different barrier-height potential [77]. The trial wavefunction is constructed as the product of the free wavefunction of hydrogen impurity and a simple auxiliary function that allows the appropriate boundary conditions to be satisfied.

In this context, the variational method here used constitutes a useful approach to study asymmetric and symmetric quantum systems confined by penetrable potentials.

#### 3.2.1. On-Axis Hydrogenic Impurity

If the nucleus of the hydrogen impurity is located on the symmetry axis of the cylindrical quantum well wire, the model Hamiltonian for the electron within the quantum well wire can be written in atomic units ( $\hbar = m_e^* = e = 1$ ) as

$$\hat{H} = -\frac{1}{2}\nabla^2 - \frac{1}{r} + V_b(\rho) \quad (114)$$

with

$$V_b(\rho) = \begin{cases} 0 & 0 \leq \rho \leq \rho_0 \\ V_0 & \rho_0 \leq \rho < \infty \end{cases} \quad (115)$$

where  $r = \sqrt{\rho^2 + z^2}$  is the electron–nucleus distance,  $\rho$  is the cylindrical coordinate parallel to  $xy$  plane,  $z$  is the coordinate along the wire axis,  $\rho_0$  is the wire radius, and  $V_0$  is the confining potential barrier.

The physical meaning of  $V_0$  in this context is to simulate, on the average, the effective potential step created by the composition difference between the quantum well wire and its surroundings.

It is well known that the Schrödinger equation for this Coulomb-type potential is not separable in cylindrical coordinates, the natural symmetry of the wire; thus we are forced to use an approximate method to calculate the ground state energy and first excited states for this system.

In order to use the variational method to solve approximately the Schrödinger equation with the Hamiltonian given by Eq. (114), we must construct a trial wavefunction  $\psi$  with the basic properties listed as follows:

$$\begin{aligned} \psi(0) & \text{ finite} \\ \psi(r) & \rightarrow 0 \text{ as } r \rightarrow \infty \\ \frac{1}{\psi(r)} \frac{\partial \psi(r)}{\partial \rho} & \text{ continua at } \rho = \rho_0 \end{aligned} \quad (116)$$

The function  $\psi$  will contain a parameter or a set of parameters that allows us to minimize the ground state energy by imposing that

$$\frac{\partial \varepsilon_0}{\partial \alpha_i} = 0 \quad (117)$$

where  $\{\alpha_i\}$  is the set of parameters mentioned earlier.

A possible ansatz wavefunction for this problem is of the form

$$\psi_{1s} = \begin{cases} \psi_i = A(\rho_0 - \alpha\rho) \exp(-\alpha r) & 0 \leq \rho \leq \rho_0 \\ \psi_o = B \exp(-\alpha r) \exp(-\beta\rho) & \rho_0 \leq \rho < \infty \end{cases} \quad (118)$$

where  $A$ ,  $B$  are normalization constants and  $\alpha$ ,  $\beta$  are the variational parameters involved in the calculation. These functions must satisfy

$$\psi_i|_{\rho=\rho_0} = \psi_o|_{\rho=\rho_0} \quad (119)$$

$$\left. \frac{\partial \psi_i}{\partial \rho} \right|_{\rho=\rho_0} = \left. \frac{\partial \psi_o}{\partial \rho} \right|_{\rho=\rho_0} \quad (120)$$

By imposing condition (120) to the function given by Eq. (118) we have that

$$\beta = \frac{\alpha}{(1 - \alpha)\rho_0} \quad (121)$$

That is, we need to find only one variational parameter to minimize the ground state energy. Furthermore, when  $V_0 \rightarrow \infty$ ,  $\alpha \rightarrow 1$ ,  $\beta \rightarrow \infty$ , and  $\psi_o \rightarrow 0$ , as expected.

The continuity condition on the boundary, Eq. (119), relates  $B$  and  $A$ :

$$B = A\rho_0(1 - \alpha) \exp\left(\frac{\alpha}{1 - \alpha}\right) \quad (122)$$

The suitable Hamiltonian for  $2p$ -type excited states is the same that given by Eq. (114), and the variational wavefunctions for  $2p_x$ ,  $2p_y$ , and  $2p_z$  states, when the nucleus of hydrogenic impurity is fixed on the symmetry axis of the wire, are of the form

$$\psi_{2p_x} = \begin{cases} \psi_i = C(\rho_0 - \gamma\rho) \\ \quad \times \exp(-\gamma r) \rho \cos \varphi & 0 \leq \rho \leq \rho_0 \\ \psi_o = D \exp(-\gamma r) \\ \quad \times \exp(-\xi\rho) \rho \cos \varphi & \rho_0 \leq \rho < \infty \end{cases} \quad (123)$$

$$\psi_{2p_y} = \begin{cases} \psi_i = C(\rho_0 - \gamma\rho) \\ \quad \times \exp(-\gamma r) \rho \sin \varphi & 0 \leq \rho \leq \rho_0 \\ \psi_o = D \exp(-\gamma r) \\ \quad \times \exp(-\xi\rho) \rho \sin \varphi & \rho_0 \leq \rho < \infty \end{cases} \quad (124)$$

$$\psi_{2p_z} = \begin{cases} \psi_i = C(\rho_0 - \gamma\rho) \\ \quad \times \exp(-\gamma r) z & 0 \leq \rho \leq \rho_0 \\ \psi_o = D \exp(-\gamma r) \\ \quad \times \exp(-\xi\rho) z & \rho_0 \leq \rho < \infty \end{cases} \quad (125)$$

where  $C$  and  $D$  are normalization constants and  $\gamma$ ,  $\xi$  are variational parameters to be determined and are related by

$$\xi = \frac{\gamma}{(1-\gamma)\rho_0} \quad (126)$$

and

$$D = C\rho_0(1-\gamma) \exp\left(\frac{\gamma}{1-\gamma}\right) \quad (127)$$

The results for the energy of the ground and  $2p_z$  states as a function of wire radius and different barrier heights are displayed in Figure 14. For a given value of the finite barrier potential the ground state (excited state) energy increases from  $-0.5$  ( $-0.125$ ) Hartrees as the wire radius is reduced. These values are characteristic of the “free” hydrogen atom.

The binding energy  $\varepsilon_b$  for the hydrogenic impurity is defined as the ground state energy of the system without Coulomb interaction  $\varepsilon_w$ , minus the ground state energy in the presence of electron–nucleus interaction  $\varepsilon_0$ ; that is,

$$\varepsilon_b = \varepsilon_w - \varepsilon_0 \quad (128)$$

The binding energy defined in this way is a positive quantity.

In Figure 15a, we display the variation of the hydrogenic impurity binding energy  $\varepsilon_b$  as a function of wire radius  $\rho_0$  for several values of finite potential barrier.

### 3.2.2. Off-Axis Hydrogenic Impurity

If the nucleus of the atom is located on the  $x$  axis, at a distance  $b$  from the axis of the wire, the electron–nucleus distance is

$$\begin{aligned} r' &= |\vec{r} - b\hat{e}_x| = \sqrt{(x-b)^2 + y^2 + z^2} \\ &= \sqrt{\rho^2 + b^2 + z^2 - 2\rho b \cos \varphi} \end{aligned} \quad (129)$$

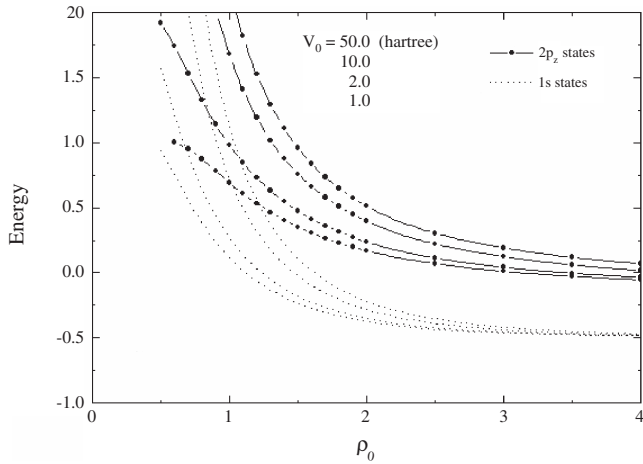


**Figure 14.** Energy of the ground and  $2p_z$  states of the hydrogenic impurity confined in a penetrable quantum well wire with the nucleus on the axis as a function of wire radius and potential barrier heights. Reprinted with permission from [205], J. L. Marín et al., in “Handbook of Advanced Electronic and Photonic Materials and Devices” (H. S. Nalwa, Ed.). Academic Press, San Diego, 2001. © 2001, Academic Press.

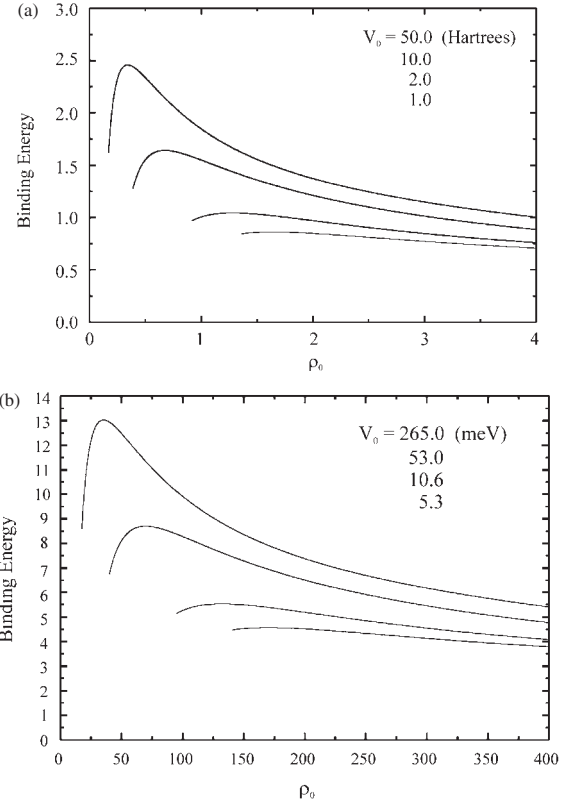


**Figure 15.** (a) Binding energy of the hydrogenic impurity confined in a penetrable quantum well wire with the nucleus on the axis as a function of the wire radius and potential barrier height. (b) Binding energy of the hydrogenic impurity confined in a penetrable GaAs–Ga<sub>1-x</sub>Al<sub>x</sub>As quantum well wire with the nucleus on the axis as a function of the wire radius and potential barrier height. Reprinted with permission from [205], J. L. Marín et al., in “Handbook of Advanced Electronic and Photonic Materials and Devices” (H. S. Nalwa, Ed.). Academic Press, San Diego, 2001. © 2001, Academic Press.

with  $\vec{r}$  the position vector of the electron relative to the origin on the wire axis. Then the suitable Hamiltonian is

$$\hat{H} = -\frac{1}{2}\nabla^2 - \frac{1}{r'} + V_b(\rho) \quad (130)$$

where  $V_b(\rho)$  is the same as that given by Eq. (115).

The trial wavefunction for the ground state energy can then be written as

$$\psi_{1s} = \begin{cases} \psi_i = A(\rho_0 - \alpha\rho) \exp(-\alpha r') & 0 \leq \rho \leq \rho_0 \\ \psi_o = B \exp(-\alpha r') \exp(-\beta\rho) & \rho_0 \leq \rho < \infty \end{cases} \quad (131)$$

where, as before,  $A$  and  $B$  are normalization constants and  $\alpha$ ,  $\beta$  are the variational parameters involved in the calculation. Again,  $\alpha$ ,  $\beta$  and  $A$ ,  $B$  are, respectively, related by Eqs. (121) and (122).

When the nucleus of hydrogenic impurity is off the symmetry axis, it is not possible to find the wavefunctions, for the  $2p_x$  and  $2p_y$  states, that satisfy the orthonormality condition as is required by the method. Therefore we will restrict to the  $2p_z$  state only. The suitable Hamiltonian is the same



that given by Eq. (116), and the variational wavefunction is given by

$$\psi_{2p_z} = \begin{cases} \psi_i = C(\rho_0 - \gamma\rho)\exp(-\gamma r')z & 0 \leq \rho \leq \rho_0 \\ \psi_o = D\exp(-\gamma r')\exp(-\xi\rho)z & \rho_0 \leq \rho < \infty \end{cases} \quad (132)$$

where, as before,  $C$ ,  $D$  are normalization constants and  $\gamma$ ,  $\xi$  are the variational parameters involved in the calculation. Again,  $\gamma$ ,  $\xi$  and  $C$ ,  $D$  are, respectively, related by Eqs. (126) and (127).

In Figure 16, we show the energy of the ground and  $2p_z$  states as a function of  $(b/\rho_0)$  for  $\rho_0 = 1.0$  Bohr and several heights of potential barrier.

In Figure 17a, we display the variation of the hydrogenic impurity binding energy  $\varepsilon_b$  as a function of  $(b/\rho_0)$  for  $\rho_0 = 1.0$  Bohr and several heights of potential barrier.

### 3.2.3. Optical Properties

To predict the absorption peak due to  $1s-2p$  transitions as a function of the wire radius and confining degree, we have calculated the transition energy between these states as well as their oscillator strengths.

The  $f_0$  oscillator strength is defined as

$$f_0 = \frac{2}{3} |\langle 1s | \vec{r} \cdot \vec{e}_r | 2p \rangle|^2 \Delta\varepsilon \quad (133)$$

where  $\vec{e}_r$  is the incident light polarization vector and  $\Delta\varepsilon = \varepsilon_{2p} - \varepsilon_{1s}$  is the transition energy between  $2p$  and  $1s$  states.

The  $1s-2p_z$  oscillator strength  $f_0$  (for  $\vec{e}_r \parallel z$ ) is shown in Figure 18 as a function of wire radius for several heights of potential barrier, when the nucleus is fixed on the center of the wire. For a given value of the finite barrier potential the oscillator strength increases from 0.139, the characteristic value of the “free” hydrogen atom, as the wire radius is reduced.

Finally, in Figure 19, we show the oscillator strength  $f_0$  (for  $\vec{e}_r \parallel z$ ) as a function of relative nucleus position  $(b/\rho_0)$

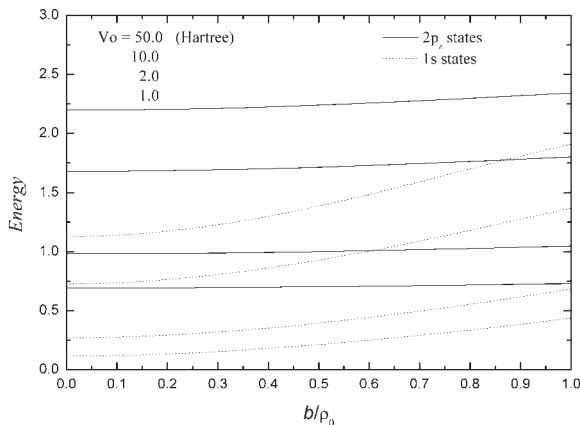


**Figure 16.** Energy of the ground and  $2p_z$  states of an off-axis hydrogenic impurity enclosed within a penetrable quantum well wire of radius  $\rho_0 = 1.0$  Bohr as a function of the relative nucleus position and potential barrier height. Reprinted with permission from [205], J. L. Marín et al., in “Handbook of Advanced Electronic and Photonic Materials and Devices” (H. S. Nalwa, Ed.). Academic Press, San Diego, 2001. © 2001, Academic Press.

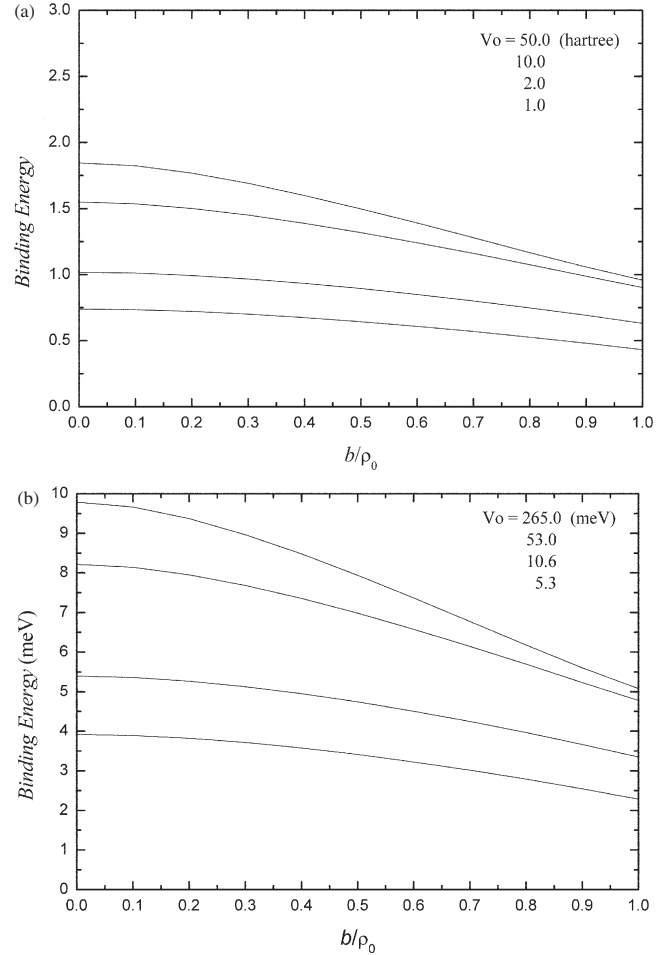


**Figure 17.** (a) Binding energy of an off-axis hydrogenic impurity enclosed within a penetrable quantum well wire of radius  $\rho_0 = 1.0$  Bohr as a function of the relative nucleus position and potential barrier height. (b) Binding energy of an off-axis hydrogenic impurity enclosed within a penetrable GaAs-Ga<sub>1-x</sub>Al<sub>x</sub>As quantum well wire of radius  $\rho_0 = 1.0$  Bohr as a function of the relative nucleus position and potential barrier height. Reprinted with permission from [205], J. L. Marín et al., in “Handbook of Advanced Electronic and Photonic Materials and Devices” (H. S. Nalwa, Ed.). Academic Press, San Diego, 2001. © 2001, Academic Press.

for  $\rho_0 = 2.0, 3.0,$  and  $4.0$  Bohr and several potential barrier heights for the off-axis case.

In Figure 14, we show the ground and first excited states energies of the hydrogenic impurity confined within cylindrical quantum dot with the nucleus on the symmetry axis, as a function of  $\rho_0$  for several  $V_0$  values. The ground state energy has a similar behavior as in [65], as well as for the hydrogen atom and for electron systems (like  $H^-$ , He,  $Li^+$ , and  $Be^{2+}$ ) within a penetrable spherical box [78]; that is, the energy diminishes as the confinement box size increases (for a given value of  $V_0$ ), and for a given size of the box the energy increases as  $V_0$  increases. Similar behavior is found by Nag and Gangopadhyay [79] who show graphically qualitative results for heavy holes and electrons within a quantum well wire with cylindrical and elliptic cross-section. They have used the physical constants of the  $Ga_{0.47}In_{0.53}As/InP$  system.

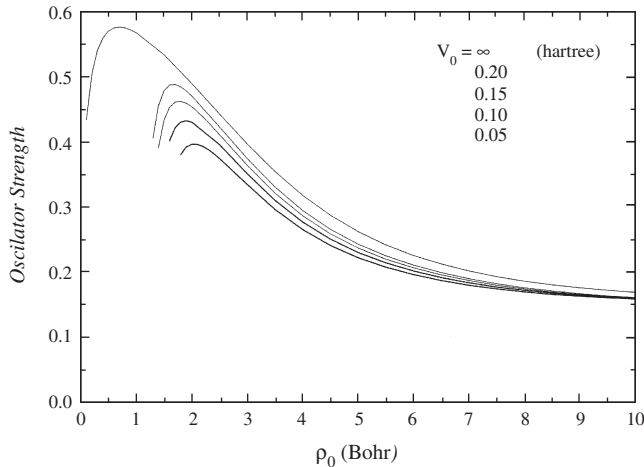


**Figure 18.**  $1s-2p_z$  oscillator strength of the hydrogenic impurity confined in a penetrable quantum well wire with the nucleus on the axis as a function of the wire radius and potential height. Reprinted with permission from [205], J. L. Marín et al., in “Handbook of Advanced Electronic and Photonic Materials and Devices” (H. S. Nalwa, Ed.). Academic Press, San Diego, 2001. © 2001, Academic Press.

This energy behavior can be understood on the basis of the uncertainty principle because when confinement dimensions are reduced the energy increases. If dimensions continue decreasing there will be a point at which the kinetic energy will be greater than the potential energy associated with internal interactions of the system. In an extreme situation of confinement the potential energy is only a perturbation of total energy for a free particle system. For attractive potentials, like Coulomb’s potential, there is a very clear competition between kinetic energy and potential energy. If  $\rho_0$  decreases, then potential energy decreases, but kinetic energy always increases because of the localization of wavefunction.

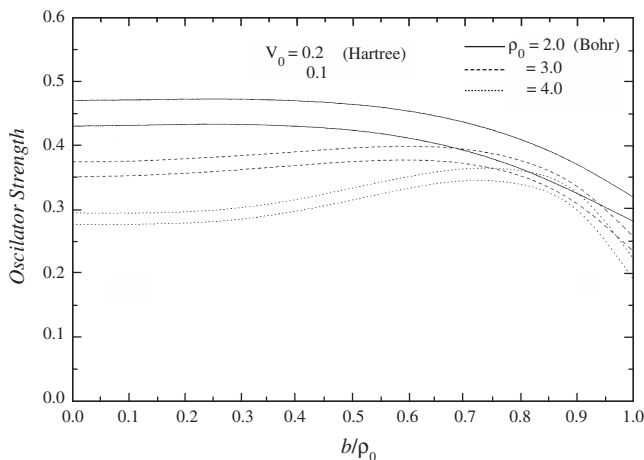


**Figure 19.**  $1s-2p_z$  oscillator strength of an off-axis hydrogenic impurity enclosed within a penetrable quantum well wire of radii  $\rho_0 = 2.0$ ,  $\rho_0 = 3.0$ , and  $\rho_0 = 4.0$  Bohr as a function of the relative nucleus position and potential height. Reprinted with permission from [205], J. L. Marín et al., in “Handbook of Advanced Electronic and Photonic Materials and Devices” (H. S. Nalwa, Ed.). Academic Press, San Diego, 2001. © 2001, Academic Press.

In Figure 15a, we display the binding energy of a hydrogenic impurity in a quantum well wire with finite potential barrier, as a function of the width of the wire. The results show that, due to the finite confining capacity of the quantum well wire, there is a critical radius for which the electron is no longer confined. Indeed, as the confining barrier increases this critical radius become smaller, as expected from simple physical considerations. For a given value of the finite barrier potential the binding energy increases from its bulk value as the wire radius is reduced, reaches a maximum value, and then drops to the bulk value characteristic of the barrier material as the wire radius goes to zero. This is due to the fact that as the wire radius is decreased the electron wavefunction is compressed thus leading to an enhancement of the binding energy. However, below a certain value of  $\rho_0$  the leakage of the wavefunction into the barrier region becomes more important, and the binding energy begins to decrease until it reaches a value that is characteristic of the barrier material as  $\rho_0 \rightarrow 0$ . This effect has been studied for heavy and light excitons confined within quantum wires [80], for hydrogen impurities within quantum well wire of  $\text{GaAs}_{1-x}\text{Al}_x\text{As}$  [81, 82], and excitons within quantum well wire in the presence of a magnetic field [83]. In Figure 15b, we show the same results for the quantum well wire of  $\text{GaAs}_{1-x}\text{Al}_x\text{As}$  for the barrier potentials  $V_0 = 265.0$ , 53.0, 10.6, 5.3 meV that correspond to the  $x = 0.36$ , 0.08, 0.016, 0.008, Al concentrations, respectively. The quantitative comparison of the curves in Figure 15b with the results of [80, 82, 83] show that our variational calculations lead to the same results.

The peak in the binding energy occurs for the smallest value of  $\rho_0$  for which the probability of electrons to be found outside the well is not significant; that is, the enhancement in binding energy occurs because the confining potential is forcing the electrons to move only in a smaller space and to spend most of their time closer the nucleus. This strong enhancement of the binding energy has important consequences for optical and transport properties of quantum well wires.

In Figure 16, we show the ground and first excited state energies for the asymmetric case. The ground state energy approaches the value calculated in [65] for the infinite potential barrier case, as the potential barrier is increased, and when the size of the quantum well wire becomes infinite and the nuclei is close to the boundary. For a given value of the finite barrier potential the energy of the  $2p_z$  excited state is almost independent of the relative position of the nuclei within the quantum well wire, as compared with the variation of the ground state energy. This is due to the orientation of the orbital in which the electron moves; a similar effect has been studied for a hydrogen atom enclosed between two impenetrable parallel planes and for a heavy exciton in a CdS film in [84].

Also, we can note that for  $\rho_0 = 1$  Bohr, the ground state energies calculated for  $V_0 = 1, 2, 10, 50$  Hartrees are in exact agreement with the ground state energies when the atom nucleus is on the symmetry axis as we can see in Figure 14. The same is true for the first excited state energies (compare Fig. 16 with Fig. 14).

In Figure 17a, we can note that the value of the binding energy for the asymmetric case decreases as the nucleus

approaching the quantum well wire is increased. A similar behavior occurs for the binding and the ground state energy of a hydrogenic impurity placed in a rectangular cross-section quantum well wire of GaAs–Ga<sub>x</sub>Al<sub>1-x</sub>As [81].

In Figure 17b, we show the same results as in Figure 17a, for the case of a hydrogenic impurity within a cylindrical quantum well wire of GaAs–Ga<sub>x</sub>Al<sub>1-x</sub>As with  $\rho_0 = 103.4 \text{ \AA}$ . The calculations were carried out for barrier potentials  $V_0 = 265.0, 53.0, 10.6, 5.3 \text{ meV}$  that correspond to aluminum concentrations  $x = 0.36, 0.08, 0.016, 0.008$ . The quantitative comparison of Figure 16b with the results of [81] shows the effect of the geometry on the binding energy.

The binding energy for  $\rho_0 = 1 \text{ Bohr}$  is in agreement with the binding energy when the nucleus is on the axis of the wire (compare Fig. 17a with Fig. 15a).

In Figure 18, the  $1s-2p_z$  transitions of the studied states in the symmetric case are shown. We note a similar behavior to that found in other systems which are confined in regions with different symmetries, for example, the heavy exciton case confined in a KCl ionic sphere for several radii and penetrabilities, in which the excitonic transitions vanish for given sphere sizes, as a consequence of the finite confining potential value, and moreover in that case the absorption peak is shifted to high energies as the sphere radius decreases. This effect has been experimentally observed in SiO<sub>2</sub> spheres [84]. In addition, for  $V_0 = \infty$ , there is a critical radius of quantum well wire for which the absorption has a maximum and then returns to bulk value as the radius continues decreasing.

In Figure 19, we show the oscillator strength  $f_0$  (for  $\vec{e}_i \parallel z$ ) as a function of relative nucleus position ( $b/\rho_0$ ) for  $\rho_0 = 2.0, 3.0, \text{ and } 4.0 \text{ Bohrs}$ , with the following potential barrier values:  $V_0 = 0.1 \text{ and } 0.2 \text{ Hartrees}$  for the off-axis case. The maximum in the absorption peak allows us to predict the optimum site for the location of the hydrogenic impurity within the quantum well wire. We can note that, for the same parameter values as those mentioned earlier, the transition intensities are in agreement with the transition intensities of the studied states in the symmetric case (compare Fig. 19 with Fig. 18).

### 3.3. Asymmetric Confinement of Hydrogen by Hard Spherical and Cylindrical Surfaces

The variational method is used to calculate the ground state energy of the hydrogen atom confined within hard spherical and cylindrical surfaces, for an atomic nucleus, which is off the center of symmetry of the confining boundary. It is shown that the wavefunction for the free hydrogen atom in spherical coordinates (referred to the center of symmetry of the confining surface) can be used, without further assumptions, to construct the trial wavefunction systematically. The latter is assumed to be the product of the free wavefunction and a simple cutoff function that satisfies the appropriate boundary conditions.

In order to show the advantage of the method we present in detail two cases: the hydrogen atom confined within hard spherical and within cylindrical surfaces. The asymmetry of these systems is due to the nucleus of the atom being shifted off the center of symmetry of the confining surface (i.e.,

either off the center of the sphere or off the axis of the cylinder). Of course, in such cases the corresponding Schrödinger equation is no longer separable.

#### 3.3.1. Applications of the Method

In this section, two explicit examples using the variational method application will be described. Both involve the hydrogen atom confined within a domain with impenetrable boundaries. In the first example, we shall consider the atom within a spherical surface where the center of surface and the nucleus of the atom differ by a constant distance  $a$ . Referring to Figure 20, the coordinates of the electron of the hydrogen atom with respect to the nucleus ( $\vec{r}$ ) and with respect to the center of the confining sphere ( $\vec{r}'$ ) are related by

$$\vec{r}' = \vec{r} - \vec{a} \quad (134)$$

The corresponding Hamiltonian can now be written as

$$\hat{H} = -\frac{1}{2}\nabla^2 - \frac{1}{|\vec{r} - \vec{a}|} + V_b(r) \quad (135)$$

where  $V_b$  is a confining potential defined as

$$V_b(\rho) = \begin{cases} +\infty & r > r_0 \\ 0 & r < r_0 \end{cases} \quad (136)$$

The ground state wavefunction for the free hydrogen atom in spherical coordinates is given as

$$\psi_0 = A \exp(-r') \quad (137)$$

where  $r'$  is the electron–nucleus distance and  $A$  is a normalization constant.

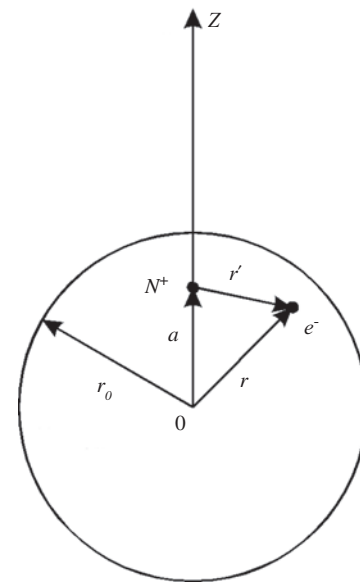


**Figure 20.** Coordinates for the off-center hydrogen atom relative to the center of the confining sphere.

Without loss of generality, we can assume that the nucleus is located on the  $z$  axis. The trial wavefunction for the ground state can be written as

$$\chi(\vec{r}) = A(r - r_0) \exp(-\alpha|\vec{r} - \vec{a}|) \quad (138)$$

where  $r_0$  is the radius of the spherical confining domain,  $A$  is a normalization constant, and

$$|\vec{r} - \vec{a}| = [r^2 + a^2 - 2ar \cos \theta]^{1/2} \quad (139)$$

Here,  $\theta$  is the usual polar angle of the spherical coordinates.

The results of the variational calculations of the ground state energy with this trial wavefunction are displayed in Table 1. A comparison with the results obtained in [85, 86] is also shown. Figure 21 shows the ground state energy for different sizes of the confining sphere as a function of  $(a/r_0)$ .

In the case of cylindrical coordinates, it is obvious that the Schrödinger equation for the Coulomb potential is nonseparable; however, the application of the variational method is still possible in the same context as could be done for spherical coordinates, as we shall see.

If the nucleus of the atom is located at the  $x$ -axis, at a distance  $\vec{b}$  (as depicted in Fig. 22), the electron–nucleus distance  $r'$  and the position of the electron relative to the origin on the axis of the cylinder  $r$  are related by

$$r' = |\vec{r}'| = |\vec{r} - \vec{b}| \quad (140)$$

That is,

$$r' = [(x - b)^2 + y^2 + z^2]^{1/2} = [\rho^2 + b^2 - 2\rho b \cos \phi + z^2]^{1/2} \quad (141)$$

The trial wavefunction can be written as

$$\chi(r) = B(\rho - \rho_0) \exp(-\alpha|\vec{r} - \vec{b}|) \quad (142)$$

where  $\rho_0$  is the radius of the cylinder and  $|\vec{r} - \vec{b}|$  is given by Eq. (141). The ground state energies resulting from the

**Table 1.** Ground state energy for the off-center hydrogen atom within an impenetrable spherical box as a function of the position of the nucleus (relative to the center of the confining sphere) for various radii of the box.

$r_0$	$a/r_0$	$\varepsilon^a$	$\varepsilon^b$	$\varepsilon^c$
4.0	0.1	-0.4804	-0.483 18	-0.483 15
	0.5	-0.4673	-0.481 05	-0.481 02
	1.0	-0.4390	-0.473 35	-0.473 42
3.0	0.1	-0.4209	-0.423 58	-0.423 58
	0.5	-0.3910	-0.413 73	-0.413 92
	1.0	-0.3223	-0.377 19	-0.378 40
2.0	0.1	-0.1198	-0.122 86	-0.122 86
	0.5	-0.0235	-0.066 07	-0.068 89
	1.0	+0.2022	+0.158 52	+0.127 51

Note: Energy units: Hartrees, distance units: Bohrs.

<sup>a</sup> Results of this subsection.

<sup>b</sup> Results of Gorecki and Byers Brown [85] obtained by boundary perturbation theory.

<sup>c</sup> Results of Brownstein [86] obtained by a variational method in which the trial wavefunction does not satisfy the boundary conditions.

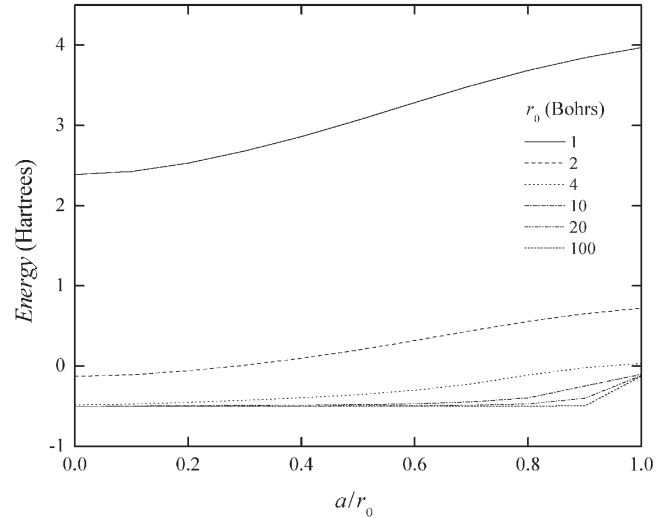


**Figure 21.** Ground state energy for an off-center hydrogen atom enclosed within an impenetrable spherical box as a function of the position of the nucleus (relative to center of the sphere), for various radii of the confining box. Note that when  $a/r_0 \gg 1$  and  $r_0 \gg 1$ , the energy approaches  $-1/8$  Hartree which corresponds to the ground state of the hydrogen atom close to an infinite planar surface. Reprinted with permission from [205], J. L. Marín et al., in “Handbook of Advanced Electronic and Photonic Materials and Devices” (H. S. Nalwa, Ed.), Academic Press, San Diego, 2001. © 2001, Academic Press.

variational calculations, using this trial wavefunction, are displayed in Table 2. A comparison with the results from [87] is also shown. In Figure 23, we show the ground state energy as a function of  $(b/\rho_0)$  for different values of  $\rho_0$ .

The trial wavefunction is accomplished by referring the electron–nucleus distance for the free atom to the origin placed at the center of symmetry of the confining surface, without further assumptions.

The results obtained by applying the direct variational method to compute the ground state energy of the hydrogen atom enclosed within spherical or cylindrical surfaces show good agreement with more elaborate calculations as can be seen from Tables 1 and 2. Furthermore, the trial wavefunctions are flexible enough to describe the case when the size of the confining surface becomes infinite and the nucleus is close to the boundary. The latter corresponds to the case when the hydrogen atom is close to a plane.

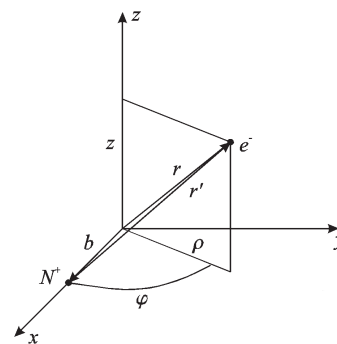


**Figure 22.** Coordinates for the off-axis hydrogen atom relative to the axis of the confining cylinder.



**Table 2.** Ground state energy for the off-axis hydrogen atom within an impenetrable cylindrical box as a function of the position of the nucleus (relative to the axis of the confining cylinder), for various radii of the box.

$\rho_0$	$b/\rho_0$	$\epsilon^a$	$\epsilon^b$
1.0	0.0	1.5854	
	0.2	1.6544	1.385 68
	0.4	1.8111	1.553 68
	0.6	2.0243	1.794 95
	0.8	2.2305	2.036 988
2.0	0.99	2.3724	2.203 82
	0.0	-0.1791	
	0.2	-0.1363	-0.247 82
	0.4	-0.0401	-0.159 586
	0.6	0.1050	0.0059 04
4.0	0.8	0.2704	0.2085 54
	0.99	0.3785	0.3369 83
	0.0	-0.4677	
	0.2	-0.4477	-0.487 374
	0.4	-0.4044	-0.467 144
10.0	0.6	-0.3291	-0.398 212
	0.8	-0.1671	-0.199 550
	0.99	-0.0388	-0.038 415
	0.0	-0.4912	
	0.2	-0.4921	-0.499 997
	0.4	-0.4859	-0.499 943
	0.6	-0.4696	-0.498 329
	0.8	-0.3988	-0.456 063
	0.99	-0.1183	-0.104 528

Note: Energy units: Hartrees, distance units: Bohrs.

<sup>a</sup> Results of this subsection.

<sup>b</sup> Results of Tsonchev and Goodfriend [87] obtained by expanding the wavefunctions in a basis of functions which depend on the polar angle  $\theta$ .

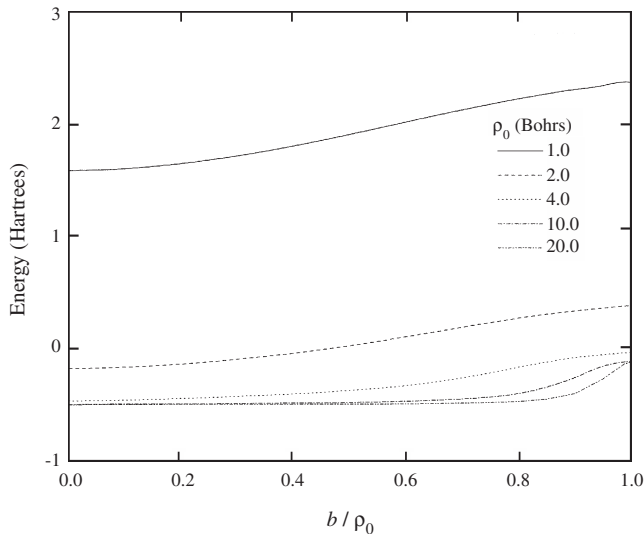


**Figure 23.** Ground state energy of an off-axis hydrogen atom enclosed within an impenetrable cylindrical box as a function of the position of the nucleus (relative to axis of the cylinder), for various radii of the confining box. Note that when  $b/\rho_0 \gg 1$  and  $\rho_0 \gg 1$ , the energy approaches  $-1/8$  Hartree which corresponds to the ground state of the hydrogen atom close to an infinite planar surface. Reprinted with permission from [205], J. L. Marín et al., in “Handbook of Advanced Electronic and Photonic Materials and Devices” (H. S. Nalwa, Ed.). Academic Press, San Diego, 2001. © 2001, Academic Press.

### 3.4. Confined Electron and Hydrogenic Donor States in a Spherical Quantum Dot

According to hydrogenic effective mass theory, exact solutions and quantum level structures are presented for confined electron and hydrogenic donor states in a spherical quantum dot of GaAs–Ga<sub>1-x</sub>Al<sub>x</sub>As [88]. Calculated results reveal that the values of the quantum levels of a confined electron in a quantum dot can be quite different for cases with finite and infinite barrier heights. The quantum level sequence and degeneracy for an electron in a quantum dot are similar to those of a superatom of GaAs–Ga<sub>1-x</sub>Al<sub>x</sub>As but different from those in a Coulombic field. There is stronger confinement and larger binding energy for a hydrogenic donor in a spherical quantum dot of GaAs–Ga<sub>1-x</sub>Al<sub>x</sub>As than in the corresponding quantum well wires and two-dimensional quantum well structures. The binding energy and its maximum of the ground state of a donor at the center of a quantum well are found to be strongly dependent on the well dimensionality and barrier height.

Because the transverse and longitudinal variables do not separate, the impurity states in two-dimensional quantum wells and quantum well wires cannot be solved exactly. Therefore approximation methods should be used. A reasonable trial function is needed to obtain a correct variational state of an impurity in two-dimensional and one-dimensional confined systems, and calculated results are more accurate if the coupling effect between the impurity and well potentials is considered using a trial function which has (or a part of which has) correctly both donor and well potential effects [89]. However, for a hydrogenic donor at the center of spherical quantum dots the exact solutions [90] can be obtained. It is interesting not only from a physical point of view but also from a mathematical point of view to compare the solutions and binding energies with those of two-dimensional and one-dimensional systems. In this section the exact solutions and quantum level structures for confined electron and hydrogenic donor states in spherical quantum dots are reported. The dependence of the quantum levels and the binding energies on the dimensionality of quantum wells is also presented.

The calculation is based on the effective mass approximation. It has been known to give excellent results for the electronic structure of GaAs–Ga<sub>1-x</sub>Al<sub>x</sub>As two-dimensional quantum wells and (AlAs)<sub>n</sub>/(GaAs)<sub>n</sub> superlattices if the well width or  $n$  is sufficiently large. The limit is estimated to be about 30 Å ( $n \approx 10$ ) [91]. Therefore it should also be valid for the GaAs–Ga<sub>1-x</sub>Al<sub>x</sub>As quantum dots, as the size (diameter for a ball) is sufficiently large. Based on the facts mentioned earlier, the limit for a ball diameter is also estimated to be the same value and equal to 30 Å. Here we treat the cases where the diameter is larger than the critical size. It is interesting to point out that the maximum quantum confinement of an electron in the GaAs–Ga<sub>1-x</sub>Al<sub>x</sub>As quantum ball is already obtained before the diameter approaches the critical value. In addition, polarization and image charge effects can be significant if there is a large dielectric discontinuity between the quantum ball and the surrounding medium [92]. However, this is not the case for the GaAs–Ga<sub>1-x</sub>Al<sub>x</sub>As quantum system; therefore we ignore such effects.

According to hydrogenic effective mass theory, the electron bound states and their binding energies have been found in two-dimensional quantum wells and quantum well wires. Normally, the effective mass equation is reliable for weakly bound states, and one might worry that the effective mass equation is inappropriate when the binding energy is greatly enhanced in spherical quantum dots of GaAs–Ga<sub>1-x</sub>Al<sub>x</sub>As. However, the bandgap of GaAs is 1.4 eV, while  $R_y^* = 5.3$  meV. Thus roughly a 100-fold enhancement of the binding energy is necessary before the effective mass equation becomes inapplicable. This difference is much greater than the enhancement seen in the cases considered here, so that the theory is still reliable for the bound states in spherical quantum dots of GaAs–Ga<sub>1-x</sub>Al<sub>x</sub>As.

Let us for definiteness consider a hydrogenic donor at the center of the quantum dot of radius  $r_0$ . The potential due to the discontinuity of the band edges at the GaAs–Ga<sub>1-x</sub>Al<sub>x</sub>As interface  $r = r_0$  is

$$V_b(r) = \begin{cases} V_0 & r \geq r_0 \\ 0 & r < r_0 \end{cases} \quad (143)$$

where  $r$  is the electron–donor distance. The barrier height  $V_0$  is obtained from a fixed ratio of the bandgap discontinuity. According to hydrogenic mass theory, the Hamiltonian for the donor is

$$\hat{H} = -\nabla^2 - \frac{2w}{r} + V_b(r) \quad (144)$$

It is written in a dimensionless form so that all energies are measured in units of the effective Rydberg  $R_y^*$  and all distances are measured in units of effective Bohr radius  $a_B^*$ .  $w$  is equal to 1.

In order to solve the Schrödinger-like equation

$$\hat{H}\psi(r, \theta, \varphi) = \varepsilon\psi(r, \theta, \varphi) \quad (145)$$

the wavefunctions of an electron with well-defined values of the orbital ( $l$ ) and magnetic ( $m$ ) quantum numbers in a spherical symmetric potential, which is the quantum well and Coulomb potential, are written in the form

$$\psi_{lm}(r, \theta, \varphi) = \psi^{(l)}(r)Y_{lm}(\theta, \varphi) \quad (146)$$

Substituting Eq. (146) in Eq. (145), we find an equation for the radial function:

$$r^2 \frac{d^2\psi^{(l)}(r)}{dr^2} + 2r \frac{d\psi^{(l)}(r)}{dr} + \{[\varepsilon(l) - V_b(r)]r^2 - l(l+1) + 2wr\}\psi^{(l)}(r) = 0 \quad (147)$$

Using the method of series expansion, we can solve Eq. (147) exactly. It should be noted that zero and infinity are a regular and an irregular singular point of Eq. (147), respectively. In the region  $0 < r$ , we have a series solution, which has a finite value at  $r = 0$  as

$$\psi^{(l)}(r) = Ar^l \sum_{n=0}^{\infty} a_n^{(l)} r^n \quad (148)$$

where  $A$  is a constant,

$$a_0^{(l)} = 1 \quad a_1^{(l)} = -\frac{1}{l+1} \quad (149)$$

and

$$a_n^{(l)} = -\left[2wa_{n-1}^{(l)} + \varepsilon(l)a_{n-2}^{(l)}\right] / n(n+2l+1) \quad n=2,3,4,\dots \quad (150)$$

In the region  $r_0 < r$ , we can obtain a normal solution [93]. It approaches zero at  $r = \infty$  and is found in the form

$$\psi^{(l)}(r) = B \exp(-K_l r) r^{\rho_l} \sum_{n=0}^N b_n^{(l)} r^{-n} \quad (151)$$

where

$$K_l = [V_0 - \varepsilon(l)]^{1/2} \quad \rho_l = -1 + \frac{w}{K_l} \quad (152)$$

and

$$b_0^{(l)} = 1 \quad b_{n+1}^{(l)} = -(\rho_l - n - 1)(\rho_l - n + l + 1)b_n^{(l)} / 2K_l(n+1) \quad n=0,1,2,\dots \quad (153)$$

$B$  is a constant. The series appears suitable for numerical computation for large  $r$  [93]. However, they are not suitable for  $r_0$  if it is small. In order to get exact value at small  $r_0$ , we find a solution of uniformly convergent Taylor series in the region  $r_0 < r \leq R_p$ , where  $R_p$  is a proper point (e.g.,  $R_p \geq 2a_B^*$ ) for using Eq. (151). For the sake of using the matching conditions at  $r = R_p$  to obtain the eigenenergy equation, it is written as

$$\psi^{(l)}(r) = C \sum_{n=0}^{\infty} c_n (r - R_p)^n + D \sum_{n=0}^{\infty} d_n (r - R_p)^n \quad (154)$$

where  $C$  and  $D$  are constants,  $c_0$  and  $d_1$  are equal to 1, and  $c_1$  and  $d_0$  are equal to 0, respectively. Noting that  $c_n$  and  $d_n$  are equal to 0 for negative  $n$ , the other  $c_n$  can be determined by the recurrence relation

$$c_n = \left\{ -2R_p(n-1)^2 c_{n-1} + [-(n-2)(n-1) + l(l+1) - 2wR_p + K_l^2 R_p^2] c_{n-2} + 2(K_l^2 R_p - w)c_{n-3} + K_l^2 c_{n-4} \right\} / [R_p^2 n(n-1)] \quad (155)$$

and the  $d_n$ 's obey a similar recurrence relation.

Using the matching conditions at the interface  $r = r_0$  and  $R_p$ , we can obtain the equation of the eigenenergies  $\varepsilon(l)$  as follows:

$$\begin{vmatrix} W_{11} & 0 & W_{13} & W_{14} \\ W_{21} & 0 & W_{23} & W_{24} \\ 0 & W_{32} & 1 & 0 \\ 0 & W_{42} & 0 & 1 \end{vmatrix} = 0 \quad (156)$$

That is,

$$W_{21}(W_{42}W_{14} + W_{32}W_{13}) - W_{11}(W_{42}W_{24} + W_{32}W_{23}) = 0 \quad (157)$$



where

$$\begin{aligned}
 W_{11} &= \sum_{n=0}^{\infty} a_n^{(l)} r_0^n & W_{13} &= \sum_{n=0}^{\infty} c_n (r_0 - R_p)^n \\
 W_{14} &= \sum_{n=1}^{\infty} d_n (r_0 - R_p)^n \\
 W_{21} &= \sum_{n=0}^{\infty} (l+n) a_n^{(l)} r_0^{n-1} & W_{23} &= \sum_{n=0}^{\infty} n c_n (r_0 - R_p)^{n-1} \\
 W_{32} &= \sum_{n=0}^N b_n^{(l)} R_p^{-n} \\
 W_{24} &= \sum_{n=1}^{\infty} n d_n (r_0 - R_p)^{n-1} \\
 W_{42} &= \sum_{n=0}^N (-n + \rho_l - K_l R_p) b_n^{(l)} R_p^{-n-1}
 \end{aligned} \tag{158}$$

can be solved numerically. Once the  $n$ th eigenenergy  $\varepsilon_n(l)$  is known, the  $A$ ,  $B$ ,  $C$ , and  $D$  [hence  $\psi_n^{(l)}(r)$ ] are known with the use of the normalized condition of  $\psi_n^{(l)}(r)$ . This  $\psi_n^{(l)}(r)$  depends on the value of  $l$ , the quantum well, Coulomb potential, and energy  $\varepsilon_n(l)$ . We should point that we have neglected the difference of the electron effective mass between GaAs and Ga<sub>1-x</sub>Al<sub>x</sub>As in the Hamiltonian and the matching conditions. If the effective mass difference is considered, similar formulas can be obtained.

If there is no Coulomb potential in the Hamiltonian of Eq. (144) (i.e.,  $w = 0$ ), using the same formulas, we can obtain wavefunction  $\psi_n^{(l)}(r, w = 0)$  and quantum levels  $\varepsilon_n(l, w = 0)$  of an electron in the quantum well. In fact, Eqs. (148) and (151) become the spherical Bessel function and Hankel function if  $w = 0$ . The equation of eigenenergies  $\varepsilon(l, w = 0)$  is

$$k_0 + K_0 \tan(k_0 r_0) = 0 \quad \text{if } l = 0 \tag{159}$$

$$\begin{aligned}
 i k_l h_l(i K_l r_0) j_{l-1}(k_l r_0) + K_l h_{l-1}(i K_l r_0) j_l(k_l r_0) &= 0 \\
 \text{if } l \geq 1 & \tag{160}
 \end{aligned}$$

and

$$k_l = [\varepsilon(l, w = 0)]^{1/2} \quad K_l = [V_0 - \varepsilon(l, w = 0)]^{1/2} \tag{161}$$

where  $j_l$  and  $h_l$  are the  $l$ th-order spherical Bessel function and Hankel functions of the first kind, respectively. Then, the same results are obtained if the wavefunctions and quantum levels are calculated with use of the Bessel and Hankel functions. Once  $\varepsilon_n(l, w = 1)$  and  $\varepsilon_n(l, w = 0)$  are obtained, the binding energy of the corresponding donor states in the spherical quantum dot is given by

$$\varepsilon_{nb}(l) = \varepsilon_n(l, w = 0) - \varepsilon_n(l, w = 1) \tag{162}$$

### 3.4.1. Quantum Levels and Binding Energies

A numerical calculation for GaAs–Ga<sub>1-x</sub>Al<sub>x</sub>As spherical quantum dots of the  $r_0$  between  $0.15a_B^*$  and  $7.0a_B^*$  with different  $V_0$  has been performed. In Table 3, the quantum levels of an electron in a spherical quantum dot with different  $r_0$  and  $V_0$  have been shown. The levels  $\varepsilon_n(l)$  are indicated by two symbols  $n$  and  $l$  as shown in Eq. (162).  $n$  is equal to the number of the root of Eqs. (158) or (159) and (160) in order of increasing magnitude (i.e.,  $n = 1, 2, 3, \dots$  and hence  $n - 1$  is the radial quantum number as usual).  $l$  is the usual notation (i.e.,  $s, p, d, \dots$ ). Thus we have  $1p, 1d, 2s, 1f$  levels (states) and so on if the  $n$  and  $l$  are used as the level notation, and we have  $1s, 2p, 3d, 2s, 4f$  levels, and so on, if the principal quantum number, which is equal to  $n + l$ , and  $l$  are used as the notation. It is interesting to point out that when  $V_0$  approaches infinity

$$\varepsilon_n(l) = (\mu_n^l / r_0)^2 \tag{163}$$

where  $\mu_n^l$  is the  $n$ th root of the  $l$ th-order spherical Bessel function. In Table 3, it is shown that the different values of  $\varepsilon_n(l)$  are obtained as  $r_0$  is equal to  $1a_B^*$  and  $2.5a_B^*$ , respectively. It is also shown that the values of quantum levels are different between infinite and finite barrier heights. The differences increase as the  $r_0$  and finite  $V_0$  decrease. There are an infinite number and a finite number of bound states for a spherical quantum dot with infinite and finite barrier heights, respectively. There is no bound state if  $r_0 < R_c = 0.5\pi/(V_0)^{1/2}$  [94]. However, the order of  $\varepsilon_n(l)$  is the same for both infinite and finite barriers [i.e., the unique level sequence  $1s, 1p(2p), 1s(3d), 2s, 1f(4f)$ , and so on]. We should note that the level order is different between both cases of a spherical quantum dot and Coulomb field, in which the level order of an electron is  $1s, 2s, 2p, 3s, 3p, 3d$ , and so on if the principal and orbital quantum numbers are used as the level notation. It is because of the lack of the deep attractive region in the vicinity of the center of a spherical quantum dot. For the motion of an electron in a Coulomb field, the quantum levels are only dependent on the principal quantum number  $n_p$  and degenerate with respect to both  $l$  (orbital quantum number) and  $m$  (magnetic quantum number). The total degree of degeneracy of a quantum level with  $n_p$  is equal to  $n_p^2$  (excluding spin degeneracy). For an electron in a spherical quantum dot, however,

**Table 3.** Quantum levels of an electron in a SQD of GaAs–Ga<sub>1-x</sub>Al<sub>x</sub>As.

$\varepsilon(l)$	$nl$	1s (1s)	1p (2p)	1d (3d)	2s (2s)	1f (4f)	2p (3p)
$r_0 = 1$	$V_0 = \infty$	9.872	20.187	33.212	39.476	48.832	59.676
	80	7.957	16.225	26.593	31.425	38.919	47.016
	60	7.702	15.679	25.642	30.191	37.420	44.789
	40	7.292	14.786	24.045	28.004	34.777	
2.5	$\infty$	1.580	3.230	5.314	6.316	7.814	9.548
	80	1.446	2.958	4.866	5.781	7.151	8.735
	60	1.427	2.919	4.800	5.702	7.054	8.613
	40	1.396	2.854	4.692	5.572	6.892	8.409

*Note:* The notation with the principal quantum number is shown in parentheses. Effective atomic units are used.

the quantum levels are dependent on both  $n$  and  $l$  and only degenerate with respect to the  $m$ . The total degree of degeneracy of a quantum level with  $n$  and  $l$  is equal to  $2l + 1$  (excluding spin degeneracy). It is worthwhile to point out that the degeneracy can be lifted in the other kinds of quantum dots. In quantum boxes with circle cross-sections, for example, the degeneracy is lifted partly. Now, we can conclude that the quantum level sequence and degeneracy for an electron in a spherical quantum dot are quite different from those in a Coulomb field, and that this distinguishing feature of levels might cause new phenomena in this type of GaAs–Ga<sub>1-x</sub>Al<sub>x</sub>As structure.

In Figure 24, the ground and first excited energy levels of an electron in a spherical quantum dot as a function of  $r_0$  for an infinite barrier height and two finite barrier heights  $V_0 = 40$  and  $80R_y^*$  were, respectively, plotted. It is shown that the differences of energy levels between different barrier heights increase as  $r_0$  is decreased and that the difference of the first excited state energy is larger than that of the ground state energy for a fixed value of  $r_0$ . It is also shown that there are no bound states for a spherical quantum dot with a finite  $V_0$  if  $r_0 < R_c$ , as mentioned earlier. In Figure 25, the binding energies of the ground and first excited states of a donor in a spherical quantum dot as a function of the  $r_0$  for three barrier heights  $V_0 = 80, 60,$  and  $40R_y^*$ , respectively, were shown. It is readily seen that as  $r_0$  decreases both the binding energies increase continuously until their maxima and then decrease fast. The values of the binding energies can be much larger than those of quantum well wire and a two-dimensional quantum well as  $r_0$  is smaller. It is interesting to point out the ratio  $\varepsilon_{1b}(0)/\varepsilon_{1b}(1)$  increases as  $r_0$  increases from some small value.  $\varepsilon_{1b}(0)$  and  $\varepsilon_{1b}(1)$  are almost independent of  $V_0$  and respectively equal to  $1.192$  and  $0.576R_y^*$  at  $r_0 = 7.0a_B^*$ . However, the ratio  $1.192/0.576$  is still much less than 4, which is the limit value of a three-dimensional hydrogenic donor as  $r_0$  (approaches infinity).

In Figures 24 and 25, it is easily seen that as the  $r_0$  decreases the binding energies with respect to different states of a donor in a spherical quantum dot increase until

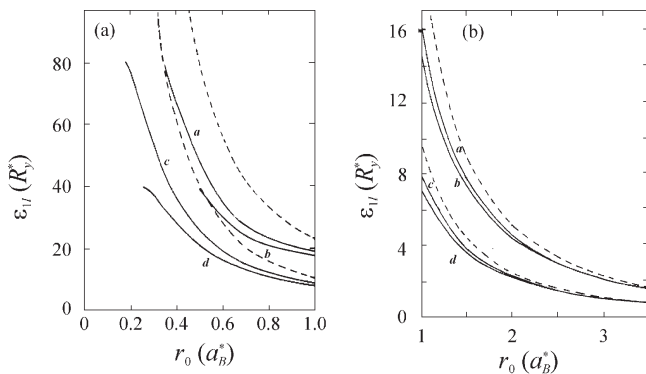


**Figure 24.** Ground state energy ( $\varepsilon_{10}$ ) and first excited state ( $\varepsilon_{11}$ ) energy levels of an electron in a spherical quantum dot versus the dot radius  $r_0$ . The top and middle dashed curves represent the levels  $\varepsilon_{11}$  and  $\varepsilon_{10}$  of the dot of  $V_0 = \infty$ , respectively. The solid curves a, b, c, and d represent the levels  $\varepsilon_{11}$  and  $\varepsilon_{10}$  of the wells of  $V_0 = 80$  and  $40R_y^*$ , respectively. Reprinted with permission from [205], J. L. Marín et al., in “Handbook of Advanced Electronic and Photonic Materials and Devices” (H. S. Nalwa, Ed.). Academic Press, San Diego, 2001. © 2001, Academic Press.

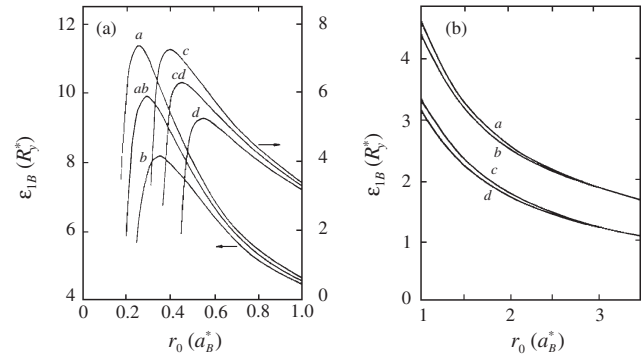


**Figure 25.** Binding energy of the ground state ( $\varepsilon_{0B}$ ) and the first excited ( $\varepsilon_{1B}$ ) states of a donor in a spherical quantum dot versus the dot radius  $r_0$ . The curves a, ab, and b represent  $\varepsilon_{0B}$  of the dot of  $V_0 = 80, 60,$  and  $40R_y^*$ , and the curves c, cd, and d represent  $\varepsilon_{1B}$  of  $V_0 = 80, 60,$  and  $40R_y^*$ , respectively. Arrows indicate the relevant vertical scales. Reprinted with permission from [205], J. L. Marín et al., in “Handbook of Advanced Electronic and Photonic Materials and Devices” (H. S. Nalwa, Ed.). Academic Press, San Diego, 2001. © 2001, Academic Press.

their maxima and that the increase of the binding energies is always much less than the increase of the energies of the corresponding states of an electron only confined by the spherical quantum dot, although the binding energies can be much larger than those in the corresponding two-dimensional quantum well and quantum well wire. It means that confinement effects [95, 96] are dominant in the range of  $r_0$ . Further, it is also true for the higher excited states. Therefore we can know what kind of quantum-level sequence we will have if the motion of an electron is confined by both a spherical quantum well and a Coulomb field with the same center. The level sequence is similar to that of a three-dimensional hydrogenic donor if  $r_0$  is much larger and quantum confinement due to the spherical quantum dot is very weak. However, it is similar to that of the electron in the spherical quantum dot if the quantum confinement of the spherical quantum dot is stronger than that of the Coulomb potential. Based on what we have mentioned, we can understand why the quantum level structure of GaAs–Ga<sub>1-x</sub>Al<sub>x</sub>As superatoms [93, 97] is similar to that of an electron in a spherical quantum dot and quite different from those of ordinary atoms and why the electronic structure of the superatoms is dominated by no-radial-node states of  $1s, 1p(2p), 1d(3d)$ , and so on.

In Figure 26, the maximum binding energies  $\varepsilon_{b\max}$  for the hydrogenic donor ground and first excited states in a spherical quantum dot as a function of the barrier height  $V_0$  were plotted. It is shown that the enhancement of the maximum is greater in a spherical quantum dot (quasi-zero-dimensional) than in the corresponding quantum well wire and two-dimensional quantum well as  $V_0$  is increased. This is because of the enhancement of the electron confinement in three dimensions in the spherical quantum dot. In Figure 27, it was shown that the maximum binding energy  $\varepsilon_{b\max}$  of ground states of a donor at the center of a different kind of quantum well depends on the well dimensionality and barrier height  $V_0$  and presents quasi-two-, one-, and zero-dimensional features of the hydrogenic donor, respectively. It is interesting to note that the mean values of

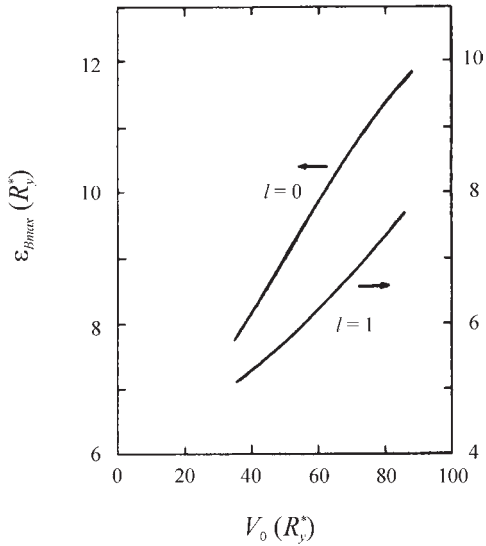


**Figure 26.** Maximum binding energies  $\varepsilon_{b\max}$  for the hydrogenic donor ground ( $l = 0$ ) and the first excited ( $l = 1$ ) states in a spherical quantum dot versus the barrier height  $V_0$ . Arrows indicate the relevant scales. Reprinted with permission from [205], J. L. Marín et al., in “Handbook of Advanced Electronic and Photonic Materials and Devices” (H. S. Nalwa, Ed.). Academic Press, San Diego, 2001. © 2001, Academic Press.

the maxima of the two-dimensional quantum well [89] and spherical quantum dot are very close to (slightly larger than) the maxima for the quantum well wire [82]. We should point out that the maximum binding energies of higher excited states can also be used to present the dimension features.

The radial Eq. (147) was solved and the exact solutions of confined electron and donor states in a spherical quantum dot were obtained. The quantum levels and binding

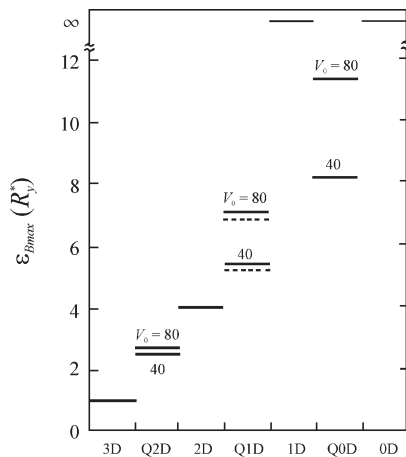


**Figure 27.** Maximum binding energies  $\varepsilon_{b\max}$  of a donor ground state in a quantum well versus the well dimensionality and the barrier height  $V_0$ . For the quasi-one-dimensional case, the dashed lines represent the maximum binding energies of quantum well wires and the solid lines represent the mean values of the maxima of the two-dimensional quantum wells and the spherical quantum dots. Reprinted with permission from [205], J. L. Marín et al., in “Handbook of Advanced Electronic and Photonic Materials and Devices” (H. S. Nalwa, Ed.). Academic Press, San Diego, 2001. © 2001, Academic Press.

energies of a donor in the spherical quantum dot are calculated numerically. The numerical results reveal that the values of the quantum levels of a confined electron in a spherical quantum dot with a finite barrier height are different from those with an infinite barrier height. The differences increase as  $r_0$  decreases. However, the quantum level order is the same for both infinite and finite barrier heights. It is also shown that the quantum level sequence and degeneracy for an electron in a spherical quantum dot are similar to those of a superatom and different from those in a Coulomb field. The quantum level structure of a donor in a spherical quantum dot is similar to that of an electron only confined by the spherical quantum dot as the quantum confinement due to the well potential is stronger than that due to the donor potential. It is useful for understanding the shell model [97] in microclusters.

On the basis of the calculated results, the crossover from three-dimensional to zero-dimensional behavior of the donor states in a spherical quantum dot is shown when the radius becomes small. The binding energy of a hydrogenic donor state in the well of GaAs–Ga<sub>x</sub>Al<sub>1-x</sub>As and its maximum are strongly dependent on the well dimensionality and the barrier height and there is a larger confinement and binding energy of a donor state in a spherical quantum dot than in a quantum well wire and quantum well. Using calculated results of quantum well and quantum well wire, it has been shown that the maxima of the binding energies of hydrogenic donors in quantum wells, quantum well wire, and spherical quantum dots of GaAs–Ga<sub>x</sub>Al<sub>1-x</sub>As can be used to present, respectively, quasi-two-, one-, and zero-dimensional features of the hydrogenic donor states. Further, it has been found that the maximum of the binding energy of donor ground state in a GaAs–Ga<sub>x</sub>Al<sub>1-x</sub>As quantum well wire is about half of the summation of the maximum binding energies in the corresponding two-dimensional quantum well and spherical quantum dot.

It should be pointed out that impurities could be located anywhere in a spherical quantum dot and that the binding energies will decrease and the level ordering will change as the impurity location shifts to the edge or out of the spherical quantum dot. Based on the exact solutions obtained, the quantum levels and binding energies of a donor located out of the center of a spherical quantum dot can be obtained by use of a variation method. The exact solutions are also useful for the calculation of excited states in a spherical quantum dot, which is a kind of quantum dot. It will be interesting to compare the calculated results about quantum levels and binding energies of impurity and exciton states in a spherical quantum dot with those of other kinds of quantum dots.

### 3.5. Shallow Donors in a Quantum Well Wire: Electric Field and Geometrical Effects

In this section the effects of an external electric field on donor binding energies in quantum well wires with cylindrical and square cross-sections are investigated. A system with a GaAs quantum well surrounded by Al<sub>x</sub>Ga<sub>1-x</sub>As potential barriers in the  $x, y$  plane has been chosen. The electron is thus free to move in the  $z$  direction, in the absence of

a Coulomb center binding the electron. A realistic finite potential well model is considered [98].

The behavior of  $\varepsilon_b$  under an electric field is different for quantum well wires of rectangular and cylindrical cross-section. While the direction of the electric field is immaterial for cylindrical wires, it is very important for wires with rectangular cross-section.

It is found that the binding energy of the hydrogenic impurities is a rather sensitive function of the geometry of the wire especially under the influence of an electric field.

It is also found that the electric field effects on  $\varepsilon_b$  are extremely sensitive to the impurity position in or outside the wire.

### 3.5.1. Theory and Calculation

It is convenient to use the Cartesian coordinates for wires of rectangular cross-section and cylindrical coordinates for wires of circular cross-section. The Hamiltonian for the wire of rectangular cross-section, lying along the  $z$  direction, is

$$\hat{H}_0 = -\frac{\hbar^2}{2m_e^*} \left( \frac{\partial^2}{\partial x^2} + \frac{\partial^2}{\partial y^2} \right) + V_b(x, y) \quad (164)$$

where

$$V_b(x, y) = \begin{cases} V_0 & x < -\frac{L_x}{2} & y < -\frac{L_y}{2} \\ 0 & -\frac{L_x}{2} \leq x \leq \frac{L_x}{2} & -\frac{L_y}{2} \leq y \leq \frac{L_y}{2} \\ V_0 & \frac{L_x}{2} < x & \frac{L_y}{2} < y \end{cases} \quad (165)$$

Thus, the electron is free to move along the  $z$  direction but is constrained along  $x$  and  $y$  directions. The wire subband structure is obtained by the variational method using the trial wavefunction

$$f_0(x, y) = N_0 \begin{cases} \exp[k_2(x+y)] & x < -\frac{L_x}{2} & y < -\frac{L_y}{2} \\ \cos(k_1 x) \cos(k_1 y) & -\frac{L_x}{2} \leq x \leq \frac{L_x}{2} & -\frac{L_y}{2} \leq y \leq \frac{L_y}{2} \\ \exp[-k_2(x+y)] & \frac{L_x}{2} < x & \frac{L_y}{2} < y \end{cases} \quad (166)$$

where  $N_0$  is the normalization coefficient, and

$$k_1 = \sqrt{2m_e^* \varepsilon_0 / \hbar^2} \quad k_2 = \sqrt{2m_e^* (V_0 - \varepsilon_0) / \hbar^2} \quad (167)$$

For the infinite potential barrier model  $V_0$  is taken to be infinite and the wavefunction outside the barrier is taken to be zero. Matching the wavefunction and its derivative at the boundaries yields

$$k_2^2 = \frac{k_1^2 (1 - \cos k_1 L)}{1 + \cos k_1 L} \quad (168)$$

where the cross-section has been taken to be a square with sides  $L_x = L_y = L$ .

Next, the effect of an electric field on the subband energies is calculated by using the Hamiltonian

$$\hat{H}_1 = \hat{H}_0 + \eta(x \cos \theta + y \sin \theta) \quad (169)$$

where  $\eta = |e|E$ .  $E$  is the electric field strength applied in the  $x, y$  plane and  $\theta$  is the angle between the electric field and the  $x$  axis. The trial function in this case is modified to be

$$\psi_1(x, y) = N_1 \psi_0(x, y) \exp[-\beta(x \cos \theta + y \sin \theta)/L] \quad (170)$$

where  $N_1$  is the normalization coefficient and  $\beta$  is the variational parameter.

With an impurity at  $(x_i, y_i, 0)$  the Hamiltonian becomes

$$\hat{H}_2 = \hat{H}_1 - \frac{\hbar^2}{2m_e^*} \frac{\partial^2}{\partial z^2} - \frac{e^2}{\kappa \sqrt{z^2 + (x - x_i)^2 + (y - y_i)^2}} \quad (171)$$

The trial function for this problem is taken to be

$$\psi_2(x, y, z) = N_2 \psi_1(x, y) \times \exp \left[ -\lambda \sqrt{z^2 + (x - x_i)^2 + (y - y_i)^2} \right] \quad (172)$$

where  $N_2$  is the normalization constant and  $\lambda$  is a variational parameter. The binding energy of the electron is written with respect to the subband energy calculated in the presence of an applied electric field. Numerical results are found for the GaAs/Ga<sub>1-x</sub>Al<sub>x</sub>As system where, within the finite barrier model that has been taken, it has been considered that the finite barrier potential and dielectric constant depend on the  $x$  concentration of Al as follows:

$$V_0 = 0.6(1.247x) \text{ eV} \quad \kappa = 12.5(1 - x) + 10.1x \quad (173)$$

For cylindrical quantum well wires, the Hamiltonian for the relative motion is given by

$$\hat{H}_0 = -\frac{\hbar^2}{2m_e^*} \left( \frac{\partial^2}{\partial r^2} + \frac{1}{r} \frac{\partial}{\partial r} + \frac{1}{r^2} \frac{\partial^2}{\partial \varphi^2} \right) + V_b(r, \varphi) \quad (174)$$

where

$$V_b(r, \varphi) = \begin{cases} 0 & r \leq r_0 \\ V_0 & r \geq r_0 \end{cases} \quad (175)$$

The wavefunction for the ground state becomes

$$\psi_0(r, \varphi) = N_0 \begin{cases} J_0(k_{10} r) & r \leq r_0 \\ \frac{J_0(k_{10} r_0)}{K_0(k_{20} r_0)} K_0(k_{20} r) & r \geq r_0 \end{cases} \quad (176)$$

where

$$k_{10} = \sqrt{\frac{2m_e^*}{\hbar^2} \varepsilon_0} \quad k_{20} = \sqrt{\frac{2m_e^*}{\hbar^2} (V_0 - \varepsilon_0)} \quad (177)$$

With an applied electric field in the  $x, y$  plane, the Hamiltonian becomes

$$\hat{H}_1 = \hat{H}_0 + \eta r \cos(\varphi - \theta) \quad (178)$$

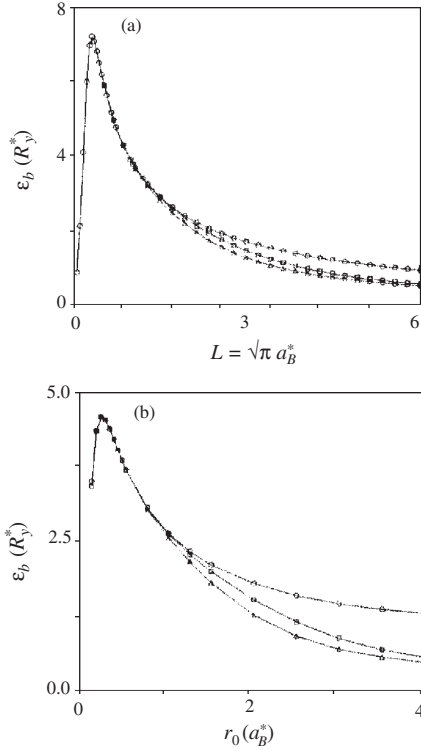


**Figure 28.** The binding energy as a function of (a) side length of the square wire and (b) radius of the cylindrical wire. For both cases  $E = 0, 10,$  and  $20$  kV/cm (from top to bottom). Reprinted with permission from [205], J. L. Marín et al., in “Handbook of Advanced Electronic and Photonic Materials and Devices” (H. S. Nalwa, Ed.). Academic Press, San Diego, 2001. © 2001, Academic Press.

The trial function in this case is taken to be

$$\psi_1(r, \varphi) = N_1 \psi_0(r, \varphi) \exp[-\beta r \cos(\varphi - \theta)/r_0] \quad (179)$$

where  $\beta$  is the variational parameter. The Hamiltonian becomes

$$\hat{H}_2 = \hat{H}_1 - \frac{\hbar^2}{2m_e^*} \left( \frac{\partial^2}{\partial z^2} \right) - \frac{e^2}{\kappa \sqrt{z^2 + (r - r_i)^2}} \quad (180)$$

The trial function for the bound electron is taken to be

$$\psi_2(r, \varphi, z) = N_2 \psi_1(r, \varphi) \exp \left[ -\lambda \sqrt{z^2 + (r - r_i)^2} \right] \quad (181)$$

where  $\lambda$  is the variational parameter.

The calculations are carried out for the model system of GaAs/Al<sub>x</sub>Ga<sub>1-x</sub>As for which the effective Bohr radius is  $a_B^* = 98.7 \text{ \AA}$  and the effective Rydberg is  $R_y^* = 5.83 \text{ meV}$  for  $x = 0.3$ . The results are in perfect agreement with previous calculations without the electric field. For example, the binding energies are found to be almost identical for wires of circular and square cross-sections if wire dimensions are taken to be comparable. The binding energies are different for finite and infinite barrier potentials. For infinite barrier potentials, the binding energy  $\varepsilon_b$  tends to infinity as the diameter of the wire tends to zero. It tends to smaller finite values for finite barrier potentials.

The behavior of the binding energy under a different electric field is shown in Figure 28a and b for wires of square and circular cross-sections, respectively. The electric field is taken to be applied along the positive axis direction with  $\theta = 0$ . Thus, the electron shifts toward the negative part of the axis. It is seen from these figures that the binding energy is a more sensitive function of the electric field for wires of cylindrical cross-section.

The impurity position dependence of the binding energy is shown in Figure 29a when the impurity position is changed along the diagonal of the square wire ( $L = \sqrt{\pi} a_B^*$ ) for different electric fields. The impurity position dependence of the binding energy is shown in Figure 29b when the impurity position is changed radially for a cylindrical wire ( $r_0 = a_B^*$ ) for different electric fields. As expected the binding energy becomes smaller for impurities located at the boundary of the wires since for this position the quantum well walls prevent the electron from feeling the full power of the Coulomb attraction.

The behavior of the binding energy is also checked as the wire dimension is increased. Figure 30a shows the binding energy as a function of impurity position along the  $x$ -axis of the square wire ( $L = \sqrt{\pi} 2a_B^*$ ) for different electric fields. Now, the binding energy is generally smaller since the walls are not pushing the electron closer to the Coulomb center.

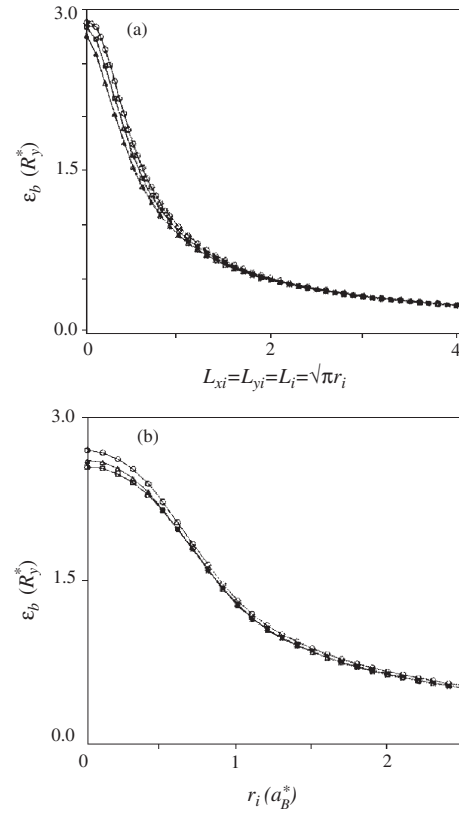


**Figure 29.** The binding energy as a function of impurity position along the (a) diagonal of the square wire ( $L = \sqrt{\pi} a_B^*$ ) and (b) radius of the cylindrical wire ( $r_0 = a_B^*$ ). Same electric field values as in Figure 28. Reprinted with permission from [205], J. L. Marín et al., in “Handbook of Advanced Electronic and Photonic Materials and Devices” (H. S. Nalwa, Ed.). Academic Press, San Diego, 2001. © 2001, Academic Press.

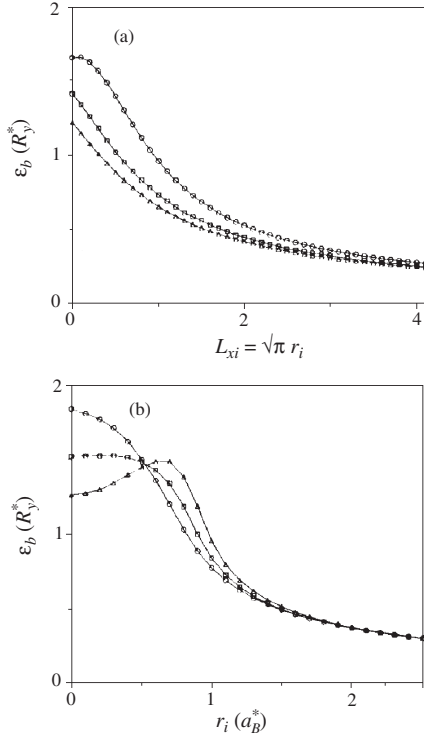


**Figure 30.** The binding energy as a function of impurity position along the (a)  $x$ -axis of the square wire ( $L = \sqrt{\pi} 2a_B^*$ ) and (b) radius of the cylindrical wire ( $r_0 = 2a_B^*$ ). Same electric field values as in Figure 28. Reprinted with permission from [205], J. L. Marín et al., in “Handbook of Advanced Electronic and Photonic Materials and Devices” (H. S. Nalwa, Ed.). Academic Press, San Diego, 2001. © 2001, Academic Press.

Figure 30b shows the binding energy as a function of impurity position along the radius of the cylindrical wire ( $r_0 = 2a_B^*$ ) for different electric fields. In this case also, the binding energy becomes generally smaller for the same reason.

The Al concentration ( $x$ ) dependence of the binding energy is shown in Figure 31. As expected, increasing the potential barrier increases the binding energy, because the electron is better pushed toward the Coulomb center when the walls are at a higher potential.

In conclusion, the variational method employed in this context is capable of giving all the correct trends for impurity binding energies as a function of the applied electric field, impurity position, and wire geometry.

### 3.6. Hydrogenic Impurities in a Spherical Quantum Dot in the Presence of a Magnetic Field

The ground state and binding energies for a hydrogenic impurity in a spherical quantum dot in the presence of a uniform magnetic field are calculated by a variational method within the effective mass approximation [99]. The simple hydrogenic trial wavefunctions used in this calculation are flexible enough to treat on-center, off-center, and edge states of impurities in a quantum dot. Overall results are in reasonable agreement when compared to other calculations. Interestingly enough, in the case of an off-center

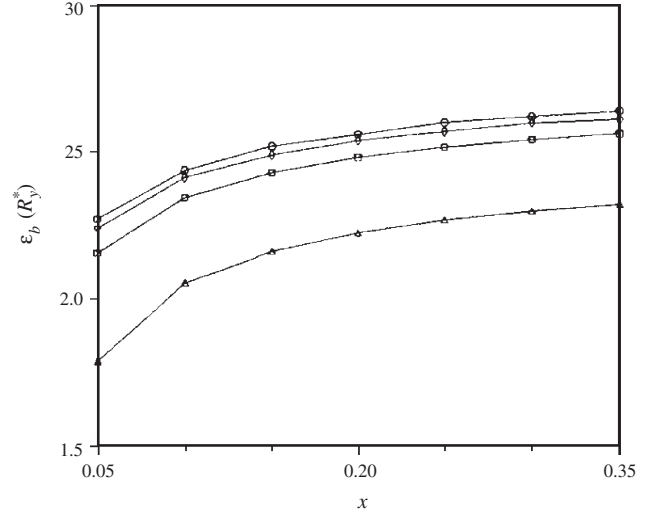


**Figure 31.** The binding energy as a function of Al concentration for hydrogenic impurities in a cylindrical wire ( $r_0 = a_B^*$ ). Same electric field values as in Figure 28. Reprinted with permission from [205], J. L. Marín et al., in “Handbook of Advanced Electronic and Photonic Materials and Devices” (H. S. Nalwa, Ed.). Academic Press, San Diego, 2001. © 2001, Academic Press.

impurity, a critical point from which bulk states change their nature (edge states) is also found.

Semiconductors composed of III–V materials usually have small effective masses, which means that the Bohr radius associated with the impurity is large compared with achievable quantum dot sizes. The binding energy of the impurity increases as the size of the confining region becomes of the order of Bohr radius, which makes possible, for instance, the fabrication of a low-threshold laser diode [100].

In this section a variational study about the effect of a magnetic field on the ground state and binding energies of a hydrogenic impurity within spherical quantum dot is made. The impurity can be located on (off) the center of symmetry to get a symmetric (asymmetric) situation, or near the boundary of quantum dot to get surfacelike states (edge states) of this system.

#### 3.6.1. Theory and Model

Within the framework of the effective mass approximation, the Hamiltonian of a hydrogenic impurity located at the center of symmetry of a spherical quantum dot of radius  $r_0$ , in the presence of magnetic field, can be written as

$$\hat{H} = \frac{1}{2m_e^*} \left( \hat{p} - \frac{e}{c} \vec{A} \right)^2 - \frac{e^2}{\kappa r} + V_b(\vec{r}) \quad (182)$$

where  $\kappa$  is the dielectric constant of material inside the quantum dot,  $m_e^*$  is the electron effective mass,  $\vec{A}$  is the vector potential, and  $V_b(\vec{r})$  is the confining potential defined by

$$V_b(\vec{r}) = \begin{cases} 0 & 0 \leq r \leq r_0 \\ \infty & r > r_0 \end{cases} \quad (183)$$

For a uniform magnetic field,  $\vec{A}(\vec{r}) = \vec{B} \times \vec{r}/2$  if the Coulomb gauge  $\nabla \cdot \vec{A} = 0$  is chosen. In spherical coordinates,



if the magnetic field is along the  $z$  direction,  $\vec{B} = B\hat{e}_z$ , the Hamiltonian can be expressed as

$$\hat{H} = -\frac{1}{2m_e^*}\nabla^2 - \frac{e^2}{\kappa r} - \frac{e}{2m_e^*c}B\hat{L}_z + \frac{e^2}{8m_e^*c^2}B^2r^2\sin^2\theta \quad (184)$$

Here,  $\hat{L}_z$  is the  $z$  component of the angular momentum operator, and  $\theta$  is the usual polar angle in these coordinates. The magnetic field preserves the azimuthal symmetry (i.e.,  $m$  is still a “good” quantum number). As only the ground state is studied, the value  $m = 0$  is required; thus the Hamiltonian [Eq. (184)] will retain the quadratic dependence on  $B$  only.

Because of confinement, the solution of the Schrödinger equation associated with Eq. (184) must satisfy

$$\psi(r = r_0, \theta, \varphi) = 0 \quad (185)$$

In order to use the variational method, the trial wavefunction for the calculation of the ground state energy is chosen as

$$\begin{aligned} \psi(r) &= N \exp(-\alpha r) \exp\left(-\frac{1}{8}Br^2\sin^2\theta\right)(r_0 - r) \\ &= N \exp(-\alpha r) \exp\left(-\frac{1}{12}Br^2\right)(r_0 - r) \end{aligned} \quad (186)$$

where  $N$  is the normalization constant and  $\alpha$  is a variational parameter to be determined. The last term has been obtained considering that in absence of  $\vec{A}$  the system holds spherical symmetry. A similar choice of the trial wavefunction to calculate the ground state energy has widely been used in the case of hydrogenic impurities within spherical quantum dots [65] and cylindrical quantum wires [77] without magnetic field.

In the case of a hydrogenic impurity displaced a constant distance  $a$  from the center of symmetry of a quantum dot, the Hamiltonian of Eq. (182) is modified as

$$\hat{H} = \frac{1}{2m_e^*}\left(\hat{p} - \frac{e}{c}\vec{A}\right)^2 - \frac{e^2}{\kappa|\vec{r} - a\hat{e}_z|} + V_b(\vec{r}) \quad (187)$$

where the confining potential,  $V_b(\vec{r})$ , is still given by Eq. (183), and  $\hat{e}_z$  is a unit vector on the  $z$ -axis. Hence, the corresponding Hamiltonian and trial wavefunction, Eqs. (184) and (186), are given by

$$\begin{aligned} \hat{H} &= -\frac{1}{2m_e^*}\nabla^2 - \frac{e^2}{\kappa|\vec{r} - a\hat{e}_z|} - \frac{e}{2m_e^*c}B\hat{L}_z \\ &\quad + \frac{e^2}{8m_e^*c^2}B^2r^2\sin^2\theta \end{aligned} \quad (188)$$

and

$$\psi(r) = N \exp(-\alpha|\vec{r} - a\hat{e}_z|) \exp\left(-\frac{1}{8}Br^2\sin^2\theta\right)(r_0 - r) \quad (189)$$

respectively.

Notice that the wavefunction [Eq. (189)] satisfies the boundary condition imposed by Eq. (185). Again, since

$m = 0$  is chosen, thus the Hamiltonian [Eq. (188)] will not have a linear dependence on magnetic field  $B$ , just like the symmetric case studied previously.

As we shall see, the trial wavefunction [Eq. (189)] is flexible enough to describe the case when the radius of the confining sphere becomes infinite and the hydrogenic impurity is close to its boundary. The latter would correspond to the case of a hydrogenic impurity close to a plane, which allows us to investigate the ground state edge level of the spherical quantum dot.

The binding energy ( $\varepsilon_b$ ) for the hydrogenic impurity is defined as the ground state energy of the system without Coulombic interaction ( $\varepsilon_w$ ) minus the ground state energy including the presence of the electron–nucleus interaction ( $\varepsilon_0$ ); that is,

$$\varepsilon_b = \varepsilon_w - \varepsilon_0 \quad (190)$$

The binding energy defined previously is a positive quantity. The  $\varepsilon_w$  term of Eq. (190) is the ground state energy of an electron confined inside a spherical quantum dot of radius  $r_0$ ; that is,

$$\varepsilon_w = \frac{\pi^2\hbar^2}{2m_e^*r_0^2} \quad (191)$$

The values of the physical parameters pertaining to a GaAs quantum dot used in these calculations, for the sake of comparison, are  $m_e^* = 0.067m_0$  and  $\kappa = 12.5$ ; thus  $a_B^* = 98.7 \text{ \AA}$  and  $R_y^* = 5.83 \text{ meV}$ . Moreover, the linear dependence term on  $B$ , in Eq. (184), can be scaled down to

$$\gamma m = \frac{e\hbar}{2m_e^*cR_y^*}Bm = \frac{m_0}{m_e^*R_y^*}\mu_0Bm \quad (192)$$

where  $\mu_0 = 5.78838263 \times 10^{-2} \text{ meV T}^{-1}$  is the Bohr magneton; then the value  $B = 6.75 \text{ T}$  corresponds to an effective Rydberg ( $\gamma = 1$ ).

The results for the symmetric case (on-center impurity) are displayed in Figure 32, in which the binding energy of the hydrogenic impurity is plotted as a function of the quantum dot radius for different magnetic field strengths. The qualitative and quantitative behaviors of the results are in good agreement with those of Xiao et al. [101] and Branis et al. [102], who studied the magnetic field dependence over the binding energies of hydrogenic impurities in quantum dots and quantum well wires, respectively. In the strong spatial confinement case, ( $r_0 < a_B^*$ ), the binding energy is relatively insensitive to the magnetic field and diverges as the dot radius  $r_0 \rightarrow 0$ , as in the case of zero magnetic field. The latter reflects that the main contribution to the binding energy is due to electron spatial confinement, which prevails over magnetic field confinement. The latter can be estimated through the magnetic length defined as

$$l_B = \sqrt{\frac{\hbar c}{eB}} = 484.82 \times B^{-1/2} \quad (193)$$

where  $l_B$  is expressed in effective Bohrs, and  $B$  is given in Teslas. For dot radius  $r_0 \cong a_B^*$ , the different magnetic field

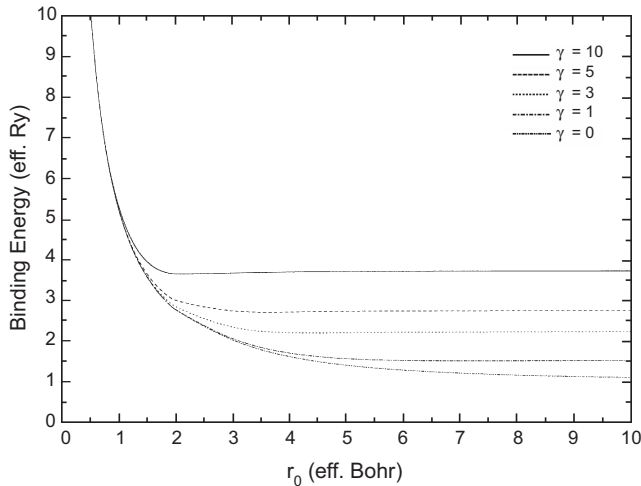


**Figure 32.** The binding energy of an on-center hydrogenic impurity as a function of the quantum dot radius for different magnetic fields. Reprinted with permission from [205], J. L. Marín et al., in “Handbook of Advanced Electronic and Photonic Materials and Devices” (H. S. Nalwa, Ed.). Academic Press, San Diego, 2001. © 2001, Academic Press.

curves deviate from each other reaching steady values as the dot radius increases. For weak spatial confinement ( $r_0 \gg a_B^*$ ), the binding energy converges asymptotically to the corresponding bulk values. In the limit of large dot radius, the binding energy for  $B = 0$  approaches its bulk value  $\varepsilon_b = 1R_y^*$ , as expected. An increase of the field strength decreases the magnetic length as compared with the dot radius; thus in this case the binding energy increases due to magnetic confinement that compels the electron to move “closer” to the on-center impurity.

Figure 33 shows the behavior of binding energy as a function of field strength for different dot radii of an on-center impurity. The variation of binding energy as the

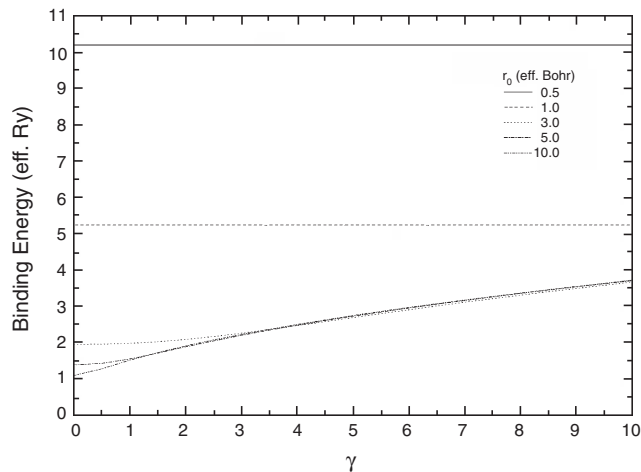


**Figure 33.** The binding energy of an on-center hydrogenic impurity as a function of the magnetic field for different dot radii. Reprinted with permission from [205], J. L. Marín et al., in “Handbook of Advanced Electronic and Photonic Materials and Devices” (H. S. Nalwa, Ed.). Academic Press, San Diego, 2001. © 2001, Academic Press.

field increases is less sensitive as dot radius decreases, thus enforcing the previous comment regarding Figure 32.

The results for the asymmetric case (off-center impurity) are plotted in Figures 34 and 35 with zero magnetic field. Figure 34 shows the ground state energy for different sizes of quantum dot versus the relative position of the off-center impurity ( $a/r_0$ ). The ground state energy increases from its on-center impurity value ( $a/r_0 = 0$ ) as the impurity is shifted off the center; this is a general behavior. For larger radii the ground state energy becomes lower, and then, for closer distances to the wall, evolves from the  $1s$  “free” hydrogen ground state ( $-1/2$  Hartree) to the  $2p_z$  “free” hydrogen first excited state ( $-1/8$  Hartree). These results are in good agreement with those of Brownstein [86], Gorecki and Byers Brown [85], and Marín et al. [65]. It is clear now that the trial wavefunction as chosen is flexible enough to describe the case when the size of the quantum dot becomes infinite and the nucleus is close to the surface. The latter corresponds to the case of a hydrogenic impurity close to a plane. This situation will be discussed later when the effect of a magnetic field on the ground state of a hydrogenic impurity near a semiconductor surface will be considered.

In Figure 35, the binding energy for different sizes of quantum dot versus the relative position of the off-center impurity ( $a/r_0$ ) was plotted. The binding energy decreases as the impurity approaches the boundary of a quantum dot. This behavior is due to the fact that wavefunctions vanish at the boundaries and thus their contributions to the binding energy of a quantum dot with an off-center impurity are smaller than a quantum dot with an on-center impurity. The results are similar to the case of a hydrogenic impurity placed in rectangular [81] or circular [77] cross-section quantum well wires, and in a spherical quantum dot [101].

The problem of a hydrogenic impurity near a crystal surface as a limit case of a hydrogenic impurity in a spherical quantum dot of very large radius will be considered next.

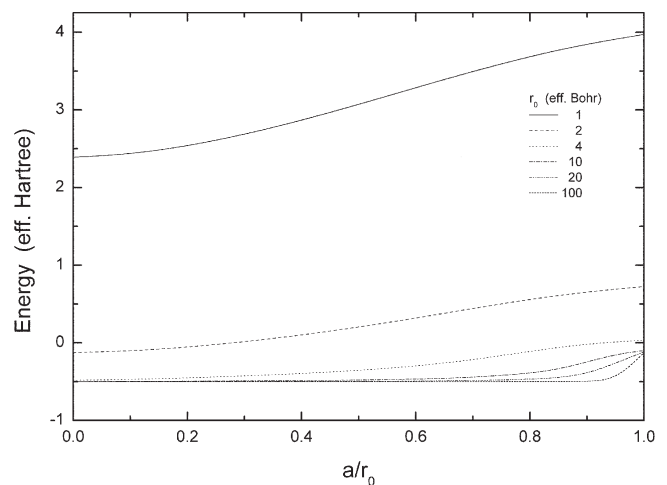


**Figure 34.** The ground state energy of an off-center hydrogenic impurity as a function of the relative position of the impurity for different dot radii. Reprinted with permission from [205], J. L. Marín et al., in “Handbook of Advanced Electronic and Photonic Materials and Devices” (H. S. Nalwa, Ed.). Academic Press, San Diego, 2001. © 2001, Academic Press.

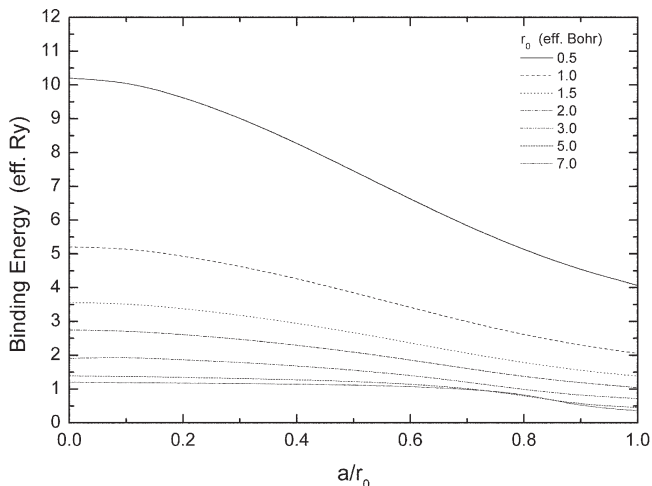


**Figure 35.** The binding state energy of an off-center hydrogenic impurity as a function of the relative position of the impurity for different dot radii. Reprinted with permission from [205], J. L. Marín et al., in “Handbook of Advanced Electronic and Photonic Materials and Devices” (H. S. Nalwa, Ed.). Academic Press, San Diego, 2001. © 2001, Academic Press.

In Figure 36, the ground state energy for different radii of quantum dot versus the relative position of the off-center impurity ( $a/r_0$ ) is shown. For very large quantum dot radii Levine’s ground state energy of an atom located precisely on the surface of a semi-infinite medium is obtained; that is, the ground state energy changes gradually from its bulk value ( $-1$  Rydberg) into Levine’s state ( $-1/4$  Rydberg) as the impurity reaches the surface.

In Figure 37, the ground state binding energy for different radii of quantum dot versus the relative position of the off-center impurity ( $a/r_0$ ) was plotted. For the too large

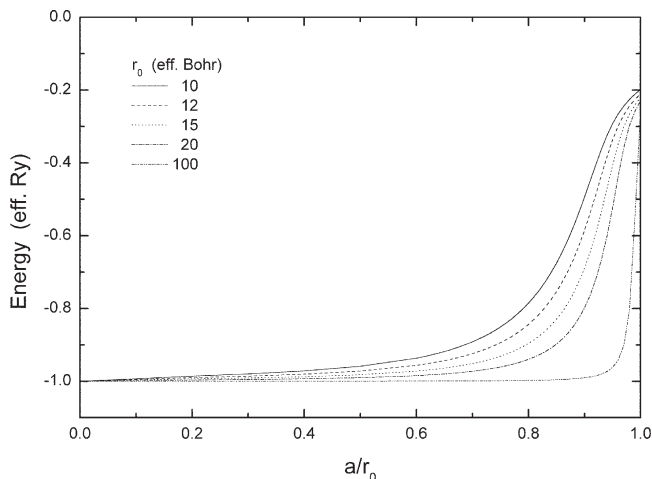


**Figure 36.** The ground state energy of a hydrogenic impurity in a spherical quantum dot of very large radius. Note that the ground state changes gradually from its bulk value ( $-1R_y^*$ ) to the Levine state ( $-1/4R_y^*$ ). Reprinted with permission from [205], J. L. Marín et al., in “Handbook of Advanced Electronic and Photonic Materials and Devices” (H. S. Nalwa, Ed.). Academic Press, San Diego, 2001. © 2001, Academic Press.

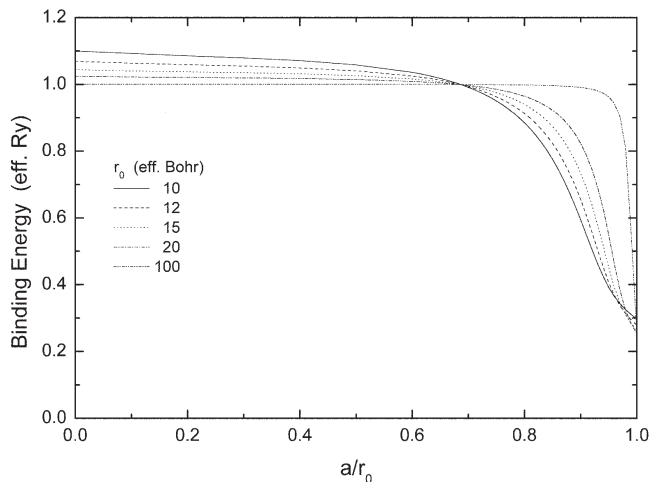


**Figure 37.** The binding state energy of a hydrogenic impurity as a function of the relative position of the impurity for large dot radii. Note that there is a point from which the edge states start to appear. Reprinted with permission from [205], J. L. Marín et al., in “Handbook of Advanced Electronic and Photonic Materials and Devices” (H. S. Nalwa, Ed.). Academic Press, San Diego, 2001. © 2001, Academic Press.

quantum dot radii considered here, binding energy curves cross one another and define a point from which the edge states begin to appear. This critical point corresponds to a hydrogenic impurity placed at the relative distance  $a/r_0 = 0.68$  from the center of the quantum dot. The associated binding energy with the quantum dot of largest radius ( $r_0 = 100$  effective Bohr) decreases from  $1R_y^*$  (effective Rydberg) for an impurity located far from a quantum dot surface to  $1/4R_y^*$  for an impurity located exactly at the surface of a quantum dot. The binding energy behavior is in reasonable agreement with that of Chen [103], who studied the problem of hydrogenic donors near semiconductor surfaces. Furthermore, starting from the critical point (near the quantum dot surface), there is an inversion of binding energy for quantum dots of different radii. This occurs because the boundary has a greater effect on binding energy when the quantum dot size increases, as a result of the strong spatial limitation due to the closeness of the impurity to the surface. When a magnetic field is applied, the critical point is removed and the binding energy curves cross one another at only one point. Moreover, crossing points are shifted away from the boundary as the magnetic field is increased, and finally a moderate field strength causes them to vanish.

### 3.7. Two-Electron Atomic Systems Confined within Spheroidal Boxes

The direct variational method is used to estimate some interesting physical properties of the He atom and  $Li^+$  ion confined within impenetrable spheroidal boxes. A comparative investigation of the ground state energy, pressure, polarizability, dipole moments, and quadrupole moments with those of He atom inside boxes with paraboloidal walls is made [104, 105]. The overall results show a similar qualitative behavior. However, for  $Li^+$  there are quantitative differences on such properties due to its major nuclear charge, as expected. The trial wavefunction is constructed as a product

of two hydrogenic wavefunctions adapted to the geometry of the confining boxes.

Nowadays there is special interest in investigation of atoms and molecules confined in nanostructures because their physical properties become highly dependent of the size and shape of the confinement volume [65, 77, 78, 105–111]. The reduction of space where the atom is located is equivalent to subjecting it to high pressures and the results of this new spatial condition are, besides other effects, the increase in total energy of the atom and the decrease of its polarizability.

The “atom in a box” model consists of replacing its interaction with neighboring particles by a potential wall. The simplest situation is to assume an infinite potential wall since for this case the wavefunction must vanish at the boundary of the box. The latter condition simplifies the calculations extremely. When a quantum system is localized in a box, the result is that the wavefunction of the system is constrained into that region.

The study of hydrogenic impurities trapped in solids has signaled the limitations of the model of confinement inside spherical boxes. For example, the observed hyperfine splitting of atomic hydrogen in  $\alpha$ -quartz shows the presence of nonvanishing anisotropic components [112], and moreover, the electron microscopy studies of semiconductor clusters show microparticles whose shapes vary from quasi-spherical to pyramidal [113]. This has motivated the use of other models involving nonspherical boxes.

The helium atom inside spherical boxes has been investigated for modeling the effect of pressure on atoms with more than one electron [106–108]. Recently the helium atom inside boxes with paraboloidal walls [105] and the helium atom in a semi-infinite space limited by a paraboloidal boundary [114] have been studied.

### 3.7.1. Variational Calculation of Ground State Energy

The prolate spheroidal coordinates  $(\xi, \eta, \varphi)$  are defined by

$$\xi = \frac{(r_1 + r_2)}{2R} \quad \eta = \frac{(r_1 - r_2)}{2R} \quad \varphi \equiv \varphi \quad (194)$$

where  $r_1$  and  $r_2$  are the distances from any point to two fixed points (foci) separated by a distance  $2R$ . In these coordinates

$$\{\xi = \text{const.} \quad -1 \leq \eta \leq 1 \quad 0 \leq \varphi \leq 2\pi\} \quad (195)$$

defines a family of ellipsoids of revolution around the  $z$ -axis, while

$$\{1 \leq \xi \leq \infty \quad \eta = \text{const.} \quad 0 \leq \varphi \leq 2\pi\} \quad (196)$$

defines a family of hyperboloids of revolution around the  $z$ -axis. In both cases  $2R$  is the focal distance and  $\varphi$  is the usual azimuth angle [115].

If the nucleus of the helium atom is located on one of the foci ( $z = -R\hat{e}_z$ ),  $r_1$  and  $r_2$  denote the location of the two electrons relative to the fixed nucleus, and  $r_{12}$  is the

interelectronic distance, then the Hamiltonian for this system formed by two electrons and one nucleus of charge  $Z$  ( $=2$ ) is given by

$$\hat{H} = -\frac{1}{2}\nabla_1^2 - \frac{1}{2}\nabla_2^2 - \frac{Z}{r_1} - \frac{Z}{r_2} + \frac{1}{r_{12}} \quad (197)$$

where it has been assumed that  $\hbar = m_e^* = e = 1$  (atomic units) and the mass of the nucleus is considered to be very large compared to the electron mass (Born–Oppenheimer approximation).

In spheroidal coordinates, the Laplacian operator can be written as

$$\nabla^2 = \frac{1}{R^2(\xi^2 - \eta^2)} \left\{ \frac{\partial}{\partial \xi} (\xi^2 - 1) \frac{\partial}{\partial \xi} + \frac{\partial}{\partial \eta} (1 - \eta^2) \frac{\partial}{\partial \eta} + \frac{\xi^2 - \eta^2}{(\xi^2 - 1)(1 - \eta^2)} \frac{\partial^2}{\partial \varphi^2} \right\} \quad (198)$$

and the electron–nucleus distances are, respectively,

$$r_1 = R(\xi + \eta) \quad r_2 = R(\xi' + \eta) \quad (199)$$

The electron–electron repulsive potential can be written as a series expansion in products of associate Legendre polynomials

$$\frac{1}{r_{12}} = \frac{1}{R} \sum_{l=0}^{\infty} (2l+1) \sum_{m=0}^l \epsilon_m i^m \left[ \frac{(l-m)!}{(l+m)!} \right]^2 \cos m(\varphi - \varphi') \times P_l^m(\eta) P_l^m(\eta') f_l^m(\xi, \xi') \quad (200)$$

where

$$f_l^m(\xi, \xi') = \begin{cases} P_l^m(\xi') Q_l^m(\xi) & \xi > \xi' \\ P_l^m(\xi) Q_l^m(\xi') & \xi < \xi' \end{cases} \quad (201)$$

$\epsilon_m$  is Neumann’s factor:  $\epsilon_0 = 1$ ,  $\epsilon_n = 2$  ( $n = 1, 2, 3, \dots$ ) [116].

If the atom is enclosed in an impenetrable prolate spheroidal box defined as

$$\{\xi = \xi_0 \quad -1 \leq \eta \leq 1 \quad 0 \leq \varphi \leq 2\pi\} \quad (202)$$

then the wavefunctions must fulfill the requirements

$$\begin{aligned} \psi(\xi = \xi_0, \eta, \varphi; \xi', \eta', \varphi') &= 0 \\ \psi(\xi, \eta, \varphi; \xi' = \xi_0, \eta', \varphi') &= 0 \end{aligned} \quad (203)$$

To obtain the ground state energy of a helium atom by using the direct variational method, the ansatz wavefunction is constructed as a product of two hydrogenic functions, namely,

$$\begin{aligned} \psi(\xi, \eta, \varphi; \xi', \eta', \varphi') &= A \exp[-\alpha R(\xi + \eta)] \\ &\quad \times \exp[-\alpha R(\xi' + \eta')] \\ &\quad \times (\xi - \xi_0)(\xi' - \xi_0) \end{aligned} \quad (204)$$

where  $A$  is a normalization constant, and  $\alpha$  is a variational parameter to be determined after minimizing the energy functional with the additional constrictions imposed by Eq. (203). To satisfy the latter, two auxiliary functions

have been included which have a similar contour to the spheroidal confinement box to allow the total wavefunction to cancel out at the boundary of the box. The kind of wavefunctions like those given in Eq. (204) have been used to investigate one- and two-electron atomic systems confined by spherical penetrable boxes [78], the H,  $H_2^+$ , and  $HeH^{2+}$  quantum systems within soft spheroidal boxes [111], and the helium atom inside boxes with paraboloidal walls [105]. In all of these confined quantum systems such simple functions can describe the symmetry in a qualitative way. Quantitatively, the results are close to those obtained by other methods [106, 107].

The evaluation of the matrix element for the electron-electron Coulomb repulsion with the trial wavefunction [Eq. (204)] involves integration over the azimuthal angles, which can be done immediately, and only the term with  $m = 0$  of Eq. (200) remains. The latter shows the symmetry of system under rotations around the  $z$ -axis. Additionally, the associate Legendre polynomials become ordinary Legendre polynomials. A complete evaluation of the leading expression for the matrix element is presented in Section 4.7.3.

The ground state energy of He and  $Li^+$  for  $R = 0.1, 0.5,$  and  $1.0$  Bohr as a function of volume of the enclosing box is displayed in Figure 38, where a comparison with results of Ley-Koo and Flores-Flores [105] for a He atom within a paraboloidal box is also made.

### 3.7.2. Pressure, Polarizability, and Dipole and Quadrupole Moments

The computed variational energy and trial wavefunctions allow calculation of some of the properties of the confined atom. The average pressure exerted by the boundary on the atom is given by

$$P = -\frac{d\varepsilon}{dV} = -\frac{3}{4\pi R^3(3\xi_0^2 - 1)} \frac{d\varepsilon}{d\xi_0} \quad (205)$$

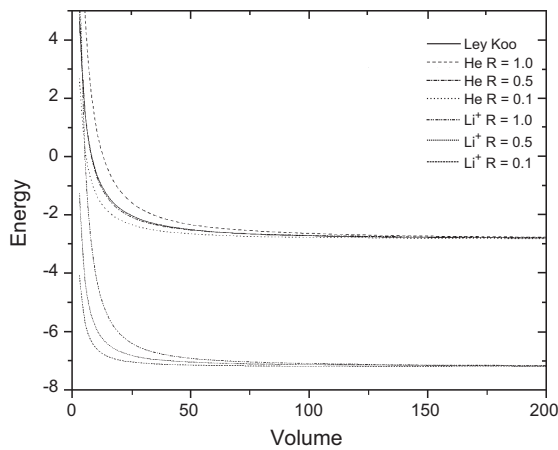


**Figure 38.** Ground state energy for the helium atom and the lithium ion versus the volume of the spheroidal box and the interfocal distance. Energy units, Hartree; volume units, Bohr<sup>3</sup>. Reprinted with permission from [205], J. L. Marín et al., in “Handbook of Advanced Electronic and Photonic Materials and Devices” (H. S. Nalwa, Ed.). Academic Press, San Diego, 2001. © 2001, Academic Press.

where  $V = 4\pi R^3 \xi_0 (\xi_0^2 - 1)/3$  is the volume of the spheroidal box and  $\varepsilon$  is the total ground state energy of the atom. The results obtained for pressure are displayed in Figure 39 for  $R = 0.1, 0.5,$  and  $1.0$  Bohr as a function of  $V$ ; they are also compared with the results of [105].

Following Ley-Koo and Flores-Flores, we used an adapted expression for the polarizability of atoms to molecules [117–119]; then the parallel and perpendicular components of the polarizability are given by

$$\alpha_{\parallel} \equiv \alpha_{zz} = \frac{4}{Z} \left\langle \sum_{i=1}^2 (z_i - \langle z \rangle)^2 \right\rangle = \frac{16}{Z} [\langle z^2 \rangle - \langle z \rangle^2]^2 \quad (206)$$

$$\alpha_{\perp} \equiv \alpha_{xx} = \alpha_{yy} = \frac{4}{Z} \left\langle \sum_{i=1}^2 x_i^2 \right\rangle = \frac{16}{Z} \langle x^2 \rangle^2 \quad (207)$$

Due to the asymmetric position of the nucleus and the asymmetric distribution of electrons inside the confinement box, the atom has an electric dipole moment, which is given by the expectation value of the electron position plus the nucleus contribution; that is,

$$\vec{d} = -RZ\hat{e}_z - \left\langle \psi \left| \sum_{i=1}^2 \vec{r}_i \right| \psi \right\rangle = -[ZR + 2\langle z \rangle]\hat{e}_z \quad (208)$$

The components of the electric quadrupole moment tensor are given by

$$\begin{aligned} Q_{zz} &= Z(2R^2) - \left\langle \sum_{i=1}^2 [2z_i^2 - x_i^2 - y_i^2] \right\rangle \\ &= Z(2R^2) - 4[\langle z^2 \rangle - \langle x^2 \rangle] \\ Q_{xx} &= Q_{yy} = -\frac{1}{2}Q_{zz} \end{aligned} \quad (209)$$

Figure 40a–c shows the polarizability components for He and  $Li^+$  as a function of the major semiaxis,  $R\xi_0$ , for

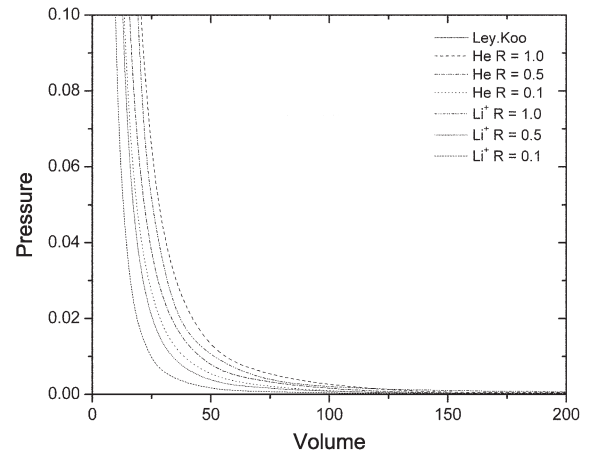


**Figure 39.** Pressure of the helium atom and the lithium ion versus the volume of the spheroidal box and the interfocal distance. The atomic unit for pressure is equivalent to  $2.94 \times 10^{13}$  Pa. Reprinted with permission from [205], J. L. Marín et al., in “Handbook of Advanced Electronic and Photonic Materials and Devices” (H. S. Nalwa, Ed.). Academic Press, San Diego, 2001. © 2001, Academic Press.

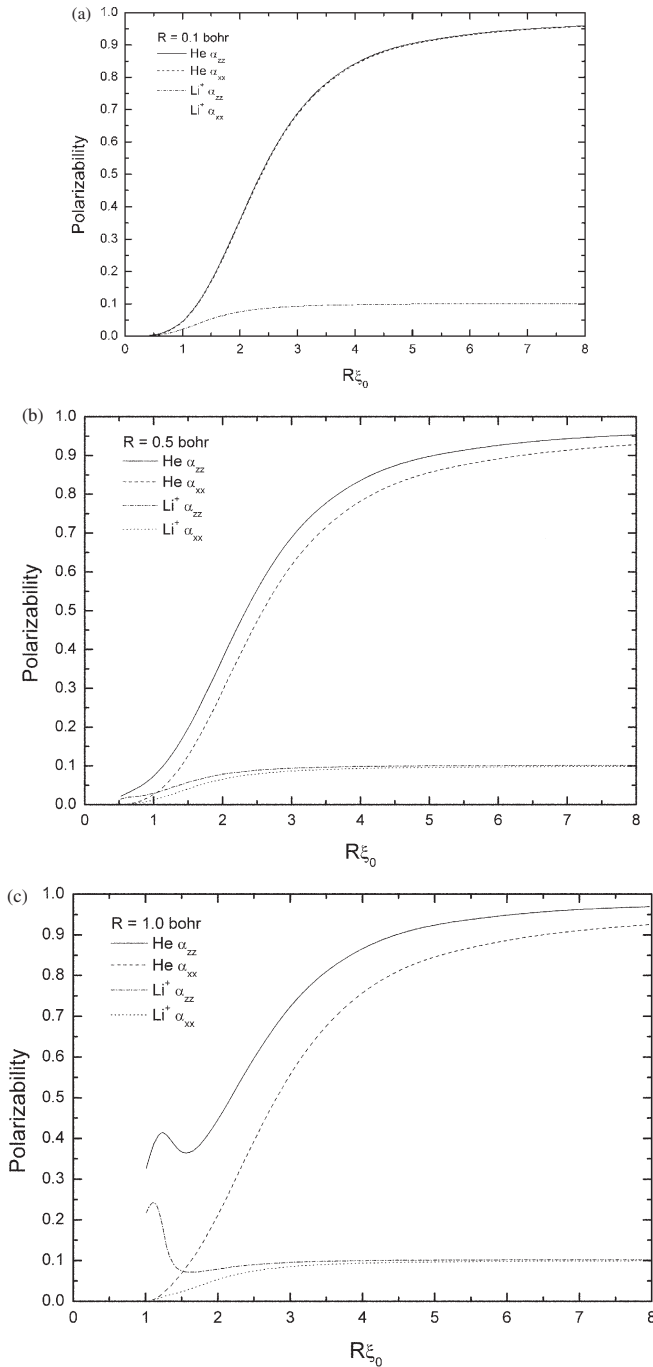


**Figure 40.** Polarizability tensor components versus major semiaxis of the spheroidal box. Polarizability units,  $\text{Bohr}^3$ ; distance units, Bohr. (a)  $R = 0.1$ , (b)  $R = 0.5$ , and (c)  $R = 1.0$ . Reprinted with permission from [205], J. L. Marín et al., in “Handbook of Advanced Electronic and Photonic Materials and Devices” (H. S. Nalwa, Ed.). Academic Press, San Diego, 2001. © 2001, Academic Press.

$R = 0.1, 0.5$ , and  $1.0$  Bohr, while Figure 41 shows the electric dipole moment as a function of  $R\xi_0$  (for the same  $R$  values given previously). Figure 42 shows the electric quadrupole moment as a function of  $R\xi_0$  for the same values of  $R\xi$ .

As can be seen in Figure 38, the qualitative behavior for confined helium atom is that the energy increases from

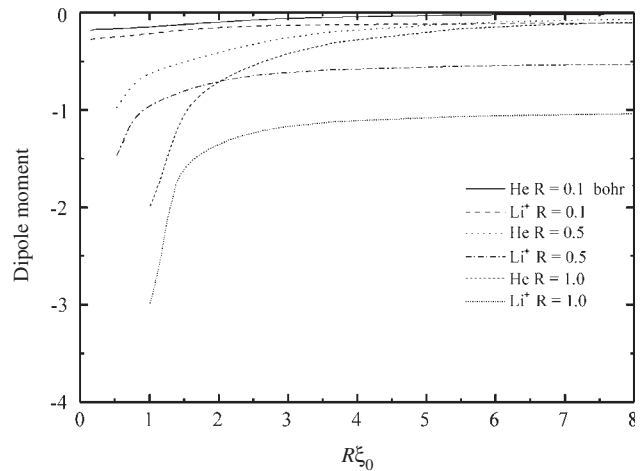


**Figure 41.** Electric dipole moment versus major semiaxis of the spheroidal box. The atomic unit for the dipole moment is equivalent to 2.54 Debye. Reprinted with permission from [205], J. L. Marín et al., in “Handbook of Advanced Electronic and Photonic Materials and Devices” (H. S. Nalwa, Ed.). Academic Press, San Diego, 2001. © 2001, Academic Press.

$-2.847656$  Hartree (corresponding to “free” helium atom) to a large positive value as a consequence of volume reduction of the confinement box. It can be also noted that for large volumes of spheroidal boxes there is a weak confinement of the atom and the eccentricity of spheroid becomes irrelevant, but for small volumes of the spheroidal box there is a strong confinement and the eccentricity plays a very important role in the energy value as can be corroborated in Figure 38. For  $R = 0.5$  Bohr, the energy curve coincides in both boxes. The latter is an important situation because it has been compared to the energy of an atom enclosed within two boxes of different shape, where additionally the nucleus of the atom for a paraboloidal box is located in the

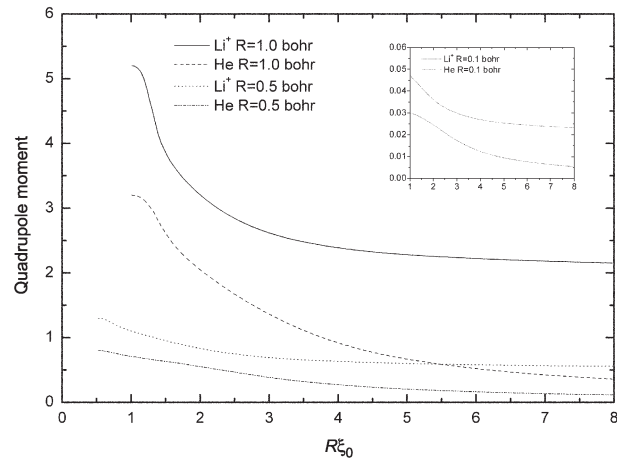


**Figure 42.** Electric quadrupole moment versus major semiaxis of the spheroidal box. The atomic unit for the quadrupole moment is equivalent to  $1.34 \times 10^{-26}$  esu  $\times$  cm<sup>2</sup>. Reprinted with permission from [205], J. L. Marín et al., in “Handbook of Advanced Electronic and Photonic Materials and Devices” (H. S. Nalwa, Ed.). Academic Press, San Diego, 2001. © 2001, Academic Press.



common focus (origin of coordinates) of paraboloids (which corresponds to a symmetric case) while for the spheroidal box the nucleus is located out of the origin, leading to an asymmetric case. It seems that for  $R = 0.5$  Bohr there is no difference for the atom to be in either of these boxes (i.e., boundary shape changes the electron distribution so that both effects combine to give the same energy for the atom). Regarding the same figure, the ground state energy for  $\text{Li}^+$  increases from its asymptotic value of  $-7.222656$  Hartree as the volume of the confinement box decreases, showing the same qualitative behavior as in the helium case. For the same confinement volume, the energy of  $\text{Li}^+$  is smaller than the energy of He due to the Coulomb attraction between the nucleus of  $\text{Li}^+$  ( $Z = 3$ ) and the electrons being greater than in helium atoms ( $Z = 2$ ).

In Figure 39, curves of pressure applied on the atom by the spheroidal box walls are displayed. In this figure we again compare with the results for helium atoms inside impenetrable paraboloidal boxes. As can be noted, the pressure curve for  $R = 0.5$  Bohr is nearest to the corresponding pressure curve for helium enclosed within a paraboloidal box. In same figure, the pressure curves for a lithium ion are also displayed. For the same  $R$  and confinement volume, the pressure on  $\text{Li}^+$  ion is smaller than for He atoms because the Coulomb attraction for the former is greater, which forces the ion electrons to move closer to the nucleus (i.e., they are farther away from the confinement walls than the He electrons).

In Figure 40a–c, the polarizability tensor components  $\alpha_{xx}$  and  $\alpha_{zz}$  are shown. When  $R = 0.1$  Bohr, they begin to decrease from their asymptotic common value  $0.986540$  (corresponding to free helium atom) to zero as the volume of the enclosing box diminishes. It can also be noted that for a nearly spherical box no differences on values of polarizability tensor components are found. For  $R = 0.5$  Bohr, the parallel component of polarizability  $\alpha_{zz}$  (which always takes a value greater than value of transversal component  $\alpha_{xx}$ ) approaches a positive value near zero as the volume of the box diminishes. Moreover, the influence of nonsphericity of the box on values of polarizability tensor components can also be observed. When  $R = 1.0$  Bohr,  $\alpha_{zz}$  has a minimum at  $R\xi_0 \cong 1.52$  Bohr, then increases to a maximum located at  $R\xi_0 \cong 1.24$  Bohr, and finally diminishes approaching a positive value greater than for the other two  $R$  values considered before. This effect in polarizability is also present for  $\text{Li}^+$ , where its polarizability decreases from its asymptotic value of  $0.153354$ . The latter is a consequence of the combination of (a) the deformation of the spheroidal box by increasing its eccentricity (given by  $1/\xi_0$ ) as the volume diminishes and (b) the proximity of the wall to the nucleus, which makes the electrons align on the  $z$  axis; thus the system reaches the maximum of its polarizability. Then, its subsequent decrease (not to zero) is due to the asymmetric reduction of space where the electrons can move.

In Figure 41, the electric dipole moments for  $R = 0.1, 0.5,$  and  $1.0$  Bohr, respectively, are displayed. The feature of this physical quantity is its decreasing behavior from zero for He atoms and from an asymptotic value (different for each value of  $R$ ) for  $\text{Li}^+$  ions to limiting negative values as  $\xi_0 \rightarrow 1$ . All these asymptotic values can immediately be determined from Eq. (208). The nonzero value of the dipole moment

is due to the asymmetric position of the nucleus inside the spheroid, which makes a permanent dipole moment ( $-ZR$ ) since  $\langle z \rangle \rightarrow 0$  as the volume approaches zero. This behavior is qualitatively different from [114] where the electric dipole moment of helium atoms in a semi-infinite space limited by a paraboloidal boundary was investigated. In the latter case, the magnitude of the electric dipole moment seems to increase monotonically from zero (free helium atom) to a limiting value as the volume is reduced. These variations show the shifting of the electron distribution away from the boundary as the latter closes in around the nucleus.

Figure 42 displays the electric quadrupole moment of He atoms increasing from its asymptotic value (corresponding to the free atom), to a positive limiting value different for each value of  $R$ , as  $\xi_0 \rightarrow 1$ . In contrast to the case studied in [105], the positive sign of the quadrupole moment indicates that the electrons preferentially distribute themselves on the major axis of the spheroid. Additionally, for this kind of confinement box, due to the asymmetric nucleus position within the spheroid, there is not a maximum for this property as in the case of paraboloidal walls where the nucleus is located on the symmetry center of the box.

### 3.7.3. Explicit Evaluation of Coulombic Interaction Term

The evaluation of the expectation value of the electron–electron repulsive potential requires performing integrals of the form

$$\begin{aligned} \left\langle \frac{1}{r_{12}} \right\rangle &= (2\pi)^2 A^2 R^5 \sum_{l=0}^{\infty} (2l+1) \\ &\times \int_1^{\xi_0} \int_{-1}^1 \int_1^{\xi_0} \int_{-1}^1 \exp[-2\alpha R(\xi + \eta)] \\ &\times \exp[-2\alpha R(\xi' + \eta')] (\xi - \xi_0)^2 (\xi' - \xi_0)^2 \\ &\times P_l(\eta) P_l(\eta') f_l(\xi, \xi') \\ &\times (\xi^2 - \eta^2)(\xi'^2 - \eta'^2) d\xi d\eta d\xi' d\eta' \end{aligned} \quad (210)$$

where  $f_l^m(\xi, \xi')$  [Eq. (201)] has been reduced to

$$f_l(\xi, \xi') = \begin{cases} P_l(\xi') Q_l(\xi) & \xi > \xi' \\ P_l(\xi) Q_l(\xi') & \xi < \xi' \end{cases} \quad (211)$$

The integration over  $\eta$  and  $\eta'$  coordinates gives the result

$$\begin{aligned} \left\langle \frac{1}{r_{12}} \right\rangle &= (2\pi)^2 A^2 R^5 \sum_{l=0}^{\infty} (2l+1) \\ &\times \int_1^{\xi_0} \int_1^{\xi_0} \exp[-2\alpha R\xi] \exp[-2\alpha R\xi'] \\ &\times (\xi - \xi_0)^2 (\xi' - \xi_0)^2 f_l(\xi, \xi') \\ &\times [\xi^2 \xi'^2 I_0^2 - (\xi^2 + \xi'^2) I_0 I_2 + I_2^2] d\xi d\xi' \end{aligned} \quad (212)$$

where  $I_0$  and  $I_2$  are integrals which involve spherical Bessel functions. That is,

$$I_0 = \int_{-1}^1 \exp(-2\alpha R\eta) P_l(\eta) d\eta$$

$$\begin{aligned}
&= \sum_{l'=0}^{\infty} \int_{-1}^1 (2l'+1) i^{l'} j_{l'}(i2\alpha R) P_{l'}(\eta) P_l(\eta) d\eta \\
&= \frac{2}{2l+1} \sum_{l'=0}^{\infty} (2l'+1) i^{l'} j_{l'}(i2\alpha R) \delta_{l'l} = 2i^l j_l(i2\alpha R) \quad (213)
\end{aligned}$$

and

$$\begin{aligned}
I_2 &= \int_{-1}^1 \eta^2 \exp(-2\alpha R \eta) P_l(\eta) d\eta \\
&= \sum_{l'=0}^{\infty} \int_{-1}^1 (2l'+1) i^{l'} j_{l'}(i2\alpha R) P_{l'}(\eta) P_l(\eta) \eta^2 d\eta \quad (214)
\end{aligned}$$

With the recurrence relation

$$\eta P_k(\eta) = \frac{k+1}{2k+1} P_{k+1}(\eta) + \frac{k}{2k+1} P_{k-1}(\eta) \quad (215)$$

the  $I_2$  integral can be written as

$$\begin{aligned}
I_2 &= \sum_{l'=0}^{\infty} \int_{-1}^1 (2l'+1) i^{l'} j_{l'}(i2\alpha R) \left\{ \frac{(l'+1)(l+1)}{(2l'+1)(2l+1)} \right. \\
&\quad \times P_{l'+1}(\eta) P_{l+1}(\eta) + \frac{l'l}{(2l'+1)(2l+1)} P_{l'-1}(\eta) P_{l-1}(\eta) \\
&\quad + \frac{(l'+1)l}{(2l'+1)(2l+1)} P_{l'+1}(\eta) P_{l-1}(\eta) \\
&\quad \left. + \frac{l'(l+1)}{(2l'+1)(2l+1)} P_{l'-1}(\eta) P_{l+1}(\eta) \right\} d\eta \\
&= 2 \left\{ \frac{(l+1)(l+2)}{(2l+1)(2l+3)} i^{l+2} j_{l+2}(i2\alpha R) + \frac{(2l^2+2l-1)}{(2l-1)(2l+3)} \right. \\
&\quad \left. \times i^l j_l(i2\alpha R) + \frac{l(l-1)}{(2l-1)(2l+1)} i^{l-2} j_{l-2}(i2\alpha R) \right\} \quad (216)
\end{aligned}$$

The integrals of Eq. (212) are evaluated numerically.

### 3.8. Quantum Systems within Penetrable Spheroidal Boxes

In this section the direct variational method is used to study some physical properties of H,  $H_2^+$ , and  $HeH^{2+}$  enclosed within soft spheroidal boxes [111]. The ground state energy, polarizability, and pressure are calculated for these systems as a function of the size and penetrability of the boxes. For these systems the ground state energy as a function of box eccentricity for different values of the barrier height is calculated. Furthermore, in order to demonstrate the applicability of the variational method, other properties of physical interest directly involving the wavefunction, such as the polarizability and the pressure, are calculated.

#### 3.8.1. H, $H_2^+$ , and $HeH^{2+}$ within Penetrable Spheroidal Boxes

The Hamiltonian for a one-electron molecular ion in the Born–Oppenheimer approximation can be written as

$$\hat{H} = -\frac{1}{2} \nabla^2 - \frac{Z_1}{r_1} - \frac{Z_2}{r_2} + \frac{Z_1 Z_2}{2R} \quad (217)$$

where the units are chosen to make  $\hbar = e = m_e^* = 1$ . The subscripts 1 and 2 denote the nucleus of charges  $Z_1$  and  $Z_2$ , respectively.

The prolate spheroidal coordinates  $(\xi, \eta, \varphi)$  are defined as [115]

$$\xi = \frac{(r_1 + r_2)}{2R} \quad \eta = \frac{(r_1 - r_2)}{2R} \quad \varphi \equiv \varphi \quad (218)$$

where  $2R$  is the interfocal distance of the prolate spheroids of revolution  $\{\xi = \text{const.}; -1 \leq \eta \leq 1; 0 \leq \varphi \leq 2\pi\}$ .

If the nuclei are located in the foci of this coordinate system, the Hamiltonian of Eq. (217) can be now expressed as

$$\hat{H} = -\frac{1}{2} \nabla^2 - \frac{Z_1}{R(\xi + \eta)} - \frac{Z_2}{R(\xi - \eta)} + \frac{Z_1 Z_2}{2R} \quad (219)$$

where the Laplacian operator is then

$$\begin{aligned}
\nabla^2 &= \frac{1}{R^2(\xi^2 - \eta^2)} \left\{ \frac{\partial}{\partial \xi} \left[ (\xi^2 - 1) \frac{\partial}{\partial \xi} \right] + \frac{\partial}{\partial \eta} \left[ (1 - \eta^2) \frac{\partial}{\partial \eta} \right] \right\} \\
&\quad + \frac{1}{R^2(\xi^2 - 1)(1 - \eta^2)} \frac{\partial^2}{\partial \varphi^2} \quad (220)
\end{aligned}$$

We now consider the system as confined within a prolate spheroidal box of eccentricity  $1/\xi_0$  and barrier height  $V_0$ . The corresponding modified Hamiltonian is then

$$\hat{H} = -\frac{1}{2} \nabla^2 + V_b(\xi, \eta) \quad (221)$$

where

$$V_b(\xi, \eta) = \begin{cases} -Z_1/R(\xi + \eta) - Z_2/R(\xi - \eta) & (1 \leq \xi \leq \xi_0) \\ V_0 & (\xi_0 \leq \xi < \infty) \end{cases} \quad (222)$$

The formal solutions of the Schrödinger equation for the inner ( $\xi \leq \xi_0$ ) and outer ( $\xi \geq \xi_0$ ) regions must satisfy continuity conditions at the boundary ( $\xi = \xi_0$ ), which are equivalent to

$$\left. \frac{1}{\psi_i} \frac{\partial \psi_i}{\partial \xi} \right|_{\xi=\xi_0} = \left. \frac{1}{\psi_o} \frac{\partial \psi_o}{\partial \xi} \right|_{\xi=\xi_0} \quad (223)$$

Equation (223) allows us to find the energy of the system if an explicit form of the wavefunction is known.

The  $V_0 = \infty$  case was studied exactly by Ley-Koo and Cruz [120]. An approximate study of these systems for finite values of  $V_0$  can be performed using a direct variational method. In this case an ansatz wavefunction  $\chi$  must be constructed. Following Refs. [78, 121], we have

$$\chi_i(\xi, \eta, \varphi) = A_i \psi_i^0(\xi, \eta, \varphi; \alpha) f(\xi, \alpha) \quad (224)$$

and

$$\chi_o(\xi, \eta, \varphi) = A_o \psi_o^0(\xi, \eta, \varphi; \alpha) f(\xi, \alpha) \quad (225)$$

where  $\psi_i^0$  and  $\psi_o^0$  are the solutions of the Schrödinger equation for the free system [122, 123],  $f$  is an auxiliary function which allows the total wavefunction to satisfy the condition shown in Eq. (223), and  $\alpha$  is a variational parameter

to be determined once the corresponding energy functional is minimized with the additional constrictions improved by Eq. (223).

Following Coulson [122], the ansatz wavefunction for the ground state is constructed as

$$\chi_i(\xi, \eta, \varphi) = A_i(\xi_0 - \alpha\xi)\exp[-\alpha(\xi + \eta)] \quad (\xi \leq \xi_0) \quad (226)$$

and

$$\chi_o(\xi, \eta, \varphi) = A_o \exp(-\beta\xi)\exp(-\alpha\eta) \quad (\xi \geq \xi_0) \quad (227)$$

where  $A_i$  and  $A_o$  are two constants related through the normalization condition on the total wavefunction. A relation between the variational parameters  $\alpha$  and  $\beta$  can be obtained through the continuity condition at  $\xi = \xi_0$  so that the energy functional is to be minimized with respect to only one parameter, either  $\alpha$  or  $\beta$ .

The energy of the ground state of H,  $H_2^+$ , and  $HeH^{2+}$  for  $V_0 = 0, 2, 8, 20$  and  $\infty R_y^*$  is displayed in Figure 43 as a function of the size of the enclosing box  $\xi_0$ . As can be noted, good agreement is found with the exact results for the case of  $V_0 = \infty$ . When  $V_0$  has a finite value, the calculations show the correct qualitative behavior, similar to that found by Ley-Koo and Rubinstein [124] for hydrogen within penetrable spherical boxes. In order to gain some confidence in the value of the ansatz wavefunctions, we have calculated the polarizability and pressure for  $H_2^+$ . In the Kirkwood approximation [119] the parallel and perpendicular components of the polarizability are given by

$$\alpha_{\parallel} \equiv \alpha_{zz} = 4\langle z^2 \rangle^2 \quad \alpha_{\perp} \equiv \alpha_{xx} = \alpha_{yy} = 4\langle x^2 \rangle^2 \quad (228)$$

Finally, the pressure on the system due to the confinement can be calculated through the relationship

$$P = -\frac{d\varepsilon}{dV} \quad (229)$$

where  $V$  is the volume of the spheroidal box and  $\varepsilon$  is the total ground state energy of the system calculated at the equilibrium bond length. The results obtained for these properties are displayed in Figure 44 for  $V_0 = 0$  and  $\infty R_y^*$  as a function of  $\xi_0$ . As can be seen, good agreement is found when our results are compared for  $V_0 = \infty$  with the calculations reported by LeSar and Herschbach [109, 110], who used a five-term James-Coolidge variational wavefunction. For finite values of  $V_0$  the correct qualitative behavior is obtained [125].

### 3.9. Confinement of One- and Two-Electron Atomic Systems by Spherical Penetrable Boxes

We explicitly treat the case of some one- and two-electron atomic systems (H,  $H^-$ , He,  $Li^{2+}$ , and  $Be^{2+}$ ) in their ground state within spherical confining barriers [66]. In all cases, a simple representation for the ansatz wavefunction is employed and the corresponding energies are given as a function of size and height of the barrier. Additionally, some

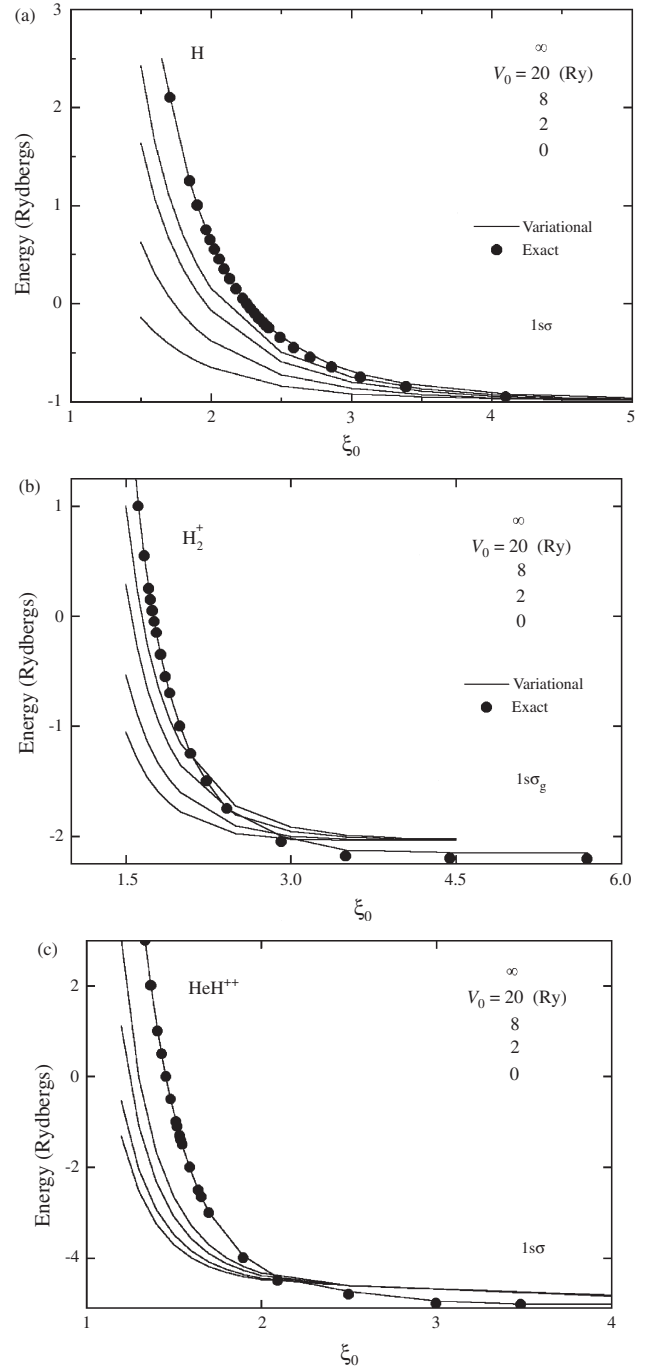


**Figure 43.** Ground state energies for H (a),  $H_2^+$  (b), and  $HeH^{2+}$  (c) enclosed within penetrable spherical boxes as a function of box size  $\xi_0$ . The nucleus are clamped and  $R = 1$  a.u. The continuous lines represent the variational calculations of this subsection. The circles are the exact results for  $V_0 = \infty$  reported in [120]. Reprinted with permission from [205], J. L. Marín et al., in “Handbook of Advanced Electronic and Photonic Materials and Devices” (H. S. Nalwa, Ed.). Academic Press, San Diego, 2001. © 2001, Academic Press.

quantities of physical interest are evaluated for the case of hydrogen.

The case of hydrogen has been thoroughly analyzed by Ley-Koo and Rubinstein [124]. Proper comparison with their

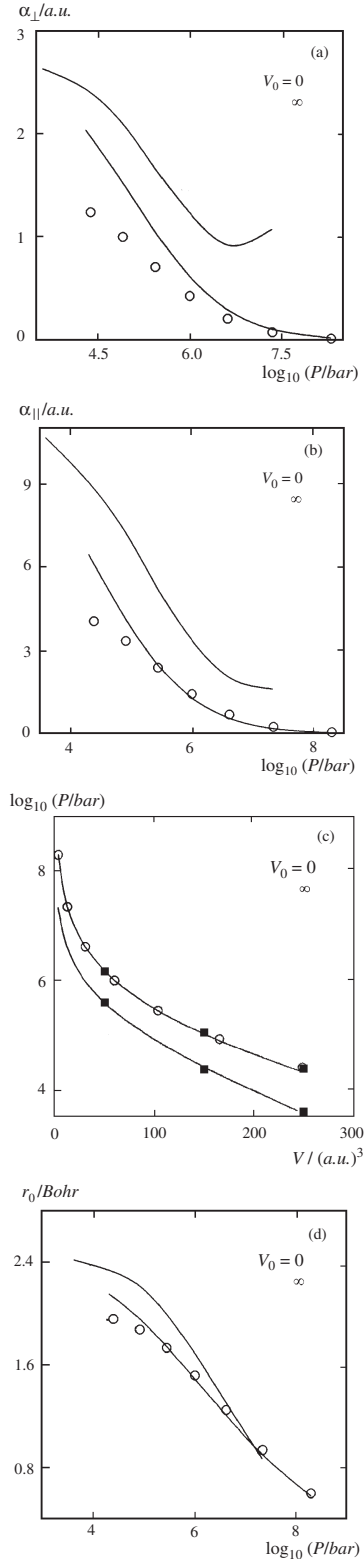


**Figure 44.** Physical properties of  $H_2^+$  enclosed within penetrable spheroidal boxes as a function of box size  $\xi_0$ . The continuous lines represent the variational calculations of this subsection. The circles are the results of [109, 110], while the squares are those of [125]. Reprinted with permission from [205], J. L. Marín et al., in “Handbook of Advanced Electronic and Photonic Materials and Devices” (H. S. Nalwa, Ed.), Academic Press, San Diego, 2001. © 2001, Academic Press.

results will yield some confidence on the capability of the procedure proposed in this work to account for the behavior of certain physical properties of the system as a function of box size and barrier height. Accordingly, for this system, in addition to the energy we evaluate the Fermi contact term, polarizability, pressure, and magnetic shielding constant.

For the rest of the systems, the estimated energies as a function of the characteristics of the confining potential and a comparison of their qualitative and quantitative behavior with available calculations for the impenetrable case by Ludeña and Gregori [107] are presented.

### 3.9.1. Model and Theory

For penetrable walls, let the ansatz wavefunction in the interior of the box be given as

$$\chi_i = \chi_{0,i} f \quad (230)$$

where  $\chi_{0,i}$  denotes the wavefunction of the free system and  $f$  denotes an auxiliary function that guarantees the adequate matching at the boundary with the exterior wavefunction

$$\chi_o = \chi_{0,e} \quad (231)$$

such that  $\chi_{0,e}$  keeps the proper asymptotic behavior characteristic of the system under study. Furthermore, the choice of the auxiliary function  $f$  must be such that it reduces to the familiar cutoff function proposed previously for an infinitely high confining potential. These requirements, together with the fulfillment of the virial theorem [126], constitute the key assumptions to be employed in order to construct our ansatz wavefunctions.

According to the direct variational method, an upper bound to the energy for a particular state may be found by requiring that

$$\langle \chi_i | \hat{H}_i | \chi_i \rangle_{\Omega} + \langle \chi_o | \hat{H}_o | \chi_o \rangle_{\Omega'} = \text{minimum} \quad (232)$$

where

$$\begin{aligned} \hat{H}_i &= -\frac{1}{2} \nabla_q^2 + V(q) & q \in \Omega \\ \hat{H}_o &= -\frac{1}{2} \nabla_q^2 + V_0 & q \in \Omega' \end{aligned} \quad (233)$$

$\Omega$  and  $\Omega'$  are the interior and exterior regions, respectively, and  $\{q\}$  represents the set of coordinates used.  $V(q)$  is the acting potential within the interior region and  $V_0$  is the height of the confining potential.

In addition to Eqs. (232) and (233), the normalization condition

$$\langle \chi_i | \chi_i \rangle_{\Omega} + \langle \chi_o | \chi_o \rangle_{\Omega'} = 1 \quad (234)$$

must be satisfied together with the requirement for continuity of the logarithmic derivative at the boundary ( $q = q_0$ ):

$$\frac{1}{\chi_i} \frac{\partial \chi_i}{\partial q} \Big|_{q=q_0} = \frac{1}{\chi_o} \frac{\partial \chi_o}{\partial q} \Big|_{q=q_0} \quad (235)$$

Indeed, if we are going to consider several states, we must impose the constraint of orthogonality among them,

both in the interior as well as in the exterior region. Note that the preceding arguments are of a general character and should apply to any system whether confined by penetrable or impenetrable walls.

### 3.9.2. Ground State of the Confined Hydrogen Atom

The potential energy associated with the Hamiltonian of the hydrogen atom confined by a spherical box with penetrable walls is given by a Coulomb term inside the box

$$V(r) = -\frac{Ze^2}{r} \quad r < r_0 \quad (236)$$

and a constant barrier height outside the box,

$$V(r) = V_0 \quad r > r_0 \quad (237)$$

with  $r_0$  the radius of the confining box.

For the purposes of this section we consider now the 1s state. For this case, the corresponding wavefunctions are chosen as

$$\begin{aligned} \chi_i(1s) &= N_i(r_0 - \gamma r)\exp(-\alpha r) & r < r_0 \\ \chi_o(1s) &= N_o r^{-1}\exp(-\beta r) & r > r_0 \end{aligned} \quad (238)$$

with  $\alpha$ ,  $\beta$ , and  $\gamma$  variational parameters and  $N_i$  and  $N_o$  normalization constants.

In contrast to the impenetrable case, we have considered three variational parameters in order to allow for more flexibility in the matching procedure at the boundary. In fact, only two of these parameters ( $\alpha$ ,  $\gamma$ ) need to be found, the third one being defined through Eq. (235) as

$$\beta = \frac{\alpha r_0(1 - \gamma) + 2\gamma - 1}{r_0(1 - \gamma)} \quad (239)$$

Following Ley-Koo and Rubinstein [124], some quantities of physical interest such as the Fermi contact term ( $A$ ), diamagnetic screening constant ( $\sigma$ ), polarizability ( $\alpha$ ), and pressure ( $P$ ) are defined, respectively, as

$$\begin{aligned} A &= \frac{2}{3}g\beta g_n\beta_n|\chi_i(1s)|_{r=0}^2 & \sigma &= \frac{e^2}{3\mu c^2}\left\langle\frac{1}{r}\right\rangle \\ \alpha &= \frac{4}{9}a_B^{-1}\langle r^2 \rangle^2 \\ P &= -\frac{1}{4\pi r_0^2}\frac{d\varepsilon}{dr_0} = \frac{1}{4\pi r_0^3}(2\varepsilon - \langle V \rangle) \end{aligned} \quad (240)$$

Fernandez and Castro [127] showed that the virial theorem for systems with sectionally defined potentials must be reformulated as compared to the case of systems constrained by Dirichlet boundary conditions. Hence, the use of Eq. (240) for  $P$  is not correct for confining potentials with finite barrier heights but, for comparative purposes, Eq. (240) will be employed for the evaluation of  $P$ .

Figures 45–49 show the values obtained by this method for the energy ( $\varepsilon$ ),  $A$ ,  $\sigma$ ,  $\alpha$ , and  $P$  for the 1s state with barrier heights of 0, 4, and 10 Ryd ( $e^2/2a_B$ ). For comparison, the corresponding exact values calculated by Ley-Koo and Rubinstein are also shown. As the reader must be aware,

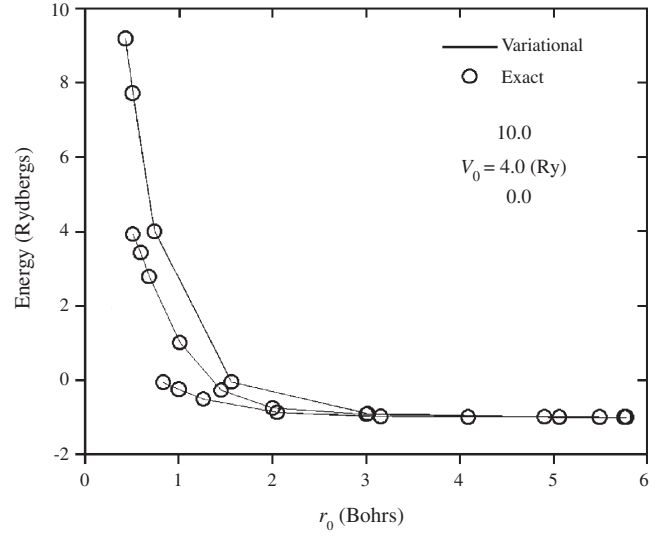


**Figure 45.** Ground state energy of H as a function of confining radius  $r_0$ , for different barrier heights. Reprinted with permission from [205], J. L. Marín et al., in “Handbook of Advanced Electronic and Photonic Materials and Devices” (H. S. Nalwa, Ed.). Academic Press, San Diego, 2001. © 2001, Academic Press.

there is a fair agreement between the energy values obtained by the method used here and the exact calculations. Also, regarding the values estimated for the various physical quantities, the agreement is also fairly good.

### 3.9.3. Ground State of Confined Two-Electron Systems

The Hamiltonian for a confined atomic system with two electrons is given as

$$\hat{H} = -\frac{1}{2}\nabla_1^2 - \frac{1}{2}\nabla_2^2 + V(\vec{r}_1, \vec{r}_2) \quad (241)$$

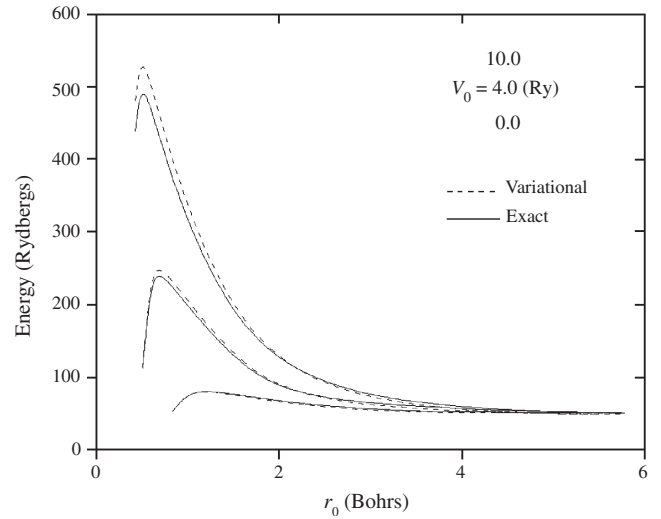


**Figure 46.** Fermi contact term ( $A$ ) for H as a function of confining radius  $r_0$ , for different barrier heights. In units of  $(2/3)g\beta g_n\beta_n = 12.690$  mT. Reprinted with permission from [205], J. L. Marín et al., in “Handbook of Advanced Electronic and Photonic Materials and Devices” (H. S. Nalwa, Ed.). Academic Press, San Diego, 2001. © 2001, Academic Press.

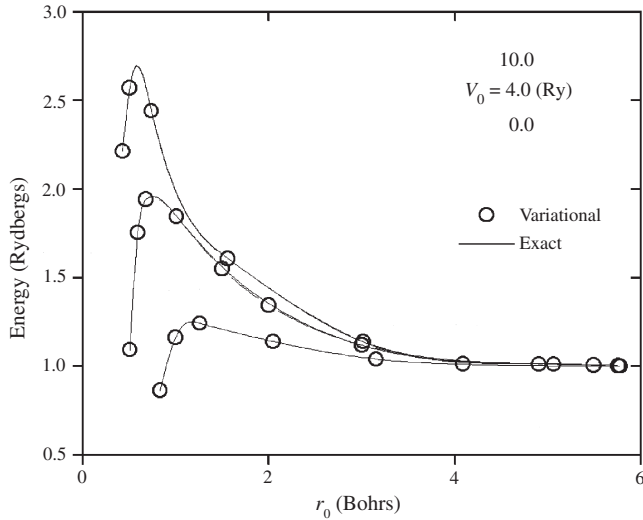


**Figure 47.** Diamagnetic screening constant ( $\sigma$ ) for H as a function of confining radius  $r_0$ , for different barrier heights. In units of  $e^2/\mu a_0 c^2$ . Reprinted with permission from [205], J. L. Marín et al., in “Handbook of Advanced Electronic and Photonic Materials and Devices” (H. S. Nalwa, Ed.). Academic Press, San Diego, 2001. © 2001, Academic Press.

with

$$V(\vec{r}_1, \vec{r}_2) = \begin{cases} -\frac{Z}{r_1} - \frac{Z}{r_2} + \frac{1}{|\vec{r}_1 - \vec{r}_2|} & r_1, r_2 \leq r_0 \\ V_0 & r_1, r_2 > r_0 \end{cases} \quad (242)$$

where  $Z$  denotes the nuclear charge,  $\vec{r}_1, \vec{r}_2$  are the electron positions relative to the nucleus, and  $r_0$  the radius of the confining box.

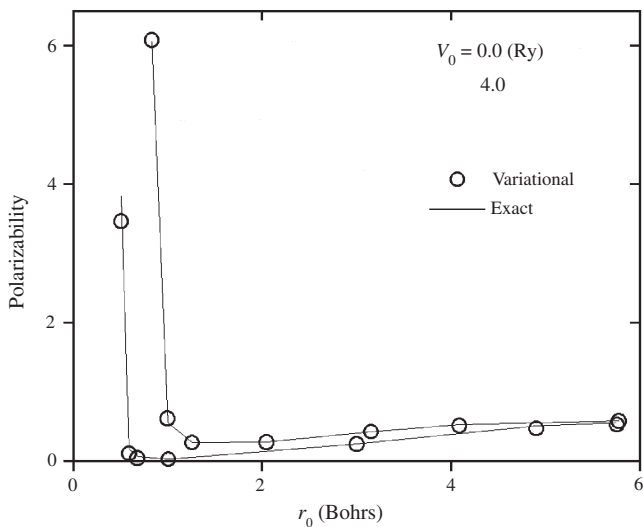


**Figure 48.** Polarizability ( $\alpha$ ) for H as a function confining radius  $r_0$ , for different barrier heights. In units of  $10^{-24} \text{ cm}^2$ . Reprinted with permission from [205], J. L. Marín et al., in “Handbook of Advanced Electronic and Photonic Materials and Devices” (H. S. Nalwa, Ed.). Academic Press, San Diego, 2001. © 2001, Academic Press.

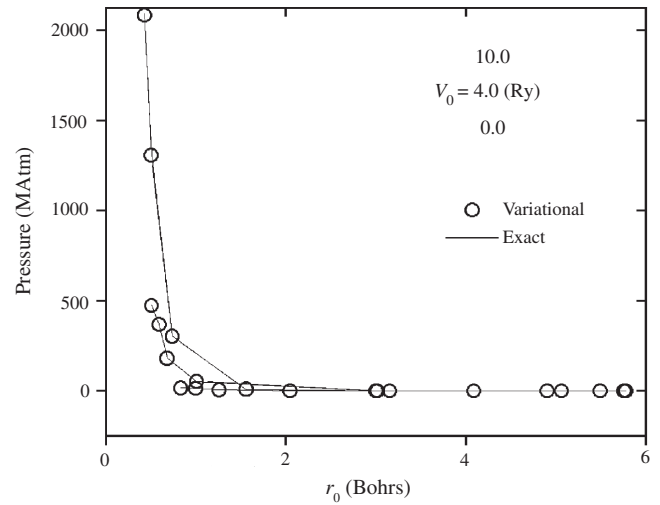


**Figure 49.** Pressure ( $P$ ) for H as a function of confining radius  $r_0$ , for different barrier heights. In units of  $10^6 \text{ atm}$ . Reprinted with permission from [205], J. L. Marín et al., in “Handbook of Advanced Electronic and Photonic Materials and Devices” (H. S. Nalwa, Ed.). Academic Press, San Diego, 2001. © 2001, Academic Press.

Considering each electron in a  $1s$  state the interior wavefunction is chosen as

$$\chi_i(r_1, r_2) = A(r_0 - \alpha r_1)(r_0 - \alpha r_2)\exp[-\alpha(r_1 + r_2)] \quad (243)$$

and the exterior function as

$$\chi_o(r_1, r_2) = B \frac{\exp[-\beta(r_1 + r_2)]}{r_1 r_2} \quad (244)$$

with  $A$  and  $B$  normalizing constants. Note that in this case we are using only two variational parameters. This choice will certainly make the trial wavefunction too rigid. However, as will be seen, even with this crude approximation fair results may be obtained.

Following the procedure outlined by Eqs. (232)–(235) the energy values for  $\text{H}^-$ ,  $\text{He}$ ,  $\text{Li}^+$ , and  $\text{Be}^{2+}$  are obtained as a function of  $r_0$  and  $V_0$ . Table 4 displays the results of this exercise for some selected barrier heights. We note first the cases of  $\text{He}$ ,  $\text{Li}^+$ , and  $\text{Be}^{2+}$  for which the qualitative and quantitative behavior of the energies tend to the correct values [107] as the barrier height approaches infinity. Note, however, that for relatively large box sizes the energy values obtained for the penetrable case lie slightly lower than those for the impenetrable case. This effect is attributed to the rigidity imposed on the input wavefunction through the assignment of a single variational parameter for the interior as well as the exterior regions.

Interestingly enough, the  $\text{H}^-$  system shows a particular sensitivity to the confining effect as may be verified from the overall trend of the energy values. Unfortunately, there are no other calculations to compare with for this confined system. The energies obtained in this work for large values of  $r_0$  correspond to the value of  $\epsilon = -0.473$  Hartree reported by Wu and Falicov [128] in their variational treatment of free  $\text{H}^-$  with a single exponential parameter. Furthermore, these authors have shown that using two exponential parameters in their trial wavefunction, the ground state energy



**Table 4.** Energy values and variational parameters as a function of box size for various heights of the potential barrier.

	$r_0(a_B)$	$V_0 = 0$		$V_0 = 10$		$V_0 = \infty$		
		$\alpha$	$\varepsilon$	$\alpha$	$\varepsilon$	$\alpha$	$\varepsilon$	
H <sup>-</sup>	0.4			0.5007	9.9141	0.3392	54.3573	
	0.6			0.5923	7.4652	0.2693	22.3108	
	0.8	0.4040	0.0000	0.6319	4.5285	0.2620	11.4966	
	1.2	0.4271	-0.0199	0.6567	1.7001	0.3163	4.1492	
	1.6	0.4550	-0.1160	0.6583	0.6222	0.3272	1.7765	
	2.0	0.4703	-0.2373	0.6507	0.1330	0.3389	0.7677	
	4.0	0.5040	-0.4433	0.5862	-0.4198	0.4054	-0.3295	
	6.0	0.5676	-0.4655	0.5725	-0.4650	0.4746	-0.4406	
He <sup>a</sup>	0.5	0.5199	-0.2412	0.6218	4.6722	0.7465	22.9229	
	1.0	0.6081	-2.0522	0.6918	-1.4621	0.8320	1.0626	
	1.5	0.6592	-2.5086	0.7329	-2.4201	0.9330	-1.8456	
	2.0	0.8438	-2.6184	0.8465	-2.6179	1.0435	-2.5285	
	3.0	1.0746	-2.7579	1.0476	-2.7579	1.2428	-2.7935	
	4.0	1.2264	-2.8054	1.2264	-2.8054	1.3701	-2.8302	
	6.0	1.3855	-2.8341	1.3855	-2.8341	1.4924	-2.8426	
Li <sup>+</sup>	0.4	0.5818	-2.1084	0.6338	1.6199	1.2102	27.8079	27.6302
	0.6	0.6346	-4.8914	0.6819	-3.7712	1.2979	3.9773	3.9284
	0.8	0.6661	-5.8925	0.7126	-5.4793	1.3962	-2.8064	-2.8612
	1.2	0.8201	-6.1460	0.8363	-6.1414	1.6171	-6.3075	-6.4047
	1.6	1.0854	-6.4588	1.0854	-6.4588	1.8383	-6.9780	-7.0869
	2.0	1.2347	-6.6033	1.2296	-6.6008	2.0190	-7.1370	-7.2356
	4.0	1.9591	-7.1300	1.9591	-7.1300	2.3967	-7.2154	-7.2783
	6.0	2.2081	-7.1979	2.2081	-7.1979	2.5037	-7.2201	-7.2784
Be <sup>2+</sup>	0.4	0.6374	-8.1952	0.6669	-6.3628	1.7401	13.7130	13.6356
	0.6	0.6835	-10.9415	0.7128	-10.4348	1.9233	-6.1782	-6.2402
	0.8	0.7324	-11.1498	0.7623	-11.0389	2.1300	-11.1522	-11.2658
	1.0	0.9958	-11.1894	0.9958	-11.1894	2.5486	-13.2248	-13.3701
	2.0	1.4081	-11.5445	1.3810	-11.4901	3.0595	-13.5616	-13.6493
	4.0	2.6901	-13.4399	2.6901	-13.4399	3.4089	-13.5931	-13.6539
	6.0	3.0308	-13.5595	3.0308	-13.5595	3.5087	-13.5959	-13.6539

Note: Energies given in Hartrees. Values in the last column for Li<sup>+</sup> and Be<sup>2+</sup> correspond to self-consistent field calculations by Ludeña and Gregori [107].

<sup>a</sup> For  $V_0 = \infty$  the energy values are taken from [121].

for H<sup>-</sup> becomes  $\varepsilon = -0.513$  Hartree, a value closer to that of  $-0.527$  reported by Pekeris [129] using a 1078-parameter wavefunction. Hence, we believe that a more flexible trial wavefunction in our treatment of two-electron confined atoms will improve the quality of the predictions.

### 3.10. Optical Properties of Impurity States in Semiconductor Quantum Dots

The optical absorption spectra associated with transitions between the  $n = 1$  valence level and the donor impurity band have been calculated for spherical GaAs quantum dots with infinite potential confinement, using a variational procedure within the effective mass approximation, following [130]. We show results either for one impurity or for a homogeneous distribution of impurities inside of the quantum dot. The interaction between the impurities has been neglected. The main features found in the theoretical spectra were an absorption edge associated with transitions involving impurities at the center and a peak related to impurities at the edge of the dot. For all sizes of the quantum dot the peak

associated with impurities located next to the edge always governs the total absorption probability.

Oliveira and Perez-Alvarez [131], Porrás-Montenegro and Oliveira [132], and Porrás-Montenegro et al. [133] have studied the optical absorption spectra associated with shallow donor impurities for both finite and infinite barrier GaAs–GaAlAs quantum wells and quantum well wires. The main features were an absorption edge associated with transitions involving impurities at the center and a peak related to impurities at the edge of the wire. For quantum well wires the situation of the bulk material is reached for radii of 1000 Å and the peak associated with transitions involving impurities at the center decreases as the radius of the structure is diminished.

Porrás-Montenegro et al. [134, 135] have calculated the impurity binding energies as functions of the radius, impurity position as well as the density of impurity states in spherical GaAs–Ga<sub>1-x</sub>Al<sub>x</sub>As quantum dots, finding two structures associated with impurities located at the center and at the edge of the quantum dots, which are expected to show up in absorption and photoluminescence spectra associated with shallow hydrogenic impurities in quantum dots, as was the

case in detailed calculations of the impurity-related optical absorption spectra in GaAs–GaAlAs quantum wells [131] and quantum well wires [133, 136].

Helm et al. [137] performed a far-infrared absorption study in lightly doped GaAs–Ga<sub>1-x</sub>Al<sub>x</sub>As superlattices and found that, at low temperatures, the absorption spectra are dominated by donor transitions. They studied the  $1s-2p_z$  donor transitions experimentally and theoretically, obtaining excellent agreement.

Otherwise experimental progress through spectroscopic techniques made possible a detailed analysis of the effects of confinement on shallow impurities in quantum wells. Far-infrared magnetospectroscopy measurements on shallow donor impurities in GaAs–Ga<sub>1-x</sub>Al<sub>x</sub>As multiple quantum well structures were performed by Jarosik et al. [138], who assigned structures in the transmission spectra to intrimpurity  $1s-2p_{\pm}$  transitions. Work on magnetic field effects on shallow impurities in GaAs–Ga<sub>1-x</sub>Al<sub>x</sub>As multiple quantum well structures was also recently reported by Yoo et al. [139].

### 3.10.1. Model and Theory

The Hamiltonian of a shallow hydrogenic impurity in a spherical quantum dot of GaAs can be written in the effective mass approximation as

$$\hat{H} = \frac{\hat{p}^2}{2m_e^*} - \frac{e^2}{\kappa|\vec{r} - \vec{R}|} + V_b(\vec{r}) \quad (245)$$

where  $V_b(\vec{r})$  is the confining potential which is zero for  $r < r_0$  and infinite for  $r > r_0$ ,  $r_0$  being the radius of the dot. The impurity position is denoted by  $\vec{R}$ .

The eigenfunction of the Hamiltonian in the absence of the impurity for the ground state ( $n = 1$  and  $l = 0$ ) and for the infinite potential well is [134]

$$\psi(\vec{r}) = \frac{\sin(k_{10}r)}{(2\pi r_0)^{1/2}r} \quad (246)$$

where  $\vec{r}$  is  $(r, \theta, \varphi)$ . In order to satisfy the boundary conditions  $\psi(r = r_0) = 0$ , the eigenenergies corresponding to Eqs. (245) and (246) are  $\varepsilon_{10} = \hbar^2 k_{10}^2 / 2m_e^*$  with  $k_{10} = \pi/r_0$ .

With inclusion of the impurity potential, one should use a variational approach to determine the ground state binding energy. The trial wavefunction considered is

$$\psi(\vec{r}) = \begin{cases} N(\vec{R}, \lambda) \frac{\sin(k_{10}r)}{r} \exp(-\lambda|\vec{r} - \vec{R}|) & r \leq r_0 \\ 0 & r > r_0 \end{cases} \quad (247)$$

with  $\lambda$  being a variational parameter and  $N(R, \lambda)$  the normalization factor. The binding energy of the impurity is given by

$$\varepsilon_b(r_0, \vec{R}) = \varepsilon_{10} - (\langle T \rangle + \langle V \rangle) \quad (248)$$

where  $\langle T \rangle$  and  $\langle V \rangle$  are kinetic and potential energies.

For transitions from the first valence level to a donor impurity level, we have, for the initial and final states,

$$\psi_{10}^i = \frac{\sin(k_{10}r)}{(2\pi r_0)^{1/2}r} u_i(\vec{r}) \quad (249)$$

$$\psi_{10}^f = N(\vec{r}, \lambda) \frac{\sin(k_{10}r)}{r} \exp(-\lambda|\vec{r} - \vec{R}|) u_f(\vec{r}) \quad (250)$$

where  $u_i(\vec{r})$ ,  $u_f(\vec{r})$  are the periodic parts of the Bloch states for the initial and final states.

Taking the energy origin at the first conduction subband as depicted in Figure 50, we have for the energy of the initial (first valence level) state

$$\varepsilon_i = -E_g \quad (251)$$

where  $E_g$  is given by

$$E_g = \varepsilon_g + \frac{\hbar^2 k_{10}^2}{2m_e^*} + \frac{\hbar^2 k_{10}^2}{2m_h^*} \quad (252)$$

with  $\varepsilon_g$  being the bulk GaAs bandgap.

The energy of the final state is

$$\varepsilon_f = -\varepsilon_b(r_0, \vec{R}) \quad (253)$$

The transition probability per unit time for valence-to-donor transitions associated with a donor impurity located at  $\vec{R}$  is proportional to the square of the matrix element of the electron–photon interaction  $\hat{H}_{el}$  between the wavefunctions of the initial state (first valence level) and final (impurity) states. That is,

$$W = \frac{2\pi}{\hbar} \sum |\langle f | \hat{H}_{el} | i \rangle|^2 \delta(\varepsilon_f - \varepsilon_i - \hbar\omega) \quad (254)$$

with  $\hat{H}_{el} = C \vec{e}_r \cdot \hat{p}$ , where  $\vec{e}_r$  is the polarization vector in the direction of the electric field of the radiation,  $\hat{p}$  is the momentum operator, and  $C$  is a prefactor which contains

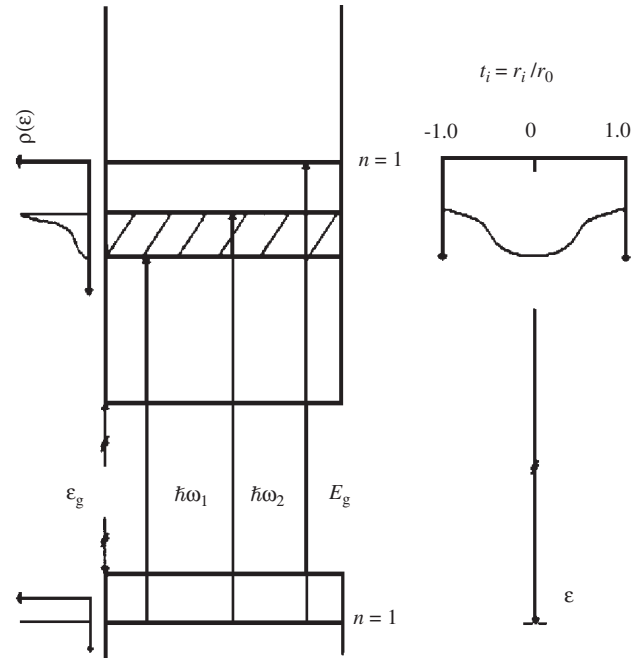


**Figure 50.** Schematic of some possible absorption transitions in an infinite GaAs–(Ga,Al)As quantum dot of radius  $r_0 = 300 \text{ \AA}$  with a donor impurity band. The density of state,  $\rho(\varepsilon)$ , from the positional dependent donor binding energy is shown schematically on the left-hand side. The dependence of the binding energy as a function of the donor impurity position is shown on the right-hand side.

the photon vector potential. Following the effective mass approximation, the foregoing matrix element may be written as [140]

$$\langle f | \widehat{H}_{e-l} | i \rangle \cong C \vec{e}_r \cdot \vec{P}_{fi} S_{fi} \quad (255)$$

with

$$\vec{P}_{fi} = \frac{1}{\Omega} \int_{\Omega} d\vec{r} u_f^*(\vec{r}) \hat{p} u_i(\vec{r}) \quad (256)$$

and

$$S_{fi} = \int d\vec{r} f_f^*(\vec{r}) f_i(\vec{r}) \quad (257)$$

where  $\Omega$  is the volume of the unit cell and  $f_f(f_i)$  is the envelope function for the final (initial) state. For the case of the donor impurity we have, for  $S_{fi} = S_{fi}(\vec{R}, \lambda)$ ,

$$S_{fi} = \left( \frac{2\pi}{r_0} \right)^{1/2} N(\vec{R}, \lambda) \int_0^{r_0} dr \sin^2(k_{10}r) \times \int_0^\pi d\theta \sin \theta \exp[-\lambda|\vec{r} - \vec{R}|] \quad (258)$$

For an infinite GaAs quantum dot of radius  $r_0$  with one impurity inside, the transition probability per unit time for valence to donor transitions is given by

$$W(\omega, \vec{R}) = W_0 \left( \frac{\pi \hbar^2}{2m_0 a_B^2} \right) S_{fi}^2 Y(\Delta) \quad (259)$$

where  $a_B$  is the Bohr radius and  $Y(\Delta)$  is the step function. In this expression we have for  $\Delta$  and  $W_0$

$$\Delta = \hbar\omega - E_g + \varepsilon_g(r_0, R) \quad (260)$$

$$W_0 = \frac{4m_0}{\hbar^3} a_B^2 |C|^2 |\vec{e}_r \cdot \vec{P}_{fi}|^2 \quad (261)$$

For a homogeneous distribution of impurities and assuming that the quantum dot radius is much larger than the lattice parameter one has for the total transition probability per unit of time

$$W_T(\omega) = \frac{3}{r_0^3} \int_0^{r_0} dR W(\omega, \vec{R}) R^2 \quad (262)$$

For the numerical computing, we used  $\kappa = 12.58$ ,  $m_c^* = 0.0665m_0$ ,  $m_h^* = 0.30m_0$ , where  $\varepsilon_g = 1.424$  eV.

A schematic representation of a GaAs quantum dot doped with a homogeneous distribution of the donor impurities is shown in Figure 50. The edges for optical absorption from the first valence subband to the donor impurity band are represented by  $\hbar\omega_1$ , and to the first conduction subband by  $E_g$ . The transition  $\hbar\omega_2$  corresponds to absorption to an impurity level associated with donors at the edges of the quantum dot. At the right we also show the density of the states for the impurity band.

In Figure 51, we display the donor binding energy as a function of the donor position inside the quantum dot for infinite potential well with different radii. The donor binding energy decreases as the donor position increases reaching a

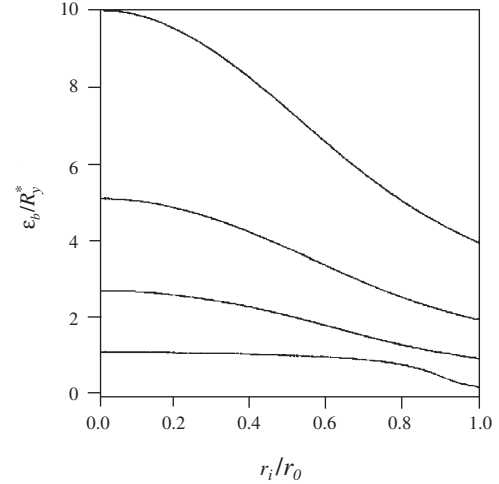


**Figure 51.** Donor binding energy as a function of the impurity position for infinite GaAs-(Ga,Al)As quantum dots with distinct dot radii. From top to bottom,  $r_0 = 50, 100, 200, 1000$  Å. Reprinted with permission from [205], J. L. Marín et al., in “Handbook of Advanced Electronic and Photonic Materials and Devices” (H. S. Nalwa, Ed.). Academic Press, San Diego, 2001. © 2001, Academic Press.

minimum as the donor position is equal to the radii of the quantum dot. The absorption probability  $W(\omega, \vec{R})$  for an infinite quantum dot with one single impurity as a function of  $\hbar\omega - \varepsilon_g$  is shown in Figure 52. In Figure 52a, we present the absorption probability for an infinite GaAs quantum dot of radius  $r_0 = 3000$  Å. We observe that there is a noticeable peak structure associated with a single impurity located at the center of the dot, which is much larger than the structure associated with a single impurity next to the edge of the dot, meaning that we have essentially reached the bulk limit. Our results for an  $r_0 = 1000$  Å and  $r_0 = 500$  Å quantum dots are shown in Figure 52b; the structure associated with a single impurity located at the center of the dot is smaller than the structure associated with a single impurity at the edge of the dot.

In Figure 53, we display the total absorption probability for an infinite GaAs quantum dot with a homogeneous distribution of impurities. For a quantum dot of  $r_0 = 3000$  Å the total absorption probability as a function of  $\hbar\omega - \varepsilon_g$  is shown in Figure 53a. An absorption edge associated with transitions involving impurities at the center of the well and a peak related with impurities next to edge of the dot are observed. The peak associated with impurities located next to the edge of the dot is much larger than the peak associated with impurities located next to the center of the dot. This behavior is quite different from that found for GaAs quantum wells and quantum well wires of comparable dimensions. This is a consequence of the quantum confinement and the homogeneous distribution of the impurities in the quantum dot.

When the radius of the quantum dot decreases we observe that the peak associated with impurities located next to the center diminishes (see Fig. 53b), which may be understood by means of the behavior of the density of the states as a function of the binding energy (see Fig. 3 in [135]). In this figure, it is seen that for small radii the density of the states

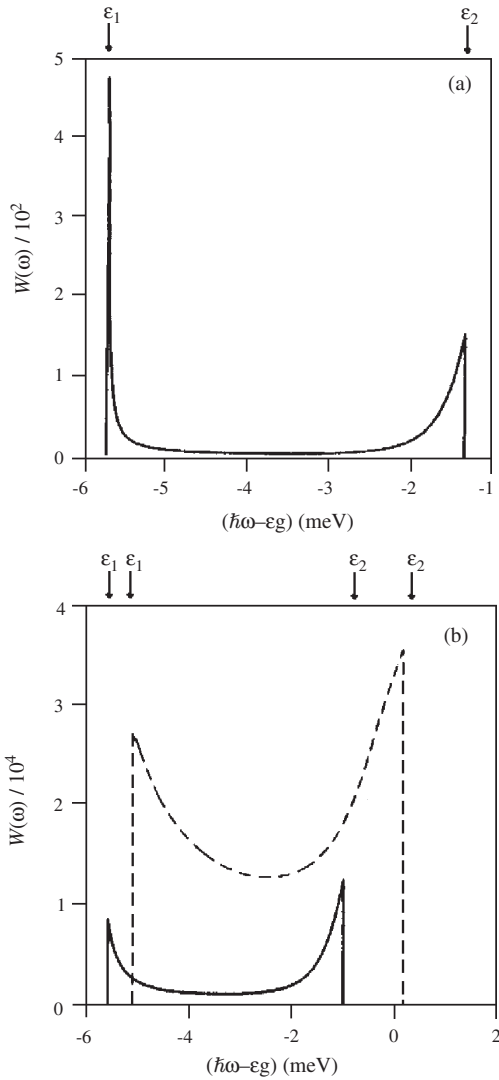


**Figure 52.** Optical absorption spectra (in units of  $W_0$ ), as a function of the  $\hbar\omega - \varepsilon_g$ , for valence to donor transitions in infinite GaAs-(Ga,Al)As quantum dots of different radii.  $r_0 = 3000 \text{ \AA}$  (a),  $r_0 = 1000 \text{ \AA}$  (full curve), and  $r_0 = 500 \text{ \AA}$  (dashed curve) (b).  $\varepsilon_1$  and  $\varepsilon'_1$  ( $\varepsilon_2$  and  $\varepsilon'_2$ ) correspond, respectively, to the onset of transitions from the first valence subband to the lower (upper) edge of the impurity band. Reprinted with permission from [205], J. L. Marín et al., in “Handbook of Advanced Electronic and Photonic Materials and Devices” (H. S. Nalwa, Ed.). Academic Press, San Diego, 2001. © 2001, Academic Press.

is a smooth function which exhibits a well-defined peak at the binding energy associated with on-edge donors. When the radius is very large, the structure of the  $\varepsilon_i^{\max}$  Van Hove-like singularity is clearly a peak associated with on-center donors, which corresponds to the bulk limit. For quantum dots of  $r_0 > 1000 \text{ \AA}$  it is observed that the peak related to on-edge donors is still significant, a situation that is very well reflected in our results. On the other hand, a remarkable difference in the total absorption probability is the absence of the peak structure associated with impurities located at wells for quantum dots with radii less than  $500 \text{ \AA}$  with quantum wells and quantum well wires.

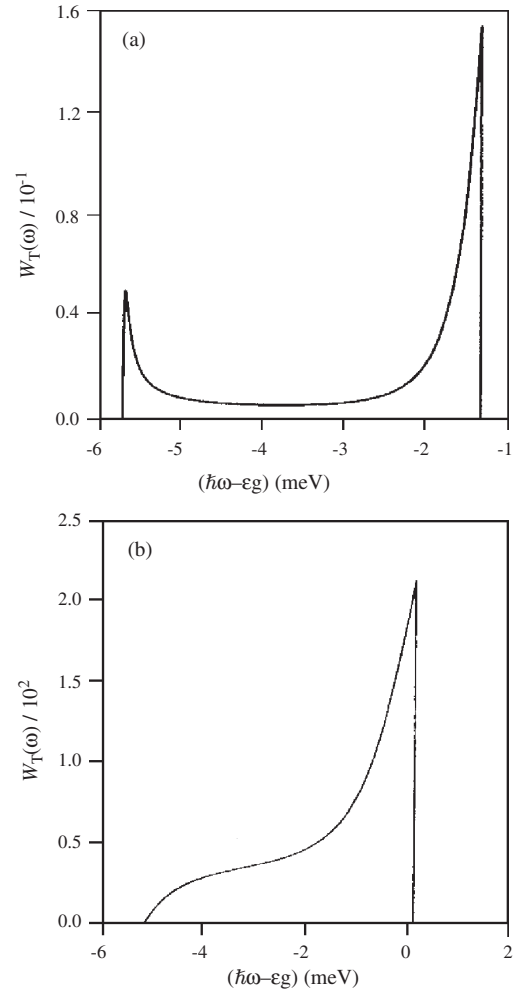


**Figure 53.** Total optical absorption spectra (in units of  $W_0$ ), as a function of the  $\hbar\omega - \varepsilon_g$ , for valence to donor transitions in infinite GaAs-(Ga,Al)As quantum dots of different radii.  $r_0 = 3000 \text{ \AA}$  (a) and  $r_0 = 500 \text{ \AA}$  (b) for a quantum dot with a homogeneous distribution of impurities, where there is no interaction between them. Reprinted with permission from [205], J. L. Marín et al., in “Handbook of Advanced Electronic and Photonic Materials and Devices” (H. S. Nalwa, Ed.). Academic Press, San Diego, 2001. © 2001, Academic Press.

## 4. NONCONVENTIONAL AND ATOMIC IDEALIZED CONFINED SYSTEMS IN NANOSTRUCTURES

### 4.1. Ground State Energy of the Two-Dimensional Hydrogen Atom Confined within Conical Curves

In this section the variational method is used to calculate the ground state energy of the two-dimensional hydrogen atom confined by impenetrable conical curves [141]. The confinement of the atom in a region limited by two intersecting parabolas as well as within a cone was also considered. The results show the transition of this system to a quasi-one-dimensional hydrogen atom when the curves are open. In the case of closed curves, a transition to a quasi-zero-dimensional hydrogen atom is observed. These limiting

cases, as well as other intermediate situations, are discussed within this section.

In particular, the ground state energy of this kind of system is calculated for different confining situations. Moreover, the behavior of the ground state energy is analyzed, as the confining region reaches an extreme value, that is, when the system becomes quasi-one-dimensional (open curves) or quasi-zero-dimensional (closed curves) as well as other intermediate situations.

The results show a very interesting behavior of this property depending upon the confinement region as well as the closed or open character of the curves.

The latter would represent an interesting research topic concerning the study of other properties of this system such as its polarizability, pressure due to the boundaries, dipole moment, etc.

#### 4.1.1. Schrödinger Equation

In atomic units ( $\hbar = e = m_e^* = 1$ ), the Schrödinger equation for the two-dimensional confined hydrogen atom in orthogonal curvilinear coordinates can be written as

$$-\frac{1}{2} \frac{1}{h_1 h_2} \left[ \frac{\partial}{\partial q_1} \left( \frac{h_2}{h_1} \frac{\partial}{\partial q_1} \right) + \frac{\partial}{\partial q_2} \left( \frac{h_2}{h_1} \frac{\partial}{\partial q_2} \right) \right] + V_{en}(q_1, q_2) + V_b(q_1, q_2) \} \psi(q_1, q_2) = \varepsilon \psi(q_1, q_2) \quad (263)$$

where  $(q_1, q_2)$  is the orthogonal curvilinear coordinate system in the plane and  $\{h_i\}$  is the scale factor, given by

$$h_i^2 = \left( \frac{\partial x}{\partial q_i} \right)^2 + \left( \frac{\partial y}{\partial q_i} \right)^2 \quad (264)$$

$V_{en}(q_1, q_2)$  is the Coulombic interaction

$$V_{en}(q_1, q_2) = -\frac{1}{r(q_1, q_2)} \quad (265)$$

while  $r(q_1, q_2)$  is the electron–nucleus separation, in this set of coordinates.

The confining potential that it will be assumed is of the form

$$V_b(q_1, q_2) = \begin{cases} +\infty & (q_1, q_2) \notin D \\ 0 & (q_1, q_2) \in D \end{cases} \quad (266)$$

where  $D$  is a given finite (or infinite) confining domain of the plane.

The solution of Eq. (263) must satisfy

$$\psi(q_1, q_2) = 0 \quad q \in \partial D \quad (267)$$

where  $\partial D$  is the boundary of  $D$ .

The model Hamiltonian for the confined quantum system under study can be written, in atomic units, as

$$\hat{H} = -\frac{1}{2} \nabla_q^2 + V_{en}(q) + V_b(q) \quad (268)$$

where  $V_{en}(q)$  and  $V_b(q)$  are given by Eqs. (265) and (266), and  $\nabla_q^2$  is derived from Eq. (263).

At this point, the variational method can be implemented to calculate the ground state energy of the system by constructing the functional

$$\varepsilon(\alpha) = \int_D \chi_i^* \left\{ -\frac{1}{2} \nabla_q^2 + V_{en}(q) \right\} \chi_i d^2 q \quad (269)$$

and minimizing it with respect to  $\alpha$ , restricted to

$$\int_D \chi_i^* \chi_i d^2 q = 1 \quad (270)$$

as usual.

The area element is given as  $d^2 q = h_1 h_2 dq_1 dq_2$ .

To this extent, the method described previously can be used to study a confined system for which the interactions with the surrounding medium are not considered (i.e., enclosed within a potential barrier of infinite depth). The next subsection is restricted to deal with the case of a typical one-electron confined system in two dimensions, namely, the case of hydrogen atoms confined within a given region of the plane with different geometries.

#### 4.1.2. Variational Wavefunctions for Different Geometries

As is well known, the Schrödinger equation for the unconfined two-dimensional hydrogen atom is separable in polar coordinates  $(r, \theta)$ ; its ground state wavefunction can be written as

$$\phi(r, \theta) = C_0 \exp(-k_0 r) \quad (271)$$

where  $C_0$  is a normalization constant,  $r$  is the electron–nucleus distance,  $k_0 = \sqrt{-2\varepsilon_0}$ ,  $\varepsilon_0 = -2$  Hartrees is its ground state energy, and the nucleus was assumed to be located at the origin.

When the atom in the plane is restricted to a given open or closed domain  $D$ ,  $\phi$  and  $\varepsilon_0$  must change to fit the new conditions accordingly. If the boundary,  $\partial D$  of  $D$ , is impenetrable for the electron, then  $\phi = 0$  at  $\partial D$ . The latter means that due to confinement, new quantization rules must be found; that is, the old “good” quantum numbers used to define the energy of the unconfined system are no longer useful to characterize the energy of the now confined system. Moreover, as the region of confinement was assumed arbitrary (in shape and size), the energy of a given state would depend on a continuous parameter associated with the size (or shape) of the domain  $D$  (or its boundary  $\partial D$ ).

In the case of the confined two-dimensional hydrogen atom, the approximate (variational) ground state energy would involve the use of a trial wavefunction given by

$$\chi(q_1, q_2) = A f(q_i, q_0) \exp[-\alpha r(q_1, q_2)] \quad (272)$$

where  $(q_1, q_2)$  is the system of coordinates compatible with the symmetry of the confining boundary,  $r(q_1, q_2)$  is the electron–nucleus distance in these coordinates,  $f(q_i, q_0)$  is a geometry-adapted auxiliary function such that  $f = 0$  at  $q_i = q_0$ ,  $q_i$  is a coordinate associated with the geometry of the boundary, and  $\alpha$  is a variational parameter.

The geometry of the confining boundary allows one to choose  $f$  in a quite simple way, namely, similar to its contours. To exemplify the latter, if the assumed confining boundary is a circle of radius  $r_0$ , then  $f = r_0 - r$  (i.e., this function maps all circles of radius  $0 \leq r \leq r_0$ , that is, the allowed region for the atomic electron). Similarly, if the confining boundary is an ellipse of “size”  $\xi_0$  (eccentricity =  $1/\xi_0$ ), then  $f = \xi_0 - \xi$  and the function would map all ellipses of size consistent with  $1 \leq \xi \leq \xi_0$ , thus generating the allowed space for the atomic electron in the plane. The definition of  $f$  can be done for other confining symmetries accordingly.

A description on the flexibility of so-constructed trial wavefunctions, to deal with a variety of confining situations, can be found in [65, 66, 78, 111, 121]. In particular, in [78, 111] other physical properties for one- and two-electron confined atoms are calculated to test the goodness of the wavefunctions. The results show good agreement compared with exact or more elaborate approximated methods.

Hence, once that coordinate system  $(q_1, q_2)$  is chosen, all necessary elements for constructing the trial wavefunction are defined and the procedure outlined in the previous section can immediately be used to calculate and minimize the energy functional. Of course, the transformation equations defining the chosen coordinate system are assumed to be known; indeed, it is usually the case and they can be found elsewhere.

It is worth mentioning that the binding energy, defined as the absolute value of the difference between the energies of the electron with and without the Coulombic interaction, has only meaning in the case of closed curves. In the case of open curves, the electron energy belongs to the continuum spectrum and the binding energy is meaningless. Moreover, in the former situation, the binding energy would behave as the total energy, that is, as the confining region becomes smaller or either grows without limit, due to the closed and impenetrable property of the confining boundary.

Figures 54a, 55a, 56a, 57a, 58a, and 59a display the confining geometries considered in this section, while Figures 54b, 55b, 56b, 57b, 58b, and 59b show the behavior of their corresponding ground state energies as a function of confining parameter, respectively.

The ground state energy of the two-dimensional hydrogen atom confined within an ellipse is displayed in Figure 54b as a function of parameter  $\xi_0$  (which defines the degree of confinement) for  $a = 0.5, 1.0,$  and  $2.0$  Bohrs, respectively. Notice that for a given  $\xi_0$  different than 1 and  $\infty$ , when  $a$  decreases, the major and minor semiaxes also decrease (i.e., the region of confinement is smaller and the energy increases). If  $\xi_0 \rightarrow 1$ , the two-dimensional hydrogen atom becomes a quasi-zero-dimensional system and the ground state energy goes to  $\infty$  (see Fig. 54a). In the case that  $\xi_0 \rightarrow \infty$ , the atom is allowed to occupy the whole plane for any value of  $a$ , thus recovering the case of an unconfined two-dimensional hydrogen atom, as expected.

In Figure 55b, the energy for the ground state of the two-dimensional hydrogen atom confined in a region of the plane limited by a hyperbola (see Fig. 55a) is displayed as a function of  $\eta_0$  (which defines the degree of confinement) for  $a = 0.5, 1.0,$  and  $1.5$  Bohrs, respectively. As can be observed, for  $\eta_0 = 0$ , the hyperbola becomes degenerate and their two

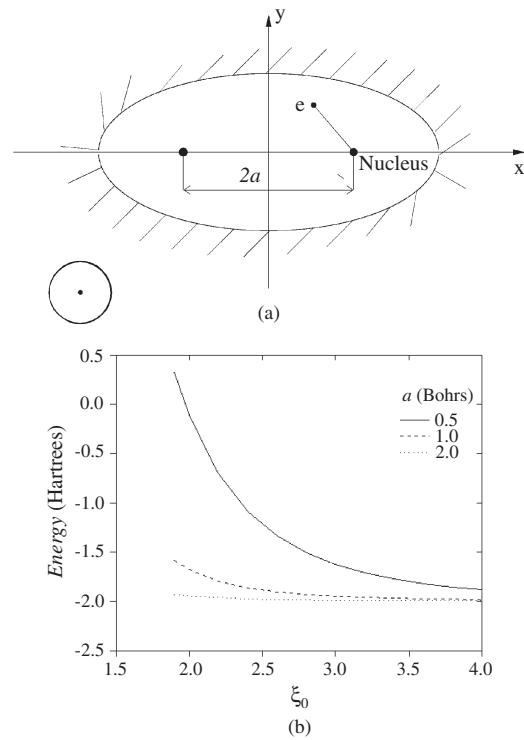


**Figure 54.** (a) Region of elliptic confinement. Limiting case: Q-zero-dimensional. (b) Ground state energy of the two-dimensional hydrogen atom confined within an ellipse as a function of the parameter  $\xi_0$ , for three values of the semidistance between foci  $a = 0.5, 1.0,$  and  $2.0$  Bohr, respectively. Reprinted with permission from [205], J. L. Marín et al., in “Handbook of Advanced Electronic and Photonic Materials and Devices” (H. S. Nalwa, Ed.). Academic Press, San Diego, 2001. © 2001, Academic Press.

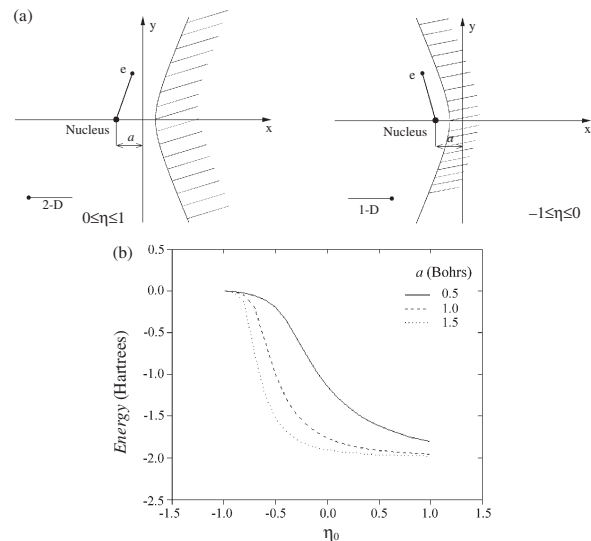


**Figure 55.** (a) Region of hyperbolic confinement. Limiting case: Q-one-dimensional. (b) Ground state energy of the two-dimensional hydrogen atom confined within a region of the plane limited by a hyperbola, as a function of  $\eta_0$ , for three values of the semidistance between foci  $a = 0.5, 1.0,$  and  $2.0$  Bohr, respectively. Reprinted with permission from [205], J. L. Marín et al., in “Handbook of Advanced Electronic and Photonic Materials and Devices” (H. S. Nalwa, Ed.). Academic Press, San Diego, 2001. © 2001, Academic Press.



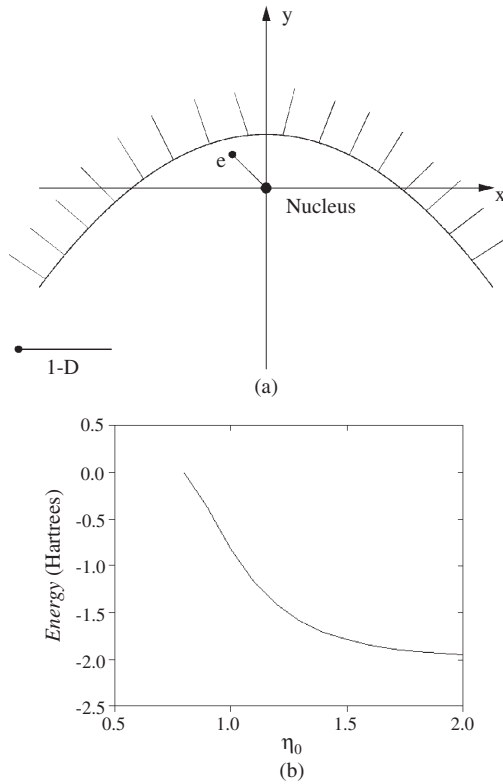


**Figure 56.** (a) Region of parabolic confinement. Limiting case: Q-one-dimensional. (b) Ground state energy of the two-dimensional hydrogen atom confined within a region of the plane limited by a parabola, as a function of  $\xi_0$ . Reprinted with permission from [205], J. L. Marín et al., in “Handbook of Advanced Electronic and Photonic Materials and Devices” (H. S. Nalwa, Ed.). Academic Press, San Diego, 2001. © 2001, Academic Press.

branches coincide with the  $y$ -axis, so that the confinement region becomes a half plane for any value of  $a$  different from zero and infinity. When  $\eta_0$  and  $a \rightarrow 0$ , the coalescence of the two branches of the hyperbola ( $\eta_0 \rightarrow 0^-$  and  $\eta_0 \rightarrow 0^+$ ) leads to a quasi-two-dimensional hydrogen atom with its nucleus at the  $y$ -axis; the ground state energy approaches  $-2/9$  Hartree. When  $a \rightarrow \infty$ , the whole plane becomes available for the atom, thus leading to the unconfined two-dimensional hydrogen atom (see Fig. 55a). Another observation is that for  $\eta_0 \rightarrow -1$  the whole plane is forbidden ( $x$ -axis is excluded), thus resulting in the one-dimensional hydrogen atom with zero energy (see Fig. 55b), which physically means that all excited states belong to the continuous spectrum or to the ionized atom. A similar behavior was found in [142, 143] for a three-dimensional hydrogen atom limited by paraboloidal or hyperboloidal surfaces.

Figure 56b shows the energy for the ground state of the two-dimensional hydrogen atom confined in a region of the plane limited by a parabola (see Fig. 56a) as a function of  $\xi_0$  (which defines the degree of confining). Notice that as  $\xi_0 \rightarrow \infty$  the parabola opens and the confinement region decreases until the whole plane is available; thus a transition occurs from a confined two-dimensional system to an unconfined two-dimensional system (see Fig. 56a), whose energy is  $-2$  Hartrees. In the same way, if  $\xi_0 \rightarrow 0$  the parabola closes

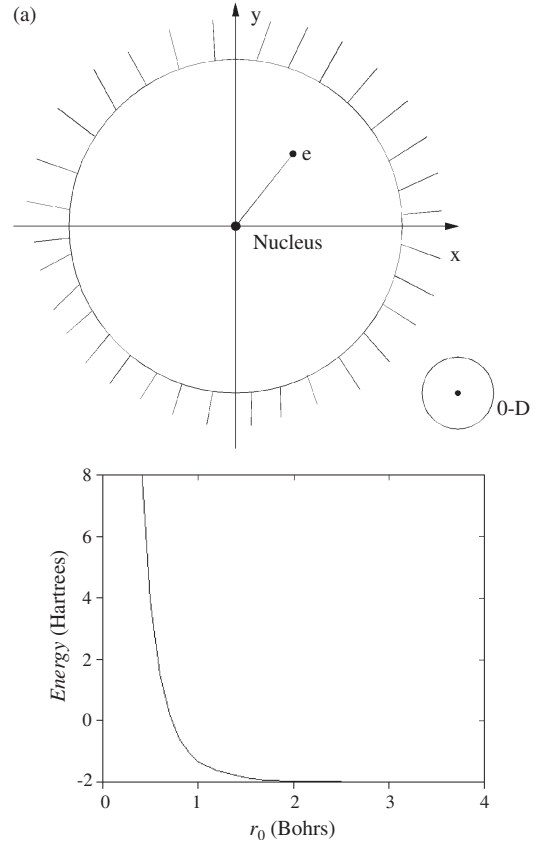


**Figure 57.** (a) Region of circular confinement. Limiting case: Q-zero-dimensional. (b) Ground state energy of the two-dimensional hydrogen atom confined within a region of the plane limited by a circle, as a function of its radius  $r_0$ . Reprinted with permission from [205], J. L. Marín et al., in “Handbook of Advanced Electronic and Photonic Materials and Devices” (H. S. Nalwa, Ed.). Academic Press, San Diego, 2001. © 2001, Academic Press.

and the forbidden region increases, confining the system in the  $-y$ -axis, thus realizing the transition from a confined two-dimensional system to a confined quasi-one-dimensional system, whose energy approaches zero (see Fig. 56b).

In Figure 57b, the ground state energy of the two-dimensional hydrogen atom confined in a circular region of the plane is depicted as a function of  $r_0$  (radius of the circle in atomic units). As can be observed, for  $r_0 \rightarrow \infty$ , the allowed space approaches the whole plane (i.e., the system becomes the unconfined two-dimensional hydrogen atom whose ground state energy is  $-2$  Hartrees). Another observation is that, when  $r_0 \rightarrow 0$ , the forbidden circular region becomes a point and a transition of the two-dimensional system to a quasi-zero-dimensional system (see Fig. 57a) with energy  $\varepsilon \rightarrow \infty$  occurs.

Figure 58b displays the ground state energy of the two-dimensional hydrogen atom confined in a region of the plane limited to a cone obtained when  $\theta = \theta_0$  and  $0 \leq r < \infty$ , as a function of  $\theta_0$  (polar angle in radians). In the limit when  $\theta_0 \rightarrow 0$  the cone decreases; then the transition of the confined two-dimensional system to the quasi-one-dimensional system with energy  $\varepsilon \rightarrow 0$  occurs, as in the previous situations. When  $\theta_0$  increases to  $2\pi$ , the allowed region grows

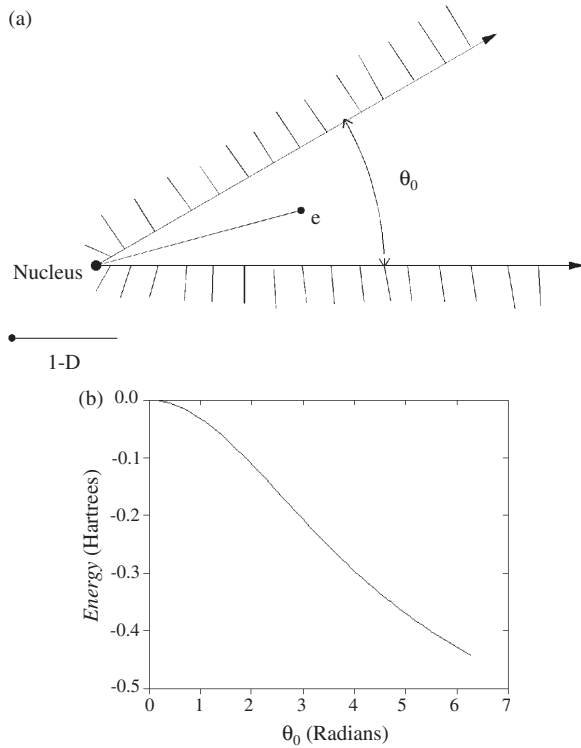


**Figure 58.** (a) Region of conical confinement. Limiting case: Q-two-dimensional. (b) Ground state energy of the two-dimensional hydrogen atom confined within a region of the plane limited by a cone, as a function of the opening angle  $\theta_0$ . Reprinted with permission from [205], J. L. Marín et al., in “Handbook of Advanced Electronic and Photonic Materials and Devices” (H. S. Nalwa, Ed.). Academic Press, San Diego, 2001. © 2001, Academic Press.

and the system behaves as a quasi-two-dimensional system; the edges of the cone are still a forbidden region (see Fig. 58a). The latter case corresponds to the minimum of the curve at 6.2856 radians ( $2\pi$ ) where the energy is  $\approx -2/9$  Hartree and coincides with the case of hyperbolic confinement in the limit  $\eta_0 \rightarrow 1$ ,  $a \rightarrow 0$  (see Figs. 55a and 58a), as expected.

Figure 59b shows the ground state energy of the two-dimensional hydrogen atom confined in a region of the plane given by the intersection of two symmetrical confocal parabolas (see Fig. 59a), as a function of  $\xi_0$  (root of the distance to the foci, in atomic units). As can be observed, when  $\xi_0 \rightarrow 0$  the two parabolas (and their intersections) are closer to the origin. The allowed region is almost a point, the transition of a confined two-dimensional system to a quasi-zero-dimensional one occurs, and accordingly, the energy becomes infinite, as expected. Moreover, in the case when  $\xi_0 \rightarrow \infty$ , the available space enlarges until the unconfined two-dimensional atom is recovered, that is, the energy approaches  $-2$  Hartrees (see Fig. 59b).

The overall results show that the ground state energy of the two-dimensional hydrogen atom confined by an impenetrable potential has two extreme limiting cases, namely: (a) In the case of closed conical curves, a transition to a quasi-zero-dimensional system occurs where the ground state energy becomes infinite, that is, the confinement region approaches a point; (b) in the case of open conical curves,

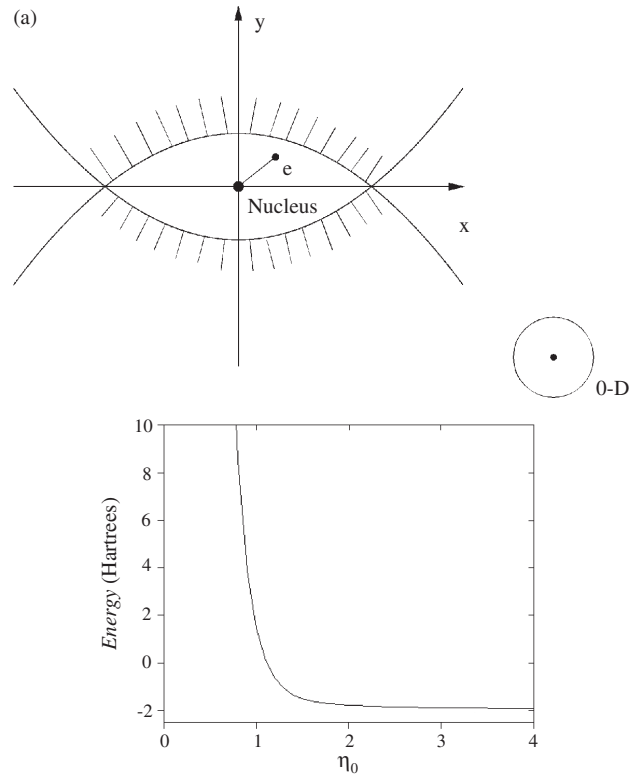


**Figure 59.** (a) Region of confinement given by the intersection of two symmetrical parabolas. Limiting case: Q-zero-dimensional. (b) Ground state energy of the two-dimensional hydrogen atom confined within a region of the plane limited by the intersection of two symmetrical confocal parabolas, as a function of  $\xi_0$ . Reprinted with permission from [205], J. L. Marín et al., in “Handbook of Advanced Electronic and Photonic Materials and Devices” (H. S. Nalwa, Ed.). Academic Press, San Diego, 2001. © 2001, Academic Press.

a transition to a quasi-one-dimensional system occurs in which the atom is confined to a straight line with origin at the nucleus and whose ground state energy becomes zero. Case (b) is closely related to the one-dimensional hydrogen atom discussed in [144–149], except that the binding energy is found to be infinite in [148]. The main difference between the limiting case (b) and the so-called Loudon one-dimensional atom [148] rests in the fact that Loudon did not take into account the energy due to the confinement because his model is one-dimensional and our limit case is quasi-one-dimensional. A discussion of this matter is made in next section. Moreover, since the binding energy of Loudon’s one-dimensional atoms is greater than the rest mass energy of the electron, the treatment of the atom should be done in a relativistic scheme, which renders a large, but finite, binding energy [150].

In summary, the confining geometries studied in this section lead us to conclude following extreme behavior:

- Circular:  $r_0 \rightarrow 0$       $\varepsilon \rightarrow \infty$
- [quasi-zero dimensional (Q-0D)]
- Elliptic:  $\xi_0 \rightarrow 1$       $\varepsilon \rightarrow \infty$      (Q-0D)

$$\text{Hyperbolic: } \begin{cases} \eta_0 \rightarrow 0 & \varepsilon = \varepsilon(a) \quad (a \neq 0) & \text{(Q-2D)} \\ \eta_0 \rightarrow 1 & \varepsilon = \varepsilon(a) & \text{(Q-2D)} \\ (\eta_0, a) \rightarrow 0 & \varepsilon \rightarrow -2/9 & \text{(Q-2D)} \\ \eta_0 \rightarrow -1 & \varepsilon \rightarrow 0 & \text{(Q-1D)} \end{cases}$$

$$\text{Parabolic (one): } \eta_0(\xi_0) \rightarrow 0 \quad \varepsilon \rightarrow 0 \quad \text{(Q-1D)}$$

$$\text{Parabolic (two): } \eta_0(\xi_0) \rightarrow 0 \quad \varepsilon \rightarrow \infty \quad \text{(Q-0D)}$$

$$\text{Cone: } \begin{cases} \theta_0 \rightarrow 0 & \varepsilon \rightarrow 0 & \text{(Q-1D)} \\ \theta_0 \rightarrow 2\pi & \varepsilon \approx -2/9 & \text{(Q-2D)} \end{cases}$$

### 4.1.3. One-Dimensional Hydrogen Atom, as a Limiting Situation

The behavior of the ground state energy of the confined two-dimensional hydrogen atom, when one dimension becomes infinitely small, will be analyzed in this section.

If the nucleus of the atom is located at the origin and the confining region is a symmetrical narrow strip of width  $2y_0$ , the Hamiltonian for the system is (in atomic units)

$$\hat{H} = -\frac{1}{2} \frac{\partial^2}{\partial x^2} - \frac{1}{2} \frac{\partial^2}{\partial y^2} + V_b(y) - \frac{1}{\sqrt{x^2 + y^2}} \quad (273)$$

where  $V_b(y)$  is the confining potential, defined as

$$V_b(y) = \begin{cases} 0 & -y_0 \leq y \leq y_0 \\ \infty & \text{otherwise} \end{cases} \quad (274)$$

The corresponding Schrödinger equation can be written as

$$\left\{ -\frac{1}{2} \frac{\partial^2}{\partial x^2} - \frac{1}{2} \frac{\partial^2}{\partial y^2} + V_b(y) - \frac{1}{\sqrt{x^2 + y^2}} \right\} \psi(x, y) = \varepsilon \psi(x, y) \quad (275)$$

where  $\varepsilon$  is the total energy and the wavefunction  $\psi(x, y)$  must satisfy the boundary condition

$$\psi(x, \pm y_0) = 0 \quad (276)$$

As has been pointed out by Jan and Lee [151], as the strip becomes very narrow (i.e.,  $y_0$  is very small), the fast motion in the  $y$ -direction allows the wavefunction to be written, approximately, as

$$\psi(x, y) \approx \chi(y) \Phi(x) \quad (277)$$

Since  $\psi(x, y)$  must satisfy the boundary condition (276), then

$$\chi(y) \approx \cos(k_0 y) \quad (278)$$

with  $k_0 = \pi/2y_0$ .

Introducing Eq. (277) into Eq. (275) and multiplying the result by  $\cos(k_0 y)$ , the integration over  $y$  from  $-y_0$  to  $y_0$  yields the equation

$$\left\{ -\frac{d^2}{dx^2} + N^2 \int_{-y_0}^{y_0} \frac{-2}{\sqrt{x^2 + y^2}} \cos^2(k_0 y) dy \right\} \Phi(x) = (\varepsilon - \varepsilon_y) \Phi(x) \quad (279)$$

where

$$N^2 = \left[ \int_{-y_0}^{y_0} \cos^2(k_0 y) dy \right]^{-1} = y_0^{-1} \quad (280)$$

is a normalization constant and  $\varepsilon_y = k_0^2 = \pi^2/4y_0^2$  is the kinetic energy of the fast motion in the  $y$ -direction due to confinement.

Equation (279) can be rewritten as

$$\left[ -\frac{d^2}{dx^2} + V_{\text{eff}}(x) \right] \Phi(x) = \varepsilon_x \Phi(x) \quad (281)$$

where  $\varepsilon_x = \varepsilon - \varepsilon_y$  and

$$V_{\text{eff}}(x) = N^2 \int_{-y_0}^{y_0} \left[ \frac{-2}{\sqrt{x^2 + y^2}} \right] \cos^2(k_0 y) dy \quad (282)$$

A similar equation was found in [151] for a hydrogenic impurity confined within a quantum well wire.

The result of averaging the two-dimensional Coulombic attraction over the fast  $y$  motion is such that Eq. (281) can be interpreted as Schrödinger equation for the one-dimensional atom under the potential  $V_{\text{eff}}(x)$ .

Moreover, a careful analysis of  $V_{\text{eff}}(x)$  in the limit  $y_0 \rightarrow 0$  reveals that this potential has the same behavior as the one-dimensional Coulomb potential, as was also pointed out by Jan and Lee [151] in the case of a three-dimensional hydrogen atom confined within a cylinder whose radius approaches zero. The energy  $\varepsilon_x$  in this limiting situation becomes the same as that obtained by Loudon [148], that is,  $-\infty$ . It can also be noted that when  $y_0 \rightarrow 0$ ,  $\varepsilon_y \rightarrow \infty$  and thus the total energy for the confined one-dimensional atom  $\varepsilon = \varepsilon_x + \varepsilon_y \rightarrow 0$ . The latter fact supports the results obtained in cases when the open confining curve approaches a straight line.

## 4.2. Geometrical Effects on the Ground State Energy of Hydrogenic Impurities in Quantum dots

The effect of nonsphericity of quantum dots on the ground state energy of hydrogenic impurities is studied in the frame of the effective mass approximation and the variational method [152]. The difference in composition of the quantum dot and the host material is modeled with a potential barrier at the boundary of the dot. To make the analysis, two symmetries are considered for the quantum dot: spherical and spheroidal. In this way, the ground state energy is calculated as a function of the volume of the quantum dot, for different barrier heights. The results show that the ground state is strongly influenced by the geometry of the dot; that is, for a given volume and barrier height, the energy is clearly different if the dot is spherical or spheroidal in shape when the volume of the dot is small (strong confinement regime). As the volume of the dot increases (weak confinement regime) the geometry becomes irrelevant, as expected.

The confinement of excitons in quantum dots and other microstructures such as quantum wells, quantum well

wires, etc. was corroborated experimentally in the past [113, 153–156]. The main feature of this effect corresponds to a frequency shift of the first excitonic peak to higher energy, compared to the mean bulk electronic peak. There have been many theoretical efforts to explain quantitatively this quantum mechanical effect [92, 157–163]. However, in all these works, the dot is assumed to be of spherical shape. This last assumption is not strictly true, since the electron microscopy studies of these systems show microparticles whose shapes vary from quasi-spherical to pyramidal [113]. The aim of this work is to analyze quantitatively the dependence of the ground state energy of a hydrogenic impurity on the geometry of the quantum dot. The latter would be of interest since it might constitute a qualitative study of the behavior of excitons confined within these microstructures. We assume that the impurity is confined within a potential barrier of finite depth, which emulates, on the average, the surrounding medium in which the dot is embedded. The calculation of the impurity ground state energy is performed using a variational approach, which previously was shown to be useful in dealing with this type of confined system in a fairly good fashion [66, 78, 111, 121]. The model Hamiltonian for the impurity is assumed to be valid within the effective mass approximation and we have considered, for the sake of comparison, spherical and spheroidal dots of the same volume and confining barrier. In this way, the ground state energy of the impurity is calculated as a function of the volume and the confining barrier heights.

#### 4.2.1. Brief Description of the Method

If  $\{q_i\}$  denotes the orthogonal set of coordinates compatible with the symmetry of the confining boundary, the trial wavefunctions can then be written as

$$\chi_i(q, \alpha) = Af(q, q_0, \alpha)\phi_i^0(q, \alpha) \quad q < q_0 \quad (283)$$

and

$$\chi_0(q, \beta) = B\phi(q, \beta) \quad q > q_0 \quad (284)$$

where  $\alpha$  and  $\beta$  are parameters to be determined,  $q_0$  is associated with the size and symmetry of the confining boundary,  $A$  and  $B$  are normalization constants,  $\phi_i^0$  is the free system wavefunction,  $\phi$  is a function with the proper asymptotic behavior as  $q_0 \rightarrow \infty$ , and  $f$  is an auxiliary function that allows the condition

$$\frac{1}{\chi_i} \frac{\partial \chi_i}{\partial q} = \frac{1}{\chi_0} \frac{\partial \chi_0}{\partial q} \quad (285)$$

at  $q = q_0$  to be satisfied.

The model Hamiltonian for the confined quantum system under study, in the effective mass approximation, can be written, in atomic units, as

$$\hat{H} = -\frac{1}{2}\nabla_q^2 + V(q) + V_b(q) \quad (286)$$

where  $V$  is the potential that accounts for the internal interactions of the components of the system and  $V_b$  is the confining potential. Here we shall assume that  $V_b$  has the form

$$V_b = \begin{cases} 0 & q < q_0 \\ V_0 & q > q_0 \end{cases} \quad (287)$$

At this point, the variational method can be implemented to calculate the energy of the ground state of the system by construing the functional

$$\varepsilon(\alpha, \beta) = \int \chi_i^* \left\{ -\frac{1}{2}\nabla_q^2 + V(q) \right\} \chi_i d^3q + \int \chi_o^* \left\{ -\frac{1}{2}\nabla_q^2 + V_0 + V(q) \right\} \chi_o d^3q \quad (288)$$

and minimizing it with respect to  $(\alpha, \beta)$ , restricted to

$$\int \chi_i^* \chi_i d^3q + \int \chi_o^* \chi_o d^3q = 1 \quad (289)$$

as usual.

#### 4.2.2. Geometry Adapted Trial Wavefunctions

In the effective mass approximation, the model Hamiltonian for an hydrogenic impurity ( $m_n^* = \infty$ ) confined within a quantum dot, in the context of the later section, can be written as

$$\hat{H} = -\frac{1}{2}\nabla_q^2 + V(q) + V_b(q) \quad (290)$$

where

$$V_b = \begin{cases} 0 & q < q_0 \\ V_0 & q > q_0 \end{cases} \quad (291)$$

and

$$V(q) = -\frac{1}{r_q} \quad (292)$$

Here  $r_q$  is the electron–nucleus separation and we have used effective atomic units. The symmetry of the confining domain determines the form of  $r_q$  in the set of coordinates compatible with it. In the following, we construct explicitly the trial wavefunctions for the chosen symmetries.

First, if we assume that the hole is located at the center of a confining sphere of radius  $r_0$ , the trial wavefunction in spherical coordinates can be written as [66]

$$\chi_i = A \exp(-\alpha r)(r_0 - \alpha r) \quad r < r_0 \quad (293)$$

and

$$\chi_o = B \exp(-\beta r)/r \quad r > r_0 \quad (294)$$

The continuity of the logarithmic derivative at  $r = r_0$ , given in Eq. (285), allows one relate  $\alpha$  and  $\beta$  by

$$\beta = \frac{\alpha r_0(1 - \alpha) + (2\alpha - 1)}{r_0(1 - \alpha)} \quad (295)$$

in such a way that only a variational parameter needs to be determined, once that the energy functional is minimized in the standard way.

If we now consider the exciton confined within the prolate spheroid

$$\{\xi = \xi_0 \quad -1 \leq \eta \leq 1 \quad 0 \leq \varphi \leq 2\pi\} \quad (296)$$

with the nucleus located at a foci, the electron–nucleus separation can then be written as

$$r_1 = R(\xi - \eta) \quad (297)$$

where  $2R$  is the interfocal distance of the spheroid. Following the solutions of Coulson and Robinson [122] for the free hydrogen atom in this coordinate system, the trial wavefunction is of the form

$$\chi_i = A \exp[-\alpha(\xi - \eta)](\xi - \alpha\xi_0) \quad \xi < \xi_0 \quad (298)$$

and

$$\chi_o = B \exp(-\beta\xi - \alpha\eta) \quad \xi > \xi_0 \quad (299)$$

Once again, the boundary condition given by Eq. (285) allows one to connect  $\alpha$  and  $\beta$  through

$$\beta = \frac{\alpha\xi_0(1 - \alpha) + \alpha}{\xi_0(1 - \alpha)} \quad (300)$$

As the reader must be aware, this form for the trial wavefunction satisfies automatically the boundary condition on its logarithmic derivative with respect to  $\eta$ , at  $\xi = \xi_0$ . As in the previous case, only a variational parameter needs to be determined when we use the variational approach.

We have to point out that the auxiliary function of the form  $(q_0 - \alpha q)$ , which was used to construct the trial wavefunction for two symmetries, is flexible enough to describe the situation in which  $V_0 \rightarrow \infty$ . In that case  $\alpha \rightarrow 1$  and correspondingly  $\beta \rightarrow \infty$  [see Eqs. (295) and (300)] so that the external wavefunction becomes vanishingly small in this limit, as expected.

In Figure 60a and b, the energy for the ground state of the hydrogenic impurity confined within spherical and prolate spheroidal quantum dots is displayed as a function of the volume, for  $V_0 = 2.0$  and  $8.0$  effective Rydbergs respectively. In both figures we have assumed an  $R = 1$  effective Bohr for the case of the prolate spheroidal dot. The effect of considering a different geometry can be noticed immediately from these figures, which supports that, for a given volume of the dot and barrier height, the ground state energy shows a dependence on the shape of the confining box that is particularly stronger for smaller sizes of the dot. The effect of including the internal interaction potential (Coulomb term) of the components of the system (electron–nucleus) in both regions (inside and outside the quantum dot) is also shown in the figures. When the Coulomb term is considered in the exterior of the quantum dot, a remarkable difference can be noticed for the smaller barrier height potential and smaller sizes of quantum dot. The latter is due to the fact that the confining capability of the box decreases and correspondingly, the probability of finding the electron in the exterior of the quantum dot is increased (see Fig. 60a). In Figure 60b, this effect is smaller. In Figure 60a, we can also observe a stronger dependence, by including the Coulomb term in the exterior of the quantum dot, for the spheroidal symmetry than for spherical one. Another observation is that, for the spheroidal symmetry, we have considered the nucleus of the impurity placed in a focus not in the origin, but in the latter case, keeping in mind the work of Marín et al. [65], the resulting geometrical effect would be stronger.

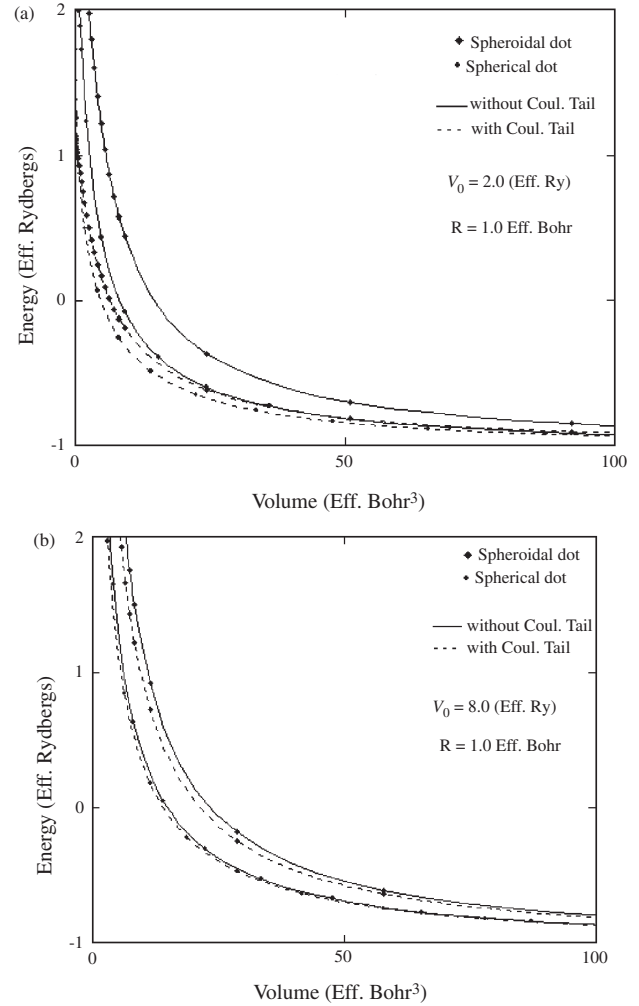


**Figure 60.** Ground state energy for a hydrogenic impurity within quantum dots of a spherical and prolate spheroidal shape as a function of their volume for a fixed value of the barrier height. (a)  $V_0 = 2.0R_y^*$ , (b)  $V_0 = 8.0R_y^*$ . Reprinted with permission from [205], J. L. Marín et al., in “Handbook of Advanced Electronic and Photonic Materials and Devices” (H. S. Nalwa, Ed.). Academic Press, San Diego, 2001. © 2001, Academic Press.

In Figure 61a, we show the energy for the ground state of the hydrogenic impurity confined in a spherical quantum dot as a function of the volume, for  $V_0 = 8.0$  and  $2.0$  effective Rydbergs. In the solid curves, the Coulomb term is not included in the external region of the quantum dot while in the dashed ones we have considered it. Figure 61b shows the same curves as in Figure 61a for the prolate spheroidal quantum dot with  $R = 1.0$  effective Bohr. A difference between the curves with and without the Coulomb term in the exterior of the quantum dot can be noticed. This difference is greater for the smaller barrier height potential and in the region of strong confinement regime (small sizes of the quantum dot). This effect is similar to that discussed earlier for Figure 60.

In Figure 62, we make a comparison of the ground state energy of the hydrogenic impurity confined within a prolate spheroidal quantum dot, for  $V_0 = 2.0$  effective Rydbergs and

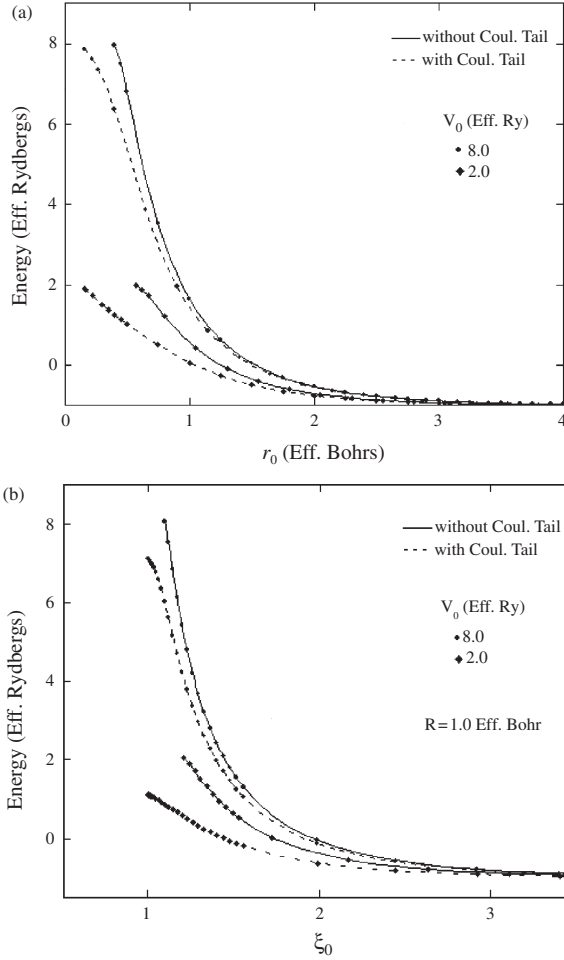


**Figure 61.** Ground state energy for a hydrogenic impurity within quantum dots of: (a) spherical symmetry as a function of the dot radius and barrier height, (b) prolate spheroidal symmetry as a function of the eccentricity and barrier height. Reprinted with permission from [205], J. L. Marín et al., in “Handbook of Advanced Electronic and Photonic Materials and Devices” (H. S. Nalwa, Ed.). Academic Press, San Diego, 2001. © 2001, Academic Press.

different interfocal distances ( $2R$ ). The solid curves correspond to  $R = 0.5$  and  $R = 1.0$  effective Rydbergs without the Coulomb term, while dashed ones are for the same values of  $R$  but the Coulomb term in the exterior of the quantum dot is included. The latter figure confirms that there is a significant variation of the energy for different interfocal distances of the spheroidal quantum dot and that the difference is greater for the lower value of  $R$  and even more significant when the Coulomb term in the exterior of the quantum dot is not included.

Thus, the previous results show that a quantitative fitting of the energy-size curves for the impurity (or, qualitatively, for the exciton) to experimental results (for a given value of  $V_0$ ) must be taken with caution, independently of the model used to make comparison. This is the case in most of the theoretical approaches dealing with semiconductor crystallites, since a spherical shape is assumed to fit the experimental results.

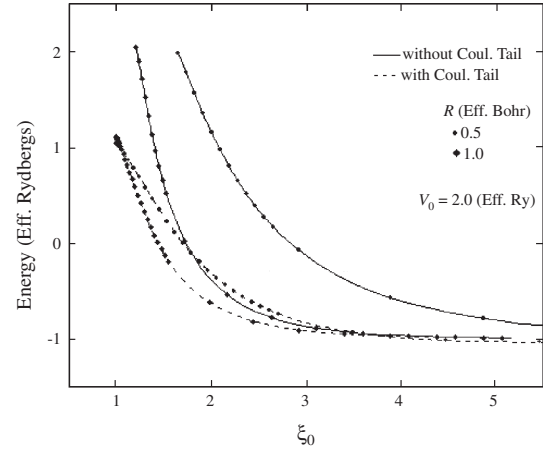


**Figure 62.** Ground state energy for a hydrogenic impurity as a function of the interfocal distance and the eccentricity for a fixed value of the barrier height. Reprinted with permission from [205], J. L. Marín et al., in “Handbook of Advanced Electronic and Photonic Materials and Devices” (H. S. Nalwa, Ed.). Academic Press, San Diego, 2001. © 2001, Academic Press.

### 4.3. Hydrogen Atom and Harmonic Oscillator Confined by Impenetrable Spherical Boxes

The direct variational method is used to study two simple confined systems, namely, the hydrogen atom and the harmonic oscillator within impenetrable spherical boxes. The trial wavefunctions have been assumed as the product of the “free” solutions of the corresponding Schrödinger equation and a simple function that satisfies the respective boundary conditions. The energy levels obtained in this way are extremely close to the exact ones, thus proving the utility of the proposed method.

#### 4.3.1. Direct Variational Approach

The exact solution for the free system can be found in any text of quantum mechanics [94]. Indeed, the corresponding energy and wavefunctions are given as

$$\varepsilon_n = -\frac{1}{n^2} \quad n = 1, 2, \dots \quad (301)$$

$$\psi_{nlm}(r, \theta, \varphi) = N_{nl}(2r/n)^l F(-n+l+1, 2l+2, 2r/n) \times \exp\left(-\frac{r}{n}\right) Y_l^m(\theta, \varphi) \quad (302)$$

where  $\hbar = m = 1$ ,  $Y_l^m(\theta, \varphi)$  are the spherical harmonics,  $F(a, b, z)$  is the confluent hypergeometric function [164], and  $N_{nl}$  is a normalization constant.

When we impose confinement on this system, the Hamiltonian is slightly modified and can be written as

$$\hat{H}' = -\frac{1}{2}\nabla^2 - \frac{1}{r} + V'(r) \quad (303)$$

where

$$V'(r) = \begin{cases} +\infty & r > r_0 \\ 0 & r \leq r_0 \end{cases} \quad (304)$$

and  $r_0$  is the radius of the confining spherical box.



The corresponding Schrödinger equation is still separable, but the resulting radial equation

$$\left[ \frac{d^2}{dr^2} + \frac{2}{r} \frac{d}{dr} - \frac{l(l+1)}{r^2} + \frac{2}{r} + 2\varepsilon \right] R(r) = 0 \quad (305)$$

must be solved with the following boundary condition:

$$R(r_0) = 0 \quad (306)$$

This means that, in order to obtain the energy spectrum, we must find the roots of Eq. (306). The new situation must be tackled in a more complicated way since we must construct a convergent series representation of  $R(r)$  and then solve it numerically.

Alternatively, we solve the same problem approximately, with the aid of the modified variational method discussed previously. We exploit the fact that the solutions of the “free” hydrogen atom are known [see Eq. (302)] in order to choose the trial wavefunctions as

$$\chi'_{nlm}(r, \theta, \varphi) = N(r_0 - r)(2\alpha r)^l F(-n + l + 1, 2l + 2, 2\alpha r) \times \exp(-\alpha r) Y_l^m(\theta, \varphi) \quad (307)$$

where  $N$  is a normalization constant that depends on  $r_0$  and  $\alpha$ , as well as on  $n$  and  $l$ .

We can note that  $1/n$  is replaced by  $\alpha$  in this choice for  $\chi'$ . The reason is that, as a result of confinement, the number  $n$  is no longer a good quantum number to specify the state of the system ( $l$  is still a good quantum number since symmetry has not been broken). This ansatz gives more flexibility to the variational wavefunctions, allowing for the calculation not only of the ground state energy, but also of excited states, with only one variational parameter. Furthermore, the quantum virial theorem for enclosed systems [165] is satisfied by these functions.

In order to show the adequacy of the method, in the following we shall restrict ourselves to states described by nodeless wavefunctions involving different symmetries.

When we use Eq. (307) as a trial wavefunction, together with the Hamiltonian given by Eq. (303), the energy can be readily found by minimizing the functional

$$\int_{\Omega} \chi'^* \hat{H} \chi' d\tau \quad (308)$$

with respect to  $\alpha$ , within the bounded volume  $\Omega$ , restricted to satisfy the constraints implied by

$$\int_{\Omega} \chi_n'^* \chi_m' d\tau = \delta_{nm} \quad (309)$$

This procedure is straightforward and can be done through direct algebraic manipulation.

Figure 63 shows the results obtained after minimizing Eq. (308) as compared to the “exact” values obtained by numerically solving Eq. (306) [124] for the ground state and the  $2p$  and  $3d$  excited states. Also shown in this figure are the results due to Fernandez and Castro [166] who used a method based on both hypervirial theorems and perturbation theory [167]. A remarkable agreement can be noticed, showing that the problem can be tackled in the simpler

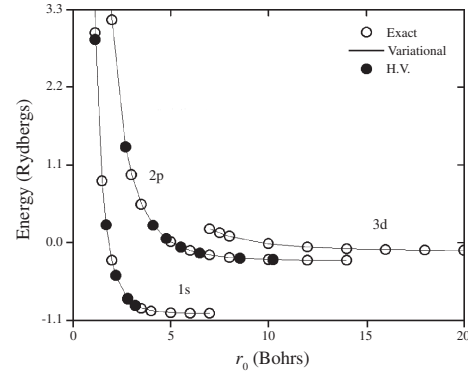


**Figure 63.** Energy levels of the enclosed hydrogen atom as a function of the radius of the box  $r_0$ . Exact and variational calculations are compared (see text). Reprinted with permission from [205], J. L. Marín et al., in “Handbook of Advanced Electronic and Photonic Materials and Devices” (H. S. Nalwa, Ed.). Academic Press, San Diego, 2001. © 2001, Academic Press.

fashion proposed here. Note that, in contrast to the hypervirial treatment, the energy values obtained by the variational method always lie as an upper bound to the exact results for all box sizes, as expected.

Incidentally, Fernandez and Castro [165] were the first to obtain the ground state energies shown in Figure 63 variationally. These authors used a trial wavefunction identical to Eq. (307) while analyzing the fulfillment of the quantum virial theorem for enclosed systems by approximate wavefunctions.

We now turn our attention to the case of the enclosed harmonic oscillator following a procedure similar to the case of the enclosed hydrogen atom.

Once again, the problem of the “free” oscillator is exactly solved and the energy and wavefunctions are given by [94]

$$\varepsilon_{nl} = 2n + l + 3/2 \quad n = 0, 1, 2, \dots \quad (310)$$

$$\psi_{nl}(r, \theta, \varphi) = N r^l F(-n, l + 3/2, r^2) \times \exp(-r^2/2) Y_l^m(\theta, \varphi) \quad (311)$$

where we have set  $\hbar = m = \omega = 1$ ,  $Y_l^m(\theta, \varphi)$  are the spherical harmonics,  $F(a, b, z)$  is the hypergeometric function, and  $N$  is a normalization constant.

As in the case of the hydrogen atom, when we impose the confinement, the Hamiltonian is modified to give

$$\hat{H}' = -\frac{1}{2} \nabla^2 + \frac{r^2}{2} + V'(r) \quad (312)$$

where

$$V'(r) = \begin{cases} +\infty & r > r_0 \\ 0 & r \leq r_0 \end{cases} \quad (313)$$

$r_0$  being the radius of the confining spherical box in units of  $(\hbar/m\omega)^{1/2}$ .

Once again, if we were to solve the problem exactly, the Schrödinger equation is separable and the resulting radial equation

$$\left[ \frac{d^2}{dr^2} + \frac{2}{r} \frac{d}{dr} - \frac{l(l+1)}{r^2} - r^2 + 2\varepsilon \right] R(r) = 0 \quad (314)$$

should be solved with the condition

$$R(r_0) = 0 \quad (315)$$

which would force us to use a numerical treatment. In the modified variational method (as in the case of the confined hydrogen atom) the symmetry of the enclosed harmonic oscillator is not broken by the confinement and  $l$  is still a good quantum number but  $n$  ceases to be so. To construct the trial wavefunctions, we simply replace  $r^2$  by  $\alpha r^2$  in the argument of the functions in Eq. (311) and we proceed, as in our previous example, to find the energy of the system for each box size.

In Table 5 we compare the exact results obtained from Eq. (315) [124] and those obtained by the application of the variational procedure, for the ground state and the first excited state. For completeness, we also show the results for the ground state, obtained through the hypervirial perturbational method using an 11-term perturbation expansion [168]. Once again, a very good agreement is observed.

An important criterion for this selection is the fulfillment of the virial theorem for these systems [165]. At this stage it is important to note that there are several papers in the literature dealing with different techniques to tackle these problems [125].

In this connection, Fernandez et al. [165, 169–171] have done a thorough study of the use of the virial theorem for quantum systems subject to Dirichlet and/or Neumann boundary conditions. As we have mentioned before, in both examples, the agreement of the results obtained by the proposed modification of the direct variational approach is remarkable, in spite of the simplicity of the method.

We note that the symmetry of the systems and their confinement were intentionally chosen to be compatible (i.e., both being of spherical symmetry).

#### 4.4. Energy States of Two Electrons in a Parabolic Quantum Dot in Magnetic Field

The energy spectra of two interacting electrons in a quantum dot confined by a parabolic potential in an applied magnetic field of arbitrary strength are obtained in this section. The

**Table 5.** Energy levels of the enclosed harmonic oscillator as a function of the radius of the box.

$r_0$	$\alpha$	Ground state ( $n = 0, l = 0$ )			First excited state ( $n = 0, l = 0$ )		
		$\varepsilon_{\text{HV}}^a$	$\varepsilon_{\text{var}}$	$\varepsilon_{\text{exact}}$	$\alpha$	$\varepsilon_{\text{var}}$	$\varepsilon_{\text{exact}}$
1.0	0.1310	5.0756	5.1313	5.0755	0.6339	10.3188	10.2822
1.5	0.1073	2.5050	5.5265	2.5050	0.3217	4.9169	4.9036
2.0	0.1365	1.7648	1.7739	1.7648	0.2402	3.2514	3.2469
2.5	0.1935	1.5517	1.5567	1.5514	0.2385	2.6901	2.6881
3.0	0.2606		1.5105	1.5061	0.2769	2.5337	2.5313
4.0	0.3530		1.5033	1.5000	0.3645	2.5015	2.5001
5.0	0.4085		1.5025	1.5000	0.4075	2.5012	2.5000

Note: Exact and variational calculations are compared. Energies in units of  $\hbar\omega$ . Radii in units of  $(\hbar/m\omega)^{1/2}$ .

<sup>a</sup> Reference [168].

shifted  $1/N$  expansion method is used to solve the effective mass Hamiltonian [172]. The influence of the electron–electron interaction on the ground state energy and its significant effect on the energy level crossings in states with different angular momentum are shown. The dependence of the ground state energy on the magnetic field strength for various confinement energies is presented.

The magnetic field dependence plays a useful role in identifying the absorption features. The effects of the magnetic field on the state of the impurity [173] and excitons [95, 159, 161, 174–176] confined in quantum dots have been extensively studied. Kumar et al. [177] have self-consistently solved the Poisson and Schrödinger equations and obtained the electron states in GaAs–GaAlAs for both cases: in zero and for magnetic fields applied perpendicular to the heterojunctions. The results of their work [177] indicated that the confinement potential can be approximated by a simple one-parameter adjustable parabolic potential. Merkt et al. [178] have presented a study of quantum dots in which both the magnetic field and the electron–electron interaction terms were taken into account. Pfannkuche and Gerhaxdts [179] have devoted a theoretical study to the magneto-optical response to far-infrared radiation (FIR) of quantum dot helium, accounting for deviations from the parabolic confinement. More recently, De Groote et al. [180] have investigated the thermodynamic properties of quantum dots taking into consideration the spin effect, in addition to the electron–electron interaction and magnetic field terms. The purpose of this section is to show the effect of the electron–electron interaction on the spectra of the quantum dot states with nonvanishing azimuthal quantum numbers and the transitions in the ground state of the system as the magnetic field strength increases.

Here we shall use the shifted  $1/N$  expansion method to obtain an energy expression for the spectra of two confined electrons in a quantum dot by solving the effective mass Hamiltonian including the following terms: the electron–electron interaction, the applied field, and the parabolic confinement potential.

##### 4.4.1. Theory and Model

Within the effective mass approximation, the Hamiltonian for an interacting pair of electrons confined in a quantum dot by parabolic potential of the form  $m_e^* \omega_0^2 r^2/2$  in a magnetic field applied parallel to the  $z$ -axis (and perpendicular to the plane where the electrons are restricted to move) in the symmetric gauge is written as

$$\hat{H} = \sum_{i=1}^2 \left\{ -\frac{\hbar^2 \nabla_i^2}{2m_e^*} + \frac{1}{2} m_e^* \omega_0^2 r_i^2 + \frac{\hbar \omega_c}{2} L_i^z \right\} + \frac{e^2}{\kappa |\vec{r}_1 - \vec{r}_2|} \quad (316)$$

where the two-dimensional vectors  $\vec{r}_1$  and  $\vec{r}_2$  describe the positions of the first and the second electron in the  $(x, y)$  plane, respectively.  $L_i^z$  stands for the  $z$ -component of the orbital angular momentum for each electron and  $\omega_c = eB/m_e^*c$ ,  $m_e^*$ , and  $\kappa$  are the cyclotron frequency, effective mass, and dielectric constant of the medium, respectively.

The frequency  $\omega$  depends on both the magnetic field  $B$  and the confinement frequency  $\omega_0$  and is given by

$$\omega = \left( \omega_0^2 + \frac{\omega_c^2}{4} \right)^{1/2} \quad (317)$$

The natural units of length and energy to be used are the effective Bohr radius  $a_B^* = \kappa \hbar^2 / m_e^* e^2$  and effective Rydberg  $R_y^* = \hbar^2 / 2m_e^* a_B^{*2}$ . The dimensionless constant  $\gamma = \hbar \omega_c / 2R_y^*$  plays the role of an effective magnetic field strength.

Upon introducing the center of mass  $\vec{R} = (\vec{r}_1 + \vec{r}_2) / \sqrt{2}$  and the relative coordinates  $\vec{r} = (\vec{r}_1 - \vec{r}_2) / \sqrt{2}$ , the Hamiltonian [180] in Eq. (316) can be written as a sum of two separable parts that represent the center of mass motion Hamiltonian,

$$\hat{H}_R = -\frac{\hbar^2}{2m_e^*} \nabla_R^2 + \frac{m_e^*}{2} \omega^2 R^2 + \frac{\hbar \omega_c}{2} L_z^R \quad (318)$$

and the relative motion Hamiltonian,

$$\hat{H}_r = -\frac{\hbar^2}{2m_e^*} \nabla_r^2 + \frac{m_e^*}{2} \omega^2 r^2 + \frac{\hbar \omega_c}{2} L_z^r + \frac{e^2}{r} \quad (319)$$

Equation (318) describes the Hamiltonian of the harmonic oscillator with the well-known eigenenergies

$$\varepsilon_{n_{cm}, m_{cm}} = (2n_{cm} + |m_{cm}| + 1) \hbar \omega + \frac{\hbar \omega_c}{2} m_{cm} \quad (320)$$

labeled by the radial ( $n_{cm} = 0, 1, 2, \dots$ ) and azimuthal ( $m_{cm} = 0, \pm 1, \pm 2, \pm 3, \dots$ ) quantum numbers. The problem is reduced to obtaining eigenenergies  $\varepsilon_{n_r, m}$  of the relative motion Hamiltonian. The energy states of the total Hamiltonian are labeled by  $CM$  and relative quantum numbers,  $|n_{cm} m_{cm}; n_r m\rangle$ . The coexistence of the electron–electron and the oscillator terms makes the exact analytic solution with the present special functions not possible.

#### 4.4.2. Shifted 1/N Expansion Method

The shifted 1/ $N$  expansion method,  $N$  being the spatial dimensions, is a pseudo-perturbative technique in the sense that it proposes a perturbation parameter that is not directly related to the coupling constant [181–184]. The aspect of this method has been clearly stated by Imbo et al. [181–183] who had displayed step-by-step calculations relevant to this method. Following their work, here we only present the analytic expressions that are required to determine the energy states.

The method starts by writing the radial Schrödinger equation, for an arbitrary cylindrically symmetric potential, in a  $N$ -dimensional space as

$$\left\{ -\frac{d^2}{dr^2} + \frac{(k-1)(k-3)}{4r^2} + V(r) \right\} \psi(r) = \varepsilon_r \psi(r) \quad (321)$$

where  $k = N + 2m$ .

In order to get useful results from 1/ $\bar{k}$  expansion, where  $\bar{k} = k - a$  and  $a$  is a suitable shift parameter, the large  $\bar{k}$ -limit of the potential must be suitably defined [185]. Since the angular momentum barrier term behaves like  $\bar{k}^2$  at large  $\bar{k}$ , so the potential should behave similarly. This will give rise

to an effective potential, which does not vary with  $\bar{k}$  at large values of  $\bar{k}$  resulting in a sensible zeroth-order classical result. Hence, Eq. (321) in terms of the shift parameter becomes

$$\left\{ -\frac{d^2}{dr^2} + \frac{\bar{k}^2 [1 - (1-a)/\bar{k}] [1 - (3-a)/\bar{k}]}{4r^2} + \frac{V(r)}{Q} \right\} \psi(r) = \varepsilon_r \psi(r) \quad (322)$$

where

$$V(r) = \frac{2}{r} + \frac{1}{4} \omega^2 r^2 + m \frac{\omega_c}{2} \quad (323)$$

and  $Q$  is a scaling constant to be specified from Eq. (325). The shifted 1/ $N$  expansion method consists of solving Eq. (322) systematically in terms of the expansion parameter  $1/\bar{k}$ . The leading contribution term to the energy comes from

$$\bar{k}^2 V_{\text{eff}}(r) = \frac{\bar{k}^2}{r_0^2} \left( \frac{1}{4} + \frac{r_0^2 V(r_0)}{Q} \right) \quad (324)$$

where  $r_0$  is the minimum of the effective potential, given by

$$2r_0^3 V'(r_0) = Q \quad (325)$$

It is convenient to shift the origin to  $r_0$  by the definition

$$x = \bar{k}^{1/2} (r - r_0) / r_0 \quad (326)$$

and expanding Eq. (322) about  $x = 0$  in powers of  $x$ . Comparing the coefficients of powers of  $x$  in the series with the corresponding ones of the same order in the Schrödinger equation for one-dimensional anharmonic oscillator, we determine the anharmonic oscillator frequency, the energy eigenvalue, and the scaling constant in terms of  $\bar{k}$ ,  $Q$ ,  $r_0$  and the potential derivatives. The anharmonic frequency parameter is

$$\bar{\omega} = \left[ 3 + \frac{V''(r_0)}{V'(r_0)} \right]^{1/2} \quad (327)$$

and the energy eigenvalues in powers of 1/ $\bar{k}$  (up to third order) read

$$\varepsilon_{n_r, m} = V(r_0) + \frac{\bar{k}^2}{4r_0} + \frac{1}{r_0^3} \left[ \frac{(1-a)(3-a)}{4} + \gamma_1 \right] + \frac{\gamma_2}{\bar{k} r_0^2} \quad (328)$$

The explicit forms of  $\gamma_1$  and  $\gamma_2$  are given in next section. The shift parameter  $a$ , which introduces an additional degree of freedom, is chosen so as to make the first term in the energy series of order  $\bar{k}$  vanish, namely,

$$\frac{\bar{k}}{r_0^2} \left[ \left( n_r + \frac{1}{2} \right) \bar{\omega} - \frac{(2-a)}{2} \right] = 0 \quad (329)$$

by requiring an agreement between  $1/\bar{k}$  expansion and the exact analytic results for the harmonic and Coulomb potentials. From Eq. (329) we obtain

$$a = 2 - (2n_r + 1)\bar{\omega} \quad (330)$$

where  $n_r$  is the radial quantum number related to the principal  $n$  and magnetic  $m$  quantum numbers by the relation  $n_r = n - |m| - 1$ . Energies and lengths in Eqs. (321)–(330) are expressed in units of  $R_y^*$  and  $a_B^*$ , respectively.

For the two-dimensional case,  $N = 2$ , Eq. (325) takes the following form:

$$\sqrt{2r_0 V'(r_0)} = 2 + 2m - a = Q^{1/2} \quad (331)$$

Once  $r_0$  (for a particular quantum state and confining frequency) is determined, the task of computing the energy is relatively simple.

The results are presented in Figures 64–68 and Tables 6 and 7. The relative ground state energy  $|00\rangle$  of the relative motion, for the zero magnetic field case, against the confinement length is displayed in Figure 64. The present results (black dots) clearly show an excellent agreement with the numerical results of [178] (dashed line). In Figure 65, the first low energy levels  $|00\rangle$ ,  $|10\rangle$ , and  $|20\rangle$  of the relative Hamiltonian are presented as a function of the effective confinement frequency  $\omega$ , using parameters appropriate to InSb, where the dielectric constant  $\kappa = 17.88$ , electron effective mass  $m_e^* = 0.014m_0$ , and confinement energy  $\hbar\omega_0 = 7.5$  meV [180]. The energy levels obviously show a linear dependence on the effective frequency. As the effective frequency  $\omega$  increases the confining energy term dominates the interaction energy term and thus the linear relationship between the energy and the frequency is maintained. This result is consistent with [180].

To investigate the effect of the electron–electron interaction on the energy spectra of the quantum dot, we plotted

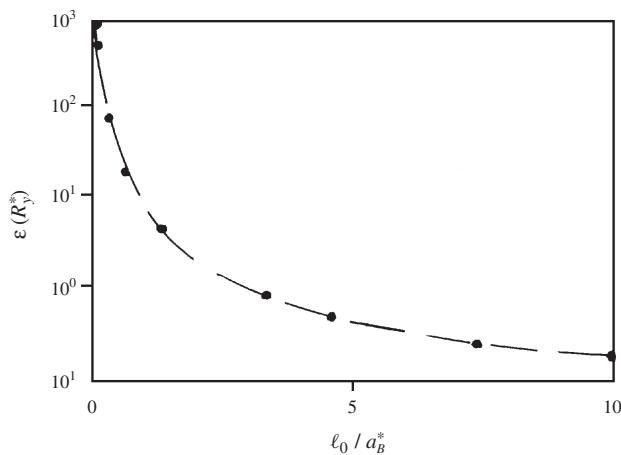


**Figure 64.** The relative ground state energy  $|00\rangle$  for the electrons in a quantum dot as a function of confinement length  $\ell_0 = (\hbar/m_e^*\omega_0)^{1/2}$  for the zero magnetic field. This section's calculations: closed circles; Ref. [178]; solid line. Reprinted with permission from [205], J. L. Marín et al., in “Handbook of Advanced Electronic and Photonic Materials and Devices” (H. S. Nalwa, Ed.). Academic Press, San Diego, 2001. © 2001, Academic Press.

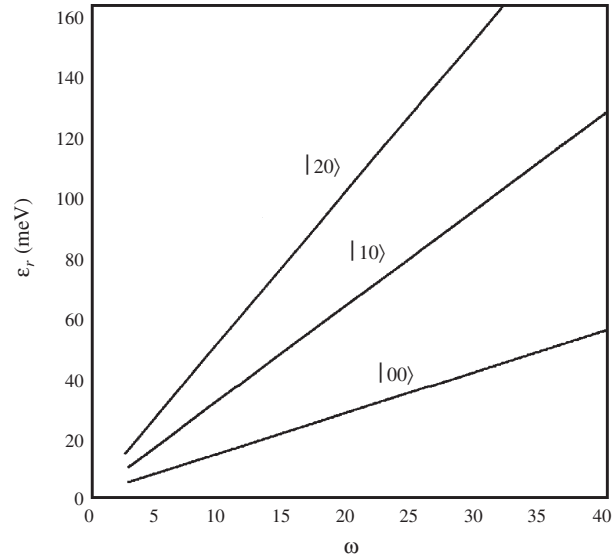


**Figure 65.** The low-lying relative states  $|00\rangle$ ,  $|10\rangle$ , and  $|20\rangle$  for two electrons in a quantum dot made of InSb as a function of confinement frequency  $\omega$ . Reprinted with permission from [205], J. L. Marín et al., in “Handbook of Advanced Electronic and Photonic Materials and Devices” (H. S. Nalwa, Ed.). Academic Press, San Diego, 2001. © 2001, Academic Press.

in Figure 66 the total ground state energy  $|00; 00\rangle$  of the full Hamiltonian for independent (solid line) and interacting (dashed line) electrons as a function of the ratio  $\omega_c/\omega_0$ . The figure shows, as we expect, a significant energy enhancement when the electron–electron Coulombic interaction term is turned on. Furthermore, as the magnetic field increases, the electrons are further squeezed in the quantum dot, resulting in an increase of the repulsive electron–electron Coulombic energy and in effect the energy levels.

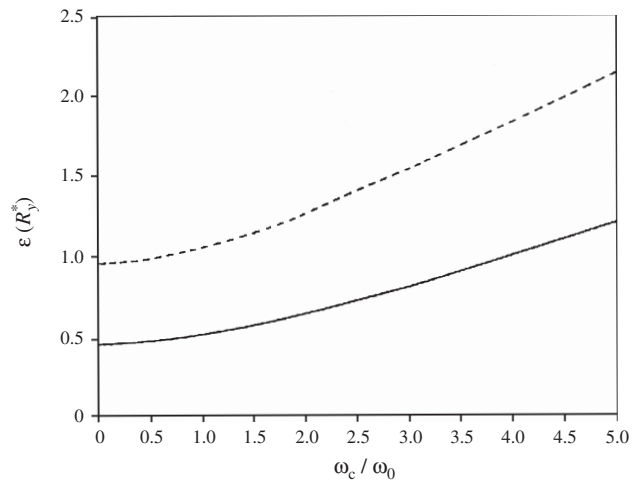


**Figure 66.** The total ground state energy  $|00; 00\rangle$  for two electrons in a quantum dot as a function of the ratio  $\omega_c/\omega_0$ . For independent (solid line) and interacting (dashed line) electrons. Reprinted with permission from [205], J. L. Marín et al., in “Handbook of Advanced Electronic and Photonic Materials and Devices” (H. S. Nalwa, Ed.). Academic Press, San Diego, 2001. © 2001, Academic Press.

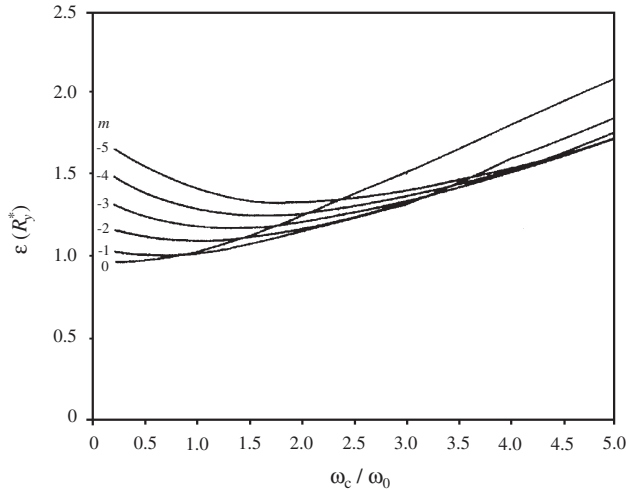


**Figure 67.** The total eigenenergies of the states  $|00; 0m\rangle$ ,  $m = 0, -1, -2, \dots, -5$ , for two interacting electrons parabolically confined in the quantum dot of size  $\ell_0 = 3a_B^*$  as a function of the ratio  $\omega_c/\omega_0$ . Reprinted with permission from [205], J. L. Marín et al., in “Handbook of Advanced Electronic and Photonic Materials and Devices” (H. S. Nalwa, Ed.). Academic Press, San Diego, 2001. © 2001, Academic Press.

The energy level crossings are shown in Figure 67. We have displayed the eigenenergies of the states  $|00; 0m\rangle$ ,  $m = 0, -1, -2, \dots, -5$ , for two interacting electrons parabolically confined in the quantum dot of size  $\ell_0 = 3a_B^*$  as a function of the ratio  $\omega_c/\omega_0$ . As the magnetic field strength increases the energy of the state  $m = 0$  increases while the energy of the states with nonvanishing quantum number  $m$  decreases, thus leading to a sequence of different ground states, as reported in [185]. In the interacting system, the higher the angular momentum of the relative motion, the lower the interaction energy. This is caused by the structure of the relative wavefunction: The larger the angular

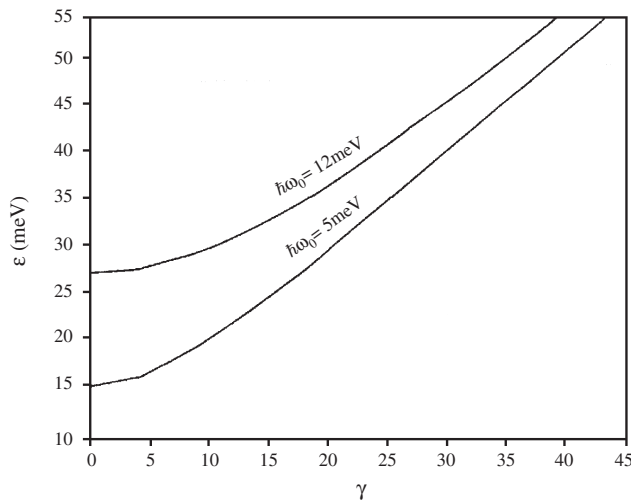


**Figure 68.** The relative ground state  $|00\rangle$  energy versus the magnetic field strength for two different confinement energies. Reprinted with permission from [205], J. L. Marín et al., in “Handbook of Advanced Electronic and Photonic Materials and Devices” (H. S. Nalwa, Ed.). Academic Press, San Diego, 2001. © 2001, Academic Press.

**Table 6.** The roots  $r_0$  determined by Eq. (684) for quantum dot states with nonvanishing azimuthal quantum number ( $m$ ) against the ratio  $\omega_c/\omega_0$ .

$m$	$\omega_c/\omega_0$	0	-1	-2	-3	-4	-5
1		4.262	4.827	5.457	6.075	6.659	7.209
2		3.692	3.682	4.212	4.719	5.193	5.635
3		3.188	2.943	3.398	3.825	4.229	4.586

momentum the larger the spatial extent and therefore, the larger the distance between the electrons [186]. To confirm this numerically, we list in Table 6 the roots  $r_0$  of the potential for the interacting electrons in the quantum dot, for states with different angular momenta. At particular values of the ratio  $\omega_c/\omega_0$ , as the azimuthal quantum number  $|m|$  increases, the root  $r_0$  also increases and thus the electron–electron interaction  $V_{ee}(r) = 2/r_0$ , in the leading term of the energy series expression, decreases.

In Figure 68, we showed the dependence of the ground state energy on the magnetic field strength for confinement energies:  $\hbar\omega_0 = 6$  and 12 meV. For constant values of the magnetic field, the larger the confinement energy, the greater the energy of the interacting electrons in the quantum dot. The spin effect can be included in the Hamiltonian, Eq. (316), added to the center of mass part as a space independent term, and Eq. (318) is still an analytically solvable harmonic oscillator Hamiltonian [180].

We have compared, in Table 7, the calculated results for the ground state energies  $|00\rangle$  of the relative Hamiltonian at different confining frequencies with the results of Taut [187]. In a very recent work, Taut has reported a particular analytical solution of the Schrödinger equation for two interacting electrons in an external harmonic potential. The table shows that as  $1/\omega$  increases the difference between both results noticeably decreases until it becomes  $\approx 1.4 \times 10^{-3}$  at  $1/\omega = 1419.47$ .

Quantum dots with more than two electrons can also be studied. The Hamiltonian for  $n_e$ -interacting electrons, provided that the electron–electron interaction term depends only on the relative coordinates between electrons  $V(|r_i - r_j|) = e^2/\kappa|r_{ij}|$ , and parabolically confined in the quantum dot, is separable into  $CM$  and relative Hamiltonians. The parabolic potential form  $V(r_i) = m_i\omega_0^2 r_i^2/2$ ,  $i = 1, 2, 3, \dots, n_e$ , is the only potential which leads to a separable Hamiltonian. The  $CM$  motion part is described by

**Table 7.** The ground state energies (in atomic units) of the relative Hamiltonian calculated by  $1/N$  expansion at different frequencies, compared with the results of Taut [187].

$1/\omega$	$1/N$ expansion	Taut
4	0.4220	0.6250
20	0.1305	0.1750
54.7386	0.0635	0.0822
115.299	0.0375	0.0477
523.102	0.0131	0.0162
1054.54	0.0081	0.0100
1419.47	0.0067	0.0081

the one-particle Hamiltonian, Eq. (318), with the electron mass replaced by the total mass  $M = n_e m_e^*$  and the electron charge replaced by the total charge  $Q = n_e e$ . The relative Hamiltonian part, which involves only the relative coordinates and momenta, has a cylindrically symmetric potential and can be handled by the  $1/N$ -expansion technique. When the confining potential is quadratic, FIR spectroscopy is insensitive to the interaction effects because of  $CM$  and relative motions. The radiation dipole operator  $\sum_i e_i \vec{r}_i = Q\vec{R}$ , being a pure  $CM$  variable, then it does not couple to  $\hat{H}_r$ , which contains all the electron–electron interactions. The dipole operator then induces transitions between the states of the  $CM$  but does not affect the states of the relative Hamiltonian. The eigenenergies for the  $CM$  Hamiltonian, Eq. (320), do not change because  $\omega_c$  in the energy expression remains the same; namely,  $QB/Mc = eB/m_e^*c$ . Consequently, the FIR absorption experiments see only the feature of the single electron energies. There are only two allowed dipole transitions ( $\Delta m = \pm 1$ ) and the FIR resonance occurs at frequencies

$$\omega_{\pm} = \sqrt{\left(\frac{\omega_c}{2}\right)^2 + \omega_0^2} \pm \frac{\omega_c}{2} \quad (332)$$

Many different experiments on quantum dots have proved the validity of Kohn's theorem and that the observed resonance frequency of an electron system in a parabolic potential is independent of electron–electron interactions and thus the actual number of electrons in the well, as reported by Wixforth et al. in a very recent review article [188].

In conclusion we have obtained the energy spectra of two interacting electrons as a function of confinement energies and magnetic field strength. The method has shown good agreement with the numerical results of Merkt et al. [178], Taut [187], and Wagner et al. [185]. Our calculations have also shown the effect of the electron–electron interaction term on the ground state energy and its significance on the energy level crossings in states with different azimuthal quantum numbers. The shifted  $1/N$  expansion method yields quick results without putting restrictions on the Hamiltonian of the system.

#### 4.4.3. Calculation of Parameters $\gamma_1$ and $\gamma_2$

The explicit forms of the parameters  $\gamma_1$  and  $\gamma_2$  are given in the following. Here  $R_y^*$  and  $a_b^*$  are used as units of energy and length, respectively

$$\gamma_1 = c_1 e_2 + 3c_2 e_4 - \bar{\omega}^{-1} [e_1^2 + 6c_1 e_1 e_3 + c_4 e_2^3] \quad (333)$$

and

$$\gamma_2 = T_7 + T_{12} + T_{16} \quad (334)$$

where

$$\begin{aligned} T_7 &= T_1 - \bar{\omega}^{-1} [T_2 + T_3 + T_4 + T_5 + T_6] \\ T_{12} &= \bar{\omega}^{-2} [T_8 + T_9 + T_{10} + T_{11}] \\ T_{16} &= \bar{\omega}^{-2} [T_{13} + T_{14} + T_{15}] \end{aligned} \quad (335)$$

with

$$\begin{aligned} T_1 &= c_1 d_2 + 3c_2 d_4 + c_3 d_6 & T_2 &= c_1 e_2^2 + 12c_2 e_2 e_4 \\ T_3 &= 2e_1 d_1 + 2c_5 e_4^2 & T_4 &= 6c_1 e_1 d_3 + 30c_2 e_1 d_5 \\ T_5 &= 6c_1 e_1 d_3 + 2c_4 e_3 d_3 & T_6 &= 10c_6 e_3 d_5 \\ T_8 &= 4e_2^2 e_2 + 36c_1 e_1 e_2 e_3 & T_9 &= 8c_4 e_2 e_3^2 \\ T_{10} &= 24c e_1^2 e_4 + 8c_7 e_1 e_3 e_4 & T_{11} &= 12c_8 e_3^2 e_4 \\ T_{13} &= 8e_1 e_3 + 108c_1 e_1 e_3 & T_{14} &= 48c_4 e_1 e_3 \\ T_{15} &= 30c_9 e_3 \end{aligned} \quad (336)$$

where  $c$ ,  $d$ , and  $e$  are parameters given as

$$\begin{aligned} c_1 &= 1 + 2n_r & c_4 &= 11 + 30n_r + 30n_r^2 \\ c_8 &= 57 + 189n_r + 225n_r^2 + 150n_r^3 & c_2 &= 1 + 2n_r + 2n_r^2 \\ c_5 &= 21 + 59n_r + 51n_r^2 + 34n_r^3 & c_3 &= 3 + 8n_r + 6n_r^2 + 4n_r^3 \\ c_6 &= 13 + 40n_r + 42n_r^2 + 28n_r^3 \\ c_9 &= 31 + 109n_r + 141n_r^2 + 94n_r^3 \\ c_7 &= 31 + 78n_r^2 + 78n_r^3 & e_j &= \kappa_j / \bar{\omega}^{j/2} & d_i &= \delta_i / \bar{\omega}^{i/2} \end{aligned} \quad (337)$$

where  $j = 1, 2, 3, 4$  and  $i = 1, 2, 3, 4, 5, 6$ :

$$\begin{aligned} \kappa_1 &= (2 - a) & \kappa_2 &= -\frac{3(2 - a)}{2} \\ \kappa_3 &= -1 - \frac{2r_0}{Q} & \kappa_4 &= \frac{5}{4} + \frac{2r_0}{Q} \\ \delta_1 &= -\frac{(1 - a)(3 - a)}{2} & \delta_2 &= -\frac{3(1 - a)(3 - a)}{4} \\ \delta_3 &= 2(2 - a) & \delta_4 &= -\frac{5(2 - a)}{2} \\ \delta_5 &= -\frac{3}{2} - \frac{2r_0}{Q} & \delta_6 &= \frac{7}{4} + \frac{2r_0}{Q} \end{aligned} \quad (338)$$

## 5. MECHANISM OF TERAHERTZ LASING IN SiGe/Si QUANTUM WELLS

Blom et al. [189] presented a theoretical calculation, which showed the formation of resonant states, and explained the origin of the observed temperature dependence of the dc conductivity under low bias voltage. Thus, it was shown that the mechanism of terahertz (THz) lasing is population inversion of the resonant state with respect to the localized impurity state. This is the same mechanism of lasing as in uniaxially stressed  $p$ -Ge THz lasers.

In an early experiment [190] published in 1992, THz radiation was observed from bulk  $p$ -Ge under uniaxial stress and a dc electric field, both applied along the same crystal axis. Eight years later measurements of the radiation spectrum characterized the observed radiation as pulse mode lasing under pumping of a strong electric field [191]. A theoretical explanation of the lasing phenomenon followed almost immediately [192], which proved the formation of resonant states as the required mechanism for achieving population inversion. Shortly thereafter, a tunable continuous



wave  $p$ -Ge THz laser was realized [193] under weak electric field pumping, accompanied by a complete theoretical interpretation [194].

The theory of population inversion based on the formation of resonant states has been given in detail very recently [195]. Under uniaxial stress the heavy hole band (HHB) in  $p$ -Ge lies lower than the light hole band (LHB) by an amount  $E_{\text{def}}$ . Dictated by the symmetry properties, one set of impurity levels is attached to the edge of the HHB, and another set is attached to the edge of the LHB. If  $E_{\text{def}}$  is greater than the hole binding energy of the lowest impurity level attached to the HHB edge, this impurity level overlaps the Bloch states in the LHB. Resonant states are then formed. Under an external electric field, the impact-ionized holes are accelerated toward the resonant level. With the proper combination of impurity concentration, temperature, electric field, stress, and scattering strength of phonons and impurities, holes have a large probability of occupying resonant states [192, 194, 195]. A resonant level population inversion with respect to those impurity levels which attach to the LHB edge is then formed, and THz lasing occurs [191, 193].

The externally applied uniaxial stress can be replaced by the strain in a QW with lattice mismatch, and a  $\text{Si}/\text{Ge}_x\text{Si}_{1-x}/\text{Si}$  QW with  $x < 0.2$  and a boron-doped well was proposed [196, 197]. In such a structure the well is stretched along the growth direction, so the HHB lies above the LHB. When impurities are added to the  $\text{SiGe}/\text{Si}$  QW system, all relevant energy levels are affected by the electric field produced by the charge redistribution in the system. It is plausible that a strong electric field in the QW may favor the formation of resonant states for THz lasing. Such a field can be achieved by employing two aspects of the sample structure. First, the Si buffer layer and the Si cap layer on each side of the well will be  $\delta$  doped with boron acceptors. Second, the existence of a thin  $\text{SiO}_2$  layer on top of the cap layer creates interface states between them. In such a structure THz lasing was indeed detected [198].

Because the carriers in a  $\text{SiGe}/\text{Si}$  QW are electrically pumped, electric transport in the well has been investigated in detail in order to clarify the relevant physical processes [197, 199]. Under a weak dc bias, the temperature behavior of the conductivity  $\sigma$ , plotted as  $\ln(\sigma)$  as a function of the inverse temperature  $1/T$ , exhibits two different linear regimes, below and above  $T \approx 20$  K, respectively, as shown by Figure 1 in [197]. Further experiments on magnetoconductivity and Hall mobility [197, 199] have indicated that the low temperature conductivity may be due to hopping. In the high temperature region, the slope of the  $\ln(\sigma)$  vs  $1/T$  curves suggests an activation energy of about 12 meV for Ge content  $x = 0.1$  and 18 meV for  $x = 0.15$ , if indeed the activation process exists. It was suggested in [197, 199] that the possible hole activation is between the two impurity levels  $E_{1s}^h$  and  $E_{1s}^l$  attached to each respective band. The present study has disproved this suggestion. The mechanism of the high temperature conductivity and its relation to the THz lasing are the questions to be answered.

In [189] an extensive numerical study of a  $\text{Si}/\text{Ge}_{0.15}\text{Si}_{0.85}/\text{Si}$  QW was performed. The system structure consisted of, in sequence, an  $n$ -Si substrate, an  $i$ -Si buffer layer of 130 nm thickness, a  $\text{Ge}_{0.15}\text{Si}_{0.85}$  well of 20 nm thickness, and an  $i$ -Si

cap layer of 60 nm thickness. Over the cap layer a thin layer of  $\text{SiO}_2$  typically appears, on which ohmic contacts were installed. The middle of the well was  $\delta$  doped with a boron concentration of  $6 \times 10^{11} \text{ cm}^{-2}$ . In both the buffer layer and the cap layer, at a distance of 30 nm from the respective QW interface, a  $\delta$  layer of boron was doped with a concentration of  $3 \times 10^{11} \text{ cm}^{-2}$ . In this system  $E_{\text{def}} = 31$  meV [200]. Using a one band variational approach given in [201], the binding energies  $E_{1s}^l$  and  $E_{1s}^h$  of the impurity levels attached to the LHB edge and the HHB edge, respectively, were calculated and both were found to have a value of about 27 meV.

One very important feature of the QW system is the interface states between the  $\text{SiO}_2$  layer and the Si cap layer, which can accumulate almost all holes from the  $\delta$  doping in the cap layer. This resulted in pinning of the chemical potential at the interface state energy level, which lay in the bandgap at  $\Delta \approx 0.4$  eV measured from the valence band top [202]. This charge redistribution inside the sample built up a strong electric field in the QW, which was detected experimentally [197, 199].

The energy level structure in the QW calculated is shown in Figure 69. The zero energy was set at the chemical potential  $\mu$ . The solid curve marks the HHB edge and the dotted curve the LHB edge. The lowest quantization energy levels  $E_1^{\text{hhb}}$  in the HHB and  $E_1^{\text{hbl}}$  in the LHB were indicated, along with the lowest impurity states attached to each band. In the case depicted ( $T = 4$  K), the electric field strength in the QW was 19 kV/cm, and  $E_1^{\text{hhb}} - E_{1s}^l = 5$  meV. The overlap of the impurity level  $E_{1s}^l$  with the  $E_1^{\text{hhb}}$  2D subband made it possible to form the resonant state required for THz lasing. Once they proved that a resonant impurity state could be formed in the structure, the theory of population inversion developed for strained bulk  $p$ -Ge [195] could be applied directly to explain the origin of the observed lasing in the  $\text{SiGe}/\text{Si}$  QW.

In order to understand the transport properties of the  $\text{SiGe}/\text{Si}$  QW system, which is relevant for the electric pumping of carriers into the resonant states, they also calculated the concentration of free holes,  $p_v(T)$ , as a function of the temperature, and their results are plotted as the solid curve in the upper panel of Figure 70. The temperature

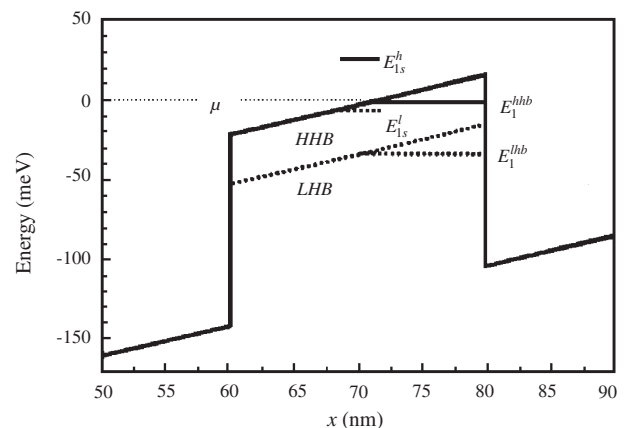


**Figure 69.** Energy level structure in the QW calculated at  $T = 4$  K. The position  $x$  is measured from the interface between the cap layer and the  $\text{SiO}_2$ . Reprinted with permission from [189], A. Blom et al., *Appl. Phys. Lett.* 79, 713 (2001). © 2001, American Institute of Physics.

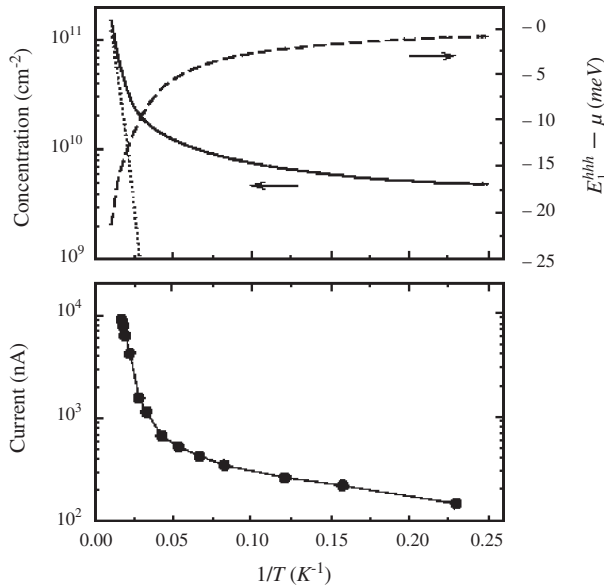


**Figure 70.** Upper panel showing the calculated temperature dependencies of the free hole concentration  $p_v(T)$  (solid curve) and the number concentration of charged acceptors in the QW (dotted curve). The dashed curve is the energy separation  $E_1^{\text{hhb}} - \mu$ . The lower panel displays the measured current as function of the temperature. Reprinted with permission from [189], A. Blom et al., *Appl. Phys. Lett.* 79, 713 (2001). © 2001, American Institute of Physics.

dependence of  $p_v(T)$  was due to the thermal excitation of holes from the chemical potential into the 2D subbands. This was governed by the energy separation  $E_1^{\text{hhb}} - \mu$ , which depends strongly on the temperature, as shown in the upper panel of Figure 70. These theoretical findings and the following experimental data will support their conjectured mechanism of THz lasing in the SiGe/Si QW.

A Si/Ge<sub>0.15</sub>Si<sub>0.85</sub>/Si QW sample with the previously specified structure was fabricated with a MBE machine. High voltage pulses of 0.3 μs duration were applied parallel to the QW via the deposited ohmic contacts. Since the δ layer of boron in the buffer layer also supplies holes to the substrate, a *pn* junction type of carrier distribution is formed, which prevents the bypass of current through the substrate. When opposite surfaces parallel to the growth direction were polished to serve as an optical resonator, strong THz radiation was detected at liquid helium temperature. The radiation intensity is orders of magnitude stronger than the intensity of spontaneous emission. In Figure 71 the radiation intensity and the corresponding electric pumping current as functions of the pulse voltage are plotted. The abrupt increase of the current around 100 V marks the onset of impact ionization of the boron acceptors in the QW. A threshold current for the radiation is clearly seen. The characteristic features of the observed THz radiation are exactly the same as those of THz lasing reported recently [203]. This was expected, because the only difference between their sample and the sample in [198, 203]

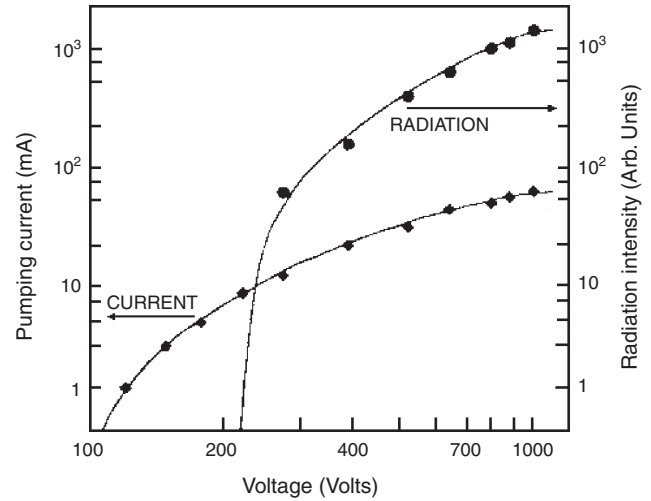


**Figure 71.** Radiation intensity and electric pumping current as functions of the pulse voltage. Reprinted with permission from [189], A. Blom et al., *Appl. Phys. Lett.* 79, 713 (2001). © 2001, American Institute of Physics.

was the concentration of δ doping in the buffer and cap layers:  $3 \times 10^{11} \text{ cm}^{-2}$  in their sample and  $4 \times 10^{11} \text{ cm}^{-2}$  in the other ones.

At a low dc bias of 2 V the current  $I$  flowing parallel to the QW was measured as a function of the temperature. The result is plotted in the lower panel of Figure 70. Similar to the temperature behavior of the free hole concentration  $p_v(T)$ , the curve  $\ln(I)$  vs  $1/T$  also displays different characteristic features below and above  $T \approx 20$  K. In fact, in the high temperature region, the slope of the  $\ln(I)$  vs  $1/T$  curve is almost the same as the slope of the  $\ln(p_v)$  vs  $1/T$  curve. They then concluded that, in this temperature region, the dependence of the current  $I$  on  $1/T$  was caused by the temperature dependence of the thermal population in the free hole levels but does not suggest an activation process as stated in [197, 199].

Then, they turned to the transport process in the low temperature region. Their calculated free hole concentration  $p_v(T)$  shown in Figure 70, although small, is non-negligible at low temperatures. However, for such low temperatures and low concentration, the mobility may be very small [204], resulting in a decrease in the current of an order of magnitude. Nevertheless, they cannot rule out completely the possibility of hopping transport for the following reason. The charged impurity ions in both the buffer layer and the cap layer create a long range random potential in the QW. At the same time the spatial variation of the alloy composition produces a short range random potential. Both effects cause fluctuation of the 2D subband edge, and their calculations gave an energy fluctuation of about 5 meV. The transport of holes in the 2D subband would then exhibit hopping behavior with an activation energy of about 2–3 meV. It is important to emphasize that such a hopping process is entirely different from that stated in [197, 199], where the transport is ascribed to the hopping of holes from one acceptor to the other within the δ layer in the well. Such a process requires partially charged acceptors. In conclusion in [189] Blom et al. calculated the number concentration of charged

acceptors in the QW and plotted it as the dotted curve in the upper panel of Figure 70. At low temperatures, the number concentration of charge acceptors in the QW is far too small to produce a measurable hopping conductivity.

It can be emphasized that the mechanism of population inversion through the formation of resonant states is essential for the realization of semiconductor QW THz lasers. A full understanding of this mechanism will allow the design of advanced THz lasers using various lattice mismatched heterostructures with different semiconductors.

## GLOSSARY

**Conduction band** Energy band in a crystalline solid partially filled by electrons.

**Confined system** A quantum system in which carriers, atoms or molecules are restricted to exist in one, two or three dimensions of the order of a few nanometers.

**Effective mass** The mass of a particle in a crystalline solid.

**Gap** Forbidden region for the electrons, which it is determined by the difference of energies between conduction and valence bands.

**Idealized confined systems** A non-real isolated quantum system whose size is of the order of few nanometers.

**Impurity** An atom or molecule embedded in a different material.

**Impurity states** The additional electron levels which appears due to the presence of an impurity.

**MBE, MOCVD and Lithography** Methods of synthesis used to the fabrication of the nanostructured materials.

**Nanostructure** Material medium whose size is of the order of few nanometers.

**Quantum dot** A quantum system, in which the carriers are confined in all directions.

**Quantum well** A quantum system, in which the carriers are confined in only one direction, the other dimensions remain free.

**Quantum well wire** A quantum system, in which the carriers are confined in two directions, the other remains free.

**Valence band** Energy band in a crystalline solid completely filled by electrons.

## REFERENCES

- H. D. Cheong and Y. H. Jeong, *Jpn. J. Appl. Phys.* 41, 1920 (2002).
- J. Kono, S. T. Lee, M. S. Salib, G. S. Herold, A. Petrou, and B. D. McCombe, *Phys. Rev. B* 52, R8654 (1995).
- M. S. Salib, H. A. Nickel, G. S. Herold, A. Petrou, B. D. McCombe, R. Chen, K. K. Bajaj, and W. Schaff, *Phys. Rev. Lett.* 77, 1135 (1996).
- J. Cerne, J. Kono, M. S. Sherwin, M. Sundaram, A. C. Gossard, and E. W. Bauer, *Phys. Rev. Lett.* 77, 1131 (1992).
- H. A. Nickel, G. S. Herold, M. S. Salib, G. Kioseoglou, A. Petrou, B. D. McCombe, and D. Broido, *Physica B* 249, 598 (1998).
- H. A. Nickel, G. S. Herold, T. Yeo, G. Kioseoglou, Z. X. Jiang, A. Petrou, B. D. McCombe, D. Broido, and W. Schaff, *Phys. Status Solidi B* 210, 341 (1998).
- R. L. Greene and K. K. Bajaj, *Phys. Rev. B* 31, 913 (1985).
- J. Zhu and S. Xu, *Phys. Rev. B* 50, 12175 (1994).
- Q. X. Zhao, M. Karlsteen, M. Willander, S. M. Wang, and M. Sadeghi, *Phys. Rev. B* 62, 5055 (2000).
- M. Sanquer, M. Specht, L. Ghenim, S. Deleonibus, and G. Guegan, *Phys. Rev. B* 61, 7249 (2000).
- Y. X. Li, J. J. Liu, and X. J. Korg, *J. Appl. Phys.* 88, 2588 (2000).
- C. Y. Hsieh and D. S. Chuu, *J. Appl. Phys.* 89, 2241 (2001).
- C. Y. Hsieh, *J. Appl. Phys.* 92, 484 (2002).
- W. Y. Ruan, K. S. Chan, H. P. Ho, and E. Y. B. Pun, *J. Phys.: Condens. Matter* 12, 3911 (2000).
- Y. N. Chen, D. S. Chuu, and Y. K. Lin, *J. Phys.: Condens. Matter* 11, 8185 (1999).
- A. Sali, H. Satori, M. Fliyou, and H. Loumhari, *Phys. Status Solidi B* 232, 209 (2002).
- E. Reyes-Gómez, A. Matos-Abiague, C. A. Perpomo-Leiva, M. de Dios-Leiva, and L. E. Oliveira, *Phys. Rev. B* 61, 13104 (2000).
- C. Yannouleas and U. Landman, *Phys. Rev. B* 61, 15895 (2000).
- F. Buonocore, D. Ninno, and G. Iadonisi, *Phys. Rev. B* 62, 10914 (2000).
- Y. Kayanuma, *Phys. Rev. B* 62, 15334 (2000).
- M. Notomi, M. Okamoto, and T. Tamamura, *J. Appl. Phys.* 75, 4161 (1994).
- B. Tanatar and A. Gold, *Phys. Rev. B* 52, 1996 (1995).
- B. S. Kandemir and A. Cetin, *Phys. Rev. B* 65, 054303 (2002).
- P. Schlottmann, *Phys. Rev. B* 65, 174407 (2002).
- P. Schlottmann, *Phys. Rep.* 181, 1 (1989).
- P. Schlottmann, *Phys. Rev. B* 65, 024420 (2002).
- P. Schlottmann, *J. Phys.: Condens. Matter* 49, 109 (1982).
- S. T. Yen, *Phys. Rev. B* 66, 075340 (2002).
- V. M. Apalkov and T. Chakraborty, *Physica E* 14, 289 (2002).
- T. J. Yang and S. Y. Hsu, *Physica E* 11, 186 (2001).
- I. Essaoudi, B. Stébé, A. Ainane, and M. Saber, *Physica E* 14, 336 (2002).
- H. S. Brandi, A. Latgé, and E. Oliveira, *Phys. Rev. B* 64, 233315 (2001).
- B. Stébé, I. Essaoudi, A. Ainane, and M. Saber, *Phys. Rev. B* 64, 085304 (2001).
- M. A. Lampert, *Phys. Rev. Lett.* 1, 450 (1958).
- T. Skettrup, M. Suffczynski, and W. Gorzkowski, *Phys. Rev. B* 4, 512 (1971).
- B. V. Shanabrook and J. Comas, *Surf. Sci.* 142, 504 (1984).
- Y. Nomura, K. Shinozaki, and M. Ishii, *J. Appl. Phys.* 58, 1864 (1985).
- X. Liu, A. Petrou, B. D. McCombe, J. Ralston, and G. Wicks, *Phys. Rev. B* 38, 8522 (1988).
- D. C. Reynolds, C. E. Leak, K. K. Bajaj, C. E. Stutz, R. L. Jones, K. R. Evans, P. W. Yu, and W. M. Theis, *Phys. Rev. B* 40, 6210 (1989).
- H. Buhmann, R. Stepniowski, G. Martinez, and B. Etienne, *Heb. Phys. Acta* 65, 323 (1992).
- L. Stauffer and B. Stébé, *Solid State Commun.* 80, 983 (1991).
- B. Stébé, L. Stauffer, and D. Fristot, *J. Phys. IV* 3, 417 (1993).
- A. Y. Cho and J. R. Arthur, *Progr. Solid State Chem.* 10, 157 (1975).
- "Collected Papers of the Second Int. Symp. On Molecular Beam Epitaxy and Clean Surface Techniques" (R. Ueda, Ed.). Japanese Society of Applied Physics, Tokyo, 1982.
- K. Ploog and K. Graf, "Molecular Beam Epitaxy of III-V Compounds—A Comprehensive Bibliography." Springer, Berlin, 1984.
- "Proc. 3rd Int. Conf. on MBE," San Francisco, 1985 (J. Arthur, Ed.), *J. Vac. Sci. Technol. B* 3, 509 (1985).
- "Technology and Physics of MBE" (E. H. C. Parker, Ed.). Plenum Press, New York, 1985.
- "Proc. 4th Int. Conf. on MBE," York, UK (C. T. Foxon and J. J. Harris, Eds.), *J. Cryst. Growth* 81, 1 (1987).
- "Molecular Beam Epitaxy in III-V Semiconductor Materials and Devices" (R. J. Marik, Ed.). Elsevier, Amsterdam, 1989.

50. "Proc. 5th Int. Conf. on MBE," Sapporo, 1988 (Y. Shiraki and H. Sakaki, Eds.), *J. Cryst. Growth* 95, 1 (1989).
51. "Proc. 6th Conf. on MBE," La Jolla, USA, 1990 (C. W. Tu and J. S. Harris, Eds.), *J. Cryst. Growth* 111 (1991).
52. Y. Yamada, in "Optical Properties of Low-Dimensional Materials" (T. Ogawa and Y. Kanemitsu, Eds.), p. 202. World Scientific, Singapore, 1995.
53. Y. Endoh and T. Taguchi, *Mater. Res. Soc. Symp. Proc.* 161, 211 (1990).
54. T. Taguchi and Y. Endoh, *Jpn. J. Appl. Phys.* 30, L952 (1991).
55. T. Taguchi, Y. Endoh, and Y. Nozue, *Appl. Phys. Lett.* 59, 3434 (1991).
56. Y. Yamada, T. Taguchi, and A. Hiraki, *Tech. Rep. Osaka Univ.* 39, 211 (1989).
57. T. Taguchi, Y. Kawakami, and Y. Yamada, *Physica B* 191, 23 (1993).
58. A. Muray, M. Isaacson, and I. Adesida, *Appl. Phys. Lett.* 45, 1289 (1984).
59. L. D. Jackel, R. E. Howard, P. M. Mankiewich, H. G. Craighead, and R. W. Epworth, *Appl. Phys. Lett.* 45, 698 (1984).
60. R. L. Kubena, F. P. Stratton, J. W. Ward, G. M. Atkinson, and R. J. Joyce, *J. Vac. Sci. Technol. B* 7, 1798 (1989).
61. G. Bastard, *Phys. Rev. B* 24, 5693 (1981).
62. G. Bastard, *Phys. Rev. B* 25, 7584 (1982).
63. D. F. Nelson, R. C. Miller, C. W. Tu, and S. K. Spitz, *Phys. Rev. B* 36, 8063 (1987).
64. D. J. Ben Daniel and C. B. Duke, *Phys. Rev.* 152, 683 (1996).
65. J. L. Marín, R. Rosas, and A. Uribe, *Am. J. Phys.* 63, 460 (1995).
66. J. L. Marín and S. A. Cruz, *Am. J. Phys.* 59, 931 (1991).
67. C. Priestler, G. Allan, and M. Lannoo, *Phys. Rev. B* 28, 7194 (1983).
68. C. Priestler, G. Allan, and M. Lannoo, *Phys. Rev. B* 29, 3408 (1984).
69. G. Bastard, *Phys. Rev. B* 24, 4714 (1981).
70. K. Tanaka, M. Nagaoka, and T. Yamabe, *Phys. Rev. B* 28, 7068 (1983).
71. S. Chaudhuri, *Phys. Rev. B* 28, 4480 (1983).
72. C. Mailhot, Y.-C. Chang, and T. C. McGill, *Phys. Rev. B* 26, 4449 (1982).
73. R. L. Greene and K. K. Bajaj, *Solid State Commun.* 45, 825 (1983).
74. R. J. Wagner, B. V. Shanabrook, J. E. Furneaux, J. Comas, N. C. Jarosik, and B. D. McCombe, in "GaAs and Related Compounds 1984" (B. De Crémoux, Ed.). Institute of Physics Conference Series 74. Hilger, Bristol, UK, 1985.
75. W. T. Masselink, Y.-C. Chang, and H. Morkoc, *Phys. Rev. B* 28, 7373 (1983).
76. R. C. Miller, A. C. Gossard, W. T. Tsang, and O. Munteanu, *Phys. Rev. B* 25, 3871 (1982).
77. A. Corella-Madueño, R. Rosas, J. L. Marín, and R. Riera, *Phys. Low-Dim. Struct.* 5/6, 75 (1999).
78. J. L. Marín and S. A. Cruz, *J. Phys. B* 25, 4365 (1992).
79. B. R. Nag and S. Gangopadhyay, *Phys. Status Solidi A* 179, 463 (1993).
80. J. W. Brown and H. N. Spector, *Phys. Rev. B* 35, 3009 (1987).
81. F. A. P. Osório, M. H. Degani, and O. Hipólito, *Phys. Rev. B* 37, 1402 (1988).
82. G. W. Bryant, *Phys. Rev. B* 29, 6632 (1987).
83. G. Li, S. V. Branis, and K. K. Bajaj, *J. Appl. Phys.* 77, 1097 (1995).
84. J. L. Marín, *Estudio de sistemas cuánticos confinados mediante el método variacional directo*, Ph.D. Thesis, Facultad de Ciencias, UNAM, 1992.
85. J. Gorecki and W. Byers Brown, *J. Phys. B* 22, 2659 (1989).
86. K. R. Brownstein, *Phys. Rev. Lett.* 71, 1427 (1993).
87. S. I. Tsonchev and P. L. Goodfriend, *J. Phys. B* 25, 4685 (1992).
88. J.-L. Zhu, J.-J. Xiong, and B.-L. Gu, *Phys. Rev. B* 41, 6001 (1990).
89. J.-L. Zhu, *J. Phys. Condens. Matter* 1, 1539 (1989).
90. J.-L. Zhu, *Phys. Rev. B* 39, 8780 (1989).
91. A. Ishibashi, Y. Mori, M. Itabashi, and N. Watanabe, *J. Appl. Phys.* 58, 2691 (1985).
92. L. E. Brus, *J. Chem. Phys.* 80, 4403 (1984).
93. A. Erdelyi, "Asymptotic Expansions." Dover, New York, 1956.
94. A. S. Davydov, "Quantum Mechanics." NEO Press, Peaks Island, ME, 1966.
95. G. W. Bryant, *Phys. Rev. B* 37, 8763 (1988).
96. G. W. Bryant, *Surf. Sci.* 196, 596 (1988).
97. T. Inoshita and H. Watanabe, in "Microstructures" (S. Sugano, Y. Nishina, and S. Ohnishi, Eds.). Springer, Berlin, 1986.
98. M. Ulas, H. Akbas, and M. Tomak, *Phys. Status Solidi B* 200, 67 (1997).
99. A. Corella-Madueño, R. Rosas, J. L. Marín, and R. Riera, *Int. J. Quantum Chem.*, in press.
100. P. Ramvall, S. Tanaka, S. Nomura, P. Riblet, and Y. Aoyagi, *Appl. Phys. Lett.* 73, 1104 (1998).
101. Z. Xiao, J. Zhu, and F. He, *J. Appl. Phys.* 79, 9181 (1966).
102. S. V. Branis, G. Li, and K. K. Bajaj, *Phys. Rev. B* 47, 1316 (1993).
103. Y. Chen, *Phys. Lett. A* 143, 152 (1990).
104. A. Corella-Madueño, R. A. Rosas, J. L. Marín, and R. Riera, to be published.
105. E. Ley-Koo and A. Flores-Flores, *Int. J. Quantum Chem.* 66, 123 (1998).
106. E. V. Ludeña, *J. Chem. Phys.* 69, 1770 (1978).
107. E. V. Ludeña and M. Gregori, *J. Chem. Phys.* 71, 2235 (1979).
108. J. Gorecki and W. Byers Brown, *J. Phys. B* 21, 403 (1988).
109. R. LeSar and D. R. Herschbach, *J. Phys. Chem.* 85, 2798 (1981).
110. R. LeSar and D. R. Herschbach, *J. Phys. Chem.* 87, 5202 (1983).
111. J. L. Marín and G. Muñoz, *J. Mol. Struct. (Teochem)* 287, 281 (1993).
112. B. D. Perlson and J. A. Weil, *J. Magn. Reson.* 15, 594 (1974).
113. Y. Wang and N. Herron, *J. Phys. Chem.* 95, 525 (1991).
114. E. Ley-Koo and K. P. Volke-Sepúlveda, *Int. J. Quantum Chem.* 65, 269 (1997).
115. G. Arfken, "Mathematical Methods for Physicists." Academic Press, New York, 1971.
116. P. M. Morse and H. Feshbach, "Methods of Theoretical Physics." McGraw-Hill, New York, 1953.
117. J. O. Hirschfelder, C. F. Curtis, and R. B. Bird, "Molecular Theory of Gases and Liquids." Wiley, New York, 1954.
118. E. A. Hylleraas, *Z. Phys.* 65, 209 (1930).
119. J. G. Kirwood, *Phys. Z* 33, 57 (1932).
120. E. Ley-Koo and S. A. Cruz, *J. Chem. Phys.* 74, 4603 (1981).
121. J. L. Marín and S. A. Cruz, *J. Phys. B* 24, 2899 (1991).
122. C. A. Coulson and P. D. Robinson, *Proc. Roy. Soc. London* 71, 815 (1958).
123. D. R. Bates, K. Ledsham, and A. L. Stewart, *Philos. Trans. Roy. Soc. London Ser. A* 246, 215 81953.
124. E. Ley-Koo and S. Rubinstein, *J. Chem. Phys.* 71, 351 (1979).
125. J. Gorecki and W. Byers-Brown, *J. Chem. Phys.* 89, 2138 (1988).
126. F. M. Fernandez and E. A. Castro, *Int. J. Quantum Chem.* 19, 533 (1981).
127. F. M. Fernandez and E. A. Castro, *J. Chem. Phys.* 75, 2908 (1981).
128. Y. Wu and L. M. Falicov, *Phys. Rev. B* 29, 3671 (1984).
129. C. L. Pekeris, *Phys. Rev.* 112, 1649 (1958).
130. J. Silva-Valencia and N. Porrás-Montenegro, *J. Appl. Phys.* 81, 901 (1997).
131. L. E. Oliveira and R. Perez-Alvarez, *Phys. Rev. B* 40, 10460 (1989).
132. N. Porrás-Montenegro and L. E. Oliveira, *Solid State Commun.* 76, 275 (1990).
133. N. Porrás-Montenegro, A. Latgé, and L. E. Oliveira, *J. Appl. Phys.* 70 (1991).
134. N. Porrás-Montenegro and S. T. Perez-Merchancano, *Phys. Rev. B* 46, 9780 (1992).
135. N. Porrás-Montenegro, S. T. Perez-Merchancano, and A. Latgé, *J. Appl. Phys.* 74, 7624 (1993).

136. A. Latgé, N. Porrás-Montenegro, and L. E. Oliveira, *Phys. Rev. B* 51, 13344 (1995).
137. M. Helm, F. M. Peeters, F. DeRosa, E. Colas, J. P. Harbison, and L. T. Florez, *Phys. Rev. B* 43, 13983 (1991).
138. N. C. Jarosik, B. D. McCombe, B. V. Shanabrook, J. Comas, J. Ralston, and G. Wicks, *Phys. Rev. Lett.* 54, 1283 (1985).
139. B. Yoo, B. D. McCombe, and W. Schaff, *Phys. Rev. B* 44, 13152 (1991).
140. F. Bassani and G. Parravicini, in "Electronic States and Optical Transitions in Solids" (R. A. Ballinger, Ed.). Pergamon, Oxford, 1975.
141. R. A. Rosas, J. L. Marín, R. Riera, and R. Núñez, *Phys. Low-Dim. Struct.* 5/6, 145 (1999).
142. E. Ley-Koo and R. M. G. García-Castelán, *J. Phys. A* 24, 1481 (1991).
143. E. Ley-Koo and S. Mateos-Cortés, *Int. J. Quantum Chem.* 46, 609 (1993).
144. R. E. Moss, *Am. J. Phys.* 55, 397 (1987).
145. M. Andrews, *Am. J. Phys.* 44, 1064 (1976).
146. M. Andrews, *Am. J. Phys.* 34, 1194 (1966).
147. M. Martin, *Am. J. Phys.* 47, 1067 (1979).
148. R. Loudon, *Am. J. Phys.* 27, 649 (1959).
149. L. S. Davtyan, G. S. Pogosyan, A. N. Sissakian, and V. M. Ter-Antonyan, *J. Phys. A: Math. Gen.* 20, 2765 (1987).
150. H. N. Spector and J. Lee, *Am. J. Phys.* 53, 248 (1985).
151. J. F. Jan and Y. C. Lee, *Phys. Rev. B* 50, 14647 (1994).
152. J. L. Marín, R. Riera, R. Rosas, and A. Uribe, *Phys. Low-Dim. Struct.* 3/4, 73 (1998).
153. L. E. Brus, *J. Phys. Chem.* 90, 2555 (1986).
154. L. E. Brus, *IEEE J. Quantum Electron.* QE-22, 1909 (1986).
155. R. A. Morgan, S. H. Park, S. W. Koch, and N. Peyghambarian, *Semicond. Sci. Technol.* 5, 544 (1990).
156. M. Yamamoto, R. Hayashi, K. Tsunetomo, K. Kohno, and Y. Osaka, *Japan J. Appl. Phys.* 30, 136 (1991).
157. L. E. Brus, *J. Chem. Phys.* 79, 5566 (1983).
158. Y. Kayanuma, *Phys. Rev. B* 38, 9797 (1988).
159. Y. Kayanuma, *Phys. Rev. B* 41, 10261 (1990).
160. Y. Wang and N. Herron, *Phys. Rev. B* 42, 7253 (1990).
161. G. T. Einevoll, *Phys. Rev. B* 45, 3410 (1992).
162. P. E. Lippens and M. Lannoo, *Phys. Rev. B* 39, 10935 (1989).
163. H. M. Schmidt and H. Weller, *Chem. Phys. Lett.* 129, 615 (1986).
164. M. Abramowitz and I. A. Stegun, "Handbook of Mathematical Functions." Dover, New York, 1970.
165. F. M. Fernandez and E. A. Castro, *Int. J. Quantum Chem.* 21, 741 (1982).
166. F. M. Fernandez and E. A. Castro, *J. Math. Phys.* 23, 1103 (1982).
167. F. M. Fernandez and E. A. Castro, *Int. J. Quantum Chem.* 22, 623 (1981).
168. F. M. Fernandez and E. A. Castro, *Phys. Rev. A* 5, 2883 (1981).
169. G. A. Arteca, F. M. Fernandez, and E. A. Castro, *J. Chem. Phys.* 80, 1569 (1984).
170. F. M. Fernandez and E. A. Castro, *Am. J. Phys.* 52, 453 (1984).
171. F. M. Fernandez and E. A. Castro, *Am. J. Phys.* 50, 921 (1982).
172. M. El-Said, *J. Phys. I France* 5, 1027 (1995).
173. K. D. Zhu and S. W. Gu, *Phys. Lett. A* 172, 296 (1993).
174. W. Que, *Phys. Rev. B* 45, 11036 (1992).
175. V. Halonen, T. Chakraborty, and M. Pietalain, *Phys. Rev. B* 45, 5980 (1992).
176. G. W. Bryant, *Phys. Rev. Lett.* 59, 1140 (1987).
177. A. Kumar, S. E. Laux, and F. Stern, *Phys. Rev. B* 42, 5166 (1990).
178. U. Merkt, J. Huser, and M. Wagner, *Phys. Rev. B* 43, 7320 (1991).
179. D. Pfannkuche and R. R. Gerhardt, *Phys. Rev. B* 44, 13132 (1991).
180. J. J. S. De Groote, J. E. M. Honos, and A. V. Chaplik, *Phys. Rev. B* 46, 12773 (1992).
181. T. Imbo, A. Pagnamento, and U. Sukhatme, *Phys. Rev. D* 29, 8763 (1984).
182. T. Imbo and U. Sukhatme, *Phys. Rev. D* 28, 418 (1983).
183. T. Imbo and U. Sukhatme, *Phys. Rev. D* 31, 2655 (1985).
184. R. Dutt, Mukherji, and Y. P. Varshni, *J. Phys. B* 19, 3411 (1986).
185. M. Wagner, U. Merkt, and A. V. Chaplik, *Phys. Rev. B* 45, 1951 (1992).
186. D. Pfannkuche and R. R. Gerhardt, *Physica B* 189, 6 (1994).
187. M. Taut, *Phys. Rev. A* 48, 3561 (1993).
188. A. Wixforth, M. Kaloudis, C. Rocke, K. Ensslin, M. Sundaram, J. H. English, and A. C. Gossard, *Semicond. Sci. Technol.* 9, 215 (1994).
189. A. Blom, M. A. Odnoblyudov, H. H. Cheng, I. N. Yassievich, and K. A. Chao, *Appl. Phys. Lett.* 79, 713 (2001).
190. I. V. Altukhov, E. G. Chirikova, M. S. Kagan, K. A. Korolev, V. P. Sinis, and F. A. Smirnov, *Sov. Phys. JETP* 74, 404 (1992).
191. I. V. Altukhov, M. S. Kagan, K. A. Korolev, V. P. Sinis, E. G. Chirikova, M. A. Odnoblyudov, and I. N. Yassievich, *JETP* 88, 51 (1999).
192. M. A. Odnoblyudov, I. N. Yassievich, M. S. Kagan, Yu. M. Galperin, and K. A. Chao, *Phys. Rev. Lett.* 83, 644 (1999).
193. Yu. P. Gousev, I. V. Altukhov, K. A. Korolev, V. P. Sinis, M. S. Kagan, E. E. Haller, M. A. Odnoblyudov, I. N. Yassievich, and K. A. Chao, *Appl. Phys. Lett.* 75, 757 (1999).
194. M. A. Odnoblyudov, I. N. Yassievich, M. S. Kagan, and K. A. Chao, *Phys. Rev. B* 62, 15291 (2000).
195. M. A. Odnoblyudov, I. N. Yassievich, M. Chistyakov, and K. A. Chao, *Phys. Rev. B* 62, 2486 (2000).
196. I. N. Yassievich, K. Schmalz, M. A. Odnoblyudov, and M. S. Kagan, *Solid-State Electron.* 40, 97 (1996).
197. M. S. Kagan, I. V. Altukhov, A. Korolev, D. V. Orlov, V. P. Sinis, K. Schmalz, S. G. Thomas, K. L. Wang, and I. N. Yassievich, *Phys. Status Solidi B* 210, 667 (1998).
198. M. S. Kagan, I. V. Altukhov, V. P. Sinis, S. G. Thomas, K. L. Wang, K. A. Chao, and I. N. Yassievich, *Thin Solid Films* 380, 237 (2000).
199. I. V. Altukhov, M. S. Kagan, V. P. Sinis, S. G. Thomas, K. L. Wang, A. Blom, and M. A. Odnoblyudov, *Thin Solid Films* 380, 218 (2000).
200. S. C. Jain, "Germanium-Silicon Strained Layers and Heterostructures," *Advances in Electronics and Electron Physics*, Suppl. 24. Academic, Boston, 1994.
201. W. Kohn and J. M. Luttinger, *Phys. Rev.* 98, 915 (1955).
202. S. M. Sze, "Physics of Semiconductor Devices," 2nd ed., p. 868. Wiley, New York, 1981.
203. I. V. Altukhov, V. P. Sinis, Yu. P. Gousev, S. G. Thomas, K. L. Wang, and M. S. Kagan, private communication.
204. K. Schmalz, I. N. Yassievich, K. L. Wang, and S. G. Thomas, *Phys. Rev.* 57, 6579 (1998).
205. J. L. Marín, R. Riera, and R. A. Rupas, in "Handbook of Advanced Electronic and Photonic Materials and Devices" (H. S. Nalwa, Ed.). Academic Press, San Diego, 2001.





# Inherently Conducting Polymer Nanostructures

Gordon G. Wallace, Peter C. Innis, Leon A. P. Kane-Maguire

*University of Wollongong, Wollongong, Australia*

## CONTENTS

1. Introduction
  2. Synthesis of Inherently Conducting Polymers Nanostructures
  3. Unique Properties and Applications of Inherently Conducting Polymers Nanostructures
  4. Conclusions
- Glossary  
References

## 1. INTRODUCTION

Inherently conducting polymers (ICPs) such as polypyrroles, polythiophenes, and polyanilines (I–III shown in Scheme 1) are extremely useful organic electronic conductors. The applications of these materials have been reviewed recently [1–3], spanning areas as diverse as nanomaterials [4], electrochromics [5], sensors [6], artificial muscles [7, 8], smart membranes [9, 10], platforms for cell culturing [11, 12] and corrosion protection [13]. Many of these applications involve electrochemical switching processes (to be discussed in more detail). In the quest to improve electrochemical switching speeds of ICPs, researchers have recently turned attention to control of the structure at the nanodomain.

It is also interesting to note that ICP macrostructures are actually composed of nanodomains of much higher conductivity than the bulk material [14–17] suggesting that nano-dimensional control will also improve the bulk conductivity of ICPs.

### 1.1. What Are ICPs?

The synthesis and electrochemical switching properties of ICPs such as polypyrroles (PPy), polythiophenes (PTh), and polyanilines (PAn) have been reviewed in recent monographs [18, 19].

The polymerization can be initiated chemically or electrochemically and involves formation of lower molecular weight oligomers via oxidation. These are then further oxidized

(at lower potentials than the initial monomer) to form a polymer that eventually precipitates or deposits onto the anode in an electrochemical cell as a critical molecular weight is exceeded:



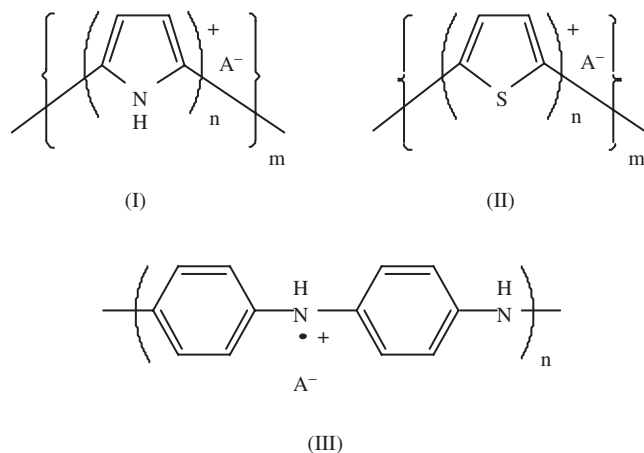
A counterion ( $\text{A}^-$ ) is incorporated during synthesis to balance the charge on the polymer backbone. The anion of the chemical oxidants used provides the dopant  $\text{A}^-$ . Electrochemical oxidation provides greater flexibility in terms of the anion that can be incorporated from the electrolyte used as the polymerization medium. Polypyrroles can be formed from neutral aqueous solutions while acidic conditions are required for aniline solubilization and polymerization. Thiophene polymerization is commonly undertaken in organic solvents due to poor monomer solubility in aqueous solutions.

#### 1.1.1. Polypyrroles

The mild oxidation potentials needed to initiate formation of polypyrrole in aqueous solution have enabled the formation of a wide range of polypyrrole structures by simply varying the dopant.

Simple metal recognition capabilities are introduced by incorporation of metal complexing groups as dopants [20, 21], or electrocatalytic effects are induced by use of appropriate dopants [22], covalently attached redox sites [23, 24], and/or inclusion of micron-sized metallic particles [25, 26]. Conducting polymers are also known to promote electron transfer into/out of biological entities [27]. Biomolecular/recognition can be introduced by incorporation of antibodies or enzymes or even nerve growth factors into the polymer at the time of synthesis, as reviewed recently [28].

The incorporation of complex biomolecules as dopants can be accomplished while retaining the unique electronic properties of the polymer backbone. For example, the



**Scheme 1.** For polypyrroles and polythiophenes,  $n$  is usually ca. 3–4. For optimal conductivity, there is a positive charge on every third or fourth pyrrole or thiophene unit along the polymer chain. For the conducting emeraldine salt form of polyaniline (III) a radical cation resides at alternate N sites.

ultraviolet-visible (UV-vis) spectrum for PPy containing DNA as dopant is shown in Figure 1. This UV-vis spectrum shows the typical polaron/bipolaron 475 nm bands of doped polypyrrole at ca. 500 nm and 900 nm. The exact location of these bands is dependent on the dopant used. As illustrated in Figure 2, when 8-hydroxyquinoline-5-sulfonic acid (HQS) is used as dopant, the lower wavelength peak is even further blueshifted. The dopant also influences the degree of absorption in the near infrared beyond 900 nm and this is attributed to changes in polymer conformation (tight coil versus expanded coil). The polymer conformation has been found to be substrate dependent, with polypyrroles deposited on hydrophilic glass displaying an absorption band at 1180 nm, which is replaced by a free carrier tail extending to 2600 nm for polymers deposited on hydrophobic surfaces [29].

As well as varying the functional properties of ICPs, the dopant plays a key role in determining the electronic (conductivity) and mechanical properties (e.g., tensile strength) of the resultant material. For example, even slight changes in the molecular structure [30] of a range of sulfonated aromatic dopants influence these properties (Table 1). The incorporation of surfactant-like dopants such as dodecylbenzene sulfonate has also proved useful in sol-

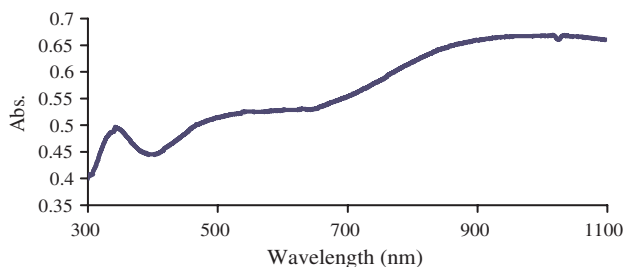


**Figure 1.** UV-visible spectrum of a PPy DNA thin film grown onto indium tin oxide (ITO) glass from a solution containing 0.2 M pyrrole and 0.2% w/v salmon sperm DNA. Reprinted with permission from [188], V. Misoska, Ph.D. Thesis, University of Wollongong, 2002.

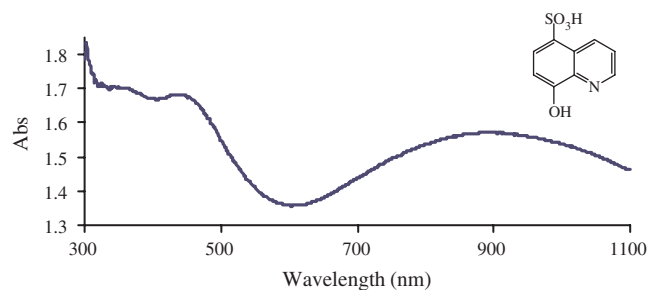
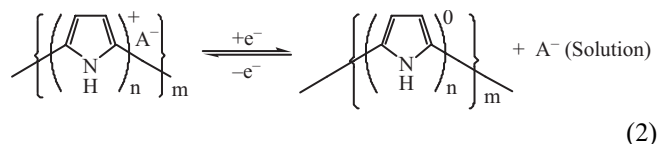


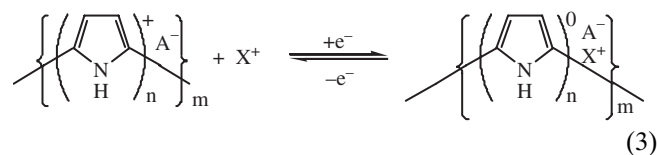
**Figure 2.** UV-visible spectrum of a PPy HQS film grown galvanostatically onto ITO glass from a solution containing 0.2 M pyrrole and 0.1 M HQS. Reprinted with permission from [188], V. Misoska, Ph.D. Thesis, University of Wollongong, 2002.

ubilizing polypyrrole in organic solvents [31, 32]. The presence of alkyl and alkoxy substituents on the backbone of polypyrrole also increases their solubility in organic solvents. In contrast, polymerization of pyrrole monomers bearing sulfonated substituents has provided water soluble polypyrroles [33]. A very useful recent advance has been the development of a facile route for the modification of pre-formed polypyrroles containing good leaving group such as *N*-hydroxysuccinamide [34].

An important feature of these ICP structures is that they are amenable to facile oxidation/reduction processes that can be initiated at moderate potentials. For polypyrrole the oxidation state can be reversibly switched, as shown in Eq. (2). The doped oxidized forms exhibit good electrical conductivity ( $\sigma = 1\text{--}100 \text{ S cm}^{-1}$ ), while the reduced forms have very low conductivity ( $\sigma \sim 10^{-8} \text{ S cm}^{-1}$ ). The dynamic character of these polymer systems, with chemical, physical, and mechanical properties being a function of applied potential, is intriguing and is the basis of their proposed use in intelligent material systems [19].

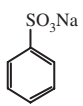
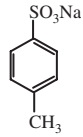
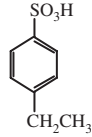
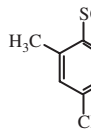
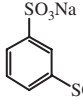
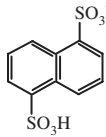


If the dopant anion ( $\text{A}^-$ ) is small and mobile (e.g.,  $\text{Cl}^-$ ), then upon reduction the anion will be efficiently ejected from the polymer [Eq. (2)]. However, extensive studies with polypyrroles have shown that if the dopant is large and immobile (e.g., if  $\text{A}^-$  is a polyelectrolyte such as polystyrene sulfonate), an electrically induced cation exchange process occurs, according to



where the cation ( $\text{X}^+$ ) is incorporated from the supporting electrolyte solution. The effect of the original dopant incorporated as well as the other ions in the electrolyte on the electrochemical switching characteristics of polypyrroles has been clearly demonstrated [30].

**Table 1.** Effect of the counterion on the tensile strength and conductivity of polypyrrole membranes [30].

Membrane	PPy/BSA	PPy/PTS	PPy/EBS	PPy/MS	PPy/BS	PPy/NPS
Counterions						
Tensile strength (MPa)	17–23	70–80	60–70	36–47	40–55	40–50
Conductivity (S/cm)	19–20	90–110	90–110	50–70	47–70	50–70

The redox processes described have a dramatic effect on the physical and chemical properties of the polymer. Conductivity will decrease, anion exchange capacity will diminish [Eq. (2)], cation exchange capacity may increase [(Eq. 3)] and hydrophobicity will be altered in a manner determined by which ion exchange process predominates. The mechanical properties are also influenced by the oxidation state with a greater elongation-to-break usually observed in the reduced materials [35]. The polymer also undergoes dramatic color changes upon redox switching (see Section 1.1.2) which is the basis of electrochromic devices based on ICPs [5].

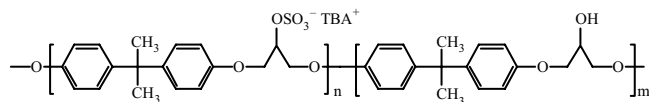
### 1.1.2. Polythiophenes

The direct polymerization of thiophene is more complicated in that the monomer oxidation occurs at potentials more positive than required to overoxidize the polymer. Hence monomers with alkyl groups attached to the 3-position [36], bithiophene [37, 38], or terthiophenes [39] are often used as starting materials since they have lower oxidation potentials.

To avoid use of organic solvents for polythiophene synthesis, monomers can be dissolved in aqueous solution using surfactants [40] or molecular inclusion compounds such as cyclodextrins [41]. While the inclusion of the extensive range of dopants available with polypyrrole is not available with polythiophenes, some functional dopants have been incorporated [42]. Specific dopants such as the polyether [43] shown in Scheme 2 induce exceptional mechanical properties into polythiophenes, with tensile strengths of the order of 120 MPa readily obtained.

The UV-visible absorption spectra obtained (Fig. 3) after polymerization of bithiophene clearly show polaron/ bipolaron absorption bands that are eliminated once the polymer is electrochemically reduced.

Given the simple synthetic chemistries available to covalently attach functional groups to thiophene substrates prior to polymerization, this has been the preferred approach to introduce functionality into polythiophenes [44]. In conjunction with our collaborators at Massey University,



**Scheme 2.** Structure of the S-PHE used in this work. TBA = tetrabutylammonium.

New Zealand, we have produced a range of substituted terthiophene precursors (Fig. 4), from which functional polymers have been produced [45].

As discussed for polypyrroles, the polythiophenes undergo reversible oxidation/reduction processes (Fig. 5). Oxidation/reduction usually occurs at more positive potentials than for the polypyrroles and is not readily achieved in aqueous solutions [45], presumably due to the hydrophobic nature of the thiophene based polymer. Some workers have attached ether groups to the polymer backbone, increasing hydrophilicity and the rate of switching in aqueous media [46].

Another interesting feature of polythiophenes is that the *n*-doped state is more readily accessible than with either polypyrroles or polyanilines. This enables the polymer to be rendered conductive at more negative potentials. A number of authors [47, 48] have highlighted the importance of substituents on the polythiophene backbone in determining the accessibility (potential required for reduction) and stability of the *n*-doped state.

### 1.1.3. Polyanilines

Like polypyrrole, conducting polyaniline (PAn) and its ring-substituted analogs are generally prepared via either chemical or electrochemical oxidation/polymerization of the appropriate aniline monomer in aqueous solution. However, acidic conditions (pH generally 0–1) are required both

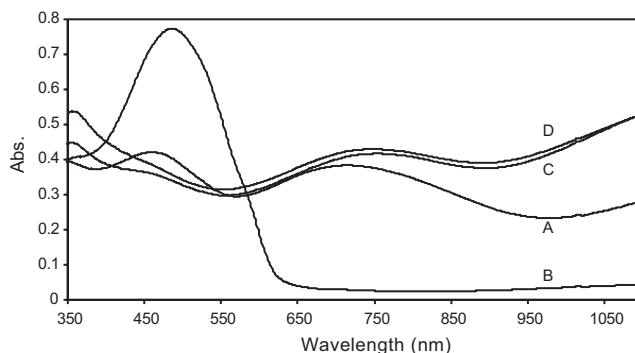


**Figure 3.** UV-vis spectra of PBT/S-PHE composite galvanostatically deposited ( $1 \text{ mA cm}^{-2}$  for 50 s) onto ITO coated glass from a solution containing 0.2 M 2,2' bithiophene and 2% S-PHE. (A) Polymer after preparation. (B)–(D) Polymer after application of an applied potential for 60 s in propylene carbonate solution containing TBAP; (B) 0 V, (C) +1.3 V (D) +1.5 V. Reprinted with permission from [43], J. Ding et al., *Synth. Met.* 110, 123 (2000). © 2000, Elsevier Science.

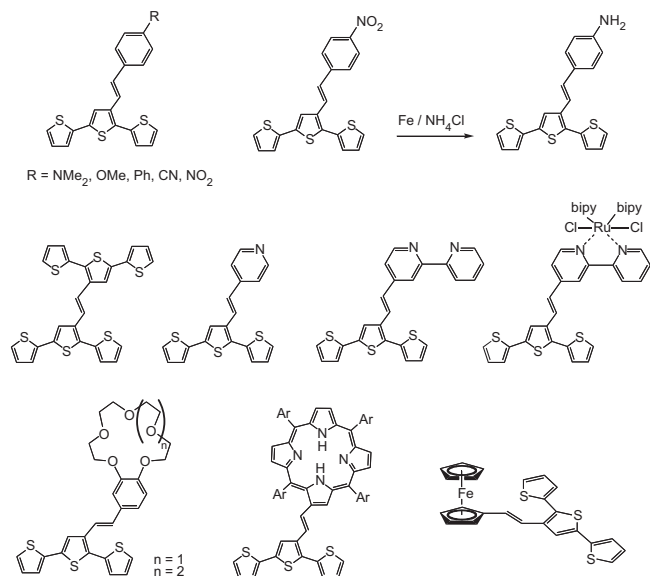


Figure 4. Styryl terthiophene monomers synthesized.

to solubilize the aniline monomer and to ensure that the conducting emeraldine salt  $\text{PAn} \cdot \text{HA}$  form of the polymer is produced [see structure (III)]. The most common chemical oxidants are ammonium persulfate or ferric chloride, in which cases  $\text{HSO}_4^-/\text{SO}_4^{2-}$  or  $\text{Cl}^-$  anions are incorporated as the dopant anions  $\text{A}^-$  at the radical cation nitrogen sites along the PAn chains.

Using electrochemical polymerization, a much wider range of dopant anions may be incorporated along the polyaniline chains, depending on the electrolyte employed. After deposition on the working electrode, films of the  $\text{PAn} \cdot \text{HA}$  may often be removed as mechanically robust, stand-alone membranes. On the other hand, chemical polymerization has the advantage of being a simple process capable of producing bulk quantities of  $\text{PAn} \cdot \text{HA}$  powders on a batch basis.

In both chemical and electrochemical polymerization the initial and rate-determining step is believed [49–51] to

be oxidation of the aniline monomer to give the radical cation of aniline. This is followed by coupling of the radicals, predominantly *N* and *para* forms, and subsequent re-aromatization to give a dimer. This undergoes more facile oxidation than the aniline monomer, leading to chain propagation and eventual deposition of the emeraldine salt from solution.

The nature of the dopant anion incorporated along the growing polymer chain during polymerization has a profound effect upon the morphology [52], conductivity [53], switching characteristics, and solubility of the resulting polyaniline salts. Incorporation of polyelectrolyte dopant anions during either chemical or electrochemical oxidation of aniline has been an area of intense recent interest. These large anions can often be preferentially incorporated even when an acid such as  $\text{HClO}_4$  is present in large excess [54]. As will be discussed further in Section 3, this can induce water “solubility” onto the resultant emeraldine salt when the anion is a polyelectrolyte such as poly(styrenesulfonate) or polyacrylate [55–57]. This approach has helped in overcoming one of the problems previously associated with polyanilines, namely their insolubility in most common solvents. It has also provided a convenient route to aqueous nanosized dispersions of conducting emeraldine salts (see Section 4). Biological polyelectrolytes such as DNA have also been incorporated into emeraldine salts using this approach [58, 59].

On the other hand, organic solvent solubility has been induced in polyanilines via the incorporation of surfactant-type dopant anions such as dodecylbenzenesulfonate, racemic 10-camphorsulfonate ( $\text{CSA}^-$ ) [60], and dinonylnaphthalene sulfonate [61]. Another significant development has been the facile generation of optically active emeraldine salts such as  $\text{PAn} \cdot (+)\text{-HCSA}$  or  $\text{PAn} \cdot (-)\text{-HCSA}$  by the simple expedience of employing chiral acids such as (+)- or (-)-HCSA as the electrolyte during electrochemical polymerization [62, 63]. These chiral conducting polyanilines are believed to preferentially adopt single-handed helical structures for their polymer chains depending on which hand of the dopant HCSA acid is employed.

A large range of substituted anilines are available. Polymerization of these has given emeraldine salts whose properties differ significantly from those of the parent unsubstituted  $\text{PAn} \cdot \text{HA}$  salts. For example, the presence of alkyl or alkoxy substituents [64] on the aniline rings imparts enhanced solubility in organic solvents on the resultant polymers. On the other hand, sulfonate groups lead to water solubility, as in poly(2-methoxyaniline-5-sulfonic acid) [65].

Postpolymerization modification of polyanilines has also been pursued to introduce added functionality into the polymer for a variety of applications. For example, treatment of the emeraldine base (EB) or leucoemeraldine base (LB) forms of polyaniline with fuming sulfuric acid has led to water-soluble, sulfonated polyanilines (SPANs) in which 50–75% of the aniline rings bear sulfonate groups [66]. These latter emeraldine salts are self-doped (i.e., ring-bound sulfonate groups provide the dopant anion for the radical cation nitrogen sites along the chain). An exciting recent development has been the synthesis of poly(aniline boronic acid) [67]. This promises to be a convenient precursor for

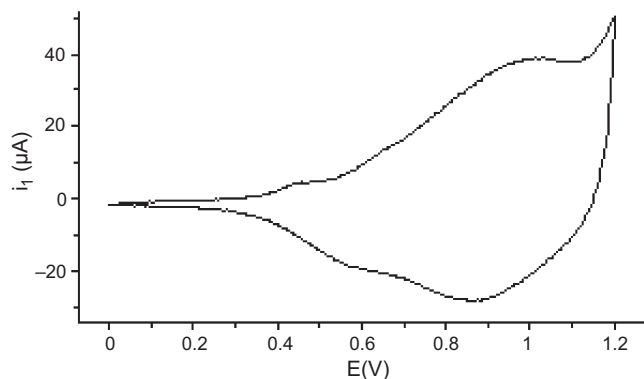


Figure 5. Cyclic voltammogram of a PBT/S-PHE coated platinum electrode obtained after immersion in a propylene carbonate solution containing 0.5 M  $\text{LiClO}_4$ , scan rate =  $100 \text{ mV s}^{-1}$ . PBT/S-PHE was prepared galvanostatically ( $1 \text{ mA cm}^{-2}$  for 3 min) using a solution containing 0.2 M 2,2'-bithiophene and 2% S-PHE.



the facile synthesis of a wide range of substituted polyanilines that are difficult to synthesize directly from their respective monomers.

Doped PAN · HA emeraldine salts are good electrical conductors, with conductivities typically in the range 1–10 S cm<sup>-1</sup>. It is generally agreed that polarons are the charge carriers responsible for this high conductivity. Evidence includes the observation of a strong electron spin resonance signal associated with the radical cation sites in structure (III) [68]. It has also been shown that bipolaron states exist in polyaniline, but these are few in number and are not associated with the conducting regions of the polymer [69].

The attachment of functional groups to the aniline rings generally decreases the conductivity of polyaniline emeraldine salts. This is attributed to steric crowding causing a marked twisting of the polymer backbone from planarity, leading to decreased conjugation along the chains. Structural defects such as those arising from undesirable *ortho*-coupling of aniline radical cations during the polymerization also lead to impaired electrical conductivity. There has been considerable recent interest in enhancing the conductivity of emeraldine salts via their exposure to “secondary dopants” such as *m*-cresol. This can cause an increase in conductivity of several orders of magnitude. The enhanced conductivity has been attributed to the adoption of an “extended coil” conformation by the polyaniline backbone, with the polarons delocalized along the chains [70].

The UV-visible near-infrared spectra of polyanilines are very sensitive to the polymer chain conformation. For example, when PAN · HCSA emeraldine salts are generated by acid doping the EB form with camphorsulfonic acid in organic solvents such as chloroform, DMSO, or NMP [Eq. (4); See Fig. 8], they typically exhibit three absorption bands in the visible region, as shown in Figure 6. The strong band observed in these cases at 750–850 nm has been assigned as a localized polaron band, while the two bands at ca. 430 and 340 nm are attributed to a second polaron band and a  $\pi$ - $\pi^*$  (bandgap) band, respectively [71]. These spectral features and the moderate electrical conductivity of such salts (ca. 1 S cm<sup>-1</sup>) are considered diagnostic of a “compact coil” conformation for the polyaniline chains. In contrast, no long wavelength localized polaron band is observed in the visible region for PAN · HCSA salts generated by analogous

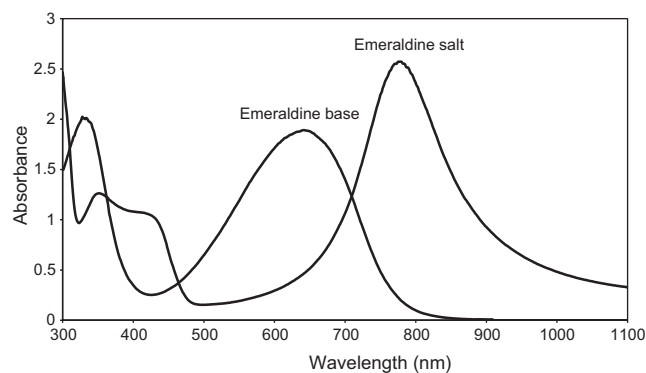
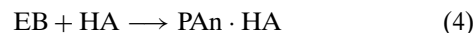


**Figure 6.** UV spectra showing EB–ES. Reprinted with permission from [189], C. Boonchu, Ph.D. Thesis, University of Wollongong, 2002.

acid doping in “secondary dopant” solvents such as *m*-cresol. These much more conducting salts ( $\delta > 100$  S cm<sup>-1</sup>) instead exhibit an intense free carrier tail in the near infrared region with an absorption maximum at ca. 2500 nm. These latter features are considered diagnostic of an “extended coil” conformation for the polyaniline backbone:



Circular dichroism (CD) spectroscopy provides a particularly powerful tool for probing the polymer chain conformation in related optically active emeraldine salts. For example, the “compact coil” form of PAN-(+)-HCSA in NMP solvent shows the characteristic bands seen in Figure 7. The strong bisignate CD bands at ca. 795 and 720 nm are associated with the localized polaron absorption at ca. 775 nm for this polymer in NMP (see Fig. 6) [72, 73]. Overlapping bisignate CD bands are also observed at lower wavelengths associated with the other two lower absorption bands seen for PAN-(+)-HCSA in Figure 6. The CD spectrum of “extended coil” PAN-(+)-HCSA (not shown) bears no similarity whatsoever to that seen in Figure 7 for the “compact coil” form [74].

Polyaniline contrasts with other ICPs in that it has three readily accessible oxidation states (fully reduced leucoemeraldine, partly oxidized emeraldine, and fully oxidized pernigraniline), as shown in Figure 8 [75]. In addition, reversible protonation/deprotonation equilibria occur for two of these oxidation states. Thus, the emeraldine salt form (ES), which is the only electrically conducting form of polyaniline, is typically dedoped at pH > 4 to give nonconducting EB. Conversely, the reverse acid doping of EB with HA acids [Eq. (4)] provides a convenient route to conducting PAN · HA emeraldine salts with a wide range of acids. The pernigraniline oxidation state of PAN can similarly exist as both a protonated pernigraniline salt or as a neutral pernigraniline base (Fig. 8). On the other hand, the fully reduced leucoemeraldine oxidation state appears to exist only in the neutral base form.

Polyaniline can be rapidly and reversibly switched between the various forms shown in Figure 8. The pH and redox switching is accompanied by marked changes in colour. For example, alkaline treatment of green PAN · HA emeraldine salts rapidly generates the blue color of EB. The associated UV-visible spectral changes caused by such alkaline dedoping are shown in Figure 8. Emeraldine base exhibits a characteristic exciton band at ca. 600 nm as well

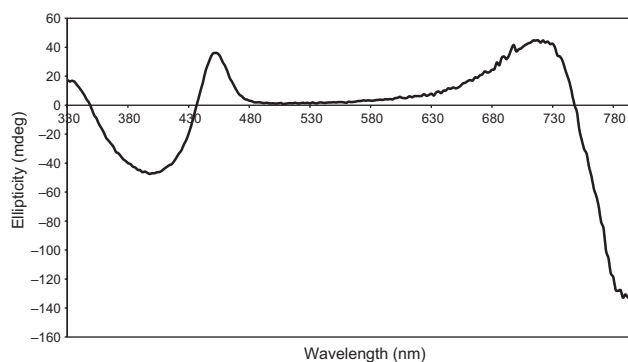


**Figure 7.** CD spectrum of PAN-(+)-HCSA.

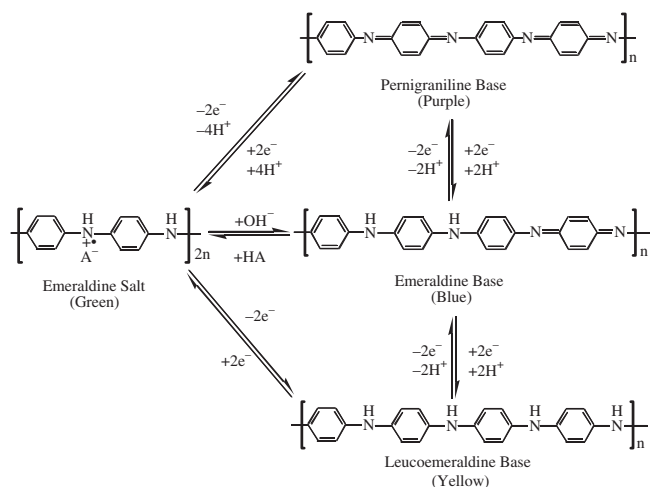


**Figure 8.** Chemical transitions observed in the oxidation/reduction of polyaniline.

as a  $\pi-\pi^*$  band at ca. 330 nm [76]. Such alkaline dedoping when performed on PAN · HA films also leads to a dramatic reduction in electrical conductivity, the EB form being an insulator.

The reversible redox switching of polyaniline films can also be readily monitored by cyclic voltammetry. For example, the cyclic voltammogram of PAN · HCl in 1 M HCl is shown in Figure 9. In the cathodic sweep, oxidation peaks are observed at ca. 0.2 and 0.7 V (vs Ag/AgCl) that may be attributed to the successive oxidations of leucoemeraldine to emeraldine to pernigraniline.

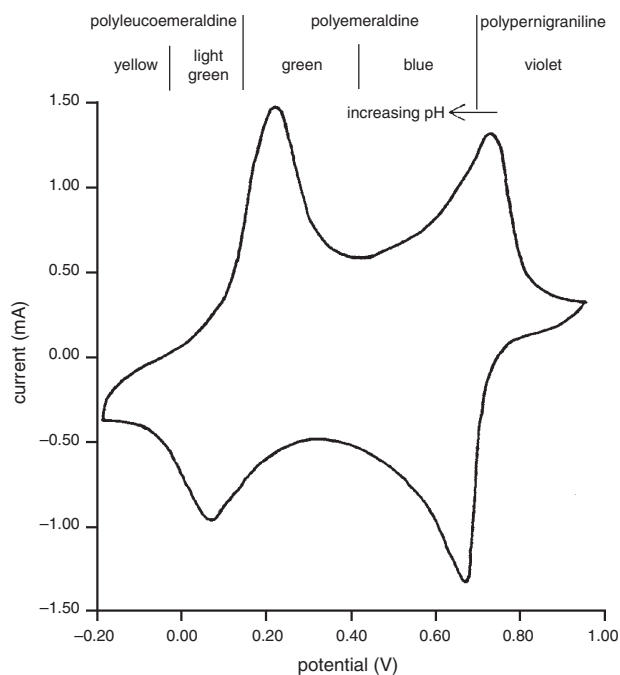


**Figure 9.** Cyclic voltammogram of polyaniline (HCl) on a glassy carbon electrode; 1 M HCl(aq); 50 mV/s. The potentials at which structure and color changes occur and the change in the potential of the second redox reaction with pH are shown as well. The second oxidation peak moves to a less positive potential with increasing pH.

## 2. SYNTHESIS OF INHERENTLY CONDUCTING POLYMERS NANOSTRUCTURES

A number of approaches have been used to produce inherently conducting polymer nanocomponents.

### 2.1. Use of Steric Stabilizers

With a view to improving the processability of inherently conducting polymers, a range of colloidal materials have been produced over the past 10 years. The conventional approach involves chemical oxidation of the monomer in the presence of a steric stabilizer such as PVA to produce stable colloidal dispersions [77–79] with particle sizes typically 10–200  $\mu\text{m}$ .

Recently this approach has been refined and oxidation of aniline in DMSO in the presence of PVA has been used to produce dispersions containing particles as small as 5 nm [80].

In our laboratory we have developed an electrohydrodynamic approach for the synthesis of inherently conducting polymer colloids [81]. This involves the use of a flow-through electrochemical reactor using a high surface area vitreous carbon electrode. Using appropriate flow-through conditions, stable colloidal dispersions containing 100–200 nm spherical particles are readily produced (Fig. 10). This electrochemical approach allows facile incorporation of a wide range of dopants during colloid formation. For example, protein-containing colloids [82], colloids containing corrosion inhibitors [83], and, more recently, optically active colloids [84] have been produced.

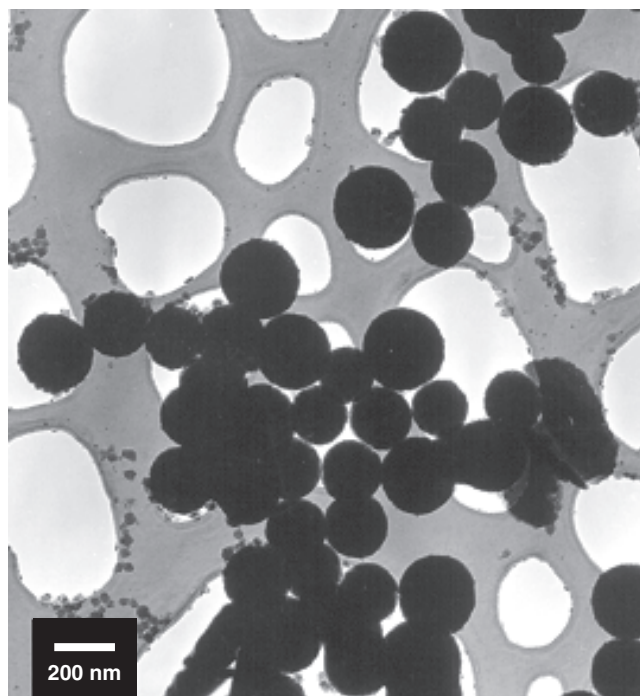


**Figure 10.** Transmission electron micrograph of colloidal polypyrrole nitrate. Reprinted with permission from [4], G. G. Wallace and P. C. Innis, *J. Nanosci. Nanotech.* 2, 441 (2002). © 2002, American Scientific Publishers.



More recent work [85] has shown that the use of Tiron (Scheme 3) as dopant enables production of monodispersed polypyrrole particles of 50 nm (Fig. 11). Tiron has previously been shown to act as an electrocatalyst in the formation of polypyrrole [86].

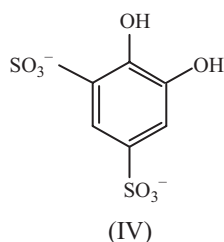
## 2.2. Micellar Polymerization and Microemulsion Routes

A novel approach to the formation of ICP nanoparticles has been developed through the use of micellar polymerization and microemulsion techniques. The advantage of such an approach is that the particle size can be predefined by establishing the appropriate size and geometry of the templating micelle (Fig. 12). For example, formation of polyaniline nanoparticles has been achieved via polymerization in a micelle approach using either sodium dodecyl sulfate (SDS) [87] or dodecylbenzenesulfonic acid [88–90] as the surfactant stabilizer. Particle sizes in the range of 10–30 nm with conductivities as high as  $24 \text{ S cm}^{-1}$  have been reported.

Poly(3,4-ethylenedioxythiophene) (PEDOT) and polyaniline nanoparticles have also been synthesised via the micellar route with sodium dodecyl sulfate and dodecylbenzenesulfonic acid [91]. Polyaniline nanoparticles were spherical and 20 to 60 nm in diameter and PEDOT was from 35 to 100 nm. The observed conductivities of 20 to  $50 \text{ S cm}^{-1}$  (by pellet) were higher than those observed for larger micrometer sized particles prepared in bulk solutions.

Control of the micelle size utilized in the formation of polyaniline nanoparticles has been achieved by tailoring the stabilizer to modify the resulting micelle dimensions. Kim et al. [92, 93] have used amphiphilic polymer molecules, hydrophobically end-capped poly(ethylene oxide), and varied the hydrophilic PEO midsection length to control the final micelle size. The micelle structures formed were referred to as flower type, with the aniline monomer and hexane cosolvent interacting with the hydrophobic end groups. The resultant nanostructures ranged from 20 to approximately 300 nm in size depending on the molecular weight of the hydrophilic PEO midsection.

Metallic and semiconducting nanoparticles have been routinely produced at the sub-5 nm scale for some time but it has been a challenge to produce polymer nanoparticles smaller than this. Jang et al. [94] have reported the synthesis of polypyrrole nanoparticles at the 2 nm scale via a microemulsion route carried out at  $3 \text{ }^\circ\text{C}$ . Pyrrole monomer was initially formed into micelles and then oxidized by ferric chloride. Typical surfactants used in



Scheme 3. Tiron.

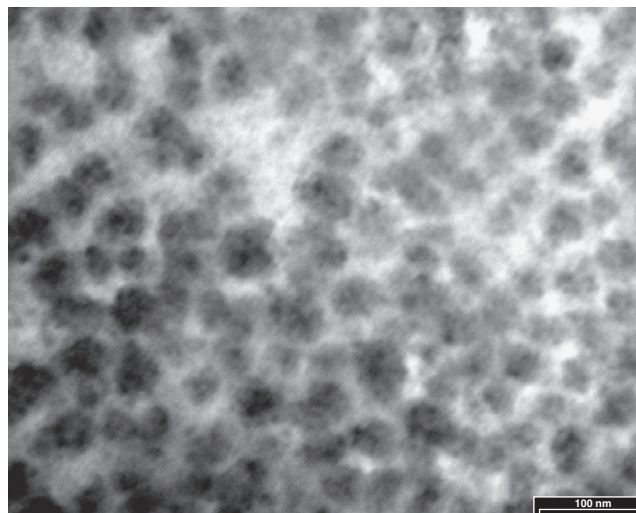


Figure 11. Transmission electron micrograph of aggregated polypyrrole tiron colloid particles ( $\times 150 \text{ K}$ ). Reprinted with permission from [4], G. G. Wallace and P. C. Innis, *J. Nanosci. Nanotech.* 2, 441 (2002). © 2002, American Scientific Publishers.

the preparation of these sub-5 nm particles were quaternary ammonium based cations such as octyltrimethylammonium bromide, decyltrimethylammonium bromide, and dodecyltrimethylammonium bromide. At room temperature these surfactants produced nanoparticles larger than 10 nm while at  $70 \text{ }^\circ\text{C}$  ca. 50 nm particles were observed.

Nanoscale patterning of polypyrrole dot structures of 80 to 180 nm diameter in self-organized arrays has also been achieved via a block copolymer surface-micelle templated approach [95]. Using this approach, micelle templates were prepared using the Langmuir–Blodgett (LB) technique to deposit an AB diblock copolymer onto a mica substrate followed by the selective chemical deposition of polypyrrole onto these templating structures. Selective deposition is achieved by exploiting the preference of polypyrrole to deposit onto hydrophobic surfaces rather than hydrophilic substrates. An advantage of this approach is that lithographic patterning techniques can be avoided due to the self-assembly of the micelle via the LB technique. Inverse structures of these PPy dots have also been prepared

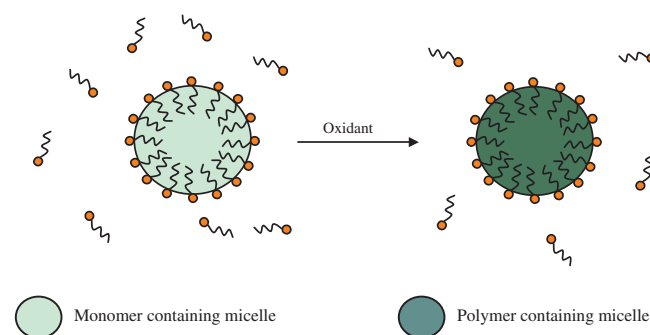


Figure 12. Schematic illustrating micellar/microemulsion nanoparticle synthesis. Reprinted with permission from [4], G. G. Wallace and P. C. Innis, *J. Nanosci. Nanotech.* 2, 441 (2002). © 2002, American Scientific Publishers.

by extended polymer synthesis in the presence of self-assembled polystyrene cores that are selectively removed by toluene.

Selvan et al. [96, 97] utilized a block copolymer micelle of polystyrene-block-poly(2-vinylpyridine) in toluene exposed to tetrachloroauric acid which was selectively adsorbed by the micelle structure. On exposure of this solution to pyrrole monomer, doped polypyrrole was observed to be synthesized concurrently with the formation of gold nanoparticles as a result of the reduction of the bound  $\text{AuCl}_4^-$ . The nanoparticles formed had a monodispersed (7–9 nm) gold core surrounded by a PPy shell after annealing at 130 °C for 1 hour. Depending on the postsynthesis treatment, different shaped nanoparticles such as spherical, cubic, tetrahedral, and octahedral shapes were formed due to micelle coagulation. Dendritic nanoaggregate structures were also reported to form via a vapor phase polymerisation of the pyrrole monomer onto cast films of the block copolymer. In related work by Zhou et al. [98, 99] metal ion reduction of Au, Pd, and Pt salts with a  $\pi$ -conjugated polymer, poly(dithiafulvene) (PDF), capable of electron donating to the metal salts thereby reducing them and itself being oxidized to provide steric and electrosteric stabilization of the nanoparticle. The resultant metal cores of the composite nanoparticles were 5–6 nm in size. Interestingly, the surface plasmon absorption band in the UV-vis spectrum for a metal nanoparticle (Pd, Pt) was significantly redshifted to 550 nm from an anticipated 510–525 nm. This shift was attributed to the electronic interaction of the oxidized PDF with the metallized cores.

Using a chemical approach involving inverse microemulsions, it has been shown that small monodisperse polyaniline particles can be produced [100–102]. Inverse microemulsion polymerization of polyaniline by Chan et al. [101] was reported to give particles of 10–35 nm diameter that were spherical and could be synthesized using either the chemical or electrochemical route. The presence of stabilizing surfactant was found to be detrimental to the electrical conductivity of these particles when dried, due to formation of an insulating barrier around the nanoparticles in the bulk. After washing to remove the surfactant, chemically prepared materials exhibited conductivities of up to 10  $\text{S cm}^{-1}$  while for electrochemically prepared materials conductivities as high as 200  $\text{S cm}^{-1}$  were reported. Gan and co-workers have used [102] an inverse microemulsion approach that involves formation of barium sulfate nanoparticles, which are then coated by polyaniline. These composite nanoparticles had a reported conductivity from 0.017 to 5  $\text{S cm}^{-1}$ , with particles ranging in size from 10 to 20 nm. Xia and Wang [103] have used ultrasonication during inverse microemulsion polymerization of polyaniline to produce spherical nanoparticles with diameters of 10–50 nm and conductivities in the order of 10  $\text{S cm}^{-1}$ . The ultrasonication was found to increase the rate of polymerization of aniline which is typically slow when the microemulsion route is used. Rate increases are obtained by acceleration of the heterogeneous liquid–liquid chemical reactions in solution. A secondary advantage is the prevention of aggregation due to particle agitation induced by ultrasonication.

Polypyrrole nanotubes have also been synthesised via an inverse microemulsion self-assembly route by Jang and

Yoon [104]. Nanotubes were synthesised by using bis(2-ethylhexyl)sulfosuccinate (20.3 mmol) in hexane (40 mL) which form tube- or rodlike micelles, due to the presence of a double tail on a small hydrophilic head group, when aqueous  $\text{FeCl}_3$  (1 mL, 9.0 M) was added. The  $\text{Fe}^{3+}$  cations are effectively trapped in the center core of the micelle. Addition of pyrrole (7.5 mmol) to this solution then results in interfacial polymerization at the micelle surface, resulting in hollow nanotubes 95 nm in diameter and up to 5  $\mu\text{m}$  in length. The electrical conductivity of these nanotubes was up to 30  $\text{S cm}^{-1}$  and was observed to be a function of the  $\text{FeCl}_3$  oxidant concentration. More interestingly, the conductivity of these materials did not appear to be limited by the presence of the surfactant molecule, which in other emulsion polymerization routes tends to lead to a thick insulating coating that limits the observable conductivity.

### 2.3. Physical Templates

Conducting polymers have been grown within zeolites [105, 106]. With channels as small as 0.3 nm this allows assembly of single molecular wires. Conductivities of  $10^{-9}$   $\text{S cm}^{-1}$  for such wires contained within zeolites have been reported and this increases to  $10^{-2}$   $\text{S cm}^{-1}$  when the polymer is extracted from the host structure.

Martin and co-workers [107–109] have used controlled pore size membranes as templates to electrochemically grow fibrillar mats of ICPs. Similar structures have also been produced using nanoporous particle track-etched polycarbonate membranes with both polypyrrole [110–113] and polyaniline [114] via chemical and electrochemical techniques. The approach involves oxidation of the monomer within the pores of a template. This is achieved electrochemically as illustrated in Figure 13. The electrode substrate used can be either a conventional flat surface system such as solid gold, platinum, or glassy carbon, resulting in structures such as shown in Figure 14a. Alternatively, more novel electrode substrates such as platinized PVDF membranes with nominal pore size of 0.45  $\mu\text{m}$  can be used (Fig. 14b).

Carbon nanotubes (CNTs) have been directly synthesized via a template carbonization of polypyrrole on an alumina template membrane (Whatman Anopore) with 0.2  $\mu\text{m}$  diameter pores and 60  $\mu\text{m}$  in total thickness [115]. Polypyrrole was chemically deposited on and through the membrane

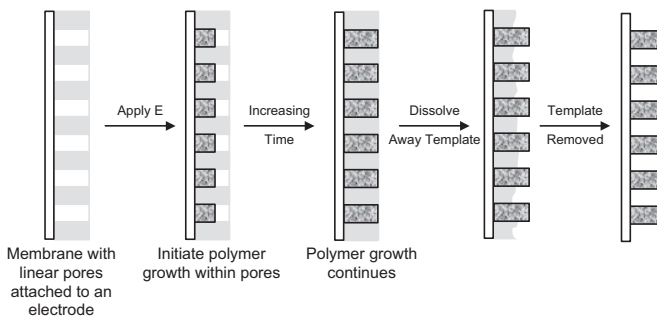


**Figure 13.** Assembly of fibrillar ICPs using controlled pore size templates. Reprinted with permission from [4], G. G. Wallace and P. C. Innis, *J. Nanosci. Nanotech.* 2, 441 (2002). © 2002, American Scientific Publishers.

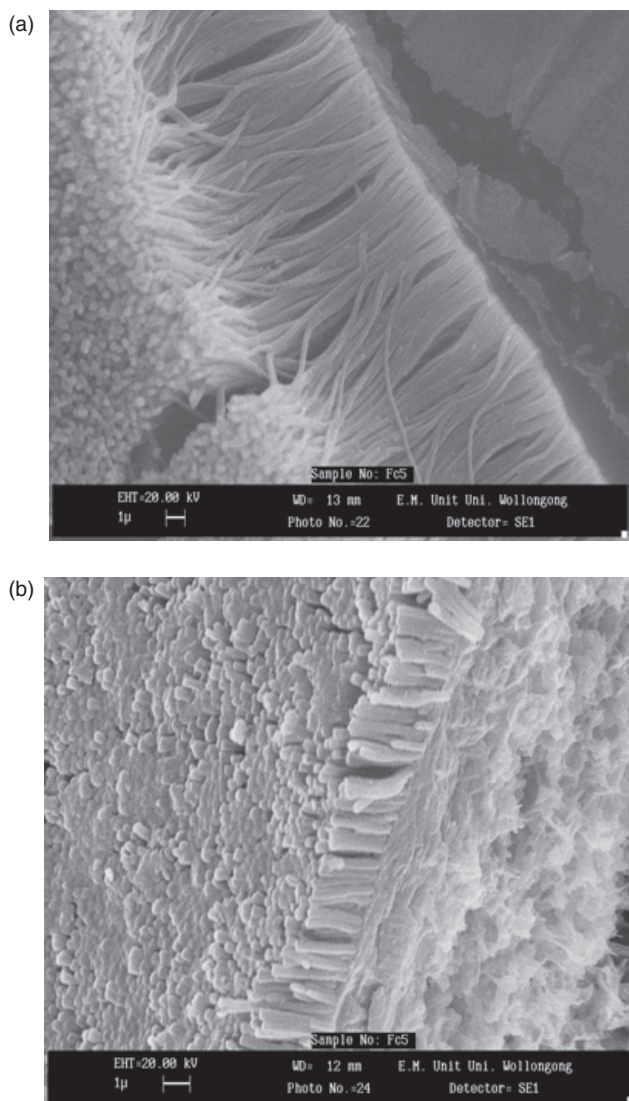


**Figure 14.** Scanning electron micrographs of fibrillar structure of PPy/pTS on (a) a flat electrode surface and (b) a PVDF membrane. Reprinted with permission from [188], V. Misoska, Ph.D. Thesis, University of Wollongong, 2002.

via a chemical oxidative process. Surface deposited polymer was removed by polishing with alumina powder and ultrasonication. This membrane was then carbonized in an Ar atmosphere and then etched in 48% HF to remove the alumina template. Metal CNTs impregnated with Pt, Pt–Ru, and Pt–WO<sub>3</sub> were prepared by treatment with the appropriate metal salt solutions prior to etching. The resulting CNTs were single wall type with diameters ranging from 1 to 5 nm. The application of these nanostructures as electrode substrates for methanol fuel cell was explored, utilizing the presence of dispersed metals such as Pt<sup>0</sup> and Ru<sup>0</sup> metal and W<sup>6+</sup> in the CNT, providing catalytic regions for methanol oxidation.

Freestanding nanotubes are formed by the selective dissolution of the templating membrane. Hollow tubes of polypyrrole are initially formed in the templating structure followed by the in-filling of these tubes at longer synthesis times. Electrical conductivities of these structures

(e.g., 375 S cm<sup>-1</sup> at 20 nm) show an enhancement over that of the bulk material (1.5 S cm<sup>-1</sup>) grown under similar conditions [110]. A similar conductivity enhancement effect based on tube diameter has also been reported by Cai et al. with conductivities up to 10<sup>3</sup> S cm<sup>-1</sup> [116, 117].

Applications of template-assisted growth of aligned polyaniline nanofibril arrays in the area of field emission have been explored by Wang et al. [118]. Nanofibril arrays were prepared by chemically depositing polyaniline into 20–200 nm pores in anodic aluminum oxide film 30 to 60 μm thick that was subsequently etched away with 0.3 M H<sub>3</sub>PO<sub>4</sub> or by ultrasonication [119]. Field emission studies revealed a low electric field threshold of 5–6 V/μm, with a minimum emission current density of ca. 0.01 mA/cm<sup>2</sup> and a maximum emission current density of 5 mA/cm<sup>2</sup>. Comparisons to other materials with lower emission current densities, such as diamond and CNTs, were made and the authors noted that aligned nanofibril arrays were attractive due to their high surface area, lower manufacturing cost, and robust mechanical properties.

Hollow ICP cigar-shaped nanotubes with sealed ends, synthesized via the track-etched polycarbonate template route, have also been reported by Mativetsky and Datars [113]. These materials exhibited a small drop in conductivity as the diameter decreased from 400 to 50 nm, contrary to the previous reports [110–112]. The small decrease in conductivity of the order of 50 mS cm<sup>-1</sup> is believed to result from an increase in the electron scattering within the nanocylinder walls or from the presence of large impedances in the nanostructure. The authors attributed this different dependence on tube diameter by treating the tube as a solid cylinder, resulting in conductivity trends observed by others, or as reported in this instance as a hollow nanostructure which gave these results.

Others have shown that the electrochemical properties of polyanilines grown in a template such as sol–gel silica or PVDF are greatly improved [120]. This is attributed to improved order at the molecular level.

Other templates used to assist assembly of nanostructured conducting polymers are synthetic opals [121–126] based on polystyrene or silica spheres. The area of synthetic opals is of interest for use as photonic bandgap crystals: materials in which photons of a given energy cannot travel through or propagate in a crystal but rather are reflected by the lattice structure [125]. Of further interest is that opal templates provide a route to establishing high range order in the nanodomain, resulting in high surface-to-volume ratios. Template opal structures (Fig. 15) are preformed from monodisperse spherical colloidal particles that are permitted to self-assemble into close packed arrays via a sedimentation process assisted by either gravity or pressure/microfiltration. After template formation, conducting polymer is formed by infiltration of monomer into the void spaces within the crystal structure, followed by subsequent oxidative polymerization. The final stage is the removal of the templating core to leave an inverse structure from the templating material with essentially the same optical properties as the original host [123] (Fig. 16). Others [121, 122] used a similar templating approach, but prepared self-assembled polystyrene (PS) latex opals onto gold substrates followed by the direct electropolymerization of PPy, PAN, and polybithiophene (PBT)



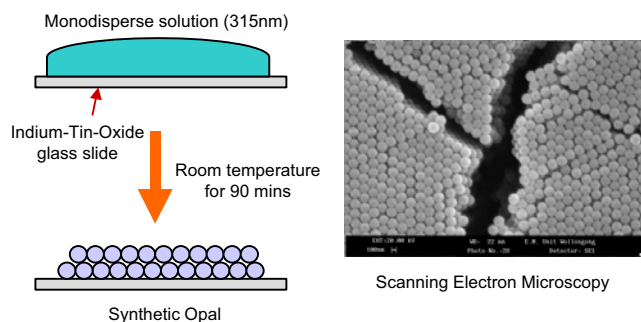


**Figure 15.** Self-assembly of opal structures onto electrode substrates via monodisperse colloidal dispersions. Reprinted with permission from [188], V. Misoska, Ph.D. Thesis, University of Wollongong, 2002.

into the interstitial void spaces of the host matrix. Upon removal of the PS, structural shrinkage was observed for PPy and PAN but PBT exhibited no such effect. Using this approach, interchanneling between adjacent template layers was evident, giving evidence for the formation of a three-dimensional (3D) macroporous nanostructure. Yoshino et al. [124] utilized  $\text{SiO}_2$  opal templates followed by the infiltration of soluble preformed poly(3-alkylthiophene) and poly(2,5-dialkoxy-*p*-phenylene vinylene) and finally removal of the  $\text{SiO}_2$  spheres by HF etching. These nanostructured materials were then investigated for photoluminescence (PL) and electroluminescence properties. A spectral narrowing of the PL and an increase in excitation intensity was observed with respect to the solution form of these polymers.

## 2.4. Molecular Templates

Distinctly different from the templating techniques described previously, this approach relies on the interaction at the molecular scale of the conducting polymer and a templating dopant or surfactant/polyelectrolyte to form a nanoparticle. The molecular template not only functions to direct morphology but it can also impart other properties to the ICP nanoparticle, as will be discussed.

Others have shown that molecular templates, such as a polyacrylate film predeposited on a carbon electrode, can be used effectively to create polypyrrole nanowires via electrochemical oxidation of pyrrole [127, 128].

Choi and Park [129] have modified surfaces with cyclodextrins to assist in the electroformation of polyaniline nanowires. Others have utilized the concept of molecular templates to form polyaniline supramolecular rods with electrical conductivity improved by 2 orders of magnitude [130].

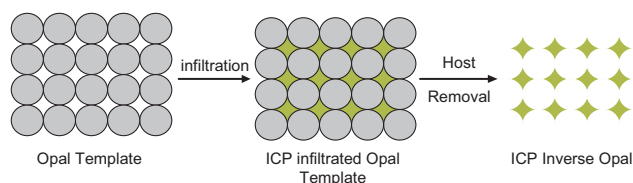


**Figure 16.** Schematic illustrating preparation of an inverse ICP opal using a synthetic opal template. Reprinted with permission from [4], G. G. Wallace and P. C. Innis, *J. Nanosci. Nanotech.* 2, 441 (2002). © 2002, American Scientific Publishers.

A template guided synthesis of water-soluble chiral conducting polyaniline in the presence of (S)-(-)- and (R)-(+)-2-pyrrolidone-5-carboxylic acid [(S)-PCA and (R)-PCA] has been reported to produce nanotubes [131]. The structures prepared have outer diameters of 80–220 nm with an inner tube diameter of 50–130 nm. It was proposed that the tubular structures form as a result of the interaction of the hydrophobic aniline being templated by the hydrophilic carboxylic acid groups of the PCA in aqueous media during chiral tube formation. The resultant tubes were shown to be optically active, suggesting that the polyaniline chains possess a preferred helical screw.

McCarthy et al. [132, 133] reported a template-guided synthesis of water-soluble chiral polyaniline nanocomposites. The nanoparticles were prepared by the physical adsorption of aniline monomer onto a templating poly(acrylic acid) in the presence of (+)- or (-)-CSA, followed by chemical oxidation. Using this approach, optically active nanocomposites of approximately 100 nm diameter were formed. Earlier work by Sun and Yang [134] using polyelectrolytes produced similar nonchiral dispersions in which the polyaniline chain is interwound with a water-soluble polymer by electrostatic forces [135]. Similar work by Samuelson et al. utilized DNA as a chiral template for polyaniline [89].

Shen and Wan [136] have shown that chemical oxidation of pyrrole (by APS) in the presence of  $\beta$ -naphthalene sulfonic acid ( $\beta$ -NSA) results in the formation of tubules down to ca. 200 nm in diameter. The tubular structures had reasonable conductivity ( $10 \text{ S cm}^{-1}$ ) and were soluble in *m*-cresol. In later work [137] it was reported that the morphology was significantly influenced by the concentration of the  $\beta$ -NSA. Granular morphologies were present when  $[\beta\text{-NSA}]$  was less than 0.2 M, while on increasing the  $\beta$ -NSA concentration fiber formation becomes the dominant morphology. At  $\beta$ -NSA concentrations above 2.9 M, a block-type morphology predominated with an associated drop in conductivity to  $2 \text{ mS cm}^{-1}$ . Monomer concentration was shown to have little effect on the resultant morphology and electrical conductivity. The morphological steps in tube formation were described as grain to short tube to long tube. Other morphology types have also been noted using the  $\beta$ -NSA anion, namely hollow microspheres ranging from 450 to 1370 nm (with inner wall thicknesses of 20 to 250 nm, respectively) and conductivities of up to  $190 \text{ mS cm}^{-1}$  [138]. A similar approach has been extended to polyaniline [139]. The influence of a secondary inorganic acid codopant has also been demonstrated, with conductivities from  $10^{-1}$  to  $10^0 \text{ S/cm}$  [140]. Others [141] have used lipid tubules as templates during chemical oxidation of pyrrole to form nanofibers with diameters between 10 and 50 nm and lengths reaching up to several hundred micrometers.

The concept of using molecular templates has been taken a step further by Zhang and Wan [142] by the incorporation of 10 nm  $\text{Fe}_3\text{O}_4$  nanomagnet particles into the  $\beta$ -NSA nanorods and nanotubes that are 80–100 nm in diameter. These PANi- $\beta$ -NSA/ $\text{Fe}_3\text{O}_4$  nanostructures were observed to exhibit superparamagnetic behavior (i.e., hysteresis loop effects). More importantly, both the electrical conductivity and magnetic properties of these nanoparticles could be

manipulated by control over the loading level of the nano-magnetic particles. Increased loading of the  $\text{Fe}_3\text{O}_4$  nanoparticle decreased the conductivity from ca.  $70 \text{ mS cm}^{-1}$  for no loading to ca.  $10 \text{ mS cm}^{-1}$  at 20 wt%, while inducing superparamagnetic behavior in the nanocomposite.

Self-assembled polyaniline nanofibers and nanotubes, which also exhibit photoisomerization functionality, have been described by Huang and Wan [143] using azobenzene-sulfonic acid (ABSA) as the molecular templating surfactant, dopant, and photoactive agent. Nanostructures formed were similar to those by Wan et al. [131, 136, 138, 140, 142] discussed previously, with diameters of 110–130 nm and fiber lengths of 3–8  $\mu\text{m}$ . The photoinduced isomerization, from *trans* to *cis*, of the ABSA dopant was observed by UV-vis spectroscopy at 430 nm ( $n-\pi^*$  transition) after irradiation of the nanocomposites at 365 nm (over 0, 2, 6, 10, and 12 min) by UV-vis spectroscopy from 300 to 800 nm. The photoisomerization of the composite material was observed to be slower than for ABSA due to steric hinderance as a result of the *trans*-ABSA interacting along the polymer backbone.

## 2.5. Nontemplated Routes

There are a number of synthetic routes that are capable of producing nanoparticles in the absence of a precursor substrate or a molecular template.

For example, He and co-workers [144] have described a technique wherein polyaniline is deposited between two nanoelectrodes to form a nanojunction. As the junction is decreased in size to just a few nanometers, abrupt switching characteristics are observed as opposed to the more gradual transition observed during electrochemical switching of polyaniline structures with larger dimensions. A further report from the same laboratory [145] added a new dimension by initiating growth of polyaniline between a scanning tunneling microscope (STM) tip and a gold substrate. The STM tip was modified to allow only a few nm to take part in the growth of the nanowire. During growth the tip and substrate were monitored at 20–100 nm resolution. After growth the nanowire could be stretched by moving the STM tip to produce wires up to 200 nm in length and with diameters as low as 6 nm. These structures had conductivities of about  $5 \text{ S cm}^{-1}$ .

Electrodeposition of polyaniline containing  $[\text{C}_{60}]$  fullerene as dopant [146, 147] has been shown to result in 2D or 3D fibrillar structures [147, 148]. Diameters from 10 to 100 nm with fibril lengths of up to 3000 nm were observed. The fibrillar network had conductivities in the range  $10\text{--}100 \text{ S cm}^{-1}$ . Two-dimensional networks have been prepared using pulsed potential techniques while 3D networks were observed to form over longer synthesis times. Via this approach there is apparent control over the density of contact points for the individual nanonetworks.

Others [148] have used electron beam lithography to create polythiophene-based nanopatterns with linewidths down to 50 nm and gaps of 10 nm. They have shown that after exposure to a 50 kV electron beam poly(3-octylthiophene) becomes less soluble in chlorobenzene, enabling development of nanotracks that have conductivity of the order of  $1 \text{ S cm}^{-1}$ .

Electrospinning [149, 150] is another recent nontemplated method. This simple approach is based on the electrostatic fiber spinning of composite fibers of polyaniline with polyethylene oxide, polystyrene, or polyacrylonitrile. These fibers are formed when a high electric field (5–14 kV) is placed between the tip of a metallic anodic spinning needle loaded with the dissolved polymer solution (0.5–4 wt% PAN and 2–4 wt% host polymer) and an opposing cathode plate separated by 20 cm. The presence of the high electric field results in the surface tension of the polymer-loaded solution at the needle tip to be exceeded, expelling a polymer fiber from the surface toward the opposing cathodic plate. The transit time from the anode tip to the cathode plate is accompanied by a desolvation and drying process in part assisted by the electrostatic charges placed upon the solvent molecules causing electrostatic repulsion. The resulting nanofiber composite is reported to have lengths in the meter range and is collected as an interwoven mesh with large surface-to-volume ratios ( $\sim 10^3 \text{ m}^2/\text{g}$ ). These fibers are ohmic in nature. Fiber dimensions of less than 100 nm have been routinely produced by this technique. More recently [149] fibers of PAN have been directly spun from a 20 wt% solution of PAN (Versicon<sup>TM</sup>) in 98% sulfuric acid at 5 kV. The electrospinning method has also been extended to produce continuous polyaniline/polyethylene oxide monofilament nanofibers down to 60 nm diameter at a maximum spin rate of 1130 m/min and a conductivity of  $33 \text{ S cm}^{-1}$  [151].

Aligned polymer nanowire structures have been developed using an electrochemical deposition technique to form aligned polyaniline arrays on smooth and textured electrode substrates without the need for a porous templating structure [152, 153]. Oriented polymer nanowires were formed using a preprogrammed constant-current deposition method where the current density was stepped down throughout the nanowire growth. In the initial stage of nanowire growth, 50 nm polymer nuclei were deposited from an aqueous electrolyte containing 0.5 M aniline and 1.0 M perchloric acid at a current density of  $0.08 \text{ mA cm}^{-2}$  over 30 min. The current density was subsequently stepped down over a 3 hr period from 0.04 to  $0.02 \text{ mA cm}^{-2}$ . Extended polyaniline growth in the initial nucleation phase resulted in the formation of a thick polymer deposit with randomly oriented, thick-branched polymer structures over the surface. Typical nanowire structures had diameters for 50 to 70 nm and lengths of approximately 0.8  $\mu\text{m}$ . Complex surface geometries have been demonstrated using this technique where nanowires have been deposited onto ordered silica spheres deposited onto the electrode substrate as well as onto textured surfaces to produce hierarchical structures. The potential for these surfaces in chemical sensing has been demonstrated for  $\text{H}_2\text{O}_2$  detection utilizing iron(III) hexacyanoferrate nanoparticle catalysts supported by the nanowire structure.

Polypyrrole nanowire have also been electrochemically synthesized on graphite/paraffin composite electrodes from a 0.2 M phosphate buffer (pH 6.86) electrolyte containing 0.2 to 2.0 M lithium perchlorate and 0.1 to 0.5 M pyrrole [154]. Nanowires were grown by cyclic voltammetry and potential step methods. Nanorod growth is directed by inducing microstructure at the electrode surface. This was achieved by predigesting the graphite rod electrode in

boiling 10% hydrochloric acid and then boiling 10% nitric acid for 30 min, respectively, resulting in a porous graphite rod surface which was subsequently in-filled with paraffin at 150 °C and finally polished. The resultant electrode surface was covered with nitro-groups to which the pyrrole monomer selectively adsorbs providing a nucleation zone for nanotube formation. The resultant tubes were unaligned and irregularly dispersed across the surface as an entangled mesh with diameters of ca. 50–200 nm.

Thin 50 to 100 nm freestanding polypyrrole nanofilms have been synthesized utilizing oxidative interfacial polymerization at a water–chloroform interface [155]. Thicker 3 to 4  $\mu\text{m}$  polypyrrole films have been produced via this method [156]. Control over the final film thickness was achieved by removal of the immiscible solvents from above and below the nucleating film after a few minutes of polymerization. Stirring of the interfacial solutions resulted in the inhibition of polymer nucleation at the interface. Thin 5 nm polypyrrole films on mica and graphite surfaces have been formed via a admicellar polymerization route [157]. The thin films were formed due to the surfactant (CTAB and SDS) in solution adsorbing to the substrate surface as a thin film micelle containing the pyrrole monomer, which was subsequently polymerized by ferric chloride solution. On the graphite surface the polypyrrole morphology consisted of thin discs and interlinked islands. On the mica surface the morphology consisted of randomly scattered islands with no continuous film formation evident.

Dip-pen nanolithography has been performed on a number of surfaces via a coated atomic force microscope (AFM) tip at the 130 nm scale up to several micrometers using SPAN as the writing ink [158]. Transfer of the conducting polymer ink from the AFM tip to the substrate is achieved via capillary action upon tip contact to the substrate surface with 0.5 nN contact force. The deposited SPAN tracks were found to electroactive.

Near-field optical lithography has also been performed to draw nanostructures of poly(*p*-phenylene vinylene) (PVP) using light delivered from a scanning near-field fiber probe, with a 40 or 80 nm optical aperture, on a scanning near-field optical microscope AFM device [159]. Polymer features are drawn by exposing the PVP soluble precursor to ultraviolet light (325 nm HeCd laser, 0.2 mW at the sample surface) rendering the exposed precursor insoluble and permitting the dissolution of the remaining polymer. Following chemical conversion for the exposed PVP precursor a fully conjugated polymer can be achieved. Two-dimensional photonic crystal arrays have been demonstrated by this method with pillars 32 nm tall, 200 nm wide (at half height) and a lattice constant of 333 nm (ca.  $30 \times 30$  dot lattice).

## 2.6. Nanocomposites

The final approach to be reviewed involves the use of preformed nanosized structures to assist in the formation of ICPs with nanodimensions. For example, Pope and co-workers introduced the concept of using silica nanoparticles to stabilize inherently conducting polymers [160]. We subsequently used this approach to produce polyaniline based silica nanocomposites [161] using an electrohydrodynamic synthesis technique. The electrochemical approach allows

direct incorporation of a wide range of dopants, including in this case the optically active camphor sulfonate ion to produce chiral particles with nanodimensional ICPs incorporated therein (Fig. 17).

Applications of conducting polymers to nanosized semiconductor particles, commonly referred to as quantum dots, have also been made to produce nanocomposite materials [162]. These materials are typically spherical semiconductor crystals of 5 to 10 nm in size, such that quantum confinement effects predominate within these structures. At this size, these nanocrystals have special optical and electronic properties resulting from these quantum effects. A prime application of these materials is that tight size control will influence the onset of absorption and the fluorescence wavelength, thereby affecting the color of the observed particles in solution. CdS and  $\text{Cu}_2\text{S}$  quantum dots were coated by mixing into an *N*-methylpyrrolidone (NMP) solution containing the EB form of polyaniline. Extended exposure of the EB to these nanoparticles resulted in the oxidation of the EB to the pernigraniline base form. Co-precipitation of the EB and nanocrystals in NMP was achieved by the addition of ethanol. For CdS, electron transfer from the polymer to the nanocrystals is energetically favorable. Similarly, excitons created on the nanocrystals can also be transferred to the polymer resulting in an electron on the nanoparticle and an electron hole in the polymer. This creates a potential to control the performance of photovoltaic devices by altering the nanocrystal's size and concentration.

In another example, Bremer and co-workers [163] polymerized polyaniline onto nanodimensional polyurethane particles dispersed using a steric stabilizer (Fig. 18). We

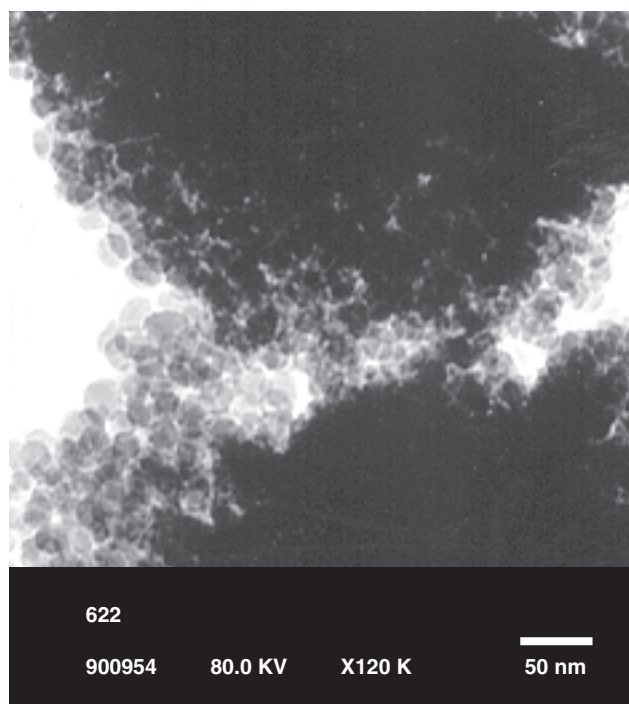


**Figure 17.** High magnification transmission electron micrograph of PAN-(+)-HCSA/silica nanocomposites. Adapted with permission from [16], V. Aboutanos et al., *Synth. Met.* 106, 89 (1999). © 1999, Elsevier Science.



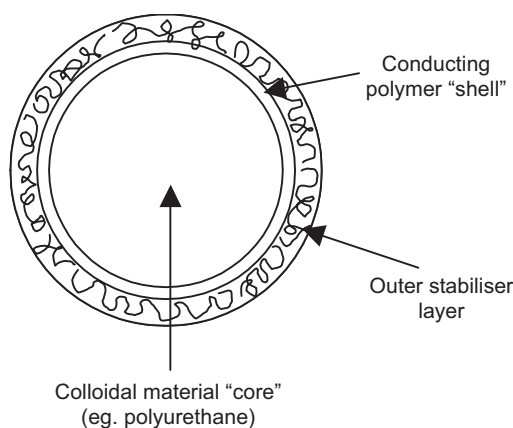


**Figure 18.** Cor-shell nanoparticles. Reprinted with permission from [4], G. G. Wallace and P. C. Innis, *J. Nanosci. Nanotech.* 2, 441 (2002). © 2002, American Scientific Publishers.

adapted this approach to produce highly optically active nanoparticles (20 nm) based on polyaniline doped with (+)-camphor sulfonate coated onto polyurethane particles [164].

A major disadvantage of using this approach is that these structures commonly aggregate to form raspberry-like structures during the polymerization process [161]. In an attempt to minimize this affect, Xia and Wang synthesized polyaniline nanosilica [165] and nanocrystalline titanium oxide composites [166] while applying ultrasonic irradiation during the chemical polymerization process. Although aggregation was evident, the resultant nanoclusters of 60 to 120 nm were obtained from the initial 15 to 40 nm SiO<sub>2</sub> cores. Similar results were observed for PAN-TiO<sub>2</sub> nanocomposites. Other morphologies that resulted from the ultrasonication included thread-like and sandwich-like aggregated structures.

Nanocomposites have also been fabricated utilizing aqueous vanadium or iron oxide sols and polyaniline to produce particles characterized by X-ray crystallography as ca. 9 and 13 nm in diameter, respectively [167]. Strong interaction between the inorganic V<sub>2</sub>O<sub>5</sub> core and its polyaniline shell indicates that the PAN-V<sub>2</sub>O<sub>5</sub> nanoparticle functions as an intercalation compound, with electron transfer from the unshared electron pair of the nitrogen atom to the V<sup>5+</sup> ion evidenced by electron paramagnetic resonance (EPR) spectroscopy. In the case of a Fe<sub>3</sub>O<sub>4</sub> core, the ferromagnetic character of the Fe<sub>3</sub>O<sub>4</sub> was the dominating feature of the EPR spectrum. However, infrared spectroscopy indicated that electronic interactions are occurring between the Fe<sub>3</sub>O<sub>4</sub> core and the conducting polymer shell.

Recent work aimed at other objectives may also provide an interesting route to the production of ICP-containing nanocomposites: this is in the use of CNTs as host “particles.” CNTs in their own right possess interesting electronic properties and when combined with other conjugated polymers synergistic effects have been observed [168, 169]. Our studies have focused on the use of aligned carbon nanotubes as templates for ICP deposition. Our recent work in this area [170] has revealed significant improvements when PPy glucose oxidase is coated onto aligned CNTs for use as biosensors (Fig. 19). We have also shown that ICPs can be highly effective dispersants for CNTs, presumably attaching

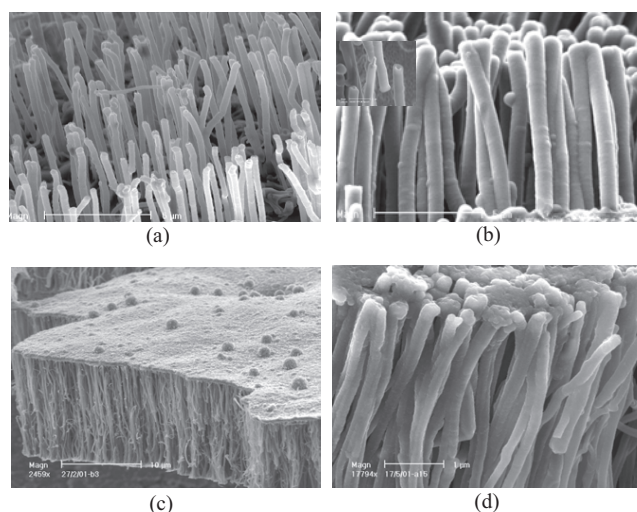


**Figure 19.** Aligned carbon nanotubes with a bioactive conducting polymer. (a) Pure CNT array before treatment. (b) Aligned CP-CNT coaxial nanowires; inset shows clear image of single tube coated with PPY. (c) PPY only deposited on the top of CNT surface due to high density of tubes. (d) Polymer formed on both outside of walls and the top of the surface of the CNT array. Reprinted with permission from [170], M. Gao et al., *Electroanalysis*, 15, 1089 (2003). © 2003, Wiley-VCH.

themselves to the CNT structure. The properties of these novel dispersants of nanomaterials are yet to be investigated.

The molecular template concept used to produce polyaniline nanotubes [136] (as discussed) has also been used prepare to sulfonated multiwalled carbon nanotubes [171]. In this instance, the sulfonated nanotube surface serves a dual role acting as an *in-situ* dopant for the polyaniline as well as providing a supramolecular template onto which the anilinium ions in solution bind. Polymerization therefore occurs predominantly at the sulfonated nanotube surface. The resultant hybrid structure consists of a 10 nm thick polyaniline coating on the CNT surface, providing a novel way of introducing and functionality of to CNTs.

## 2.7. ICP Surfaces for Facilitating Metal Nanoparticle Growth

Utilizing ICPs as potential platforms for supporting nanoscale structures has been investigated to provide novel supported catalysts. The concept of embedded metal nanoparticles was recently presented by Zhou et al. [98, 99]. In this instance the metal nanoparticles were embedded in the polymer matrix and therefore protected from the chemical environment. Wang and co-workers [172] employed a similar approach by chemical reduction of AuCl<sub>3</sub> or Pd(NO<sub>3</sub>)<sub>2</sub> by polyaniline powder in either aqueous dispersions or in NMP, a common solvent for the EB form of PAN. Reduction of palladium nanoparticles was slow with EB; hence the polyaniline was initially reduced to the leucoemeraldine base form in order to facilitate reduction of the Pd<sup>2+</sup> to its metallic state. The nanoparticle sizes for the Au and Pd were observed to be 20 nm from NMP solution and 50–200 nm from polyaniline powder. Gold-polyaniline nanocomposites have been prepared by the chemical reduction of

$\text{HAuCl}_4$  and simultaneous polymerization of aniline to produce 26 nm Au nanoparticles dispersed in the polyaniline powder matrix [173].

Platinum and platinum oxide nanoparticles, 4 nm in size, have been successfully deposited onto polypyrrole/polystyrene sulfonate colloidal dispersions (with dimensions ranging from 30 to 1000 nm) [174] for use as catalysts.  $\text{Pt}(\text{NH}_3)_4\text{Cl}_2$  and  $\text{Na}_6\text{Pt}(\text{SO}_3)_4$  metal salts were reduced by formaldehyde or  $\text{H}_2\text{O}_2$  respectively in order to form Pt nanoparticles on the ICP colloid surface. These nanocomposite dispersions have been reported to be effective catalysts for oxygen reduction in a proton exchange membrane fuel cell, indicating that the metal catalytic particles are accessible for chemical interaction.

Polythiophene has also been investigated as a potential substrate for the formation of catalytic platinum nanoparticles, 2–4 nm in size, for oxygen reduction. The Pt nanoparticles were homogeneously deposited across a predeposited polythiophene film by direct electrodeposition from a solution of 12.5 M  $\text{H}_2\text{SO}_4$  and 4 mM  $\text{H}_2\text{PO}_4$ . The resulting composite was produced in a similar fashion as other electrocatalysts such as carbon-supported platinum.

### 3. UNIQUE PROPERTIES AND APPLICATIONS OF INHERENTLY CONDUCTING POLYMERS NANOSTRUCTURES

As ICPs approach nanodimensions a number of trends become evident which involve either the preservation of the bulk properties of the ICP and/or the enhancement of the properties of the nanomaterial such as conductivity. Some of these influences of nanostructure reported in the literature are discussed.

He et al. [144, 145] have created a conducting polymer nanojunction switch with abrupt switching characteristics that are attributed to a single nanocrystalline domain in which the individual polymer strands collectively undergo the usual insulator–conductor transition.

Nanoelectronics will be an expanding area of application for ICPs. A recent example has been illustrated for the fabrication of organic photodiodes and light emitting diodes [175]. Fullerene derivatives grafted onto soluble polythiophene, based upon the PEDOT system, have been utilized to form an integrated donor–acceptor polymer system. Nanopatterned electrodes were prepared by using a silicone rubber replica stamp which was used to transfer an organic resist image of an optical grating (280 nm periodicity) on top of a metal film. This film was subsequently etched to form a nanopatterned metal electrode substrate, onto which the polymer was cast forming the electronic device. Short sub-micrometer/nanoscale distances between the metallic electrodes were important due to the polymer layer having a low charge carrier mobility (exciton), emphasizing the importance of nanofabrication for these devices.

Numerous reports have discussed the fact that nanocomponents have inherently greater conductivity than the macroscopic analog [111]. This is not surprising given the model described by Epstein [176] and Kaiser [177] in which the bulk properties of ICPs arise from crystalline (highly

conductive) nanodomains in a sea of amorphous (less conductive) material. A number of experimental approaches [178] have been used to verify the presence of these domains.

Formation of these nanodomains provides us with a unique opportunity to access these regions of high order and subsequently higher conductivity. A challenge in accessing enhanced electrical properties is that many approaches for the formation of nanoparticles require the use of an insulating surfactant. This was noted by Chan et al. [101] where removal of the insulating surfactant required for nanoparticle formation caused the conductivity to increase. Others [179] have shown that dramatic improvements in specific capacitance for polythiophene tubules can be obtained, increasing from 4 C/g polymer for a flat film up to 140 C/g polymer and 148 C/g polymer for micro- and nanotube formations, respectively.

The realization of efficient photovoltaic devices based on inherently conducting polymers also depends on the ability to control structure at the nanodimension [180, 181]. Such materials generate electron/hole pairs (excitons) upon irradiation. The ability to generate electricity from these charge pairs depends on our ability to split these charges at appropriate interfaces. Unfortunately, the lifetime of excitons is short and only those formed within 10 nm of an interface will ever reach it. The development of efficient nanostructures is therefore critical to this area.

Metallic nanoparticles exhibit well-documented phenomena of surface plasmon absorption processes where the free electrons at the surface of the nanoparticle generate a dipole moment to interact with visible wavelengths [182, 183] when the particle is too small itself to interact with light by Bragg scattering processes. It has been reported that the surface plasmon absorption can interact with an encapsulating  $\pi$ -conjugated polymer when it is oxidized [98, 99]. This interaction is reported to be due to the direct electronic communication of the surface electrons of the metal nanoparticle with the encapsulating polymer. The result of this interaction is a redshift of the optical plasmon absorption band with respect to a lone metal nanoparticle. This shift in absorption can be achieved by an aggregation process of the metal nanoparticle, but no such aggregation was evident implying direct electronic interaction with the polymer and metal electron.

Xia and Wang [103] elegantly demonstrated the advantages and pitfalls to be encountered as we enter the nanoworld. As particle size decreases the degree of doping and crystallinity increases, with a concomitant increase in conductivity. They also showed crystalline domain sizes ranging from 10 to 40 nm and that as size decreases lattice defects may occur causing the crystalline structure to be broken due to the smaller size.

An industrial application of polyaniline utilizing nanodispersions of the ICP into corrosion inhibiting paint latexes has been developed whereby 70 nm particles are dispersed to form a self-organised complex of ultrafine network [184]. For a number of years it has been demonstrated that ICPs can impart corrosion resistance to metal substrates. When these nanoparticles have been melt dispersed with a loading of 1% w/v in paint, the composite material is observed to have similar metallic properties to the bulk

material. This arises due to the nanoparticle forming a network structure permitting electron tunneling via a continuous conducting pathway [185]. A clear advantage of utilizing these nanodispersions is that a similar corrosion inhibitor activity is achieved to that found using larger particle sizes, requiring higher polymer loading, or coated films.

Mandal has shown that the use of polyaniline nano-components results in extraordinarily low (0.03 vol%) percolation thresholds in polyvinylalcohol [186].

Polypyrrole-iron oxide nanocomposites have been prepared for application as humidity and gas sensors [187]. Improved sensor sensitivity is achieved by increasing the surface area based upon microstructure. By this approach nanoparticles were prepared by the reaction of ferric nitrate and methoxyethanol in the presence of pyrrole to produce a nanostructured aggregate with the appropriate morphology and surface area to function as a sensor.

Recently we have used aligned carbon nanotube platforms to fabricate inherently conducting polymer based biosensors with excellent performance characteristics [170].

## 4. CONCLUSIONS

The unique properties of materials brought about by control of structure at the nanodimension have generated much excitement in the research community in recent times. Those of us interested in the modification and efficient utilization of inherently conducting polymers have not escaped the nanotechnology euphoria.

Potentially, the benefits to be reaped from control of the ICP structure from the nanoscale to the microdomain and beyond are substantial. The more highly ordered structures obtained are expected to yield novel electronic, electrochemical, mechanical, chemical, and photoelectrochemical properties. Researchers have developed innovative strategies and approaches that enable controlled dimension nanocomponents to be produced. As with all areas of nanotechnology, the challenge is to assemble these nanocomponents into devices or structures that display the benefits of nanodimensional control.

## GLOSSARY

**Dopant** An anionic additive incorporated into the matrix of an inherently conducting polymer to provide electrostatic neutrality to the cationic charges on the polymer backbone and to modulate the electrical properties of the polymer.

**Emeraldine (salt or base)** The half oxidized state of polyaniline. When protonated as the salt polyaniline is conducting. As the base the polymer is an insulator or poorly conducting.

**Inherently conducting polymer** A polymeric material which conducts and electrical current by means of its electronic structure, namely via  $\pi$ -bond conjugation along the polymer backbone, and has no other conducting fillers added. Conductivity can be modulated by the addition of dopant anions to the polymer matrix and controlling the polymer oxidation level.

**Leucoemeraldine (base)** The fully reduced and insulating form of polyaniline.

**Monomer** A single repeat unit within a polymer chain structure.

**Pernigraniline (salt or base)** The fully oxidized and non conducting form of polyaniline.

**Polyelectrolyte** A polymer which has either anionic or cationic functionality attached directly to or as a part of the monomer repeat unit. Anionic or cationic character can be controlled by the number of repeat units, with these functionalities, incorporated into the polyelectrolyte structure.

**Polymerization** The process whereby single monomer units are reacted to form a larger continuous molecular chain structure.

**Redox** Reduction (electron loss) and oxidation (electron gain) processes.

## REFERENCES

1. G. M. Spinks, P. C. Innis, T. W. Lewis, L. A. P. Kane-Maguire, and G. G. Wallace, *Mater. Forum* 24, 125 (2000).
2. D. deLeeuw, *Physics World* 31 (1999).
3. F. Hide, M. A. Diaz-Garcia, B. J. Swartz, and A. J. Heeger, *Acc. Chem. Res.* 30, 430 (1997).
4. G. G. Wallace and P. C. Innis, *J. Nanosci. Nanotech.* 2, 441 (2002).
5. B. L. Groenendaal, F. Jonas, D. Freitag, and H. Pielartzik, *Adv. Mater.* 12, 481 (2000).
6. M. R. Smyth, H. Zhao, and G. G. Wallace, *TrAC* 18, 245 (1999).
7. R. H. Baughman, *Synth. Met.* 78, 339 (1996).
8. T. W. Lewis, S. E. Moulton, G. M. Spinks, and G. G. Wallace, *Synth. Met.* 85, 1419 (1997).
9. A. C. Partridge, C. B. Milestone, C. O. Too, and G. G. Wallace, *J. Memb. Sci.* 152, 61 (1999).
10. D. Zhou, C. O. Too, A. M. Hodges, A. W. H. Mau, and G. G. Wallace, *Reactive Functional Polymers* 45, 217 (2000).
11. B. Garner, A. Georgevich, A. J. Hodgson, L. Liu, and G. G. Wallace, *J. Biomed. Mater. Res.* 44, 121 (1999).
12. B. Garner, A. J. Hodgson, P. A. Underwood, and G. G. Wallace, *J. Mater. Sci. Mater. Med.* 10, 19 (1999).
13. T. A. Skotheim, R. C. Elsenbaumer, and J. R. Reynolds (Eds.), "Handbook of Conducting Polymers" 2nd ed. Dekker, New York, 1998.
14. J. N. Barisci, R. Stella, G. M. Spinks, and G. G. Wallace, *Synth. Met.* 124, 407 (2001).
15. T. Hernandez-Perez, M. Morales, N. Matina, and M. Salmon, *J. Electrochem. Soc.* 148, C369 (2001).
16. A. B. Kaiser, *Adv. Mater.* 13, 927 (2001).
17. J. Too, S. M. Long, J. P. Pouget, E. J. Oh, A. G. MacDiarmid, and A. Epstein, *Phys. Rev. B* 57, 9567 (1998).
18. P. Chandrasekhar, "Conducting Polymers: Fundamentals and Applications," Kluwer, Boston 1999.
19. G. G. Wallace, G. M. Spinks, P. R. Teasdale, and L. A. P. Kane-Maguire, "Conductive Electroactive Polymers: Intelligent Material Systems," 2nd ed. CRC Press, Boca Raton, 2003.
20. A. Deronzier and J. C. Moulet, *Coord. Chem. Rev.* 147, 339 (1996).
21. B. R. Saunders, K. S. Murray, R. J. Fleming, and Y. Karbathieh, *Chem. Mater.* 5, 809 (1993).
22. P. Weng and Y. Li, *J. Electroanal. Chem.* 408, 77 (1996).
23. E. Simon, E. Sable, H. Handel, and M. Litter, *Electrochim. Acta* 45, 855 (1999).
24. M. Boopathi, M. S. Won, Y. H. Kim, S. C. Shin, and Y. B. Shim, *J. Electrochem. Soc.* 149, E265 (2002).
25. S. W. Huang, K. G. Neoh, E. T. Kang, H. S. Han, and K. L. Tan, *J. Mater. Chem.* 8, 1743 (1998).

26. S. W. Huang, K. G. Neoh, C. W. Shih, D. S. Lim, E. T. Kang, H. S. Hen, and K. L. Tan, *Synth. Met.* 96, 117 (1998).
27. K. S. Ryder, D. G. Morris, and J. M. Cooper, *Biosensors Bioelectron.* 12, 721 (1997).
28. G. G. Wallace and L. A. P. Kane-Maguire, *Adv. Mater.* 14, 953 (2002).
29. Z. Huang, P. C. Wang, J. Feng, A. G. MacDiarmid, Y. Xia, and G. M. Whitesides, *Synth. Met.* 85, 1375 (1997).
30. H. Zhao, W. E. Price, and G. G. Wallace, *J. Memb. Sci.* 87, 47 (1994).
31. J. Y. Lee, D. Y. Kim, K. T. Song, S. Y. Kim, and C. Y. Kim, *Mol. Cryst. Liq. Cryst.* 280, 135 (1996).
32. J. Y. Lee, D. Y. Kim, and C. Y. Kim, *Synth. Met.* 74, 103 (1995).
33. S. A. Ashraf, F. Chen, C. O. Too, and G. G. Wallace, *Polymer* 37, 2811 (1996).
34. P. Godillot, H. Korri-Youssoufi, P. Srivastava, A. Kassmi, and F. Garnier, *Synth. Met.* 83, 117 (1996).
35. P. M. Murray, G. Spinks, G. G. Wallace, and R. Burford, *Synth. Met.* 874, 847 (1997).
36. L. Zhou, S. Jin, and G. Xue, *Macromol. Chem. Phys.* 197, 3309 (1996).
37. K. Faid, R. Cloutier, and M. Leclerc, *Synth. Met.* 55, 1272 (1993).
38. B. Krische, M. Zagorska, and J. Hellberg, *Synth. Met.* 58, 295 (1993).
39. C. Visy, J. Lukkari, and J. Kankare, *Macromolecules* 27, 3322 (1994).
40. M. Fall, J. J. Aaron, N. Sakmeche, M. M. Dieng, M. Jouini, S. Aeiyaich, J. C. Lacroix, and P. C. Lacaze, *Synth. Met.* 93, 175 (1998).
41. C. Lagrost, J. C. Lacroix, S. Aeiyaich, M. Jounini, K. Chane-Ching, and P. C. Lacaze, *Chem. Comm.* 489 (1998).
42. D. Singh, S. Dubey, B. M. Prasad, and R. A. Misra, *J. Appl. Polym. Sci.* 73, 91 (1999).
43. J. Ding, W. E. Price, S. F. Ralph, and G. G. Wallace, *Synth. Met.* 110, 123 (2000).
44. J. Pencali, *J. Mater. Chem.* 9, 1875 (1999).
45. A. K. Burrell, J. Chen, G. E. Collis, D. K. Grant, D. L. Officer, C. O. Too, and G. G. Wallace, *Synth. Met.* 135, 97 (2003).
46. S. A. Chen and C. C. Tsai, *Macromolecules* 26, 2234 (1993).
47. H. A. Ho, H. Brisset, E. H. Elandaloussi, P. Fiere, and J. Roncali, *Adv. Mater.* 8, 990 (1996).
48. P. Miao, C. Y. Zhang, H. S. O. Chan, and S. C. Ng, *Macromol. Chem. Phys.* 202, 1 (2001).
49. E. M. Genies, C. Tsintavis, and A. A. Syed, *Mol. Cryst. Liq. Cryst.* 121, 181 (1985).
50. E. M. Genies, A. Boyle, M. Lapkowski, and C. Tsintavis, *Synth. Met.* 36, 139 (1990).
51. D. E. Stilwell and S.-M. Park, *J. Electrochem. Soc.* 135, 2254 (1998), and references cited therein.
52. T. L. Porter, D. Minove, and A. G. Sykes, *J. Vac. Sci. Technol.* 1286 (1995).
53. S. Mu and J. Kan, *Synth. Met.* 92, 149 (1998).
54. K. Hyodo and M. Nozaki, *Electrochim. Acta* 33, 165 (1988).
55. L. Sun, H. Liu, R. Clark, and S. C. Yang, *Synth. Met.* 84, 67 (1997), and references cited therein.
56. M. Angelopoulos, M. Patel, J. M. Shaw, N. C. Labianca, and S. A. Rishton, *J. Vac. Sci. Technol. B* 11, 2794 (1993).
57. S.-A. Chen and H.-T. Lee, *Macromolecules* 28, 2858 (1995).
58. W. Liu, A. L. Cholli, R. Nagarajan, J. Kumar, S. K. Tripathy, F. F. Bruno, and L. Samuelson, *J. Am. Chem. Soc.* 121, 11345 (1999).
59. R. Nagarajan, W. Liu, J. Kumar, S. K. Tripathy, F. F. Bruno, and L. Samuelson, *Macromolecules* 34, 3921 (2001).
60. Y. Cao, P. Smith, and A. J. Heeger, *Synth. Met.* 48, 91 (1992).
61. P. J. Kinlen, J. Liu, Y. Ding, C. R. Graham, and E. E. Remsen, *Macromolecules* 31, 1735 (1998).
62. M. R. Majidi, L. A. P. Kane-Maguire, and G. G. Wallace, *Polymer* 45, 3113 (1994).
63. M. R. Majidi, L. A. P. Kane-Maguire, and G. G. Wallace, *Aust. J. Chem.* 51, 23 (1998).
64. M. Leclerc, J. Guay, and L. H. Dao, *Macromolecules* 22, 649 (1989).
65. D. Zhou, P. C. Innis, G. G. Wallace, S. Shimizu, and S.-I. Maeda, *Synth. Met.* 114, 287 (2000).
66. X.-L. Wei, Y. Z. Wang, S. M. Long, C. Bobeczko, and A. J. Epstein, *J. Am. Chem. Soc.* 118, 2545 (1996), and references therein.
67. E. Shoji and M. S. Freund, *Langmuir* 17, 7183 (2001).
68. A. J. Epstein, J. M. Ginder, F. Zuo, R. E. Biegelow, H. S. Wou, D. B. Tanner, A. F. Fichter, W. S. Huang, and A. G. MacDiarmid, *Synth. Met.* 18, 303 (1987).
69. D. A. Bonnell and M. Angelopoulos, *Synth. Met.* 33, 301 (1989).
70. A. G. MacDiarmid and A. J. Epstein, *Synth. Met.* 65, 103 (1994).
71. Y. Xia, J. M. Wiesinger, A. G. MacDiarmid, and A. J. Epstein, *Chem. Mater.* 7, 443 (1995).
72. M. R. Majidi, L. A. P. Kane-Maguire, and G. G. Wallace, *Polymer* 36, 3597 (1995).
73. M. R. Majidi and L. A. P. Kane-Maguire, *Polymer* 37, 359 (1996).
74. I. D. Norris, L. A. P. Kane-Maguire, and G. G. Wallace, *Macromolecules* 31, 6529 (1998).
75. W. S. Huang, B. D. Humphrey, and A. G. MacDiarmid, *J. Chem. Soc. Faraday Trans.* 82, 2385 (1985).
76. R. P. McCall, J. M. Ginder, J. M. Leng, H. J. Ye, S. K. Manohar, J. G. Masters, G. E. Asturias, A. G. MacDiarmid, and A. J. Epstein, *Phys. Rev. B* 41, 5202 (1990).
77. M. R. Simmons, P. A. Chaloner, and S. P. Armes, *Langmuir* 11, 4222 (1995).
78. P. M. Beadle, S. P. Armes, S. J. Greaves, and J. F. Watts, *Langmuir* 12, 1784 (1996).
79. M. Aldissi and S. P. Armes, *Prog. Org. Coat.* 19, 21 (1991).
80. P. Gosh, S. K. Siddhanta, S. R. Haque, and A. Chakrabarti, *Synth. Met.* 123, 83 (2001).
81. J. N. Barisci, J. Mansouri, G. M. Spinks, G. G. Wallace, C. Y. Kim, and D. Y. Kim, *Colloids Surfaces* 126, 129 (1997).
82. J. N. Barisci, A. J. Hodgson, L. Liu, G. G. Wallace, and G. Harper, *React. Funct. Polym.* 39, 269 (1999).
83. P. C. Innis, G. Spinks, and G. G. Wallace, *Antec.* 1224 (1998).
84. P. C. Innis, I. D. Norris, L. A. P. Kane-Maguire, and G. G. Wallace, *Macromolecules* 31, 6521 (1998).
85. M. Gustavsson, "Particle size control of conducting polymer colloids" Master of Science Thesis, Department of Chemistry, University of Wollongong, 2000.
86. B. Zinger, *Synth. Met.* 28, 37 (1989).
87. B. J. Kim, S. G. Oh, M. G. Han, and S. S. Im, *Synth. Met.* 122, 297 (2001).
88. M. G. Han, S. K. Cho, S. G. Oh, and S. S. Im, *Synth. Met.* 126, 53 (2002).
89. L. Samuelson, W. Liu, R. Nagarajan, J. Kuman, F. F. Bruno, A. Cholli, and S. Tripathy, *Synth. Met.* 119, 271 (2001).
90. S. E. Moulton, P. C. Innis, L. A. P. Kane-Maguire, O. Ngamna, and G. G. Wallace, *Current Appl. Phys.*, in press.
91. S.-G. Oh and S.-S. Im, *Current Appl. Phys.* 2, 273 (2002).
92. D. Kim, J. Choi, J.-Y. Kim, Y.-K. Han, and D. Sohn, *Macromolecules* 35, 5314 (2002).
93. D. Kim, J.-Y. Kim, E.-R. Kim, and D. Sohn, *Mol. Cryst. Liq. Cryst.* 377, 345 (2002).
94. J. Jang, J. H. Oh, and G. D. Stucky, *Angew. Chem. Int. Ed.* 41, 4016 (2002).
95. M. Goren and R. B. Lennox, *Nano Lett.* 1, 735 (2001).
96. S. T. Selvan, *Chem. Commun.* 351 (1998).
97. S. T. Selvan, J. P. Spatz, H.-A. Klok, and M. Moller, *Adv. Mater.* 10, 132 (1998).
98. Y. Zhou, H. Itoh, T. Uemura, K. Naka, and Y. Chujo, *Chem. Commun.* 613 (2001).

99. Y. Zhou, H. Itoh, T. Uemura, K. Naka, and Y. Chujo, *Langmuir* 18, 277 (2002).
100. L. M. Gan, C. H. Chew, H. S. O. Chan, and L. Ma, *Polym. Bull.* 31, 347 (1993).
101. H. S. O. Chan, L. M. Gan, C. H. Chew, L. Ma, and S. H. Seow, *J. Mater. Chem.* 3, 1109 (1993).
102. L. M. Gan, L. H. Zhang, H. S. O. Chan, and C. H. Chew, *Mater. Chem. Phys.* 40, 94 (1995).
103. H. Xia and Q. Wang, *J. Nanopart. Res.* 3, 401 (2001).
104. J. Jang and H. Yoon, *Chem. Commun.* 720 (2003).
105. C. G. Wu and T. Bein, *Science* 264, 1757 (1994).
106. L. Zuppiroli, F. Beuneu, J. Mory, P. Enzel, and T. Bein, *Synth. Met.* 55, 5081 (1993).
107. V. M. Cepak and C. R. Martin, *Chem. Mater.* 11, 1363 (1999).
108. C. R. Martin, *Acc. Chem. Res.* 28, 61 (1995).
109. C. R. Martin, *Science* 266, 1961 (1994).
110. J. Duchet, R. Legras, and S. Demoustier-Champagne, *Synth. Met.* 98, 113 (1998).
111. S. Demoustier-Champagne, J. Duchet, and R. Legras, *Synth. Met.* 101, 20 (1999).
112. S. Demoustier-Champagne and P.-Y. Stavaux, *Chem. Mater.* 11, 829 (1999).
113. J. M. Mativetsky and W. R. Datars, *Physica B* 324, 191 (2002).
114. M. Delvaux, J. Duchet, P.-Y. Stavaux, R. Legras, and S. Demoustier-Champagne, *Synth. Met.* 113, 275 (2000).
115. B. Rajesh, V. Karthik, A. Karthikeyan, K. R. Thampi, J.-M. Bonard, and B. Viswanathan, *Fuel* 81, 2177 (2002).
116. Z. Cai, J. Lei, W. Liang, V. Menon, and C. R. Martin, *Chem. Mater.* 3, 960 (1991).
117. Z. Cai and C. R. Martin, *J. Am. Chem. Soc.* 111, 4138 (1989).
118. C. Wang, Z. Wang, M. Li, and H. Li, *Chem. Phys. Lett.* 341, 431 (2001).
119. Z. Wang, M. Chen, and H.-L. Li, *Mater. Sci. Eng. A* 328, 33 (2002).
120. S. Neves, C. Polo Onseca, R. A. Zoppi, D. E. Cord Oba, and S. I. Torressi, *J. Solid State Electrochem.* 5, 412 (2001).
121. V. Misoska, W. Price, S. F. Ralph, and G. G. Wallace, *Synth. Met.* 121, 1501 (2001).
122. P. N. Bartlett, P. R. Birkin, M. A. Ghanem, and C. S. Toh, *J. Mater. Chem.* 11, 849 (2001).
123. D. Wang and F. Caruso, *Adv. Mater.* 13, 350 (2001).
124. Y. Yoshino, Y. Kawagashi, S. Tatsuhara, H. Kajii, S. Lee, A. Fujii, M. Ozaki, A. Zakhidov, Z. V. Vardeny, and M. Ishikawa, *Microelectron. Eng.* 47, 49 (1999).
125. T. Cassagneau and F. Caruso, *Adv. Mater.* 14, 34 (2002).
126. T. F. Krauss and R. De La Rue, *Progr. Quantum Elect.* 23, 51 (1999).
127. C. Jerome, D. Labaye, I. Bodart, and R. Jerome, *Synth. Met.* 101, 3 (1999).
128. C. Jerome and R. Jerome, *Agnew. Chem. Int. Ed.* 37, 2488 (1998).
129. S. J. Choi and S. M. Park, *Adv. Mater.* 12, 1547 (2000).
130. H. Kosenen, J. Ruokolainen, M. Knaapila, M. Torkkeli, K. Jokela, R. Serimaa, G. T. Brinke, W. Bras, A. P. Mankman, and O. Ikkala, *Macromolecules* 33, 8671 (2000).
131. M. Wan and Y. Yang, *J. Mater. Chem.* 12, 897 (2002).
132. P. A. McCarthy, J. Huang, S.-Z. Yang, and H.-L. Wang, *Langmuir* 18, 259 (2002).
133. W. Li, P. A. McCarthy, D. Liu, J. Huang, Z.-C. Yang, and H.-L. Wang, *Macromolecules* 35, 9975 (2002).
134. L. Sun and S. C. Yang, *Mater. Res. Soc. Symp. Proc.* 328, 167 (1994).
135. L. Sun, H. Liu, R. Clark, and S. C. Yang, *Synth. Met.* 84, 67 (1997).
136. Y. Shen and M. Wan, *J. Polym. Sci.* 37, 1443 (1999).
137. J. Liu and M. Wan, *J. Mater. Chem.* 11, 404 (2001).
138. Z. Wei and M. Wan, *Adv. Mater.* 14, 1314 (2002).
139. M. Wan, J. Huang, and Y. Shen, *Synth. Met.* 101, 708 (1999).
140. Z. Zhang, Z. Wei, and M. Wan, *Macromolecules* 35, 5937 (2002).
141. Z. Qi and R. B. Lennox, *Electrochem. Proc.* 5, 173 (1997).
142. Z. Zhang and M. Wan, *Synth. Met.* 132, 205 (2003).
143. K. Huang and M. Wan, *Chem. Mater.* 14, 3486 (2002).
144. H. He, J. Zhu, J. Tao, L. A. Nagahara, I. Amlani, and R. Tsui, *J. Am. Chem. Soc.* 123, 7730 (2001).
145. H. X. He, C. Z. Li, and N. J. Tao, *App. Phys. Lett.* 78, 811 (2001).
146. J. J. Langer and I. Czajkowski, *Adv. Mater. Opt. Electr.* 7, 149 (1997).
147. J. J. Langer, G. Franski, and R. Joachimiak, *Synth. Met.* 121, 1281 (2001).
148. S. H. Magnus Persson, P. Dyreklev, and O. Inganas, in "Atomic and Molecular Wires" pp. 119–128. (S. Joachim, and S. Roth, Eds.), Kluwer, Dordrecht, 1997.
149. A. G. MacDiarmid, W. E. Jones, I. D. Norris, J. Gao, A. T. Johnson, N. J. Pinto, J. Hone, B. Han, F. K. Ko, H. Okuzaki, and M. Llaguno, *Synth. Met.* 119, 27 (2001).
150. I. D. Norris, M. M. Shaker, F. K. Ko, and A. G. MacDiarmid, *Synth. Met.* 114, 109 (2000).
151. S.-H. Lee, J.-W. Yoon, and M. H. Suh, *Macromol. Res.* 10, 282 (2002).
152. J. Liu, Y. Lin, L. Liang, J. A. Voigt, D. L. Huber, Z. R. Tian, E. Coker, B. McKenzie, and M. J. McDermott, *Chem. Eur. J.* 9, 604 (2003).
153. L. Liang, J. Liu, C. F. Windisch, G. J. Exarhos, and Y. Lin, *Angew. Chem. Int. Ed.* 41, 3665 (2002).
154. D. Ge, J. Wang, Z. Wang, and S. Wang, *Synth. Met.* 132, 93 (2002).
155. U. Sree, Y. Yamamoto, B. Deore, H. Hiigi, and T. Nagaoka, *Synth. Met.* 131, 161 (2002).
156. Y. Lu, G. Shi, C. Li, and Y. Liang, *J. Appl. Polym. Sci.* 70, 2169 (1998).
157. W.-L. Yuan, E. A. O'Rear, B. P. Grady, and D. T. Glatzhofer, *Langmuir* 18, 3343 (2002).
158. J.-Y. Lim and C. A. Mirkin, *Adv. Mater.* 14, 1274 (2002).
159. R. Riehn, A. Charas, J. Morgado, and F. Cacialli, *Appl. Phys. Lett.* 82, 526 (2003).
160. M. R. Pope, S. P. Armes, and P. J. Tarcha, *Bioconj. Chem.* 7, 436 (1996).
161. V. Aboutanos, J. N. Barisci, L. A. P. Kane-Maguire, and G. G. Wallace, *Synth. Met.* 106, 89 (1999).
162. R. L. N. Chandrakanthi and M. A. Careem, *Thin Solid Films* 417, 51 (2002).
163. L. G. B. Bremer, M. W. C. G. Verbong, M. A. M. Webers, and M. A. M. M. Jan Doorn, *Synth. Met.* 84, 355 (1997).
164. V. Aboutanos, L. A. P. Kane-Maguire, and G. G. Wallace, *Synth. Met.* 114, 313 (2000).
165. H. Xia and Q. Wang, *J. Appl. Polym. Sci.*, 87, 1811 (2003).
166. H. Xia and Q. Wang, *Chem. Mater.* 14, 2158 (2002).
167. V. D. Pokhodenko, V. A. Krylov, Y. I. Kurys, and O. Y. Posudievsky, *Phys. Chem. Chem. Phys.* 1, 905 (1999).
168. M. Cochet M., W. K. Maser, A. M. Benito, M. A. Callejas, M. T. Martinez, J. M. Benoit, J. Schreiber, and O. Chauret, *Chem. Comm.* 1450 (2001).
169. J. Fan, M. Wan, D. Zhu, B. Chang, Z. Pan, and S. Xie, *J. Appl. Polym. Sci.* 74, 2605 (1999).
170. M. Gao, L. Dai, and G. G. Wallace, *Electroanalysis*, 15, 1089 (2003).
171. Z. Wei, M. Wan, T. Lin, and L. Dai, *Adv. Mater.* 15, 136 (2002).
172. J. Wang, K. G. Neoh, and E. T. Kang, *J. Colloid Interface Sci.* 239, 78 (2001).
173. T. K. Sarma, D. Chowdhury, A. Paul, and A. Chattapadhyay, *Chem. Commun.* 1048 (2002).
174. Z. Qi and P. G. Pickup, *Chem. Commun.* 15 (1998).
175. T. Nyberg, F. Zhang, and O. Inganas, *Current Appl. Phys.* 2, 27 (2002).
176. A. J. Epstein, *Springer Ser. Mater. Sci.* 41, 3 (2001).
177. A. B. Kaiser, *Adv. Mater.* 13, 927 (2001).

178. J. N. Barisci, R. Stella, G. M. Spinks, and G. G. Wallace, *Electrochim. Acta* 46, 519 (2000).
179. M. Fu, Y. Zhu, R. Tan, and G. Shi, *Adv. Mater.* 24, 1874 (2001).
180. K. Yoshino, K. Tada, A. Fujii, E. M. Conwell, and A. A. Zakhidov, *IEEE Trans. Electron. Devices* 44, 1315 (1997).
181. G. G. Wallace, P. Dastoor, C. O. Too, and D. O. Officer, *Chem. Innov.* 15 (2000).
182. P. Mulvaney, *Langmuir* 12, 788 (1996).
183. Y. Xia, P. Yang, Y. Sun, Y. Wu, B. Mayers, B. Gates, Y. Yin, F. Kim, and H. Yan, *Adv. Mater.* 15, 353 (2003).
184. B. Wessling and J. Posdorfer, *Synth. Met.* 102, 1400 (1999).
185. B. Wessling, *Synth. Met.* 102, 1396 (1999).
186. B. M. Mandal, *Bull. Mater. Sci.* 21, 161 (1998).
187. K. Suri, S. Annapoorni, A. K. Sakar, and R. P. Tandon, *Sensors Actuators B* 81, 277 (2002).
188. V. Misoska, Ph.D. Thesis, University of Wollongong, 2002.
189. C. Boonchu, Ph.D. Thesis, University of Wollongong, 2002.



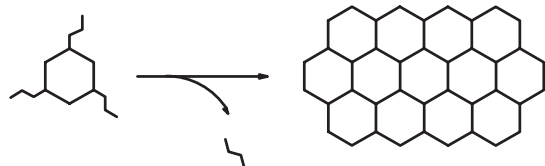
# Inorganic Nanomaterials from Molecular Templates

Sanjay Mathur, Hao Shen

*Institute of New Materials, Saarbrücken, Germany*

## CONTENTS

1. Introduction
  2. Chemical Synthesis of Nanomaterials
  3. The Metal-Organic Precursor Approach
  4. Methods for Molecule-to-Material Transformation
  5. Molecular Clusters as Building Blocks to Nanoparticles and Nanostructured Films
  6. Conclusions
- Glossary  
References



*All things began in order, so shall they end, and so shall they begin again; according to the ordainer of order and mystical mathematics of the city of heaven.*

—Sir Thomas Browne, 1658

## 1. INTRODUCTION

Typically, a nanostructure is a material structure assembled from a layer or cluster of atoms with size on the order of nanometers [1–5]. A number of methods exist for the synthesis of nanostructured materials, including synthesis from atomic or molecular precursors (chemical or physical vapor deposition, gas condensation, chemical precipitation, aerosol reactions, biological templating, etc.), processing of bulk precursors (mechanical attrition, crystallization from the amorphous state, phase separation, etc.), and processes

in nature (e.g., biological systems) [6–12]. Although it is general, this definition underlines the fact that a positional control over constituting atomic or molecular units is inherently associated with the synthesis of nanostructured materials. When evaluated dimensionally, the domain of nanoscale structures (<100 nm) lies between that of ordinary, macroscopic or mesoscale products and microdevices on the one hand, and single atoms or molecules on the other. For this reason, nanostructured materials comprising a countable number of polyatomic or molecular units represent a scale of matter where entirely new properties, not known in the bulk counterparts, are manifested and dominate their behaviors. The most well-known example is the change in color of CdS nanocrystals when their size is reduced to a few nanometers [13]. Such mechanisms include quantum effects, statistical time variations of properties and their scaling with structure size, dominant surface interactions, and the absence of defects in the volume of nanocrystals. These effects endow nanoscale particles and structures thereof with unique mechanical, electronic, magnetic, optical, chemical, etc. properties [6, 8, 14]. Bulk materials constructed from nanoparticles also exhibit new properties such as enhanced plasticity and surface reactivity, and more uniform structures [15].

The unique properties of assembled nanostructures largely attributed to their small size are responsible for the great strides in the development of new synthetic methodologies that would allow the prescribed synthesis of any desired nanostructured material. Methods for controlling the shape and size of inorganic nanocrystals are evolving rapidly with the increasing understanding of basic size-dependent scaling laws, which are important for a wide range of applications. Furthermore, nanoparticulate systems display some special properties like dispersability of an immiscible phase, light weight, extremely high surface area, control over the scattering of light and electronic states (useful in optoelectronic features), and the relatively higher energetic state of atoms and molecules present at the surface of a nanoparticle when compared with those in the bulk. The higher energy associated with the surface also drives

the growth of phases and poses the greatest challenge to the controlled synthesis of nanosized particles [7, 8].

The various possibilities for fabricating nanomaterials through the control of the sizes of their constituent clusters or particles can be broadly divided in the so-called *top-down* (transformative) and *bottom-up* (synthetic) approaches. The top-down processes are based on the transformation of bulk materials into nanoscaled components, largely by mechanical methods, whereas the bottom-up approach relies on the synthesis of large architectures from smaller, well-defined nanosized units. Conventional materials with a grain size anywhere from hundreds of microns ( $\mu\text{m}$ ) to millimeters (mm) are also made of polyatomic or molecular assemblies of matter, where the distribution (ordered or statistical) and multiplicity of such building units are responsible for the familiar averaged properties of bulk materials. Because these macroscale properties effectively extend down to the microscale, traditional manufacturing techniques are experiencing a miniaturization trend for the fabrication of microstructures (e.g., in microelectronics) in a top-down approach. On the other hand, well-known monoatomic or molecular units offer the ultimate building blocks for an atom-by-atom or molecule-by-molecule synthesis of nanostructures in a bottom-up fashion. However, the possibility of building extended solid-state structures from molecular building blocks demands a comprehensive and thorough analysis of synthesis and the composition-structure-property relationship. This review is intended to provide an overview of the efforts made in the chemical synthesis of nanomaterials with the use of molecular metal-organic precursors, with special emphasis given to single-source precursors (SSPs) [16–31]. The term “single source” in a strict sense applies to compounds containing all of the phase-forming elements in a single molecular source (e.g.,  $(\text{Me}_2\text{AlNH}_2)_3$  for AlN) that can be used to perform a one-step synthesis of the desired (nano)material. In addition to the inherent advantages (low-temperature synthesis, phase purity, better composition, and morphology control, etc.) of chemical methods, this concept allows the “preformation” of a solid-state material on the molecular scale.

The research work reviewed here is focused on molecular routes to inorganic nanomaterials and will not refer to the progress of molecular nanotechnology, which is largely related to the understanding of molecular phenomena involved in the self-assembly or self-organization of molecular building blocks to form supramolecular structures that interact to form a higher ordered material (aggregate or crystalline) [32–34]. The emphasis in this contribution will be on the state of the art of molecular concepts developed to obtain inorganic nanoparticles or nanostructured films by chemical routes.

## 2. CHEMICAL SYNTHESIS OF NANOMATERIALS

There is a growing realization that the knowledge of fundamental molecular interactions and processes (=chemistry) is of central importance for the progress of nanoscience, which deals with matter at a scale where the properties are dominated by molecular behaviors, including single molecules and molecular assemblies. Despite clear practical implications of nanocrystalline materials, there exists a deficit in

the ability to produce materials with desired intrinsic properties and a precise control over size, shape, and composition [35]. This situation is distressing, especially in view of the fact that most of the recent advances in nanomaterials are based on novel materials with extraordinary properties (e.g., fullerenes, carbon nanotubes, quantum dots, 1-D oxide wires, etc.) as well as new processing routes (e.g., aerosol nucleation, mechanochemistry, templated growth in mesoporous matrices, hydrothermal methods, etc.).

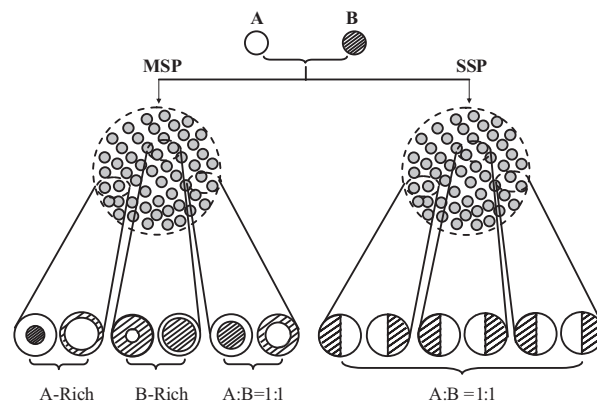
Chemistry has profoundly influenced the emergence of advanced materials through the development and application of novel chemical routes for the synthesis of nanosized powders and nanostructured films. The “nano-movement” in materials chemistry is partly triggered by the observation that the predefined metal stoichiometry and reaction chemistry of molecular precursors can enforce a molecular-level homogeneity in the obtained materials [36–38]. In solid-state processing, the solid precursors (such as metal oxides, carbonates, and salts) must be brought into contact by grinding and mixing and subsequently heat-treated at high temperatures to facilitate the diffusion of atoms or ions in the reaction mixture. Since the diffusion process depends on the temperature of the reaction and grain interfaces, the mixing and grinding steps are usually repeated throughout the heat treatments to prepare fresh surfaces for further reactions. When compared with solid-state processing, the diffusion of matter in the vapor or liquid phase is typically many orders of magnitude higher. Moreover, the chemical reactions allow a controlled interaction of atoms or molecules to form uniformly dispersed solid particles. The atomic-scale mixing of the phase-forming elements results in a faster nucleation of the product at low temperature, which makes kinetic control over the process possible. As a result it is possible to suppress the preferred formation of thermodynamically favored substances and to perform a phase-selective synthesis of metastable compounds.

Although the concept of synthesizing materials from molecules has long been suggested as a mild approach (the so-called soft chemistry methods), the interest, for a long period of time, was to apply these routes to known materials. It is only recently that attention has been shifted to the synthesis of new materials with novel compositions. To decipher how molecular interactions give rise to complexity, it is chemical synthesis that can provide new compounds to manipulate molecular interactions and thereby control the process of material formation as well as the properties of the resulting materials. The chemical techniques use direct, often very simple, chemical reactions to produce the solid of interest. In addition, chemical processing allows control of chemical structure, morphology, and dimension required on several scales of magnitude. For instance, with the manipulation of the reaction kinetics so as to encourage particle nucleation over particle growth, ultrafine particles can be obtained. The nucleation kinetics are easily regulated by varying the amounts or ratios of the reactants or reaction time, for example, by massively exceeding the supersaturation ratio in precipitation reactions or by increasing the amount of water added in an alkoxide-based sol-gel process to drive hydrolysis at the expense of condensation reactions. Furthermore, the reaction kinetics can also be influenced by adjustment of the thermal energy input or thermal energy

distribution in the reaction vessel. The enhanced degree of mixing achieved by ultrasonic irradiation can accelerate reaction kinetics by two orders of magnitude and yield nanometric particles [39]. Sonic and ultrasonic agitation methods are used to create small bubbles, in a reaction pool, to accelerate reaction kinetics by cavitation. This method, known as sonochemical synthesis, relies on the phenomenon of acoustic cavitation (a point where the intensity of ultrasound exceeds the intramolecular forces, and, as a result, the molecular structure collapses and a cavity is formed) that results from enormous stresses (500–1000 atm) and elevated temperatures ( $\sim 3000$  K) induced in the reaction medium by the application of ultrasound (20 kHz to 10 MHz). Another example of accelerated chemical reaction strategy is the straightforward synthesis of hexagonal gallium nitride (GaN) nanocrystals by detonation of gallium azides [40, 41].

In basic chemistry terms, the starting materials (input) of a chemical reaction are the *reactants* and the material (output) to which the reactants are converted, the *product*. In most of the chemical methods in practice, the starting materials are commonly available reagents, which are close to the desired composition but need a heat-treatment step to attain the final composition. For example, the calcination of  $\text{CaCO}_3$  eliminates  $\text{CO}_2$  and results in the formation of  $\text{CaO}$ . Similarly, firing  $\text{Al}(\text{OH})_3$  drives off water to produce  $\text{Al}_2\text{O}_3$ . In such cases, where the “precursor” is an infusible solid, the size of the particles in the precursor will impose a minimum limit for the size of the particles in the final calcined material. However, particles can grow larger because of fusion (necking) that takes place at elevated temperatures. Further problems associated with such powders are (i) that particles are rarely round (spherical powders pack better), (ii) the presence of dense agglomerates of much smaller crystallites formed during firing and crystallization, and (iii) the external contamination of particles during milling or grinding steps that are necessary to break down the larger agglomerates. For these reasons, minimizing the calcination temperature and steps is a prerequisite in the preparation of nanocrystalline materials by conventional chemical techniques. An elegant way to limit the particle size at the precursor stage is to use well-defined molecules that can be seen as “molecular fragments” of the solid-state structure. A number of methods have been devised to control the final particle size by performing the reactions in spatially confined reaction pools, for example, hydrolysis in aqueous reaction pools separated by an intervening liquid (water-in-oil micro(nano)emulsion) or pyrolysis of small droplets of precursor solution separated from each other by a gaseous phase (aerosol). The methods are not straightforward in predicting the final particle size because of chemical exchange and agglomeration between pools in the microemulsion method, whereas coalescence and drying of droplets in the case of aerosol technique lead to a size distribution and chemical inhomogeneities in the final material. In addition, the chemical reaction occurring within the droplets and the nature of different chemical intermediates can further complicate the synthesis. Since no *positional control* is offered, the different compounds present in the reaction mixture randomly collide to form various intermediate species with metal ratios unfavorable for obtaining

a single-phase material. As a consequence, phase separation and element segregation are present at the nanometer scale, although the global stoichiometry of the product corresponds to the desired composition. This is a common observation in the conventional material synthesis procedures (e.g., solid-state reactions, coprecipitations, combustion reactions, etc.) where the intrinsic chemical behaviors (e.g., different hydrolysis rates of the reactants in solution-phase reactions or different vapor pressure or thermal stability in the gas-phase reactions) of the different components present in a reaction mixture make the stoichiometry of the target material highly susceptible to inaccuracies. For instance, a simple mixing of two chemical precursors A and B, to produce the binary system AB (multisource precursor, MSP), may produce a visibly homogeneous mixture, but the molecular-level scenario can be different, and, despite a correct global stoichiometry, the precursor “cocktail” may have element segregation and non-ideal A:B ratios at the nanometer scale that may be carried forward to the end product (Scheme 1).



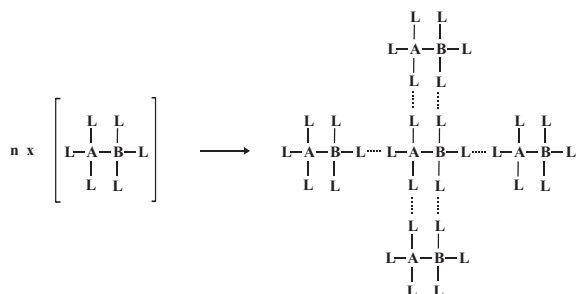
**Scheme 1.** Chemical aspects of multisource precursor (MSP) and single-source precursor (SSP) processes.

In this context, the SSP containing predetermined metal-ligand interactions (e.g., metal-carbon for carbides, metal-nitrogen for nitrides, metal-oxygen for oxides, etc.) are an attractive choice for obtaining materials that are homogeneous at the atomic level. The superior potential of molecular-level synthesis has been demonstrated in several cases. For instance, the metal organic chemical vapor deposition (MOCVD) of group III nitrides ( $\text{AlN}$ ,  $\text{GaN}$ ,  $\text{InN}$ ) has traditionally been carried out with mixtures of the corresponding metal alkyls with ammonia ( $\text{NH}_3$ ). However, the high thermal stability of  $\text{NH}_3$  (<5% pyrolyzed at  $700^\circ\text{C}$ ) necessitates very high substrate temperatures ( $>1000^\circ\text{C}$ ), and high  $\text{NH}_3:\text{MR}_3$  ( $\text{M} = \text{Al}, \text{Ga}, \text{In}$ ) ratios (e.g., 2000:1) are required to inhibit nitrogen desorption. This severely limits the choice of substrate material, and the inefficient use of toxic ammonia demands gas-scrubbing systems. On the other hand, the use of molecular sources  $[\text{Me}_2\text{AlNH}_2]_3$  and  $[\text{Et}_2\text{GaNH}_2]_3$  containing preformed aluminum-nitrogen and gallium-nitrogen bonds gives crystalline  $\text{AlN}$  and  $\text{GaN}$  films at  $400\text{--}800$  and  $650^\circ\text{C}$ , respectively.

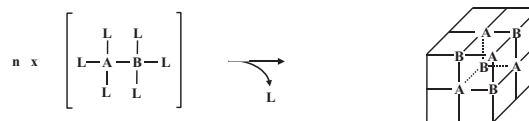
Finally, the chemical routes are simple and thus cost-effective when compared with the physical methods, which require sophisticated technology and expensive experimental set-ups. The synthesis of materials is achieved at relatively lower temperatures than those required for conventional processing methods, and it is possible to process large quantities and high throughput. Moreover, they offer enormous versatility with respect to composition, allowing, for instance, tailoring of the composition. It is possible to cosynthesize another material in the same medium. For this reason, various chemical routes have been proposed based on the application of molecular compounds to produce inorganic materials. A brief description of the common chemical methods (sol-gel, CVD, aerosol, microemulsion, and hydrothermal synthesis) applied to the synthesis of nanophase materials from molecular precursors is presented in the following section. In addition, some other methods (coprecipitation and the polymeric precursor route) not using the single-source approach but based on a molecular-level mixing of the components are also discussed because examples taken for a comparative evaluation of conventional and molecular chemistry routes necessitates their understanding.

### 3. THE METAL-ORGANIC PRECURSOR APPROACH

The synthesis of materials prepared from molecular components is a growing research thrust in nanomaterials science because it allows the use of molecular building blocks for the rational design and construction of new materials [42]. Novel molecular and extended networks constructed from organic and inorganic building blocks have been found to behave like molecule-based conductors and superconductors, optically active compounds, and magnets. In addition, the versatility of molecular based materials allows for the design of hybrid materials with the possibility of synergy effects. At this stage it is necessary to differentiate between the two popular strategies of obtaining materials from molecules, namely molecule-based nanomaterials (MBNs) and molecule-derived nanomaterials (MDNs). Both approaches are based on the use of molecules or molecular ions and their interactions to design a (nano)material in a *bottom-up* fashion. However, in the case of molecule-based materials, the molecular integrity of the building units is maintained in the final configuration (Scheme 2), whereas in the case of molecule-derived synthesis the features of the parent molecular framework are not necessarily maintained in the final material (Scheme 3).



Scheme 2.



Scheme 3.

In addition, the nature of bonding is generally different in the two cases; the class of MBNs is dominated by molecular architectures and assemblies based largely on noncovalent interactions, where the main driving forces for the formation of a network are metal-ligand interaction, hydrogen bonding,  $\pi$ - $\pi$  stacking, ion templation, chiral interactions, etc. On the other hand, the MDNs are based on covalent and/or ionic interaction. Furthermore, in the case of an MBN, the common principles of synthetic organic, organometallic, inorganic, and polymer chemistry are used to obtain the desired material. This methodology is also used to obtain the precursors to MDNs; however, the target nanomaterial is obtained only after a few processing steps, which involve the loss of organic ligands, structural fragments, or elements to reach the final solid. Moreover, a molecular building block of an MDN may contain many more elements than those required to form the end product. For instance, iron pentacarbonyl ( $\text{Fe}(\text{CO})_5$ ) is used as a source of iron nanoparticles, and nanostructured films contain C and O as carbonyl ligands, which are knocked off during the processing steps to nanocrystalline iron. Similarly, titanium isopropoxide ( $\text{Ti}(\text{OPr}^i)_4$ ) loses the organic periphery in the formation of titanium dioxide ( $\text{TiO}_2$ ).

The molecular self-assembly, which can be seen as a case of MBN, seems to open new pathways to nanostructures formed by the organization of molecular building blocks through controlled molecular interactions. A representative example is shown in Figure 1, which displays a supramolecular ribbon structure based on hydrogen bonding between barbituric acid and 2,4,6-triaminopyrimidine units [32].

It must be emphasized that despite significant differences, the distinction between the MBN and MDN approaches is not absolute because examples are now known in which the structural features of an MDN source are carried forward to the extended solid network. For instance, the use of cubane precursor molecules,  $[(\text{Bu}^t)\text{GaS}]_4$ , in the MOCVD process results in the growth of a new cubic GaS phase, whereas using the dimeric species  $[(\text{Bu}^t)_2\text{GaS}]_2$  as molecular precursor forms the thermodynamically stable hexagonal GaS. It has been shown that the formation of cubic GaS is a consequence of the retention of the cubane  $\text{Ga}_4\text{S}_4$  core during the deposition and growth process (Scheme 4). Interestingly, the cubic phase is not obtained by other routes and precursors. In view of the general definitions applied to MBN and

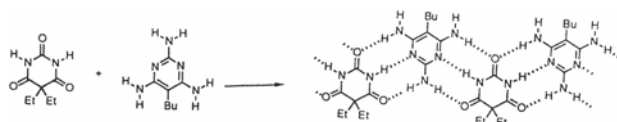
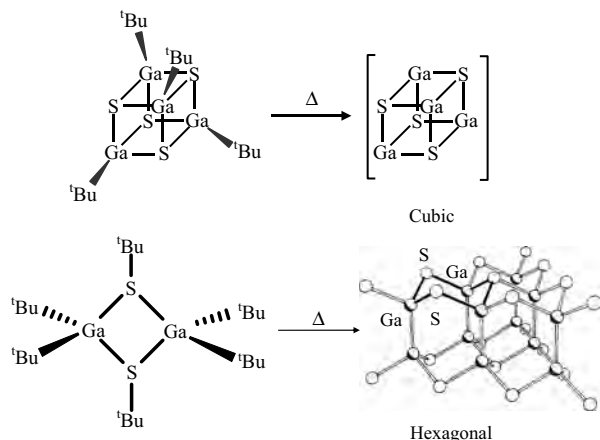


Figure 1. Self-assembly of a supramolecular ribbon from barbituric acid and 2,4,6-triaminopyrimidine units. Reprinted with permission from [32], J. M. Lehn et al., *J. Chem. Soc., Perkin Trans. 2*, 461 (1992). © 1992, Royal Society of Chemistry.

MDN, the cubic phase of GaS might be termed an MBN and the hexagonal GaS an MDN.



Scheme 4.

### 3.1. The Single-Source Concept

When one considers that precursor structure and metal-ligand connectivity determine the composition of nanomaterial from a legal perspective, the role of suitable precursors in the designed synthesis of nanomaterials becomes immediately apparent. It is reasonable to assert that solid-state structures can be templated at the nanometer scale by employing well-defined molecular clusters containing metallic elements in a ratio compatible with the targeted ceramic or composite, the so-called SSPs [16–31, 43–51]. The defined metal-ligand interactions in such *nano-synthons* initiates the growth of nanomaterials at lower temperatures by providing intact nuclei for a bulk material. A large number of different expressions like molecular building blocks, molecular subunits, or modular building units are used to describe metal-organic compounds used as single molecular source.

However, the expression “single-source precursor” is also applied to a mixture of constituents mixed homogeneously either as a powdery mixture (solid) or in a common solvent (liquid) system. While the precursor system in the first case is a physical mixture, the validity of the expression is rather questionable in the second case because it is used to define a precursor cocktail, although no investigations of the nature of the species present in the solution is made, in most of the cases. The use of a mixture of different chemical compounds, corresponding to the elements present in the desired material (e.g., individual Y, Ba, and Cu sources to obtain  $\text{YBa}_2\text{Cu}_3\text{O}_{7-\delta}$ ), complicates the situation in the multiple-precursor route, mainly because of the different chemical nature of the individual chemical species present in the precursor-complex. The composition and phase purity of the material are difficult to control because the intrinsic behaviors of single components, for example, solubility, susceptibility to hydrolysis, etc., in solution-based methods and differential vapor pressures, thermal stability, etc., in the gas-phase synthesis make the stoichiometry highly susceptible to inaccuracies due to an increased number of process variables. In view of the above, the examples described in this article are based on the conversion of defined molecular

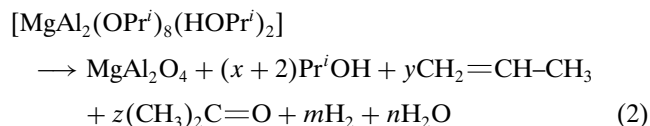
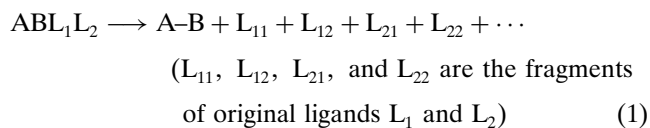
clusters, which have been characterized with respect to their chemical structure and composition before being applied as molecular sources to nanostructured materials.

In the past few years, the use of molecular compounds as precursors to thin films and powders has been extensively explored. There are many excellent examples of the use of SSPs for one-, two-, three-, and four-component systems and even biphasic composites [16, 19, 20, 29, 43, 44, 47, 52–315].

The salient examples of compounds used as a single source to solid-state phases are assembled in Tables 1–4. A broad and arbitrary classification of the single molecular source,  $[\text{ABL}_1\text{L}_2]$ , based on experimental results, is presented in the following section (Eqs. 1–6, A and B, are the phase-forming elements;  $\text{L}_1$  and  $\text{L}_2$  are ligands that can be similar or different). The concept is elaborated on the basis of different Mg- and Al-containing alkoxides that have been used as precursors to  $\text{MgAl}_2\text{O}_4$  particles or films [104, 259, 260, 263, 316, 317].

#### 3.1.1. Case I: Stoichiometric Assembly of the Phase-Forming Elements

The SSPs belonging to the subcategory outlined in Eq. (1) are based on an appropriate ratio of the phase-forming elements that should be compatible with the desired inorganic phase. The chemical nature (neutral, anionic, chelating), steric bulk, and the decomposition chemistry of the ligand(s) are not the prime concern in the selection of a suitable precursor. Nevertheless, the existence of similar molecular frameworks with different ligands offers the possibility to choose the precursor most suited for a particular process or



application. For example, the mixed-metal Mg-Al alkoxide,  $[\text{MgAl}_2(\text{OPr}^i)_8(\text{Pr}^i\text{OH})_2]$ , possesses the cation ratio required for the formation of  $\text{MgAl}_2\text{O}_4$  spinel. The thermal decomposition of the precursor is associated with the formation of several products based on radical and/or ionic fragmentation of the ligands (Eq. (2)). The mutual stoichiometry of the by-products depends upon the reaction conditions. The molecule exists as an isopropyl alcohol adduct in the solid-state (Fig. 2a), and the observed arrangement of  $\text{Mg}^{2+}$  and  $\text{Al}^{3+}$  ions is also maintained in the solution, as confirmed by molecular weight studies [318]. Because of the appropriate Mg:Al ratio,  $[\text{MgAl}_2(\text{OPr}^i)_8(\text{Pr}^i\text{OH})_2]$  has been used for the synthesis of ultrafine spinel particles by the sol-gel method [260]. The hydrolysis of the heterometal precursor was investigated by rheological measurements and  $^{27}\text{Al}$  NMR spectroscopy, which suggested that the bimetallic unit survives

**Table 1.** Selected single-source precursors for one-component systems.

Material	Method	Precursor	Properties and application potentials	Ref.
Ag	CVD	Ag(C <sub>4</sub> F <sub>7</sub> )	Catalyst, quantum dots	[52]
	Thermolysis	AgC <sub>14</sub> H <sub>29</sub> O		[53]
Al	CVD	AgC <sub>5</sub> H <sub>7</sub> O <sub>2</sub>	Interconnects, microelectronics	[54]
	CVD	( $\eta^5$ -C <sub>5</sub> H <sub>5</sub> )Ag(PR <sub>3</sub> )		[55]
	CVD	Al( <i>i</i> -Bu) <sub>3</sub>		[52]
Al	CVD	Al(BH <sub>4</sub> ) <sub>3</sub> , AlH <sub>2</sub> (BH <sub>4</sub> )N(CH <sub>3</sub> ) <sub>3</sub>	Interconnects, microelectronics	[56]
	CVD	AlH <sub>3</sub> ·NR <sub>3</sub> , R = Me, Et, Me <sub>2</sub> Et		[57, 58]
	CVD	Me <sub>2</sub> Au(hfac), hfac = C <sub>5</sub> HF <sub>6</sub> O <sub>2</sub>		[52]
Au	CVD	[(CF <sub>3</sub> ) <sub>2</sub> Au(OSiMe <sub>3</sub> ) <sub>2</sub> ] <sub>2</sub>	Catalyst, quantum dots	[59]
	CVD	MeAu(CNMe)		[60]
Au <sub>55</sub>	Sol-gel	Au <sub>55</sub> {P(C <sub>6</sub> H <sub>5</sub> ) <sub>3</sub> } <sub>12</sub> Cl <sub>6</sub>	Quantum dots, microelectronic	[61]
Co	CVD	Co{N(SiMe <sub>3</sub> ) <sub>2</sub> } <sub>2</sub>	Catalyst, magnetic	[47]
	CVD	Co( $\eta^5$ -C <sub>5</sub> H <sub>5</sub> ) <sub>2</sub>		[62]
Cr	CVD	( $\eta^5$ -C <sub>5</sub> H <sub>5</sub> )Co(CO) <sub>2</sub>	Protective coatings, wear-resistant coatings	[62]
	CVD	Cr(CH <sub>2</sub> CMe <sub>3</sub> ) <sub>4</sub>		[63]
	CVD	Cr(C <sub>9</sub> H <sub>12</sub> ) <sub>2</sub>		[64, 65]
Cu	Thermolysis	Cr(CO) <sub>4</sub>	Microelectronics, integrated circuits	[66]
	CVD	[Cu(O <sup><i>i</i></sup> Bu) <sub>4</sub> ]		[52]
Cu	CVD	Cu(tbaoac) <sub>2</sub> , tbaoac = C <sub>8</sub> H <sub>13</sub> O <sub>2</sub>	Microelectronics, integrated circuits	[67]
	CVD	CuN(SiMe <sub>3</sub> ) <sub>2</sub>		[47]
	CVD	(O <sup><i>i</i></sup> Bu)Cu(PMe <sub>3</sub> )		[68]
	CVD	Cu(O <sup><i>i</i></sup> Bu)(OR <sub><i>F</i></sub> )		[69]
Fe	CVD	Fe(C <sub>5</sub> H <sub>5</sub> ) <sub>2</sub>	Magnetic, catalyst	[52]
	CVD	Fe{N(SiMe <sub>3</sub> ) <sub>2</sub> } <sub>3</sub>		[47]
Ge	CVD	Ge{N(SiMe <sub>3</sub> ) <sub>2</sub> } <sub>2</sub>	Semiconductor	[47]
	CVD	GeC <sub>10</sub> H <sub>18</sub> , GeC <sub>11</sub> H <sub>20</sub> , GeC <sub>9</sub> H <sub>16</sub> , C <sub>8</sub> H <sub>14</sub> Ge		[70]
Hf	CVD	HfI <sub>4</sub>	Optoelectronic	[71]
Pd	CVD	Pd(C <sub>5</sub> H <sub>5</sub> ) <sub>2</sub> , ( $\eta^5$ -C <sub>5</sub> H <sub>5</sub> )Pd(C <sub>3</sub> H <sub>5</sub> )	Optical, protective coatings	[72]
		Pt(acac) <sub>2</sub> , acac = C <sub>5</sub> H <sub>7</sub> O <sub>2</sub>		[72]
Pt	CVD	(C <sub>5</sub> H <sub>5</sub> )PtMe(CO), (C <sub>5</sub> H <sub>7</sub> O <sub>2</sub> )PtMe <sub>3</sub>	Catalyst	[52]
	CVD	(C <sub>5</sub> H <sub>4</sub> Me)PtMe <sub>3</sub>		[73–75]
	CVD	(C <sub>5</sub> H <sub>5</sub> )PtMe <sub>3</sub>		[76–79]
	CVD	Mn[N(SiMe <sub>3</sub> ) <sub>2</sub> ] <sub>2</sub>		[76]
Mn	CVD	Mn[N(SiMe <sub>3</sub> ) <sub>2</sub> ] <sub>2</sub>	Electric circuits	[47]
	CVD	(Me <sub>3</sub> C <sub>6</sub> H <sub>3</sub> )Mo(CO) <sub>3</sub> , ( $\eta^6$ -C <sub>6</sub> H <sub>6</sub> )Mo(CO) <sub>3</sub>		[80]
Mo	CVD	Mo(allyl) <sub>3</sub> , N = C <sub>3</sub> H <sub>5</sub>	Copper, nickel metallization	[81]
	CVD	Ni(CO) <sub>4</sub>		[52]
Ni	CVD	Ru(od) <sub>3</sub> , od = C <sub>8</sub> H <sub>13</sub> O <sub>2</sub>	Magnetic, catalyst	[82]
	Sol-gel	Ru(bipyr) <sub>3</sub> , bipyr = C <sub>10</sub> H <sub>8</sub> N <sub>2</sub>		[83]
Ru	CVD	Sn{N(SiMe <sub>3</sub> ) <sub>2</sub> } <sub>2</sub>	Electrically conductive layers	[47]
	Thermolysis	Sn(O <sup><i>i</i></sup> Pr) <sub>2</sub>		[84]
Sn	CVD	TiI <sub>4</sub>	Semiconductor	[85]
	Thermolysis	( $\eta^5$ -C <sub>5</sub> H <sub>5</sub> ) <sub>2</sub> Ti		[86]
Ti	CVD	Zr(CH <sub>2</sub> <sup><i>i</i></sup> Bu) <sub>4</sub>	Protective coatings	[87, 88]

**Table 2.** Selected single-source precursors for two-component systems.

Material	Method	Precursor	Properties and application potentials	Ref.
AIB	CVD	Al(BH <sub>4</sub> ) <sub>3</sub>	Films operating at high current densities	[56]
AlN	CVD	[Me <sub>2</sub> Al- $\mu$ -N(H)NMe <sub>2</sub> ] <sub>2</sub> ,	Passivation, dielectric	[89]
		[Et <sub>2</sub> Al- $\mu$ -N(H)NMe <sub>2</sub> ] <sub>2</sub>		
Al <sub>2</sub> O <sub>3</sub>	CVD	AlMe <sub>3</sub> ·NR <sub>3</sub>	Wear-resistant and corrosion-protective coating	[90]
	CVD	Al(CH <sub>3</sub> ) <sub>2</sub> (O <sup><i>i</i></sup> C <sub>3</sub> H <sub>7</sub> )		[91]
	ALD	Al(O <sup><i>i</i></sup> Pr) <sub>3</sub>		[92]
	Sol-gel	AlCl <sub>3</sub> , Al(O <sup><i>i</i></sup> Pr) <sub>3</sub>		[93]
	Sol-gel	Al(O-sec-Bu) <sub>3</sub>		[94, 95]
AlSb	CVD	[H <sub>2</sub> Al(OC <sub>4</sub> H <sub>9</sub> ) <sub>2</sub> ] <sub>2</sub>	Midinfrared lasers	[96]
	CVD	[Et <sub>2</sub> AlSb(SiMe <sub>3</sub> ) <sub>2</sub> ] <sub>2</sub> ,		[97]
BN	CVD	[(Bu <sub>2</sub> AlSb)-Bu <sup><i>i</i></sup> -(SiMe <sub>3</sub> ) <sub>2</sub> ] <sub>2</sub>	Low-density, high-temperature application, hard coatings	[98]
		(C <sub>2</sub> H <sub>5</sub> ) <sub>3</sub> N·BH <sub>3</sub>		[99]
	Polymeric route	Et <sub>3</sub> BNH <sub>2</sub> R, R = <sup><i>i</i></sup> Pr, Bu		[99]
		[B <sub>3</sub> N <sub>3</sub> H <sub>4</sub> ] <sub><i>n</i></sub>	Electric insulator, oxidation resistant	[100]

continued



Table 2. Continued

Material	Method	Precursor	Properties and application potentials	Ref.	
Bi <sub>2</sub> S <sub>3</sub>	CVD	Bi(S <sub>2</sub> CNEt <sub>2</sub> ) <sub>3</sub> , Bi(S <sub>2</sub> CNMeHex) <sub>3</sub> , Hex = C <sub>6</sub> H <sub>13</sub>	Thermoelectric cooler, photodiode array	[101]	
Cd <sub>3</sub> P <sub>2</sub>	Thermolysis	[MeCdP <sup><i>i</i></sup> Bu <sub>2</sub> ] <sub>3</sub>	Semiconductor	[102]	
CdS	Thermolysis	Cd{S <sub>2</sub> CN-Me(C <sub>6</sub> H <sub>13</sub> ) <sub>2</sub> }	Semiconductor, quantum dots	[103]	
	CVD	Cd(Et <sub>2</sub> NCOS) <sub>2</sub>	Electronic	[104]	
CdSe	Thermolysis	[Cd(S <sub>2</sub> CNMe(C <sub>18</sub> H <sub>37</sub> )) <sub>2</sub> ]	Optical coatings, solid-state solar cell windows, photoconductor	[105]	
	CVD	Cd(S <sub>2</sub> O <sub>2</sub> C <sub>16</sub> H <sub>34</sub> N <sub>2</sub> )	Electronic, optical, optoelectronic	[106]	
	Pyrolysis	Cd(SC <sub>7</sub> H <sub>7</sub> ) <sub>2</sub>		[107]	
	Sol-gel	Cd(S <sub>2</sub> CNMeC <sub>6</sub> H <sub>13</sub> ) <sub>2</sub>		[108]	
	Thermolysis	[Cd(SePh) <sub>2</sub> ] <sub>2</sub>	Semiconductor, optical, quantum dots	[109]	
	CVD	[Cd <sub>10</sub> Se <sub>4</sub> (SC <sub>6</sub> H <sub>5</sub> ) <sub>16</sub> ] <sub>4</sub>		[110]	
CdTe	Sol-gel	Cd(Se <sub>2</sub> CNMeC <sub>6</sub> H <sub>13</sub> ) <sub>2</sub>		[108]	
	CVD	Cd{Te(ox)} <sub>2</sub> , ox = C <sub>11</sub> H <sub>13</sub> NO <sub>3</sub>	Semiconductor, optical	[111]	
CeO <sub>2</sub>	Sol-gel	(NH <sub>4</sub> ) <sub>2</sub> Ce(NO <sub>3</sub> ) <sub>6</sub>	Efficient UV absorber, oxidation catalyst	[112]	
	CVD	Ce(fod) <sub>4</sub> , fod = C <sub>3</sub> F <sub>7</sub> COCHCOC <sub>4</sub> H <sub>9</sub>	Buffer layer for superconductors	[113]	
	Pyrolysis	Ce(C <sub>5</sub> H <sub>7</sub> O <sub>2</sub> ) <sub>4</sub>		[114]	
	CVD	[Ce(C <sub>5</sub> F <sub>6</sub> HO <sub>2</sub> ) <sub>3</sub> (MeO(C <sub>2</sub> H <sub>4</sub> O) <sub><i>n</i></sub> Me)], <i>n</i> = 1, 2, 3		[115]	
CoGa		(CO) <sub>4</sub> CoGaEt <sub>2</sub> L	Schottky contacts for GaAs	[116]	
CoSi	CVD	(CO) <sub>4</sub> CoSiH <sub>3</sub>	Schottky contacts for Si	[117]	
Co <sub>2</sub> Si, CoSi, CoSi <sub>2</sub>	CVD	Co(SiCl <sub>3</sub> )(CO) <sub>4</sub>	Gate, contact, and interconnect materials in IC	[118]	
CoSn, Co <sub>3</sub> Sn <sub>2</sub>	CVD	R <sub>3</sub> SnCo(CO) <sub>4</sub> , R = Me, C <sub>6</sub> H <sub>5</sub>	Anticorrosion protection, solar energy devices, magnetic tapes	[119]	
CoSn	CVD	Me <sub>3</sub> SnCo(CO) <sub>4</sub> , Ph <sub>3</sub> SnCo(CO) <sub>4</sub>	Alloy, catalyst	[119]	
CrC	CVD	Cr{N(SiMe <sub>3</sub> ) <sub>2</sub> } <sub>3</sub>	Abrasive, conductor	[47]	
CrN	CVD	Cr{N(SiMe <sub>3</sub> ) <sub>2</sub> } <sub>3</sub>		[47]	
CuS, CuSe	CVD	Cu{E <sub>2</sub> CNMe(C <sub>6</sub> H <sub>13</sub> ) <sub>2</sub> }	Semiconductor	[120]	
Er <sub>2</sub> O <sub>3</sub>	CVD	Er(tmhd) <sub>3</sub> , tmhd = C <sub>11</sub> H <sub>19</sub> O <sub>2</sub>	Corrosion resistance, photoluminescent	[121]	
Eu <sub>2</sub> O <sub>3</sub>	Sol-gel	Eu(TTA) <sub>3</sub> C <sub>6</sub> H <sub>5</sub>	Photoluminescent, infrared emission	[122]	
Fe <sub>2</sub> O <sub>3</sub>	Sol-gel	Fe(O <sup><i>i</i></sup> Bu) <sub>3</sub>	Gas sensing, inorganic pigment, paint	[123]	
	Sol-gel	Fe(OEt) <sub>3</sub>		[124]	
	Sonication	Fe(CO) <sub>5</sub>		[125]	
	Sol-gel	Fe(NO <sub>3</sub> ) <sub>3</sub> ·9H <sub>2</sub> O-C <sub>3</sub> H <sub>8</sub> O <sub>2</sub> -C <sub>5</sub> H <sub>8</sub> O <sub>2</sub>		[126]	
	CVD	Fe(O <sup><i>i</i></sup> Bu) <sub>3</sub>	Magnetic application, semi-metal behavior	[123]	
Fe <sub>3</sub> O <sub>4</sub>	CVD	Fe(C <sub>5</sub> H <sub>7</sub> O <sub>2</sub> ) <sub>3</sub>		[127]	
	Sonication	Fe(CO) <sub>5</sub>		[125]	
	Sol-gel	Fe(NO <sub>3</sub> ) <sub>3</sub> ·9H <sub>2</sub> O-C <sub>3</sub> H <sub>8</sub> O <sub>2</sub> -C <sub>5</sub> H <sub>8</sub> O <sub>2</sub>		[125]	
	CVD	Fe <sub>2</sub> (μ-S <sub>2</sub> )CO <sub>6</sub>	Solar cells, solid-state batteries, catalyst	[128]	
FeS <sub>2</sub>	CVD	Fe(S <sub>2</sub> CNMePr <sup><i>i</i></sup> ) <sub>2</sub>	Magnetic	[129]	
FeSi, FeSi <sub>2</sub>	CVD	Fe(SiCl <sub>3</sub> ) <sub>2</sub> (CO) <sub>4</sub>	Optoelectronic	[130]	
FeSn <sub>2</sub> , FeSn	CVD	(C <sub>5</sub> H <sub>5</sub> )Fe(CO) <sub>2</sub> (SnMe <sub>3</sub> ), (C <sub>5</sub> H <sub>5</sub> )Fe(CO) <sub>4</sub> (SnMe <sub>3</sub> ) <sub>2</sub>	Alloys	[131]	
FeSn	CVD	CpFe(CO) <sub>2</sub> (SnMe <sub>3</sub> )	Alloy, catalyst	[131]	
GaAs	Thermolysis	[Et <sub>2</sub> GaAs(SiMe <sub>3</sub> ) <sub>2</sub> ] <sub>2</sub> , [Et <sub>2</sub> GaSb(SiMe <sub>3</sub> ) <sub>2</sub> ] <sub>2</sub> , [Ga{As(NMe <sub>2</sub> ) <sub>3</sub> }] <sub>3</sub>	Semiconductor Optoelectronic	[132, 133] [16]	
	Pyrolysis	[Me <sub>2</sub> Ga(μ-AsR <sub>2</sub> )] <sub>3</sub> , R = <sup><i>i</i></sup> Pr, Me, <sup><i>t</i></sup> Bu		[134]	
	Thermolysis	[H <sub>2</sub> GaNH <sub>2</sub> ] <sub>3</sub>	Luminescent, blue LEDs	[135]	
GaN	CVD	[Et <sub>2</sub> GaNH <sub>2</sub> ] <sub>3</sub>	Semiconductor lasers	[43]	
	CVD	H <sub>2</sub> GaN <sub>3</sub>		[136]	
	Pyrolysis	(Me <sub>3</sub> N)Ga(N <sub>3</sub> ) <sub>3</sub>		[137]	
	CVD	Cl <sub>2</sub> GaN <sub>3</sub> , GaC <sub>3</sub> N <sub>3</sub> , LiGaC <sub>4</sub> N <sub>4</sub>		[138]	
	Thermolysis	(R <sub>3</sub> N)Ga(N <sub>3</sub> ) <sub>3</sub> , R = CH <sub>3</sub> , C <sub>2</sub> H <sub>5</sub>		[139]	
	CVD	(N <sub>3</sub> ) <sub>2</sub> Ga(CH <sub>2</sub> ) <sub>3</sub> N(CH <sub>3</sub> ) <sub>2</sub>		[140]	
	CVD	[HClGaNH <sub>2</sub> ] <sub>4</sub>		[141]	
	Ga <sub>2</sub> O <sub>3</sub>	CVD	Ga(OR) <sub>3</sub> , R = <sup><i>i</i></sup> Pr, <sup><i>t</i></sup> Bu	H <sub>2</sub> sensor, <i>n</i> -type semiconductor	[142]
		CVD	Ga(O <sup><i>i</i></sup> Bu) <sub>3</sub>		[143]
		Sol-gel	Ga(C <sub>5</sub> H <sub>7</sub> O <sub>2</sub> ) <sub>3</sub>		[144]
GaP	Sol-gel	(Et <sub>2</sub> GaP(SiMe <sub>3</sub> ) <sub>2</sub> ) <sub>2</sub>	Photonic application	[145]	
GaS	CVD	[ <sup><i>t</i></sup> Bu)GaS] <sub>4</sub>	Surface passivation material for GaAs	[146]	

continued

Table 2. Continued

Material	Method	Precursor	Properties and application potentials	Ref.
Ga <sub>2</sub> S <sub>3</sub>	CVD	[Ga(S' Bu) <sub>2</sub> (μ-S' Bu)] <sub>2</sub>	Surface passivation material for GaAs	[147]
	CVD	Ga(S <sub>2</sub> CNMeHex) <sub>3</sub> , Hex = C <sub>6</sub> H <sub>13</sub>	Photovoltaic, optoelectronic applications	[148]
GaSb	CVD	[ <sup>t</sup> Bu <sub>3</sub> Ga-Sb( <sup>t</sup> Bu) <sub>3</sub> ], [ <sup>t</sup> Bu <sub>3</sub> Ga-Sb( <sup>i</sup> Pr) <sub>3</sub> ]	Semiconductor	[132, 133]
GaSe	CVD	[(R)Ga(μ <sub>3</sub> -Se)] <sub>4</sub> R = CMe <sub>3</sub> , CEtMe <sub>2</sub> , CEt <sub>2</sub> Me	Semiconductor, optical	[149]
	CVD	[ <sup>t</sup> Bu)GaSe] <sub>4</sub>		[150]
GaTe	CVD	[(R)Ga(μ <sub>3</sub> -Te)] <sub>4</sub> , R = CMe <sub>3</sub> , CEtMe <sub>2</sub> , CEt <sub>2</sub> Me	Semiconductor, optical	[149]
GeO <sub>2</sub>	CVD	Ge(O' Bu) <sub>4</sub>	Optical	[143]
	Sol-gel	Ge(OEt) <sub>4</sub>		[151]
Gd <sub>2</sub> O <sub>3</sub>	Sol-gel	(Me <sub>3</sub> N) <sub>6</sub> (Ge <sub>32</sub> O <sub>64</sub> )(H <sub>2</sub> O) <sub>4.5</sub>		[152]
	Sol-gel	Gd(O' Pr) <sub>3</sub>	Transparent conducting oxide, optoelectronic	[153]
HfB <sub>2</sub>	CVD	Hf(BH <sub>4</sub> ) <sub>4</sub>	Hard coating, high melting point, chemical inertness	[154]
HfN	CVD	Hf(NMe <sub>2</sub> ) <sub>4</sub>	Insulator	[155]
HfO <sub>2</sub>	CVD	[Hf(μ-C <sub>5</sub> H <sub>11</sub> O)(OC <sub>5</sub> H <sub>11</sub> ) <sub>2</sub> ], Hf(O' Bu) <sub>4</sub> , Hf(tfac) <sub>4</sub> , tfac = C <sub>5</sub> H <sub>4</sub> F <sub>3</sub> O <sub>2</sub>	High dielectric constant	[156]
	Thermolysis	[Hf(OtBu) <sub>2</sub> (mmp) <sub>2</sub> ], [Hf(mmp) <sub>4</sub> ], mmp = C <sub>5</sub> H <sub>11</sub> O		[157]
HgS	Thermolysis	CHgSR, R = C <sub>6</sub> H <sub>5</sub> , <sup>i</sup> Pr	Optical, electrical	[158]
InN	CVD	(N <sub>3</sub> ) <sub>3</sub> In(C <sub>5</sub> H <sub>5</sub> N) <sub>3</sub>	Optoelectronic, semiconductor, blue light emitter	[29]
	CVD	[(CF <sub>3</sub> SO <sub>3</sub> )In{(CH <sub>2</sub> ) <sub>3</sub> NMe <sub>2</sub> }] <sub>2</sub> · (μ-N <sub>3</sub> )In{(CH <sub>2</sub> ) <sub>3</sub> NMe <sub>2</sub> }] <sub>n</sub>		[159]
In <sub>2</sub> O <sub>3</sub>	CVD	{(N <sub>3</sub> )In[(CH <sub>2</sub> ) <sub>3</sub> NMe <sub>2</sub> ]} <sub>2</sub> , N <sub>3</sub> In{C <sub>3</sub> H <sub>6</sub> NMe <sub>2</sub> }} <sub>2</sub>	Transparent conductive oxide	[160]
	CVD	[Et <sub>2</sub> InOH-Et <sub>2</sub> InNH <sub>2</sub> ], [(Pr <sub>2</sub> InOH)·(Pr <sub>2</sub> InNH <sub>2</sub> )]		[161]
InP	Photolysis	[Me <sub>2</sub> In(acac)] <sub>2</sub> , acac = C <sub>5</sub> H <sub>7</sub> O <sub>2</sub>		[162]
	Sol-gel	In(C <sub>5</sub> H <sub>7</sub> O <sub>2</sub> ) <sub>3</sub>		[163]
InS	Sol-gel	In(O' C <sub>3</sub> H <sub>7</sub> ) <sub>3</sub>	Infrared optical emitter	[164]
	CVD	[R <sub>2</sub> InP(SiMe <sub>3</sub> ) <sub>2</sub> ] <sub>2</sub>	Optoelectronic, photovoltaic	[165]
In <sub>2</sub> S <sub>3</sub>	Sol-gel	In(S <sub>2</sub> CNEt <sub>2</sub> ) <sub>3</sub>		[166]
	CVD	[In(SOCNEt <sub>2</sub> ) <sub>3</sub> ]	Semiconductor	[167]
InSb	CVD	In{(SOCNPr <sub>2</sub> ) <sup>i</sup> Pr} <sub>3</sub>		[168]
	Thermolysis	[Et <sub>2</sub> InSb(SiMe <sub>3</sub> ) <sub>2</sub> ] <sub>3</sub>	Electronic	[169]
InSe	CVD	[ <sup>t</sup> Bu) <sub>2</sub> In(μ-Se' Bu)] <sub>2</sub> , [(Me <sub>2</sub> EtC)In(μ <sub>3</sub> -Se)] <sub>4</sub>	Optoelectronic, photovoltaic	[170]
	CVD	In(Se <sub>2</sub> CNEt <sub>2</sub> ) <sub>3</sub>	Semiconductor	[166]
In <sub>2</sub> Se <sub>3</sub>	CVD	[(EtMe <sub>2</sub> C)InSe] <sub>4</sub>		[150]
	CVD	Me <sub>2</sub> InSePh		[171]
In <sub>2</sub> Se <sub>3</sub>	CVD	In(Se <sub>2</sub> CNMe <i>n</i> -hexyl) <sub>3</sub> , hexyl = C <sub>6</sub> H <sub>13</sub>	Optical, semiconductor	[172]
	CVD	In{SeC(SiMe <sub>3</sub> ) <sub>3</sub> }} <sub>3</sub>		[19]
La <sub>2</sub> O <sub>3</sub>	CVD	In(SePh) <sub>3</sub>		[171]
	CVD	La(C <sub>11</sub> H <sub>19</sub> O <sub>2</sub> ) <sub>3</sub>	Fuel cells	[173]
MgO	CVD	La(C <sub>5</sub> F <sub>6</sub> HO <sub>2</sub> ) <sub>3</sub>		[174]
	CVD	Mg(C <sub>11</sub> H <sub>19</sub> O <sub>2</sub> ) <sub>2</sub> , Mg(C <sub>5</sub> H <sub>7</sub> O <sub>2</sub> ) <sub>2</sub>	Buffer layer for HTc thin films	[175]
MnGa	CVD	MeMgO' Bu		[176]
	CVD	C <sub>32</sub> H <sub>62</sub> N <sub>4</sub> MgO <sub>2</sub>		[177]
MnGa	CVD	C <sub>13</sub> H <sub>26</sub> MgO <sub>4</sub>		[178]
	ALE	Mg(C <sub>5</sub> H <sub>5</sub> ) <sub>2</sub>		[179]
MoO <sub>2</sub> , MoO <sub>3</sub>	CVD	(CO) <sub>5</sub> MnGaEt <sub>2</sub> (NR <sub>3</sub> ), NR <sub>3</sub> = N(CH <sub>3</sub> ) <sub>3</sub> , NC <sub>7</sub> H <sub>13</sub> , [CO <sub>5</sub> Mn]Ga <sub>2</sub> [(CH <sub>2</sub> ) <sub>3</sub> NMe <sub>2</sub> ] <sub>2</sub>	Magnetic multilayer	[180]
	Sol-gel	MoO(OEt) <sub>4</sub> , MoO <sub>2</sub> (OEt) <sub>2</sub>	Catalyst	[181]
MoS <sub>x</sub>	Sol-gel	[(H <sub>3</sub> NC <sub>n</sub> H <sub>2n</sub> NH <sub>3</sub> )MoS <sub>4</sub> ]	Solar-cell application	[182]
Mo-Si	CVD	(C <sub>5</sub> H <sub>5</sub> ) <sub>2</sub> Mo(H)(SiH <sub>3</sub> )	High-temperature structural application	[183]
Nb <sub>2</sub> O <sub>5</sub>	Sol-gel	Nb(OEt) <sub>5</sub>	Catalyst, sensor	[184]
	Solvothermal	Nb(O' Bu) <sub>5</sub>	Semiconductor, photocatalyst	[185]
Nd <sub>2</sub> O <sub>3</sub>	CVD	Nd(tmhd) <sub>3</sub> , tmhd = C <sub>11</sub> H <sub>19</sub> O <sub>2</sub>	Dielectric resonator, ceramic filter, multilayer capacitor	[186]
	CVD	Ni(S <sub>2</sub> COCHMe <sub>2</sub> ) <sub>2</sub>	Optical	[187]
PbS	Pyrolysis	Pb(SC <sub>7</sub> H <sub>7</sub> ) <sub>2</sub>	Electronic, optical, optoelectrons	[107]
PbSe	Thermolysis	Pb{Se <sub>2</sub> CNEt <sub>2</sub> }} <sub>2</sub> , Pb{Se <sub>2</sub> CNMe(C <sub>6</sub> H <sub>13</sub> )}} <sub>2</sub>	Quantum dots	[188]
PdCu	CVD	PdCu(C <sub>5</sub> H <sub>7</sub> O <sub>2</sub> ) <sub>2</sub>	Catalyst	[189]

continued

Table 2. Continued

Material	Method	Precursor	Properties and application potentials	Ref.
PdRu	Thermolysis	$[\text{Pd}_6\text{Ru}_6(\text{CO})_{24}]^{2-}$	Catalyst	[190]
PdS	CVD	$\text{Pd}(\text{S}_2\text{COCHMe}_2)_2$	Optical	[187]
RhSn	Thermolysis	$\text{Rh}(\text{SnBu}_{4-x})_x$	Catalyst	[191]
SiC	Sono-chemical	$\text{MeSiH}_3$ , $\text{Me}_2\text{EtSiH}$	Hard coating, abrasive, optical coating, microelectric buffer layer	[192]
	Sono-chemical	$(\text{H}_3\text{Si-CH}_3)$		[193]
SiO <sub>2</sub>	Sol-gel	$\text{R-Si}(\text{OR})_3$ , $\text{R} = \text{Et, Me, } ^i\text{Pr}$	Microelectric	[194]
SnO <sub>2</sub>	CVD	$\text{Sn}(\text{O}^i\text{Bu})_4$	Gas-sensing behavior, semiconductor	[143]
	CVD	$\text{Sn}(\text{NO}_3)_4$		[195]
	CVD	$(\text{EtNH})_2\text{Me}_2\text{Sn}$		[196]
	Sol-gel	$\text{Sn}(\text{OEt})_4$ , $\text{Sn}(\text{ethylhexanoate})_4$		[197]
	Sol-gel	$\text{Sn}(\text{OR}^1)\text{F}[(\text{RC}_3\text{HO}_2\text{R}^2)-\text{C}_2]_2$ , $\text{R}^1 = ^i\text{Pr, Et, C}_5\text{H}_{11}\text{O}$ , $\text{R}^2 = \text{Me, } ^i\text{Bu}$		[198]
	CVD	$\text{Me}_4\text{Sn}$		[199]
SnS	Pyrolysis	$[(\text{C}_7\text{H}_7)_3\text{Sn}]_2\text{S}$	Semiconductor, optical	[200]
SnS, SnS <sub>2</sub> , Sn <sub>2</sub> S <sub>3</sub>	CVD	$[\text{Sn}(\text{SCH}_2\text{CH}_2\text{S})_2]$	Semiconductor, solar energy collector, photovoltaic	[201]
SnSe	Pyrolysis	$[(\text{C}_7\text{H}_7)_3\text{Sn}]_2\text{Se}$	Photoelectric, memory-switching devices	[200]
SnSe, SnTe	CVD	$[\text{Sn}\{(\text{SiMe}_3)_2\text{CH}\}_2(\mu\text{-E})]_2$ , $\text{E} = \text{Se, Te}$ , $(\text{Bn}_2\text{SnTe})_3$ , $\text{Bn} = \text{CH}_2\text{C}_6\text{H}_5$	Narrow-band semiconductor	[202]
				[203]
TaN	CVD	$\text{Ta}(\text{NEt}_2)_4$	Diffusion barrier, wear, corrosion resistance	[204]
	CVD	$\text{Ta}(\text{N}^i\text{Bu}(\text{or Pr}^i))(\text{}^i\text{Bu}_2\text{Pz})_3$		[205]
	CVD	$(\text{Bu}^i\text{N})\text{Ta}(\text{NEt}_2)_3$		[206]
	Thermolysis	$[(^i\text{BuCH}_2)_2\text{TaN}]_5$		[20]
Ta <sub>2</sub> O <sub>5</sub>	CVD	$[\text{Ta}(\text{OEt})_5]$	Microelectronic, dielectric gate	[207]
	CVD	$[\text{Ta}(\text{OEt})_4(\text{C}_5\text{H}_7\text{O}_2)]$ , $[\text{Ta}(\text{OEt})_4(\text{C}_{11}\text{H}_{19}\text{O}_2)]$		[208]
TiC	Colloidal	$\text{Ti}(n\text{-Bu})_4$	Hard coating	[209]
TiN	CVD	$[\text{Ti}(\text{NMe}_2)_2(\text{N}_3)_2(\text{bipy})]$ , $\text{bipy} = \text{C}_{10}\text{H}_8\text{N}_2$	Hard wear-resistant coating, diffusion barrier in microelectronics	[210]
		$[\text{Ti}(\text{NMe}_2)_3(\text{N}_3)(\text{bipy})]$ , $\text{bipy} = \text{C}_{10}\text{H}_8\text{N}_2$	High chemical resistivity, electrical conductor, optical	
	CVD	$[\text{Ti}_2\text{Cl}_4(\text{NN}(\text{CH}_3)_2)_2(\text{NH}_2\text{N}(\text{CH}_3)_2)_2]$		[211]
	Sol-gel	$\text{Ti}\{\text{N}(\text{SiMe}_3)_2\}_3$		[212]
	Sol-gel	$\text{TiH}_2(\text{NHMe})(\text{NH}_2)$		[213]
		$\text{Ti}(\text{NMe}_2)_4$		[155]
	CVD	$\text{Ti}(\text{NH}_2)_2\text{NH}$		[214]
TiO <sub>2</sub>	Sol-gel	$\text{Ti}(\text{O}^i\text{Bu})_4$	Photocatalyst, cosmetic industry	[215]
	Sol-gel	$\text{Ti}(\text{OEt})_4$		[216]
	CVD	$\text{Ti}(\text{NO}_3)_4$		[195]
	Sol-gel	$(^i\text{PrO})_2\text{Ti}(\text{Etacac})$ , $\text{acac} = \text{C}_5\text{H}_7\text{O}_2$		[217]
	CVD	$\text{Ti}(\text{OC}_3\text{H}_7)_4$		[218]
	CVD	$[\text{Ti}(\mu\text{-C}_5\text{H}_{11}\text{O})(\text{OC}_5\text{H}_{11})_3]_2$		[156]
Ti <sub>2</sub> O <sub>3</sub>	CVD	$\text{Ti}(\text{C}_5\text{H}_5)_3$ , $\text{Ti}(\text{C}_5\text{H}_4\text{Me})_3$	Thallium-containing HT superconductor	[219]
WO <sub>3</sub>	Sol-gel	$\text{WO}(\text{OEt})_4$ , $\text{WO}_2(\text{OEt})_2$	Catalyst, optical	[181]
WSi	CVD	$(\text{C}_5\text{H}_5)_2\text{W}(\text{H})(\text{SiCl}_3)$	Hard material	[183]
VO <sub>2</sub>	Sol-gel	$\text{OV}(\text{OR})_3$	Electrochromic displays	[220]
	CVD	$\text{VO}(\text{C}_5\text{H}_7\text{O}_2)_2$	Reversible cathodes for lithium batteries	[221]
	Sol-gel	$\text{OV}(\text{OC}_3\text{H}_7)_3$		[222]
Y <sub>2</sub> O <sub>3</sub>	CVD	$\text{Y}(\text{thd})_3$ , $\text{Y}(\text{thd})_3(\text{bipy})$ , $\text{bipy} = \text{C}_{10}\text{H}_8\text{N}_2$ , $\text{Y}(\text{C}_{11}\text{H}_{19}\text{O}_2)_3(\text{C}_{10}\text{H}_8\text{N}_2)$	Insulator, laser	[223]
ZrB <sub>2</sub>	CVD	$\text{Zr}(\text{BH}_4)_4$	Electrical	[224]
ZrN	Sol-gel	$\text{Zr}(\text{NEt}_2)_4$	High hardness, chemical resistance	[225]
ZrO <sub>2</sub>	CVD	$\text{Zr}(\text{C}_5\text{H}_7\text{O}_2)_2(\text{hfp})_2$ , $\text{hfp} = \text{OCH}(\text{CF}_3)_2$	Protective coating, dielectric	[226]
	CVD	$\text{Zr}\{\text{OC}(\text{CH}_3)_3\}_4$	High dielectric constant	[227]
	CVD	$[\text{Zr}(\text{O}^i\text{Bu})_2(\text{mmp})_2]$ , $[\text{Zr}(\text{mmp})_4]$ , $\text{mmp} = \text{C}_5\text{H}_{11}\text{O}$		[157]
	Sol-gel	$\text{Zr}(\text{OPr}^n)_4$		[228]
	CVD	$[\text{Zr}(\mu\text{-C}_5\text{H}_{11}\text{O})(\text{OC}_5\text{H}_{11})_3]_2$		[229]
	CVD	$\text{Zr}(\text{C}_5\text{H}_7\text{O}_2)_4$ , $\text{Zr}(\text{C}_{11}\text{H}_{19}\text{O}_2)_4$		[156]
	CVD	$\text{Zr}(\text{O}^i\text{Pr})_2(\text{C}_{11}\text{H}_{19}\text{O}_2)_2$ , $\text{Zr}_2(\text{O}^i\text{Pr})_6(\text{C}_{11}\text{H}_{19}\text{O}_2)_2$		[156]

continued

Table 2. Continued

Material	Method	Precursor	Properties and application potentials	Ref.
ZnO	CVD	[MeZnOSiMe <sub>3</sub> ] <sub>4</sub>	Optoelectronic, transparent UV protection	[230]
	CVD	Zn <sub>4</sub> O(C <sub>2</sub> H <sub>3</sub> O <sub>2</sub> ) <sub>6</sub>	Optical modulator, solar-cell coating	[231]
	Sol-gel	Zn(NO <sub>3</sub> )(C <sub>3</sub> H <sub>7</sub> O <sub>2</sub> )	Chemical sensor	[232]
ZnS	CVD	MeZn(OR), R = <sup>i</sup> Pr, <sup>t</sup> Bu		[233]
	Thermolysis	Zn{S <sub>2</sub> CN-Me(C <sub>6</sub> H <sub>13</sub> ) <sub>2</sub> }	Semiconductor, quantum dots, optical, electronic	[234]
	CVD	Zn(S <sub>2</sub> COCHMe <sub>2</sub> ) <sub>2</sub>	Optical coatings, solar-cell windows, photoconductor	[235]
	CVD	Zn{S <sub>2</sub> CN(C <sub>2</sub> H <sub>5</sub> ) <sub>2</sub> }		[236]
	Pyrolysis	Zn(SC <sub>7</sub> H <sub>7</sub> ) <sub>2</sub>		[107]
	CVD	Zn(S <sub>2</sub> O <sub>2</sub> C <sub>16</sub> H <sub>34</sub> N <sub>2</sub> )		[106]
	Sol-gel	Zn(S <sub>2</sub> CNMeC <sub>6</sub> H <sub>13</sub> ) <sub>2</sub>		[108]
ZnSe	Thermolysis	Zn[Se <sub>2</sub> CN-Me(C <sub>6</sub> H <sub>13</sub> ) <sub>2</sub> ]	Semiconductor, quantum dots	[234]
	CVD	[Zn <sub>10</sub> Se <sub>4</sub> (SC <sub>6</sub> H <sub>5</sub> ) <sub>16</sub> ] <sub>4</sub>		[110]
	Sol-gel	Zn(Se <sub>2</sub> CNMeC <sub>6</sub> H <sub>13</sub> ) <sub>2</sub>		[108]

Table 3. Selected single-source precursors for three-component systems.

Material	Method	Precursor	Properties and application potentials	Ref.
AgInS <sub>2</sub>	Pyrolysis	[(Ph <sub>3</sub> P) <sub>2</sub> AgIn(SC{O}Me) <sub>4</sub> ]	Linear and nonlinear optics	[237]
AgIn <sub>5</sub> S <sub>8</sub>	CVD	[(Ph <sub>3</sub> P) <sub>2</sub> AgIn(SC{O}Ph) <sub>4</sub> ]	Photovoltaic, solar-cell applications	[237]
Al(PO <sub>3</sub> ) <sub>3</sub>	Thermal	Al[N(P(O)Cl <sub>2</sub> ) <sub>2</sub> ] <sub>3</sub>	Ionic exchanger, ionic conductor, nonlinear optical material	[238]
BCN	CVD	Et <sub>3</sub> NBH <sub>3</sub>	High-temperature protective layer	[239]
	CVD	BN <sub>3</sub> H <sub>2</sub> (CH <sub>2</sub> ) <sub>6</sub>		[240]
BaTiO <sub>3</sub>	Thermolysis	Ba <sub>2</sub> Ti <sub>2</sub> (C <sub>11</sub> H <sub>19</sub> O <sub>2</sub> ) <sub>4</sub> (μ <sub>3</sub> -OEt) <sub>2</sub> ·(μ-OEt) <sub>4</sub> (OEt) <sub>2</sub> (EtOH) <sub>2</sub>	Dielectric	[44]
	Thermolysis	BaTi(OCH(CH <sub>3</sub> ) <sub>2</sub> ) <sub>6</sub> ·C <sub>6</sub> H <sub>6</sub>		[241]
	Polymeric	BaTi(C <sub>2</sub> H <sub>4</sub> O <sub>2</sub> ) <sub>3</sub> ·4C <sub>2</sub> H <sub>6</sub> O <sub>2</sub> ·H <sub>2</sub> O		[242]
BaZrO <sub>3</sub>	Sol-gel	[BaZr(OPr <sup>i</sup> ) <sub>5</sub> (OH)(Pr <sup>i</sup> OH) <sub>3</sub> ] <sub>2</sub>	Dielectric	[243]
CoAl <sub>2</sub> O <sub>4</sub>	Sol-gel	[CoAl <sub>2</sub> (OR) <sub>8</sub> ]	Ceramic pigment, coating, catalyst	[244]
CoFe <sub>2</sub> O <sub>4</sub>	Sol-gel	[CoFe <sub>2</sub> (OR) <sub>8</sub> ]	Ferromagnetic	[245]
CoGa <sub>2</sub> O <sub>4</sub>	Sol-gel	[CoGa <sub>2</sub> (OR) <sub>8</sub> ]	Ceramic pigment	[246]
CoMn <sub>2</sub> O <sub>4</sub>	Thermolysis	CoMn <sub>2</sub> (CO <sub>3</sub> ) <sub>3</sub>	Catalyst	[247]
CrCN	CVD	Cr(NEt <sub>2</sub> ) <sub>4</sub>	Hard coating	[248]
Cr-O-Si	Thermolysis	(O <sup>i</sup> Bu) <sub>3</sub> CrOSi(O <sup>i</sup> Bu) <sub>3</sub> , (O <sup>i</sup> Bu) <sub>2</sub> Cr[OSi(O <sup>i</sup> Bu) <sub>3</sub> ] <sub>2</sub>	Ethylene polymerization	[249]
CuAl <sub>2</sub> O <sub>4</sub>	Sol-gel	[CuAl <sub>2</sub> (OR) <sub>8</sub> ]	Catalyst	[244]
CuFe <sub>2</sub> O <sub>4</sub>	Sol-gel	[CuFe <sub>2</sub> (O <sup>i</sup> Bu) <sub>8</sub> ]	Dielectric	[245]
CuInS <sub>2</sub> , CuInSe	CVD	[{PBu <sub>3</sub> } <sub>2</sub> Cu(SEt') <sub>2</sub> In(SEt') <sub>2</sub> ]	Solar cell	[250]
	CVD	[{PPH <sub>3</sub> } <sub>2</sub> Cu(SEt') <sub>2</sub> In(SEt') <sub>2</sub> ]		[251]
	CVD	[{ER <sub>3</sub> }Cu(YR) <sub>2</sub> In(YR) <sub>2</sub> ] E = P, Y = S, Se, R, R' = alkyl, aryl		[252]
CuMn <sub>2</sub> O <sub>4</sub> , Cu <sub>1.5</sub> Mn <sub>1.5</sub> O <sub>4</sub>	Thermolysis	CuMn <sub>2</sub> (CO <sub>3</sub> ) <sub>3</sub> , CuMn(CO <sub>3</sub> ) <sub>2</sub>	Catalyst	[247]
GaAs <sub>x</sub> P <sub>3-x</sub>	Thermolysis	Ga <sub>2</sub> (As, P)Cl <sub>3</sub>	Semiconductor	[253]
GaIn <sub>1-x</sub> N	Pyrolysis	[(Br) <sub>2</sub> In((CH <sub>2</sub> ) <sub>3</sub> NMe <sub>2</sub> )] (Et <sub>3</sub> N)Ga(N <sub>3</sub> ) <sub>3</sub>	Semiconductor	[254]
GdFeO <sub>3</sub>	Sol-gel	[{GdFe(O <sup>i</sup> Pr) <sub>6</sub> }(HOPr <sup>i</sup> ) <sub>2</sub> ]	Magnetic	[255]
LaAlO <sub>3</sub>	Sol-gel	LaAl(O <sup>i</sup> Pr) <sub>6</sub>	Buffer layer for HTc, optical	[256]
LiMO <sub>2</sub> , M = Al, Ga	CVD	[Li(OCH <sub>2</sub> CH <sub>2</sub> OMe) <sub>2</sub> MMe <sub>2</sub> ] <sub>2</sub> , M = Al, Ga	Substrate for GaN	[257]
LiNbO <sub>3</sub>	Sol-gel, CVD	[LiNb(OEt) <sub>6</sub> ], [LiNb(O <sup>i</sup> Bu) <sub>6</sub> ]	Holographic recording material, ferroelectric	[258]
MgAl <sub>2</sub> O <sub>4</sub>	CVD	[MgAl <sub>2</sub> (OR) <sub>8</sub> ], R = <sup>i</sup> Pr or sec-Bu		[259]
	Sol-gel			[260]
	Polymeric route	Al <sub>2</sub> C <sub>18</sub> H <sub>36</sub> MgN <sub>3</sub> O <sub>9</sub>		[261]
	Sol-gel	[MgAl <sub>2</sub> (OPr <sup>i</sup> ) <sub>8</sub> ]		[262]
	CVD	[MgAl <sub>2</sub> H <sub>4</sub> (O <sup>i</sup> Bu) <sub>4</sub> ]		[243]
	CVD	MgAl <sub>2</sub> (O <sup>i</sup> Pr) <sub>8</sub> , MgAl <sub>2</sub> Me <sub>4</sub> (OR) <sub>4</sub> , R = <sup>i</sup> Pr, <sup>t</sup> Bu		[263]

continued

Table 3. Continued

Material	Method	Precursor	Properties and application potentials	Ref.
MgNb <sub>2</sub> O <sub>6</sub>	Sol-gel	MgNb <sub>2</sub> (OEt) <sub>12</sub>	Dielectric	[264]
NdAlO <sub>3</sub>	Sol-gel	[NdAl(O <sup>i</sup> Pr) <sub>6</sub> (HO <sup>i</sup> Pr) <sub>2</sub> ]	Optical	[265]
NiAl <sub>2</sub> O <sub>4</sub>	Sol-gel	[NiAl <sub>2</sub> (OR) <sub>8</sub> ]	Catalyst	[244]
NiFe <sub>2</sub> O <sub>4</sub>	Sol-gel	[Ni(H <sub>2</sub> O) <sub>6</sub> ] – [FeC](EDTA)H <sub>2</sub> ·4H <sub>2</sub> O	Magnetic	[266]
NiFe <sub>2</sub> O <sub>4</sub>	Sol-gel	[NiFe <sub>2</sub> (O <sup>i</sup> Bu) <sub>8</sub> ]		[245]
PbTiO <sub>3</sub>	Thermolysis	[PbTi <sub>2</sub> (μ <sub>4</sub> -O)(OOCCH <sub>3</sub> )(OCH <sub>2</sub> CH <sub>3</sub> ) <sub>7</sub> ] <sub>2</sub>	Dielectric	[267]
PbZrO <sub>3</sub>	CVD	PbZr(O <sup>i</sup> Bu) <sub>6</sub>	Microelectronic, optical	[268]
PrAlO <sub>3</sub>	Sol-gel	[PrAl(O <sup>i</sup> Pr) <sub>6</sub> (HO <sup>i</sup> Pr) <sub>2</sub> ]	Optical	[269]
Si <sub>3</sub> B <sub>3</sub> N <sub>7</sub>	Pyrolysis	Cl <sub>3</sub> SiNH <sub>2</sub> BH <sub>3</sub>	Monochromator	[270]
SiCN	Sol-gel	[Si(CN <sub>2</sub> ) <sub>2</sub> ] <sub>n</sub> , [H <sub>3</sub> CSi(CN <sub>2</sub> ) <sub>1.5</sub> ] <sub>n</sub>	High-temperature material	[271]
	CVD	Si <sub>2</sub> NH(CH <sub>3</sub> ) <sub>6</sub>		[272]
	CVD	Si <sub>2</sub> NH(CH <sub>3</sub> ) <sub>6</sub>	Tribological applications	[273]
Si <sub>1-x-y</sub> Ge <sub>x</sub> C <sub>y</sub>	CVD	Ge(SiMe <sub>3</sub> ) <sub>4</sub>	Semiconductor	[274]
SmFeO <sub>3</sub>	Sol-gel	Sm(Fe(CN) <sub>6</sub> ) <sub>4</sub> ·4H <sub>2</sub> O	Catalyst, fuel cell, NO <sub>2</sub> gas sensors	[275]
SrSnO <sub>3</sub> , Sr <sub>2</sub> SnO <sub>4</sub>	Hydrothermal	Sr <sub>2</sub> Sn(OH) <sub>8</sub>	Dielectric	[276]
SrTa <sub>2</sub> O <sub>6</sub>	CVD	[Sr{Ta(OEt) <sub>5</sub> (C <sub>7</sub> H <sub>17</sub> N <sub>2</sub> O)} <sub>2</sub> ]	Ferroelectric	[277]
	CVD	[Sr{Ta(O <sup>i</sup> Pr) <sub>6</sub> ] <sub>2</sub> ·2Pr <sup>i</sup> OH		[278]
SrZrO <sub>3</sub>	Pyrolysis	[SrZrO(C <sub>2</sub> O <sub>4</sub> ) <sub>2</sub> ·6H <sub>2</sub> O]	Fuel cell, protonic conductor	[279]
TaCN	CVD	Ta(NEt <sub>2</sub> ) <sub>5</sub>	Interconnecting material for circuit devices	[280]
	CVD	Ta(NEt <sub>2</sub> ) <sub>4</sub>	Diffusion barrier	[204]
TiAl <sub>2</sub> O <sub>5</sub>	Sol-gel	TiAl <sub>2</sub> (O <sup>i</sup> Pr) <sub>10</sub>	Photocatalyst	[281]
WCoO <sub>4</sub> , W <sub>n</sub> Co <sub>n</sub> C, n = 3, 6	Pyrolysis	(η <sup>5</sup> -C <sub>5</sub> H <sub>5</sub> )(CO) <sub>3</sub> WCo(CO) <sub>4</sub>	Coating on cutting tools	[282]
YAlO <sub>3</sub>	Sol-gel	YAl(O <sup>i</sup> Pr) <sub>6</sub>	Optical	[283]
YFeO <sub>3</sub>	Sol-gel	[YFe(OPr <sup>i</sup> ) <sub>6</sub> (Pr <sup>i</sup> OH) <sub>2</sub> ]	p-Type semiconductor, ethanol-sensing sensor	[284]
YGaO <sub>3</sub>	Sol-gel	[YGa(OPr <sup>i</sup> ) <sub>6</sub> (Pr <sup>i</sup> OH) <sub>2</sub> ]	Optical	[285]
ZnAl <sub>2</sub> O <sub>4</sub>	Sol-gel	[ZnAl <sub>2</sub> (OR) <sub>8</sub> ]	Semiconductor	[286]
ZnFe <sub>2</sub> O <sub>4</sub>	Sol-gel	[ZnFe <sub>2</sub> (O <sup>i</sup> Bu) <sub>8</sub> ]	Magnetic storage device, TV deflection units	[245]
ZnGa <sub>2</sub> O <sub>4</sub>	Sol-gel	ZnGa <sub>2</sub> (OR) <sub>8</sub>	Semiconductor	[287]
ZnIn <sub>2</sub> S <sub>4</sub>	CVD	Et <sub>2</sub> In(S <sub>2</sub> CNEt <sub>2</sub> )·ZnEt(S <sub>2</sub> C)	Photoconductor	[288]
Zr <sub>(1-x)</sub> Si <sub>x</sub> O <sub>2</sub>	CVD	Zr(acac) <sub>2</sub> (OSiMe <sub>3</sub> ) <sub>2</sub> , acac = C <sub>5</sub> H <sub>7</sub> O <sub>2</sub> Zr(acac) <sub>2</sub> (OSi <sup>i</sup> BuMe <sub>2</sub> ) <sub>2</sub> , acac = C <sub>5</sub> H <sub>7</sub> O <sub>2</sub>	High-dielectric material	[289]

during hydrolysis and gelation and does not break down into constituent alkoxides.

Although [MgAl<sub>2</sub>(OPr<sup>i</sup>)<sub>8</sub>(Pr<sup>i</sup>OH)<sub>2</sub>] is suitable to produce stoichiometric powders or films of MgAl<sub>2</sub>O<sub>4</sub> by the sol-gel process, it is not a convenient precursor for gas-phase synthesis of spinel particles or films because of its thermal instability [263, 317]. When this compound is heated under low-pressure conditions (LP-MOCVD) or stored for long time periods, the coordinated isopropyl alcohol molecules are knocked off, creating a coordinative insaturation at the Mg center. As a result the compound undergoes a structural change, giving rise to new Mg-Al species such

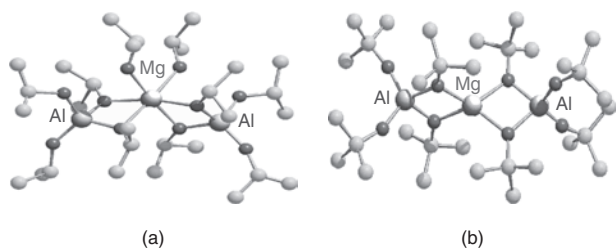


Figure 2. Molecular structures of [MgAl<sub>2</sub>(OPr<sup>i</sup>)<sub>8</sub>(Pr<sup>i</sup>OH)<sub>2</sub>] (a) and [MgAl<sub>2</sub>(OBu<sup>t</sup>)<sub>8</sub>] (b), precursors to MgAl<sub>2</sub>O<sub>4</sub>.

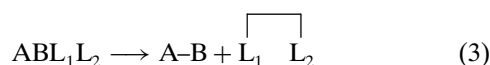
as [Mg<sub>2</sub>Al<sub>3</sub>(OPr<sup>i</sup>)<sub>13</sub>], which do not possess the Mg:Al ratio ideal for MgAl<sub>2</sub>O<sub>4</sub> [263]. The problem of thermal instability can be overcome by replacing the isopropoxide ligands with bulkier *tert*-butoxide ligands. The *tert*-butoxide derivative, [MgAl<sub>2</sub>(OBu<sup>t</sup>)<sub>8</sub>] [319], contains no coordinated alcohol molecules (Fig. 2b) and is thermally robust. In view of the above, it can be used in gas-phase reactions to obtain stoichiometric spinel films. However, the thermal stability acquired through the introduction of the bulky *tert*-butoxy ligands (–OC<sub>4</sub>H<sub>9</sub>) also imparts a low vapor pressure and higher organic contamination in the final material. This necessitates treatment at higher temperatures to remove the residual carbon content, however, only at the expense of grain growth. Such problems are typical in the chemical or molecular synthesis of materials and represent an area that has not been investigated from the viewpoint of (nano)materials chemistry. A probable solution would be a judicious choice of ligands and/or novel ligand combinations that undergo a clean stripping by intramolecular mechanisms, a strategy that is still not popular in the context of inorganic materials. The principles of organometallic chemistry permit the engineering of a *new generation* of precursors; the designed decomposition opens up new routes to high-purity nanomaterials at low temperatures.

**Table 4.** Selected single-source precursors for four-component systems and composites.

Material	Method	Precursor	Properties and application potentials	Ref.
CuCoMnO <sub>4</sub>	Thermolysis	CuCoMn(CO <sub>3</sub> ) <sub>3</sub>	Catalyst	[247]
SiBN <sub>3</sub> C	Pyrolysis	Cl <sub>3</sub> Si-NH-BCl <sub>2</sub>	High-temperature protective layer	[290]
Si <sub>2</sub> B <sub>2</sub> N <sub>5</sub> C <sub>4</sub>	Sol-gel	BC <sub>2</sub> Cl <sub>3</sub> H <sub>4</sub> Si	High-temperature resistant	[291]
SrBi <sub>2</sub> Ta <sub>2</sub> O <sub>9</sub>	Sol-gel	SrBi <sub>2</sub> Ta <sub>2</sub> (OCH <sub>2</sub> CH <sub>2</sub> OCH <sub>3</sub> ) <sub>18</sub>	Fatigue-free ferroelectric	[292]
TiSiCN	CVD	Cp <sub>2</sub> TiCH <sub>2</sub> Si(Me <sub>2</sub> )NSiMe <sub>3</sub>	Hard material	[293]
Ag/SiO <sub>2</sub>	Sol-gel	[AgSCH <sub>2</sub> Si(Me)(OEt) <sub>2</sub> ][AgCl] <sub>3</sub>	Electronic	[294]
Al <sub>x</sub> O <sub>3</sub> Si <sub>z</sub>	Thermolysis	Al{OSi(O <sup>i</sup> Bu) <sub>3</sub> } <sub>3</sub> (THF), Al{OSi(O <sup>i</sup> Bu) <sub>3</sub> } <sub>3</sub> (HO <sup>i</sup> Pr)-0.5[Al(O <sup>i</sup> Pr) <sub>3</sub> ] <sub>4</sub> , [( <sup>i</sup> PrO) <sub>2</sub> AlOSi(O <sup>i</sup> Bu) <sub>3</sub> ] <sub>2</sub>	Catalyst	[295]
BaCeO <sub>3</sub> /BaO	Sol-gel	Ba <sub>4</sub> Ce <sub>2</sub> O(C <sub>11</sub> H <sub>19</sub> O <sub>2</sub> ) <sub>4</sub> (O <sup>i</sup> Pr) <sub>10</sub> , BaCe <sub>2</sub> (C <sub>5</sub> H <sub>7</sub> O <sub>2</sub> )(O <sup>i</sup> Pr) <sub>9</sub>	Ionic conductor	[296]
CeAlO <sub>3</sub> /Al <sub>2</sub> O <sub>3</sub>	Sol-gel	[CeAl <sub>3</sub> (O <sup>i</sup> Pr) <sub>12</sub> ]	Automotive catalyst, oxygen storage capacity	[297]
Cu/Al <sub>2</sub> O <sub>3</sub>	Microemulsion	[CuAl <sub>2</sub> (O <sup>i</sup> Pr) <sub>8</sub> ]	Catalyst	[298]
Cu/SiO <sub>2</sub> , CuO/SiO <sub>2</sub>	Sol-gel	[CuOSi(O <sup>i</sup> Bu) <sub>3</sub> ] <sub>4</sub>	Heterogeneous catalyst	[299]
Cu/SiO <sub>2</sub>	Sol-gel	CuCl[PPPh <sub>2</sub> CH <sub>2</sub> CH <sub>2</sub> Si(OEt) <sub>3</sub> ] <sub>3</sub>	Catalyst	[194]
ErAlO <sub>3</sub> /Al <sub>2</sub> O <sub>3</sub>	Sol-gel	ErAl <sub>3</sub> (O <sup>i</sup> Pr) <sub>12</sub>	Optical	[300]
HfO <sub>2</sub> /SiO <sub>2</sub>	Pyrolysis	Hf{OSi(O <sup>i</sup> Bu) <sub>3</sub> } <sub>4</sub>	Antireflective thin film coating, catalyst	[301]
	Sol-gel	Hf{OSi(O <sup>i</sup> Bu) <sub>3</sub> } <sub>4</sub>		[301]
Ga/Ga <sub>2</sub> O <sub>3</sub>	CVD	[HGa(O <sup>i</sup> Bu) <sub>2</sub> ] <sub>2</sub>	Microelectronic, semiconductor	[302]
Ge/GeO <sub>2</sub>	CVD	[Ge(O <sup>i</sup> Bu) <sub>2</sub> ] <sub>2</sub>	Optical, catalytic	[143]
Ge/SiO <sub>2</sub>	Sol-gel	Me <sub>3</sub> GeS(CH <sub>2</sub> ) <sub>3</sub> Si(OMe) <sub>3</sub>	Optical	[303]
LaAlO <sub>3</sub> /Al <sub>2</sub> O <sub>3</sub>	Sol-gel	LaAl <sub>3</sub> (O <sup>i</sup> Pr) <sub>12</sub>	Automotive catalyst	[256, 297]
NdAlO <sub>3</sub> /Al <sub>2</sub> O <sub>3</sub>	CVD/sol-gel	[NdAl <sub>3</sub> (O <sup>i</sup> Pr) <sub>12</sub> (HO <sup>i</sup> Pr)]	Optical	[269]
Ni/Al <sub>2</sub> O <sub>3</sub>	Sol-gel	[NiAl <sub>2</sub> (OPr <sup>i</sup> ) <sub>8</sub> ]	Catalyst, pigment	[243]
NiO/ZnO	Sol-gel	Ni <sub>3</sub> Zn <sub>2</sub> (OH) <sub>8</sub> (CH <sub>3</sub> COO) <sub>2</sub> ·2H <sub>2</sub> O	Sorbent, catalyst, filter, structural material	[304]
Ni <sub>3</sub> Sn <sub>4</sub> /SnO <sub>2</sub>	CVD	Ni <sub>2</sub> Sn <sub>2</sub> (O <sup>i</sup> Bu) <sub>8</sub>	Catalyst	[305]
Os/SiO <sub>2</sub>	Sol-gel	OsCl <sub>2</sub> (η <sup>6</sup> -cumene){PPh <sub>2</sub> CH <sub>2</sub> CH <sub>2</sub> Si(OMe) <sub>3</sub> }	Electronic	[294]
Pb/PbO <sub>2</sub>	CVD	[Pb(O <sup>i</sup> Bu) <sub>2</sub> ] <sub>3</sub>		[143]
Pd/SiO <sub>2</sub>	Sol-gel	Pd(C <sub>8</sub> H <sub>22</sub> N <sub>2</sub> O <sub>3</sub> ) <sub>2</sub>	Catalyst	[306]
	Sol-gel	PdBr <sub>2</sub> {PEt <sub>2</sub> CH <sub>2</sub> CH <sub>2</sub> Si(OEt) <sub>3</sub> } <sub>2</sub>		[294]
PrAlO <sub>3</sub> /Al <sub>2</sub> O <sub>3</sub>	CVD/sol-gel	[PrAl <sub>3</sub> (O <sup>i</sup> Pr) <sub>12</sub> (HO <sup>i</sup> Pr)]	Optical	[269]
Pt/SiO <sub>2</sub>	Sol-gel	PtCl <sub>3</sub> {PPh <sub>2</sub> CH <sub>2</sub> CH <sub>2</sub> Si(OMe) <sub>3</sub> } <sub>2</sub>	Catalyst	[294]
Re/SiO <sub>2</sub>	Sol-gel	[Re(CO) <sub>5</sub> {PPh <sub>2</sub> CH <sub>2</sub> CH <sub>2</sub> Si(OMe) <sub>3</sub> }][BF <sub>4</sub> ]	Catalyst	[294]
Ru/SiO <sub>2</sub>	Sol-gel	Ru <sub>3</sub> (CO) <sub>10</sub> (H){SC <sub>3</sub> H <sub>6</sub> Si(OMe) <sub>3</sub> }	Catalyst	[294]
Si <sub>3</sub> N <sub>4</sub> /SiC	Pyrolysis	[CH <sub>3</sub> Si(H)NH] <sub>n</sub>	Mechanical properties	[307]
Sn/SnO <sub>2</sub>	CVD	[Sn(O <sup>i</sup> Bu) <sub>2</sub> ] <sub>2</sub>	Sensing and electric properties	[143]
TeO <sub>2</sub> /SiO <sub>2</sub>	Sol-gel	<sup>i</sup> Bu <sub>2</sub> Si(O <sup>i</sup> TeCl) <sub>2</sub>	Catalyst	[308]
TiO <sub>2</sub> /SiO <sub>2</sub>	Sol-gel	[Ti(O <sup>i</sup> Pr) <sub>2</sub> (SiOR) <sub>2</sub> ] <sub>2</sub>	Epoxidation catalyst	[309]
	CVD	(TiX <sub>2</sub> ) <sub>2</sub> O <sub>4</sub> (SiBu <sub>2</sub> ) <sub>2</sub> (X = Cl, Br, I)	Catalyst, antireflection films	[310]
	Pyrolysis	Ti[OSi(O <sup>i</sup> Bu) <sub>3</sub> ] <sub>4</sub>		[311]
	CVD	[ <sup>i</sup> C <sub>4</sub> H <sub>9</sub> O] <sub>3</sub> Si-O-Ti[O <sup>i</sup> C <sub>4</sub> H <sub>9</sub> ] <sub>3</sub>		[312]
V <sub>2</sub> O <sub>5</sub> /SiO <sub>2</sub>	Sol-gel	[ <sup>i</sup> Bu <sub>2</sub> SiOV(O)ClO] <sub>3</sub> , [OV(OSiO <sup>i</sup> Bu) <sub>3</sub> ]	Catalyst	[308]
	Sol-gel	OV[OSi(O <sup>i</sup> Bu) <sub>3</sub> ] <sub>3</sub>		[313]
ZrO <sub>2</sub> /Al <sub>2</sub> O <sub>3</sub>	Sol-gel	ZrAl <sub>2</sub> (O <sup>i</sup> Pr) <sub>10</sub>	Thermal barrier coatings	[314]
ZrO <sub>2</sub> /SiO <sub>2</sub>	Pyrolysis	Zr{OSi(O <sup>i</sup> Bu) <sub>3</sub> } <sub>4</sub>	Antireflective thin-film coating, catalyst	[301]
	Sol-gel	Zr{OSi(O <sup>i</sup> Bu) <sub>3</sub> } <sub>4</sub>		
ZrO <sub>2</sub> /Y <sub>2</sub> O <sub>3</sub>	Sol-gel	[ZrY <sub>2</sub> (OR) <sub>10</sub> ]	Catalyst, optical, high-temperature applications	[315]

### 3.1.2. Case II: Controlled Stoichiometry and Designed Ligand Elimination

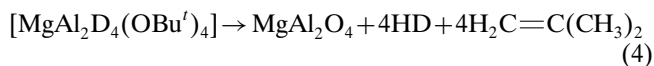
This class of precursors is based on a controlled ligand elimination pathway. With the use of the principles of organometallic chemistry, the ligands or combination of ligands in the precursor is judiciously chosen so that stripping of the organic periphery, which is usually the source of contamination in MDN, is simple and clean (Eq. (3)).



In the case of Mg-Al heterometal alkoxide precursors discussed here, the modification of the precursor by the introduction of hydride or alkyl ligands uses the  $\beta$ -elimination pathway on the metal centers. For example, Kim et al. have synthesized alkyl-modified derivatives of the general formula [Mg( $\mu$ -OR)<sub>2</sub>AlMe<sub>2</sub>]<sub>2</sub> (R = Pr<sup>i</sup>, Bu<sup>i</sup>) and successfully used them as single sources to deposit stoichiometric MgAl<sub>2</sub>O<sub>4</sub> films on Si(001) substrates [263]. Both of the precursors are much more volatile than MgAl<sub>2</sub>(OR)<sub>8</sub> compounds; Mg[( $\mu$ -O<sup>i</sup>Pr)<sub>2</sub>AlMe<sub>2</sub>]<sub>2</sub> can be vapor-transported at room temperature, whereas Mg[( $\mu$ -O<sup>i</sup>Bu)<sub>2</sub>AlMe<sub>2</sub>]<sub>2</sub> should be heated to 60 °C. Veith et al. have designed a more elegant



strategy in which the terminal alkoxide ligands on Al centers were replaced by hydride ligands [320] to obtain a hydride-modified Mg-Al *tert*-butoxide,  $[\text{MgAl}_2\text{H}_4(\text{O}i\text{Bu}^t)_4]$ . As a consequence of the drastic reduction in the molecular weight, an enhanced volatility is observed for the modified precursors ( $[\text{MgAl}_2(\text{O}i\text{Bu}^t)_8]$ , 100 °C;  $[\text{MgAl}_2\text{Me}_4(\text{O}i\text{Bu}^t)_4]$ , 60 °C;  $[\text{MgAl}_2\text{H}_4(\text{O}i\text{Bu}^t)_4]$ , 45 °C).



Both modification schemes are based on the abstraction of  $\beta$ -hydrogen (by an incipient carbanion) from the alkoxy group to eliminate methane ( $[\text{MgAl}_2\text{Me}_4(\text{O}i\text{Bu}^t)_4]$ ) or dihydrogen ( $[\text{MgAl}_2\text{H}_4(\text{O}i\text{Bu}^t)_4]$ ) and isobutene (Eq. (4)). This phenomenon is well established in organometallic chemistry and has been exploited for the deposition of ZnO and MgO from methyl zinc alkoxide and methyl magnesium alkoxide, respectively [233]. Figure 3 shows the ligand elimination mechanism operative in the alkyl- and hydride-modified Mg-Al alkoxides. The on-line mass spectral analysis performed during the chemical vapor deposition of  $[\text{MgAl}_2\text{H}_4(\text{O}i\text{Bu}^t)_4]$  revealed isobutylene and dihydrogen to be the only volatile by-products. Veith et al. verified further the proposed mechanism by investigating the thermal decomposition of deuterated compound,  $[\text{MgAl}_2\text{D}_4(\text{O}i\text{Bu}^t)_4]$  [320]. The observation of a new peak at  $m/z = 3$  instead of the peak due to molecular hydrogen ( $m/z = 2$ ) confirmed the abstraction of  $\beta$ -hydrogen by the terminal deuteride ligands, resulting in the formation of HD. The above example illustrates that a careful selection of ligands can be used to design the decomposition behavior of the precursor compound. Since all of the thermolysis products are volatile organic compounds, "organic-free" nanomaterials can be obtained at low temperatures.

### 3.1.3. Case III: Single-Step Formation of Multiphase Materials

This class of precursors represents a rather new strategy where two discrete solid phases can be obtained from a single molecular species. This approach uses precursors with unusual stoichiometry or oxidation states. In the first case, the driving force is often the phase separation from a metastable matrix to give two or more thermodynamically stable phases, whereas the disproportionation of a

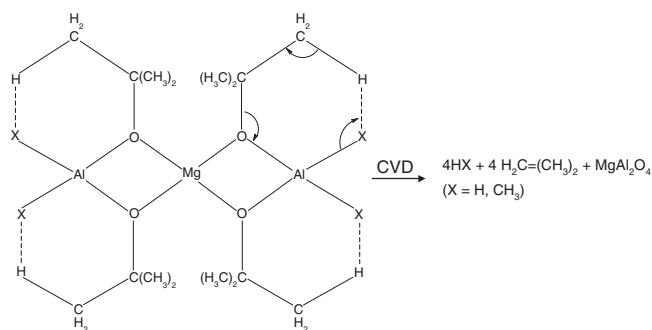
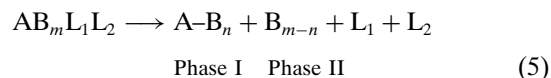
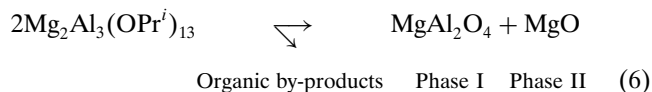


**Figure 3.** Ligand elimination mechanism in hydride- and alkyl-modified Mg-Al *tert*-butoxides.

metastable precursor is responsible, in the latter case, for the formation of a composite material. The thermolysis of alkyl silicon alkoxides ( $\text{R}_x\text{-Si}(\text{OR})_{4-x}$ ) to produce SiC/SiO<sub>2</sub> composite or that of  $\text{LaAl}_3(\text{OPr}^i)_{12}$  to form  $\text{LaAlO}_3/\text{Al}_2\text{O}_3$  belongs to the first category, whereas the disproportionation of a Cu(I) precursor to give Cu(0) and Cu(II) species from a single source exemplifies the second category. Since these composites originate from a single chemically homogeneous source, the different phases are homogeneously interdispersed, and it is possible to control their three-dimensional structures and the grain sizes of the individual phases.



For instance, the Mg-Al isopropoxide,  $[\text{Mg}_2\text{Al}_3(\text{OPr}^i)_{13}]$  (Fig. 4), which can be prepared in good yield by reacting Mg and  $\text{Al}(\text{OPr}^i)_3$  in refluxing isopropyl alcohol [317], serves as a unimolecular source to obtain a biphasic oxide-oxide composite of composition  $\text{MgAl}_2\text{O}_4/\text{MgO}$  [321]. The X-ray powder diffractogram of the oxide-oxide nanocomposite



obtained from the above precursor shows that both phases are crystalline (Fig. 5). The TEM image revealed a homogeneous biphasic material in which MgO grains are evenly dispersed in a nanocrystalline matrix of spinel particles.

The current interest in the design of nanomaterials at the molecular scale is largely driven by the ability of chemical methods to permit the control of size, shape, and purity, which ultimately influence the final properties of the nanomaterials. In this context, the use of SSPs is highly favored to achieve an atomic-scale mixing of the elements in target nanomaterial. The concept of using a single molecular source or a molecular building block is derived in principle from biomolecular, supramolecular, or polymeric structures where a repetitive arrangement of one or more fundamental structural units can lead to novel architectures and properties [33]. However, for inorganic materials, the molecular

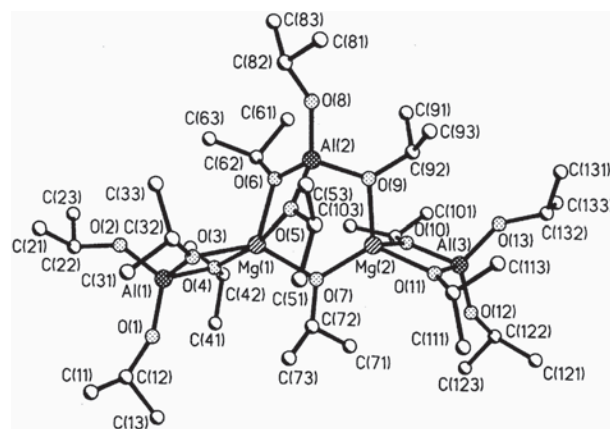


**Figure 4.** Molecular structure of  $[\text{Mg}_2\text{Al}_3(\text{OPr}^i)_{13}]$ . Reprinted with permission from [317], J. A. Meese-Marktscheffel et al., *Chem. Mater.* 5, 755 (1993). © 1993, American Chemical Society.

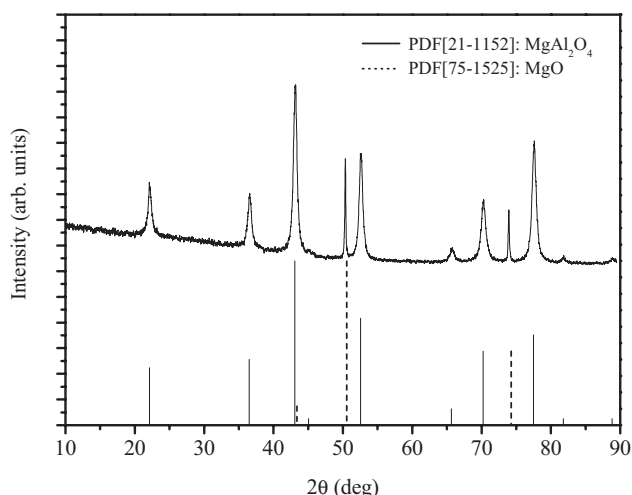


**Figure 5.** XRD pattern of  $\text{MgAl}_2\text{O}_4/\text{MgO}$  nanocomposite obtained from  $[\text{Mg}_2\text{Al}_3(\text{OPr})_{13}]$  precursor.

building units are intermediates between the extended network and the atoms forming it. Attention is paid to the connectivity between the elements that should be present in the final material after all of the processing steps have been performed. In other words, the molecular precursor for MDN provides intermediate control of the process of formation of large structures.

Some of the salient features and promises of the single molecular source approach are (i) the possibility of tuning the metal and organic contents in a molecule according to the requirements of the material; (ii) low decomposition/crystallization temperatures, since the metals are already mixed on a molecular scale and no diffusion of ions is necessary; and (iii) ultrahigh purity of the resulting ceramics or composites because of the neat decomposition processes that can be tuned by the appropriate ligand elimination mechanism. In addition, the use of a single molecular species avoids phenomena like preferential hydrolysis or crystallization during solution processing and selected pyrolysis of one of the constituents in thermolysis reactions, which are typical features of a multisource synthesis. A large number of chemical compounds belonging to different organometallic groups have been exploited to obtain solid materials of different compositions. The main classes of precursors used in (nano)material synthesis are presented in Table 5.

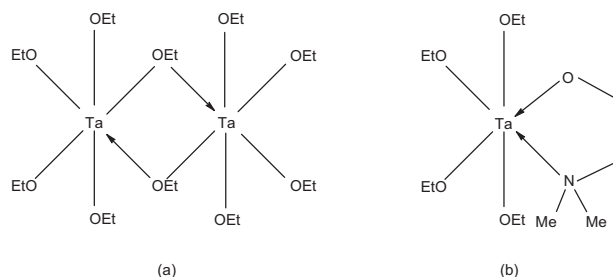
One of the major advantages of using metal-organics in processing new materials is the flexibility of varying both the organic and metallic parts of the molecular source. In the case of metal alkoxides, a common problem is their propensity to expand the coordination number at the metal center, either by intermolecular association (oligomerization) or by reaction with adventitious water or oxygen [45, 49–51, 322–326]. This adversely affects their properties, such as volatility, which is an important feature for their easy transport in the gas phase. A simple approach to preventing this is to modify the alkoxide precursor with chelating or donor functionalized ligands, that produces species with coordinatively saturated metal centers. Jones et al. have shown that dimeric Nb and Ta alkoxides can be modified by alkoxide groups containing one donor function, such as dimethyl

**Table 5.** Commonly used precursors<sup>a</sup> in the synthesis of (nano)-materials.

Hydrides/halides	$\text{MH}_x$ , $\text{R}_x\text{MH}_y$ , $\text{M}(\text{BH}_4)_x$ , $\text{MHal}_x$ , Hal = F, Cl, Br, I
Nitrates	$\text{M}(\text{NO}_3)_x$ , $\text{M}(\text{NH}_4)_x(\text{NO}_3)_y$ , $\text{M}(\text{NO}_3)_x \cdot y\text{H}_2\text{O}$
Oxalates, acetates	$\text{M}(\text{HOOCOO})_x$ , $\text{M}(\text{CH}_3\text{COO})_x$
Alkyls	$\text{MR}_x$ , $\text{MR}_x\text{R}'_y$
Carbonyls	$\text{M}(\text{CO})_x$ , $(\text{CO})_x\text{ML}_y$ , L = donor ligand
Cyclopentadienylides	$\text{M}(\text{C}_5\text{H}_5)_x$ , $(\text{C}_5\text{H}_5)\text{M}(\text{CO})_x\text{R}_y$ , $(\text{N}_3)_x\text{M}(\text{C}_5\text{H}_5\text{N})_y$
Amides	$\text{MR}_x(\text{NH}_2)_y$ , $\text{M}(\text{NR}_2)_x$ , $(\text{N}_3)_x\text{M}(\text{RN})_y$
Silanes	$\text{R}_x\text{SiL}_y$ , L = OR, halide
Silazanes	$\text{M}\{\text{N}(\text{SiR}_3)_2\}_x$
$\beta$ -diketonates	$\text{M}(\beta\text{-dik})_x$ , $\beta\text{-dik}$ = acac, dpm, tmhd, od, hfac, fod
Alkoxides	$\text{M}(\text{OR})_x$ , $\text{LM}(\text{OR})_x$ , L = R, O, OH, halide
Siloxanes	$\text{M}(\text{OSiR})_x$ , $\text{R}_3\text{Si-O-MR}_x$ , $\text{M}(\text{R})_x(\text{OSiR}_3)_y$
Thiolates (selenolates, tellurates)	$\text{M}(\text{ER})_x$ , E = S, Se, Te
Thiocarbamates	$\text{M}(\text{R}_2\text{NCOS})_x$

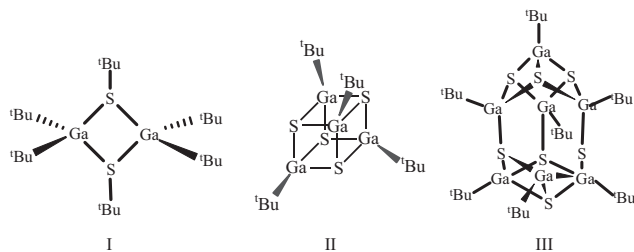
<sup>a</sup>M = Metal; R = Me, Et, <sup>i</sup>Pr, <sup>t</sup>Bu, <sup>n</sup>Bu, <sup>i</sup>Bu, Ph, and substituted alkyl or phenyl groups.

aminoethoxide ( $\text{OCH}_2\text{CH}_2\text{NMe}_2$ ), to obtain monomeric species (Scheme 5) with a 10-fold increase in the vapor pressure ( $\text{Ta}_2(\text{OEt})_{10}$ , 0.075 torr/108 °C;  $\text{Ta}(\text{OEt})_4(\text{OCH}_2\text{CH}_2\text{NMe}_2)$ , 0.75 torr/108 °C) [327]. Furthermore, multidentate ligands can be used to modify the reactivity of alkoxide precursors, for example, by decreasing the number of hydrolyzable (terminal) ligands. The modification of ligand sets not only alters the physical and chemical properties of the precursor systems, but also seems to have a pronounced influence on the properties of the resulting materials. Boyle et al. have investigated the densification behavior of  $\text{TiO}_2$  films obtained with the use of various carboxylic acid-modified titanium alkoxides in a sol-gel process. The structure of the Ti–O framework depends on the steric bulk of the ligands and the  $\text{Ti}(\text{OR})_4/\text{carboxylic acid}$  ratio [328]. The results indicate that small nuclearity clusters favored fully dense materials, which illustrates the relationship between precursor structure and final film properties. If the modification of precursor is achieved with polymerizable organic ligands such as methacrylic acid or methyl methacrylate, clusters capable of undergoing polymerization or cross-linking reactions are obtained. Such organically modified clusters entail a synergetic combination of the properties typical of each of the constituents, giving rise to the class of inorganic-organic hybrid materials [329].



**Scheme 5.**

Another significant advantage of the molecular precursor approach is the production of metastable materials. Since the molecule-to-material transformations operate far from equilibrium conditions, kinetically rather than thermodynamically favored products are formed. Barron et al. have shown that the easy formation of metastable cubic GaS is determined by the cubane structure of the precursor compound,  $[(t\text{Bu})\text{GaS}]_4$ , which is preserved under MOCVD conditions. The structure of the precursor was determined and found to be identical at 25 and 250 °C by single-crystal X-ray diffraction and gas-phase electron diffraction studies [149, 330]. Their work on several other gallium thiolates and selenolates is an elegant effort to elucidate the role of precursor structure in determining the phase of the material. The different GaS compounds (Scheme 6) were found to produce different solid-state phases in the films deposited by their chemical vapor deposition), which may be related to the symmetry of the core structures. For example, chemical vapor deposition) of the dimer  $[(\text{Bu}')_2\text{Ga}(\text{SBU}') ]_2$  (I), possessing a  $\text{Ga}_2\text{S}_2$  core of  $C_{2v}$  symmetry, yields poorly crystalline hexagonal GaS. On the other hand, the highly symmetrical  $\text{Ga}_4\text{S}_4$  core of  $[(t\text{Bu})\text{GaS}]_4$  (II) provides a template for a high-symmetry solid phase (cubic GaS). In a similar manner, the lack of any but  $C_3$  symmetry in heptameric  $[(t\text{Bu})\text{GaS}]_7$  (III) should result, if the core is retained during the deposition, in an amorphous film. The  $\text{Ga}_7\text{S}_7$  core of  $[(t\text{Bu})\text{GaS}]_7$  has a  $C_3$  axis with no possibility of ordered close packing. Thus, during CVD a random array of Ga and S atoms is incorporated into the film. Indeed, an amorphous film is obtained when  $[(t\text{Bu})\text{GaS}]_7$  is used in the MOCVD process [18].



Scheme 6.

Furthermore, the SSPs can facilitate the formation of those ceramic materials (e.g., nitrides) whose syntheses are severely constrained by the reaction conditions. Transition metal nitrides possess free energies of formation that are extremely less favorable than corresponding oxides, principally because of the tremendous strength of the  $\text{N}=\text{N}$  bond ( $227 \text{ kcal mol}^{-1}$ ) relative to  $\text{O}_2$  ( $119 \text{ kcal mol}^{-1}$ ). Consequently, the preparation of  $[\text{MN}_n]$  from the respective elements is entropically disfavored at the high temperatures necessary to ensure sufficient diffusion rates. In this case, the metal amides, given the covalent nature of metal–nitrogen bonds, act as convenient SSPs to obtain metal nitride phases at low temperatures.

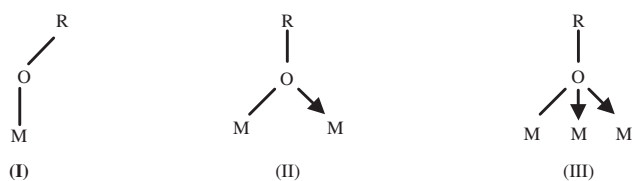
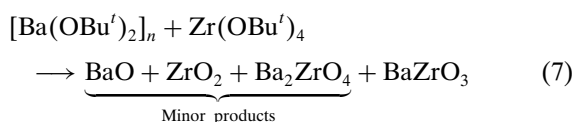
Given the importance of molecular chemistry routes in the synthesis of nanomaterials, the challenge is to develop synthetic rationales for a customized assembly of molecular building blocks from the fundamental components (metals and ligands) that would facilitate a prefabrication of suitable precursor to any desired nanomaterial. However, it

would be overly simplistic to assume that a single molecular source is the only structure from which target material can be obtained. Given the versatility and development of synthetic chemistry, the range of potential molecular structures that can be used to obtain new materials and nanomaterials appears to be unlimited. A major bottleneck in this regard is the fact that molecular control of materials is not a predictive science, and it is difficult to anticipate the phase structure of the resulting solid from the knowledge of the precursor design. Most of the work performed to demonstrate the strength of molecular chemistry methods in achieving better control over the phase purity and composition of the materials is based on an explanation with hindsight, achieved after the experiment was concluded. In this context, there is an urgent need to develop an understanding of the precursor–material relationship based on the mechanism of precursor decomposition and the structural and chemical factors that govern (or disfavor) molecular control over the process of material formation. The ability to answer the question, Can the molecular structure of the precursor species influence the phase of the final solid product? is the driving force for the current quest for SSPs to nanoscale materials.

Despite the potential advantages of metal–organic precursors as molecular sources for the low-temperature synthesis of nanomaterials, their application to most of the materials is limited because of the unavailability of compounds containing all of the phase-forming elements in a single source. In most of the cases, the selection of a suitable precursor is dictated by the requirements of the material and the synthesis methods. Subject to the processing conditions (solid, solution, or gas phase), the inherent properties of the precursor can impose limitations on the building-block approach. For example, the pyrophoric nature, poor solubility, and extremely low vapor pressure of a compound can limit its application in solid-state, liquid, and gas-phase synthesis, respectively. The other related and equally important parameters are the stability of the molecular framework and stoichiometry of the cations. The fact that the construction of metal–organic species (e.g., alkoxides, amides, metal–metal bonded clusters, etc.) is based on the principles of charge neutrality and electron count limits the choice when precursors to nonstoichiometric compounds or doped materials are sought.

To understand what precursor chemistry implies, the isolation and characterization of preceramic aggregates are necessary, because similar molecular building blocks can arrange themselves in different ways to produce compounds with different metal stoichiometries. For example, heterometal alkoxides are invariably formed in a mixture of constituent alkoxides; however, a simple mixing of two alkoxides,  $\text{M}(\text{OR})_x$  and  $\text{M}'(\text{OR})_y$ , is no guarantee of the formation of a single precursor species  $\text{MM}'(\text{OR})_{x+y}$  mainly due to the structure potential (I, II, and III, Scheme 7) of alkoxide ligands. As a result, in addition to the desired precursor, several other compounds may be present in an uncharacterized precursor mixture, depending upon the chemical requirements of the individual components and reaction conditions. For example, Ba and Zr(Ti) alkoxides can combine in different ways to produce mixed-metal Ba–Zr(Ti) clusters with different structures and metal ratios [331]. Of course, the

formation of a particular framework is subject to the chemical nature (neutral or anionic) and steric profile of the ligands. Some examples of alkoxide clusters based on different Ba:Zr(Ti) ratios are shown in Figure 6. As a consequence of this combinatorial effect, the synthesis of BaZrO<sub>3</sub> from a mixture of Ba and Zr precursors was associated with traces of Ba and Zr phases or their products in the final ceramic material, whereas BaZrO<sub>3</sub> could be selectively synthesized from the single-source Ba-Zr precursor [BaZr(OH)(OPr<sup>i</sup>)<sub>5</sub>(Pr<sup>i</sup>OH)<sub>3</sub>]<sub>2</sub> (Eqs. (7) and (8)) [332].



Scheme 7.

To act as a suitable chemical source for material synthesis, the precursor compound should fulfill a set of requirements. The basic criteria for designing and synthesizing a metal-organic precursor are

- Simple and scalable synthesis
- High purity and purifiability by sublimation or distillation
- Easy handling and long shelf life
- Clean decomposition behavior

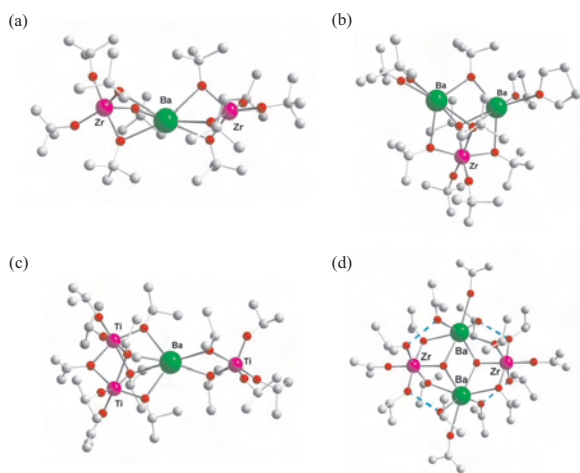


**Figure 6.** Molecular structure of different Ba-Zr(Ti) alkoxide clusters: (a) [BaZr<sub>2</sub>(OBU<sup>i</sup>)<sub>10</sub>] (Ba:Zr = 1:2), (b) [Ba<sub>2</sub>Zr(OBU<sup>i</sup>)<sub>8</sub>(HOBU<sup>i</sup>)<sub>2</sub>(THF)] (Ba:Zr = 2:1), (c) [BaTi<sub>3</sub>(OPr<sup>i</sup>)<sub>14</sub>] (Ba:Ti = 1:3) and (d) [BaZr(OPr<sup>i</sup>)<sub>5</sub>(OH)(HOPr<sup>i</sup>)<sub>3</sub>]<sub>2</sub> (Ba:Zr = 1:1). Reprinted with permission from [23], M. Veith, *J. Chem. Soc., Dalton Trans.* 2405 (2002). © 2002, Royal Society of Chemistry.

- Must not form stable residues
- Decomposition at low temperatures
- No(?) chemical hazards (nontoxic and noncorrosive by-products).

In addition to the above attributes, metal-organics should meet the following requirements to be SSPs:

- Appropriate element ratio compatible with the target material
- Sufficient stability of the molecular framework to survive different experimental conditions (e.g., thermolysis and hydrolysis)
- Low molecular weight and low nuclearity to achieve acceptable vapor pressure
- Predefined reaction/decomposition chemistry
- Minimum heteroatom content in the ligands used to build or stabilize the molecule.

Further properties of a “tailor-made” precursor are subject to the nature and condition of the processing methods. These specific criteria, for example, can be high vapor pressure, a large temperature window between evaporation and decomposition, and thermal lability for the methods involving gas-phase decomposition, whereas high solubility, stability in solution (no dissociations or rearrangements), and high reactivity are of interest for solution-based transformation. It must be pointed out that all of these conditions are seldom met in a single molecular species, and the quest for an “ideal” precursor is responsible for the rapidly increasing chemistry–material science interface.

Although a wealth of information on the synthesis and characterization of inorganic molecular derivatives is available, a continuous input based on new synthetic principles and reaction chemistry is desired to discover a provisional and plausible sequence of transformation that will convert a starting configuration (molecular precursor) into the desired final state (nanomaterial). The current approach of using molecular building blocks to grow nanomaterials is backward chaining, where the role of precursor chemistry in determining the structure and purity of the synthesized material is analyzed in a retrosynthetic manner. The concept of designing molecular precursors to mimic and act as preforms for known solid-state structures is still in its infancy and needs a systematic exploration to elucidate the potential of this methodology in terms of obtaining device-quality materials with improved performance when compared with materials obtained by conventional routes. Furthermore, the diversity of molecular structures and structural motifs available to synthetic chemists acts as a pointer for future research dealing with the synthesis of inorganic materials with unusual structures, new compositions, and possibly unknown properties.

#### 4. METHODS FOR MOLECULE-TO-MATERIAL TRANSFORMATION

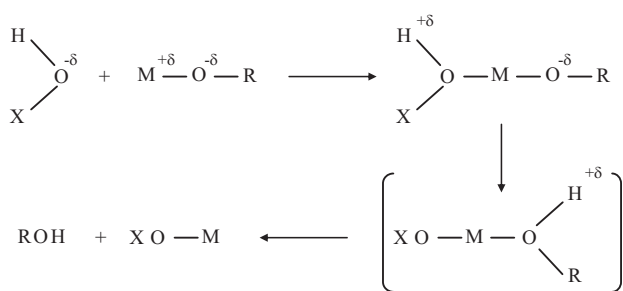
The chemical methods commonly applied to the synthesis of nanomaterials involve reactions in different phases: solid (mechanical attrition, mechanochemical synthesis,



sonochemical treatment), solution (sol-gel, coprecipitation, hydrothermal synthesis, electrochemical, micro(nano)-emulsion and polymeric precursor methods), and gas (chemical vapor deposition, aerosol synthesis, atomic layer deposition). The methods described in the following section are only a subset of the wide variety of chemical routes being investigated for the preparation of nanomaterials. The underlying criterion for the selection of these chemical methods is the fact that either they rely on the availability of molecular chemical compounds as precursors or the inherent advantages of the method(s) are fortified by the use of metal-organic precursors. There has been no attempt to be comprehensive, but we have tried to provide an overall picture of the developments in material synthesis from chemical methods.

#### 4.1. Sol-Gel Process

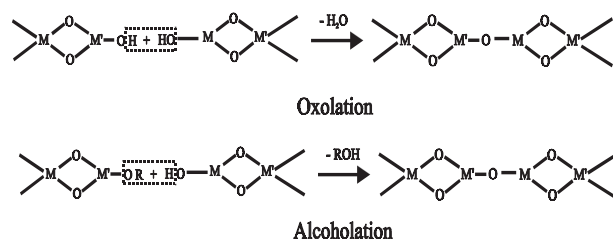
The sol-gel technique refers to a room-temperature chemical route that is used for preparing oxide materials by the hydrolysis of metal-organic compounds (particularly metal alkoxides) carried out under controlled pH, amount of water, and alkoxide concentration [333]. The process involves initially a homogeneous solution of metal alkoxide derivatives such as  $M(OR)_x$  or  $MM'(OR)_{x+y}$ , which is “activated” by a careful hydrolysis to initiate inorganic polymerization reactions that produce species containing M–O–M or M–O–M’ linkages [194]. The fundamental reaction in the hydrolysis of metal alkoxides is a nucleophilic substitution ( $SN^2$ ) that involves a nucleophilic addition of an  $OH^-$  group to the electrophilic metal center ( $M^{+\delta}$ ). As a result, the coordination number of the metal atom is increased in the transition state, which leads to the migration of a proton toward an alkoxy group, consequently knocking off the protonated ROH ligand (Scheme 8).



Scheme 8.

The metal species bearing a terminal hydroxy group react with other species in the solution to form oligomeric structures linked by oxo- or hydroxo- ligands, which can be transformed into polymeric gels by aging. The polymerization reactions and the subsequent drying and thermal treatments result in the elimination of water (oxolation) and alcohol (alcoholation) to finally produce a solid material (Scheme 9). These modified molecular entities arrange themselves via hydrolysis and cross-condensation reactions

to form oxo- or hydroxo-macromolecular networks, thus favoring the gelation process.



Scheme 9.

The stage where the molecular structure of the precursor is no longer reversible is called a sol-gel transition. The gel is an elastic solid filling the same volume as the solution; it shrinks upon drying to give a rigid oxide skeleton with interconnected porosity that can be tailored in terms of size, shape, and volume. The natural drying of gels results in xerogels, whereas removal of the solvent under hypercritical conditions (without disturbing the gel structure) produces aerogels [334]. A schematic representation of the various steps of the sol-gel processing is given in Figure 7.

The partially hydrolyzed alkoxides can be viewed as molecular building blocks for the development of sol (particulate) or gel (polymeric), which can be used to obtain films by spin- or dip-coating and spray methods. Modifying the alkoxide precursors with less hydrolyzable or polymerizable groups can chemically control the condensation reactions [37, 335, 336]. Finally, the chemical reactivity of metal alkoxides toward nucleophilic reactions mainly depends on the strength of the nucleophile, the electrophilic character of the metal atom (an electronegativity-related property characterized by the positive charge on the metal atom), and its ability to increase the coordination number  $N$ : the degree of unsaturation at the metal center can be simply expressed by the difference  $N - Z$ , where  $N$  is the coordination number usually found in the oxide and  $Z$  is the oxidation state. A comparison of these values for some tetravalent metal alkoxides is made in Table 6. The above facts underline the critical role of the precursor chemistry when materials are

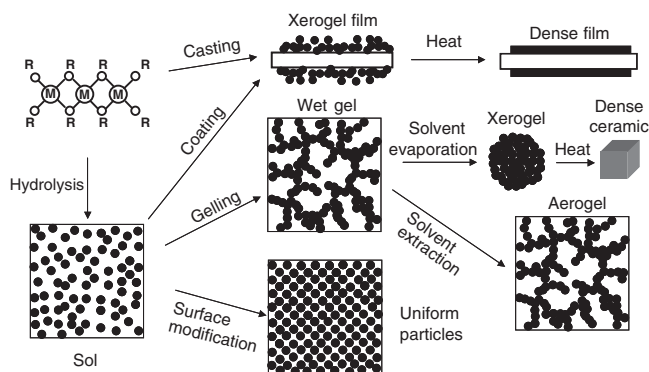


Figure 7. Various steps of sol-gel processing starting from a molecular alkoxide.

**Table 6.** A comparison of electronegativity, ionic radius, and preferred coordination number in some tetravalent metal alkoxides.

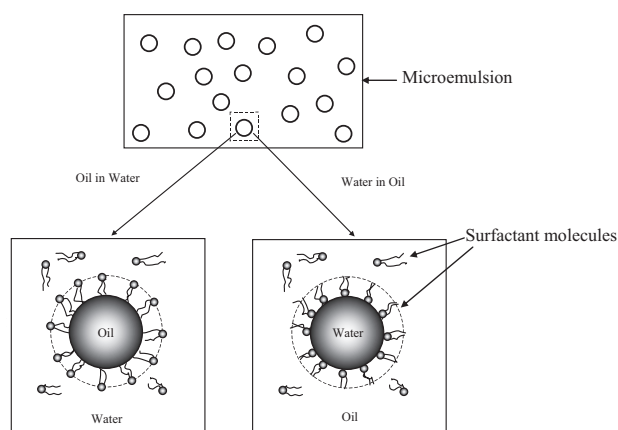
Alkoxide	Electronegativity ( $\chi$ )	Ionic radius ( $\text{\AA}$ )	Oxide	$N$	$N - Z$
$\text{Si}(\text{OPr}^i)_4$	1.74	0.40	$\text{SiO}_2$	4	0
$\text{Sn}(\text{OPr}^i)_4$	1.89	0.60	$\text{SnO}_2$	6	2
$\text{Ti}(\text{OPr}^i)_4$	1.32	0.64	$\text{TiO}_2$	6	2
$\text{Zr}(\text{OPr}^i)_4$	1.29	0.87	$\text{ZrO}_2$	7	3
$\text{Ce}(\text{OPr}^i)_4$	1.17	1.02	$\text{CeO}_2$	8	4

synthesized from chemical methods, but at the same time it offers the possibility of chemical control over the molecule-to-material transformation process.

The main advantages of sol-gel processing are easy control over the microstructure of the material from the earliest stages of the processing, higher purity, low or high porosity, and greater homogeneity. In addition, it allows facile synthesis of homogeneously doped systems, biphasic nanocomposites [337, 338]. In terms of economic potential, net-shape casting, extrusion, and coatings on large and complex surfaces are the major engineering advantages [194]. On the other hand, the long processing times, costs of the precursors, large shrinkage, production of volatiles, and fragmentation of the green body due to internal stresses are some of the limitations associated with this technique.

## 4.2. Microemulsion Technique

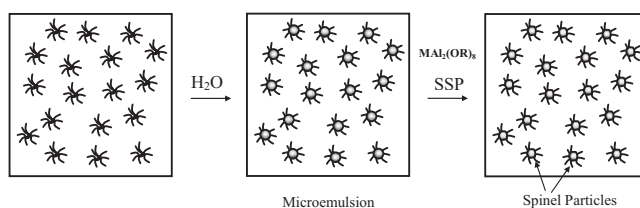
Microemulsions are transparent, isotropic dispersions of oil and water (two immiscible liquids) stabilized by the presence of carefully adjusted emulsifier(s) (surfactant molecules that can be cationic, anionic, or neutral), which are located at the interfaces between oil and water domains [339] (Scheme 10).

**Scheme 10.**

These systems are clear and thermodynamically stable, and they are prized for their stability and small particle size. The use of microemulsion technique in the synthesis of nanoparticles is based upon the use of two nonmiscible phases homogenized with the help of surface-active agents, ligands, and/or polymers, for assisting the growth of nanocrystals in small water droplets homogeneously entrapped in a hydrocarbon solvent. The most common examples are the water-in-oil (W/O) and the oil-in-water (O/W) micro-emulsions, as

shown in Scheme 10. The important properties are governed mainly by the water-to-surfactant molar ratio. Typically, the droplets are spherical and have a small polydispersity, in terms of size. The radii of the drops are usually one to four times the thickness of the surfactant film.

The reverse micelle technique is suitable for tailoring small and uniform nanoparticles of discrete nanoscaled oxides or hydroxides with controlled size distribution ( $<10$  nm) [244, 340–351]. The principal advantage of the method is that the concentration of metal-organic in the water droplets is very high, so that the reaction easily forms particles that are gelled throughout. This method has been used to prepare spherical submicrometer particles of titania, zirconia, and alumina [352]. However, a controlled formation of oxide materials is subject to the reactivity of the starting material with water and the reaction parameters, which actually determine the size and agglomeration effects in the final powder. As a consequence, the results can be different for similar precursors. For example, in the microemulsion-based hydrolysis of titanium, alkoxides have yielded uncontrolled aggregation and flocculation [353]; however,  $\text{TiO}_2$  particles with diameters less than 10 nm were prepared by controlled hydrolysis of titanium iso-propoxide in reverse micelles of sodium bis(2-ethylhexyl)sulfosuccinate-hexane-water [354]. Similarly, transition metal aluminum heterometal alkoxides of the general formula  $\text{MAI}_2(\text{OR})_8$  have been successfully used to perform a size-selective synthesis of nanocrystalline  $\text{MAI}_2\text{O}_4$  spinels (Scheme 11).

**Scheme 11.**

The emulsion method provides a physical means of controlling particle size and shape while still exploiting the advantages of sol-gel processing. The principal limitation of emulsion methods is that the emulsion structure is not at thermodynamic equilibrium and should be stabilized by the addition of surfactants that lower the interfacial tension between the phases and decrease the rate at which the droplets coalesce. Furthermore, the surfactant molecules have large molecular weights, and even a small amount of unremoved (uncracked) surfactant can result in significant organic contamination in the ceramic material.

## 4.3. Colloidal and Polymeric Routes

A well-known approach to the synthesis of multicomponent oxide powders is based on Pechini-type methods where the metal ions present in an aqueous solution are complexed with the help of organic ligands to form polybasic chelates [355–357]. This method generally allows for the use of readily available reagents such as oxides, carbonates, or nitrate as cation sources, with the added advantage that it requires no special apparatus or atmosphere control. The commonly used ligands are  $\alpha$ -hydroxycarboxylic acid (e.g., citric acid,



$\text{HOC}(\text{CH}_2\text{COOH})_2\text{-COOH}$ ). The polyhydroxy-metal complex, when treated with a polyfunctional alcohol (e.g., ethylene glycol,  $\text{HOCH}_2\text{CH}_2\text{OH}$ ), undergoes a polyesterification reaction with the concurrent formation of a water molecule and the formation of a mixed-cation precursor (Fig. 8).

A number of variations of this methodology are used to obtain stoichiometric powders, with the use of different chelating reagents like citric acid, tartaric acid, glycol, acrylic acid, etc. The common idea is to achieve an atomistic distribution of the cations within the polymer resin. The utility of the method relies on the chemical bonding of the cations to the polymer chains (Fig. 8). It is assumed that various cations are homogeneously mixed with little or no segregation of the components, and the rigid transparent glassy mass is a “single” preceramic precursor [356]. The organic molecules used as a complexing aid not only function as chelating agents and a resin vehicle but also provide combustion heat for calcinations; however, excess organic content can have a negative effect by raising the temperature too high during calcination. Moreover, the composition of the polymeric precursor is important for the final agglomerate morphology and particle size because when compared with a dense resin, a foamy, voluminous precursor is expected to produce loosely bound aggregates. Although these methods claim the advantages of molecular-level mixing and the formation of mixed-metal polymeric precursors, evidence is not always available. However, the characterization of a Ba-Ti precursor to  $\text{BaTiO}_3$  (Pechini method) by  $^{13}\text{C}$  NMR spectroscopy indicates that the coordination of Ba and Ti in the mixed-metal complex remains unchanged at both solution and resin stages. Nevertheless, this approach represents a low-temperature route to multicomponent material. For example, nanocrystalline yttrium aluminum garnet

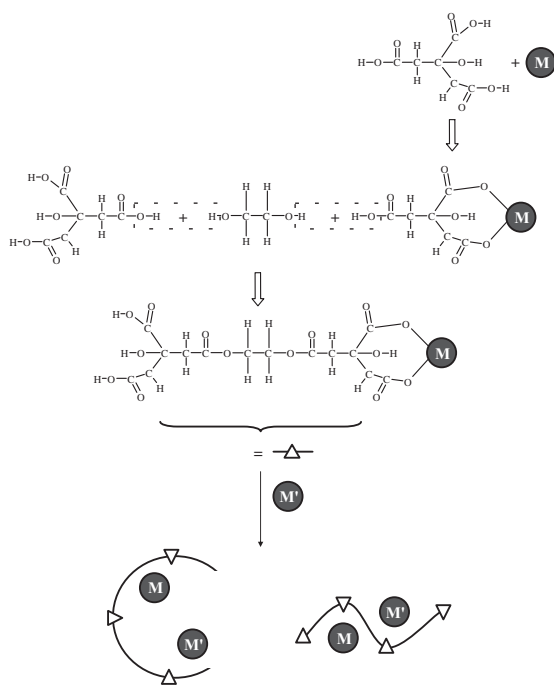


**Figure 8.** Illustration of the formation of mixed-cation precursor in Pechini-type processes.

( $\text{Y}_3\text{Al}_5\text{O}_{12}$ ) could be obtained at  $1000\text{ }^\circ\text{C}$ , compared with the  $1600\text{ }^\circ\text{C}$  required for the solid-state reaction [358–360]. In another example, the refractory mixed oxide calcium aluminate ( $\text{CaAl}_2\text{O}_4$ ) was prepared in high purity at  $900\text{ }^\circ\text{C}$ , whereas the solid-state reaction between calcia ( $\text{CaO}$ ) or calcium carbonate ( $\text{CaCO}_3$ ) requires temperatures in excess of  $1400\text{ }^\circ\text{C}$  to complete the reaction, which still contains undesirable  $\text{CaAl}_4\text{O}_7$ ,  $\text{Ca}_{12}\text{Al}_{14}\text{O}_{33}$ , and unreacted starting materials [361]. Further advantages of the Pechini-type synthesis are the ability to prepare complex compositions, homogeneous mixing of the cations, and easy scalability.

Another strategy for the *in-situ* formation of single molecular species as precursors utilizes the complexing abilities of triethanol amine ( $\text{N}(\text{C}_2\text{H}_4\text{OH})_3$ ) and ethylene glycol ( $\text{C}_2\text{H}_4(\text{OH})_2$ ). This concept has been put forward as an inexpensive alternative to metal-organic precursors but is similar to the Pechini-type methods; the molecular structure of these alkoxide precursors remains ambiguous because of the lack of appropriate characterization. For example, Laine et al. have synthesized a precursor to Mg-Al spinel [362, 363] by heating  $\text{Al}(\text{OH})_3$ ,  $\text{MgO}$ , and a stoichiometric amount of  $\text{N}(\text{C}_2\text{H}_4\text{OH})_3$  in ethylene glycol. A plausible ionomer-like structure (Fig. 9) based on the mass spectral and NMR data [362] was proposed for the precursor compound wherein magnesium ion is encapsulated by a TEA molecule bridging two alumatrane units [364]. Following this approach, single precursors to mullite ( $\text{Al}_6\text{Si}_2\text{O}_{13}$ ) and cordierite ( $\text{Mg}_2\text{Al}_2\text{Si}_5\text{O}_{18}$ ) have been developed and used to synthesize high-purity phases [362].

The other commonly used solution method for the synthesis of multicomponent oxide ceramics is coprecipitation reactions producing a “mixed” precipitate comprising two or more insoluble species that are simultaneously removed from solution. The precursors used in this method are mostly inorganic salts (nitrate, chloride, sulfate, etc.) that are dissolved in water or any other suitable medium to form a homogeneous solution with clusters of ions. The solution is then subjected to pH adjustment or evaporation to force those salts to precipitate as hydroxides, hydrous oxides, or oxalates [365–367]. A careful control of pH is important for achieving a quantitative precipitation because the precipitating species is a product of the neutralization reaction between the inorganic precursor and the base. The crystal growth and their aggregation are influenced by the concentration of salt, temperature, the actual pH, and the rate of pH change. After precipitation, the solid mass is collected, washed, and gradually dried by heating to the boiling point of the medium. The washing and drying procedures applied for coprecipitated hydroxides affect the degree of agglomeration in the final powder and must be considered

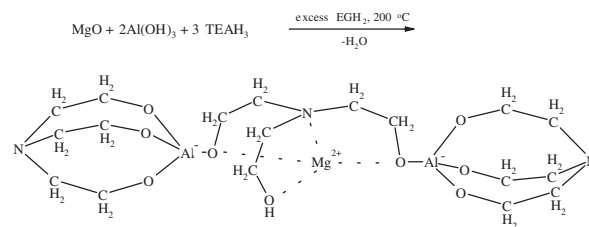


**Figure 9.** Proposed arrangements of cations in the trane precursor to  $\text{MgAl}_2\text{O}_4$  (adapted from [362]).

when nanosized powders are the intended product. Generally, a calcination step is necessary to transform the hydroxide into crystalline oxides. Although the precipitate is not structurally characterized, the association of ions to form mixed-metal hydroxides (e.g.,  $\text{MgAl}_2(\text{OH})_8$  for  $\text{MgAl}_2\text{O}_4$ ) offers the advantages of molecular-scale mixing of the components. This strategy is a commercially viable alternative method for obtaining high-quality oxide powders; however, the method is plagued by the problems of contamination due to anionic ligands (halides, nitrates, etc.), which are detrimental to the material properties if not removed during the calcination steps. In addition, an incomplete precipitation of one of the ions can lead to phase segregation or non-stoichiometric products. In most of the binary, ternary, and quaternary systems, a crystallization step is necessary, which is generally achieved by calcinations or, more elegantly, by a hydrothermal procedure in high-pressure autoclaves.

A large number of reports are available on the synthesis of ultrafine oxide powders ( $\text{Fe}_3\text{O}_4$  [368],  $\text{ZrO}_2$  [369],  $\text{BaTiO}_3$  [340],  $\text{NiTiO}_3$  [370],  $\text{MnFe}_2\text{O}_4$  [371],  $\text{ZnAl}_2\text{O}_4$  [372], oxide-oxide composites  $\text{CeO}_2/\text{ZrO}_2$  [373], and bio-material  $[\text{Ca}_5(\text{PO}_4)_3(\text{OH})_2$  [374]) by coprecipitation reactions. Nanocrystalline yttria-stabilized zirconia (grain size < 100 nm), consolidated and sintered to a nanostructured ceramic has been prepared by coprecipitation reactions [375]. Figure 10 shows the scheme employed to produce  $\text{BaTiO}_3$  nanopowders from a barium titanate oxalate precursor,  $\text{BaTiO}(\text{C}_2\text{O}_4)_2 \cdot 4\text{H}_2\text{O}$ .

The advantages of coprecipitation reactions are (i) the homogeneity of component distribution, (ii) the relatively low reaction temperature, (iii) the fine and uniform particle size with weakly agglomerated particles, and (iv) the low cost. However, these reactions are highly susceptible

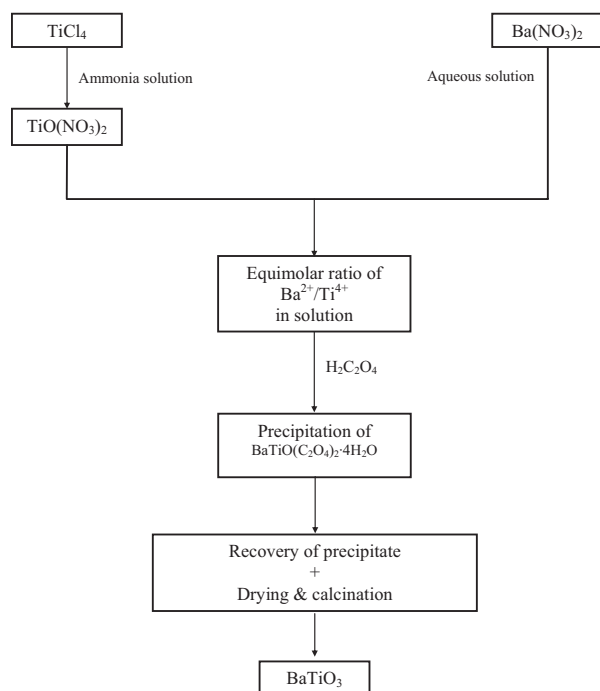
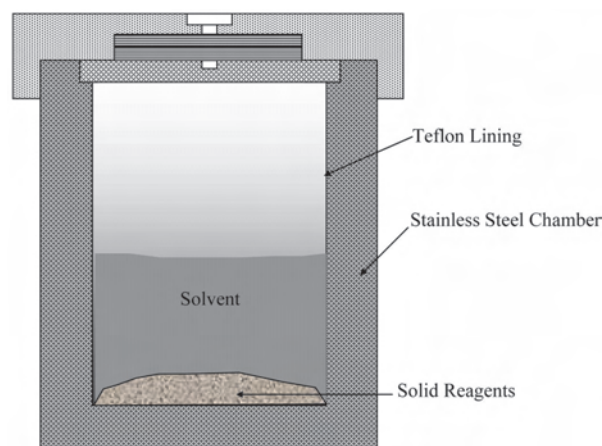


**Figure 10.** A schematic of various steps involved in the preparation of  $\text{BaTiO}_3$  by a coprecipitation technique.

to the reaction conditions, and, because of incomplete precipitation of the metal ions, control over the stoichiometry of the precursors is rather difficult to achieve. In addition, the coprecipitation reactions are not suited for certain oxides/hydroxides, for instance, in the case of amphoteric systems.

#### 4.4. Solvothermal Synthesis

Solvothermal processes can be defined as chemical reactions or transformations in a solvent under supercritical conditions [36, 376]. The specific physico-chemical properties of solvents near such a pressure-temperature (100 MPa, 300 °C) domain can markedly improve the diffusion of chemical species [377]. These processes are used to synthesize new materials (meta-stable phases) as well as to develop new processes for obtaining functional materials and the shaping of materials, for example, monodispersed nanosized particles [378–380]. Although water is largely used as the reaction medium (hydrothermal synthesis) in most solvothermal reactions, several nonaqueous solvents (e.g., ammonia, hydrazine, alcohols) have been investigated for the preparation of different materials [381]. The first step of a hydrothermal reaction is either a sol-gel precipitation or a coprecipitation process, the precursors mostly being alkoxides, nitrates, chlorides, or sulfates, which are first dissolved in a suitable medium or water to form a homogeneous solution. Typically, sol-gel or coprecipitation-derived precipitates are amorphous in nature, which are hydrothermally treated in Teflon-lined steel autoclaves at constant temperature to induce crystallization (Scheme 12). Finally, the crystallized powders are repeatedly washed and dried at room temperature. Hydrothermal synthesis does not require expensive precursors and apparatus. Moreover, it is possible to predict the optimum synthesis conditions by theoretical methods based on electrolyte thermodynamics. One of the peculiar advantages of the hydrothermal synthesis is that besides the synthesis of inorganic materials, it is also possible to synthesize new crystalline precursors that can be structurally characterized. For example, a new hydroxo-stannate,  $\text{Sr}_2\text{Sn}(\text{OH})_8$ , has been obtained from hydrothermal studies of the  $\text{SrO-SnO}_2$  system. The compound acts as a single source for  $\text{SrSnO}_3$  (<700 °C) and  $\text{Sr}_2\text{SnO}_4$  (>900 °C) [382], subject to the thermal treatment.



**Scheme 12.**

Solvothermal methods offer a simple, direct, and low-temperature route for obtaining nanometric particles with narrow size dispersions and represent an alternative to calcinations for promoting crystallization under milder temperatures. Another feature of the hydrothermal treatment performed under near-supercritical conditions concerns the morphology of the materials that can be governed by monitoring temperature, pressure, reaction time, and the nature of the solvent. The easy access to the shaping of materials (crystal growth, preparation of fine microcrystallites) and low crystallization temperatures make hydrothermal synthesis an attractive method for producing submicrometer particles with a narrow size distribution, avoiding the firing steps required in sol-gel processing; however, interest in this method is limited compared with sol-gel methods. The drawbacks include the trial-and-error nature of the method to understand the chemical reactivity of supercritical fluids, which governs the course of the hydrothermal synthesis and consequently the composition, structure, and morphology of the nanomaterial. There are many experimental variables, like composition of the starting mixture (stoichiometric or not), choice of reagents, temperature, reaction time, and percentage fill of the reaction vessel. In addition, it remains difficult to predict the outcome of new reactions. Furthermore, observation of the reaction course is difficult because the reaction takes place in a sealed vessel. The future of hydrothermal processing for nanocrystal growth and materials synthesis requires lower pressure and temperature, which will facilitate *in-situ* observation of the reaction. Finally, the use of molecular compounds as stoichiometric synthons can substantially augment the advantages of solvothermal routes to produce nanopowders with high crystallinity and regular morphology.

#### 4.5. Chemical Vapor Deposition

The acronym MOCVD designates a gas-phase process in which metal-organic compounds (precursor) are converted into a solid film by their decomposition on a hot substrate [383–386]. In addition to the four important parameters (i.e., temperature, deposition time, pressure, and surface specificity), the chemical nature of the precursor substance is of paramount importance in determining the quality of the film in terms of homogeneity, morphology, and contamination. The film growth involves the conversion of atoms and/or molecules in the gas phase into atoms or molecules at the surface of the film, which can then be incorporated into it [52, 387]. This process takes place by adsorption of the gas-phase species on the substrate surface. Depending upon the interactions of the adatoms with the surface, the surface adsorption can be physical (essentially van der Waals interaction) or chemical (covalent linkage between the molecule and the surface) in nature. The adsorbed molecules may wander on the surface and react with other surface species to form the solid deposit. The mobility of surface species is largest on metallic and semiconducting surfaces, where bonding is not very directional. In the case of dielectrics, the highly directional covalent bonds tend to hold the chemisorbed molecules, thereby limiting their mobility. The volatile by-products released in the gas-phase decomposition, collision, and surface reactions can be removed in vacuum and

analyzed on-line by infrared spectroscopy or mass spectrometry to control the decomposition process as well as to elucidate the thermal decomposition of the precursor molecule. In a simplified view of the surface, it is assumed that there are a fixed total number of reactive sites upon which an incoming atom (“adatom”) or molecule can adsorb. Once a site is occupied, a second molecule will not adsorb on it. This is equivalent to the assumption that the number of atoms adsorbing is equal to those desorbing, if no reaction is taking place. The number of atoms or molecules adsorbing on the surface is proportional to the concentration of the gas-phase species or, in other words, equivalent to the partial pressure. Some of the fundamental processes occurring during the CVD of a metal-organic compound are depicted in Figure 11.

Since the conversion of an organometallic precursor to a useful thin film involves stripping most of the coordinated ligands, a well-understood decomposition chemistry is a prerequisite. The efficiency of the CVD process depends crucially on ligands that decompose by way of chemically productive pathways and with a low activation barrier. The precursors based on ligands with complex concomitant fragmentation reactions usually lead to the incorporation of heteroatoms such as C, B, N, O, or Si [383–386]. Furthermore, the intact vapor transport of the molecular precursor is highly essential to control over the process. The thermal instability or dissociative tendency of the precursor can initiate a cascade of reactions leading to nonideal geometry or undesirable deposits [305].

### 5. MOLECULAR CLUSTERS AS BUILDING BLOCKS TO NANOPARTICLES AND NANOSTRUCTURED FILMS

#### 5.1. One-Component Systems ( $E_x$ )

The nanoparticles (NPs) and nanostructured films of different metallic elements (Fe, Co, Ni, Cu, Ge, Ag, Au, Pd, Pt, Ru, etc.) have been the focus of intense research in recent years (Table 1) [12, 13, 386, 388]. A large number of methods have been devised for a controlled and size-tunable synthesis of colloidal nanoparticles. A variety of solution chemical methods such as laser pyrolysis and thermal

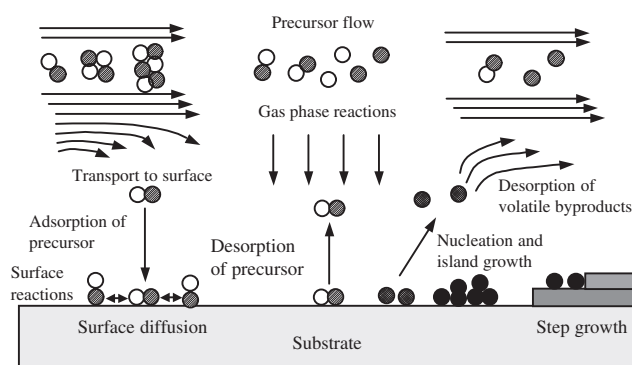
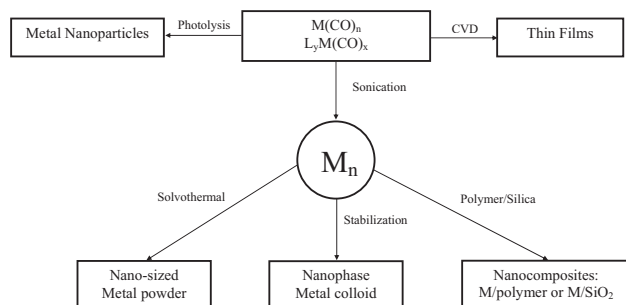


Figure 11. Fundamental processes active in the CVD process.

decomposition of organometallic compounds have recently been used to generate nanostructured materials [389, 390]. Fendler and Meldrum have reviewed the colloidal methods applied to generate nanostructured materials [391]. In terms of size selectivity and standardized procedures, this area has reached a certain level of maturity, due in particular to the large number of methods applied and efforts dedicated to the synthesis of monodisperse metal nanoparticles. However, the following section contains only selected examples that are related or show a close relevance to the scope of this article.

One general scheme for preparing nearly monodisperse (standard deviation, <5%) 3d transition metal nanoparticles relies on producing a single short nucleation event followed by slower growth on the nuclei formed. This is best achieved by introducing thermally unstable, zero-valent metal precursors, usually carbonyl compounds (e.g.,  $\text{Fe}(\text{CO})_5$ ,  $\text{Co}_2(\text{CO})_8$  [392, 393],  $\text{Ni}(\text{CO})_4$  for Fe, Co, and Ni NPs), into a hot solution containing colloidal stabilizers (Scheme 13) [394–396]. Alternatively, the metal precursors (e.g., acetates, halides) can be reduced by appropriate reagent (e.g., hydrides, polyols) to the elemental form [397, 398]. Metal carbonyls are interesting SSPs for the preparation of metallic nanoparticles and thin films (Table 1) because the metals within these compounds are formally in the zero-valent state and the departing CO ligand is by itself a stable noncondensable gas. For this reason, thermolysis, even in the absence of a reducing environment, can, in principle, produce high-quality metallic films or nanoparticles. The as-produced metal nanoparticles can be collected and consolidated to obtain nanopowders of metals. Alternatively, they can be capped with appropriate passivating agents to obtain stable colloids or can be incorporated within the pores of mesoporous organic or inorganic matrices to obtain composite materials (Scheme 13). Furthermore, a number of metal carbonyls are reasonably stable under ambient conditions and possess sufficient volatility to be transported in the vapor phase at relatively low temperatures. The volatility and stability of carbonyl compounds depend upon their nuclearity and can be altered through the stabilization of the metal center via donor ligands. Both simple and modified metal carbonyl precursors (Table 5) have been used in the CVD process to deposit metallic films of a huge number of metals (CVD BOOK).



Scheme 13.

Although the choice of metal precursor is commonly based on the ease of handling and ready availability of the starting material, a judicious choice may nevertheless affect the process parameters. For instance, the size of NPs in the case

of thermal or sonochemical reduction of metal sources can be controlled by adjusting the temperature and precursor-to-surfactant ratio, whereas the chemical reduction of metal ions (minimum two sources) is additionally subject to the influence of the concentration of the reducing agent and the kinetics of the reduction (e.g., a fast reduction step will produce a large number of nuclei). The presence of inert atmosphere and surfactant is necessary to avoid the oxidation of NPs, which otherwise results in the isolation of metal oxide particles [399]. The adsorbed surfactant molecules provide a dynamic organic shell that mediates growth, stabilizes the particles in solution, and limits oxidation after synthesis. The chemical strength of NP-surfactant interaction can also be used to monitor the size; for example, a combination of tight (e.g., long-chain carboxylic acid that binds strongly because of the strong affinity of metal for oxygen) and weak (e.g., tri-octyl or butyl phosphines) binding surfactants will favor slow and rapid growth, respectively. Although weak binding surfactants are important in mediating the growth of NPs, the surfactants that remain coordinated to the metal surface upon the isolation of NPs are the ones that bind tightly. Similarly, the steric profile of the surfactant molecules can be changed to tune the NP size. Furthermore, the surfactant can be exchanged for surfactants of different length or chemical functionality. In the case of transition metal NPs, the carbonyl decomposition methodology is scalable to large quantities for the production of magnetic fluids [400, 401]. With the use of molecular precursors, metal nanoparticles can be synthesized with a very narrow size dispersion that allows investigation of the scaling effect on the fundamental properties of the material. For instance, the magnetization data on cobalt nanoparticles of different sizes clearly show that the saturation magnetization decreases with the decreasing particle size (Fig. 12) [402, 403]. The coercivity  $H_c$ , the field required to reverse the magnetization, decreases with decreasing nanocrystal size, as seen in  $M$  versus  $H$  loops measured at 5 K (Fig. 12) for a series of hcp Co nanoparticles [401].

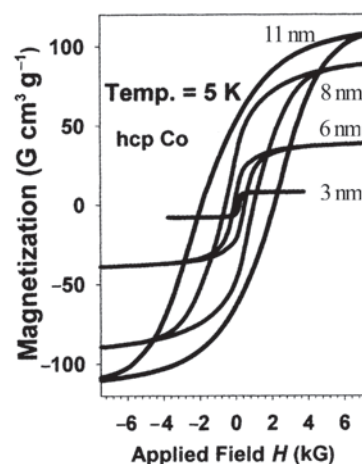


Figure 12. Magnetization versus applied field hysteresis ( $M$  vs.  $H$ ) loops of cobalt NPs of different sizes. Reprinted with permission from [401], C. B. Murray et al., *MRS Bull.* 26, 985 (2001). © 2001, Materials Research Society.



Suslick et al. have introduced the sonochemical reactions of volatile organometallic compounds as a general approach to the synthesis of nanophase materials [404]. The chemical effects of ultrasound result from acoustic cavitation, the formation, growth, and implosive collapse of bubbles within a liquid. The collapsing bubbles generate localized hot spots ( $T \approx 5000$  K) where molecular species decompose, and the resulting metal atoms agglomerate to form nanostructured metals that are often amorphous. A variety of metals, alloys and carbides have been produced using this approach [405]. A scanning electron micrograph of amorphous nanostructured iron obtained by the sonication of iron pentacarbonyl (Fig. 13) shows agglomerated nanometric particles (ca. 20 nm), which were shown by transmission electron microscopy to consist of smaller (4–6 nm) nanocrystals.

Thin films of Fe [406], Ru [407], and Os [407] have been formed by thermal decomposition of metal pentacarbonyls. Since pentacarbonyls are difficult to handle because of their air-, light-, and temperature-sensitive nature, Shore et al. have used trinuclear precursors  $M_3(CO)_{12}$  ( $M = Fe, Ru, Os$ ) to deposit metallic films; however, a dynamic vacuum of  $10^{-5}$  torr was necessary to transport the metal carbonyls to the heated substrate [408]. An exhaustive account of the CVD of a variety of metals, including the basic principles of precursor design and a classification of the precursors, is available in the book "The Chemistry of Metal CVD," authored by Kodas and Hampden-Smith [386].

The technological importance of films of single metals, multilayers, and alloys, together with the increasing demand of materials with improved performance, has led to a great deal of interest in nanostructured device-quality films. High-purity, dense metal films with controlled crystallite size and smooth surfaces deposited at relatively low temperatures with high deposition rates are required for microelectronic applications [409]. Precursors for CVD of metals (Table 1) can be broadly classified into three categories: (i) inorganic precursors, which do not contain carbon such as metal halides; (ii) metal-organic precursors, which contain organic

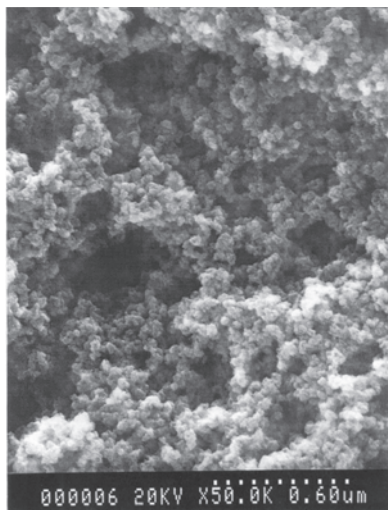
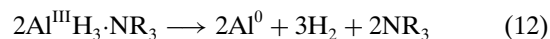
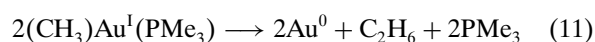


**Figure 13.** Scanning electron micrograph of nanostructured iron. Reprinted with permission from [403], K. S. Suslick et al., *Chem. Mater.* 8, 2172 (1996). © 1996, American Chemical Society.

ligands but do not possess metal-carbon bonds, such as metal alkoxides, metal amides, and metal hydrides; and (iii) organometallic precursors that contain organic ligands and metal-carbon bonds, for example, metal carbonyls, metal alkyls, and metallocenes [52, 387].

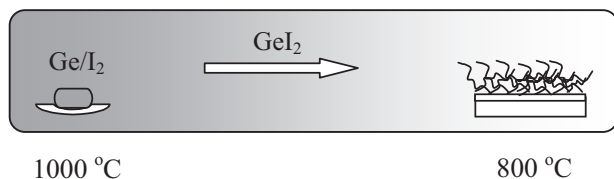
Inorganic precursors such as metal halides typically need high temperatures ( $>600$  °C) and a reducing agent such as  $H_2$  to produce pure metal films. Furthermore, they are inexpensive, commercially available precursors that can easily be purified. However, most of them are solids, and homogeneous precursor delivery into the CVD reactor is difficult. In contrast, the metal-organic or organometallic molecular precursors decompose at lower temperatures and possess high vapor pressures, and most of them are liquids or can be obtained as liquids by changing the ligands. The major disadvantage is the incorporation of heteroelements (C, O, F, N, P), which is difficult to control, particularly in the case of reactive metals. However, there are many examples where high-purity metal films have been deposited from single-source molecular precursors without coreactant like reactive (reducing) gas. This requires a decomposition mechanism where the organic ligands are removed intact from the reaction chamber or in which a reaction pathway exists to form volatile species that desorb easily from the surface [52, 387]. Disproportionation of Cu(I) compounds yields elemental Cu and a volatile Cu(II) species [410], and the metal-carbon bond is cleaved by  $\beta$ -hydrogen elimination in  $Al(iBu)_3$  [411], homolytic scission of Au–C bonds in  $(CH_3)Au(PMe_3)$  [412] and the use of precursors, which do not contain metal-carbon bonds such as  $AlH_3 \cdot NR_3$  [413]. The chemical transformations of these precursors are displayed in Eqs. (9)–(12).



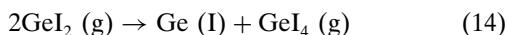
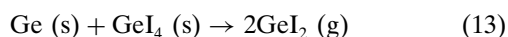
In the case of metal CVD, precursors devoid of a metal-carbon bond or a low metal-carbon bond order are preferred because of the low carbon contamination in the deposits. The possibility of carbon incorporation is increased because of the increased strength of M–C bonding. For example, CVD of Fe using  $Fe(CO)_5$  produces relatively pure films when compared with the decomposition of ferrocene ( $Fe(C_5H_5)_2$ ), in the absence of any reducing agent [406].

Among elemental semiconductors, germanium crystals, wires, and films of nanoscopic dimensions are receiving increasing attention because of their novel electronic and optical properties that are intrinsically associated with the low dimensionality and quantum confinement effect in semiconductor materials. The quantum confinement effect enables indirect band gap semiconductors like Si and Ge to become more efficient light emitters. Compared with Si, Ge nanostructures are of particular interest, since the Bohr exciton radius is larger in Ge than in Si, which consequently should lead to more prominent quantum confinement effects. Ge nanocrystals have been synthesized by different physical, chemical transport [414–416], CVD [70], and sol-gel [417] methods. Yang et al. have used chemical

vapor transport for rational synthesis of random and aligned growth of 1-D structures [414–416, 418, 419]. In a typical synthesis, a mixture of Ge powder and I<sub>2</sub> and a gold-coated Si wafer were placed at the high-temperature (1000 °C) and low-temperature (800 °C) ends, respectively. Ge reacts with I<sub>2</sub> to form GeI<sub>2</sub> vapor at the hot end, which is then transported to the cold end. GeI<sub>2</sub> then decomposes into Ge and I<sub>2</sub> vapor to form Ge nanowires on the Au-coated Si substrate (Scheme 14). Although the starting material is a mixture of two different chemical species, the precursor to Ge nanowires is the single compound germanium diiodide, which is formed in the gas phase as a single source.



Scheme 14.



The molecular precursor strategy is less investigated for Ge-based nanostructures, largely because of the unavailability of suitable precursors. Chisholm et al. have used germanium bis(trimethyl)silylamide to deposit metallic Ge; however, the films were found to contain small amounts of N and O incorporated because of inefficient decomposition of precursor and partial oxidation of the films, respectively [47]. The most commonly used germanium precursor is tetrahydrogermane, GeH<sub>4</sub>. Since the germane precursor is pyrophoric in nature, the replacement of one of the hydrogen atoms in GeH<sub>4</sub> by appropriate organic groups with leaving group characteristics should lead to alternative germanium precursors. Jutzi et al. have synthesized the cyclopentadienyl germanes (RGeH<sub>3</sub>; R = substituted cyclopentadienyl groups) as new liquid precursors for the deposition of thin germanium films [70]. These precursors are easy to handle and decompose at low temperatures (<400 °C) to allow the deposition of Ge films under mild conditions; however, the films contain a significant amount of carbon (8 at.%). The quality of the films is comparable to the quality of those obtained from the decomposition of GeEt<sub>4</sub> above 500 °C [420]. The high organic contamination in Ge deposits (Ge: 92 at.%; C: 8 at.%) obtained from substituted cyclopentadienyl precursors was due to the high stability of the ligands and their fragments. We have used a simple germanium bis-cyclopentadienylide (Ge(C<sub>5</sub>H<sub>5</sub>)<sub>2</sub>) as a SSP to obtain high-purity germanium nanowires (Fig. 14a) as well as nanostructured films (Fig. 14b) at the lowest temperature (<350 °C) reported so far for the CVD of Ge [421]. Ge(C<sub>5</sub>H<sub>5</sub>)<sub>2</sub> is different from GeH<sub>4</sub> or cyclopentadienyl germanes because of the weak dipolar interactions of the cyclopentadienyl groups with the metal centers, which results in the easy formation of metallic nanostructures. The micro-EDX analysis showed the Ge content to be more than 99 at.%, and carbon and oxygen contents were negligible. The

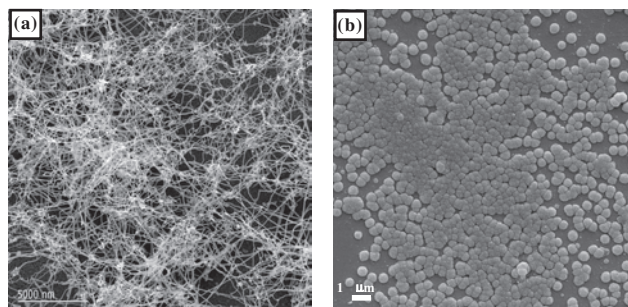


Figure 14. SEM image of (a) as-obtained Ge nanowires and (b) nanocrystalline Ge islands obtained by the CVD of Ge(C<sub>5</sub>H<sub>5</sub>)<sub>2</sub>.

thermal decomposition of Ge(C<sub>5</sub>H<sub>5</sub>)<sub>2</sub> proceeds possibly by the cleavage of the Ge–Cp bond. This is supported by the observation of C<sub>5</sub>H<sub>5</sub><sup>+</sup>, (C<sub>5</sub>H<sub>5</sub>)<sub>2</sub><sup>+</sup>, and Ge<sup>+</sup> species in the mass spectral analysis of the gaseous products formed during the thermolysis of Ge(C<sub>5</sub>H<sub>5</sub>)<sub>2</sub> [421].

A high-resolution transmission electron microscope (HR-TEM) image (Fig. 15) shows the wires to be homogeneous and straight, which indicates that they are free of defects. The average diameter of the wires was found to be 15 nm. The selective area diffraction pattern of these structures exhibits sharp spots corresponding to their highly crystalline nature. The preferred growth direction was found to be [112].

Molecular compounds, together with standard nanostructure fabrication methods, can be used for obtaining patterned nanowires or dots. For instance, Himpsel et al. have obtained self-assembled Fe nanowires by pyrolysis (nitrogen laser) of ferrocene (Fe(C<sub>5</sub>H<sub>5</sub>)<sub>2</sub>), selectively adsorbed between CaF<sub>2</sub> stripes on Si(111) [422]. Ferrocene is a suitable precursor because each molecule contains one Fe atom sandwiched between two cyclopentadienyl rings,

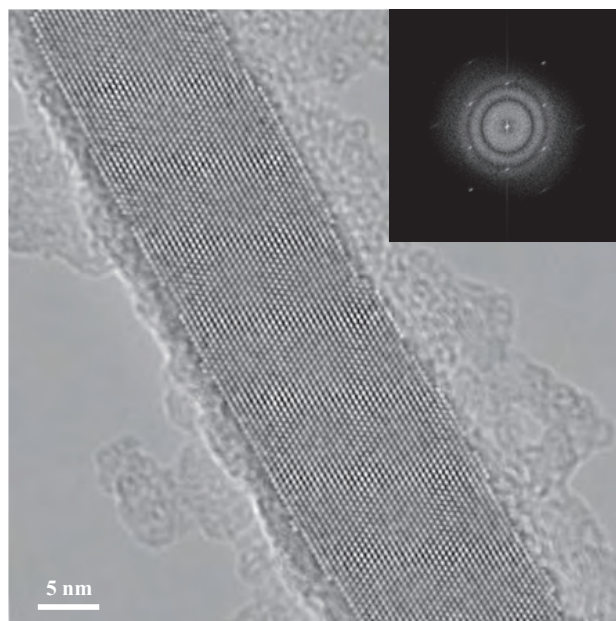


Figure 15. HR-TEM image showing the lattice fringes of a single-crystal Ge wire.



and, owing to the nonreactive nature of the precursor, the ferrocene-covered substrate is passive unless it is exposed to ultraviolet photons. The Fe nanowires were fabricated in three steps: (1) preparation of a Si template by annealing vicinal Si(111), (2) creation of continuous  $\text{CaF}_2$  stripes on a  $\text{CaF}_1/\text{Si}(111)$  surface by the growth of one or two monolayers of  $\text{CaF}_2$ , and (3) selective adsorption of ferrocene molecules in  $\text{CaF}_1$  trenches between the  $\text{CaF}_2$  stripes. Figure 16 shows the initial and final stages during Fe nanowire growth.

## 5.2. Two-Component Systems ( $\text{AE}_x$ )

In the context of monophasic binary materials (e.g.,  $\text{MgO}$ ,  $\text{Al}_2\text{O}_3$ ,  $\text{Y}_2\text{O}_3$ ,  $\text{AlN}$ ,  $\text{GaN}$ ,  $\text{CdS}$ ,  $\text{ZnSe}$ ,  $\text{SiC}$ ,  $\text{TiC}$ , etc.), the decomposition of metal-organic precursors has been successfully used to obtain nanoparticles and nanostructured films. The following text contains some outstanding examples of nanoparticles and nanostructured films obtained from well-defined single-source molecules.

### 5.2.1. Oxide Ceramics

The class of binary metal oxides represents a very important group of materials as both grains and coatings because of their mechanical (e.g.,  $\text{ZrO}_2$ ,  $\text{HfO}_2$ ), dielectric (e.g.,  $\text{Al}_2\text{O}_3$ ), conducting (e.g.,  $\text{SnO}_2$ ), photocatalytic (e.g.,  $\text{TiO}_2$ ), optical (e.g.,  $\text{Eu}_2\text{O}_3$ ), biocidal (e.g.,  $\text{ZnO}$ ), and magnetic (e.g.,  $\text{Fe}_3\text{O}_4$ ) applications. Nanocrystalline aluminum oxide is used for a large number of applications such as insulating layers, optical filters, wear-resistant coatings, and corrosion-protective films. In addition, high-surface-area aluminum oxides are used as catalyst support and adsorbents in industrial processes. The synthesis of so-called active aluminas by Yoldas [423] from aluminum alkoxides represents one of the fundamental steps taken toward the processing of high-performance materials from molecular precursors, which has been extended and modified during the last three decades, by several working groups (Tables 1–4).

Iron oxide films and nanoparticles are currently being extensively investigated because of their applications in catalysis, magnetic recording media, gas sensors, and anticorrosion protective paints [424–427]. Nanosized iron oxides

with a size of a few nanometers exhibit unique properties (e.g., high coercivity, superparamagnetism, enhanced surface sensitivity) not shown by their bulk phases, which has generated a great deal of technological and fundamental interest in the size and phase-selective synthesis of iron oxide particles and films. The functional properties of iron oxides are strongly dependent on their chemical composition, microstructure, and phase purity. The control over morphology, microstructure, and composition poses a synthetic challenge and is influenced by the preparation method, specific synthesis conditions, and pyrolytic or hydrolytic properties of the precursor [123] under processing conditions. The production of magnetic nanoparticles has improved enormously in recent years, although the synthesis of high-purity iron oxide nanoparticles a few nanometers in size with controlled size and distribution is still a challenging problem [124–127, 428–430] despite the application of different physical (e.g., molecular beam epitaxy (MBE) [431], reactive sputtering [432], and pulsed laser deposition (PLD) [433]) and chemical (e.g., sol–gel [434], electrochemical synthesis [435], ball milling [436], aerosol synthesis [437], and CVD [438]) methods. In view of the above, the use of iron alkoxide clusters as precursors to nanocrystalline oxides is a convenient route for controlling the composition and morphology of the target oxide. Furthermore, it allows a phase-selective synthesis, which is of significant importance, especially in the case of oxides, for instance, the  $\text{Fe}_x\text{-O}_y$  system, where several phases (hematite ( $\text{Fe}_2\text{O}_3$ ), maghemite ( $\gamma\text{-Fe}_2\text{O}_3$ ), magnetite ( $\text{Fe}_3\text{O}_4$ ), etc.) can be simultaneously formed in a narrow processing window.

Kiyomura and Gomi [127] has used iron (III) acetylacetonate complex (Fig. 17) in a plasma-assisted MOCVD process to grow magnetite films on Si(111) with a uniform morphology at 400 °C; however, the carbon content in the deposited film was rather high (2–6 at.%) because of the thermally robust nature of the precursor.

Armelaio and Artigliato [124] have used iron ethoxide  $[\text{Fe}(\text{OEt})_3]_n$  as a single molecular source for the sol–gel synthesis of nanocrystalline and transparent hematite thin films. The crystalline phase was obtained by thermal treatment of a homogeneous and amorphous material. The crystallite dimensions were controlled by varying the temperature, and the coatings were found to be nanostructured, even after

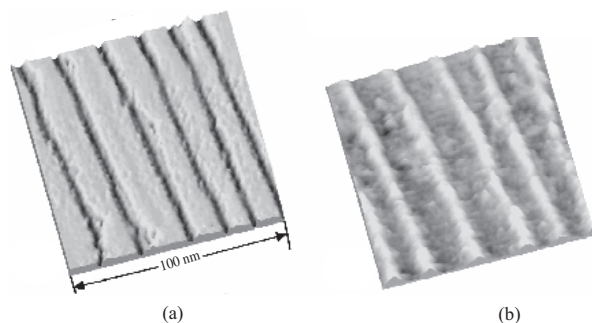


**Figure 16.** STM images of the initial and final stages in the self-assembly of Fe nanowires obtained by selective adsorption of ferrocene molecules. (a)  $\text{CaF}_2$  stripes separated by  $\text{CaF}_1/\text{Si}(111)$  trenches at a coverage of 1.9 monolayers of  $\text{CaF}_2$ . (b) Linear array of Fe nanowires 3 nm wide and 0.8 nm thick. Reprinted with permission from [422], J. L. Lin et al., *Appl. Phys. Lett.* 78, 829 (2001). © 2001, American Institute of Physics.

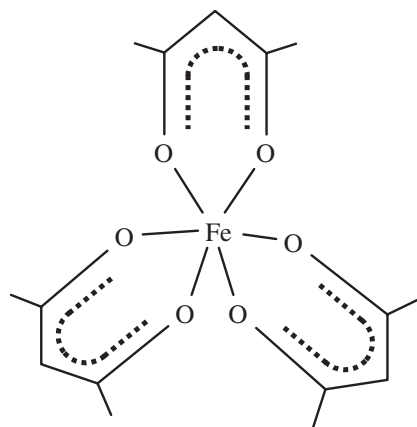


**Figure 17.** Molecular structure of  $\text{Fe}(\text{acac})_3$ .

prolonged heating. The iron sites were found to be octahedrally coordinated in both the crystalline and amorphous states, which shows the inherent advantage of using a single molecular source, which results in a chemically homogeneous matrix. As a result, the microstructural evolution is consistent and stable [124]. Although iron ethoxide is an interesting precursor for solution methods, its application in gas-phase techniques is limited because of its poor volatility. The attempted volatilization ( $200\text{ }^{\circ}\text{C}/10^{-2}\text{ torr}$ ) results in the formation of a polynuclear iron cluster,  $\text{Fe}_9\text{O}_3(\text{OC}_2\text{H}_5)_{21}(\text{C}_2\text{H}_5\text{OH})$ , with low vapor pressure [439]. The molecular structure of this species reveals a cyclic arrangement of Fe–O rings based on the different coordination of Fe(III) centers (Fig. 18). The oxo-alkoxide species represent a molecular intermediate that is probably involved in the alkoxide-to-oxide conversion.

The thermal instability of iron ethoxide is related to the degree of association of the ethoxide molecule in the solid state. It is known that the corresponding aluminum compound is an infusible solid due to the extensive polymerization of  $\text{Al}(\text{OEt})_3$  through alkoxy-bridging. The bridging tendency in alkoxide species is governed by the propensity of the metal center to increase their coordination state [49–51], which can be tuned either through an increase in the steric bulk of the alkoxide ligands or through the use of chelating ligands [440, 441]. Indeed, the higher alkoxide analogue  $[\text{Fe}(\text{O}i\text{Bu})_3]_2$  was found to be an excellent precursor for the deposition of different iron oxide phases. The molecular structure of  $[\text{Fe}(\text{O}i\text{Bu})_3]_2$  exhibits a centrosymmetric dimer where two tetrahedrally coordinated Fe (III) centers are linked via bridging  $-\text{O}i\text{Bu}$  groups (Fig. 19).

The decomposition temperature of  $[\text{Fe}(\text{O}i\text{Bu})_3]_2$  needed to form iron oxide was determined by thermogravimetric analysis performed under nitrogen. The major weight loss occurs in a single decomposition step around  $180\text{ }^{\circ}\text{C}$  corresponding to the elimination of the organic ligands to form the inorganic oxide. This demonstrates the inherent advantage of SSPs in obtaining pure compounds with control over the phase purity and particle size in the resulting ceramic material. Such a single-step decomposition behavior is not observed in other precursor systems, for example, the organic derivatives of the inorganic iron salts like glycolates, citrates,  $\beta$ -diketonates, etc., where the precursor degrades in several

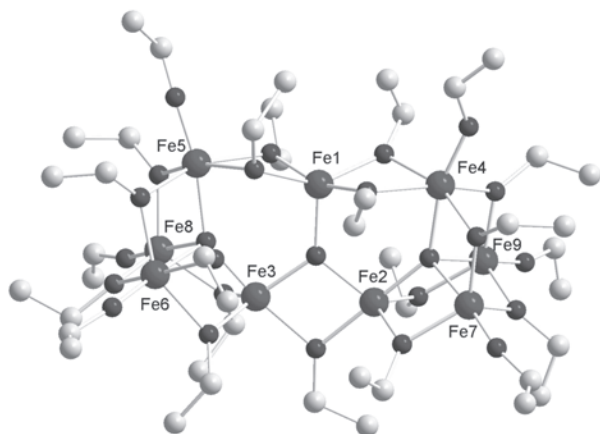


**Figure 18.** Molecular structure of  $\text{Fe}_9\text{O}_3(\text{OC}_2\text{H}_5)_{21}(\text{C}_2\text{H}_5\text{OH})$ .

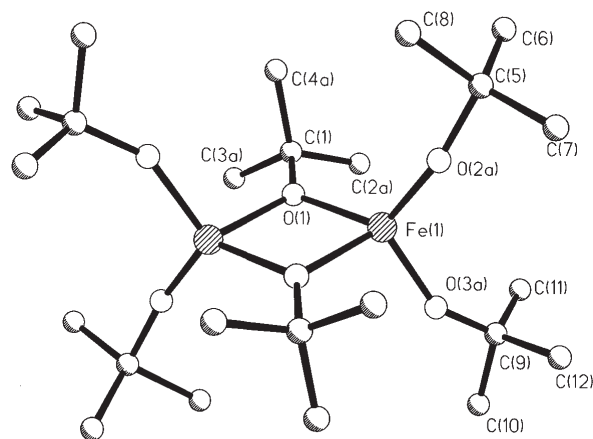
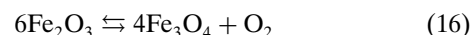
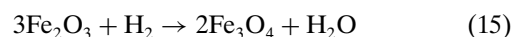


**Figure 19.** Molecular structure of  $[\text{Fe}(\text{O}i\text{Bu})_3]_2$ .

steps, because of the stability of intermediate species; consequently higher temperatures are necessary for a complete decomposition of the precursor to form the oxide [442]. The DTA curve shows a small endothermic peak around  $150\text{ }^{\circ}\text{C}$  corresponding to the melting temperature of the precursor, and the exothermic transition at  $225\text{ }^{\circ}\text{C}$  is possibly due to the oxidative degradation of the iron alkoxide, resulting in the liberation of the organic by-products. The crystallization of hematite is observed as a small exothermal peak around  $370\text{ }^{\circ}\text{C}$ .  $[\text{Fe}(\text{O}i\text{Bu})_3]_2$  was used in a horizontal cold-wall reactor to deposit hematite films at  $400\text{ }^{\circ}\text{C}$ , whereas magnetite films were obtained at  $450$  and  $500\text{ }^{\circ}\text{C}$ , as confirmed by the X-ray diffraction (XRD) data (Fig. 20). It was shown that the  $\text{Fe}_3\text{O}_4$  phase results from the reduction of  $\alpha$  and  $\gamma$  ferric oxides [123, 428]. Apparently, the dangling oxygen bonds on the surface of ferric oxide nanocrystals cleave upon heating in a vacuum, thereby eliminating oxygen. However, the reduction of  $\text{Fe}^{3+}$  to  $\text{Fe}^{2+}$  by dihydrogen liberated during the decomposition of  $[\text{Fe}(\text{O}i\text{Bu})_3]_2$  cannot be ruled out (Eqs. (15) and (16)).



Subject to the nature of the metal atom, a thermally activated fragmentation of the metal *tert*-butoxides produces,

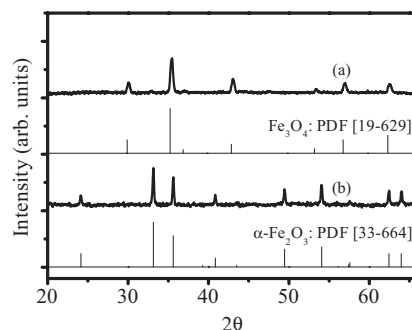


**Figure 20.** XRD patterns of magnetite (a) and hematite (b) iron oxide films deposited on silicon. Reprinted with permission from [428], S. Mathur, et al. *Chem. Vap. Deposition* 8, 277 (2002). © 2002, Wiley-VCH.

generally by an intramolecular process, *tert*-butyl alcohol, isobutene, and dihydrogen as the by-products [143]. This pathway was first proposed by Bradley and Maxfactor in their pioneering work on the thermolysis of Zr-*tert*-butoxide [443]. In other studies [227], it has been shown that isobutene results from  $\beta$ -H elimination of adsorbed *tert*-butoxy groups, whereas *tert*-butyl alcohol is formed by reaction of a *tert*-butoxide fragment with an adsorbed hydroxy group. All of these compounds are volatile and can easily be removed from the deposition zone to obtain oxides with minimum carbon contamination. The carbon content in the CVD deposits was shown to be low (<0.2 at.%), which exhibits a clean ligand stripping in the thermolysis of  $[\text{Fe}(\text{O}'\text{Bu})_3]_2$ . SEM analysis of the CVD films reveals characteristic morphologies for different iron oxide phases (Fig. 21). The hematite films display nanocrystalline spindle-like grains, whereas densely packed faceted crystallites were observed for the magnetite layers.

The nanostructured nature of the films is reflected in their magnetic behavior. The hysteresis loop of the  $\text{Fe}_3\text{O}_4$  film shown in Figure 22 can be considered as the superposition of a paramagnetic line a and a ferrimagnetic loop b. The weak magnetization when compared with polycrystalline  $\text{Fe}_3\text{O}_4$  probably results from the presence of a superparamagnetic phase. If a sample consists of small particles, its total magnetization decreases with particle size. As the size of the magnetic particle approaches the critical size required for a single-domain behavior, it becomes difficult to switch the magnetization from one direction to another. In the case of nanostructured materials (<50 nm), the total magnetization decreases with decreasing particle size, owing to the increased dispersion in the exchange integral and finally reaches the superparamagnetic state, where each particle acts as a spin with suppressed exchange interaction between the particles. In the case of magnetite films, the mean particle size (ca. 10–12 nm) is smaller than the critical (50–80 nm) size reported in the literature for single-domain behavior [444]. The higher coercivity of the  $\text{Fe}_3\text{O}_4$  film (4000 Oe) when compared with coarse-grained  $\text{Fe}_3\text{O}_4$  material (ca. 400 Oe) provides additional evidence for superparamagnetic behavior. The advantages of having molecular control over the growth process was also demonstrated by the deposition of different iron oxide phases on the silicon cantilever of an atomic force microscope with a conformal coverage and homogeneous morphology (Fig. 23).

$[\text{Fe}(\text{O}'\text{Bu})_3]_2$ , when used in a sol-gel process, produced hematite nanocrystals with a regular size and narrow size

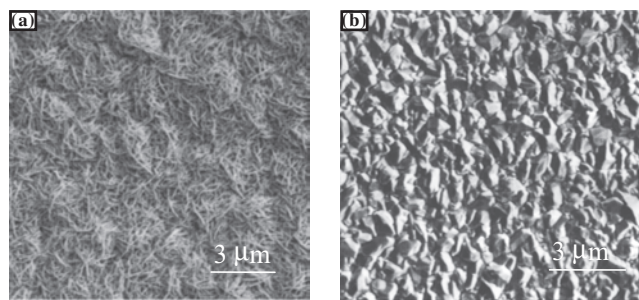


**Figure 21.** SEM images of iron oxide phases. (a) Hematite. (b) Magnetite.

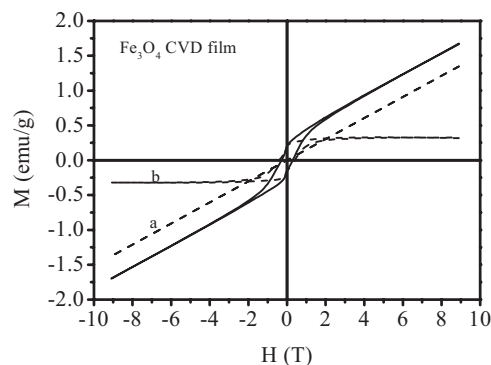


**Figure 22.** Room temperature magnetization curve of  $\text{Fe}_3\text{O}_4$  deposited at 450 °C on silicon. Reprinted with permission from [428], S. Mathur et al., *Chem. Vap. Deposition* 8, 277 (2002). © 2002, Wiley-VCH.

distribution. TEM images revealed a homogeneous distribution of highly faceted hematite particles (Fig. 24).

Although the magnetic properties of these samples reproduce reported data on  $\alpha$ - $\text{Fe}_2\text{O}_3$ , for the first time the existence of thermal hysteresis of both structural and magnetic hyperfine parameters at the Morin transition was observed (Fig. 25). The detailed Mössbauer measurements revealed a jump in hyperfine parameters (HPs) at  $T \sim T_M$ , a distinctive feature of Morin transition observed at 256(2) K [445]. The analysis of HPs as a function of temperature discards the coexistence of low- and high-temperature phases with different crystal symmetries as the possible origins of this hysteretic behavior.

Nanocrystalline  $\text{TiO}_2$  has received significant attention because of its improved properties and numerous potential applications, including nanoporous solar

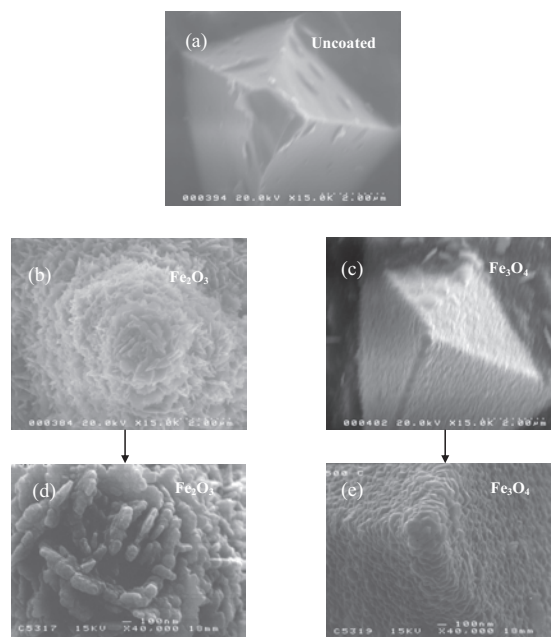


**Figure 23.** SEM images of AFM cantilever uncoated (a) and coated with hematite (b and d) and magnetite (c and e). Reprinted with permission from [428], S. Mathur et al., *Chem. Vap. Deposition* 8, 277 (2002). © 2002, Wiley-VCH.



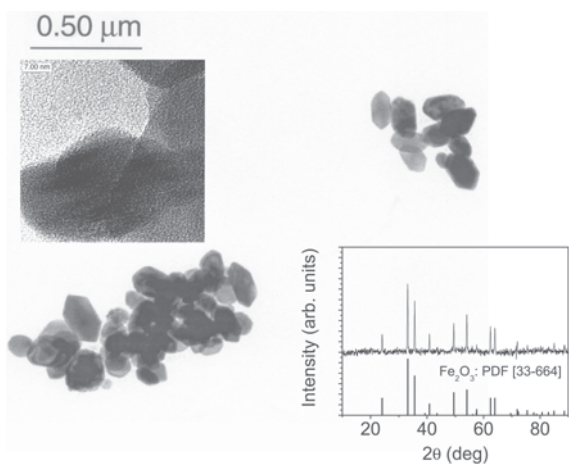


**Figure 24.** HR-TEM micrographs and XRD pattern of the  $\alpha$ - $\text{Fe}_2\text{O}_3$  particles.

cells, photochemical applications and optical coatings, etc. [446–448]. The photocatalytically active  $\text{TiO}_2$  is currently used for so-called self-cleaning coatings in which titanium oxide nanocrystals are deposited as a porous film on the desired substrate. When illuminated, these materials oxidize the organic compounds present in the system, eventually degrading these compounds to water and carbon dioxide.

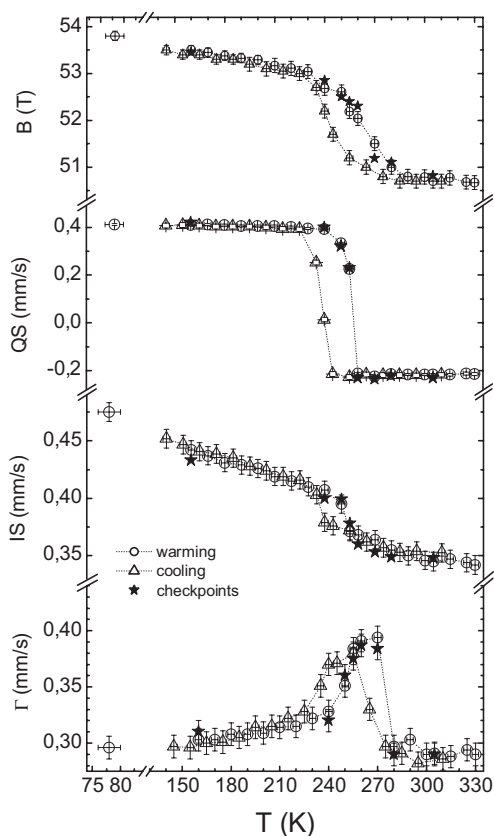
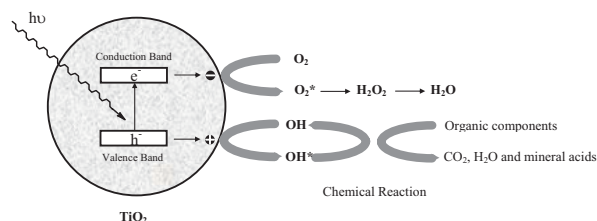


**Figure 25.** Mössbauer hyperfine parameters: (a) Hyperfine field  $B_{hyp}$ . (b) Quadrupole splitting (QS). (c) Isomer shift IS. (d) Linewidth  $\Gamma$  measured in heating and cooling cycles. The solid star-shaped symbols are checkpoints from the repeated measurements.

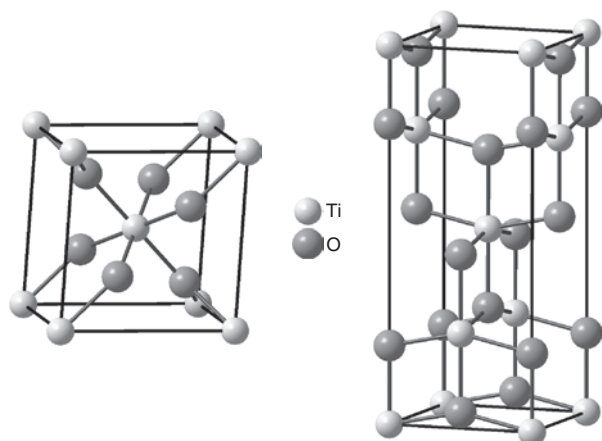
The energy of sunlight, mainly the UV part of the spectrum (360–380 nm), excites titanium dioxide nanoparticles, creating a photogenerated electron and a highly oxidizing hole in the conduction and valence band of the semiconductor [449, 450]. The electron can be scavenged by oxygen, and the hole can react with surface-bound OH on the  $\text{TiO}_2$ , creating a highly reactive  $\text{OH}^*$  radical that can completely mineralize organic components [451, 452] (Scheme 15).



**Scheme 15.**

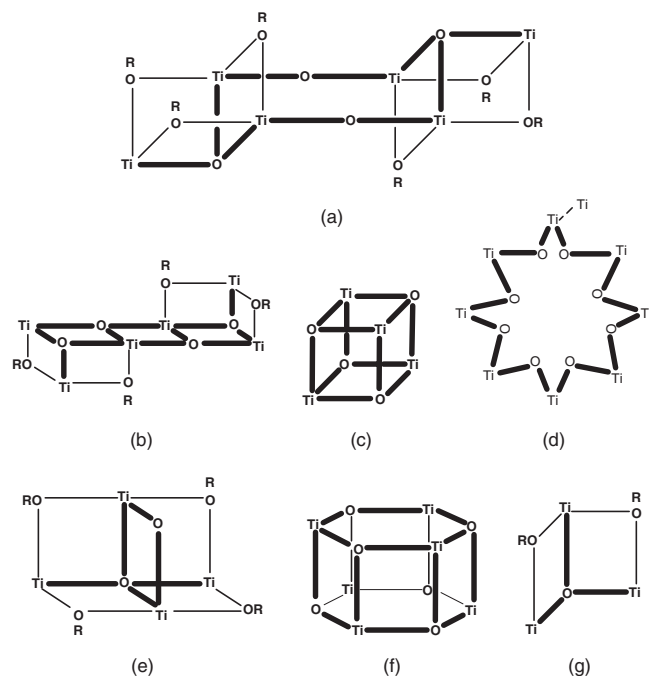
In view of the growing technological potential of nanocrystalline titania, several chemical synthesis routes have been employed to prepare very fine particles [453–455]. The above-mentioned physical properties of  $\text{TiO}_2$  depend on the specific crystallographic structure (Scheme 16), as it is known to exhibit three different crystallographic forms, namely anatase, rutile, and brookite. In nanosized titania, anatase and rutile phases are inhomogeneously distributed, and postsynthesis thermal treatments are necessary to induce phase transformation and/or to improve the crystallinity. Solar energy conversion devices and chemical sensors make use of the anatase form of  $\text{TiO}_2$ , which is difficult to prepare in pure form and is generally accompanied by the rutile modification that dominates at high temperatures. For this reason, control over the solid-state structure is highly desirable. Although the anatase-to-rutile phase transformation in nanocrystalline samples is not well understood, a new kinetic model proposes the combined interface nucleation at certain contact areas between two anatase particles and formation and growth of rutile nuclei to be the transformation steps. Over shorter reaction times, the net transformation rate is determined by the rate of nucleation, which is initiated from rutile-like structural elements in the contact area. The activation energy of 165.6 kJ/mol for rutile nucleation within nanocrystalline anatase particles is much lower than values previously measured for rutile nucleation in coarse anatase samples (>330 kJ/mol). Over longer reaction times, the net transformation rate is determined by both nucleation and nuclei growth. These results quantitatively explain the origin of the size dependence of phase transformation rates in nanocrystalline  $\text{TiO}_2$ . However, the anatase phase can be selectively obtained when the material is formed under mild conditions; for example, Rambabu et al. have used titanium tetraisopropoxide,  $\text{Ti}(\text{OPr}^i)_4$ , as a SSP to obtain nanocrystalline oxide (5–7 nm) at temperatures as low as 85 °C by the *in-situ* conversion of titania sol [456]. Interestingly,  $\text{Ti}(\text{OPr}^i)_4$ , when used in a hydrothermal synthesis, produces rutile nanoparticles, indicating the role of high-temperature

and high-pressure conditions in the structure of the resulting nanoparticles.



**Scheme 16.**

It is well known that hydrolysis and condensation rates of alkoxide precursors can be tailored through the addition of multidentate ligands. However, the influence of the precursor structure on the physical properties of the resulting nanocrystalline material has received less attention. Boyle et al. have synthesized and characterized a series of carboxylic acid-modified titanium alkoxides [328] that display a rich structural diversity in the titanium-oxygen arrangements, depending upon the steric situation around the metal center (Scheme 17).



**Scheme 17.** Structural motifs of the titanium-oxygen cores in carboxylic acid-modified  $\text{Ti}(\text{OR})_4$ .

These compounds were used in a sol-gel process to obtain  $\text{TiO}_2$  films. The density of the films (Table 7) was found to vary for different precursors, which is probably related to the

**Table 7.** Influence of precursor structure on the density of resulting  $\text{TiO}_2$  films.

Compound	Core structure (Scheme 17)	$n_f$	$\rho$
$\text{Ti}_3(\text{O})(\text{ONep})_8(\text{OFC})_2$	g	2.185	101.8
$\text{Ti}_3(\text{O})(\text{ONep})_8(\text{OAc})_2$	g	2.173	101.1
$\text{Ti}_4(\text{O})_2(\text{OPr}^i)_{10}(\text{OFC})_2$	e	2.170	100.7
$[\text{Ti}(\text{ONep})_4]_2$	h	2.133	99.04
" $\text{Ti}(\text{OPr}^i)_4$ "	Oil	2.113	97.95
$\text{Ti}(\text{OPr}^i)_4 + \text{HOPc}$	—	2.082	96.20
$\text{Ti}_6(\text{O})_6(\text{ONep})_6(\text{OPc})_6$	f	2.095	96.97
$\text{Ti}_6(\text{O})_4(\text{OPr}^i)_{12}(\text{OAc})_4$	a	2.038	93.65
$\text{Ti}_6(\text{O})_4(\text{OPr}^i)_{12}(\text{ONc})_4$	b	1.937	89.24
$\text{Ti}_3(\text{O})(\text{ONep})_8(\text{ONc})_2$	g	1.966	87.46
$[\text{Ti}(\text{ONep})_3(\text{OBC})]_2$	h	1.923	86.52
$[\text{Ti}(\text{OPr}^i)_3(\text{OBC})]_2 \cdot \text{HOPr}^i$	h	1.802	78.26

gel structure and the geometry of the basic unit (Scheme 17) forming the three-dimensional network, which is corroborated by the fact that the solid-state structures are maintained in the solution. The most desirable precursors that were found to generate fully dense  $\text{TiO}_2$  films were those having small nuclearities, few terminal alkoxides, and a low overall carbon content. This study clearly shows the influence of precursor structure on material property.

### 5.2.2. Metal Chalcogenides, Nitrides, Pnictides

The changes in the fundamental properties of materials as a function of the size, evolving from the isolated atoms or molecular clusters to a bulk phase, are most remarkably manifested in the case of semiconductor nanoparticles. The observation of quantum-confinement effects has generated substantial interest in their applications in device technology based on their novel optical and transport properties [457, 458]. For example, the bandgap in CdS can be tuned between 4.5 and 2.5 eV as the size is varied from the molecular regime to the macroscopic crystal, and the radiative lifetime for the lowest allowed optical excitation ranges from tens of picoseconds to several nanoseconds [14, 459]. The colloidal processing methods, based on controlled nucleation and rapid termination of growth, are commonly used to prepare II-VI compound semiconductor nanoparticles. These methods allow easy access to large quantities of nanomaterials, but with relatively large dispersities ( $\sim 10\%$ ). In this context, the use of SSPs containing metal-chalcogen bonds templated in molecular compounds is a promising route for controlled growth of nanomaterials. These clusters exist as discrete molecular species and can be seen as a fragment of the bulk lattice [22, 110]. O'Brien et al. have studied the thermolysis of metal dithio- and diselenocarbamate complexes ( $\text{M}\{\text{E}_2\text{CNMe}(\text{C}_6\text{H}_{13})\}_2$ ) as single molecular precursors for a one-pot synthesis of CdS, ZnS, CdSe, and ZnSe nanoparticles [103, 105, 234]. The fabrication of semiconductor nanocrystals from these molecular precursors (Fig. 26) is a one-step process, typically performed in the temperature range of 200–250 °C. This approach has been extended to the synthesis of PbS and PbSe from lead(II) alkyldithio- or alkyldiselenocarbamates, respectively [22, 188, 460].

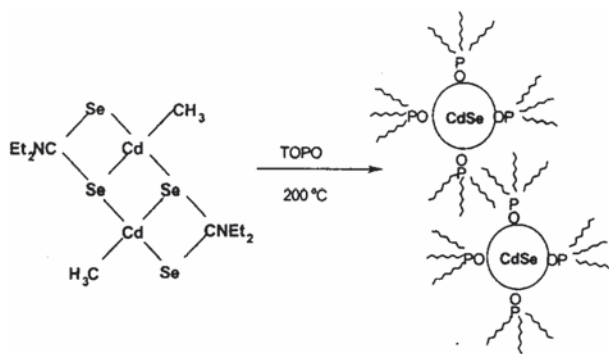
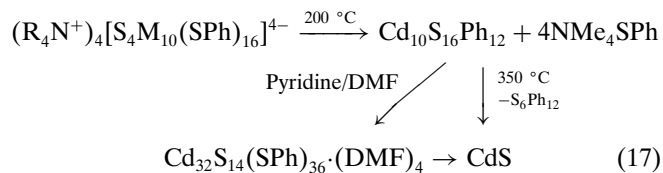


**Figure 26.** Single-source approach for preparing semiconductor nanocrystallites in TOPO. Reprinted with permission from [22], T. Trindade et al., *Chem. Mater.* 13, 3843 (2001). © 2001, American Chemical Society.

The importance of using small molecular clusters as synths to extended solid-state structures is especially evident in those examples where a structurally characterized molecular species reveals the metal-ligand interactions and coordination present in solid-state material. Several examples of well-defined polynuclear molecular clusters, possessing the elemental ratio suitable for the formation of a solid-state phase, are known; these represent the small (molecular) size regime where the properties are more like those of molecules than like those of bulk [461]. Farneth et al. have investigated the mechanism of the solid-state conversion of a series of II–VI precursors of general formula  $(R_4N^+)_4[S_4M_{10}(SPh)_{16}]^{4-}$  ( $R = Me, Et; M = Cd, Zn$ ) to the bulk metal sulphide structure [17]. The transformation as followed by combined TGA and mass spectroscopy proceeds in two discrete reaction steps: the first reaction, occurring around 200 °C, is characterized as a nucleophilic substitution or elimination reaction of a fragment ( $NMe_4SPh$ ) of the anion cluster with the tetraalkylammonium counterion. The loss of the cluster counteranions produces a new molecular solid of stoichiometry  $Cd_{10}S_{16}Ph_{12}$ , which has been isolated and characterized. This intermediate composition gave a broad XRD pattern that indicated very small (<25 Å) sphalerite-phase (cubic) crystals of CdS. It undergoes a second reaction around 350 °C, whereupon  $S_6Ph_{12}$  is eliminated, leaving a solid residue that was shown to be phase-pure CdS in the Wurtzite structure (Eq. (17)). The compound  $Cd_{10}S_{16}Ph_{12}$  is highly soluble in pyridine and was recrystallized by the addition of dimethylformamide (DMF). The solid-state structure determined by X-ray crystallography confirmed the formation



of a cluster with  $Cd_{32}S_{14}(SPh)_{36} \cdot (DMF)_4$  (Fig. 27). This molecule is much larger than the original  $Cd_{10}S_{16}Ph_{12}$  precursor-cluster, suggesting that the  $Cd_{32}$  cluster results from the assembly of CdS and  $SC_6H_5$  species of various nuclearities, which were shown by  $^{113}\text{Cd}$  NMR spectroscopy

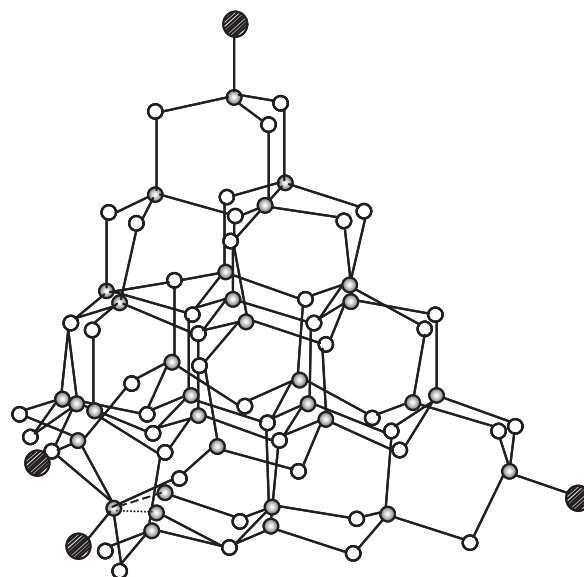


**Figure 27.** Molecular structure of  $Cd_{32}S_{14}(SPh)_{36} \cdot (DMF)_4$  cluster (drawn after [461]).

to be in rapid exchange [17]. The structural details reveal a chunk of sphalerite form of bulk CdS whose dangling surface bonds have been terminated by wurtzite-like (hexagonal) CdS units at four tetrahedral corners (Fig. 27). This corresponds to an overall cluster size of  $\sim 15$  Å.

The lowest absorption band of  $Cd_{32}S_{14}(SPh)_{36} \cdot (DMF)_4$  located at 358 nm shows a significant “blue-shift” compared with the bulk CdS (Fig. 28).

The two main implications of this work are (i) the formation of molecular cluster solids as tractable intermediates, which display the features of nanocrystalline solids, and (ii) the possibility of exploiting the ligand chemistry to control the microstructure of the final nanocrystalline solids. Similarly, CdSe (2–9 nm) and ZnSe (2–5 nm) nanoparticles have been prepared from the corresponding selenides. Although the molecular precursors  $(R_4N^+)_4 \cdot [S_4M_{10}(SPh)_{16}]^{4-}$  and the resulting nanocrystals have been the subject of intensive investigations, the chemical reaction associated with this transformation, which could uncover the nucleation mechanism, has been not well studied. Strouse et al. [110] have investigated the decomposition of  $(R_4N^+)_4 \cdot [Se_4M_{10}(SPh)_{16}]^{4-}$  to form MSe ( $M = Zn, Cd$ ). The Cd:Se ratio in  $[Se_4Cd_{10}(SPh)_{16}]^{4-}$  is significantly higher

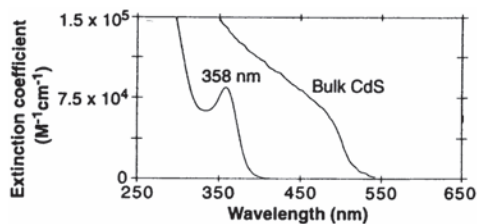


**Figure 28.** Absorption spectrum of  $Cd_{32}S_{14}(SPh)_{36} \cdot (DMF)_4$  in THF at room temperature compared with the bulk CdS absorption spectrum. Reprinted with permission from [461], N. Herron et al., *Science* 259, 1426 (1993). © 1993, American Association for the Advancement of Science.



(2.5:1) than required for the final product.  $\text{Cd}(\text{SPh})_3^-$  has been suggested as a labile fragment that would yield a Cd:Se stoichiometry of 1.5:1 based on the  $\text{Cd}_6\text{Se}_4$  core of the cluster. Since the CdSe nanomaterial grown in hexadecylamine is strictly stoichiometric, unidentified Cd by-products are required to balance the reaction stoichiometry. Several mechanisms for nucleus formation have been put forward, for instance, the fragmentation of the  $\text{M}_{10}$  cluster into  $\text{M}^{2+}$  and  $\text{Se}^{2-}$  or  $(\text{CdSe})_n$  species that can reassemble to form the nucleus or the alternative possibility that the cluster remains intact, acting as partial nuclei, and that the nanomaterial growth proceeds through scavenging of free M and Se atoms. Moreover, a combination of fragmentation via ring opening and subsequent ligand exchange, proposed for other metal chalcogenide clusters [462, 463], seems to be probable as well (Fig. 29). Apparently the  $\text{Cd}_{10}$  cluster grows (to  $\text{Cd}_{32}$ ) by ring opening followed by attack of the exposed Cd atom at the trigonally passivated chalcogenide ions and subsequent loss of the apical  $\text{Cd}(\text{SPh})_3^-$  caps (Fig. 29). As a consequence, nucleus formation occurs through ligand exchange, and in effect the cluster acts as a template for the formation of larger-nuclearity clusters. The transformation of molecular metal-chalcogenide systems into semiconductor nanocrystals with narrow size and shape dispersions demonstrates the versatility of templating nanomaterial growth by providing molecular inorganic clusters as intact nuclei. In view of the above, the use of SSPs in the deposition of thin film semiconductors by CVD techniques has been extensively studied [106, 464, 465]. Cadmium bis(diethylmonothiocarbamate),  $\text{Cd}(\text{Et}_2\text{mtc})_2$ , was shown to be a suitable source for the deposition of nanocrystalline and transparent CdS films at low temperatures (300–450 °C) (Fig. 30) [104].

Gallium nitride (GaN) has promising applications for blue and ultraviolet optoelectronic devices and has attracted much attention recently after the successful fabrication of high-efficiency blue light-emitting diodes [466]. GaN possesses a range of interesting properties, such as a wide bandgap (3.45 eV), high chemical inertness, radiation resistance, and capability of working at high temperatures, which make it an interesting candidate for optoelectronic devices.

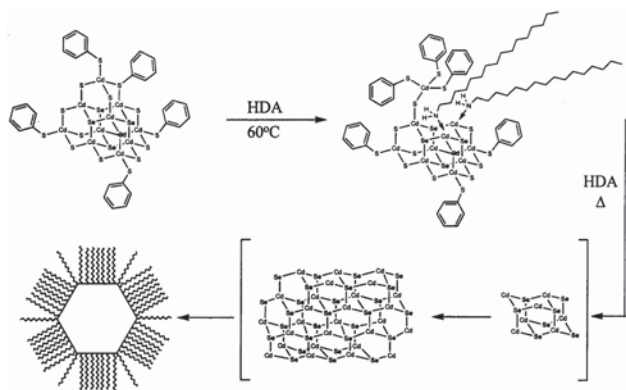


**Figure 29.** Proposed reaction mechanism for the formation of CdSe nanocrystals from cluster precursors. The thiol and amine ligands for the clusters and nanomaterials are not shown. Reprinted with permission from [110], S. L. Cumberland et al., *Chem. Mater.* 14, 1576 (2002). © 2002, American Chemical Society.

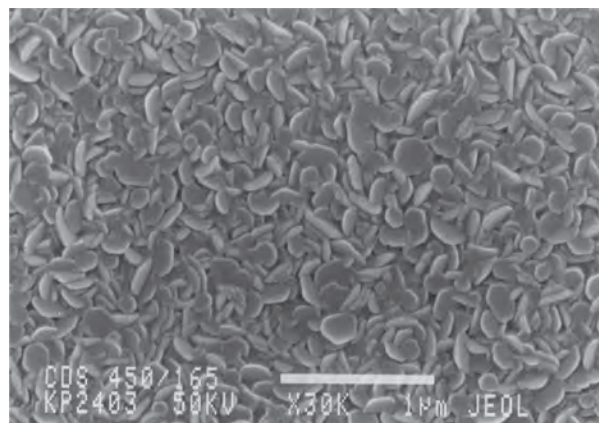


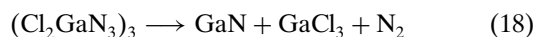
**Figure 30.** SEM image of CdS thin film deposited on the GaAs(100) substrate. Reprinted with permission from [104], M. Chunggaze et al., *Adv. Mater. Opt. Electron.* 7, 311 (1998). © 1998, John Wiley & Sons.

For the above reasons, there is growing interest in the synthesis of GaN nanocrystals and nanostructured films. The established method of depositing device-quality GaN by MOCVD utilizes high-temperature interaction of  $(\text{CH}_3)_3\text{Ga}$ , with a large excess of  $\text{NH}_3$ . However, the high stability of the N–H bond in  $\text{NH}_3$  requires reaction temperatures in excess of 1000 °C and the inefficient use of toxic  $\text{NH}_3$ . Therefore, the choice of substrate material is limited by a high substrate temperature, which may result in residual strains in the deposited layers. To overcome the limitations of this process, alternative methods based on SSPs that incorporate direct Ga–N bonds and do not contain any strong N–H bonds, or even organic groups, offer the potential for significant improvements in the growth process and film quality [137, 467–469]. The major advantages of using molecular precursors with pre-formed Ga–N bonds include lower deposition temperatures, exclusion of  $\text{NH}_3$  from the process, reduction in N vacancies, and elimination or drastic reduction of carbon impurities [470, 471].

Recently, a large number of routes for synthesizing freestanding nanocrystals and films (nanostructured and epitaxial) of GaN have been reported. For example, the pyrolyses of  $[\text{Ga}(\text{NH}_2)_{3/2}]_n$  (450 °C) [472],  $[\text{H}_2\text{GaNH}_2]_3$  (600 °C) [473],  $[\text{Ga}\{\text{N}(\text{CH}_3)_2\}_3]_2$  (600 °C) [474],  $[\text{H}_2\text{GaN}_3]$  (350 °C) [467], and  $[\text{Ga}(\text{N}_3)_3]_n$  (280 °C) [475] gave nanocrystalline GaN powders. Although all of the precursors produced chemically homogeneous GaN, the temperature of crystallization and the amount of organic contamination depend on the organic content in the precursor molecule. In the case of large organic groups, high temperatures are required for their dissociation and complete decomposition. Despite several promises, the single-source route implies problems, such as low volatility of precursors and carbon contamination of the nitride films from undecomposed organic fragments. Therefore, a single precursor should be carefully designed so that it follows a clean decomposition pathway to produce the desired phase with a minimum level of impurities and the lowest possible decomposition temperature.

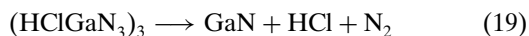
In a nonconventional approach, Fischer et al. have used detonation of gallium azides,  $(\text{R}_3\text{N})\text{-Ga}(\text{N}_3)_3$ , to obtain phase-pure nanocrystals of hexagonal GaN [137]. Kouvetakis et al. have reported several related routes for GaN synthesis

utilizing a carbon- and hydrogen-free SSP,  $\text{Cl}_2\text{GaN}_3$ , to grow thin oriented films of high-quality GaN on sapphire at 700 °C. The main limitation of this approach is the extremely low vapor pressure of  $\text{Cl}_2\text{GaN}_3$ , which is an involatile polymeric solid at room temperature, and the inherent loss of substantial quantities of  $\text{GaCl}_3$  (Eq. (18)) at the growth temperature:

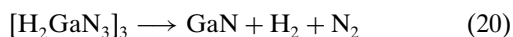


In view of the above, an alternative monohydride precursor,  $(\text{HClGaN}_3)_3$ , was synthesized [136, 141], which is a moderately volatile molecular system consisting of interconnected tetrameric  $\text{Ga}_4\text{N}_4$  units (Fig. 31).

The compound decomposes easily at low temperatures by elimination of  $\text{HCl}$  and  $\text{N}_2$  to grow GaN on Si and sapphire (Eq. (19)).



An obvious extension of the above approach suggests the simpler dihydride analog of  $(\text{Cl}_2\text{GaN}_3)_3$  to be a potential precursor, as it could be expected to be more volatile (low molecular weight and increased covalent character). Indeed,  $[\text{H}_2\text{GaN}_3]_3$  is an air-sensitive liquid, volatile at room temperature, that can be distilled readily at 40 °C (0.2 torr). This simple hydride analog is particularly desirable as a CVD source [467] because it eliminates benign  $\text{H}_2$  and  $\text{N}_2$  by-products to yield stoichiometric GaN at temperatures as low as 150 °C (Eq. (20)).



$[\text{H}_2\text{GaN}_3]_3$  exists as a trimer of  $C_{3v}$  symmetry in the gas phase, as indicated by *ab initio* calculations. The  $\text{Ga}_3\text{N}_3$  cyclic core of the structure (Fig. 32) represents the basic building block that is structurally consistent with the tetrahedral structures of the group III nitrides, including those of GaN.

The dihydrido compound was successfully used to obtain high-purity GaN films free of carbon, oxygen, or hydrogen

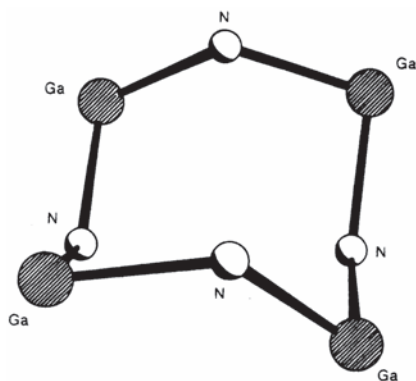


**Figure 31.** Representation of the  $\text{Ga}_4\text{N}_4$  cyclic core of  $(\text{HClGaN}_3)_4$ . Reprinted with permission from [136], J. McMurran et al., *Inorg. Chem.* 37, 6638 (1998). © 1998, American Chemical Society.

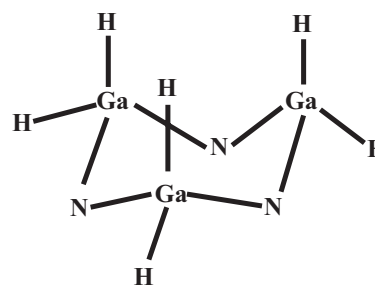
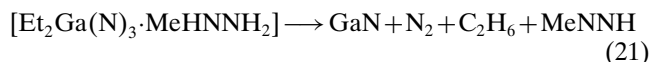


**Figure 32.** Gas-phase structure of  $(\text{H}_2\text{GaN}_3)_3$ . The  $\text{N}_2$  portion of the  $\text{N}_3$  group is omitted for clarity (adapted from [467]).

impurities. Heteroepitaxial growth (Fig. 33) of wurzite GaN on sapphire was achieved at 650 °C [467].

Although  $[\text{H}_2\text{GaN}_3]_3$  is a versatile CVD source for GaN, the high reactivity of this molecule, which is a significant advantage with respect to the formation of GaN, requires a careful manipulation of the pure product. The pronounced tendency of this precursor to decompose in an exothermic reaction liberating nitrogen is a typical feature of metal azide chemistry. Nevertheless, it is possible to control the pyrophoric nature of the azide precursors by using ligands capable of intramolecular coordination [468, 476]. Kim et al. have synthesized mononuclear  $[\text{Et}_2\text{Ga}(\text{N}_3)\cdot\text{MeHNNH}_2]$  as a Lewis acid-base adduct for low-temperature deposition of *h*-GaN films on Si(111). The compound decomposes via loss of stable molecular species (Eq. (21)), yielding high-quality GaN films with little contamination [476].



In addition to the gas-phase synthesis, these precursors can be employed for the solution-based synthesis of GaN

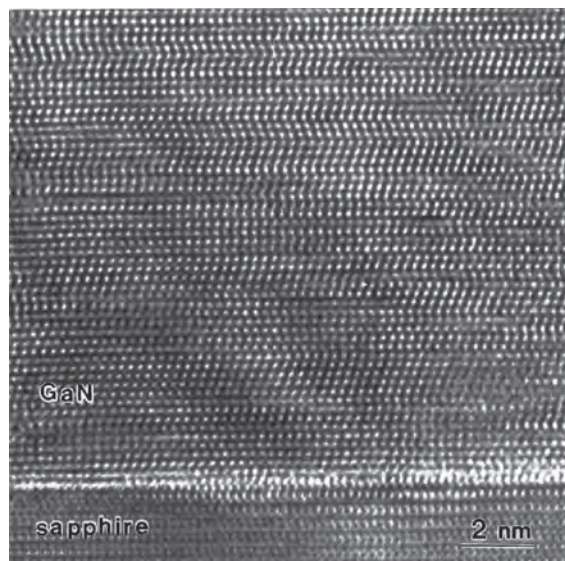
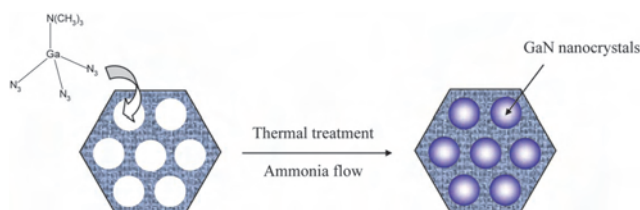


**Figure 33.** High-resolution cross-sectional electron micrograph showing heteroepitaxial growth of wurzite GaN on sapphire at 650 °C. Reprinted with permission from [467], J. McMurran et al., *Appl. Phys. Lett.* 74, 883 (1999). © 1999, American Institute of Physics.

nanocrystals. Gladfelter et al. have used a cyclotrigallazane, prepared by the reaction of  $[\text{GaH}_3(\text{NMe}_3)]$  in supercritical ammonia. This compound dehydrogenates in the solid state to form nanocrystalline GaN. The thermal instability of gallium azides can be used to obtain colloids of GaN. Thermolysis of  $[\text{Et}_2\text{Ga}(\text{N}_3)]_3$ ,  $[(\text{N}_3)_3\text{Ga}\{\text{NMe}_2(\text{CH}_2)_3\}]$ , and  $[(\text{Et}_3\text{N})\text{Ga}(\text{N}_3)_3]$  in triglyme has produced nanometric GaN particles [469] (Scheme 18). Furthermore,  $[(\text{Et}_3\text{N})\text{Ga}(\text{N}_3)_3]$  has been used to grow nanocrystals of GaN in a regular porous matrix. For this purpose, the mesoporous molecular sieve MCM-41 was impregnated by the precursor solution and heat-treated ( $500\text{ }^\circ\text{C}$ ) to achieve a spatially confined nucleation of GaN nanoparticles [469] (Scheme 18).



**Scheme 18.**

The above examples clearly illustrate the potential of molecular-level design in controlling the vapor pressure and reactivity of the precursor compounds. Furthermore, an appropriate selection of ligands can enforce a neat thermal decomposition mechanism to offer high-purity inorganic materials at low temperatures. Another advantage of suitable liquid precursors is the possibility of growing nanoparticles by spatially restricting the molecular species in ordered channels or pores of mesoporous matrices.

Metal pnictides are best represented by the 13–15 compounds, such as GaAs, and are well known for their electronic and optoelectronic applications. The single-source approach to the preparation of these materials has been intensively investigated and reviewed by Maury [422] and Cowley [464], who have also actively contributed to the field [134, 477–486]. The use of III–V adducts as substitutes for highly reactive group III alkyls by Benz et al. [487, 488] was among the pioneering steps in this direction. Maury et al. have used Lewis acid-base adducts of formulae  $\text{ClR}_2\text{Ga} \leftarrow \text{ER}'_3$  ( $\text{E} = \text{As}, \text{P}$ ;  $\text{R}$  and  $\text{R}' = \text{Me}$  or  $\text{Et}$ ) to overcome the problem of the high reactivity and toxicity of conventional dual sources [487, 489]. Films of GaP [490, 491] and InP [491] were successfully grown from the cyclic trimers of general formula  $[\text{Et}_2\text{M}-\text{P}(\text{Et})_2]_3$  ( $\text{M} = \text{Ga}, \text{In}$ ) with covalent metal-phosphorus bonds [487, 492]. Epitaxial growth of GaAs was achieved with  $\text{ClR}_2\text{Ga} \leftarrow \text{AsR}'_3$  ( $\text{R} = \text{Me}, \text{Et}$ ). The thermal decomposition of two series of molecular precursors was achieved with the general formulae  $(\text{C}_6\text{F}_5)_{3-n}\text{Me}_n\text{Ga} \leftarrow \text{AsEt}_3$  ( $n = 0$  or  $2$ ) and  $[\text{ClR}_2\text{Ga} \leftarrow \text{AsEt}_2]_2\text{CH}_2$  ( $\text{R} = \text{Me}, \text{Et}$ ). The relative stabilities of the central M–E bond with respect to peripheral M–ligand and E–ligand interactions was evaluated by two different approaches. The first case deals with the use of Lewis acid-base dative bonds, whose strength can be tuned by means of the more or less electron-donating nature of the alkyl groups, and varied admixture of halogen (Cl) or pseudo-halogen ( $\text{C}_6\text{F}_5$ ) substituents; the rather fragile M–E bonds are a major limitation

in this approach, causing loss in volatility and surface mobility, whereas in the second approach complexes with covalent M–E bonds were used [289, 493, 494].

Cowley and Jones have used a variety of single-source organometallics that involve  $\sigma$ -bonding between group III and group V elements [16, 487, 495]. They have tested different Ga–As precursors, such as  $[\text{Me}_2\text{Ga}(\mu\text{-AsBu}'_2)]_2$  [484, 485, 487, 495–497],  $[\text{Me}_2\text{Ga}(\mu\text{-AsBu}'_2)]_2$  [487, 487, 498], and  $[\{\text{Ga}(\text{AsBu}'_2)\}_3]$  [487, 497]. The films deposited with the use of the methyl derivative  $[\text{Me}_2\text{Ga}(\mu\text{-AsBu}'_2)]_2$  were arsenic-deficient [487, 496]. On the other hand, epitaxial films could be obtained with  $[\text{Et}_2\text{Ga}(\mu\text{-AsBu}'_2)]_2$ ; however, the films exhibited anomalously low Hall mobilities due to the formation of gallium islands.

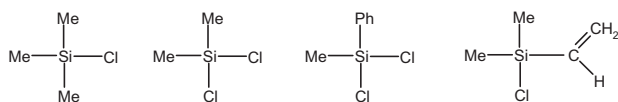
The antimonides of group 13 elements are narrow direct bandgap semiconductors with small bandgaps ( $E_g$  (eV) = 1.60 (AlSb), 0.67 (GaSb), 0.16 (InSb)) and high electron mobility that render them very attractive for potential applications in optoelectronic devices. For instance, GaSb is used for the production of light-emitting and light-detecting devices operating in the  $2\text{-}\mu\text{m}$  wavelength range (GaSb: 1), field effect transistors (GaSb: 2), and infrared detectors (GaSb: 3). The growth of thin films of group 13 nitrides, phosphides, and arsenides by CVD typically involves group 13 alkyls and group 15 hydrides; however, an analogous process is not possible for the preparation of group 15 antimonides because  $\text{SbH}_3$  is thermally very unstable (decomposes below  $-60\text{ }^\circ\text{C}$ ), which is also true for primary ( $\text{RSbH}_2$ ) and secondary stibines ( $\text{R}_2\text{SbH}$ ). Furthermore, an excess of stibine during film growth may lead to the formation of elemental Sb on the substrate, which has to be strictly avoided because of the low volatility of elemental Sb. For these reasons, group 13 trialkyls ( $\text{R}_3\text{M}$ ) and tri-organostibines ( $\text{R}_3\text{Sb}$ ) are used as the common precursors (GaAs: 12). However, the inability to produce atomic hydrogen during pyrolysis, as well as the high stability of metal-carbon bonds, favor the incorporation of large amounts of carbon in the resulting material. GaSb has been grown from  $\text{Sb}(\text{NMe}_2)_3$ , which contains weaker Sb–N bonds [499, 500]. The alternative pathway is based on the use of heterocycles  $[\text{R}_2\text{MER}'_2]_x$  that are attractive SSPs, particularly because of their lower metal-carbon bond energies when compared with pure group 13 and 15 alkyls. Schulz et al. have used  $\text{Bu}'_3\text{Ga}-\text{Sb}(\text{Bu}')_3$  and  $\text{Bu}'_3\text{Ga}-\text{Sb}(\text{Pr}')_3$  as single-molecule precursors for the synthesis of highly oriented carbon-free GaSb nanocrystals and whiskers [97].

### 5.2.3. Silicon Oxide, Nitride, and Carbide

Because of the covalent character of the chemical bonds, the nonoxide amorphous and nanocrystalline refractory ceramics exhibit a very high ( $\sim 3000\text{ }^\circ\text{C}$ ) melting point, low mobility of atoms, low plasticity, and high hardness at temperatures up to  $2000\text{ }^\circ\text{C}$ . Therefore these materials can substitute for metals, alloys, and intermetallics in many high-temperature engineering, chemical, and electronic applications. The synthesis of silicon-containing ceramics (oxide, carbide, nitride, etc.) is an active research field in its own right, and, since the early investigations of organometallic oligomers and polymers in the 1970s [501], numerous new organometallic compounds have been developed as precursors to all kinds of nonoxide ceramics like SiC,  $\text{Si}_3\text{N}_4$ , AlN, BN,  $\text{B}_4\text{C}$ , TiC, and TiN.



The low-temperature synthesis (without sintering aid) of two- and three-component silicon-containing ceramics that are homogeneous on an atomic scale is possible only through organometallic precursors [502]. The most salient application of organometallic precursors is in the liquid phase synthesis of silicon nitride and carbide ceramics, which are of significant technological interest because of their high strength and thermal and chemical stability. The use of molecular precursors for refractory materials affords potential advantages in terms of controlling the composition, deposition temperature, and microstructure of the deposited product [30]. The need to control these factors is critical to achieve the extraordinary properties of the above materials, which are sensitive to local variations in composition and/or microstructure. The choice of organometallic molecules for use as SSPs has been largely an empirical process, with few guidelines available relating to the molecular structure of the precursor and the chemical composition of the final material. In the preparation of silicon preceramic polymers, compounds containing Si-Si, Si-H, Si-N, Si-C, and Si-Cl bonds or molecular units based on these linkages are used as precursor species [503] that are derived from different alkyl chlorosilanes (Scheme 19). Since most of the precursor compounds are viscous or oily, their structural characterization is generally based on NMR and mass spectral data [504].

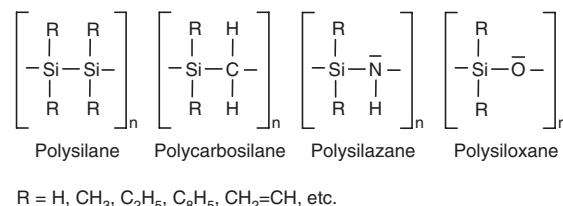


**Scheme 19.** The alkyl chlorosilanes used as building blocks in the synthesis of organometallic precursors.

The versatility of this class of polyceramic precursors originates from the facile chemical (cross-linking, dechlorination) reaction producing, sometimes by thermal treatments, tractable, soluble, and fusible precursor compounds. These stable coordinations are not always directly accessible. For example, the chlorosilanes  $\text{SiHCl}_3$ ,  $\text{SiH}_2\text{Cl}_2$ , and  $\text{SiH}_3\text{Cl}$  are stable compounds and do not split off HCl, whereas the corresponding aminosilane  $\text{SiCl}(\text{NH}_2)_3$  would decompose into  $\text{NH}_4\text{Cl}$  and solid diimide  $\text{Si}(\text{NH}_2)_2$ , which seems to be an attractive precursor from its chemical composition, but is unsuitable because of its physical properties. Similarly, the tetra-amide  $\text{Si}(\text{NH}_2)_4$  is an unstable compound. Although polymeric precursors for  $\text{Si}_3\text{N}_4$  with the ideal atomic ratio  $\text{Si}:\text{N}:\text{C} = 3:4:0$  cannot be directly prepared, various polysilazanes have been shown to convert to pure  $\text{Si}_3\text{N}_4$  [505–508].

This route offers the possibility of improving the compositional homogeneity and tailoring the composition and molecular structure of the ceramic powders. Furthermore, the solubility and rheology of polymeric precursors provide potential processing routes to binders, to sintering aids, and to the formation of nanosized thin films and fibers. In addition, this methodology produces nanosized powders, which are often difficult or impossible to achieve by the more traditional ceramic processing techniques. For example, a single class of preceramic polymer, polysilazanes, has been shown to convert to either pure  $\text{Si}_3\text{N}_4$  or a combination of  $\text{Si}_3\text{N}_4$  and SiC, depending on the chemistry of the polymer and pyrolysis conditions [509]. Polysilazanes are silicon compounds based

on an alternating Si–N backbone that may or may not contain organic substitutes (Scheme 20). The amount of carbon present in the polymer is decisive for the composition of the ceramic material. Minimizing the amount of carbon results in a ceramic with a stoichiometry closer to  $\text{Si}_3\text{N}_4$ , whereas the  $\text{Si}_3\text{N}_4/\text{SiC}$  composite is formed in the case of carbon-rich precursors [509]. In contrast to the sintering step applied for conventional ceramic powder processing, the polymeric precursors are solidified by pyrolysis, whereby the key concern is the ceramic yield determined by thermogravimetric analysis and corroborated by mass spectral studies of the pyrolysis products.



**Scheme 20.** General representation of organometallic precursors to silicon-containing ceramics.

Silicon carbide is an attractive material for demanding mechanical and high-temperature applications and is extensively used as an abrasive and erosive medium. In addition, it is tough, possesses low-friction characteristics, and is second only to diamond in wear resistance. Conventional SiC chemical vapor deposition processes generally utilize separate Si (e.g.,  $\text{SiH}_4$ ,  $\text{SiCl}_4$ ,  $\text{SiBr}_4$ ) and C (e.g.,  $\text{CH}_4$ ,  $\text{C}_2\text{H}_2$ ,  $\text{C}_3\text{H}_8$ ) sources and require temperatures in excess of  $1000^\circ\text{C}$  for the phase formation. High temperatures cause significant deformation of released polycrystalline-Si microstructures, making postprocess SiC coating challenging [510]. Moreover, control over microstructure and composition is difficult at high temperatures. Such limitations clearly illustrate the need for low-temperature alternatives. Lee and co-workers have obtained epitaxial cubic-SiC films with the use of 1,3-disilabutane ( $[\text{SiH}_2\text{CH}_2]_2$ , I, Scheme 21a) as a single precursor, at temperatures as low as  $900^\circ\text{C}$  [511]. Polycrystalline SiC films were obtained at  $650^\circ\text{C}$ . The molecular source, a liquid with high vapor pressure, simplifies the handling compared with conventional dual-source CVD, thereby eliminating the need for an elaborate gas-handling system and ensuring strict stoichiometry control. Using the same precursor, Maboudian et al. have deposited conformal SiC films on Si atomic force microscopy cantilevers at  $780^\circ\text{C}$ . Figure 35 displays a cross section of a SiC film deposited with the use of a molecular precursor on a Si AFM cantilever; an excellent conformal coverage with no void formation at the SiC/Si interface was observed. The disilacyclobutane CVD process was also successfully used to coat released poly-Si microstructures (Fig. 34). This observation reveals the potential for integrating this process into the fabrication technology for microelectromechanical systems (MEMS) [512].

Although 1,3-disilabutane is an ideal SiC precursor, it is not suitable for large-scale applications because it is expensive. Similarly, the simple carbosilanes such as  $\text{CH}_3\text{SiCl}_3$  afford little advantage in terms of either improved stoichiometry control or lowered deposition temperature [513]. Interrante et al. have used substituted disilacyclobutanes

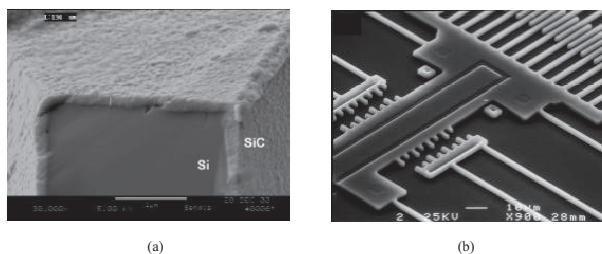
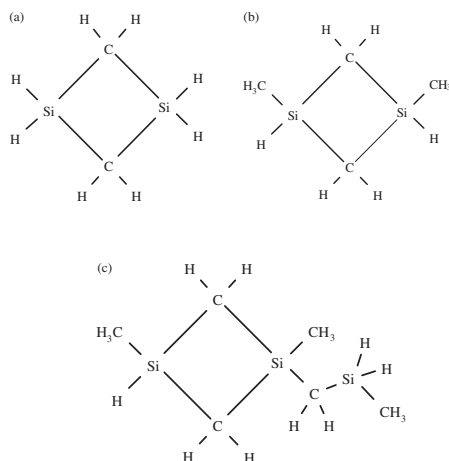


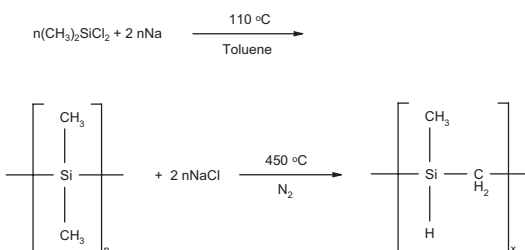
**Figure 34.** SEM images of (a) the cross section of a 130-nm thick SiC film deposited on a Si AFM cantilever and (b) a released poly-Si lateral resonator coated with a thin SiC film. Reprinted with permission from [615], C. R. Stoldt, *Sens. Actuators, A* 97-8, 410 (2002). © 2002, Elsevier Science.

[MeSi(H)- $\mu$ -(CH<sub>2</sub>)<sub>2</sub>Si(Me)CH<sub>2</sub>SiH<sub>2</sub>Me] (II) and [Si(Me)-HCH<sub>2</sub>]<sub>2</sub> (III) (Scheme 21b, c) as alternative single precursors to SiC [514, 515]. Their results indicate that the decomposition chemistry is complicated in the case of II and III because of molecular rearrangements that adversely affect the product purity.



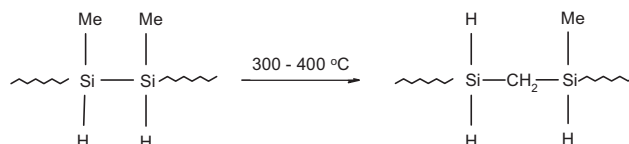
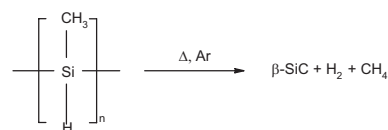
**Scheme 21.**

In contrast to the sol-gel and other processing methods, synthetic organometallic polymers obtained from well-defined building units can be used directly in applications such as coatings, fibers, or bulk shapes and subsequently pyrolyzed to the desired ceramic. The repetition and/or combination of modular units shown in Scheme 22 allows the fabrication of different organometallic precursors. Polycarbosilanes used as precursors to silicon carbide (SiC) can be synthesized with different alkyl groups according to the following equation [333]:



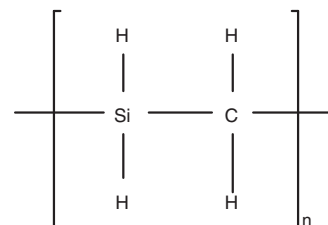
**Scheme 22.**

The polymeric route to silicon-based ceramics was developed by Yajima et al., who used polycarbosilane ( $-\text{[MeHSiCH}_2\text{]}_x-$ ) as a precursor to SiC [502, 516–518]. One of the drawbacks of this method was the initial Si:C ratio of 1:2, which resulted in excess carbon in the final product. The nonstoichiometric product offers mechanical properties inferior to those of bulk stoichiometric SiC [519]. To overcome these problems, pure and modified polymethylsilane (PMS) precursors with a Si:C ratio of 1:1 were successfully used by Laine et al. to obtain stoichiometric SiC [520]. Unmodified PMS,  $-\text{[MeSiH]}-$  [521, 522], with the stoichiometry required to form SiC, offers the potential to be the SSP to SiC. The only gaseous species that should be released in the pyrolytic conversion of PMS is H<sub>2</sub> with the retention of the Si:C ratio. However, unmodified PMS undergoes a rearrangement upon heating [520, 523] and loses 7–8 wt.% by releasing CH<sub>4</sub> and H<sub>2</sub> (Scheme 23). As a consequence, pyrolysis of unmodified PMS gives a mixture of SiC and excess Si, which shows the importance of molecular architecture and its inherent chemical behavior for the composition of the final material. The functionalization of PMS by vinyl groups was shown to compensate for the carbon loss by introducing additional carbon content. Depending upon the functionality of the vinyl groups, it is possible to adjust the composition from silicon rich to stoichiometric SiC and to carbon-rich ceramic.



**Scheme 23.**

Furthermore, new molecular precursors such as hydriodopolycarbosilane (Scheme 24), which is a single-component liquid source, have been developed to obtain high-purity SiC [524].

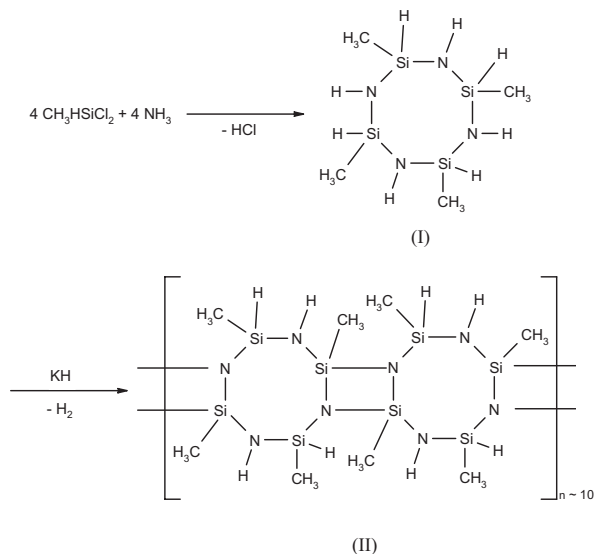


**Scheme 24.**

Polysilazanes are prepared in a straightforward reaction of  $(\text{CH}_3)_n\text{SiCl}_{4-n}$  with  $\text{NH}_2(\text{H}, \text{R})$ , whereby HCl is eliminated and a low-molecular compound is formed that can be polymerized by employing dehydrocoupling catalysts like KH,  $\text{Ru}_3(\text{CO})_{12}$ , etc. [525] (Scheme 25). The synthesis route



is especially suitable in the case where  $n = 1$  and  $R = \text{CH}_3$  [526, 527].



**Scheme 25.**

The pyrolysis of polysilazane II in a  $\text{NH}_3$  atmosphere produces colorless  $\text{Si}_3\text{N}_4$  in high yield (82%). The decomposition of polysilazanes involves different reaction products such as  $\text{CH}_4$  and  $\text{H}_2$ , which determine the ceramic yield. The highly branched polysilazanes with low carbon content exhibit higher ceramic yield. The split-off of oligosilazanes or loss of volatile silazanes by thermolytic retroversion and transamination should be suppressed to increase the ceramic yield.

Boron nitride has attracted a growing interest for technological applications because of its excellent characteristics, namely high hardness, chemical inertness, and dielectric behavior. Hexagonal boron nitride (*h*-BN) with a layered and  $sp^2$ -bonded structure is similar to graphite and is the stable ordered phase under ambient conditions. On the other hand, cubic boron nitride (*c*-BN) has a zinc blende structure with  $sp^3$ -bonding resembling that of diamond. In fact, *c*-BN is better suited for electronic device applications as a high-temperature semiconductor because of the wide direct energy bandgap (6.4 eV). Moreover, it can easily be doped both *n*-type and *p*-type with Si and Be, respectively. Significant progress has been made in the synthesis of *c*-BN by various physical and chemical deposition methods [528]. However, the major disadvantage of *c*-BN films is that they are much more difficult to synthesize than diamond because of their narrow phase stability region, high compression stress, and problems in controlling boron and nitrogen sources [529, 530]. To overcome these problems, Boo et al. have used isopropyl amine and *tert*-butylamine complexes of triethylborane ( $(i\text{Pr})\text{H}_2\text{NBET}_3$ ,  $(t\text{Bu})\text{H}_2\text{NBET}_3$ ) as SSPs with boron and nitrogen in a 1:1 ratio to grow a crack-free *h*-BN film on Si(100) at 850 °C [99].

#### 5.2.4. Intermetallics

Heterometallic nanoparticle catalysts such as Pt-Re, Ir-Sn, Pt-Ru, Ag-Ru, Cu-Ru, and Pd-Ru occupy an important position in heterogeneous catalysis [531]. Published reports

[190, 532–534] on such catalyst systems reveal that enhanced catalytic performance apparently arises from the synergy between the component elements at the nanoscale, which is absent in solid solutions of the two bulk metals. Furthermore, the thin films of intermetallic combinations of a group 13 element and a transition metal are thermodynamically stable metal/semiconductor interfaces that can act as ohmic contacts or as Schottky barriers [535]. Although molecular beam epitaxy is used to deposit such materials, a large number of reports have appeared on the deposition of binary metal alloys by the gas-phase decomposition of single-source organometallic sources, which demonstrate the possibilities of controlling the stoichiometry of intermetallics.

Thomas and Johnson and co-workers have obtained discrete nanoparticles of the Pd-Ru bimetallic catalyst by gentle thermolysis of the mixed-metal Pd-Ru carbonylate cluster  $[\text{Pd}_6\text{Ru}_6(\text{CO})_{24}]^{2-}$  (Fig. 35) [190]. HR-TEM revealed that the Pd-Ru bimetallic nanoparticles were of uniform size (ca. 1.7 nm diameter). A uniform distribution of nanoparticles within the pores of mesoporous silica offers a highly active catalyst for hydrogenation of alkenes and unsaturated aromatic systems [190]. The easy formation of Pd-Ru nanoparticles is due to the ability of the anionic molecular precursor to shed its cloak of carbonyl groups under mild thermal treatment (180 °C). A comparison of the catalytic performance with monometallic Ru and Pd clusters reveals that the bimetallic catalysts are far superior in performance to their monometallic analogs, suggesting a possible synergism between the two bimetallic nanoparticles [190].

Kaeszi and co-workers have deposited stoichiometric films of intermetallics containing a group 14 element and a transition metal [536–538]. Precursor complexes with metal-metal bonds (e.g.,  $(\text{CO})_4\text{-CoGaCl}_2(\text{THF})$ ) [537] as well as those in which the metal centers are connected by bridging ligands such as  $[(\text{py})(\text{Et})\text{Co}(\text{dmg}\cdot\text{GaEt}_2)_2]$  [538],  $[\text{Ni}(\text{dmg}\cdot\text{GaEt}_2)_2]$  [538], and  $[\text{Pt}(\text{dmg})(\text{GaMe}_2)_2]$  [536] have been used to deposit CoGa, NiGa, and PtGa<sub>2</sub>, respectively. Since the Co–Ga phase diagram mainly comprises the  $\beta$ -CoGa phase, which extends on either side of the 1:1 atomic ratio, the CoGa films were consistently monophasic. On the other hand, the phase diagrams in the Ga–Pt and Ga–Ni systems comprise several phases, and as a result a small amount of Pt<sub>2</sub>Ga<sub>3</sub> is formed with the major and expected PtGa<sub>2</sub> phase

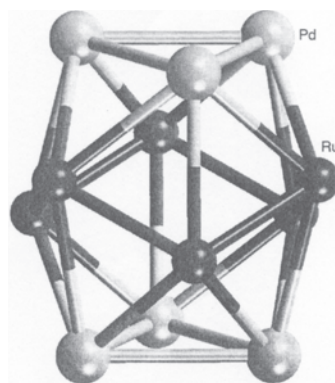


**Figure 35.** Structure of the  $\text{Pd}_6\text{Ru}_6$  core of the  $[\text{Pd}_6\text{Ru}_6(\text{CO})_{24}]^{2-}$  cluster. Reprinted with permission from [190], R. Raja et al., *Chem. Commun.* 1571 (1999). © 1999, Royal Society of Chemistry.

and the films obtained from the Ni-Ga precursor contained NiGa, NiGa<sub>4</sub>, Ni<sub>2</sub>Ga<sub>3</sub>, and NiGa<sub>4</sub>. Deposition from (CO)<sub>4</sub>-CoGaCl<sub>2</sub>(THF) in the temperature range 250–350 °C gave nearly stoichiometric CoGa films with some chlorine contamination. A mass spectral study (EI-MS) of the precursor showed the abundance (15%) of the stripped heterobimetallic species [CoGa]<sup>+</sup> corresponding to the stability of the Co–Ga bond [537]. The chlorine content in the films decreased at higher temperatures (350–400 °C), but the film became cobalt-rich, indicating that a decrease in the chlorine contamination is associated with a loss of gallium. This is probably due to the formation of volatile GaCl<sub>3</sub>, which is favored by the dissociation of Co–Ga bonds occurring above 350 °C. This example shows the relevance of investigating the gas-phase behavior of precursors, particularly in view of the different fragmentation mechanisms operative in the thermal degradation of the molecule, depending on the decomposition temperature.

Fischer et al. have performed extensive studies on the CVD of intermetallics from molecular precursors containing metal-metal bonds between *d* and *p* block elements [539–542]. Volatile heterodinuclear organometallic compounds L(CO)<sub>3</sub>Co–GaR<sub>2</sub>(D) and L(CO)<sub>3</sub>Co–Ga[(CH<sub>2</sub>)<sub>3</sub>NR<sub>1</sub>]<sub>2</sub>(R) (R = H, CH<sub>3</sub>, C<sub>2</sub>H<sub>5</sub>, CH<sub>2</sub>Bu', CH<sub>2</sub>SiMe<sub>3</sub>; D = THF, NMe<sub>3</sub>, NC<sub>7</sub>H<sub>13</sub>; L = CO, PMe<sub>3</sub>, PPh<sub>3</sub>; R<sup>1</sup> = CH<sub>3</sub>, C<sub>2</sub>H<sub>5</sub>) were studied as single molecular precursors for the deposition of binary CoGa alloy thin films. The films, grown in a hot wall reactor, had Co/Ga atomic ratios in the range of 1 to 3, depending upon the substrate temperature and the type of substituents at the gallium atom. The molecular structure of a prototype of the compound series L(CO)<sub>3</sub>Co–GaR<sub>2</sub>(D) is shown in Figure 36. The deviation in the Co:Ga ratio when compared with that in the precursor was observed when the deposition was performed at low temperatures. The formation of thermally stable gallium alkyl complexes was suggested as a probable reason for the Ga deficiency in the deposits [539].

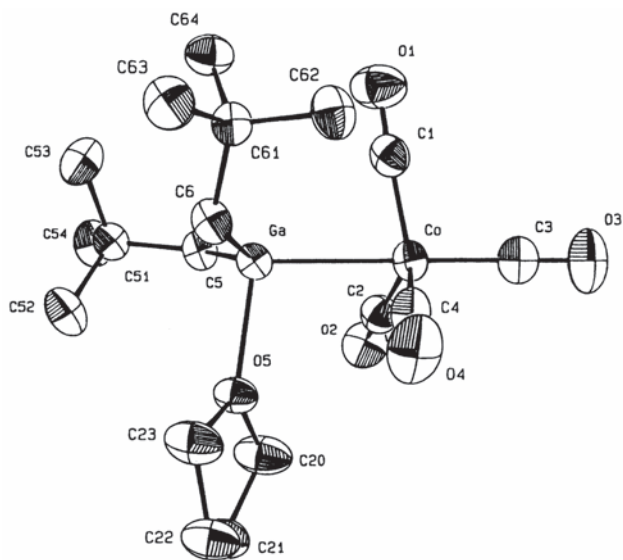
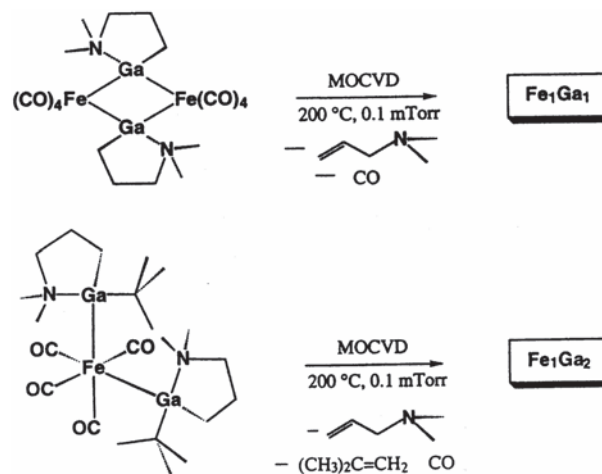


**Figure 36.** Molecular structure of (CO)<sub>4</sub>Co-Ga(CH<sub>2</sub>'Bu)<sub>2</sub>(C<sub>8</sub>H<sub>8</sub>O). Reprinted with permission from [539], R. A. Fischer and A. Miehr, *Chem. Mater.* 8, 497 (1996). © 1996, American Chemical Society.

Similarly, a series of complexes based on Fe–Ga bonds [540] was used to deposit films with different Fe:Ga ratios. [(CO)<sub>4</sub>FeGa{(CH<sub>2</sub>)<sub>3</sub>NMe<sub>2</sub>}]<sub>2</sub>, a tetranuclear species with a preformed Fe<sub>2</sub>Ga<sub>2</sub> ring, and the gallium-rich complex [(CO)<sub>4</sub>Fe{Ga(CH<sub>2</sub>)<sub>3</sub>NMe<sub>2</sub>}(Bu')]<sub>2</sub> (Scheme 26) produced Fe-Ga films with strict control of the stoichiometry. The efficient elimination of ligands due to β-H elimination was proposed to be the reason for excellent film quality and low deposition temperatures (200–250 °C). Shore et al. have used HFeCo<sub>3</sub>(CO)<sub>12</sub> and H<sub>2</sub>FeRu<sub>3</sub>(CO)<sub>12</sub> as single sources for the CVD of FeCo<sub>3</sub> and FeRu<sub>3</sub> alloy films [408]. When occurring in cold wall reactors, partial decomposition of the HFeCo<sub>3</sub>(CO)<sub>12</sub> into volatile organo-iron compounds and less volatile cobalt species was observed, resulting in iron enrichment of the films. Nevertheless, pure heterobimetallic films could be obtained from photochemical vapor deposition by irradiation with a mercury arc lamp, with CO as a carrier gas. Chi et al. have used the Fe–Sn compounds (C<sub>5</sub>H<sub>5</sub>)Fe(CO)<sub>2</sub>(SnMe<sub>3</sub>) and *cis*-Fe(CO)<sub>4</sub>(SnMe<sub>3</sub>)<sub>2</sub> based on different Fe:Sn ratios to grow FeSn and FeSn<sub>2</sub> films [131]. Pure FeSn films were obtained with (C<sub>5</sub>H<sub>5</sub>)Fe(CO)<sub>2</sub>(SnMe<sub>3</sub>), whereas films composed of the FeSn<sub>2</sub> phase with a minor constituent of FeSn were obtained with *cis*-Fe(CO)<sub>4</sub>(SnMe<sub>3</sub>)<sub>2</sub>. Similarly, CoSn films with small amounts of α-Co<sub>3</sub>Sn<sub>2</sub> were prepared by CVD of Me<sub>3</sub>SnCo(CO)<sub>4</sub> and Ph<sub>3</sub>SnCo(CO)<sub>4</sub> [119].



**Scheme 26.**

The formation of intermetallic compounds from organometallic precursors is highly sensitive to the experimental conditions and requires an optimization of the deposition process for a phase-selective synthesis, especially in those cases where a large number of phases coexist in the binary phase diagrams.

### 5.3. Three-Component Systems (ABE<sub>x</sub>)

#### 5.3.1. Heterometal Oxides

The preparation of three-component systems poses a challenge for the molecular design of the precursor because of the compatibility of the intrinsic physicochemical properties of the individual building units. Moreover, it demands unambiguously characterized precursors with element ratios corresponding to that of the nanomaterial of choice. A variety

of interesting molecular precursors have been synthesized and/or modified for a size- and phase-selective synthesis of nanomaterials (Table 2), which provide the proof of the concept for the molecular-level synthesis of materials.

Stoichiometric  $\text{MgAl}_2\text{O}_4$  films have been successfully prepared from magnesium-aluminum isopropoxide containing the appropriate Mg:Al ratio (1:2) [259–261]. However, for the preparation of transition metal-aluminum, -gallium, or -iron spinels, the fusion of component oxides [543, 544] at high temperatures (1000–1600 °C), ball milling [545], self-propagating combustion synthesis [546], coprecipitation reactions [547], polymer route [548], and hydrothermal synthesis [549] have been used. Wickham et al. have used mixed acetates,  $\text{M}_3\text{Fe}_6(\text{OOCCH}_3)_{17}(\text{O})_3(\text{OH}) \cdot 12\text{pyridine}$  ( $\text{M} = \text{Ni}, \text{Co}, \text{Mn}$ ), as crystalline precursors to stoichiometric ferrites. These complexes contain a large number of pyridine molecules of crystallization, and rapid removal of the coordinated ligands can lead to the segregation of ions. Moreover, they require high temperatures (800–1000 °C) to transform into the respective ferrites. Apblett et al. synthesized a water-soluble Ni–Fe complex,  $[\text{Ni}(\text{H}_2\text{O})_6][\text{FeCl}(\text{EDTA})\text{H}]_2 \cdot 4\text{H}_2\text{O}$  [266], as a single precursor to nickel ferrite; however, the pyrolysis of this compound leads to phase separation, and the sample heat-treated at 600 °C shows  $\text{Fe}_2\text{O}_3$  and  $\text{NiFe}_2\text{O}_4$  as the crystalline phases. Further heating at 900 °C is essential for obtaining stoichiometric nickel ferrite.

Mathur et al. [244, 550] have used heterobimetallic precursors of the type  $[\text{MM}'_2(\text{OR})_8]$  ( $\text{M} = \text{Co}, \text{Zn}$ ;  $\text{M}' = \text{Al}, \text{Ga}, \text{Fe}$ ) for low-temperature synthesis of high-purity spinel particles by the microemulsion method. For a comparative evaluation of the single- and multicomponent approaches, the  $\text{CoAl}_2\text{O}_4$  spinel was synthesized from the single source  $[\text{CoAl}_2(\text{O}i\text{Pr})_8]$  (Fig. 37) and by the use of a stoichiometric mixture of  $[\text{Al}(\text{O}i\text{Pr})_3]_4$  and  $\text{Co}(\text{OR})_2$  ( $\text{R} = -\text{C}(\text{C}_6\text{H}_5)_3$ ). The XRD patterns (Fig. 38) of the two  $\text{CoAl}_2\text{O}_4$  samples reveal that the single-source synthesis yields, under similar experimental conditions, higher phase purity and crystallinity compared with the spinel obtained from a stoichiometric mixture of Al and Co sources. The expected differences in the hydrolysis susceptibility of the isopropoxide and phenoxide derivatives [551] cause different hydrolysis kinetics that adversely affect the homogeneity (with respect to the cation distribution) of the precursor solution. As a result, minor phase separation occurs in the dual-source system (Fig. 38).

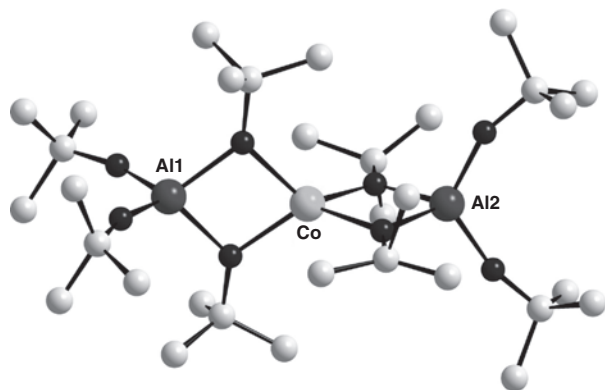


Figure 37. Molecular structure of  $[\text{CoAl}_2(\text{O}i\text{Pr})_8]$ .

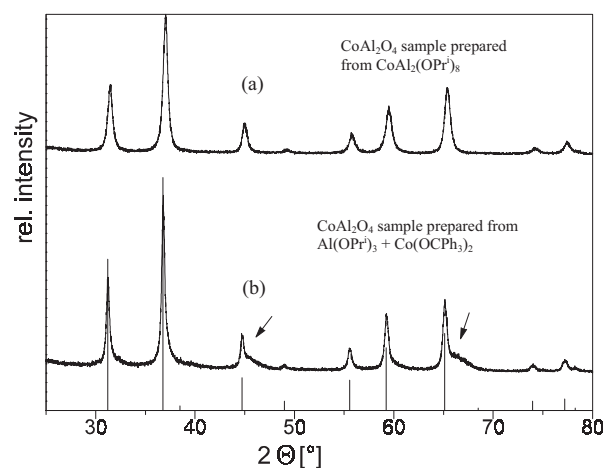


Figure 38. X-ray diffractograms of two  $\text{CoAl}_2\text{O}_4$  samples prepared by multicomponent (a) and single-source (b) precursor routes. Reprinted with permission from [244], F. Meyer et al., *J. Mater. Chem.* 9, 1755 (1999). © 1999, Royal Society of Chemistry.

Similarly, nanocrystalline  $\text{CuAl}_2\text{O}_4$  and  $\text{NiAl}_2\text{O}_4$  could be obtained by processing  $[\text{CuAl}_2(\text{O}i\text{Bu}')_8]$  and  $[\text{NiAl}_2(\text{O}i\text{Bu}')_8]$ , respectively.

Similarly, zinc aluminate ( $\text{ZnAl}_2\text{O}_4$ ), a well-known wide bandgap semiconductor with a spinel structure, was prepared by the sol-gel processing of the bimetallic precursor shown in Figure 39. Recent investigations of  $\text{ZnM}_2\text{O}_4$  ( $\text{M} = \text{Al}, \text{Ga}$ ) compounds have shown these systems to be new transparent and conductive materials [552]. The optical bandgap of polycrystalline  $\text{ZnAl}_2\text{O}_4$  (3.8 eV) indicates the material to be transparent for light with a wavelength larger than 320 nm. Thus it can be utilized for UV-photoelectronic devices. Moreover, the  $\text{ZnAl}_2\text{O}_4$  spinel is useful in many catalytic reactions, such as cracking, dehydration, hydrogenation, and dehydrogenation [553]. The XRD pattern of the sample calcined at 400 °C shows zinc aluminate (Gahnite) to be the only crystalline phase. This is the lowest reported temperature for the formation of single-phase crystalline  $\text{ZnAl}_2\text{O}_4$ . The crystallite size calculated from the line shape analysis of the diffraction peaks showed a log normal grain growth with increasing calcination temperature (Fig. 40). The above observations are in accordance with the TEM observations showing a systematic crystal growth (Fig. 41).

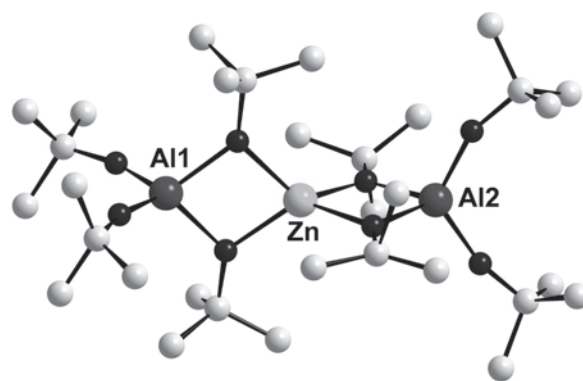
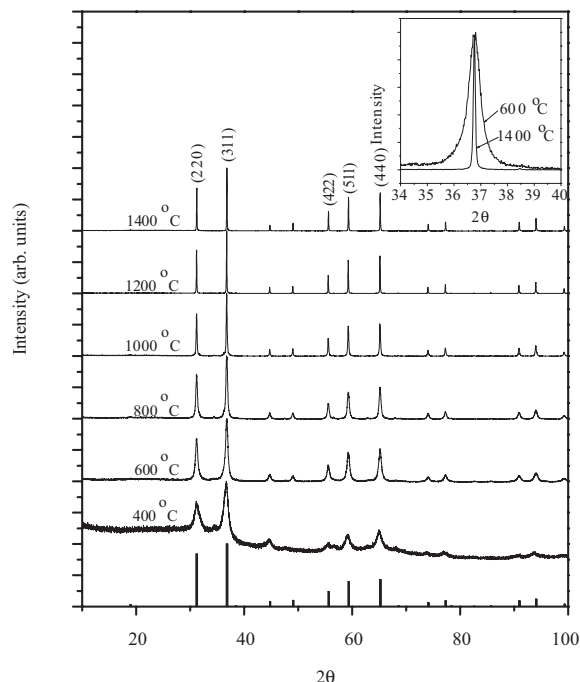


Figure 39. Molecular structure of  $[\text{ZnAl}_2(\text{O}i\text{Pr})_8]$ .





**Figure 40.** XRD traces of  $\text{ZnAl}_2\text{O}_4$  ceramic calcined at different temperatures. Reprinted with permission from [286], S. Mathur et al., *J. Am. Ceram. Soc.* 84, 1921 (2001). © 2001, American Ceramics Society.

The absorbance spectra (Fig. 42) of  $\text{ZnAl}_2\text{O}_4$  nanoparticles heat-treated (6 h) at 700, 800, 1000, 1200, and 1400 °C reveal a systematic shift in the absorption maxima. The absorbance edge became steeper with increasing the calcination temperature, and a “red shift” (4.5 to 4.0 eV) was observed (Fig. 42). Since the bandgap,  $E_g$ , of a nanocrystalline specimen scales with its diameter,  $d$ , as  $E_g \approx 1/d$ ,

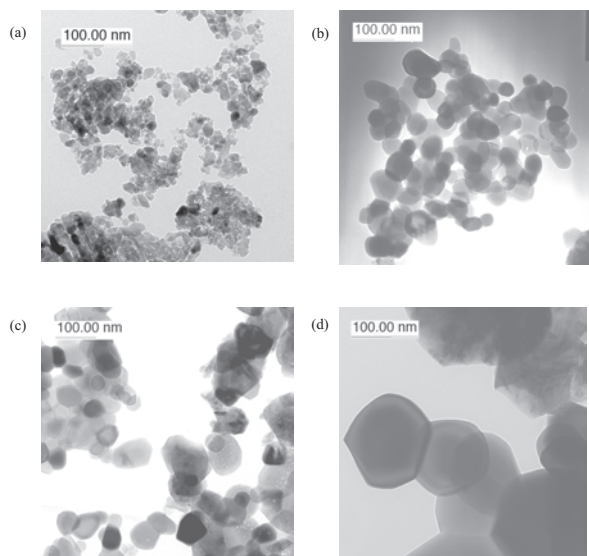


**Figure 41.** TEM micrographs of  $\text{ZnAl}_2\text{O}_4$  ceramic calcined at 600 (a), 800 (b), 1000 (c), and 1200 °C (d). Reprinted with permission from [286], S. Mathur et al., *J. Am. Ceram. Soc.* 84, 1921 (2001). © 2001, American Ceramics Society.

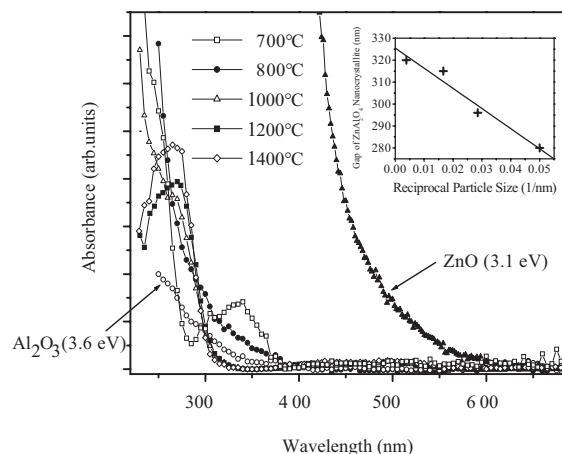


**Figure 42.** Absorbance spectra of  $\text{ZnAl}_2\text{O}_4$  calcined at 700, 800, 1000, 1200, and 1400 °C, respectively. Reprinted with permission from [286], S. Mathur et al., *J. Am. Ceram. Soc.* 84, 1921 (2001). © 2001, American Ceramics Society.

it can be surmised that the observed variation in absorption is relevant to a strong change in the particle size, reflecting the transition of the spinel from nanocrystalline to the micron (bulk) state (inset, Fig. 42).

The class of spiro compounds with the general formula  $\text{M}^{\text{II}}\text{M}_2^{\text{III}}(\text{OR})_8$  was extended by introducing divalent cobalt and trivalent iron into a molecular framework to obtain a single molecular precursor to cobalt ferrite, which is the first example of a Co-Fe mixed-metal alkoxide (Fig. 43) [245]. The decomposition of the Co-Fe precursor in the sol-gel or CVD process produced stoichiometric  $\text{CoFe}_2\text{O}_4$  particles and films, respectively. The X-ray diffractogram (Fig. 44) of the sol-gel-derived material shows a monophasic spinel with nanosized grains ( $\langle d \rangle$ , 35 nm) [246].

One of the major strengths of the chemical methods is the selective synthesis of metastable phases. In contrast to the conventional processing that largely relies on brute force (mixing, milling, and firing), the molecular precursor approach provides a kinetic control over the process (see Section 2). A unique example in this regard is the selective synthesis of single-phase orthoferrite,  $\text{GdFeO}_3$ , which is difficult to obtain because of the easy formation of the thermodynamically favorable  $\text{Gd}_3\text{Fe}_5\text{O}_{12}$  (garnet) phase [554]. Orthoferrites are gaining attention as materials for

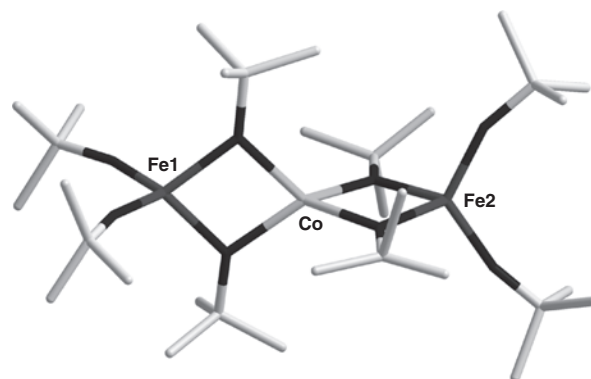


**Figure 43.** Molecular structure of  $\text{CoFe}_2(\text{O}'\text{Bu})_8$ .

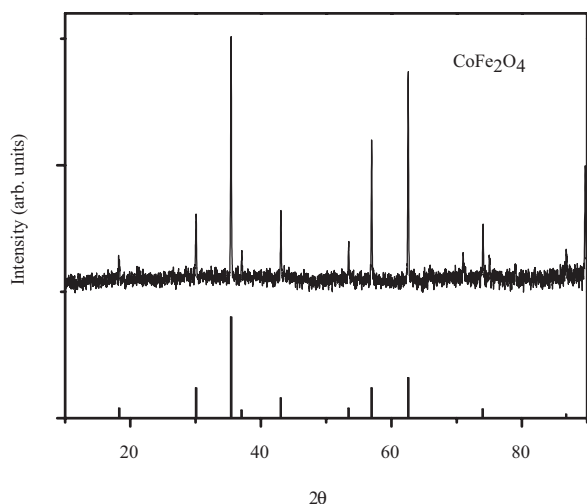


**Figure 44.** XRD pattern of  $\text{CoFe}_2\text{O}_4$  derived by the sol-gel method.

magneto-optical data storage devices and because of their unique magnetic properties [555, 556]. Access to metastable rare earth iron perovskites with the general formula  $\text{LnFeO}_3$  ( $\text{Ln}$  = any lanthanide ion) was provided, for the first time, by a designed assembly of trivalent lanthanide and iron ions in a molecular framework [255] (Fig. 45). The problem commonly encountered in the selective synthesis of  $\text{LnFeO}_3$  compounds is the formation of thermodynamically favored garnet and secondary iron oxide phases resulting from the use of a mixture of  $\text{Ln}^{3+}$  and  $\text{Fe}^{3+}$  constituents as the precursor. In the absence of any chemical control (bonding) on the ions, the lanthanide and iron compounds in the admixture randomly collide to form various intermediate species with metal ratios unfavorable for obtaining a single-phase material. The result is the coexistence of undesired phases (e.g.,  $\text{Ln}_3\text{Fe}_5\text{O}_{12}$  and  $\text{Fe}_3\text{O}_4$  in the synthesis of  $\text{LnFeO}_3$ ) in the final ceramic material. In view of the above, more stable garnet ( $\text{Ln}_3\text{Fe}_5\text{O}_{12}$ ) and magnetite ( $\text{Fe}_3\text{O}_4$ ) phases are easily formed that, in view of their higher magnetic moments, hinder specific investigations of the weak ferrimagnetic behavior of the orthoferrite,  $\text{LnFeO}_3$ . In this context, the precursors with the required cation ratio and preformed  $\text{Ln-O-Fe}$  bonds are a major breakthrough in the selective synthesis of orthoferrite films and particles [255]. A controlled hydrolysis of Gd-Fe heterometal alkoxide produced

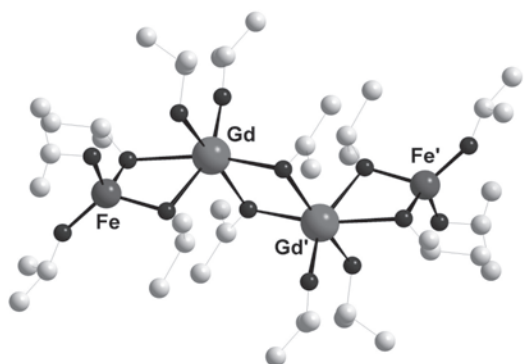


**Figure 45.** Molecular structure of  $[\{\text{GdFe}(\text{OPr}^i)_6\}(\text{HOPr}^i)]_2$ .

faceted nanocrystallites of nearly uniform size ( $\sim 60$  nm) (Fig. 46). The crystalline  $\text{GdFeO}_3$  is formed at a temperature much lower than those required for the solid-state reaction with  $\text{Gd}_2\text{O}_3$  and  $\text{Fe}_2\text{O}_3$  powders ( $\sim 1800$  °C). Furthermore, the crystalline  $\text{GdFeO}_3$  forms directly from an amorphous precursor without the crystallization of any intermediate phases, which in the absence of any phase segregation or crystallization of other stoichiometries confirms the compositional purity of the sample and the contention that the chemical mixing of the ions is retained during the various stages of the processing.

It is interesting to note that using a mixture of component alkoxides does not result in the formation of monophasic material. Kominami et al. have used a mixture of lanthanum and iron alkoxide in a glycothermal synthesis to obtain pure  $\text{LaFeO}_3$ , but the precursor was found to be contaminated by  $\text{LaCO}_3\text{OH}$  [557], whereas Traversa et al. could synthesize pure  $\text{LaFeO}_3$  powders by thermal decomposition of a heteronuclear cyanide complex,  $\text{La}\{\text{Fe}(\text{CN})_6\}\cdot 5\text{H}_2\text{O}$  [558]. In analogy,  $\text{Sm}\{\text{Fe}(\text{CN})_6\}\cdot 4\text{H}_2\text{O}$  was used as a single source for preparing  $\text{SmFeO}_3$  powders and to deposit films on alumina substrates [275]. They have also performed, for comparisons sake, a solid-state reaction between  $\text{Sm}_2\text{O}_3$  and  $\text{Fe}_2\text{O}_3$  powders. The XRD data (Fig. 47) for the two samples show that a single-phase  $\text{SmFeO}_3$  is present at 700 °C in the powder obtained from the Sm-Fe precursor, whereas single metal oxides were present as the major phases up to 1000 °C, in the ball-milled sample (Fig. 47).

Alkaline earth stannate, titanate, zirconate, and hafnate based on the perovskite structure are finding extensive applications as high dielectric constant, ferroelectric, and gas-sensing materials [559–562]. The conventional preparation of these electro-ceramics is based on the solid-state reactions of common inorganic precursors like oxides, chlorides, and carbonates, which require repeated cycles of milling and calcinations at high temperatures ( $>1400$  °C), to achieve complete diffusion and phase formation. Moreover, the

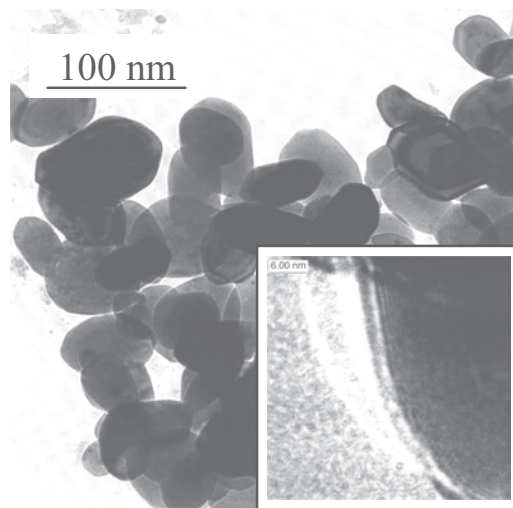


**Figure 46.** TEM and HREM images of  $\text{GdFeO}_3$  ceramic calcined at 1000 °C. Reprinted with permission from [255], S. Mathur et al., *Adv. Mater.* 14, 1405 (2002). © 2002, Wiley-VCH.



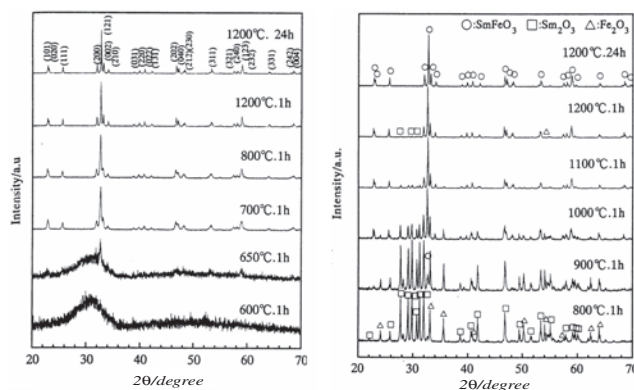


**Figure 47.** XRD profiles of (a)  $\text{Sm}\{\text{Fe}(\text{CN})_6\}\cdot 4\text{H}_2\text{O}$  complex decomposed at different temperatures and (b) the mixture of  $\text{Sm}_2\text{O}_3$  and  $\text{Fe}_2\text{O}_3$  ball-milling calcined at different temperatures. Reprinted with permission from [275], H. Aono et al., *J. Am. Ceram. Soc.* 84, 341 (2001). © 2001, American Ceramics Society.

powders exhibit a wide grain size distribution and contamination due to impurities incorporated from abrasive particles or incomplete reactions. Many of these characteristics are symptomatic of inhomogeneous chemical reactions and exert an adverse effect on the useful properties of the material. In contrast to the powder-processing methods, liquid-phase processing (e.g., solution-sol-gel technique) provides a molecular-level mixing of the individual components, which reduces the diffusion path in the nanometer range to yield crystalline material at much lower temperatures than normally required for the solid-state reactions [563–566].

The alkoxide-based synthesis of perovskite powders has its origin in the pioneering works of Mazdiyasi et al., who utilized simultaneous hydrolytic decomposition of titanium and barium alkoxides [567]; however, the precise structure and composition of the precursor was not known in their studies. Several mechanisms have been suggested for the formation of perovskite phases in solution methods [566, 568]. Two mechanisms have been postulated for the formation of barium titanate. The first mechanism involves an acid-base-type reaction in which an anion with the formula  $\text{Ti}(\text{OH})_6^{2-}$  is initially formed during the hydrolysis of Ti alkoxide and later neutralized by the alkaline earth cations [569]. A second type of mechanism suggests the formation of negatively charged  $\text{TiO}_2$  particles (due to the absorption of hydroxyl groups) in which the alkaline earth cations diffuse to counterbalance the negative charge. The above mechanisms do not take into account the formation of heterometal species in the alkoxide or partially hydrolyzed solution, which is a prominent feature of alkoxide chemistry [45, 49, 50, 323, 570]. The nature and chemical composition of intermediate species play a dominant role in determining the purity and temperature of crystallization of the desired phase. For example, the formation of the ortho-titanate or zirconate phase ( $\text{Ba}_2\text{MO}_4$ ;  $\text{M} = \text{Ti}, \text{Zr}$ ) in sols containing individual Ba and Ti(Zr) precursors requires high ( $>1000^\circ\text{C}$ ) temperatures to decompose into  $\text{BaMO}_3$  [332].

The potential of heterometal alkoxide precursors to “preform” the ceramic on a molecular level is promising for nanoscaled perovskite powders (Tables 2–4). High-purity nanocrystalline  $\text{BaTiO}_3$  and  $\text{BaZrO}_3$  oxides [332] have been

synthesized from single-source Ba-Ti(Zr) alkoxide precursors. The improved homogeneity and phase purity and lower crystallization temperatures for gel  $\rightarrow$  oxide conversion are attributed to the use of mixed-metal compounds containing preformed Ba–O–Ti and Ba–O–Zr bonds. The TEM images of barium-titanate (Fig. 48) and zirconate powders revealed homogeneous nanoparticles, which were shown to be monophasic perovskites by powder XRD studies [332].

The strict control over the metal ratios through stoichiometric clusters allows the crystallization of perovskite nanoparticles at low temperatures. For comparative evaluation,  $\text{BaTiO}_3$  was also prepared through the use of common inorganic salts of individual elements in a classic sol-gel route. The X-ray powder diffractograms (Fig. 49) reveal that the powder obtained by the conventional method is contaminated even at  $1200^\circ\text{C}$  by undesired side products like  $\text{BaCO}_3$  and  $\text{Ba}_2\text{TiO}_4$ , whereas a single-phase material is obtained with the mixed-metal alkoxide precursor. In addition, the volume- and number-weighted size dispersion is significantly narrow for the perovskite powders obtained from alkoxide precursors (Fig. 50), which is not the case for powders obtained by the hydroxide route.

A large number of pure and  $\beta$ -diketonate-modified alkoxide derivatives of lead and alkaline earth metals with various tetravalent cations (Ti, Zr, Hf, Ce) are known [50, 267, 571–575], but most of them do not possess the cation ratio required for perovskite materials. The correct metal ratio in the molecular precursor with respect to the solid-state phase is a prerequisite for chemical control over the phase formation. For example, the decomposition of Pb-Ti heterometal precursor,  $[\text{PbTi}_2(\text{O})_4(\text{OOCCH}_3)(\text{OCH}_2\text{CH}_3)_7]_2$  [267], based on the Pb:Ti ratio 1:2, produced a mixture of  $\text{TiO}_2$ ,  $\text{PbTiO}_3$ , and  $\text{PbTi}_5\text{O}_7$  phases, whereas the precursor  $[\text{Pb}_2\text{Ti}_2(\text{O})_4(\text{OOCCH}_3)_2(\text{OCH}_2\text{CH}_3)_8]_2$  (Pb:Ti = 1:1), with similar ligands but an ideal cation ratio, could be converted into single-phase  $\text{PbTiO}_3$  at  $600^\circ\text{C}$  [575]. Figure 51 shows the molecular structures of the two precursors and the powder X-ray diffractograms of the residue obtained from their pyrolytic decomposition.

Hubert-Pfalzgraf et al. have prepared mixed-ligand Ba-Ti and Sr-Ti complexes (Fig. 52) that possess a metal ratio suitable for the synthesis of  $\text{BaTiO}_3$  and  $\text{SrTiO}_3$  [44, 564].

In an elegant study of the alkoxide-to-oxide transformation, Gaskins and Lannutti have prepared barium titanate at room temperature by reacting a barium titanium oxo-alkoxide,  $\text{Ba}_4\text{Ti}_4\text{O}_4(\text{OPr}^i)_{16}(\text{Pr}^i\text{OH})_3$  (Fig. 53), with acetone

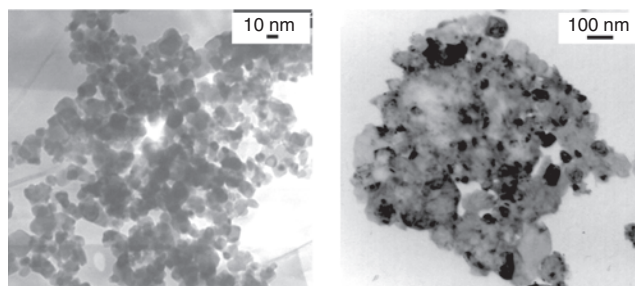


**Figure 48.** TEM micrographs of  $\text{BaTiO}_3$  ceramic obtained at  $800^\circ\text{C}$  from a single-source heterometal alkoxide (a) and hydroxide route (b).

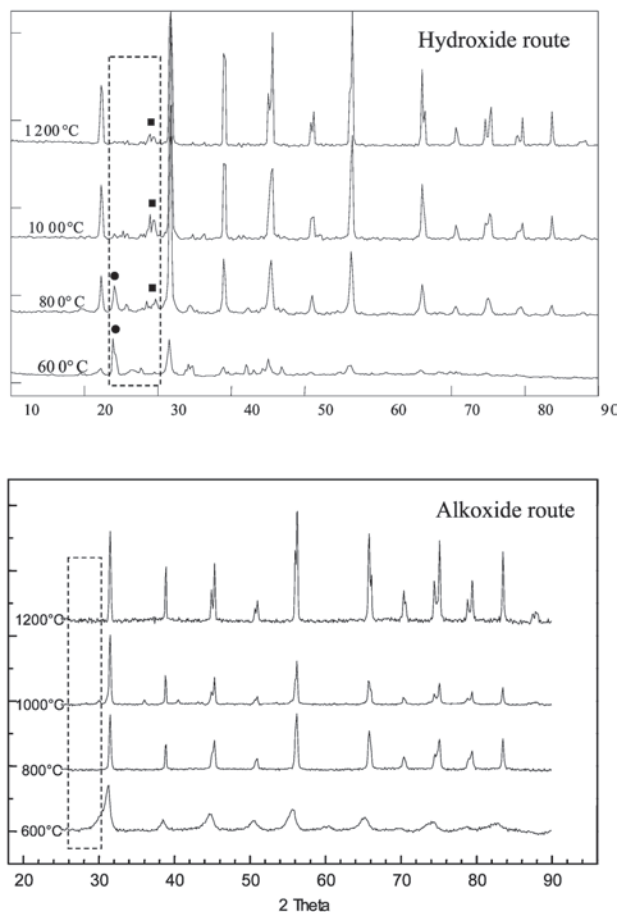


**Figure 49.** XRD patterns of  $\text{BaTiO}_3$  particles obtained by hydroxide and alkoxide sol-gel methods ( $\text{BaCO}_3$  (●) and  $\text{Ba}_2\text{TiO}_4$  (■)).

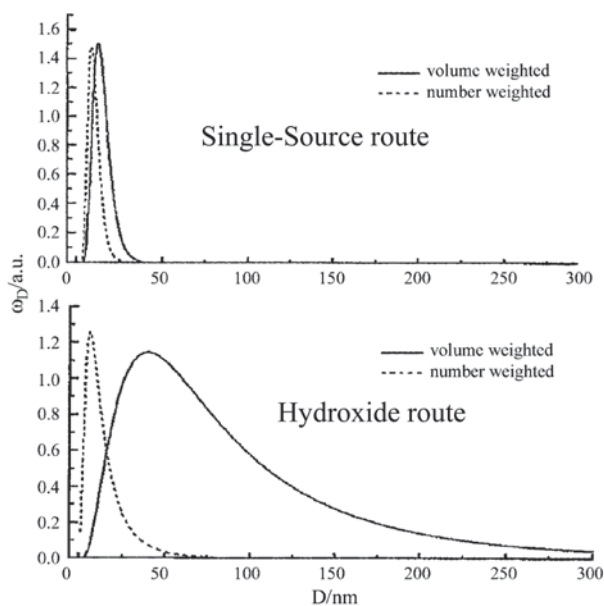


**Figure 50.** Particle size-distribution curves for  $\text{BaZrO}_3$  powders obtained from the alkoxide single source precursor (SSP) and conventional hydroxide routes. Reprinted with permission from [23], M. Veith et al., *J. Chem. Soc., Dalton Trans.* 2405 (2002). © 2002, Royal Society of Chemistry.

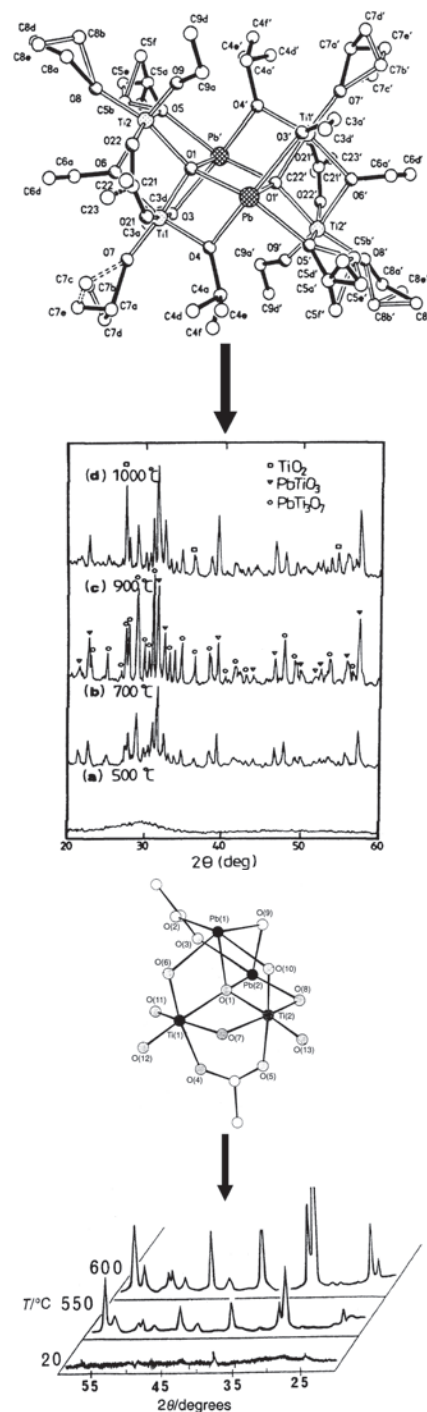


**Figure 51.** (a) Molecular structure of a Pb-Ti precursor  $[\text{PbTi}_2(\text{O})_4(\text{OOCCH}_3)(\text{OCH}_2\text{CH}_3)_2]_2$  and XRD patterns for the thermal decomposition of this precursor at 500, 700, 900, and 1000 °C. Reprinted with permission from [267], H. K. Chae et al., *Chem. Mater.* 6, 1589 (1994). © 1994, American Chemical Society. (b) Molecular structure of  $[\text{Pb}_2\text{Ti}_2(\text{O})_4(\text{OOCCH}_3)_2(\text{OCH}_2\text{CH}_3)_8]_2$  and XRD patterns at various temperatures. Reprinted with permission from [575], L. G. Hubert-Pfalzgraf et al., *J. Mater. Chem.* 7, 753 (1997). © 1997, Royal Society of Chemistry.

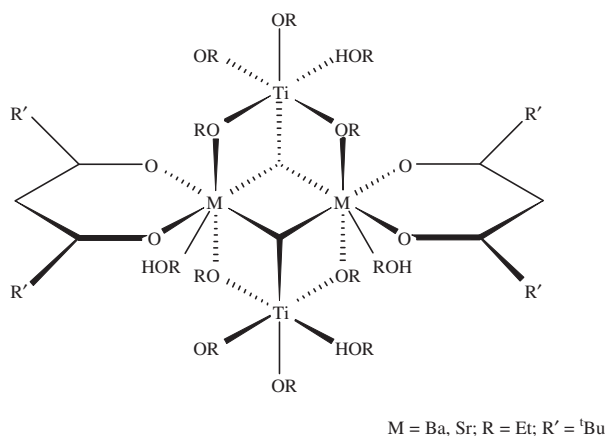


**Figure 52.** The tetranuclear structure of  $\text{Ba}_2\text{Ti}_2(\text{thd})_2(\text{OEt})_{10}(\text{EtOH})_4$ .

[576]. The transient oxo species formed in the transformation of the molecular cluster possess oxygen coordination numbers for the metals that are necessarily lower than those found for the extended solid-state structure of  $\text{BaTiO}_3$ . As a consequence, the cluster grows (condenses) through oxygen supplied by the acetone molecules, a reaction called aldol condensation. The deficiency in oxygen coordination as the two alkoxide groups are replaced by an oxo unit provides a driving force for the cluster growth. A close look at the metal-oxygen core of the oxo-alkoxide molecule reveals a resemblance to a  $\text{BaTiO}_3$  structural subunit (Fig. 53). This structural similarity probably helps in lowering the barrier to a direct molecule-to-material conversion.

### 5.3.2. Heterometal Chalcogenides

Ternary chalcopyrite materials such as copper indium diselenide ( $\text{CuInSe}_2$ ), copper indium disulfide ( $\text{CuInS}_2$ ), and copper gallium diselenide ( $\text{CuGaSe}_2$ ) are potential solar cell materials, given that their direct bandgaps are nearly optimal for the absorption of the solar spectrum. High-quality thin films of solar-cell materials with high specific power ( $\text{W kg}^{-1}$ ) are required to fabricate efficient devices. Nanocrystalline films are an attractive alternative to single-crystalline devices that are currently used. Since the microstructure and secondary phases (surface layers) may have a large influence on the transport properties of the films [577], optimal control over the purity of films is necessary. Moreover, the current thin-film technologies are limited by the requirement of

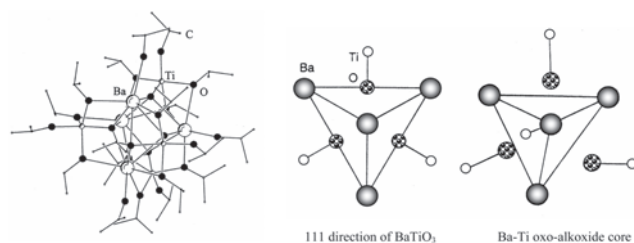
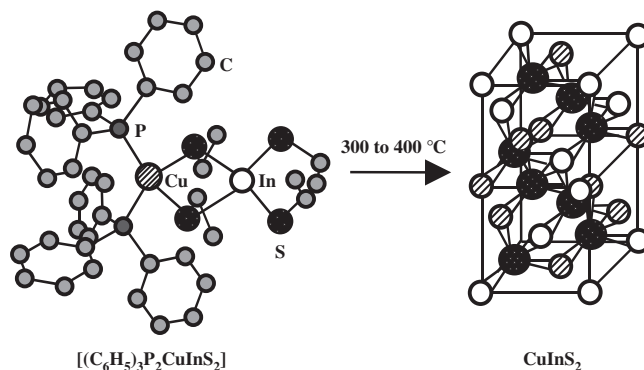


**Figure 53.** (a) Molecular structure of Ba-Ti oxo-alkoxide. (b) Comparison of the core structure of monoclinic barium-titanium oxoisopropoxide with the  $\text{BaTiO}_3$  structure viewed along the 111 direction. Reprinted with permission from [576], B. C. Gaskins and J. J. Lannutti, *J. Mater. Res.* 11, 1953 (1996). © 1996, Materials Research Society.

high-temperature deposition processes that are incompatible with all polyimide or other polymer substrate materials. To eliminate or minimize the problems associated with differences between the coefficients of thermal expansion of the substrate and functional film, new approaches to depositing chalcopyrite materials at reduced temperatures are desired. One interesting solution to this problem is the use of ternary SSPs to obtain single-phase materials at low temperatures.

Banger et al. have tested molecular precursors with the general formula  $[\{\text{ER}_3\}_2\text{Cu}(\text{YR}')_2\text{In}(\text{YR}')_2]$  ( $\text{E} = \text{P, As, Sb}$ ;  $\text{Y} = \text{S, Se}$ ; and  $\text{R} = \text{alkyl, aryl}$ ). Besides the appropriate elemental ratio required to form the chalcopyrite phase, another key feature of this class of precursors is the number of tunable sites within the complex that allow engineering of the molecular architecture to direct properties (liquid state, high volatility, thermal stability) that best meet the requirements of the deposition process. An important illustration of the flexibility of the  $[\{\text{ER}_3\}_2\text{Cu}(\text{YR}')_2\text{In}(\text{YR}')_2]$  architecture is the phosphine stabilized complexes  $[\{\text{P}(\text{Bu}^n)_3\}_2\text{Cu}(\text{SEt})_2\text{In}(\text{SEt})_2]$  (**A**) and  $[\{\text{P}(\text{Bu}^n)_3\}_2\text{Cu}(\text{SPr}^n)_2\text{In}(\text{SPr}^n)_2]$  (**B**) that represent the first liquid precursor for the deposition of  $\text{CuInS}_2$ . The low-temperature differential scanning calorimetry (DSC) profiles of the two compounds (Fig. 54) show an absence of an endotherm assignable to a melting phase transition, thus confirming their liquid state. The exothermic peaks at 250 and 268 °C correspond to the decomposition of the samples.

$[\{\text{PPh}_3\}_2\text{Cu}(\text{SEt})_2\text{In}(\text{SEt})_2]$  was used to deposit well-adherent mirror-like films of  $\text{CuInS}_2$  at 390 °C [252] (Scheme 27). The films were dense, with a columnar grain growth and grain size of ca. 500 nm. No evidence of phosphorus or carbon contamination was obtained, indicating a clean decomposition of the precursor [250].



**Scheme 27.**

Vittal et al. have synthesized and structurally characterized molecular precursors (Fig. 55) to ternary silver indium sulfide phases,  $\text{AgInS}_2$  and  $\text{AgIn}_5\text{S}_8$ . Pyrolysis of  $[\{\text{PPh}_3\}_2\text{AgIn}(\text{SCOR})_4]$  ( $\text{R} = \text{Me, Ph}$ ) compounds results in the formation of  $\text{AgInS}_2$ , whereas aerosol-assisted CVD (AACVD) produced dark red films of  $\text{AgIn}_5\text{S}_8$ .

Mixed-metal perovskites are well known for their technological significance to electrochemical applications. In view of their unique ferroelectric, pyroelectric, piezoelectric, and dielectric properties, these materials are finding applications in transducers, light modulation, charge storage, and non-volatile memory devices [46, 559, 560]. The columbite-like phase of  $\text{MgNb}_2\text{O}_6$  (MN) has attracted interest because of



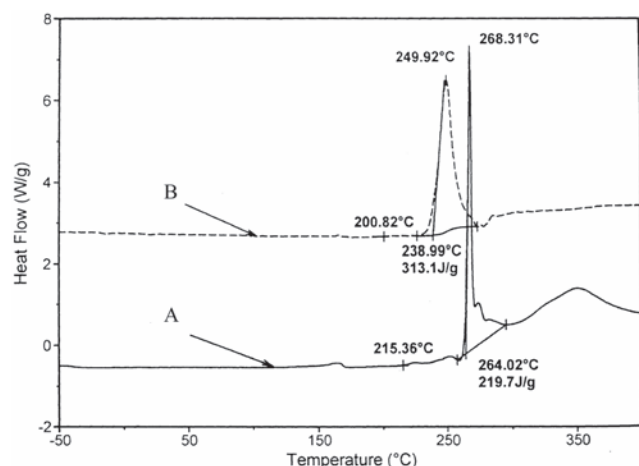


**Figure 54.** Low-temperature DSC for  $[\{P(\text{Bu}^n)_3\}_2\text{Cu}(\text{SET})_2\text{In}(\text{SET})_2]$  (A) and  $[\{P(\text{Bu}^n)_3\}_2\text{Cu}(\text{SPr}^n)_2\text{In}(\text{SPr}^n)_2]$  (B). Reprinted with permission from [252], K. K. Banger et al., *Thin Solid Films* 403–404, 390 (2002). © 2002, Elsevier Science.

its use in the synthesis of microwave dielectric materials such as  $\text{Ba}(\text{Mg}_{1/3}\text{Nb}_{2/3})\text{O}_3$  (BMN). Moreover,  $\text{MgNb}_2\text{O}_6$  is the key material for the successful preparation of single-phase perovskite,  $\text{Pb}(\text{Mg}_{1/3}\text{Nb}_{2/3})\text{O}_3$  (PMN), which is becoming increasingly important for multilayer ceramic capacitor, electrostrictor, and actuator applications [578, 579]. However, the synthesis of single-phase  $\text{MgNb}_2\text{O}_6$  by solid-state methods is not straightforward, because of the formation of a corundum-like  $\text{Mg}_4\text{Nb}_2\text{O}_9$  phase [580], as observed in the XRD data for the powder calcined at high temperatures (Fig. 56). The transmission electron micrograph and selective area electron diffraction suggested the coexistence of orthorhombic  $\text{MgNb}_2\text{O}_6$  and hexagonal  $\text{Mg}_4\text{Nb}_2\text{O}_9$  phases, which was confirmed by micro-EDX analysis of the grains (Fig. 56).

The use of metal organic precursors ( $\beta$ -diketonate derivatives of Pb and Mg and  $\text{Nb}(\text{OR})_5$ ) also suffer from the problem of compatibility due to the differential hydrolysis rates of alkoxide and  $\beta$ -diketonate precursors [581]. A potential solution to this problem is mixed-metal precursors like

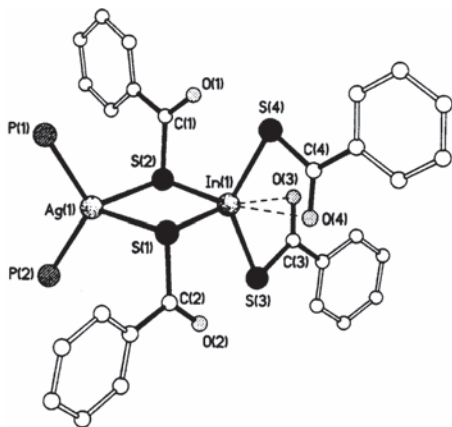


**Figure 55.** Molecular structure of  $[\{P\text{Ph}_3\}_2\text{AgIn}(\text{SCOPh})_4]$ . Reprinted with permission from [237], T. D. Devaraj et al., *Chem. Commun.* 2304 (2001). © 2001, Royal Society of Chemistry.

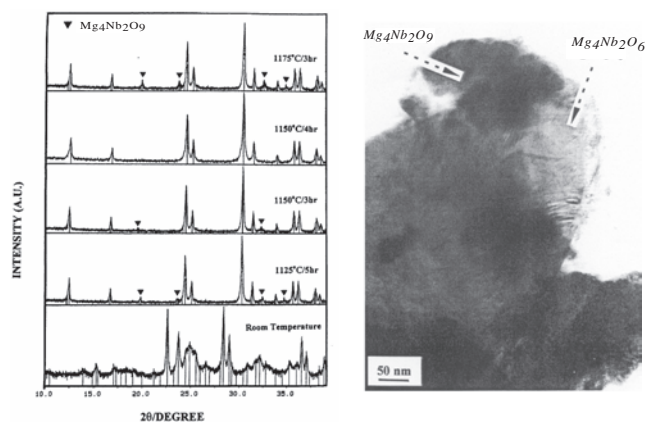


**Figure 56.** (a) Powder XRD patterns of the calcined  $\text{MgNb}_2\text{O}_6$  powders prepared from a dual source after calcination at different temperatures and times. (b) TEM micrograph of the calcined  $\text{MgNb}_2\text{O}_6$  powder, which shows the coexistence of a parasitic  $\text{Mg}_4\text{Nb}_2\text{O}_9$  phase. Reprinted with permission from [580], S. Ananta et al., *J. Eur. Ceram. Soc.* 19, 355 (1992). © 1992, Elsevier Science.

$\text{MgNb}_2(\text{OEt})_{12}(\text{EtOH})_2$  (Fig. 57) containing Mg and Nb in a single molecule and appropriate ratio [278]. The Mg-Nb ethoxide has been successfully used to deposit stoichiometric films of  $\text{MgNb}_2\text{O}_6$  [264]. The evaporation of  $\text{MgNb}_2(\text{OEt})_{12}(\text{EtOH})_2$  occurs in the range of 200–320 °C, which is comparable to the evaporation temperature of  $\text{Pb}(\text{thd})_2$  ( $\text{thd} = 2,2,6,6\text{-tetramethylheptane-3,5-dionate}$ ), showing that the volatilities of the two precursor systems (Mg-Nb and Pb) are well matched for liquid injection applications. This approach is of help, especially in the case of systems based on three or four different elements for which the precursor systems have not been investigated. The Mg-Nb bimetallic alkoxide is stable only at low deposition temperatures ( $<450$  °C); at higher temperatures the coordinating EtOH ligands dissociate to leave an unsaturated four-coordinate Mg center that is highly susceptible to attack by oxygen. This leads to interaction between the ligands (liberated from the  $\text{Pb}(\text{thd})_2$  precursor) to form Mg-thd species (e.g.,  $\text{Mg}(\text{thd})_2$  or  $\text{EtOMg}(\text{thd})$ ), which have a high thermal stability and lead to Mg-deficient films [264]. The reactivity of pure Mg-Nb alkoxide may be controlled by introducing chelating acetate ligands to obtain a modified acetato-alkoxide precursor,  $\text{MgNb}_2(\mu\text{-OAc})_2(\text{OPr}^i)_{10}$  (Fig. 58) [323]. Similarly,  $\text{Ba}(\text{Mg}_{1/3}\text{Nb}_{2/3})\text{O}_3$  ceramics could

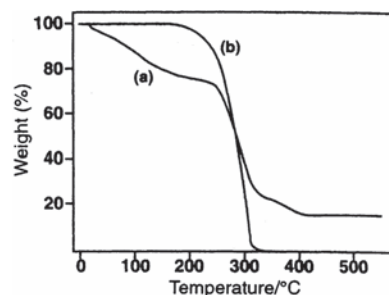


**Figure 57.** TGA data for (a)  $\text{Mg}[\text{Nb}(\text{OEt})_6]_2 \cdot 2\text{EtOH}$  and (b)  $\text{Pb}(\text{thd})_2$ . Reprinted with permission from [278], A. C. Jones et al., *J. Mater. Chem.* 11, 544 (2001). © 2001, Royal Society of Chemistry.

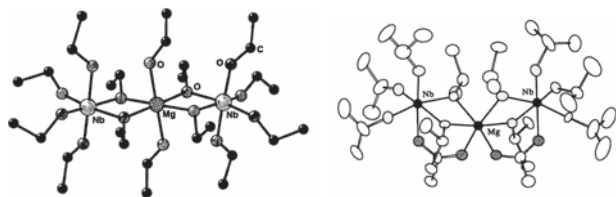


**Figure 58.** (a) Molecular structure of  $\text{Mg}\{\text{Nb}(\text{OEt})_6\}_2(2\text{EtOH})$ . Reprinted with permission from [264], H. O. Davies et al., *Adv. Mater. Opt. Electron.* 10, 177 (2000). © 2000, John Wiley & Sons. (b) Molecular structure of  $\text{MgNb}_2(\mu\text{-OAc})_2(\text{O}^i\text{Pr})_{10}$ . Reprinted with permission from [323], L. G. Hubert-Pfalzgraf et al., *Polyhedron* 13, 1181 (1994). © 1994, Elsevier Science.

be prepared by a sol-gel method involving the reaction of the heterometallic  $\text{MgTa}_2(\text{OEt})_{12}$  with a barium precursor [582].

A SSP is not always a guarantee of control over stoichiometry, and heterometallic precursors may become a disadvantage when they disproportionate during the gas-phase transport, as observed for  $\text{SrTa}_2(\text{OR})_{12}$  compounds, because of the large disparity in the vapor pressure of the parent alkoxides [277]. Nevertheless, the replacement of simple (monoanionic) alkoxide ligands by chelating alkoxides (donor functionalized) offers the possibility of increasing the strength of the  $\text{Sr}(\text{O})\text{R}-\text{Ta}$  bridge. Jones et al. have used dimethyl aminoethanol (dmae) and bis(dimethylamino) isopropanol (bis-dmap) to obtain novel Sr-Ta heteroleptic alkoxides,  $\text{SrTa}_2(\text{OEt})_{10}(\text{R})_2$  ( $\text{R} = \text{dmae}, \text{bis}(\text{dmap})$ ). It can be discerned from the solid-state structure of the dmap derivative (Fig. 59) that in contrast to  $\text{SrTa}_2(\text{OPr}^i)_{12}(\text{Pr}^i\text{OH})_2$ , the Sr atom in  $\text{SrTa}_2(\text{OEt})_{10}(\text{bis-dmap})_2$  more highly coordinated (C. N. = 8) (Fig. 59). The use of  $\text{SrTa}_2(\text{OEt})_{10}(\text{dmae})$  in MOCVD has produced crystalline films of  $\text{SrTa}_2\text{O}_6$  [277].

#### 5.4. Four-Component Systems ( $\text{ABCE}_x$ ) and Composites ( $\text{AE}_x/\text{ABE}_x$ )

In general, the synthesis of multicomponent nanomaterials such as  $(\text{Ba},\text{Zr})\text{TiO}_3$ ,  $\text{Pb}(\text{ZrTi})\text{O}_3$ , and  $\text{Pb}(\text{MgNb})\text{O}_3$  by chemical methods is plagued by the unavailability of suitable precursors. The mismatch in the compatibility (vapor pressure, decomposition temperature, chemical properties) of individual components often leads to unwanted side reactions that are unfavorable for obtaining a single-phase

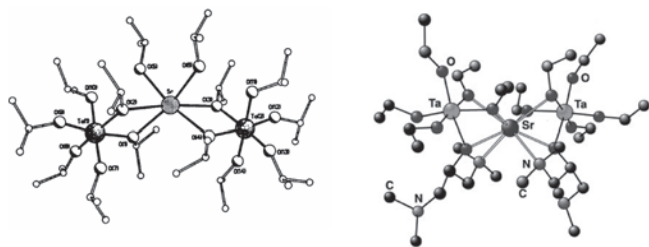
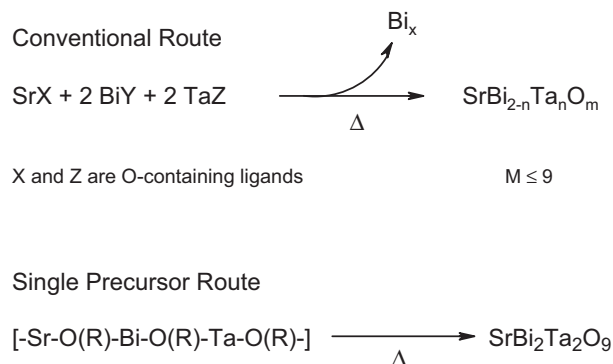


**Figure 59.** (a) Molecular structure of  $\text{Sr}\{\text{Ta}(\text{OPr}^i)_6\}_2\cdot\text{Pr}^i\text{OH}$ . Reprinted with permission from [278], A. C. Jones et al., *J. Mater. Chem.* 11, 544 (2001). © 2001, Royal Society of Chemistry. (b) Molecular structure of  $[\text{Sr}\{\text{Ta}(\text{OEt})_5(\text{bis-dmap})\}_2]$ . Reprinted with permission from [277], M. J. Crosbie et al., *Chem. Vap. Deposition* 5, 9 (1999). © 1999, Wiley-VCH Publishers.

nanomaterial. For instance, the control of stoichiometry in the synthesis of strontium bismuth tantalite,  $\text{SrBi}_2\text{Ta}_2\text{O}_9$  (SBT), is still a knotty problem because of the relatively high volatility of the bismuth components. Recently attempts have been made to obtain SBT films and powders from a mixture of  $\text{SrTa}_2(\text{OEt})_{12}$  and  $\text{Bi}(\text{CH}_3)_3$  or by mixing of individual alkoxides, but none of these reports deals with a single-source SBT system [583, 584]. Lee et al. have prepared a complex alkoxide,  $[\text{SrBi}_2\text{Ta}_2(\text{OCH}_2\text{CH}_2\text{OCH}_3)_{18}]$ , which was characterized by solution NMR studies [292]. Since the complex exhibits just one set of alkoxide ligands indicating the same chemical environment, the formation of a single source was assumed. However, such a simplified spectrum may also result from a fast exchange of alkoxide groups present on different alkoxide centers. Nevertheless, the intrinsic role of a single alkoxide source is corroborated by the formation of single-phase SBT films. The common chemical routes to SBT (Scheme 28) employ a 20–30% excess of Bi component, which seems to be a must to compensate for the loss of Bi during the heat treatments [292, 585]. The use of Sr-Bi-Ta methoxyethoxide, however, shows that excess Bi is not necessary for the formation of a pure ferroelectric phase. The TGA analysis shows that the dried alkoxide precursor decomposed gradually and monotonously, with no abrupt heat release characteristic of a heterogeneous mixture. The low-temperature (350 °C) synthesis of SBT films with a homogeneous and dense grain structure, together with the TGA analysis, suggests a chemical network of Sr, Bi, and Ta ions that is responsible for retarding the loss of the Bi component.



**Scheme 28.**

The continuous quest to obtain materials with improved properties and the possibility of improving the compositional homogeneity and tailoring the composition through new organometallic molecular or polymeric precursors has led to investigations of new preceramic precursors based on additional elements (e.g., B-C-N and Si-B-N-C systems). The approach of synthesizing nonoxide ceramic materials from multicomponent precursor molecules already containing the basic structure (coordination) and bonds desired in the final ceramic product has proved to be of great value. Among ternary nonoxide ceramics, boron-carbon-nitrogen is gaining increasing attention because of the outstanding properties of boron carbonitride,  $\text{BC}_x\text{N}_y$ . These compounds are superhard like diamond and cubic boron nitride and show remarkable stability against oxidation at elevated temperatures [586].



When compared with diamond, which decomposes to carbon dioxide at 800 °C in air, cubic boron nitride (*c*-BN) is resistant to oxidation up to 1600 °C. However, the application of *c*-BN is complicated because of high internal stresses in thin films. Boron carbonitride possesses high hardness and oxidation resistance by low internal stresses; these properties make it an interesting alternative material. The starting materials pyridine borane ( $C_5H_5N \cdot BH_3$ ) and triazaborabicyclodecane ( $BN_3H_2(CH_2)_6$ ) containing boron, carbon, and nitrogen have been used as SSPs to deposit ultrahard  $BC_xN_y$  on low-melting-point materials like aluminum and polymers [240]. Riedel et al. have made a comparative evaluation of the suitability of  $C_5H_5N \cdot BH_3$  and  $BN_3H_2(CH_2)_6$  in a plasma-assisted CVD process. They found that the atomic hydrogen produced by the decomposition of precursor in the plasma reduces the carbon content in the films. Since  $BN_3H_2(CH_2)_6$  contains a higher amount of hydrogen, BCN films produced with this precursor revealed a lower carbon content. This example illustrates the role auxiliary elements (ligands) can play in the final composition of the material [271].

In view of the higher thermal stability of amorphous Si-C-N ceramics compared with binary Si-N or Si-C amorphous compounds, a large number of organometallic precursors such as polyorganosilazane [587], polymethyldisilazanes [588], and polyorganosilylcarbodiimides [589] have been used to obtain Si-C-N systems. It was observed that a dual-source precursor system consisting of polysilazane (Si-N) and polycarbosilane (Si-C) did not provide sufficiently homogeneous Si-C-N precursors to prevent the crystallization of SiC. On the other hand, single-source Si-C-N precursors with a similar C:Si ratio led to products that were amorphous at rather high temperatures [590].

Jansen et al. [591] have prepared amorphous ceramics with the chemical compositions  $Si_3B_3N_7$  and  $SiBN_3C$  by the pyrolysis of the single-source trichlorosilylamino-dichloroborane,  $Cl_3Si-NH-BCl_2$ , under ammonia and inert gas atmospheres, respectively. These ceramics possess optimized mechanical properties compared with material prepared from modified polymers or by copolymerization [592]. The borosilicon nitride  $Si_3B_3N_7$  and the borosilicon carbonitride  $SiBN_3C$  remain amorphous on heating in vacuum or in a  $N_2$  atmosphere up to 1800 and 1900 °C, respectively, and no separation into thermodynamically stable crystalline phases was observed. In addition, an extremely high resistance against oxidation up to 1550 °C was observed for  $SiBN_3C$ , which is simply too high for a metastable nonoxide ceramic [592]. The exceptional properties of these amorphous compounds seem to have their origin in the precursor chemistry and preorganized Si-N-B bonds. The atomic arrangement in the precursor (Fig. 60) is an important condition for the homogeneous elemental distribution, and it avoids regional inhomogeneity due to boron- or silicon-enriched clusters [593]. Si-B-N-C ceramics prepared from other precursors show segregation into crystalline  $Si_3N_4$  and turbostratic BN at temperatures over 1400 °C [594, 595].

Whereas  $SiBN_3C$  fibers can easily withstand temperatures of up to 1800 °C in nonoxidizing atmospheres and up to 1500 °C under oxidizing conditions for long periods (<50 h), the commercial HiNicalon fibers (Nippon Carbon), when

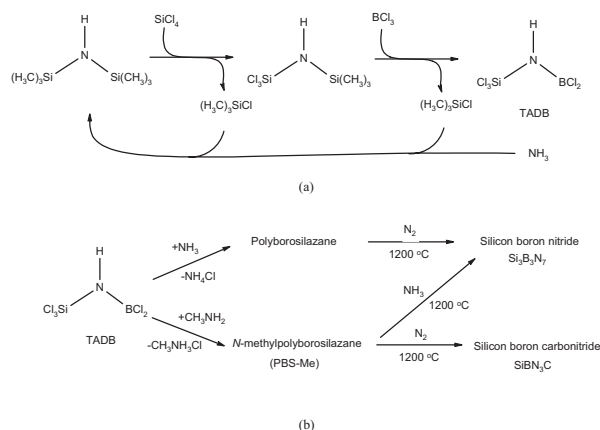


**Figure 60.** (a) Synthesis of the precursor molecule TADB. (b) Pyrolysis and polymerization of TADB.

aged in air at 1500 °C for 15 h, develop a crystalline oxide layer that contains several cracks and debonds from the fiber core (Fig. 61). The above example shows the advantage of molecular precursors in achieving a high degree of connectivity in the amorphous ceramic that is responsible for the unusual properties of the fibers prepared from it.

The definition of nanocomposite material encompasses a large variety of systems, such as one-dimensional, two-dimensional, three-dimensional, and amorphous materials, made of distinctly dissimilar components and mixed at the nanometer scale [337] (Scheme 29). Nanocomposites are of intense current interest for potential applications

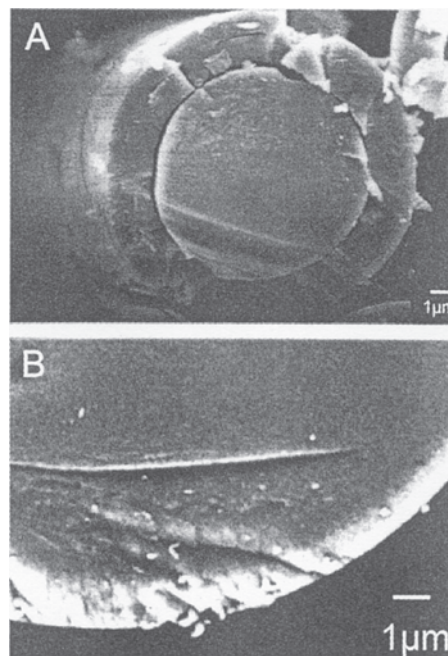
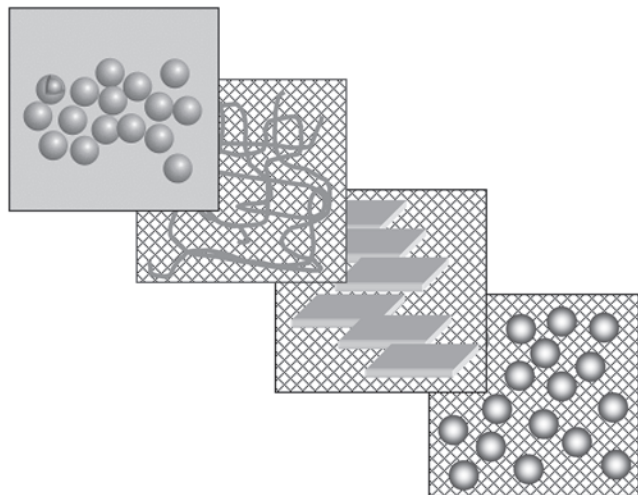


**Figure 61.** Oxidation resistance of Siboramic compared with HiNicalon fibers (Nippon Carbon). (A) Fracture surface of HiNicalon fibers after exposure to air (15 h, 1500 °C). (B) Fracture surface of  $SiBN_3C$  fibers after exposure to air (50 h, 1500 °C). Reprinted with permission from [616], P. Baldus et al., *Science* 285, 699 (1999). © 1999, American Association for the Advancement of Science.

in catalytic, magnetic, electronic, and optical applications [596–602].



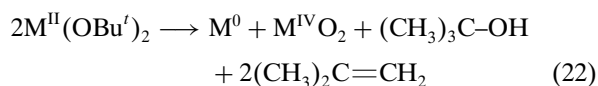
**Scheme 29.**

The combination of two discrete phases with different properties, at the molecular level, provides an avenue to the design of new hybrid materials as well as the possibility of modulating the properties of one or more of the components. It is also a unique way to generate materials that have special properties that are unknown in the individual components or new compositions (materials) not known before. The concept of dispersing an active phase into a supporting phase (matrix) is not new, and a large number of examples are available where functional nanoparticles have been embedded in polymer, glass, or ceramic matrices to modify the properties [289, 296, 299, 301, 303, 306, 308, 309]. Since the properties of nanocomposite materials depend not only on the properties of their individual parents but also on their degree of mixing and interfacial characteristics, considerable efforts are focused on the development of new chemical routes for producing these systems. The phase segregation poses a challenge in the synthesis of compositionally different nanocomposites because a uniform intermingling of two different phases cannot be obtained by mechanical blending. The above problem nevertheless can be addressed by using single-molecule precursors in which the elements required to form the two phases (dispersoid and matrix) are assembled in a molecular framework.

Composites of a metal and metal oxide phase could be interesting in view of their special material properties, like hardness, plasticity, luminescence, conductivity, photoelectric properties etc. The strategy to obtain such biphasic nanocomposites in a *single-step* approach is based on the use of molecular precursors containing either a zerovalent or a meta-stable (unusual oxidation state) metallic center [410]. On thermal treatments, the meta-stable oxidation state disproportionates via a redox reaction to form a more stable higher oxidation state and the elemental form. For example, Cu(I) species have been used in sol-gel and CVD processes to obtain the Cu/Cu<sub>2</sub>O system.

A particularly interesting example is the formation of biphasic composites from the CVD of *tert*-butoxides of bivalent germanium, tin, and lead with the general formula

$M(\text{O}^t\text{Bu})_2$  ( $M(\text{II}) = \text{Ge, Sn, Pb}$ ) [143]. Veith et al. have studied the gas-phase pyrolysis (450–550 °C) of  $M^{\text{II}}(\text{O}^t\text{Bu})_2$  compounds to obtain composite films where metal particles are wrapped in oxide shells (Eq. (22)).



The molecular structure of the Ge precursor is shown in Figure 62. The formation of biphasic particles is chemically driven because the electron transfer necessary for the observed redox process ( $2M^{\text{II}} \rightarrow M^0 + M^{\text{IV}}$ ) occurs in a molecular entity, which enforces a narrow size distribution and self-organization of the two phases in the CVD deposit. The SEM images of the films show a regular distribution of spherical particles. The globular morphology of metal-metal oxide composite particles was investigated by nanoindentation and X-ray photoelectron spectroscopy (XPS) studies [603].

The Ge 3d XPS spectrum (Fig. 63) of the Ge/GeO<sub>2</sub> films exhibits two peaks, where the signal located at the lower binding energy is due to the germanium metal. Pure GeO<sub>2</sub> films (obtained by the CVD of Ge(OPr<sup>i</sup>)<sub>4</sub> under identical conditions) showed a peak corresponding only to the Ge-O phase (Fig. 63), which confirmed the formation of a composite material.

The Ge content in the composite film was found to increase upon argon sputtering. This suggested that the metal particles are possibly wrapped in an oxide matrix that was peeled off during the sputtering process. To confirm that the sputter process does not lead to the reduction of germanium oxide to elemental germanium, the GeO<sub>2</sub> sample was also sputtered with Ar<sup>+</sup> ions, but no Ge(0) was detected, even after a long sputtering time (Fig. 63). The nanomechanical characterization [603] of the Ge/GeO<sub>2</sub> films with an atomic force microscope-coupled nanoindenter (NI-AFM) supported a core-shell-type structure. Figure 64 shows the AFM images of the composite film before and after nanoindentation. The triangular impressions are due to indentations with different load forces. The applied force versus displacement (penetration depth) gave the hardness profile across the film. The hardness increased with increasing indented depth, reached a maximum value (7.2 GPa), and

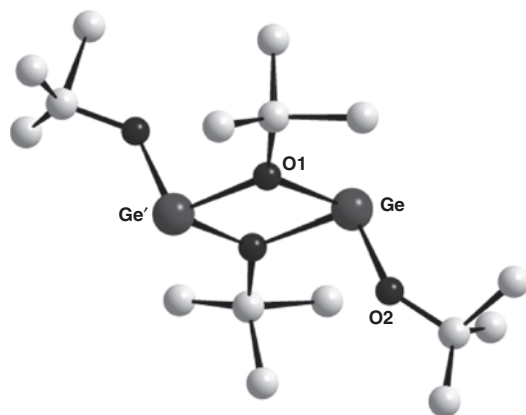


**Figure 62.** Molecular structure of  $[\text{Ge}(\text{O}^t\text{Bu})_2]_2$ .

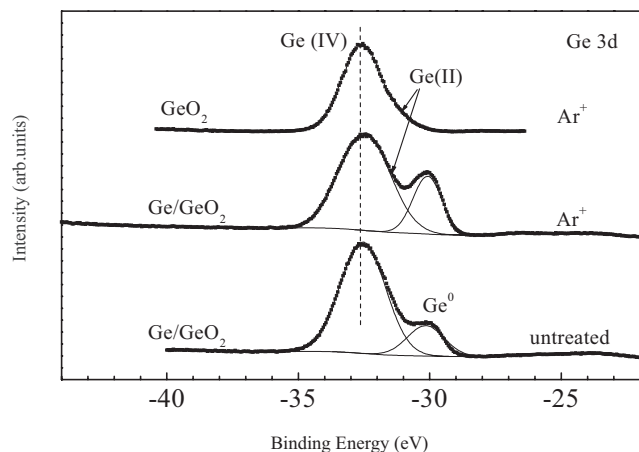


**Figure 63.** Ge 3d XPS spectra of the as-deposited and Ar<sup>+</sup>-sputtered Ge/GeO<sub>2</sub> and GeO<sub>2</sub> films. Reprinted with permission from [24], S. Mathur et al., *Mater. Sci. Forum* 386–388, 341 (2002). © 2002, Trans Tech Publications.

then gradually decreased to the initial value (6.0 GPa); the hardness value at the maximum corresponds to the hardness of bulk Ge (7.6 GPa). The indented depth-dependent variation of hardness (Fig. 64) indicated that the composite was composed of a harder constituent at the core. The indented depth corresponding to the maximum hardness can be assigned to the center of a spherical particle, which indicates that the mean particle diameter is about the twice the indented depth (ca. 120 nm), a fact borne out by the AFM image (Fig. 64), which shows the average particle size to be ca. 120–130 nm.

The redox chemistry observed for divalent Ge, Sn, and Pb species is also valid in their heterometal compounds;

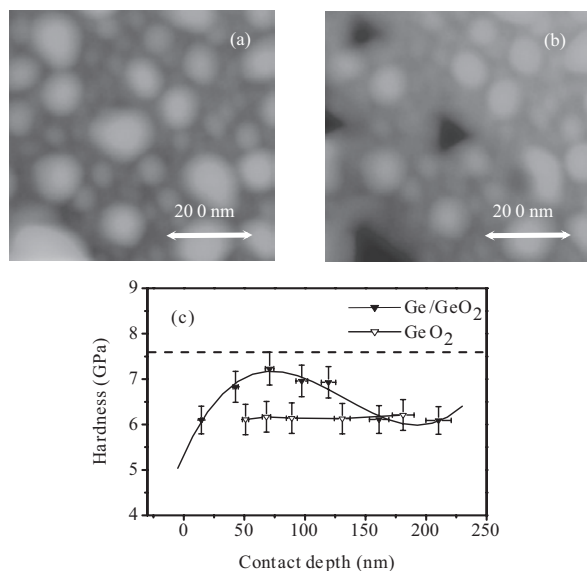
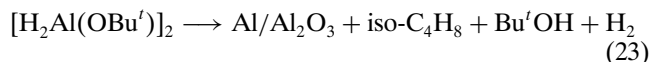


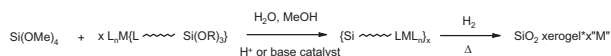
**Figure 64.** AFM images of Ge/GeO<sub>2</sub> sample obtained before (a) and after (b) indentation experiments and the variation of the hardness with the contact depth. Reprinted with permission from [24], S. Mathur et al., *Mater. Sci. Forum* 386–388, 341 (2002). © 2002, Trans Tech Publications.

for example, thermolysis of BaSn<sub>2</sub>(OBU')<sub>6</sub> (formed by the Lewis acid-base reaction of Ba(OBU')<sub>2</sub> and Sn(OBU')<sub>2</sub> [325]) produces a two-phase material (Sn/BaSnO<sub>3</sub>) where metallic tin particles are dispersed in a barium stannate matrix [604]. Veith et al. have extended this approach to those metal centers for which a meta-stable oxidation state is not easily accessible [605] by incorporating reducing ligands into the precursor. Thus, hydride-modified aluminum *tert*-butoxide, [H<sub>2</sub>Al(OBU')]<sub>2</sub>, disproportionates upon pyrolysis (450–550 °C) to yield an Al/Al<sub>2</sub>O<sub>3</sub> composite [605]. A similar observation was made with the Ga compound [H<sub>2</sub>Ga(OBU')]<sub>2</sub> (Table 4), which produced a Ga/Ga<sub>2</sub>O<sub>3</sub> composite [302].



Silica-supported metal particles constitute a large class of important heterogeneous catalysts [532, 606]. The efficiency of such catalytic systems depends on the size and shape of the metal particles and on the nature of particle-support interactions. For this reason, considerable attention has been paid to the development of synthetic strategies to tailor metal/silica (M/SiO<sub>2</sub>) composite materials.

Lukehart et al. have incorporated complexes of various metals (Ge, Ag, Cu, Os, Pd, Pt, Re, and Ru) in silica xerogel matrices (Table 4) to obtain molecularly doped xerogels [294, 303].

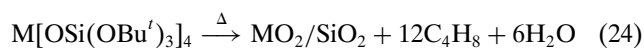


**Scheme 30.**

Subsequent thermal treatment of the doped xerogels afforded metal nanoclusters highly dispersed in the bulk of the xerogel matrix [294, 303], which is chemically controlled because of the covalent bonding of the metal complex in the matrix (Scheme 30). When a dinuclear complex such as *cis*-Pt(PPh<sub>3</sub>)<sub>2</sub>-(Ph)(SnPh<sub>2</sub>Cl), with a bimetallic core (Pt:Sn = 1:1) is used, a nanocomposite containing nanocrystals of PtSn (niggliite) intermetallic dispersed in silica matrix is formed (Fig. 65). The selective formation of single-phase PtSn particles demonstrates that control over the composition of the nanomaterial can be achieved through proper choice of the core structure of the molecular precursor [607].

Tilley et al. have used tris(alkoxy)siloxo derivatives of different metals such as Cu, Al, Ti, Zr, Hf, V, and Cr to obtain metal/silica and metal oxide/silica nanocomposites [103, 249, 299, 301, 311, 313] and have investigated their catalytic behavior. The molecular structure of the copper(I) derivative, [Cu(OSi(OBU')<sub>3</sub>)<sub>4</sub>], is shown in Figure 66.

The precursors of the general formula M[OSi(OBU')<sub>3</sub>]<sub>n</sub> are well-defined oxygen-rich compounds that can be thermolyzed to amorphous, homogeneous metal oxide/silica materials at low temperatures, via the elimination of isobutene and water. For example, the group 4 complexes, M[OSi(OBU')<sub>3</sub>]<sub>4</sub> (M = Ti, Zr, Hf), convert readily to high-surface-area MO<sub>2</sub> · 4SiO<sub>2</sub> materials at temperatures as low as 135 °C (Eq. (24)).





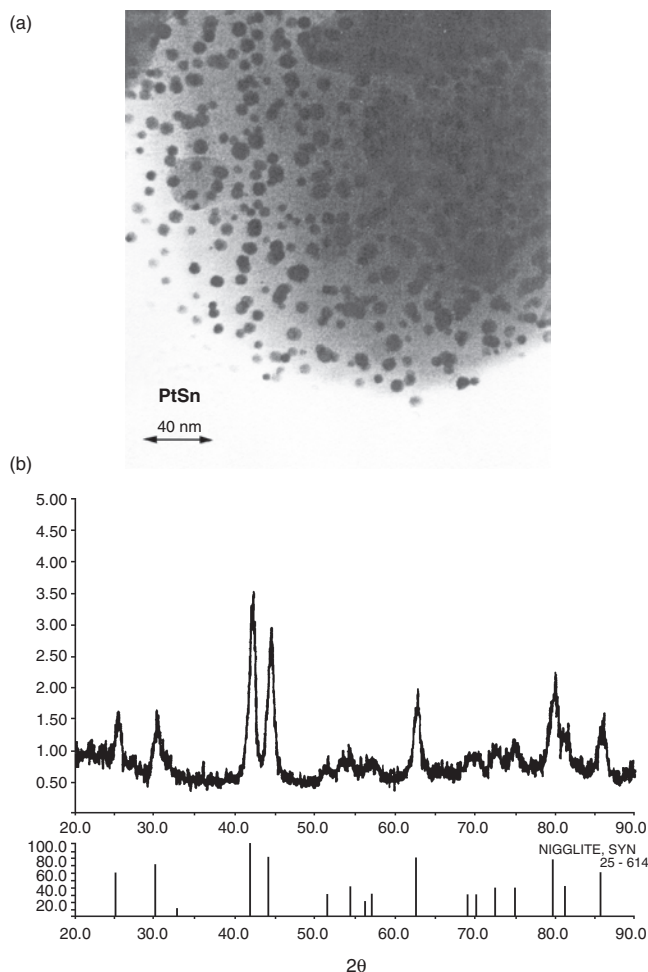


**Figure 65.** (a) TEM micrograph of silica xerogel nanocomposite containing PtSn nanoclusters and (b) the corresponding XRD trace. Reprinted with permission from [607], J. P. Carpenter et al., *Inorg. Chim. Acta* 251, 151 (1996). © 1996, Elsevier Science.

The thermolytic conversion of molecular precursors to metal oxide-silica materials occurs in theoretical yields with a homogeneous distribution of silicon and the transition metal in the oxide matrix that can be attributed to the preservation of molecular-level homogeneity in the transition from precursor to ceramic material. The solid-state transformation gives relatively ordered porous structures, indicating that the precursor's crystalline lattice may function as a template to orient the condensation reactions in particular directions. The microstructure of the heat-treated  $ZrO_2/SiO_2$  material shows a smooth silica matrix containing spherical  $ZrO_2$  particles that grow in size at higher temperatures (Fig. 67).

Roesky et al. have reported on the preparation and chemical properties of a large number of heterometallosiloxane compounds that represent an interesting class of model compounds and precursors to silica-based materials [608]. For example, Dhameincourt et al. have used eight-membered titanium-containing halo-siloxane rings  $[(TiX_2)_2O_4(SiBu_2)_2]$  ( $X = Cl, Br, I$ ) (Scheme 31) as SSPs, prepared according to Scheme 31, to homogeneous  $TiO_2/SiO_2$  material [310].

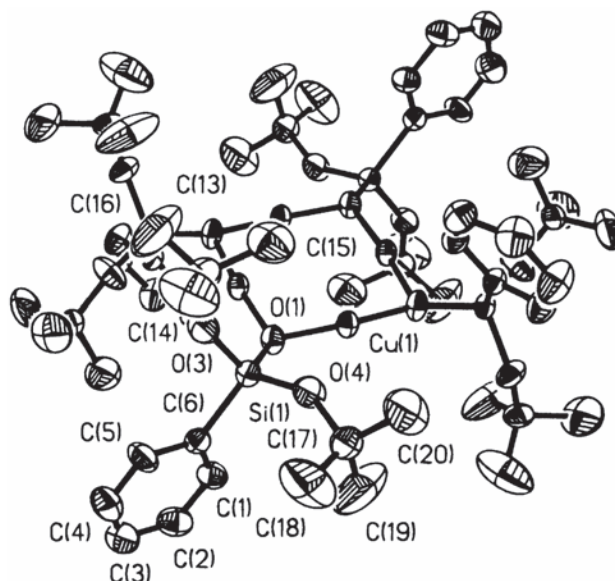
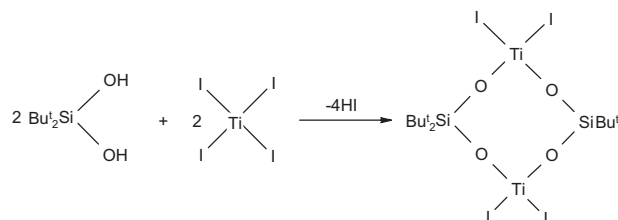


**Figure 66.** ORTEP view of the molecular structure of  $[Cu(OSi(OBu')_3)_4]$ . Reprinted with permission from [299], K. W. Terry et al., *Chem. Mater.* 8, 274 (1996). © 1996, American Chemical Society.

One of the interesting findings of their study is the role of halogen atoms, in the precursor, in determining the phase of the resulting ceramic. For instance, the precursors containing chloride and iodide ligands produced silica mixed with anatase, whereas the bromide derivative yielded silica mixed with rutile [310].



**Scheme 31.**

The (alkoxy)siloxides are also interesting precursors for depositing biphasic thin films. Narula et al. have used  $[(Bu'O)_3Si-O-Ti(OBu')_3]$  as a SSP for obtaining antireflection  $TiO_2-SiO_2$  coatings by atmospheric pressure CVD process [312]. Recently, Schubert et al. have prepared titanium alkoxides modified with a  $\beta$ -diketonate group

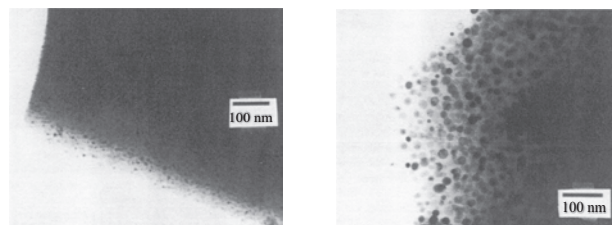


**Figure 67.** TEM photographs of xerogel derived from  $Zr[OSi(OBu')_3]_4$  after calcination under  $O_2$  at 1200 and 1400 °C. Reprinted with permission from [301], K. W. Terry et al., *J. Am. Chem. Soc.* 119, 9745 (1997). © 1997, American Chemical Society.

containing a hydrolyzable alkoxy silane moiety [609]. The hydrolytic conversion of these compounds produced dispersed silica-titania powders. The amount of silica in the final material could be tuned by increasing the number of alkoxy silane groups in the precursors. The presence of silica matrix inhibits the growth of titania nanoparticles; as a result, in the  $\text{TiO}_2\text{:2SiO}_2$  system the anatase phase was observed, whereas the formation of rutile was favored in the  $\text{TiO}_2\text{:SiO}_2$  system [609]. For anatase-rutile transformation, the titania particles must exceed a certain size, and particle growth is favored in the system containing lower silica content.

Recent reports on nanocomposite systems have shown that the matrix materials not only act as passive hosts in sustaining and protecting the nanocrystallites, but also provide a special environment the dispersoids [610–612]. For example, the change in the emission peak observed in the  $\text{CdSe/BaTiO}_3$  composite system has been attributed to the dielectric environment effects of the matrix on the electronic structure of the embedded  $\text{CdSe}$  quantum dots [613]. In the context of optical materials, composites containing lanthanide elements or their phases dispersed in an isotropic matrix are of immense technological value and current interest. The neodymium-doped materials are useful as solid-state laser media, phosphors, and optical amplifiers [600–602]. A homogeneous dispersion of high concentrations of  $\text{Nd}^{3+}$  ions in a fully connected host matrix like  $\text{SiO}_2$  is difficult because of the absence of nonbridging oxygen atoms. As a result, the coordinatively unsaturated  $\text{Nd}^{3+}$  ions form interaction clusters, resulting in quenching of the luminescence quantum yield. The addition of alumina as a codopant can control the clustering of rare-earth ions by forming  $\text{Nd-O-Al}$  bonds, which improves the ill-coordinated state of lanthanide centers [614]. Mathur et al. have put forward a new concept of controlling the quenching problem by restricting the movement of lanthanide ions in the host matrix. Since the  $\text{Nd-Nd}$  separation plays a decisive role in the quenching process, adding the dopant phase in the form of nanocrystals containing  $\text{Nd-O-Al}$  units is expected to offer positional control with respect to the minimum  $\text{Nd-Nd}$  separation. A higher amount of alumina can serve as an active matrix by interacting with the surface  $\text{Nd}$  atoms of the  $\text{NdAlO}_3$  nanocrystals to form further  $\text{Nd-O-Al}$  bonds. Moreover, alumina is a suitable matrix because it allows the incorporation of a high concentration of  $\text{Nd}^{3+}$  ions, and, in comparison to silica, alumina possesses a higher refractive index and optical transparency. To avoid short  $\text{Nd-Nd}$  distances, heterometallic precursors

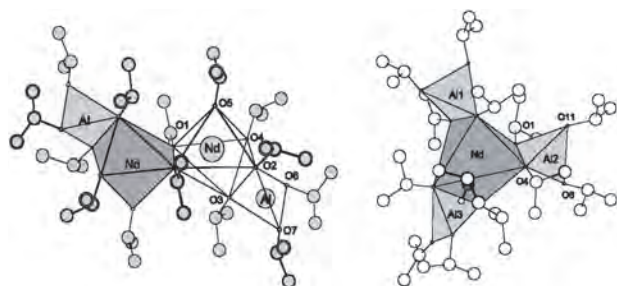


**Figure 68.** Molecular structures of the NA and NA3 systems. Reprinted with permission from [265], S. Mathur et al., *Chem. Mater.* 14, 568 (2002). © 2002, American Chemical Society.

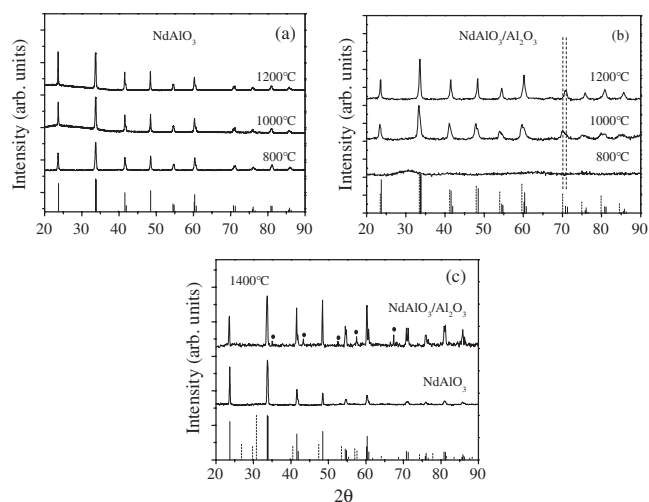
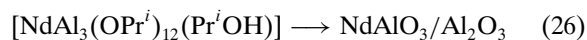
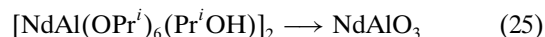


**Figure 69.** X-ray diffraction profiles of  $\text{NdAlO}_3$  (a) and  $\text{NdAlO}_3/\text{Al}_2\text{O}_3$  (b and c) systems calcined at 800, 1000, 1200 and 1400 °C. Reprinted with permission from [265], S. Mathur et al., *Chem. Mater.* 14, 568 (2002). © 2002, American Chemical Society.

$[\text{NdAl}_3(\text{OPr}^i)_{12}(\text{Pr}^i\text{OH})]$ , containing single, isolated  $\text{Nd}$  ions surrounded by optically silent metal atoms, were used as precursors. The validity of this hypothesis was verified by investigation of the optical properties of (i) monophasic  $\text{NdAlO}_3$  and (ii)  $\text{NdAlO}_3$  nanocrystals evenly dispersed in alumina matrix ( $\text{NdAlO}_3/\text{Al}_2\text{O}_3$ ).

The precursors,  $[\text{NdAl}(\text{OPr}^i)_6(\text{Pr}^i\text{OH})]_2$  (NA) and  $[\text{NdAl}_3(\text{OPr}^i)_{12}(\text{Pr}^i\text{OH})]$  (NA3), possess the  $\text{Nd}:\text{Al}$  ratio required for the formation of  $\text{NdAlO}_3$  and  $\text{NdAlO}_3/\text{Al}_2\text{O}_3$  (Fig. 68). The molecular frameworks in NA and NA3 formed by the bidentate chelation of tetrahedral isopropoxo aluminate group(s) [297] fulfill the condition of preformed  $\text{Nd-O-Al}$  bonds.

Both compounds, when subject to controlled hydrolysis, produce homogeneous xerogels that can be calcined to obtain mono- and biphasic nanomaterials (Eqs. (25)–(26)).



The XRD patterns of the calcined powder obtained from NA show neodymium aluminate to be the only crystalline

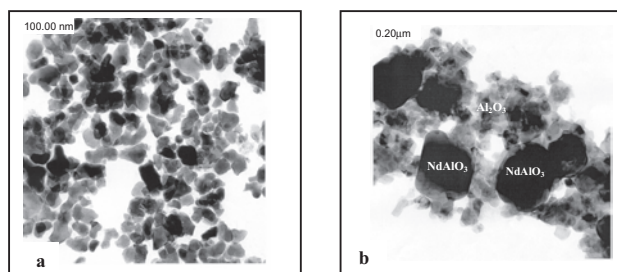


**Figure 70.** TEM images of (a)  $\text{NdAlO}_3$  and (b)  $\text{NdAlO}_3/\text{Al}_2\text{O}_3$  calcined at 1000 and 1200 °C, respectively. Reprinted with permission from [265], S. Mathur, et al., *Chem. Mater.* 14, 568 (2002). © 2002, American Chemical Society.



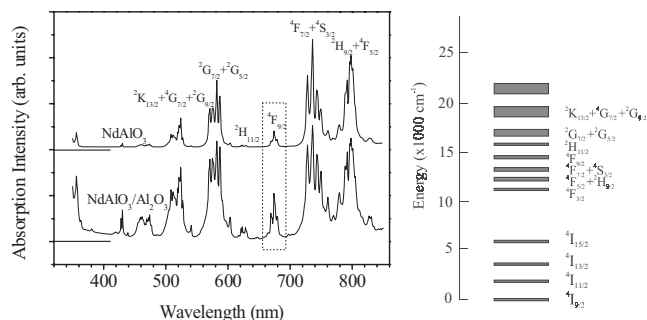


**Figure 71.** Overview absorption spectra of  $\text{NdAlO}_3$  and  $\text{NdAlO}_3/\text{Al}_2\text{O}_3$  systems obtained at room temperature. Reprinted with permission from [265], S. Mathur et al., *Chem. Mater.* 14, 568 (2002). © 2002, American Chemical Society.

phase up to 1400 °C (Fig. 69), whereas in the case of the  $\text{NdAl}_3\text{O}_6$  sample, crystallization of aluminas (mixture of  $\gamma$ ,  $\kappa$ , and  $\delta$  phases) was observed around 1300 °C (Fig. 69). This observation was corroborated by the formal composition ( $\text{NdAl}_3\text{O}_6$ ) of the oxide material, indicating  $\text{Al}_2\text{O}_3$  to be amorphous up to 1200 °C. The TEM image of  $\text{NdAlO}_3$  exhibits crystallites with regular size and narrow size distribution, whereas a bimodal mixture of particles was present in calcined **NA3** powder (Fig. 70). The analytical electron microscopy of the composite material revealed large  $\text{NdAlO}_3$  grains (ca. 150 nm) regularly dispersed in an alumina matrix made up of tiny crystallites (ca. 20 nm) [265].

A comparative evaluation of the optical properties of  $\text{Nd}^{3+}$  ions in  $\text{NdAlO}_3$  and  $\text{NdAlO}_3/\text{Al}_2\text{O}_3$  revealed the absorption coefficient to be much larger (especially in the 350–700-nm region) for the  $\text{NdAlO}_3$  crystallites embedded in an  $\text{Al}_2\text{O}_3$  matrix than that observed for pure  $\text{NdAlO}_3$  (Fig. 71). The high-resolution absorption spectra (Fig. 72) of  $\text{NdAlO}_3$  and  $\text{NdAlO}_3/\text{Al}_2\text{O}_3$  recorded at 10 K correspond to the  $^4\text{I}_{9/2}(1) \rightarrow ^4\text{F}_{9/2}(1)$  transition. The  $\text{NdAlO}_3$  spectrum shows a single peak, whereas the  $\text{NdAlO}_3/\text{Al}_2\text{O}_3$  composite exhibits, besides the main peak, a series of satellites. The photoluminescence (PL) spectra (Fig. 72) of the two systems excited at 4 K by 351-nm radiation ( $\text{Ar}^+$  ion laser) reveal an enhanced PL intensity (X35 times) for the  $\text{NdAlO}_3/\text{Al}_2\text{O}_3$  sample. These improved optical properties of the oxide-oxide composite can be attributed to the influence of the  $\text{Al}_2\text{O}_3$  matrix on the electronic structure of  $\text{Nd}^{3+}$  ions in  $\text{NdAlO}_3$  particles. It is plausible that the much smaller alumina crystallites form a solvation shell around the  $\text{NdAlO}_3$

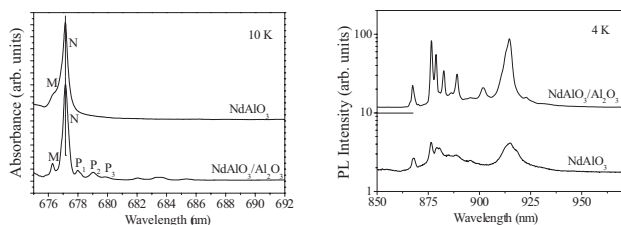


**Figure 72.** (a) High-resolution absorption and (b) photoluminescence spectra of  $\text{Nd } 4f \ ^4\text{F}_{3/2} \rightarrow ^4\text{I}_{9/2}$  emission in  $\text{NdAlO}_3$  and  $\text{NdAlO}_3/\text{Al}_2\text{O}_3$  systems. Reprinted with permission from [265], S. Mathur et al., *Chem. Mater.* 14, 568 (2002). © 2002, American Chemical Society.

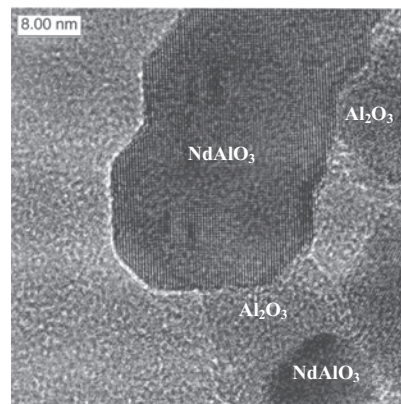


**Figure 73.** HR-EM image of  $\text{NdAlO}_3/\text{Al}_2\text{O}_3$  composite showing crystalline and amorphous domains. Reprinted with permission from [265], S. Mathur et al., *Chem. Mater.* 14, 568 (2002). © 2002, American Chemical Society.

crystallites, thereby amending some of the surface defects of  $\text{NdAlO}_3$  nanocrystals and eliminating the clustering of Nd centers. Indeed, the high-resolution TEM images reveal crystalline domains of  $\text{NdAlO}_3$  linked together by amorphous alumina grains (Fig. 73). The observed higher absorption coefficient and photoluminescence of the **NA3** sample indicate that energy transfer from the alumina matrix to the  $\text{Nd}^{3+}$  cations is operative in the composite material, which additionally populates the excited state of  $\text{Nd}^{3+}$ , resulting in enhanced luminescence efficiency. The surface defects in the nanoparticles are the source of nonradiative quenching sites in the luminescent materials, which decrease the luminescence intensity. In the composite material, the  $\text{NdAlO}_3$  crystallites are in close contact with neighboring alumina grains (Fig. 73), which may compensate for some of the surface defects and simultaneously act as a passivating medium to

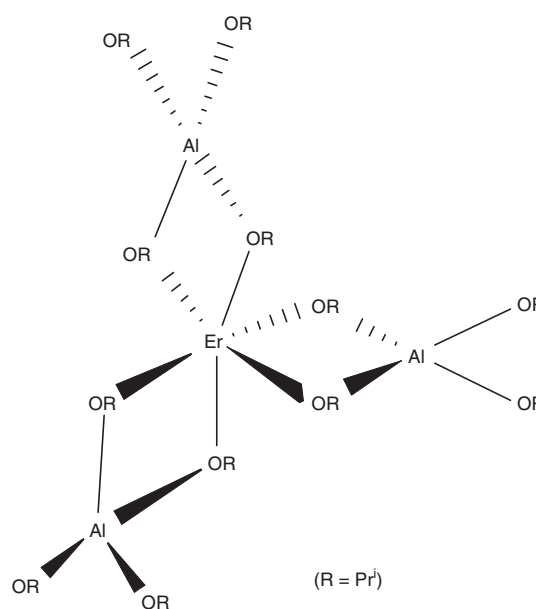


**Figure 74.** Molecular structure of  $\text{ErAl}_3(\text{OR})_{12}$ .

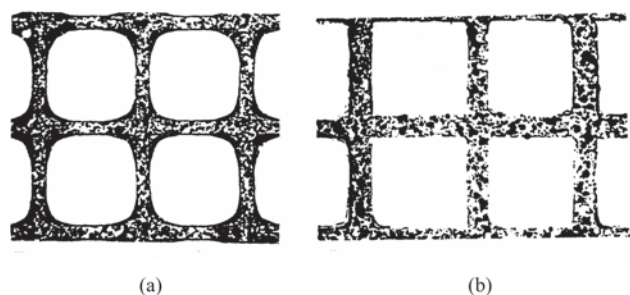
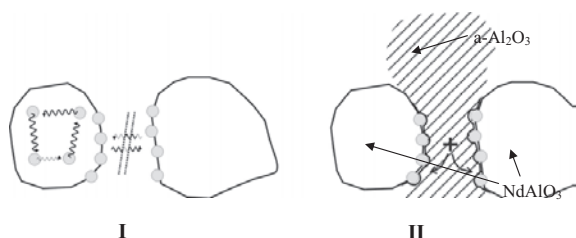


**Figure 75.** Commercial (a) and sol-gel (b) processed wash coat. Reprinted with permission from [256], C. K. Narula, *Mater. Res. Soc. Symp. Proc.* 271, 181 (1992). © 1992, Materials Research Society.

keep the neodymium aluminate centers effectively isolated (Scheme 32).



**Scheme 32.**

The lanthanide-containing oxide-oxide system represents a two-phase structure, where the optically active phase is crystalline and the matrix is amorphous. The processing of these composites can offer materials with properties that are glass-like in most respects, except for the spectroscopy, where they are crystal-like.

Westin et al. have used  $\text{ErAl}_3(\text{OPr}^i)_{12}$  in a sol-gel process to obtain Er-doped Al-Si-Ti oxide glasses (Fig. 74) [614]. The optical characterization of the material shows that using a SSP as the doping source endows a high homogeneity with respect to the cation dispersion, and the films were free from Er-rich clusters, which is the case in conventionally prepared Ln-doped material. The high dispersivity of Er ions in the matrix is reflected in the high emission in the infrared region.

Narula et al. have used lanthanum and cerium alkoxy-aluminates ( $\text{MAl}_3(\text{OPr}^i)_{12}$ ;  $\text{M} = \text{La}, \text{Ce}$ ) in a sol-gel process to obtain high-surface-area alumina incorporating lanthanum and cerium for automotive catalyst substrate applications [256, 297]. The NMR experiments performed to follow the hydrolysis reactions show that lanthanides remain bonded to aluminum in the early stages of hydrolysis. They have impregnated the wash coat of automotive catalysts with alkoxy-derived sols and compared it with the commercial wash coat for the oxidation of hydrocarbons and CO and the reduction of  $\text{NO}_x$ . As shown in Figure 75, a higher channel volume was achieved in the sol-gel-processed wash coat.

## 6. CONCLUSIONS

Nanotechnology demands maneuvering materials atom by atom, which renders the conventional macroscopic material processing methods (mixing, milling, and heating) crude and imprecise. The need for methods enabling controlled

growth of nanomaterial has led to the use of SSPs, which inherently possess the requirements of the nanomaterial (element combination and bonding features of the solid phase) in the molecular state. This review underlines the potential of molecular templating of nanomaterials of different compositions and shows that original solutions can be achieved through the chemical design of the precursor. The directed manipulation of molecular aggregates as elementary fragments of solid-state structure seems to be an efficient strategy for the preconceived synthesis of nanomaterials at the atomic level.

The incorporation of different elements into a molecular source to obtain the target material from a single source simplifies the material synthesis by drastically reducing the process parameters. The SSPs with a predefined metal stoichiometry and reaction (decomposition) chemistry can enforce a molecular-level homogeneity in the obtained materials. The hydrolytic or pyrolytic transformations of molecular derivatives have been used for the phase-selective synthesis of a large variety of ceramics and composites, which illustrates the potential of molecular clusters to “preform” the material on a molecular level (Tables 1–4). Although the field is still far from maturity, the continuing efforts of a large number of research groups in controlling various aspects of the molecule source strategy, such as enhanced volatility, low decomposition temperature, clean and efficient ligand elimination mechanisms, and control of stoichiometry, have boosted the use of single-molecule sources in the synthesis of functional nanomaterials, both films and particles, as is evident from the rapid increase in the publications dealing with this concept and the diversity of the composition of the materials synthesized (Tables 1–4). However, it should be noted that a significant number of reports have emerged from the material curiosity of a synthetic chemist, and the targeted development of experimental chemical methods, necessary to achieve nanoscopic structures by controlled and/or self-organized growth, needs greater attention.

A better understanding of underlying principles of chemical synthesis and the process of molecule-to-material conversion can make possible the rational synthesis of new inorganic materials. The current status of nanomaterials chemistry can be analyzed from two viewpoints: one corresponds to the synthesis of a material from an available precursor followed by the analysis of the nature of the precursor (chemical reactivity, stability, fragmentation, etc.) in light of the results obtained and can be termed as a *synthetic* approach; the other is from a *retrosynthetic* direction, which involves going backward from a target material to molecular starting materials by performing conceivable retro-reactions (subject to the knowledge base) to design the material at the molecular scale. The second case, which in principle forms the basis for illustrating the potential of molecular design, is less practiced for obvious reasons. Although the basic principles of the building-block approach to (nano)materials can obviously be extended to inorganic materials/phases hitherto “unknown,” the lack of systematic investigations regarding the molecular templating or the conditions under which a molecular compound can be transformed into an extended solid poses an application barrier. Consequently, a large number of metal-organic compounds are potential “assemblers” for the controlled assembly of meso- and nanoscopic

structures, yet remain underutilized synthons in the growth of nanomaterials. In view of the above, future research needs in the chemical synthesis of nanophase materials are:

- New synthesis strategies for a directed (chemically driven) synthesis
- Better control over chemical and structural homogeneity, the latter feature being crucial for nanocomposites
- Combinatorial methods for the exploration of complete thermodynamic space
- New chemical principles for designed texture, microstructure, and size-tuning
- Computational methods applicable to complex systems
- Development of precursor systems for nonstoichiometric compounds and doped materials
- Isolation and characterization of high-nuclearity molecular clusters (e.g., partially hydrolyzed species isolated from the sol-gel process), which can reveal the intermediate stages of the molecule-to-material conversion process
- Laboratory validation of discrete steps in the synthetic pathways and a knowledge base to guide the material scientist from the initial conception of a chemical synthesis to a reasonable strategy
- Up-scaling of laboratory procedures by development of commercially viable production methods.

The search for new materials is subject to rationales for providing chemical composition and structures, which constitute the feedback for new synthetic approaches and composition-structure-property relationships. This requires identification of new materials by both experimental (e.g., combinatorial materials synthesis) and computational (energy landscapes of different chemical systems to identify kinetically stable structures) methods. Finally, serious efforts at a complete characterization and proved improvement in the properties of the synthesized nanomaterial is needed from the chemistry community, especially to overcome mindsets and biases about molecular chemistry routes, for instance, the general (mis)conception that a multicomponent molecular precursor would definitely dissociate under experimental conditions to produce a mixture of individual components.

## GLOSSARY

**Chemical vapor deposition (CVD)** Chemical vapor deposition is a generic name for a group of processes that involve depositing a solid material from a gas-phase process by the decomposition of volatile precursors at a suitable temperature either in the gaseous state or on the substrate, thereby eliminating organic fragments as by-products.

**Molecule-based materials (MBM)** Material systems fabricated from molecular subunits, where the molecular integrity of the building units is maintained in the final configuration.

**Molecule-derived materials (MDM)** Materials derived from molecular precursors in which the parent molecular framework is not (necessarily) maintained in the final material.

**Single-source precursor (SSP)** A molecular source containing all of the phase-forming elements in a single chemical

compound, for example, gallium (*tris*)amide ( $\text{Ga}(\text{NR}_2)_3$ ) for gallium nitride (GaN).

**Sol-gel** A room-temperature chemical method used for preparing high-purity ceramics by the hydrolysis of metal-organic compounds in particular metal alkoxides carried out under controlled pH, amount of water, and alkoxide concentration, which involves the transition of a liquid “sol” into a solid “gel” phase.

## ACKNOWLEDGMENTS

S.M. thanks Prof. Michael Veith for his valuable suggestions and continuing encouragement. The authors are thankful to Eva Hemmer, Gabriele Koster, Nicole Donia, Rasa Rapalaviciute, Thomas Rügamer, and Vladimir Sivakov for discussions and help in reading the draft of this review. The financial support of the German Science Foundation (SFB 277) and the Alexander von Humboldt Foundation, Germany, is gratefully acknowledged.

## REFERENCES

1. H. Gleiter, J. Weissmüller, O. Wollersheim, and R. Würschum, *Acta Mater.* 49, 737 (2001).
2. H. Gleiter, *Acta Mater.* 48, 1 (2000).
3. H. Gleiter, *Nanostruct. Mater.* 6, 3 (1995).
4. H. Gleiter, *Nanostruct. Mater.* 1, 1 (1992).
5. R. W. Siegel, in “Advanced Topics in Materials Science and Engineering” (J. L. Moran-Lopez and J. M. Sanchez, Eds.), p. 1273. Plenum, New York 1993.
6. C. B. Murray, C. R. Kagan, and M. G. Bawendi, *Annu. Rev. Mater. Sci.* 30, 545 (2000).
7. J. H. Fendler, Ed., “Nanoparticles and Nanostructured Films.” Wiley-VCH, Weinheim/New York 1998.
8. A. S. Edelstein and R. C. Cammarata, “Nanomaterials: Synthesis, Properties and Applications.” Institute of Physics, Bristol/Philadelphia 1996.
9. J. Chen and N. C. Seeman, *Nature* 350, 631 (1991).
10. Y. Zhang and N. C. Seeman, *J. Am. Chem. Soc.* 114, 2656 (1992).
11. Y. Zhang and N. C. Seeman, *J. Am. Chem. Soc.* 116, 1661 (1994).
12. G. Schmid, M. Bäuml, M. Geerkens, I. Heim, C. Osemann, and T. Sawitowski, *Chem. Soc. Rev.* 28, 179 (1999).
13. A. Henglein, *Chem. Rev.* 89, 1861 (1989).
14. A. P. Alivisatos, *Science* 271, 933 (1996).
15. M. J. Mayo, *Int. Mater. Rev.* 41, 717 (1997).
16. A. H. Cowley and R. A. Jones, *Angew. Chem.* 101, 1235 (1989).
17. W. E. Farneth, N. Herron, and Y. Wang, *Chem. Mater.* 4, 916 (1992).
18. A. N. MacInnes, M. B. Power, and A. R. Barron, *Chem. Mater.* 5, 1344 (1993).
19. J. Cheon, J. Arnold, K. M. Yu, and E. Bourret, *Chem. Mater.* 7, 2273 (1995).
20. M. M. B. Holl, P. T. Wolczanski, D. Proserpio, A. Bielecki, and D. B. Zax, *Chem. Mater.* 8, 2468 (1996).
21. M. Lazell, P. O’Brien, D. J. Otway, and J.-H. Park, *J. Chem. Soc., Dalton Trans.* 4479 (2000).
22. T. Trindade, P. O’Brien, and N. L. Pickett, *Chem. Mater.* 13, 3843 (2000).
23. M. Veith, *J. Chem. Soc., Dalton Trans.* 2405 (2002).
24. S. Mathur, M. Veith, H. Shen, and S. Hüfner, *Mater. Sci. Forum* 386–388, 341 (2002).
25. S. Mathur, M. Veith, H. Shen, and S. Hüfner, *Ceram. Eng. Sci. Proc.* 23, 557 (2002).

26. S. Mathur, in "Chemical Physics of Thin Film Deposition Processes for Micro- and Nano-Technologies" (Y. Pauleau, Ed.), p. 91. Kluwer Academic, Dordrecht, the Netherlands 2002.
27. A. C. Jones, *Chem. Soc. Rev.* 101 (1997).
28. A. Devi, W. Rogge, A. Wohlfart, F. Hipler, H. W. Becker, and R. A. Fischer, *Chem. Vap. Deposition* 6, 245 (2000).
29. R. A. Fischer, H. Sussek, A. Miehr, H. Pritzkow, and E. Herdtweck, *J. Organomet. Chem.* 548, 73 (1997).
30. M. Jansen, *Solid State Ionics* 101-103, 1 (1997).
31. J. P. Carpenter, C. M. Lukehart, S. B. Milne, S. R. Stock, J. E. Wittig, B. D. Jones, R. Glosser, and J. G. Zhu, *J. Organomet. Chem.* 557, 121 (1998).
32. J. M. Lehn, M. Mascal, A. DeCian, and J. Fischer, *J. Chem. Soc., Perkin Trans. 2*, 461 (1992).
33. J. M. Lehn, "Supramolecular Chemistry." VCH, Weinheim 1995.
34. J. D. Hartgerink, E. Beniash, and S. I. Stupp, *Science* 294, 1684 (2001).
35. R. W. Siegel, E. Hu, and M. C. Roco, "... " WTEC Panel Report on Nanostructure Science and Technology: R&D Status and Trends in Nanoparticles, Nanostructured Materials, and Nanodevices. Kluwer, Dordrecht, the Netherlands 1999.
36. D. Segal, *J. Mater. Chem.* 7, 1297 (1997).
37. U. Schubert, *J. Chem. Soc., Dalton Trans.* 3343 (1996).
38. H. Schmidt, R. Nass, M. Aslan, K.-P. Schmitt, T. Benthien, and S. Albayrak, *J. Phys. IV* 3, 1251 (1993).
39. T. J. Trebtlar, R. Suryanarayanan, S. M. L. Sastru, and W. E. Buhro, *Mater. Sci. Eng.* 204, 193 (1995).
40. A. C. Frank, F. Stowasser, C. R. Miskys, O. Ambacher, M. Giersig, and R. A. Fischer, *J. Am. Chem. Soc.* 120, 3512 (1998).
41. M. J. Mayo, *Int. Mater. Rev.* 41, 85 (1996).
42. A. Alivisatos, P. F. Barbara, A. W. Castleman, J. Chang, D. A. Dixon, M. L. Klein, G. L. McLendon, J. S. Miller, M. A. Ratner, P. J. Rossky, S. I. Stupp, and M. E. Thompson, *Adv. Mater.* 10, 1297 (1998).
43. H. S. Park, S. D. Waezsada, A. H. Cowley, and H. W. Roesky, *Chem. Mater.* 10, 2251 (1998).
44. V. G. Kessler, L.-G. Hubert-Pfalzgraf, and S. Daniele, *Chem. Mater.* 6, 2336 (1994).
45. K. G. Caulton and L. G. Hubert-Pfalzgraf, *Chem. Rev.* 90, 969 (1990).
46. C. D. Chandler, C. Roger, and M.-J. Hampden-Smith, *Chem. Rev.* 93, 1205 (1993).
47. D. V. Baxter, M. H. Chisholm, G. J. Gama, A. L. Andrew, and I. P. Parkin, *Chem. Vap. Deposition* 1, 49 (1995).
48. D. C. Bradley, *Polyhedron* 13, 1111 (1994).
49. R. C. Mehrotra, A. Singh, and S. Sogani, *Chem. Soc. Rev.* 215 (1994).
50. R. C. Mehrotra and A. Singh, *Chem. Soc. Rev.* 1 (1996).
51. R. C. Mehrotra, A. Singh, and S. Sogani, *Chem. Rev.* 94, 1643 (1994).
52. M. J. Hampden-Smith and T. T. Kodas, *Chem. Vap. Deposition* 1, 10 (1995).
53. S. Y. Ma, Z. C. Ma, W. H. Zong, H. X. Han, Z. P. Wang, G. H. Li, G. Qin, and G. G. Qin, *J. Appl. Phys.* 84, 559 (1998).
54. M. J. Shapiro, "Chemical Vapor Deposition of Silver for Superconducting Wire Applications," p. 543 1992.
55. A. Erbil, U.S. Patent 4880670, 1989.
56. J. A. Glass, Jr., S. S. Kher, and J. T. Spencer, *Chem. Mater.* 4, 530 (1992).
57. D. L. Schmidt and R. Hellmann, U.S. Patent 3462288, 1969.
58. M. G. Simmons and E. C. Phillips, *Chemtronics* 5, 155 (1991).
59. H. Schmidbaur and M. Bergfeld, *Inorg. Chem.* 5, 2069 (1966).
60. R. J. Puddephatt and A. I. Treunicht, *J. Organomet. Chem.* 319, 129 (1987).
61. P. Hoffmann, G. Ben Assayag, J. Gierak, J. Flicstein, M. Maar-Stumm, and H. van den Bergh, *J. Appl. Phys.* 74, 7588 (1993).
62. G. J. M. Dormans, *J. Cryst. Growth* 108, 806 (1991).
63. N. M. Rutherford and C. E. Larson, *Mater. Res. Soc. Symp. Proc.* 131, 439 (1989).
64. R. Tomono and E. Yagi, *J. Met. Finishing Soc. Jpn.* 16, 210 (1965).
65. B. D. Nash and T. T. Cambel, Report 7112, U.S. Bureau of Mines, Washington DC, 1968.
66. B. B. Owen and R. T. Webber, *Met. Technol.* 15, 230 (1948).
67. A. Devi, J. Goswami, S. A. Shivashankar, and S. Chandrasekaran, *J. Mater. Res.* 13, 687 (1998).
68. M. J. Hampden-Smith and T. T. Kodas, *Chem. Mater.* 2, 636 (1990).
69. T. Wu and R. A. Autlaw, *J. Appl. Phys.* 74, 4990 (1993).
70. K. Dittmar, P. Jutzi, J. Schmallhorst, and G. Reiss, *Chem. Vap. Deposition* 7, 193 (2001).
71. E. S. Vlahov and K. A. Gesheva, *Mater. Lett.* 6, 58 (1987).
72. J. E. Cozum and D. M. Pollina, *J. Am. Chem. Soc.* 110, 2688 (1988).
73. R. Kumar and S. Roy, *Polyhedron* 8, 551 (1989).
74. B. Nixon and P. R. Norton, *Chem. Mater.* 3, 222 (1991).
75. N. H. Dryden and R. Kumar, *Chem. Mater.* 3, 677 (1991).
76. Z. Xue and H. Thridandam, *Chem. Mater.* 4, 162 (1992).
77. Z. Xue and N. J. Strouse, *J. Am. Chem. Soc.* 111, 8779 (1989).
78. Y. J. Chen and H. D. Kaesz, *Appl. Phys. Lett.* 53, 1591 (1988).
79. J. E. Gozum and J. A. Jensen, *J. Am. Chem. Soc.* 110, 2668 (1988).
80. J. A. Papke and R. D. Stevenson, in "Proceedings of the Conference on CVD of Refractory Metals and Alloys," American Nuclear Society, p. 1293, 1967.
81. M. E. Gross and K. S. Krang, *J. Vac. Sci. Technol., B* 6, 1548 (1988).
82. J. W. Lee, K. M. Kim, H. S. Song, K. C. Jeong, J. M. Lee, and J. S. Roh, *Jpn. J. Appl. Phys.* 40, 5201 (2001).
83. M. M. Collinson and B. Novak, *Anal. Chem.* 72, 2914 (2000).
84. D. J. Teff, C. D. Minear, D. V. Baxter, and K. G. Caulton, *Inorg. Chem.* 37, 2547 (1998).
85. I. E. Campbell and R. I. Jaffee, *J. Electrochem. Soc.* 93, 271 (1948).
86. H. J. Homer, U.S. Patent 2887406, 1959.
87. C. P. Boekel and J. H. Teuber, *J. Organomet. Chem.* 81, 371 (1974).
88. R. Moorancho and J. Petit, "Proceedings of the 7th International Conference on CVD," ECS Princeton, p. 593, 1979.
89. Y. Kim, J. H. Kim, J. E. Park, B. J. Bae, B. Kim, J. T. Park, K. S. Yu, and Y. Kim, *Thin Solid Films* 339, 200 (1999).
90. R. L. Puurunen and A. Root, *Appl. Surf. Sci.* 165, 193 (2000).
91. D. Barreca, G. A. Battiston, R. Gerbasi, and E. Tondello, *J. Mater. Chem.* 10, 2127 (2000).
92. M. Ritala, K. Kukli, A. Rahtu, P. I. Räisänen, M. Leskelä, T. Sajavaara, and J. Keinonen, *Science* 288, 319 (2000).
93. D. M. Ibrahim, F. F. AbdelMohsen, and Y. M. AbouAyana, *Br. Ceram. Trans.* 95, 146 (1996).
94. S. Kureti and W. Weisweiler, *Appl. Catal.* 225, 251 (2002).
95. K. Kamiya, J. Yotani, R. Senba, and H. Nasu, *J. Ceram. Soc. Jpn.* 104, 685 (1996).
96. M. Veith and S. Faber, *J. Mater. Sci.* 31, 2009 (1996).
97. H. S. Park, S. Schulz, H. Wessel, and H. W. Roesky, *Chem. Vap. Deposition* 5, 179 (1999).
98. J. H. Boo, C. Rohr, and W. Ho, *J. Cryst. Growth* 189-190, 439 (1998).
99. J.-H. Boo, S.-B. Lee, K.-S. Yu, Y. Kim, Y.-S. Kim, and J. T. Park, *J. Korean Phys. Soc.* 34, 532 (1999).
100. T. Wideman and L. G. Sneddon, *Chem. Mater.* 8, 3 (1996).
101. O. C. Monteiro, T. Trindade, J. H. Park, and P. O'Brien, *Chem. Vap. Deposition* 6, 230 (2000).
102. M. Green and P. O'Brien, *Adv. Mater.* 10, 527 (1998).
103. T. Trindade, P. O'Brien, and X. Zhang, *Chem. Mater.* 9, 523 (1997).
104. M. Chunggaze, M. A. Malik, and P. O'Brien, *Adv. Mater. Opt. Electron.* 7, 311 (1998).
105. M. Lazell and P. O'Brien, *Chem. Commun.* 2041 (1999).

106. M. Nyman, K. Jenkins, M. J. Hampden-Smith, T. T. Kodas, E. N. Duesler, A. L. Rheingold, and M. L. Liable-Sands, *Chem. Mater.* 10, 914 (1998).
107. P. Boudjouk, B. R. Jarabek, D. L. Simonson, D. J. Seidler, D. G. Grier, G. J. McCarthy, and L. P. Keller, *Chem. Mater.* 10, 2358 (1998).
108. M. A. Malik, N. Revaprasadu, and P. O'Brien, *Chem. Mater.* 13, 913 (2001).
109. J. G. Brennan, T. Siegrist, P. J. Carrol, S. M. Stuczynski, L. E. Brus, and M. Steigerwald, *J. Am. Chem. Soc.* 111, 4141 (1989).
110. S. L. Cumberland, K. M. Hanif, A. Javier, G. A. Khitrov, G. F. Strouse, S. M. Woessner, and C. S. Yun, *Chem. Mater.* 14, 1576 (2002).
111. G. Mugesh, H. B. Singh, and R. J. Butcher, *J. Organomet. Chem.* 577, 243 (1999).
112. X. H. Liao, J. M. Zhu, J. J. Zhu, J. Z. Xu, and H. Y. Chen, *Chem. Commun.* 937 (2001).
113. K. Fröhlich, J. Souc, D. Machjdić, M. Jergel, J. Snauwaert, and L. Melleman, *Chem. Vap. Deposition* 4, 216 (1998).
114. S.-Y. Wang and W. Wang, *Solid State Ionics* 133, 211 (2000).
115. K. D. Pollard and H. A. Jenkins, *Chem. Mater.* 12, 701 (2000).
116. R. A. Fischer and J. Behm, *Angew. Chem.* 105, 776 (1993).
117. P. J. Aylett and A. A. Tannakil, *Vacuum* 35, 435 (1985).
118. J. Prokop, C. E. Zybilla, and S. Veprek, *Thin Solid Films* 359, 39 (2000).
119. T. H. W. Sun, H. F. Wang, and K. M. Chi, *J. Mater. Chem.* 10, 1231 (2000).
120. M. Kemmler and M. Lazell, *J. Mater. Sci., Mater. Electron.* 13, 531 (2002).
121. K. M. Hubbard and B. F. Espinoza, *Thin Solid Films* 366, 175 (2000).
122. W. Zhu and Q. Jiang, *Thin Solid Films* 363, 167 (2000).
123. S. Mathur, M. Veith, V. Sivakov, H. Shen, and H. B. Gao, *J. Phys. IV* 11, 487 (2001).
124. L. Armelao and A. Artigliato, *J. Mater. Res.* 12, 1441 (1997).
125. X. Cao, R. Prozorov, Yu. Koltypin, G. Kataby, I. Felner, and A. Gedanken, *J. Mater. Res.* 12, 402 (1997).
126. T. Hashimoto, T. Yamada, and T. Yoko, *J. Appl. Phys.* 80, 3184 (1996).
127. T. Kiyomura and M. Gomi, *J. Phys. IV* 7, C1-611 (1997).
128. S. G. Shyu, J. S. Wu, and K. M. Chi, *J. Am. Chem. Soc.* 119, 16 (1997).
129. P. O'Brien, D. J. Otway, and J. H. Park, *Chem. Proc. Dielectrics Insulators Electron. Ceram.* 606, 127 (2000).
130. L. Luo, C. E. Zybilla, H. G. Ang, S. F. Lim, D. H. C. Chua, J. Lin, A. T. S. Wee, and K. L. Tan, *Thin Solid Films* 325, 87 (1998).
131. K. M. Chi, S. H. Liu, and S. H. Chien, *Chem. Mater.* 14, 2028 (2002).
132. E. E. Foos, R. J. Jouet, R. L. Wells, A. L. Rheingold, and L. M. Liable-Sands, *J. Organomet. Chem.* 582, 45 (1999).
133. A. Kuczkowski, S. Schulz, and W. Assenmacher, *J. Mater. Chem.* 11, 3241 (2001).
134. J. E. Miller, M. A. Mardones, J. W. Nail, A. H. Cowley, R. A. Jones, and J. G. Ekerdt, *Chem. Mater.* 4, 447 (1992).
135. J. A. Jegier, S. McKernan, and W. L. Gladfelter, *Chem. Mater.* 10, 2041 (1998).
136. J. McMurrin, D. Dai, K. Balasubramanian, C. Steffek, J. Kouvetakis, and J. L. Hubbard, *Inorg. Chem.* 37, 6638 (1998).
137. A. C. Frank and R. A. Fischer, *Adv. Mater.* 10, 961 (1998).
138. J. Kouvetakis, M. Okeeffe, M. Brouseau, J. McMurrin, D. Williams, and D. J. Smith, *III-IV Nitrides* 449, 313 (1997).
139. A. C. Frank, F. Stowasser, O. Stark, H. T. Kwak, H. Sussek, A. Rupp, H. Pritzkow, O. Ambacher, M. Giersig, and R. A. Fischer, *Adv. Mater. Opt. Electron.* 8, 135 (1998).
140. A. Devi, W. Rogge, R. A. Fischer, F. Stowasser, H. Sussek, H. W. Becker, J. Schafer, and J. Wolfrum, *J. Phys. IV* 9, 589 (1999).
141. J. McMurrin, J. Kouvetakis, D. C. Nesting, D. J. Smith, and J. L. Hubbard, *J. Am. Chem. Soc.* 120, 5233 (1998).
142. M. Valet and D. M. Hoffman, *Chem. Mater.* 13, 2135 (2001).
143. M. Veith, S. J. Kneip, A. Jungmann, and S. Hüfner, *Z. Anorg. Allg. Chem.* 623, 1507 (1997).
144. T. Minami and T. Shirai, *Jpn. J. Appl. Phys., Part 2* 39, L524 (2000).
145. R. J. Jouet, R. L. Wells, A. L. Rheingold, and C. D. Incarvito, *J. Organomet. Chem.* 601, 191 (2000).
146. A. B. Hopcus, S. I. Yi, C. H. Chung, R. I. Pelzel, and W. H. Weinberg, *Surf. Sci.* 446, 55 (2000).
147. S. Suh and D. M. Hoffman, *Chem. Mater.* 12, 2794 (2000).
148. M. R. Lazell, P. O'Brien, D. J. Otway, and J. H. Park, *Chem. Mater.* 11, 3430 (1999).
149. E. G. Gillan and A. R. Barron, *Chem. Mater.* 9, 3037 (1997).
150. S. L. Stoll, E. G. Gillan, and A. R. Barron, *Chem. Vap. Deposition* 2, 182 (1996).
151. J. H. Jang and J. Koo, *J. Am. Ceram. Soc.* 83, 1356 (2000).
152. T. Conradsson and M. S. Dadachov, *Microporous Mesoporous Mater.* 41, 183 (2000).
153. A. Garciamurillo and C. Leluyer, *Opt. Mater.* 16, 39 (2001).
154. A. L. Wayda, L. F. Schneemeyer, and R. L. Opila, *Appl. Phys. Lett.* 53, 361 (1988).
155. R. Fix and R. G. Gordon, *Chem. Mater.* 3, 1138 (1991).
156. R. C. Smith and T. Ma, *Adv. Mater. Opt. Electron.* 10, 105 (2000).
157. P. A. Williams, J. L. Roberts, A. C. Jones, P. R. Chalker, N. L. Tobin, J. F. Bickley, H. O. Davies, L. M. Smith, and T. J. Leedham, *Chem. Vap. Deposition* 8, 163 (2002).
158. G. Kräuter, B. Neumüller, V. L. Goedken, and W. S. Rees, Jr., *Chem. Mater.* 8, 360 (1996).
159. J. Schäfer, J. Wolfrum, R. A. Fischer, and H. Sussek, *Chem. Vap. Deposition* 5, 205 (1999).
160. P. Lobinger, H. S. Park, H. Hohmeister, and H. W. Roesky, *Chem. Vap. Deposition* 7, 105 (2001).
161. J. H. Park, G. A. Horley, P. O'Brien, A. C. Jones, and M. Motevalli, *J. Mater. Chem.* 11, 2346 (2001).
162. T. Tsuchiya and A. Watanabe, *Jpn. J. Appl. Phys., Part 2* 38, L1112 (1999).
163. C. Cantalini and W. Wlodarski, *Thin Solid Films* 350, 276 (1999).
164. T. Douglas and K. H. Theopold, *Inorg. Chem.* 30, 594 (1991).
165. A. N. MacInnes, W. M. Cleaver, A. R. Barron, M. B. Power, and A. F. Hepp, *Adv. Mater. Opt. Electron.* 1, 229 (1992).
166. N. Revaprasadu, M. A. Malik, J. Carstens, and P. O'Brien, *J. Mater. Chem.* 9, 2885 (1999).
167. G. A. Horley, M. Chunggaze, P. O'Brien, A. J. P. White, and D. J. Williams, *J. Chem. Soc., Dalton Trans.* 4205 (1998).
168. G. A. Horley, P. O'Brien, J. H. Park, A. J. P. White, and D. J. Williams, *J. Mater. Chem.* 9, 1289 (1999).
169. E. E. Foos, R. J. Jouet, R. L. Wells, and P. S. White, *J. Organomet. Chem.* 598, 182 (2000).
170. S. L. Stoll and A. R. Barron, *Chem. Mater.* 10, 650 (1998).
171. H. J. Gysling and A. A. Wernberg, *Chem. Mater.* 4, 900 (1992).
172. P. O'Brien, D. J. Otway, and J. R. Walsh, *Chem. Vap. Deposition* 3, 227 (1997).
173. M. Nieminen and M. Putkonen, *Appl. Surf. Sci.* 174, 155 (2001).
174. G. G. Condorelli and S. Gennaro, *Chem. Vap. Deposition* 7, 151 (2001).
175. J. H. Boo, S.-B. Lee, K. S. Yu, W. Koh, and Y. Kim, *Thin Solid Films* 341, 63 (1999).
176. M. M. Sung, C. Kim, C. G. Kim, and Y. Kim, *J. Cryst. Growth* 210, 651 (2000).
177. J. S. Matthews and O. Just, *Chem. Vap. Deposition* 6, 129 (2000).
178. H. O. Davies and A. C. Jones, *Chem. Vap. Deposition* 6, 71 (2000).
179. M. Putkonen and T. Sajavaara, *J. Mater. Chem.* 10, 1857 (2000).
180. R. A. Fischer, A. Miehr, and T. Metzger, *Thin Solid Films* 289, 147 (1996).
181. M. I. Yanovskaya and I. E. Obvintseva, *J. Non-Cryst. Solids* 124, 155 (1990).



182. J. Putz and M. A. Aegerter, *Thin Solid Films* 351, 119 (1999).
183. S. H. A. Petri, B. Neumann, H. G. Stammler, and P. Jutzi, *J. Organomet. Chem.* 553, 317 (1998).
184. T. Sun and J. Y. Ying, *Nature* 389, 704 (1997).
185. H. Kominami, K. Oki, M. Kohno, S.-I. Onoue, Y. Kera, and B. Ohtani, *J. Mater. Chem.* 11, 604 (2001).
186. J. Chevalier and G. Bonnet, *Appl. Surf. Sci.* 167, 125 (2000).
187. J. W. Cheon, D. S. Talaga, and J. I. Zink, *Chem. Mater.* 9, 1208 (1997).
188. T. Trindade, O. C. Monteiro, P. O'Brien, and M. Motevalli, *Polyhedron* 18, 1171 (1999).
189. A. Renooprez and K. Lebas, *J. Mol. Catal., A: Chem.* 120, 217 (1997).
190. R. Raja, G. Sankar, S. Hermans, D. S. Shephard, S. Bromley, J. M. Thomas, and B. F. G. Johnson, *Chem. Commun.* 1571 (1999).
191. P. Reyes and M. C. Aguirre, *J. Mol. Catal., A: Chem.* 184, 431 (2002).
192. J. H. Boo, S. A. Ustin, and W. Ho, *Thin Solid Films* 343–344, 650 (1999).
193. S. A. Ustin, C. Long, and W. Ho, *Solid-State Electron.* 42, 2321 (1998).
194. L. L. Hench and J. K. West, *Chem. Rev.* 90, 33 (1990).
195. D. G. Colombo, D. C. Gilmer, V. G. Young, S. A. Campbell, Jr., and W. L. Gladfelter, *Chem. Vap. Deposition* 4, 220 (1998).
196. D. Barreca and S. Garom, *J. Phys. IV* 9, 667 (1999).
197. C. Savaniu and A. Arnautu, *Thin Solid Films* 349, 29 (1999).
198. A. Gamarol and B. Jousseau, *Inorg. Chem.* 38, 4671 (1999).
199. P. H. Wei and G. B. Li, *J. Electrochem. Soc.* 146, 3536 (1999).
200. P. Boudjouk, M. P. Remington, D. J. Seidler, B. R. Jarabek, D. G. Grier, B. E. Very, R. L. Jarabek, and G. J. McCarthy, *Mater. Res. Bull.* 34, 2327 (1999).
201. I. P. Parkin, L. S. Price, T. G. Hibbert, and K. C. Molloy, *J. Mater. Chem.* 11, 1486 (2001).
202. I. S. Chuprakov, K. H. Dahmen, J. J. Schneider, and J. Hagen, *Chem. Mater.* 10, 3467 (1998).
203. P. Boudjouk, M. P. Remington, D. G. Grier, W. Triebold, and B. R. Jarabek, *Organometallics* 18, 4534 (1999).
204. Y. Ohshita and A. J. Ogura, *J. Cryst. Growth* 220, 604 (2000).
205. K. R. Gust, M. J. Heeg, and C. H. Winter, *Polyhedron* 20, 805 (2001).
206. H.-T. Chiu, S.-H. Chuang, C.-E. Tsai, G.-H. Lee, and S.-M. Peng, *Polyhedron* 17, 2187 (1998).
207. Y. S. Lai and J. S. Chen, *Jpn. J. Appl. Phys., Part 1* 40, 4593 (2001).
208. K. D. Pollard and R. J. Puddephatt, *Chem. Mater.* 11, 1069 (1999).
209. Y. H. Chang and C. V. Chinn, *J. Mater. Chem.* 12, 2189 (2002).
210. C. J. Carmalt, A. H. Cowley, R. D. Culp, R. A. Jones, Y. M. Sun, B. Fitts, S. Whaley, and H. W. Roesky, *Inorg. Chem.* 36, 3108 (1997).
211. J. T. Scheper, P. J. McKarns, T. S. Lewkebandara, and C. H. Winter, *Mater. Sci. Semicond. Proc.* 2, 149 (1999).
212. D. V. Baxter, M. H. Chisholm, G. J. Gama, V. F. DiStasi, A. L. Hector, and I. P. Parkin, *Chem. Mater.* 8, 1222 (1996).
213. T. R. Cundari and J. M. Morse, Jr., *Chem. Mater.* 8, 189 (1996).
214. J. B. Cross, S. M. Smith, and H. B. Schlegel, *Chem. Mater.* 13, 1095 (2001).
215. L. M. Gan, L. W. Chen, and Z. J. Xu, *J. Inorg. Mater.* 16, 846 (2001).
216. M. J. van Bommel and T. N. M. Bernards, *J. Sol-Gel Sci. Technol.* 8, 459 (1997).
217. R. K. Roeder and E. B. Slamovich, *J. Mater. Res.* 14, 2364 (1999).
218. T. Nakamura and H. Asai, *Appl. Surf. Sci.* 142, 182 (1999).
219. P. Zanella and G. A. Battiston, *Adv. Mater. Process* 282, 123 (1998).
220. J. Livage, *Coord. Chem. Rev.* 192, 391 (1999).
221. D. Barreca and G. A. Battiston, *J. Phys. IV* 9, 529 (1999).
222. E. A. Meulenkamp and V. Vanklinken, *Solid State Ionics* 126, 235 (1999).
223. M. Putkonen and Sajavaara, *Chem. Vap. Deposition* 7, 44 (2001).
224. J. W. Sung, D. M. Goedde, G. S. Girolami, and J. R. Abelson, *J. Appl. Phys.* 91, 3904 (2001).
225. F. Cheng and Y. Sugahara, *Chem. Lett.* 2, 138 (2000).
226. M. Morstein, I. Pozsgai, and N. D. Spencer, *Chem. Vap. Deposition*, 151 (1999).
227. D. J. Bursleson, J. T. Roberts, W. L. Gladfelter, S. A. Campbell, and R. C. Smith, *Chem. Mater.* 14, 1269 (2002).
228. R. Caruso and N. Pellegrini, *J. Sol-Gel Sci. Technol.* 3, 241 (1994).
229. J. J. Gallegos and T. L. Ward, *Chem. Vap. Deposition* 6, 21 (2000).
230. K. Merz, R. Schoenen, and M. Driess, *J. Phys. IV* 11, 467 (2001).
231. M. H. Koch, A. J. Hartmann, R. N. Lamb, M. Neuber, and M. Grunze, *J. Phys. Chem. B* 101, 8231 (1997).
232. M. Toyoda and J. Watanabe, *J. Sol-Gel Sci. Technol.* 16, 93 (1999).
233. J. Auld, D. J. Houlton, A. C. Jones, S. A. Rushworth, M. A. Malik, P. O'Brien, and G. W. Critchlow, *J. Mater. Chem.* 4, 1249 (1994).
234. B. Ludolph, M. A. Malik, P. O'Brien, and N. Revaprasadu, *Chem. Commun.* 1849 (1998).
235. J. Cheon, D. S. Talaga, and J. I. Zink, *J. Am. Chem. Soc.* 119, 163 (1997).
236. N. H. Tran and R. N. Lamb, *J. Phys. Chem. B* 106, 352 (2002).
237. T. C. Devaraj, J. H. Park, M. Afzaal, P. O'Brien, and J. J. Vital, *Chem. Commun.* 2305 (2001).
238. A. Meliani, H. Bali, A. Mazzah, R. de Jaeger, M. Drache, and L. Gengembre, *Phosphorus, Sulfur Silicon Relat. Elem.* 174, 133 (2001).
239. M. L. Kosinova, N. I. Fainer, Y. M. Rumyantsev, and F. A. Kuznetsov, *J. Phys. IV* 9, 915 (1999).
240. D. Hegemann, R. Riedel, W. Dreßler, C. Oehr, B. Schindler, and H. Brunner, *Chem. Vap. Deposition* 3, 257 (1997).
241. Y. Suyama and M. Nagasawa, *J. Am. Ceram. Soc.* 77, 603 (1994).
242. V. W. Day, T. A. Eberspacher, M. H. Frey, W. G. Klemperer, S. Liang, and D. A. Payne, *Chem. Mater.* 8, 330 (1996).
243. M. Veith, A. Altherr, N. Lecerf, S. Mathur, K. Valtchev, and E. Fritscher, *Nanostruct. Mater.* 12, 191 (1999).
244. F. Meyer, R. Hempelmann, S. Mathur, and M. Veith, *J. Mater. Chem.* 9, 1755 (1999).
245. S. Mathur and H. Shen, *J. Phys. IV*, 12, Pr4-1 (2002), and references therein.
246. M. Haas, S. Mathur, and M. Veith, unpublished results.
247. P. A. Wright, S. Natarajan, J. M. Thomas, and P. L. Gai-Boyes, *Chem. Mater.* 4, 1053 (1992).
248. F. Ossola and F. Maury, *Chem. Vap. Deposition* 3, 137 (1997).
249. K. L. Furdala and T. D. Tilley, *Chem. Mater.* 13, 1817 (2001).
250. K. K. Banger, J. Cowen, and A. F. Hepp, *Chem. Mater.* 13, 3827 (2001).
251. J. A. Hollingsworth, A. F. Hepp, and W. E. Buhro, *Chem. Vap. Deposition* 5, 105 (1999).
252. K. K. Banger, J. D. Harris, J. E. Cowen, and A. F. Hepp, *Thin Solid Films* 403–404, 390 (2002).
253. S. R. Aubuchon, M. S. Lube, and R. L. Wells, *Chem. Vap. Deposition* 1, 28 (1995).
254. R. A. Fischer, H. Sussek, H. Parala, and H. Pritzkow, *J. Organomet. Chem.* 592, 205 (1999).
255. S. Mathur, H. Shen, N. Lecerf, H. Fjellvag, and G. F. Goya, *Adv. Mater.* 14, 1405 (2002).
256. C. K. Narula, *Mater. Res. Soc. Symp. Proc.* 271, 181 (1992).
257. E. Jung, S. H. Yoo, T.-M. Chung, C. G. Kim, Y. Kim, and D. Y. Jung, *Inorg. Chem. Commun.* 5, 439 (2002).
258. D. Saulys, V. Joshkin, M. Khoudiakov, T. F. Kuech, A. B. Ellis, S. R. Oktyabrsky, and L. McCaughan, *J. Cryst. Growth* 217, 287 (2000).
259. R. E. Rocheleau, Z. Zhang, J. W. Gilje, and J. A. Meese-Marktscheffel, *Chem. Mater.* 6, 1615 (1994).
260. K. Jones, T. J. Davies, H. G. Emblem, and P. Parkes, *Mater. Res. Soc. Symp. Proc.* 73, 111 (1986).
261. C. R. Bichmore, K. F. Waldner, and R. M. Laine, *J. Am. Ceram. Soc.* 79, 1419 (1996).

262. F. Meyer, A. Dierstein, C. Beck, W. Härtl, R. Hempelmann, S. Mathur, and M. Veith, *Nanostruct. Mater.* 12, 71 (1999).
263. W. Koh, S.-J. Ku, and Y. Kim, *Chem. Vap. Deposition* 4, 192 (1998).
264. H. O. Davies, A. C. Jones, T. J. Leedham, P. J. Wright, M. J. Crosbie, P. A. Lane, A. Steiner, and J. F. Bickley, *Adv. Mater. Opt. Electron.* 10, 177 (2000).
265. S. Mathur, M. Veith, H. Shen, S. Hüfner, and M. Jilavi, *Chem. Mater.* 14, 568 (2002).
266. A. W. Apblett, L. A. Cubano, G. D. Georgieva, and J. T. Mague, *Chem. Mater.* 8, 650 (1996).
267. H. K. Chae, D. A. Payne, Z. Xu, and L. Ma, *Chem. Mater.* 6, 1589 (1994).
268. B. A. Vaartstra, *Mater. Res. Soc. Symp. Proc.* 282, 689 (1993).
269. M. Veith, S. Mathur, H. Shen, N. Lecerf, S. Hüfner, and M. Jilavi, *Chem. Mater.* 13, 4041 (2001).
270. R. M. Hagenmayer, U. Muller, C. J. Benmore, J. Neuefeind, and M. Jansen, *J. Mater. Chem.* 9, 2865 (1999).
271. Y. Iwamoto, W. Volger, E. Kroke, R. Riedel, T. Saitou, and K. Matsunaga, *J. Am. Ceram. Soc.* 84, 2170 (2001).
272. M. L. Kosinova, N. I. Fainer, Y. M. Romyantsev, M. Terauchi, K. Shibata, F. Satoh, M. Tanaka, and F. A. Kuznetsov, *J. Phys. IV* 11, 987 (2001).
273. N. I. Fainer, M. L. Kosinova, Y. M. Romyantsev, and F. A. Kuznetsov, *J. Phys. IV* 9, 769 (1999).
274. H. T. Chiu, C. S. Shie, and S. H. Chuang, *J. Mater. Res.* 10, 2257 (1995).
275. H. Aono, M. Sato, E. Traversa, M. Sakamoto, and Y. Sadaoka, *J. Am. Ceram. Soc.* 84, 341 (2001).
276. M. Wu and X. Li, *J. Solid State Chem.* 151, 56 (2000).
277. M. J. Crosbie, P. J. Wright, H. O. Davies, A. C. Jones, T. J. Leedham, P. O'Brien, and G. W. Critchlow, *Chem. Vap. Deposition* 5, 9 (1999).
278. A. C. Jones, H. O. Davies, T. J. Leedham, P. J. Wright, M. J. Crosbie, A. Steiner, J. F. Bickley, P. O'Brien, A. J. P. White, and D. J. Williams, *J. Mater. Chem.* 11, 544 (2001).
279. H. S. Potdar and S. B. Deshpande, *Mater. Chem. Phys.* 65, 178 (2000).
280. G. C. Jun, S. L. Cho, K. B. Kim, H. K. Shin, and D. H. Kim, *Jpn. J. Appl. Phys.* 37, L30 (1998).
281. S. Tudyka, K. B. Pflanz, F. Aldinger, H. Borrmann, P. Fischer, and H. Brunner, *Z. Anorg. Allg. Chem.* 623, 1163 (1997).
282. S. G. Shyu, C. S. Wu, Y. S. Sung, and K. M. Chi, *J. Am. Ceram. Soc.* 82, 1436 (1999).
283. S. M. Sim and K. A. Keller, *J. Mater. Sci.* 35, 713 (2000).
284. S. Mathur, M. Veith, R. Rapalaviciute, and H. Shen, manuscript in preparation.
285. S. Mathur and M. Veith, to be published.
286. S. Mathur, M. Veith, M. Haas, H. Shen, N. Lecerf, V. Huch, S. Hüfner, R. Haberkorn, H. P. Beck, and M. Jilavi, *J. Am. Ceram. Soc.* 84, 1921 (2001).
287. N. Lecerf, personal communication.
288. R. Nomura, H. Matsuda, T. Miyai, and A. Baba, *Thin Solid Films* 342, 108 (1999).
289. S. Zurcher, M. Morstein, N. D. Spencer, M. Lemberger, and A. Bauer, *Chem. Vap. Deposition* 8, 171 (2002).
290. G. M. Brown and L. Maya, *J. Am. Ceram. Soc.* 71, 78 (1988).
291. H. Jungermann and M. Jansen, *Mater. Res. Innov.* 2, 200 (1999).
292. Y. Kim, H. K. Chae, K. S. Lee, and W. I. Lee, *J. Mater. Chem.* 8, 2317 (1998).
293. B. Chansou, R. Choukroun, and L. Valade, *Appl. Organomet. Chem.* 11, 195 (1997).
294. J. P. Carpenter, C. M. Lukehart, S. B. Milne, D. O. Henderson, R. Mu, and S. R. Stock, *Chem. Mater.* 9, 3164 (1997).
295. C. G. Lugmair, K. L. Furdala, and T. D. Tilley, *Chem. Mater.* 14, 888 (2002).
296. L.-G. Hubert-Pfalzgraf, C. Sirio, and C. Bois, *Polyhedron* 17, 821 (1998).
297. C. K. Narula, W. H. Weber, J. Y. Ying, and L. F. Allard, *J. Mater. Chem.* 7, 1821 (1997).
298. M. Veith, S. Kneip, S. Faber, and E. Fritscher, *Mater. Sci. Forum* 269–272, 303 (1998).
299. K. W. Terry, C. G. Lugmair, P. K. Gantzel, and T. D. Tilley, *Chem. Mater.* 8, 274 (1996).
300. G. Westin, M. Wijk, M. Moustiakimov, and M. Kritikos, *J. Sol-Gel Sci. Technol.* 13, 125 (1998).
301. K. W. Terry, C. G. Lugmair, and T. D. Tilley, *J. Am. Chem. Soc.* 119, 9745 (1997).
302. S. Faber, Ph.D. Thesis, Saarland University, Germany 1996.
303. J. P. Carpenter, C. M. Lukehart, D. O. Henderson, R. Mu, B. D. Jones, R. Glosser, S. R. Stock, J. E. Wittig, and J. G. Zhu, *Chem. Mater.* 8, 1268 (1996).
304. M. Rajamathi, S. Thimmaiah, P. E. D. Morgan, and R. Seshadri, *J. Mater. Chem.* 11, 2489 (2001).
305. M. Veith, S. Mathur, N. Lecerf, H. Shen, and S. Hüfner, *Chem. Mater.* 11, 3103 (1999).
306. B. Heinrichs and F. Noville, *J. Catal.* 170, 366 (1997).
307. D. Seyferth and C. Strohmann, *Chem. Mater.* 7, 2058 (1995).
308. A. Haoudi, P. Dhamelincourt, A. Mazzah, M. Drache, and P. Conflant, *Int. J. Inorg. Mater.* 3, 357 (2001).
309. R. Murugavel, in "Advances in Metallo-Organic Chemistry" (R. Bohra, Ed.), p. 77. RBSA Publishers, India 1999.
310. A. Haoudi, P. Dhamelincourt, A. Mazzah, M. Drache, P. Conflant, and M. Lazraq, *J. Mater. Chem.* 10, 1001 (2000).
311. M. P. Coles, C. G. Lugmair, K. W. Terry, and T. D. Tilley, *Chem. Mater.* 12, 122 (2000).
312. C. K. Narula, A. Varshney, and U. Riaz, *Chem. Vap. Deposition* 2, 13 (1996).
313. R. Rulkens, J. L. Male, K. W. Terry, B. Olthof, A. Khodakov, A. T. Bell, E. Iglesia, and T. D. Tilley, *Chem. Mater.* 11, 2966 (1999).
314. S. Mathur, M. Veith, and D. Nicole, unpublished results.
315. S. Mathur and M. Veith, manuscript submitted for publication.
316. J. Zhang, G. T. Stauf, R. Gardiner, P. van Buskirk, and J. Steinbeck, *J. Mater. Res.* 9, 1333 (1994).
317. J. A. Meese-Marktscheffel, R. Fukuchi, M. Kido, G. Tachibana, C. M. Jensen, and J. W. Gilje, *Chem. Mater.* 5, 755 (1993).
318. J. Sassmannshausen, R. Riedel, K. B. Pflanz, and H. Z. Chmiel, *Z. Naturforsch.* 48, 7 (1993).
319. M. Veith, S. Mathur, and C. Mathur, *Polyhedron* 17, 1005 (1998).
320. M. Veith, A. Altherr, and H. Wolfanger, *Chem. Vap. Deposition* 5, 87 (1999).
321. S. Mathur and H. Shen, to be published.
322. T. P. Hanusa, *Chem. Rev.* 93, 1023 (1993).
323. L. G. Hubert-Pfalzgraf, *Polyhedron* 13, 1181 (1994).
324. W. A. Herrmann, N. W. Huber, and T. Priermeier, *Angew. Chem.* 106, 102 (1994).
325. M. Veith, *Chem. Rev.* 90, 3 (1990).
326. D. C. Bradley, R. C. Mehrotra, and D. P. Gaur, "Metal Alkoxides." Academic Press, London 1978.
327. A. C. Jones, *Chem. Vapor Deposition* 4, 169 (1998).
328. T. J. Boyle, R. P. Tyner, T. M. Alam, B. L. Scott, Z. W. Ziller, and B. G. Potter, *J. Am. Chem. Soc.* 121, 12104 (1999).
329. B. Morar, N. Hüsing, C. Kickelbick, U. Schubert, P. Fratzl, and H. Peterlik, *Chem. Mater.* 14, 2732 (2002).
330. W. M. Cleaver, M. Späth, D. Hoyk, G. McMurdo, M. B. Power, M. Stuke, D. W. H. Rankin, and A. R. Barron, *Organometallics* 14, 690 (1995).
331. M. Veith, S. Mathur, V. Huch, and T. Decker, *Eur. J. Inorg. Chem.* 1327 (1998).
332. M. Veith, S. Mathur, N. Lecerf, V. Huch, and T. Decker, *J. Sol-Gel Sci. Technol.* 15, 145 (2000).
333. R. West, in "Ultrastructure Processing of Ceramics, Glasses and Composites" (L. L. Hench and D. R. Ulrich, Eds.), p. 235. Wiley-Interscience, New York 1984.

334. L. C. Klein, "Sol-Gel Technology for Thin Films, Fibers, Preforms, Electronics and Specialty Shapes." Noyes Publications, Park Ridge, NJ 1988.
335. C. Sanchez, F. Ribot, and B. Lebeau, *J. Mater. Chem.* 9, 35 (1999).
336. J. Livage, *Mater. Sci. Forum* 152-153, 43 (1994).
337. S. Komarneni, *J. Mater. Chem.* 2, 1219 (1992).
338. S. Komarneni, *J. Sol-Gel Sci. Technol.* 6, 127 (1996).
339. J. H. Schulman, W. Stocckenius, and L. M. Prince, *J. Phys. Chem.* 63, 1977 (1959).
340. J. Wang, J. Fang, S.-C. Ng, L.-M. Gan, C.-H. Chew, X. Wang, and Z. Shen, *J. Am. Ceram. Soc.* 82, 873 (1999).
341. M. L. Steigerwald, A. Alivisatos, J. M. Gibson, T. D. Harris, R. Kortan, A. J. Muller, A. M. Thayer, T. M. Duncan, D. C. Douglass, and L. E. Brus, *J. Am. Ceram. Soc.* 110, 3046 (1998).
342. P. D. Moran, J. R. Bartlett, G. A. Bowmaker, J. L. Woolfrey, and R. P. Cooney, *J. Sol-Gel Sci. Technol.* 15, 251 (1999).
343. G. K. Lim, J. Wang, S. C. Ng, and L. M. Gan, *Langmuir* 15, 7472 (1999).
344. M. Maugey and A.-M. Bellocq, *Langmuir* 15, 8602 (1999).
345. S. P. Moulik, G. C. De, A. K. Panda, B. B. Bhowmik, and A. R. Das, *Langmuir* 15, 8361 (1999).
346. H. S. Lee and W. C. Lee, *J. Appl. Phys.* 85, 5231 (1999).
347. L. Porcar and J. Marignan, *J. Sol-Gel Sci. Technol.* 13, 99 (1999).
348. M. Roth and R. Hempelmann, *J. Mater. Chem.* 9, 493 (1999).
349. M. Li, H. Schnablegger, and S. Mann, *Nature* 402, 393 (1999).
350. J. Fang, J. Wang, S. C. Ng, C. H. Chew, and L. M. Gan, *J. Mater. Sci.* 34, 1943 (1999).
351. W. B. Ng, J. Wang, S. C. Ng, and L. M. Gan, *J. Am. Ceram. Soc.* 82, 529 (1999).
352. H. Herrig and R. Hempelmann, *Mater. Lett.* 27, 287 (1996).
353. K. Osseo-Asare and F. J. Arriagada, in "Better Ceramics Through Chemistry III" (C. J. Brinker, D. E. Clark, and D. R. Ulrich, Eds.). Materials Research Society, Pittsburgh 1988.
354. P. D. Moran, J. R. Bartlett, J. L. Woolfrey, G. A. Bowmaker, and R. P. Cooney, in "Ceramic Transaction: Ceramic Processing Science and Technology" (H. Hausner, G. L. Messing, and S. Hirano, Eds.). American Ceramic Society, Westerville, OH 1995.
355. M. P. Pechini, U.S. Patent 3330694, 1967.
356. P. A. Lessing, *Ceram. Bull.* 68, 1002 (1998).
357. N. G. Eror and H. U. Anderson, in "Better Ceramics Through Chemistry II," Materials Research Society Symposia Proceedings (C. J. Brinker, D. E. Clark, and D. R. Ulrich, Eds.), p. 571. Materials Research Society, Pittsburgh 1996.
358. M. Veith, S. Mathur, A. Kareiva, M. Jilavi, M. Zimmer, and V. Huch, *J. Mater. Chem.* 9, 3069 (1999).
359. A. Ikesue, K. Yoshida, and K. Kamata, *J. Am. Ceram. Soc.* 79, 507 (1996).
360. J. M. Yang, S. M. Jeng, and S. Chang, *J. Am. Ceram. Soc.* 79, 1218 (1996).
361. M. A. Gülgün, O. O. Popolla, and W. M. Kriven, *J. Am. Ceram. Soc.* 77, 531 (1994).
362. R. M. Laine, D. R. Treadwell, B. L. Mueller, C. R. Bickmore, K. F. Waldner, and T. R. Hinklin, *J. Mater. Chem.* 6, 1441 (1996).
363. C. R. Bickmore, K. F. Waldner, D. R. Treadwell, and R. M. Laine, *J. Am. Ceram. Soc.* 79, 1419 (1996).
364. R. Narayanan and R. M. Laine, *Appl. Organomet. Chem.* 11, 919 (1997).
365. E. Matijevic, *Acc. Chem. Res.* 14, 22 (1981).
366. E. Matijevic, *Chem. Mater.* 5, 412 (1993).
367. M. Stockenhuber, H. Mayer, and J. A. Lercher, *J. Am. Ceram. Soc.* 76, 1185 (1993).
368. J. Lee, T. Isobe, and M. Senna, *Colloids Surf. A* 109, 121 (1996).
369. M. Dechamps, B. Diuricic, and S. J. Pickering, *J. Am. Ceram. Soc.* 78, 2873 (1995).
370. M. Hasegawa, *Ceram. Forum Int.* 70, 490 (1993).
371. T. Kodama, M. Ookubo, S. Miura, and Y. Kitayama, *Mater. Res. Bull.* 31, 1501 (1996).
372. J. Gang, Y. Feng, L. Mingqiang, and L. Jinhuai, *Sensors* 2, 71 (2002).
373. J. Lin and J. Duh, *J. Am. Ceram. Soc.* 80, 92 (1997).
374. L. Wang, Y. Zhang, and M. Muhammed, *J. Mater. Chem.* 5, 309 (1995).
375. C. D. Sagel-Ransijn, A. J. A. Winnubst, A. J. Burgraaf, and H. Verweij, in "Ceramic Transactions," Vol. 51, Ceramic Processing Science and Technology (H. Hausner, G. L. Messing, and S. Hirano, Eds.), p. 33. American Ceramic Society, Westerville, OH, 1995.
376. D. Barb, L. Diamandescu, A. Rusi, D. Tarabasani-Mihaila, M. Morariu, and V. Teodorescu, *J. Mater. Sci.* 21, 1118 (1986).
377. G. Demazeau, *J. Mater. Chem.* 9, 15 (1999).
378. Q. Feng, H. Kanoh, Y. Miyai, and K. Ooi, *Chem. Mater.* 7, 1226 (1995).
379. K. Yanagisawa, *J. Mater. Sci. Lett.* 12, 1842 (1993).
380. S. Somiya, Ed., "Hydrothermal Preparation of Fine Powders, Advanced Ceramics III." Elsevier Applied Science Publishers, UK 1990.
381. A. Wang, F. Capitain, V. Monnier, S. Matar, and G. Demazeau, *J. Mater. Synth. Proc.* 5, 235 (1997).
382. M. Wu, X. Li, G. Shen, J. Li, R. Xu, and D. M. Proseripos, *J. Solid State Chem.* 151, 56 (2000).
383. G. B. Stringfellow, "Organometallic Vapor-Phase Epitaxy: Theory and Practice." Academic Press, New York 1989.
384. H. O. Pierson, "Handbook of Chemical Vapour Deposition." Noyes Publications, Park Ridge, NJ 1992.
385. W. S. Rees, Jr., "CVD of Nonmetals." Wiley, New York 1996.
386. T. T. Kodas and M. J. Hampden-Smith, in "The Chemistry of Metal CVD" (T. T. Kodas and M.-J. Hampden-Smith, Eds.). VCH, Weinheim, 1994.
387. M.-J. Hampden-Smith and T. T. Kodas, *Chem. Vapor Deposition* 1, 39 (1995).
388. G. Schmid, *J. Chem. Soc., Dalton Trans.* 1077 (1998).
389. A. S. Lisitsyn, A. V. Golovin, A. L. Chuvilin, V. L. Kuznetsov, A. V. Romanenko, A. F. Danilyuk, and Y. I. Yermakov, *Appl. Catal.* 55, 235 (1989).
390. J. Chaiken, *Chem. Ind.* 751 (1993).
391. J. H. Fendler and F. C. Feldrum, *Adv. Mater.* 7, 607 (1995).
392. P. H. Hess and P. Parker, *J. Appl. Polym. Sci.* 10, 1915 (1996).
393. E. Papirer, P. Horny, H. Balard, R. Anthore, C. Petipas, and A. Martinet, *J. Colloid Interface Sci.* 94, 207 (1983).
394. S. Sun and C. B. Murray, *J. Appl. Phys.* 85, 4325 (1999).
395. C. B. Murray, C. R. Kagan, and M. G. Bawendi, *Science* 270, 1335 (1995).
396. X. Peng, J. Wickham, and A. Alivisatos, *J. Am. Chem. Soc.* 120, 5343 (1998).
397. F. Fievet, J. P. Lagier, and M. Figlarz, *MRS Bull.* 14, 29 (1989).
398. G. M. Chow, L. K. Kurihara, K. M. Kemner, P. E. Schoen, W. T. Elam, A. Ervin, S. Keller, Y. D. Zhang, J. Budnick, and T. Ambrose, *J. Mater. Res.* 10, 1546 (1995).
399. J. S. Yin and Z. L. Wang, *J. Phys. Chem., B* 101, 8979 (1997).
400. B. M. Berkovskii and V. G. Bashtovio, "Magnetic Fluids and Applications." Begell House, New York 1996.
401. C. B. Murray, S. Sun, H. Doyle, and T. Betley, *MRS Bull.* 26, 985 (2001).
402. D. V. Berkov, P. Gornert, N. Buske, C. Gansau, J. Mueller, M. Giersig, W. Neumann, and D. Su, *J. Phys. D: Appl. Phys.* 33, 331 (2000).
403. C. B. Murray, *Phys. Rev. B* 64, 7913 (2001).
404. K. S. Suslick, T. Hyeon, and M. Fang, *Chem. Mater.* 8, 2172 (1996).
405. K. S. Suslick, in "Encyclopedia of Materials Science and Engineering" (R. W. Cahn, Ed.). Pergamon, Oxford 1993.
406. R. Kaplan and N. Bottka, *Appl. Phys. Lett.* 41, 972 (1982).
407. A. D. Berry, D. J. Brown, R. Kaplan, and E. Cukauskus, *J. Vac. Sci. Technol., A* 4, 215 (1986).

408. E. P. Boyd, D. R. Ketchum, H. Deng, and S. G. Shore, *Chem. Mater.* 9, 1154 (1997).
409. M. L. Hitchman and K. F. Jensen, "Chemical Vapour Deposition: Principles and Applications." Academic, San Diego 1993.
410. P. M. Jeffries and G. S. Girolami, *Chem. Mater.* 1, 8 (1989).
411. B. E. Bent, R. G. Nuzzo, and L. H. Dubois, *J. Am. Chem. Soc.* 111, 1634 (1989).
412. M. M. Banaszek Holl, P. F. Seidler, S. P. Kowalczyk, and F. R. McFeely, *Inorg. Chem.* 33, 510 (1994).
413. W. L. Gladfelter, *Chem. Mater.* 5, 1372 (1993).
414. T. Hanrath and B. A. Korgel, *J. Am. Chem. Soc.* 124, 1424 (2002).
415. Y. Wu, H. Q. Yan, M. Huang, B. J. Messer, J. H. Song, and P. D. Yang, *Chem. Eur. J.* 8, 1261 (2002).
416. Y. Wu and P. D. Yang, *Adv. Mater.* 13, 520 (2001).
417. H. Yang and X. Wang, *J. Cryst. Growth* 236, 371 (2002).
418. Y. Wu and P. D. Yang, *Appl. Phys. Lett.* 77, 43 (2000).
419. Y. Wu and P. D. Yang, *Chem. Mater.* 12, 605 (2000).
420. J. ElBoucham, F. Maury, and R. Morancho, *J. Anal. Appl. Pyrolysis* 44, 153 (1998).
421. S. Mathur, H. Shen, and V. Sivakov, *Chem. Mater.*, in press.
422. J. L. Lin, D. Y. Petrovykh, A. Kirakosian, H. Rauscher, J. F. Himpfel, and P. A. Dowben, *Appl. Phys. Lett.* 78, 829 (2001).
423. B. E. Yoldas, *Am. Ceram. Soc. Bull.* 54, 286 (1975).
424. B. Ao, L. Kummerl, and D. Harrer, *Adv. Mater.* 7, 495 (1995).
425. H. Hibst, *J. Magn. Magn. Mater.* 74, 173 (1988).
426. F. N. Bradley, "Materials for Magnetic Functions." Hayden, New York 1976.
427. H. Sun, C. Cantalini, M. Faccio, M. Pelino, M. Catalano, and L. Tapfer, *J. Am. Ceram. Soc.* 79, 927 (1996).
428. S. Mathur, M. Veith, V. Sivakov, H. Shen, V. Huch, U. Hartmann, and H. B. Gao, *Chem. Vap. Deposition* 8, 277 (2002).
429. J. S. Miller, *Adv. Mater.* 14, 1105 (2002).
430. V. S. Arunachalam and E. L. Fleischer, *MRS Bull.* 26, 1020 (2001).
431. C. Pascal, J. L. Pascal, F. Favier, M. L. Elidrissi Moubtassim, and C. Payen, *Chem. Mater.* 11, 141 (1999).
432. P. Matteazzi and G. Le Caer, *Mater. Sci. Eng., A* 149, 135 (1991).
433. Z. X. Tang, S. Nafis, C. M. Sorensen, G. C. Hadjipanayis, and K. J. Klabunde, *J. Magn. Magn. Mater.* 80, 285 (1998).
434. S. Dhara, A. C. Rastogi, and B. K. Das, *Thin Solid Films* 239, 240 (1994).
435. K. Kandori, N. Ohkasi, A. Yasukawa, and I. Ishikawa, *J. Mater. Res.* 13, 1698 (1998).
436. M. P. Morales, C. de Julien, J. M. Gonzalez, and C. J. Serna, *J. Mater. Res.* 9, 135 (1994).
437. M. P. Morales, J. M. Gonzalez, and C. J. Serna, *J. Mater. Res.* 7, 2538 (1992).
438. M. V. Cabanas, M. Vallet-Regi, M. Labeau, and J. M. Gonzalez-Calbet, *J. Mater. Res.* 8, 2694 (1993).
439. M. Veith, F. Grätz, and V. Huch, *Eur. J. Inorg. Chem.* 367 (2001).
440. R. C. Mehrotra, A. Singh, and U. M. Tripathi, *Chem. Rev.* 91, 1287 (1991).
441. W. A. Herrmann, A. Egli, E. Herdtweck, R. Alberto, and F. Baumgärtner, *Angew. Chem.* 108, 486 (1996).
442. S. Mathur, H. Shen, N. Lecerf, M. H. Jilavi, V. Cauniene, J.-E. Jorgensen, and A. Kareiva, *J. Sol-Gel Sci. Technol.* 24, 57 (2002).
443. D. C. Bradley, *Chem. Rev.* 89, 1317 (1989).
444. T. Brousse, G. Poullain, J. F. Hamet, H. Murray, and B. Raveau, *Physica C* 170, 545 (1990).
445. G. F. Goya, M. Veith, R. Rapalaviciute, H. Shen, and S. Mathur, to be published.
446. B. O. Regan and M. Graetzel, *Nature* 353, 737 (1991).
447. I. Sopyan, M. Watanabe, S. Murasawa, K. Hashimoto, and A. Fujishima, *Chem. Lett.* 69 (1996).
448. W. T. Pawlewicz, G. J. Exarhos, and W. E. Conaway, *Appl. Opt.* 22, 1837 (1983).
449. R. Asahi, T. Morikawa, T. Ohwaki, K. Aoki, and Y. Taga, *Science* 293, 269 (2001).
450. S. Malato, S. Blanco, C. Richter, and M. I. Maldonado, *Appl. Catal., B* 25, 31 (2000).
451. C. S. Turchi and D. F. Ollis, *J. Catal.* 122, 178 (1990).
452. M. Ranchella, C. Rol, and G. V. Sebastiani, *J. Chem. Soc., Perkin Trans. 2*, 311 (2000).
453. Q. Xu and M. A. Anderson, *J. Am. Ceram. Soc.* 77, 1939 (1994).
454. V. J. Nagpal, R. M. Davis, and S. B. Desu, *J. Mater. Res.* 10, 3068 (1995).
455. R. Zhang and L. Gao, *Mater. Res. Bull.* 36, 1957 (2001).
456. K. I. Gnanasekar, V. Subramanian, J. Robinson, J. C. Jiang, F. E. Posey, and B. Rambabu, *J. Mater. Res.* 17, 1507 (2002).
457. L. Banyai and S. W. Koch, "Semiconductor Quantum Dots." World Scientific, Singapore 1993.
458. U. Waggon, "Optical Properties of Semiconductor Quantum Dots." Springer-Verlag, Berlin 1997.
459. T. Vossmeier, L. Katsikas, M. Giersig, I. G. Popovic, K. Diesner, A. Chemseddine, A. Eychmüller, and H. Weller, *J. Phys. Chem.* 98, 7665 (1994).
460. T. Trindade, P. O'Brien, X. Zhang, and M. Motevalli, *J. Mater. Chem.* 7, 1011 (1997).
461. N. Herron, J. C. Calabrese, W. E. Farneth, and Y. Yang, *Science* 259, 1426 (1993).
462. T. Lover, W. Henderson, G. Bowmaker, J. M. Seakins, and R. P. Cooney, *Inorg. Chem.* 36, 3711 (1997).
463. N. Herron, A. Suna, and Y. Wang, *J. Chem. Soc., Dalton Trans.* 2329 (1992).
464. A. H. Cowley and R. A. Jones, *Polyhedron* 13, 1149 (1994).
465. P. O'Brien and R. Nomura, *J. Mater. Chem.* 5, 1761 (1995).
466. S. Nakamura, S. Pearton, and G. Fasol, "The Blue Laser Diode: The Complete Story." Springer-Verlag, Berlin/New York 2000.
467. J. McMurran, J. Kouvetakis, and D. J. Smith, *Appl. Phys. Lett.* 74, 883 (1999).
468. J. Müller and S. Bendix, *Chem. Commun.* 911 (2001).
469. H. Winkler, A. Devi, A. Manz, A. Wohlfart, W. Rogge, and R. A. Fischer, *Phys. Status Solidi A* 177, 27 (2000).
470. A. C. Jones, C. R. Whitehouse, and J. S. Robert, *Chem. Vap. Deposition* 1, 65 (1995).
471. D. A. Neumayer and J. G. Ekerdt, *Chem. Mater.* 8, 9 (1996).
472. J. F. Janik and R. L. Wells, *Chem. Mater.* 8, 2708 (1996).
473. J.-W. Hwang, J. P. Compbell, J. Kozubowski, S. A. Hanson, J. F. Evans, and W. L. Gladfelter, *Chem. Mater.* 7, 517 (1995).
474. K. E. Gonsalves, G. Carlson, S. P. Rangarajan, M. Benaissa, and M. J. Jose-Yacamán, *J. Mater. Chem.* 6, 1451 (1996).
475. R. A. Fischer, A. Miehr, E. Herdtweck, M. R. Mattner, O. Ambacher, T. Metzger, E. Born, S. Weinkauff, C. R. Pulham, and S. Parsons, *Chem. Eur. J.* 2, 1353 (1996).
476. M. M. Sung, C. Kim, S. H. Yoo, C. G. Kim, and Y. Kim, *Chem. Vap. Deposition* 8, 50 (2002).
477. F. Maury and G. Constant, *Polyhedron* 3, 581 (1984).
478. F. Maury, G. Constant, P. Fontaine, and J. P. Biberian, *J. Cryst. Growth* 78, 185 (1986).
479. F. Maury and G. Constant, *J. Cryst. Growth* 62, 568 (1983).
480. F. Maury, A. E. Hammadi, and G. Constant, *J. Cryst. Growth* 68, 88 (1984).
481. A. E. Hammadi, F. Maury, G. Muller, J. Bensoam, and G. Constant, *C. R. Acad. Sci. Paris, Ser. II* 299, 1255 (1984).
482. F. Maury and A. E. Hammadi, *J. Cryst. Growth* 91, 97 (1988).
483. F. Maury and A. E. Hammadi, *J. Cryst. Growth* 91, 105 (1988).
484. A. H. Cowley, R. A. Jones, M. A. Mardones, and C. M. Nunn, *Organometallics* 10, 1635 (1991).
485. J. E. Miller, K. B. Kidd, A. H. Cowley, A. C. Jones, J. G. Ekerdt, H. J. Gysling, A. A. Wernberg, and T. N. Blanton, *Chem. Mater.* 2, 589 (1990).
486. A. H. Cowley, A. C. Jones, M. A. Mardones, and C. M. Nunn, *Organometallics* 10, 1635 (1991).
487. A. N. Gleizes, *Chem. Vap. Deposition* 6, 155 (2000).

488. K. W. Benz, H. Renz, J. Weidlein, and M. H. Pilkuhn, *J. Electron. Mater.* 10, 185 (1981).
489. A. Zaouk, E. Salvatat, J. Sakaya, F. Maury, and G. Constant, *J. Cryst. Growth* 55, 135 (1981).
490. F. Maury, M. Combes, G. Constant, R. Carles, and J. B. Benucci, *J. Phys. C1* (Suppl. 10), 347 (1982).
491. F. Maury, M. Combes, and G. Constant, in "Proceedings of EUROCV4" (J. Bloem, G. Verspui, and L. R. Wolff, Eds.), Philips Centre for Manufacturing Technology, Eindhoven, the Netherlands 1983.
492. K. A. Aitchison, J. D. J. Backer-Dirks, D. C. Bradley, M. M. Faktor, D. M. Frigo, M. B. Hursthouse, B. Hussain, and R. L. Short, *J. Organomet. Chem.* 366, 11 (1989).
493. F. Maury, *Adv. Mater.* 3, 542 (1991).
494. F. Maury, in "Transformation of Organometallics into Common and Exotic Materials: Design and Activation" (R. M. Laine, Ed.), NATO ASI Series E, p. 195. Martinus Nijhoff, the Netherlands 1988.
495. A. H. Cowley, B. L. Benac, J. G. Ekerdt, A. C. Jones, K. B. Kidd, J. Y. Lee, and J. E. Miller, *J. Am. Chem. Soc.* 110, 6248 (1988).
496. J. E. Miller and J. G. Ekerdt, *Chem. Mater.* 4, 7 (1992).
497. J. G. Ekerdt, Y. M. Sun, M. S. Jackson, V. Lakhota, K. A. Pacheco, S. U. Koschmieder, A. H. Cowley, and A. C. Jones, *J. Cryst. Growth* 124, 158 (1992).
498. A. H. Cowley, A. C. Jones, C. M. Null, and D. L. Westmorland, *Chem. Mater.* 2, 221 (1990).
499. J. Shin, A. Verma, G. B. Stringfellow, and R. W. Gedridge, *J. Cryst. Growth* 143, 15 (1994).
500. S. H. Li, C. A. Larsen, G. B. Stringfellow, and R. W. Gedridge, *J. Elect. Mater.* 20, 457 (1991).
501. R. W. Rice, *Am. Ceram. Soc. Bull.* 62, 889 (1982).
502. S. Yajima, K. Okamura, J. Hayashi, and M. Omori, *J. Am. Ceram. Soc.* 59, 324 (1975).
503. M. Peuckert, T. Vaahs, and M. Brück, *Adv. Mater.* 2, 398 (1990).
504. N. Auner and J. Weis, "Organosilicon Chemistry IV: From Molecules to Materials." Wiley Europe 2000.
505. G. E. Legrow, T. F. Lim, J. Lipowitz, and R. S. Reaach, *Am. Ceram. Soc. Bull.* 66, 363 (1987).
506. C. R. Blanchard and S. T. Schwab, *J. Am. Ceram. Soc.* 77, 1729 (1994).
507. K. J. Wynne and R. W. Rice, *Annu. Mater. Sci.* 14, 297 (1984).
508. M. Arai, S. Sakurada, T. Isoda, and T. Tomizawa, *Polym. Prepr.* 34, 286 (1993).
509. K. B. Schwartz, D. J. Rowcliffe, Y. D. Blum, and R. M. Laine, 407 (1986).
510. F. Maseeh and S. D. Senturia, *Sens. Actuators, A* 23, 861 (1990).
511. K. W. Lee, K. S. Yu, and Y. Kim, *J. Cryst. Growth* 179, 153 (1997).
512. C. R. Stoldt, M. C. Fritz, C. Carraro, and R. Maboudian, *Appl. Phys. Lett.* 79, 347 (2001).
513. J. Schlichting, *Powder Met. Ind.* 12, 141 (1980).
514. L. V. Interrante, D. J. Larkin, and C. Amato, *Mater. Res. Soc. Symp. Proc.* 250, 283 (1992).
515. B. Han and J. B. Hudson, *Mater. Res. Soc. Symp. Proc.* 282, 457 (1993).
516. S. Yajima, J. Hayashi, M. Omori, and K. Okamura, *Nature* 261, 683 (1976).
517. S. Yajima, T. Shishido, and H. Kayano, *Nature* 73, 525 (1978).
518. S. Yajima, *Am. Ceram. Soc. Bull.* 62, 893 (1983).
519. Z. F. Zhang, C. S. Scotto, and R. M. Laine, *J. Mater. Chem.* 8, 2715 (1998).
520. Z. F. Zhang, F. Babonneau, R. M. Laine, Y. Mu, J. F. Harrod, and J. A. Rahn, *J. Am. Ceram. Soc.* 74, 670 (1990).
521. D. Seyferth, T. G. Wood, H. J. Tracy, and J. L. Robinson, *J. Am. Ceram. Soc.* 75, 1300 (1992).
522. D. Seyferth and H. Lang, *Organometallics* 10, 151 (1991).
523. T. Kobayashi, T. Sakakura, T. Hayashi, M. Yumura, and M. Tanaka, *Chem. Lett.* 1157 (1992).
524. L. V. Interrante, C. W. Whitmarsh, W. Sherwood, H.-J. Wu, R. Lewis, and G. Maciell, in "Hydridopolycarbosilane Precursors to Silicon Carbide: Synthesis, Pyrolysis and Application as a SiC Matrix Source" (J. F. Harrod, and R. M. Laine, Eds.), NATO ASI Series E, p. 173. Kluwer Academic Publishers, Dordrecht, the Netherlands 1995.
525. Y. B. Blum, K. B. Schwartz, and R. M. Laine, *J. Mater. Sci.* 24, 1707 (1989).
526. D. Seyferth and G. H. Wiseman, *J. Am. Ceram. Soc.* 67, 132 (1984).
527. D. Seyferth, G. H. Wiseman, and C. Prudhomme, *Mater. Sci. Rev.* 17, 263 (1984).
528. H. Saitoh and W. A. Yarbrough, *Diamond Relat. Mater.* 1, 137 (1992).
529. O. Mishima, K. Era, J. Tanaka, and S. Yamaoka, *Appl. Phys. Lett.* 53, 962 (1988).
530. C. Comez-Aleixandre, A. Essafi, M. Fernandez, J. L. G. Fierro, and J. M. Albella, *J. Phys. Chem.* 100, 2148 (1996).
531. J. M. Thomas and W. J. Thomas, "Principles and Practice of Heterogeneous Catalysis." Wiley-VCH, Weinheim 1997.
532. B. C. Gates, *Chem. Rev.* 95, 511 (1995).
533. D. M. Somerville and J. R. Shapley, *Catal. Lett.* 52, 123 (1998).
534. M. S. Nasher, A. I. Frenkel, D. L. Adler, J. R. Shapley, and R. G. Nuzzo, *J. Am. Chem. Soc.* 119, 7760 (1997).
535. R. S. Williams, *Appl. Surf. Sci.* 60-61, 613 (1992).
536. Y. J. Chen, H. D. Kaesz, Y. K. Kim, H. J. Müller, R. S. Williams, and Z. Xue, *Appl. Phys. Lett.* 55, 2760 (1989).
537. F. Maury, L. Brandt, and H. D. Kaesz, *J. Organomet. Chem.* 449, 159 (1993).
538. B. Fraser, L. Brandt, W. K. Stovall, H. D. Kaesz, and S. I. Khan, *J. Organomet. Chem.* 472, 317 (1994).
539. R. A. Fischer and A. Miehr, *Chem. Mater.* 8, 497 (1996).
540. R. A. Fischer, A. Miehr, and M. M. Schulte, *Adv. Mater.* 7, 58 (1995).
541. A. Miehr, R. A. Fischer, O. Lehmann, and M. Stuke, *Adv. Mater. Opt. Electron.* 6, 27 (1996).
542. R. A. Fischer, A. Miehr, M. M. Schulte, and E. Herdtweck, *Chem. Commun.* 337 (1995).
543. J. W. Mellor, *Trans. Ceram. Soc.* 36, 1 (1937).
544. J. A. Hedvall and J. Heuberger, *Z. Anorg. Chem.* 116, 137 (1921).
545. G. F. Goya and H. R. Rechenberg, *J. Appl. Phys.* 84, 1101 (1998).
546. W. W. Cross, L. Affleck, M. V. Koznetsov, I. P. Parkin, and Q. A. Pankhurst, *J. Mater. Chem.* 9, 2545 (1999).
547. M. A. Valenzuela, P. Bosch, G. Aguilar-Rios, A. Montoya, and I. Schifter, *J. Sol-Gel Sci. Technol.* 8, 107 (1997).
548. M. Zayat and D. Levy, *Chem. Mater.* 12, 2763 (2000).
549. M. Hirano, M. Imai, and M. Inagaki, *J. Am. Ceram. Soc.* 83, 977 (2000).
550. S. Mathur and H. Shen, in "Nanoscience and Nanoengineering" (D. Dascalu and I. Kleps, Eds.). Romanian Academy of Science, Bucharest 2003.
551. D. C. Bradley, R. C. Mehrotra, I. Rothwell, and A. Singh, "Alkoxo and Aryloxo Derivatives of Metals." Academic Press, London 2001.
552. S. K. Sampath and J. F. Cordaro, *J. Am. Ceram. Soc.* 81, 649 (1998).
553. Th. El-Nabarawy, A. A. Attia, and M. N. Alaya, *Mater. Lett.* 24, 319 (1995).
554. S. Music, S. Popovic, I. Czakonagy, and F. Gashi, *Mater. Sci. Lett.* 12, 869 (1993).
555. D. S. Schmool, N. Keller, M. Guyot, R. Krishnan, and M. Tessier, *J. Magn. Magn. Mater.* 195, 291 (1999).
556. D. S. Schmool, N. Keller, M. Guyot, R. Krishnan, and M. Tessier, *J. Appl. Phys.* 86, 5712 (1999).
557. H. Kominami and H. Inoue, *J. Am. Ceram. Soc.* 85, 2148 (1990).



558. E. Traversa, M. Sakamoto, and Y. Sadaoka, *J. Am. Ceram. Soc.* 79, 1401 (1996).
559. A. J. Moulson and J. M. Herbert, "Electroceramics: Materials, Properties and Applications." Chapman and Hall, London 1986.
560. G. Goodman, in "Ceramic Materials for Electronics" (R. C. Buchanan, Ed.). Dekker, New York 1986.
561. R. E. Riman, in "High-Performance Ceramics" (R. Pugh and L. Bergstrom, Eds.). Dekker, New York 1993.
562. E. Wu, K. C. Chen, and J. D. Mackenzie, "Better Ceramics Through Chemistry." North-Holland, Amsterdam 1984.
563. M. A. McCormick and E. B. Slamovich, *J. Am. Ceram. Soc.* 83, 442 (2000).
564. E. P. Turevskaya, D. V. Berdyev, and N. Ya. Turova, *J. Sol-Gel Sci. Technol.* 8, 111 (1997).
565. P. P. Phule and S. H. Risbud, *J. Mater. Sci.* 25, 1169 (1990).
566. M. I. Diaz-Guemes, T. G. Carreno, C. J. Serna, and J. M. Palacios, *J. Mater. Sci.* 24, 1011 (1989).
567. K. S. Mazdiyassani, R. T. Dolloff, and J. S. Smith II, *J. Am. Ceram. Soc.* 52, 523 (1969).
568. C. Lemoine, B. Gilbert, B. Michaux, J.-P. Pirard, and A. J. Lecloux, *J. Non-Cryst. Sol.* 175, 1 (1994).
569. R. C. Pastor, *Mater. Res. Bull.* 21, 761 (1986).
570. K. A. Easom, K. J. Klabunde, and C. M. Sorensen, *Polyhedron* 13, 1197 (1994).
571. Z. A. Starikova, A. I. Yanovsky, N. M. Kotova, M. I. Yanovskaya, N. Ya. Turova, and D. Benlian, *Polyhedron* 16, 4347 (1997).
572. L. Ma and D. A. Payne, *Chem. Mater.* 6, 875 (1994).
573. B. A. Vaarstra, J. C. Huffman, W. E. Streib, and K. G. Caulton, *Inorg. Chem.* 30, 3068 (1991).
574. J. Bates, Q. Zhang, L. Spiccia, and B. O. West, *J. Sol-Gel Sci. Technol.* 2, 29 (1994).
575. L. G. Hubert-Pfalzgraf, S. Daniele, R. Papiernik, M. C. Massiani, B. Septe, J. Vaissermann, and J. C. Daran, *J. Mater. Chem.* 7, 753 (1997).
576. B. C. Gaskins and J. J. Lannutti, *J. Mater. Res.* 11, 1953 (1996).
577. C. H. de Groot and J. S. Moodera, *J. Appl. Phys.* 89, 4336 (2001).
578. S. L. Swartz and T. R. Shrout, *Mater. Res. Bull.* 17, 1245 (1982).
579. K. Sreedhar and A. Mitra, *Mater. Res. Bull.* 32, 1643 (1997).
580. S. Ananta, R. Brydson, and N. B. Thomas, *J. Eur. Ceram. Soc.* 19, 355 (1999).
581. S. Stemmer, G. R. Bai, N. D. Browning, and S. K. Streiffer, *J. Appl. Phys.* 87, 3526 (2000).
582. O. Renoult, J.-P. Boilot, F. Chaput, R. Papiernik, L.-G. Hubert-Pfalzgraf, and M. Lejeune, *J. Am. Ceram. Soc.* 75, 3337 (1992).
583. H. Kadokura, Y. Okuhara, M. Mitsuya, and H. Funakubo, *Chem. Vap. Deposition* 6, 225 (2000).
584. K. Amanuma, T. Hase, and Y. Miyasaka, *Appl. Phys. Lett.* 66, 221 (1995).
585. C. T. Chen, T. Li, X. Zhang, and S. B. Desu, *J. Mater. Res.* 12, 1569 (1997).
586. L. Vel, G. Demazeau, and J. Etourneau, *Mater. Sci. Eng.* 10, 149 (1991).
587. H. N. Hahn, D. A. Lindquist, J. S. Haggerty, and D. Seyferth, *Chem. Mater.* 4, 705 (1992).
588. J. He, M. Scarlete, and J. F. Harrod, *J. Am. Ceram. Soc.* 78, 3009 (1995).
589. R. Riedel, E. Kroke, A. Greiner, A. O. Gabriel, L. Ruwisch, J. Nicolish, and P. Kroll, *Chem. Mater.* 10, 2964 (1998).
590. G. Guerrero, P. H. Mutin, and A. Vioux, *Chem. Mater.* 12, 1268 (2000).
591. H. P. Baldus, M. Jansen, and O. Wagner, *Key Eng. Mater.* 88-91, 75 (1994).
592. H. P. Baldus and M. Jansen, *Angew. Chem.* 109, 338 (1997).
593. H. Jüngeremann and M. Jansen, *Mat.-Wiss. Werkstofftech.* 29, 573 (1998).
594. A. Jalowiecki, J. Bill, F. Aldinger, and J. Mayer, *Composites Part A* 27A, 717 (1996).
595. J. Mayer, D. V. Szabo, M. Rühle, M. Seher, and R. Riedel, *J. Eur. Ceram. Soc.* 15, 717 (1995).
596. J. H. Sinfelt and G. D. Meitzner, *Acc. Chem. Res.* 26, 1 (1993).
597. M. L. Steigerwald and L. E. Brus, *Acc. Chem. Res.* 23, 183 (1990).
598. Y. Wang, *Acc. Chem. Res.* 24, 133 (1991).
599. H. Weller, *Adv. Mater.* 5, 88 (1993).
600. L. L. Beecroft and C. K. Ober, *Chem. Mater.* 9, 1302 (1997).
601. B. M. Tissue, *Chem. Mater.* 10, 2837 (1998).
602. G. Blasse, *Chem. Mater.* 1, 294 (1989).
603. M. Veith, S. Mathur, H. Shen, V. Sivakov, and X. K. Meng, *J. Mater. Res.*, in press.
604. M. Veith and S. Kneip, *J. Mater. Sci. Lett.* 13, 335 (1994).
605. M. Veith, S. Faber, R. Hempelmann, S. Janssen, J. Prewo, and H. Eckerlebe, *J. Mater. Sci.* 31, 2009 (1996).
606. D. W. Goodman, *Chem. Rev.* 95, 523 (1995).
607. J. P. Carpenter, C. M. Lukehart, S. B. Milne, S. R. Stock, and J. E. Wittig, *Inorg. Chim. Acta* 251, 151 (1996).
608. R. Murugavel, A. Voigt, M. G. Walawalkar, and H. W. Roesky, *Chem. Rev.* 96, 2205 (1996).
609. W. Rupp, N. Hüsing, and U. Schubert, *J. Mater. Chem.* 12, 2594 (2002).
610. S. K. Bera, S. Chaudhuri, and A. K. Pal, *J. Phys. D: Appl. Phys.* 33, 2326 (2000).
611. C. M. Bender, J. M. Burtlich, D. Barber, and C. Pollock, *Chem. Mater.* 12, 1969 (2000).
612. J. Zhou, L. F. Li, Z. L. Gui, S. Buddhudu, and Y. Zhou, *Appl. Phys. Lett.* 76, 1540 (2000).
613. M. Fujii, A. Mimura, S. Hayashi, and K. Yamamoto, *Appl. Phys. Lett.* 75, 184 (1999).
614. G. Westin, A. Ekstrand, E. Zangellini, and L. Börjesson, *J. Phys. Chem. Solids* 61, 67 (2000).
615. C. R. Stoldt, *Sens. Actuators, A* 97-98, 410 (2002).
616. P. Baldus, M. Jansen, and D. Sporn, *Science* 285, 699 (1999).



# *In-situ* Microscopy of Nanoparticles

Mark Yeadon

*National University of Singapore, Singapore*

## CONTENTS

1. Introduction
  2. Instrumentation for Dynamic *In-situ* Studies
  3. Special Concerns for *In-situ* Nanostructure Studies
  4. *In-situ* Studies Using Conventional Microscopes
  5. *In-situ* Studies Using Ultrahigh Vacuum Microscopes
  6. *In-situ* Studies Using Environmental Microscopes
  7. Conclusions
- Glossary  
References

## 1. INTRODUCTION

The detailed characterization of samples of nanoparticles and nanostructured materials presents a considerable challenge to the materials scientist. The importance of the task of determining basic characteristics such as size, structure, and chemical composition is in no doubt. However, the range of techniques available to comprehensively determine these properties in a single experiment is limited, and a survey of the published literature reveals an overwhelming emphasis on the use of electron microscopy, and in particular the transmission electron microscope (TEM).

The principal advantage of the TEM is its unprecedented spatial resolution, combined with the possibility of spatially localized reciprocal space examination using transmission electron diffraction. The ability to probe the local structure of a sample by electron diffraction is a unique advantage to the transmission electron microscopist. The reasonable penetration of high-energy electrons has enabled for example the characterization of buried interfacial structures, and this has been of immense importance to the development of our understanding of nucleation and growth mechanisms in heteroepitaxial thin films.

The TEM is ideally suited to the investigation of nanostructured materials; nanoparticles are among the simplest of TEM specimens, requiring no mechanical thinning to

achieve electron transparency and thus the least amount of sample preparation. Typically they need only be dispersed on a “holey” or “lacey” carbon support film prior to electron imaging.

In any situation involving materials characterization, an ideal microscopy technique will provide (1) sufficient spatial resolution to form interpretable images and (2) a method of preparing and mounting the sample that will avoid substantial modification and/or the introduction of artifacts. The first requirement is readily satisfied, since modern transmission electron microscopes typically have a resolution better than 2.5 Å. The second requirement, however, must be given careful consideration in any proposed experiment. One of the properties of nanoparticles that makes them attractive for certain key technologies, such as catalysis and biosensing, is their enhanced chemical activity due to their large surface area to volume ratio (a direct consequence of their small diameter). This has made nanoparticles of immense interest to the chemical and biomedical industries. However, as a consequence of this enhanced reactivity, atmospheric degradation (and in particular, oxidation) may substantially change the chemical and structural properties of the sample before analysis is complete.

Materials such as metal oxides and inert metals such as gold may suffer little or no effects. However, more reactive metals such as copper and many semiconductor materials such as silicon may experience substantial oxidation. Thus, in order to understand the structural properties of these nanomaterials as-synthesized, examination should ideally be made before exposure to ambient atmosphere occurs.

In situations where the examination of as-grown nanoparticles or nanoscale deposits is the main requirement, embedding of the particles or the film in a protective medium either during or immediately following growth has proved remarkably effective [1]. Sputtered silicon oxide layers have been widely used for this purpose. Metallic or semiconducting nanoparticles embedded in insulating media such as SiO<sub>2</sub> are an intrinsic part of the structure of some nanoelectronic device structures [2].

In addition to the characterization of the structures synthesized, we are also interested in understanding the dynamic processes that occur either during the growth of the nanomaterial or during subsequent processing. One of

the key advantages of dynamic observations is the ability to identify elusive metastable intermediate phases and probe structural evolution both within the bulk of a sample and at the sample surface. A comprehensive understanding of the influence of service environment on the bulk structure and surface morphology of the nanostructure is of immense interest. As our understanding of these processes and their mechanisms develop, we will become better able to intelligently design structures of the highest utility and efficiently predict the conditions most favorable to their realization.

We conclude then that there are situations where it is desirable to study the structure of nanoparticles before any exposure to atmosphere has taken place, in order to characterize the “intrinsic” properties of the nanomaterial. In addition, we wish to gain an understanding of the structural and morphological developments that may take place during exposure to a variety of service environments.

## 2. INSTRUMENTATION FOR DYNAMIC *IN-SITU* STUDIES

For our present purpose, we will define an *in-situ* observation as one that occurs either (a) during the *synthesis* of a nanostructured material, with no temporal interruption of the growth process, or (b) during postsynthesis *processing* of the nanostructure, such as during an anneal or other heat treatment. Depending upon the material and its specific application, the processing of interest may take place under conditions ranging from ultrahigh vacuum ( $<10^{-9}$  Torr), through high vacuum ( $\sim 10^{-8}$ – $10^{-6}$  Torr), to atmospheric or near-atmospheric pressure in a variety of different gases. We consider first the conditions our sample will experience during transmission electron imaging using conventional electron microscopes.

The gun, column, and camera chambers of an electron microscope are by necessity maintained in the high vacuum pressure regime or better, since electrons are scattered strongly in air. An ion-pumped TEM column will typically equilibrate at a pressure of order  $10^{-7}$ – $10^{-8}$  Torr during electron observation. Older and less well pumped systems may be at least an order of magnitude higher in pressure. The presence of a substantial partial pressure of hydrocarbon species in the high vacuum environment is almost unavoidable due to the presence of rotary oil pumps and perhaps oil diffusion pumps.

In addition, the area under observation is subjected to irradiation by fast electrons with energies typically in the range 100–300 keV. Hydrocarbon molecules are readily “cracked” by the electron beam, and anticontamination devices such as liquid nitrogen-cooled cold traps are commonly mounted close to the specimen to help reduce the total pressure.

## 3. SPECIAL CONCERNS FOR *IN-SITU* NANOSTRUCTURE STUDIES

Nanostructured materials are well known for their enhanced reactivity, due at least in part to their increased surface area:volume ratio. This has a positive influence on their catalytic properties; increased catalytic activity observed in

nanostructured materials such as supported metal particles in zeolite structures is a strong motivation to develop our understanding of the science, and thus the technology, of nanostructured materials.

However, as a consequence of their enhanced reactivity, atmospheric degradation (and in particular, oxidation) of nanostructured materials is an important consideration once they have been synthesized. Some materials are more sensitive to the effects of atmospheric exposure or electron irradiation than others. Ceramic materials, for example, are typically more stable under the electron beam and more resistant to chemical modification. Other materials such as metals and semiconductors, however, are rather more sensitive, and *in-situ* processing must be performed under ultrahigh vacuum (“ultraclean”) conditions.

In order to address the issues of (i) avoiding contamination for atmosphere-sensitive materials and (ii) achieving a controlled high pressure gaseous environment, two parallel streams of instrumentation development have developed. These are, respectively, instruments operating under ultrahigh vacuum conditions (with a base pressure below  $10^{-9}$  Torr), and instruments operating under controlled atmosphere conditions, enabling background gas pressures of up to 50 mbar or more to be sustained in the specimen region under electron irradiation.

In the following sections we provide a survey of published *in-situ* TEM studies of nanocrystals. The specific examples discussed are intended to illustrate some of the wide diversity of interests that exist and experiments that have been performed. Several examples are drawn from the author’s own research for reasons of familiarity. The interested reader is encouraged to refer to the references presented and those contained therein.

## 4. *IN-SITU* STUDIES USING CONVENTIONAL MICROSCOPES

At elevated temperatures, reaction and/or diffusion of atomic species often leads to significant modifications to the microstructure of the material. The ability to observe these in real time can often provide invaluable insight into nanoscale phenomena. The development of *in-situ* heating holders (or “hot stages”) capable of heating samples to medium or high temperatures has led to a number of exciting discoveries in materials science.

Hot stages most commonly comprise a resistively heated ring-shaped furnace, capable of receiving a standard TEM sample (3 mm disc). Temperatures between 800 and 1300 °C are generally attainable, at least for short periods of time, under electron observation.

Ceramic nanoparticles are typically reasonably robust to atmospheric exposure and may be readily prepared for TEM observation in atmosphere. Rankin [3] and Rankin and Boatner [4] studied the high-temperature sintering characteristics of nanoparticles of  $ZrO_2$  and  $MgO$  using a conventional TEM equipped with a furnace-type hot stage. Their investigations centered around direct observations of the development of interparticle contacts during sintering.

The evolution of neck profiles during high temperature annealing processes is not well characterized, due in

part to the experimental difficulties of neck profile inspection. There is particular interest in nanoscale sintering phenomena, where continuum theories of neck formation are expected to break down.

Rankin performed dynamic observations of the formation of neck growth between pairs of ceramic nanoparticles in point contact, at temperatures between  $\sim 830$  and  $890$  °C. The results revealed that the relative orientations of the particles prior to heat treatment are critical in determining the subsequent microstructural evolution.

The lowest energy configuration of two particles in contact is of course one in which the two particles coalesce to form a single particle with no grain boundaries and an equilibrium shape determined by the Wulff construction. Such a global equilibrium may not always be achievable, however, since substantial mass transport and particle rotation may be required; instead, the system may assume a local metastable equilibrium.

During the experimental observations, particles with relatively small misalignments showed evidence of rotation to full alignment and the formation of curved necks between the particles which were entirely epitaxial with both particles [3]. In the case of particle pairs with larger initial misorientations, in each case the orientation of one particle was found to dominate the neck formation, with a large faceted neck region forming in only one of the particles. In Figure 1a, the faceted edge of one particle (lower right corner) is initially in contact with the “rough” (highly stepped) surface of a second particle (upper left corner); after 15 minutes at high temperature, the neck region has almost completely filled. Further annealing apparently led to little change in the neck profile suggesting local equilibrium conditions had been achieved.

In Figure 2, two particles both with rough surfaces in contact are shown, after (a) 54 minutes and (b) 68 minutes annealing. Again, it is apparent that material is adding in registry with only one of the particles (the right hand particle in this case).

This study provides an excellent example of the breakdown of continuum theory as the dimensions of a material

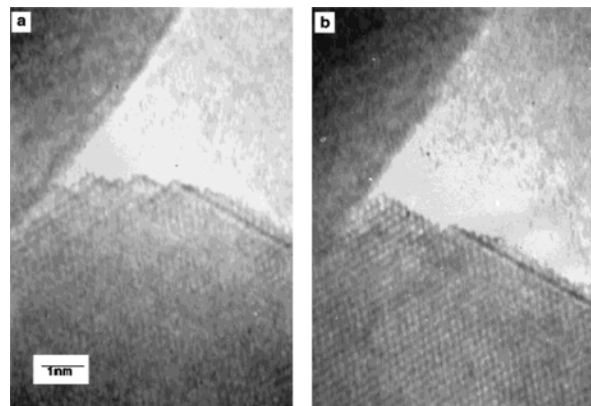


**Figure 1.** Two particles in facet–rough contact and the neck which forms epitaxially between them after (a)  $\sim 5$  and (b)  $\sim 20$  minutes. Reprinted with permission from [3], J. Rankin, *J. Am. Ceram. Soc.* 82, 1560 (1999). © 1999, American Ceramic Society.

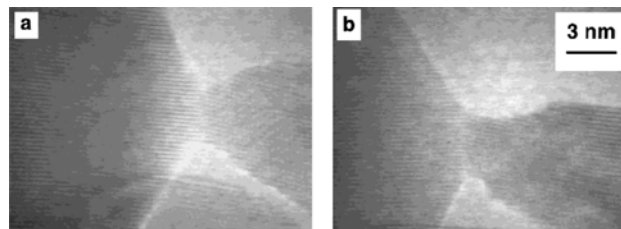


**Figure 2.** Two particles in rough–rough contact and the neck which forms epitaxially between them after (a) 54 and (b) 68 min. Reprinted with permission from [3], J. Rankin, *J. Am. Ceram. Soc.* 82, 1560 (1999). © 1999, American Ceramic Society.

move in to the nanoscale size regime, where expectations based on classical models must be revised.

Suspended wire-type holders have also been used for studies of nanoparticles, the advantage being that higher temperatures may be achieved for longer periods than with furnace-type holders [5]. Nanoparticles may be attached to a fine wire (e.g., W, of diameter  $20\text{--}30$   $\mu\text{m}$ ) by solvent evaporation, which can then be resistively heated to in excess of  $1500$  °C by a dc current. The relatively small mass of the heating element reduces significantly the thermal load on the electron microscope compared to other holders.

By placing a second wire in parallel with the first, and coating this second wire with a low melting point, high vapor pressure material such as gold, it is possible to perform relatively crude *in-situ* evaporation. Kamino and Saka [6] used this technique to vapor-deposit gold nanocrystals onto single crystal silicon particles. Upon annealing the particles wet the Si surface, resulting in the desorption of the native oxide and the formation of a reconstructed, highly faceted surface. Their experiments were performed in a conventional high resolution electron microscope with no vacuum modification, over a relatively short time scale. Portions of the surface could thus be preserved in a relatively clean condition for short periods. More well controlled conditions require the use of ultrahigh vacuum instrumentation.

## 5. IN-SITU STUDIES USING ULTRAHIGH VACUUM MICROSCOPES

Ultrahigh vacuum (UHV) electron microscopes have been developed in order to allow sample heating and *in-situ* deposition under ultraclean conditions similar to those found in molecular beam epitaxy (MBE) systems. Their development has occurred at a slower pace than conventional electron microscopes due in part to the hardware costs involved in following UHV design rules. To build a TEM entirely of UHV materials, from the gun to the viewing chamber, is still prohibitively expensive for most applications. One of the key design issues, then, becomes the ability to establish a continuous path for the electron beam between the gun ( $\sim 10^{-8}$  Torr), the specimen chamber ( $\sim 10^{-10}$  Torr), and the camera chamber ( $\sim 10^{-7}$  Torr). The same issue must be addressed for the environmental cell TEM where, in this case, the pressure in the specimen chamber (up to 50 mbar) is much higher than that in the gun and camera chambers.



The most common solution is to use a system of differential pumping apertures (see for example [7, 8] and references therein). Furthermore, to achieve base pressures in the region of  $10^{-10}$  Torr, only a select range of materials can be used for the specimen chamber, based on their propensity to outgas under UHV conditions. All components sharing the vacuum must be bakeable to in excess of 100 °C, to remove adsorbed water vapor from the interior surfaces of the vacuum chamber. The use of polymer-based vacuum seals is avoided due to outgassing and the need for high temperature baking; construction is dependent upon all-metal seals of high purity materials (such as low-oxygen copper). Since the sample is mounted in the polepiece of the objective lens, this also must be constructed with care.

The earliest UHV TEMs were developed in-house by modifying commercial high vacuum TEMs for UHV. To achieve UHV conditions, either local cryopumping of the sample chamber was employed, or a UHV sidechamber was attached to the microscope, or both [9–16]. More recently, UHV TEMs have become commercially available [17–22] with various modifications by different research groups, including an *in-situ* scanning tunneling microscope (STM) within the objective polepiece [23].

A number of studies of the structures of nanocrystals under electron beam irradiation have been published, both in UHV [24–26] and non-UHV [27–31] environments. Studies of nanoparticle structures by UHV TEM have focused on *in-situ* grown nanoparticles, prepared by either (i) condensation of a vapor onto the substrate surface, (ii) inert gas condensation of nanoparticles in a carrier gas, followed by deposition onto a surface, or (iii) chemical vapor deposition (CVD) onto a substrate. We consider examples of each of these experiments in the following sections.

### 5.1. MBE-Deposited Nanoparticles

One of the most technologically important materials today is silicon, and considerable attention has been given to the growth of materials for microelectronic device applications on the silicon surface. Native oxide which forms readily on the silicon surface is typically removed by heating to high temperature in order to form clean surfaces of reproducible structure. Upon cooling, a  $(7 \times 7)$  surface reconstruction is observed in the case of Si(111), and a  $(2 \times 1)$  reconstruction in the case of Si(100).

Using a UHV TEM with field emission gun (JEOL 2000VF), Tanaka et al. studied the formation of Pd islands on the Si(111) and Si(110) surfaces by electron beam evaporation of Pd [32]. Upon annealing at 673 K Pd<sub>2</sub>Si was observed to form, with a  $(3 \times 3)$  reconstructed surface as determined by an *in-situ* STM. The STM measurements were performed in a side chamber of the electron microscope sharing the same vacuum, following growth of the nanocrystals in the column of the electron microscope. Similar *in-situ* growth of Mo [20] and In [33] nanocrystals using MBE was also performed using the same instrument. HREM images identified size-dependent structural variations of the In nanocrystals. Crystals ~3 nm in diameter formed after relatively short deposition times were found to exhibit face-centered cubic (fcc) stacking; however, those formed after longer periods with diameters above 7 nm

exhibit the tetragonal structure similar to bulk In. Nanocrystals in excess of 10 nm in diameter were found to show transitions between single crystal, single twin, and decahedral multiply twinned structures.

### 5.2. Sputter-Deposited Nanoparticles

An alternative approach to nanoparticle synthesis is by Gleiter's inert gas condensation technique [34]. The technique involves the condensation of a vapor of the material of interest (formed, e.g., by evaporation, sputtering, etc.) by collision with inert gas molecules to form nanocrystals *prior* to deposition on a surface. Olynick and co-workers constructed a UHV sputtering chamber and connected the system directly to the column of a modified JEOL 200CX UHV TEM with *in-situ* sample heating and a base pressure of  $1 \times 10^{-9}$  Torr [35, 36]. Copper nanoparticles were synthesized by sputtering a high purity copper target (99.99%) in ~1 Torr of Ar (<1 ppb O<sub>2</sub>), producing particles in the size range ~5–20 nm and with a log-normal size distribution. The particles were then injected into the polepiece of the electron microscope. Upon entering the microscope, some of the particles were deposited on an electron transparent membrane mounted on the sample stage where they could be imaged under the electron beam. Immediately following deposition, the residual Ar gas was evacuated and electron observation performed within 30 s of deposition.

Sputtering of the Cu target was typically performed for a period of 30 s, before injection of the particles into the microscope column. If the particles were allowed to remain inside the sputtering chamber for a short period (30–120 s) following termination of the sputtering process, and before injection into the microscope, the as-deposited particles were found to have agglomerated, with up to 10 or more particles comprising each agglomerate.

In order to understand the effects of O<sub>2</sub> exposure on the sintering properties of nanocrystalline copper, a comparison was made between the structures of nanoparticle agglomerates prepared with and without a deliberate leak of O<sub>2</sub> during sputtering. In the absence of an O<sub>2</sub> leak, examination of the particles immediately after injection revealed the presence of “necks” between the particles, with some grain growth. The particles were icosahedral in shape and multiply twinned in structure, which is known from theory and experiment to be the lowest energy state for clean fcc particles with diameters less than 4–7 nm [37–39].

In the case of sputtering in Ar with trace amounts of O<sub>2</sub>, or in an unbaked system, the outlines of individual particles could be clearly discerned, with little or no “neck” growth between particles and no evidence of grain growth. It was concluded that trace amounts of oxygen slow the particle grain growth and sintering kinetics of icosahedral particles. This was shown to be consistent with a change in the kinetics of the surface diffusion of Cu in the presence of oxygen.

The ability to control grain growth and agglomeration in particle ensembles is attractive since these processes are detrimental to the properties of nanophase materials, leading to an increase in size and reduction in surface area. However, the formation of an oxide may not be beneficial to the particular application in view and thus the identification of a surfactant that might play the same role as oxygen in

reducing surface diffusivity would be an attractive solution to prevent particle sintering [35].

Having considered particle–particle interactions, particle–substrate interactions were then explored in a series of experiments using the same instrument. Cu [40], Ag [41], and Co [42, 43] nanoparticles were deposited onto single crystal copper as a model substrates. Electron transparent copper foils were prepared *ex-situ* by electron beam evaporation of copper onto cleaved NaCl(100), followed by flotation in deionized water onto 200  $\mu\text{m}$  thick silicon supports,  $\sim 3\text{ mm} \times 2\text{ mm}$  in size and with a central perforation. The portion of the copper foil overlying the perforated region could be imaged under the electron beam. The sample could also be resistively heated to several hundred Celsius; at a temperature of  $\sim 300\text{ }^\circ\text{C}$  an anomalous desorption of the native oxide covering the foil was observed leading to the formation of a clean, oxide-free Cu(100) surface [44]. Reproducible substrate surfaces could thus be obtained for each experiment.

For each material, the nanoparticles were found to assume random orientations on the Cu(100) substrate as determined by transmission electron diffraction. The particles were also stable in location and orientation until the substrate was heated.

In the case of Cu nanocrystals, upon heating to  $\sim 250\text{ }^\circ\text{C}$ , the particles appeared to vanish from the bright field images. Examination of the corresponding dark field images obtained using a  $\text{Cu}_{220}$  reflection revealed, however, that the particles were in fact still present in the same locations on the surface, being made visible by thickness fringe contrast as variations in the thickness of the substrate. An example of this contrast is presented in Figure 3. By slightly tilting the angle of incidence of the electron beam, the dark/bright thickness fringe contrast due to each particle (e.g., areas “A,” “B,” and “C” in Fig. 3a) can be reversed, as can be seen by comparing Figure 3a and b. The particles have thus reoriented, exhibiting the same crystallographic orientation as the substrate. A classical mechanism of sintering and grain growth was proposed.

The significance of the experiment was the observed time scale over which grain growth occurred. Gleiter and

co-workers studied the formation of low energy grain boundaries in copper by sintering a randomly oriented array of macroscopic single crystal copper spheres  $\sim 100\text{ }\mu\text{m}$  in diameter on a Cu(100) surface. Over a period of several hundred hours at a temperature close to the melting point, necks were found to form between the particles and the substrate. The sintering of spherical particles exhibits an  $r^4$  time dependence, where  $r$  is the radius of the sphere [45]. A time scale on the order of  $10^3$  hours was required for substantial neck formation in the case of a sphere  $\sim 100\text{ }\mu\text{m}$  in diameter. In the case of nanoparticles, however, where the radius is several orders of magnitude smaller, the time required for neck formation and grain growth is predicted to be  $< 1\text{ s}$  even at temperatures well below the melting point, consistent with the experimental observations [40].

When Ag nanoparticles were deposited instead of Cu, the results were a little different. An example of a selected area diffraction pattern recorded immediately after particle deposition on Cu(100) is shown in Figure 4a. The diffraction pattern again shows the Debye–Scherrer rings corresponding to randomly oriented nanocrystals as observed in the case of copper nanocrystals. However, superimposed on the Debye–Scherrer rings are two distinct single crystal diffraction patterns corresponding to the epitaxial orientation relationship:

$$(111)_{\text{Ag}} // (001)_{\text{Cu}}$$

$$[110]_{\text{Ag}} // [110]_{\text{Cu}}$$

This orientation relationship corresponds to four possible orientations of Ag, two of which are equivalent by a twin relationship. Two  $\text{Ag}_{220}$  reflections ( $^1\text{Ag}_{220}$  and  $^2\text{Ag}_{220}$ ) corresponding to these two distinct orientations are labeled in the figure. Dark field images were recorded using electrons from both the randomly oriented material and the epitaxially oriented material. In Figure 4b, we present an image recorded using the  $^1\text{Ag}_{220}$  reflection labeled in Figure 4a. From this and other images recorded using electrons from different portions of the Debye–Scherrer rings it was concluded that the majority of the Ag nanocrystals comprised both epitaxial and nonepitaxial material.

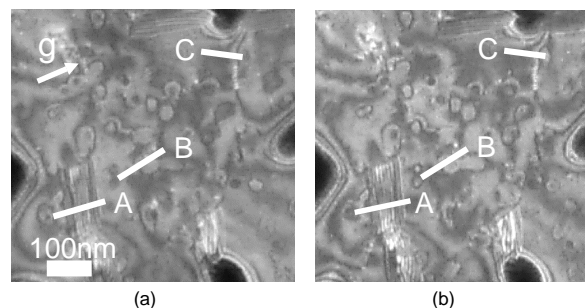


**Figure 3.** Weak-beam dark field image of the sample using a  $\text{Cu}_{220}$  reflection. The particles labeled A, B, and C show opposite contrast in images (a) and (b) due to a small change in the tilt of the electron beam, confirming that the particles have now assumed the same orientation as the substrate. Reprinted with permission from [40], M. Yeadon et al., *Appl. Phys. Lett.* 71, 1631 (1997). © 1997, American Institute of Physics.

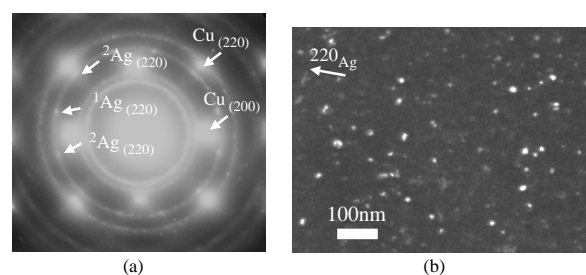


**Figure 4.** (a) Selected area diffraction pattern obtained immediately after nanoparticle deposition revealing a preferred orientation of the silver deposit. (b) Dark-field image obtained using the  $^1\text{Ag}_{220}$  epitaxial reflection, revealing the epitaxial interfacial layers between the particles and the substrate. Reprinted with permission from [41], M. Yeadon et al., *Appl. Phys. Lett.* 73, 3208 (1998). © 1998, American Institute of Physics.

Comparison of these findings with molecular dynamics computer simulations of “soft” landings of Ag nanocrystals on the Cu(100) surface showed remarkably consistent results. In Figure 5, the results of the simulations are presented in the form of [100] slices, 12 Å in thickness, through the nanoparticle and a portion of the substrate. After 5 ps of contact between the deposited Ag nanoparticle and the Cu surface, Figure 5a, ordering of Ag lattice planes close to the interface is occurring; after 2 ns, the first three lattice planes show good epitaxial registry with the substrate, Figure 5b. This phenomenon was termed “contact epitaxy” by the authors, since the epitaxial orientation is apparently established almost instantly upon contact. Neck growth then proceeds by stress-assisted diffusion (Fig. 5b), and the Ag atoms begin to “wet” the substrate surface.

The surface energy of Ag ( $\sim 1.25 \text{ J m}^{-2}$ ) is lower than that of Cu ( $\sim 1.8 \text{ J m}^{-2}$ ); in the final experiment, Co nanoparticles were deposited on the Cu(00) surface. Co is also immiscible in Cu, but the surface energy ( $\sim 2.55 \text{ J m}^{-2}$ ) is higher than that of Cu. One might therefore expect a tendency for the Cu substrate atoms to wet the Co particles in this case, rather than the particles wetting the substrate, as was observed in the case of Ag on Cu.

Upon annealing the Co nanoparticles, a significant change in the image contrast due to the particles was immediately observed. In Figure 6 we present bright field images of the sample (a) before and (b) after heating to 600 K. Inspection of electron diffraction patterns recorded following the anneal revealed that the particles were now entirely epitaxial with the substrate.

The image contrast in Figure 6b is similar to that observed by Ashby and Brown [46] and corresponds to strain contrast arising from the presence of Co particles coherently strained with the Cu(100) matrix. The lattice parameter mismatch between Cu and Co is small (Co is 1.9% smaller than Cu). The contrast is similar to that observed from self-assembled Ge quantum dots on Si(100), where the Ge epilayer is coherently strained with the underlying Si lattice.

The question as to where the particles were located, with respect to the substrate surface, was then considered. The strain state of the sample will vary depending upon the location of the nanoparticle (i.e., whether it is on the surface of the substrate, partially buried below the surface, or

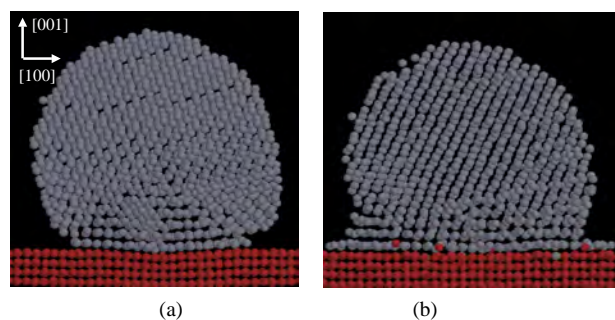


**Figure 5.** Molecular dynamics simulations of the particle–substrate interactions, (a) 5 ps and (b) 2 ns after contact. The diagram represents a (100) slice, 12 Å in thickness, through the substrate and nanoparticle. Reprinted with permission from [41], M. Yeadon et al., *Appl. Phys. Lett.* 73, 3208 (1998). © 1998, American Institute of Physics.

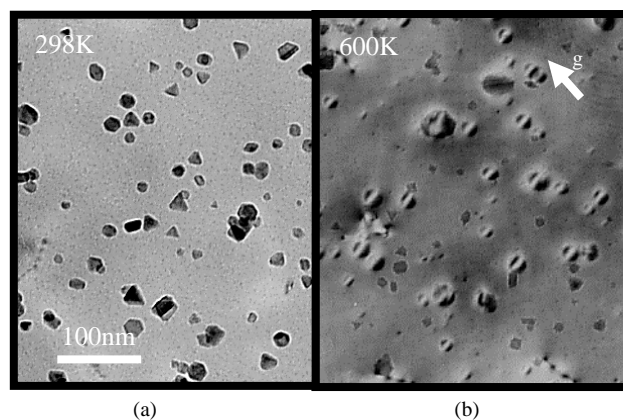


**Figure 6.** Bright-field images of Co nanoparticles on Cu(100) at (a) 300 K and (b) 600 K.

fully buried). Cross-sectional TEM of *in-situ* grown samples was inconclusive, and so a new quantitative TEM technique for strain measurement [47] was combined with molecular dynamics simulations of the strain state of particles as a function of depth below the surface. Quantitative comparison suggested that the particles were in fact fully buried in the copper substrate.

The driving force for burrowing was attributed to the reduction in free energy of the system by exchanging the Co–vacuum interface with a Co–substrate interface below the surface without increasing the substrate area or, significantly, the elastic strain. The process most likely occurred by (1) wetting of the particle by substrate material, followed by (2) burrowing. In both steps the total free energy of the system is reduced. Analysis of the burrowing time was also presented and was estimated to be less than 0.1 s at 600 K for a 13 nm diameter cluster. At room temperature, the time scale for burrowing to occur would be of the order of months [42].

### 5.3. CVD-Deposited Quantum Dots

Ross and co-workers studied the growth of Ge quantum dots on Si(100) using a Hitachi 9000UHV TEM modified for low-pressure chemical vapor deposition [48]. These and later low energy electron microscope studies brought new and exciting insights into the remarkable phenomenon of strain-mediated self-assembly. Self-assembled heteroepitaxial islands are of considerable technological interest for application in novel quantum dot optoelectronic and nanoelectronic systems and the model system Ge/Si(100) has attracted considerable attention [49–56].

The lattice mismatch between Ge and Si is similar to that between Co and Cu. Below a critical size, Ge islands grow under strained conditions to maintain a coherent interface between the island and substrate. Strain fields are generated in both the island and the substrate, and repulsive forces are exerted on neighboring islands through strain field interactions, reducing dramatically the probability of island coalescence events. Above a critical island size, it becomes energetically favorable for the introduction of dislocations to relieve the lattice strain.

In order to obtain data on the dynamics of island nucleation and growth, real-time observations of the nucleation and growth of Ge islands on the Si(100) surface were made. A partial pressure of  $2 \times 10^{-7}$  Torr of digermane was established in the microscope column and an electron transparent Si(100) substrate held at a temperature of 640 °C. Dark-field images of the sample were recorded on videotape as a function of digermane exposure [48]. Above a dose of  $\sim 50$  L of digermane, the nucleation and growth of Ge islands was observed. In Figure 7, a series of histograms of island size distribution are presented together with the corresponding dark field image. The images were recorded (a) 21, (b) 51, (c) 98, and (d) 180 s after the earliest evidence of strain contrast could be observed, corresponding to the nucleation of the islands.

From these data it is clear that the island size distribution, which is initially bimodal, becomes progressively narrower during growth, corresponding to extensive Ostwald ripening processes. The observed bimodal size distribution is known to correspond to two distinct island shapes—a pyramidal shape in the case of the smaller islands, and a dome shape in the case of the larger islands [56]. The processes involved in the transition between shapes have been the subject of much debate; these experiments provide direct evidence that the chemical potential of an island experiences an abrupt change when the equilibrium shape transitions between the pyramid and dome configurations. The model proposed by Ross and co-workers demonstrated that the shape transition could occur at a critical island volume where the dome energy becomes lower than the pyramid energy and may be

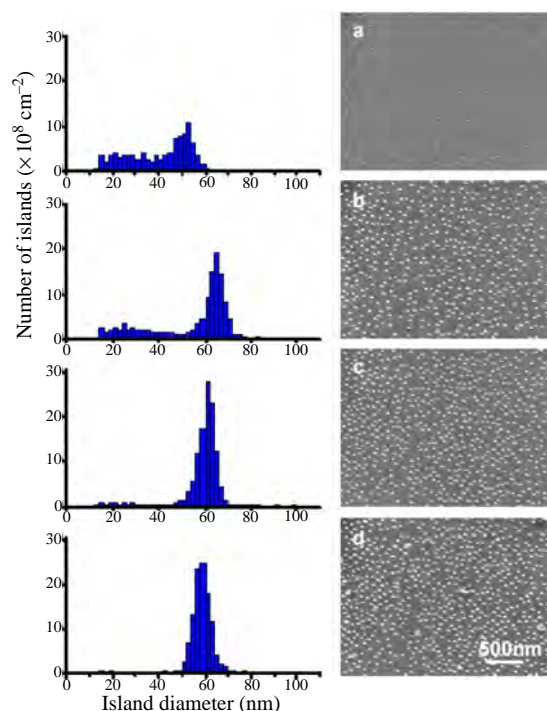


**Figure 7.** A series of histograms of island size distribution with corresponding dark field TEM images inset. The images were recorded after (a) 21, (b) 51, (c) 98, and (d) 180 s after the appearance of the earliest island strain contrast.

relevant to other heteroepitaxial systems involving bimodal size distributions.

## 6. IN-SITU STUDIES USING ENVIRONMENTAL MICROSCOPES

### 6.1. Catalyst Particles

Environmental electron microscopes permit controlled atmospheres of reducing, oxidizing, or other gases to be established in the polepiece and maintained for extended periods of time in the presence of the electron beam. Pressures of up to  $\sim 50$  mbar may be routinely achieved using modified microscopes [57].

Nanoscale particles find important applications in industrial catalysis for the chemical industry, constituting a critical component in a host of multibillion dollar global enterprises. Critical issues in the study of catalytic reactions and degradation mechanisms include metal–ceramic interfaces. Strong metal–support interactions (SMSI) in the gas environment, together with particle sintering, can lead to deactivation of the catalyst and loss of activity [57].

Gai and Boyes [57, 58] studied gas-phase reactions using a modified electron microscope at,  $N_2$  gas pressures of a few mbar, the instrument was capable of resolving gold and graphite lattice fringes at 700 °C [57]. Greater pressures of lighter gases such as  $H_2$  may in fact be tolerated, since electron scattering is strongly  $Z$ -dependent (where  $Z$  is the atomic mass of the scattering atom).

Recognizing the enormous potential of controlled environment TEM, Gai and Boyes studied the model intermetallic alloy catalyst Cu–Pd, supported on carbon. Fine particles were heated to 250 °C in both a  $H_2/He$  environment and a  $CO/He$  environment, for comparison. Particles were observed to be more strongly faceted in  $CO$  than in  $H_2$  and to sinter more quickly in a  $H_2$  atmosphere. High resolution imaging of the particles revealed that their (100) surfaces were also enriched with Pd.  $CO$  is known to bind more strongly to Pd than to Cu; the (110) surfaces, however, did not appear to show such enrichment [57–61].

Studies of nanoscale novel xerogel catalysts were also performed, important in the hydrogenation reaction of adiponitrile in Nylon 6,6 synthesis. Figure 8 shows a dynamic observation of Ru/titania xerogel catalyst in an  $H_2$  gas environment recorded (a) at room temperature and (b) during reaction at 280 °C after 2 hours. SMSI were not observed in the xerogel system, with the clusters appearing stable, with only very limited sintering and reaction. This has important implications for the use of xerogel catalysts in the selective hydrogenation reaction where stability is paramount.

Following the pioneering work of Gai and Boyes, Hansen and co-workers developed a similar *in-situ* environmental TEM capability, again based on the Philips CM300 [62]. They studied the shapes of Cu nanocrystals supported on ZnO and silica under different reaction conditions [63]. Copper nanocrystals find applications as catalysts in the synthesis of methanol, and in hydrocarbon conversion processes for fuel cells. They observed reversible shape changes of the nanocrystals, depending on the nature of the background gas.

The samples were prepared by impregnation of ZnO or silica supports with aqueous Cu-acetate solution, followed



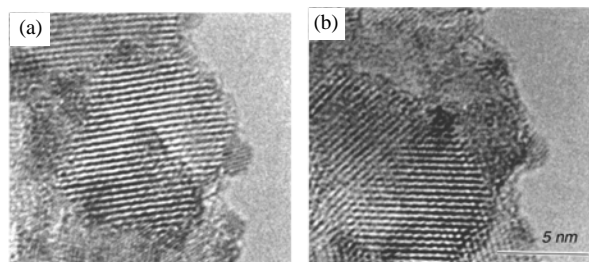


**Figure 8.** *In-situ* environmental cell high resolution TEM image of a Ru/titania xerogel catalyst in  $H_2$  gas environment recorded (a) prior to reaction at room temperature, and (b) during reaction at  $280\text{ }^\circ\text{C}$  for 2 h.

by *in-situ* reduction of the CuO precursor by heating to  $\sim 280\text{ }^\circ\text{C}$  in flowing  $H_2$  (5 mbar). The influence of the gas composition on the structure and shape of the nanocrystals was then investigated by adding  $H_2O$  to the  $H_2$  flow (to produce more oxidizing conditions) or CO (to produce more reducing conditions).

The particles were observed to undergo significant shape changes with each change in gas composition. In Figure 9, the profile of a single copper nanocrystal supported on ZnO is presented, during exposure to sequential gas compositions of (a) 1.5 mbar  $H_2$ , (b) 1.5 mbar  $H_2:H_2O$  (3:1), and (c) 1.5 mbar  $H_2$ . A transition from a relatively high aspect-ratio profile to a pronounced low aspect-ratio profile is immediately apparent. From these and other HREM images, the faceted surfaces of the nanocrystals were identified, including that of the facet in contact with the substrate. The surface free energies and work of adhesion were subsequently calculated using the Wulff construction.

Under a pure  $H_2$  atmosphere, the majority of the Cu particles shared their (111) facet with the ZnO surface (as in the case of UHV deposition of Cu onto various atomically clean ZnO surfaces) indicating a weak particle-support interaction. With the addition of water vapor, the more spherical shape of the particles suggests that the (110) and (100) facets are stabilized with respect to the (111) planes, although the (111) facet in contact with the support remains unchanged.

The observations clearly suggest that water adsorption on the different exposed Cu facets is the main driving force for the gas-induced shape changes. This model is consistent with

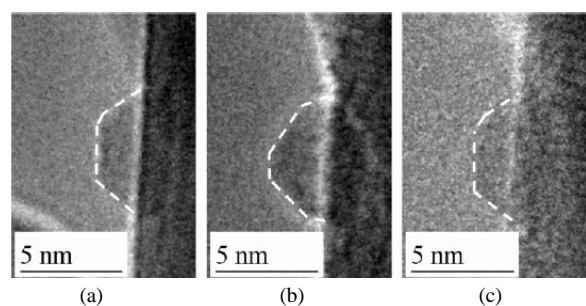


**Figure 9.** TEM images showing the reversible shape change of a Cu nanocrystal. The same Cu nanocrystal is imaged at  $220\text{ }^\circ\text{C}$  under (a)  $H_2$  at 1.5 mbar, (b)  $H_2:H_2O$  (3:1) at a total pressure of 1.5 mbar, and (c)  $H_2$  at 1.5 mbar. Reprinted with permission from [63], P. L. Hansen et al., *Science* 295, 2053 (2002). © 2002, American Association for the Advancement of Science.

the reversible nature of the shape changes, and the observation that the same changes are also observed on silica supports [63].

## 6.2. Carbon Nanostructures

In 1985, Kroto and co-workers [64] made the exciting discovery of a third form of Carbon—the  $C_{60}$  fullerene molecule, comprising a spherical, closed “shell” of 60 carbon atoms. Since this discovery, there has been substantial interest in understanding the structure and mechanisms of formation of fullerenes and related nanostructures [65, 66]. Fullerenes, carbon nanotubes, and carbon nanocages are commonly synthesized in arc-discharge chambers in the presence of He gas [67]. Processing conditions in these chambers vary widely with location within the chamber [68], and a variety of processing conditions have been explored [69]. It is believed that fullerene formation takes place in a He atmosphere below 100 mbar, with nanotubes being formed at pressures of order 500 mbar [65], and current densities of between 200 and  $700\text{ A cm}^{-2}$ .

The TEM has played a crucial role in the discovery and exploration of carbon nanostructures. The high energy electron beam has also been used to stimulate microstructural changes in carbonaceous materials leading for example to the formation of Bucky-onions (continuous concentric spherical shells of C) under electron irradiation [70, 71]. Electron beam current densities of  $\sim 150\text{ A cm}^{-2}$  were employed in these experiments, similar to those found in arc-discharge chambers. Burden and Hutchison used a modified JEOL 4000 controlled environment high resolution TEM [72, 73] to study the *in-situ* growth of fullerenes under conditions as close as possible to those found in the arc-discharge chamber [74]. Single crystal graphite particles (with *c*-axis oriented normal to the electron beam) were irradiated in a partial pressure of He of 25 mbar. At room temperature, amorphous spheres of carbon of up to 50 nm in diameter were formed within the samples during irradiation. Upon heating to  $500\text{ }^\circ\text{C}$ , the crystalline stability of the graphite was enhanced dramatically, and under prolonged irradiation ( $\sim 1200\text{ s}$ ), single graphene sheets were observed to peel away from the single crystal particles, rolling up to form discrete single shells with circular profiles. The experiments provided initial evidence of the possibility of fullerene formation directly from graphene sheets, as opposed to condensed, amorphous carbon.

In later experiments, the formation of fullerene molecules on the surface of untreated carbon black was observed. The surface of carbon black comprises fragmented and overlapping graphene layers. The sample was subjected to 25 mbar of He gas and was heated to  $550\text{ }^\circ\text{C}$ . An electron beam current density of  $\sim 6.4\text{ A cm}^{-2}$  was applied [75], during which curling of the graphene sheets was again observed, with the formation of features consistent with closed fullerene shells of  $C_{60}$  and  $C_{70}$  bucky-balls [76]. In contrast to their prior observations of fullerene formation on single crystal graphite, none of the graphene sheets comprising the carbon black were large enough to roll up to form tubular structures. It was therefore concluded that the electron beam interaction with the He atmosphere led to a *sputtering* of fragments of graphene from the carbon black surface,



from which the growth of the observed fullerene molecules proceeded.

The authors also present a careful assessment of prior TEM experiments where, in some cases, formation of fullerene molecules in the absence of controlled environmental conditions was observed [70, 77–79], while in other cases (where very clean vacuum conditions were maintained), fullerene molecules did not form [77]. It was concluded that residual hydrocarbons present in the vacuum systems of some electron microscopes were likely a key factor determining the ability to synthesize fullerenes *in-situ*. This assessment is consistent with the results of their experiment, where ionized He ions cause local sputtering of the carbon black surface and provide a very high local density of C molecules for fullerene formation.

### 6.3. Boron Nitride Nanostructures

Burden and Hutchison also studied *h*-BN particles subjected to similar conditions as carbon black in their experiments [74, 75]. The structure of BN is analogous to that of graphite, the hexagonal polymorph possessing a comparable interlayer spacing. Evidence of curling of the *h*-BN sheets was also observed during irradiation; however, curling sufficient to result in closure was not observed even after extended periods of irradiation.

More recently, the synthesis of *h*-BN nanomaterials was investigated by Bengu and Marks [80] and Yeadon et al. [81] using ultrahigh vacuum transmission electron microscopes. Using a modified Hitachi 9000 UHV TEM Bengu and Marks synthesized single walled BN nanotubes in the sidechamber of the UHV TEM by electron beam evaporation of B in the presence of excited nitrogen. The profiles of the as-synthesized nanostructures were subsequently examined under the electron beam without atmospheric exposure. Comparison with computer simulations of shape as a function of structure led to a conclusive and elegant determination of their structure. In Figure 10, a high resolution TEM image of a typical BN “nanomountain” is shown, as grown on the tungsten substrate in the side chamber of the microscope. To the right, a structural model of the nanomountain determined using a molecular modeling software package is presented. Boron atoms are shown in red;

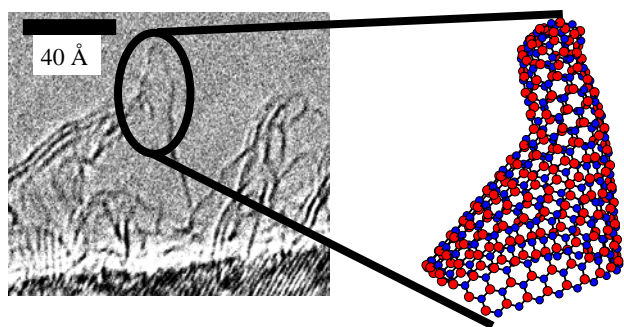


**Figure 10.** Single walled BN “nanomountain” grown on a tungsten substrate. The substrate lattice fringes correspond to W(100),  $d = 0.223$  nm. A computer model of the structure is shown to the right. Red spheres correspond to boron atoms; blue spheres correspond to nitrogen atoms.

nitrogen atoms are shown in blue. A high resolution image of a “nanodome” is presented in Figure 11, again with the corresponding structural model.

High resolution TEM images were subsequently simulated for the molecular models; it was found that only the presence of four-, six-, and eight-membered rings could lead to correct reproduction of the angles seen in the experimental high resolution images. Atomic models with five-, six-, and seven-membered rings (as per C nanostructures) failed to reproduce the observed angles, and this is believed to be due to the unfavorable nature of B–B and N–N bonds in odd-membered rings.

Using a modified JEOL 2000V UHV TEM with *in-situ* gas injection capability, Yeadon and co-workers synthesized *h*-BN nanocages under the electron beam by nitridation of FeB catalyst particles in an ammonia atmosphere. The UHV electron microscope was modified to permit reactive gas injection into the polepiece of the objective lens, thus enabling real time observations.

Nanoparticles of FeB were prepared by ball milling under an Ar atmosphere and then cast onto electron-transparent silicon supports by solvent evaporation. The Si supports could be resistively heated to  $\sim 1200$  °C.

In Figure 12a, a bright field image of a representative area of the sample is presented. Agglomerates of nanoparticles can be seen; the image was recorded at room temperature prior to  $\text{NH}_3$  injection. An electron energy loss spectroscopy (EELS) spectrum recorded from the sample at this stage is shown in Figure 12b (lower trace). The spectrum shows the presence of the B *K*-edge, together with a small peak due to C.

A partial pressure of  $\sim 5 \times 10^{-6}$  Torr  $\text{NH}_3$  was then stabilized in the sample chamber in the presence of the electron beam, and the sample was heated to 1000 °C. Sintering and agglomeration of the nanoparticles was observed during the ramp to 1000 °C, after which the particles appeared to stabilize. The particle profiles exhibited liquidlike fluctuations despite being several hundred Celsius below their melting temperature.

After a short period of time the profiles of the particles began to take on a faceted appearance, and the formation of a shell around the particles was observed. After further

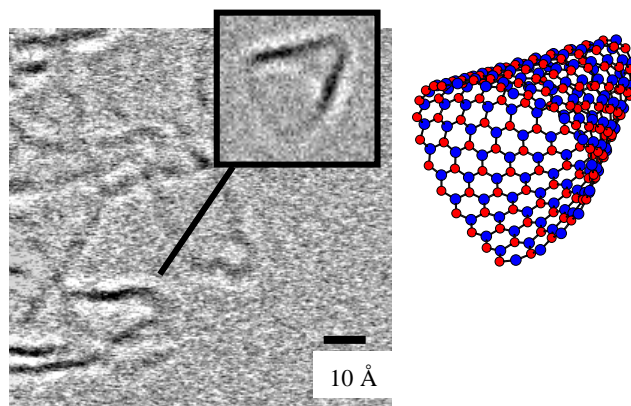


**Figure 11.** Single walled BN “dome” grown on a tungsten substrate together with the corresponding structural model (right). Red spheres correspond to boron atoms; blue spheres correspond to nitrogen atoms.

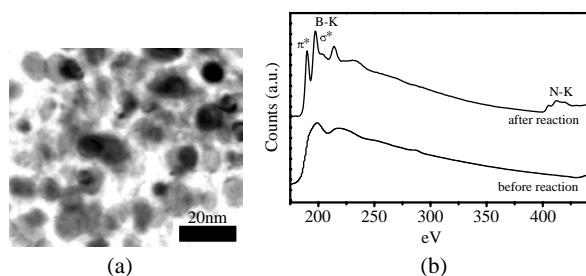


**Figure 12.** (a) FeB nanocrystals at room temperature prior to ammonia exposure. (b) EELS spectra recorded before (lower trace) and after (upper trace) ammonia exposure at  $\sim 1000$  °C.

exposure ( $\sim 150$  s), in certain instances some of the particles were observed to spontaneously “eject” from their shells. The particles then remained in contact with the shell while a second shell formed around them. They were again spontaneously ejected from this second shell after a similar period of time.

In Figure 13, a bright field image recorded at room temperature after 4 of these events had occurred is presented. It is apparent that a chain of nanocages has formed, with the last nanocage still encapsulating the Fe–B particle (labelled “P”). The corresponding EELS spectrum is presented in Figure 12b (upper trace) and shows the characteristic energy loss peaks corresponding to *h*-BN. No evidence of the presence of C could be found.

Similar chains of nanocages and nanobamboo structures have been observed *ex-situ* by other groups for both carbon [82, 83] and BN [84, 85], although the exact mechanism by which the structures form is still not well understood. The *in-situ* data suggest that the nanocages grow by diffusion of nitrogen species to the FeB interface, where reaction with boron can occur. Ejection is most likely a consequence of compressive stress within the particle as a consequence of the inward growth of the *h*-BN layers. Cage growth and particle ejection continue until the B content of the nanoparticle is substantially depleted.

The liquidlike motion of the particles observed *in-situ* provides direct confirmation that, even at temperatures well below the melting point, substantial particle mobility is possible thus making possible the observed multiple expulsion mechanism of formation [86].

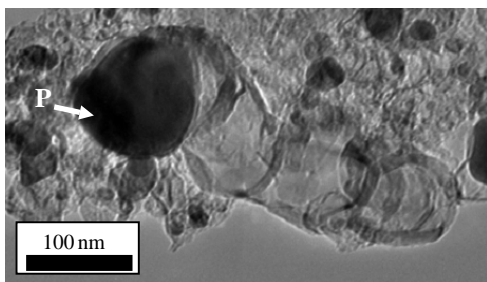


**Figure 13.** Bright field TEM image of the sample after cooling to room temperature showing the formation of a chain of *h*-BN nanocages. The particle responsible for the chain formation is labeled “P.”

## 7. CONCLUSIONS

*In-situ* transmission electron microscopy studies of the synthesis and processing of nanoparticles have considerably increased our understanding of fundamental materials processes in the science and technology of nanomaterials. The relative ease with which TEM samples of nanoparticles can typically be prepared has made electron microscope analysis more accessible to the nonspecialist and provided an efficient route to comprehensive nanoparticle characterization. As instrumentation of greater flexibility and enhanced performance continues to be developed, we can look forward to further exciting developments in the field of *in-situ* microscopy at the nanoscale.

## GLOSSARY

**Diffusion** Thermally activated movement of individual atoms through the crystal lattice or over the surface of a material.

**Inert gas condensation** The process of nanoparticle formation by which a vapour of atomic species cools by collision with an inert gas, the atomic species condensing to form fine particles of nanoscopic dimensions.

**In-situ** In the normal or natural position. In the present context, the characterization of materials synthesis and processing phenomena by reproducing the phenomena in a manner accessible to the characterisation technique of interest.

**Molecular beam epitaxy** The formation of crystals whose orientation is related to that of the substrate (i.e. epitaxial) by directing a molecular beam at a crystalline substrate under ultrahigh vacuum conditions.

**Sintering** The process by which fine particles of a material become chemically bonded by a process involving diffusion of atomic species at a temperature below the melting point.

**Sputtering** The emission of particles from a solid surface as a consequence of the impingement of energetic ionized particles with the surface.

## REFERENCES

1. G. Fuchs, D. Nieman, and H. Poppa, *Thin Solid Films* 207, 65 (1992).
2. H. Ahmed, *J. Vac. Sci. Technol. B* 15, 2101 (1997).
3. J. Rankin, *J. Am. Ceram. Soc.* 82, 1560 (1999).
4. J. Rankin and L. A. Boatner, *J. Am. Ceram. Soc.* 77, 1987 (1994).
5. T. Kamino and H. Saka, *Micros. Microanal. Microstruct.* 4, 127 (1993).
6. T. Kamino and H. Saka, *Mater. Res. Soc. Symp. Proc.* 404, 19–24 (1996).
7. M. T. Marshall, M. L. McDonald, X. Tong, M. Yeadon, and J. M. Gibson, *Rev. Sci. Instrum.* 69, 440 (1998).
8. E. D. Boyes and P. L. Gai, *Mater. Res. Soc. Symp. Proc.* 404, 53 (1996).
9. H. Poppa, *J. Vac. Sci. Technol.* 2, 42 (1965).
10. R. B. Marcus, C. J. Calbick, and T. T. Sheng, *Rev. Sci. Instrum.* 41, 1319 (1970).
11. A. Barna, P. B. Barna, and J. F. Poczka, *Vacuum* 17, 219 (1967).
12. G. Honjo and K. Yagi, *J. Vac. Sci. Technol.* 6, 576 (1969).
13. D. N. Braski, J. R. Gibson, and E. H. Kobisk, *Rev. Sci. Instrum.* 39, 1806 (1968).

14. R. Anton, in "Proceedings of the Sixth International Congress for Electron Microscopy," p. 339. Maruzen, Nihonbashi, Tokyo, 1986.
15. A. L. Aseev, A. V. Latyshev, and S. I. Stenin, in "Proceedings of the 10th International Congress on Electron Microscopy," Hamburg, West Germany, 1982, p. 1215.
16. R. J. Wilson and P. M. Petroff, *Rev. Sci. Instrum.* 54, 534 (1983).
17. L. D. Marks, M. Kubozoe, M. Tomita, M. Ukiana, T. Furutsu, and I. Matsui, in "Proceedings of the 46th Annual MSA Meeting" (G. W. Bailey, Ed.), p. 658. San Francisco Press, San Francisco, 1988.
18. M. Hammar, F. K. Le Goues, J. Tersoff, M. C. Reuter, and R. M. Tromp, *Surf. Sci.* 349, 129 (1996).
19. Y. Kondo and K. Takayanagi, *Science* 289, 606 (2000).
20. M. Tanaka, K. Furuya, M. Takeguchi, and T. Honda, *Thin Solid Films* 319, 110–114 (1998).
21. T. Suzuki, H. Minoda, Y. Tanishiro, and K. Yagi, *Thin Solid Films* 343–344, 423 (1999).
22. R. K. K. Chong, M. Yeadon, W. K. Choi, E. A. Stach, and C. B. Boothroyd, *Appl. Phys. Lett.*, in press.
23. Y. Naitoh, K. Takayanagi, Y. Oshima, and H. Hirayama, *J. Electron. Microsc.* 49, 211 (2000).
24. L. D. Marks and P. M. Ajayan, *J. Mater. Res.* 5, 1496 (1990).
25. Y. Oshima, K. Takayanagi, and H. Hirayama, *Z. Phys. D* 40, 534 (1997).
26. D. L. Olynick, J. M. Gibson, and R. S. Averback, *Philos. Mag. A* 77, 1205 (1998).
27. M. J. Yacaman, S. Fuentes, and J. M. Dominguez, *Surf. Sci.* 106, 472 (1981).
28. S. Iijima and T. Ichihashi, *Phys. Rev. Lett.* 56, 616 (1986).
29. S. Iijima, *Jpn. J. Appl. Phys.* 26, 357 (1987).
30. D. J. Smith, A. K. Petford-Long, L. R. Wallenburg, and J.-O. Bovin, *Science* 233, 872 (1986).
31. R. Anton and I. Schneider, *Phys. Rev. B* 58, 13874 (1998).
32. M. Tanaka, M. Takeguchi, and K. Furuya, *J. Cryst. Growth* 237–239, 254 (2002).
33. M. Tanaka, M. Takeguchi, and K. Furuya, *Surf. Sci.* 433–435, 491 (1999).
34. H. Gleiter, *Progr. Mater. Sci.* 33, 1 (1990).
35. D. L. Olynick, J. M. Gibson, R. S. Averback
36. M. L. McDonald, J. M. Gibson, and F. C. Unterwald, *Rev. Sci. Instrum.* 60, 700 (1989).
37. S. Ogawa and S. Ino, "Advances in Epitaxy and Endotaxy" (H. G. Schneider and V. Ruth, Eds.), pp. 183–225. VEB Deutscher Verlag Fur Grundstoffindustrie, Leipzig.
38. P.-A. Buffat, M. Flueli, R. Spycher, P. Stadelmann, and J.-P. Borel, *Faraday Discuss.* 92, 173 (1991).
39. G. D'Agostino, *Philos. Mag. B* 68, 903 (1993).
40. M. Yeadon, J. C. Yang, R. S. Averback, J. W. Bullard, D. L. Olynick, and J. M. Gibson, *Appl. Phys. Lett.* 71, 1631 (1997).
41. M. Yeadon, M. Ghaly, J. C. Yang, R. S. Averback, and J. M. Gibson, *Appl. Phys. Lett.* 73, 3208 (1998).
42. C. G. Zimmermann, M. Yeadon, K. Nordlund, J. M. Gibson, R. S. Averback, U. Herr, and K. Samwer, *Phys. Rev. Lett.* 83, 1163 (1999).
43. C. G. Zimmermann, K. Nordlund, M. Yeadon, J. M. Gibson, R. S. Averback, U. Herr, and K. Samwer, *Phys. Rev. B* 64, 085419-1 (2001).
44. J. C. Yang, M. Yeadon, B. Kolasa, and J. M. Gibson, *Appl. Phys. Lett.* 70, 3522 (1997).
45. F. A. Nichols and W. W. Mullins, *J. Appl. Phys.* 36, 1826 (1965).
46. M. F. Ashby and L. M. Brown, *Philos. Mag.* 8, 1083 (1963).
47. P. D. Miller, C. P. Liu, and J. M. Gibson, *Ultramicroscopy* 84, 225 (2000).
48. F. M. Ross, J. Tersoff, and R. M. Tromp, *Phys. Rev. Lett.* 80, 984 (1998).
49. M. Zinke-Allmang et al., *Phys. Rev. B* 39, 7848 (1989).
50. D. J. Eaglesham and M. Cerullo, *Phys. Rev. Lett.* 64, 1943 (1990).
51. A. A. Williams et al., *Phys. Rev. B* 43, 5001 (1991).
52. J. Knall and J. B. Pethica, *Surf. Sci.* 265, 156 (1992).
53. F. LeGoues et al., *Phys. Rev. Lett.* 73, 300 (1994).
54. P. Schittenhelm et al., *Appl. Phys. Lett.* 67, 1292 (1995).
55. M. Hammar et al., *Surf. Sci.* 349, 129 (1995).
56. G. Medeiros-Ribeiro, A. M. Bratkovski, T. I. Kamins, D. A. A. Ohlberg, and R. S. Williams, *Science* 279, 353 (1998).
57. P. L. Gai and E. D. Boyes, "In-situ Microscopy in Materials Research" (P. L. Gai, Ed.). Kluwer, Norwell, MA, 1997.
58. E. D. Boyes and P. L. Gai, *Ultramicroscopy* 67, 219 (1997).
59. P. L. Gai, in "Electron Microscopy in Heterogeneous Catalysis." Institute of Physics Publishing, London, 2002.
60. P. L. Gai, *Top. Catalysis* 8, 97 (1999).
61. P. L. Gai and K. Kourtakis, *Science* 267, 661 (1995).
62. T. W. Hansen, J. B. Wagner, P. L. Hansen, S. Dahl, H. Topsoe, and C. J. H. Jacobsen, *Science* 294, 1508 (2001).
63. P. L. Hansen, J. B. Wagner, S. Helveg, J. R. Rostrup-Nielsen, B. S. Clausen, and H. Topsoe, *Science* 295, 2053 (2002).
64. H. W. Kroto, J. R. Heath, S. C. O'Brien, R. F. Curl, and R. E. Smalley, *Nature* 318, 162 (1985).
65. S. Iijima, *Nature* 354, 56 (1991).
66. T. W. Ebbesen and P. M. Ajayan, *Nature* 358, 220 (1992).
67. W. Kratschmer, L. D. Lamb, K. Fostiropoulos, and D. R. Huffman, *Nature* 347, 354 (1990).
68. P. J. F. Harris, *Microsc. Anal.* 9, 13 (1994).
69. S. Seraphin, D. Zhou, J. Jiao, J. C. Withers, and R. Loutfy, *Carbon* 31, 685 (1993).
70. D. Ugarte, *Chem. Phys. Lett.* 207, 473 (1993).
71. D. Ugarte, *Europhys. Lett.* 22, 45 (1993).
72. R. C. Doole, G. M. Parkinson, M. J. Goringe, and P. J. F. Harris, *JEOL News* 30E, 30 (1992).
73. R. C. Doole, G. M. Parkinson, and J. M. Stead, *Am. Inst. Phys. Conf. Ser.* 119, 157 (1991).
74. A. P. Burden and J. L. Hutchison, *J. Cryst. Growth* 158, 185 (1996).
75. A. P. Burden and J. L. Hutchison, *Carbon* 36, 1167 (1998).
76. S. Iijima, *J. Phys. Chem.* 91, 3466 (1987).
77. P. J. F. Harris, S. C. Tsang, J. B. Claridge, and M. L. H. Green, *J. Chem. Soc., Faraday Trans.* 90, 2799 (1994).
78. M. S. Zwanger and F. Banhart, *Philos. Mag. B* 72, 149 (1995).
79. G. Lulli, A. Parisini, and G. Mattei, *Ultramicroscopy* 60, 187 (1995).
80. E. Bengu and L. D. Marks, *Phys. Rev. Lett.* 86, 2385 (2001).
81. M. Yeadon, M. Lin, C. B. Boothroyd, H. Zheng, and K. P. Loh, submitted for publication.
82. S. Seraphin, S. Wang, D. Zhou, and J. Jiao, *Chem. Phys. Lett.* 228, 506 (1994).
83. Y. Saitoh, T. Yoshikawa, M. Okuda, N. Fujimoto, K. Sumiyama, K. Suzuki, A. Kasuya, and Y. Nishina, *J. Phys. Chem. Solids* 54, 1849 (1993).
84. T. Oku and K. Sukanuma, *Diam. Rel. Mater.* 10, 1205 (2001).
85. H. Kitahara, T. Oku, T. Hirano, and K. Sukanuma, *Diam. Rel. Mater.* 10, 1210 (2001).
86. M. Yeadon, L. Ming, K. P. Loh, C. B. Boothroyd, G. Fu, and Z. Hu, unpublished (2003).



# *In-situ* Nanomeasurements of Individual Carbon Nanotubes

Zhong Lin Wang

Georgia Institute of Technology, Atlanta, Georgia, USA

## CONTENTS

1. Introduction
  2. Bending Modulus of Carbon Nanotubes
  3. Field Emission from Carbon Nanotubes
  4. Electric Transport of Carbon Nanotubes
  5. Summary
- Glossary  
References

## 1. INTRODUCTION

Due to the great size and structure selectivity of nanomaterials, their physical properties can be quite diverse, depending on their atomic-scale structure, size, and chemistry. To maintain and utilize the basic and technological advantages offered by the size specificity and selectivity of the nanomaterials, there are three key challenges that we need to overcome for future technological applications of nanomaterials. First, the synthesis of size, morphology, and structurally controlled nanomaterials, which are likely to have precisely designed and controlled properties [1]. Second, novel techniques for characterizing the properties of individual nanostructures and their collective properties. This is essential for understanding the characteristics of the nanostructures. Finally, the integration of nanomaterials with the existing technology is the most important step for their applications, especially in nanoscale electronics and optoelectronics.

Characterizing the physical properties of individual carbon nanotubes is a challenge for many existing testing and measuring techniques because of the following constraints [2]. First, the size (diameter and length) is rather small, prohibiting the application of well-established testing techniques. Second, the small size of the nanotubes makes their manipulation rather difficult, and specialized techniques are needed for picking up and installing an individual nanostructure. Therefore, new methods and methodologies must

be developed to quantify the properties of individual nanotubes. The objective of this chapter is to introduce the theory and techniques that have been developed for characterizing the mechanical, field emission, and electric transport properties of carbon nanotubes. Our study is based on *in-situ* transmission electron microscopy (TEM), so that the one-to-one correspondence of structure and property is maintained.

## 2. BENDING MODULUS OF CARBON NANOTUBES

### 2.1. Experimental Approach

In property measurement in nanoscale, the main challenge comes from the ultrasmall size of the nanotube that prohibits the application of conventional techniques. We first have to see the nanotube, and then measure its properties. Apparently, we must rely on electron microscopy. To carry out the property measurement of a nanotube, a specimen holder for a 100 kV TEM was built to apply a voltage across a nanotube and its counterelectrode (Fig. 1) [3, 4]. In the area that is loading a specimen in conventional TEM, an electromechanical system is built that allows not only the lateral movement of the tip, but also applying a voltage across the nanotube with the counterelectrode. This setup is similar to the integration of the scanning probe technique with TEM. The static and dynamic properties of the nanotubes can be obtained by applying a controllable static and alternating electric field.

The nanotubes used in the study are produced by an arc-discharge technique, and the as-prepared nanotubes are agglomerated into a fiber-like rod. The carbon nanotubes have diameters of 5–50 nm and lengths of 1–20  $\mu\text{m}$ , and most of them are nearly defect-free. The fiber is glued using silver paste onto a gold wire, through which the electric contact is made. The counterelectrode is an Au/Pt ball of diameter  $\sim 0.25$  mm. The nanotube to be used for property



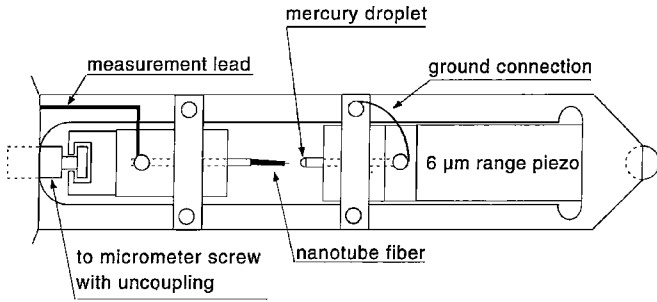


**Figure 1.** Schematic diagram of the TEM specimen holder for *in-situ* measurements.

measurements is directly imaged under TEM (Fig. 2), and electron diffraction patterns and images can be recorded from the nanotube. The information provided by TEM directly reveals both the surface and the intrinsic structure of the nanotube. This is a unique advantage over scanning probe microscope (SPM) techniques. The distance from the nanotube to the counterelectrode is controllable.

## 2.2. The Fundamental Resonance Frequency and Nonlinear Effect

A carbon nanotube can be charged by an externally applied voltage; the induced charge is distributed mostly at the tip of the carbon nanotube, and the electrostatic force results in the deflection of the nanotube. Alternatively, if an applied voltage is an alternating voltage, the charge on the tip of the nanotube is also oscillating, and so is the force. If the applied frequency matches the natural resonance frequency of the nanotube, mechanical resonance is induced. By tuning the applied frequency, the first and second harmonic resonances can be observed (Fig. 3). The analysis of the information provided by the resonance experiments relies on the theoretical model for the system. The most established theory for modeling a mechanical system is the continuous elasticity theory, which is valid for a large-size object. For atomic scale mechanics, we may have to rely on molecular

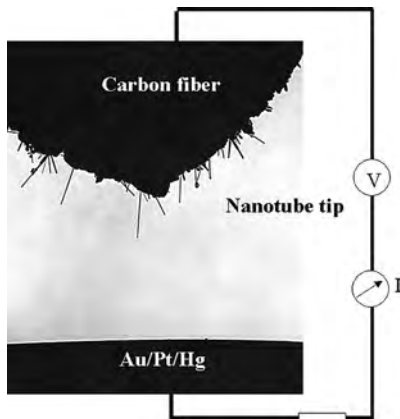


**Figure 2.** TEM image showing carbon nanotubes at the end of the electrode and the other counterelectrode. A constant or alternating voltage can be applied to the two electrodes to induce electrostatic deflection or mechanical resonance.

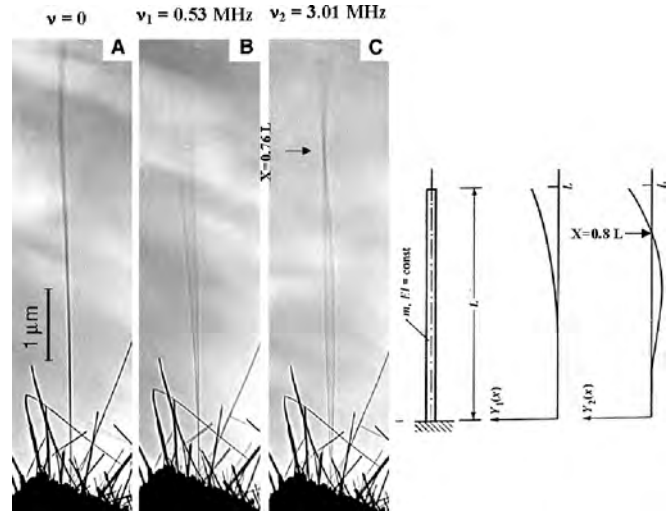


**Figure 3.** A selected carbon nanotube at (A) stationary, (B) the first harmonic resonance ( $\nu_1 = 1.21$  MHz), and (C) the second harmonic resonance ( $\nu_2 = 5.06$  MHz). The right-hand side shows the shape predicted based on elasticity theory for a uniform macroscopic beam. Reprinted with permission from [3], P. Poncharal et al., *Science* 283, 1513 (1999). © 1999, American Association for the Advancement of Science.

dynamics. We first examine the validity of applying the classical elasticity theory for the data analysis.

We have compared the following three characteristics of the results predicted by the elasticity theory and the experimental results shown in Figure 3. First, the theoretical node for the second harmonic resonance occurs at  $0.8L$ , and the experiment showed  $\sim 0.76L$ . Second, the frequency ratio between the second and the first modes is  $\nu_2/\nu_{21} = 6.27$  theoretically, while the observed one is  $\nu_2/\nu_{21} = 5.7$ . The agreement is reasonably good if one looks into the assumptions made in the theoretical model: the nanotube is a uniform and homogeneous beam, and the root of the clamping side is rigid. The latter, however, may not be realistic in practical experiments. Finally, the shape of the nanotube during resonance has been compared quantitatively with the shape calculated by the elasticity theory, and the agreement is excellent. Therefore, we still can use the elasticity theory for the data analysis.

If the nanotube is approximated as a uniform solid bar with one end fixed on a substrate, from classical elasticity theory, the resonance frequency is given by [5]

$$\nu_i = \frac{\beta_i^2}{8\pi} \frac{1}{L^2} \sqrt{\frac{(D^2 + D_i^2)E_b}{\rho}} \quad (1)$$

where  $D$  is the tube outer diameter,  $D_i$  is the inner diameter,  $L$  is the length,  $\rho$  is the density, and  $E_b$  is the bending modulus. The resonance frequency is nanotube selective, and it is a specific number for a nanotube.

The correlation between the applied frequency and the resonance frequency of the nanotube is not trivial. We know that there are some electrostatic charges built on the tip of the carbon nanotube. With consideration of the difference between the surface work functions of the carbon nanotube and the counterelectrode (Au), a static charge exists even

when the applied voltage is withdrawn. Therefore, under an applied field, the induced charge on the carbon nanotube can be represented by  $Q = Q_0 + \alpha V_0 \cos \omega t$ , where  $Q_0$  represents the charge on the tip to balance the difference in surface work functions,  $\alpha$  is a geometrical factor, and  $V_0$  is the amplitude of the applied voltage. The force acting on the carbon nanotube is

$$F = \beta(Q_0 + \alpha V_0 \cos \omega t)V_0 \cos \omega t \\ = \alpha\beta V_0^2/2 + Q_0\beta V_0 \cos \omega t + \alpha\beta V_0^2/2 \cos 2\omega t \quad (2)$$

where  $\gamma$  is a proportional constant. Thus, resonance can be induced at  $\omega$  and  $2\omega$  at vibration amplitudes proportional to  $V_0$  and  $V_0^2$ , respectively. The former is a linear term in which the resonance frequency equals the applied frequency, while the latter is a nonlinear term, and the resonance frequency is twice the applied frequency. In practical experiments, the linear and nonlinear terms can be distinguished by observing the dependence of the vibration amplitude on the magnitude of the voltage  $V_0$ . This is an important process to ensure the detection of the linear term.

Another factor that one needs to consider is to identify the true fundamental resonance frequency [6]. From Eq. (1), the frequency ratio between the first two modes is 6.27. In practice, if resonance occurs at  $\omega$ , resonance could also occur at  $2\omega$ , which is the double harmonic. Figure 4 shows the resonance of a bent nanotube in such a case. To identify the fundamental frequency, one needs to examine the resonance at a frequency that is half or close to half of the observed resonance frequency; if no resonance occurs, the observed frequency is the true fundamental frequency.

The diameters of the tube can be directly determined from TEM images with a high accuracy. The determination of length has to consider the 2-D projection effect of the tube. It is essential to tilt the tube and to catch its maximum length in TEM, which is likely to be the true length. This requires a TEM that gives a tilting angle as large as  $\pm 60^\circ$ . Also, the operation voltage of the TEM is important to minimize radiation damage. The 100 kV TEM used in our experiments showed almost no detectable damage to a carbon nanotube, while 200 kV electrons could quickly

damage a nanotube. The threshold for radiation damage of carbon nanotubes is  $\sim 150$  kV.

After a systematic study of the multiwalled carbon nanotubes, the bending modulus of nanotubes was measured as a function of their diameters (Fig. 5). The bending modulus is as high as 1.2 TPa (as strong as diamond) for nanotubes with diameters smaller than 8 nm, and it drops to as low as 0.2 TPa for those with diameters larger than 30 nm. A decrease in the bending modulus with an increase of the tube diameter is attributed to the wrinkling effect of the wall of the nanotube during small bending [3]. The deformation is elastic, and the nanotube recovers its shape after relieving. This effect is pronounced, especially for larger size nanotubes; thus, the geometrical shape makes a significant contribution to the measured bending modulus (different from Young's modulus) [7]. However, with the decrease in the nanotube diameter, the bending modulus approaches Young's modulus.

The *in-situ* TEM technique demonstrated here provides a powerful approach toward nanomechanics of fiber-like nanomaterials with well-characterized structures. It can be applied to measure the mechanical properties of a wide range of nanowires, such as SiC, silica, and Si nanowires [8], and carbon nanotubes with defects [9]. This is a universal approach for nanomechanics.

### 2.3. Nanobalance

In analogy to a spring pendulum, the mass of a particle attached at the end of the spring can be determined if the vibration frequency is measured, provided that the spring constant is calibrated. This principle can be adopted to determine a very tiny mass attached at the tip of the free end of the nanotube. The resonance frequency drops more than  $\sim 40\%$  as a result of adding a small mass at its tip (Fig. 6). The mass of the particle thus can be derived by a simple calculation using an effective mass in the calculation of the momentum of inertia. This newly discovered "nanobalance" has been shown to be able to measure the mass of a particle as small as  $22 \pm 6$  fg ( $1f = 10^{-15}$ ).

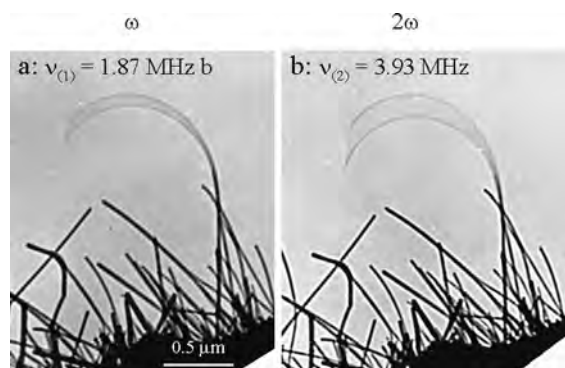


**Figure 4.** Resonance of a bent carbon nanotube at (a)  $\nu_{(1)} = 1.87$  MHz;  $V_0 = 2$  V and (b)  $\nu_{(2)} = 3.93$  MHz;  $V_0 = 5$  V, showing the multiple-harmonic effect.

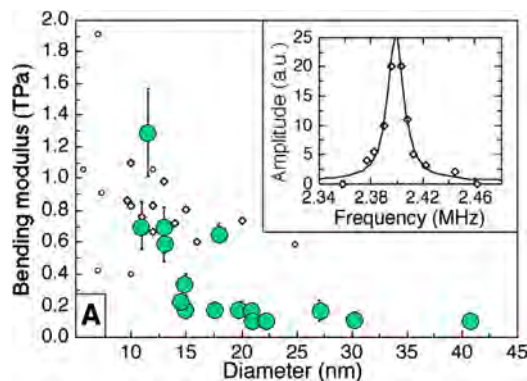


**Figure 5.** Bending modulus of the MWNT produced by arc discharge as a function of the outer diameter of the nanotube. The inner diameter of the nanotubes is  $\sim 5$  nm, independent of the outer diameter. The FWHM of the resonance peak is inserted.

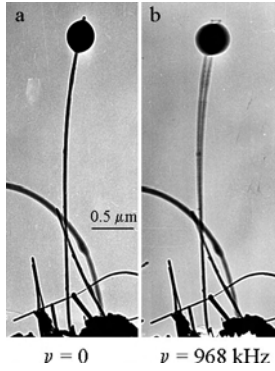


**Figure 6.** A small particle attached at the end of a carbon nanotube at (a) stationary and (b) first harmonic resonance ( $\nu = 0.968$  MHz). The effective mass of the particle is measured to be  $\sim 22$  fg ( $1 \text{ f} = 10^{-15}$ ). Reprinted with permission from [3], P. Poncharal et al., *Science* 283, 1513 (1999). © 1999, American Association for the Advancement of Science.

### 3. FIELD EMISSION FROM CARBON NANOTUBES

Carbon nanotubes possess various superior properties for use as field emitters, such as sharp tips with a nanometer-scale radius of curvature [10], high mechanical stiffness [11–13], high chemical stability [14], and unique electrical properties [15, 16]. Due to the unique tip geometry of the carbon nanotubes, their field-emission property is one of the most attractive applications [17], which has been extensively studied using the classical technique. In this chapter, we introduce a few novel applications of TEM in characterizing the field-emission properties of carbon nanotubes, with focus on the characteristics of individual carbon nanotubes.

#### 3.1. Work Function at the Tips of Carbon Nanotubes

An important physical quantity in electron field emission is the surface work function, which is well documented for elemental materials. For emitters such as carbon nanotubes (NTs), most of the electrons are emitted from the tips of the carbon NTs, and it is the local work function that matters to the properties of the NT field emission. The work function is measured from the  $\ln(J/E^2)$  versus  $1/E$  characteristic curve, where  $E$  is the macroscopic applied electric field that is an average over all of the aligned carbon NTs that are structurally diverse in diameter, length, and helical angle, and  $J$  is the emitted current density. We have developed a technique for the measurement the work function at the tip of a single carbon nanotube [18].

Our measurement is based on the electric-field-induced mechanical resonance of carbon nanotubes, but with a slight modification. The principle for work function measurement is schematically shown in Figure 7a. We consider a simple case in which a carbon nanotube, partially soaked in a carbon fiber produced by arc discharge, is electrically connected to a gold ball. Due to the difference in the surface work functions between the NT and the counter Au electrode, a static charge  $Q_0$  exists at the tip of the NT to balance this potential difference, even at zero applied voltage [19]. The

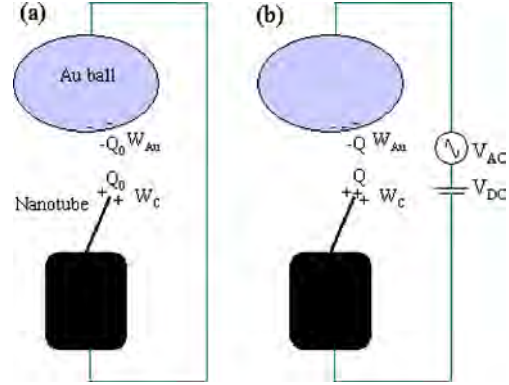


**Figure 7.** (a) Schematic diagram showing the static charge at the tip of carbon nanotube as a result of difference in work functions between the nanotube and the gold electrode. (b) Schematic experimental approach for measuring the work function at the tip of a carbon nanotube.

magnitude of  $Q_0$  is proportional to the difference between work functions of the Au electrode and the NT tip (NTT),  $Q_0 = \alpha(W_{\text{Au}} - W_{\text{NTT}})$ , where  $\alpha$  is related to the geometry and distance between the NT and the electrode.

The measurement relies on the mechanical resonance of the carbon NT induced by an externally applied oscillating voltage with tunable frequency. In this case, a constant voltage  $V_{\text{DC}}$  and an oscillating voltage  $V_{\text{AC}} \cos 2\pi ft$  are applied onto the NT, as shown in Figure 7b, where  $f$  is the frequency and  $V_{\text{AC}}$  is the amplitude. The total induced charge on the NT is

$$Q = Q_0 + \alpha e(V_{\text{DC}} + V_{\text{AC}} \cos 2\pi ft) \quad (3)$$

The force acting on the NT is proportional to the square of the total charge on the nanotube:

$$\begin{aligned} F &= \beta [Q_0 + \alpha e(V_{\text{DC}} + V_{\text{AC}} \cos 2\pi ft)]^2 \\ &= \alpha^2 \beta \{ [(W_{\text{Au}} - W_{\text{NTT}} + eV_{\text{DC}})^2 + e^2 V_{\text{AC}}^2 / 2] \\ &\quad + 2eV_{\text{AC}}(W_{\text{Au}} - W_{\text{NTT}} + eV_{\text{DC}}) \cos 2\pi ft \\ &\quad + e^2 V_{\text{AC}}^2 / 2 \cos 4\pi ft \} \end{aligned} \quad (4)$$

where  $\beta$  is a proportional constant. In Eq. (5), the first term is constant, and it causes a static deflection of the carbon NT; the second term is a linear term, and resonance occurs if the applied frequency  $f$  approaches the intrinsic mechanical resonance frequency  $f_0$  of the carbon NT (Fig. 8a). The last term in Eq. (4) is the second harmonics. The most important result of Eq. (4) is that, for the linear term, the resonance amplitude  $A$  of the NT is proportional to  $V_{\text{AC}}(W_{\text{Au}} - W_{\text{NTT}} + eV_{\text{DC}})$ . By fixing the  $V_{\text{DC}}$  and measuring the vibration amplitude as a function of  $V_{\text{AC}}$ , a linear curve is achieved (Fig. 8c).

Experimentally, we first set  $V_{\text{DC}} = 0$ , and tune the frequency  $f$  to find the mechanical resonance induced by the applied field. Secondly, under the resonance condition of keeping  $f = f_0$  and  $V_{\text{AC}}$  constant, slowly change the magnitude of  $V_{\text{DC}}$  from zero to a value that satisfies  $W_{\text{Au}} - W_{\text{NTT}} + eV_{\text{DC}0} = 0$  (Fig. 8b); the resonance amplitude  $A$  should be zero, although the oscillating voltage is still in effect.  $V_{\text{DC}0}$

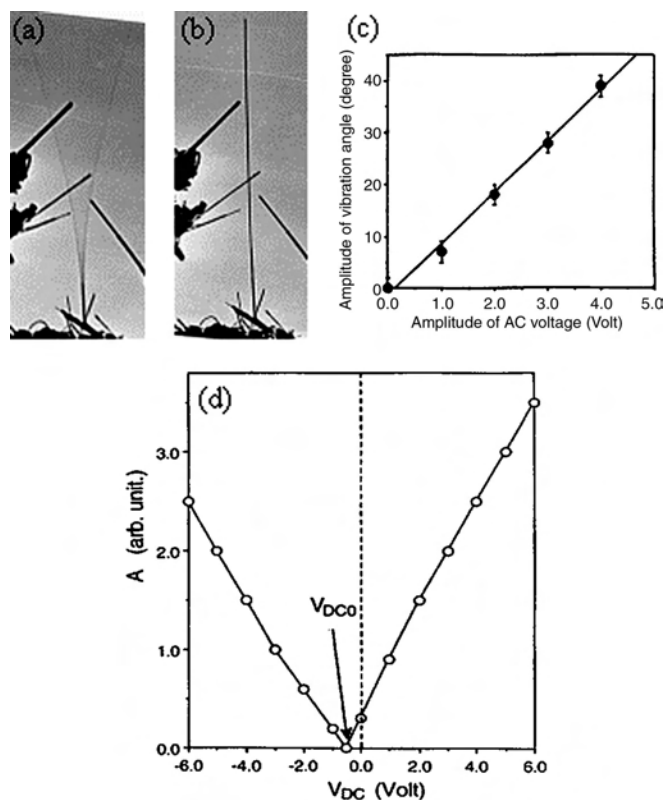


**Figure 8.** (a) Mechanical resonance of a carbon nanotube induced by an oscillating electric field. (b) Halting the resonance by meeting the condition of  $W_{Au} - W_{NTT} + eV_{DC0} = 0$ . (c) Plot of vibration amplitude of a carbon nanotube as a function of the amplitude of the applied alternating voltage  $V_{AC}$ . (d) Plot of vibration amplitude of a carbon nanotube as a function of the applied direct current voltage  $V_{DC}$ , while the applied frequency is 0.493 MHz and  $V_{AC} = 5$  V.

is the  $x$ -axis interception in the  $A$ - $V_{DC}$  plot (Fig. 8d). Thus, the tip work function of the NT is  $W_{NTT} = W_{Au} + eV_{DC0}$  [18].

Several important factors must be carefully checked to ensure the accuracy of the measurements. The true fundamental resonance frequency must be examined to avoid higher order harmonic effects. The resonance stability and frequency drift of the carbon nanotubes must be examined prior to and after each measurement to ensure that the reduction of vibration amplitude is solely the result of  $V_{DC}$ . The NT structure suffers no radiation damage at 100 kV, and the beam dosage shows no effect on the stability of the resonance frequency. Figure 9 gives the plot of the experimentally measured  $V_{DC0}$  as a function of the outer diameter of the carbon NTs. The data show two distinct groups:  $-0.3$  to  $-0.5$  eV and  $\sim +0.5$  eV. The work function shows no sensitive dependence on the diameters of the NTs, at least in the range considered here. 75% of the data indicate that the tip work function of carbon NTs is 0.3–0.5 eV lower than the work function of gold ( $W_{Au} = 5.1$  eV), while 25% of the data show that the tip work function is  $\sim 0.5$  eV higher than that of gold. This discrepancy is likely due to the nature of some nanotubes being conductive and some being semiconductive, depending on their helical angles. In comparison to the work function of carbon ( $W_C = 5.0$  eV), the work function at the tip of a conductive multiwalled

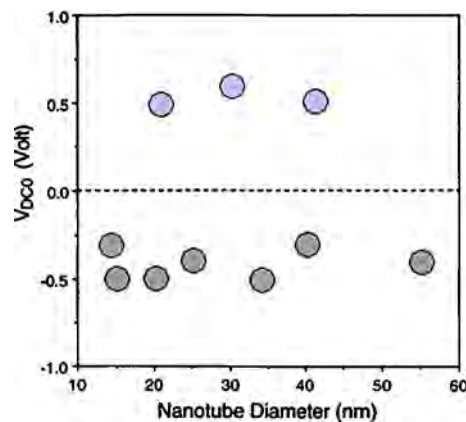


**Figure 9.** Experimentally measured  $V_{DC0}$  as a function of the outer diameter of the carbon nanotube.

carbon NT is 0.2–0.4 eV lower. This is important for electron field emission.

### 3.2. Electrostatic Charges on Carbon Nanotubes

Using the *in-situ* TEM setup that we built, some of the interesting aspects of electron field emission from carbon nanotubes can be revealed. To observe the electrostatic field distribution due to the charges on a carbon nanotube, we use the beam deflection effect introduced by the electrostatic force. If the nanotube is positively charged (Fig. 10a), the electrons passing through the two sides of a nanotube are deflected toward each other due to electrostatic attraction, resulting in a weak diffuse scattering in the electron diffraction pattern around the central transmission beam. By selecting a portion of the diffusely scattered electrons using a small-size objective aperture, the field distribution around the nanotube can be revealed. Figure 10b and c shows two images of the nanotubes acquired by placing the objective aperture at the b and c positions, as indicated in Figure 10a, corresponding, respectively, to the dark-field and bright-field images of the nanotubes that are emitting electrons. The nonuniform contrast adjacent to a defect clearly shows the build up of charges. Therefore, electrostatic charges accumulate not only at the tips and bodies of the nanotubes, but

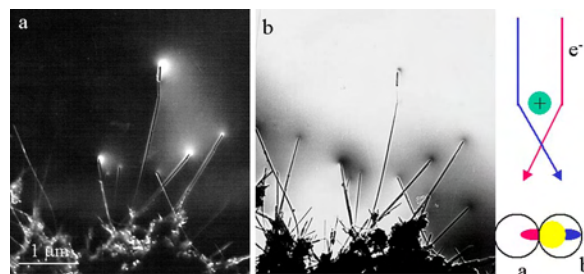


**Figure 10.** (a) Bright- and (b), (c) dark-field images of carbon nanotubes recorded by selecting the electrons scattered off the center beam due to the electrostatic deflection produced by the nanotubes under an applied voltage of 40 V, showing the electric field distribution at the tips, from where the electrons are emitting.



also at the defect sites. These observations are consistent with the expected results from electrostatics to preserve the carbon nanotube, if conductive, as an equal potential object.

### 3.3. Field-Emission-Induced Structural Damage

Due to the large aspect ratio of carbon nanotubes, the electric field at the tips of the nanotubes can be rather large; thus, the local temperature could be very high at field emission. It is possible to induce structural damage at the tips. The classical definition of turn-on field  $E_t = V/d$ , where  $V$  is the applied voltage and  $d$  is the distance from the tip of the field emitter to the surface of the counterelectrode, may not be an adequate measurement of the local field at the tips of the carbon nanotube due to its sharp needle geometry.

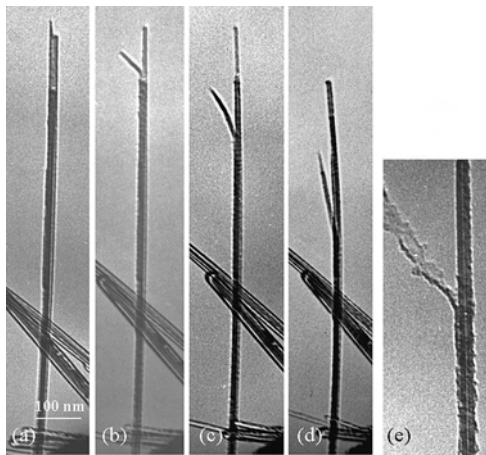
An important phenomenon of our study is the observation of the structural damage of a carbon nanotube during field emission under a higher voltage [20]. This study is useful in determining the structural stability of the nanotubes. Figure 11 shows a series of images of a nanotube that was being damaged by an applied voltage. The structural damage is apparent as the applied voltage increases. The damage occurs in such a way that the walls of the nanotubes are split patch by patch and segment by segment. A closer image of the splitting is shown in Figure 11e. This damage process is different from the unraveling process proposed by Rinzler et al. [21], who believed that the nanotubes are damaged following a string-by-string removal of the carbon atoms along the circumference of the graphitic layer.

Figure 12 shows a “stripping” process of a carbon nanotube under the applied electric field. The diameter and length of the nanotube  $A$  decrease as it being damaged by the field. This is a sharpening process of the multiwalled

nanotube. The structure of nanotube  $B$  is almost totally damaged by the field, and finally becomes a graphitic structure.

The mechanisms of the field-induced damage are believed to be due to two processes. First, the electrostatic force acting on the tip of the nanotube can split the nanotube piece by piece and segment by segment, such as the one shown in Figure 11. The second process is likely due to the local temperature created by the flow of emission current, which may “burn” the nanotube layer by layer, resulting in the sharpening process, as presented in Figure 12. The emission current is likely to flow along the nanotube through the most outer graphitic layers, which was first proposed by Frank et al. [22] for interpreting the quantum conductance of a multiwalled carbon nanotube at room temperature. This process has recently been used for removing the walls of carbon nanotubes [23, 24].

It was reported by Rinzler et al. [21] that the current emitted by nanotubes fluctuates almost randomly as a function of time at a time scale of a couple of seconds; this phenomenon was interpreted owing to an unraveling process of the carbon atom ring. Through *in-situ* TEM observation, we found that the fluctuation in emission current is due to a “head-shaking” effect of the nanotube while emitting electrons. The nanotube bends toward the counterelectrode at an applied voltage. The emission of electrons from a nanotube is likely to be a “ballistic” emission process in which the electrons are emitted as groups, although each emission can release many electrons. When the nanotube is fully charged prior to emission, the distance between the nanotube tip and the counterelectrode is the smallest due to the strongest electrostatic attraction; as soon as the electrons are emitted as a group, the electrostatic force between the nanotube



**Figure 11.** “Splitting” process in structural damage. (a)–(d) Series of TEM images showing the structural damage of a carbon nanotube during field emission, in which the applied voltage and the emission current are: (a)  $V = 80$  V,  $I = 10$   $\mu$ A, (b)  $V = 90$  V,  $I = 40$   $\mu$ A, (c)  $V = 110$  V,  $I = 100$   $\mu$ A, and (d)  $V = 130$  V,  $I = 250$   $\mu$ A. The distance from the tip of the nanotube to the counterelectrode was  $\sim 2$   $\mu$ m. (e) A nanotube that is experiencing the splitting of its outer layers during the damage. Reprinted with permission from [20], Z. L. Wang et al., *Appl. Phys. Lett.* 80, 856 (2002). © 2002, American Institute of Physics.

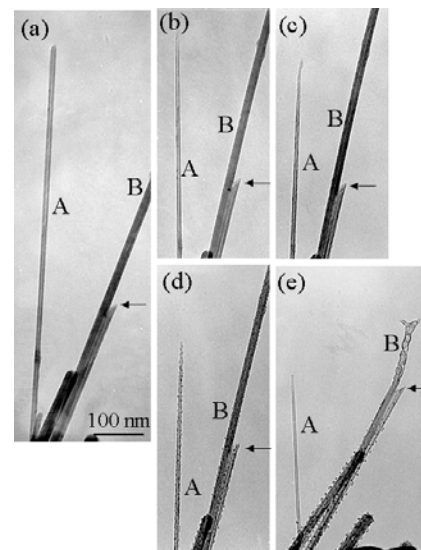


**Figure 12.** “Stripping” effect in structural damage. (a)–(e) Series of TEM images showing the structural damage of a carbon nanotube during field emission. The applied voltages were (a)  $V = 100$  V, (b)  $V = 120$  V, (c)  $V = 140$  V, (d)  $V = 160$  V, and (e)  $V = 200$  V. The distance from the tip of the nanotube to the counterelectrode was  $\sim 4$   $\mu$ m. Reprinted with permission from [20], Z. L. Wang et al., *Appl. Phys. Lett.* 80, 856 (2002). © 2002, American Institute of Physics.



and the electrode drops slightly, resulting in the recovery of the nanotube shape and a larger distance from the electrode. The head shaking of the nanotube due to “ballistic” emission results in a variation in the distance of its tip from the electrode, thus leading to a fluctuation in the emission current. This may also account for the blinking of the emission current from carbon nanotubes. The ballistic emission is possible because the small size of a nanotube can only hold a small amount of electrons at its tip. A rough estimation indicates that losing one electron at the tip can change the tip potential by  $\sim 0.15$  V for a 20 nm diameter nanotube. The head shaking is a result of its large aspect ratio, which leads to body swing during field emission.

#### 4. ELECTRIC TRANSPORT OF CARBON NANOTUBES

Electrical transport in single-walled nanotubes (SWNTs) and multiwalled nanotubes (MWNTs) is of great importance for their applications in electronics. Measurements of nanotube conductance mainly use two techniques. Using lithographically made gold electrodes, a carbon nanotube is laid down across two electrodes, and the  $I$ - $V$  characteristic is measured [25]. The other technique takes advantage of using liquid mercury as a soft contacting electrode; a nanotube is inserted into the mercury, and the conductance is monitored as a function of the depth that the nanotube is inserted into the mercury [26]. The latter has been carried out *in-situ* in TEM. This chapter intends to review the progress in applying the second technique in the electrical property characterization of nanotubes. A comprehensive review of all of the existing literature and a comparison of data in electrical characterization can be found in [27].

##### 4.1. Ballistic Quantum Conductance at Room Temperature

Our original technique involved two contact measurements on free-standing MWNTs in air. An arc-produced fiber composed of MWNTs was attached to a conducting tip of a scanning probe microscope, and dipped into various liquid metals. The conductance was recorded as a function of the depth  $L$  that the nanotube penetrated into the liquid metal. Figure 13 shows a schematic diagram of the measurements in an atomic force microscope (AFM). This experiment has three main advantages: 1) the carbon nanotube is as-synthesized without contamination; 2) the soft metal contact reduces the contact resistance, allowing a sensitive measurement on the conductance of the nanotube; and 3) the length of the nanotube exposed outside the liquid metal surface is a variable that allows a direct measurement of the conductance of the nanotube as its length is being reduced.

If  $Z$  represents the depth of the nanotube into the mercury surface, the conductance traces revealed quantized conductance steps with step heights of about  $1 G_0$  (Fig. 14), with  $G_0 = 2e^2/h = 1/(12.9 \text{ k}\Omega)$ . For a single tube, the conductance is  $G_0$ , and the jump to  $2G_0$  occurs once the second nanotube touches the mercury. This effect appears only if the carbon nanotube is defect-free, which means that the tubes are produced by arc discharge rather than catalytic

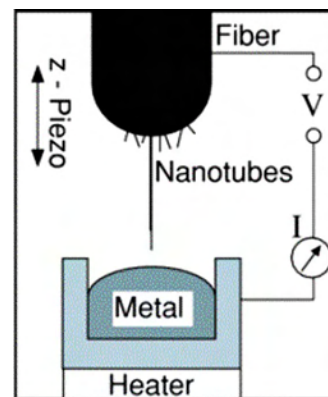


Figure 13. Experimental setup for measuring the electrical conductance of a single MWNT using the soft contact method in an AFM apparatus.

growth. The conductance is quantized, and it is independent of the length of the carbon nanotube. No heat dissipation was observed in the nanotube. This is the result of ballistic conductance, and it is believed to be a result of single graphite layer conductance. A recent observation using a different technique has confirmed our result [28].

The quantized steps typically develop only after many dipping cycles: the initial dipping cycles do not show steps, but rather sequences of sloping structures. Despite a lack of sophistication, these measurements consistently produce the highest measured two-point conductances for closed MWNTs, which points to reproducible low-contact resistances. In about 80 fibers that we tested, we did not observe nanotubes with conductances (significantly) greater than  $1 G_0$ , although anomalous low ultimate conductances have been observed. In this work, we arrived at the following conclusions: 1) MWNTs are one-dimensional conductors; 2) the current in closed MWNTs flows on the outer surface; 3) MWNTs can sustain very large current densities; 4) transport in MWNTs is quantized with  $1 G_0$  at room temperature, suggesting ballistic conduction, but with half the expected value; and 5) the average current density carried out by the nanotube over its cross section can exceed  $10^7 \text{ A/cm}^2$ .

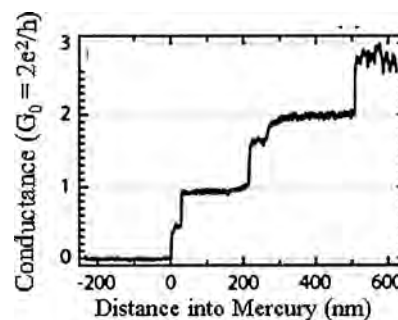


Figure 14. Conductance of a carbon nanotube as a function of the depth  $z$  the nanotube is inserted into the mercury surface, showing the quantum conductance of the nanotube. The flat plateau indicates that, within a certain length, the conductance of the nanotube is independent of its length.

## 4.2. In-Situ Measurement

The conductance measurement of individual carbon nanotubes has also been carried out using the *in-situ* technique introduced in Section 2.1. The same specimen holder used for the mechanical property measurements was used for the conductance measurement, except that the counterelectrode is replaced by a mercury droplet, which served as the soft contact for the measurement. Figure 15 shows the contact of a carbon nanotube with the mercury electrode, and a conductance of  $G_0$  was observed. It is also interesting to note that the contact area between the nanotube and the mercury surface is curved. This is likely due to the difference in surface work function between the nanotube and mercury; thus, electrostatic attraction could distort the mercury surface. This effect effectively reduces the contact resistance between the nanotube and the Hg electrode.

*In-situ* nanotube conductances are determined by applying a voltage difference of 100 mV between the Hg droplet and the nanotube fiber, and measuring the current. Three types of behavior are found. For type 1, more than half of the nanotubes that clearly contact the Hg surface (as seen from a slight bowing of the nanotube, as for example in Fig. 16a, or a distortion of the Hg surface) have resistances  $R$  that are out of our range, that is,  $>1$  M $\Omega$ . For type 2 tubes, the conductance is  $13$  k $\Omega$   $< R < 15$  k $\Omega$ . For the remainder,  $15$  k $\Omega$   $< R < 100$  k $\Omega$  (type 3). We have not observed nanotubes whose resistance is significantly less than  $13$  k $\Omega$  (i.e.,  $6.5$  k $\Omega$ , as expected for  $2 G_0$ ). This observation is consistent with the in-air experiments.

We previously measured currents up to  $1$  mA through the tubes before they are damaged, implying current densities at the outer layer of up to  $10^{10}$  A/cm $^2$  for a  $10$  nm diameter tube (assuming surface conduction). Higher currents ( $>1$  mA) damage the nanotubes. We observed that defective nanotubes tend to break at the defects (Fig. 17), while type 2 nanotubes invariably break near the Hg contact (Fig. 16b). In particular, type 2 nanotubes do not break halfway between the contacts, which is where the temperature would be the greatest for freely suspended nanotubes if the nanotubes were dissipative conductors. Hence, we

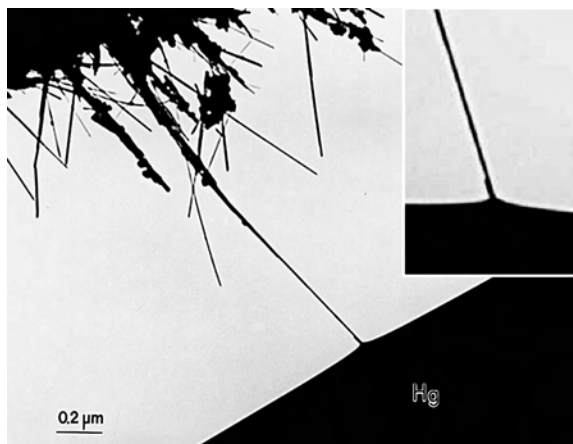


**Figure 15.** *In-situ* TEM image showing the conductance measurement through a single carbon nanotube. The inset is the contact area of the nanotube with the mercury surface.

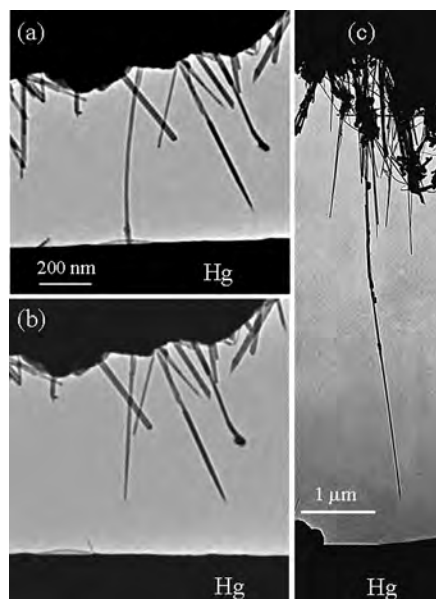


**Figure 16.** *In-situ* observation of electric transport through a single carbon nanotube. (a) Applied voltage  $V = 0.1$  V, current  $I = 7.3$   $\mu$ A, resistance of the carbon  $R = 12.7$  k $\Omega$ , which corresponds to a conductance  $G = (12.7$  k $\Omega)^{-1} = 1.02 G_0$ . (b) After applying a  $4$  V voltage, the nanotube was broken, and the break occurred at the contact of the nanotube and the Hg. (c) The conductance of this carbon nanotube contaminated with graphitic particles is  $0.25 G_0$ .

conclude that the heat dissipation occurs primarily at the contacts, consistent with (but not conclusive evidence for) ballistic transport.

## 4.3. Top-Layer Conductance in MWNT

We now examine the origin of quantum conductance in MWNT at room temperature. Graphite has a unique layer structure, in which the conductivity parallel to the graphitic

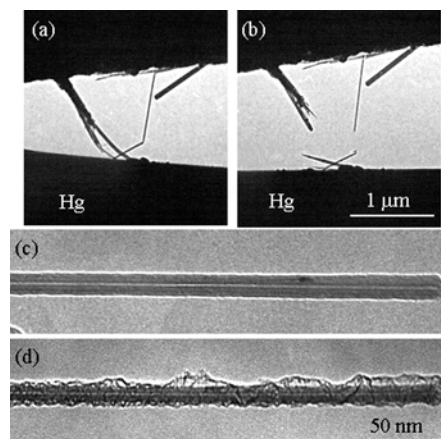


**Figure 17.** Examples of nanotube failure modes. MWNTs (a) before and (b) after passing a large current, showing the breakpoints at the defect sites. (c), (d) An MWNT before and after passing a large current through it. In (d), the tip of the MWNT had been contacted to an Au surface, and current was passed through it. Only the outer layer, starting at the contact point, has been damaged, suggesting that the current flows over the surface.

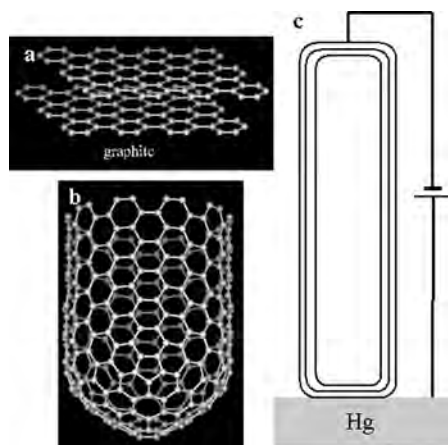


**Figure 18.** (a) Atomic structure of graphitic sheets. (b) A carbon nanotube model with a closed end. (c) Top-layer conductance of a defect-free, closed-end MWNT.

plane ( $a$ - $b$  axis plane) is about 50 times higher than that along the  $c$  axis (Fig. 18a). If the applied voltage is small, so that the interlayer tunneling effect can be ignored, and the end of the nanotube is closed (Fig. 18b), the electric current mainly flows along the top surface layer, provided the tube is perfect and there is no defect. Since the layer thickness of  $\sim 0.34$  nm is comparable to the electron wavelength of 0.5 nm in the graphitic plane, quantum conductance is possible. The unique structure of the nanotube greatly reduces the phonon density of states; thus, the mean-free-path length of the electron is longer than  $10 \mu\text{m}$  [29], possibly resulting in a room-temperature quantum effect. This is possible for a structurally perfect nanotube with closed ends (Fig. 18c). If the applied voltage is large, interlayer tunneling among the nanotube walls is inevitable; the effective size of the object that carries the current is large, finally destroying the quantum conductance effect. On the other hand, if there is a defect, the density of phonons near the defect is different from the rest of the nanotube; a reduced mean-free-path length of the electron at the defect site results in the disappearance of the quantum effect as well. Therefore, nanotubes grown by the CVD process that contain a large density of defects are unlikely to exhibit quantum conductance.

Figure 7d shows an MWNT after passing a large current, which was brought into contact with an Au surface (which replaced the Hg droplet in this experiment). Due to the flow of the shock short-circuit current, the surface of the nanotube is disrupted starting at the contact point, while the interior layers are not visibly affected. This observation provides further evidence that the electronic current passes over the surface layers of the nanotube, for example, single-layer conductance. The observation of Aharonov-Bohm oscillations in carbon nanotubes also supports the top-layer conductance [30].

## 5. SUMMARY

This chapter has reviewed the experimental methods for *in-situ* nanomeasurements of carbon nanotubes based on transmission electron microscopy. The static and dynamic properties of the nanotubes can be obtained by applying

controllable static and alternating electric fields. Resonance of the carbon nanotubes can be induced by tuning the frequency of the applied voltage. The technique is powerful in such a way that it can directly correlate the atomic-scale microstructure of the carbon nanotube with its physical properties, providing a one-to-one correspondence in structure-property characterization. This is a new approach toward nanomechanics.

The work function at the tips of individual multiwalled carbon nanotubes has been measured by an *in-situ* transmission electron microscopy technique. The tip work function shows no significant dependence on the diameter of the nanotubes in the range of 14–55 nm. The majority of the nanotubes have a work function of 4.6–4.8 eV at the tips, which is 0.2–0.4 eV lower than that of carbon. Field emission of the individual carbon nanotubes was observed by *in-situ* transmission electron microscopy. A fluctuation in emission current was due to a variation in the distance between the nanotube tip and the counterelectrode owing to a “head-shaking” effect of the nanotube during field emission.

We also presented the conductance measurements of individual carbon nanotubes using the two-electrode contacting technique. We discovered that freely suspended MWNTs are 1-D conductors with quantum conductance at room temperature. A large current density is sustained, and the current is carried out by the outermost layer of the MWNT. Carbon nanotubes contaminated on the surface either by graphitic particles or during lithographical manipulation do not show quantum conductance. Defects can destroy quantum conductance, resulting in heat dissipation.

## GLOSSARY

**Ballistic transport** Elastic transport process during which an electron experiences no inelastic collision; thus, no heat is generated. This is possible if the length of the transport wire is shorter than the inelastic mean-free-path length of the electron in the material.

**Bending modulus** Elastic property of a tubular structure that describes its inherent stiffness. It is determined not only by the Young’s modulus of the materials that are made of the tubular structure, but also by the geometrical parameters of the tube.

**Field emission** Emission of electrons from a solid surface under an externally applied electric field.

**Quantum conductance** Electron wave elastic transmission through a solid wire without inelastic collision; the trace of the transmission coefficient derived from quantum scattering theory is defined to be the electric conductance  $G$ , which is a multiple of  $G_0 = 2e^2/h = 1/(12.9 \text{ k}\Omega)$ , depending on the number of conduction channels, but independent of the length of the wire, provided that the length of the transport wire is shorter than the inelastic mean-free-path length of the electron.

**Work function** Energy required to extract an electron from a semi-infinite solid surface to infinity.

**Young’s modulus** Elastic property of solids that describes the inherent stiffness of the material. It is the slope of the stress-strain curve in the elastic region.

## ACKNOWLEDGMENTS

The author thanks the contributions made by Prof. W. A. de Heer, Dr. P. Poncharal, and Dr. Ruiping Gao on the work reviewed in this chapter.

## REFERENCES

1. Z. L. Wang, Y. Liu, and Z. Zhang, Eds., "Handbook of Nanophase and Nanostructured Materials," Vol. I-IV. Tsinghua University Press, Beijing and Kluwer Academic, New York, 2002.
2. Z. L. Wang, Ed., "Characterization of Nanophase Materials." VCH-Wiley, 2000.
3. P. Poncharal, Z. L. Wang, D. Ugarte, and W. A. de Heer, *Science* 283, 1513 (1999).
4. Z. L. Wang, P. Poncharal, and W. A. De Heer, *J. Phys. Chem. Solids* 61, 1025 (2000).
5. L. Meirovich, "Elements of Vibration Analysis." McGraw-Hill, New York, 1986.
6. Z. L. Wang, P. Poncharal, and W. A. De Heer, *Pure Appl. Chem.* 72, 209 (2000).
7. J. Z. Liu, Q. S. Zheng, and Q. Jiang, *Phys. Rev. Lett.* 86, 4843 (2001).
8. Z. L. Wang, Z. R. Dai, Z. G. Bai, R. P. Gao, and J. Gole, *Appl. Phys. Lett.* 77, 3349 (2000).
9. R. P. Gao, Z. L. Wang, Z. G. Bai, W. A. de Heer, L. M. Dai, and M. Gao, *Phys. Rev. Lett.* 85, 622 (2000).
10. S. Iijima and T. Ichihashi, *Nature* 363, 603 (1993).
11. M. M. J. Treacy, T. W. Ebbesen, and J. M. Gibson, *Nature* 381, 678 (1996).
12. E. W. Wong, P. E. Sheehan, and C. M. Lieber, *Science* 277, 1971 (1997).
13. P. Poncharal, Z. L. Wang, D. Ugarte, and W. A. de Heer, *Science* 283, 1513 (1999).
14. T. W. Ebbesen, P. M. Ajayan, H. Hiura, and K. Tanigaki, *Nature* 367, 519 (1994).
15. T. W. Ebbesen, H. J. Lezec, H. Hiura, J. W. Bennett, H. F. Ghaemi, and T. Thio, *Nature* 382, 54 (1996).
16. S. Frank, P. Poncharal, Z. L. Wang, and W. A. de Heer, *Science* 280, 1744 (1998).
17. W. A. de Heer, A. Chatelain, and D. Ugarte, *Science* 270, 1179 (1995).
18. R. P. Gao, Z. W. Pan, and Z. L. Wang, *Appl. Phys. Lett.* 78, 1757 (2001).
19. Z. L. Wang, *Adv. Mater.* 12, 1295 (2000).
20. Z. L. Wang, R. P. Gao, W. A. de Heer, and P. Poncharal, *Appl. Phys. Lett.* 80, 856 (2002).
21. A. G. Rinzler, J. H. Hafner, P. Nikolaev, L. Lou, S. G. Kim, D. Tomanek, P. Nordlander, D. T. Colbert, and R. E. Smalley, *Science* 269, 1550 (1995).
22. S. Frank, P. Poncharal, Z. L. Wang, and W. A. de Heer, *Science* 280, 1744 (1998).
23. J. Cumings, P. G. Collins, and A. Zettle, *Nature* 406, 586 (2000).
24. P. G. Collins and P. Avouris, *Nanolett* 1, 453 (2001).
25. S. J. Tans, M. H. Devoret, H. Dai, A. Thess, R. E. Smalley, L. J. Geerligs, and C. Dekker, *Nature* 386, 474 (1997).
26. S. Frank, P. Poncharal, Z. L. Wang, and W. A. de Heer, *Science* 280, 1744 (1998).
27. P. Poncharal, C. Berger, Y. Yi, Z. L. Wang, W. A. de Heer, and *J. Phys. Chem. B* (2002).
28. M. S. Fuhrer, J. Nygard, L. Shih, M. Forero, Y. G. Yoon, M. S. C. Mazzoni, H. J. Choi, J. Ihm, S. G. Louie, A. Zettl, and P. L. McEuen, *Science* 288, 494 (2000).
29. C. T. White and T. N. Todorov, *Nature* 393, 240 (1998).
30. A. Bachtold, C. Strunk, L. P. Salvetat, J. M. Bonard, L. Forro, T. Nussbaumer, and C. Schonenberger, *Nature* 397, 673 (1999).

# Integrated Passive Components

Richard Ulrich

University of Arkansas, Fayetteville, Arkansas, USA

## CONTENTS

1. Introduction
  2. Motivation and Challenges
  3. Applications for Integrated Passives
  4. Integration of Resistors
  5. Integration of Capacitors
  6. Integration of Inductors
  7. Status of Passive Integration
  8. The Future of Integrated Passives
- Glossary  
References

This chapter is excerpted from *Integrated Passive Component Technology*, by Richard Ulrich and Leonard Schaper, © 2002 IEEE Press, and is used by permission of IEEE Press/John Wiley & Sons, Inc. Reproduction, adaptation, or any further distribution of this material is expressly prohibited without permission of John Wiley & Sons, Inc.

## 1. INTRODUCTION

Tremendous progress has been made in the past four decades in miniaturizing and integrating transistors and capacitors for logic applications onto silicon. By comparison, passive components (resistors, capacitors, and inductors) at the circuit board level have made only incremental advances in size and density. Consequently, passive components occupy an increasingly larger area and mass fraction of electronic systems, and are a major hurdle to the miniaturization of many electronic systems. This is particularly true for analog and mixed-signal applications that use a larger number of passives than typical digital applications. The surface of cell phone boards can be over 50 percent occupied by passives.

Almost no through-hole axial-leaded resistors and disk capacitors are used anymore; they have been replaced with smaller rectangular surface-mount components with solder joints at both ends. The size of these modern discretes is described by a number such as 0603, which indicates a size of  $60 \times 30$  mils ( $1.5 \times 0.75$  mm). The 0402 ( $1.0 \times 0.5$  mm) size

is commonly used, and the smallest discrete passives today are 0201 ( $0.50 \times 0.25$  mm), which represents a considerable challenge in handling and attachment. About a trillion passive devices were placed in electronic systems in 2000, with the vast majority utilizing surface-mount technology. Today, each mounted passive costs about half a cent to purchase, and about 1.3 cents for conversion (assembly) for a total of 1.8 cents. Therefore, the present total market for passive devices is around \$18 billion annually [1–3].

If passive components could be integrated in somewhat the same manner as transistors have been on integrated circuits, they might enjoy the same economy of manufacture, functional density, and performance enhancements. For that reason it is an active area of research and development in the microelectronics systems industries. The “nano” aspect of this comes about because of the use of very thin films, under  $500 \text{ \AA}$  in many cases, to achieve passive integration into circuit boards.

### 1.1. Definitions

The concept of “integrated,” “integral,” “embedded,” “arrayed,” or “networked” passives involves manufacturing them as a group in or on a common substrate instead of in their own individual packages. The distinction with present technology is as follows:

Discrete passive component is a single passive element in its own leaded or surface mount technology (SMT) package. An example would be a single resistor, capacitor, or inductor in an 0402 package. This will typically have two contacts to be soldered to the board. Presently, the vast majority of passives are utilized in this manner and this is what passive integration seeks to eliminate. (Fig. 1.)

Integrated passive component (IP) is a general term for multiple passive components that share a substrate and packaging. They may be housed inside the layers of the primary interconnect substrate, which would give them the sub-designation of an “embedded passive component,” or they may be on the surface of a separate substrate that is then placed in an enclosure and surface mounted on the primary interconnect substrate, in which case they would be called “passive arrays” or “passive networks.” (Fig. 2.)



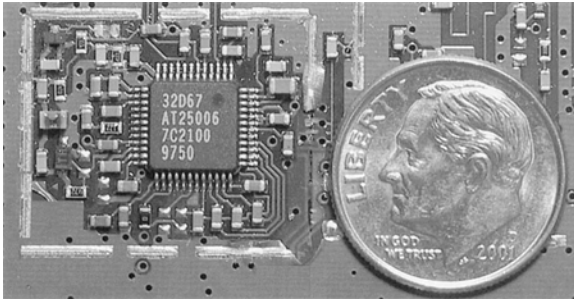


**Figure 1.** Cell phone RF section utilizing 0402 surface mount passives grouped around a single integrated circuit.

## 1.2. Types of Interconnect Substrates

There is a vast array of materials, processing methods, and configurations in use as interconnect substrates—from resin-impregnated paper with printed conductors on the low end to single-crystal silicon with photolithographic thin film build-up layers on the high end. In between there is FR4, ceramic, polymer film, and rigid inorganics, each of which can be composed of a multitude of specific materials and processed in dozens of ways. The number of possible interconnect substrates times the number of processes to achieve them times the number of materials and processes for integrated passives equals an impossible number to describe individually. In order to make this manageable, the types of substrates must be grouped.

The primary natural division is into organic and inorganic designations. “Organic” means that there is a polymer material, either thermoset or thermoplastic, in the board even if it makes up a small fraction by mass. This will limit the maximum temperature for any processing to around 200 °C–300 °C and possibly lower for some steps. Inorganic substrates, such as alumina, can withstand well over 700 °C–1,000 °C and are usually limited by the softening point of the metals. Integrated passives are highly developed in ceramic substrates, but these make up only a small fraction of the total boards sold, especially in consumer products. The major emphasis in integrated passive research

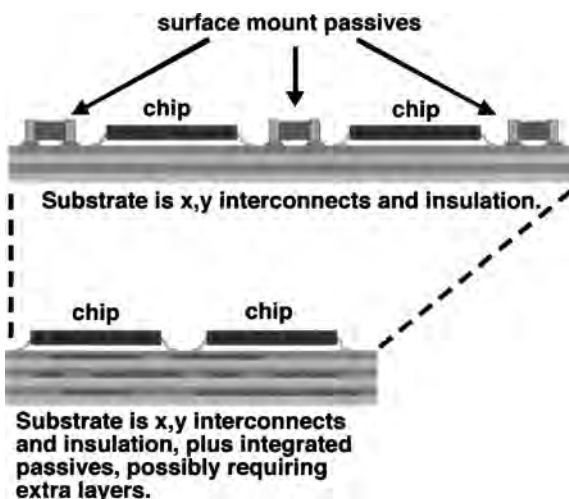


**Figure 2.** Integration of passive components into a system's substrate.

today is for organic-containing materials such as FR4, BT, and flex, which make up about 85 percent of the boards manufactured today and a larger fraction of boards in consumer products. Therefore, the necessity for low processing temperatures is an important consideration in integrated passive development.

## 1.3. Overview of Integrated Passive Fabrication

At present, neither the optimal materials nor methods for fabricating integrated passives on organic substrates have been established. This is a limiting factor in their use in the most common substrates. Due to the planar nature of integrated passives, the formation and patterning of films are central to this technology. There are three broad classes of films required: conductive, resistive, and dielectric. Conductive films are those that are needed for carrying current with a minimum of voltage loss, such as the top and bottom plates of capacitors and the spiral windings of a planar inductor. There is no advantage to having parasitic resistance in this type of film; that would only degrade the performance of the capacitor or inductor. Therefore, these would normally be metals or else very conductive metal-filled polymer thick films with resistances less than about 0.1  $\Omega$ /square. Narrow tolerance and repeatability is not a major issue as long as the overall resistance is low enough for the application. Of course, it would be desirable for integrated passives to utilize the same metal used as interconnect on the substrate. Resistive films would be used in making integrated resistors only, and would be specified on the basis of providing predictable, reproducible values of resistance in a sufficiently small footprint. A wide variety of materials could be used for this, ranging from resistive alloys (NiCr, CrSi, TaN<sub>x</sub>, TiN<sub>x</sub>O<sub>y</sub>) to ceramic-metal nanocomposites (cermets) to carbon-filled polymers. Resistivities of 100 to 10,000  $\Omega$ /square are required. Dielectric films would be used to form integrated capacitors, and a vast array of materials with a wide range of dielectric constants are feasible from simple unfilled polymers for small-valued capacitors ( $k = 2$ –5) to amorphous metal oxides ( $k = 9$ –50) to highly ordered mixed oxides for the highest possible dielectric constants ( $k > 1,000$ ). There are essentially no fabrication issues for inductors; they are simply shaped conductors made from the interconnect metallization already present in the boards.

These three types of films can be formed subtractively or additively by sputtering, CVD, evaporation, anodization, dry oxidation, sol-gel, spin-on, doctor blade coating, chemical conversion, and many others. Etching options include liquids and a variety of reactive and unreactive, directed or nondirected plasmas. Also, they can be modified by annealing. Integrated passives are not a new idea; they have been used for decades in ceramic substrates and on various substrates under the name “hybrids.” Thick-film pastes of conductors and dielectrics are used to form resistors, capacitor dielectrics, and spiral inductors that are fired simultaneously with the green tape of the insulating layers. However, the firing requirements mean that this technology is not transferable to heat-sensitive organic substrates. Glass has been used for integrated passive substrates by Intarsia, and silicon had a brief period of use as an MCM substrate; Bell

Labs and N-Chip utilized an integrated decoupling capacitor as part of the buildup over a silicon substrate for their MCM designs. Organic substrates make up the vast majority of interconnect boards due to their low cost, and it is here that integrated passive efforts are most important. Because organic boards cannot tolerate temperatures much above about 250 °C, many processing options are not possible including all involving fired ceramic thick films. Whatever methods and materials are chosen must be compatible with the board's conductors and insulation layers already in place, integrated passives already in place, and any fabrication following.

## 2. MOTIVATION AND CHALLENGES

Both technical and economic issues should be considered in order to determine the ultimate worth of changing technologies. Deciding which engineering option will provide a higher return on each dollar invested cannot be based solely on the goal of lowering the cost to make the same product; the implications are much more nebulous and include concepts such as increased functionality, added product value, higher consumer appeal, and the ability to make products that cannot be realized with the older technology. Some of these issues are difficult to quantify; for instance, what is the added dollar value to a cell phone that is made 20 percent smaller? There is a real worth to this type of improvement, but it is a function of consumer psychology, which is notoriously difficult to enumerate. The merely technical issues often can be quantified fairly accurately.

### 2.1. Reasons for Integrating Passives

For integrated passives, the reasons in favor of integration can be broken down into these motivations:

1. *Reduced system mass, volume, and footprint.* Individual packages are eliminated and passives can go underground leaving more room on the surface for ICs.
2. *Improved electrical performance.* Integrated passives can have lower parasitics, particularly much lower inductance in capacitors.
3. *Increased design flexibility.* The component's resistance, capacitance, or inductance can be sized to any desired value within the technology's range.
4. *Improved reliability.* Solder joints are eliminated.
5. *Reduced unit cost.* Integrated passives can be formed simultaneously and with very low incremental cost. Also, they are inherently lead-free.

Not all integrated passives have smaller footprints than the surface mount devices they might replace. In fact, the higher values of integrated capacitors and inductors would occupy a much larger area. For example, a 100 nF integrated capacitor formed by sputtering 3,000 Å of Al<sub>2</sub>O<sub>3</sub> onto a circuit board would require almost 4 cm<sup>2</sup> of area, compared to only 0.01 cm<sup>2</sup> for a 0402 surface mount capacitor plus its associated keep-away distance. Similarly, a 50 nH planar spiral inductor could be made from five turns of 5 mil conductor, but would have an outer diameter of 3.3 mm. Furthermore, this inductor would require a keep-away distance on all layers of the substrate—not just one like a

capacitor or a resistor—about equal to its radius to avoid interference from other metal with its electromagnetic field that would reduce its effective value. Its total area would be 0.34 cm<sup>2</sup> and would be effectively multiplied times the number of layers in the substrate that must be kept clear. Integrated resistors and small-valued capacitors are much closer to, or even smaller than, their surface mount size. The reduction in system form factor with integrated passive technology would come from the fact that integrated passives, regardless of their footprint, can be fabricated under the surface of the board, which frees up top-surface area that was formerly occupied by surface mount passives. Since many wireless and mixed-signal systems have something like half of the board surface occupied by passives, the footprint reduction can be significant. Additionally, system mass may be reduced by stripping an integrated resistor, capacitor, or inductor down to only its electrically active portions, leaving less than a milligram of metal and/or dielectric. The integrated passive would depend on the substrate for mechanical support and the layers above and below it for environmental protection, thus eliminating the mass and volume of the individual package.

The price paid for this integration is that additional board layers may be required to accommodate these passives in their integrated form, adding cost and complexity to the manufacturing process, which can offset some of the benefits of freeing up surface area and reducing volume or mass. This is an important tradeoff in passive integration and will be a major driving force in the economic viability of any integrated approach. It is not clear that more layers will always be required for integrated passives; savings in wiring and, especially, vias required to route all passive connections to the surface may be significant if the passives can be placed on any desired layer. As previously mentioned, active logic devices can be scaled down to nanometer scales, principally by improvements in processing technology, since they can operate with arbitrarily few electrical quanta. But passives may have to maintain values of resistance, capacitance, and inductance regardless of their size, and footprint reduction can come about only by improvements in materials to give higher specific values per unit area. This is particularly problematic for integrated capacitors.

Due to their simplified structure and lack of leads and contacts, integrated capacitors and resistors tend to have considerably less parasitic inductance than their surface mount counterparts. Also, short leads to the integrated capacitor or inductor can result in less parasitic resistance. As a result, integrated passives tend to be “purer” components with less undesired properties to be taken into account in the design phase. Lower parasitic inductance is particularly important for capacitors in high-frequency applications such as decoupling and RF filtering, since, above the self-resonance frequency, the inductive properties of the capacitor dominate the component's behavior, making it act completely like an inductor. Integrated capacitors can be fabricated that have far higher self-resonant frequencies and therefore a larger usable frequency range than is possible with any discrete capacitor, no matter how much the latter is optimized for low inductance. This is a major motivation for integrating capacitors, as will be discussed next.

An additional electrical advantage comes about because the value of integrated passives can be specified exactly. If an 18.2 nF capacitor, a 2,360  $\Omega$  resistor, and a 14.6 nH inductor are needed for a design, the integrated passives can be sized to give those values (within tolerance limits); it is not necessary to choose the next closest value from a catalog of discrete passives or to create the values by stringing together discretely in series and/or parallel. Using multiple discretely may take up a large amount of board space, require a large number of lead attach steps, and exacerbate problems associated with parasitics.

With regard to reliability, the use of integral passives does eliminate two solder joints per passive, which are major failure points for systems with discrete components. However, the use of new materials and fabrication methods necessary for integration may bring with them new failure modes that have not been fully revealed. There is much research to be done to validate the conjecture that integrated passives enhance system reliability. The standard environmental and thermal stress tests will still apply, but, while discrete components may be tested on their own to identify failure modes not associated with the solder joints, integrated passives must always be tested in the systems that they will occupy, since the interconnect substrate forms their packaging. Of particular concern is the result of mechanical stresses on large-area capacitors and long resistors brought about by CTE mismatch, layer-to-layer slippage during fabrication, and flexure.

Because integrated passives can be formed simultaneously, the incremental cost of producing just one more is nearly zero. This characteristic is attractive for systems that require dense placement of passives, the direction in which most systems are heading. A major issue in business models for integrated passives is whether all of them can be integrated or only some. If they can all be integrated, then there is no need for any pick-and-place equipment for surface mount passives, just for the ICs, and the cost model needs to consider only one technology set for passives: integration. However, if only most of them can be integrated, then it may be more difficult to be cost-competitive, since the manufacturing facility must support both technologies at once. Some passives, such as large-value capacitors and inductors, may be very challenging to integrate due to their large footprints, even in buried layers, and may be best left as surface mounts. On the plus side, integrated passives are inherently lead-free. At present, economic analysis to determine the feasibility of integrated passives is specific to both the application and the integrated passive technology.

## 2.2. Problems with Integrating Passive Devices

The problems with implementing integrated passives on organic boards are as well-understood as their potential benefits.

1. *Indecision on materials and processes.* Research continues on many resistor materials and capacitor dielectrics.
2. *Lack of design tools.* For both component sizing and system layout.

3. *Requires vertical integration.* The same company must manufacture both substrates and passives.
4. *Yield issues.* One bad component can scrap the entire board.
5. *Tolerance issues.* Integrated passives cannot be pre-sorted prior to inclusion on the board.
6. *Lack of standardization.* The various segments of the integrated passive industry aren't speaking the same language [4].
7. *Surface mount technology is improving.* Moving toward 01005.
8. *Lack of costing models.* It's not easy to tell when integrated passives might be more cost effective.

It's not that it cannot be done; scores of research projects have shown that the full required range of  $R$ ,  $C$ , and  $L$  values are achievable on just about any substrate. The problem is that the optimal materials and processes have not been identified, if they exist for a given substrate, and that the infrastructure does not yet exist in the industry for their design and manufacture. The physical integration of passive components into circuit boards necessitates the integration of the corresponding business units. For example, a manufacturer that previously made only boards but now expands into integrated passives finds itself in the business of making passive components instead of simply buying them out of a catalog. That means having to understand issues of passive performance, fabrication, sizing, tolerance, parasitics, and reliability, which were previously taken care of by a separate entity.

There are two main aspects to the design issue: designing the individual components and designing the components into a system. Taking the narrower one first, designing individual integrated resistors and capacitors is easy but dependent on the materials used, since this will influence the value density of the structure, such as the number of nF/cm<sup>2</sup> for an integrated capacitor. If the ohms/square of the resistor film or the nF/cm<sup>2</sup> of the dielectric film are known, then it is a simple matter to size the component for a required overall value. Therefore, the component's material and processing technology have to be established before components can be sized. For inductors, the design situation is much more complex. Accurate sizing of a spiral inductor from first principles requires solving Maxwell's equations for a spiral shape on a Cartesian geometry with various other conductors from the eventual system layout present to distort the magnetic field. Although there are some excellent approximate design tools for isolated spirals, the presence of other conductive materials nearby means that the design of the integrated inductor usually can't be done as a standalone component. Trial and error with physical prototypes sometimes will be required.

With regard to overall layout, only a few programs are capable of taking integrated passives into consideration by incorporating them from SPICE-like electrical models, autorouting around them, or optimizing their placement on and among layers. Doing all of these by hand is possible but can be quite tedious, and very few designers are experienced with integrated passives to the extent of knowing the pertinent layout issues necessary for taking advantage of their unique electrical and size characteristics. However, progress is being made in this area by design and layout software vendors, and there is no major technological hurdle to enabling

these programs to utilize integrated passives effectively and with the same ease of operation as they do for surface mount boards. Again, the processes must be established first.

On the assembly side, attachment of surface mount discretes is one of the last steps to be performed on a circuit board prior to its inclusion in the overall system. All of the layers and conductors are fully formed and tested before the passives go on. The only concession made by the board designers to the eventual presence of the surface mount passives, and ICs for that matter, is that proper attach metallurgy be available and that the board be able to withstand the temperatures associated with the attachment process. The attachment typically uses reflowed or wave solder, requiring about 250 °C for up to a few minutes, or else uses conductive epoxies, which usually have even milder thermal requirements. However, if integrated passives are utilized, they will be fabricated as part of the board's manufacturing flow, and the portions of the board already formed will have to be able to withstand not only the thermal stresses that a particular integrated passive technology requires, but also any chemical and mechanical exposures that are involved. Subsequent interconnect/insulator processing must not degrade any integrated passives that are already in place, and any integrated passive processing must not degrade the board layers already in place. Not only are the passives integrated into the board, but their processing requirements are mixed in as well.

The same yield problem exists for integrated passives as is well known for integrated circuits; one bad component out of many can force the entire board to be scrapped. The problem might not be apparent until the substrate is completed, so a considerable amount of fabrication may be wasted if the bad component is formed early on. Rework might be possible, but few procedures for this have been developed or reported in the literature. This same problem was identified and solved for active integration, enabling tens of millions of components to be formed on silicon with IC yields routinely over 75 percent. The same issue impacts tolerance; discrete passives may be presorted by value while the values for planar integrated passives will be ruled by sizing tolerances associated with film patterning or printing. In the case of integrated capacitors, because they are area-ruled, the resulting variation in value will be higher than the variation in one-dimensional sizing. Attempting to make smaller integrated passives will result in less exact values. Trimming technology for integrated passives requires further development. The use of singulated and embedded passives might help to alleviate these problems by enabling sorting for yield and tolerance.

Meanwhile, surface mount technology continues to improve. On the average, surface mount passives have gone down by about one case size every four years. Sizes as small as 0201 ( $0.50 \times 0.25$  mm) are in use and, although it is hard to imagine them becoming much smaller, there is work in progress for 01005 components. With a 10 mil keep-away distance, the theoretical density for 0402s is 107 components/cm<sup>2</sup> and for 0201 it is 270/cm<sup>2</sup>. However, in some instances, integrated passives may be the only way to make the product possible. This situation is rapidly approaching in the case of decoupling upcoming generations of microprocessors that will draw very high bursts of current

from the board's power and ground planes. Surface mount capacitors may exhibit too much inductance to do the job, and integrated capacitors may be the only way to enable these chips to function.

### 2.3. Cost Modeling

The greater the detail necessary to accurately model a system, the less general and more application-specific are the results. This is the situation with integrated passives on organic boards. Because the specific processes and materials have not yet been reduced to a manageable number, it is not currently possible to say when passive integration is and is not economically feasible. No generalized models exist to aid the manufacturer. This sounds like a chicken-and-egg problem, but it can be cracked by first assuming a specific and feasible material and process set for the existing manufacturing infrastructure and for the potential product, and then performing the costing based on that [5, 6].

What is the impact of passive integration on an existing board design that utilized surface mounts? Of primary importance is that the number of layers will probably increase due to the need to accommodate subsurface passives. Also, if reduced board form factor is desired, this will also add pressure to increase the number of layers simply to accommodate the interconnects. PWB cost goes about linearly with number of layers. Adding another signal layer to a controlled impedance board actually requires the addition of two layers, since a ground or power layer has to be added as well between the signal planes. The decrease in board area will result in a more compact product, but the benefit of this is harder to put into terms of dollars than is the cost. It does have the advantage of increasing throughput since there can be more boards per panel, but board yield will probably decrease, for the reasons discussed earlier in this section. There may be some decrease in wiring and, particularly, via density due to the reduced need to route to specific areas on the surface to accommodate surface mount units. Instead, it may be possible to put the passive in any given layer and position where it is needed. Overall, each design needs to be considered on a case by case basis, at least until much more experience with these designs has been accumulated.

## 3. APPLICATIONS FOR INTEGRATED PASSIVES

In principle, integrated passives can replace discretes in any application, but in what forms will they find widespread use? Except for decoupling, the circuit schematic will not generally change if integrated passives are used instead of discretes, though slightly fewer integrated passives may be used if exact component values can be made in one unit instead of having to string discretes together in series or parallel to achieve a specific value. Therefore, replacement of resistors and most capacitors will be at a ratio of one to one. This section will discuss some of the most likely initial applications and describe what factors will motivate the switch from surface mount to integration.

### 3.1. Replacing Surface Mount Discretes with Arrays and Networks

Individual surface mount discrete passives can be replaced with a smaller number of integrated passives formed, not inside the primary interconnect board, but on a separate substrate that is then mounted on the surface of the primary board. This integration approach is referred to as passive arrays or passive networks and can result in significant assembly cost savings with a minimum of design and process changes. Arrays will have the same number of total contacts but are achieved with fewer component placements. Passive networks contain internal connections that result in fewer mounted components and contacts. Not only are there fewer components to mount, but each one is bigger than the individual units it replaces, and therefore easier to handle, but it has a smaller total footprint on the board than the group it replaces. Since this brings almost all of the advantages of passive integration with few of the problems, both listed above, this trend is well underway and represents the majority of integrated passive usage today, especially for units mounted on organic boards. The reason this approach has gained rapid acceptance is that it maintains the separation between passive integration issues and substrate issues. The only concession for the board is that pads be moved to accommodate the layout of the integrated surface mount units. The board maker does not have to be in the passive manufacturing business and the integrated units can be pre-sorted and tested to avoid yield and tolerance problems.

Numerous configurations of  $R + C$  networks are available in quantity from reputable vendors, and custom arrangements are possible. Integrated inductors are also available. Off-the-shelf versions include filters, terminators, and low-inductance decouplers. With diodes and transistors added to silicon substrates, networks can include ESD protection, oscillators and amplifiers. RC termination is a popular application for passive networks, since densely packed groups of resistors and capacitors are required to terminate wide bus lines. Integrated RC termination networks can be formed in single packages with footprints to match the physical bus width on the board and will require only half the number of pads since there are internal R-C connections within the unit.

There is much more to be squeezed out of this approach as the passive networks become merged with active devices to form what NEMI refers to as “functional modules,” which could include, for instance, Bluetooth or GPS subsystems mounted as surface units on the primary interconnect board. There is tremendous potential flexibility with little downside. For example, a cell phone maker could include a GPS receiver in the form of a surface mount module that would include integrated passives and integrated antennas, as well as integrated transistors on one piece of silicon in a single chip scale package. The company would not have to worry about going into the business of manufacturing GPS systems and could also upgrade or switch vendors when required, possibly with the same surface pad layout. At this point, the distinction between which is the primary interconnect substrate and which is the add-on module becomes blurred. In the limit, the main board may have no passives at all and simply provide interconnection among various functional modules.

### 3.2. Decoupling

High-frequency operation of digital logic circuitry places severe demands on power distribution systems to supply stable, noise-free power during the clock-driven simultaneous switching of millions of transistor gates. Decoupling capacitors are necessary to supply these large current surges, ramping as fast as 500 A/ns, to high-power microprocessor and logic ICs during the switching portions of the clock cycles. The purpose of this is to ensure that unacceptable drops in logic voltage levels do not occur due to the high current demands on a power supply that may be located many inches away down narrow conductor paths. Between cycles of current demand, the power distribution system recharges these capacitors in preparation for the next switching cycle. It's not too simplistic to think of the capacitors as actually providing the power to run the chips with the power supply merely acting as a battery charger during low-demand periods. In other terms, the impedance of the power supply is too high to prevent voltage drop during high demand periods, so the capacitors must provide low impedance power to the chip [7, 8].

Sizable groups of surface mount decoupling capacitors can be seen surrounding the microprocessor on almost any circuit board. Even memory chips are starting to draw enough power to require decoupling capacitors. The two main requirements for these capacitors are that they provide sufficient charge to run the chip for one clock cycle and that they provide that power at low impedance to prevent excessive voltage drop during moments of high current draw by the chip. Of these two criteria, the low impedance issue is the more challenging to surface mount capacitors. The inherent parasitic inductance of surface mounts requires that many separate capacitors be arranged in parallel in order to lower the overall inductance, resulting in a large number of small caps instead of a few large-valued units. That means using more board area near the microprocessor, where space is at a premium anyway, and more solder joints. Also, the temperature extremes are higher near the chip, which can cause a variety of reliability problems, including failure of those solder joints.

The much lower parasitic inductance of integrated capacitors, the ability to bury them beneath the surface of the board, and the lack of solder joints makes them very attractive for replacing surface mount capacitors in decoupling. Because of their inherently low inductance, there is no need to use multiple capacitors in parallel; a single large integrated capacitor will suffice. The inductance is so low that, when using integrated capacitors, the designer must consider the inductance of the vias and interconnects from the power/ground planes to the capacitor, while these contributions are usually negligible compared to the inductance of surface mount capacitors. The major unknown in replacing surface mount decoupling capacitors is how much capacitance is needed. With surface mount, an excess of capacitance is usually present because of all the units placed in parallel to lower the total inductance, but, with integrated capacitors, probably much less will suffice. Exactly how much less is not fully understood and can only be determined with a combination of modeling and power/ground voltage measurements with a variety of integrated capacitor values.



### 3.3. DC/DC Conversion

One application for integrated capacitors, either on a substrate or on the ICs themselves, is as charge storage elements in DC-to-DC converters. For example, charging capacitors in series and discharging them in parallel achieves a step-down function. If the switching frequency is high enough, relatively small capacitors can be used for small (~1 W) converters. Localized power conversion of this type becomes more and more important as IC supply voltages decrease and large currents must be supplied.

### 3.4. Passive Replacement in FR4

Developing passive integration for commodity FR4 will open up a huge market. Because it is such a large target, there is a concerted effort to solve the problems associated with integration onto this platform. In October 1998, NIST funded the Advanced Embedded Passives Technology Consortium (AEPT) to develop the materials, design, and processing technology for embedding passive devices onto circuit board substrates. This combination of industrial partners and associations is tackling the parallel issues of processing, materials, design software, cost modeling, standardization, testing, and reliability for FR4. AEPT made this task manageable by selecting a small number of integration technologies (materials and processes) and building the modeling, reliability, and costing efforts around those. As the results and products come onto the market over the next few years, many of the obstacles will be solved or made manageable, enabling integration to penetrate this market.

### 3.5. Passive Replacement in HDI

The various forms of HDI interconnect will employ processing steps not common in the FR4 domain such as sputtering, buildup, spin on, dry etching, and more. A wider spectrum of metals and dielectrics will also be used. This provides the opportunity to employ a variety of possible integrated passive processes and materials into this maturing technology. If these are all developed in parallel, integrated passives will arrive as part of the infrastructure instead of as an add-on.

## 4. INTEGRATION OF RESISTORS

Integrated resistors are fabricated either by depositing and patterning a layer of resistive material or by printing resistive paste in series with an interconnect line on an insulating substrate. In keeping with the concept of a planar, stacked assembly, the resistor will be a film of material, probably between a few hundred angstroms and a few microns thick [9, 10].

Assuming that all of the resistance is in the resistor material and not in the interconnects, the resistance of the structure is

$$R = \frac{\rho L}{Wt}$$

where  $R$  = resistance,  $\Omega$ ,  $\rho$  = resistivity of the material,  $\Omega$ -cm,  $L$  = length of the strip, cm,  $W$  = width of the strip, cm and  $t$  = thickness of the strip, cm.

The resistivity of a material is an intrinsic property and is a function of composition and microstructure. For thin films, the resistivity can be somewhat different from that of bulk materials, and is generally higher.

Sheet resistance is defined by

$$R = \left(\frac{\rho}{t}\right)\left(\frac{L}{W}\right) = R_s N_s$$

where  $R_s = \rho/t$  = sheet resistance,  $\Omega$ /square,  $N_s = L/W$  = the number of squares, and  $L$  = length of the strip, cm.

The sheet resistance is the resistance of a square of material ( $L = W$ ) when the electrical contacts cover opposite edges completely. The size of the square is irrelevant as long as length equals width and the contacts completely cover two opposing sides. When long, narrow materials are used, the resistor is thought of as squares in series.

Resistors consisting of many squares are usually formed in a serpentine pattern to fit into an allocated substrate area with corner squares counted as somewhat less than a full square, 0.556 squares, since the current does not have to traverse the entire side-to-opposite-side distance. Thus, a material with a resistivity of 1 m $\Omega$ -cm, that is, 1  $\mu$ m thick would have a sheet resistance of 10  $\Omega$ /square, and this number, multiplied by the number of squares, would give the value of the resistor in Ohms. The benefit of expressing films of resistor materials in  $\Omega$ /square is that it does not matter what the resistivity or the thickness is as long as it gives the desired sheet resistance. For example, in sputtering TaN<sub>x</sub> resistors, the sputtering conditions such as vacuum level, temperature, power, gas composition, etc. may be varied to affect both the material's film thickness and resistivity. It may be impossible to change conditions so that only resistivity or film thickness is adjusted to desired values due to the inevitable cross-dependencies of processing conditions. However, if the sheet resistance is the target variable, processing conditions can be optimized to give the desired value of  $\Omega$ /square without having to measure or specify both the thickness and resistivity. Also, the sheet resistance is a quantity easily measured with standard four-point probes or from simple test structures, again without having to measure either of its two constituent variables.

Once a resistor material and process are selected, it is a simple matter to determine the length/width ratio to give any required value of resistance from the Ohms/square of the material. However, to separate these two measures out of the ratio and establish the actual footprint of the resistor, other factors must be considered such as the following:

- **Heat dissipation.** Integrated resistors must be designed so that the temperature rise during use will not heat them to the point that their value drifts significantly or that failure mechanisms are accelerated to the point of affecting their reliability. Large area resistors are favored regardless of their number of squares. For resistors integrated into circuit boards, three-dimensional thermal simulations are necessary to predict operating temperatures at all parts of the components and assembly.
- **Tolerance.** Tolerance and precision improves for larger areas.  $\pm 10\%$  value precision is considered acceptable for most resistors, but many applications require tolerances down to 1%.

- **Parasitic capacitance.** Long serpentine resistors will exhibit characteristics of capacitors at high frequencies due to coupling between adjacent strips, resulting in a drop in resistor impedance. Small numbers of squares and large strip spacing are favored to minimize this, regardless of the total area.

#### 4.1. Materials for Integrated Resistors

A resistor's performance is a direct function of its composition, microsegregation of composition, crystal structure, film thickness, temperature, and voltage, at least. These, in turn, are functions of processing conditions such as pressure, temperature, power, gas flow, etc. for sputtering, CVD, or evaporation of thin films and cure time and temperature for thick films. Subsequent anneals, which alter crystal structure and composition microsegregation, are often used to modify resistor properties. Some useful reviews of this topic are available [11].

The use of integrated resistors, and capacitors and inductors for that matter, requires that the design and process engineers work together to an extent that is not necessary when off-the-shelf discretely are used. The selection of an integrated resistor technology for a given application requires the simultaneous consideration of electrical performance issues (resistivity, temperature effects, stability) and compatibility with the materials and processing of other parts of the substrate/interconnect/passive assembly. No resistor material should be considered that cannot be deposited, cured, and/or patterned by techniques and chemicals that do not harm the pre-existing substrate, interconnects, and other passive components in place. For these reasons, the integrated passive engineer must understand the potential resistor film materials and processing methods, how those methods affect the composition and structure of

the films, and how the resulting composition and structure affect the electrical properties.

Resistor materials that can be processed at under about 250 °C can generally be used on polymer board materials or organic buildup layers. Of course, these same technologies could also be used on inorganic substrates such as glass, silicon, or ceramic since these are typically more thermally and chemically robust than polymer. There are two restrictions to transferring the technology to ceramic substrates: (1) The ceramic surface may be significantly rougher than organics, resulting in yield and tolerance problems with thin film devices, and (2) ceramic substrates are fired at temperatures usually exceeding 600 °C, which may not be tolerated by some resistor materials.

Most integrated passive resistor applications can be realized using two ranges of sheet resistance: about 100 Ω/square and about 10,000 Ω/square. The lower range can be obtained using any one of several materials, including TaN<sub>x</sub>, CrSi, NiCr, and TiN<sub>x</sub>, and the high end of the resistance range can be covered by cermet or, perhaps, TiN<sub>x</sub>O<sub>y</sub> and LaB<sub>6</sub>. Polymer thick film materials (PTF) can accommodate the entire range, but problems with value stability exist at this time. Elemental metals are generally too conductive to be used for anything but very low valued current sensing applications. Table 1 shows the status of these materials on organic substrates. It should be remembered that these films, formed by any method, cannot subsequently be annealed at high temperature on organic substrates for the purposes of modifying their structure and properties.

#### 5. INTEGRATION OF CAPACITORS

A very wide range of capacitor dielectric materials is potentially useful for integration; some of the most important are shown in Table 2. Ideally, this dielectric constant should

**Table 1.** Materials for integrated resistors.

Material	Resistivity range (μΩ-cm)	Film thickness	Sheet resistance (Ω/square)	TCR (ppm/°C)
Ag	1.6	2 μm	0.0080	4,100
Cu	1.7	2 μm	0.0085	4,330
Au	2.4	2 μm	0.0120	4,000
Al	2.7	2 μm	0.0135	
Ni	6.9	2 μm	0.0345	6,750
Ta	bcc: 13 beta: 180	500 Å	2.6	3,800
Cr	13	500 Å	2.6	3,000
Ti	42	500 Å	8.4	
TaN <sub>x</sub> , CrSi, NiCr, TiN <sub>x</sub> , NiP	100–500	500 Å	20–100	+/-50 with process optimization
NiP	~2,000	1,000–4,000 Å	up to 250 1,000 in development	0–100
TiN <sub>x</sub> O <sub>y</sub>	up to 7,000	500 Å	up to 1,400	+/-100 with process optimization
LaB <sub>6</sub>	10 <sup>7</sup>	10 μm	10,000	+/-200
PTF	very wide, depending on filler	1–2 mil	10–10 <sup>7</sup>	~200
nanocomposite cermets	10 <sup>4</sup> –10 <sup>10</sup> depending on metal/glass ratio	1 μm	100–10 <sup>8</sup>	close to zero or slightly negative

**Table 2.** Dielectric constants for paraelectric and ferroelectric dielectrics.

Material	Dielectric constant	Dissipation factor (%)
Teflon	2.0	0.02
polyethylene	2.3	0.02
BCB	2.7	0.1
parylene	2.7	0.01–0.1
Low e BT Resin	2.7	0.2
BPA Cyanate	3.1	0.4
polycarbonate	3.1	0.1
Mylar	3.2	0.4
SiO <sub>2</sub>	3.7	0.03
polyimide	3–4	0.2–1.0
epoxies	3–6	0.4–0.7
epoxy resin for FR4	3.9	1.2
FR4	3–5	0.5–1.5
E glass	5	0.09
SiO	5.1	0.01
Si <sub>3</sub> N <sub>4</sub>	7–9	
AlN	9	
Al <sub>2</sub> O <sub>3</sub>	9	0.4–1
Si <sub>3</sub> N <sub>4</sub>	9.4	<1
BaTiO <sub>3</sub> (amorphous)	17	
NbO <sub>x</sub>	20	
Ta <sub>2</sub> O <sub>5</sub> (amorphous)	24	0.2–1
SiC	40	
HfO	23, 40	~1
Ta <sub>2</sub> O <sub>5</sub> (polycrystalline)	50	
TiO <sub>2</sub>	31 (anatase) 78 (brookite) 117 (polycrst) ~40–60 (film)	2–5
BaTiO <sub>3</sub> (tetragonal)	up to thousands	5
BaSrTiO <sub>3</sub>	up to thousands	
PbZr <sub>x</sub> Ti <sub>1-x</sub> O <sub>3</sub>	up to thousands	
Ba <sub>0.8</sub> Pb <sub>0.2</sub> (Zr <sub>0.12</sub> Ti <sub>0.88</sub> )O <sub>3</sub>	up to thousands	

be flat with regard to frequency, temperature, voltage, and time. The dielectric should be capable of being bent and stretched to a reasonable degree so that it will not suffer from the effects of CTE mismatch with other board materials during normal temperature excursions and so it can be used in applications with little packaging such as smart cards. It should be amendable to mass production at an economic cost using common materials and patterning techniques that do not harm other parts of the board or components already in place. Certainly, any material and process technology will compromise on some of these issues, which is why no one perfect integrated capacitor dielectric has yet been identified from the hundreds of journal and proceedings articles to date.

There are two broad classes of dielectrics: paraelectrics and ferroelectrics (Table 3). The distinguishing feature between the two is that ferroelectric materials do not lose their ionic polarization when the field is removed and paraelectrics do. Because of lattice hindrances in ferroelectrics, the electric field can pull the ions into configurations that do not relax back to the previous state once the field is removed. As a result, ferroelectrics, analogous to ferromagnetic materials, can possess a residual polarization after the field is removed. Furthermore, this

**Table 3.** Comparison of paraelectric and ferroelectric dielectrics.

<i>k</i>	Paraelectrics 2–50	Ferroelectrics up to 1,000s
<i>k</i> vs. <i>T</i>	little dependence, <500 ppm/°C	Can be highly dependent due to crystal phase transitions and ion mobility
<i>k</i> vs. frequency	little dependence	Decreases significantly, typically above a few GHz
<i>k</i> vs. film thickness	no dependence since amorphous	Highly dependent due to effects on crystal structure
<i>k</i> vs. bias dielectric fatigue	no dependence none	Decreases with DC bias <i>k</i> can decrease significantly with cycles and time
<i>k</i> vs. film structure cure requirements	little or no dependence none	Film must be crystalline May require up to 700 °C in O <sub>2</sub>

residual polarization can be oriented in one direction or the other depending on the direction of the last field. It is this trait that gives them utility in nonvolatile memories. Paraelectric materials are those which cannot be left with a residual polarization once the field is removed because they do not have a mobile charged atom with more than one stable lattice position. This residual polarizability defines ferroelectric and paraelectric materials, but this feature is irrelevant to any projected substrate-level integrated capacitor application. The important difference from the point of view of integrated passives is that ferroelectrics generally have much greater dielectric constants than do paraelectrics, sometimes by as much as three orders of magnitude, because of the mobile ionic charge. For example, the common ferroelectric barium titanate is a perovskite crystal with a Ti cation at the center that can shift back and forth within the confines of this crystal a distance larger than the ions can move in a typical paraelectric such as tantalum oxide. This motion creates a considerably larger dipole arm than is possible in Ta<sub>2</sub>O<sub>5</sub>, resulting in a much larger dielectric constant for BaTiO<sub>3</sub>. Incidentally, it is the fact that this Ti ion can remain shifted to one side or the other after the field is removed that gives BaTiO<sub>3</sub> its ferroelectric residual polarization behavior. However, to achieve this very high dielectric constant, ferroelectrics must be in an oriented, single-crystal form, which usually requires a curing temperature in oxygen far in excess of what can be tolerated by organic boards. Adapting ferroelectric dielectrics to organics is a major goal of capacitor integration development.

The fact that so many different dielectric materials have been evaluated in just the past few years for applications as integrated capacitors is indicative of the uncertainty in this area. Scores of dielectrics representing all classifications of these materials (oxides, polymers, ceramics, etc.) have been evaluated experimentally in order to identify the technical advantages and disadvantages with regard to fabrication, electrical performance, and reliability as an integrated component. In any new technology, this is a necessary procedure to both cull out the materials that are clearly impractical and to provide the information to establish the economical viability of those that are feasible. The list includes almost every material that has ever been used as a capacitor dielectric as

well as one class of material that was invented specifically for the purpose: ferroelectric nanopowders dispersed in curable epoxy. As it turns out, very few out of this multitude are completely impractical for use as in integrated capacitors, which means that there is a large number of choices that have passed the technical challenges and remain to be evaluated economically.

There is a tremendous amount of research currently underway on high specific capacitance materials and structures, not only for integrated passives, but also for gate dielectrics and memory cells for ICs. Many of the same goals are sought for all capacitor development programs: high specific capacitance, low leakage, high breakdown, and sufficient stability. However, what are considered good properties is very much a function of application. A gate dielectric with a leakage of a mA/cm<sup>2</sup> at 5 V may be considered a low-leakage material for that application, but this is a tremendous amount of leakage for an integrated passive capacitor used in, for instance, an A/D converter. Similarly, a capacitor that might be considered very stable against frequency for energy storage applications might be far too variable to be used as a filter element. There are several excellent overviews of dielectric materials, some written long before integrated passives were conceived [12].

Because integrated capacitors are planar and area-ruled, the best way to express their value is as capacitance per unit area or “specific capacitance.” The following equation uses convenient units:

$$\text{specific capacitance in } \frac{\text{nF}}{\text{cm}^2} = 0.885 \frac{\text{dielectric constant}}{\text{dielectric thickness in } \mu\text{m}}$$

One of these factors is a function of the dielectric material itself and the other depends on its form (film thickness). See Table 4.

Figure 3 shows the length required for the side of a square integrated capacitor to provide a given amount of capacitance for various dielectric materials. The *x*-axis is the total capacitance of the structure, not the specific capacitance, and the *y*-axis is the required length of one side of the square plate of dielectric material in mils. Since integrated capacitors are area-ruled, the lines have a slope of

**Table 4.** Specific capacitance achievable from integratable dielectrics.

Dielectric	Dielectric constant	Thickness (μm)	Specific capacitance (nF/cm <sup>2</sup> )	Energy density at 5 V (μJ/cm <sup>2</sup> )
BCB	2.7	2.0	1.2	0.015
SiO <sub>2</sub>	3.7	0.2	16	0.20
Ferroelectric nanopowders in an epoxy matrix	90	5.0	16	0.20
SiO	6	0.2	27	0.34
Al <sub>2</sub> O <sub>3</sub>	9	0.2	40	0.50
Ta <sub>2</sub> O <sub>5</sub>	24	0.2	110	1.40
TiO <sub>2</sub>	40	0.2	180	2.30
Barium titanate	~2000	1.0	1800	22

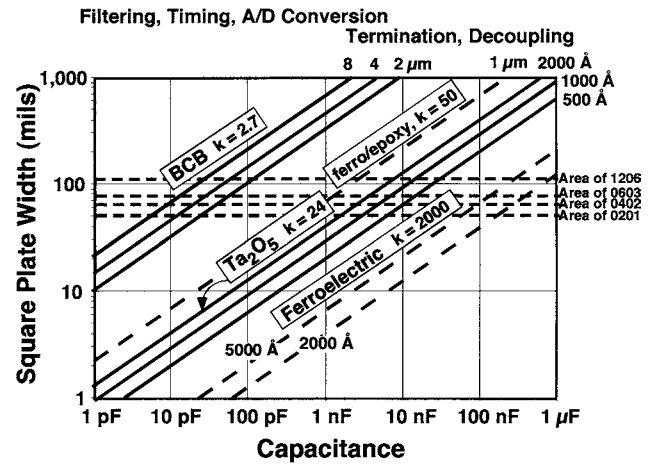


**Figure 3.** Square plate sizes required for various integrated capacitor technologies.

1/2 on log-log coordinates. A few representative dielectrics are shown for some practical thicknesses. Other dielectric materials of known dielectric constant and thickness may be interpolated into the diagram to show their required sizes. The four horizontal dashed lines represent the areas of common surface mount components along with a 10 mil keep-away distance. For comparison purposes, these surface mount components were converted to square areas so that the “square plate width” for these units is the average side length required. It is clear from this diagram that integrated capacitors do not necessarily have a smaller footprint than their surface mount counterparts. For instance, using 2,000 Å of a paraelectric such as Al<sub>2</sub>O<sub>3</sub> or Ta<sub>2</sub>O<sub>5</sub> would result in a smaller footprint only for capacitor values below a few nF. For micron thicknesses of BCB, polyimide, SiO<sub>2</sub>, or SiN, the crossover is around 10–100 pF. However, integrated passives are placed below the surface of the interconnect substrate so, no matter their footprint, they take up no surface area, enabling the system to either be smaller or to have more ICs.

## 6. INTEGRATION OF INDUCTORS

Integrated inductors are the easiest of the IPs to fabricate since they are usually spirals of the conductor material, but they are the most difficult to accurately model. Also, since inductors are magnetic devices, they pose an integration problem not shared by resistors and capacitors: They perform best when there is a sufficient volume of space to allow their magnetic fields to be unimpeded by other structures. As a result, a “keep-away” distance is required for inductors in order to avoid loss of inductance relative to an isolated structure and to prevent interference with nearby signal lines and ground planes from the inductor’s field. Inductors perform poorly over conductive substrates such as doped Si and over dense layers of interconnects due to the magnetic field’s interaction with conductive materials.

The easiest way to fabricate integrated inductors is to simply form a spiral out of the interconnect material, typically 1 to 8 turns with a total outer diameter of 0.2–2.0 mm,

which will provide an inductance of around 1–40 nH. Unfortunately, the prediction of the resulting inductance for integrated spirals, or other inductor shapes, is very complex due to the interaction of magnetic fields with the structure's width, spacing, number of turns, inner diameter, spacing to ground, and the presence of nearby conductors. There are several empirical and semi-empirical methods that can be used to approximate these parameters, most of which use the mutual and self-inductance of concentric rings to approximate a spiral form. A more direct but computationally intensive method involves solving Maxwell's equations with a finite element field solver, which takes into account the distortion of the inductor's fields due to nearby conductive structures.

There are several strategies for increasing the value of integrated inductors. Ferromagnetic alloys such as Fe/Ni can be plated around the windings in order to efficiently guide and focus the fields. However, this means increased cost because of considerably more processing and can also result in the addition of parasitic capacitance between the coil and the plated metal. Ideally, the conductors would be completely embedded within the ferromagnetic material, but almost any geometry of core material addition around the conductors is beneficial. Several other topologies, such as solenoids, toroids, and meanders, are also useful. Two-layer spirals yield approximately double the  $L$ , but with about double the resistance and additional capacitive coupling between the spirals. In addition to applications in signal filtering, these electromagnetic devices have applications in driving MEMS, power conversion, and magnetic sensing. These devices continue to be a focus of intense research.

## 7. STATUS OF PASSIVE INTEGRATION

Embedded passives in primary interconnect boards are not a new idea; they have been used in ceramic substrates for decades. Favored materials and processes for resistors, capacitors, and inductors in LTCC are well-characterized with regard to manufacturing requirements, performance, and economics, and there is a large infrastructure supporting them. A company wishing to use them on ceramics can find accurate and well-developed design tools, cost models, and performance information, and can then buy fully supported equipment and processes from vendors. The main drawback with embedded passives in ceramic is that tolerance is rarely better than around 10 percent due to printing variations, firing variations, shrinkage, and the inability to trim component values. Ceramic substrates, while growing in use with the rest of the industry, will never approach organic boards in sales volume.

Integrated passives are also widely available as surface mount arrays or networks, usually fabricated on Si, that can be mounted onto the surface of ceramic or organic boards using the same sort of infrastructure used for surface mount discretes. This technology is rapidly gaining market share due to the obvious economic advantages with a minimum of changes in board design or on the factory floor for implementation.

To date, integrated passives have not been utilized as embedded structures in organic substrates to a significant degree, particularly with FR4, which makes up the vast

majority of boards sold today. Penetration into this very large market is the driving force for R&D in the area. The problems with this implementation are well understood; both academia and industry are doing their parts in their own ways to solve these issues. Literature, conferences, and workshops for integrated passives on organic substrates began to appear in the mid-90s, and the typical journal article or conference presentation is a demonstration of a material or a process to make resistor, capacitor, or inductor test structures, or else to make a simple multicomponent device such as a filter or terminator. The striking characteristic about the literature is the vast array of materials and processes that have been investigated for integrated resistors or capacitor dielectrics. The list is very long and varied, including metals, ceramics, and polymers, as well as nano- and microcomposites of these materials that can be formed and patterned in dozens of candidate processes. It will take years for the set of candidate processes to be reduced for FR4 and flex. Also, there is very little in the way of design software that is capable of performing automated layout, although some is under development. It will ultimately be economics that determines which integrated passive technologies are suitable for implementation on a given substrate for a proposed application. Although the literature does contain many good papers on economic analysis, the large number of candidate processes and the application-specific nature of the problem make it difficult to give general conclusions. All of these issues must be solved at the same time to create a set of viable commercialized processes.

### 7.1. Issues for Implementation on Organic Substrates

A comprehensive economic evaluation of using an integrated passive technology versus a discrete passive technology must take into account the following:

1. *Electrical design issues.* Schematic differences due to differences in component characteristics.
2. *Board design issues.* Footprint, routing, number of layers.
3. *Fabrication issues.* Materials, processes, tolerances, yield.
4. *Manufacturing issues.* Implementation and scale up of fabrication technology to produce a volume process.
5. *Added value to the product.* Increased customer appeal resulting from smaller form factor and mass, performance.

A summary of the status of these issues and a brief description of the remaining challenges follows,

#### 7.1.1. Electrical Design Issues

Embedded passives in primary interconnect boards are not new; they have been used in ceramic substrates for decades. Favored materials and processes for resistors, capacitors, and inductors in LTCC are well-characterized with regard to manufacturing requirements, performance, and economics, and there is a large infrastructure supporting them. The main technical drawback with embedded passives in between



ceramic layers is that tolerance is rarely better than around 10 percent due to variations in printing, firing, and shrinkage, and to the inability to trim component values. If passives are formed on the surface of the ceramic substrate (“hybrids”), they can be trimmed after firing. Ceramic substrates, while growing in use with the rest of the industry, will never approach organic boards in sales volume, and, therefore, will continue to host only a small fraction of the overall passives produced, discrete or integrated.

Integrated passives are also widely available as arrays or networks, usually fabricated on IC-sized Si using basic front-end technologies, that can be surface mounted onto ceramic or organic boards using the same sort of infrastructure used to install discretely. This technology is rapidly gaining market share due to the obvious economic advantages with a minimum of changes in board design or on the factory floor for implementation.

To date, integrated passives have not been utilized as embedded structures in organic substrates to a significant degree, particularly with FR4, which makes up the vast majority of boards sold today. This potentially very large market is the driving force for R&D in the area. The problems with this implementation are well understood; both academia and industry are doing their parts in their own ways to solve these issues. Literature, conferences, and workshops for integrated passives on organic substrates began to appear in the mid-90s, and the typical journal article or conference presentation since then is a demonstration of a material or a process to make resistor, capacitor, or inductor test structures, or else to make a simple multicomponent device such as a filter or terminator. The striking characteristic about the technical literature is the vast array of materials and processes that have been investigated for integrated resistors and for capacitor dielectrics. The list is very long and diverse, including metals, ceramics, polymers as well as nano- and microcomposites of these materials that can be formed and patterned through many different processes. Methodology from the ceramic side is difficult to port to organics because these processes typically require much higher processing temperatures than can be tolerated by organic board materials and can only be applied if processed separately and laminated onto the board afterwards. A more manageable number of candidate processes, together with design software, costing models, and supply infrastructure, must be developed before embedded passives can move into organic boards.

### 7.1.2. Board Design Issues

The impact of passive integration on board design will be profound. The main effect will be to increase the number of layers since some considerable area must now be created to accommodate the planar integrated components. This is based on the assumption that integrated components will require more area per component than the discretely they replace, and this will be true for the most part. A secondary effect is the change in routing requirements since not all passives must be connected at the surface.

The size gap is largest for capacitors. At the time of this writing, an 0402 can be purchased with 2.2  $\mu\text{F}$  which, even with keep-away distance figured in, amounts to

230,000 nF/cm<sup>2</sup>. The highest values from the various processes becoming available for commercialization are much lower: up to about 1 nF/cm<sup>2</sup> for unfilled polymers, maybe 30 for ferroelectric-filled polymers, 50 for fired ferroelectric-coated foils for lamination, and the low hundreds for sputtered or anodized paraelectric. Ferroelectric thin films cured in place might reach over 1,000 nF/cm<sup>2</sup>, but that technology seems the farthest away. Only the smallest-valued capacitors can be replaced on a size-competitive basis with embedded components. Somewhere above that range, the remaining driving forces include economy of manufacture, replacement of solder joints, and very low inductance for decoupling. It may rarely make sense to attempt to integrate the largest capacitors on the board, those over about a micro-Farad that are generally used for energy storage. Larger capacitor areas not only occupy more layer space, but also pose a higher reliability risk.

Since a range of six decades or more of capacitance is required for many common systems, no one dielectric could provide the entire range with reasonable footprints regardless of its specific capacitance. Even if the lowest-valued capacitors can be fabricated, say, 10 mils across with acceptable tolerance, the highest-valued would then be unacceptably large at 10 inches. For this reason, it might be useful to employ the board’s interlayer dielectric for the low-valued components and a more exotic high-*k* material for the large values. The low-valued capacitors generally require paraelectric-type performance, matching most common board dielectrics. The other technology should have as high a specific capacitance as possible in order to embed the most components.

The size of integrated resistors is ruled by the number of squares and only indirectly by the specific resistance of the material. The lower limit of resistor linewidth is set by either thermal or tolerance issues. Large numbers of squares are to be avoided due to capacitive coupling between the meanders, resulting in a decrease in impedance at high frequencies. Resistor materials need to span between about 100 and 10,000  $\Omega$ /square to cover the entire range of values normally required in electronic systems. The available thin film processes such as TaN<sub>x</sub>, CrSi, and NiP are limited to only a few hundred  $\Omega$ /square at most. There is some promise of achieving 10,000  $\Omega$ /square with metal-deficient compounds or sputtered cermets, but more development is needed. Fired thick film materials on foil, borrowed from LTCC technology, and polymer thick films can cover the entire range with no more than a few squares. If the fundamental problems of reliability and value drift can be solved, PTF will be hard to beat as a flexible, economical process.

The number of extra board layers required for an embedded passive approach can be estimated. The total area requirements of proposed integrated passives from a schematic can be calculated for given set of integratable *R*, *C*, and *L* technologies. This can greatly exceed the interconnect area on the board in some applications. Dividing the total required area by the desired circuit board footprint will give a good estimate of the number of layers needed. Layout optimization may alter this number a bit, but this alone may indicate the worth of embedding for a specific application.

### 7.1.3. Fabrication and Manufacturing Issues

Materials and their processes are inextricably connected in passive integration, so choosing a material usually sets the processing method, while choosing a processing method usually restricts the number of materials. For instance, if  $TaN_x$  is desired as the resistor material, about the only way to deposit it is by sputtering. Conversely, if plating is desired, the number of resistor materials is reduced to only a few candidates. It is possible to categorize these groups as follows.

**Processes Requiring Vacuum** Sputtering and CVD are necessary for most thin film processes. These tend to be subtractive techniques requiring photolithography, and they are capable of excellent tolerance. An extensive range of component values is enabled by this, particularly with thin film dielectrics that make possible specific capacitances over the limit of about 20 nF/cm<sup>2</sup>, that is, available with thick film methods and as high as several hundred nF/cm<sup>2</sup>. Many tried-and-true materials are possible for resistors, but most are under a couple of hundred  $\Omega$ /square; considerable work remains to be done to achieve values over 1,000  $\Omega$ /square, which are needed for the high end of resistor values. Inductor materials up to a few microns can be deposited in this way, but they may be too thin to achieve high  $Q$  at high inductance values. Complete integrated and interconnected  $R$ ,  $C$ , and  $L$  systems have been demonstrated using thin film methods, and they are well suited to HDI and buildup technologies. However, they are relatively expensive and it may not make economic sense to include vacuum processes solely for the purpose of creating integrated passives, especially on low-cost commodity boards.

**Polymer Thick Film** These are additive processes using screenprinted preformulated inks. For resistors, a very wide range of  $\Omega$ /square is available, enabling almost any practical resistor value to be fabricated with no more than 10 squares. For capacitors, the maximum may be in the low tens of nF/cm<sup>2</sup> with ferroelectric characteristics using high  $k$  nanopowders dispersed in curable polymers. Tolerances are no better than about 10 percent for either, and resistor inks tend to have unstable values with regard to humidity, temperature, and time; extensive research is underway to improve this. The attractive feature of PTF is the low cost of capital equipment, inks, and processing. If value drift problems of PTF resistors can be solved, they will find widespread use for integration on almost any platform. Trimming has already been demonstrated to improve tolerance. PTF capacitor inks should be useful for decoupling, especially if specific capacitance can approach 100 nF/cm<sup>2</sup>, since tolerance and stability are not so important in this application.

**Integrated passives Formed Before Inclusion in the Board** Separating the processing of capacitor dielectrics and resistor materials from the board enables the use of a host of materials that have been long used on ceramic substrates such as  $BaTiO_3$  dielectrics and  $RuO_2$  and  $LaB_6$  resistors. Commercialized processes are soon to be released

from DuPont that involve printing resistors and capacitors that are fired onto Cu foil and provided for lamination into FR4 or flex film stacks. The metal is then photodefined to create the separated passive components. Ohmega-Ply® has provided plated NiP resistors on Cu foil for some years, and has seen some commercial use. Costs are probably intermediate between PTF and vacuum processes.

Table 5 is taken, for the most part, from p. 6 of the Passives chapter of the 2000 *NEMI* roadmap, with some updates by the author of this article.

## 8. THE FUTURE OF INTEGRATED PASSIVES

The implementation of integrated passives will be an evolution, not a revolution. Passive arrays and networks will continue to increase their market share as they replace terminators, filters, and other natural groups of passives. This should top out at some fraction of total passives, probably less than a quarter. The use of embedded capacitors for decoupling is a certainty since their parasitic inductance is lower than can be achieved with any surface mount components. Upcoming high-current and high-speed microprocessors cannot be decoupled any other way. Penetration into commodity boards is an important goal that will be realized gradually as the interrelated issues are resolved. Once cost savings are demonstrated, market share should increase steadily.

How far can this concept go? Figure 4 shows a hypothetical system with passives, chips, and other subsystems integrated together. In this format, all individual component packaging is discarded, and the layers of the “board” become the mechanical and environmental protection for each part so that there is very little mass that does not have electrical function. The chips are thinned to fit within one layer of the stack, and the surface is left only for those components that require access to the outside world. The system could hardly be smaller or have shorter interconnects. On our way to this ideal, integrating passive components is essential.

Between the current rapid development of integrated passive component technology and the increasing requirements of future electronic systems, significant commercial

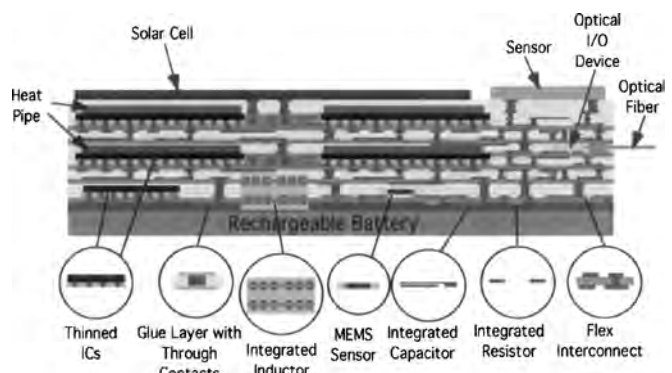


Figure 4. The complete integration of an electronic system.

**Table 5.** Implementation issues for integrated passives.

	Discretes	Integrated arrays and networks	Integrated passives
Cost	Good—the benchmark for all other technologies	Better when local densities have 4–8 devices close together	Better when the average component density is above 3/cm <sup>2</sup> , cost is panel-size dependent, number of layers is increased by integration. Pb-free technology
Size	Good—board area required for each and every device	Better—50% and greater board area savings over discretes	Best—no surface board area required since the devices are buried, but more total area required
Frequency range	Good, but self resonates at low frequencies	Better—higher self resonant frequency	Best—very high self resonant frequencies due mainly to decreased lead length and avoidance of inductive current loops
Reliability	Good—heavy use of solder joints	Better—reduces the number of solder joints	Best—eliminates solder joints
Flexibility	Best—most flexible for both design and manufacturing	Better than integrated, not quite as good as discretes	Good, but requires modeling and simulation up front, cannot be reworked
Time to market	Best—flexibility allows quick turns	Better—simple networks and arrays can be quickly designed and manufactured	Fair—most board shops require 5–7 days to build an integrated passive board
Value range	Best—all values available at commodity prices	Good—more work needed on high sheet resistance and high specific capacitance processes	Good—more work needed on high sheet resistance and high specific capacitance processes
Tolerances	Best—tight tolerances available at commodity prices	Better—can be presorted like discretes, with slightly more loss of parts	Good—10% achievable as formed, and trimming possible

use appears assured, but when? For those of us “in the business,” this never happens fast enough. There is always a gap between what can be done technically and what is economically viable at a given time, which is a challenge when drawing up roadmaps. For passive integration, this gap is especially large because of the vast number of materials and processes that have been demonstrated. Now, the infrastructure needs of design tools, costing models, and supply chains must be established, and this will happen as a few tentative processes are commercialized in the coming years. Once at least some technologies are available for OEMs to consider, the first pieces of their associated infrastructure will provide nucleation for the simultaneous solution of the interrelated issues of passive integration.

What year will more than half of passives be integrated? The microelectronics industry is full of cautionary tales; many of us remember other questions such as “What year will more than half of ICs be made from GaAs instead of Si?” or “What year will more than half of chip connections be TAB instead of wirebond?” But some technologies prove their economic viability and become industry standards, such as surface mounting. Is passive integration economically viable? Certainly for decoupling it is and, in fact, may be the only way to handle the future generations of high-power, high-frequency microprocessors. For discrete replacement in general, the best processes and materials are still being identified, and this is the most important task now. If we find suitable technologies, then passive integration will probably show a long, steady climb to dominance in a manner similar to surface mount as the

infrastructure, supply chain, and industry acceptance grow simultaneously.

## GLOSSARY

**Cermet** A nanocomposite of ceramic and metal used as a resistor material.

**Decoupling** Installing a capacitor between a power supply and an integrated circuit chip so that the capacitor actually powers the chip and the power supply simply recharges the capacitor.

**Ferroelectric** A dielectric material that can hold polarization after the electric field is removed and that typically exhibits a very high dielectric constant, up to thousands.

**FR4** A polymer-based circuit board material commonly used in consumer electronics.

**Integrated passive** A resistor, capacitor, or inductor fabricated directly into the printed wiring board instead of mounted on top as a separate component.

**Nanocomposite dielectric** A capacitor dielectric made from a nanodispersion of high-*k* ceramic in a low-*k* matrix.

**National Electronic Manufacturing Initiative (NEMI)** An industry consortium to identify major manufacturing issues in the field of electronics.

**Paraelectric** A dielectric material that cannot hold polarization after the electric field is removed and that typically exhibits a dielectric constant of 2–50.

**PTF** Polymer thick film.

## REFERENCES

1. R. Ulrich and L. Schaper, "Integrated Passive Component Technology." IEEE Press, 2003.
2. R. Frye, *The International Journal of Microcircuits and Electronic Packaging* 19, 483 (1996).
3. K. Paik, *Proceedings of 1995 Japan International Electronic Manufacturing Technology*, 1995 Japan IEMT Symposium, 1996, p. 365.
4. D. McGregor, Advanced Embedded Passives Technology Web site: <http://aept.ncms.org/papers.htm> (2001).
5. J. Rector, *Proceedings of the 48th Electronic Components and Technology Conf.*, IEEE, 1998, p. 218.
6. B. Etienne and P. A. Sandborn, *Proceedings of the IMAPS Advanced Packaging Materials Processes, Properties and Interfaces Symposium*, Braselton, GA, 2001, pp. 399–404.
7. L. D. Smith, R. E. Anderson, D. W. Forehand, T. J. Pelc, and T. Roy, *IEEE Trans. on Adv. Pack.* 22, 284 (1999).
8. Z. Wu, Y. Chen, and J. Fang, *Proceedings of the 44th Electronic Components and Technology Conference*, Washington, DC, May 1994, p. 945.
9. R. Berry, P. Hall, and M. Harris, "Thin Film Technology," p. 271. D. Van Nostrand Co., Inc., 1968.
10. L. Maissel and R. Glang, "Handbook of Thin Film Technology," p. 13–1. McGraw-Hill, 1970.
11. R. Kennedy, *Advancing Microelectronics*, p. 12 Sept./Oct. 1999.
12. R. Ulrich, L. Schaper, D. Nelms, and M. Leftwich, *IMAPS Journal* 23, 172 (2000).





# Interatomic Potential Models for Nanostructures

H. Rafii-Tabar

*Institute for Studies in Theoretical Physics and Mathematics, Tehran, Iran*

G. A. Mansoori

*University of Illinois at Chicago, Chicago, Illinois, USA*

## CONTENTS

1. Introduction
  2. Computer-Based Simulation Methods
  3. Interatomic Potentials
- Glossary  
References

## 1. INTRODUCTION

Over the last decade, nanoscience and nanotechnology [1–4] have emerged as two of the pillars of the research that will lead us to the next industrial revolution [5] and, together with molecular biology and information technology, will map the course of scientific and technological developments in the 21st century. This progress has been largely due to the development of sophisticated theoretical and experimental techniques, and practical tools, for understanding, characterizing, and manipulating nanoscale structures, processes, and systems. On the experimental front, the most significant developments were brought about by the invention of the scanning tunneling microscope (STM) in 1982 [6], followed by the atomic force microscope (AFM) [7] in 1986. These are tip-based devices which allow for a nanoscale manipulation of the morphology of the condensed phases and the determination of their electronic structures. These probe-based techniques have been extended further and are now collectively referred to as scanning probe microscopy (SPM). The SPM-based techniques have been improved considerably, providing new tools in research in such fields of nanotechnology as nanomechanics, nanoelectronics, nanomagnetism, and nanooptics [8].

The fundamental entities of interest to nanoscience and nanotechnology are the isolated individual nanostructures and their assemblies. Nanostructures are constructed from

a countable (limited) number of atoms or molecules. Their sizes are larger than individual molecules and smaller than microstructures. Nanoscale is a magical point on the dimensional scale: Structures in nanoscale (called *nanostuctures*) are considered at the borderline of the smallest of human-made devices and the largest molecules of living systems. One of their characteristic features is their high surface-to-volume ratio. Their electronic and magnetic properties are often distinguished by quantum mechanical behavior, while their mechanical and thermal properties can be understood within the framework of classical statistical mechanics. Nanostructures can appear in all forms of condensed matter, be it soft or hard, organic or inorganic, and/or biological. They form the building blocks of nanotechnology, and the formation of their assemblies requires a deep understanding of the interactions between individual atoms and molecules forming the nanostructures. Accordingly, nanotechnology has been specialized into three broad areas, namely, wet, dry, and computational nanotechnology.

Wet nanotechnology is mainly concerned with the study of nanostructures and nanoprocesses in biological and organic systems that exist in an aqueous environment. An important aspect of research in wet nanotechnology is the design of smart drugs for targeted delivery using such nanostructures as nanotubes and self-assembling materials [9, 10] as platforms. Dry nanotechnology, on the other hand, addresses the electronic and mechanical properties of metals, ceramics, focusing on fabrication of structures in carbon (e.g., fullerenes and nanotubes), silicon, and other inorganic materials.

Computational nanotechnology is based on the fields of mathematical modeling and computer-based simulation [11], which allow for computation and prediction of the underlying dynamics of nanostructures and processes in condensed matter physics, chemistry, materials science, biology, and genetics. Computational nanotechnology, therefore, covers

the other domains of nanofields by employing concepts from both classical and quantum mechanical many-body theories. It can provide deep insight into the formation, evolution, and properties of nanostructures and mechanisms of nanoprocesses. This is achieved by performing precise atom-by-atom numerical experiments (modeling and simulation) on many aspects of various condensed phases. The precision of such calculations depends on the accuracy of the interatomic and intermolecular potential energy functions at hand.

At the nanoscale, the implementation of the computational science leads to the study of the evolution of physical, chemical, and biophysical systems on significantly reduced length, time, and energy scales. Computer simulations at this scale form the basis of computational nanoscience. These simulations could allow for an understanding of the atomic and molecular scale structures, energetics, dynamics, and mechanisms underlying the physical and chemical processes that can unfold in isolated nanostructures, and their assemblies, under different ambient conditions.

This review is concerned with one of the most important elements of the computational approach to the properties of, and processes involving, nanoscale structures, namely, the phenomenological interatomic and intermolecular potentials. The mathematical expressions for the phenomenological forces and potential energies between atoms and molecules necessary for prediction of bulk (macroscopic) fluid and solid properties are rather well understood [12–14]. There are sufficient, effective phenomenological intermolecular potential energy functions available for the statistical mechanics prediction of macroscopic systems [13–17]. Parameters of phenomenological interaction energies between atoms and simple molecules can be calculated through such measurements as X-ray crystallography, light scattering, nuclear magnetic resonance spectroscopy, gas viscosity, thermal conductivity, diffusivity, and the virial coefficients data [18]. Most of the present phenomenological models for interparticle forces are tuned specifically for statistical mechanical treatment of macroscopic systems. However, such information may not be sufficiently accurate in the treatment of nanosystems where the number of particles are finite and the statistical averaging techniques fail.

Nanostructures consist of many-body systems, and a rigorous modeling of their properties has to be placed within the quantum mechanical domain, taking into account the electronic degrees of freedom. For simple atoms and molecules, the quantum mechanical *ab initio* calculation methods [19] have been successful in producing accurate intermolecular potential functions. While *ab initio* calculations may be satisfactory for simple molecules, for complex molecules and macromolecules they may not be able to produce the accurate needed information. However, even with today's enhanced computational platforms and sophisticated quantum mechanical techniques [20], the nanostructures that can be studied from a quantum mechanical, or *ab initio*, basis are those composed of at most a few hundred atoms. Consequently, the use of phenomenological interatomic and intermolecular potentials in simulations is still necessary. This allows modeling of nanostructures consisting of several mil-

lions of atoms, and recently simulations involving more than  $10^9$  atoms have been performed.

To motivate the use of interatomic and intermolecular potentials and show how they enter into nanoscale modeling, we consider, in Section 2, two of the widely used methods for numerical modeling at the nanoscale. This is followed, in Section 3, by a description of several types of state-of-the-art interatomic potentials that are in current use for modeling the energetics and dynamics of several classes of materials, including metals, semimetals, and semiconductors. We will then briefly review the applications of these potentials in specific computational modeling studies.

## 2. COMPUTER-BASED SIMULATION METHODS

Computer simulations applied in nanoscience consist of computational “experimentations” conducted on an assembly of a countable number of molecules with the assumption of predefined intermolecular interaction models. Computer simulations can direct an experimental procedure and have the potential of replacing an experiment if accurate intermolecular potentials are used in their development.

Computer simulation modeling of the physics and chemistry of nanostructures composed of several millions to several hundreds of millions of atoms can be performed by employing several distinct approaches. The most widely used approaches include (1) Monte Carlo simulation and (2) molecular dynamics simulation.

The cell in which the simulation is performed is replicated in all spatial dimensions, generating its own periodic images containing the periodic images of the original  $N$  atoms. This is the periodic boundary condition, and is introduced to remove the undesirable effects of the artificial surfaces associated with the finite size of the simulated system. The forces experienced by the atoms and molecules are obtained from prescribed two-body or many-body interatomic and intermolecular potentials,  $H_I(r_{ij})$ , according to

$$F_i = - \sum_{j>i} \nabla_{r_i} H_I(r_{ij}) \quad (1)$$

where  $r_{ij}$  is the separation distance between two particles  $i$  and  $j$ .

### 2.1. Monte Carlo Simulation Methods

The Metropolis Monte Carlo (MC) simulation methods can be used in nanoscience to simulate various complex physical phenomena, including prediction of phase transitions, thermally averaged structures, and charge distributions, just to name a few [21]. A variety of MC simulations are used depending on the nanosystem under consideration and the kind of computational results in mind. They include, but are not limited to, classical MC, quantum MC, and volumetric MC. In classical MC, the classical Boltzmann distribution is used as the starting point to perform various property calculations. Through the use of quantum MC, one can compute quantum mechanical energies, wave functions, and electronic structure using Schrödinger's equation. The volumetric MC is used to calculate molecular volumes and sample molecular phase space surfaces [22].

## 2.2. Molecular Dynamics Simulation Methods

In the molecular dynamics (MD) simulation methods [23–25], the emphasis is on the motion of individual atoms within an assembly of  $N$  atoms, or molecules, that make up the nanostructure under study. The dynamical theory employed to derive the equations of motion is either the Newtonian deterministic dynamics or the Langevin-type stochastic dynamics. The initial data required are the initial position coordinates and velocities of the particles, in either a crystalline or an amorphous state, located in a primary computational cell of volume  $V$ .

To save computational time, the simplifying assumption is made that each particle interacts with its nearest neighbors, located in its own cell as well as in the image cells, that are within a specified cutoff radius. The  $3N$  coupled differential equations of motion can then be solved by a variety of numerical finite-difference techniques, one of which is the velocity Verlet algorithm [23], according to which the positions,  $r_i$ , and velocities,  $v_i$ , of the particles of mass,  $m_i$ , are updated at each time step,  $dt$ , by

$$\begin{aligned} r_i(t + dt) &= r_i(t) + v_i(t) dt + \frac{1}{2} dt^2 \frac{F_i(t)}{m_i} \\ v_i\left(t + \frac{dt}{2}\right) &= v_i(t) + \frac{1}{2} dt \frac{F_i(t)}{m_i} \\ v_i(t + dt) &= v_i\left(t + \frac{dt}{2}\right) + \frac{1}{2} dt \frac{F_i(t + dt)}{m_i} \end{aligned} \quad (2)$$

The dynamical history of a particular microstate of the system, constructed initially, is followed by computing the space–time trajectories through the phase space via (2). At each instant of the simulation time, the exact instantaneous values of the observables, such as pressure, temperature, and thermodynamics response function, are also obtained, leading to time-average values at the conclusion of the simulation.

### 2.2.1. Constant-Temperature Molecular Dynamics Simulation: Nosé–Hoover Dynamics

For a large class of problems in the physics and chemistry of nanostructures, the type of system that is considered is a closed one. This is a system with a fixed volume,  $V$ , a fixed number of particles,  $N$ , maintained at a constant temperature,  $T$ . Within statistical mechanics, such a system is represented by a constant ( $NVT$ ), or canonical, ensemble [26], where the temperature acts as a control parameter.

A constant-temperature MD simulation can be realized in a variety of ways. A method that generates the canonical ensemble distribution in both the configuration space and the momentum space parts of the phase space was proposed by Nosé [27–29] and Hoover [30] and is referred to as the extended-system method. According to this method, the simulated system and a heat bath couple to form a composite system. This coupling breaks the energy conservation that otherwise restricts the behavior of the simulated system and leads to the generation of a canonical ensemble. The conservation of energy still holds in the composite system,

but the total energy of the simulated system is allowed to fluctuate.

The mathematical formulation of the method is based on the extension of the space of dynamical variables of the system beyond that of the coordinates and momenta of the real particles to include one additional *phantom coordinate*,  $s$ , and its conjugate momentum,  $p_s$  [31]. This extra degree of freedom acts as a heat bath for the real particles. There are, therefore, four systems to consider, namely, the real  $(r_i, p_i)$  system, the virtual  $(\tilde{r}_i, \tilde{p}_i)$  system, the real extended  $(r_i, p_i, s, p_s)$  system, and the virtual extended  $(\tilde{r}_i, \tilde{p}_i, s, p_s)$  system. The aim of Nosé’s approach is to show that there is a method for selecting the Hamiltonian of the extended system and, simultaneously, to relate the variables of the real system to those of the virtual system, such that the micro-canonical partition function of the extended virtual system is proportional to the canonical partition function of the real system [31].

The Hamiltonian of the virtual extended system is

$$H^* = \sum_{i \rightarrow N} \frac{\tilde{p}_i^2}{2ms^2} + H_I(\tilde{r}_{ij}) + \frac{p_s^2}{2Q} + gk_B T \ln s \quad (3)$$

where  $g$  is the number of degrees of freedom,  $k_B$  is the Boltzmann constant,  $Q$  is a parameter that behaves like a “mass” associated with the motion of the coordinate  $s$ , and  $r_i, p_i$  and  $\tilde{r}_i, \tilde{p}_i$  are the canonical position and momentum coordinates of all the particles in the real and virtual systems, respectively. The virtual coordinates, and the time, are related to the corresponding real coordinates via the transformations

$$\begin{aligned} r_i &= \tilde{r}_i \\ p_i &= \frac{1}{s} \tilde{p}_i \\ dt &= \frac{1}{s} d\tilde{t} \end{aligned} \quad (4)$$

Since  $H_I$  in (3) is the potential energy for both the real and the virtual systems, the first two terms on the right-hand side of (3) represent the kinetic and potential energies of the real system, respectively, and the last two terms correspond to the kinetic and potential energies, respectively, associated with the extra degree of freedom.

From this Hamiltonian, the equations of motion of the real system are

$$\begin{aligned} \frac{dr_i}{dt} &= \frac{p_i}{m_i} \\ \frac{dp_i}{dt} &= F_i - \eta p_i \\ \frac{d\eta}{dt} &= \frac{1}{Q} \sum_i \frac{p_i^2}{m_i} - gk_B T \end{aligned} \quad (5)$$

where  $\eta$  is called the friction coefficient of the bath. This coefficient is not a constant and can take on both positive and negative values. This gives rise to what is called a negative-feedback mechanism. The last equation in (5) controls the functioning of the heat bath. From this equation, we observe that if the total kinetic energy is greater than

$gk_B T/2$ , then  $d\eta/dt$ , and hence  $\eta$ , is positive. This prompts a friction inside the bath and, correspondingly, the motion of the atoms is decelerated to lower their kinetic energy to that of the bath. On the other hand, if the kinetic energy is lower than  $gk_B T/2$ , then  $d\eta/dt$  will be negative, the bath will heat up, and the motion of the atoms will be accelerated. Equations (5) are collectively referred to as the Nosé–Hoover thermostat.

### 2.2.2. Equations of Motion

The implementation of the Nosé–Hoover dynamics substantially modifies (2), the equations of motion. A velocity Verlet version of this dynamics formulation can be given by the following expressions [32]:

$$\begin{aligned} r_i(t+dt) &= r_i(t) + v_i(t)dt + \frac{1}{2}dt^2 \left[ \frac{F_i(t)}{m_i} - \eta(t)v_i(t) \right] \\ v_i\left(t + \frac{dt}{2}\right) &= v_i(t) + \frac{dt}{2} \left[ \frac{F_i(t)}{m_i} - \eta(t)v_i(t) \right] \\ \eta\left(t + \frac{dt}{2}\right) &= \eta(t) + \frac{dt}{2Q} \left[ \sum_{i \rightarrow N} m_i v_i^2(t) - gk_B T \right] \\ \eta(t+dt) &= \eta\left(t + \frac{dt}{2}\right) \\ &\quad + \frac{dt}{2Q} \left[ \sum_{i \rightarrow N} m_i v_i^2\left(t + \frac{dt}{2}\right) - gk_B T \right] \\ v_i(t+dt) &= 2 \frac{[v_i(t + \frac{dt}{2}) + dt F_i(t+dt)/(2m_i)]}{[2 + \eta(t+dt)dt]} \end{aligned} \quad (6)$$

A particular parameterization of  $Q$  is given by

$$Q = gk_B T \tau^2 \quad (7)$$

where  $\tau$  is the relaxation time of the heat bath, normally of the same order of magnitude as the simulation time step,  $dt$ . It controls the speed with which the bath damps down the fluctuations in the temperature. The number of degrees of freedom is given by  $g = 3(N - 1)$ .

## 3. INTERATOMIC POTENTIALS

To study nanostructures composed of several hundred to several million atoms or molecules, the computationally most efficient method is the use of phenomenological interatomic and intermolecular potentials. This is because the existing quantum mechanical techniques are able to deal with at most a few hundred atoms.

The phenomenological potentials are obtained by using phenomenological approaches of selecting a mathematical function and fitting its unknown parameters to various, experimentally determined, properties of the system, such as its lattice constant.

Interatomic and intermolecular potentials must be able to model the energetics and dynamics of nanostructures, and this fact lies at the very foundation of computer-based modeling and simulations. Potentials describe the physics of the model systems, and the significance of much of the modeling and simulation results, their accuracy, and the extent

to which they represent the real behavior of nanostructures, and their transitions, under varied conditions, depends in a critical manner on the accuracy of the interatomic and intermolecular potentials employed.

A great deal of effort has been expended over the years to develop phenomenological intermolecular potentials to model the bonding in various classes of materials, such as metallic, semimetallic, semiconducting, and organic atoms and molecules. For a review, see [11, 33, 34].

Basically, intermolecular potential energies include pairwise additive energies, as well as many-body interactions. The interparticle interaction potential energy between atoms and molecules is generally denoted by  $H(r) = H_{\text{rep}} + H_{\text{att}}$ , where  $r$  is the intermolecular distance,  $H_{\text{rep}}$  is the repulsive interaction energy, and  $H_{\text{att}}$  is the attractive interaction energy; see Figure 1. From the equation above, the interaction force is

$$\mathbf{F} = -\nabla H(\mathbf{r}) = \mathbf{F}_{\text{rep}} + \mathbf{F}_{\text{att}}$$

For neutral and spherically symmetric molecules when the separation ( $r$ ) is very small, an exponential repulsive term,  $H_{\text{rep}} = \alpha \exp(-\beta r)$ , dominates, and the potential is strongly positive. Hence, the  $H_{\text{rep}} = \alpha \exp(-\beta r)$  term describes the short-range repulsive potential due to the distortion of the electron clouds at small separations. For neutral and spherically symmetric molecules when the separation ( $r$ ) is large, the London dispersion forces dominate.

Among pairwise additive energies, one can mention the repulsive potentials, van der Waals energies, interactions involving polar and polarization of molecules, interactions involving hydrogen bonding, and strong intermolecular energies, including covalent and Coulomb interactions [35, 36]. Among many-body interactions, one can name the Axilrod–Teller triple–dipole interactions [37–39].

To be effective for computational nanotechnology, interatomic and intermolecular potentials must possess the following properties [40, 41]:

- Flexibility.* A potential energy function must be sufficiently flexible that it could accommodate as wide a range as possible of fitting data. For solid systems, these data might include lattice constants, cohesive energies, elastic properties, vacancy formation energies, and surface energies.
- Accuracy.* A potential function should be able to accurately reproduce an appropriate fitting database.
- Transferability.* A potential function should be able to describe at least qualitatively, if not with quantitative accuracy, structures not included in a fitting database.

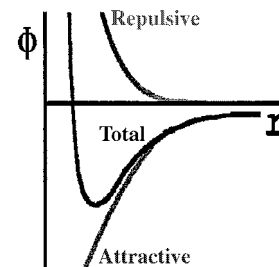


Figure 1. Pair interaction energy.

- (d) *Computational efficiency.* Evaluation of the function should be relatively efficient depending on quantities such as system sizes and time scales of interest, as well as available computing resources.

In this section, we shall describe some of the potential functions that meet these criteria and are widely used in computational nanoscience.

### 3.1. Interatomic Potentials for Metallic Systems

Bonding in metallic systems operates over the range of 0.2 to 0.5 nm [42]. At large interatomic distances, the predominant forces arise from van der Waals interactions, which are responsible for long-range cohesion. Metallic bonding, like covalent bonding, arises from the sharing of electrons, and hence its proper description requires the consideration of the many-body effects. Two-body potentials are incapable of describing this bonding [43, 44] since:

- For most cubic metals, the ratio of the elastic constants,  $C_{12}$  to  $C_{44}$ , is far from unity, whereas a pairwise potential leads to the Cauchy relation, that is,  $C_{12} = C_{44}$ .
- The prediction of the unrelaxed vacancy formation energy gives values around the cohesive energy, which is completely incorrect for metals. The relaxation energy for metals is quite small, and the experimental data suggest that the vacancy formation energy for metals is about one-third of the cohesive energy.
- The interatomic distance between the first and second atomic layers within an unreconstructed surface structure (bulk cross section) is predicted to be expanded by pairwise potentials. This is in contrast with the experimental data, which suggest a contraction of the open-surface lattice spacing; that is, pair potentials fail to predict an inward relaxation of the metallic surfaces.
- Pairwise potentials overestimate the melting point by up to 20% of the experimental value.
- Potentials with a functional form having only one optimum at the diatomic equilibrium distance cannot be fitted properly to the phonon frequencies.

Two approaches have been proposed for going beyond pair potentials and incorporating many-body effects into two-body potentials.

The first approach is to add a term, which is a functional of the local electronic density of a given atom, to the pairwise term. This method has itself led to several alternative potentials that mimic the many-body effects. These many-body potentials are known as the embedded-atom model (EAM) potentials [45–47], which have been employed in several studies involving elemental metals and their alloys [48–53], the glue model potentials [54], the Finnis–Sinclair potentials for the body-centered cubic (bcc) elemental metals [55], which have also been developed for the noble metals [56], the Sutton–Chen (SC) potentials [57] for the 10 face-centered cubic (fcc) elemental metals, and the Rafii-Tabar–Sutton potentials [58] for the fcc random binary alloys, which have also been used in several modeling studies [11, 59–61].

The second approach is to go from pair potentials to cluster potentials by the addition of higher order interactions, for example, three-body and four-body terms, with appropriate functional forms and symmetries. This has led to potentials, such as the Murrell–Mottram cluster potentials [44]. Inclusion of higher order terms provides a more accurate modeling of the energetics of the phenomena than is given by pair potentials alone. In the following sections, we consider the potentials pertinent to each approach.

#### 3.1.1. Many-Body Embedded-Atom Model Potentials

The many-body EAM potentials were proposed [45–47] to model the bonding in metallic clusters. They were the first alternatives to the traditional pair potential models. Their construction is based on the use of density functional theory (DFT), according to which the energy of a collection of atoms can be expressed exactly by a functional of its electronic density [62]. Similarly, the energy change associated with embedding an atom into a host background of atoms is a functional of the electronic density of the host before the new atom is embedded [63, 64]. If we can find a good approximation to the embedding functional, then an approximate expression for the energy of an atom in a metal can be constructed.

The total electron density of the host atoms is approximated as a linear superposition of the electron densities (charge distributions) of individual host atoms. To zeroth order, the embedding energy can be equated to the energy of embedding an atom in a homogeneous electron gas, whose density,  $\rho_{h,i}$ , matches the host density at the position of the embedded atom, augmented by the classical electrostatic interaction with the atoms in the host system [65]. The embedding energy for the homogeneous electron gas can be calculated from an *ab initio* basis. Computation of  $\rho_{h,i}$  from a weighted average of the host density over the spatial extent of the embedded atom improves the description by accounting for the local inhomogeneity of the host density. The classical electrostatic interaction reduces to a pairwise sum if a frozen atomic charge density is assumed for each host atom [65]. This approach, called the quasi-atom method [63], or the effective-medium theory [64], provides the theoretical basis of the EAM and similar methods.

In the EAM, the total energy of an elemental system is, therefore, written as

$$H_I^{\text{EAM}} = \sum_i F_i[\rho_{h,i}] + \frac{1}{2} \sum_i \sum_{j \neq i} \phi_{ij}(r_{ij}) \quad (8)$$

where  $\rho_{h,i}$  is the electron density of the host at the site of atom  $i$ ;  $F_i[\rho]$  is the embedding functional, that is, the energy to embed atom  $i$  into the background electron density,  $\rho$ ; and  $\phi_{ij}$  is a pairwise central potential between atoms  $i$  and  $j$ , separated by a distance  $r_{ij}$ , and represents the repulsive core–core electrostatic interaction. The host electron density is a linear superposition of the individual contributions and is given by

$$\rho_{h,i} = \sum_{j \neq i} \rho_j^*(r_{ij}) \quad (9)$$



where  $\rho_j^*$ , another pairwise term, is the electron density of atom  $j$  as a function of interatomic separation. It is important to note that the embedding functional,  $F_i[\rho]$ , is a universal functional that does not depend on the source of the background electron density. This implies that the same functional can be employed to compute the energy of an atom in an alloy as that employed for the same atom in a pure elemental metal [48]. Indeed, this is one of the attractive features of these potentials. For a solid at equilibrium, the force to expand, or contract, due to the embedding function is exactly balanced by the force to contract, or expand, due to the pairwise interactions. At a defect, this balance is disrupted, leading to the displacements as atoms move to find a new balance [65]. The positive curvature of  $F$  plays a key role in this process, by defining the optimum tradeoff between the number of bonds and the length of those bonds.

The expression for the Cauchy pressure for a cubic crystal can be found from (8) and is seen to depend directly on the curvature of the function  $F$  as described in [46]:

$$C_{11}-C_{44} = \frac{1}{\Omega} \frac{d^2 F}{d\rho_{h,i}^2} \left[ \sum_j \frac{d\rho}{dr_{ij}} \frac{x_{ij}^2}{r_{ij}} \right]^2 \quad (10)$$

where  $\Omega$  is the atomic volume and  $x_{ij}$  is the  $x$  component of the  $r_{ij}$ .

To apply these potentials, the input parameters required are the equilibrium atomic volume, the cohesive energy, the bulk modulus, the lattice structure, as well as the repulsive pair potentials and the electron density function [50]. Among the extensive applications of these potentials, we can list their parameterization and use in the computation of the surface energy and relaxation of various crystal surfaces of Ni and Pd and the migration of hydrogen impurity in the bulk Ni and Pd [46], the computation of the formation energy, migration energy of vacancies and surface energies of a variety of fcc metals [48], the calculation of the surface composition of the Ni–Cu alloys [66], the computation of the elastic constants and vibrational modes of the Ni<sub>3</sub>Al alloy [49], the self-diffusion and impurity diffusion of the fcc metals [51], the computation of the heats of solution for alloys of a set of fcc metals [52], and the computation of the phase stability of fcc alloys [53]. There has also been an application of these potentials to covalent materials such as Si [67].

In a recent application [68], the second-order elastic moduli ( $C_{11}$ ,  $C_{12}$ ,  $C_{44}$ ) and the third-order elastic moduli ( $C_{111}$ ,  $C_{112}$ ,  $C_{123}$ ,  $C_{144}$ ,  $C_{166}$ ,  $C_{456}$ ), as well as the cohesive energies and lattice constants, of a set of 12 cubic metals with fcc and bcc structures were used as input to obtain the corresponding potential parameters for these metals [69]. The resulting potentials were then used to compute the pressure–volume ( $P$ – $V$ ) curves, the phase stabilities, and the phonon frequency spectra, with excellent agreement obtained for the  $P$ – $V$  curves with the experimental data, and a reasonable agreement obtained for the frequency curves.

The EAM potentials can also be written for ordered binary alloys [65]. We can write

$$H_{\text{alloy}}^{\text{EAM}} = \sum_i F_i[\rho_{h,i}] + \frac{1}{2} \sum_i \sum_{j \neq i} \phi_{t_i, t_j}(r_{ij}) \quad (11)$$

where  $\phi$  now depends on the type of atom  $t_i$  and atom  $t_j$ . The host electron density is now given by

$$\rho_{h,i} = \sum_{j \neq i} \rho_{t_j}^*(r_{ij}) \quad (12)$$

where the terms in the sum each depend on the type of neighbor atom  $j$ . Therefore, for a binary alloy with atom types A and B, the EAM energy requires definitions for  $\phi_{AA}(r)$ ,  $\phi_{BB}(r)$ ,  $\phi_{AB}(r)$ ,  $\rho_A(r)$ ,  $\rho_B(r)$ ,  $F_A(\rho)$ , and  $F_B(\rho)$ .

### 3.1.2. Many-Body Finnis–Sinclair Potentials

The Finnis–Sinclair (FS) potentials [55] were initially constructed to model the energetics of the transition metals. They avoid the problems associated with using pair potentials to model metals, for example, the appearance of the Cauchy relation between the elastic constants  $C_{12} = C_{44}$  which is not satisfied by cubic crystals. They also offer a better description of the surface relaxation in metals.

In the FS model, the total energy of an  $N$ -atom system is written as

$$H_I^{\text{FS}} = \frac{1}{2} \sum_{i \rightarrow N} \sum_{j \neq i} V(r_{ij}) - c \sum_i (\rho_i)^{1/2} \quad (13)$$

where

$$\rho_i = \sum_{j \neq i} \phi(r_{ij}) \quad (14)$$

The function  $V(r_{ij})$  is a pairwise repulsive interaction between atoms  $i$  and  $j$ , separated by a distance  $r_{ij}$ ,  $\phi(r_{ij})$  are two-body cohesive pair potentials, and  $c$  is a positive constant. The second term in (13) represents the cohesive many-body contribution to the energy. The square root form of this term was motivated by an analogy with the second-moment approximation to the tight-binding model [70]. To see this, we start with the tight-binding approach [71] in which the total electronic band energy, that is, the total bonding energy, which is given as the sum of the energies of the occupied one-electron states, is expressed by

$$E_{\text{tot}} = 2 \int_{-\infty}^{E_f} E n(E) dE \quad (15)$$

where  $n(E)$  is the electron density of states,  $E_f$  is the Fermi level energy, and the factor 2 refers to spin degeneracy.  $E_{\text{tot}}$  is an attractive contribution to the configurational energy, which is dominated by the broadening of the partly filled valence shells of the atoms into bands when the solid is formed [72]. It is convenient to divide  $E_{\text{tot}}$  into contributions from individual atoms

$$E_{\text{tot}} = \sum_i E_i = 2 \sum_i \int_{-\infty}^{E_f} E n_i(E) dE \quad (16)$$

where

$$n_i(E) = \sum_v |\langle \Psi_v | i \rangle|^2 \delta(E - E_v) \quad (17)$$

is the projected density of states on site  $i$  and  $|\Psi_v\rangle$  are the eigenfunctions of the one-electron Hamiltonian. As has

been discussed in [72], to obtain  $n_i(E)$  exactly, it is, in principle, necessary to know the positions of all the atoms in the crystal. Furthermore,  $n_i(E)$  is a very complicated functional of these positions. However, it is not necessary to calculate the detailed structure of  $n_i(E)$ . To obtain an approximate value of quantities such as  $E_i$ , which involves integrals over  $n_i(E)$ , we need only information about its width and gross features of its shape. This information is conveniently summarized in the moments of  $n_i(E)$ , defined by

$$\mu_n^i = \int_{-\infty}^{\infty} E^n n_i(E) dE \quad (18)$$

The important observation, which allows a simple description comparable to that of interatomic potentials, is that these moments are rigorously determined by the local environment. The exact relations are [72]:

$$\begin{aligned} \mu_2^i &= \sum_j h_{ij}^2 \\ \mu_3^i &= \sum_{jk} h_{ij} h_{jk} h_{ki} \\ \mu_4^i &= \sum_{jkl} h_{ij} h_{jk} h_{kl} h_{li} \end{aligned} \quad (19)$$

where

$$h_{ij} = \langle \chi_i | H | \chi_j \rangle \quad (20)$$

$\chi_i$  is the localized orbital centered on atom  $i$ , and  $H$  is the one-electron Hamiltonian. Therefore, if we have an approximate expression for the  $E_i$  in terms of the first few  $\mu_n^i$ , the electronic band energy can be calculated with essentially the same machinery used to evaluate the interatomic potentials. Now, the exact evaluation of  $E_i$  requires the values of all the moments on site  $i$ . However, a great deal of information can be gained from a description based only on the second moment,  $\mu_2^i$ . This moment provides a measure of the squared valence band width and thus sets a basic energy scale for the problem. Therefore, a description using only  $\mu_2^i$  assumes that the effects of the structure of  $n_i(E)$  can be safely ignored, since the higher moments describe the band shape. Since  $E_i$  has units of energy and  $\mu_2^i$  has units of (energy)<sup>2</sup>, we have

$$E_i = E_i(\mu_2^i) = -A\sqrt{(\mu_2^i)} = -A\sqrt{\sum_j h_{ij}^2} \quad (21)$$

where  $A$  is a positive constant that depends on the chosen density of states shape and the fractional electron occupation [65].

The functions  $\phi(r_{ij})$  in (14) can be interpreted as the sum of squares of hopping (overlapping) integrals. The function  $\rho_i$  can be interpreted as the local electronic charge density [45] constructed by a rigid superposition of the atomic charge densities  $\phi(r_{ij})$ . In this interpretation, the energy of an atom at site  $i$  is assumed to be identical to its energy within a uniform electron gas of that density. Alternatively,  $\rho_i$  can be interpreted [55] as a measure of the local density of atomic sites, in which case (13) can be considered as a

sum consisting of a part that is a function of the local volume, represented by the second term, and a pairwise interaction part, represented by the first term. The FS potentials, Equation (13), are similar in form to the EAM potentials in (8). However, their interpretations are quite different. The FS potentials, as has been shown above, were derived on the basis of the tight-binding model and this is the reason their many-body parts, which correspond to the  $F_i[\rho_{n,i}]$  functionals in the EAM potentials, are in the form of square root terms. Furthermore, the FS potentials are less convenient than the EAM potentials for a conversion from the pure metals to their alloys. Notwithstanding this difficulty, FS potentials have been constructed for several alloy systems, such as the alloys of the noble metals (Au, Ag, Cu) [56].

### 3.1.3. Many-Body Sutton–Chen Long-Range Potentials

The Sutton–Chen (SC) potentials [57] describe the energetics of 10 fcc elemental metals. They are of the FS type and therefore similar in form to the EAM potentials. They were specifically designed for use in computer simulations of nanostructures involving a large number of atoms.

In the SC potentials, the total energy, written in analogy with (13), is given by

$$H_I^{\text{SC}} = \varepsilon \left[ \frac{1}{2} \sum_i \sum_{j \neq i} V(r_{ij}) - c \sum_i (\rho_i)^{1/2} \right] \quad (22)$$

where

$$V(r_{ij}) = \left( \frac{a}{r_{ij}} \right)^n \quad (23)$$

and

$$\rho_i = \sum_{j \neq i} \left( \frac{a}{r_{ij}} \right)^m \quad (24)$$

where  $\varepsilon$  is a parameter with the dimensions of energy,  $a$  is a parameter with the dimensions of length and is normally taken to be the equilibrium lattice constant, and  $m$  and  $n$  are positive integers with  $n > m$ . The power law form of the potential terms was adopted so as to construct a unified model that can combine the short-range interactions, afforded by the  $N$ -body second term in (22) and useful for the description of surface relaxation phenomena, with a van der Waals tail that gives a better description of the long-range interactions. For a particular fcc elemental metal, the potential in (22) is completely specified by the values of  $m$  and  $n$ , since the equilibrium lattice condition fixes the value of  $c$ . The values of the potential parameters, computed for a cutoff radius of 10 lattice constants, are listed in Table 1. These parameters were obtained by fitting the experimental cohesive energies and lattice parameters exactly. The indices  $m$  and  $n$  were restricted to integer values, such that the product  $m \times n$  was the nearest integer to  $18\Omega^f B^f / E^f$ , Equation (9) in [57], where  $\Omega^f$  is the fcc atomic volume,  $B^f$  is the computed bulk modulus, and  $E^f$  is the fitted cohesive energy.

The SC potentials have been applied to the computation of the elastic constants, bulk moduli, and cohesive energies

**Table 1.** Parameters of the Sutton–Chen potentials.

Element	$m$	$n$	$\varepsilon$ (eV)	$c$
Ni	6	9	$1.5707 \times 10^{-2}$	39.432
Cu	6	9	$1.2382 \times 10^{-2}$	39.432
Rh	6	12	$4.9371 \times 10^{-3}$	144.41
Pd	7	12	$4.1790 \times 10^{-3}$	108.27
Ag	6	12	$2.5415 \times 10^{-3}$	144.41
Ir	6	14	$2.4489 \times 10^{-3}$	334.94
Pt	8	10	$1.9833 \times 10^{-2}$	34.408
Au	8	10	$1.2793 \times 10^{-2}$	34.408
Pb	7	10	$5.5765 \times 10^{-3}$	45.778
Al	6	7	$3.3147 \times 10^{-2}$	16.399

of the fcc metals, and the prediction of the relative stabilities of the fcc, bcc, and hexagonal close-packed (hcp) structures [57]. The results show reasonable agreement with the experimental values. These potentials have also been used in modeling the structural properties of metallic clusters in the size range of 13 to 309 atoms [73].

### 3.1.4. Many-Body Murrell–Mottram Potentials

The Murrell–Mottram (MM) potentials are an example of cluster-type potentials and consist of sums of effective two- and three-body interactions [44, 74, 75]:

$$U_{\text{tot}} = \sum_i \sum_{j>i} U_{ij}^{(2)} + \sum_i \sum_{j>i} \sum_{k>j} U_{ijk}^{(3)} \quad (25)$$

The pair interaction term is modeled by a Rydberg function, which has been used for simple diatomic potentials. In the units of reduced energy and distance, it takes the form

$$\frac{U_{ij}^{(2)}}{D} = -(1 + a_2 \rho_{ij}) \exp(-a_2 \rho_{ij}) \quad (26)$$

where

$$\rho_{ij} = \frac{r_{ij} - r_e}{r_e} \quad (27)$$

$D$  is the depth of the potential minimum, corresponding to the diatomic dissociation energy at  $\rho_{ij} = 0$ , that is, for  $r_{ij} = r_e$ , with  $r_e$  the diatomic equilibrium distance.  $D$  and  $r_e$  are fitted to the experimental cohesive energy and lattice parameter, respectively. The only parameter involved in the optimization of the potential is  $a_2$ , which is related to the curvature (force constant) of the potential at its minimum [44, 74, 75]. The three-body term must be symmetric with respect to the permutation of the three atom's indices,  $i$ ,  $j$ , and  $k$ . The most convenient way to achieve this is to create functional forms that are combinations of interatomic coordinates,  $Q_1$ ,  $Q_2$ , and  $Q_3$ , which are irreducible representations of the  $S_3$  permutation group [76]. If we construct a given triangle with atoms  $(i, j, k)$ , then the coordinates  $Q_i$  are given by

$$\begin{bmatrix} Q_1 \\ Q_2 \\ Q_3 \end{bmatrix} = \begin{bmatrix} \sqrt{1/3} & \sqrt{1/3} & \sqrt{1/3} \\ 0 & \sqrt{1/2} & -\sqrt{1/2} \\ \sqrt{2/3} & -\sqrt{1/6} & -\sqrt{1/6} \end{bmatrix} \begin{bmatrix} \rho_{ij} \\ \rho_{jk} \\ \rho_{ki} \end{bmatrix} \quad (28)$$

where

$$\rho_{\alpha\beta} = \frac{r_{\alpha\beta} - r_e}{r_e} \quad (29)$$

and  $r_{\alpha\beta}$  represents one of the three triangle edges ( $r_{ij}$ ,  $r_{jk}$ ,  $r_{ki}$ ). These interatomic coordinates have specific geometrical meanings.  $Q_1$  represents the perimeter of the triangle in reduced units;  $Q_2$  and  $Q_3$  measure the distortions from an equilateral geometry [44]. All polynomial forms that are totally symmetric in  $\rho_{\alpha\beta}$  can be expressed as sums of products of the so-called integrity basis [44], defined as

$$Q_1, \quad Q_2^2 + Q_3^2, \quad Q_3^3 - 3Q_3Q_2^2 \quad (30)$$

A further condition that must be imposed on the three-body term is that it must go to 0 if any one of the three atoms goes to  $\infty$ . The following general family of functions can be chosen for the three-body part to conform to the functional form adopted for the two-body part:

$$\frac{U_{ijk}^{(3)}}{D} = P(Q_1, Q_2, Q_3) F(a_3, Q_1) \quad (31)$$

where  $P(Q_1, Q_2, Q_3)$  is a polynomial in the  $Q$  coordinates and  $F$  is a damping function, containing a single parameter,  $a_3$ , which determines the range of the three-body potential. Three different kinds of damping functions can be adopted:

$$\begin{aligned} F(a_3, Q_1) &= \exp(-a_3 Q_1) && \text{exponential} \\ F(a_3, Q_1) &= \frac{1}{2} \left[ 1 - \tanh\left(\frac{a_3 Q_1}{2}\right) \right] && \tanh \\ F(a_3, Q_1) &= \text{sech}(a_3 Q_1) && \text{sech} \end{aligned} \quad (32)$$

The use of the exponential damping function can lead to a problem; namely, for large negative  $Q_1$  values (i.e., for triangles for which  $r_{ij} + r_{jk} + r_{ki} \ll 3r_e$ ), the function  $F$  may be large so that the three-body contribution swamps the total two-body contribution. This may lead to the collapse of the lattice. To overcome this problem, it may be necessary, in some cases, to add a hard wall function to the repulsive part of the two-body term.

The polynomial,  $P$ , is normally taken to be

$$\begin{aligned} P(Q_1, Q_2, Q_3) &= c_0 + c_1 Q_1 + c_2 Q_1^2 + c_3 (Q_2^2 + Q_3^2) \\ &\quad + c_4 Q_1^3 + c_5 Q_1 (Q_2^2 + Q_3^2) \\ &\quad + c_6 (Q_3^3 - 3Q_3 Q_2^2) \end{aligned} \quad (33)$$

This implies that there are seven parameters to be determined. For systems where simultaneous fitting is made to data for two different solid phases, the following quartic terms can be added:

$$C_7 Q_1^4 + C_8 Q_1^2 (Q_2^2 + Q_3^2) + C_9 (Q_2^2 + Q_3^2)^2 + C_{10} Q_1 (Q_3^3 - 3Q_3 Q_2^2) \quad (34)$$

The potential parameters for a set of elements are given in Table 2.

**Table 2.** Parameters of the Murrell–Mottram potentials.

Element	$a_2$	$a_3$	$D$ (eV)	$r_c$ (nm)	$c_0$	$c_1$	$c_2$
Al	7.0	8.0	0.9073	0.27568	0.2525	-0.4671	4.4903
Cu	7.0	9.0	0.888	0.2448	0.202	-0.111	4.990
Ag	7.0	9.0	0.722	0.2799	0.204	-0.258	6.027
Sn	6.25	3.55	1.0	0.2805	1.579	-0.872	-4.980
Pb	8.0	6.0	0.59273	0.332011	0.18522	0.87185	1.27047

Element	$c_3$	$c_4$	$c_5$	$c_6$	$c_7$	$c_8$	$c_9$	$c_{10}$
Al	-1.1717	1.6498	-5.3579	1.6327	0.0	0.0	0.0	0.0
Cu	-1.369	0.469	-2.630	1.202	0.0	0.0	0.0	0.0
Ag	-1.262	-0.442	-5.127	2.341	0.0	0.0	0.0	0.0
Sn	-13.145	-4.781	35.015	-1.505	2.949	-15.065	10.572	12.830
Pb	-3.44145	-3.884	155.27033	2.85596	0.0	0.0	0.0	0.0

### 3.1.5. Many-Body Rafii-Tabar–Sutton Long-Range Alloy Potentials

We now consider the case of many-body interatomic potentials that describe the energetics of metallic alloys, in particular, the fcc metallic alloys. The interatomic potential that models the energetics and dynamics of a binary, A–B, alloy is normally constructed from the potentials that separately describe the A–A and the B–B interactions, where A and B are the elemental metals. To proceed with this scheme, a combining rule is normally proposed. Such a rule would allow for the computation of the A–B interaction parameters from those of the A–A and B–B parameters. The combining rule reflects the different averaging procedures that can be adopted, such as arithmetic or geometric averaging. The criterion for choosing any one particular combining rule is the closeness of the results obtained, when computing with the proposed A–B potential obtained with that rule, with the corresponding experimental values where they exist.

The RTS potentials [11, 58] are a generalization of the SC potentials and model the energetics of the metallic fcc random binary alloys. They have the advantage that all the parameters for the alloys are obtained from those for the elemental metals without the introduction of any new parameters. The basic form of the potential is given by

$$\begin{aligned}
 U^{\text{RTS}} = & \frac{1}{2} \sum_i \sum_{j \neq i} \hat{p}_i \hat{p}_j V^{\text{AA}}(r_{ij}) + (1 - \hat{p}_i)(1 - \hat{p}_j) V^{\text{BB}}(r_{ij}) \\
 & + [\hat{p}_i(1 - \hat{p}_j) + \hat{p}_j(1 - \hat{p}_i)] V^{\text{AB}}(r_{ij}) \\
 & - d^{\text{AA}} \sum_i \hat{p}_i \left[ \sum_{j \neq i} \hat{p}_j \Phi^{\text{AA}}(r_{ij}) + (1 - \hat{p}_j) \Phi^{\text{AB}}(r_{ij}) \right]^{1/2} \\
 & - d^{\text{BB}} \sum_i (1 - \hat{p}_i) \left[ \sum_{j \neq i} (1 - \hat{p}_j) \Phi^{\text{BB}}(r_{ij}) + \hat{p}_j \Phi^{\text{AB}}(r_{ij}) \right]^{1/2}
 \end{aligned} \quad (35)$$

The operator  $\hat{p}_i$  is the site occupancy operator and is defined as

$$\begin{aligned}
 \hat{p}_i &= 1 & \text{if site } i \text{ is occupied by an A atom} \\
 \hat{p}_i &= 0 & \text{if site } i \text{ is occupied by a B atom}
 \end{aligned} \quad (36)$$

The functions  $V^{\alpha\beta}$  and  $\Phi^{\alpha\beta}$  are defined as

$$\begin{aligned}
 V^{\alpha\beta}(r) &= \varepsilon^{\alpha\beta} \left[ \frac{a^{\alpha\beta}}{r} \right]^{n_{\alpha\beta}} \\
 \Phi^{\alpha\beta}(r) &= \left[ \frac{a^{\alpha\beta}}{r} \right]^{m_{\alpha\beta}}
 \end{aligned} \quad (37)$$

where  $\varepsilon$  and  $\beta$  are both A and B. The parameters  $\varepsilon^{\text{AA}}$ ,  $c^{\text{AA}}$ ,  $a^{\text{AA}}$ ,  $m^{\text{AA}}$ , and  $n^{\text{AA}}$  are for the pure element A, and  $\varepsilon^{\text{BB}}$ ,  $c^{\text{BB}}$ ,  $a^{\text{BB}}$ ,  $m^{\text{BB}}$ , and  $n^{\text{BB}}$  are for the pure element B, given in Table 1.

$$\begin{aligned}
 d^{\text{AA}} &= \varepsilon^{\text{AA}} c^{\text{AA}} \\
 d^{\text{BB}} &= \varepsilon^{\text{BB}} c^{\text{BB}}
 \end{aligned} \quad (38)$$

The mixed, or alloy, states are obtained from the pure states by assuming the combining rules:

$$V^{\text{AB}} = (V^{\text{AA}} V^{\text{BB}})^{1/2} \quad (39)$$

$$\Phi^{\text{AB}} = (\Phi^{\text{AA}} \Phi^{\text{BB}})^{1/2} \quad (40)$$

These combining rules, based on purely empirical grounds, give the alloy parameters as

$$\begin{aligned}
 m^{\text{AB}} &= \frac{1}{2} (m^{\text{AA}} + m^{\text{BB}}) \\
 n^{\text{AB}} &= \frac{1}{2} (n^{\text{AA}} + n^{\text{BB}}) \\
 a^{\text{AB}} &= (a^{\text{AA}} a^{\text{BB}})^{1/2} \\
 \varepsilon^{\text{AB}} &= (\varepsilon^{\text{AA}} \varepsilon^{\text{BB}})^{1/2}
 \end{aligned} \quad (41)$$

These potentials were used to compute the elastic constants and heat of formation of a set of fcc metallic alloys [58], as well as to model the formation of ultrathin Pd films on a Cu(100) surface [59]. They form the basis of a large class of MD simulations [11, 33].

### 3.1.6. Angular-Dependent Potentials

Transition metals form three rather long rows in the periodic table, beginning with Ti, Zr, and Hf and terminating with Ni, Pd, and Pt. These rows correspond to the filling of 3d, 4d, and 5d orbital shells, respectively. Consequently, the d-band interactions play an important role in the energetics of these metals [77], giving rise to angular-dependent forces that contribute significantly to the structural and vibrational characteristics of these elements. Pseudopotential models are commonly used to represent the intermolecular interaction in such metals [78, 79]. Recently, an *ab initio* generalized pseudopotential theory [80] was employed to construct an analytic angular-dependent potential for the description of the element Mo [81], a bcc transition metal. According to this prescription, the total cohesive energy is expressed as

$$\begin{aligned}
 H_I^{\text{Mo}} = & H_{\text{vol}}(\Omega) + \frac{1}{2N} \sum_i \sum_{j \neq i} V_{2(ij)} \\
 & + \frac{1}{6N} \sum_i \sum_{j \neq i} \sum_{k \neq i, j} V_{3(ijk)} \\
 & + \frac{1}{24N} \sum_i \sum_{j \neq i} \sum_{k \neq i, j} \sum_{l \neq i, j, k} V_{4(ijkl)} \quad (42)
 \end{aligned}$$

where  $\Omega$  is the atomic volume,  $N$  is the number of ions,  $V_3$  and  $V_4$  are, respectively, the angular-dependent three- and four-ion potentials, and  $H_{\text{vol}}$  includes all one-ion intratomic contributions to the cohesive energy. The interatomic potentials,  $V_{2(ij)}$ ,  $V_{3(ijk)}$ , and  $V_{4(ijkl)}$ , denote

$$\begin{aligned}
 V_{2(ij)} &\equiv V_2(r_{ij}; \Omega) \\
 V_{3(ijk)} &\equiv V_3(r_{ij}, r_{jk}, r_{ki}; \Omega) \\
 V_{4(ijkl)} &\equiv V_4(r_{ij}, r_{jk}, r_{kl}, r_{li}, r_{ki}, r_{lj}; \Omega) \quad (43)
 \end{aligned}$$

where  $r_{ij}$ , for example, is the ion-ion separation distance between ions  $i$  and  $j$ . These potentials are expressible in terms of weak pseudopotential and d-state tight-binding and hybridization matrix elements that couple different sites. Analytic expressions for these functions are provided [80, 81] in terms of distances and angles subtended by these distances.

The potential expressed by (42) was employed to compute the values of a set of physical properties of Mo, including the elastic constants, the phonon frequencies, and the vacancy formation energy [81]. These results clearly show that the inclusion of the angular-dependent potentials greatly improves the computed values of these properties as compared with the results obtained exclusively from an effective two-body interaction potential,  $V_2^{\text{eff}}$ . Furthermore, the potential was employed in an MD simulation of the melting transition of Mo, the details of which can be found in [81].

## 3.2. Interatomic Potentials for Covalently Bonding Systems

### 3.2.1. Tersoff Many-Body C–C, Si–Si, and C–Si Potentials

The construction of Tersoff many-body potentials is based on the formalism of an analytic bond order potential, initially suggested by Abell [82]. According to Abell's

prescription, the binding energy of an atomic many-body system can be computed in terms of pairwise nearest neighbor interactions that are, however, modified by the local atomic environment. Tersoff employed this prescription to obtain the binding energy in Si [83–85], C [86], Si–C [85, 87], Ge, and Si–Ge [87] solid-state structures.

In Tersoff's model, the total binding energy is expressed as

$$H_I^{\text{TR}} = \sum_i E_i = \frac{1}{2} \sum_i \sum_{j \neq i} V(r_{ij}) \quad (44)$$

where  $E_i$  is the energy of site  $i$  and  $V(r_{ij})$  is the interaction energy between atoms  $i$  and  $j$ , given by

$$V(r_{ij}) = f_c(r_{ij})[V^{\text{R}}(r_{ij}) + b_{ij}V^{\text{A}}(r_{ij})] \quad (45)$$

The function  $V^{\text{R}}(r_{ij})$  represents the repulsive pairwise potential, such as the core–core interactions, and the function  $V^{\text{A}}(r_{ij})$  represents the attractive bonding due to the valence electrons. The many-body feature of the potential is represented by the term  $b_{ij}$ , which acts as the bond order term and which depends on the local atomic environment in which a particular bond is located. The analytic forms of these potentials are given by

$$\begin{aligned}
 V^{\text{R}}(r_{ij}) &= A_{ij} \exp(-\lambda_{ij} r_{ij}) \\
 V^{\text{A}}(r_{ij}) &= -B_{ij} \exp(-\mu_{ij} r_{ij}),
 \end{aligned}$$

$$f_c(r_{ij}) = \begin{cases} 1 & \text{for } r_{ij} < R_{ij}^{(1)} \\ \frac{1}{2} + \frac{1}{2} \cos \left[ \frac{\pi(r_{ij} - R_{ij}^{(1)})}{R_{ij}^{(2)} - R_{ij}^{(1)}} \right] & \text{for } R_{ij}^{(1)} < r_{ij} < R_{ij}^{(2)} \\ 0 & \text{for } r_{ij} > R_{ij}^{(2)} \end{cases}$$

$$\begin{aligned}
 b_{ij} &= \chi_{ij} [1 + (\beta_i \zeta_{ij})^{n_i}]^{-0.5n_i} \\
 \zeta_{ij} &= \sum_{k \neq i, j} f_c(r_{ik}) \omega_{ik} g(\theta_{ijk}) \quad (46)
 \end{aligned}$$

$$g(\theta_{ijk}) = 1 + \frac{c_i^2}{d_i^2} - \frac{c_i^2}{d_i^2 + (h_i - \cos \theta_{ijk})^2}$$

$$\lambda_{ij} = \frac{\lambda_i + \lambda_j}{2} \quad \mu_{ij} = \frac{\mu_i + \mu_j}{2}$$

$$\omega_{ik} = \exp[\mu_{ik}(r_{ij} - r_{ik})]^3$$

$$A_{ij} = \sqrt{A_i A_j} \quad B_{ij} = \sqrt{B_i B_j}$$

$$R_{ij}^{(1)} = \sqrt{R_i^{(1)} R_j^{(1)}} \quad R_{ij}^{(2)} = \sqrt{R_i^{(2)} R_j^{(2)}}$$

where the labels  $i$ ,  $j$ , and  $k$  refer to the atoms in the  $ijk$  bonds and  $r_{ij}$  and  $r_{ik}$  refer to the lengths of the  $ij$  and  $ik$  bonds whose angle is  $\theta_{ijk}$ . Singly subscripted parameters, such as  $\lambda_i$  and  $n_i$ , depend only on one type of atom, for example, C or Si. The parameters for the C–C, Si–Si, and Si–C potentials are listed in Table 3. For C, the parameters



**Table 3.** Parameters of the Tersoff potentials for C and Si.

Parameter	C	Si
$A$ (eV)	$1.3936 \times 10^3$	$1.8308 \times 10^3$
$B$ (eV)	$3.467 \times 10^2$	$4.7118 \times 10^2$
$\lambda$ (nm <sup>-1</sup> )	34.879	24.799
$\mu$ (nm <sup>-1</sup> )	22.119	17.322
$\beta$	$1.5724 \times 10^{-7}$	$1.1000 \times 10^{-6}$
$\eta$	$7.2751 \times 10^{-1}$	$7.8734 \times 10^{-1}$
$c$	$3.8049 \times 10^4$	$1.0039 \times 10^5$
$d$	4.384	16.217
$h$	-0.57058	-0.59825
$R^{(1)}$ (nm)	0.18	0.27
$R^{(2)}$ (nm)	0.21	0.30
$\chi$	1	1
$\chi_{C-Si}$	0.9776	

were obtained by fitting the cohesive energies of carbon polytypes, along with the lattice constant and bulk modulus of diamond. For Si, the parameters were obtained by fitting to a database consisting of cohesive energies of real and hypothetical bulk polytypes of Si, along with the bulk modulus and bond length in the diamond structure. Furthermore, these potential parameters were required to reproduce all three elastic constants of Si to within 20%.

### 3.2.2. Brenner–Tersoff-Type First-Generation Hydrocarbon Potentials

The Tersoff potentials correctly model the dynamics of a variety of solid-state structures, such as the surface reconstruction in Silicon [83, 84] or the formation of interstitial defects in carbon [86]. However, while these potentials can give a realistic description of the C–C single-, double-, and triple-bond lengths and energies in hydrocarbons, solid graphite, and diamond, they lead to nonphysical results for bonding situations intermediate between the single and double bonds, such as the bonding in the Kekulé construction for graphite where, due to bond conjugation, each bond is considered to be approximately one-third double bond and two-thirds single bond in character. To correct for this, and similar problems in hydrocarbons, as well as to correct for the nonphysical overbinding of radicals, Brenner [88] developed a Tersoff-type potential for hydrocarbons that can model the bonding in a variety of small hydrocarbon molecules as well as in diamond and graphite. In this potential, (44) and (45) are rewritten as

$$H_i^{\text{Br}} = \frac{1}{2} \sum_i \sum_{i \neq j} V(r_{ij}) \quad (47)$$

and

$$V(r_{ij}) = f_c(r_{ij}) [V^{\text{R}}(r_{ij}) + \bar{b}_{ij} V^{\text{A}}(r_{ij})] \quad (48)$$

where

$$\begin{aligned} V^{\text{R}}(r_{ij}) &= \frac{D_{ij}}{S_{ij} - 1} \exp\left[-\sqrt{2S_{ij}}\beta_{ij}(r_{ij} - R_{ij}^{\text{c}})\right] \\ V^{\text{A}}(r_{ij}) &= \frac{-D_{ij}S_{ij}}{S_{ij} - 1} \exp\left[-\sqrt{(2/S_{ij})}\beta_{ij}(r_{ij} - R_{ij}^{\text{c}})\right] \\ \bar{b}_{ij} &= \frac{b_{ij} + b_{ji}}{2} + F_{ij}(N_i^{(\text{t})}, N_j^{(\text{t})}, N_{ij}^{\text{conj}}) \\ b_{ij} &= [1 + G_{ij} + H_{ij}(N_i^{(\text{H})}, N_i^{(\text{C})})]^{-\delta_i} \\ G_{ij} &= \sum_{k \neq i, j} f_c(r_{ik}) G_i(\theta_{ijk}) \\ &\quad \times \exp[\alpha_{ijk}\{(r_{ij} - R_{ij}^{\text{c}}) - (r_{ik} - R_{ik}^{\text{c}})\}] \\ G_c(\theta) &= a_0 \left[1 + \frac{c_0^2}{d_0^2} - \frac{c_0^2}{d_0^2 + (1 + \cos \theta)^2}\right] \end{aligned} \quad (49)$$

The quantities  $N_i^{(\text{C})}$  and  $N_i^{(\text{H})}$  represent the number of C and H atoms bonded to atom  $i$ ,  $N_i^{(\text{t})} = (N_i^{(\text{C})} + N_i^{(\text{H})})$  is the total number of neighbors of atom  $i$ , and its values, for neighbors of the two carbon atoms involved in a bond, can be used to determine if the bond is part of a conjugated system. For example, if  $N_i^{(\text{t})} < 4$ , then the carbon atom forms a conjugated bond with its carbon neighbors.  $N_{ij}^{\text{conj}}$  depends on whether an  $ij$  carbon bond is part of a conjugated system. These quantities are given by

$$\begin{aligned} N_i^{(\text{H})} &= \sum_{l \neq i, j}^{\text{hydrogen atoms}} f_c(r_{il}) \\ N_i^{(\text{C})} &= \sum_{k \neq i, j}^{\text{carbon atoms}} f_c(r_{ik}) \\ N_{ij}^{\text{conj}} &= 1 + \sum_{k \neq i, j}^{\text{carbon atoms}} f_c(r_{ik}) F(x_{ik}) \\ &\quad + \sum_{l \neq i, j}^{\text{carbon atoms}} f_c(r_{jl}) F(x_{jl}) \\ F(x_{ik}) &= \begin{cases} 1 & \text{for } x_{ik} \leq 2 \\ \frac{1}{2} + \frac{1}{2} \cos[\pi(x_{ik} - 2)] & \text{for } 2 < x_{ik} < 3 \\ 0 & \text{for } x_{ik} \geq 3 \end{cases} \\ x_{ik} &= N_k^{(\text{t})} - f_c(r_{ik}) \end{aligned} \quad (50)$$

The expression for  $N_{ij}^{\text{conj}}$  yields a continuous value as the bonds break and form, and as the second-neighbor coordinations change. For  $N_{ij}^{\text{conj}} = 1$ , the bond between a pair of carbon atoms  $i$  and  $j$  is not part of a conjugated system, whereas for  $N_{ij}^{\text{conj}} \geq 2$  the bond is part of a conjugated system.

The functions  $H_{ij}$  and  $F_{ij}$  are parameterized by two- and three-dimensional cubic splines, respectively, and the potential parameters in (47)–(50) were determined by first fitting to systems composed of carbon and hydrogen atoms only, and then the parameters were chosen for the mixed hydrocarbon systems. Two sets of parameters, consisting of 63

and 64 entries, are listed in [88]. These parameters were obtained by fitting a variety of hydrocarbon data sets, such as the binding energies and lattice constants of graphite, diamond, simple cubic and fcc structures, and the vacancy formation energies. The complete fitting sets are given in Tables I, II, and III in [88].

### 3.2.3. Brenner–Tersoff-Type Second-Generation Hydrocarbon Potentials

The potential function, expressed by (47)–(50) and referred to as the first-generation hydrocarbon potential, was recently further refined [41, 89] by including improved analytic functions for the intramolecular interactions and by an extended fitting database, resulting in a significantly better description of bond lengths, energies, and force constants for hydrocarbon molecules, as well as elastic properties, interstitial defect energies, and surface energies for diamond. In this improved version, the terms in (48) are redefined as

$$\begin{aligned}
 V^R(r_{ij}) &= f_c(r_{ij}) \left[ 1 + \frac{Q_{ij}}{r_{ij}} \right] A_{ij} \exp(\alpha_{ij} r_{ij}) \\
 V^A(r_{ij}) &= -f_c(r_{ij}) \sum_{(n=1,3)} B_{ijn} \exp(\beta_{ijn} r_{ij}) \\
 \bar{b}_{ij} &= \frac{p_{ij}^{\sigma\pi} + p_{ji}^{\sigma\pi}}{2} + p_{ij}^{\pi} \\
 p_{ij}^{\pi} &= \pi_{ij}^{\text{rc}} + \pi_{ij}^{\text{dh}} \\
 p_{ij}^{\sigma\pi} &= [1 + G_{ij} + P_{ij}(N_i^{(\text{H})}, N_i^{(\text{C})})^{-1/2}] \\
 G_{ij} &= \sum_{k \neq i, j} f_c(r_{ik}) G_i[\cos(\theta_{jik})] \exp[\lambda_{ijk}(r_{ij} - r_{ik})] \\
 \pi_{ij}^{\text{rc}} &= F_{ij}(N_i^{(\text{t})}, N_j^{(\text{t})}, N_{ij}^{\text{conj}}) \\
 N_{ij}^{\text{conj}} &= 1 + \left[ \sum_{k \neq i, j}^{\text{carbon atoms}} f_c(r_{ik}) F(x_{ik}) \right]^2 \\
 &\quad + \left[ \sum_{l \neq i, j}^{\text{carbon atoms}} f_c(r_{jl}) F(x_{jl}) \right]^2 \\
 \pi_{ij}^{\text{dh}} &= T_{ij}(N_i^{(\text{t})}, N_j^{(\text{t})}, N_{ij}^{\text{conj}}) \\
 &\quad \times \left[ \sum_{k \neq i, j} \sum_{l \neq i, j} (1 - \cos^2 \omega_{ijkl}) f_c(r_{ik}) f_c(r_{jl}) \right] \\
 \cos \omega_{ijkl} &= e_{ijk} e_{ijl}
 \end{aligned} \tag{51}$$

$Q_{ij}$  is the screened Coulomb potential, which goes to  $\infty$  as the interatomic distances approach 0. The term  $\pi_{ij}^{\text{rc}}$  represents the influence of radical energetics and  $\pi$ -bond conjugation on the bond energies, and its value depends on whether a bond between atoms  $i$  and  $j$  has a radical character and is part of a conjugated system. The value of  $\pi_{ij}^{\text{dh}}$  depends on the dihedral angle for the C–C double bonds.  $P_{ij}$  represents a bicubic spline, and  $F_{ij}$  and  $T_{ij}$  are tricubic spline functions. In the dihedral term,  $\pi_{ij}^{\text{dh}}$ , the functions  $e_{jik}$  and  $e_{ijl}$  are unit vectors in the direction of the cross products  $\mathbf{R}_j \times \mathbf{R}_k$  and  $\mathbf{R}_j \times \mathbf{R}_l$ , respectively, where the  $\mathbf{R}$ 's

are the interatomic vectors. The function  $G_c[\cos(\theta_{jik})]$  modulates the contribution that each nearest-neighbor makes to  $\bar{b}_{ij}$ . This function was determined in the following way. It was computed for the selected values of  $\theta = 109.47^\circ$  and  $\theta = 120^\circ$ , corresponding to the bond angles in diamond and graphitic sheets, and for  $\theta = 90^\circ$  and  $\theta = 180^\circ$ , corresponding to the bond angles among the nearest neighbors in a simple cube lattice. The fcc lattice contains angles of  $60^\circ$ ,  $90^\circ$ ,  $120^\circ$ , and  $180^\circ$ . A value of  $G_c[\cos(\theta = 60^\circ)]$  was also computed from the above values. To complete an analytic function for the  $G_c[\cos(\theta)]$ , sixth-order polynomial splines in  $\cos(\theta)$  were used to obtain its values for  $\theta$  between  $109.47^\circ$  and  $120^\circ$ . For  $\theta$  between  $0^\circ$  and  $109^\circ$ , for a carbon atom  $i$ , the angular function

$$g_c = G_c[\cos(\theta)] + Q(N_i^{(\text{t})})[\gamma_c \cos(\theta) - G_c\{\cos(\theta)\}] \tag{52}$$

is employed, where  $\gamma_c \cos(\theta)$  is a second spline function, determined for angles less than  $109.47^\circ$ . The function  $Q(N_i^{(\text{t})})$  is defined by

$$Q(N_i^{(\text{t})}) = \begin{cases} 1 & \text{for } N_i^{(\text{t})} \leq 3.2 \\ \frac{1}{2} + \frac{1}{2} \cos \left[ \frac{\pi(N_i^{(\text{t})} - 3.2)}{3.7 - 3.2} \right] & \text{for } 3.2 < N_i^{(\text{t})} < 3.7 \\ 0 & \text{for } N_i^{(\text{t})} \geq 3.7 \end{cases} \tag{53}$$

The large database of the numerical data on parameters and spline functions was obtained by fitting the elastic constants, vacancy formation energies, and formation energies for interstitial defects for diamond.

## 3.3. Interatomic Potential for C–C Nonbonding Systems

The nonbonding interactions between carbon atoms are required in many of the simulation studies in computational nanoscience and nanotechnology. These can be modeled according to various types of potentials. The Lennard-Jones and Kihara potentials can be employed to describe the van der Waals intermolecular interactions between carbon clusters, such as  $C_{60}$  molecules, and between the basal planes in a graphite lattice. Other useful potentials are the exp-6 potential [90], which also describes the  $C_{60}$ – $C_{60}$  interactions, and the Ruoff–Hickman potential [91], which models the  $C_{60}$ –graphite interactions.

### 3.3.1. Lennard-Jones and Kihara Potentials

The total interaction potential between the carbon atoms in two  $C_{60}$  molecules, or between those in two graphite basal planes, could be represented by the Lennard-Jones potential [92]:

$$H_I^{IJ}(r_{ij}^{IJ}) = 4\epsilon \sum_i \sum_{j>i} \left[ \left( \frac{\sigma}{r_{ij}^{IJ}} \right)^{12} - \left( \frac{\sigma}{r_{ij}^{IJ}} \right)^6 \right] \tag{54a}$$

where  $I$  and  $J$  denote the two molecules (planes) and  $r_{ij}$  is the distance between atom  $i$  in molecule (plane)  $I$  and atom

$j$  in molecule (plane)  $J$ . The parameters of this potential ( $\varepsilon = 0.24127 \times 10^{-2}$  eV,  $\sigma = 0.34$  nm) were taken from a study of graphite [93]. The Kihara potential is similar to the Lennard-Jones potential except that a third parameter,  $d$ , is added to correspond to the hard-core diameter, that is,

$$H_I^{LJ}(r_{ij}^{JJ}) = \begin{cases} 4\varepsilon \sum_i \sum_{j>i} \left[ \left\{ \frac{\sigma - d}{r_{ij}^{JJ} - d} \right\}^{12} - \left\{ \frac{\sigma - d}{r_{ij}^{JJ} - d} \right\}^6 \right] & \text{for } r > d \\ \infty & \text{for } r \leq d \end{cases} \quad (54b)$$

### 3.3.2. exp-6 Potential

This is another potential that describes the interaction between the carbon atoms in two  $C_{60}$  molecules

$$H_I^{\text{EXP6}}(r_{ij}^{JJ}) = \sum_i \sum_{j>i} \left[ A \exp(-\alpha r_{ij}^{JJ}) - B/(r_{ij}^{JJ})^6 \right] \quad (55)$$

Two sets of parameter values are provided, and these are listed in Table 4. These parameters have been obtained from the gas phase data of a large number of organic compounds, without any adjustment. The measured value of the  $C_{60}$  solid lattice constant is  $a = 1.404$  nm at  $T = 11$  K. The calculated value using set 1 was  $a = 1.301$  nm and using set 2 was  $a = 1.403$  nm. The experimentally estimated heat of sublimation is equal to  $-45$  kcal/mol (extrapolated from the measured value of  $-40.1 \pm 1.3$  kcal/mol at  $T = 707$  K). The computed value using set 1 was  $-41.5$  kcal/mol and using the set 2 was  $-58.7$  kcal/mol. We see that whereas set 2 produces a lattice constant nearer the experimental value, the thermal properties are better described by set 1.

### 3.3.3. Ruoff–Hickman Potential

This potential, based on the model adopted by Girifalco [94], describes the interaction of a  $C_{60}$  molecule with a graphite substrate by approximating these two systems as continuum surfaces on which the carbon atoms are “smeared out” with a uniform density. The sums over the pair interactions are then replaced by integrals that can be evaluated analytically. The  $C_{60}$  is modeled as a hollow sphere having a radius  $b = 0.355$  nm, and the C–C pair interaction takes on a Lennard-Jones form

$$H_I(r_{ij}) = c_{12}r^{-12} - c_6r^{-6} \quad (56)$$

with  $c_6 = 1.997 \times 10^{-5}$  [eV · (nm)<sup>6</sup>] and  $c_{12} = 3.4812 \times 10^{-8}$  [eV · (nm)<sup>12</sup>] [94]. The interaction potential between the hollow  $C_{60}$  and a single carbon atom of a graphite substrate, located at a distance  $z > b$  from the center of the

sphere, is then evaluated as

$$V(z) = V_{12}(z) - V_6(z) \quad (57)$$

where

$$V_n(z) = [c_n/2(n-2)][N/(bz)] \times [1/(z-b)^{n-2} - 1/(z+b)^{n-2}] \quad (58)$$

where  $N$  is the number of atoms on the sphere ( $N = 60$  in this case) and  $n = 12, 6$ . The total interaction energy between the  $C_{60}$  and the graphite plane is then obtained by integrating  $V(z)$  over all the atoms in the plane, giving

$$H_I(R) = E_{12}(R) - E_6(R) \quad (59)$$

where

$$E_n(R) = \{c_n/[4(n-2)(n-3)]\}(N^2/b^3) \times [1/(R-b)^{n-3} - 1/(R+b)^{n-3}] \quad (60)$$

and  $R$  is the vertical distance of the center of the sphere from the plane.

## 3.4. Interatomic Potential for Metal–Carbon System

In modeling the growth of metallic films on semimetallic substrates, such as graphite, a significant role is played by the interface metal–carbon potential since it controls the initial wetting of the substrate by the impinging atoms and also determines the subsequent diffusion and the final alignments of these atoms. This potential has not been available, and we have used an approximate scheme, based on a combining rule, to derive its general analytic form [95]. To construct a mixed potential to describe the interaction of an fcc metallic atom (M) with C, we assumed a generalized Morse-like potential energy function

$$H_I^{\text{MC}}(r_{ij}) = \sum_i \sum_{j>i} E_{\text{MC}} \left[ \exp\{-N\alpha(r_{ij} - r_w)\} - N \exp\{-\alpha(r_{ij} - r_w)\} \right] \quad (61)$$

and to obtain its parameters, we employed a known Morse potential function

$$H_I^{\text{CC}}(r_{ij}) = \sum_i \sum_{j>i} E_{\text{C}} \left[ \exp\{-2\alpha_1(r_{ij} - r_d)\} - 2 \exp\{-\alpha_1(r_{ij} - r_d)\} \right] \quad (62)$$

that describes the C–C interactions [96] and a generalized Morse-like potential function

$$H_I^{\text{MM}}(r_{ij}) = \sum_i \sum_{j>i} E_{\text{M}} \left[ \exp\{-m\alpha_2(r_{ij} - r_0)\} - m \exp\{-\alpha_2(r_{ij} - r_0)\} \right] \quad (63)$$

**Table 4.** Parameters of the exp-6 potential for C.

	A (kcal/mol)	B [kcal/mol × (nm) <sup>6</sup> ]	$\alpha$ (nm) <sup>-1</sup>
Set 1	42,000	$3.58 \times 10^8$	35.8
Set 2	83,630	$5.68 \times 10^8$	36.0

that describes the M–M interactions [97]. Several combining rules were then tried. The rule giving the satisfactory simulation results led to

$$\begin{aligned} E_{\text{MC}} &= \sqrt{E_{\text{C}}E_{\text{M}}} \\ r_{\text{w}} &= \sqrt{r_{\text{d}}r_0} \\ \alpha &= \sqrt{\alpha_1\alpha_2} \\ N &= \sqrt{2m} \end{aligned} \quad (64)$$

Since a cutoff is normally applied to an interaction potential, the 0 of this potential at a cutoff,  $r_{\text{c}}$ , was obtained according to the prescription in [96], leading to

$$\begin{aligned} H_i^{\text{MC}}(r_{ij}) &= \sum_{i>j} \sum E_{\text{MC}}[\exp\{-N\alpha(r_{ij}-r_{\text{w}})\} \\ &\quad - N \exp\{-\alpha(r_{ij}-r_{\text{w}})\}] \\ &\quad - E_{\text{MC}}[\exp\{-N\alpha(r_{\text{c}}-r_{\text{w}})\} \\ &\quad - N \exp\{-\alpha(r_{\text{c}}-r_{\text{w}})\}] \\ &\quad - E_{\text{MC}}N\alpha/\eta[1 - \exp\eta(r_{ij}-r_{\text{c}})] \\ &\quad \times [\exp(-N\alpha(r_{\text{c}}-r_{\text{w}})) - \exp(-\alpha(r_{\text{c}}-r_{\text{w}}))] \end{aligned} \quad (65)$$

where  $\eta$  is a constant whose value was chosen to be  $\eta = 20$ . This was a sufficiently large value so that the potential (65) was only modified near the cutoff distance. The parameters pertinent to the case when the metal atoms were silver, that is,  $M = \text{Ag}$ , are listed in Table 5. The parameters for (62) were obtained by fitting the experimental cohesive energy and the interplanar spacing,  $c/2$ , of the graphite exactly, and the parameters for (63) were obtained by fitting the experimental values of the stress-free lattice parameter and elastic constants  $C_{11}$  and  $C_{12}$  of the metal.

### 3.5. Atomic-Site Stress Field

In many modeling studies involving the mechanical behavior of nanostructures, such as the simulation of the dynamics of crack propagation in an atomic lattice, it is necessary to compute a map of the stress distribution over the individual atomic sites in a system composed of  $N$  atoms.

The concept of atomic level stress field was developed by Born and Huang [98] using the method of small homogeneous deformations. Applying small displacements to a pair of atoms  $i$  and  $j$ , with an initial separation of  $r_{ij}$ , it can be shown that [99] the Cartesian components of the stress tensor at site  $i$  are given by

$$\sigma_{\alpha\beta}(i) = \frac{1}{2\Omega_i} \sum_{j>i} \frac{\partial \Phi(r_{ij})}{\partial r_{ij}} \frac{r_{ij}^{\alpha} r_{ij}^{\beta}}{r_{ij}} \quad (66)$$

**Table 5.** Parameters of the Ag–C potential.

$\alpha_1$	$49.519 \text{ (nm)}^{-1}$
$\alpha_2$	$3.7152 \text{ (nm)}^{-1}$
$E_{\text{C}}$	3.1 eV
$E_{\text{Ag}}$	0.0284875 eV
$m$	6.00
$r_0$	0.444476 nm
$r_{\text{d}}$	0.12419 nm

where  $\alpha, \beta = x, y, z$ ,  $\Phi(r_{ij})$  is the two-body central potential, and  $\Omega_i$  is the local atomic volume, which can be identified with the volume of the Voronoi polyhedron associated with the atom  $i$  [100].

For the many-body potential energy given by (35), the stress tensor is given by

$$\begin{aligned} \sigma_{\alpha\beta}^{\text{RTS}}(i) &= \frac{1}{2\Omega_i} \left[ \sum_{j \neq i} \frac{\partial V(r_{ij})}{\partial r_{ij}} - \frac{1}{2} d^{\text{AA}} \hat{p}_i \right. \\ &\quad \times \sum_{j \neq i} \left( \frac{1}{\sqrt{\rho_i^{\text{A}}}} + \frac{1}{\sqrt{\rho_j^{\text{A}}}} \right) \frac{\partial \Phi^{\text{A}}(r_{ij})}{\partial r_{ij}} - \frac{1}{2} d^{\text{BB}} (1 - \hat{p}_i) \\ &\quad \times \sum_{j \neq i} \left( \frac{1}{\sqrt{\rho_i^{\text{B}}}} + \frac{1}{\sqrt{\rho_j^{\text{B}}}} \right) \frac{\partial \Phi^{\text{B}}(r_{ij})}{\partial r_{ij}} \left. \right] \frac{r_{ij}^{\alpha} r_{ij}^{\beta}}{r_{ij}} \end{aligned} \quad (67)$$

which for an elemental lattice with the two-body potentials given in [37] reduces to (see also [101])

$$\begin{aligned} \sigma_{\alpha\beta}^{\text{RTS}}(i) &= \frac{\varepsilon}{a^2} \frac{1}{2\Omega_i} \left[ \sum_{j \neq i} -n \left( \frac{a}{r_{ij}} \right)^{n+2} + cm \left( \frac{1}{\sqrt{\rho_i}} + \frac{1}{\sqrt{\rho_j}} \right) \right. \\ &\quad \times \left. \left( \frac{a}{r_{ij}} \right)^{m+2} \right] \frac{r_{ij}^{\alpha} r_{ij}^{\beta}}{r_{ij}} \end{aligned} \quad (68)$$

where only the contribution of the virial component to the stress field has been included and the contribution of the kinetic energy part (momentum flux) has been ignored as we are only interested in the low-temperature stress distributions. The volumes associated with individual atoms,  $\Omega_i$ , can be obtained by computing numerically their corresponding Voronoi polyhedra according to the prescription given in [23].

### 3.6. Direct Measurement of Interparticle Forces by Atomic Force Microscopy

The invention of the atomic force microscope (AFM) [7] in 1986 and its modification to optical detection [102] has opened new perspectives for various micro- and nanoscale surface imaging in science and industry. The use of AFM not only allows for nanoscale manipulation of the morphology of various condensed phases and the determination of their electronic structures, it can be also used for direct determination of interatomic and intermolecular forces.

However, its use for measurement of interparticle interaction energies as a function of distance is getting more attention for various reasons. For atoms and molecules consisting of up to 10 atoms, quantum mechanical *ab initio* computations are successful in producing rather exact force-distance results for interparticle potential energy. For complex molecules and macromolecules, one may produce the needed intermolecular potential energy functions directly only through the use of atomic force microscopy (AFM). For example, atomic force microscopy data are often used to develop accurate potential models to describe the intermolecular interactions in the condensed phases of such molecules as  $\text{C}_{60}$  [103].

The atomic force microscope is a unique tool for direct study of intermolecular forces. Unlike traditional microscopes, AFM does not use optical lenses, and therefore it provides very high resolution range of various sample properties [7, 104, 105]. It operates by scanning a very sharp tip across a sample, which “feels” the contours of the surface in a manner similar to the stylus tracing across the grooves of a record. In this way, it can follow the contours of the surface and so create a topographic image, often with subnanometer resolution.

This instrument also allows researchers to obtain information about the specific forces between and within molecules on the surface. The AFM, by its very nature, is extremely sensitive to intermolecular forces and has the ability to measure force as a function of distance. In fact, measurement of interactions as small as a single hydrogen bond have been reported [106–110]. Noncontact AFM will be used for attractive interaction force measurement. Contact AFM will be used for repulsive force measurement. Intermittent-contact AFM is more effective than noncontact AFM for imaging larger scan sizes.

In principle, to perform such a measurement and study with AFM, it is necessary to specially design the tip for this purpose [102, 111, 112]. Sarid [8] has proposed force–distance relationships when the tip is made of a molecule, a sphere, and a cylinder assuming van der Waals dispersion attractive forces. Various other investigators have developed the methodologies for force–distance relationships for other tip geometric shapes, including cylinder, paraboloid, cone, pyramid, a conical part covered by the spherical cap, and so on [105, 111, 113–119]. For example, Zanette et al. [111] present a theoretical and experimental investigation of the force–distance relationship in the case of a pyramidal tip. Data analysis of interaction forces measured with the atomic force microscope is quite important [120]. Experimental recordings of direct tip–sample interaction can be obtained as described in [121], and recordings using flexible cross-linkers can be obtained as described in [122, 123]. The noise in the typical force–distance cycles can be assumed to be, for example, Gaussian.

Recent progress in AFM technology will allow the force–distance relationship measurement of inter- and intramolecular forces at the level of individual molecules of almost any size.

Because of the possibility to use the AFM in liquid environments [109, 124], it has become possible to image organic micelles, colloids, biological surfaces such as cells and protein layers, and generally organic nanostructures [4] at nanometer resolution under physiological conditions. One important precaution to be considered in the force measurement is how to fix micelles, colloids, and biological cells on a substrate and a probe securely enough for measuring force but flexible enough to keep the organic nanostructure intact and, in the case of biological cells, keep it biologically active [124]. A variety of techniques for this purpose has been proposed, including the use of chemical cross-linkers, flexible spacer molecules [125], inactive proteins as cushions in the case of biological systems [126], and self-assembled monolayers [127]. An important issue to consider in liquid state force–distance measurements is the effect of pushing the organic nanostructures on to the substrate and AFM probe.

As the AFM probe is pushed onto the nanostructure, there is a possibility of damaging it or adsorbing it to the probe physically.

Also making microelectrophoretic measurements of the zeta potential will allow us to calculate the total interparticle energies indirectly. From the combined AFM and microelectrophoretic measurements, accurate force–distance data can be obtained. From the relationship between force and distance, an interparticle force vs. distance curve can be created. Then, with the use of the phenomenological potential functions presented in this review, the produced data can be readily fitted to a potential energy function for application in various nanotechnology and nanoscience computational schemes.

### 3.7. Conclusions

In this chapter, we have presented a set of state-of-the-art phenomenological interatomic and intermolecular potential energy functions that are widely used in computational modeling at the nanoscale. We have also presented a review of direct measurement of the interparticle force–distance relationship from which intermolecular potential energy functions data can be generated. There is still a great deal of work to be done in order to develop a thorough database for interatomic and intermolecular potential energy functions to be sufficient for applications in nanoscience and nanotechnology. This is because, to control the matter atom by atom, molecule by molecule, and/or at the macromolecular level, which is the aim of nanotechnology, it is necessary to know the exact intermolecular forces between the particles under consideration. In the development of intermolecular force models applicable for the study of nanostructures, which are at the confluence of the smallest of human-made devices and the largest molecules of living systems, it is necessary to reexamine the existing techniques and come up with more appropriate intermolecular force models.

It is understood that formidable challenges remain in the fundamental understanding of various phenomena on the nanoscale before the potential of nanotechnology becomes a reality. With the knowledge of better and more exact intermolecular interactions between atoms and molecules, it will become possible to increase our fundamental understanding of nanostructures. This will allow development of more controllable processes in nanotechnology and optimization of production and design of more appropriate nanostructures, such as nanotubes [128], and their interactions with other nanosystems.

## GLOSSARY

**Atomic force microscope (AFM)** An instrument for analyzing the material surface all the way down to the atoms and molecules level. A combination of mechanical and electronic probe is used in AFM to magnify surfaces up to 100,000,000 times to produce 3-D images of them.

**Body-centered cubic crystalline (BCC) structure** A structure in which the simplest repeating unit consists of nine equivalent lattice points, eight of which are at the corners of a cube and the ninth of which is in the center of the body of the cube.



**Embedded-atom model (EAM)** This is a type of interatomic potential, first suggested by Friedel, which describes the bonding of an atom in terms of the local electronic density.

**Face-centered cubic crystalline (FCC) structure** A structure in which the simplest repeating unit consists of fourteen equivalent lattice points, eight of which are at the corners of a cube and another six in the centers of the faces of the cube. Found in cubic closest-packed structures.

**Hexagonal close pack (HCP) crystalline structure** HCP structure is a special case of a hexagonal structure with alternating layers shifted so its atoms are aligned to the gaps of the preceding layer, and with  $c/a = \sqrt{8/3} = 1.633\dots$ . With this ratio, the atomic separation within a layer (on the x-y plane) is the same as the separation between layers.

**Molecular dynamics (MD)** This consist of the study of intramolecular conformations and molecular motions, using computational simulations taking into account the.

**Monte Carlo (MC) method of computation** This is a stochastic technique of computation/simulation which uses random numbers.

**Scanning tunneling microscope (STM)** This is an instrument able to image conducting surfaces to atomic accuracy; has been used to pin molecules to a surface. This is a more powerful device than AFM.

## REFERENCES

1. K. E. Drexler, "Nanosystems: Molecular Machinery, Manufacturing and Computation." Wiley, New York, 1992.
2. <http://www.foresight.org>.
3. H. S. Nalwa, Ed., "Handbook of Nanostructured Materials and Nanotechnology," Vols. 1-5. Academic Press, San Diego, 1999.
4. G. A. Mansoori, "Nanotechnology: The Emerging Cutting-Edge Technology," UN Tech Monitor. United Nations, New York, 2002.
5. M. C. Roco, S. Williams, and P. Alivisatos, Eds., "Nanotechnology Research Directions: IWGN Workshop Report—Vision for Nanotechnology R&D in the Next Decade," 1999.
6. G. Binnig and H. Rohrer, *Helv. Phys. Acta* 55, 726 (1982).
7. G. Binnig, C. F. Quate, and C. Gerber, *Phys. Rev. Lett.* 56, 933 (1986).
8. D. Sarid, "Scanning Force Microscopy with Applications to Electric Magnetic and Atomic Forces." Oxford Univ. Press, Oxford, 1994.
9. J. M. Frechet and D. A. Tomalia, "Dendrimers and Other Dendritic Polymers." Wiley, New York, 2001.
10. S. Priyanto, G. A. Mansoori, and A. Suwono, *Chem. Eng. Sci.* 56, 6933 (2001).
11. H. Rafii-Tabar, *Phys. Rep.* 325, 239 (2000).
12. J. M. Haile and G. A. Mansoori, Eds., "Molecular-Based Study of Fluids," *Advances in Chemistry Series*, Vol. 204. Am. Chem. Soc., Washington, DC, 1983.
13. W. Gans and J. C. A. Boeyens, Eds., "Intermolecular Interactions." Plenum, New York, 1998.
14. P. L. Huyskens, W. A. P. Luck, and T. Zeegers-Huyskens, Eds., "Intermolecular Forces: An Introduction to Modern Methods and Results." Springer-Verlag, New York, 1991.
15. A. R. Massih and G. A. Mansoori, *Fluid Phase Equilib.* 10, 57 (1983).
16. A. Stone, "The Theory of Intermolecular Forces," *International Series of Monographs on Chemistry*, Vol. 32. Oxford Univ. Press, London, 1997.
17. K. Terakura and H. Akai, "Interatomic Potential and Structural Stability: Proceedings of the 15th Taniguchi Symposium," 1993.
18. M. Edalat, F. Pang, S. S. Lan, and G. A. Mansoori, *Int. J. Thermophys.*, 1, 177 (1980).
19. R. L. Rowley, Y. Yang, Pakkanen, and A. Tapani, *J. Chem. Phys.* 114, 6058 (2001).
20. R. Car and M. Parrinello, *Phys. Rev. Lett.* 55, 2471 (1985).
21. D. H. E. Gross, "Microcanonical Thermodynamics: Phase Transitions in "Small" Systems," *World Scientific Lecture Notes in Physics*, Vol. 66. World Scientific, Singapore, 2001.
22. K. Esfarjani, Y. Kawazoe, and K. Ohno, "Computational Materials Science: From Ab Initio to Monte Carlo Methods," *Springer Series in Solid State Sciences*, Vol. 129. Springer-Verlag, Berlin, 1999.
23. M. P. Allen and D. J. Tildesley, "Computer Simulation of Liquids." Clarendon, Oxford, 1987.
24. J. M. Haile, "Molecular Dynamics Simulation: Elementary Methods." Wiley, New York, 1992.
25. D. C. Rapaport, "The Art of Molecular Dynamics Simulation." Cambridge Univ. Press, Cambridge, UK, 1995.
26. R. K. Pathria, "Statistical Mechanics." Pergamon, Oxford, 1972.
27. S. Nosé, *J. Chem. Phys.* 81, 511 (1984).
28. S. Nosé, *Mol. Phys.* 52, 255 (1984).
29. S. Nosé, *Prog. Theor. Phys. Suppl.* 103, 1 (1991).
30. W. G. Hoover, *Phys. Rev. A* 31, 1695 (1985).
31. J. Jellinek and R. S. Berry, *Phys. Rev. A* 38, 3069 (1988).
32. A. P. Sutton, J. B. Pethica, H. Rafii-Tabar, and J. A. Nieminen, in "Electron Theory in Alloy Design" (D. E. Pettifor and A. H. Cottrell, Eds.), p. 191. Institute of Materials, London, 1994.
33. H. Rafii-Tabar, *Phys. Rep.* 365, 145 (2002).
34. S. Erkoç, *Phys. Rep.* 278, 79 (1997).
35. P. L. Huyskens, W. A. P. Luck, and T. Zeegers-Huyskens, Eds., "Intermolecular Forces: An Introduction to Modern Methods and Results." Springer-Verlag, New York, 1991.
36. W. Gans and J. C. A. Boeyens, Eds., "Intermolecular Interactions." Plenum, New York, 1998.
37. B. M. Axilrod, *J. Chem. Phys.* 19, 719 (1951).
38. B. M. Axilrod and E. Teller, 11, 711 (1943).
39. E. H. Benmekki and G. A. Mansoori, *Fluid Phase Equilib.* 41, 43 (1988).
40. T. J. Frankcombe, R. Stranger, and H. W. Schranz, *Internet J. Chem.* 1, 12 (1998).
41. D. W. Brenner, *Phys. Status Solidi B* 271, 23 (2000).
42. J. Israelachvili, "Intermolecular and Surface Forces." Academic Press, New York, 1995.
43. F. Ercolessi, M. Parrinello, and E. Tosatti, *Philos. Mag. A* 58, 213 (1988).
44. H. Cox, R. L. Johnston, and J. N. Murrell, *J. Solid State Chem.* 517, 145 (1999).
45. M. S. Daw and M. I. Baskes, *Phys. Rev. Lett.* 50, 1285 (1983).
46. M. S. Daw and M. I. Baskes, *Phys. Rev. B* 29, 6443 (1984).
47. M. S. Daw, S. M. Foiles, and M. I. Baskes, *Mater. Sci. Rep.* 9, 251 (1993).
48. S. M. Foiles, M. I. Baskes, and M. S. Daw, *Phys. Rev. B* 33, 7983 (1986).
49. S. M. Foiles and M. S. Daw, *J. Mater. Res.* 2, 5 (1987).
50. R. A. Johnson, *Phys. Rev. B* 37, 3924 (1988).
51. J. B. Adams, S. M. Foiles, and W. G. Wolfer, *J. Mater. Res.* 4, 102 (1989).
52. R. A. Johnson, *Phys. Rev. B* 39, 12554 (1989).
53. R. A. Johnson, *Phys. Rev. B* 41, 9717 (1990).
54. F. Ercolessi, E. Tosatti, and M. Parrinello, *Phys. Rev. Lett.* 57, 719 (1986).
55. M. W. Finnis and J. E. Sinclair, *Philos. Mag. A* 50, 45 (1984).
56. G. J. Ackland and V. Vitek, *Phys. Rev. B* 41, 19324 (1990).
57. A. P. Sutton and J. Chen, *Philos. Mag. Lett.* 61, 139 (1990).
58. H. Rafii-Tabar and A. P. Sutton, *Philos. Mag. Lett.* 63, 217 (1991).

59. J. E. Black, *Phys. Rev. B* 46, 4292 (1992).
60. Yi.-G. Zhang and G. J. Guo, *Phys. Earth. Planet. Int.* 122, 289 (2000).
61. A. Ghazali and J.-C. S. Levy, *Surf. Sci.* 486, 33 (2001).
62. P. Hohenberg and W. Kohn, *Phys. Rev. B* 136, 864 (1964).
63. M. J. Stott and E. Zaremba, *Phys. Rev. B* 22, 1564 (1980).
64. J. K. Norskov and N. D. Lang, *Phys. Rev. B* 21, 2131 (1980).
65. A. F. Voter, in "Intermetallic Compounds: Principles" (H. Westbrook and R. L. Fleischer, Eds.), Vol. 1, p. 77. Wiley, London, 1994.
66. S. M. Foiles, *Phys. Rev. B* 32, 7685 (1985).
67. M. I. Baskes, *Phys. Rev. Lett.* 59, 2666 (1987).
68. S. Chantasirawan and F. Milstein, *Phys. Rev. B* 48, 14080 (1996).
69. S. Chantasirawan and F. Milstein, *Phys. Rev. B* 58, 5996 (1998).
70. G. J. Ackland, G. Tichy, V. Vitek, and M. W. Finnis, *Philos. Mag. A* 56, 735 (1987).
71. W. A. Harrison, "Electronic Structure and Properties of Solids." Freeman, San Francisco, 1984.
72. A. E. Carlsson, *Solid State Phys.* 43, 1 (1990).
73. J. Uppenbrink and D. J. Wales, *J. Chem. Phys.* 96, 8520 (1992).
74. B. R. Eggen, R. L. Johnston, S. Li, and J. N. Murrell, *Mol. Phys.* 76, 619 (1992).
75. L. D. Lloyd and R. L. Johnston, *Chem. Phys.* 236, 107 (1998).
76. B. S. Wherrett, "Group Theory for Atoms, Molecules and Solids." Prentice Hall, New York, 1986.
77. D. G. Pettifor, *J. Phys. C* 3, 367 (1970).
78. W. Harrison, "Elementary Electronic Structure." World Scientific, River Edge, NJ, 1999.
79. G. A. Mansoori, C. Jędrzejek, N. H. Shah, and M. Blander, in "Chemical Metallurgy—A Tribute to Carl Wagner" (N. A. Gokcen, Ed.), pp. 233–240. Metallurgical Society of AIME, 1981.
80. J. A. Moriarty, *Phys. Rev. B* 42, 1609 (1990).
81. J. A. Moriarty, *Phys. Rev. B* 49, 12431 (1994).
82. G. C. Abell, *Phys. Rev. B* 31, 6184 (1985).
83. J. Tersoff, *Phys. Rev. Lett.* 56, 632 (1986).
84. J. Tersoff, *Phys. Rev. B* 37, 6991 (1988).
85. J. Tersoff, *Phys. Rev. B* 38, 9902 (1988).
86. J. Tersoff, *Phys. Rev. Lett.* 61, 2879 (1988).
87. J. Tersoff, *Phys. Rev. B* 39, 5566 (1989).
88. D. W. Brenner, *Phys. Rev. B* 42, 9458 (1990).
89. D. W. Brenner, O. A. Shenderova, J. A. Harrison, S. J. Stuart, B. Ni, S. B. Sinnott, and J. A. Harrison, *J. Phys.: Condens. Matter* 14, 783 (2002).
90. D. Dharamvir and V. K. Jindal, *Int. J. Mod. Phys. B* 6, 281 (1992).
91. R. S. Ruoff and A. P. Hickman, *J. Phys. Chem.* 97, 2494 (1993).
92. A. Cheng and M. L. Klein, *Phys. Rev. B* 45, 1889 (1992).
93. W. A. Steele, "The Interaction of Gases with Solid Surfaces." Pergamon, New York, 1974.
94. L. A. Girifalco, *J. Chem. Phys.* 96, 858 (1992).
95. H. Rafii-Tabar, H. Kamiyama, and M. Cross, *Surf. Sci.* 385, 187 (1997).
96. D. J. Oh and R. A. Johnson, *Mater. Res. Soc. Symp. Proc.* 141, 51 (1989).
97. F. Milstein, *J. Appl. Phys.* 44, 3825 (1973).
98. M. Born and K. Huang, "Dynamical Theory of Crystal Lattices." Clarendon, Oxford, 1954.
99. N. Nishioka, T. Taka, and K. Hata, *Philos. Mag. A* 65, 227 (1992).
100. D. Srolovitz, K. Maeda, V. Vitek, and T. Egami, *Philos. Mag. A* 44, 847 (1981).
101. R. M. Lynden-Bell, *J. Phys.: Condens. Matter* 7, 4603 (1995).
102. G. Meyer and N. M. Amer, *Appl. Phys. Lett.* 53, 1045 (1988).
103. Z. Gamba, *J. Chem. Phys.* 97, 553 (1992).
104. J. L. Hutter and J. Bechhoefer, *J. Appl. Phys.* 73, 4123 (1993).
105. J. L. Hutter, and J. Bechhoefer, *J. Vac. Sci. Technol., B* 12, 2251 (1994).
106. B. V. Derjaguin, Y. I. Rabinovich, and N. V. Churaev, *Nature* 272, 313 (1978).
107. A. Diehl, M. C. Babosa, and Y. Levin, *Europhys. Lett.* 53, 86 (2001).
108. W. A. Ducker, T. J. Senden, and R. M. Pashley, *Nature* 353, 239 (1991).
109. W. A. Ducker, T. J. Senden, and R. M. Pashley, *Langmuir* 2, 1831 (1992).
110. T. Hugel and M. Seitz, *Macromol. Rapid Commun.* 22, 989 (2001).
111. S. I. Zanette, A. O. Caride, V. B. Nunes, G. L. Klimchitskaya, F. L. Freire, Jr., and R. Prioli, *Surf. Sci.* 453, 10 (2000).
112. R. Wiesendanger, "Scanning Probe Microscopy and Spectroscopy." Cambridge Univ. Press, Cambridge, UK, 1994.
113. E. V. Blagov, G. L. Klimchitskaya, A. A. Lobashov, and V. M. Mostepanenko, *Surf. Sci.* 349, 196 (1996).
114. E. V. Blagov, G. L. Klimchitskaya, and V. M. Mostepanenko, *Surf. Sci.* 410, 158 (1998).
115. Yu. N. Moiseev, V. M. Mostepanenko, V. I. Panov, and I. Yu. Sokolov, *Phys. Lett. A* 132, 354 (1988).
116. Yu. N. Moiseev, V. M. Mostepanenko, V. I. Panov, and I. Yu. Sokolov, *Sov. Phys. Tech. Phys. (USA)* 35, 84 (1990).
117. M. Bordag, G. L. Klimchitskaya, and V. M. Mostepanenko, *Surf. Sci.* 328, 129 (1995).
118. U. Hartman, *Phys. Rev. B* 43, 2404 (1991).
119. C. Argento and R. H. French, *J. Appl. Phys.* 80, 6081 (1996).
120. W. Baumgartner, P. Hinterdorfer, and H. Schindler, *Ultramicroscopy* 82, 85 (2000).
121. K. Schilcher, Ph.D. Thesis, University of Linz, 1997.
122. P. Hinterdorfer, W. Baumgartner, H. J. Gruber, K. Schilcher, and H. Schindler, *Proc. Natl. Acad. Sci. U.S.A.* 93, 3477 (1996).
123. P. Hinterdorfer, K. Schilcher, W. Baumgartner, H. J. Gruber, and H. Schindler, *Nanobiology* 4, 177 (1998).
124. H. Sekiguchi, H. Arakawa, T. Okajima, and A. Ikai, *Appl. Surf. Sci.* 188, 28 (2002).
125. O. H. Willemsen, M. M. E. Snel, K. O. Werf, B. G. Grooth, J. Greve, P. Hinterdorfer, H. J. Gruber, H. Schindler, Y. Kooyk, and C. G. Figdor, *Biophys. J.* 75, 2220 (1998).
126. U. Dammer, M. Hegner, D. Anselmetti, P. Wagner, M. Dreier, W. Huber, and H.-J. Güntherodt, *Biophys. J.* 70, 2437 (1996).
127. K. A. N. A. Wadu-Mesthrige and G. Y. Liu, *Scanning* 22, 380 (2000).
128. R. E. Smalley, *Mater. Sci. Eng., B* 19, 1 (1993).



# Interfacial Defects in Nanostructures

I. A. Ovid'ko

*Russian Academy of Sciences, St. Petersburg, Russia*

## CONTENTS

1. Introduction
  2. Classification of Interfaces in Nanostructured Materials
  3. Specific Features of Interfaces and Interfacial Defects in Nanocrystalline (Nanograined) Films and Coatings
  4. Grain Boundary Dislocations as Misfit Defects in Nanocrystalline Films and Coatings
  5. Misfit Disclinations at Grain Boundaries in Nanocrystalline Films and Coatings
  6. Partial Misfit Dislocations in Nanoscale Films
  7. Grain Boundary Dislocations and Enhanced Diffusion in Nanocrystalline Bulk Materials
  8. Interfacial Defects and Deformation Mechanisms in Nanocrystalline Bulk Materials
  9. Nanodefects in Nanostructures
  10. Concluding Remarks
- Glossary  
References

## 1. INTRODUCTION

Nanostructured materials exhibit outstanding physical, mechanical, and chemical properties opening a range of new applications in high technologies; see, for example, [1–7]. These outstanding properties of nanostructured materials are due to the interface and nanoscale effects. In particular, interfaces—grain and interphase boundaries—play the crucial role in physical and chemical processes occurring in nanocrystalline bulk materials and films where the volume fraction of the interfacial phase ranges from 10 to 50%. At the same time, the structure and the properties of interfaces in nanostructured materials are strongly influenced by technological parameters of their fabrication. In these circumstances, in order to technologically control, design, and

enhance functional characteristics of nanostructured materials, it is very important to understand the behavior of interfaces in them.

In description of the effects of interfaces on the properties of nanostructured materials, of special interest are theoretical models of interfaces. Such models represent a very essential constituent in a description of the relationship between fabrication technologies, structure, and functional properties of nanomaterials. Models of interfaces include, in particular, computer, geometric, and continuum models. Computer models commonly concentrate on simulations of the atomic structure of interfaces. Geometric models of solid/solid interfaces are concerned with their translational and rotational symmetries, in which case interfacial defects are treated as local violations of these symmetries. Continuum models use results of geometric and/or computer models in description of interfaces and interfacial defects as sources of internal stress fields, contributing to structural stability, mechanical, transport, and other properties of nanomaterials. Continuum models, in fact, provide a link between descriptions of the structure of interfaces and their properties. In this chapter we give a review of geometric and continuum models describing the specific structural and behavioral peculiarities of interfaces in nanostructured materials, with focuses placed on interfacial defects. In doing so, we will consider classification of interfaces in nanostructured materials (Section 2), specific features of interfaces and interfacial defects in nanostructured bulk materials and films (Sections 2 and 3), interfacial defects playing the role as misfit defects (causing relaxation of residual stresses) in nanocrystalline films and coatings (Sections 4 and 5), partial misfit dislocations at interphase boundaries in nanoscale films (Section 6), and grain boundary defects and their effects on diffusion and plastic deformation processes in nanocrystalline bulk materials (Sections 7 and 8). Finally, we will discuss the notion of nanodefects in nanostructures, extending the notion of defects to the case of assembled nanostructures, and we will summarize results of a theoretical description of interfacial defects in diverse nanostructured materials (Sections 9 and 10).

## 2. CLASSIFICATION OF INTERFACES IN NANOSTRUCTURED MATERIALS

Following Gleiter [3, 8], nanostructured materials can be divided into the following three basic categories, depending on both their structure and the shape of the crystallites: materials in the form of (isolated, substrate-supported, or embedded) nanometer-sized particles, thin wires, and films; materials in which the nanometer-sized microstructure is limited to a thin (nanometer-sized) surface region of a bulk solid; and bulk materials with a nanometer-sized microstructure. These categories are rather general, in which case nanostructured materials belonging to one category contain interfaces with very different structures and properties. In this context, for aims of this review focused on defects at solid/solid interfaces in nanostructured materials, we suggest classification of such interfaces, which takes into account their structural geometry as well as crystalline structure and phase content of solids adjacent to interfaces. In doing so, internal (solid/solid) interfaces in nanostructured materials can be divided into the following basic categories: (i) plane interphase boundaries between single crystalline nanoscale films and single crystalline substrates (Fig. 1a), and between single crystalline nanolayers in multilayered coatings (Fig. 1b); (ii) short and curved grain boundaries in nanocrystalline bulk materials (Fig. 1c), thin films (Fig. 1d), and thick coatings; (iii) plane and short interphase boundaries between grains of nanocrystalline films and single crystalline substrate (Fig. 1d); (iv) short and curved interphase boundaries in nanocomposites consisting of equaxed nanoparticles (Fig. 1e); (v) curved interphase boundaries in nanocomposites consisting of nanowires embedded into a matrix (Fig. 1f); (vi) striplike interphase boundaries between freestanding nanowires and single crystalline substrates (Fig. 1g); (vii) squarelike interphase boundaries between freestanding nanoislands (quantum dots) and substrate (Fig. 1h); (viii) short and curved interphase boundaries surrounding quantum dots embedded into nanowires (Fig. 1i).

Crystalline structure and phase content of adjacent solids cause the existence of geometrically necessary or, in other terms, intrinsic defects at solid/solid interfaces. In particular, these intrinsic defects are associated with misorientation inherent to grain boundaries, and provide a partial relaxation of misfit stresses occurring due to geometric mismatch between different crystalline lattices of different phases matched at interphase boundaries. The intrinsic defects exist also at solid/solid interfaces in conventional materials (with micrometer-sized structure), where interfaces are tentatively plane and have large dimensions. Interfaces in conventional materials are commonly modeled as plane interfaces of infinite extent. In doing so, ensembles of intrinsic interfacial defects are modeled as infinite, periodically arranged structures. However, these theoretical representations of interfaces and interfacial defects are oversimplified in the case of the nanostructured materials, in which most interfaces are curved and short (see Fig. 1). Owing to curved geometry of interfaces in nanostructured materials, high-density ensembles of their junctions, first of all, triple junctions of grain and interphase boundaries, exist in such materials. They have both the structure and properties different from

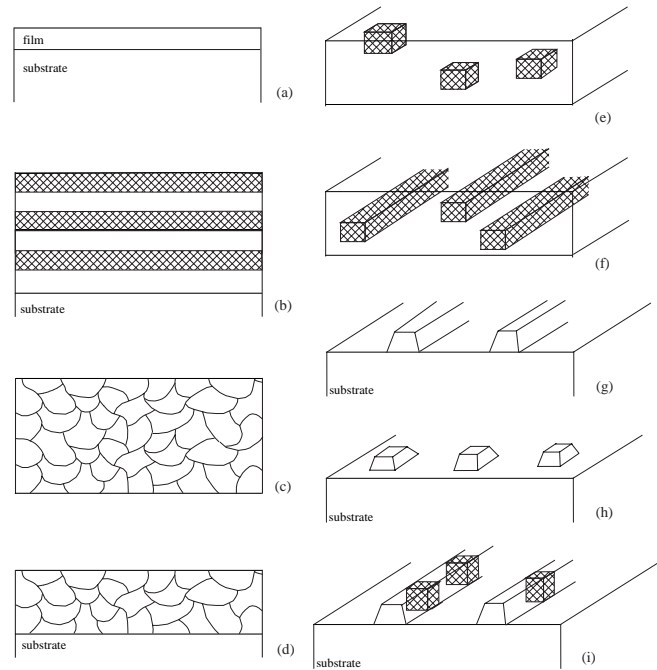


**Figure 1.** Interfaces in nanostructured materials: (a) plane interphase boundaries between single crystalline nanoscale film and single crystalline substrate; (b) plane interphase boundaries between single crystalline nanolayers in multilayered coatings; (c) short and curved grain boundaries in nanocrystalline (nanograined) bulk materials; (d) short and curved grain boundaries in nanocrystalline (nanograined) film as well as plane and short interphase boundaries between grains of nanocrystalline film and single crystalline substrate; (e) short and curved interphase boundaries in nanocomposite consisting of equaxed nanoparticles embedded into a matrix; (f) curved interphase boundaries in nanocomposite consisting of nanowires embedded into a matrix; (g) striplike interphase boundaries between freestanding nanowires and single crystalline substrate; (h) squarelike interphase boundaries between freestanding nanoislands (quantum dots) and substrate; (i) interphase boundaries surrounding quantum dots embedded into nanowires.

those of interfaces that they adjoin; see, for example, [9]. As a result, triple junctions treated as interfacial defects of the special type are capable of strongly influencing functional properties of nanostructured materials. In addition, interfaces in diverse nanostructured materials are short, in which case their length is of the same order as periods of arrangements of intrinsic defects at interfaces in conventional materials. With finite extent of interfaces and influence of triple junctions, arrangement of intrinsic interfacial defects is different from conventionally modeled periodic arrangement (see, e.g., [9–13]), causing these defects to exhibit behavior different from that of interfacial defects at interfaces in conventional materials.

In the case of plane interphase boundaries between nanoscale films and single crystalline substrates (Fig. 1a) or between nanoscale layers in multilayered coatings (Fig. 1b), geometry of interphase boundaries is similar to that in conventional films. Nevertheless, nanoscale effects come into play in this case, causing the formation of specific interfacial structures such as partial misfit dislocations associated with

V-shaped stacking faults in films of nanoscale thickness (see Section 6) and amorphization of interphase boundaries (see experimental data [14] and a theoretical model [15]).

Parallel with structural geometry and phase content, conditions of fabrications of nanostructured materials strongly affect interfacial defect structure of interfaces. More precisely, nanostructured materials are commonly fabricated by highly nonequilibrium methods causing the formation of so-called extrinsic interfacial defects, that is, defects which are not geometrically necessary at interfaces. Grain boundaries with high densities of extrinsic defects are called nonequilibrium boundaries and exhibit specific properties different from those of equilibrium grain boundaries containing intrinsic defects only [16–22]. It is believed that the nonequilibrium grain boundaries are responsible for the very unusual mechanical properties of nanostructured materials produced by severe plastic deformation [20, 21]. By analogy with the notion of nonequilibrium grain boundaries [16–22], it is natural to define nonequilibrium interphase boundaries as those containing high-density ensembles of extrinsic defects. Such nonequilibrium interphase boundaries are expected to exist in nanocomposites fabricated at highly nonequilibrium conditions.

In this chapter we will consider theoretical models of intrinsic and extrinsic defects and their ensembles at interfaces in nanostructured materials. Focuses are placed on defects in nanocrystalline bulk materials, films, and coatings, because the theory of such defects is well developed. Theoretical representations of such defects can serve as a basis for a theoretical description of interfacial defects in nanocomposite systems.

### 3. SPECIFIC FEATURES OF INTERFACES AND INTERFACIAL DEFECTS IN NANOCRYSTALLINE (NANOGRAINED) FILMS AND COATINGS

Nanocrystalline thin films (thick coatings) (Fig. 1a) can be treated as polycrystalline films (coatings) in the limiting case, where the grain size is on the order of a few nanometers. As a corollary, nanocrystalline films have the “conventional” structural and behavioral features that are inherent to both nanocrystalline and polycrystalline films as well as the “specific” structural and behavioral features associated with their nanoscale structure.

The existence of both grain boundaries and interphase (film/substrate) boundaries causes the “conventional” features of nanocrystalline and polycrystalline films, which are as follows: (a) There is a strong elastic interaction between grain boundaries in a nanocrystalline (or polycrystalline) film and the film/substrate interface which is a source of misfit stresses. (b) Film/substrate interfaces are complicately arranged; each interface consists of fragments with various structures and properties, bounded by junctions of grain boundaries and the film/substrate interface. Due to the features (a) and (b), grain boundaries and film/substrate interfaces strongly affect both the structure and the properties of each other in nanocrystalline and polycrystalline films.

In addition, interfaces in nanocrystalline films (Fig. 1d) have the following “specific” features related to their nanoscale structure:

- (1) The volume fraction of the interfacial phase is extremely high in nanocrystalline films.
- (2) Grain boundaries are short and curved.
- (3) There is a strong elastic interaction between neighboring interfaces, because (extremely short) distances between them are close to the characteristic scales of their stress fields.
- (4) In nanocrystalline films there is a strong effect of triple junctions and nanograins on interfaces and vice versa, because the volume fraction of triple junctions is extremely high in nanocrystalline solids and because nanograins commonly are more distorted than conventional grains in polycrystalline films.
- (5) Formation of nanocrystalline films frequently occurs at highly nonequilibrium conditions that essentially influence the interfacial structures.<sup>1</sup>

The points under discussion should be definitely taken into account in a theoretical description of interfaces and interfacial defects in nanocrystalline films, which, in most cases, can not be unambiguously identified with the help of contemporary experimental methods. With these points, let us consider interphase boundaries between nanocrystalline films and (single crystalline) substrates (Fig. 1d). To do so, first let us discuss structural geometry of interphase boundaries between single crystalline films and single crystalline substrates. In general, such interphase boundaries can be coherent, incoherent, or semicoherent, depending on the structural and chemical features of the matched phases as well as on external factors such as temperature and the geometric sizes (e.g., thickness) of the matched crystalline samples. In doing so, according to a qualitative description of the coherent, incoherent, and semicoherent states of interfaces given by Möbus et al. [23], the key classifying factor for these states is supposed to be the way in which the mismatch (geometric misfit) between the adjacent crystalline lattices (Fig. 2a) is accommodated.

- (1) For a coherent interface between a thin film and a thick substrate, the mismatch is accommodated completely by straining the lattice of the adjacent film (Fig. 2b). In this event, misfit stresses (stresses occurring due to the mismatch at interface) are characterized by the spatial scale being the film thickness.
- (2) For a semicoherent interface, localized misfit dislocations (misfit dislocations) provide at least partial compensation of long-range misfit stresses (Fig. 2c) (for more details, see reviews [24–29]).
- (3) A completely incoherent interface can be treated as resulted from a rigid contact of two crystalline lattices distorted only at the contact regions (Fig. 2d).

Incoherent interfaces do not induce long-range strains; there are only short-range distortions occurring due to faults in

<sup>1</sup>The same features are inherent also to bulk nanocrystalline materials.



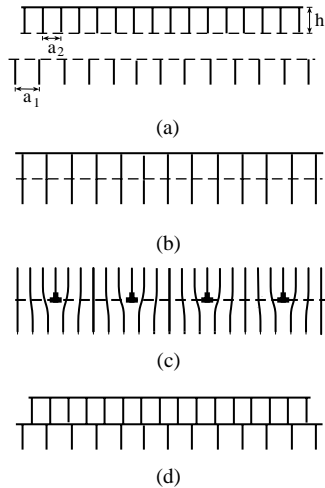


**Figure 2.** Interphase boundaries between single crystalline films and substrates. (a) Origin of dilatation misfit stresses is the geometric mismatch between crystal lattice parameters,  $a_1$  and  $a_2$ , of film and substrate. (b) Coherent boundary. (c) Semicoherent boundary. (d) Incoherent interphase boundary.

chemical binding at the interface. Such distortions are characterized by a spatial scale close to interatomic distances in the adjacent phases.

Now let us turn to a consideration of structural geometry of interphase boundaries between nanocrystalline films and single crystalline substrates. As it has been noted in Section 2, any nanocrystalline film/substrate interface consists of many fragments bounded by junctions of grain boundaries and the interface. Grains of the film that are adjacent to the film/substrate interface are misoriented relative to each other and, generally speaking, relative to the substrate. As a corollary, fragments of the film/substrate boundary are characterized by the misorientation and the dilatation misfit between the crystalline lattices of the film grains and the substrate. Each fragment of the film/substrate interface is either coherent, incoherent, or semicoherent, depending on its misfit and misorientation parameters and the structural and chemical features of the matched grain and the substrate, as well as on external factors such as temperature and the film thickness. Thus, in general, the nanocrystalline film/substrate interface is partly coherent, semicoherent, and incoherent; it consists of coherent, semicoherent, and incoherent fragments (Fig. 3). In this situation, the film/substrate interface contains defects of the two types: dilatation misfit defects (responsible for partial compensation of dilatation misfit stresses generated due to mismatch between the crystal lattice parameters of the film and the substrate) and misorientation defects (that provide misorientation between the adjacent grains of the film and the single crystalline substrate). More than that, misfit defects can be generated not only at film/substrate interfaces, but also at grain boundaries of the film. In Sections 4 and 5 we will consider geometric and continuum models of interfacial defects in nanocrystalline films with focuses placed on misfit defects at grain boundaries in these films.

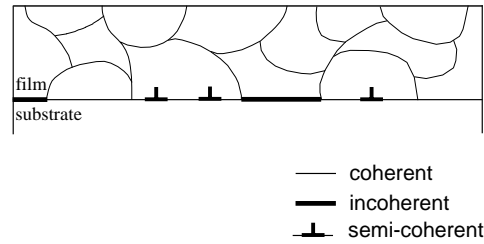


**Figure 3.** Partly coherent, semicoherent, and incoherent interphase boundary between nanocrystalline film and single crystalline substrate.

#### 4. GRAIN BOUNDARY DISLOCATIONS AS MISFIT DEFECTS IN NANOCRYSTALLINE FILMS AND COATINGS

Misfit stresses occur in crystalline films due to the geometric mismatch at interphase boundaries between crystalline lattices of films and substrates. In most cases a partial relaxation of misfit stresses in single crystalline films is realized via generation of misfit dislocations that form dislocation rows in interphase boundary plane (Fig. 2c) or more complicatedly arranged configurations; see, for example, experimental and theoretical works [23–41]. Generally speaking, the formation of misfit dislocation rows at interphase boundaries is either desirable or disappointing, from an applications viewpoint, depending on the roles of films and interphase boundaries in applications of film/substrate composite solids. So, if the properties of a film are exploited, the formation of misfit dislocation rows commonly is desirable as it results in a (partial) compensation of misfit stresses in the film. If the properties of an interphase boundary are exploited, the formation of misfit dislocation rows commonly is undesirable, since the formed misfit dislocation cores violate the pre-existent ideal (coherent) structure of the interphase boundary.

The structure and the properties of nanocrystalline films are different from those of single crystalline films. Therefore, relaxation of misfit stresses in nanocrystalline films, in general, can occur via micromechanisms that are different from the standard micromechanism, the formation of rows of perfect misfit dislocations (Fig. 2c). In particular, we think that, due to the existence of grain boundaries in nanocrystalline films, an effective alternative to the standard physical micromechanism for relaxation of misfit stresses in such films is the formation of grain boundary dislocations as misfit defects. These grain boundary dislocations (with Burgers vectors being displacement-shift-complete lattice vectors which characterize grain boundary translation symmetries) induce stress fields that compensate for, in part, misfit stresses and are located at grain boundaries and triple junctions of interphase and grain boundaries (Fig. 4). The formation of grain boundary dislocations as misfit defects does not induce any extra violations of coherent fragments of interphase boundaries and, therefore, does not lead to degradation of their functional properties used in applications. In this section we, following [29], will discuss the behavioral peculiarities of nanocrystalline and

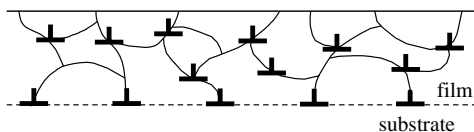


**Figure 4.** Grain boundary dislocations as misfit defects in nanocrystalline film.

polycrystalline films with grain boundary dislocations as misfit defects.

First, let us discuss a scenario for the formation of grain boundary dislocations as misfit defects. Nanocrystalline films are often synthesized at highly nonequilibrium conditions, in which case grain boundaries in these films are highly distorted and are characterized by misorientation parameters which, in general, vary along grain boundary planes. Each distorted boundary contains both the so-called “equilibrium” or, in other terms, intrinsic grain boundary dislocations (which provide the mean misorientation characterizing the boundary) and “nonequilibrium” or extrinsic grain boundary dislocations (which provide local deviations of the distorted boundary misorientation from its mean value) (Fig. 5) [16–19]. Nonequilibrium dislocations in a grain boundary, after some relaxation time interval, disappear via entrance to a free surface of a sample and/or via annihilation of dislocations with opposite Burgers vectors (Fig. 5a). As a result of the relaxation processes discussed, a distorted grain boundary commonly transforms into its equilibrium state with the misorientation being (tentatively) constant along the boundary plane.

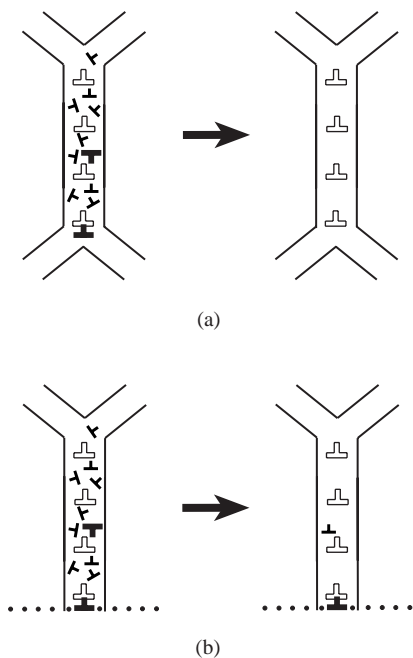


**Figure 5.** “Equilibrium” and “nonequilibrium” dislocations (shown as open and solid dislocation signs, respectively) in distorted and low-energy grain boundaries. (a) “Nonequilibrium” dislocations completely disappear after relaxation. (b) Some “nonequilibrium” dislocations keep existing as misfit defects (compensating for misfit stresses generated at interphase boundary shown as dotted line) after relaxation.

However, the relaxation processes result in complete disappearance of nonequilibrium grain boundary dislocations in materials with initially distorted grain boundaries, only if there are not sources of long-range stresses affecting evolution of defects in the grain boundary phase (Fig. 5a). In nanocrystalline films with initially distorted grain boundaries, the misfit stresses (generated at film/substrate interfaces) influence evolution of nonequilibrium dislocations. More precisely, we expect that the low-energy (equilibrium) state of a nanocrystalline film corresponds to the existence of not only equilibrium grain boundary dislocations, but also some residual nonequilibrium grain boundary dislocations that play the role of misfit defects (Figs. 4 and 5b) compensating for misfit stresses in the film. In other words, in the framework of the scenario discussed, fabrication of nanocrystalline films at nonequilibrium conditions produces high-density ensembles of nonequilibrium grain boundary dislocations, while misfit stresses generated at interphase (film/substrate) boundaries cause some nonequilibrium grain boundary dislocations to keep existing, even after relaxation, as misfit defects compensating for these misfit stresses (Fig. 5b).

In general, the most spatially homogeneous distribution of misfit dislocations is characterized by the minimal elastic energy density and, therefore, is most stable. Grain boundary dislocations commonly are characterized by Burgers vectors being essentially lower than those of perfect misfit dislocations being crystal lattice dislocations. This specific feature allows grain boundary dislocations to be more homogeneously distributed along an interphase boundary as compared with perfect misfit dislocations, if the sum Burgers vectors of ensembles of misfit, grain boundary and perfect, dislocations are the same per unit of the boundary plane area. As a corollary, the existence of grain boundary dislocations as misfit dislocations often is more energetically favorable than that of perfect misfit dislocations [19]. This statement is supported by data of experiments dealing with measurements of residual stresses in nanocrystalline films and coatings. So, as it has been noted in [42], residual stresses are low in nanocrystalline cermet coatings (fabricated by thermal spray methods at highly nonequilibrium conditions), resulting in a capability for producing very thick coatings. So, nanocrystalline coatings were fabricated up to 0.65 cm thick and could probably be made with arbitrary thickness [42]. At the same time, in a conventional polycrystalline cermet coating, stress buildup limits coating thickness to typically 500–800  $\mu\text{m}$ . This is naturally explained as caused by a misfit stress relaxation micromechanism (in the situation discussed, the formation of grain boundary misfit dislocations) which comes into play in nanocrystalline films and coatings, and is different from and more effective than the standard micromechanism, the formation of perfect misfit dislocations.

In general, as with ensembles of dislocations with identical Burgers vectors (Fig. 4), complicately arranged configurations of grain boundary dislocations with various Burgers vectors are capable of effectively contributing to accommodation of misfit stresses in nanocrystalline solids. In particular, following a theoretical model [43], dislocation dipoles at grain boundaries can play the role of misfit defect configurations. This statement is indirectly supported by the

experimentally detected fact that misfit dislocation dipoles exist in a single crystalline GaInP film deposited onto a GaAs substrate [44].

## 5. MISFIT DISCLINATIONS AT GRAIN BOUNDARIES IN NANOCRYSTALLINE FILMS AND COATINGS

Parallel with nonequilibrium dislocations and their configurations, the so-called grain boundary disclinations (rotational defects) are generated in nanocrystalline materials fabricated at highly nonequilibrium conditions [18, 45]. Such disclinations, after some relaxation time interval, annihilate in the absence of sources of long-range stresses affecting the grain boundary phase evolution. In nanocrystalline films containing grain boundary disclinations, the misfit stresses (generated at film/substrate interfaces) influence evolution of disclinations. More precisely, in the general situation, the low-energy (equilibrium) state of a nanocrystalline film is expected to correspond to the existence of not only some residual nonequilibrium dislocations, but also some residual grain boundary disclinations that play the role of misfit defects (Fig. 6). In this section we, following theoretical models [29, 46], will briefly discuss the behavioral peculiarities of nanocrystalline films with grain boundary disclinations as misfit defects.

So, relaxation of misfit stresses through the formation of misfit disclinations (defects of the rotational type) (Fig. 6) [29, 46] is an alternative to the formation of misfit dislocation rows (Fig. 2b). The effective action of the disclination micromechanism for stress relaxation has been experimentally detected in semiconducting polycrystalline films [47–49]. Also, the disclination relaxation micromechanism is capable of effectively contributing to relaxation of residual stresses in crystalline films deposited on amorphous substrates (see a theoretical model [50]) as well as diverse nanocrystalline and polycrystalline films [51–55]. Owing to the presence of the grain boundary phase in nanocrystalline films, disclinations at grain boundaries play the role as misfit disclinations in such films (Fig. 6). The specific feature of the disclination micromechanism for relaxation of misfit stresses in nanocrystalline films is that cores of grain boundary disclinations playing the role as misfit defects are located at existent grain boundaries (either at boundaries in film interior or at junctions of interphase and grain boundaries) and, therefore, do not induce any extra violations of the interphase boundary structure. The disclination micromechanism for relaxation of misfit stresses is of particular importance in nanocrystalline films, because of the fact that grain

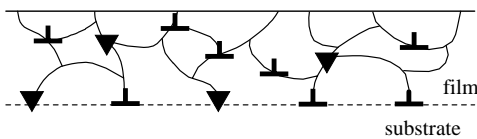


**Figure 6.** Grain boundary dislocations and disclinations as misfit defects in nanocrystalline film.

boundary disclinations are intensively generated in nanocrystalline materials synthesized at highly nonequilibrium conditions (see, e.g., [45]) and because of extremely high volume fraction of the grain boundary phase in nanocrystalline films.

Following [46], let us consider a model composite system consisting of a thin nanocrystalline film of thickness  $h$  deposited onto a semifinite substrate (Fig. 7). The film and substrate are assumed to be isotropic solids having the same values of the shear modulus  $G$  and the same values of the Poisson ratio  $\nu$ . Interphase (film/substrate) boundary is a semicoherent interface which induces misfit stresses and contains misfit disclinations at junctions of grain boundaries and the interface. For simplicity, misfit disclinations are assumed to be arranged periodically (Fig. 7) and to be characterized by identical value,  $\omega$ , of the disclination strength.

In the framework of the model discussed, Kolesnikova et al. [46] have calculated the basic characteristics (stored elastic energy density, equilibrium residual strain, critical values of film thickness) of a film with misfit disclinations. According to these calculations, the difference,  $\Delta E = E_{discl} - E_{coher}$ , between the energy densities of the interphase boundary with misfit disclinations and the coherent interphase boundary is as follows:

$$\Delta E = \frac{G}{4\pi(1-\nu)} \omega^2 l \Phi \left( \frac{h}{l} \right) - \frac{G}{(1-\nu)} \omega f \frac{h^2}{l} \quad (1)$$

where  $h$  denotes the film thickness,  $l$  the distance between neighboring disclinations (or, in other words, period of the misfit disclination array),  $G$  the shear modulus,  $\nu$  the Poisson ratio,  $f$  the misfit parameter (defined as  $f = 2(a_2 - a_1)/(a_1 + a_2)$ , with  $a_1$  and  $a_2$  being the crystal lattice parameters of the substrate and the film, respectively),

$$\begin{aligned} \Phi = \int_{-\tilde{h}}^0 \left[ \frac{1}{2} \ln \frac{\cosh 2\pi(\tilde{x} + \tilde{h}) - 1}{\cosh 2\pi(\tilde{x} - \tilde{h}) - 1} \right. \\ + \pi(\tilde{x} + \tilde{h}) \frac{\sinh 2\pi(\tilde{x} + \tilde{h})}{\cosh 2\pi(\tilde{x} + \tilde{h}) - 1} \\ - \pi(\tilde{x} + 3\tilde{h}) \frac{\sinh 2\pi(\tilde{x} - \tilde{h})}{\cosh 2\pi(\tilde{x} - \tilde{h}) - 1} \\ \left. - 4\pi^2 \tilde{x} \tilde{h} \frac{1}{\cosh 2\pi(\tilde{x} - \tilde{h}) - 1} \right] (\tilde{x} + \tilde{h}) d\tilde{x} \quad (2) \end{aligned}$$

If  $\Delta E < 0$  ( $> 0$ , respectively), the formation of misfit disclinations at the interphase boundary (Fig. 7) is energetically favorable (unfavorable respectively).

From Eq. (1) it follows that the characteristic energy of difference  $\Delta E$  depends on four parameters of the film with misfit disclinations at the interphase boundary: disclination strength  $\omega$ , the misfit parameter  $f$ , the film thickness  $h$ ,

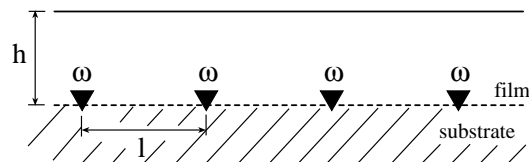


**Figure 7.** Model of interphase boundary with misfit disclinations.

and the distance  $l$  between neighboring disclinations. Analysis [46] of the relationships (given by Eqs. (1) and (2)) between  $\Delta E$ ,  $\omega$ ,  $f$ ,  $h$ , and  $l$  shows the following. The critical thickness for generation of misfit disclinations in nanocrystalline (and polycrystalline) films is 0, if disclination strength ranges from 0 to some value  $\omega_0$  denoted as the optimum disclination strength. More precisely, the formation of misfit disclinations is more energetically favorable ( $\Delta E < 0$ ) than the coherent state of the interphase boundary at any value of the film thickness, below some value  $h_0$  denoted as the optimum thickness. (It is contrasted to the situation with “conventional” misfit dislocations (see, e.g., [24–27]) whose formation in a thin film is energetically favorable compared to the coherent state, only if the film thickness exceeds some critical value.) As a corollary, the discussed micromechanism for relaxation of misfit stresses—generation of misfit disclinations at grain boundaries (Fig. 6)—serves as an effective alternative to the standard micromechanism—generation of misfit dislocations (Fig. 2b)—in nanocrystalline films characterized by low values of film thickness, in particular, in films with nanoscaled thickness. The effective action of the disclination micromechanism for relaxation of misfit stresses in nanocrystalline films can be responsible for the experimentally observed fact that residual stresses are low in nanocrystalline cermet coatings synthesized by thermal spray methods (see discussion in [42] and Section 4).

## 6. PARTIAL MISFIT DISLOCATIONS IN NANOSCALE FILMS

Now let us turn to a discussion of interfacial defects at plane interphase boundaries between nanoscale single crystalline films and substrates (Fig. 1a). One of the structural features of nanoscale films is the experimentally observed [56–60] enhanced formation of partial misfit dislocations (associated with stacking faults) at film/substrate boundaries. In this section we, following [41, 61], consider a model describing generation and evolution of configurations of partial misfit dislocations associated with V-shaped stacking faults in nanolayer/substrate composites.

In general, misfit dislocations formed at film/substrate interfaces are either perfect (Fig. 2b) or partial (Fig. 8). Perfect misfit dislocations are characterized by Burgers vectors being crystal lattice vectors and just locally, at dislocation line cores, violate the ideal crystalline structure; see, for example, [23–29] (Fig. 2b). Partial misfit dislocations are characterized by Burgers vectors that commonly are lower than crystal lattice vectors and have line cores which bound plane stacking faults, in which case the ideal crystalline structure is violated at both line cores and plane stacking faults; see, for example, [56–60] (Fig. 8). In most situations the formation of perfect misfit dislocations is more energetically favorable compared to partial misfit dislocations. Therefore, the perfect misfit dislocations are the traditional subject of theoretical and experimental studies. However, there are also film/substrate systems in which the enhanced formation of partial misfit dislocations is experimentally detected [56–60]. Following theoretical analysis [41, 61], the formation of partial misfit dislocations associated with V-shaped stacking faults is energetically favorable in

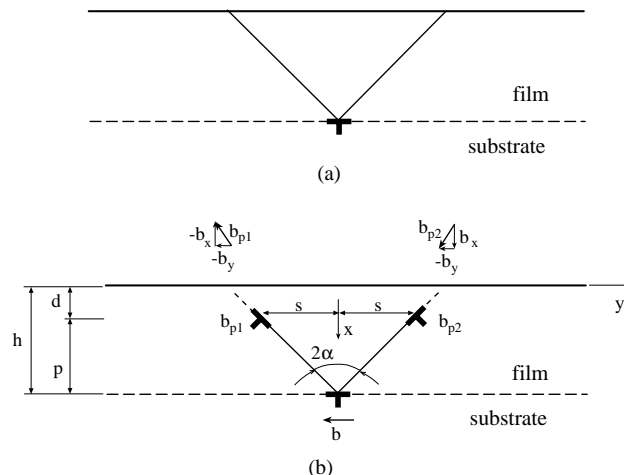


**Figure 8.** Configurations of partial misfit dislocations in nanolayer/substrate composites: (a) single partial misfit dislocations associated with V-shaped stacking faults; and (b) complicatedly arranged configurations of partial misfit dislocations.

film/substrate systems characterized by low (nanoscale) values of film thickness and large misfit between crystal lattice parameters of the film and substrate. This statement (directly supported by experimental data [60]) is highly interesting due to rapidly growing industrial needs in technologies exploiting nanofilm/substrate systems characterized by large misfit parameters.

Let us consider both generation and evolution of complicatedly arranged configurations of partial misfit dislocations, namely the experimentally observed [60] configurations each consisting of three partial misfit dislocations located at respectively the top line and the two edge lines that bound a V-shaped stacking fault in a film (Fig. 8b). In the limiting case where the partial misfit dislocations located at the edge lines of the stacking fault reach the film free surface, the complicatedly arranged configuration (Fig. 8b) transforms into a simple configuration consisting of one partial misfit dislocation at top of the V-shaped stacking fault, that connects the film free surface and the film/substrate boundary (Fig. 8a). Such simple configurations of partial misfit dislocations have been observed in experiments [59].

Let us consider characteristics of complicatedly arranged configurations of partial misfit dislocations (Fig. 8b) in heteroepitaxial (nanofilm/substrate) systems (for details, see [61]). In doing so, for definiteness, we will focus our consideration on partial misfit dislocations in heteroepitaxial systems GaAs/Si (001) that are interesting for applications. One of the important characteristics of a thin solid film is its critical thickness, defined as the thickness at which the formation of misfit dislocations in film/substrate system becomes energetically favorable; see, for example, [24–27]. In the situation discussed (Fig. 8b), the critical thickness  $h_c$  of a film is defined as the thickness at which the formation of one complicatedly arranged configuration of partial misfit dislocations is energetically favorable in the film.

Let us consider a model heteroepitaxial system consisting of an elastically isotropic semi-infinite crystalline substrate and an elastically isotropic thin film with thickness  $h$ . The shear modulus  $G$  and the Poisson ratio  $\nu$  are assumed to

be identical for the substrate and the film. For definiteness, hereinafter we confine our examination to the situation with one-dimensional misfit  $f = 2(a_2 - a_1)/(a_1 + a_2) > 0$ , where  $a_1$  and  $a_2$  are the crystal lattice parameters of the substrate and the film, respectively. In the initial state with a coherent interphase boundary, owing to the geometric mismatch between the crystalline lattices of the film and the substrate, the film is elastically uniformly distorted. It is characterized by the elastic strain  $\varepsilon = -f < 0$ .

Now let us turn to a consideration of the model heteroepitaxial system with a complicatedly arranged configuration of partial misfit dislocations (Fig. 8b). Let the “top” partial misfit dislocation be located at line  $(h, 0)$  which bounds the top of V-shaped stacking fault, and the partial misfit dislocations of the  $90^\circ$  type be located at lines  $(d, \pm s)$  that bound the edges of V-shaped stacking fault. Let the top misfit dislocation be characterized by Burgers vector  $\mathbf{b}$ , and the “lateral” misfit dislocations be characterized by Burgers vectors  $\mathbf{b}_{p1} = -\mathbf{b}_x - \mathbf{b}_y$  and  $\mathbf{b}_{p2} = \mathbf{b}_x - \mathbf{b}_y$ , respectively. For our further consideration, the lateral misfit dislocation at line  $(d, s)$  (line  $(d, -s)$ , respectively) can be effectively represented as the superposition of two edge dislocations with Burgers vectors  $\mathbf{b}_y$  and  $\mathbf{b}_x$  ( $-\mathbf{b}_x$ , respectively); see Figure 8b. The V-shaped stacking fault bounded by the top and lateral misfit dislocations (Fig. 8b) is characterized by top angle  $2\alpha$ .

According to calculations [61], the critical film thickness  $h_c$  at which the formation of a complicatedly arranged configuration of misfit dislocations (Fig. 8b) in a film becomes energetically favorable can be found from the following transcendental equation:

$$\begin{aligned}
& 2b_p^2 - 8\pi f(1 + \nu)(bh + 2b_y d) + \frac{8\pi\gamma(1 - \nu)(h - d)}{G \cos \alpha} \\
& + b^2 \left( 1 - \ln \frac{b}{2h - b} - \frac{2h(h - b)}{(2h - b)^2} \right) \\
& - 2bb_y \left( \ln \frac{(h - d)^2 + s^2}{(h + d)^2 + s^2} - \frac{2s^2}{(h - d)^2 + s^2} \right. \\
& \quad \left. + \frac{2(s^2 + 2dh)}{(h + d)^2 + s^2} - \frac{8dhs^2}{[(h + d)^2 + s^2]^2} \right) \\
& + 2bb_x s \left( \frac{2(h - d)}{(h - d)^2 + s^2} - \frac{2(h - d)}{(h + d)^2 + s^2} \right. \\
& \quad \left. - \frac{8dh(h + d)}{[(h + d)^2 + s^2]^2} \right) - \frac{4b_x b_y s d^3}{(d^2 + s^2)^2} \\
& - b_y^2 \left( \ln \frac{b_y^2 s^2}{(d^2 + s^2)(2d - b_y)^2} + \frac{4d(d - b_y)}{(2d - b_y)^2} \right. \\
& \quad \left. - \frac{d^2(d^2 + 3s^2)}{(d^2 + s^2)^2} \right) \\
& - b_x^2 \left( \ln \frac{b_x^2(d^2 + s^2)}{s^2(2d - b_x)^2} + \frac{4d(d - b_x)}{(2d - b_x)^2} \right. \\
& \quad \left. - \frac{d^2(3d^2 + s^2)}{(d^2 + s^2)^2} \right) = 0 \tag{3}
\end{aligned}$$

where  $\gamma$  is the stacking fault energy density (per unit area). Equation (3) allows one to analyze relationships between characteristics (critical thickness, misfit parameter)

of nanofilm/substrate composites with perfect misfit dislocations (Fig. 2b), single partial misfit dislocations associated with V-shaped stacking faults (Fig. 8a), and complicatedly arranged configuration of partial misfit dislocations (Fig. 8b).

In particular, theoretical analysis [61] based on Eq. (3) shows the following. The formation of perfect misfit dislocations is energetically favorable in composites with comparatively small values of misfit parameter ( $f < 0.1$ ). At the same time, during growth of the films (nanolayers) with comparatively large values of misfit parameter (tentatively  $f > 0.01$ ), the formation of single partial misfit dislocations is energetically favorable, if the film thickness  $h$  is in the range  $h_c < h < h'_c$ . In the situation discussed, when the film thickness  $h$  exceeds the critical value  $h'_c$  (which commonly is in the range of a few nanometers and decreases with increase of misfit parameter  $f$ ), single partial misfit dislocations associated with V-shaped stacking faults (Fig. 8a) transform into complicatedly arranged configurations of partial misfit dislocations (Fig. 8b). Further growth of the film thickness leads to the merging of the three partial misfit dislocations (elements of a complicatedly arranged configuration) into a perfect misfit dislocation at the interphase (film/substrate) boundary, in which case the stacking fault disappears.

The statement that partial misfit dislocations transform into perfect misfit dislocations during growth of films, resulted from theoretical analysis [61], is in agreement with experimental data [60]. These data are indicative of the fact that the density of perfect misfit dislocations increases and the density of partial misfit dislocations decreases with increase of film thickness.

It should be noted that, according to theoretical analysis [34], the generation of partial misfit dislocations effectively competes with that of conventional perfect dislocations also in germanium pyramid-like quantum dots (nanoisland films) on silicon substrate. In doing so, different partial dislocation structures are energetically preferred in different regions of the interface. Single partial dislocation is generated near lateral free surface of a nanoisland. Then, during its motion towards the nanoisland base center, the second partial dislocation is generated [34].

## 7. GRAIN BOUNDARY DISLOCATIONS AND ENHANCED DIFFUSION IN NANOCRYSTALLINE BULK MATERIALS

Let us turn to a discussion of interfacial defects and their effects on physical processes occurring in bulk nanocrystalline materials. In this section, we consider grain boundary defects and their role in diffusion processes in bulk nanocrystalline materials. Diffusion properties of bulk nanocrystalline materials, in general, are different from those of conventional coarse-grained polycrystals. Thus, following [62–66], bulk nanocrystalline materials exhibit the anomalously enhanced diffusion. For instance, the boundary diffusion coefficients in bulk nanocrystalline materials fabricated by high-pressure compaction and severe plastic deformation methods are several orders of magnitude larger than those in conventional polycrystalline materials with the

same chemical composition [62–66]. With these experimental data, the anomalously fast diffusion is treated as the phenomenon inherent to only nanocrystalline materials and is attributed to their specific structural and behavioral peculiarities [8, 62]. At the same time, however, there are experimental data indicating that the boundary diffusion coefficients in dense bulk nanocrystalline materials are lower than those measured in [62, 64–66] and similar to the boundary diffusion coefficients in conventional coarse-grained polycrystals or a little higher [67–71]. These data form a basis for the viewpoint that the atomic diffusion in nanocrystalline materials is similar to that in conventional coarse-grained polycrystals. In doing so, the difference in the diffusivities between nanocrystalline and coarse-grained materials is treated to be related to only the difference in the volume fraction of the grain boundary phase.

Thus, in general, there are controversial experimental data and theoretical representations of diffusion processes in nanocrystalline materials. Nevertheless, mechanically synthesized nanocrystalline bulk materials are definitely recognized to exhibit enhanced diffusion properties compared to those of nanocrystalline materials fabricated by nonmechanical (more equilibrium than mechanical) methods and those of coarse-grained polycrystals; see [64–66]. The experimentally documented phenomenon in question can be naturally explained as that occurring due to the deformation-induced nonequilibrium state of grain boundaries, in which case the grain boundary diffusivity highly increases. In this section we will consider theoretical models of diffusion processes in nanocrystalline materials with special attention being paid to the role of extrinsic defects at nonequilibrium grain boundaries in the diffusion enhancement occurring in mechanically synthesized nanocrystalline bulk materials.

Theoretical models of diffusion in nanocrystalline materials can be divided into the three following basic categories: (1) Models that describe grain boundary diffusion in conventional coarse-grained polycrystals and are directly extended to the situation with nanocrystalline materials, with nanoscale effects neglected. (2) Models focused on the specific features of diffusion in nanocrystalline materials in the general situation, taking into account the nanoscale effects, but neglecting the influence of preparation technologies on the structure and the diffusion properties of nanocrystalline materials. In short, such models deal with the “nanostructure-diffusion” relationship. (3) Models focused on the structural and behavioral peculiarities of grain boundaries in nanocrystalline materials, taking into account the peculiarities of their fabrication. In short, such models are concerned with the “preparation-nanostructure-diffusion” relationship.

Theoretical models of the first type and their applications to a description of diffusion in nanocrystalline materials have been reviewed in detail by Larikov [72]. Such models are, in particular, those [73–77] describing spatial distributions of diffusion species within and near grain boundaries in polycrystals, models [78–86] focused on macroscopic mechanisms of grain boundary diffusion, and models [87–94] dealing with diffusion-assisted processes (diffusional creep, diffusion-induced grain boundary migration, transformations of grain boundary dislocations and disclinations, etc.) in polycrystals. Now let us turn to a brief discussion of models

describing the enhanced diffusion in nanocrystalline materials in the general situation, with the specific features of their preparation being neglected. In [95, 96] it has been demonstrated that nanocrystalline materials exhibit much larger variety of possible kinetic diffusion regimes compared to coarse-grained polycrystals. In particular, together with conventional A-, B-, and C-regimes occurring in polycrystals [77], the additional diffusion kinetic regimes have been distinguished, depending on the grain size, diffusion temperature and time, the grain boundary segregation level in the case of impurity diffusion, and other parameters [96].

Gleiter [62] considered the anomalously fast diffusion in nanocrystalline materials as the phenomenon related to the three following factors: (i) The diffusion in nanocrystalline materials is essentially enhanced due to the existence of high-density network of grain boundary junction tubes which commonly are characterized by more increased diffusion rate than grain boundaries themselves. (The highly enhanced diffusivity of triple junctions of grain boundaries is experimentally identified in polycrystals; see [97–102] and discussion in review article [9] concerning grain boundary junctions.) (ii) Rigid body relaxation of grain boundaries that occurs via relative translational displacements of their adjacent crystallites and reduces the boundary free volume is hampered in nanocrystalline materials. This is related to the fact that rigid body relaxations of the various boundaries surrounding every nanocrystallite require its different displacements due to their different atomic structure. (iii) In grain boundaries of nanocrystalline materials, the concentration of impurities that often reduce boundary diffusivity is lower than that in grain boundaries in conventional polycrystals.

Let us discuss factors (i)–(iii) in terms of Arrhenius formula for diffusivity in solids. The coefficient  $D$  of self-diffusion occurring via transfer of vacancies<sup>2</sup> is given by the following Arrhenius relationship (e.g., [86])

$$D = D_0 \exp[-(\varepsilon_f + \varepsilon_m)/kT] \quad (4)$$

where  $D_0$  denotes the constant dependent on parameters of the ideal crystalline lattice,  $k$  the Boltzmann's constant,  $T$  the absolute temperature,  $\varepsilon_f$  and  $\varepsilon_m$  the energies of respectively formation and migration of vacancies. In nanocrystalline materials (characterized by extremely high volume fraction of the grain boundary phase), self-diffusion processes occur mostly via transfer of grain boundary vacancies. In these circumstances, all the factors (i)–(iii) discussed by Gleiter [62] induce the characteristic boundary free volume to be increased and, as a corollary, both formation and migration of boundary vacancies to be facilitated in nanocrystalline materials as compared to those in conventional polycrystals. In terms of Arrhenius formula (4), the diffusion coefficient  $D$  is increased in nanocrystalline materials, because their characteristic energies,  $\varepsilon_f$  and  $\varepsilon_m$ , are decreased due to factors (i)–(iii) discussed in [62].

Now let us discuss theoretical models describing the enhanced diffusion in nanocrystalline materials fabricated

<sup>2</sup> In general, diffusion processes in crystals occur via transfer of point defects of different types. However, self-diffusion occurring via transfer of vacancies is most effective; it is characterized by the largest coefficient of diffusion, e.g., [86, 103].



at highly nonequilibrium conditions (say, by severe plastic deformation methods). Following [104–107], together with factors (i)–(iii) discussed by Gleiter [62], the existence and transformations of ensembles of grain boundary dislocations and disclinations strongly enhance diffusion processes in nanocrystalline materials fabricated at highly nonequilibrium conditions. The effects of such defects on diffusion are briefly as follows [106, 107]:

(a) Disorderedly distributed grain boundary dislocations and disclinations are formed in nanocrystalline materials fabricated at highly nonequilibrium conditions. Such dislocations and disclinations rearrange to annihilate or to form more ordered, low-energy configurations, in which case they move to new positions. Climb of (grain boundary) dislocations is accompanied by generation of new point defects [103, 108]—vacancies and interstitial atoms—serving as new carriers of diffusion. In this situation, generation of new vacancies at grain boundaries occurs under the action of the driving force related to a release of the elastic energy of “nonequilibrium” or, in other words, extrinsic grain boundary dislocations during their transformations. The action of the driving force in question facilitates diffusion processes in nanocrystalline materials. The effect discussed is quantitatively described by Eq. (4) with the sum  $\varepsilon_f + \varepsilon_m$  being replaced by  $\varepsilon_f - W_v + \varepsilon_m$ , where  $W_v (>0)$  is the energy release due to the climb of a grain boundary dislocation, per one vacancy emitted by the dislocation.

(b) Cores of grain boundary dislocations and disclinations are characterized by excess free volume, in which case their presence in grain boundaries increases the total free volume that characterizes the grain boundary phase in nanocrystalline materials. This decreases values of  $\varepsilon_f$  and  $\varepsilon_m$  and, therefore, enhances diffusion processes occurring by vacancy mechanism.

(c) Dilatation stress fields of grain boundary dislocations and disclinations influence migration of vacancies. More precisely, in spirit of the theory of diffusion in stressed solids [109], the elastic interaction between vacancies and grain boundary dislocations and disclinations is characterized by the energy

$$\varepsilon_{int} = -\sigma_{ii}\Delta V/3 \quad (5)$$

where  $\sigma_{ii}$  denotes the sum of dilatation components (say, components  $\sigma_{xx}$ ,  $\sigma_{yy}$ , and  $\sigma_{zz}$  written in  $(x, y, z)$ -coordinates) of stress fields created by grain boundary defects, and  $\Delta V$  the excess free volume associated with a vacancy. To minimize  $\varepsilon_{int}$ , vacancies migrate to regions where compressive stresses exist. This vacancy migration contributes to the enhanced diffusion in nanocrystalline materials. The effect discussed is quantitatively described by Eq. (4) with the sum  $\varepsilon_f + \varepsilon_m$  being replaced by the sum  $\varepsilon_f + \varepsilon_m + \varepsilon_{int}$ .

Thus, the factor (a) gives rise to the diffusion enhancement owing to the influence of grain boundary dislocations on the generation of vacancies. The factors (b) and (c) facilitate the vacancy migration and therefore, cause the diffusion enhancement in nanocrystalline materials. According to the theoretical analysis [106], the most essential contribution to the diffusion enhancement is due to the dislocation climb in grain boundaries (see factor (a)). With this taken into

account, below we will consider the effects of grain boundary dislocations on diffusion in nanocrystalline materials, with focuses placed on the climb of grain boundary dislocations composing dipole configurations.

Nanocrystalline materials are effectively fabricated by mechanical methods at highly nonequilibrium conditions (see, e.g., [19–22, 110]), in which case “nonequilibrium” or, in other words, extrinsic defect structures are formed at grain boundaries (Fig. 5a). During some relaxation time interval after mechanical synthesis of a nanocrystalline sample, extrinsic grain boundary dislocations with opposite Burgers vectors move (climb and glide) to each other and annihilate, and the geometrically necessary dislocations move (climb and glide) to their equilibrium positions (Fig. 5a).

The climb of grain boundary dislocations during the relaxation time interval is accompanied by both emission and absorption of point defects: vacancies and interstitial atoms. In these circumstances, emission of vacancies (“take-off” of vacancies from dislocation cores and their consequent displacement into the surrounding grain boundary phase) is more intensive than that of interstitial atoms, because vacancies are essentially more mobile compared to interstitial atoms [103]. Also, it should be noted that absorption of vacancies, which accompanies the climb of grain boundary dislocations, needs vacancies to permanently move to dislocation cores from a surrounding material, while emission of vacancies is not related to such a restrictive condition. As a corollary, emission of vacancies occurs more intensively than absorption of vacancies and absorption of slow interstitial atoms. With the aforesaid taken into account, in the following we will focus our consideration on the effects of only those processes of grain boundary dislocation climb that are accompanied by emission of vacancies.

The largest contribution to energy of “nonequilibrium” defect structures at grain boundaries commonly is related to the existence of extrinsic grain boundary dislocations. Therefore, climb and annihilation of such dislocations, which are accompanied by emission of vacancies, are characteristic processes of relaxation of grain boundaries in nanocrystalline materials.

Let us discuss the effect of dislocation-climb-induced emission of vacancies on diffusion in nanocrystalline materials. The coefficient of diffusion occurring via vacancy mechanism (which commonly is most effective) in the absence of extrinsic grain boundary defects is given by Eq. (4), where factor  $\exp(-\varepsilon_f/kT)$  characterizes equilibrium concentration of vacancies (when dislocation climb and dilatation stresses do not influence vacancy formation). The vacancy concentration in vicinity of the climbing dislocations (Fig. 9) is higher than the equilibrium concentration, because vacancy formation is facilitated due to the climb of dislocations. The effect in question is quantitatively described by the following change of the vacancy formation energy:  $\varepsilon_f \rightarrow \tilde{\varepsilon}_f = \varepsilon_f - W_v$  and by the corresponding local change of diffusion coefficient:  $D \rightarrow D^*$ . Here  $W_v(\lambda)$  is the decrease of the dislocation dipole energy  $W$  due to emission of one vacancy, related to the climb of the dislocations composing the dipole, and  $D^*$  in vicinity of the climbing dislocations (Fig. 9) is given as

$$D^* = D \exp\left(\frac{W_v}{kT}\right) \quad (6)$$

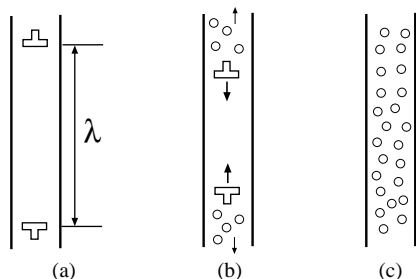


**Figure 9.** Climb and annihilation of grain boundary dislocations composing dipole configuration.

Following [106, 107], the energy decrease  $W_v(\lambda)$  is

$$W_v(\lambda) = \frac{a}{d} \Delta W(\lambda) = \frac{a}{d} (W(\lambda) - W(\lambda - a)) \quad (7)$$

for  $\lambda > 2a$ , and

$$W_v(\lambda) = \frac{Gb^2 a (\ln 2 + Z)}{4\pi(1 - \nu)} \quad (8)$$

for  $\lambda \leq 2a$ . With the dependence  $W_v(\lambda)$  given by Eqs. (7) and (8), for  $G = 50$  GPa,  $a \approx 0.3$  nm,  $b \approx a/3$ ,  $Z \approx 1$ , and  $\nu \approx 1/3$ , let us estimate the diffusion coefficient in vicinity of the climbing dislocations. In doing so, with factor  $\exp(W_v/kT)$  averaged on  $\lambda$  (ranging from 0 to  $10a$ ), we find that  $D^* \approx 300D$ .

In nanocrystalline materials during relaxation time interval (after synthesis at highly nonequilibrium conditions, say, after fabrication by severe plastic deformation method), almost all grain boundaries contain nonequilibrium defect structures, in particular, extrinsic dislocations whose annihilation enhances diffusion. In this situation,  $D^*$  plays the role of grain boundary diffusion coefficient in nanocrystalline materials fabricated at highly nonequilibrium conditions. To summarize, estimations [106, 107] allow us to conclude that the climb of grain boundary dislocations (Fig. 9) essentially enhances diffusion processes in nanocrystalline materials (in particular, nanocrystalline materials fabricated by severe plastic deformation), causing increase of the grain boundary diffusion coefficient by about two orders. Thus, the climb of grain boundary dislocations is capable of strongly contributing to the experimentally observed (see [63–66]) anomalously fast diffusion in nanocrystalline materials during some relaxation time interval after their synthesis at highly nonequilibrium conditions.

Following [104–107], the elastic interactions between the diffusing species and grain boundary dislocations and disclinations (see point (c)) facilitate migration of vacancies and impurities, causing the diffusion enhancement in vicinities of grain boundaries. In this situation, the diffusion rate is increased by factor  $M \sim 1 \div 5$  in vicinities of grain boundaries. The effect discussed is small compared to that related to the climb of grain boundary dislocations.

Thus, there are controversial experimental data and theoretical representations on diffusion processes in nanocrystalline materials. At the same time, diffusion in mechanically synthesized bulk nanocrystalline materials is definitely recognized as the strongly enhanced diffusion compared to

that in coarse-grained polycrystals and nanocrystalline materials fabricated by nonmechanical (more equilibrium than mechanical) methods. This experimentally documented phenomenon is naturally explained as that occurring due to the deformation-induced nonequilibrium state of grain boundaries, in which case extrinsic grain boundary dislocations strongly enhance the boundary diffusivity.

## 8. INTERFACIAL DEFECTS AND DEFORMATION MECHANISMS IN NANOCRYSTALLINE BULK MATERIALS

Nanocrystalline materials exhibit the unique mechanical behavior due to nanoscale and interface effects; see, for example, [111–113]. High-density ensembles of grain boundaries in nanocrystalline materials serve as effective obstacles for lattice dislocation slip which dominates in coarse-grained polycrystals. In addition, the image forces acting in nanometer-sized grains cause the difficulty in forming lattice dislocations in such nanograins [114, 115]. In these circumstances, the grain refinement hampers the lattice dislocation slip. At the same time, grain boundaries provide the effective action of alternative deformation mechanisms occurring via motion of grain boundary defects. As a corollary, the grain refinement leads to the competition between the lattice dislocation slip and deformation mechanisms associated with the active role of grain boundaries. It is believed that nanocrystalline matter represents the arena for the discussed competition which causes unique mechanical properties of nanocrystalline materials [116–125]. In this context, identification of effective deformation mechanisms and their contributions to plastic flow is very important for understanding the fundamentals of the mechanical behavior of nanocrystalline materials as well as development of technologies based on plastic forming of nanostructures.

The deformation mechanisms in nanocrystalline materials, in many cases, cannot be unambiguously identified with the help of contemporary experimental methods, because of high precision demands on experiments at the nanoscale. Therefore, theoretical modeling of defects and plastic deformation processes is a very important constituent of both fundamental and applied research of nanostructured materials. In this section, we briefly review theoretical models of deformation mechanisms and grain boundary defects being carriers of plastic flow in nanocrystalline materials with focuses placed on new deformation modes.

Let us consider plastic deformation mechanisms in nanocrystalline materials. The specific deformation behavior of nanocrystalline materials, in particular, is exhibited in the so-called abnormal Hall–Petch effect which manifests itself as the softening of a material with reduction of the grain size  $d$  [111–113]. The most theoretical models relate the abnormal Hall–Petch dependence to the competition between deformation mechanisms in nanocrystalline materials; for example, [116–125]. In the framework of this approach, deformation mechanisms associated with the active role of grain boundaries dominate over conventional lattice dislocation motion in nanocrystalline materials, in which case the grain refinement leads to a softening of a material. In doing so, generally speaking, standard and new deformation

mechanisms associated with the active role of grain boundaries can contribute to plastic flow in nanocrystalline materials. The standard deformation mechanisms are the grain boundary sliding and Coble creep related to enhanced diffusional mass transfer along grain boundary planes [116–123]. This idea is originated, in fact, from the classical theory of creep and superplasticity of microcrystalline materials where these mechanisms play the essential role; see, for example, [126, 127]. We think that, together with these two standard deformation mechanisms associated with the active role of grain boundaries, nonconventional (new) deformation mechanisms are capable of effectively contributing to plastic flow in nanocrystalline bulk materials and coatings. In particular, such specific deformation mechanisms are creep associated with enhanced diffusion along triple junctions of grain boundaries [124] and rotational deformation mode [128, 129].

First, let us consider the triple junction diffusional creep. In general, in recent years, triple junctions of grain boundaries have been recognized as defects with the structure and properties being essentially different from those of grain boundaries that they adjoin [9]. For instance, from experimental data and theoretical models it follows that triple junctions play the role of enhanced diffusion tubes [97–99, 102], nuclei of the enhanced segregation of the second phase [100, 130], strengthening elements and sources of lattice dislocations [114–116, 131–133] during plastic deformation, and drag centers of grain boundary migration during recrystallization processes [134, 135]. Also, as it has been shown in experiments [98], creep associated with enhanced diffusion along triple junctions contributes to plastic flow of coarse-grained polycrystalline aluminum. Actually, since triple junction diffusion coefficient  $D_{ij}$  highly exceeds grain boundary diffusion coefficient  $D_{gb}$  [97–99, 102], enhanced diffusional mass transfer along triple junction tubes occurs under mechanical stresses and contributes to plastic forming of a mechanically loaded material. The contribution in question is characterized by a rather specific dependence of plastic strain rate on grain size  $d$ . More precisely, grain size exponent is  $-4$  in this case [98], in contrast to grain boundary diffusional creep (Coble creep) and bulk diffusional creep characterized by grain size exponents  $-3$  and  $-2$ , respectively:

$$\dot{\epsilon}_{ij} \propto D_{ij} \cdot d^{-4} \quad (9)$$

$$\dot{\epsilon}_{gb} \propto D_{gb} \cdot d^{-3} \quad (10)$$

$$\dot{\epsilon}_{bulk} \propto D_{bulk} \cdot d^{-2} \quad (11)$$

Here  $\dot{\epsilon}_{ij}$ ,  $\dot{\epsilon}_{gb}$ , and  $\dot{\epsilon}_{bulk}$  are plastic strain rates that correspond to triple junction diffusional creep, grain boundary diffusional creep, and bulk diffusional creep, respectively.  $D_{bulk}$  denotes the bulk self-diffusion coefficient.

Fedorov et al. [124] suggested a theoretical model describing the yield stress dependence on grain size in fine-grained materials, based upon competition between conventional dislocation slip, grain boundary diffusional creep, and triple junction diffusional creep. It has been shown that the contribution of triple junction diffusional creep increases with

reduction of grain size, causing a negative slope of the Hall–Petch dependence in the range of small grains. The results of model [124] are compared with experimental data [136–140] from copper and shown to be in rather good agreement.

Now let us turn to a discussion of a rotational deformation mechanism in nanocrystalline materials. The primary carriers of the rotational plastic deformation in solids are believed to be dipoles of grain boundary disclinations [141]. A grain boundary disclination represents a line defect that separates two grain boundary fragments with different misorientation parameters (Fig. 10). That is, grain boundary misorientation exhibits a jump at disclination line. A disclination dipole consists of two grain boundary disclinations of opposite signs. Motion of a disclination dipole causes plastic deformation accompanied by crystal lattice rotation (Fig. 10). It is called the rotational deformation

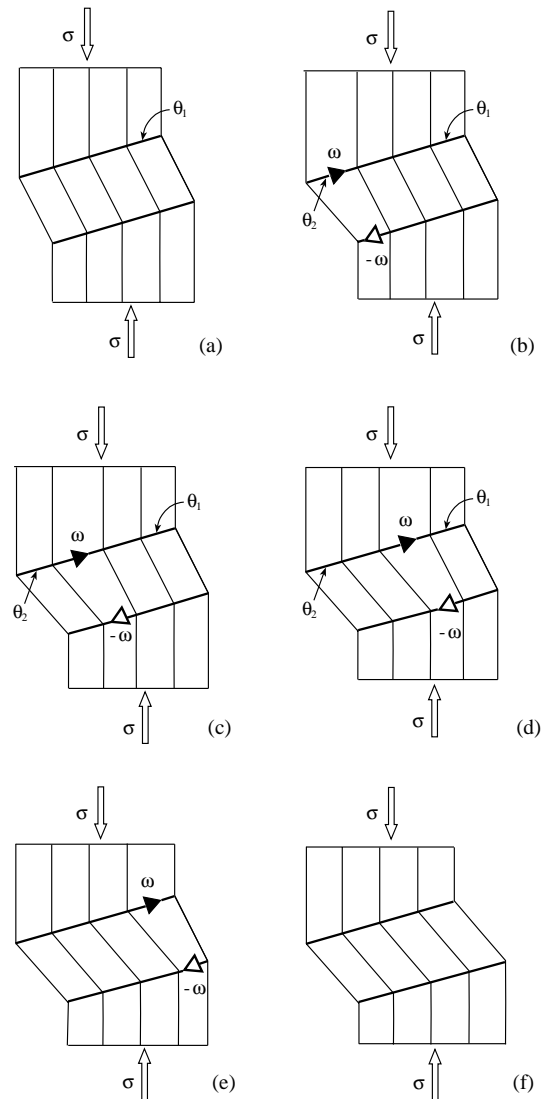


**Figure 10.** Rotational deformation occurs through movement of a dipole of grain boundary disclinations. Grain boundary fragments separated by disclination of strength  $\omega$  are characterized by misorientation parameters  $\theta_2$  and  $\theta_1$ , where  $\omega = \theta_2 - \theta_1$ .

mode. Conventional electron microscopy experiments are indicative of the essential role of the rotational plastic flow in coarse-grained materials under high-strain deformation (for a review, see [142, 143]). It is supported also by experimental observation of grain rotations in superplastically deformed microcrystalline materials [127, 144].

The rotational deformation is capable of being very intensive in nanocrystalline materials [128]. Actually, the volume fraction of grain boundaries is extremely high in nanocrystalline materials, in which case grain boundary disclinations can be formed, roughly speaking, in every point of a mechanically loaded sample. In addition, the elastic energy of a disclination dipole rapidly diverges with increasing distance between disclinations [141]. Therefore, such dipoles are energetically permitted mostly for grain boundary disclinations that are close to each other. It is the case of nanocrystalline materials where the interspacings between neighboring grain boundaries are extremely small. Finally, nanocrystalline materials contain high-density ensembles of triple junctions where the crossover from the conventional grain boundary sliding to the rotational deformation effectively occurs. Murayama et al.'s atomic-level observation of disclination dipoles in deformed nanocrystalline materials [145] supports the theoretical statement [128] on the rotational deformation in nanostructures.

Thus, owing to interface and nanoscale effects in nanocrystalline materials, the set of deformation mechanisms in these materials is richer than that in conventional coarse-grained polycrystals. In particular, triple junction diffusional creep and the rotational deformation mode (Fig. 10) are capable of essentially contributing to plastic flow of nanocrystalline bulk materials and coatings. These deformation mechanisms should be definitely taken into account in further research of plastic flow processes in nanocrystalline materials, including the phenomenon of high-strain-rate superplasticity [146, 147].

## 9. NANODEFFECTS IN NANOSTRUCTURES

In this section, we will discuss the notion of nanodefects in ordered nanostructures, which extends the conventional notion of interfacial defects in solids. New physical, chemical, and biological properties are exhibited by ordered nanostructures that represent assemblies of crystallites with at least one characteristic size being on the order of a few nanometers [1–7]. Examples of such nanostructures are self-assembled ordered arrays of semiconductor quantum dots and wires [148–152], self-assembled ordered arrays of carbon nanotubes [153, 154], and nanoparticles embedded into organic matter [1–7, 155]. Their unique properties are due to the combined nanoscale, interface, and interaction effects. The nanoscale effect occurs because many fundamental processes in solids are associated with particular length scales being on the order of a few nanometers. The interface effect comes into play because a large fraction of atoms (up to 50%) of each nanosized crystallite are located at interfaces where their behavior is different from that in the bulk. The interaction between assembled nanosized crystallites causes

their unique collective properties which are more than just a sum of properties of individual crystallites.

Spatial arrangement of nanocrystallites and uniformity in their size and shape are among the most important issues for the combined nanoscale, interface, and interaction effects crucially affecting the functional properties of ordered nanostructures. In the first approximation self-assembled ordered nanostructures are commonly treated as regular, periodically ordered arrays of identical nanocrystallites, in which case a theoretical description of their properties is simplified. However, real self-assembled nanostructures, as it is well documented experimentally, are not regular. There are deviations of spatial positions, sizes, and shapes of their structural units from ideal ones. In addition, there are topological defects which violate nanoscale translational order inherent to self-assembled periodic nanostructures, similar to topological defects in conventional crystal lattices [155–160]. That is, symmetry of a periodically ordered nanostructure relative to translation by a period (being commonly on the order of nanometers) is locally violated by topological defects. Examples of such topological defects are interphase-boundary-like defects in ordered assemblies of two different sizes of CdSe nanoparticles [155] (Fig. 11a), vacancy-like defects in self-assembled superlattice films of FePt nanoparticles with partial chemical ordering [157] (Fig. 11b), carbon nanohorns [158], X-, Y-, and T-like junctions of carbon nanotubes [159] (Fig. 11c), interstitial-like defect in lithographically synthesized supramolecular pillar arrays in a thin polymer melt [160] (Fig. 11d), impurity-like defect (double crystal) in a chain of nanoparticles in magnetostatic bacteria [156] (Fig. 11e), impurity-like defects (dome nanoislands) in ordered arrays of pyramid quantum dots [148, 149] (Fig. 11f). With their generic definition as topological defects of nanoscale translational order inherent to nanostructures, we will call such defects nanodefects.

Nanodefects are formed during fabrication and processing of nanostructures at highly nonequilibrium conditions. In some cases, they are capable of strongly influencing the behavior of ordered nanostructures. For instance, the formation of impurity-like defects (dome nanoislands) in ordered arrays of pyramid quantum dots dramatically breaks uniformity of quantum dots in size and shape, giving rise to degradation of their functional characteristics highly desired for applications [148, 149]. In general, new properties of nanostructures may arise due to the presence of nanodefects. For instance, carbon nanotubes with such nanodefects as Y- and T-like junctions could act as multiterminal electronic devices [161].

Thus, the definition of nanodefects in ordered nanostructures as topological defects violating nanoscale periodic translational order inherent to nanostructures is generic for diverse nanostructures. Analysis of data in the literature shows that nanodefects are experimentally found in diverse periodically ordered nanostructures where they are capable of strongly influencing functional properties. Use of the notion of nanodefects may allow researchers involved in science and engineering of different nanostructures to share views and develop interdisciplinary ideas.

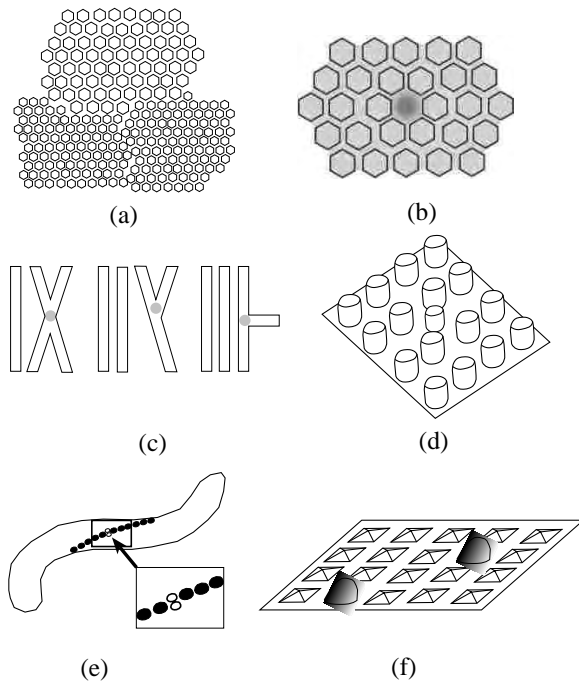


**Figure 11.** Nanodefects in ordered nanostructures (schematically). (a) Interphase-boundary-like defects in ordered assemblies of two different sizes of CdSe nanoparticles. (b) Vacancy-like defects in self-assembled superlattice films of FePt nanoparticles with partial chemical ordering. (c) X-, Y-, and T-like junctions of carbon nanotubes. (d) Interstitial-like defect in lithographically synthesized supramolecular pillar arrays in a thin polymer melt. (e) Impurity-like defect (double crystal) in a chain of nanoparticles in magnetostatic bacteria. (f) Impurity-like defects (dome nanoislands) in ordered arrays of pyramid quantum.

## 10. CONCLUDING REMARKS

Thus interfaces in nanostructured materials are characterized by the specific structural and behavioral features associated with generation and evolution of interfacial defects in these materials (see Sections 2 and 3). In particular, the elastic interaction between grain boundary defects and interphase boundaries in nanocrystalline film/substrate composites causes extrinsic grain boundary defects—dislocations and disclinations (Figs. 4–6)—to serve as misfit defects compensating for misfit stresses. The effective contribution of grain boundary defects to relaxation of misfit stresses in nanocrystalline films explains the experimentally documented (see discussion in [42]) fact that residual stresses are low in nanocrystalline coatings synthesized by thermal spray methods, compared to their coarse-grained counterparts.

One of the behavioral structural features of nanoscale single crystalline films (Fig. 1a) is the experimentally observed [56–60] enhanced formation of partial misfit dislocations associated with stacking faults. Partial misfit dislocations at interphase (film/substrate) boundaries (Fig. 8) transform into perfect misfit dislocations with increase of film thickness. This statement, resulted from theoretical analysis [61] (see also Section 6), is in agreement with experimental data [60] which are indicative of the fact that density of perfect

misfit dislocations increases and density of partial misfit dislocations decreases with increase of film thickness.

Diffusion in mechanically synthesized bulk nanocrystalline materials is definitely recognized as the strongly enhanced diffusion compared to that in coarse-grained polycrystals and nanocrystalline materials fabricated by nonmechanical (more equilibrium than mechanical) methods [64–66]. This experimentally documented phenomenon is naturally explained as that occurring due to the deformation-induced nonequilibrium state of grain boundaries, in which case transformations of extrinsic grain boundary dislocations strongly enhance the boundary diffusivity (see Section 7).

Owing to interface and nanoscale effects in nanocrystalline materials, the set of deformation mechanisms in these materials is richer than that in conventional coarse-grained polycrystals. In particular, triple junction diffusional creep and the rotational deformation mode (Fig. 10) are capable of essentially contributing to plastic flow of nanocrystalline bulk materials and coatings (see Section 8).

To summarize, the effects of interfacial defects should be definitely taken into account in experimental research and theoretical description of the structure and behavior of advanced nanostructured bulk materials and films. Identification and systematic study of these effects in nanostructures are important for both understanding the fundamentals of the combined nanoscale, interface, and interaction effects and development of current and novel technologies exploiting nanostructures.

## GLOSSARY

**Grain boundary disclinations** Disclinations—defects of rotational type—located at grain boundaries.

**Grain boundary dislocations** Dislocations located at grain boundaries.

**Misfit defects** Defects creating stresses that compensate for, in part, misfit stresses in films.

**Misfit stresses** Stresses occurring due to geometric mismatch at interphase boundaries between crystalline lattices of adjacent films and substrates.

**Nanodefects** Topological defects locally violating nanoscale translational order inherent to assembled periodic nanostructures.

**Rotational deformation mode** Plastic deformation accompanied by crystal lattice rotation in grain interiors.

## ACKNOWLEDGMENTS

This work was supported in part by the Office of US Naval Research (Grant N00014-01-1-1020), the Russian Fund of Basic Research (Grant 01-02-16853), St. Petersburg Scientific Center of Russian Academy of Sciences, and “Integration” Program (Grant B0026). The author thanks M. Yu. Gutkin, A. L. Kolesnikova, K. N. Mikaelyan, A. B. Reizis, A. E. Romanov, and A. G. Sheinerman for permanent collaboration, valuable contributions, fruitful discussions, and encouragements.

## REFERENCES

1. G.-M. Chow and N. I. Noskova, Eds., "Nanostructured Materials: Science and Technology," NATO ASI Series. Kluwer, Dordrecht, 1998.
2. H. S. Nalwa, Ed., "Handbook of Nanostructured Materials and Nanotechnology," Vols. 1–5. Academic Press, San Diego, 1999.
3. H. Gleiter, *Acta Mater.* 48, 1 (2000).
4. G.-M. Chow, I. A. Ovid'ko, and T. Tsakalakos, Eds., "Nanostructured Films and Coatings," NATO Science Ser. Kluwer, Dordrecht, 2000.
5. M. C. Roco, R. S. Williams, and P. Alivisatos, Eds., "Nanotechnology Research Directions." Kluwer, Dordrecht, 2000.
6. S. Ankem, C. Pande, I. Ovid'ko, and S. Ranganathan, Eds., "Science and Technology of Interfaces." TMS, Warrendale, PA, 2002.
7. H. S. Nalwa, Ed., "Nanoclusters and Nanocrystals." American Sci. Publ., California, 2003.
8. H. Gleiter, *Nanostruct. Mater.* 6, 3 (1995).
9. A. H. King, *Interf. Sci.* 7, 251 (1999).
10. A. H. King and L. Balasubramanian, *Mater. Sci. Forum* 189–190, 143 (1995).
11. I. A. Ovid'ko, *Mater. Sci. Eng. A* 280, 355 (2000).
12. A. A. Fedorov, A. L. Kolesnikova, and I. A. Ovid'ko, *Mater. Phys. Mech* 5, 49 (2002).
13. A. H. King, L. Balasubramanian, and R. T. Catalano, *Mater. Sci. Forum* 207–209, 125 (1996).
14. A. F. Jankowski, P. Sandoval, and J. P. Hayes, *Nanostruct. Mater.* 5, 497 (1995).
15. M. Yu. Gutkin and I. A. Ovid'ko, *J. Phys.: Cond. Matter* 11, 8607 (1999).
16. A. A. Nazarov, A. E. Romanov, and R. Z. Valiev, *Acta Metall. Mater.* 41, 1033 (1993).
17. A. A. Nazarov, A. E. Romanov, and R. Z. Valiev, *Solid State Phenom.* 35–36, 381 (1994).
18. A. A. Nazarov, A. E. Romanov, and R. Z. Valiev, *Scr. Mater.* 34, 729 (1996).
19. J. Y. Huang, Y. T. Zhu, H. Jiang, and T. C. Lowe, *Acta Mater.* 49, 1497 (2001).
20. R. K. Islamgaliev, R. Z. Valiev, R. S. Misra, and A. K. Mukherjee, *Mater. Sci. Eng. A* 304–306, 206 (2001).
21. R. S. Mishra, R. Z. Valiev, S. X. McFadden, R. K. Islamgaliev, and A. K. Mukherjee, *Phil. Mag. A* 81, 37 (2001).
22. R. Z. Valiev, I. V. Alexandrov, Y. T. Zhu, and T. C. Lowe, *J. Mater. Res.* 17, 5 (2002).
23. G. Möbus, E. Schummann, G. Dehm, and M. Rühle, *Phys. Stat. Sol. (a)* 150, 77 (1995).
24. J. H. van der Merve, *Crit. Rev. Sol. State Mater. Sci.* 17, 187 (1991).
25. E. A. Fitzgerald, *Mater. Sci. Rep.* 7, 87 (1991).
26. S. C. Jain, J. R. Willis, and R. Bullough, *Adv. Phys.* 39, 127 (1990).
27. S. C. Jain, A. H. Harker, and R. A. Cowley, *Philos. Mag. A* 75, 1461 (1997).
28. S. Mahajan, *Acta Mater.* 48, 137 (2000).
29. I. A. Ovid'ko, in "Nanostructured Films, and Coatings," NATO Science Series (G.-M. Chow, I. A. Ovid'ko, and T. Tsakalakos, Eds.), p. 231. Kluwer, Dordrecht, 2000.
30. J. H. van der Merve, *Proc. Phys. Soc. London A* 63, 616 (1950).
31. N. Burle, B. Pichaud, N. Guelton, and R. G. Saint-Jacques, *Phys. Stat. Sol. (a)* 149, 123 (1995).
32. K. Jagannadham and J. Narayan, *J. Electron. Mater.* 20, 767 (1991).
33. W. Wunderlich, G. Frommeyer, and P. V. Carnowski, *Mater. Sci. Eng. A* 164, 421 (1993).
34. I. A. Ovid'ko, *Phys. Rev. Lett.* 88, 046103 (2002).
35. T. J. Gosling and J. R. Willis, *Philos. Mag. A* 69, 65 (1994).
36. J. P. Hirth, *Acta Mater.* 48, 93 (2000).
37. X. H. Liu, F. M. Ross, and K. W. Schwarz, *Phys. Rev. Lett.* 85, 4088 (2000).
38. I. A. Ovid'ko and A. G. Sheinerman, *J. Phys.: Condens. Matter* 13, 7937 (2001).
39. J. de la Figuera, K. Pohl, O. Rodriguez, A. K. Schmid, N. C. Bartelt, C. B. Carter, and R. Q. Hwang, *Phys. Rev. Lett.* 86, 3819 (2001).
40. G. Springholz and K. Wiesauer, *Phys. Rev. Lett.* 88, 015507 (2002).
41. M. Yu. Gutkin, K. N. Mikaelyan, and I. A. Ovid'ko, *Phys. Sol. State* 40, 1864 (1998).
42. L. Kabacoff, in "Nanostructured Films and Coatings," NATO Science Ser. (G.-M. Chow, I. A. Ovid'ko, and T. Tsakalakos, Eds.), p. 373. Kluwer, Dordrecht, 2000.
43. I. A. Ovid'ko and A. G. Sheinerman, *J. Nanosci. Nanotechnol.* 1, 215 (2001).
44. Q. Wang, Z. L. Wang, T. Brown, A. Brown, and G. May, *Appl. Phys. Lett.* 77, 223 (2000).
45. V. G. Gryaznov and L. I. Trusov, *Progr. Mater. Sci.* 37, 289 (1993).
46. A. L. Kolesnikova, I. A. Ovid'ko, and A. E. Romanov, *Solid State Phen.* 87, 265 (2002).
47. F. K. LeGoues, M. Copel, and R. Tromp, *Phys. Rev. Lett.* 63, 1826 (1989).
48. F. K. LeGoues, M. Copel, and R. Tromp, *Phys. Rev. B* 42, 11690 (1990).
49. C. S. Ozkan, W. D. Nix, and H. Gao, *Appl. Phys. Lett.* 70, 2247 (1997).
50. I. A. Ovid'ko, *Phil. Mag. Lett.* 79, 709 (1999).
51. J. S. Speck, A. C. Daykin, A. Seifert, A. E. Romanov, and W. Pompe, *J. Appl. Phys.* 78, 1696 (1995).
52. A. E. Romanov, M. J. Lefevre, J. S. Speck, W. Pompe, S. K. Streifer, and C. M. Foster, *J. Appl. Phys.* 83, 2754 (1998).
53. I. A. Ovid'ko, *J. Phys.: Cond. Matter* 11, 6521 (1999).
54. I. A. Ovid'ko, *J. Phys.: Cond. Matter* 13, L97 (2001).
55. S. V. Bobylev, I. A. Ovid'ko, and A. G. Sheinerman, *Phys. Rev. B* 64, 224507 (2001).
56. B. C. De Cooman and C. B. Carter, *Acta Metall.* 37, 2765 (1989).
57. B. C. De Cooman, C. B. Carter, K. T. Chan, and J. R. Shealy, *Acta Metall.* 37, 2779 (1989).
58. J. Zou and D. J. H. Cockayne, *Appl. Phys. Lett.* 69, 1083 (1996).
59. M. Loubradou, R. Bonnet, A. Vila, and P. Ruterana, *Mater. Sci. Forum.* 207–209, 285 (1996).
60. M. Tamura, *Appl. Phys. A* 63, 359 (1996).
61. M. Yu. Gutkin, K. N. Mikaelyan, and I. A. Ovid'ko, *Phys. Sol. State* 43, 000 (2001).
62. H. Gleiter, *Progr. Mater. Sci.* 33, 223 (1989).
63. J. Horvath, R. Birringer, and H. Gleiter, *Solid State Comm.* 62, 391 (1987).
64. H.-E. Schaefer, R. Wurschum, T. Gessmann, G. Stockl, P. Scharwaechter, W. Frank, R. Z. Valiev, H.-J. Fecht, and C. Moelle, *Nanostruct. Mater.* 6, 869 (1995).
65. Yu. R. Kolobov, G. P. Grabovetskaya, I. V. Ratochka, and K. V. Ivanov, *Nanostruct. Mater.* 12, 1127 (1999).
66. Yu. R. Kolobov, G. P. Grabovetskaya, K. V. Ivanov, R. Z. Valiev, and T. C. Lowe, in "Investigations and Applications of Severe Plastic Deformation," NATO Science Ser. (T. C. Lowe, and R. Z. Valiev, Eds.), p. 261. Kluwer, Dordrecht, 2000.
67. R. Wurschum, K. Reimann, S. Größ, P. Farber, A. Kübler, P. Scharwaechter, W. Frank, O. Kruse, H. D. Carstanjen, and H.-E. Schaefer, *Phil. Mag. B* 76, 407 (1997).
68. H. Tanimoto, P. Farber, R. Wurschum, R. Z. Valiev, and H.-E. Schaefer, *Nanostruct. Mater.* 12, 681 (1999).
69. H. Tanimoto, L. Pasquini, R. Prümmer, H. Kronmüller, and H.-E. Schaefer, *Scripta Mater.* 42, 961 (2000).
70. H.-E. Schaefer, K. Reimann, W. Straub, F. Philipp, H. Tanimoto, U. Brossmann, and R. Wurschum, *Mater. Sci. Eng. A* 286, 24 (2000).
71. R. Wurschum, A. Kübler, S. Größ, P. Scharwaechter, W. Frank, R. Z. Valiev, R. R. Mulyukov, and H.-E. Schaefer, *Annales de Chimie (Fr.)* 21, 471 (1996).
72. L. N. Larikov, *Metal. Phys. Appl. Tech.* 17, 1 (1995).
73. J. C. Fischer, *J. Appl. Phys.* 22, 74 (1951).



74. R. T. P. Whipple, *Phil. Mag.* 45, 1225 (1954).
75. T. Suzuoka, *Trans. Jap. Inst. Metals* 2, 25 (1961).
76. P. Benoist and G. Martin, *Thin Solid Films* 25, 181 (1975).
77. G. Harrison, *Trans. Faraday Soc.* 57, 1191 (1961).
78. B. S. Bokshstein, "Diffusion in Metals," *Metallurgiya*, Moscow, 1978. [In Russian.]
79. V. T. Borisov, V. M. Golikov, and G. V. Shcherbedinskii, *Fiz. Met. Metalloved.* 17, 881 (1964). [In Russian.]
80. R. W. Balluffi, T. Kwok, P. D. Bristowe et al., *Scripta Met.* 15, 951 (1981).
81. P. D. Bristowe, A. Brokman, T. Spaepen, and R. W. Balluffi, *Scripta Met.* 14, 943 (1980).
82. A. Brokman, P. D. Bristowe, R. W. Balluffi et al., *Appl. Phys.* 52, 6116 (1981).
83. T. Kwok, P. S. Ho, S. Yip, and R. W. Balluffi, *Phys. Rev. Lett.* 47, 1148 (1981).
84. L. M. Klinger and D. A. Gorbunov, "Structure and Properties of Interfaces in Metals." Nauka, Moscow, 1988. [In Russian.]
85. Q. Ma and R. W. Balluffi, *Acta Metall. Mater.* 42, 1 (1994).
86. A. P. Sutton and R. W. Balluffi, "Interfaces in Crystalline Materials." Oxford Science Publications, Oxford, 1996.
87. R. Z. Valiev, V. Yu. Gertsman, and O. A. Kaibyshev, *Phys. Stat. Sol. (a)* 61, K95 (1980).
88. P. H. Pumphrey and H. Gleiter, *Philos. Mag.* 30, 593 (1974).
89. A. A. Nazarov, A. E. Romanov, and R. Z. Valiev, *Scripta Metall. Mater.* 24, 1929 (1990).
90. A. A. Nazarov, *Annales de Chimie (Fr.)* 21, 461 (1996).
91. A. A. Nazarov, *Mater. Sci. Forum* 243–245, 31 (1997).
92. A. V. Osipov and I. A. Ovid'ko, *Appl. Phys. A* 54, 517 (1992).
93. I. A. Ovid'ko and A. B. Reizis, *J. Phys. D* 32, 2833 (1999).
94. E. S. Smirnova and V. N. Chuvil'deev, *Fiz. Met. Metalloved.* 88, 74 (1999). [In Russian.]
95. H. J. Hoefler, H. Hahn, and S. Averback, *Defect Diffusion Forum* 68, 99 (1993).
96. Yu. Mishin and Ch. Herzig, *Nanostruct. Mater.* 6, 859 (1995).
97. V. B. Rabukhin and A. S. Panikarskii, *Poverkhnost* 5, 150 (1986). [In Russian.]
98. V. B. Rabukhin, *Poverkhnost* 7, 126 (1986). [In Russian.]
99. G. Palumbo and K. T. Aust, *Mater. Sci. Eng. A* 113, 139 (1989).
100. K. M. Yin, A. H. King, T. E. Hsieh, F. R. Chen, J. J. Kai, and L. Chang, *Microscopy Microanalysis* 3, 417 (1997).
101. U. Czubyko, V. G. Sursaeva, G. Gottstein, and L. S. Shvindlerman, in "Grain Growth in Polycrystalline Materials III" (H. Weiland, B. L. Adams, and A. D. Rollett, Eds.) p. 423. TMS, Pittsburg, PA, 1998.
102. B. Bokstein, V. Ivanov, O. Oreshina, A. Peteline, and S. Peteline, *Mater. Sci. Eng. A* 302, 151 (2001).
103. V. I. Vladimirov, "Einführung in die Physikalische Theorie der Plastizität, and Festigkeit." VEB Deutscher Verlag für Grundstoffindustrie, Leipzig, 1975.
104. R. A. Masumura and I. A. Ovid'ko, *Mater. Phys. Mech.* 1, 31 (2000).
105. A. A. Nazarov, *Phil. Mag. Lett.* 80, 221 (2000).
106. I. A. Ovid'ko, A. B. Reizis, and R. A. Masumura, *Mater. Phys. Mech.* 1, 103 (2000).
107. I. A. Ovid'ko and A. B. Reizis, *Phys. Sol. State* 43, 35 (2001).
108. J. P. Hirth and J. Lothe, "Theory of Dislocations." McGraw-Hill, New York, 1968.
109. L. A. Girifalco and D. O. Welch, "Point Defects and Diffusion in Strained Metals." Gordon and Breach, New York, 1967.
110. R. Z. Valiev and I. V. Alexandrov, "Nanostructured Materials Fabricated by Severe Plastic Deformation." Logos, Moscow, 2000. [In Russian.]
111. K. A. Padmanabhan, *Mater. Sci. Eng. A* 304–306, 200 (2001).
112. F. A. Mohamed and Y. Li, *Mater. Sci. Eng. A* 298, 1 (2001).
113. C. C. Koch, D. G. Morris, K. Lu, and A. Inoue, *MRS Bulletin* 24, 54 (1999).
114. V. G. Gryaznov, I. A. Polonsky, A. E. Romanov, and L. I. Trusov, *Phys. Rev. B* 41, 42 (1991).
115. A. E. Romanov, *Nanostruct. Mater.* 6, 125 (1995).
116. H. Hahn, P. Mondal, and K. A. Padmanabhan, *Nanostruct. Mater.* 9, 603 (1997).
117. H. Hahn and K. A. Padmanabhan, *Philos. Mag. B* 76, 559 (1997).
118. D. A. Kostantinidis and E. C. Aifantis, *Nanostruct. Mater.* 10, 1111 (1998).
119. R. A. Masumura, P. M. Hazzledine, and C. S. Pande, *Acta Mater.* 46, 4527 (1998).
120. H. van Swygenhoven, M. Spavzer, A. Caro, and D. Farkas, *Phys. Rev. B* 60, 22 (1999).
121. H. van Swygenhoven, M. Spavzer, and A. Caro, *Acta Mater.* 473, 117 (1999).
122. H. S. Kim, Y. Estrin, and M. B. Bush, *Acta Mater.* 48, 493 (2000).
123. V. Yamakov, D. Wolf, S. R. Phillpot, and H. Gleiter, *Acta Mater.* 50, 61 (2002).
124. A. A. Fedorov, M. Yu. Gutkin, and I. A. Ovid'ko, *Scr. Mater.* 47, 51 (2002).
125. M. Yu. Gutkin, I. A. Ovid'ko, and C. S. Pande, *Rev. Adv. Mater. Sci.* 2, 80 (2001).
126. J. Pilling and N. Ridley, "Superplasticity in Crystalline Solids." The Institute of Metals, London, 1989.
127. M. G. Zelin and A. K. Mukherjee, *Mater. Sci. Eng. A* 208, 210 (1996).
128. I. A. Ovid'ko, *Science* 295, 2386 (2002).
129. M. Yu. Gutkin, A. L. Kolesnikova, I. A. Ovid'ko, and N. V. Skiba, *J. Metast. Nanocryst. Mater.* 12, 47 (2002); *Philos. Mag. Lett.* (2003), in press.
130. M. Yu. Gutkin and I. A. Ovid'ko, *Philos. Mag. A* 70, 561 (1994).
131. O. A. Kaibyshev, *Mater. Sci. Forum* 304–306, 21 (1999).
132. K. Owusu-Boahen and A. H. King, *Acta Mater.* 49, 237 (2001).
133. A. A. Fedorov, M. Yu. Gutkin, and I. A. Ovid'ko, *Acta Mater.*, in press.
134. G. Gottstein, A. H. King, and L. S. Shvindlerman, *Acta Mater.* 48, 397 (2000).
135. L. S. Shvindlerman and G. Gottstein, *Mater. Sci. Eng. A* 302, 141 (2001).
136. A. H. Chokshi, A. Rosen, J. Karch, and H. Gleiter, *Scr. Metal.* 23, 1679 (1989).
137. C. J. Youngdahl, P. G. Sanders, J. A. Eastman, and J. R. Weertman, *Scr. Mater.* 37, 809 (1997).
138. R. Suryanarayana, C. A. Frey, S. M. L. Sastry, B. E. Waller, S. E. Bates, and W. E. Buhro, *J. Mater. Res.* 11, 439 (1996).
139. P. G. Sanders, J. A. Eastman, and J. R. Weertman, *Acta Mater.* 45, 4019 (1997).
140. P. G. Sanders, J. A. Eastman, and J. R. Weertman, in "Processing and Properties of NC Materials" (C. Suryanarayana, J. Singh, and F. H. Froes, Eds.), p. 397. TMS, Warrendale, 1996.
141. A. E. Romanov and V. I. Vladimirov, in "Dislocations in Solids" (F. R. N. Nabarro, Ed.), Vol. 9, p. 191. North-Holland, Amsterdam, 1992.
142. P. Klimanek, V. Klemm, A. E. Romanov, and M. Seefeldt, *Adv. Eng. Mater.* 3, 877 (2001).
143. M. Seefeldt, *Rev. Adv. Mater. Sci.* 2, 44 (2001).
144. R. Z. Valiev and T. G. Langdon, *Acta Metall.* 41, 949 (1993).
145. M. Murayama, J. M. Howe, H. Hidaka, and S. Takaki, *Science* 295, 2433 (2002).
146. S. X. McFadden, R. S. Misra, R. Z. Valiev, A. P. Zhilyaev, and A. K. Mukherjee, *Nature* 398, 684 (1999).
147. R. Z. Valiev, I. V. Alexandrov, Y. T. Zhu, and T. C. Lowe, *J. Mater. Res.* 17, 5 (2002).
148. G. Medeiros-Riberto, A. M. Bratkovski, T. I. Kamins, D. A. A. Olberg, and R. S. Williams, *Science* 279, 353 (1998).
149. F. M. Ross, R. M. Tromp, and M. C. Reuter, *Science* 279, 353 (1998).

150. Y. Cui and C. M. Lieber, *Science* 291, 851 (2001).
151. Y. Huang, X. Diang, Q. Wei, and C. M. Lieber, *Science* 291, 630 (2001).
152. M. S. Gudiksen, L. J. Lauhon, J. Wang, D. C. Smith, and C. M. Lieber, *Nature* 415, 617 (2002).
153. B. Q. Wei, R. Vajtai, Y. Jung, J. Ward, R. Zhang, G. Ramanath, and P. M. Ajayan, *Nature* 416, 495 (2002).
154. H. W. Zhu, C. L. Xu, D. H. Wu, B. Q. Wei, R. Vajtai, and P. M. Ajayan, *Science* 296, 88 (2002).
155. C. B. Murray, C. R. Kagan, and M. G. Bawendi, *Annu. Rev. Mater. Sci.* 30, 545 (2000).
156. R. E. Dunin-Borkowski, M. R. McCartney, R. B. Frankel, D. A. Bazylinski, M. Posfai, and P. R. Buseck, *Science* 282 (1998) 1868.
157. J. W. Harrell, *Appl. Phys. Lett.* 79, 4393 (2001).
158. P. M. Ajayan, M. Terrones, A. de la Guardia, V. Huc, N. Grobert, B. Q. Wei, H. Lezec, G. Ramanath, and T. W. Ebbesen, *Science* 296, 705 (2002).
159. M. Terrones, F. Banhart, N. Grobert, J.-C. Charlier, H. P. Terrones, and M. Ajayan, *Phys. Rev. Lett.* 89, 75505 (2002).
160. S. Y. Chou and L. Zhuang, *J. Vac. Sci. Technol. B* 17, 3197 (1999).
161. A. N. Andriotis, M. Menon, D. Srivastava, and L. Chernozatonskii, *Phys. Rev. Lett.* 87, 066802 (2001).



# Interfacial Effects in Nanocrystalline Materials

K. T. Aust

*University of Toronto, Toronto, Ontario, Canada*

G. Hibbard, G. Palumbo

*Integran Technologies Inc., Toronto, Ontario, Canada*

## CONTENTS

1. Introduction
  2. Interfacial Structure
  3. Intercrystalline Defects and Properties of Nanocrystalline Materials
  4. Grain Boundary Engineered Nanostructures
  5. Summary
- Glossary  
References

## 1. INTRODUCTION

Nanostructured materials were first introduced as interfacial materials over two decades ago by Gleiter [1]. The main characteristic of these materials is the enhanced volume fraction of their interface component, namely, grain boundaries and triple junctions (*i.e.*, an intersection line of three or more grain boundaries), compared with their conventional polycrystalline counterparts. A three-dimensional study by Palumbo, Thorpe, and Aust [2], assuming a grain boundary thickness of 1 nm and a tetrakaidecahedron as the grain shape (and later generalized to any grain shape [3]), has shown that the grain boundary volume fraction increases rapidly from a few percent at a grain size of 100 nm to about 45% at a grain size of 3 nm, for example, Figure 1. For grain sizes below 20 nm, the triple junction volume fraction reaches significant values and exhibits greater grain size dependence than does the grain boundary volume fraction. Over the range of reasonable grain boundary thickness values, that is, 0.5 to 1.5 nm, the relative grain boundary and triple junction contributions to the volume fraction are

not significantly changed [4]. Several of the unusual properties observed for nanocrystalline materials, to be discussed herein, are directly associated with grain boundaries and/or triple junctions.

Another type of interfacial structural element is the quadruple node, that is, the intersection of (usually four) triple lines [3]. The contribution of quadruple nodes to the volume fraction of the intercrystalline component can be significant for grain sizes below about 5 nm, and may be important in the transition from the nanocrystalline state to the amorphous or noncrystalline state [3]. The quadruple node will not be considered in detail herein, since very few investigations have been conducted with nanomaterials having grain sizes below 5 nm and, consequently, little is known concerning its contribution to the properties of nanomaterials.

## 2. INTERFACIAL STRUCTURE

### 2.1. Grain Boundaries

Gleiter [1] first recognized that the intercrystalline component of a material will form a distinct microstructural constituent when processing the material to have a nanocrystalline structure. Initially, according to Gleiter [5], the interfacial component of a nanocrystalline material was considered as a structure, exhibiting no short-range order. This did not imply that grain boundaries are disordered: every boundary was assumed to have a two-dimensionally ordered structure, the periodicity and interatomic spacings of which are different from boundary to boundary.

Several studies have suggested that grain boundaries in nanocrystalline materials are more disordered than those in conventional polycrystalline materials. One study suggested a gas-like disorder at the grain boundaries [6]. In another

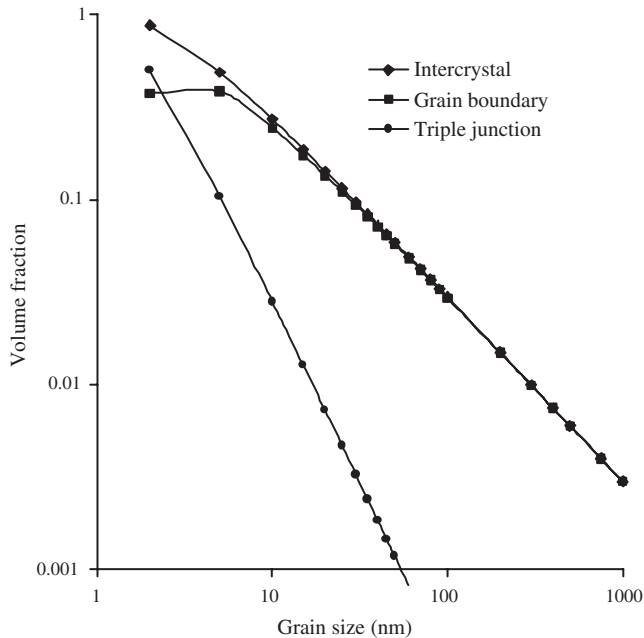


**Figure 1.** The effect of grain size on calculated volume fractions for intercrystalline regions, grain boundaries, and triple junctions, assuming a grain boundary thickness of 1 nm. Reprinted with permission from [2], G. Palumbo, S. J. Thorpe, and K. T. Aust, *Scripta Met. Mater.* 24, 1347 (1990). © 1990, Elsevier Science.

study, Wunderlich, Ishida, and Maurer [7], using high-resolution electron microscopy (HREM), concluded that grain boundaries in nanocrystalline Pd have an “extended” structure not typically observed in conventional systems. In addition, it was concluded from simulation studies that materials with very small grain sizes, generally  $<10$  nm, show “amorphous” grain boundaries [8–10], at least for highly idealized microstructures with randomly oriented grains and mainly high-energy grain boundaries. As was pointed out in [10], “it would be interesting to know the degree to which grain misorientations in actual nano materials are truly random and the degree to which agglomeration, sintering, and grain growth lead to the formation of lower-energy and hence crystalline grain boundaries.” It would be expected that maximum energy grain boundaries are highly disordered and thus appear to have an “amorphous-like” structure. However, how many such grain boundaries occur in nanomaterials may well depend on the method of synthesis of the material.

In contrast to the above studies, there are several studies that appear to indicate that the structure of grain boundaries is the same in both nanocrystalline and coarse-grained materials. For example, Thomas, Siegel, and Eastman [11], using HREM, observed that the interfacial structure of nano Pd is consistent with that typically observed in coarse-grained materials. It was also concluded from comparisons of diffraction data from nanocrystalline and coarse-grained Pd samples that grain boundaries in nano Pd are reasonably ordered [12, 13]. In addition, lattice parameter measurements indicated no significant grain boundary excess volume in nano Pd; therefore, the reduced density typically observed in nano Pd samples must be due to porosity associated with

the specific processing method, that is, vapor condensation and compaction. In agreement with this latter conclusion, a maximum porosity of only  $0.3 \pm 0.1\%$  was measured in nano Ni produced by electrodeposition and the intercrystalline density of this material was only about 2% less than the density of single crystal nickel [14]. High-resolution electron microscopy has revealed that the grain boundary structure in electrodeposited nanocrystalline nickel is similar to the structure found in conventional polycrystalline materials [15]. Twinning and low angle boundaries with misfit dislocations similar to what is found in materials with large grain size were also observed [15]. As will be seen in the subsequent discussion of interfacial effects on properties, many property studies of nanocrystalline materials support the view of ordered grain boundary structures.

## 2.2. Triple Junctions

A microstructural element, which has been largely overlooked in the interpretation of nanocrystal properties, is the triple junction. Theoretical and experimental studies have demonstrated that triple junctions can be considered distinct structural defects, capable of possessing a unique line energy [16–18].

Several complementary models for the structure of triple junctions have been advanced. Bollmann [19–21] has shown that the application of the O-lattice model for grain boundaries intersecting at a triple line leads to two distinct classes of triple junctions: (1) those for which the adjoining grain boundary dislocation arrays (as calculated through the nearest neighbor relationships) form nodes where the Burgers vectors balance to zero (I-lines), and (2) those for which the crystallographic arrangement precludes such a nodal balance (U-lines). In the latter case, the triple line can be considered a crystalline defect with distinct physical characteristics [19–21]. Support for Bollmann’s treatment has been obtained in electron microscopy studies [22, 23] and in experimental studies of corrosion [24] and superplasticity [25].

Doni and Bleris [26] evaluated the geometric characteristics of triple junctions composed of low  $\Sigma$  coincidence site lattice (CSL) grain boundaries, and have shown that these “special” triple junctions can be structurally characterized through the symmetry of the CSL, that is, CSL displacement shift complete (DSC) relaxations. Palumbo and Aust [27] have shown that a one-dimensional periodicity along the triple junction, arising through low-index planar continuity, can be achieved when the sequence of crystallographic rotations describing the junction can be represented about a low-index axis. This coincident axial direction (CAD) approach to the structural characterization of triple junctions is analogous to plane matching [28] and CAD [29] models of interface structure. However, the one-dimensional periodicity associated with the CAD model may be of greater significance to linear triple junctions than to planar grain boundaries. The CAD approach is considered the one-dimensional limit to Bollmann’s three-dimensional disclination treatment of triple lines and is applicable when nodal balancing of adjoining grain boundary dislocation arrays cannot occur (U-lines).

Cahn and Kalonji [30] have derived a triple-junction classification scheme that is independent of the character of the adjoining interfaces, and based solely upon crystallographic symmetry restrictions arising from the presence of adjoining junctions. Such a treatment may be of particular significance to nanostructured materials where the mean distance between adjacent triple junctions becomes very small.

In all models considered, it should be noted that increasing randomness in global and local crystallographic texture of the material would lead to an enhanced frequency of occurrence of triple junctions possessing “defect” character [31, 32]. Commonly applied nanocrystalline processing methods (*e.g.*, mechanical attrition, vapor condensation and compaction, high current density pulse electroplating) would be expected to yield such highly random distributions of crystals.

### 2.3. Impurity Segregation

The problem of harmful impurity segregation to the nanocrystalline interfaces is not thought to be a factor in their properties, due to the impurity dilution associated with typically about  $10^{19}$  boundaries per  $\text{cm}^3$  [5]. For example, by applying an equation developed for the intercrystalline volume fraction (*i.e.*, cumulative volume fraction of grain boundaries and triple junctions) (*e.g.* Fig. 1) [2], and assuming complete segregation of bulk impurities, the maximum grain boundary concentration attainable for a given average grain size is depicted in Figure 2 [33]. It is evident that even with conventional material of high purity, for example, 10 ppm total bulk impurities with  $10\ \mu\text{m}$  average grain size, grain boundary solute concentrations can be greater than 3 at %; decreasing the grain size of this material to  $<30\ \text{nm}$  results in a maximum grain boundary solute concentration of  $<0.01$  at % [33]. However, it was concluded

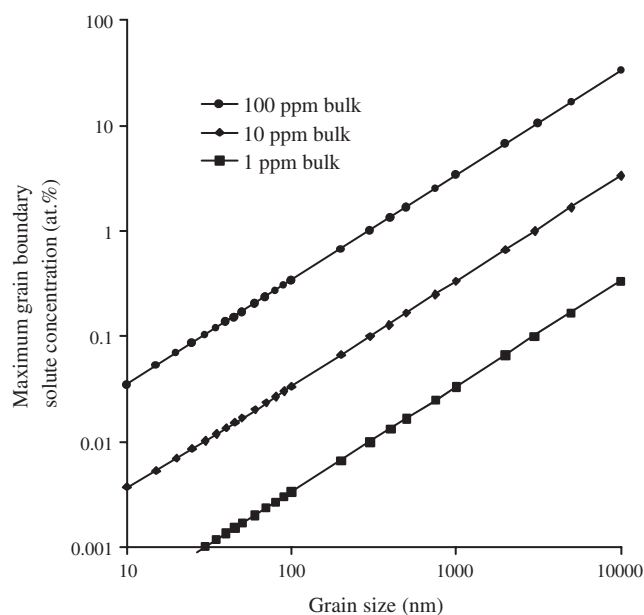


**Figure 2.** Solute dilution at grain boundaries from extreme reduction in grain size. Reprinted with permission from [33], G. Plumbo and U. Erb, *MRS Bulletin* 24, 27 (1999). © 1999, Materials Research Society.

that uncontaminated samples are required before definitive information can be obtained regarding the nature of the grain boundary structure in nanocrystalline materials such as Cr [13]. Klement et al. [34] using energy dispersive X-ray (EDX) measurements in a scanning transmission electron microscope (STEM) determined the presence of S segregation at intercrystalline defects in annealed nano Ni containing 0.16 wt % S produced by electrodeposition [35]. Figure 3 shows the S concentration along and normal to a grain boundary of initially 10 nm Ni annealed for 30 min at 493 K. After this anneal, a dual-sized grain structure was present: 10–20 nm grain size matrix and grains produced by abnormal grain growth with a size from 50 to 130 nm. Along the grain boundary of the larger grains, the S content fluctuates (Fig. 3(a)), which may suggest a dependency on the local grain boundary structure. Triple junctions are known for their special properties compared with grain boundaries and bulk materials [36], for example, preferred sites (sinks) for solutes. This is evident at position “0” in Figure 3(a), which was at a triple junction, showing higher S content than at the grain boundary. Normal to the grain boundary, Figure 3(b), a large difference in the S content within the grains and directly at the grain boundary was detected. The observed solute (S) segregation at grain boundaries and triple lines may play a significant role in the properties of nano materials, at least in the annealed condition.

## 3. INTERCRYSTALLINE DEFECTS AND PROPERTIES OF NANOCRYSTALLINE MATERIALS

### 3.1. General

In recent years, wide ranges of novel property measurements have been attributed to the large interfacial volume fraction in nanocrystalline materials. However, a number of these novel properties were not strictly due to the increased intercrystalline volume fraction associated with the ultrafine grain size, but rather to other secondary defects that were introduced during synthesis. It is instructive, therefore, to consider a nanostructured material as having two types of defect structures. The first is the primary defect structure, which is the set of grain boundaries, triple lines, and quadruple nodes that form the ultra-fine interfacial network. The other is a secondary defect structure, which may be composed of

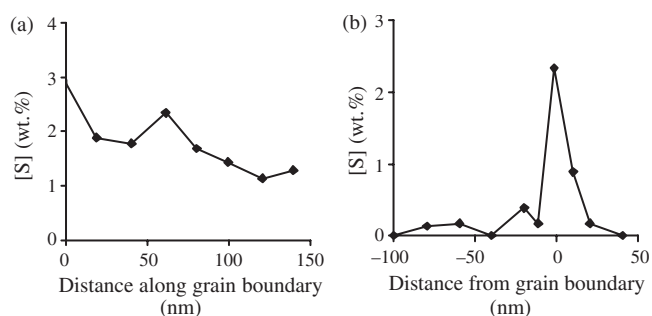


**Figure 3.** EDX measurements showing the S concentration (a) along and (b) normal to a grain boundary in nanocrystalline Ni after annealing at 493 K for 30 min [34].



entrained porosity, residual amorphous regions, lattice dislocations, and extrinsic grain boundary dislocations.

The nature of the secondary defect structure is strongly dependent on the synthesis method used to obtain the ultrafine intercrystalline network. For example, nanocrystalline materials produced in powder form (through inert gas condensation, ball milling, etc.) followed by consolidation, can have entrained porosity that significantly affects certain materials properties [37]. While crystallization of amorphous precursors, recrystallization following severe plastic deformation, and electrodeposition, can all produce fully dense nanostructures, the first two can also introduce relatively extensive secondary defect structures. For example, amorphous grain boundary structures [38, 39] and residual amorphous regions [40] have been reported in nanocrystalline materials produced from melt-spun precursors. For nanocrystalline materials produced by severe plastic deformation, substantial extrinsic grain boundary dislocations and a subgrain boundary network have been observed [41]. In contrast, high resolution transmission electron microscopy of electrodeposited nanocrystalline Ni and Ni-1.2 wt % P showed very low densities of lattice dislocations, and the grain boundary structures were found to be qualitatively the same as those in conventional polycrystalline materials [15]. Electrodeposition can produce nanostructured materials, which are relatively unencumbered by such secondary defect structures. This presents an opportunity to study material properties that fundamentally scale with the dimensions of the intercrystalline network.

In the present section, only those observations on properties of nanocrystalline materials will be discussed in relation to their primary defect structures. In considering the intercrystalline region to consist of distinct grain boundary and triple junction defects, the influence of these defects on the bulk properties of nanocrystalline materials will depend upon their relative volume fraction contributions (e.g., Fig. 1) and on their specific structural and chemical character (Section 2). Several material properties are significantly affected by changes in the scale of the interfacial network, while others remain essentially unchanged [42]. Properties that depend strongly on the interactions of grain boundaries with other microstructural defect structures (e.g., dislocations, vacancies, solute, second-phase particles, domain walls, etc.) are greatly influenced by the decrease in grain size. Examples include hardness, yield and tensile strength, and ductility [43]. In contrast, those material properties that depend predominantly on the local bond structure are relatively insensitive to changes in grain size down to 10 nm. Examples include saturation magnetization, heat capacity, thermal expansion, and Young's modulus [43].

## 3.2. Thermal Stability and Grain Growth in Nanocrystalline Materials

### 3.2.1. General

One of the most significant effects of the large volume fraction of intercrystalline interfaces is the strong thermodynamic potential for microstructural transformation through grain growth. While there have been numerous studies, grain growth in nanostructured materials is not well understood

at present. In part, this is due to the intrinsic difficulties of studying nm-scale microstructural evolution. It is also due to the complexities introduced by the interaction of migrating grain boundaries and the secondary defect structures that were introduced during synthesis of the nm-scale intercrystalline network. It is difficult, therefore, to draw meaningful comparisons between grain growth observations of nanocrystalline materials produced by different synthesis methods [37].

Perhaps the most significant differences in secondary defect structures are between those methods that produce nanostructured powders requiring further consolidation and those methods that produce fully dense nanostructures in one processing step. For instance, entrained porosity has been observed to have a considerable effect on the rate of grain growth. Nanostructured TiO<sub>2</sub> samples having similar starting grain sizes, but different entrained porosity (~25% and ~10%), were studied [44]. After comparable annealing treatments, the sample with the larger porosity had an annealed grain size of ~30 nm, while the sample with ~10% porosity had an annealed grain size of ~500 nm. Significant differences have also been observed between nanostructures that are both fully dense and fully crystalline, but are produced by different synthesis methods. For example, it was found [45] that the grain boundary diffusivity of nanostructured nickel produced by severe plastic deformation was several orders of magnitude higher than the diffusivity of nanostructured nickel produced by electrodeposition. The difference was attributed to the presence of extrinsic grain boundary dislocations that were formed during severe plastic deformation.

It is relatively difficult, therefore, to directly compare grain growth studies of nanostructured materials produced by different synthesis methods because of the intrinsic differences in the effects of the secondary defect structures on grain boundary migration. By contrast, the class of electrodeposited nanocrystalline materials is relatively unencumbered by secondary defect structures such as porosity, residual amorphous regions, and extrinsic grain boundary dislocations and is, therefore, a good system to study the thermodynamic effects of large volume fractions of internal intercrystalline interfaces.

### 3.2.2. Thermal Stability

The thermal stability of nanostructured electrodeposits has been most frequently studied by calorimetry. The enthalpy release during grain growth is typically measured as a function of annealing temperature at a constant scan rate. In the calorimetric (enthalpic) transformation signals for 20-nm starting grain size nanocrystalline Ni [46] and Co [47], there is a broad, low-energy exotherm followed by a main heat release peak in both cases. This type of curve has been reported in several studies of Ni [34, 46, 48–50], Ni-Fe alloys [49], and Ni-1.9 wt % P [51]. A qualitatively similar transformation signal has also been obtained using *in-situ* electrical resistivity measurements of electrodeposited nanocrystalline Co, Ni, and Ni-Fe alloys during annealing [52].

Integrating the area under the thermal signals provides the enthalpy released during grain growth. For the thermal signals of Figure 4, this yields 15.8 J/g for Ni and 17.1 J/g

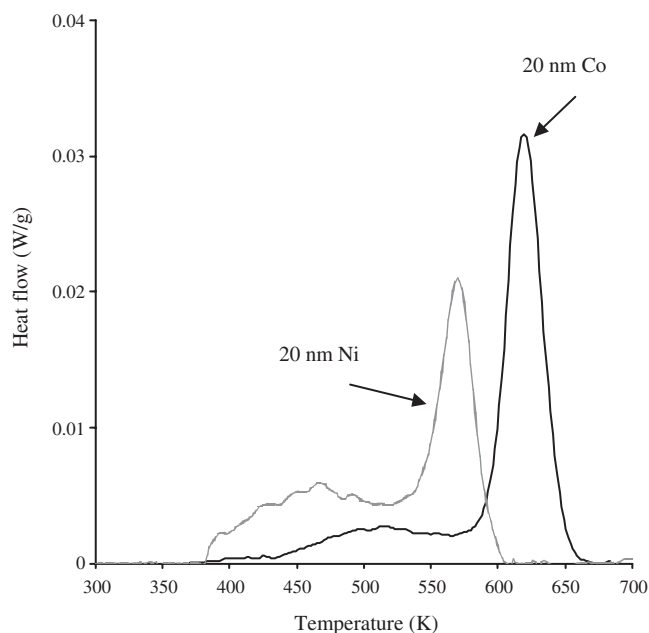


**Figure 4.** Thermal signal of grain growth obtained by modulated differential scanning calorimetry for 20 nm electrodeposits of Ni [46] and Co [47]. Reprinted with permission from [64], G. Hibbard et al., *Mat. Sci. Forum* 386–388, 387 (2002). © 2002, Trans. Tech.

for Co. If this enthalpy release is related to the reduction in intercrystalline volume fraction during growth (requiring a model of intercrystalline volume fraction as a function of grain size *e.g.*, [2]), then an average interfacial enthalpy can be estimated. Using the heat releases reported in previous studies of electrodeposited nickel [34, 46, 48, 49], values in the range of 0.6 to 1.2 J/m<sup>2</sup> are obtained. The excess interfacial enthalpy of nanostructured Co was found to be similar—1.1 J/m<sup>2</sup> [47]. The values for nickel correspond well with the extrapolated value for grain boundary energy (1.0 J/m<sup>2</sup>) determined from conventional polycrystalline nickel [53], and are not enhanced such as the 2.8 J/m<sup>2</sup> value reported for 12-nm nanocrystalline Ni produced by mechanical attrition [54].

The peak temperature,  $T_p$ , of the thermal signal has been used both as a relative measure of stability and to obtain the effective activation energy for grain growth,  $Q$ . Physically, the peak temperature indicates the point of maximal heat release from the sample during the scan. From the change in peak temperature with scanning rate, an activation energy can be obtained. Figure 5 shows a modified Kissinger plot [55] for representative examples of Ni [46], Ni-1.2 wt % P [15], Ni-20 wt % Fe [49], and Co [47]. In general terms, those systems exhibiting higher peak temperatures during calorimetry are further to the left in Figure 5, while those with higher activation energies have steeper slopes. The activation energy for nanostructured nickel electrodeposits has been obtained in several studies with values ranging from 1.20 eV to 1.46 eV. For polycrystalline Ni, the activation energies for lattice and grain boundary self-diffusion have been reported as 2.9 eV and 1.2 eV, respectively [56]. This has led several studies to suggest that grain growth in nanostructured nickel electrodeposits is controlled by grain boundary self-diffusion [48, 49, 57].

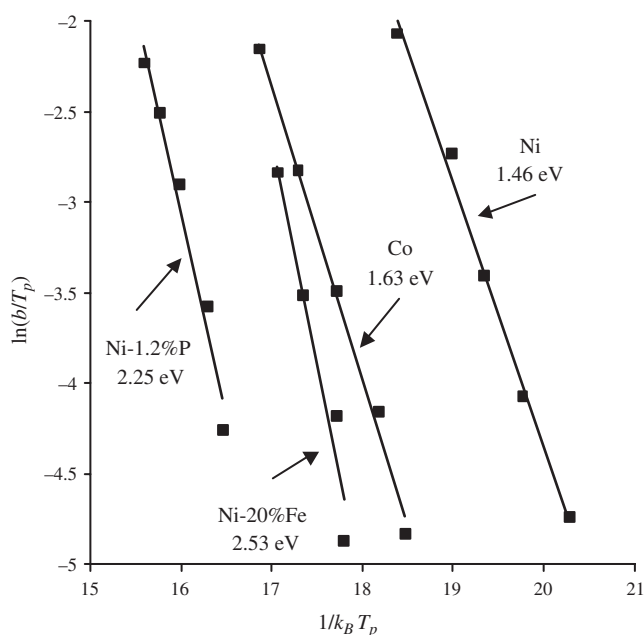


**Figure 5.** Modified Kissinger analysis for calorimetric studies of Ni [46], Ni-1.2 wt % P [15], Ni-20 wt % Fe, [49] and Co [47]. Reprinted with permission from [64], G. Hibbard et al., *Mat. Sci. Forum* 386–388, 387 (2002). © 2002, Trans. Tech.

A substantial increase in thermal stability can be obtained by alloying nanostructured Ni electrodeposits with P. The activation energy increases from ~1.2–1.4 eV for nickel electrodeposits to 2.25 eV [15] with 1.2 wt % P addition and 2.63 eV [51] with 1.9 wt % P addition. In addition, the peak temperatures increase from ~538–573 K for Ni to over 673 K with P additions. A similar increase in thermal stability can be obtained by alloying nanostructured Ni electrodeposits with Fe. The activation energy increases to 1.61 eV [52] for Ni-10 wt % Fe and to 2.43 eV [52] or 2.53 eV [49] for Ni-20 wt % Fe electrodeposits. Based on X-ray diffraction (XRD) of annealed structures, this trend of increasing thermal stability with increasing Fe content was also seen for nanostructured Pd-Fe electrodeposits [58, 59]. For Co electrodeposits, the activation energies and peak temperatures of grain growth were higher than for Ni electrodeposits. This suggests the possibility that alloying nanostructured Co electrodeposits with Fe or P may yield nanostructures with even greater thermal stability than that obtained thus far with Ni-Fe or Ni-P electrodeposits.

### 3.2.3. Grain Growth

A review of the suggested transformation mechanisms for grain growth in nano materials reveals substantially less agreement between studies than among the calorimetric observations. Several methods have been used to study the grain growth transformation mechanisms in nanostructured electrodeposits. The most frequently used method has been a decoupled annealing/characterization approach in which growth mechanisms are inferred from quenched-in transformed microstructures. A range of characterization techniques, including transmission electron microscopy (TEM) [15, 34, 46–48, 52, 57, 60–64], XRD [50, 51, 58, 59, 65],

scanning electron microscopy (SEM) [52, 66], atom probe field ion microscopy (APFIM) [51], and 3-dimensional atom probe (3DAP) [67, 68] have been used. Transformation mechanisms have also been inferred from *in-situ* annealing experiments (*i.e.*, coupled characterization and annealing) using TEM [15, 60, 62], XRD [50], and electrical resistivity measurements [52].

The most extensive observations of annealed microstructures have come from the nanocrystalline Ni system [34, 46, 48, 50, 52, 60, 61, 64, 66]. Direct TEM observation of annealed Ni has shown a wide range of annealed microstructures and it is instructive to consider this range in some detail. The first type was obtained during *in-situ* TEM annealing at 573 K and resulted in a  $\sim 30$ -nm stabilized (through 20.5 h) nanostructure [60]. For isothermal annealing at temperatures below 573 K, a second type of annealed structure with a nonuniform grain structure having grains in the size range of  $\sim 100$  to  $\sim 1000$  nm embedded in a nanocrystalline matrix, was obtained [34, 52]. For isothermal annealing in the temperature range of 573 K to 693 K, a third type was obtained, which had a uniform grain structure with mean grain size on the order of  $\sim 500$  nm [34, 57]. A fourth type, obtained by annealing at 773 K for 1 h, had a nonuniform grain structure with 12- to  $50\text{-}\mu\text{m}$  sized grains having planar interfaces surrounded by submicron-sized matrix grains [66]. A fifth type was obtained during annealing at still higher temperatures (*e.g.*, 873 K for 3 h) and showed a uniform grain structure with grains in the size range of  $\sim 50$  to  $100\ \mu\text{m}$  [52].

Taken individually, these disparate annealing structures have implied distinct growth mechanisms, which may become active over different temperature ranges. Indeed, the following mechanisms have been suggested. A-Sherik et al. [60] reported uniform growth followed by a stabilization. It was also suggested that abnormal growth occurred at lower annealing temperatures (less than 593 K) and that normal growth occurred at higher annealing temperatures [34]. A transition from abnormal growth to normal growth with increasing scanning temperature was noted [48]. It was also claimed that growth changed from normal to abnormal with increasing annealing time at a constant temperature [50]. Other work [52, 69] suggested that there was concurrent abnormal and normal grain growth.

A recent comprehensive study [64, 70] examined the structural evolution of nanocrystalline Ni at 493 K, 593 K, and 693 K over a period of annealing times ranging from  $\sim 1$  s to 432 ks (120 h). It has shown that the microstructural evolution during annealing of nanocrystalline Ni occurs sequentially, through at least four distinct stages of growth, and that these individual stages can explain the previously observed annealed nanocrystalline nickel structures. An example of this multistaged grain growth is shown in Figure 6, in which low magnification, bright-field TEM images are shown of nanocrystalline Ni after annealing for  $\sim 1$  s, 3.6 ks (1 h), 39.6 ks (11 h), and 432 ks (120 h) at 693 K. Four distinct microstructures can be seen: a nonuniform annealed microstructure with 100 to 700 nm grains in a nanocrystalline matrix (Fig. 6a); a uniform microstructure with  $\sim 500$  nm grain size (Fig. 6b); a nonuniform microstructure with large grains of size  $\sim 5$  to  $50\ \mu\text{m}$  with planar growth

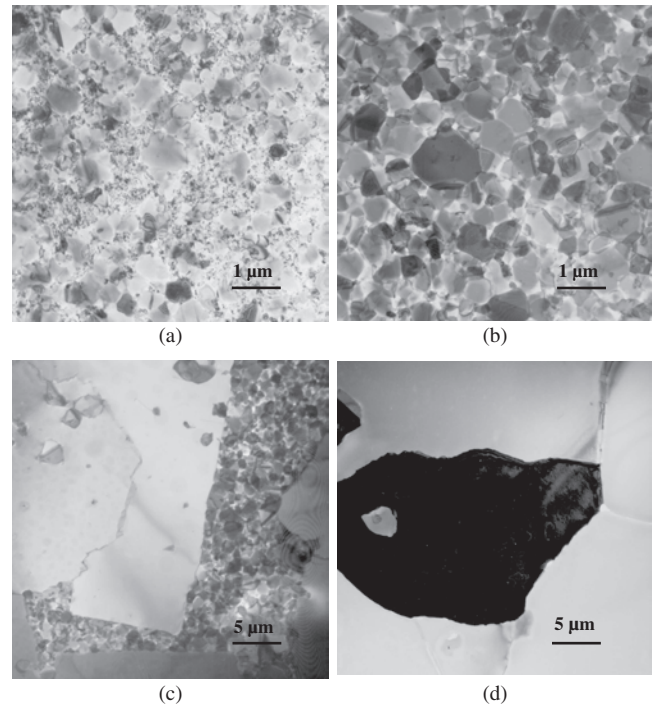


**Figure 6.** Bright-field TEM images of 20 nm Ni after the following annealing times at 693 K:  $\sim 1$  s (a), 3.6 ks (1 h) (b), 39.6 ks (11 h) (c), and 432 ks (120 h) (d) [70]. Reprinted with permission from [64], G. Hibbard et al., *Mat. Sci. Forum* 386–388, 387 (2002). © 2002, Trans Tech.

interfaces (Fig. 6c); and a uniform microstructure with a grain size of  $\sim 50\ \mu\text{m}$  (Fig. 6d).

Of the five types of annealed structures listed in the previous section, only the stabilized nanostructure (*i.e.*, type 1) was not observed during the microstructural evolution at 693 K. Indeed, there was no evidence of a stabilized nanostructure at either of the other two annealing temperatures (493 K and 593 K) through 120 h of annealing [70]. The previous observations of a stabilized nanostructure [60] were likely due to grain boundary pinning by the free surfaces during *in-situ* TEM annealing.

During the first stage of growth, the nanocrystalline matrix is consumed by a small fraction of the grains growing abnormally into the nanocrystalline matrix. There are several dragging forces to consider in rationalizing this type of growth behavior. First, nanostructured nickel electrodeposits typically have sulfur impurities in the range of 100 to 1000 ppm due to bath additives [71]. However, sulfur may not be the major dragging force at the outset of growth, because of solute dilution from the large intercrystalline volume fraction [33]. In fact, 3DAP of nanostructured Ni in the as-deposited condition has shown sulfur impurities to be evenly distributed through the electrodeposit [67]. Other dragging mechanisms may be of more significance at the start of abnormal growth. In particular, it has been suggested that triple line drag [*e.g.*, 72, 73] and vacancy drag [*e.g.*, 74] may become increasingly important as the grain size is reduced. Once growth has begun, however, it is expected that solute pinning effects will increase in importance as the abnormal growth front consumes the matrix,

collecting sulfur as it migrates. Indeed, significant sulfur enrichment was observed at the interface between large abnormally growing grains and the nanocrystalline matrix in nanostructured nickel annealed for 30 min at 493 K using HREM (e.g., see Fig. 3b [34]).

Perhaps one of the most dramatic effects of sulfur segregation in a nanocrystalline material can be seen in Figure 7. The characteristic feature of this late-stage abnormal grain growth is the migration of planar interfaces into a submicron, grain-sized matrix. EDX and STEM of the planar interface region showed sulfur-rich, second-phase precipitates that appeared to wet the interface [70, 75]. Initiation of this second stage of abnormal grain growth is likely linked to a redistribution of sulfur during the prolonged period of uniform (second stage) growth (Fig. 6b), during which the system approaches thermodynamic equilibrium with respect to nickel-sulfide precipitation and grain boundary, structure-dependent segregation [70, 75].

### 3.3. Mechanical Properties

As expected, the plastic deformation behavior of nanocrystalline materials is strongly dependent upon the interfacial volume fraction. Much of the early work was concerned with room temperature micro-hardness measurements (e.g., Fig. 8). This figure shows the results obtained for room temperature Vickers hardness measurements of Ni-P electrodeposits [76]. Also shown are the results on nanocrystalline Pd and Cu produced by the inert gas condensation technique [77]. Initial increases, followed by significant decreases in hardness, are noted with decreasing grain size ( $d$ ) in the nanocrystal range of  $d \leq 20$  nm. The observed decreases in hardness are contrary to the Hall-Petch behavior [78, 79] and consistent with results reported elsewhere [80, 81] for nanocrystalline materials. Others have only reported a reduction in the Hall-Petch slope in the nanometer range (e.g., [82]). Results of hardness and compressive yield stress measurements on nanocrystalline Cu, made by inert gas condensation and compaction with grain sizes from about 20 nm to 16 nm, suggest a deviation from linearity at the smallest grain sizes measured [83]. However, Erb et al. [84, 85], in

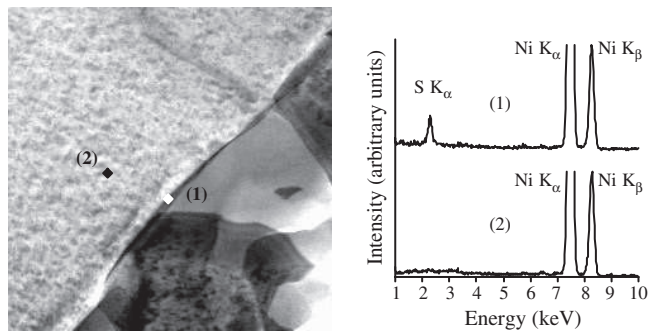


**Figure 7.** STEM micrograph of the planar abnormal growth interface showing the wetting, sulfur-rich second phase at the interface between the abnormal grain (left) and matrix grains (right). Also shown are EDX spectra corresponding to positions 1 and 2 [70], Reprinted with permission from [75], G. Hibbard et al., *Scripta Mat.* 47, 83 (2002). © 2002, Elsevier Science.

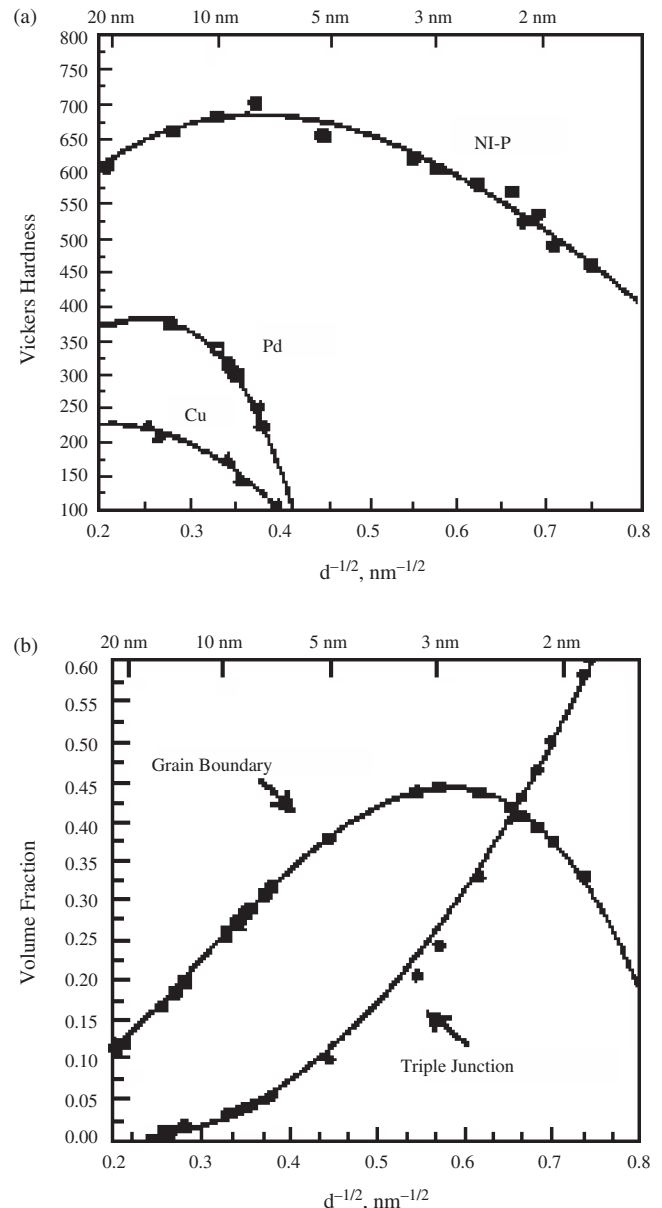


**Figure 8.** (a) Vickers hardness measurements for nanocrystalline Ni-P, Pd, Cu, (b) corresponding intercrystalline volume fractions. Reproduced with permission from [76], G. Palumbo et al., *Scripta Met. Mater.* 24, 2347 (1990). © 1990, Elsevier Science.

an extensive study of electrodeposited Ni, found a strong deviation from linearity below about 25 nm grain size and a negative Hall-Petch slope between 11 nm and 6 nm, as depicted in Figure 9.

Chokshi et al. [77] interpreted their results for Pd and Cu seen in Figure 8 in terms of room temperature Coble creep, arising from the disorder associated with large intercrystalline fractions. However, in one study [86], it appeared that grain boundary diffusional creep is not an appreciable factor in determining the room temperature mechanical behavior of nanocrystalline Cu and Pd. Modified dislocation pile-up theories involving small numbers of dislocations [87, 88] can be used to explain the deviation behavior of the Hall-Petch



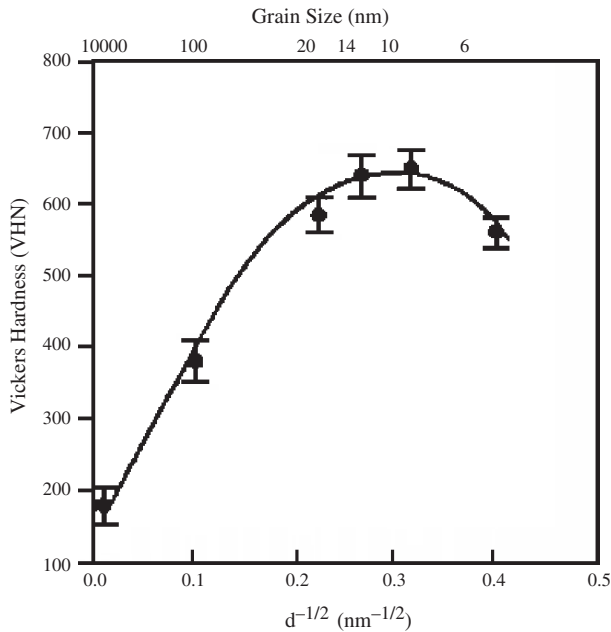


**Figure 9.** Hardness of nanocrystalline Ni as a function of grain size [84, 85].

relationship but not the negative slopes shown in Figures 8 and 9. A significant reduction in the Hall–Petch slope was predicted to occur for the extreme case of only one dislocation loop being expanded against the grain boundary obstacle stress [89]. Scattergood and Koch [90] concluded from their model that a continued drop in dislocation line tension with decreasing grain size leads to a negative Hall–Petch slope. Wang et al. [91] concluded that the dislocation pile-up mechanism no longer applies to nanocrystalline materials below a critical grain size, for example, about 10 nm for FCC metals. In agreement with the latter conclusion, computer simulation results [92, 93] indicate that no dislocation activity occurs below a critical grain size (of the order of 10 nm for metals) and that plastic deformation then occurs entirely by grain boundary sliding.

Using a two-component model of grain boundaries and grains, Carsley et al. [94] calculated the hardness of nanocrystalline metals as a function of grain size. They assumed Hall–Petch behavior for the grains down to the finest grain sizes, while the hardness of the assumed amorphous grain boundaries was estimated from a relation between hardness and shear modulus in the glassy state. The shear modulus of the amorphous state is assumed to be about one-half of the crystalline value. Using a simple rule of mixtures to obtain the hardness of the two combined phases, their Hall–Petch plot [94] agreed with some data for Ni [84, 95].

A composite model based upon geometric considerations, in terms of the volume fraction of crystalline and intercrystalline components, was proposed by Wang et al. [91, 96] to evaluate the strength of nanocrystalline materials. It was shown that this model can be used for interpreting the various observations involving deviation from the Hall–Petch relationship and a negative Hall–Petch slope. In addition to grain boundaries and triple junctions, this analysis also included quadruple nodes where triple lines (usually four) are linked up [3]. The strength contributions

for grain boundaries ( $\sigma_{gb}$ ), triple lines ( $\sigma_{tl}$ ), and quadruple nodes ( $\sigma_{qn}$ ) was shown to have the following sequence [96]:  $\sigma_{gb} > \sigma_{tl} > \sigma_{qn}$ . The result of comparing the measured yield strength of nanocrystalline Ni electrodeposits to the composite model incorporating strength contributions from grain boundaries, triple junctions, and quadruple nodes is shown in Figure 10. The experimental yield strength data not only fit the composite model reasonably well but also show a behavior consistent with that of the hardness studies of bulk nano Ni electrodeposits (e.g., Fig. 9).

It should be noted that the onset of decreasing strength, that is, deviation from Hall–Petch behavior, in these systems (Figs. 8, 9, and 10) occurs at grain sizes where triple lines begin to comprise a significant fraction of the bulk specimen volume (Fig. 8b). The observed phenomena are in general agreement with the triple-line softening effects first reported by Rabukhin [97], who investigated the effect of triple junctions on the room-temperature tensile properties of conventional polycrystalline wires (Al, Cu, W) having various grain sizes. By electrochemical thinning of the wires to a diameter less than the average grain size, triple junctions could be eliminated from the microstructure. In all cases, an increase in strength and decrease in ductility was noted on such a transition from an equiaxed (with triple lines) to bamboo grain structure (no triple lines). The grain size dependence of the proof stress was found to obey the Hall–Petch relationship; however, at constant grain size, low values of proof stress were always obtained with the equiaxed geometry. Using a similar approach, Lehockey et al. [98] confirmed triple-line softening effects in Ni.

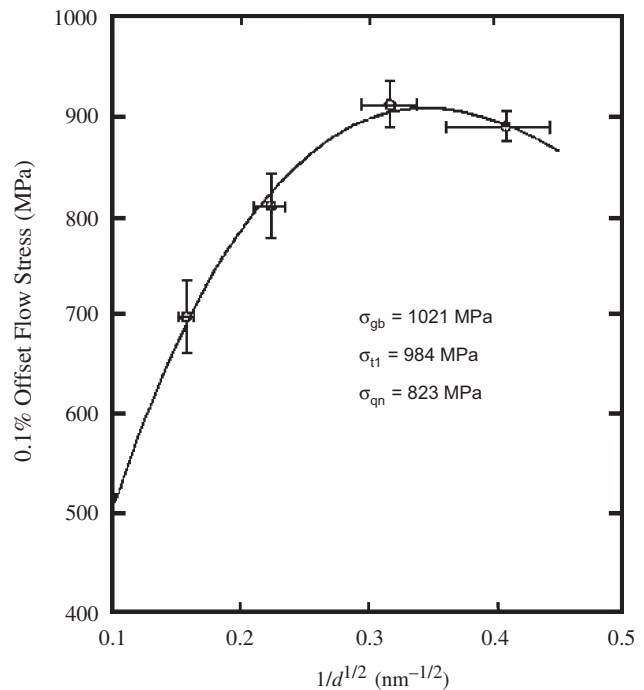


**Figure 10.** The result of fitting the yield strength of nanocrystalline nickel electrodeposits to a composite model incorporating strength contributions from grain boundaries ( $\sigma_{gb}$ ), triple lines ( $\sigma_{tl}$ ), and quadruple nodes ( $\sigma_{qn}$ ). Reprinted with permission from [96], N. Wang et al., *Mat. Sci. Eng. A*, 237, 150 (1997). © 1997, Elsevier Science.

Wang et al. [96] also derived an analytical expression for assessing the creep rate of nanocrystalline materials by a diffusion mechanism, including triple line diffusion. The overall creep rate is the sum of the creep rate due to lattice diffusion, grain boundary diffusion, and triple line diffusion. It was predicted that the creep rate due to triple line diffusion will exhibit a stronger grain size dependence than that due to grain boundary diffusion. For example, the contribution of triple line diffusion to steady-state creep rate appears to be the inverse of  $d^4$  ( $d$  = grain size), which is one order of magnitude higher than grain boundary diffusion and two orders higher than lattice diffusion in terms of grain size dependence. In addition, the secondary creep rate is still linearly proportional to the applied tensile stress, compared to the dislocation mechanism in which the exponent of the applied stress is usually greater than three.

It is evident from the work of Wang et al. [91, 96] that at high stress levels, grain boundary sliding is the major room temperature deformation mechanism in nanocrystalline Ni electrodeposits. However, the contribution from creep mechanisms through intercrystalline regions can be significant for smaller grain size. A negative Hall–Petch slope was observed when the grain size was below about 10 nm. It was suggested [96] that the deviation from the Hall–Petch relationship can be attributed to a dynamic creep process due to intercrystalline diffusion mechanisms.

Contrary to earlier measurements on nanocrystalline materials prepared by consolidation of precursor powder particles, [5, 86, 99] nanocrystalline nickel electrodeposits showed little grain size dependence of Young's modulus, at least for grain sizes larger than about 10 nm [100]. This result provides further support for the findings of Krstic et al. [101] and Zugic et al. [102], which demonstrated that the previously reported large reductions in modulus with nanoprocessing were likely the result of high residual porosity. Subsequent measurements [83, 103] on compacted nanocrystalline metals with lower residual porosity confirmed that the initially reported large reductions in Young's modulus were indeed mainly the result of residual porosity.

Zhou et al. [104] recently measured Young's modulus as a function of grain size for grain sizes ranging from about 30 nm to less than 5 nm in nano Ni-P samples having fully dense structure and constant P content (2 wt %). As shown in the comparison between Young's modulus and the interfacial volume fraction of Figure 11, a continuous decrease in Young's modulus at grain sizes below 30 nm was observed, which is considered to be the result of all interface contributions. The large drop in Young's modulus at a grain size of 4 nm is mainly due to the sharp increase of triple junction volume fraction indicated in Figure 11. Using a simple composite model, the Young's moduli of the grain boundary and triple junction components were determined to be 184 GPa and 143 GPa, respectively [104]. In this same study [104], nanoindentation measurements revealed a transition from regular to an inverse Hall–Petch relationship with decreasing grain size; this was explained in terms of triple junction contributions.

With respect to the hardness curve for Ni-P shown in Figure 8a, it should be noted that the grain size for the smallest grain sizes (<3 nm) was derived from X-ray line broadening measurements. However, the XRD scans for

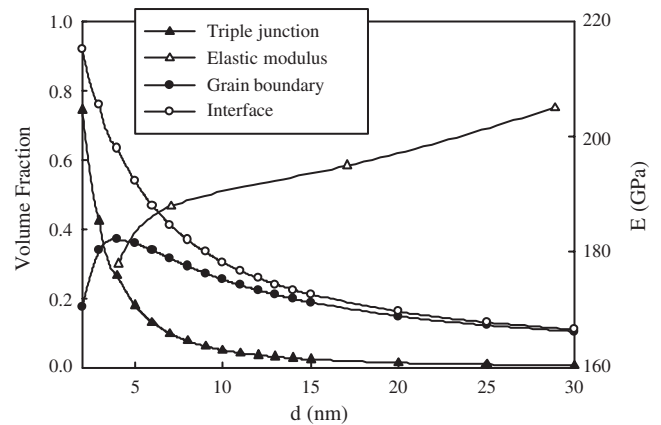


**Figure 11.** A comparison between the measured Young's modulus for nanocrystalline Ni-P and the calculated interfacial volume fraction, as a function of grain size. Reprinted with permission from [104], Y. Zhou et al., *Scripta Mater.* 48, 825 (2003). © 2003, Elsevier Science.

these particular samples resembled those typically obtained for amorphous structures. These electrodeposits contained increasing P content with decreasing grain size and it has been previously shown [105, 106] that there is a smooth, but not fully characterized, transition from the nanocrystalline to the amorphous structure. The smooth decrease in hardness through the nanocrystalline to the amorphous transition in Figure 8a indicates that a common structural element may be responsible for ductilization in both the nanocrystalline and amorphous states. This transition coincides with the region following the plateau in the grain boundary volume fraction at a grain size of  $\sim 3$  nm (Fig. 8b) below which the triple junction volume fractions assume relatively large values. Figure 12 schematically illustrates a limiting case for this phenomenon [107]. When the mean grain size becomes very small, individual atoms can be better represented as spherical clusters of atoms. Under these conditions, the grain boundary is shown by the point of contact between adjacent spherical clusters, while the triple junction region assumes a relatively large volume. Thus, the transition to the non-nanocrystalline state is defined as the crystal (cluster) size, where the ratio of triple junction to grain boundary volume fraction begins to approach infinite values [107]. It was

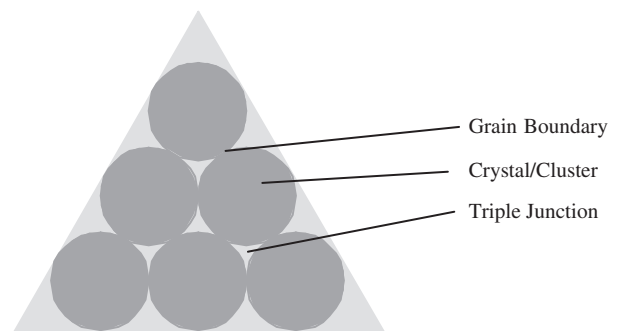


**Figure 12.** Schematic representation of a postulated limiting grain size for crystallinity, where the triple junction to grain boundary volume fraction ratio approaches infinite values [107].



suggested that the common structural element, which could be responsible for the ductilization, is the disclination [76].

### 3.4. Physical Properties

#### 3.4.1. Magnetic Properties

Many of the earlier studies on nanocrystalline materials have reported that there is a large reduction in saturation magnetization ( $M_s$ ) with increasing interfacial volume fraction (*i.e.*, decreasing grain size) [5, 108–111]. For example, a 40% decrease in saturation magnetization for nano Fe (6 nm grain size) was found compared to bulk  $\alpha$ -Fe [5]. It was also reported [112] that the spontaneous magnetization of nano Gd samples was about 75% of the value for polycrystalline Gd. All of these previous nano materials were produced using the gas condensation method, which yields materials with high internal porosity that can provide large surface areas for oxide formation after exposing the samples to air. In contrast, Aus et al. [113] reported that the saturation magnetization of nanocrystalline Ni was not strongly dependent on the grain size. In this study, the grain sizes of Ni varied from 100  $\mu\text{m}$  to 10 nm; for the Ni with the smallest grain size, the observed saturation magnetization was only 10% less than conventional polycrystalline Ni. These results were obtained on bulk nanocrystalline Ni produced by electrodeposition and were explained in terms of the negligible porosity/oxide formation in this material. Other studies [114–117] have generally confirmed the initial results of Aus et al. [114]. Kisker et al. [118] presented results for gas-condensed Ni, which showed the saturation magnetization to be independent of grain size as long as the material was not exposed to air. However, after exposure to air,  $M_s$  decreased to about 80% of its original value.

Studies were conducted on the effect of structural disorder introduced by grain boundaries, on the magnetic properties of nanocrystalline metals [119–121]. Grain boundary configurations representing various degrees of disorder were generated using molecular dynamics simulations with embedded atom potentials. These boundary configurations ranged from  $\Sigma 3$  boundaries with minimum structural disorder through  $\Sigma 5$  and  $\Sigma 13$  special grain boundaries of intermediate structural disorder to random amorphous grain boundaries with maximum disorder. Electronic structure calculations were performed using the tight-binding linear muffin-tin orbital atomic-sphere-approximation method. These calculations have shown that the magnetic moment is rather insensitive to the degree of structural disorder associated with grain boundaries. Even when all the material was amorphous, the average moment was found to be reduced by only 15%. It was concluded that, for the case of nanocrystalline Ni with a grain size of 10 nm at which the grain boundary atoms comprise about 30% of the volume, the overall effect of structural disorder on the average moment is very small, in good agreement with the experimental data reported by Aus et al. [113] for electrodeposited nickel.

Further experimental evidence and detailed calculations for nanocrystalline Ni-Fe, Ni-P, Co, and Co-W [122, 123] also indicate that the structural disorder introduced by grain boundaries and triple junctions has an insignificant effect

on saturation magnetization compared with chemical disorder introduced by alloying additions. In addition, Tamimoto et al. [124] have shown that the magnetization of fully dense and highly pure nanocrystalline Fe (density increased by explosive compaction) is almost the same as that of polycrystalline Fe. The grain boundaries in the high-density nano metals are not so disordered as the “gas-like” state originally proposed in the early days of nano materials [5, 6], and their magnetic behavior is quite similar to that of conventional grain boundaries in polycrystalline metals [124].

#### 3.4.2. Electrical Properties

Grain boundaries have long been recognized to affect the electrical properties of metals [125]. Conventional polycrystalline metals (grain size  $>1 \mu\text{m}$ ) contain a relatively low volume fraction of grain boundaries, and therefore their influence on the electrical resistivity is only significant at low temperatures [126–129]. For nanocrystalline materials (grain size  $<100 \text{ nm}$ ), however, the grain boundary volume fraction can increase to levels that are comparable to that of the crystalline component (*e.g.*, Fig. 1) and thus the effects of the grain boundaries quickly become a significant factor. Consequently, an increase in the electrical resistivity of various nanocrystalline materials has been reported even at room temperature [5, 116, 130–132].

A comparison of results of electrical property measurements performed on nanostructured materials produced by different synthesis routes (*e.g.*, gas condensation [5], electrodeposition [116, 130, 132]) show very similar trends. In most cases, the electrical resistivity was observed to increase with decreasing grain size. For example, the room temperature resistivity for Ni was increased from about  $6 \mu\Omega \text{ cm}$  at 100  $\mu\text{m}$  grain size in fully annealed material, to about  $22 \mu\Omega \text{ cm}$  at 11-nm grain size in electrodeposited material [130]. This can be attributed to electron scattering at defects, such as grain boundaries and triple junctions. In fact, a linear relationship between excess resistivity—defined as the total resistivity of the nanocrystalline material minus the resistivity of conventional polycrystalline material (100  $\mu\text{m}$  grain size) with negligible intercrystalline volume fraction—was observed for nanocrystalline Ni of varying grain size [130].

A more comprehensive study [52, 133] has recently shown that the contribution to the electrical resistivity from the grain boundaries in nano Ni, Co, and Ni-Fe alloy varies linearly with the grain boundary area. It was also shown that the grain boundary contribution can be quantified in terms of a specific electrical resistivity. The specific grain boundary resistivity (SGBR) for electrodeposited pure Ni and Co at 295 K was found to be  $2.82 \times 10^{-6} \mu\Omega \text{ cm}^2$  and  $3.26 \times 10^{-6} \mu\Omega \text{ cm}^2$ , respectively. The SGBR values for electrodeposited Ni with 16%, 31%, and 34% Fe were 3.01, 3.09, and  $2.99 \times 10^{-6} \mu\Omega \text{ cm}^2$ , respectively [52]. These SGBR values for electrodeposited Ni, Co, and Ni-Fe alloy were determined to be independent of temperature. The SGBR values determined from measurements on nano materials were similar to those previously determined for polycrystalline Cu, Al, and Al bicrystals [52, 133]. This indicates that the structure of grain boundaries in nano materials is similar to that in polycrystalline materials at least with respect to electron scattering effects.

### 3.5. Corrosion Properties

The corrosion behavior of nanocrystalline materials produced by crystallization of amorphous precursor materials has shown both beneficial and detrimental effects (e.g., [134–139]). The conflicting results may largely be due to the difficulty of correlating the complex microstructures and chemical compositions of the crystallized-amorphous materials to the corrosion resistance. However, nanostructured materials produced by electrodeposition have shown considerable advances in the understanding of the role of primary defect structures on the corrosion properties [140–145].

The corrosion behavior of nanocrystalline Ni has been extensively studied using potentiostatic and potentiodynamic polarizations in various corrosion environments: 2 N H<sub>2</sub>SO<sub>4</sub> solution (pH = 0), 30 wt % KOH solution (pH = 13), and 3 wt % Na Cl solution (pH = 7) [140–143]. While the overall corrosion rate in the passive region was somewhat higher for nanocrystalline than polycrystalline Ni, localized corrosion at grain boundaries and triple junction was found to disappear with decreasing grain size [140, 141]. X-ray photoelectron spectroscopy of the specimens polarized in the passive region showed that the passive film formed on the nanostructured specimen is more defective than that formed on the polycrystalline specimen, while the thickness of the passive layer was the same on both specimens [146]. This higher defective film on the nanocrystalline specimen allows for a more uniform breakdown of the passive film, which in turn leads to a more uniform corrosion. In contrast, as shown previously [24, 147], in coarse-grained Ni the breakdown of the passive film occurs first at the triple junctions and grain boundaries rather than the crystal surface, leading to a preferential attack at these defects.

Similar observations were made for the corrosion behavior in HCl of nanocrystalline 304 stainless steel (grain size 25 nm) produced by sputtering [148]. The reduced susceptibility to localized corrosion was attributed to the fine-grained microstructure, which allowed for a uniform distribution of Cl<sup>-</sup> ions. Further tests, (American Society for Testing and Materials (ASTM) G28-susceptibility to intergranular attack; ASTM G35, G36, and G44-susceptibility to stress corrosion cracking) have shown that nanostructured Ni is intrinsically resistant to intergranular attack and intercrystalline stress corrosion cracking [144]. The material was also found to be resistant to pitting attack and only slightly susceptible to crevice corrosion (ASTM G 48) [144].

Potentiodynamic polarization in conjunction with energy dispersive X-ray spectroscopy was used to investigate the role of sulfur on the passivation behavior of nanocrystalline Ni with an average grain size of about 30 nm and a sulphur content of about 1080 ppm [149]. Several of the as-deposited nano Ni samples were annealed at 1223 K for 15 min in order to obtain polycrystalline Ni through grain growth with the same overall sulfur content as in nano Ni. In addition to extensive grain growth, this anneal also resulted in sulfur segregation to grain boundaries and subsequent formation of grain boundary precipitates. In 0.25 M Na<sub>2</sub>SO<sub>4</sub> solution (pH = 6.5), the presence of 1080 ppm sulfur reduced the passivity of both as-plated and annealed nano Ni, as compared to polycrystalline Ni 200 (<100 ppm S). However, even at such a high concentration of sulfur, as-plated nano Ni is highly resistant to localized corrosion while the

annealed polycrystalline counterpart with the same sulfur content resulted in highly localized attack with grain dropping. This is demonstrated in Figure 13. For the annealed nanocrystalline Ni, the localized grain boundary corrosion penetrated as deep as 130 μm into the sample, which resulted in “grain dropping” in some areas. However, in the case of nanocrystalline Ni, the corrosion attack due to uniformly distributed surface pitting is very shallow, usually less than 2 μm in depth. At higher pH (pH = 11.5, 1 vol% NH<sub>4</sub>OH solution), both as-plated and annealed nanocrystalline Ni with 1080 ppm sulfur displayed passive behavior comparable to that of conventional polycrystalline Ni 200. However, the passive current density for the annealed nano Ni was approximately one order of magnitude higher and localized grain boundary/triple junction attack on Ni sulfide precipitates was observed.

Uniform surface dissolution was observed in electrodeposited nanocrystalline Co, grain size 12 nm, (containing 440 ppm S and 290 ppm C) after potentiodynamic polarization in a deaerated 0.25 M Na<sub>2</sub>SO<sub>4</sub> solution at pH of 6.5 [150]. Uniform metal dissolution can be expected when it is assumed that the S impurities are evenly dispersed throughout the nanocrystalline structure, similar to what has been observed in a 3-D atom probe study by Warren et al. [67] in electrodeposited nanocrystalline Ni containing 550 ppm (by weight) of S. However, the surface of annealed nanocrystalline Co, (average grain size 10 μm) and containing the same total amount of impurities as the electrodeposited nanocrystalline Co, showed considerable preferential attack along the grain boundaries [150], where segregation of S would be expected after the anneal (15 min at 1223 K) [34]. The results of these studies [149, 150] support the previous considerations (Fig. 2 [33]) that solute dilution by nano processing can be used as an effective method to improve the overall intergranular degradation resistance.

### 3.6. Hydrogen Diffusion and Activity

The dependence of diffusion or local atomic jumps of hydrogen on the hydrogen concentration may be used as a local probe to obtain information on the spectra of available trapping sites in interfaces. The spectrum of hydrogen sites in

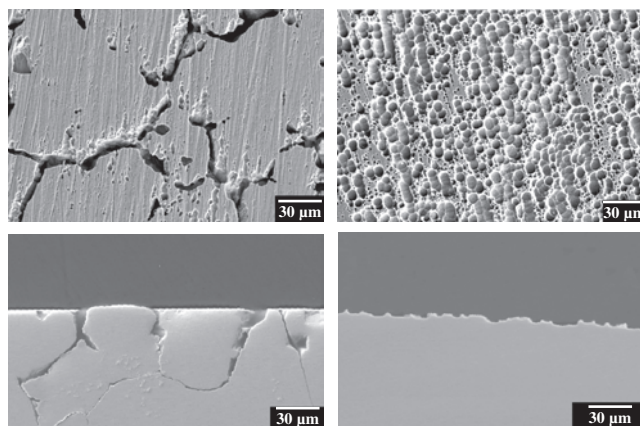


**Figure 13.** Surface (top) and cross-sectional (bottom) corrosion morphologies of nickel containing 1080 ppm sulfur. Left-annealed nanocrystalline Ni (1223 K for 15 min); right-as-plated nanocrystalline Ni [149].

the interfaces of nano Pd, prepared by gas condensation and compaction, appears to differ from that in amorphous alloys, for example, amorphous  $\text{Pd}_{83}\text{Si}_{17}$  [151]. For example, the energy distribution of the hydrogen sites, as deduced from the variation of hydrogen diffusivity with concentration, is enhanced by about 30% compared to amorphous  $\text{Pd}_{83}\text{Si}_{17}$ . However, the hydrogen diffusivity in nano Pd at low hydrogen concentrations with respect to that in the crystalline state is more greatly reduced than in amorphous  $\text{Pd}_{83}\text{Si}_{17}$  [151]. This indicates that the interfacial traps in the nano Pd have higher binding energies than in amorphous alloys. As was concluded in [152], this behavior is in contrast to that observed in nanocrystalline alloys prepared by crystallization from the amorphous state, and fits the different interface structures found for cluster-compacted nano metals and crystallized alloys by means of positron lifetime spectroscopy [153, 154]. It should be noted in this regard that a study [124] using explosion densified nanocrystalline Fe (density >95% of theoretical value) indicated that the self-diffusivity was close to that for conventional polycrystalline grain boundary diffusion expected from the extrapolation of high temperature data. It was concluded that the grain boundary structure of high-density nano metals is similar to that of conventional grain boundaries in coarse-grained metals [124]. In another study [155], a misorientation dependence of grain boundary diffusion of Ni in nanocrystalline thin films of nickel silicide (grain size 40–60 nm) was observed. Again, it was concluded that “the grain boundaries in our samples are well structured and do not consist of an amorphous phase” [155].

The transport behavior of hydrogen in electrodeposited nanocrystalline Ni foil (average grain size of 17 nm) at 293 K was determined using an electrochemical double cell [156]. Figure 14 shows a typical hydrogen permeation curve, where the anodic exit current density is plotted as a function of cathodic charging time. Three distinct breakthrough events are evident, as indicated by the arrows in Figure 14. On the basis of determined diffusivities, permeation flux values, and area (volume) fraction considerations [156], these breakthrough events were considered to be due to hydrogen transport through distinct triple junction, grain boundary,

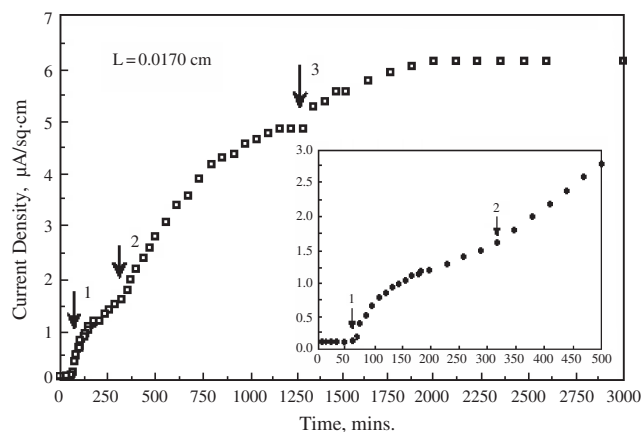


**Figure 14.** Anodic exit current density as a function of cathodic charging time at  $0.1 \text{ mA/cm}^2$  for nanocrystalline Ni (17-nm grain size) foil of 0.17-mm thickness. Reprinted with permission from [156], G. Palumbo et al., *Scripta Met. Mater.*, 25, 679 (1991). © 1991, Elsevier Science.

and lattice paths, respectively. The triple junction diffusivity was determined to be approximately three times faster than grain boundary diffusivity and 70 times faster than lattice diffusion. Other studies [157] have also shown that diffusive transport occurs at a considerably faster rate through the triple junctions than along the adjoining grain boundaries. These results provide support for the defect character of triple junctions. Furthermore, the existence of a “measurable” triple junction diffusivity in nanocrystalline Ni indicates the importance of triple junction defects in the bulk properties of nanocrystalline materials.

Nanocrystalline Ni electrodeposits having an average grain size of 20 nm are also observed to display higher electrocatalytic behavior when compared to cold worked, fine grained, and fully annealed reference structures, with regard to the hydrogen evolution reaction (HER) for alkaline water electrolysis at room temperature [158]. The enhanced HER kinetics are considered to be the direct result of the high area fraction of grain boundaries, and to some extent, triple junctions which intersect the free surface of the electrode. It has been also shown [159] that the HER kinetics can be further enhanced by alloying nanocrystalline Ni with molybdenum.

An additional study [158] into the transport behavior of hydrogen in nickel as determined by an electrolytic-charging technique revealed that substantial increases in hydrogen diffusivity and capacity are obtained when Ni is in nanocrystalline form. Figure 15 illustrates three representative permeation transients corresponding to hydrogen transport through nanocrystalline (20 nm), fine-grained (1  $\mu\text{m}$ ), and single-crystal Ni foils of 140- $\mu\text{m}$  thickness. Detection of permeated hydrogen in the Ni bielectrodes of identical thickness is observed in the following order: (1) nanocrystalline, (2) fine grained, and (3) single crystal structures. In addition,

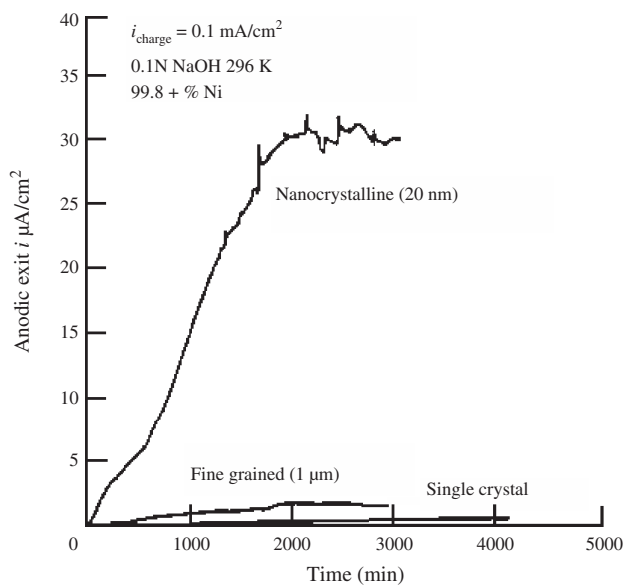


**Figure 15.** Hydrogen permeation transient showing anodic exit current density (flux) versus time for nanocrystalline, fine-grained, and single-crystal Ni foils (0.14-mm thickness). Reprinted with permission from [158], D. M. Doyle et al., *Acta Met. Mater.* 43, 3027 (1995). © 1995, Elsevier Science.

the apparent concentration of hydrogen in the 20-nm grain size sample is found to be about 60 times greater than that of the single crystal structure with regard to the permeation transients shown in Figure 15. The increased hydrogen diffusivity and capacity are attributed to the high intercrystalline content, which provides: (1) a high density of short circuit diffusion paths, and (2) large free volumes to which increased segregation of hydrogen can occur.

Permeation experiments were also conducted in a double chamber, ultra-high vacuum system separated by a test nickel specimen [160]. Hydrogen permeabilities and diffusivities through microcrystalline and nanocrystalline Ni were measured in the temperature range of 303 K to 473 K. Steady-state permeability measurements indicate that nanocrystalline Ni (average grain size of 78 nm) displays enhanced permeability below 323 K (*e.g.*, a factor of six at 303 K), as compared to the microcrystalline Ni (average grain size of 3  $\mu\text{m}$ ). Also, diffusivity measurements in combination with hydrogen trapping site density measurements suggest that there are more intercrystalline hydrogen trapping sites in the nanocrystalline Ni.

#### 4. GRAIN BOUNDARY ENGINEERED NANOSTRUCTURES

Grain boundary engineering involves the deliberate control of both the (1) density and (2) types of grain boundaries in a polycrystalline aggregate in a effort to improve the overall mechanical, physical, and chemical properties of materials. In recent years, grain boundary engineering has emerged as an effective method which can alleviate intergranular degradation concerns in many polycrystalline metals, alloys, and metal matrix composites [161, 162]. As discussed in Section 3, the primary grain boundary engineering concept as applied to nanocrystals was the consideration of the grain and triple junction volume fraction enhancement by grain size reduction. In addition to these geometric considerations, solute segregation to grain boundaries must also be considered a major cause of cracking and corrosion susceptibility in many materials. Despite attempts at “cleaner” melting, casting, and fabrication processes, even small residual impurity contents (*i.e.*, ppm range) can represent large grain boundary concentrations owing to large enrichment factors [36]. Structurally ordered “special” low  $\Sigma$  boundaries are less prone to solute segregation and their increased population in materials can provide significant resistance to solute segregation. However, even more substantive improvements may be attainable by using nanocrystalline materials. As was discussed in Section 2 and depicted in Figure 2, nano processing may be applied to allow for greater tolerance of prevalent impurity levels [33]. In addition, the grain boundaries in these ultra-fine grained materials likely represent the “cleanest” grain boundaries ever produced, thus providing large potential for significantly enhanced intergranular degradation resistance. This subject is discussed in more detail in [163].

The structure-property relationships presented in Section 3 were mainly for nanostructures with little consideration of the second concept of grain boundary engineering—the types or structures of grain boundaries,

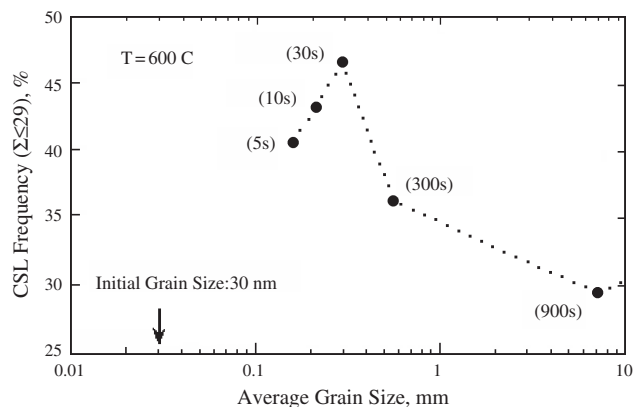


**Figure 16.** CSL frequency as a function of average grain size for Ni-15% Fe. Values in parentheses indicate annealing times. Reprinted with permission from [165], G. Palumbo and K. T. Aust, in “Grain Growth in Polycrystalline Materials III,” p. 311, 1998. © 1998, The Minerals, Metal, and Materials Society.

that is, the grain boundary character distribution. For conventional polycrystalline materials, the optimization of boundary character distribution to achieve a high population of low  $\Sigma$  CSL boundaries has recently emerged as a technically viable and cost-effective means of achieving significant performance improvements (*e.g.*, enhanced ductility, creep resistance, fracture resistance, corrosion resistance) in practical engineering materials [164]. For polycrystalline materials, it has been shown that mobility differences between low  $\Sigma$  and general grain boundaries during grain growth can be used to optimize conventional metallurgical thermomechanical processes in order to achieve significant increases in the population of low  $\Sigma$  CSL boundaries [165]. In order to assess the possibility to achieve high frequencies of special boundaries in nanocrystalline materials by annealing, a series of experiments have been conducted on nanocrystalline Ni-15 wt % Fe having an initial average grain size of 30 nm. Specimens were annealed at 873 K for annealing times in the range of 5 s to 900 s and subsequently analyzed by electron backscatter diffraction [165]. Initial results from this analysis as shown in Figure 16 are encouraging. The low  $\Sigma$  CSL population is found to increase with increasing grain size in the range of 150 nm to 300 nm and then subsequently decrease with increasing grain size in the range 300 nm to 7  $\mu\text{m}$ . These measurements must be extended to grain sizes below 100 nm and with other nanocrystalline materials to evaluate the effect of optimized grain boundary character distribution in nanocrystals on the materials performance. Post-deposition annealing of nanostructured electrodeposits has been proposed [162] as a means of optimizing grain boundary character distributions, which could result in further property improvements of these materials.

#### 5. SUMMARY

Experimental results are discussed concerning the influence of primary intercrystalline defects, that is, grain boundaries and triple junctions, on the properties of nanocrystalline materials. The properties considered are largely based on nanostructured materials relatively free of secondary



defects introduced during synthesis, such as porosity, residual amorphous regions, lattice dislocations, and extrinsic grain boundary dislocations. These property studies include thermal stability and grain growth, mechanical, physical, corrosion, hydrogen diffusion, and activity.

For nanocrystalline materials having grain sizes above about 10–20 nm, grain boundaries play a dominant role, for example, increased strength and electrical resistivity, resistance to intergranular degradation, enhanced hydrogen diffusivity, and enhanced electrocatalytic behavior. At smaller grain sizes, triple junctions appear to exert a stronger influence, as in softening effects observed in measurements of hardness, yield strength, and Young's modulus.

In addition to some high-resolution electron microscopy and diffraction studies, property measurements such as grain boundary energy and diffusivity, grain growth, magnetic behavior, and specific grain boundary resistivity support the view of ordered grain boundary structures in nanocrystalline materials, similar to those in polycrystalline materials. The presence of low angle ( $\Sigma 1$ ) and twin ( $\Sigma 3$ ) boundaries has been observed in materials having <100 nm grain size and  $\Sigma \leq 29$  boundaries found for larger grain sizes. Further enhancement of the properties of nanostructured materials is, therefore, possible by optimization of the grain boundary character distribution.

## GLOSSARY

**Abnormal grain growth** Movement of grain boundaries by diffusion in which a bimodal grain size distribution usually emerges as some grains became very large at the expense of small grains.

**Activation energy** The energy required to cause a specific reaction to occur. In diffusion-related processes, the activation energy is related to the energy required to move an atom from one lattice site to another.

**Amorphous materials** Materials that have no regular repetitive arrangement of atoms in a solid which extends over a very large distance.

**Creep rate** The rate at which a material deforms when a stress is applied usually at a high temperature.

**Grain boundaries** Regions between grains or crystals of a polycrystalline or nanocrystalline material. The grain has a different orientation on either side of the grain boundary.

**Hall–petch behavior** A specific relationship between yield strength or hardness and grain size in a metallic material.

**Impurity segregation** Increased concentration of elements at structural defects in the material, such as at grain boundaries and triple junctions. The impurities often originate from processing or raw materials and usually have a deleterious effect on the properties or processing of a material.

**Interfacial effects** Influence of grain boundaries and triple junctions (i.e. intersection of three or more grain boundaries) on properties such as mechanical, physical, and chemical.

**Intergranular corrosion** Corrosion at grain boundaries due to local galvanic cells produced by grain boundary energy, segregation, or precipitation.

**Nanostructure** Structure of a material at a nano-scale, i.e. length-scale 1–100 nm.

**Saturation magnetization** All the magnetic moments have been aligned by the magnetic field producing the maximum magnetization.

**Twin boundary** A surface defect across which there is a mirror image misorientation of the crystal structure.

**Young's modulus** The slope of the linear part of a stress-strain curve in the elastic region.

## ACKNOWLEDGMENTS

Financial support from the Natural Sciences and Engineering Research Council of Canada, and Integran Technologies is gratefully acknowledged.

## REFERENCES

1. H. Gleiter, "Second Riso International Symposium Metals and Materials Science" (N. Hansen, Ed.), p. 15. Riso Nat. Laboratroy, Denmark, 1981.
2. G. Palumbo, S. J. Thorpe, and K. T. Aust, *Scripta Met. Mater.* 24, 1347 (1990).
3. N. Wang, G. Palumbo, Z. Wang, U. Erb, and K. T. Aust, *Scripta Met. Mater.* 28, 253 (1993).
4. K. T. Aust, U. Erb, and G. Palumbo, "Mechanical Properties and Deformation Behaviour of Materials having Ultra-Fine Microstructures" (M. Nastasi, D. M. Parkin, and H. Gleiter, Eds.), p. 107. Kluwer Academic Publishers, The Netherlands, 1993.
5. H. Gleiter, *Prog. Mater. Sci.* 33, 224 (1989).
6. R. Birringer, *Mater. Sci. Eng.* A117, 33 (1989).
7. W. Wunderlich, Y. Ishida, and R. Maurer, *Scripta Metall.* 24, 403 (1990).
8. S. R. Phillpot, D. Wolf, and H. Gleiter, *Scripta Met. Mater.* 33, 1245 (1995).
9. P. Keblinski, S. R. Phillpot, D. Wolf, and H. Gleiter, *Acta Mater.* 45, 987 (1997).
10. P. Keblinski, D. Wolf, S. R. Phillpot, and H. Gleiter, *Scripta Mater.* 41, 631 (1999).
11. G. J. Thomas, R. W. Siegel, and J. A. Eastman, *Scripta Metall.* 24, 201 (1990).
12. J. A. Eastman, M. R. Fitzsimmons, and J. Thompson, *Phil. Mag.* B66, 667 (1992).
13. J. A. Eastman, *Mat. Sci. Forum* 126–128, 813 (1993).
14. T. R. Haasz, K. T. Aust, G. Palumbo, A. M. El-Sherik, and U. Erb, *Scripta Met. Mater.* 32, 423 (1995).
15. S. C. Mehta, D. A. Smith, and U. Erb, *Mat. Sci. Eng.* A204, 227 (1995).
16. D. McLean, "Grain Boundaries in Metals," p. 49. Clarendon Press, Oxford, 1957.
17. G. Nishimura, M.A.Sc. thesis, University of Toronto, Canada, 1973.
18. P. Fortier, G. Palumbo, G. D. Bruce, W. A. Miller, and K. T. Aust, *Scripta Met.* 25, 177 (1991).
19. W. Bollmann, *Phil. Mag. A* 49, 73 (1984).
20. W. Bollmann, *Phil. Mag. A* 57, 637 (1988).
21. W. Bollmann, *Mat. Sci. Eng. A* 113, 129 (1989).
22. L. M. Clarebrough and C. T. Forwood, *Phil. Mag. A* 55, 217 (1987).
23. G. Palumbo and K. T. Aust, *Mat. Sci. Eng. A* 205, 254 (1996).
24. G. Palumbo and K. T. Aust, *Mat. Sci. Eng. A* 113, 139 (1989).
25. V. Randle, *Acta Met. Mater.* 43, 174 (1995).
26. E. G. Doni and G. L. Bleris, *Phys. Stat. Sol. A* 110, 383 (1988).
27. G. Palumbo and K. T. Aust, *Scripta Met. Mater.* 24, 1771 (1990).
28. P. H. Pumphrey, *Scripta Met.* 6, 107 (1972).

29. V. Randle and B. Ralph, *J. Mater. Sci.* 23, 934 (1988).
30. J. W. Cahn and G. Kalonji, *J. Phys. Chem. Sol.* 55, 1017 (1994).
31. E. G. Doni, G. Palumbo, and K. T. Aust, *Scripta Met.* 24, 2325 (1990).
32. P. Fortier, K. T. Aust, and W. A. Miller, *Acta Met. Mater.* 43, 339 (1995).
33. G. Palumbo and U. Erb, *MRS Bulletin* 24, 27 (1999).
34. U. Klement, U. Erb, A. M. El-Sherik, and K. T. Aust, *Mat. Sci. Eng. A* 203, 177 (1995).
35. U. Erb, A. M. El-Sherik, G. Palumbo, and K. T. Aust, *Nanostruct. Mater.* 2, 383 (1993).
36. G. Palumbo and K. T. Aust, "Materials Interfaces" (D. Wolf and S. Yip, Eds.), p. 190. Chapman and Hall, London, England, 1992.
37. H. Gleiter, *Acta Mater.* 48, 1 (2000).
38. G. Hampel, A. Pundt, and J. Hesse, *J. Phys. Cond. Mater.* 4, 3195 (1992).
39. M. A. Al-Khafaji, I. Ahmad, W. M. Rainforth, H. A. Davies, and R. A. Buckley, *Phil. Mag. A* 81, 11 (2001).
40. A. Revesz, J. Lendvai, and I. Bakonyi, *Nanostructured Mater.* 11, 1351 (1999).
41. R. Z. Valiev, R. K. Islamgaliev, and I. V. Aleksandrov, *Prog. Mater. Sci.* 45, 102 (2000).
42. U. Erb, G. Palumbo, R. Zugic, and K. T. Aust, in "Processing and Properties of Nanocrystalline Materials" (C. Suryanarayana, J. Singh, and F. H. Froes, Eds.), p. 93. The Minerals, Metals, and Materials Society, Warrendale, PA, 1996.
43. U. Erb, K. T. Aust, G. Palumbo, J. McCrea, and F. Gonzalez, in "Processing and Fabrication of Advanced Materials IX" (T. S. Srivatsan, R. A. Varin, and K. A. Khor, Eds.), p. 253. ASM, Materials Park, OH, 2001.
44. H. Hahn, J. Logos, and R. S. Averbach, *J. Mater. Res.* 5, 609 (1990).
45. Y. R. Kolobov, G. P. Grabovestkaya, M. B. Ivanov, A. P. Zhilyaev, and R. Z. Valiev, *Scripta Mater.* 44, 873 (2001).
46. G. Hibbard, U. Erb, K. T. Aust, and G. Palumbo, *Mat. Res. Soc. Symp. Proc.* 580, 183 (2000).
47. G. Hibbard, K. T. Aust, G. Palumbo, and U. Erb, *Scripta Mater.* 44, 513 (2001).
48. N. Wang, Z. Wang, K. T. Aust, and U. Erb, *Acta Mater.* 45, 1655 (1997).
49. T. Turi, Ph.D. thesis, Queen's University, Kingston, Ontario, Canada, 1997.
50. H. Natter, M. Schmelzer, and R. Hempelmann, *J. Mater. Res.* 15, 1186 (1998).
51. T. H. Hentschel, D. Isheim, R. Kirkchheim, F. Muller, and H. Kreye, *Acta Mater.* 48, 933 (2000).
52. J. L. McCrea, Ph.D. thesis, University of Toronto, Toronto, Ontario, Canada, 2001.
53. L. E. Murr, "Interfacial Phenomenon in Metals and Alloys." Addison-Wesley Publishing, London, 1975.
54. J. Eckert, J. C. Holzer, C. E. Krill, III, and W. L. Johnson, *J. Mater. Res.* 7, 1751 (1992).
55. L. C. Chen and F. Spaepen, *J. Appl. Phys.* 69, 679 (1991).
56. I. Kaur, W. Gust, and L. Kozma (Eds.), "Handbook of Grain and Interphase Boundary Diffusion Data." Ziegler Press, Stuttgart, 1989.
57. M. C. Iordache, S. H. Whang, Z. Jiao, and Z. M. Wang, *Nanostructured Mater.* 11, 1343 (1999).
58. K. J. Bryden and J. Y. Ying, *Nanostructured Mater.* 9, 485 (1997).
59. K. J. Bryden and J. Y. Ying, *J. Electrochem. Soc.* 145, 3339 (1998).
60. A. M. El-Sherik, K. Boylan, U. Erb, G. Palumbo, and K. T. Aust, *Mat. Res. Soc. Symp. Proc.* 238, 727 (1992).
61. A. Cziaraki, Zs. Tonkovics, I. Gerocs, B. Fogarassy, I. Groma, E. Toth-Kadar, T. Tarnoczi, and I. Bakonyi, *Mat. Sci. Eng. A* 179-180, 531 (1994).
62. K. Boylan, D. Ostrander, U. Erb, G. Palumbo, and K. T. Aust, *Scripta Met. Mater.* 25, 2711 (1991).
63. D. Osmola, P. Nolan, U. Erb, G. Palumbo, and K. T. Aust, *Phys. Stat. Sol. (A)* (131) 569 (1992).
64. G. Hibbard, U. Erb, K. T. Aust, U. Klement, and G. Palumbo, *Mat. Sci. Forum* 386-388, 387 (2002).
65. F. Czerwinski, H. Li, M. Megret, J. A. Szpunar, D. G. Clark, and U. Erb, *Scripta Mater.* 37, 1967 (1997).
66. C. Xiao, R. A. Mirshams, S. H. Whang, and W. M. Yin, *Mat. Sci. Eng. A301*, 35 (2001).
67. P. J. Warren, M. Thuvander, M. Abraham, H. M. Lane, A. Cerezo, and G. D. W. Smith, *Mat. Sci. Forum* 343-346, 701 (2000).
68. M. Abraham, M. Thuvander, H. M. Lane, A. Cerezo, and G. D. W. Smith, *Mat. Res. Soc. Symp. Proc.* 581, 517 (2000).
69. M. Thuvander, M. Abraham, A. Cerezo, and G. D. W. Smith, *Mater. Sci. Tech.* 17, 961 (2001).
70. G. Hibbard, Ph.D. thesis, University of Toronto, Toronto, Ontario, Canada, 2002.
71. A. M. El-Sherik and U. Erb, *J. Mat. Sci.* 30, 5743 (1995).
72. S. G. Srinivasan, J. W. Cahn, H. Jonsson, and G. Kalonji, *Acta Mater.* 47, 2821 (1999).
73. G. Gottstein, A. H. King, and L. S. Shvindlerman, *Acta Mater.* 48, 397 (2000).
74. Y. Estrin, G. Gottstein, and L. S. Shvindlermann, *Scripta Mater.* 41, 385 (1999).
75. G. Hibbard, J. L. McCrea, G. Palumbo, K. T. Aust, and U. Erb, *Scripta Mater.* 47, 83 (2002).
76. G. Palumbo, U. Erb, and K. T. Aust, *Scripta Met. Mater.* 24, 2347 (1990).
77. A. H. Chokshi, A. H. Rosen, J. Karch, and H. Gleiter, *Scripta Met. Mater.* 23, 1679 (1989).
78. E. O. Hall, *Proc. Roy. Soc. London* B64, 474 (1951).
79. N. J. Petch, *J. Iron Steel Inst.* 174, 25 (1953).
80. K. Lu, W. D. Wei, and J. T. Wang, *Scripta Met. Mater.* 24, 2319 (1990).
81. T. Christman and M. Jain, *Scripta Met. Mater.* 25, 767 (1991).
82. G. W. Neiman, J. R. Weertman, and R. W. Siegel, *Nanostr. Mat.* 1, 185 (1992).
83. P. G. Sanders, C. J. Youngdahl, and J. R. Weertman, *Mater. Sci. Eng. A234-36*, 77 (1997).
84. A. M. El-Sherik, U. Erb, G. Palumbo, and K. T. Aust, *Scripta Met. Mater.* 27, 1185 (1992).
85. U. Erb, *Nanostr. Mater.* 6, 533 (1995).
86. G. W. Nieman, J. R. Weertman, and R. W. Siegel, *Scripta Met. Mater.* 24, 145 (1990).
87. R. W. Armstrong, Y. T. Chow, R. M. Fisher, and N. Louat, *Phil. Mag.* 14, 943 (1966).
88. C. S. Pande, R. A. Masumura, and R. W. Armstrong, *Nanostr. Mater.* 2, 323 (1993).
89. T. R. Smith, R. W. Armstrong, P. M. Hazzledine, R. A. Masumura, and C. S. Pande, *Mat. Res. Soc. Symp. Proc.* 362, 31 (1995).
90. R. D. Scattergood and C. C. Koch, *Scripta Met. Mater.* 27, 1195 (1992).
91. N. Wang, Z. Wang, K. T. Aust, and U. Erb, *Acta Met. Mater.* 43, 519 (1995).
92. J. Schulz, F. DiTella, and K. Jacobson, *Nature* 391, 561 (1988).
93. H. van Swiggenhoven, M. Spaczer, and A. Caro, *Acta Mater.* 47, 3117 (1999).
94. J. E. Carsley, J. Ning, W. W. Milligan, S. A. Hackney, and E. C. Aifantis, *Nanostr. Mater.* 5, 441 (1995).
95. G. D. Hughes, S. D. Smith, C. S. Pande, H. R. Johnson, and R. W. Armstrong, *Scripta Met.* 20, 93 (1986).
96. N. Wang, Z. Wang, K. T. Aust, and U. Erb, *Mat. Sci. Eng. A* 237, 150 (1997).
97. V. B. Rabukhin, *Phys. Met. Metalloved* 43, 3027 (1995).
98. E. M. Lehigh, G. Palumbo, K. T. Aust, U. Erb, and P. Lin, *Scripta Met.* 39, 341 (1998).
99. G. W. Nieman, J. R. Weertman, and R. W. Siegel, *J. Mat. Res.* 6, 1012 (1991).



100. L. Wong, D. Ostrander, U. Erb, G. Palumbo, and K. T. Aust, in "Nanophase and Nanocrystalline Structures" (R. D. Shull and J. M. Sanchez, Eds.), p. 85. Met. Soc. AIME, Warrendale, PA, 1994.
101. V. Krstic, U. Erb, and G. Palumbo, *Scripta Met. Mater.* 29, 1501 (1993).
102. R. Zugic, B. Szpunar, V. Krstic, and U. Erb, *Phil. Mag. A* 75, 1041 (1997).
103. P. G. Sanders, J. A. Eastman, and J. R. Weertman, *Acta Mat.* 45, 4019 (1997).
104. Y. Zhou, U. Erb, K. T. Aust, and G. Palumbo, *Scripta Mater.* 48, 825 (2003).
105. G. McMahon and U. Erb, *Microstr. Sci.* 17, 447 (1989).
106. G. McMahon and U. Erb, *J. Mat. Sci. Lett.* 8, 865 (1989).
107. G. Palumbo, K. T. Aust, and U. Erb, *Mat. Sci. Forum* 225–227, 281 (1996).
108. W. Ging, H. Li, Z. Zhao, and J. Chen, *J. Appl. Phys.* 69, 5119 (1991).
109. S. Gangopadhyay, G. C. Hadjipanayis, B. Dale, C. M. Sorensen, and K. J. Klabunde, *Nanostr. Mat.* 1, 77 (1992).
110. H. E. Schaefer, H. Kisker, H. Kronmüller, and R. Würschum, *Nanostr. Mat.* 9, 455 (1997).
111. Y. D. Yao, Y. Y. Chen, C. M. Hsu, H. M. Lin, C. Y. Tung, M. F. Tai, D. H. Wang, K. T. Wu, and C. T. Suo, *Nanostr. Mat.* 6, 933 (1995).
112. C. E. Krill, F. Merzoug, W. Krauss, and R. Birringer, *Nanostr. Mat.* 9, 455 (1997).
113. M. J. Aus, B. Szpunar, A. M. El-Sherik, U. Erb, G. Palumbo, and K. T. Aust, *Scripta Met. Mater.* 27, 1639 (1992).
114. L. Daroczi, D. L. Beke, G. Posgay, G. F. Zhou, and H. Bakker, *Nanostr. Mat.* 2, 512 (1993).
115. L. Daroczi, K. L. Beke, G. Posgay, and M. Kis-Varga, *Nanostr. Mat.* 6, 981 (1995).
116. I. Bakonyi, E. Toth-Kadar, J. Toth, T. Tarnoczi, and Cziraki, in "Processing and Properties of Nanocrystalline Materials" (C. Suryanarayana, J. Singh, and F. H. Froes, Eds.), p. 465. The Minerals, Metals, and Materials Society, Warrendale, PA, 1996.
117. J. Weissmüller, R. D. McMichael, J. Barker, H. J. Brown, U. Erb, and R. D. Shull, *Mat. Res. Soc. Symp. Proc.* 457, 231 (1997).
118. H. Kisker, T. Gessmann, R. Würschum, H. Kronmüller, and H. E. Schaefer, *Nanostr. Mat.* 6, 925 (1995).
119. B. Szpunar, U. Erb, K. T. Aust, G. Palumbo, and L. Lewis, *Mat. Res. Soc. Symp. Proc.* 318, 477 (1994).
120. B. Szpunar, R. Zugic, U. Erb, and L. Lewis, *Can. Met. Quart.* 349, 281 (1995).
121. B. Szpunar, U. Erb, G. Palumbo, K. T. Aust, and L. Lewis, *Phys. Rev. B* 53, 5547 (1996).
122. M. J. Aus, C. Cheung, B. Szpunar, U. Erb, and J. A. Szpunar, *Mater. Sci. Lett.* 17, 1949 (1998).
123. B. Szpunar, M. J. Aus, C. Cheung, U. Erb, G. Palumbo, and J. A. Szpunar, *J. Magn. Magn. Mat.* 187, 325 (1998).
124. H. Tamimoto, L. Pasquini, R. Prümmer, H. Krommüller, and H. E. Schaefer, *Scripta Mater.* 42, 961 (2000).
125. A. Seeger and G. Schottky, *Acta Met.* 7, 495 (1959).
126. P. V. Andrews, M. B. West, and C. R. Robenson, *Phil. Mag.* 19, 887 (1969).
127. M. B. Kasen, *Phil. Mag.* 21, 599 (1970).
128. A. Gangulee, *J. Appl. Phys.* 43, 867 (1972).
129. I. Nakamichi, *J. Sci. Horoshima Univ.* 54A, 49 (1990).
130. M. J. Aus, B. Szpunar, U. Erb, A. M. El-Sherik, G. Palumbo, and K. T. Aust, *J. Appl. Phys.* 75, 3632 (1994).
131. M. J. Aus, B. Szpunar, U. Erb, G. Palumbo, and K. T. Aust, *Mat. Res. Soc. Symp. Proc.* 318, 39 (1994).
132. I. Bakonyi, E. Toth-Kadar, T. Tarnoczi, I. K. Varga, A. Cziraki, I. Gerocs, and B. Fogarassy, *Nanostr. Mat.* 3, 155 (1993).
133. J. L. McCrea, K. T. Aust, G. Palumbo, and U. Erb, *Mat. Res. Soc. Symp. Proc.* 581, 461 (2000).
134. R. B. Diegle and J. E. Slater, *Corrosion* 32, 155 (1976).
135. K. Hashimoto, K. Osada, T. Masumoto, and S. Shimodaira, *Corrosion Sci.* 16, 71 (1976).
136. M. Naka, K. Hashimoto, and T. Masumoto, *Corrosion* 36, 679 (1980).
137. J. C. Turn and R. M. Latanison, *Corrosion* 39, 271 (1983).
138. S. J. Thorpe, B. Ramaswami, and K. T. Aust, *J. Electrochem. Soc.* 135, 2162 (1988).
139. P. Bragagnola, Y. Waseda, G. Palumbo, and K. T. Aust, *MRS Int. Mtg. Adv. Mat.* 4, 469 (1989).
140. R. Rofagha, R. Langer, A. M. El-Sherik, U. Erb, G. Palumbo, and K. T. Aust, *Scripta Met. Mater.* 25, 2867 (1991).
141. R. Rofagha, R. Langer, A. M. El-Sherik, U. Erb, G. Palumbo, and K. T. Aust, *Mat. Res. Soc. Symp. Proc.* 238, 751 (1992).
142. R. Rofagha, U. Erb, D. Ostrander, G. Palumbo, and K. T. Aust, *Nanostr. Mat.* 2, 1 (1993).
143. S. Wang, R. Rofagha, P. R. Roberge, and U. Erb, *Electrochem. Soc. Proc.* 95–98, 224 (1995).
144. F. Gonzalez, A. M. Brennenstuhl, G. Palumbo, U. Erb, and P. C. Lichtenberger, *Mat. Sci. Forum* 225–227, 831 (1996).
145. G. Palumbo, F. Gonzalez, A. M. Brennenstuhl, U. Erb, W. Shmayda, and P. C. Lichtenberger, *Nanostr. Mat.* 9, 737 (1997).
146. R. Rofagha, S. J. Splinter, U. Erb, and S. N. McIntyre, *Nanostr. Mat.* 4, 69 (1994).
147. G. Palumbo and K. T. Aust, *Acta Met. Mat.* 38, 2343 (1990).
148. R. B. Inturi and Z. Szklarska-Smialowska, *Corrosion* 48, 398 (1992).
149. S. H. Kim, K. T. Aust, U. Erb, G. Ogundele, and F. Gonzalez, *AESF Sur/Fin Proc.* 225 (2002), accepted.
150. S. H. Kim, K. T. Aust, U. Erb, F. Gonzalez, and G. Palumbo, *Scripta Mater.* 48, 1379 (2003).
151. R. Kirchheim, T. Mütchele, W. Kreninger, H. Gleiter, R. Birringer, and T. D. Koblé, *Mat. Sci. Eng.* 99, 457 (1988).
152. R. Würschum, V. Brossmann, and H. E. Schaefer, in "Nanostructured Materials" (C. C. Koch, Ed.), p. 267. Noyes Publications, Norwich, NY, 2002.
153. R. Würschum, W. Greiner, R. Z. Valiev, M. Rapp, W. Sigle, O. Schneeweiss, and H. E. Schaefer, *Scripta Met. Mater.* 25, 2451 (1991).
154. R. Würschum and H. E. Schaefer, in "Nanomaterials; Synthesis Properties and Applications" (A. S. Edelsteinand and R. C. Cammarata, Eds.), p. 277. Inst. Phys. Bristol, UK, 1996.
155. W. Losch and P. M. Jardim, *Scripta Mater.* 38, 1857 (1998).
156. G. Palumbo, D. M. Doyle, A. M. El-Sherik, U. Erb, and K. T. Aust, *Scripta Met. Mater.* 25, 679 (1991).
157. V. B. Rabukhin and A. S. Panikarski, *Phys. Chem. Mech. Surf.* 5, 1304 (1990).
158. D. M. Doyle, G. Palumbo, K. T. Aust, A. M. El-Sherik, and U. Erb, *Acta Met. Mater.* 43, 3027 (1995).
159. S. Wang, Ph.D. thesis, Queen's University, Kingston, Ontario, Canada, 1997.
160. A. R. A. Haasz, K. T. Aust, W. T. Shmayda, and G. Palumbo, *Fusion Techn.* 28, 1169 (1995).
161. U. Erb and G. Palumbo (Eds.), "Grain Boundary Engineering," Canadian Institute of Metallurgy, Mining, and Petroleum, Montreal, Quebec, Canada, 1993.
162. U. Erb, G. Palumbo, and K. T. Aust, in "Nanostructured Films and Coatings" (G. M. Chow, I. A. O'Vidko, and T. Tsakalakos, Eds.), Kluwer, Dordrecht, The Netherlands, 2000.
163. U. Erb, P. Lin, S. Kim, K. T. Aust, F. Gonzalez, and G. Palumbo, in "Processing and Fabrication of Advanced Materials X" (T. S. Srivatsan and R. A. Varin, Eds.), p. 3. ASM International, Materials Park, OH, 2002.
164. G. Palumbo, E. M. Lehockey, and P. Lin, *JOM* 50, 40 (1998).
165. G. Palumbo and K. T. Aust, in "Grain Growth in Polycrystalline Materials III" (H. Weiland, B. L. Adams, and A. D. Rollett, Eds.), p. 311. The Minerals, Metals, and Materials Society, Warrendale, OH, 1998.

# Ion Implanted Nanostructures

Karen J. Kirkby, Roger P. Webb

*University of Surrey, Guildford, Surrey, United Kingdom*

## CONTENTS

1. Introduction
  2. Ion Implantation in Semiconductors
  3. Other Applications of Ion Beam Synthesis
  4. Conclusions
- Glossary  
References

## 1. INTRODUCTION

Ion implantation can trace its roots back to the Manhattan project of the 1940's and the development of the world's first atomic bombs. At the heart of the ion implanter is the mass analyzer, which was developed during the Manhattan project as a means of separating the different uranium isotopes.

Ion implantation involves the formation of a plasma using either a gaseous, solid, or occasionally liquid source containing the isotope which is to be implanted. Ions (usually positively charged) are then extracted from the plasma and accelerated to the desired energy (from several hundred eV to MeVs). The mass analyzer then selects the desired isotope, which is then implanted into a target. The beam is either electrostatically scanned over a single target, or a number of targets are mechanically scanned in front of the ion beam. Ion implantation is used in a number of applications, namely,

- semiconductor doping,
- synthesis of compound layers,
- materials modification,
- understanding the effects of radiation on living tissue.

This chapter deals primarily with nanostructures formed in semiconductor and semiconductor-related structures using ion implantation. It then proceeds to examine emerging fields of research where materials as diverse as superconductors and living cells are beginning to be probed and modified using ion implantation techniques.

## 2. ION IMPLANTATION IN SEMICONDUCTORS

### 2.1. Introduction

Different regions of semiconductor devices conduct via electrons or positive holes, with the dominant conducting species being termed the majority carrier and the lesser the minority carrier. In order to make a region of a semiconductor electron or hole rich, impurity atoms have to be introduced into the semiconductor lattice. These impurities can either donate electrons (e.g., arsenic (As), phosphorous (P), or antimony (Sb) in silicon (Si)) or accept electrons and thereby create positive holes (e.g., boron (B) in silicon (Si)). These impurity atoms are called dopants.

At least two ion implantation steps are used in the manufacture of over 99% of silicon chips and many semiconductor fabrication processes use more implantation steps. Ion implantation is used because of the controllability and precision it affords in placing the desired dopant at the required location within the semiconductor device.

The depth at which an implanted dopant comes to rest beneath the surface of the semiconductor is dependent on:

- mass of the dopant ion,
- energy of dopant ion,
- mass of the target atoms,
- implantation angle,
- orientation of the target,
- implantation temperature.

The processes responsible for slowing down the incoming dopant atom within the target are termed electronic and nuclear stopping.

Electronic stopping occurs via the excitation of the target electrons by the incoming dopant atom. It is an inelastic process and can be likened to the viscous drag experienced by a ball bearing when dropped into a jar of syrup.

Nuclear stopping, as the name suggests, is the slowing down of the incoming atom through elastic "collisions" between the incoming dopant atom and the target nuclei. These collisions can be described by classical Newtonian mechanics and can be likened to the collisions experienced by snooker balls.

The peak in the nuclear stopping occurs when the energy of the ion in keV is approximately equal to the atomic mass of the ion, so for boron (B), this is  $\sim 11$  keV, for arsenic (As)  $\sim 75$  keV, and for phosphorous (P)  $\sim 31$  keV. Electronic stopping becomes the predominant mechanism at about twice this value, with the peak in electronic stopping occurring when the energy in MeV is approximately equal to the mass of the ion, that is,  $\sim 11$  MeV for boron,  $\sim 75$  MeV for arsenic (As), and  $\sim 31$  MeV for phosphorous (P). Obviously, where each atom comes to rest, is a statistical process with some atoms coming to rest close to the surface while others come to rest at depth [1] (Fig. 1).

During the nuclear stopping process, target atoms can be given sufficient energy (10–20 eV) to displace them from their lattice sites and they in turn can displace other target atoms. Thus, in the region where nuclear stopping predominates the track of the incoming dopant atom is surrounded by the tracks of recoiling target atoms—termed the collision cascade (Fig. 2). For heavy ions (e.g., As, Sb) in a target such as silicon, the collision cascade is dense and starts close to the surface (Figs. 2c and 2d). For lighter ions (e.g., B Fig. 2a and P Fig. 2b), the collision cascade contains far fewer recoils, occurs close to the end of range, and is fairly diffuse. The damage produced during implantation is in the form of vacancies and interstitials, which can form defect clusters, dislocation clusters, and even extended defects as the implant progresses. When adjacent collision cascades overlap, the local energy within the system can be sufficient

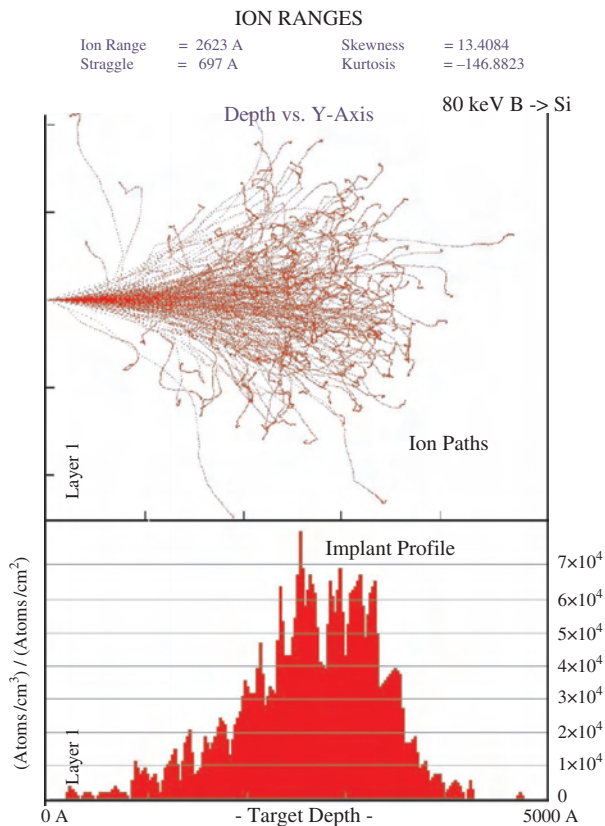


**Figure 1.** Simulation of 80 keV B implantation into silicon, showing individual ion paths and depth distribution of implanted B atoms.

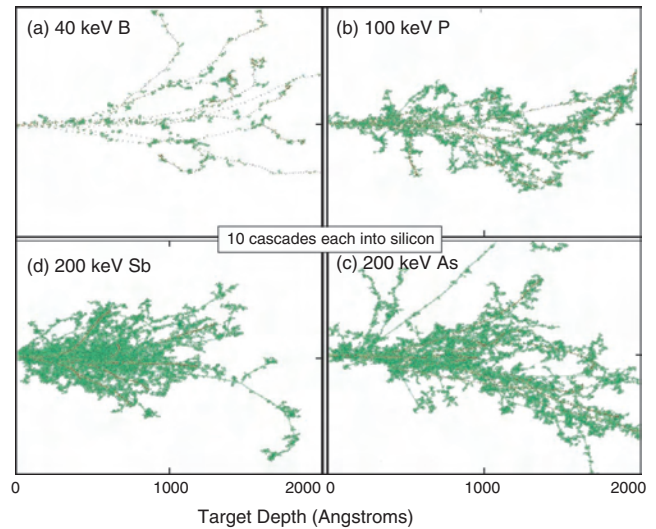


**Figure 2.** Simulated collision cascades from different elements implanted into silicon: (a) B; (b) P; (c) As; and (d) Sb.

to facilitate a local crystalline  $\rightarrow$  amorphous phase transformation and if the dose is increased still further, an amorphous layer can be produced.

Annealing subsequent to implantation is used to activate the implanted dopant atoms by placing them on substitutional lattice sites. Annealing is also used to remove, as far as is possible, the residual radiation damage resulting from implantation and to regrow regions that have been amorphized.

Doping, as mentioned previously, is used to modify the electrical properties of a semiconductor. However, by increasing the dose of implanted ions, it is possible to synthesize another compound within the target substrate. This often occurs at temperatures well below those required for conventional equilibrium growth. This phenomenon is thought to occur because some of the bonds within the target lattice have been broken by the incoming ion, and as the energetic reactants are intimately mixed the reaction can proceed immediately. Subsequent to implantation, the structure is normally annealed to remove as much of the implantation-induced damage as possible and to redistribute the implanted species. The process of ion beam synthesis (IBS) is shown schematically in Figure 3.

The size of the synthesized precipitates fabricated by IBS depends on:

- the implanted dose
- the implanted energy
- the number of nucleation sites available
- the implantation temperature
- annealing temperature and time

Before going on to look at the formation of ion-implanted nanostructures, it is pertinent to consider the mechanisms by which they nucleate and grow.

## 2.2. Precipitate Nucleation and Growth

The nucleation of ion beam synthesized phases depends on the implanted ion and the substrate material. The first step in the nucleation of the synthesized phase is

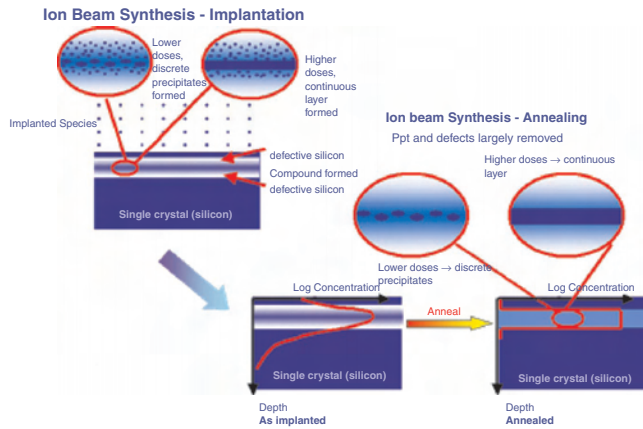


**Figure 3.** Schematic showing the process of ion beam synthesis.

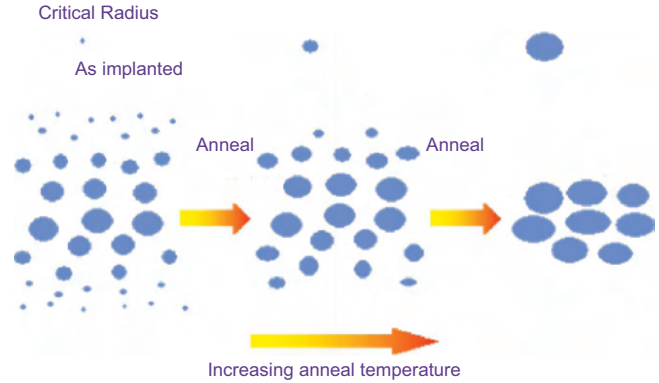
thought to be via the occupation of interstitial sites by the implanted atom [2]. Extended X-ray absorption fine structure (EXAFS) studies [3] on the early stages of  $\text{CoSi}_2$  synthesis indicates the presence of  $\text{CoSi}_3$  cores, which subsequently grow into  $\text{CoSi}_2$  precipitates with the eightfold coordination of the nuclei reflected in the  $\text{CaF}_2$  structure of the  $\text{CoSi}_2$  phase.

The growth of the precipitates during implantation and the subsequent annealing phase is governed by thermally induced precipitate coarsening (Oswald ripening), the local concentration of the implanted atoms, and diffusion. Consider a system in which the concentration of solute (implanted atoms) remains constant. Then at a given temperature,  $T$ , if the solute concentration exceeds the solid solubility limit of the matrix, discrete precipitates of either a pure solute phase or a solute-matrix compound will form. If  $T_E$  is defined as the equilibrium temperature at which all the solute is in solid solution with the matrix, then providing the solid solubility decreases with temperature, when  $T < T_E$  precipitates will form. The degree of solute supersaturation is proportional to  $T_E - T$ . If  $r_c$  is the critical radius of a precipitate at an annealing temperature  $T_A$ , then precipitates with radii equal or greater than  $r_c$  will be stable at  $T_A$ , whereas those with smaller radii will be unstable and will dissolve. As  $T_A$  increases,  $r_c$  increases and the solute atoms released by the dissolution of the smaller unstable precipitates migrate to larger stable precipitates. As an implant profile roughly corresponds to a gaussian, the largest precipitates are found at the peak and the smallest in the wings. Thus, during annealing, as the temperature rises, the larger precipitates at the peak appear to suck in solute atoms from the wings. This is shown schematically in Figure 4.

The following sections examine specific examples of ion-beam synthesized nanostructures for a number of applications.

### 2.3. Light Emission from Silicon

The development of silicon-based, integrated circuit technology has more or less followed Moore's law for the past three decades. Moore's law was developed by Gordon Moore, one of the cofounders of Intel in 1965, states that "the number of transistors that can be placed on the same area of a microprocessor doubles every eighteen months." As silicon chips have



As temperature increases the critical radius of a precipitate increases

**Figure 4.** Schematic showing how the critical radius of the ion beam synthesized precipitates increases with increasing anneal temperature.

become smaller and faster, the feature size has decreased such that device technology nodes are now measured in nm. In 2002, Intel demonstrated fully functional chips using 90-nm node technology with 330 million transistors incorporated onto a single chip. It is true to say that ion-implanted nanostructures are already part of our everyday life.

The point is now being reached, however, where the delay time in the devices and interconnects, means that further miniaturization and increases in packing density are posing severe technological problems and are not yielding the increases in circuit speed required for the next generation of integrated circuits. One route to further improvements would be to utilize light rather than electrons for on-chip data transfer. Significant research into silicon-based optoelectronics has, therefore, been undertaken over the past 10–15 years to see whether conventional silicon circuit components can be integrated with optical components on a single chip. This research interest is not surprising given the potential impact such a technology would have on the computer and communications industries—especially if it were compatible with ultra large scale integration (ULSI) processing and integrated with optical fibers. With respect to the latter, the 1.5  $\mu\text{m}$  wavelength is of particular interest, as this corresponds to the wavelength window preferred for optical communication systems. However, the indirect nature of the bandgap in silicon would at first sight appear to preclude this as a possibility. Thus, the search has been to find a method of achieving optical emitters, waveguides, and detectors in silicon. Several alternatives have been tried; at present, some of the most promising utilize ion-implanted nanostructures.

### 2.4. Ion Beam Synthesis in Silicon

Before going on to look at light-emitting, silicon nanostructures, it is important to look at the development of ion beam synthesis. During the 1980's, it had been shown [4, 5] that when high doses (typically  $1.8 \times 10^{18} \text{ O}^+ \text{ cm}^{-2}$ ) of energetic (typically 200 eV) oxygen ions were implanted into silicon at elevated temperatures ( $\sim 600^\circ\text{C}$ ), a buried dielectric layer some 3000  $\text{\AA}$  thick was formed beneath a single crystal silicon overlayer (2000  $\text{\AA}$  thick). These structures termed separation by implanted oxygen (SIMOX) [6]



could be processed like conventional silicon but had the additional advantages that devices fabricated on them were much more tolerant to ionizing radiation and much less prone to parasitic transistor action between adjacent devices (latch-up). Early device characteristics were, however, inferior to those in conventional silicon because of residual defects and SiO<sub>2</sub> precipitates in the silicon overlayer (Fig. 5). The breakthrough came in 1986 [7, 8] when higher annealing temperatures were used. Before this the maximum annealing temperature had been 1200 °C, but by increasing this annealing temperature to 1300 °C for 6 h or 1405 °C for 30 min, the SiO<sub>2</sub> precipitates and the defects in the silicon overlayer were almost entirely removed (Fig. 6). The evolution of the SIMOX structure with annealing temperature is a good illustration of thermally induced precipitate growth and dissolution. By 1300 °C, the buried oxide layer is the only stable precipitate and all of the implanted oxygen tends to segregate towards it. Device characteristics from SIMOX structures annealed at  $\geq 1300$  °C showed significant improvements over those annealed at lower temperatures and by the late 1980's commercial implanters [9] had been produced for the fabrication of SIMOX wafers. More recently, SIMOX and other silicon on insulator (SOI) substrates have been used to enable further reductions in the feature size of complementary metal oxide semiconductor (CMOS) devices, enabling higher speeds and lower power consumption to be realized.

The success of SIMOX technology encouraged research in other types of ion beam synthesis, particularly in silicon. In 1987, White et al. [10] at AT&T Bell Laboratories reported the successful fabrication of hetero-epitaxial CoSi<sub>2</sub> in silicon. The ion beam synthesized CoSi<sub>2</sub> was found to have a very low resistivity [11] (12  $\mu\Omega$  cm) and was seen as having applications in novel hot electron devices, vertical devices, and high-speed interconnects. Discrete wires [12], dots, and buried structures [13] have all been fabricated using IBS CoSi<sub>2</sub>. Other metallic silicides were also synthesized using ion beams. These included NiSi<sub>2</sub> [14], CrSi<sub>2</sub> [15], YSi<sub>2</sub> [16], ErSi [17, 18], HfSi<sub>2</sub> [19] and WSi<sub>2</sub> [20]. Apart from the conducting silicides, semiconducting materials such as SiC [21] were also investigated. In the early 1990's, interest turned to IBS of semiconducting  $\beta$ FeSi<sub>2</sub>.

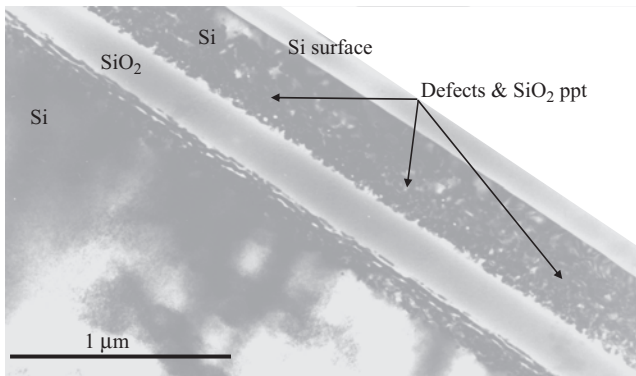


**Figure 5.** SIMOX structure implanted at  $1.8 \times 10^{18}$  O cm<sup>-2</sup> 200 keV and annealed at 1150 °C 2 h.

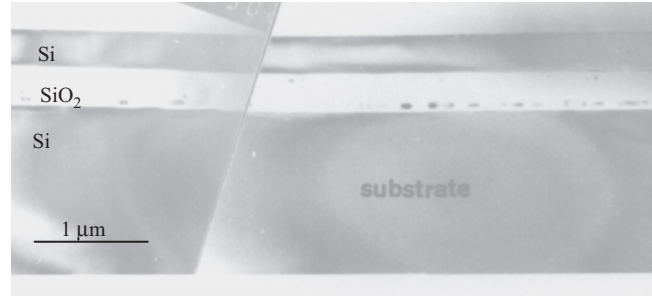


**Figure 6.** SIMOX structure implanted at  $1.7 \times 10^{18}$  O cm<sup>-2</sup> 200 keV and annealed at 1300 °C 2 h.

## 2.5. Light-Emitting $\beta$ FeSi<sub>2</sub>

$\beta$ FeSi<sub>2</sub> was of interest as it is a semiconductor with a bandgap of 0.87 eV. If it has a direct bandgap, then it has the potential to emit light at 1.5  $\mu$ m, which would make it compatible with optical fiber technology and facilitate the integration of electronic and optoelectronic components on a single chip. The potential impact of such a technology on the computer and communications industries would be enormous and thus significant research has been devoted to investigating the materials—optical and electronic properties of  $\beta$ FeSi<sub>2</sub>—over the past 10 years.

There has been some debate in the literature about the nature of the bandgap in  $\beta$ FeSi<sub>2</sub>. Band structure calculations [22, 23] predicted a direct energy gap of approximately 0.85 eV and an indirect energy gap at slightly lower energies. Some experimental observations [24–27] had concluded that the bandgap was indirect, while other experimental results [28–33] indicated a direct bandgap of 0.87–0.89 eV. The reason for this apparent discrepancy was attributed by some to the presence of defects in the surrounding silicon, in particular the D1 dislocation related line (0.81 eV) [34]. It was claimed the observed photoluminescence originated from these defects rather than from the  $\beta$ FeSi<sub>2</sub> itself. Obviously, if  $\beta$ FeSi<sub>2</sub> was to be seriously considered as a good candidate for optoelectronic devices, this particular controversy had to be resolved.

In 1997, Leong et al. [33] published results on an electroluminescent device operating at 1.5  $\mu$ m, in which a layer of  $\beta$ FeSi<sub>2</sub> precipitates had been fabricated by IBS above a silicon p-n junction. More recent theoretical studies by Miglio and Merregalli [35, 36] have concluded that the extreme sensitivity of the electronic bands to lattice deformation and the strong electron phonon coupling may account for the different experimental observations. They concluded that the growth conditions may be critical in determining whether the  $\beta$ FeSi<sub>2</sub> has a direct or an indirect bandgap.

To date, two methods [33, 37, 38] have been successfully employed to achieve room temperature electroluminescence (albeit rather weak) from silicon-based structures incorporating nano-precipitates of  $\beta$ FeSi<sub>2</sub>. These are:

### 2.5.1. Ion Beam Synthesis

Ion beam synthesis uses high dose Fe<sup>+</sup> implantation, at elevated temperatures, (500°–600 °C) into a silicon p-n junction, followed by a 900 °C, 18-h anneal in a nitrogen ambient [33, 37]. A schematic of this structure is shown in Figure 7a. The

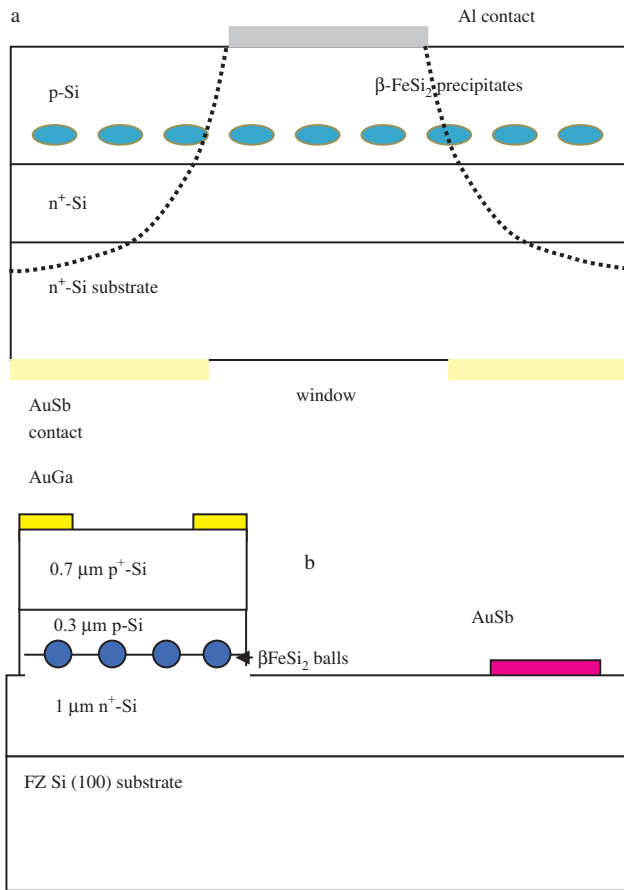


**Figure 7.** (a) Schematic of the  $\beta\text{FeSi}_2/\text{Si}$  light emitting device fabricated by IBS; (b) Schematic of the  $\beta\text{FeSi}_2/\text{Si}$  LED fabricated by RDE.

optimum results to date were found for samples implanted with a dose of  $1.5 \times 10^{16}$  Fe  $\text{cm}^{-2}$ . It has also been found that the best results are obtained when the  $\beta\text{FeSi}_2$  precipitates are buried well below the silicon surface. This is thought to be because this allows carrier injection and direct recombination to occur in relatively undamaged silicon, whereas for the samples implanted at lower energies, this region is much thinner and contains a higher number of defects. The quenching of the EL signal for the IBS samples, is found to depend on the doping density of the p-type layer, and hence the proximity of the  $\beta\text{FeSi}_2$  precipitates to the depletion region. The best results were achieved for the highest p-type doping density ( $1 \times 10^{18}$  B  $\text{cm}^{-3}$ ).

### 2.5.2. Reaction Deposition Epitaxy

Using the reaction deposition epitaxy (RDE) technique, Suemasu et al. [38] deposited a thin ( $\sim 10$  nm), continuous layer of epitaxial  $\beta\text{FeSi}_2$  on a pregrown p-n junction. After which, the sample was annealed in ultra-high vacuum at  $850^\circ\text{C}$  for 1 h and then  $0.3 \mu\text{m}$  of p-type silicon was deposited, at  $500^\circ\text{C}$  by molecular beam epitaxy (MBE). The structure was then annealed in an argon ambient at  $900^\circ\text{C}$  for 14 h. A schematic of this structure is shown in Figure 7b. Using this technique, the  $\beta\text{FeSi}_2$  nano-balls are fabricated across the p-n junction. The room temperature electroluminescence (EL) increased superlinearly with injected current

density and a reasonable EL signal was observed at room temperature for injection currents above  $10 \text{ A cm}^{-2}$ .

The weak room temperature electroluminescence observed from  $\beta\text{FeSi}_2$  means that although this material is an interesting candidate for silicon-based optoelectronics, unless significant improvements are made in the intensity of the emitted light, it is not a serious candidate for commercial devices.

## 2.6. Ion-Implanted LEDs in Silicon-Dislocation Engineering

In 2001, Ng et al. [39] reported room temperature electroluminescence from a boron-implanted device, which the authors attribute to “Dislocation Engineering.” In this study, they implanted B to a dose of  $1 \times 10^{15}$  B  $\text{cm}^{-2}$  at an energy of 30 keV into an n-type silicon substrate (CZ  $2\text{--}4 \Omega \text{ cm}$ ). The sample was then annealed at  $1000^\circ\text{C}$  in a nitrogen ambient for 20 min. The implantation of B meant that a p-n junction was produced; the B implantation also produced small dislocation loops  $80\text{--}100$  nm in diameter located  $\sim 100$  nm below the junction. The authors claim that the strain field associated with these dislocation loops leads to an increase in the local bandgap of  $0.35\text{--}0.7$  eV, causing a blocking potential barrier that confines the carriers within the junction region and allows room temperature electroluminescence to be achieved. The main peak of the room temperature electroluminescence spectrum is found at  $1.16 \mu\text{m}$ . The authors claim an external quantum efficiency of  $2 \pm 0.1 \times 10^{-4}$  for this device, making it a promising candidate for silicon-based optoelectronics (for comparison, commercial GaAs infrared LED have external quantum efficiencies of typically  $\times 10^{-2}$ ).

In order to see whether this dislocation engineering approach could be used to fabricate devices operating at different wavelengths, Lourenco et al. [40] incorporated it with known radiative centers (such as  $\beta\text{FeSi}_2$  precipitates and Er). Nonradiative defect centers in the bulk and at the surface are thought to be responsible for the thermal quenching observed in  $\beta\text{FeSi}_2$  precipitate structures and those incorporating Er. The authors claim that the provision of a barrier between the surface and the bulk, in the dislocation engineered samples enables the recapture of blocked carriers, enhancing the radiative routes and significantly reducing the thermal quenching. The results presented [40] appear to support this supposition, although apart from wavelength tuning, the authors do not appear to have significantly improved on the efficiency of their original device.

In parallel to work on light emission from nanostructures in silicon, work has also been progressing on nanostructures in silicon dioxide both for light emission and novel device applications. These will be discussed in the following two sections.

## 2.7. Light Emission from Silicon Nanocrystals in Silicon Dioxide

Over the past decade, there has been significant interest in silicon nanocrystals fabricated in silicon dioxide layers on silicon. These materials are of interest for applications in optoelectronics and their potential uses in volatile memory devices [41, 42]. The nanocrystals are either produced by the implantation of silicon ions into silicon dioxide [43–47]



or by the annealing of sub-stoichiometric  $\text{SiO}_x$  layers (Si  $\sim$  46 at %) on silicon [48] fabricated using plasma-enhanced, chemical vapor deposition (PECVD). The implantation of silicon is seen as a particularly attractive route for the formation of these nanocrystals, since it is fully compatible with silicon process technology and enables precise amounts of atoms to be placed at controlled depths. It also allows the samples to be masked so that nanocrystals can be placed in discrete regions of a device.

Silicon nanocrystals formed by implantation are fabricated using high doses (typically  $1 \times 10^{15}$ – $1 \times 10^{17}$  ions  $\text{cm}^{-2}$ ) of silicon implanted into silicon dioxide at energies of 25–200 keV, such that the peak concentration of the implanted ions ranges from 0.3 to 46 Si at %. The samples are normally implanted at room temperature. Subsequent to implantation, the samples are annealed in an inert ambient at temperatures  $>950$  °C for times ranging from 1–20 h. Most of the experiments have been undertaken on thermally grown silicon dioxide layers on  $\langle 100 \rangle$  silicon wafers. The oxide layers are typically 100–600 nm thick, although Linros et al. [49] used films of 10–100 nm thick. The oxidation temperature is typically around 1100 °C and both wet and dry oxidation methods have been used. For thin layers of silicon dioxide, a single energy implant is normally used for which the projected range of the implanted ions is approximately one-third the oxide thickness. For thicker oxide layers, multiple energy implants are used to give an approximately constant concentration of implanted ions over a depth range commensurate with the oxide thickness (typically 100–400 nm).

After implantation, most of the implanted atoms exist as small, elemental, crystalline, nanoprecipitates with a smaller amount of the implanted species in a solid solution with the silicon dioxide. Silicon nanocrystals have been shown to be responsible for the strong red PL which is found at  $\sim 1.7$  eV [43, 44, 46, 50, 51]. It is now generally recognized that there is a strong correlation between the wavelength of the emitted light and the size of the silicon nanocrystals. More recently Lopez et al. [45] have shown that the photoluminescence (PL) intensity follows the volume fraction of precipitates. Figure 8 shows the results for silicon nanocrystals fabricated by both implantation and PECVD for a range of annealing temperatures and times. The nanocrystals fabricated by PECVD are generally smaller than those formed by implantation and appear to have a more uniform size distribution. Lopez et al. [45] have described two regimes with respect to the density of silicon nanocrystals. The first is when the concentration of silicon in the silicon dioxide layer falls below a certain critical value (Lopez et al. [45] suggest  $\leq 10\%$  at % Si, but other authors [46] think the value is lower). In this regime, the system should be treated as dilute, that is, each silicon nanocrystal can be treated as a discrete entity which is unaffected by other silicon nanocrystals since these are so far away from it that their influence is negligible. This is especially valid given the low diffusion coefficient of silicon in silicon dioxide, which is thought to be between  $5 \times 10^{-18}$  and  $1 \times 10^{-16}$   $\text{cm}^2 \text{s}^{-1}$  [52, 53]. For higher doses, Lopez et al. [45] suggest that this regime can no longer be treated as a dilute system and that the interaction between nanocrystals must also be taken into account.

Most reports on silicon-implanted nanostructures report a PL peak at around 1.7 eV (728 nm). However, Rebohle

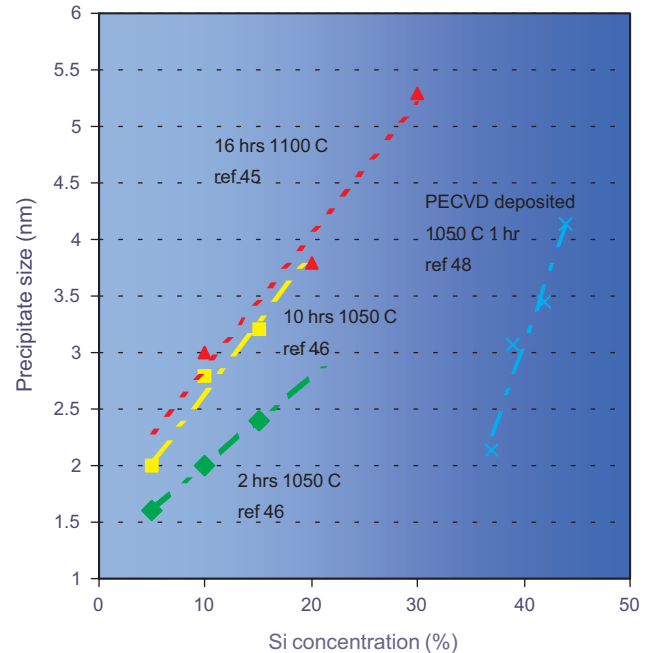


**Figure 8.** Variation in precipitate diameter with Si concentration and annealing time for Si nanocrystals in  $\text{SiO}_2$ . Adapted with permission from [45], M. Lopez et al., *Nucl. Instrum. Meth. B* 178, 89 (2001). © 2001, Elsevier Science; [46], T. S. Iwayama et al., *Surf. Coatings Technology* 158–159, 712 (2002). © 2002, Elsevier Science; [47], C. Bonafos et al., *Nucl. Instrum. Meth. B* 178, 17 (2001). © 2001, Elsevier Science.

et al. [54] report blue-violet PL (2.7 eV) in silicon-implanted samples, while [54–56] report PL at 3.2 eV for Ge-implanted samples and [54] report intense PL at 3.1 eV for Sn-implanted samples. The PL in the blue appears to come from an oxygen deficiency center rather than the nanocrystals themselves.

Considering the luminescence at around 1.7 eV, most authors agree the exact position of this peak appears to be dependent on the implanted dose of silicon [45, 46, 57, 58], with a red shift in PL peak position generally being observed with an increasing dose. Most agree that this red shift only occurs after a certain critical dose [45, 46, 59], although the magnitude of this dose appears to be influenced by the experimental conditions. Electron paramagnetic resonance (EPR) results [43, 45] show the presence of an  $E'$  center. After this paramagnetic center is associated with oxygen vacancy related defects [60, 61] the paramagnetic center associated with dangling bonds at the Si/SiO<sub>2</sub> interface is also observed ( $P_b$  center). During annealing, the  $E'$  centers are quickly annealed out and the intensity of the  $P_b$  signal at first decreases and then saturates.

The highest PL peak intensity is reported [45, 46] for samples containing  $\sim 10$  at % Si. For samples containing  $\leq 10$  at %, the PL intensity is found to initially increase with annealing time, after which it saturates [47]. Lopez et al. [45] suggest that during the initial stages of annealing, the silicon nanocrystals grow and some kind of surface passivation takes place (to account for the observed reduction in the EPR signal due to  $P_b$  centers). The nanocrystals then reach the critical radius for that annealing temperature and their size stabilizes, as does the number of dangling bonds at the

silicon/silicon dioxide interface. Interestingly, Cheylan and Elliman [62] have found that using a second stage anneal at 500 °C in forming gas (95% N<sub>2</sub>, 5% H<sub>2</sub>) results in an increase in PL intensity and a red shift in the emission peak. They have concluded that this increase in PL intensity may be a consequence of the passivation of nonradiative defects (e.g., silicon-dangling bonds).

There is some debate in the research about the mechanisms responsible for the luminescence at 1.7 eV. Some investigations have concluded that the observed PL is a result of quantum confinement (direct recombination of electrons and holes confined within the silicon nanocrystal), while others have concluded that it results from surface states in the interfacial layer between the silicon nanocrystal and the surrounding silicon dioxide. At first sight, the red shift observed in the PL peak position with increasing silicon dose [45, 46, 63], would appear to support the quantum confinement supposition. However, at lower doses, although the precipitates increase in size with annealing temperature (Fig. 8), the PL peak position does not change. Moreover, for samples annealed in forming gas [62] the precipitate size remains approximately constant and a red shift in the peak intensity is observed, which tends to suggest that the interface states at the silicon dioxide interface are also involved in the light emission.

The model that is most widely accepted for the observed light emission from silicon nanocrystals [46, 64–66] is that the light comes from the recombination of a quantum-confined exciton which is self-trapped [59, 60] in a size-dependent Si = O level [67] at the silicon-crystal/silicon dioxide interface. These interface states appear to be critically dependent on both the surface configuration [47] and the density of the silicon nanocrystals [48].

## 2.8. Er-Implanted Silicon Nanocrystals

Very recently, Pacifici et al. [66] has shown that if Er is implanted into a structure containing silicon nanostructures fabricated by PECVD, intense room temperature electroluminescence at 1.54 μm is observed. The silicon nanocrystals were ~1 nm in diameter and Er was implanted to a dose of  $7 \times 10^{14}$  Er cm<sup>-2</sup>, at an energy to place its peak in the center of the silicon dioxide layer where the nanocrystals are located. When an LED incorporating this structure is forward biased, the EL is quite intense even at room temperature. The authors suggest that strong coupling between the silicon nanocrystals and the implanted Er atoms effectively enables the nanocrystals to pump the Er, that is, each silicon nanocrystal absorbs energy that is preferentially transferred to the Er atom. This is observed in the strong increase of the excitation cross-section of the Er atom in the presence of silicon nanocrystals when compared to Er in the pure oxide host. Quoted quantum efficiencies larger than 1% have been claimed for this type of device [68]. Moreover, Er-doped silicon nanocrystals could, in principle, form the basis of a silicon laser as they combine the advantages of silicon (efficient excitation) and SiO<sub>2</sub> (negligible thermal quenching of luminescence), while avoiding their disadvantages (low excitation efficiency of SiO<sub>2</sub> and strong nonradiative processes in bulk Si). In contrast, the dislocation engineered structures

are unlikely to prove suitable for the fabrication of a silicon laser, since they are likely to still suffer from the two main problems encountered in bulk silicon which prevent population inversion, for example, Auger recombination and free-carrier absorption [68].

## 2.9. Combined Si and C Implants into Silicon Dioxide

González-Verona et al. [69] implanted both C and Si into SiO<sub>2</sub> layers. They implanted Si first at two energies in order to obtain a rectangular implant profile, buried 100 nm–300 nm from the surface, with a silicon excess of ~30%. They then implanted C so that the peak of the implant lay at the center of the implanted silicon distribution, with the peak C concentration  $2 \times 10^{22}$  C cm<sup>-3</sup> being approximately equal to that of Si in this region. Subsequent to implantation, the samples were annealed at 1100 °C for 4 h. Samples implanted with just silicon showed a strong red luminescence from silicon nanostructures, whereas those that had also been implanted with carbon showed a strong white emission. Photoluminescence analysis of this white emission shows three distinct peaks at 1.45 eV (854 nm), 2.1 eV (590 nm), and 2.8 eV (442 nm). These are thought to correspond to silicon nanocrystals (~4 nm in diameter), carbon rich amorphous clusters, and 6H-SiC nanocrystals (~7 nm in diameter), respectively. These results demonstrate the versatility of IBS and a potential method of tuning the emitted light.

## 2.10. Blue Emission from Group IV Implanted Silicon Dioxide

Germanium-doped silica glasses are known to exhibit a strong absorption band at 5 eV. More recently, blue EL has been observed from silicon implanted layers [54, 70, 71], violet EL from Ge-implanted layers [54–56, 72, 73], and blue-violet EL from Sn-implanted SiO<sub>2</sub> layers [51]. It is thought that the light emission in these structures arises from an oxygen deficiency center rather than the nanocrystals themselves. However, a power efficiency of 0.5% has been achieved for Ge-implanted silicon dioxide layers and the first successfully integrated optocoupler has been demonstrated [74].

## 2.11. Other Implants into Silicon Dioxide

Apart from the work mentioned above, a wide variety of other compounds have been synthesized in silicon dioxide. These include GaAs [75], ZnS [76], and ZnTe [77].

## 2.12. Smart Cut

High-dose ion implantation does not always lead to the formation of compound layers or discrete elemental nanocrystals. This section describes how high doses of inert ions can be used as atomic scalpels to allow thin layers of crystalline material to be placed on any kind of substrate (dielectric, glass, plastic, quartz, amorphous silicon, crystalline semiconductor, etc.). The Smart Cut™ process developed in the LETI Laboratories, Grenoble, France,

in 1991 involves the implantation of  $H^+$  ions into a target substrate (usually silicon). These hydrogen atoms then form small bubbles and microcavities, the size and density of which is dependent on the implantation parameters. These structures grow during implantation in a manner that again depends on the implanted dose, implantation energy, dose rate, implant temperature, and thermal history of the implanted wafer. When the distance between cavities falls below a certain threshold value, intercavity fractures occur that propagate through a percolation-type process [78]. This leads to a structure where all the microcavities are joined and expressed on the surface of the wafer by the formation of a blister. The driving force behind the formation of this blister is the gas pressure in the microcavities and stresses within the layer. By bonding another substrate to the implanted wafer, blister formation is suppressed and instead, a homogeneous force exists throughout the surface layer, enabling the surface layer to be split away from the underlying material with relative ease. After this, the sample undergoes a high temperature anneal and surface polish. Figure 9 shows a schematic of the Smart Cut™ process.

Smart Cut™ can be used in any material where microcavities can be produced by hydrogen or inert gas implantation. The fact that it uses implantation allows the thickness of the Smart Cut™ layer to be tailored for each specific application. Smart Cut™ silicon on insulator substrates

have been in commercial production since 1996, where along with SIMOX they provide a route for the realization of high speed, low-power consumption CMOS ICs. Recently [79], Smart Cut™ has been used in crystalline SiC structures which have enabled it to be bonded onto silicon substrate. The process has been used successfully in GaAs and InP [79–81].

### 3. OTHER APPLICATIONS OF ION BEAM SYNTHESIS

#### 3.1. Superconducting Nanocrystals Synthesized by IBS

Another very recent application of ion beam synthesis is in the fabrication of superconducting  $MgB_2$  nanocrystals. Although superconductors based on the YBaCuO system have been found with high superconducting transition temperatures ( $T_c$ ), they cannot be readily deposited as thin films. The superconductor that can readily be deposited as a thin film is Nb, but this has a very low  $T_c$  of 5 K. The recent discovery of a superconducting phase transition with a high  $T_c$  value of 39 K in ceramic  $MgB_2$ , has stimulated a new wave of worldwide research into the superconducting properties of this material and other related  $AlB_2$ -type compounds [82, 83], since these have the potential of being grown as thin films.

So far, various thin film preparation methods have been explored for the fabrication of  $MgB_2$  in many different laboratories with different substrates [84–87]. It is worth noting here that the most important factor influencing the  $T_c$  value appears to be related to the deposition method rather than the substrate materials used. A survey of the available literature reveals a number of major technical problems, which stand in the way of realizing high  $T_c$   $MgB_2$  thin films using conventional growth techniques. These include possible MgO contamination, poor stoichiometry control, and the need for a high temperature post-deposition anneal. The annealing temperature normally employed for producing the high  $T_c$  superconducting thin films is generally between 600° and 1000 °C, suggesting that these growth methods involve Mg diffusion into the solid B. As Mg starts to melt and  $MgB_2$  starts to dissociate at temperatures around 620 °C [88, 89], such a high annealing temperature are obviously undesirable for superconductor fabrication.

In order to avoid the unwanted high temperature step while still maintaining favorable  $MgB_2$  formation conditions, IBS has been used [90]. This involved the implantation of  $^{11}B$  into a solid Mg target. Peng et al. [80] have shown that  $MgB_2$  thin films can be successfully fabricated by high dose  $^{11}B$  implantation into commercial Mg ribbon followed by a relatively low temperature anneal at 500 °C. Figure 10 shows a XTEM image of a Mg sample implanted with  $1 \times 10^{18} \text{ cm}^{-2}$   $^{11}B$  at 80 keV and annealed at 500 °C for 15 min in flowing Ar gas. Figure 10 shows a buried layer containing small nano-precipitates of  $MgB_2$ . Magnetic susceptibility measurements on these samples reveal both the low temperature superconducting transition at 15 K and the high temperature transition at 36 K. Preliminary studies on these structures also indicate that the size of the  $MgB_2$  nano-precipitates play

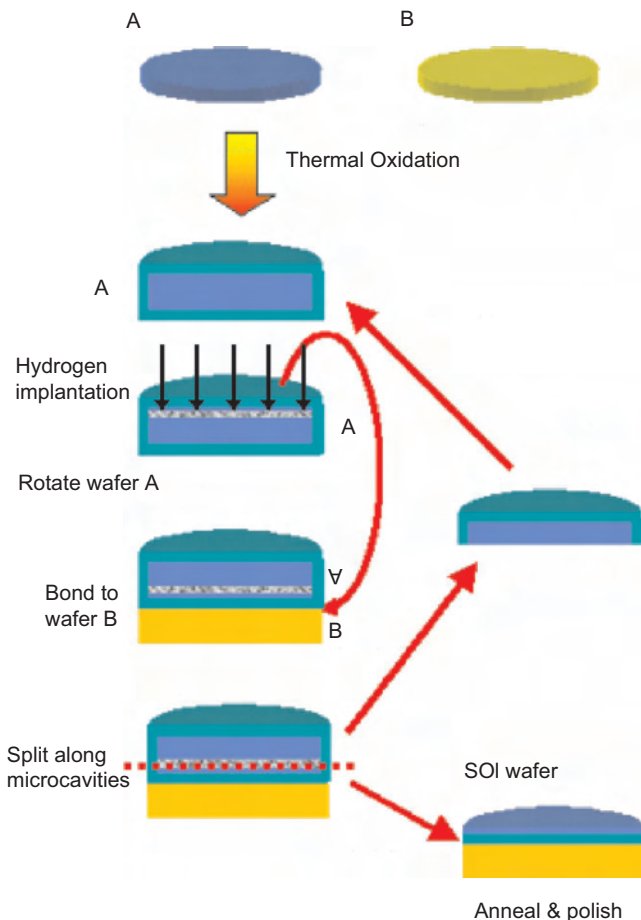
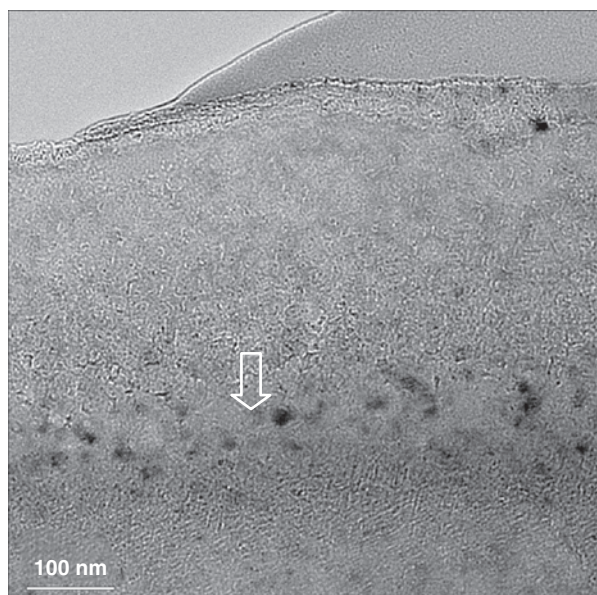


Figure 9. Schematic of Smart Cut™ process.



**Figure 10.** XTEM image of IBS MgB<sub>2</sub>.

a crucial role in determining the magnitude of the higher temperature transition temperature.

All of the work discussed thus far uses relatively high doses of ions to form discrete nanostructures. The work discussed in the final section considers much lower doses and looks at their impact in a wide diversity of areas.

### 3.2. Medical and Future Applications of Ion Implantation

The smallest structures that can be envisaged are those where only a single ion is implanted. This technique is already being employed to target living cells in order to better understand the way in which ionizing radiation interacts with biological material [91]. Such research has important implications both for the development of radiation treatment strategies for cancer [92, 93] and for identifying potential risks from low-level radiation. By targeting cells individually, using submicron ion beams that deliver a precise number of ions to each cell (usually 1), it is possible to address a number of important radiobiological questions not easily studied by other methods. There are three areas where this technique excels:

- the ability to irradiate selected targets within individual cells;
- the ability to selectively target one or more cells within a population of cells;
- the ability to deliver exact low doses of particles to one or more cells, or to a whole population of cells.

The recent application of microbeam techniques to radiobiology is already yielding important information regarding the effect of ionizing radiations on cells and tissues, particularly at low doses relevant to risk. The microbeam provides an elegant method for accurately delivering single particles to cellular and subcellular targets *in vitro*, which experimentally mimics what happens with

environmental exposure to  $\alpha$ -particle emitting radionuclides (i.e., from radon, which represents the largest single contribution to our overall background dose). Microbeams will also be an important tool in the development of improved radiotherapy treatment strategies. The unique ability of a microbeam to probe effects at the individual cell and subcellular level will ultimately lead to a better understanding of both the mechanisms involved in tumor cell killing by radiations and those involved in cancer induction to nearby healthy tissue from low doses outside the treatment field.

Of relevance to both clinical and risk related studies, is the role of so-called “nontargeted” effects where cells respond indirectly to energy deposited by radiations. One such effect is the occurrence of damage arising from radiation-induced cell signaling, both intracellular (i.e., from the cytoplasm to the nucleus) and intercellular (from cell to cell and referred to as the “bystander effect”). In fact, recent discoveries have revealed a number of radiobiological effects that are known to cause significant deviations from the assumed dose-effect relationship, particularly at low doses. Such effects include the bystander effect, genomic instability (where damage is revealed in cells several generations after the initial exposure), and low-dose hypersensitivity. The ability of a microbeam to selectively irradiate subcellular targets and individual cells, and give the ultimate low dose of particles (i.e., just a single particle), make it ideal for the study of these effects. As the understanding develops of the responses of subcellular targets to irradiation, so potential targets for new drug development may emerge.

In addition to their applications in radiobiology, ion microbeams and the new generation of nanobeams are likely to play an increasingly important role in the future where potential applications include:

- study of single event upsets in digital electronic devices;
- study of selective radiation damage and strain fields in ultra-large scale integrated circuits;
- nano-lithography in polymers using precisely defined single-ion tracks;
- surface modification of catalysts for improved chemical reaction yields and selectivity;
- nano-implantation into semiconductors for direct writing of quantum dots and wires;
- quantum computing using the implantation of single ions.

## 4. CONCLUSIONS

In this chapter, the history of the technique of ion beam synthesis has been reviewed from the development of atomic weapons to cancer therapy. It has been shown that IBS structures have enabled high-speed, radiation-tolerant integrated circuits to be developed and that this technology will provide an important route for the realization of even smaller devices for future generations of integrated circuits. Ion implanted nanostructures may also play a key role in the development of silicon-based optoelectronics, as they provide routes for the fabrication of both laser and light-emitting devices (LED) structures. In addition, IBS superconducting films are just beginning to be developed; these may allow the full potential of commercial superconductivity



to be realized and exploited. In the future, the development of nano-beams offers a huge diversity of opportunities from quantum computing to cancer therapy.

## GLOSSARY

**Å** Angstrom =  $10^{-10}$  m.

**Amorphous** Random arrangement of atoms.

**CaF<sub>2</sub> structure** Cubic structure type with Ca coordination number 8 and fluorine coordination number 4.

**Complementary metal oxide semiconductor (CMOS)** Basic building block of computer memory chips. Contains two transistors of opposing polarities, when one is off the other is on.

**CZ** Silicon grown by the Czochralski technique which involves dipping a seed crystal into a crucible of molten silicon and drawing out a single crystal silicon ingot.

**Doping** Introduction of impurities into a semiconductor lattice to modify electrical conduction.

**Electroluminescence** Light is emitted in response to an applied electric current.

**Electron paramagnetic resonance (EPR)** Technique which involves flipping the spin of an electron associated with a paramagnetic centre in a magnetic field.

**eV** Electron volt =  $1.60218 \times 10^{-19}$  J = 23.053 kcal/mol.

**Exciton** Electron hole pair found in semiconductors and insulators in an excited state. The hole behaves as a positive charge and the electron is attracted to it, to form an exotic atom state similar to a hydrogen atom.

**Extended X-ray absorption fine structure (EXAFS)** Technique for probing the local structure around almost any element in the periodic table (except the lightest). Gives information about near neighbours and average interatomic distances.

**Interstitials** Sites between crystal lattice planes where an impurity or host atom can be located. These atoms are not bonded to the crystal lattice.

**Ion beam synthesis** Synthesis of a compound layer within a target substrate using ion implantation.

**MeV** Mega electron volt = 1 million eV.

**Phonon** Quantum of lattice vibration.

**Photoluminescence light (PL)** Directed onto a sample where it is absorbed, and imparts excess energy to the material via a process of photon excitation. One mechanism by which this excess energy can be liberated is via the emission of light (luminescence) if this process involves photoexcitation the emitted light is termed photoluminescence.

**Superconductivity** is the ability for a material to conduct electricity with practically zero resistance.

**Ultra large scale integration (ULSI)** Refers to how many circuit elements can be placed on a single chip. Where very large scale integration (VLSI) stops and ULSI starts is unclear but it is generally thought that above 1 million circuit elements on a chip is ULSI.

**Vacancies** Sites in a crystal lattice where an atom is missing.

**Waveguide** A material medial that guides and confines a propagating electromagnetic wave.

## REFERENCES

1. J. F. Ziegler, J. P. Biersack, and U. Littmark, "The Stopping and Range of Ions in Solids," Vol. 1. Pergamon Press, New York, 1984.
2. S. Mantl, *Material Sci. Reports* 8, 1–95 (1995).
3. Z. Tan, J. F. Budnik, F. H. Sanchez, G. Tourillion, F. Navamar, and H. C. Hyden, *Phys Rev B* 40, 6368 (1989).
4. E. A. Maydell-Ondrusz and I. H. Wilson, *Thin Solid Films* 114, 357–366 (1984).
5. P. L. F. Hemment, E. A. Maydell Ondrusz, K. G. Stephens, J. Butcher, D. Ioannou, and J. Alderman, *Nucl. Instrum. Meth. B* 209/210, 157–164 (1983).
6. K. Izumi, M. Doken, and H. Ariyoshi, *Electron. Lett.* 14, 593 (1978).
7. M. Bruel, J. Margail, C. Jaussaud, A. J. Auberton-Hervé, and J. Stoemenos, *Microelectronic Engineering* 8, 149–161 (1988).
8. K. J. Reeson, A. K. Robinson, P. L. F. Hemment, C. D. Marsh, K. N. Christensen, G. R. Booker, R. J. Chater, J. A. Kilner, G. Harbeke, E. F. Steigmeir, and G. K. Celler, *Microelectronic Engineering* 8, 163–186 (1988).
9. Andrew B. Wittkower and Michael A. Guerra, *Nucl. Instrum. Methods B* 37–38, 512–517 (1989).
10. A. E. White, K. T. Short, R. C. Dynes, J. P. Garno, and J. M. Gibson, *Appl. Phys. Lett.* 50, 95 (1987).
11. R. S. Spraggs, K. J. Reeson, B. J. Sealy, A. De Veirman, and J. Van Landuyt, *Nucl. Instrum. Meth.* B55, 836 (1991).
12. T. L. Alford, M. Mitan, T. Marek, and J. W. Mayer, *Ion Implant Technology IIT2002*, Taos, NM, September 2002, IEEE (to appear).
13. U. Weidenmuller, J. Meijer, P. Baving, H. Rocken, H. H. Bukow, and C. Rolf, *Microelec. Eng.* 53, 385–388 (2000).
14. J. K. N. Lindner, T. Klassen, and E. H. te Kaat, *Nucl. Instrum. Methods B* 59–60, 655–659 (1991).
15. A. E. White, K. T. Short, and D. J. Eaglesham, *Appl. Phys. Lett.* 56, 1260 (1990).
16. T. J. Alford and J. C. Barbour, *Mater. Res. Soc. Proc.* 157, 137 (1988).
17. A. Golanski and C. W. White, *Nucl. Instrum. Methods B* 63, 384 (1992).
18. S. M. Hogg, A. Vantomme, M. F. Wu, and G. Langouche, *Micro. Eng.* 50, 211–215 (2000).
19. A. R. Ramos, J. G. Marques, M. R. da Silva, O. Conde, M. F. da Silva, and J. C. Soares, *Nucl. Instrum. Methods B* 161–163, 909–912 (2000).
20. J. H. Liang and D. S. Chao, *Surf. Coat. Technol.* 140, 116–121 (2001).
21. K. J. Reeson, J. Stoemenos, and P. L. F. Hemment, *Thin Solid Films* 191, 147 (1990).
22. R. Eppenga, *J. Appl. Phys.* 68, 3027 (1990).
23. N. E. Christensen, *Phys. Rev.* B42, 7148 (1990).
24. S. Mantl, *Nucl. Instrum. Methods B* 84, 127 (1994).
25. K. Radermacher, A. Shuppen, and S. Mantl, *Solid State Electron.* 37, 443 (1994).
26. R. Radermacher, S. Mantl, C. Dieker, and H. Lüth, *Appl. Physics Lett.* 59, 2145 (1991).
27. R. Radermacher, S. Mantl, Ch. Dieker, and H. Lüth, *Mat. Sci. Eng.* B12 115 (1992).
28. H. Katsumata, Y. Makita, N. Kobayashi, H. Shibata, M. Hasegawa, I. Aksenov, S. Kimura, A. Obara, and S. Uekusa, *J. Appl. Phys.* 80, 5995 (1996).
29. C. A. Dimitriadis, J. H. Werner, S. Logothetidis, M. Stutzmann, J. Weber, and R. Nesper, *J. Appl. Phys.* 68, 1726 (1990).
30. K. Lefki, P. Muret, N. Cherief, and R. C. Cinti, *J. Appl. Phys.* 69, 352 (1991).
31. K. J. Reeson, M. S. Finney, M. A. Harry, S. V. Hutchinson, Y. S. Tan, D. Leong, T. R. Bearda, Z. Yang, G. Curello, K. P. Home-wood, R. M. Gwilliam, and B. J. Sealy, *Nucl. Instrum. Methods B* 106, 364 (1995).

32. D. Leong, M. A. Harry, K. J. Reeson, and K. P. Homewood, *Appl. Phys. Lett.* 68, 1649 (1996).
33. D. Leong, M. A. Harry, K. J. Reeson, and K. P. Homewood, *Nature* 387, 686 (1997).
34. R. Sauer, J. Weber, J. Stoltz, E. R. Weber, K. H. Kuster, and H. Alexander, *Appl. Phys. A* 36, 1 (1985).
35. L. Miglio and V. Meregalli, *J. Vac. Sci. Technol. B* 16, 1604–1609 (1998).
36. L. Miglio and V. Meregalli, *Mat. Res. Soc. Symp. Proc.* 402, 367–372 (1996).
37. K. J. Kirkby, M. Lourenco, T. M. Butler, K. Homewood, and C. M. McKinty, *Phys. Chem. Appl. Nano. World Scientific* 76–87 (2001).
38. T. Suemasu, Y. Negishi, K. Takakura, and F. Hasegawa, *Jpn. J. Appl. Phys.* 39 (2000).
39. W. L. Ng, M. A. Lourenco, R. M. Gwilliam, S. Ledain, G. Shao, and K. P. Homewood, *Nature* 410, 192–194 (2001).
40. M. A. Lourenco, M. S. A. Siddiqui, R. M. Gwilliam, G. Shao, and K. P. Homewood, *Phys. E*, in press.
41. M. Y. Hao, H. Hwang, and J. C. Lee, *Appl. Phys. Lett.* 62, 1530 (1993).
42. K. H. Heinig, B. Schmidt, A. Markwitz, R. Grotzchel, M. Strobel, and S. Oswald *Nucl. Instrum. Meth. B* 148, 969–974 (1999).
43. Y. Kanemitsu, N. Shimizu, T. Komoda, P. L. F. Hemment, and B. J. Sealy, *Phys. Rev. B* 54, 14329 (1996).
44. T. S. Iwayama, N. Kurumadho, D. E. Hole, and P. Townsend, *J. Appl. Phys.* 83, 6018 (1998).
45. M. Lopez, B. Garrido, C. Bonafos, A. Perez-Rodriguez, J. R. Morante, and A. Claverie, *Nucl. Instrum. Meth. B* 178, 89–92 (2001).
46. T. S. Iwayama, T. Hama, D. E. Hole, and I. W. Boyd, *Surf. Coatings Technol.* 158–159, 712–716 (2002).
47. C. Bonafos, B. Columbeau, A. Altibelli, M. Carrada, G. Ben Assayag, B. Garrido, M. Lopez, A. Perez Rodriguez, J. R. Morante, and A. Claverie, *Nucl. Instrum. Meth. B* 178, 17–24 (2001).
48. F. Iacona, G. Franzo, and G. Spinella, *J. Appl. Phys.* 87, 1295 (2000).
49. J. Linnros, A. Galeckas, N. Lalic, and V. Grivickas, *Thin Solid Films* 297, 167–170 (1997).
50. T. S. Iwayama, M. Ohshima, T. Nilmi, S. Nakao, K. Saitoh, T. Fujita, and N. Itoh, *J. Cond. Mater.* 5, L375 (1993).
51. M. L. Brongersma, A. Polman, K. S. Min, E. Boer, T. Tambo, and H. A. Atwater, *Appl. Phys. Lett.* 72, 2577 (1998).
52. L. A. Nesbit, *Appl. Phys. Lett.* 46, 38 (1985).
53. M. Agarwal and S. T. Dunham, *J. Appl. Phys.* 78 (1995).
54. L. Rebohle, J. von Borany, H. Frob, T. Gebel, M. Helm, and W. Skorupa, *Nucl. Instrum. Meth. B* 188, 28–35 (2002).
55. H. Z. Song and X. M. Bao, *Phys. Rev. B* 55, 6988 (1997).
56. L. Rebohle, T. Gebel, J. von Borany, H. Frob, D. Borchert, and W. Skorupa, *Mat. Sci. Eng. C* 19, 373–76 (2002).
57. M. L. Brongersma, A. Plolman, K. S. Min, E. Boer, T. Tambo, and H. A. Atwater, *Appl. Phys. Lett.* 72, 2577 (1998).
58. S. Cheylan and R. G. Elliman, *Nucl. Instrum. Meth. B* 148, 986–990 (1999).
59. S. A. Trushin, A. N. Mikhaylov, D. I. Tetelbaum, O. N. Gorshkov, D. G. Revin, and D. M. Gaponova, *Surf. Coat. Technol.* 158–159, 717–719 (2002).
60. C. Bonafos, B. Columbeau, A. Altibelli, M. Carrada, G. Ben Assayag, B. Garrido, M. Lopez, A. Perez-Rodriguez, J. R. Morante, and A. Claverie, *Nucl. Instrum. Meth. B* 178, 17–24 (2001).
61. R. C. Barklie, T. J. Ennis, P. L. F. Hemment, and K. J. Reeson, *Nucl. Instrum. Meth. B* 332, 433 (1987).
62. S. Cheylan and R. G. Elliman, *Nucl. Instrum. Meth. B* 148, 986–990 (1999).
63. M. L. Brongersma, A. Polman, K. S. Min, E. Boer, T. Tambo, and H. A. Atwater, *Appl. Phys. Lett.* 72, 2577 (1998).
64. K. S. Zhuralev and A. Yu, *Kobitski Semiconductors* 34, 1203 (2000).
65. A. Yu Kobitski, K. S. Zhuralev, H. P. Wagner, and D. R. T. Zahn, *Phys. Rev. B* 63, 115423 (2001).
66. D. Pacifici, A. Irrera, G. Franzo, M. Miritello, F. Iacona, and F. Priolo, *Phys. E*, in press.
67. M. V. Wolkin, J. Jorne, P. M. Fauchet, G. Allan, and C. Delarue, *Phys. Rev. Lett.* 82, 197 (1999).
68. L. Parvesi, “Optoelectronic Integration in Silicon” (David J. Robbins and G. E. Jabbour, Eds.). *Proc SPIE*, in press.
69. O. González, V. A. Pérez-Rodriguez, B. Garrido, C. Bonafos, M. López, J. R. Morante, J. Montserrat, and R. Rodriguez, *Nucl. Instrum. Meth. B* 161–163, 904–908 (2000).
70. F. Kozlowski, H. E. Porteanu, V. Petrova-Koch, and F. Koch, *Mater. Res. Soc. Proc.* 452, 657 (1997).
71. P. Knapek, B. Rezek, D. Muller, J. J. Grob, R. Levy, K. Luternova, J. Kocka, and I. Pelant, *Phys. Status Solid A* 167, R5 (1998).
72. J. P. Zou, Y. F. Mei, J. K. Shen, J. H. Wu, X. L. Wu, and X. M. Bao, *Phys. Lett. A* 301 (2002).
73. J.-Y. Zhang, Y.-H. Ye, and X.-M. Bao, *J. Non. Cryst. Solids* 241, 184–189 (1998).
74. L. Rebohle, J. von Borany, D. Borchert, H. Frob, T. Gebel, M. Helm, W. Moller, and W. Skorupa, *J. Electrochem. Soc. Electrochem. Solid State Lett.* 7, G57 (2001).
75. Y. Kanemitsu, H. Tanaka, T. Kushida, K. S. Min, and H. A. Atwater, *Phys. E*: 7, 322–325 (2000).
76. K. Y. Gao, H. Karl, I. Grosshans, W. Hipp, and B. Stritzker, *Nucl. Instrum. Meth. B* 196, 68–74 (2002).
77. I. Großhans, H. Karl, and B. Stritzker, *Nucl. Instrum. Meth. B* 190, 865–868 (2002).
78. A. J. Auberton-Herve and M. Bruel, *Int. J. High Speed Electron. Systems* 10, 131–146 (2000).
79. L. Di Cioccio, Y. Leitec, F. Letertre, C. Jassaud, and M. Bruel, *Electron. Lett.* 32, 1144 (1996).
80. E. Jalaguier, B. Aspar, S. Pocas, J. F. Michaud, M. Zussy, and M. Bruel, *Electron. Lett.* 34, 408 (1998).
81. E. Jalaguier, N. Dessaud, B. Aspar, S. Pocas, A. M. Papon, and M. Bruel, *Temes Journées Nationales de Microelectronique et Optoelectronique*, Egat, France 6–8 Jan. 1999.
82. J. Nagamatsu, N. Nakagawa, T. Muranaka et al., *Nature* 410, 63 (2001).
83. C. Buzea and T. Yamashita, *Supercond. Sci. Technol.* 14, R115 (2001).
84. X. H. Zeng, A. Sukiasyan, X. X. Xi et al., *Appl. Phys. Lett.* 7, 1840 (2001).
85. W. N. Kang, H. J. Kim, E. M. Choi et al., *Science* 292, 1512 (2001).
86. K. Ueda and M. Naito, *Appl. Phys. Lett.* 79, 2046 (2001).
87. A. Plecenik, L. Satrapinsky, P. Kus et al., *Physica C* 363, 224 (2001).
88. Z. K. Liu, Y. Zhong, D. G. Schlom et al., *CALPHAD* 25, 299 (2001).
89. P. Villars and L. D. Clvert, “Pearson’s Handbook of Crystallographic Data for Intermetallic Phases,” pp. 127–128. ASM International, Materials Park, OH, 1991.
90. N. Peng, C. Jeynes, R. P. Webb et al., *Appl. Phys. Lett.* 2002, submitted.
91. M. Folkard, B. Vojnovic, K. M. Prise, and B. D. Michael, *Nucl. Instrum. Meth. B* 188, 49–54 (2002).
92. N. F. Kirkby, N. G. Burnet, and D. B. F. Faraday, *Nucl. Instrum. Meth. B* 188, 210–215 (2002).
93. D. B. F. Faraday, P. Hayter, and N. F. Kirkby, *Biochem. Eng. J.* 7, 49–68 (2001).





# Ion Sputtering on Metal Surfaces

C. Boragno, F. Buatier de Mongeot, U. Valbusa

*INFM-UdR Genova, Genova, Italy*

## CONTENTS

1. Introduction
2. Ion Sputtering
3. Morphological Modifications Induced by Ion Sputtering on Metals
4. Other Materials
5. Theoretical Models
6. Applications
7. Conclusions
- Glossary
- References

## 1. INTRODUCTION

In this chapter, we review the recent results on the modification of surfaces (especially metal surfaces) induced by ion sputtering. The method is very common in so-called surface science since it provides a simple tool which can be used for many different purposes, such as material deposition and chemical analysis. Ion sputtering, which will be presented in greater detail in the next paragraph, consists of the bombardment of a target by ions (generally of noble gases like argon, neon, and xenon) accelerated by an electric field, in order to get typical kinetic energies in the range 0.1–10 keV ( $1 \text{ eV} = 1.6 \cdot 10^{-19} \text{ J}$ ). Roughly speaking, when the ion hits the target, it can penetrate for many nanometers in the solid, causing the displacement of many thousands of atoms from their original position and the ejection of few (typically less than ten) other atoms in the vacuum.

In many cases, one may be interested to collect the ejected atoms, for example, by inducing their deposition onto a substrate: if so, we speak about “sputter deposition,” which represents a convenient tool to produce thin films also on a large scale. On the other hand, performing an analysis of the ejected atoms (for example, by means of a mass spectrometer, like in the SIMS) one can obtain the composition of the target.

In many instances, one can use ion sputtering only to clean a surface, removing the first layers, and then exposing a fresh surface for other analysis or material deposition.

Within our scope, we are interested in the surface damage induced by ion sputtering. We will show that this damage can be “driven” to obtain morphologies characterized by a long-range order and a characteristic size on the nanometer scale. These nanopatterns can be used as substrates for subsequent depositions, or to modify the chemical properties of the target, or to produce electronic devices.

On these topics, many recent reviews have been published in specialized scientific journals [1–3].

## 2. ION SPUTTERING

The process of ion sputtering may remind one of sandblasting, the erosion of materials with a stream of abrasive particles: a projectile is accelerated in order to transfer its kinetic energy to the atoms of the target. As a consequence of the impact, atoms are removed from the target. In both methods, the erosion rate depends on the angle of incidence, but the physical processes involved are quite different since the average kinetic energy per atom in sandblasting (a few millielectron volts) is much lower than that in sputtering (electronvolts to several kiloelectronvolts). Unlike the abrasive particles, ions can penetrate deep into the target, and energy and momentum transfer occur on a different scale. An important experimental observation is that ion erosion occurs even in the limit of a small flux, and the sputter yield is independent of the flux. In other words, even a single ion can remove target atoms.

The first explanation of the sputtering process came from Stark [4]: ion bombardment leads to heating of the target, and subsequent boiling of atoms from the surface region. Actually, molecular dynamics simulations have shown that thermal spikes do occur [5]. When crystalline materials are bombarded with kiloelectronvolt ions, part of the material in the path of the ions has the radial distribution function of a liquid, consistent with local heating of the target. However, the sputter yield from such heating is low due to the short-lived nature of the spikes, typically a few picoseconds. There just is not enough time for atoms to boil off from the target.

A better description has been developed by Sigmund [4, 6, 7] and Thompson [8] (transport theory): the incident ion loses its energy to the target atoms through a series of collisions, as schematically shown in Figure 1. The target atoms

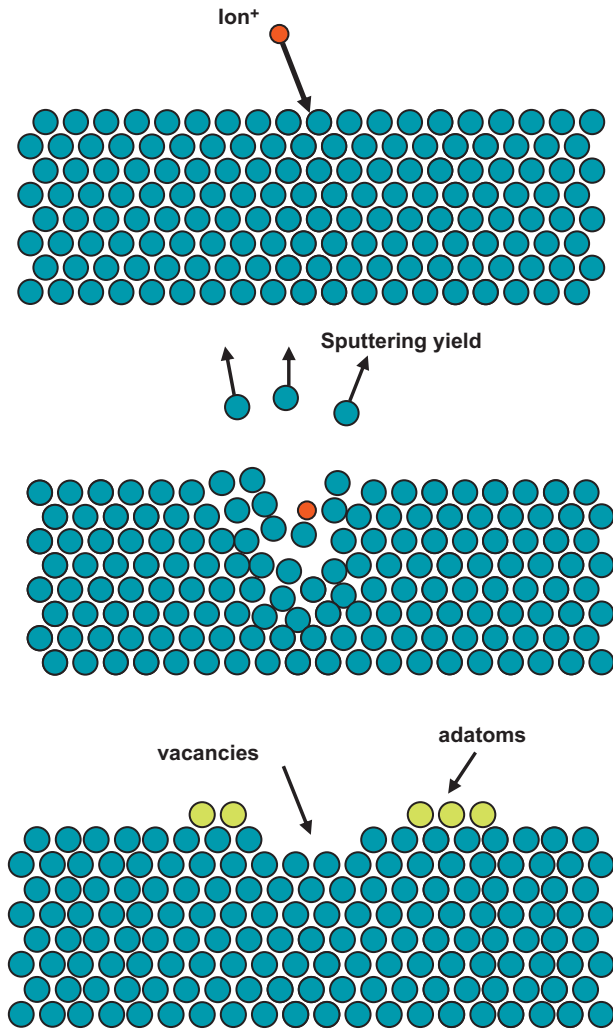


**Figure 1.** Schematic drawing of the collision cascade induced in a crystal by an energetic ion.

involved in these collisions, in turn, undergo further collisions, thereby setting up collision cascades. Some atoms near the surface receive a sufficient kick in these cascades to leave the target. In order to understand what happens when an ion impinges on a surface, we have to consider the way in which an energetic ion loses its energy through collisions. Two mechanisms must be considered: scattering with the nuclei and with the electrons. This view is so correct that the penetration range of the ions can be determined to a good approximation by treating the nuclear stopping and the electronic stopping independently. For all except the light ions (such as  $H^+$ ,  $He^+$ ), the nuclear energy loss dominates at low (kiloelectronvolt) energies. The nuclear energy loss can be calculated by modeling the interaction of the ion and the target nucleus with a (repulsive) screened Coulomb potential. Lindhard, Scharff, and Schafer wrote a universal expression for the nuclear stopping cross section (nuclear energy loss per unit path length per unit atomic density), now called the LSS expression, for any ion–target combination [9]. The transport theory incorporates the ideas of the stopping theory of Lindhard and co-workers. Being a continuum theory, it applies best to amorphous and polycrystalline targets.

While the mathematical treatment of the ion transport is sophisticated, the results take a simple form. The sputter yield  $Y$  (i.e., the number of target atoms ejected per incident ion) has the expression  $Y \approx \alpha NS(E)/E_b$ , where  $N$  is the atom density of the target,  $S(E)$  is the stopping power (a function of the incident energy  $E$ ),  $E_b$  is the binding energy for a surface atom in the target, and  $\alpha$  contains material and geometric parameters.

The consequences of the transport theory have been verified with great accuracy in the past since it was a crucial model for the development of the ion-implantation technique which is now commonly used in semiconductor technology. All of the results showed that this theory describes the ion sputtering quite well.

Before concluding this paragraph, we want to remark that the simulation of a collision cascade in a solid represented in past years a challenge for the development of fast computer codes and molecular dynamics techniques. Today, various PC programs are very popular among researchers in the field (the most famous is the TRIM code).

### 3. MORPHOLOGICAL MODIFICATIONS INDUCED BY ION SPUTTERING ON METALS

In the previous paragraph, we saw that, when an energetic ion hits the target, it dissipates its kinetic energy by multiple collisions with the atoms. As computer simulations show, the dissipative process occurs in a few picoseconds ( $1 \text{ ps} = 10^{-12} \text{ s}$ ). The final result is that many thousands of atoms are moved from their original position, and a few are ejected into vacuum. Of course, this atomic arrangement is out of equilibrium, and then the system tends to recover an energetically stable configuration. When the target is a metal, the main mechanism by which the atoms try to find their equilibrium is surface diffusion. From these simple considerations, we can deduce some general rules about the effect of ion sputtering on metals.

1. While the dissipation of the kinetic energy can be considered temperature independent, the mechanism for the equilibrium recovery is strongly temperature dependent since it depends on surface diffusion. Surface diffusion is a thermally activated process; generally speaking, an adatom (i.e., an atom on the surface) can move in different ways, and each way has an energy cost  $E$ . The rate  $v$  at which an adatom tries to follow a particular diffusion path can be written

$$v = v_0 \exp(-E/kT) \quad (1)$$

where  $v_0$  is on the order of  $10^{13} \text{ s}^{-1}$ ,  $k$  is the Boltzmann constant, and  $T$  is the surface temperature.

From 1, it is clear that, at high enough temperatures, the adatoms can follow many different paths to gain an equilibrium position, and so the damage recovery is very effective and fast. But lowering the temperature, the contrary happens, and the damage recovery is slow.

In conclusion, the surface morphology is due to a competition between the induced damage and the recovery by surface diffusion.

2. The surface morphology must depend on the rate at which the ions arrive on the surface [ion flux  $\Phi$ , expressed in ions/(cm<sup>2</sup> · s)]. In fact, since the damage happens in a few picoseconds, if the ion flux is low, the target has a sufficient time to recover, and the next ion again sees a surface in equilibrium. With the typical ion flux used in the laboratory, some milliseconds can pass between two hits in the same area.
3. Also, the total number of ions hitting the surface (ion dose  $D$ , expressed in ions/cm<sup>2</sup>) is a crucial parameter to determine the surface morphology. In fact, if the time delay between two ion hits is not long enough, the damage cumulates, and the final morphology is determined by the history of the ion sputtering process.

In light of these preliminary considerations, we can start to examine the experimental evidence. The recent studies on the present topic have been done with essentially three methods.

1. Surface microscopy: Since the typical spatial range of the structures present on an ion-bombarded surface is the nanometer, electron microscopy (SEM) and scanning probe microscopy (STM, AFM) have been extensively used. These techniques allow us to directly visualize the effect of the ion sputtering, but generally, they are applied in a nonreal-time mode: the sample is first processed, and then imaged with the microscope. Often, the time delay between the two stages is so long that it is not guaranteed that the surface morphology visualized by the microscope is really the same produced at the end of the ion sputtering since the smoothing mechanisms continue to act. Further, if one is interested in the statistical properties of the ion-bombarded surface (we will show that a statistical approach can be very convenient to analyze the data), many tens of images must be acquired, and the method can become very time consuming
2. Electron diffractive methods: LEED and SPA-LEED overcome some limitation of the previous techniques, in particular, they allow us to analyze a relatively large region of the sample, so it is an easy task to measure the statistical properties of the surface. However, rarely have these techniques been applied to real-time studies since the technical difficulties are relevant.
3. X-ray diffractive methods: In the last few years, diffraction techniques based on the scattering of X-rays have been successfully applied. The most interesting experiments have been carried out at synchrotron radiation facilities since the X-ray beam is characterized by high brilliance and monochromaticity. By means of these methods, it is possible to follow the evolution of the surface morphology in real time, during the ion sputtering.

### 3.1. Single Impacts

We begin our presentation of experimental results with the direct observations done on the surface damage induced by a single ion on a metallic surface. To perform this kind of study, the ion flux is reduced to very low rates,

and the sputtering time is so short that it is possible to image (with an appropriate microscopy, especially STM in an ultrahigh-vacuum environment) the effect of a single impact.

Figure 2 reports the result on an Ag(100) surface. Ar<sup>+</sup> ions, with an energy of 1 keV, are directed against the surface. Each dark spot represents a vacancy island corresponding to a single ion impact (the number of these holes corresponds very well with the ion dose). Around the hole, few islands are present (the bright spots in the figure). The interpretation of this image is straightforward. An ion impinging on the surface causes two kinds of defects: a vacancy island and some adatom clusters around it. The hole has a depth of one layer, and also the adatom clusters generally have a thickness of one layer. Quite similar results have been obtained by analyzing the single impacts on Pt(111) [10] and Al(111) [11]. By means of a detailed analysis of many images, and following the evolution of the surface morphology with increasing temperature, the authors showed that the adatom clusters come out from an inner layer, a few atoms are ejected from the surface, and many vacancies are frozen in subsurface layers.

From these results, we can deduce that such a mechanism is quite general for metals, and it is different from what happens in semiconductors, where a single ion impact causes only the ejection of a few atoms and the creation of a vacancy island, but not of adatom clusters (see Section 4).

This is the starting point for the interpretation of the experiments shown in the next paragraph: increasing the ion flux and dose, we induce many of these islands that interact between them to form the final surface morphology. In this sense, ion sputtering seems to be quite similar to the deposition of adatom and vacancy clusters at the same time.

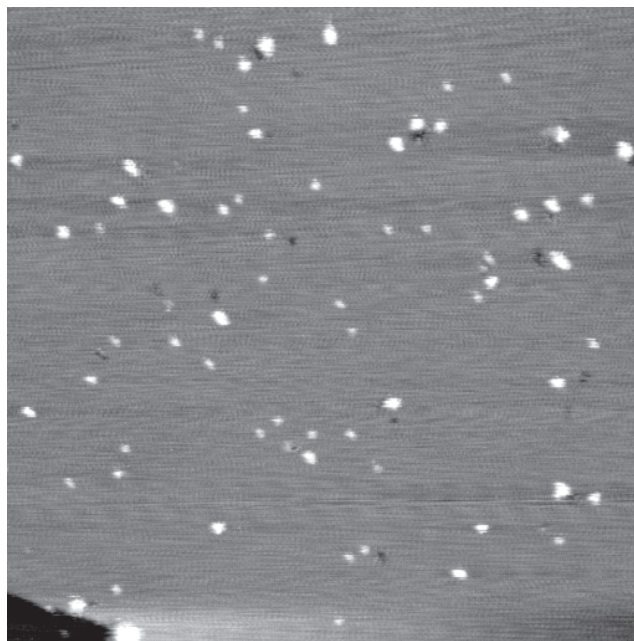


**Figure 2.** Top: typical surface morphology after single ion impact experiment in Ag(100) at  $T = 115$  K (scan area  $40 \times 23$  nm<sup>2</sup>).



### 3.2. Submonolayer Regime

Increasing the ion dose, the surface defects created by a single impact (adatoms and vacancies) begin to self-organize on the surface. By carefully controlling the dose, it is possible to observe how this self-organization happens. Figure 3 shows the morphology of an Ag(110) surface bombarded with an ion dose of about 0.2 ML (here and in the following, we will use the monolayer (ML) as a unit, that is, a number of ions or atoms per  $\text{cm}^2$  equal to the surface density of the target). An array of holes, one layer deep, is visible. These holes are oriented along the (1–10) direction, where the diffusion of surface defects created by a single ion impact can diffuse easily (for more details, see Section 3.4). No adatoms are present on the surface, indicating that they diffuse faster than vacancies, then attaching to atomic steps or falling into the vacancy clusters. Of course, this particular morphology can be created only in a restricted temperature range: at lower temperatures, adatom clusters are also present, while at higher temperatures, the surface has sufficient energy to completely recover the damage.

Starting from a similar situation, it is possible to study the diffusion mechanism of adatom and vacancy clusters, as reported, for example, in [12–15]. In all of these experiments, ion sputtering is used to form on a metal surface a well-controlled distribution of holes, and then their time evolution is followed by collecting STM images on the same surface area. By the analysis of images, energetic barriers for the movement of surface defects can be inferred.

### 3.3. Isotropic Surfaces

In this paragraph, we will analyze the results obtained on isotropic surfaces. By this term, we mean metal surfaces in which free adatoms and vacancies diffuse in all of the allowed directions with the same probability. For example,

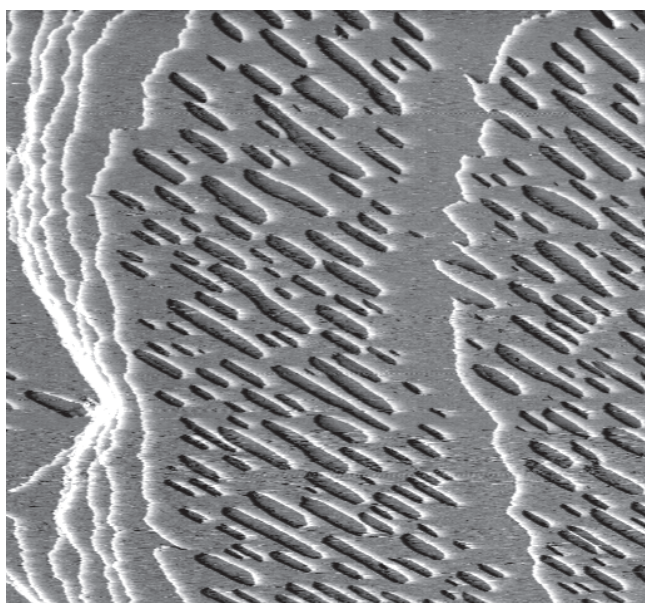


**Figure 3.** STM topography of Ag(110) surface after ion bombardment at a dose of about 0.2 ML ( $T = 130$  K, scan area  $120 \times 120$  nm<sup>2</sup>).

in a (111) surface of an fcc crystal, there are three equivalent directions, due to threefold surface symmetry, while in the (100) surface of an fcc crystal, the equivalent directions are four. Of course, the diffusion probability is not the same when the adatoms or vacancies are moving along a step since the bonds between atoms are different.

The surface morphology induced by ion sputtering on Pt(111) has been extensively studied in the past [16–19]. In Figure 4, we present a collection of typical images taken after different ion doses. They used Xe ions with an energy of 1 keV and an ion density current of  $0.3 \mu\text{A}/\text{cm}^2$ . This flux corresponds to an ion flux of 0.0013 ML/s. The temperature was fixed at 600 K. In the first panel, the ion dose was 0.093 ML, which corresponds to an eroded amount of 0.26 ML. This value is equal to the ion flux times the sputtering yield, which has been measured to be 2.8 in this experimental condition. Many vacancy islands, but no adatom clusters are present. With respect to the situation reproduced in Figure 2, this means that the surface temperature is high enough that adatom clusters are broken, and their atoms are moved around until they are incorporated

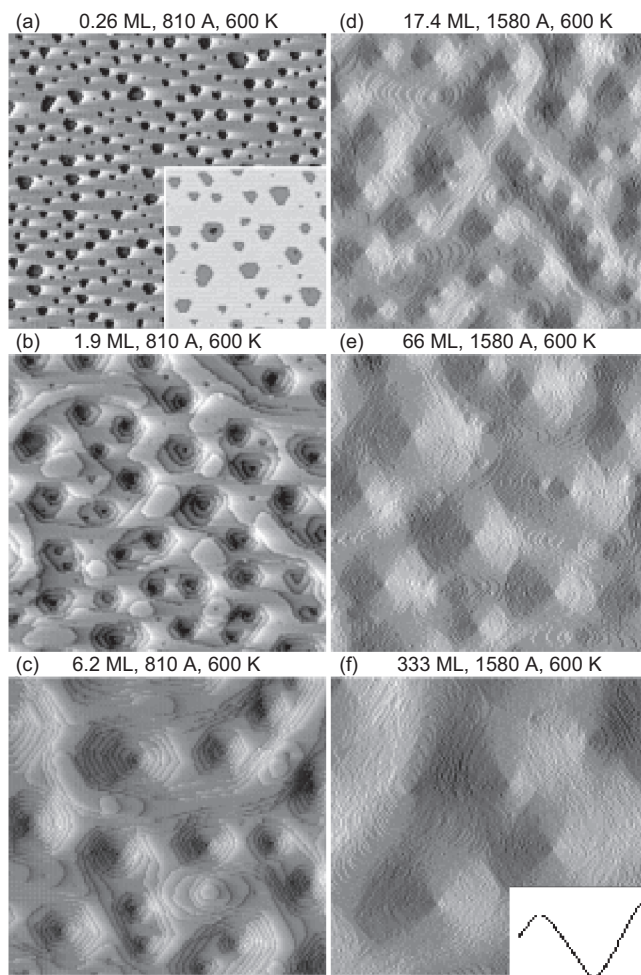


**Figure 4.** STM topographies of Pt(111) after ion erosion at 600 K. Scan area is  $81 \times 81$  nm<sup>2</sup> for (a)–(c) images and  $156 \times 156$  nm<sup>2</sup> for (d)–(f) images. Inset in (a): higher magnification gray-scale topography. Inset in (f): line scan through pit. Reprinted with permission from [16], M. Kalff et al., *Surf. Sci.* 486, 103 (2001). © 2001, Elsevier Science.

at steps or in the vacancy islands. These vacancy islands are more or less equally spaced. Increasing the amount of removed material, the holes become more and more deep, but it is more important to observe that these holes have the tendency to self-organize. After the removal of 333 ML, the self-organization is well evident: the shape of the holes reflects the surface symmetry, while the slope of each valley is quite regular and fixed.

Also, sputtering on Ag(100) produces very similar results [20]. Of course, now the holes are square since the symmetry of the surface is fourfold. In Figure 5, a series of images is shown, taken after the same ion dose, but at different temperatures. At low temperature, the surface appears rough, without any evidence of self-organization. Increasing  $T$ , holes and mounds appear, which become more and more pronounced and well organized. At high temperature, the surface is again flat.

From these images, we can calculate the average roughness of the surface. Plotting this quantity versus temperature, we obtain a characteristic bell-shaped behavior, reported in Figure 6. This curve presents a marked maximum and a rapid decrease of the roughness at low and

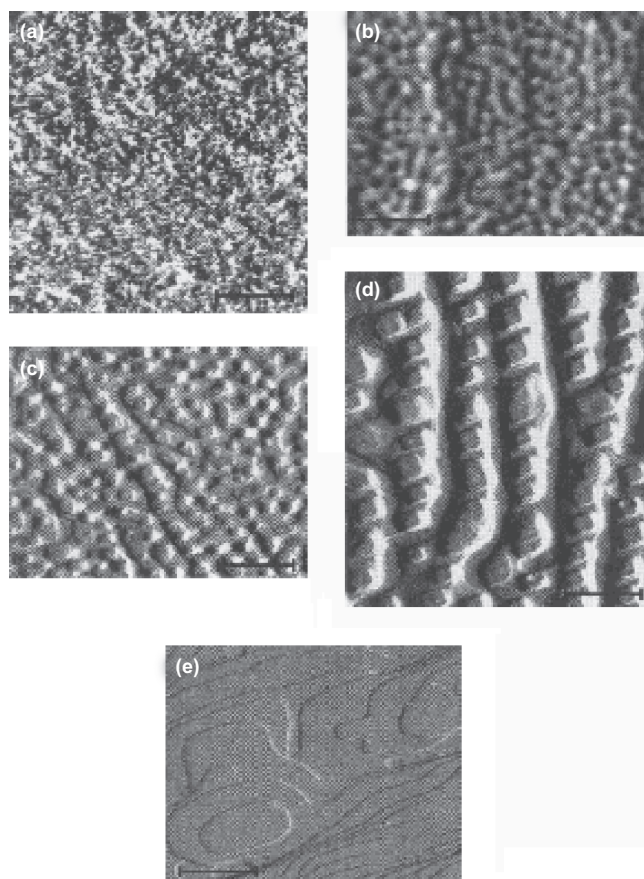


**Figure 5.** STM topographies of Ag(100) after ion erosion at different temperatures: (a)  $T = 180$  K, (b)  $T = 240$  K, (c)  $T = 300$  K, (d)  $T = 380$  K, and (e)  $T = 440$  K. For all images, ion energy 1 keV, ion flux 0.02 ML/s, and ion dose 36 ML. The bar corresponds to a length of 50 nm for images (a)–(b) and to 100 nm for images (c)–(e). Reprinted with permission from [20], G. Costantini et al., *Surf. Sci.* 416, 245 (1998). © 1998, Elsevier Science.

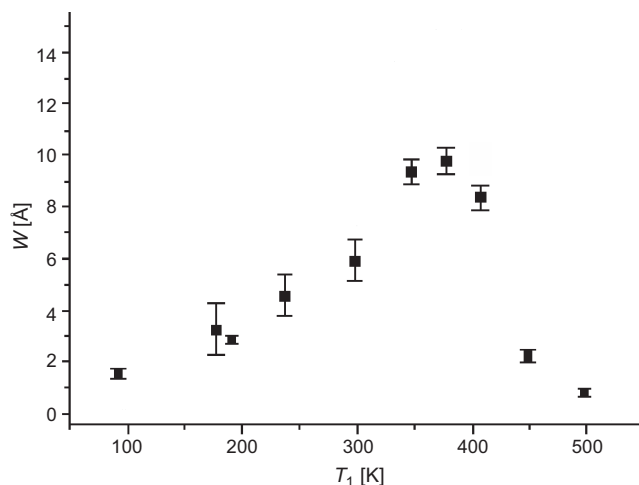


**Figure 6.** Surface roughness  $W$  as a function of the sputtering temperature  $T_s$  in the case of Ag(100). Reprinted with permission from [20], G. Costantini et al., *Surf. Sci.* 416, 245 (1998). © 1998, Elsevier Science.

high temperature. A similar behavior has been reported for other isotropic surfaces, like Cu(100) [21, 22].

From the experimental results presented in this section, we can deduce several consequences.

1. The surface morphology modifications induced by ion sputtering are not due to a random process, contrary to what one would think at first sight: after a sufficiently high dose, the surface self-organizes in structures of typical dimensions of some nanometers. The shape of these structures reflects the surface symmetry, suggesting that the surface diffusion of adatoms and vacancies must have a crucial role in the determination of the final morphology.
2. Lowering the temperature, surface diffusion decreases, and as a consequence, the recovery of the damage and its reorganization are less effective; on the contrary, at high temperature, diffusion is so fast that the surface can recover the damage in a short time, and the surface is also flat after high doses. When the balance between the two processes (damage and diffusion) is correct, the roughness increases, and large holes and mounds appear.
3. As in growth experiments, increasing the ion flux has the same effect as lowering the temperature since the system has less time to recover the damage.
4. The average distance between holes or mounds increases with dose. This means that ion sputtering induces a relevant coarsening on the surface: small islands coalesce to form large ones. Mass transport is important both in-layer and intralayer.
5. The morphology depends weakly on the angle at which the ions impinge on the surface, at least in some range close to normal incidence, which depends on temperature. This point will be developed later in greater detail.
6. The morphology depends on the ion used since the damage depends on the ratio between the masses of the projectile and target. Also, ion energy can change some details of the surface morphology, but not the general trend.



### 3.4. Anisotropic Surfaces

A typical example of an anisotropic surface is represented by the (110) surface of an fcc crystal. In this surface, the atoms are arranged in channel: they are more compact along the  $\langle 1-10 \rangle$  direction (the neighbor distance is  $a/\sqrt{2}$ , where  $a$  is the lattice constant). Along this direction, often called the “in-channel” direction as opposed to the “cross channel,” the adatom and vacancy diffusion is faster, so the mass transport is strongly asymmetric.

The first systematic study of the morphology induced by ion sputtering on such surfaces was done in 1997 by Rusponi et al. [23]. The main result is reported in Figure 7, where the morphology after the same dose, but at different temperatures is reported. The experimental conditions were:  $\text{Ar}^+$  ions, ion flux 0.03 ML/s, ion dose 27 ML, ion energy 1 keV.

The general behavior is quite similar to that reported in Figure 5: at low  $T$ , the surface is rough, while at high  $T$ , the surface is flat. However, in the intermediate temperature range, the situation is much more complicated. At 230 K, a clear organization along the  $\langle 100 \rangle$  is visible: we recall that, along this direction, surface diffusion is slow. At 270 K,

rectangular mounds are present on the surface, while at 290 and 320 K, well-developed ripples are now present, but aligned along the “in-channel” direction. The ripple structure rotates by  $90^\circ$  passing from 230 to 320 K: this rotation is characteristic of anisotropic surfaces since the two principal directions are inequivalent for surface diffusion. We observed a similar behavior on other anisotropic surfaces like Cu(110) [24] and Rh(110), thus concluding that ripple formation and rotation with temperature are general behavior for these surfaces.

In order to explain this effect in terms of surface diffusion, we need to introduce a more complicated model with respect to the isotropic case. In fact, we could expect ripples aligned along  $\langle 1-10 \rangle$  since, in this direction, the atoms can rearrange easily, but the observation of ripples along  $\langle 100 \rangle$  at 230 K seems to require a pronounced mass transport along this direction. To solve this question, a more accurate analysis of the surface diffusion barriers is required.

Up to now, we considered only the possibility for an adatom (or vacancy) to move freely along one direction on a large terrace; but in a real surface, the adatom can do many other movements: for example, it can move along a step, or detach from it, or try to descend a step. All of these processes have the appropriate energetic barrier, and then at a fixed temperature, the rate for each process can be more or less high. It is the competition among all of these processes which determines the shape and orientation of the nanostructures induced by ion sputtering. In particular, kinetic Monte Carlo simulations and other considerations suggest that an important role is played by the so-called Ehrlich–Schwoebel (ES) process: when an adatom tries to descend from a step, it must overcome an extra barrier due to the repulsion that the step takes against the atom. In other words, the adatom must have more energy to descend the step than to move on a terrace. In this way, the mass transport between different layers is frustrated, at least until the temperature is high enough to give sufficient energy to the moving adatom to overcome the ES barrier. It is clear that, if an adatom cannot descend from a step, it can continue to move on a terrace, and when it hits another adatom on the same terrace, a new condensation cluster is formed. In this way, material is continuously accumulated in the upper layers, and the mass transport is unbalanced: the growth of mounds and ripples is favored.

Obviously, this scenario is also valid for isotropic surfaces, but we present it in this section because it is most important in the case of anisotropic surfaces.

In this light, we can sketch a model for the results presented in Figure 7.

1. At low temperature, the diffusion of adatoms and vacancies is inhibited. The damage caused by an ion cannot be recovered, and the morphology is only due to the accumulation of the damage.
2. At 230 K, diffusion is fast enough along the in-channel direction, favoring the motion of adatoms; a nonzero probability exists that two adatoms running along two neighboring channels stick together, forming an island elongated in the cross-channel direction. These islands form the condensation nuclei for the growing ripples: when further material reaches the islands, it

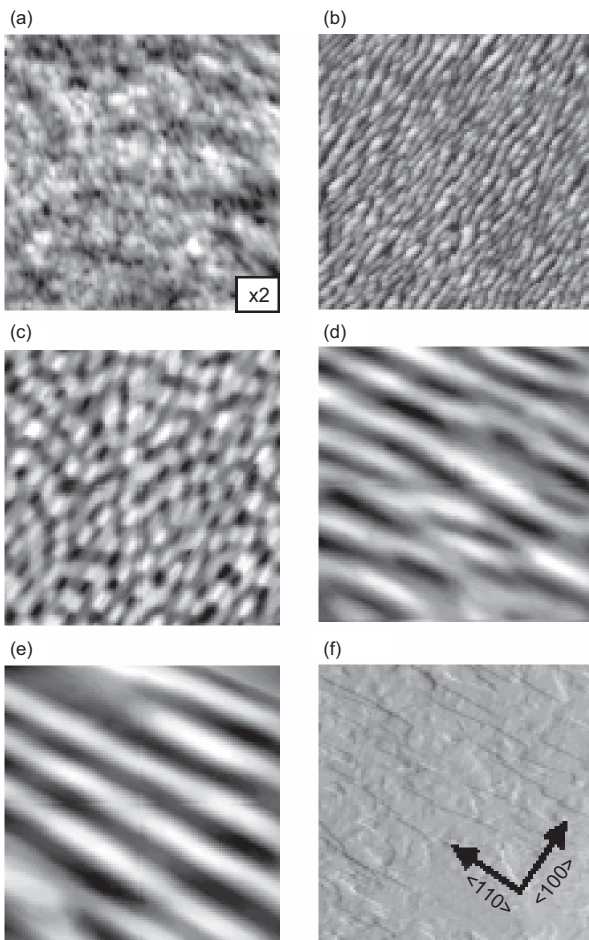


**Figure 7.** Six STM topographies taken after normal sputtering of Ag(110) by means of 1 keV  $\text{Ar}^+$ ; ion flux  $F = 0.03$  ML/s, ion dose 27 ML. The sputtering temperatures are, respectively, (a) 160 K, (b) 230 K, (c) 270 K, (d) 290 K, (e) 320 K, (f) 350 K. The scan size is  $175 \times 175$  nm<sup>2</sup> for image (a) and  $350 \times 350$  nm<sup>2</sup> for images (b)–(f).

accumulates as the ES barrier along the in-channel direction cannot be surpassed. Thus, the ripples grow along the cross-channel direction. We call this phase low-temperature ripple (LTR).

3. At 270 K, there is a balance between the rate at which the adatom can surmount the ES barrier along the in-channel direction and the probability to form islands in the cross-channel direction. Thus, almost rectangular mounds appear on the surface. We call this phase intermediate-temperature mounds (ITMs).
4. At 290 K, the bond between adatoms in adjacent channels is not more sufficient to stabilize the cross-channel islands, and so the condensation nuclei are now formed by islands elongated along the channel. The ES barrier along  $\langle 1-10 \rangle$  can be surpassed, and a relevant mass transport sets in along the in-channel direction. Then the original islands become more and more elongated, but also increase in height. Ripples are now formed along the easy diffusion direction. That is the high-temperature ripple phase (HTR).
5. At higher temperatures, the adatoms have sufficient energy to overcome the ES barrier along both directions: the recovery of the damage is now very effective, and the surface becomes flat.

The model depicted briefly above has been tested by means of kinetic Monte Carlo simulations [25] in a more simple situation, when only adatoms are deposited on the surface. The results are in good agreement with an experiment done under similar conditions [26].

Up to now, we have established that ion bombardment induces the formation of regular nanostructures on anisotropic surfaces, and that these nanostructures can assume different shapes, depending on temperature. However, the STM studies cannot answer the following question: How do these structures grow, starting from a flat surface? As mentioned in Section 3, the experiments based on microscopy generally do not allow following in real time the evolution of the surface morphology. For this reason, we performed a series of experiments by using X-ray diffraction. These experiments were carried out at the European Synchrotron Radiation Facility in Grenoble, France. We did two different kinds of diffraction experiments: in the first, the X-ray beam impinges on the sample at grazing angles (about  $1^\circ$  from the surface), and the scattered intensity is taken again at very low angles. In this way, the scattering of the photon holds in a few microns under the surface: the out intensity is modulated by the surface morphology, and collecting it as function of the exit angle, we can analyze the periodicity of the structures on the surface. This method is called grazing incidence small-angle X-ray scattering (GISAXS).

The second method consists of collecting the scattered intensity around a Bragg peak: in this case, called a crystal truncation rod (CTR) scan, the intensity is modulated by the shape of the nanostructures. Both methods can be applied during ion sputtering, so they allow following the growth of the nanostructures in real time.

In Figure 8, we report the spatial periodicity as a function of the ion dose in the case of Cu(110). The experimental conditions were:  $\text{Ar}^+$  ions, ion flux 0.015 ML/s, and ion

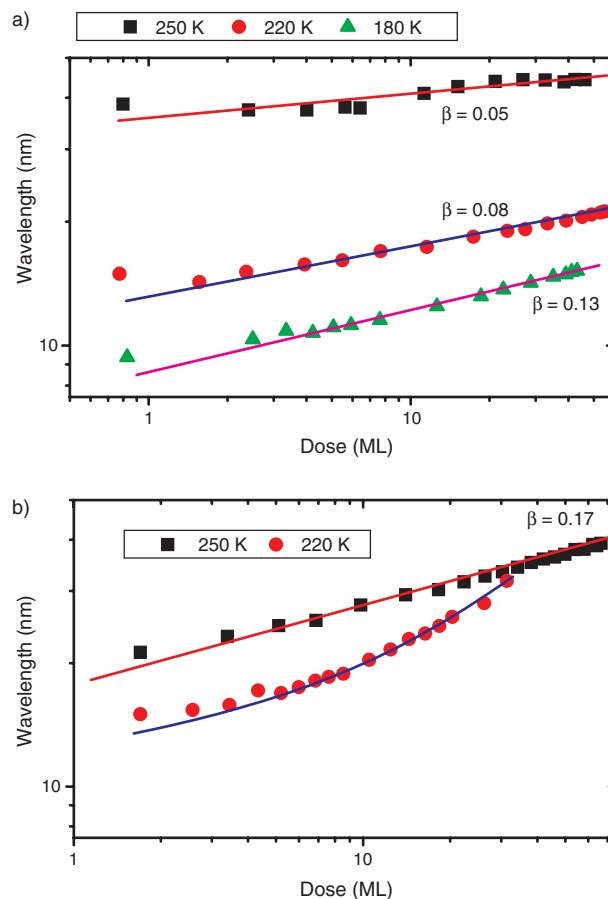


**Figure 8.** Ripple wavelength as a function of the ion dose in the case of Cu(110) at different temperatures, as determined by X-ray diffraction. (a) shows the slope of the facets along the  $\langle 100 \rangle$  direction, and (b) the slope of the facets along the  $\langle 1-10 \rangle$  direction.

energy 1 keV. The spatial periodicity was measured along the two principal surface axes,  $\langle 1-10 \rangle$  and  $\langle 100 \rangle$ . At 180 K, only the periodicity along  $\langle 100 \rangle$  can be observed: this situation corresponds to the LTR phase described before. The wavelength increases with the dose, following a simple power law  $L \sim D^b$ , with  $b = 0.13$ . At other temperatures, periodicity is seen along both directions, indicating that we were in the ITM phase. Also in this case, the distance between features increases with the dose, but with a different  $b$ . We notice that, within the experimental time range, no saturation in the wavelength has been observed.

The increase of the spatial periodicity with dose indicates that, during sputtering, a coarsening of the ripples occurs. We do not have any clear indication, but it seems that, at the beginning, small ripples are formed, which coalesce and mix in greater structures when sputtering proceeds. This result is quite important since, in nonmetallic materials, as will be shown in the next paragraph, the spatial periodicity does not change with the dose, indicating that, in these two classes of material, the formation of ripples or mounds has a common origin, but a different time evolution. This has to do with the much higher diffusivity on the metal surfaces.

In Figure 9, we report the evolution of facets slope for Cu(110) as deduced from CTR scans acquired during sputtering. Due to the particular geometry used in the

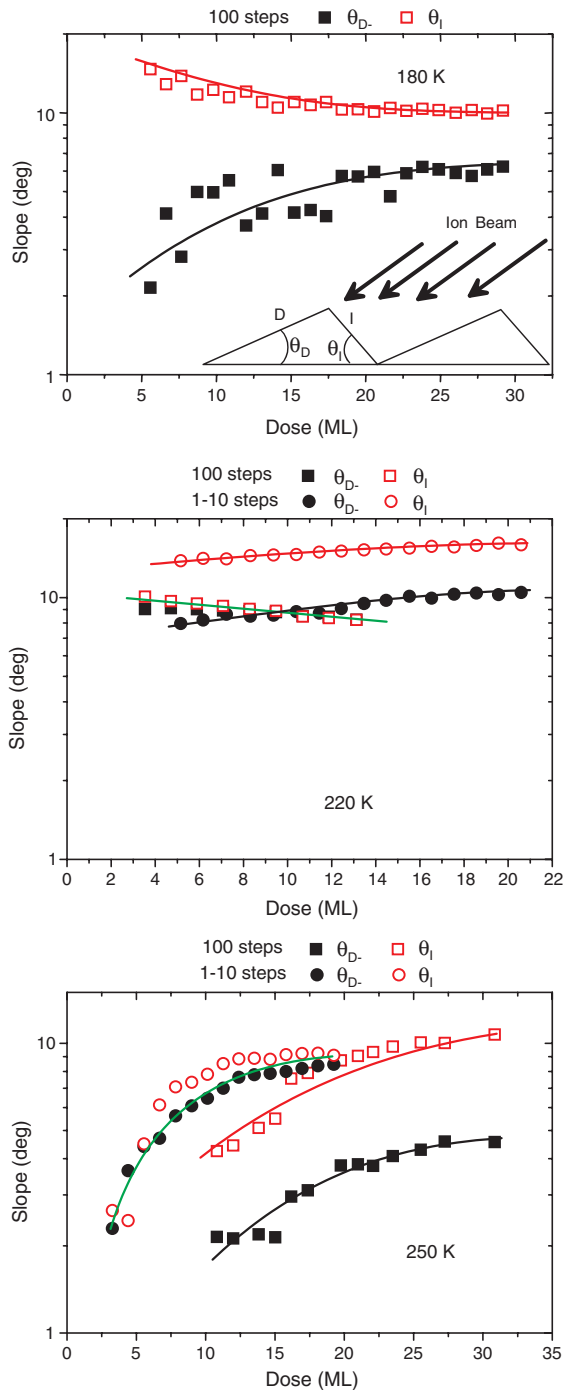


**Figure 9.** Time evolution of the local slope in the case of Cu(110). In the inset, the sputtering geometry is shown. The incident angle is  $54^\circ$  with respect to the flat surface.

experiment (see the inset in Fig. 9), the nanostructures formed on the surface are asymmetric: the side in front of the beam (illuminated *I* side) has a slope different from the other (dark *D* side). The results are quite interesting: at 180 K, the *I* side is very steep at the beginning, while the *D* side is almost flat. Increasing the dose, the system evolves toward a more symmetric shape, gaining an equilibrium value after about 20 ML. At 230 K, the situation is

completely different: for the step along  $\langle 100 \rangle$ , the slopes of both sides change very slowly with the dose, and they have almost the same value; also, for the steps along  $\langle 1-10 \rangle$ , the change is not too great, but the difference between the *I* and *D* sides is more relevant. Increasing the temperature to 250 K, the situation changes again: now, the evolution of the slopes along the two directions is quite high, with the difference that also, at this temperature, the steps along  $\langle 100 \rangle$  have the same slope, while there is a difference of about  $5^\circ$  in the other direction.

How can we interpret these results? First, it is clear that the nanostructures evolve in time, not only in spatial periodicity, but also in their shape. The system gains an equilibrium only after about 20 ML. Moreover, this evolution depends on the temperature, indicating again that are diffusion processes which play a key role in the determination of the surface morphology. Another important aspect to consider is the nature of the ion impacts: as depicted in [16], the effect of an ion hit is different, depending on the surroundings of the impact point. If it is in a flat region (like a large surface terrace), adatom and vacancy islands are created, and they can move or coalesce, as explained before. But if the ion impinges on a stepped region (i.e., a region in which the terraces have a size of a few atomic spaces), the defects created by the impact are efficiently annihilated and incorporated at steps, leaving the morphology unchanged (cf. [20, Fig. 6]).

We notice that, unfortunately, the simulations of the sputtering process are more complicated than the molecular growth. First, two different time scales are involved: the damage is completely determined in a few picoseconds, while the diffusion of the surface defects (adatoms and vacancies) occurs in milliseconds. This great difference in time scale does not allow us to develop practical codes for the simulations. Second, since the defects created by the ions are mainly clusters, the number of possible atomistic processes increases considerably (movement of the clusters, detachment of atoms and vacancies from the clusters, coarsening, periphery diffusion), again hindering the development of a suitable code.

GISAXS measurements, but also He beam scattering and SPA-LEED experiments, have been applied to study another important aspect of the ripple or mound morphology: the decay in time of these nanostructures. In fact, in metals, the nanostructures are unstable in time since the diffusion processes tend to smoothen the surface in order to obtain a lower free energy. Of course, this process depends on temperature and on the particular material: for Cu and Ag, room temperature is high enough to cause a smoothening of the surface in few hours, while for Rh and Pt, it is necessary to increase  $T$  up to about 600–700 K before observing the disappearance of the nanostructures.

The decay of the nanostructures induced on metals can prevent their use in applications like nanostamping or as substrates to induce order in organic or nematic thin films (see Section 6). In some cases, we can prevent the decay by a simple oxidation procedure. The method has been tested on Ag, Cu, and Al. In Cu(100) [27], the method allows us to stabilize for several days nanostructures that would otherwise decay in a few hours at room temperature.



### 3.5. Erosive Regime

In the previous paragraphs, we summarized the results obtained on simple metals, but in all of the experiments reported, a common aspect must be emphasized: the angle of incidence of the ions was always close to normal (say in a cone of about  $30^\circ$ ). In this condition, the damage induced is well described as in Section 3.1, and the final morphology is mainly due to the diffusion processes as reported in Sections 3.2 and 3.3. We call this experimental condition a “diffusive regime.” The nanostructures do not depend on the azimuthal angle, that is, nothing changes if the ion impinges on the target along one surface direction or another.

What happens if this condition is not fulfilled, that is, if the ion impinges on the target at angles close to grazing incidence? The answer to this question is the topic of the present paragraph.

We have seen that the damage caused by a single ion does not depend on temperature since the energy released is much higher than the cohesive energy between atoms in the target, but temperature is important to determine how this damage can be removed. If the sputtering is done at grazing incidence (angle  $\vartheta > 60^\circ$  from normal), nothing changes if the temperature is high enough. The picture changes completely if the sputtering is done at grazing incidence and low temperature: in this case, the defect diffusion is very slow, and increasing the dose, a pile up of defects occurs. When the roughness is high enough, the dominant effect becomes the erosion caused by the impinging ion. The evolution of this particular morphology is shown in Figure 10. Ag(100) is bombarded with  $\text{Ar}^+$  ions (energy 1 keV) at a very low flux (0.01 ML/s). The incidence angle is fixed at  $70^\circ$ . The white arrow in the first image corresponds to the projection on the surface of the ion beam. After 1 s, the single impact defects are visible on the surface; they are completely equivalent to that reported in Figure 2 (produced at normal incidence). If we look at the spatial distribution of the adatom islands around the ion crater, we do not recognize any elongation along the beam direction, but only an isotropic distribution around the impact point. This observation is very important: the single impact induces the same kind of defects independently on the impact angle at least in the range  $0\text{--}70^\circ$ . Then the formation of ripples cannot be attributed to the shape of the damage caused by a single ion.

After 30 s ( $D = 0.3$  ML), we see that the damage is accumulated on the surface, but there is still no evidence of any self-organization. After 720 s ( $D = 7.2$  ML), the self-organization along the ion beam direction is evident. The last image shows the autocorrelation function of the STM image, which clearly evidences the orientation of the structure along the ion beam.

To distinguish this experimental condition from the ones described in the previous paragraphs, we call it an “erosive regime.” The surface diffusion still plays a role: in fact, if the temperature is lowered enough, the time to observe ripples increases substantially. Now, the ripple direction is not related to any surface direction; it is only determined by the ion beam, as clearly shown in Figure 11. In this experiment on Cu(110) [24], we fixed  $T = 180$  K,  $E = 1$  keV,  $F = 0.03$  ML/s, and  $D = 27$  ML. Only the incidence angle

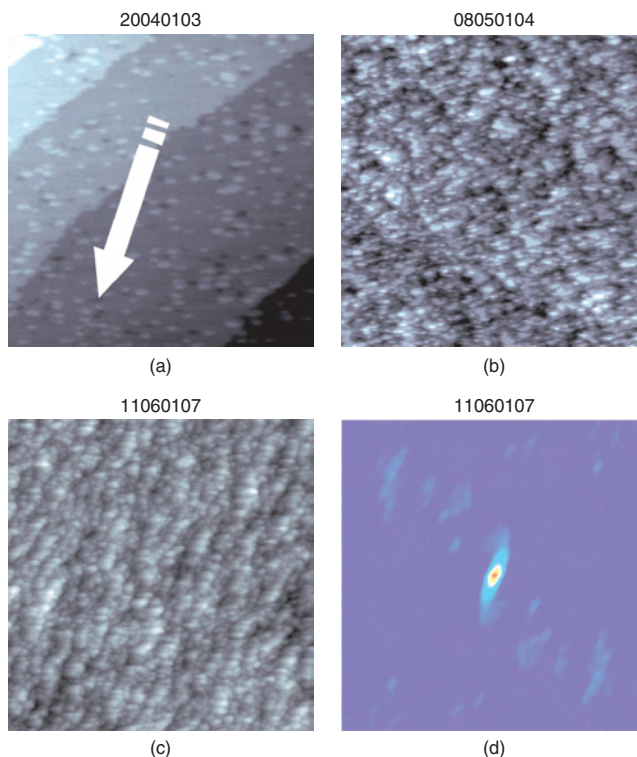


**Figure 10.** STM topographies of the initial stages of the nanostructuring of Cu(110) in erosive regime ( $\text{Ar}^+$ , ion energy 1 keV, ion flux 0.01 ML/s,  $T = 180$  K). The (a) image has been acquired after 1 s (scan size  $90 \times 90$  nm<sup>2</sup>), (b) after 30 s (scan size  $200 \times 200$  nm<sup>2</sup>), and (c) after 720 s (scan size  $200 \times 200$  nm<sup>2</sup>). In (d), the autocorrelation function of the (c) image is reported.

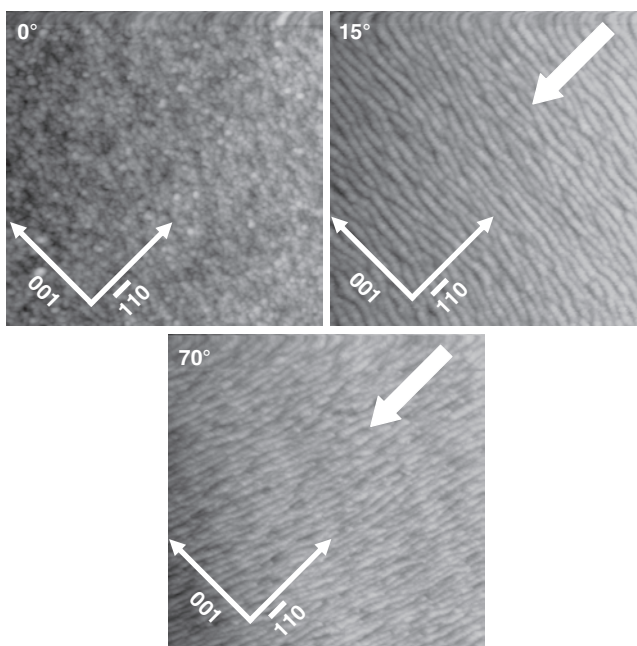


**Figure 11.** The role of the incidence angle  $\theta$  in the transition from the diffusive to the erosive sputtering regime for Cu(110) at  $T = 180$  K. The white arrow shows the ion-beam scattering plane. For all images,  $\text{Ar}^+$  sputtering at  $E_i = 1$  keV, ion flux 0.03 ML/s, ion dose 27 ML. Image size  $400 \times 400$  nm<sup>2</sup>.

is varied from 0 to 70°. At normal incidence, the surface appears rough, while for  $\vartheta$  between 15 and 55°, the ripples are aligned along the  $\langle 100 \rangle$  direction: the system is in the LTR phase depicted in Section 3.3. For  $\vartheta > 65^\circ$ , the ripples rotate along the ion beam projection, which in this experiment was along the  $\langle 1-10 \rangle$  direction. We emphasize that this 90° rotation is quite different from the previously reported (Section 3.2) as there, the temperature is fixed.

In the “erosive regime,” the surface symmetry directions play no role in determining the final ripple alignment: we observed quite similar ripples on Ag(110), Ag(100), Cu(100), and Cu(110) [28], independent of the direction on which the ions hit the target. The spatial periodicity increases with the dose, but more slowly than in the diffusive regime. In this sputtering regime, mound formation has never been observed. In many aspects, the ripples so created are similar to those produced on nonmetallic materials (see Section 4).

Before concluding this paragraph, we want to mention an interesting work done by Poelsema and collaborators [29] on Cu(100). They bombarded the surface at a very grazing incidence (about 80°). Under these conditions, vacancy islands one or two layers deep are formed, with a spatial periodicity that can be changed by varying the temperature. Also in this case, the elongation direction is independent of the surface symmetry, but is parallel to the ion beam.

### 3.6. Sputtering and Growth

So far, we have investigated the effect of ion sputtering on metal surfaces, showing that all of the observed morphologies are related to the damage from the ion impact and the recovery of it via surface diffusion of defects. Since a single impact causes the formation of a vacancy cluster and few adatom clusters, it is a natural consequence to suggest that ion sputtering is quite similar to the deposition process, with the only difference being that, in the latter, only (single) adatoms are deposited. This analogy is the topic of this paragraph.

In a recent experiment, Buatier de Mongeot et al. [30] deposited Ag on Ag(110) at different temperatures, following the morphology with high-resolution electron diffraction (SPA-LEED). Also in this case, the presence of regular structures is evident: at 130 K, they observed elongated features (ripples) oriented along the  $\langle 001 \rangle$  direction, exactly what happens on the sputtered surface at a low temperature (LTR phase). Increasing  $T$ , the symmetry of the diffraction pattern becomes fourfold, indicating that rectangular mounds are now present (ITM phase). Finally, ripples appear again at 210 K, but rotated by 90° with respect to those observed at low  $T$  (HTR phase).

However, the temperature at which the rotation sets in is different between the two cases: about 170 K in growth and about 270 K in sputtering. This difference is easily explained since the movement of the clusters produced in the ion impact requires a greater activation energy. The observation that the morphologies created by the two methods (erosion and deposition) are quite similar, eventually in a different temperature range, also has been done by Busse et al. [11] on Al(111). They bombarded the surface with different rare gas ions, and surprisingly, they did not

observe an “eroded” surface like on Pt(111) (cf. Fig. 4), but an unexpected island and mound structure, typical of atomic deposition.

Before we conclude this paragraph, we want to emphasize another aspect of the analogy sputtering—deposition. In many computer simulations, ion erosion has been seen as a “vacancy deposition,” in which a beam of “vacancies” is directed against a surface [31, 32]. This method allows us to obtain results in agreement with experimental data, but can be applied only if the sputtering temperature is high enough [33].

## 4. OTHER MATERIALS

In 1956, Navez et al. [34], by bombarding a glass surface with an ion beam of air, observed for the first time a curious phenomenon: the bombardment produced a new morphology depending mainly on the incidence angle  $\theta$  of the ion beam. A clean glass surface was exposed for 6 h to the ion beam at incidence angles ranging from 30 to 80°. The surface was covered by wave-like structures (ripples) separated by distances ranging from 30 ( $\vartheta = 80^\circ$ ) to 120 nm ( $\vartheta = 30^\circ$ ), which are stable under ambient conditions after the ion bombardment is finished. For incident angles close to  $\vartheta = 0^\circ$ , the ripples are perpendicular to the ion beam direction, while they rotate by 90° when the beam reaches the surface at grazing incidence. In contrast, when the bombardment is performed at normal incidence, one observes a regular structure formed by elements of a diameter of about 40 nm. The authors did not provide an accurate explanation at that time, but simply tried to find analogies with macroscopic phenomena such as the ripple structures formed by wind over a sandbed. After this pioneering experiment, other groups investigated the effects of ion bombardment on semiconductor and amorphous materials.

First, we examine the results of a single ion impact on a semiconductor surface. At low energies (<5 keV), which are of interest in this chapter, sputtering of atoms by direct knock-on effects is observed [35, 36]: each ion causes the ejection of one or a few atoms from the surface, but not the growth of adatoms islands around the crater. Sometimes, bumps have been observed, but they have been interpreted as a mechanism to relax strain, induced in a subsurface region by the collision cascade caused by the ion. Similar effects also have been reported for HOPG.

These results represent the first important difference between the sputtering on metal and nonmetal materials: in the latter, the surface morphology is dominated only by vacancies, and the internal damage is quite relevant, leading to the amorphization of the near surface layers as sputtering proceeds. Basing on this conclusion, we can foresee that the accumulation of damage (i.e., for increasing doses) has quite different consequences in the two classes of materials.

Ripples produced by off-normal ion scattering have been observed on SiO<sub>2</sub> [37], HOPG surfaces with (0001) orientation [38, 39], diamond [40], Si [41], GaAs [42], and Ge [43].

The results obtained on nonmetal materials can be summarized in the following way.

1. Ripples can be produced, but only at nonnormal angles of incidence.

2. A critical angle  $\vartheta_c$  exists, for which, if  $\vartheta < \vartheta_c$ , the ripples are perpendicular to the ion beam, and if  $\vartheta > \vartheta_c$ , they are parallel. Thus, the ripple orientation is determined by the beam direction, and not by the crystal symmetry.
3. The spatial periodicity does not change in time, but it depends on ion flux and temperature.
4. The time evolution is much slower than in metals: for comparable ion fluxes, ripples appear on nonmetal material in a time which can be ten times greater. That means that the mass transport on such materials is quite reduced with respect to metals.
5. Mounds can be formed only if  $\vartheta = 0^\circ$ .
6. Structures are stable in time up to elevated temperatures.

It is evident from these considerations that nanopatterning by ion sputtering leads to quite different results in the two classes of materials. The closest results are found in the “erosive regime” since, here also for metals, the surface symmetry does not influence the ripple morphology. However, as we will show briefly in the next section, from a theoretical point of view, the sputtering process can be described in a quite general framework.

## 5. THEORETICAL MODELS

Starting from Sigmund’s theory of sputtering, Bradley and Harper in 1988 [44] proposed the first model (in the following, referred to as the BH model), which explains why ion bombardment produces periodic height modulations on the surface of amorphous solids.

The rate at which the material is sputtered from a point  $O$  of a surface is proportional to the power dissipated there by the random distribution of the incoming ions. They penetrate the surface and transfer their kinetic energy to the atoms of the substrate, which may start secondary collisions, thereby generating other recoiling atoms. A small fraction of the atoms is sputtered away, while some of them are permanently removed from their sites, making the substrate locally amorphous. In the limit of low energy of the incoming ions, the average energy deposited at  $O$  because of an ion penetrating into the crystal follows the Gaussian law:

$$E(r') = \frac{\varepsilon}{(2\pi)^{3/2} \alpha \beta^2} \exp[-(z')^2/2\alpha^2 - (x'^2 + y'^2)/2\beta^2] \quad (2)$$

where  $a$  is the mean range of ion penetration,  $\alpha$  is the longitudinal and  $\beta$  is the lateral straggling width, and  $\varepsilon$  is the total energy deposited;  $a$ ,  $\alpha$ , and  $\beta$  define the atomic collision cascade. The model calculates the normal component of the velocity of erosion at a generic point  $O$  of the interface when a uniform flux  $J$  hits the surface. The details are reported in [44].

Here, we limit ourselves to reporting the most important steps. For simplicity, let us reduce the model to a (1 + 1)-dimensional one. The incoming beam direction forms an angle  $\varphi$  with the direction normal to the surface  $Y$ .  $Y$  and the trajectory of the incoming ion beam form a plane containing the  $X$  axis. We point out that  $\varphi$  changes from point to point along the surface. The radius of curvature at  $O$

is  $R_X$  (positive when the surface is concave, and negative when the surface is convex). Let us define the velocity of erosion  $v(\varphi, R_X)$  as the velocity at which the surface retracts because the atom loosens. The sputtering yield  $Y(\varphi)$  is related to  $v(\varphi, R_X)$  by the following expression:

$$Y(\varphi) = nv(\varphi, R_X)/J \cos(\varphi) \quad (3)$$

where  $n$  is the number of atoms per unit volume in the amorphous solid and  $J$  is the flux of the incoming ions. Bradley and Harper showed that Eq. (3) in the limit  $a/R_X \ll 1$  can be approximated to the first order in  $a/R_X$ , giving the following expression for the erosion velocity:

$$v(\varphi, R_X) = \frac{J}{n} Y_0(\varphi) [\cos(\varphi) - \Gamma_X(\varphi) a/R_X] \quad (4)$$

In Eq. (4),  $Y_0(\varphi)$  corresponds to the sputtering yield of a flat surface, and depends only on the parameters that define the collision cascade ( $\varepsilon, \alpha, \beta$ ) and on the angle  $\varphi$ . The expression  $Y_0(\varphi)$  deduced by Bradley and Harper is an increasing function of  $\varphi$ , and therefore limits the model to angles not too close to grazing incidence, where the sputtering yield starts to decrease with  $\varphi$ .  $\Gamma_X(\varphi)$  is a function of  $\varphi$  and of the parameters  $\alpha$  and  $\beta$ . For  $a = \alpha = \beta$ , that is, for a spherical distribution of the deposited energy,

$$\Gamma_X(\varphi) = \sin^2(\varphi) \sin^2(\varphi/2) - \cos^2(\varphi/2) \quad (5)$$

The dependence of the erosion velocity on the curvature is in the term  $\Gamma_X(\varphi) a/R_X$ . For instance, for normal ion incidence,  $\Gamma_X(\varphi = 0)$  is negative, while the curvature is positive in the trough and negative in the crest; then the product  $\Gamma_X(\varphi = 0) a/R_X$  is negative in the trough and positive in the crest. The velocity of erosion is therefore faster for the trough than for the crest. The results are easily generalized [44] to arbitrary surfaces:

$$v(\varphi, R_X, R_Y) = \frac{J}{n} Y_0(\varphi) [\cos(\varphi) - \Gamma_X(\varphi) a/R_X - \Gamma_Y(\varphi) a/R_Y] \quad (6)$$

Until now, the above equations are written in a local frame, referred to the impact point  $O$ . More useful expressions can be expressed in the laboratory frame  $(x, h)$ , where  $h$  is the normal to the initial flat surface. The ion beam forms with  $h$  an angle  $\theta$ , while the plane containing  $h$  and the ion trajectory identifies the  $x$  axis. The time evolution of the surface is described by the height function  $h(x, t)$  measured from the initial flat configuration and  $\varphi = \theta + (\partial h/\partial x)$ .  $\theta$  is a fixed angle, while  $\varphi$  changes from point to point along the surface. The equation of motion is obtained by writing the normal component along  $h$  of the velocity of erosion, assuming that the surface height varies slowly. Equation (3) becomes

$$\begin{aligned} \frac{\partial h}{\partial t} = & -\frac{J}{n} Y_0(\theta) \cos(\theta) + \frac{J}{n} \frac{\partial}{\partial \theta} [Y_0(\theta) \cos(\theta)] \frac{\partial h}{\partial x} \\ & + \frac{Ja}{n} Y_0(\theta) \left[ \Gamma_X(\theta) \frac{\partial^2 h}{\partial x^2} \right] \end{aligned} \quad (7)$$

The first term is the rate of erosion of the unperturbed planar surface and the two other terms contain the dependence of the sputtering yield on the local curvature. This is the



fundamental equation in the BH model, written in (1 + 1) dimensions.

It is easy to generalize it to an arbitrary surface  $h(x, y, t)$  [44]. In Eq. (7), all terms concern the erosion of the surface by ions, but Bradley and Harper recognized that a smoothing mechanism is needed to explain the presence of ripples. Then they added a term which takes into account the diffusion of atoms on the surface. After some manipulation, Eq. (7) becomes

$$\frac{\partial h}{\partial t} = -v_0(\theta) + \frac{\partial v_0(\theta)}{\partial \theta} \frac{\partial h}{\partial x} + v_x(\theta) \frac{\partial^2 h}{\partial x^2} + v_y(\theta) \frac{\partial^2 h}{\partial y^2} + K \nabla^2 \nabla^2 h + \eta(x, y, t) \quad (8)$$

where  $K$  is a coefficient which depends on the surface self-diffusivity  $D$ , the free energy per unit area  $\gamma$ , and the number of atoms per unit area moving across the surface, and  $\eta(x, y, t)$  is a Gaussian white noise with zero mean and variance proportional to the ion flux  $J$ , which takes into account the stochastic arrival of the ions.

In this expression, the sputtering yield dependence on local curvature is now in the terms  $v_x(\theta)$ ,  $v_y(\theta)$ , which can change sign as the angle of incidence of the ion is varied.

Bradley and Harper did a stability analysis of this equation, imposing a sinusoidal form for the function  $h(x, y, t)$ , and looking for its time evolution. This approach is based on the observation that any periodical corrugation, as ripples are, can be expressed as a sum of sinusoidal amplitudes. Applying this analysis to the BH model, it is possible to demonstrate that a ripple with a defined wavelength can grow during the sputtering process. Its spatial periodicity is equal to

$$\lambda_i = 2\pi \sqrt{2K/|v_i|} \quad (9)$$

where  $i$  refers to the direction ( $x$  or  $y$ ) along which the associated  $|v_i|$  is the largest. We point out that the direction  $x$  is along the ion beam, while  $y$  is perpendicular to it. Since the coefficients  $v_x(\theta)$ ,  $v_y(\theta)$  change magnitude and sign in dependence on the incidence angle, a critical value  $\theta_c$  exists so that, for  $\theta < \theta_c$ , the ripple is perpendicular to the ion beam, and for  $\theta > \theta_c$ , it is parallel. Due to its intrinsic approximations, the BH model works well at intermediate ion doses, when erosion produces ripples with a small local slope.

The consequences of the BH model have been verified in many experiments on amorphous and semiconductor materials. The ripple rotation at grazing incidence angles has been verified in graphite, glass, SiO<sub>2</sub>, diamond, Si, GaAs, and Ge.

The dependence of the ripple structure on the ion energy is in the erosive terms  $v_{x,y}(\theta)$ : they depend on the way in which the energy is released in the surface, and then they are related to the penetration depth of the ion, which is a function of energy. Then we expect that the ripple wavelength is a function of the energy. More precisely, we expect that

$$\lambda_{x,y} \propto E^p \quad (10)$$

Such a behavior has been verified on graphite [39] ( $p = 1$ ), Si [45] ( $p = 0.8$ ), and diamond [40] ( $p = 1$ ). However, the

BH model foresees a flux dependence of the ripple wavelength ( $\lambda \sim \Phi^{1/2}$ ) which has been observed only in Si [41].

In the BH model, the behavior of the wavelength with temperature is determined by the surface mobility of the diffusing species. By writing the surface diffusivity  $D$  as

$$D = D_0 \exp\left(-\frac{E_a}{k_B T}\right) \quad (11)$$

where  $E_a$  is the activation energy for surface self-diffusion, the coefficient  $K$  of Eq. (8) depends on the temperature as

$$K = \frac{D_0 \gamma^\sigma}{n^2 k_B T} \exp\left(-\frac{E_a}{k_B T}\right) \quad (12)$$

and on the wavelength as

$$\lambda_{x,y} \propto T^{1/2} \exp\left(-\frac{E_a}{2k_B T}\right) \quad (13)$$

The effect of surface mobility during ion-beam treatment has been studied experimentally on graphite. The experiment shows that the ripple wavelength increases slowly with temperature, from 70 to 110 nm between 300 and 450 K as expected, due to the increase of the surface mobility. Comparing the results with the BH model, Habenicht obtained an activation energy of  $E_a = 0.14$  eV, which is rather small compared to others. He ascribes this fact to radiation-enhanced diffusion effects that should be taken into account. However, the energy deposition of the ion beam into the near surface region can affect several parameters of the surface mobility, such as the density of diffusing species, the surface free energy, and the activation energy for surface diffusion.

The model cannot account for the formation of ripples at low temperature since it considers only a thermal mechanism of smoothing. Additional mechanisms have been proposed to explain the inadequacy of BH model. In particular, Makeev and Barabasi [46] demonstrated that ion sputtering could produce an effective surface diffusion (ESD) that does not imply mass transport. The ESD explains the presence of ripples at low temperatures where the surface diffusion is not activated, and was predicted in the computer simulation of the ripple formation on amorphous carbon [47] and observed in the case of GaAs [48].

Besides its ability to explain most of the experimental results, the BH model fails when the ion dose becomes larger and larger. Cuerno and Barabasi [49] revisited the BH model, introducing two new terms in the equation:

$$\frac{\partial h}{\partial t} = -v_0(\theta) + \frac{\partial v_0(\theta)}{\partial \theta} \frac{\partial h}{\partial x} + v_x(\theta) \frac{\partial^2 h}{\partial x^2} + v_y(\theta) \frac{\partial^2 h}{\partial y^2} + \frac{\eta_x}{2} \left(\frac{\partial h}{\partial x}\right)^2 + \frac{\eta_y}{2} \left(\frac{\partial h}{\partial y}\right)^2 + K \nabla^2 \nabla^2 h + \eta(x, y, t) \quad (14)$$

The coefficients  $\eta_x$ ,  $\eta_y$  depend on parameters such as the penetration depth and the angle of incidence. In this way, the equation becomes nonlinear, and the temporal evolution of the height  $h$  shows a transition from a periodic to a fractal behavior, as found in the experiments.

We have seen that the BH model (and its modifications) is able to reproduce most of the experimental findings in semiconductors and amorphous materials. But when we try to apply it to the metal case, some difficulties arise. First, the spatial periodicity increases in time, both in the diffusive and erosive regime. This effect is out of the model. Second, periodic patterns also appear at normal incidence, while in the model, no regular pattern can grow if  $\vartheta = 0^\circ$ . Finally, the nanostructures on metals are crucially dependent on temperature (in shape and periodicity). On the other hand, many features have their behavior foreseen by the model: the periodicity depends on the ion flux as  $\Phi^{1/2}$ , at grazing incidence the ripples are always parallel to the ion beam, and so on.

In order to explain these differences, we proposed to modify the diffusion terms in Eq. (14) [24]. In fact, while the erosive terms have an expression that is quite general, which depends only on the parameters of the sputtering, the diffusion terms are too simple, as they do not take into account many aspects of the diffusion processes in metals: the existence of different energetic barriers, the directionality of the diffusion, and the existence of different diffusing species. However, a detailed study of the equation and its consequences is still in progress.

## 6. APPLICATIONS

In this section, we illustrate some applications of the ion sputtering in different fields. The advantage of the method is that it is very easy to perform, can be used to nanostructure large samples (several  $\text{cm}^2$ ), and the results depend on easily controlled parameters, such as ion beam energy, incidence angle, ion species, ion flux and dose, and substrate temperature.

Ion erosion has interesting applications in chemistry. Creating and controlling the density of artificial defects may lead to the growth of materials with unusual catalytic properties. In fact, artificially created surface defects can enhance the surface reactivity. One illuminating example of this possibility is the experiment of Costantini and co-workers [50, 51], who recently demonstrated that the dissociation probability of  $\text{O}_2$  on  $\text{Ag}(100)$  can be enhanced by orders of magnitude after modification with ion sputtering. The most interesting result is that the reactivity can be tuned by changing the angle of sputtering. The dissociation probability of  $\text{O}_2$  molecules changes from less than  $10^{-3}$  on the flat surface to 0.1 on the rippled surface. In perspective, this straightforward result opens up the possibility to control the chemical properties of a surface by modifying *in-situ* its morphology, that is, by creating different amounts and different kinds of defects, like kinks at step edges, on which the reactivity of the chemisorbed species can be enhanced. The recent observation of similar structures on  $\text{Rh}(110)$ , which were investigated by X ray diffraction, suggests possible applications in catalysis.

The fabrication of quantum dots (QDs) is currently a topic of great interest due to the potential applications in optoelectronics. However, the methods available for their fabrication are rather limited because the actual lithographic techniques cannot produce QDs of appropriate size and density for device applications. Facsko et al. gave the first

evidence of QD fabrication via ion erosion in the case of  $\text{GaSb}(100)$  [52, 53]. They observed that ion erosion creates dots remarkably well ordered and uniformly distributed. The method of ion erosion may therefore open a new road for nanofabricating large-area surfaces patterned at low cost.

But the potential applications are also in other fields of material science. Using ion erosion, it was recently possible to fabricate magnetic wires structures in the case of a Co film deposited on a  $\text{Cu}(100)$ . The experiment shows a remarkable change in the magnetization anisotropy of the film after bombardment by ions. 5 ML of Co have been deposited on a  $\text{Cu}(100)$  surface at  $T = 180$  K. The sample has been successively bombarded with  $\text{Ar}^+$  ions at an incident angle of  $70^\circ$  (erosive regime),  $E = 1$  keV; in this condition, the ripples supported on  $\text{Cu}(100)$  are elongated along the projection of the ion beam on the surface.

Finally, ion erosion can produce nanoscale patterned substrates for deposition methods either on metallic substrate or glasses [54]. Rippled glasses are also expected to be good candidates as templates, for instance, for aligning liquid crystals or organic molecules.

## 7. CONCLUSIONS

In this chapter, we reviewed the results on surface nanostructuring by ion sputtering, mainly in the case of metal surfaces. The surface morphology is found to be dependent on surface symmetry if the temperature is high enough and the incidence angle is close to zero (normal incidence). In this diffusive regime, the diffusion of the surface defects (adatom and vacancy clusters) created by the ion impact determines the evolution of the morphology. On the contrary, in the erosive regime (low temperature and grazing incidence), the ripples created are determined only by the ion beam direction. The possibility to pattern metal surfaces on a nanometer scale opens a new route to many applications in nanotechnology since the ion sputtering method can be applied easily and also adapted to large-scale production.

## GLOSSARY

**Atomic force microscope (AFM)** Microscope based on a cantilever with a sharp tip, which is deflected by the forces acting between the surface and the tip. An AFM can resolve atoms on insulating materials.

**Low energy electron diffraction (LEED)** Instrument based on the reflection of electrons from a surface. It gives information on the symmetry of the surfaces.

**Scanning tunneling microscopy (STM)** Microscope based on the tunneling effect, able to resolve atoms on a metallic surface.

**Secondary ions mass spectroscopy (SIMS)** Analytical technique that uses ion sputtering to extract other ions from the surface. These secondary ions are analyzed with a mass spectrometer, in order to get information on the chemical species present on the surface.

**Spot profile analyzer-LEED (SPA-LEED)** A variance of normal LEED, used to observe symmetry on a larger scale.

## REFERENCES

1. M. V. Ramana Murty, *Surf. Sci.* 500, 523 (2002).
2. G. Carter, *J. Phys. D: Appl. Phys.* 34, R1 (2001).
3. U. Valbusa, C. Boragno, and F. Buatier de Mongeot, *J. Phys.: Condens. Matter* 14, 8153 (2002).
4. P. Sigmund, "Sputtering by Particle Bombardment I" (R. Behrisch, Ed.), Vol. 47. Springer, Berlin, 1981.
5. T. Diaz de la Rubia, R. S. Averback, R. R. Benedek, and W. E. King, *Phys. Rev. Lett.* 1930 (1987).
6. P. Sigmund, *Phys. Rev.* 84, 383 (1969).
7. P. Sigmund, *Phys. Rev. B* 184, 383 (1969).
8. M. W. Thompson, *Philos. Mag.* 18, 377 (1968).
9. M. Nastasi, J. W. Mayer, and J. K. Hirvonen, "Ion-Solid Interactions: Fundamentals and Applications." Cambridge, Cambridge University Press, 1996.
10. T. Michely and C. Teichert, *Phys. Rev. B* 50, 11156 (1994).
11. C. Busse, C. Engin, H. Hansen, U. Linke, T. Michely, and H. M. Urbassek, *Surf. Sci.* 488, 346 (2001).
12. S. Rusponi, C. Boragno, R. Ferrando, F. Hontinfinde, and U. Valbusa, *Surf. Sci.* 440, 451 (1999).
13. K. Morgenstern, E. Laegsgaard, I. Stensgaard, and F. Besenbacher, *Phys. Rev. Lett.* 83, 1613 (1999).
14. K. Morgenstern, G. Rosenfeld, E. Laegsgaard, F. Besenbacher, and G. Comsa, *Phys. Rev. Lett.* 80, 556 (1998).
15. G. Rosenfeld, K. Morgenstern, I. Beckmann, W. Wulfhekel, E. Laegsgaard, F. Besenbacher, and G. Comsa, *Surf. Sci.* 404, 401 (1998).
16. M. Kalff, G. Comsa, and T. Michely, *Surf. Sci.* 486, 103 (2001).
17. T. Michely and G. Comsa, *Phys. Rev. B* 44, 8411 (1991).
18. T. Michely and G. Comsa, *Surf. Sci.* 256, 217 (1991).
19. T. Michely and G. Comsa, *Nucl. Inst. Meth. B* 82, 207 (1993).
20. G. Costantini, S. Rusponi, R. Gianotti, C. Boragno, and U. Valbusa, *Surf. Sci.* 416, 245 (1998).
21. H. J. Ernst, *Surf. Sci.* 383, L755 (1997).
22. M. Ritter, M. Stindtmann, M. Farle, and K. Baberschke, *Surf. Sci.* 348, 243 (1996).
23. S. Rusponi, C. Boragno, and U. Valbusa, *Phys. Rev. Lett.* 78, 2795 (1997).
24. S. Rusponi, G. Costantini, C. Boragno, and U. Valbusa, *Phys. Rev. Lett.* 81, 4184 (1998).
25. F. Hontinfinde, R. Ferrando, and A. C. Levi, *Physica A* 248, 288 (1998).
26. C. De Giorgi, P. Aihemaiti, F. Buatier de Mongeot, C. Boragno, R. Ferrando, and U. Valbusa, *Surf. Sci.* 487, 49 (2001).
27. D. Sekiba, S. Bertero, R. Buzio, F. Buatier de Mongeot, C. Boragno, and U. Valbusa, *Appl. Phys. Lett.* 81 (2002).
28. S. Rusponi, G. Costantini, F. Buatier de Mongeot, C. Boragno, and U. V. Valbusa, *Appl. Phys. Lett.* 75, 3318 (1999).
29. S. van Dijken, D. de Bruin, and B. Poelsema, *Phys. Rev. Lett.* 86, 4608 (2001).
30. F. Buatier de Mongeot, G. Costantini, C. Boragno, and U. Valbusa, *Phys. Rev. Lett.* 84, 2445 (2000).
31. C. Teichert, C. Ammer, and M. Klaua, *Phys. Status Solidi A* 146, 223 (1994).
32. R. M. V. Murty, T. Curcic, A. Judy, B. H. Cooper, A. R. Woll, J. D. Brock, S. Kycia, and R. L. Headrick, *Phys. Rev. Lett.* 80, 4713 (1998).
33. G. Costantini, F. Buatier de Mongeot, C. Boragno, and U. Valbusa, *Phys. Rev. Lett.* 86, 838 (2001).
34. M. Navez, C. Sella, and D. Chaperot, *Compt. Rend.* 254, 240 (1962).
35. X.-S. Wang, R. J. Pechman, and J. H. Weaver, *J. Vac. Sci. Technol. B* 13, 2031 (1995).
36. H. J. W. Zandvliet, H. B. Elswijk, E. J. van Loenen, and I. S. T. Tsong, *Phys. Rev. B* 46, 7581 (1992).
37. T. M. Mayer, E. Chason, and A. J. Howard, *J. Appl. Phys.* 76, 1633 (1994).
38. S. Habenicht, W. Bolse, K. P. Lieb, K. Reimann, and U. Geyer, *Phys. Rev. B* 60, R2200 (1999).
39. S. Habenicht, *Phys. Rev. B* 63, 125419 (2001).
40. A. Datta, Y.-R. Wu, and Y. L. Wang, *Phys. Rev. B* 63, 125407 (2001).
41. J. Erlebacher, M. J. Aziz, E. Chason, M. B. Sinclair, and J. A. Floro, *Phys. Rev. Lett.* 82, 2330 (1999).
42. D. Datta, S. R. Bhattacharyya, T. K. Chini, and M. K. Sanyal (2001).
43. D. P. Adams, T. M. Mayer, E. Chason, B. K. Kellerman, and B. S. Swartzentruber, *Surf. Sci.* 371, 445 (1997).
44. R. M. Bradley and J. M. E. Harper, *J. Vac. Sci. Technol. A* 6, 2390 (1988).
45. J. J. Vajo, R. E. Doty, and E. Cirlin, *J. Vac. Sci. Technol. A* 14, 2709 (1996).
46. M. A. Makeev and A. L. Barabasi, *Appl. Phys. Lett.* 71, 2800 (1997).
47. I. Koponen, M. Hautala, and O.-P. Sievanen, *Phys. Rev. Lett.* 78, 2612 (1997).
48. S. W. MacLaren, J. E. Baker, N. L. Finnegan, and C. M. Loxton, *J. Vac. Sci. Technol. A* 10, 468 (1992).
49. R. Cuerno and A. L. Barabasi, *Phys. Rev. Lett.* 74, 4746 (1995).
50. G. Costantini, F. Buatier de Mongeot, S. Rusponi, C. Boragno, U. Valbusa, L. Vattuone, U. Burghaus, L. Savio, and M. Rocca, *J. Chem. Phys.* 112, 6840 (2000).
51. L. Vattuone, U. Burghaus, L. Savio, M. Rocca, G. Costantini, F. Buatier de Mongeot, C. Boragno, S. Rusponi, and U. Valbusa, *J. Chem. Phys.* 115, 3346 (2001).
52. S. Facsko, T. Bobek, T. Dekorsy, and H. Kurz, *Phys. Status Solidi B* 224, 537 (2001).
53. S. Facsko, T. Dekorsy, C. Koerdt, C. Trappe, H. Kurz, A. Vogt, and H. L. Hartnagel, *Science* 285, 1551 (1999).
54. C. C. Umbach, R. L. Headrick, and K.-C. Chang, *Phys. Rev. Lett.* (2001).

# Ionic Conduction in Nanostructured Materials

Philippe Knauth

Université de Provence—CNRS, Marseille, France

## CONTENTS

1. Introduction
2. Theory of Ionic Conduction in the Bulk
3. Ionic Conduction At and Near Interfaces
4. Nanocrystalline Ceramics and Thin Films
5. Nanocomposites
6. Conclusions

Glossary

References

Electrolytes, as respects their insulating and conducting forces, belong to the general category of bodies; and if they are in the solid state (as nearly all can assume that state), they retain their place presenting then no new phenomenon.

Michael Faraday On induction, in "Experimental Researches in Electricity," Volume 1, p. 1344, Series XII. Taylor and Francis, London, 1839.

## 1. INTRODUCTION

Ceramics have been a part of human culture for thousands of years. Ceramic objects, including bricks, tiles, and pottery, can be traced back to the ancient civilizations of Mesopotamia, Egypt, and Asia. From a materials scientist's point of view, ceramics can be defined as nonmetallic, dense, polycrystalline solids that are prepared by shaping and high temperature firing, typically around 1000 °C. A large part of conventional ceramics is based on aluminosilicates, especially clay. From the 19th century on, the physical and chemical properties of these ionocovalent materials were investigated in earnest. It was then recognized that their electrical properties were quite different from those of the earlier investigated metallic solids.

As early as 1833, Michael Faraday reported experiments on ionic conducting inorganic solids: "There is no other body with which I am acquainted, that, like sulphuret of silver, can compare with metals in conducting power for electricity at low tension when hot, but which, unlike them, during

cooling, loses in power, whilst they, on the contrary, gain. Probably, however, many others may, when sought for, be found" [1]. The large enhancement of the electrical conductivity of silver sulfide  $\text{Ag}_2\text{S}$  with increasing temperature was difficult to interpret at that time, because it was in strong contradiction to the behavior of metals.

The first major invention based on solid electrolytes was an electric lightning device using the "Nernst mass," a mixture of zirconia with rare earth oxides, including the particularly favorable composition 85% zirconia and 15% yttria [2]. Although the Nernst lamp was finally not used extensively in practice—it was replaced in 1905 by the simpler tungsten filament lamp—this discovery gave a major impulse to the development of solid state ionics. Around 1850, Gaugain had already discovered the principle of solid electrolyte fuel cells: "air and alcohol vapor separated by a glass envelope and heated up to high temperature can form a couple capable to develop electricity" [3]. Gaugain obtained similar results with a porcelain tube and with other gaseous fuels. Nearly one century later, after fruitless efforts with liquid electrolytes, Baur and Preiss proposed a great number of solid electrolytes for fuel cells, including glasses, porcelains, clays, and different oxide mixtures, and concluded that "unsurpassed is the Nernst mass" [4], even if degradation problems remained.

The role of temperature, doping, and stoichiometry variations influencing the electrical conductivity and ionic diffusivity in solids, often described as "defect chemistry," was treated in pioneering papers in the 1920s and 1930s. Joffé investigated the ionic conductivity of  $\text{NaCl}$ ,  $\text{SiO}_2$ , and  $\text{CaCO}_3$  crystals [5]. Based on these observations, Frenkel postulated the existence of point defects in order to understand the diffusion properties of solids [6]. Wagner and Schottky applied the methods of statistical thermodynamics to the problem of disorder in an ordered binary compound  $\text{AB}$  in 1930 [7]. Wagner also introduced the term excess electron and electron defect and comprehensively discussed the consequences of electronic and ionic disorder on the electrical conductivity of ionic solids [8]. He had already noticed that these concepts could be used to deduce quantitatively

the dependence of conductivity on the partial pressure of the electronegative component.

The main conclusion of these researches is that the electrical conductivity at moderate temperatures of many ionocovalent solids is not due to electronic carriers only but contains a more or less important contribution of mobile ions. The discipline that deals with the preparation, characterization, modeling, and applications of such solid materials supporting ionic motion is called “solid state ionics.” Progress in solid state ionics is related to major technological developments in the domains of energy storage and conversion (batteries and fuel cells) and environmental monitoring and control (chemical sensors).

The presence of interfaces, recognized 50 years ago to play a key role in semiconductor science and microelectronics, strongly impacts also the ionic conductivity. The evaluation of multiphase materials, commonly designated as “composites,” containing heterophase boundaries was started after Liang discovered in 1973 an ionic conduction enhancement in a heterogeneous material: dispersion of small alumina particles in a matrix of the moderate ionic conductor LiI leads to 50 times higher ionic conductivity as compared with pure LiI [9]. The conductivity enhancement is a consequence of the formation of space charge regions with enhanced ionic carrier concentration near the interfaces. Similar effects, although somewhat smaller, are expected in polycrystalline materials, where grain boundaries are present. Logically, the enhancement should be particularly significant in systems with a high density of grain or phase boundaries, like in nanocrystalline ceramics and thin films or in nanocomposites. The objective of this chapter is to present the current knowledge on this topic and to review different classes of nanomaterials where an important ionic conductivity has been reported. But before that and for those not familiar with the subject, let us summarize the essential concepts on ionic conduction in the bulk and at, or near, interfaces.

## 2. THEORY OF IONIC CONDUCTION IN THE BULK

The total electrical conductivity  $\sigma$  of a solid at a given temperature is the sum of the partial conductivities of ionic and electronic charge carriers:

$$\sigma = \sum_i q_i \mu_i c_i \quad (1)$$

In this equation,  $q_i$  is the charge,  $\mu_i$  is the mobility, and  $c_i$  is the concentration of the charge carrier  $i$ . It is thus apparent that two parameters can be modified in order to increase the conductivity of a solid: the carrier concentration and/or mobility.

The **concentration** of ionic defects may be increased in one of several ways, as shown in Figure 1 for the case of silver chloride AgCl.

- (1) Deviation from stoichiometry (Fig. 1a and b): a reduction or oxidation of the compound produces simultaneously electronic species and point defects, thereby leading to mixed conduction.

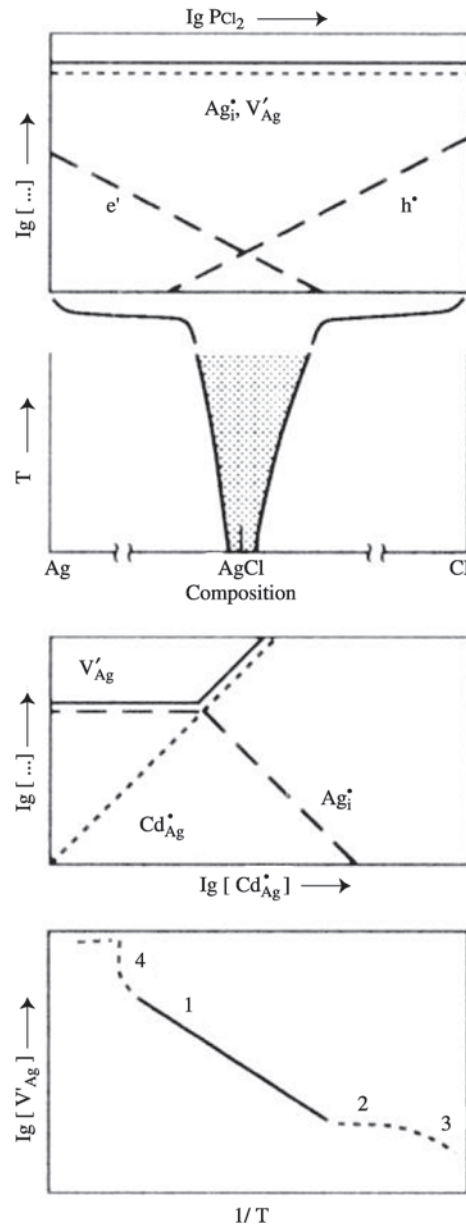


**Figure 1.** Defect chemistry in the bulk of AgCl. From top to bottom: (a) charge carrier concentration as function of compound stoichiometry, (b) “phase diagram”: composition range of the homogeneous compound, (c) influence of doping by  $\text{Cd}^{2+}$  ions, (d) Arrhenius diagram of silver vacancy concentration. The Kröger–Vink nomenclature is explained in Section 2. Reprinted with permission from [48], J. Maier, Nanoionics and soft materials science, in “Nanocrystalline Metals and Oxides—Selected Properties and Applications” (P. Knauth and J. Schoonman, Eds.), p. 84. Kluwer Academic, Boston, 2002. © 2002, Kluwer Academic Publishers.

- (2) Doping (Fig. 1c): the addition of aliovalent impurities requires the generation of ionic defects with opposite charge in order to maintain electrical neutrality.
- (3) Intrinsically disordered solids: many solids pass through an order–disorder transition as the temperature is increased (e.g., point 4 in Fig. 1d or the  $\beta$ – $\alpha$  transition in AgI, three-dimensional disorder). In other cases, the disorder is limited to disordered



planes (intercalation compounds, e.g., Na- $\beta$ -alumina) or one-dimensional channels (tunnel compounds). Likewise, amorphous phases (inorganic glasses and polymers) present a high intrinsic disorder and, in certain cases, also exhibit ionic conductivity.

- (4) Formation of space charge regions in the vicinity of interfaces: the space charge forms in response to a plane of opposite charge adsorbed on the surface or segregated at a grain boundary. This phenomenon will be discussed in some detail.

The ionic **mobility** depends on a number of factors. The most important is the height of the potential barrier that the ion must overcome in order to pass from one well to an adjacent well. In general, the barrier height depends on a number of factors, including the strain energy that needs to be expended for the ion to “squeeze” through the bottleneck, the polarizability of the lattice, and the electrostatic interactions between the ion and its surroundings. Perhaps the easiest to visualize is the strain energy and one is therefore tempted to assume that solids or interfaces with the highest free volume should exhibit the highest mobility. While this is often the case, as in short circuit diffusion at extended defects (e.g., grain boundaries and dislocations), there are many examples where solids with smaller channels support higher mobilities than those with larger channels, due to polarization effects.

## 2.1. Defect Chemistry: Kröger–Vink Nomenclature

Let us introduce now the commonly used nomenclature for the description of defect chemical reactions, proposed in 1956 by Kröger and Vink [10]. The point defects are considered as dilute species and the solid plays the role of the solvent. Several analogies can be found between intrinsic defect formation and self-dissociation of water.

- (1) A pair of charged defects is formed, which is responsible for electrical conduction.
- (2) Defect formation is thermally activated. A mass action law constant using defect activities (or concentrations for dilute species) describes the defect equilibrium.
- (3) An acidity–basicity concept can be introduced [11].

In the Kröger–Vink notation, the subscript shows the site of a defect; the subscript  $i$  stands for an interstitial site. The effective defect charge is written as a superscript, relative to the ideal lattice: a dot ( $\cdot$ ) stands for a positive and a prime ( $'$ ) for a negative charge. The vacancy is written V. For example,  $O_i^{\cdot\cdot}$  represents a doubly charged oxygen interstitial ion,  $V_O^{\cdot\cdot}$  is a doubly charged oxygen vacancy. Bulk defect chemical reactions must obey:

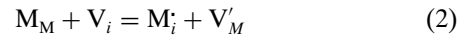
- (1) mass balance,
- (2) balance of lattice sites,
- (3) charge balance (global electrical neutrality).

The electrical neutrality condition is, however, not respected near interfaces, where deviations can occur.

In a binary ionic compound  $M^+X^-$ , four types of intrinsic ionic disorder can be generated by permutation of the elementary defects, ion vacancies, and interstitial ions, but only

three types are experimentally observed. The predominant disorder type depends mainly on the solid’s crystal structure.

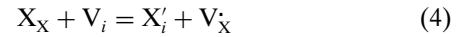
(1) **Cation Frenkel disorder** corresponds to the formation of a cation interstitial plus a cation vacancy:



$K_{Fr}$  is the Frenkel equilibrium constant:

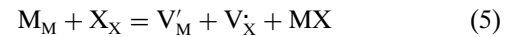
$$K_{Fr} = c(M_i)c(V'_M) = \exp(-\Delta_{Fr}G^\circ/kT) \quad (3)$$

$\Delta_{Fr}G^\circ$  is the standard Gibbs free energy of the Frenkel reaction. Obviously, interstitial formation is easier for small ions and/or in relatively open lattices. Therefore, cationic Frenkel disorder is more often found than the corresponding anionic Frenkel disorder (also called anti-Frenkel type), because anions are generally larger. The **anion Frenkel reaction** can be written



Due to the small radii of silver and copper ions, silver halides (such as AgCl, see Fig. 1) and copper halides belong to this group, but also certain anion conductors with the relatively open fluorite-type lattice (e.g., ceria or zirconia).

(2) **Schottky disorder** is due to the coupled formation of cation and anion vacancies:



$MX$  represents ions, which have been displaced to “new” interfacial sites.  $K_{Sch}$  is the Schottky equilibrium constant:

$$K_{Sch} = c(V'_M)c(V'_X) = \exp(-\Delta_{Sch}G^\circ/kT) \quad (6)$$

$\Delta_{Sch}G^\circ$  is the standard Gibbs free energy of the Schottky reaction. One already imagines that this type of disorder will be found mainly in dense crystal lattices. For example, close-packed alkali halides (including NaCl) show Schottky-type disorder. The fourth theoretically possible defect combination, a pair of cation and anion interstitials, is not found in reality, because it is very difficult to create interstitials on both sublattices.

(3) In addition to intrinsic ionic disorder by point defects, one must take into account **intrinsic electronic disorder** by creation of electron–hole pairs, which can be written



This process can be thermally activated or due to photons. The excess electrons are in the conduction band, whereas electron holes are located in the valence band of the compound. The temperature-dependent equilibrium constant of this reaction is

$$K_{el}(T) = c(h')c(e') = A \exp(-E_g/kT) \quad (8)$$

The prefactor  $A$  contains the effective mass of hole and electron;  $E_g$  is the bandgap energy of the compound.

Intrinsic electron–hole pair formation and vacancy–interstitial pair creation (Frenkel reaction) can both be represented in level diagrams, like those used in solid state physics. Figure 2 shows this type of diagram for the case

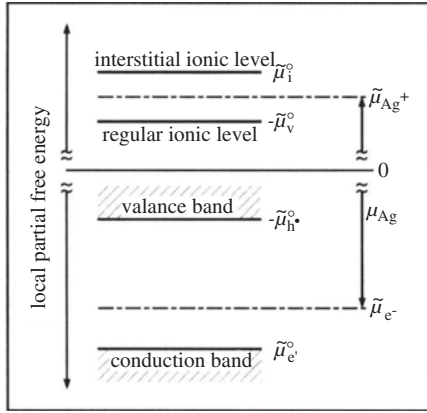


**Figure 2.** Level diagrams of ionic and electronic disorder in AgCl. The electrochemical potentials  $\mu_i$  of silver ions and electrons are connected via the chemical potential of silver  $\mu_{Ag}$ , in other words the exact stoichiometry of the compound. The indicated prevailing  $n$ -type semiconductivity corresponds to a slight Ag excess in AgCl. Reprinted with permission from [48], J. Maier, Nanoionics and soft materials science in “Nanocrystalline Metals and Oxides—Selected Properties and Applications” (P. Knauth and J. Schoonman, Eds.), p. 82. Kluwer Academic, Boston, 2002. © 2002. Kluwer Academic Publishers.

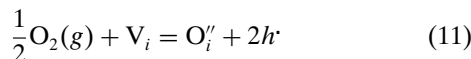
of AgCl. If equilibrium is established, the electrochemical potentials of electrons [ $\eta(e^-)$ , i.e., the Fermi level] and ions [ $\eta(\text{Ag}^+)$ ] are connected via the chemical potential of one of the components, here Ag [ $\mu(\text{Ag})$ ] (i.e., by the exact compound stoichiometry):



$$\mu(\text{Ag}) = \eta(\text{Ag}^+) + \eta(e^-) \quad (10)$$

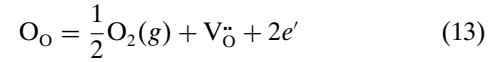
(4) “**Antisite**” disorder describes the interchange of ions between two sublattices. While such exchange between cation and anion sites is not observed in binary ionic systems due to trivial electrostatic reasons, “antisite” disorder can be observed in ternary and higher order compounds in which cations disorder between two different cation sublattices: this is common, for example, in solids with the spinel structure [12].

(5) As one can easily verify in Eqs. (2), (4), and (5), the intrinsic defect reactions do not modify the composition of the exactly stoichiometric solid (the “Daltonide”). In addition to these intrinsic disorder types, one can also observe “**extrinsic**” disorder due to composition changes of the solid, be it the presence of foreign ions (impurities or dopants) or a nonstoichiometry. The latter is induced by chemical potential changes of one of the components, for example oxygen in the case of oxides. Oxidation or reduction of the material results in deviations from stoichiometry (corresponding to a “Berthollide”) and the formation of both ionic and electronic charge carriers. For example, electron holes and oxygen interstitials are created in a Frenkel-disordered oxide by the oxidation reaction



$$K_{\text{ox}} = c(\text{O}_i')c(h)^2P(\text{O}_2)^{-1/2} = \exp(-\Delta_{\text{ox}}G^\circ/kT) \quad (12)$$

$K_{\text{ox}}$  is the equilibrium constant and  $\Delta_{\text{ox}}G^\circ$  is the standard Gibbs free energy of the oxidation reaction. Excess electrons and oxygen vacancies are formed in the reduction reaction



$$K_{\text{red}} = c(\text{V}_\text{O}'')c(e')^2P(\text{O}_2)^{1/2} = \exp(-\Delta_{\text{red}}G^\circ/kT) \quad (14)$$

$K_{\text{red}}$  is the equilibrium constant and  $\Delta_{\text{red}}G^\circ$  is the standard Gibbs free energy of the reduction reaction.

As a consequence, the  $p$ -type or  $n$ -type conductivity increases together with the deviation from stoichiometry. At reduced temperature, impurities (or dopants) will dominate near stoichiometry, while under reducing or oxidizing conditions, defects associated with nonstoichiometry will control the electrical properties of the material. The electrical properties eventually become intrinsic when the temperature increases to sufficiently high values. Kröger and Vink discussed various aspects of stoichiometry deviations in inorganic compounds and developed diagrams that show defect concentrations as a function of the chemical potential of the components. These diagrams can be much simplified under the assumption of only two majority defects, according to the so-called Brouwer approximation [13]. A general discussion of these phenomena is outside the scope of this chapter but can be found in many standard texts [14].

## 2.2. Ionic Conduction in the Bulk: Hopping Model

Ionic conduction in solids [15] is due to thermally activated ion hopping [16, 17]. Assuming Boltzmann statistics, the diffusion coefficient  $D_i$  is a function of the jump distance  $a$ , the characteristic attempt frequency  $\nu_0$  (typically  $\approx 10^{13} \text{ s}^{-1}$ ) and the free energy of migration  $\Delta_{\text{migr}}G = \Delta_{\text{migr}}H - T\Delta_{\text{migr}}S$ :

$$D_i = \gamma a^2 \nu_0 \exp(-\Delta_{\text{migr}}G/kT) \quad (15)$$

The factor  $\gamma$  takes into account geometrical and so-called correlation effects. For example, the backward jump has a slightly higher probability than the forward jump, but, on the other hand, cooperative motion can lead to higher diffusion coefficients than isolated jumps. The Nernst–Einstein equation relates the ionic mobility  $\mu_i$  to the diffusion coefficient ( $k$  is Boltzmann’s constant):

$$\mu_i = D_i q_i / kT \quad (16)$$

Using Eqs. (1), (15), and (16), the ionic conductivity can be expressed as

$$\sigma_{\text{ion}} = (q_i^2/kT)c_i \gamma a^2 \nu_0 \exp(\Delta_{\text{migr}}S/k) \exp(-\Delta_{\text{migr}}H/kT) \quad (17)$$

A general equation representing the ionic conductivity can thus be written with a prefactor  $\sigma_0$ :

$$\sigma_{\text{ion}} = \sigma_0 / T \exp(-\Delta_{\text{act}}H/kT) \quad (18)$$

Most crystalline and amorphous fast ion conductors (the latter below their glass transition temperature) satisfy this equation. For crystalline fast cation conductors (such as

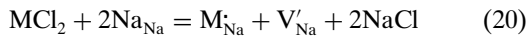
$\alpha$ -AgI), the activation enthalpy  $\Delta_{\text{act}}H$  is typically below 0.5 eV; for anion conductors, it is normally larger (0.5–1.0 eV). The activation enthalpy can contain different contributions.

- (1) If the concentration of the mobile ionic defects is fixed by charged **background impurities and dopants**, as in the case of Y-stabilized  $\text{ZrO}_2$  [ $2c(\text{V}_{\text{O}}^{\bullet}) = c(\text{Y}_{\text{Zr}}')$ ], the activation enthalpy  $\Delta_{\text{act}}H$  represents only the defect migration enthalpy  $\Delta_{\text{migr}}H$  (cf. curve 2 in Fig. 1d).
- (2) Assuming a **thermally activated defect creation**, the carrier concentration  $c_i$  has a temperature dependence such as Eq. (3) or (6):

$$c_i = c_{i0} \exp(-\Delta_{\text{form}}H^\circ/2kT) \quad (19)$$

In this “intrinsic” case,  $\Delta H_{\text{act}}$  is the sum of the defect migration and formation enthalpies ( $\Delta_{\text{act}}H = \Delta_{\text{migr}}H + \Delta_{\text{form}}H^\circ/2$ ; cf. curve 1 in Fig. 1d).

- (3) If **deviations from stoichiometry** are observed, the activation enthalpy can be related to reaction enthalpies, such as the oxidation enthalpy for metal deficient oxides, cf. Eq. (12), or the reduction enthalpy for oxygen deficient oxides, cf. Eq. (14).
- (4) At low temperatures, **defect association** phenomena can be observed. These issues were discussed early on by Lidiard [18]. Dreyfus and Nowick investigated such point defect association phenomena in doped sodium chloride [19]. In the case of NaCl, doping with divalent cations requires the formation of sodium vacancies for charge compensation:



At low temperature, defect association due to Coulomb interactions between the oppositely charged defects begins to predominate:

$$\text{M}_{\text{Na}} + \text{V}_{\text{Na}}' = (\text{M}_{\text{Na}}, \text{V}_{\text{Na}}') \quad (21)$$

$(\text{M}_{\text{Na}}, \text{V}_{\text{Na}}')$  refers to a bound dopant–vacancy pair. In the temperature domain in which association occurs, the conductivity has an effective activation enthalpy ( $\Delta_{\text{act}}H = \Delta_{\text{migr}}H + \Delta_{\text{ass}}H/2$ , where  $\Delta_{\text{ass}}H$  is the association enthalpy; cf. curve 3 in Fig. 1d). There are other important experimental consequences from such association:

- (1) The formation of vacancy–dopant pairs leads to a weaker overall enhancement of conductivity.
- (2) The pairs act as dipoles and contribute to dielectric relaxation processes. Haven established the presence of loss peaks due to defect pairing in 1953 [20].
- (3) The dopant ion being in the immediate vicinity of a vacancy, it can be expected to diffuse faster than the host cation.

In addition to the formation of defect pairs, Lidiard showed that long-range defect interactions also play a role and adapted the Debye–Hückel theory of aqueous electrolytes

to the case of ionic crystals [18]. The resulting activity variations can often be described by a cube root law of the defect concentrations [21]. The electrostatic interactions are also the origin of the frequency dependence of the ionic conductivity and dielectric permittivity of structurally disordered solid electrolytes (cf. the “universal dielectric response”) [22, 23].

### 3. IONIC CONDUCTION AT AND NEAR INTERFACES

An interface is a two-dimensional region separating two parts of a system. The word interface is used in the following synonymous with the term boundary. One can differentiate two main types:

- (1) Phase boundaries separate two phases with different chemical composition and/or structure; they are found in polyphase materials, also called composites.
- (2) Grain boundaries separate two grains of identical composition and structure; they are found in polycrystalline materials.

At reduced temperature, boundaries can significantly enhance the ionic conductivity of polycrystalline or composite materials and thin films as compared with single crystals of identical composition. However, boundaries can also block ionic charge carriers and reduce the ionic conductivity of a material.

To understand this behavior, one has to take into account the anisotropy of boundary properties: transport might be facilitated along an interface or blocked across the interface (parallel and perpendicular effects). For microcrystalline materials, study of bulk and interface effects is experimentally possible by impedance spectroscopy, because the different electrical properties of bulk and interface regions usually lead to a significant difference of the time constants  $\tau$ :

$$\tau = \varepsilon/\sigma \quad (22)$$

In this equation,  $\varepsilon$  is the dielectric permittivity and  $\sigma$  is the electrical conductivity of the respective region. Therefore, bulk and boundary responses can often be clearly separated in the complex impedance plane as function of the signal frequency. For nanocrystalline materials, the overall electrical response is, however, more complex and the theoretical discussion of impedance spectra is not trivial [24]. For a general discussion of impedance spectra of solid ionic conductors, the reader can consult a standard textbook [25].

Let us now review the atomic mechanisms involved in the enhanced ionic conductivity at and near interfaces: one can distinguish enhanced boundary core diffusion and equilibrium (and out-of-equilibrium) space charge layer effects.

#### 3.1. Boundary Core Diffusion

High resolution electron micrographs of grain boundaries in oxides (e.g., NiO) show that the disordered region between grains is typically only a few atomic layers thick, not unlike the “grain boundary width” postulated for the interpretation of grain boundary diffusion data in metals (0.5 nm) [26]. The defects create a new periodic interface structure with

regularly repeating structural units. Ordinary boundaries are formed by portions of such special boundaries.

The boundary core is a fast diffusion path and can act as a short-circuiting pathway for diffusion at reduced temperature. This mechanism has been known in metallurgy for quite a long time but applies obviously also in ionic materials. The enhancement of the oxygen ion diffusion coefficient, due to surface and grain boundary diffusion, was already recognized in 1960 by comparison of single crystalline and polycrystalline  $\text{Al}_2\text{O}_3$  [27]. More recently, Atkinson showed that the grain boundary diffusion coefficient in nickel oxide NiO is as much as six orders of magnitude larger than the bulk one [28].

Accelerated diffusion in the boundary core can be expected for two reasons:

- (1) the large defect concentration at interface sites (high percentage of displaced atoms), corresponding to a low defect formation energy,
- (2) the large excess free volume, which enhances the defect mobility, corresponding to a low defect migration energy.

The activation energy for interfacial diffusion is therefore significantly lower than for bulk diffusion, because defect formation and migration need less energy at interface sites. This is the origin of the fast boundary diffusion at low temperature. In the “neutral core model,” the interface core is also held responsible for an ionic conductivity enhancement (see Section 4 for more details).

In usual microcrystalline materials, the cross-sectional area of grain boundaries is, however, very small: using an elementary brick layer model, the ratio of cross-sectional areas of grain boundaries (gb) of width  $d$  and cubic grains of size  $L$  is

$$A(\text{gb})/A(\text{bulk}) = 2d/L \quad (23)$$

The general conclusion from these considerations is that grain boundary diffusion is the main diffusion contribution at low temperature. It leads to a significant enhancement of mass transport in comparison with single crystals, if the grain size is sufficiently small.

### 3.2. Space Charge Layer Models

Boundary core diffusion is, however, not the only and generally not the most important origin for an ionic conductivity enhancement, but space charge effects are. Space charge regions are formed near interfaces in ionic materials to compensate charged defects and dopants, which segregate to surfaces and grain and phase boundaries. Two segregation modes are commonly recognized: one is segregation of over- or undersized dopants to the boundary core, due to elastic relaxation, and the second is segregation of charged defects in the space charge regions, due to electrostatic interactions.

Space charge effects have been known to be important in colloid systems for some time: Verwey and Overbeek established the electrostatic theory applicable to these systems in 1948 [29]. Grimley and Mott discussed boundary conditions at Ag/AgBr and AgBr/liquid electrolyte interfaces in 1947 [30]. Lehovc calculated the distribution of lattice defects

and the space charge potential at the surface of ionic crystals following a statistical thermodynamic approach in 1952 and already mentioned the implications for ionic conduction [31]. Kliewer and Koehler applied these concepts to the case of NaCl in 1965 [32]. Poeppl and Blakely extended this treatment by taking the density of surface sites into account [33]. Wagner used the space charge layer concept in 1972 to explain conductivity effects in two-phase materials, such as metallic inclusions in a semiconducting oxide or mixtures of two semiconducting oxides [34]. Space charge segregation of dopants was studied in a number of systems, for example, in  $\text{TiO}_2$  and  $\text{CeO}_2$  by Chiang and co-workers [35–37].

The first evidence for the importance of space charge effects in solid state ionics was the experimental work of Liang published in 1973. The ionic conductivity of the moderate  $\text{Li}^+$  ion conductor LiI was enhanced by a factor of almost 50 by dispersing small alumina particles in the ion conductor matrix. A large number of papers confirmed this “heterogeneous doping” effect on other ionic conductor composites, with a major contribution by the group of Saki and Wagner [38]. Similar enhancement effects can be predicted if dislocations are present. However, the number of experimental studies is smaller, given their difficulty: Nowick studied the conductivity of plastically deformed NaCl crystals [39]. Dudney investigated the enhancement of conductivity due to dislocations and stress effects in AgCl composites [40].

The space charge layer theory of ionic conductor systems was largely developed by Maier since 1984 [41]. The fundamental idea is that ionic defects (or dopants) can be trapped at an interface. This corresponds to an interfacial segregation process that can modify the excess (positive or negative) interface core charge  $\varphi$  and the interface potential  $\phi$ . All species with an opposite charge are enriched in the adjacent space charge region (accumulation layer), whereas the species with the same charge are depleted (depletion layer):

$$q_i \partial c_i / \partial \phi < 0 \quad (24)$$

A so-called “inversion” layer is observed for a species that is the majority carrier in the bulk but a minority carrier in the space charge region [42].

Space charge effects are relevant for different ionic conducting materials, including ionic conductor–insulator composites, thin films, and polycrystalline solids; the higher the interfacial area in these materials, the higher the expected conductivity effect.

- (1) Composites: The driving force for trapping can be the presence of a second phase with chemical affinity for a mobile ion. For example, “basic” oxides present many nucleophilic hydroxide surface groups, which can attract and fix cations. The space charge regions are then enriched in mobile cation vacancies, which are often majority ionic charge carriers at low temperature. The space charge layers represent then high conductivity regions that can short-circuit the bulk, if they percolate [43]. An optimized effect is expected when the two phases have a nanometric size.
- (2) Thin films: The interaction with a gas phase can also lead to a space charge effect, particularly if the solid

ionic conductor is in thin-film form [44]. For example, ammonia is known to form strong complexes with copper ions in aqueous solution. Copper ions can also be trapped at the surface of a solid copper ion conductor in contact with a gas phase containing ammonia. This effect can be used for ammonia gas detection [45]. Large conductivity effects are also expected in ionic conductor heterolayers with small periodicity (cf. Section 4.4).

- (3) Polycrystalline materials: Ions can be trapped at the grain boundary core, which has a larger free volume than the bulk [46]. Obviously, the trapping effects can be particularly important in nanocrystalline solids, which present a very large grain boundary density.

Space charge effects on conductivity depend on whether one considers:

- (1) transport along or across a boundary,
- (2) accumulation, depletion, or inversion layers,
- (3) “Gouy–Chapman” or “Mott–Schottky” situations.

However, the impact of space charge layers on conductivity can always be expressed by the relation

$$\partial \ln \sigma_i(x) / \partial (\phi(x)/kT) = -q_i \quad (25)$$

$\phi(x)$  is the space charge potential relative to the bulk, modifying the charge carrier concentration in the space charge region. Let us consider now the assumptions and detailed relations for the two cases of complete and partial charge carrier equilibrium.

### 3.2.1. Complete Equilibrium: “Gouy–Chapman” Model

If all defects are in local thermodynamic equilibrium, the boundary can be described by a model similar to the classical electrochemical model of the electrode–electrolyte interface, outlined around 1910 by Gouy and Chapman [47]. The formation of space charge layers is a consequence of local thermodynamic defect equilibrium: since the boundary core has its own defect chemistry, a defect redistribution between bulk and boundary core leads to space charge layers adjacent to the core. For a Frenkel disordered material  $M^+X^-$ , the defect reaction can be written:



Here,  $V_S$  and  $M'_S$  are respectively an empty interface site and a metal ion trapped at this site. The metal vacancies  $V'_M$  are distributed in the region adjacent to the interface, which becomes electrically charged (space charge region). It is assumed that the bulk defect thermodynamic properties, such as the standard chemical potential  $\mu^\circ$  or the Frenkel equilibrium constant [cf. Eq. (3)] and also the bulk defect mobility remain unchanged inside the space charge region, up to the boundary core. This is certainly an oversimplification, because it is known that the local structure changes more gradually and not in a steplike manner. However, a similar assumption is made in semiconductor physics and the conclusions obtained by the space charge model are validated by experiments in a number of cases, including

composite and nanocrystalline ionic conductors, as we will see later.

At equilibrium, the electrochemical potentials  $\eta_i$  of charged species are constant across the interface, but the chemical potentials  $\mu_i$  change ( $\phi$  is the internal electrical potential):

$$d\eta_i = d\mu_i + q_i d\phi = 0 \quad (27)$$

Using the relation between the chemical potential of the species  $i$  and its thermodynamic activity  $a_i$ , it follows that

$$kT d \ln a_i = -q_i d\phi \quad (28)$$

For small defect concentrations, the activity can be replaced by the concentration and the defect concentration profile in the space charge region can be formulated as function of the bulk carrier concentration  $c_{i\infty}$ :

$$c_i(x)/c_{i\infty} = \exp[-q_i(\phi(x) - \phi_\infty)/kT] = \exp[-q_i\phi(x)/kT] \quad (29)$$

The local concentration in the space charge region  $c_i(x)$  depends on the difference between the local and the bulk electrical potential,  $\phi(x)$  and  $\phi_\infty$ , which is in the following consistently taken as  $\phi_\infty = 0$  to simplify the equations. For positive values of  $\phi(x)$ , the concentrations of all negative defects are raised by the exponential factor, while those of the positive defects are reduced by the same factor and vice versa for negative values (Fig. 3a). The divergence of

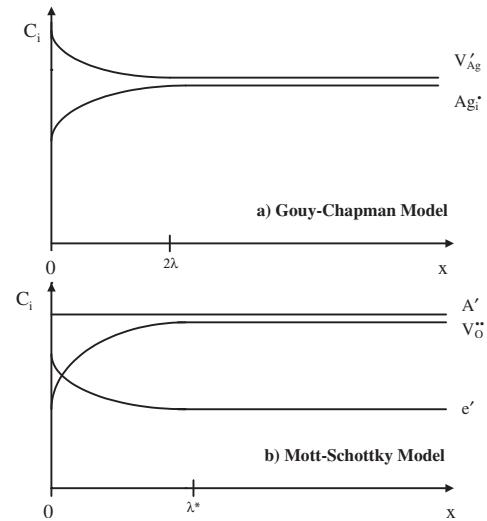


**Figure 3.** Defect concentration profiles near an interface (at  $x = 0$ ) with a positive interface charge [positive interface potential  $\phi(0)$ ]. The upper part (a) represents the Gouy–Chapman situation, where complete defect equilibrium is established. The defect profiles of depleted silver interstitials and accumulated silver vacancies are observed inside the space charge layer width  $2\lambda$ , where  $\lambda$  is the Debye length [cf. Eq. (30)]. The lower part (b) represents the Mott–Schottky case, where the defect equilibrium is only partially established. Here, the acceptor dopant ( $A'$ ) is assumed to be immobile at the temperature of the experiment: its concentration is constant up to the interface. The defect profiles of depleted oxygen vacancies and accumulated electrons are observed inside the space charge zone  $\lambda^*$  [cf. Eq. (39)]. The depicted situation corresponds to an inversion layer.



defect profiles is observed over a distance proportional to the Debye length  $\lambda$  that is conveniently defined, as in semiconductor and liquid electrolyte theory, with respect to the bulk concentration  $c_{i\infty}$  of the majority defect ( $\varepsilon$  is the dielectric permittivity):

$$\lambda^2 = \varepsilon kT / (2q_i^2 c_{i\infty}) \quad (30)$$

From this relation, one recognizes immediately that an enhancement of the bulk carrier concentration, by appropriate doping or temperature increase, reduces the Debye length and thus the space charge layer width. Space charge effects are thus low temperature effects and can have a considerable influence on the electrical properties of ionic conductor ceramics with reduced charge carrier concentrations, because the space charge layer width (approximately twice the Debye length) can be orders of magnitude larger than the typical grain boundary core width of a few atomic distances.

Let us calculate now the conductivity along a boundary for charge carrier accumulation. This requires integration of the concentration profile of the accumulated carrier, called 1, from the boundary ( $x = 0$ ) to the bulk:

$$\sigma_1^{\parallel} = 1/L \int_0^L \sigma_1^{\parallel}(x) dx = q_1 \mu_1 / L \int_0^L c_1(x) dx \quad (31)$$

It is assumed that the defect mobility  $\mu_1$  takes the bulk value also in the space charge region. This total conductivity  $\sigma_1^{\parallel}$  can be separated into the bulk conductivity  $\sigma_{\infty}$  and the space charge layer conductivity  $\sigma_{\text{isc}}^{\parallel}$ . For large accumulation of carrier 1, one obtains, using Eq. (30), a square-root concentration dependence for the space charge layer conductivity [48]:

$$\sigma_{\text{isc}}^{\parallel} = q_1 \mu_1 (2\lambda)(c_{10} c_{1\infty})^{1/2} / L = (2\varepsilon k T c_{10})^{1/2} \mu_1 / L \quad (32)$$

$c_{10}$  is the concentration in the first layer adjacent to the boundary core ( $x = 0$ ). The effective concentration of the species 1 is the geometrical mean of bulk and “interface” concentration; the effective thickness of the space charge region is  $2\lambda$ .

The Gouy–Chapman model permits a quantitative interpretation of conductivity measurements where complete charge carrier equilibrium is established, for example on composite materials with a matrix of a low temperature ion conductor, such as AgCl [43]. Here, the silver vacancy concentration is enhanced in the space charge region (accumulation layer), due to  $\text{Ag}^+$  adsorption on the second phase nanoparticles. The simplified distribution topology of the two phases is expressed by geometrical factors [41]. An equation of type (32) can also be used to estimate the conductivity of  $\text{CaF}_2/\text{BaF}_2$  heterolayers [49], as long as the space charge regions can be considered semi-infinite, in other words as long as they do not overlap.

### 3.2.2. Mesoscopic Effects (Thin Films and Nanostructured Materials)

Interfaces in systems with very small lateral dimensions (e.g., extremely thin films, nanocrystalline, or nanocomposite materials) can be expected to have a more important effect

on ionic conduction. Apart from the ionic conductivity enhancement due to the increased interface area, which can easily be extrapolated, an additional conductivity increase can be observed when the Debye length becomes comparable to the grain size. In that case, the space charge regions overlap; in other words, the defect density no longer reaches the “normal” bulk value, even at the center of the particles (Fig. 4). Mathematically; the model of semi-infinite space charge layers breaks down. In the limit of very small grains, local charge neutrality is nowhere satisfied and a full depletion (or accumulation) of charge carriers can occur with major consequences for ionic and electronic conductivity. This is equivalent to a flat-band situation, where the conductivity is homogeneous over the whole nanocrystallite, and corresponds to a change of the standard electrochemical potential. The defect thermodynamic [50], electrical, and mass transport properties then cannot be extrapolated from conventional size scaling laws and become truly grain-size dependent.

In this case, the ionic conductivity should not depend linearly on the grain size  $L$ . The supplementary enhancement can be estimated introducing a “nanosize” factor  $g$  that can be obtained from [48]

$$g = (4\lambda/L)[(c_{10} - c_1^*)/c_{10}]^{1/2} \quad (33)$$

$c_1^*$  is the defect concentration in the grain center. For a large effect ( $c_{10} \gg c_1^*$ ),  $g = 4\lambda/L$ , and with a grain size  $L = 0.4\lambda$ ,

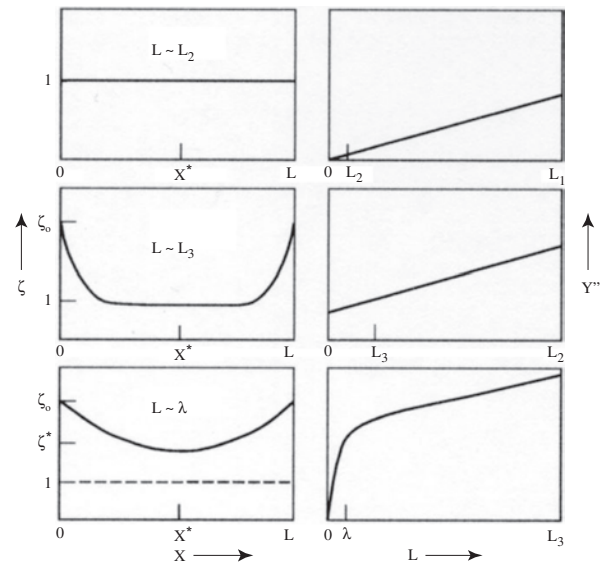


**Figure 4.** Left: Defect concentration profiles as function of the particle size  $L$ .  $\zeta$  is the normalized defect concentration (i.e., divided by the bulk concentration). The two top figures show the macroscopic situation, when the grain size  $L$  is much larger than the Debye length  $\lambda$  [cf. Eq. (30)]. Separate space charge regions are observed. Bottom: mesoscopic situation of very small particles:  $L \approx \lambda$ . The space charge regions overlap: the “normal” bulk defect concentration is not reached. Right: Parallel conductances for thin films of various thickness ( $L_3 \ll L_2 \ll L_1$ ). Reprinted with permission from [48], J. Maier, *Nanoionics and soft materials science*, in “Nanocrystalline Metals and Oxides—Selected Properties and Applications” (P. Knauth and J. Schoonman, Eds.), p. 96. Kluwer Academic, Boston, 2002. © 2002, Kluwer Academic Publishers.



the conductivity would be enhanced by a supplementary order of magnitude. A major objective of experiments is to check the validity of this prediction by studying systems with small grain size and/or low bulk carrier concentration. Mesoscopic effects due to overlapping space charge regions have for example been observed in very thin heterolayers [49].

### 3.2.3. Partial Equilibrium: “Mott–Schottky” Model

The Mott–Schottky model corresponds to the case found in doped silicon at ambient temperature: if a dopant is assumed to be immobile (frozen-in) at the temperature of the experiment, the bulk dopant concentration  $c_D$  is constant up to the boundary (Fig. 3b). In that case, Poisson’s equation must be integrated with a constant charge density related to the dopant density and the charge of the ionized dopant ( $\varphi = c_D q_D$ ), in the one-dimensional case for an acceptor:

$$d^2 \phi(x)/dx^2 = -\varphi/\varepsilon = c_D q_D/\varepsilon \quad (34)$$

The required two boundary conditions for this second-order differential equation are determined by the potential in the bulk and the absence of electric field outside the depletion layer:

$$\phi = 0 \quad \text{and} \quad d\phi/dx = 0 \quad \text{for } x > \lambda^* \quad (35)$$

A solution of Poisson’s equation gives the potential profile in the depletion region [51, 52] ( $x \leq \lambda^*$ ):

$$\phi(x) = (\lambda^* - x)^2 c_D q_D / 2\varepsilon \quad (36)$$

The interface potential at  $x = 0$  is

$$\phi(0) = \lambda^{*2} c_D q_D / 2\varepsilon \quad (37)$$

One can easily show that the relation between the two potentials is

$$\phi(x) = \phi(0)(1 - x/\lambda^*)^2 \quad (38)$$

Given that equilibrium is only partially established, the interface potential  $\phi(0)$  is not determined by the thermodynamic boundary conditions alone but can be modified externally, for example, by applying a voltage. This corresponds to so-called Mott–Schottky experiments in liquid electrolyte or to Mott–Schottky semiconductor–metal contacts. The width of the space charge region  $\lambda^*$  depends on the interface potential  $\phi(0)$  and is not exclusively determined by the bulk carrier concentration, from Eqs. (37) and (30):

$$\lambda^* = [2\varepsilon\phi(0)/c_D q_D]^{1/2} = 2\lambda(q_D \phi(0)/kT)^{1/2} \quad (39)$$

Even in heavily doped situations, where the Debye length  $\lambda$  is very small,  $\lambda^*$  can be perceptible if the boundary potential  $\phi(0)$  is large. Inserting Eq. (36) into Eq. (29) and using Eq. (39), it is easy to calculate, this time for a depleted species called 2, a Gaussian-type concentration profile:

$$c_2(x)/c_{2\infty} = \exp[-(q_2/q_D)[(x - \lambda^*)/2\lambda]^2] \quad (40)$$

$c_{2\infty}$  is the bulk carrier concentration of the depleted species.

The resistivity across a boundary  $\rho_2^\perp$  can be obtained by integration of the concentration profile of the depleted species 2 in the space charge region, using Eqs. (39) and (40):

$$\rho_2^\perp = (\sigma_2^\perp)^{-1} = 1/L \int_0^L (\sigma_2(x))^{-1} dx = 1/(Lq_2\mu_2) \int_0^L dx/c_2(x) \quad (41)$$

One can notice that

$$\lambda^* = 2\lambda(q_2\phi(0)/kT)^{1/2} = 2\lambda[\ln(c_{2\infty}/c_{20})]^{1/2} \quad (42)$$

$c_{20}$  is the concentration in the first layer adjacent to the boundary core ( $x = 0$ ). The separation into the bulk resistivity  $\rho_{\text{bulk}}$  and the grain boundary resistivity  $\rho_{\text{gb}}^\perp$  leads to [48]

$$\rho_{\text{bulk}} = 1/(q_2\mu_2 c_{2\infty}) = 1/[q_2\mu_2 c_{20} \exp(q_2\phi(0)/kT)] \quad (43)$$

$$\begin{aligned} \rho_{\text{gb}}^\perp &= \lambda^* [Lq_2\mu_2 2c_{20} \ln(c_{2\infty}/c_{20})] \\ &= \lambda^* / [Lq_2\mu_2 2c_{20} (q_2\phi(0)/kT)] \end{aligned} \quad (44)$$

The effective thickness of the space charge layer is  $\lambda^*$  and the effective concentration  $[2c_{20} \ln(c_{2\infty}/c_{20})]$ .

Two electric properties can be used to estimate the interface potential  $\phi(0)$ , which is the main parameter influencing the defect chemistry in the space charge region.

- (1) The grain boundary capacitance ( $A$ : sample cross-sectional area) is related to the effective grain boundary thickness. By insertion of Eq. (30) into Eq. (39), one easily gets

$$C/A = \varepsilon/\lambda^* = [\varepsilon q_2 c_{2\infty} / (2\phi(0))]^{1/2} \quad (45)$$

This equation is related to the well-known Mott–Schottky equation that allows determination of a dopant density in semiconductors from interfacial capacitance measurements [53].

- (2) Using Eqs. (43) and (44), one gets easily the ratio of grain boundary resistivity  $\rho_{\text{gb}}$  and bulk resistivity  $\rho_{\text{bulk}}$ :

$$\rho_{\text{gb}}/\rho_{\text{bulk}} = \exp(q_2\phi(0)/kT) / [2q_2\phi(0)/kT] \quad (46)$$

At the reduced measurement temperature generally used for nanocrystalline materials, one can often reasonably assume that dopants are immobile, so that the Mott–Schottky model will be useful for a quantitative interpretation of conductivity measurements on nanoceramics, including the model system of pure and acceptor-doped ceria discussed in Section 4. Furthermore, the Mott–Schottky model was used to interpret the grain boundary resistivity of highly pure zirconia ceramics. In this refractory compound, dopants can still be considered immobile at quite high measurement temperatures [54].

### 3.3. Percolation Models for Composites

Although analytical equations, such as Eq. (32), are in good agreement with experimental conductivity data for many ionic conductor composites, these expressions cannot describe the behavior near critical points. Two thresholds exist in ionic conductor/insulator composites. For a small concentration of insulator, the space charge regions around the phase boundaries are isolated in the matrix of the ionic conductor and do not effectively contribute to ionic conductivity enhancement. There exists a first critical concentration, where a continuous network of highly conducting paths extends through the whole sample. With further increase of insulator concentration, the conductivity increases drastically: this is the domain where the analytical equations describe the experimental data satisfactorily. At large volume fractions of insulator, a second critical concentration is attained, where conduction paths become disrupted, because continuous layers of insulator grains are formed (conductor–insulator transition). The conductivity drops sharply after this second threshold.

Effective medium theories are unable to describe the behavior near critical points, because property fluctuations are important here. Critical phenomena can, however, be described in the framework of percolation theory, first applied to the problem of ionic conductor/insulator composites by Bunde et al. [55]. However, the assumptions made in their model (i.e., randomly distributed ionic conductor and insulator particles having identical sizes) do not correspond to the experimental evidence. In the experiments, ionic conductor and insulator have usually a different mean grain size and the interfacial interactions lead to the formation of continuous layers of insulator around the ionic conductor grains. Both experimental facts were taken into account in an improved percolative transport model [56, 57]. A particularly important conductivity enhancement is predicted when both phases have nanosized grains: percolation theory was applied to discuss the ionic conductivity of nanocrystalline  $\text{Li}_2\text{O}:\text{B}_2\text{O}_3$  composites [58]. The percolation models are complementary to the analytical approach; in both cases the physical model is based on the space charge layer concept.

## 4. NANOCRYSTALLINE CERAMICS AND THIN FILMS

The synthesis, processing, and characterization of nanocrystalline ceramics (“nanoceramics”) and thin films belong to the emerging and rapidly growing field called nanotechnology. Substantial progress has been achieved in the last decades in the preparation of ultrafine grained precursor materials [59, 60]. Nanoceramics (i.e., three-dimensional solids composed of crystallites with a mean size below 100 nm [61]) can be prepared from precursor nanopowders by hot-pressing, where shaping and sintering are performed during a unique procedure, typically around 600 °C under several thousand bars [62].

Nanocrystalline ceramics can present improved mechanical properties, hardness combined with ductility [63], which

are outside the scope of this chapter. There seems to be convincing evidence now that the crystallites in nanoceramics present few extended lattice imperfections. Structural investigations of nanocrystalline oxides showed crystallites with a high degree of perfection, separated by sharp grain boundaries without indication of amorphous regions [64]. The high order in the grain interior can be understood by the existence of a large number of grain boundaries, which can act as defect sinks, in atomic proximity. Extended X-ray fine structure studies of nanocrystalline oxides showed that the grain boundary structure appears to be essentially similar to that in conventional microcrystalline materials [65, 66]. The gaslike or glasslike grain boundary structure sometimes postulated in the early literature was not confirmed.

Solute segregation at grain boundaries and surfaces in nanocrystalline solids can lead to an apparent solubility enhancement for solutes with low bulk solubility: the large increase of the apparent copper solubility in nanocrystalline  $\text{CeO}_2$  was attributed to interfacial segregation and correlated with the mean grain size of the ceria particles [67, 68]. The dopant segregation can tune the activity of nanostructured catalysts [69].

Let us review now major studies on ionic conduction in nanocrystalline ceramics and thin films, with emphasis on model investigations. The domain of “nanoionics” is currently expanding at a fast pace, like the whole sector of nanoscience and nanotechnology. A few recent reviews on this topic can be found in [70–76].

### 4.1. A Model System: Pure and Doped $\text{CeO}_2$

Ceria is the most studied nanocrystalline oxide so far, given its importance as solid electrolyte [77] and for oxygen storage [78], when appropriately doped, and for catalysis. Nominally undoped  $\text{CeO}_2$  nanoceramics [64] remain *n*-type semiconducting even at high oxygen partial pressure, in contrast to conventional microcrystalline samples that are ionically conducting, due to acceptor doping, and become mixed conducting only under reducing conditions. The large increase of the electronic conductivity, the decrease of ionic conductivity, and reduction enthalpy as compared with microcrystalline samples are striking results, confirmed by several experimental investigations [79, 80]. Similar results were also obtained for  $\text{CeO}_2$  thin films [81–83]. Grain-size dependent conductivity data of various authors are reported in Figure 5. Two competing models can be used for interpretation:

- (1) the neutral boundary core model, where charge effects are neglected,
- (2) the space charge concept, where charge effects are paramount.

#### 4.1.1. Neutral Boundary Core Model

In the “neutral core model,” the enhancement of conductivity is explained by the high disorder in the boundary core, due to a significantly lower standard reduction enthalpy

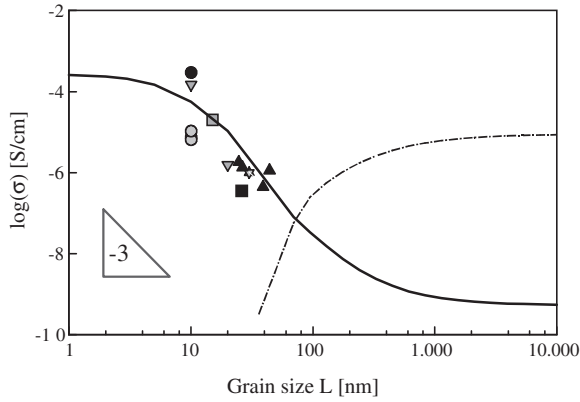
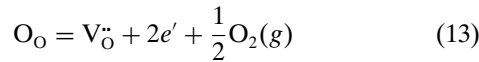


**Figure 5.** Grain size dependence of the conductivity of nanocrystalline ceria ceramics. The solid line represents the calculated electronic conductivity, based on analytical equations for grain size in the micrometer range, numerical calculations for nanometric sizes. The dotted line represents the calculated ionic conductivity. The symbols stand for electronic conductivity data of various authors. Reprinted with permission from [92], A. Tschöpe, *Mater. Res. Soc. Symp. Proc.* © Material Research Society.

$\Delta_{\text{red}}H^{\circ}$  at interface sites, making the reduction reaction much easier:



One can write the equilibrium constant of the reduction reaction at interface sites [cf. Eq. (14)] as

$$K_{\text{red}'} = c(\text{V}_{\text{O}}^{\bullet\bullet})c(e')^2P(\text{O}_2)^{1/2} = A \exp(-\Delta_{\text{red}}H^{\circ}/kT) \quad (47)$$

In order to obtain the experimentally observed slope  $-1/6$  in the  $\ln \sigma$  vs  $\ln P(\text{O}_2)$  dependence, one has to assume an electrical neutrality relation:

$$2c(\text{V}_{\text{O}}^{\bullet\bullet}) = c(e') \quad (48)$$

In other words, the defect concentrations due to the reduction reaction are assumed so high that doping can be neglected, so that the vacancy concentration is not fixed by acceptor impurities, like in conventional samples. One then obtains

$$c(e')^3 = 2A \exp(-\Delta_{\text{red}}H^{\circ}/kT)P(\text{O}_2)^{-1/2} \quad (49)$$

Using Eq. (1), one gets finally the experimentally observed power law:

$$\ln \sigma = \ln[e\mu_e(2A)^{1/3}] - 1/6 \ln P(\text{O}_2) - (\Delta_{\text{hop}}H + \Delta_{\text{red}}H^{\circ}/3)kT \quad (50)$$

$\Delta_{\text{hop}}H$  is the small polaron hopping enthalpy (around 0.4 eV in ceria [84]). Using the data of [64], the standard reduction enthalpy is strikingly lower ( $\Delta_{\text{red}}H^{\circ} \approx 2$  eV) than in conventional  $\text{CeO}_2$  (4.7 eV [85]). This implies a corresponding enhancement of the oxygen deficiency to values of the order  $10^{-6}$ – $10^{-5}$ , in comparison with typically  $10^{-9}$  for microcrystalline samples. This is not unrealistic: the fraction of reduced interface oxygen sites can be estimated from the

interface-to-volume ratio and for a 10 nm mean grain size, only one out of 10,000 grain boundary sites needs to be reduced to dominate the defect and transport behavior of the nanoceramics [64]. Even larger oxygen deficiencies, up to values of  $10^{-3}$ , were actually measured on nanocrystalline  $\text{CeO}_2$ , using coulometric titration with oxygen solid electrolyte cells [86].

An exceptionally high oxygen deficiency was also determined in nanocrystalline ceria–praseodymia solid solutions with high Pr content:  $x > 0.1$  in  $\text{Pr}_{0.7}\text{Ce}_{0.3}\text{O}_{2-x}$  at 640 °C [87]. In this system, two factors contribute to the high nonstoichiometry:

- (1) the easy valence change of praseodymium ions ( $\text{Pr}^{4+}/\text{Pr}^{3+}$ ),
- (2) the high interface density.

Large deviations from stoichiometry can significantly improve the oxygen storage capacity of nanocrystalline oxides.

The existence of many interfaces improves also the oxygen exchange kinetics and the oxygen diffusivity. Coulometric titration experiments using oxygen concentration cells gave high chemical diffusion coefficients (around  $10^{-6}$   $\text{cm}^2/\text{s}$  at 600 °C) with an exceptionally low activation energy (0.3 eV). These results are also suspected to reflect the presence of a large density of fast diffusion pathways with reduced defect migration energy [88] and can be interpreted in the framework of a “neutral core model.” This conclusion remains, however, to be validated for other solid solutions and by different techniques.

In conclusion, the “neutral core model” treats changes of defect thermodynamic and transport properties as solely related to the boundary core and neglects charge effects, so that an electrical neutrality condition, such as Eq. (48), can still be applied.

#### 4.1.2. Space Charge Layer Model

Mason and Hwang [89] found a reduced ionic conductivity and an enhanced activation energy for ionic conduction in  $\text{CeO}_2$  nanoceramics (1.6 eV, about twice the value for microcrystalline  $\text{CeO}_2$ ) that cannot be understood in the “neutral core model,” because the ionic conductivity should also be enhanced in the boundary core. Tschöpe first proposed a consistent model, where the increase of electronic conductivity and the decrease of ionic conductivity in nanocrystalline ceria is explained by the existence of space charge regions [90]. Kim and Maier checked the consistency of this model using defect thermodynamic considerations [91]. If the bulk defect thermodynamic properties are unchanged inside the space charge zone, the defect concentrations are subjected to the following consistency condition, cf. mass-action law (47):

$$\begin{aligned} c_0(\text{V}_{\text{O}}^{\bullet\bullet})c_0(e')^2 &= c_{\infty}(\text{V}_{\text{O}}^{\bullet\bullet})c_{\infty}(e')^2 \\ &= A \exp(-\Delta_{\text{red}}H^{\circ}/kT)P(\text{O}_2)^{-1/2} \end{aligned} \quad (51)$$

$c_0$  is the concentration in the first layer adjacent to the boundary core;  $c_{\infty}$  is the bulk concentration. Concerning the

$P(\text{O}_2)$  and  $T$  dependencies, one sees easily that the following equations should be observed locally:

$$\partial \ln c_0(V_{\text{O}}^{\bullet\bullet}) / \partial \ln P(\text{O}_2) + 2\partial \ln c_0(e') / \partial \ln P(\text{O}_2) = -1/2 \quad (52)$$

$$\partial \ln c_0(V_{\text{O}}^{\bullet\bullet}) / \partial (1/T) + 2\partial \ln c_0(e') / \partial (1/T) = -\Delta_{\text{red}}H^\circ/k \quad (53)$$

The excellent fulfillment of these consistency criteria, demonstrated in [91], and the quantitative interpretation of  $P(\text{O}_2)$  exponents and activation energies for ionic and electronic conduction are very strong arguments for the space charge model in the case of pure and doped ceria.

Very recently, Tschöpe [92] succeeded in determining the grain size dependence of the electrical conductivity of ceria from micro- to nanometer range in excellent agreement with the experiment, as shown in Figure 5, using analytical equations for large grain sizes and numerical calculations for the smallest ones, where analytical equations break down. The large set of experimental investigations and the detailed theoretical analysis permit one to draw already a few general conclusions:

- (1) A positive boundary charge is observed in ceria, probably due to boundary reduction. Space charge potentials between 0.3 [91] and 0.7 V [93] have been calculated; they depend only weakly on temperature and oxygen partial pressure. This leads to severe depletion of oxygen vacancies and strong accumulation of electrons in the space charge regions.
- (2) The electron accumulation strongly enhances the electronic conductivity of the nanoceramics, which becomes dominant in nominally undoped ceria.
- (3) The transition from predominantly ionic to electronic conductivity upon grain size reduction has been confirmed by measurements of the grain-size dependent thermopower [93, 94].
- (4) Experiments on very small particle sizes, to investigate quantitatively nontrivial size effects by space charge overlap, remain to be done.

The oxygen vacancy depleted space charge regions should be an obstacle to oxygen ion transport across grain boundaries, enhancing the grain boundary resistivity of nanoceramics compared with conventional samples. Experimentally, the opposite is observed: the specific grain boundary resistivity of fully dense  $\text{CeO}_2$  nanoceramics [64, 95] is orders of magnitude lower as compared with microcrystalline samples. However, it is well known that in most cases, grain boundary blocking is actually due to segregated impurities. One can assume that the dilution of segregants, given the larger grain boundary area in nanoceramics, is the origin of the enhancement of the conductivity across the grain boundary. For a more detailed study of the grain boundary blocking effect, let us turn now to the case of doped zirconia.

## 4.2. Doped $\text{ZrO}_2$

Ca- or Y-doped zirconia is the most prominent crystalline oxygen ion conductor, with paramount importance for potentiometric oxygen sensors and solid oxide fuel cells. The grain boundary resistance in this compound was studied several times. In conventional stabilized  $\text{ZrO}_2$ , Ca and Si

segregation has been correlated with variations of the blocking grain-boundary conductivity. A significant enhancement of the blocking grain boundary conductivity was observed at grain sizes below  $2 \mu\text{m}$ , because the grain boundary coverage by segregated solutes obviously decreased with decreasing grain size [95].

In nanocrystalline materials, solute segregation occurs on a large grain boundary area and the mean grain boundary concentration of segregated solutes is much lower than in microcrystalline materials with the same solute content. This should further enhance the conductivity across a grain boundary in nanoceramics. Indeed, nanocrystalline tetragonal Y-doped  $\text{ZrO}_2$  presents a grain boundary conductivity one to two orders of magnitude higher than comparable microcrystalline samples, with a low, grain-size independent activation energy [96]. Both results can be attributed to a reduced grain-boundary concentration of Si, in other words a “dilution” of segregated impurities over the very large grain boundary area.

In highly pure Y-doped zirconia, where no siliceous intergranular phases leading to flux constriction are observed, there is now sufficient evidence that the blocking grain boundary resistance is related to oxygen vacancy depletion layers, consecutive to boundary reduction. The oxygen-vacancy depletion layers can be described in the framework of the Schottky–Mott model (see Section 3.2.3), as shown recently [97]. The space charge potential and oxygen vacancy profiles can be calculated quantitatively using interfacial capacitance and resistance data [cf. Eq. (45) and (46)], obtained from impedance spectroscopy. The results are in good agreement although a discrepancy remains concerning the widths of the space charge layers.

A particular effort has been devoted to the preparation and study of phase-pure nanocrystalline zirconia samples with tetragonal or monoclinic structure. Nanocrystalline tetragonal  $\text{ZrO}_2$  was successfully prepared using electrostatic spray deposition [98] and the grain size effect on the tetragonal–monoclinic phase transition was studied by Raman spectroscopy and X-ray diffraction [99–101]. The dopant-size effect on the transport properties was also investigated [102]. In tetragonal Y-doped  $\text{ZrO}_2$  nanoceramics, the ionic conductivity was similar to that of microcrystalline samples [96].  $^{18}\text{O}$  diffusion profiles in nominally undoped fully dense nanocrystalline  $\text{ZrO}_2$  with monoclinic structure showed grain boundary diffusion at deeper penetration [103]. Within the entire temperature range between 450 and 950 °C, the grain boundary diffusion coefficient was three to four orders of magnitude higher than the bulk diffusion coefficient, the latter being similar to earlier results on monoclinic samples. The grain boundary diffusion coefficient remained, however, below the diffusion coefficient in coarse-grained cubic Ca- or Y-stabilized zirconia, which is related to a high bulk vacancy concentration [103]. A complete analysis applying the space charge models is certainly worthwhile.

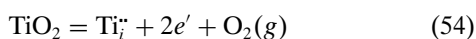
## 4.3. $\text{TiO}_2$ : Anatase and Rutile

Titanium dioxide is an oxide of uttermost importance for applications in dye-sensitized solar cells, for photocatalysis or in resistive oxygen sensors, especially in metastable

anatase modification. Furthermore,  $\text{TiO}_2$  is a model mixed conductor that can be doped with acceptor or donor ions and can present departures from stoichiometry and domains of ionic or electronic conductivity. The energetics of nanocrystalline  $\text{TiO}_2$  modifications, rutile, anatase, brookite, were recently reviewed [104]; the electrical properties are only partially investigated.

Nanocrystalline anatase  $\text{TiO}_2$  ceramics show a conductivity plateau at high oxygen partial pressures, indicating an uncommon domain of ionic conductivity at reduced temperature (450–600 °C) with a plausible activation energy ( $\approx 1$  eV) [105]. Nanocrystalline rutile [106] ceramics, obtained with the addition of about 1 mol%  $\text{SnO}_2$ , show a similar plateau with an identical activation energy ( $\approx 1$  eV) [107]. Predominant ionic conduction in a rutile single crystal was found at a significantly higher temperature (900 °C) and with a higher activation energy (1.6 eV) [108]. The different behavior can be attributed to the existence of a large density of interfacial diffusion paths in the nanoceramics, where ionic transport is enhanced with reduced migration energy.

A steep increase of electronic conductivity with an unusually large partial pressure exponent ( $-1/2$ ) is observed at low  $P(\text{O}_2)$  [105]. The large pressure dependence is certainly of interest for sensor applications. The  $-1/2$  exponent can be interpreted in a neutral layer model by assuming that the majority ionic defects are not completely ionized, in other words that the concentrated ionic (titanium interstitials) and electronic defects are partially associated. The reduction reaction can for example be written with doubly ionized titanium interstitials:



$$K_{\text{red}} = [\text{Ti}_i^{2+}][e']^2 P(\text{O}_2) = B \exp(-\Delta_{\text{red}}H^\circ/kT) \quad (55)$$

Given the large  $\text{Na}^+$  acceptor concentration in these samples ( $>1000$  ppm), which remains from the precipitation process of the anatase precursor using sodium hydroxide [62], one can assume that the interstitial concentration is fixed by the acceptor impurity concentration ( $2[\text{Ti}_i^{2+}] = [A'_{\text{Ti}}]$ ). One then gets the  $P(\text{O}_2)$  and  $T$  dependence of the conductivity:

$$\ln \sigma = \ln(e\mu_e(2B/[A'_{\text{Ti}}])^{1/2}) - 1/2 \ln P(\text{O}_2) - \Delta_{\text{red}}H^\circ/2kT \quad (56)$$

The calculated standard reduction enthalpy ( $\Delta_{\text{red}}H^\circ = 7.8$  eV) is well below the value in conventional microcrystalline  $\text{TiO}_2$  ( $\approx 10$  eV), indicating a reduced defect formation enthalpy at interface sites. One can notice that the estimated Debye length, taking into account the large acceptor density, is very small so that a “neutral layer model,” disregarding space charge effects, might be sufficient to explain the experimental data in this case. A more complete investigation of nanocrystalline anatase is currently in progress.

#### 4.4. $\text{CaF}_2$ and Related Materials

Calcium fluoride is a well-known solid  $\text{F}^-$  ion conductor. In nanocrystalline  $\text{CaF}_2$  ceramics, a largely increased ionic conductivity can be observed [109], as shown in Figure 6.

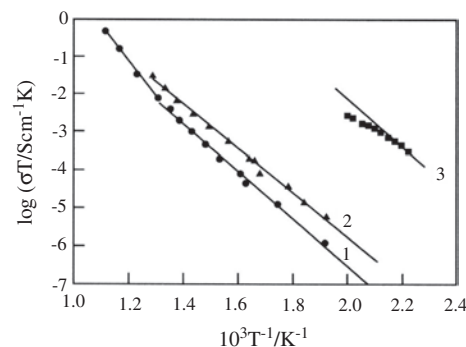


**Figure 6.** Ionic conductivity of  $\text{CaF}_2$ . (1) Microcrystalline  $\text{CaF}_2$ ; mean grain size  $\sim 0.2$   $\mu\text{m}$ . (2) Microcrystalline  $\text{CaF}_2$  activated with  $\text{SbF}_5$ . (3) Nanocrystalline  $\text{CaF}_2$ ; mean grain size  $\sim 10$  nm. Adapted with permission from [48], J. Maier, Nanoionics and soft materials science, in “Nanocrystalline Metals and Oxides—Selected Properties and Applications” (P. Knauth and J. Schoonman, Eds.), p. 91. Kluwer Academic, Boston, 2002. © 2002, Kluwer Academic.

Conductivity values and activation energy suggest dominating transport in space charge layers. By simply scaling up the space charge effects observed in microcrystalline samples according to the increased interface density, the correct order of magnitude of conductivity is obtained (Fig. 5). A systematic deviation at higher measurement temperatures is related to grain coarsening during the experiments. The activation energy corresponds to the migration energy of fluoride vacancies and suggests an accumulation of  $\text{F}^-$  vacancies in the space charge regions. Given the Na background concentration in the studied samples, the computed Debye length (1 nm) is well below the grain size, so that an observation of mesoscopic space charge effects is not expected; this requires highly pure nanocrystalline samples.

Sata et al. succeeded in growing multilayer structures of  $\text{BaF}_2/\text{CaF}_2$  by molecular beam epitaxy on alumina substrates at 500 °C [110]. The multilayer period was varied between 16 and 430 nm with an overall thickness of 500 nm (Fig. 7). At low temperature, the activation energy is dominated by  $\text{BaF}_2$ , in accordance with the larger vacancy mobility in this compound, whereas the activation energy at higher temperature seems to be determined by space charge layer conduction in  $\text{CaF}_2$ . This indicates a transfer of  $\text{F}^-$  ions from  $\text{BaF}_2$  to  $\text{CaF}_2$  rather than phase boundary core segregation of  $\text{F}^-$  ions.

The conductivities along the phase boundaries increase linearly with the number of heterojunctions provided that the period is greater than 100 nm. Films with smaller periods exhibit an anomalous conductivity increase. Calculation of the Debye length (15 nm) revealed that this effect is related to an overlap of space charge regions. Such heterostructures, routinely prepared by the semiconductor community, open up the possibility to measure properties reproducibly on a scale normally inaccessible in solid state ionics and to design devices which take advantage of the size and scale of such structures.

Other papers on nanocrystalline inorganic ion conductors can be found in [111, 112].



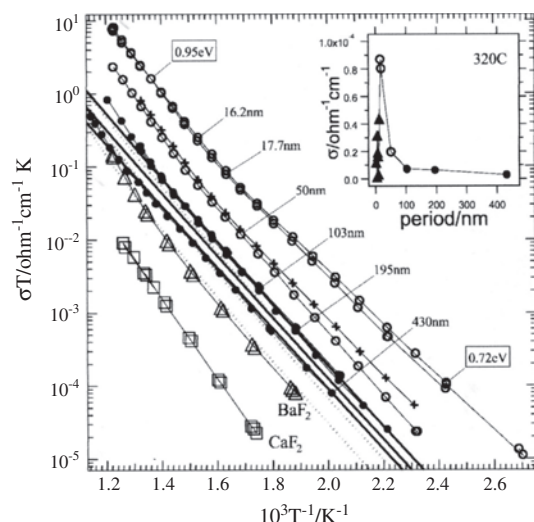


**Figure 7.** Arrhenius plots of conductivity of BaF<sub>2</sub>/CaF<sub>2</sub> heterolayers, BaF<sub>2</sub> (open triangles) and CaF<sub>2</sub> (open squares) thin films. The numbers indicate the BaF<sub>2</sub>/CaF<sub>2</sub> period. The inset shows the thickness dependence of conductivity at 320 °C. One observes an anomalous increase of conductivity for thicknesses comparable to 4  $\lambda$ , where  $\lambda$  is the Debye length. Reprinted with permission from [49], N. Sata et al., *Solid State Ionics* 154–155, 497 (2002). © 2002, Elsevier Science.

## 5. NANOCOMPOSITES

### 5.1. Ceramic and Glass Nanocomposites

The development of ionic conducting ceramic and glass nanocomposites started with the discovery by Liang of a conductivity enhancement in a two-phase material and, in the same period, of ionic conducting glasses.

Mesoscopic effects highlighting the importance of interfaces in nanocomposites are the stabilization of metastable phases and the variation of phase transition temperatures [113]. Interfacial interaction energies of the order of 0.5 eV in composite materials with alumina are great enough to cause phase transitions in a polymorphic compound, such as AgI. Furthermore, Coulomb interactions at high defect concentrations near interfaces can naturally lead to order-disorder phase transitions. The considerable enhancement of ionic conductivity observed in AgI–Al<sub>2</sub>O<sub>3</sub> composites, by more than three orders of magnitude [114], is outside the range of conventional space charge effects but can be explained by a nanosized ionic heterostructure  $\beta$ -AgI/ $\gamma$ -AgI with a layer thickness below the Debye length, so that mesoscopic conductivity effects result from overlapping space charge regions with considerable disorder in the Ag<sup>+</sup> sublattice. This kind of heterostructure can also be viewed as a succession of stacking faults (Fig. 8). The total AgI exists in the seven-layer polytype form if the alumina concentration exceeds 30 mol% [115]. This striking enhancement of ionic conductivity may also be expected for other structures in which structural units alternate with a typical distance below the Debye length and efforts should be directed to such ionic heterostructures. The study of ionic conductivity in microporous materials, such as zeolites [116–118], that contain tailored channels with nanometric dimensions might become another future highlight.

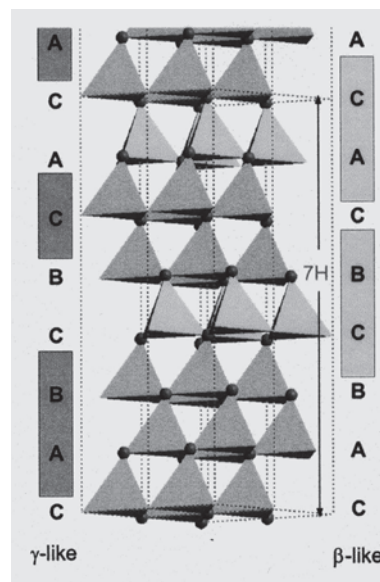


**Figure 8.** Stacking fault arrangement at the Al<sub>2</sub>O<sub>3</sub>/AgI boundary, which is equivalent to a sequence of subnanometer heterolayers of  $\beta$ - and  $\gamma$ -AgI, leading to pronounced disorder in the cation sublattice. Reprinted with permission from [48], J. Maier, *Nanoionics and soft materials science*, in “Nanocrystalline Metals and Oxides—Selected Properties and Applications” (P. Knauth and J. Schoonman, Eds.), p. 103. Kluwer Academic, Boston, 2002. © 2002, Kluwer Academic.

Glass ceramics, formed by crystalline inclusions inside a glassy matrix, are often nanocomposites, because the size of the crystallites is very small. Dispersed  $\alpha$ -AgI nanocrystals in AgI-based glass matrices of composition AgI–Ag<sub>2</sub>O–M<sub>x</sub>O<sub>y</sub> (M<sub>x</sub>O<sub>y</sub> = B<sub>2</sub>O<sub>3</sub>, GeO<sub>2</sub>, WO<sub>3</sub>) were discovered by Tatsumisago et al. [119–121]. These glass ceramics exhibit high ionic conductivities and low activation energies at room temperature. The larger activation energies observed at lower temperatures were attributed to a positional ordering of Ag<sup>+</sup> ions in the microcrystals. The pronounced conductivity increase observed during initial stages of devitrification of some AgI–Ag<sub>2</sub>O–M<sub>x</sub>O<sub>y</sub> glasses depends on the interfacial area between the glass and the low conductivity crystalline inclusions. This suggests the existence of a highly conducting interfacial region, possibly due to a mobility change close to the interface [122]. In the AgI–Ag<sub>2</sub>O–V<sub>2</sub>O<sub>5</sub> system [123], the increase depends on the interfacial area between glass and crystalline Ag<sub>8</sub>I<sub>4</sub>V<sub>2</sub>O<sub>7</sub> inclusions. An interface related effect is also responsible for the conductivity enhancement in partially crystallized AgI–Ag<sub>2</sub>O–P<sub>2</sub>O<sub>5</sub> glasses. The absence of conductivity enhancement in the AgI–Ag<sub>2</sub>O–B<sub>2</sub>O<sub>3</sub> system was explained by formation of  $\alpha$ -AgI microcrystals. When the conductivity of the crystallites is higher than that of the glassy matrix, the interface region is short-circuited. The research activity on glass and ceramic composites slowed down in recent years due to persisting mechanical problems which are difficult to resolve.

Other papers on ceramic and glass nanocomposites can be found in [124–138].



## 5.2. Polymer Nanocomposites

Polymer electrolytes are actively developed as separator material in solid lithium batteries and proton exchange membrane fuel cells (PEMFCs). The search of polymer nanocomposites with high ionic conductivity and good mechanical properties has been pursued in the past decade with the objective to provide flexible, compact solid membranes free from leakage and available in variable geometry.

Most PEMFCs rely on the transport of protons through hydrated regions of Nafion, which has become the industry standard virtually by default, or other polymers containing sulfonate groups. Complications arise from the hydrated nature of the polymer electrolytes, because humidification is required to maintain ion conduction and prevent irreversible dehydration damage. This excludes thermal excursions to higher temperatures. However, nanocomposite Nafion + SiO<sub>2</sub> membranes can retain water at higher temperatures [139–142] and were found able to operate at 130 °C or more. Membranes with nanocrystalline TiO<sub>2</sub> were also described [143]. With too much water, on the other hand, degradation of the mechanical properties of the polymer is observed due to swelling. This is the reason for investigations on water-free systems, including polymer–ceramic composites (e.g., Nafion + SiO<sub>2</sub> membranes doped with heteropolyacids, such as phospho- or silicotungstic acid) [144–146].

An even larger effort has been devoted to polyethyleneoxide (PEO) based systems for lithium ion batteries, which include:

- (1) The solid (PEO-LiX) type. It reaches practically useful ionic conductivity values only at 60–80 °C. The ionic conductivity is often enhanced in amorphous polymer electrolytes, which behave as rubberlike “soft solids.”
- (2) The hybrid polymer electrolyte (gel type). It contains organic molecules (“plasticisers”), such as ethylene or propylene carbonate, and is gel-like, losing to some extent the advantages of solid polymer electrolytes: mechanical stability and processing flexibility.
- (3) The inorganic filler-containing composite type. A simple strategy is to blend conventional polymer electrolytes with dry ceramic powders [147], which can improve ion conductivity and mechanical stability.

The polymer composites development started in the 1980s initially to improve the elastic and tensile properties of glasses and ceramics, which are often too hard and brittle to be useful as solid electrolytes. Skaarup et al. [148] made polymer-ceramic composites using a large percentage of Li<sub>3</sub>N in doped PEO and insulating polyethylene matrices. Surprisingly, the latter, supposedly isolating, were actually more conducting than the PEO composites. This indicates that the polymer mainly holds the ceramic particles together but does not provide an ionic conduction pathway. Mixtures of Nasicon with doped PEO showed smaller dc conductivity than either the pure ceramic or the pure polymer electrolyte. The considerably enhanced interface resistance was probably due to a poor contact between the two phases [149]. Mixtures of a Li-ion conducting Li<sub>1-x</sub>Al<sub>x</sub>Ti<sub>2-x</sub>(PO<sub>4</sub>)<sub>3</sub> ceramic with an amorphous copolymer ethylene oxide-propylene oxide showed conductivities

approaching bulk ceramic values, but the importance of pores was confirmed [150]. Tortet et al. presented a percolation model of proton-conducting composites made with an inert polymer (PPS) and brushite (CaHPO<sub>4</sub>·2H<sub>2</sub>O) [151, 152].

Weston and Steele [153] first mixed PEO-LiClO<sub>4</sub> complexes with  $\alpha$ -alumina powder in order to improve the mechanical strength of the polymer electrolyte. A significant ionic conductivity enhancement was obtained using  $\gamma$ -Al<sub>2</sub>O<sub>3</sub> as inorganic filler [154]. An important contribution was made by Croce and co-workers, who first added  $\beta''$ -alumina or LiAlO<sub>2</sub> to PEO electrolytes in order to improve the mechanical properties of the polymer [155] and later succeeded in preparing a polymer composite with dispersed TiO<sub>2</sub> nanoparticles with a largely enhanced conductivity [156, 157]. A significant increase of the ionic conductivity and of the Li ion transference number and a decrease of activation energy were observed in polyacrylonitrile composites with dispersed  $\alpha$ -Al<sub>2</sub>O<sub>3</sub> [158].

The discussion of the mechanism of the conductivity enhancement and improvement of Li<sup>+</sup> ion transport number is far from being terminated and various explanations have been given.

- (1) It was attributed to hydroxide groups on the oxide nanoparticle surface [159], providing an additional route for fast Li<sup>+</sup> ion transport, possibly involving a space charge effect [160]. In principle, modifications of local defect distribution are expected near any type of interface, but they are more or less important, depending on the chemical affinity between the two phases.
- (2) It was ascribed to interactions between Lewis acid sites on the nanoparticle surface, probably OH groups, and anions or PEO segments, which help release more free Li<sup>+</sup> ions and suppress crystallization of amorphous regions [161–163].
- (3) A recent study using differently heat-treated SnO<sub>2</sub> nanoparticles as second phase concluded that oxygen vacancies on the oxide surface act as Lewis acid sites [164]. In this model, the oxygen vacancies are assumed to compete with Li ions to coordinate with PEO segments, preventing PEO crystallization on one hand and releasing free Li<sup>+</sup> ions on the other. Furthermore, ClO<sub>4</sub><sup>-</sup> ions are also bound to oxygen vacancies, decreasing the tendency to ion association.
- (4) Other structural factors, such as a change of the glass transition temperature, have also been discussed [165].

However, preparation problems, notably poor adhesion, pores, and gaps at the phase boundaries, make the theoretical discussion of conductivity effects in polymer nanocomposites in the present status a difficult task. More preparative and theoretical efforts are definitely needed to better understand and further improve the properties of polymer–ceramic nanocomposites. This is a major challenge that should be met in the future.

Other papers on polymer nanocomposites can be found in [166–183].

## 6. CONCLUSIONS

After the first decade of research on ionic conduction in nanostructured materials, a few general conclusions can already be drawn.

Concerning nanocrystalline materials, the main conclusion so far is that space charge theory seems to provide an adequate interpretation of “bulk” conductivity at least for the most studied model compound,  $\text{CeO}_2$ . In this case, space charge regions lead actually to a counterintuitive decrease of ionic conductivity due to oxygen vacancy depletion. So far, clear ionic conductivity enhancement has been found in  $\text{CaF}_2$ -based systems, either nanocrystalline ceramics or heterolayer thin films with small periodicity. In the case of the most prominent oxygen ion conductor, doped  $\text{ZrO}_2$ , the results are ambivalent. However, the effect of impurity segregation and charge carrier depletion layers on the grain boundary resistance seems now to be reasonably well understood.

Concerning nanocomposites, especially polymer-based systems, there is much greater uncertainty on mechanistic details related to less mastered synthesis conditions. This leads to a wide variety of interpretations for conductivity changes, including microstructural effects, like amorphous versus crystalline regions in the polymer, and defect chemical ones, like the existence of cation–anion pairs or cation adsorption on inorganic filler particles. A more careful sample preparation will be necessary before better understanding and predictability of nanocomposite performance can be achieved. Given the importance of polymer nanocomposites in energy storage and conversion, continuing progress in this field can safely be foreseen.

## GLOSSARY

**Interface (synonym: boundary)** Two-dimensional transition region in a material separating (a) two phases (e.g. in composites), also called phase boundary, (b) two crystallites with different orientation (e.g. in ceramics), also called grain boundary. The interface core has a width of a few atomic layers only. The presence and density of interfaces greatly influence many materials properties, including the electrical conductivity.

**Percolation** Geometrical model used for the description of disordered or random systems, introducing scaling laws with universal parameters. Near a critical value, property fluctuations become important: e.g. ionic conductor-insulator transitions in solid state ionics.

**Solid ionic conductor** Ionocovalent solid, in which the electrical conduction is essentially due to mobile ions.

**Space charge layer** Region in proximity of extended defects (such as interfaces or dislocations), where electroneutrality is not observed due to the symmetry break. The space charge compensates the interface core charge. These regions can present very different electrical properties than the bulk, due to enhanced or reduced charge carrier concentrations.

## REFERENCES

1. M. Faraday, On conducting power generally, in “Experimental Researches in Electricity,” Vol. 1, p. 439. Series IV. Taylor and Francis, London, 1839.
2. W. Nernst, Material for Electric-Lamp Glowlers, U.S. Patent 685, 730, 1901.
3. J.-M. Gaugain, *C. R. Acad. Sci.* 37, 82 (1853).
4. E. Baur and H. Preiss, *Z. Elektrochem.* 43, 727 (1937).
5. A. Joffé, *Ann. Phys.* 72, 461 (1923).
6. J. Frenkel, *Z. Phys.* 35, 652 (1926).
7. C. Wagner and W. Schottky, *Z. Phys. Chem. B* 11, 163 (1930).
8. C. Wagner, *Z. Phys. Chem. B* 22, 181 (1933).
9. C. C. Liang, *J. Electrochem. Soc.* 120, 1289 (1973).
10. F. A. Kröger, “The Chemistry of Imperfect Crystals,” 2nd ed. North-Holland, Amsterdam, 1974.
11. J. Maier, *Chem. Eur. J.* 7, 4762 (2001).
12. See, for example, R. Röttger, H. Schmalzried, and M. Günter, *Ber. Bunsenges. Phys. Chem.* 101, 1083 (1997).
13. C. Brouwer, *Philips Res. Rep.* 9, 366 (1954).
14. See, for example, “Handbook of Solid State Electrochemistry” (P. J. Gellings and H. J. M. Bouwmeester, Eds.). CRC Press, Boca Raton, 1997.
15. A. V. Chadwick, *Defect Diffusion Forum* 95–98, 1015 (1993).
16. W. Jost, *J. Chem. Phys.* 1, 466 (1933).
17. N. F. Mott and M. J. Littleton, *Trans. Faraday Soc.* 34, 485 (1936).
18. A. B. Lidiard, *Phys. Rev.* 94, 29 (1954).
19. R. W. Dreyfus and A. S. Nowick, *J. Appl. Phys. Suppl.* 33, 473 (1962).
20. Y. Haven, *J. Chem. Phys.* 21, 171 (1953).
21. N. Hainovsky and J. Maier, *Phys. Rev. B* 51, 15789 (1995).
22. K. Funke, *Ber. Bunsenges. Phys. Chem.* 90, 661 (1986).
23. K. Funke and R. D. Banhatti, *Mater. Res. Soc. Symp. Proc.*, 756, 3 (2003).
24. R. Bouchet, P. Knauth, and J.-M. Laugier, *J. Electrochem. Soc.*, 150, 348 (2003).
25. J. R. MacDonald, “Impedance Spectroscopy Emphasizing Solid Materials and Systems.” Wiley, New York, 1987.
26. K. L. Merkle, *J. Phys. Chem. Solids* 55, 991 (1994).
27. Y. Oishi and W. D. Kingery, *J. Chem. Phys.* 33, 905 (1960).
28. A. Atkinson, *Solid State Ionics* 28–30, 1377 (1988).
29. J. W. Verwey and J. Th. G. Overbeek, “Theory of the Stability of Lyophobic Colloids.” Elsevier, New York, 1948.
30. T. B. Grimley and N. F. Mott, *Discuss. Faraday Soc.* 1, 3 (1947).
31. K. Lehovec, *J. Chem. Phys.* 21, 1123 (1953).
32. K. L. Kliewer and J. S. Koehler, *Phys. Rev.* 140, 1226 (1965).
33. R. B. Poeppel and J. M. Blakely, *Surf. Sci.* 15, 507 (1969).
34. C. Wagner, *J. Phys. Chem. Solids* 33, 1051 (1972).
35. J. A. S. Ikeda and Y.-M. Chiang, *J. Am. Ceram. Soc.* 76, 2437 (1993).
36. J. A. S. Ikeda, Y.-M. Chiang, A. J. Garratt-Reed, and J. B. VanderSande, *J. Am. Ceram. Soc.* 76, 2447 (1993).
37. D. A. Blom and Y.-M. Chiang, *Mater. Res. Soc. Symp. Proc.* 458, 127 (1997).
38. K. Saki and J. B. Wagner, *Appl. Phys. Lett.* 37, 757 (1980).
39. A. S. Nowick, *Annu. Rev. Mater. Sci.* 26, 1 (1996).
40. N. J. Dudney, *J. Am. Ceram. Soc.* 70, 65 (1987).
41. J. Maier, *Progr. Solid State Chem.* 23, 171 (1995).
42. J. Maier and B. Reichert, *Ber. Bunsenges. Phys. Chem.* 90, 666 (1986).
43. J. Maier, *J. Phys. Chem. Solids* 46, 309 (1985).
44. J. Maier and U. Lauer, *Ber. Bunsenges. Phys. Chem.* 94, 973 (1990).
45. M. Bendahan, C. Jacolin, P. Lauque, J.-L. Seguin, and P. Knauth, *J. Phys. Chem. B* 105, 8327 (2001).
46. J. Maier, *Ber. Bunsenges. Phys. Chem.* 90, 26 (1986).
47. G. Gouy, *J. Phys.* 9, 457 (1910); D. L. Chapman, *Philos. Mag.* 25, 475 (1913).

48. J. Maier, Nanoionics and soft materials science, in "Nanocrystalline Metals and Oxides—Selected Properties and Applications" (P. Knauth and J. Schoonman, Eds.), pp. 81–110. Kluwer, Boston, 2002.
49. N. Sata, N. Y. Jin-Phillipp, K. Eberl, and J. Maier, *Solid State Ionics* 154–155, 497 (2002).
50. J. Maier, *Solid State Ionics* 131, 13 (2000).
51. S. M. Sze, "Physics of Semiconductor Devices," 2nd ed., p. 372. Wiley, New York, 1981.
52. P. A. Cox, "The Electronic Structure and Chemistry of Solids." Oxford Univ. Press, Oxford, 1987.
53. A. J. Bard and L. R. Faulkner, "Electrochemical Methods: Fundamentals and Applications." Wiley, New York, 1980.
54. X. Guo, W. Sigle, J. Fleig, and J. Maier, *Solid State Ionics* 154–155, 555 (2002).
55. A. Bunde, W. Dieterich, and E. Roman, *Solid State Ionics* 18–19, 147 (1986).
56. J.-M. Debierre, P. Knauth, and G. Albinet, *Appl. Phys. Lett.* 71, 1335 (1997).
57. P. Knauth, *J. Electroceram.* 5, 111 (2000).
58. S. Indris, P. Heitjans, H. E. Roman, and A. Bunde, *Phys. Rev. Lett.* 84, 2889 (2000).
59. M. P. Pileni, Nanomaterials production by soft chemistry, in "Nanostructured Materials, Selected Synthesis Methods, Properties and Applications" (P. Knauth and J. Schoonman, Eds.), pp. 1–22. Kluwer, Boston, 2002.
60. O. Schäf, H. Ghobarkar, and P. Knauth, Hydrothermal synthesis of nanomaterials, in "Nanostructured Materials, Selected Synthesis Methods, Properties and Applications" (P. Knauth and J. Schoonman, Eds.), pp. 23–42. Kluwer, Boston, 2002.
61. H. Gleiter, *Acta Mater.* 48, 1 (2000).
62. P. Knauth, R. Bouchet, O. Schäf, A. Weibel, and G. Auer, Functionalized TiO<sub>2</sub> nanoparticles for pigments, photoelectrochemistry, and solid state chemical sensors, in "Synthesis, Functionalization and Surface Treatments of Nanoparticles" (M.-I. Baraton, Ed.). American Scientific, Stevenson Ranch, CA, 2002.
63. R. Valiev, *Nature* 419, 887 (2002).
64. Y. M. Chiang, E. B. Lavik, I. Kosacki, H. L. Tuller, and J. Y. Ying, *J. Electroceram.* 1, 7 (1997).
65. A. V. Chadwick and G. E. Rush, Characterization of nanocrystalline materials by EXAFS spectroscopy, in "Nanocrystalline Metals and Oxides—Selected Properties and Applications" (P. Knauth and J. Schoonman, Ed.), pp. 133–164. Kluwer, Boston, 2002.
66. G. E. Rush, A. V. Chadwick, I. Kosacki, and H. U. Anderson, *J. Phys. Chem. B* 104, 9597 (2000).
67. P. Knauth, G. Schwitzgebel, A. Tschöpe, and S. Villain, *J. Solid State Chem.* 140, 295 (1998).
68. P. Knauth and H. L. Tuller, *Solid State Ionics* 136–137, 1215 (2000).
69. A. Tschöpe, W. Liu, M. Flytzani-Stephanopoulos, and J. Y. Ying, *J. Catal.* 157, 42 (1995).
70. J. Schoonman, *Solid State Ionics* 135, 5 (2000).
71. H. L. Tuller, *Solid State Ionics* 131, 143 (2000).
72. P. Knauth, *J. Solid State Electrochem.* 6, 165 (2002).
73. J. Schoonman, *Solid State Ionics* 157, 319 (2003).
74. J. Maier, *Solid State Ionics* 154–155, 291 (2002).
75. J. Maier, *Solid State Ionics* 157, 327 (2003).
76. J. Maier, *Solid State Ionics* 148, 367 (2002).
77. C. Kleinlogel and L. J. Gauckler, *Solid State Ionics* 135, 567 (2000).
78. M. Boaro, A. Trovarelli, J.-H. Hwang, and T. O. Mason, *Solid State Ionics* 147, 85 (2002).
79. Y.-M. Chiang, E. B. Lavik, and D. A. Blom, *Nanostructured Mater.* 9, 633 (1997).
80. A. Tschöpe, *Solid State Ionics* 139, 255 (2001).
81. I. Kosacki, T. Suzuki, V. Petrovsky, and H. U. Anderson, *Solid State Ionics* 136–137, 1225 (2000).
82. T. Suzuki, I. Kosacki, H. U. Anderson, and P. Colomban, *J. Am. Ceram. Soc.* 84, 2007 (2001).
83. T. Suzuki, I. Kosacki, and H. U. Anderson, *Solid State Ionics* 151, 111 (2002).
84. H. L. Tuller and A. S. Nowick, *J. Phys. Chem. Solids* 38, 859 (1977).
85. H. L. Tuller and A. S. Nowick, *J. Electrochem. Soc.* 126, 209 (1979).
86. O. Porat, H. L. Tuller, E. B. Lavik, and Y.-M. Chiang, in "Nanophase and Nanocomposite Materials II" (S. Komarneni, J. Parker, and H. Wollenberger, Eds.), p. 99. MRS, Pittsburgh, 1997.
87. P. Knauth and H. L. Tuller, *Ceramic Trans.* 92, 15 (1999).
88. P. Knauth and H. L. Tuller, *J. Europ. Ceram. Soc.* 19, 831 (1999).
89. T. O. Mason and J. H. Hwang, *Z. Phys. Chem.* 207, 21 (1998).
90. A. Tschöpe, *Solid State Ionics* 139, 267 (2001).
91. S. Kim and J. Maier, *J. Electrochem. Soc.* 149, 373 (2002).
92. A. Tschöpe, *Mater. Res. Soc. Symp. Proc.*, in press.
93. A. Tschöpe, S. Kilassonia, B. Zapp, and R. Birringer, *Solid State Ionics* 149, 261 (2002).
94. M. Vennekamp and J. Janek, *Solid State Ionics* 118, 43 (1999).
95. M. Aoki, Y.-M. Chiang, I. Kosacki, L. J. R. Lee, H. L. Tuller, and Y. Liu, *J. Am. Ceram. Soc.* 79, 1169 (1996).
96. P. Mondal, A. Klein, W. Jaegermann, and H. Hahn, *Solid State Ionics* 118, 331 (1999).
97. X. Guo and J. Maier, *J. Electrochem. Soc.* 148, E121 (2001).
98. T. Nguyen and E. Djurado, *Solid State Ionics* 138, 191 (2001).
99. E. Djurado, L. Dessemond, and C. Roux, *Solid State Ionics* 136–137, 1249 (2000).
100. E. Djurado, P. Bouvier, and G. Lucazeau, *J. Solid State Chem.* 149, 399 (2000).
101. F. Boulc'h and E. Djurado, *Solid State Ionics* 157, 335 (2003).
102. F. Boulc'h, L. Dessemond, and E. Djurado, *Solid State Ionics* 154–155, 143 (2002).
103. H. E. Schaefer, K. Reimann, W. Straub, F. Phillipp, H. Tanimoto, U. Brossmann, and R. Würschum, *Mater. Sci. Eng. A* 286, 24 (2000).
104. M. R. Ranade, A. Navrotsky, H. Z. Zhang, J. F. Banfield, S. H. Elder, A. Zaban, P. H. Borse, S. K. Kulkarni, G. S. Doran, and H. J. Whitfield, *PNAS* 99, 6476 (2002).
105. P. Knauth and H. L. Tuller, *J. Appl. Phys.* 85, 897 (1999).
106. C. Real, L. García, M. D. Alcalá, and J. M. Criado, *Solid State Ionics* 141–142, 671 (2001).
107. C. Demetry and X. Shi, *Solid State Ionics* 118, 271 (1999).
108. J. Nowotny, M. Radecka, M. Rekas, S. Sugihara, E. R. Vance, and W. Weppner, *Ceramics Int.* 24, 571 (1998).
109. W. Pui, S. Rodewald, R. Ramlau, P. Heitjans, and J. Maier, *Solid State Ionics* 131, 159 (2000).
110. N. Sata, K. Eberman, K. Eberl, and J. Maier, *Nature* 408, 946 (2000).
111. Y. Wang, L. Huang, H. He, and M. Li, *Physica B* 325, 357 (2003).
112. A. Hartridge, M. Ghanashyam Krishna, A. K. Bhattacharya, A. Attia, and J. R. Owen, *Solid State Ionics* 144, 287 (2001).
113. J. Maier, *J. Europ. Ceram. Soc.* 19, 675 (1999).
114. K. Shahi and J. B. Wagner, *J. Electrochem. Soc.* 128, 6 (1981).
115. J.-S. Lee, St. Adams, and J. Maier, *Solid State Ionics* 136–137, 1261 (2000).
116. H. Ghobarkar, O. Schäf, and U. Guth, *Progr. Solid State Chem.* 27, 293 (1999).
117. H. Ghobarkar, O. Schäf, and P. Knauth, *Angew. Chem. Int. Ed.* 40, 3831 (2001).
118. O. Schäf, H. Ghobarkar, F. Adolf, and P. Knauth, *Solid State Ionics* 143, 433 (2001).
119. M. Tatsumisago, Y. Shinkuma, and T. Minami, *Nature* 354, 217 (1991).
120. M. Tatsumisago, K. Okuda, N. Itakura, and T. Minami, *Solid State Ionics* 121, 193 (1999).
121. N. Kuwata, J. Kawamura, Y. Nakamura, K. Okuda, M. Tatsumisago, and T. Minami, Ag-109 NMR study of AgI-based glasses

- containing frozen  $\alpha$ -AgI nanocrystals, *Solid State Ionics* 136–137, 1061 (2000).
122. St. Adams, K. Hariharan, and J. Maier, *Solid State Ionics* 86–88, 503 (1996).
  123. H. Takahashi, K. Shishitsuka, T. Sakuma, Y. Shimojo, and Y. Ishii, *Solid State Ionics* 113–115, 685 (1998).
  124. E. Bychkov, A. Bychkov, A. Pradel, and M. Ribes, *Solid State Ionics* 113–115, 691 (1998).
  125. G. Dotelli, R. Volpe, I. Natali-Sora, and C. M. Mari, *Solid State Ionics* 113–115, 325 (1998).
  126. N. Bamba, Y.-H. Cho, T. Sekino, and K. Niihara, *Solid State Ionics* 111, 171 (1998).
  127. A. Yuzaki and A. Kishimoto, *Solid State Ionics* 116, 47 (1999).
  128. V. G. Ponomareva, G. V. Lavrova, and L. G. Simonova, *Solid State Ionics* 118, 317 (1999).
  129. M. Nagai and T. Nishino, *Solid State Ionics* 117, 317 (1999).
  130. V. G. Ponomareva, G. V. Lavrova, and L. G. Simonova, *Solid State Ionics* 119, 295 (1999).
  131. G. Ardel, D. Golodnitsky, E. Peled, Y. Wang, G. Wang, S. Bajue, and S. Greenbaum, *Solid State Ionics* 113–115, 477 (1998).
  132. G. V. Lavrova, V. G. Ponomareva, and N. F. Uvarov, *Solid State Ionics* 136–137, 1285 (2000).
  133. N. F. Uvarov, L. I. Brezhneva, and E. F. Hairetdinov, *Solid State Ionics* 136–137, 1273 (2000).
  134. P. Ghigna, M. Di Muri, P. Mustarelli, C. Tomasi, and A. Magistris, *Solid State Ionics* 136–137, 479 (2000).
  135. R. C. Agrawal, M. L. Verma, R. K. Gupta, and S. Thaker, *Solid State Ionics* 136–137, 473 (2000).
  136. G. Senthil Murugan and K. B. R. Varma, *Solid State Ionics* 139, 105 (2001).
  137. A. Robledo, N. J. Garcia, and J. C. Bazan, *Solid State Ionics* 139, 303 (2001).
  138. M. Carewska, G. B. Appetecchi, F. Cardellini, and S. Passerini, *Solid State Ionics* 139, 211 (2001).
  139. P. L. Antonucci, A. S. Aricò, P. Cretì, E. Ramunni, and V. Antonucci, *Solid State Ionics* 125, 431 (1999).
  140. K. T. Adjemian, S. J. Lee, S. Srinivasan, J. Benziger, and A. B. Bocarsly, *J. Electrochem. Soc.* 149, A256 (2002).
  141. D. Carrière, P. Barboux, F. Chaput, O. Spalla, and J. P. Boilot, *Solid State Ionics* 145, 141 (2001).
  142. N. Miyake, J. S. Wainright, and R. F. Savinell, *J. Electrochem. Soc.* 148, A898 (2001).
  143. H. Uchida, Y. Ueno, H. Hagihara, and M. Watanabe, *J. Electrochem. Soc.* 150, A57 (2003).
  144. P. Staiti, A. S. Aricò, V. Baglio, F. Lufrano, E. Passalacqua, and V. Antonucci, *Solid State Ionics* 145, 101 (2001).
  145. I. Honma, H. Nakajima, and S. Nomura, *Solid State Ionics* 154–155, 707 (2002).
  146. H. Nakajima and I. Honma, *Solid State Ionics* 148, 607 (2002).
  147. C. Capiglia, J. Yang, N. Imanishi, A. Hirano, Y. Takeda, and O. Yamamoto, *Solid State Ionics* 154–155, 7 (2002).
  148. S. Skaarup, K. West, P. M. Julian, and D. M. Thomas, *Solid State Ionics* 40/41, 1021 (1990).
  149. J. Plochanski and W. Wiczorek, *Solid State Ionics* 28–30, 979 (1988).
  150. K. M. Nairn, A. S. Best, P. J. Newman, D. R. MacFarlane, and M. Forsyth, *Solid State Ionics* 121, 115 (1999).
  151. L. Tortet, J.-R. Gavarri, J. Musso, G. Nihoul, and A. K. Sarychev, *J. Solid State Chem.* 141, 392 (1998).
  152. J. R. Gavarri, L. Tortet, and J. Musso, *Solid State Ionics* 117, 75 (1999).
  153. J. E. Weston and B. C. H. Steele, *Solid State Ionics* 7, 75 (1982).
  154. J. Plochanski, W. Wiczorek, J. Przulski, and K. Such, *Appl. Phys. A* 49, 55 (1989).
  155. F. Croce, S. Passerini, A. Selvaggi, and B. Scrosati, *Solid State Ionics* 40/41, 375 (1990).
  156. F. Croce, G. B. Appetecchi, L. Persi, and B. Scrosati, *Nature* 394, 456 (1998).
  157. F. Croce, L. Persi, F. Ronci, and B. Scrosati, *Solid State Ionics* 135, 47 (2000).
  158. Y. W. Chen-Yang, H. C. Chen, F. J. Lin, and C. C. Chen, *Solid State Ionics* 150, 327 (2002).
  159. F. Croce, L. Persi, B. Scrosati, F. Serraino-Fiory, E. Plichta, and M. A. Hendrickson, *Electrochim. Acta* 46, 2457 (2001).
  160. M. Forsyth, D. R. MacFarlane, A. Best, J. Adebahr, P. Jacobsson, and A. J. Hill, *Solid State Ionics* 147, 203 (2002).
  161. D. Golodnitsky, G. Ardel, and E. Peled, *Solid State Ionics* 147, 141 (2002).
  162. M. Marcinek, A. Zalewska, G. Żukowska, and W. Wiczorek, *Solid State Ionics* 136–137, 1175 (2000).
  163. B. Kumar and S. J. Rodrigues, *J. Electrochem. Soc.* 148, A1336 (2001).
  164. H.-M. Xiong, K. K. Zhao, X. Zhao, Y.-W. Wang, and J.-S. Chen, *Solid State Ionics*, in press.
  165. C. G. Joo, L. M. Bronstein, R. L. Karlinsey, and J. W. Zwanziger, *Solid State Nuclear Magnetic Resonance* 22, 235 (2002).
  166. M. M. Doeff and J. S. Reed, *Solid State Ionics* 113–115, 109 (1998).
  167. C. Capiglia, P. Mustarelli, E. Quartarone, C. Tomasi, and A. Magistris, *Solid State Ionics* 118, 73 (1999).
  168. I. Honma, S. Hirakawa, K. Yamada, and J. M. Bae, *Solid State Ionics* 118, 29 (1999).
  169. I. Honma, Y. Takeda, and J. M. Bae, *Solid State Ionics* 120, 255 (1999).
  170. B. Kumar and L. G. Scanlon, *Solid State Ionics* 124, 239 (1999).
  171. A. S. Best, A. Ferry, D. R. MacFarlane, and M. Forsyth, *Solid State Ionics* 126, 269 (1999).
  172. B. Kumar, S. J. Rodrigues, and L. G. Scanlon, *J. Electrochem. Soc.* 148, A1191 (2001).
  173. J. Ibañez, C. Pecharroman, R. Jimenez, P. Duran-Martin, M. G. Lazarraga, and J. M. Rojo, *J. Electrochem. Soc.* 148, J31 (2001).
  174. M. J. G. Jak, M. S. Pontfoort, N. Van Lanschoot, A. S. Best, E. M. Kelder, D. R. MacFarlane, M. Forsyth, and J. Schoonman, *Solid State Ionics* 143, 57 (2001).
  175. Th. Joykumar Singh, T. Mimani, K. C. Patil, and S. V. Bhat, *Solid State Ionics* 154–155, 21 (2002).
  176. Z. Wen, M. Wu, T. Itoh, M. Kubo, Z. Lin, and O. Yamamoto, *Solid State Ionics*, 148, 185 (2002).
  177. R. A. Zoppi and M. C. Gonçalves, *Solid State Ionics* 147, 157 (2002).
  178. H. Nakajima, S. Nomura, T. Sugimoto, S. Nishikawa, and I. Honma, *J. Electrochem. Soc.* 149, A953 (2002).
  179. L. Persi, F. Croce, B. Scrosati, E. Plichta, and M. A. Hendrickson, *J. Electrochem. Soc.* 149, A212 (2002).
  180. R. Bissessur, D. Gallant, and R. Brüning, *Solid State Ionics* 158, 205 (2003).
  181. Y. W. Chen-Yang, H. C. Chen, F. J. Lin, C. W. Liao, and T. L. Chen, *Solid State Ionics* 156, 383 (2003).
  182. P. P. Chu, M. Jaipal Reddy, and H. M. Kao, *Solid State Ionics* 156, 141 (2003).
  183. H. J. Walls, P. S. Fedkiw, T. A. Zawodzinski, Jr., and S. A. Khan, *J. Electrochem. Soc.* 150, E165 (2003).

# Kelvin Probe Technique for Nanotechnology

G. Koley, M. G. Spencer

*Cornell University, Ithaca, New York, USA*

## CONTENTS

1. Introduction
  2. Kelvin Probe Technique: Basic Concepts
  3. Experimental Details
  4. Applications
  5. Summary
- Glossary  
References

## 1. INTRODUCTION

The Kelvin probe technique has established itself as an important tool in material characterization. Named after Lord Kelvin, the technique was first demonstrated by him to the Royal Society in 1897 [1]. In his experiment, he demonstrated for the first time the use of a null method to quantitatively measure the work function difference between two dissimilar metals, such as copper and zinc. As the technique became more popular, modifications were made to the original measurement apparatus as well as to the measurement procedure. In 1932, Zisman [2] modified the measurement procedure by mechanically vibrating one plate of the condenser (consisting of two plates of dissimilar metals) and nullifying the contact potential difference (CPD) by an audiofrequency amplifier arrangement. Later, in 1976, Besocke and Berger [3] replaced the mechanical drive and feedthrough with a piezoelectric oscillator and used a lock-in amplifier and feedback mechanism to nullify the CPD automatically and continuously. A further modified version of the ac Kelvin probe was demonstrated by Weaver and Abraham in 1991 [4], in which an ac voltage was applied to the probe tip in addition to a dc voltage that was used to nullify the CPD (through measurement of force rather than current as before). In the same year, Nonnenmacher, O'Boyle, and Wickramasinghe reported on Kelvin probe measurements performed in conjunction with atomic force

microscopy (AFM) [5]. With this technique the lateral resolution of the potential measurement could be improved quite significantly ( $<50$  nm), and simultaneous imaging of the surface morphology and the surface potential was made possible. In modern systems (e.g., those manufactured by TM Microscopes, Veeco Metrology Group) the Kelvin probe measurements are usually performed in a scanning mode together with the surface morphology imaging. This mode of operation is called scanning Kelvin probe microscopy (SKPM) and has become very popular for various materials and semiconductor device characterization. Another common electrical characterization technique is called electrostatic force microscopy (EFM), which is based on the same basic principles as SKPM and is performed in a similar way. However, in EFM the output signal is the electrostatic force between the tip and the sample, whereas in SKPM a feedback loop is used that generates a voltage (the output signal) that is applied to the probe tip to nullify the force between the tip and the sample. This feedback voltage is exactly equal to the CPD if the electrostatic force can be totally nullified. Thus with the Kelvin probe technique a direct and quantitative measurement of the surface charge density, work function, and applied bias is possible.

Over the years, the Kelvin probe technique has become quite popular, and much work has been done to characterize a wide variety of materials. In this article, we have discussed the underlying principles, experimental procedures, and important practical applications of this method (as relevant to nanotechnology). Not much coverage has been provided to hardware and detection systems, detailed treatment of which can be found elsewhere [6]. Freedom has been exercised in treating different topics at different depths as found necessary. Efforts have been made to make this review more practically oriented without being superficial in discussing the underlying physical principles. Since modern instruments available today perform simultaneous imaging of surface potential (by SKPM) and surface morphology (by AFM), we have discussed the various aspects of Kelvin probe measurement from that viewpoint. We start with a discussion of the basic concepts involved with this technique

in Section 2. The different origins of the electrostatic force between the probe tip and the sample have been discussed, and the basic equations governing the Kelvin probe operation have been developed in this section. Section 3 is devoted to the experimental procedures pertaining to this technique. Here we discuss the basic components of this system and the possible modes of operation. An overview of the different forces acting on the tip is also presented. The versatility of this technique leads to a host of important applications, which are discussed in Section 4. A general discussion of the applications of this technique to the characterization of materials important to nanotechnology (such as insulators and semiconductors) is presented first, followed by the applications specific to nanotechnology. Applications to surface photovoltage (SPV) measurements and devices and integrated circuits have been treated separately as deemed necessary. Additionally, the limitations of this technique and possible sources of inaccuracies have been pointed out. We conclude this chapter with a summary of this technique and some pertinent remarks in Section 5.

## 2. KELVIN PROBE TECHNIQUE: BASIC CONCEPTS

### 2.1. Origins of the Electrostatic Force

The Kelvin probe measurement technique, in its present form, is based on the detection of the electrostatic force between the tip and the sample. This electrostatic force can originate from a number of different factors, such as (i) the electrochemical potential difference between the tip and the sample, (ii) an external electrical bias applied to the sample, and (iii) uncompensated charges on an insulating sample. The total force acting on the tip can be, in general, a sum of the individual forces arising from the factors mentioned above. However, in most cases the situation can be simplified and useful insight can be obtained by eliminating one or two of the above factors. The total electrostatic force on the tip depends on the three factors described above, as well as on the capacitance gradient of the system consisting of the sample and the tip-cantilever assembly. So, to obtain information about those three factors, through measurement of the electrostatic force, the capacitance gradient has to be determined. In general, because of the complicated and often unknown geometry of the tip, the theoretical computation of this capacitance gradient is extremely difficult and unreliable. The other way is to measure it directly with a lock-in amplifier, as will be discussed later. However, in the Kelvin probe technique, there is no need to compute or measure the capacitance gradient because the desired information can easily be obtained by nullifying the electrostatic force between the tip and the sample with the use of a feedback loop. This is discussed in detail later in this section, where a quantitative formulation is developed. Each of the individual factors responsible for the electrostatic force is briefly discussed.

#### 2.1.1. Contact Potential Difference

In general, any two dissimilar materials will have different electrochemical potentials. So, when two different materials are brought into intimate contact, they equilibrate via

transfer of electrons from one to the other (see Fig. 1a and b). For example, if two metals, Zn and Cu, are brought into intimate contact, then electrons will flow from Zn to Cu because of the higher work function of Cu. Thus Cu will be negatively charged and Zn will be positively charged. The electrostatic potential difference arising from such a transfer of charges is called the contact potential difference (CPD). Since the electrons will continue to flow until the electrochemical potentials of the two materials are the same, the CPD is given by

$$V_{\text{con}} = (\phi_{\text{Cu}} - \phi_{\text{Zn}})/q \quad (1)$$

where  $\phi_{\text{Cu}}$  and  $\phi_{\text{Zn}}$  are the work functions of Cu and Zn, respectively. In an actual measurement, the probe tip and the sample, when connected externally, exchange charges and equilibrate to give rise to the CPD. This charge exchange causes an electrostatic force of attraction between the tip and the sample. Such an attractive force forms the basis of measurement by the Kelvin probe technique (in its modern form) and can be nullified by an externally applied bias, leading to the measurement of CPD (Fig. 1c). The knowledge of CPD is very important for the characterization of materials, especially semiconductors.

#### 2.1.2. Charges on the Surface

Charges present on the surface of a sample will induce image charges (of opposite polarity) on the tip and therefore give rise to electrostatic forces between them. The charges on the sample can be present naturally, like charged domains in triglycine sulfate (TGS) [7], or can be deposited by external means, such as the probe tip itself [8, 9]. For charges to be deposited by the tip, and for the deposited charges to stay for a sufficiently long time to be measured again by the tip, the surface of the sample should be fairly insulating. Insulators such as polymethyl methacrylate (PMMA) and  $\text{SiO}_2$  are well suited for such measurements [8, 9]. Usually for the measurement of surface charge the operating distance between the tip and the sample is kept as small as possible for higher measurement accuracy [7].

#### 2.1.3. Externally Applied Bias

When an external bias is applied to the sample the situation is quite similar to the cases discussed above. The only difference is that in this case the charge separation is deliberately created between the tip and the sample by the externally applied bias. Measurement of such biases becomes very important for the study of nanoscale devices and integrated circuits (ICs). In such cases the SKPM probe tip can act as a “nano-voltmeter” and can be used for troubleshooting and reliability studies.

## 2.2. Quantitative Formulation

One of the principal advantages of the Kelvin probe technique is that it can be very accurate quantitatively. With modern lock-in and feedback techniques, it is possible to obtain a high degree of accuracy that is sufficient for most practical purposes. Figure 2a shows the tip-sample configuration during measurement along with the electrical biases,



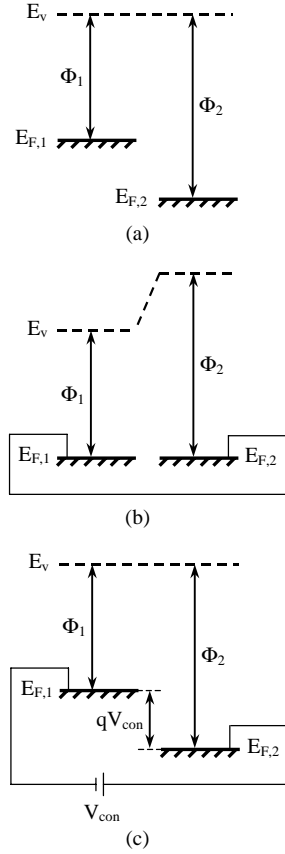


**Figure 1.** Schematic band diagrams showing the principles of operation of the Kelvin probe technique. The Fermi levels (denoted by  $E_F$ ) and the local vacuum levels (denoted by  $E_v$ ) are shown for two dissimilar metals (a) before contact, (b) after they are brought into contact and the Fermi levels reach equilibrium by transfer of charges creating an electric field between them, and (c) after the electric field is nullified by the application of an external potential  $V_{con}$ .

and Figure 2b shows the schematic band diagrams for the tip and the sample. Two different voltages are applied to the tip, namely, a sinusoidal ac voltage at a certain reference frequency,  $\omega$  (usually a few kHz), and a dc feedback voltage. Based on the discussions in the previous section, the total electrostatic force of attraction between the tip and the sample (the effect of the cantilever has been neglected for simplicity and is dealt with in Section 4.3),  $F_{tot}$ , is given by a capacitive component,  $F_{capa}$ , and a coulombic component,  $F_{coul}$ . The capacitive component itself comprises two parts: a part due to the difference in work function between the tip and the sample, and another due to any externally applied bias. The total force on the probe tip (at a distance  $z$  from the sample) is therefore given by the expression [8, 10–12]

$$F_{tot} = F_{capa} + F_{coul} = \frac{1}{2} \frac{\partial C}{\partial z} (V_{app} - V_{con})^2 + \frac{Q_s Q_t}{4\pi\epsilon_0\epsilon_r z^2} \quad (2)$$

where  $Q_t$  is the charge on the tip,  $Q_s$  is the charge on the surface,  $V_{con}$  is the CPD (where  $qV_{con}$  is equal to the difference in work functions of the tip and the material to be probed ( $\phi_{tip} - \phi_{mat}$ )), and  $\epsilon_r$  is the dielectric constant

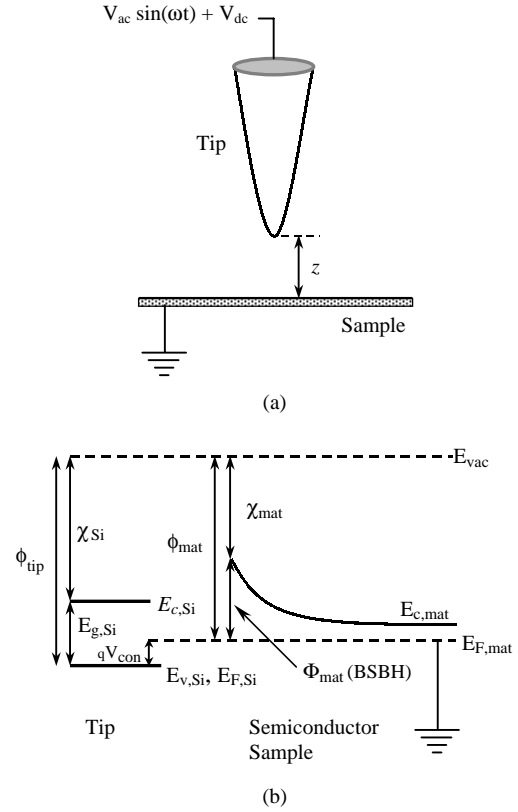


**Figure 2.** (a) Schematic diagram illustrating the tip-sample configuration and the electrical biases applied to the tip and the sample during measurement. An external bias can also be applied to the sample, if desired. (b) Schematic band diagram showing the Fermi levels and the vacuum level for the tip and a semiconductor sample. A  $p^+$ -doped Si tip is shown here, for which the Fermi level will almost coincide with the valence band. For a typical semiconductor, a surface band bending exists because of the presence of the surface space charge region. The Kelvin probe technique can be used to measure the surface barrier height  $\Phi_{mat}$  directly from the knowledge of  $V_{con}$  if the electron affinity of the semiconductor  $\chi_{mat}$  is known.

of the medium between the tip and the sample (air here). The capacitive term arises because of changes in the capacitive energy stored in the tip-sample capacitance ( $C$ ), and the Coulombic term arises because of the interaction between charges present on the surface and those on the tip. The negative sign in the capacitive component has been absorbed in the  $\partial C/\partial z$  term, which is a negative quantity. We have  $V_{app} = V_{dc} + V_{ac} \sin(\omega t)$ , and  $Q_t$  is given by the sum of the image charge on the tip,  $-Q_s$  and  $Q_c = CV_{app}$ . The total force,  $F_{tot}$ , is then obtained after simplification of Eq. (2) as

$$\begin{aligned} F_{tot} &= \frac{1}{4} \frac{\partial C}{\partial z} V_{ac}^2 + \frac{1}{2} \frac{\partial C}{\partial z} (V_{dc} - V_{con})^2 - \frac{Q_s(Q_s - CV_{dc})}{4\pi\epsilon_0\epsilon_r z^2} \\ &\quad + \left[ \frac{\partial C}{\partial z} (V_{dc} - V_{con}) + \frac{CQ_s}{4\pi\epsilon_0\epsilon_r z^2} \right] V_{ac} \sin(\omega t) \\ &\quad - \frac{1}{4} \frac{\partial C}{\partial z} V_{ac}^2 \cos(2\omega t) \\ &= F_{const} + F_{\omega} + F_{2\omega} \end{aligned} \quad (3)$$

Thus the total force is a sum of three components: a constant term,  $F_{\text{const}}$ ; one varying with frequency  $\omega$ ,  $F_\omega$ ; and another varying with frequency  $2\omega$ ,  $F_{2\omega}$ . From Eq. (3),  $F_\omega$  is given by

$$F_\omega = \left[ \frac{\partial C}{\partial z} (V_{\text{dc}} - V_{\text{con}}) + \frac{CQ_s}{4\pi\epsilon_0\epsilon_r z^2} \right] V_{\text{ac}} \sin(\omega t) \quad (4)$$

where  $V_{\text{dc}}$  is the dc feedback voltage generated by the feedback loop with respect to the sample bias (ground potential). In feedback mode,  $V_{\text{dc}}$  applied to the probe tip nullifies  $F_\omega$ .  $V_{\text{dc}}$  is therefore given by simplification of Eq. (4) as

$$V_{\text{dc}} = V_{\text{con}} - \frac{CQ_s}{4\pi\epsilon_0\epsilon_r z^2 \left( \frac{\partial C}{\partial z} \right)} \quad (5)$$

When operated in feedback mode at a distance sufficiently far from the surface, it is possible to neglect the Coulombic term, and the dc feedback voltage  $V_{\text{dc}}$  becomes exactly equal to the contact potential  $V_{\text{con}}$ . The work function is then given by

$$\phi_{\text{mat}} = \phi_{\text{tip}} - qV_{\text{dc}} \quad (6)$$

Equation (6) is of course valid if surface charges are altogether absent. For semiconductors, often the bare surface barrier height (BSBH),  $\Phi_{\text{mat}}$ , of the sample (see Fig. 2b) is an important parameter to measure. From Eq. (6) and Figure 2b, we obtain

$$\Phi_{\text{mat}} = \phi_{\text{tip}} - \chi_{\text{mat}} - qV_{\text{dc}} \quad (7)$$

where  $\chi_{\text{mat}}$  is the electron affinity of the semiconductor sample. From Eq. (3) it can be observed that the expression of  $F_{2\omega}$  explicitly contains the capacitance gradient of the tip-sample configuration,  $\partial C/\partial z$ . Thus, from the measurement of the magnitude of  $F_{2\omega}$ ,  $\partial C/\partial z$  can be obtained directly. Knowledge of  $\partial C/\partial z$  can be quite important, as pointed out in Section 4.3.

For electrostatic force microscopy, which is performed without a feedback loop, Eqs. (2) and (3) are still valid, and the surface work function,  $\phi_{\text{mat}}$ , or the BSBH,  $\Phi_{\text{mat}}$ , can be obtained by taking the ratio of  $F_\omega$  and  $F_{2\omega}$ . In the absence of any surface charge, we have from Eq. (3) after simplification

$$V_{\text{con}} = V_{\text{ext}} + \frac{1}{4} \frac{F_\omega V_{\text{ac}}}{F_{2\omega}} \quad (8)$$

where  $V_{\text{ext}}$  is the known external dc bias applied to the tip instead of the feedback voltage  $V_{\text{dc}}$ . Therefore,  $\Phi_{\text{mat}}$  can be obtained from Eq. (7) as

$$\Phi_{\text{mat}} = \phi_{\text{tip}} - \chi_{\text{mat}} - q \left( V_{\text{ext}} + \frac{1}{4} \frac{F_\omega V_{\text{ac}}}{F_{2\omega}} \right) \quad (9)$$

The coulombic term in Eq. (2) was written simply as an interaction between two point charges (on the sample and on the tip). This is valid to an appreciable extent when the diameter of the localized charged area to be measured is less than or equal to the diameter of the tip. Such situations are possible when nanoparticles are being characterized [10]. However, in cases where extended areas of charges are present on the surface, such as charged domains, it is

more convenient to use an alternative expression developed by Hong et al. [7]. The coulombic component of the total force in that case is given by the interaction between the charge on the tip and the electric field created by the uniform charge density,  $\sigma_s$ , on the surface. Neglecting any effect of contact potential for insulators, and assuming half the field lines going outward from the surface toward the tip,<sup>1</sup> we have  $F_\omega$  given by

$$F_\omega = \left[ \frac{\partial C}{\partial z} V_{\text{dc}} + \frac{\sigma_s C}{2\epsilon_0\epsilon_r} \right] V_{\text{ac}} \sin(\omega t) \quad (10)$$

When the feedback loop is employed to make  $F_\omega$  zero, we get  $\sigma_s$  as

$$\sigma_s = -\frac{2\epsilon_0\epsilon_r}{C} \frac{\partial C}{\partial z} V_{\text{dc}} \quad (11)$$

Using the parallel plate approximation, we have

$$\sigma_s = \frac{2\epsilon_0\epsilon_r}{z} V_{\text{dc}} \quad (12)$$

As discussed earlier, an external electrical bias applied to the sample can be measured in the same way as the work function difference. Therefore, if a dc bias,  $V_{\text{ext}}$ , is applied to the sample, then to make the electrostatic force between the tip and the sample go to zero, the feedback voltage applied to the tip has to be incremented by the exact amount,  $V_{\text{ext}}$ . Using Eq. (5), and assuming an absence of any surface charge, the feedback voltage is then given by

$$V_{\text{dc}} = V_{\text{ext}} + V_{\text{con}} \quad (13)$$

Incidentally, a quick way to verify that proper feedback mode operation of the SKPM has been achieved is to check whether  $V_{\text{dc}}$  changes appropriately with a change in dc sample bias. If the change in  $V_{\text{dc}}$  equals the change in the sample bias, then proper feedback has been established. Any external dc bias applied to the sample can be measured easily and quite accurately if the area to which it is applied is much larger than the projected area of the tip and the cantilever (on the sample surface). However, for smaller features where the applied bias varies rapidly within the projected area, such measurements are not always accurate, because of the finite tip size and the effect of the cantilever. These effects are discussed in Section 4.3. In addition, if the externally applied bias varies rapidly with time (faster than the feedback loop response), then the measurements will be inaccurate and might be altogether impossible.

<sup>1</sup> The charge on the surface of an insulating layer is usually modeled as having the probe tip on one side, separated by the air gap, and a conducting plane on the other, separated by the insulating layer (see [68]).

### 3. EXPERIMENTAL DETAILS

#### 3.1. Components of the SKPM System

The primary components of the SKPM measurement setup are the tip, the cantilever holding the tip, and the sample that is to be probed. The configurations of each of these components are important for proper measurement of the surface potential. We discuss each of these individual components in detail in what follows. Apart from these core components, there are hardware and electronics that are used for the measurements, which are mentioned briefly in the discussion of the measurement procedure. We start with the basic operational procedure to get an overview of the measurement technique and then move on to discuss the tip-cantilever assembly and the sample.

##### 3.1.1. Basic Operational Procedure

As mentioned earlier, the SKPM is performed in conjunction with AFM (almost always in noncontact mode). This is important because, apart from providing valuable surface morphology information simultaneously, it helps maintain a constant distance between the tip and the sample during measurements, so that a clean and stable surface potential signal is obtained. Therefore, two feedback loops are used for the measurements, one for surface morphology, and the other for surface potential [11]. The cantilever and the tip are usually mounted on a ceramic holder, and the whole assembly is made to oscillate at a particular frequency near the resonance frequency,  $\omega_{\text{res}}$ , of the tip. Usually the natural frequency of oscillation of commercially available tips ranges from a few tens to a few hundreds of kHz, depending on the spring constant. A laser beam is directed toward the tip, and the reflected light is sensed by an array of photosensitive position detectors (PSPDs). The output of the PSPDs is used by both the surface morphology loop and the surface potential loop as the input signal. As the tip approaches the surface, the van der Waals force field causes the resonance frequency of the cantilever to shift. From the shift in resonance frequency the surface morphology image is obtained in noncontact mode. Detailed discussion of the principles of AFM can be found elsewhere [6].<sup>2</sup>

For the measurement of surface potential, an ac signal,  $V_{\text{ac}} \sin(\omega t)$ , is applied to the probe tip in addition to a dc feedback voltage,  $V_{\text{dc}}$ , as discussed in Section 2.2. In the surface potential loop, the output of the PSPDs is used as an input to the lock-in amplifier, and the amplitude of the signal varying at frequency  $\omega$  is obtained at the output of the lock-in amplifier. That signal is used by the feedback circuitry to eliminate the electrostatic force of attraction between the tip and the sample, as described in detail in Section 2.2. To keep the topography feedback loop from interacting with the surface potential feedback loop, the frequencies are usually chosen to be wide apart. However, away from the resonance frequency the amplitude of oscillation decreases, and therefore the sensitivity of the measurement decreases. One remedy to this problem is to have a tip that has two different resonance frequencies that are

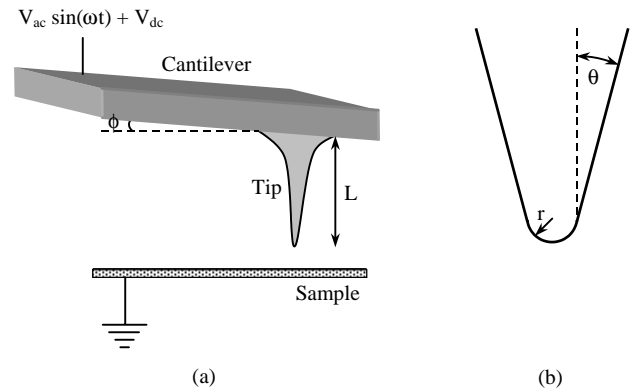


**Figure 3.** (a) The geometrical configuration of the tip-cantilever assembly and the sample during actual measurements. Note that the cantilever is slanted at an angle  $\phi$  with respect to the horizontal. (b) A magnified image of the tip apex is shown, assuming a cone and a sphere model, with the cone half-angle  $\theta$  and the sphere radius  $r$ .

widely separated. In that case the topography signal could be obtained near one of the resonance frequencies while the Kelvin probe signal could be obtained at another resonance frequency [13, 14]. However, manufacturing such tips is not easy, and usually, with a frequency sufficiently far from the resonant frequency, reasonably good results can be obtained. For resonance frequencies of  $\sim 100$  kHz, an ac signal frequency of  $\sim 17$  kHz has been used to obtain good results [10, 11, 15].

##### 3.1.2. Tip and the Cantilever

The nature and geometry of the tip and the cantilever play a very important role in the SKPM measurements. Different types of tips manufactured for AFM can also be used for SKPM, with the requirement that the tip must be electrically conducting so that it can interact with the sample. Commercial tips available today are usually made of *n*-doped or *p*-doped Si and are sometimes coated with metals. A schematic diagram of the tip-cantilever assembly is shown in Figure 3a, and a magnified view of the tip (spherical apex with a truncated conical body) is shown in Figure 3b. For commercially available Si tips, the radius  $r$  usually varies from 10 to 20 nm, and the length  $L$  can vary from a few to more than 10  $\mu\text{m}$ . The cone half-angle  $\theta$  of the tip apex is usually  $10^\circ$  to  $20^\circ$ . For special applications such as imaging deep trenches with very steep sidewalls, 3-D micro-optics, etc., very high-aspect-ratio tips fabricated with a focused ion beam (FIB) technique can be used. These tips can have a base diameter of  $\sim 0.4$   $\mu\text{m}$ , an apex radius less than 20 nm, and a tip height greater than 4  $\mu\text{m}$ .<sup>2</sup> Another type of high-aspect-ratio tip is made of high-density carbon (HDC). High-density or amorphous carbon is very hard and hydrophobic, and tips manufactured from it can have an apex radius less than 10 nm, an apex half-angle less than  $4^\circ$ , and a length that is easily up to 5  $\mu\text{m}$ .<sup>3</sup> Sometimes for special purposes, such as for calibration, tips can be coated with different metals. However, it has been found out that metal-coated tips are usually much more unstable compared with

<sup>2</sup> Refer to Thermomicroscopes (Veeco metrology group) website at [www.tmmicro.com](http://www.tmmicro.com).

<sup>3</sup> Refer to NanoTOOLS website at [www.nano-tools.com](http://www.nano-tools.com).

normal Si tips, as the metal coating can easily be destroyed [16, 17]. In the past few years, carbon nanotube tips have been used for AFM, yielding much superior results compared with conventional tips [18]. Recently these tips have also been used for EFM and SKPM [19–22]. These tips are particularly suited for SKPM applications because they are strong and less prone to surface contamination or electrical conduction, and have a very high aspect ratio, minimizing the finite tip size effect [19]. However, the manufacturing process for carbon nanotube tips is quite complicated, time consuming, and not very well controlled, which results in their being very expensive at present. Nevertheless, it has been demonstrated that these tips yield enhanced spatial and voltage resolution [19, 21] and may be used more commonly once larger demand brings down their price. The dimensions of the cantilever holding the tip can vary from tens to hundreds of micrometers. As mentioned earlier, the finite size of the tip and the cantilever reduces the measurement accuracy for very small features at a surface potential different from that of their surroundings. This is due to the fact that the tip and the cantilever “feel” the total electrostatic force arising from all of the individual features, rather than that arising from only the intended one. For features with dimensions much larger than the tip diameter but smaller than the projected area of the cantilever, only the effect of the cantilever is relevant. However, for feature sizes smaller than or comparable to the tip diameter, both the tip and the cantilever will contribute to measurement inaccuracies. It will be shown later that tips that are longer and held by cantilevers that have a smaller projected area will result in more accurate measurements. Alternatively, to reduce the parasitic effects of the measurement probe, it can be shielded from its surroundings by a guard electrode [23, 24]. More recently probes with fully integrated guard rings, to probe nanostructures, were fabricated by Nabhan et al., which resulted in enhanced sensitivity and lateral resolution [25]. The use of dielectric cantilevers, with a narrow conductive layer up to the tip apex, has also been suggested as a way to reduce parasitic capacitances [26]. In their design, Nabhan et al. used a tungsten probe on which they deposited a thin layer of aluminum that was oxidized electrochemically. On the aluminum oxide layer, they deposited a fresh layer of aluminum that acted as the guard ring (kept grounded) and prevented parasitic interaction between the cantilever and the body of the tip with the sample. The method can be easily modified for commercially available silicon tips [27]. In this technique, the tip-cantilever assembly is covered with a thin layer of native oxide, and a metal film is deposited to act as the guard ring. This process is currently under development.

### 3.1.3. Sample

Characteristics of the sample are very important and influence the surface potential measurements to a significant extent. Since the Kelvin probe feedback voltage applied to the tip is with respect to the sample Fermi level, a good ohmic contact must be made with the sample to keep the sample Fermi level at a reference potential, usually ground. The feedback voltage (and the ac signal) can also be applied to the sample, which will then be equal in magnitude but

opposite in sign to the normal tip feedback voltage [28]. Samples stored in air can become covered with a thin film of water, and some samples may form oxides etc. on their surface. These layers can affect the surface barrier as well as the electron affinity of the sample and reduce the accuracy of the surface potential measurements. For surface potential imaging over an extended area (especially by EFM), unwarranted potential fluctuations can occur because of variations in oxide layer thickness, surface depletion depth, and dielectric constant of the contaminant layers [15]. Additional variations may also be caused by charging of the contaminant layers and dust particles present on the surface. Therefore, it is important to carefully prepare the sample before surface potential measurements. The native oxide layer on semiconductors can usually be etched away with HF-based solvents. Organic contaminants on the surface can be removed by ultrasonic cleaning with organic solvents to yield good results [11, 28]. For semiconductor samples it has been found that air-exposed samples (due to chemisorption of  $O_2$ ) can have different electron affinities compared with samples under high vacuum by as much as  $\sim 0.6$  eV [29]. Therefore, for accurate measurements of the surface barrier it is advisable to conduct the measurements in an ultrahigh vacuum. Reference samples (usually metals such as gold) should also be used for good quantitative measurements.

## 3.2. Forces on the Tip

There can be several forces acting on the tip when it is in close proximity to a surface. A detailed discussion of the intermolecular and surface forces can be found elsewhere [30]. For our purposes, the most important forces are the van der Waals force and the electrostatic force. As mentioned before, the former is the basis for surface morphology image, and the latter is the basis for a surface potential image. These two forces will be discussed in some detail below. Of the other forces, the capillary force can also become significant. This arises because of the presence of a thin layer of water on the surface and the tip and becomes important only in a sufficiently humid environment [31].

### 3.2.1. Interatomic Forces

When the tip is sufficiently close to the sample the interatomic forces become significant. Very close to the sample surface (within a few Å) there is a repulsive interaction between the tip and the sample as the electron clouds of the respective atoms start to overlap. Farther from the sample the force first becomes zero and then becomes attractive. This is the van der Waals force regime arising from the dipolar interaction between the atoms, which can exist up to hundreds of angstroms from the sample surface. The repulsive potential is usually given by one of several empirical forms, such as  $A/z^{12}$  or  $Be^{-z/z_0}$ , and the van der Waals potential is of the form  $-C/z^6$ , where  $A$ ,  $B$ ,  $C$ , and  $z_0$  are constants and  $z$  is the tip-sample distance [32]. The total potential of the tip-sample system can be obtained by integration over the volume of the tip and the sample. The force can then be obtained by simple differentiation [33]. The variation of the force on the tip and its gradient (with its axis reversed for easier comparison) with tip-sample distance is shown

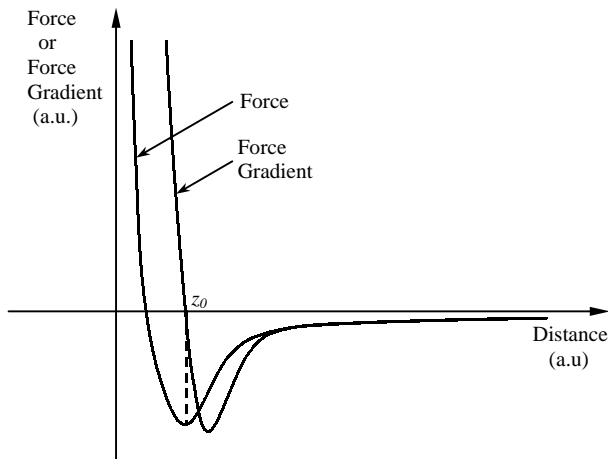


**Figure 4.** Variation of the total interatomic force on the tip and its gradient with the tip-sample distance. The repulsive force is considered positive. The force gradient axis has been reversed for easier comparison of the force gradient curve with the force curve. The magnitude of the force gradient (always positive in the noncontact region) determines the shift in noncontact mode oscillation frequency. At  $z_0$ , the force gradient is zero.

schematically in Figure 4. In contact-mode AFM the tip is very close to the surface, so that it experiences a repulsive force, whereas in the noncontact mode the tip is much farther away and experiences an attractive force. The contact and noncontact modes of operation, as relevant to SKPM, will be discussed in detail later.

### 3.2.2. Electrostatic Force

As discussed before, the electrostatic force on the tip originates from (a) the contact potential difference between the tip and the sample, (b) externally applied bias, and (c) charges on the surface. Since electrostatic force is a long-range force, at larger distances from the surface, that is, in the noncontact force regime, it can easily dominate the van der Waals force [33]. The respective force gradients can also be comparable. This has important consequences in the coupling of the morphology and surface potential feedback loops, as will be discussed in the next section. The expression for the total electrostatic force with an ac voltage applied to the tip was developed before (Eq. (3)). It depends directly on the differential capacitance of the tip-sample system. A theoretical calculation of the total electrostatic force on the tip can be made, assuming a special shape of the tip, usually as a truncated cone with a spherical apex, as shown in Figure 3b. It can be shown that for  $z \ll r$ , the contribution of the spherical apex is dominant, whereas for  $z \gg r$ , the contribution of the conical part is dominant [33]. In general, for noncontact mode operation where  $z$  is usually a few times  $r$ , the forces arising from both the parts are important and should be taken into consideration [33, 34].

## 3.3. Modes of Operation

During simultaneous measurements of surface morphology and surface potential, two separate feedback loops are in operation, as mentioned before. The morphology (usually

noncontact AFM) feedback loop is useful for surface morphology imaging as well as maintenance of a constant tip-sample distance for stable surface potential measurements. In the process, however, the two feedback loops may interfere and spurious signals may be obtained [7, 35, 36]. To avoid such interference, contact-mode operation has been proposed, with better isolation between the feedback loops [7, 36]. Following we will discuss the operation of SKPM in both contact and noncontact AFM modes.

### 3.3.1. Noncontact Mode

The noncontact-mode AFM is operated at a relatively larger  $z$  of a few to a few tens of nanometers. The operating regions for noncontact and contact modes are shown in Figure 5. The noncontact mode operation is in the region of the positive force gradient (refer also to Fig. 4 and note that the axis for the force gradient is reversed). The force on the tip is attractive, but its magnitude is much smaller in comparison with the contact mode. Therefore, a very sensitive detection technique, based on the shift in resonance frequency of the cantilever (due to the presence of the positive force gradient), is employed to get the surface morphology image. However, in noncontact mode, if the surface potential feedback loop is not operating properly, the electrostatic force gradient cannot be distinguished from the actual van der Waals force gradient, and the morphology feedback loop will pick up spurious signals. This can also happen the other way around, especially at the edge of large morphology features. Thus, there is always a chance of undesirable intermixing of the two signals [7, 36]. Usually the morphology signal becomes corrupted, as the force gradient associated with the electrostatic forces can be quite large. A possible way to avoid intermixing of the signals is to measure the surface morphology first and then measure the surface potential after the tip is lifted to a certain height from the sample surface [9]. However, in that case a constant distance from the sample surface is not guaranteed during surface potential imaging and the measurement resolution may be reduced.

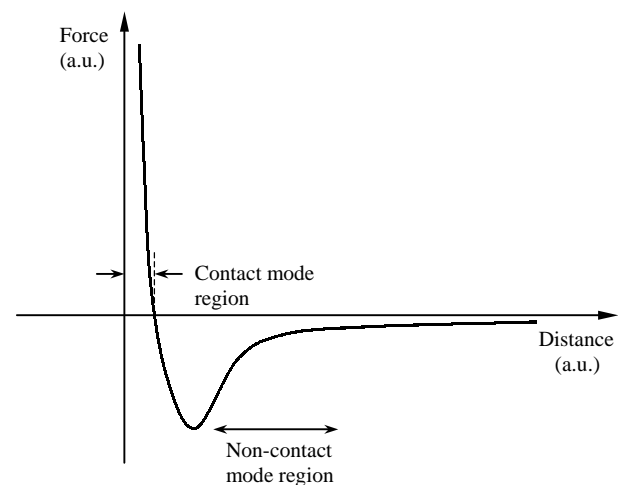


**Figure 5.** Contact and noncontact mode operation regions in the force vs. distance curve.

### 3.3.2. Contact Mode

In contact mode operation the tip is very close to the surface (within a few angstroms) in the repulsive force regime (see Fig. 5). Since the repulsive force is much larger in magnitude compared with the van der Waals force, the morphology signal is obtained by detecting the cantilever deflection directly. It has been shown that the intermixing of the surface morphology and surface potential signals can be avoided by operating SKPM with contact-mode AFM [7, 36]. This is due to the fact that the morphology signal in this case is obtained by monitoring the static deflection of the cantilever caused by a large repulsive force instead of the resonance frequency shift caused by a change in the force gradient. The disadvantage of this technique is that it is not easy to get sufficiently large oscillation amplitude of the tip in contact mode to generate the surface potential signal. Furthermore, since the tip is placed very close to the sample surface, there can be a tunneling current between the tip and the sample, which can alter their electrostatic configuration. Furthermore, the geometrical configuration of the tip can change rather dramatically because of the enhanced probability of crashing.

## 4. APPLICATIONS

The Kelvin probe measurement technique has numerous applications in a large number of fields ranging from biological sciences to electrical engineering. Since this technique is noncontact, quantitative, and straightforward and has nanoscale resolution (achieved through simultaneous operation with AFM), it is very suitable for the characterization of a wide range of materials and devices. In this review we will focus mainly on the applications that are relevant to nanotechnology. First we will discuss the applications to materials important to nanotechnology, such as insulators and semiconductors, and then move on to discuss applications that are specific to nanotechnology. Applications of this technique to SPV characterization and to devices and integrated circuits will be treated in separate subsections because of their importance. Since the EFM and SKPM are based on the same principles and are performed in almost the same way, we will discuss the applications of both techniques.

### 4.1. Insulating Materials

Insulators form a class of materials in which charges cannot move around freely. Therefore, if some charges are deposited at a certain position, they are expected to remain there for a long time. Characterization of insulators is important for a variety of reasons, including their ability to provide electrical isolation, passivate exposed surfaces of semiconductors, and act as a dielectric layer between the semiconductor and the gate of a device. Studies of charge storage and decay in insulators are also important because of their possible applications in memory devices. A large number of studies have been made on charging and discharging of insulators. Charge exchange processes between the probe tip and insulators (such as polycarbonate and PMMA) with submicron resolution were studied by Terris et al. by EFM

[37]. Decay of charges deposited on  $\text{Si}_3\text{N}_4$  film by thermionic emission was studied by Schönenberger et al. by EFM [38], where a single charge carrier resolution could be obtained. Moreover, storage and decay of charges in Co nanoclusters embedded in  $\text{SiO}_2$  were studied by Schaadt et al. [9], and charging of self-assembled silicon quantum dots was studied by Shimizu et al. [39] by EFM and SKPM, respectively. In all of the above cases the tip itself was used to deposit charges by applying a suitable bias to it with respect to the sample. An elegant demonstration of charge storage and measurement with the SKPM technique was made by Jacobs and Stemmer [40], in which an entire picture was imprinted on  $\text{SiO}_2$  and subsequently read out. Studies have also been reported on charging and discharging of electron beam resist films [41], as well as of polyethylene samples obtained from industrial cables [42]. Apart from intentionally deposited charges on insulators, charged domains already present on samples have also been characterized by SKPM [7].

### 4.2. Semiconductors

The Kelvin probe measurement technique has been widely used to characterize several important properties of semiconductors, such as surface work function, surface barrier, doping, diffusion length, and surface state density. The Kelvin probe technique is a unique way to measure surface work functions of semiconductors, which leads to an estimation of surface barrier height if the electron affinity of the semiconductor is known (refer to Section 2.2). The other quantities, such as doping, diffusion length, and surface state density, can be determined from the knowledge of either the surface work function or the surface barrier height. It is quite easy to make measurements on a homogeneous material, but measurements on a heterogeneous material are more complicated, as several optimizations are necessary. Of course, it is always advisable to standardize these measurements against metal work functions that can be measured easily and fairly accurately. It has been observed that measurement of the surface work function for a homogeneous sample can be made most accurately more than a micrometer from the sample surface, as the van der Waals and other short-range interactions can be completely avoided at such a distance [11]. Such techniques have been fruitfully employed for the measurement of the surface barrier height of GaN [11]. However, for nonhomogeneous materials, the measurement resolution will be much reduced at large distances from the sample surface. Therefore, for characterization of such samples the tip has to be operated very close to the surface. This might not be a problem for most cases if only relative values are important. Tanimoto and Vatel reported Kelvin probe measurements on Si  $p^+-p$ ,  $p^+-n$  junctions (with and without illumination) and cleaved AlGaAs/GaAs multilayer structures with a lateral resolution of 40 nm [43], and Chavez-Pirson et al. measured the band profile for a GaAs/AlGaAs  $n-i-p-i$  multiple quantum well structure [44]. Measurements of cross-sectional potential distribution (and electric field from it) were made on a cleaved  $n^+-\text{InP}/\text{InGaAs}/p^+-\text{InP}$   $p-i-n$  laser diode [45], and band profile changes under different illumination conditions were studied for cleaved GaAs/GaInP layers [40]. Antiphase



boundaries in GaAs film grown on Ge were also characterized with the use of EFM [15]. Surface state density and the corresponding energy level for GaN were found by EFM measurements with tips coated with different metals [12]. The surface state density has also been calculated from the measurement of surface barrier height of GaN films with different doping [11]. Characterization of dislocations in GaN and AlGaIn/GaN heterostructures by SKPM has also become quite popular [28, 46, 47] since the initial demonstration [46]. There is considerable interest in dopant profiling by the Kelvin probe technique; however, quantitative measurement with high lateral resolution is not easy [48]. In addition, the doping resolution that can be obtained is not very satisfactory [49]. Further applications of this technique to semiconductor materials are presented in Section 4.4, where SPV effects are discussed. SPV studies are very important and form a separate branch by themselves; therefore they merit a separate discussion. In the studies on heterogeneous materials, though qualitative agreements with theoretical predictions could be achieved, it was found to be difficult to obtain exact quantitative results. This is because of the finite size of the tip and the cantilever contributing to stray capacitance effects in the surface potential measurements. This is discussed in detail in the following section.

### 4.3. Devices and Integrated Circuits

The SKPM technique can be used very fruitfully to characterize devices and ICs because of its nanoscale resolution. The surface potential studies can provide rare insight into actual device operation, as well as help in troubleshooting and reliability studies. Since the morphology information is available simultaneously with potential, the tip can be positioned virtually anywhere on the device or IC. Furthermore, as the measurements are noncontact, there is no device degradation due to the measurements, and even working devices can be characterized. However, certain problems are usually faced in the application of this technique to characterize nanoscale devices or ICs. Perhaps the biggest challenge is to avoid the effect of stray (parasitic) capacitances contributed by the finite tip size and the cantilever. This leads to inaccurate measurements and reduced spatial resolution, as mentioned in the previous section. If the area to be measured is small compared with the area of the cantilever but much bigger than the tip diameter, then only the cantilever will cause most of the inaccuracies. However, if the area is smaller than or comparable to the tip diameter (a few tens of nanometers), then even the tip (and its sidewalls) will contribute to the inaccuracies. However, it should be noted that if the potential at the surface is homogeneous, then there will not be any inaccuracy in the measurements due to stray capacitances. In this section we will develop the mathematical formulation highlighting the effect of the cantilever only, with the assumption that the tip measures an accurate potential (of the region directly below the tip). In this way the effect of the cantilever can be deconvoluted to get more accurate results. The cases where the finite size of the tip also contributes to the inaccuracies are not easy to deconvolute without computer simulations.

Figure 6 shows a schematic diagram of the different capacitances associated with the tip and the cantilever when measurement is made over regions with different potentials. The parasitic capacitances associated with the tip sidewalls have been omitted for simplicity. Neglecting any fixed charge on the surface of the sample, the total amplitude of the  $\omega$ -component of the force  $F_{\omega, \text{tot}}$  acting on the tip is given by [11, 34]

$$F_{\omega, \text{tot}} = V_{\text{ac}} \left[ \frac{\partial C_{\text{tip}}}{\partial z} (V_{\text{dc}} - V_{\text{con}} - V_{\text{surf}}) + \frac{\partial C_{\text{canti}}}{\partial z} (V_{\text{dc}} - V_{\text{con}} - \langle V_{\text{surf}} \rangle) \right] \quad (14)$$

where  $V_{\text{con}} = (\phi_{\text{tip}} - \phi_{\text{mat}})/q$ ,  $V_{\text{surf}}$  is the electrostatic potential applied to the region of the sample directly below the tip (the intended region of measurement),  $\langle V_{\text{surf}} \rangle$  is the average potential measured by the cantilever (this is due to the projection of the cantilever over regions with different electrostatic bias), and  $(\partial C_{\text{tip}}/\partial z)$  and  $(\partial C_{\text{canti}}/\partial z)$  are the capacitance gradients of the tip and the cantilever, respectively. In feedback mode, the force on the tip  $F_{\omega, \text{tot}}$  is made to go to zero, and therefore from Eq. (1) after rearrangement,  $V_{\text{dc}}$  is given by

$$V_{\text{dc}} = V_{\text{con}} + [V_{\text{surf}} + \langle V_{\text{surf}} \rangle R] / [1 + R] \quad (15)$$

where  $R = (\partial C_{\text{canti}}/\partial z) / (\partial C_{\text{tip}}/\partial z)$ . The estimate  $V_{\text{est}}$  of the applied bias  $V_{\text{surf}}$  is given by  $V_{\text{dc}} - V_{\text{con}}$ .  $V_{\text{est}}$  tends to  $V_{\text{surf}}$  for very small tip-sample distance ( $R \ll 1$ ) and to  $\langle V_{\text{surf}} \rangle$  for large distances ( $R \gg 1$ ). However, if the whole sample surface has a single bias  $V_{\text{surf}}$  everywhere, then  $\langle V_{\text{surf}} \rangle = V_{\text{surf}}$ , and so  $V_{\text{est}}$  is equal to  $V_{\text{surf}}$ , and there is no effect of the cantilever on the measurements. For simplicity we have assumed the same value of  $V_{\text{con}}$  for all of the different regions with different potentials. If  $V_{\text{con}}$  differs significantly for these regions, then an average  $V_{\text{con}}$  should be used, which can be clubbed together with  $\langle V_{\text{surf}} \rangle$  in Eq. (14). The ratio  $R$  can be obtained theoretically by calculating  $(\partial C_{\text{tip}}/\partial z)$  and  $(\partial C_{\text{canti}}/\partial z)$ , assuming a particular geometry of the tip (see Fig. 3b), and from the dimensions specified by the manufacturer [34]. Alternatively, and more realistically,  $(\partial C_{\text{canti}}/\partial z)$  can be measured at a large distance from the sample where

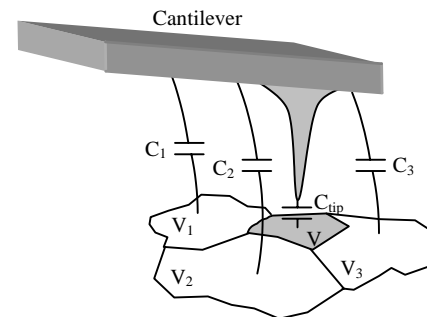


**Figure 6.** Schematic diagram showing the main tip capacitance and the parasitic capacitances associated with the cantilever when measurement is made over regions with different surface potentials. As a result of the parasitic capacitances the cantilever “senses” an average potential (in addition to the correct potential  $V$  measured by the tip apex) and reduces the measurement accuracy. The parasitic capacitances associated with the sidewalls of the tip are not included for simplicity.

( $\partial C_{\text{tip}}/\partial z$ ) will be negligible.<sup>4</sup> Then ( $\partial C_{\text{tip}}/\partial z$ ) at any  $z$  can be obtained by simply subtracting ( $\partial C_{\text{canti}}/\partial z$ ) (modified appropriately to include the distance dependence of a slanted plate capacitor [34]) from the total capacitance value at that  $z$ . Thus from the knowledge of  $R$  and the average potential measured by the cantilever,  $\langle V_{\text{surf}} \rangle$ , the deconvoluted value of the surface potential,  $V_{\text{surf}}$ , can be obtained from Eq. (15) after rearrangement as

$$\begin{aligned} V_{\text{surf}} &= (V_{\text{dc}} - V_{\text{con}}) + R(V_{\text{dc}} - V_{\text{con}} - \langle V_{\text{surf}} \rangle) \\ &= V_{\text{est}} + R(V_{\text{dc}} - V_{\text{con}} - \langle V_{\text{surf}} \rangle) \end{aligned} \quad (16)$$

It follows from Eq. (16) that longer tip lengths and smaller areas of cantilevers give more accurate results as  $R$  decreases (refer also to Fig. 6). It should be noted that in the above derivation it has been assumed that the sidewalls of the tip do not contribute a significant capacitance gradient, and whatever it contributes can be mostly grouped with that of the cantilever. This is true to a large extent since the area of the sidewalls increases significantly only near the base of the tip, which is much farther from the sample. More accurate measurements can perhaps be made with tips with integrated guard rings (see Section 3.1.2). However, the effectiveness of such designs has yet to be adequately studied.

Measurements on a saw device, where alternate fingers were maintained at 0 and 5 V, have been made to illustrate the effect of the cantilever [34]. Back in 1991, measurements on an operational amplifier IC were performed by Weaver and Abraham [50]. Jacobs et al. reported measurements on a test structure with different finger widths [51] to study resolution, and on externally biased high electron mobility transistors (HEMTs) [40], and potentiometry measurements on polymer field-effect transistors have been reported by Bürgi et al. [52]. Mizutani et al. performed detailed measurements of the two-dimensional potential profile of a cleaved GaAs/AlGaAs/InGaAs/AlGaAs HEMT in operation by SKPM [53]. Simultaneously obtained surface potential and surface morphology images on a dc biased AlGaN/GaN heterostructure field effect transistor (HFET) are shown in Figure 7. As can be seen, the measurement accuracy is about 80–85%. Work is under way to automatically deconvolute the effect of the cantilever for more accurate measurements. The ability to place the tip at any position on the device has led to certain rare insights into device degradation mechanisms. Simultaneous measurements of drain current and surface potential near the gate (on the drain side) of an AlGaN/GaN HFET device after it is subjected to high stress has led to the conclusion that charges (electrons) are injected from the gate into the surface states. These electrons trapped at the surface states can increase the surface depletion region near the gate, causing the observed drain current degradation commonly associated with these devices [54]. Recently, Wang et al. observed the movement of charges under applied drain

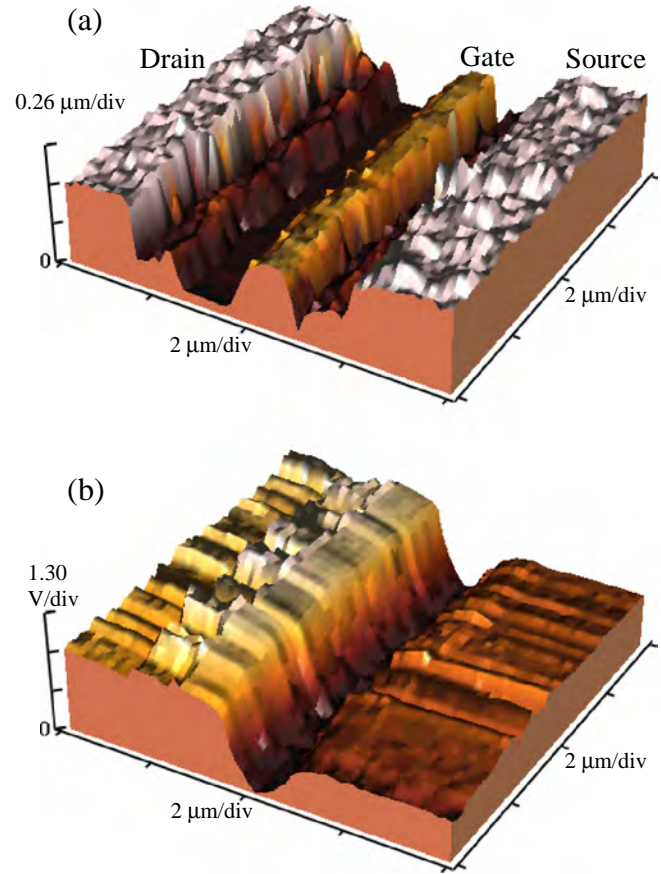


**Figure 7.** (a) Surface morphology and (b) surface potential images obtained simultaneously for a dc biased AlGaN/GaN heterostructure field effect transistor device. A drain bias of 2 V and a gate bias of  $-1.5$  V were applied for surface potential imaging. A potential offset is applied by software to the surface potential image for better rendering and clarity.

bias in silicon nitride film deposited on an n-channel Si field effect transistor under applied drain bias and calculated the surface charge density [55]. Furthermore, measurements on GaAs metal-semiconductor field effect transistors with and without a low-temperature-grown GaAs cap layer have been made by Matsunami et al. [56]. So far we have only dealt with the measurements of dc potential applied to the sample. For applications to integrated circuits it is sometimes useful to be able to measure the high-frequency ac periodic signal applied at different points in the circuit. Such measurements can be made with various techniques such as heterodyne/nulling, pulse width modulation, and amplitude modulation techniques [57–59].

#### 4.4. SPV Measurements

SPV measurements form a separate field by themselves, though they are commonly based on Kelvin probe measurements. In the SPV technique, which has been exclusively developed to study semiconductors, the sample is subjected to super bandgap or sub-bandgap illumination, and the change in surface barrier height is measured. From these measurements, a large variety of semiconductor surface and

<sup>4</sup> At any distance from the sample surface  $z$ ,  $F_{2\omega}$  in Eq. (3) will be given by  $-\frac{1}{4}(\partial C_{\text{tip}}/\partial z + \partial C_{\text{canti}}/\partial z)V_{\text{ac}}^2 \cos(2\omega t)$  when the force on the cantilever is also included in the total force. At a large distance from the sample  $\partial C_{\text{tip}}/\partial z$  will be negligible and  $\partial C_{\text{canti}}/\partial z$  can be obtained from the magnitude of  $F_{2\omega}$ .

bulk properties can be determined. Excellent in-depth treatment of this technique is available elsewhere [60]. In this section we will discuss only three of the most important measurements that can be made with this technique, namely, (a) minority carrier diffusion length, (b) surface band bending, and (c) surface state density. It is hoped that a discussion of these applications will provide some flavor of the usefulness and versatility of the SPV technique.

#### 4.4.1. Measurement of Minority Carrier Diffusion Length

The measurement of diffusion length is perhaps one of the most important direct applications of the SPV technique. We will discuss briefly the underlying principles for this measurement. More detailed treatment can be found in [60]. For front surface illumination, the generation rate as a function of distance is given by

$$G(x) = \alpha I \exp(-\alpha x) \quad (17)$$

where  $I$  is the effective photon flux (incident photon flux times the surface optical transmission and quantum efficiency), and  $\alpha$  is the absorption coefficient. Assuming a low-level injection condition, the continuity equation for electrons (assumed minority carriers here) is then given by [61]

$$D \frac{d^2 \delta n(x)}{dx^2} - \frac{\delta n(x)}{\tau} + \alpha I \exp(-\alpha x) = 0 \quad (18)$$

where  $\tau$  is the minority carrier lifetime and  $D$  is the diffusion coefficient. With the boundary conditions  $\delta n(\infty) = 0$  (at the back surface of a thick sample), and  $D \frac{d\delta n(x)}{dx} \Big|_{x=w} = S \delta n(w)$  (at the edge of the space charge region), and assuming  $w \ll 1/\alpha$  and  $w \ll L$ , we have the excess minority carrier density at the edge of the space charge region given by

$$\delta n(w) = \frac{\alpha L}{1 + \alpha L} \cdot \frac{1}{S + D/L} I \quad (19)$$

Equation (19) forms the basis for measuring the minority carrier diffusion length. Indeed, if at different wavelengths the SPV is kept constant (see Fig. 8a for the measurement setup), then  $\delta n(w)$  is also expected to remain constant and Eq. (18) can be rearranged (showing explicit variations with wavelength  $\lambda$ ) as

$$I(\lambda) = C_1 \left( \frac{1}{\alpha(\lambda)} + L_n \right) \quad (20)$$

where  $C_1$  is a constant. Thus, from the plot of  $I(\lambda)$  vs.  $\alpha^{-1}(\lambda)$  we can find the diffusion length,  $L_n$ , from the intercept on the negative  $x$  axis. This technique is very useful for the solar cell community, as the minority carrier diffusion length is one of the most important parameters controlling the conversion efficiency of solar cells. Moreover, this technique can be used to monitor the presence of metallic impurities such as iron in silicon and has become quite popular in the silicon industry.

#### 4.4.2. Measurement of Surface Band Bending

Surface band bending for a semiconductor material is an important parameter that can be measured with the SPV technique. Figure 8a shows the general experimental setup, and Figure 8b shows the steady-state band diagrams with and without illumination. We can see from Figure 8b that the surface band bending and the  $(E_c - E_F)$  value in the bulk together determine the surface barrier height. The surface barrier height can also be calculated from the surface work function if the electron affinity of the semiconductor is known (see Section 2.2). However, the electron affinity of a semiconductor may not always be known unambiguously. The surface band bending is caused by trapping of charges by the surface states present within the bandgap. These trapped charges are compensated for by opposite charges in the bulk forming a charge dipole near the surface. Under super bandgap illumination electron-hole pairs are generated, which reduce the surface band bending (Fig. 8b). This can happen in two ways [60]: (a) by the screening of the built-in electric field at the surface by the excess carriers, and (b) by preferential trapping of the charges of opposite polarity at the surface, reducing the net surface charge. Therefore, referring to Figure 8b, it is intuitively expected that under illumination of high enough intensity, the surface band bending will disappear. Thus, from the change in surface potential (SPV) measured by the Kelvin probe, the surface band bending can be determined, as well as the surface barrier if the  $(E_c - E_F)$  value in the bulk is known. The way to check if a flat-band condition has been achieved is to increase the illumination intensity and see if the SPV saturates with increasing intensity. The value at which the photovoltage saturates is the value of the surface band bending (with opposite sign). This technique is not applicable if the SPV does not saturate. In such cases other techniques have to be adopted [60]. An interesting case has been observed for AlGaIn/GaN heterostructures, where the photogenerated carriers under super bandgap illumination become spatially separated and reduce the surface barrier by screening the built-in electric field in the AlGaIn layer. However, after the illumination is turned off, the charge carriers cannot recombine immediately, and a long tail of the

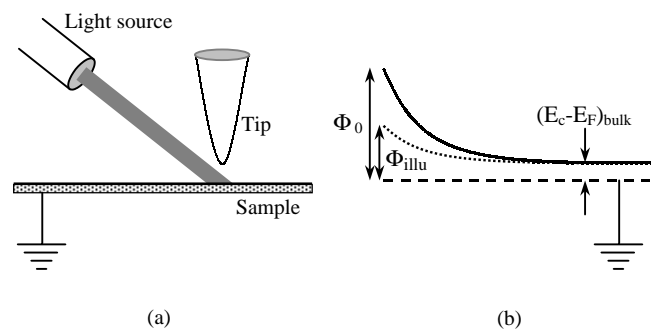


**Figure 8.** (a) Schematic diagram showing the surface photovoltage measurement setup. (b) The surface barrier of the sample decreases from  $\Phi_0$  before illumination to  $\Phi_{\text{illu}}$  under illumination. With increasing intensity of illumination the flat-band condition can be achieved, and hence the surface band bending (before illumination) can be measured.

surface potential recovery transient is observed (stretched over a few days or even weeks!). This long decay transient can be modeled by a thermionic emission process, and the surface barrier before illumination can be calculated without the photosaturation technique [62].

**4.4.3. Measurement of Surface State Density**

Surface state density,  $\sigma_s$ , of a semiconductor is another important material parameter that one often needs to know for many reasons, including its effects on Schottky barrier height. Surface state density can also be determined from surface photovoltage measurements. The basic procedure for this technique was described by Lam [63]. Though Lam used a SiO<sub>2</sub> dielectric for his metal-insulator-semiconductor (MIS) structure, a contactless MIS structure can be used with the air film as the dielectric between the “gate” and the semiconductor. Through a change in the voltage  $V_g$  on the metal “gate,” the surface charge density  $Q_{ss}$  and the bulk compensating charge density  $Q_{sc}$  can be altered. Naturally, this will also alter the surface barrier  $\Phi_s$ . Using the charge conservation law,  $dQ_g + dQ_{ss} + dQ_{sc} = 0$ , where  $Q_g$  is the charge density on the “gate.” Moreover, from Kirchhoff’s voltage law, we have  $dV_g = dV_{ins} + d\Phi_s$ . From these equations, the surface state density,  $N_t$ , ( $= -(1/q)dQ_{ss}/d\Phi_s$ ) at any surface barrier  $\Phi_s$  can be obtained as

$$qN_t(\Phi_s) = C_{ins} \left( \frac{dV_g}{d\Phi_s} - 1 \right) + \frac{dQ_{sc}}{d\Phi_s} \quad (21)$$

where  $C_{ins}$  is the capacitance of the air layer per unit area. For a particular  $\Phi_s$ , the term  $dV_g/d\Phi_s$  can be obtained experimentally from the curve of gate voltage vs. surface barrier (obtained with the photosaturation technique described in Section 4.4.2 for each  $V_g$ ), and  $dQ_{sc}/d\Phi_s$  can be obtained

from the standard relation that exists between  $Q_{sc}$  and  $\Phi_s$  for a known bulk doping level [61].

**4.5. Applications to Nanotechnology**

In the previous sections we discussed the important applications of the Kelvin probe technique in general. In this section we discuss the applications that are specific to nanotechnology. As pointed out earlier, because of its inherent nanoscale resolution, this technique is very suitable for characterizing nanoscale devices and systems (through measurement of electrical quantities such as surface charge, surface work function, and applied bias). The applications of this technique in different areas of nanotechnology are shown in Figure 9. Following we will discuss each of these areas of application, except for the nanoscale devices that have already been treated in detail in Section 4.3.

Thin films, especially of semiconductors, are very important for nanotechnology. This due to the fact that a vast majority of nanoscale devices, such as transistors, emitters, detectors, etc., are made of semiconductor thin films. The electrical characterization of these thin films becomes especially critical for epitaxially grown layers (required for high-speed and optoelectronic devices) because strict control of the electronic properties of such layers is required for proper device operation. This technique has been used to characterize Langmuir-Blodgett (LB) films. LB films consisting of a 1:1 molar mixture of arachidic acid and partially fluorinated carboxylic acid on a silicon (100) substrate were studied by Yasutake et al. [64]. They measured a potential difference of ~50–60 mV between the two regions with an improved version of SKPM capable of 1-mV voltage resolution and 10-nm lateral resolution. Iwamoto and Itoh [65] systematically studied the surface potential variation with film thickness for LB films of polyimide and Cu-tetra-(*tert*-butyl)-phthalocyanine deposited at different temperatures

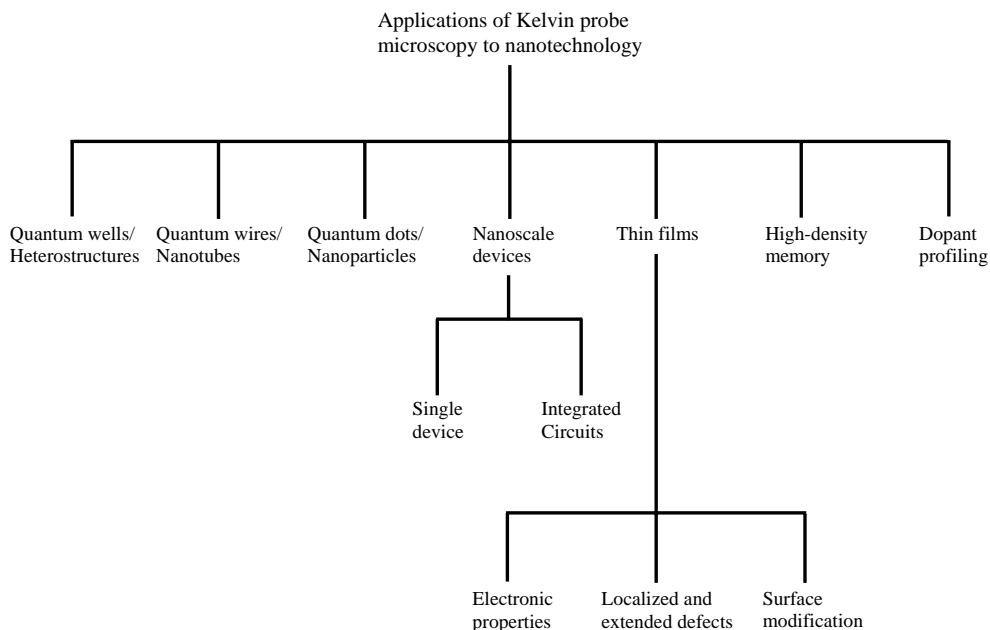


Figure 9. Schematic chart showing different applications of Kelvin probe microscopy to nanotechnology.

on Au-, Cu-, and Al-based electrodes. From the variation of surface potential with thickness, the charge density in the LB film could be obtained for each thickness corresponding to each base electrode. O'Boyle et al. [66] applied this technique to the study of Al/Cu intermetallic decorating Al/Cu lines (Cu 5%) deposited on silicon. Whereas the intermetallic regions were not distinguishable in the regular topography image, they readily showed up in the surface potential image, underlining the efficacy of this technique in alloy surface studies. Using dynamic contact-mode EFM, Hong et al. [7] characterized nanoscale charged domains in single-crystal triglycine sulfate. They measured the charge density in the domains as well as the domain charge dynamics after the sample was heated above Curie temperature. The semiconductor surface work function is strongly dependent on the presence of surface layers, atomic arrangement, and chemical composition. Therefore, to obtain information about the surface contaminant layers the measurement of the surface work function becomes very useful. Baikie et al. [67] compared the variation of surface work function of silicon (111) with oxide layer thickness for a clean Si surface and an Ar ion-bombarded Si surface. The Ar-sputtered Si surface showed a dramatic reduction in the magnitude of surface potential change due to oxygen incorporation at the surface. The variation at higher temperature was also correspondingly lower. They also studied Al (lower work function than Ru) deposition on Ru (0001) and found that with increasing Al deposition thickness the work function decreases as the film growth progresses from the initial island growth to flat island growth to monolayer growth. Kitamura and Iwatsuki [68] studied a Si (111) surface with Au deposited and observed a potential difference of 0.5 eV between the  $7 \times 7$  (higher) and  $5 \times 2$  (lower) phases. They also observed a potential difference of 20 mV between the work function of the Ag islands (higher) compared with the clusters. They demonstrated atomic-level resolution for both noncontact AFM images and surface potential images. The Kelvin probe technique has also been used by DeVecchio and Bhusan [69] to study nanoscale wear on Al, Au, Si, and alumina samples. Wear studies are important to the magnetic recording industry, microelectromechanical systems industry, and other nanoscale industries. In their studies, the initial nanoscale wears were simulated by abrading the samples in contact mode, which was followed by tapping-mode morphology imaging and lift mode (see Section 3.3.1) surface potential imaging. They observed very significant changes in surface potential caused by the nanoscale wears, and they attributed these to a combination of chemical and structural changes in the sample surface.

A large number of defect studies of materials, especially semiconductors, have used the Kelvin probe technique. This is due to the fact that the defect sites usually become electrically charged and can easily be studied by Kelvin probe or EFM. Sommerhalter et al. [14] studied work function variations on highly oriented pyrolytic graphite (HOPG), *n*-GaAs, and *p*-WSe<sub>2</sub>. They could identify the positively and negatively charged defects on *p*-WSe<sub>2</sub> and measure the work function difference between the stepped edges and flat surfaces for HOPG and *n*-GaAs. The work functions for different crystal facets of polycrystalline CuGaSe<sub>2</sub> deposited on ZnSe (100) and Mo/glass substrates were measured by

Sadewasser et al. [70] with a lateral resolution of 25 nm and a voltage resolution of 5 mV. CuGaSe<sub>2</sub> films are used in making solar cells based on chalcopyrite materials. Constant surface work functions were observed for different well-defined faces of the nanosized crystals of the film grown on ZnSe. For the film grown on Mo/glass the absolute values of the work functions for different faces were different from the film on ZnSe, though the difference between any two faces was almost the same. Xu and Hsu [15] studied antiphase boundaries of GaAs grown on Ge by EFM and found that the surface potential at the antiphase boundaries (APBs) are consistently higher than the domains by about 30 mV because of Fermi-level pinning at the APBs closer to the valence band than at the domains. They also observed wedge-shaped depressions where the surface potential was lower by about 25 mV compared with the surroundings, indicating that the Fermi level shifted relatively closer to the conduction band. The two positions of the Fermi level for the two defect types can be attributed to the difference in defect state densities (as a function of energy) in the two cases. Recently studies have been made of electronic characteristics of dislocations in GaN [28, 46, 47]. It has been observed that dislocations in GaN and AlGaN/GaN heterostructures are negatively charged, as indicated by the upward bending of the conduction band at the dislocation sites (by a few tenths of an eV). Although the exact magnitude of the band bending is difficult to measure because of the parasitic capacitance effects, the fact that dislocations charge is nevertheless important, as they are widely believed to scatter electrons during AlGaN/GaN HFET operation.

Because the Kelvin probe can measure the surface barrier height there is considerable interest in using this technique for dopant profiling of semiconductors. However, there are several limitations to such use. The surface barrier obtained gives only a relative estimate of the separation between the conduction band and the Fermi level, and therefore quantitative measurement is difficult. Frequently, for atmospheric measurements, the electron affinity of the semiconductor might change, giving rise to errors. Moreover, calibration samples have to be used for better measurement accuracy. Last, the spatial resolution is limited by parasitics, and the voltage resolution (which controls the doping resolution that can be achieved by this technique), by noises. In spite of the above limitations, good qualitative characterization of the doping profile is possible with this technique. Si and GaAs *p-n* junctions have been studied by several groups [13, 43, 48] and the limitations have been pointed out [13, 48]. A good review of the Kelvin probe technique in comparison with other scanning probe microscopy techniques for the measurement of doping has been made by De Wolf et al. [49].

The Kelvin probe technique can also be used to "write" potential images in insulating films as well as "read" them. A Kelvin probe was used to measure charge storage effects and effects of UV illumination in aluminum oxide films as early as 1977 by Rageh et al. [71]. However, writing on insulating films and reading them was first successfully demonstrated by Stern et al. [72] and Terris et al. [8]. They used a bias of 100 V for 25 ms to deposit the charges (writing) and obtained a lateral resolution of  $\sim 1 \mu\text{m}$  in reading. A positive or a negative charge on sufficiently insulating film

can be deposited by applying a suitable bias to the probe tip (placed very close to the surface) for a certain interval of time. Schönenberger and Alvarado [38] studied the deposition ( $\sim 10$  V dc for 10 ms) and subsequent decay of charge in  $\text{Si}_3\text{N}_4$  films. They found that the charge decay follows a thermionic emission process and could obtain single-electron resolution in their measurements. Usually the insulators used for writing and reading charges are of four types: polymers, silicon dioxide, nitride-oxide-silicon (NOS), and oxide-nitride-oxide-silicon (ONOS), as discussed in detail by Wright and Chetwynd [73]. They concluded that the NOS and ONOS structures give the best lateral resolution, and the charges persist for days or months. In 1999, Jacobs and Stemmer [74] reported on the use of computer control to write patterns on  $\text{SiO}_2$  film (2–4-nm native oxide on Si) with pulses of selectable duration (2.5–400  $\mu\text{s}$ ) and magnitude (10–30 V). With their technique they could even write a photograph on a  $\text{SiO}_2$  surface and successfully read it. They have obtained a resolution of around 200 nm, and the patterns stayed for at least 24 h. Recently, charge writing on fluorocarbon polymer film has been demonstrated by Mesquida et al. [75]. For writing they used pulses of 10- $\mu\text{s}$  to 1-ms duration with a magnitude varying from  $-60$  to  $60$  V and obtained a lateral resolution of 20 nm for fluorocarbon film on Si. They also studied the influence of the film thickness and the substrate on the measured potential and the influence of the humidity and the substrate on the charge decay time. Apart from the charge storage in films, storage on nanoparticles has also been studied. Schaadt et al. [9] reported on the charging of Co nanoclusters embedded in  $\text{SiO}_2$  layer by applying  $\pm 12$  V for 10 s. They estimated the radius of the charged area to be 20 nm and showed that one electron per Co nanocluster is added or removed under the charging conditions they used. The advantage of writing charges with the Kelvin probe technique is that charges and patterns can be stored virtually without any processing steps, and the bits can be a few tens of nanometers in diameter. However, the disadvantage is that both reading and writing have to be done serially and cannot be done too fast without compromising the accuracy of the reading and writing steps.

A large number of measurements of heterostructures and quantum wells made with the Kelvin probe technique have been reported in the literature. These studies are important, as they give an idea of the band profile along the interface, which can be used to obtain the electric field and in some cases the charge densities in the various layers. These data are very important for ensuring proper operation of the devices, especially those consisting of structures grown by epitaxial techniques. Early characterization results of semiconductor devices and processes were reported by Tanimoto and Vatel [43]. They measured the surface potential profile on cleaved  $\text{AlGaAs}/\text{GaAs}$  heterostructures and cleaved Si  $p^+-p$ ,  $p^+-n$  junctions with and without illumination. They found that the potential measurements (performed with  $<40$ -nm resolution) were sensitive to the Al mole fraction and helped in the estimation of band structures of the cleaved samples. In addition, they could determine the lateral impurity profile under an ion implantation mask through calibration of the potential profile with the use of spreading resistance measurements. Chavez-Pirson et al. [44] measured the potential

profile of a cleaved  $\text{GaAs}/\text{AlGaAs}$   $n-i-p-i$  multiple quantum well (MQW) structure with and without illumination. They found that the measured potential profile was in good agreement with the calculated profile, taking into account the estimated surface band bending corresponding to the doping level in the layers. Under illumination the potential modulations of the  $n-i-p-i$  layer decreased because of screening of the built-in electric field by the photogenerated carriers. Similar cross-sectional potential measurements on a cleaved  $n^+-\text{InP}/\text{InGaAs}/p^+-\text{InP}$   $p-i-n$  laser diode were made by Robin et al. [45]. The potential measurements were corrected for tip convolution for comparison with two-dimensional simulation with a commercially available package from Silvaco (Santa Clara, CA). Very good agreement between the measurements and the simulation could be obtained by taking into consideration partial ionization of the  $n^+-\text{InP}$  layer and the presence of surface states. Similar measurements were also made on cleaved  $\text{GaAs}/\text{AlAs}$  MQWs and  $\text{InAlAs}/\text{InGaAs}$  layered structures with a resolution of 40 nm [76]. Breymesser et al. [77] measured cross-sectional potentials of cleaved Si  $p-i-n$  diodes (solar cells) and obtained the charge density profile by differentiating the potential profile twice. The potential measurements led to the conclusion that a graded donor like defect distribution and a constant boron concentration were present in the intrinsic layer. Ruzin et al. [78] also applied this technique to the study of neutron implantation effects in a silicon  $p-i-n$  particle detector. Weitz et al. [79] applied the Kelvin probe technique (modified for low-temperature applications) to investigate the 2DEG under quantum Hall conditions with submicron resolution. They succeeded in observing the sawtooth-like variation of the chemical potential with increasing magnetic field resulting from the expected depopulation of the Landau levels. To avoid the undesirable retarding effect of the high-frequency signal used for minimizing force (in high resistive areas) and to enhance the contributions of the tip-sample interactions, they minimized the force gradient with the use of an ac signal with very low frequency (3.4 Hz) to measure the shift in resonance frequency. They also developed a normalized measurement technique and used it to measure the Hall-potential profiles under an applied magnetic field.

Lower dimensional structures, like quantum wires and nanotubes, have also been characterized with this technique. Characterization of quantum wires grown by MBE on patterned  $\text{GaAs}$  surfaces ((100) and (311)) was done by Yoh and Takabayashi [80]. From EFM measurements they could identify the amphoteric nature of the Si dopants (depending on the facet orientation) and could clearly determine the width of the quantum wire, which was not unambiguously possible with AFM alone. Ono et al. [81] characterized  $\text{InAs}$  nanowires grown on a  $\text{GaAs}$  (110) plane with a  $3^\circ$  offset toward the (111) plane and found evidence of electron accumulation in the nanowires. Carbon nanotubes have been successfully characterized with EFM by Bachtold et al. [82]. They found that this technique can be used very fruitfully to identify a break in the nanotube, which would be very difficult to identify from the morphology image. Through potential measurements on nanotubes they could also conclude that multiwalled carbon nanotubes (MWNTs) behave as diffusive conductors (since they had a linear voltage drop



along their length), whereas single-walled carbon nanotubes (SWNTs) support ballistic transport (since there was no voltage drop along their length). Using potential measurements, they could also measure the nanotube resistance per unit length, as well as the contact resistances between the carbon nanotube and the gold electrodes. Gekhtman et al. [83] studied the thermodynamic density of states (TDOS) of Bi quantum wires by measuring the electrostatic force gradient as a function of diametrical ( $x$ ) position, axial ( $z$ ) position, and bias voltage. From their measurements they could estimate the L-point quasi-gap for various radii of the quantum wires. They also found out that the TDOS increases toward the wire boundaries compared with the center, and this difference increases with decreasing radius.

Quantum dots (QDs) and nanoparticles have been characterized quite extensively with this technique. Silver nanoparticles dispersed on graphite have been characterized by NCAFM and EFM with a lateral resolution of 4–5 nm [10]. It was found that the silver particles were positively charged, as expected from the lower work function of silver with respect to the graphite basal plane. As discussed before, cobalt nanoclusters embedded in  $\text{SiO}_2$  have been charged and imaged with the use of EFM [9]. Krauss and Brus [84] used EFM to study the dielectric constant and electrostatic charges in CdSe nanocrystals. They found that the dielectric constant was uniform; however, the charge per nanocrystal was nonuniform. They also found that photoexcitation with light of frequencies greater than the bandgap of the nanocrystals resulted in their becoming positively charged. There has been considerable interest in the study of Si nanocrystals and nanostructures, especially for the fabrication of nonvolatile floating gate memory that can be directly integrated into the baseline Si process. Shimizu et al. [85] studied the charging (both positive and negative) of Si QDs (average height 5.4 nm) formed on  $\text{SiO}_2$  and was able to calculate the number of electrons added to or removed from the QDs. Guillemot et al. [86] also studied charging

of Si QDs embedded in  $\text{SiO}_2$  by phase-contrast EFM imaging and calculated the charge present in each QD and the charge decay time (30 min to 3 h). Shiota and Nakayama [87] used NCAFM to create nanostructures on a Si (111)  $7 \times 7$  surface that were higher by  $\sim 1 \text{ \AA}$  and showed a surface potential lower by  $\sim 0.1 \text{ V}$  compared with the surrounding regions. From SKPM and NCAFM measurements made on quenched Si they concluded that the nanostructure was indeed  $1 \times 1 \text{ Si}$ . Takahashi et al. [88] characterized the near-surface band structure of InAs dots covering an  $n\text{-GaAs}$  (100) surface with a lateral resolution better than 20 nm. They found from the force images of  $\omega$  and  $2\omega$  that the surface depletion is more suppressed under the dots, possibly because of electron accumulation in the InAs dots. From the above discussion it should be quite obvious that the Kelvin probe technique (or the EFM) has been used extensively by the scientific community to characterize nanostructures. A summary of the different applications of this technique to nanotechnology is given in Table 1. In spite of the extensive use of this technique for nanocharacterization, its resolution (lateral) and accuracy are limited by parasitics, as discussed in Section 4.3. This problem will be discussed again in the following section.

#### 4.6. Miscellaneous Applications

In the previous sections we discussed the important applications of the Kelvin probe measurement technique to nanotechnology and related materials. The versatility of this technique allows itself to be used for many more applications than the ones discussed above. We will briefly mention some of the other interesting applications in this section. Biological applications of the Kelvin probe technique were demonstrated by Baikie et al. [89] with the use of a multitip setup, where they measured biopotentials developed along a growing plant shoot (corn seedling). Measurements of surface photovoltage on a semiconductor ( $p\text{-InP}$  (100))

**Table 1.** Summary of the applications of Kelvin probe technique to nanotechnology.

Type of application	Quantity measured	Significance of measurement	Comments
Thin films	Charge, potential	Defects, electronic properties, surface modification studies	Characterization very important for thin film growth and deposition
Quantum wells/heterostructures	Charge, potential	Study of conduction band profile, electric field, defects, 2DEG	Quite important for characterization, but lateral resolution limited by parasitics
Quantum wires/nanotubes	Charge, potential	Band profile, conduction, carrier properties	Quite useful, but lateral resolution limited by parasitics
Quantum dots/nanoparticles	Charge, potential	Study of charging and discharging	Quite useful, but lateral resolution limited by parasitics
Nanoscale devices	Charge, potential, applied bias	Potential profile, troubleshooting, reliability studies	Quite useful for surface and cross-sectional measurements; holds good promise if parasitics can be reduced
High-density memory	Charge	Memory write and read in insulators and nanostructures	Slow and serial reading and writing; lateral resolution limited by parasitics
Dopant profiling	Potential	Doping variation data	Lateral resolution limited by parasitics; surface-related problems

immersed in different liquid etchants were made by Bastide et al. [90]. Though only relative changes in surface potential could be measured with their setup, the validity of such measurements was nevertheless established by comparison with measurements performed directly on the InP sample. Measurements of liquid “work functions” are also possible and have been discussed in [91] and [92]. Development of a special probe to carry out such measurements has also been discussed [93]. This technique has also been widely used to measure the modification of the work function and corrosion of metals [94–97]. Examples of some other applications of this method include studies of organic light-emitting diodes [98, 99], the study of diamond work function variation [100], and chemistry [101].

In spite of the versatility of the Kelvin probe measurement technique, it has several limitations that should be addressed. In addition, certain issues must be kept in mind to ensure proper operation of the technique. Surface contamination and consequent alteration of the contact potential can be an issue if the measurements are performed in an atmosphere. However, contamination-related problems can be avoided to a large extent by proper cleaning of the samples just before measurement, or best by performing the measurements in a vacuum. Another possible source of inaccuracy is the ac signal applied to the tip, which has been shown to cause significant changes in the surface potential [102]. However, if the ac signal magnitude is kept low enough, such problems can be avoided [15]. The Kelvin probe station itself must be isolated from the environment with a floating air table to avoid errors resulting from mechanical vibrations. Measurement inaccuracies can also be caused by the microphonic signals (ac electrical signals produced by vibrating conductors and insulators) associated with the vibration of the tip-cantilever assembly (in noncontact mode). This can give rise to spurious distance variation of the feedback signal. However, it has been shown that the effects of microphonics can be minimized with the use of coaxial cables together with vibration damping and isolation, or by the introduction of a suitable dc offset in the feedback loop [103]. As discussed before, simultaneous measurement of surface potential and surface morphology in the scanning mode can lead to a significant error in surface potential measurements due to intermixing of signals (when the morphology feedback cannot maintain a constant  $z$ ), especially if the morphology features are big enough. Furthermore, changes in the tip work function, especially if the tip is coated with a metal film (due to peeling of the metal film), can contribute to errors. In addition, stray charges on the surface can give rise to irregularities in the potential scan.

Apart from the above causes of inaccuracies, there are problems of spatial and potential resolution. The spatial resolution is limited by the stray capacitances associated with the cantilever and the tip. Such stray capacitances depend on the geometry of the tip-cantilever system, as well as on the operating distance,  $z$ . Based on semiempirical techniques, McMurray and Williams [104] obtained a relationship between the probe diameter  $d$  and tip-sample distance  $z$ , with the distance  $\Delta L_{50}$  between the points corresponding to 25% and 75% of the total change in Kelvin potential (measured across a step change in potential between two regions with a straight line boundary) in the form

$\Delta L_{50} = K_1 z + K_2 d$ , where  $K_1$  and  $K_2$  are constants. They found that  $\Delta L_{50}$  (and hence the lateral resolution) is dominated by  $d$  for smaller  $z$ , and by  $z$  itself at larger  $z$ . To minimize parasitic effects it is important to use long tips and cantilevers with the smallest possible areas and perform the measurements as close to the sample as possible (see discussion in Section 4.3). In addition, a metal shield can be fabricated around the tip cylindrical body and the cantilever bottom face to avoid parasitic capacitance effects [25, 27]. Therefore, a shielded tip with a very small radius and high aspect ratio (like a carbon nanotube) should be ideal for obtaining the highest resolution. Alternatively, it has been proposed that the resolution can be improved by using the force gradient as the signal source [105, 106], because the contribution of the tip apex to the total force gradient is much greater than that of the cantilever and the tip sidewall for small  $z$  (which is experimentally important).

The voltage resolution of the Kelvin probe technique is limited by the electrical and thermal noise. These noises can be generated by the electronics, the signal wires, the ac signal source for tip bias, the piezoelectric chip, the laser, and the photodetectors [5, 6, 106, 107]. Usually, the combined effect of all of these sources leads to a voltage resolution of  $\sim 1$  mV to  $\sim 10$  mV. Moreover, since a lock-in amplifier and feedback loop are used in the measurements, there is an inherent reduction in the signal-to-noise ratio as the signal is minimized to achieve a null condition. To avoid such a problem, a data acquisition-based off-null measurement technique has been proposed by Baikie et al. [107]. One of the significant drawbacks of the Kelvin probe technique is that its temporal resolution is not good because of the large time constant usually associated with the lock-in amplifier to reduce noise. Usually the overall time constant of measurement varies from a few tens to a few hundreds of milliseconds. Therefore, it is not easy to measure time-varying signals with this technique.

## 5. SUMMARY

In this chapter we have discussed the various aspects of the Kelvin probe measurement technique in a fairly detailed manner, covering the origins of the electrostatic force, the components of the measurement system, the forces on the tip, and the modes of operation. We have also discussed the applications (with a particular focus on nanotechnology) and the limitations of this technique. The technique has been used for about a century, and it was not possible to cover every aspect of this technique in the limited span of this review. Instead, we have tried to explain the more important aspects of this technique fairly rigorously (both in words and by equations, wherever appropriate), keeping in mind the broad spectrum of readers for whom this article is intended. The Kelvin probe technique is rapidly evolving, and newer applications are discovered every year. Therefore, while writing this review we put a strong emphasis on bringing out the general principles of the measurements, without merely trying to list all of the experiments that have been performed. Of course, special attention was paid to covering as fully as possible the various applications of this technique to nanoscience and nanotechnology. Today, the Kelvin probe technique has wide-ranging applications in the

fields of basic sciences, material science, and engineering. Because of its inherent nanoscale resolution (made possible by using it simultaneously with AFM), the technique is very suitable for nanocharacterization, as has been stressed again and again in the review. Kelvin probe measurements using carbon nanotube tips are just becoming popular and hold much promise for the future. The applications to integrated circuits and biopotentiometry are also very promising. Additionally, unique applications of nanoscale charge storage and readout for high-density memory are emerging. However, to realize its full potential this technique must overcome the limitations in spatial resolution and time constant. The spatial resolution can be improved to a significant extent by special tip design and force gradient detection technique. Quantitative measurements of high-frequency periodic signals have also been made possible. Considering all of the aspects of the Kelvin probe, it is indeed safe to say that this is one of the most versatile nanocharacterization tools available today and should be found to be increasingly useful by the researchers of the “nano-world.”

## GLOSSARY

**Contact potential difference (CPD)** The potential difference that develops between two dissimilar materials (with different work functions) through transfer of charges when they are brought into contact.

**Electrostatic force microscopy (EFM)** Microscopy based on electrostatic force between the probe and the sample. It is different from SKPM in that no feedback loop is used to null the electrostatic force.

**Kelvin probe** A probe that measures the difference in work function between itself and the sample, with the use of an electrostatic force nulling technique in a two-plate capacitor configuration.

**Nanotechnology** The technology involving the fabrication and characterization of nanoscale devices and structures.

**Scanning Kelvin probe microscopy (SKPM)** The Kelvin probe measurement performed in a scanning mode in conjunction with atomic force microscopy.

## ACKNOWLEDGMENTS

Our work with the Kelvin probe measurement technique is supported by the Office of Naval Research MURI on semiconductor interface electronics under contract N00014-99-1-0714 under the direction of Dr. Colin E. C. Wood.

## REFERENCES

1. Lord Kelvin, *Philos. Mag.* 46, 82 (1898).
2. W. A. Zisman, *Rev. Sci. Instrum.* 3, 367 (1932).
3. K. Besocke and S. Berger, *Rev. Sci. Instrum.* 47, 840 (1976).
4. J. M. R. Weaver and D. W. Abraham, *J. Vac. Sci. Technol., B* 9, 1559 (1991).
5. M. Nonnenmacher, M. P. O'Boyle, and H. K. Wickramasinghe, *Appl. Phys. Lett.* 58, 2921 (1991).
6. Dror Sarid, “Scanning Force Microscopy.” Oxford University Press, New York, 1994.
7. J. W. Hong, K. H. Noh, S. Park, S. I. Kwun, and Z. G. Khim, *Phys. Rev. B* 58, 5078 (1998).
8. B. D. Terris, J. E. Stern, D. Rugar, and H. J. Mamin, *Phys. Rev. Lett.* 63, 2669 (1989).
9. D. M. Schaadt, E. T. Yu, S. Sankar, and A. E. Berkowitz, *Appl. Phys. Lett.* 74, 472 (1999).
10. R. M. Nyffenegger, R. M. Penner, and R. Schierle, *Appl. Phys. Lett.* 71, 1878 (1997).
11. G. Koley and M. G. Spencer, *J. Appl. Phys.* 90, 337 (2001).
12. P. M. Bridger, Z. Z. Bandić, E. C. Piquette, and T. C. McGill, *Appl. Phys. Lett.* 74, 3522 (1999).
13. A. Kikukawa, S. Hosaka, and R. Imura, *Appl. Phys. Lett.* 66, 3510 (1995).
14. C. Sommerhalter, T. W. Matthes, T. Glatzel, A. Jäger-Waldau, and M. C. Lux-Steiner, *Appl. Phys. Lett.* 75, 286 (1999).
15. Q. Xu and J. W. P. Hsu, *J. Appl. Phys.* 85, 2465 (1999).
16. H. O. Jacobs, H. F. Knapp, and A. Stemmer, *Rev. Sci. Instrum.* 70, 1756 (1999).
17. S. J. O'Shea, R. M. Atta, and M. E. Welland, *Rev. Sci. Instrum.* 66, 2508 (1995).
18. H. Dai, J. H. Hafner, A. G. Rinzler, D. T. Colbert, and R. E. Smalley, *Nature* 384, 147 (1996).
19. S. B. Arnason, A. G. Rinzler, Q. Hudspeth, and A. F. Hebard, *Appl. Phys. Lett.* 75, 2842 (1999).
20. C. Maeda, N. Ozeki, S. Kishimoto, T. Mizutani, T. Sugai, and H. Shinohara, *Jpn. J. Appl. Phys.* 41, 2615 (2002).
21. S. Takahashi, T. Kishida, S. Akita, and Y. Nakayama, *Jpn. J. Appl. Phys.* 40, 4314 (2001).
22. S. V. Kalinin, D. A. Bonnell, M. Freitag, and A. T. Johnson, *Appl. Phys. Lett.* 81, 754 (2002).
23. P. P. Craig and V. Radeka, *Rev. Sci. Instrum.* 41, 258 (1970).
24. M. Wolff, A. E. Guile, and D. J. Bell, *J. Phys. E* 2, 921 (1969).
25. W. Nabhan, B. Equer, A. Broniatowski, and G. De Rosny, *Rev. Sci. Instrum.* 68, 3108 (1997).
26. J. Colchero, A. Gil, and A. M. Baró, *Phys. Rev. B* 64 245403 (2001).
27. G. Koley, Z. Yang, and M. G. Spencer, unpublished observations.
28. B. S. Simpkins, D. M. Schaadt, E. T. Yu, and R. J. Molnar, *J. Appl. Phys.* 91, 9924 (2002).
29. V. M. Bermudez, *J. Appl. Phys.* 80, 1190 (1996).
30. U. Hartmann, *Ultramicroscopy* 42–44, 59 (1992).
31. M. Binggeli and C. M. Mate, *J. Vac. Sci. Technol., B* 13, 1312 (1995).
32. J. L. Hutter and J. Bechhoefer, *J. Appl. Phys.* 73, 4123 (1993).
33. M. Saint Jean, S. Hudlet, C. Guthmann, and J. Berger, *J. Appl. Phys.* 86, 5245 (1999).
34. G. Koley, M. G. Spencer, and H. R. Bhangale, *Appl. Phys. Lett.* 79, 545 (2001).
35. R. Lüthi, H. Haefke, K.-P. Meyer, E. Meyer, L. Howald, and H.-J. Güntherodt, *J. Appl. Phys.* 74, 7461 (1993).
36. J. W. Hong, S. Park, and Z. G. Khim, *Rev. Sci. Instrum.* 70, 1735 (1999).
37. B. D. Terris, J. E. Stern, D. Rugar, and H. J. Mamin, *Phys. Rev. Lett.* 63, 2669 (1989).
38. C. Schönenberger and S. F. Alvarado, *Phys. Rev. Lett.* 65, 3162 (1990).
39. N. Shimizu, M. Ikeda, E. Yoshida, H. Murakami, S. Miyazaki, and M. Hirose, *Jpn. J. Appl. Phys.* 39, 2318 (2000).
40. H. O. Jacobs and A. Stemmer, *Surf. Interface Anal.* 27, 361 (1999).
41. M. Bai, R. F. W. Pease, C. Tanasa, M. A. McCord, D. S. Pickard, and D. Meisburger, *J. Vac. Sci. Technol., B* 17, 2893 (1999).
42. A. D. Bass, P. Cloutier, and L. Sanche, *J. Appl. Phys.* 84, 2740 (1998).
43. M. Tanimoto and O. Vatel, *J. Vac. Sci. Technol., B* 14, 1547 (1996).
44. A. Chavez-Pirson, O. Vatel, M. Tanimoto, H. Ando, H. Iwamura, and H. Kanbe, *Appl. Phys. Lett.* 67, 3069 (1995).
45. F. Robin, H. Jacobs, O. Homan, A. Stemmer, and W. Bächtold, *Appl. Phys. Lett.* 76, 2907 (2000).

46. G. Koley and M. G. Spencer, *Appl. Phys. Lett.* 78, 2873 (2001).
47. Y. Eguchi, S. Kishimoto, and T. Mizutani, *Jpn. J. Appl. Phys.* 40, L589 (2001).
48. T. Hochwitz, A. K. Henning, C. Levey, C. Daghljan, and J. Slinkman, *J. Vac. Sci. Technol., B* 14, 457 (1996).
49. P. De Wolf, R. Stephenson, T. Trenkler, T. Clarysse, T. Hantschel, and W. Vandervorst, *J. Vac. Sci. Technol., B* 18, 361 (2000).
50. J. M. R. Weaver and D. W. Abraham, *J. Vac. Sci. Technol., B* 9, 1559 (1991).
51. H. O. Jacobs, P. Leuchtman, O. J. Homan, and A. Stemmer, *J. Appl. Phys.* 84, 1168 (1998).
52. L. Bürgi, H. Sirringhaus, and R. H. Friend, *Appl. Phys. Lett.* 80, 2913 (2002).
53. T. Mizutani, M. Arakawa, and S. Kishimoto, *IEEE Electron Device Lett.* 18, 423 (1997).
54. G. Koley, V. Tilak, L. F. Eastman, and M. G. Spencer, *IEEE Trans. Electron Device Lett.*, submitted for publication.
55. Z. Wang, J. Bao, H. Zhang, and W. Guo, *Appl. Phys. Lett.* 81, 1300 (2002).
56. K. Matsunami, T. Takeyama, T. Usunami, S. Kishimoto, K. Maezawa, T. Mizutani, M. Tomizawa, P. Schmid, K. M. Lipka, and E. Kohn, *Solid-State Electron.* 43, 1547 (1999).
57. G. E. Bridges, R. A. Said, M. Mittal, and D. J. Thomson, *Rev. Sci. Instrum.* 65, 3378 (1994).
58. R. A. Said, S. P. Cheung, and G. E. Bridges, *J. Vac. Sci. Technol., B* 18, 626 (2000).
59. Z. Weng, C. J. Falkingham, G. E. Bridges, and D. J. Thomson, *J. Vac. Sci. Technol., A* 20, 999 (2002).
60. L. Kronik and Y. Shapira, *Surf. Sci. Rep.* 37, 1 (1999).
61. S. M. Sze, "Physics of Semiconductor Devices," 2nd ed. Wiley, New York, 1981.
62. G. Koley, H. Cha, C. I. Thomas, and M. G. Spencer, *Appl. Phys. Lett.* 81, 2282 (2002).
63. Y. W. Lam, *J. Phys. D: Appl. Phys.* 4, 1370 (1971).
64. M. Yasutake, D. Aoki, and M. Fujihira, *Thin Solid Films* 273, 279 (1996).
65. M. Iwamoto and E. Itoh, *Thin Solid Films* 331, 15 (1998).
66. M. P. O'Boyle, T. T. Hwang, and H. K. Wickramasinghe, *Appl. Phys. Lett.* 74, 2641 (1999).
67. I. D. Baikie, U. Petermann, and B. Lägel, *Surf. Sci.* 433–435, 770 (1999).
68. S. Kitamura and M. Iwatsuki, *Appl. Phys. Lett.* 72, 3154 (1998).
69. D. DeVecchio and B. Bhusan, *Rev. Sci. Instrum.* 69, 3618 (1998).
70. S. Sadewasser, T. Glatzel, M. Rusu, A. Jäger-Waldau, and M. C. Lux-Steiner, *Appl. Phys. Lett.* 80, 2979 (2002).
71. M. S. I. Rageh, D. V. Morgan, and A. E. Guile, *J. Phys. D: Appl. Phys.* 10, 2269 (1997).
72. J. E. Stern, B. D. Terris, H. J. Mamin, and D. Rugar, *Appl. Phys. Lett.* 53, 2717 (1988).
73. W. M. D. Wright and D. G. Chetwynd, *Nanotechnology* 9, 133 (1998).
74. H. O. Jacobs and A. Stemmer, *Surf. Interface Anal.* 27, 361 (1999).
75. P. Mesquida, H. F. Knapp, and A. Stemmer, *Surf. Interface Anal.* 33, 159 (2002).
76. T. Usunami, M. Arakawa, S. Kishimoto, T. Mizutani, T. Kagawa, and H. Iwamura, *Jpn. J. Appl. Phys.* 37, 1522 (1998).
77. A. Breymesser, V. Schlosser, D. Peiró, C. Voz, J. Bertomeu, J. Andreu, and J. Summhammer, *Sol. Energy Mater. Sol. Cells* 66, 171 (2001).
78. A. Ruzin, N. Croitoru, G. Lubarsky, and Y. Rosenwaks, *Nucl. Instrum. Methods Phys. Res., Sect. A* 461, 229 (2001).
79. P. Weitz, E. Ahlswede, J. Weis, K. V. Klitzing, and K. Eberl, *Appl. Surf. Sci.* 157, 349 (2000).
80. K. Yoh and S. Takabayashi, *J. Vac. Sci. Technol., B* 18, 1675 (2000).
81. S. Ono, M. Takeuchi, and T. Takahashi, *Ultramicroscopy* 91, 127 (2002).
82. A. Bachtold, M. S. Fuhrer, S. Plyasunov, M. Forero, E. H. Anderson, A. Zettl, and P. L. McEuen, *Phys. Rev. Lett.* 84, 6082 (2000).
83. D. Gekhtman, Z. B. Zhang, D. Adderton, M. S. Dresselhaus, and G. Dresselhaus, *Phys. Rev. Lett.* 82, 3887 (1999).
84. T. D. Krauss and L. E. Brus, *Phys. Rev. Lett.* 83, 4840 (1999); T. D. Krauss and L. E. Brus, *Mater. Sci. Eng. B* 69–70, 289 (2000).
85. N. Shimizu, M. Ikeda, E. Yoshida, H. Murakami, S. Miyazaki, and M. Hirose, *Jpn. J. Appl. Phys.* 39, 2318 (2000).
86. C. Guillemot, P. Budau, J. Chevrier, F. Marchi, F. Comin, C. Alandi, F. Bertin, N. Buffet, C. Wyon, and P. Mur, *Europhys. Lett.* 59, 566 (2002).
87. T. Shiota and K. Nakayama, *Appl. Surf. Sci.* 1–5, 9450 (2002).
88. T. Takahashi, T. Kawamukai, and I. Kamiya, *Appl. Phys. Lett.* 75, 510 (1999).
89. I. D. Baikie, P. J. S. Smith, D. M. Porterfield, and P. J. Estrup, *Rev. Sci. Instrum.* 70, 1842 (1999).
90. S. Bastide, D. Gal, D. Cahen, and L. Kronik, *Rev. Sci. Instrum.* 70, 4032 (1999).
91. I. R. Peterson, *Rev. Sci. Instrum.* 70, 3418 (1999).
92. W. N. Hansen and K. B. Johnson, *Surf. Sci.* 316, 373 (1994).
93. K. B. Johnson and W. N. Hansen, *Rev. Sci. Instrum.* 66, 2967 (1995).
94. G. Grundmeier and M. Stratmann, *Appl. Surf. Sci.* 141, 43 (1999).
95. L. T. Han and M. Mansfeld, *Corros. Sci.* 39, 199 (1997).
96. R. W. Zehner, B. F. Parsons, R. P. Hsung, and L. R. Sita, *Langmuir* 15, 1121 (1999).
97. A. Tahara and T. Kodama, *Corros. Sci.* 42, 655 (2000).
98. S. M. Tadayyon, K. Griffiths, P. R. Norton, C. Tripp, and Z. Popovic, *J. Vac. Sci. Technol., A* 17, 1773 (1999).
99. Y. Shen, D. B. Jacobs, G. G. Malliaras, G. Koley, M. G. Spencer, and A. Ioannidis, *Adv. Mater.* 13, 1234 (2001).
100. K. W. Wong, Y. M. Wang, S. T. Lee, and R. W. M. Kwok, *Appl. Surf. Sci.* 140, 144 (1999).
101. M. Josowicz, H. S. Li, K. Domansky, and D. R. Baer, *Electroanalysis* 11, 774 (1999).
102. Y. Leng, C. C. Williams, L. C. Su, and G. B. Stringfellow, *Appl. Phys. Lett.* 66, 1264 (1995).
103. F. Rossi, *Rev. Sci. Instrum.* 63, 4174 (1992).
104. H. N. McMurray and G. Williams, *J. Appl. Phys.* 91, 1673 (2002).
105. J. Colchero, A. Gil, and A. M. Baró, *Phys. Rev. B* 64, 245403 (2001).
106. P. Girard, *Nanotechnology* 12, 485 (2001).
107. I. D. Baikie, S. Mackenzie, P. J. Z. Estrup, and J. A. Meyer, *Rev. Sci. Instrum.* 62, 1326 (1991).

# Kinesin and Nanoactuators

Konrad J. Böhm, Eberhard Unger

*Molecular Cytology Group, Jena, Germany*

## CONTENTS

1. Introduction
  2. Kinesin Biochemistry and Biophysics
  3. Configuration of a Kinesin-Based Transport Device
  4. Possible Applications and Outlook
- Glossary  
References

## 1. INTRODUCTION

Motility is a crucial feature of living matter existing in very different forms. To maintain all the diverse processes of motility on each single level of organization within a given organism, nature has evolved both *rotary motors*, including the flagellar motors of bacteria [1, 2] and the adenosine triphosphate (ATP) synthase [3–5], and *linear* (forward propulsive) *motors*, including ribonucleic acid (RNA) polymerases [6, 7] and cytoskeleton-associated motors.

Within the last two decades, it has been realized that cell locomotion, muscle contraction, and the active intracellular transport of organelles and macromolecules are generally based on the functional activity of specialized proteins called motor proteins or mechanochemical proteins. Motor proteins are defined as proteins that convert the chemical energy of adenosine triphosphate (ATP) into mechanical energy to move along the surface of suited proteinaceous filamentous rails constituting the complex cytoskeleton network. The cytoskeletal motor proteins comprise different types of myosins, dyneins, and kinesins, expressed ubiquitously in eukaryotic organisms.

From a structural point of view, the motor proteins appear as elongated (often long-stretched) molecules with characteristic head domains that attach the motor to the cytoskeletal filament and generate force for the movement. The distal end of these proteins is linked to membranous vesicles or biomacromolecule complexes, which constitute the *cargo* to be moved along the filament [8].

According to their cellular functions, cytoskeletal motors can be divided into three subgroups:

1. Motors involved in intracellular transport processes (kinesins, cytoplasmic dyneins, cytoplasmic myosins, e.g., myosin V)
2. Motors responsible for cell locomotion and cell surface transport (axonemal dynein, myosin I)
3. Motors for muscle contraction (sarcomeric myosin II)

Another classification made on the basis of the type of cytoskeletal filament along which these motors move results in the following two subgroups:

1. Microtubule-associated motors (kinesins, cytoplasmic and axonemal dyneins)
2. Actin microfilament-associated motors (cytoplasmic and muscle myosins)

The myosins (for reviews, see, e.g., [9, 10]), dyneins (for reviews, see, e.g., [11, 12]), and kinesins constitute large protein families with a great number of functionally specialized, different members. So far, nearly 150 kinesin isoforms and related proteins from 31 species have been described for animal and plant cells as well as for lower eukaryotic organisms [13]. It seems that every kind of cellular cargo requires its own motor to be transported. Besides a set of basic features that all the kinesin isoforms share, single members of the kinesin superfamily reveal specific properties, making them favorite above the others with regard to their potential usability for nanotechnological applications.

The present contribution is focused on conventional kinesin, which belongs to the KHC protein family [13]. It was first discovered in the axoplasm of the squid giant axon [14] and is now one of the best characterized motor proteins. This kinesin walks in discrete nanometer-sized steps in a defined direction along the surface of microtubules. Furthermore, it is known to be a highly processive motor protein, moving over relatively long distances without being released from its microtubule rail [15]. The energy required for the movement is delivered by the kinesin itself, using an intrinsic molecular power station hydrolyzing the ubiquitously occurring biological fuel ATP in a specialized catalytic center with ATPase activity. The microtubules do not only

fulfill static but also regulatory functions: They determine the direction the kinesin moves, and they are involved in the regulation of the efficiency of energy transformation performed by the kinesin. For these and some other reasons, conventional kinesin appears to be well suited to be used to develop novel linear motor microdevices.

## 2. KINESIN BIOCHEMISTRY AND BIOPHYSICS

### 2.1. Molecular Structure of Kinesin

Conventional kinesin is a dimer [16] consisting of two identical 120- to 130-kDa chains, commonly known as heavy chains. When kinesin is purified from brain homogenates, two light chains (60–70 kDa) are found to be associated with the dimers [17]. These light chains, which are involved in the kinesin binding to organelles, are not essential for motility generation [18] and seem to have regulatory functions [19].

In the electron microscope, the conventional kinesin molecules appear to be rod shaped. The rods were found to have a diameter of 2–4 nm and a length of approximately 80–100 nm [20]. One end of each heavy chain reveals a globular head, while the opposite end is fan shaped [21]. Combining electron microscopic observations with data from limited proteolytic digestion and sequence analyses, the kinesin molecule can be divided into distinct structural domains (Fig. 1): a N-terminal head (or motor) domain comprising the amino acids 1 to 325, the neck region (up to position 374), a long-stretched stalk (up to 800), and the C-terminal tail domain (up to 963) [17].

The kinesin head domain, which is known to be a highly conserved region characteristic of very different members of the kinesin superfamily, contains both the microtubule-binding domain and the ATP-hydrolyzing center [17]. It has the shape of an arrowhead with dimensions of approximately 7.5 nm × 4.5 nm × 4.5 nm [23]. X-ray structural analysis revealed a central, eight-stranded  $\beta$ -sheet with three  $\alpha$ -helices on either side [23, 24].

The neck domain, which is conserved within certain kinesin classes [25], is believed to be essentially implied in

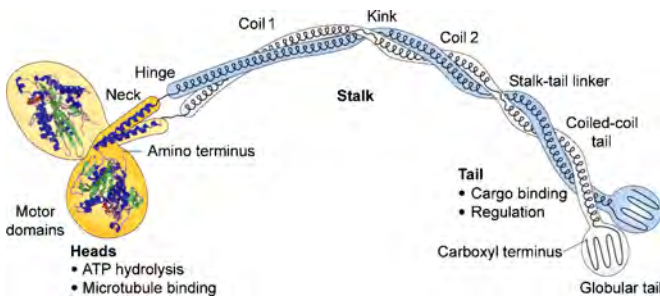


**Figure 1.** Domain structure of the conventional kinesin heavy-chain dimer, showing the crystal structure of the catalytic domains and the neck. The structure of the stalk and the tail are inferred from electron microscopic images and coiled-coil prediction analyses. Regions predicted to form coiled coils (neck, coil 1, coil 2, coiled-coil tail) and flexible regions (hinge, kink, stalk-tail linker) are indicated. Reprinted with permission from [22], G. Woehlke and M. Schliwa, *Nat. Rev. Mol. Cell Biol.* 1, 53 (2000). © 2000, Macmillan Magazines Ltd.

the dimerization of the kinesin heavy chains and in processive movement (see Section 2.4). Vale and co-workers [26] reported that deleting the neck coiled coil decreases processivity 10-fold, whereas elongating it by seven residues results in a threefold increase in processivity, indicating that the structural features of the neck coiled coil can tune the efficiency of the motor. It has been shown that the sequence 330–369 is mainly responsible for the formation of a two-stranded  $\alpha$ -helical coiled coil [27, 28]. Moreover, it was concluded that the kinesin neck linker functions as a mechanical amplifier for motion [29] and that directional bias of the working stroke is dependent on interactions of the neck with the motor core [30].

The stalk region is predominantly composed of an  $\alpha$ -helical coiled coil. The percentage of  $\alpha$ -helix formation depends on the temperature: At 4 °C up to 85–90% of the stalk was found to be  $\alpha$ -helices [31]. The poorly conserved C-terminal globular tail domain is implicated presumably together with the stalk in cargo binding. Unlike the head region, which is nearly neutral and the stalk region which is acidic, the tail is basic. This feature is highly relevant with respect to the electrostatic interaction between the heavy chain and the negatively charged surfaces of, for example, glass coverslips and latex beads [32].

The activity of soluble kinesin has been found to be repressible by an interaction between the N-terminal motor and the C-terminal cargo-binding tail domains [33].

The actual molecular structure of the kinesin molecule functionally depends on the state of the mechanochemical cycle; that is, it is coupled to microtubule binding, ATP binding, ATP hydrolysis, and the release of the hydrolysis products adenosine diphosphate (ADP) and  $P_i$  [34, 35].

### 2.2. Molecular Structure of Microtubules

Microtubules are obligate proteinaceous macromolecule complexes found in nearly all eukaryotic cells. In cooperation with other components of the cytoskeleton, namely, actin microfilaments and intermediate filaments, they constitute a functional unit that is involved in diverse cell physiological processes such as segregation of genetic material, intracellular transport, maintenance of cell shape, positioning of cell organelles, extracellular cilia-supported transport, and movement of cells by means of flagella and cilia. Irreversible elimination or functional inactivation of microtubules causes cell death.

Microtubules are described as hollow cylinders with outer and inner diameters of about 25 nm and 14 nm, respectively. Their lengths vary from a few to some tens of micrometers. The main constituent of the microtubules is tubulin, which is a globular protein existing in the native state as a heterodimer of an  $\alpha$  and a  $\beta$  form. Both monomers have a molecular mass of approximately 50 kDa and a diameter of about 4–5 nm. The longitudinal dimension of the dimer, which is 8 nm, defines the unitary step size of kinesin movement.

In the electron microscope, microtubules reveal characteristic subfilaments (called protofilaments) formed by longitudinal association of  $\alpha$ - and  $\beta$ -tubulin dimers. In mammalian neuronal cells, microtubules are composed of 13 protofilaments. In particular, the microtubules of lower



eukaryotes show a greater tendency to deviate from the 13-protofilament pattern. They were observed to have between 11 and 17 protofilaments [36]. Dependent on diverse factors, the protofilament number of microtubules assembled from purified tubulin under *in vitro* conditions varies from 8 to 18 [37]. It can be affected, for example, by a set of accessory proteins (microtubule-associated proteins, MAPs) [37], ionic strength [38], or special drugs like taxol [37, 39].

MAPs are known to inhibit kinesin attachment to microtubules [40]. Therefore, to study kinesin-driven motility, *in vitro* microtubules assembled from tubulin depleted of MAPs were usually used, which were stabilized by the addition of taxol (an anticancer drug obtained from the yew tree). Such microtubules are typically composed of 12 protofilaments [37] known to be tilted with respect to the tubule long axis, resulting in a right-handed helix with a supertwist pitch of 3.4  $\mu\text{m}$  [41]. The protofilaments of microtubules with 14 protofilaments revealed a left-handed helix with a 6.2- $\mu\text{m}$  supertwist pitch [41]. In the case of microtubules with a 13-protofilament pattern, the protofilaments run nearly parallel to the tubule long axis [41]. The orientation of protofilaments relative to the long axis defines the track along which the kinesin molecule moves (see Section 2.4).

Because of the dimeric character of the tubulin and the strict alternation of  $\alpha$  and  $\beta$ , one end of the protofilament is terminated by an  $\alpha$  subunit and the opposite one by a  $\beta$  subunit. This provides the protofilament a certain kind of polarity. The microtubule wall is composed of protofilaments laterally associated with the same polarity, which is reflected in cryoelectron microscope images and in three-dimensional reconstructions [42]. Consequently, one microtubule end exposes  $\alpha$  subunits (minus end) and the opposite end  $\beta$  subunits (plus end) only [43]. When the steady state of microtubule assembly is reached, at the plus end more dimers are added than lost. Conversely, at the minus end more dimers are released than new ones reassociate. This means that the microtubule is growing at the plus end while it is shrinking at the minus end. The direction the kinesin moves along a microtubule is related to its structural and kinetic polarity.

### 2.3. Conditions of *In Vitro* Motility Generation

The molecular mechanisms of movement and transport can be studied in a cell-free environment either by gliding of taxol-stabilized microtubules across kinesin-coated glass surfaces [14, 44] or by translocation of kinesin-coated polymer beads along immobilized microtubules [45]. The velocities of motility generated by conventional neuronal kinesin are typically found to be between 0.4 and 0.9  $\mu\text{m/s}$  [14, 46–48]. To generate kinesin-mediated motility, ATP is required as an energy source and  $\text{Mg}^{2+}$  ions as an obligate co-factor [49].

The application of ATP in the absence of  $\text{Mg}^{2+}$  or of nonhydrolyzable ATP analogues results in stopping motility. The  $\text{Mg}^{2+}$  ions can be replaced by some other divalent metal ions, among them  $\text{Ca}^{2+}$  and  $\text{Mn}^{2+}$  [50, 51]. Whereas the velocities of kinesin movement in the presence of  $\text{Ca}^{2+}$  were only about one-fourth compared with  $\text{Mg}^{2+}$ , the efficiency of  $\text{Mn}^{2+}$  was similar to that of  $\text{Mg}^{2+}$ .

Binding of the kinesin heads to a microtubule boosts the ATPase activity by a factor of up to 1000 [52–54]. Cargo binding also enhances the hydrolytic activity of kinesin [55]. The kinesin–microtubule system can be regarded as a self-regulating motor that utilizes its substrate resources very economically. Nature seems to have phylogenetically optimized the energy consumption of kinesin (as well as other motor proteins). Only very small amounts of ATP are hydrolyzed by kinesin in a nonactive state, that is, when it is not linked to microtubules or a cargo.

The velocity of kinesin-driven microtubule motility is fairly uniform from pH 6 to 9, with almost no motility outside this range [48, 56]. Kinesin was demonstrated to generate motility within the temperature interval from (at least) 5 to 45  $^{\circ}\text{C}$  [57]. Using temperature pulse microscopy, it has recently been shown that under favorable conditions kinesin can work for 30 min even at a temperature of 50  $^{\circ}\text{C}$ , where its velocity reached 3.68  $\mu\text{m/s}$  [58]. However, it has to be mentioned that kinesin purified from porcine brain gradually exhibits denaturation at temperatures above 45  $^{\circ}\text{C}$  [57].

It is known that each tubulin dimer of a microtubule is able to bind one kinesin head [59]. But Howard and co-workers [60] demonstrated that one kinesin molecule is sufficient to move a microtubule over micrometer distances. To support microtubule gliding, the density of kinesin immobilized to a given surface might be as low as 3.4 and 17 molecules per square micrometer for microtubules shorter and longer than 10  $\mu\text{m}$ , respectively [61]. The gliding velocity was found to be inversely proportional to the number of kinesin molecules involved in motility generation [48, 61].

### 2.4. Mechanism of Movement, Processivity, and Duty Ratio

Each tubulin dimer of a microtubule is capable of binding one kinesin motor domain. In the case of the two-headed (dimeric) conventional kinesin, two consecutive binding sites can be occupied on the microtubule [62], depending on the phase in the mechanochemical cycle. Whereas the binding to the microtubule was shown to be realized mainly via the  $\beta$ -tubulin subunit [63, 64], recent studies demonstrated that the two flanking  $\alpha$ -monomers can also be involved [65]. Interaction of kinesin with  $\beta$ -tubulin appears to be mediated mainly by electrostatic force [65]. For microtubule binding, it does not matter whether there is an  $\alpha$ - or a  $\beta$ -tubulin monomer in the lateral neighborhood to the protofilament track along which the kinesin is moving [64]. For the fast fungal kinesin from *Neurospora*, an additional interaction of the L11 structural part with the C-terminal region of the  $\beta$ -tubulin of the adjacent protofilament has been suggested [65].

Kinesin generates motility by walking step by step and hand over hand along the outer surface of a given microtubule protofilament [66]. As alternatives to the hand-over-hand model for movement, recently an “inchworm” model [67, 68] and a biased diffusion [67] model of processive movement have been proposed. Contrary to the hand-over-hand model, in the inchworm model the two heads do not change their positions relative to the walking direction.

This means that there is no net neck rotation during the mechanochemical cycle [68].

During its movement, kinesin follows one and the same protofilament [41, 64, 69]. Corresponding to this model, microtubules with 12 and 14 protofilaments, which are helically oriented around the tubule long axis (see Section 2.2), rotate as they glide across a kinesin-coated surface, depending on the pitch and the handedness of the supertwist. In contrast, 13-protofilament microtubules, whose protofilaments run more or less parallel to the tubule axis, do not rotate during gliding [41]. Interestingly, most of the cytoplasmic microtubules of higher eukaryotic cells are composed of 13 protofilaments [36]. Due to the different protofilament arrangements, an organelle moving along a 13-protofilament microtubule should reach the microtubule end in a shorter time than an organelle moving along a 12-protofilament microtubule of the same length. Obviously, nature has favored the 13-protofilament microtubule pattern for realizing efficient organelle transport with minimal energy consumption.

The kinesin heads translocate by turns in 16-nm steps, resulting in 8-nm center-of-mass shifts [34, 70]. Using an assay that resolves nanometer displacements with microsecond accuracy, Nishiyama and co-workers [71] demonstrated that the 8-nm shifts of the kinesin can be resolved into fast and slow substeps, each corresponding to a center-of-mass displacement of approximately 4 nm.

Conventional kinesin is a highly processive molecular motor that takes several hundred steps per encounter with a microtubule without dissociating [72–74]. One of the heads remains bound to the microtubule while the second one moves [41, 75]. Kinesin processivity is based on mechanical and chemical coordination between the ATP hydrolysis cycles of the two heads [76], resulting in conformational changes and coordinated consecutive translocations. Recently, it has been shown that one-headed members of the kinesin superfamily (e.g., KIF1A) can also realize movement in a processive fashion. This was explained by the existence of two microtubule-binding motifs in one head [77].

In governing the run length, that is, the distance a single motor protein travels per microtubule encounter, the neck coiled-coil region of kinesin was shown to play an important role. By adding positive charge to the neck coiled coil, Thorn and co-workers [78] created ultraprocessive kinesin mutants with fourfold longer run lengths than the wild-type motor, but with normal ATPase activity and motor velocity. Conversely, the addition of negative charge to the neck coiled coil resulted in a decrease in the run length. Furthermore, processivity is suppressible by either proteolytic cleavage of the negatively charged C-terminus of tubulin or an increase in the ionic strength, suggesting that processivity modulation by the neck coiled coil is based on an electrostatic binding mechanism with the COOH terminus of tubulin [78].

Besides the ionic strength, the processivity of kinesin can be also affected by other physicochemical parameters adjusted in its microenvironment: For example, it has been found that the average run length at around 50 °C was approximately 9  $\mu\text{m}$ , which significantly exceeds that at 20 °C [58]. Addition of ADP, released after ATP hydrolysis and competing for the ATP-binding site, was found to

decrease the run length even in the presence of saturating ATP [79]. The greatest run lengths that have been measured in a single molecule assay performed with a GFP kinesin construct containing the motor and a part of the stalk domain of conventional kinesin were about 10  $\mu\text{m}$  [40].

The question arises as to what limits processive movement. According to Hackney [80], ATP hydrolysis at the first head that is attached to the microtubule before the tethered second head can release its ADP and become tightly bound seems to be one cause of processivity limitation. We suppose that the helical arrangement of the protofilaments within a microtubule (see Section 2.2) might also decrease the kinesin run length, especially in cases where the motor protein transports a cargo along a microtubule immobilized to a substratum. Besides, restrictions of kinesin run length might be due to irregularities in microtubule structure, for example, incorrect dimer positioning, partially denatured dimers with alterations in their kinesin recognition site, or any other discontinuities within the protofilaments that hinder the kinesin in finding the next binding place on the microtubule.

In the context of possible nanotechnological applications of the kinesin motor, methodological approaches have to be developed that enable the transport of a cargo over distances exceeding the run length of a single kinesin molecule (see Section 3.8).

There is another relevant parameter that has to be considered in characterizing the mechanism of motor protein movement along a filamentous track. This is the so-called duty ratio, which is defined as the ratio of the time an intermittently operating device is working to the total time available [81]. In the case of motor proteins, the duty ratio indicates the fraction of time that a motor domain remains attached to the track during one full ATP hydrolysis cycle [82]. Compared to skeletal muscle myosin [83, 84], conventional kinesin has a high duty ratio, which is about 0.5 [18]. This means that a kinesin head is attached to the microtubule track over half of a full mechanochemical cycle. A high duty ratio seems to be the basis for the movement of kinesin along a microtubule over micrometer distances [82].

## 2.5. Directionality and Forces Generated by Conventional Kinesin

The direction of kinesin movement depends on both the microtubule polarity and the intrinsic molecular structure of kinesin [82, 85, 86].

Conventional kinesin is known to be a plus-end-directed motor. There are a few other kinesin-like motors that move to the minus end: Examples are the nonclaret disjunctional protein *ncd* [87] and the yeast *Kar3* [88], both required for chromosome distribution, and *KIFC3*, involved in the apical transport of renal tubular epithelial cells [89]. The direction in which the kinesin motor moves obviously depends on the location of the motor domain. Dimeric constructs with the motor domains either at the N- or the C-terminal end of the heavy chain were shown to move toward microtubule plus or minus ends, respectively [90]. The directionality of kinesin seems to be also dependent on neck/motor core interactions [30].

Several approaches have been used to measure forces generated by single kinesin molecules, including movement against a viscous load [61], a centrifuge microscope-based motility assay [91], optical trapping interferometry to track movement [92, 93], and a bead assay in an optical microscope equipped with optical tweezers [94]. Forces in the range of 4–8 pN were determined. So far, we do not know what forces are generated when *more than one kinesin molecule* contributes cooperatively to the transport of a cargo (see Fig. 2) and whether or not the kinesin molecules are self-synchronizing in such a case.

## 2.6. Advantages of Kinesin for Nanoactuatoric Systems

The movement of dimeric kinesin involves a highly coordinated interaction between both heads of the kinesin molecule and the microtubule rail. Both heads alternate in their binding. When one of the heads is released from the microtubule surface, the second one is bound, resulting in a permanent attachment of the kinesin to the microtubule, which is in contrast to, for example, myosin II [95]. Consequently, the kinesin is able to walk over distances up to some micrometers before being detached, which makes it suitable for conveying a cargo steadily and reliably to its destination.

Besides dimeric kinesins, some myosins, namely, myosin V [96] and myosin VI [97] as well as cytoplasmic dynein [98],

also reveal processivity. However, their usability in artificial transport systems seems to be strongly limited for the following reasons:

- Myosins walk along the microfilaments. For microfilaments, a mean flexural rigidity of  $7.3 \times 10^{-26} \text{ N m}^2$  was measured [99], which seems to be too low to form rigid stable rails supporting a nearly straight-line movement of the motor.
- Although cytoplasmic dynein also uses microtubules as rails, its processivity seems to be a more complex mechanism, requiring the activity of additional regulator proteins [98]. Processivity of the 22S subunit of axonemal dynein has been shown to be induced at low ATP concentration [100] only. A diminished ATP supply, however, might decrease the lifetime of the motor system.
- While much progress has been made on the biochemistry and mechanochemical cycles of conventional kinesin and myosin II [101], significantly less is known about cytoplasmic dynein. One main reason for this is the high complexity of the dynein molecule, which consists of two heavy chains and 8 to 11 diverse accessory polypeptides [98].

On the contrary, kinesin has some striking advantages favoring its use for nanoactuatoric systems:

- Kinesin is known to be a motor with high directional stability. It moves along one and the same microtubule protofilament [102]; that is, the lateral deviation from the track line is within the limits of 5 nm (protofilament diameter).
- The microtubules are believed to be more suitable for forming a stable straight-line rail as they have a much higher flexural rigidity ( $2.1 \times 10^{-23} \text{ N m}^2$  [99]) than the microfilaments.
- Kinesin has a relatively low torsional stiffness of approximately  $4 \times 10^{-21} \text{ J}$ , which allows for twisting a kinesin molecule at room temperature through more than  $360^\circ$  from its resting orientation [103]. This high flexibility might explain how several motors can efficiently work together even if they are randomly oriented on the surface of a cargo or on the substratum [103].
- Kinesin is able to utilize not only ATP as fuel but also some other nucleoside triphosphates such as GTP. If some kinesins with GTP specificity could be found or created by molecular engineering, they could be involved in a transport device together with other motors requiring exclusively ATP, for example, together with the oppositely directed cytoplasmic dynein, to get shuttle systems with forward and backward movement.

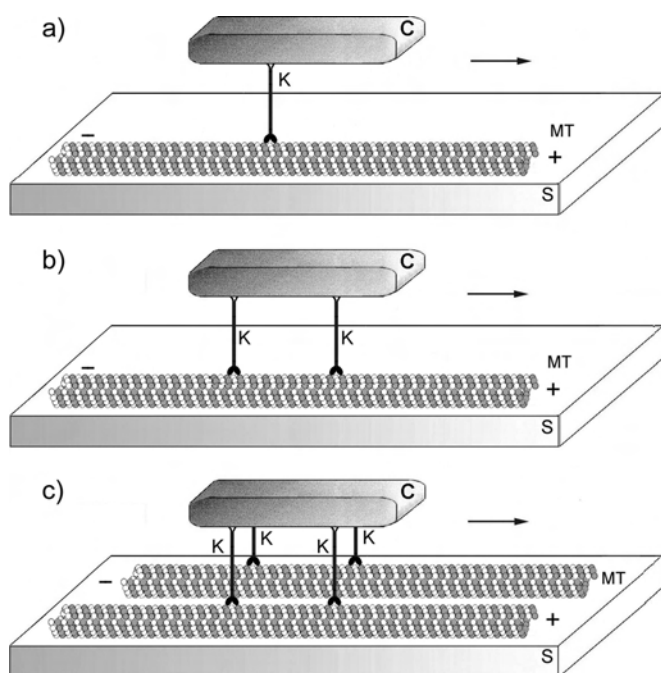


**Figure 2.** Principal schemes of kinesin-based nanoactuators realizing the transport of a cargo: (a) elementary motor unit (a single kinesin molecule), involving one microtubule in the transport; (b) serial alignment of motor units, involving more than one kinesin molecule moving along one and the same microtubule rail; (c) serial and parallel (isopolar) alignment of motor units (the transport is realized by different kinesin molecules moving along different microtubule rails). C, cargo; S, substratum; K, kinesin dimer; MT, microtubule with plus and minus ends.

There is another important argument related to the present state of methodological know-how that makes the kinesin force-generating system superior to other motors for nanoactuatoric applications: This concerns the possibility of preparing chemically stabilized arrays with microtubules arranged in parallel and isopolar fashion. Such arrays were demonstrated to be suitable rails for kinesin to transport a cargo in a predetermined direction [104, 105].

### 3. CONFIGURATION OF A KINESIN-BASED TRANSPORT DEVICE

#### 3.1. Basic Requirements

A kinesin molecule can be regarded as an engine moving with nanometer precision along fixed proteinaceous rails (Fig. 2). Converting the chemical energy of the biofuel ATP into mechanical energy, it conveys different kinds of nano- and micrometer-sized cargoes to their destination points.

Within the last five years, great efforts have been made to introduce the kinesin-microtubule machinery into the development of miniaturized technical transport devices. However, before this biomotor can be really exploited, numerous methodological and technical problems have to be solved. Complex studies have to be performed to learn, for example, to regulate the velocity and to increase the lifetime of the kinesin motor, to find out technically relevant materials enabling its work in a cell-free environment, to perform transport events with nanometer precision, or to control the direction of force generation.

Another problem concerns the lengths of the transport tracks. In single-molecule experiments, the distance a kinesin molecule can move was found to be limited to its maximum run length of about 10  $\mu\text{m}$  [40] and to the lengths of the microtubules used as rails, which were on the order of magnitude of some tens of micrometers. Some special nanotechnological applications might require methodological approaches enabling the transport of a cargo over distances greater than the kinesin run length and the microtubule length.

Furthermore, the clearance allowing for kinesin force generation seems to be important to work out the basic configuration of a kinesin-driven motor device incorporated into a spatially limited system (chambers or pipes with submicrometer heights or diameters, respectively). Interesting first approaches have been published (see [106]), contributing to the solution of these problems and being large steps on the way to engineering complex nanoactuators and nanorobots driven by biomotors.

#### 3.2. Preparation of the Protein Constituents

**Microtubules** Microtubules are ubiquitous structures found in eukaryotic cells. Neuronal tissue is known for its high tubulin content. In rat brain, the percentage of tubulin in the soluble protein fraction is about 33% at birth and 20% 15 days after birth, respectively [107]. Therefore, mammalian brain routinely serves as a source for microtubule isolation.

Standard protocols, used in many laboratories throughout the world for purification of microtubule protein especially from brain tissue, are based on temperature-dependent assembly-disassembly cycles in combination with ultracentrifugation [108]. It has to be mentioned that the protein preparations obtained in this way contain a defined set of accessory proteins called MAPs. The quantity and quality of MAPs, including the high-molecular-weight MAP1 and MAP2 (280–320 kDa) and the group of  $\tau$  proteins (65–70 kDa), depend on details of the preparation protocol. The amount of MAPs co-purified can be lowered, for example,

by adding glycerol or by increasing the ionic strength within the buffer [109, 110]. Both high-molecular-weight MAPs and  $\tau$  proteins are described to hinder kinesin binding to microtubules [40]. Therefore, MAP-free microtubules have to be used in kinesin motility assays. The MAPs can be separated from tubulin by phosphocellulose column chromatography [111]. Using the assembly-disassembly protocol of Shelanski and co-workers [108] in combination with phosphocellulose column chromatography, one obtains about 100 mg tubulin from 1 kg porcine brain.

Recently, a protocol has been published that enables tubulin synthesis in *Escherichia coli* [112]. The most critical point in recombinant tubulin preparation was to get assembly-competent protein. Shah and co-workers employed rabbit reticulocyte lysate, containing both the cytoplasmic chaperonin CCT and its co-factors, to form  $\alpha$ - $\beta$ -tubulin dimers that self-assemble into microtubules of normal morphology [112]. This approach offers a good chance for large-scale production of tubulin with reproducible quality. The availability of recombinant tubulins is also a main goal of pharmaceutical biotechnology, which needs standardized tubulins for the sophisticated search of novel cancerostatic drugs and for their evaluation.

The microtubules used in kinesin-based motility assays can be formed by 20-min incubation of pure tubulin at 37 °C with 1 mM GTP and 10  $\mu\text{M}$  taxol as assembly promoter and microtubule stabilizer. It is possible to store these microtubules in a frozen state for some months.

To obtain a matrix of densely packed microtubules, about 40 ng tubulin per square millimeter or 40 mg per square meter are required.

**Kinesin** To functionalize a 1-mm<sup>2</sup> surface, approximately 2–4 ng kinesin are needed. Kinesin can be purified from different organisms, tissues, and cells. Special protocols are available for fungi (*Neurospora*) [47], HeLa cells [113], *Dictyostelium amoeba* [114], and mammalian brain [52, 115].

Besides some others (see, e.g., [70]), a standard purification procedure was published for brain tissue by Kuznetsov and Gelfand [52, 115], which includes homogenization and preparation of a high-speed supernate followed by ion-exchange chromatography, tripolyphosphate-supported microtubule affinity binding, and gel filtration. This procedure yields about 2 mg kinesin from 1 kg brain with both ATPase and motility-generating activity, which can be frozen and stored in liquid nitrogen for several months.

Biochemical isolation of motor proteins from their natural sources has some distinct advantages: First, the motor will be properly folded and has normal posttranslational modifications. Second, the motor will carry with it a normal complement of associated proteins. Studies of kinesin-associated proteins will be important in learning how this motor accomplishes its tasks *in vivo* [116]. Today, it is well proved that for motility generation in a cell-free environment kinesin does not need any accessory proteins. Therefore, recombinant kinesins are produced with constant quality in relatively large amounts. Different expression systems for conventional kinesins are described, for example, by Navone and co-workers [117] and Niclas and co-workers [118]. Moreover, genetic engineering has proved its ability to supply numerous kinesin constructs with specialized properties,

for example, with improved processivity or higher velocity [76, 119] (see also Section 2.3). Genetic engineering is also expected to contribute to prolongation of kinesin lifetime. Another task arising in connection with nanotechnological requirements might be the addition of a specific cargo-binding domain to the kinesin tail that recognizes different kinds of materials.

### 3.3. Regulation of Transport Velocity

The velocities of microtubule gliding supported by conventional kinesin, measured in a cell-free environment at  $Mg^{2+}$  and ATP concentrations both around 1 mM and at room temperature, were about 0.4–0.9  $\mu\text{m/s}$ . For comparison, a conventional kinesin from the fungus *Neurospora* was found to walk significantly faster (up to 3.8  $\mu\text{m/s}$  [47]). In contrast, the mitotic kinesin Eg5, which is another plus-end-directed motor, moves only at about 0.06  $\mu\text{m/s}$  [120].

Kinesin-driven microtubule gliding can be accelerated by increasing the ratio of  $Mg^{2+}$  to ATP concentration [48, 74] and by temperature elevation [57]. At high temperature (50–60 °C), velocities up to 3.7  $\mu\text{m/s}$  were measured for kinesin purified from brain [58].

Howard and co-workers [60] demonstrated that microtubule gliding still occurs at kinesin densities as low as one molecule within an area of about 700 nm  $\times$  700 nm. When the surface density of kinesin bound to the substratum was increased, the velocity of microtubule movement across kinesin-coated glass surfaces was found to be lowered [48, 61].

It is known that under conditions of saturation each kinesin dimer occupies two microtubule-binding sites, provided that there is a free one close by [62] and that movement does not start before the next binding site at the microtubule surface has become free. Consequently, the higher the kinesin density, the higher should be the probability that the next binding site is occupied, resulting in a decrease in the mean velocity of kinesin translocation.

Another explanation for the slowdown in kinesin movement as a result of elevating kinesin surface density might be the asynchronous work of single kinesin molecules collectively contributing to the transport of a given cargo (see Fig. 2). At high density, more than one kinesin molecule might bind to one and the same protofilament of a gliding microtubule. It seems to be even likely that in such a case kinesin molecules binding to adjacent protofilaments contribute to the movement of the microtubule. In this context, the question of the self-synchronization of kinesin work has to be discussed.

Further ways to throttle the velocity of kinesin movement are the addition of polyhydroxy compounds [121], lowering the  $Mg^{2+}/\text{ATP}$  ratio [48], or the replacement of the  $Mg^{2+}$  ions by  $Ca^{2+}$  and other alkaline earth metal ions [50]. Alternatively, certain drugs might be applied to slow down kinesin movement. In a single-molecule motility assay, local anesthetics such as tetracaine and lidocaine reversibly inhibited the motility of individual kinesin molecules in a dose-dependent manner [122].

Regulation of the velocity is tightly correlated with the problem of how to start or stop kinesin movement within the shortest time intervals. The kinesin motor works with 8-nm

feed. This means that at velocities between 0.4 and 0.9  $\mu\text{m/s}$  each step takes about 9–20 ms (in the case of *Neurospora* kinesin, even about 2 ms). To stop movement with nanometer precision, the motor should be switched off in millisecond ranges. By “chemical switching” such as the removal of ATP or  $Mg^{2+}$  or the introduction of additives slowing down kinesin movement, the motor can be started or stopped only within a few tens of seconds. A first approach to cope with this challenging task is the application of hexokinase and 1-(4,5-dimethoxy-2-nitrophenyl) ethyl-caged ATP instead of the usual (noncaged) ATP [123], which is converted from an inactive state into an active state during exposure to ultraviolet (UV) light. This system enables one to switch kinesin movement within some seconds.

### 3.4. Lifetime and Energy Supply

Kinesin-based motility generation can be maintained in a cell-free environment at least over three hours when desiccation is avoided and ATP is available in sufficient quantity [48]. Thereafter, the binding strength of kinesin to the glass support and/or the microtubule rails was found to be lowered rapidly, obviously due to protein degradation.

Our own investigations indicated that chambers with microtubules gliding across kinesin-coated surfaces can be stored for some days in a frozen state. After rethawing, the microtubules continued to move (not published).

ATP complexed with  $Mg^{2+}$  is commonly known to supply the energy for kinesin motility. Other nucleoside triphosphates, including guanosine triphosphate (GTP) and uridine triphosphate (UTP), can also be used as an energy source, but the velocity of kinesin movement is remarkably lower in these cases [56].

Both ATPase activity and kinesin-driven microtubule gliding follow Michaelis–Menten kinetics with an apparent  $K_m$  value of approximately 60  $\mu\text{M}$  [46, 48, 56]. Kinesin-driven microtubule gliding as well as the translocation of kinesin-coated beads is usually performed at an ATP concentration of 0.5 mM, corresponding to  $0.3 \times 10^{15}$  ATP molecules within a chamber of 1  $\mu\text{L}$  volume. Each kinesin molecule consumes one molecule ATP to translocate a 200-nm silica bead over a distance of 8 nm [124]. This means that with  $0.3 \times 10^{15}$  ATP molecules a bead can be theoretically moved over distances up to  $2.4 \times 10^6$  m. An alternative calculation gives  $4.8 \times 10^9$  beads that can be transported over a track length of 5 mm. However, it should be mentioned that the adenosine diphosphate (ADP) released during the mechanochemical cycle of kinesin acts as a feedback effector with inhibiting activity. Whereas the kinesin run length at zero-load condition was observed to be independent of the ATP concentration from micromolar to millimolar concentrations, the addition of ADP in the presence of saturating ATP decreased both the velocity and the run length. At 2 mM ATP and 2 mM ADP, a 50% inhibition of the kinesin run length and velocity was measured [79]. To get over this problem especially in cases of high ATP turnover rates, an ATP-regenerating enzymatic system was proposed [106]. Such a system, however, comprises further more or less sensitive proteins whose activities might be nonstable in a cell-free environment. Alternatively, the ATP concentration can be maintained on a nearly constant level by a permanent exchange of the ATP-containing soluble phase.

### 3.5. Cargo Materials and Surface Requirements

The cargoes to be transported by kinesin or the supports used to carry the biomolecular force-generating motor unit can be made from a broad variety of materials, including glass, quartz, carbon, gold, polystyrene, and the microtechnologically outstanding silicon [125]. The main transport parameters (e.g., velocity, maximum distance the load is transported, and lifetime) were found to be practically independent of the kind of material used.

For functioning of the motor system, the quality of the surface to which the kinesin binds seems to be of great importance. One main requirement on which kinesin-mediated motility generation crucially depends is a low surface roughness and a minimum of contaminating surface-bound particles. Silicon wafers with etched steps of defined height and edge steepness were used to find out the critical height difference kinesin-driven gliding microtubules tolerate. It was observed that such microtubules could overcome steps upwards up to at least 280 nm at an edge angle of 60°–70° [104]. Under favorable conditions when the gliding microtubule approaches the step at low angle, even steps of 1  $\mu\text{m}$  can be climbed up [123]. These observations suggest that knolls and dells on the surface as well as dust particles (provided that they are without any microtubule-binding affinity) with dimensions up to 1  $\mu\text{m}$  do not prevent transport processes realized by kinesin-driven gliding microtubules.

The requirements concerning surface purity and evenness seem to be remarkably higher for transport systems where kinesin drives a bead along immobilized microtubules. In this case, beads were often observed to stop when they encounter a micrometer-sized obstacle on the microtubule and/or the glass surface [105]. This problem might be solved using arrays of densely packed isopolar microtubules and loading the beads with a higher number of kinesin molecules. Under such conditions, moving beads were seen to go around the obstacle, obviously using adjacent microtubule rails [105].

### 3.6. Critical Clearance

Concrete tasks in the development of kinesin-based machinery might be the relative displacement of two thin plates against each other or the transport of a cargo into or through pipes with diameters in the nanometer range. In this context, it is necessary to determine the minimal distance between the cover and the bottom surface (clearance), which still allows kinesin-dependent force generation.

Stracke and co-workers [104] studied kinesin-driven microtubule gliding in clefts of defined height to measure the clearance the kinesin requires. Such clefts can be formed by a slightly curved coverslip (made by thermal deformation under one-sided pressure), which was approximated by a small vacuum chamber with convex side down to a glass slide. Around the contact point between the coverslip and the slide, Newton rings appear, enabling interferometric determination of the distance between both glasses. Using this approach, gliding was observed, in principle, down to approximately 100 nm [104], which crudely corresponds to

the length of the kinesin molecule (80–100 nm) plus the diameter of the microtubule rail (25 nm). When the height of the gap was lowered to values below 100 nm, only in single cases were microtubules observed to migrate and their leading edges often stuck and the tails revealed a fishtailing-like movement [104]. Thus, a height of 100 nm is proposed to be the critical clearance for kinesin moving along a microtubule.

It has to be mentioned, however, that the velocity of gliding microtubules was significantly reduced in clefts with heights just below 5  $\mu\text{m}$ . This effect is at least partially due to limitations in fuel supply and can be minimized by increasing the ATP concentration [104].

### 3.7. Regulation of Transport Direction

A crucial point in the development of cell-free kinesin-based machinery is the predetermination and control of the transport direction. Both microtubules gliding across a kinesin-coated surface and kinesin-coated beads translocating along immobilized microtubules are experimental approaches in which motility is generated in two-dimensional systems. The first step on the way to control the transport direction is the restriction of motility generation to one dimension, resulting in shuttle systems with forward and backward movements.

In recent years, it has been shown that the kinesin-dependent transport can be limited to one dimension using different kinds of guiding channels: Wittmann and Smith [126] described a shear deposition method by which glass surfaces can be coated with thin polytetrafluorethylen (Teflon) films, leaving parallel nanometer-deep grooves free of the polymer. Whereas the Teflon does not bind proteins, kinesin is attached to the polymer-free surface on the bottom of the grooves. Dennis and co-workers [127] demonstrated that such kinesin-coated grooves can serve as channels to guide gliding microtubules in nearly straight lines.

Turner and co-workers [128] prepared lithographically patterned silane surfaces to which microtubules were attached under the action of an external flow field. Under such conditions, the microtubules adhered in parallel fashion, retaining their ability to serve as rails for the transport of kinesin-coated beads [128]. Limberis and Stewart succeeded in moving even large kinesin-coated silicon microchips (10  $\mu\text{m} \times 10 \mu\text{m} \times 5 \mu\text{m}$ ) along parallel microtubules immobilized to trimethoxysilylpropyl-diethylenetriamine silane-treated glass coverslips during flow field action [129]. Remarkably, the maximum velocity at which the microchips moved (0.8  $\mu\text{m}$ ) was in the same range as determined for microtubules gliding across a kinesin-coated surface (see Section 2.3).

Another remarkable contribution toward guiding kinesin movement was made by Hess and co-workers [130]. These authors introduced a pinwheel pattern of tracks selectively binding the motor protein and open 1- $\mu\text{m}$ -deep and 2.5- $\mu\text{m}$ -wide guiding channels to realize the one-directional sorting of kinesin-based shuttles. They suggested that a Brownian ratchet mechanism is the basis of this kind of sorting in the case when the pattern includes motor protein-rich and motor protein-free surface regions and the directional change of the molecular shuttle is caused by Brownian motion.



The approaches described above allow the kinesin to be guided in linear parallel tracks. The transport direction is unpredictable, however, so that the load can be moved forward and backward, depending on the orientation of the majority of microtubules contributing to the transport. To guide the kinesin to a desired destination point, it is necessary to align the microtubule rails not only in parallel fashion but additionally with equal polarity. Otherwise, the elementary forces generated along adjacent microtubules act in a different direction and may neutralize each other more or less completely. Therefore, procedures in which the microtubules are not aligned with the same polarity are not well suited for efficient transport of large cargoes binding to more than one microtubule and, consequently, can find only a limited application in nanotechnology.

So far, three promising approaches were described to regulate the direction of kinesin-supported movement: Microtubules were aligned in parallel and isopolar fashion during gliding across kinesin-coated glass surfaces by application of flow fields (Figs. 3 and 4) [104]. However, when the flow was abolished the microtubules immediately started to move again in a directionally uncontrolled manner. It is known that microtubules treated by glutaraldehyde retained their potency to serve as tracks for kinesin movement [131]. Using this protocol, the aligned microtubules can be immobilized with isopolar orientation. When the microtubules were applied at high density, the stable microtubule arrays were formed able to transport kinesin-coated particles into a predetermined direction in the absence of flow [105]. This approach has the advantage that large areas of a given substratum surface can be densely covered with isopolar microtubules, along which the transport can be realized over

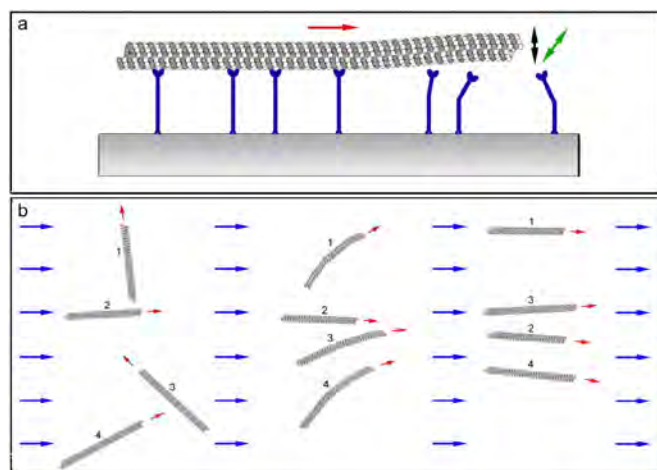


**Figure 3.** Mechanism of isopolar microtubule alignment in flow fields. (a) Especially in cases of relatively low kinesin densities, the leading end (minus end) of a microtubule gliding across a kinesin-coated substratum is often observed lifting off from the surface and wobbling in the  $y$  direction [104]. (b) When a transverse force (generated, e.g., by a flow field) acts laterally on this end, it turns in the flow direction guiding the whole microtubule in the flow direction. Blue arrow, direction of force exerted by the flow field; black arrow, lifting off of the microtubule end from the substratum; green arrow, wobbling of the microtubule end in the  $y$  direction; red arrow, direction of the resulting force driving the microtubule. The numbers indicate individual microtubules.

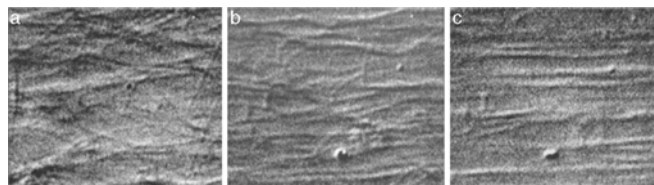


**Figure 4.** Flow field-induced isopolar orientation of microtubules gliding across a kinesin-coated substratum, visualized by video-enhanced differential interference contrast microscopy: (a) stochastic microtubule gliding; (b) and (c) consecutive microtubule alignment after application of a flow field. The leading (minus) end of the microtubules is turned in the flow direction. The bars represent  $5 \mu\text{m}$ .

distances exceeding the length of an individual microtubule (see Section 3.8).

Another efficient approach to obtain isopolar microtubule rails to direct kinesin-mediated transport in a desired direction has been published by Limberis and co-workers [132] who attached a histidine-tagged anti- $\alpha$ -tubulin antibody to a hydrophobic glass coverslip (Fig. 5). This antibody fixes the microtubules selectively by their minus ends onto the glass. When a fluid flow was applied, these one-point fixed microtubules turned into the flow direction. As a result, about 90% of the microtubules were found to be oriented with their minus ends pointing upstream. Reorientation of the microtubules could be prevented by the addition of a 0.2% solution of methyl cellulose [132].

Alternatively, Hiratsuka et al. [133] produced linear microlithographic tracks on glass surfaces supplemented with mechanical rectifiers of an arrowhead pattern (Fig. 6). When the surface of such channel-like tracks was functionalized with kinesin, gliding microtubules were forced to move preferentially in one direction. The efficiency of unidirectional rectification of gliding microtubules correlated to the arrowhead geometry. Using a surface on which the tracks form a complex meander, a cargo bound to a microtubule can be transported precisely from one point to another within a two-dimensional system (Fig. 7). Microlithography allows for the production of not only linear but also circular tracks, enabling unidirectional rotational movement of the microtubules (Fig. 8) [133].

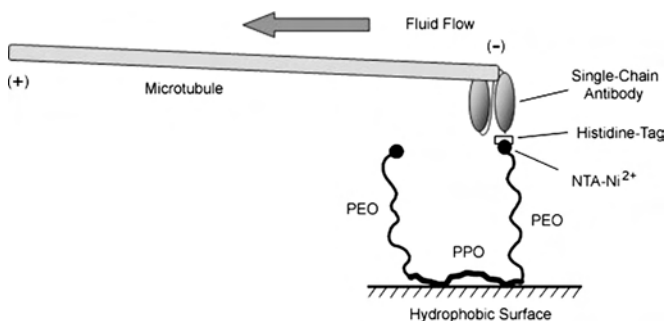


**Figure 5.** Immobilization and polar alignment of microtubules. A metal-chelating Pluronic surfactant is used to immobilize the minus end of the microtubules on a hydrophobic microscope coverslip using a histidine-tagged  $\alpha$ -tubulin single-chain antibody. The microtubules are polar aligned by fluid flow in a flow chamber. Reprinted with permission from [132], L. Limberis et al., *Nano Lett.* 1, 279 (2001). © 2001, American Chemical Society.

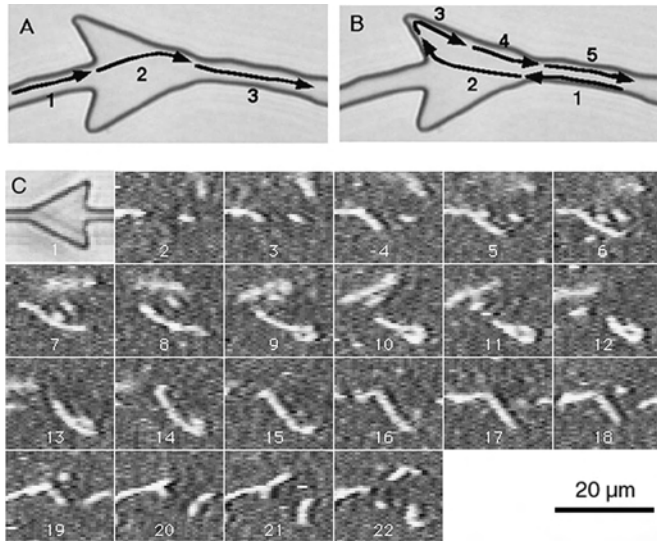


**Figure 6.** Arrowhead pattern functioning as a rectifier of microtubule movements. A shows that a microtubule entering the arrowhead from the correct direction (from the left-side entrance) passes through the arrowhead pattern. B demonstrates schematically how a microtubule entering the arrowhead from the wrong direction (from the right-side entrance) makes a 180° turn and moves out in the correct direction. C is the actual sequence of fluorescence images showing the turning of a microtubule in an arrowhead pattern. Images were captured with an SIT camera at a rate of 8 s per frame. Reprinted with permission from [133], Y. Hiratsuka et al., *Biophys. J.* 81, 1558 (2001). © 2001, Biophysical Society.

### 3.8. Length of Transport Tracks

The parameter run length was introduced to characterize the distance a *single* motor protein molecule walks along its filament. The maximal run length of kinesin that has

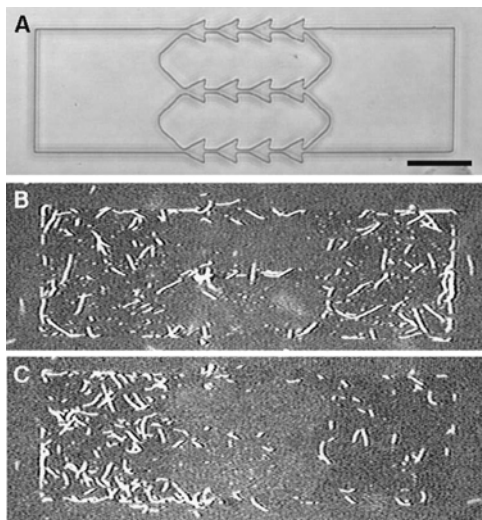


**Figure 7.** Active transport between two pools of micrometer scales: (A) transmission micrograph; (B) fluorescence image of rhodamine-labeled microtubules taken before the addition of ATP; (C) taken 18 min after the addition of ATP. Scale bar, 30 μm. A movie of this movement is available online at <http://unit.aist.go.jp/genediscry/motility/biophysj/moviedl.html>. Reprinted with permission from [133], Y. Hiratsuka et al., *Biophys. J.* 81, 1558 (2001). © 2001, Biophysical Society.

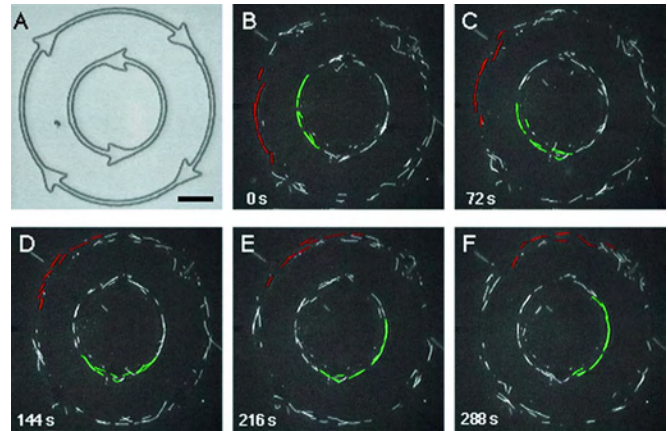


**Figure 8.** Unidirectional rotational movement of microtubules along circular tracks. The photographs represent snapshots of the movement of rhodamine-labeled microtubules taken at intervals of 72 s, 20 min after the addition of ATP (B–F). A shows an image of the transmission microscopy. Selected filaments were colored to allow tracking of groups of microtubules. Microtubules in the outer circle are moving clockwise (red), whereas those in the inner circle are moving counter-clockwise (green). Scale bar, 20 μm. A movie of this movement is available online at <http://unit.aist.go.jp/genediscry/motility/biophysj/moviedl.html>. Reprinted with permission from [133], Y. Hiratsuka et al., *Biophys. J.* 81, 1557 (2001). © 2001, Biophysical Society.

been reported so far was near 10 μm [40]. This seems to be the first limitation when a cargo has to be transported by the kinesin–microtubule machinery over longer distances. The second one is related to the length of individual microtubules used as transport rails. Taxol-stabilized microtubules formed from MAP-free tubulin under laboratory conditions in a cell-free environment are usually about 5–40 μm long, depending on the tubulin concentration, the speed of increasing temperature to start assembly, and the time the microtubules were held at the assembly temperature (own observation).

Therefore, the question arises as to how to support the cargo transport over distances significantly exceeding the microtubule length. Howard [69] reported that, at high kinesin density, microtubules gliding across a surface with immobilized kinesin can cover distances much greater than their length. This can be realized only in the case when the surface density of kinesin is high enough to ensure that the moving microtubule is able to encounter in its nearer surrounding the next active kinesin molecule.

When a cargo should be transported by kinesin along microtubule rails over distances exceeding the microtubule length, a second requirement has to be fulfilled besides a sufficiently high kinesin surface density. This concerns special conditions ensuring the efficient transition of the cargo from one microtubule to an adjacent one. Using small polystyrene beads (0.1 μm in diameter) to get a high resolution, such transition events have been directly observed by real-time video interference contrast microscopy [105]. The beads were found to change microtubule rails without remarkable interruption of movement after reaching the end of the microtubule rail.

With micrometer-sized beads and densely packed isopolar microtubule arrays, the transition probability proved



to be remarkably higher. Under such conditions, different kinds of cargoes (latex, glass, gold beads, flat glass particles) were transported by kinesin over some millimeter distances. Böhm and co-workers [105] succeeded in driving large kinesin-coated flat particles ( $24 \mu\text{m} \times 12 \mu\text{m}$  and  $2\text{--}5 \mu\text{m}$  thickness) across the surface of isopolar microtubule arrays without interruption over a distance of  $130 \mu\text{m}$ . Such particles, which were shown by laser scanning microscopy to contact more than one microtubule, moved unidirectionally at velocities of  $0.5\text{--}0.6 \mu\text{m/s}$ , known for microtubule gliding or the translocation of  $100\text{-nm}$  beads. Comparable control experiments performed with microtubules nonaligned in an isopolar fashion also revealed moving particles. However, the distances they could cover were only in the range of a few micrometers. Especially, large particles were found to rotate or to go forward and within some seconds back again. Similar observations were made when the translocation of silicon microchips across arrays of geometrically parallel microtubules with different polarity was followed [129]. This behavior can be explained by counteracting forces generated by kinesin moving along nonisopolar microtubules.

The finding that the track lengths of kinesin-driven cargoes can significantly exceed the lengths of individual microtubules is of eminent practical value. It demonstrates that it is not necessary to produce long individual microtubules when distances in the millimeter range should be covered.

#### 4. POSSIBLE APPLICATIONS AND OUTLOOK

Recently, a first interesting application of the kinesin motor system has been introduced by Hess and co-workers [134], who assembled a piconewton forcemeter consisting of two microtubules (Fig. 9): Whereas the first microtubule serves as a molecular cantilever fixed with one end and freely swinging with the opposite one, the second microtubule moves across a kinesin-coated surface perpendicular to the first microtubule. After contact, the cantilevered microtubule is bent when a link through the receptor/ligand complex of interest is established. The applied force is calculated from the known flexural rigidity of the microtubules [134].

Potential applications of cell-free nanomotors and nanoactuators include the following:

- Switchable linear motor devices and molecular machines working with nanometer precision, which might be applied for directionally controlled displacement of objects or for specific and directed substance transport over nanometer, micrometer, or millimeter distances. Such devices can contribute to nanostructure assembly and nanostructure fabrication.
- Transport of chemical components or catalysts into or out of microreactors, used, for example, for enhancing and controlling reactions.
- Development of intracellular sensors for diagnostic purposes.
- Delivery systems to convey drugs to pathological targets.

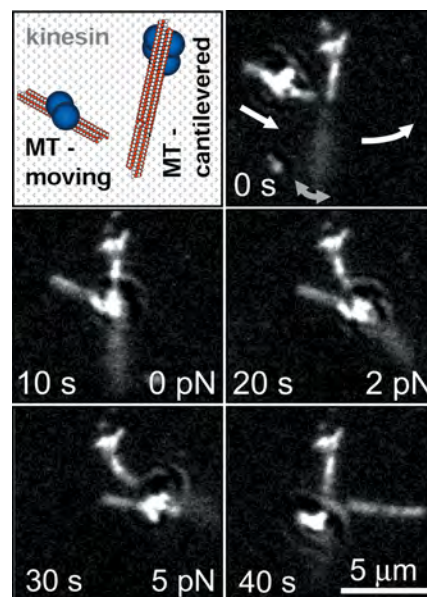


**Figure 9.** The cantilevered microtubule (MT) is attached on one end to a clump of beads, while the other end is suspended above the surface. Swiveling due to Brownian motion causes the smeared-out appearance of the free end. The moving microtubule is propelled by kinesin motor proteins adsorbed on the surface and carries a clump of beads. The snapshots show how the moving microtubule approaches (0 s), makes contact (10 s), bends (20 s, 30 s), and releases (40 s) the cantilevered microtubule. Reprinted with permission from [134], H. Hess et al., *Nano Lett.* 2, 1113 (2002). © 2002, American Chemical Society.

- Screening systems for developing novel therapeutic drugs targeting cellular movement.
- Autonomously working power units to drive implantable sensors using the cell ATP.
- Cell biological tools to study functional or regulatory mechanisms of motor protein-based force generation.

Although long-term technological impacts are difficult to predict, it seems to be realistic that motor protein-based force generation might be involved in the future development of novel nanoactuatoric systems, including miniaturized energy conversion and biofuel cells, implantable microdevices and sensors, separation techniques, as well as the assembly of nanotechnical circuits or microrobots.

Taken together, the design and control of kinesin-based nanoactuatoric devices have been advanced, but several basic problems remain to be solved until such a device can be introduced as an integral part into complex nanoactuatoric machines or robots. One main point that has to be addressed in the future is the regulation of starting and stopping force generation under cell-free conditions in the millisecond range, that is, with nanometer precision. Further unsolved problems concern the maximum load mass that can be moved by a collective of kinesin molecules and the synchronization of the great number of kinesin molecules contributing to the transport of one and the same cargo.

On the ambitious way toward the nanoactuatoric application of biomotors, further cell biological, biochemical, biophysical, and developmental work has to be done to improve the technical performance of these motors.

## GLOSSARY

**Adenosine triphosphate** A ubiquitous biofuel that supplies the energy required for various biological processes of transport and movement.

**Kinesin** A specialized motor protein that, moving along microtubules, is responsible for the transport of cell organelles and biomacromolecules.

**Microtubules** Proteinaceous hollow cylindrical filaments of 25 nm diameter and lengths in the micrometer range that constitute the rail for movement of kinesin (and some other motor proteins).

**Motor protein** A protein with catalytic (enzymatic) activity that converts the chemical energy of adenosine triphosphate into mechanical energy to move along the surface of suitable proteinaceous filamentous rails. The direction of its movements is strongly related to both the intrinsic molecular structure of the motor protein and the polarity of the filament.

**Polarity** The feature of a proteinaceous filament to expose two ends with different dissociation constants of the subunits that form the filament.

**Processivity** The feature of a motor protein to remain bound to the filament it moves along and to hydrolyze substrate molecules through several repetitious hydrolytic cycles.

**Run length** The distance a single motor protein molecule walks along the filament without being released from its surface.

## ACKNOWLEDGMENT

The authors are grateful to Roland Stracke for helpful discussions, numerous advice, and a critical reading the manuscript.

## REFERENCES

- H. C. Berg, *Biophys. J.* 68, 163S (1995).
- H. C. Berg, *Philos. Trans. R. Soc. London, Ser. B* 355, 491 (2000).
- S. Engelbrecht and W. Junge, *FEBS Lett.* 414, 485 (1997).
- R. L. Cross, *Biochim. Biophys. Acta* 1458, 270 (2000).
- C. Montemagno and G. Bachand, *Nanotechnology* 10, 225 (1999).
- J. Gelles and R. Landick, *Cell* 93, 13 (1998).
- M. D. Wang, *Curr. Opin. Biotechnol.* 10, 81 (1999).
- J. M. Lackie and J. A. T. Dow, "The Dictionary of Cell and Molecular Biology," 3rd ed. Academic Press, London, 1999.
- J. R. Sellers, *Biochem. Biophys. Acta* 1496, 3 (2000).
- L. M. Coluccio, *Am. J. Physiol.* 273, C347 (1997).
- A. R. Reilein, S. L. Rogers, M. C. Tuma, and V. I. Gelfand, *Int. Rev. Cytol.* 204, 179 (2001).
- A. S. Reddy, *Int. Rev. Cytol.* 204, 97 (2001).
- A. J. Kim and S. A. Endow, *J. Cell Sci.* 113, 3681 (2000).
- R. D. Vale, T. S. Reese, and M. P. Sheetz, *Cell* 42, 39 (1985).
- K. S. Thorn, J. A. Ubersax, and R. D. Vale, *J. Cell Biol.* 151, 1093 (2000).
- K. Hirose and L. A. Amos, *Cell. Mol. Life Sci.* 56, 184 (1999).
- F. J. Kull, in "Essays in Biochemistry. Molecular Motors" (G. Banting and S. J. Higgins, Eds.), p. 61. Portland Press, London, 2000.
- J. Howard, *Nature* 389, 561 (1997).
- K. J. Verhey, D. L. Lizotte, T. Abramson, L. Barenboim, B. J. Schnapp, and T. A. Rapoport, *J. Cell Biol.* 143, 1053 (1998).
- L. A. Amos, *J. Cell Sci.* 87, 105 (1987).
- N. Hirokawa, K. K. Pfister, H. Yorifuji, M. C. Wagner, S. T. Brady, and G. S. Bloom, *Cell* 56, 867 (1989).
- G. Woehlke and M. Schliwa, *Nat. Rev. Mol. Cell Biol.* 1, 50 (2000).
- F. J. Kull, E. P. Sablin, R. Lau, R. J. Fletterick, and R. D. Vale, *Nature* 380, 550 (1996).
- S. Sack, J. Müller, A. Marx, M. Thormählen, E.-M. Mandelkow, S. T. Brady, and E. Mandelkow, *Biochemistry* 36, 16155 (1997).
- R. D. Vale, R. Case, E. Sablin, C. Hart, and R. Fletterick, *Philos. Trans. R. Soc. London, Ser. B* 355, 449 (2000).
- L. Romberg, D. W. Pierce, and R. D. Vale, *J. Cell Biol.* 140, 1407 (1998).
- B. Tripet, R. D. Vale, and R. S. Hodges, *J. Biol. Chem.* 272, 8946 (1997).
- B. Tripet and R. S. Hodges, *J. Struct. Biol.* 137, 220 (2002).
- R. B. Case, S. Rice, C. L. Hart, B. Ly, and R. D. Vale, *Curr. Biol.* 10, 157 (2000).
- S. A. Endow and H. Higuchi, *Nature* 406, 913 (2000).
- M. de Cuevas, T. Tao, and L. S. Goldstein, *J. Cell Biol.* 116, 957 (1992).
- K. S. Kosik, L. D. Orecchio, B. Schnapp, H. Inouye, and R. L. Neve, *J. Biol. Chem.* 265, 3278 (1990).
- D. S. Friedman and R. D. Vale, *Nat. Cell Biol.* 1, 293 (1999).
- E. Mandelkow and K. A. Johnson, *Trends Biochem. Sci.* 23, 429 (1998).
- K. Hirose, J. Lowe, M. Alonso, R. A. Cross, and L. A. Amos, *Mol. Biol. Cell* 10, 2063 (1999).
- E. Unger, K. J. Böhm, and W. Vater, *Electron Microsc. Rev.* 3, 355 (1990).
- K. J. Böhm, W. Vater, H. Fenske, and E. Unger, *Biochim. Biophys. Acta* 800, 119 (1984).
- K. J. Böhm, W. Vater, P. Steinmetzer, and E. Unger, *Acta Histochem. Suppl.* 39, 365 (1990).
- J. F. Diaz, J. M. Valpuesta, P. Chacon, G. Diakun, and J. M. Andreu, *J. Biol. Chem.* 273, 33803 (1998).
- A. Seitz, H. Kojima, K. Oiwa, E. M. Mandelkow, Y. H. Song, and E. Mandelkow, *EMBO J.* 21, 4896 (2002).
- S. Ray, E. Meyhöfer, R. A. Milligan, and J. Howard, *J. Cell Biol.* 121, 1083 (1993).
- H. Sosa and D. Chrétien, *Cell Motil. Cytoskeleton* 40, 38 (1998).
- E. Nogales, S. G. Wolf, and K. H. Downing, *Nature* 391, 199 (1998).
- B. J. Schnapp, B. Crise, M. P. Sheetz, T. S. Reese, and S. Khan, *Proc. Natl. Acad. Sci. U.S.A.* 87, 10053 (1990).
- S. C. Kuo, J. Gelles, E. Steuer, and M. P. Sheetz, *J. Cell Sci. Suppl.* 14, 135 (1991).
- A. von Massow, E. M. Mandelkow, and E. Mandelkow, *Cell Motil. Cytoskeleton* 14, 562 (1989).
- G. Steinberg and M. Schliwa, *J. Biol. Chem.* 271, 7516 (1996).
- K. J. Böhm, R. Stracke, and E. Unger, *Cell Biol. Int.* 24, 335 (2000).
- S. A. Cohn, *Mol. Chem. Neuropathol.* 12, 83 (1990).
- K. J. Böhm, P. Steinmetzer, A. Daniel, W. Vater, M. Baum, and E. Unger, *Cell Motil. Cytoskeleton* 37, 226 (1997).
- K. J. Böhm, R. Stracke, and E. Unger, *Eur. J. Cell Biol. Suppl.* 49, 50 (1999).
- S. A. Kuznetsov and V. I. Gelfand, *Proc. Natl. Acad. Sci. U.S.A.* 83, 8530 (1986).
- T. G. Huang and D. D. Hackney, *J. Biol. Chem.* 269, 16493 (1994).
- K. A. Johnson and S. P. Gilbert, *Biophys. J.* 68, 173S (1995).
- D. S. Friedman and R. D. Vale, *Nat. Cell Biol.* 1, 293 (1999).
- S. A. Cohn, A. L. Ingold, and J. M. Scholey, *J. Biol. Chem.* 264, 4290 (1989).
- K. J. Böhm, R. Stracke, M. Baum, M. Zieren, and E. Unger, *FEBS Lett.* 466, 59 (2000).
- K. Kawaguchi and S. Ishiwata, *Cell Motil. Cytoskeleton* 49, 41 (2001).
- A. Hoenger, S. Sack, M. Thormählen, A. Marx, J. Müller, H. Gross, and E. Mandelkow, *J. Cell Biol.* 141, 419 (1998).

60. J. Howard, A. J. Hudspeth, and R. D. Vale, *Nature* 342, 154 (1989).
61. A. J. Hunt, F. Gittes, and J. Howard, *Biophys. J.* 67, 766 (1994).
62. A. Hoenger, M. Thormahlen, R. Diaz-Avalos, M. Doerhoefer, K. N. Goldie, J. Muller, and E. Mandelkow, *J. Mol. Biol.* 297, 1087 (2000).
63. Y. H. Song and E. Mandelkow, *Proc. Natl. Acad. Sci. U.S.A.* 90, 1671 (1993).
64. M. Kikkawa, T. Ishikawa, T. Nakata, T. Wakabayashi, and H. Hirokawa, *J. Cell Biol.* 127, 1965 (1994).
65. Y. H. Song, A. Marx, J. Muller, G. Woehlke, M. Schliwa, A. Krebs, A. Hoenger, and E. Mandelkow, *EMBO J.* 20, 6213 (2001).
66. K. Kawaguchi and S. Ishiwata, *Science* 291, 667 (2001).
67. S. A. Endow and D. S. Baker, *Annu. Rev. Physiol.* 65, 161 (2003).
68. W. Hua, J. Chung, and J. Gelles, *Science* 295, 844 (2002).
69. J. Howard, *Annu. Rev. Physiol.* 58, 703 (1996).
70. H. Kojima, E. Muto, H. Higuchi, and T. Yanagida, *Biophys. J.* 73, 2012 (1997).
71. M. Nishiyama, E. Muto, Y. Inoue, T. Yanagida, and H. Higuchi, *Nat. Cell Biol.* 3, 425 (2001).
72. S. M. Block, L. S. Goldstein, and B. J. Schnapp, *Nature* 348, 348 (1990).
73. I. M. Crevel, A. Lockhart, and R. A. Cross, *J. Mol. Biol.* 273, 160 (1997).
74. W. O. Hancock and J. Howard, *J. Cell Biol.* 140, 1395 (1998).
75. F. Kozielski, I. Arnal, and R. H. Wade, *Curr. Biol.* 8, 191 (1998).
76. W. O. Hancock and J. Howard, *Proc. Natl. Acad. Sci. U.S.A.* 96, 13147 (1999).
77. W. R. Schief and J. Howard, *Curr. Opin. Cell Biol.* 13, 19 (2001).
78. K. S. Thorn, J. A. Ubersax, and R. D. Vale, *J. Cell Biol.* 151, 1093 (2000).
79. J. Yajima, M. C. Alonso, R. A. Cross, and Y. Y. Toyoshima, *Curr. Biol.* 12, 301 (2002).
80. D. D. Hackney, *Biochemistry* 41, 4437 (2002).
81. C. Morris, Ed., "Dictionary of Science and Technology." Academic Press, San Diego, 1992.
82. G. Woehlke and M. Schliwa, *Biochim. Biophys. Acta* 1496, 117 (2000).
83. J. T. Finer, A. D. Mehta, and J. A. Spudich, *Biophys. J.* 68, 291S (1995).
84. A. Ishijima, H. Kojima, H. Higuchi, Y. Harada, T. Funatsu, and T. Yanagida, *Biophys. J.* 70, 383 (1996).
85. U. Henningsen and M. Schliwa, *Nature* 389, 93 (1997).
86. R. A. Cross, *Nature* 406, 839 (2000).
87. K. A. Foster, A. T. Mackey, and S. P. Gilbert, *J. Biol. Chem.* 276, 19259 (2001).
88. S. A. Endow, S. J. Kang, L. L. Satterwhite, M. D. Rose, V. P. Skeen, and E. D. Salmon, *EMBO J.* 13, 2708 (1994).
89. Y. Noda, Y. Okada, N. Saito, M. Setou, Y. Xu, Z. Zhang, and N. Hirokawa, *J. Cell Biol.* 155, 77 (2001).
90. R. H. Wade and F. Kozielski, *Nat. Struct. Biol.* 7, 456 (2000).
91. K. W. Hall, D. G. Cole, Y. Yeh, J. M. Scholey, and R. J. Baskin, *Biophys. J.* 68, S71 (1995).
92. K. Svoboda and S. M. Block, *Cell* 77, 773 (1994).
93. I. Crevel, N. Carter, M. Schliwa, and R. Cross, *EMBO J.* 18, 5863 (1999).
94. K. Kawaguchi and S. Ishiwata, *Biochem. Biophys. Res. Commun.* 272, 895 (2000).
95. H. Higuchi and S. A. Endow, *Curr. Opin. Cell Biol.* 14, 50 (2002).
96. H. Tanaka, K. Homma, A. H. Iwane, E. Katayama, R. Ikebe, J. Saito, T. Yanagida, and M. Ikebe, *Nature* 415, 192 (2002).
97. S. Nishikawa, K. Homma, Y. Komori, M. Iwaki, T. Wazawa, A. Hikikoshi Iwane, J. Saito, R. Ikebe, E. Katayama, T. Yanagida, and M. Ikebe, *Biochem. Biophys. Res. Commun.* 290, 311 (2002).
98. S. J. King and T. A. Schroer, *Nat. Cell Biol.* 2, 20 (2000).
99. F. Gittes, B. Mickey, J. Nettleton, and J. Howard, *J. Cell Biol.* 120, 923 (1993).
100. E. Hirakawa, H. Higuchi, and Y. Y. Toyoshima, *Proc. Natl. Acad. Sci. U.S.A.* 97, 2533 (2000).
101. R. D. Vale and R. A. Milligan, *Science* 288, 88 (2000).
102. A. Hoenger, M. Thormahlen, R. Diaz-Avalos, M. Doerhoefer, K. N. Goldie, J. Muller, and E. Mandelkow, *J. Mol. Biol.* 297, 1087 (2000).
103. A. J. Hunt and J. Howard, *Proc. Natl. Acad. Sci. U.S.A.* 90, 11653 (1993).
104. R. Stracke, K. J. Böhm, J. Burgold, H. J. Schacht, and E. Unger, *Nanotechnology* 11, 52 (2000).
105. K. J. Böhm, R. Stracke, P. Mühligh, and E. Unger, *Nanotechnology* 12, 238 (2001).
106. H. Hess and V. Vogel, *J. Biotechnol.* 82, 67 (2001).
107. H. Schmitt, I. Gozes, and U. Z. Littauer, *Brain Res.* 121, 327 (1977).
108. M. L. Shelanski, F. Gaskin, and C. R. Cantor, *Proc. Natl. Acad. Sci. U.S.A.* 70, 765 (1973).
109. K. J. Böhm, W. Vater, P. Steinmetzer, and E. Unger, *Acta Histochem. Suppl.* 39, 365 (1990).
110. W. Vater, K. J. Böhm, and E. Unger, *Acta Histochem. Suppl.* 33, 123 (1986).
111. M. D. Weingarten, A. H. Lockwood, S. Y. Hwo, and M. W. Kirschner, *Proc. Natl. Acad. Sci. U.S.A.* 72, 1858 (1975).
112. C. Shah, C. Z. Xu, J. Vickers, and R. Williams, *Biochemistry* 40, 4844 (2001).
113. J. G. DeLuca, C. N. Newton, R. H. Himes, M. A. Jordan, and L. Wilson, *J. Biol. Chem.* 276, 28014 (2001).
114. G. McCaffrey and R. D. Vale, *EMBO J.* 8, 3229 (1989).
115. S. A. Kuznetsov and V. I. Gelfand, in "Kinesin Protocols" (I. Vernos, Ed.), pp. 1–7. Humana Press, Totawa, NJ, 2001.
116. W. M. Saxton, *Methods Cell Biol.* 44, 279 (1994).
117. F. Navone, J. Niclas, N. Hom-Booher, L. Sparks, H. D. Bernstein, G. McCaffrey, and R. D. Vale, *J. Cell Biol.* 117, 1263 (1992).
118. J. Niclas, F. Navone, N. Hom-Booher, and R. D. Vale, *Neuron* 12, 1059 (1994).
119. A. Kallipolitou, D. Deluca, U. Majdic, S. Lakamper, R. Cross, E. Meyhofer, L. Moroder, M. Schliwa, and G. Woehlke, *EMBO J.* 20, 6226 (2001).
120. A. Lockhart and R. A. Cross, *Biochemistry* 35, 2365 (1996).
121. K. J. Böhm, R. Stracke, W. Vater, and E. Unger, in "Micro- and Nanostructures of Biological Systems" (H.-J. Hein and G. Bischoff, Eds.), p. 153. Shaker-Verlag, Aachen, 2001.
122. Y. Miyamoto, E. Muto, T. Mashimo, A. H. Iwane, I. Yoshiya, and T. Yanagida, *Biophys. J.* 78, 940 (2000).
123. H. Hess, J. Clemmens, D. Qin, J. Howard, and V. Vogel, *Nano Lett.* 1, 235 (2001).
124. D. L. Coy, M. Wagenbach, and J. Howard, *J. Biol. Chem.* 274, 3667 (1999).
125. E. Unger, R. Stracke, J. Beeg, and K. J. Böhm, in "Sensoren im Fokus neuer Anwendungen—Dresdener Beiträge zur Sensorik" (J. P. Baselt and G. Gerlach, Eds.), Vol. 16, p. 45. University of Dresden, 2002.
126. J. C. Wittmann and P. Smith, *Nature* 352, 414 (1991).
127. J. R. Dennis, J. Howard, and V. Vogel, *Nanotechnology* 10, 232 (1999).
128. D. C. Turner, C. Chang, K. Fang, S. L. Brandow, and D. B. Murphy, *Biophys. J.* 69, 2782 (1995).
129. L. Limberis and R. J. Stewart, *Nanotechnology* 11, 47 (2000).
130. H. Hess, J. Clemmens, C. M. Matzke, G. D. Bachand, B. C. Bunker, and V. Vogel, *Appl. Phys. A* 75, 309 (2002).
131. D. Turner, C. Y. Chang, K. Fang, P. Cuomo, and D. Murphy, *Anal. Biochem.* 242, 20 (1996).
132. L. Limberis, J. J. Magda, and R. J. Stewart, *Nano Lett.* 1, 277 (2001).
133. Y. Hiratsuka, T. Tada, K. Oiwa, T. Kanayama, and T. Q. P. Uyeda, *Biophys. J.* 81, 1555 (2001).
134. H. Hess, J. Howard, and V. Vogel, *Nano Lett.* 2, 1113 (2002).





# Kinetics in Nanostructured Materials

V. V. Skorokhod, I. V. Uvarova, A. V. Ragulya

*Institute for Problems of Materials Science, Kiev, Ukraine*

## CONTENTS

1. Classification of Nanostructured Systems
2. Genesis of Nanostructured Systems
3. Surface Relaxation in Nanosized Systems
4. Thermal Stability of Nanostructured Systems

Glossary

References

## 1. CLASSIFICATION OF NANOSTRUCTURED SYSTEMS

Dispersed systems can be represented by the following structure levels:

1. atomic-molecular (0.1–1 nm)
2. macromolecular and cluster (0.5–5 nm)
3. microscopic or grain-heterophased (>5 nm to 1000  $\mu\text{m}$ )
4. macroscopic (>1000  $\mu\text{m}$ )

Nanostructured systems are a special group of physicochemical systems with unique properties determined by the small size of the structural elements composing them. Important physical and practical phenomena can be observed in the transition of structural elements up to the nanoscale. As a whole, nanostructured systems should be viewed as a part of a wider class of dispersed systems. From the viewpoint of physics, they are determined as heterogeneous systems consisting of at least two or more phases with well-developed interfaces; one of the phases is very dispersed, and the medium surrounding it is called a dispersing medium. By aggregate state, it can be gas, liquid, or solid. Depending on this, the system may be flowable or solid. The latter includes a great number of dispersed systems such as minerals, rocks, composite materials, heterophased alloys, organic tissues, and even microorganisms.

In general, dispersed systems are divided into coarsely dispersed and ultrafine ones. In the former the average characteristic size of structural elements is more than  $10^{-6}$  m. The fine systems have structural elements smaller than  $10^{-6}$  m and ultrafine ones smaller than  $10^{-7}$  m. Fine and ultrafine

systems are well known in colloid chemistry as liquid dispersed media, such as emulsions, suspensions, colloidal solutions (sols), and the products of their coagulation (gels). Such systems as sprays, vapors, smoke, and especially solid dispersed structures have not been given enough attention by colloid chemistry. Modern physics pays a lot of attention to solid dispersed structures, especially to physical methods for small-particle structural study, formation of nonequilibrium phases, and so on. Dispersed structures generated by the decomposition of supersaturated solid solutions are studied by physical materials science [1]. Such solid dispersed structures as catalysts and sorbents are studied by classical physical chemistry.

Detachment of nanostructured systems with a particle size of  $10^{-9}$  to  $10^{-7}$  m (1–100 nm) from the ultrafine class has been performed by physicists who have discovered many specific physical properties of such systems in the last 15–20 years. An interest in studies of the systems has grown after the discovery of their new unique properties as construction and functional materials. As a result of this, the central problem in understanding their nature and the possibility of controlling nanostructured material technology is the genesis and evolution of nanosized particle structure. Based on the conception of material structure, it is possible to establish the functional bonds of the chemical composition and technology with structure, on the one hand, and of the structure with the properties of the material, on the other hand. As a whole, technology consists of a number of individual technological processes, each of which influences the structure.

Technological processes are also connected with such kinetic phenomena as heterophase chemical reactions, diffusion and self-diffusion, coagulation and coalescence, sintering, phase transformation, crystallization and recrystallization, and so on.

Thus, physicochemical kinetics of solid heterogeneous nanostructured media is the scientific basis for most technological processes in the preparation of nanostructured materials with optimal structure and optimal physical, physicochemical, and mechanical properties. By investigating kinetic regularities for each physicochemical process, one can forecast all of the stages of the structural evolution from ultrafine powder to sintered nanocrystalline material.

In the study of kinetics, modern physical methods are used to examine fine structure, which is the main distinctive feature of microstructural in comparison with macrostructural physicochemical kinetics.

Dispersed systems, the structural elements of which are grains, phase components, inclusions, and layers with non-coherence interfaces, are the most important for nanoscale materials. In such systems, the structural elements are limited by free surfaces or solid-gas interfaces. First of all, nanostructured systems should be classified by topological parameters. One hundred nanometers is considered to be the upper limit for nanostructured materials [2], but the action of dimension factors is more significant in the range of 10–50 nm.

Some cluster structures, glass amorphous alloys, and nonequilibrium decomposition structures, as well as macromolecules such as fullerene, nanotubes, organic molecules, belong to nanostructured systems, too. Nanostructured objects can be subdivided into three groups in accordance with the shape of their structural elements.

Isolated or weakly bound small particles, thin fibers, and films with nanosizes in one, two, or three directions belong to the first group. The second group contains surface layers of nanoscale thickness connected with a massive base but differing from it in chemical composition and structure. Such layers can be nanostructured, because they consist of nanosized grains. Within the surface layer, the structure can be homogeneous, heterogeneous, periodically laminated, or gradient. Massive nanostructured materials, monophase (micro-uniform) or heterophase (micro-nonuniform) and remaining macro-uniform belong to the third group. Structural elements in these materials have a crystalline texture and nanosizes. In this case the interfaces are called high-angle grain boundaries.

A significant characteristic of nanostructured systems is a level of physical property anisotropy; in other words, their properties have a vectorial nature. Fibrillar and laminar structures are very anisotropic and granular ones are isotropic.

Nanostructured systems can also be distinguished by the character of the reciprocal arrangement of their structural elements. From this point of view, they can be divided into regular and irregular (or stochastic).

Regular structures, as a rule, have elements of symmetry, but there are also aperiodic regular ones [3]. Regular granular structures are characterized by the location of isodiametric particles in the sites of spatial lattice with elements of symmetry. If the structural elements have no spherical symmetry or are characterized by some particle size distribution, the structure, as a whole, reserving regularity has no corresponding elements of symmetry. However, in most cases, such structures can be regarded as regular ones, for example, in the calculation of physical properties. Irregular (stochastic) structures have many peculiarities and can be distinguished from one another.

Fibrillar structures can be regular if the fibers forming them are oriented in space. Such orientation can be in one, two, or three dimensions. Special regular structures result from weaving or netting fibers.

Regular laminar structures are formed by parallel plates with the same or periodically changing thickness. Such struc-

tures are called orthotropic. Their properties change in one direction and are isotropic on surfaces perpendicular to this direction. The orthotropic structures can also be observed in fibrillar systems formed by layers of two-dimensional net or textile. Such structures are intermediate between laminar and fibrillar ones. Nonregular laminar structures can be imagined as textures in which layers are not exactly parallel.

There are many more complicated structures that cannot be described by these simple types, for example, dendrites and similar structures with fractal properties.

Nanostructured surface layers on a massive substrate belong to the second group not having such morphological variety as the objects of the first group. These systems are divided into single-layer and multilayer ones. They can be viewed as nanosized in accordance with such characteristics as the layer thickness and the average size of grain or other structural elements composing the layer. Within the limits of the layer, the structure can be uniform or nonuniform. The layers can be unbroken or broken. There are two types of discontinuity. The first type is porosity where pores are nanosized. Such a structure is typical for relatively thick layers. For very thin layers and films the surface discontinuity is characteristic. In this case, the whole coating is divided into separate sections with the same or different composition. Such a structure of a surface layer or thin film is called a discontinuous film. As a rule, the interface between the surface layer and substrate is noncoherent, but on a monocrystalline substrate, coherent epitaxial layers can be formed.

Multilayer materials have the same structural types as single-layer materials. Structures with many layers with a thickness of 10–100  $\mu\text{m}$  or more should be viewed as belonging to the third group of nanostructured systems, that is, as massive macroscopic homogeneous solids.

There are monophased and multiphased systems in the third nanostructured group. The monophased nanostructures have one critical linear parameter only, namely, the average size of grain or crystallite. Multiphased structures are more complicated. The so-called stochastic systems consist of structural elements with the same geometry and different chemical composition and crystalline structure. The nanoporous structures regard to stochastic. A peculiarity of such systems is the structural identity of all of the phases forming them. They have a main continuous spatial matrix phase and phases of inclusions separated by the matrix. The classification of matrix structures by inclusion topology is similar to that for nanostructured systems given above. The inclusions can be equilibrium (isodiametric) or nonequilibrium (gaunt or flattened out along one axis). The former are called globular; the latter are needle- or scale-shaped. If the inclusions transform into continuous fibers or thin plates, the system loses its matrix character.

The interfaces in mono- and multiphased nanostructures are incoherent except for cluster structures (1–5 nm) with a segregate nature, in other words, they differ from the matrix in chemical composition. Cluster structures are not phases according to thermodynamics. They have no interface between a cluster and matrix; that is, there is continuous transformation of structures into one another at a distance of nearly the cluster size. The systems with cluster structure are well known in physical material science, as many alloys in which the disintegration of metastable solid solutions begins

have such structures. A typical example of a cluster is the well-known Ginye-Preston's zones appearing at the stage of preaging. It is also known that clusters are formed in disintegrating martensite.

### 1.1. Nanosized Powders

The most important feature of nanosized powders, composed of 10–100-nm particles and having very large interfaces, is an excess of free surface energy. The physical properties of solids may be considered constant only in the case if solids have no limited sizes and interfaces. In real solids, the equilibrium and nonequilibrium properties change with a change in external sizes or in the sizes of internal structure elements with interfaces.

The dependence of physical properties of solids on their linear sizes has a fundamental character because the correlation between the number of atoms on the surface and that in the crystal volume, that is, between the surface and volume crystal energies, depends on the sizes and morphology. From a microscopic point of view, the difference in energy of atoms on the surface or in the volume of crystal results from disfunction of coordination for surface atoms and a decrease in the number of neighboring atoms interacting with them. Thus the surface atoms have an excess of free energy. Direct experimental methods for the free surface energy measurement are very complex, but there are many versions of its calculation, based on experimentally determined thermodynamic quantities such as the enthalpy of sublimation or atomization [4].

One of the simplest formulas for calculation of the surface energy in metals and simple covalent compounds is as follows:

$$\sigma_s = \Delta H_s / f N_A^{1/3} V_M^{2/3} \quad (1)$$

where  $\Delta H_s$  is the enthalpy of sublimation,  $V_M$  is the molecular volume,  $N_A$  is Avogadro's number, and  $f$  is an empirical factor depending on the crystal lattice type.

For composites, another formula in which the surface energy is normalized to the enthalpy of atomization ( $\Delta H_{at}$ ) was proposed by Kisly and Kusenkova [4]. The coordination number for a volume of crystal,  $K$ , is determined as the sum of coordination numbers for atom types, the coordination number on the crystal surface with the index (hkl) being taken into account. In this case, the algebraic number of disrupted atomic bonds on the surface is  $n = (1 - K_{(hkl)}/K)$ , and the specific surface energy for a plane (hkl) may be calculated by the formula

$$\sigma_s = \Delta H_{at} n / 4 S_{at} m N_A \quad (2)$$

where  $S_{at}$  is a surface with one atom per plane (hkl) and  $m$  is the number of atoms in a molecule. The surface crystal energy can be calculated by averaging all of the crystal planes.

The two formulas have the same physical meaning, namely, the number of unrealized atomic bonds determines the free surface energy. For monoatomic crystal, formula (2) changes to (1). The specific surface energy depends on the sublimation energy and atomic density. Calculation of the

specific energy for internal interfaces is more complex. It is supposed to be equal to one-third of the specific surface energy. The surface energy in nanostructured systems is a big part of the total energy.

As a result of development of the available methods for nanosized powder preparation, many advanced new materials have appeared. There are two directions in nanosized powder preparation:

1. Physical: the phase transformation of the first type occurs without chemical reactions.
2. Chemical: the phase transformation is accompanied by chemical reactions.

In the first case, different condensation methods, in which a new material forms because of collectivization of molecules or clusters into nuclei of a new phase through a transition state after the achievement of the needed sizes and formation of interfaces, are the most prevailing. The simple breakage of coarsely dispersed particles in high-energy, high-frequency, colloidal, and ultrasonic mills is considered to be a physical method as well.

The breakage of brittle solids by mechanical or acoustic disintegration is one of the prevailing methods for ultrafine powder, suspension, and aerosol preparation. The process of disintegration includes stages of mechanical deformation and relaxation. From the atomic-molecular point of view, there are three main stages of deformation. The first stage is a disorder of structure, the result of which can be amorphization without destruction of the crystal. The second stage is considered to be a type of special mobility appearance caused by weakening of internal tensions (which, in their turn, can be caused by the multiplication and movement of dislocations) and the appearance and growth of cracks. The result of the third stage is structure relaxation connected with the moving and disappearance of defects and aspiration of the system to return to equilibrium.

During chemical transformation, the formation of a new phase can occur in two ways: because of a gradual change in properties and structure throughout the whole volume of the initial solid or because of the formation of small areas with the properties of the final or intermediate products. A strict mathematical approach to the problem is only available for the second case, that is, for the phase transformation of the first type, when a new nucleus is formed in the matrix of the initial phase. The new phase can be solid, gas, or liquid. At the same time, an interface between the new and old phases is formed; the old phase partially disappears. This new interface is responsible for the chemical reaction. For two interacting solids, a solid-phase reaction takes place; for interacting solids with a liquid or gas, a heterogeneous one does.

Reduction of metal from oxide in the presence of catalysts and surface stabilizers and the methods of thermal decomposition, solution chemistry, aqueous electrolysis and electrodeposition, hydrothermal and plasma-chemical synthesis, chemical condensation in gas, laser ablation, fast drying by dispersion, synthesis with the controlled rate of transformation, and combustion synthesis are the best known chemical methods for nanosized powder preparation [4–12]. The condensation methods for nanosized powder preparation are based on the formation of particles at the molecular level

during synthesis. The gas-phase synthesis is submitted to the main physicochemical dependencies of material deposition from a vapor-gas mixture, and the processes of volume condensation take place in the tongue of flame. The method of fast drying by dispersion is based on the dispersion of liquids containing unstable initial phases. The synthesis with the controlled rate of transformation is performed at moderate temperatures and rates of heating. By modeling the back-coupling between the transformation rate and temperature, it is possible to control the size distribution of particles.

The common characteristics of all these methods are a high rate of nucleation and a small rate of nucleus growth. On the basis of taking into account the kinetic competition of different transformation mechanisms activated by thermal treatment, an optimization of all these processes can be achieved by varying the rates of nucleation and nuclei growth. One of the most important characteristics of nano-sized particles formed under very nonequilibrium conditions is a strong interaction with the components of the surrounding medium. As a result, a common shortcoming of chemical methods is the possibility of particle agglomeration and formation of polydisperse assemblies with a wide particle size distribution.

## 1.2. Nanocrystalline Bulk Systems

The thermodynamic nonequilibrium of nanosized powder systems, connected with an excess of the free surface energy, causes relaxation processes leading to an increase in equilibrium degree, that is, to a decrease in the surface area. This demands mass transport, which results in structural changes and system transformation from powder into bulk.

The most physical properties are characterized by extreme behavior at the achievement of a certain critical grain size. Such behavior is called the “size effect” [13]. It is the key point in solving the problem of production, study, and use of nanocrystalline objects [14–20]. However, the physical properties are determined not only by the structural element size, but also by the boundary conditions under which the object exists. R. A. Andrievsky has indicated four principal features of size effect in nanocrystalline bulk systems [20]. The first is the increase in the role of interfacial defects (grain boundaries, triples, etc). The second is the properties of these interfacial defects, which can be different in nanosized and conventional materials. The third is the overlapping of the grain size with characteristic physical length. The fourth is the possibility of a quantum effect revelation. All of these can result in the presence of some specific points in size dependencies and the availability of nonmonotonous change in the properties.

### 1.2.1. Change in the Equilibrium Temperature of Phase Transformation

The temperature of phase transformation to a great extent is determined by the surface energy of a system. The size dependence of the phase transformation temperature is well known, as is that of the formation of disperse phases with small surface energy and more compact packing of atoms. Commonly, an increase in volume free energy due to the formation of a phase with nonequilibrium structure under given

conditions (temperature, pressure) is compensated for by a decrease in the free surface (interface or grain boundary) energy, provided that the corresponding decrease is caused by the phase transformation.

Another fundamental phenomenon connected with small particle sizes is Laplace (or capillary) pressure. It is defined by the surface curvature of a solid and appears to be due to the presence of surface tension. The value of the Laplace pressure is

$$P_L = \sigma_s(1/r_1 + 1/r_2) \quad (3)$$

where  $r_1$  and  $r_2$  are the main radii of curvature. If  $r_1 = r_2 = r$  (spherical surface),  $P_L = 2\sigma_s/r$ . For quasispherical particles the radius of curvature is equal to half their linear size. Thus, small particles are cramped by great Laplace pressure (equal to 150–200 MPa at  $r = 10^{-8}$  m (10 Hm) and  $\sigma_s = 1.5\text{--}2$  kJ/m<sup>2</sup>).

The main fundamental size effect connected with Laplace pressure is a decrease in the crystal lattice parameter  $a$  with decreasing particle radius [21]:

$$\Delta a/a = -2\sigma_s k_T/3r \quad (4)$$

where  $k_T$  is the isothermal compression (equal to  $10^{-11}$  (Pa)<sup>-1</sup> for metals). The interatomic distance can decrease to a critical value at which the phase transformation connected with reconstruction of the crystal lattice occurs. The size effect can result in stabilization of either high-pressure phases (under normal conditions) or high-temperature phases. The latter are very important for many oxide systems with several structural crystal modifications. With rising temperatures, transformation from less symmetric modifications to more symmetric and denser ones takes place. Some data on phase transformation connected with the size effect are given in Table 1 for some oxide systems.

### 1.2.2. Size Dependence of Kinetic and Mechanical Properties

Kinetic properties define the rate or intensity of transfer of heat (heat conduction), mass (diffusion), and charge (electroconduction). The size dependence of the phonon constituent of the heat conductivity in a polycrystalline material results from peculiarities of the phonon behavior in solids, which have inner edges able to dissipate phonons.

**Table 1.** Size dependence of phase transformation in oxide systems.

Material	Phase transformation	Structure state	Critical size (nm)
ZrO <sub>2</sub>	M–T	Powder	>30
	T–C	Powder	20
BaTiO <sub>3</sub>	T–C	Powder	100–120
		Ceramics	40–50
PbTiO <sub>3</sub>	T–C	Powder	90–100
		Ceramics	8–12
Y <sub>2</sub> O <sub>3</sub> (R <sub>2</sub> O <sub>3</sub> )	O–C	Powder	8–10

Note: Structures: M, monocline; T, tetragonal; C, cubic; O, orthorhombic  
Source: Reprinted with permission from [4], V. V. Skorokhod et al., “Physicochemical Kinetics in Nanostructured Systems.” *Academperiodica*, Kiev, 2001 (in Ukrainian). © 2001, *Academperiodica*.

In nanocrystalline materials, the length of the free phonon run is defined by grain size. The possibility of further lowering the heat conductivity for low-heat-conducting materials is of great practical importance. It has been theoretically proved that there is a possibility of decreasing the heat conductivity of  $ZrO_2$  (having a very low heat conductivity and used as a thermo-barrier material on freezing blades) by 2–3 times with decreasing grain size to 20–30 nm, whereas the durability, heat resistance, fracture toughness, and adhesion between  $ZrO_2$ -based coating and substrate improve. The possibility of the structural regulation of heat kinetic properties is of great scientific importance.

The diffusion coefficients of nanostructured materials, as a rule, are several orders of magnitude greater than those of monocrystalline or conventional ones because of the special role of grain boundaries. A decrease in grain size increases the concentration of boundaries, for which the diffusion coefficient is bigger and the activation energy is 2–2.5 times lower [21, 22]. The self-diffusion parameters for nanosized and conventional copper and nickel are listed in Table 2.

A common empirical regularity of the grain structure influence on the mechanical properties of different materials is an increase in their hardness with decreasing grain size. In most cases, the durability increases, too, although it depends on cohesion on the grain boundary. This regularity is based on the well-known Petch-Xoll equation, according to which the stress of plastic deformation for a multicrystal is inversely proportional to the square root of the grain size. However, the hardness for many materials has an extreme size dependence, which is mostly observed for hard materials. The maximum hardness in these cases is due to the formation of structure with a grain size of some nanometers.

### 1.3. Thin and Multilayer Films

The burst of research in modern industry has become possible thanks to the development of new superhard, super-strong, heat- and wear-resistant bulk materials, especially coatings. The advancement of coating properties, particularly hardness, abrasion and corrosion resistance, and a decrease in size of some details due to coating and film deposition, has become a reality as grain has been brought into the nanorange. The appearance of new methods for

nanostructured coating and film deposition and improvement of available ones have changed, in a number of cases, the rules for using them. Among the well-known physical and chemical methods, such as thermal evaporation, chemical vapor deposition, thermal decomposition of precursors, nitration and aquation are prevalent. Different types of surface modification, deposition of new material particles, implantation of atoms and defects, and different types of interaction take place under the influence of irradiation, depending on beam type and energy. Peculiarities of coating use determine the choice of method. By controlling the process of deposition one can change the microstructure and produce mono- or multicrystals or amorphous films and coatings. [23].

Vapor atoms on the substrate surface have an energy higher than  $\kappa T$ . The rate of evaporation,  $N_e$ , can be estimated by Lengmur's equation,

$$N_e = 3513 \cdot 10^{22} p_e \sqrt{1/MT} \quad (5)$$

where  $p_e$  is the pressure,  $T$  is the temperature, and  $M$  is the molecular mass.

In spite of the fact that the molecules (atoms) move very fast, they are not transmitted at large distances, because of frequent collisions with the other gas atoms or molecules. The free path for the molecules (atoms) of gas is inversely proportional to the gas pressure:

$$\lambda = \frac{V}{N} \cdot \frac{1}{\pi d^2 \sqrt{2}} = \frac{kT}{p_e \pi d^2 \sqrt{2}} \quad (6)$$

where  $d$  is the molecular diameter and  $p_e$  is the pressure. The gas atoms gravitate toward the surface, forming doublets and quadrupoles and losing the rate of displacement.

The level of thermal equilibrium is described by the coefficient of thermal accommodation,  $\alpha_T$ :

$$\alpha_T = \frac{E_v - E_r}{E_v - E_s} = \frac{T_v - T_r}{T_v - T_s} \quad (7)$$

where  $E_v$  is the energy of vapor atoms,  $E_r$  is the energy of desorbed atoms at equilibrium with substrate,  $E_s$  is the surface energy, and  $T_v$ ,  $T_r$ , and  $T_s$  are the corresponding temperatures.

**Table 2.** The self-diffusion parameters for nanosized and conventional copper and nickel.

Object	Porosity (%)	Method	Activation energy (kJ/mol)	Self-diffusion coefficient $D_0$ (m <sup>2</sup> /c)	$D$ at 393 K, (m <sup>2</sup> /c)
Nano-Cu	20	NMR	66.5	$3 \cdot 10^{-9}$	$1.8 \cdot 10^{-17}$
Nano -Cu	20	Isotopic	61.7	$2 \cdot 10^{-5}$	$1.3 \cdot 10^{-31}$
Cu (volume)		Isotopic	197		
Cu (boundary)		Isotopic	104	$1 \cdot 10^{-5}$	$1.7 \cdot 10^{-19}$
Cu (surface)			66.5	$1 \cdot 10^{-7}$	$1.4 \cdot 10^{-16}$
Nano -Ni	7–8	Isotopic	50.7	$1.2 \cdot 10^{-3}$	$1.9 \cdot 10^{-10}$
Ni (volume)		Isotopic	275	0.48	$3.5 \cdot 10^{-37}$
Ni (boundary)		Isotopic	115		$3 \cdot 10^{-12}$
Ni (surface)			75		

Source: Reprinted with permission from [4], V. V. Skorokhod et al., "Physicochemical Kinetics in Nanostructured Systems." *Academperiodica*, Kiev, 2001 (in Ukrainian). © 2001, *Academperiodica*.

The use of different methods for deposition and different substrate types makes it possible to prepare different structures: discontinuous and multilayer films and columnar structures. Today multilayer structures and combinations of thin films and coatings are of great interest.

Chemical methods for thin-layer and coating deposition can be discussed on the basis of the laws of electrolysis. The mass of deposit on the unit surface,  $G/S$ , is equal to

$$G/S = JtE\alpha \quad (8)$$

where  $J$  is the current density,  $t$  is the time,  $E$  is the electrochemical equivalent, and  $\alpha$  is the current index (experimental/theoretical ratio equal to 0.5–1). The process of chemical deposition permits one to prepare deposits of metals, semiconductors, and insulators. Thin films and coatings prepared by physical or chemical vapor deposition ensure a high level of functional properties when used in optics, electronics, chemistry, and so on [24, 25].

The best properties were revealed with the transition to nanoscale multilayer coatings such as TiN-TiCN, TiN-TiC, TiN(TiC), Al<sub>2</sub>O<sub>3</sub>, and so on. Ten years ago the thickness of each layer in multilayer coating was  $\approx 0.5 \mu\text{m}$ , and the whole thickness was  $\approx 5\text{--}10 \mu\text{m}$ . In recent years, a new class of multilayer coatings deposited by magnetron scattering, with a smaller thickness (2–10 nm) and a hardness of  $>5000 \text{ kg/mm}^2$ , has appeared [26]. This hardness is not far from those of cubic boron nitride and diamond. The diffusion of dislocation is less possible in multilayer coatings than in composite ones. It is possible to prepare multilayer coatings with different shear moduli and a shear fracture close to the theoretical one.

Nanocomposite coatings are also very important for use as thermal barrier coatings [27–30]. Such coatings, in addition to their good mechanical properties, possess high-thermal and high-temperature corrosion and wear resistance. The possible creation of gradient structures in surface layers shows great promise.

In addition to the old methods for composite coating deposition with nanosized fillers, some new directions, particularly the deposition of nanocomposite electrolytic coatings under the action of pulsatile current, should be mentioned [31]. With the use of direct current, coatings with disperse fillers in the matrix structure were produced [32]. With the use of pulsatile current, composite electrolytic coatings with 30-nm Ni particles (matrix) and 80-nm filler particles were prepared [31]. Subsequent thermal, chemical thermal, and laser treatments can change the properties of the coatings prepared.

## 2. GENESIS OF NANOSTRUCTURED SYSTEMS

### 2.1. Homogeneous and Heterogeneous Systems

Homogeneous systems are physicochemical systems with one phase. They have no interfaces, in which the contiguous parts of systems usually have different compositions and properties. The constituent parts cannot be divided mechanically. Chemical components of homogeneous systems are

distributed as molecules, atoms, or ions. The best examples of homogeneous systems are ice, liquid, or solid alloys; gas mixture; water vapor; and so on. Homogeneous systems can be physically uniform or nonuniform. The composition and properties of uniform systems are the same in their different parts, whereas in nonuniform systems they can differ in different places in the system but change continuously. For example, gas is a uniform system in the absence of gravity, but under the action of gravity it has a different density in the upper substratum of the atmosphere. Aqueous solutions are chemically nonuniform systems.

Heterogeneous physicochemical systems consist of two or more phases and have interfaces between uniform parts with different compositions and properties. These parts can be separated. Colloidal systems with particles with a size between a molecule and particles of heterogeneous systems occupy an intermediate position.

Homogeneous reactions proceed in the volume of phase, while heterogeneous ones proceed on the interfaces. The reaction rate is determined by the number of chemical events taking place per unit time in a unit volume (for homogeneous reactions) or per unit interface (for heterogeneous reactions) and depends on the material composition, temperature, and other parameters, such as the electrode potential in electrochemical reactions, the light intensity in photochemical reactions, and the dosage rate in radiochemical reactions. The reactions can be one-stage or multistaged and have intermediate products.

To establish a reaction mechanism, the experimental kinetic data are compared with theoretical equations based on definite suppositions about the mechanism [33]. Practically a single method of representation for phenomena, taking place in the theory of change, is a method of mathematical modeling that includes differential equations and dimensioned correlation [34].

In the ideal gas mixture or ideal liquid solution, the reaction rates obey the law of active masses; that is, the evidence of collisions of molecules of the initial material is the first and necessary demand. A peculiarity of heterogeneous reactions is the processes of transportation of initial reaction components out of volume to interfaces and of the products in the opposite direction. The influence of the transportation processes on the reaction rate is not constant, and changes depend on many factors, including the temperature and pressure. Under slowed diffusion in the pores of a solid, the reaction with a noticeable rate occurs only on the outer surfaces or in layers bordering them. In this case, the reaction is said to take place in the internal diffusion regime. In the external diffusion regime, the reaction rate is determined by the mass transport to the outer surface of a solid reacting with a gas or liquid. With large enough diffusion rates, the reaction occurs in the kinetic region.

In chemical transformation, the formation of a new phase can be realized in two ways [4]:

- owing to a gradual change in the properties and structure of the whole volume of the initial solid;
- owing to the formation of regions (nuclei) with a small size and to the properties of the final or intermediate products.

Exact mathematical calculations are possible only in the second case, that is, for the phase transformation of the first



type, when the nucleus of a solid forms in the initial solid matrix. The new phase of chemical reaction may be a solid, gas, or liquid. The solid-phase reaction takes place in the interaction between two or more solids; heterogeneous reactions are determined by the interaction of a solid with a gas or liquid.

The main demand for nanosized powder preparation in heterogeneous reactions is a high rate of nucleation and a small rate of nuclei growth. At the high rates of chemical reactions occurring at very high temperatures or at low ones in the presence of catalyst, fast condensation and hardening are favorable for the formation of a nonequilibrium state of particles at their growth. One of the important characteristics of nanosized particles formed under highly nonequilibrium conditions is their intense interaction with the components of the medium in which they are formed. The probability of consolidation, coagulation, and coalescence is very significant, even in the case of inert media. Thus, the common deficiency of all chemical methods is the formation of polydisperse aggregates with a wide particle size distribution.

## 2.2. Topochemical Reactions

Solid and heterogeneous reactions occurring with a change of phase composition in the places of contact between two or more solids or on the surface of a solid in contact with a gas or liquid are called topochemical reactions. The reactions accompanied by partial or total transfer of one or more solid reaction components in a gas or liquid cannot be viewed as topochemical reactions. A place where a topochemical reaction can occur is the surface between phases (interface).

Most heterogeneous and solid reactions can be referred to as topochemical or gas-transport reactions, depending on temperature. For example, some reactions of metal reduction from oxide are topochemical at low temperatures. They begin with the adsorption of gas (reducing agent) on the oxide surface, and, by following the interaction with it, but at higher temperatures, one can observe a partial outlet of solid reagent in gas and the interaction of the components in gas following the transfer of the reaction product to the solid surface. The latter case is a gas-transport reaction.

The gas-transport reaction is a more complicated process, the first stage of which is heterogeneous nucleation on the solid surface, and the following one is the partial transfer of the initial phase or intermediate products to gas. Such reaction products as water vapor (in reduction by hydrogen) and carbon oxide (in reduction by carbon) can initiate a transfer of solid products to gas, and these reactions mostly occur near equilibrium. Gas-transport reactions can be avoided with the use of low temperatures.

The interface ( $S$ ) in solid and heterogeneous reactions is the sum of zones formed by all of the reacting nuclei, which appear by the time  $t$ :

$$S = \int_0^t \varphi(t, y) \left[ \frac{dN}{dt} \right]_{t=y} dy \quad (9)$$

where  $\varphi(t, y)$  is the function describing the size of the reaction zone by the time  $t$  for nuclei appearing at the moment  $y$ , and  $dN/dt$  is the change in nuclei number by the time  $t$ .

Beginning at some definite moment, the growing nuclei join one another and the reaction zone begins to decrease after the maximum size is achieved. The rate of solid or heterogeneous reaction for this stage is expressed by the equation for the shrinking reaction zone. For example, if a reaction zone of a spherical shape is formed, the rate of the process is described by the equation of the reducing zone [33]:

$$1 - \sqrt[3]{1 - \alpha} = kt \quad (10)$$

where  $\alpha$  is the degree of transformation.

The dependence of fractional conversion on time is plotted with an  $S$  curve, and the dependence of the reaction rate on fractional conversion has a maximum. A peculiarity of such reactions is evidence of an incubation period and self-catalysis. At the same time, not each reacting substance but only part of them in contact with the initial phase undergoes the self-catalyzed action. In other words, the catalytic action of the reaction product on a unit surface of the reaction zone remains constant during the whole process, provided the product state does not change during the reaction.

It has been assumed [35] that when simultaneous multiple nucleation develops at the nanometer scale, each nucleation event is confined in a supply region of radius  $R$  from which the embryo can be fed up to its critical size. The amount of atoms  $A$  in this region must be significantly larger than the number of atoms  $N^*$  in the critical nucleus. Otherwise the region would be much too depleted, giving an important increase in the barrier of nucleation able to suppress the transformation. The condition to be fulfilled for nucleation to occur is

$$R \gg \left( \frac{X_1 v_1}{X_0 v} \right)^{1/3} r^* \quad (11)$$

where  $r^*$  is the critical radius of nuclei. Taking  $r^* = 10^{-9}$  m,  $X_0 = 0.2$ , and  $v/v_1 \sim 1$ ,  $X_1 = 0.7$ , one obtains for the radius  $R$  of the supply region  $R \gg 1.5$  nm. When  $R < 1.5$  nm, nucleation is absolutely impossible. It appears that even when  $R$  is on the order of 5 nm, the nucleation barrier will be substantially larger than in the case of infinite matrix.

Dispersion of products in topochemical reduction reactions occurs because of;

1. Formation of porous agglomerates taking the form of the initial reagent particles due to the large difference between oxide and metal volumes.
2. Disintegration of matrix oxide into small particles in the absence of coherence between oxide and metal or intermediate phase.
3. Disintegration of surface layers, bursting and peeling.

In the first case, dispersion is determined by the size of some structural elements (dendrites) formed on the base of the matrix phase. In the second case, the size of particles is connected with the number of nuclei on the unit of surface or volume. In the third case, dispersion results from the high intensity of destruction of the crystal matrix, which stimulates movement of the reaction front.

### 2.3. Kinetics of Nucleation and Nucleus Growth

The main characteristic determining the size of growing nuclei is the correlation between the rates of nucleation and nuclei growth, which, in its turn, depends on the correlation between the activation energy of these processes and the number of active centers on the crystal surface. Significant characteristics are also anisotropy of crystal growth, reproduction of reaction nuclei at their development, change in surface spots where nuclei can be formed, diffusion through product layers, and so on.

The comparison of experimental kinetic data with theoretical curves describing various mechanisms of topochemical (solid and heterogeneous) reactions may help to approximate the reaction mechanism, but for its final determination a direct observation of the rates of nucleation and nuclei growth, a study of product state change during nuclei growth, and so on should be carried out. From the point of view of formal kinetics, the processes of nucleation on a surface and in a volume can be described by the same laws. In the first case, the examination is carried out in a two-dimensional area, in the second case in three-dimensional one [33]. In a description of the new phase appearance, the spatial characteristics of the forming nuclei, such as isotropy or anisotropy in both the matrix phase and nucleus, should be taken into account.

The appearance of new phase nuclei in a metastable system results in the transition of substance in a thermodynamically stable state. In a homogeneous nucleation in a metastable phase, homogeneous spontaneous formation of ensembles of different compositions from the atoms of the matrix phase occurs because of atom association. At the same time, the metastable phase is in a quasi-equilibrium state: the rate of formation of spontaneous growing associates of supercritical sizes is small, and the equilibrium statistic size distribution of the associates is not broken and almost does not change with time up to the critical size.

For topochemical (solid and heterogeneous) reactions such explicit description is not available, although nuclei of a new phase have been investigated experimentally in many chemical reactions [36–37]. Simultaneously with the new phase formation, the interface between new and old phases is formed, the surface of the old phase partially disappears, and in its place a new surface between the new phase and gas appears. For the new surface formation, some work is expended. It can be described by the following equation [36]:

$$A = \sigma S = \sigma b r^2 \quad (12)$$

where  $\sigma$  is the surface energy,  $S$  is the surface area,  $b$  is a constant depending on the nucleus shape, and  $r$  is the characteristic nucleus size.

The work expended on the new surface formation emerges as a free energy of formation ( $\Delta q_f$ ) at the transition to a thermodynamically stable state. This energy is proportional to the specific free transition energy  $q$  and nucleus volume  $V$  (or characteristic size),

$$\Delta q_f = qV = qbr^3 \quad (13)$$

By summarizing these equations, one can determine some critical size  $r_c$ ; for the lower range of  $r_c$  the energy expended on the new surface formation exceeds the free formation energy, and for the higher range of  $r_c$  an inverse relationship is observed. Thus, to form a molecular cluster or heterogeneous fluctuation exceeding the critical size  $r_c$ , an incubation period is needed. Its presence explains the possibility of overheating liquid to temperatures higher than the boiling temperature and the absence of crystallization from a supersaturated solution. At the same time, the reaction rate in a liquid or gas is proportional to the concentrations of reacting substances [37]:

$$dn/dt = K(n_a, n_b, \dots) \quad (14)$$

and in heterogeneous systems it also depends on the surface on which the reaction occurs:

$$dn/dt = K(n_a, n_b, \dots)qS \quad (15)$$

A chemical reaction can occur because of the collision of particles of different chemical natures, but not every collision results in an interaction. The probability of chemical interaction leading to new compound formation is determined by the availability of a resource of energy that is enough to overcome the potential barrier. A specificity of solid and heterogeneous reactions is their dependence not only on chemical and phase composition, but also on the state of the crystal lattice in a solid and the presence of different defects.

The normal and active states of a solid are known. A solid in the normal state is defective only because of its lattice disorder. The active state is a result of the presence of nonequilibrium defects influencing the differently reactive abilities of solids. To operate the activity of solids in concrete processes, it is necessary to know their nonequilibrium structure. This permits one to create definite defects initiating the chosen chemical reactions. The influence of defects in crystals on their reactive ability has been studied by many researchers, and now ways to realize many physicochemical processes are known.

Crystal defects are of importance not only for the acceleration of the initial stage in topochemical reactions, but also for the formation of the new phase structure. The activity of a solid can be increased in reactions accompanied by a change in volume due to the strained state at the nucleus-matrix boundary.

In heterogeneous reactions, adsorption of gas or liquid takes place on the most defective places of a solid. It can be accompanied by solution of the adsorbed reaction component in the lattice. In this case, the theory of oversaturated solution can be used. The X-ray and electron-microscopical investigations of oversaturated solid solution showed the possibility of Ginye-Preston zone formation. These zones are the smallest segregation of composition formed as a result of atom redistribution in the crystal lattice of a homogeneous solid solution. After the achievement of a definite level of oversaturation, the Ginye-Preston zones are replaced by stable or intermediate metastable phases; that is, the nucleus of a new phase appears.

The phase transformations are the result of chemical reactions also in the case when the rate of phase transformation

limits the appearance of an intermediate layer, which divides the area of chemical and phase transformation in space and time.

The problem of nucleus size and shape control is the least decisive in the investigation of phase transformation. If the deformation energy in the two-dimensionally growing nucleus prevails, a new phase aspires to follow the shape of the matrix solid phase. According to Boldurev's supposition [36] the nucleus shape can be connected with the values of two components surrounding the nucleus. They are  $K_s$  (the component of deformation depending on interfacial energy) and  $K_v$  (the component of deformation resulting in a change of volume during conversation). If  $K_s$  is large, the nucleus tries to form a shape with the minimum ratio of surface to volume. For an isotropic medium the spherical shape is characteristic. If  $K_v$  is big, the nucleus is flat and elongated along the surface. The combination of these factors results in a variety of nucleus shapes.

The most direct mathematical calculation can be made in the case where all of the nuclei appear simultaneously and have a spherical shape. Then the rates of their appearance, growth, and interarrangement should be taken into account, and the shape of product particles, their sizes, and some physicochemical properties connected with dispersion composition of powder material can be established.

Delmon [33] accomplished these tasks on the basis of the following hypotheses of the kinetic theory:

1. Samples consist of particles of the same shape.
2. Nucleation occurs with the same probability or the potential nuclei take part in the process.
3. Nuclei are distributed along the surface in such a way that the probability that each of them will stay at any point is the same.
4. Nucleus growth is isotropic; that is, it proceeds with the same rate in different directions, and the rate of growth does not change with time.

These hypotheses are the simplest and can be taken into consideration for real conditions only approximately.

The crystal structure and the presence of defects influence the nucleation rate. By increasing the number of potential nuclei or using catalytic additions, surfactant admixtures, and promoters, one can change the nucleation rate. The reaction products and the appearance of tension round the nucleus due to the difference between the volumes of matrix and product phases can also influence the nuclei growth rate. As a result, dislocations are formed and the reaction on them proceeds with a higher rate.

## 2.4. Genesis of Bulk Nanostructured Materials

The genesis of nanostructure is the key feature in the preparation of nanocrystalline materials with powder methods. The structure of particles is connected with synthesis conditions: the density of defects, such as twins, domains, stacking faults, core and shells, as well as particle aggregates and agglomerates, depends on process parameters. All of this defines the behavior of powder during consolidation and affects the structure of a monolithic sample. Such heredity was known for coarse particles and micrometer-grained bulk

materials [38]. Refining particles and grains to the nanoscale leads to the escalation of a material's structural sensitivity. Today we can make powders of the same particle size distribution and shape; however, different techniques for synthesis commonly result in different defect structures and, therefore, in different sintering behaviors and properties of sintered bodies. The most important achievement of today's techniques for synthesis and consolidation of nanoparticles is flexible control over properties [4].

Thermodynamic nonequilibrium of nanosized systems connected with a high excess of free surface energy leads to relaxation processes increasing the equilibrium extent, that is, decreasing the surface area. It can be possible only because of mass transport, which can appear only during thermal activation accompanied by increasing atomic mobility. The transport processes cause structural changes, which result in the evolution of the system from nanosized to nanostructured monolithic materials. The kinetics of transport processes has a physicochemical nature, as it depends on the chemical nature of materials of which the system consists, the state of the particle surface, the chemical activity of the gas phase, and so on. Chemical reactions occurring simultaneously in multicomponent disperse systems influence the rate and character of mass transport to a great extent.

A disperse system is characterized not only by a big free surface area, but also by its curvature, resulting in Laplace pressure. This pressure influences the equilibrium conditions along the boundary between two phases divided by a curved surface. The surface curvature of each disperse phase is equal to  $L = 2r_c$ , where  $r_c$  is the equivalent particle radius. The conditions of equilibrium of two phases divided by a curved surface were shown to correspond to local equilibrium near the surface, but the system as a whole remains in nonequilibrium because of the excess of free energy.

## 2.5. Genesis of Thin and Multilayer Films

Today, many different coating techniques for depositing thin and thick films are known. The genesis of thin and multilayer films is determined by the method chosen for deposition, materials used for films and coatings, diffusion processes, and so on. For example, in using the diffusion method for film and coating deposition, one should take into account the energetic state of gas as contributing to diffusing component transfer on the surface of the material under saturation, phenomena on the material boundary, and diffusion of chemisorbed elements into the material. The main physicochemical parameters determining the genesis of films and coatings are the same as in topochemical heterogeneous reactions.

Electrophoresis is a method for coating deposition from a highly dispersive suspension when the rate of sedimentation is lower than that of electrophoresis. The latter for each particle is  $V = f(\xi\varepsilon_1 E/\pi\eta)$ , that is, it is determined by the coefficient of particle form ( $f$ ), electrochemical potential ( $\xi$ ), medium permittivity ( $\varepsilon_1$ ), intensity of the electric field ( $E$ ), and the viscosity of the dispersive medium ( $\eta$ ). The genesis of such films and coatings is determined by the conditions of electrophoresis and the chemical nature and dispersion of deposited powder particles.

Vapor deposition of thin and thick films is defined by hydrodynamics, heat and mass transport. Here the elementary chemical reactions occurring on the surfaces do not differ from those on individual particles. The rate of product formation is proportional to the reaction rate per unit surface ( $w'$ ) and the size of active place ( $s$ ):

$$w = w's \quad (16)$$

With small reagent concentrations, the reaction rate is determined by a diffusion process.

Thus, the presence of essential deviation from the equilibrium conditions of crystallization and repression of heat-activated processes of structural and phase transformations at a solid-phase stage play the determining role in nanostructured state formation. The formation of new metastable phases (absent in the equilibrium diagrams), ultrafine dendrite or globular microstructures, and amorphization of crystal materials are the result of nanostructured thin and thick film deposition.

### 3. SURFACE RELAXATION IN NANOSIZED SYSTEMS

The technology of small particles is close to that of conventional powder materials; however, for nanosized particles, the effect of disperse system evolution on the transition of ensembles of free particles into a monolithic nanostructured material already becomes apparent at the stage of small particle formation, when the van der Waals interaction forces between particles are substantial enough to result in adhesion of particles and a decrease in the density of packing. Such a spontaneous aggregation of small particles plays an important role in the formation of mesostructure within the green body.

Heating of the ensemble of small particles leads not only to the fast growth of interparticle necks, but also to coagulation and coalescence processes in a nanosized system, which can decisively affect densification kinetics and structure evolution under high-temperature sintering.

The final high-temperature sintering stage, following the intermediate stage, has many specific features. Among them there is a distinct tendency toward local (differential) shrinkage and formation of large pores. In this case the heredity of mesostructure formed at the first technological stage develops. With the high density of a nanostructured body, an abrupt dependence of mean grain size on both the absolute residual porosity and geometry and topology of pores is observed at this stage.

#### 3.1. Coalescence and Coagulation of Nanosized Particles

When heated, the green body compacted from nanosized particles tends to undergo relaxation processes, which substantially reduce the free surface energy of particles and proceed without marked variation in the density of the system as a whole. These processes are thermally activated and can proceed at temperatures sufficient for surface and grain boundary diffusion [38]. The surface area relaxation

begins with the formation of contact necks and their subsequent growth. German proposed the use of the surface area decrease as a measure for characterizing the particulate system at the initial stage of sintering [39]. Let us consider several of the simplest relations defining the reduction of the surface area in the system of identical spherical particles due to the formation and growth of interparticle necks.

The specific surface area in such a system is equal to

$$S_v = \frac{4\pi R^2}{4/3\pi R^3} = \frac{3}{R} \left[ \frac{\text{cm}^2}{\text{cm}^3} \right] \quad (17)$$

where  $R$  is the radius of a particle.

Formation of interparticle contacts of radius  $R$  results in a specific surface area decrease:

$$S_v^{(x)} = S_v^0 \left( 1 - \frac{n_c x^2}{8 R^2} \right) \quad (18)$$

where  $n_c$  is the average coordination number for a given packing of particles and  $x$  is the neck radius. For regular and dense packing  $n_c = 12$ . In real porous structures, however,  $n_c$  can be arbitrary but less than 12, depending on relative density. For very loose packing  $n_c = 3 \div 4$ . Taking into consideration the fact that the maximum value of relative neck size,  $x/R$ , is close to 0.7 (spherical particles in dense packing transform into polyhedrons and loose, chainlike structures, and chains of particles transform into cylindrical fibers), one can estimate the maximum value of relative decrease in the specific surface area due to growth of the necks.

In accordance with formula (3.2), for the densest packing ( $n_c = 12$ )  $\Delta S_v^{\text{max}}/S_v^{(0)} = 0.74$ , and for very loose packing ( $n_c = 3$ )  $\Delta S_v^{\text{max}}/S_v^{(0)} = 0, 2$ . The kinetics of the neck radius growth is defined by the well-known relation

$$\left( \frac{x}{R} \right)^n = Mt \quad (19)$$

where  $n = 7$  for surface diffusion and the kinetic constant  $M$  is inversely proportional to  $R^4$ :

$$M \approx \frac{100 D_s \sigma \Omega \delta}{kTR^4} \quad (20)$$

where  $D_s$  is the coefficient of surface diffusion,  $\sigma$  is the surface tension, and  $\Omega$  and  $\delta$  are the atomic volume and size, respectively. Taking into consideration relations (19) and (20), the kinetics of surface area decrease follows the relation

$$\left[ \frac{\Delta S_v}{S_v^{(0)}} \right]^\gamma = M_1 t \quad (21)$$

where  $\gamma = n/2 = 3 \div 3.5$  and  $M_1 = M(n_c/8)^\gamma$ .

Elaborated in [39], the analysis of experimental data required for calculation of the specific surface area reduction during isothermal firing of ultrafine oxide systems in oxidizing media shows the validity of Eq. (21) in many cases. However, a substantial number of experiments do not correlate with this simple theory: the exponent is very often higher than 3.5 (4 and higher), and the general surface area decrease greatly exceeds the one estimated above for loose packing ( $\Delta S_v^{\text{max}}/S_v^0 \approx 0.2$ ).

Such deviations originate from particle coarsening due to coalescence and coagulation. To describe the kinetics of surface diffusion controlling coalescence in the system with small adjacent particles, the author [40] proposed the following relation:

$$R^4 = R_0^4(1 + Bt) \quad (22)$$

where  $B$  is the kinetic constant, which is close to  $1/3 M$  in Eq. (19).

It was assumed that the initial particle size distribution following the formula

$$\chi_0 = \frac{R_0^{\max} - R_0^{\min}}{\bar{R}_0} \quad (23)$$

is rather wide (about 1). Equation (22) is in good correlation with many experimental data obtained for oxide and metallic powders [39]. It follows from this that  $\gamma$  can be equal to 4 in Eq. (21).

If the initial particle size distribution is narrow ( $\chi_0 \ll 1$ ), the kinetics of coalescence substantially changes. If a particle size distribution is taken into account, the mathematic solution of this task becomes much more complicated. The general case gives

$$\begin{aligned} & \frac{1}{4} \left[ \left( \frac{R}{R_0} \right)^4 - 1 \right] + \frac{1}{3} (1 - \chi_0) \left[ \left( \frac{R}{R_0} \right)^3 - 1 \right] \\ & + \frac{1}{2} (1 - \chi_0)^2 \left[ \left( \frac{R}{R_0} \right)^2 - 1 \right] + (1 - \chi_0)^3 \left[ \left( \frac{R}{R_0} \right) - 1 \right] \\ & + (1 - \chi_0)^4 \ln \left( \frac{R/R_0 + \chi_0}{\chi_0} \right) = \frac{B}{4} t \end{aligned} \quad (24)$$

When  $\chi_0$  is small, the logarithmic addend predominates and the kinetics of mean particle size growth can be described by an S-type curve at the early stages of the process (curve 2 in Fig. 1). As the coalescence is in progress and  $\chi$  increases, the curve 2 tends to curve 1, corresponding to Eq. (25), which is a particular case derived from (24) at  $\chi_0 = 1$ . Thus, in a monodisperse system, the initial stage of coalescence has a character similar to that of chemical reactions with an explicit incubation period [40]:

$$R_m^4 = R_0^4 + B_1 \sigma_s D_s \Omega \delta t / kT \quad (25)$$

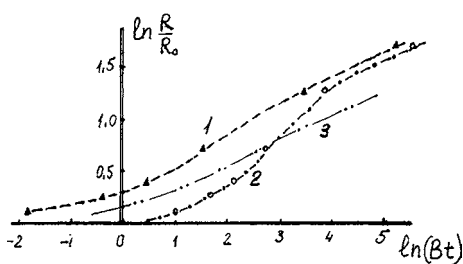


**Figure 1.** The coalescence kinetics for different values of the  $\chi_0$  parameter. 1,  $0.5 < \chi_0 < 1$ ; 2,  $\chi_0 \ll 1$  ( $\sim 0.01$ ); 3, kinetics of coagulation ( $B_1 \ll B$ ). Reprinted with permission from [4], V. V. Skorokhod et al., "Physicochemical Kinetics in Nanostructured Systems." Academperiodica, Kiev, 2001 (in Ukrainian). © 2001, Academperiodica.

where  $B_1$  is a numeral factor near 2 and  $D_s$  is a coefficient of surface self-diffusion.

The coalescence in the particulate system does not mean any mobility of particles, and mass transfer proceeds only through the diffusion mechanism.

In colloidal systems, coarsening of particles and, accordingly, a decrease in their surface area may occur through coagulation. This mechanism assumes substantial mobility of particles in the surrounding medium, their collisions, and further formation of agglomerates, which gradually transform into coarser particles.

The classic equation of kinetic coagulation can be written here:

$$\frac{dN}{dt} = -KN^2 \quad (26)$$

where  $N$  is the number of particles per unit volume and  $K$  is the kinetic constant of coagulation. If particle motion follows the Brawn law, then

$$K = \frac{4 kT}{3 \eta} \quad (27)$$

where  $\eta$  is the viscosity of a system,  $k$  is Boltzmann's constant,  $T$  is the absolute temperature. Integration results in hyperbolic dependence of  $N$  on  $t$ :

$$N = N_0(1 + KN_0t)^{-1} \quad (28)$$

and the mean particle radius  $R$  increases with time as a cubic parabola:

$$\bar{R}^3 = \bar{R}_0^3 + K_1 t \quad (29)$$

where the new constant  $K_1$  is proportional to the volume concentration of particles in the colloidal medium  $C_{\text{vol}} = \frac{4}{3} \pi \bar{R}^3 N$ .

If particles are rather mobile, processes like coagulation may proceed in systems with small contiguous particles. Indeed, such a process is a local sintering, which results in the formation of agglomerates consisting of several particles. In this case, the reduction of free surface energy occurs because of reorganization of the outer surfaces of particles into the inner surfaces of grain boundaries. Nevertheless, we can apply the formalism of coagulation kinetics to the description of such a local sintering.

To do this, it appears sufficient for the coagulation constant in Eq. (26) to be replaced by the kinetic constant defining the rate of interparticle sliding or rotation controlled by grain boundary diffusion. The driving force for such a particle rearrangement is locally asymmetric Laplacian forces [41, 42]. As a first approximation, we can write

$$K_{\text{eff}} = \frac{AD_{\text{gb}}\sigma\Omega\Delta_b}{R} kT \quad (30)$$

where  $D_{\text{gb}}$  is the coefficient of grain boundary diffusion,  $\sigma$  is the surface tension,  $\Omega$  is the atomic volume,  $\Delta_b$  is the width of the interparticle boundary, and  $A$  is a constant. Since  $K_{\text{eff}}$  is inversely proportional to  $R$ , one can derive the following relation for  $R$  as a fourth-power parabola

$$\bar{R}^4 = \bar{R}_0^4(1 + B_1 t) \quad (31)$$

where  $B_1$  is the summarized kinetic constant equal to

$$B_1 = \frac{A_1 D_{gb} \sigma \Omega \Delta_b}{kT} \quad (32)$$

and  $A_1$  is a new numerical constant.

This relation is fair for stationary coagulation because at the earliest stage the rate of interparticle sliding strongly depends on the interparticle neck size. In other words, we suggest that the specific time necessary to double  $R$  is substantially more than that of neck growth up to value  $x/R \approx 1$ . Equation (31) coincides with Eq. (22) for coalescence kinetics; the kinetic constant  $B_1$  in (31), however, is substantially less than in (22), as their ratio is proportional to the ratio of the grain boundary to surface diffusion coefficients at the same temperature.

Despite this fact, the coagulation in the system of ultrafine particles with a very narrow size distribution can prevail over coalescence because of the reasons stated above. It should be noted that the surface diffusion controlling coalescence is not accompanied by change in the mean density of a system (no change in distance between particles), and coagulation like a local sintering can lead to some densification of the system as a whole.

Experimental study of the competitive role of both coalescence and coagulation at the second stage of technology is of interest because surface impurities are inevitably inherent in ultrafine media. These impurities behave differently in the two processes. During coalescence a substantial refinement of surface can be expected. When particles coagulate, the impurities may pinch off and place themselves on the interfaces or grain boundaries.

Both coalescence and coagulation processes play a main role in decreasing driving forces for sintering.

### 3.2. Sintering of Nanosized Systems

One of the characteristic features of sintering in the ultrafine media is a tendency toward local densification or differential shrinkage. Local densification usually becomes apparent as an increase in the mean pore size at the stage of open porosity during sintering of micron- and submicron-sized particles. At the late sintering stages, the homogeneity of densification can be restored and a high density of sintered materials can be achieved. Local densification, however, is usually irreversible, and pores, which are tens or hundreds of times larger than the particles, form and cannot be eliminated even if the temperature is increased to fusion temperatures.

It is known that in the nanosized particle system there is a tendency toward inhomogeneous spatial distribution as green packing is prepared. Such inhomogeneity may intensify because of coagulation at the early sintering stages. In addition to the formation of a mesostructure, it proves to be possible to create an inhomogeneity of much larger density than that of the mesoelement. Finally, in the systems of polydisperse powders and especially two-modal particle size distribution, the local variation of mean pore size and therefore variation of Laplacian pressure become possible [43, 44]. Under sintering, such inhomogeneity can provoke the appearance of zones with tensile stresses and, as a result,

macro-cracking inside a sintered body [45]. Thus, the characteristics of the initial powder, the methods of green sample compacting, and the degree of particle coagulation in heating play a determinant role in attainment a high-density material and conservation of homogeneous and fine-grained structure.

It was experimentally found that the main part of volume shrinkage on sintering (up to 85–95% of the theoretical density) of nanocrystalline powders occurs during heating. The sintering temperature is commonly tens or hundreds of degrees lower compared with that for micron-sized particles. The beginning of the isothermal hold is accompanied by abrupt retardation of shrinkage and intensive grain growth.

The key feature of sintering of nanocrystalline materials is a competition of two main processes: shrinkage (densification) and coarsening of microstructure. Both processes are under the control of the main mechanisms of mass transport in sintering: surface and grain boundary diffusion. Parameters of thermal activation are close for both mechanisms, and, consequently, densification and evolution of microstructure occur in parallel. Thus, to make sintering an effective technology for the consolidation of a material with a density close to the theoretical one and a grain size less than 100 nm, it is necessary to separate densification and grain growth in time and temperature. The most approved approaches are rapid-rate sintering, pressure-assisted sintering, and application of dopants, which permit the acceleration of densification and retard grain growth. The first and second of these are the basis of today's consolidation practice, and the third is a method of powder preparation.

#### 3.2.1. Volume Shrinkage in Isothermal and Nonisothermal Sintering

The temperature dependence of volume shrinkage has a classical S-like shape, which commonly consists of three ranges: interparticle necks are formed at the first stage, the cylinder-like channel pores appear and evolve at the second stage, and isolated pores define porosity at the third stage. As for nanostructured ceramics, these three stages are described carefully enough in [46].

For nanosized particles, the two initial sintering stages proceed and are complete during heating, long before an isothermal hold. The initial stage of isothermal hold often coincides with the third sintering stage. This division is rather arbitrary; however, in most experiments, this approach is quite convenient and appropriate for understanding how the residual porosity can be removed for several hours at temperatures lower than the temperature of recrystallization. For some materials this approach is actual, but for others it is not. Table 3 demonstrates several of the best examples of sintering of nanostructured ceramics.

From Table 3 one can see that the isothermal sintering regimes resulted in almost poreless materials with grain sizes less than 100 nm, but only for the ceramics characterized by the high activation energy of grain boundary migration ( $ZrO_2$ , TiN). Barium titanate demonstrates a high migration activity of grain boundaries at temperatures of 1300 °C and above, and this fact becomes a reason for abnormal grain growth, leading to isolated pore entrapment inside the



**Table 3.** Characteristics of the best samples of nanocrystalline ceramics obtained by sintering in a ramp-and-hold regime.

Material	Particle size (m)	Sintering regime	Density (% of theor.)	Grain size (nm)	Grain growth factor	Ref.
3YSZ	8	1050 °C, 5 h, air	99.9	90	11	[47]
3YSZ	6	1070 °C, 2 h, air	99.9	80	13	[48]
3YSZ	4	970, 2 h, air	99	60	15	[49]
BaTiO <sub>3</sub>	26	1300, 1 h, air	99.0	500	20	[50]
TiN	70	1600, 1 h, vacuum	98	800	11	[51]
TiN	12	1200 °C, 1 h, 0.1 MPa N <sub>2</sub>	99.0	140	12	[52]
TiN	40	1400 °C, vacuum	98	400	10	[53]

Source: Reprinted with permission from [4], V. V. Skorokhod et al., "Physicochemical Kinetics in Nanostructured Systems." *Academperiodica*, Kiev, 2001 (in Ukrainian). © 2001, *Academperiodica*.

grains. Grain growth factor exceeds 10 in all of the examples; therefore isothermal sintering can be used in manufacturing dense nanograined ceramics, but for particles of sizes less than 10 nm.

Grain size is the integral of growth rate, which depends on temperature, pore structure, dopant concentration, and other factors. Therefore, it appears to be difficult to predict when the contributions of these factors to the integral become larger: either in the case of isothermal hold or during the permanent heating to higher temperatures. In any case, the sintering of nanocrystalline powders is a non-isothermal process, and transition to the final stage of densification strongly depends on "successful" implementation of the initial and intermediate stages, because they are responsible for pore and grain microstructure. Attention must be paid to both stages, initial and intermediate, especially taking into consideration their dependence on the heating rate.

The temperature dependence of the densification rate very often has two extrema, the first of which at rather low temperatures corresponds to interagglomerate sintering or rearrangement of particles. The interagglomerate pore coarsening occurs because of the action of both tensile stresses between agglomerates and surface-diffusion-controlled coalescence of pores and grains inside the agglomerates. Widening of pore size distribution was revealed in the sintered sample compared with the green one.

### 3.2.2. Rapid Sintering

Selection of heating rate is stipulated by the kinetics of heat and mass transfer, shrinkage, and the evolution of microstructure. First an idea of rapid sintering at the initial stage was postulated by Harmer and Brook [54] and was experimentally examined for alumina and barium titanate. Lynn Johnson proposed an idea of ultrarapid sintering of thin-wall tubes during transport of plasma [55]. Palmour used Harmer's idea of rapid heating at the initial stage of rate-controlled sintering [56]. The competition between different sintering mechanisms was put into the background of nonisothermal sintering and rapid sintering. The sintering schedule was rationalized by rapid heating at the first stage to surpass the temperature interval, where surface

diffusion, responsible for coarsening microstructure, predominates over grain boundary or bulk diffusion, which is responsible for densification. If the green body is rapidly heated, a high driving force of sintering is retained up to temperatures where densification prevails over coarsening. Nanocrystalline powders are an ideal object for the investigation of rapid sintering because of the huge specific surface area and, therefore, the high surface diffusion activity [57]. The heating rate, however, is restricted.

The influence of the heating rate on sintering of nanocrystalline zirconia powder was studied in [57]. Heating was carried out in the rate interval of 2–200 °C/min up to the same temperature in the range from 1050 to 1300 °C. Then an isothermal hold was provided for 2 h. The higher the heating rate was, the lower the final density of sintered ceramics was. There have been cases where the porosity increase was revealed instead of densification.

A similar result was described in [58], where BaTi<sub>5</sub>O<sub>11</sub> underwent ramp-and-hold sintering with a heating rate of 1–100 °C/min. The main reason for the porosity increase under rapid rate heating conditions is the localized shrinkage (differential sintering) [58], which, in its turn, is a sequence of agglomeration and temperature gradient. Because of the low thermal conductivity of zirconia (2 W/m K<sup>-1</sup>) and the high heating rate, the shell of the specimen was heated to a higher temperature than the core. Therefore, the shell had a higher density than the core. This phenomenon was described by Geguzin as "shell sintering" [21]. The difference in densification rates in adjacent microvolumes leads to stresses of different signs, including tensile stresses, which cause a local pore growth, or sometimes porosity. To estimate the stresses originating from the shrinkage rate difference, Evans introduced the following ratio [59]:

$$\sigma_m(t) = -\frac{4f}{1-f} \int_0^1 \Delta \dot{\epsilon}_s(t) \cdot F(G, K, \eta, t-u) du \quad (33)$$

where  $\Delta \dot{\epsilon}_s(t) = \Delta \dot{\epsilon}_s^1 - \Delta \dot{\epsilon}_s^2$ ,  $\Delta \dot{\epsilon}_s^i = \dot{\rho}^i / 3\rho^i$  is the variation in the densification rate,  $f$  is the concentration of inhomogeneities,  $\Delta \dot{\epsilon}_s^1$  is the densification rate in the microvolume where the fluctuation of density is observed, and  $\Delta \dot{\epsilon}_s^2$  is the shrinkage rate of the porous body as a whole. Thus, the

densification rate of a structurally nonhomogeneous material can be written as [59]

$$\dot{\rho} = A \left( 1 - \frac{\rho}{\rho_f} \right)^\alpha \left[ \frac{\Sigma - \sigma_m}{\Sigma} \right] \cdot l^{-a} \quad (34)$$

where  $A$  is a temperature-dependent function,  $\rho$  is the instantaneous density,  $\rho_f$  is the theoretical density,  $\Sigma$  is the "sintering potential,"  $\Sigma = \gamma_s(r + 2\gamma_b/l)$  for the homogeneous state,  $\gamma_s$ ,  $\gamma_b$  are the surface and grain boundary energies, respectively,  $l$  is the curvature radius, and  $\alpha$  and  $a$  are power indexes. From Eq. (34) it can be concluded that the densification rate approaches zero if  $\sigma_m = \Sigma$ . Thus, the higher the instantaneous densification rate, the higher the instantaneous difference  $\Delta\dot{\epsilon}_s$  and the higher the value of  $\bar{\sigma}_m$ . An increase in  $\bar{\sigma}_m$  results in a decrease in the driving force of sintering. One can conclude that for each fractional density there is a range of optimal densification rates corresponding to the minimum variation of density.

If sintering is carried out without isothermal hold, the final fractional density of sintered material depends strongly on the heating rate, and this feature is inherent in nanocrystalline powders of ceramics and metals [60]. It is worth mentioning that the heating rate corresponding to the maximum density increases with particle size decrease.

Thus, rapid heating leads to pore growth due to differential densification, owing to strong temperature gradient. On the other hand, slow heating does not result in full densification because of pore coalescence and premature pinching off of channel pores. At low temperatures, the coalescence of pores is under the control of surface diffusion and prevails over densification, which is under the control of boundary diffusion, because the surface area exceeds the area of grain boundaries and the surface diffusion coefficient is three orders of magnitude higher than that of grain boundary diffusion at the same temperature. In real nanostructure systems, it becomes impossible to avoid coalescence completely and prevent differential densification. It appears to be possible to minimize their influence by flexibly affecting the competition between coarsening of microstructure and densification during nonisothermal sintering. The optimal heating rate is the best evidence of this statement.

#### 4. THERMAL STABILITY OF NANOSTRUCTURED SYSTEMS

A dissipative system aspirates to decreasing free surface energy, which is the driving force of sintering (a thermodynamically reversible process). Let us consider densification as a rheological process, where the densification rate is defined by the effective viscosity of the dissipative system and the value of the driving force. On the other hand, a decrease in free surface energy proceeds through surface diffusion-controlled coalescence. The two processes are in temperature-driven competition, which can be controlled by temperature variation in the course of sintering. Since the technological purpose of sintering is to bring the density of a material close to its theoretical value, it is reasonable to accelerate the first process and retard or impede the second one.

The specific surface area of a porous body or a loose powder is the surface area of the pores,  $S$ , divided by the volume,  $V_m$ :  $s_s = S/V_m$  (where  $s_s$  is in  $\text{cm}^2/\text{cm}^3$ ). Thus,  $s_s$  is proportional to the ratio  $A/L$ , where  $A$  is a constant ( $3 \div 4$ ) and  $L$  is a structural parameter (mean particle size of the powder, or the average pore size in a porous body, for cylinder-shaped pores,  $L = 2R_{\text{cyl}}$ ). If the volume of a body  $V$  and  $L$  are independent variables, the full differential of  $s_s$  can be written [40] as

$$ds_s = \frac{\partial s_s}{\partial V} \Big|_{L=\text{const}} dV + \frac{\partial s_s}{\partial L} \Big|_{V=\text{const}} dL \quad (35)$$

In accordance with the rheological theory of sintering, which uses the statistical model of a porous body, the second addend can be omitted if we suppose that the only shrinkage affect variation is in the surface area. This assumption is reliable if the grain size is larger than  $10^{-3}$  cm. In the case of ensemble of nanosized particles, the surface area changes at the initial sintering stage because of variation in the structural parameter (coalescence). Shrinkage and coalescence make a combined contribution to the reduction of the surface area at the intermediate sintering stage.

#### 4.1. Coalescence of Pores and Inclusions

The initial stage of volume shrinkage occurs because of mechanisms with low activation energies. According to different assumptions, mutual particle rotation and sliding leading to rearrangement of particles, accommodation of facets in adjacent particles, and other modes correspond to this requirement. First, such assumptions and mechanisms were described by Geguzin and Thoelen in [21, 61], and today they are in the focus again. Particle rearrangement and accommodation, however, are restricted by package density.

The intermediate stage of shrinkage denotes the formation of a peculiar structure, namely, channel-like porosity, due to simultaneous action of grain boundary and surface diffusion mechanisms. This structure evolves specifically through changes in pore diameter, while their length remains unchanged. Pinching off the channel pores occurs locally, in those places where pore diameter becomes smaller than the critical value, defined from the ratio of Raleigh. The fragmentation of channels results in pore isolation and formation of close porosity, which is usually localized on grain boundaries or in triple junctions. Elimination of such porosity depends on grain boundary mobility, temperature, and sintering duration.

Both initial and intermediate stages can be attributed to low-activation-energy mechanisms. Comparative characteristics of nanograined and conventional micrograined ceramics are presented in Table 4. However, all of these parameters are rather close to the activation energy of surface diffusion obtained for coarse-grained materials.

Mayo suggested that such a low activation energy can be explained by the mechanism of facet accommodation. In [62], a contact formation mechanism was proposed for the initial stage of sintering if the diffusion coefficient is a function of the contact geometry and decreases surface diffusion coefficient to grain boundary diffusion one.

**Table 4.** Effective sintering activation energies for nanocrystalline powders and corresponding activation parameters of diffusion in some substances.

Substance	$E_a$ (experiment) (kJ/mol)	$E_a$ (grain bound.) (kJ/mol)	$E_a$ (surface) (kJ/mol)	$E_a$ (volume) (kJ/mol)
ZrO <sub>2</sub> -3mol.% Y <sub>2</sub> O <sub>3</sub> (3YSZ)	88–100	190 ([O <sup>2-</sup> ], in m-ZrO <sub>2</sub> ) 115 (O-vacancies, 4YSZ)	~100 (O-vacancies, 3YSZ) 400–530 (Zr <sup>4+</sup> , 3YSZ)	125 ([O <sup>2-</sup> ], in t-3YSZ) 90 (O-vacancies, 4YSZ)
Al <sub>2</sub> O <sub>3</sub>	234			
TiO <sub>2</sub>	96.2			
BaTiO <sub>3</sub>	50–60	96–120	44–50	48 [34] ([O <sup>2-</sup> ], single crystal) 372[35] ([Ba <sup>2-</sup> ], single crystal)
Ni	70–100	120	58.6	279

Source: Reprinted with permission from [4], V. V. Skorokhod et al., "Physicochemical Kinetics in Nanostructured Systems." *Academperiodica*, Kiev, 2001 (in Ukrainian). © 2001, *Academperiodica*.

At low and moderate temperatures, sintering of nanoparticles is controlled by the mechanism of surface self-diffusion. In this case, the kinetic equation is easily derived for isothermal variation of a structural parameter with the modified equation of diffusion coalescence [53]:

$$L^4 = L_0^4 + \frac{32\sigma D_s \delta^4}{kT} t \quad (36)$$

where  $D_s$  is the coefficient of surface self-diffusion,  $\sigma$  is the surface tension,  $\delta$  is the thickness of a surface layer,  $L_0$  is the initial value of the structural parameter,  $k$  is the Boltzmann constant, and  $T$  is the temperature. Equation (36) is valid for a description of coalescence in nanostructured systems, such as ensembles of pores. Relaxation of the pore surface occurs when pores coalesce, making the microstructure coarser. At the same time, the surface area decreases simultaneously with porosity reduction and decreasing mean pore size. The competition between shrinkage and coalescence as a function of the heating rate is represented in Figure 2.

For nanocrystalline powders, which tend toward coarsening through the mechanism of surface self-diffusion, Eq. (36) is correct and the assumption of linear viscous flow accompanied by interparticle sliding under the action of capillary forces becomes reasonable [21, 63]. In this case, the viscosity of the system is reversely proportional to the third power of the linear size of the structural element [21, 63]:

$$\frac{1}{\eta} = 100 \frac{\Omega b D_b}{kTL^3} \quad (37)$$

where  $\Omega$  is the atomic volume,  $D_b$  is the grain boundary diffusivity, and  $b$  is the width of the grain boundary.

To build this graph, the coalescence of pores (the region between curves 2 and 3) and densification (curves 4 and 5) was calculated and compared with experimental data (curve 1) [4]. At low heating rates (curves 3 and 5), there is a temperature interval (300–500 °C) in which the coalescence prevails over densification, that is, it makes the main contribution to the reduction of surface area. The higher the

heating rate, the smaller is the contribution of pore coalescence to the surface area reduction. At high heating rates, densification prevails over coalescence in the whole temperature interval, and pore growth is impeded. Thus, during sintering of nanosized powders there exists the dependence of structure on heating rate, which influences the driving forces of sintering.

It was experimentally shown that the coarsening of pores and grains at the initial stage of sintering proceeds simultaneously. Actually, if a small particle is located inside a pore and is surrounded by coarser particles, it divides the pore into several small ones and porosimetry shows a small pore size. During heating, the particle gradually coalesces, with the coarser particles redistributing substance all over the surface and filling the contact necks between the coarse particles. At the same time, the pore becomes larger. In this case, coarse particles and large pores increase in size while small particles and pores disappear. The process of coarsening is shown in Figure 3.

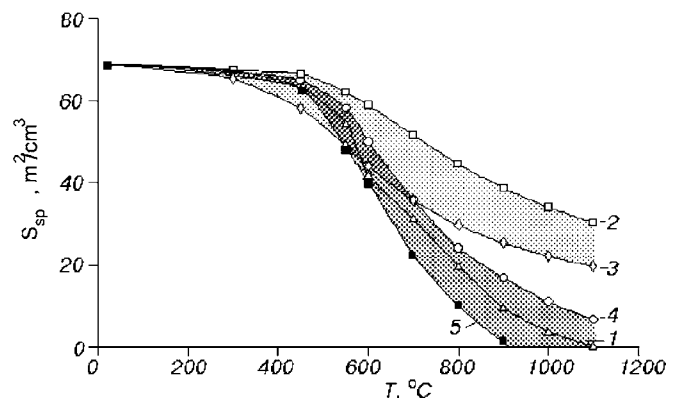


**Figure 2.** Temperature dependence of specific pore surface for nano-sized Ni. Rates of heating: 1, 2, 4, 0.44 °C/c; 3, 5, 0.18 °C/c. 1, experimental data; 2–5, calculated data; 2, 3, for coalescence; 4, 5, for compaction. Reprinted with permission from [4], V. V. Skorokhod et al., "Physicochemical Kinetics in Nanostructured Systems." *Academperiodica*, Kiev, 2001 (in Ukrainian). © 2001, *Academperiodica*.

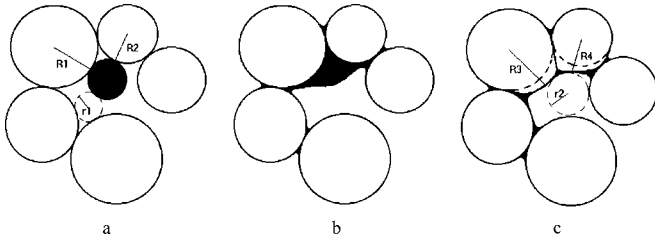


**Figure 3.** Schematic drawing of coalescence increase of pores and grains at the initial stage of sintering when shrinkage is absent. Reprinted with permission from [4], V. V. Skorokhod et al., "Physicochemical Kinetics in Nanostructured Systems." Academperiodica, Kiev, 2001 (in Ukrainian). © 2001, Academperiodica.

Particles of sizes  $R1$  and  $R2$  increase to  $R3$  and  $R4$ , respectively, owing to coalescence with small particles (shown in black). The pore inside the agglomerate also increases: a pore of the maximum size  $r1$  is transformed into a pore of size  $r2$  after coalescence. At this stage of sintering, the pores change in size and shape, which reduces the free surface energy as well. Figure 4 presents the results of calculations and experiments, both for coalescence growth, which takes place under nonisothermal conditions. The only coalescence provides a rapid growth, but it cannot be observed in practice because of the competitive contribution of shrinkage.

When the porosity is large and the structure of the pores is well developed, the intensive densification of the porous body is the reason for the suppression of grain growth. As shown, the maximum contribution of coalescence to coarsening microstructure doubles the mean linear size of the structural element. A correctly selected heating regime at the initial stage of sintering, however, and a homogeneous green microstructure as a result of the optimal scheme of compaction can minimize the effect of coalescence coarsening the microstructure at the initial stage of sintering.

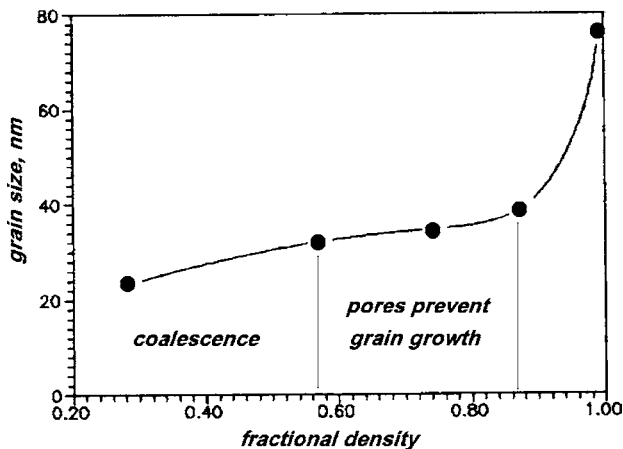


**Figure 4.** Temperature dependence of coalescence growth of grains and pores of nanopowder at constant initial rate of sintering. Reprinted with permission from [4], V. V. Skorokhod et al., "Physicochemical Kinetics in Nanostructured Systems." Academperiodica, Kiev, 2001 (in Ukrainian). © 2001, Academperiodica.

General theoretical calculations allowed the following equations to be deduced:

$$f(\theta) \frac{d\theta}{dt} \approx \frac{A\sigma D}{a^n kT} \quad (38)$$

$$a^n = a_0^n + \frac{B\sigma D'}{kT} t \quad (39)$$

where  $t$  is time,  $m$  and  $n$  are indexes of power,  $a$  is the middle grain size, and  $D$  and  $D'$  are the effective diffusion coefficients, corresponding to densification and grain growth, respectively. A detailed analysis of the two competitive processes can be carried out. First of all, it is necessary to note that densification does not depend on the heating rate if  $m = n$ . If grain boundary diffusion prevails over bulk diffusion at the initial and intermediate stages of sintering, the index of densification is equal to  $m = 4$ . At the same time, the index of grain growth is equal to  $n = 4$ , provided either the nanoparticles coalesce from the beginning of sintering by means of surface mass transport or grain growth is restricted by porosity and inclusions of the second phase. Thus, the case of  $n = 4$  can be suitable for the nonisothermal stage of densification as a whole. Actually, the heating rate independence of the temperature derivative of density remains unchanged in many experiments. For nanocrystalline titanium nitride, nickel, barium titanate, and composition  $B_4C-TiB_2$  this was confirmed in [64]. If  $m > n$ , the temperature derivative of density (or porosity) is directly proportional to the heating rate, and, vice versa, for  $m < n$  it is reversely proportional to the heating rate. Both cases were revealed experimentally at the late stage of sintering at high temperatures, where the contribution of volume diffusion is much higher than that of grain boundary diffusion and the contribution of surface mass transfer is negligibly small. There is an interval of heating rate (about 1) where densification does not depend on the ratio  $m/n$ . Since the contribution of different mechanisms of mass transport to the kinetics of total densification changes synchronously, the ratio  $m/n$  is variable. Thus, the heating rate must be variable to optimize the densification process as a whole and instantaneous density in particular. This statement is the basis for rate-controlled sintering, which is the most profitable in the manufacture of dense nanostructured materials.

## 4.2. Recrystallization and Grain Growth

New ideology and experimental achievements of rate-controlled thermally activated processes of synthesis and sintering are very useful in the manufacture of nanosized powders and nanograined materials. The rate-controlled processes differ strikingly from the conventional synthesis and sintering due to back-coupling established between transformation degree (completeness of chemical reaction or shrinkage) and instantaneous temperature. During the process, the transformation degree is a dependent parameter, whereas the temperature is an independent parameter. sintering, chemical synthesis, and phase transformations proceed through the competition between densification and grain growth or new phase nucleation and nuclei growth. This competition results in the possibility of controlling particle and grain size within the nanoscale range, where a useful "size effect" takes place.

The size effect is the most attractive fundamental problem in nanocrystalline materials since it directly answers the question of whether these extremely fine-grained materials are worth producing. Variations in properties with size and shape of structural element occur in all solids, because the relative contributions from surface and volume energies are both size- and shape-dependent and are different for particles, fibers, films, and polycrystals.

The final stage of sintering is characterized by fast reducing densification and an intensive grain growth. At this stage, the process of shrinkage of nanocrystal material and an intensive grain growth are both complete. In a number of cases, fully dense and nanostructured materials cannot be produced. At the intermediate stage, the two processes can keep in balance. However, at the final stage it is difficult to restrain grain growth because of the essential decrease in the driving force of sintering. To clear up the question of whether this is the result of imperfections of procedures used to produce a nanostructured material or it is an inherent trait of the latter, the evolution of the structure during sintering of ideally packed powders with different dispersities was investigated [4]. It was found that the grain growth at the final stage could be described by the following exponential expression:

$$a^m = a_0^m + K_0 \exp(-Q/RT) \quad (40)$$

where  $a$ ,  $a_0$  are the current and initial sizes of a grain,  $Q$  is the energy of grain growth activation, and  $m$  is an index of the level of grain growth. The index  $m$  is defined by the mechanism of grain growth and changes from 1 to 4, but in some cases it can reach 20. When a grain growth is abnormal,  $m = 1$ ; for normal growth,  $m = 2$ ; in the case of deceleration of the grain growth caused by impurities or of sintering of powders of solid solutions,  $m = 3$ . For dense nanostructured metals, the index  $m$ , however, is equal to 20 at low temperatures and, under heating, decreases to 2. As for normal grain growth, it is seldom observed in nanostructured materials.

The "classical" curve of the grain growth against the density, the so-called trajectory of sintering, has three distinct regions corresponding to three stages of sintering. At the initial (where coalescence is dominant) and intermediate (where deceleration of grain growth takes place) stages, the grain growth changes very slowly. When the density reaches 0.84 of its theoretical value, a very sharp increase in grain size (by 2 times) begins.

The most attractive process from the point of view of the possibility of controlling the evolution of microstructure under nonisothermal sintering is deceleration of the grain growth by pores and inclusions.

Gupta et al. [65] summed up experimental data for different polycrystalline materials by drawing density dependences of the grain size. The increase in grain size proved to be linear in the density range from the initial value to 90% of the theoretical one. With increasing density, a more intensive (by 2–3 times) grain growth was observed. Other investigators obtained similar results.

In the common case, the mechanisms of densification and grain growth have different dependences on the scale. In practice, a change in grain growth leads to a change in the

temperature of isothermic sintering, which, in its turn, influences the trajectory of sintering. Thus, the following two cases can be distinguished:

- Activation energies for densification and size growth are equal.
- Activation energy for densification is higher than that for size growth (coarsening the microstructure).

In the first case, the influence of temperature and heating rate is minimal or absent. In the second case, a great heating rate can confer essential advantages because at high temperatures shrinkage is accelerated more than grain growth.

An algorithm for the calculation of the trajectory of sintering was proposed in [66] on the basis of the suggestion that deceleration caused by pores and internal grain boundary diffusion can be interpreted as mechanisms of densification during sintering. The slope of the trajectory of sintering is described by the expression

$$\frac{dg}{d\rho} = \frac{\dot{G}}{G_0 \dot{\rho}} \quad (41)$$

where  $g = G/G_0$ ,  $\rho$  is the density, and the symbols with dots denote derivatives with respect to time. If grain growth is reduced by pores, the expression can be transformed as follows:

$$\frac{dg}{d\rho} = g \frac{\delta_s D_s^0}{\delta_b D_b^0} \exp\left(-\frac{Q_s - Q_b}{kT}\right) \rho^{-1} K_1(\psi) \quad (42)$$

If the mobility of grain boundaries is responsible for grain growth,

$$\frac{dg}{d\rho} = g^3 G_0^2 \frac{M_b^0}{\Omega \delta_b D_b^0} kT \exp\left(-\frac{Q_M - Q_b}{kT}\right) \rho^{-1} K_2(\psi) \quad (43)$$

where  $K_2(\psi)$ ,  $K_1(\psi)$  are functions describing the contact geometry and dihedral angle, and  $M_b$  and  $Q_M$  are a preexponent and the energy of grain boundary mobility activation, respectively. Equation (42) corresponds to the intermediate stage of shrinkage, where the competition between shrinkage and coalescence is changed by the competition between shrinkage and grain growth limited by channel porosity and independent of the initial grain size. The final stage of sintering proceeds under conditions when pores do not prevent grain growth. However, they are dependent on the initial grain size, and Eq. (43) defines the conditions of competitions of the mechanisms at this stage. It is worth noticing that the only competition between shrinkage and grain growth limited by boundary migration can lead to a poreless material. In addition, in this case the process becomes sensitive to the heating rate and, as in the initial stage, optimization of heating conditions is actual. In practice, this is taken into account in the method for sintering with the controlled rate of shrinkage.

Thus, by taking into account the competition between the rates of nucleation and nuclei growth in heterogeneous or solid-state reactions and the competition between the rates of densification and the grain growth, it can be possible to create nanosized powders and nanostructured sintered materials.

## GLOSSARY

**Coagulation** A process of reducing free surface energy in the system followed by coarsening of nanoparticles and maintaining the interfaces.

**Coalescence** A process of reducing free surface energy in the system followed by coarsening of nanoparticles and disappearance of interfaces between them.

**Genesis** Genesis of nanostructured systems is a structural heredity of powders from precursors and nanograined materials from powders.

**Kinetics** Kinetics in nanostructured systems is a complex of characteristics determining the change of properties in solids during a process.

**Sintering** A process of reducing free surface energy in the system of nanoparticles and pores resulting in healing of pores, transformation of particles into grains and grain growth.

## REFERENCES

1. "Physical Metallurgy." R. W. Cahn, North-Holland, Amsterdam, 1965.
2. H. Gleiter, *Nanostruct. Mater.* 6, 3 (1995).
3. V. V. Skorokhod, *Powder Metallurgy* 53 (1995).
4. V. V. Skorokhod, I. V. Uvarova, and A. V. Ragulya, "Physicochemical Kinetics in Nanostructured Systems." *Academperiodica*, Kiev, 2001 (in Ukrainian).
5. G. M. Chow, in "Proceedings of NATO Conference Functional Gradient Materials and Surface Layers, Prepared by Fine Particle Technology" (M.-I. Baraton and I. Uvarova, Eds.), Vol. 16, p. 33. Kluwer Academic, Dordrecht/Boston/London, 2001.
6. O. Vasyukiv and Y. Sakka, *J. Am. Ceram. Soc.* 83, 9 (2000).
7. B. H. Kear and P. R. Strutt, *Nanostruct. Mater.* 6, 227 (1995).
8. J. S. Haggerty and R. W. Cannon, "Laser Induced Chemical Processes" (J. I. Steinfeld, Ed.), Plenum, New York, 1981.
9. X.-C. Yang and W. Riehemann, *Scripta Mater.* 45, 435 (2001).
10. Z. Yao, J. J. Stiglich, and T. S. Sudarshan, *Metal Powder Rep.* 53, 26 (1998).
11. A. V. Ragulya, *Nanostruct. Mater.* 10, 349 (1998).
12. T. V. Anuradha, S. Ranganathan, Tanu Mimani, and K. C. Patil, *Scripta Mater.* 44, 2237 (2001).
13. H. Gleiter, *Acta Mater.* 48, 1 (2000).
14. M. Alexe, C. Harnagea, A. Visinoui, A. Pignolet, D. Hesse, and U. Gosele, *Scripta Mater.* 44, 1175 (2001).
15. R. Schmechel, H. Winkler, Li Xiaomao, M. Kennedy, M. Koble, A. Benker, M. Winterer, R. A. Fisher, H. Hahn, and H. Von Seggern, *Scripta Mater.* 44, 1213 (2001).
16. H. Fugunaga and H. Nakamura, *Scripta Mater.* 44, 1341 (2001).
17. S. Takeuchi, *Scripta Mater.* 44, 1183 (2001).
18. J.-M. Greneche, *J. Metastable Nanocrystalline Mater.* 1, 159 (1999).
19. V. I. Zubov, J. N. Teixeira Rabelo, and I. V. Mamontov, *J. Metastable Nanocrystalline Mater.* 8, 57 (2000).
20. R. A. Andrievski, in "Science of Sintering in the XXI Century" (V. Nikolic and N. Nikolic, Eds.), p. 27. Serbian Academy of Science and Art, Belgrade, Yugoslavia, 2002.
21. Ya. E. Gegusin, "Physics of Sintering." Science, Moscow, 1984 (in Russian).
22. Yu. R. Kolobov, G. P. Grabovetskaya, M. B. Ivanov, A. P. Zhilyaev, and R. Z. Valiev, *Scripta Mater.* 44, 873 (2001).
23. T. M. Nenadovic, "Atomic Collision on Surfaces and Material Implementation Advanced Materials for High Technology Applications." Transtec Publication, Switzerland/Germany/UK/USA, 1995.
24. P. Nesladek and S. Veprek, *Phys. Status Solidi.* 177, 53 (2000).
25. J. Musil, P. Zeman, H. Hruby, and Mayrhofer, *Surf. Coat. Technol.* 120/121, 173 (1999).
26. P. C. Yaspar and W. D. Sproul, *Vacuum* 55, 179 (1999).
27. W. A. Nelson and R. M. Orenstein, *J. Thermal Spray Technol.* 6, 176 (1997).
28. M. B. Beardsley, *J. Thermal Spray Technol.* 6, 181 (1997).
29. R. A. Miller, *Curr. Status Thermal Barrier Coat. Overview Surf. Coat. Technol.* 30 (1987).
30. R. Vasen and D. Stover, in "Proceedings of NATO Conference on Functional Gradient Materials and Surface Layers, Prepared by Fine Particle Technology" (M.-I. Baraton and I. Uvarova, Eds.), Vol. 16, p. 199. Kluwer Academic, Dordrecht/Boston/London, 2001.
31. J. Steinbach and H. Ferkel, *Funct. Mater.* 189 (2001).
32. I. Uvarova, *J. Adv. Mater.* 32, 26 (2000).
33. B. Delmon, "a la Cinetique Heterogene." Editions Technip., Paris, 1969.
34. B. I. Bondarenko and V. K. Besugly, "Potentials of Components in Physicochemical Systems." *Academperiodica*, Kiev, 2002 (in Ukrainian).
35. A. S. Shirinyan, A. M. Gusak, and P. J. Desre, *J. Metastable Nanocrystalline Mater.* 7, 17 (2000).
36. V. V. Boldurev, *Prog. Chem.* 42, 1161 (1973).
37. V. V. Boldurev, *Kinet. Catal.* 1, 203 (1960).
38. V. V. Skorokhod, Yu. M. Solonin, and I. V. Uvarova, "Chemical, Diffusion and Rheological Processes in Technology of Powder Materials." Naukova Dumka, Kiev, 1990.
39. R. M. German, *Sci. Sintering* 10, 11 (1978).
40. V. V. Skorokhod, in "Sintering '85" (G. C. Kuczynski, D. P. Uskokovic, H. Palmour III, and M. M. Ristic, Eds.). Plenum, New York/London, 1987.
41. M. F. Ashby and R. Verrall, *Acta Metall.* 21, 53 (1973).
42. H. E. Exner, *Rev. Powder Metallurgy Phys. Ceram.* 1, 7 (1979).
43. V. V. Skorokhod, V. V. Panichkina, and A. V. Ragulya, *Funct. Mater.* 6, 215 (1999).
44. V. V. Skorokhod, *Powder Metallurgy Metal Ceram.* 38, 350 (1999).
45. C. A. Handwerker, J. E. Blendell, and R. L. Coble, in "Science of Sintering: New Direction for Materials Processing and Microstructural Control" (D. P. Uskokovic, H. Palmour III, and R. M. Spriggs, Eds.). Plenum, New York/London, 1989.
46. M. Mayo, *Int. Mater. Rev.* 41, 85 (1996).
47. M. Mayo, in "Nanostructured Materials: Science and Technology" (G.-M. Chow and N. I. Noskova, Eds.), Vol. 50, p. 361. Kluwer Academic, Dordrecht, the Netherlands, 1998.
48. P. Duran, M. Villegas, J. F. Fernandes, F. Capel, and C. Moure, *Mater. Sci. Eng.* A232, 168 (1997).
49. V. V. Srdic, M. Winterer, and H. Hahn, *J. Am. Ceram. Soc.* 84, 729 (2000).
50. A. V. Ragulya, *Nanostruct. Mater.* 10, 349 (1998).
51. V. V. Skorokhod and A. V. Ragulya, in "Proceedings of the 14th International Plansee Seminar" (G. Kneringer, Ed.), Vol. 3, p. 735. Plansee AG, Reutte, 1997.
52. D. T. Castro and J. Y. Ying, in "Proceedings of the International Conference: Fine, Ultrafine and Nano Powders '98," 1998, p. 356.
53. R. Nass, S. Albayrak, M. Alsan, and H. Schmidt, *Adv. Sci. Technol.* 11, 47 (1995).
54. M. P. Harmer and R. J. Brook, *J. Br. Ceram. Soc.* 80, 147 (1981).
55. S. K. Joung and D. Lynn Johnson, *Am. Ceram. Soc. Bull.* 62, 620 (1983).
56. H. Palmour III, M. L. Huckabee, and T. M. Hare, in "Material Science Monographs," Vol. 4, p. 46. Elsevier, Amsterdam, 1979.
57. D.-J. Chen and M. J. Mayo, *J. Am. Ceram. Soc.* 79, 906 (1996).
58. T. Fukui, C. Sakurai, and M. Okuyama, *J. Mater. Res.* 7, 192 (1992).
59. C. H. Shuch, A. G. Evans, R. M. Caimon, and R. J. Brook, *Acta Met* 34, 927 (1986).



60. V. V. Skorokhod and A. V. Ragulya, in "Nanostructured Materials: Science and Technology" (G.-M. Chow and N. I. Noskova, Eds.), p. 387. Kluwer Academic, Dordrecht, the Netherlands, 1998.
61. S. A. Sethi and A. Thoenen, in "Mechanical Properties and Deformation Behavior of Materials Having Ultra-Fine Microstructure," p. 157. Kluwer Academic, Boston/London, 1993.
62. A. V. Ragulya and V. V. Skorokhod, *Powder Metallurgy* 23 (1992).
63. V. V. Skorokhod and S. M. Solonin, "Physicomettallurgical Foundation of Powder Sintering." Metallurgy, Moscow, 1984 (in Russian).
64. V. V. Skorokhod, M. V. Vljajic, and V. D. Krstic, in "Proceedings of Yugoslav Conference on New Materials, YUGOMAT'97," 1998.
65. T. K. Gupta, *J. Am. Ceram. Soc.* 55, 276 (1972).
66. M. Stech, P. Reynders, and J. Roedel, *J. Am. Ceram. Soc.* 83, 1889 (2000).



# Kondo Effect in Quantum Dots

H. Matsumura, R. Ugajin

*Sony Corporation, Hodogaya-ku, Yokohama, Japan*

## CONTENTS

1. Introduction
2. Historical Background on Metal Nanostructures
3. Kondo Resonance in a Quantum Dot
4. Related Topics
  - Glossary
  - References

## 1. INTRODUCTION

Recent progress in microfabrication techniques has made it possible to realize low dimensional electronic systems in semiconductor structures. The motion of electrons inside microfabricated structures (whose size is comparable to the Fermi wavelength) is quantized. This is known as the quantum size effect. This effect was first observed in two-dimensional electronic systems confined in the Si/SiO<sub>2</sub> surface of metal-oxide semiconductor transistors, followed by experiments with semiconductor heterostructures such as GaAs/GaAlAs systems. One can also realize electronic systems of low dimensions, such as a one-dimensional quantum wire and a zero-dimension quantum dot, using electrostatic confinement potentials inside the surface. Owing to the quantum size effect, the discreteness of energy levels becomes apparent. Moreover, it is obvious that in such small structures, the Coulomb interaction between electrons is enhanced. In an analogy with an atom, which is a small system with a few electrons occupying discrete energy levels and interacting with each other by Coulomb repulsion, semiconductor quantum dots are sometimes called “artificial atoms.” They differ from real atoms in several ways. For example, they are larger than the atomic size and the confining potential is different from the  $1/r$  potential of real atoms.

Confinement of electrons can be achieved in two ways. One way is by confining them in the depletion region of

a semiconductor. Here, we confine electrons in the depletion region, which can be modeled by a parabolic potential [1–8]. The second way is by confining the electrons using compound semiconductor heterostructures, such as GaAs/AlGaAs. Here, the size of the confining structure can be on the order of 10 nm [9–14]. In the second way, the electron density inside a dot can be tuned, that is, the number of electrons in a dot can be counted [15].

In comparison with metallic particles, quantum dots fabricated on the semiconductor heterojunctions are clean and highly symmetric. Further, they can be made sufficiently small that the dot size is comparable to the Fermi wavelength. Two types of quantum dots, the lateral dot and the vertical dot, have been used in transport experiments. A lateral-dot device can be made in a two-dimensional electron system by fabricating metal electrodes on the surface of semiconductor heterostructures, for example AlGaAs/InGaAs/AlGaAs, as shown in Figure 1 [16]. Metals are deposited in a particular pattern to form Schottky electrodes above the two-dimensional electron system, where anti-bias voltage is applied so that electrons are confined inside the small region surrounded by the electrodes. Electrons can move by tunneling only through two paths, which are pinched off by these electrodes. The tunneling rate can be controlled by adjusting the gate voltage.

A vertical-dot device is also useful in experiments on transport through a quantum dot. Mesa-shaped structures are carved out of a semiconductor double-barrier structure in order to obtain a quantum dot sandwiched between two tunneling barriers, as shown in Figure 2 [17]. Electrons inside the dot are confined by the heterostructure potential barrier perpendicular to the layers. On the other hand, parallel to these layers, the depletion-layer potential originating from the gate electrode fabricated on the side of the dot confines these electrons using a parabolic potential. The vertical dot has two advantages over the lateral dot. One is that the number of electrons inside the dot can be adjusted, since the electrons are essentially independent from those outside. The other advantage is that the electronic states can be determined using a simple calculation because the shape of the region where electrons dwell is almost cylindrical due to the confining potential.

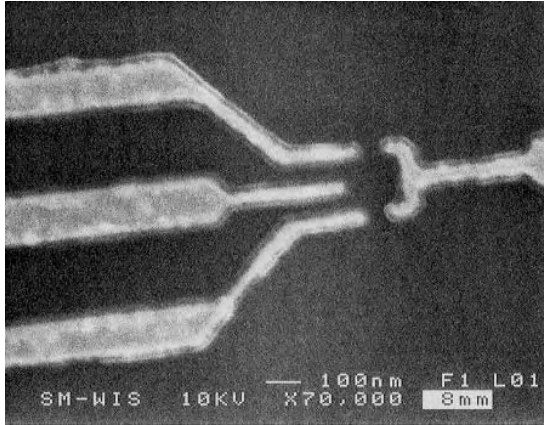


**Figure 1.** Transmission electron micrograph (TEM) image of a lateral dot structure used in the experiment involving the Kondo effect. Three electrodes (right one and left upper and lower ones) adjust the tunneling barriers between the dot and the leads, while the electrode at the center of the left side modifies the gate voltage. Reprinted with permission from [16], D. Goldhaber-Gordon et al., *Nature* 391, 156 (1998). © 1998, Macmillan Magazines Ltd.

We review some recent work on quantum dots featuring spin-related phenomena, for example Kondo effects [18], in which the magnetic moment of electrons is elicited in localized sites coupled to metallic reservoirs. We note that electron–electron interaction is important in describing these spin-related phenomena. Before spin-related phenomena in quantum dots are discussed, let us consider the history of research on small metallic particles, including the Kubo effect of electrons.

## 2. HISTORICAL BACKGROUND ON METAL NANOSTRUCTURES

### 2.1. Ultrafine Particles

Particles about 1–100 nm in size are called ultrafine particles. Electronic states confined in an ultrafine particle have discrete Eigen energies whose level spacing is about 1–100 K. The electronic properties of ultrafine particles (e.g., specific heat and spin susceptibility) are different from those of bulk metal owing to this discreteness of energy levels.

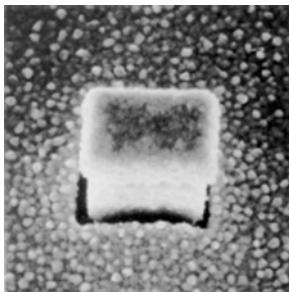


**Figure 2.** TEM image of a vertical quantum dot used in the Kondo-effect experiment. Reprinted with permission from [17], S. Sasaki et al., *Nature* 405, 764 (2000). © 2000, Macmillan Magazines Ltd.

A prominent feature of the electronic properties of ultrafine particles is single electron tunneling, which was first posited in the 1950s [19, 20]. At sufficiently low temperatures, where the charging energy (typically 100–1,000 K) is much higher than the thermal energy, the number of electrons inside the particle is constant. In electron transport across the particle, electrons go into and out of the particle one by one, which results in steplike  $I$ – $V$  characteristics. Differential conductance is often plotted in the  $V_g$ – $V_{SD}$  plane, where  $V_g$  and  $V_{SD}$  are the gate and source-drain voltage, respectively. The resulting diagram, which is sometimes called “Coulomb diamonds,” is a series of diamonds inside which no current flows due to the Coulomb blockade, as shown in Figure 3 [21]. When the dot region is superconducting, a Cooper pair can be manipulated by the bias voltage [22]. Note that these effects, which are due to the high charging energy of an island of electrons, can be distinguished from the Coulomb blockade effect, in which the electric current is suppressed by high charging energy via a capacitor with low capacitance.

The difference in electronic properties depending on whether the number of electrons in the particle is even or odd is caused by the Kubo effect [23, 24]. For example, spin susceptibility shows anomalies at sufficiently low temperatures, where the thermal energy is less than the level spacing. When the number of electrons is odd, the highest occupied single-particle level of the multielectron ground state has only one electron, and thus the state has a free spin of  $\hbar/2$ . Therefore, spin susceptibility obeys Curie’s law and diverges in proportion to the inverse of the temperature. On the other hand, when the number of electrons is even, all the energy levels of the ground state are occupied with two electrons with opposite spins. In this case, charge excitation is needed so that the fine particle has a finite magnetization, which requires energy equal to the level spacing. When the

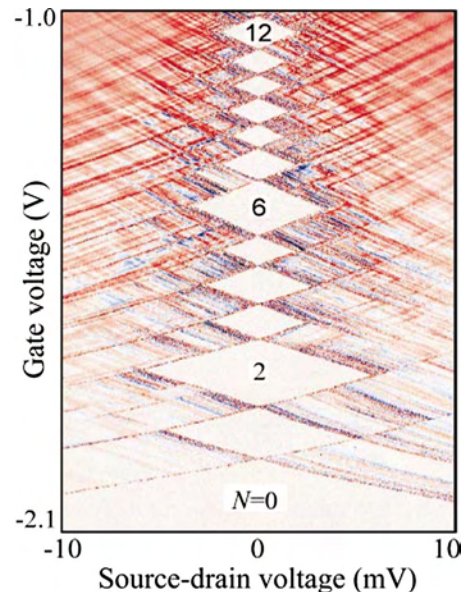


**Figure 3.** An example of Coulomb diamonds. Differential conductance is plotted in  $V_g$ – $V_{SD}$  plane. Reprinted with permission from [21], L. P. Kouwenhoven et al., *Science* 278, 1788 (1997). © 1997, American Association for the Advancement of Science.

system is in thermal equilibrium, the spin susceptibility starts to decrease at the temperature where the thermal energy is equal to the level spacing.

The report on the Kubo effect [23] is the first study to emphasize the importance of the odd/even difference of the electron number inside nanoscale structures. Later, we shall see that the same phenomena appear in transport through the quantum dot. Recently, metallic fine particles have provoked the interest of chemists from the viewpoint of chemical functionalizing using ligands in order to obtain nanoscale optical and electronic devices [25].

## 2.2. Kondo Effect

One of the puzzles of low-temperature physics has been the anomaly in the resistance of metals with magnetic impurities [26], which was first noted in the 1930s [27]. At low temperatures, elastic scattering brings about residual resistance, which remains finite at  $T = 0$  and is independent of temperature, while there is no contribution of inelastic scattering to resistance when the temperature is near zero. Thus, resistance is expected to decrease as the temperature goes down, followed by a saturation in residual resistance. Experimentally, however, resistance takes a minimum, then increases with decreasing temperature. After some thirty years, the cause of this phenomenon was reported by Kondo [28]. Resistance was calculated perturbatively up to the second order of Born approximation with respect to the interaction between conduction electrons in metals and the localized spin of a magnetic impurity. Conduction electrons are scattered by the localized spin through exchange interaction. A temperature called the Kondo temperature ( $T_K$ ) has been identified, below which the higher-order terms of perturbation cause a large scattering amplitude of conduction electrons and thus enhance resistance. This effect is now known as the Kondo effect. The Kondo effect describes the interplay between a quantum spin and conduction electrons with energy under the Fermi energy  $E_F$ . In fact, the Kondo temperature is related to the strength of exchange interaction ( $J_K$ ) and the electron density of states at the Fermi energy [ $N(E_F)$ ] as  $k_B T_K \propto \exp[-1/J_K N(E_F)]$ .

## 3. KONDO RESONANCE IN A QUANTUM DOT

### 3.1. Spectroscopy

Electron phenomena in semiconductor quantum-dot structures have drawn much attention [29–52]. Quantum dots can be regarded as “artificial atoms” whose ground and excited states can be probed electrically using single-electron tunneling spectroscopy [53–55].

When a small bias  $V$  is applied across the dot between the source and the drain contacts, the ground states of a few electrons inside the quantum dot can be investigated directly by observing the  $I$ – $V$  characteristics of the current through the dot as the voltage  $V_g$  is varied. When no current flows (that is, a Coulomb blockade is apparent), the number of electrons is specified by integer  $N$ . On the other hand, when current flows the number of electrons can oscillate between  $N$  and  $N + 1$ . By raising the gate voltage,  $N$  can

be increased from zero, so a series of sharp current peaks due to the charging of the dot, which are called Coulomb oscillations [56], can be observed, as shown in Figure 4 [57]. For a large dot containing a large number of electrons, as in the above case of metallic particles, the Coulomb oscillations are periodic because the charging effect can be treated in a mean-field manner, and the single-electron charging energy is determined by classical theory using only the total dot capacitance.

For a dot containing only a few electrons, however, quantum effects reflecting both the discrete energy levels formed inside the dot and the electron–electron interactions become more important as the dot size is reduced. This leads to Coulomb oscillations that are no longer periodic. One can modify the energy levels by tuning parameters such as the magnetic-field strength. The electron–electron correlation effect is enhanced when the crossing of two energy levels occurs. This effect is shown in the observed spectrum shown in Figure 5 [21].

### 3.2. Kondo Effect of an Odd Number of Electrons in a Dot

Semiconductor quantum dots provide a new type of Kondo effect [58–79]. Quantum dots containing a few electrons, which are coupled with two conducting leads via tunneling barriers, act as a single artificial “impurity,” and the Kondo effect *enhances* the conductance *through* the impurity [80–96]. Assume that there are no degenerate energy levels of electrons inside the quantum dot. If the dot has an even number of electrons, its total magnetic moment is zero since

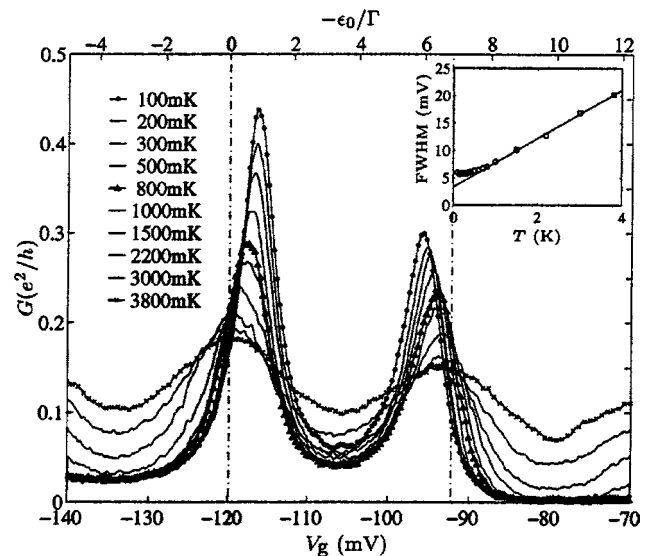


**Figure 4.** Conductance of a lateral quantum dot as a function of the gate voltage plotted for various temperatures. Around the Coulomb oscillation peaks, conductance grows with decreasing temperature. As to the Coulomb blockade regions, conductance continues to decrease outside the peaks, while it exhibits saturation inside the peaks. The temperature dependence is logarithmic, as is shown in the inset. These conditions are caused by the Kondo effect. Reprinted with permission from [57], D. Goldhaber-Gordon et al., *Phys. Rev. Lett.* 81, 5225 (1998). © 1998, American Physical Society.

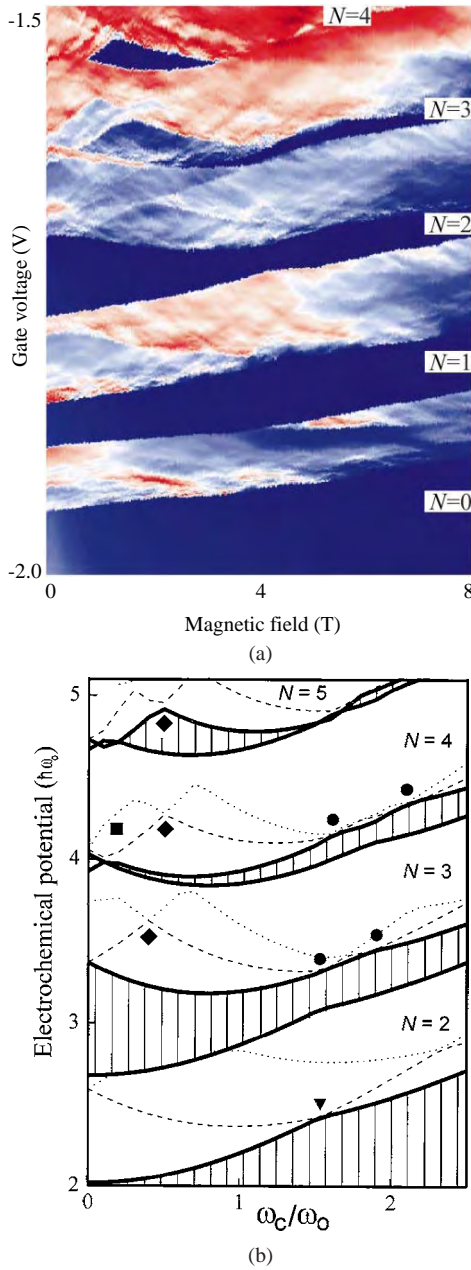


**Figure 5.** Energy spectrum obtained from tunneling current spectroscopy with the corresponding calculated energy spectrum. Reprinted with permission from [21], L. P. Kouwenhoven et al., *Science* 278, 1788 (1997). © 1997, American Association for the Advancement of Science.

the occupied states have a pair of electrons with both up and down spins. If the number of electrons is odd, on the other hand, the situation is the same except for the highest occupied state with an unpaired electron, which makes the total magnetic moment equal to  $\hbar/2$ .

Figure 6 shows a schematic illustration of a quantum dot with an odd number of electrons, coupled to two electrodes (which are referred to as source and drain) via tunneling barriers. The energy level of the highest occupied state ( $\varepsilon$ ), which can be controlled by the gate voltage, is shown inside the dot, as well as the Fermi energy of the electrodes ( $E_F$ ).

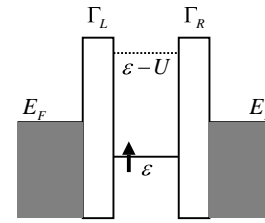


**Figure 6.** Schematic illustration of a quantum dot with odd number of electrons.

The tunneling rates to the electrodes are denoted as  $\Gamma_L$  and  $\Gamma_R$ , the sum of which gives the width of the resonance peak of conductance as a function of the gate voltage ( $\Gamma = \Gamma_L + \Gamma_R$ ). Let  $U$  be the charging energy of the dot. Consider the case where  $\varepsilon < E_F < \varepsilon + U$ ,  $|E_F - \varepsilon| > \Gamma$ , and  $|\varepsilon + U - E_F| > \Gamma$ . The transport property of an electron through the dot is significantly altered when the temperature is sufficiently low, so that the discreteness of the energy levels is clear. At higher temperatures, an electron from one electrode, say the left one, cannot enter the dot because otherwise its energy would be higher than the Fermi energy due to the charging energy. Thus, tunneling through the dot is inhibited (by the Coulomb blockade), and the number of electrons remains odd. In this case, the profile of the conductance is a series of peaks (Coulomb oscillation), as depicted by the dotted line in Figure 7. Peaks occur when the Fermi energy is equal to the addition energy, which is the energy required to add one electron to the dot.

On the other hand, if one decreases the temperature below the Kondo temperature ( $T_K$ ), conduction electrons in the electrodes start to couple with the electron at the highest occupied state inside the dot in order to form a singlet bound state (the Kondo effect), resulting in the screening of the magnetic moment of the dot and the coherent transmission of electrons through the dot [97]. This mechanism modifies the conductance at the gate voltage where an odd number of electrons remains inside the dot at higher temperature. Within this range, the conductance grows with decreasing temperature and finally reaches its maximum  $G = (2e^2/\hbar)(4\Gamma_L\Gamma_R/\Gamma^2)f(T/T_K)$  [98, 99], where  $f(T/T_K)$  has logarithmic dependence ( $\log T^{-1}$ ) at  $T \sim T_K$  and approaches unity as  $T \ll T_K$ . It should be noted that the Kondo temperature depends on the gate voltage as

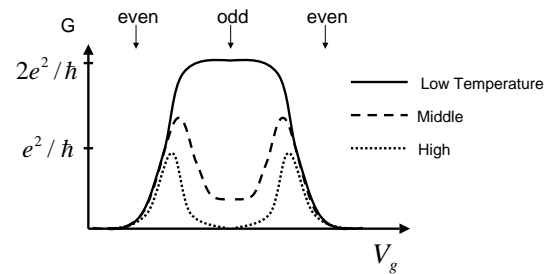


**Figure 7.** Conductance profile of quantum dot. Coulomb peaks are plotted by dotted lines. As the temperature decreases, conductance grows in the Coulomb blockade region where there are an odd number of electrons inside the dot, while conductance remains the same in the region of even number of electrons.



$k_B T_K \sim (\sqrt{\Gamma U}/2) \exp[-\pi \delta \varepsilon (U - \delta \varepsilon)/\Gamma U]$ , where  $\delta \varepsilon = \varepsilon - E_F$ . Correspondence with the conventional Kondo effect can be seen as follows: When the energy level of the dot is near the Fermi energy ( $\varepsilon \ll U$ ),  $k_B T_K \propto \exp(-\pi \delta \varepsilon/\Gamma)$ . Let  $t$  be the transfer integral between the dot state and the lead. Then, the tunneling rate is given by Fermi's golden rule:  $\Gamma \propto t^2 N(E_F)$ . An electron with a spin antiparallel to the spin in the dot state can transit virtually to and back from the unoccupied state, which causes an antiferromagnetic exchange interaction:  $J_K = t^2/\delta \varepsilon$ . Thus,  $k_B T_K \propto \exp[-\pi/J_K N(E_F)]$ , as stated above.

The temperature dependence of the conductance differs with the gate voltage. Conductance grows around the Coulomb peaks, while it hardly changes inside these peaks. This feature can be seen in Figure 7, with broken and solid lines. This effect has been observed experimentally [16, 57, 100–103]. These experiments using lateral quantum dots have several features in common. Zero-bias ( $V_{SD} = 0$ ) conductance in the Coulomb-blockade regions increases with decreasing temperature, and this conductance depends logarithmically on the temperature, as suggested by the Kondo effect. Conductance disappears when  $V_{SD}$  is applied; the Kondo effect no longer applies because of the enhancement of inelastic scattering. The peak structure appearing in the conductance as a function of  $V_{SD}$  splits in the presence of magnetic fields, as described by the Zeeman effect.

The effect of microwave radiation was also investigated, both theoretically [104] and experimentally [105], on the transport properties through quantum dots in the Kondo regime. With increasing power of the microwave of the frequency between 10 GHz and 50 GHz, the Kondo anomaly in conductance tends to disappear. This phenomenon is ascribed to dephasing of the spin states inside the quantum dot, which is introduced by external irradiation.

### 3.3. Kondo Effect of an Even Number of Electrons in a Dot

Thus far, we have assumed that the energy levels are not degenerate. We shall see that a new type of Kondo effect occurs when the electronic states inside the dot that contribute to the transport are degenerate.

In the previous section, we saw that the energy levels inside the dot can be adjusted by varying the strength of the applied magnetic field, and that two levels with different spatial symmetry can cross. Let us consider the case where the number of electrons is even. In this case, the total magnetic moment is zero, and the Kondo effect on transport phenomena would ordinarily not be expected to appear. In fact, it does appear, however, if one can adjust the strength of the magnetic field so that multiple states are involved in the transport. The key to realizing this situation is for two electrons at the highest occupied level to form a singlet state ( $S^0$ ) and three triplet states ( $S^1_0, S^1_1, S^1_{-1}$ ).

The degeneracy of a few electron states can be realized by coupling to a heat bath [106, 107] and also by an external magnetic field [108–113]. There are two types of magnetic-field effects. The first is due to the Zeeman effect, which was realized in an experiment using carbon nanotubes with a  $g$  factor larger than that of semiconductor heterostructures

[114, 115]. The second is due to the deformation of multielectron wave functions, yielding spin-singlet-spin-triplet transitions in a parabolic dot [116] and parity oscillation in a square-well dot [117].

## 4. RELATED TOPICS

### 4.1. Interacting Electrons in Double Dots

Tunneling transfer  $t_{cd}$  between adjacent dots plays an important role in coupled quantum dots, where the effect of Coulomb interaction between electrons is enhanced by a sufficiently small  $t_{cd}$  [118, 119]. When this happens, the ground state of two electrons in double dots has an antiferromagnetic correlation as in a Mott insulator [120–123].

Ono et al. [124] observed what they called a “spin blockade” effect [125, 126] due to Pauli's exclusion principle in the  $I$ - $V$  characteristics of a vertical double-dot system. In this experiment, the energy difference between the spin-singlet state and the three spin-triplet states formed inside the dot is much larger than that between two dots. In such a situation, a spin blockade occurs only in one bias direction, while an electron always resides in one dot.

Due to couplings to a heat bath, the spin-singlet state and spin-triplet states of two electrons can be degenerate, as in a dot with a certain strength of external magnetic field, yielding a resonance similar to that of the Kondo effect [127–139]. Kikoin and Avishai proposed that Kondo resonance could be observed in a double-dot system connected to reservoirs by applying asymmetric gate voltage [140]. If electrons are confined by a heterostructure of compound semiconductors, strongly correlated electron states of double dots can have a quasisresonance between multielectron states belonging to the same sector, classified by the discrete symmetries of the dots [141].

### 4.2. Tunneling Effects Related to Antiferromagnetic Correlated States

In an array of coupled quantum dots in which electrons can tunnel through the barriers of a heterostructure between adjacent quantum dots, we can expect electrons to have various phases [142–148]. When the density of electrons in a quantum-dot chain is lower than that in a chain of half-filled electrons, the system acts as a metal of correlated electrons with no antiferromagnetic order, as in a Tomonaga–Luttinger liquid, of an infinite chain. On the other hand, when the chain is half filled, a Mott–Hubbard gap opens, and the system becomes a Mott insulator with an antiferromagnetic spin correlation, where the upper Hubbard band is empty and the lower Hubbard band is fully occupied by electrons.

If an array of very small quantum dots of GaAs is embedded in bulk AlGaAs, a field effect caused by a depletion region or an external electric field causes parabolic confinement over the array. Hubbard-gap tunneling, which can be thought of as quasisresonance, is expected in these quantum-dot chains [149]. The Tomonaga–Luttinger liquid and a Mott insulator can be thought of as a single system when the overall parabolic potential confines electrons with a density

less than that of half-filled electrons. When an overall confining potential is imposed, the density of electrons in the center becomes higher. When the density of electrons in this region approaches that of half-filled, a Mott insulating state is produced, resulting in a quasi-Hubbard gap in the center of the chain. There is a metallic electron located to the left of the Mott-insulating electrons in the center of the chain in the multielectron state  $|L\rangle$ , and there is a metallic electron located to the right of the Mott-insulating electrons in the multielectron state  $|R\rangle$ . The ground state of our quantum-dot chain can be written as the bonding state of these multielectron states:  $(|L\rangle + |R\rangle)/\sqrt{2}$ , in which an electron tunnels between the right-hand side and the left-hand side, where the tunneling effect depends on the number of electrons confined in the quantum-dot chain [150]. Note that our system has multiple electrons whose wave functions are totally asymmetric and  $|L\rangle$  and  $|R\rangle$  are really multielectron states [151].

### 4.3. A Dot Coupled to Various Leads

Resonant Andreev tunneling in quantum dots coupled to a superconducting lead and a metallic lead has been investigated when the Kondo effect plays a great role [152–158]. It was found that the interplay between Kondo resonance and two-particle tunneling causes an anomalous feature in  $I$ - $V$  characteristics, which depends on the relative strength of the gap energy to the Kondo temperature. Transport through a quantum dot coupled to two superconducting leads was also investigated [159, 160].

Let us turn to a quantum dot coupled to ferromagnetic leads. When both leads have the same orientation of magnetic moments, the existence of a spin-dependent renormalization of the localized levels in a quantum dot was shown theoretically [161]. When a quantum dot is connected to two ferromagnetic leads whose magnetic moments are oriented at an angle with respect to each other, the current has been calculated using Keldysh–Green’s function and has been shown to be dependent on the angle [162].

### 4.4. Composite Quantum Structures in a Magnetic Field

Tunneling conductance through disconnected double dots threaded by an Aharonov–Bohm (AB) flux has been calculated in a wide temperature range [163–165]. Various types of AB oscillations appear depending on the temperature and the potential depth of the dots. Especially, AB oscillations have strong higher-harmonics components as a function of the magnetic flux when the potential of the dots is deep.

Let us turn our attention to a quantum dot embedded in a mesoscopic ring [166]. It is shown that the persistent current accompanied by the Kondo resonance is large in comparison with the current flowing either when the dot is at a single-particle resonance or along a simple ring of the same length. The possibility of detection of the Kondo effect by means of a persistent-current measurement is proposed [167–170]. The transmission phase shift of a quantum dot in an AB ring was discussed in the context of the Kondo effect [171]. It was proposed that this system should allow the direct observation of the well-known scattering phase

shift of  $\pi/2$  expected at zero temperature for an electron forming a Kondo singlet. The influence by the spin fluctuations on the persistent current was also investigated [172].

Simon and Affleck discussed the persistent currents induced by the AB effect in a closed ring that either embeds or is directly side-coupled to a quantum dot at Kondo resonance [173]. They mentioned that the persistent current is very sensitive to the ratio between the length of the ring and the size of the Kondo screening cloud, as suggested by a scaling theory of the Kondo effect.

### 4.5. The 0.7 Anomaly in Transport Through a Quantum Point Contact

In 1988, it was found that the conductance through a quantum point contact, that is, a narrow constriction whose size is comparable to the Fermi wavelength of the conducting electron, is quantized in units of  $2e^2/h$  [174, 175]. A single-particle description is useful in explaining the quantized conductance through a quantum point contact [176]. Besides these conductance plateaus, Thomas et al. observed an extra structure close to  $0.7(2e^2/h)$  [177–184]. The peak of the differential conductance at the bias zero suggests that the 0.7 structure is caused by the formation of Kondo-like spin states. Therefore, the description of a localized state coupled to a heat bath can be used in explaining the extra structure. Meir et al. analyzed an Anderson model, which explains the observed gate-voltage, temperature, magnetic-field, and bias-voltage dependences [185].

## GLOSSARY

**Addition energy** The energy required in an addition of an electron to a dot.

**Aharonov–Bohm effect** The effect of a gauge potential on quantum motion without any electromagnetic field.

**Anderson model** A lattice fermion model in which electrons interact with each other only at a single site.

**Andreev reflection** A phenomenon in which one of the electrons consisting a Cooper pair only reflects at a superconductor-normal junction.

**Charging energy** Energy of excess charge in a capacitor.

**Cooper pair** Paired electrons which carries a superconducting current.

**Coulomb blockade** Suppression of a tunneling current through a small junction around zero bias voltage due to the large charging energy.

**Coulomb oscillation** A periodic structure in conductance through a dot.

**Curie’s law** Power-law decay of spin susceptibility with decreasing temperatures.

**Depletion region** A semiconductor region accompanied with an imbalance of carriers and impurities.

**Exchange interaction** The effective interaction between adjacent spins.

**Fermi’s golden rule** A general formula which gives the quantum transition probability.

**Fermi wavelength** The length determined by the inverse of wave number of an electron at the Fermi surface.

**g factor** The coefficient measuring the strength of the Zeeman effect.

**Half-filled** A state of electrons on a lattice where each site has a single electron on the average.

**Heat bath** A completely thermalized system in which electrons have continuous density of states.

**Hubbard band** Two sets of states forming bands separated from each other by a Hubbard gap.

**Hubbard gap** A gap of the single-particle density of states due to electron–electron interaction when electrons are on a lattice.

**Keldysh Green’s function** A non-equilibrium Green’s function.

**Mean field** An approximation method ignoring fluctuations around the average value.

**Mott insulator** An insulator because of the existence of a Hubbard gap.

**Parity** The symmetry accompanied with a mirror-reflection transformation.

**Pauli’s exclusion principle** The law of physics stating that any quantum states cannot be occupied by two or more quantum particles which obey the Fermi statistics, e.g., electrons.

**Persistent current** Non-dissipative current due to mesoscopic effects.

**Quantum dots** A zero-dimensional quantum system which has a discrete spectrum of energy eigenstates.

**Quantum point contact** A nanometer-size waveguide in which ballistic electrons go.

**Quantum size effect** The effect of confinement of electrons which is coherent over a mesoscopic structure.

**Quasiresonance** Resonant tunneling between multiparticle states belonging the same sector classified by the discrete symmetries of the system.

**Schottky electrodes** A contact between a semiconductor and a metal where currents are rectified.

**Semiconductor heterostructures** A material’s interface composed of two different species of atoms epitaxially grown on a substrate.

**Singlet** A nonmagnetic two-spin state.

**Spin susceptibility** The degree of response of a spin to an applied magnetic field.

**Tomonaga–Luttinger liquid** A metallic state of one-dimensional electrons characterized by the absence of the Fermi surface (actually, points) due to electron–electron interaction.

**Transfer integral** An energy measuring the mobility between two states.

**Triplet** A two-spin state with magnetic moment  $\hbar$ .

**Zeeman effect** The energy splitting of spin states due to an applied magnetic field.

## REFERENCES

1. M. A. Reed, J. N. Randall, R. J. Aggarwal, R. J. Matyi, T. M. Moore, and A. E. Wetsel, *Phys. Rev. Lett.* 60, 535 (1988).
2. S. Tarucha, Y. Hirayama, T. Saku, and T. Kimura, *Phys. Rev. B* 41, 5459 (1990).
3. P. A. Maksym and T. Chakraborty, *Phys. Rev. Lett.* 65, 108 (1990).
4. F. M. Peeters, *Phys. Rev. B* 42, 1486 (1990).
5. N. F. Johnson and M. C. Payne, *Phys. Rev. Lett.* 67, 1157 (1991).
6. M. Tewardt, L. Martin-Moreno, J. T. Nicholls, M. Pepper, M. J. Kelly, V. J. Law, D. A. Ritchie, J. E. F. Frost, and G. A. C. Jones, *Phys. Rev. B* 45, 14407 (1992).
7. R. C. Ashoori, H. L. Stormer, J. S. Weiner, L. N. Pfeiffer, K. W. Baldwin, and K. W. West, *Phys. Rev. Lett.* 71, 613 (1993).
8. P. Hawrylak, *Phys. Rev. Lett.* 71, 3347 (1993).
9. G. W. Bryant, *Phys. Rev. Lett.* 59, 1140 (1987).
10. P. C. Sercel and K. J. Vahala, *Appl. Phys. Lett.* 57, 1569 (1990).
11. T. Fukui, S. Ando, Y. Tokura, and T. Toriyama, *Appl. Phys. Lett.* 58, 2018 (1991).
12. J. Oshinowo, M. Nishioka, S. Ishida, and Y. Arakawa, *Appl. Phys. Lett.* 65, 1421 (1994).
13. Y. Arakawa, *Solid-State Electron.* 37, 523 (1994).
14. R. Ugajin, *Phys. Rev. B* 53, 6963 (1996).
15. B. Meurer, D. Heitmann, and K. Ploog, *Phys. Rev. Lett.* 68, 1371 (1992).
16. D. Goldhaber-Gordon, H. Shtrikman, D. Mahalu, D. Abusch-Magder, U. Meirav, and M. A. Kastner, *Nature* 391, 156 (1998).
17. S. Sasaki, S. De Franceschi, J. M. Elzerman, W. G. van der Wiel, M. Eto, S. Tarucha, and L. P. Kouwenhoven, *Nature* 405, 764 (2000).
18. B. G. Levi, *Phys. Today* 51, 17 (1998).
19. C. J. Gorter, *Physica* 17, 177 (1951).
20. “Single Charge Tunneling,” H. Grabert and M. H. Devoret, Eds., Plenum, New York, 1992.
21. L. P. Kouwenhoven, T. H. Oosterkamp, M. W. S. Danoastro, M. Eto, D. G. Austing, T. Honda, and S. Tarucha, *Science* 278, 1788 (1997).
22. Y. Nakamura, Yu. A. Pashkin, and J. S. Tsai, *Nature* 398, 786 (1999).
23. R. Kubo, *Phys. Lett.* 1, 49 (1962).
24. W. P. Halperin, *Rev. Mod. Phys.* 58, 533 (1986).
25. See, for example, “Metal Nanoparticles,” D. L. Feldheim and C. A. Foss Jr., Eds., Marcel Dekker, Inc., New York, 2002.
26. P. W. Anderson, *Phys. Rev.* 124, 41 (1961).
27. A. C. Hewson, “The Kondo Problem to Heavy Fermions,” Cambridge University Press, Cambridge, 1993.
28. J. Kondo, *Prog. Theor. Phys.* 32, 37 (1964).
29. K. Obermayer, W. G. Teich, and G. Mahler, *Phys. Rev. B* 37, 8096 (1988).
30. W. G. Teich, K. Obermayer, and G. Mahler, *Phys. Rev. B* 37, 8111 (1988).
31. U. Bockelmann and G. Bastard, *Phys. Rev. B* 42, 8947 (1990).
32. T. Inoshita and H. Sakaki, *Phys. Rev. B* 46, 7260 (1992).
33. C. S. Lent, P. D. Toungaw, and W. Porod, *Appl. Phys. Lett.* 62, 714 (1993).
34. S.-R. Eric, A. H. MacDonald, and M. D. Johnson, *Phys. Rev. Lett.* 71, 3194 (1993).
35. G. W. Bryant, *Phys. Rev. B* 47, 1683 (1993).
36. N. Taniguchi and B. L. Altshuler, *Phys. Rev. Lett.* 71, 4031 (1993).
37. V. N. Prigodin, B. L. Altshuler, K. B. Efetov, and S. Iida, *Phys. Rev. Lett.* 72, 546 (1994).
38. R. Ugajin, *J. Appl. Phys.* 77, 5509 (1995).
39. K. B. Efetov, *Phys. Rev. Lett.* 74, 2299 (1995).
40. C. I. Duruöz, R. M. Clarke, C. M. Marcus, and J. S. Harris, Jr., *Phys. Rev. Lett.* 74, 3237 (1995).
41. Y. Alhassid and C. H. Lewenkopf, *Phys. Rev. Lett.* 75, 3922 (1995).
42. K. Nomoto, R. Ugajin, T. Suzuki, and I. Hase, *J. Appl. Phys.* 79, 291 (1996).
43. C. W. J. Beenakker, *Rev. Mod. Phys.* 69, 731 (1997).
44. R. J. Warburton, C. S. Dürr, K. Karrai, J. P. Kotthaus, G. Medeiros-Ribeiro, and P. M. Petroff, *Phys. Rev. Lett.* 79, 5282 (1997).

45. D. L. Klein, R. Roth, A. K. L. Lim, A. P. Alivisatos, and P. L. McEuen, *Nature* 389, 699 (1997).
46. J. König, Y. Gefen, and G. Schön, *Phys. Rev. Lett.* 81, 4468 (1998).
47. J. A. Folk, S. R. Patel, K. M. Birnbaum, C. M. Marcus, C. I. Duruöz, and J. S. Harris, Jr., *Phys. Rev. Lett.* 86, 2102 (2001).
48. B. I. Halperin, A. Stern, Y. Oreg, J. N. H. J. Cremers, J. A. Folk, and C. M. Marcus, *Phys. Rev. Lett.* 86, 2106 (2001).
49. I. L. Aleiner and V. I. Fal'ko, *Phys. Rev. Lett.* 87, 256801 (2001).
50. K. Kanisawa, M. J. Butcher, Y. Tokura, H. Yamaguchi, and Y. Hirayama, *Phys. Rev. Lett.* 87, 196804 (2001).
51. S. Sauvage, P. Boucaud, R. P. S. M. Lobo, F. Bras, G. Fishman, R. Prazeres, F. Glotin, J. M. Ortega, and J.-M. Gérard, *Phys. Rev. Lett.* 88, 177402 (2002).
52. W. Sheng and J.-P. Leburton, *Phys. Rev. Lett.* 88, 167401 (2002).
53. M. A. Kastner, *Rev. Mod. Phys.* 64, 849 (1992).
54. Y. Tanaka and H. Akera, *Phys. Rev. B* 53, 3901 (1996).
55. P. Recher, E. V. Sukhorukov, and D. Loss, *Phys. Rev. Lett.* 85, 1962 (2000).
56. R. A. Jalabert, A. D. Stone, and Y. Alhassid, *Phys. Rev. Lett.* 68, 3468 (1992).
57. D. Goldhaber-Gordon, J. Göres, M. A. Kastner, H. Shtrikman, D. Mahalu, and U. Meirav, *Phys. Rev. Lett.* 81, 5225 (1998).
58. A. Kawabata, *J. Phys. Soc. Jpn.* 60, 3222 (1991).
59. Y. Meir, N. S. Wingreen, and P. A. Lee, *Phys. Rev. Lett.* 70, 2601 (1993).
60. T. Inoshita, A. Shimizu, Y. Kuramoto, and H. Sakaki, *Phys. Rev. B* 48, 14725 (1993).
61. N. S. Wingreen and Y. Meir, *Phys. Rev. B* 49, 11040 (1994).
62. T. Inoshita, A. Shimizu, Y. Kuramoto, and H. Sakaki, Correlated electron transport through a real-life quantum dot (J. Lockwood, Ed.). "Proceedings of the 22nd International Conference on the Physics of Semiconductors," World Scientific, Singapore, 3, 1931 (1995).
63. F. Yamaguchi, M. Yamaga, and K. Kawamura, *J. Magn. Magn. Mater.* 140, 1207 (1995).
64. M. Yamaga and K. Kawamura, *J. Magn. Magn. Mater.* 140, 1209 (1995).
65. Y. Funabashi, K. Ohtsubo, M. Eto, and K. Kawabata, *Solid-State Electron.* 42, 1367 (1998).
66. R. López, R. Aguado, G. Platero, and C. Tejedor, *Phys. Rev. Lett.* 81, 4688 (1998).
67. A. Kaminski, Yu. V. Nazarov, and L. I. Glazman, *Phys. Rev. B* 62, 8154 (2000).
68. M. Plihal, D. C. Langreth, and P. Nordlander, *Phys. Rev. B* 61, R13341 (2000).
69. U. Gerland, J. v. Delft, T. A. Costi, and Y. Oreg, *Phys. Rev. Lett.* 84, 3710 (2000).
70. A. Rosch, J. Kroha, and P. Wölfle, *Phys. Rev. Lett.* 87, 156802 (2001).
71. P. Coleman, C. Hooley, and O. Parcollet, *Phys. Rev. Lett.* 86, 4088 (2001).
72. A. L. Chudnovskiy and S. E. Ulloa, *Phys. Rev. B* 63, 165316 (2001).
73. Y. Yu, T. C. Au Yeung, W. Z. Shangquan, and C. H. Kam, *Phys. Rev. B* 63, 205314 (2001).
74. I. Affleck and P. Simon, *Phys. Rev. Lett.* 86, 2854 (2001).
75. M. Keller, U. Wilhelm, J. Schmid, J. Weis, K. v. Klitzing, and K. Eberl, *Phys. Rev. B* 64, 033302 (2001).
76. R. López, R. Aguado, G. Platero, and C. Tejedor, *Phys. Rev. B* 64, 075319 (2001).
77. P. G. Silvestrov and Y. Imry, *Phys. Rev. B* 65, 035309 (2002).
78. Y. Ji, M. Heiblum, and H. Shtrikman, *Phys. Rev. Lett.* 88, 076601 (2002).
79. Y.-W. Lee and Y.-L. Lee, *Phys. Rev. B* 65, 155324 (2002).
80. Y. Wan, P. Phillips, and Q. Li, *Phys. Rev. B* 51, 14782 (1995).
81. J. König, H. Schoeller, and G. Schön, *Phys. Rev. Lett.* 76, 1715 (1996).
82. J. König, J. Schmid, H. Schoeller, and G. Schön, *Phys. Rev. B* 54, 16820 (1996).
83. W. Izumida, O. Sakai, and Y. Shimuzu, *J. Phys. Soc. Jpn.* 67, 2444 (1998).
84. F. Simmel, R. H. Blick, J. P. Kotthaus, W. Wegscheider, and M. Bichler, *Phys. Rev. Lett.* 83, 804 (1999).
85. S.-J. Xiong and Y. Xiong, *Phys. Rev. Lett.* 83, 1407 (1999).
86. O. Takagi and T. Saso, *J. Phys. Soc. Jpn.* 68, 2894 (1999).
87. L. P. Rokhinson, L. J. Guo, Y. Chou, and D. C. Tsui, *Phys. Rev. B* 60, R16319 (1999).
88. A. L. Yeyati, F. Flores, and A. Martín-Rodero, *Phys. Rev. Lett.* 83, 600 (1999).
89. O. Tsuchiya, I. Ichinose, and Y. Kayama, *Phys. Rev. B* 60, 2350 (1999).
90. L. Craco and K. Kang, *Phys. Rev. B* 59, 12244 (1999).
91. D. Matsumoto, *J. Phys. Soc. Jpn.* 69, 1449 (2000).
92. R. M. Konik, H. Saleur, and A. W. W. Ludwig, *Phys. Rev. Lett.* 87, 236801 (2001).
93. W. Izumida, O. Sakai, and S. Suzuki, *J. Phys. Soc. Jpn.* 70, 1045 (2001).
94. D. Sprinzak, Y. Ji, M. Heiblum, D. Mahalu, and H. Shtrikman, *Phys. Rev. Lett.* 88, 176805 (2002).
95. D. Gerace, E. Pavarini, and L. C. Andreani, *Phys. Rev. B* 65, 155331 (2002).
96. N. Sergueev, Q.-F. Sun, H. Guo, B. G. Wang, and J. Wang, *Phys. Rev. B* 65, 165303 (2002).
97. "Kondo Effect and Dephasing in Low-Dimensional Metallic Systems," V. Chandrasekhar, C. v. Haesendonck, and A. Zawadowski, Eds., Kluwer Academic Publishers, The Netherlands, 2000.
98. L. I. Glazman and M. E. Raikh, *JETP Lett.* 47, 452 (1988).
99. T. K. Ng and P. A. Lee, *Phys. Rev. Lett.* 61, 1768 (1988).
100. S. M. Cronenwett, T. H. Oosterkamp, and L. P. Kouwenhoven, *Science* 281, 540 (1998).
101. F. Simmel, R. H. Blick, J. P. Kotthaus, W. Wegscheider, and M. Bichler, *Phys. Rev. Lett.* 83, 804 (1999).
102. J. Schmid, J. Weis, K. Eberl, and K. v. Klitzing, *Phys. Rev. Lett.* 84, 5824 (2000).
103. W. G. van der Wiel, S. De Franceschi, T. Fujisawa, J. M. Elzerman, S. Tarucha, and L. P. Kouwenhoven, *Science* 289, 2105 (2000).
104. A. Kaminski, Yu. V. Nazarov, and L. I. Glazman, *Phys. Rev. Lett.* 83, 384 (1999).
105. J. M. Elzerman, S. de Franceschi, D. Goldhaber-Gordon, W. G. vander Wiel, and L. P. Kouwenhoven, *J. Low Temp. Phys.* 118, 375 (2000).
106. M. Eto and Y. V. Nazarov, *Phys. Rev. Lett.* 85, 1306 (2000); *Phys. Rev. B* 64, 085322 (2001).
107. Y. Imai and N. Kawakami, *J. Phys. Soc. Jpn.* 70, 1851 (2001).
108. D. Giuliano and A. Tagliacozzo, *Phys. Rev. Lett.* 84, 4677 (2000); D. Giuliano, B. Jouault, and A. Tagliacozzo, *Phys. Rev. B* 63, 125318 (2001).
109. M. Pustilnik, Y. Avishai, and K. Kikoin, *Phys. Rev. Lett.* 84, 1756 (2000).
110. M. Pustilnik and L. I. Glazman, *Phys. Rev. Lett.* 85, 2993 (2000); *Phys. Rev. Lett.* 87, 216601 (2001).
111. W. Izumida, O. Sakai, and S. Tarucha, *Phys. Rev. Lett.* 87, 216803 (2001).
112. C. Tejedor and L. Martín-Moreno, *Phys. Rev. B* 63, 035319 (2001).
113. B. Dong and X. L. Lei, *Phys. Rev. B* 63, 235306 (2001).
114. J. Nygård, D. H. Cobden, and P. E. Lindelof, *Nature* 408, 342 (2000).
115. M. R. Buitelaar, A. Bachtold, T. Nussbaumer, M. Iqbal, and C. Schonenberger, *Phys. Rev. B* 68, 156801 (2002).
116. M. Wagner, U. Merkt, and A. V. Chaplik, *Phys. Rev. B* 45, 1951 (1992).
117. R. Ugajin, *Surf. Sci.* 432, 1 (1999).
118. R. Ugajin, T. Suzuki, K. Nomoto, and I. Hase, *J. Appl. Phys.* 76, 1041 (1994).

119. T. H. Oosterkamp, S. F. Godijn, M. J. Uilenreef, Y. V. Nazarov, N. C. van der Vaart, and L. P. Kouwenhoven, *Phys. Rev. Lett.* 80, 4951 (1998).
120. R. Ugajin, *J. Appl. Phys.* 76, 2833 (1994).
121. D. Loss and D. P. Divincenzo, *Phys. Rev. A* 57, 120 (1998).
122. G. Burkard, G. Seelig, and D. Loss, *Phys. Rev. B* 62, 2581 (2000).
123. C. A. Büsser, E. V. Anda, A. L. L. Lima, M. A. Davidovich, and G. Chiappe *Phys. Rev. B* 62, 9907 (2000).
124. K. Ono, D. G. Austing, Y. Tokura, and S. Tarucha, *Science* 297, 1313 (2002).
125. D. Weinmann, W. Häusler, and B. Kramer, *Phys. Rev. Lett.* 74, 984 (1995).
126. T. Fujisawa, D. G. Austing, Y. Tokura, Y. Hirayama, and S. Tarucha, *Phys. Rev. Lett.* 88, 236802 (2002).
127. C. Niu, L.-J. Liu, and T.-H. Lin, *Phys. Rev. B* 51, 5130 (1995).
128. T. Ivanov, *Phys. Rev. B* 56, 12339 (1997).
129. N. Andrei, G. T. Zimányi, and G. Schön, *Phys. Rev. B* 60, R5125 (1999).
130. S. M. Maurer, S. R. Patel, C. M. Marcus, C. I. Duruöz, and J. S. Harris, Jr., *Phys. Rev. Lett.* 83, 1403 (1999).
131. A. Georges and Y. Meir, *Phys. Rev. Lett.* 82, 3508 (1999).
132. K. Kikoin and Y. Avishai, *Phys. Rev. B* 62, 4647 (2000).
133. D. Giuliano and A. Tagliacozzo, *Phys. Rev. Lett.* 84, 4677 (2000).
134. W. Izumida and O. Sakai, *Phys. Rev. B* 62, 10260 (2000).
135. R. Aguado and D. C. Langreth, *Phys. Rev. Lett.* 85, 1946 (2000).
136. D. Loss and E. V. Sukhorukov, *Phys. Rev. Lett.* 84, 1035 (2000).
137. T. Aono and M. Eto, *Phys. Rev. B* 63, 125327 (2001); *Phys. Rev. B* 64, 073307 (2001).
138. H. Jeong, A. M. Chang, and M. R. Melloch, *Science* 293, 2221 (2001).
139. P. A. Orellana, G. A. Lara, and E. V. Anda, *Phys. Rev. B* 65, 155317 (2002).
140. K. Kikoin and Y. Avishai, *Phys. Rev. Lett.* 86, 2090 (2001); *Phys. Rev. B* 65, 115329 (2002).
141. R. Ugajin, *Appl. Phys. Lett.* 68, 2657 (1996); *J. Appl. Phys.* 81, 2693 (1997).
142. H. Sakaki, *Jpn. J. Appl. Phys.* 28, L314 (1989).
143. K. Ismail, W. Chu, A. Yen, D. A. Antoniadis, and H. I. Smith, *Appl. Phys. Lett.* 54, 46 (1989).
144. C. A. Stafford and S. Das Sarma, *Phys. Rev. Lett.* 72, 3590 (1994).
145. F. R. Waugh, M. J. Berry, D. J. Mar, and R. M. Westervelt, *Phys. Rev. Lett.* 75, 705 (1995).
146. F. R. Waugh, M. J. Berry, C. H. Crouch, C. Livermore, D. J. Mar, R. M. Westervelt, K. L. Campman, and A. C. Gossard, *Phys. Rev. B* 53, 1413 (1996).
147. R. Ugajin, *Phys. Rev. B* 53, 10141 (1996).
148. R. Ugajin, *Physica E* 1, 226 (1997).
149. R. Ugajin, *Phys. Rev. Lett.* 80, 572 (1998); *Phys. Rev. B* 59, 4952 (1999).
150. R. Ugajin, *Physica B* 240, 128 (1997).
151. R. Ugajin, *Int. J. Mod. Phys. B* 13, 2689 (1999).
152. K. Kang, *Phys. Rev. B* 58, 9641 (1998).
153. R. Fazio and R. Raimondi, *Phys. Rev. Lett.* 80, 2913 (1998).
154. R. Raimondi and P. Schwab, *Superlattices Microstruct.* 25, 1141 (1999).
155. P. Schwab and R. Raimondi, *Phys. Rev. B* 59, 1637 (1999).
156. K. Kang, *Phys. Rev. B* 65, 033302 (1998).
157. Q.-F. Sun, H. Guo, and T.-H. Lin, *Phys. Rev. Lett.* 87, 176601 (2001).
158. J. C. Cuevas, A. L. Yeyati, and A. Martin-Rodero, *Phys. Rev. B* 63, 094515 (2001).
159. T. Ivanov, *Phys. Rev. B* 59, 169 (1999).
160. D. Matsumoto, *J. Phys. Soc. Jpn.* 70, 492 (2001).
161. J. Fransson, O. Eriksson, and I. Sandalov, *Phys. Rev. Lett.* 88, 226601 (2002); *Phys. Rev. Lett.* 89, 179903 (2002).
162. N. Sergueev, Q. Sun, H. Guo, B. G. Wang, and J. Wang, *Phys. Rev. B* 65, 165303 (2002).
163. W. Izumida, O. Sakai, and Y. Shimzu, *J. Phys. Soc. Jpn.* 66, 717 (1997).
164. W. Izumida, O. Sakai, and Y. Shimzu, *Physica B* 259, 215 (1999).
165. O. Sakai, S. Suzuki, and W. Izumida, *J. Phys. Soc. Jpn.* 68, 1640 (1999).
166. M. Büttiker and C. A. Stafford, *Phys. Rev. Lett.* 76, 495 (1996).
167. V. Ferrari, G. Chiappe, E. V. Anda, and M. A. Davidovich, *Phys. Rev. Lett.* 82, 5088 (1999).
168. K. Kang and S.-C. Shin, *Phys. Rev. Lett.* 85, 5619 (2000).
169. K. Kang and L. Craco, *Phys. Rev. B* 65, 033302 (2001).
170. J. König and Y. Gefen, *Phys. Rev. B* 65, 045316 (2001).
171. U. Gerland, J. v. Delft, T. A. Costi, and Y. Oreg, *Phys. Rev. Lett.* 84, 3710 (2000).
172. S. Y. Cho, K. Kang, C. K. Kim, and C. Ryu, *Phys. Rev. B* 64, 033314 (2001).
173. P. Simon and I. Affleck, *Phys. Rev. B* 64, 085308 (2001).
174. B. J. van Wees, H. van Houten, C. W. J. Beenakker, J. G. Williamson, L. P. Kouwenhoven, D. van del Marcel, and C. T. Foxon, *Phys. Rev. Lett.* 60, 848 (1988).
175. D. A. Wharam, T. J. Thornton, R. Newbury, M. Pepper, H. Ahmed, J. E. F. Frost, D. G. Hasko, D. C. Peacock, D. A. Ritchie, and G. A. Jones, *J. Phys. C* 21, 209 (1988).
176. A. Kawabata, *J. Phys. Soc. Jpn.* 58, 372 (1989).
177. K. J. Thomas, J. T. Nicholls, M. Y. Simmons, M. Pepper, D. R. Mace, and D. A. Ritchie, *Phys. Rev. Lett.* 77, 135 (1996).
178. K. J. Thomas, J. T. Nicholls, N. J. Appleyard, M. Y. Simmons, M. Pepper, D. R. Mace, W. R. Tribe, and D. A. Ritchie, *Phys. Rev. B* 58, 4846 (1998).
179. K. J. Thomas, J. T. Nicholls, M. Y. Simmons, W. R. Tribe, A. G. Davies, and M. Pepper, *Phys. Rev. B* 59, 12252 (1999).
180. K. J. Thomas, J. T. Nicholls, M. Pepper, W. R. Tribe, M. Y. Simmons, and D. A. Ritchie, *Phys. Rev. B* 61, 13365 (2000).
181. A. Kristensen, H. Bruus, A. E. Hansen, J. B. Jensen, P. E. Lindelof, C. J. Marckmann, J. Nygård, and C. B. Sorensen, *Phys. Rev. B* 62, 10950 (2000).
182. D. J. Reilly, G. R. Facer, A. S. Dzurak, B. E. Kane, R. G. Clark, P. J. Stiles, R. G. Clark, A. R. Hamilton, J. L. O'Brien, and N. E. Lumpkin, *Phys. Rev. B* 63, 121311 (2001).
183. K. Hirose and N. S. Wingreen, *Phys. Rev. B* 64, 073305 (2001).
184. S. M. Cronenwett, H. J. Lynch, D. Goldhaber-Gordon, L. P. Kouwenhoven, C. M. Marcus, K. Hirose, N. S. Wingreen, and V. Umansky, *Phys. Rev. Lett.* 88, 226805 (2002).
185. Y. Meir, K. Hirose, and N. S. Wingreen, *Phys. Rev. Lett.* 89, 196802 (2002).





# Laser-Scanning Probe Microscope Assisted Nanofabrication

Piero Morales

*Unità Materiali e Nuove Tecnologie, Centro Ricerche della Casaccia, Rome, Italy*

## CONTENTS

1. Introduction
  2. Pulsed Laser Desorption and Ablation
  3. Resonance Enhanced Multiple Photon Ionization
  4. Matrix Assisted Laser Desorption Ionization
  5. Proximity Enhancement of the Electromagnetic (EM) Field
  6. Thermal Expansion in the Laser Field
  7. Nanopatterning of Metallic Layers
  8. Small Cluster and Single Atom Depositions on Flat Surfaces
  9. Laser-Scanning Probe Microscope (SPM) Assisted Shadow Mask Deposition
  10. Conclusions
- Glossary  
References

## 1. INTRODUCTION

This chapter will describe some recent attempts in nanofabrication aiming to exploit the use of lasers and scanning probe instruments in conjunction. More than reviewing fully established techniques, we aim to introduce the reader to ideas and technologies which, although in part still in their infancy, represent the essence of the “bottom up” nanotechnological fabrication process.

Why is the “bottom up” approach important? Building matter or devices starting from single atoms or molecules has been recognized from the very beginning of the attempts toward nanotechnology as the conceptually ideal methodology, in spite of the fact that this approach is intrinsically slow and perhaps inadequate to parallel mass fabrication. Not all that is valuable is necessarily addressed to a large market, however; all pieces of fine arts, and in general all achievements of knowledge, for example, are unique examples of “bottom up” methodology that have a universally

recognized intrinsic high value. But there are also many high value technological products that are built in a limited number, like high performance nuclear magnetic resonance imagers for clinical use, or machineries for specific productions. In the nanoscopic realm, where humanity has no direct perception, art may not be an important issue; bottom up nanotechnologies, however, will help in achieving a deeper understanding in materials science, an advancement of human knowledge of high intrinsic value. They will also soon enable us to fabricate unique high value devices in the fields of nanomedicine and surgery, of neural prostheses, of sensing, beyond supplying prototypes for nanoelectronics and more and more sophisticated devices for nanoscopic mass productions. Thus, although the present industrial approach to micro- and nanofabrication of highly integrated electronic circuits still relies completely on the high throughput, parallel, “top-down” approach represented by optical lithography, as early as in 1992 a paradoxical but significant statement was made by pioneers in nanoscience: that “lithography in nanofabrication is like building the Golden Gate bridge by carving it out of a single block of steel” [1]. On the other hand, an equally paradoxical and important statement is often made today, that “if technology is represented by computers and cellular phones, or more simply by motor cars or washing machines, then in nanotechnology we are today at the pickaxe stage.” The most used “pickaxe” is the scanning probe instrument, or microscope (SPM), whose nanometric controllable tip is also employed to carve and drill surfaces [2], or to accumulate small amounts of material in nanometrically resolved spots, like in silicon nanooxidation lithography [3], or even to move around and put together little “bricks” represented by atoms [4], molecules [5], or self-assembled nanostructures (such as fullerenes and nanotubes of different sorts) [6, 7].

If we are to continue with the analogy, scientists often perform their bottom up nanoassemblage with the pickaxe in their hands and a very limited supply of bricks (atoms or molecules) somewhere close to their working location. When they finish the supply, although they have learned a lot on the art of “nanomasonry” (a huge value in itself), they have not completed the building, unless it is so elementary to be of little practical use. Unfortunately we do not have

a nanoscopic truck to carry more atomic components easily, but we shall see in the following that lasers may contribute to carry or produce new bricks.

Thus, in order to tackle real technological challenges, bottom up nanotechnology needs to turn into something more than the mere use of a nanometric “pickaxe.” There are of course many other challenges beyond easy and unlimited delivery of atomic or molecular components; for example, in order to meet the requirement of faster bottom up assembly, scientists hire a large team of pickaxe workers, or in other words develop arrays of scanning probes controlled by computer, which will perform their building tasks in parallel [8]. Very recent developments have achieved arrays of  $32 \times 32$  scanning force cantilevers, capable of printing 40 nm size spots, which can be used to encode information with a density of 1 Gb/mm<sup>2</sup>. Further, not always do we necessarily need to use simple bricks to assemble our nanodevices. Sometimes it is convenient to put together preassembled elements, like the fullerenes that we already mentioned, but also more complex ones. In the nanoworld the preassembly step is often conveniently performed by chemistry or biology, which therefore have received increasing attention recently [9–13]. Positioning of complex “smart” molecules, capable of performing specific tasks, in nanometrically predetermined locations on the surface of a microelectronic chip is thus one important goal that is pursued by several research groups [14–16] in spite of the difficulties of dealing with delicate soft matter that easily loses its smart properties. Again, as we shall see, lasers have recently given an important contribution to “soft” deposition techniques, the bases of which are therefore described in Sections 3 and 4.

One further, very important requirement of any bottom up assembling technique is the ability to see, characterize, and test what we have produced. Scanning probe instruments of course are almost ideal instruments to this aim. Here we find that the pickaxe analogy no longer holds. These rather simple manipulation tools turn into sophisticated sensors not only of the morphology of what we have done, but also of its stiffness, its external force fields, its electrical conductivity, and even, through its optical and spectroscopic characteristics, its physical chemical state. Once more we have a hint that lasers, as intense sources of well manageable light, may have something to do with such characterizations, well beyond their common use in sensing the deflection of scanning force cantilevers. We refer here to the exciting very recent area of near-field optics and spectroscopy, pursued both by tapered optical fibers, as in “conventional” scanning near-field optical microscopes [17] and by the exploitation of the near-field scattered by metallic tips, [18, 19] for spectroscopic characterizations [20, 21].

Lasers as a nanotechnological tool, and in particular deep ultraviolet (UV) lasers, are being commonly used nowadays for optical lithography in the 100 nm range, allowing fast parallel processing of large surfaces through the multistep procedures of lithography. This type of technology is based on location specific degradation of a polymeric resist, its removal followed by the subsequent deposition of a uniform layer of the desired material, and finally the removal of the unwanted portions by means of the removal of the remaining resist. It is a complex procedure that allows parallel deposition of the same material in different locations,

the procedure to be repeated for each material for a total of 20 or 30 times in modern industrial technology. But the use of lasers in nanotechnology can be much more than this.

First of all they are successfully used as a tool to vaporize materials to be deposited [22]; laser fabrication of layered thin films has gained enormous importance in recent times, the current literature being extremely rich. Pulsed laser ablation or desorption in particular has been used for deposition of intact delicate materials such as polymers and organic or biological molecules. They may thus represent an important and convenient source of vapor phase material, particularly suitable in micro- and nanotechnology because, due to ease of focusing, they can act upon very small amounts of valuable materials. Desorption (i.e., the transfer in vapor phase of atoms and molecules adsorbed on a surface without affecting the surface structure) and ablation, or bulk evaporation of the material with strong damage of the surface, will be shortly described in Section 2, with some insight into the threshold of plasma ignition for ablated materials and into integrity of vaporized large molecules.

Second, lasers are used to ionize vapor phase molecules, both directly, acting on neutral vapors (in which case the ionization process can be made extremely material selective, by exploiting resonance enhanced multiple photon ionization, described in Section 3) or indirectly by proton adduction following extensive molecular fragmentation [as in the case of the matrix assisted laser desorption ionization (MALDI) technique, described in Section 4]. Ionization can then be used to direct molecular ions at will; use of an electric field applied to the SPM tips, or of very fine movable masks driven by the piezo actuators of the SPM, can produce nanometric patterning when coupled to laser ablation/ionization. Recent work performed in this direction will be reported in Section 9. In this respect laser radiation and the applied electric fields may well play the role of the molecular carrier, or “truck,” that we wished to have. In perspective, we can foresee that nanofabrication strategies based on supplying a burst of laser ionized gaseous material finely directed at the SPM tip, where a voltage pulse steers selected ions to hit the device surface, would be most appealing due to its flexibility (almost any material can be vaporized and ionized) and speed (pulsed lasers can be operated at high repetition rates).

Furthermore, in conjunction with the fine tips of SPMs, lasers can supply resolution beyond the diffraction limit in optical lithography, exploiting the near EM field scattered by the nanometric tip, that we have already briefly mentioned with respect to characterization rather than fabrication. This near-field enhancement of the incident radiation, which will be described in Section 5, has typical dimensions of the order of the tip apex rather than of the wavelength of the incident light; it can then be exploited to reach the ionization threshold, or for field induced desorption, surface melting, and even manipulation [23, 24] all limited to the nanometric region close to the tip apex. As we have mentioned, the same process can also be used in the characterization step: the enhancement of Raman spectral intensities due to EM field enhancement caused by surface nanostructures (often called SERS, surface enhanced Raman scattering), also occurs in the proximity of the SPM tip; it is thus possible to obtain Raman spectra from regions of the surface

that have comparable dimensions to that of the facing tip apex, easily nanometer sized [20]. This means that we are in principle capable of characterizing spectroscopically single molecules or small clusters immediately after performing a nanostructured deposition.

Finally, laser induced thermal effects can also be extremely important in localized nanostructuring of surfaces. We shall thus spend some time in Section 6 to show some possible models of thermal expansion and to highlight the important parameters that affect this process. It is commonly recognized that a laser pulse focused at the scanning tunneling microscope tip will cause a thermal expansion of the tip; this is normally considered a drawback of laser-SPM techniques. It can, however, also be used to mechanically affect the surface and, more subtly, to couple the heating effect due to light absorption to the additional heating caused by the exponential increase of the tunneling current, to thermally desorb single atoms or molecules from the tip. Furthermore, thermal recrystallization of the substrate surface may occur under strong laser irradiance, leading to a variation of the electric field distribution between tip and surface. Field enhancement effects may arise both from the tip and from the recrystallized surface, causing atoms or molecules to be moved to or from the surface.

As mentioned at the beginning, laser assisted SPM nanofabrication is not a fully established technique yet. In spite of early attempts soon after the invention of the STM, these methodologies are not as widely used as other nanotechniques. Beyond the obvious fact that bottom up methods are less interesting for the present electronic industry, this is probably due partly to the high cost and complexity of the experimental apparatus, reducing the number of research groups active on the subject, but even more to the high number of parameters playing a role at the STM gap. This caused early experiments to be unreliable, not easy to reproduce, and even less to interpret. With the progress of theory, mainly on thermal effects and field enhancement, the role of each important parameter is becoming more clear, so that interest is being revived and fascinating possibilities can be seen.

This chapter will only deal with laser assisted SPM nanostructuring, referring the reader to the excellent recent review by Grafstrom for the important fields of optically assisted scanning probe microscopy and scanning probe assisted spectroscopy, where most exciting achievements have also been obtained recently [25].

## 2. PULSED LASER DESORPTION AND ABLATION

Pulsed lasers have been used for many years to remove material from a sample and transfer it onto a substrate with or without the assistance of electric fields. There are thousands of publications on this mature subject, regarding all classes of materials and applications, from polymers like PTFE, PMMA, or polycarbonate [26, 27], to composites as magnetic [28] and piezoelectric materials [29], from organic semiconductors [30] to biological macromolecules [31, 32], from hard coatings of diamondlike carbon [33] to single wall carbon nanotubes films encapsulated in amorphous carbon [34], and of course to metals and semiconducting materials

[35, 36], quoting only a very small selection of recent work. Useful recent reviews of the subject are those by Haglund [22], Voevodin and Donley [33], and Zhigilei et al. [37], particularly insofar as modeling of the MALDI technique is concerned. The fundamentals of the subject can be found in the books by von Allmen [38] and Lubman [39].

When a laser beam interacts with a solid, light absorbing surface, energy is transferred from the radiation field into the solid. Dissipation of this energy leads to heating of the solid, which can be so strong as to cause melting and vaporization of material. For example, continuous wave lasers are industrially used to drill and cut metals, wood, or textiles or to weld metals. Further, the evaporated material can absorb the incident radiation, mainly by multiple photon absorption, and become strongly ionized. Above a threshold irradiance (or power density, measured in  $\text{W}/\text{cm}^2$ ), easily reached by pulsed lasers, plasma ignition is normally observed. The physical processes involved are too complicated and interdependent to be treated in any depth here; we shall only spend some time on two aspects of desorption and ablation that are particularly relevant to organic and biological molecules, that is, maintenance of molecular integrity through selective breakage of the adsorption bonds, and plasma ignition threshold. The MALDI technique, of particular relevance for biological molecules, will be described in the following section.

Let us consider a molecular species adsorbed on a solid surface, in the common case in which the total adsorption energy is higher than the internal binding energy of the weakest bond. If laser irradiation goes on for a long time, the temperature can increase to values where adsorbed molecules are dissociated as the amount of energy transferred from the surface to the internal degrees of freedom of the molecule exceeds the covalent molecular binding energies. The process is analogous to heating molecules on a flame, simply producing molecular dissociation. However, while the phonons in the heated solid may easily exchange energy with the low frequency modes of the adsorption weak interactions, being entirely off resonance with the higher frequency modes of the intramolecular covalent bonds, they experience a “bottleneck” in exciting the molecular vibrational modes [40]. Therefore, use of a short laser pulse tuned away from the molecular absorption band will help in desorbing intact molecules by concentrating the energy input in times much shorter than the time necessary to overcome the bottleneck. If  $\tau$  is the excitation duration, this can be expressed by

$$\tau < 1/k$$

where  $k = \nu \exp(-\xi)$  is the rate constant for energy transfer between the weak adsorption mode of low frequency  $\nu$  and the internal molecular vibrations, and the adiabaticity parameter  $\xi = 2\pi T/T'$  (with  $T$  and  $T'$  the characteristic times of motions of the adsorption mode and of the intramolecular vibrational mode respectively) is a measure of the difficulty of energy exchange between adsorption and covalent modes. If  $D$  is the weak bond energy to the surface, the condition for desorption of intact molecules is

$$\tau < (h/D) \exp \xi$$

where  $h$  is Planck's constant.

The important parameters are thus the heating rate  $1/\tau$  which, to the aim of obtaining vapor phase intact molecules, must be as high as possible, the decoupling between modes (or adiabaticity)  $\xi$ , which should also be large, and the adsorption energy  $D$ , which should be as low as possible. Typical values for  $\xi$ , according to Zare and Levine [40], are around 10, which, considering binding energies of about 0.12 eV (a typical adsorption energy), requires heating rates of the order of  $10^{11}$  or  $10^{12}$  K/s. It has been proved experimentally since the mid 1980s that indeed nanosecond laser excitation yields desorption of intact  $\text{CH}_3\text{OH}$  and  $\text{C}_2\text{H}_4$  [41, 42] whereas at much lower heating rates there is complete fragmentation. Other examples of intact desorption of fairly labile molecules concern, for example, amino acids [43, 44].

We have described so far the so-called desorption process. Increasing the power density of the light impinging on the surface will lead to disruption of the surface and ejection of material, which is commonly termed ablation. Ablation is normally associated with a large amount of ejected material that is visually observable and because of its shape has been named the “plume.” The plume has a variable degree of ionization and, unlike desorption, requires a threshold power density that is of the order of  $10^7$ – $10^9$  W/cm<sup>2</sup>. Interestingly, the threshold energies are orders of magnitude higher than the cohesive energy of the outermost monolayer (estimated in the range of 0.1–1 mJ), suggesting that a large amount of energy is dissipated into relaxation processes not leading to material ejection. As we have already mentioned laser ablation at high laser irradiances can produce a plasma. When plasma ignition occurs, molecules within the plasma are in large part destroyed, although the sudden sublimation of the area immediately surrounding the plasma region is rich in intact molecules as has been observed by measuring the biological activity of enzymes ablated in these conditions [45]. It should also be noted that plasma ignition strongly increases the total ablation rate, including that of intact molecules, at least in a limited irradiance range.

The plasma ignition threshold is influenced by several factors; the main ones are the material ionization potential, the absorption coefficient, and the particle number density [46]. It is found that the plasma ignition takes place more easily for low ionization potential materials and for high particle density. High absorbances favor plasma ignition up to the point where the gas becomes opaque to radiation. Further, plasma ignition was found to be easier with long wavelength lasers than with UV lasers. Typical fluence thresholds for plasma ignition with organic molecules are between 0.1 and 1 J/cm<sup>2</sup>.

A review on the characterization of laser ablation plasmas can be found in [47].

### 3. RESONANCE ENHANCED MULTIPLE PHOTON IONIZATION

Atoms and molecules in the gaseous phase can be ionized by laser excitation up to a nonbound electronic state. Normally ionization thresholds lie at energies of several eV so that photons in the UV to deep UV are needed to reach such energies. It is possible, however, to reach the same excitation levels by simultaneous or sequential absorption of

two or more photons of lower energies, following one of the schemes of Figure 1. The fundamentals of multiple photon excitation can be found in several books [48–50] mainly about its important application in mass spectrometry.

The probability that an atom or molecule is excited to the upper level by a two frequency field  $\underline{E}(\omega_1, \omega_2) = 1/2[\underline{e}_1 E_1 \exp(i(\underline{k}_1 \underline{r} - \omega_1 t)) + \underline{e}_2 E_2 \exp(i(\underline{k}_2 \underline{r} - \omega_2 t))] + \text{complex conjugate}$ , if the energy difference between initial and final state is equal to the sum of the energies of the two photons (which is always true when the total energy of the two photons is above the ionization threshold) and neglecting line broadening, is given by

$$W_{gf} = [2(h/2\pi)^4]^{-1} |A_{gf}|^2 E_1^2 E_2^2$$

where the transition matrix element between states  $g$  (ground) and  $f$  (final) is given by

$$A_{gf} = \sum_n \{ [\underline{p} \cdot \underline{e}_1]_{gn} [\underline{p} \cdot \underline{e}_2]_{nf} / (\omega_{ng} - \omega_1) + [\underline{p} \cdot \underline{e}_2]_{gn} [\underline{p} \cdot \underline{e}_1]_{nf} / (\omega_{ng} - \omega_2) \} \quad (1)$$

where  $p$  is the electric dipole operator and where the sum runs over all intermediate states  $n$  [51, 52].

If the energy of one photon matches an energy level of the atom or molecule (resonance condition), then we see from Eq. (1) that the probability of the two photon process is greatly enhanced. This has also another important consequence, that the resonant ionization process is extremely species selective, particularly so in the case of atoms that have very narrow resonances. Further, since the transition from the excited state to the ionization continuum is unstructured, ionization has a spectral dependence that reflects only the intermediate state. Measuring the ion current as a function of the excitation wavelength thus gives us the spectral fingerprint of the ionized molecules. The intensity dependence of simultaneous and sequential absorption is quite different. If no real resonances are present, the excitation rate depends on the probability that two photons are available at the molecule at strictly the same time

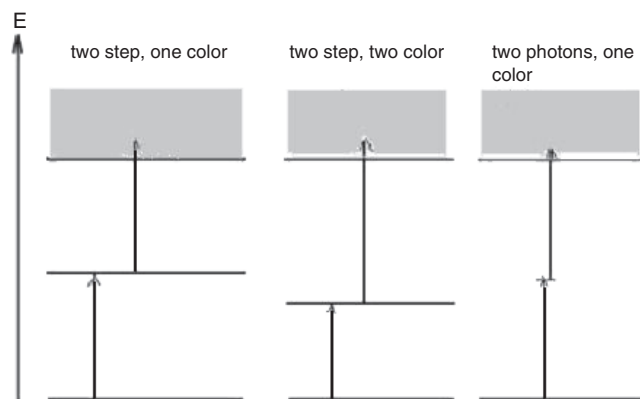


**Figure 1.** Three possible multiple photon excitation ways to the ionization continuum. The resonance enhancement mechanism is often termed multistep excitation, while multiphoton excitation (right) occurs with simultaneous absorption of photons via a virtual state when the irradiance is very high.

(in the theoretical description of the process the two photon absorption occurs via a virtual intermediate state, arising from the photon-matter interaction, which has very short lifetime). If, on the other hand, one photon is resonant with an intermediate permanent energy level, the second photon has to be available within its lifetime. Thus we may expect an intensity dependence of the form  $I^n$  with  $n = 2$  for a two photon process without resonance and  $n = 1$  in case of resonance with a very long lived intermediate state. In  $\text{UF}_5$ , for example,  $n$  is 1.2 for resonant excitation and about 2 off resonance [53]. A further advantage of multiple photon excitation, when dealing with narrow resonances (atoms or cold molecules), is that by arranging that the two photons being absorbed travel in opposite directions, Doppler broadening effects can be eliminated [54]. This is mainly useful for isotope separation purposes, but it can in principle be also exploited for the selection of specific molecular conformations that have only slightly different excitation wavelengths.

Molecular vibroelectronic energy levels are arranged in ladderlike schemes, along which excitation “climbs” (resonantly or nonresonantly) until either dissociation or ionization is reached. If the dissociation threshold is lower than the ionization level, depending on the lifetime of the dissociative state, a percentage of fragments will be formed, which can again absorb radiation along their vibrational states “ladder” and then dissociate and ionize and so on until, for very high photon densities, complete atomization of the molecule is achieved. This is described by the “ladder switching” model of Boesl and co-workers [55] (excitation switches from the energy ladder of the parent molecule to that of the primary ion and so on). Ladder climbing up to energies above the ionization level of the parent molecule and ladder switching to the fragments ionization are often competitive processes. With laser pulses longer than the dissociative state lifetime, the ladder switching process tends to dominate, increasing fragment ions with respect to parent ions; use of picosecond or femtosecond pulses limits excitation to the ladder climbing process and, if the dissociative state lifetime is not too short, it can be effective in optimizing the yield of unfragmented ions. The comparison of the effects of nanosecond and pico- or femtosecond pulses is reviewed in a recent paper by Ledingham and Singhal [56]. Although it is not the purpose of this chapter to go into the details of the fragmentation process that may follow multiple photon excitation, we want to underline here that fine tuning of the experimental parameters (wavelength, intensity, pulse length) can indeed supply a soft ionization methodology by controlling the fragmentation rate, from complete atomization to molecular integrity.

By this method it was shown, from the late 1970's onward, that molecular ions of molecules such as benzene [57], amines [58, 59],  $\text{UF}_5$  [60], sugars and polymers [61], amino acids, and peptides [62], to mention only a few, could be obtained. The technique was obviously applied mainly to mass spectrometry, and in particular to time-of-flight mass spectrometry exploiting nanosecond pulsed laser excitation. Very high mass resolution, of the order of 10,000, was achieved by introducing in the flight tube devices to compensate the kinetic energy spread of the ions produced (reflectron devices) [63].

With regard to the issue of spatial control and resolution of the ionization process, which can be very relevant to micro- and nanotechnologies, we note that although resonance enhanced ionization is extremely species selective (isotopic separation is also effected by this method), nonresonant multiphoton excitation, due to its higher dependence on intensity, can be in principle more efficiently localized in space.

#### 4. MATRIX ASSISTED LASER DESORPTION IONIZATION

In spite of the “softness” of the multiple photon ionization method (MPI), it was not possible to obtain the mass spectra of intact complex biological molecules until the MALDI technique was developed by Karas et al. in 1987 [64]. Due to the importance of biomolecules in nanotechnology we shall thus briefly describe this technique which produces controlled ionization of unfragmented large biomolecules like DNA [65], enzymes, and antibodies [66, 67]. The underlying idea in this technique is to exploit a different molecular species, to be mixed in large excess (of the order of  $10^3$  M) with the biomolecule of interest, to couple the laser energy into the sample. The absorption band of this matrix must have minimal overlap with the absorption of biomolecules (which is dominated by the absorption of aromatic amino acids of proteins and of nitrobases of nucleic acids and thus is limited to the region below 300 nm). Strong excitation of the matrix by short laser pulses will not directly affect biomolecules but will lead to evaporation of the sample with minimal energy transfer to the analyte biomolecules. Minimization of the energy transfer relies on the rapid adiabatic expansion in the vacuum environment, so that excitation of matrix molecules will have too short a time to be transferred efficiently into the analyte. Detailed descriptions of the vaporization process and maintenance of molecular integrity can be found in the early paper by Vertes and Levine [68], and in a more recent review by Zhigilei and co-workers [37]. Vaporization alone would not supply ionized analytes, however. If excitation of the matrix molecules is strong enough to cause ionization, subsequent absorption, dissociation, and further ionization/dissociation of the fragments, as described by the ladder switching model mentioned in the previous paragraph, we will end up with plenty of small fragment ions and protons. These are easily captured by the uneven charge distribution on the surface of protein molecules, causing a net charge on the molecule that can be exploited for mass selection purposes or, more generally, to direct molecules on the desired locations.

While the integrity of organic molecules is commonly checked by mass spectrometry, loss of small fragments from the bulk of a large macromolecule is not easily detected, unless very high resolution spectrometers are used. Furthermore, since conformation plays a crucial role in the biological functionality of biomolecules, a check of their mass integrity is not enough to decide that they have not been damaged. Moreover, if deposition is effected, denaturation may occur as a consequence of dissipation of kinetic energy on impact onto the deposition substrate. However, measurement of both enzyme and antibodies activity deposited by

such a method on glass or metal surfaces was demonstrated in the author's laboratory [45, 69].

The main drawback of this technique is that, together with the ions we are interested in, it yields a large amount of ionized fragments. These are small enough to be confined to an entirely different region of the mass spectrum with respect to the heavy biomolecules. For deposition purposes, however, it implies the need for some sort of mass filter to avoid contamination with the matrix fragments. Due to the commercial interest of MALDI based mass spectrometers, a large number of possible matrix molecules have been investigated [70–72], some of which minimize fragmentation.

A recent development of this technique allows atmospheric pressure analysis of samples by coupling the mass analyzer to the atmospheric ambient through a thin capillary [73, 74].

## 5. PROXIMITY ENHANCEMENT OF THE ELECTROMAGNETIC (EM) FIELD

Much interest has been devoted in recent times to electromagnetic field enhancement in the near field of nanoscopic objects, and in particular of metal tips, analogous to the mechanism responsible for SERS [75, 76]. The area of near-field optics developed with the aim of extending optical microscopy and the related fields of spectroscopy and lithography beyond the diffraction limit. Furthermore it was also applied to the recent technological achievement of optical trapping (optical tweezers), as the high spatial confinement of near-field emission allows manipulation of loose matter on the molecular scale [23, 77]. The basic idea underlying near-field optics is that the charges oscillating in an assembly of atoms under the influence of external radiation will in turn reradiate, or scatter, an oscillating field, which results in a strong enhancement of the radiation intensity in regions comparable to the size of the atom assembly [78]. It was found experimentally that silver nanoparticles were most efficient in enhancing the Raman scattered intensity, although most surfaces with an appropriate degree of roughness show enhanced scattering. Several models were therefore developed.

The electromagnetic model, which was first developed, considers the large EM fields that are produced when the incident light frequency is in resonance with collective excitation frequencies of the surface charges (surface plasmons). For a nanometric spherical object whose dimensions are much less than the incident light wavelength, the real part of the dielectric constant associated with the  $n$ th surface collective excitation mode is  $\varepsilon(\omega_n) = -(n+1)/n$  [79], and considering that the polarization of the sphere is [80]

$$\underline{\mathbf{P}} = \alpha \underline{\mathbf{E}} = 3/4\pi(\varepsilon - 1)/(\varepsilon + 2)\underline{\mathbf{E}}$$

the surface mode with  $n = 1$  yields a resonance in the polarization of the sphere. A resonance is also observed when the real part of the dielectric constant is  $\varepsilon(\omega) = -2$ .

Objects other than spheres are usually described by the model for an ellipsoid of volume  $V$ , which changes this equation into

$$\underline{\mathbf{P}} = \underline{\mathbf{E}}V(\varepsilon - 1)/[1 + \eta_i(\varepsilon - 1)]$$

where  $\eta_i$  is the depolarization form factor  $\eta = (ab^2/2) \int_0^\infty ds / [(s + a^2)^{3/2}(s + b^2)]$  with  $a$  and  $b$  the spheroid semiaxes.

We can see that excitation of plasmons may lead to strongly increased polarization and scattered intensity, and that the enhancement depends on the dielectric function and the elongation of the scattering nanostructure.

A further source of field enhancement, even in absence of resonances, is given by the concentration of field lines with the strong curvature typical of SPM conductive tips. This effect, often called the “lightning rod” effect, adds to the resonance effects to reach calculated field enhancement factors  $g$ ,  $10 < g < 1000$ .

A different way of modeling the field enhancement is to consider the SPM tip as both a receiving and an emitting antenna at optical frequencies [81]. This approach also yields the dependence of the field enhancement on the main parameters affecting the electromagnetic interaction: the polarization and incidence angle dependence, the dielectric constant of the tip and substrate material, the tip aspect ratio, and the tip to substrate distance. It is found that the field enhancement is greatest for incidence close to the substrate (i.e., almost perpendicular to the tip axis) and polarization parallel to the tip, for high conductivity metals of both tip and sample (silver tip on gold surface gives enhancements five times greater than on a glass surface), for high tip aspect ratio, and for short tip to sample distances. The same model calculates the temperature increase of the substrate surface subject to EM emission from the tip antenna. The authors of the model obtain

$$\Delta T_0 = \pi^{1/2} I_0 (1 - r) g w_0 / 8\lambda$$

where  $g = I_{\text{loc}}/I_0 =$  field enhancement,  $w_0$  is the near-field spot size (at  $1/e$  of the maximum),  $r$  is the sample reflectivity at normal incidence, and  $\lambda$  is the thermal conductivity of the sample.

The sample surface temperature calculation is important to the aim of laser-SPM assisted surface nanostructuring, as temperatures as high as the metal melting or boiling point could be achieved. In the case considered by these authors, where the calculated near-field spot size is 60 nm,  $g = 525$ ,  $r = 0.64$ ,  $\lambda = 2.44$  W/cm K, to reach the melting temperature of gold (1338 K) a threshold laser irradiance of 13 MW/cm<sup>2</sup> would be necessary. As we shall see, this is consistent with that reported by other authors. The problem of calculating the heat transferred from the laser enhanced near field to a sample and its diffusion in thick and thin films on a dielectric was studied in detail by Geshev and co-workers using a finite-difference numerical method [82]. The results they obtain in terms of temperature rise in a thin metal film are similar to those of Lu and co-workers (i.e., hundreds or thousands of degrees for irradiances in the order of 10 MW/cm<sup>2</sup>). This is certainly an easily accessible power density range that, if suitable control of all the experimental parameters is reached, would allow controlled material transfer to and from the sample with molecular size resolution.



## 6. THERMAL EXPANSION IN THE LASER FIELD

When a laser beam is focused at the tip/substrate gap, the focal volume being much larger than the gap, both the tip and the substrate partially absorb the laser radiation so that their temperatures rise considerably and thermal expansion of both occurs. This in turn reduces the gap distance and exponentially increases the tunneling current. These phenomena are always observed in laser-SPM experiments.

In order to understand the basic mechanisms and the important parameters and to evaluate the expected order of magnitude of expansion we shall briefly outline in the following some of the existing theories. Grafstrom and co-workers investigated the thermal expansion of a tip subject to a periodically modulated laser beam [83]; they solve the differential equation for the temperature modulation generated by a heat flow that is composed of a periodically modulated input and of an output toward the tip holder that is considered at constant temperature. No heat flows out of the tip apex. Setting the modulating frequency to zero, they find for the temperature rise of the apex

$$T_{\text{apex}} = 2PA/(\lambda\pi^2 w \tan \phi) + PA \tan \phi(1 - lc)/\lambda\pi^2 R^2$$

and on integrating the temperature variation on the whole tip,  $\Delta z_{\text{therm}} = \sigma \int_{0,l} T(z) dz$

$$\Delta z_{\text{therm}} = (\sigma PA \tan \phi / \lambda \pi^2) [(\ln(l_c/w) + 1/2) / \tan^2 \phi + l^2 / 2R^2] \quad \text{for the tip}$$

where  $\sigma$  is the coefficient of thermal expansion,  $P$  is the laser power,  $A$  is the absorption coefficient of the material,  $\phi$  is the half angle of the tip cone,  $w$  is the illuminated tip length (spot radius),  $\lambda$  is the heat conductivity,  $l_c$  is the tip cone length,  $l$  is the total tip length, and  $R$  is the radius of the cylindrical tip shaft, although we are mainly interested in pulsed laser irradiation, this result shows the important aspects of tip expansion: the first term is related to the conical part of the tip, while the second depicts thermal expansion of the cylindrical tip shaft. Furthermore, for narrow tip angles, the  $\tan^2 \phi$  denominator means that thermal expansion is dominated by the cone, as the thermal diffusion through the narrow conical region is slow and the temperature rises considerably. The authors also calculate the sample thermal expansion

$$\Delta z_{\text{therm}} = [\sigma PA / (2\pi\lambda)] \ln(2t/w) \quad \text{for the sample}$$

$t$  is the sample or substrate thickness.

Comparison of the latter equation to that for a small angle tip shows that sample expansion is negligible with respect to tip expansion, due to three-dimensional heat flow in the bulk.

In the assumption of pulsed irradiation, a different, simpler model [84] neglects thermal diffusivity along the tip axis and simply assumes that the heat content of a portion or slice of the conical tip diffuses uniformly into the whole slice; slices further away from the apex, however, are wider and therefore heat and expand less. The temperature increase of the  $i$ th slice is

$$\Delta T(i) = J_{\text{laser}} A s_i / (c_v V_i \rho)$$

while its thermal expansion is

$$\Delta z_{\text{therm}}(i) = \sigma \Delta T(i) \Delta l_i$$

The thin regions closer to the apex thus heat much more than those away from it. Integration of the thermal expansions of all the slices between the apex and the tip length  $l$  gives

$$\Delta z_{\text{therm}} = [(2\sigma A J_{\text{laser}} / \pi w^2) / c_v \rho \pi] \int_{0,l} dz / (R + z \tan \phi)$$

where  $J_{\text{laser}}$  is the energy of a laser pulse,  $R$  is the tip apex radius,  $c_v$  is the specific heat of the tip material,  $\rho$  is the material density,  $s_i$  is the cross section of the  $i$ th slice, and  $V_i$  is the  $i$ th slice volume.

The typical expansions, in good agreement with experimental findings in spite of the model simplicity, range from approximately 5 Å at 1 μJ to 15 Å at 30 μJ.

In both models the tip aperture angle is the critical factor; the slimmer the tip apex, the higher the temperature being reached.

A third, simple model by Ukraintsev and Yates obtains the temperature increase of the tip considering only the tip volume corresponding to the thermal diffusion length [85]. From  $\Delta T = Q / c_v m_{\text{tip}}$  (where  $Q$  is the heat absorbed by the tip from the laser pulse and  $m_{\text{tip}}$  is the mass of the tip portion affected by the temperature increase), defining the volume and cross section area of the tip within the thermal diffusion length from the apex as

$$V_{\text{th}} = 2\pi(1 - \cos \phi) \lambda_{\text{th}}^3 / 3 \quad \text{and} \quad A_{\text{th}} = \lambda_{\text{th}}^2 \phi$$

and considering that only a fraction of the laser beam hits the tip, which has a reflectivity  $r$ , the absorbed heat is

$$Q = J_{\text{laser}}(1 - r) A_{\text{th}} / \pi D^2$$

Ukraintsev and Yates obtain

$$\Delta T_{\text{tip}} = 6\phi J_{\text{laser}}(1 - r) / [\pi^2 \lambda_{\text{th}} D^2 c_v \rho (1 - \cos \phi)]$$

and

$$\begin{aligned} \Delta z_{\text{therm}} &= \sigma h_{\text{exp}} \Delta T_{\text{tip}} \\ &= \sigma h_{\text{exp}} 6\phi J_{\text{laser}}(1 - r) / [(1 - \cos \phi) \pi^2 \lambda_{\text{th}} D^2 C_v \rho] \end{aligned}$$

where  $h_{\text{exp}}$  is the portion of the tip subject to  $z$ -expansion (not all the tip portion affected by the focused beam expands but only the thinnest portion, where expansion occurs primarily in the tip axis direction),  $h_{\text{exp}} = \eta \lambda_{\text{th}}$ ,  $1 < \eta < 3$  being the tip geometry factor.  $D$  is the laser beam diameter in the focal region and  $\lambda_{\text{th}} = \lambda t_{\text{pulse}}$  is the thermal diffusion length.

To have a feeling of the orders of magnitude of temperature increase and expansion in typical experimental conditions [ $D = 250 \mu\text{m}$ ,  $\phi = 15^\circ$ ,  $t_{\text{pulse}} = 8 \text{ ns}$ ,  $\sigma = 0.7 \text{ cm}^2/\text{s}$ ,  $c_v = 0.14 \text{ J/g K}$ ,  $\rho = 19.4 \text{ g/cm}^3$  (tungsten),  $r = 0.5$ ,  $\lambda_{\text{th}} = 0.75 \mu\text{m}$ ] a 1 μJ pulse causes a temperature increase of 18 K and a tip expansion, for a geometry factor  $\eta = 2$  of 1.2 Å.

A further model by Geshev and co-workers [86] is based on the transformation of the Poisson problem for the temperature distribution into the Laplace problem for the

modified temperature and on its solution by the boundary element method. This work shows that the temperature rise in a tungsten tip is 10–100 times that of the substrate, that is, of the order of 100 degrees for irradiances of 10 MW/cm<sup>2</sup>, corresponding to focused pulse energies of the order of hundreds of  $\mu$ J, while for silver, due to its lower absorption and its higher thermal conductivity, substrate and tip temperatures can rise by similar amounts. As we have seen in the previous section, due to enhanced field absorption, a thin metal layer on a low thermal conductivity substrate can raise its maximum temperature by several hundred degrees. Particularly when applied to small metal islands on a dielectric substrate, this model supplies extremely high temperatures of local structures, which may be responsible for melting or evaporation of nanometric features, opening the way to controlled nanometric machining.

As a conclusion we observe that all models supply the same order of magnitude for the evaluation of thermal expansion, in the range of several nanometers for irradiances of the order of tens of MW/cm<sup>2</sup>. Furthermore, all models show that expansion depends on the tip material and even more on the tip conicity; the sharper the cone, the lower the heat dissipation and thus the higher the temperature increase and the expansion. As we shall see in the following, even if thermal expansion is dominant over field enhancement effects, it may still be used to effect high resolution patterning, adding one more possibility to the set of available tools for bottom up nanotechnologies.

## 7. NANOPATTERNING OF METALLIC LAYERS

Illumination of a SPM tip–surface nanometric gap by a laser pulse normally gives rise to a fast variation of the tunneling current [87–89], very often accompanied by the formation of nanostructures on the surface. Most experiments concern the creation of pits and trenches in the metal layer, while some also produce hillocks. Several mechanisms can contribute to nanostructuring of metal layers, which makes modeling of the experiments quite complicated. The main phenomena involved are thermal expansion of the illuminated tip and localized field enhancement due to the tip. Either of these can in principle be the dominant effect in creating nanostructures, depending on the fine details of the experiment.

The first experiments on laser/STM metal layer nanostructuring were performed by Gorbunov and Pompe at Dresden in 1993–94 [90]. They were based on the expectation that the laser EM field would be strongly enhanced in the proximity of the sharp tip. They used polished silver STM tips because silver has the highest electrodynamic resonance in the electric polarization of a small particle [79]. Radiation of 800 nm from a mode locked Ti:sapphire laser was mildly focused (30 cm focal length) on the STM tip gap and switched on for 100 ms. The substrate was a gold film evaporated on glass. The film, consisting of 10 nm grains, was recrystallized by laser pulses until 100 nm crystallites were created. The STM tip was then positioned on the flat top of the largest ones and 100 W/cm<sup>2</sup> laser radiation was applied for 5 ms, producing 20–40 nm sized hillocks.

These hillocks could also be erased by application of the recrystallizing laser pulses (200 W/cm<sup>2</sup> for 100 ms). No interpretation of the mechanism of mound formation was given at the time, but it was noted that the same hillocks could be produced by applying voltage pulses.

Shortly after these experiments Jersch and co-workers performed similar work at Munster, again based on the idea of exploiting the enhancement of the electromagnetic radiation in the near field of the tip [91–93]. They used 5 ns, 532 nm, Nd-YAG laser pulses impinging on bare tungsten tips to produce holes and trenches or on silver coated tungsten tips to produce mounds. Figure 2 shows the mechanism of surface nanostructuring in the particular case of a flat apex tungsten tip and the resulting nanostructure as evidenced by STM imaging. According to the

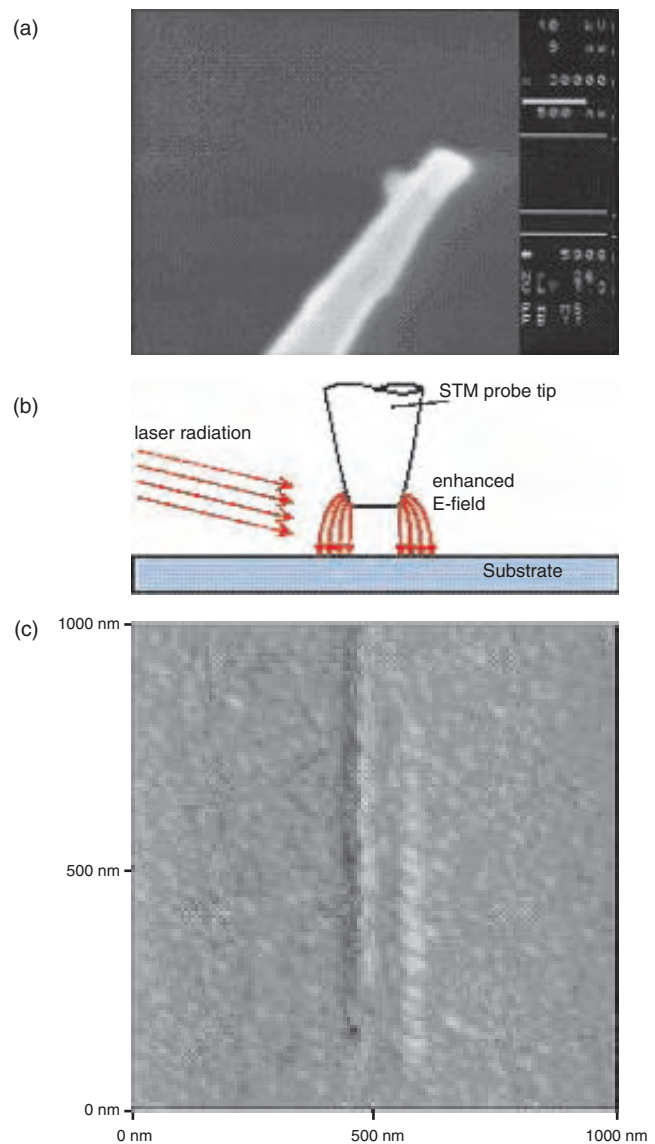


**Figure 2.** Nanostructuring using a tungsten STM tip with a flat top (a) and a double structure obtained with this tip on a gold layer (c). (b) shows the fabrication mechanism. Reprinted with permission from [92], J. Jersch et al., *Appl. Phys. A* 66, 29 (1998). © 1998, Springer-Verlag.

authors, this particular result is an indication of the fact that nanostructuring is not the effect of thermal expansion, which would produce one single wide trace on sweeping the tip across the surface, but rather of the “lightning rod” enhancement at the tip corners. However, the size of the trace does not exactly match that of the tip shown, leaving some doubt about the mechanism. Figure 3 shows mounds created on using silver coated tungsten tips on a gold substrate, both as isolated features and as quasi-continuous line. The latter shows also the effect of increasing size with increasing irradiance from 13 to 20 MW/cm<sup>2</sup>. A threshold intensity was necessary to produce mound of 10 MW/cm<sup>2</sup> for silver and silver coated tungsten and 30 MW/cm<sup>2</sup> for Pt/Ir tips. Mound material was proven to be different from the substrate material (gold, on mica) by observing different tunneling spectroscopy characteristics. Thermal expansion of the tip was not considered a possible mechanism on the observation that focusing of the laser beam on the tip above the apex did not produce any structure. As we have seen in Section 5, however, this was probably a wrong assumption as the high thermal loss through the thick shaft toward the tip holder prevents substantial heating. Figure 4 shows a set of parallel grooves carved in a gold layer by sweeping a tungsten tip across the surface with a pulse energy of 15 MW/cm<sup>2</sup>, slightly above the threshold. For groove spacing less than the gold grain size, it is observed that grains are removed. The enhanced field induced mechanism was shown to be a possible explanation for such grain extrusion. With intensities much higher than the threshold, the structures showed very different features, possibly explained by field evaporation. Figure 4b also shows a convex structure obtained on polycarbonate using a Si tip. Threshold intensity

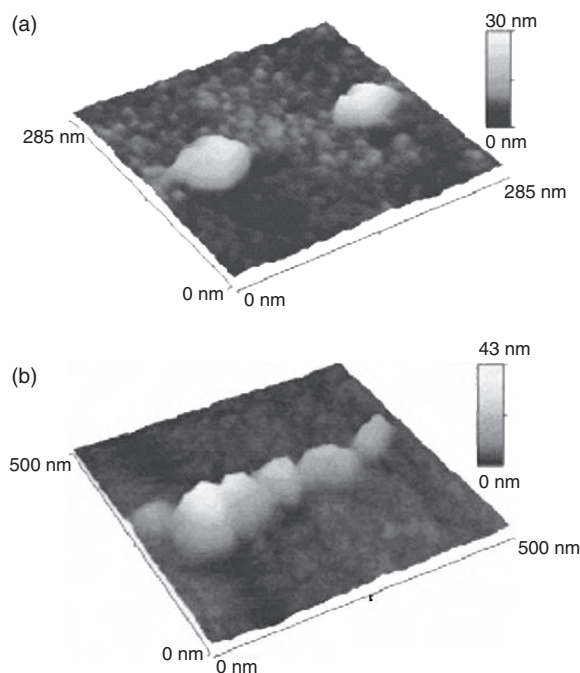


**Figure 3.** STM images of (a) two hillocks and (b) a nearly continuous nanostructure made with a silver coated tungsten tip on a gold substrate. Reprinted with permission from [91], J. Jersch and K. Dickmann, *Appl. Phys. Lett.* 68, 868 (1996). © 1996, American Institute of Physics.

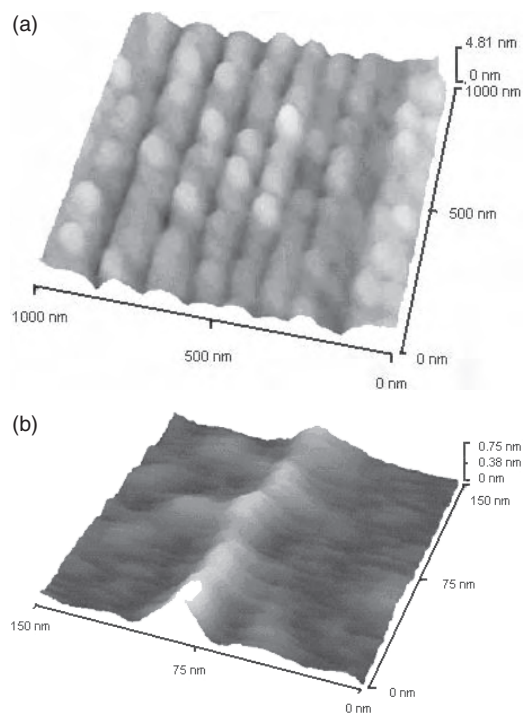


**Figure 4.** (a) Parallel nanogrooves on a gold layer produced by laser STM with a tungsten tip in a configuration similar to that of Figure 3. (b) Convex structure on polycarbonate illuminated from beneath in total internal reflection mode so that the AFM silicon tip can only scatter the evanescent field, ruling out thermal expansion effects. Reprinted with permission from [92], J. Jersch et al., *Appl. Phys. A* 66, 29 (1998). © 1998, Springer-Verlag.

was much lower in this case, only 2 MW/cm<sup>2</sup>, and this structure was explained by polymer softening due to absorption from the enhanced field. No definite explanation was attempted on the mechanisms of pit formation with tungsten or Pt–Ir tips and mound formation with silver or silver coated tips.

A remarkable observation throughout all these experiments is that the tips did not show any sign of wear or distortion after thousands of laser shots. A further remarkable fact is that nanostructuring is strongly polarization dependent, the strongest effect being observed with the polarization vector parallel to the tip axis.

The most recent experiments, by Huang and co-workers at the National University of Singapore, created nm resolution pits and carved lines into approximately 30 nm thick gold and copper layers, using 30 nm radius atomic force microscope (AFM) silicon tips in contact mode and 7 ns green light pulses from the second harmonic of a Nd-YAG laser [94, 95]. Formation of the structures requires a threshold intensity of the laser pulse that is of the order of 7.5 MW/cm<sup>2</sup>, above which the depth of these structures becomes linear with the laser intensity with a coefficient of about 1 nm/(MW/cm<sup>2</sup>) for copper and about twice this figure for gold. Typical widths of the pits are a few tens of nm. (Fig. 5). The depth increases also with the number of laser pulses, but it saturates above approximately 10 pulses. On slowly scanning the AFM tip while the laser is operated at 10 Hz, neat trenches are created with a depth similar to that

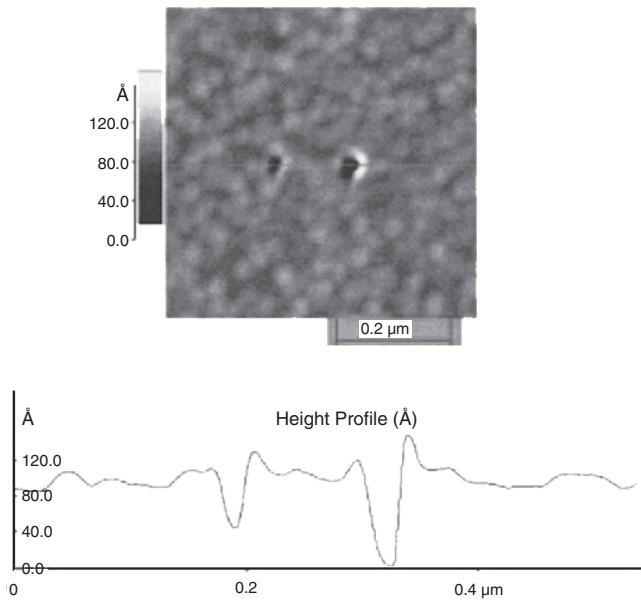


**Figure 5.** AFM topographic image and the height profiles of nanoholes created by one laser pulse with irradiance of 9 (left) and 11 (right)  $\text{MW}/\text{cm}^2$ , respectively, on a gold on silicon film with an AFM boron doped silicon tip. Reprinted with permission from [94], S. M. Huang et al., *J. Vac. Sci. Technol. B* 20, 1118 (2002). © 2002, American Institute of Physics.

of single pulse pits, in spite of the fact that the laser shoots several times within the dimension of the structure. Figure 6 reports such patterning in a gold layer, showing a maximum linewidth of about 10 nm and trench depth of about 3.5 nm. The authors believe that the dominant mechanism is metal melting and evaporation due to the temperature increase of the surface caused by absorption of the strongly enhanced EM field in the tip proximity. The calculated field energy enhancement factor is of the order of 15 to 30 but it is not clear how the incidence angle of the enhanced field should be calculated. The authors estimate that a field enhancement of 1.5 and 2.5 would bring the temperature to the melting point of Cu and Au, respectively, while enhancements by a factor 8 and 10 are necessary to reach their boiling points. They exclude hard mechanical contact due to thermal expansion of the tip on the basis of the observation that the tip shape remains unaffected after thousands of laser pulses. However, their calculation of the temperature increase of the tip is in the range 350–800 °C, corresponding to a thermal expansion of 2–5 nm, of the same order as the pit depth. According to most models, the full expansion of the tip is reached approximately at the end of the laser pulse, when the increased field absorption may have already caused melting of the surface. The decrease of the tip to surface distance caused by thermal expansion may contribute to further field enhancement in the later part of the laser pulse.

The authors also underline that direct surface heating by the laser pulse is essential to obtain nanostructures. Their calculation of the surface heating due to a  $10 \text{ MW}/\text{cm}^2$  beam incident at a  $10^\circ$  angle on the metal film deposited on an insulating substrate amounts to only about 80 °C. Experimentally, for the smoothest films, with roughness below

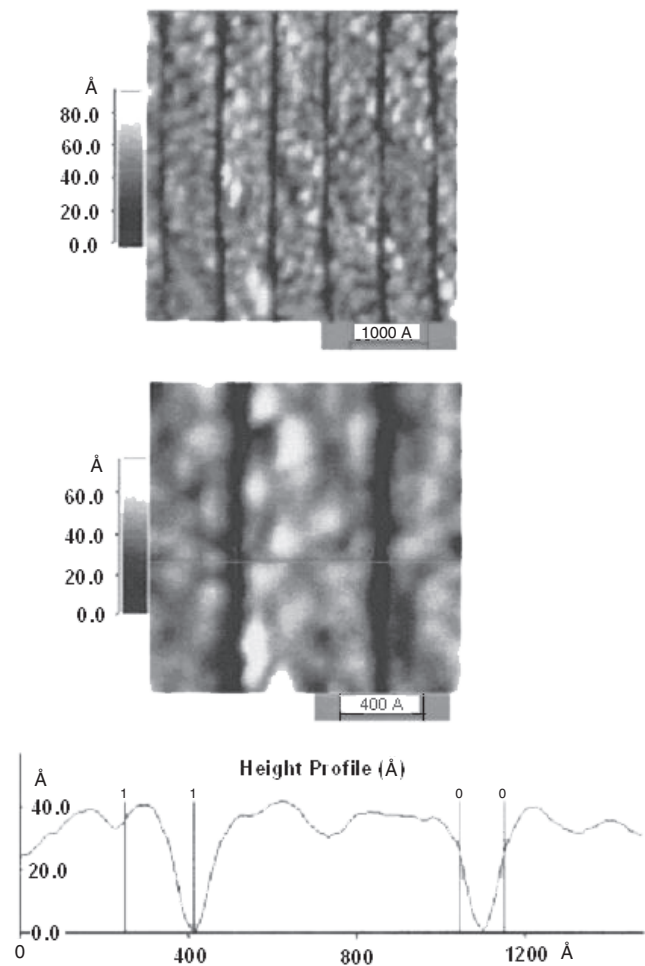


**Figure 6.** AFM topographic images and height profile of multiple nanolines created by laser pulses with intensity of  $7.5 \text{ MW}/\text{cm}^2$ . Reprinted with permission from [94], S. M. Huang et al., *J. Vac. Sci. Technol. B* 20, 1118 (2002). © 2002, American Institute of Physics.

1 nm, no single pulse carving occurs even at the highest laser intensities, which causes significant distortion of the tip. After several laser shots, the surface roughness increases and nanostructuring occurs at an average roughness of 2 nm, which the authors believe to substantially increase absorption and decrease thermal conductivity. The importance of surface heating is also confirmed by the fact that no nanostructuring is obtained on the highly reflective Al films. Thus the description of the structuring mechanism given by the authors is compatible with the experimental evidence, but the relative roles played by mechanical indentation and enhanced field absorption remain unclear.

The thermal expansion of a Pt–Ir STM tip due to laser pulse heating was experimentally measured by Boneberg and co-workers [96]. From the transient increase in tunneling current caused by pulsed laser heating of a tip that is retracted known distances from a reference tunneling distance, they obtain a thermal expansion of the tip of the order of a few angstroms for energy densities at least 10 times smaller than the threshold for nanostructure formation. They also obtain unequivocal experimental evidence that the expansion is strongly dependent on the polarization



of the incident light, parallel and perpendicular orientation of the polarization vector with respect to the tip axis being the angles at which absorption by the ellipsoidal tip end occurs. This is also confirmed on shifting the laser focus position on a thicker, cylindrical part of the tip, where neither expansion nor polarization effects are observed. Furthermore the transient behavior of the tunneling current occurs on a time scale that is much longer than the laser pulse, ruling out any direct effect of the light pulse, such as photoelectric emission or enhanced field electron emission. These experimental findings agree with those of Huang et al. and confirm that at nanometric distances thermal expansion of the tip cannot be neglected. Interestingly Boneberg and co-workers, using an STM Pt–Ir tip positioned within tunneling distance on a 150 nm thick gold film and again green light pulses from a Nd-YAG source ( $400 \text{ mJ/cm}^2 = 57 \text{ MW/cm}^2$ ), obtain hillocks on the gold surface rather than pits. Their interpretation of the mechanism of nanostructuring is almost opposite compared to that of Huang and co-workers: although they do not exclude a contribution from enhanced field absorption, these authors believe that the main factor responsible is mechanical contact and adhesion of the gold layer to the Pt–Ir tip. This interpretation is confirmed by their measurement of quantized conductance, obtained in the slow retraction phase following the laser pulse, where the current decreases in steps of  $2e^2/h$  as expected [97]. The same interpretation of mechanical adhesion is also given by other authors who obtain dips and hillocks simply on establishing a contact with the surface [98].

Another assessment of the importance of thermal expansion comes from Huber and co-workers who measured the thermal expansion of a tungsten STM tip by the deflection of an AFM cantilever in near contact with it [99]. They obtain values as high as 16 nm for tungsten, although with energy density 3 times higher than in the work of Boneberg et al. and more than 20 times higher than in the experiments of Huang et al. All these values of thermal expansion are therefore roughly equivalent.

While both enhanced field and thermal expansion mechanisms are undoubtedly active, there is thus at present no definite answer to the question of which is the dominant one and in what exact experimental configuration. The experiments of Huang et al. and Boneberg et al. are not identical (different tip material, one STM and one AFM, different laser pulse energies), so that it is difficult to make proper comparisons.

Recently Boneberg and co-workers, who had demonstrated the importance of thermal expansion in the interpretation of carvings, have also demonstrated the potential of locally enhanced fields for surface nanostructuring, using isolated polystyrene spheres dispersed on silicon or glass surfaces [100]. In their work, using spheres of different sizes, they show that local melting of the surface occurs just beneath the spheres illuminated by a laser beam.

If thermal expansion were the only mechanism, then there would probably be little interest in the use of lasers coupled to SPMs for carving, which could be more simply performed by control of the piezo vertical voltage. There is, however, no doubt that the tip integrity and the fact that there is little outspread material (as compared both to common tip

collision damages and to the carved volume itself) around the beautifully neat carvings reported by Huang et al. are good reasons to carry on further investigation. For example it would be interesting to check if the maintenance of tip is due melting of the surface, decreasing the forces experienced by the tip on dipping into the molten surface.

## 8. SMALL CLUSTER AND SINGLE ATOM DEPOSITIONS ON FLAT SURFACES

The first pioneer work on this deposition technique dates back to 1990 and is due to Yau and co-workers at the University of Urbana, IL [101, 102]. They photodissociated and photoionized a gaseous metal compound, trimethylaluminum (TMA), in order to obtain  $\text{Al}^+$  single ions in the STM tunneling gap region. The applied electric field between tip and surface drives  $\text{Al}^+$  ions to the surface, where they are imaged by the STM. The experiment was performed at a pressure of  $10^{-8}$  Pa on atomically flat highly oriented pyrolytic graphite. In order to obtain three photon dissociation of TMA and four photon ionization of Al atoms, exploiting the  $4300 \text{ \AA}$  resonance of the Al excitation, the laser intensity is very high, of the order of  $100 \text{ MW/cm}^2$ . The authors checked that no deposition occurs in the absence of TMA in the vacuum vessel and also that deposition is only rarely observed when the laser is detuned by only  $5 \text{ \AA}$  from the resonant excitation wavelength of Al. Deposits are well evident in the STM images and the atomic structure of graphite, also well detected by STM, is used for an accurate calibration of their dimensions (Fig. 7). The thickness of the deposit is strongly dependent on the applied electric field, ranging from 2 to  $53 \text{ \AA}$  (i.e., from a “monolayer” of four to five atoms to a thick mound of hundreds of atoms); the horizontal dimensions range from approximately 1 to 16 nm.

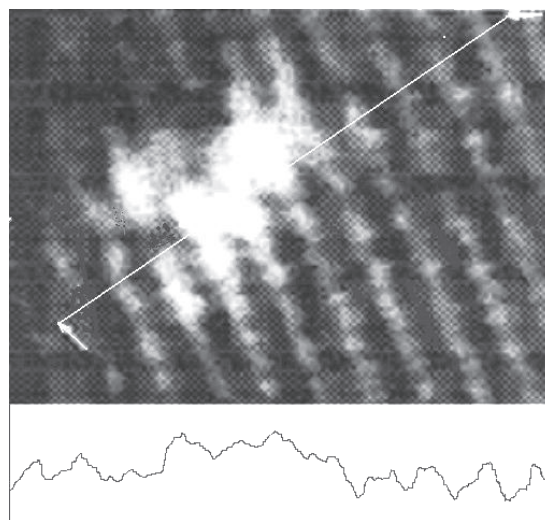


**Figure 7.** STM image ( $27 \text{ \AA} \times 27 \text{ \AA}$ ) of an Al deposit consisting of four components produced by one laser pulse at a tip bias of 1 V. The vertical span of the gray scale is  $2 \text{ \AA}$ . The crystal lattice of graphite is clearly visible. White arrows indicate the endpoints of the line profile ( $28.5 \text{ \AA}$ ), the maximum variation of which is  $1.4 \text{ \AA}$ . Reprinted with permission from [101], S. T. Yau et al., *Appl. Phys. Lett.* 57, 2913 (1990). © 1990, American Institute of Physics.

In the thinnest depositions, discrete round structures can be observed, their dimensions being compatible with that of single Al atoms. Although the amount of deposited material was too small to attempt electronic spectroscopy measurements in order to determine its elemental composition, the authors presume its different nature, in comparison with the graphite substrate, from the recorded  $I$ - $V$  curves that are linear over the deposition (typical of metals) and show a bandgap over clean graphite.

The authors also showed that holes created in the highly oriented pyrolytic graphite surface by voltage pulse application could easily be filled by aluminum deposited in such way; they could even erase their depositions by further laser pulses, although no explanation of this latter observation can be given.

In this work, on the basis of the experimental observation that no surface modification is obtained in the absence of TMA or with nonresonant radiation, no account of thermal expansion phenomena is given, which may sound strange nowadays, particularly considering a  $100 \text{ MW/cm}^2$  intensity. The authors explicitly state that in order to avoid tip ablation, which may produce extended deposition, they focus the laser beam ahead of the tip, but no quantitative estimate of the radiation intensity at the tip is given. If the power density there is too low to produce appreciable thermal expansion, it may still be enough for enhanced field dissociation/ionization processes; but then it is not clear why such large energy pulses should be used.

This work aroused a large interest since it was the first (and even today one of the few) attempt to add material to a surface in a controlled fashion, with truly nanometric resolution and with a virtually infinite source of material. The metal compound (TMA) was carefully chosen, having the atomic resonance used for the enhanced multiphoton ionization within the wide molecular absorption band used for photodissociation of the molecule, so that a single wavelength is necessary. However, it is obvious that, with fairly straightforward variations of the experiment (using more wavelengths, according to Fig. 1), the methodology could be of very general use. There are indeed many gaseous metal compounds (e.g., metal carbonyls) that can be used and in fact are used to deposit metals in electron or ion beam assisted deposition.

A few years later Ukraintsev and Yates at the University of Pittsburgh [85] obtained very repeatable single atom deposition on an atomically flat Si surface using 7 ns, 532 nm laser pulses to heat a W tip up to the point of evaporating its apex atoms (Fig 8). Several atoms were deposited while the STM was performing one scan line (the laser repetition rate was 10 Hz and the line scan time 1 s). Thus, in the scan lines that immediately followed it was possible to image the deposited atoms. The authors ascribe their results to low atomic coordination of the apex atoms (apex diameter of 25 nm) and also to a “chemical” interaction of the tip with the silicon surface, which is supposed to decrease the W atom binding energy. The experiment is performed in ultra-high vacuum. Although the calculated laser induced direct heating only accounts for about 100 °K, a further 350 °K temperature increase would be due to Nottingham heating, or heating of the apex bound to the strong increase of the tunneling current that is observed when thermal expansion

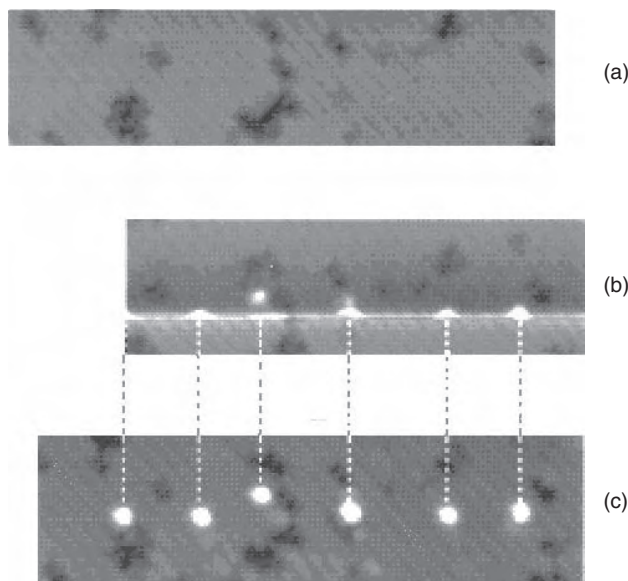


**Figure 8.** Laser induced single W atom transfer. Laser irradiance  $3 \text{ MW/cm}^2$  at 532 nm; sample bias =  $-1.3 \text{ V}$ . (a) STM image before atom transfer. The Si lattice structure and some impurities useful for identification of the deposition location are observable. (b) STM image during transfer: scan direction is left to right and bottom to top, laser shoots every 42 nm of one horizontal scan only, and the deposited atoms are already detected by the scan lines that follow immediately. (c) STM image of the whole deposition area after atom transfer. Reprinted with permission from [85], V. A. Ukraintsev and J. T. Yates, *J. Appl. Phys.* 80, 2561 (1996). © 1996, American Institute of Physics.

causes a tip approach of 8 Å. No tip damage was observed, however, and the transient tunneling current was limited to  $15 \mu\text{A}$  at most. The dependence of the transient tunneling current on both the laser intensity and on the tip to sample bias voltage showed that the thermal expansion cannot be the only mechanism to govern the current.

Very recently in the author’s laboratory at ENEA, Rome, some deposition experiments have been performed aimed at much lower resolution but in the sure knowledge that no thermal expansion consequences could be produced on the surface (i.e., keeping the tip hundreds of nanometers away from it). For such low resolution work no crystalline flat surface was required and the vacuum was in the range  $10^{-5} \text{ Pa}$ . These experiments aimed to establish an even more general technique (not necessarily relying on gaseous compounds) and therefore used one laser to vaporize solid material and a second laser, finely tuned on an electronic resonance of the atomic species as in the work of Yau and co-workers, to effect ionization (Fig. 9a). Lead was used in the first experiments, again because of its convenient spectroscopic properties, its resonant intermediate level being a little higher in energy than one-half the ionization threshold. The ionization charge signal was collected across the STM tip-sample gap as a function of the ionizing wavelength, showing the very narrow line, typical of atomic transitions, reported in Figure 9b. No charges are created and collected if the radiation is detuned by as little as  $1 \text{ \AA}$  from the lowest lead electronic resonance. The vaporizing laser is a pulsed Nd-YAG source at 1064 nm (8 ns) supplying an intensity at the solid lead surface of  $50 \text{ MW/cm}^2$ ; ionization is performed by an



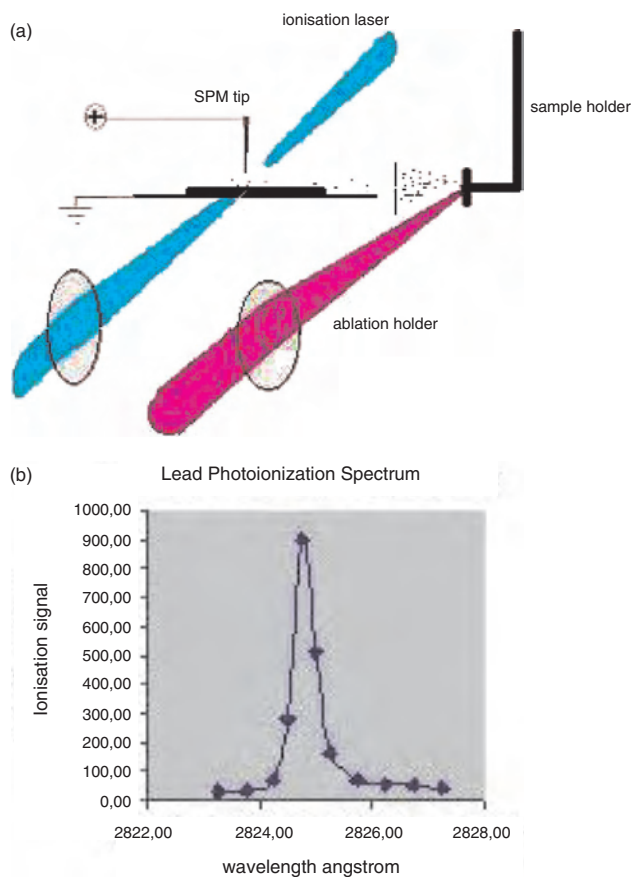


**Figure 9.** (a) Scheme of the laser ablation/ionization apparatus. The ablation laser is focused on the sample that produces a burst of vapor phase atoms or molecules in high vacuum. These are collimated toward the tip-sample gap where a suitably delayed and tuned laser beam causes resonant enhanced two photon ionization. The tip is biased with 1 V. (b) The charge signal collected at the tip-sample gap when the burst of laser vaporized lead atoms is resonantly ionized by two photons, vs laser wavelength. Detuning by  $0.5 \text{ \AA}$  from the intermediate atomic energy level excitation causes ionization to drop to nearly zero. This signal is not observed when either of the two lasers is turned off.

excimer laser pumped, frequency doubled dye laser, supplying approximately  $5 \text{ MW/cm}^2$  at the STM gap with a suitable delay to account for the transit time from the neutral atoms source to the STM tip apex (15 mm ca.). We check that no deposition and no charge signal are present when either of the two lasers is absent. Figure 10 reports three different lead spots deposited on a gold coated silicon wafer surface, keeping the tip at three different distances from the surface. As expected, the spot becomes progressively smaller on approaching the tip; it is interesting that the dimensions of these deposits are much smaller than the focal region of the laser beam ( $200 \mu\text{m}$ ) and have fairly well defined edges, suggesting that ions must be produced in a region of the order of the tip apex size (a few tens of nm), rather than in the whole focal volume. However, whether this is the effect of the enhanced EM field at the tip proximity or merely of the effective electric field driving the ions to the surface (which might be strongly influenced by the first deposited clusters) is still difficult to decide. The scanning electron microscope analysis of the surface reveals that deposition is influenced

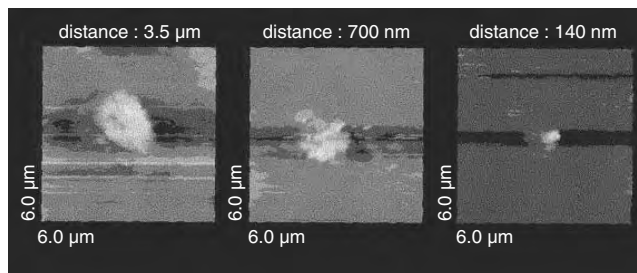


**Figure 10.** STM image of three lead spots obtained by resonance enhanced multiphoton ionization of laser ablated lead on holding the STM tip at different distances from the substrate. Spot size increases with increasing distance but it is always incomparably smaller than the beam focal dimension ( $200 \mu\text{m}$ ).

by the local electric field intensity that is determined by surface asperities. For example, the edges of submicrometer scratches produced by polishing powders on metals act as attractors for ionized material [32]; it is thus conceivable that any deposition protruding above the surface will focus new ions on itself.

Depositions can also be performed while scanning the tip in a raster fashion, in order to coat very small areas uniformly. A first attempt in this direction is reported in Figure 11, which shows a STM image recorded immediately after decorating the gold surface with lead ions. The tip was held 1200 nm away from the surface. Tip bias was +1 V; scan size was  $3 \mu\text{m} \times 3 \mu\text{m}$ . The deposition was effected with 300 laser shots over 1 min. The underlying gold structure of the original surface is observable; within the deposition, a large crater with outburst of material due to an unwanted crash of the tip into the sample is also visible.

Similar results were obtained with the amino acid tryptophan and tryptophan containing di- and tripeptides,

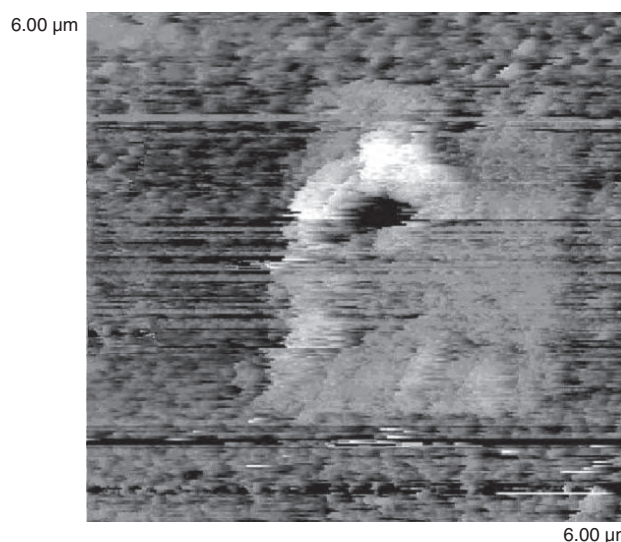


**Figure 11.** Painting a gold surface with a square of photoionized lead atoms by a scanning polarized tungsten tip (STM image). The consequences of an accidental collision of the tip into the deposit are observable. The underlying evaporated gold structure is also visible.

vaporized from a frozen aqueous solution under high vacuum and resonantly ionized by two photons at 286 nm. A time of flight mass analysis of these ionized biological materials shows that tryptophan reaches the deposition surface without measurable fragmentation, while peptide dissociation is of the order of 10% (Fig. 12). Separation of the ablation step from the two photon ionization step also allows measurement of the kinetic energy distribution of the vaporized material in the different phases of ablation, by measuring the collected ions signal as a function of the delay

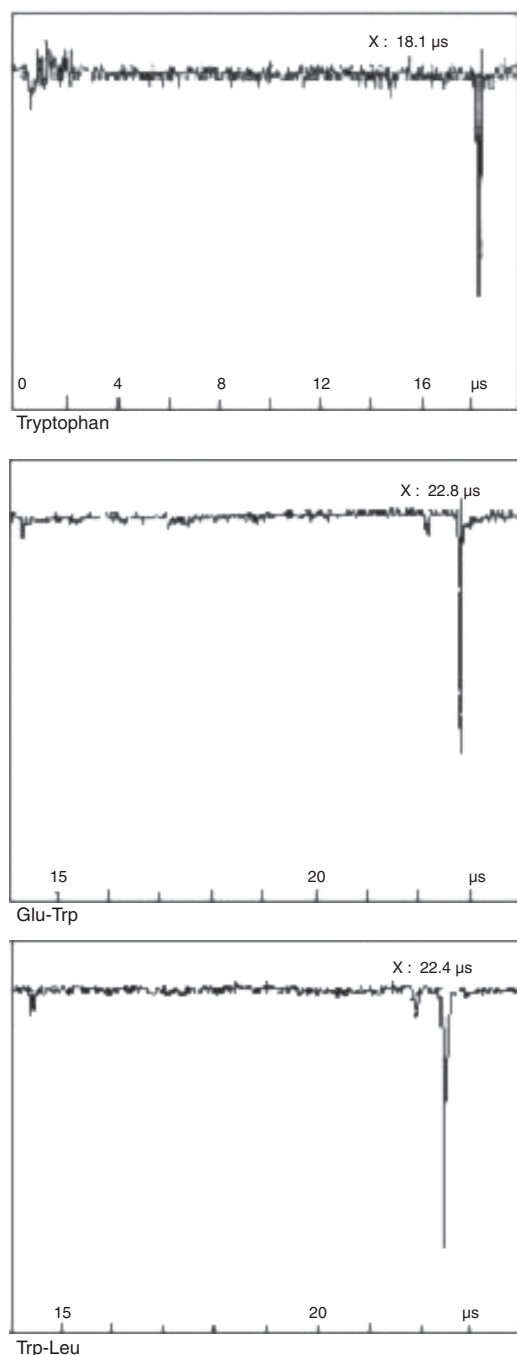


**Figure 12.** Time of flight mass spectra of laser ablated (at 355 nm) and two photon ionized (at 286 nm) tryptophan and dipeptides, showing that deposited molecules are only minimally dissociated.

between the two laser pulses, which are focused at a fixed distance of about 15 mm from one another. Hansen measured the time of flight distribution of the masses detected following ablation of several polymers [103]. He found that in all cases at least two different waves of material are produced, the fastest ones being largely dissociated. For each component he extracted a velocity distribution, which was well fitted by an offset Maxwell–Boltzmann distribution, with an offset velocity of about  $5 \times 10^6$  cm/s and a transverse translational temperature of about 10,000 K. In the case of tryptophan and peptides only one component was measured in the ENEA laboratories, with the fastest part being made of unfragmented material while the late arrivals, ejected by the slowly cooling sample, show dissociation of the order of 20 to 50%. The desorption (or ablation) and ionization technique thus allows a very detailed characterization and control of the material to be deposited. It should also be observed that other spectroscopic characterizations of the vaporized jet of material, beyond photoionization spectra, are possible. Also, if entrained in a supersonic beam of monoatomic gases, molecules in specific conformational states could even be selectively ionized, and thus deposited, exploiting the strong narrowing of ro-vibronic lines at the low temperatures achieved in the supersonic expansion.

Although of very general applicability, this technique has some important drawbacks, particularly at the submicrometer scale. Most important of all, contamination from neutrals is observed on very large areas of the sample. Although careful skimming of the atomic or molecular beam can be easily introduced in the experiment, contamination will always occur on a surface area that is larger than our desired deposition. For thermally resistant materials, heating the substrate may reduce the problem. A second problem arises with neutral atom contamination of the STM tip, on which metal dendrites easily grow during the experiment. Such dendrites reduce the spatial resolution of the technique and often cause problems in subsequent imaging. It was found, however, that this can be minimized by frequent application of voltage pulses to the tip.

## 9. LASER-SCANNING PROBE MICROSCOPE (SPM) ASSISTED SHADOW MASK DEPOSITION

Shadow masks, or stencils, are commonly used in microtechnologies to produce patterned depositions by evaporation of metals through their open features. Normally they are clamped in close contact with the surface to be patterned. If they are moved with high resolution, controlling the distance from the surface so that they neither scratch it nor lift too much away, then this may become a neat bottom up fabrication method. Atomic force microscopes are of course the best suited instruments to control soft contact with the surface. A recent work by the IBM Ruschlikon and University of Cambridge groups used a modified AFM cantilever and an evaporation source to directly write Cu features on a flat substrate in ultrahigh vacuum (UHV) [104]. This methodology has the great advantage of being simple. It allows high resolution, it has no need for resists and surface chemistry,

and it even allows parallel writing of different features. Basically, what is needed is small apertures through the AFM cantilevers or movable shadow masks. Using focused ion beams, 50 nm apertures can be opened, but even smaller features can be written by increasing the angle between the vapor beam and the opened channel in the cantilever. A further advantage of this method is that written features can immediately be read and possibly modified by the AFM. Figure 13 shows some of the features created. Obviously pulsed lasers are an extremely convenient source of vaporization in UHV as they can supply small bursts of vapor in the immediate vicinity of the cantilever from a spatially well defined source, thus implying less stringent demands for collimation of the beam. As we have seen, the use of selective resonant ionization also allows high purity in the deposited materials, while laser soft ionization techniques allow delicate biological materials to be deposited. Very high resolution patterns of biologically functional monolayers have been obtained recently in the author's laboratory by means of e-beam lithography and laser deposition [105]. The following step has been to use piezoelectrically moved micro- and nanostencils to produce both metallic and biological material patterns. Figure 14 shows a micrometric square deposition of chromium, obtained through a movable micrometric stencil a few micrometer away from the surface. The second part of the figure shows a nanometric pattern of the enzyme horseradish peroxidase, softly vaporized, ionized, and shadowed by a nanostencil in close contact with the silicon wafer surface.

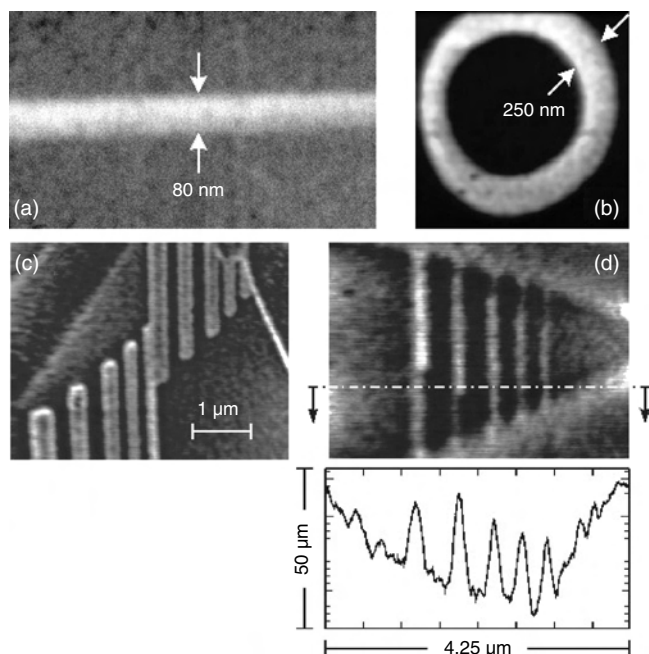


**Figure 13.** AFM images of Cu wire structures created by the nanostencil technique with thermal evaporation from a 60 mm distant source. Reprinted with permission from [104], R. Luthi et al., *Appl. Phys. Lett.* 75, 1314 (1999). © 1999, American Institute of Physics.

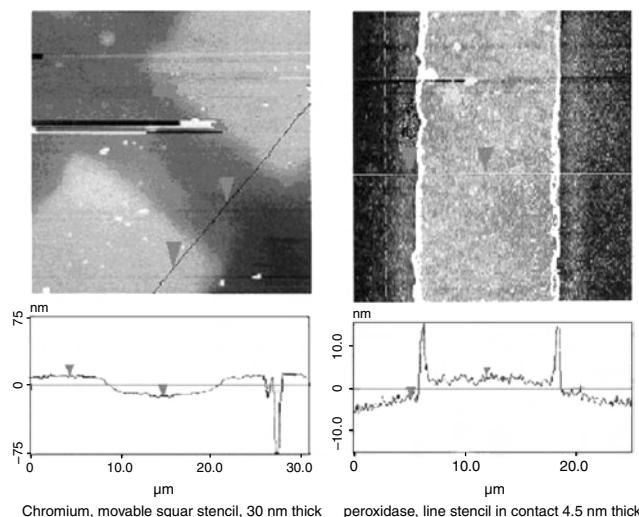


**Figure 14.** Deposition of chromium (left) and of the enzyme horseradish peroxidase (right) through movable stencils. Note the difference between a suspended stencil (left) and one in close contact with the surface (right). Depositions are 30 nm thick (chromium) and 4.5 nm thick (peroxidase).

## 10. CONCLUSIONS

We have shown that laser-SPM techniques, which are paradigmatic examples of bottom up nanoassembling, have produced in the last decade structures that range from single atoms to hundreds of nanometers. To the author's view laser-SPM coupling will become increasingly important mainly for two issues: unlimited supply of ionized material at the junction and high resolution heating, molecular transfer, or ionization, due to enhancement of the near field. Progress in this field has not been as fast as in other nanotechnological work, like silicon nanooxidation [3], because of the high number of parameters involved. Although too little experience has been gained so far on the subject, we have seen for example that the choice of the correct laser beam polarization, the tip material, and the tip shape may influence drastically both field enhancement and thermal expansion. Modeling of the involved processes has improved recently and will certainly improve even more in the near future, allowing more accurate planning of the experiments and almost certainly much better repeatability. Controlled evaporation of material from the sample surface due to a nanometrically localized EM field and ejection of single atoms from the tip are the most valuable results for ultrahigh resolution fabrication that, however, need better control by a deeper theoretical understanding of the processes.

Multiphoton ionization of gaseous precursors has also supplied atomic resolution deposits, while lower resolution but no dependence on tip thermal expansion has been obtained on holding the tip hundreds of nanometers away from the surface by pulsed laser vaporization and ionization in separate steps. Soft ionization techniques coupled to SPM localization seem ideal for the deposition of functional biological and organic material with nanometric resolution, and the first steps in this direction are being taken. In fact, nanometric resolution patterning of monolayers of

functional biological molecules has been obtained in conjunction with e-beam lithography, while somewhat lower resolution with both metals and biomolecules is achieved by movable shadow masks that need no other processing. First attempts of deposition of unfragmented amino acids and peptides, as well as of metals, in the localized SPM tip field are also being made, for the moment at lower resolution. For biomolecular work, these methods will have to compete with the beautiful technique of “dip pen” nanolithography, which recently succeeded in writing nanometric features of functional biomolecules by flowing a solution of a suitable chemical intermediate along the tip onto the substrate [14]. A problem posed by this latter method is that of reloading the tip with the “ink.” In perspective, controlled laser vaporization and ionization could accomplish this task, both with biomolecules and with metals, in a high vacuum environment. A disadvantage of the laser ionization technique (we have seen that excessive tip contamination leads to loss of resolution in deposition and of imaging capabilities) if suitably controlled may thus turn into a further powerful nanofabrication tool. And of course optical trapping of molecules within a focused laser beam could be a viable alternative to refill the tip.

Fascinating perspectives can also be foreseen with optical trapping in the tip enhanced radiation near field, where in principle modulation of the laser irradiance may lead to nanometrically controlled pick and release of nanoparticles or molecules. Although we have not discussed it as a fabrication technology, only one experimental attempt having been made so far in this direction [24], this methodology seems highly promising, and it may become soon a true fabrication tool, particularly for work in solution with large molecules.

We have not addressed in this short chapter the beautiful and exciting recent results on molecular resolution imaging or spectroscopic characterization obtained exploiting scanning near-field optical microscopes or fluorescence excited by SPM near-field enhancement, which are not properly nanofabrication techniques. These techniques, however, will stimulate the field of light assisted scanning probe nanofabrication, because of both buildup of experience on near-field optics and deeper and more general characterization of the fabricated nanostructures at the molecular level.

Nanotechnology is a multidisciplinary branch: beyond sophisticated engineering, it uses quantum solid state physics and surface science, but also chemistry and biology. Many processes in these fields are photoactivated. Single molecule scale photochemistry and photobiology seem nowadays not so far, so that soon the way may be opened to a wealth of achievements of hardly imaginable dimensions.

## GLOSSARY

**Atomic force microscope (AFM)** One instrument of the family of scanning probe microscopes based on the deflection of an elastic cantilever with a thin tip attached to it that interacts with the electronic cloud of the sample. Interaction causes weak deflection toward the sample at long distance range and strong repulsion at short distances.

**Highly oriented pyrolytic graphite (HOPG)** A form of crystalline graphite with very long range order, particularly

easy to cleave along crystalline planes so that freshly exposed atomically perfect flat surfaces are easily obtained.

**Multiple photon ionization (MPI)** Ionization of atoms or molecules by simultaneous or sequential absorption of two or more photons, whose energies are individually lower than the ionization threshold.

**NMR imaging** A tomographic imaging technique based on the nuclear magnetic resonance signal from the elementary magnets (spins) of hydrogen atoms contained in water and fats present in living tissues. Unlike X-rays tomography it does not use harmful ionizing radiation.

**Polymethylmethacrylate (Perspex) (PMMA)** Beyond being an ubiquitous lightweight transparent material, optically similar to glass, it is also a commonly used polymeric resist in electron beam lithography techniques.

**Polytetrafluoroethylene (Teflon) (PTFE)** Widely used polymer particularly suited for coating purposes where high temperature resistance and low friction are important.

**Scanning near-field optical microscope (SNOM)** One instrument of the family of scanning probe microscopes based on the detection of “optical tunneling” (evanescent wave) to or from a suitably tapered optical waveguide brought to nanometric distances from the sample.

**Scanning tunneling microscope (STM)** One instrument of the family of scanning probe microscopes based on the detection of the tunneling current between tip and sample brought to within one nm from each other. Since the tunneling current depends exponentially on distance only one atom of the tip practically contributes to the current so that the resolution is extremely high.

**Surface enhanced Raman scattering (SERS)** Inelastic scattering of radiation enhanced by nanometric corrugations of the surface.

**Ultrahigh vacuum (UHV)** Vacuum in the range of less than  $10^{-8}$  mbar.

## REFERENCES

1. J. Hopfield, citation by P. Ball and L. Garwin, in *Nature* 355, 761 (1992).
2. S. Akita, H. Nishijima, T. Kishida, and Y. Nakayama, *Japan J. Appl. Phys.* 39, 7086 (2000).
3. M. Tello, F. Garcia, and R. Garcia, *J. Appl. Phys.* 92 4075 (2002).
4. J. A. Stroschio and D. M. Eigler, *Science* 254, 1319 (1991).
5. T. A. Jung, R. R. Schlittler, J. K. Gimzewski, H. Tang, and C. Joachim, *Science* 271, 181 (1996).
6. C. Thelander and L. Samuelson, *Nanotechnology* 13, 108 (2002).
7. H. W. C. Postma, M. de Jonge, Z. Yao, and C. Dekker, *Phys. Rev. B* 62, 10653 (2000).
8. M. Lutwyche, C. Andreoli, G. Binnig, J. Brugger, U. Drechsler, W. Häberle, H. Rohrer, H. Rothuizen, P. Vettiger, G. Yaralioglu, and C. Quate, *Sens. Actuat. A* 73, 89 (1999).
9. J. M. Laval, P.-E. Mazeran, and D. Thomas, *Analyst* 125, 29 (2000) and references therein.
10. R. A. G. Cinelli, V. Pellegrini, A. Ferrari, P. Faraci, R. Nifosi, M. Tyagi, M. Giacca, and F. Beltram, *Appl. Phys. Lett.* 79, 3353 (2001).
11. E. Braun, Y. Eichen, U. Sivan, and G. Ben-Yoseph, *Nature* 391, 775 (1998).
12. C. Dekker and M. A. Ratner, *Phys. World* 14, 29 (2001).
13. I. Lee, J. W. Lee, and E. Greenbaum, *Phys. Rev. Lett.* 79, 3294 (1997).

14. K.-B. Lee, S.-J. Park, C. A. Mirkin, J. C. Smith, and M. Mrksich, *Science* 295, 1702 (2002).
15. A. A. Bergman, *Langmuir* 14, 6785 (1998).
16. M. E. Browning-Kelly, K. Waud-Mesthrige, V. Hari, and G.-Y. Liu, *Langmuir* 13, 343 (1997).
17. D. W. Pohl, U. C. Fischer, and U. T. Durig, *J. Microsc.* 152, 853 (1986).
18. W. Denk and D. W. Pohl, *J. Vac. Sci. Technol. B* 9, 510 (1991).
19. A. V. Bragas, *Phys. Low Dim. Struct.* 9/10, 1 (1998).
20. N. Hayazawa, Y. Inouye, Z. Sekkat, and S. Kawata, *Chem. Phys. Lett.* 335, 369 (2001).
21. E. J. Sanchez, L. Novotny, and X. S. Xie, *Phys. Rev. Lett.* 82, 4014 (1999).
22. R. F. Haglund, *Appl. Surf. Sci.* 96–98, 1 (1996).
23. L. Novotny, R. X. Bian, and X. S. Xie, *Phys. Rev. Lett.* 79, 645 (1997).
24. M. S. Anderson and W. T. Pike, *Rev. Sci. Instr.* 73, 1198 (2002).
25. S. Grafstrom, *J. Appl. Phys.* 91, 1717 (2002).
26. Y. Tsuboi, H. Adachi, and E. Yamamoto, *Jpn. J. Appl. Phys.* 1 41, 885 (2002).
27. T. Smausz, B. Hopp, and N. Kresz, *J. Phys. D* 35, 1859 (2002).
28. H. Jenniches, M. Klaua, H. Hoche, and J. Kirschner, *Appl. Phys. Lett.* 69, 3339 (1996).
29. Z. Y. Yang, Y. C. Zhou, X. J. Zheng, Z. Yan, and G. Bignall, *J. Mater. Sci. Lett.* 21, 1541 (2002).
30. C. Hong, H. B. Chae, K. H. Lee, S. K. Ahn, C. K. Kim, T. W. Kim, N. I. Cho, and S. O. Kim, *Thin Solid Films* 409 37 (2002).
31. R. T. Phadke and G. Agarwal, *Mater. Sci. Eng. C* 5 237 (1998).
32. P. Morales, A. Pavone, M. Sperandei, G. Leter, L. Mosiello, L. Nencini, L. Grifoni, and S. Santucci, *Mater. Sci. Eng. C* 2, 173 (1995).
33. A. A. Voevodin and M. S. Donley, *Surf. Coat. Technol.* 82, 199 (1996).
34. H. Schittenhelm, D. B. Geohegan, G. E. Jellison, A. A. Puretzky, M. J. Lance, and P. F. Britt, *Appl. Phys. Lett.* 81, 2097 (2002).
35. A. A. Gorbunov, W. Pompe, A. Sewing, S. V. Gaponov, A. D. Akhsakhalyan, I. G. Zabrodin, I. A. Kaskov, E. B. Klyenkov, A. P. Morozov, N. N. Salaschenko, R. Dietsch, H. Mai, and S. Vollmar, *Appl. Surf. Sci.* 96, 649 (1996); K. Sturm, S. Fahler, and H. U. Krebs, *Appl. Surf. Sci.* 154, 462 (2000); V. Dureuil, C. Ricolleau, M. Gandais, C. Grigis, J. P. Lacharme, and A. Naudon, *J. Cryst. Growth* 233, 737 (2001).
36. R. D. Vishpute, S. Choopun, R. Enck, A. Patel, V. Talyansky, R. P. Sharma, T. Venkatesan, W. L. Sarney, L. Salamanca-Riba, S. N. Andronescu, A. A. Iliadis, and K. A. Jones, *J. Electr. Mat.* 28, 275 (1999); Y. F. Lu, Z. M. Ren, T. C. Chong, B. A. Cheong, S. K. Chow, and J. P. Wang, *J. Appl. Phys.* 87, 1540 (2000); D. W. Kim, D. H. Kim, T. W. Noh, Oh E, H. C. Kim, and H. C. Lee, *Solid State Comm.* 121, 631 (2002).
37. L. V. Zhigilei, B. S. Kodali, and B. J. Garrison, *J. Phys. Chem. B* 102, 2845 (1998).
38. M. von Allmen, "Laser-Beam Interactions with Materials," Springer Series in Materials Science. Springer-Verlag, Berlin, 1986.
39. N. S. Nogar and R. C. Estler, Laser desorption/ablation with detection by resonance ionization spectroscopy, in "Lasers and Mass Spectrometry" (D. M. Lubman, Ed.). Oxford Univ. Press, London, 1990; W. B. Emary, O. W. Hand, and R. G. Cooks, Laser for the generation and excitation of ions in tandem mass spectrometry, in "Lasers and Mass Spectrometry" (D. M. Lubman, Ed.). Oxford Univ. Press, London, 1990.
40. R. N. Zare and R. D. Levine, *Chem. Phys. Lett.* 136, 593 (1987).
41. R. B. Hall and A. M. DeSantolo, *Surface Sci.* 137, 421 (1984).
42. M. G. Sherman, J. R. Kinsey, J. C. Hemminger, and R. T. McIver, *Anal. Chim. Acta* 178, 79 (1985).
43. J. Grotemeyer and E. W. Schlag, *Acc. Chem. Res.* 22, 399 (1989).
44. F. Engelke, J. H. Hahn, W. Henke, and R. N. Zare, *Anal. Chem.* 59, 909 (1987).
45. P. Morales and M. Sperandei, *Appl. Phys. Lett.* 64, 1042 (1994).
46. A. Vertes, M. De Wolf, P. Juhasz, and R. Gijbels, *Anal. Chem.* 61, 1029 (1989).
47. S. Amoruso, R. Bruzzese, N. Spinelli, and R. Velotta, *J. Phys. B* 32, R131 (1999).
48. G. S. Hurst and M. G. Payne, "Principles and Applications of Resonance Ionization Spectroscopy." Hilger, Bristol Philadelphia, 1988.
49. V. S. Letokhov, "Laser Photoionization Spectroscopy." Academic Press, London, 1987.
50. "Lasers and Mass Spectrometry" (D. M. Lubman, Ed.). Oxford Univ. Press, London, 1990.
51. V. S. Lethokov and V. P. Chebotayev, "Nonlinear Laser Spectroscopy," Ch. 4, Springer Series in Optical Sciences. Springer-Verlag, Berlin, 1977.
52. N. Bloembergen and M. D. Levenson, "High Resolution Laser Spectroscopy," Ch. 8, Topics in Applied Physics. Springer-Verlag, Berlin/Heidelberg, New York, 1976.
53. P. Dore, M. I. Schisano, M. Menghini, and P. Morales, *Chem. Phys. Lett.* 116, 521 (1985).
54. A. L. Chebotayev, A. L. Golger, and V. S. Letokhov, *Chem. Phys.* 7, 316 (1975).
55. U. Boesl, H. J. Neusser, and E. W. Schlag, *J. Chem. Phys.* 72, 4327 (1980); W. Dietz, H. J. Neusser, U. Boesl, E. W. Schlag, and S. H. Lin, *Chem. Phys.* 66, 105 (1982); U. Boesl, H. J. Neusser, and E. W. Schlag, *Chem. Phys. Lett.* 87, 1 (1982).
56. K. W. D. Ledingham and R. P. Singhal, *Int. J. Mass Spectr. Ion Proc.* 163, 149 (1997).
57. R. Weinkauff, P. Aicher, G. Wesley, J. Grotemeyer, and E. W. Schlag, *J. Phys. Chem.* 98, 8381 (1994).
58. J. E. Mathis and R. N. Compton, *J. Chem. Phys.* 104, 8341 (1996).
59. P. W. Werner and E. Schamiloglu, *J. Appl. Phys.* 79, 2728 (1996).
60. M. Stuke, H. Reisler, and C. Wittig, *Appl. Phys. Lett.* 39, 201 (1981).
61. R. J. Cotter, *Anal. Chim. Acta* 195, 45 (1987).
62. J. Grotemeyer and E. W. Schlag, *Acc. Chem. Res.* 22, 3999 (1989).
63. K. Walter, U. Boesl, and E. W. Schlag, *Int. J. Mass Spectr. Ion Proc.* 71, 309 (1986) and references therein.
64. M. Karas, D. Bachmann, U. Bahr, and F. Hillenkamp, *Int. J. Mass Spectr. Ion Proc.* 78, 53 (1987).
65. L. J. Romano and R. J. Levis, *J. Am. Chem. Soc.* 113, 9665 (1991).
66. F. Hillenkamp, M. Karas, R. C. Beavis, and B. T. Chait, *Anal. Chem.* 63, 1193A (1991).
67. M. Karas, U. Bahr, A. Ingendoh, E. Nordhoff, B. Stahl, K. Strupat, and F. Hillenkamp, *Anal. Chim. Acta* 241, 175 (1990).
68. A. Vertes and R. D. Levine, *Chem. Phys. Lett.* 171, 284 (1990).
69. P. Morales, A. S. Pavone, M. Sperandei, G. Leter, L. Mosiello, and L. Nencini, *Biosensors Bioelectr.* 10, 847 (1995).
70. M. C. Fitzgerald, G. R. Parr, and L. M. Smith, *Anal. Chem.* 65, 3204 (1993).
71. D. S. Cornett, M. A. Duncan, and I. J. Amster, *Anal. Chem.* 65, 2608 (1993).
72. R. C. Beavis and B. T. Chait, *Rapid Comm. Mass Spectr.* 3, 432 (1989).
73. V. V. Laiko, M. A. Baldwin, and A. L. Burlingame, *Anal. Chem.* 72, 652 (2000).
74. M. C. Galicia, A. Vertes, and J. H. Callahan, *Anal. Chem.* 74, 1891 (2002).
75. "Surface Enhanced Raman Scattering" (R. K. Chang and T. E. Furtak, Eds.). Plenum, New York, 1982.
76. T. E. Furtak and J. Reyes, *Surface Sci.* 93, 35 (1980).
77. D. W. Pohl, in "Forces in Scanning Probe Methods" (H. J. Guntherodt, D. Anselmetti, and E. Meyer, Eds.), NATO Advanced Study Institutes, Ser. E, Vol. 286. Kluwer, Dordrecht, 1995.
78. C. Girard and A. Dereux, *Rep. Progr. Phys.* 59, 657 (1996).
79. J. Gersten and A. Nitzan, *J. Chem. Phys.* 73, 3023 (1980).

80. L. Landau and E. Lifshits, "Electrodynamics of Continuous Media." MIR, Moscow, 1966.
81. Y.-F. Lu, Z.-H. Mai, and W.-K. Chim, *Jpn. J. Appl. Phys.* 38, 5910 (1999).
82. P. I. Geshev, F. Demming, J. Jersch, and K. Dickmann, *Thin Solid Films* 368, 156 (2000).
83. S. Grafstrom, P. Schuller, and J. Kowalski, *J. Appl. Phys.* 83, 3453 (1998).
84. R. Huber, M. Koch, and J. Feldmann, *Appl. Phys. Lett.* 73, 2521 (1998).
85. V. A. Ukraintsev and J. T. Yates, Jr. *Appl. Phys.* 80, 2561 (1996).
86. P. I. Geshev, F. Demming, J. Jersch, and K. Dickmann, *Appl. Phys. B* 70, 91 (2000).
87. J. Jersch, F. Demming, I. Fedotov, and K. Dickmann, *Appl. Phys. A* 68, 637 (2001).
88. I. Lyubinetsky, Z. Dohnalek, V. A. Ukraintsev, and J. T. Yates, Jr., *J. Appl. Phys.* 82, 4115 (1997).
89. J. Boneberg, M. Tresp, M. Ochmann, H.-J. Munzer, and P. Leiderer, *Appl. Phys. A* 66, 615 (1998).
90. A. A. Gorbunov and W. Pompe, *Phys. Status Solidi A* 145, 333 (1994).
91. J. Jersch and K. Dickmann, *Appl. Phys. Lett.* 68, 868 (1996).
92. J. Jersch, F. Demming, L. J. Hildenhagen, and K. Dickmann, *Appl. Phys. A* 66, 29 (1998).
93. J. Jersch, F. Demming, and K. Dickmann, *Appl. Phys. A* 64, 29 (1997).
94. S. M. Huang, M. H. Hong, B. S. Lukyanchuk, Y. F. Lu, W. D. Song, and T. C. Chong, *J. Vac. Sci. Technol. B* 20, 1118 (2002).
95. S. M. Huang, M. H. Hong, B. S. Lukyanchuk, Y. F. Lu, W. D. Song, and T. C. Chong, *J. Appl. Phys.* 91, 3268 (2002).
96. J. Boneberg, M. Tresp, M. Ochmann, H. J. Munzer, and P. Leiderer, *Appl. Phys. A* 66, 615 (1998).
97. J. I. Pascual, J. Méndez, J. Gomez Herrero, A. M. Barò, N. Garcia, U. Landmann, W. D. Luedtke, E. N. Bogachev, and H. P. Cheng, *Science* 267, 1795 (1995).
98. J. Gimzewski and R. Moller, *Phys. Rev. B* 36 1284 (1987).
99. R. Huber, M. Koch, and J. Feldmann, *Appl. Phys. Lett.* 73, 2521 (1998).
100. H. J. Munzer, M. Mosbacher, M. Bertsch, J. Zimmermann, P. Leiderer, and J. Boneberg, *J. Microsc.* 202, 129 (2001).
101. S. T. Yau, D. Saltz, and M. H. Nayfeh, *Appl. Phys. Lett.* 57, 2913 (1990).
102. S. T. Yau, D. Saltz, and M. H. Nayfeh, *J. Vac. Sci. Technol. B* 9, 1371 (1991).
103. S. G. Hansen, *J. Appl. Phys.* 66, 3329 (1989).
104. R. Luthi, R. R. Schlittler, J. Brugger, and P. Vettiger, *Appl. Phys. Lett.* 75, 1314 (1999).
105. A. Gerardino, A. Notargiacomo, and P. Morales, *Microelectr. Eng.*, 67, 923 (2003).



# Laser Fusion Target Nanomaterials

Keiji Nagai, Takayoshi Norimatsu, Yasukazu Izawa, Tatsuhiko Yamanaka

*Osaka University, Suita, Osaka, Japan*

## CONTENTS

1. Introduction
  2. Laser Fusion Target Fabrication Technique
  3. Laser Fusion Target Materials
  4. Summary
- Glossary  
References

## 1. INTRODUCTION

Nuclear fusion is the power source of luminous stars. The final goal of laser fusion research is to make an artificial microstar on the earth as an alternative clean energy source to maintain a healthy global environment. Although laser fusion research started later than magnetic fusion research, laser fusion has an attractive feature, that is, separability of the system and a simple, compact reactor due to high reaction efficiency [1–3]. The center plasma of laser fusion is very small even for the actual reactor size ( $\sim 200 \mu\text{m}$  in diameter) and of very high density ( $\sim 2000$  times solid density) which is achieved by keeping a highly spherical implosion process. The ignition temperature is  $\sim 10^7$  K, which is far from the conventional nanotechnology region, but the fine structured plasma should be well controlled to ignite fusion reaction. Therefore, laser fusion research should be overlap with the nanotechnology research field. The implosion process for the fusion reactor stands on laser and target technology. Laser is a quite low entropy photon flux; therefore most laser devices have precise structure related to nanotechnology. On the other hand, laser plasma generates high quality (for example monochromic [4]) X-rays,  $\gamma$ -rays, high temperature ions, electrons, positrons, etc., which depend on the combination of a tailored irradiating laser and an irradiated target. These features can be summarized such as an input of nanotechnology to the target and laser makes an output of another nanotechnology through laser plasma as shown in Figure 1.

## 2. LASER FUSION TARGET FABRICATION TECHNIQUE

Capsule fabrication is the most important technology in fabrication of laser fusion targets. The capsules of laser fusion have roles as fuel containers and ablaters to compress the fuel (Fig. 2). Previous capsules were composed of glass and designed with the large aspect ratio of capsule diameter/thickness [5]. The capsules exhibited high neutron yield [6, 7], but the compression density was not sufficiently high due to shock heating and X-ray preheating effects from high atomic number silicon. Therefore, recent design have a relatively thick capsule composed of light atoms such as carbon to obtain high fuel compression. Capsule size has been designed to be 5 mm in diameter for a future reactor and 0.5–2 mm for current fundamental experiments depending on laser power. In the case of fundamental experiments, some capsules contain probe atoms to estimate fuel density or fuel temperature.

For an indirect driven system such as the National Ignition Facility (NIF), targets consist of a capsule and a hohlraum. The laser directly irradiates the inner surface of the hohlraum and the inner fuel capsule is compressed by X-rays from the hohlraum. There are three candidate materials of the capsules: beryllium, polyimide, and glow discharge polymer (GDP) for NIF targets. These specifications are summarized including the range of values for all targets and the variation in value allowed in a specific target of that group (Table 1). The NIF specification is shown in Table 2 [8, 9], where the out-of-roundness in mode 2 must be less than 500 nm and that in mode 10 should be less than 4 nm. In the direct driven system, the high power laser light directly irradiates the capsule; therefore it is no longer necessary and the material component is different than the indirect driven system.

### 2.1. Plastic Capsule Fabrication

#### 2.1.1. Coating Method

GDP capsules [10] have been fabricated and used in the United States and France to supply fundamental experiments as summarized in Table 1. The capsule scale depends on the laser power. GDP capsules are prepared using

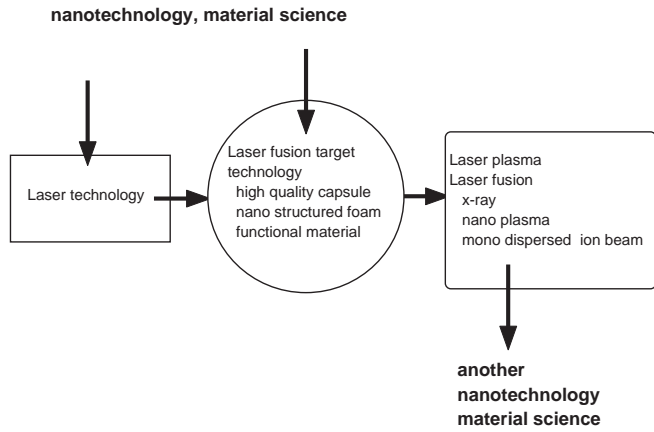


**Figure 1.** Relation between laser fusion target and nanotechnology.

the depolymerizable mandrel technique (Fig. 3). Poly( $\alpha$ -methylstyrene) (PAMS) mandrels were coated with GDP. After the coating of GDP, the PAMS mandrel is thermally decomposed via depolymerization and the remaining GDP capsule is used as a target. The thickness control is difficult for thick capsules ( $\sim 200 \mu\text{m}$ ). These dimensions are well beyond those currently fabricated on a routine basis [11, 12].

In French laser fusion experiments using laser integration line and the future megajoule laser systems, the coatings are prepared by GDP with *trans*-2-butene and hydrogen. Theobald et al. presented the first microshells obtained at the CEA with a GDP coater. Amorphous hydrogenated carbon shells of  $175 \mu\text{m}$  with 1 or 2.4 mm diameter have been prepared. The measured roughness at high modes is lower than 10 nm for a  $30 \times 30 \mu\text{m}$  characterization area [13, 14].

Thin walled polymer shells are required for cryogenic laser experiments with the OMEGA laser system at Rochester University [15]. These capsules need to be about  $900 \mu\text{m}$  in diameter and as thin as possible ( $\sim 1\text{--}2 \mu\text{m}$ ), while having enough strength to be filled with a equivalent deuterium–tritium mixture (DT) as fast as possible to about 1000 atm. They have found that by optimizing the coating parameters in the GDP deposition system, they can routinely make robust,  $\sim 1.5 \mu\text{m}$  thick,  $900 \mu\text{m}$  diameter GDP

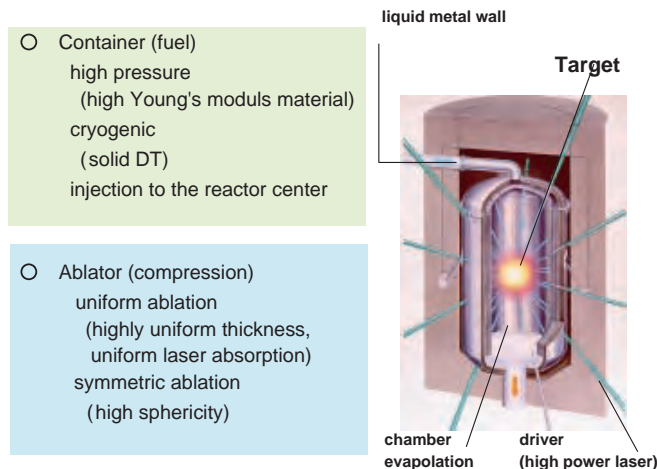


**Figure 2.** Roles of laser fusion target as container and ablator.

**Table 1.** Various specs of GDP capsules for high power laser implosion experiments.

Laser system	Laser power	Capsule diameter	Capsule thickness
NIF	1.8 MJ	2 mm	200 $\mu\text{m}$
Omega (CRYO)	40 kJ	900 $\mu\text{m}$	as thin as possible
LIL	60 kJ	1 mm	
LMJ	1.8 MJ	2.4 mm	175 $\mu\text{m}$
Gekko XII	25 kJ	500 $\mu\text{m}^a$	7 $\mu\text{m}^a$

<sup>a</sup> A polystyrene capsule has been used and a GDP capsule has not been used.

shells with buckle strength of over 0.3 atm. Shells as thin as  $0.5 \mu\text{m}$  have been made. This is twice the strength of shells made prior to the optimization and it is comparable to values quoted for polyimide shells. In addition, these shells were found to be approximately three times more permeable and over 20% denser than previously made GDP shells. The combination of higher strength and permeability is ideal for direct drive cryogenic targets at OMEGA.

The composition and chemical structure of GDP capsules have been studied by Nikroo et al. [16, 17]. The investigation was carried out using combustion and Fourier transform infrared (FTIR) analysis. The strongest coatings were obtained when the polymer had the lowest hydrogen content or hydrogen/carbon (H/C) ratio ( $\sim 0.9$ ), whereas the weakest coating had the highest hydrogen content or H/C ratio ( $\sim 1.3$ ). Good agreement was observed between composition results obtained from combustion and FTIR analysis, where the strongest coating had less terminal methyl groups and more double bonds or olefinic structures. Strong GDP coatings that were aged in air reacted more with oxygen and moisture than standard GDP coatings. In addition to the more olefinic structures, there may also be more free-radical sites present in strong GDP coatings, which leads to a greater oxygen uptake.

Polyimide capsules are being developed for implosion experiments. Vapor-deposited polyimide capsules for the NIF were developed [18–22] by improving the capsule surface finish through better understanding of the origin of surface roughness created during the deposition processes and implementation of a postdeposition vapor smoothing procedure to imidation. They have determined that the most important factors during the deposition process that impact surface finish include mandrel quality, monomer mixing,

**Table 2.** The allowed long wavelength deviation from sphericity for low modes of the outer surface and ablator and fuel thickness.

Mode	Outer radius (nm)	Ablator thickness (nm)	Fuel thickness (nm)
1	—	50	400
2	500	75	400
3	400	75	400
4	120	75	400
5	50	25	400
6	25	17	120
7	10	10	80
8	6	8	70
9	5	7	50
10	4	6	40

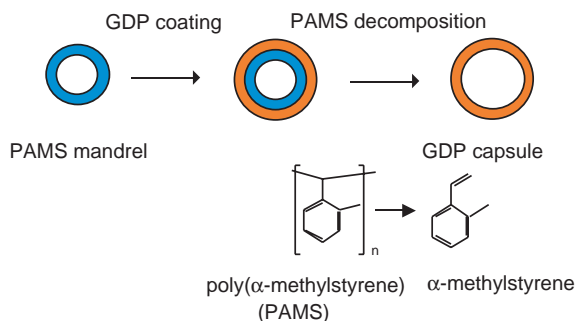


**Figure 3.** Fabrication of GDP capsule using poly(2-methylstyrene) mandrel.

self-shadowing, and abrasion. They showed that the high rate deposition (above  $10 \mu\text{m/h}$ ) is effective at reducing roughness, which is due to the shorter total time of shell agitation in a bouncer pan. By adjusting the coating conditions, coating up to  $160 \mu\text{m}$  thick was reproducibly fabricated with  $300 \text{ nm}$  root mean square (rms) roughness. Solvent vapor smoothing using dimethyl sulfoxide, a new technique also developed at Lawrence Livermore National Laboratory, improves the surface to  $30 \text{ nm rms}$ .

The processing conditions for vapor-depositing polyimide shells were studied to improve the surface finish, the tensile properties, and the gas permeability for inertial confinement fusion application [23, 24]. The vapor-deposited polyimide possessed distinct properties from solution-cast Kapton, resulting perhaps from being physically or chemically cross-linked. The vapor-deposited polyimide was characterized as semicrystalline with molecular chains parallel to the shell's surface. Varying the imidization conditions (i.e., using different atmospheres, heating rates, and heating durations) increased the permeability while maintaining the Young's modulus. Plastically deforming the shells under biaxial stress increased the permeability up to 1000-fold, which could be reversed when shells were heated to  $350 \text{ }^\circ\text{C}$ . Analyses using X-ray diffraction, infrared spectroscopy, and solubility tests indicated that these modifications in properties may have arisen from changes in the crystallinity, cross-linking, and molecular weight. The low-mode (2 to 20) surface roughness was reduced when the shells were slightly inflated; the high-mode roughness (coating-induced bumps) was increased when the substrate was heated to a temperature of  $90$  to  $140 \text{ }^\circ\text{C}$ .

### 2.1.2. Emulsion Technique

The emulsion technique to prepare capsules is well known by polymer scientists [25, 26], but vacuole formation during microencapsulation is a serious problem for laser fusion targets [27]. Highly spherical and uniformly thick capsules without a vacuole have been developed in the field of laser fusion targets. In particular, the polystyrene capsule [28] provided the highest density implosion, 600 times that of solid density [29, 30]. In a future power plants, high repetition implosion is required in the reactor. For mass production of shells with monodispersed diameter and uniform thickness, a droplet generator (Fig. 4) was utilized to prepare emulsions [31].

However, the process in which a uniform wall is formed was not clearly known. Norimatsu et al. [32, 33] and Gresho

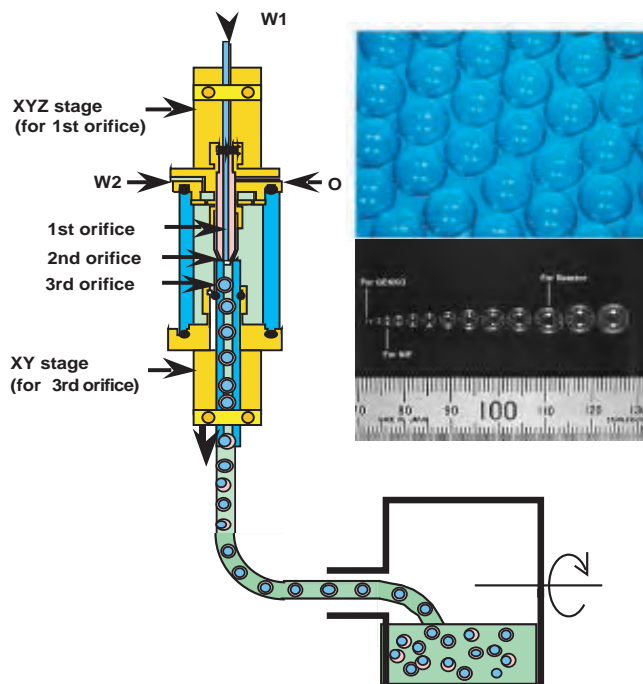


**Figure 4.** Monodispersed sized emulsion generator (left), polystyrene capsules from the emulsion (upper right), and various capsule size range (lower right).

[34] proposed a model (Fig. 5) to numerically simulate the emulsion process to improve the shell fabrication process. When some external force such as collisions with the stirring propeller deforms a water/oil/water ( $W_1/O/W_2$ ) emulsion, the deformation force is transferred to the inner water core through the oil phase. If the force is inversely proportional to the thickness of the oil phase, a centering force appears and the core moves toward the center of the emulsion. Because some important assumptions were made in the model, they compared the model with an experiment, where equipment was established to mechanically deform a  $W_1/O/W_2$  emulsion by a vertically vibrating rod instead of the deformation during stirring. Experimental results obtained using a mechanical driver are shown in Figure 6. The densities of  $W_1$  and  $O$  measured before making the compound emulsion were  $0.998$  and  $1.024 \text{ g/cc}$ , respectively. Their values were estimated to be  $0.999$  and  $1.017 \text{ g/cc}$  during the centering experiment because of diffusions of 1, 2-dichloroethane into the  $W_1$  and  $W_2$ . The viscosity of  $O$  was  $0.1 \text{ P}$  ( $\pm 15\%$ ). Their model calculations could explain experimental results obtained by emulsions with the large

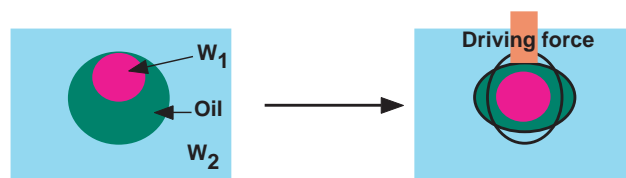


**Figure 5.** A schematic view of an emulsion (left) and the core  $W_1$  phase of the emulsion centered by the deformation of emulsion due to the sloshing (right).

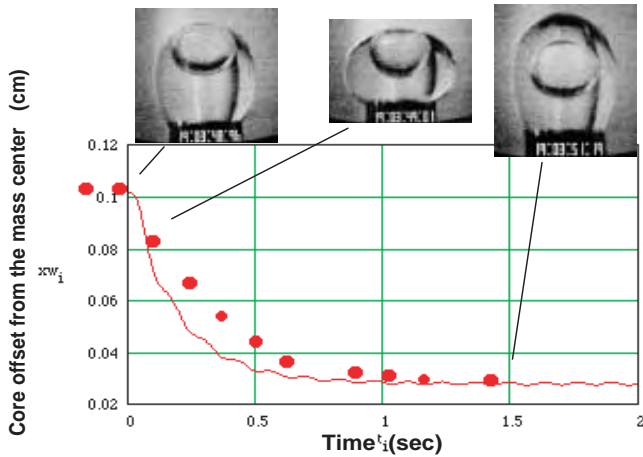


**Figure 6.** Comparison of the centering process of a compound emulsion with the Norimatsu model. The oscillation is in sloshing mode. The vertical axis is the offset of the core in mm and the horizontal axis is the time in seconds. In the set of photographs, the left and middle photographs show the first vertically lengthened phase and the first compressed phase, respectively. The right photograph shows the final equilibrium position in the lengthened phase. Time origins for experiment and simulation are arbitrary.

and small core oscillating in sloshing mode. However, the centering speed of the small core was faster than calculations. The recommended aspect ratio  $\lambda$  (=inner radius of O/outer radius of O) was  $0.5 < \lambda < 0.8$ .

The mass transfer of the solvents was experimentally measured in the oil, water, and distillate phases during the curing process of highly spheric monodispersed 4-mm-diameter polystyrene capsules of uniform thickness (Fig. 7) [35]. It was determined that the water solubility of the solvents is crucial in the solvent selection in order to prepare the capsules by this method. The curing process started from the

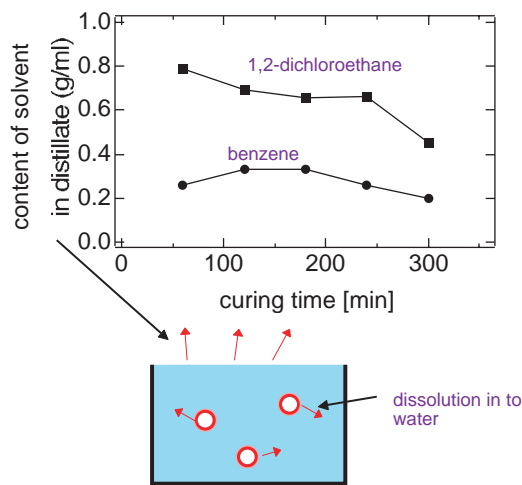


**Figure 7.** At the early time of the emulsion curing process ( $\sim 30$  min), the distillate ratio of 1, 2-dichloroethane/benzene was higher than that at the later time (above). This means that the curing was not governed by the boiling point (benzene:  $\sim 80^\circ\text{C}$ , 1, 2-dichloroethane:  $\sim 83^\circ\text{C}$ ) but rather the solubility in water (benzene: 0.2 g/100 g, 1, 2-dichloroethane: 1.0 g/100 g at  $50^\circ\text{C}$ ).

water/oil/water emulsions, where the boiling temperature and the densities of the oil were well matched by mixing benzene and 1, 2-dichloroethane. The masses of the solvents were measured for the oil phases and the distillate and then calculated for the water phase. The analysis of the solvents in the water phase indicated that the process was governed by the kinetics of the dissolving from the oil phase to the outer water phase rather than by the vapor pressure of the solvents in the early stage before the oil phase lost its fluidity. The time at losing the centering motion of the emulsion core was measured experimentally and gave a procedure of the highly spheric PAMS mandrel [36–38].

The surface finish of the final shells was examined using atomic force microscopy (AFM) and scanning electron microscopy (SEM). A clear dependence of the spectrum of final GDP shell on the quality of the initial PAMS mandrel was observed. These shells with various thicknesses have very similar power spectra, indicating little coating deterioration of shell surface finish due to GDP coating processes [39].

Surface ripples of mode 10 in IFE shells were a serious problem for NIF ignition. PAMS spherical shells made by microencapsulation show a surface roughness ( $\sim 30$  nm) within the mode range 7–20 (Fig. 8). The roughness mode number corresponds with theoretical models of Marangoni convection cells formed during the curing of the initial wet shells. The roughness was removed by reducing the curing rate so that the concentration gradient across the wall was less than the threshold of Marangoni convection [40].

Takagi et al. developed a new method for making spherical PAMS mandrels, where a small amount ( $< 0.1$  wt%) of high-molecular-weight poly(acrylic acid) (PAA) was utilized instead of poly(vinyl alcohol) in the suspending medium, which substantially increases the interfacial tension during curing and yields extremely round capsules. The poly(acrylic acid) is also beneficial for centering of the core water, leading to exceptionally concentric capsules. However, fully cured capsules made by this method displayed a significant level of high frequency surface debris that became especially problematic when the mandrels were subsequently overcoated with GDP. To overcome this problem, they examined the use of poly(acrylic acid) in conjunction with poly(vinyl alcohol) in order to reduce these surface features

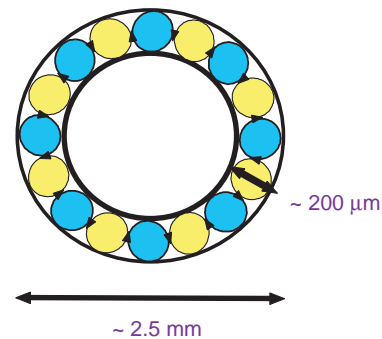


**Figure 8.** The PAMS capsule showed a surface roughness  $\sim 30$  nm within mode 7–20. The roughness mode number corresponds with theoretical modes of Marangoni convection cells formed during the curing of emulsion.



and explored numerous variations of concentration and timing of the poly(vinyl alcohol) addition. The conditions were optimized for the initial use of poly(acrylic acid) for centering and symmetry of the mandrel, followed by exchange to poly(vinyl alcohol) solution. GDP shells made from these mandrels satisfy the ignition capsule design requirements [41, 42].

The capsule characteristics mainly depend on the number of average molecular weight, molecular weight dispersion, and finally the atomic composition. It was shown that the surface quality of the capsule is directly connected to the polydispersity index. The best results have been obtained using polystyrene which exhibited a dispersity index inferior to 1.20.

Thin-walled shells with polystyrene or its copolymers were fabricated using a conventional emulsion technique [43]. The wall thickness of the resultant shells was found to be 3  $\mu\text{m}$  for the 1 mm diameter. The reduced thickness was due to the low concentration oil of polystyrene derivatives and the high temperature water phase.

Recently high quality polyimide capsules have been fabricated using an emulsion technique (Fig. 9), while the previous emulsion method succeeded only for conventional soluble and noncrystalline polymers such as polystyrene and poly(methyl methacrylate). The polyimide capsule is one of the leading designs for IFE experiments and is prepared using a chemical vapor deposition process [18–24], which requires expensive apparatus. By curing an emulsion containing nonvolatile *N, N*-dimethylacetamide, 0.5–5 mm capsules of highly spheric poly(amic acid) were fabricated [44]. Although the sphericity of the capsule (>99%) obtained by the emulsion method was slightly lower than the highest millimeter-sized polystyrene capsule, its surface was smooth without irregular deviation. The curing for high sphericity capsules required stabilization and deformation, which were governed by several conditions such as the concentration of PAA, the viscosity of the emulsion matrix, the stirring speed, and the temperature. The PAA capsule was imidized by a chemical process.

Metal particle (20–30 nm) doped polystyrene capsules were fabricated using an emulsion technique. The capsule will be applied to suppress Rayleigh–Taylor instability [45]. Another polystyrene hollow pellet with a high atomic number atom boundary irradiator is fabricated for inertial confinement fusion experiments. The pellet adsorbs high *Z* micro- or nanoparticles on its inner surface to emit characteristic X-rays of the high *Z* materials. A triphasic

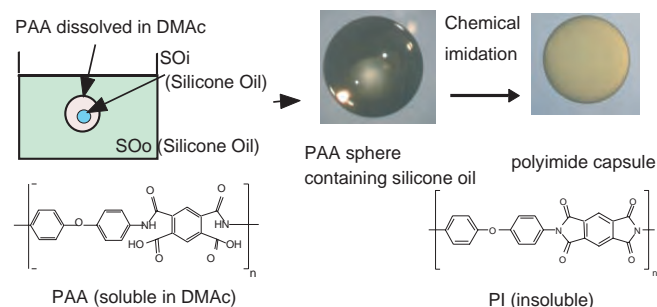


**Figure 9.** A polyimide capsule was obtained using the emulsion technique via a soluble precursor of the poly(amic acid) capsule and the chemical imidation process.

emulsion of  $W_1/O/W_2$  is used for the fabrication processes. The  $W_1$  is a high *Z* microparticle (alumina) mixture in water. After drying, high *Z* microparticles 300 nm in diameter remain on the inner surface of the pellet [46].

### 2.1.3. Other Problems with Capsule Treatment

Stephens et al. reported unique capsule fabrication using a heated drop tower. Polystyrene capsules in the 1 to 1.5 mm diameter range were prepared employing solid polystyrene pellet feed [47].

The capsules need to be characterized in detail. A wall mapping apparatus and a sphere mapping apparatus were investigated to determine thickness along the same paths as the surface profiles [48]. In the system, a capsule was mounted on a horizontally rotating vacuum chuck. Sphere mapping was done using AFM, while wall mapping was monitored using optical fiber connected to a light source to illuminate the capsule. Both mapping circles were on the equatorial face of the capsule.

The economic viability of target fabrication is a crucial issue for the feasibility of future IFE power plants. Current targets produced for IFE ignition experiments are estimated to cost about \$2500 each. Design studies of cost-effective power production from IFE have found a cost requirement of about \$0.25 each. While a four orders of magnitude cost reduction may seem at first to be a significant challenge, there are many factors that suggest this is an achievable goal. Goodin et al. summarized the major steps in cost reduction that will be taken to economically supply targets for IFE power plant fueling [49].

Target delivery to the reactor center is important problem. In order for the driver to properly ignite the target, the target and laser beams must come together at the center of the reactor chamber with precise timing ( $\pm 10$  ms) and positioning ( $\pm 10$   $\mu\text{m}$ ). The cryogenic target must not melt [50, 51]. A preliminary injection system was constructed at the Institute of Laser Engineering (ILE) in Osaka to ascertain the initial perturbations in the injection speed and the direction (Fig. 10). The system is composed of two sets of coils. Each consists of three pairs of two coils triggered by a 120 degree delay in the phase. The coils in the first and second stage are powered with 300 V, 1980  $\mu\text{F}$  and 840 V,

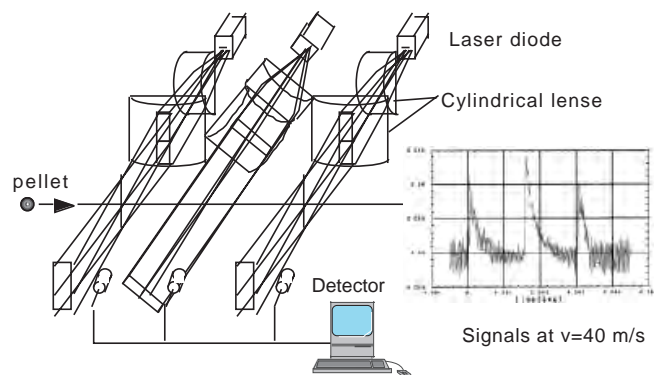


**Figure 10.** Tracking system developed at ILE Osaka and the typical signal obtained from a 5 mm polystyrene shell at  $v = 40$  m/s.

366  $\mu\text{F}$  capacitors, respectively. This system can launch a 98 mm long, 12.5 mm diameter, 0.5 mm thick aluminum sabot with a 5 mm diameter polystyrene shell inside at a speed of 10 m/s.

## 2.2. Inorganic Capsule Fabrication

Glass microspheres were the principal fuel container for laser fusion targets. In particular, high-aspect-ratio targets produced thermonuclear neutron yields exceeding  $10^{12}$  with the 12-beam green GEKKO XII laser [6, 7]. Two methods were developed for the specific purpose of supplying high-quality glass microspheres: liquid droplet and the sol-gel methods. The liquid droplet method involves the formation of highly uniform droplets of aqueous glass solutions by breaking up a capillary jet flow of the solution. The droplets are subsequently dried and fused to form the desired hollow glass microspheres. In the sol-gel method, a solution of glass-forming oxides is dried to form gel. After crushing and sieving to a suitable particle size, the gel particle drops through a high-temperature furnace to form a glass microsphere. The two methods are complementary in many aspects. Reference [52] summarizes both methods briefly.

Recent developments in making glass shells from metal doped GDP deposited by plasma polymerization (where metal is Si or Ti) have significantly expanded the diameter and wall thickness obtainable by the process. Further, the wall uniformity of glass shells made by the process is generally superior to those made by the traditional drop-tower approach. Hoppe enabled pressurization of a glass shell with argon by taking advantage of permeability properties of the glass before it is converted to full density where it becomes essentially impermeable to most gases [53].

## 2.3. Cryogenic Solid Hydrogen Layering

Cryogenic targets with solid deuterium/tritium layers are very important in laser fusion and have occupied a large area in target development. The hollow, spherical solid density fuel can be efficiently imploded due to the initially higher density and lower isentropy compared with gaseous fuel with the same mass. This means such targets reduce the energy to compress it to a high density and high temperature. A cryogenic target system with low density plastic foam was developed 10 years ago [54, 55] and supplied for the fundamental experiments [56], while very recently the first results from a cryogenic target without foam have been supplied for implosion experiments at Rochester University [57].

It is difficult to form a uniform layer because of gravity and polycrystallization during the solidification process. Many techniques have been proposed and studied to overcome the difficulties. The first cryogenic target was fabricated by cooling a fuel-filled glass sphere with direct thermal conduction through a supporting copper fiber [58]. The second technique, fast isothermal freezing, did not use the supporting fiber which disturbs the implosion symmetry [59–62].

The  $\beta$ -heating technique uses  $\beta$ -decay-induced redistribution of a DT-filled fuel container to be cooled uniformly below the freezing point. Because the DT fuel generates heat due to  $\beta$  decay, the temperature of the inner surface of the thicker area is higher than that of the thinner area

when it is cooled uniformly. The solid DT at the thicker area is redistributed to the thinner areas through a sublimation–condensation process. The maximum rate at which the redistribution occurs was given by  $d\delta/dt = -\delta/\theta_{\text{TC}}$ , where  $\delta = \text{DT ice thickness in excess of that for a uniform layer}$  and  $\theta_{\text{TC}} = \text{a time constant } \sim 1500 \text{ s}$  [63]. The apparatus was summarized in the [64], and  $\theta_{\text{TC}}$  was reported depending on the  $^3\text{He}$  content (the age of  $^3\text{T}$  [63]).

Norimatsu et al. developed a plasma layering technique in which a nonuniform solid fuel layer is redistributed into a uniform one, with a glow discharge initiated in the void by an external intense microwave field. Reactor sized frozen deuterium was demonstrated with the redistribution time constant of  $\sim 80 \text{ s}$  [31, 66, 67]. Mapoles et al. reported a technique to generate a heat flux across the fuel surface by applying an electric field to the DT layer in the center of the shells. The vapor has a small but significant conductivity due to ionization caused by  $\beta$  decay of tritium in the vapor and the solid [68].

The IR heating method is also a powerful candidate for future reactor use. Pumping the IR collision induced vibration–rotation band in solid  $\text{D}_2$  ( $3.15 \mu\text{m}$ ) and (HD, heated deuterium-hydride  $2.57 \mu\text{m}$ ) redistributes the solid depending on IR intensity profile [69]. HD layers 150–250  $\mu\text{m}$  thick formed near the triple point have a surface roughness rms between 1 and 3  $\mu\text{m}$  and become rougher with decreasing temperature. When solid DT in an isothermally cooled shell is heated, the solid DT layer becomes uniform through a process similar to  $\beta$ -heating. Solid growth dynamics have a significant impact on the quality of the resultant layer. The solid layers slowly grown from the melt were much smoother [70]. Koziowski et al. reported results of modeling and experiments on infrared HD layers in hohlraums [71]. A 2 mm diameter, 40  $\mu\text{m}$  thick shell with 100–400  $\mu\text{m}$  thick HD ice inside a NIF scale gold hohlraum is heated by pumping the HD vibrational bands. Models indicate control of the low-mode layer shape by adjusting the infrared distribution along the hohlraum walls. They have experimentally demonstrated control of the layer symmetry perpendicular to the hohlraum axis.

The cryogenic foam target consists of a low-density, plastic foam shell to sustain liquid fuel and an outer thin film to prevent the fuel from boiling off (Fig. 11). The uniformity

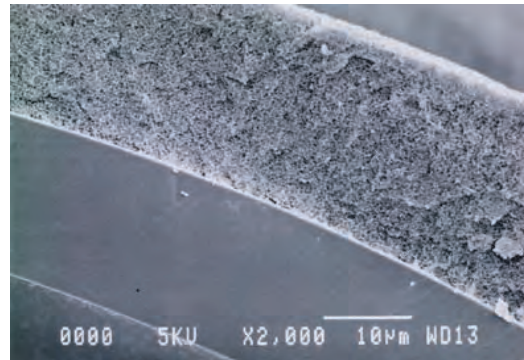


**Figure 11.** Cross section of foam shell obtained from macromonomeric acrylate with multifunctional groups.



of the liquid fuel layer is confirmed by that of the foam shell. The carbon in the foam material was considered to be an acceptably low-content impurity for the fusion plasma. A recent target design by Phillips et al. indicated that the impurity of carbon is preferable to absorb laser efficiently [72].

Layering indirect drive targets with the capsule already assembled in the hohlraum would be advantageous. One way to accomplish this is to layer targets in controlled temperature tubes while they are being staged for feeding to the injection system. Successful layering requires maintaining a specially tailored temperature profile on the hohlraum surface. Tritium decay heat removal from the filled capsule depends upon the thermal properties of the tube material, the capsule material, and other materials filling the hohlraum. Pulsifer et al. evaluated various techniques for achieving adequate thermal control during the in-hohlraum layering process. Results provided feedback to target designers on design techniques which will be important in order to make in-hohlraum layering possible [73].

All the cryogenic targets mentioned previously were supported, for example, by a stork. Technologies based on using freestanding targets (FST) are important for the next step fuel production. In each production step (fuel filling, fuel layering, and target delivery) the research has been intensively explored at the Lebedev Physical Institute. The layering apparatus can form 30–100  $\mu\text{m}$   $\text{H}_2$  and  $\text{D}_2$  solid layers on the inner surface of millimeter sized polystyrene shells. Layering time was less than 30 sec. Based on their advances, the FST technologies are now at the stage of extension on a reactor target design for the IFE power plant [74–76].

To form the smooth cryogenic layer inside laser targets a new approach is in progress which shares basic principles of fabrication of finely dispersed compounds (solid solutions) with little doping that slows crystalline grain growth. This approach has been demonstrated experimentally with a  $\text{H}_2/\text{HD}$  mixture where the amount of HD is less than 1%. As a result the transparent solid layer has been formed inside 500  $\mu\text{m}$  glass shells. The layer keeps its transparency at cycling heat treating in the range of 5 to 16–20 K [77].

Concerning cryogenic targets, cooling-induced deformation of fuel capsules was experimentally characterized in detail by Endo et al. In the experiments, polystyrene shells were cooled using liquid nitrogen and observed with an optical microscope. Pictures of each shell were recorded at various temperatures, and they were compared with each other. As a result of precise error estimation, it was found that any polystyrene shell showed deformation in varying degrees. It has been found that thinner shells deform more remarkably than thicker shells [78, 79].

## 2.4. Porous Foam Fabrication

Foam targets have been used not only for the cryogenic target [54–56] but also for the study of laser shock [80, 81] and laser–plasma interactions [82–84], for which the foam fabrication technique has also been investigated over a wide range of element compositions, densities, and microstructures.

Ultra-low-density foams provide a plasma under the cutoff density ( $n_{cr}$ ) which allows the penetration and interaction of laser light with the frequency of  $\omega_L$ , and the relation is [85]

$$\omega_L = [(e^2 n_{cr}) / (\epsilon_0 m_e)]^{1/2} \quad (1)$$

where  $e$ ,  $\epsilon_0$ , and  $m_e$  are the elementary charge, vacuum permittivity, and electron mass, respectively.

In addition to the ultra-low-density foams, recent laser–plasma experiments have required finer structures such as submicro- and nanostructures, for example, the high-power laser-induced D–D reaction indicated a size effect of the atomic cluster where the maximum nuclear yield was given at the cluster size of 6 nm [86]. Therefore, a variety of micro- and nanostructures of the foam materials are important in controlling the laser plasma.

Poly(4-methyl-1-pentene) (denoted as PMP) foams [82, 87–96] have been investigated for the following reasons: (1) they contain no oxygen which interferes with X-ray diagnostics, (2) they have the potential for heavy atom doping, and (3) they can be fabricated by dissolving the polymer by heat, cooling to coagulation, and removal of the solvent. See Table 3.

Generally, the removal of the solvent from a gel to the corresponding foam has been carried out by the freeze-drying method or the supercritical fluid extraction (SFE) method; either way a neat density polymer should be obtained. Ultra-low-density foams were prepared by the freeze-drying method to give a density of 2.5  $\text{mg}/\text{cm}^3$  [87–90], and their structure, for example for a PMP foam prepared from durene/naphthalene solution, was  $\sim 20 \mu\text{m}$  in size.

Recently, the coagulant effect for microstructures was observed in PMP foam from its gel of hexanol derivatives via supercritical fluid  $\text{CO}_2$ . The obtained ultra-low-density PMP foams have various microstructures depending on coagulant alcohols (Fig. 12). Although alcohols do not dissolve PMP, they have an alkyl group that interacts with the main and side chains of PMP [96].

The silicon doped CH foams were prepared by a thermally induced phase-inversion technique, with PMP, durene/naphthalene, and  $\text{SiO}_2$  as the foam skeleton material, the solvent/nonsolvent, and the doping materials, respectively. Foam density was 5–80  $\text{mg}/\text{cm}^3$ , and the weight percentage of Si was less than 10% [92].

One method of production of low-density polymeric foams is to dissolve a multifunctional monomer and initiator in a solvent and to polymerize by means of free-radical polymerization. The gel produced is precipitated in a non-solvent and subsequent SFE drying produces a low-density

**Table 3.** Characteristics of low-density foam of poly(4-methyl-1-pentene) prepared from alcoholic gel.

Coagulant	Foam density ( $\text{mg}/\text{cm}^3$ )	Disk size at the cutoff ( $\mu\text{m}$ )	Wavelength density ( $\mu\text{m}$ )
1-Hexanol	12	$\sim 10$	0.55
2-Methyl-1-pentanol	5.0	$\sim 3$	0.84
2-Ethyl-1-butanol	2.0	$\sim 6$	1.3

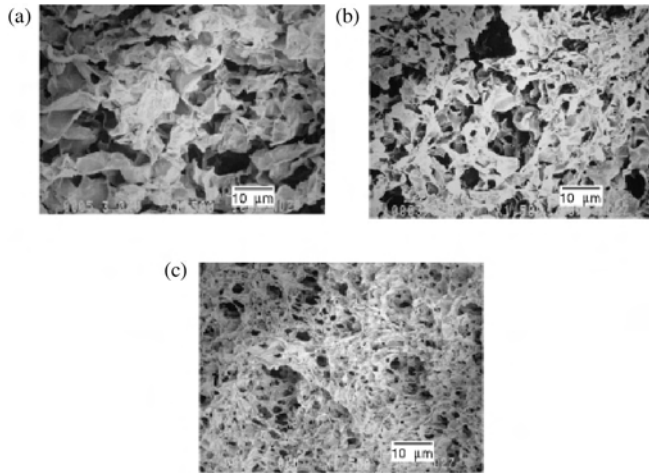


**Figure 12.** Scanning electron microscope image of poly(4-methyl-1-pentene) foam prepared from (a) 1-hexanol, (b) 2-methyl-1-pentanol, and (c) 2-ethyl-1-butanol.

microporous foam, which has a finer structure than that prepared by the freeze-drying process [93].

The cross-linked acrylic polymer exhibited fine structure of  $\sim 200$  nm [97–99] and was widely used as foam capsules with a gas barrier and foam-coated cryogenic targets (Fig. 11). The metal doping was done using lead and titanium [97]. Other cross-linked polymers provide fine foam, for example, phenol resin [100] and copolymer containing divinylbenzene. Resolsinol/formaldehyde foam, a kind of phenol resin foam, exhibited fine structure and opacity for laser light [101].

A middle density, foam layer coating was proposed to protect direct-drive, cryogenic targets from melting due to surface heating by residual gas in a laser fusion reactor. A  $100 \mu\text{m}$  thick,  $50 \text{ mg/cm}^3$  foam layer can prevent melting of the solid DT layer injected into the latest heat of Pb vapor. A thermal insulator coating on the target surface, or a sabot-in-chamber scheme, is necessary to protect the direct-drive, cryogenic target [102, 103].

To characterize foam, SEM and optical interferometric techniques are used. The latter method is limited by scattering caused by the foam structure. Foam parameters were estimated using model calculations to enable adequate foam shell characterization for a baseline capsule [104].

## 2.5. Cluster Target

Vapor atomic clusters and large molecules are attractive as targets for intense ultrashort pulse lasers. For example, Ditmire et al. reported D–D fusion at high pressure and low temperature gas jet, where  $10^2$ – $10^6$  molecules of  $\text{D}_2$  were coupled through van der Waals interaction [86, 105]. Such a system has a high atomic density similar to solids, but the average density is low: as a consequence the absorption of laser light is more than 90%. The efficiently absorbed laser light stripped almost all electrons, and the following ion acceleration is called a Coulomb explosion, reaching kinetic energy as high as 1 MeV. The neutron yield of the D–D fusion reached  $10^4$ .

Another difference of the cluster target from gas and solid is well-ordered molecular orientation. This phenomenon

provides fundamental prospects to design not only neutron generation but also generation of bright X-rays [106–109], high energy ions [110], etc.

## 2.6. Other Techniques

Due to the recent progress in ultra-high-intensity lasers, the “fast ignition” scenario enables heating of ultra-high-density plasma [111, 112]. The target structure is shown in Figure 13 where a gold cone is inserted in a spherical poly(d8-styrene) capsule. The gold cone was fabricated by electrochemical gilding on a brass mandrel.

To fabricate the cryogenic gold cone guided target, a foam technique is useful because the required cooling uniformity is not as important as that for beta layering and IR heating. The fuel will be loaded into the void through a gas feeder pipe at a cryogenic temperature although normal targets are loaded by diffusion across the wall at room temperature. This technique can significantly reduce the inventory of tritium in a future target factory. The liquefied fuel penetrates into the foam leaving a void inside (Fig. 14) [113].

To examine hydrodynamic instability during high power laser irradiation, targets with perturbed surfaces have been prepared by, for example, the thermal-press method [114], Fourier laser machining, the laser interference ablation technique, etc.

Nanoadhesion of metal foils was achieved to provide a precise thickness ( $\sim 20 \mu\text{m}$ ) of an adhered step target for ultrahigh pressure, laser shock experiments [115]. The technique involves two processes: single molecule coating on the metal surface and fastening the two surfaces together. For the two  $20 \mu\text{m}$  aluminum targets of single foil and adhered foils, a negligible difference in laser shock speed was observed in comparison with laser energy and target thickness (Fig. 15).

## 3. LASER FUSION TARGET MATERIALS

### 3.1. Light Atom Materials

A beryllium capsule has been designed and has multi-mode hydrodynamic instability in implosion simulations. In comparison with a CH capsule, the instability of a beryllium capsule is much less sensitive to DT ice roughness

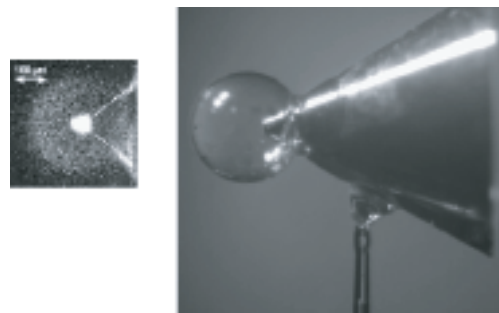


**Figure 13.** Right: The implosion target for efficient heating of the highly compressed plasma. A gold cone is attached to a poly(d8-styrene) capsule. Left: An X-ray image of the implosion.

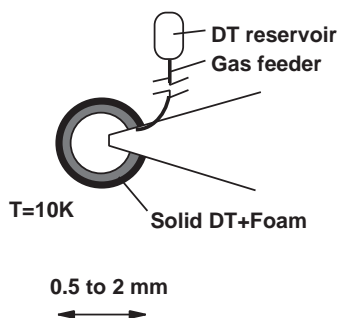


**Figure 14.** Structure of cryogenic foam target with gold cone guide. Gaseous DT is filled into the target using the gas feeder shown in the figure.

[116, 117]. Capsule fabrication of micrometer sized beryllium metal and its alloy has been investigating at Los Alamos National Laboratory [118]. Chemical vapor deposition of beryllium was done by using dialkylberyllium derivatives [119], bis(cyclopentadienyl)beryllium [120].

Amorphous beryllium has a grain structure, and a model study was done taking into account the possible effect of beryllium grain sound speed anisotropy in capsule implosions, where effects of crystallographic texture on sound velocity propagation in polycrystalline beryllium were discussed [121].

Recently light atom hydride was fabricated as low-density foam. Beryllium-containing materials were foamed to be

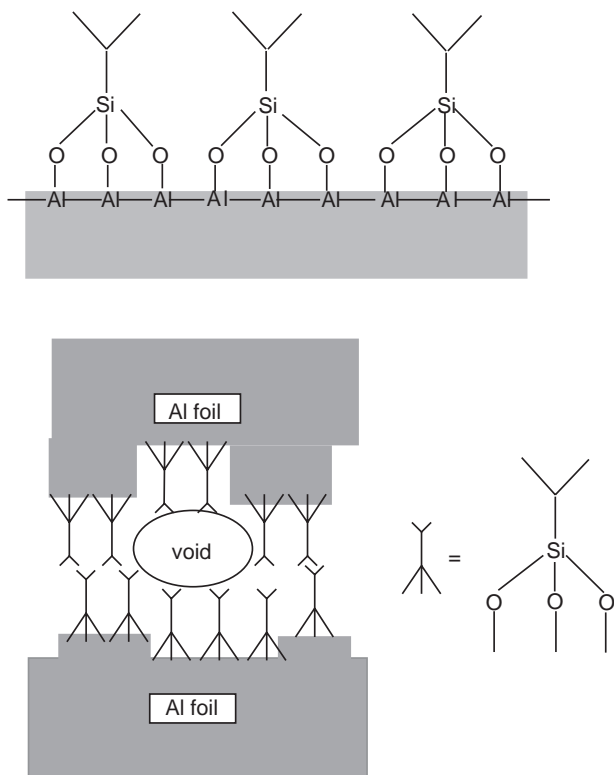


**Figure 15.** Schematic structure of single molecular membrane glue. Left: ideal modified surface with isopropylsiloxo groups on the aluminum surface. Right: possible mechanism of adhesion.

less than 0.1 g/cc in density and pore sizes of  $\sim 10 \mu\text{m}$  could be used. Such structures could be obtained in the course of thermal transformation of beryllium hydride (deuteride) [122, 123] as well as mixtures of beryllium hydride and lithium hydride. Heavy elements can be admixed to the low-density beryllium and their distribution can be controlled over layer thickness.

### 3.2. Photovoltaic Target to Prevent Laser Shine-Through

In the direct-driven ICF implosions, where laser light directly irradiates the target, hydrodynamic instabilities such as Rayleigh–Taylor instability during the implosion are seeded by initial imprint due to laser irradiation nonuniformity, along with the original target surface roughness. These perturbations are accompanied by rippled shock propagation before the shock breaks out the inner surface, and they grow due primarily to the Rayleigh–Taylor instability after the shock breakout. The perturbations grown on the outer surface are then fed through on the inner surface. These, together with inner surface roughness, will grow again during the spark and the main fuel, which could quench the ignition and burn. The precise structures of the fuel capsule have been designed and fabricated based on the strategy mentioned previously, and a number of experiments on the rippled shock waves, initial imprint, and Rayleigh–Taylor instability in direct drive as well as indirect drive have been done [124].

There is another problem in which the previous scenario does not take into account, called the laser shine-through effect. Recent experiments indicated that sparklike damages are nucleated inside the capsule layer during the very early phase of the laser pulse. The damages are considered to be due to penetration of laser light into the transparent capsule materials such as GDP and polystyrene before the laser intensity reaches high intensity to ionize the capsule materials. A similar damage pattern and damage threshold are well known in high-power laser optical materials, such as potassium dihydrogenphosphate and silica glasses, in which the damage threshold values are  $1 \times 10^{10}$ – $3 \times 10^{11} \text{ W/cm}^2$  [125, 126]. This damage inside the laser optical materials has been characterized to be traces of self-focusing of the laser beam, where both the nonlinear growth of small scale beam break-up and the whole-beam self-focusing alter the focusing properties of the system (Fig. 16).

Organic material is one of the promising materials to be engineered for this purpose due to its feasibility based on advanced synthetic chemistry. Such organic functional materials will provide us not only functionality of the IFE target to suppress initial perturbations but also an efficient yield of IFE because they consist of low  $Z$  atoms. Experiments [127, 128] showed a uniform laser ablation in a polystyrene film coated with a photovoltaic perylene/phthalocyanine [129] bilayer when an incident took place at an intensity range of  $10^9$ – $10^{10} \text{ W/cm}^2$  ( $\lambda = 1064 \text{ nm}$ ) as shown in Figure 17b. Without the bilayer coating, the laser pulse formed spiky structures in the polystyrene film as self-focusing traces of the laser pulse, while for the coated film, the uniform surface ablation trace without the spiky interior structures was observed (Fig. 17a).

Irradiation of High Power Laser

-Amplification of initial perturbation-

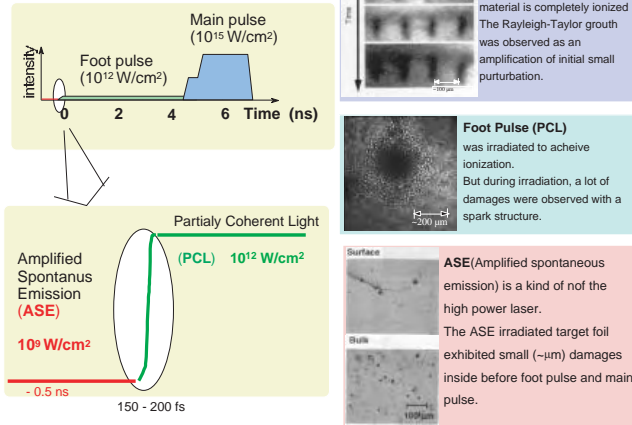


**Figure 16.** Pulse shape of high power laser (left) and the perturbation growth of the capsule surface and damage generation in the capsule during laser irradiation.

In the case of a laser incidence of 532 nm where the coating material exhibits no reflection, such a difference depending on the coating was not observed [130]. These phenomena were coupled with the reflection and conduction properties via the photovoltaic effect and agreed with the required ablation to reduce the initial damage and to achieve high-density compression of the fuel capsule for inertial fusion energy. The property indicates a functionality of organic materials, where a possible scenario is presented in Figure 18.

3.3. Magnetic Materials

The next step of direct driven implosion experiments demands high symmetrical irradiation for which a nonsupported pellet is useful. Sakagami et al. reported the first description concerned with fundamental studies of magnetic suspension of a target: how one can coat the ferromagnetic thin film over the pellet, how a magnetically suspended pellet behaves in low temperature, and how the optical forces damp unexpected horizontal oscillation of them [131]. Yoshida et al. designed and tested a magnetic suspension system (“MINO” series) to suspend a Ni coated plastic capsule without mechanical contact [132]. MINO-2 is composed

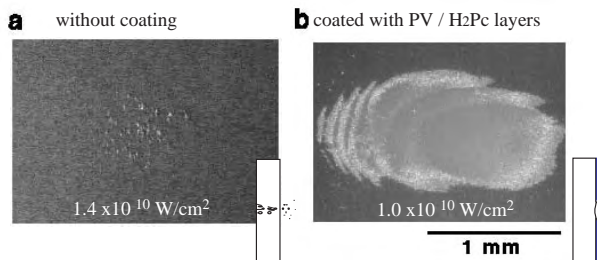


**Figure 17.** Laser ablation trace of polystyrene film (4 μm thickness); 1060 nm input beam in a 1.1 ns (full width half maximum) pulse with a 1/e<sup>2</sup> beam diameter of 750 μm.

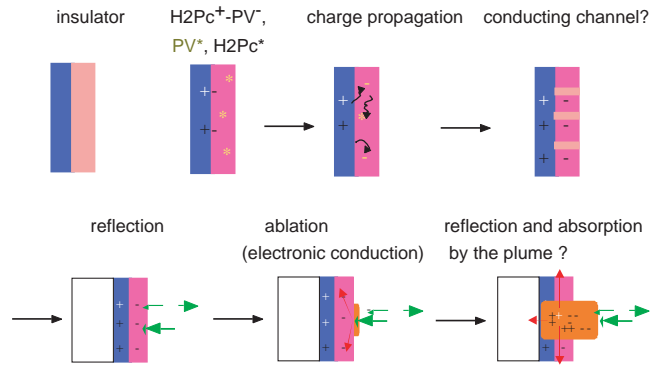


**Figure 18.** Mechanism of uniform laser ablation utilizing organic photovoltaic materials.

of four compact units: the gas puff unit to detach a Ni coated capsule into the detective area, the capsule detection unit within 5 μm accuracy, the pellet control unit to achieve less than 5 μm vertical vibration amplitude, and the pellet suspension unit not to obstruct laser irradiation using a small solid angle electromagnet (Fig. 19). Recently they succeeded in suspension of Ni coated capsules in a hohlraum.

In the fusion reactor chamber, the irradiation frequency is ~4 Hz, which requires an injection system for capsule delivery to the reactor center. Survival of the cryogenic target during acceleration and during its transit across the high-temperature target chamber is also an issue. A combination of thermal analyses, modeling, materials property measurements, and demonstration tests with representative injection equipment is being employed to demonstrate IFE plant fueling [133].

A prototype of the facility for a reactor target repetitive production and injection with the rate of 1–6 Hz has been designed by Osipov et al. [134]. The most important elements of the design are the unit for the protective sabot-and-target cryogenic assembly, and the double-stage accelerator combining the coil gun for target preacceleration and the gas gun for target final acceleration up to 200 m/sec. This approach contributes to a considerable reduction of the dimensions of the injector, increasing the reproducibility of the injection velocity as well as increasing the reliability of the device operation without mechanical and heat target damage.

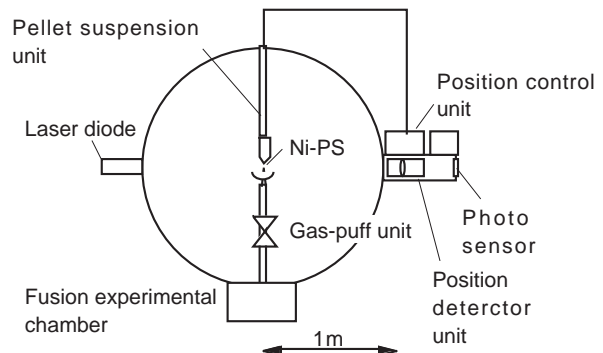


**Figure 19.** Schematic diagram of magnetic suspension system for laser fusion target “MINO-2,” where a nickel coated polystyrene capsule was magnetically centered within 5 μm accuracy.



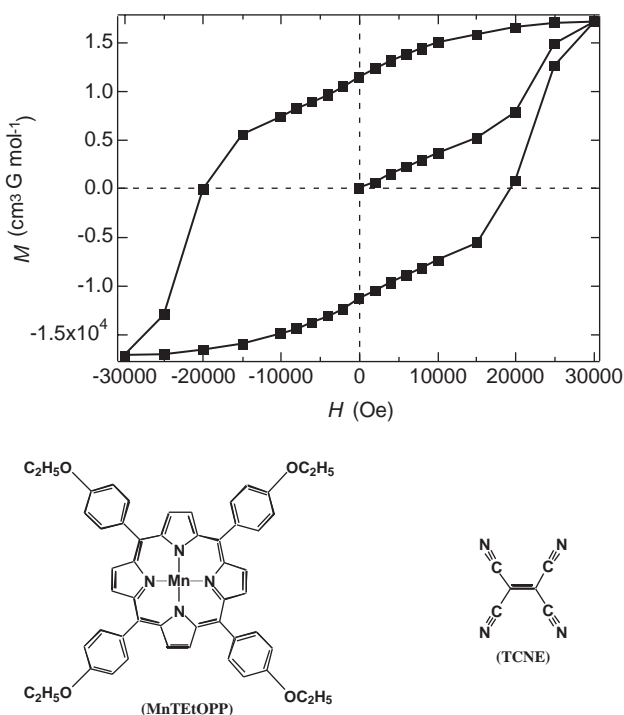


**Figure 20.** Magnetic hysteresis of the hardest molecular based magnet of MnEtOPP/TCNE at 2 K and its chemical structure.

For both capsule levitation and injection, coating of magnetic material is a promising technique. Actually, in the MINO system, conventional metals have been used as magnetic material. A light atom magnet is preferable as a coating material for the same reason that one avoids X-ray generation. Fourteen years ago, two organic magnets were discovered of which one exhibits very low critical temperature ( $T_c$ ) with well-characterized spin source and the other with high  $T_c$  with unknown organic spin source. The field has been investigated as molecular-based magnet, which unfortunately has not provided high  $T_c$  with a well-characterized spin source. The IFE target with solid DT is used at cryogenic temperature; therefore a molecular-based magnet with low  $T_c$  is applicable as a magnetic material for levitation. For example, manganese(tetraethoxyphenylporphyrin)/tetracyanoethylene (MnEtOPP/TCNE,  $\text{C}_{58}\text{H}_{44}\text{MnN}_8\text{O}_4$ , Fig. 20) and its derivatives contains about 1% metal ion, but it has an extremely high coercive force (20,000 Oe) [135].

#### 4. SUMMARY

We have summarized the present status of the research field of laser fusion target fabrication, especially capsule fabrication, low-density foam fabrication, cryogenic hydrogen layering, and related materials. The present field will be developed with further investigation of material chemistry, cryogenic technology, and nanotechnology. In addition to these improvement, the demands from laser plasma physics and fusion reactor technologies are also important and will contribute to the present field.

#### GLOSSARY

**Cryogenic target** A target with hollow, spherical solid density fuel is called as the cryogenic target and known to be more efficiently imploded than a target with a gaseous fuel with the same mass because of its higher initial density and lower isentrope in the compression process.

**Inertial fusion energy (IFE)** A future energy source to generate electric power. Fuel (typically deuterium and tritium) is instantaneously heated to a high-temperature and high-density plasma by laser or heavy ion beams to complete nuclear reactions before it expands.

**Laser fusion target** Used to feed fuel to the burning position of the IFE power plant. The typical target is a plastic capsule filled with hollow, solid deuterium-tritium fuel. The design and fabrication of the target is one of the key technologies of the Laser Fusion Energy.

**Ultralow density foam** A key material of the fusion targets. The usage of the foam includes supporting the liquid deuterium-tritium fuel, protective coating on the target against thermal radiation in the reactor and supporting the fuel capsule in a cavity target. Foams whose electron density is less than  $10^{20}/\text{cc}$  is especially called ultralow density foam and laser light can deeply penetrate into the foam plasma.

#### REFERENCES

1. "Energy from Inertial Fusion." International Atomic Energy Agency, Vienna, 1995.
2. J. D. Lindl, "Inertial Confinement Fusion: The Quest for Ignition and Energy." Springer-Verlag, New York, 1998.
3. "Inertial Fusion Science and Applications 2001" (K. A. Tanaka, D. D. Meyerhofer, and J. Meyer-ter-Vehn, Eds.). Elsevier, Amsterdam, 2002.
4. T. Zh. Esirkepov, S. V. Bulanov, K. Nishihara, T. Tajima, F. Pegoraro, V. S. Khoroshkov, K. Mima, H. Daido, Y. Kato, Y. Kitagawa, K. Nagai, and S. Sakabe, *Phys. Rev. Lett.* 89, 175003 (2002).
5. T. Norimatsu, H. Tajima, M. Takagi, S. Nakai, and C. Yamanaka, *J. Vac. Sci. Technol. A* 6, 2552 (1988).
6. C. Yamanaka, S. Nakai, T. Yamanaka, Y. Izawa, Y. Kato, K. Mima, K. Nishihara, T. Mochizuki, M. Yamanaka, M. Nakatsuka, T. Sasaki, T. Yabe, K. Yoshoda, H. Azachi, H. Nishimura, T. Norimatsu, S. Ido, N. Miyanaga, S. Sakabe, H. Takabe, J. Jitsuno, and M. Takagi, *Nucl. Fusion* 27, 19 (1987).
7. C. Yamanaka and S. Nakai, *Nature* 319, 757 (1986).
8. S. W. Haan, T. Dittrich, G. Strobel, S. Hatchett, D. Hinkel, M. Marinak, D. Munro, O. Jones, S. Pollaine, and L. Suter, *Fusion Sci. Technol.* 41, 164 (2002).
9. R. B. Stephens, S. W. Haan, and D. C. Wilson, *Fusion Sci. Technol.* 41, 226 (2002).
10. S. A. Letts, E. M. Feason, S. R. Buckley, M. D. Saculla, L. M. Allison, and R. Cook, *Fusion Technol.* 28, 1797 (1995).
11. M. L. Hoppe, *Fusion Technol.* 38, 42 (2000).
12. A. Nikroo, J. M. Pontelandolfo, and E. R. Castillo, *Fusion Sci. Technol.* 41, 220 (2002).
13. M. Theobald, P. Baclet, O. Legaie, and J. Durand, *Fusion Technol.* 38, 62 (2000).
14. S. Charton, F. Dano, J.-Y. Godefroy, and P. Baclet, *Fusion Sci. Technol.* 41, 242 (2002).
15. A. Nikroo, D. G. Czechowics, E. R. Castillo, and J. M. Pontelandolfo, *Fusion Sci. Technol.* 41, 214 (2002).
16. A. Nikroo and J. M. Pontelandolfo, *Fusion Technol.* 38, 58 (2000).
17. D. G. Czechowics, E. R. Castillo, and A. Nikroo, *Fusion Sci. Technol.* 41, 188 (2002).

18. R. Cook, *Fusion Technol.* 38, 74 (2000).
19. F.-Y. Tsai, D. R. Harding, S.-H. Chen, T. N. Blanton, and E. L. Alfonso, *Fusion Sci. Technol.* 41, 178 (2002).
20. S. A. Letts, A. E. H. Nissen, P. J. Orthion, S. R. Buckley, E. Fearon, C. Chancellor, C. C. Roberts, B. K. Parrish, and R. C. Cook, *Fusion Sci. Technol.* 41, 268 (2002).
21. F.-Y. Tsai, E. L. Alfonso, S.-H. Chen, and D. R. Harding, *Fusion Technol.* 38, 83 (2000).
22. D. Marsacq and F. Jousse, *Fusion Technol.* 38, 90 (2000).
23. C. C. Roberts et al., *Fusion Technol.* 38, 94 (2000).
24. F.-Y. Tsai, E. L. Alfonso, D. R. Harding, and S.-H. Chen, *J. Phys. D* 34, 3011 (2001).
25. H. Kawaguchi, *Progr. Polym. Sci.* 25, 1171 (2000).
26. "Microspheres, Microcapsules, and Liposomes" (R. Arshady, Ed.). Citus Books, London, 1999.
27. U. Kubo and H. Tsubakihara, *J. Vac. Sci. Technol. A* 4, 1134 (1989).
28. G. Wilemski, T. Boone, L. Cheung, D. Nelson, and R. Cook, *Fusion Technol.* 28, 1773 (1995).
29. M. Takagi, T. Norimatsu, T. Yamanaka, and S. Nakai, *J. Vac. Sci. Technol. A* 9, 2145 (1991).
30. H. Azechi, T. Jitsuno, T. Kanabe, M. Katayama, K. Mima, N. Miyanaga, M. Nakai, S. Nakai, H. Nakaishi, M. Nakatsuka, A. Nishiguchi, P. A. Norrays, M. Takagi, M. Yamanaka, and C. Yamanaka, *Laser Particle Beams* 9, 193 (1991).
31. T. Norimatsu, C. M. Chen, K. Nakajima, M. Takagi, Y. Izawa, T. Yamanaka, and S. Nakai, *J. Vac. Sci. Technol. A* 12, 1293 (1994).
32. T. Norimatsu, Y. Izawa, K. Mima, and P. M. Gresho, *Fusion Technol.* 35, 147 (1999).
33. T. Norimatsu, T. Takaki, M. Nakajima, K. Nagai, Y. Izawa, and K. Mima, *Kobunshi Ronbunshu (Jpn. J. Polym. Sci. Technol.)* 56, 415 (1999) [in Japanese].
34. P. M. Gresho, *Fusion Technol.* 35, 157 (1999).
35. K. Nagai, M. Nakajima, T. Norimatsu, Y. Izawa, and T. Yamanaka, *J. Polym. Sci. A* 38, 3412 (2000).
36. T. D. Bonne, *J. Moscow Phys. Soc.* 8, 79 (1998).
37. M. Takagi, R. Cook, R. Stephens, J. Gibson, and S. Paguio, *Fusion Technol.* 38, 50 (2000).
38. M. Takagi, R. Cook, R. Stephens, J. Gibson, and S. Paguio, *Fusion Technol.* 38, 54 (2000).
39. A. Nikroo, J. M. Pontelandolfo, and E. R. Castillo, *Fusion Sci. Technol.* 41, 220 (2002).
40. B. W. McQuillan and M. Takagi, *Fusion Sci. Technol.* 41, 209 (2002).
41. M. Takagi, R. Cook, R. Stephens, J. Gibson, and S. Paguio, *Fusion Technol.* 38, 46 (2000).
42. M. Takagi, R. Cook, B. McQuillan, F. Elsner, R. Stephens, A. Nikroo, J. Gibson, and S. Paguio, *Fusion Sci. Technol.* 41, 278 (2002).
43. H. Nakano and T. Fukuda, *Fusion Technol.* 35, 189 (1999).
44. K. Nagai, T. Takaki, T. Norimatsu, and T. Yamanaka, *Macromol. Rapid Commun.* 22, 1344 (2001).
45. K. K. Mishra, R. K. Khardekar, R. Singh, H. C. Pant, N. G. Borisenko, A. I. Gromov, and Ju. A. Merkul'ev, *Plasma Phys. Control. Fusion* 43, 1723 (2001).
46. R. Tsuji and Y. Ogushi, *Fusion Eng. Design* 34, 811 (1997).
47. R. B. Stephens, T. Mroczkowski, and J. Gibson, *Fusion Sci. Technol.* 38, 132 (2000).
48. A. A. Akunets, V. M. Dorogotovsev, Y. A. Merkuliev, S. A. Startev, and R. Cook, *Fusion Technol.* 28, 1781 (1995).
49. D. T. Goodin, G. E. Besenbruch, J. P. Dahlburg, K. R. Schultz, A. Nobile, and E. M. Campbell, in "Proceedings of Inertial Fusion Science and Applications 2001," pp. 827. Elsevier, Amsterdam, 2002.
50. R. W. Petzoldt, D. Goodin, and N. Siegel, *Fusion Technol.* 38, 22 (2000).
51. T. Norimatsu, K. Nagai, T. Takaki, and T. Yamanaka, *Fusion Eng. Design* 55, 387 (2001).
52. Y. Izawa and T. Norimatsu, in "Nuclear Fusion by Inertial Confinement" (G. Velarde, Y. Ronen, and J. M. Martinez-Val, Eds.), p. 515. CRC Press, Boca Raton, 1993.
53. M. L. Hoppe, *Fusion Sci. Technol.* 41, 234 (2002).
54. H. Katayama, T. Norimatsu, Y. Kato, T. Yamanaka, and S. Nakai, *Appl. Phys. Lett.* 55, 2660 (1989).
55. H. Katayama, T. Norimatsu, C. Chen, T. Yamanaka, S. Nakai, and Y. Nishino, *J. Vac. Sci. Technol. A* 9, 2140 (1991).
56. A. Richard, K. A. Tanaka, K. Nishihara, M. Nakai, M. Katayama, Y. O. Fukuda, T. Kanabe, Y. Kitagawa, T. Norimatsu, M. Nakatsuka, M. Kado, T. Kawashima, C. Chen, M. Tsukamoto, and S. Nakai, *Phys. Rev. E* 49, 1520 (1994).
57. C. Specki, C. Chiritescu, J. A. Delettrez, R. Epstein, V. Yu. Glebov, D. R. Harding, R. L. Keck, S. J. Loucks, L. D. Lund, R. L. McCrory, P. W. McKenty, F. J. Marshall, D. D. Meyerhofer, S. F. B. Morse, S. P. Regam, P. B. Radha, S. Roberts, T. C. Sangster, W. Seka, S. Skupsky, V. A. Smalyuk, C. Sorce, J. M. Soures, R. P. J. Town, J. A. Frenje, C. K. Li, R. D. Petraso, F. H. Seguin, K. Fletcher, S. Paladino, C. Freeman N. Izumi, R. Lerche, and T. W. Phillips, *Phys. Plasma* 9, 2195 (2002).
58. T. M. Henderson and R. R. Johnson, *Appl. Phys. Lett.* 31, 18 (1977).
59. J. R. Miller, *Adv. Cryo. Eng.* 23, 669 (1978).
60. K. Kim, B. J. Smoot, R. L. Woerner, and C. D. Hendricks, *Appl. Phys. Lett.* 34, 282 (1979).
61. D. L. Musinski, T. M. Henderson, R. J. Simms, T. R. Pattinson, and R. B. Jacobs, *J. Appl. Phys.* 51, 1394 (1980).
62. V. Varadarajan, K. Kim, and T. P. Bernat, *J. Vac. Sci. Technol. A* 6, 1876 (1988).
63. A. J. Martin, R. J. Simms, and R. B. Jacobs, *J. Vac. Sci. Technol. A* 6, 1885 (1988).
64. M. T. Mruzek, J. S. Ankney, and D. N. Decker, *J. Vac. Sci. Technol. A* 6, 1889 (1988).
65. J. K. Hoffer and L. R. Foreman, *Phys. Rev. Lett.* 60, 1310 (1988).
66. C. M. Chen, T. Norimatsu, Y. Izawa, T. Yamanaka, and S. Nakai, *J. Vac. Sci. Technol. A* 13, 2908 (1995).
67. T. Norimatsu, M. Takagi, Y. Izawa, T. Yamanaka, and K. Mima, in "Proceedings of the 16th International Conference on Fusion Energy Organized by the International Atomic Energy Agency," Montreal, Canada, October 1996, p. 171.
68. E. R. Mapoles, J. Sater, J. Pipes, and E. Monsler, *Phys. Rev. E* 55, 3473 (1997).
69. G. M. Collins, D. N. Bittner, E. Monsler, S. Letts, E. R. Mapoles, and T. P. Bernat, *J. Vac. Sci. Technol. A* 14, 2897 (1996).
70. D. N. Bittner, G. W. Collins, E. Monsler, and S. Letts, *Fusion Technol.* 35, 244 (1999).
71. B. J. Kozioziemski, R. L. McEachern, R. A. London, and D. N. Bittner, *Fusion Sci. Technol.* 41, 296 (2002).
72. L. Phillips, J. H. Gardner, S. E. Bodner, D. Colombant, S. P. Obenshain, A. J. Schmitt, J. P. Dahlburg, T. Lehecka, M. Klapisch, and A. Bar-Shalom, *Laser Particle Beams* 17, 225 (1999).
73. J. E. Pulsifer, M. S. Tillack, D. T. Goodin, and R. W. Petzoldt, in "Proceedings of the Inertial Fusion Science and Applications 2001," Kyoto, Japan, September 2002, p. 802.
74. I. V. Aleksandrova, E. R. Koresheva, I. E. Osipov, S. M. Tolokonnikov, L. A. Rivkis, V. P. Veselov, A. A. Belolipetskiy, G. D. Baranov, V. I. Listratov, V. G. Soloviev, I. D. Timofeev, G. S. Usachev, and L. S. Yaquzhinskiy, *Fusion Technol.* 38, 166 (2000).
75. I. V. Aleksandrova, S. V. Bazdenkov, V. I. Chtcherbakov, E. R. Koresheva, and I. E. Osipov, in "Proceedings of the Inertial Fusion Science and Applications 2001," Kyoto, Japan, September 2002, p. 762.
76. E. R. Koresheva, I. E. Osipov, T. P. Timasheva, and L. S. Yaguzinskiy, in "Proceedings of the Inertial Fusion Science and Applications 2001," Kyoto, Japan, September 2002, p. 767.
77. I. E. Osipov, E. R. Koresheva, G. D. Baranov, I. D. Timofeev, V. G. Kapralov, and B. V. Kuteev, in "Proceedings of the Inertial Fusion



- Science and Applications 2001,” Kyoto, Japan, September 2002, p. 810.
78. T. Endo, K. Shibata, K. Kobayashi, M. Yasuda, Y. Fujima, and T. Norimatsu, *Fusion Sci. Technol.* 41, 248 (2002).
  79. T. Endo, K. Shibata, Y. Fujima, and T. Norimatsu, *Fusion Technol.* 38, 34 (2000).
  80. Y.-G. Kang, K. Nishihara, H. Nishimura, H. Takabe, A. Sunahara, T. Norimatsu, K. Nagai, H. Kim, M. Nakatsuka, H. J. Kong, and N. J. Zabusky, *Phys. Rev. E* 64, 047402 (2001).
  81. A. Benuzzi, M. Koenig, J. Krishman, B. Faral, W. Nazarov, M. Temporal, D. Batani, L. Müller, F. Torsiello, T. Hall, and N. Grandjouan, *Phys. Plasmas* 5, 2827 (1998).
  82. D. Hoarty, L. Barringer, C. Vickers, O. Willi, and W. Nazarov, *Phys. Rev. Lett.* 82, 3070 (1999).
  83. W. L. Perry, R. C. Dye, P. G. Apen, L. Foreman, and E. Peterson, *Appl. Phys. Lett.* 66, 314 (1995).
  84. N. Elliott, C. W. Barnes, S. H. Batha, R. D. Day, J. Elliott, P. Gobby, V. Gomez, D. Hatch, N. E. Lanier, G. R. Magelssen, R. Manzanarez, R. Perea, T. Pierce, G. Rivera, D. Sandoval, J. M. Scott, W. Steckle, D. L. Tubbs, S. Rothman, C. Horefield, A. M. Dunne, and K. W. Parker, *Fusion Sci. Technol.* 41, 196 (2002).
  85. J. J. Duderstadt and G. A. Moses, “Inertial Confinement Fusion,” p. 143. Wiley, New York, 1982.
  86. J. Zweiback, R. A. Smith, T. E. Cowan, G. Hays, K. B. Wharton, V. P. Yanovsky, and T. Ditmire, *Phys. Rev. Lett.* 84, 2634 (2000).
  87. W. L. Perry, R. C. Dye, P. G. Apen, L. Foreman, and E. Peterson, *Appl. Phys. Lett.* 66, 314 (1995).
  88. A. J. Antolak, D. H. Morse, D. E. Hebron, R. J. Leeper, and D. Schroen-Carey, *Fusion Eng. Design* 46, 37 (1999).
  89. I. G. Schneir and B. McQuillan, *Fusion Technol.* 28, 1849 (1995).
  90. M. A. Mitchell, P. Gobby, and N. Elliott, *Fusion Technol.* 28, 1844 (1995).
  91. K. Okada, S. Sakabe, H. Shiraga, T. Mochizuki, and C. Yamanaka, *Jpn. J. Appl. Phys.* 21, L257 (1982).
  92. Z. Lin, L. Xian, and D. Kai, in “Proceedings of the Inertial Fusion Science and Applications 2001,” Kyoto, Japan, September 2002, p. 772.
  93. W. Nazarov and P. G. McGivern, *Fusion Technol.* 38, 110 (2000).
  94. N. G. Borisenko, A. I. Gromov, Yu. A. Merkul’ev, A. V. Mitrofanov, and W. Nazarov, *Fusion Technol.* 38, 115 (2000).
  95. N. G. Borisenko, A. I. Gromov, Yu. A. Merku’ev, and A. V. Mitri-fanov, *Fusion Technol.* 38, 115 (2000).
  96. K. Nagai, B.-R. Cho, Y. Hashishin, T. Norimatsu, and T. Yama-naka, *Jpn. J. Appl. Phys.* 41, L431 (2002).
  97. N. Miele-Pajot, L. G. Hubert-Pfalzgraf, R. Papiernik, J. Vaisser-mann, and R. Collier, *J. Mater. Chem.* 46, 37 (1999).
  98. M. Takagi, M. Ishihara, T. Norimatsu, Y. Izawa, and S. Nakai, *J. Vac. Sci. Technol. A* 11, 2837 (1993).
  99. M. Takagi, T. Norimatsu, T. Yamanaka, and S. Nakai, *J. Vac. Sci. Technol. A* 9, 820 (1991).
  100. S. M. Lambert, G. E. Overturf, G. Wilemski, S. A. Letts, D. Schroen-Carey, and R. C. Cook, *J. Appl. Polym. Sci.* 65, 2111 (1997).
  101. G. E. Overturf III, R. Cook, S. A. Letts, S. R. Buckley, and M. R. McClellan, *Fusion Technol.* 28, 1803 (1995).
  102. T. Norimatsu, A. Sunahara, K. Nagai, and T. Yamanaka, *Fusion Technol.* 38, 28 (2000).
  103. T. Norimatsu, K. Nagai, T. Takaki, and T. Yamanaka, *Fusion Eng. Design* 55, 387 (2001).
  104. R. B. Stephens, *Fusion Technol.* 28, 1809 (1995).
  105. T. Ditmire, J. Zweiback, V. P. Yanovsky, T. E. Cowan, G. Hays, and K. B. Wharton, *Nature* 398, 489 (1999).
  106. A. McPherson, B. D. Thompson, A. B. Borisov, K. Boyer, and C. K. Rhodes, *Nature* 370, 631 (1994).
  107. T. Ditmire, T. Donnelly, R. W. Falcone, and M. D. Perry, *Phys. Rev. Lett.* 75, 3122 (1995).
  108. T. Ditmire, J. W. G. Tisch, E. Sprigate, M. B. Mason, N. Hay, and R. A. Smith, *Nature* 386, 54 (1997).
  109. K. Kondo, M. Mori, and T. Shiraiishi, *Appl. Surf. Sci.* 197, 138 (2002).
  110. M. Lezius, S. Dobosz, D. Normand, and M. Schmidt, *Phys. Rev. Lett.* 80, 261 (1998).
  111. R. Kodama, P. A. Norris, K. Mima, A. E. Dangor, R. G. Evans, H. Fujita, Y. Kitagawa, K. Krushelnick, T. Miyakoshi, N. Miyanaga, T. Norimatsu, S. J. Rose, T. Shozaki, K. Shigemori, A. Sunahara, M. Tampo, K. A. Tanaka, Y. Toyama, T. Yamanaka, and M. Zepf, *Nature* 412, 798 (2001).
  112. R. Kodama and the Fast-Ignitor Consortium, *Nature* 418, 933 (2002).
  113. T. Norimatsu, K. Nagai, T. Yamanaka, T. Endo, H. Yoshida, and Y. Sakagami, *Fusion Eng. Design* 63, 587 (2002).
  114. T. Sakaiya, H. Azechi, M. Matsuoka, N. Izumi, M. Nakai, K. Shige-mori, H. Shiraga, A. Sunahara, H. Takabe, and T. Yamanaka, *Phys. Rev. Lett.* 88, 145003 (2002).
  115. K. Nagai, T. Norimatsu, T. Yamanaka, T. Nishibe, N. Ozaki, K. Takamatsu, T. Ono, M. Nakano, and K. A. Tanaka, *Jpn. J. Appl. Phys.* 41, L1186, (2002).
  116. M. M. Marinak, S. W. Haan, T. R. Dittrich, R. E. Tipton, and G. B. Zimmerman, *Phys. Plasmas* 5, 1125 (1998).
  117. D. C. Wilson, P. A. Bradley, S. R. Goldman, N. M. Hoffman, R. M. Margeevicius, R. B. Stephens, and R. E. Olson, *Fusion Technol.* 38, 16 (2000).
  118. K. Salazar, S. G. Pattillo, and M. Trkula, *Fusion Technol.* 38, 69 (2000).
  119. R. Brusasco, T. Dittrich, and R. Cook, *Fusion Technol.* 28, 1854 (1995).
  120. R. W. Margevicius, *Fusion Sci. Technol.* 41, 286 (2002).
  121. R. Cook, *Fusion Sci. Technol.* 41, 155 (2002).
  122. N. G. Borisenko, V. M. Dorogotovsev, A. I. Gromov, S. Yu. Guskov, Yu. A. Markushkin, N. A. Chirin, A. K. Shikov, and V. F. Petrunin, *Fusion Technol.* 38, 161 (2000).
  123. Yu. A. Markushkin, V. V. Gorlevsky, and V. F. Petrunin, *J. Moscow Phys. Soc.* 8, 373 (1998).
  124. H. Azechi, M. Nakai, K. Shigemori, N. Miyanaga, H. Shiraga, H. Nishimura, M. Honda, R. Ishizaki, J. G. Wouchuk, H. Takabe, K. Nishiara, K. Mima, A. Nishiguchi, and T. Endo, *Phys. Plasmas* 4, 4079 (1997).
  125. H. Yoshida, T. Jitsuno, H. Fujita, M. Nakatsuka, M. Yoshimura, T. Sasaki, and K. Yoshida, *Appl. Phys. B* 70, 195 (2000).
  126. K. Yoshida, H. Yoshida, T. Kamimura, and N. Kuzuu, *Jpn. J. Appl. Phys.* 37, 1882 (1998).
  127. K. Nagai, T. Norimatsu, N. Miyanaga, and T. Yamanaka, *Fusion Sci. Technol.* 41, 257 (2002).
  128. K. Nagai, K.-I. Morishita, H. Yoshida, T. Norimatsu, N. Miyanaga, Y. Izawa, and T. Yamanaka, *Synth. Met.* 121, 1445 (2001).
  129. T. Morikawa, C. Adachi, T. Tsutsui, and S. Saito, *Nippon Kagaku Kaishi* 962 (1990).
  130. K. Nagai, H. Yoshida, T. Norimatsu, N. Miyanaga, Y. Izawa, and T. Yamanaka, *Appl. Surf. Sci.* 197, 808 (2002).
  131. Y. Sakagami, H. Yoshida, R. Itou, T. Terasawa, and T. Fuseya, in “Proceedings of Inertial Fusion Science and Applications 2001,” p. 819. Elsevier, Amsterdam, 2002.
  132. H. Yoshida, Y. Sakagami, Y. Hasegawa, and T. Fuseya, in “Pro-ceedings of Inertial Fusion Science and Applications 2001,” p. 819. Elsevier, Amsterdam, 2002.
  133. D. Goodin, N. B. Alexander, C. R. Gibson, A. Nobile, R. W. Pet-zoldt, N. P. Siegel, and L. Thompson, *Nucl. Fusion* 41, 527 (2001).
  134. I. E. Osipov, E. R. Koresheva, G. D. Baranov, I. D. Timofeev, V. G. Kapralov, and B. V. Kuteev, in “Proceedings of Inertial Fusion Science and Applications 2001,” p. 810. Elsevier, Amster-dam, 2002.
  135. K. Nagai, T. Iyoda, A. Fujishima, and K. Hashimoto, *Solid State Commun.* 102, 809 (1997).



# Laser Induced Surface Nanostructuring

Yuji Kawakami, Eiichi Ozawa

*Vacuum Metallurgical Co. Ltd, Chiba, Japan*

Isamu Miyamoto

*Osaka University, Suita, Osaka, Japan*

## CONTENTS

1. Laser Induced Surface Nanostructuring
2. Laser Induced Periodic Surface Structures
3. Cone/Column Type Surface Structuring
4. Nanometer-Sized Protuberance  
Coherent Array
5. Recent Topics  
Glossary  
References

## 1. LASER INDUCED SURFACE NANOSTRUCTURING

Laser processing has a wide range of industrial applications from macroprocessing-like welding to ultraprecision machining using laser lithography technologies. Laser induced surface nanostructuring is a type of ultraprecision machining and deals with the surface phenomenon whose size is on the order of laser wavelength, that is, from hundreds of nanometers to 10  $\mu\text{m}$ . Laser induced surface nanostructuring is being actively studied in the United States, Europe, and Japan. In this chapter, the authors systematically explain in detail their interesting reports.

In the past 37 years, the surface structuring of various materials from a micrometer to nanometer size that is induced by laser irradiation has been observed. Most of the primary research was done by Birnbaum [1], who studied the ruby laser irradiated damage of a semiconductor and observed the damage morphology. The parallel straight line pattern was then discovered and therefore the research was likely the initial one for surface structuring by a laser.

The target materials dealt with until now were metals (Al alloy, brass,  $\text{Ni}_x\text{P}_{1-x}$ , iron, etc.) [2–8], semiconductors (Si, Ge, GaAs, etc.) [1, 3, 9–13], polymers [14–29], and recently, multilayer materials [30–33], inorganic materials [34–39], superconductor [40], fullerite [41], and diamond crystals and microclusters [42]. The main interest of the researchers was how the structures were formed on the irradiated surface. Some researchers observed laser induced periodic surface structures (LIPSS) on the irradiated material like a silicon single-crystal surface using  $\text{CO}_2$ , Nd:YAG, and excimer lasers. They explained the cause of the formation of the periodic structure focusing on the relationship between the optical characteristics of the laser beam such as the incident wavelength and polarization and the periodic surface ripples with spacing and direction. These structures were formed with the morphology of several hundreds of nanometers to tens of micrometer size.

On the other hand, many investigations of cone and column type micronanostructuring by laser ablation have also been carried out. The target materials used were silicon (Si) [43–51], a polymer (polyimide, etc.) [52–58], oxides ( $\text{YBa}_2\text{Cu}_3\text{O}_{7-x}$ ,  $\text{ZrO}_2$ ) [59–62], nitride ( $\text{Si}_3\text{N}_4$ ) [61], and metal (Co, Ti, W, etc.) [63–70] to examine the microcones and microcolumns. Two lasers such as a KrF (248 nm) excimer laser and a Ti:sapphire (800 nm) laser have been utilized for the laser ablation of the Si substrate, and the influence of the ambient gas species such as  $\text{SF}_6$ ,  $\text{Cl}_2$ , and air was examined. The formation of micro-nano-sized protuberances was considered by many different mechanisms such as the shielding effect of the particulate impurities [53, 54] and the solvent [53, 54, 59, 60], the debris particles [61], capillary waves [43–45], catalyst-free VLS (vapor-liquid-solid) [46–50], etc., depending on the materials.

Finally, a coherent array with hundreds of nm-sized protuberances was discovered by the authors for single crystal tungsten substrates [71–74]. The influence of laser fluence, wavelength, polarization, surface crystal structure, etc., was examined. This study will be discussed later.

In this chapter, the various surface micro–nano-scale structuring processes are described and the phenomena and the formation mechanisms are also discussed. In particular, the authors deal with in detail the effect of the surface modification parameters on both the process and the product by using a pulsed laser ablation technique. This chapter is composed of three interesting topics that include laser induced periodic surface structures, cone and column type surface structuring, and nanometer-sized protuberance coherent array.

## 2. LASER INDUCED PERIODIC SURFACE STRUCTURES

It is well known that laser ablation induces some interesting phenomena on an irradiated surface. For instance, the surface structuring by laser ablation includes the phenomenon of a LIPSS. Some researchers observed a kind of fringe, grating, and ripple pattern on the irradiated material surface. They discussed these phenomena focusing on the relationship between the optical characteristics of the laser beam and periodic surface ripples with spacing and direction. Based on their discussions, the periodic ripples were related to the number of laser shots. The first pulse caused only a rough surface while subsequent pulses created periodic ripples [69]. The ripples depended on the incident wavelength, polarization, and the angle of incidence. The ripple spacing was calculated from Rayleigh's diffraction condition [2, 3, 5, 9–11],

$$\Lambda = \frac{\lambda}{(1 \pm \sin \theta)} \quad (1)$$

where  $\Lambda$  is the ripple spacing,  $\lambda$  is the laser wavelength, and  $\theta$  is the angle of incidence relative to the surface normal.

Some other researchers considered it from the polarization ( $p$ -polarized incident beam) of the incident laser beam [3, 5, 9–11]. In this case, the ripple direction should be perpendicular to the polarization of the normal incident beam and parallel to the plane of the incident beam at  $\theta \geq 45^\circ$  [9]. The ripple spacing of the incident beam at  $\theta \geq 45^\circ$  was calculated from  $\lambda/\cos \theta$  [9]. When the laser beam was circularly polarized, no ripples were observed [10]. In a recent report about inorganic materials irradiated by an ArF excimer laser, the influence of polarization on the patterns was not confirmed. This research was planned to modify the geometric surfaces of the inorganic materials. In the case of a single crystalline  $\text{CaF}_2$ , the structure of the laser-irradiation marking depended on the crystal surface structure [35, 36]. The LIPSS induced on metallic surfaces did not depend on the laser light polarization or wavelength. A more important factor seems to be related to the characteristics of the material and its molten phase rather than those of the laser [7].

### 2.1. Metals and Alloys

When Emmony et al. [2] investigated the damage of a germanium-made mirror by  $\text{CO}_2$  laser irradiation, they discovered a periodic pattern on the mirror surface. One of the explanations for the formation of the pattern was the scattering effect coming from dust or other particles on the mirror surface. Interference between the scattered and cavity radiations might proceed so that interference fringes could occur with a spacing corresponding to the wavelength of the laser. The most interesting feature in the surface damage was the predominantly parallel nature of the damage bars with a spacing calculated from Eq. (1), which might be explained by the interference mechanism. In the two cases of spacing, the scattered radiation has a component of velocity toward or away from the incident laser beam. If the radiation intensity falls rapidly in all directions except along the direction parallel to the surface of the laser electrodes, high radiation intensity will only occur in the interference fringes along this direction.

Isenor [5] irradiated a  $\text{CO}_2$  laser on the surface of  $\text{Ni}_x\text{P}_{1-x}$  used as a mirror material and the periodic ripple pattern was also observed on the irradiated area. In the report, the influence of the polarization and laser intensity and the atmospheric gas species on the surface pattern were investigated in detail. The ripple wave fronts were normal to the electric field and varied in spacing from a laser wavelength at normal incidence to half the laser wavelength for  $\pi$  polarization at grazing incidence. The damage was produced on the  $\text{Ni}_x\text{P}_{1-x}$  surface in a vacuum and Ar and  $\text{N}_2$  atmospheres. However, no distinct ripple pattern was observed under these conditions. In air,  $\text{O}_2$ , or  $\text{CO}_2$ , the ripple pattern was observed so that an oxygen atmosphere may be needed for the pattern formation. The following formation mechanism was also suggested. The combination of the incident, reflected, and diffracted waves could produce a complicated electric field distribution that would drive the localized plasma oscillations, which would give a locally stronger heating which would result in a greater erosion of the surface in the “valleys” of the ripple pattern.

Fuh has successfully obtained laser-induced ripple patterns on various ferric metal surfaces by using a  $Q$ -switched Nd:YAG laser [6]. Changes of the local magnetic properties associated with the rippled areas were then investigated to determine a possible reading method. All these observations are consistent with the theory of Young et al. [9] for ripple formation. Significant magnetic changes associated with a steel/chromium formation of the ripples were found on a steel substrate precoated with a layer of chromium. This technique can be used as the basis of a machine-readable laser marking system on steel surfaces, or even other surfaces that could be film coated.

For the iron with point defects, a point defect scattering center produced patterns consisting of confocal circles while a linear scatter induced fringes parallel to the linear scratches. The spacing is determined by Eq. (1). The initial surface state underwent a succession of melting and solidification by rapid quenching [7]. It could not be simply explained by the interference of light on a nonpolished iron surface and the spacing was also different. The authors take account of hydrodynamic sputtering for the formation. Non-homogeneities (asperities) were sometimes formed on the

surface of the target during the laser irradiation. It might come from an additional expansion of the asperities relative to the molten surface. Since cooling took place at the bottom of the liquid target, there was a tendency for the asperities to move away from the target. The formation of a particle (droplet) is related to the surface tension of the liquid phase. It decreased with temperature and the liquid tended to be pulled away from the hotter region to the cooler one. This process resulted in a broadening of the valleys and a narrowing of the hills. The crucial parameter for the surface patterning of iron was surface temperature and there was no simple relation to the wavelength of the incident beam. Moreover, as the beam was polarized differently for the two studied wavelengths, the theories based on beam polarization should also be neglected. The more important factors seemed to be the characteristics of the material and its molten bath rather than those of the laser. The given temperature range, higher than the melting point but lower than the ablation threshold and in which the ejection–re-deposition of the droplet occurred, was necessary for obtaining the steady state rippled surface patterning, whenever the initial state of the surface was observed.

Yu and Lu report an alternative LIPSS that was produced on Ni–P disks under low fluence near the melting threshold of Ni–P. The ripple structures induced in Ni–P disks by 248 nm excimer laser pulses are experimentally investigated by varying laser fluence (175–270 mJ/cm<sup>2</sup> for 150 pulses) and pulse number (400–1000 pulses for 118 mJ/cm<sup>2</sup>) [8]. A quantity of  $R_a/(\Lambda/2)$  was proposed to characterize as the real contact area at the head–disk interface. This quantity was defined as the ratio of roughness height  $R_a$  to half ripple period ( $\Lambda/2$ ). The maximum shear stress and the plasticity index were derived to analyze the ability of ripple structures to withstand stress and the head-ripple contact mode, respectively. Increasing fluence and pulse number may lead to an increase in ripple periodicity and, on the contrary, decreases in corresponding maximum shear stress, real contact area [ $R_a/(\Lambda/2)$ ], and plasticity index. The control of the laser parameters (fluence and pulse number) is an effective way to improve the tribology of the head–disk interface through the laser-induced ripple pattern such as periodicity and roughness height. The laser irradiation with lower fluence and fewer pulses is helpful in order to introduce required ripple structures in magnetic media. This structure could meet the requirements of elastic contacts between head and disk, and less deformation under stress, although with a slight sacrifice in contact-area reduction.

## 2.2. Semiconductors

The periodic structure was observed on the edge of the laser-annealed spots on the ion-implanted silicon [10]. The direction of the periodic fringes was always found to be perpendicular to the electric vector of the light for linearly polarized beams. No fringe pattern was observed for the circular polarization. They suggested that the observed pattern was due to heating by a standing wave resulting from the interference of the impinging wave and a radial scattered wave.

The ripple structure was observed on Si and gallium arsenide (GaAs) after picosecond laser irradiation [11]. The ripple spacing was considered to depend on Eq. (1) for the *p*-polarized waves and  $\lambda$  for the *s*-polarized waves. When the laser beam was circularly polarized, ripples could not be observed. Large and small spacings sometimes coexisted in the same region. This phenomenon seemed to disagree with the defect-scattering theory used by Emmony et al. They suggested that these surface ripples developed as the result of an exponentially growing interaction between the incident laser wave front and a scattered surface optical wave. For GaAs, the arsenic was locally evaporated and redeposited at the peaks of the ripples so that a pitlike structure was formed.

In the  $\langle 111 \rangle$  single crystalline germanium, the surface structure was a hexagonal system coming from the similar underlying symmetry of the  $\langle 111 \rangle$  surface of germanium [12]. When the incident beam irradiated the surface at an oblique incident beam, the observed high-order grating patterns became quite complex, but the observed patterns generally reflected over rectangular rather than hexagonal surface symmetry. Here, LIPSS was discussed as the formation mechanism relating to the spacing and direction of the ripple determined by the wavelength and incidence angle of the laser light. Moreover, LIPSS was discussed related to the number of laser pulses of the laser irradiation and the first pulse produced a surface roughness. That is, the spacing for the new ripples could be interpreted from the reinforcement of the initially incident weak and straggling surface disturbances caused by the interference between the incidence beam and successively scattered waves [13].

## 2.3. Polymers

Tonyali et al. examined the response of highly stressed polyimide films to excimer laser radiation (20 ns pulses at 248 nm wavelength) in a vacuum [14]. They reported changes in surface topography due to surface/near-surface damage, crack initiation, and eventually crack growth over a wide range of applied stress. The morphology of the stressed material had a significant influence on the resulting damage and suggested that the regions of highest damage were those experiencing the highest local stress.

When the laser with a wavelength of the absorption edge was irradiated on a polymer with a high glass transition temperature, a microstructure with a periodicity of about 1  $\mu\text{m}$  was formed. In this case, the XeCl laser was irradiated on polyethersulfone [15]. The optimization of the laser fluence and polarization of the laser could lead to the anisotropy and periodicity of the patterns [16]. For example, although the microstructure of the random fingerprint-like pattern was obtained by irradiation of the nonpolarized laser beam, the anisotropy of the microstructure gradually increased if the degree of polarization was increased. The grating pattern was observed for the irradiation of the plane polarized beam. Moreover, the periodicity increased as the laser intensity increased. The periodicity was 1  $\mu\text{m}$ , three times larger than the laser wavelength, and there was no effect by the interference of the incidence beams. Therefore, the thermal processes of the surface during and after the

laser radiation play a significant role in the formation of the microstructures.

Dyer and Farley reported that periodic surface structures were observed on organic polymers that were photoablated using low coherence excimer lasers [17]. Both unpolarized and linearly polarized radiation at 248 and 308 nm produced well ordered, micrometer-scale structures over dimensions greatly exceeding the coherence area of the laser at the surface. The formation of such structures was understood through effects by surface scattered wave effects.

Periodic line structures with a period of 167 nm and linewidths varying from 35 to 100 nm were produced on polyimide by direct ablation with a KrF laser using an interferometric technique [18]. Since ablation is a nonlinear process, the resolution can exceed that expected from the wavelength and numerical aperture of the system; the linewidth can be controlled by varying the laser fluence. This externally generated period of 167 nm prevents the spontaneous growth of periodic surface structures due to radiation remnants.

Bolle and Lazare contributed many papers on laser nanostructuring of polymers [19–21]. A controlled submicrometer-level rough surfaces is desired in many applications. For the first time, pure LIPSS (without any ablation or any larger structure) of submicrometer size (spacing and amplitude of 0.2  $\mu\text{m}$ ) was developed on polymer surfaces (polyethylene terephthalate, polybutylene terephthalate, polystyrene, polycarbonate, etc.) by irradiation with 1000 pulses of the polarized beam of an ArF (193 nm) and KrF (248 nm) excimer laser [19, 20]. Fluence should be below the ablation threshold of polymers and chosen in a narrow window that depends on the polymer and the wavelength. Structures were obtained also by irradiation of thin films (200 nm) coated on silicon wafers. The mechanism of ripple formation is related to the surface wave. Owing to the simplicity of this irradiation procedure large-scale surface treatments could be done. Surface properties such as friction, adhesion, and so on could be very much improved.

Periodic ripples and dot patterns with spacing smaller than 200 nm were produced on various highly absorbent polymers (polyethylene terephthalate, polybutylene terephthalate, polystyrene, polycarbonate, etc.) using a polarized beam of an ArF and KrF excimer laser [21]. The period of the structures increases with the wavelength used and with the angle of incidence of the beam, whereas the ripple direction was parallel to the polarization direction. The fluence interval in which the pattern could be produced was far below the ablation threshold of the polymer but probably allowed local melting or photolysis of the surface. For polystyrene, a strong influence of the presence of oxygen was observed, which led to the conclusion that photo-oxidative processes played a major role in the structure growing mechanisms.

Periodic structures of sub-half-micrometer size were produced on the surface of different polymers [polyethylene terephthalate, polyimide-type Kapton (DuPont), and polyimide-type XU 293 (Ciba-Geigy)] by Nd:YAG laser irradiation at 266 nm wavelength [22]. A phenomenological explanation for the ripple formation in terms of generating waveguide modes on the polymer surface was proposed.

A branched dendritic surface structure on polyethylene terephthalate (PET) could be observed after 248 nm KrF laser irradiation in a vacuum [23, 24]. These structures consisted of independent objects with lateral dimensions of several micrometers and a substructure starting at a certain center. These structures were henceforth denoted as surface dendrites. They were upheaving above the surface by about 5–30 nm and extended into the surface by about the same amount. The formation of these dendrites was most pronounced for single-pulse irradiation and fluences around the ablation threshold (for PET about 40  $\text{mJ}/\text{cm}^2$  at 248 nm). The dendrites are probably polymeric crystallites, which grew within the amorphous surface layer formed by laser irradiation of the semicrystalline polymer foil. The crystalline dendrites were formed through the process of melting and solidification. The lateral growth rate of dendrites was of the order of 100 nm/h.

Periodic surface structures generated by linearly polarized ArF excimer laser (193 nm) were studied on PET, in a narrow fluence region (3–5  $\text{mJ}/\text{cm}^2$ ) [25]. A homemade kinematic base plate ensured the reproducible positioning of the sample with respect to the atomic force microscope (AFM) and the laser beam. The main subsequent phases of the LIPSS formation were identified as laser light scattering on the originally existing granules, formation of elliptical structures around the granules, and the transformation of ellipses into ripple-shape modulation. The LIPSS generating feedback mechanism was described: the incident beam and the beams scattered on the granules and already existing LIPSS interfere causing spatially modulated melting and crystallization, which developed the structure. The dependence of the LIPSS period on the wavelength and on the angle of incidence was studied. The structure's height and surface-roughness vs the number of laser shots was measured. The experimental results were in good agreement with the theory of self-organized diffraction gratings. It was proved experimentally that the LIPSSs were formed by redistribution of the material on the surface, without significant material removal.

Some applications of polymer films required microstructuring of partly uneven substrates. This could not be achieved by conventional photolithography, casually performed with ultraviolet short-pulse lasers (excimer, fourth harmonic Nd:YAG) [26, 27]. When processing is thermally sensitive or polymers were undoped ones with low optical absorption, the precision of ablation could be improved by using femtosecond laser pulses and the heat-affected zone would be reduced. Then, a Ti:sapphire laser system was employed to perform ablation experiments on polyimide. Highly oriented ripple structures, which were related to the polarization state of the laser pulses, were observed in the cavities. The relationship between the ablation threshold fluence and the number of laser pulses shot to the same spot was described in accordance with an incubation model.

The dichroism of the laser-induced periodic microstructure on a polyimide surface was studied with polarized reflectance infrared spectroscopy. The experimental results showed that the polar C=O groups in the polyimide exhibit a greater tendency of orienting in the direction parallel to the microlines while the nonpolar C–C–C linkages between



the two benzene rings in the diamine moiety tended to orient in a direction perpendicular to the nanolines [28]. This result indicates that the polyimide molecule chains tend to orient in a direction perpendicular to the nanolines.

Surface modification on a polyimide film by pulsed ultraviolet (UV) laser irradiation with a fluence below its ablation threshold was examined [29]. It was observed that a photochemical reaction occurred and hydrophilic groups, such as -OH and -COOH, were formed on the polyimide surface after irradiation. A ripple microstructure was formed on the surface when the angle of incidence of the laser beam was 20–50°. The contact angle of the polyimide surface with water decreased and the adsorption ability of the surface to a water-soluble dye clearly increased after laser irradiation.

## 2.4. Multilayer Materials

An analytical model was proposed in order to predict the LIPSS formation on silicon dioxide/silicon and silicon dioxide/aluminum interfaces [30]. The freezing of surface waves was considered to understand the dominant mechanism for ripple formation. The model precisely predicts a linear relationship between the interface periodicity and the silicon dioxide thickness. The ripple periodicity in the substrates could hence be adjusted by varying the thickness of the SiO<sub>2</sub> overlayer. This process was expected to be useful in laser microtexturing for magnetic media of high storage density, which requires microtextures to be well controlled within a certain roughness to prevent stiction failure. The theoretical calculation had good agreement with the experimental results.

The LIPSSs by excimer laser at the interfaces of silicon dioxide/silicon have been investigated experimentally [31]. It was found that a stable, fine, and homogeneous ripple structure was preferentially generated under a comparatively larger laser beam. The ripple periodicity seemed to have no angular dependence and was enhanced with increased laser pulses for the first few pulses. The initial substrate temperature also represented an important parameter that could be used to control the interface ripple structures. The threshold pulse number for the ripple formation at different laser fluences, or at different oxide thicknesses was studied as well. This study will be helpful to understand the physics of laser-induced ripple formation and hence be useful in controlling ripple structures within the range required for the laser texturing of high density magnetic recording media.

Rapid thermal processing was reported to be capable of improving film properties [32]. In this study, the effects of rapid thermal annealing (RTA) on rapid-thermal-annealed radio-frequency-sputtered silicon oxide films and hence on LIPSS by excimer laser at the silicon dioxide/silicon interface were investigated. It was found that the RTA of the oxide film done by increasing either annealing temperature or annealing time could enhance the ripple growth but did not change the topography of the ripple structure. The ellipsometric measurements indicated that the optical constants of the film, and hence the calculated film density, increased with an increment of annealing temperature or annealing time. The increase in film density is balanced by the decrease in the corresponding film thickness. An analytical model by

Yu and Lu predicted that the increase in ripple period was a result of enhanced energy absorption caused by the decrease in equivalent reflectivity of SiO<sub>2</sub>/Si after RTA. The calculation was identified to be consistent with the experiment.

The periodicity of the ripple for a material like a multilayer film with SiO<sub>2</sub>/polysilicon/SiO<sub>2</sub>/single crystal silicon by XeCl excimer laser (wavelength: 308 nm, pulse duration: 35 ns, repetition rate: 5 Hz, pulse number: 10 pulses, fluence: 340 mJ/cm<sup>2</sup>) irradiation could not be explained using Rayleigh's diffraction condition. The ripple wave fronts were chaotic patterns rather than parallel lines [33]. The ripple wave fronts were controllable by changing the polysilicon surface topology. Moreover, since molten silicon would not be wet a SiO<sub>2</sub> surface, these ripples likely formed in order to release stress in the polysilicon film upon solidification.

## 2.5. Inorganic Materials

Ihlemann et al. reported on the ablation of fused silica using several excimer lasers (20–30 ns pulse duration at 193, 248, and 308 nm) and a short pulse laser system (500 fs at 248 nm) [34]. Ablation rates ranged from several hundred nm/pulse (193 nm or fs-laser) up to about 6 μm/pulse (308 nm). The performance of the ablation not only depended on wavelength and pulse duration but also on the existing surface condition or laser induced surface quality (e.g., roughness) of the material. Special ablation phenomena were observed there. That is, at 193 nm and moderate fluence (3 J/cm<sup>2</sup>) ablation took place at the rear side of a plate without affecting the front side, whereas at higher fluence normal ablation at the front side occurs. At 248 nm (28 ns pulse duration) the existence of two consecutive ablation phases was observed: smooth ablation at a low rate was followed by explosive ablation at high rate. The smooth shaped holes using fs-pulse lasers were formed during the first pulses, whereas high pulse numbers caused the development of a ripple structure in the ablation craters. So two different ablation mechanisms were involved. The first was based on two photon bulk absorption while the second was based on controlled surface damage in relation to (partially laser induced) singularity conditions at the surface.

When microstriae were formed by ArF excimer laser irradiation on inorganic materials such as synthetic silica glass, soda-lime glass, quartz, corundum, and calcium fluoride, the relationship between the microstriae and polarization of the laser beam was not confirmed [35, 36]. The direction of the microstriae depended on the incidence angle of laser. As the incident angle approached 90°, the directivity of the microstriae became strong and the striae line became longer. Polarization did not affect the directivity of the microstriae. The microstriae were also formed on quartz as well as on silica glass. Since soda-lime glass had the high absorption coefficient, almost all of the laser beams were absorbed and removed near the surface so that the surface became smooth. When corundum and calcium fluoride surfaces were irradiated and removed, the cleavage fracture occurred with preference to the crystal direction having a weak binding energy.

Regular structures on Al<sub>2</sub>O<sub>3</sub> surfaces were observed on the bottom of the ablation pit after Ti:sapphire laser (wavelength: 800 nm, pulse duration: 120–300 fs, repetition rate: 1 kHz) ablation by linearly polarized laser pulses [37]. These

structures did not comply with conventional ripple patterns. Instead, they more nearly resemble wickerwork and were aligned perpendicular to the laser beam polarization. They observed parallel chains, 1–2  $\mu\text{m}$  long and about 250 nm wide, both on the bottom and on the edge of the pit. Neither the general structure nor the spacing of about  $3/\lambda$  changed with the angle of incident, the pulse duration, the fluence, or the number of pulses. A similar morphology was obtained by arc discharge erosion at AgCdO electrodes, suggesting that explosive laser ablation might be characterized by high electric field effects and self-organization in the ablation craters.

Laser processing of sapphire using a Ti:sapphire laser at 790 and 395 nm and pulse widths varying between 200 fs and 5 ps was reported [38]. A clear improvement in quality was demonstrated for multishot processing with sub-ps laser pulses. For fluences between 3 and 12  $\text{J}/\text{cm}^2$  two ablation phases were observed, which was in agreement with previous work from Tam et al. using 30 ps, 266 nm laser pulses [39]. During the “gentle ablation” phase, periodic wavelike structures like ripples were observed on the  $\text{Al}_2\text{O}_3$  surface. The structures were perpendicular to the laser polarization and their spacing was almost equal to the laser wavelength, indicating metallic-like behavior of sapphire in a thin surface region due to the long lifetime of free electrons in the conduction band. The ripple modulation depth was on the order of a few tens of nm. For fluences between 1 and 2.5  $\text{J}/\text{cm}^2$ , below the single-shot surface damage threshold and at a pulse width above 200 fs, microstructures could be produced at the rear side of a 1 mm thick sapphire substrate without affecting the front surface.

## 2.6. Others

For the  $\text{Bi}_2\text{Sr}_2\text{CaCu}_2\text{O}_8$  (BSCCO) superconductor [40], the hexagonal microstructure, with the diagonal of each hexagon being about 0.7–0.9  $\mu\text{m}$  and 10 nm heights, was formed. However, the formation mechanism had not been clarified. According to the theory of a two-dimensional phase transition, a single crystal should melt into a so-called intermediate “hexatic” phase. The experimental results of the charged colloidal particles formed under a two-dimensional plasma system supported the idea of hexagonal structure formation during melting [75–77]. It is well known that the plasma formed during laser ablation and the surface molten layer have little interaction with the solid surface. Therefore, the theory of two-dimensional phase transition might be able to be applied to this case. These structures were formed during the solidification process of the laser induced thin liquid layer of BSCCO. Moreover, a crack of 0.1  $\mu\text{m}$  depth by 5 laser pulses ran in accordance with the *a*-axis and *b*-axis. The crack might be formed by the thermal stress induced on the surface of the target. When the number of laser irradiation pulses increased to 50, the crack became 2  $\mu\text{m}$  in depth. Furthermore, it had a pyramid-type projection of 3  $\mu\text{m}$  height by increasing the number of laser shots up to 1200 pulses. Consequently, it was based on the influence of the surface structure.

For the fullerite surface [41], the sharp regular pattern of ripples was observed on the circumference of the laser spot. In the process of ablating the surface area in the laser

spot, a wavelike morphology was created. Also, a crater in the rough surface became clearer and it became sharper as the number of laser pulses increased. The sharp ripple could be reproduced and it was observed that the ripple spacing depended on the incidence angle. The spacing by  $\lambda/\cos\theta$  was realized from the 20° incident angle. This is based on interference of the incident field with a surface scattered field. The surface field can be generated by electronic excitations or defects already present or created by the laser irradiation. If there is anything like a scratch, the spacing of a fringe from interference is given by Eq. (1). The morphology of the periodic nanostructures can be controlled by the laser conditions such as laser fluence, angle of incidence, and wavelength. On the other hand, the laser pulses of a 266 nm wavelength produced patterns similar to those observed under analogous conditions in polymers. Thermal effects were responsible for the formation of bubblelike structures and the annealing of the surfaces.

On the diamond surface [42], ripple grooves were formed perpendicular to the direction of the electric field. The spacing of the ripple was on the order of the wavelength, which was in agreement with the previous report relating to interference. However, a ripple with the small spacing of 50–100 nm was also formed besides the spacing with the wavelength order. The formation of the secondary spacing could be attributed to the out-of-phase superposition of the electromagnetic fields due to the laser pulses. It was hypothesized that the scattered wave was not only produced by the interference but also by a thin waveguide etched on the surface. When the unpolished surface was irradiated, two surface ripple trains crossed each other on the side of a crystal wall and a crosshatch pattern was created. The spacing of the ripples was not in agreement with the value calculated from Eq. (1). The consistent periodicity ( $\lambda/2$ ) observed on all the clusters nucleated along the ablation path indicated that the formation of circular corrugations on these clusters might not be due to random stacking faults, which occurred during the growth process. The periodicity of these ripples was significantly influenced by the surface roughness and morphology of the surface. On an extremely smooth surface of a single crystal and a diamond surface, an interaction was produced only between the incidence wave and the wave reflected from the surface. However, for a surface with polycrystalline grains (i.e., for pyramids with smooth facets, an unpolished diamond surface, or spherical random features on a laser-processed diamond), the interaction among the incident wave, the scattered one, and backscattered ones became more complex.

Many investigations of LIPSS have been carried out on various materials. In almost all cases, the formation of a periodic structure was taken into account from the standpoint of the laser beam characteristics. That is, the relationship between the optical characteristics of the laser beam, such as the incident wavelength and polarization, and the periodic surface ripples with spacing and direction was discussed. Some parameters characteristic of the material, the crystal structure of the material, and surface roughness were also considered to be very important since researchers think that such parameters are key factors.

### 3. CONE/COLUMN TYPE SURFACE STRUCTURING

The laser ablation method has attracted much attention with respect to the surface patterns induced by laser irradiation as mentioned in the previous session. Besides the surface patterns, microcones and microcolumns induced by laser ablation have been studied. Many target materials have been used in order to clarify this formation mechanism. They include semiconductors (Si, Ge) [45–51, 64], oxides ( $\text{YBa}_2\text{Cu}_3\text{O}_{7-x}$ ,  $\text{ZrO}_2$ ,  $\text{Al}_2\text{O}_3\text{-TiC}$ ) [59–62], a nitride ( $\text{Si}_3\text{N}_4$ ) [61], a polymer (polyimide, etc.) [52–58], metals (Co, Ti, W, etc.) [63–68], and alloys [69, 70]. The lasers used were an excimer laser, a Nd:YAG laser, and a Cu vapor laser to form the microcone and column. Nowadays, even a femtosecond laser (Ti:sapphire) is used. This research field will be more actively studied from year to year.

#### 3.1. Semiconductors

The KrF (248 nm) excimer laser and a Ti:sapphire (800 nm) laser were mainly used for the Si substrate ablation. Since the column formation was related to the ambient gas species, the influence of the ambient gas species such as  $\text{SF}_6$ ,  $\text{Cl}_2$ , and air was also examined. The microcones could not be produced in an inert (Ar) gas atmosphere and did not have sharp conical spikes in a vacuum [51]. Therefore, it was concluded that their growth was driven by the chemical reaction with the chemical gases.

Sánchez et al. [43–45] reported the growth of whisker-like columnar structures on (100) silicon targets in air by ArF excimer laser (193 nm, 23 ns) irradiation. Microcolumns were not formed with preferential etching of the surrounding materials. The obtained results showed the dynamics of the hydrodynamical growth leading to the formation of the columns. These columns were typically 1–2  $\mu\text{m}$  in diameter and never below 1  $\mu\text{m}$  and presented a dispersion in height. Some of them were as high as 20–30  $\mu\text{m}$  in a 0.3- $\mu\text{m}$ -deep crater. In this case, the dependence of the evaporation was slight. The growth process of the columns was as follows. At first, small micrometer-sized depressions (Fig. 1a) on the flat surface appeared after more than 100 laser pulse shots. With more shots, the formed depressions increased in area (Fig. 1b) but did not develop so significantly in depth. Simultaneously, other depressions appeared and the result was the constriction of the nondepressed area and the formation of an elevated reticular network with a mesh size of some micrometers (Fig. 1c). The original surface was no longer identifiable and a quite flat new one appeared in the inner part of the polygons defined by the network (Fig. 1c). With additional pulses, the material of the network tended to have fewer branches and accumulated at nodes. As a consequence of this process, the branches became slim and broke, and isolated hillocks were formed (Fig. 1d). As the laser irradiation continued, the base material crawled up to the top of the hillocks along the hillock surface so that the structure became columnar (Fig. 1e). This process gradually advanced and the initial conical shape evolved into a cylindrical one after more pulses (Fig. 1f). Tall columns resulted with diameters between 1 and 2  $\mu\text{m}$ , whose height could increase as high as 15  $\mu\text{m}$  in 100 pulses. The movement of

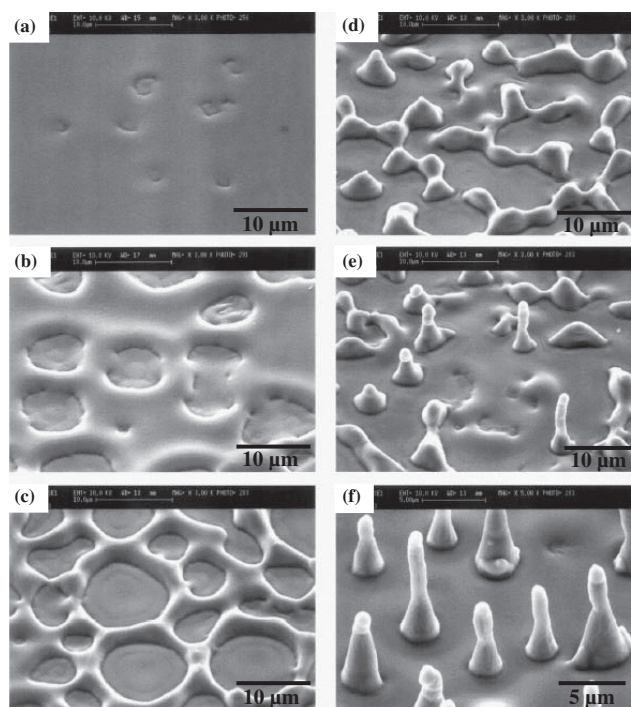


**Figure 1.** 45° SEM views of Si microcolumns obtained after irradiation at the laser fluence of 2 J/cm<sup>2</sup> from the initial depressions (a) to the final columns (f) [note that magnification of (f) is higher]. Reprinted with permission from [43], F. Sánchez et al., *Appl. Phys. Lett.* 69, 620 (1996). © 1996, American Institute of Physics.

silicon atoms in the radial direction was presumably promoted due to the thermocapillarity as a consequence of differences in temperature and then in surface tension. Liquid silicon has a higher density (2.52 g/cm<sup>3</sup>) than solid silicon (2.32 g/cm<sup>3</sup>) so that the liquid will go up as the solid–liquid interface advances during solidification (the volume of the solidified layer is greater than that of the liquid phase and the volume expansion of the solidified liquid at the top layer occurs in a short time).

Pedraza et al. [46–50] researched most actively in this field and proposed that microcolumn growth occurred through a combination of the tip melting of the columns by pulsed-laser shots and the condensation of silicon from the silicon-rich vapor produced by ablation of the foot area of the columns. This growth process is conceptually similar to the VLS method used to grow silicon whiskers so that they called it the “catalyst-free” VLS mechanism. The impurities related to any growth mechanism through surface tension effects [78] or thermal expansion of the liquid [79] might affect their morphology with the tip becoming thinner. However, the experimental results showed that the columns did not become thinner as their length became longer. Moreover, the cumulated thermal expansion model [79] is not applicable here because the microcolumn formation and growth strongly depended on the ambient atmosphere. It strongly suggests that growth advanced due to the condensation of small atom clusters and/or molecular reactions at the tips of individual columns. The fact that an oxygen atmosphere promoted column growth indicates that chemical reactions and/or oxidized species exist at the growing

tip. The column growth did not occur in an argon atmosphere or vacuum. Figure 2 shows the conical arrays of the walled silicon structure produced in 1 atm of  $\text{SF}_6$  by KrF excimer laser irradiation with 2040 pulses and the fluence of  $1.5 \text{ J/cm}^2$ . In an oxygen atmosphere, silicon microcolumns are produced as in Figure 1f. However, extremely long structures are produced in  $\text{SF}_6$ , and at first, they look like walls surrounding very deep central holes. The conical arrays formed in  $\text{SF}_6$  were more complex. They showed a kind of melted droplet-shaped morphology not only at the tips of the cones and walls but also on their sides. The axis of a column remained the same as the axis of a solid and a column grew upward along with the flow of gas, not along the liquid between columns. The top of a column was higher than the original surface. Since the tip of a microcorn is exposed to the high-density plasma generated by laser ablation, it may be etched so that the growth might be suppressed. The maximum height of a corn decreased with the increase in atmospheric pressure. From a heat balance equation, solidification of the molten silicon occurred before the melted Si moved to a tip site (time is too short) so that it deposited again with gas and made the column grow. Column formation was done with the ablation plasma induced from the pulse laser irradiation.

Her et al. produced an array of sharp conical spike microcones using a femtosecond laser [51]. The influence of the ambient gas on the shape of the spikes indicates that the chemical reaction between  $\text{SF}_6$  or  $\text{Cl}_2$  and silicon contributes to the formation of the spike shapes. The sharp spikes did

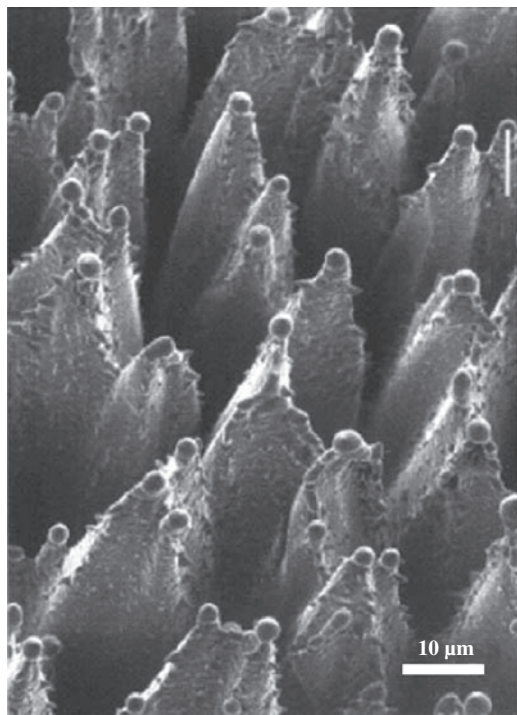


**Figure 2.** Walled Si structure produced by 2040 laser pulses at  $1.5 \text{ J/cm}^2$  in 1 atm of  $\text{SF}_6$ . Reprinted with permission from [46], A. J. Pedraza et al., *Appl. Phys. Lett.* 74, 2322 (1999). © 1999, American Institute of Physics.

not form in a vacuum,  $\text{N}_2$ , or He so that the chemical reaction was considered to be very important.

### 3.2. Polymers

Many studies of the photochemical processing of polymer films using excimer lasers have been reported. The direct etching of polyethylene terephthalate film using a XeCl laser was investigated and was shown to be consistent with a thermal model for degradation. Microstructure revealed by deep etching suggests that the UV laser might prove useful for studying polymeric materials. Polyimide and photoresist film was also directly etched [52]. Dyer et al. [53, 54] discovered polyimide cones using excimer laser ablation (Fig. 3). The cones were produced by the shielding effect of the seeding particles. Therefore, the cone density of the area was changed by the size of the seeding particles. In this case, the areal cone density and cone full angle decreased with increasing laser fluence. The microcones were also produced by the shielding effect of particulate impurities by laser ablation.

The surface of polyethylene terephthalate obtained by irradiation with the 193 nm pulsed radiation of the ArF excimer laser ( $10^7 \text{ W/cm}^2$ ) in air or the 185 nm low-intensity ( $2.5 \text{ mW/cm}^2$ ) radiation of the mercury lamp in a vacuum was studied by Lazare and Srinivasan [55]. The X-ray photoelectron spectroscopy (XPS) analysis revealed that both were depleted in oxygen, but the efficiency of the change was intensely dependent on nonlinear effects at high intensity. The pulsed radiation gave ablative photodecomposition when the energy of the pulse was  $\geq 40 \text{ mJ/cm}^2$ . The radiation area yielded a rough surface that was composed of tiplike structures of submicrometer size. The roughness increased with the accumulation of pulses and the maximum spacing of the roughness reached  $1\text{--}2 \mu\text{m}$  at 10 pulses. The roughness also showed some periodicity. Since the chemical composition of the laser-treated surface dose not vary with the accumulation of pulses, the increase in the advancing contact angle with water was interpreted as depending on roughness. Labeling reactions and XPS were used in order to probe the reactivity of the modified surface. Carboxylic acids, alcohols, and olefins were qualitatively and quantitatively probed. The laser treatment had a superior ability to create new functionalities.

The ablation of PET by ArF laser radiation was studied at different fluences for amorphous and semicrystalline samples [56]. The surface structure created on PET was interpreted as resulting mainly from a difference in the etch rate and not the ablation threshold between amorphous and semicrystalline PET. UV laser etching was proposed as a quick and easy method for observing the crystalline subsurface structure of aromatic semicrystalline polymers, as long as low fluence and a low pulse repetition rate were used. The melting of the PET surface occurred at high fluence ( $\geq 80$  to  $100 \text{ mJ/cm}^2$ ). The ablative photodecomposition process threshold was about  $20 \text{ mJ/cm}^2$ . At higher fluence of  $150 \text{ mJ/cm}^2$ , ripples were observed but looked more like “quenched drops” than those at  $120 \text{ mJ/cm}^2$ . For this structure, Novis et al. suggested that the “hills” corresponded to the more crystalline material and the “valleys” to more



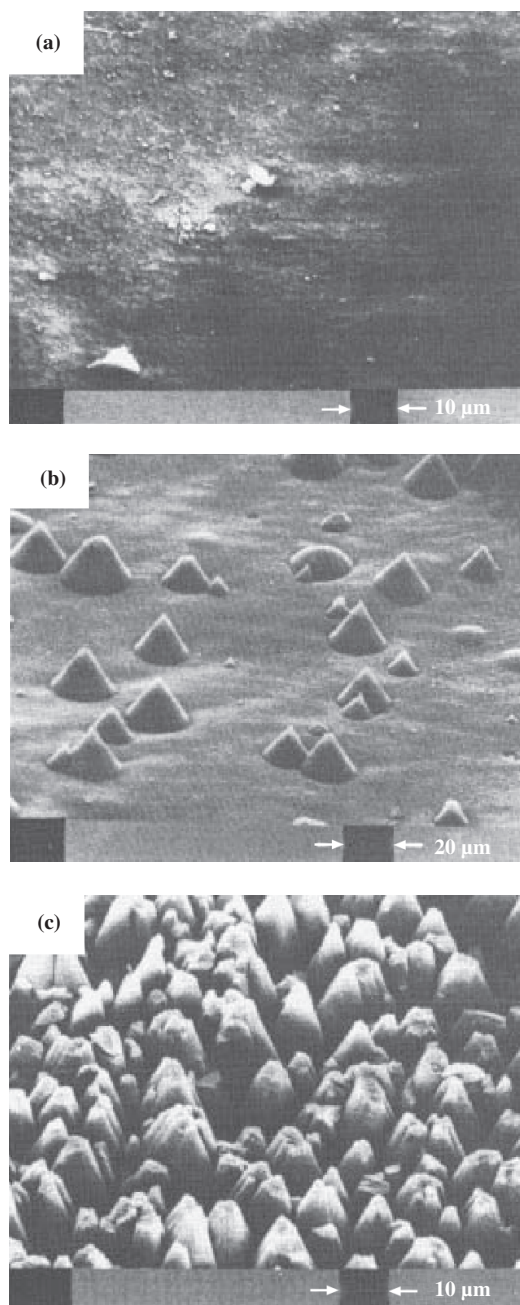


**Figure 3.** XeCl laser etched polyimide (300 shots at  $70 \text{ mJ/cm}^2$ ). SEM images showing (a) unseeded spun-on film, (b) seeding with  $\sim 0.05\text{-}\mu\text{m}$ -diameter particles, and (c) seeding with  $\sim 3\text{-}\mu\text{m}$ -diameter particles. Reprinted with permission from [53], P. E. Dyer et al., *Appl. Phys. Lett.* 49, 453 (1986). © 1986, American Institute of Physics.

amorphous material. The droplike shape of the top of the hills was easily recognized.

Excimer-laser-induced ablation of polymers was often accompanied by a modification of the surface morphology at the irradiated regions [57]. The models by Novis et al. [56] were proposed for this effect. The origin was sought for in the different reflectivity or absorbance, or a higher energetic stability of crystalline and amorphous material. A study by Bahners and Schollmeyer on synthetic fibers irradiated by

UV laser was conducted to examine that assumption and gave evidence of a thermal contribution to laser–polymer interaction. Furthermore, a strong influence of internal or external stress fields was found. On this basis a synergetic understanding of the surface structures was proposed.

Niino et al. investigated the laser ablation of an elastomer composite with picosecond (ps) and femtosecond (fs) pulsed UV lasers (ps laser:  $\lambda = 263 \text{ nm}$ ,  $\tau = 8 \text{ ps}$ ; fs laser:  $\lambda = 248 \text{ nm}$ ,  $\tau = 500 \text{ fs}$ ) [58]. Upon laser irradiation, a unique microstructure on the surface of the elastomer composite (acrylate polymer) containing carbon black (particle size:  $18\text{--}30 \text{ nm}$ ) was observed. The laser-ablated surfaces were analyzed by scanning electron microscopy (SEM) and XPS. The formation mechanism was discussed in terms of thermal effects induced by the different pulse durations of the lasers. Intrinsic laser ablation without thermal effects was experimentally demonstrated by fs-laser ablation of the composite, where the heat-affected zone on the surface during laser irradiation was negligible. These advantages of fs lasers indicated that it is a very promising technique for various applications in precise material processing.

### 3.3. Oxides and Nitrides

For the  $\text{YBa}_2\text{Cu}_3\text{O}_{7-x}$  microcone formation, the yttrium concentration increased at the cone tip during the initial step of the microcone growth; this yttrium-rich shell seemed to suppress the laser vaporization [59, 60], which enabled us to consider an impurity shielding mechanism for the cone formation. Such phase segregation could provide the mechanism for column formation. The top of the columns must be at the level of the initial target surface or below the level.

Miyamoto and Maruo [61] explained that a  $\text{Si}_3\text{N}_4$  microcone formation mechanism was related to the debris particles (Fig. 4). (1) During the first step, debris particles produced by the laser irradiation stuck to the laser irradiated area, then (2) small protuberances were produced by an alternative ablation around the debris particles, (3) the fluences were reduced on the side of the protuberance, and (4) after these processes, the conical protuberance with a high aspect ratio was generated. Therefore, this process mainly occurs due to the etching of the base material and not to the redeposition of base material on the tip. Consequently, the top level of the microcone is below the level of the initial target surface.

For  $\text{Al}_2\text{O}_3\text{--TiC}$  [62], the mechanism comes from the shielding effect. Column growth started with the formation of small globules of solidified TiC. With subsequent laser pulses, the globules coalesced, leading to an increase in the mean globule diameter. This process continued until the surface was completely covered by the globule. At this point, a further increase in the number of pulses lead to the evolution of the globules into a columnar topography.

### 3.4. Metals and Alloys

For metals, two cone formation mechanism models were proposed. One is a kind of growth model. The nucleation of cones is considered to occur only during the stage of initial laser irradiation. Once a surface relief is created, it is accelerated to grow through the appearance of “hot” valleys,

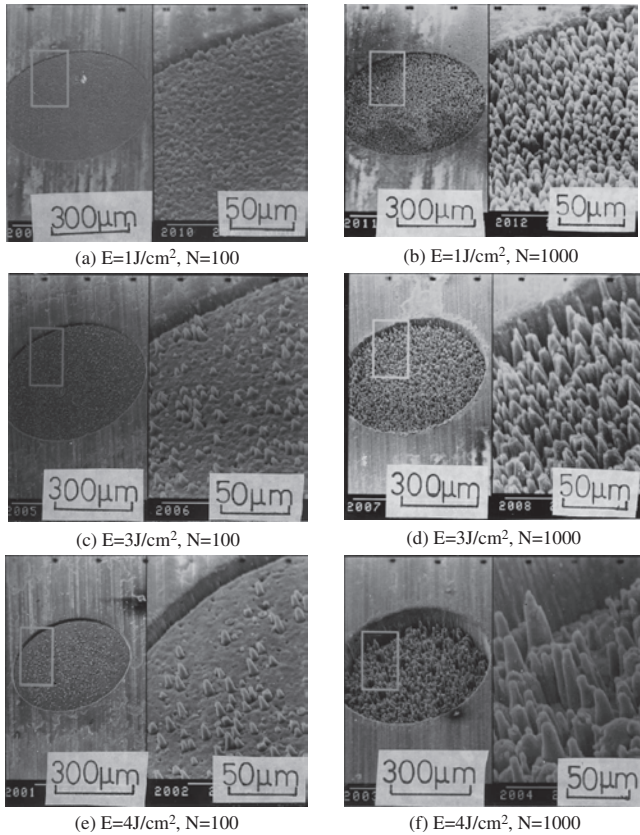


**Figure 4.** Surface appearance of  $\text{Si}_3\text{N}_4$  irradiated by KrF excimer laser. (a)  $1 \text{ J/cm}^2$ , 100 pulses, (b)  $1 \text{ J/cm}^2$ , 1000 pulses, (c)  $3 \text{ J/cm}^2$ , 100 pulses, (d)  $3 \text{ J/cm}^2$ , 1000 pulses, (e)  $4 \text{ J/cm}^2$ , 100 pulses, and (f)  $4 \text{ J/cm}^2$ , 1000 pulses. Reprinted with permission from [61], I. Miyamoto et al., *Proc. SPIE* 1279, 66 (1990). © 1990, International Society for Optical Engineering.

where the electromagnetic energy of the light wave sustains the cone growth. As a result of this effect, the depth of the valleys increases and the cone structure becomes more and more pronounced [63]. The other was developed by Dolgaev et al. [64], who produced the microcone by combination of Si, Ge, and Ti materials and a copper vapor laser. Figure 5 shows the Ge and Ti microcones irradiated in a vacuum. The nuclei were formed by the capillary waves, which induced different reflective areas on the surface. The bottom of the wave was ablated more than the top of the wave so that the evaporation produced a metal vapor, which could deposit on the top of the wave. Cones were then produced with a height of  $20\text{--}30 \mu\text{m}$ . Both mechanisms indicate that microcones grow by the process of evaporation and deposition of metal vapor. In these papers, the densities of the cones and the irregular arrays were not mentioned.

Krebs and Bremert investigated microcones using the pulsed KrF excimer laser ablation with a laser fluence of  $7 \text{ J/cm}^2$  on thin metallic alloys of  $\text{Fe}_{50}\text{Nb}_{50}$  [70]. In the outer part with a lower energy density, microcolumnar structures evolved, which were aligned in the direction of the incident laser beam due to the recrystallization process after laser irradiation, although the laser plume emanated normal to the target surface. Most columns were narrowed in the upper part and covered on top by small droplets, but

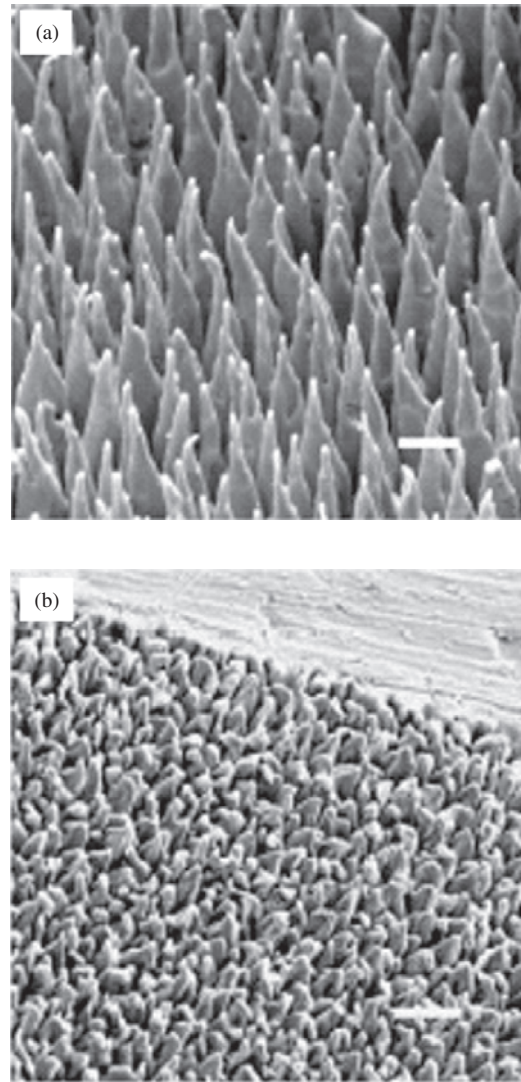


**Figure 5.** Conical structures on the surface of a single-crystal Ge (a) and polycrystalline Ti (b). Irradiation in vacuum, laser fluence of  $1 \text{ J/cm}^2$ . Space bar denotes (a)  $20$  and (b)  $40 \mu\text{m}$ . Reprinted with permission from [64], S. I. Dolgaev et al., *Appl. Phys. A* 73, 177 (2001). © 2001, Springer-Verlag.

underneath cracks were visible. They investigated the stoichiometry transfer from the target to deposited films by pulsed laser ablation. However, they did not define the formation mechanism of the microcolumns in detail.

The authors examined the tungsten microcone using Nd:YAG laser ablation [65–68]. Figure 6 shows the SEM micrographs of tungsten microcones obtained after irradiation at the laser fluence of  $2.6 \text{ J/cm}^2$  with 1–2400 pulses. The initial few hundred pulses by the laser produced only a rough surface (Fig. 6a–d) and subsequent pulses created the microcone arrays (Fig. 6e–g). The morphology of the microcone was strongly affected by the number of laser pulses. The irradiation with more than 1200 pulses (Fig. 6f) produced microcones up to a  $20 \mu\text{m}$  height with about a  $1.5 \mu\text{m}$  diameter at the tip. This experimental result showed that the cone's height increased with the number of pulses, so that a multiplicity of pulses was required to get a cone with a



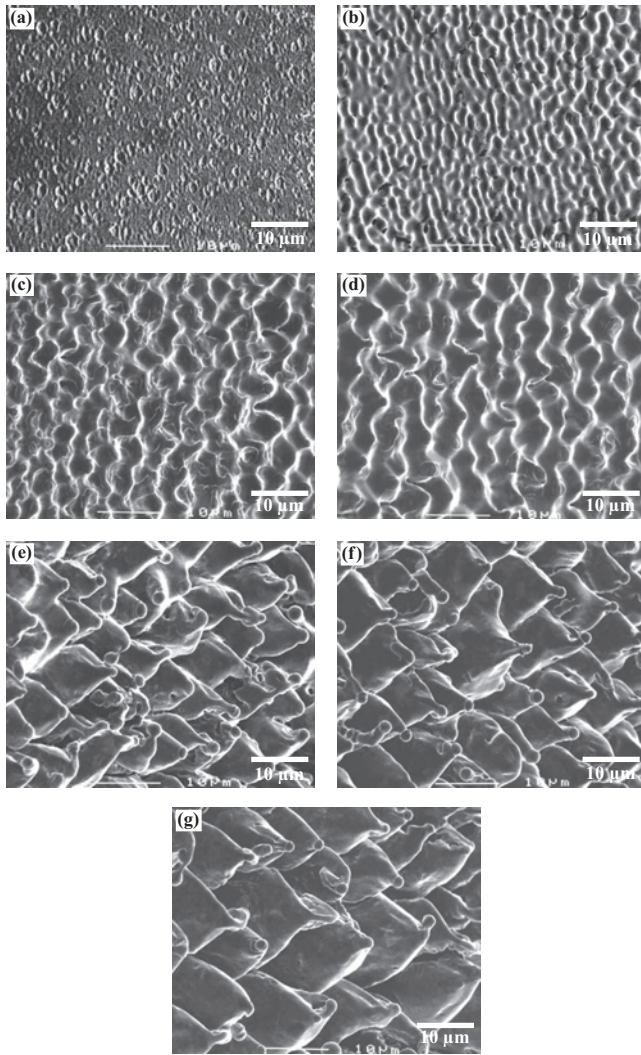


**Figure 6.** 45° SEM views of tungsten microcone obtained after irradiation at the laser fluence of 2.6 J/cm<sup>2</sup> in 4 KPa of He gas: (a) 1, (b) 30, (c) 100, (d) 300, (e) 600, (f) 1200, and (g) 2400 pulses. Reprinted with permission from [65], Y. Kawakami et al., *Appl. Phys. A* 74, 59 (2002). © 2002, Springer-Verlag.

high aspect ratio. Figure 7 shows the relationship between the density, height of the microcones, and number of laser pulses. The microcone density decreased and height rapidly increased until about 600 pulses. They then gradually began to saturate. The cause of the decrease in the microcones was due to the absorption of the smaller microcones by the larger ones as if they were following a kind of capillary since the smaller ones were more easily melted than the larger ones during the laser irradiation. The authors also examined the effect of laser fluence on the morphology of the microcone arrays. Microcones were also formed with about a 10 μm height when the irradiation was done at the lower laser fluence of 1.5 J/cm<sup>2</sup> after 2400 pulses. Therefore, the microcone growth rate depended on the laser fluence.

For a high laser fluence, microcones were not created because the irradiated surface has been significantly melted, etched, and ablated by the very high laser fluence. The authors then observed a random pattern or a ring structure.

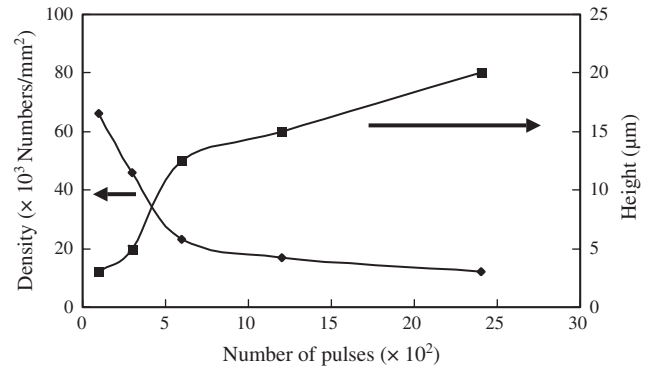


**Figure 7.** Relationship between the density, height of microcones, and number of laser pulses. Reprinted with permission from [65], Y. Kawakami et al., *Appl. Phys. A* 74, 59 (2002). © 2002, Springer-Verlag.

Such a different pattern growth might be due to a thermal strain wave, thermal expansion, temperature gradient, and nonuniform temperature by various spatial distributions of intensity in the laser spot. The pattern formation might be affected by the laser plasma plume because it depended on the size of the plume. These patterns were also confirmed in the laser fluence at 6.8 J/cm<sup>2</sup>. The critical laser fluence to change the morphology from microcones to the random structure was 4–5 J/cm<sup>2</sup> under these experimental conditions.

The microcone and silicon whisker growth by the VLS method [46–50] showed an analogous morphology. The growth of silicon whiskers could be attributed to the presence of various impurities. For the silicon laser ablation, chemical gases such as SF<sub>6</sub>, Cl<sub>2</sub>, and air were used to form a silicon microcolumn and microcone. However, the authors used neither an impurity nor chemical gases. The authors thought that the growth mechanism of the microcone was different from that of the silicon whisker. Their experimental results showed that the melted tungsten induced by the repetition of the pulsed laser irradiation played a significant role in the formation of the microcone. That is, the initial laser pulse produced only a rough surface like a crater structure (Fig. 8a). Successive several tens of pulse

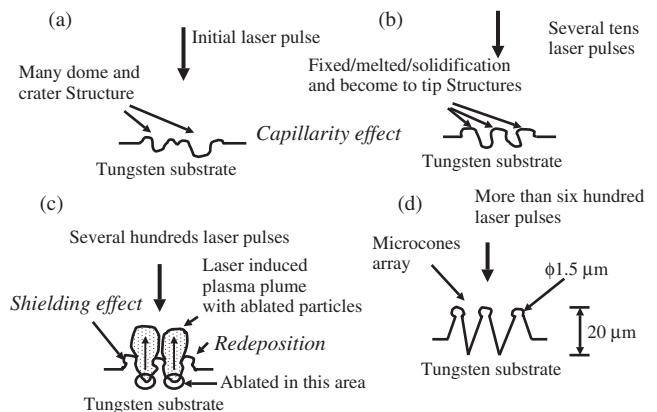


**Figure 8.** Schematic illustrations of growth mechanism of tungsten microcones by laser irradiation. Reprinted with permission from [65], Y. Kawakami et al., *Appl. Phys. A* 74, 59 (2002). © 2002, Springer-Verlag.

irradiations could create the melted/solidification tungsten hemispheres. The decrease in the number of hemispheres was due to the *capillarity* among the random protrusions (Fig. 8b). The large hemispheres absorbed smaller ones because the surface energy could decrease. The morphology of the microcone was strongly affected by the number of laser pulses. In this process, resolidification of the slightly induced liquid tungsten took place. The protuberance and dome structures of the rough surface are easily created due to the initial melt generation. The spherical tip like a mushroom during the next several hundreds pulses (Fig. 8c) was produced by the high surface tension of tungsten (2500 mN/m) compared with Si (865 mN/m). The small mushroom structures were produced by a preferential ablation and etching around the tungsten tip. The fluence was reduced on the side of the mushroom structure. After these processes, the microcone array grew under the *shielding effect* of the tungsten tip (Fig. 8d). The top of the cones and their bottom area were easily ablated, because the top of the cones had a high efficiency of heat absorption and the bottom area had a high ablation rate compared with the side of the cones. Once the mushroom structure appears, the top of the mushroom induces the *shielding effect* on the side. Then evaporated tungsten atom and cluster from the bottom area are *deposited* on the top and side of the cones to make the cone grow. Consequently, the melting and solidification process of the tungsten tips becomes very important for producing the microcone structure.

For tungsten, the influence of various ambient gas atmospheres on the morphology of the microcone arrays was confirmed. The microcones were formed in He and air under the described experimental conditions. In  $\text{SF}_6$ , the chemical reaction between  $\text{SF}_6$  and tungsten contributed to the formation of the microcones with a blunt spike due to the etching effect, and it could not redeposit to form on the top portions of the microcones. Tungsten tips were also etched/vaporized due to a dense  $\text{SF}_6$  gas around the top sections of the microcones. Therefore, the height of the microcones was limited. In air, the vapor pressure of tungsten oxide was so highly that air acted as a highly efficient etching agent. However, the oxide vapor formation did not influence the formation of the microcones. Only oxidation of the top area occurred and left an oxide after the laser pulses stopped.

In order to investigate the influence of the laser wavelength, a KrF excimer laser (wavelength: 248 nm) was used. The laser fluence was set up with a sufficiently larger value than an ablation threshold one. The influence of the laser pulses on the formation of the tungsten microcorn by using the KrF excimer laser irradiation was investigated. The experimental result is shown in Figure 9. The large growth of microcones did not take place, although the formation of the tip was observed. The evolution of the microcorns done with different laser fluences is shown in Figure 10. The size of the tip significantly changed with different fluences, which was about  $1 \mu\text{m}$  at  $0.9 \text{ J/cm}^2$ , about  $2 \mu\text{m}$  at  $1.5 \text{ J/cm}^2$ , and further,  $3 \mu\text{m}$  at  $3 \text{ J/cm}^2$ . It was found that the density of the tips decreased with the increasing laser fluence. Furthermore, when it was  $6.3 \text{ J/cm}^2$ , it became a rocklike structure and a decrease in density took place. These results suggest that the microcorn does not grow and the tip size changes

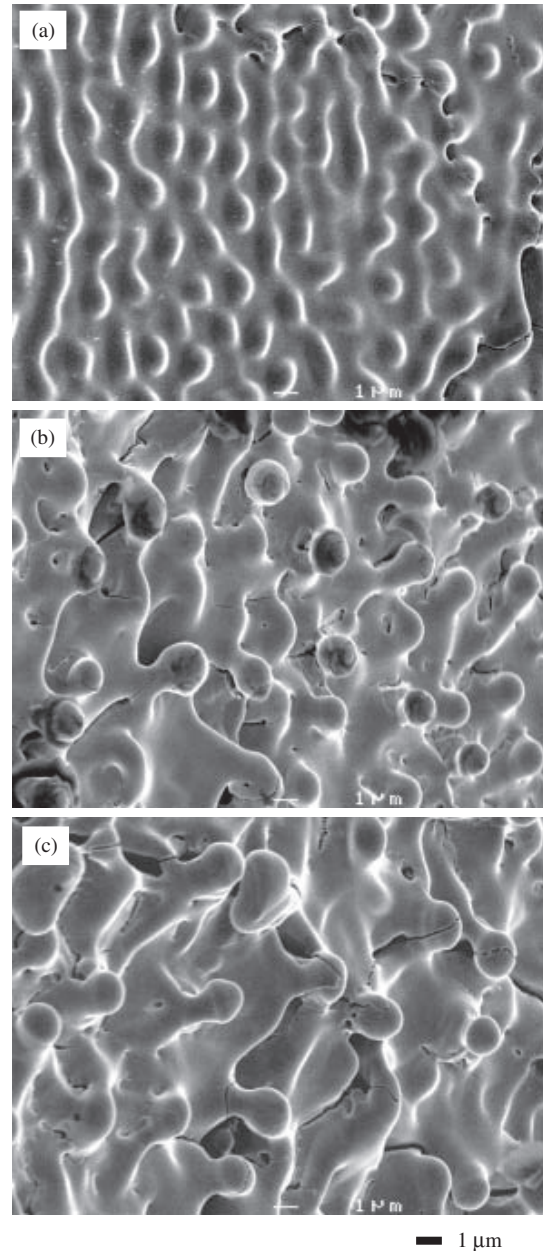


**Figure 9.** SEM microphotograph of tungsten microcone obtained after irradiation by KrF excimer laser in air (248 nm,  $1.7 \text{ J/cm}^2$ , 20 Hz): (a) 100 pulses, (b) 600 pulses, (c) 1200 pulses.

due to the change in the temperature and quantity of the melted tungsten.

Recently, many investigations concerning the microstructuring formation of a ripple or corn under the polarization of a femtosecond laser have been carried out. For example, Baudach et al. studied the ripple orientation of a polyimide and found that it was always parallel to the electric vector of the light for linearly polarized light and that the spacing was nearly the same as the wavelength. Moreover, it had a corn structure toward the center of the cavity bottom when circularly polarized light was used [26, 27]. At the top of each cone, a small hole was observed. In order to investigate the influence of the pulse width on the nanostructuring, the



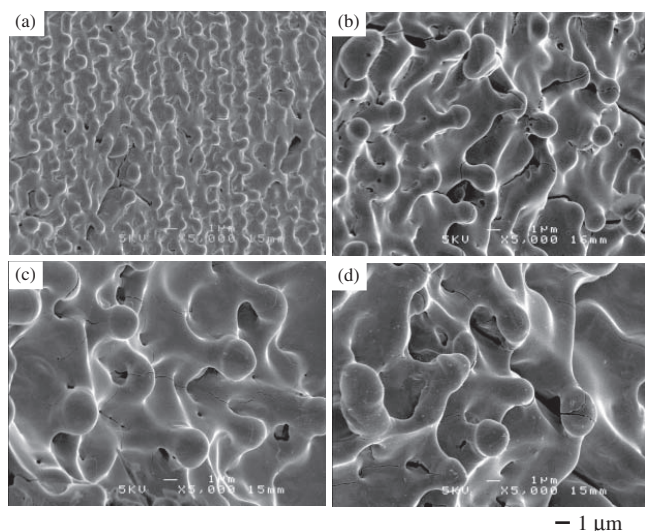


**Figure 10.** SEM micrographs of tungsten microcone obtained after irradiation at various laser peak fluences after 1200 pulses in air: (a) 0.9, (b) 1.5, (c) 2.0, (d) 3.0 J/cm<sup>2</sup>.

authors used a Ti:sapphire laser (energy: 100  $\mu$ J, damage area: 0.01 mm<sup>2</sup>, wavelength: 800 nm, pulse width: 120 fs, repetitions: 200 Hz). Figure 11 shows the influence of the polarization on tungsten nanostructuring. These morphologies were almost the same as in previous reports.

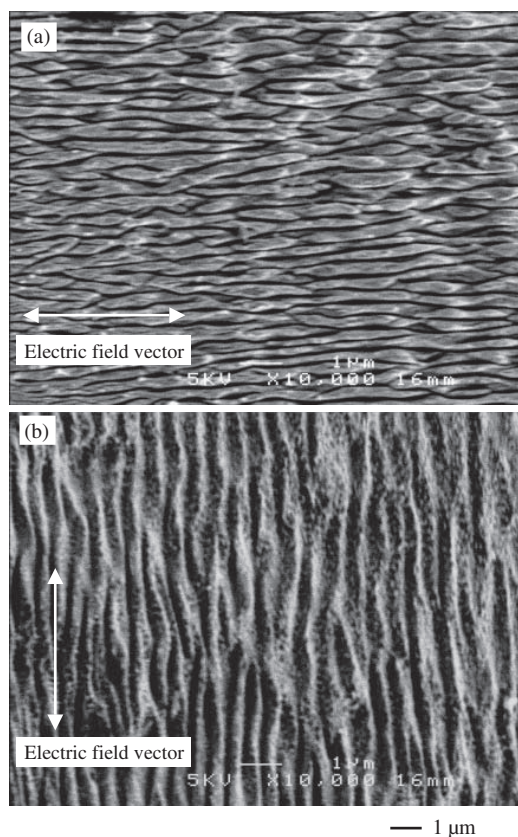


**Figure 11.** Effect of the polarized waves of tungsten surface modification obtained after irradiation by Ti:sapphire laser in air: (a) *p*-polarized waves, (b) *s*-polarized waves.

In order to form the sharper tip of the microcone, chemical etching was tried. This result is shown in Figure 12. Figure 12c and d shows very sharp tips that were etched in boiling hydrogen peroxide and distilled water. Especially, the tips etched for 90 sec shown in Figure 12d had the sharper microcone tip. The high magnification of a typical sharper tip of the microcone before and after the etching under the conditions described in Figure 12d is shown in Figure 13. It is clearly shown that facets in the crystal appear after etching. A specific crystal side was preferentially etched. Therefore, this etching technique might be able to be used to make a sharp edge that might have a significant potential for widely diversified industrial applications ranging from emission cathodes for a field emission display to microelectronic devices, since it was less than 100 nm in diameter.

Many investigations of cone- and column-type micro-nanostructuring have been carried out using laser ablation techniques. Silicon, a polymer, oxides, a nitride, and metals were used to form the microcones and microcolumns. The formation mechanisms has been proposed depending on both the target materials and laser ablation conditions such as the shielding effect of the particulate impurities and the solvent, the debris particles, capillary waves, catalyst-free VLS, and so on.

#### 4. NANOMETER-SIZED PROTUBERANCE COHERENT ARRAY

A self-assembled coherent array of tungsten protuberances was discovered around a laser-irradiated mark on a single-crystal tungsten surface [71]. The tungsten protuberances were about 150 nm in diameter and their spacing was hundreds of nm [73]. The substrates were irradiated by a *Q*-switched Nd:YAG laser at a wavelength with the fundamental (1064 nm) and the second harmonic (532 nm) at low

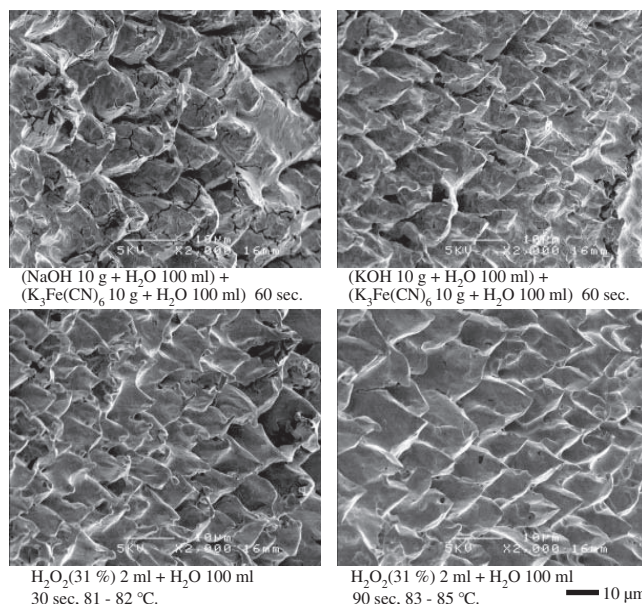


**Figure 12.** Modification of tip tungsten microcone by chemical etching [laser fluence: 2.6 J/cm<sup>2</sup>, pulse number: 1200 pulses, ambient gas: He (4 kPa)].



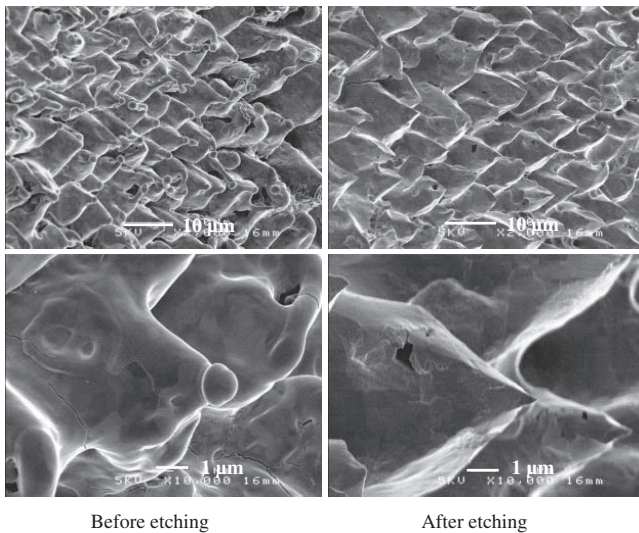


**Figure 13.** High resolution of typical tungsten microcone in the conditions of Figure 12d [ $\text{H}_2\text{O}_2$  (31%) 2 ml +  $\text{H}_2\text{O}$  100 ml, 90 sec, 83–85 °C].

pressure in an inert gas atmosphere. As it was a very interesting phenomenon, the authors investigated the influence of the laser fluence, wavelength, polarization, surface crystal structure, etc., on the arrangement and spacing of the protuberances in order to clarify the formation mechanism.

Figure 14a shows a SEM microphotograph of a laser-irradiated mark (wavelength; 1064 nm) on the orientation

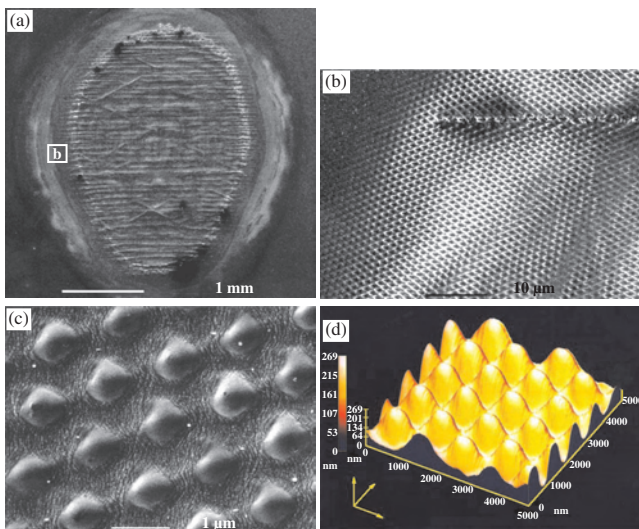


**Figure 14.** (a) SEM microphotograph of a tungsten surface irradiated by the Nd:YAG laser. We can observe many cracks on the laser-irradiated mark due to the effect of crystal orientation on the tungsten surface. (b) SEM microphotograph around the laser-irradiated mark on the tungsten surface, irradiated at an angle of incidence  $\theta = 4^\circ$  with the  $p$ -polarized beam. A coherent array of ultrafine particles was observed around the laser-irradiated mark. (c) The highly magnified SEM microphotograph of the ultrafine particles arranged like a hexagonal system with about a  $1.3 \mu\text{m}$  array spacing. (d) AFM trace of the ultrafine particles arranged like a hexagonal system with about a  $1.3 \mu\text{m}$  array spacing, of which the hemisphere height was about 270 nm. Reprinted with permission from [73], Y. Kawakami et al., *Appl. Phys. A* 71, 453 (2000). © 2000, Springer-Verlag.

of the (110) surface of a single crystal tungsten with a laser fluence at  $19.6 \text{ J/cm}^2$ . Many cracks on the laser-irradiated mark were found. They might be created by thermal shock to the single-crystal tungsten. The laser-irradiation markings observed on the three types of single-crystal tungsten surfaces such as (100), (110), and (111) were square, rectangular, and triangular, respectively [72]. These phenomena were related to the cleavage plane of tungsten. That is, when the tungsten surfaces were irradiated, the cleavage fracture occurred with preference to the crystal direction having a weak binding energy. Figure 14b shows a SEM microphotograph around the laser-irradiated mark on the tungsten surface. The rapid resolidification of a highly melted layer of tungsten was observed. Figure 14c and d shows a highly magnified SEM microphotograph and Figure 14b shows the AFM trace. The authors could observe a coherent array of protuberances of about 750 nm with the spacing at  $1.3 \mu\text{m}$  around the laser-irradiated mark. The spacings of 1.0 or  $1.1 \mu\text{m}$  were calculated from Eq. (1). The spacing values from the SEM observations were different from the calculated one. In the case of the  $17.4 \text{ J/cm}^2$  fluence, the spacing of the coherent array was also different from the calculated spacing [71]. Therefore, the surface patterns depended on the laser fluence rather than the wavelength and the angle of incidence. For another region in the same sample, it was observed that the array was like a two-dimensional cubic system based on the AFM trace of Figure 15. The array spacing was also about  $1 \mu\text{m}$ . Two types of arrays, namely, a cubic system and a hexagonal one, were finally confirmed. In the case of the angle of incidence of  $\theta = 4^\circ$  with an  $s$ -polarized beam, nearly the same results were obtained [71, 72]. This was also confirmed for the other orientations of the single-crystal surface. The array was not observed on the polycrystalline tungsten surface [73].

Figure 16a and b shows a SEM microphotograph in/around a laser-irradiated mark (wavelength; 532 nm) on the (100) surface of the single-crystal tungsten with a laser fluence of  $5.2 \text{ J/cm}^2$ . Column structures are observed in the laser-irradiated mark. This formation mechanism was explained in Section 3 of this chapter. The lower fluence might be compensated by a decrease in the reflection coefficient at 532 nm. The protuberances of about 150 nm (radius of curvature: 70–80 nm) were coherently arranged with a spacing at 640 nm. However, the array could not be observed

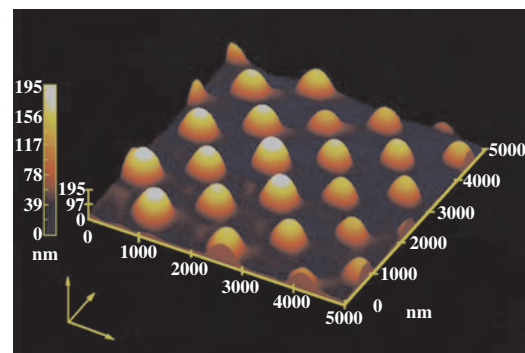


**Figure 15.** AFM trace of the ultrafine particles arranged like a cubic system. Reprinted with permission from [71], Y. Kawakami et al., *Appl. Phys. Lett.* 74, 3954 (1999). © 1999, American Institute of Physics.

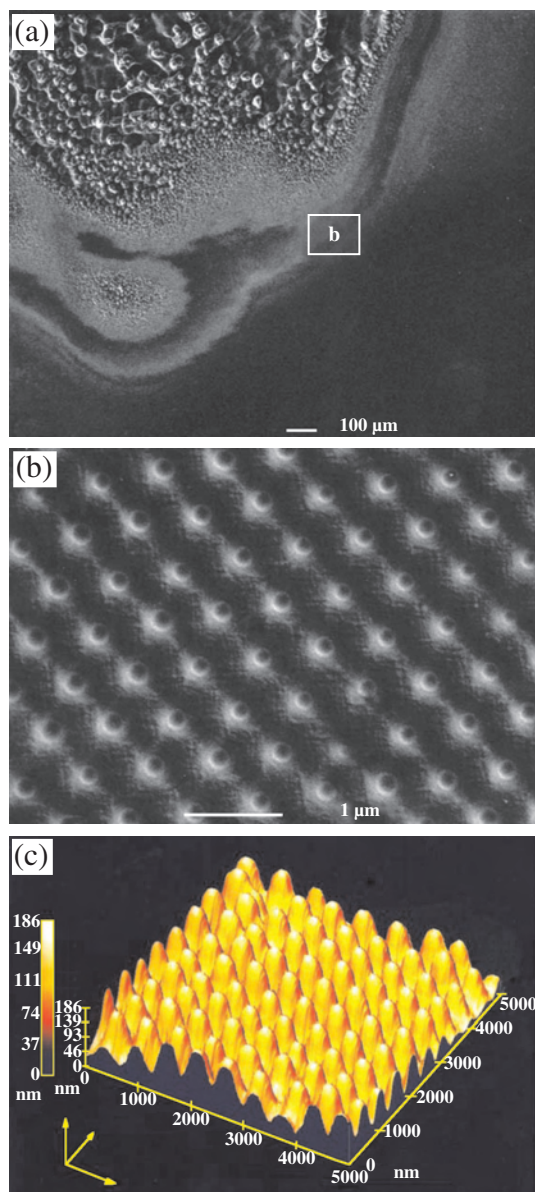


**Figure 16.** (a) SEM microphotograph of a tungsten surface irradiated by the Nd:YAG laser irradiated at an angle of incidence  $\theta = 4^\circ$  with the *p*-polarized beam. We can observe many columns on the laser-irradiated mark due to a temperature high enough to induce melting and solidification by rapid quenching on the tungsten surface. (b) The highly magnified SEM microphotograph of the ultrafine particles arranged like a hexagonal system with about a 640 nm array spacing. (c) AFM trace of the ultrafine particles arranged like a hexagonal system with about a 640 nm array spacing, of which the hemisphere height was about 180 nm. Reprinted with permission from [73], Y. Kawakami et al., *Appl. Phys. A* 71, 453 (2000). © 2000, Springer-Verlag.

for the specimens with several tens of  $\text{J}/\text{cm}^2$  irradiation but many droplets were observed instead. For the higher laser fluence, many droplets were produced due to the increment of expansion on the inside of the tungsten. The spacing calculated from Eq. (1) was 490 or 570 nm. These values are very different from the ones observed by SEM. Figure 16c shows an AFM trace of the same area in Figure 16b. The hundreds of nm-sized protuberances were arranged like a

two-dimensional hexagonal system. Their hemisphere height was about 180 nm.

In order to investigate the influence of the laser fluence, three fluences of 2.6, 5.2, and  $10.5 \text{ J}/\text{cm}^2$  were tuned. The array structures of the protuberances at 2.6 and  $5.2 \text{ J}/\text{cm}^2$  are clearly observed. The protuberances of about 380–500 nm are coherently arranged with a spacing at 595 nm ( $2.6 \text{ J}/\text{cm}^2$ ) and 683 nm ( $5.2 \text{ J}/\text{cm}^2$ ). For the higher laser fluence of  $10.5 \text{ J}/\text{cm}^2$ , the arrays could not be found but many droplets and peeling of the surface layer induced by thermal expansion of the tungsten were observed. The spacing calculated from Eq. (1) was 453 or 644 nm. These values were very different from the ones obtained from the experimental results. For the  $17.4 \text{ J}/\text{cm}^2$  laser fluence at 1064 nm and  $5.2 \text{ J}/\text{cm}^2$  laser fluence at 532 nm, the spacing of the coherent array was also different from the calculated spacing [73]. That is, the surface patterns depended on the laser fluence rather than the wavelength of the laser.

Judging from a cross-sectional transmission electron microscope image of the protuberances, the protuberances composing the coherent array seemed to grow from the matrix surface as if they rose continuously from the base material. No grain boundary between the protuberances and the matrix surface was detected. From this experimental result, it was concluded that the formation of protuberances depended on the kind of crystal growth and that the controlling factors for the formation were the laser fluence, the crystal surface structure preferential growth direction of the crystal, cooling rate and its direction, etc. Anyway, the recrystallization of the slightly melted tungsten on the top surface induced by the repeated laser irradiation should play a vital role in the formation of the array.

In order to more fully understand this phenomenon, more studies should be necessary. The rapid solidification process of the molten tungsten induced by the laser beam should be examined more carefully especially about the rapid solidification rate, heat flow on the specimen, surface temperature, etc. The fluence also seems to be a very important factor for inducing the coherent array, since the spacing of the array was changed by the intensity of the laser fluence. The effect of the surface structure, crystal growth (dendrite), surface tension (surface energy), thermal effect, and standing wave should be carefully considered. The formation mechanism of a Coulomb crystal [75–77] formed from the Coulomb potential energy due to the charge between the protuberances might also be considered.

In summary, the authors formed different spacing coherent arrays with 150–700 nm-sized protuberances using the short-pulse Nd:YAG laser irradiation technique. The cause of the formation of the two-dimensional coherent arrays could not be explained by only the laser's characteristics such as the wavelength, incident angle, and polarization of the cones as previously mentioned. The interesting points of the coherent arrays are as follows: (1) the ultrafine tungsten protuberances of 150 nm were coherently arranged in several lattice directions, (2) two types of arrays, namely, a cubic system and a hexagonal one, were confirmed, (3) the formation of coherent patterns will not be affected by the wavelength of the laser, (4) the spacing of arrays depends on the intensity of the laser fluence, (5) coherent arrays could be observed only on the surface of single-crystal tungsten,

and (6) the recrystallized texture on the surface was confirmed for the protuberances. A much more detailed discussion should be necessary to understand this phenomenon. It is a very interesting topic for science such that a more detailed examination is expected.

## 5. RECENT TOPICS

Morphological changes during dehydration of single crystals containing lattice  $\text{H}_2\text{O}$  (hydrates) were dramatic. Surfaces became rough, polycrystalline, and laden with defects. Ionic crystal surfaces containing point defects readily desorbed energetic positive ions under UV excimer laser irradiation. Kawaguchi et al. examined the consequences of thermally pretreated single crystal brushite ( $\text{CaHPO}_4 \cdot 2\text{H}_2\text{O}$ ) exposed to 30 ns pulses of 248 nm laser irradiation and showed that the surface modifications strongly enhanced the emission of  $\text{Ca}^+$  and other positive ions [80]. When they were gently irradiated on the untreated brushite surface in a vacuum with 248 nm laser irradiation only, they produced "microflowers," where laser-induced heating alone activated efflorescence.

Nonerasable micrograting structures were successfully encoded in amorphous  $\text{SiO}_2$  thin film on silicon wafers by colliding a pair of focused pulses split from a single femtosecond pulse from a 10 Hz mode-locked Ti:sapphire laser with a regenerative amplifier (wavelength:  $\lambda = 800$  nm, pulse duration: 100 fs, pulse energy:  $\sim 3$  mJ/pulse). The encoded periodic spacing varied with the angle,  $\theta$ , between the two crossed pulses according to  $d = \lambda / (2 \sin(\theta/2))$ . A minimum periodic spacing of  $\sim 430$  nm was achieved for a laser wavelength of 800 nm. Volume compaction resulting from structural alterations of the silica network in amorphous  $\text{SiO}_2$  induced by intense femtosecond laser irradiation was responsible for the formation of these grating structures. Further, an array of dot structures was fabricated in amorphous  $\text{SiO}_2$  thin films by encoding two perpendicular gratings [81].

Li et al. investigated a periodic microstructure induced by a 355 nm ultraviolet polarized laser on a polyimide surface and the dependence of the structures on laser parameters. Laser-induced periodic surface structures of submicrometer size were generated on three kinds of polyimide films by a polarized Nd:YAG laser of 355 nm within a wide range of laser fluence. The formation of LIPSS was greatly influenced by the chemical structure of the polyimide, the film-making process, the number of laser pulses, and the laser fluence. The periodicity of LIPSS was decided by the wavelength, the incidence angle of the laser beam, and the apparent refractive index of the material [82].

Ripple structures by KrF excimer laser irradiation were observed on a silicon surface capped with a thin layer of patterned silicon oxide. The ripples were highly dependent on the patterns of the silicon oxide. They were centered and enhanced at the boundaries of the opened windows, forming a radial wavelike structure. The formation of the ripples was attributed to the combined effect of surface stress, surface scattered wave, and boundary effects [83].

Relatively low-energy laser illumination, specifically the second harmonic ( $\lambda = 532$  nm) of a Nd:YAG laser, was used to prepare laser-induced periodic surface structures on surfaces of polymers doped and grafted with Dispersed Red 19.

This dye strongly absorbed the laser light, and the use of 532 nm wavelength irradiation avoided the photolysis reactions on polymers that often accompanied the use of UV lasers. Li et al. found that LIPSS could be obtained on grafted polyurethane-imide film. Effects of scanning speed, laser fluence, and the angle of incidence on formation of LIPSS were examined. Nonpolarized and polarized transmission Fourier transform infrared spectroscopy was applied to characterize the orientation of azobenzene side groups, which were found to tend to align in the plane perpendicular to the direction of LIPSS [84].

Crater morphology was investigated after femtosecond laser ablation of wide bandgap insulators ( $\text{BaF}_2$  and  $\text{CaF}_2$ ) [85]. Experiments performed at a weak laser ablation rate showed a particular elastic, sound-wave-like structure, frozen on the surface, with a periodicity on the order of some micrometer and a modulation depth up to 500 nm. A superimposed and periodic fine structure (ripples) was generated, the origin of which could not be explained by the classical ripple model. Costache et al. [85] observed a periodicity ranging from 100 to 500 nm, dependent on the laser intensity rather than on the laser wavelength. Based on their recent results, demonstrating an explosive surface decomposition, they assumed self-organizing relaxation of a nonequilibrium surface to be responsible for the structures.

Pedraza and et al. reported on an interesting topic, the formation of linear arrays of nanoparticles by pulsed-laser irradiation [86, 87]. Periodic undulations,  $\sim 10$  nm high, were formed when flat Si substrates were irradiated with polarized laser light. These periodic structures had a wavelength that was a function of the light wavelength and the angle of incidence of the laser beam. At a slightly higher laser fluence,  $\sim 40$ -nm-diameter nanoparticles were formed on the surface of laser irradiated flat Si specimens. Linear arrays of Si nanoparticles with fairly uniform size were observed in a microstructured region. These nanostructures were explained within the framework of the LIPSS theory.

Laser-induced surface structuring of Si was studied using fluences close to the melting threshold and in a He gas background atmosphere. The effects of an initial surface microstructured region and of light polarization on the evolution of the surface topography were investigated. The microstructured surface topography consisted of an array of microholes surrounded by microcones of 2–3  $\mu\text{m}$  tip diameter and over 20  $\mu\text{m}$  high. Pulsed laser irradiation of laser-microstructured Si induced nanostructures. Nanocolumns having a diameter of 100 to 200 nm and a height of up to 3  $\mu\text{m}$  upon cumulative laser pulses grew on top of every microcone. The mechanisms of nanocolumn origin and growth were analyzed [86].

Sequential pulsed-laser irradiation of silicon in a  $\text{SF}_6$  atmosphere induced the formation of an ensemble of microholes and microcones. Profilometry measurements and direct imaging with an intensifying charge-coupled device camera were used to study the evolution of this microstructure and the laser-generated plume. Both the partial pressure of  $\text{SF}_6$  and the total pressure of an  $\text{SF}_6$ -inert gas mixture strongly influenced the maximum height. The height of microcones was attained over the initial surface. The cones first grew continuously with the number of pulses, reached a maximum, and then began to recede as the number of



laser pulses increased further. The growth of the cones was closely connected with the evolution of the laser-generated plume [88].

For the application of field electron emission (FEE), Karabutov et al. reported low-threshold FEE for periodic arrays of microtips produced by laser ablation of Si wafers [89]. The best samples had threshold fields as low as 4–5 V/ $\mu\text{m}$  for *n*-type Si substrates and 1–2 V/ $\mu\text{m}$  for *p*-type Si substrates, as measured with a flat-screen technique.

György et al. reported micrometer-sized crownlike structure growth on a Ti surface by multipulse Nd:YAG ( $\lambda = 1.064 \mu\text{m}$ ,  $\tau = 170 \text{ ns}$ ) laser irradiation in air at atmospheric pressure [90]. The irradiation was performed at  $8 \times 10^7 \text{ W/cm}^2$  laser-pulse intensity, below the ablation threshold. A ring-shape structure was created in the center of the irradiation spot after the action of five laser pulses. The further increase of the laser-pulse number led gradually to a crownlike structure, which had a height of 120–140  $\mu\text{m}$  for 150 pulses higher than the nonirradiated Ti surface. The forming crater's depth did not exceed the height of the grown structure. In the neighboring zone, after the action of 25 laser pulses, microcracks of the oxide surface layer developed. With the next pulses this led to the formation of a surface microrelief. Molten material movement attributed to the laser-induced plasma-recoil pressure might lead to the crownlike structure.

Polyimides were known to exhibit large ablation rates with excimer laser because of their high absorbance in the UV and low fluorescence yield [91]. Metayer et al. studied different regimes of laser ablation according to the fluence and the structures resulting from carbon product deposition. For fluences larger than the polyimide ablation threshold, but lower than the carbon one, the development of one structure was the dominant process, whereas large ablation rates led to polyimide etching above the carbon ablation threshold. The deposition of a carbon layer on the walls of ablated slits was in particular investigated using an original experimental technique. Optical microscopy and MEB showed that this carbon layer covered the main height of the ablated holes whereas a threshold (bare polyimide) for carbon condensation was evidenced at the bottom of the ablated hole. Raman spectroscopy and conductivity measurements revealed that the carbon phase was mainly graphitic. Dependence of the carbon condensation threshold on the slit width was made clear and discussed in relation to the angle of ejection of ablation debris. A procedure was developed to render the bare polyimide of the threshold region conductive. Lastly, the conductive properties of the walls of the ablated holes were exploited to perform an electrolytic metallization. Implications for the production of interconnection vertical interconnections in high density printed circuits were addressed.

This research field will evolve and generate many reports.

## GLOSSARY

**Ablation threshold** The laser fluence  $E_{th}$  [ $\text{J/cm}^2$ ] of threshold while the surface is ablated.

**Capillary wave** The wave which occurs on the liquid surface by surface tension.

**Coulomb crystal** When a coulomb interaction occurs between the charged particles and the interaction energy significantly exceeding the thermal kinetic energy of a particle, the “Coulomb crystal” is denoted by the regular arrangement between the charged particles such as the atomic arrangement in a solid crystal.

**Debris particles** Large-sized particles of hundreds of nm to several micrometers, which are contained in the laser-induced plasma plume formed by a large quantity of particles emitted from a solid by laser ablation.

**Dendrite** Many crystals, which have the shape of a branch due to the solidification texture of the melted metal.

**Field emission display (FED)** One of the various types of flat-panel displays. A field emission display has the advantages of both the CRT and liquid-crystal displays, having a high display quality while being thin and lightweight with a low power consumption.

**Laser** Light amplification by stimulated emission of radiation.

**Laser ablation** A sputtering process in which the material removal rates typically exceed one-tenth a monolayer per pulse; the surface is structurally or compositionally modified at mesoscopic length scales; and particle yields are superlinear functions of the density of excitation.

**Laser fluence** The energy density,  $E$  [ $\text{J/cm}^2$ ], of the product between the power density and pulse width of a laser.

**Laser induced periodic surface structures (LIPSS)** A very general phenomenon. It occurs from the interference of scattered light from a rough surface with the incident laser beam.

**Vapor-liquid-solid (VLS) method** The growth mechanism in which the three phases of vapor, liquid, and solid are simultaneously involved. It is used especially for the growth of a whisker.

## ACKNOWLEDGMENTS

The authors gratefully thank Dr. Shinya Sasaki of the National Institute of Advanced Industrial Science and Technology (AIST) for valuable discussions, Dr. Tomokazu Sano, Hirokazu Yamada, and Makoto Murai of Osaka University for the laser-induced tungsten microcone experiments, Dr. Yasuhisa Ando of AIST for the AFM study, and Masaru Iwashina of Vacuum Metallurgical Co., Ltd., for the chemical etching tests.

This author's work was supported by the R&D Institute for Photonics Engineering entrusted from the Advanced Photon Processing and Measurement Technologies Program of the New Energy and Industrial Technology Development Organization of Japan.

## REFERENCES

1. M. Birnbaum, *J. Appl. Phys.* 36, 3688 (1965).
2. D. C. Emmony, R. P. Howson, and L. J. Willis, *Appl. Phys. Lett.* 23, 598 (1973).
3. A. K. Jain, V. N. Kulkarni, D. K. Sood, and J. S. Uppal, *J. Appl. Phys.* 52, 4882 (1981).
4. H. M. van Driel, J. E. Sipe, and J. F. Young, *Phys. Rev. Lett.* 49, 1955 (1982).

5. N. R. Isenor, *Appl. Phys. Lett.* 31, 148 (1977).
6. A. Y. G. Fuh, *Appl. Phys. A* 54, 176 (1992).
7. A. Dauscher, V. Feregotto, P. Cordier, and A. Thomy, *Appl. Surf. Sci.* 96–98, 410 (1996).
8. J. J. Yu and Y. F. Lu, *Appl. Surf. Sci.* 148, 248 (1999).
9. J. F. Young, J. E. Sipe, J. S. Preston, and H. M. van Driel, *Appl. Phys. Lett.* 41, 261 (1982).
10. M. Oron and G. Sørensen, *Appl. Phys. Lett.* 35, 782 (1979).
11. P. M. Fauchet and A. E. Siegman, *Appl. Phys. Lett.* 40, 824 (1982).
12. P. M. Fauchet and A. E. Siegman, *Appl. Phys. A* 32, 135 (1983).
13. N. Tsukada, S. Sugata, and Y. Mita, *Appl. Phys. A* 42, 424 (1983).
14. K. Tonyali, L. C. Jensen, and J. T. Dickinson, *J. Vac. Sci. Technol. A* 6, 941 (1988).
15. H. Niino, M. Shimoyama, and A. Yabe, *Appl. Phys. Lett.* 57, 2368 (1990).
16. H. Niino and A. Yabe, *J. Photochem. Photobiol. A: Chem.* 65, 303 (1992).
17. P. E. Dyer and R. J. Farley, *Appl. Phys. Lett.* 57, 765 (1990).
18. H. M. Phillips, D. L. Callahan, R. Sauerbrey, G. S. Zabo, and Z. Bor, *Appl. Phys. Lett.* 58, 2761 (1991).
19. M. Bolle, S. Lazare, M. L. Blanc, and A. Wilmes, *Appl. Phys. Lett.* 60, 674 (1992).
20. M. Bolle and S. Lazare, *Appl. Surf. Sci.* 65–66, 349 (1993).
21. M. Bolle and S. Lazare, *J. Appl. Phys.* 73, 3516 (1993).
22. H. Hiraoka and M. Sendova, *Appl. Phys. Lett.* 64, 563 (1994).
23. J. Heitz, E. Arenholz, D. Bäuerle, H. Hibst, A. Hagemeyer, and G. Cox, *Appl. Phys. A* 56, 329 (1993).
24. J. Heitz, E. Arenholz, D. Bäuerle, and K. Schilcher, *Appl. Surf. Sci.* 81, 103 (1994).
25. M. Csete and Z. Bor, *Appl. Surf. Sci.* 133, 5 (1998).
26. S. Baudach, J. Bonse, and W. Kautek, *Appl. Phys. A* 69, S395 (1999).
27. S. Baudach, J. Krüger, and W. Kautek, *Rev. Laser Eng.* 29, 705 (2001).
28. Q. H. Lu, Z. G. Wang, J. Yin, Z. K. Zhu, and H. Hiraoka, *Appl. Phys. Lett.* 76, 1237 (2000).
29. Q. H. Lu, M. Li, J. Yin, Z. K. Zhu, and Z. G. Wang, *J. Appl. Polym. Sci.* 82, 2739 (2001).
30. Y. F. Lu, J. J. Yu, and W. K. Choi, *Appl. Phys. Lett.* 71, 3439 (1997).
31. Y. F. Lu, J. J. Yu, and W. K. Choi, *Jpn. J. Appl. Phys.* 37, 3471 (1998).
32. J. J. Yu and Y. F. Lu, *Appl. Surf. Sci.* 154–155, 670 (2000).
33. G. K. Giust and T. W. Sigmon, *Appl. Phys. Lett.* 70, 3552 (1997).
34. J. Ihlemann, B. Wolff, and P. Simon, *Appl. Phys. A* 54, 363 (1992).
35. K. Ohsawa and H. Tokura, *J. Jpn. Soc. Precision Eng.* 64, 121 (1998).
36. H. Tokura, *Jpn. Soc. Laser Technol.* 23, 45 (1998).
37. M. Henyk, N. Vogel, D. Wolfframm, A. Tempel, and J. Reif, *Appl. Phys. A* 69, S355 (1999).
38. D. Ashkenasi, A. Rosenfeld, H. Varel, M. Wahmer, and E. E. B. Campbell, *Appl. Surf. Sci.* 120, 65 (1997).
39. A. C. Tam, J. L. Brand, D. C. Cheng, and W. Zapka, *Appl. Phys. Lett.* 55, 2045 (1994).
40. I. Kawayama, J. J. Dubowski, H. Nishikawa, and T. Kawai, *Appl. Surf. Sci.* 143, 313 (1998).
41. P. Milani and M. Manfredini, *Appl. Phys. Lett.* 68, 1769 (1996).
42. A. M. Ozkan, A. P. Malshe, T. A. Railkar, W. D. Brown, M. D. Shirk, and P. A. Molian, *Appl. Phys. Lett.* 75, 3716 (1999).
43. F. Sánchez, J. L. Morenza, R. Aguiar, J. C. Delgado, and M. Varela, *Appl. Phys. Lett.* 69, 620 (1996).
44. F. Sánchez, J. L. Morenza, R. Aguiar, J. C. Delgado, and M. Varela, *Appl. Phys. A* 66, 83 (1998).
45. F. Sánchez, J. L. Morenza, and V. Trtik, *Appl. Phys. Lett.* 75, 3303 (1999).
46. A. J. Pedraza, J. D. Fowlkes, and D. H. Lowndes, *Appl. Phys. Lett.* 74, 2322 (1999).
47. A. J. Pedraza, J. D. Fowlkes, and D. H. Lowndes, *Appl. Phys. A* 69, S731 (1999).
48. D. H. Lowndes, J. D. Fowlkes, and A. J. Pedraza, *Appl. Surf. Sci.* 154–155, 647 (2000).
49. J. D. Fowlkes, A. J. Pedraza, and D. H. Lowndes, *Appl. Phys. Lett.* 77, 1629 (2000).
50. A. J. Pedraza, J. D. Fowlkes, and D. H. Lowndes, *Appl. Phys. Lett.* 77, 3018 (2000).
51. T. H. Her, R. J. Finlay, C. Wu, S. Deliwala, and E. Mazur, *Appl. Phys. Lett.* 73, 1673 (1998).
52. J. E. Andrew, P. E. Dyer, D. Forester, and P. H. Key, *Appl. Phys. Lett.* 43, 717 (1983).
53. P. E. Dyer, S. D. Jenkins, and J. Sidhu, *Appl. Phys. Lett.* 49, 453 (1986).
54. P. E. Dyer, S. D. Jenkins, and J. Sidhu, *Appl. Phys. Lett.* 52, 1880 (1988).
55. S. Lazare and R. Srinivasan, *J. Phys. Chem.* 90, 2124 (1986).
56. Y. Novis, J. J. Pieaux, A. Brezini, E. Petit, R. Caudano, P. Lutgen, G. Feyder, and S. Lazare, *J. Appl. Phys.* 64, 365 (1988).
57. T. Bahners and E. Schollmeyer, *J. Appl. Phys.* 66, 1884 (1989).
58. H. Niino, J. Ihlemann, S. Ono, and A. Yabe, *Macromol. Symp.* 160, 159 (2000).
59. S. R. Foltyn, R. C. Dye, K. C. Ott, E. Peterson, K. M. Hubbard, W. Hutchinson, R. E. Muenchausen, R. C. Estler, and X. D. Wu, *Appl. Phys. Lett.* 59, 594 (1991).
60. S. R. Foltyn, in “Pulsed Laser Deposition of Thin Films” (D. B. Chrisey and G. K. Hubler, Eds.), Ch. 4, p. 89. Wiley, New York, 1994.
61. I. Miyamoto and H. Maruo, *Proc. SPIE* 1279, 66 (1990).
62. V. Oliveira and R. Vilar, *Proc. Laser Mater. Processing Conf. LIA* 92/93, 1852 (2001).
63. A. Usoskin, H. C. Freyhardt, and H. U. Krebs, *Appl. Phys. A* 69, S823 (1999).
64. S. I. Dolgaev, S. V. Lavrishev, A. A. Lyalin, A. V. Simakin, V. V. Voronov, and G. A. Shafeev, *Appl. Phys. A* 73, 177 (2001).
65. Y. Kawakami and E. Ozawa, *Appl. Phys. A* 74, 59 (2002).
66. Y. Kawakami and E. Ozawa, *Appl. Surf. Sci.* 218, 175 (2003).
67. Y. Kawakami and E. Ozawa, *Proc. SPIE* 4274, 323 (2001).
68. Y. Kawakami and E. Ozawa, *Proc. SPIE* 4426, 158 (2002).
69. Z. Ball and R. Sauerbrey, in “Laser Ablation and Desorption” (J. C. Miller and R. F. Haglund, Eds.), Vol. 30, p. 41. Academic Press, San Diego, 1998.
70. H. U. Krebs and O. Bremert, *Appl. Phys. Lett.* 62, 2341 (1993).
71. Y. Kawakami, E. Ozawa, and S. Sasaki, *Appl. Phys. Lett.* 74, 3954 (1999).
72. Y. Kawakami, S. Sasaki, and E. Ozawa, *Surf. Eng.* 16, 218 (2000).
73. Y. Kawakami and E. Ozawa, *Appl. Phys. A* 71, 453 (2000).
74. Y. Kawakami and E. Ozawa, *Proc. SPIE* 4088, 228 (2000).
75. Y. Hayashi and K. Tachibana, *Jpn. J. Appl. Phys.* 33, L804 (1994).
76. J. H. Chu and I. Lin, *Phys. Rev. Lett.* 72, 4009 (1994).
77. H. Thomas, G. E. Morfill, V. Demmel, J. Goree, B. Feuerbacher, and D. Möhlmann, *Phys. Rev. Lett.* 73, 652 (1994).
78. M. L. Dowes, J. T. Dickinson, L. C. Jensen, and S. C. Langford, *Nanotechnology* 5, 101 (1994).
79. R. Kelly and A. Miotello, in “Pulsed Laser Deposition of Thin Films” (D. B. Chrisey and G. K. Hubler, Eds.), Ch. 3, p. 55. Wiley, New York, 1994.
80. Y. Kawaguchi, M. L. Dawes, S. C. Langford, and J. T. Dickinson, *J. Appl. Phys.* 88, 647 (2000).
81. K. Kawamura, E. Motomitsu, M. Hirano, and H. Hosono, *Jpn. J. Appl. Phys.* 41, 4400 (2002).
82. M. Li, Q. H. Lu, J. Yin, S. Y. Luo, and Z. G. Wang, *Chin. Phys. Lett.* 19, 255 (2002).
83. X. Y. Chen, Y. F. Lu, B. J. Cho, Y. P. Zeng, J. N. Zeng, and Y. H. Wu, *Appl. Phys. Lett.* 81, 1344 (2002).

84. M. Li, Q. H. Lu, J. Yin, Y. Sui, G. Li, Y. Qian, and Z. G. Wang, *Appl. Surf. Sci.* 193, 46 (2002).
85. F. Costache, M. Henyk, and J. Reif, *Appl. Surf. Sci.* 186, 352 (2002).
86. A. J. Pedraza, J. D. Fowlkes, and Y. Guan, *SPIE Proc.* 4760, 164 (2002).
87. J. D. Fowlkes, A. J. Pedraza, D. A. Blom, and H. M. Meyer III, *Appl. Phys. Lett.* 80, 3799 (2002).
88. S. Jesse, A. J. Pedraza, J. D. Fowlkes, and J. D. Budai, *J. Mater. Res.* 17, 1002 (2002).
89. A. V. Karabutov, V. D. Frolov, E. N. Loubnin, A. V. Simakin, and G. A. Shafeev, *Appl. Phys. A* 76, 412 (2003).
90. E. György, I. N. Mihailescu, P. Serra, A. P. D. Pino, and J. L. Morenza, *Appl. Phys. A* 74, 755 (2002).
91. P. Metayer, J. Davenas, and J. M. Bureau, *Nucl. Instrum. Methods B* 185, 156 (2001).



# Layer-by-Layer and Langmuir–Blodgett Films from Nanoparticles and Complexes

Marysilvia Ferreira

*Universidade Federal do Rio de Janeiro, Rio de Janeiro, RJ, Brazil*

Valtencir Zucolotto, Marystela Ferreira, Osvaldo N. Oliveira, Jr.

*Universidade de São Paulo, São Carlos, SP, Brazil*

Karen Wohnrath

*Universidade Estadual de Ponta Grossa, Campus de Uvaranas, Ponta Grossa, PR, Brazil*

## CONTENTS

1. Introduction
  2. The Langmuir–Blodgett (LB) Method
  3. The Layer-by-Layer (LBL) Method
  4. Nanoparticles in LBL Films
  5. LBL Films from Aluminosilicates
  6. LBL Films from Macrocyclic Systems
  7. Dendrimers in LBL Films
  8. LB Films from Metallic Complexes
- Glossary  
References

## 1. INTRODUCTION

Recent developments in nanoscience and nanotechnology have provided fresh motivation for the search of innovative nanostructured materials. As far as organic materials are concerned, two main techniques have been used to fabricate ultra-thin, nanostructured films, namely, the Langmuir–Blodgett (LB) and the layer-by-layer (LBL) techniques. The LB method was conceived several decades ago [1], following developments in surface chemistry dating from the early 20th century [2]. It was originally proposed for deposition of multilayers of amphiphilic organic compounds, but has been extended considerably to a variety of substances, including polymers [3] and other macromolecules [4]. The LBL technique is much more recent; its first form employed chemical adsorption of suitably derivatized molecules [5]. A more versatile method was proposed by Decher et al. [6], in which

physical adsorption is driven by ionic attraction. A number of review articles and book chapters have been produced recently on LB and LBL methods [7–9]. In addition to emphasizing the wide variety of materials that can be employed with these techniques, in some cases the reviews address specific issues such as the characterization techniques [7], the films formed from conducting polymers [8], the applications in opto-electronics and photonics [9], or the physical principles involved in film assembling [9]. In this article, we shall focus on the use of LBL and LB techniques for producing supramolecular structures involving inorganic compounds combined with organic materials. Particular emphasis will be placed on the special characteristics due to the nanostructured nature of the films, in comparison to the corresponding bulk or thicker film properties.

The main aim in producing hybrid inorganic/organic supramolecular structures lies in the possibility of obtaining new physical, chemical, electronic, and optical properties due to specific interactions at the molecular level and/or quantum confinement. Polymeric thin films can be used, for instance, as a matrix for inorganic particle growth in a strategy for controlling size, shape, and spatial distribution. Additionally, the build-up of structures comprising organic/inorganic layers of appropriate molecules is a well-known strategy to improve properties such as photoluminescence, catalysis, and photochromism. In electrochemical and sensing applications, in particular, nanostructured films formed from spherical particles like dendrimers or polyoxometalates were found to provide a porous architecture where specific ions can easily diffuse through. Therefore, the development of composites that can be manipulated at the supramolecular level has potential application within opto-electronic and biotechnology industries.

Before describing in detail the latest findings in LBL and LB films from inorganic/organic structures, we shall present in Sections 2 and 3 a brief description of the techniques where the focus will be in the issues directly associated with the manipulation of macromolecules and nanoparticles. Section 4 covers the extensive works carried out in the fabrication of LBL films with nanoparticles, while Section 5 is dedicated to LBL films from aluminosilicates. The use of macrocyclic compounds and dendrimers in LBL films is described in Sections 6 and 7, respectively. Because extensive literature already exists in LB films from metallic complexes, we focused on recent developments of our group exploiting ruthenium complexes. This is aimed at providing a sample of the possibilities to combine organic and inorganic compounds, particularly in the case of mixtures of ruthenium compounds with conducting polymers.

## 2. THE LANGMUIR-BLODGETT (LB) METHOD

The LB method is named after two eminent scientists that worked at General Electric (USA) in the early 20th century. Irving Langmuir was responsible for putting on a solid scientific basis the field of monolayers from amphiphilic materials spread onto aqueous subphases. Following previous work by Pockels [10] and Lord Kelvin [11], Langmuir introduced experimental, as well as theoretical procedures, to manipulate and interpret the thermodynamic properties of such monolayers, now referred to as Langmuir films or Langmuir monolayers. One such monolayer is spread from a volatile, organic solvent solution containing a small aliquot of the amphiphile onto the aqueous subphase. By employing movable barriers, the monolayer may be compressed until forming a condensed film that may be highly organized. The presence of this film is sensed by the decrease in surface tension of the subphase, which has been traditionally referred to as surface pressure. With pressure area per molecule isotherms, one can investigate the various phases formed during compression. Figure 1 shows a typical pressure-area isotherm for stearic acid, one of the most investigated amphiphiles. At large areas per molecule, the interaction between molecules is negligible and the surface pressure

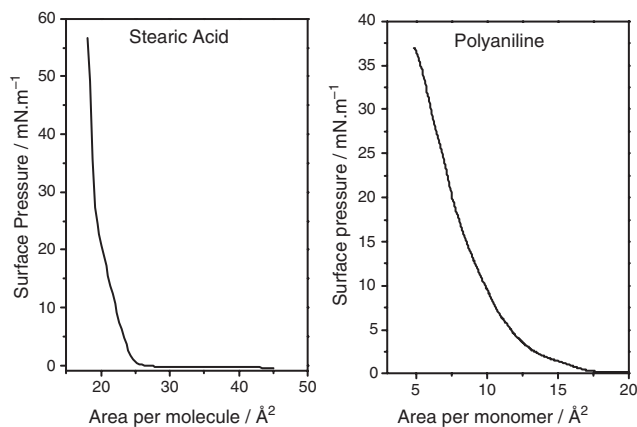


**Figure 1.** Pressure-area isotherms for an Stearic acid (SA) and polyaniline monolayers.

is null. Upon compression, the monolayer suffers a phase transition to a liquid-condensed phase, denoted by an almost linear increase in pressure with the change in area. Also shown in the figure is an isotherm from a polymer film. The latter is usually nonmonomolecular in nature due to the aggregation of material at the air/water interface. Several strategies must be sought to obtain stable polymer films and therefore research into Langmuir films is a prerequisite for any further application. A review on the strategies to overcome the difficulties in processing polymers for Langmuir monolayers is given in [12].

The film in the liquid-condensed or condensed phase can be transferred onto a solid substrate by immersing and withdrawing the substrate vertically across the film. If several immersions and withdrawals are made, a multilayer film is formed. The deposited film is referred to as an LB film, even when only one layer is deposited. While transfer of stable Langmuir monolayers from amphiphilic materials is relatively straightforward, the same does not apply when more complex molecules are to be deposited. For example, polymer films at the air/water interface may be too rigid for deposition. Furthermore, films from nonamphiphilic materials such as ruthenium complexes [13] and lignins [14] tend to contain aggregates and the deposition of good-quality LB films requires optimization of experimental conditions such as the speed of immersion and withdrawal of the substrate, the surface pressure to be kept fixed during transfer, the subphase, and even the speed of compression of the Langmuir film.

## 3. THE LAYER-BY-LAYER (LBL) METHOD

Spontaneous adsorption of several monolayers onto a single substrate may be achieved by covalent bonding of derivatized groups of the monolayers with the substrate for the first layer and with the molecules of the adjacent layer for the following layers. This process leads to chemically adsorbed multilayers, also referred to as self-assembly [5] for the obvious reason that monolayers spontaneously self-assemble on each other. There are many advantages in using this strategy to build a multilayer, the main one perhaps being the high stability of the films. However, chemical adsorption requires highly specific groups to establish the covalent bonds, and this restricts the type of material that can be employed. Moreover, adsorption is easily precluded by defects on the top layer. In the more versatile version proposed by Decher et al. [6, 15], multilayer adsorption is driven by ionic attraction. Originally applied to polyelectrolytes, the method was extended to conjugated polymers [16–19] and then to a variety of materials with adsorption being driven not only by ionic interactions but also by secondary interactions such as H-bonding [20].

Because a multitude of materials are now employed, the characteristics of LBL films may vary enormously. A convenient way of classifying LBL films is based on identifying the mechanism responsible for adsorption. Oliveira et al. [9] have suggested that four main types of film may be produced.

1. Highly charged polyelectrolytes lead to molecularly thin films as originally proposed by Decher et al.



[6, 15], with adsorption via ionic attraction. This is by far the most common class of LBL films.

2. When partially charged, weak polyelectrolytes are used, much thicker layers may be obtained. Ionic attraction is still the main driving force in the process though the amount of adsorbed material may vary by one order of magnitude due to the so-called anomalous adsorption [21].
3. Secondary interactions such as H-bonding [20] can also be responsible for adsorption, either in conjunction with ionic interactions or on their own. The amount of material adsorbed depends on an even larger number of parameters, and nonself-limiting adsorption may occur [22].
4. Finally, LBL films produced with very specific interactions are also reported in the literature. In this case, multilayers may be formed with polyelectrolytes of the same charge [23].

#### 4. NANOPARTICLES IN LBL FILMS

Inorganic particles with nanometer dimensions form a new class of materials with size-dependent properties, which are unique due to the large surface area compared to their volume. These materials are relevant to diverse fields, ranging from opto-electronics which rely on quantum confinement effects in semiconductors, to magnetism, catalysis, and biotechnology. They have been studied in the form of micelles, vesicles, sol-gel glasses, zeolites, LB films, and polymers [24–29]. The immobilization of nanoparticles in supramolecular structures is an endeavor, where the main aim is to achieve confined structures that may possess properties that differ considerably from those of the same materials in other forms. Clear examples of applications of nanoparticles are the use of  $\text{Fe}_3\text{O}_4$  nanoparticles for exploiting magnetic-related phenomena, and of  $\text{TiO}_2$  and  $\text{MnO}_2$  for their catalytic and photovoltaic activity, in addition to the use in the paint, paper, and food industries as pigments, fillers, and whiteners. One of the difficulties in obtaining nanoparticles in solid films is to preserve their nanosized nature by avoiding aggregation and to achieve organization of the particles in order to maximize the potential application. This may be circumvented if the LBL technique is employed. In this context, use is made of the various extensions of the LBL technique proposed in recent years, which have extended the original paradigm of adsorption of alternated, oppositely charged polymer layers. For gold particles, for example, aggregation is avoided if the Au particles are assembled with a generation 5 dendrimer [30]. In this approach, a few atoms of Au can be located in the hollow structure of the dendrimers, avoiding aggregation. Many reports have demonstrated the use of weak and strong polyelectrolytes to prepare multilayers combining various materials including conjugated polymers, dyes, proteins, etc.

The formation of organic/inorganic nanocomposites is achieved by incorporation of nanoparticles in LBL structures, either by selective growth inside a previously built LBL organic structure which operates as a matrix for controlling particle structure, size, and distribution, or by assembling inorganic particles to replace one of the polymeric components during the film build-up process, resulting in a

layered organic/inorganic film. Since surface charge is the main requirement for film growth, in order to have an effective increase in film thickness, the inorganic spherical particles that have been used were, in most cases, modified by incorporation of a charged capping layer.

The choice of the substrates onto which nanoparticles will be assembled depends, in almost all the cases, on the application desired for the film as well as the techniques employed in film characterization. Reports have been made on the growth of LBL films onto hydrophilic, hydrophobic, or indium-tin-oxide (ITO)-coated glass, silicon wafers, polymeric-colloidal particles, etc. It should also be mentioned that identical particles may lead to films with different properties, since the polymeric counterpart in the incorporation process determines the particle distribution and interaction. Therefore, the polymer is crucial for the final film properties, which extends the capabilities of the LBL approach for nanocomposites.

In the following subsections we shall illustrate several successful attempts to obtain nanoparticles. For the sake of clarity, the description will be split into two topics: nanoparticles growing within LBL films, and layers of nanoparticles assembled in conjunction with charged species in the films.

##### 4.1. Nanoparticle Growth in a LBL Polymeric Matrix

Layer-by-layer polymer films have been employed as a matrix for growth of several crystals and nanoparticles. The strength of the polyelectrolytes is critical in determining the final characteristics of the particles and therefore their properties of interest. A matrix is comprised, for example, by poly(diallyldimethylammonium chloride) (PDDA) and sulfonated polystyrene (SPS) bilayers [31], where assembly of nickel and cobalt compounds, PbS, and manganese oxide has been obtained. The polymer base imparts the ability of sulfonate groups from SPS to act as strong binding sites for metal ions, which conversely are available for further chemical reactions. Hence, by appropriate chemistry, it is possible to convert the metallic ion into the desired oxide, hydroxide, or oxihydroxide compound. Additionally, the polymorphic crystal structure may be controlled. That is an important feature since for nickel and cobalt compounds, for instance, the less stable  $\alpha$  form presents better electrochemical properties due to larger d-space. Several reports are found in the literature employing such an approach. Fojas et al. [32] reported the nucleation of  $\text{Ni}(\text{OH})_2$  by cycling polymer-coated substrates in  $\text{Ni}^{2+}$  and NaOH solutions. Fourier transform infrared (FTIR) results indicated that the Ni particles grown are  $\alpha$ - $\text{Ni}(\text{OH})_2$ , which was corroborated by transmission electron microscopy (TEM) micrographs. Such crystals are reported in the literature [33, 34] as ribbon-like-shaped and fibrous, consistent with the microcrystals observed in [32].  $\beta$ - $\text{Ni}(\text{OH})_2$  crystals are reported [35] to be hexagonal platelet-like structures. X-ray diffraction (XRD) data showed that the d-spacing was consistent with a  $\beta$ - $\text{Ni}(\text{OH})_2$  form. The authors pointed out that  $\alpha$ - $\text{Ni}(\text{OH})_2$  may be converted to the  $\beta$ -form over time or by thermal treatment or exposure to alkali solutions.

Co and Fe compounds were studied by Stroeve et al. [31, 36, 37] for their catalytic, electric, and magnetic properties. Transition-metal layered structures can be used to enhance the electrochemical performance of nickel electrodes by modifying conductivity and chargeability. In [31], Co compounds were obtained inside a PDDA/SPS matrix previously deposited on quartz slides. UV-vis absorption data showed linear growth of the polymeric matrix as well as growth of the crystalline particles. Crystals were preferentially deposited inside the SPS layer and were not confined in a given SPS layer but rather grew within the whole film, since an increase in the number of SPS layers led to an increase in the number of crystals. Three types of crystalline structures ( $\alpha$ ,  $\beta$ , and an oxyhydroxy phase) were obtained depending on the number of cycles and environment ( $N_2$  or  $O_2$ ), again indicating that the polymorphic form can be chosen by controlling the environment and film fabrication parameters. Iron compounds were also built and the morphology and type of final crystal depended on the starting material. Lepidocrocite ( $\gamma$ -FeOOH), for example, is formed when ferric nitrate is employed and akaganéite ( $\beta$ -FeOOH) is obtained by using ferric chloride [36, 37]. The latter authors also found that the polymeric matrix restrains crystal growth in specific directions depending on the morphology of the free space (or cavities) formed by polymer chains.

Stroeve et al. nucleated PbS nanoparticles inside a LBL matrix [38]. They were particularly interested in controlling particle size and film structure, which is mandatory in exploiting quantum-confinement effects that determine size-dependent opto-electronic properties. The procedure was similar to that employed for Ni, Co, and Fe compounds: nucleation was achieved by absorption of  $Pb^{2+}$  into the polymer film followed by water rinsing and exposure to  $H_2S$  vapor. The UV-vis spectrum was redshifted and widened as the number of cycles increased, which was associated with the escalation of particle size. The crystals grow in a rhomboid form with a broad size distribution due to the constrained geometry of the void space. The XRD pattern was found to be consistent with PbS particles, and small amounts of  $PbSO_4$  impurities were possibly present.

A further step in controlling particle size and distribution into a polymeric LBL matrix was achieved by Joly et al. [39]. They observed that by using weak polyelectrolytes which allow chemistry afterwards, nanoparticles are grown selectively and controllably within specific regions of a multilayer polyelectrolyte thin film. The use of strong polyelectrolyte such as SPS tends to form layers in which all of the strong acidic anionic groups are compromised with the cationic groups of the previous layer, leaving few or no active sites available for subsequent chemistry. When weak polyacids are used, the change in pH allows control of the number of free acid groups in the final structure and the use of different bilayer combinations results in a multilayer heterostructure in which nanocluster growth is restricted to specific regions. The authors used a poly(acrylic acid) (PAA) and poly(allylamine hydrochloride) (PAH) matrix. Ag and PbS particles were obtained by immersion on a silver acetate solution or lead acetate using low salt concentrations to decrease precipitation. Oxidation was carried out in air for

silver and by exposure to  $H_2S$  for PbS. The selective deposition of the nanoparticles was confirmed by energy dispersive X-ray spectroscopy (EDXS) profiles in TEM micrographs.

## 4.2. Nanoparticles Assembled in Conjunction with Charged Species in LBL Films

### 4.2.1. LBL Nanostructures of Organic/Inorganic Composites

An alternative procedure for fabrication of LBL nanocomposites uses charged nanoparticles as a substitute for one of the polymeric materials. This was, in fact, the first approach employed and has been demonstrated for several types of particles. Usually, inorganic particles must be surface-modified by a suitable molecule that provides the necessary surface charge for LBL film growth. It seems that the kinetics of adsorption for most of the systems is similar to a polymer/polymer process. One of the earliest works in building organized organic/inorganic multilayers was reported by Kleinfelde and Ferguson [40] employing synthetic hectorite, a mica-type, layered silicate that serves as an electrical insulator, diffusional barrier, or for mediating electron transfer. The research in [40] describes a method for stepwise preparation of ordered multilayered films from ultrathin ( $\sim 1$  nm) layers of PDDA and exfoliated sheets of synthetic hectorite onto 100 single-crystal silicon wafers having a native oxide layer. Films with a thickness up to  $0.2 \mu m$  were fabricated by dripping solutions of both materials alternately onto the substrates, instead of the standard dipping procedure usually employed for polymer film build-up. Adsorption of approximately two hectorite layers per cycle occurred, indicating that some loosely bound polymer interpenetrates into the inorganic material allowing adsorption of an extra hectorite layer. This suggests that the amount of hectorite adsorbed can be varied by controlling the amount of polymer in each layer. X-ray diffraction data confirmed the structural order of the films, and the absence of reflection corresponding to the structure of the three-dimensional starting material indicated preferential orientation of the sheets parallel to the surface and the absence of the crystalline precursor within the film structure. Also, in 1994, Keller et al. [41] reported the build-up of several organic/inorganic systems, though there was no systematic study on film growth. Use was made of surface-modified particles with a loose coating layer which can be displaced by the ionic groups of the polymer in the film fabrication process, using the standard dipping procedure. Therefore, electrostatic attraction was the driving force for the film build-up. Keller et al. [41] reported the sequential layering of structurally well-defined, two-dimensional colloidal polyanions containing Zr, Al, or cytochrome compounds with a variety of polymeric cations.

Other zircon-based nanocomposites were later studied in a more detailed work [42], which was aimed at fabricating dense, polycrystalline zirconia hard coatings. Up to 150 bilayers were built onto quartz and 111 silicon wafers using a zirconia nanocluster commercial solution and SPS. The film thickness was estimated using ellipsometry to be of the

order of 2 nm. Atomic force microscopy showed a defect-free surface comprising well and densely packed structures. These films had a Vickers micro-hardness of 25 GPa, which according to the authors is higher than for zirconia coatings deposited by other methods such as sputtering, thermal spray, or laser treatment. This good performance was attributed to the high molecular packing density of the film, the ultra-small size of the zirconia nanoclusters, and the absence of voids. Heat treatments resulted in even better packing arrangements and improved structure of zirconia layers due to the burnout of the polymeric matrix layer.

#### 4.2.2. LBL Films from Magnetic Nanoparticles

The possibility of obtaining an assembly of magnetic nanoparticles/polymer with no phase segregation and the opportunity of selecting particles according to size and shape prior to deposition providing a better control over the final properties was explored by several authors [43–45]. An interesting magnetic structure comprises metallic and ferromagnetic nanoparticles encapsulated by ultra-thin graphite shells. Such structures have potential application in data storage and/or biomedicine, and metals such as Co, Cu, and Ag can be successfully cosputtered with graphite resulting in encapsulated carbon cages. Cassagneau and Fendler [43] were able to assemble Ag-GO (graphite oxide) magnetic-caged particles alternated with PDDA in an LBL-type structure. Films were found to grow linearly with the number of deposition steps and have a very flat surface, as indicated in AFM images. It was also observed that the polymer reorganizes itself around the particles.

An important issue in magnetic storage is to achieve a high signal-to-noise ratio, which can be done by partial magnetic isolation of the grains by cosputtering of chromium, carbon, and SiO<sub>2</sub> [46–48]. The nonmagnetic layer prevents cooperative switching and zigzag noises. One limitation to this approach is the poor regularity between layers and the particle size, which reduces the capability of tailoring the desired properties. Aliev et al. [44] suggested that control over spatial distribution of the particles could be achieved with the LBL approach, with the additional advantage of film fabrication under ambient conditions without the need of post-annealing. This allows the use of any type of substrate. The nanoclusters employed were superparamagnetic Fe<sub>3</sub>O<sub>4</sub> (plain and SiO<sub>2</sub>-coated) and the polyelectrolyte PDDA. Adhesion to the substrate was reported to be outstanding, since no peeling or cracks were observed after intense physical stress. Optical microscopy and atomic force microscopy (AFM) results confirmed the physical integrity of the samples after the stress experiments, and also the stability of the LBL films after 1 year of fabrication. Superparamagnetic properties were observed for films prepared from both plain and coated particles, revealing drastic reduction of the cooperative magnetization between adjacent nanoparticles with the coating layer.

Yttrium iron garnet (YIG) nanoparticles and barium ferrite were also assembled using the LBL approach and PDDA again for preventing phase segregation [45]. The authors observed that the domains might grow laterally in a two-dimensional (2D) mechanism instead of the regular vertical

fashion normal to the film growth direction observed for polymeric systems. They claim that both mechanisms cannot be differentiated by standard kinetic procedures, since lateral growth also depends on the number of layers. For high-quality films, it is important to have nanoparticle dispersion solutions, where the surface potential of the colloids must overcome attractive forces between the particles. This is achieved by the right solution parameters. Therefore, control of ionic strength and pH are crucial for determining growth kinetics. Scanning electron microscopy (SEM) results showed that YIG does not form uniform layers but rather forms domains of 0.5 to 1.5 μm. Such domains expanded laterally (and linearly) with the number of layers, regardless of the nature of the substrate.

Interesting work involving magnetic particles was developed by Mamedov and Kotov [49]. They were interested in building free-standing LBL films to act as ultra-thin membranes. The availability of mechanically resistant free-standing films may open new possibilities and applications, including nanofiltration and nanoseparation, taking advantage of the organized structure of the films. Their approach was to build up PDDA and negatively charged colloidal magnetite nanoparticles onto a cellulose acetate (CA) film that was previously placed onto a glass support. The choice of the substrate was based on its hydrophilic and solubility properties. After film deposition, CA plus LBL film was removed from the support and placed in acetone which caused dissolution of the substrate, thus leaving a free-standing ultra-thin film. Measurements indicated that the magnetic properties were preserved.

#### 4.2.3. LBL Films from Oxides

Oxide nanoparticles were largely explored using the LBL technique. Lvov et al. [50] investigated the adsorption of surface-modified nanoparticles of manganese oxide, alternated with PDDA or myoglobin (Mb) layers onto silver, quartz, and rough pyrolytic graphite substrates. Mb/MnO<sub>2</sub> structures were built to produce electroactive films. The saturation time for adsorption of the nanoparticles, measured with a quartz crystal microbalance (QCM), was similar to those typically measured for polymeric systems. The bilayer thickness for the PDDA particle system was 23 ± 2 nm where approximately 21 nm is due to the nanoparticle layer. This thickness is increased if particles are aged for 2 weeks indicating aggregation, although films were found to be stable for up to 6 months. X-ray photoelectron spectroscopy (XPS) results indicated a surface rich in carbon and oxygen with less than 7% of manganese and nitrogen. Manganese had two valences (Mn<sup>4+</sup> and Mn<sup>3+</sup>), and nitrogen appeared in two different environments suggesting the formation of contact ion pairs and long-distance charge pair formation between the Mn particles and PDDA.

Colloidal oxide particles were studied by Lvov et al. [51], using PDDA and SPS and colloidal dispersions of several SiO<sub>2</sub>-size particles (diameter of 25 ± 5, 45 ± 5, and 78 ± 5 nm), CeO<sub>2</sub>, and anionic TiO<sub>2</sub>. All systems were investigated using QCM. For SiO<sub>2</sub> layers alternated with PDDA, the thickness per layer depended on the particle concentration and the ionic strength of the solution. For 45-nm particles, for example, ca. 70% coverage was found when a

100-mg mL<sup>-1</sup> was used and there was only a sparse coverage for 0.1 mg mL<sup>-1</sup> for all particle sizes. Other assemblies were made from oxide particles (CeO<sub>2</sub> and anionic TiO<sub>2</sub>) and complex layer architectures using, in addition to polymers, glucose oxidase (GOD) (SiO<sub>2</sub>/PDDA/GOD/PDDA or SiO<sub>2</sub>-PDDA complex/SPS). A flat and smooth surface was found for these films but cross-section SEM images showed no long-range order. Atomic force microscopy measurements pointed to individual particles on the film surface. The large difference in size, morphology, and charge density between the particle and the polymer appeared to cause formation of long-distance charge pairs. Hence, the assembly was strongly dependent on ionic strength and particle concentration. Rinsing with water did not lead to desorption of the SiO<sub>2</sub> layer.

Ichinose et al. [52] described the build-up of LBL films from molybdenum oxide layers obtained via ammonium octamolybdate alternated with PAH layers. These compounds, whose generic name is polyoxometalates, have potential applications in catalysis, solid-state devices, photo and electrochromic displays, and in biochemistry and medicine. The assembly of oxide layers and PAH was found to be highly dependent on the pH of the PAH solution, which should be between 2.5 and 3.0. Saturation in the adsorption of the inorganic compound was attributed to the loss of negative charge on the molybdenum oxide layer during the adsorption, as the species in solution are not restricted to the ions—there are also protonated and condensed species. Therefore, the formation of a PAH layer at regular intervals is essential for growth control of the Mo oxide. The film thickness measured with a QCM varied with deposition time with a growth ratio of 5.7 Å/min. Scanning electron microscopy showed a very smooth surface in spite of the presence of cracks, which were attributed to the vacuum drying process for the microscopic studies.

Titanium oxides (TiO<sub>2</sub>) were employed for LBL film fabrication using PAH [53] or sulfonated polystyrene (SPS) [54] following the same approach of using modified surface particles. Cassagneau et al. [53] were able to use the TiO<sub>2</sub>/polymer structure sandwiched between ITO and gold to fabricate Schottky diodes. The presence of a capping layer did not prevent the TiO<sub>2</sub> electroactivity, which means that this approach can be extended to any oxide particle.

Nanocomposites of V<sub>2</sub>O<sub>5</sub> and polyaniline (PANI) were fabricated with the LBL technique [55], as an alternative to the previously used xerogel method [56]. It was found that obtaining nanocomposites was much easier with the LBL technique, probably due to the intimate contact between the adjacent layers of oxide and PANI, since the thickness per bilayer was only ca. 2.5 nm. Such intimate contact was reflected in the film characteristics, which differed from those of films from the separate materials or cast films from mixtures of V<sub>2</sub>O<sub>5</sub> and PANI. For example, a large shift in the V = O bands of FTIR spectra was observed, which was attributed to a more effective H-bonding between the polymer and oxide in the LBL films. Figure 2 shows the proposed structure for the PANI/V<sub>2</sub>O<sub>5</sub> LBL films, in which the architecture of the film can be controlled. Interestingly, the film properties depended on which material is the top layer [57], as demonstrated by UV-vis and Raman characterization. When the top layer was V<sub>2</sub>O<sub>5</sub>, the absorption

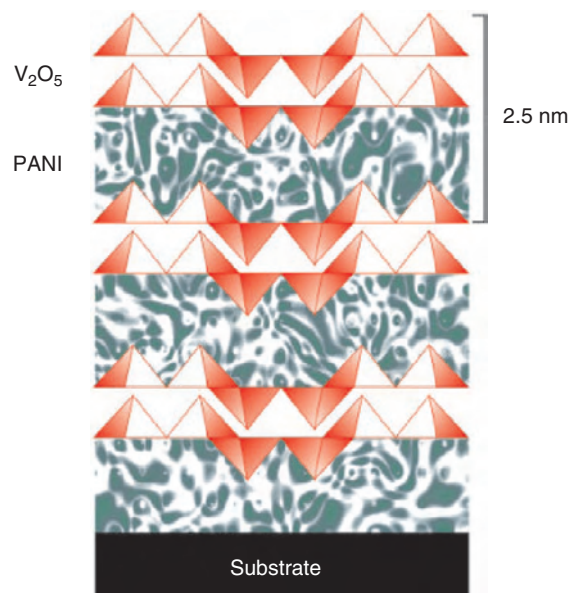


**Figure 2.** Schematic representation of PANI/V<sub>2</sub>O<sub>5</sub>/LBL films. Reprinted with permission from [55], M. Ferreira et al., *J. Nanosci. Nanotech.* 2, 29 (2002). © 2002, American Scientific Publishers.

spectrum peaks were at ca. 600 nm, which is characteristic of undoped PANI and/or PANI in the pernigraniline form. When the top layer was PANI, the absorption maximum shifted to ca. 800 nm, which is characteristic of doped PANI. Raman experiments were also carried out with a 20-bilayer PANI/V<sub>2</sub>O<sub>5</sub> LBL film whose last layer of PANI was partially overlaid by a 6-nm Ag film to achieve the surface enhanced phenomenon. The spectra remained similar to that obtained with no Ag coating, showing that Ag does not chemically interact with the PANI/V<sub>2</sub>O<sub>5</sub> film. The main changes were observed for the bands at 575 cm<sup>-1</sup> (benzene radical) and 1410 cm<sup>-1</sup> (C-N-C and C = N stretch), which became more intense for the Ag overlaid film. When the last layer of V<sub>2</sub>O<sub>5</sub> was also partially overlaid by a 6-nm Ag film, a more drastic change in the spectra was observed, if not in terms of new bands at least in terms of relative intensities. The spectra from the Ag overlaid film were dominated by the band at 576 cm<sup>-1</sup>. Raman scattering experiments were carried out where the LBL films with a PANI top layer were submitted to HCl vapor. The intensity of the 1336 cm<sup>-1</sup> (polaronic structures (C-N<sup>+</sup>)) band increased upon this treatment, thus indicating that PANI was in the emeraldine form, but the intensity was less than for a cast film (doped PANI). For V<sub>2</sub>O<sub>5</sub> as the top layer, the intensity of this band decreased. One possible explanation for such effects is deprotonation or overoxidation of PANI, but the latter is more plausible because V<sub>2</sub>O<sub>5</sub> is an acid semiconductor, which is unlikely to deprotonate the emeraldine salt.

More complex oxide structures can be devised for LBL film fabrication. One example is the interest on highly dielectric thin films. Available techniques for producing structures with such characteristics, for example, magnetron sputtering, laser ablation, chemical vapor deposition (CVD), and sol-gel, require high processing temperatures, vaporization of the bulk dielectric material, or use of soluble precursors. This requirement has associated problems of

undesired elements in device fabrication. Fang et al. [58] took advantage of the LBL technique for fabrication of films from previously exfoliated perovskite-type oxides and polymeric cations that could be converted into a three-dimensional structure by means of chemical reactions. The oxides employed were  $\text{Ca}_2\text{Nb}_3\text{O}_{10}$  and  $\text{HTiNbO}_5$ , whose layers were alternated with PAH layers onto p-type Si wafers and borosilicate glass. A unilamellar colloid structure was obtained as a pure phase for  $\text{pH} \geq 8.5$ . Both oxides form dense monolayers onto PAH at  $\text{pH} 8.5\text{--}9.0$ , with only a single layer of the colloid being deposited, which suggests repulsive interactions between the sheets. X-ray diffraction data showed relatively strong Bragg peaks indicating well-ordered stacks of the oxide layers. The lamellar films could be further converted into three-dimensional (3D) structures by chemical condensation reactions, which were confirmed by thermal analysis.

Some compounds are obtained as platelets rather than particles and those are also easily assembled in a LBL structure as demonstrated by Cassagneau et al. [59], who used oxidized graphite. The adsorption process of these films is affected by the extent of oxidation of graphite that can be selectively controlled. Layer-by-layer films deposited on ITO and  $\text{SiO}_x$ -coated glass and quartz were analyzed with QCM, surface plasmon spectroscopy, UV-vis, FTIR, and AFM. The thickness of graphite-oxide (GO/PDDA) or poly(ethylene oxide) GO/(PEO) layers increased linearly with the number of bilayers, while the GO layer depended on the underlayer, as can be observed in Figure 3 that shows the schematics for three different sequential growths studied and the respective absorbance at 230 nm versus the number of layers. Poly(diallyldimethylammonium chloride) was always found to render higher coverage and thicker films compared to PEO, as expected since the first is a positively charged material and PEO is a neutral polymer.

#### 4.2.4. Metallic Nanoparticles in LBL Films

Metallic nanoparticles can be assembled in LBL films, similarly to what was described for oxide particles. The surface of the particles is modified to form a colloidal suspension.

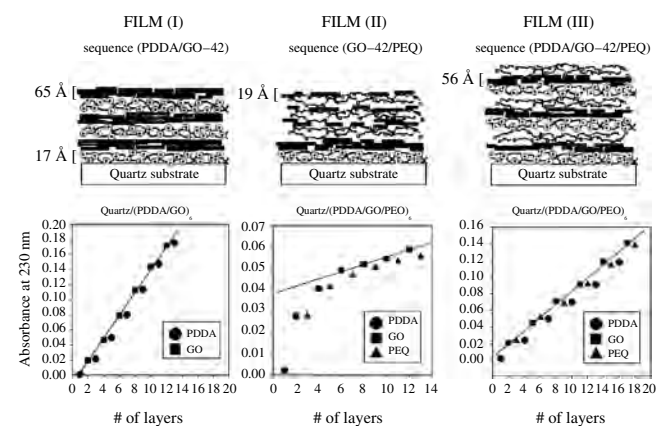


**Figure 3.** Schematics of S-(PDDA/GO-42)<sub>6</sub>, S-PDDA/(GO-42/PEO)<sub>6</sub>, and S-(PDDA/GO-42/PEO)<sub>6</sub> films (top) and plots of absorbances versus number of layers self-assembled onto a quartz substrate (bottom). Reprinted with permission from [59], T. C. Cassagneau et al., *Langmuir* 16, 7318, (2000). © 2000, American Chemical Society.

The first example of layered nanocomposite films prepared from colloidal metal particles and polyelectrolyte appears to be that of Schmitt et al. [60]. The interest in this kind of composite is in tailoring optical and electrical properties such as photo-induced charge separation for energy storage applications. The superlattices formed by gold particles and polyelectrolyte could either be layered or disordered structures, depending upon the thickness of the polymer interlayer. In [60], gold particles were prepared in a colloidal suspension with a narrow size distribution [61] and then used to produce the LBL films. Silicon wafers or glass substrates were alternately immersed into the colloidal dispersion and in a poly(ethyleneimine) (PEI) solution. For the film structure (PEI/SPS/PAH)<sub>1</sub>/(Au/PAH)<sub>4</sub> X-ray reflectivity data showed that the polymer layer was not thick enough to prevent interparticle interaction, that is, the systems were highly interpenetrated. Spacing layers were then used as control layers in film structures, such as PEI/[SPS/PAH]<sub>3</sub>/[Au/PAH]<sub>4</sub>, and X-ray reflectivity measurements showed multiple Bragg reflections indicating the well-defined layers of gold nanoparticles. The separating layers play no active role in the film. This approach to control particle interactions was extended to other polymers, with the nanoparticles being covered by different groups such as carboxylic acids or pyridine groups. The presence of gold particles was well evidenced by FTIR spectroscopy.

Control of interaction among gold nanoparticles of spherical and triangular shape in layer-by-layer (LBL) films was achieved by Malikova et al. [62]. Interaction was assessed by measuring the surface plasmon frequency, which was affected because oscillations of free electrons are largely dependent on the space available. The shape of the particles is also relevant. For example, electrons in rods can oscillate in transversal and longitudinal paths generating two well-defined surface plasmon peaks [63]. On the other hand, metallic spherical shells also display two surface plasmon bands, but these depend on the thickness and diameter of the sphere [64]. In [62], gold particles dispersed in solution were LBL processed with PDDA, with the gold particles being assembled with a flat conformation on the substrate as shown by TEM and AFM. The appearance of a new band at 650 nm attributed to interparticle interactions between adjacent monolayers occurred after four bilayers had been deposited. Particle interaction could be diminished by interposing spacing bilayers of PDDA/PAA. Such control is important for applications in catalysis, surface plasmon resonance, and to enhance nonlinear optical properties. Gold nanoparticles could also be assembled using hydrogen bonding as the driving force [65].

A direct synthesis method of 3D nanoparticle multilayers on carbon electrodes functionalized with 4-aminobenzoic acid (4-ABA) was proposed in [66]. The Pd nanoparticles were obtained from QPVP-Os (a quaternized poly(4-vinylpyridine)) complexed with [(Os(bpy)<sub>2</sub>Cl)<sup>2+</sup> and PdCl<sub>4</sub><sup>2-</sup>. After build-up, the film was electrochemically reduced to yield zero-valence 3D Pd nanoparticles. This was indeed confirmed by XPS results showing that the reduction takes place within the whole film thickness. Film growth was followed by the redox current of the Os-complex that increased linearly with the number of layers. Atomic force microscopy

images showed that before reduction, a poor surface morphology was observed. After reduction, however, Pd nanoparticles could be readily observed. The average diameter was estimated to be around 3–7 nm. The catalytic current increased with the number of layers and the particles did not show clear interfaces, which is favorable for charge transfer through the film. The nanoparticles could effectively catalyze the reduction of O<sub>2</sub> and the oxidation of hydrazine compounds.

#### 4.2.5. Quantum Dot-Type Nanoparticles

Quantum dots are nanoparticles with very well-defined emission wavelength that can be tuned by size variation associated with high fluorescence efficiency. Those characteristics put them as promising structures for electroluminescent device fabrication. Additionally, such particles can be easily assembled with several polymers rendering different LBL structures [67–72]. Gao et al. [67] took advantage of CdSe quantum dot opto-electronic properties by combining them with poly(*p*-phenylene vinylene) (PPV) electroluminescent devices. Such devices can be easily built with the LBL technique and it has been shown that the structure and material combination are determining for the emission properties [73, 74]. The large quantum efficiency of quantum dots contributes to improving external quantum efficiency of polymeric devices. Negatively charged CdSe nanoparticles, PAH, SPS, PPV (deposited as precursor and converted at 130 °C under 10<sup>-5</sup> bar vacuum for 11 hours) were used to assemble several device structures. Since emission of quantum dots depends on their size, the same device fabrication process and structure can be used for tuning different colors. The LBL technique also provides a means of controlling particle interaction using polymeric inert spacing layers, thus tailoring the final color emission. Gao et al. [67] studied several device structures, changing the composition of blocks: SPS/PPV, CdSe/PPV, CdSe/PAH, and CdSe/PAH-SPS/PPV. For CdSe/PPV, emission was found to come from CdSe rather than from PPV, which worked better as a hole injection layer. Emission from CdSe/PAH was redshifted by about 50 nm compared to CdSe/PPV, implying that there are some deep trap sites formed at the particle's surface during measurements. The two-block device was observed to be more stable. The most interesting result is that the nanoparticles were oxidized but this was prevented in the presence of PPV. X-ray reflectivity results indicated the presence of domains with an inhomogeneous distribution of CdSe particles, and with the average thickness being smaller than the particle diameter, that is, coverage was incomplete. CdSe nanoparticles were also studied by Hao and Lian [70], where assembly was made with H-bonding as the driving force.

In [42], Rosidian et al. reported on LBL films of HgTe nanocrystals. These materials display strong emission in the infrared region, therefore being relevant for the telecommunication industry. The average particle size used was 3.5 nm with size deviation of 30% as detected by TEM. Poly(diallyldimethylammonium chloride) was used as the assembling material and adsorption of the nanoparticles saturated after 80 min. The nanoparticle layer was 8-nm thick, which represents 2–3 monolayers in spite of the electrostatic repulsion. The film roughness estimated with scanning tunneling microscopy (STM) was slightly larger than

the quantum dot diameter. Layer-by-layer films showed strong emission around 1600 nm with no effect from solvent reabsorption.

Zhang et al. [72] proposed a new approach where CdTe nanoparticles are assembled with a special polymer, nitro-containing diazoresin (NDR), relying on ionic bonds. The ionic bonds are converted into covalent bonds by photoreaction of the photosensitive precursor film exposed to ultraviolet irradiation. Diazonium groups from the polycation were easily decomposed under UV irradiation forming cationic phenyl groups which could further react with the nucleophile of carboxylic acid groups and convert ionic to covalent bonds. This was achieved in 20-bilayer films, with decomposition being monitored by UV-vis and FTIR spectroscopy. The assembly of the nanoparticles was verified by XPS. The high stability of the irradiated film was checked by etching with a solvent mixture (H<sub>2</sub>O-dimethyl-formamide (DMF)-ZnCl<sub>2</sub>). For films irradiated during 30 min, only 11.9% of the particles were removed whereas 47.3% were removed for the nonirradiated film.

Finally, “coupled” nanoparticles can also be used. Those structures are anticipated to have potential applications in photocatalysis and solar energy conversion. They are large bandgap semiconductor particles with energetically low-lying conduction band. Such particles were LBL-assembled [75], using TiO<sub>2</sub>/PbS “coupled” nanoparticles and SPS. Poly(ethylene oxide) was used to modify the substrate surface and promote adhesion. The first step consisted of the preparation and characterization of the semiconducting particles. The LBL films displayed a morphology characteristic of well-packed layers.

## 5. LBL FILMS FROM ALUMINOSILICATES

The use of layered aluminosilicates in potential technological applications is limited due to their powdery nature. The conventional route to film formation is casting, spraying, or sometimes simply painting a suitable substrate with a polymer-nanoparticle mixture. However, these approaches do not allow control of film thickness, typically ranging from a few nanometers to a few micrometers, or of the particle orientation within the film. Furthermore, using these methods partial phase separation of the polymer/nanoparticle solutions may occur, leading to microheterogeneities in the film. Due to the strong negative surface charge of layered aluminosilicates, the LBL technique is suitable for the production of films in the nanometer range with vertical organization of different sandwich-like layers. In LBL films, aluminosilicate layers are alternated with positively charged polyelectrolytes, where the host lattice can have an ordered molecular arrangement. A further advantage is that the thermal and oxidative stability of organic molecules is improved when they are confined to interlamellar spaces of host lattices, owing to the reduced thermal motion and a quasi-absence of oxygen [76].

Although the mechanisms involved in the physical adsorption of clays are believed to be the same as for polyelectrolytes, significant differences have been observed in the times involved in the adsorption process. Table 1 summarizes the data for the adsorption kinetics of inorganic and



**Table 1.**

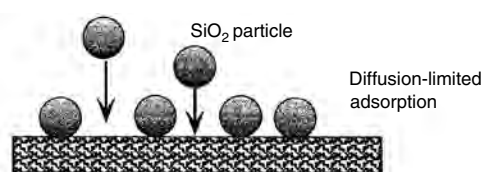
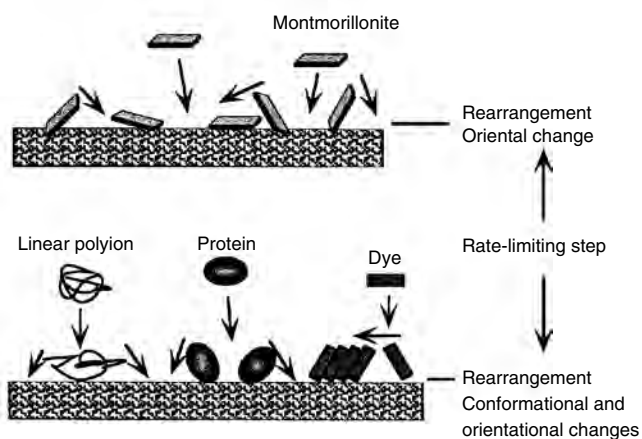
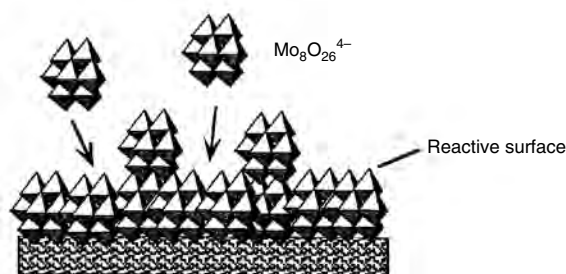
Adsorbent	Time for adsorption/saturation	Ref.
<b>Organic materials</b>		
Linear polyions	8–10 min	[78]
Anionic dye polymer	20–40 min	[79]
SPS and PAH	5 min	[80]
Anionic polythiophene derivatives	10 min	[81]
Anionic polyaniline derivatives	5 min	[81]
Ionene polymers	15 min	[82]
Proteins	10–20 min	[83]
Ionic dyes	15–20 min	[84]
PDDA (onto SiO <sub>2</sub> layer)	40 s (20 s <sup>a</sup> )	[77]
<b>Inorganic materials</b>		
SiO <sub>2</sub> nanoparticles	10 s (2 s <sup>a</sup> )	[77, 51]
Montmorillonite	5–6 min	[85]
Molybdenum oxide	Infinite growth	[52]

<sup>a</sup>Minimum adsorption time for successful assembly.

Source: Reprinted with permission from [87], K. Ariga et al., *Appl. Clay Sci.* 15, 137 (1999). © 1999, Elsevier Science.

organic materials. The inorganic species assemblies show quite large differences in saturation time, while adsorption of most of the organic materials reaches saturation within 5 to 20 min. These characteristics can be explained by plausible models shown in Figure 4. Adsorption of rigid, spherical SiO<sub>2</sub> particles appeared to be diffusion-limited (Fig. 4A). The diffusion time of SiO<sub>2</sub> from solution onto the surface is estimated to be 2 s using a diffusion coefficient of  $1.1 \times 10^{-7} \text{ cm}^2 \text{ s}^{-1}$ . Lvov et al. [77] demonstrated that 2 s are sufficient for SiO<sub>2</sub> assembly. If this diffusion rate is applied to the adsorption of PDDA at a concentration of  $3 \text{ mg mL}^{-1}$ , one should expect hundreds of monolayers to be adsorbed within 20 s, which was actually the minimum PDDA adsorption time required for only one SiO<sub>2</sub>-PDDA bilayer. It was concluded that the adsorption process of PDDA was not determined simply by its diffusion rate, for rearrangement of the adsorbed polymer chains may slow down the PDDA adsorption. Furthermore, the adsorption process depends on the clay nature. While adsorption of montmorillonite microplates is similar to that of organic materials (Fig. 4B) due to the flexibility of the polyions that change their conformation to achieve an efficient interaction with surface-bound opposite charges, the adsorption of molybdenum oxide is different (Fig. 4C). In the latter, protonation and condensation allow films to grow without excessive accumulation of the surface charges and the adsorption does not saturate. For montmorillonite, the adsorbed plates may reorient on the film surface to give the most stable or packed arrangement as in the case of proteins and dyes. The adsorption of montmorillonite microplates may resemble a dye assembly as most dye molecules possess rigid nonsymmetrical shapes. Their slower adsorption times (15–20 min for saturation) probably arise from rearrangement of adsorbed species to achieve stable aggregates and effective electrostatic attraction.

Several clays were demonstrated to render well-defined LBL polymeric/clay structures, among which montmorillonite is the most popular [85–90], followed by hectorite [91] and laponite [92, 93]. The polycations used are generally the

**(A) Fast adsorption**

**(B) Slow adsorption**

**(C) Infinite growth**


**Figure 4.** Schematic illustration of adsorption processes of inorganic materials in alternate LBL assembly. Reprinted with permission from [87], K. Ariga et al., *Appl. Clay Sci.* 15, 137 (1999). © 1999, Elsevier Science.

common polyelectrolytes for LBL film fabrication, but there are cases in which PPV [86] or dyes such as coumarin [94] have been employed. Montmorillonite as polyanion in LBL films was investigated by Lvov et al. [85]. Well-structured layered films or solid gels could be obtained depending on the concentration of the two components and on the preparation methods. The authors suggested that the assembly process of montmorillonite/polycation multilayers occurs with precise control of its architecture. As a result, LBL films and highly hydrated gels could be obtained, giving rise to useful functional materials. It was shown later on that the individual aluminosilicate-polyelectrolyte sheets were unexpectedly flexible and oriented in parallel to the substrate plane [89]. The LBL aluminosilicate-polyelectrolyte composites exhibited exceptionally high mechanical strength and resilience to crack proliferation [89], thus making this system promising material for gas separation and other membranes.

In a new approach, LBL films were produced under an applied electric field [90]. Positively charged PDDA was

found to bind strongly to the surface of anionic montmorillonite platelets in aqueous dispersions up to a saturation beyond which reversible physisorption occurred. The LBL films were prepared under an electric potential in a standard three-electrode electrochemical cell. Glass slides coated by Cr and Au were used as substrates. The substrate was connected to the bias source (in a potentiostat/galvanostat), immersed into a solution of PDDA (or dispersion of montmorillonite), and the desired potential was applied for 10–15 min. When the potential-assisted assembly of montmorillonite or PDDA was completed, the substrate was rinsed with ultra-pure water, dried with a stream of nitrogen, and introduced into a dispersion of montmorillonite (or solution of PDDA). In a given LBL film, only one of the components, either PDDA or montmorillonite, was assembled under a potential. The thickness of the montmorillonite layer was found to depend on the external voltage applied. The layer thickness increased when positive potentials or large negative voltages were applied but decreased slightly for films produced under a small negative potential.

Rigid platelets of Laponite with low surface charge density were obtained in LBL films where the Laponite polyanion was alternated with a cationic copolymer [93]. Film thickness increased linearly with the number of dipping cycles, as measured by ellipsometry. The characterization of these LBL films was accompanied by studies of LBL films from strong polyelectrolytes, where the influence of charge density of the polyelectrolytes on the growth of LBL multilayers from pure aqueous solutions was studied. For example, the analysis of the cationic copolymer/SPS system revealed that a critical linear charge density ( $\lambda_c$ ) of 0.036 elementary charge/Å of contour length is necessary to obtain stable multilayer growth in pure water. Above  $\lambda_c$ , the thickness per layer varies with the linear charge density of the cationic copolymers, in good agreement with current theories of polyelectrolyte solutions. Analogous results were obtained for the variation of the basal spacing of internally structured hybrid multilayers (cationic copolymer/hectorite). However, in contrast to the first system, no critical linear charge density was found for the hybrid system. This was explained by the authors due to the existence of nonelectrostatic interactions between the clay platelets and the formamide fragment.

Some applications have been suggested for alluminosilicate LBL films, including the production of inorganic hollow spheres for microencapsulation [92], humidity sensors [91], and in optoelectronics and photonics devices [86, 94]. The applicability of the LBL technique for the formation of a range of polymer-core, inorganic-shell particles and inorganic hollow spheres was demonstrated by Caruso et al. [92]. Composite particles comprising a polystyrene (PS) core and  $\text{TiO}_2$ ,  $\text{SiO}_2$ , or Laponite nanoparticle/PEI multilayers were fabricated. The influence of nanoparticle type, shape, and size on the formation of multilayer shells was examined by TEM and SEM. The LBL technique for coating polymer spheres is adaptable with small variations in the coating steps used to optimize the nanoparticle coatings of different materials. The number of polyelectrolyte multilayers separating the nanoparticle layers and the number of nanoparticle/polyelectrolyte depositions cycles may be varied to generate uniformly coated nanocomposite spheres.

The hybrid core-shell particles were subsequently calcinated to create well-defined hollow spheres with predetermined diameters.

Eckle and Decher [86] fabricated organic light emitting diodes (OLEDs) based on the PPV/Poly(methacrylic acid) (PMA) system including an insulating layer of montmorillonite. Multilayers of the cationic precursor polyelectrolyte (pre-PPV) and PMA were prepared by a cyclic immersion of PEI-coated substrates in pre-PPV and PMA solutions. Thermal conversion from pre-PPV to PPV was carried out at 270 °C for 12 h under vacuum. They demonstrated that a single clay layer affects the devices, lowering the current densities and increasing the light output in comparison with other polymer systems. Figure 5 shows the luminescence versus current density curves, whose slopes indicate the relative efficiency of the devices. Furthermore, when the distance between the clay layer and the ITO anode increases, the efficiency becomes slightly smaller. The device performance increased by a factor of at least 14 in the presence of a barrier layer. The authors also showed that the subnanometer positioning of this insulating barrier within the active medium with respect to both electrodes, which is easily controlled by the LBL technique, had an important role for the electro-optical properties of the diodes.

Nanocomposites containing a layered aluminosilicate with an expandable lattice such as hectorite and a coumarin dye were prepared using the LBL technique [94]. The aluminosilicate/coumarin dye was alternated with PDDA and deposited on hydrophilic glass substrates. The films exhibited blue fluorescence emission centered at 465 nm when excited at 386 nm and had an outstanding thermal stability. The intercalation of the dye causes the molecules to adopt

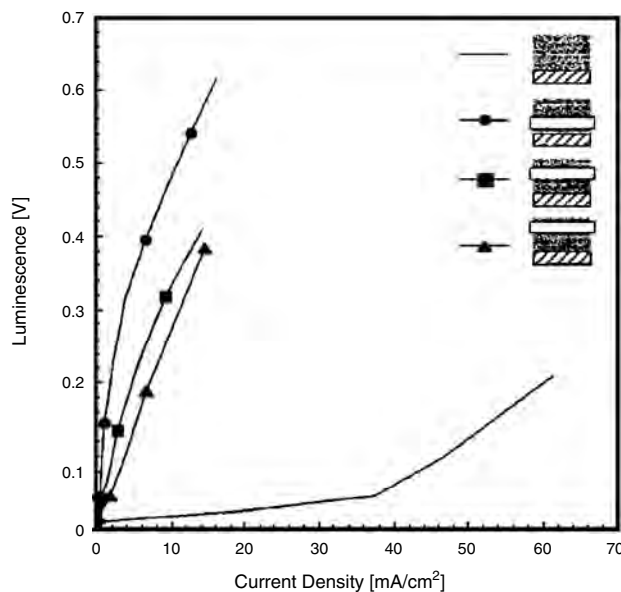


**Figure 5.** Luminescence-current density profiles showing the greatly enhanced performance of OLEDs containing a montmorillonite layer. The device without a clay layer (MLA-1, straight line) has a somewhat lower relative efficiency than those with an insulating layer. Device efficiency is further increased when the insulating inorganic layer is close to the ITO anode (MLA-2, filled circles). Reprinted, with permission from [86], M. Eckle and Decher, *Nano. Lett.* 1, 45 (2001). © 2001, American Chemical Society.

a flat conformation. The same authors observed [94] that the linear build-up of the multilayer films containing up to 20 cycles resulted in transparent films which exhibited strong blue-green fluorescence due to coumarin dye molecules adhered to the exfoliated hectorite platelets. These organic/inorganic core-shell nanoparticles may be promising building blocks for ordered ultra-thin nanocomposite films with high mechanical strength, chemical resistance, and thermal stability. Such properties are probably associated with the layered architecture and the ionic interaction with the cationic polyelectrolytes.

## 6. LBL FILMS FROM MACROCYCLIC SYSTEMS

Macrocyclic porphyrins and phthalocyanines have been widely reported as being suitable for microelectronics, photoresponsive materials, modified electrodes for catalyses, gas sensing, etc. The main characteristics exhibited by this class of materials are semiconductivity, well-defined redox activity, and high thermal stability. The fabrication of thin films of porphyrins and phthalocyanines is relevant for many fields because of the basic advantages to work with solid-state films where thickness and molecular engineering can be tailored for specific applications. The limited solubility of most metallic phthalocyanines has led researchers to employ vapor deposition techniques for film fabrication. Nevertheless, reports have been made on the preparation of ultra-thin films of substituted phthalocyanines using the LB and the LBL technique. The fabrication of LB films from phthalocyanines dates from decades ago and interesting results have been reported by a variety of groups [95–97]. Here we shall not cover such works, but rather concentrate on the more recent use of phthalocyanines in LBL films. A key for the production of LBL films has been the incorporation of sulfonated groups to metallic phthalocyanines, allowing LBL active layers of tetrasulfonated phthalocyanines to be alternated with cationic polyelectrolytes. In these films, interactions between the components may be maximized due to the nanostructured nature of the films.

The possibility of assembling sulfonated water-soluble phthalocyanines as active layers in LBL films was first reported by Lütt et al. [98]. In this seminal work, nickel tetrasulfonated phthalocyanine (NiTsPc) was assembled with PDDA. Growth of the multilayers was confirmed via UV-vis spectroscopy. Lütt et al. [98] observed significant differences between deposition of PDDA/NiTsPc onto silicon and glass substrates mainly regarding the thickness of the layers. When Si substrates were used, the thickness of the bilayers was ca. 2 nm for the few first bilayers, decreasing with the number of deposited layers to 0.8 nm after 40 bilayers had been deposited. Deposition on glass substrates did not show such dependency, with the thickness per bilayer being constant at ca. 1 nm. The latter implied that NiTsPc molecules were adsorbed in a standing up conformation onto the Si substrate (orthogonally in relation to the substrate plane) during the first layers. From X-ray reflectivity it was found that the electron density of the first deposited bilayer was not affected by the subsequent depositions [98].

In a subsequent work, Li et al. [99] presented a detailed study on film fabrication and optical properties of LBL

films made of PDDA and NiTsPc. The multilayers were grown by electrostatic attraction onto glass and silicon-charged substrates. X-ray reflectivity analysis showed that the PDDA/NiTsPc LBL films displayed a thickness of about 1.1 nm per bilayer with surface roughness of 0.2–0.7 nm (rms). Such thickness values were applied as constraints for ellipsometry measurements in order to obtain optical parameters such as refractive index,  $n$ , and extinction coefficient,  $k$ . The refractive index varied from 1.6 to 1.8. The use of LBL films from tetrasulfonated phthalocyanines in rectifying devices was evaluated by Li et al. [100]. The main scope of the work was to investigate the influence of bilayers of NiTsPc and poly(*p*-quaterphenylene-disulfonic-dicarboxylic acid) (PPP) assembled with PDDA on the potential barrier at the interface of rectifying devices made of aluminum and a *p*-type silicon semiconductor. The authors aimed at reducing the Schottky barrier across the metal/semiconductor interface. Through I-V characterization, it was found that the devices containing organic active layers did not show a Schottky behavior but rather a power-law dependence of current on voltage (at forward bias),  $J \sim V^\alpha$ , with  $\alpha = 1.4, 2.2,$  and  $2.7$  for PDDA/PPP, PDDA monolayer and PDDA/NiTsPc, respectively. This research opened up the possibility of exploiting phthalocyanines LBL films in electroluminescent devices as hole-transport layers.

L. S. Li et al. [101, 102] studied the electronic properties of conductive surfaces modified by the deposition of polyelectrolyte/NiTsPc layers. They evaluated the changes in work function of an ITO-modified glass when NiTsPc was assembled with PDDA [101] or an oligomeric viologen: oligo(hexylene 4,4'-bipyridinium dibromide) (OHBP) [102], respectively. The films were characterized by FTIR at an external grazing-angle reflection configuration and X-ray reflectivity. The work function of the films was obtained using the Kelvin probe technique. Preferential orientation for both PDDA and NiTsPc was inferred by FTIR at the grazing angle configuration [101] on drop cast films in comparison with the bulk materials. The same orientation was found in the LBL films, that is, the NiTsPc molecules seem to lie flat on the surface of the PDDA layer. Fourier transform infrared spectra also confirmed the presence of salt bridges between  $\text{SO}_3^-$  and  $\text{Me}_2\text{N}^+$  ( $1227$  and  $1200 \text{ cm}^{-1}$ ), which acted as binding forces between PDDA and NiTsPc. Kelvin probe measurements showed that the work function of the surface could be changed from 500 mV to 100 mV depending on whether the outermost layer was PDDA or NiTsPc (for any number of deposited bilayers). A possible explanation for the periodic variation on the work function of the film is that when one monolayer of PDDA is deposited atop ITO, there is an increase in the current due to the presence of dipoles from the PDDA configuration. When a NiTsPc layer is added atop the PDDA layer, a decrease in the current is observed due to the presence of another dipole layer that cancels the dipoles from PDDA.

The control of electronic properties on surfaces through molecular engineering was also demonstrated in [102], where the hole conductor behavior of NiTsPc and the electron acceptor characteristic of viologens were exploited to control the work function and photovoltaic characteristics of

LBL films made from OHBP and NiTsPc. In agreement with the results from [101], the work function of the film surface varied from 450 mV to 100 mV, depending on the terminal layer (OHBP or NiTsPc, respectively). Figure 6 shows the photovoltaic behavior of OHBP-NiTsPc on ITO evaluated by surface photovoltage spectroscopy. When one layer of OHBP is deposited on ITO (curve a), the photovoltaic response drops from 200 mV to about 105 mV at 350 nm. With the addition of one layer of NiTsPc to the film, about 30 mV of the photovoltaic response is recovered. Although this effect repeats with the deposition of additional layers of OHBP and NiTsPc, the photovoltaic effect diminishes with each addition of OHBP layer. The Kelvin probe technique and surface photovoltage spectroscopy were employed in another work by Li et al. [103] in the study of electronic and photovoltaic effects of LBL layers from PDDA and NiTsPc deposited onto conducting and semiconducting ITO and TiO<sub>2</sub> surfaces, respectively. The work aimed at investigating the charge-transfer properties between PDDA and NiTsPc. As expected, the work function of the films

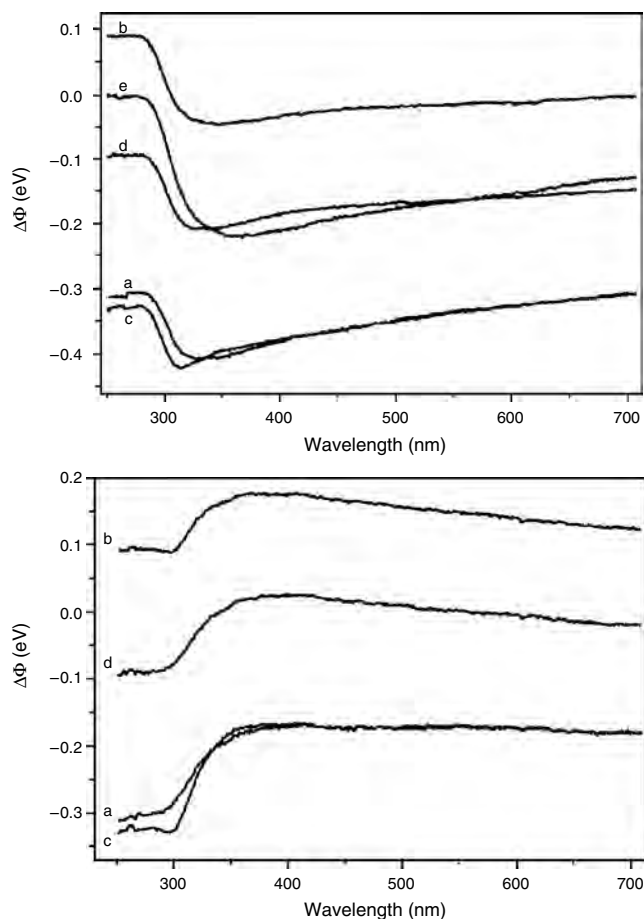


**Figure 6.** Top: Surface photovoltage spectra dependence on the terminating layer of OHBP and NiPc. (a) OHBP/ITO; (b) NiPc-OHBP/ITO; (c) OHBP-NiPc-OHBP/ITO; (d) NiPc-OHBP-NiPc-OHBP/ITO; (e) blank ITO. Bottom: Photovoltage spectra after the correction from blank ITO, that is,  $\phi_{\text{sam}} - \phi_{\text{ITO}}$ . Reprinted with permission from [102], L. S. Li and A. D. Q. Li, *J. Phys. Chem. B* 105, 10022 (2001). © 2001, American Chemical Society.

differed by approximately 300 mV depending on the top layer, whether it was from PDDA or NiTsPc. This occurred for ITO and TiO<sub>2</sub> substrates—in the dark or under illumination. Using surface photovoltage spectroscopy, it was shown [103] that the effect of the terminal layer is not significant when the PDDA/NiTsPc system is deposited on ITO. However, the presence of PDDA/NiTsPc layers seems to have a more remarkable effect for films deposited on TiO<sub>2</sub>, especially for excitation beyond the bandgap.

The electrochemical properties of LBL films comprising cobalt and iron tetrasulfonated phthalocyanines (CoTsPc and FeTsPc) were investigated by Lvov et al. [104] and Zucolotto et al. [105, 106], respectively. In these works, LBL films from phthalocyanines are used to modify electrodes for electrochemical analysis. Investigating the ion transport phenomena inside the films, Lvov et al. [104] showed that the redox process of PDDA/CoTsPc films containing one to five bilayers is controlled by charge diffusion. The diffusion coefficient for charge transport,  $D$ , was estimated as  $10^{-13}$  cm<sup>2</sup>/s for a 5-bilayer film.

In the works cited above, the assembling of tetrasulfonated phthalocyanines is expected to occur via the sulfonated group from phthalocyanine and the positively charged moiety of the polycation (e.g., PDDA, PAH). However, unusual interactions binding tetrasulfonated phthalocyanine and the polycation were observed in PAH/FeTsPc films [105]. Such specific interactions occurred between the metallic center of the phthalocyanine and the unprotonated NH<sub>2</sub> groups from PAH, as schematically illustrated in Figure 7.

Reports have been made of porphyrins in LBL films [107–111], where in addition to the study of basic concepts and film characterization, the films have been proposed for sensing [107] and to modify electrodes for electrochemical analysis [108]. The first report appears to be due to Araki et al. [107], where studies were made with two porphyrin species bearing opposite charges, viz. tetraruthenated zinc

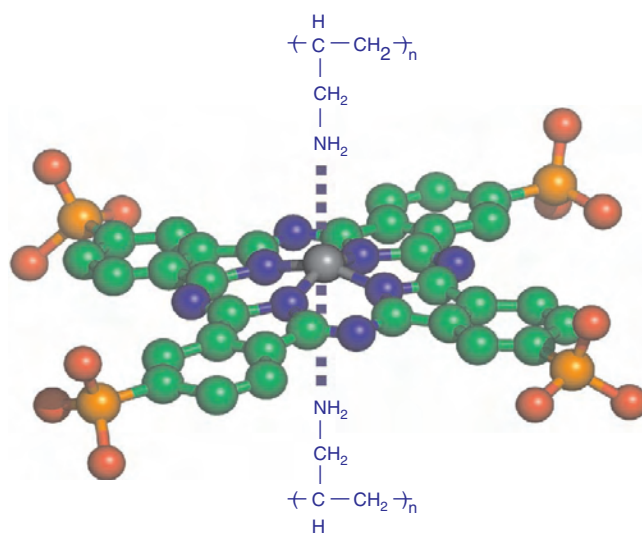


**Figure 7.** Schematic illustration suggesting the additional interaction binding the Fe atom and unprotonated NH<sub>2</sub> groups from PAH. Reprinted with permission from [105], V. Zucolotto et al., *J. Phys. Chem. B*, in press. © —, American Chemical Society.

porphyrin ( $\text{ZnTPyPBpy}^{4+}$ ) and meso-tetra phenyl porphyrin sulfonate ( $\text{M-TPPS}^{4-}$ ). The deposition process was driven primarily by electrostatic attraction between the charged species. The multilayer structured films displayed microcrystalline morphology, with grain size of  $0.12 \mu\text{m}$ . The thickness of each bilayer was approximately  $1.27 \text{ nm}$ . The latter suggested a slip-stacked configuration with the molecules oriented coplanar with the substrate. Also worth mentioning is the work by Jiang et al. [111 and references therein] on the fabrication of LBL-patterned structures. It focuses on the assembly of several polyelectrolytes with a PPV derivative or an organometallic ruthenium electroluminescent dye (sulfonated ruthenium polybipyridyl complex): ( $\text{Ru}(\text{phen}')_3^{4+}$ ). Direct multilayer patterning of different dyes could be obtained based on the selective adsorption of polyelectrolytes onto surface templates made of carboxylic acid and oligoethylene glycol (EG) self-assembled monolayers (SAMs). By using the two dyes assembled with different polyelectrolytes it was possible to grow LBL films specifically on the COOH or on EG-modified regions of the patterned template. This new approach allows the formation of multilayer films placed in a side-by-side arrangement on the surface. The main interest in side-by-side deposition is the fabrication of patterned electrochemiluminescent devices.

## 7. DENDRIMERS IN LBL FILMS

The development of a new class of polymers, referred to as *dendrimers*, is relevant for several fields, particularly in the so-called *wet chemistry*. The interest in the fundamental understanding and application of dendrimers comes from the unique properties presented by these materials, such as monodispersity, tree-like architecture, well-defined functionalities, and the ability to self-organize into superstructures. In addition, a series of conducting or semiconducting particles can be placed into the hollow structure of the dendrimer. Dendrimers with specific properties can be successfully tailored by adjusting the functionality of the end groups. These features allow the use of dendrimers in a wide range of applications especially in the form of thin films. Nanostructured thin films made from dendrimers, in particular, may serve as active surface layers for sensing, nano-reactors, reservoirs for conductive particles, and as modified electrodes for electrochemical analysis.

The LBL technique is suitable in producing nanostructured films of dendrimers due to their water-solubility, stability, and presence of functional end groups. These groups allow the fabrication of layered structures made from dendrimers in conjunction with a number of charged species such as polyelectrolytes, biomaterials, polyoxometalates, and even with other dendrimers. The first report of LBL films from dendrimers was made by Watanabi et al. [112], where only one type of dendrimer was used. In that seminal work, polyamidoamine dendrimers (PAMAM) were assembled on themselves by functionalization of the end groups with  $\text{K}_2\text{PtCl}_4$  after each dendrimer layer had been adsorbed. This functionalization process provided sites where a further layer of dendrimer could attach. This process allowed the deposition of 8-nm thick layers at each deposition step. In a similar approach, Wang et al. [113] produced covalently bonded LBL multilayers of PAMAM G1.5 dendrimer and

nitro-containing diazoresin (NDR). The multilayered films were initially built via electrostatic attraction and then irradiated with UV light which promoted the conversion of the bonds from electrostatic to covalent.

Tsukruk et al. [114] produced LBL films with two types of dendrimers bearing opposite charges. Polyamidoamine dendrimers presenting surface amino groups for generation 4, 6, and 10 (G4, G6, and G10) and carboxylic groups for generations 3.5, 5.5, and 9.5 (G3.5, G5.5, and G9.5) were adsorbed onto each other driven by electrostatic attractions between the amino and carboxylic functional groups. An important result was that the thickness of a dendritic monolayer in the layered structure was smaller than the diameter of ideal spherical dendritic macromolecules as estimated from molecular models or from chromatography data of dendritic solutions [114 and references therein]. Such behavior can be explained by the strong interaction of the sticky groups of adjacent dendritic layers leading to the formation of a compressed, flattened structure for the dendrimers. The structural state of dendrimers on air-solid (self-assembled films) and air-water (Langmuir monolayers) interfaces was further investigated in [115].

Evidence of unexpected compressed multilayers was also found by Casson et al. [116] for LBL films assembled with a propyleneimine generation 3 dendrimer and azobenzene-containing polymer poly[1-[4-(3-carboxy-4-hydroxyphenylazo)benzenesulfonamido]-1,2-ethanediyl, sodium salt], (PAZO). When PAZO was the top layer, it adsorbed as a loosely packed layer due to electrostatic repulsion of the negative charges, resulting in a thicker layer. With a subsequent dendrimer deposition, the PAZO layer collapsed to a more compact form, as seen in Figure 8. The latter occurs due to a screening effect as the dendritic layer

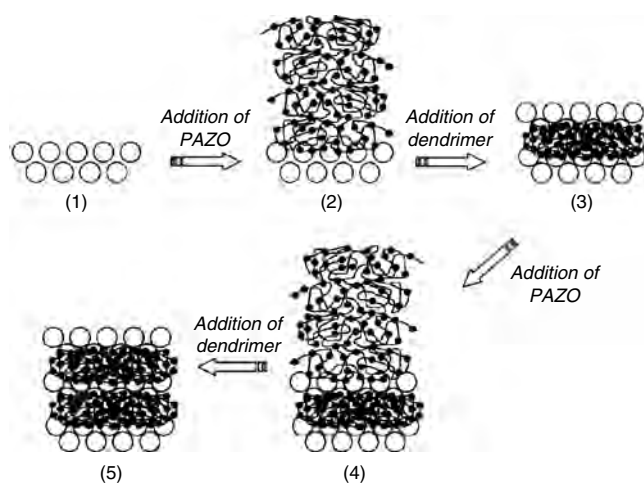


**Figure 8.** Schematic diagram of the dendrimer/PAZO multilayer system showing the interpenetration of the dendrimer molecules into the PAZO polymer and the collapse of the film. (1) a terminal dendrimer layer; (2) a loosely packed layer of PAZO on a dendrimer layer; (3) a collapse of the PAZO layer when dendrimer is adsorbed onto it; (4) another layer of loosely packed PAZO on top of the dendrimer and collapsed PAZO layers; (5) a second collapse of the underlying PAZO layer when dendrimer is adsorbed. Reprinted with permission from [116], J. L. Casson et al., *J. Phys. Chem. B* 106, 1697 (2002). © 2002, American Chemical Society.

interpenetrates in the PAZO layer shielding the charges and allowing the PAZO molecules to pack close together.

The use of dendrimers as encapsulating materials or nanoreservoir materials was exploited by He et al. [30] and Khopade and Caruso [117], using multilayers built up with a PAMAM dendrimer and an anionic polyelectrolyte, SPS. Layer-by-layer films from dendrimers encapsulating gold nanoparticles were produced by He et al. [30]. The insertion of gold particles within the hollow structure of a PAMAM G5 dendrimer was carried out by mixing an aqueous solution of  $\text{AuCl}_4^-$  with an aqueous solution of the PAMAM dendrimer (at a molar ratio of 10 gold atoms per dendrimer) followed by a reduction reaction with hydrazine. Figure 9 depicts the structure of the Au-dendrimer nanocomposite. The final solution with concentration of 3.78 g/L for dendrimer and 0.58 g/L for gold was used in the fabrication of LBL films with SPS onto solid substrates modified with a monolayer of PDDA. The adsorption process was monitored by UV-vis spectroscopy showing that the growth of the Au-dendrimer/SPS multilayer nanocomposites was uniform after the sixth bilayer. The effectiveness of incorporation of Au into the dendritic structure was probed by TEM performed on Au-dendrimer/SPS layers deposited onto carbon-covered copper grids. The results showed that Au appears as nanoparticles (5–20 nm) aggregated within the Au-dendrimer structure. The nanostructure of the films was observed via AFM that showed uniform spherical gold-dendrimer nanoclusters packed on the surface.

Khopade and Caruso [117] showed that multilayers of PAMAM G4 dendrimer assembled with SPS can act as nanoreservoirs. The LBL films of PAMAM/SPS were assembled onto PS colloidal particles (925 nm). In the sequence, the SPS/PAMAM-coated PS particles were exposed to an aqueous solution containing a model fluorescent dye (4,5 Carboxyfluorescein (CF)). The presence of entrapped dye molecules in the LBL films was confirmed by photoluminescence experiments and confocal laser scanning microscopy (CLSM). In the CLSM images, the fluorescence of the entrapped dye molecules appeared as a ring on the

dendrimer/SPS-coated particles. Since CF is not expected to bind SPS, the entrapment is due to interactions of CF with amino groups of the PAMAM dendrimer. Furthermore, it was observed that ca. 80–90% of the entrapped dye molecules could be released under physiological conditions by exposing the dendrimer/SPS-coated PS particles to a stirred solution of 0.154 M NaCl at pH 6.5 (isotonic saline solution), thus suggesting the potential use of these films as drug delivery materials.

The versatility of addressing specific functional sites as end groups in dendrimers contributed to the development of a new approach concerning the mechanisms of adsorption in LBL films [23, 118]. Multilayer films fabricated with biotin-labeled polyamines and avidin were reported by Anzai et al. [23]. Despite the fact that avidin and polyamines are both positively charged, multilayer growth was possible due to the very specific interaction between avidin and biotin, since the avidin-biotin interactions are stronger than the ionic repulsion. The latter was confirmed by the fact that multilayers could not form when unmodified polyamines were used. Differences in deposition behavior and structure of the LBL films were observed depending on the geometry of the modified polyamine. Films prepared with a modified dendritic polyamine (PAMAM) provided the deposition of a monomolecular layer of avidin. Such behavior, however, was not observed when avidin was assembled with branched poly(ethyleneimine) and linear poly(allyllamine).

The nanometer-scale porous structure presented by dendrimers has become of special interest in applications where diffusion of molecules is required, such as heterogeneous catalysis and sensing. Layer-by-layer dendritic films, in particular, have been reported as modified electrodes for electrochemical catalysis [119] and bio [120, 121] or vapor sensing [122, 123]. The reason is that the porous structure of dendrimers may facilitate ion exchange throughout the film. Layer-by-layer films especially designed for electrocatalysis were prepared by Cheng and Cox [119]. The films were made up of PAMAM G4 dendrimers assembled with two different polyoxometalates (POMs), viz.  $\text{PMo}_{12}\text{O}_{40}^{3-}$  (Keggin-structure) and  $\text{P}_2\text{W}_{18}\text{O}_{62}^{6-}$  (Dawson-structure). The structure of the LBL films is shown in Figure 10. The growth of the multilayers was uniform according to UV-vis and cyclic voltammetry data. The catalytic effect of the films was confirmed via cyclic voltammetry where the electrochemical reduction of iodate and nitrite was analyzed. In addition to the catalytic effect, the stability of POM into the layered structure was improved.

The feasibility of LBL dendritic films for biosensing applications was demonstrated by Yoon et al. [120, 121]. Multilayer structured films were assembled alternating PAMAM G4 dendrimer with periodate ( $\text{IO}_4^-$ ) oxidized glucose oxidase (GOx) onto a gold electrode surface [120]. Thin films containing 1 to 5 bilayers (ca. 5.2 nm per bilayer) were used for detecting glucose via electrochemical analysis using ferrocenemethanol as an electron-transfer mediator. Glucose was detected by the increase in the anodic current plateau as a function of its concentration. Besides, the modified electrodes displayed thickness-dependent sensitivity. A linear increase of the anodic current was observed as a function of the number of bilayers in the presence of 20 mM of glucose. The sensitivity of the 5-bilayer film was

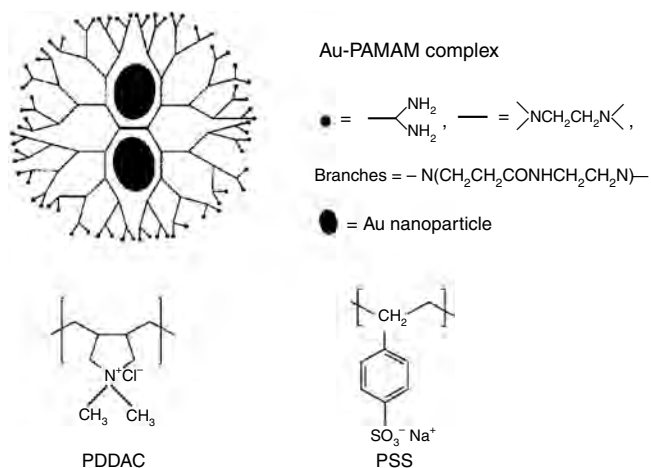


**Figure 9.** Structures of the polyelectrolytes and Au-dendrimer (G5 PAMAM) nanocomposites for electrostatic LBL assembly. Reprinted with permission from [30], J.-A. He et al., *Chem. Mater.* 11, 3268 (1999). © 1999, American Chemical Society.



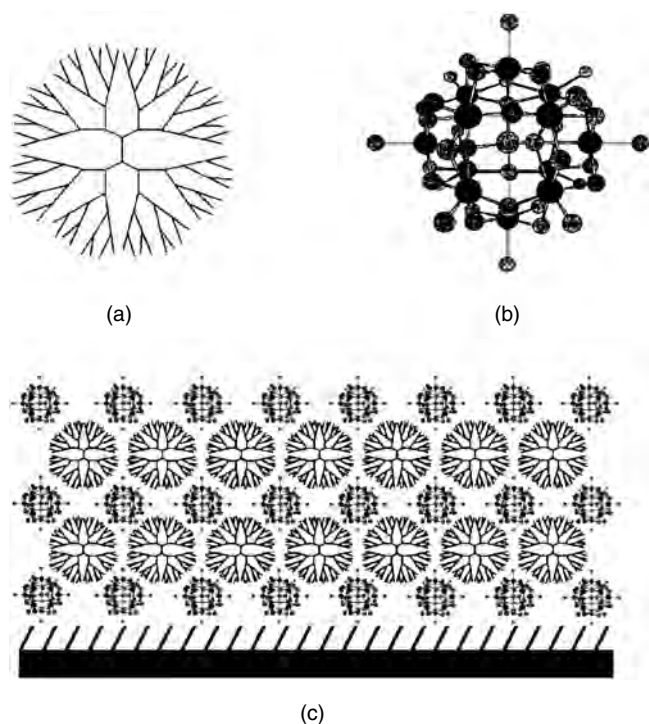


**Figure 10.** Structures of: (a) PAMAM and (b)  $\text{PMo}_{12}\text{O}_{40}^{3-}$ . In the PAMAM structure, the branching site is  $-\text{N}<$  and the surface is  $-\text{NH}_2$ . In the  $\text{PMo}_{12}\text{O}_{40}^{3-}$  structure, the dark ball represents Mo atom, while the shadowed ball represents an O atom with the exception that the central shadow ball is a P atom. (c) The conceptual model of a multilayer of  $\text{Au}|4\text{-ATP}|(3) \text{PMo}_{12}\text{O}_{40}^{3-}|(2)\text{PAMAM}$ . Note: the sizes of PAMAM and  $\text{PMo}_{12}\text{O}_{40}^{3-}$  drawn are not to scale. Reprinted with permission from [119], L. Cheng and J. A. Cox, *Electrochem. Comm.* 3, 285 (2001). © 2001, Elsevier Science.

$14.7 \mu\text{A} \cdot \text{mM}^{-1} \text{glucose} \cdot \text{cm}^{-2}$ . In order to produce reagentless biosensors, modified gold electrodes were produced for glucose detection, using a PAMAM-functionalized dendrimer and GOx [121]. The primary amine end groups of a PAMAM G4 dendrimer were chemically modified with ferrocene carboxaldehyde leading to the ferrocenyl-tethered dendrimer (Fc-D). As in the case previously discussed [120], the sensitivity of the LBL modified electrodes built with Fc-D could be tuned by adjusting the number of bilayers of the films. Dendrimers exhibiting 32% of modification provided the optimum balance between conjugation with enzyme and electrocatalytic activity.

Dendrimers as building blocks for porous LBL films were exploited by Vossmeier et al. in vapor-sensing devices [122, 123]. The devices comprised gold nanoparticles assembled with different types of dendrimers onto lithographic interdigitated electrodes. High selectivity could be achieved in the devices upon appropriate choice of dendrimers with hydrophilic, amphiphilic, or hydrophobic character. Electrical conductivity was provided by the Au nanoparticles. The use of dendrimers allowed the assembly of Au nanoparticles in addition to the fact that they provided specific sites for the sorption of the analyte molecules. Three different types of dendrimers were employed, viz. polyphenylene dendrimer (PPh) (hydrophobic), poly(propyleneimine) dendrimer G4 (amphiphilic) (PPI), and poly(amidoamine)

PAMAM G3 (hydrophilic) (PAMAM). The sensor characteristics of the LBL films were evaluated by monitoring the changes in the film electrical conductivity in the presence of toluene, 1-propanol, or water vapors. Figure 11 illustrates the electrical responses of the devices in the presence of 5000 ppm of the solvents. The sensing mechanism is attributed to a swelling effect of the film in the presence of the solvent, which increases the tunneling distance between the Au particles, thus diminishing the film conductivity. Such a mechanism explains the high selectivity of the films since the swelling effect depends on the affinity between solvent and dendrimer.

## 8. LB FILMS FROM METALLIC COMPLEXES

The scientific interest in the fabrication of ultra-thin films from organometallic materials [124–127] is motivated by the possible extension of applications that today are based on inorganic compounds, especially semiconductors. The LB

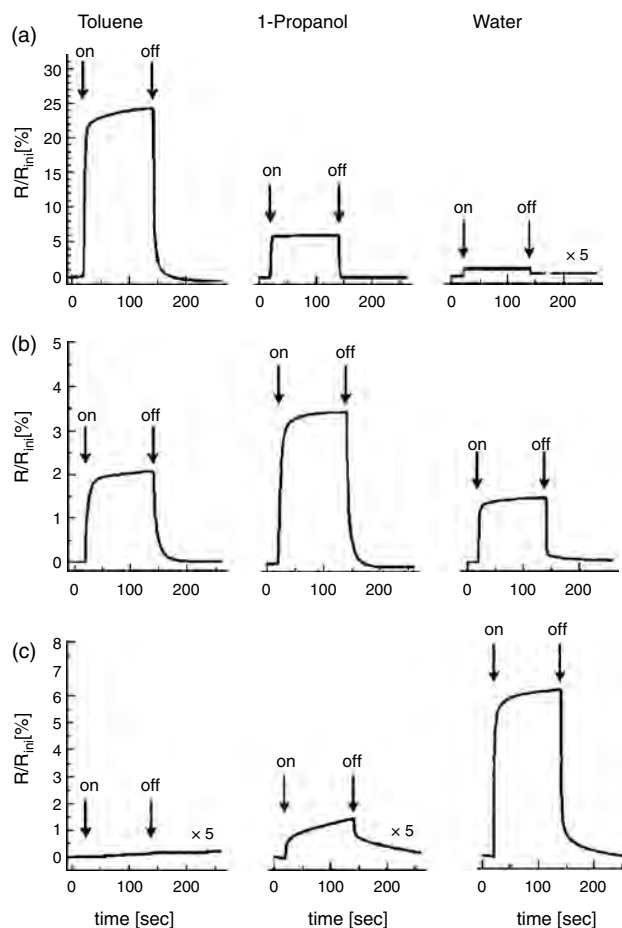


**Figure 11.** Response traces measured by dosing the Au/dendrimer films with toluene, 1-propanol, and water: (a) Au/PPh; (b) Au/PPI; (c) Au/PAMAM. In each case the vapor concentration was 5000 ppm, and the temperature of the sensor cells was kept constant at  $39^\circ\text{C}$ . The arrows indicate switching between carrier gas (dry, purified air) and the test vapor. Reprinted with permission from [123], N. Krasteva et al., *Nano. Lett.* 2, 551 (2002). © 2002, American Chemical Society.

technique has been exploited in this context due to the control over film thickness and architecture [128, 129], in addition to the intimate contact between distinct materials in heterostructures. Complexes of transition metals, for example, are advantageous when containing ligands with low-energy  $\pi$  electrons coupled to metal ions with various redox states [130]. In order to exploit the advantages of the LB technique, one has to optimize film fabrication conditions since most materials do not readily form stable LB films. The LB technique was conceived for amphiphilic, small molecules that are efficiently spread on an aqueous subphase and suitable rigidity to allow transfer onto a solid substrate. For macromolecules or semi-amphiphilic materials, a number of difficulties may arise. The first one comes from the poor spreadability of the material, particularly when the hydrophilic and hydrophobic parts of the molecules are not well defined. Such compounds tend to form aggregates with a consequent decrease in monolayer stability. This is an important issue as the fabrication of high-quality LB films requires stable monolayers. In the case of macromolecules, there are additional difficulties associated with the rigidity of the monolayer which hampers transfer onto a substrate. Furthermore, Langmuir films from macromolecules are most often not true monolayers, that is, they are not monomolecular layers. In any case, special strategies must be used to produce LB films. A number of such strategies have been used in the recent past, and perhaps the most frequent one is the mixture of the nonamphiphilic material with a traditional amphiphile like a fatty acid [131].

### 8.1. LB Films from Ru Complexes

Ruthenium complexes are certainly among the most used metallic complexes for the fabrication of Langmuir and LB films. Such compounds may be classified as semi-amphiphilic or nonamphiphilic—their spreading ability is generally low. As a result, stable monolayers are only formed after optimization of experimental conditions. The first attempts to produce LB films from amphiphilic ruthenium compounds, including those with long alkyl chains, were unsuccessful [132–135], mainly because the Langmuir films were unstable due to hydrolysis of the ester groups. Zhang and Bard [136, 137] and Obeng and Bard [138] investigated the electrochemical properties of LB films of  $[\text{Ru}(\text{bpy})_2(\text{bpy}-\text{R})]^{2+}$  (bpy = 2,2'-bipyridine; R is a long alkyl chain) and suggested that the monolayer of ruthenium complexes tends to aggregate on the water surface, thus leading to unstable films. In later works, it was shown, however, that stable Langmuir films could be formed. For example, while producing mixed LB films of stearic acid (SA) and the complex  $[\text{Ru}(\text{dppen})_3]^{2+}$  (dppen = 4,7-diphenyl-1,10-phenanthroline), Murakata et al. [139] showed that long alkyl chains are not required in the ruthenium complex for the formation of stable Langmuir films. Murakata et al. [139] proposed a mechanism of monolayer formation consistent with the ion-pair interaction, as depicted in Figure 12, where the metallic complex interacts with the carboxylate of SA. In the experiments by Murakata et al. [139], the incorporation of the complex alters the surface pressure isotherm of stearic acid, by introducing a phase transition between the liquid-expanded and liquid-condensed phases, which is not

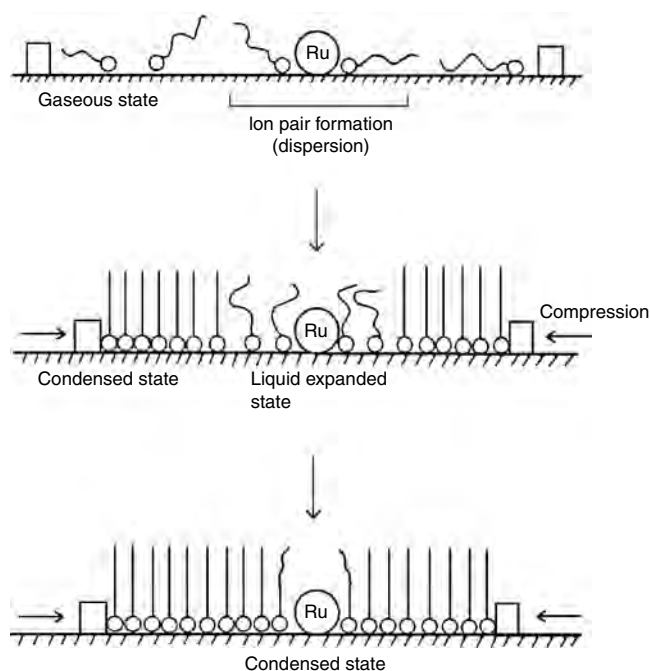


**Figure 12.** Schematic diagram for the formation of the Langmuir monolayer via ion-pair interaction. Reprinted with permission from [139], T. Murakata et al., *J. Phys. Chem.* 92, 6040 (1988). © 1998, American Chemical Society.

present for the pure acid. The plateau characteristic of this phase transition was attributed to the interaction between the metallic complex and the carboxylate.

Langmuir films from other ionic Ru complexes were fabricated by DeArmond et al. [140], where the complex was dissolved in the aqueous subphase on which a fatty acid monolayer was spread. This was motivated by Palacin et al.'s work [141, 142] for cobalt(II) phthalocyanines. The area per molecule for the fatty acid condensed monolayer on a subphase containing Ru complex is 23–24 Å<sup>2</sup>, compared to 20 Å<sup>2</sup> for the monolayer on pure water. This increase was attributed to the ionic interaction between the complex and stearic acid molecules. It is known that when the subphase contains CdCl<sub>2</sub>, a stearic acid monolayer displays no liquid-expanded phase [143]. However, when Ru<sup>2+</sup> were present in the subphase, the packing of the stearic acid molecules was less efficient and the liquid-expanded phase appeared [141].

Samha and DeArmond [144] investigated Langmuir films from mixtures of stearic acid and Ru(II) ionic complexes ( $[\text{Ru}(\text{N}-\text{N})_3]^{2+}$ , where N-N = 4,4',5,5'-tetramethyl-2,2'-bipyridine, 1,10-phenanthroline, 4,7-diphenyl-1,10-phenanthroline) dissolved in the subphase solutions compared with films of stearic acid on pure water. They showed that equilibrium is reached for monolayers of these complexes within 30–60 min after spreading. Immediately after spreading, however, the collapse pressure decreased and tended to the collapse pressure of stearic acid. The area per stearic acid unit in the compressed film of stearic acid on the surface of the ruthenium complex subphase (23–24 Å<sup>2</sup>) is larger than that on the pure water subphase (20 Å<sup>2</sup>). Such behavior is due to the ion-pair interaction between the stearic acid and the metal complex ions. This was attributed to the

migration of molecules of the complex into the subphase. The collapse pressure of the film decreased with time (in the range of 30 to 60 min) becoming the same of the collapse pressure of pure stearic acid (55–65 mN/m, 120 min) [144], which indicates the migration of the complex molecules from the surface to underneath the stearic acid layer, as shown schematically in Figure 13.

The interaction of Ru complexes with fatty acids in Langmuir films has been investigated in [145]. Arachidic acid (AA) monolayers were spread on subphases containing tris(1,10-phenanthroline)ruthenium(II) chloride hexahydrate. The electrostatic interaction between Ru(II) ions and AA molecules is similar to that with  $\text{Cd}^{2+}$  ions, which caused the monolayer to be more stable. The only difference was that the Ru(II) complex kept AA molecules further apart than in the case of cadmium ions. The red shift in the UV-vis absorption spectra of the mixed LB films, in relation to the spectra of Ru(II) in acetonitrile, can probably be assigned to aggregates and a counterion effect. Interaction with fatty acid (arachidic acid) monolayers was also studied for  $[\text{Ru}(\text{L})(\text{totpy})(\text{OH}_2)](\text{ClO}_4)$  ( $\text{L} = \text{Ph}_2\text{AsCH}_2\text{CH}_2\text{AsPh}_2$ ); 4-totpy = 4'-(4-tolyl-2,2':6',2''-terpyridine) complex (2:1). The surface pressure ( $\pi$ ) versus surface area ( $A$ ) isotherms obtained for the Langmuir films showed a phase transition between the expanded and liquid-condensed states, which is not present in the  $\pi$ - $A$  curves for pure AA monolayers. In surface potential,  $\Delta V$ , versus area,  $A$ , isotherms, the critical area corresponding to the onset for the surface potential increased considerably with the incorporation of the ruthenium complex. Also, the difference between the minimum and maximum surface potential increased with the concentration of the ruthenium complex in the mixed monolayer. UV-vis, and FTIR spectroscopy of the LB films from the mixture confirmed the partial dissociation of the acid [146]. This mixed monolayer approach was also employed for

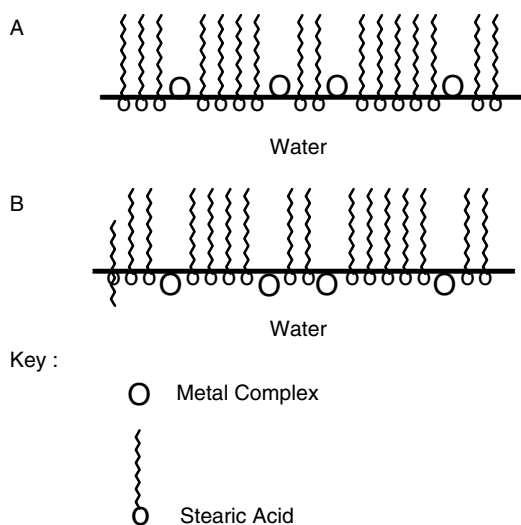


**Figure 13.** Schematic illustration of the migration of the metal complex molecules from (A) the surface of the subphase (surface film) to (B) beneath the stearic acid monolayer (subphase film). Reprinted with permission from [144], H. Samha and M. K. De Armond, *Langmuir* 10, 4157 (1994). © 1994, American Chemical Society.

other ionic ruthenium complex, for example,  $[\text{Ru}(\text{dppe})(4'\text{-totpy})(\text{H}_2\text{O})]\text{ClO}_4$ , where  $\text{dppe} = \text{PPh}_2(\text{CH}_2)_2\text{PPh}_2$  and 4'-totpy = 4'-(4-tolyl-2,2':6',2''-terpyridine) [147]. In the latter, FTIR characterization confirmed that the acid molecules were ionized and complexed with the ruthenium complex molecules.

The properties of Langmuir films from  $[\text{Ru}(\text{L}_{18})(\text{tPY-PO}_3\text{H})]\text{PF}_6$  complex, where  $\text{L}_{18} = 2,6\text{-bis}(\text{N-octadecylbenzimidazol-2-yl})\text{pyridine}$  and  $\text{tPY-PO}_3\text{H} = 2,2';6',2''\text{-terpyridine-4'-phosphonic}$  were strongly affected by the pH of the subphase and by the metal coordination [148]. The surface pressure-area isotherms displayed a smaller area per molecule at lower pHs. The *in-situ* UV-vis absorption spectra of the Ru complex at the air-water interface also depended on the pH of the subphase, because as the subphase becomes acidic, the absorption band at 363 nm from the intraligand  $\pi - \pi^*$  transitions is sharpened with a slight red shift, which reveals the formation of molecular aggregates at the air-water interface.

Uemura et al. [149] reported hybrid multilayers of natural saponite and the amphiphilic ruthenium(II) complex  $[\text{Ru}(\text{phen})_2(\text{dcCl}_2\text{bpy})]^{2+}$  ( $\text{phen} = 1,10\text{-phenanthroline}$ ,  $\text{dcCl}_2\text{bpy} = 4,4'\text{-carboxyl-2,2'-bipyridyl didodecyl ester}$ ) prepared by two methods: in method A (Fig. 14a), the hybrid monolayer was deposited by a horizontal dipping one after another; in method B (Fig. 14b) a hydrophilic surface of the transferred hybrid monolayer was dipped in an aqueous solution of an alkylammonium salt to render the surface hydrophobic with alkylammonium cations. The isotherms obtained for the films of  $[\text{Ru}(\text{phen})_2(\text{dcCl}_2\text{bpy})]^{2+}$  spread on pure water and on clay suspensions showed a dependence

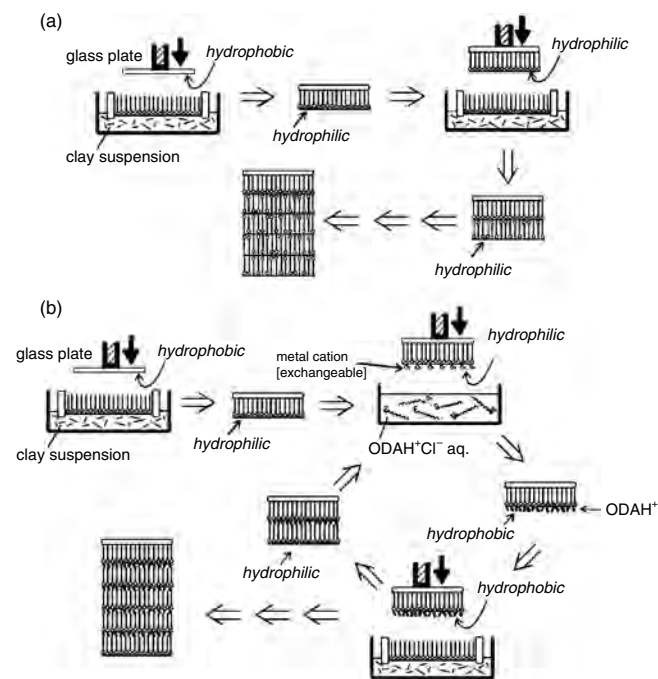


**Figure 14.** Preparation methods of hybrid LB multilayers of amphiphilic ruthenium(II) complex cations and clay platelets: (a) Method A and (b) Method B. Reprinted with permission from [149], Y. Uemura et al., *J. Am. Chem. Soc.* 124, 992 (2002). © 2002, American Chemical Society.

on the clay concentration (10, 50, and 100 ppm), suggesting the formation of a hybrid monolayer of the complex and the clay at the air-suspension interface. The difference in orientation resulting from the application of the two methods was apparent in the area per cation for the multilayer. It was concluded that in method A, the multilayer was produced LBL, but the orientation of the Ru(II) complex cation in the layer was disturbed [149]. The multilayer prepared by method B was also built in a LBL fashion, but with a better defined structure with the layer oriented in one direction, that is, the hydrophobic alkyl chains of the Ru(II) complex cation would be directed to the alkylammonium salt layer, and the hydrophilic head group of the complex cation and phenanthroline ligands would face the clay layer [149].

A fullerene-ruthenium-porphyrin complex was employed in the fabrication of LB films, building upon previous experiences [150] with fulleropyrrolidines functionalized at the nitrogen with hydrophilic chains possessing the correct hydrophobic-hydrophilic balance to form stable monomolecular layers at the air-water interface [151]. The existence of a true monolayer was confirmed by means of  $\pi$ - $A$  isotherms. The  $\pi$ - $A$  isotherm for a 1:20 molar mixture of ruthenium complex and AA displayed different phases as the dyad molecules were squeezed out from the film. When  $\pi > 35 \text{ mN} \cdot \text{m}^{-1}$ , the dyad molecules were virtually on top of the hydrophobic arachidic acid layer. Photophysical studies, performed by transient absorption spectrophotometry, demonstrated that electron transfer occurs in the solid film with a lifetime of  $2.2 \mu\text{s}$ .

Another class of ligands for transition metals comprises the tertiary phosphines that may be strongly bonded to transition metal ions. Phosphines may be employed to stabilize isolated compounds or intermediates in homogeneous catalysis [152, 153], as well as in chemotherapy agents [154]. Because they possess a reasonably strong *trans* effect, phosphines lead to easily labile complexes that are essential for homogeneous catalysts [152, 155, 156]. Ru-containing catalysts with chelated biphosphine ligands for asymmetric hydrogenation have been used since the 1970's [157], and in recent years applied in classical catalytic reactions (e.g., hydrogenation, isomerization, decarbonylation, homologation of amines) [158, 159], in the activation of C-H species in the coupling of olefines [160], for oxidation [161] and incorporation of carboxylic acid in alkynes [162], hydrogenation of styrene [163], and imines [164, 165]. With regard to LB films from phosphine-containing metallic complexes, in 1993 Fu et al. [166] reported the use of a long-chain phosphine ligand,  $\text{P}(\text{C}_{18}\text{H}_{37})_3$ , coordinated to the complex  $[\text{Ru}(\text{P}(\text{C}_{18}\text{H}_{37})_3)(\text{DTBSq})]$  ( $\text{DTBSq} = 3,5$ -di-*tert*-butyl-*o*-benzosemiquinonato). These LB films were characterized using UV-vis spectroscopy, and *in-situ* cyclic voltammetry. Santos et al. [147] employed the achiral biphosphine ligand dppe with the complex  $[\text{Ru}(\text{dppe})(4'$ -totpy) $(\text{H}_2\text{O})]\text{ClO}_4$ , and the resulting LB films were assessed as electrode modifiers. Enhanced electrochemical activity was observed with the immobilization of the complex within the matrix formed by the LB film, due to the orientation conferred by the LB technique that assists the electron transport.

The molecular-level interaction between a biphosphine ruthenium complex,  $\text{mer-}[\text{RuCl}_3(\text{dppb})(4\text{-Mepy})]$

( $\text{dppb} = \text{PPh}_2(\text{CH}_2)_4\text{PPh}_2$ ; 4-Mepy = 4-methylpyridine) ( $\text{Ru-pic}$ ) [167] (Fig. 15) and stearic acid was investigated in LB films by Wohnrath et al. [168]. Langmuir-Blodgett films could also be produced from pure Ru-pic, but in this case the films that were spread on the water/air interface were not true monolayers. Transferability was considerably enhanced upon mixing Ru-pic with stearic acid. Nevertheless, the LB films from pure Ru-pic displayed higher electroactivity, partially because there was no insulating matrix of stearic acid and also because the resulting films had higher roughness. Cyclic voltammetry results also indicated that the irreversible behavior of this complex in the LB films was associated with its spatial rearrangement when Ru(III) was converted into Ru(II), which caused the electron transfer rate between film and substrate to be lower than for the compound in solution. In the latter, such restructuring induced different species. It should be stressed that cast films from Ru-pic were not electroactive, which demonstrates that this property depends on the order induced in the LB technique.

A parent biphosphine ruthenium complex,  $\text{mer-}[\text{RuCl}_3(\text{dppb})(\text{py})]$ , ( $\text{py} = \text{pyridine}$ ) ( $\text{Rupy}$ ), was also investigated for a molecular-level interaction with stearic acid in

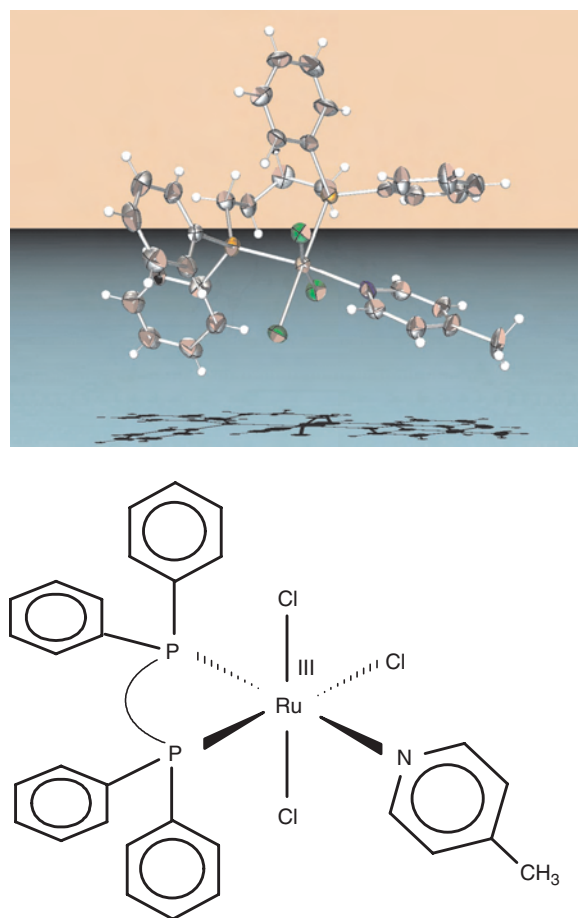


**Figure 15.** Three-dimensional illustration and chemical structure of the complex  $\text{mer-}[\text{RuCl}_3(\text{dppb})(4\text{-Mepy})]$ . Reprinted with permission from [168], K. Wohnrath et al., *Thin Solid Films* 402, 272 (2002). © 2002, Elsevier Science.

Langmuir and Langmuir–Blodgett films [169]. The interaction was demonstrated in the Langmuir films by a non-linear increase in the area per molecule and in surface potential with the relative concentration of the ruthenium complex in the mixture. Interaction with stearic acid in the LB films occurred via complexation with the ruthenium complex, even though Rupy is not charged. It was suggested [169] that one of the chlorides was labilized to promote complexation and keep the Ru(III) oxidation state of the complex. Complexation was confirmed through FTIR spectroscopy. Another interesting feature of the LB films from Ru-pic and Rupy was the color change in comparison to cast films or solutions of the complexes in organic solvents, as illustrated in Figure 16. This color change was attributed to an order-induced effect caused by the LB fabrication process, and was enhanced due to the interaction with stearic acid.

In the previous paragraphs, we mentioned LB films from mononuclear ruthenium complexes. Langmuir–Blodgett films have also been produced from binuclear Ru species with mixed valence. The behavior of the organized monolayers of the dyad Ru(II)-Rh(III) (water soluble)

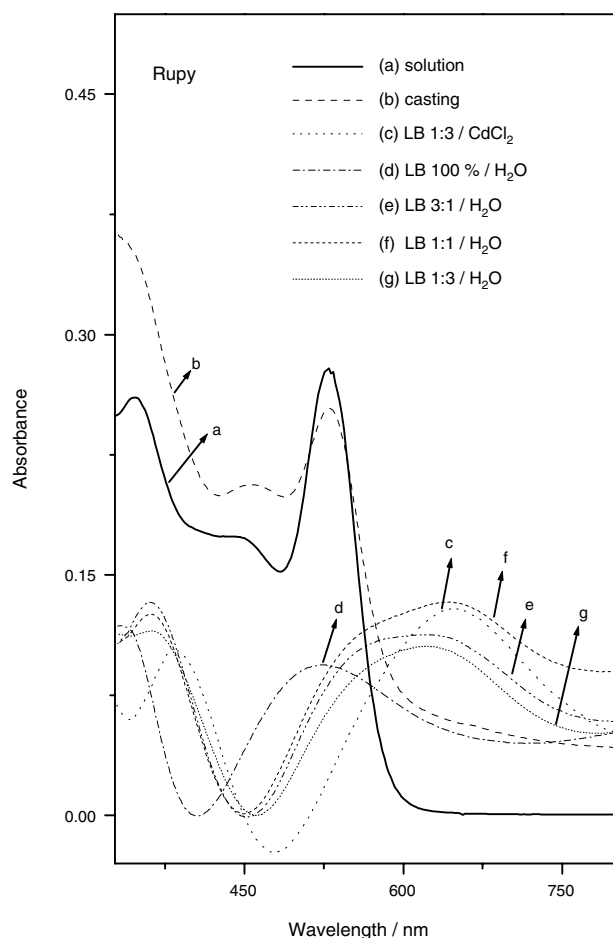


**Figure 16.** Electronic absorption spectra recorded for Rupy in various forms: in chloroform solution (a), as neat cast film (b), in neat LB films (d), or mixed LB films (c, e, f, g). Reprinted with permission from [169], M. Ferreira et al., *J. Phys. Chem. B* 106, 7272 (2002). © 2002, American Chemical Society.

and monolayers of opposite head-group charge such as dimyristoyl-phosphatidic acid (DMPA) and protonated eicosylamine (EA) has been studied [170]. The Rh(II) subunit has two 2,2'-bi-(4,4'-dicarboxy)-pyridine ligands and the bipyridine-residual of the bridging 1,2-di-(4,4-(2,2'-bi(4',4'-dimethyl)-pyridine))-ethane, which also acts as a ligand of the octahedral Ru(II) subunit with two further 1,10-dimethyl-phenanthroline ligands. The dyad has a net positive charge of  $1^+$ , if all four COOH groups in the Rh moiety are ionized. The Ru moiety has the charge  $2^+$  (Fig. 17). The surface pressure area isotherms indicated that the pure dyad is water soluble and forms no monolayer at the air-water interface. The polar heads of DMPA bind electrostatically not only to the Ru(II) center but also interact with Rh(III). The COOH groups of the Rh(III) ligands and the charge of the metal ions provide a variety of possibilities to bind the dyad to a charged monolayer and/or to incorporate a subunit into the hydrophobic moiety of the lipid monolayer. The isotherms of dyad-EA demonstrated that the dyad with a net positive charge also interacts with a positively charged monolayer: the positive head group of the EA monolayer with three deprotonated carboxyl groups of the Rh subunit while the Ru subunit was oriented towards the subphase.

The system Ru(II)-Rh(III) dyad [171] was incorporated in monolayers at the air/water interface by cospreading with a positively EA or negatively SA charged amphiphile. The morphologies of the two resulting systems after transfer onto mica were determined using two scanning probe techniques, scanning probe microscopy (SPM) and scanning force microscopy (SFM). No dyad was lost with SA upon compression and transfer of the monolayer. In contrast, much less dyad remained at the water/interface with EA as the lipid anchor.

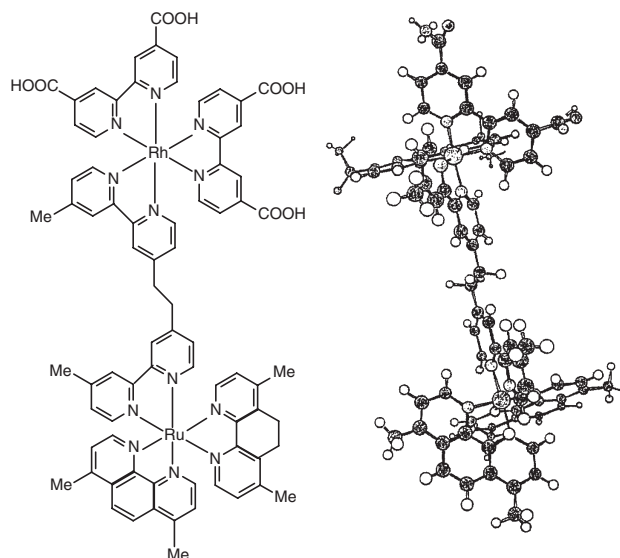


**Figure 17.** The Ru-RH dyad: Chemical structure (left), and three-dimensional model of the dyad (right). Reprinted with permission from [170], H. Huesmann et al., *Thin Solid Films* 284–285, 62 (1996). © 1996, Elsevier Science.

## 8.2. LB Films from Metallic Complexes Other than Ru

A great deal of work has been done in organometallic materials in the form of LB monolayers and multilayers. A review of the topic was published by Nalwa and Kakuta in 1992 [172], where the electrical and nonlinear optical properties of LB films from several systems were discussed. Such systems included organoruthenium complexes, ferrocene derivatives, metal(4,5-dimercapto-1,3-dithiol-2-dithiolene)<sub>2</sub> complexes, metallophthalocyanines, metalloporphyrins, metal(dibenzotetra-aza[14]annulene)s, and siloxane polymers. Details were also given of the possible applications of these organometallic LB films in sensors, electrochromic devices, and optical switches.

Recently, LB films have also been produced from other metallic complexes as described in the review article by De Armond and Fried [124]. For instance, Zhang et al. [173] obtained a stable monolayer of the molecules Eu(TTA)<sub>3</sub>Phen and Sm(TTA)<sub>3</sub>Phen ( $\beta$ -diketone 2-thenoyltrifluoroacetone), (TTA) using a composite subphase—an aqueous solution saturated with TTA, Phen and Eu(TTA)<sub>3</sub>Phen. The reason for reproducible  $\pi$ -A isotherms and homogeneous crystalline monolayer is that the dissolution and dissociation of Eu(TTA)<sub>3</sub>Phen are effectively inhibited by the composite subphase [174]. Gao et al. [174] were the first to report the influence of different compounds introduced in organized molecular films for the fluorescence of rare earth complexes. They reported the fabrication of 10 alternate LB films: each of the two rare earth complexes was alternated with AA, trin-octyl phosphine oxide (TOPO), a long chain Schiff base (SB), 5,50,15,20-tetra-4-oxy(2-stearic acid)phenyl porphyrin (TPP(-COOH)), and a long ferrocene derivative (Fc). The results indicated that TOPO and SB enhanced while Fc and TPP(-COOH) strongly quenched the fluorescence of the rare earth complexes. The reason why TOPO and SB enhanced the fluorescence intensity of the complexes is that they can absorb energy in the ultraviolet range. The energy can be transferred to the rare earth ions either from the ligands or directly from TOPO and SB.

Monolayers of three biferrocene derivatives (BiFc) and mixed ones with AA (1:1 molar ratio) were investigated for their electrochemical properties [175]. Cyclic voltammograms on modified ITO electrodes are similar for these systems. The currents for the electrochemical reaction of  $\text{Fe}(\text{CN})_6^{3-}/\text{Fe}(\text{CN})_6^{4-}$  on each kind of mixed LB monolayer-modified ITO electrode were higher than those on the bare ITO electrode. The oxidation peak potential of  $\text{Fe}(\text{CN})_6^{4-}$  was more negative and the reduction peak potential of  $\text{Fe}(\text{CN})_6^{3-}$  was more positive. The electrochemical redox reaction of  $\text{Fe}(\text{CN})_6^{3-}/\text{Fe}(\text{CN})_6^{4-}$  could be catalyzed by ITO electrodes modified with the mixed monolayer of BiFc and AA. BiFc films were found to be more efficient for the electrochemical reaction than the LB films from ferrocene derivatives containing one redox center and long alkyl chains [176]. A variety of reports have been made on LB films from porphyrin and phthalocyanine complexes [177–187], which include proposals of applications [188–192]. For example, LB films of a porphyrin complex CoPPC<sub>18</sub>, Cobalt(II) 5,10,15-tri(*p*-octadecyloxyphenyl)-20-(*p*-hydroxyphenyl)porphyrin [192] were suitable for optical

sensing upon exposure of the films to NO<sub>2</sub>. Interaction between NO<sub>2</sub> molecules with the active layers of the LB films resulted in a change of the films refractive index. This effect was reversible and could be monitored using a Mach-Zender interferometer. Another sensor was made with LB films from a metallic porphyrin, copper(II) tetra-(*tert*-butyl)-5,10,15,20-tetraazporphyrin, [CuPaz(*t*-Bu)<sub>4</sub>] [193]. The UV-vis spectra of the 20-layer LB films were dramatically changed after being exposed to the saturated vapors of benzene, toluene, and hexane. Shifts in the Soret and Q bands were observed due to the interactions between porphyrin of the [CuPaz(*t*-Bu)<sub>4</sub>] molecules and the organic solvent molecules. The gas sensing ability for benzene and toluene was also demonstrated via QCM measurements.

## 8.3. LB Films from Mixtures of Metallic Complexes and Polymers

A large number of papers reporting the build-up of LB films from mixtures of metallic complexes and polymers have been published in recent years. The motivation for such studies arises from the potential application of these films in sensors [194], catalytic systems [191], and molecular electronic devices [195]. In order to provide a flavor of the interesting results that may be obtained, we shall concentrate mostly on recent work of our group, followed by a description of a few articles from other authors.

The interaction between ruthenium complexes and polyaniline in monolayer and LB films was studied by Ferreira et al. [196, 197]. Langmuir monolayers and LB films were produced from polyaniline and a biphosphinic ruthenium complex, referred to as Rupy. Strong, repulsive interaction between the two components led to a nonlinear change in area per molecule and surface potential with the concentration of Rupy in the mixed film. Molecular interaction was also denoted in the spectroscopic and electrochemical properties of the Y-type LB transferred films. Upon increasing the amount of Rupy in PANI, a blue shift was observed in the peak attributed to the quinoid species of the PANI UV-vis spectra [197], and the Raman spectra of mixed PANI-Rupy films also indicated the oxidation of PANI. With PANI being oxidized by Rupy, the electroactivity of the mixed films decreased with the amount of Rupy, to become undetectable when the mixed LB film was 50% mol in Rupy. In contrast, cast films from PANI and Rupy always exhibited electroactivity, because in these films the molecules are randomly oriented and interaction between the components is not strong as in the LB films [198]. The interest in combining PANI with the ruthenium complexes is to enhance the properties of the polymer films for possible applications in electronic devices and sensors. Besides, the presence of the Ru complex brings the transfer ratio close to one for the fabrication of LB films, similarly to the effect widely reported for fatty acids.

The interaction between ruthenium complexes and conducting polymers was exploited to produce sensing units [194] for artificial taste sensors—the so-called electronic tongue [199]. In this approach, nanostructured LB or LBL films are deposited onto interdigitated gold electrodes and serve as sensing units for liquid media, in which the principle of detection is impedance spectroscopy. Riul et al. [199]



showed that high sensitivity may be obtained because the films are ultra-thin and probably organized, and that sensor arrays with a combination of 4–6 sensing units can distinguish low quantities of substances corresponding to the basic tastes—salty, sour, bitter, and sweet. These tastes are represented by aqueous solutions of NaCl, HCl, quinine, and sucrose, respectively. This ability can also be employed to distinguish among samples of different liquid media, including coffee [200], coconut water [194], and to detect trace amounts of impurities in a liquid, as is the case of metals in water [199]. The electrical response of the units—that is, the impedance for various frequencies—is treated theoretically with an equivalent circuit that represents the sensor immersed in an electrolyte [200]. The figure of merit chosen is usually the capacitance associated with the nanostructured film at a given frequency, say 1 kHz, and one value is taken for each and every liquid sample tested. Obviously, the amount of data collected is enormous and statistical methods must be used to treat the data. One such method is the principal component analysis (PCA) [201], which allows one to cluster similar electrical responses among a variety of data. By way of illustration, we show a PCA plot in Figure 18, which demonstrates that beverages and solutions with different tastes and inorganic contaminants can be distinguished. In the context of applications of LB films from metallic complex, we should mention that an electronic tongue has been produced in which the sensing units were made from conducting polymers and the Rupy complex [194]. This sensor array could identify sucrose, quinine, NaCl, and HCl at the parts per billion (ppb) level, being in some cases three orders of magnitude below the human threshold. With a direct comparison with results obtained

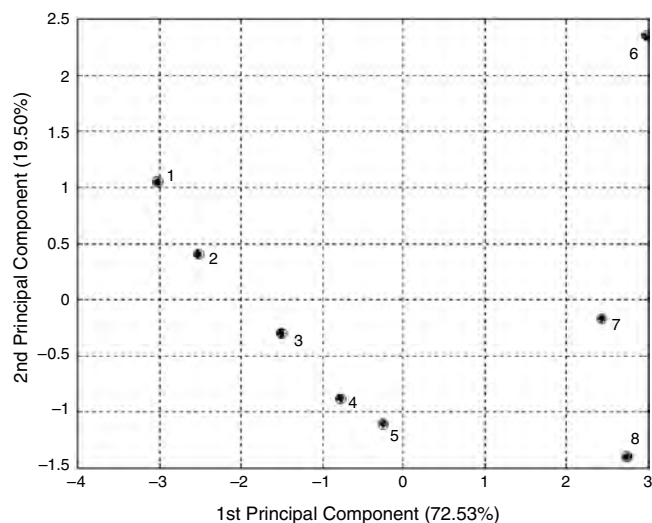


**Figure 18.** Principal component analysis plot for sensing commercial beverages with the set of six units from LB films. Sensing units used were made from LB films of the following materials: (1) Rupy; (2) PANI; (3) PPy; (4) PPy-Rupy 30%; (5) PANI-Rupy 10%; (6) PANI-Rupy 30%; 1 = ultra-pure water; 2 = distilled water; 3 = tap water; 4 = mineral water A; 5 = mineral water B; 6 = natural coconut water; 7 = commercial coconut water A; 8 = commercial coconut water B. Reprinted with permission from [194], M. Ferreira et al., *Anal. Chem.* 75, 953 (2003). © 2003, American Chemical Society.

with cast films of the same materials, it was possible to show for the first time the superior performance of the nanostructured LB films [194].

The formation of LB films from a coordination complex involving metals ions ( $K^+$ ,  $Mg^{2+}$ , and  $Fe^{3+}$ ) and a ligand monolayer (an amphiphilic polymeric imidazole, poly(N-(2-(4-imidazolyl)ethyl)maleimide-*alt*-1-octadecene), IM-O) was reported by Jeong et al. [202] to explore the possibility of obtaining ion sensors using LB films. Surface pressure isotherms for IM-O indicated that the monolayers were not affected by changing the subphase, and that the area per molecule was slightly reduced for metal ion-containing subphases compared with that of pure water at the same surface pressure. Using XPS, they showed that the concentration of metal ions incorporated into the LB films obeyed the order  $Fe^{3+} > Mg^{2+} > K^+$ . The SEM micrographs showed that these LB films can be used in sensors or for the selective permeation of gases. Langmuir–Blodgett films that did not contain the metal ions were rarely seen over the pores. However, the metal ion-containing LB films could be placed over the pores with a few layers. This self-supporting capability of the LB films on porous substrates may therefore be exploited in the applications mentioned. Other interesting pieces of work were carried out by Miyashita et al. on the electrical and electrochemical properties of polymer Ru-based LB films [203–214]. As an example, one could mention their use of surface plasmon resonance to photoexcite the  $[Ru(bpy)_3]^{2+}$  complex in an LB film containing poly(N-dodecylacrylamide) [203] and deposited onto silver substrates. They found that the photocurrent was enhanced by a factor of 23.6 by increasing the distance between the Ru layer and the silver electrode, in a way that the quenching of silver surface states is avoided.

The redox and photoelectrochemical properties of hybrid LB films containing Prussian blue (PB) and a surfactant derivative of the ruthenium tris(bipyridine) in aqueous KCl solutions were studied in [215]. The interest in PB and  $Ru(bpy)_3$  stem from their application in various molecular devices. A large cathodic photocurrent was recorded when the LB films were irradiated with polychromatic light at a negative applied potential, indicating that both PB and the derivative of ruthenium tris(bipyridine) complex play an important role in the light-energy conversion process. This photoelectrochemical behavior resulted from the association at the molecular level of the organic and inorganic entities in the lamellar systems [215].

Hybrid, multilayered LB films were obtained by Miyashita et al. [208] with two kinds of polymer, viz. poly(N-dodecylacrylamide-co-ferrocenylmethylacrylate) (Fc copolymer) and poly(N-dodecylacrylamide-co-(4-(acryloylmethyl)-4'-methyl-2,2'-bipyridine)-bis(2,2'-bipyridine) ruthenium diperchlorate) (Ru copolymer). The cyclic voltammograms of the hetero-deposited redox polymer LB films showed current rectifying and charge storage properties. Upon light irradiation, an anodic photocurrent was observed for the films comprising a Ru copolymer LB film as an inner layer and a Fc copolymer LB film as an outer layer on the ITO (Fc/Ru/ITO) electrodes. On the other hand, cathodic currents were observed at the reverse layered structures (Ru/Fc/ITO). This is demonstration that the direction of the

photocurrent flow can be controlled by altering the architecture of the hetero-deposited LB films from redox polymers. Aoki and Miyashita [216] described a structural effect on the electrochemical behavior of hetero-deposited LB films consisting of Ru copolymer LB film (three layers) as an inner layer and Fc copolymer LB film (two layers) as an outer layer on ITO electrodes. These hetero-deposited films were prepared at different surface pressures (25 and 28 mN m<sup>-1</sup>). The results for the LB films deposited at 28 mN m<sup>-1</sup> indicated that the redox behavior of the ferrocene moiety in the outer Fc copolymer LB film was controlled by the redox condition of the ruthenium complex in the inner Ru copolymer LB film, and not directly influenced by the electrode potential. On the other hand, in the LB films prepared at a pressure less than 25 mN m<sup>-1</sup>, such behavior was not observed because the inner Ru copolymer LB films were not able to act as an insulator between the outer Fc copolymer LB films and the ITO electrode. These results indicated that the insulating property of the inner layer is improved and the electron transfer rate is decreased, when higher deposition surface pressures are employed. This is attributed to the formation of highly packed alkyl side-chains in the LB films at high surface pressures.

## GLOSSARY

**Aluminosilicate** Group of minerals with some of the Si<sup>4+</sup> ions in silicates replaced by Al<sup>3+</sup> ions. For each Si<sup>4+</sup> ion replaced by an Al<sup>3+</sup>, the charge must be balanced by having other positive ions such as Na<sup>+</sup>, K<sup>+</sup>, and Ca<sup>2+</sup> ions.

**Amphiphilic** From the Greek meaning “both” (amphi) and “lover” (philos), an amphiphile is a molecule that has a strong attraction towards both polar solvents, such as water (hydrophilic), and non-polar solvents (hydrophobic), and will be generally located at the interface between the two. When dispersed in either a polar or non-polar solvent an amphiphile has a tendency to form capsules with the ends of the molecules that are not compatible with the solvent on the inside. Stearic acid is an example with a long history.

**Composite** Multiphase material formed from a combination of materials which differ in composition or form, remains bonded together, and retains their identities and properties. Composites maintain an interface between components and act in concert to provide improved specific or synergistic characteristics not obtainable by any of the original components acting alone. Composites include: (1) fibrous (composed of fibers, and usually in a matrix), (2) laminar (layers of materials), (3) particulate (composed of particles or flakes, usually in a matrix), and (4) hybrid (combinations of any of the above).

**Electronic tongue** System for automatic analysis and recognition (classification) of liquids, including arrays of non-specific sensors, data collectors and data analysis tools. Electronic tongues may be used to identify a liquid sample and estimate its concentration and characteristic properties.

**Langmuir–Blodgett (LB)** Method used to create a molecular film of a surfactant at the air-water interface and transfer onto a solid substrate, named after the American scientists Irving Langmuir and Katherine Blodgett. (1) The surfactant is spread on the water surface with a highly

volatile solvent. After solvent evaporation of the solvent, the amphiphilic molecules start to reorganize. At this point, the molecules need place and the film is not continuous. (2) Then a barrier on the water surface pushes the molecules. A feedback (Wilhelmy plate) controls the position of the barrier and thus the pressure. Before this step, the pressure-area isotherms of the surfactant must be studied, in order to obtain information about the stability of the film, the reorientation of the molecules, the phase transitions and the conformational transformations. After this step, the deposition on a solid substrate can be performed.

**Layer-by-layer technique** Thin film fabrication technique which involves the assembly of multilayers onto a solid substrate via physical adsorption of oppositely charged layers or via secondary interactions.

**Phthalocyanine** Any of several stable, light-fast, blue or green organic pigments derived from the basic compound (C<sub>6</sub>H<sub>4</sub>C<sub>2</sub>N)<sub>4</sub>N<sub>4</sub> and used in enamels, printing inks, linoleum, and plastics.

**Polyamidoamine dendrimers (Pamam)** Dendrimers containing tertiary amines (a nitrogen (N) atom bonded to three carbon (C) atoms) as branching points and amide groups (carbon (C), oxygen (O) and nitrogen (N) atoms).

**Polyelectrolyte** An electrolyte (a solution that conducts electricity) of high molecular weight.

**Principal component analysis (PCA)** Mathematical procedure that transforms a number of (possibly) correlated variables into a (smaller) number of uncorrelated variables, referred to as principal components. The first principal component accounts for as much of the variability in the data as possible, and each succeeding component accounts for as much of the remaining variability as possible.

## ACKNOWLEDGMENTS

The authors are grateful to the financial support from FAPESP and CNPq (Brazil).

## REFERENCES

1. K. B. Blodgett, *J. Am. Chem. Soc.* 56, 495 (1934).
2. I. Langmuir, *J. Am. Chem. Soc.* 38, 2221 (1916).
3. C. S. Winter, R. H. Tredgold, A. J. Vickers, E. Khoshdel, and P. Hodge, *Thin Solid Films* 134, 49 (1985).
4. C. J. L. Constantino, A. Dhanabalan, A. A. S. Curvelo, and O. N. Oliveira, Jr., *Thin Solid Films* 327–329, 47 (1998).
5. L. Netzer and J. Sagiv, *J. Am. Chem. Soc.* 105, 674 (1983).
6. G. Decher, J. D. Hong, and J. Schmitt, *Thin Solid Films* 210/211, 831 (1992).
7. M. C. Petty, “Langmuir–Blodgett Films: An Introduction.” Cambridge University Press, Cambridge, 1996.
8. O. N. Oliveira, Jr., M. Raposo, and A. Dhanabalan, in “Handbook of Surfaces and Interfaces of Materials” (H. S. Nalwa, Ed.), Academic Press, San Diego, CA, 2001, Vol. 4, p. 1.
9. O. N. Oliveira, Jr., J.-A. He, V. Zucolotto, S. Balasubramanian, L. Li, H. S. Nalwa, J. Kumar, and S. K. Tripathy, in “Handbook of Polyelectrolytes and Their Applications” (J. Kumar and H. S. Nalwa, Ed.), American Scientific Publishers, Los Angeles, CA, 2002, Vol. 1, p. 1.
10. A. Pockels, *Nature* 43, 437 (1891).
11. L. Kelvin, *Philos Mag.* 46, 82 (1898).

12. P. Dynarowicz-Latka, A. Dhanabalan, and O. N. Oliveira, Jr., *Adv. Colloid Interf. Sci.* 91, 221 (2001).
13. K. Wohnrath, S. V. Mello, M. A. Pereira-da-Silva, and O. N. Oliveira, Jr., *Synthetic Metals* 121, 1425 (2001).
14. C. J. L. Constantino, L. P. Juliani, V. R. Botaro, D. T. Balogh, M. R. Pereira, E. A. Ticianelli, A. A. S. Curvelo, and O. N. Oliveira, Jr., *Thin Solid Films* 284–285, 191 (1996).
15. G. Decher, *Science* 277, 1232 (1997).
16. A. C. Fou, O. Onitsuka, M. Ferreira, M. F. Rubner, and B. R. Hsieh, *J. Appl. Phys.* 79, 7501 (1996).
17. W. B. Stockton and M. F. Rubner, *Macromolecules* 30, 2717 (1997).
18. M. Raposo, R. S. Pontes, L. H. C. Mattoso, and O. N. Oliveira, Jr., *Macromolecules* 30, 6095 (1997).
19. M. K. Ram, M. Salerno, M. Adami, P. Faraci, and C. Nicolini, *Langmuir* 15, 1252 (1999).
20. P. T. Hammond, *Curr. Opin. Coll. Interf. Sci.* 4, 430 (2000).
21. S. Y. Park, C. J. Barrett, M. F. Rubner, and A. M. Mayes, *Macromolecules* 34, 3384 (2001).
22. R. S. Pontes, M. Raposo, C. S. Camilo, A. Dhanabalan, M. Ferreira, and O. N. Oliveira, Jr., *Physica Status Solidi (a)* 173, 41 (1999).
23. J. Anzai, Y. Kobayashi, N. Nakamura, M. Nishimura, and T. Hoshi, *Langmuir* 15, 221 (1999).
24. C. Petit, P. Lixon, and M. P. Pileni, *J. Phys. Chem.* 94, 1598 (1990).
25. M. T. Kennedy, B. A. Korgel, H. G. Montbouquette, and J. A. Zasadinski, *Chem. Mater.* 10, 2116 (1998).
26. T. Rajh, M. I. Vuemilovic, N. M. Dimitrijevic, O. I. Micic, and A. J. Nozik, *Chem. Phys. Lett.* 143, 305 (1988).
27. G. A. Ozin, M. R. Steele, and A. J. Holmes, *Chem. Mater.* 6, 999 (1994).
28. X. K. Zhao, L. D. McCormick, and J. H. Fendler, *Adv. Mater.* 4, 93 (1992).
29. V. Sankaran, C. C. Cummins, R. R. Schrock, R. E. Cohen, and R. J. Silbey, *Chem. Mater.* 5, 1133 (1993).
30. J.-A. He, R. Valluzzi, K. Yang, T. Dolukhanyan, C. Sung, J. Kumar, S. K. Tripathy, L. Samuelson, L. Balogh, and D. A. Tomalia, *Chem. Mater.* 11, 3268 (1999).
31. L. Zhang, A. K. Dutta, G. Jarero, and P. Stroeve, *Langmuir* 16, 7095 (2000).
32. A. M. Fojas, E. Murphy, and P. Stroeve, *Ind. Eng. Chem. Res.* 41, 2662 (2002).
33. P. Jeevanadam, Y. Kolytyn, and A. Gedanken, *Nanoletters* 1, 263 (2001).
34. J. Zhang, S. Yang, and Q. Xue, *J. Mat. Res.* 15, 541 (2000).
35. M. Rajamathi, G. N. Subanna, and P. V. Kamath, *J. Mat. Chem.* 7, 2293 (1997).
36. A. K. Dutta, G. Jarero, L. Zhang, and P. Stroeve, *Chem. Mater.* 12, 176 (2000).
37. S. Dante, Z. Hou, S. Risbud, and P. Stroeve, *Langmuir* 15, 2176 (1999).
38. A. K. Dutta, T. Ho, L. Zhang, and P. Stroeve, *Chem. Mater.* 12, 1042 (2000).
39. S. Joly, R. Kane, L. Radzilowski, T. Wang, A. Wu, R. E. Cohen, E. L. Thomas, and M. F. Rubner, *Langmuir* 16, 1354 (2000).
40. E. R. Kleinfelde and G. S. Ferguson, *Science* 265, 370 (1994).
41. S. W. Keller, H.-N. Kim, and T. E. Mallouk, *J. Am. Chem. Soc.* 116, 8817 (1994).
42. A. Rosidian, Y. Liu, and R. O. Claus, *Adv. Mater.* 10, 1087 (1998).
43. T. Cassagneau and J. H. Fendler, *J. Phys. Chem. B* 103, 1789 (1999).
44. F. G. Aliev, M. A. Correa-Duarte, A. Mamedov, J. W. Ostrander, M. Giersig, L. M. Liz-Marzán, and N. A. Kotov, *Adv. Mater.* 11, 1006 (1999).
45. J. W. Ostrander, A. A. Mamedov, and N. A. Kotov, *J. Am. Chem. Soc.* 123, 1101 (2001).
46. G. Choe, S. J. Chung, and R. M. Walser, *Thin Solid Films* 259, 231 (1995).
47. I. Kaitsu, A. Inomata, I. Okamoto, and M. Shinohara, *IEEE Trans. Magn.* 34, 1591 (1998).
48. A. Murayama, K. Ohshima, M. Miyamura, M. Maekawa, and S. Kondoh, *J. Appl. Phys.* 79, 7916 (1996).
49. A. A. Mamedov and N. A. Kotov, *Langmuir* 16, 5530 (2000).
50. Y. Lvov, B. Munge, O. Giraldo, I. Ichinose, S. L. Suib, and J. F. Rusling, *Langmuir* 16, 8850 (2000).
51. Y. Lvov, K. Ariga, M. Onda, I. Ichinose, and T. Kunitake, *Langmuir* 13, 6195 (1997).
52. I. Ichinose, H. Tagawa, S. Mizuke, Y. Lvov, and T. Kunitake, *Langmuir* 14, 187 (1998).
53. T. Cassagneau, J. H. Fendler, and T. E. Mallouk, *Langmuir* 16, 241 (2000).
54. Y. Liu, A. Wang, and R. Claus, *J. Phys. Chem. B* 101, 1385 (1997).
55. M. Ferreira, V. Zucolotto, F. Huguenin, R. M. Torresi, and O. N. Oliveira, Jr., *J. Nanosci. Nanotech.* 2, 1 (2002).
56. Y.-J. Liu, D. C. DeGroot, J. L. Schindler, C. R. Kannewurf, and M. G. Kanatzidis, *J. Chem. Soc., Chem. Commun.* 593 (1993).
57. M. Ferreira, V. Zucolotto, C. J. L. Constantino, M. L. A. Temperini, R. M. Torresi, and O. N. Oliveira, Jr., *Synthetic Metals* 137, 931 (2003).
58. M. Fang, C. H. Kim, G. B. Saupe, H.-N. Kim, C. C. Waraksa, T. Miwa, A. Fujishima, and T. E. Mallouk, *Chem. Mater.* 11, 1526 (1999).
59. T. Cassagneau, F. Guérin, and J. H. Fendler, *Langmuir* 16, 7318 (2000).
60. J. Schmitt, G. Decher, W. J. Dressik, S. L. Brandow, R. E. Geer, R. Shashidhar, and J. M. Calvert, *Adv. Mater.* 9, 61 (1997).
61. D. A. Handley, "Colloidal Gold: Principles, Methods and Applications" (M. A. Hayat, Ed.). Academic Press, San Diego, 1989.
62. N. Malikova, I. Pastoriza-Santos, M. Schierhorn, N. A. Kotov, and L. M. Liz-Marzán, *Langmuir* 18, 3694 (2002).
63. B. M. I. van der Zande, M. R. Bömher, L. G. Fokkink, and C. Schöneberger, *Langmuir* 12, 788 (1996).
64. S. J. Oldenburg, R. D. Averitt, S. L. Westcott, and N. J. Halas, *J. Chem. Phys. Lett.* 288, 243 (1998).
65. E. Hao and T. Lian, *Chem. Mater.* 12, 3392 (2000).
66. J. Liu, L. Cheng, Y. Song, B. Liu, and S. Dong, *Langmuir* 17, 6747 (2001).
67. M. Gao, B. Richter, S. Kirstein, and H. Möhwald, *J. Phys. Chem. B* 102, 4096 (1998).
68. L. I. Halaoui, *Langmuir* 17, 7130 (2001).
69. M. Gao, X. Zhang, B. Yang, F. Li, and J. Shen, *Thin Solid Films* 284, 242 (1996).
70. E. Hao and T. Lian, *Langmuir* 16, 7879 (2000).
71. A. L. Rogach, D. S. Koktysh, M. Harrison, and N. A. Kotov, *Chem. Mat.* 12, 1526 (2000).
72. H. Zhang, B. Yang, R. Wang, G. Zhang, X. Hou, and L. Wu, *J. Coll. Inter. Sci.* 247, 361 (2002).
73. A. C. Fou, O. Onitsuka, M. Ferreira, B. Hsieh, and M. F. Rubner, *J. Appl. Phys.* 79, 7501 (1996).
74. O. Onitsuka, A. C. Fou, M. Ferreira, B. Hsieh, and M. F. Rubner, *J. Appl. Phys.* 80, 4067 (1996).
75. Y. Sun, E. Hao, X. Zhang, B. Yang, J. Shen, L. Chi, and H. Fuchs, *Langmuir* 13, 5168 (1997).
76. D. W. Kim, A. Blumstein, J. Kumar, and S. K. Tripathy, *Chem. Mater.* 13, 243 (2001).
77. Y. Lvov, J. F. Rusling, D. L. Thomsen, F. Papadimitrakopoulos, T. Kawakami, and T. Kunitake, *Chem. Comm.* 1229 (1998).
78. Y. Lvov, K. Ariga, M. Onda, I. Ichinose, and T. Kunitake, *Coll. Surf. A* 146, 337 (1999).
79. K. Asano, K. Miyano, H. Ui, M. Shimomura, and Y. Ohta, *Langmuir* 9, 3587 (1993).
80. J. Ramsden, Y. Lvov, and G. Decher, *Thin Solid Films* 254, 246 (1995).
81. M. Ferreira and M. Rubner, *Macromolecules* 28, 7107 (1995).

82. A. Advincula, E. Aust, W. Meyer, and W. Knoll, *Langmuir* 12, 3536 (1996).
83. Y. Lvov, K. Ariga, I. Ichinose, and T. Kunitake, *J. Am. Chem. Soc.* 117, 6117, (1995).
84. K. Ariga, Y. Lvov, and T. Kunitake, *J. Am. Chem. Soc.* 119, 2224 (1997).
85. Y. Lvov, K. Ariga, I. Ichinose, and T. Kunitake, *Langmuir* 12, 3038 (1996).
86. M. Eckle and G. Decher, *Nano Lett.* 1, 45 (2001).
87. K. Ariga, Y. Lvov, I. Ichinose, and T. Kunitake, *Appl. Clay Sci.* 15, 137 (1999).
88. A. Mamedov, J. Ostrander, F. Aliev, and N. A. Kotov, *Langmuir* 16, 3941 (2000).
89. N. A. Kotov, S. Magonov, and E. Tropscha, *Chem. Mater.* 10, 886 (1998).
90. N. A. Kotov, T. Haraszti, L. Turi, G. Zavala, R. E. Geer, I. Dékány, and J. H. Fendler, *J. Am. Chem. Soc.* 119, 6821 (1997).
91. E. R. Kleinfeld and G. S. Ferguson, *Chem. Mater.* 7, 2327 (1995).
92. R. A. Caruso, A. Susha, and F. Caruso, *Chem. Mater.* 13, 400 (2001).
93. K. Glinel, A. Moussa, A. M. Jonas, and A. Laschewsky, *Langmuir* 18, 1408 (2002).
94. D. W. Kim, A. Blumstein, J. Kumar, and S. K. Tripathy, *Chem. Mater.* 13, 1916 (2001).
95. R. Aroca, H. Bolourchi, D. Battisti, and K. Najafi, *Langmuir* 9, 3138 (1993).
96. L. Gaffo, C. J. L. Constantino, W. C. Moreira, R. F. Aroca, and O. N. Oliveira, Jr., *Langmuir* 18, 3561 (2002).
97. M. Tsuchida, W. Tsujita, Y. Majima, and M. Iwamoto, *Coll. Surfaces A* 198, 729 (2002).
98. M. Lütt, M. R. Fitzsimmons, and D. Q. Li, *J. Phys. Chem. B* 102, 400 (1998).
99. D. Q. Li, M. Lütt, M. R. Fitzsimmons, R. Synowicki, M. E. Hawley, and G. W. Brown, *J. Am. Chem. Soc.* 120, 8797 (1998).
100. D. Q. Li, A. Bishop, Y. Gim, X. B. Shi, M. R. Fitzsimmons, and Q. X. Jia, *Appl. Phys. Lett.* 73, 2645 (1998).
101. L. S. Li, R. Wang, M. Fitzsimmons, and D. Q. Li, *J. Phys. Chem. B* 104, 11195 (2000).
102. L. S. Li and A. D. Q. Li, *J. Phys. Chem. B* 105, 10022 (2001).
103. L. S. Li, Q. X. Jia, and A. D. Q. Li, *Chem. Mater.* 14, 1159 (2002).
104. Y. M. Lvov, G. N. Kamau, D.-L. Zhou, and J. F. Rusling, *J. Coll. Int. Sci.* 212, 570, (1995).
105. V. Zucolotto, M. Ferreira, M. R. Cordeiro, C. J. L. Constantino, D. T. Balogh, A. R. Zanatta, W. C. Moreira, and O. N. Oliveira, Jr., *J. Phys. Chem. B* 107, 3733 (2003).
106. V. Zucolotto, M. Ferreira, M. R. Cordeiro, C. J. L. Constantino, W. C. Moreira, and O. N. Oliveira, Jr., *Synthetic Metals* 137, 909 (2003).
107. K. Araki, M. J. Wagner, and M. S. Wrighton, *Langmuir* 12, 5393 (1996).
108. C. M. N. Azevedo, K. Araki, L. Angnes, and H. Toma, *Electroanalysis* 10, 467 (1998).
109. H. Jiang, W. Su, J. Hazle, J. T. Grant, V. V. Tsukruk, T. M. Cooper, and T. J. Bunning, *Thin Solid Films* 372, 85 (2000).
110. H. Byrd, C. H. Holloway, J. Pogue, S. Kircus, R. C. Advincula, and W. Knoll, *Langmuir* 16, 10322 (2000).
111. X.-P. Jiang, S. L. Clark, and P. T. Hammond, *Adv. Mater.* 13, 1669 (2001).
112. S. Watanabi and S. L. Regen, *J. Am. Chem. Soc.* 116, 8855 (1994).
113. J. Wang, J. Chen, X. Jia, W. Cao, and M. Li, *Chem. Commun.* 511 (2000).
114. V. V. Tsukruk, F. Rinderspacher, and V. Bliznyuk, *Langmuir* 13, 2171 (1997).
115. V. V. Tsukruk, *Adv. Mater.* 10, 253 (1998).
116. J. L. Casson, H.-L. Wang, J. B. Roberts, A. N. Parikh, J. M. Robinson, and M. S. Johal, *J. Phys. Chem. B* 106, 1697 (2002).
117. A. J. Khopade and F. Caruso, *Nano. Lett.* 2, 415 (2002).
118. J.-I. Anzai, Y. Kobayashi, Y. Suzuki, H. Takeshita, Q. Chen, T. Osa, T. Hoshi, and X.-Y. Du, *Sensors and Actuators B* 52, 3, (1998).
119. L. Cheng and J. A. Cox, *Electrochem. Comm.* 3, 285 (2001).
120. H. C. Yoon and H.-S. Kim, *Anal. Chem.* 72, 922 (2000).
121. H. C. Yoon, M.-Y. Hong, and H.-S. Kim, *Anal. Chem.* 72, 4420 (2000).
122. T. Vossmeier, B. Guse, I. Besnard, R. E. Bauer, K. Müllen, and A. Yasuda, *Adv. Mat.* 14, 238 (2002).
123. N. Krasteva, I. Besnard, B. Guse, R. E. Bauer, K. Müllen, A. Yasuda, and T. Vossmeier, *Nano. Lett.* 2, 551 (2002).
124. M. K. De Armond and G. A. Fried, *Prog. Inorg. Chem.* 44, 97 (1997).
125. R. Des Enfants, T. Martinez, and M. K. De Armond, *ACS Symp. Series* (T. Bein, Ed.), 1992.
126. A. K. Kakkar, *Chem. Rev.* 102, 3579 (2002).
127. K. Töllner, R. Popovitz-Biro, M. Lahav, and D. Milstein, *Science* 278, 2100 (1997).
128. A. Ulman, "An Introduction to Ultrathin Organic Films." Academic, New York, 1991.
129. M. C. Petty, "Langmuir-Blodgett Films: An Introduction." Cambridge University Press, New York, 1996.
130. K. Kalyanasundaram, *Coord. Chem. Rev.* 46, 159 (1982).
131. K. P. Seefeld, D. Möbius, and H. Kuhn, *Heb. Chim. Acta* 60, 2608 (1977).
132. P. Delavie, J. R. Lee, H. W. Sprintschnik, H. Abruna, T. J. Meuer, and D. Whiteen, *J. Am. Chem. Soc.* 99, 7094 (1977).
133. G. L. Gaines, Jr., P. E. Behnken, and S. J. Valenty, *J. Am. Chem. Soc.* 100, 6549 (1979).
134. S. J. Valenty, D. E. Behnken, and G. L. Gaines, Jr., *Inorg. Chem.* 18, 2160 (1979).
135. H. Daifuku, K. Aoki, K. Tokuda, and H. Matsuda, *J. Electroanal. Chem.* 140, 179 (1985).
136. X. Zhang and A. J. Bard, *J. Phys. Chem.* 92, 5566 (1988).
137. X. Zhang and A. J. Bard, *J. Am. Chem. Soc.* 111, 8098 (1989).
138. Y. S. Obeng and A. J. Bard, *Langmuir* 7, 191 (1991).
139. T. Murakata, T. Miyashita, and M. Matsuda, *J. Phys. Chem.* 92, 6040 (1988).
140. M. K. De Armond, H. Samha, and O. Dvorak, *Langmuir* 10, 343 (1994).
141. S. Palacin and A. Barraud, *J. Chem. Soc. Chem. Commun.* 45 (1989).
142. S. Palacin, A. Ruadel, and A. Barraud, *J. Phys. Chem.* 93, 7195 (1989).
143. G. Roberts, "Langmuir-Blodgett Films." Plenum Press, New York, 1990.
144. H. Samha and M. K. De Armond, *Langmuir* 10, 4157 (1994).
145. W. X. Lu, H. L. Zhou, P. S. He, and W. H. Guo, *Thin Solid Films* 365, 67 (2000).
146. J. P. Santos, M. E. Zaniquelli, C. Batalani, and W. F. De Giovanni, *Thin Solid Films* 105, 1780 (2001).
147. J. P. Santos, M. E. Zaniquelli, C. Batalani, and W. F. De Giovanni, *Thin Solid Films* 349, 238 (1999).
148. K. Wang, M. Haga, M. D. Hossain, H. Shindo, K. Hasebe, and H. Monjushiro, *Langmuir* 18, 3528 (2002).
149. Y. Uemura, A. Yamagishi, R. Schoonheydt, A. Persoons, and F. De Schryver, *J. Am. Chem. Soc.* 124, 992 (2002).
150. T. Da Ros, M. Prato, M. Carano, P. Ceroni, F. Paolucci, S. Roffia, L. Valli, and D. M. Guldi, *J. Organomet. Chem.* 599, 62 (2000).
151. P. Wang, B. Chen, R. M. Metzger, T. Da Ros, and M. Prato, *J. Mater. Chem.* 7, 2397 (1997).
152. G. W. Parshall and S. D. Ittel, "Homogeneous Catalysis." John Wiley & Sons, New York, 1992.
153. T. Naota, H. Takaya, and S.-I. Murahashi, *Chem. Rev.* 98, 2599 (1998).
154. S. L. Queiroz and A. A. Batista, *Química Nova* 19, 651 (1996).
155. H. A. Mayer and W. C. Kaska, *Chem. Rev.* 94, 1239 (1994).

156. C. A. McAuliffe and W. Levason, "Phosphine, Arsine and Stibine Complexes of the Transition Elements." Elsevier, New York, 1979.
157. B. R. James and D. K. W. Wang, *Canad. J. Chem.* 58, 245 (1980).
158. F. H. Jardine, *Prog. Inorg. Chem.* 31, 265 (1984).
159. S. L. Queiroz, A. A. Batista, G. Oliva, M. T. Gambardella, R. H. A. Santos, K. S. MacFarlane, S. J. Rettig, and B. R. James, *Inorg. Chim. Acta* 267, 209 (1998).
160. S. Murai, F. Kakiuchi, S. Sesekine, Y. Tanaka, A. Kamatani, M. Sonoda, and N. Chatani, *Pure Appl. Chem.* 66, 1527 (1994).
161. S. I. Murahashi, T. Naota, and N. Hirai, *J. Org. Chem.* 58, 7318 (1983).
162. H. Doucet, B. Martinvaca, C. Bruneau, and P. H. Dixneuf, *J. Org. Chem.* 60, 7247 (1995).
163. A. M. Joshi, K. S. McFarlane, and B. R. James, *J. Organomet. Chem.* 488, 161 (1995).
164. D. E. Fogg, B. R. James, and M. Kilner, *Inorg. Chim. Acta* 222, 85 (1994).
165. B. R. James, *Catal. Today* 37, 209 (1997).
166. Y. Fu, J. Ouyang, and A. B. P. Lever, *J. Phys. Chem.* 97, 13753 (1993).
167. K. Wohnrath, M. P. de Araujo, A. A. Batista, L. R. Dinelli, G. Oliva, E. E. Castellano, and J. Ellena, *J. Chem. Soc. Dalton Transitions* 19, 3383 (2000).
168. K. Wohnrath, J. R. Garcia, F. C. Nart, A. A. Batista, and O. N. Oliveira, Jr., *Thin Solid Films* 402, 272 (2002).
169. M. Ferreira, K. Wohnrath, A. Riul, Jr., J. A. Giacometti, and O. N. Oliveira, Jr., *J. Phys. Chem. B* 106, 7272 (2002).
170. H. Huesmann, C. A. Bignozzi, M. T. Indelli, L. Pavanin, M. A. Rampi, and D. Möbius, *Thin Solid Films* 284–285, 62 (1996).
171. H. K. Kirsh, A. Schaper, H. Huesmann, M. A. Rampi, D. Möbius, and T. M. Jovin, *Langmuir* 14, 3895 (1998).
172. H. S. Nalwa and A. Kakuta, *Appl. Organometal. Chem.* 6, 645 (1992).
173. R.-J. Zhang, H.-G. Liu, C.-R. Zhang, K.-Z. Yang, G.-Y. Zhu, and H.-W. Zhang, *Thin Solid Films* 302, 223 (1997).
174. X. Gao, H.-G. Liu, R.-J. Zhang, and K.-Z. Yang, *Thin Solid Films* 284–285, 39 (1996).
175. C.-R. Zhang, K.-Z. Yang, and W.-R. Jin, *Thin Solid Films* 284–285, 533 (1996).
176. Y. Lin and X. R. Xiao, *Acta Chem. Sinica* 52, 960 (1994).
177. N. Kobayashi, *Coordin. Chem. Rev.* 227, 129 (2002).
178. L. Zhang, Y. Zhang, H. B. Tao, X. J. Sun, Z. J. Guo, and L. G. Zhu, *Thin Solid Films* 413, 224 (2002).
179. C. L. Honeybourne, D. Portus, N. M. Ratcliffe, T. Richardson, and G. L. Ashwell, *Pol. J. Chem.* 76, 367 (2002).
180. L. Gaffo, D. Gonçalves, A. Dhanabalan, W. C. Moreira, and O. N. Oliveira, Jr., *Synthetic Metals* 124, 351 (2001).
181. V. Huc, F. Armand, J. P. Bourgoin, and S. Palacin, *Langmuir* 17, 1928 (2001).
182. E. Vuorimaa, T. Vuorinen, N. Tkachenko, O. Cramariuc, T. Hukka, S. Nummelin, A. Shivanyuk, K. Rissanen, and H. Lemmetyinen, *Langmuir* 17, 7327 (2001).
183. O. Korth, T. Hanke, J. von Gersdorff, H. Kurreck, and B. Roder, *Thin Solid Films* 382, 240 (2001).
184. H. G. Liu, X. S. Feng, Q. B. Xue, L. Wang, and K. Z. Yang, *Thin Solid Films* 340, 265 (1999).
185. S. Yamada, K. Kuwata, H. Yonemur, and T. Matsuo, *J. Photochem. Photobiol. A-Chem.* 87, 115 (1995).
186. R. Bonnett, S. Ioannou, C. Pearson, M. C. Petty, M. Rogersevans, and R. F. Wilkins, *J. Mater. Chem.* 5, 237 (1995).
187. Y. Liu, J. Liu, X. S. Feng, J. Mu, and K. Z. Yang, *Thin Solid Films* 210, 545 (1992).
188. I. O. Benitez, B. Bujoli, L. J. Camus, C. M. Lee, F. Odobel, and D. R. Talham, *J. Am. Chem. Soc.* 124, 4363 (2002).
189. F. Armand, P. A. Albouy, F. Da Cruz, M. Normand, V. Huc, and E. Goron, *Langmuir* 17, 3431 (2001).
190. W. C. Moreira and R. Aroca, *Spectrochimica Acta-A* 51, 2325 (1995).
191. D. Abatti, M. E. Zaniquelli, Y. Iamamoto, and Y. M. Idemori, *Thin Solid Films* 310, 296 (1997).
192. Y. Liu, Q. Liang, Y. Xu, F. Chen, and D. Zhu, *Solid State Comm.* 99, 167 (1996).
193. H. Ding, V. Erokhin, M. K. Ram, S. Paddeu, L. Valkova, and C. Nicolini, *Thin Solid Films* 379, 279 (2000).
194. M. Ferreira, A. Riul, Jr., K. Wohnrath, F. J. Fonseca, O. N. Oliveira, Jr., and L. H. C. Mattoso, *Anal. Chem.* 75, 953 (2003).
195. M. C. Petty, M. R. Bryce, and D. Bloor, "An Introduction to Molecular Electronics." Edward Arnold, London, 1995.
196. M. Ferreira, K. Wohnrath, R. M. Torresi, C. J. L. Constantino, R. F. Aroca, J. A. Giacometti, and O. N. Oliveira, Jr., *Langmuir* 18, 540 (2002).
197. M. Ferreira, K. Wohnrath, R. M. Torresi, J. A. Giacometti, and O. N. Oliveira, Jr., *Mol. Cryst. Liq. Cryst.* 374, 235 (2002).
198. M. Ferreira, K. Wohnrath, and O. N. Oliveira, Jr., *Synthetic Metals* 135–136C, 443 (2003).
199. A. Riul, D. S. dos Santos, K. Wohnrath, R. Di Tommazo, A. C. P. L. F. Carvalho, F. J. Fonseca, O. N. Oliveira, D. M. Taylor, and L. H. C. Mattoso, *Langmuir* 18, 239 (2002).
200. A. Riul, Jr., A. M. Gallardo Soto, S. V. Mello, S. Bone, D. M. Taylor, and L. H. C. Mattoso, *Synthetic Metals* 132, 109 (2003).
201. K. R. Beebe, R. J. Peel, and M. B. Seasholtz, "Chemometrics: A Practical Guide." Wiley, New York, 1998.
202. H. Jeong, B.-J. Lee, W. J. Cho, and C.-S. Ha, *Polymer* 41, 5525 (2000).
203. J. F. Chen, M. Mitsuishi, A. Aoki, and T. Miyashita, *Chem. Commun.* 23, 2856 (2002).
204. N. Fukuda, M. Mitsuishi, A. Aoki, and T. Miyashita, *J. Phys. Chem. B* 106, 7048 (2002).
205. A. Aoki and T. Miyashita, *Electrochem.* 69, 929 (2001).
206. N. Fukuda, M. Mitsuishi, A. Aoki, and T. Miyashita, *Chem. Lett.* 5, 378 (2001).
207. T. Miyashita, J. F. Chen, M. Yuasa, and M. Mitsuishi, *Polymer J.* 31, 1121 (1999).
208. T. Miyashita, A. Aoki, and Y. Abe, *Mol. Cryst. Liq. Cryst.* 327, 77 (1999).
209. T. Miyashita, T. Taniguchi, Y. Fukasawa, and Y. Chin, *J. Poly. Sci.* 17, 75 (1999).
210. T. Taniguchi, Y. Fukasawa, and T. Miyashita, *J. Phys. Chem. B* 103, 1920 (1999).
211. T. Taniguchi and T. Miyashita, *Chem. Lett.* 4, 295 (1997).
212. A. Aoki and T. Miyashita, *Chem. Lett.* 7, 563 (1996).
213. T. Yatysue, M. Matsuda, and T. Miyashita, *J. Phys. Chem.* 96, 10125 (1992).
214. T. Miyashita, H. Saito, and M. Matsuda, *Chem. Lett.* 5, 859 (1991).
215. G. R. Torres, E. Dupart, C. Mingotaud, and S. Ravaine, *J. Phys. Chem. B* 104, 9487 (2000).
216. A. Aoki and T. Miyashita, *J. Electroanal. Chem.* 473, 125 (1999).





# Layer-by-Layer Nanoarchitectonics

Katsuhiko Ariga

ERATO Nanospace Project, Tokyo, Japan

## CONTENTS

1. Introduction
  2. Basics of Layer-by-Layer Adsorption
  3. Analyses of Layering Processes and the Layered Structures
  4. Preparation of Layered Nanostructures
  5. Applications
  6. Conclusions
- Glossary  
References

## 1. INTRODUCTION

Technologies to create precisely controlled structures have been energetically researched for many years. However, the level of structural precision is drastically changing these days; that is, microfabrication now turns into nanofabrication. This change is driven by our demands in daily life, because we realize the advantages of highly miniaturized functional systems. For example, this fact appears in the rapidly spreading use of cellular phones and mobile computers. Scientists and engineers are now requested to create and develop more and more new technologies in nanofabrication, because the development of small intelligent devices will improve our life-style with portable, easily accessible, less energy-consuming, and pollution-minimizing processes.

Although the production of three-dimensionally defined nanolevel structures is quite a difficult target to achieve, preparation of layered structures with molecular-level precision in thickness is rather easily accomplished. Construction of a controlled layer structure on a solid support sounds simple but actually involves very important techniques of surface modification and device preparation. The Langmuir-Blodgett (LB) method is well known as a technique for providing molecular layer structures of organic molecules. The LB technique provides multilayer structures of amphiphilic molecules by transferring their monolayers from water surface to solid support in a layer-by-layer manner. The procedure of the LB method usually requires formation of a well-packed monolayer on water. Amphiphilic molecules are

mainly used in this research, and some attractive materials such as proteins are not a suitable substance for this method. Some modified techniques allow us to prepare protein-containing LB films, but the well-packed nature of the film is sometimes disadvantageous in function exhibition because of the limited diffusion process in the film [1, 2].

Recently, alternating layer-by-layer adsorption has attracted much attention as a technique for providing nanometer-level layer-by-layer architectures by a rather simple procedure [3–10]. This technique is applicable mainly to water-soluble charged materials, including conventional and functional polyelectrolytes; biopolymers such as proteins, DNAs, virus, and sugars; colloidal particles and other inorganic materials; and dyes and molecular assemblies, including bolaamphiphile monolayers, lipid bilayers, and LB films. The films obtained are less ordered and less dense compared with the fine-structured LB films. Therefore, the alternating layer-by-layer films can compensate for the disadvantages observed in the LB films and are more useful in some kinds of applications. In this chapter, novel types of layered nanofabrication based on alternating layer-by-layer adsorption are introduced as *layer-by-layer nanoarchitectonics*.

## 2. BASICS OF LAYER-BY-LAYER ADSORPTION

In 1966, the concept of alternating layer-by-layer adsorption was first proposed for charged colloidal particles by Iler [3]. The concept was widely realized by Decher and co-workers, who demonstrated various assemblies, mainly using linear polyelectrolytes or bolaamphiphiles [4]. This method is basically conducted through electrostatic interaction, although several modified methods, such as stereo-complex assembly, charge-transfer assembly, and biospecific assembly, have recently been proposed as described later in this chapter.

The basic mechanism of the alternating layer-by-layer adsorption is illustrated in Figure 1, together with the materials used. Major driving forces in the assembly process are charge neutralization and resaturation. As illustrated in Figure 1, a cationic polyelectrolyte is adsorbed on a negatively charged surface of a solid support, and the surface charges on the two materials effectively quench each other.

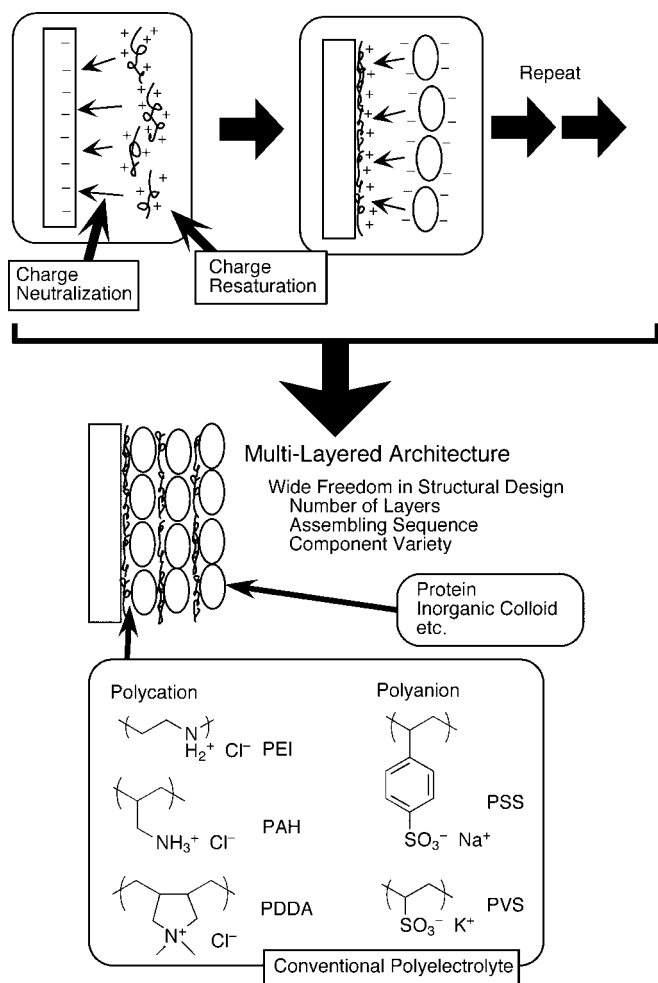


**Figure 1.** The assembly mechanism and characteristics of the assembled film of alternating layer-by-layer adsorption. Formulae of polyelectrolytes frequently used in this method are also shown.

However, overadsorption usually occurs to make the surface charge reversed (positively charged in this example) at relatively high concentrations of the polyelectrolytes. The next adsorption of an anionic material again reverses the surface charge. Alternation in the surface charges allows us to fabricate the layered structure continuously. Kunitake and co-workers experimentally proved the charge reversal by a surface force measurement [11].

The simplicity of the assembly process confers a huge versatility on the applicable materials. Recent progress with alternating layer-by-layer adsorption has revealed that various materials such as polyelectrolytes and aggregated small molecules can be used in the assembly. This method is also available for various biorelated materials and inorganic substances. Atomic force microscopic (AFM) observation revealed that spontaneous saturation in adsorption results in a remarkably uniform film surface [12].

The inexpensive nature of the assembly procedure is one of the most prominent advantages of this method, because the only instruments required in this procedure are beakers and tweezers. A solid support with a charged surface is immersed in a solution containing an oppositely charged polyelectrolyte. After the solid support is rinsed in pure

water, the support is immersed in a solution of an oppositely charged material. Repeating both adsorption processes leads to alternation of the surface charge and multilayer formation of polycations and polyanions in an alternating sequence. The prepared multilayers provide wide freedom in structural design. The number of layers and the layering sequence are controlled simply by selecting the number of dipping cycles and their sequences, respectively. As easily imagined, this simple procedure can be automatically conducted. Clark and Hammond [13] and Shiratori and Yamada [14–16] separately proposed an automatic dipping machine for these procedures.

### 3. ANALYSES OF LAYERING PROCESSES AND THE LAYERED STRUCTURES

Analytical methods that are applicable to other thin films can generally be used for the evaluation of alternately assembled films. The adsorption amount can be detected by UV-vis and FT-IR spectroscopies if the adsorbed materials have specific absorption bands. The thickness of the adsorbed layers can be evaluated by X-ray reflectivity [17], surface plasmon resonance (SPR) [18], and scanning angle reflectometry (SAR) [19].

A quartz crystal microbalance (QCM) that provides the weight increase from shifts in its resonant frequency is a unique device for evaluating the assembly process [20–23]. Because all kinds of adsorbents have weight, this technique is theoretically applicable to all of the assembled materials. In addition, we can evaluate the weight of every layer with precision at the nanogram-level because of the high sensitivity of this measurement. The QCM evaluation can be conducted by assembling the films directly on the QCM plate (Fig. 2) [24]. The QCM frequency shifts in the assembly processes of three sizes of SiO<sub>2</sub> particles (25 nm, 45 nm, and 78 nm in diameter) are shown in Figure 2B as examples where larger and smaller steps correspond to the adsorption of SiO<sub>2</sub> particles and poly(diallyldimethylammonium chloride) (PDDA), respectively. A linear increase in the film mass was observed for all kinds of SiO<sub>2</sub> particles. The growth steps are 520, 910, and 1350 Hz for the 25-nm, 45-nm, and 78-nm SiO<sub>2</sub> particles, respectively, corresponding to ca. 70% coverage of the surface on the assumption of hexagonal packing of the particles.

The morphology of the films can also be analyzed by various microscopies. For example, cross-sectional observation of the protein-polyelectrolyte film can be conducted by scanning electron microscopy (SEM), revealing the constant thickness of the film. Surface roughness of the assembled films can be evaluated by atomic force microscopy (AFM). A few examples are shown later in this chapter.

## 4. PREPARATION OF LAYERED NANOSTRUCTURES

### 4.1. Polyelectrolytes

Polyelectrolytes frequently used in this method are also summarized in Figure 1. Poly(allylamine hydrochloride) (PAH), PDDA, and poly(ethyleneimine) (PEI) are used as

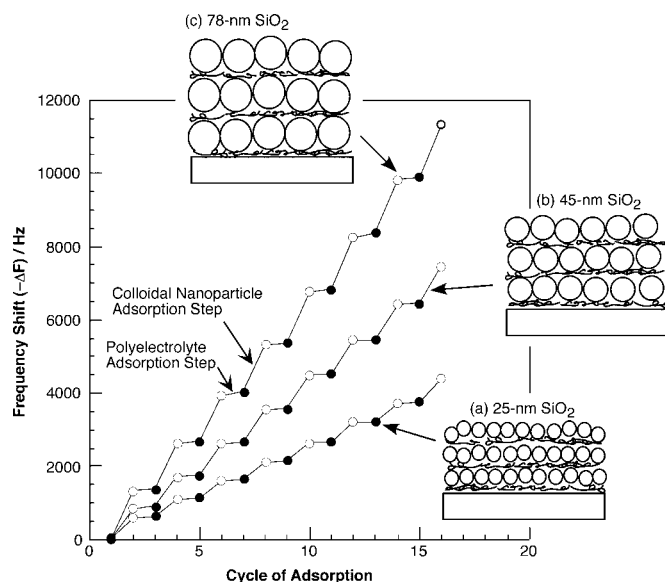


**Figure 2.** QCM frequency changes in the alternating layer-by-layer adsorption of SiO<sub>2</sub> and PDDA at 22 °C: SiO<sub>2</sub>, 10 mg ml<sup>-1</sup>, pH 10; PDDA, 3 mg ml<sup>-1</sup>; adsorption time, 15 min. Plots of open circles and solid circles represent SiO<sub>2</sub> adsorption and PDDA adsorption, respectively. Three different SiO<sub>2</sub> particles (a, 25-nm-diameter SiO<sub>2</sub>; b, 45-nm-diameter SiO<sub>2</sub>; c, 78-nm-diameter SiO<sub>2</sub>) were used. Reprinted with permission from [94], K. Ariga et al., *Appl. Clay Sci.* 15, 137 (1999). © 1999, Elsevier Science.

polycation components, and poly(sodium styrenesulfonate) (PSS) and poly(potassium vinylsulfonate) (PVS) are used as polyanions.

Since polyelectrolyte assembly [12–16, 25–60] is the most fundamental process, physicochemical factors that affect the assembly amount and structures of the films have been extensively researched at the initial stage of this technology. In particular, solution pH and ionic strength are quite important parameters in the assembly process, because charged state and electrostatic interaction are easily modified by these parameters. Combined analyses of AFM, SEM, and QCM have revealed that practical procedures such as washing and drying affect film thickness and roughness [25]. Experiments using PSS/PAH assemblies have demonstrated that drying the film at every step increases the thickness of adsorbed films because of the enhanced surface roughness of the film. Frequent drying during the assembly process is not profitable for preparing films of good quality. In contrast, water washing between the consecutive adsorptions was effective for successful alternating adsorption. About 10% of an adsorbed polyelectrolyte layer was removed by 5-min washing, probably because of removal of the loosely attached materials.

Alternating layer-by-layer adsorption was, of course, applied to functional polyelectrolytes. Rubner and co-workers presented several reports on layered assemblies of conjugate polymers [49, 50]. They demonstrate the fabrication of light-emitting diodes using poly(*p*-phenylenevinylene) (PPV). In this case, the cationic precursor of PPV was first assembled with polyanion, and then thermal treatment created conjugate chains of PPV. Yamada and co-workers reported nonlinear optical effects in

alternately assembled films between azobenzene-containing polycation and polyanion [51]. Second-harmonic generation intensity was sensitively influenced by the assembling cycles.

Polyelectrolytes do not have to be linear, as demonstrated by spherical dendrimer assembly with counterionic polyelectrolytes. Poly(amidoamine) dendrimers (PAMAM) have positive charges at the proper pH and can be alternatively assembled with anionic PSS [52]. A gold-dendrimer composite in which gold nanoparticles are immobilized in the compartment of the PAMAM dendrimer was also successfully assembled with PSS [53].

Assembly of UV-reactive polyelectrolytes can lead to micropatterned thin films [54]. A multilayered film of diazoresin (DAR) and poly(acrylic acid) (PAA) was assembled through the electrostatic alternating adsorption, and UV irradiation on the assembled film resulted in covalent linking between the two components through ester formation. Surfactant solution can dissolve the unirradiated film but not the irradiated film. Therefore, the UV irradiation on the assembled film through a patterned mask resulted in micrometer-scale patterns with defined thickness.

The alternating layer-by-layer adsorption can be driven by various forces other than simple electrostatic interaction. Hydrogen bonding between donor and acceptor polymers can be similarly applied in alternating layer-by-layer adsorption [49, 55]. As an interesting example, an alternating layer-by-layer adsorption based on stereocomplexation of hydrophobic poly(methyl methacrylate) (PMMA) was demonstrated by Akashi and co-workers [56, 57]. The assembly processes were conducted with acetonitrile solution of two types of PMMA. The isotactic PMMA physically adsorbed on the solid support because of its lower solubility in acetonitrile. In contrast, the syndiotactic PMMA, with a higher solubility, did not adsorb to a bare substrate, but it could be adsorbed to the isotactic-PMMA-exposed surface through stereocomplex formation. Alternating repetition of the physical adsorption and stereocomplexation led to multilayer formation between noncharged polymers.

Preparation of alternately assembled films through charge transfer interaction was reported by Ito and co-workers, who used an electron-donating polymer [poly(2-(9-carbazoyl)ethylmethacrylate)] and an electron-accepting polymer (poly(2-((3,5-dinitrobenzoyl)oxy)ethylene methacrylate)) [58–60]. The layers of their charge transfer complex are sandwiched between the donor and acceptor layers. Nonlinear optical properties of similarly assembled films were also achieved by copolymerization of a nonlinear optical dye with a donor polymer.

## 4.2. Biomaterials

Construction of multilayer structures of biological materials is an attractive focus for investigation, because such layered structures provide artificial sequences of biologically important functions [8, 17–19, 61–92]. Many highly sophisticated functions expressed in the biological world are based on controlled protein arrays. Such elegant constructions can be mimicked by this method. Typical advantages of protein immobilization by this method are summarized.

(i) *Wide Applicability of Proteins* Because most proteins, especially water-soluble proteins, have charged sites on

their surface, they are generally assembled by electrostatic layer-by-layer adsorption. QCM research using 18 proteins revealed that the assembly process with counterionic polyelectrolytes proceeded for unlimited numbers of cycles with high reproducibility in all cases [62, 63]. Except for some examples, the estimated thickness of the protein layer is approximately comparable to the protein dimensions.

(ii) *Rich Variety of Layered Structures* The film thickness and layering sequence are also easily controllable. Therefore, we can prepare protein-polyelectrolyte films with desirable thickness and layering sequences. This is an important feature for optimizing the reactor structure, as demonstrated later in this chapter.

(iii) *Minimization of Protein Denaturation* In this method, the proteins are simply adsorbed from their aqueous solution; that is, the assembly procedure is not conducted under severe physical conditions. Unnecessary disturbance of the protein structure would be minimized.

One crucial point in successful protein assembly is control of the protein solution pH; that is, the pH value should be set apart from the isoelectric point of the protein. Interestingly, control of the pH makes it possible to assemble the same protein in both a positively charged form and a negatively charged form [63]. For example, hemoglobin is positively charged at pH 4.5 and was assembled with anionic PSS, and hemoglobin in anionic form was assembled at pH 9.2 alternately with cationic PDDA. Albumin was similarly assembled with anionic heparin and cationic PDDA at pH 3.9 and 8, respectively.

Other charged biological materials can also be assembled with suitable partner polyelectrolytes. Negatively charged DNA can be assembled with various cationic materials [84–89]. Charged polysaccharides, chitosan and chondroitin sulfate, were assembled with PSS and PDDA, respectively [90]. As a remarkable example, alternating assembly between charged virus and polyelectrolyte was successfully demonstrated by Lvov et al. [17].

Some kinds of biomolecules possess specific recognition ability for specific functional groups. Such biospecific interactions are also utilized for protein assembly by alternating layer-by-layer adsorption. Concanavalin A (Con A) from *Canavalia ensiformis* (isoelectric point, ca. 5) is known to recognize specific sugar functionalities. It can be assembled with polycation PEI through electrostatic interaction and with glycogen (branched polyglucose) (Fig. 3) [91]. Similarly, a biospecific assembly was also reported for a biotin-avidin pair [92].

### 4.3. Colloidal Nanoparticles

Organic-inorganic layered nanohybrids have recently attracted attention. A convenient method for the preparation of nanohybrid films is solvent casting. Although preparations of uniformly ordered particles in two dimensions have been reported, it was not possible to create multilayers with precisely known numbers of layers. The LB method is the most powerful technique for providing defined layered structures. However, the LB technique is

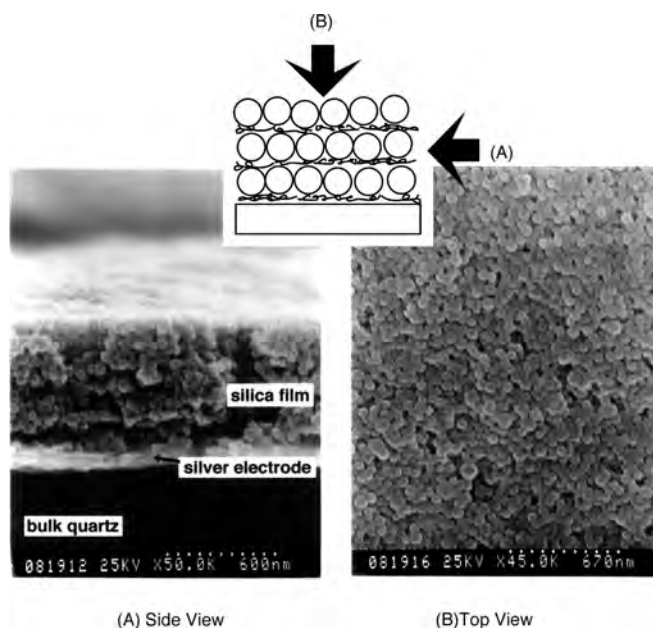


**Figure 3.** Scanning electron micrographs (SEMs) of  $(\text{PDDA/PSS})_2 + \text{PDDA} + (\text{SiO}_2/\text{PDDA})_8$  film on a silver electrode of a QCM plate. (A) Cross section. (B) Top view. Assembly conditions:  $\text{SiO}_2$ , 45 nm,  $10 \text{ mg} \cdot \text{ml}^{-1}$ , 0.1 M NaCl, pH 10; PDDA,  $3 \text{ mg} \cdot \text{ml}^{-1}$ ; adsorption time, 15 min. The QCM plate with assembled films was cut and coated with 20-Å-thick Pt with the use of an ion-coater (Hitachi E-1030 ion sputter, 15 mA/10 Pa) under an argon atmosphere. The SEM images were obtained with a Hitachi S-900 instrument at an acceleration voltage of 25 kV. Reprinted with permission from [24], Y. Lvov et al., *Langmuir* 13, 6195 (1997). © 1997, American Chemical Society.

not generally applicable to inorganic materials and is rather complicated and requires specialized machines. In contrast, alternating layer-by-layer adsorption possesses both advantages, that is, simplicity in procedure and controllability in structure [9, 24, 93–114].

As previously demonstrated in Figure 2, silica colloidal particles were successfully assembled alternately with a polycation. Next, the effect of the adsorption time of  $\text{SiO}_2$  particles was investigated by successively changing the adsorption time [24]. The film growth estimated by the QCM analysis remained exactly the same when the adsorption time was changed from 20 min to 15 s. This directly demonstrates the ease of this method; that is, the adsorption process is completed within a minute. The minimum  $\text{SiO}_2$  adsorption time was separately reported to be only 2 s at a concentration of  $10 \text{ mg} \cdot \text{ml}^{-1}$  [97].

QCM frequency shifts upon the assembly of 45-nm  $\text{SiO}_2$  in alternation with polycation PDDA were monitored at various  $\text{SiO}_2$  concentrations. The frequency shifts per  $\text{SiO}_2$  step increased as the  $\text{SiO}_2$  concentration increased [24]. The effect of the copresence of NaCl in the  $\text{SiO}_2$  solution was also examined, and the magnitude of the growth step increased as the ionic strength increased. Charge shielding by increased ionic strength may explain the salt effect. The repulsive force among the effective negative charges would be suppressed by increased ionic strength, leading to a larger adsorption amount at saturation. The results obtained

suggest that film thickness and surface coverage can be optimized through adjustment of the solution composition.

Film morphology was also affected by the concentration and ionic strength of the  $\text{SiO}_2$  solution, and the best quality film with a smooth surface and constant thickness would be obtained by optimizing the concentration of  $\text{SiO}_2$  particles and the ionic strength. SEM images of the optimized  $\text{SiO}_2$ -PDDA assembled film are shown in Figure 3 [24]. The internal structure of the film can readily be seen in the cross-sectional image, where the  $\text{SiO}_2$  particles are closely packed in the layer, but long-range ordering is not found (Fig. 3A). Well-packed particles in a two-dimensional plane were also confirmed in the top image (Fig. 3B).

The surface morphology was investigated by AFM in the noncontact mode (Fig. 4) [24]. In the image of the PSS-PDDA precursor film, a height difference of only 1 nm was detected over 500 nm in the horizontal distance (Fig. 4A). In contrast, individual  $\text{SiO}_2$  particles are clearly seen in the AFM image of a  $\text{SiO}_2$ -assembled film (Fig. 4B). The observed height difference of the 10–20-nm particles reasonably agrees with the actual particle radius of 23 nm. Their relatively larger horizontal profile is probably due to the bluntness of the scanning AFM tip.

Recently, Kotov and co-workers reported detailed observation of the surface image of assembled films of yttrium iron garnet nanoparticles (YIG) with PDDA [99]. They

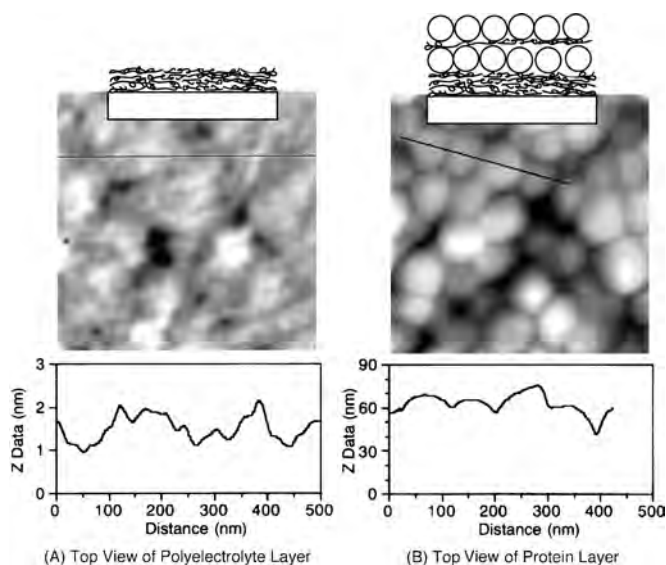


**Figure 4.** Noncontact mode AFM images ( $500 \text{ nm} \times 500 \text{ nm}$ ) of the surface of the assembled films. (A) Mica +  $(\text{PDDA}/\text{PSS})_4$  + PDDA film. (B) Mica +  $(\text{PDDA}/\text{PSS})_4$  +  $(\text{PDDA}/\text{SiO}_2)$  film. Assembly conditions:  $\text{SiO}_2$ , 45 nm, 10  $\text{mg ml}^{-1}$ , 0.1 M NaCl, pH 10; PDDA, 3  $\text{mg ml}^{-1}$ ; adsorption time, 15 min. Bottom figures represent height profiles along the line in the upper image. In the latter profiles, Z data represent the relative height versus the lowest point of the whole two-dimensional image. The observation was made with a TMX-2000 SPM System (TopoMetrix) in noncontact mode with a 2- $\mu\text{m}$  scanner. Measurements were carried out in the air. Silicon nitride cantilevers with spring constants of 38–66  $\text{N m}^{-1}$  were used as purchased. The resonance frequency of the cantilever was in the range of 130–150 kHz. Scanning rates were 3  $\mu\text{m s}^{-1}$ . Reprinted with permission from [24], Y. Lvov et al., *Langmuir* 13, 6195 (1997). © 1997, American Chemical Society.

noticed the two kinds of assembly modes in nanoparticle deposition, that is, layer growth and lateral growth mode. The latter mode should be avoided for preparation of a sophisticated layered structure. Grafting of the charged polymer on the nanoparticles significantly increases particle/polyelectrolyte and particle/particle interaction, resulting in the formation of a densely packed particle layer and avoidance of unfavorable lateral growth deposition.

#### 4.4. Clay Microplates, Polyoxometalates, and Other Inorganic Materials

Alternating layer-by-layer adsorption is applicable to inorganic materials other than spherical particles [115–135]. As flat-textured materials, clay microplates (montmorillonite) whose average size is  $1 \times 500 \times 500 \text{ nm}$  were used [115]. Regular changes in the QCM frequency response upon the alternating assemblies between negatively charged clay microplates and polycations were confirmed. Interestingly, the frequency shifts remained unchanged regardless of the concentration of the aqueous clay dispersion from 0.03 to 1 wt%. The flat texture of the clay plates would induce efficient contact with the underlying polycations. Effective charge neutralization and resaturation suppress the effect of the remaining charges that was observed in the assembly of spherical colloidal particles. In fact, a SEM photograph of the assembled film containing the clay microplates and PEI shows the remarkable uniformity of the film thickness. An AFM observation in a lateral-force mode detected the clay sheets that lay flat one on another with a typical step of ca. 1 nm that corresponds to the single clay-plate thickness.

Assembly of a large nonspherical inorganic substance by alternating layer-by-layer adsorption was recently demonstrated by Yoon and co-workers [124]. They used micrometer-sized cationically modified zeolite crystals and PSS for the assembly of components. SEM observation revealed a beautifully stacked assembly of tablet-like crystals with even thickness. Successful assembly of two-dimensional perovskite sheets with polyelectrolytes was also reported [132].

Polyoxometalates are an interesting target as an assembly unit, because they are useful for catalysts, solid-state devices, photo- and electrochromic displays, biochemistry, and medicine. Research on alternating layer-by-layer adsorption between ammonium octamolybdate ( $(\text{NH}_4)_4[\text{Mo}_8\text{O}_{26}]$ ) and PAH was reported by Kunitake and co-workers [120]. The film growth was reproducibly constant when the adsorption time was exactly fixed. However, the adsorption amount of molybdenum oxide increased when the immersion time was elongated. Reflection-adsorption IR spectroscopy and X-ray photoelectron spectroscopy (XPS) of the prepared films suggested that polymerized octamolybdates, such as  $(\text{NH}_4)_{2n}^{2n+} \cdot [\text{Mo}_8\text{O}_{26}]_n^{2n-}$ , would be formed via protonation and condensation of  $[\text{Mo}_8\text{O}_{26}]^{4-}$  ions. The molybdenum oxide layer can grow infinitely, because the surface charge of the molybdenum oxide is kept low because of condensation.

Alternating layer-by-layer adsorption of three kinds of inorganic materials, colloidal nanoparticles, clay microplates, and polyoxometalate clusters, displayed unique characteristics in adsorption kinetics (Fig. 5) [94]. Adsorption of rigid, spherical  $\text{SiO}_2$  particles is quite fast and

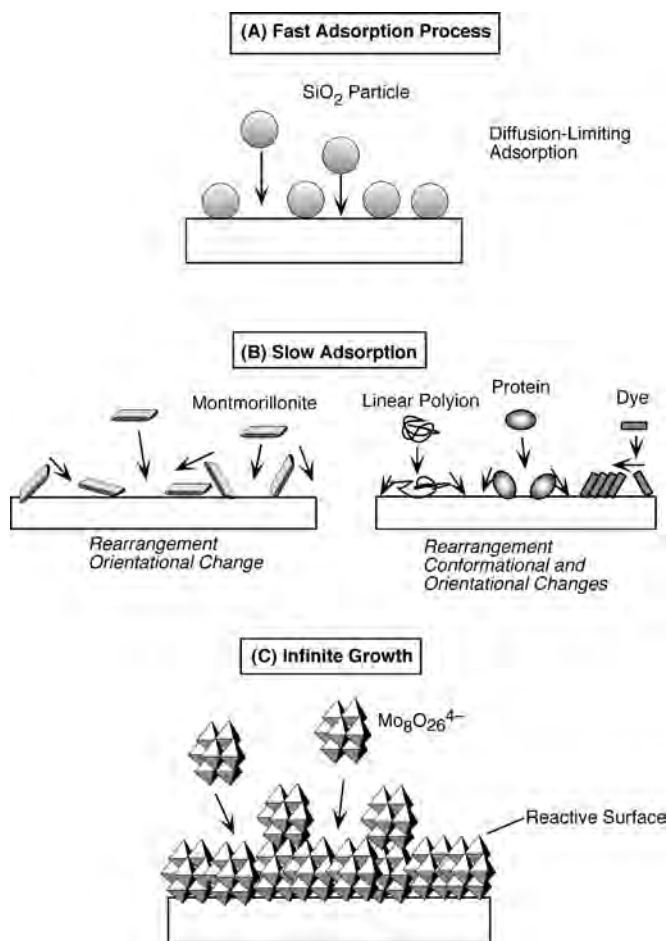


**Figure 5.** Plausible adsorption mechanisms of various inorganic materials. (A) Adsorption of silica particles is based on a diffusion-limiting process, and the adsorption is completed within a short period. (B) Most of the materials require rearrangement and conformational change in their adsorption process, resulting in relatively slow adsorption. (C) Adsorbed molybdates expose the reactive surface to the solution phase, and adsorption continues indefinitely. Reprinted with permission from [94], K. Ariga et al., *Appl. Clay Sci.* 15, 137 (1999). © 1999, Elsevier Science.

appeared to be diffusion-limited. The diffusion time of SiO<sub>2</sub> from solution onto the surface was estimated to be 2 s, with the use of a diffusion coefficient of  $1.1 \times 10^{-7} \text{ cm}^2 \cdot \text{s}^{-1}$  by Lvov et al. [97]. In contrast, the adsorption behavior of montmorillonite microplates is in the range of 10–20 min, similar to those of organic materials. Relatively long adsorption times would be attributed to the rearrangement process. The planar shape of montmorillonite can produce a tight contact with an oppositely charged surface, and rearrangement of the montmorillonite microplates requires a longer time. A similar rearrangement process, such as conformational and/or orientational changes, is required for the adsorption of soft organic materials. The mode of adsorption of molybdenum oxide is a nonsaturation-type. Protonation and condensation induce infinite film growth without excessive accumulation of surface charges.

## 4.5. Organic–Inorganic Hybrids

Hierarchical assemblies are attractive targets for study because hierarchically assembled structures express high functions in biological systems. For example, lipid molecules spontaneously form a bilayer structure that constitutes a cell membrane, and the cells assemble into organisms, tissues, and our bodies. Therefore, a layer-by-layer assembly of lipid vesicles, which can be regarded as an artificial cell, would be an interesting approach to creating artificial tissues. However, exposure of the lipid vesicles to counterionic polyelectrolytes sometimes induces vesicle destruction due to strong electrostatic interaction and results in an assembly alternating between a planar bilayer and a polyelectrolyte (see below). Therefore, the development of nondestructive vesicles is indispensable for this purpose.

We have recently developed a novel class of Organic–Inorganic hybrid vesicles, cerasomes, which form cell-like lipid bilayer structures with a ceramic-like inorganic skin (Fig. 6) [136–140]. The cerasomes can be obtained from amphiphiles bearing a triethoxysilyl head and a dialkyl tail by a conventional vesicle preparation procedure. Control of solution pH is an important factor in the cerasome preparation; that is, the triethoxysilyl group was moderately hydrolyzed and polymerized into polysiloxane under weakly acidic conditions. A spherical structure with a multibilayer skin was confirmed by transmission electron microscopic observation.

Because the prepared cerasome bears anionic charge on its surface, it can be alternately assembled with cationic components. As a first example, an anionic cerasome was alternately assembled with polycation PDDA [138]. The assembly process was monitored by QCM measurement, and regular growth in film weight was confirmed. AFM observation on the surface morphology of the assembled film revealed that the spherical structures of the cerasomes remained and were closely packed. Such a vesicular assembly was not obtained when conventional anionic vesicles from dihexadecyl phosphate were used in the assembly.

A cationic cerasome was prepared from another amphiphile with a quarternary ammonium group as well as the triethoxysilyl group and a dialkyl tail. Direct assembly between an anionic cerasome and a cationic cerasome was also demonstrated by the QCM measurement [137]. AFM observation confirmed the packing of spherical cerasome structures at both cerasome layers. The size of the cationic cerasome is smaller than that of the anionic cerasome, and thus their images can be distinguished. This is the first example of a hierarchically integrated vesicular assembly without serious destruction of the vesicle sphere. The assembly process looks like stone paving, and the structure obtained resembles biological tissues composed of living cell assemblies.

## 4.6. Dye and Lipid Assemblies

Assemblies of charged molecules form a multicharged surface, and thus they are applicable to alternating layer-by-layer adsorption. Bolaamphiphile monolayers [141–149], bilayers [71, 150], and LB films [151] can be assembled alternately with countercharged polyelectrolytes. Multicharged



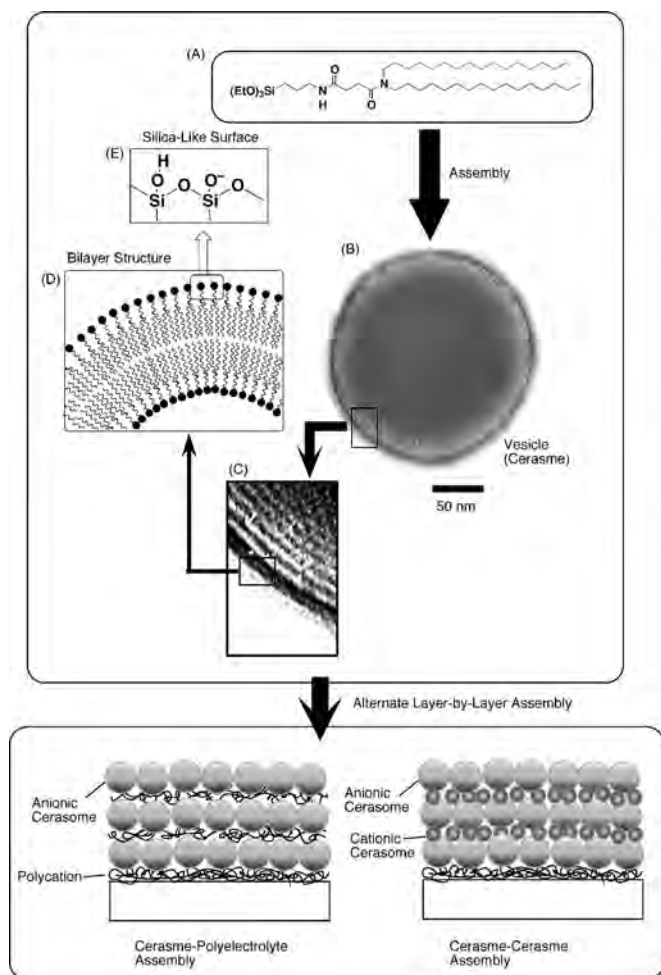


**Figure 6.** Formation of an Organic-Inorganic hybrid vesicle (“cerasome”) from a dialkyl amphiphile with a triethoxysilane head. The cerasome has a bilayer structure like that of a cell membrane and silicate walls like silica particles. It is expected to form a structure like a silica particle assembly. (A) Lipid. (B, C) TEM images of cerasome. (D) Bilayer structure. (E) Siloxane linkage on the cerasome surface. Two modes of the alternating assemblies (anionic cerasome and polycation, anionic cerasome and cationic cerasome) are also depicted.

dye molecules were also assembled with polyelectrolytes by stacking of the dye molecules [152–163].

In particular, hybrid assemblies between proteins and lipid bilayers are interesting because biomimetic structures composed of these components would be constructed by a procedure much easier than the LB technique. The QCM frequency shifts for the films from cationic lipid bilayer and anionic enzyme lactate dehydrogenase (LDH) are plotted in Figure 7, where successful assemblies between the bilayer and the enzyme are clearly demonstrated [71]. A similar assembly method was successfully applied to alcohol dehydrogenase (ADH). Calculation based on a ball-packing model indicates that these proteins form a monolayer or a bilayer structure in a single adsorption process.

The adsorption behavior of dye aggregates on a polyelectrolyte surface provides insight into alternating layer-by-layer adsorption [152]. QCM analyses of assembly processes of various dyes and counterionic polyelectrolytes allow us to

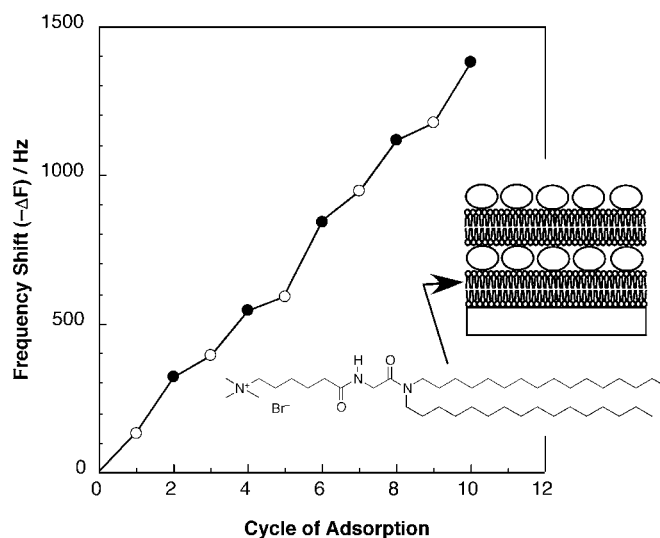


**Figure 7.** Frequency shift upon alternating layer-by-layer adsorption between LDH (●) ( $0.2 \text{ mg ml}^{-1}$ ) and lipid bilayer (○) (lipid concentration,  $1 \text{ mM}$ ) and LDH; [HEPES buffer],  $10 \text{ mM}$  (pH 7.0); room temperature.

guess the orientation of the adsorbed dye. The experimentally estimated thickness of Congo Red on PDDA is  $12 \text{ \AA}$ , which is smaller than the long axis of the molecule ( $19 \text{ \AA}$ ) but is significantly larger than the short axis ( $5 \text{ \AA}$ ). Congo Red molecules probably adsorbed on PDDA in edge-on orientation with a tilted orientation, which was also supported by red-shifted UV characteristics. In contrast, side-on orientation was suggested for Acid Red 26 and Ponceau S. Data on various dye adsorbents revealed a set of general rules on adsorption orientation. The dye exposes its charged side to the polyelectrolyte surface by maintaining at least one charged site in contact with the outer solution phase. This adsorption mode satisfies charge neutralization on polyelectrolyte surfaces and avoids unfavorable contact of the hydrophobic side of dye molecules with water.

#### 4.7. Hybrid Layering

As previously described, alternating layer-by-layer adsorption offers freedom in film construction. This characteristic allows us to design and prepare various kinds of hybrid layering structures. Silica colloidal particles with different sizes were assembled in the same film in two kinds of structural designs for demonstration [24]. The consecutive assembly of two kinds of layers was done in a separated layer mode; that is, the first four layers were made from  $45\text{-nm SiO}_2$  and the following six layers were assembled with  $25\text{-nm SiO}_2$ . QCM responses on growth steps for the two sizes of  $\text{SiO}_2$  particles are highly constant. Another example was demonstrated in a neighboring layer mode; that is, a four-unit layer ( $45\text{-nm SiO}_2/\text{PDDA}/25\text{-nm SiO}_2/\text{PDDA}$ ) was repeatedly assembled. Interestingly, individual growth steps in this film were identical to the corresponding adsorption steps in the former assembly. Therefore, it is concluded that individual adsorption steps are not affected by the previous adsorption sequences.

Hybrid assemblies were also demonstrated with the use of biological materials and inorganic material. Glucose oxidase (GOD) was assembled with clay microplates with the help of polycationic PEI [63]. Figure 8 shows the QCM responses upon the assembly of four-unit layers (GOD/PEI/clay/PEI) on clay/PEI underlayer films. The observed QCM changes showed strange profiles. The frequency shift showed the adsorption of a thicker GOD layer, and negative growth in the next PEI adsorption steps, implying peeling out of some GOD molecules during immersion of the film in the PEI solution. Somehow, excess adsorption occurs in the first GOD adsorption step, but the extra GOD in the excess layer is self-excluded during the cationic PEI adsorption step. The clay sheets stably adsorbed on the resulting surface in the third step, and the formation of a superlattice unit was completed by the final PEI adsorption. Assemblies between rigid components such as clay microplates and enzymes were usually reported to be unsuccessful. PEI can bridge two negatively charged rigid substances as a flexible glue. Similar heterogeneous assemblies were achieved between  $\text{SiO}_2$  particles and GOD, with PDDA as the glue.

#### 4.8. 3D Assembly

The fundamentals of alternating layer-by-layer adsorption have been established, and several modification methods for producing more elaborate assemblies have recently been proposed. Intercalation of dye molecules into inorganic platelets makes it possible to prepare three-component inorganic/dye/polyelectrolyte assemblies [119]. Alternating

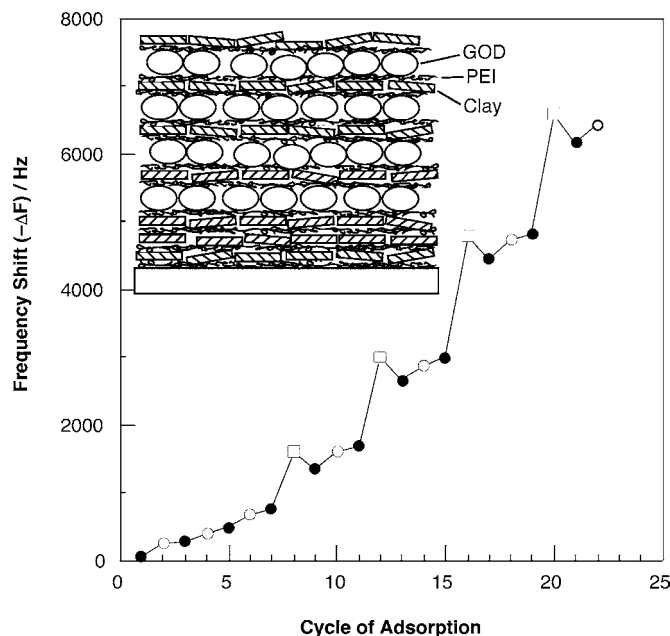


**Figure 8.** QCM frequency changes in three-component alternating layer-by-layer adsorption between PEI, clay microplate, and glucose oxidase at 22 °C: clay microplate, 0.3 mg ml<sup>-1</sup> at pH 6.5; PEI, 1.5 mg ml<sup>-1</sup>; glucose oxidase, 2 mg ml<sup>-1</sup>; adsorption time, 20 min. Open circles, solid circles, and open squares represent montmorillonite, PEI, and glucose oxidase adsorption processes, respectively. Reprinted with permission from [63], Y. Lvov et al., *J. Am. Chem. Soc.* 117, 6117 (1995). © 1995, American Chemical Society.

assembly of CdTe nanocrystals with PDDA was controlled by electrical fields, and patterned assemblies were deposited on a multielectrode support [121]. A patterned structure of assembled films of nanoparticles and polyelectrolyte was also achieved by a lithographic approach [112]. Alignment of chromophores in an assembled film of azobenzene polymer with PDDA was controlled by polarized light irradiation [29].

Among various modifications, the most pronounced improvement in alternating layer-by-layer adsorption is three-dimensional assembly on an invisible colloidal support. So far, solid supports in a visible size such as a quartz plate have mainly been used for this method. However, the assembly mechanism of this technique does not require the use of these solid supports; that is, microscopic materials can be used for this method. Three-dimensional (3D) assembly on colloidal particles has recently been reported by several groups [164–171].

The first example is a 3D assembly for biological substances. Precursor layers of polyelectrolytes were first assembled on colloidal particles. Charge alteration upon polyelectrolyte adsorption can be monitored by surface potential measurement. On the precursor layer, proteins were sequentially assembled in a manner similar to that of conventional assemblies on a plate surface. This strategy would be more fruitful than a reactor prepared on a macroscopic support, because the particle system has an inherently high surface area. Preparation of a multienzyme film on polystyrene particles and their coupling reaction were demonstrated by Caruso and Schüller [165]. A more interesting assembly design was proposed that combined an enzyme and magnetic particles ( $\text{Fe}_3\text{O}_4$ ). Prior to enzyme layer assembly, magnetic particles were assembled on a polystyrene particle, resulting in the production of particles with both enzymatic and magnetic properties. These particles can be collected by an external magnet. Therefore, they can be regarded as a reusable biocatalyst.

The 3D assembly can be similarly applied to inorganic materials [167]. As illustrated in Figure 9, multilayer assemblies between  $\text{SiO}_2$  nanoparticles and polyelectrolyte were first prepared on support particles. Destruction of the center particles provides hollow spheres. Dissolution of the center particles upon exposure of the particles to appropriate

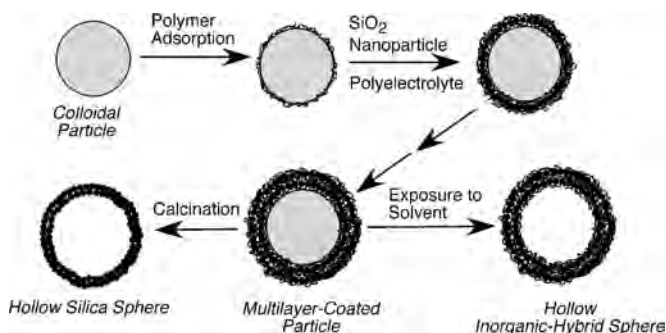


**Figure 9.** Three-dimensional alternating layer-by-layer adsorption on a colloidal template provides multilayer-coated particles, hollow inorganic spheres, and hollow hybrid spheres. Reprinted with permission from [167], F. Caruso et al., *Science* 282, 1111 (1998). © 1998, American Association for the Advancement of Science.

solvents results in hollow organic–inorganic hybrid spheres. Hollow inorganic spheres without an organic component were similarly prepared by calcination.

Hollow spheres prepared by 3D assembly can be used for encapsulation of guest substances, because permeability through the sphere skin would be controllable by several perturbations [172–177]. Polycation PAH and polyanion PSS were alternately assembled on a melamine formaldehyde core that can be decomposed at low pH. The permeability of the polyelectrolyte capsule obtained was controlled by changing the dielectric environment of the surrounding solvent system. Usually, a polyelectrolyte shell cannot be penetrated by macromolecules such as proteins. However, the capsules became permeable even by proteins when the capsules were exposed to a water/ethanol mixture. Resuspension of the capsules in water closed the opened pores, resulting in encapsulation of the enzymes. The polyelectrolyte skin is permeable by small materials such as substrates for enzymatic reaction; therefore, the enzyme-entrapped polyelectrolyte capsule can be used as a biocatalytic reactor.

## 5. APPLICATIONS

### 5.1. Nanobioreactor

Alternating layer-by-layer adsorption has led to the imagination of functional applications, because highly functionalized materials such as protein and microparticles can easily be assembled in controlled layer structures. As one of the straightforward applications, preparation of multienzyme reactors was demonstrated [61, 67, 68]. The reaction scheme used for the reactor function is depicted in Figure 10. Two enzymes, glucoamylase (GA) and GOD, were assembled in the film, and another enzyme, peroxidase (POD), was used in solution phase for a coloring assay reaction. The substrate is starch that is hydrolyzed into glucose through hydrolysis of the glycoside bond in starch by GA. The glucose produced is converted to gluconolactone by GOD with  $\text{H}_2\text{O}_2$  as a coproduct. POD in solution oxidizes DA67 (indicator) with  $\text{H}_2\text{O}_2$  as an oxidant. The reaction can easily be followed by monitoring the strong absorbance of the oxidized DA67 at 665 nm.

A multienzyme reactor composed of GOD and GA was examined with the experimental setup depicted in Figure 10. The enzyme film was assembled on an ultrafilter (limiting molecular weight 5000). The substrate, water-soluble starch, in 0.1 M 1,4-piperazinediethanesulfonic acid (PIPES) buffer (pH 7.0), was placed on enzyme-immobilized ultrafilters in the upper cup. The starch solution was passed through the enzyme film by pressure from a syringe. The filtrate obtained was assayed by POD and DA67 to quantify the resulting  $\text{H}_2\text{O}_2$ . The concentration of unreacted starch was assayed by the iodostarch reaction, but the unreacted starch was not detected in the filtrate at all.

Free design of multienzyme films allows us to examine the effect of the film construction on reactor performance. In order to investigate the influence of layer order and layer separation, the reactor performance of four kinds of films was examined. The film structure and the order of reactor performance (yield of the product  $\text{H}_2\text{O}_2$ ) are schematically

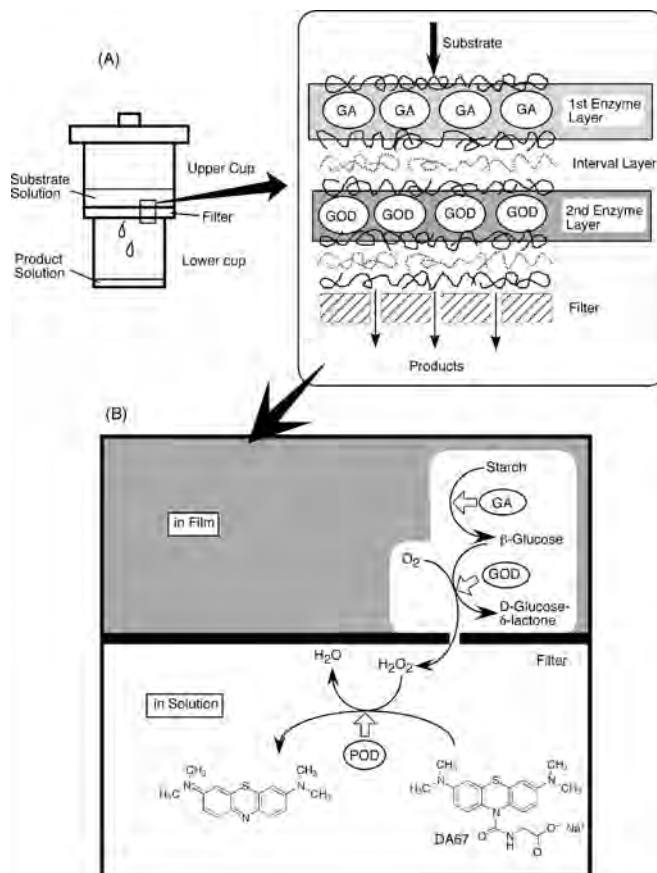


**Figure 10.** (A) Structure of a multienzyme reactor composed of GA and GOD. (B) Sequential reaction catalyzed by the multienzyme reactor. To evaluate the reaction, DA67 oxidation by POD in the filtrate is coupled with the sequential reaction in the film.

summarized in Figure 11. All of the films have a precursor layer [(PEI/PSS)<sub>4</sub>] on the filter. Inner enzyme layers and outer enzyme layers are separated by a (PEI/PSS)<sub>n</sub> interval layer, and the outermost surface was covered by a single layer of PEI.

Film A and film B have inner layers of GOD and GA outer layers and showed the best and the second best performances, respectively. Matching in the direction of reactant flow and the sequence of the enzyme layers resulted in a higher yield of the product. The difference between these films is the separation between the two kinds of enzyme layers. Inhibition of GA by gluconolactone, which is the product of the glucose oxidation, may be more effectively suppressed in film A, having a larger spacer layer between GOD and GA. Film C has a reversed ordering of the enzyme layers and provides less efficient reactor performance. In this film, glucose has to diffuse against the solution flow, and that process is apparently disadvantageous. Film D has two mixed layers of GA and GOD and showed the worst yield. The coexistence of GA and GOD might result in the lowest activity because of the inhibition of GA by gluconolactone [178, 179]. The above-mentioned results strongly support the superiority of controlled layering than random immobilization.

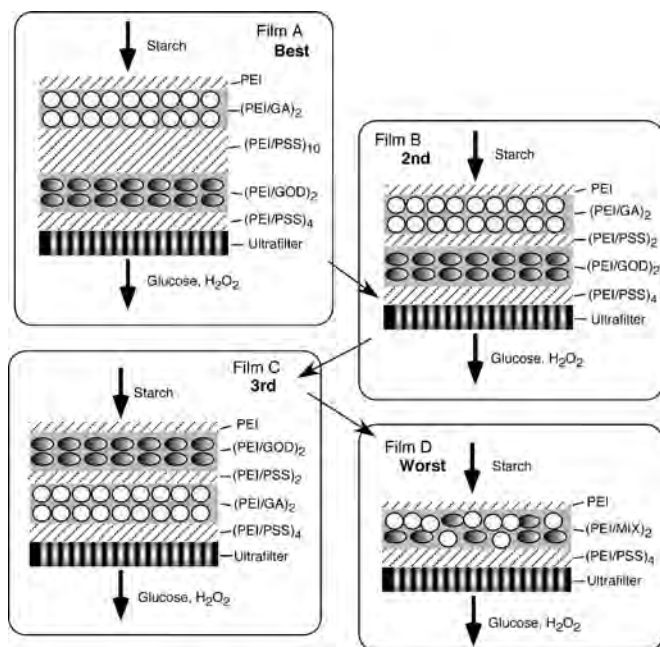


**Figure 11.** Reaction efficiency of various films. (A) Film composed of GA outer layers and GOD inner layers with thick spacer layers (the highest efficiency). (B) Film composed of GA outer layers and GOD inner layers with thin spacer layers (the second highest efficiency). (C) Film composed of GOD outer layers and GA inner layers with thin spacer layers (the second lowest efficiency). (D) Film composed of GA and GOD mixed layers (the lowest efficiency).

Here the advantages of the multienzyme reactors prepared by the alternating layer-by-layer adsorption between proteins and polyelectrolytes are briefly summarized. The most pronounced advantage is freedom of film construction. Various film structures are easily prepared through changes in the dipping number and sequence, and thus optimization of the reactor structures can be achieved rather easily. Simplicity of the procedure excludes usage of specialized equipment, making the method inexpensive, which is an important feature for practical purposes. An increase in thermal and duration stabilities of the enzyme immobilized in the assembled film was also demonstrated [64]. Alternating layer-by-layer adsorption does not have special requirements for a solid support. The support just has to bear some degree of charge, and charge introduction treatment is widely established.

## 5.2. Electrochemical Application and Sensors

The layer-by-layer adsorption method is easily applied to many kinds of solid surfaces. Therefore, modification of an electrode by this method would be useful for molecular device development. Here, some recent applications of alternating layer-by-layer adsorption to electrochemical usages are introduced.

An enzyme-coated electrode provides the basis of a biocatalytic device including an enzymatic bioreactor. When an electron is directly exchanged between the electrode and

an enzyme, a chemical mediator is omitted and the system is simplified. Rusling et al. reported redox behavior and chemical conversion at an electrode modified by the alternating layer-by-layer adsorption technique [77]. Epoxidation of styrene by myoglobin-containing, alternately assembled films was demonstrated. Myoglobin is directly reduced at the electrode and oxygen is converted to hydrogen peroxide. Metmyoglobin ( $\text{MbFe}^{\text{III}}$ ) is converted to an active oxidant form, ferrylmyoglobin ( $\text{MbFe}^{\text{IV}}=\text{O}$ ), upon conversion of the hydrogen peroxide to water, and the latter form may oxidize styrene. Similar catalytic activity was achieved with cytochrome P450-containing film.

Electrically wired enzymes have attracted attention because of their potential application in biosensors and molecular devices. Layer-by-layer structures composed of alternating layers of charged enzymes and countercharged redox polyelectrolytes would easily make electrochemical contact with an electrode. Calvo et al. demonstrated that glucose oxidase, lactate oxidase, and soybean peroxidase were electrically wired to an underlying electrode through poly(allylamine) with a covalently attached osmium complex [73]. Lactate oxidation by the corresponding enzyme was driven indirectly by an electrode. A bienzyme system with glucose oxidase and peroxidase was also proposed.

Thin-film characteristics are favorable for a quick sensing system, and thus alternating films on appropriate device surfaces are quite suitable for sensor preparation. As easily imagined from the above-mentioned examples, enzyme multilayers immobilized on an electrode surface provide wide variety in sensor preparation. For example, a cholesterol sensor was recently proposed that included an alternating film containing cholesterol oxidase [83]. Much simpler polyelectrolyte assemblies are also useful for sensor devices. Alternating assembled films of PEI and poly(maleic acid-co-ethylenimine) was used for the detection of copper and nickel ions [48]. Uptake of these ions to the films is monitored by SPR. As a unique application, a smoke sensor was proposed that would include films of PAH and PAA alternately assembled on a QCM device [16]. Exposure of the film to smoke from tobacco induced an incredible shift of the resonance frequency. The frequency response upon smoke adsorption was recovered by heat treatment.

## 5.3. Electronics and Photonics

For the construction of molecular photoelectrical devices, immobilization of bacteriorhodopsin is an attractive research target. Its long-term resistance to thermal, chemical, and photochemical degradation makes bacteriorhodopsin one of the most promising biological candidates for biophotonics. Tripathy et al. reported that layer-by-layer assemblies using cationic PDDA and the anionic bacteriorhodopsin were successfully constructed by the alternating layer-by-layer adsorption technique. Generation of photocurrent from the assemblies confirmed the biological activity of bacteriorhodopsin after the assembly process [74, 75].

Many applications of alternately assembled film of non-biological materials have also been extensively researched. In particular, assemblies of inorganic materials and conductive polymers were used for various electronic and photonic

devices, such as a rectifying junction device and light-emitting diodes.

Alternating assembled film can incorporate metallic components as a coordination complex. Rubner et al. reported light-emitting devices based on alternating layer-by-layer adsorption of Ru(bpy)<sub>3</sub> complex polyelectrolyte and poly(acrylic acid) (PAA) [33]. The Ru(bpy)<sub>3</sub> complex is known to emit light in an electrogenerated chemiluminescence process. When a thin insulating layer (PAH/PAA layer) existed at an anodic electrode, the luminescence level of these devices was significantly diminished. Therefore, luminescence intensity was observed to be controlled by the film construction and bias types. Great freedom of film construction in alternating layer-by-layer adsorption makes it possible to design vectorially functioning devices.

The importance of layering sequences was also pointed out in these functions. For example, Eckle and Decher fabricated organic light-emitting diodes based on poly(*p*-phenylenevinylene) and poly(methacrylic acid) that included an isolating layer of clay microplates [116]. Introduction of the clay layer lowered the current density and increased the luminescence intensity in comparison with a pure polymer assembly, and these characteristics were easily modified by the deposition sequences of these components. The most important advantage in alternating layer-by-layer adsorption, freedom in layering construction, can lead to easy device optimization.

Diode nanowire devices were prepared by combining template synthesis and the layer-by-layer adsorption. Kovtyukhova and co-workers assembled nanoparticles (TiO<sub>2</sub> and ZnO) and PSS between metals in a matrix of porous alumina membrane [125]. Removal of the matrix resulted in free-standing nanowire with the nanoparticle assembly film sandwiched by the metals. The prepared nanowire showed current-rectifying behavior.

## 6. CONCLUSIONS

Preparation of well-controlled structures in nanometer-level precision is an indispensable research target for the current development of nanoscience and nanotechnology. In particular, the formation of layered nanostructures is more easily accomplished than the total construction of three-dimensional structures. We need a simple and inexpensive methodology that can be generally applied to various materials. Alternating layer-by-layer adsorption satisfies these requirements. Recent developments in this method have expanded the application area from the visible range (2D assembly on visible support) to a microscopic scale (3D assembly on invisible particles). The potential and recent progress of this method could lead to various practical applications, from electronic devices to medical uses.

## GLOSSARY

**Alternating layer-by-layer adsorption** Method to produce thin film through alternating adsorption of materials. Electrostatic interaction between cationic and anion polyelectrolytes is mainly used as an adsorption force.

**Atomic force microscopy (AFM)** Microscopy for observation of surface morphology with molecular-level resolution produced by controlling atomic force between sample surface and monitoring tip.

**Cerasome** Lipid vesicle with a ceramic-like surface.

**Langmuir–Blodgett (LB) film** Thin film prepared by layer-by-layer transfer of monolayers from water surface to solid support.

**Quartz crystal microbalance (QCM)** Device to monitor mass change with nanogram precision through the resonance frequency shift of quartz crystal based on its piezoelectric property.

## REFERENCES

1. Y. Okahata, T. Tsuruta, K. Ijio, and K. Ariga, *Langmuir* 4, 1373 (1988).
2. Y. Okahata, T. Tsuruta, K. Ijio, and K. Ariga, *Thin Solid Films* 180, 65 (1989).
3. R. K. Iler, *J. Colloid Interface Sci.* 21, 569 (1966).
4. G. Decher, *Science* 277, 1232 (1997).
5. W. Knoll, *Curr. Opin. Colloids Interfaces* 1, 137 (1996).
6. S. K. Tripathy, J. Kumar, and H. S. Nalwa, Eds., "Handbook of Polyelectrolytes and Their Applications," Vols. 1–3. American Scientific Publishers, Los Angeles, 2002.
7. R. C. Advincula, in "Handbook of Polyelectrolytes and Their Applications," Vol. 1 (S. Tripathy, J. Kumar, and H. S. Nalwa, Eds.), Chap. 3, p. 65. American Scientific Publishers, Los Angeles, 2002.
8. K. Ariga, in "Handbook of Polyelectrolytes and Their Applications," Vol. 1 (S. Tripathy, J. Kumar, and H. S. Nalwa, Eds.), Chap. 4, p. 99. American Scientific Publishers, Los Angeles, 2002.
9. K. Ariga, in "Handbook of Polyelectrolytes and Their Applications," Vol. 1 (S. Tripathy, J. Kumar, and H. S. Nalwa, Eds.), Chap. 5, p. 127. American Scientific Publishers, Los Angeles, 2002.
10. M. Shimomura, in "Handbook of Polyelectrolytes and Their Applications," Vol. 1 (S. Tripathy, J. Kumar, and H. S. Nalwa, Eds.), Chap. 6, p. 150. American Scientific Publishers, Los Angeles, 2002.
11. P. Bernt, K. Kurihara, and T. Kunitake, *Langmuir* 8, 2486 (1992).
12. M. Onda, Y. Lvov, K. Ariga, and T. Kunitake, *Jpn. J. Appl. Phys.* 36, L1608 (1997).
13. S. L. Clark and P. T. Hammond, *Adv. Mater.* 10, 1515 (1998).
14. S. S. Shiratori and M. Yamada, *Polym. Adv. Technol.* 11, 810 (2000).
15. S. S. Shiratori, T. Ito, and T. Yamada, *Colloids Surf., A* 198–200, 415 (2002).
16. M. Yamada and S. S. Shiratori, *Sens. Actuators, B* 64, 124 (2000).
17. Y. Lvov, H. Haas, G. Decher, H. Möhwald, A. Mikhailov, B. Mchedlishvili, E. Morgunova, and B. Vainstein, *Langmuir* 10, 4232 (1994).
18. F. Caruso, K. Niikura, N. Furlong, and Y. Okahata, *Langmuir* 13, 3427 (1997).
19. G. Ladam, P. Schaaf, F. J. G. Cuisinier, G. Decher, and J.-C. Voegel, *Langmuir* 17, 878 (2001).
20. G. Sauerbrey, *Z. Phys.* 155, 206 (1959).
21. Y. Okahata, K. Kimura, and K. Ariga, *J. Am. Chem. Soc.* 111, 9190 (1989).
22. K. Ariga and Y. Okahata, *Langmuir* 10, 2272 (1994).
23. K. Ariga and Y. Okahata, *Langmuir* 10, 3255 (1994).
24. Y. Lvov, K. Ariga, M. Onda, I. Ichinose, and T. Kunitake, *Langmuir* 13, 6195 (1997).
25. Y. Lvov, K. Ariga, M. Onda, I. Ichinose, and T. Kunitake, *Colloids Surf., A* 146, 337 (1999).
26. I. Ichinose, S. Mizuki, S. Ohno, H. Shiraiishi, and T. Kunitake, *Polym. J.* 31, 1065 (1999).

27. J. Ramsden, Y. Lvov, and G. Decher, *Thin Solid Films* 254, 246 (1995).
28. A. Baba, M.-K. Park, R. C. Advincula, and W. Knoll, *Langmuir* 18, 4648 (2002).
29. M.-K. Park and R. C. Advincula, *Langmuir* 18, 4532 (2002).
30. A. Advincula, E. Aust, W. Meyer, and W. Knoll, *Langmuir* 12, 3536 (1996).
31. S. S. Shiratori and M. F. Rubner, *Macromolecules* 33, 4213 (2000).
32. D. Yoo, S. S. Shiratori, and M. F. Rubner, *Macromolecules* 31, 4309 (1998).
33. A. Wu, D. Yoo, J.-K. Lee, and M. F. Rubner, *J. Am. Chem. Soc.* 121, 4883 (1999).
34. M. Ferreira and M. Rubner, *Macromolecules* 28, 7107 (1995).
35. E. J. Calvo and A. J. Wolosiuk, *J. Am. Chem. Soc.* 124, 8490 (2002).
36. L. Krasemann and B. Tieke, *Langmuir* 16, 287 (2000).
37. M. C. Hsieh, R. J. Farris, and T. J. McCarthy, *Macromolecules* 30, 8453 (1997).
38. X. Jiang and P. Hammond, *Langmuir* 16, 8501 (2000).
39. J. Ruths, F. Essler, G. Decher, and H. Riegler, *Langmuir* 16, 8871 (2000).
40. D. Cochran and A. Laschewsky, *Macromol. Chem. Phys.* 200, 609 (1999).
41. S. T. Dubas, T. R. Farhat, and J. B. Schlenoff, *J. Am. Chem. Soc.* 123, 5368 (2001).
42. G. Zotti, S. Zecchin, A. Berlin, G. Schiavon, and G. Giro, *Chem. Mater.* 13, 43 (2001).
43. M. Raposo and O. N. Oliveria, Jr., *Langmuir* 16, 2839 (2000).
44. J. Sun, T. Wu, F. Liu, Z. Wang, X. Zhang, and J. Shen, *Langmuir* 16, 4620 (2000).
45. M. Ginzburg, J. Galloro, F. Jäkle, K. N. Power-Billard, S. Yang, I. Sokolov, C. N. C. Lam, A. W. Neumann, I. Manners, and G. A. Ozin, *Langmuir* 16, 9609 (2000).
46. M. Onoda and K. Yoshino, *Jpn. J. Appl. Phys.* 34, L260 (1995).
47. M. Breit, M. Gao, G. von Piessen, U. Lemmer, J. Feldmann, and S. T. Cundiff, *J. Chem. Phys.* 117, 3956 (2002).
48. C. Pearson, J. Nagel, and M. C. Petty, *J. Phys. D: Appl. Phys.* 34, 285 (2001).
49. W. B. Stockton and M. F. Rubner, *Macromolecules* 30, 2717 (1997).
50. A. C. Fou, O. Onitsuka, M. Ferreira, M. Rubner, and B. R. Hsieh, *J. Appl. Phys.* 79, 7501 (1996).
51. Y. Lvov, S. Yamada, and T. Kunitake, *Thin Solid Films* 300, 107 (1997).
52. A. J. Khopade and F. Caruso, *Langmuir* 18, 7669 (2002).
53. J.-A. He, R. Valluzzi, K. Yang, T. Dolukhanyan, C. Sung, J. Kumar, S. K. Tripathy, L. Samuelson, L. Balogh, and D. A. Tomalia, *Chem. Mater.* 11, 3268 (1999).
54. F. Shi, B. Dong, D. Qiu, J. Sun, T. Wu, and X. Zhang, *Adv. Mater.* 14, 805 (2002).
55. S. A. Sukhishvill and S. Granick, *Macromolecules* 35, 301 (2002).
56. T. Serizawa, K. Hamada, T. Kitayama, N. Fujimoto, K. Hatada, and M. Akashi, *J. Am. Chem. Soc.* 122, 1891 (2000).
57. T. Serizawa, K. Hamada, T. Kitayama, K. Katsukawa, K. Hatada, and M. Akashi, *Langmuir* 16, 7112 (2000).
58. Y. Shimazaki, R. Nakamura, S. Ito, and M. Yamamoto, *Langmuir* 17, 953 (2001).
59. Y. Shimazaki, S. Ito, and N. Tsutsumi, *Langmuir* 16, 9478 (2000).
60. Y. Shimazaki, M. Mitsuishi, S. Ito, and M. Yamamoto, *Langmuir* 14, 2768 (1998).
61. K. Ariga and T. Kunitake, in "Protein Architecture-Interfacing Molecular Assemblies and Immobilization Biotechnology" (Y. Lvov and H. Möhwald, Eds.), p. 169. Dekker, New York, 2000.
62. Y. Lvov, in "Protein Architecture-Interfacing Molecular Assemblies and Immobilization Biotechnology" (Y. Lvov and H. Möhwald, Eds.), p. 125. Dekker, New York, 2000.
63. Y. Lvov, K. Ariga, I. Ichinose, and T. Kunitake, *J. Am. Chem. Soc.* 117, 6117 (1995).
64. M. Onda, K. Ariga, and T. Kunitake, *J. Biosci. Bioeng.* 87, 69 (1999).
65. F. Caruso, D. N. Furlong, K. Ariga, I. Ichinose, and T. Kunitake, *Langmuir* 14, 4559 (1998).
66. K. Ariga, M. Onda, Y. Lvov, and T. Kunitake, *Chem. Lett.* 25 (1997).
67. M. Onda, Y. Lvov, K. Ariga, and T. Kunitake, *Biotechnol. Bioeng.* 51, 163 (1996).
68. M. Onda, Y. Lvov, K. Ariga, and T. Kunitake, *J. Ferment. Bioeng.* 82, 502 (1996).
69. Y. Lvov, K. Ariga, I. Ichinose, and T. Kunitake, *Thin Solid Films* 284/285, 797 (1996).
70. Y. Lvov, K. Ariga, and T. Kunitake, *Chem. Lett.* 2323 (1994).
71. K. Ariga, Y. Sasaki, H. Horiguchi, N. Horiuchi, and J. Kikuchi, in "Soft Chemistry Leading to Novel Materials Defect and Diffusion Forum" (R. P. Agarwala, Ed.), Vol. 191, p. 35. Trans Tech Publications, Zürich, 2001.
72. E. S. Forzani, M. Otero, M. A. Perez, M. L. Teijelo, and E. J. Calvo, *Langmuir* 18, 4020 (2002).
73. E. J. Calvo, F. Battaglini, C. Danilowicz, A. Wolosiuk, and M. Otero, *Faraday Discuss.* 116, 47 (2000).
74. J.-A. He, L. Samuelson, L. Li, J. Kumar, and S. Tripathy, *Langmuir* 14, 1674 (1998).
75. J.-A. He, L. Samuelson, L. Li, J. Kumar, and S. K. Tripathy, *J. Phys. Chem. B* 102, 7067 (1998).
76. H. Ma, N. Hu, and J. F. Rusling, *Langmuir* 16, 4969 (2000).
77. Y. M. Lvov, Z. Lu, J. B. Schenkman, X. Zu, and J. F. Rusling, *J. Am. Chem. Soc.* 120, 4073 (1998).
78. X. Zhang, Y. Sun, and J. Shen, in "Protein Architecture-Interfacing Molecular Assemblies and Immobilization Biotechnology" (Y. Lvov and H. Möhwald, Eds.), p. 229. Dekker, New York, 2000.
79. W. Kong, L. P. Wang, M. L. Gao, H. Zhou, X. Zhang, W. Li, and J. C. Shen, *J. Chem. Soc., Chem. Commun.* 1297 (1994).
80. W. Li, Z. Wang, C. Sun, M. Xian, and M. Zhao, *Anal. Chim. Acta* 418, 225 (2000).
81. J. Anzai, T. Hoshi, and N. Nakamura, *Langmuir* 16, 6306 (2000).
82. S. V. Rao, K. W. Anderson, and L. G. Bachas, *Biotechnol. Bioeng.* 65, 389 (1999).
83. M. K. Ram, P. Bertonecello, H. Ding, S. Paddeu, and C. Nicolini, *Biosens. Bioelectron.* 16, 849 (2001).
84. G. Sukhorukov, H. Möhwald, G. Decher, and Y. Lvov, *Thin Solid Films* 284, 220 (1996).
85. Y. Lvov, G. Decher, and G. Sukhorukov, *Macromolecules* 26, 5396 (1993).
86. J. Lang and M. Liu, *J. Phys. Chem. B* 103, 11393 (1999).
87. X. Shi, R. J. Sanedrin, and F. Zhou, *J. Phys. Chem. B* 106, 1173 (2002).
88. X. Chen, J. Ling, and M. Liu, *Thin Solid Films* 409, 227 (2002).
89. L. Luo, J. Liu, Z. Wang, X. Yang, S. Dong, and E. Wang, *Biophys. Chem.* 94, 11 (2001).
90. Y. Lvov, M. Onda, K. Ariga, and T. Kunitake, *J. Biomater. Sci., Polym. Ed.* 9, 345 (1998).
91. Y. Lvov, K. Ariga, I. Ichinose, and T. Kunitake, *J. Chem. Soc., Chem. Commun.* 2313 (1995).
92. J.-D. Hong, K. Lowack, J. Smitt, and G. Decher, *Prog. Colloid Polym. Sci.* 93, 98 (1993).
93. K. Ariga, Y. Lvov, M. Onda, I. Ichinose, and T. Kunitake, *Chem. Lett.* 125 (1997).
94. K. Ariga, Y. Lvov, I. Ichinose, and T. Kunitake, *Appl. Clay Sci.* 15, 137 (1999).
95. T. Yonezawa, H. Matsune, and T. Kunitake, *Chem. Mater.* 11, 33 (1999).
96. Y. Lvov, B. Munge, O. Giraldo, I. Ichinose, S. L. Suib, and J. F. Rusling, *Langmuir* 16, 8850 (2000).
97. Y. M. Lvov, J. F. Rusling, D. L. Thomsen, F. Papadimitrakopoulos, T. Kawakami, and T. Kunitake, *Chem. Commun.* 1229 (1998).



98. N. Malikova, I. Pastoriza-Santos, H. Schierhorn, N. A. Kotov, and L. M. Liz-Marzan, *Langmuir* 18, 3694 (2002).
99. J. W. Ostrander, A. A. Mamedov, and N. Kotov, *J. Am. Chem. Soc.* 123, 1101 (2001).
100. I. Pastoriza-Santos, D. S. Koktysh, A. A. Mamendov, M. Giersig, N. A. Kotov, and L. M. Liz-Marzán, *Langmuir* 16, 2731 (2000).
101. A. Mamedov, J. Ostrander, F. Aliev, and N. A. Kotov, *Langmuir* 16, 3941 (2000).
102. A. A. Mamedov and N. A. Kotov, *Langmuir* 16, 5530 (2000).
103. F. G. Aliev, M. A. Correa-Duarte, A. Mamedov, J. W. Ostrander, M. Giersig, L. M. Liz-Marzán, and N. A. Kotov, *Adv. Mater.* 11, 1006 (1999).
104. T. Cassagneau, J. H. Fendler, and T. E. Mallouk, *Langmuir* 16, 241 (2000).
105. T. Cassagneau, J. H. Fendler, S. A. Johnson, and T. E. Mallouk, *Adv. Mater.* 12, 1363 (2000).
106. T. Cassagneau, J. H. Fendler, and T. E. Mallouk, *J. Am. Chem. Soc.* 120, 7848 (1998).
107. N. A. Kotov, I. Dekany, and J. H. Fendler, *J. Phys. Chem.* 99, 13065 (1995).
108. J. F. Hicks, Y. Seok-Shon, and R. W. Murray, *Langmuir* 18, 2288 (2002).
109. L. I. Halaoui, *Langmuir* 17, 7130 (2001).
110. M. Gao, X. Zhang, B. Yang, F. Li, and J. Shen, *Thin Solid Films* 284/285, 242 (1996).
111. S. Joly, R. Kane, L. Radzilowski, T. Wang, A. Wu, R. E. Cohen, E. L. Thomas, and M. F. Rubner, *Langmuir* 16, 1354 (2000).
112. F. Hua, Y. Lvov, and T. Cui, *J. Nanosci. Nanotechnol.* 3/4, 357 (2002).
113. A. A. Mamedov, A. Belov, M. Giersig, N. N. Mamedova, and N. A. Kotov, *J. Am. Chem. Soc.* 123, 7738 (2001).
114. S. Westenhoff and N. A. Kotov, *J. Am. Chem. Soc.* 124, 2448 (2002).
115. Y. Lvov, K. Ariga, I. Ichinose, and T. Kunitake, *Langmuir* 12, 3038 (1996).
116. M. Eckle and G. Decher, *NanoLetters* 1, 45 (2001).
117. N. A. Kotov, T. Haraszi, L. Turi, G. Zavala, R. E. Geer, I. Dékány, and J. H. Fendler, *J. Am. Chem. Soc.* 119, 6821 (1997).
118. D. Cochin, M. Passmann, G. Wilbert, R. Zentel, E. Wischerhoff, and R. Zentel, *Macromolecules* 30, 4775 (1997).
119. D. W. Kim, A. Blumstein, and S. K. Tripathy, *Chem. Mater.* 13, 1916 (2001).
120. I. Ichinose, H. Tagawa, S. Mizuki, Y. Lvov, and T. Kunitake, *Langmuir* 14, 187 (1998).
121. M. Gao, J. Sun, E. Dulkeith, N. Gaponik, U. Lemmer, and J. Feldmann, *Langmuir* 18, 4098 (2002).
122. T. Sasaki, Y. Ebina, T. Tanaka, M. Harada, M. Watanabe, and G. Decher, *Chem. Mater.* 13, 4661 (2001).
123. S. Bharathi, M. Nogami, and S. Ikeda, *Langmuir* 17, 7468 (2001).
124. G. S. Lee, Y.-J. Lee, and K. B. Yoon, *J. Am. Chem. Soc.* 123, 9769 (2001).
125. N. I. Kovtyukhova, B. R. Martin, J. K. N. Mbindyo, P. A. Smith, B. Razavi, T. S. Mayer, and T. E. Mallouk, *J. Phys. Chem. B* 105, 8762 (2001).
126. N. I. Kovtyukhova, P. J. Oliver, B. R. Martin, T. E. Mallouk, S. A. Chizhik, E. V. Buzaneva, and A. D. Gorchinskiy, *Chem. Mater.* 11, 771 (1999).
127. M. Fang, C. H. Kim, G. B. Saupe, H.-N. Kim, C. C. Waraksa, T. Miwa, A. Fujishima, and T. E. Mallouk, *Chem. Mater.* 11, 1526 (1999).
128. H. Lee, L. J. Kepley, H.-G. Hong, S. Akhter, and T. E. Mallouk, *J. Phys. Chem.* 92, 2597 (1988).
129. T. Cassagneau, F. Guérin, J. H. Fendler, and T. E. Mallouk, *Langmuir* 16, 7318 (2000).
130. T. Cassagneau and J. H. Fendler, *J. Phys. Chem. B* 103, 1789 (1999).
131. I. Moriguchi and J. H. Fendler, *Chem. Mater.* 10, 2205 (1998).
132. R. E. Schaak and T. E. Mallouk, *Chem. Mater.* 12, 2513 (2000).
133. T. Mitsui, K. Yamaguchi, Y. Takeoka, M. Rikukawa, and K. Sanui, *Chem. Commun.* 1094 (2002).
134. S. Liu, D. G. Kurth, and D. Volkmer, *Chem. Commun.* 976 (2002).
135. F. Caruso, D. G. Kurth, D. Volkmer, M. J. Koop, and A. Müller, *Langmuir* 14, 3462 (1998).
136. K. Katagiri, R. Hamazaki, K. Ariga, and J. Kikuchi, *J. Sol-Gel Sci. Technol.* 26, 393 (2003).
137. K. Katagiri, R. Hamazaki, K. Ariga, and J. Kikuchi, *J. Am. Chem. Soc.* 124, 7892 (2002).
138. K. Katagiri, R. Hamazaki, K. Ariga, and J. Kikuchi, *Langmuir* 18, 6709 (2002).
139. K. Katagiri, K. Ariga, and J. Kikuchi, *Chem. Lett.* 661 (1999).
140. K. Katagiri, K. Ariga, and J. Kikuchi, in "Studies in Surface Science and Catalysis 132" (Y. Iwasawa, N. Oyama, and H. Kunieda, Eds.), p. 509. Elsevier, Amsterdam, 2001.
141. M. Lösche, J. Schmitt, G. Decher, W. G. Bouwman, and K. Kjaer, *Macromolecules* 31, 8893 (1998).
142. D. Korneev, Y. Lvov, G. Decher, J. Schmitt, and S. Yaradaikin, *Physica B* 213/214, 954 (1995).
143. G. Decher, J. D. Hong, and J. Schmitt, *Thin Solid Films* 210/211, 831 (1992).
144. G. Decher, Y. Lvov, and J. Schmitt, *Thin Solid Films* 244, 772 (1994).
145. Y. Lvov, G. Decher, and H. Möhwald, *Langmuir* 9, 481 (1993).
146. G. Decher and J.-D. Hong, *Ber. Bunsenges. Phys. Chem.* 95, 1430 (1991).
147. G. Decher and J.-D. Hong, *Makromol. Chem., Macromol. Symp.* 46, 321 (1991).
148. A. Toutianoush, F. Saremi, and B. Tieke, *Mater. Sci. Eng.* C8-9, 343 (1999).
149. J. Locklin, J. H. Youk, C. Xia, M.-K. Park, X. Fan, and R. C. Advincula, *Langmuir* 18, 877 (2002).
150. I. Ichinose, K. Fujiyoshi, S. Mizuki, Y. Lvov, and T. Kunitake, *Chem. Lett.* 257 (1996).
151. Y. Lvov, F. Essler, and G. Decher, *J. Phys. Chem.* 97, 13773 (1993).
152. K. Ariga, Y. Lvov, and T. Kunitake, *J. Am. Chem. Soc.* 119, 2224 (1997).
153. S. Das and A. J. Pal, *Langmuir* 18, 458 (2002).
154. K. E. Van Cott, M. Guzy, P. Neyman, C. Brands, J. R. Heflin, H. W. Gibson, and R. M. Davis, *Angew. Chem. Int. Ed.* 41, 3236 (2002).
155. D. M. Kaschak, J. T. Lean, C. C. Waraksa, G. B. Saupe, H. Usami, and T. E. Mallouk, *J. Am. Chem. Soc.* 121, 3435 (1999).
156. C. Tedeschi, H. Möhwald, and S. Kirstein, *J. Am. Chem. Soc.* 123, 954 (2001).
157. C. Tedeschi, F. Caruso, H. Möhwald, and S. Kristein, *J. Am. Chem. Soc.* 122, 5841 (2000).
158. E. Rousseau, M. Van der Auweraer, and F. De Schryver, *Langmuir* 16, 8865 (2000).
159. S. L. Clark, E. S. Handy, M. F. Rubner, and P. T. Hammond, *Adv. Mater.* 11, 1031 (1999).
160. S. Yamada, A. Harada, T. Matsuo, S. Ohno, I. Ichinose, and T. Kunitake, *Jpn. J. Appl. Phys.* 36, L1110 (1997).
161. K. Araki, M. J. Wagner, and M. S. Wrigton, *Langmuir* 12, 5393 (1996).
162. T. Cooper, A. Campbell, and R. Crane, *Langmuir* 11, 2713 (1995).
163. N. Kometani, H. Nakajima, K. Asami, Y. Yonezawa, and O. Kajimoto, *Chem. Phys. Lett.* 294, 619 (1998).
164. H. Ai, M. Fang, S. A. Jones, and Y. M. Lvov, *Biomacromolecules* 3, 560 (2002).
165. F. Caruso and C. Schüler, *Langmuir* 16, 9595 (2000).
166. F. Caruso and H. Möhwald, *J. Am. Chem. Soc.* 121, 6039 (1999).
167. F. Caruso, R. A. Caruso, and H. Möhwald, *Science* 282, 1111 (1998).

168. R. A. Caruso, A. Sussha, and F. Caruso, *Chem. Mater.* 13, 400 (2001).
169. F. Caruso, M. Spasova, A. Sussha, M. Giersig, and R. A. Caruso, *Chem. Mater.* 13, 109 (2001).
170. F. Caruso, R. A. Caruso, and H. Möhwald, *Chem. Mater.* 11, 3309 (1999).
171. F. Caruso, H. Lichtenfeld, M. Giersig, and H. Möhwald, *J. Am. Chem. Soc.* 120, 8523 (1998).
172. Y. Lvov, A. A. Antipov, A. Mamendov, H. Möhwald, and G. B. Sukhorov, *NanoLetters* 1, 125 (2001).
173. M. J. McShane, J. Q. Brown, K. B. Guice, and Y. M. Lvov, *J. Nanosci. Nanotechnol.* 3/4, 411 (2002).
174. G. Berth, A. Voigt, H. Dautzenberg, E. Donath, and H. Möhwald, *Biomacromolecules* 3, 579 (2002).
175. F. Caruso, D. Trau, H. Möhwald, and R. Renneberg, *Langmuir* 16, 1485 (2000).
176. S. Leporatti, A. Voigt, R. Mitlöchner, G. Sukhorukov, E. Donath, and H. Möhwald, *Langmuir* 16, 4059 (2000).
177. E. Donath, G. B. Sukhorukov, F. Caruso, S. A. Davis, and H. Möhwald, *Angew. Chem. Int. Ed.* 37, 2202 (1998).
178. M. Dixon and E.-C. Webb, in "Enzymes," 2nd ed., p. 315. Academic Press, New York, 1964.
179. M. Ohnishi, T. Yamashita, and K. Hiromi, *J. Biochem.* 79, 1007 (1976).

# Lead Sulfide Nanoparticles

Jochen Fick

*INPG-UJF-CNRS, Grenoble, France*

Alessandro Martucci

*Università di Padova, Padova, Italy*

## CONTENTS

1. Introduction
  2. Theoretical Investigations
  3. Synthesis
  4. Characterization
  5. Discussion of Optical Properties
  6. Applications
  7. Conclusion
- Glossary  
References

## 1. INTRODUCTION

Lead sulfide nanoparticles are subject of increasing research interest. On the one hand, this research is motivated by the opportunity to study quantum confinement effects inside zero-dimensional structures [1]. On the other hand, the optical properties of semiconductor nanoparticle-doped materials can be precisely engineered by choosing their composition, size, and the host matrix. Moreover, some interesting properties, such as the optical nonlinearity, are significantly enhanced with respect to the corresponding bulk materials [2]. Thus, the realization of improved or new optical devices becomes possible.

Historically, semiconductors other than lead sulfide were much more intensively studied. Most of the work was done in Cd(S,Se)-doped glasses, partly because they are commercially available as sharp cut-off optical filters. For example, the strong optical nonlinearity of semiconductor nanoparticles was first observed in Cd(S,Se)-doped glasses [3]. Other semiconductors, such as CuS or HgS, are seldom studied. The interest in lead sulfide is, however, strongly increasing over the last few years. In the 1980's and 1990's, many groups studied the linear and nonlinear optical properties of semiconductor-doped glasses and observed original features such as the blue shift of the absorption edge

or the high optical nonlinearity. The theoretical work that accompanied the experimental work provided explanations for most of these observations by the quantum confinement of free carriers inside the nanoparticle.

Bulk PbS was primarily studied for near-infrared detector applications. PbS is a narrow bandgap semiconductor with its absorption band in the near infrared around 3  $\mu\text{m}$ . In nanoparticles, the absorption resonance can be shifted to the visible wavelength region by choosing an appropriate particle size. Thus the 1–2  $\mu\text{m}$  wavelength region can be easily covered. This spectral region is of paramount interest for telecommunication devices or sensors. A further specific feature of PbS is its very large exciton Bohr radius. Hence, strong quantum confinement is obtained relatively easy. This is an important fact, as theoretical considerations predict that for this case the most interesting quantum confinement features can be observed.

During the last 20 years, many different techniques have been developed for semiconductor nanocrystal synthesis. For both fundamental research studies and applications, it is necessary to control the average size of the particles, in order to obtain a very narrow size distribution of particle sizes, control the electronic surface states, and also to control the shape and organization of the particles. Most of the developed synthesis methods aim to overcome these problems, and to obtain semiconductor nanocrystals inside a specific host material as for many application, it is often necessary to embed the nanocrystals in a solid matrix.

This entry is considered a concise introduction to lead sulfide quantum dots only. Great care was taken to consider all important aspects of the field and to include all available recent results. For more detailed information, the reader should consult the cited references or the more general introductions to the exciting field of semiconductor quantum dots that can be found in [4–7].

The organization of this article is as follows: the theoretical investigations of lead sulfide nanoparticles are described in Section 2. Section 3 gives an overview on the extensive particle elaboration techniques, followed by the results of the particle characterization illustrated in Section 4.

Some important optical features of lead sulfide nanoparticles are discussed in more details in Section 5. The last section deals with the application of PbS nanoparticles. Tables 1–4 provide an overview on research done on the theoretical considerations, the material elaboration, its characterization, and its nonlinear optical properties, respectively.

## 2. THEORETICAL INVESTIGATIONS

### 2.1. Quantum Confinement

The optical properties of lead sulfide nanoparticles are fundamentally changed with respect to the bulk material. This modification is caused by the confinement of the free carriers

into the volume of the nanoparticle. Thus, the available electron and hole states are modified, which, in turn, affects the particle-light interactions. As this characteristic feature can only be explained in the framework of quantum theory, it was named quantum confinement and, consequently, the semiconductor nanoparticles are often denoted as quantum dots. The quantum confinement influences the absorption and the emission as well as the carrier dynamics of the semiconductor.

One of the most striking quantum confinement effects is the blue shift of the linear optical absorption offset. This effect can be understood in a very straightforward way. In a bulk semiconductor, the conduction electrons and holes are free to move around. However, in a confined geometry,

**Table 1.** Theoretical considerations concerning PbS nanoparticles.

Studied property	Theoretical model	Specific features	Ref.
exciton ground state energy	cluster model	local tight binding Hamiltonian use basic set of $sp^3$ pseudofunctions	[12]
exciton ground state energy	hyperbolic band model	modified effective mass approximation infinite confinement potential	[12]
exciton ground state energy	effective mass approach (EMA)	strong confinement regime spherical confinement geometry finite confinement potential	[16]
electronic bandgap density of states	tight-binding approach	spin-orbit coupling Lanczos recursion	[19]
electronic structure (PbS molecule)	scattered-wave method	relativistic approach	[181]
electronic band structure (bulk) density of states	Löwdin process	atomic orbitals combination of Slater and Koster Vogel basis $\{sp^3s^*\}$	[22]
optical absorption spectra	four-band kp method	anisotropy effects	[24]
exciton energy levels	anisotropic four-band envelop function formalism (AFBEF)	non-parabolicity of $e/h$ bands enhanced consideration of anisotropy of $e/h$ bands	[25]
exciton energy levels	isotropic four wave envelope function formalism (IFBEF)	spin-orbit interactions non-parabolicity of $e/h$ bands anisotropy of $e/h$ bands (perturbative approach)	[25, 26]
electronic band structure (bulk) volume dependence of the energy gap density of states	scalar-relativistic full-potential linearized augmented plane wave method	spin-orbit interactions Slater–Koster Hamiltonian local density approximation	
polar optical phonons		generalized gradient approximation spin-orbital coupling coupling between longitudinal and transverse modes phonon dispersion up to quadric terms coupling of vibration displacement to electrostatic potential	[32]
Raman spectra	one phonon Raman scattering model	complete description of phonon modes of spherical structures embedded in a matrix correct treatment of mechanical and electrostatic conditions at the surface	[34]
selection rules for Raman scattering		Fröhlich interaction	
Raman spectra photoluminescence spectra	electrical dipole approximation	phonon-assisted optical transitions nonadiabaticity of exciton-phonon system	[36, 37]
Raman scattering spectra selection rules for Raman scattering photoluminescence spectra	Kubo	nonadiabatic approach (Jahn–Teller effects) multiphonon transitions	[38]

the carriers feel confined. Thus, in a first approximation, their wavefunctions have to be zero at the surface of the particle. This problem corresponds to the well-known particle-in-a-box problem, resulting in discrete energy levels and an increase of the ground state energy.

The first theoretical description of quantum confinement in semiconductor nanoparticles was published in 1981 [8]. In this joint effective mass and particle in a sphere approach, the electron wavefunctions are forced to zero at the particle surface. The nature of the confinement is governed by the relationship between three lengths:  $a$ ,  $a_e$ , and  $a_h$  ( $a$  is the crystal radius,  $a_{e,h}$  the electron/hole Bohr radii:  $a_{e,h} = \hbar^2 \kappa / m_{e,h} e^2$ ,  $\kappa$  the semiconductor static permittivity, and  $e$  the electron charge). In lead sulfide, the electron and hole radii are both in the order of  $a_{e,h} \approx 9$  nm [9], that is, bigger than the nanoparticle size of most elaborated particles ( $\approx 2$ –5 nm). Consequently, lead sulfide nanoparticles can be described in the so-called strong confinement limit which is defined by  $a \ll a_{h,e}$  [8]. In this case, the confinement energy separation between electron/hole energy levels is dominant over the Coulomb interaction energy. Therefore, in a first-order approximation, the electrons and holes can be considered as two independent particles confined inside a spherically symmetrical energy wall with infinitely high potential wells. The effective bandgap of the nanoparticle can be calculated by

$$E_g = E_g^{\text{bulk}} + \frac{\hbar^2 \pi^2}{2\mu a^2} - 1.786 \frac{e^2}{\varepsilon a} - 0.248 E_{\text{Ry}}^* \quad (1)$$

where  $E_g^{\text{bulk}}$  is the bulk energy gap,  $\mu = m_e m_h / (m_e + m_h)$  the reduced mass,  $\varepsilon$  is the semiconductor dielectric constant, and  $E_{\text{Ry}}^* \equiv \mu e^4 / (2\kappa^2 \hbar^2)$  the exciton effective Rydberg energy. The second and most important term scales with the inverse of the square of the sphere radius and the inverse of the reduced mass. The two further terms are small corrections, which describe the electron-hole Coulomb interaction (third term) and the remnant of the exciton effect, that is, the spatial correlation between the two particles (fourth term) [10]. One can notice that because of the small effective electron/hole mass in PbS, the actual value of  $E_g$  is very sensitive to small changes in the particle size.

This basic model provides an understanding of the confinement effect and its dependence on the particle size. However, especial for very small particles, some of its assumptions, such as the parabolic band structure or the infinite confinement potential, are not realistic. For example, the potential barrier between nanoparticles and the matrix in PbS-doped Langmuir–Blodgett (LB) films was experimentally evaluated to 4.5 eV [11]. Moreover, the band nonparabolicity has been described by a two-band model, using a basis set of  $sp^3$  pseudo wavefunctions centered at the Pb and S atoms [12]. Actually, this improved model was successfully applied to explain the blue shift of PbS particles with sizes as low as 2.5 nm. Further modified models were published (see Table 1), including a nonparabolic band structure [13, 14] or an infinite confinement potential at the semiconductor glass interface [15, 16].

A different approach to explain the electronic properties of semiconductor nanoparticles is given by the tight-binding method. It starts from one atom and its electronic

orbit structure. The semiconductor nanoparticle is then constructed by adding more and more atoms and calculating the electronic energy structure of the resulting particle [17–20]. This appropriate approach is feasible because of the rather small number of atoms in one particle. For example, a 3.5-nm diameter PbS nanoparticle contains only 912 atoms. Kane et al. applied this approach to describe the size effects on the absorption spectra of PbS nanoparticles and observed good agreement with experimental results [19]. This model was also used to study the influence of the particle shape on the absorption spectra. This is a very important feature as very small crystals are rarely of perfect spherical shape. Calculations for CdSe nanoparticles show that the first transition energy is only dependent on the smallest particle dimension, whereas higher transitions are affected by the particle anisotropy [20]. This shape dependence of the optical absorption spectra was experimentally verified in PbS nanoparticles of different shape [21].

The calculation of the lowest optical absorption can be extended to the calculation of the entire electronic energy structure. Some important differences between the band structure of bulk PbS [22, 23] and PbS nanoparticles [24–26] were found. Exact theoretical analysis of the energy spectra in the framework of a four-band  $kp$  method with a full account of anisotropy effects results in pronounced optical transitions, which are forbidden in an isotropic approximation. The band anisotropy effects are more pronounced for excited states and increase with the confinement.

The application of most of these theoretical models are limited by the fact that they include specific material parameters (such as  $\varepsilon$  or  $n$ ) which are only known with precision for the bulk material. These parameters can change drastically for nanoparticles. For example, the size dependence of the refractive index was experimentally investigated [27]. For particles with average diameters below 25 nm, the refractive index decreases with decreasing particle size from the bulk value of  $n_{\text{bulk}} = 4$  to  $n = 2.1$  for 3-nm sized particles.

## 2.2. Phonon Coupling

Similar to the confinement of electrons or holes to the nanoparticle volume, size quantization also effects the phonons. The effects of confinement on the vibrational modes of PbS nanoparticles are dramatic, owing to the dispersive phonons and unusual dielectric properties of the bulk material. In a basic model, the phonon wavefunction is confined to the nanoparticle while the bulk dispersion relations are retained. More appropriate treatments use a classical dielectric model, which couples the phonon amplitude to the electrostatic potential, but still neglect phonon dispersion [28, 29]. The application of spherical boundary conditions results in confined longitudinal and surface modes.

The modified electronic structure of PbS nanoparticles affects the exciton-phonon coupling efficiency. In bulk PbS coupling of electrons and holes to polar phonons is strong because of their high ionicity. In nanoparticles, this coupling is expected to be much smaller. In fact, in the strong confinement limit, the size quantized electron and hole states ideally have identical wave functions and can be thought of as lying on top of each other, thus cancelling each other's coupling to the lattice. Therefore, the coupling to polar phonons

should vanish. Coupling to acoustic phonons occurs through deformation potential and piezoelectric interactions. The sodium chloride crystal structure of lead sulfide is centrosymmetric and thus not piezoelectric, so the deformation potential coupling is isolated. PbS nanoparticles are thus well-suited to test theoretical predictions of the vibronic nature of the excited states and the homogeneous line shape.

Once the electronic wave functions and vibrational modes are known, they can be used to calculate the coupling of excitons to optical modes. Measurements of the exciton photon coupling showed that the actual coupling to optical phonons is very small due to the net charge neutrality and is at least 10 times smaller than values obtained for nanoparticles in other material systems [30]. Moreover, the coupling to acoustic modes is larger than the coupling to optical modes. These conclusions are consistent with the original theoretical predictions for nanoparticles in the strong quantum confinement limit [31].

For a more accurate treatment of materials with dispersive phonons, it is essential to satisfy the appropriate mechanical as well as electromagnetic boundary conditions. It was shown that correct boundary conditions demand the coupling of longitudinal and transverse modes [32]. In the special case where the vibrational amplitude is completely confined to the nanoparticle, the modes can be classified as coupled spheroidal and uncoupled torsional modes. The uncoupled modes are purely transverse, have no associated electrostatic potential, and hence are not expected to be optically active. The coupled solutions have a mixed longitudinal and transverse character involving the mechanical amplitude and the electrostatic potential. Since they involve the electrostatic potential, the coupled modes should be optically active, which was experimentally confirmed [33].

These calculations can be extended in order to determine the Raman cross-section of the phonon modes [34]. However, when measured by time-integrated Raman scattering, the electron-phonon coupling was found to be about four times more important than expected [35]. This discrepancy was explained by trapped charges built up on the nanoparticle surface during steady-state Raman measurement. The resulting local field enhances the coupling of excitons to polar phonons by at least an order of magnitude. The use of short excitation pulses should resolve this problem.

Devreese et al. developed a theory of phonon-assisted optical transitions in semiconductor nanoparticles, which takes into account the nonadiabaticity of the exciton-phonon system [36–38]. The role of the nonadiabaticity was shown to be of paramount importance in spherical particles, where the lowest one-exciton state can be degenerated or quasi-degenerated. In nanoparticles of lower symmetry, the effects of nonadiabaticity reveal themselves mainly due to the phonon-induced mixing of states which belong to different energy levels.

### 2.3. Nonlinear Optical Properties

The overall polarizability  $\chi = \varepsilon - 1$  of a medium is defined in its scalar form as  $\chi^{(3)}E = P/\varepsilon_0 = \chi^{(1)}E + \chi^{(2)}E^2 + \chi^{(3)}E^3 + \dots$  [4]. The first term describes the linear response; the second term corresponds to frequency doubling, summation,

and subtraction; and the third term describes four-wave mixing and other processes. It can be shown that in centrosymmetric media, such as most semiconductor nanoparticles, the even order terms must be zero [39]. In the case of PbS nanoparticles, the most important term is  $\chi^{(3)}$  corresponding to the third order or Kerr-type nonlinearity. This effect can also be interpreted as a nonlinear dephasing and one introduces the complex nonlinear refractive index  $n_2$  by  $n = n_0 + n_2 \cdot I$ , where  $n_0$  is the complex linear refractive index and  $I$  the light intensity.

The nonlinear optical properties of bulk semiconductors are mostly of electronic nature. Near the electronic bandgap, absorption saturation leads to a strong negative optical nonlinearity. The response time of the nonlinearity is, however, relatively long, as its mechanism is based on real electronic transitions with quite slow decay rates ( $\approx 10$  ns<sup>-1</sup>). It was shown that the spectral region near half the bandgap is more favorable for nonlinear optical applications [40]. In this case, the nonlinearity is somewhat smaller, but its response time is much faster and the linear absorption is significantly lower.

Similar to the linear optical properties of semiconductor quantum dots, the effects of the quantum confinement on the nonlinear optical properties depend on the size of the particle in respect to the different Bohr radii. Different theoretical models for the nonlinear optical properties of semiconductor nanoparticles in the strong confinement limit were published [2, 31]. The separation between the discrete energy levels inside the valence and conduction bands, is large. Thus, in a first approximation, electronic intraband transitions can be neglected with respect to state filling of the lowest interband transition. Hence, the nonlinear response of quantum dots can be described in the framework of a saturated two level system [31]. Using a nonlinear Kramers–Kronig relation [41], the real part of the nonlinear refractive index  $n_2$  can be calculated from the absorption changes induced by the saturation of the absorption. In this theory, the nonlinearity will saturate as  $n_2 = n_2'(1 + I/I_S)$ . The main improvement of nanoparticles, with respect to bulk material, is that the absolute absorption change and, consequently, the nonlinear refractive index change can be much larger before the transition saturates. This is particularly important for nonlinear devices, where in the case of bulk semiconductors, the transition already saturates before sufficient index change, that is, dephasing occurs. The larger saturation intensity in quantum dots is partially caused by their much faster recombination. However, the theory predicts that relatively complete saturation of absorption should be possible in quantum dots, because there are no competing mechanisms such as bandgap renormalization that inhibit strong absorption saturation in bulk.

At present, only a limited number of articles dealing with the nonlinear properties of PbS nanoparticles are published. Thus, the reading of some articles not directly dealing with lead sulfide can be useful for the understanding of the nonlinear properties of PbS nanoparticles [7, 42–44].

## 3. SYNTHESIS

Table 2 summarizes the main synthesis methods of PbS nanoparticles reported up to the present. The different synthesis methods will be reviewed with particular consideration



**Table 2.** Main PbS nanoparticles synthesis method. The synthesis have been divided into to main groups: PbS not embedded in a matrix and embedded in a host material. In the dimension row it is reported the mean diameter for spherical particles and the width x length for road or wire shaped particles. The presence or not of structured absorption spectra is reported in the abs row. Particles shape is abbreviated as follow: s = spherical; c = cubic; r = road; tp = triangular pyramid; w = wire. (n.r = not reported).

Not embedded in a matrix							
Precursors	Method	Stabilizer	Solvent	Dimension (nm)	Shape	Abs	Ref.
Pb(NO <sub>3</sub> ) <sub>2</sub> , H <sub>2</sub> S	colloidal	EDTA	H <sub>2</sub> O	7.4 ± 0.4–12.0 ± 1.6	c	n.r.	[45]
Pb(ClO <sub>4</sub> ) <sub>2</sub> ·6H <sub>2</sub> O, Na <sub>2</sub> S	colloidal		acetonitrile	2.7 ± 0.7	s	no	[46]
			ethanol/methanol	2.8 ± 1.3	s		
Pb(NO <sub>3</sub> ) <sub>2</sub> , Na <sub>2</sub> S	colloidal	PEG	acetonitrile	2–3, 5–20	s	no	[47]
Pb(ClO <sub>4</sub> ) <sub>2</sub> , H <sub>2</sub> S	colloidal	PVA	H <sub>2</sub> O	1.5–2.5 × 18	r	yes	[48]
		PVA	methanol		n.r.	yes	
		PEG	acetonitrile		n.r.	yes	
		PF	H <sub>2</sub> O		n.r.	no	
Pb(CH <sub>3</sub> CO <sub>2</sub> ) <sub>2</sub> , H <sub>2</sub> S	colloidal	PVA	H <sub>2</sub> O	3.5–5	s	yes	[49]
		3-mercapto-1,2propanediol		1–5	s	no	
Pb(NO <sub>3</sub> ) <sub>2</sub> , Na <sub>2</sub> S	colloidal	PVP	H <sub>2</sub> O	6–8	s	CdS@PbS	no [50]
Pb(CH <sub>3</sub> CO <sub>2</sub> ) <sub>2</sub> , Na <sub>2</sub> S	colloidal	4-ATP	methanol	2.8 ± 0.5; 2.7 ± 0.4	s	no	[51]
Pb(NO <sub>3</sub> ) <sub>2</sub> , Na <sub>2</sub> S	colloidal		H <sub>2</sub> O	3	s	TiO <sub>2</sub> /PbS	no [52]
Pb(CH <sub>3</sub> CO <sub>2</sub> ) <sub>2</sub> , CH <sub>3</sub> CSNH <sub>2</sub>	colloidal	TMD, TETA, EDTA, and gelatin,	H <sub>2</sub> O	100	s, c	n.r.	[53]
Pb(ClO <sub>4</sub> ) <sub>2</sub> , H <sub>2</sub> S	colloidal	HPC	ethanol	4.7 ± 0.6	s	yes	[54]
Pb(CH <sub>3</sub> CO <sub>2</sub> ) <sub>2</sub> , Na <sub>2</sub> S	colloidal	DDP	ethanol and H <sub>2</sub> O	5	s	n.r.	[55]
Pb(NO <sub>3</sub> ) <sub>2</sub> , Na <sub>2</sub> S	colloidal	PVA	H <sub>2</sub> O	4–6	s	yes	[21]
		PVP		8–12	s, n, c	no	
		gelatin		8–12	s, n, c	yes	
		DNA		4–6	s	no	
Pb(CH <sub>3</sub> CO <sub>2</sub> ) <sub>2</sub> , Na <sub>2</sub> S	colloidal	1-hexanethiol	toluene	2.5 ± 1.1–4.0 ± 1.1	s	no	[57]
Pb(NO <sub>3</sub> ) <sub>2</sub> , Na <sub>2</sub> S	Micelles mediated colloids	CTAB	H <sub>2</sub> O, CH <sub>2</sub> Cl <sub>2</sub>	3.5	s	no	[56]
	Micelles mediated colloids	DBS	H <sub>2</sub> O, toluene	3.2	s	no	
	colloidal	PVA	H <sub>2</sub> O	3.5	s	yes	
Pb(ClO <sub>4</sub> ) <sub>2</sub> , H <sub>2</sub> S	Micelles mediated colloids	PS-P4VP	methanol, toluene	2 ± 0.5 × 5–15	r	yes	[58]
				1–2	s	no	
				6–7	c	n.r.	
Pb(NO <sub>3</sub> ) <sub>2</sub> , Na <sub>2</sub> S	micelles mediated colloids	AOT/n-dodecanethiol	H <sub>2</sub> O, chloroform	4.9 ± 0.6	s	no	[59]
Pb(CH <sub>3</sub> CO <sub>2</sub> ) <sub>2</sub> ·2H <sub>2</sub> O, S	sonochemistry	1-decanethiol	Ethylenediamine	20	c	n.r.	[60]
Pb(NO <sub>3</sub> ) <sub>2</sub> , Na <sub>2</sub> S	supercritical fluid process	PVP	ammonia and ethanol	3.9–4.3 ± 0.6–0.8	s	yes	[61]
			methanol and ethanol	4.1–4.2 ± 0.5–0.8	s	n.r.	
			acetone and ethanol	4.5–4.6 ± 0.7–1	s	yes	
Pb(S <sub>2</sub> CNEtPr) <sub>2</sub>	thermolysis of single molecule precursor	TOPO	toluene	6.3 ± 1.4; 85 ± 23	s, c	no	[62]
Pb(SCH <sub>2</sub> C <sub>6</sub> H <sub>5</sub> ) <sub>2</sub>	thermolysis of single molecule precursor			20–40	s	n.r.	[63]
PbS	gas phase			3–20 ± 1	s	n.r.	[64]
Pb(OH) <sub>2</sub> , Na <sub>2</sub> S·9H <sub>2</sub> O	solid state reaction			40	s	n.r.	[65]
Pb(NO <sub>3</sub> ) <sub>2</sub> , Na <sub>2</sub> S	epitaxial growth on AA monolayer			50.9 ± 9.7; 60.7 ± 13.3	tp	n.r.	[66]
PbS	molecular beam epitaxy on InP(100)			0.8–1.5 ± 0.1–0.18	tp	n.r.	[67]
Embedded in a matrix							
Precursors	Method	Matrix	Composition	Dimension (nm)	Shape	Abs	Ref.
			<i>Film</i>				
Pb(CH <sub>3</sub> CO <sub>2</sub> ) <sub>2</sub> , H <sub>2</sub> S	ionomers	polymer	E-MAA	2.5–12.5	s	no	[12]
Pb(CH <sub>3</sub> CO <sub>2</sub> ) <sub>2</sub> , H <sub>2</sub> S	ionomers	polymer	NAFION	16–40	s	no	[68]

continued

Table 2. Continued

Precursors	Method	Embedded in a matrix		Dimension (nm)	Shape	Abs	Ref.
		Matrix	Composition				
Pb(CH <sub>3</sub> CO <sub>2</sub> ) <sub>2</sub> , H <sub>2</sub> S	ionomers	polymer	styrene	2.0–2.3		n.r.	[69]
(C <sub>2</sub> H <sub>5</sub> ) <sub>4</sub> Pb, H <sub>2</sub> S	ionomers	polymer	MTD/NORCOOH	4–12	s, w	no	[116]
(C <sub>7</sub> H <sub>9</sub> CH <sub>2</sub> C <sub>3</sub> H <sub>4</sub> ) <sub>2</sub> Pb, H <sub>2</sub> S	ionomers	polymer	polynorbornene	1–5	s	n.r.	[70]
Pb(C <sub>p</sub> <sup>N</sup> OTf, H <sub>2</sub> S	ionomers	polymer	MTD	2–13	s, w	yes	[71]
[PMMA-MAA]-Pb <sup>II</sup> , H <sub>2</sub> S	ionomers	polymer	PMMA-MAA	1.8–8.7	s	no	[72]
Pb(CH <sub>3</sub> CO <sub>2</sub> ) <sub>2</sub> , H <sub>2</sub> S	ionomers	polymer	PAH/PAA	2.5	s	n.r.	[73]
Pb(CH <sub>3</sub> CO <sub>2</sub> ) <sub>2</sub> , H <sub>2</sub> S	coprecipitation	polymer	PEO	19	s	n.r.	[74]
			gelatin	15–20	s		
Pb(NO <sub>3</sub> ) <sub>2</sub> , Na <sub>2</sub> SO <sub>4</sub>	electropolymerization	polymer	polyaniline	2.6	n.r.	yes	[75]
PbS	cryochemical	polymer	PPX	4.5	n.r.	no	[76]
	vapor deposition						
Pb(AOT) <sub>2</sub> , H <sub>2</sub> S	template mediate crystallization	polymer	PVB/AOT	2200 ± 20 × 10 ± 3	r	no	[77]
Pb(NO <sub>3</sub> ) <sub>2</sub> , H <sub>2</sub> S	template mediate crystallization	polymer	PDDA/PSS	1–100	s, c	no	[78]
Pb(NO <sub>3</sub> ) <sub>2</sub> , H <sub>2</sub> S	template mediate crystallization	polymer-BLM	PS/GMO/STYRS		s	yes	[79]
Pb(CH <sub>3</sub> CO <sub>2</sub> ) <sub>2</sub> , H <sub>2</sub> S	template mediate crystallization	polymer-LB	stearate		w	yes	[80]
Pb(NO <sub>3</sub> ) <sub>2</sub> , H <sub>2</sub> S	template mediate crystallization	polymer-LB	n-alkanoates		w	yes	[81]
n.r., H <sub>2</sub> S	template mediate crystallization	polymer-LB	behenates	1.1–1.2 × 5–10	w	n.r.	[82]
Pb(NO <sub>3</sub> ) <sub>2</sub> , H <sub>2</sub> S	template mediate crystallization	polymer-LB	behenates		w	n.r.	[83]
Pb(NO <sub>3</sub> ) <sub>2</sub> , H <sub>2</sub> S	gas-aerosol	polymer	PVA	4.4 ± 0.7	s	NO	[84]
Pb(CH <sub>3</sub> CO <sub>2</sub> ) <sub>2</sub> , CH <sub>3</sub> CSNH <sub>2</sub>	Sol-gel	hybrid	ZrO <sub>2</sub> -ORMOSIL (TMSPM)	4.8 ± 0.8	s	NO	[86]
Pb(CH <sub>3</sub> CO <sub>2</sub> ) <sub>2</sub> , CH <sub>3</sub> CSNH <sub>2</sub>	Sol-gel	glass	SiO <sub>2</sub> -TiO <sub>2</sub>	2.3 ± 0.46–3.5 ± 0.3	s	NO	[85]
Pb(CH <sub>3</sub> CO <sub>2</sub> ) <sub>2</sub> , H <sub>2</sub> S	Sol-gel	hybrid	SiO <sub>2</sub> -ORMOSIL (TMSPM-GPTMS)	9.56 ± 0.58–14.07 ± 0.17	s	NO	[87]
Pb(CH <sub>3</sub> CO <sub>2</sub> ) <sub>2</sub> or Pb(NO <sub>3</sub> ) <sub>2</sub> , H <sub>2</sub> S	Sol-gel	ceramic	TiO <sub>2</sub>	≥3	n.r.	NO	[88, 89]
Pb(CH <sub>3</sub> CO <sub>2</sub> ) <sub>2</sub> , CH <sub>3</sub> CSNH <sub>2</sub>	Sol-gel	ceramic	ZrO <sub>2</sub>	3	s	no	[90]
Pb(CH <sub>3</sub> CO <sub>2</sub> ) <sub>2</sub> , NH <sub>4</sub> SCN	Sol-gel	ceramic	ZrO <sub>2</sub>	4.5	s	NO	[91]
PbS	RF-sputtering	glass	SiO <sub>2</sub>	2–12	s	no	[92]
PbS	evaporation	glass	SiO <sub>2</sub>	1–3	s	no	[93]
			<i>Bulk</i>				
Pb(MA) <sub>2</sub> , H <sub>2</sub> S	ionomers	polymer	styrene, MAA	4–11	s	no	[94]
[PMMA-MAA]-Pb <sup>II</sup> , H <sub>2</sub> S	ionomers	polymer	PMMA-MAA	1.8–8.7	s	no	[72]
Pb(CH <sub>3</sub> CO <sub>2</sub> ) <sub>2</sub> , H <sub>2</sub> S	coprecipitation	polymer	PEO	4 ± 2–80 ± 35	s	n.r.	[27]
Pb(NO <sub>3</sub> ) <sub>2</sub> or Pb(CH <sub>3</sub> CO <sub>2</sub> ) <sub>2</sub> , Na <sub>2</sub> S	template mediated crystallization	polymer	PEO/SDS	10–15 × 500–1000	s, r	no	[95, 96]
Pb(CH <sub>3</sub> CO <sub>2</sub> ) <sub>2</sub> , CS <sub>2</sub>	template mediated crystallization	polymer	PMMA	30 ± 2	s	n.r.	[97]
Pb(CH <sub>3</sub> CO <sub>2</sub> ) <sub>2</sub> , CS <sub>2</sub>	γ-irradiation	polymer	acrylonitrile	8	s	n.r.	[98]
PbO, H <sub>2</sub> S	sol-gel	glass	SiO <sub>2</sub>	2–10	s	no	[101]
Pb(ClO <sub>4</sub> ) <sub>2</sub> , H <sub>2</sub> S	sol-gel	xerogel	Al <sub>2</sub> O <sub>3</sub> -SiO <sub>2</sub> , ZrO <sub>2</sub> -SiO <sub>2</sub>	11 ± 3.4	s	n.r.	[99]
Pb(NO <sub>3</sub> ) <sub>2</sub> , Na <sub>2</sub> S	sol-gel	xerogel	SiO <sub>2</sub>	2–4	s	no	[100]
Pb(NO <sub>3</sub> ) <sub>2</sub> , H <sub>2</sub> S	sol-gel	xerogel	SiO <sub>2</sub>	3.5–16	n.r.	no	[102]
PbO, H <sub>2</sub> S	sol-gel	glass ceramic	PbO-ZrO <sub>2</sub> -TiO <sub>2</sub>	3.5 ± 1.6–15.3 ± 1.5	s	n.r.	[103]
Pb(CH <sub>3</sub> CO <sub>2</sub> ) <sub>2</sub> , CH <sub>3</sub> CSNH <sub>2</sub>	sol-gel	hybrid	SiO <sub>2</sub> -ORMOSIL (PDMS)	6.5 ± 0.9	s	no	[104]
				10.5 ± 1.2	s, c		
				7 × 10–20	r		

continued

Table 2. Continued

Precursors	Method	Embedded in a matrix					
		Matrix	Composition	Dimension (nm)	Shape	Abs	Ref.
Pb(CH <sub>3</sub> CO <sub>2</sub> ) <sub>2</sub> , CH <sub>3</sub> CSNH <sub>2</sub>	sol-gel	xerogel	TiO <sub>2</sub>	10	s	no	[105]
PbAc <sub>2</sub> , HS(CH <sub>2</sub> ) <sub>3</sub> Si(CH <sub>3</sub> O) <sub>3</sub>	sol-gel	mesoporous	SiO <sub>2</sub>	5–6 × ~100	w	n.r.	[106]
PbO, S	melting 1350 °C/ annealing 450 °C	glass	SiO <sub>2</sub> -Al <sub>2</sub> O <sub>3</sub> - Na <sub>2</sub> O-ZnO	7.6–13.3	s	yes	[9]
PbO, H <sub>2</sub> S	melting 1300 °C/ annealing 650 °C	glass	SiO <sub>2</sub> -Na <sub>2</sub> O-CaO- PbO-Bi <sub>2</sub> O <sub>3</sub>	2.5 ± 1.3–12.9 ± 1.4	s	n.r.	[108]
PbO, S	melting 1100 °C/ annealing 390–440 °C	glass	P <sub>2</sub> O <sub>5</sub> -Ga <sub>2</sub> O <sub>3</sub> -ZnO- AlF <sub>3</sub> -Na <sub>2</sub> O	2–15 ± 0.2–3	s	yes	[107]
Pb, S	ion implantation	glass, ceramic	SiO <sub>2</sub> , Al <sub>2</sub> O <sub>3</sub>	6.8 ± 3.4–8.5–9.5	s	n.r.	[109]
Pb(NO <sub>3</sub> ) <sub>2</sub> , Na <sub>2</sub> S	diffusion	zeolite	Na <sub>2</sub> O-SiO <sub>2</sub> -Al <sub>2</sub> O <sub>3</sub>	0.6–1.3		yes	[110]
Pb(CH <sub>3</sub> CO <sub>2</sub> ) <sub>2</sub> , H <sub>2</sub> S	diffusion	zeolite	Na <sub>2</sub> O-SiO <sub>2</sub> -Al <sub>2</sub> O <sub>3</sub>	2–10	r	no	[111]
Pb(CH <sub>3</sub> CO <sub>2</sub> ) <sub>2</sub> , H <sub>2</sub> S	diffusion	Layered metal phosphate	Zr(O <sub>3</sub> PCH <sub>2</sub> · CH <sub>2</sub> CO <sub>2</sub> H) <sub>2</sub>	3–5	s	n.r.	[112]

Note: 4-ATP = 4-aminothiophenol; AOT = sodium dioctyl sulfosuccinate; BLM = bilayer lipid membrane; C<sub>p</sub><sup>N</sup> = 2-(cyclopentadienylmethyl)norborn-5-ene; CTAB = cetyltrimethylammonium bromide; DBS = dodecyl benzene sulphonate; DDP = di-n-hexadecyldithiophosphate; EDTA = ethylenediaminetetraacetic acid; E-MAA = ethylene-methacrylic acid; GMO = glyceryl monooleate; GPTMS = glycidoxypropyltrimethoxysilane; MAA = methacrylic acid; MTD = methyltetraacyclododecane; NAFION = perfluorosulfonate; NORCOOH = 2-norbornene-5,6-dicarboxylic acid; ORMOSIL = organic modified silicate; HPC = hydroxypropyl cellulose; PAA = polyacrylic acid; PAH = polyallylaminehydrochloride; Pb(AOT)<sub>2</sub> = bis(2-ethylhexyl)sulfosuccinate; Pb(MA)<sub>2</sub> = lead methylacrylate; PDDA = polydiallyldimethylammonium chloride; PEG = polyethylene glycol; PMMA = polymethylmethacrylate; PS = phosphatidylserine; PSS = polystyrenesulfonate sodium salt; PS-P4VP = polystyrene-b-poly(4)vinylpyridine; PVA = polyvinyl alcohol; PVB = poly(vinyl butyral); PVP = polyvinyl pyrrolidone; STYRS = [n-C<sub>15</sub>H<sub>31</sub>CO<sub>2</sub>(CH<sub>2</sub>)<sub>2</sub>N<sup>+</sup>(CH<sub>3</sub>)CH<sub>2</sub>C<sub>6</sub>H<sub>4</sub>CH=CH<sub>2</sub>.Cl<sup>-</sup>]; TETA = triethylenetetraamine; TMD = trimethylenediamine; TMSPM = trimethoxysilpropylmethacrylate; TOPO = tri-n-octylphosphine oxide.

to particle's average size and size distribution, particle's surface states, and particles shape. The different approaches for nanoparticles fabrication have been divided into two main groups considering particles not embedded in a host matrix and materials doped with PbS nanocrystals.

### 3.1. Particles Not Embedded in a Host Matrix

One of the most used chemical routes to PbS nanoparticles dispersed in solvents is colloidal chemistry [21, 45–57]. This method consists in the reaction of the lead precursor (typically a lead salt: lead acetate, nitrate, or perchlorate) and the sulfur precursor (very often H<sub>2</sub>S or Na<sub>2</sub>S) in suitable solvents, while the nucleation and growth process are controlled through suitable stabilizer (also called capping agent) and/or controlling the environment conditions (pH, temperature, solvents). Using this approach, PbS nanoparticles can be prepared both in polar and nonpolar solvents with the surface covered by many different capping agents. The obtained particle size is normally in the nanometer range, with a size distribution ranging from 5% up to 25% (standard deviation). The capping agent plays a very important role also in controlling the surface states and hence the optical properties of the PbS quantum dots. For example, PbS colloids stabilized with PVA [21, 48, 49, 56] or hydroxypropyl cellulose (HPC) [54] showed structured absorption spectra, while the use of other stabilizers very often did not cause structured absorption spectra. The shape of the particle is also strongly dependent on the used surface capping agent. For example Patel et al. [21] have found that the shape of particles stabilized with PVA is spherical, while particles stabilized with PVP or gelatin have a mixture

of needle, cubic, and spherical shapes. It is worth noting that both the size and shape of the particles are influenced not only by the used stabilizer, but also by pH, temperature, concentration, and solvents.

Colloidal core-shell CdS-PbS [50] nanoparticles were synthesized by Pb<sup>2+</sup> ions displacing Cd in Cd-S bonds on the surface of CdS colloids. TiO<sub>2</sub>/PbS coupled semiconductors were also obtained by colloidal chemistry [52]. PbS nanoparticles are formed in a water solution containing TiO<sub>2</sub> colloids, by reacting lead nitrate and sodium sulfide in the presence of mercapto acetic acid, which is used for linking the TiO<sub>2</sub> and PbS nanoparticles. It was found that TiO<sub>2</sub> acts as a stabilizer in the PbS growth. TiO<sub>2</sub>/PbS nanocomposite films were also obtained by depositing the colloidal solution on a substrate whose surface is appropriately activated.

Colloidal PbS nanoparticles have also been prepared without using any stabilizer [46]. In this case, the growth processes are slowed down by carrying out at low temperature just above the solvent freezing point.

PbS nanoparticles have also been synthesized using a micelles-mediated colloids method [56, 58, 59]: Lin and Xicheng [56] prepared a microemulsion in the system water/surfactant/apolar solvent, allowing the reaction between the lead and sulfur precursors inside the micelles. Size and size distribution of the particles depends on size and size distribution of the micelles, which in turn, depends on the nature and concentration of used surfactants. The surface of the nanoparticles is covered by the surfactant molecules used for the preparation of the microemulsion. As in microemulsion, micelles are generally spherical; PbS particles also maintain the same shape. Yang et al. [58] used a bicontinuous cubic phase in which monodispersed lead sulfide nanoparticles with 4–14 nm in diameters have been grown. They used a sodium dioctyl

sulfosuccinate (AOT)/water/ $\text{Na}_2\text{S}$  system in which sodium dioctyl sulfosuccinate (AOT) forms a mesoporous phase with long-range, three-dimensional periodicity called bicontinuous cubic phase, where the aqueous pores are interconnected through small channels. Lead sulfide nanoparticles have been grown inside the pores and then transferred into a chloroform solution by functionalizing the surface by *n*-dodecanethiol. Schneider et al. [59] used the micellar organization of a block copolymer, polystyrene-*b*-poly(4-vinylpyridine) (PS-P4VP), composed of blocks with different solubility properties. Toluene is used as a selective solvent for the PS block. By adjusting the lead-to-polymer ratio, temperature and pH, PbS particles of different sizes (2–20 nm) and morphology (sphere, cubes, or needles) have been obtained.

Sonochemistry [60] was used for synthesizing round-shaped PbS nanoparticles starting with lead acetate and sulfur. In fact, when ultrasound is applied to a solution, bubbles are formed in the liquid. During the implosive collapse of the bubbles, a localized hotspot is generated and a temperature up to 4700 °C and pressures up to 180 MPa can be reached. In these extreme conditions, elemental sulfur and lead ions can react to provide PbS nanocrystals. Also in this case, the growth of the nanoparticles can be controlled by using stabilizers.

Formation of PbS spherical nanoparticles in ethanol was obtained using a supercritical fluid process [61]. A supercritical ammonia/ $\text{Pb}(\text{NO}_3)_2$  solution at 160 °C and 24 MPa is rapidly expanded in a  $\text{Na}_2\text{S}$ -ethanol solution containing polyvinyl pyrrolidone (PVP) as a stabilizer, to produce PbS nanoparticles with a size distribution of about 12–15%.

Synthesis methods, using just a single source precursor for PbS, were also investigated. Trindade et al. [62] injected a solution of lead(II) dithiocarbamate complexes dissolved in toluene into tri-*n*-octylphosphine oxide (TOPO) at 150–250 °C, obtaining spherical nanoparticles with a size distribution of about 20%. More recently, Boudjouk et al. [63] used metal bis(benzylthiolates) for the synthesis of pure PbS and PbS-CdS solid solution nanoparticles. Both the size and shape of the nanoparticles depends on the pyrolysis temperature, which can be carried out in the presence or not of solvents.

Formation of PbS nanoparticles was also obtained through gas phase synthesis [64]. Lead sulfide aerosol is formed at normal pressure by sublimating PbS powders in a tube furnace blowing  $\text{N}_2$  and charged by a radioactive  $\beta$ -source ( $\text{Kr}^{85}$ ). In a differential mobility analyzer, the charged particles are size-selected on the basis of their electric mobility, which is a function of their charge level, mass, and shape, and then subjected to a second heating step. Spherical particles ranging from 5 to 20 nm can be obtained. For bigger particles, the standard deviation is about 5%, while for smaller particles it is approximately 20–30%.

Solid state reaction leading to 40-nm diameter PbS particles was reported by Ye et al. [65]. PbS nanocrystals were prepared at room temperature through self-propagating, solid-state reactions of  $\text{Pb}(\text{OH})_2$  and  $\text{Na}_2\text{S} \cdot 9\text{H}_2\text{O}$ .

PbS nanocrystals were also epitaxially grown on an arachidic acid (AA) monolayer [66] or on an InP(110) substrate [67]. In the first case, AA monolayers are formed at the water-air interface of a water solution containing lead nitrate. Equilateral triangular pyramidal nanocrystals have

been *in-situ* generated by exposing the AA monolayer to  $\text{H}_2\text{S}$ . In the second case, the formation of self-assembled PbS nanodots was obtained through molecular beam epitaxy in an ultra-high vacuum chamber onto a *in-situ* cleaved InP(100) surface. Triangular pyramidal PbS dots were also obtained in this case.

### 3.2. Particles Embedded in a Host Matrix

PbS nanoparticles have been embedded in many different kinds of host materials, both as film and as bulk. Films will be discussed first and then bulk materials (both monoliths and powders) will be considered.

#### 3.2.1. Thin Films

Polymers are one of the most used matrices to embed PbS nanoparticles. Several types of ion-containing polymers have been used for the preparation of polymer films doped with PbS quantum dots. Ionomers, defined as ion-containing copolymers, are frequently used because microphase separation of the ionic polymer part results in the formation of ionic aggregates within a matrix of the nonionic polymer component. This micro- or nano-ionic aggregate can react with lead ions and then can be exposed to  $\text{H}_2\text{S}$  to form the PbS nanoparticles [12, 19, 68, 69]. In a different approach, lead complexes are directly attached to one block of the copolymer, leading to the direct formation of lead ions containing microdomains, and then exposed to  $\text{H}_2\text{S}$  [70–72].

Control of particle size, size distribution, and shape, can be achieved controlling the ionomer aggregate sizes. In fact, it was demonstrated that these aggregates serve as micron/nano reactors for the synthesis of PbS quantum dots [19, 69, 71]. In general, spherical nanoparticles a few nanometers in diameter have been obtained.

Nanoreactors have also been obtained in multi-layer thin films of polyelectrolytes. Such multilayer films are constructed using a layer-by-layer process scheme involving the alternate absorption of oppositely charged polymers onto a substrate. By choosing suitable polyelectrolytes and adjusting the pH of the deposition solution, it is possible to control the ionic aggregate, which will react with the forming nanoparticles. Spherical PbS nanoparticles with a 2.5 nm diameter have been obtained in polyallylaminehydrochloride/polyacrylic acid (PAH/PAA) multilayer films by immersing it first in a lead acetate, aqueous solution and then exposing it to  $\text{H}_2\text{S}$  [73].

Incorporation of PbS in polymer films was also obtained in poly(ethylene oxide) (PEO) or gelatin by the coprecipitation method [74]. In this case,  $\text{H}_2\text{S}$  is added to a water solution of PEO-lead acetate or gelatin-lead acetate. The final solution is deposited on a suitable substrate and then dried.

Gaponik and Sviridov [75] deposited polyaniline films doped with PbS quantum dots on an indium tin oxide (ITO) glass slide. In this case,  $\text{Pb}^{2+}$  ions were trapped in the polymer matrix by electrodeposition of a solution of aniline,  $\text{HNO}_3$ , and  $\text{Pb}(\text{NO}_3)_2$ . PbS nanoparticles are formed after the immersion of the film in  $\text{Na}_2\text{S}$  solution.

Poly-*p*-xylylene-PbS nanocomposite films were synthesized by cryochemical solid-state synthesis [76]. It is based on the low-temperature, co-condensation of metal sulfide

and monomer vapors followed by the low-temperature solid state polymerization of the obtained condensates. With this method, polymerization proceeds at temperatures below the glass transition temperature of the forming polymer matrix. Thus, it is possible to obtain very fine particles (around 4 nm) dispersed in an hydrophobic polymer matrix with very low particles/matrix interaction.

PbS nanoparticles in polymer films or membranes have also been obtained through template-mediated crystallization. The templates create a micro/nano reactor in which nucleation and growth of PbS takes place. Moreover, they control size, size distribution, morphology, and organization of nanoclusters.

Wang and Yang [77] used lead bis(2-ethylhexyl) sulfosuccinate ( $\text{Pb}(\text{AOT})_2$ ) as a surfactant, which can self-assemble into an ordered structure in solution also containing poly(vinyl butyral) (PVB). Films can be obtained by depositing the solution on suitable substrates. Rod-shaped PbS nanoparticles are formed inside the template upon exposure to  $\text{H}_2\text{S}$  of the  $\text{Pb}(\text{AOT})_2$ -loaded PVB films. Dutta et al. [78] used a layer-by-layer deposition technique for building supramolecular multilayers on solid substrates by alternating layers of polydiallyldimethylammonium chloride (PDDA) and polystyrenesulfonate sodium salt (PSS). *In-situ* nucleation of PbS particles was achieved by immersing the PDDA-PSS multilayer film into a aqueous solution of  $\text{Pb}(\text{NO}_3)_2$  and subsequent exposure to  $\text{H}_2\text{S}$ . Spherical and cubic nano- and micro-particles can be obtained with a very broad size distribution. *In-situ* generation of confined lead sulfide has also been obtained in bilayer lipid membranes (BLM) [79] and in Langmuir–Blodgett (LB) films [80–83]. Langmuir–Blodgett and bilayer films are organized, molecularly assembled, multilayer films characterized by alternating stacking of hydrophilic and hydrophobic layers. The formation of metal semiconductor particles can take place if the hydrophilic head group of the constructing molecules has a metal-ion binding ability. The amount and spatial arrangement of the precursor metal ions are controlled by the self-assembled head groups. Upon exposure to  $\text{H}_2\text{S}$ , these metal ions react with the sulfur ions forming the confined metal sulfide nanostructure. In general, PbS wires have been obtained in LB films [80–83].

PbS nanoparticles in PVA films were also obtained by a gas aerosol method [84]. An aerosol of microdroplets can be used to create a microreactor in which nanoparticles can nucleate and grow. With this method, microdroplets of a solution of PVA and lead nitrate are electrostatically generated applying a very high voltage to a stainless capillary inside a reaction chamber where a substrate is placed at a ground potential. PbS nanoparticles are formed in the solution microdroplets by reaction with  $\text{H}_2\text{S}$ , generated inside the reaction chamber, by the reaction of sodium sulfide and diluted hydrochloric acid. Spherical particles of a 4.4-nm diameter can be obtained in PVA films with a size distribution better than 15%.

Glass or ceramic films doped with PbS quantum dots have been obtained by sol–gel. Three different approaches have been used for obtaining sol–gel films doped with lead sulfide quantum dots. One approach consists of the independent preparation of semiconductor nanoclusters and the matrix sol and their successive mixing. Following this

method Martucci et al. [85, 86] prepared PbS-doped  $\text{SiO}_2$ - $\text{TiO}_2$  and  $\text{ZrO}_2$ -organic modified silicate (ORMOSIL) planar waveguides by doping a matrix solution containing the matrix precursor with a colloidal solution of PbS stabilized with 3-mercaptopropyltrimethoxysilane. With this procedure, spherical PbS nanoparticles with a size distribution of about 10% have been obtained. A different approach consists in the preparation of a porous matrix containing lead oxide or lead ions, followed by exposure to  $\text{H}_2\text{S}$ . del Monte et al. [87] used this approach for preparing PbS nanoparticles in  $\text{SiO}_2$ -ORMOSIL films. Homogeneous lead salt distribution at the solution stage was obtained through the use of glycidoxypropyltrimethoxysilane (GPTMS), which can coordinate the lead acetate through the epoxy group, while 3-mercaptopropyltrimethoxysilane was used for controlling the aggregation process. Homogeneously dispersed PbS nanoparticles with size distribution as low as 5% were obtained. PbS nanoclusters were also adsorbed on the internal surface of  $\text{TiO}_2$  by dipping  $\text{TiO}_2$ -porous, sol–gel films into a concentrated solution of coated lead ions followed by impregnation in  $\text{Na}_2\text{S}$  solution [88, 89]. With this process, particles of about 3 nm have been obtained, while larger particles are obtained when the coating process is repeated several times. The last approach consists in the preparation of a deposition solution containing all the precursors both for the matrix and the lead sulfide. Lead sulfide nanoparticles precipitate in the matrix after heat treatments. Using this approach,  $\text{ZrO}_2$  films doped with PbS quantum dots have been fabricated [90, 91].

$\text{SiO}_2$  glass films doped with PbS spherical nanoparticles were also obtained by RF-sputtering [92]. The used target was a  $\text{SiO}_2$  glass plate over which several different PbS polycrystalline pellets were placed. The size of the particles depends on the relative surface area of PbS pellets in the composite target.

PbS nanoparticles have been embedded in  $\text{SiO}_2$  glass film by a co-evaporation method [93]. The two evaporation sources ( $\text{SiO}_2$  and PbS) were placed in a vacuum chamber and well separated from each other by mechanical shields. The substrates were placed onto a rotating sample holder for alternating exposure to the two evaporation sources. By adjusting the evaporation rate of the sources and the post-deposition heat treatments, it is possible to control the size and volume fraction of the PbS nanocrystals.

### 3.2.2. Bulk Materials

Polymers are one of the most used matrices also in the case of bulk materials doped with PbS nanocrystals. The synthesis procedures are very often the same as for the polymer films; so with the same method both bulk and films can be prepared.

Bulk polymeric matrices doped with spherical PbS nanoparticles have been prepared using ionomers [72, 94] and a co-precipitation method [27], whose methodology has already been described for films.

Leontidis et al. [95, 96] used the template-mediated, crystallization method to control the shape of lead sulfide nanoparticles in bulk polymers. Micelles were formed using an ionic surfactant (sodium dodecyl sulfate (SDS)) and water soluble nonionic polymer (polyethyleneoxide (PEO)).

By adding lead and sulfur ions to the PEO/SDS solution, lead sulfide nanocrystals are formed on the polymer-bound micelles. The shape of the nanoparticles is controlled by the shape of the micelles, which are strongly affected by the pH of the solution. PbS nanoparticles encapsulated in polymethylmethacrylate (PMMA) nanocages have been synthesized by Qiao et al. [97] using PMMA as a template to control the growth of PbS nanocrystals. Spherical particles of 30 nm with a size distribution of about 6% have been obtained.

PbS nanoparticles have been embedded in a polymer matrix using a  $\gamma$ -irradiation process [98] for promoting both the polymerization and the reaction between sulfur and lead precursors.

The sol-gel technique was used widely for preparing bulk glass or ceramic materials doped with PbS QD. As for the films, three different approaches have been used. Xerogels (*i.e.*, dried gel) doped with PbS have been obtained by independent preparation of PbS nanoclusters (by colloidal chemistry) and matrix sol and their successive mixing [99, 100]. Gacoin et al. [99] prepared colloids stabilized with 3-mercaptopropyltrimethoxysilane while Pellegrini et al. used reverse micelles [100].

Monolith SiO<sub>2</sub> glass [101], SiO<sub>2</sub> xerogel [102], and PZT (PbO-ZrO<sub>2</sub>-TiO<sub>2</sub>) glass ceramics [103] doped with spherical PbS nanoparticles have been obtained through the preparation of a porous matrix containing lead oxide or lead ions, followed by exposure to H<sub>2</sub>S. Moreover, PbS nanocrystals have been precipitated in SiO<sub>2</sub>-ORMOSIL [104] and TiO<sub>2</sub> xerogel [105] from a one-pot solution containing all the precursors—both for the matrix and the lead sulfide.

The sol-gel method was also used for the preparation of mesoporous silica powders doped with PbS nanowires [106]. The mesophase was synthesized by using a pluronic P123 as a template and tetraethyl ortosilicate as a silica precursor. After calcination, the surface channels of the mesopores were functionalized with thiol groups (SH), then impregnated with lead ions, and finally PbS nanowires were grown inside the channels by heat treatments in N<sub>2</sub> at high temperatures. The obtained nanowires are a several hundred nanometers in length and 6 nm in diameter.

Glasses doped with PbS nanoparticles have also been obtained by a traditional glass-melting technique. Borelli and Smith [9] and Lipovskii et al. [107] melted the raw materials (including sulfur) at a temperature higher than 1000 °C, then promoted the nucleation and growth of the nanocrystals annealing the samples just over the glass transition temperature in reducing atmosphere. Mukherjee et al. [108] prepared a lead silicate glass and precipitated the lead sulfide nanocrystals annealing the glass in a H<sub>2</sub>S atmosphere. The size and size distribution is strictly related to the heat treatment schedule.

Ion implantation was used to synthesize PbS nanoparticles in SiO<sub>2</sub> glass and Al<sub>2</sub>O<sub>3</sub> single crystal ceramic [109]. Lead and sulfur ions beams are impinging onto the substrate and then annealed in reducing atmosphere. The size and size distribution of the particles mainly depend on the ion dose and energy and on the annealing conditions. Generally, very broad size distributions are obtained.

PbS nanostructures have also been grown inside the pores of zeolite [110, 111]. Zeolites are sodium (or potassium)

alumino silicate ceramics with an interconnected porous structure. Sodium ions can be exchanged with lead ions, and semiconductor nanocrystals can be grown inside the pores after H<sub>2</sub>S exposure. The particle size and size distribution depends not only on the zeolite structure but also on the ion exchange conditions.

PbS quantum dots with 3–5 nm diameters were grown in the interlamellar region of layered zirconium phosphonate powders [112]. Zirconium phosphonate crystals have a layered structure in which semiconductor nanoparticles can be grown. First, the phosphonate crystals are immersed in a NaOH solution in order to adsorb sodium ions, then lead cations are exchanged into the interlamellar region and finally exposed to H<sub>2</sub>S.

## 4. CHARACTERIZATION

### 4.1. Morphology

As already pointed out in the previous sections, most of the properties of PbS nanoparticles depend on their size, size distribution, and shape. The transmission electron microscopy (TEM) is the most frequently used investigation technique for evaluating the morphology of nanocrystals (see Table 3). This technique is used in almost all the references reported in the synthesis section. It enables one to resolve particles with a diameter lower than 1 nm, and using high resolution electron microscopy (HRTEM), it is also possible to resolve the lattice planes and measure the distance between them (see, *e.g.*, Figure 1). For quantum dots (QD) dispersed in a solvent, a few drops are deposited on copper grids covered with a carbon membrane and allow the solvent evaporate. For particles embedded in a solid matrix (bulk or film), fragments of materials are deposited (sometimes first dispersing it in a solvent) on copper grids covered with a carbon membrane (sometimes a holey carbon membrane). A more complex sample preparation is necessary for cross-sectional TEM [109].

The morphology of PbS nanoparticles has also been investigated by atomic force microscopy (AFM) [66, 67, 113, 114]. Particles have been grown on different substrates (InP(110) [67], or LB film [66]) and size and shape of particulate films have been studied with AFM. Atomic force microscopy images of triangular pyramidal PbS dots with an average lateral size as low as 15 nm are reported [67]. Atomic force microscopy images of PbS QD prepared by a colloidal [113] or gas condensation method [114] and then deposited on a suitable substrate have also been taken, but with a lower resolution.

### 4.2. X-Ray Diffraction

The crystal structure of nanoparticles can be studied by X-ray diffraction (XRD); moreover, from the line broadening of the diffraction peaks it is also possible to evaluate the mean particle diameters through the Scherrer formula [115]. An XRD spectra of PbS nanoparticles has been reported by many authors, both embedded in a matrix [9, 12, 27, 68, 71, 72, 76–78, 83, 85–87, 90, 92, 93, 96, 99, 101, 102, 104–107, 112, 116, 117] and not embedded in a matrix [21, 48, 55, 58, 60, 61, 63]. The PbS nanoparticles showed a cubic rock-salt



**Table 3.** Experimental results of PbS nanoparticles.

State	Optical absorption	PL	XRD	TEM	Others	Ref.
powder	$E_g = 2.0$ $d = 5.5$		powders $d = 5.5$	$d = 5.5$ (30%)		[81, 117]
powder			<i>crp</i> $a = 5.9288$ $d = 23.1$	cubic shape $d = 22.6$		[182]
powder	$\lambda_{exc}: 500\text{--}1000^*$		<i>crp</i> $d = 5\text{--}10^*$		<b>XPS:</b> $S_{2p}^3/2: 161.9 \text{ eV}^\ddagger$ $Pb_{4f}^{7/2}: 138.3 \text{ eV}^\ddagger$ $Pb_{4f}^{5/2}: 143.3 \text{ eV}^\ddagger$	[113, 143]
powder			sphalrite phase $d = 20$	rectangular $20 \times 15$	<b>EDAX:</b> Pb:S = 43:57 <b>XPS:</b> $S_{2p}^{3/2}: 160.8 \text{ eV}$ $S_{2p}^{1/2}: 161.8 \text{ eV}$ $Pb_{4f}^{7/2}: 137.7 \text{ eV}$ $Pb_{4f}^{5/2}: 142.6 \text{ eV}$	60
powder			<i>crp</i> $a = 5.94$	rod-shape $70\text{--}160 \times 150\text{--}700$		[183, 184]
powder	$\lambda_{ab} = 540$ ( <i>fl</i> )		<i>crp</i>	spherical $d = 10\text{--}15$	<b>XPS:</b> $S_{2p}^{3/2}: 160.5 \text{ eV}$ $S_{2p}^{1/2}: 161.5 \text{ eV}$ $Pb_{4f}^{7/2}: 137.5 \text{ eV}$ $Pb_{4f}^{5/2}: 142.4 \text{ eV}$	154
Alkanethiolate-protected particles	$\chi(d > 3 \text{ nm})$ $560 \text{ nm}$ ( $d = 2.5 \text{ nm}$ )	$\lambda_{em} = 804$ $\lambda_{ex} = 610/665$		$d = 2\text{--}4^*$	<b>EDX:</b> PbS $L_\beta: 12.650 \text{ keV}$ $L: 10.550 \text{ keV}$ $M: 2.346 \text{ keV}$	[57]
CD-coated particles	<i>fl</i>				<b>PP:</b> $\tau = 150 \text{ fs}$	[142]
DNA-capped	$\lambda_{exc}: 538/350$		<i>crp</i> $d = 4.98$	spherical shape $d = 4\text{--}6$	<b>PP:</b> $\tau = 1.5/45 \text{ ps}$	[21]
particles on gold electrode	$\lambda_{exc} = 290/380$ $/450$ $E_g = 2.08$			<i>crd</i> spherical shape $d = 6.5$ (30%)	<b>IMPS*</b>	[173]
P-PbS solution	$\lambda_{ab} = 600\text{--}800$ ( <i>fl</i> )	$\lambda_{em} = 600$		colloidal solutions <i>crd</i> $d = 4$		[94, 122, 140]
PP stabilized aqueous solution	$\lambda_{ab} = 700$ ( <i>fl</i> )	$\lambda_{em} = 750$				[48]
PS-capped PVA stabilized aqueous solution	$\lambda_{ab} = 650$ ( <i>fl</i> ) $1S_c\text{-}1S_h: 600$	$\lambda_{em} = 630$	$d = 3$		<b>PP:</b> $\tau = 1.5/45 \text{ ps}$	[21] [48]
PVA stabilized aqueous solution	$\lambda_{exc}: 596/385/291$ $\lambda_{ab} = 670$	$\lambda_{em} = 667$				[49]
PVA stabilized aqueous solution	$1S_c\text{-}1S_h: 600$ $1S_c\text{-}1P_h: 400$ $1P_e\text{-}1P_h: 300$	$\lambda_{em} = 690$			<b>PP:</b> oscillations	[119, 145]
PVA stabilized aqueous solution	$1S_c\text{-}1S_h: 600$ $1S_c\text{-}1P_h: 400$ $1P_e\text{-}1P_h: 300$				<b>PP:</b> $\tau = 160 \text{ fs}$	[122, 142]
PVA capped in aqueous solution	$\lambda_{exc} = 581/390/290$			spherical shape $d = 4\text{--}6$	<b>PP:</b> $\tau = 1.5/45 \text{ ps}$	[21]

continued

Table 3. Continued

State	Optical absorption	PL	XRD	TEM	Others	Ref.
PVP capped in aqueous solution	$\lambda_{ab} = 800$ ( <i>fl</i> )			needle, cubic spherical $d = 8-12$	<b>PP:</b> $\tau = 1.5/45$ ps	[21]
PVA stabilized methanol solution	$E_g = 2.11$ $d = 2-3$		<i>crp</i> $a = 5.96 \text{ \AA}$ $d = 13 \text{ nm}$ $d = 10 \text{ nm}$ (SAXS)	$d = 11$ (30%)		[99]
PVA stabilized methanol solution	$1S_c-1S_h: 590$	$\lambda_{em} = 600$				[48]
PVA stabilized solution	$\lambda_{exc}: 550$ $\lambda_{ab} = 700$		<i>crp</i> $d = 2.7$	$d = 4$ (17%)		[61]
in PVA sol	$\lambda_{ab} = 700$ ( <i>fl</i> )	$\lambda_{em} = 1100$				[131]
HPC stabilized ethanolic solution	$1S_c-1S_h: 537$ $1P_c-1P_h: 372$ $1D_c-1D_h: 282$ $\lambda_{ab} = 625$	$\lambda_{em} = 691/636$	<i>crp</i> $d = 3.2$ (200) $d = 3.6$ (220)	spherical $d = 4.7$ (12%)		[54, 167]
gelatin in aqueous solution	$\lambda_{exc}: 581/390$			needle, cubic spherical $d = 8-12$	<b>PP:</b> $\tau = 1.5/45$ ps	[21]
DDP coated in paraffin			<i>crp</i>		<b>XPS:</b> $S_{2p}: 163.7 \text{ eV}$ $Pb_{4f}^{7/2}: 140.1 \text{ eV}$	[55, 185]
in ethylenediamine			<i>crp</i> $d = 60$	rectangular shape	<b>XPS:</b> $S_{2p}: 161.0 \text{ eV}$ $P_{2p}: 137.7$	[138]
organo-sol	$\lambda_{ab} = 500-700^*$ ( <i>fl</i> )			cubic shape $d = 12$ <i>crp</i>		[144]
			solid matrix			
SDG	$1S_c-1S_h: 1200-2300^*$		<i>crp</i> $d = 8-13^*$	$d = 10^\dagger$		[9, 132]
SDG				$d = 2.5-13$ (52-11%)		[108]
SDG	$1S_c-1S_h: 946$ $d = 4$	$\lambda_{em} = 540^\dagger$				[139, 151]
silica glass	$E_g = 0.9-2.2^*$ ( <i>fl</i> )		<i>crp</i> $d = 3.0-8.5^*$ $a = 5.89-5.93^*$	$d = 2.9-8.0^{ast}$		[101]
silica	$\lambda_{ab} = 700-3200^*$ ( <i>fl</i> )		<i>crp</i> $a = 5.85-5.95$			[102, 150]
silica	$\lambda_{ab} = 900-1100^*$ ( <i>fl</i> )	$\lambda_{em} = 605$ $\lambda_{ex} = 475$				[130]
silica aerogel	$E_g = 0.73-2.3^*$ ( <i>fl</i> )		<i>crp</i> $6.7-14.1$	$d = 4-5$ (colloid)		[156]
silica gel	$\lambda_{ab} = 800-1000^*$ ( <i>fl</i> )					[100]
phosphate glass	8 peak adsorption spectrum					[24]
phosphate glass	$\lambda_{exc} = 1130-3100^*$		<i>crp</i>			[107]
phosphate glass	$\lambda_{exc} = 832-1450^*$ $d = 2.2-10^*$					[149]
titania	$\lambda_{ab} = 440$ ( <i>fl</i> )	$\lambda_{em} = 447$	<i>crp</i> $a = 5.94$ $d = 9.8$ (200)	$d = 10$	<b>FTIR:</b> P-S not visible	[105]

continued

Table 3. Continued

State	Optical absorption	PL	XRD	TEM	Others	Ref.
lead zirconate titanate			<i>crp</i>	3.5–15.5* (10–45%)		[103, 186]
Si-ORMOSIL in polyvinyl acetate	<i>fl</i>		<i>crp</i> <i>crp</i>	$d = 6.5\text{--}11^*$ (14–11%) tubular shape $30 \times 80$		[104] [187]
Nafion	$E_g = 2.14\text{--}1.5 * 5(fl)$ $\lambda_{em} = 590^\dagger$		<i>crp</i> 1.6–4.0* (111)	$d = 2.0\text{--}10.5^*$		[68]
PEO/SDS	$\lambda_{ab} = 600\text{--}800 (fl)$		<i>crp</i> $d = 4(110)$	needles $10\text{--}15 \times 500\text{--}1000$	<b>XPS:</b> $S_{2p}$ : 162 eV $Pb_{4f}^{7/2}$ : 138.9 eV $Pb_{4f}^{5/2}$ : 143.7 eV* <b>NMR:</b> broad $^{207}Pb$ peak	[95, 96]
PMMA matrix polyacrylamide	$\lambda_{ab} = 600 (fl)$		$d = 13\text{--}32^*$ $a = 5.903$ $-5.942^*$	<i>crp</i> $d = 10\text{--}2^*$ (17–11%)	<b>PP:</b> $\tau = 1.5/45$ ps	[21] [188, 189]
in polyacrylonitrile			<i>crp</i> $d = 7.8$	$d = 8$	<b>FTIR:</b> Pb-S: 1110/1160 /835 $cm^{-1}$	[98]
AOT-capped nanoparticle film	$\lambda_{ab} = 500\text{--}700^* (fl)$		thin film		<b>photocurrent</b> <sup>#</sup>	[148]
nanoparticle film	$\lambda_{exc}: 470$	$\lambda_{em} = 500\text{--}750$ (3 peaks)	<i>crp</i> $d = 17.5 (200)$		<b>PIXE:</b> no impurity <b>RBS:</b> P/S = 0.9; thickness = 60 nm <b>AFM:</b> $d = 20$ nm <b>Raman:</b> 1LO: 210; SP: 205 $cm^{-1}$ <b>current-voltage behavior</b> <sup>#</sup>	[147] [120, 163, 175]
silica films			<i>crp</i>	particles	<b>XPS:</b> $S_{2p}$ : 161 eV	[92]
silica films					<b>XPS:</b> $S_{2s}$ : 225.4–227.2 eV* $Pb_{4f}^{7/2}$ : 137.9–138.9 eV* $Pb_{5d}^{5/2}$ : 19.1–20.0 eV*	[190]
silica films	$E_g = 2.7\text{--}5.5 (fl)$ $d = 1.5\text{--}2.0$	$\lambda_{em} = 446$ $\lambda_{ex} = 311$	<i>crp</i> $a = 5.94$ $d = 1.0\text{--}3.1$		<b>XPS:</b> $S_{2s}$ : 227.2 eV $Pb5d^{5/2}$ : 20.0 eV	[93]
silica titania film	$E_g = 0.88\text{--}1.45^* (fl)$		<i>crp</i> $d = 2\text{--}3 (220)$	$d = 2\text{--}3 (10\%)$	<b>RBS:</b> Pb:S = 0.8–0.9*	[6, 85, 123, 141, 146, 157, 159, 174]
titania film	$E_g = 1.24\text{--}1.6^* (fl)$				<b>Photoconductance</b> <sup>#</sup>	[89]
zirconia film	$\lambda_{ab} = 770\text{--}885^* (fl)$	$\lambda_{em} = 900\text{--}1300$	<i>crp</i>	$d = 3$		[90]
zirconia film	$E_g = 1.42\text{--}1.92^*$	$\lambda_{em} = 775\text{--}1159^*$		nearly spherical, $d = 4.5^\dagger$	<b>current-voltage behavior</b> <sup>#</sup>	[91, 153, 164]
Zr-ORMOCER films	$\lambda_{ab} = 650\text{--}900^* (fl)$		$d = 11\text{--}14^*$	$d = 10\text{--}14^*$ (2–6%)		[87]
Zr-ORMOCIL films	$E_g = 0.90 (fl)$	$\lambda_{em} = 1000\text{--}13000^*$	<i>crp</i>	$d = 4.8 (17\%)$	<b>RBS:</b> Pb:S = 1 : 1	[86, 158, 159]
ZSUR	$E_g = 1.28\text{--}2.60^* (fl)$	$\lambda_{em} = 885\text{--}1000^*$		spherical $d = 4.0\text{--}8.0$		[161]
polymer film	$\lambda_{ab} = 800\text{--}900$ $1S_c\text{--}1S_h: 600$		<i>crp</i>	feathery crystallites- rhomboid structures		[78]

continued

Table 3. Continued

State	Optical absorption	PL	XRD	TEM	Others	Ref.
polymer film	<i>fl</i>	$\lambda_{em} = 459/539/290$ $t = 1/20 \mu s$ (biexp.) $\lambda_{ex} = 359$		$d = 2.1$ (15%)		[125]
polymer film	$\lambda_{ab} = 530\text{--}3200^*$ ( <i>fl</i> )		<i>crp</i> $d = 1.3\text{--}13$			[12]
polymer film	rods: $\lambda_{ab} = 750$ ( <i>fl</i> ) spheres: $\lambda_{ab} = 750$ 1S <sub>c</sub> -1S <sub>h</sub> : 600 1S <sub>c</sub> -1P <sub>h</sub> : 400 1P <sub>c</sub> -1P <sub>h</sub> : 300		<i>crp</i> rods are oriented	rods: $2.2 \times 0.1$ spheres: 1–20 disks: 20–200		[72, 77, 155]
poly- <i>p</i> -xylylene film	$E_g = 1.58$ ( <i>fl</i> )		WAXS: <i>crp</i> $d = 4.5$ (220) SAXS: $d = 4.0$ (50%)		<b>Photoconductance</b> <sup>#</sup>	[76]
tetracosanediote film	$\lambda_{ab} = 600$ ( <i>fl</i> )			2.5 (30%)	XPS: Pb <sub>4f</sub> <sup>7/2</sup> : 137.5 eV Pb <sub>4f</sub> <sup>5/2</sup> : 142.4 eV	[117]

<sup>#</sup> see text for results

\* from different samples

†: value of one sample

‡: peak composed of several peaks, position of the most intense is given

*fl*: featureless, i.e. no excitonic peak visible

*crp*: crystallized in the cubic rocksalt structure

$\lambda_{ab}$ : absorption offset [nm]

$\lambda_{exc}$ : position of undefined exciton transition [nm]

$\lambda_{em}$ : position of photoluminescence emission peak [nm]

$\lambda_{ex}$ : position of photoluminescence excitation peak [nm]

$E_g$ : electronic energy gap [eV]

$d$ : particle diameter [nm]

(hkl) XRD peak used for calculation using Scherrer formula

(10%) particle size dispersion

$a$ : crystal lattice constant [Å]

1S<sub>c</sub>-1S<sub>h</sub>: absorption peak position of corresponding exciton transition [nm]

Note: AOT: dioctyl sulfosuccinate; CD: 2,6-O-diallyl- $\beta$ -CD organosol; CTAB: cetyltrimethylammonium bromide; DBS: dodecyl benzene sulphonate; IMPS: intensity-modulated photocurrent spectroscopy; FTIR: Fourier transformation infrared spectroscopy; PIXE: proton induced X-ray emission; PP: optical absorption in pump-probe configuration; DDP: di-*n*-hexadecyldithiophosphate; HPC: hydroxypropyl cellulose; PEO/SDS: Pb<sup>II</sup>/S<sup>-II</sup>/poly(ethylene oxide)/sodium dodecyl sulfate; PMMA: polymethylmethacrylate; PP: polyphosphate; P-PBS: polymeric surface modified PbS; PS: polystyrene; PVA: polyvinyl alcohol; PVP: polyvinyl-pyrrolidone; SDG: semiconductor-doped glass; SAXS: small angle X-ray scattering; TEM: transmission Electron microscopy; XPS: X-ray photoelectron spectroscopy; XRD: X-ray diffraction; ZSUR: zirconia-silica-urethane.

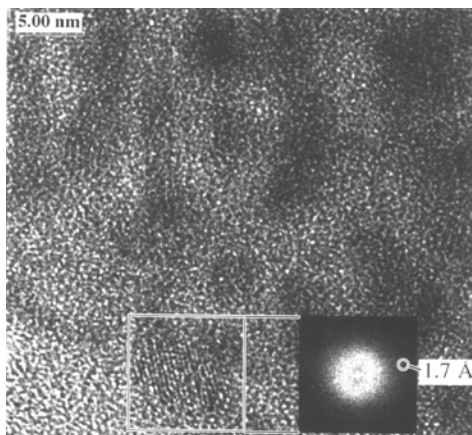


**Figure 1.** High resolution image of PbS-doped SiO<sub>2</sub>-TiO<sub>2</sub> film elaborated by sol-gel. In the inset is reported the Fourier transform of the indicated nanoparticle. The indicated lattice distance corresponds to the (222) crystalline plane. Reprinted with permission from [85], A. Martucci et al., *J. Appl. Phys.* 86, 79 (1999). © 1999, American Institute of Physics.

structure (galena) corresponding to JCPDS #5-592. A typical XRD spectra of PbS nanocrystals embedded in a glass matrix is reported in Figure 2. From the image, it is evident the effect on the line broadening of the particle mean diameter as the particle diameter increases the full width at half maximum of diffraction peaks decreases. In general, PbS nanocrystals with an average diameter as low as 2–3 nm can be evaluated using the line broadening of diffraction peaks but the size evaluated by XRD is not always in good agreement with the size evaluated by TEM measurements. Differences can be originated by a very broad size distribution, variation in shape, and also when PbS nanoparticles are partially amorphous. Wang and Heron [118] examined the validity of the Scherrer's equation by using a direct simulation of Bragg diffraction from PbS nanoparticles, and they obtained an empirical relationship relating the Scherrer's cluster diameter  $d_s$  (in Å) to the real cluster diameter  $d$ :  $d = 0.45 + 1.14d_s$ .

Information on the size distribution can also be obtained by the Fourier analysis of the profile of isolated reflections [76], but this method is not often used and TEM measurements are preferred.

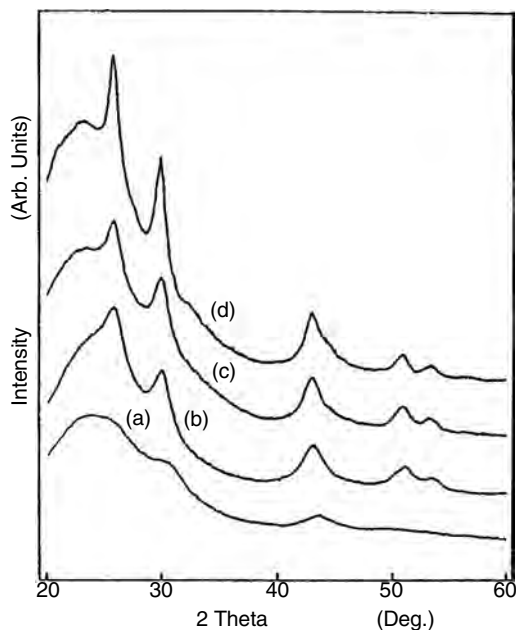


**Figure 2.** X-ray diffraction patterns of glasses containing 4.5 wt.% PbO reacted with  $H_2S$  gas at (a) 25, (b) 200, (c) 250, and (d) 400 °C. The PbS particle size is 3.0, 4.3, 5.7, and 8.5 nm, respectively. Reprinted with permission from [101], M. Nogami et al., *J. Non-Cryst. Solids* 126, 87 (1990). © 1990, Elsevier.

From the XRD spectra, it is also possible to evaluate the lattice constant of PbS nanocrystals [101, 102], it is reported that the lattice constant of PbS nanoparticles in glass is constant for particle diameters larger than 4.5 nm, while it decreases for smaller particles [101].

Preferred lattice plane orientation of PbS rods in PVB film has been observed from XRD patterns [77]. In fact, when preferred orientation of the PbS nanocrystal structure is present, the intensity distribution of the observed diffraction peaks deviates from those reported in the JCPDS cards for bulk PbS.

### 4.3. Vibrational Spectroscopy

Raman and infrared spectroscopy are well-established techniques in studying the structure of crystalline and amorphous materials by evaluating the lattice vibrations. Many studies demonstrated that the vibrational modes of PbS nanocrystals are not the phonons of the bulk crystals [33, 35, 38, 119–121].

In bulk semiconductors, the observed Raman shifts usually correspond to the longitudinal optical phonons (LO), while other modes such as the transverse optic (TO) and the surface phonon (SP) modes, in general, are not observable because of the symmetry restriction and low intensities, respectively. As the surface-to-volume ratio is large in nanoparticles, it is possible to observe SP modes; moreover, multiphonon processes are also detected.

A Raman spectra of 2-nm diameter PbS nanocrystals stabilized with PVA [33] showed the presence of an intense band at  $217\text{ cm}^{-1}$  due to the first-order LO mode, while a shoulder around  $190\text{ cm}^{-1}$  was attributed to SP mode. A very sharp peak centered at  $68\text{ cm}^{-1}$  was attributed to TO modes and a small peak around  $275\text{ cm}^{-1}$  was assigned to

two phonon processes. Similar results were also obtained for nanocrystals prepared by an electrochemical technique [120] and a frequency shift of the main band at  $217\text{ cm}^{-1}$  towards the lower side with increasing crystalline size is observed.

Both Machol et al. [119] and Krauss et al. [33] reported far infrared spectrum of small (2 and 4.3 nm, respectively) PbS colloids stabilized with PVA, which showed a broad and intense peak centered at  $90\text{ cm}^{-1}$  due to coupled modes (they have a mixed longitudinal and transverse character), while a smaller and even more broader peak centered around  $275\text{ cm}^{-1}$  is assigned to two phonon processes. The spectra were essentially temperature-independent within the range 15–300 K.

Infrared (IR) vibration bands centered at 1175, 1160, 1110, 990, and  $835\text{ cm}^{-1}$  were attributed to Pb-S bonds by Parvathy et al. [102] in PbS/SiO<sub>2</sub> sol-gel nanocomposite, accordingly to the IR vibrations of bulk PbS.

### 4.4. Optical Absorption Spectroscopy

The optical absorption spectroscopy is the most widespread characterization technique applied to lead sulfide nanoparticles [1, 9, 11, 12, 16, 21, 24, 27, 46–52, 54, 56–61, 68, 71, 72, 74, 76–78, 84–93, 95, 96, 99–102, 104–107, 110, 113, 116, 119, 122–173].

Absorption spectroscopy is available to most research groups and it enables a fast and straightforward proof for the existence of nanoparticles. The quantum confinement of the carriers into the nanoparticles causes a strong blue shift of the bulk optical absorption band to visible or near-infrared wavelengths. By using adequate theoretical models, it is even possible to deduce the nanoparticle size from the position of the absorption offset or the first excitonic transition. The experimental results can be divided into featureless absorption spectra and spectra resolving the signature of room temperature excitonic transitions.

Most research groups, especially those dealing with thin film samples, record a broad, featureless absorption band [12, 21, 48, 68, 76, 85–87, 89, 90, 93, 95, 96, 100–102, 104, 105, 122, 123, 125, 130, 140–142, 144, 146, 148, 150, 156–159, 161]. The absorption offset position varies in general between  $\lambda_{ab} = 500$  and 1100 nm, as a function of the particle size. These wavelengths correspond to band energies of  $E_g = 1.1$  to 2.5 eV. The absorption curves of silica-titania thin films with different PbS-doping ratios is displayed in Figure 3. The arrows indicate the expected position of the first excitonic peak. In general, the lack of the excitonic shoulder can be explained by the poor precision of thin film absorption measurements. Further problems are due to inhomogeneous broadening due to the finite size distribution of the PbS nanoparticles. Moreover, the exciton can be quenched due to the large dielectric constant, the small effective mass, and the relatively large Bohr radius of the electrons and holes in lead sulfide. These features also explain the very broad absorption band that are observed.

In some cases it was, however, possible to resolve one [9, 48, 57, 61, 78, 99, 113, 132, 137, 139, 142, 143, 147, 149, 151, 163] or even more [21, 54, 72, 77, 119, 122, 142, 145, 155, 167, 173] excitonic peaks in the optical absorption spectra. Most of these results are obtained in powders or colloidal

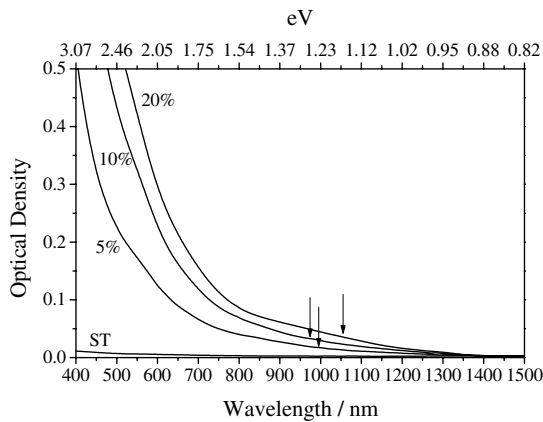


**Figure 3.** Absorption spectra of  $\text{SiO}_2\text{-TiO}_2$  films doped with 5, 10, and 25 mol% of PbS, and one undoped film (ST). The arrows indicate the expected position of the first excitonic peak for particles with the mean diameters obtained from XRD measurements. Reprinted with permission from [85], A. Martucci et al., *J. Appl. Phys.* 86, 79 (1999). © 1999, American Institute of Physics.

solutions, which are known to show the smallest size distribution. Moreover, colloidal solutions allow very efficient surface passivation which further increases the optical quality of the nanoparticles. Figure 4 displays the absorption spectra of PbS-doped glass. The first two excitonic transitions are clearly resolved and the particle size dependence of their position is evident. The position of the first excitonic transition ( $1S_c-1S_h$ ) is situated in the same wavelength region as the absorption offset in the case of featureless spectra. In the case of multiple excitonic peaks, the second and third peaks are in general in the 350–400 nm and 280–300 nm region, respectively.

#### 4.5. Photoluminescence

Photoluminescence (PL) [38, 48, 49, 54, 57, 68, 91, 93, 105, 106, 119, 125, 130, 131, 139, 140, 145, 147, 151, 153, 158–161, 164] and photoluminescence excitation (PLE) [57, 93,

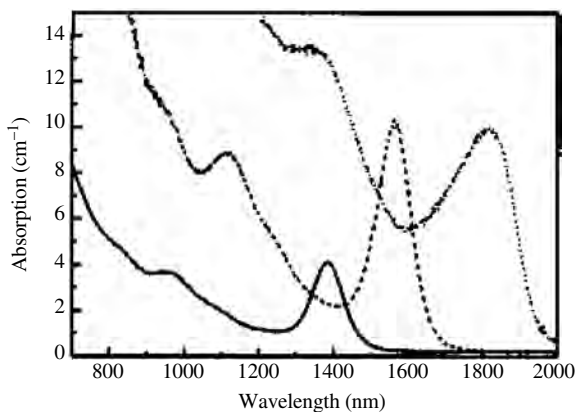


**Figure 4.** Room temperature absorption spectra of glasses with PbS quantum dots. Diameters are: 6.6 (solid line), 7.5 (dashed line), and 9.3 (dotted line). Reprinted with permission from [132], P. T. Guerreiro et al., *Appl. Phys. Lett.* 71, 1595 (1997). © 1997, American Institute of Physics.

125, 130] spectroscopy is used less frequently than optical absorption. Photoluminescence measurements allow the resolution of well-defined emission peaks on thin films, which displays only broad absorption features in the absorption spectra. Most of the published results contain only one emission peak which can be attributed to the lead sulfide nanoparticles. Typical PL and PLE spectra of small PbS nanoparticles are shown on Figure 5. In general, the PL position varies in-between 450 and 1100 nm as a function of the PbS particle size. Lu et al. observed two [54], Lifshitz et al. [125] three, and Nanda and Sahu [147] even four emission peaks. The observed PL excitation peak is situated at 260–475 nm, about 100–130 nm below the corresponding emission peaks. Only Chen et al. found two excitation maxima at 610 and 665 nm conjointly with one single emission band at 804 nm [57].

#### 4.6. Optical Pump-Probe Measurements

Pump probe measurements or transient absorption spectroscopy allow the characterization of the time evolution of the optical absorption and thus the electron dynamics inside lead sulfide nanoparticles. In this experiment, a strong pump beam causes absorption bleaching or induced absorption which is then probed by a time-delayed probe beam. Patel et al. used a pump probe scheme with a regeneratively amplified mode-locked femtosecond Ti-sapphire laser system to measure the transient absorption of PbS nanoparticles stabilized with PVA [21]. They found that the absorption decay is governed by two processes with decay times of 1.2 and 45 ps, which are independent from pump power, probe wavelength, particle size and shape, and surface capping (see Fig. 6). The fast decay is possibly due to trapping, while the slower decay can be attributed to electron-hole recombination mediated by a high density of trap states.

Guo et al. measured transient-induced absorption peaks in surface-capped lead sulfide particles [142]. The decay time

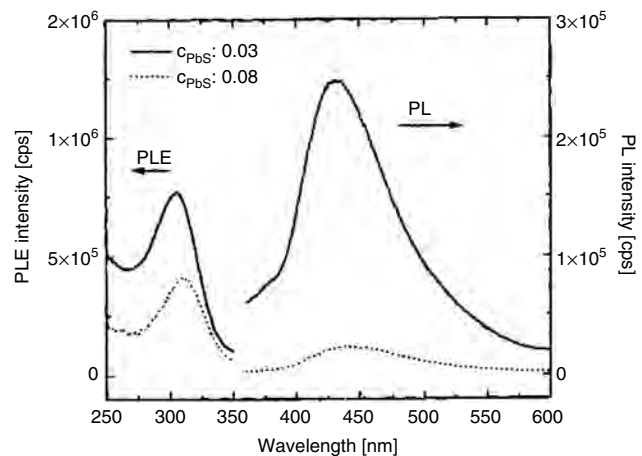


**Figure 5.** Photoluminescence excitation (PLE) and photoluminescence (PL) spectra of two doped  $\text{SiO}_2$  films with PbS volume fractions of 0.03 and 0.08. The excitation wavelength was 311 nm. Reprinted with permission from [93], R. Thielsch et al., *Nano Struc. Mater.* 10, 131 (1998). © 1998, Acta Metallica Inc.



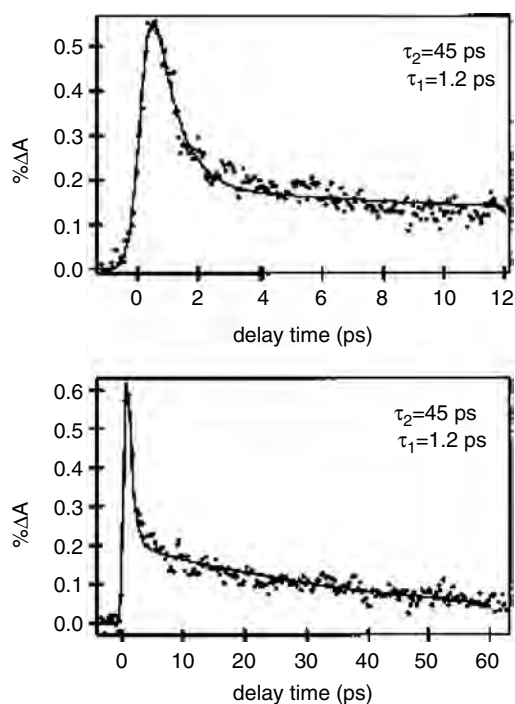


**Figure 6.** Transient absorption decay profiles of photoinduced electrons in PbS nanoparticles stabilized with PVA (circles). The short (top) and intermediate (bottom) scans are fit simultaneously to a double-exponential function deconvolved with a Gaussian of 400 fs FWHM representing the instrument response (solid lines). Time constants of 1.2 and 45 ps for the two decay components are generated from the fitting. Reprinted with permission from [21], A. A. Patel et al., *J. Phys. Chem. B* 104, 11598 (2000). © 2000, American Chemical Society.

was in the order of 150 to 160 fs. It was suggested that this feature arises from the trapped carrier-induced Stark effect.

Machol et al. studied the dynamics of the excitons strongly confined in lead sulfide nanoparticles by using 90 fs laser pulses generated by a mode locked dye laser [119]. The relatively small damping of the exciton transition allowed the observation of the ground state biexcitons as well as an ultra-fast sinusoidal relaxation. This oscillatory response was attributed to quantum beats involving confined TO phonons in the nanoparticles.

#### 4.7. Optical Nonlinear Characterization

The nonlinear properties of lead sulfide nanoparticles have been studied using different experimental techniques: nonlinear M-line spectroscopy [85, 86, 123, 174], degenerated four-wave mixing (DFWM) [85, 123, 174], Z-scan [90, 124, 131]; third harmonic generation (THG) [126], or pump probe spectroscopy [56, 122, 128]. A detailed summary of these techniques can be found in [6]. The use of different techniques is necessary to characterize different types of samples (bulk, thin films, or colloidal solutions) and to obtain complementary information (see Table 4). However, great care has to be taken when comparing results from different nonlinear experiments. In fact, the experimental conditions are rarely comparable. Moreover, it is important to know which element of the nonlinear susceptibility tensor is actually probed. Nevertheless, good agreement was observed, for example, for results from M-line and DFWM measurements made under equivalent experimental conditions [123].

**Table 4.** Nonlinear optical properties of PbS nanoparticles.

State	Method	Pulse duration, rep. rate	$\lambda$ [nm]	$\chi^{(3)}$ [esu]	$n_2$ [cm <sup>2</sup> /W]	Time constant	Ref.
P-PbS solution	OKE-spectroscopy	165 fs, 76 MHz	647	$5.6 \cdot 10^{-12}$	—	~165 fs	[122]
DBS stab. solution	OKE-spectroscopy	165 fs, 76 MHz	647	$9.3 \cdot 10^{-12}$	—	<165 fs	[56, 122, 137]
CTAB stab. solution	OKE-spectroscopy	165 fs, 76 MHz	647	$8.7 \cdot 10^{-13}$	—	<165 fs	[56, 137]
surface modified PbS solution	Z-scan	150 fs, 76 MHz	780	—	$-4.7 \cdot 10^{-12}$	—	[124, 166]
PVA solution	Z-scan	50 ps, 1 Hz	530	$7.3 \cdot 10^{-9}$	—	—	[131]
			1064	$1.1 \cdot 10^{-9}$	—	—	
PVA solution/film	DFWM	25 ns	585–630	$1.1 \cdot 10^{-5}$	—	—	[167]
polymer	Z-scan	150 fs, 76 MHz	780	—	$-6.8 \cdot 10^{-12}$	—	[162]
silica-titania thin film	m-line	8 ns, 10 Hz	532	—	$-2 \cdot 10^{-10}$	—	[85, 174]
silica titania thin film	DFWM	30 ps, 5 Hz	532	—	$5 \cdot 10^{-12}$	<30 ps	[85, 174]
silica titania thin film	m-line	10 ns, 10 Hz	1064	—	$n' = 1.2 \cdot 10^{-11}$	<30 ps	[85, 123]
	DFWM	35 ps, 5 Hz			$I_s = 115 \text{ to } 840 \text{ MW/cm}^2$		
zirconia film	Z-scan	10 ns	1064	—	$-10^{-8} \text{ to } -10^{-9}$	—	[90]
zirconia-ORMOSIL thin film	m-lines	10 ns, 10 Hz	1064	—	$-10^{-11} \text{ to } -10^{-12}$	—	[86]
silica gel	DFWM	8 ns	532	$1.95 \cdot 10^{-11}$	—	—	[100]
Langmuir–Blodgett film	THG	—	1064	$10^{-12}$	—	—	[126]

Note: CTAB: cetyltrimethylammonium bromide; DBS: dodecyl benzene sulphonate; DFWM: degenerated four-wave mixing; OKE: optical kerr effect; P-PBS: polymeric surface modified PbS; PVA: polyvinyl alcohol; THG: third harmonic generation.

PbS nanoparticles show high negative nonlinear response for resonant and nonresonant wavelengths. The nonlinearity is several orders of magnitude higher than for bulk lead sulfide. The nonlinear refractive index of PbS-doped silica titania thin films at 1.064  $\mu\text{m}$  wavelength is in the order of  $n_2 = -10^{-10}$  to  $-10^{-11}$   $\text{cm}^2/\text{W}$  for nanosecond excitation and  $-10^{-12}$  to  $-10^{-13}$   $\text{cm}^2/\text{W}$  for picosecond excitation [85, 123, 174]. These measurements were done on films elaborated by the sol-gel technique. In this case, the main particle size was  $\sim 3$  nm and the doping concentration was 5–25 mol%. At 532 nm wavelength, the measured  $n_2$  was about 10 times higher than at 1.064  $\mu\text{m}$ , and the difference between the nanosecond and picosecond experiments was comparable.

Similar results were observed in PbS-doped zirconia-ORMOSIL thin films [86]. For a 2.9- $\mu\text{m}$  thick film doped with 10 mol% PbS, the  $n_2$  was measured to  $-6 \cdot 10^{-11}$   $\text{cm}^2/\text{W}$  at 1.064  $\mu\text{m}$  with nanosecond excitation. This value is about twice as high as for corresponding silica-titania films. Looking at the absorption spectra, it can be seen that the blue shift of the absorption offset is less important in the case of the ORMOSIL film. This feature is confirmed by HRTEM measurements, which show that in this case the PbS nanoparticles are about twice as large (4.8 nm instead of 2.3 nm). Consequently, the excitation is nearly resonant, explaining the higher  $n_2$  values.

Using picosecond excitation, the nonlinear refractive index of PbS nanoparticles dissolved in polyvinyl alcohol (PVA) is  $-2 \cdot 10^{-10}$  and  $-2 \cdot 10^{-11}$   $\text{cm}^2/\text{W}$  at 532 nm and 1.064  $\mu\text{m}$ , respectively [131]. In the case of surface-modified PbS nanoparticles in microemulsion (PbS concentration of  $2 \cdot 10^{-3}$  mol/l),  $n_2$  was measured at 780 nm to  $-5 \cdot 10^{-12}$   $\text{cm}^2/\text{W}$  (femtosecond excitation) [124]. Third harmonic generation measurements were used for PbS nanoparticles embedded in L-B films. By pumping at 1.064  $\mu\text{m}$ ,  $\chi^{(3)}$  values of the order of  $10^{-20}$  V/m (corresponding to  $n_2 \approx 10^{-14}$   $\text{cm}^2/\text{W}$ ) could be observed [126]. The highest published nonlinearity was measured in PbS-doped  $\text{ZrO}_2$  films [90]. Using Z-scan with nanosecond excitation at 1.064  $\mu\text{m}$ ,  $n_2$  was measured to  $-10^{-8}$  to  $-10^{-9}$   $\text{cm}^2/\text{W}$ .

The difference between the values measured for nanosecond and picosecond excitation is coherent with the fact that the nonlinear response can be explained by a saturated two-level system. In fact, the important parameter is not the pulse duration, but the light intensity. The peak intensity is typically in the order of 10–100  $\text{MW}/\text{cm}^2$  and 1–10  $\text{GW}/\text{cm}^2$  for nanosecond and picosecond excitation, respectively. The typical saturation intensity for PbS nanoparticles is in the order of 100–900  $\text{MW}/\text{cm}^2$ , just in-between the intensities applied in the two cases. This interpretation could be confirmed experimentally by measuring  $n_2$  for different light intensity in-between 10 and 4000  $\text{MW}/\text{cm}^2$ . The experimental curve fits very well to the corresponding theory (see Fig. 7). For a 25 mol% PbS-doped silica-titania film at 1.064  $\mu\text{m}$ ,  $I_s = 840$   $\text{MW}/\text{cm}^2$ , and  $n' = 1.2 \cdot 10^{-11}$   $\text{cm}^2/\text{W}$  could be deduced [123]. The saturated two-level system is, however, only applicable for wavelengths below or near the absorption threshold of the semiconductor. For longer wavelengths, two-photon absorption is supposed to be responsible for the nonlinear response [131].

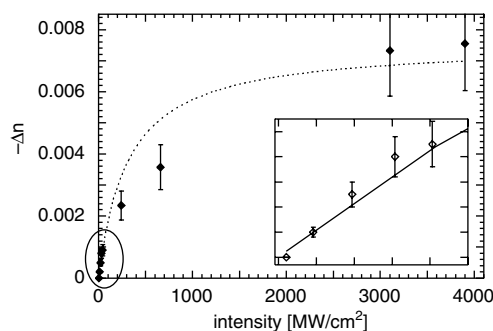


**Figure 7.** Absolute refractive index change as a function of the guided intensity for a 25 mol% PbS-doped  $\text{SiO}_2$ - $\text{TiO}_2$  thin film.

In most experiments, the response time of the nonlinearity was observed to be in the order or below the laser pulse duration [85], even for femtosecond excitation [56, 122]. This is a considerable improvement comparing to bulk semiconductors, where the nonlinear response time is typically in the order of  $\geq 10$  ns.

The nonlinear response of the PbS nanoparticles is dominant in respect to the contributions of the matrix or solvent. Moreover, the module of  $n_2$  is, in general, linearly proportional to the PbS concentration [85, 124], suggesting that for doping concentrations below 25 mol%, one can neglect interactions between the single particles.

The important role of the nanoparticle surface was investigated by studying different surface-capping agents. With this purpose, different kinds of PbS nanoparticles were produced and characterized under the same conditions [56, 122]: (i) PbS modified with polymers, (ii) cetyl-trimethyl-ammonium-bromide capped PbS (CTAB), and (iii) PVA stabilized and sodium-dodecyl-benzene-sulphonate (DBS) capped PbS. The transient nonlinear optical properties were measured using femtosecond, time-resolved optical Kerr effect spectroscopy. For the three samples, similar  $n_2$  values were measured:  $3.8 \cdot 10^{-14}$ ,  $5.9 \cdot 10^{-15}$ , and  $6.3 \cdot 10^{-15}$   $\text{cm}^2/\text{W}$  for i, ii, and iii, respectively. This large nonlinearity of the PbS nanoparticles is attributed to the reduction of surface trapped electrons and the corresponding surface-induced charge separation due to the static electrical field effect. The main difference between the two capped samples consist in lower surface losses for the CTAB-modified particles ( $\chi^{(3)}/\alpha = 3.6 \cdot 10^{-21}$  for (ii) and  $1.1 \cdot 10^{-21}$   $\text{cm}^2/\text{V}$  for (iii)). The higher nonlinearity of the polymer-modified sample (i) can be explained by the local concentration effect due to cross-linking of the nanoparticles by the polymer chains through -Pb-COO- groups.

#### 4.7. Electric Measurements

Hoyer and Könenkamp studied the photoconduction in heterogeneous thin films consisting of a porous titania matrix and PbS nanoparticles adsorbed in the pores of the  $\text{TiO}_2$  matrix [89]. They found that titania serves as the interconnecting matrix to isolated PbS particles. Particles smaller than 2.5 nm act as efficient sensitizers in the visible wavelength region. Upon illumination, photogenerated electrons are injected from the PbS into the insulating titania and give rise to photoconductance with typical values of  $10^{-10}$  ( $\Omega\text{cm}$ ) $^{-1}$  at illumination levels around 10  $\mu\text{W}/\text{cm}^2$ .

The photoelectrical properties of poly-*p*-xylylene PbS nanocomposite films were investigated by Nikolaeva et al. [76]. The dark conductivity was found to be characterized by a linear current-voltage dependence. Ultra-violet irradiation leads to a reversible increase of the conductivity. This phenomena was observed even under irradiation at wavelengths over 630 nm corresponding to an energy below 2 eV.

Yang et al. prepared photoelectrochemical electrodes by chemical deposition of PbS nanoparticles on titania nanocrystalline films and followed by the modification with thiols [136]. These electrodes generated photocurrents as high as 542  $\mu\text{A}/\text{cm}^2$  under irradiation with 400 nm light. However, they underwent photodegradation. The modification with thiols increased the photostability, although it decreases the photocurrent due to the resistance brought about by the carbon chains of thiols.

Using intensity-modulated photocurrent spectroscopy (IMPS), Bakkers et al. studied the electronic structure and decay dynamics of a long-lived photoexcited state in lead sulfide nanoparticles absorbed as a monolayer on a gold surface [173]. By scanning the Fermi level of the gold, they found that the excited state consists of an electron in a deep trap and a hole in the highest occupied molecular orbital (HOMO). It was found that the trapped charge carrier has a lower tunneling probability than the free carrier, indicating that distance is the determining parameter for electron tunneling.

Ogawa et al. measured the photoelectrochemical properties of lead sulfide nanoparticles incorporated in self-assembled monolayers (SAMS) on gold [148]. They found either cathodic or anodic photocurrents, depending on the nature of the solution mediator (hole or electron scavenger) and the applied potential.

Kundu et al. measured the piezoelectric coefficients of lead zirconate titanate doped with lead sulfide nanoparticles [103]. The samples were poled in a bath of silicone oil at a temperature of 353 K for 10 min at an applied electrical field of 25 kV/cm. The measured values of saturation polarization, remnant polarization, and coercive fields increased with increasing PbS particle size. Moreover, an improvement of the piezoelectric and pyroelectric behavior was noticed for the composites as compared to the base glass ceramics.

In order to study the electrical properties of PbS nanoparticle-doped, zirconia films, Sashchiuk et al. deposited them on ITO/glass substrates, followed by their coverage with gold contacts [91, 153]. The current-voltage characteristics depended on the PbS particle size and exhibited nonlinear, nearly symmetric curves, associated with the space-charge limited current or the tunneling of carriers through the nanocrystalline film.

Nanda and Sahu fabricated a self-assembled heterojunction by means of an electrochemical deposition of PbS nanoparticles on indium tin oxide substrate [175]. A large current and large capacitance were observed in the case of a device from particles of a smaller size, which was believed to be due to the large surface area contact. The rectifying behavior of the heterojunction was found to be weak as compared to the usual *p-n* junctions.

## 5. DISCUSSION OF OPTICAL PROPERTIES

### 5.1. Excitons-Absorption Spectra

In semiconductor nanoparticles, the bulk model of conduction and valence bands has to be replaced by discrete electron and hole energy levels. In this case, the effective bandgap energy can be defined as the minimal energy that is required for creating one electron-hole pair or exciton. This quasi-particle corresponds to the hydrogen-like bound state of an electron-hole pair which interacts via the Coulomb potential. The excitonic states usually lie slightly below the bottom of the conduction band. In bulk semiconductors, the exciton binding energy is low (few tens of meV) and excitons are often thermally dissipated. Thus, low temperature spectroscopy is necessary to study bulk excitons. In nanoparticles, the two charged carriers of the exciton are confined to the same volume. Thermal dissipation requires much higher temperatures and the exciton structure becomes visible even at room temperature. The observation of an exciton absorption feature in PbS nanoparticles is, however, difficult. PbS is a narrow bandgap semiconductor with weak exciton binding energy due to strong Coulomb screening. Moreover, the enhanced sensibility to particle size dispersion widens the exciton peaks.

The excitonic absorption line of nanoparticles saturates much faster than the absorption band of the corresponding bulk semiconductor. In addition, this saturation is accompanied by induced absorption near resonance. This feature is due to the formation of biexcitons via absorption of a second phonon. Thus, the ground state biexciton (two electron-hole pair states) is visible as an induced absorption line on the low energy side of the exciton resonance. Its experimental observation is dependent on weak dumping of the exciton transition. This condition is fulfilled for PbS nanoparticles. Thus, the biexciton ground state could be observed in a pump-probe experiment [119]. By using time-resolved pump-probe experiments, it was even shown that bleaching and induced absorption has a similar time evolution [128]. Fast ( $\sim 10$  ps) and slow ( $\sim$  ns) decay components are clearly distinguished with the same time-constant. The fast component is attributed to the recombination of free carriers or carriers trapped in shallow traps, whereas the slow one is assigned to trapped carriers.

The excitonic absorption of PbS nanoparticles is also influenced by external carriers. It was shown that the injection of electrons into PbS colloids in aqueous solution leads to a blue shift of the absorption edge [49]. This effect was explained by trapping of the excess carriers into surface states of the particles. In fact, colloidal semiconductors are usually synthesized with a very high density of surface defects. The appearance of the shift actually depends critically on the method of colloid preparation. PbS colloids prepared at  $\text{pH} < 6$  have long-living bleaching of the initial absorption, which disappears several seconds after the injection of the electrons. After the addition of hydroxide ions to the colloids solution ( $\text{pH} > 8$ ), the absorption bleaching disappears. In fact, the hydroxide ions saturate the surface defects on which the electrons are trapped. However, the absorption spectrum is only very weakly influenced by the pH change.

The quantum confinement has also an influence on the temperature-dependence of the bandgap. In bulk semiconductors, this temperature-dependence is linked to lattice thermal expansion and to electron-phonon coupling. In PbS nanoparticles the position of the exciton absorption should be nearly temperature-independent. First, the influence of thermal lattice expansion diminishes with decreasing particle size as the energy levels become determined by the particle size instead of the lattice constants. Second, the electron-phonon coupling intensity decreases with decreasing particle size due to increasing energy separation of the discrete phonon and electron energy levels. This feature was experimentally confirmed by studying the temperature-dependence of the absorption spectra of PbS nanoparticles embedded in a glass matrix [127]. For larger particles with diameters above 8.5 nm, bulk-like temperature-dependence was observed. With decreasing size, the temperature coefficient decreases by more than one order of magnitude from the bulk value. The exciton energy of 4.5-nm sized particles was found to be almost independent of temperature as for isolated atoms.

## 5.2. Carrier Dynamics–PL

Time-resolved PL measurements show that decay mechanisms are complex, consisting of multi-exponential processes. After excitation, the first step of relaxation is the electronic relaxation inside the conduction band and the hole relaxation inside the valence band. This is mainly due to electron-phonon interactions and is expected to be on the timescale of 100 fs or less. Once the electron is relaxed to the bottom of the conduction band and the hole to the top of the valence band, they can recombine radiatively or non-radiatively. If there are few or no bandgap states, the recombination should be primarily radiative, that is, strong band edge luminescence is observed. The corresponding lifetime is in the order of nanoseconds or longer. In a more precise description of semiconductor nanoparticles, the bands have to be replaced by excitonic states. Thus, the absorption of a photon will create an exciton in an excited state. The electron and hole of the exciton will recombine after relaxation to the exciton ground state.

When electron states are present within the bandgap due to surface or internal defects, they act to trap the charge carriers on time-scales faster than radiative recombination, typically a few picoseconds to tens of picoseconds. Further trapping from shallow trap states to deep trap states can take place on the tens of ps to hundreds of ps timescales. The trapped charge carriers can recombine nonradiatively or radiatively, producing trap state emission that is red shifted with respect to bandedge emission. The trap state varies significantly in their energy levels or trap depth, which in turn determines how fast the trapping occurs and how long the trap states live. The trap states have lifetimes on the timescale from tens of picoseconds to nanoseconds, microseconds, or even longer.

Consequently, two emission lines are observed from semiconductor nanoparticles: excitonic and trapped-electron luminescence [68, 130]. The excitonic emission is sharp and is located near the absorption edge of the material, whereas the trap emission is broad and stokes-shifted towards longer

wavelengths. For most applications, the sharp excitonic luminescence is preferable. Thus, great care has to be taken in order to limit the number of electronic trap states at the surface of the nanoparticles.

Low temperature PL measurements show even three emission features [125]. UV-excitation at 340 nm of PbS nanoparticles embedded in a polymer film reveals an excitonic emission in the blue (450–490 nm) and two additional nonexcitonic bands in the green ( $\approx 550$  nm) and red ( $\approx 633$  nm). The blue emission was assigned to exciton emission. Thus, its position depends on the particle size. The red and green bands correspond to trap states, deep inside the bandgap, and therefore, they are independent of the particle size. In addition, the intensity of the red band is enhanced for the smallest particles. The red emission can, therefore, be associated with surface defects, as for small samples the surface-to-volume ratio is maximal. The green band may be associated with trapped electron-hole recombination at a stoichiometric defect site, located at the interior part of the nanoparticles, as its intensity is decreasing for decreasing sample size.

The temperature-dependence of the PL spectra reveals information on the relaxation processes and the mutual interaction among states. The continuous decrease of the luminescence intensity of the blue band with an increase in temperature suggests a coupling to lattice phonon that enables a transfer of carriers into nonradiative states. The increase in luminescence intensity of the green and red emission band up to 65 K, suggests that the corresponding states are thermally populated by carrier transfer from exciton states. Above 65 K, thermal activation competes with quenching of nonradiative transitions, and thus, the intensity of the green and red bands decreases with a further increase in temperature. This thermal activation model was also suggested for other semiconductors.

The great influence of the surface properties on the PL could be shown by studying PbS nanoparticles in solutions with different pH values [49]. Poly vinyl alcohol stabilized PbS colloids, prepared at pH 5, have a weak broad emission from 600 to 800 nm with a low quantum yield, indicating that radiationless carrier recombination is the dominant relaxation process. Addition of hydroxide ions to adjust the pH to 10 increases the excitonic bandedge luminescence by about a factor of four. At the same time, the long-wavelength luminescence, which is assigned to surface-trap relaxation, only increases very slightly. This result confirms the fact that hydroxide is very efficient for saturating surface traps.

The influence of the nanoparticle shape on the carrier dynamics was found to be insignificant. The shape of PbS nanoparticles can be monitored from mostly spherical to needle or cubic shape by changing the surface capping polymer. While the absorption spectrum depends on the shape of the nanoparticle, the electronic relaxation dynamics remains about the same for the apparently different-shaped particles [21]. The electric relaxation was found to feature a double exponential decay with time constants of 1.2 and 45 ps, independent of probe wavelength and excitation density. The shape independence can be attributed to the dominant influence of the surface properties on the electronic relaxation. While shapes are different, the different samples should have similar surface properties. Therefore, if the

dynamics are dominated by the surface, changes in shape may not affect the electronic relaxation dynamics substantially. The extremely short lifetime of trapped electrons in PbS nanoparticles is most likely due to the high density of trap states.

## 6. APPLICATIONS

The great research effort made with PbS nanoparticles results in improved elaboration processes as well as in an increasing understanding of their physics. In the continuation of this research, the implementation of PbS nanoparticles in some applications was proposed and realized. It could be shown that their specific properties may be very beneficial for the device operating.

### 6.1. Optical Amplification

Due to their strong light-emission, semiconductor nanoparticle-doped materials are good candidates for infrared emitting materials with high quantum efficiency. Potential applications are wideband optical amplifiers or laser sources for telecommunication purposes [176]. The emission wavelength can be easily chosen by monitoring the mean size of the particles, and the emission width is defined by the size dispersion. Moreover, in comparison with epitaxially grown semiconductor structures presently used for infrared lasers, semiconductor-doped glasses are inexpensive as well as robust materials. Despite the presence of highly efficient intrinsic Auger recombination, room temperature optical gain could be obtained in different semiconductor quantum dot materials [177–180], including PbS-doped glass [129]. When pumping into the first-excited exciton transition, optical gain was observed in the vicinity of the ground-state exciton resonance. The spectral position of the emission peak could be changed from 1317 to 1352 nm by tuning the pump wavelength between 900 and 980 nm. This tunability relies on the strong carrier confinement and the inhomogeneous broadening in the sample due to the particle-size distribution. The actual spectral width and position of the gain was limited by the pump pulse.

### 6.2. Passive Q-Switching

The fast absorption bleaching of PbS-doped glass was successfully used for passive Q-switching of Cr:forsterite [132] and erbium-doped glass lasers [133, 134]. Compared to active Q-switching, passive Q-switching with a saturable absorber is simpler, more compact, more robust, and does not require auxiliary electronics. These points are of paramount interest for erbium-doped, eye-safe lasers used in telemetry and ranging. Most of currently used absorbers for Er-doped lasers have relatively high saturation intensities in the order of 40–200 MW/cm<sup>2</sup>, whereas the low saturation intensity of PbS-doped glass in the 60–180 kW/cm<sup>2</sup> range allows complete bleaching with intensities achievable with standard micro-lasers. Laser pulses of 110 ns duration and 0.2 mJ energy were obtained with 6 nm PbS nanoparticle-doped glass inside an Er<sup>3+</sup>:glass laser cavity [134]. 1 μJ, 30–50 ns long pulses at 1–2 kHz repetition rate were observed in a different experiment [133]. In the case of the Cr:forsterite laser, nearly

transformed limited, 4.6 ps long laser pulses at 110 MHz repetition rate and a tunability range from 1.207 to 1.307 μm were reported [132]. In that case, the absorption saturation intensity of the PbS-doped glass containing 6.6-nm sized nanoparticles was estimated to be 200 kW/cm<sup>2</sup>. It was shown that the nonlinearity in the glass host limits the maximum intracavity power, which can be saturated by nanoparticle absorption [135]. Above a fluence of around 10 mJ/cm<sup>2</sup>, bright third-harmonic generation is detected and the PbS-doped glass no longer operates as a saturable absorber.

### 6.3. Refractive Index Modification

Bulk PbS has a refractive index of  $n_b = 4$ , which decreases for nanoparticles. It has been shown that nanocomposites of polymers and semiconductors may exhibit optical properties that cannot be obtained with pure polymers alone. The introduction of PbS nanoparticles into a polymer matrix increases its refractive index to values of up to  $n_{nc} = 3.0$  [27, 74]. This value has to be compared with the maximum refractive index of pure organic polymers of about 1.7. Thus, the composite material becomes suitable for some optical applications, such as the manufacture of improved efficiency solar cells. The refractive index was found to be nearly constant in the 1000 to 2500 nm wavelength region. Moreover, the engineering of the refractive index is straightforward as it scales quasi-linearly with the PbS concentrations.

In the case of these polymer films, light scattering losses at the high index nanoparticles could be reasonably limited by choosing particles with average diameters below 50–100 nm. However, the very low waveguiding losses required for integrated optic devices may be a problem. The scattering losses depend on the refractive index difference between particles and matrix, the size, and the form of the particles. The scattering losses for a slab waveguide of homogeneously PbS nanoparticle-doped glass can be evaluated by using a simplified Mie scattering algorithm [123]. For spherical particles (size: 3 nm; PbS concentration: 5 vol%) in a silica glass host ( $n = 1.51$ ), the calculated scattering losses are about 0.047 dB/cm at 1.064 μm and 0.021 dB/cm at 1.3 μm. Hence, the contribution of the scattering losses to the overall waveguide losses can be neglected. However, for larger particles (>10 nm) scattering losses represent a serious limitation. By using high index host materials, such as chalcogenide glasses, the scattering losses can be considerably reduced and the presence of large particles becomes feasible.

### 6.4. Light-Converting Devices

A further application field of lead sulfide is the fabrication of light-converting electrodes which can be obtained by sensitizing porous titania with PbS nanoparticles [88, 89, 136]. In this device, visible light is absorbed by the semiconductor particles, followed by electron transfer into the porous TiO<sub>2</sub> films. The use of PbS nanoparticles implies several advantages as compared to organic dyes: the bandgap and, thereby, the absorption range are easily adjustable by the size of the particle, and the bandedge type of absorption behavior is most favorable for effective light harvesting. Internal photocurrent quantum yield of more than 80% and open circuit photovoltages of 300 mV were realized.

## 7. CONCLUSION

Over the last few years, lead sulfide nanoparticles were the subject of vigorous research activities. This work enabled a better understanding of their physical properties which, in turn, allowed the enhancement of the particle fabrication techniques. Important improvements of the characterization techniques are accompanying this process. Particle size dispersion and problems with the particle surface quality have been the most important limitations of PbS nanoparticles. However, the improved elaboration techniques, including surface passivation, can resolve these problems.

It seems that the most interesting properties of lead sulfide nanoparticles are their saturable absorption, their strong emission, and their capacity to sensitize dielectric matrices for photoelectric devices. Some early devices were already demonstrated in the laboratory and commercial devices can be expected in the near future. In parallel, the increasing quality of lead sulfide nanoparticles will enable us to continue the exciting investigation of strong quantum confinement effects.

## GLOSSARY

**Blue shift** Shift of the optical absorption edge due to the quantum confinement of electrons and holes inside semiconductor quantum wells or nanoparticles.

**Exciton** Quasi particle inside semiconductors similar to an hydrogen atom and consisting of an electron and hole linked by the Coloumb interaction. In contrast to bulk semiconductors, in quantum dots excitons are observable at room temperature.

**Quantum confinement** Confinement of electrons and holes inside semiconductor nanoparticles. The quantum confinement changes radically the optical properties of the semiconductor. It enhances especially its nonlinear optical properties.

**Sol-gel** Recently developed chemical processing route for the fabrication of glasses and ceramics as thin film or bulk materials. Sol-gel allows to elaborate high purity materials, does in general not require high temperature processing, and requires only low investment.

**Surface passivation** Saturation of electronic trap states at the surface of semiconductor nanoparticles. Surface passivation enhances significantly the linear and nonlinear optical properties of the nanoparticles.

## REFERENCES

1. F. W. Wise, *Acc. Chem. Res.* 33, 773 (2000).
2. L. Banyai, Y. Z. Hu, M. Lindberg, and S. W. Koch, *Phys. Rev. B* 38, 8142 (1988).
3. R. K. Jain and R. C. Lind, *J. Opt. Soc. Am.* 73, 647 (1983).
4. S. V. Gaponenko, "Optical Properties of Semiconductor Nanocrystals." Cambridge University Press, Cambridge, 1998.
5. U. Woggon, "Properties of Semiconductor Nanocrystals." Springer-Verlag, Berlin, 1997.
6. J. Fick, in "Handbook of Surfaces and Interfaces of Materials" (H. S. Nalwa, Ed.) Vol. 3, p. 311. Academic Press, San Diego, 2001.
7. V. I. Klimov, in "Handbook of Nanostructured Materials and Nanotechnology" (H. S. Nalwa, Ed.) Vol. 4, p. 563. Academic Press, San Diego, 2000.
8. A. L. Efros and A. L. Efros, *Sov. Phys. Semicon.* 16, 772 (1982).
9. N. F. Borrelli and D. W. Smith, *J. Non-Cryst. Solids* 180, 25 (1994).
10. Y. Kayanuma, *Phys. Rev. B* 38, 9797 (1988).
11. Y. N. Savin, A. V. Tolmachev, and Y. A. Tolmacheva, *JETP Lett.* 75, 163 (2002).
12. Y. Wang, A. Suna, W. Mahler, and R. Kasowski, *J. Chem. Phys.* 87, 7315 (1987).
13. A. L. Efros and M. Rosen, *Phys. Rev. B* 58, 7120 (1998).
14. G. T. Einevoll, *Phys. Rev. B* 45, 3410 (1992).
15. Y. Kayanuma and H. Momiji, *Phys. Rev. B* 41, 10261 (1990).
16. J. L. Marín, R. Riera, and S. A. Cruz, *J. Phys.: Cond. Matt.* 10, 1349 (1998).
17. P. E. Lippens and M. Lannoo, *Phys. Rev. B* 39, 10935 (1989).
18. L. M. Ramaniah and S. V. Nair, *Phys. Rev. B* 47, 7132 (1993).
19. R. S. Kane, R. E. Cohen, and R. Silbey, *J. Phys. Chem.* 100, 7928 (1996).
20. V. Albe, C. Jouanin, and D. Bertho, *Phys. Rev. B* 58, 4713 (1998).
21. A. A. Patel, F. Wu, J. Z. Zhang, C. L. Torres-Martinez, R. K. Mahra, Y. Yang, and S. H. Risbud, *J. Phys. Chem. B* 104, 11598 (2000).
22. J. A. Valdivia and E. Barberis, *J. Phys. Chem. Sol.* 56, 1141 (1995).
23. M. Lach-Hab, D. A. Papaconstantopoulos, and M. J. Mehl, *J. Phys. Chem. Solids* 62, 833 (2002).
24. A. D. Andreev and A. A. Lipovskii, *Phys. Rev. B* 59, 15402 (1999).
25. G. E. Tudury, M. V. Marquezini, L. G. Ferreira, L. C. Barbosa, and C. L. Cesar, *Phys. Rev. B* 62, 7357 (2000).
26. I. Kang and F. W. Wise, *J. Opt. Soc. Am. B* 14, 1632 (1997).
27. T. Kyprianidou-Leodidou, W. Caseri, and U. W. Suter, *J. Phys. Chem.* 98, 8992 (1994).
28. M. C. Klein, F. Hache, D. Ricard, and C. Flytzanis, *Phys. Rev. B* 42, 11123 (1990).
29. S. Nomura and T. Kobayashi, *Phys. Rev. B* 45, 1305 (1992).
30. T. D. Krauss and F. W. Wise, *Phys. Rev. Lett.* 79, 5102 (1997).
31. S. Schmitt-Rink, D. A. B. Miller, and D. S. Chemla, *Phys. Rev. B* 35, 8133 (1987).
32. E. Roca, C. Trallero-Giner, and M. Cardona, *Phys. Rev. B* 49, 13704 (1994).
33. T. D. Krauss, F. W. Wise, and D. B. Tanner, *Phys. Rev. Lett.* 76, 1376 (1996).
34. M. P. Chamberlain, C. Trallero-Giner, and M. Cardona, *Phys. Rev. B* 51, 1680 (1995).
35. T. D. Krauss and F. W. Wise, *Phys. Rev. B* 55, 9860 (1997).
36. J. T. Devreese, V. M. Fomin, and S. N. Klimin, *Int. J. Mod. Phys. B* 15, 3579 (2001).
37. J. T. Devreese, V. M. Fomin, V. N. Gladilin, E. P. Pokatilov, and S. N. Klimin, *Nanotech.* 13, 163 (2002).
38. V. M. Fomin, E. P. Pokatilov, J. T. Devreese, S. N. Klimin, V. N. Gladilin, and S. N. Balaban, *Solid State Electron.* 42, 1309 (1998).
39. P. N. Butcher and D. Cotter, "The Elements of Nonlinear Optics." Cambridge University Press, Cambridge, 1990.
40. M. Sheik-Bahae, A. A. Said, D. J. Hagan, M. J. Soileau, and E. W. Van Stryland, *Opt. Eng.* 30, 1228 (1991).
41. D. C. Hutchings, M. Scheik-Bahae, D. J. Hagan, and E. W. Van Stryland, *Opt. Quantum Electron.* 24, 1 (1992).
42. E. Vanagas, J. Moniatte, M. Mazilu, P. Riblet, B. Hönerlage, S. Juodkazis, F. Paille, J. C. Plenet, J. G. Dumas, M. Petruskas, and J. Vaitkus, *J. Appl. Phys.* 81, 3586 (1997).
43. G. P. Banfi, V. Degiorgio, D. Fortusini, and H. M. Tan, *J. Non. Opt. Phys. Mater.* 5, 205 (1996).
44. D. Ricard, M. Ghanassi, M. C. Schanne-Klein, and C. Flytzanis, *SPIE Vol.* 2801, 47 (1995).
45. G. Chui and E. J. Meehan, *J. Coll. Interf. Sci.* 49, 160 (1974).
46. R. Rossetti, R. Hull, J. M. Gibson, and L. E. Brus, *J. Chem. Phys.* 83, 1406 (1985).
47. A. J. Nozik, F. Williams, M. T. Nenadovic, T. Rajh, and O. I. Micic, *J. Phys. Chem.* 89, 397 (1985).
48. S. Gallardo, M. Gutiérrez, A. Henglein, and E. Janata, *Ber. Bunsenges. Phys. Chem.* 93, 1080 (1989).



49. M. T. Nenadovic, M. I. Comor, V. Vasic, and O. I. Micic, *J. Phys. Chem.* 94, 6390 (1990).
50. H. S. Zhou, I. Homma, H. Komiyama, and J. W. Haus, *J. Phys. Chem.* 97, 985 (1993).
51. T. Torimoto, T. Sakata, H. Mori, and H. Yoneyama, *J. Phys. Chem.* 98, 3036 (1994).
52. Y. Sun, E. Hao, X. Zhang, B. Yang, J. Shen, L. Chi, and H. Fuchs, *Langmuir* 13, 5168 (1997).
53. T. Sugimoto, S. Chen, and A. Muramatsu, *Colloids Surfaces A* 135, 207 (1998).
54. S. Lu, U. Sohling, T. Krajewski, M. Mennig, and H. Schmidt, *J. Mater. Sci. Lett.* 17, 2071 (1998).
55. S. Chen, W. Liu, and L. Yu, *J. Mater. Res.* 14, 2147 (1999).
56. G. Lin and A. Xicheng, *Mater. Chem. and Phys.* 63, 30 (2000).
57. S. Chen, L. A. Truax, and J. M. Sommers, *Chem. Mater.* 12, 3864 (2000).
58. J. P. Yang, S. B. Qadri, and B. R. Ratna, *J. Phys. Chem.* 100, 17255 (1996).
59. T. Schneider, M. Haase, A. Kornowski, S. Nased, H. Weller, S. Förster, and M. Antonietti, *Ber. Bunsenges. Phys. Chem.* 101, 1654 (1997).
60. J. Zhu, S. Liu, O. Palchik, Y. Koltypin, and A. Gedanken, *J. Solid State Chem.* 153, 342 (2000).
61. Y.-P. Sun, R. Guduru, F. Lin, and T. Whiteside, *Ind. Eng. Chem. Res.* 39, 4663 (2000).
62. T. Trindade, P. O'Brien, X. Zhang, and M. Motevalli, *J. Mater. Chem.* 7, 1011 (1997).
63. P. Boudjouk, B. R. Jarabek, D. L. Simonson, D. J. Seidler, D. G. Grier, G. J. McCarthy, and L. P. Keller, *Chem. Mater.* 10, 2358 (1998).
64. F. E. Kruijs, K. Nielsch, H. Fissan, B. Rellinghaus, and E. F. Wassermann, *Appl. Phys. Lett.* 73, 547 (1998).
65. X. R. Ye, D. Z. Jia, J. Q. Yu, X. Q. Xin, and Z. Xue, *Adv. Mater.* 11, 941 (1999).
66. X. K. Zhao, J. Yang, L. D. Mc Cormic, and J. H. Fendler, *J. Phys. Chem.* 96, 9933 (1992).
67. A. B. Preobrajenski, K. Barucki, and T. Chassé, *Phys. Rev. Lett.* 85, 4337 (2000).
68. H. Miyoshi, M. Yamachika, H. Yoneyama, and H. Mori, *J. Chem. Soc. Faraday Trans.* 86, 815 (1990).
69. M. Moffitt and A. Eisenberg, *Chem. Mater.* 7, 1178 (1995).
70. V. Sankaran, C. C. Cummins, R. R. Schrock, R. E. Cohen, and R. J. Silbey, *J. Am. Chem. Soc.* 112, 6858 (1990).
71. R. Tassoni and R. R. Schrock, *Chem. Mater.* 6, 744 (1994).
72. Z. Zeng, S. Wang, and S. Yang, *Chem. Mater.* 11, 3365 (1999).
73. S. Joly, R. Kane, L. Radzilowski, T. Wang, A. Wu, R. E. Cohen, E. L. Thomas, and M. F. Rubner, *Langmuir* 16, 1354 (2000).
74. W. Caseri, *Macromol. Rapid Commun.* 21, 705 (2000).
75. N. P. Gaponik and D. V. Sviridov, *Ber. Bunsenges. Phys. Chem.* 101, 1657 (1997).
76. E. V. Nikolaeva, S. A. Ozerin, A. E. Grigoriev, S. N. Chvalun, G. N. Gerasimov, and L. I. Trakhtenberg, *Mater. Sci. Engin.* C 8-9, 217 (1999).
77. S. Wang and S. Yang, *Langmuir* 16, 389 (2000).
78. A. K. Dutta, T. Ho, L. Zhang, and P. Stroeve, *Chem. Mater.* 12, 1042 (2000).
79. X. K. Zhao, S. Baral, R. Rolandi, and J. H. Fendler, *J. Am. Chem. Soc.* 110, 1012 (1988).
80. I. Moriguchi, H. Nii, K. Hanai, H. Nagaoka, Y. Teraoka, and S. Kagawa, *Colloids Surfaces A* 102, 173 (1995).
81. S. Guo, R. Popovitz-Biro, T. Arad, G. Hodes, L. Leiserowitz, and M. Lahav, *Adv. Mater.* 10, 657 (1998).
82. F. N. Dultsev and L. L. Sveshnikova, *Thin Solid Films* 322, 303 (1998).
83. L. Konopny, M. Berfeld, R. Popovitz-Biro, I. Weissbuch, L. Leiserowitz, and M. Lahav, *Adv. Mater.* 13, 580 (2001).
84. O. V. Salata, P. J. Dobson, P. J. Hull, and J. L. Hutchison, *Adv. Mater.* 6, 772 (1994).
85. A. Martucci, J. Fick, J. Schell, G. Bataglin, and M. Guglielmi, *J. Appl. Phys.* 86, 79 (1999).
86. A. Martucci, P. Innocenzi, J. Fick, and J. D. Mackenzie, *J. Non-Cryst. Solids* 244, 55 (1999).
87. F. del Monte, Y. Xu, and J. D. Meckenzie, *J. Sol-Gel Sci. Technol.* 17, 37 (2000).
88. R. Vogel, P. Hoyer, and H. Weller, *J. Phys. Chem.* 98, 3183 (1994).
89. P. Hoyer and R. Könenkamp, *Appl. Phys. Lett.* 66, 349 (1995).
90. W. Huang and J. Shi, *J. Mater. Res.* 15, 2343 (2000).
91. A. Sashchiuk, E. Lifshitz, R. Reisfeld, T. Saraidarov, M. Zelner, and A. Willenz, *J. Sol-Gel Sci. Technol.* 24, 31 (2002).
92. H. Nasu, H. Yamada, J. Matsuoka, and K. Kamiya, *J. Non-Cryst. Solids* 183, 290 (1995).
93. R. Thielsch, T. Böhme, R. Reiche, D. Schläfer, H.-D. Bauer, and H. Böttcher, *Nano Struct. Mater.* 10, 131 (1998).
94. M. Gao, Y. Yang, F. Bian, and J. Shen, *J. Chem. Soc., Chem. Commun.* 2779 (1994).
95. E. Leontidis, T. Kyprianidou-Leodidou, W. Caseri, and K. C. Kyriacou, *Langmuir* 15, 3381 (1999).
96. E. Leontidis, T. Kyprianidou-Leodidou, W. Caseri, P. Robyr, F. Krumeich, and K. C. Kyriacou, *J. Phys. Chem. B* 105, 4133 (2001).
97. Z. Qiao, G. Xie, J.-M. Huang, S.-Y. Zhao, and X.-M. Chen, *J. Mater. Chem.* 12, 611 (2002).
98. Z. Qiao, Y. Xie, Y. Zhu, and Y. Qian, *J. Mater. Chem.* 9, 1001 (1999).
99. T. Gacoin, C. Train, F. Chaput, J.-P. Boilot, P. Aubert, M. Gandais, Y. Wang, and A. Lecomte, *SPIE* Vol. 1758, 565 (1992).
100. N. Pellegrini, R. Trebojevich, O. De Sanctis, and K. Kadono, *J. Sol-Gel Sci. Technol.* 8, 1023 (1997).
101. M. Nogami, K. Nagasaka, and K. Kotani, *J. Non-Cryst. Solids* 126, 87 (1990).
102. N. N. Parvathy, A. Venkateswara Rao, and G. M. Pajonk, *J. Non-Cryst. Solids* 241, 79 (1998).
103. T. K. Kundu, D. Chakravorty, and L. E. Cross, *J. Mater. Res.* 14, 1796 (1999).
104. R. Erce-Montilla, M. Piñero, N. dela Rosa-Fox, A. Santos, and L. Esquivias, *J. Mater. Res.* 16, 2572 (2001).
105. H. Su, P. Gao, Y. Xiong, and Y. Qian, *J. Mater. Chem.* 11, 684 (2001).
106. F. Gao, Q. Lu, X. Liu, Y. Yan, and D. Zhao, *Nano Lett.* 1, 743 (2001).
107. A. A. Lipovskii, E. V. Kolobkova, A. Olkhovets, V. D. Petrikov, and F. W. Wise, *Physica E* 5, 157 (2000).
108. M. Mukherjee, A. Datta, and D. Chakravorty, *J. Mater. Res.* 12, 2507 (1997).
109. A. Meldrum, E. Sonder, R. A. Zuhr, I. M. Anderson, J. D. Budai, C. W. White, L. A. Boatner, and D. O. Henderson, *J. Mater. Res.* 14, 4489 (1999).
110. K. Moller, T. Bein, N. Herron, W. Mahler, and Y. Wang, *Inorg. Chem.* 28, 2914 (1989).
111. M. Wark, N. I. Jaeger, W. Lutz, and O. P. Tkachenko, *Ber. Bunsenges. Phys. Chem.* 101, 1635 (1997).
112. G. Cao, L. K. Rabenberg, C. M. Nunn, and T. E. Mallouk, *Chem. Mater.* 3, 149 (1991).
113. V. S. Gurin, *J. Cryst. Growth* 191, 161 (1998).
114. R. Houbertz, W. Krauss, R. Birringer, and U. Hartmann, *Nano Struct. Mater.* 9, 339 (1997).
115. H. P. Klug and L. E. Alexander, "X-Ray Diffraction Procedures." John Wiley, New York, 1954.
116. R. S. Kane, R. E. Cohen, and R. Silbey, *Chem. Mater.* 8, 1919 (1996).
117. S. Guo, R. Popovitz-Biro, I. Weissbuch, H. Cohen, G. Hodes, and M. Lahav, *Adv. Mater.* 10, 121 (1998).
118. Y. Wang and N. Herron, *J. Phys. Chem.* 95, 525 (1991).
119. J. L. Machol, F. W. Wise, R. C. Patel, and D. B. Tanner, *Phys. Rev. B* 48, 2819 (1993).
120. K. K. Nanda, S. N. Sahu, R. K. Soni, and S. Tripathy, *Phys. Rev. B* 58, 15405 (1998).

121. E. P. Pokatilov, S. N. Klimin, V. M. Fomin, J. T. Devreese, and F. W. Wise, *Phys. Rev. B* 65, 075316 (2002).
122. X. C. Ai, L. Guo, Y. H. Zou, Q. S. Li, and H. S. Zhou, *Mater. Lett.* 38, 131 (1999).
123. J. Fick, A. Martucci, M. Guglielmi, and J. Schell, *Fiber and Integrated Optics* 19, 43 (2000).
124. H. P. Li, B. Liu, Y. L. Lam, W. X. Que, L. M. Gan, C. H. Chew, and G. Q. Xu, *Opt. Mater.* 14, 321 (2000).
125. E. Lifshitz, M. Sirota, and H. Porteanu, *J. Cryst. Growth* 196, 126 (1999).
126. I. Moriguchi, K. Hanai, Y. Teraoka, S. Kagawa, S. Yamada, and T. Matsuo, *Jpn. J. Appl. Phys. Part 2* 3A, L323 (1995).
127. A. Olkhovets, R.-C. Hsu, A. A. Lipovskii, and F. W. Wise, *Phys. Rev. Lett.* 81, 3539 (1998).
128. G. Tamulaitis, V. Gulbinas, G. Kodis, A. Dementjev, L. Valkunas, I. Motchalov, and H. Raaben, *J. Appl. Phys.* 88, 178 (2000).
129. K. Wundke, J. Auxier, A. Schülzgen, N. Peyghambarian, and N. F. Borrelli, *Appl. Phys. Lett.* 75, 3060 (1999).
130. P. Yang, C. F. Song, M. K. Lü, X. Yin, G. J. Zhou, D. Xu, and D. R. Yuan, *Chem. Phys. Lett.* 345, 429 (2001).
131. B. Yu, G. Yin, C. Zhu, and F. Gan, *Opt. Mater.* 11, 17 (1998).
132. P. T. Guerreiro, S. Ten, N. F. Borrelli, J. Butty, G. E. Jabbour, and N. Peyghambarian, *Appl. Phys. Lett.* 71, 1595 (1997).
133. J. F. Philipps, T. Töpfer, H. Ebendorff-Heidepriem, D. Ehr, R. Sauerbrey, and N. F. Borrelli, *Appl. Phys. B* 72, 175 (2001).
134. A. M. Malyarevich, I. A. Denisov, V. G. Savitsky, K. V. Yumashev, and A. Lipovskii, *Appl. Opt.* 39, 4345 (2000).
135. K. Wundke, S. Pötting, J. Auxier, A. Schülzgen, and N. Peyghambarian, *Appl. Phys. Lett.* 76, 10 (2000).
136. S.-M. Yang, Z.-S. Wang, and C.-H. Huang, *Synth. Met.* 123, 267 (2001).
137. L. Guo, Z. Wu, X. Ai, Q. Li, H. Zhu, and S. Yang, *Opt. Mater.* 14, 247 (2000).
138. M. Chen, Y. Xie, H. Chen, Z. Qiao, and Y. Qian, *J. Coll. Interf. Sci.* 237, 47 (2001).
139. N. O. Dantas, R. S. Silva, and F. Qu, *Phys. Stat. Sol. (A)* 232, 177 (2002).
140. M. Gao, Y. Yang, B. Yang, J. Shen, and X. Ai, *J. Chem. Soc. Faraday Trans.* 91, 4121 (1995).
141. M. Guglielmi, A. Martucci, E. Menegazzo, G. C. Righini, S. Pelli, J. Fick, and G. Vitrant, *J. Sol-Gel Sci. Technol.* 8, 1017 (1997).
142. L. Guo, K. Ibrahim, F. Q. Liu, X. C. Ai, Q. S. Li, H. S. Zhu, and Y. H. Zou, *J. Lumin.* 82, 111 (1999).
143. V. S. Gurin, K. N. Kasparov, and E. A. Tyavlovskaya, *Coll. Surf. A* 139, 1 (1998).
144. E. Hao, B. Yang, S. Yu, M. Gao, and J. Shen, *Chem. Mater.* 9, 1598 (1997).
145. J. L. Machol, F. W. Wise, R. Patel, and D. B. Tanner, *Physica A* 207, 427 (1994).
146. A. Martucci, M. Guglielmi, and K. Urabe, *J. Sol-Gel Sci. Technol.* 11, 105 (1998).
147. K. K. Nanda and N. Sahu, *Adv. Mater.* 13, 280 (2001).
148. S. Ogawa, K. Hu, F.-R. F. Fan, and A. J. Bard, *J. Phys. Chem.* 101, 5707 (1997).
149. T. Okuno, A. A. Lipovskii, T. Ogawa, I. Amagai, and Y. Masumoto, *J. Lumin.* 87–89, 491 (2000).
150. N. N. Parvathy, G. M. Pajonk, and A. Venkateswara Rao, *J. Cryst. Growth* 179, 249 (1997).
151. F. Qu, R. S. Silva, and N. O. Dantas, *Phys. Stat. Sol. (A)* 232, 95 (2002).
152. C. Ricolleau, M. Gandais, T. Gacoin, and J. P. Boilot, *J. Cryst. Growth* 166, 769 (1996).
153. A. Sashchiuk, E. Lifshitz, R. Reisfeld, and T. Saraidarov, *Mater. Sci. Engin. C* 19, 67 (2002).
154. W. Wang, Y. Liu, C. Zheng, and G. Wang, *Mater. Res. Bul.* 36, 1977 (2001).
155. S. Yang, S. Wang, and K. K. Fung, *Pure Appl. Chem.* 72, 119 (2000).
156. L. Z. Yao, C. H. Ye, C. M. Mo, W. L. Cai, and L. D. Zhang, *J. Cryst. Growth* 216, 147 (2000).
157. J. Fick, J. Schell, A. Martucci, and M. Guglielmi, *SPIE Vol.* 3620, 198 (1999).
158. P. Di Benedetto, A. Martucci, and J. Fick, *SPIE Vol.* 4808 (2002).
159. A. Martucci, M. Guglielmi, J. Fick, and M. Post, *SPIE Vol.* 4804, 52 (2002).
160. R. Plass, S. Pelet, J. Krueger, and M. Grätzel, *J. Phys. Chem. B* 106, 7578 (2002).
161. T. Saraidarov, R. Reisfeld, A. Sashchiuk, and E. Lifshitz, *J. Sol-Gel Sci. Technol.* 26, 533 (2003).
162. B. Liu, H. Li, C. H. Chew, W. Que, Y. L. Lam, C. H. Kam, L. M. Gan, and G. Q. Xu, *Mater. Lett.* 51, 461 (2001).
163. K. K. Nanda, F. E. Kruis, H. Fissan, and M. Acet, *J. Appl. Phys.* 91, 2315 (2002).
164. R. Reisfeld, *J. Alloys Compounds* 341, 56 (2002).
165. Y. Savin, T. Pak, and A. Tolmachev, *Mol. Cryst. Liq. Cryst.* 361, 223 (2001).
166. H. Li, B. Liu, C. H. Kam, Y. L. Lam, W. X. Que, L. M. Gan, C. H. Chew, and X. G. Q., *SPIE Vol.* 3899, 376 (1999).
167. S. W. Lu, U. Sohling, M. Mennig, and H. Schmidt, *Nanotech.* 13, 669 (2002).
168. T. Trindade, P. O'Brian, and X.-M. Zhang, *J. Mater. Res.* 14, 4140 (1999).
169. Y. Sun, E. Hao, X. Zhang, B. Yang, M. Gao, and J. Shen, *Cem. Commun.* 2381 (1996).
170. S. Mochizuki, *J. Lumin.* 70, 60 (1996).
171. A. M. Malyarevich, V. G. Savitsky, I. A. Denisov, P. V. Prokoshin, K. V. Yumashev, E. Raaben, A. A. Zhilin, and A. A. Lipovskii, *Phys. Stat. Sol. (B)* 224, 253 (2001).
172. A. Henglein, *J. Phys. Chem.* 103, 9302 (1999).
173. E. P. A. M. Bakkers, J. J. Kelly, and D. Vanmaekelbergh, *J. Electroana. Chem.* 482, 48 (2000).
174. J. Fick, J. Schell, R. Lévy, A. Martucci, and M. Guglielmi, *Pure Appl. Opt.* 6, 527 (1997).
175. K. K. Nanda and S. N. Sahu, *Appl. Phys. Lett.* 79, 2743 (2001).
176. S. V. Kershaw, M. Harrison, A. L. Rogach, and A. Kornowski, *IEEE J. Selected Topics in Quantum Electron.* 6, 534 (2000).
177. J. Butty, N. Peyghambarian, Y. Kao, and J. D. Mackenzie, *Appl. Phys. Lett.* 69, 3224 (1996).
178. Y. A. Vlasov, K. Luterova, I. Pelant, B. Hönerlage, and V. N. Astratov, *Thin Solid Films* 318, 93 (1998).
179. A. A. Mikhailovsky, A. V. Malko, J. A. Hollingsworth, M. G. Bawendi, and V. I. Klimov, *Appl. Phys. Lett.* 80, 2380 (2002).
180. V. I. Klimov, A. A. Mikhailovsky, S. Xu, A. Malko, J. A. Hollingsworth, C. A. Leatherdale, H. J. Eisler, and M. G. Bawendi, *Science* 290, 314 (2000).
181. C. Y. Yang and S. Rabii, *J. Chem. Phys.* 69, 2497 (1978).
182. Y. Jiang, Y. Wu, B. Xie, S. Yuan, X. Liu, and Y. Qian, *J. Cryst. Growth* 231, 248 (2001).
183. M. Chen, Y. Xie, Z. Yao, Y. Qian, and G. Zhou, *Mater. Res. Bul.* 37, 247 (2002).
184. M. Chen, Y. Xie, Z. Y. Yao, X. M. Liu, and Y. Qian, *Mater. Chem. and Phys.* 74, 109 (2002).
185. S. Chen, W. Liu, and L. Yu, *Wear* 218, 153 (1998).
186. T. K. Kundu, M. Mukherjee, D. Chakravorty, and L. E. Cross, *J. Appl. Phys.* 83, 4380 (1998).
187. Z. Qiao, M. Chen, J. Xu, and Y. Qian, *Chem. Phys. Lett.* 321, 504 (2000).
188. M. Mukherjee, A. Datta, and D. Chakravorty, *Appl. Phys. Lett.* 64, 1159 (1994).
189. M. Mukherjee, A. Datta, S. K. Pradhan, and D. Chakravorty, *J. Mater. Sci. Lett.* 15, 645 (1996).
190. R. Reiche, R. Thielsch, S. Oswald, and K. Wetzig, *J. Elec. Spectros.* 104, 161 (1999).

# Light-Harvesting Nanostructures

Teodor Silviu Balaban

Forschungszentrum Karlsruhe, Institute for Nanotechnology, Karlsruhe, Germany;  
and University of Karlsruhe, Karlsruhe, Germany

## CONTENTS

1. Introduction
  2. Mechanistic Aspects of Energy Transfer
  3. Light-Harvesting in Natural Photosynthesis
  4. Artificial Light-Harvesting Nanostructures
  5. Conclusions: Artificial Photosynthesis—Perspectives and Future Goals
- Glossary  
References

## 1. INTRODUCTION

Higher life on Earth depends on photosynthesis. The ability to convert sunlight into biochemical energy has helped proliferate not only photosynthetic organisms but also those with heterotrophic metabolisms which thus indirectly depend upon efficient light-harvesting, the first step of a very complex orchestration of photophysical, biochemical, and biological processes. Recent breakthroughs in structural biology have permitted insight into the architecture, at molecular level, of the apparatus involved. Functionality is in all cases obtained by engineering into supramolecular assemblies different molecular components with tailored properties. The result is not just the summation of the parts' properties, but fully new ensemble characteristics emerge which are essential for its function. Because the dimensions of these discrete functional units are well within the 2 to 100 nm range the term *nanostructure*<sup>1</sup> seems appropriate. Nature has learned through evolution that it is easier to fabricate copies of such discrete functional nanostructures than to synthesize directly larger microstructures. This results in a considerable information and atom economy both at the

<sup>1</sup> To our knowledge, the first to use the term *nanostructure* was the French paleontologist A. M. Mangin in 1975 who described *nanostructures* of silicified limestones in *C. R. Hebd. Acad. Sc. Ser. D*, 281, 973 and 1079. Presently "nanostruct" appears either as title or keyword in more than 6000 publications each year.

genetic as well as at the molecular level. In this chapter we shall focus on nanostructures which perform the function of light-harvesting. At first we will describe the natural light-harvesting systems, or photosynthetic antennae; then we will review efforts in mimicking this process with fully synthetic molecules. Finally some implications useful for designing efficient artificial photosynthetic systems will be addressed.

One of the first membrane proteins to be crystallized was the bacterial photosynthetic reaction center of the bacterium *Rhodospseudomonas viridis* and its structural elucidation by means of X-ray crystallography in 1985 [1] was a feat which only three years later was honored by awarding the Chemistry Nobel Prize to R. Huber, H. Michel, and J. Deisenhofer. The high resolution structure (initially at 3 Å resolution) has allowed unprecedented insight into the architecture of this molecular machinery which after excitation by light leads to charge separation and after a cascade of electron transfer steps charge recombination is prohibited. The so-formed exciton reaches a final state where the electron and the hole (positive charge) are on opposite sides of the photosynthetic membrane. The thus created potential energy is used to pump protons across the membrane. The protons in turn serve for driving the adenosine triphosphate (ATP) synthase. This rotary nanomachine (for whose study P. D. Boyer and J. E. Walker shared the 1997 Chemistry Nobel Prize) converts adenosine diphosphate to ATP which, having an energy rich phosphate bond, is used by all living cells as energy currency and thus to drive uphill biochemical endergonic reactions. Solving crystal structures of reaction centers from other bacteria (*Rhodobacter sphaeroides*) at improved resolutions, such as 2.65 Å [2], or of light and dark adapted reactions centers [3] has led to further understanding of the rather intricate phenomenological events which occur post-light-harvesting. Studies of bacterial mutants, where by targeted point mutations amino acid residues in the protein matrix have been interchanged, have revealed the role of the proteinaceous scaffold in accelerating or retarding the electron transfer rates between the various cofactors. Ample excellent reviews and books [4, 5] have been dedicated to bacterial reaction centers. This research effort, which has included structural biologists, biochemists,

and especially photophysicists, has triggered, for more than a decade, synthetic efforts by chemists to assemble manmade (nano)devices mimicking the elementary processes in reaction centers. This field has also been amply reviewed [6–9]. This chapter describes the energy transfer events related to light-harvesting which precede the electron transfer cascades in the reaction centers.

One interesting evolutionary observation is that different photosynthetic organisms have developed widely different light-harvesting systems. These match the illumination conditions of the habitat so it is not surprising that bacteria which live at 10 m under the water surface have different antennae and other pigments which collect light at other wavelengths than the bacteria or algae living at water surface, which in turn have different light-harvesting complexes than the plants. Thus, there are many ways in which capture of light has been optimized under the pressure of evolution. However, this is in stark contrast with the photosynthetic reaction centers which all have the same genetic ancestor. Only recently, by solving the crystal structures of photosystem II (PSII) at 3.8 Å resolution [10] and that of photosystem I (PSI) and 2.5 Å resolution [11], a remarkable feat of the Berlin research groups around Horst-Tobias Witt and Wolfram Saenger, was it possible to show the great similarity of these reaction centers to the bacterial reaction center. Apparently, once archaeobacteria have learned how to effect photoinduced charge separation and to convert this into useful energy by avoiding the charge recombination, this was carefully conserved during evolution. In other words, photosynthetic species with a different mechanistic cascade have not survived and are presently not known.

Figure 1 represents schematically the essence of a photosynthetic apparatus, either natural or artificial. A light-harvesting nanostructure, or antenna, is coupled to the reaction center by means of an energetic trap. Within the antenna rapid energy transfer steps occur which eventually funnel the energy within the trap. From the trap the reaction center is excited and here successive electron transfer reactions take place. Of course, one can trigger the electron transfer cascade by exciting directly the primary

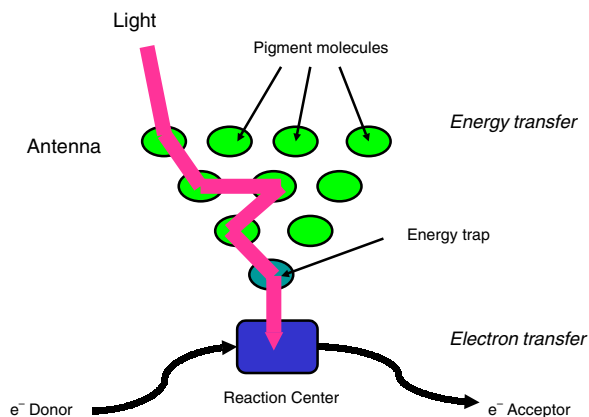


**Figure 1.** Photosynthetic antenna and reaction center. Adapted with permission from [12], R. E. Blankenship, in “Research Opportunities in Photochemical Sciences” (A. D. Nozik, Ed.), NREL/CP-450-21097, DE96007867, 1996.

electron donor, an excitonically coupled pair of (bacterio)chlorophylls, the so-called “special pair.” The presence of the antenna is, however, beneficial for three reasons: (i) a much larger cross section is achieved so that the probability of capturing a photon is greatly increased, (ii) a broader range of wavelengths can be used so that not only the rather narrow absorption of special pairs from the solar spectrum is filtered out, and (iii) the reaction center can be cycled much more rapidly, in some species even about 8000 times per second.

An analogy of the rapid cycling of the reaction centers coupled to antennas is the following: When a photographer uses a flash to capture the image of a fashion model, the strong photoexcitation causes the model to close the eyes. Several seconds may pass before (s)he can reopen the eyes and be composed for the next flash and picture. This is why photoshooting sessions are usually done in daylight, sometimes at dusk or dawn, and many pictures are taken successively, with modern cameras, several times per second. This improves the yield in obtaining usable pictures and shortens the duration of sometimes costly photosessions. Similarly, by using an antenna, diffuse and even dim light may be used by reaction centers which are closed only for a few tens of nanoseconds which is sufficient for the electron transfer to be completed successfully.

## 2. MECHANISTIC ASPECTS OF ENERGY TRANSFER

Two different mechanisms exist for excitation energy transfer (EET), one which operates between weakly coupled molecules, the so-called dipolar mechanism as initially proposed by Förster [13, 14], and one which occurs between closely spaced molecules which interact strongly due to orbital overlap and here an electron exchange mechanism may function, as proposed by Dexter [15].

In both cases a donor molecule  $D^*$  in its singlet excited state transfers its energy to an acceptor molecule  $A$ , initially in its ground state.

In Figure 2 the Förster mechanism is represented in the upper part. While the electron from the donor lowest unoccupied molecular orbital (LUMO) flips to the highest occupied molecular orbital (HOMO), at the same time an electron from the acceptor is promoted into the excited state. Note that this is not an optical phenomenon (i.e., the photon which is emitted by the donor upon returning to the ground state is not the same photon as the one absorbed by the acceptor). In the Dexter mechanism the orbitals of the donor and acceptor have to overlap to allow an electron exchange as indicated by the arrows (lower part of Fig. 2). The rate of the Förster energy transfer  $k_{\text{EET}}$  is given by the equation

$$k_{\text{EET}} = \frac{9\kappa^2(\ln 10)c^4}{128\pi^5 n^4 N \tau_R^D R_{DA}^6} \int_0^\infty f_D(\nu) \epsilon_A(\nu) \frac{d\nu}{\nu^4}$$

where  $\kappa^2$  is an orientation factor due to the scalar product between the transition dipole moments of the donor ( $\mu_D$ ), respectively acceptor ( $\mu_A$ ), and the distance vector  $R_{DA}$ :

$$\kappa^2 = [\vec{\mu}_D \cdot \vec{\mu}_A - 3(\vec{\mu}_D \cdot \vec{R}_{DA})(\vec{\mu}_A \cdot \vec{R}_{DA})]$$

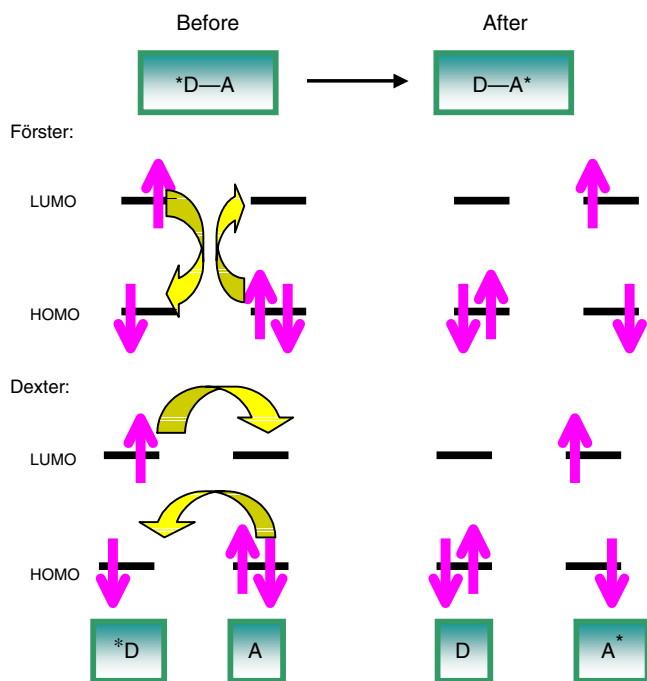


**Figure 2.** Schematic representation of the two possible energy transfer mechanisms from an excited singlet state donor ( $D^*$ ) to an acceptor molecule (A).

After the standard definition of the unit vectors, if  $\alpha$  is the angle between the transition moments of the donor and acceptor,  $\beta_1$  is the angle between  $\mu_D$  and the distance vector  $R_{DA}$  connecting the donor and the acceptor and  $\beta_2$  is the angle between  $\mu_A$  and  $R_{DA}$  one may write

$$\kappa^2 = \cos \alpha - 3 \cos \beta_1 \cos \beta_2$$

It is clear that  $\kappa^2$  may vary between 0 and 4 accounting for accelerating or slowing down the excitation energy transfer for certain orientations.

An other important factor in determining  $k_{\text{EET}}$  is the integral which describes the spectral overlap between the fluorescence of the donor  $f_D(\nu)$  and the absorbance of the acceptor,  $\varepsilon_A(\nu)$ , being the molar decadic extinction coefficient. Other constants are the speed of light  $c$  (in  $\text{m s}^{-1}$ ), the refraction index of the medium  $n$ , and the number of molecules per millimole  $N$  (Avogadro's number  $\times 10^{-3}$ ). Furthermore,  $\tau_R^D$  is the radiative fluorescence lifetime (measured in s) of the donor which also depends on the fluorescence quantum yield  $\tau_R^D = \tau^D/\Phi_D$ , where  $\tau^D$  is the lifetime of the first excited singlet state of the donor in the absence of any energy and/or electron transfer processes.

A more convenient way of rewriting this Förster equation is to compress the constants and the overlap between the donor fluorescence with intensity normalized to unity, and the acceptor absorbance into the so-called Förster radius  $R_0$ . If the integration is done in the wavenumber scale ( $\text{cm}^{-1}$ ) then the following expression is obtained [22]:

$$R_0^6 = \frac{8.785 \times 10^{17}}{n^4} \int f_D(\nu) \varepsilon_A(\nu) \frac{d\nu}{\nu^4} \quad (\text{in nm}^6 \text{ units})$$

Accordingly, the Förster equation becomes

$$k_{\text{EET}} = \frac{\kappa^2}{\tau_R^D} \left( \frac{R_0}{R_{DA}} \right)^6$$

Distances between donor and acceptor of over 5 nm may be encountered where this mechanism still operates. Typical rates encountered in nanostructures are of the order  $10^{10}$  to  $\sim 10^{12} \text{ s}^{-1}$  which translate in hopping times of ps to a few hundred fs between adjacent pigments.

The Dexter mechanism which can only function at close range is similar to an electron transfer which allows a mutual exchange of the electrons. For an efficient transfer the requirement is that the excited state of the donor  $D^*$  exceeds energetically that of the acceptor A. In the usual electron transfer beside the energy of the excited state also the redox potentials of the donor and acceptor dictate the rate of the process. In contrast to the Förster mechanism, not only does energy transfer between the singlet states of the chromophores occur but also triplet-triplet exchanges may take place. Using the classical formalism adopted for nonadiabatic electron transfer [16–19] one may calculate  $k_{\text{EET}}$  by the equations

$$k_{\text{EET}} = \nu_{\text{EET}} e^{-\frac{\Delta G^\ddagger}{RT}}$$

$$\nu_{\text{EET}} = \frac{2H^2}{h} \sqrt{\frac{\pi^3}{\lambda RT}}$$

$$\Delta G^\ddagger = \frac{\lambda}{4} \left( 1 + \frac{\Delta G^0}{\lambda} \right)^2$$

where  $H$  is the intercomponent electronic interaction (or matrix element describing the electronic coupling),  $\Delta G^0$  is the Gibbs free energy change of the process, and  $\lambda$  is the reorganizational energy. In the case of an energy transfer process  $\lambda$  is mainly due to the reorientation of bond angles and adjustment of bond lengths upon excitation from the ground to the excited state. The original formulas due to Dexter [15] are usually written as

$$k_{\text{EET}} = \frac{4\pi^2 H^2}{h} e^{-\beta_{\text{EET}}(R_{DA}-R_C)} J_D$$

where  $J_D$  is the following overlap integral:

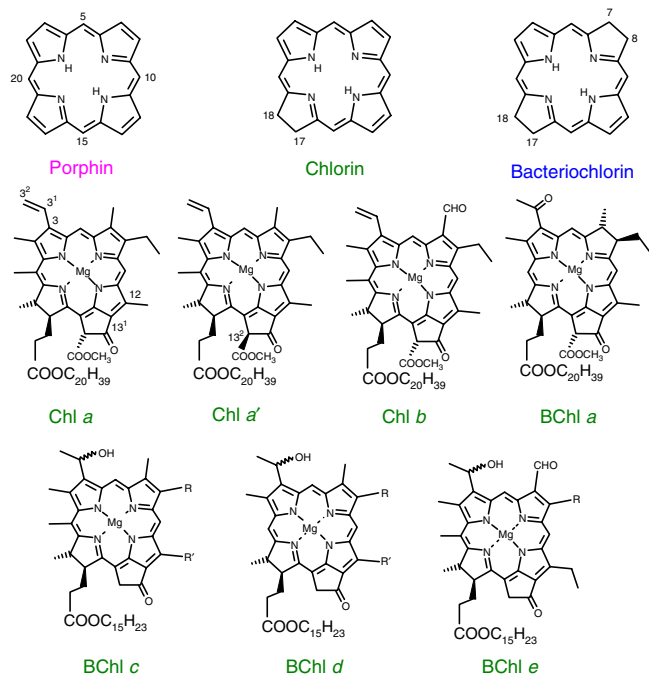
$$J_D = \frac{\int f_D(\nu) \varepsilon_A(\nu) d\nu}{\int f_D(\nu) d\nu \int \varepsilon_A(\nu) d\nu}$$

As in electron transfer phenomena  $\beta_{\text{EET}}$ , is an attenuation factor (also termed damping factor, i.e., a constant) which depends on the nature of the bridge connecting the donor D and acceptor A separated by  $R_{DA}$  and which have a contact distance  $R_C$ .

An important aspect is that both mechanisms may sometimes operate in one and the same particular case.

### 3. LIGHT-HARVESTING IN NATURAL PHOTOSYNTHESIS

In order to absorb daylight, molecules need to have an extended conjugated  $\pi$ -system, the so-called chromophore or color bearing group. An increase of the conjugation leads to a narrowing of the HOMO–LUMO gap and electronic transitions are allowed at increasing wavelengths. With different pigments, the solar spectrum filtered by the atmosphere can be spanned. Scheme 1 summarizes the chemical formulae of some chromophores encountered in natural light-harvesting nanostructures. Two main classes of pigments have evolved, namely carotenoids (Car) which are rather rigid, rodlike, conjugated polyenic molecules with absorption in the ultraviolet (UV) and high energy side of the visible spectrum, and tetrapyrrolic chromophores which have two strong absorptions at both ends of the visible spectrum. Among the tetrapyrroles one distinguishes the chlorophylls (Chl) of plants and bacteriochlorophylls (BChl) from photosynthetic bacteria, both which are cyclic tetrapyrroles. The parent, fully unsaturated system is the  $22\pi$  electron system of porphyrins (Por). According to Hückel's  $4n + 2$  rule, this system, with  $n = 5$ , has aromatic character and thus high stability, and diatropic ring current. Due to their high thermal stability porphyrins are frequently encountered in oil (petro- and geoporphyris) and serve as a geological clock for tracing the transformations within sediments. While heme, the blood pigment in vertebrates, is a typical porphyrin, porphyrins are less used in photosynthesis. This is because of the high symmetry of the conjugated  $\pi$ -system. The redshifted transitions (so-called Q bands) are of low extinction coefficient and thus inefficient for light harvesting. The degeneracy of these transitions is lifted



**Scheme 1.** Main cyclic tetrapyrrolic chromophores with their atom numbering. Note that Chl *a* and Chl *a'* are epimers differing only by the configuration at carbon  $13^2$ .

by reducing one or two of the conjugated double bonds. A  $20 \pi$ -electron system thus forms chlorins while an  $18 \pi$ -electron system forms bacteriochlorins. In both these systems, the Q bands are due to electronic transitions which are now strongly allowed and thus have at least an order of magnitude higher extinction coefficients than porphyrins and are thus perfectly suited for light harvesting. Heme and chlorophylls are also known as the *pigments of life*, the first being used in respiration which represents the reversed energetic process of photosynthesis, the latter being based mainly on chlorophylls. Confusion sometimes arises due to the nonsystematic nomenclature of these tetrapyrroles. Thus, while all chlorophylls are chlorins having a fused five-membered ring, there are bacteriochlorophylls which are also chlorins and not bacteriochlorins (see Scheme 1). Open chain tetrapyrroles or bilins such as phycocyanobilin from cyanobacteria and biliverdin are cousins of porphyrins and chlorophylls which share their metabolic pathway up to a point and/or are degradation products. Photosynthetic organisms have evolved differently by fine-tuning the main absorption characteristics, namely wavelength range and extinction coefficient of their antenna systems. This has led to a wide variety of light-harvesting nanostructures.

#### 3.1. Structural Features of Natural Antenna Systems

Our present understanding of natural photosynthesis is based upon the notion of the photosynthetic unit (PU) introduced in 1936 by Emerson and Arnold [20]. By experimenting with light flashes they could convincingly show that for one  $\text{CO}_2$  molecule, which plants reduce to " $\text{CH}_2\text{O}$ " or " $\text{C}\cdot\text{H}_2\text{O}$ ", the empirical formula of carbohydrates, several hundreds of Chl molecules must be involved. Thus only relatively few Chls actively take part in transforming light energy into chemical energy. These special chlorophylls which are involved in electron transfer were assigned to the reaction center (RC), another fundamental notion introduced by Hans Gaffron [21]. Most of the other chlorophylls in the photosynthetic unit have more a spectator role: each one of them can be hit by a photon whereby the excitation energy is rapidly and efficiently transferred toward the RC. Due to the large number of these antenna Chls, the probability or cross section for harvesting photons is greatly increased. Energetically the process runs "downhill" and has often been compared to a funnel. The most redshifted antenna pigments trap eventually the whole energy and from there it is transferred to the RC which absorbs light at still longer wavelengths (are further redshifted). This directionality of energy transfer ensures the high quantum yield due to the fact that back energy transfer is inhibited. Figure 3 presents schematically these events. An excellent review by van Grondelle et al. on energy trapping in antenna systems discusses in detail these processes bringing not only photophysical evidence but also the mathematical interpretation of the data [22]. More recent studies on the major light-harvesting complex of plants are summarized in [23].



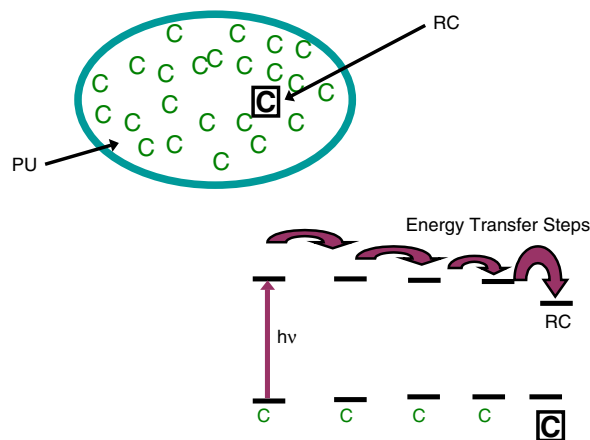


**Figure 3.** Schematic representation of a photosynthetic unit (PU) and the energy transfer steps toward the reaction center. Adapted with permission from [21], L. Stryer, “Biochemistry,” 3rd ed., p. 520. Freeman, New York, 1988. © 1988, Freeman.

### 3.1.1. Self-Assembling Light-Harvesting Nanostructures of Green Photosynthetic Bacteria

Early during evolution, when synthetic and genetic economy was stringent for photosynthetic organisms, in order that these could build large and efficient antenna systems, which could harvest sunlight even under water as deep as 100 m, self-assembly of chromophores was used. This very simple architectural principle, which is frequently encountered in nature, for instance in viruses, is based on the fact that it is much easier to fabricate several copies of the same building block (or tecton, i.e., molecular brick) and then induce self-assembly to a desired nanostructure than to build on the basis of a complicated blueprint large functional components for which a multitude of genes and molecules are needed. The self-assembly algorithm, once it is allowed to proceed correctly, ensures that due to a fine balance between entropy and enthalpy, in the end, only the desired structure is obtained. The final architecture is encoded within the structure of the tectons and the supramolecular interactions for which they have been programmed [24]. Figure 4 illustrates such a self-assembly process where from monomers, under appropriate conditions, one can form dimers, oligomers, and finally large nanostructures.

Misplaced components, for instance the tecton in the upper left which kinetically might be stable, are allowed to disassemble so that actually a repair mechanism operates. It is essential that the final nanostructure serves a function which the components alone could not have fulfilled. In our case the desired function is efficient light harvesting. This can be ensured by amplifying the cross section for capturing photons by a relatively large number of chromophoric tectons but which all must transfer their excitation energy to collectors (i.e. energetic traps) within the photosynthetic units.

Green photosynthetic bacteria (*Chlorobiineae*) have evolved for this purpose an unique organelle—the chlorosome, or green sac. Both the *Chlorobiaceae* (such as *Chlorobium tepidum*) and the *Chloroflexaceae* (e.g., *Chloroflexus*

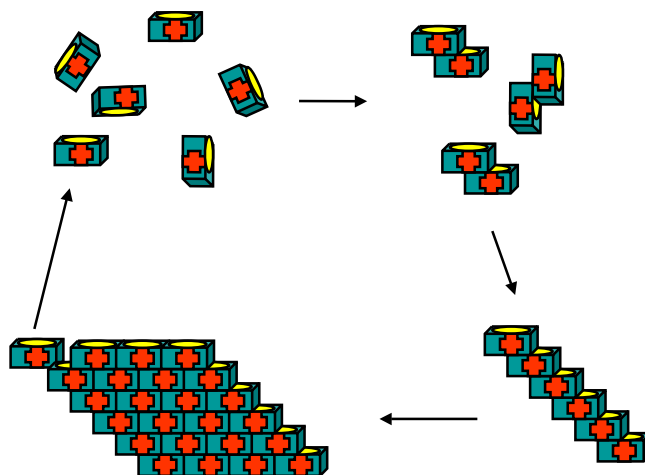


**Figure 4.** Illustration of a typical self-assembly process.

*aurantiacus*) which are, however, phylogenetically quite distant, have well-developed chlorosomes. Chlorosomes are typically oblong ellipsoids resembling a flattened nanocigar with dimensions of approximately  $10 \times 25 \times 100$  nm which is attached via a baseplate to the inner side of the cytoplasmic membrane. The sizes and number of chlorosomes are dependent not only on the species but also on illumination conditions showing that light harvesting is strongly genetically regulated. Early electron microscopy images employing freeze-fractured membranes have shown that within the interior of the chlorosome, long cylindrical rods are encountered and these are separated from the cytosol by a monolayer lipid membrane [25, 26]. Figure 5 presents an artist’s view of this intriguing organelle which has been the object of intense study and debate. It is now generally accepted that the chlorosomal rods are constituted of self-assembled bacteriochlorophyll molecules [27, 28], and that proteins do not have a structural role in the organization of the chromophores.

Very recently, by sequencing the entire genome of the photosynthetic bacterium *Chlorobium tepidum* [30], genetic evidence has been brought forth that the 10 chlorosomal proteins (CsmA, CsmB, . . . CsmH, CsmI, CsmJ, and CsmX) are embedded in the membrane and that various mutants where the genes of these proteins have been knocked out are still forming fully functional chlorosomes [31, 32]. This has shattered the dogma that only proteins can function as scaffolds for light-harvesting pigments. For an excellent biochemical review see [33].

Another interesting aspect of the chlorosome, studied in depth by Frigaard et al., is related to the redox active components and the role of quinones which act as quenchers for the fluorescence of BChl *c* aggregates if exogenously added [34–37]. Also studied was the role of oxygen which triggers in *Chlorobium tepidum* an uncoupling of the chlorosome antenna under aerobic conditions in order to prevent degradation by formation of toxic singlet oxygen species and radicals [38]. In contrast to this, chlorosomes of *Chloroflexus aurantiacus* were not affected by oxygen.

We have been involved relatively early in investigating the structural details of how BChl molecules self-assemble.

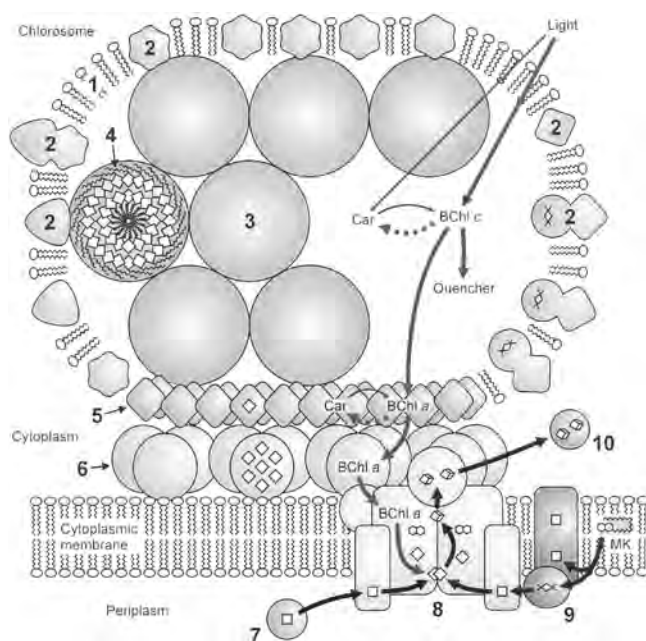


**Figure 5.** The chlorosome organelle. Graphic courtesy of Nils-Ulrik Frigaard (Pennsylvania State University). Arrows denoting the energy transfer are gray and pointing downward while arrows denoting the electron transfer pathway are black and pointing mostly upward. **1** Monolayer lipid membrane. **2** Chlorosomal proteins which are part of the chlorosome envelope [29]. **3** Chlorosomal rod element containing self-assembled BChl *c*. **4** Detail of how BChl *c* self-assembles into circular aggregates—note that the long chain alcohol chains esterifying the 17-propionic acid residue are all pointing either to the exterior of the rod ensuring hydrophobic inter-rod interactions and with the monolayer lipids, or all toward the inside [49]. **5** Chlorosomal baseplate. **6** Fenna–Matthews–Olson protein trimers which act as an energy trap. **7** Cytochrome *c*. **8** Reaction center—note that the energy transfer cascade ends at the special pair of chlorophylls where charge separation occurs and the electron reaches the iron sulfur centers which are shown as cubes. **9** Rieske’s protein involved in electron transfer from the menaquinone (MK). **10** Ferredoxin.

Various spectroscopic techniques such as resonance Raman [39, 40], UV-visible absorption [41], Fourier transform infrared (FT-IR) [42], circular dichroism (CD) [43] and solid state nuclear magnetic resonance (NMR) with  $^{13}\text{C}$ -labelled [44, 45] BChls have ascertained the primary binding scheme indicated in Figure 6 and that the BChls are assembled into stacks.

On the basis of our experimental evidence, a crude model of the chlorosomal rods was proposed as early as 1994 by Holzwarth and Schaffner employing a heuristic molecular modeling approach [46]. For the first time this model explained satisfactorily most of the accumulated structural evidence and described how the cylindrical rods are formed by self-assembled BChls. Thus, stacks of BChl molecules formed by the relatively strong ligation of the central magnesium atom by hydroxy groups of the 3-(1-hydroxyethyl) group which can have either *R* or *S* chirality are joined together by multiple cooperative hydrogen bonds having the same hydroxyl group as donor and the  $^{13}\text{C}$ -carbonyl groups as acceptors. Cooperative interactions imply that for instance a hydrogen bond operating

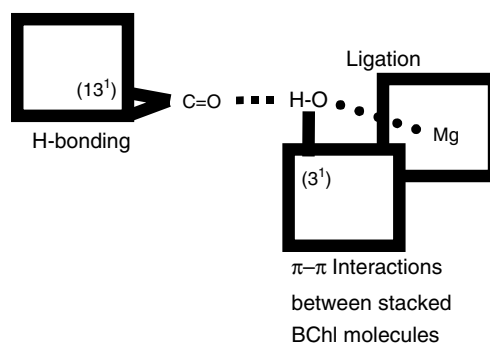


**Figure 6.** Schematic supramolecular interactions between bacteriochlorophyll molecules in a nonpolar environment. Essentially, the magnesium atom of one BChl is ligated by a hydroxy group in a second BChl and due to its strong polarization the same hydroxy group acts as donor in a hydrogen bond to an acceptor carbonyl group in a third BChl. Between the off-setted, helical stacks of BChl molecules,  $\pi$ - $\pi$  interactions are encountered.

simultaneously with metal ligation is stronger than if these occurred independently or that multiple hydrogen bonds (e.g.,  $n$ ) reinforce each other and are stronger than  $n$  times one hydrogen bond between similar groups. This cooperative bonding was evident from sigmoidal curves describing the kinetics of the self-assembly process [47] which shows a pronounced dependency on the concentration, temperature, and medium polarity. These hydrogen bonds stitch together adjacent stacks leading to a curvature with a helical arrangement of the BChl molecules. This helicity is independent of the *R/S* configuration of the 3-(1-hydroxyethyl) group [43] and shows a counterclockwise arrangement of the transition dipole moments of the chromophores (i.e., negative chirality according to the exciton chirality theory) [48]. Figure 6 presents a view perpendicular to the stacks in such a crude model employing BChl *d*. Due to the curvature angle given by the hydrogen bonding between the stacks, 18 or more stacks may form a tubular structure. Convincingly, the diameter of the modeled helical tubes corresponded well with those observed for the chlorosomal rods in different bacterial species. Thus the increase in diameter from ca. 5 nm in *Chloroflexus* rods to over 6 nm in *Chlorobium* rods could be explained on the basis of different peripheral substituent sizes.

Remarkable is the fact that this cylindrical arrangement of chromophores was proposed before the first X-ray crystallographic structure of the LH2 system of purple photosynthetic bacteria was solved (see Section 3.1.2) heralding the importance of a closed ring structure in the delocalization of excitons and ensuring rapid energy transfer. Other models have been proposed which differ mainly in the parallel versus antiparallel orientation of the BChl molecules and these have been reviewed [27, 28]. More recently, van Rossum et al. have proposed a refined model, where in the interior of the cylinder in Figure 7, a second more curved aggregate of BChls is positioned [49]. This newer model was based on multidimensional solid state NMR studies conducted both on isolated chlorosomes and on purified BChl *c* uniformly labelled with  $^{13}\text{C}$  which was induced to self-assemble [44, 50].

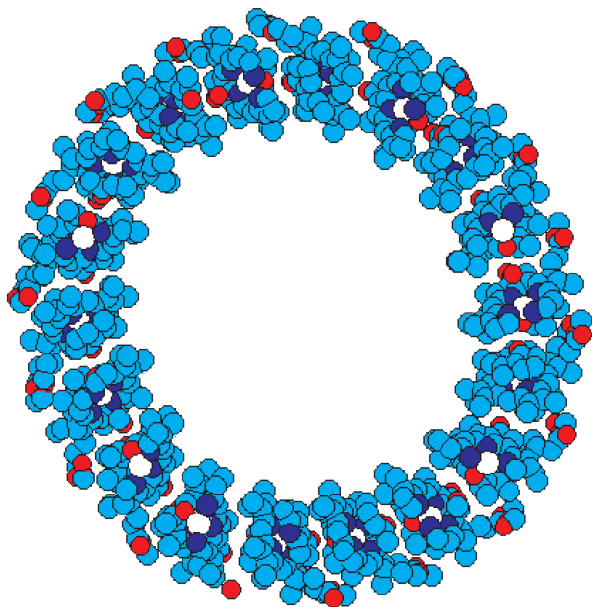


**Figure 7.** Holzwarth–Schaffner initial model for chlorosomal self-assembled BChl *d* with the long chain alcohol esterifying the 17-propionyl ester residue shortened to a methyl group. Carbon atoms are represented as cyan, nitrogens as blue, oxygen as red, and magnesiums as white spheres. 18 Stacks are viewed from above the helical cylinder.

Credit is here due to the pioneering works of several chemists who have brought forth evidence for the self-assembly of (B)Chls in spite of rebuke from their more biological oriented colleagues. Thus Krasnovskii and co-workers were the first to observe that BChl *c* self-assembles *in vitro* [51, 52], while Smith et al., in a seminal paper, have shown that the redshifted absorption spectra of the natural system can be fully reproduced with self-assembled BChls [53]. Worcester and co-workers, using small angle neutron scattering, have subsequently shown that hydrated Chl *a* forms micellelike assemblies [54, 55]. Olson and co-workers have performed several early spectroscopic studies on BChl *c* in nonpolar solvents [56–60] or aqueous solutions [61, 62] and have discovered the so-called “hexanol effect” [63]. This curious effect deserves a brief description. It consists initially of disruption of the self-assembled BChls within the chlorosomes which is associated with a blueshift and sharpening of the absorption maximum. This is common also in smaller alcohols, amines, or pyridine which all compete for the ligation of the magnesium atoms and disrupt any hydrogen bonding. This transformation is usually irreversible, but in the case of hexanol, when water is used to partially remove it, a reassembly of BChls occurs with almost entire recovery of the redshifted absorption spectrum and CD signals [64]. The excitation energy transfer to the BChl *a* protein complex which acts as an energetic trap (see Fig. 5 and discussion) within the baseplate is perturbed [65] and also the transmission electron microscopy images show that swelling is the main morphological change [66] of such hexanol and then water treated chlorosomes. Both in nonpolar solvents as in aqueous medium, the self-assembled BChls have rather close contacts which lead to strong excitonic interactions with

broad and redshifted absorption maxima and intense CD signals. These assemblies have, however, different molecular structures. In an aqueous medium, the hydrophobic interactions between the long alcohol tails force the relatively large macrocycles into close  $\pi$ – $\pi$  interactions. Additionally, due to the aqua–magnesium complexes which being polar are well solvated, this ensures a micellelike segregation similar to the one encountered in surfactants. Hexanol apparently has the right hydrophilic/hydrophobic ratio to allow the transformation from one nanostructure into the other one.

Another interesting effect associated with the BChl *c*, *d*, and *e* nanostructures as well as with chlorosomal preparations is the variability of CD signals. It is now again accepted that this is mainly due to size variations and the related contributions of Rayleigh light scattering and the linear dichroism to the CD signal. In DNA-based nanostructures this effect has been studied and termed “giant CD” or “polymer and salt induced CD” [67–69]. Thus if the size of the nanostructures is larger than about a tenth of the wavelength at which a Cotton effect is observed, then enhancements and distortions of the signal are possible. With supramolecular associations of chromophores which absorb light at, for example, 500 nm, if these nanostructures are larger than about 50 nm, due to this effect, the stereochemical interpretations must be done with caution.

A lot of effort has been invested in characterizing the energy transfer processes in chlorosomes and BChl assemblies and these have been sufficiently reviewed. Ultrafast spectroscopies [70, 71] have shown that the energy transfer rates within the chlorosomal rods are very similar to those of the BChl self-assemblies. Both exhibit a very fast component of about 10 fs stemming from the initial coherent oscillations, and similar kinetics in their isotropic and anisotropic absorption difference spectra together with a 1–2 ps component which does not represent single step energy transfer between neighboring BChl *c* pigments but long range energy transfers which span many pigments within one rod. A second relatively fast component may represent inter-rod transfer which is in the range of 7–10 ps. Slight differences exist between the chlorosomes of *Chlorobium* and *Chloroflexus*, due to the different BChl *c* substitution patterns, as well as between the isolated BChl *c* aggregates, which reflect small differences in the transition moment organization and a somewhat more disordered structure in the aggregates. The component which is completely absent in the self-assembled BChl *c* aggregates and is important in the intact chlorosomes is the energy transfer from the BChl *c* rods to the BChl *a* protein complex (also known as the Fenna–Matthews–Olson or FMO complex) in the 30–40 ps range. In other species containing also BChl *d* and *e* this energy trapping by the more red shifted BChl *a* FMO complex (which absorbs light at about 800 nm) spans a 30–160 ps range [72, 73]. Thus the energy funnelling principle illustrated in Figure 1 is realized by efficient light capture by the self-assembled BChl rods (with a relatively broad absorption at 730–760 nm), very rapid energy transfer steps by incoherent excitation hopping, and final trapping within the BChl *a* protein complex. From there the special pair in the reaction center is photoexcited for triggering the electron transfer cascade. If the energy trap is absent, as in the case of self-assembled BChl aggregates, trapping occurs by diffusing the excitation to

randomly positioned redox active defect sites which act as quenchers. This was proved by adding sodium dithionite as reducing agent which greatly increases the BChl *c* fluorescence yield [74]. If, however, a covalently linked semisynthetic BChl *a* trap is included in the BChl *c* aggregate, efficient trapping occurs as demonstrated by Tamiaki et al. in the first supramolecular artificial light-harvesting device to be assembled [75]. Incorporation of BChl *a* into vesicles or liposomes containing BChl *c* aggregates [76, 77] is also effective. Very recently fluorescence from single chlorosomes as well as atomic force microscopy images were recorded by Tamiaki and his colleagues [78].

### 3.1.2. Pigment–Protein Complexes

A different organizational principle of chromophores is encountered in the pigment–protein complexes. These function either as light-harvesting systems, intermediate energy traps, or reaction centers. Here the carefully engineered protein matrix ensures the exact orientation of the pigments which allows a fine tuning of the direction of transition dipole moments and thus of the energy transfer rates and efficiencies according to the Förster mechanism (Section 2). In the reaction centers the electron transfer rates are also finely tuned by the protein. Furthermore, by positioning close to the chromophores special amino acids either as charged residues (Arg, Glu, etc.), hydrogen bonding (Ser, Tyr, etc.), or aromatic ones (Trp, Phe, Tyr, etc.) capable of  $\pi$ -stacking, the absorption properties can be influenced quite dramatically. Evolution, of course, has optimized these complex nanostructured machineries. Histidines are by far the preferred ligand for magnesium atoms of (B)Chls while carotenoids are usually bound only by weak hydrophobic interactions without a specific ligand. Several examples of such pigment–protein complexes will be briefly discussed.

**PSI Antenna of *Synechococcus elongatus*** In plants two photosystems I and II (PSI and PSII) are present and act in conjunction. Their individual isolation and purification are difficult from the plant thylakoid membranes. However, in the much simpler photosynthetic bacteria, either PSI or PSII can be expressed and these have very high sequence homology to the photosystems encountered in different plants. Berlin researchers have achieved the crystallization and structural elucidation of both PSI [5] and of PSII from *Synechococcus elongatus*, a thermophilic cyanobacterium [4]. While PSI is trimeric, resembling a clover leaf, PSII is a homodimer. Figure 8 describes schematically the main differences between the two photosystems. Thus while PSII has relatively isolated light-harvesting nanostructures, in PSI one can distinguish an inner core antenna system engulfing the reaction center and a peripheral antenna. Both PSI and PSII reaction centers are in overall architecture remarkable similar to the earlier known bacterial reaction centers [1, 2] emphasizing that there is only one common ancestor for achieving light induced charge separation. The electrochemical potentials are, however, different and this is probably due to the fact that the special pair of chlorophylls in PSI (P700) is actually a heterodimer composed of a Chl *a* and the epimeric Chl *a'* (see Scheme 1) and the ligation of their Mg atoms by methionine residues. Other slight differences

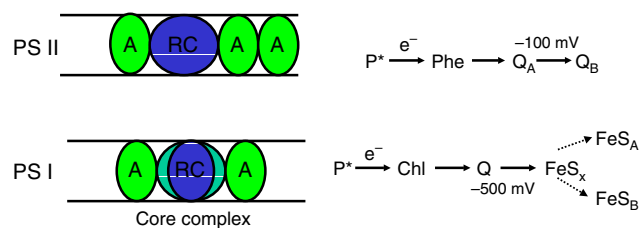


**Figure 8.** Schematic differences between PSI and PSII. Abbreviations: A = Antenna, RC = reaction center, P\* = excited special pair: P670 for PSII and P700 for PSI, Phe = pheophytin, Q = quinones, FeS<sub>x</sub> = iron sulfur clusters. Arrows indicate electron transfer steps. Adapted with permission from [21], L. Stryer, “Biochemistry,” 3rd ed., p. 520. Freeman, New York, 1988. © 1988, Freeman.

are that in PSII, like in the bacterial reaction center, the primary electron acceptor is a chlorophyll which has lost its magnesium atom, namely a pheophytin, and that the final electron acceptors are a quinone for PSII and iron sulfur centers for PSI. The lower resolution of the PSII crystal structure does not yet allow one to discern fine stereochemical features allowing assignment of the direction of transition moments in antenna Chls or to exactly elucidate the ligands of the tetramanganese cluster involved in water splitting. For this reason we will not discuss the PSII chlorophyll–protein complexes here.

The much higher resolution of PSI has allowed us very recently to elucidate an important structural feature of its core complex which is instrumental for the energy funnelling from the peripheral antenna toward the reaction center [79]. (B)Chls have two nonidentical sides from which the magnesium atom can bound be a fifth ligand giving rise to two diastereoisomeric complexes. Figure 9 shows the crystal structure of PSI with the magnesium atoms highlighted as spheres. In total there are 96 chlorophyll molecules.

We have denoted as *anti*-ligated (B)Chls the diastereoisomer where the magnesium ligand is on the opposite side

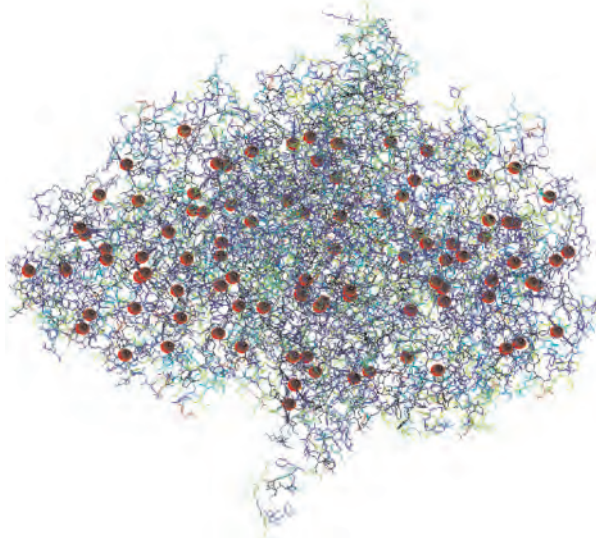


**Figure 9.** PSI viewed in the membrane plane luminal side up, stromal side down. Spheres represent magnesium atoms of chlorophylls.



of the 17-propionic acid residue which is esterified with a long chain alcohol such as phytol in plants [43]. The other diastereomer is denoted as *syn*. Figure 10 shows two Chls from the PSI crystal structure both coordinated by histidine residues one being in a typical *anti* configuration and the other one being *syn*.

A simple counting of the *syn* Chls revealed that these are only 14 out the total 96 which translates by a crude Boltzmann distribution into an energetic difference of 1.1 kcal/mol. The *syn* Chls are not only less stable than the *anti* ones but if coordinated by a histidine, their absorption spectrum, according to semiempirical ZINDO calculations, is slightly shifted by about 4 nm. Astonishingly, however, is the very controlled position of these *syn* Chls carefully engulfing the reaction center [79]. The Chl ligands have been strictly conserved during evolution, as could be seen from the sequence alignment in different plant and bacterial species, a fact which implies that the incorporation of Chls in the protein matrix is a nonrandom process. Probably a highly stereoselective self-assembly process occurs which allows binding of the magnesium atom only from the desired side. An enzymatic process requiring two different enzymes for chaperoning *syn*- or *anti*-ligation appears less probable. Figure 11 shows the disposition of the *syn* Chls which are exclusively in the core antenna system.

Recently Byrdin et al., also on the basis of the PSI crystal structure, have interpreted the energy transfer kinetics using a detailed modeling of the system by applying excitonic coupling theory [80]. The *syn* Chls are interconnected into clusters characterized by medium to rapid energy transfer rates in the 3 to 11 ps<sup>-1</sup> range. They appear not to be strongly redshifted having assigned “colors” between 670 and 680 nm. Far more redshifted are, however, two dimers of *syn-syn* Chls which are situated some 2.5 nm from P700, the special pair of PSI. It thus appears probable that the energy funnelling occurs also in this case cascadelike, from the peripheral antenna, to the inner core rich in *syn* Chls which are not redshifted to dimeric Chls which are redshifted and finally to the P700 heterodimer, which absorbs

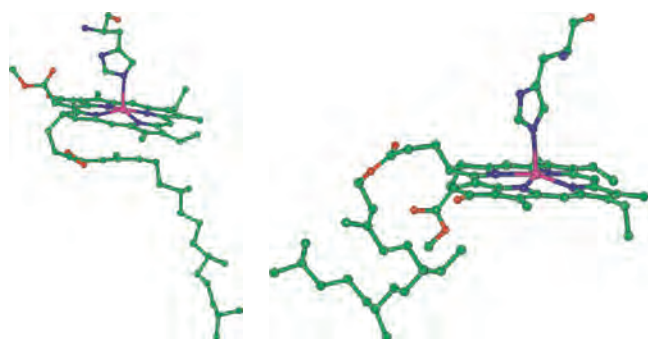


**Figure 10.** The two different diastereomeric configurations of histidine coordinated Chls. At left a typical *anti*-ligated Chl. Note the sharp curling of the phytol chain on the opposite side of the histidine ligand. At right a *syn*-ligated Chl. Note that in this case the propionic acid residue is on the same side as the histidine ligand while the esterifying phytol curls back to the other side. The role of the phytol chain is to ensure a hydrophobic environment thus steering the coordination of magnesium from the other side which is more hydrophilic.

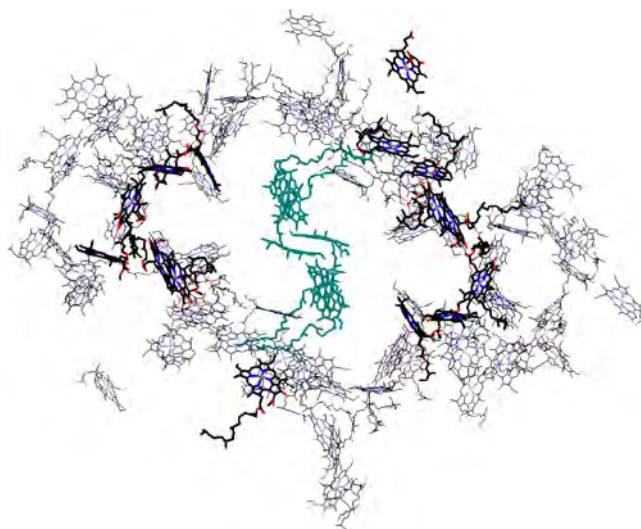


**Figure 11.** Disposition of the *syn* chlorophylls (colored in red) around the electron transfer chain chlorophylls (colored in blue) of the reaction center. Green chlorophylls are all *anti* coordinated. Note that for the upper right chlorophyll the ligand is uncertain. Reprinted with permission from [79], T. S Balaban et al., *Biochim. Biophys. Acta* 1556, 1 (2002). © 2002, Elsevier.

light at 700 nm (as its name implies) where charge separation occurs. Carotenoid–Chl interactions are also different for the *syn* and *anti* configurations affecting most importantly the Soret band.

**The Fenna–Matthews–Olson Complex** John Olson was historically the first to be able to isolate a (bacterio)-chlorophyll–protein complex from the green bacterium *Prosthecochloris aestuarii* (previously named *Chlorobium limicola*) and to crystallize it. Apparently serendipity played here a role but it was the prepared mind who realized the importance of this discovery [81]. The crystal structure was solved at an astonishingly high resolution for that time (2.8 Å) by Fenna and Matthews [82] and since then this complex has been the workhorse for spectroscopic investigations and for testing various theoretical models of energy transfer and trapping [83, 84]. The FMO complex is a trimer and energy trapping occurs from the chlorosomal antenna in one unit and is transferred to the other two units before excitation of the reaction center. Only seven BChl *a* per monomer are present, two of which are *syn*-ligated, confirming the higher stability and thus propensity of the *anti* Chls. Blankenship and co-workers have shown by crystallizing and solving the structure of the FMO complex from *Chlorobium tepidum* that it has a similar architecture which enables it to function as the energy sink of the antenna, although some differences are encountered for the BChl *a* molecules [85]. Figure 12 shows the BChl *a* molecules from a monomer in the latter structure together with their ligands in their original orientations and without the protein matrix. Also in this case the *syn* Chls appear to be “special” and are most probably the energetic trap as they are closely situated, having a Mg–Mg distance of 12.5 Å forming thus a redshifted *syn-syn* dimer ligated on two consecutive histidines (red in Fig. 12). The central *syn* BChl *a* (#7 in the original numbering [82]) of this dimer has been recognized before as the energetic trap having the largest intersubunit

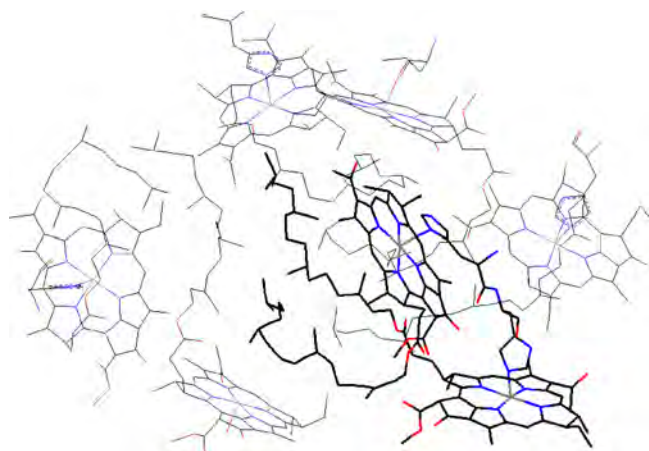


**Figure 12.** The seven Chls of an FMO monomer. *Anti* chls are green; *syn* Chls which are on two consecutive histidines are red.

interactions within the trimer. For evidence that BChl #6 is the reddest pigment see [86].

As BChl *a* absorbs at longer wavelengths than the antenna BChls (which are actually chlorins; see Scheme 1) a downhill energy transfer is operating. The reaction center absorbs light at still longer wavelengths and must be supplied from the energetic trap. If the *syn* Chls are involved either in the intertrimer energy transfers or act as the traps remains to be ascertained. We have written a thought-provoking article discussing this feature [87].

Recently Oba and Tamiaki have also counted *anti*-ligated Chls (which they denote as back-face ligated) and *syn* Chls (denoted as front-face ligated) in all known chlorophyll protein complexes and have also concluded that *anti*-ligation is energetically more favorable [88, 89].

**The LH2 of Purple Bacteria (*Rhodospseudomonas acidophila* and *Rhodospirillum molischianum*)** Purple bacteria have a fascinating peripheral light-harvesting complex, the LH2, which is an integral membrane complex consisting of two rings of BChl *a* molecules embedded in an aggregate of polypeptide matrices. The first X-ray crystallographic structure to be solved was from *Rhodospseudomonas acidophila*, strain 10050, which has involved almost a decade of research and crystallization trials by Cogdell and co-workers [90, 91]. Crystals with heavy atom derivatives could be prepared in order to solve the phase problem. Based on these coordinates, the crystal structure of a second LH2 complex from *Rhodospirillum molischianum* could be solved soon thereafter in a collaborative effort between the research groups of Klaus Schulten and Hartmut Michel [92]. Both nanostructures have the same overall architecture, the main difference being the oligomerization state and thus their symmetry: while the *acidophila* LH2 is a nonamer, the *molischianum* LH2 has eightfold symmetry. This implies that the function of light harvesting and energy transfer is actually independent of the symmetry and almost the same optical properties are encountered. These are determined by the disposition of the pigments and the orientation of the transition dipole moments. One ring of *anti*-ligated BChl *a* molecules, which are loosely coupled, absorbs light at about 800 nm and has been denoted as B800

(B stands for bulk Chl). The second ring, denoted as B850, is formed of dimers which are closely spaced and are red-shifted absorbing light at about 850 nm. Interestingly all the B850 BChls are *syn*-ligated. Figure 13 shows a view of the BChls in the *acidophila* LH2 from above the ring of the 18 B850 BChls *a* as well as a view in the plane of the membrane. One *syn-syn* BChl dimer and one B800 BChl are precisely oriented (almost perpendicular to each other) by two polypeptides which are  $\alpha$ -helical and span the membrane. Furthermore, a carotenoid molecule is also present having close contact with both the dimer and the B800 monomer. The two polypeptides which are termed  $\alpha$  and  $\beta$  together with the associated pigments form a so-called protomer [93]. Interprotomer interactions lead to self-assembly of the circular structure. Nine protomers come together in the *acidophila* LH2 leading to a disposition of the  $\beta$ -polypeptides on a outer circle having a diameter of 6.8 nm while the  $\alpha$ -polypeptides form an inner circle with 3.6 nm diameter. While the Mg to Mg distance in opposite BChls from the B800 ring is 6 nm, the corresponding distance in the B850

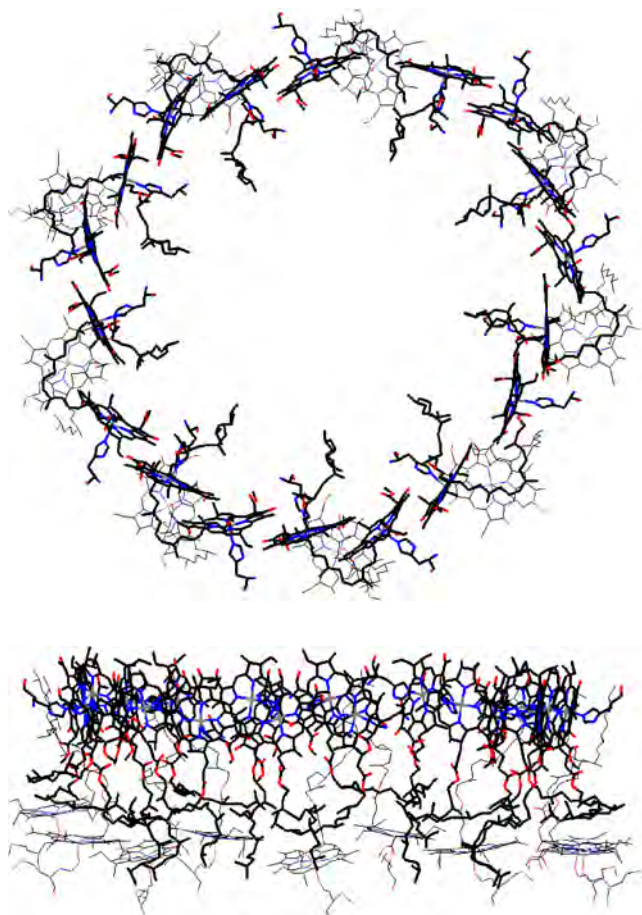


**Figure 13.** The BChl *a* molecules in *acidophila* LH2 with their ligands. The B800 BChls are green (ligated *anti* by an *N*-formylmethionine residue) while the B850 BChls are red (ligated *syn* by histidines). Note the different orientation of the BChl planes in the two rings. The BChl *c* ligands have carbon atoms colored cyan, nitrogen blue, oxygen red, and sulfur yellow. The figure was produced with HyperChem® using the PDB coordinates.



ring is ca. 5 nm. Only eight protomers self-assemble in the *molischianum* LH2 leading to a similar architecture.

The B800 BChls are situated nearer to the cytosolic side of the membrane. Their role is to function as antenna and to transfer the singlet excitation energy to the B850 ring via a Förster mechanism (see Section 2). Detailed investigations of the energy transfer kinetics in the LH2 of the purple bacteria *Rhodobacter sphaeroides* and *Rhodospseudomonas palustris* using femtosecond pump-probe techniques have been performed [94].

These studies could distinguish between intra- and inter-ring energy transfer processes. Within the B800 BChls which have a Mg-Mg distance of 2.1 nm a very fast energy transfer occurs with a time constant of 400 fs. The B800 to B850 inter-ring energy transfer occurs slower within 700 fs although the average separation between the Mg atoms is smaller, namely 1.8 nm. Both these processes involve the Förster mechanism, which as discussed in detail in Section 2, beside the distance dependence involves a spectral overlap between the fluorescence of the donor and the absorption of the acceptor as well as an orientation factor of the transition dipole moments. The latter two factors are more favourable for the intra-ring energy transfer, although the distance is larger. Once the excitation has been transferred to the B850 ring, because of the extensive  $\pi$ - $\pi$  overlap of these BChls, a different mechanism operates. A delocalized exciton coupling mechanism of Dexter type which involves orbital overlap occurs in this case. The B850 BChls have Mg-Mg distances of under 1 nm (9.6 Å within a protomer and 8.9 Å between adjacent protomers) being ideally suited to delocalize and to store the energy within this ring until it can be transferred further to the LH1 complex. This process occurs within 3 to 5 ps and is followed by a slower 35 ps energy transfer process to the reaction center [95]. The overall efficiency for the excitation transfer from the LH2 to the LH1 and from there to the RC is extremely high (about 95%) due to the optimal orientation of pigments within the complexes.

The carotenoids (rhodopin glucoside in the *Rps. acidophila* LH2 and lycopene in the *Rs. molischianum* LH2) are also involved in light harvesting but at lower wavelengths (about 500 nm) than the BChls. Due to their low fluorescence yield they transfer sluggishly the excitation energy via the Förster mechanism but having close contacts with both the B800 and B850 again the Dexter mechanism can operate. Energy can in principle be transferred directly from the carotenoid  $S_2$  state or after the fast (100 fs) radiationless decay from the  $S_2$  to the  $S_1$  state, from the latter (see Fig. 14). Due to the unfavourable orientation of the  $S_1$  transition dipole which is oriented along the long molecular axis and thus being almost perpendicular to the  $Q_x$  and  $Q_y$  transitions of the B800 BChls, excitation transfer from this carotenoid to B800 is rather limited. In contrast, due to its proximity to the  $\alpha$ -B850 BChl *a* (5.4 Å to the central Mg atom) and to the  $\beta$ -B850 BChl *a* (8 Å to the central Mg atom) and to the parallel alignment to the  $Q_x$  transition a favourable  $S_2$ - $S_2$  transfer occurs. Beside this dipolar or Coulombic, Förster-type singlet-singlet energy transfer, a Dexter type mechanism involving electron exchange can occur also between the triplet states which has been shown much earlier to involve only the B850 BChls [96]. A second carotenoid molecule per protomer which in the initial

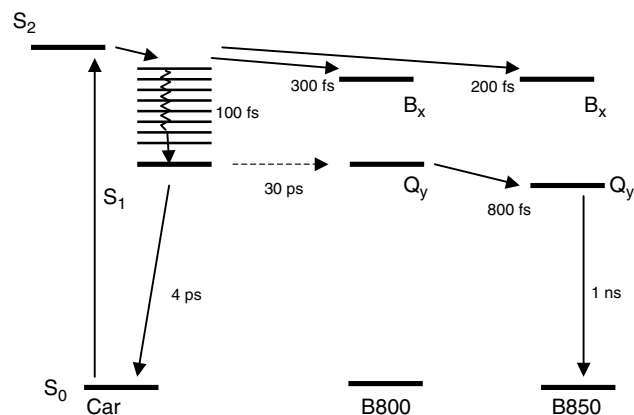


**Figure 14.** Schematic energy diagram with the energy transfer pathways and time constants from the carotenoid  $S_2$  state to the B800 and B850 BChls. The dotted line indicates that only a small amount (5%) is transferred from the internal conversion state  $S_1$  to the BChls. There is no back transfer from BChl to the Car due to energy funneling. Adapted with permission from [102], J. L. Herek et al., *Nature* 417, 533 (2002). © 2002,

structure [90] was not seen in the electron density map, probably due to local disorder, has later been put into evidence [93]. It is certain that beside their light harvesting role, carotenoids play an important structural role in holding chlorophyll-protein complexes together. Being rather stiff and nonpolar they interact with hydrophobic amino acids ensuring rigidity to the nanostructure. Carotenoidless mutants assemble much more labile complexes. The third role of carotenoids involves efficient quenching of the BChl triplet states, again through electron exchange mechanism. This prevents generation of the reactive species singlet oxygen [ $O_2(^1\Delta_g)$ ] which may generate subsequently radicals and thus could lead to cell damage. The protective role of carotenoids has made them wide spread in natural photosynthesis being the second most abundant pigment class, after chlorophylls.

Several studies related to the *Rs. molischianum* LH2 complex have also been performed and these have been reviewed [97–99]. Molecular modeling of the LH2 complexes surrounding the LH1 complex (which is discussed below) and which engulfs the reaction center have been reported [100, 101]. The exact number of LH2's surrounding the larger LH1 may vary between different purple bacterial species as well as with illumination conditions. Under dim light the ratio LH2/LH1 increases.

**The LH3 of *Rhodospseudomonas acidophila*** The crystal structure of the smaller LH3 light-harvesting complex which is also present in some purple bacteria such as *Rhodospseudomonas acidophila* and which absorbs light at higher energies having B800 and B820 absorbing BChls was recently disclosed by Cogdell and co-workers [103]. Surprisingly, the overall structure resembles closely that of the LH2 complex consisting of a ring of 9 loosely coupled *anti* BChls *a* responsible for the 800 nm absorption band and a tightly coupled ring of 18 *syn*-ligated BChls *a* which absorb at 820 nm. It is very interesting to understand the structural

difference which leads to the blueshift of the B850 ring in LH2 to B820 in LH3 (see Fig. 14). Apparently it is not the coupling energy which is different, as the distances and the orientations between the BChls are almost identical. Rather it is the site energy which is different. That is, due to slight variations in the geometry of the individual BChls, the absorption is blueshifted. Most notably, the 3-acetyl group which has its carbonyl group coplanar with bacteriochlorin plane in the B850 LH2 ring, due to the more extended conjugation, leads to the redshifted absorption. In the LH3 BChls this acetyl group, due to subtle interactions with the protein matrix, has its carbonyl group twisted out of the plane and is thus not in conjugation, a fact which explains nicely the 30 nm blueshift. Figure 15 presents the very similar arrangement of three consecutive *syn* BChls while Figure 16 shows the different orientation of the 3-acetyl groups.

Another reason for the blueshift lies in the more ruffled conformation of the bacteriochlorin ring in the LH3 complex, whereas in the LH2 complex a more domed conformation is encountered. Extensive theoretical calculations by John Shelnutt and Craig Medforth coupled with experimental data supplied by Kevin Smith and Jack Fajer have convincingly shown that conformationally perturbed cyclic tetrapyrroles have not only very different absorption characteristics but also different fluorescence and excited states lifetimes [104–108]. This shows that the protein can very finely tune the spectroscopic properties of the bound pigments.

To a similar conclusion, namely that the difference in the absorption wavelengths between the LH3 and the LH2 complexes is due to the difference in site energies and not from the coupling energy, comes a recent study by optical single-molecule fluorescence spectroscopy of Aartsma and co-workers [109].

**The LH1 of Purple Bacteria** Electron microscopy images of two-dimensional crystals of the LH1 complex from *Rhodospirillum rubrum* obtained by Gosh and co-workers have shown also a circular structure but with a 16-fold symmetry [110]. Again  $\alpha\beta$  heterodimeric polypeptides with  $\alpha$ -helices spanning the membrane are used for positioning the pigments. Absorption occurs at about 875 nm, more redshifted than the B850 ring of the LH2. Furthermore, within the membrane plane the positioning of the LH1 hexadecagon formed by the BChls coincides with the depth at which the B850 ring is embedded.

The reaction center complex fits well within the ring of LH1, although it sits deeper within the membrane. From

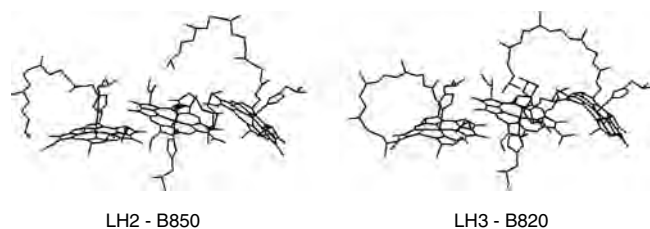


**Figure 15.** Similarities in the chromophore arrangement in the LH2 and LH3 complexes.

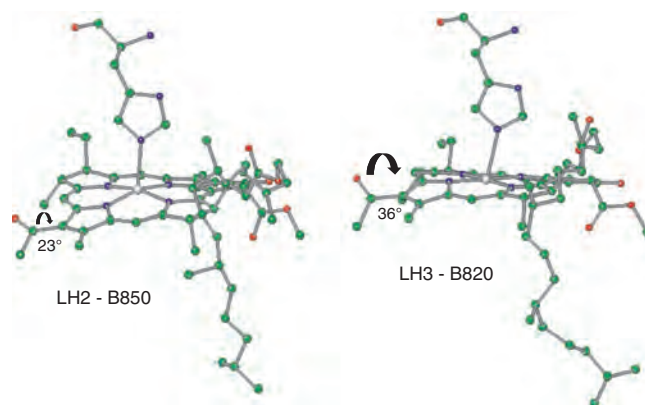


**Figure 16.** The arrows indicate the OC–CC torsion angle of the carbonyl group which is more conjugated in the LH2 complex.

some species the isolation of LH1 cannot be performed without the RC. The energetic cascade is realized by initial light harvesting of the B800 ring of the LH2, transfer to the neighboring B850 ring then to the LH1, and from there to the reaction center. Here the special pair is photoexcited. Hu and Schulten have argued that the long debated role of the accessory BChls could actually be that they trap the energy from LH1 and transfer it then efficiently to the special pair [98]. Thus they appear to be involved in an initial energy transfer while their role in electron transfer, once the special pair has been excited and the electron is ejected, has been the subject of debate. Whether this electron actually resides on one of these accessory BChls or whether the latter has just a spectator role as the electron is passed directly onto the magnesium-free pheophytin has different mechanistic implications. For an excellent discussion with stimulating concepts and synthetic models for studying the superexchange mechanism see the book chapters by Paddon-Row (Chapter 1, Vol. 3 in [19] and/or [111]).

**The Peridinin Complex** The high resolution structure of this light-harvesting complex from *amphidinium carterae* has shown that the carotenoid peridinin is the main pigment and eight carotenoids are being associated closely with two Chl *a* molecules [112]. The complex is a trimer and having reversed the usual stoichiometry between pigments absorbs light predominantly at shorter wavelengths. Figure 17 shows a monomeric unit highlighting the close contacts between the carotenoid and Chls.

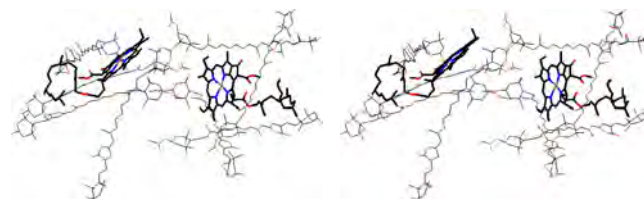


**Figure 17.** Stereoview of the monomeric unit in the peridinin light-harvesting complex. Carotenoids are light (yellow) and the Chls are dark (green).

**The LHCII of Plants** This light-harvesting complex of photosystem II of plants is the largest and outermost antenna complex which due to its abundance accounts for about half of the pigments in plant photosynthesis. Its structure has been determined by Kühlbrandt et al. using electron diffraction of two-dimensional crystals to a resolution of 3.4 Å [113]. Three membrane-spanning  $\alpha$ -helices bind 12 Chl *a* and Chl *b* molecules together with 3 carotenoids. In the initial structure the assignment of the Chl *a* or Chl *b* as well as their orientations was uncertain due to the low resolution. Furthermore, only two of the carotenoids, namely two central lutein molecules, were visible. A lot of effort has been invested into assigning the Chl *a* and *b* binding sites as well as the position of the third carotenoid molecule, neoxanthin. These have included mutagenesis studies where mutant apoproteins were expressed in *Escherichia coli* and after isolation were reconstituted in the presence of chlorophyll and carotenoid cofactors. By replacing the Mg binding residues with noncoordinating amino acids the spectral characteristics of each chlorophyll molecule could be assessed [114]. A similar procedure was used for determining the binding site and orientation of the elusive neoxanthin molecule [115, 116]. Interestingly, while occupation of the binding sites with at least one lutein is essential for correct protein folding, the neoxanthin occupancy does not influence the folding process.

A recent detailed femtosecond transient absorption study has unravelled the carotenoid to chlorophyll energy transfer processes by using recombinant LHCII reconstituted with different carotenoid contents [117]. The data analysis has shown that most of the energy transfer occurs directly from the initially excited state  $S_2$  of the carotenoids to Chls with time constants under 100 fs. Only a relatively small part of the energy transfer (under 20%) occurs after relaxation from  $S_2$  to the  $S_1$  carotenoid state. The two luteins have transfer times of about 50 and 75 fs while the neoxanthin has about 90 fs and it transfers its energy almost exclusively to Chl *b*. Three different Chl *b* molecules could be distinguished which receive energy directly from the carotenoids. As there are five Chl *b* and seven Chl *a* there is less energy transferred directly to Chl *b* as estimated in a previous study in the LHCII of *Arabidopsis thaliana* [118]. Figure 18 shows the energy levels and the proposed energy transfer pathways.

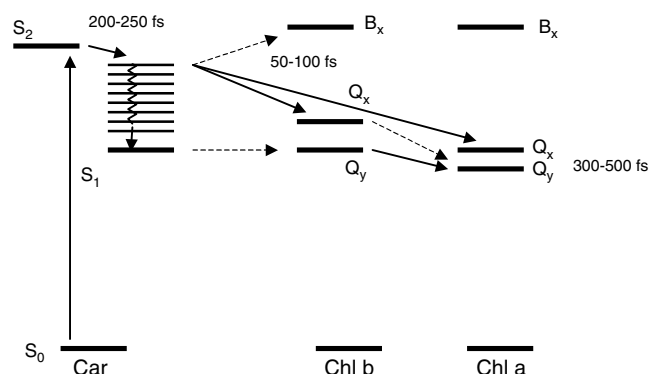
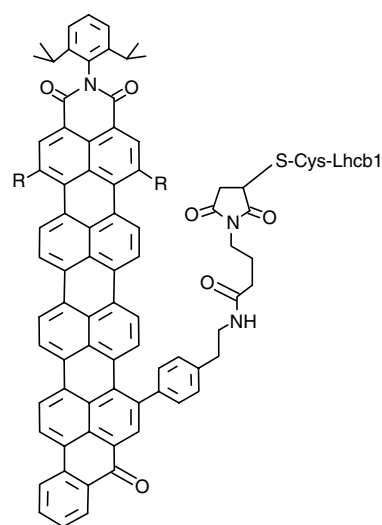


**Figure 18.** Qualitative kinetic scheme for the energy transfer from carotenoids to chlorophylls in LHCII. Adapted with permission from [118], J. P. Connelly et al., *Biochemistry* 36, 281 (1997). © 1997,

While the energy transfer from carotenoids to Chl *b* involves both the  $B_x$  and  $Q_x$  state, the transfer to Chl *a* occurs only via the  $Q_x$  Chl state.

Investigations on the smaller chlorophyll-protein (CP) complexes from plants which have a high degree of homology to LHCII such as CP29 have also been performed [119]. The inner-antenna subunits CP43 and CP47 flank the PSII reaction center and contain 12 and respectively 14 Chl molecules and their role is to transfer the excitation energy from the outer LHCII antenna to the reaction center, in an energetic cascade similar to that encountered in bacterial photosynthesis.

Worth mentioning here are also Paulsen's reconstitution studies of LHCII with artificial dyes such as terrylene which acts as an energy trap [120]. A single cysteine residue has been inserted near the *N*-terminus and the dye benzoylterrylene-3,4-dicarboximide (BTI) could be covalently coupled via a maleimido linker. The site specificity was verified by the fact that maleimido-BTI was not bound by a mutant apoprotein containing no cysteine at all. Reconstitution of this apoprotein containing the artificial energy trap was effected with the natural pigments in the usual way [121, 122]. Quenching of the donor (Chl *a*) fluorescence allowed an estimation of the energy transfer efficiency to BTI to be 70% at 297 K and 85% at 77 K. Elegant proof of this high efficiency was provided by digestion with trypsin which cleaves only the *N*-terminal part leaving intact the pigment binding domains. The fluorescence in the trypsin digested LHCII labeled with BTI rose to the level of the nonlabeled complex. Thus in this biomimetic study, for the first time a self-assembled recombinant light-harvesting complex from higher plants has been shown to mimic perfectly the efficient light harvesting and subsequent energy transfer to an artificial trap. However, in this case no charge separation occurs, as in the fully functional natural system.



Shown is maleimido-BTI attached to the Lhcb1 recombinant apoprotein via a cysteine residue near the *N*-terminus (R is a *tert*-butylphenol group).

Very recently, single molecule spectroscopy of oriented LHCIIb as trimers has been performed in collaboration between the groups of Paulsen and Wrachtrup [123]. Photobleaching in one step was observed for most complexes a fact which indicates energy transfer between the subunits. An excellent feature article on the energy transfer in LHCII was published recently by van Amerongen and van Grondelle [23].

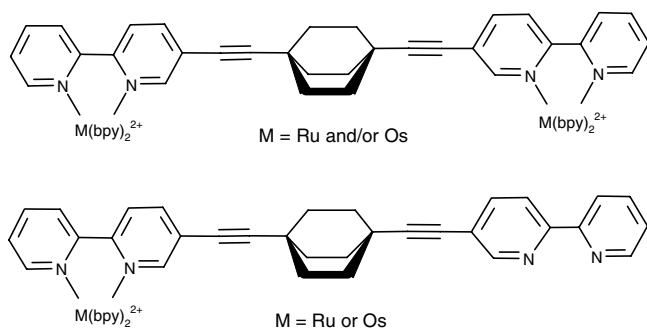
## 4. ARTIFICIAL LIGHT-HARVESTING NANOSTRUCTURES

In this section we review recent synthetic efforts to construct artificial nanostructures mimicking the natural light-harvesting apparatus described. Two different approaches have been followed: (i) covalent assembly of large molecular structures having nanometer dimensions and (ii) a supramolecular approach where noncovalent interactions are engineered between chromophoric molecules.

### 4.1. Covalent Arrays

The evolution of synthetic chemistry has allowed the construction of impressive architectures which are covalently linked. This tedious bond-by-bond construction mode makes use of well optimized synthetic procedures, such as palladium catalyzed cross-coupling reactions, acetylene scaffolding, esterifications, or amide bond linkages where from small molecular building blocks nanostructures can be accessed. A precise control of the architecture is possible so that geometry and device performance can be finely tuned. The major disadvantage of this procedure resides in the limited amount of material which one obtains in the end of such a multistep synthetic sequence which then is available for photophysical studies.

An early investigation of a rigid rodlike nanostructure encompassing ruthenium and/or osmium trisbipyridyl complexes was a collaborative effort between German and Swiss synthetic chemists and Italian photophysicists in Bologna [124]. This was the first example where two metal chelating units were separated by a rigid bridging ligand with linear geometry which restricted the electronic communication between the metal centers due to a [2,2,2]-bicyclooctane insulating spacer. Model compounds served the monometallic complexes of the same ligand as well as ruthenium and osmium trisbipyridine complexes.



The bisacetylenic-[2,2,2]-bicyclooctane spacer, as could be inferred from its X-ray structure, is 1 nm long and assures a separation of 1.7 nm between two metal centers chelated by the bispyridine (bpy) ligands. The absorption and luminescence spectra of the mixed [Ru–Os]<sup>4+</sup> complex is exactly the sum of the mononuclear complexes showing that there is no electronic communication between the metal centers. Eloquently, the absorption spectra of the three complexes [Ru–Ru]<sup>4+</sup>, [Ru–Os]<sup>4+</sup>, and [Os–Os]<sup>4+</sup> show two isosbestic points (at 416 and 466 nm) where each metal complex unit absorbs 50% of the incident light. Also the electrochemical measurements show constant values for the halfwave potentials versus the standard calomel electrode ( $E_{1/2}$  vs SCE) of ca. 1.26 V for a [Ru]<sup>2+</sup> complex and 0.84 V for a [Os]<sup>2+</sup> complex having the same coordinating ligands. As the [Os]<sup>2+</sup> unit has a more bathochromically shifted absorption and the lower  $E_{1/2}$  value than the [Ru]<sup>2+</sup> unit, a unidirectional energy transfer can occur from the donor [Ru]<sup>2+</sup> metal center to the [Os]<sup>2+</sup> metal center which acts as acceptor.

Upon irradiation at the isosbestic points, the fluorescence of the Ru-based luminescence in the [Ru–Os]<sup>4+</sup> complex, after correction for 50% absorption of the Os-based unit, shows a pronounced quenching (about 10 times smaller quantum yield) than the model compounds [Ru–Ru]<sup>4+</sup> or the monometallic complex [Ru]<sup>2+</sup>. At the same time there is no quenching of the Os-based luminescence, the quantum yield being about the same as in the [Os–Os]<sup>4+</sup> or [Os]<sup>2+</sup> model complexes. Furthermore, the excited state lifetime of the Ru-based unit is drastically decreased from 231 ns in the [Ru–Ru]<sup>4+</sup> complex to 22 ns in the mixed [Ru–Os]<sup>4+</sup> complex and concomitantly, with practically the same lifetime (21 ns) there is a rise in the luminescence of the Os-based unit. This is direct evidence that energy is transferred *intramolecularly* from the Ru-based center to the Os-based center. The rate for this energy transfer can be calculated from the experimentally determined lifetimes  $\tau$  of the [Ru–Os]<sup>4+</sup> complex and  $\tau^0$  of the [Ru–Ru]<sup>4+</sup> complex, that is, in the presence and respectively absence of the energy transfer with the equation.

$$k_{\text{EET}} = \frac{1}{\tau} - \frac{1}{\tau^0} = 4.1 \times 10^7 \text{ s}^{-1}$$

The theoretical rate calculated by a Förster dipole–dipole mechanism gives a value for  $k_{\text{EET}}$  of the same order of magnitude, albeit a little smaller, namely  $2.4 \times 10^7 \text{ s}^{-1}$ . For this calculation, in the Förster formula (see Section 2) the value of the overlap integral was calculated as  $4.7 \times 10^{-14} \text{ M}^{-1} \text{ cm}^{-3}$ ,  $R_{DA}$  was taken as 1.7 nm,  $\tau_R^D = \tau^D / \Phi_D$ , where  $\tau^D$ , the radiative lifetime of the Ru-based donor in the absence of energy transfer, was 231 ns and the fluorescence quantum yield of the Ru-based donor  $\Phi_D$  was 0.015.

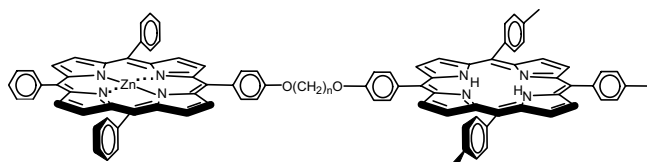
If exclusively a Dexter exchange mechanism is considered, in order to explain the observed energy transfer rate, a value of  $0.4 \text{ cm}^{-1}$  is obtained for the through-bond electronic interaction energy  $H$  between the two metal centers. The reorganization energy  $\lambda$  could be estimated as ca. 0.2 eV from the Stokes shift, while the free energy  $\Delta G^0$  could be calculated to be  $-0.33 \text{ eV}$  from the difference between the spectroscopic energies of the Ru-based donor and the Os-based acceptor measured from their luminescence maxima at 77 K. If the Dexter mechanism would

operate only 50% to the observed energy transfer, then the corresponding value for  $H$  would have been  $0.3 \text{ cm}^{-1}$ . Clearly in this case there is a contribution from both mechanisms to the energy transfer process as the Förster mechanism alone cannot explain the observed energy transfer rate unless the real orientation factor  $\kappa$  is different than the one assumed.

#### 4.1.1. Multiporphyrinic Nanostructures

Porphyrins have been the most used pigments in artificial light-harvesting nanostructures as they are available synthetically by various procedures, are thermally quite robust, and show interesting photophysics. Several excellent reviews have appeared describing mainly covalent assemblies of porphyrins [125, 126]. While the former review focuses on the structure, several examples of crystal structures obtained by the group of K. M. Smith being described, the second review describes synthetic routes to such multiporphyrin arrays. Neither theme will be treated here and the interested reader is referred to these fairly recent sources.

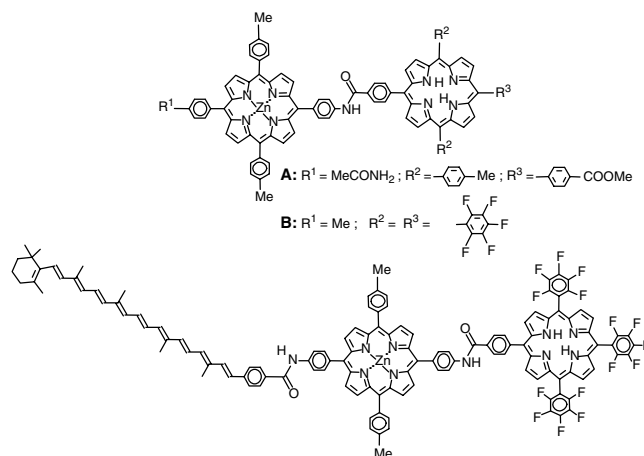
Among the first series of molecules to be constructed with the aim of studying the energy transfer among different chromophores was the following series with  $n = 3, 4,$  and  $6$  [127]:



Harriman and co-workers together with the late Lord Porter have studied both by stationary and time-resolved fluorescence the zinc metallated tetraphenylporphyrin covalently linked via different dialkoxy chains to a tetratolyl free base porphyrin. In the case for  $n = 2$  and the ethyleneglycol unit links both *ortho* positions of the phenyl rings, a strong ground state interaction by exciton coupling was encountered between the porphyrin rings. In all cases, upon excitation of the zinc porphyrin energy is transferred to the free base acceptor porphyrin. The efficiency of the energy transfer ( $\Phi_{\text{EET}}$ ) could be estimated from the fluorescence quenching at  $605 \text{ nm}$ , where only the zinc donor emits. For the  $n = 2$  case, with *ortho*-linkage the  $\Phi_{\text{EET}}$  was almost quantitative (94%) and occurred with a rate constant of  $8$  to  $9 \times 10^9 \text{ s}^{-1}$  depending whether measured in benzene or the more polar dimethylformamide as solvent. As the linker length is increased,  $\Phi_{\text{EET}}$  drops to 75% for  $n = 3$ , and only 35% for  $n = 4$ , while the rates decrease to  $5$  and  $4 \times 10^9 \text{ s}^{-1}$  respectively. Interestingly as the chain length is further increased to  $n = 6$ ,  $\Phi_{\text{EET}}$  becomes 48% indicating that a flexible conformation with more closely spaced donor and acceptor can now be populated. If Förster-type calculations are performed, the measured rates indicate separations between the donor and acceptor smaller than estimated from molecular models in a fully extended conformation. Furthermore, a random orientation of the transition dipole moments has to be considered in this case which leads to an averaging of the

factor  $\kappa^2$ . From the time-resolved measurements it was concluded that a slow equilibration exists between an open conformation with increased separation between the Zn donor and the free base porphyrin and a more closed conformation. Triplet-triplet energy transfer processes, which in principle can occur only via a Dexter mechanism, were found to be negligible.

Also an early and very thorough study of energy transfer coupled with electron transfer which deserves mention is due to Gust and co-workers at the Center for the Study of Early Events in Photosynthesis, Arizona State University, in collaboration with De Schryver in Leuven, Belgium and Bensasson and Rougée in Paris [128]. This work was based on previous studies of various dyad, triad, tetrad, and pentad molecules which were specially constructed to generate long-lived charge-separated states upon photoexcitation and multistep electron transfer reactions mimicking thus natural reaction centers (for earlier reviews see [6, 7, 129]). Various porphyrinic dyads of type  $P_{\text{Zn}}-P$  and triads of type  $C-P_{\text{Zn}}-P$  (where  $C$  is a carotenoid moiety) were synthesized and their photophysics was investigated. The novelty consisted of a fine tuning of the redox properties and thus of the excited state energies by introducing electron withdrawing groups, such as pentafluorophenyl, for stabilizing the radical anions formed upon electron transfer.



The absorption spectra of dyads **A** and **B** are essentially a superposition of the spectra corresponding to the monosubstituted porphyrins (denoted as  $P_{\text{Zn}}$  and  $P$ ) which thus act as independent chromophores. Due to the amide linkage, which has partial double bond character, a folded conformation where the porphyrin rings could  $\pi$ -stack is excluded and this was supported by the solution NMR studies where no aberrant shielding effects were seen for the protons and no close interporphyrin contacts could be put into evidence by nOe studies. Time resolved studies by single photon timing showed that in a dyad of type **A** where both porphyrins are free bases, there is no quenching of the porphyrin singlet excited states by any electron or energy transfer process. Thus upon excitation at  $590 \text{ nm}$  a decay of the fluorescence was observed which could be fitted by a single exponential with a lifetime of  $7.8 \text{ ns}$  which is comparable to that of the separated free base porphyrins with the same substituents ( $7.9$  and  $8.3 \text{ ns}$ ). The energetic diagram shown in

Figure 19 could be inferred by estimating the energies of the first excited singlet states of the porphyrins from the difference in energies (or frequencies) between the longest wavelength absorption maxima and the shortest wavelength emission maxima. Furthermore, the energy of the state after electron transfer,  $P_A^{\bullet+}-P_B^{\bullet-}$ , could be estimated from the first oxidation potentials of the isolated donor porphyrin  $P_A$  and the first reduction potential of the acceptor porphyrin  $P_B$  measured by cyclic voltammetry in the model compounds having the same substitution patterns.

As the state  $P_A^{\bullet+}-P_B^{\bullet-}$  lies about 0.2 eV above the first excited singlet states of the two electronically similar porphyrins, it is expected that it would be populated only very slowly. Accordingly the  $^1P$  states can relax only by intersystem crossing to the triplet state, by internal conversion, or by fluorescence with a normal lifetime.

The situation is different for dyad **A** when the left porphyrin is metalated with zinc ( $P_{Zn}-P$ ). Although again the absorption spectrum is a linear combination of the constituent chromophores, in emission the fluorescence of the zinc porphyrin is almost entirely quenched so that only fluorescence from the free base can be detected by stationary methods. This could be due to either an energy or an electron transfer process. A nice confirmation that only an energy transfer process occurs could be obtained by time-resolved fluorescence measurements by exciting at 590 nm and recording at different wavelengths the decays which were then analyzed by the global technique method developed by Wendler and Holzwarth [130]. Good fits were obtained for three components with lifetimes of 42 ps, 1.5 ns, and 7.9 ns over the whole spectral range between 630 and 730 nm of the Q bands. By scaling the relative amplitudes of the three components, at each wavelength where the decays were measured, to the corrected steady-state fluorescence spectrum, the so-called decay associated spectrum was obtained. While the 1.5 ns component had a negligible amplitude at all wavelengths and could be ignored, the slow 7.9 ns component reflected the emission spectrum of the free base porphyrin having a *meso*-methylbenzoate group.

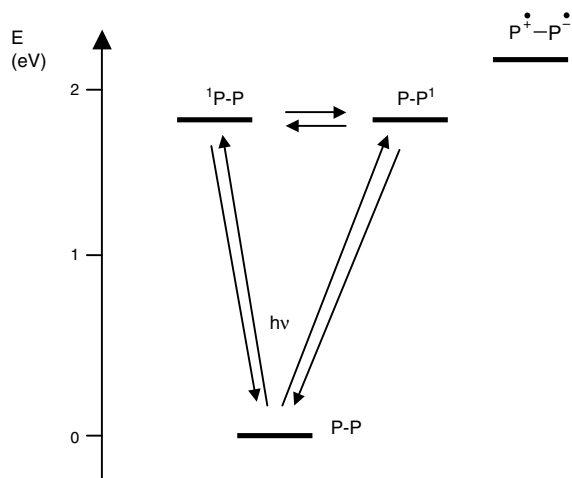


**Figure 19.** Energy diagram for the model dyad P-P. Adapted with permission from [128], D. Gust et al., *J. Am. Chem. Soc.* 113, 3638 (1991). © 1991, American Chemical Society.

This value is also comparable to the lifetime which was measured in the model monoporphyrinic compounds. The fast component is typical for an energy transfer process as it shows a positive amplitude at ca. 635 nm [i.e., only where the decay of the zinc-metallated porphyrin occurs and a negative amplitude, i.e., a rise (or growth in fluorescence) at 710 nm where only the free base porphyrin can fluoresce]. This proves unambiguously that energy is being transferred from  $P_{Zn}$  to P. The energy diagram is presented in Figure 20.

In this case due to the higher energy of the first excited singlet state of the  $^1P_{Zn}-P$  (estimated at 2.08 eV) than that of the corresponding free base ( $P_{Zn}-P^1$  estimated at 1.90 eV), energy transfer from the zinc donor to the free base can occur while the reverse case must be very slow. Again the rate of the excitation energy transfer can be calculated from the measured lifetimes with the formula

$$k_{EET} = \frac{1}{\tau} - \frac{1}{\tau^0} = 2.3 \times 10^{10} \text{ s}^{-1}$$

where  $\tau$  is the measured lifetime of the zinc porphyrin first excited singlet state in the dyad (42 ps) and  $\tau^0$  is the lifetime in the absence of energy transfer, taken as 1.6 ns in a model zinc porphyrin substituted with a *meso*-acetamidobenzoate group. The efficiency of the energy transfer  $\Phi_{EET}$  can be calculated as a quantum yield from the product of the lifetime and rate constant ( $\Phi_{EET} = \tau \times k_{EET} = 0.97$ ) which means that the energy transfer is not only very fast but also almost quantitative. The much slower rate constant of the reverse process ( $k_{-1}$ ) can be estimated from the free energy difference  $\Delta G^0$  which in this case measures  $-0.18$  eV assuming an equilibrium constant  $K = k_{EET}/k_{-1}$  and that  $\Delta G^0 = -RT \ln K$ . At 298 K,  $k_{-1}$  equals  $2.1 \times 10^7 \text{ s}^{-1}$  and is thus three orders of magnitude slower. Also negligible is the formation of the  $P_{Zn}^{\bullet+}-P^{\bullet-}$  state as the rate of the singlet-singlet excitation energy transfer process is much faster than that of an electron transfer process with a driving force  $\Delta G^0 = -0.19$  eV.

The situation changes in case of dyad **B** which consists of a *meso* tris-*p*-tolyl-zinc porphyrin linked to a *meso* tris-pentafluorophenyl free base porphyrin ( $P_{Zn}-P_F$ ). Due to the

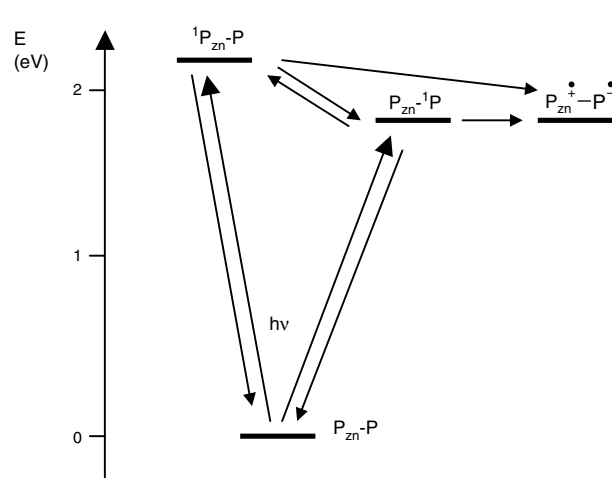


**Figure 20.** Energy diagram for the model dyad  $P_{Zn}-P$ . Adapted with permission from [128], D. Gust et al., *J. Am. Chem. Soc.* 113, 3638 (1991). © 1991, American Chemical Society.



electron-withdrawing pentafluorophenyl groups an anionic charge on the free base is in this case stabilized increasing the driving force so there is a competing electron transfer pathway to the  $P_{Zn}^{\bullet+}-P_F^{\bullet-}$  state. Figure 21 presents the energetics and interconversion pathways between the various states.

Similarly to the dyad discussed before, upon excitation at 550 nm, almost the entire fluorescence of the zinc porphyrin at 600 nm is being quenched. By time-resolved studies and global analysis of the decays at several wavelengths in the 640–725 nm region, two components were found with lifetimes of 82 ps and 2.7 ns. Again the faster component showed a decay at 650 nm, where the zinc porphyrin emits and a rise at 710 nm where only the free base is emitting. Accordingly, the fast component is due to the singlet-singlet energy transfer and the lifetime of the  $^1P_{Zn}-P$  state is 82 ps. In this case, however, a second quenching process may occur, as indicated in Figure 21 by an electron transfer process to the  $P_{Zn}^{\bullet+}-P_F^{\bullet-}$  state in an exergonic process by nearly 0.5 eV. This process could be put into evidence by recording the steady state fluorescence excitation spectra at the free base emission at 720 nm. The corrected excitation spectrum is significantly lower than the absorption spectrum of the dyad, especially for the bands due to the zinc moiety at 550 and 590 nm. Thus the energy transfer is incomplete and its quantum yield could be estimated from these spectra at about 0.77. The rate of the energy transfer process  $k_{EET}$  could be calculated from the equation  $\Phi_{EET} = \tau k_{EET}$  where  $\tau$  is the measured 82 ps lifetime. Thus  $k_{EET}$  is  $9.4 \times 10^9 \text{ s}^{-1}$ . From the energy difference between the  $^1P_{Zn}-P$  and  $P_{Zn}^{-1}P$  states of 0.16 eV, the equilibrium constant at 298 K is calculated to be 510 which makes the rate for the reverse process to the energy transfer  $1.8 \times 10^7 \text{ s}^{-1}$ . As this much slower rate can be neglected, only the three rate constants contribute to the observed lifetime of the  $^1P_{Zn}-P$  state,

$$\frac{1}{\tau} = k_{EET} + k_0 + k_{eT}$$

where  $k_0$  is the rate in the absence of any energy and electron transfer process and can be estimated as  $6.3 \times 10^8 \text{ s}^{-1}$

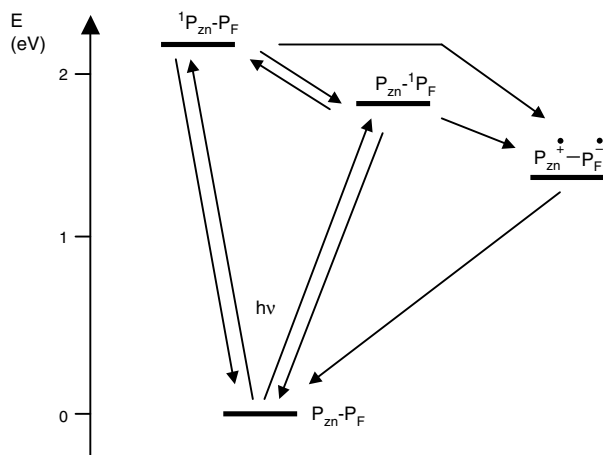


**Figure 21.** Energy diagram for the model dyad  $P_{Zn}-P_F$ . Adapted with permission from [128], D. Gust et al., *J. Am. Chem. Soc.* 113, 3638 (1991). © 1991, American Chemical Society.

from the fluorescence lifetime of 1.6 ns encountered in a similarly substituted zinc porphyrin without the free base acceptor. From this equation, the electron transfer rate  $k_{eT}$  can now be calculated as  $2.2 \times 10^9 \text{ s}^{-1}$  and the quantum yield  $\Phi_{eT}$  for the direct transformation of  $^1P_{Zn}-P$  into the  $P_{Zn}^{\bullet+}-P_F^{\bullet-}$  state is  $\Phi_{eT} = 82 \times 10^{-12} \times 2.2 \times 10^9 = 0.18$ .

The longer lived component of 2.7 ns which can be attributed to the decay of the free base of the  $P_{Zn}^{-1}P$  state has an appreciably shorter lifetime than the one encountered a model free base porphyrin substituted with three *meso*-pentafluorophenyl groups (8.5 ns). This lifetime shortening must be due to another quenching process, namely the electron transfer process from the  $P_{Zn}^{-1}P$  into the  $P_{Zn}^{\bullet+}-P_F^{\bullet-}$  state which according to the Figure 21 is exergonic by ca. 0.32 eV. The rate of this process,  $k'_{eT}$ , can be evaluated from the two lifetimes  $\tau$  and  $\tau_0$ ,

$$k'_{eT} = \frac{1}{\tau} - \frac{1}{\tau_0} = 2.5 \times 10^8 \text{ s}^{-1}$$

where  $\tau$  is the 2.7 ns lifetime and  $\tau_0$  is the fluorescence lifetime in the absence of electron transfer (i.e., the 8.5 ns obtained for the same model free base porphyrin). The quantum yield for this electron transfer process is  $\Phi'_{eT} = \tau k'_{eT} = 0.68$ . This example has shown how the two very related process, namely energy and electron transfer, can be distinguished by a combination of stationary and time-resolved fluorescence techniques.

Finally we turn to the analysis for the carotenodiporphyrin triad  $C-P_{Zn}-P_F$ . Also in this case the absorption spectra are a linear combination of the separate chromophoric systems indicating no electronic interactions among the different parts of the triad. The fluorescence spectra upon excitation of the Soret band at 425 nm show almost complete quenching of the zinc porphyrin fluorescence and only bands from the free base porphyrin at ca. 640 and 710 nm. Again a combination of energy and electron transfer processes could be the cause of this quenching effect. The energetic diagram and the states involved are summarized Figure 22.

From time-resolved single fluorescence by single photon timing again after global analysis of the decays, two exponential components were found having lifetimes of 62 ps and 2.9 ns. The fast component showing a decay at 650 nm and a

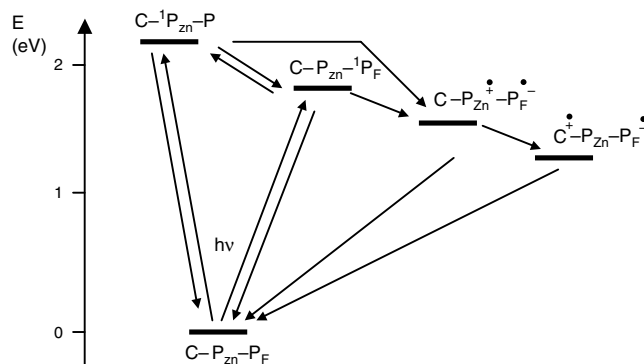


**Figure 22.** Energy diagram for the triad  $C-P_{Zn}-P_F$ . Adapted with permission from [128], D. Gust et al., *J. Am. Chem. Soc.* 113, 3638 (1991). © 1991, American Chemical Society.

rise where only the free base fluoresces (at ca. 710 nm) can be ascribed to the singlet–singlet energy transfer from the  $C^{-1}P_{Zn}-P_F$  state to the  $C-P_{Zn}^{-1}P_F$  state. The fluorescence decay of a model compound consisting of a carotenoid-zinc-porphyrin dyad, where no energy transfer can occur, showed a lifetime of 0.31 ns which is much shorter than the lifetime of a zinc porphyrin lacking the carotenoid. This shortening is indicative of a quenching process probably due to the formation by photoinduced electron transfer of the species  $C-P_{Zn}^{*+}-P_F^{-}$ . Following a similar reasoning as in the case of dyad **B**, the rate for the energy transfer process  $k_{EET}$  could be estimated as  $9.4 \times 10^9 \text{ s}^{-1}$  and the  $\Phi_{EET} = \tau k_{EET} = 0.58$  while the rate for the competing electron transfer process  $k_{eT}$  was found to be  $2.3 \times 10^8 \text{ s}^{-1}$  and the corresponding quantum yield for formation of the  $C-P_{Zn}^{*+}-P_F^{-}$  state by way of  $C-P_{Zn}^{-1}P_F$  was calculated to be 0.67. The same state can, however, also be accessed directly from the  $C^{-1}P_{Zn}-P_F$  and the overall quantum yield may vary with the excitation wavelength. Based on the total light absorbed at 590 nm, the quantum yield of the  $C-P_{Zn}^{*+}-P_F^{-}$  state by all paths was determined to be 0.64. From this species, by a secondary electron transfer step the long-lived charge separated state  $C^{*+}-P_{Zn}-P_F^{-}$  is formed as put into evidence by transient absorption spectroscopy where the radical cation of the carotenoid absorption could be measured at about 960 nm and having a monoexponential decay of 240 ns. The quantum yield based upon the total light absorbed at the excitation wavelength of 590 nm for this state was calculated to be 0.32. This means that 50% of the  $C-P_{Zn}^{*+}-P_F^{-}$  state indeed undergoes the secondary electron transfer to the desired long-lived charge separated state.

Calculation of the energy transfer rates by means of the Förster formula taking into account the orientation factor  $\kappa^2$ , which due to the amide linkage with variable orientations can have limiting values between 0.25 and 2.25, shows a large discrepancy to the experimentally measured rates in both dyads **A** and **B**. The measured rates are a factor of 14 faster for dyad **A** and a factor of 80 faster for dyad **B** than those predicted by the Förster mechanism for an orientation factor with random conformation. This discrepancy was attributed to the existence of another mechanism involving stronger electronic coupling, of Dexter type. That this was indeed the case could be proved by the simultaneous occurrence of photoinduced electron transfer which must proceed via electron exchange interactions. All the measured rates for the zinc porphyrin-free base systems are in the “normal” and not in the “inverted” Marcus region [16, 131]. Charge recombination occurs probably by direct electron transfer from the fluorinated porphyrin to the carotenoid and due to the large spatial separation between the charges this explains why the charge-separated state is long-lived. For applications in photovoltaic devices it is a stringent requirement that the energy rich charge-separated state produced upon photoexcitation has a long lifetime and that the unproductive charge recombination is inhibited allowing the energy to be used in further steps.

More recent work has involved elegant synthesis of covalently assembled multichromophoric arrays in the group of

Lindsey [132–137] which has also been recently reviewed [138]. Much of the synthetic effort has been possible only after extensive optimization of reaction conditions involving porphyrin syntheses [139–144], functional group manipulations, and devising of special protective groups adapted for porphyrin chemistry [145]. The photophysical studies and nanostructure design and synthesis have run in parallel to optimize light-harvesting or optoelectronic properties. Complex architectures have been rationally designed comprising Zn (or Mg) metalated porphyrins as energy donors and free base porphyrins (**Fb**) as energy acceptors. The preferred linkage between the porphyrin macrocycles was a diarylethylene group which, besides the advantage of being readily assembled, induces only a weak electronic coupling between the units. The thus assembled nanostructures have absorption and redox properties which are essentially the sum of the corresponding units, allowing a modular, bottom-up approach to the construction of complicated architectures with desired functions. The weak electronic coupling is due to the limited orbital overlap between the diarylethylene bridge with the extended porphyrin orbitals which are thus almost orthogonal. A further advantage of this linker group is its rigidity which leads to architectures with well defined geometries. Apart from slight rotation, the overall geometry remains constant allowing Förster-type calculations to be performed.

A further increase of the steric hindrance of the linker by adding *ortho*-methyl groups restricts the torsional mobility leading to slower energy transfer rates from the Zn to the FB moieties. Thus while in the unhindered dimer (**ZnFbU**)  $k_{Zn \rightarrow Fb} = 24 \text{ ps}^{-1}$ , introduction of the xyl group either in distal position to the Zn porphyrin (**ZnFbD**) or in proximal position (**ZnFbP**) leads to a slowing down by a factor of two of the  $k_{EET}$  to 45 and 48  $\text{ps}^{-1}$ , respectively. A bis-hindered linker (as in **ZnFbB**) leads to further slowing down to 88  $\text{ps}^{-1}$ . These structures are shown in Figure 23.

In the tetrameric array depicted in Figure 24, the measured energy transfer rate (26  $\text{ps}^{-1}$ ) is essentially the same as in the unhindered dimer **ZnFbU**, a fact which indicates that the same electronic communication among the porphyrin units exists. The observed rates are by a factor of up to 25 times more rapid than those predicted by the Förster equation for a pure through-space energy-transfer process. Accordingly an important through-bond contribution of electron exchange must operate in these systems. Understanding the factors controlling these rates have allowed the design of very efficient artificial light-harvesting units.

Strong influence on the frontier orbitals and thus upon  $k_{EET}$  can be achieved by either modifying the position of the linker from the *meso*- to a  $\beta$ -pyrrolic position on the porphyrin macrocycle, or by replacing the mesityl group by the electron-withdrawing group pentafluorophenyl (Fig. 25).

The pentafluorophenyl enhances the electronic communication in the  $\beta$ -position by a factor of more than 2 and at the same time causes a 10-fold attenuation in the *meso*-position. This fact was nicely explained by the switching of ordering of the  $a_{1u}/a_{2u}$  frontier orbitals and electron density distribution which changes with the position of linker attachment. Also important are whether the *meso*- or  $\beta$ -pyrrolic positions are unsubstituted. Thus, if one

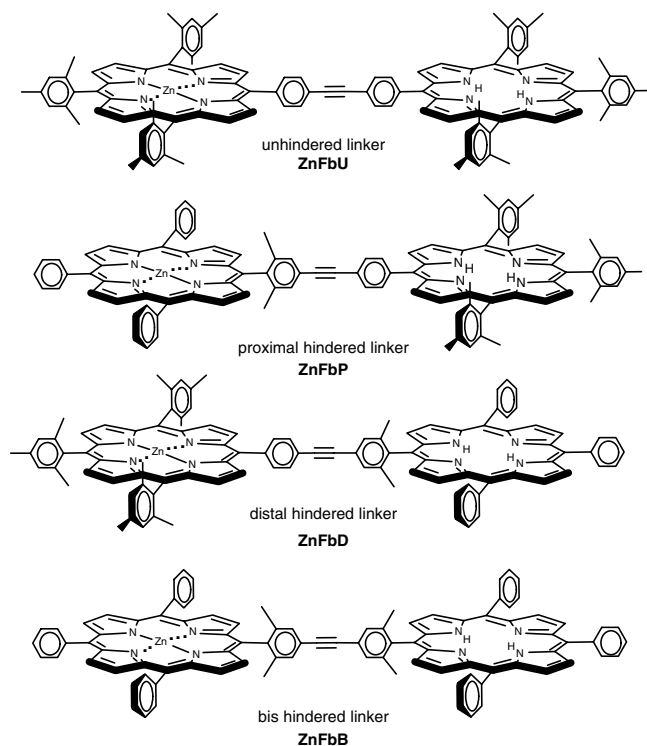
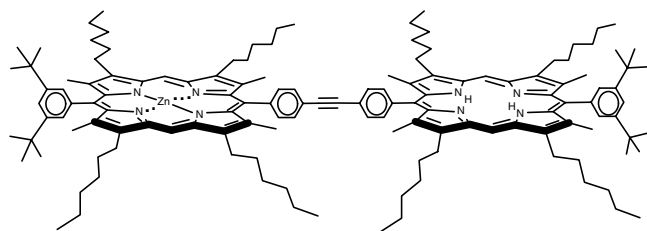


**Figure 23.** Dimeric structures for studying the effects of the torsional mobility of the diarylethylene linker on the  $k_{\text{EET}}$  rates.

compares the rate  $k_{\text{Zn} \rightarrow \text{Fb}}$  of  $24 \text{ ps}^{-1}$  in **ZnFbU** with the much slower rate encountered in a similarly linked dimer but with another substitution pattern of the porphyrin, which was prepared earlier by Osuka and co-workers [146], one can see how subtle substitution differences in these compounds drastically alter their behavior.



This compound has shown a rate  $k_{\text{Zn} \rightarrow \text{Fb}}$  of  $417 \text{ ps}^{-1}$  and an lower energy transfer efficiency  $\Phi_{\text{EET}}$  of 78% although

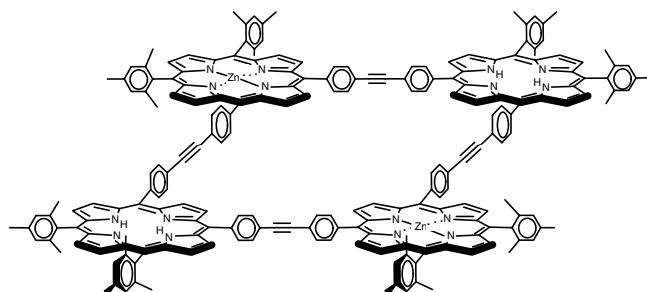


**Figure 24.** Tetrameric array with  $k_{\text{Zn} \rightarrow \text{Fb}} = 26 \text{ ps}^{-1}$ .

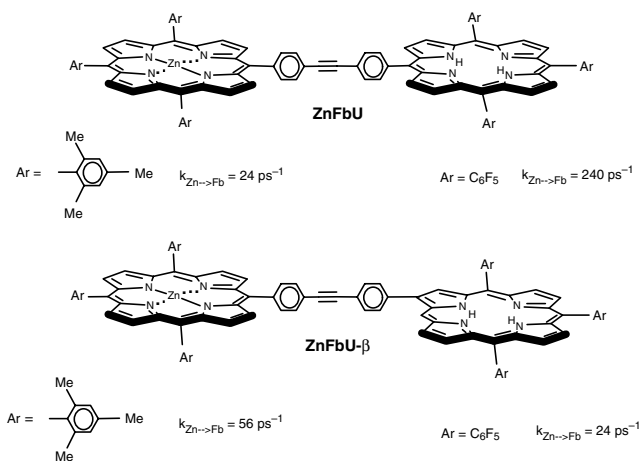
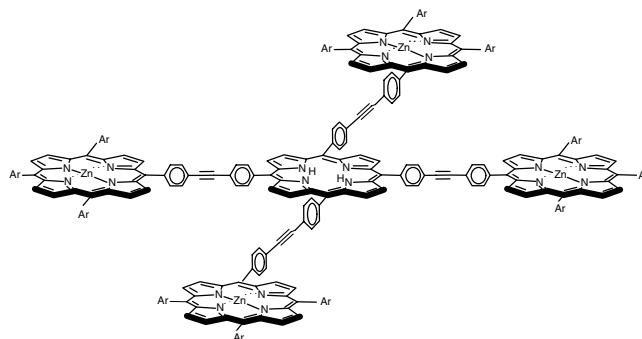


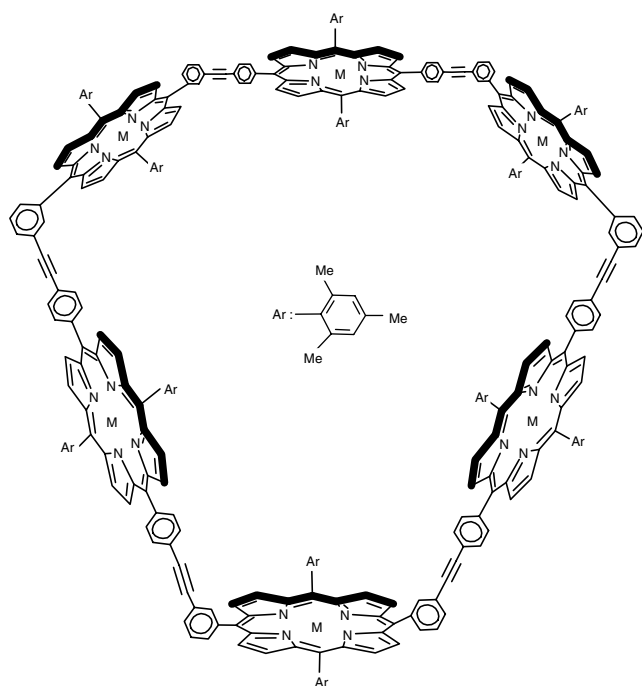
**Figure 25.** Influence of the free base (**Fb**) linkage in the *meso* or  $\beta$ -pyrrolic positions on the energy transfer rate constants.

the same diphenylethyne linker is present. Due to the four flanking methyl groups in the  $\beta$ -pyrrolic positions in this case electronic communication is almost completely hindered.

The following light-harvesting array has four antenna Zn porphyrins linked to a central free base energy acceptor (Ar = 2,6-dimethoxyphenyl group). Architecturally similar to the earlier Harriman system, this second generation antenna is more efficient due to the rigidity of the linkers and of the through-bond operating Dexter mechanism.



A hexameric wheel of porphyrins consisting of alternating zinc metalated and free base porphyrins has also been prepared [136]. Due to the *meta*-phenylene linkages a somewhat slower energy transfer process is observed,  $k_{\text{Zn} \rightarrow \text{Fb}}$  of  $34 \text{ ps}^{-1}$ , than in the case of the dimeric assembly **ZnFbU** ( $k_{\text{Zn} \rightarrow \text{Fb}}$  of  $24 \text{ ps}^{-1}$ ) although the center-to-center distance is smaller. Within the completely Zn-metalated hexameric cavity, a spindle consisting of a dipyridil-substituted free base porphyrin could be complexed [147]. This host-guest complex combines the covalent approach for construction of the preorganized wheel-like guest cavity and of the spoke with a supramolecular approach using self-assembly for forming the complex.

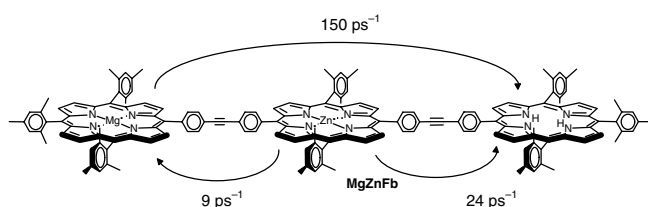


M = 2H or Zn

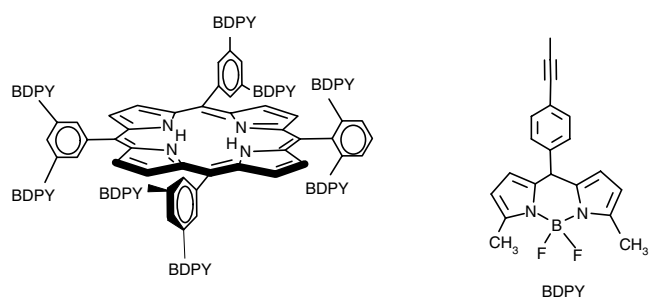
In the case of *p*-phenylene linkers, due to the shorter distance, larger electronic couplings are encountered which lead to increased rates. Only  $3.5 \text{ ps}^{-1}$  are needed for the transfer rate from a trimesityl substituted zinc porphyrin to the free base linked by a *p*-phenylene bridge. If instead of the mesityl group a pentafluorophenyl group is inserted, again a slowing down to  $10 \text{ ps}^{-1}$  was encountered.

The central metal atom also affects the energy transfer rates. Within a series of diphenylethyne linked dimers the energy transfer rates decrease from **CdFbU** ( $15 \text{ ps}^{-1}$ ), to **ZnFbU** ( $24 \text{ ps}^{-1}$ ) to **MgFbU** ( $31 \text{ ps}^{-1}$ ). For the Cd derivative, the energy transfer efficiency  $\Phi_{\text{EET}}$  also drops from nearly quantitative ( $>99\%$ ) to 87% mainly due to the very short inherent lifetime ( $\sim 100 \text{ ps}$ ) of the photoexcited Cd porphyrin. Energy transfer may be effected also between a Zn porphyrin as donor and a Mg porphyrin as acceptor; in this case a  $k_{\text{Zn} \rightarrow \text{Mg}}$  of only  $9 \text{ ps}^{-1}$  was measured.

In trimeric assemblies a branching energy transfer can occur as the energy of the lowest excited singlet state of porphyrins decreases in the order  $\text{Zn} > \text{Mg} \gg \text{Fb}$ . Thus excitation of the zinc porphyrin, if it is in a central position, can lead to branched transfer both to the  $\text{Mg}^*$  or  $\text{Fb}^*$ . A second transfer step may then occur directly from  $\text{Mg}^*$  to Fb:

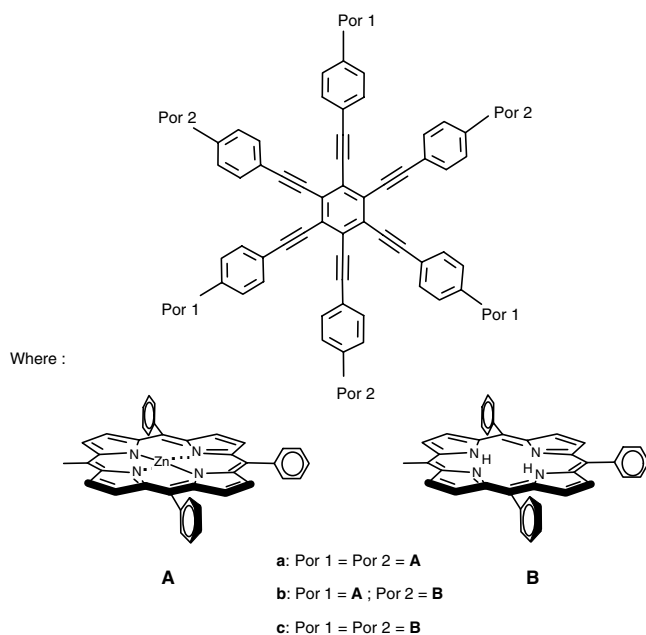


This modulation of the transfer rates closely mimics the one encountered in natural systems where stepwise transfers occur between different pigment pools. This versatile covalent building block bottom-up construction principle has also been used by Lindsey and co-workers to construct mixed arrays incorporating accessory pigments besides porphyrins such as boron-dipyrin [135, 148], perylene [149], and/or phthalocyanines [150]. The latter will be presented in Section 4.1.2.



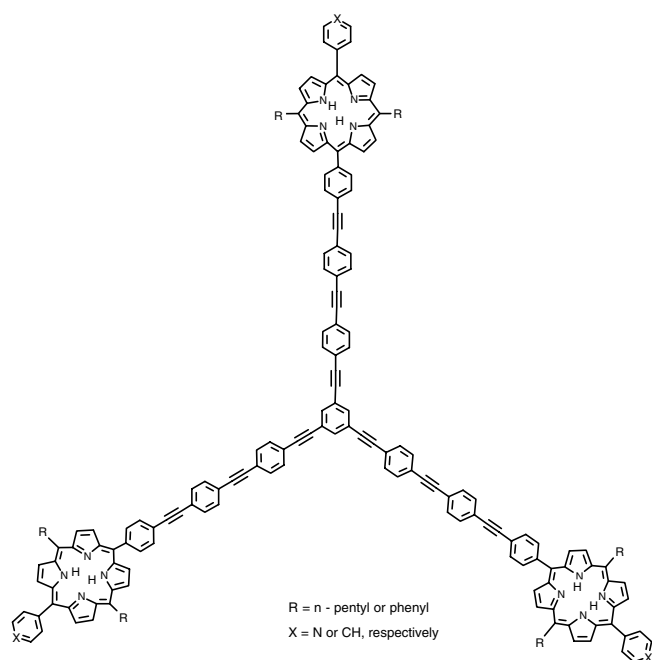
In this molecule eight highly fluorescent boron-dipyrin (BDPY) antenna molecules transfer their energy to the central free base porphyrin. The blue-green BDPY absorption cumulated over eight molecules is comparable in intensity to the porphyrinic Soret band. Dual fluorescence with exponential decays with time constants of  $\sim 2$  and  $\sim 20 \text{ ps}$  were encountered and explained by the existence of two excited state conformers, which differ in the orientation of the 5-phenylethynyl ring of the BDPY units.

Gossauer and co-workers have elaborated aesthetically very pleasing architectures, such as the niphaphyrins, and have demonstrated fast and very efficient ( $>98\%$ ) intramolecular energy transfer [151–153] in the niphaphyrin **b** depicted from the Zn porphyrins to the free bases. Here again the Dexter mechanism was invoked to explain the encountered fast rates for energy transfer:



Among the covalent architectures investigated are also ones having threefold symmetry due to a 1,3,5-triethynylbenzene as the central radialene unit or even tetraedric symmetry imposed by a central tetraphenylmethane unit. By varying the number of rigid phenylethynyl units, the porphyrin units become increasingly separated. In the smaller arrays with center-to-center distances of 2.3 nm, through a careful analysis which included time resolved fluorescence studies and the anisotropy decay, it could be established that the energy transfer occurs through both Förster and Dexter mechanisms at a ratio of about 1:3 respectively. At a larger distance of ca. 3.5 nm, the Förster mechanism is less present, the ratio being 1:10. This is because of the very good through-bond communication enabled by the spacers. At still larger distances 4.7 nm as in the array to be shown, there is a drop in the Dexter mechanism and the Förster mechanism dominates, their ratio being in this case ca. 2.1:1.

Two such nanometric covalent arrays having threefold symmetry due to Gossauer are shown:

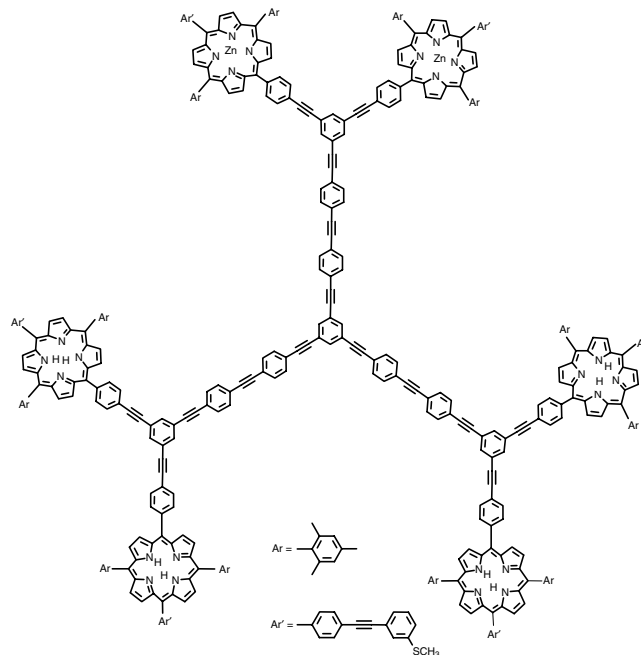


Note that introduction of the pyridine rings allows further elaboration by supramolecular interactions, as will be shown in Section 4.2.

A  $\beta_{\text{EET}}$  value of  $0.15 \text{ \AA}^{-1}$  for the attenuation factor was found by a linear regression of the logarithmic rate constants for EET versus the distance  $R_{DA}$  in several such arrays where the Dexter mechanism prevails and which shows an exponential distance dependence. As mentioned before a power  $-6$  distance dependence is encountered for the Förster mechanism. This small attenuation constant again indicates that the phenylethynyl spacers induce good through-bond communication. A much higher value for  $\beta_{\text{EET}}$  of  $1.7 \text{ \AA}^{-1}$  was reported earlier for triplet-triplet energy transfer between a donor and an acceptor separated by saturated cyclohexanediyl spacers [154]. According to Marcus and Sutin [16] the attenuation factor in the distance dependence

of electron transfer is  $\beta_{eT}$  and because actually the Dexter energy transfer process is a double electron transfer, the following relationship holds:  $\beta_{\text{EET}} \approx 2\beta_{eT}$ .

As electron transfer mediated by a variety of covalent linkers has been much more extensively studied than the energy transfer, this represents a very useful approximation to just double the  $\beta_{eT}$  values known for certain linkers and thus obtain the  $\beta_{\text{EET}}$  values. For an excellent recent review on the comparison between electron and energy transfer see [111] by Paddon-Row.

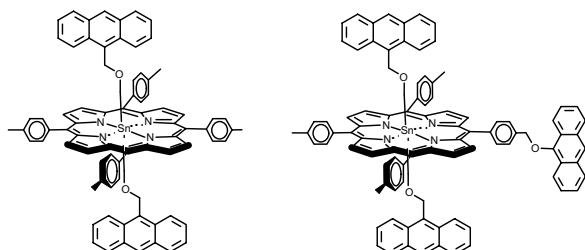


Important for the efficiency of the excitation energy transfer is also the excited state lifetime of the chromophores. Transfer between two Zn-metallated porphyrins is faster by a factor of 4 than between two free base tetraarylporphyrins. However, the efficiency is higher in the latter case due to the longer lifetime of the free base porphyrins. Ni-metallated porphyrins are not to be used in efficient antennas due to their short excited lifetime and the high energy of the singlet state which makes energy transfer both to the free base or Zn-metallated porphyrins an endergonic process by more than 0.7 eV.

Notable in the previous nanostructure is the insertion of a thiomethyl group which should allow selective attachment to gold nanoelectrodes and direct measurements of current versus voltage curves. Such studies have not been reported yet on these superb molecules, although electron conduction through thiol derivatized porphyrins synthesized by either the Lindsey or Tour group has been amply reported by Reed and co-workers [155, 156].

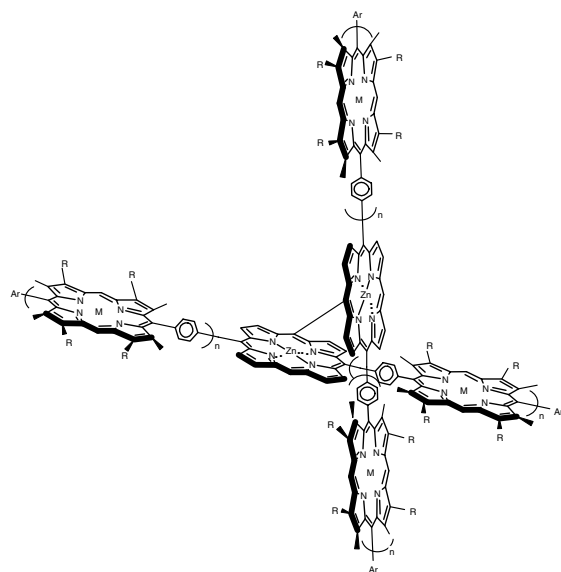
A very interesting orientation dependence of the energy transfer efficiency from anthracene donors to a porphyrin acceptor was recently reported by Indian chemists [157]. In the following tin-metallated porphyrin which accepts two axial oxo ligands, either hydroxy groups or the depicted 9-oxymethylene-anthracenes, energy transfer occurs only from

the anthracene group in the *meso*-position:

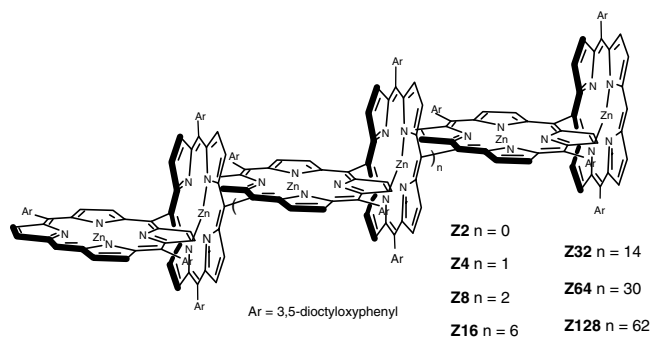


Thus, while the *meso*-tetratolyl-bis-anthryl compound on the left shows very low energy transfer efficiencies (<10%), due to an unfavorable Förster orientation factor  $\kappa$ , the compound on the right shows efficient fluorescence quenching of the *meso*-situated anthracene group by the porphyrin moiety. This was nicely demonstrated also by a model compound where the same anthracene-substituted porphyrin has the central tin atom ligated by only two hydroxy groups which shows almost complete (>90%) fluorescence quenching of the anthracene upon 250 nm irradiation. Further proof was that the fluorescence excitation spectra, with emissions collected at the porphyrin emission maxima, matched well the absorption spectra of the model with axial dihydroxy ligands and the compound on the right, but not the one on the left. This represented a clear demonstration that the directionality of energy transfer is critically dependent on the geometry of the system.

Japanese chemists have designed the most extended covalent porphyrinic architectures to date. Osuka and co-workers, after developing an efficient synthetic method for oxidative *meso-meso* coupling of porphyrins using  $\text{Ag}^{\text{I}}$  ions [158], could prepare orthogonal windmill-like porphyrin arrays. The metalated multiporphyrinic arms harvest energy and transmit it to an energy sink represented by the central *meso*-linked dimer which gives a characteristic split Soret band [159]. In this formula R is a *n*-hexyl solubility inducing group,  $n = 1, 2$  or 3, and  $\text{M} = \text{Ni}$  or  $\text{Zn}$ :



Similar reaction conditions were developed which allowed oligomerization of porphyrins having two free *meso* positions [160]. Using this synthetic methodology in a controlled and repetitive manner, the longest manmade nonpolymeric molecule was constructed by Osuka et al. comprising 128 consecutive *meso*-linked porphyrin units [161]. Here the nanostructures merge into the microstructure world having dimensions of over 0.1  $\mu\text{m}$ . The calculated length amounts to 106 nm (for  $n = 62$  in the formula below) if one estimates that one porphyrin unit is 0.835 nm long.



The photophysical properties of such rigid, extremely long rodlike molecules are very interesting and have been studied in detail [162, 163]. Additionally, resonance Raman studies have been undertaken when, by irradiating the sample at certain wavelengths corresponding to electronic transitions, the vibrational Raman spectrum is accumulated [164]. Rapid energy transfer due to the well defined geometry and the lack of any energy sink which could disrupt the energy flow along equivalent porphyrins make such light-harvesting arrays ideal candidates for molecular photonic wires. Due to the orthogonal orientation of the porphyrin rings, the electronic communication is largely inhibited so that each unit retains its individual character. However, exciton coupling occurs which leads to splitting of the Soret bands. The absorption spectra change systematically as the number of porphyrins increases. While the high energy Soret band remains constant (at ca. 413 nm), the low energy band of this couplet shifts batho- and hyperchromically upon increasing the number of porphyrin units indicating a progressive increase of the splitting energy. This is in agreement with the simple point dipole approximation of the exciton coupling theory developed by Kasha et al. [165, 166] although multipole interactions might give a better description. For an excellent earlier review on chlorophyll singlet excitons see [167].

In a monomeric porphyrin the two transitions  $B_x$  and  $B_y$  are degenerate but even in the simplest case of a dimer **Z2**, due to exciton coupling, the  $B_x$  transitions oriented along the long molecular axis become split with the energy  $\Delta E$  (also known as Davydov splitting [168]), while the  $B_y$  and the equivalent  $B_z$  transitions, being perpendicular, remain unperturbed as shown in Figure 26. Accordingly the Soret band becomes split having a redshifted  $B_x$  component while the  $B_y$  and  $B_z$  remain as in the monomer.  $\Delta E$  for a dimer can be calculated with the formula

$$\Delta E = \frac{\mu^2}{2\pi \epsilon_0 R^3}$$



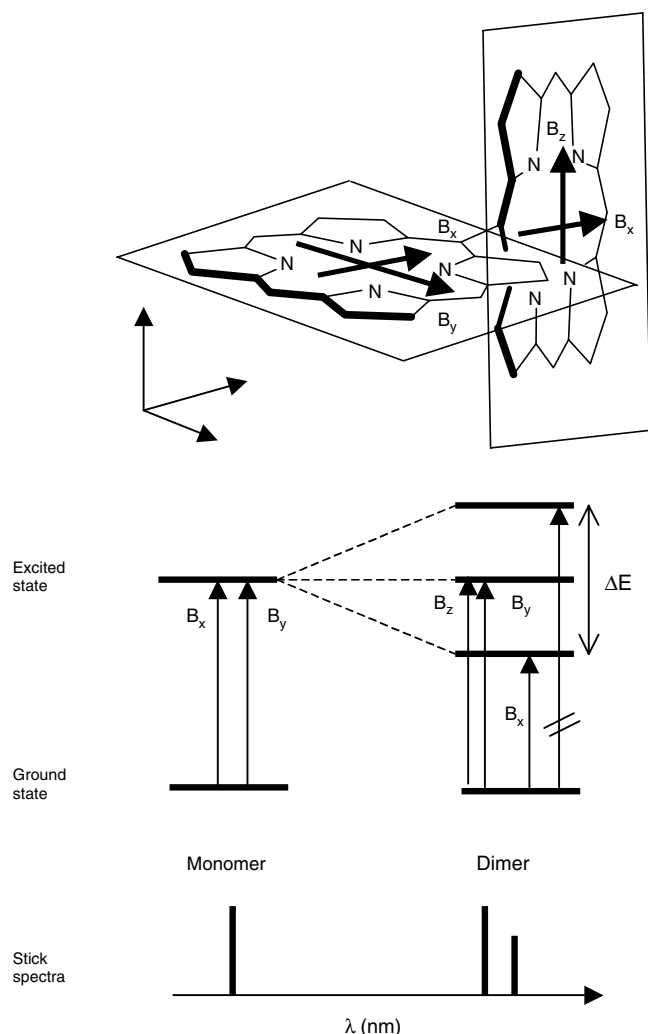


**Figure 26.** Transitions in a monomer and *meso-meso* coupled dimeric porphyrin. Adapted with permission from [163], Y. H. Kim et al., *J. Am. Chem. Soc.* 123, 76 (2001). © 2001, American Chemical Society.

where  $\mu$  represents the transition dipole moment and  $R$  is the center-to-center distance between the chromophores.

For  $N$  interacting chromophores the following relation is valid:

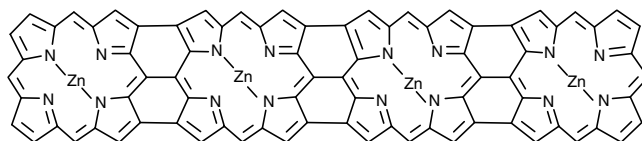
$$\Delta E = E_0 \cos[\pi/(N + 1)]$$

$\Delta E$  is thus twice the energy difference between the red-shifted  $B_x$  band and the unperturbed  $B_{yz}$  peaks and can be read directly from the absorption spectra. A linear relationship was obtained for  $\Delta E$  with increasing number of porphyrins  $N$  when plotted as a function of  $\cos[\pi/(N + 1)]$  having a slope  $E_0$  of  $4250 \text{ cm}^{-1}$ . Importantly, as the length of the array increases, the absorptivity is greatly enhanced and for **Z64** extinction coefficients as high as  $10^6 \text{ M}^{-1}\text{cm}^{-1}$  were measured. The Q bands are hardly affected as the length of the array increases. As the whole visible region of the spectrum is covered these nanostructures are very efficient light harvesters.

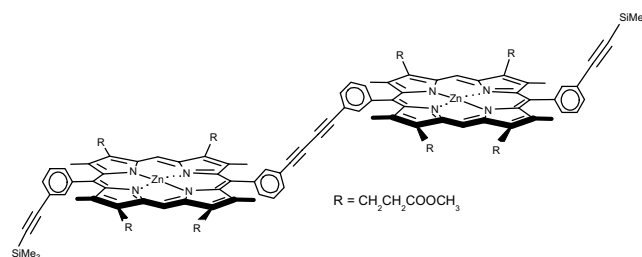
In the arrays longer than **Z8**, exciton-exciton annihilation processes become operative as seen from the appearance of

fast decay components in time resolved fluorescence measurements by single photon timing. From the cooperative spontaneous emission, also termed as superradiance, the coherence length could be estimated. The superradiance coherent length is defined as the ratio of the radiative decay rate of the porphyrin array to that of the monomeric porphyrin **Z1** (which has a lifetime of 2.64 ns). This length reflects the degree of excitonic intermolecular coherence and for the B850 ring of LH2 (and LH1) it has been estimated to be comprise about four BChl *a* units. In the previous porphyrin arrays, 6 to 8 units were estimated to be the radiative coherence length. This increased length is probably due to the direct covalent linkage of the porphyrins which keeps a center-to-center distance of only 0.84 nm which is somewhat shorter than the separation between the magnesium atoms of the BChl *a* ligated by the LH2 polypeptides.

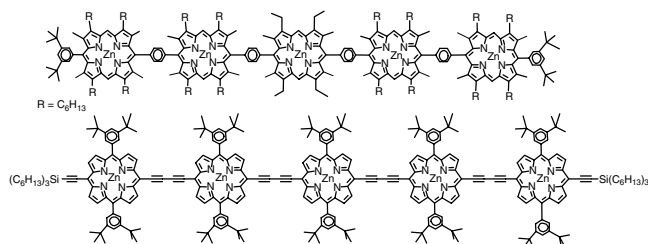
In an extension of this work, Tsuda and Osuka, devising a novel oxidative coupling using in conjunction scandium trifluoromethanesulfonate and 2,3-dichloro-5,6-dicyano-1,4-benzoquinone, have prepared from the above *meso-meso*-linked porphyrin oligomers, fully conjugated porphyrin tapes [169]. The dimer **Z2** cyclized in 86% yield while the tetramer below was obtained from the corresponding **Z4** tetramer in 78% yield. In contrast to the noninteracting *meso-meso*-linked porphyrins the fused porphyrin rings are fully conjugated having one of the strongest electronic interactions encountered so far which manifests itself by shifting the visible absorption maxima into the infrared region of the spectrum.



These fully conjugated porphyrin oligomers may be of use as molecular wires. Other linkages which have been shown to facilitate electronic communication between porphyrin rings were simultaneously and independently pioneered by Therien et al. [170–173] and Anderson et al. [174–179] and since then have been reviewed [180] and further developed. These include the *meso*-butadiyne-bridged porphyrin arrays which besides showing molecular wire behavior have extremely high second order polarizabilities being of use in the fabrication of nonlinear optical materials. A *meta*-phenylene linkage in a porphyrin dimer with a butadiyne bridge is, however, fully insulating but can give rise to *cis*-oid and *trans*-oid conformations which could be imaged by Sanders and co-workers using scanning tunneling microscopy (STM) [181].



A very different behavior was encountered in porphyrin oligomers with increasing lengths having 1,4-butadiynylene and 1,4-phenylene bridges between the porphyrin rings [178]. By flash-photolysis time-resolved microwave conductivity measurements it could be shown that the 1,4-phenylene type bridges lead to a singlet state  $S_1$  with a very small excess polarizability ( $<20 \text{ \AA}^3$ ) which is characteristic of a tightly bound Frenkel-type exciton. In contrast, the butadiynylene linked oligomers have very large excess polarizabilities for their  $S_1$  states which increases up to  $960 \text{ \AA}^3$ , with increasing oligomer length, a characteristic for loosely bound, Wannier–Mott type excitons. The optical absorption and fluorescence spectra also indicate strong electronic interactions in this case. However, the triplet excited state of the latter oligomers is much more localized having an excess polarizability of  $50 \text{ \AA}^3$ . In a preliminary previous study it was shown that in a similar oligomeric butadiyne-linked porphyrins with ca. 10 units, the photoinduced charge separation is long-lived having a half life of ca. 100 ns [182].



Because energy transfer and electron transfer are very related phenomena, as can be seen from the two mechanisms described earlier (see Section 2) which often operate in conjunction, and because conduction is a higher form of electron transfer some explanatory remarks may be in order here. It is interesting how mathematicians, physicists, and chemists evolve for the same phenomena completely different terminology which sometimes also hampers interdisciplinary synergistic collaborations. Chemists due to chemical formulae and systematic nomenclature have evolved a very precise archiving system of their research and thanks to modern databases can retrieve within seconds complete information on a certain molecule such as if it has been prepared before or its properties such as toxicity, melting point, color, odor, etc. Physicists, working on different problems, may come across the same phenomena and as their literature searches are done primarily by keywords, which are arbitrary, thus nonsystematic, and also nonexhaustive. Systematization of information in mathematics is even worse, and here often knowledge of related problems and solutions can be retrieved only by consulting experts in the field.<sup>2</sup>

<sup>2</sup> Henry Poincaré was known as the last universal expert in mathematics. Currently “experts” exist only in limited branches of the field. An anecdotal case of a researcher trying to solve analytically a very complicated triple integral which he could not solve numerically or find either tabulated or in the literature is by the method of Fock: He writes the problem to be solved clearly on a piece of paper and knocks at the door of Academician Fock. The next day he had the solution.

Solid-state physics has long ago elaborated the description of phenomena encountered upon photoexcitation of molecular crystals composed of chromophores. In such a multichromophoric assembly, *excitons* are formed which are neutral, electron–hole pairs. These may differ in properties, and by the way these are described (or derived), from the excited state of an individual chromophore. This is also the point where chemists and physicists sometimes start diverging in terminology due to their different backgrounds. Once charge separation has occurred, a combination of electrostatic and electron-exchange interactions with other nonspectator molecules in the vicinity may take place. If electron exchange is inhibited, due to large distances and/or noninteracting orbitals, then the interchromophoric interactions are mainly electrostatic and the exciton resides exclusively on a single molecule and thus is called tightly bound or Frenkel type [183]. Excitation energy transfer among adjacent chromophores occurs in this case by the Förster mechanism by way of collapse of the exciton on one chromophore and transfer mediated by a virtual photon to the adjacent chromophore which becomes thus a “new” exciton. For long, one-dimensional, Osuka-type **Z** oligomers or the *p*-phenylene-linked oligomers, this leads to a “photonic wire” behavior. On the contrary, for the Osuka tapes, or the butadiynylene oligomers, due to the strong electronic interaction either by direct orbital overlap or by mixing with the bridge orbitals, electron exchange occurs (i.e., a Dexter mechanism operates). In this case the electron and hole forming the exciton may become distonic and thus reside on different chromophores within the time frame of the observation. One speaks in this is the case of weakly bound electron–hole pairs or of Wannier–Mott type excitons [184, 185].

In the *p*-phenylene bridged oligomers the porphyrin units are isolated from each other, just as in the Osuka-type **Z** oligomers. Beginning with the dimer also here the Soret band shows a Davydov splitting while the Q bands are hardly affected. Upon excitation, as a negligible increase of polarizability is observed, only localized Frenkel-type excitons are formed. In contrast to the *p*-phenylene bridge, a 1,4-butadiynylene bridge mediates strongly electronic communication between the porphyrin rings. The strong orbital delocalization mediated by the bridge is seen in increased batho- and hyperchromic shifts of the Q bands as the number of porphyrin units within one oligomer increases. The singlet excited state is neutral but highly polarizable, which speaks for the formation of a loosely bound Wannier–Mott-type exciton, the correlation length being estimated as 3 to 4 porphyrin units. Within a such polymeric nanostructure with more than 10 porphyrinic units, dissociation of the exciton is expected into separate mobile charges. However, the triplet state  $T_1$  is localized on only one porphyrin unit, irrespective of the nature of the bridge linking the porphyrin units. These observations can be nicely accounted for by a relatively large contribution of a planar singlet excited state where the 1,4-butadiynylene bridge adopts a cumulenic limiting structure (Fig. 27). Such a planar limiting structure is not possible with a 1,4-phenylene bridge due to severe steric hindrance between the  $\beta$ -pyrrolic hydrogens and the *ortho*-hydrogens within a *para*-quinoid structure. According to molecular models, these hydrogen atoms

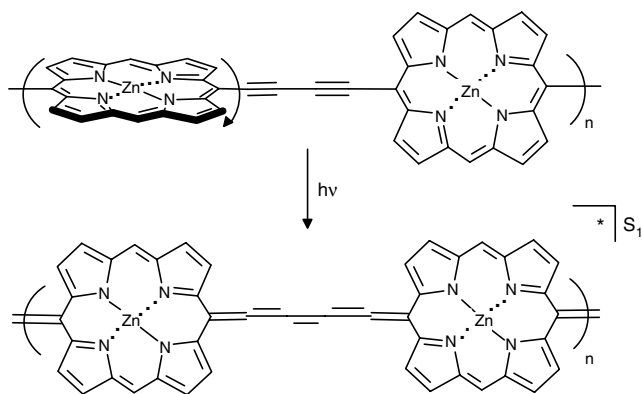


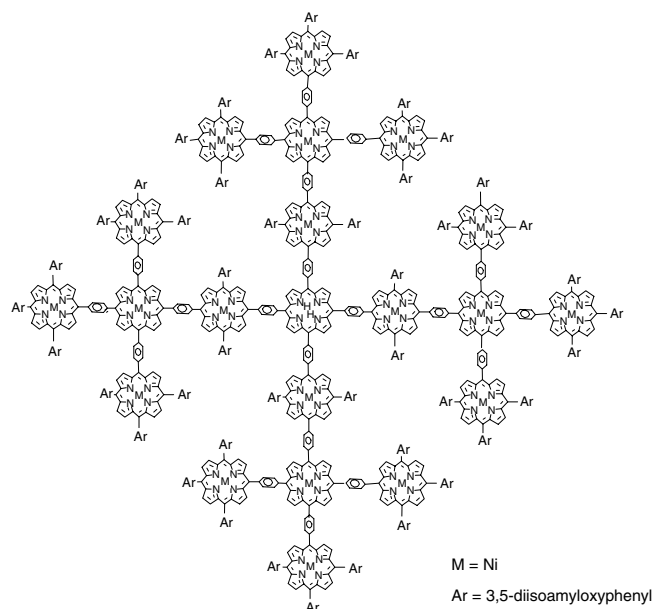
**Figure 27.** Photoinduced formation of a cumulenenic structure of the butadiynylene bridge with the + and – charges being localized on other porphyrinic rings. Solubility inducing substituents have been omitted for clarity.

would approach less than 0.5 Å in a fully planar structure which is thus energetically unacceptable. The uniqueness of the 1,4-butadiynylene bridge resides in the absence of hydrogens which would prevent planarization and thus fully delocalized molecular orbitals. We expect that a 1,4-bis-ethynylphenyl linker would also mediate efficiently electronic communication between porphyrin units attached in the *meso*-positions. Due, however, to the increased linker length and separation of the chromophores, a smaller super-radiance coherent length is in this case to be predicted. In a crystal structure of a dimer ( $n = 1$ ) the porphyrin planes are actually coplanar [176]. In solution and in more extended oligomers deviation from planarity can occur as the rotation barrier around the porphyrin-ethynyl single bonds is expected to be lower than 1 kcal/mol. For comparison, the rotation barrier in 1,2-diphenylethyne is 2.4 kJ/mol in the ground state but rises to ca. 20 kJ/mol in the singlet excited state [186].

An important aspect, often neglected, is that high solubility has to be ascertained in order to allow purification and full characterization of such nanoarrays by decorating the porphyrins with certain groups. A special such group is the 3,5-di-*tert*-butylphenyl group introduced to porphyrin chemistry initially by Crossley and Burn [187, 188] also for making extended porphyrin wires having conjugated benzo and polyazabenzofused groups. The molecular electronic properties of such fused rigid oligoporphyrin wires have also been subsequently investigated [189]. These wires have dimensions of up to 5.6 nm and thus are able to span a membrane. Due to the excellent solubility induced by the 3,5-di-*tert*-butylphenyl group this length could be doubled in only one synthetic step accessing thus molecular wires suitable for contacting with microelectrodes. We propose to name the 3,5-di-*tert*-butylphenyl group as “Crossley’s crutch” because it helps porphyrin chemists not only to solubilize extremely well complicated architectures but also to visualize these either by scanning probe microscopy techniques [190, 191] or X-ray diffraction techniques as these voluminous groups pack well into crystal structures [192]. Furthermore, selective electrophilic chemistry may be performed on the porphyrin ring leaving intact the *meso*-aryl groups due to the steric hindrance of the *t*-butyl groups

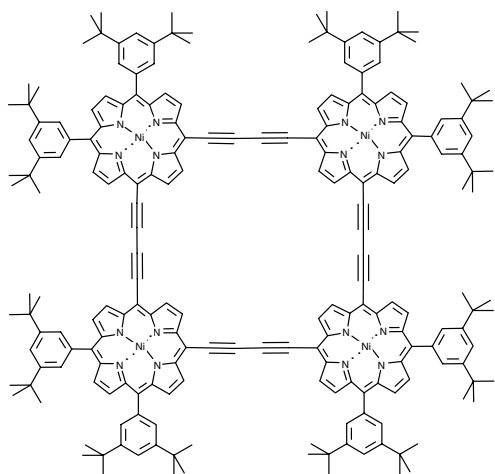
[193, 194]. Even better solubilizing groups such as the 3,5-bis(octyloxy)phenyl or 3,5-bis(isoamyloxy)phenyl have since been devised but extrapolation of the photophysical properties from one substituted porphyrin to another should be done with care. This is mainly because the rotational diffusion times become slower and also affected are the fluorescence lifetimes [163]. No crystal structures have yet been reported with such groups. The longest alkyl chains which could be appended onto a porphyrin and from which crystals suitable for X-ray analysis could be grown were two *meso*-undecyl sidechains [195]. There is a trade-off between solubility, molecular complexity, and ability to crystallize which has to be taken into account when devising porphyrinic architectures with desired properties. Apparently the *n*-hexyl sidechains, as has been systematically explored by Sanders, are a good compromise which confer enough solubility but still yield crystals which are the best way to obtain structural information on the assembly of such nanostructures.

Sakata and co-workers have not only prepared the first *meso*-tetrakis-3,5-di-*tert*-butylphenyl copper porphyrine which could be successfully imaged [190], dawning thus the era of “photogenic molecules” [196], but could also prepare a unique “Mandala-type” porphyrin array [197] having 21 porphyrin units with an impressive molecular formula of  $C_{1244}H_{1350}N_{84}Ni_{20}O_{88}$  with a molecular mass of over 20 kDa as evidenced by matrix-assisted laser ionization, time-of-flight (MALDI-TOF) and dimensions of roughly 6.5 nm which were successfully imaged by STM on a Cu(111) surface as distinct squares having a fine structure. Although photophysical studies were not performed, this would be a very interesting study if different metalated and free base porphyrins could be inserted into desired positions. This architecture can be actually considered as a dendrimer made only out of porphyrin units. Dendrimers are considered in Section 4.1.3.



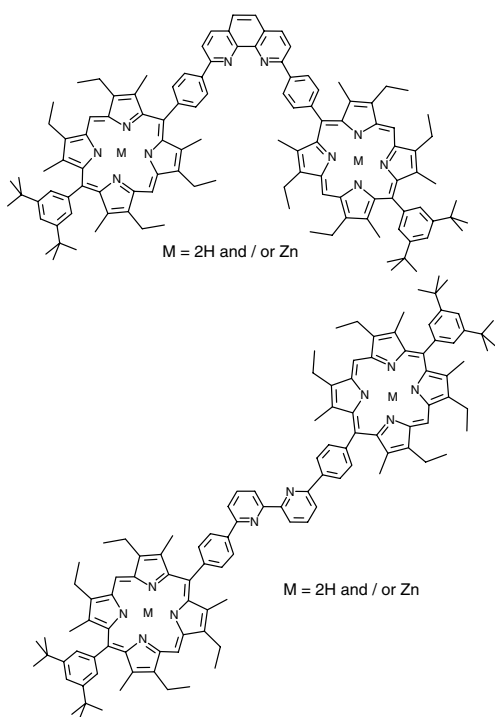
Another interesting covalent nanostructure synthesized more recently in the laboratories of the same Japanese

chemists is the following tetramer with butadiyn linkages. Astonishingly, the copper mediated Glaser–Hay coupling employed in the synthesis does not lead to higher oligomers [198]. In this case in their design the authors combined the Therien–Anderson 1,3-butadiyn linkage which facilitates electronic communication with the overall geometry of the Lindsey-type tetramer having *meso*-aryl linkages:



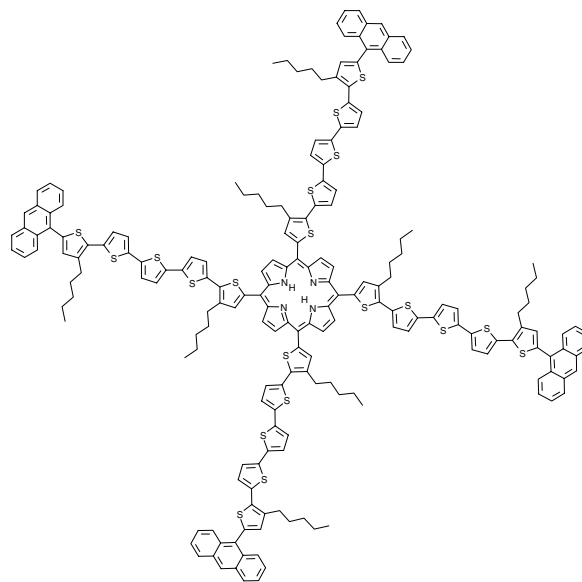
The photophysical studies of this nice porphyrin square, which shows absorption spectra similar to the corresponding Anderson linear tetramers [176], although announced as being under investigation, have not yet been reported.

A thorough investigation of the intramolecular energy transfer in bisporphyrins has shown a sixfold increase in the transfer rate in the case of a *cis*-phenantroline bridge (which leads to 1.3 nm center-to-center distance) compared to an  $\alpha$ - $\alpha$ -bipyridine bridge (2.3 nm) [199]:



For the bipyridine linker, also a folded *syn*-conformer is present to about 30% due to the unrestricted rotation around the 2,2'-bipyridyl single bond. In this conformer as well as in the phenantroline case a pure Förster mechanism cannot account for the observed energy transfer rates and this is explained by the large size of the porphyrins which have comparable dimensions to their center-to-center separation, and thus considerable exchange (Dexter-type) interactions may occur. Very interesting in these or similar systems would be to be able to switch between conformers and thus between the energy transfer mechanisms by using, for example, weakly complexing metal ions to the bipyridine.

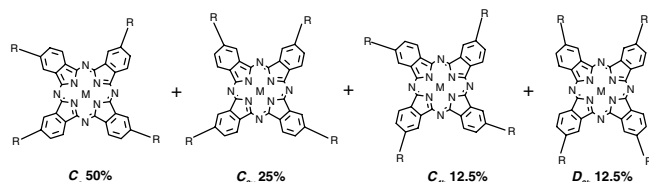
In conclusion of this section describing covalent nanostructures encompassing porphyrins devised for studying energy transfer, the study of Vollmer et al. deserves mention [200]. In this study, a molecular photonic wire having a porphyrin core and four pentathiophene arms terminated by anthryl groups has been synthesized in a multistep sequence. Different chromophores have thus been linked by the pentathiophene bridge which mediates efficiently electronic communication. Singlet–singlet energy transfer occurs upon selective excitation of the four anthracene donors within less than 10 ps, the resolution time of the experimental setup. However, no clear-cut mechanistic conclusions could be drawn in this particular case, due probably to a mixing of Dexter and Förster contributions to the energy transfer rate. Replacement by saturated spacer molecules, which interrupt the conjugation of the oligothiophene bridges, but keep the same overall geometry, could shed light upon this problem.



#### 4.1.2. Phthalocyanine-Based Nanostructures

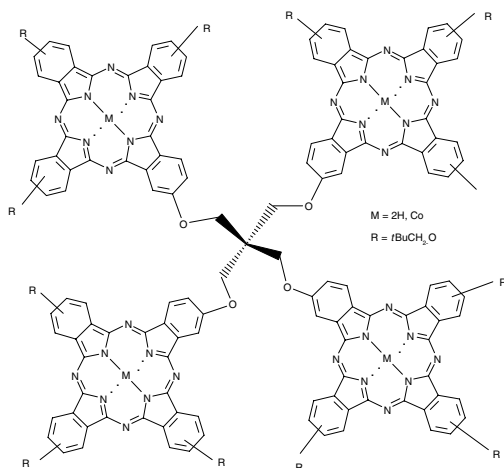
Phthalocyanines (Pc's) are extremely robust chromophores having applications as industrial dyes and pigments. Their stability and high absorption coefficients in the visible region make them better candidates for light-harvesting purposes than porphyrins. However much fewer studies have been performed with Pc's due to two main synthetical difficulties which have to be circumvented. The first difficulty is related

to a much lower solubility in organic solvents which is associated with the need for tailored substituents in order to allow chemical reactions and chromatographic purifications to be performed for accessing nanostructures. The second obstacle is due to the complex isomeric mixtures which are usually obtained for substituted Pc's. For example, a tetrasubstituted phthalocyanine can have the following four isomers if only one substituent is present in each benzoannulated pyrrole ring, as is the case when a metal templated reaction is used for Pc formation:

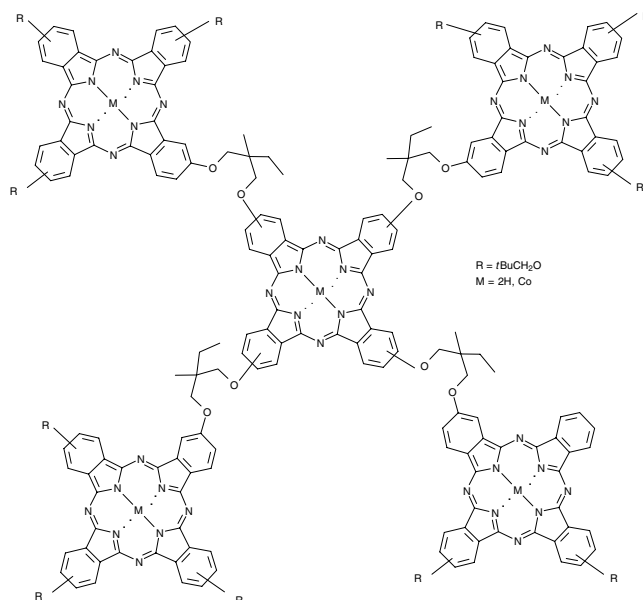


The percentages show the statistical expectation with which the isomers, indicated by their symmetry group, should be formed assuming thermodynamic control of the reaction and similar energies. Significant deviations from the expected ratio have been observed depending also on the templating metal atom or the precursor used for the tetracondensation. This is usually a phthalodinitrile or synthetic equivalent such as the diamide, anhydride, or diiminoisoindoline. In many cases further elaboration of functional nanostructures has been performed without isomer separation, a fact which leads also to inhomogeneous photophysical properties. Sometimes very different physical and chemical behaviors are encountered between these regioisomers. Recently, we could show that for tetrasulfonated Pc's ( $R = SO_3^-$ ) isomer specific rates are encountered for the loss of an electron from the tetra-anions in the gas phase [201]. Also the self-assembly properties of these isomers differ. The alternative to working with inhomogeneous preparations, thus exhibiting properties which are hard to quantify, is of course to symmetrize the Pc's with identical disubstituted benzoannulated pyrrole rings.

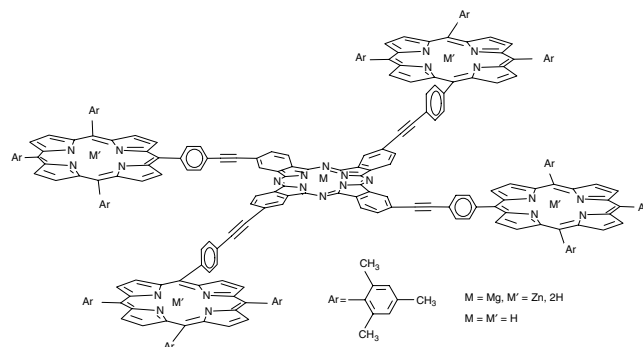
The first covalently linked nanostructures with several Pc's were synthesized by Leznoff and co-workers, of which two examples, a tetranuclear [202] and a pentanuclear array [203–205], are presented here:



In these cases, due to the nonconjugated linkers, no electronic communication occurs between the Pc macrocycles.



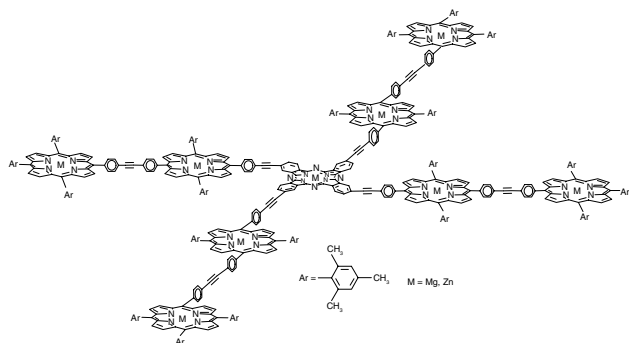
Several light-harvesting pentads having a phthalocyanine core and porphyrins as antennas were prepared by Lindsey and co-workers and the photophysical properties were investigated by Bocian and Holten [150]:



Various metals, such as Mg or Zn, or the free bases could be selectively inserted in the pentads which were actually mixtures of the four isomers described. Rapid energy transfer occurs from the porphyrins to the Pc. Excitation of the free base porphyrins at 515 nm leads to emission exclusively from the phthalocyanine with high quantum yields. The energy transfer is very fast (time constant of ca. 1 ps) and quantitative for the free base and zinc metallated pentads. In the case of the magnesium pentads, due to the matching energy levels, some competing electron transfer occurs from the excited porphyrins. Furthermore absorption over a very wide wavelength range (from 400 to 750 nm) together with good electronic communication mediated by the phenylethynyl groups makes these star-shaped arrays excellent light-harvesting nanostructures. The complex kinetic behavior observed might also be due to slightly different behavior among the isomers.

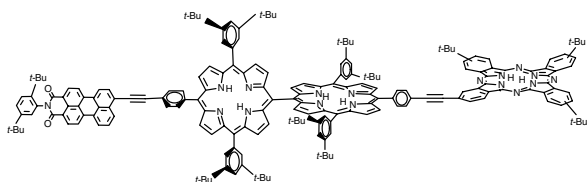
An even more impressive covalent nanostructure having eight porphyrin units tightly coupled to a central

phthalocyanine was synthesized by Li and Lindsey [206]:



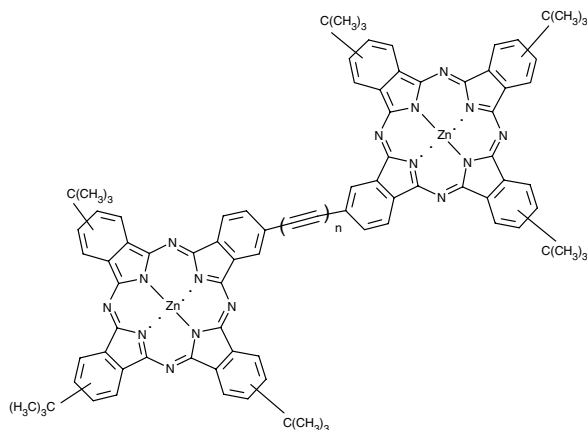
This nonamer also absorbs light across the solar spectrum and exhibits rapid and efficient energy transfer from the porphyrins to the Pc.

In an extension of these two studies, a strongly coupled linear array comprising a perylene unit a bis-porphyrin and a Pc light trap has been synthesized and investigated for rapid energy funneling [207]:

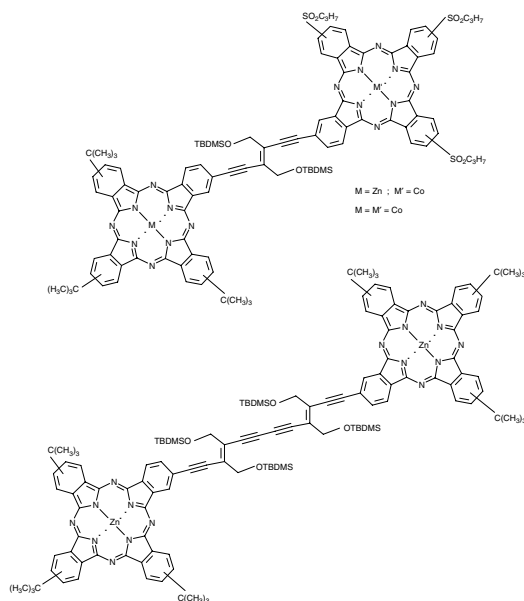


By selective excitation of the perylene unit (at 490 nm) exclusively fluorescence from the Pc is observed, with a high quantum yield ( $\Phi_f = 0.78$ ). A rapid energy cascade occurs from the perylene via the two porphyrins and finally to the Pc whose excited state is formed with time constants of 2 (90% of the amplitude) and 13 ps (10%). This energy transfer “wire” is superior to the ones based exclusively on porphyrins, being 5 to 10 times faster than the single step energy transfer from a zinc porphyrin to a free base porphyrin covalently linked in the *meso*-positions by a bis-(*p*-phenylene)ethyne linker.

Different linkers which mediate electronic communication between Pc's, synthesized also with push-pull substituents in view of applications for nonlinear optical materials, have been elaborated by Maya et al. [208–209]:



Somewhat weaker electronic communication than in these cases with ethynyl ( $n = 1$ ) and buta-1,3-diyndiyl-bridge ( $n = 2$ ) are encountered with these mono and bis-(*E*)-1,2-diethynylethene-(*E*)-hex-3-ene-1,5-diyne-bridges:



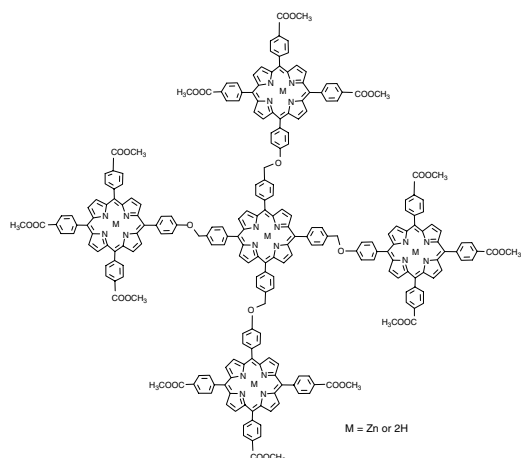
The increase in conjugation does not lead to significant changes in the ground state absorption spectra. This might be due either to reaching the limit of the conjugation length or to slight deviations from planarity of the sterically encumbered tetrasubstituted *E*-double bonds.

An excellent review on the ground and excited state optical properties of Pc's linked to porphyrins and porphyrazines was written by Tran-Thi [210].

#### 4.1.3. Dendrimers

Dendrimers are an elegant approach for obtaining covalent nanostructures using repetitively the same reaction sequences enabling transformation from one generation ( $G_n$ ) to the next ( $G_{n+1}$ ).

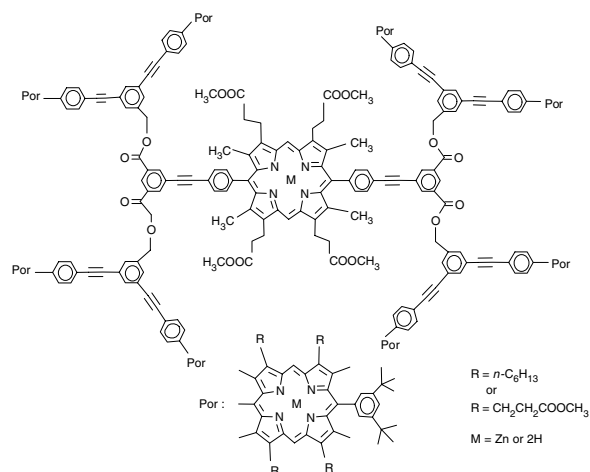
Porphyrinic dendrimers have been synthesized in several groups. Thus Norsten and Branda have obtained in relatively good yield (48% after purification by column chromatography) the following first generation ( $G_1$ ) dendrimer [211]:





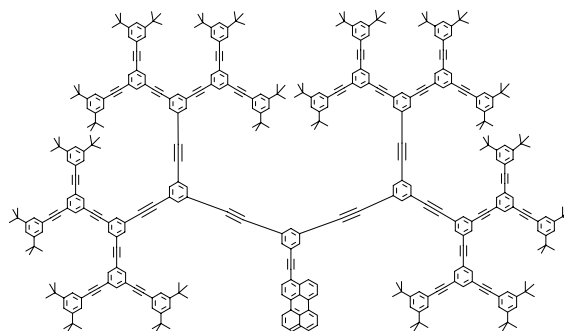
The synthetic strategy involved conversion of the 4-carbomethoxyphenyl groups first by  $\text{LiAlH}_4$  reduction into the benzylic alcohol, then into the corresponding chloromethyl derivative which was afterwards used to append four other porphyrins by ether linkages. The resulting pentaporphyrin has now 12 carbomethoxy groups which can be similarly elaborated to a second generation porphyrinic dendron, as the ether linkages should be stable to all reaction conditions involved. Apparently, the absorption spectrum indicates no ground state interaction between the porphyrin rings, being the sum of the individual components. Remarkable is also the relatively high solubility in solvents such as dichloromethane and chloroform of the free base derivative and in tetrahydrofuran of the pentazinc metalated dendrimer.

A different, more convergent approach was followed in the Sanders group for preparing a nonmetalated zinc porphyrinic dendron with folding arms. Pd-mediated coupling of phenylacetylenic groups appended into the *meso*-position of porphyrins allowed construction of the sidearms as well as coupling of the central porphyrin to a 5-iodoisophthalic acid moiety. Esterification under mild Mitsunobu conditions provides a wedge having four porphyrin units linked upon the iodobenzene derivative which in the final step connects two wedges via the central porphyrin. The yields of the sequence are remarkably high (about 78% per coupling step) and involve no protection/deprotection steps. By MALDI-TOF mass spectrometry the correct molecular ion for  $\text{C}_{660}\text{H}_{804}\text{N}_{36}\text{O}_{16}\text{Zn}_9$  nanostructure was encountered at 10,087 Da. The folding arms were used to bind DABCO molecules, a fact which could be followed by visible absorption changes in the Soret band which becomes redshifted, and an exciton coupling between two DABCO linked porphyrins becomes visible. It is thus possible to modulate the physical and photophysical properties such as viscosity, solubility, or excited state lifetimes through complexation with a bidentate ligand which affects profoundly the conformation of this dendrimer.

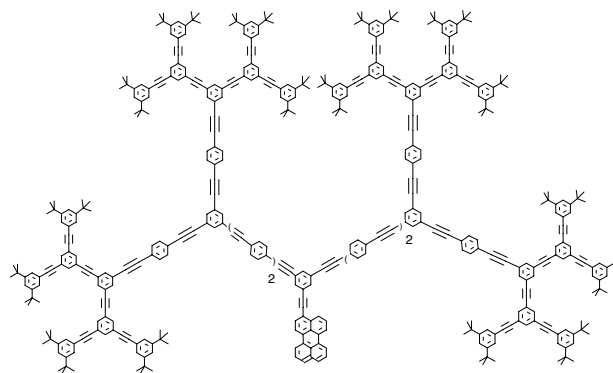


Earlier studies by Fréchet and co-workers have shown that indeed the absorption and emission are profoundly affected by encapsulation within third or fourth generation poly(benzylether) dendrimers [212]. Using a *p*-nitroaniline core as solvatochromic probe, when nonpolar solvents such

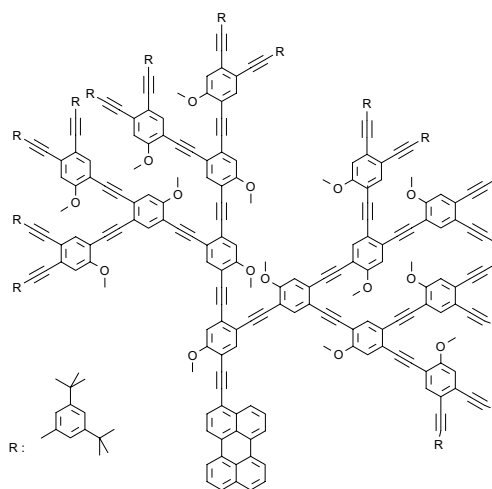
as carbon tetrachloride or toluene are used, a strong bathochromic shift occurs in the higher generation dendrimers when solvent access at the core is prevented. The core's local polarity corresponds to that of highly polar solvents such as dimethylformamide. Similar abrupt shifts in the fluorescence emission were found in phenylacetylene dendrimers synthesized by Moore and co-workers upon passing from the fourth to the fifth generation [213]. An energy gradient can be formed due to a special arrangement of the linear phenylacetylenic chains [214, 215]. More recently Melinger et al. have studied the photophysics of such phenylacetylene dendrons with unsymmetrical branching having a perylene trap [216].



Symmetrical branched dendrimer.



Symmetrical branched dendrimer with extended phenylacetylenic arms [349].

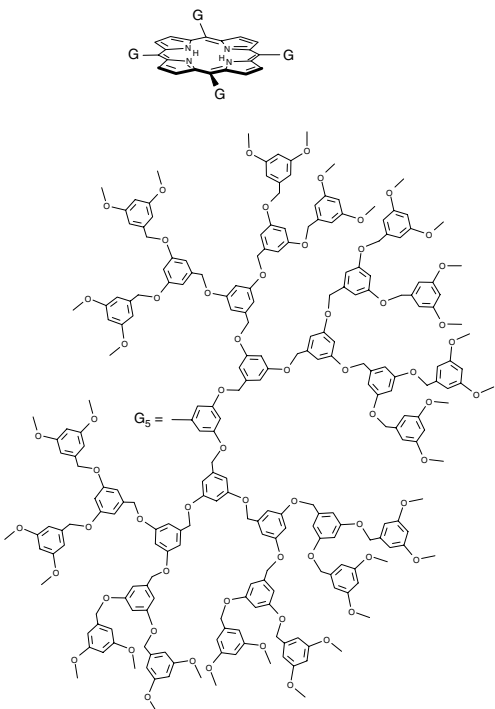


### Unsymmetrical branched dendrimer.

Without the perylene trap the higher generation dendrons have large molar extinction coefficients ( $>10^5 \text{ M}^{-1}\text{cm}^{-1}$ ) and exhibit high fluorescence quantum yields (65–81%). With the perylene trap rapid energy transfer occurs with over 90% efficiency. While the symmetrical branched dendrons depicted have *meta*-phenylene linkages which do not allow extended conjugation, the *ortho*- and *para*-phenylene linkages permit the delocalization of electrons through the contribution of *ortho*- and respectively *para*-quinoid limiting structures. This is manifested by a large bathochromic shift (ca. 50 nm) of the absorption maxima of the perylene trap as well as of the phenylacetylenic backbone.

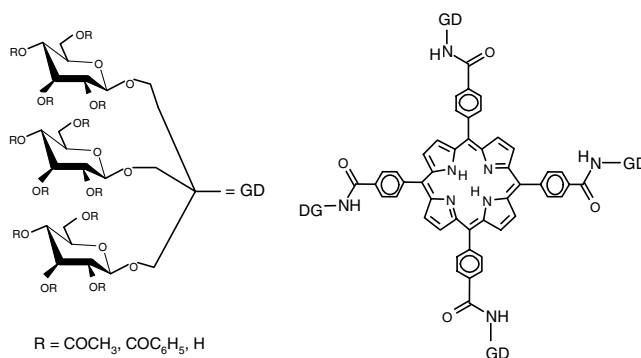
Dendritic architectures having an anthracene core, phenylacetylene scaffolding, and triphenylamine as terminating antenna groups, which are also effective hole transporters, have been assembled into an electroluminescent device [217] of organic light emitting diode type. Although the phenylacetylenic backbone was efficient in mediating the energy transfer, the device performance was limited by self-quenching effects due to aggregation on the solid support. Better performances were achieved in modular devices with dendrimers having a coumarin or pentatiophene cores which also allow color tuning [218, 219].

Jiang and Aida have prepared a poly(benzylether) dendrimer attached to a porphyrin core [220]. Only a limited amount of overlap occurred between the fluorescence of the dendritic arms and the Soret absorption of the porphyrin core allowing some energy transfer to be observed upon excitation in the UV region (280 nm). The transfer efficiency was quite high ( $\sim 80\%$ ) only in the tetrasubstituted fourth and fifth generation dendrimers ( $G_4$  and  $G_5$ ). If, instead of a *meso*-tetraakis-substituted porphyrin only three, two, or one dendritic arms were present, due to the increased mobility and conformational freedom,  $\Phi_{\text{EET}}$  dropped to 32, 20, and 10% respectively.

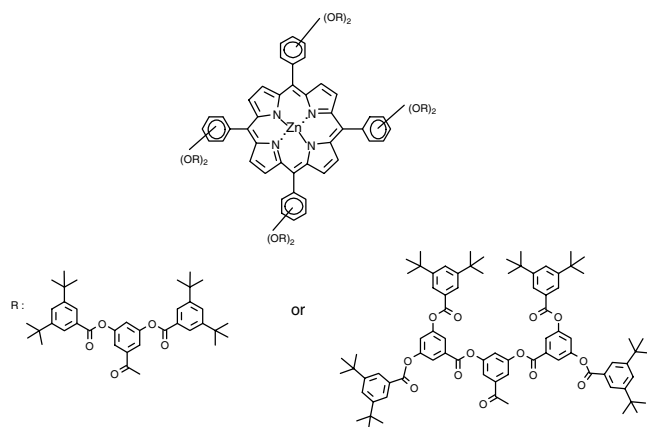


If instead of the poly(benzyl ether) dendrons triphenylene-type dendrimers are attached to the porphyrin core, due to the better spectral overlap, higher efficiencies were encountered even in lower generations of dendrimers [221]. One problem associated with the dendrimer architecture is that energy collected at the periphery is transferred to the interior and thus it is not available for further use such as charge separation, as in natural light-harvesting nanostructures. However, a spectacular application was shown earlier by Jiang and Aida where instead of the porphyrinic core, an azobenzene core was used which could be isomerized from *cis* to *trans* upon irradiation [222]. An unusual rate acceleration by two orders of magnitude was observed only in the high generation poly(benzyl ether) dendrimers upon irradiation with low flux infrared (IR) frequencies matching the vibration mode of the aromatic rings ( $\sim 1600 \text{ cm}^{-1}$ ). This result was interpreted that the dendritic shell insulates the azobenzene core from collisional deactivation and that at the same time it acts as a IR photon antenna.

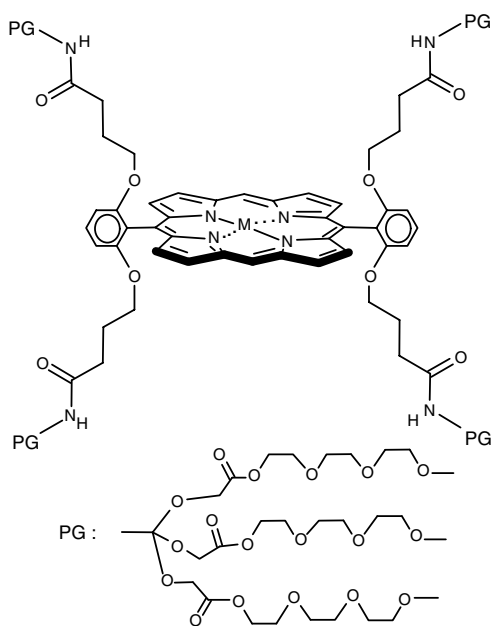
A similar *meso*-tetraarylporphyrinic core was very recently incorporated into a glycodendrimer by Stoddart and co-workers [223]. Either peracetylated, perbenzoylated, or hydrolyzed sugar units were used. As expected the glycodendrons do not show any electronic interaction with the porphyrin core. When exciting at 230 nm in the case of benzoate substituted dendrimer, complete quenching of the porphyrin emission was observed. This was explained by the absence of an energy transfer from the benzoate groups to the porphyrin core and by either a very fast radiationless deactivation or by an electron transfer process which quenches the luminescence. Also in this case dual fluorescence behavior was observed with two lifetimes, one shorter than the usual porphyrin decay which was attributed to the existence of multiple conformations in solution due to the bulky  $\beta$ -D-glycopyranoside units.



Suslik and co-workers have prepared several polyphenyl ester dendrimers with a *meso*-tetraarylporphyrin core and have studied the binding of various nitrogen ligands to the central zinc atom [224]. A certain shape selectivity of the binding constants was observed but no photophysical measurements were performed in that study.



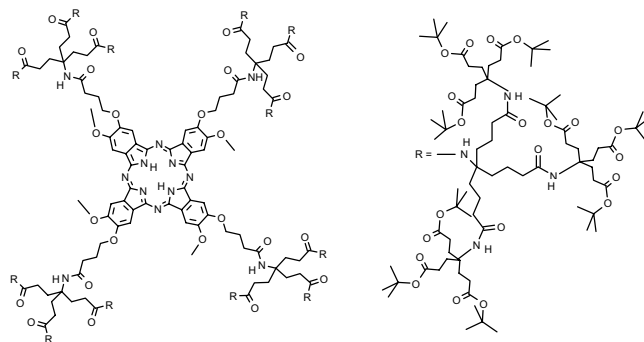
Diederich and collaborators were among the first to have synthesized water soluble dendrimers having a porphyrin core and have studied their spectroelectrochemistry [225].



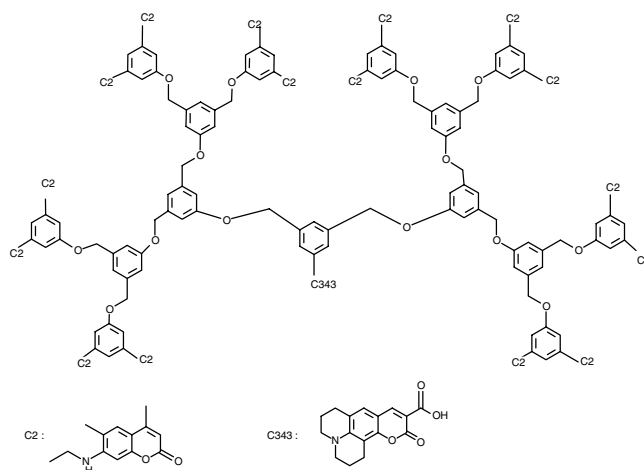
Very recently, by STM investigations, single physisorbed dendrimers having a porphyrinic core could be imaged [226].

Several phthalocyanine dendrimers were also synthesized. As shown in the previous section, the existence of multiple isomers must be considered in cases where the macrocycle periphery is functionalized by different groups. Only one example is given here where the usual phthalocyanine aggregation by  $\pi$ - $\pi$  stacking was prevented by encapsulation within an ether-amide dendrimer [227]. The phthalocyanine dendrimers have been much less employed in energy transfer studies, although the favorable optical properties

and the high stability of phthalocyanines should make these excellent candidates for applications.



Fréchet and co-workers have synthesized a large number of dendrimers encapsulating different chromophores and have studied the energy transfer processes encountered therein [228]. Some of this work has also been reviewed [229, 230].

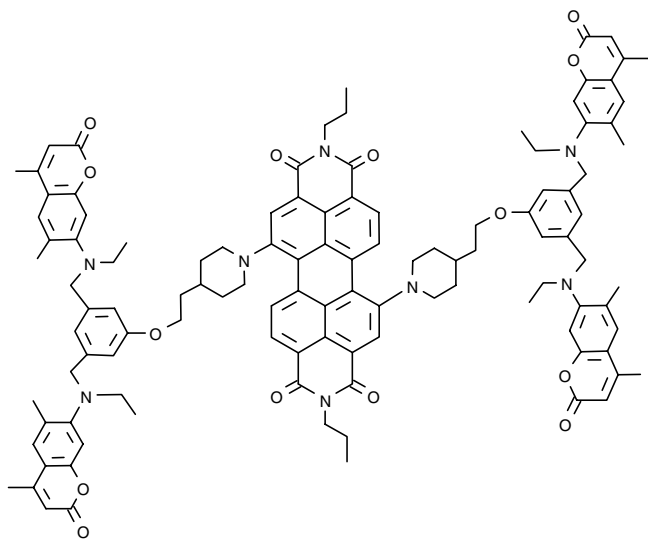


Laser dyes based on 7-aminocoumarin were appended into Fréchet-type [poly(arylether)] dendrimers. The julolidine coumarin C<sub>343</sub> was inserted at the dendritic core by esterifying the 3 carboxy group while the periphery at each successive generation was functionalized with the 7-aminoethylcoumarin C<sub>2</sub> by alkylation of the NH group with benzylic halides. The formula presents the third generation G<sub>3</sub> dendrimer. Energy transfer from the C<sub>2</sub> donors absorbing at 310–380 nm and the C<sub>343</sub> acceptor absorbing between 400 and 480 nm is almost quantitative in the lower generations G<sub>1</sub>–G<sub>3</sub> and decreases slightly for the fourth generation to 93%. No ground state interactions were observed in the dendrons, the absorption spectra being the sum of the individual chromophores, and the poly(aryl ether) backbone is transparent in the 300–500 nm region. Due to a perfect overlap between the emission of the donor C<sub>2</sub> and the absorption of the C<sub>343</sub> the Förster mechanism was expected to operate. Calculations of the average distances between donor and acceptor, based on multiple conformations, gave 1.4 nm for the G<sub>3</sub> and 1.8 nm for the G<sub>4</sub>

dendrons. The observed energy transfer rates  $k_{\text{EET}}$  were  $2.0 \times 10^{10} \text{ s}^{-1}$  for  $G_4$ , somewhat slower than the theoretically expected Förster rate ( $5.3 \times 10^{10} \text{ s}^{-1}$ ). For  $G_3$ , the theoretical rate was  $19.9 \times 10^{10} \text{ s}^{-1}$  reflecting the power six distance dependence. The measured rate for the smaller dendrimers  $G_1$ – $G_3$  was faster than the instrument response so only a lower value could be given. An important aspect is that “energy hopping” from one donor  $C_2$  molecule to another apparently does not occur in this case due to the large Stokes shift which makes the donor–donor overlap integral two orders of magnitude smaller than the donor–acceptor one.

Films cast from these dendrimers have just been investigated by photoluminescence scanning near-field optical microscopy (PL SNOM) and formation of redshifted excimers could be put into evidence for the  $G_1$ – $G_3$  dendrimers [231]. The spatially resolved PL SNOM images of the red edge emission show pronounced nanoscopic domains in  $G_1$ , which due to site isolation of the luminescent core chromophore  $C_{343}$  become more homogeneous in  $G_2$  and  $G_3$ . In  $G_4$  the site isolation in this light-harvesting dendrimer film is fully accomplished.

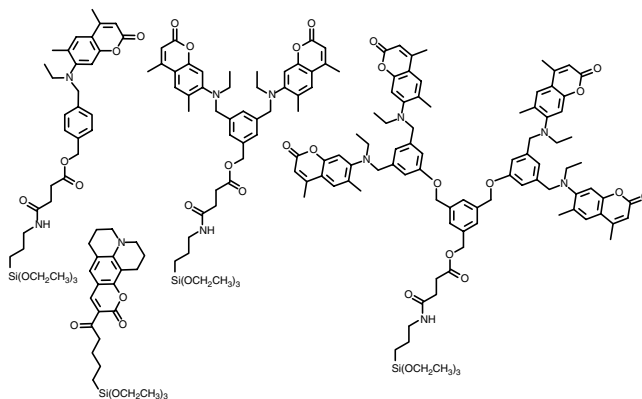
Design principles learned from these studies were recently put to use in preparing a UV to near-IR frequency converter based on fluorescence resonance energy transfer [232]. In this study a first generation dendrimer with four  $C_2$  coumarine dyes was prepared with a perylene core in 31% yield based on the commercial starting material 3,4,9,10-perylenetetracarboxylic acid dianhydride.



Upon excitation of the donor  $C_2$  coumarine at 345 nm, the donor emission was completely quenched indicating over 99% energy transfer to the perylene core. Simultaneously an increase of emission from the core in the 720–800 nm NIR region was observed in comparison to the model perylene compound lacking  $C_2$  donors. This amplification has sometimes been termed the “antenna effect,” a fact which may cause confusion. Rather, due to the increased number of chromophores at the periphery of the dendrimer, the photon capture cross section is correspondingly increased. Due to the efficient energy transfer, emission from the

core is enhanced in comparison with the case when direct excitation of the core is performed. Similarly, in the natural systems, where several energy transfer steps occur, a funnelling of the energy to the reaction center takes place (see Section 1).

Moving toward applications, Fréchet and co-workers have prepared dendrimers having coumarine chromophores as antennas and groups suitable for formation of self-assembled monolayers on silicon wafers [233].

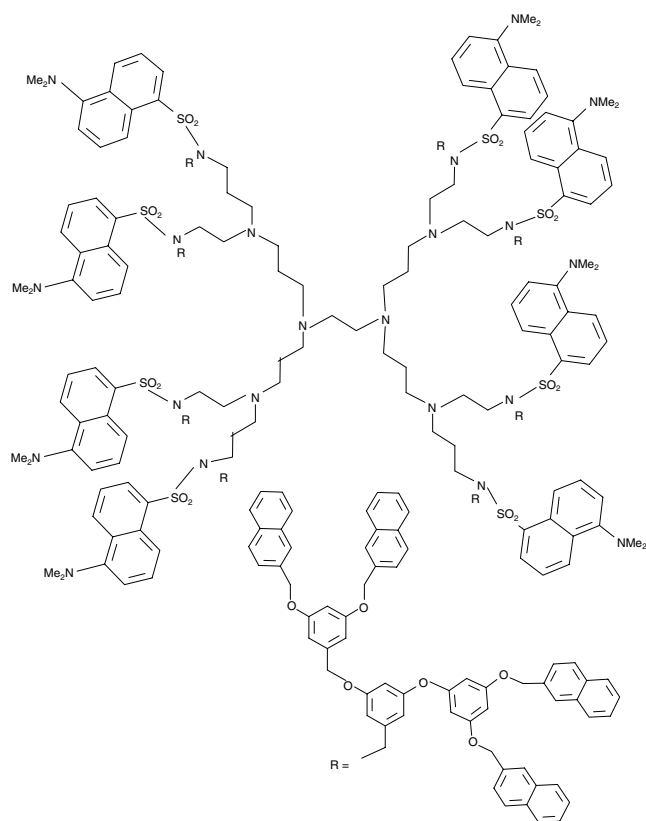


Mixed monolayers encompassing coumarine  $C_2$  as donors and the julolidine derived coumarine  $C_{343}$  as energy acceptors were prepared which showed photophysical properties dependent on the molar ratio of donors and acceptors as well as on the nature of the dendritic architecture.

Campagna et al. have extended the elegant studies of electron and energy transfer in metal complexes also to the nanoscale size by investigating various dendrimeric nanostructures. If in a ruthenium tris-bipyridine complex one of the pyridine rings is replaced by a 1,4-pyrazine, this can function as a ligand to two ruthenium centers and thus acts as branching point in a dendrimer which can be constructed in a controlled manner, either in a “complexes-as-metals” or “complexes-as-ligands” fashion [234]. The luminescence originates from the MLCT (metal-to-ligand-charge-transfer) band which is the excited state with the lowest energy. An important feature is that the energy gradient is in this case reversed; the innermost chromophores are higher in energy and act as antennas for the peripheral complexes which are lower in energy.

In collaboration with Vögtle, the Bologna photophysics school of Balzani has studied various other dendrimers [235, 236]. In dendrimers having poly(ether-amide) or poly(benzylether) linkers and a tris(bipyridine) ruthenium core, when full encapsulation is achieved in the higher dendrimer generations, the fluorescence quantum yields as well as the excited-state lifetimes are considerably increased in aerated solutions. This was explained by the low diffusion rates and solubility of oxygen molecules which quench the triplet states. The longer lifetime and bathochromically shifted emission (by 30 nm) in the poly(ether-amide) dendrimers compared to the poly(benzylether) ones is due to the better stabilization of the MLCT excited state by the more polar former dendrimers. In a very recent and important study,

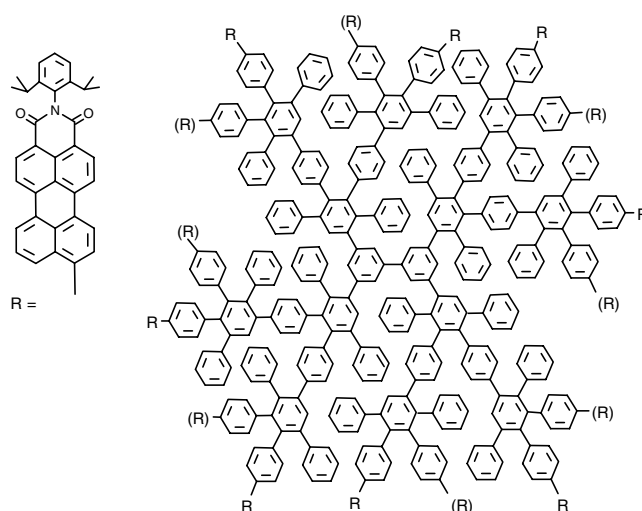
a cascade of energy transfer steps was engineered in the dendritic architecture shown [237].



Three different chromophores were hierarchically mounted on a polyamine core: (i) 8 dansyl (5-dimethylamino-1-naphthalenesulfonyl) units, (ii) 24 3,5-dimethoxybenzene units, and (iii) 32 naphthalene units at the periphery. The chromophores do not interact electronically with each other as judged by their unshifted absorption spectra in comparison with the isolated chromophores. Upon excitation of the naphthalenes, enhanced fluorescence from the dansyl units is detected. Interestingly this fluorescence can be effectively quenched upon addition of a fourth chromophore, which is still further redshifted, namely eosin, together with [18]crown-6 used for solubilizing this anionic dye in dichloromethane, the solvent used for the photophysical measurements. This effect could be explained by encapsulation of eosin as guest molecules (presumably in their monoprotonated forms) within the dendritic polyamine host. Thus eosin can be extracted from an aqueous phase by a dichloromethane solution of the depicted dendrimer. After extraction, the dansyl fluorescence is quenched which indicates that eosin is efficiently encapsulated within the dendrimer. It is likely that it is positioned within the polyamine core by an acid–base type of interaction, as poly(benzylether) dendrimers containing naphthalene units do not bind eosin. Proof that the fluorescence quenching is indeed due to energy transfer was provided by recording the excitation spectrum (at the wavelength corresponding to the eosin maximum) which closely matched the absorption spectrum of the host

dendrimer indicating that all three chromophores (i)–(iii) contribute to supplying light energy to the eosin trap. As the fluorescence lifetime of the dansyl groups is 16 ns, the rate constant for its quenching by eosin must be over  $1.2 \times 10^9 \text{ s}^{-1}$  which is in very good agreement with the value obtained by calculation of a Förster-type energy transfer with a reasonable separation of 1 nm between donors and the eosin acceptors. Because two exponential decays of the eosin fluorescence were observed, even at very low eosin concentration, it was concluded that this trap molecule can occupy two “substantially different” sites within the dendrimer.

A very thorough investigation of light-harvesting dendrimers synthesized by Müllen and co-workers has been made [238, 239] by single molecule fluorescence spectroscopy. The following second generation pentaphenyl derived dendrimer having eight perylenedicarboximide (PMI) chromophores either in the positions indicated by R or by (R) has been studied:



Collective on/off jumps of the fluorescence intensity were observed for single dendrimer molecules, a fact which was also encountered during the observation of single natural light-harvesting antenna systems LH2 [240, 241]. Thus, although the system contains eight chromophores it behaves like a single emitting quantum system. Due to folding of the branches, two chromophores can become closely spaced giving rise to a dimerlike entity. This has different optical properties, such as emission wavelength and lifetime, than an isolated monomeric dye at the dendron’s periphery.

More recently, a tour de force regarding the synthesis of a more elaborate polyphenylene architecture encompassing three different chromophores which enable a vectorial energy transfer has been realized by Müllen and co-workers [242]. The dendritic nanostructure (shown in Fig. 28) has at its core a single terrylene tetracarboxydiimide (TDI) chromophore which absorbs at ca. 650 nm and emits at ca. 700 nm. An inner shell is composed of four perylenedicarboximide (PMI) with two absorption maxima at ca. 490 and 520 nm. Its emission peaks at 550 nm but has a

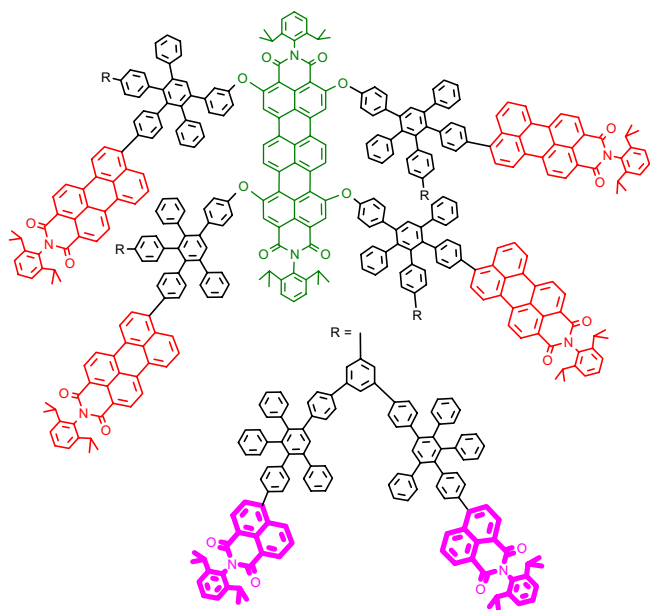


**Figure 28.** Shape persistent vectorial energy transfer dendrimer of Weil et al. [242]. The central TDI chromophore is presented in green, the four intermediate PMI chromophores are red, and the eight outer antenna NMI pigments are yellow, while the pentaphenyl linkers, which confer rigidity and prevent a collapse of the dendritic arms, are presented in black.

redshifted tail which overlaps with a blueshifted shoulder of the TDI absorption band. Finally, an outer shell amounting to eight naphthalene dicarboxmonoimide (NMI) consists of the main light-harvesting unit absorbing below 400 nm and which emits at about 400 nm. Again the tail of this emission band overlaps with the blue wing of the PMI absorption, making this system one of the best optimized so far.

The PMI chromophore can be viewed as a pericondensed naphthaleno homolog of NMI. Similarly, extension of the chromophoric system by one perinaphthaleno unit and another dicarboxmonoimide transforms the PMI into the central energy trap TDI. An important aspect is that the Förster energy transfer, for which a radius  $R_0 = 6$  nm has been calculated from the overlap of the PMI fluorescence and TDI absorption, occurs sequentially (i.e., stepwise from NMI to PMI and only afterwards to the energy trap TDI) just as in the natural systems. No transfer can occur directly from the outer antenna NMI to the trap due to the zero spectral overlap. By exciting the NMI periphery, a strong fluorescence from the TDI trap is detected which is about threefold more intense than if irradiating directly in the TDI absorption. Similarly, by exciting the intermediate PMI chromophores, only a slightly reduced fluorescence intensity is emitted from the TDI trap as compared to the case when the outer NMI antenna is irradiated at its absorption maximum. Our interpretation of these results is that there is no “amplification effect” of fluorescence intensity. Rather, the increased number of antenna chromophores have a larger cross section for capturing photons than only one central TDI trap. Through the four intermediate PMI chromophores, the excitation is efficiently

transferred to the trap from any excited NMI molecule which leads to about the threefold increase in fluorescence observed from the trap compared to the case when exciting directly the trap. The pentaphenyl linkers are instrumental in maintaining the separation between the pigments so that no aggregation, excimer formation, and self-quenching effects occur. These findings allow an optimization of multichromophoric assemblies for photonic devices. Their high thermal and temporal stability make them suitable candidates for solar-cell applications. However, we are skeptical that it would be easily feasible to trigger artificial reaction centers in the inner core of a dendritic architecture. To be able to use the thus created chemical potential, access of reactant species should be possible; otherwise, charge recombination and thermal deactivation are the most likely processes to occur. Very recently nanotubes were synthesized by an elegant cross-linking of dendrimeric porphyrins [350].

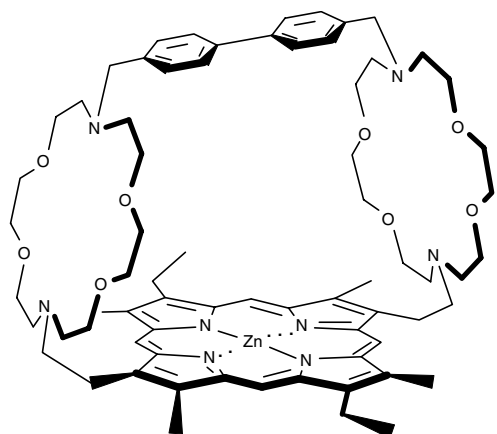
## 4.2. Supramolecular Assemblies

The alternative way of constructing multichromophoric arrays with light-harvesting properties is to use noncovalent interactions by applying the principles of supramolecular chemistry [24]. The major advantage is that instead of constructing the nanostructures in a bond-by-bond manner, employing only weak interactions one can access large functional architectures in a tecton-by-tecton manner. The disadvantage is that a strict control of the assembly process has to be assured in order not to have large dispersions in size (i.e., nonunique nanostructures). Besides ligation of metal ions, which is also the strongest supramolecular interaction, hydrogen bonding,  $\pi$ - $\pi$  interactions, as well as hydrophobic or dispersive forces may be used for constructing supramolecular assemblies. Some excellent reviews by Lawrence et al. [243] and Stoddart and co-workers are available [244–247]. A visionary survey of this field is to be found in [248]. A shorter but useful review dealing with electron and energy transfer in supramolecular systems is due to Ward [249]. Special emphasis on the photophysics for driving molecular machines is to be found in [250, 251].

An early photophysical study on the effects of complexation of cations such as  $\text{Na}^+$ ,  $\text{K}^+$ ,  $\text{Cu}^{2+}$ ,  $\text{Ni}^{2+}$ , and  $\text{Eu}^{3+}$  into the voids of benzocrown ethers attached to the *meso*-position of metalated terta-arylporphyrins (the central metal being Zn, Mn, or Sn) has shown a pronounced luminescence dependency on the nature of the cation [252]. When  $\text{Eu}^{3+}$  was complexed, an intramolecular electron transfer takes place from the excited triplet state of the porphyrin. The reverse electron transfer was found to be diffusion controlled and a bimolecular process. An interesting zinc porphyrin host molecule, comprising two [18]- $\text{N}_2\text{O}_4$  macrocycles preorganized by a biphenylene strap, underwent intense fluorescence quenching upon addition of silver triflate [253]. As potassium triflate had no effect on the fluorescence of the host, and low concentrations of silver triflate also do not quench the fluorescence of a normal zinc porphyrin such as zinc-octaethylporphyrin, it could be unambiguously proved that the observed effect is due to an intramolecular electron transfer process involving the



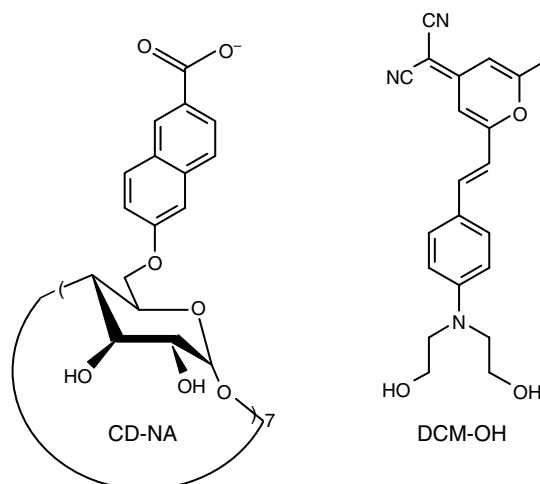
complexed  $\text{Ag}^+$  ions by the crown macrocycles:



From titration experiments it was concluded that an average of about 2.6 silver ions were bound per molecule. Upon irradiation of the silver complex, the singlet excited state has a main deactivation pathway, which explains the observed quenching of the fluorescence, by forming a charge separate state which was long-lived. The charge recombination is retarded probably by the displacement or even dissociation of the  $\text{Ag}^+$  ions and it involves thus a large reorganization energy.

These two examples show that one of the simplest supramolecular interactions, such as metal ion chelation, can lead to drastic changes in luminescence behavior. Using these interactions in the assembly of functional light-harvesting nanostructures has to be done with caution as the energy transfer processes may become secondary. Additionally, if heavy metal atoms which also have rich coordination chemistry are employed, fluorescence quantum yields may drop by orders of magnitude due to the heavy-atom effect [254].

A pioneering series of synthetic, physical, and photochemical studies involving cyclodextrins chemically modified by attaching covalently on their periphery several chromophore molecules and which can additionally form within their hydrophobic cavity inclusion complexes with different dye molecules, which can thus act as energy traps, have been performed by the research groups of Jean-Marie Lehn and Bernard Valeur [255–259]. In view of the circular nature of the arrangement of the “antenna” chromophores imposed by the  $\beta$ -cyclodextrin scaffold composed of seven D-(+)-glucopyranose units, there is an obvious resemblance to the natural LH1, LH2, and LH3 purple bacterial complexes. It is worth mentioning that these circular, smaller, synthetic nanostructures have been studied well before the first structural data became available on the natural complexes and both the energy hopping and trapping mechanisms appear to be very similar.



At left, is depicted the formula of the  $\beta$ -cyclodextrin to which seven naphthyl chromophores have been covalently linked. At right is presented the laser dye molecule DCM-OH, a 2-sytryl-derivative of a 4-(dicyanomethylene)-4H-pyran which can be tightly bound within the cone shaped cavity formed by the seven glucose units. The definition introduced in these studies, “an enhancement of light sensitivity due to an increase of the overall cross section for light absorption is called the ‘antenna effect’,” is the one which has been generally adopted. By “light sensitivity” it is meant that the reaction center traps more efficiently and rapidly photons as in the case when it is itself directly excited. With 7 or 14 naphthyl (or the more polar naphthoate) chromophores fast energy hopping occurs which is directed toward the “red,” lower energy chromophores. As the geometry is not fixed, various orientations of the naphthyl residues and accidental  $\pi$ -stacking which may lead to the formation of red-shifted dimers (or excimers) can occur. In the case when a guest molecule is present, good spectral overlap between the naphthoate emission and the DCM-OH absorption lead to an efficient energy transfer, as confirmed by the fluorescence quenching of the naphthyl emission upon titrating increasing amounts of the dye to the cyclodextrin host in buffered aqueous solution at pH 10 containing 5% (v/v) ethanol. Simultaneously increased fluorescence is emitted from the dye molecule at about 610 nm. A Job plot, at two different excitation wavelengths, confirmed efficient complexation with a 1:1 stoichiometry of the dye guest molecule. By carefully correcting the amount of light directly absorbed by the dye, the authors could conclude that the quantum yield of complexed DCM-OH molecules is much higher than that of buffered solvated molecules and that the efficiency of the energy transfer must be very close to 1 (i.e., nearly quantitative). By time resolved experiments, it could be shown that energy transfer must be fast, well under 45 ps, the time resolution of the apparatus. Further thermodynamic characterization of the complex has demonstrated that the association constant is one of the largest ever measured for a  $\beta$ -cyclodextrin derivative ( $\log K = 5.1$ ) and that there is a large entropic contribution (ca. 70%) to the free energy of

complexation. Only a small part of the dye molecules is laterally complexed as concluded by comparison with unsubstituted  $\beta$ -cyclodextrin which should laterally complex equally well. Complexation by inclusion within the heptanaphthoate cyclodextrin is much more favorable due to  $\pi$ - $\pi$  interactions with the naphthyl groups. Assuming a random orientation of the naphthyl chromophores and thus an average orientation factor  $\kappa$  of 0.67, rates of  $1.8 \times 10^{12}$  to  $2.8 \times 10^{10} \text{ s}^{-1}$  could be calculated with the Förster formula for the energy transfer. These are well within the measured order of magnitudes, especially if one takes into account the formation of excimers which have broader and more redshifted spectra with increased overlap with the DCM absorption which thus account for faster energy transfer than from isolated monomers. Another important aspect of these studies was that apparently once a naphthoate chromophore is excited, it transfers the excitation energy directly to the entrapped dye molecule. Because of the Stokes shift, the energy hopping between adjacent equivalent chromophores, which could be put into evidence in the absence of guest molecules, is much less favorable than the energy trapping. In the words of the authors "heterotransfer" of energy is faster than the "homotransfer." The same phenomenon is encountered in the natural antenna systems coupled to reaction centers.

#### 4.2.1. Multiporphyrinic Arrays

Various research groups have been involved in building supramolecular architectures with porphyrinic tectons. Again the advantages of the well combed porphyrin chemistry [260] such as versatile synthetic methods and attractive photophysical properties have been put to use. These nanostructures can be classified by the type of the strongest supramolecular interaction which is used to self-assemble the tectons. We will differentiate between metal complexes and exclusively hydrogen-bonded assemblies. Only short reviews have appeared on this topic, describing mainly some of the work carried out in the groups of the respective authors [261].

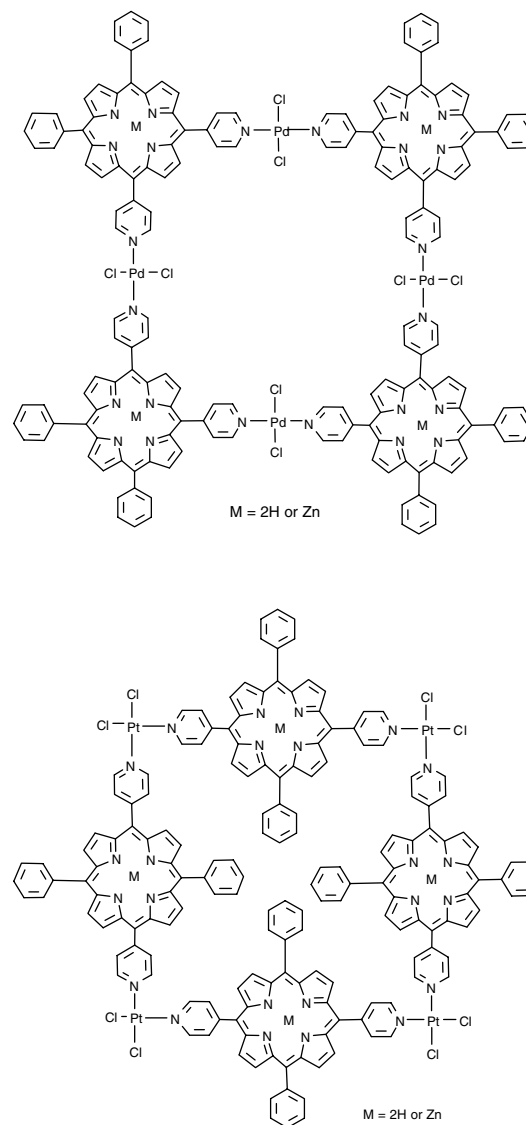
##### Assembly of Porphyrinic Nanostructures Using Metal Ligation

The rich coordination chemistry of metal ions has made possible the tailored construction, by means of self-assembly, of various aesthetically pleasing multiporphyrinic architectures. However, as mentioned, for artificial light-harvesting purposes only special metal atoms which do not quench the assembly's fluorescence can be used. Only a few selected examples can be presented here.

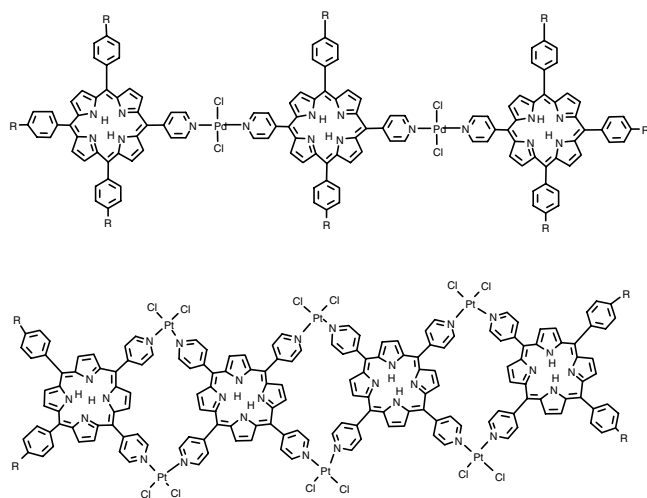
Some early nanostructures where palladium atoms were used to stitch together *meso*-4-pyridyl substituted porphyrins are due to Drain and Lehn [262]. By using the ability of 4-pyridyl groups to form linear complexes using *trans*-dichloropalladium(II) but kinked complexes when using *cis*-dichloroplatinum(II) discrete assemblies can be formed. Dimers and the following tetramers (or "squares" as the authors name them), either as porphyrin free bases or as zinc complexes, could be prepared. Heating to 50 °C for 48 hr leads to preferential formation of the squares while other oligomeric species are disassembled.

The control of the architecture is assured by the *cis* or *trans* heavy metal bis(benzonitrile) dichloride square planar

precursor and by having either adjacent or "vicinal" *meso*-4-pyridyl groups (i.e., in positions 5,10) or what we call "distal" positions (i.e., 5,15) of the porphyrin macrocycle. In the jargon of porphyrin chemists these disubstituted *meso* positions are sometimes incorrectly referred as *cis* and *trans*, respectively. Notable is the fact that although the overall size and architecture of the porphyrin squares depicted are similar, in the first case the "heavy" Pd atoms which stitch the porphyrins are situated on the square edges while the Pt atoms act as corners. Photophysical measurements have shown that the Soret absorption bands are broadened in the dimers and even more in the tetramers while the heavy atom effect was responsible for the observed fluorescence quenching, in comparison to the monomeric porphyrins. Formation of polymeric species was observed by mixing in a 1:1 ratio the distal and the vicinal bis-*meso*-4-pyridyl porphyrins isomers with *trans*-Pd(NCPh)<sub>2</sub>Cl<sub>2</sub>. The excitation spectra of this species was completely depolarized, in contrast to that of the corresponding dimers or tetramers. It would be interesting to investigate whether modern microscopy techniques can distinguish between the two photogenic squares shown.

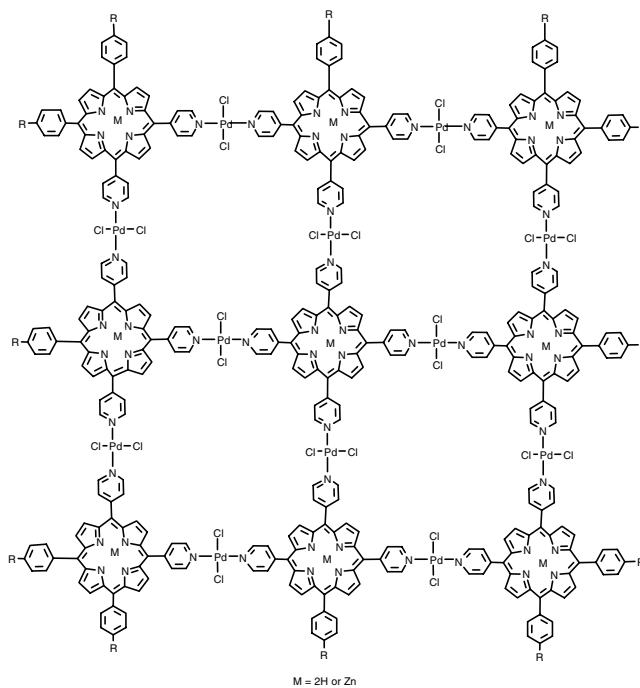


In later independent studies Drain et al. extended this concept to access in a controlled manner various architectures. The self-assembly process is dictated by the stoichiometry of the tectons and thus an oligomeric nanostructure is obtained by controlling the amount of different porphyrins and either palladium or platinum metal ions. Linear tapes or nonamers could be obtained by design [263].



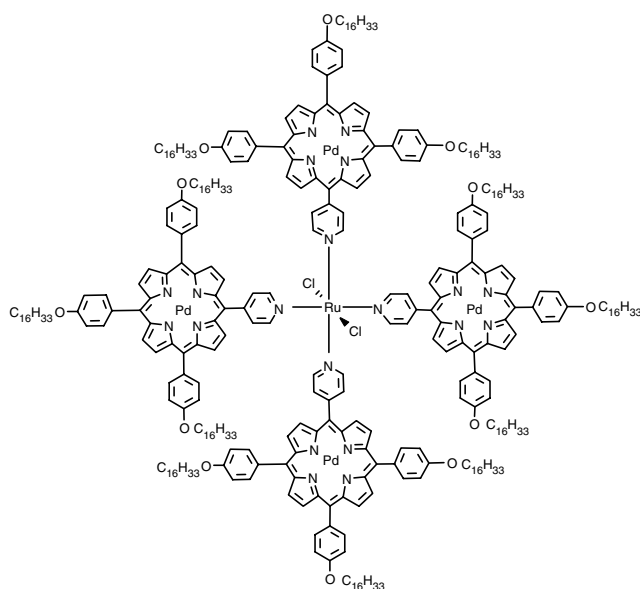
Here R is either a methyl or a *tert*-butyl group which induces better solubility to these “tapes.” By mixing two equivalents of the mono-pyridyl porphyrin to two equivalents of the distal disubstituted one and two equivalents of the labile benzonitrile palladium complex a mixture of dimer, trimer, and tetramer is formed in a 3:8:2 ratio. Only the trimer is shown. Similarly, by mixing the vicinal disubstituted pyridyl porphyrin (termed by the authors an “L-shaped porphyrin”) with equimolar amounts of the tetra-4-pyridylporphyrin (X-shaped) and the corresponding platinum precursor (3 equivalents) after 4–5 days at 50 °C, a mixture of the trimer, tetramer, and pentamer in a ratio 2:4:1 is obtained as determined by electrospray mass spectrometry. Only the tetramer LXXL is shown. Instrumental in these cases is the reversibility of the metal–pyridyl coordination which assures that the thermodynamically stable product is favored in the end. This coordination is more stable for platinum than the palladium complex.

Spectacular in what can be achieved by using this stoichiometry control is the preferential formation of the nonamer depicted as follows in over 90% yield. The reaction is completed within 30 minutes of mixing of the following reactants: 12 equivalent Pd precursor benzonitrile complexes, 1 “X”-shaped central tetrapyrrolyl substituted porphyrin, 4 “L”-shaped vicinal dipyrrolyl porphyrins for the corners, and 4 “T”-shaped tripyridyl porphyrins for the edges. R is the *tert*-butyl group. Evidently by using differently metalated porphyrins assembly of polymetal complexes with controlled architecture and thus interesting material properties can be achieved.



The nonamers are extremely stable and by  $\pi$ – $\pi$  interactions tend to stack strongly with a stacking energy which has been estimated at ca. 5 kcal/mol per porphyrin face. Formation of columns was observed by atomic force microscopy (AFM) which, after deconvolution of the tip profile, indicated dimensions of approximately 5 × 5 × 5 nm. Interesting photonic applications are envisageable with these polymetalated porphyrinic nanostructures.

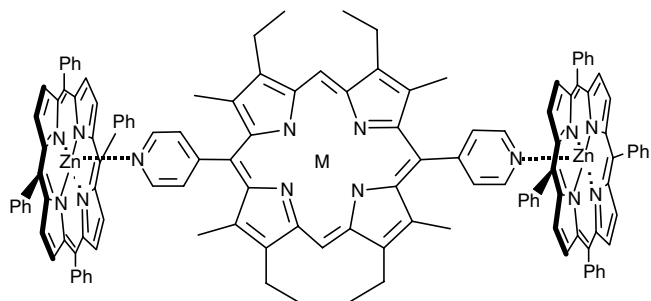
Similar architectures have been more recently constructed in the group of Nolte where the R group has been replaced by a long chain alcohol group and the self-assembly at the air–water interface has been investigated [264]. Also other multiporphyrinic assemblies such as the ruthenium complex depicted were investigated:



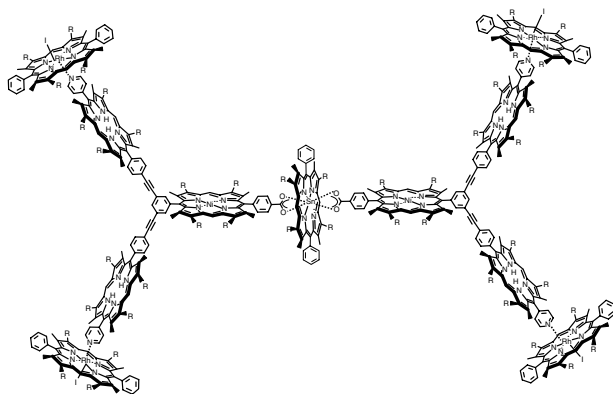
The scope of this study was to prepare stable chromophoric monolayers which could be transferred by Langmuir–Blodgett technique to a glass surface with good transfer ratios. Compression of the films leads to well ordered layers with tetraporphyrin metal squares which are orthogonal to the surface. The fatty hexadecyloxy chains (cetyl) are responsible for adopting the perpendicular orientation to the water surface while  $\pi$ – $\pi$  stacking of the multiporphyrin planar nanostructures induce the high stability of the monolayers toward collapse.

A mixed layer-by-layer deposition onto a hydrophobic glass substrate mediated by  $\text{PdCl}_4^{2-}$  ions was performed by alternatively transferring monolayers of *meso*-tetrakis-(4-pyridyl)porphyrin and *meso*-tetrakis-(4-carboxymethoxyphenyl) free base porphyrins [265]. Here the ionic (or electrostatic) pairing between the carboxy and pyridyl groups is expected to be important at the air–water interface, in addition to the palladium coordination as proposed by the authors.

An assembly in which it would have been interesting to study the energy transfer was synthesized by Burrell et al. The crystal structure could be solved by X-ray diffraction [261]. The perpendicular arrangement of two antenna zinc porphyrins to the central free base energy trap ( $M = 2\text{H}$ ) should have an unfavorable Förster orientation factor  $\kappa$  for the energy transfer but a through-bond mechanism involving the two distal pyridine ligands could operate in this case:

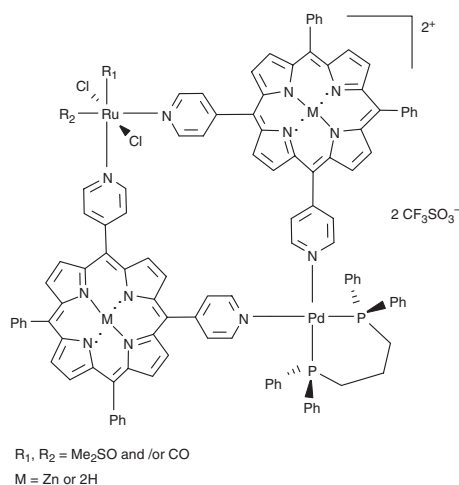


Other interesting nanostructures assembled by the coordination of the central metal atom within porphyrins were reported recently by several groups. Sanders and co-workers, in an extensive study which included the syntheses and X-ray structural characterization of several porphyrinic coordination arrays, described the formation of the undecamer depicted as follows [266]. Here the axial ligation of the central tin porphyrin is engineered using benzoic carboxyl groups of two *meso*-substituted porphyrins, while the four peripheral rhodium(III) substituted porphyrins are ligated by 4-pyridyl substituents. An iodine atom completes the Rh coordination sphere.

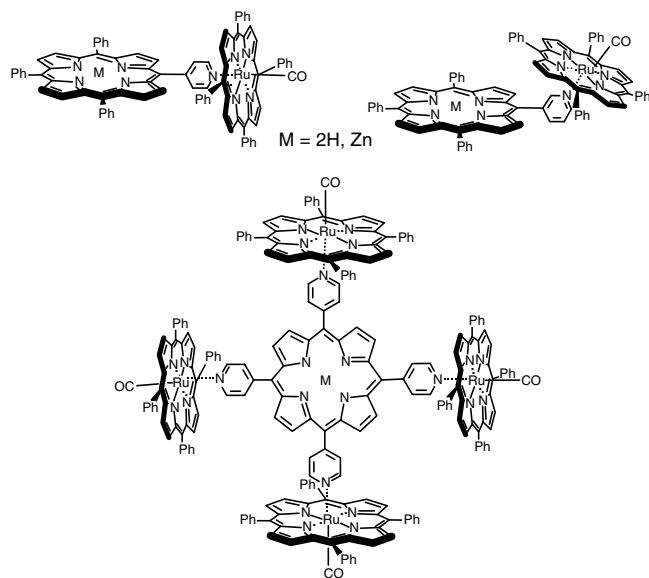


The R group is *n*-hexyl, the ideal substituent when solubility is desired but also for obtaining suitable crystals for envisaged X-ray diffraction studies. If instead of Rh and Ni porphyrins, which have low fluorescence quantum yields, other lighter metals could have been employed for building this nanostructure, it would have been very interesting to study the energy transfer. A perpendicular orientation of the porphyrin rings as imposed by axial ligation should also lead to an unfavorable orientation factor  $\kappa$  by the Förster mechanism. However, in this case, also the Dexter mechanism would not be very efficient due to the reduced orbital overlap due to the *meta*-phenylene linkage of the phenylacetylene bridges.

The following mixed metal complex incorporating also a ruthenium center and resembling the Drain–Lehn dimers was assembled in a modular stepwise manner [267]. First the octahedral ruthenium bis-“L”-shaped (following Drain’s nomenclature) porphyrin complex was formed after which the square planar “diphos” corner was closed. The authors name their assemblies “heterobimetallic molecular squares of porphyrins.” As only two porphyrins are involved, the term “square of porphyrins” which implies a pseudo- $D_{4h}$  symmetry is maybe misleading, as well as “molecular” which is actually supramolecular. Furthermore, in the case of zinc metallated porphyrins, the complexes are actually “heterotrimetallic.” Although photophysical studies were in this study not undertaken, both synthetic and photochemical extensions of this work are envisageables.

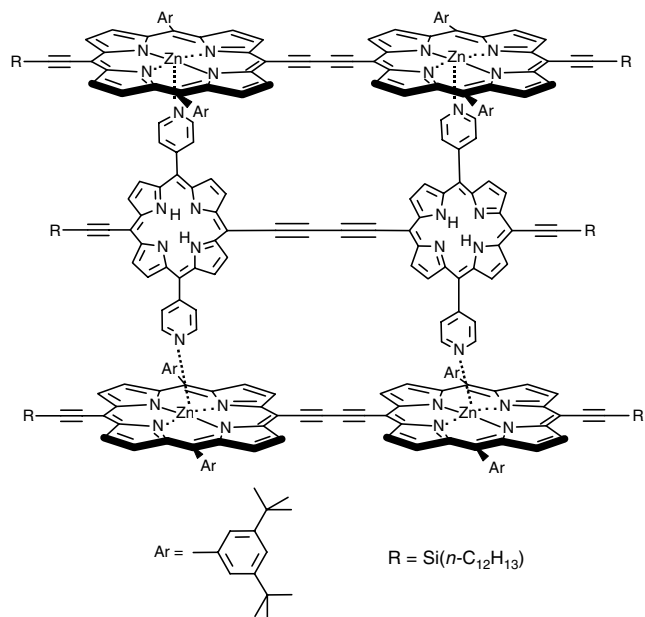


A more thorough study by other Italian chemists and photophysicists was undertaken on the following ruthenated porphyrin dimers and pentamers with a side-to-face coordination staged also through pyridyl ligands [268]:



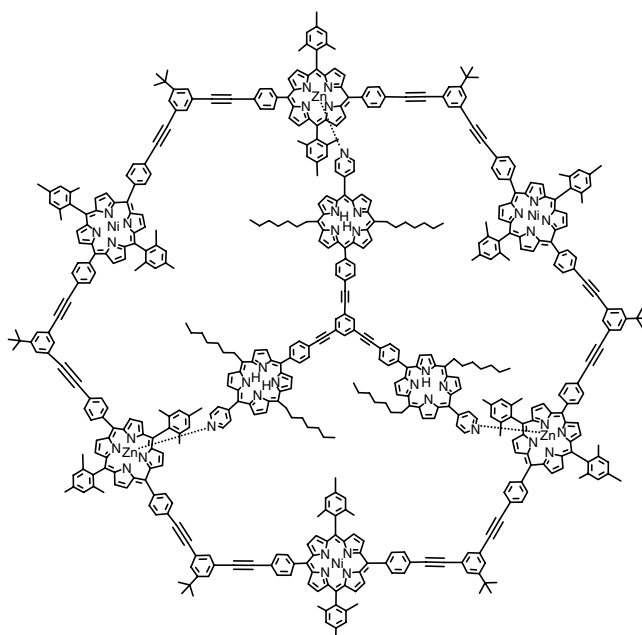
The axial 4- or 3-pyridyl-Ru ligation is more stable than a pyridyl-Zn bond ensuring preferential formation instead of oligomers of the previous species which are stable toward dissociation even in dilute toluene solutions which were used for detailed photophysical studies. The ruthenium porphyrin units are higher in energy, both as singlet and triplet states, than the corresponding free bases or zinc metalated porphyrins. The supramolecular assemblies differ markedly in their photochemical behavior from the corresponding monomers. The Ru monomer undergoes from the singlet level efficient (100%) intersystem crossing (ISC) to the longer lived triplet state. However, in the case when it is axially coordinated by either a 3- or 4-pyridyl-*meso*-porphyrin strong fluorescence quenching of the free base or zinc porphyrins was observed due to the heavy atom effect of the nearby situated ruthenium center. This causes an enhanced ISC in the free base or Zn porphyrins to the triplet states from where efficient triplet-triplet energy transfer takes place. The driving force  $\Delta G$  is large in the case of the free base so that the transfer from the ruthenium moiety to the free base triplet is irreversible and has rate constants between  $10^8$  and  $10^9$  s<sup>-1</sup>. In the case of the Zn-porphyrin assemblies,  $\Delta G$  is small so that an equilibrium is established between the states prior to deactivation.

Wilson and Anderson have linked one porphyrinic molecular wire into a supramolecular nanostructure by ligating the zinc atoms with distal bis-4-pyridyl substituted free base porphyrins [269].



It would be interesting to study the energy transfer mechanisms between the two antenna zinc dimers and the central free base dimer which can act as the energy trap. Due to the butadiyne linkages the overlap integral would be different from all systems studied so far.

Gossauer and co-workers have synthesized the pyridyl derivatized porphyrinic tripods mentioned before or star-shaped hexaethynylbenzene (niphaphyrins) and studied the complexation with their macrocyclic covalent assemblies of porphyrins [270]. Only one example is shown having a longer linker of the central tripod guest molecule:



The binding constants are extremely high, between  $1.4 \times 10^9$  and  $1.1 \times 10^{10}$  M<sup>-1</sup>, which explains the high stability of such complexes which can survive even the ionization during mass spectrometric investigations by

MALDI-TOF. Peaks corresponding to the 1:1 complex were found in the positive mode which were greatly increased in intensity by using the aprotic matrix DCTB (2-[(2*E*)-3-(4-*tert*-butylphenyl)-2-methylprop-2-enylidene]malononitrile) dissolved in chloroform [271] instead of the common MALDI matrix 1,8,9-anthracenetriol, which being protic and in large excess, can compete for complexation of the zinc atoms and displace the polypyridyl ligand.

Hunter and Hyde have also constructed several elaborate supramolecular assemblies which make use of pyridyl groups to ligate porphyrins (Fig. 29).

In Figure 29, the meso-aryl substituents having either alkyl or alkoxy long chains have been omitted for clarity. Energy and photoinduced electron transfer were studied in these systems [272]. While the terephthaloyl diamide spacer in the first formula is inert, the naphthalenediimide spacer acts as an electron acceptor. A stability constant of  $3 \pm 1 \times 10^8 \text{ M}^{-1}$  was determined for these complexes which dissociate in very dilute solutions ( $>10^{-8} \text{ M}$ ). In the case of the terephthaloyl linker, the fluorescence of the zinc porphyrins is significantly reduced at concentrations where complexation occurs, compared to dilute solutions having

uncomplexed units. This effect is due to *intracomplex* excitation energy transfer from the zinc porphyrins to the free base. In case of the naphthalenediimide spacer, the free base fluorescence at ca. 650 nm is quenched to an extent of 70% and this is attributed to an *intracomplex* electron transfer process from the singlet state of the free base porphyrin to the naphthalene diimide electron acceptor. While a through-bond electron transfer mechanism would involve 24 bonds (i.e., ca 3.5 nm) the through-space separation is only about 1 nm. Probably the high rate of the observed electron transfer is due to a through-space or a solvent mediated mechanism involving the solvent molecules within the void between the chromophores in the complex. The bis zinc-porphyrin unit linked by the naphthalenediimide spacer shows only weak fluorescence which upon complexation is not altered. This fact speaks that also here *intramolecular* electron transfer occurs from the excited zinc porphyrins to the naphthalenediimide electron sink. This relatively early study has shown the potential of a supramolecular approach which allows one through choice of concentration to switch on and off electron and energy transfer processes within carefully engineered assemblies.

In a later study [273] Hunter and co-workers assembled a 2:1 complex between a Zn metalated bis-porphyrin and a *meso*-tetrakis-aryl free base porphyrin having 4-formamidopyridyl groups in such a way that all four zinc atoms of the energy donors can be ligated by the four pyridyl groups in the energy trap. The binding constant for a one zinc-pyridine coordination has been estimated at ca.  $10^3 \text{ M}^{-1}$  [272, 274, 275]. In this case the 2:1 complex shows cooperativity between two identical binding sites with association constants of  $(2.0 \pm 0.5) \times 10^6 \text{ M}^{-1}$  per binding event. Vapor pressure osmometry confirmed the formation of the 2:1 complex whereas mass spectrometric techniques failed to put into evidence associated species indicating that upon ionization the complex dissociates. The rate of the energy transfer which occurred with high efficiency was estimated at  $10^9 \text{ s}^{-1}$ .

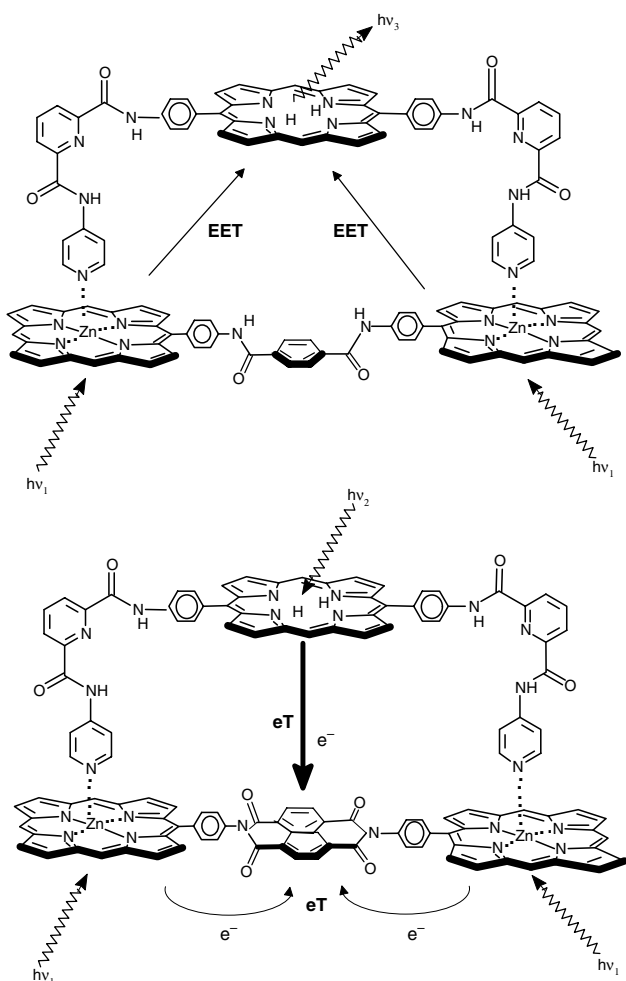
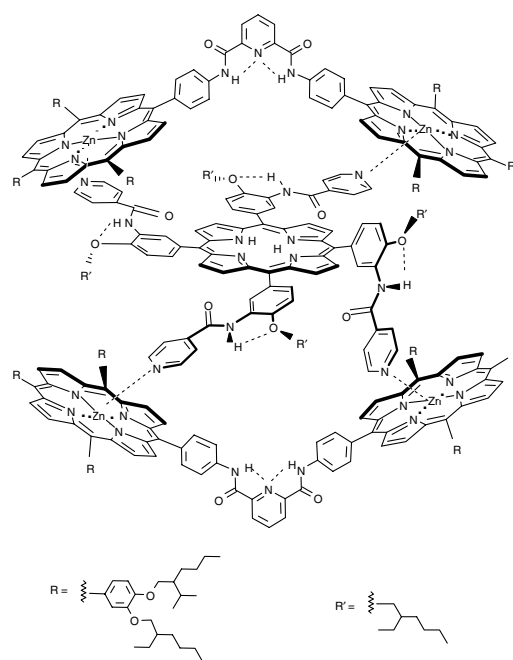


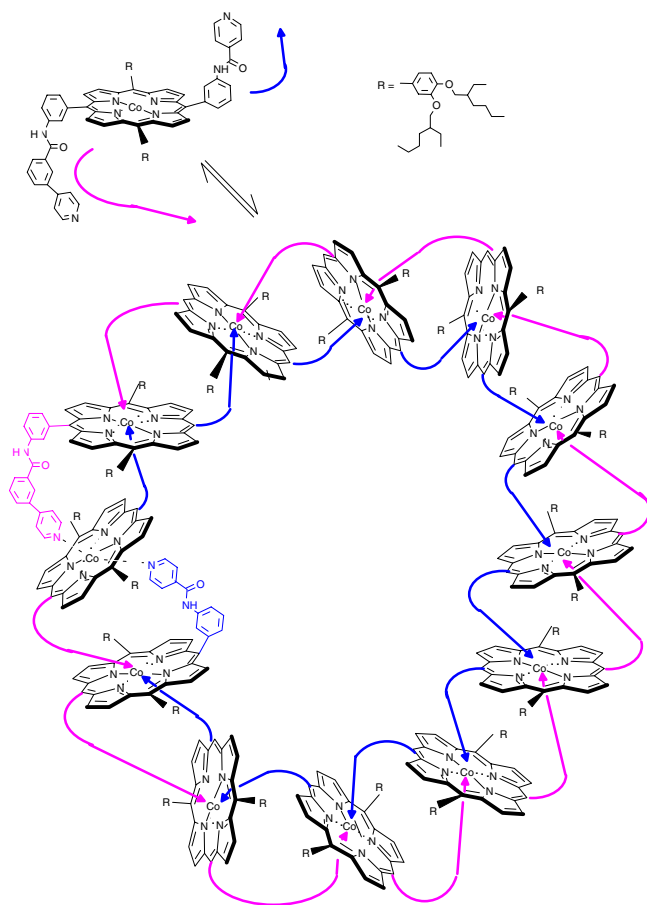
**Figure 29.** Excitation energy transfer and electron transfer events shown schematically in supramolecular porphyrin assemblies formed by pyridine-Zn ligations.





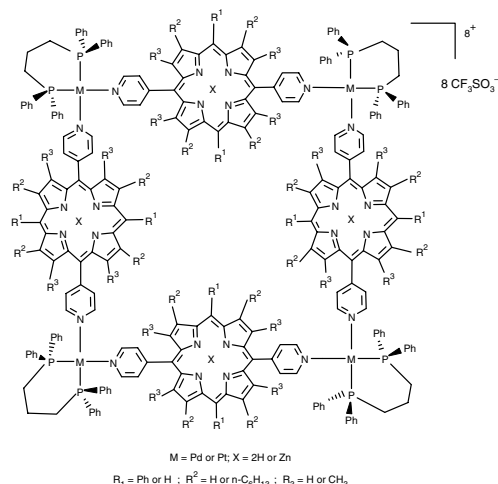
In this formula the coordination of the bisporphyrin clip is depicted as being from the vicinal (5,10) *meso* position of the central free base porphyrin which acts as the energy trap. However, a distal (5,15) coordination also appears to be possible. Molecular modeling calculations which might shed light on the stabilities of the two nonequivalent structures or other structural evidence were not yet presented for this interesting complex.

More recently, by using different 4-formamidopyridyl groups and cobalt atoms which form six-coordinated porphyrin complexes, complex oligomeric arrays could be prepared [276]. For a dodecamer the following cyclic geometry was proposed where the arrows stand for the respective substituted 4-pyridyl ligands.

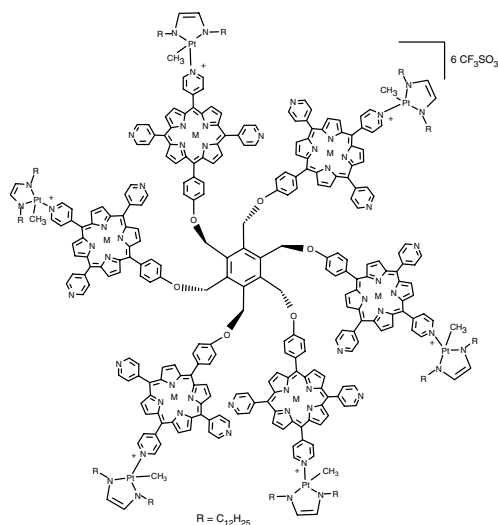


Stang and co-workers, elaborating on their concept of preparing macrocyclic arrays using biphosphine-coordinated transition metals as building blocks, have also made use of pyridyl groups. However, the pyridyl nitrogen is used here to coordinate the heavier metal atoms and not the central zinc inside the porphyrin [277].

Several other porphyrinic cyclic arrays were prepared, some of them displaying interesting chirality imposed by (*R*) or (*S*) BINAP-phosphines which lead to mirror imaged and very intense excitonic couplets of the Soret band in the CD spectra. As mentioned due to the heavy atoms these arrays have low fluorescence quantum yields and very short lifetimes and thus would be of little use as light-harvesting nanostructures.

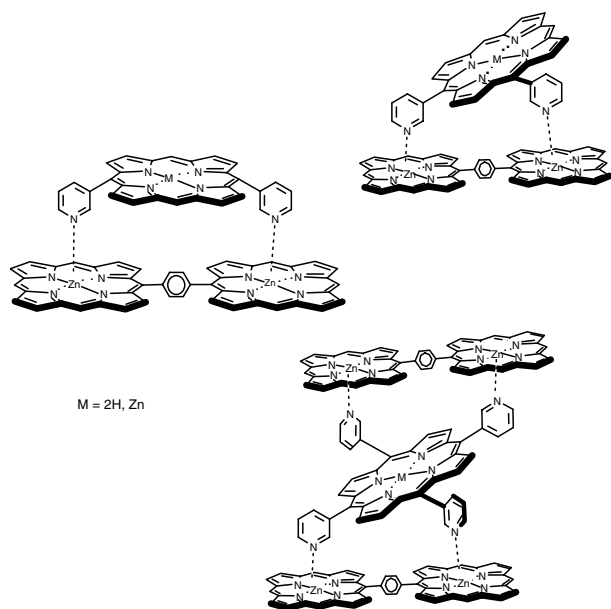


A hexakis pyridyl-functionalized porphyrinato-benzene was recently synthesized and the ability of the pyridyl ligands to form platinum complexes was put into evidence [278]. Of course instead of the platinum complex substituted with long dodecyl chains which confer an amphiphilic character to the sixfold charged cation (the counterion being trifluoromethanesulfonate), zinc porphyrins could have been used to construct hierarchically a light-harvesting nanostructure by coordination. Interestingly, due to steric hindrance only 6 of the 18 pyridyl nitrogens bind platinum atoms. The assembly was further characterized both in solution, using resonance light scattering, a very useful technique to study chromophore aggregation perfected by Pasternack [279–282], and on solid supports by transmission electron microscopy. While in solution, little or no aggregation was observed; from chloroform solutions by aggregation on carbon-coated copper grids, very large, micrometer-size rings were formed. These “porphyrin wheels,” as previous studies by Nolte and other Dutch and Belgian researchers have termed such assemblies [283, 284], are formed mainly by  $\pi$ - $\pi$  interactions which in this case appear not to be disturbed by the presence of multiple charges. Deposition upon solid supports of such self-assembling microstructures might have important applications in solar cell technology.



In this formula, both the implied orientation of the 5-(benzyloxy)-porphyrinato groups around the central benzene ring as well as the positioning of the platinum atoms only on the 15-(4-pyridyl) groups, although probable, may actually not be true. Upon complexation of 2–4 equivalents of the platinum diimine ligands the porphyrin fluorescence was completely quenched due to the heavy atom effect.

Several other pyridyl substituted porphyrins and phenylene-bridged zinc-bis-porphyrins (with or without additional electron acceptor groups such as quinones or pyrromellitimide) were synthesized by Shulga and the photophysics of the supramolecular assemblies, formed upon complexation of the zinc metalated porphyrins by the pyridyl groups, were performed by Zenkevich and von Borzyskowski [285–288]. The following formulae show typical such assemblies where other nonpyridinic peripheral porphyrin substituents have been omitted for clarity.

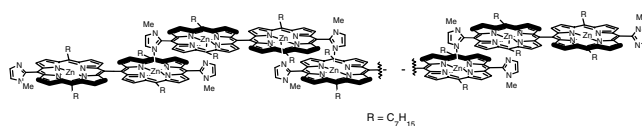


Again in these studies, by using pentafluorophenyl groups, the potentials are shifted so that vectorial photoinduced electron transfer to the electron sinks is made possible. However, a detailed structural characterization of the supramolecular assemblies (such as by high-field NMR or X-ray analysis) which would clearly differentiate between the 2:1 complexes shown and complexes (or oligomers) with other stoichiometries is lacking. This is also maybe why, in some cases, a clear distinction between the energy and electron transfer rates, from the time-resolved fluorescence and absorbance studies, was not possible. The interested reader can consult a recent review of this work [289].

As a final example of a porphyrin self-assembly mediated by pyridyl groups, a very nice structure presented by Fujita et al. deserves mention [290]. A porphyrin triangular prism comprised of three porphyrins ligated by six  $[\text{Pd}^{\text{II}}(\text{en})]^{2+}$  building blocks (where *en* stands for ethylenediamine) was obtained and its crystal structure could be solved. The palladium atoms hinge together two 3-pyridyl groups situated in the *meso*-positions of adjacent porphyrins. All coordination

sites are thus equally satisfied. This example illustrates the preferential formation of discrete nanoarchitectures by self-assembly. Upon complexation of a pyrene molecule within the prism, the  $D_{3h}$  conformation was desymmetrized to a  $C_2$  complex as inferred from 800 MHz  $^1\text{H-NMR}$  studies. Strong  $\pi$ - $\pi$  interactions between the pyrene guest and the porphyrin walls of the host must occur in order explain the observed redshift of the porphyrin Q bands upon complexation. Interesting photophysical properties are expected from such a nanoprism.

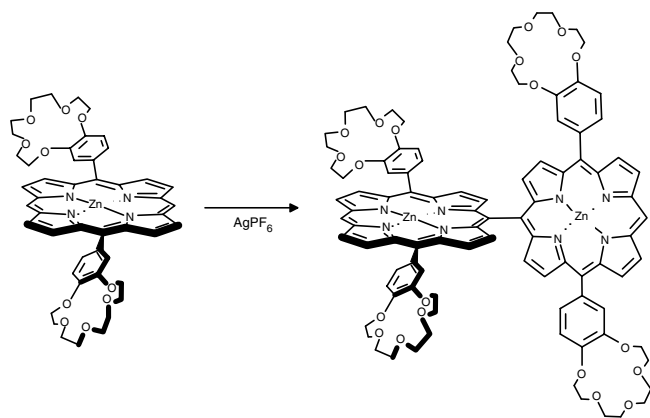
As an alternative to pyridyl groups as the ligand of central metal atoms in porphyrins, Ogawa and Kobuke have prepared an imidazolyl substituted porphyrin dimer that self-coordinates showing an oligomeric distribution which peaks at about 150 porphyrin units. According to molecular modeling, if a linear geometry presumed, the array should have a length of about 110 nm [291]. Due to the R-substituents, which in this case was *n*-heptyl, these coordination nanostructures are still remarkably soluble in organic solvents such as chloroform. This is also an indication that due to the nearly perpendicular geometry of the *meso*-linked unit extended  $\pi$ - $\pi$  interactions between oligomeric strands are not possible. This is in contrast to the large planar coordination arrays presented previously.



The monomeric 5-(1-methylimidazol-2-yl)-porphyrinc building block with a free *meso*-position dimerizes in solution by coordination of the zinc atom by the 3-imidazolyl nitrogen. Upon oxidative Osuka coupling of this monomer and formation of the *meso*-linked dimer, in the absence of polar solvents, extensive oligomerization occurs. Very recently it was shown that these oligomers have extremely large third-order optical nonlinearities and, as expected from the Osuka-type *meso*-linkage of the dimers, the Soret band is split [292].

Another similar interesting polymeric assembly of porphyrins mediated by metal ion ligations but using crown ethers as the ligands was very recently presented by Shinmori et al. [293]. A detailed complexation study of alkaline ions was shown to induce dimerization of a distal bis-substituted benzo-15-crown-5-porphyrin which is especially favorable for potassium ions. Additional *face-to-face* stabilization leads to an increased stability constant (ca.  $10^{18} \text{ M}^{-3}$ ) for a 2:2 complex. When different metals are introduced within the porphyrin additional ligands may be coordinated. The dimer formation was not only inhibited but also dissociation occurred in the case of a cobalt porphyrin in presence of dimethylaminopyridine (DMAP). Thus the bis-cobalt ligation by DMAP is stronger than the *face-to-face* aggregation assisted by metal ion complexation. By silver ion promoted oxidation the *meso-meso* linked Osuka-type dimer shown at right could be obtained in 13% yield. Due to the perpendicular orientation of the two porphyrin rings, dimer formation upon complexation within

the benzo-crown ethers of  $K^+$  is in this case not possible. Instead an extended oligomer was formed which had a molecular weight of ca. 100 kDa which corresponds to an aggregate with a distribution peaking at ca. 50 bis-porphyrin units. From simple molecular modeling (Fig. 30), if a linear geometry is inferred, an approximate length of over 100 nm is to be expected. However, multiple conformations of the crown ethers may exist so that a linear geometry may not be maintained for the longer oligomers.



Potassium ions do not quench the fluorescence of the aggregate and thus such large antenna systems would be suitable for artificial light-harvesting.

In the previous structure, if instead of potassium, silver ions would be used (similar to the example presented in the beginning of this section [253]), although for light-harvesting purposes this would not be a useful construct, maybe molecular electronics applications could be envisageable. Electron transport, mediated by metalated porphyrins between the silver atoms, could be possible on the decinometer scale. Additionally, such a wire composed of discrete silver atoms would appear to be insulated due to the crown ether ligands and the perpendicular bisporphyrins, so that interstrand electron jumps would be much less probable. A linear silver(I)-mediated network of *meso*-tetrakis(4-pyridylporphyrin) could be characterized by X-ray diffraction of single crystals [294]. Within the voids of the  $\pi$ -stacked network, solvent molecules and the hexafluorophosphate counterions were clathrated. This silver network showed interesting redox behavior and the fluorescence was apparently not quenched in the solid state. Very recently, the self-assembly of this same tetrapyrrolyl porphyrin was studied on gold [Au(111)] electrodes using STM showing that it

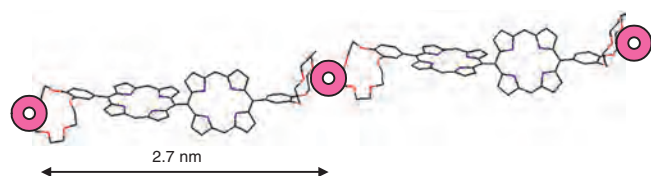
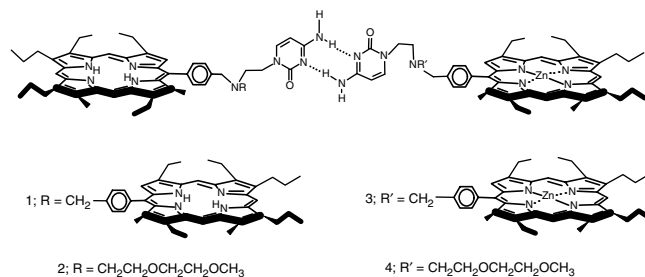


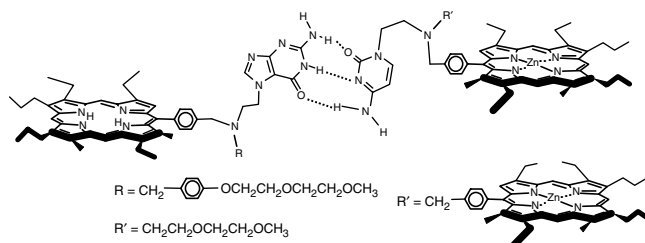
**Figure 30.** An extended metal ligated oligomer from the Shinmori et al. bis-porphyrins decorated with benzo-15-crown-5 ethers. Metal ions are shown as disks.

is possible to tune surface interaction and to modulate the surface mobility by the electrode potential [295].

**Assembly of Porphyrinic Nanostructures Using Hydrogen Bonding** The first to synthesize hydrogen bonded supramolecular species and to show by detailed photophysical measurements that energy transfer can occur efficiently in such assemblies were Harriman, Magda and Sessler [296, 297]. Several nucleic acid bases were covalently attached onto porphyrins. In solution, due to multiple hydrogen bonding base-pairing was induced as depicted in this formula for cytosine derivatives:



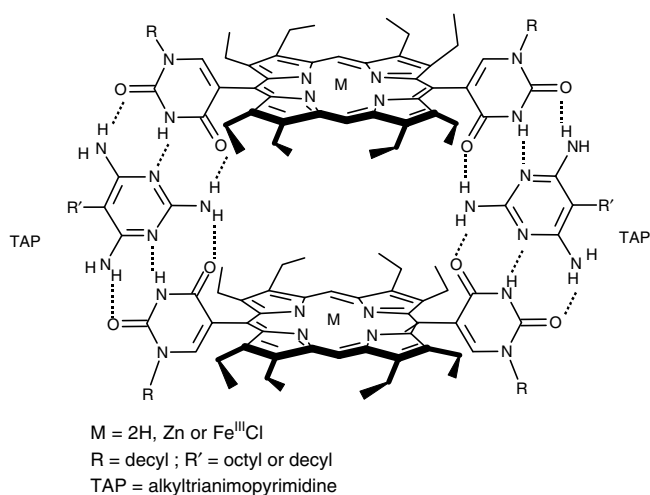
Alternatively, the stronger guanine–cytosine (G–C) base pair was used to enhance the association constant:



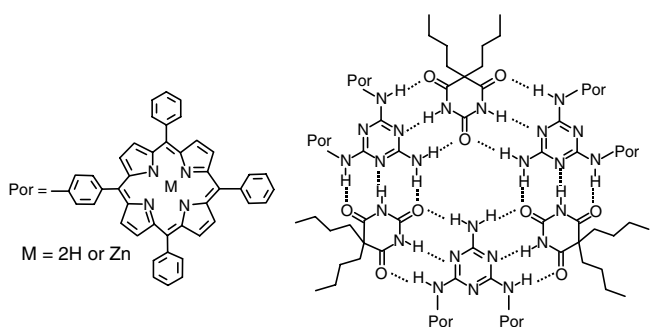
The photophysical properties of the assemblies were compared to those of model compounds such as the free base octaethylporphyrin (OEP) and the zinc-metallated counterpart (ZnOEP). Even at high concentrations (in the molar range), equimolar mixtures of OEP and ZnOEP behave exactly as the separated noninteracting molecules. In the porphyrin conjugates where the hydrogen bonding group has been connected by an amine linkage there is a decrease both in the fluorescence quantum yields and in the lifetimes in comparison to the corresponding OEP models. This was attributed to an intramolecular electron transfer process from the tertiary amino group in the linker. There is little or no energy transfer from the Zn donor to the free base acceptor in this case. At higher concentrations, depending on the strength of the association constant, additional fluorescence quenching of the zinc donor occurs which indicates that energy transfer is occurring. This was confirmed by time-resolved measurements from which also the respective rate constants could be differentiated into those occurring for a singlet–singlet excitation energy transfer process in the  $(2-9) \times 10^{-8} \text{ s}^{-1}$  range and those for a triplet–triplet process occurring in the  $(5-100) \times 10^{-5} \text{ s}^{-1}$  range. The association constants between the different conjugates varied by one order of magnitude between ca. 24 and 225  $\text{M}^{-1}$ , the weakest being for guanine–guanine self-association and

the strongest for the cytosine–guanine base pairs. An important aspect is that the rate of the energy transfer, once an assembly is formed by hydrogen bonding, is practically independent of the nature of the connecting zipper bases (termed also “recognition groups”) and increases strongly upon increasing the number of zinc-porphyrin donors. This is in accord with the Förster mechanism due to the increased probability of matching an excited donor moiety with an acceptor moiety at a preferred orientation and smaller separation. Additionally, due to the flexible linkers, a Dexter mechanism may occur at small separations when the orbitals of a donor and an acceptor overlap.

Drain while in the group of Lehn [298, 299] and later independently [300] has also engineered self-assembly of porphyrins exclusively by hydrogen bonding. By using different complementary recognition groups, discrete multiporphyrin arrays could thus be built in a controlled manner. The following “bisporphyrin supramolecular cage” was formed by stitching with a alkyltriaminopyrimidine (TAP) “wedge” two bis *meso*-uracyl OEP molecules, either as free bases, zinc, or chloroferric complexes [298]:

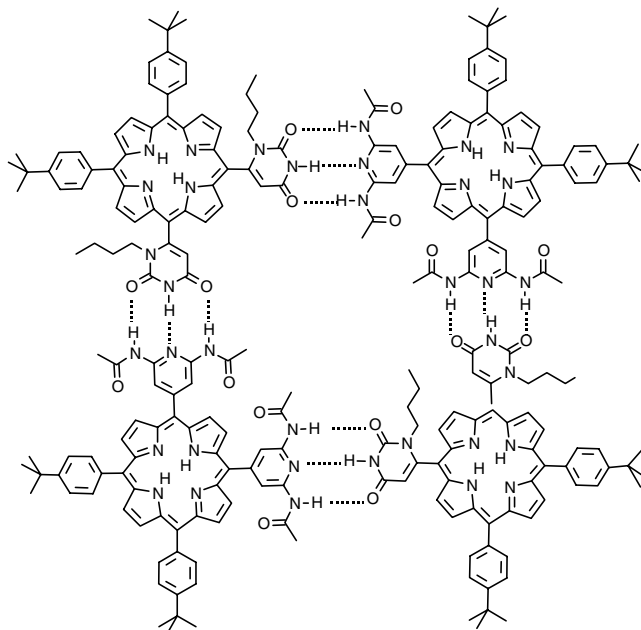


Alternatively, a “rosette” is formed by appending two porphyrins on a 1,3,5-triazine and stitching each donor–acceptor–donor face by a complementary acceptor–donor–acceptor barbituric acid wedge [299]:



By using the complementary 2,6-diacetamidopyridine and uracyl recognition groups introduced by Lehn and

co-workers [301], Shi et al. recently showed by NMR, electrospray ionisation mass spectrometry (ESI-MS) and vapor phase osmometry (VPO) that preferentially a tetrameric assembly is formed from vicinal *meso*-disubstituted porphyrins in chloroform solutions [300]:



In the same study [300], a nice crystal structure could be solved for the free base 5,10-bis-(2,6-diacetamido-4-pyridyl)porphyrin, where water molecules mediate hydrogen bonding in the crystal lattice.

In an attempt to mimic the self-assembly of natural bacteriochlorophylls (BChls) encountered in chlorosomes (see Section 3.1.1) Balaban et al. have synthesized various zinc metallated porphyrins where a hydroxy group and a carbonyl group were appended onto *p*-phenylene spacers situated in vicinal or distal *meso* positions of porphyrins having also two other long chain solubilizing groups [195]. A hydrogen bonding network acting cooperatively with  $\pi$ – $\pi$  interactions was put into evidence in the crystal structure of such a free base porphyrin. Here the inner pyrrolic nitrogens devoid of hydrogen atoms, which could be localized in the electron density map, act as hydrogen bond acceptors while the hydroxy group is the hydrogen bond donor as shown in Figure 31.

In Figure 31 the central porphyrin is a hydrogen bond acceptor from two neighboring porphyrins, one from above and one from below. At the same time it is a hydrogen bond donor through the hydroxymethylene groups to two other porphyrins not shown in the figure. Note the different orientation of the porphyrin planes and the very regular extension of the otherwise flexible undecyl sidechain which has a kink allowing it to deviate above and below the porphyrin plane. Due to the deviation of the *meso-p*-phenylene groups from the porphyrin plane (dihedral angle of 65°), ligation of a zinc metallated porphyrin by a 4-hydroxymethylenephyl group is energetically disfavored in a  $\pi$ -stacked arrangement. Thus, although all the functional groups encountered

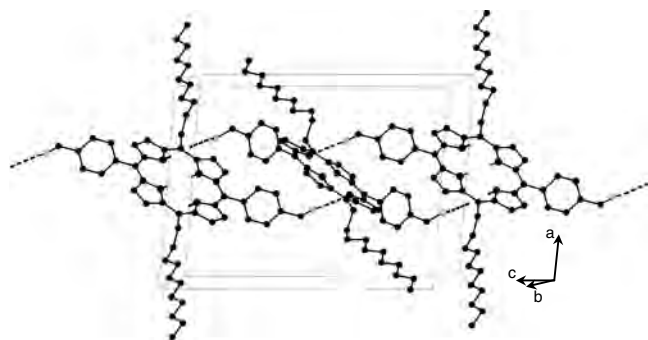
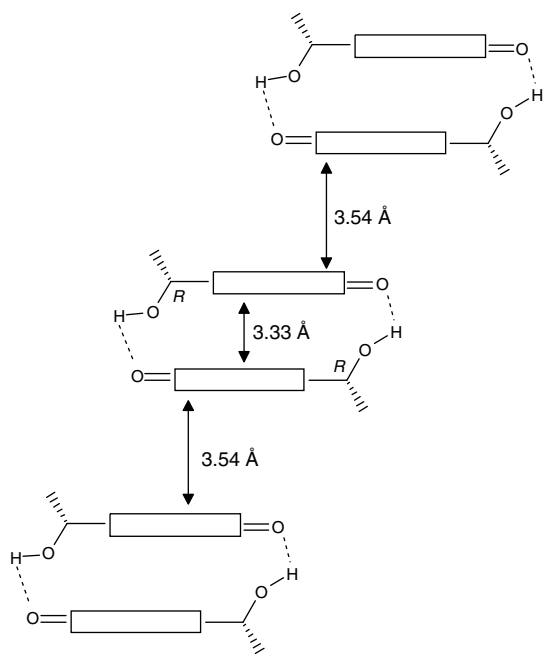


Figure 31. Hydrogen-bonding network in the crystal.

in BChls are presented, the self-assembly algorithm cannot operate in the same manner. For better tailored systems see the following.

Similar hydrogen bonding to the inner pyrrolic nitrogens was more recently put into evidence in other crystal structures of 5,15-diarylporphyrins synthesized by the group of Sanders [266, 302].

In another earlier interesting crystallographic study by Barkigia et al. which was related to models for the antenna complexes of green photosynthetic bacteria, it was shown that a zinc porphyrin analog of BChl *d* forms stacked dimers of the type shown schematically [303]:



Surprisingly, the 3-hydroxyethyl group (in which the 3<sup>1</sup> carbon atom had *R* configuration) does not bind as expected

the central zinc atom and prefers to hydrogen bond the carbonyl group of an antiparallel stacked porphyrin. There is a slightly shorter interplane distance within such a doubly hydrogen bonded dimer than between the dimers: 3.33 Å intradimer and 3.54 Å interdimer. However the  $\pi$ - $\pi$  overlap is almost uniformly offset showing that its cooperative action with double hydrogen bonding may win over the stronger zinc chelation.

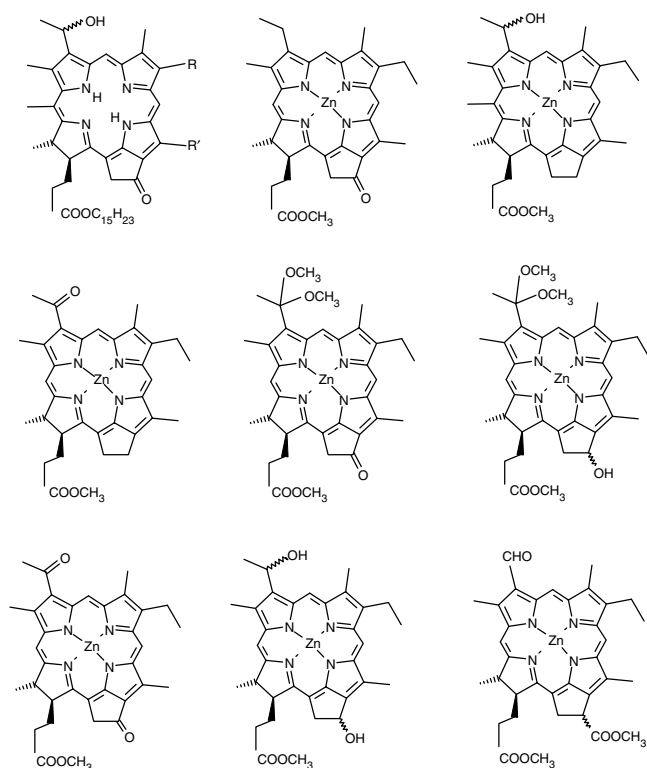
### Cooperative Interactions between Porphyrinic Chromophores Using Metal Ligation and Hydrogen Bonding

When a ligand binds to a metal atom and at the same time the ligand can function as a hydrogen bonding group, cooperativity effects may occur. This is the case presently believed to operate for the natural light-harvesting systems of green photosynthetic bacteria, the chlorosomes, discussed before (see Section 3.1.1) which involve BChl *c*, *d* and *e*. Numerous studies of the natural system first in collaboration with Schaffner and Holzwarth [39–47] were then continued independently by Tamiaki and Balaban with nonnatural systems. While Tamiaki has used exclusively semisynthetic compounds derived either from Chl *a* (usually isolated from algae such as *Spirulina geitleri*) or BChl *a* (isolated for example from the purple bacterium *Rhodobacter sphaeroides*), Balaban has taken a fully synthetic approach with robust pigments such as porphyrins or phthalocyanines. In view of applications, the latter way is better yielding and does not rely on culturing and tedious isolation techniques, usually involving high performance liquid chromatography (HPLC) separations.

Jesorka et al. were the first to show that the BChl *c* and *d* skeleton is tolerant to rather wide variations and can still be induced to self-assemble [304]. Thus when the positions of the 3<sup>1</sup>-hydroxy groups and 13<sup>1</sup> carbonyl groups are interchanged self-assembly still occurs. However, if the central metal atom (zinc or magnesium) is missing (i.e., the corresponding free base chlorins) or if either the hydroxyl and/or the carbonyl groups are removed or protected the ability to form a light-harvesting system by self-assembly is inhibited. Thus the simultaneous presence of a metal atom, carbonyl group, and hydroxyl group on a macrocyclic scaffold capable of  $\pi$ -stacking is essential. Scheme 2 presents structures which cannot self-assemble.

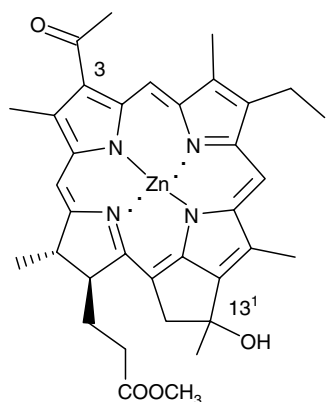
Scheme 3 shows the semisynthetic mimics of BChl *c*, *d*, and *e* (for their formulas see Scheme 1) which can self-assemble and have large redshifted and usually broad absorption maxima, reminiscent of J-aggregates [41, 304–306].

Newer studies from Tamiaki's laboratory include the asymmetric reduction of the 3-acetyl group using oxazaborolidines as chiral auxiliaries [307] or insertion in the 3-position of  $\omega$ -hydroxyalkyl groups [308] instead of the hydroxy(m)ethyl group. Also synthesized were similar compounds having a tertiary 3<sup>1</sup>-hydroxy group [309] or "inverted" compounds having a tertiary hydroxy group in the

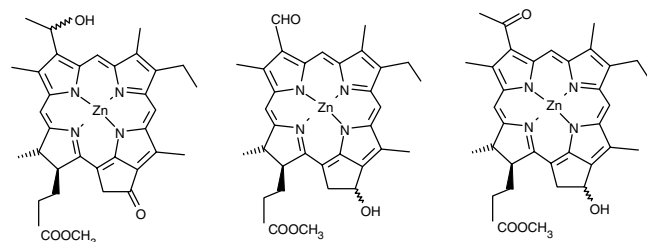


**Scheme 2.** BChl analogs which do not self-assemble.

13<sup>1</sup>-position and a 3-acetyl group [310]:

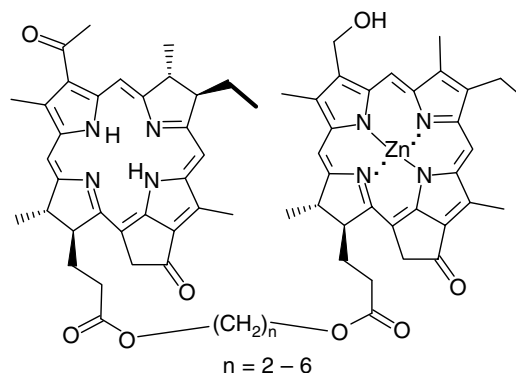


Important proof that functional devices can be obtained by self-assembly was made by generating light-harvesting



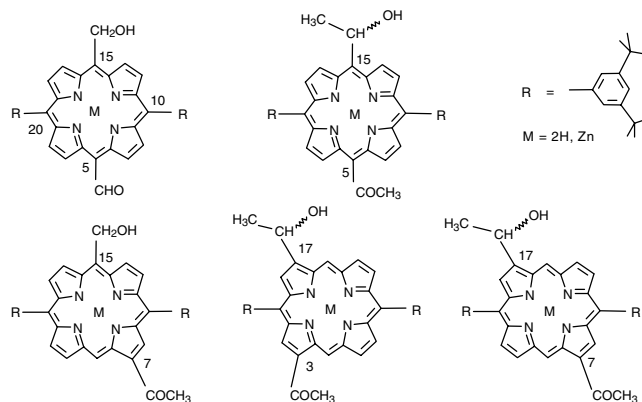
**Scheme 3.**

nanostructures with such BChl *c* (or *d*) mimics which had additionally incorporated an energy trap of BChl *a* type [75–77]:



These covalent linked dyads have the BChl *a* energy trap (left moiety) bound to the semisynthetic chlorin mimic (right part) which, having the same functional groups, inserts itself within the self-assembling antenna formed only from the right half molecules. The energy absorbed by the self-assembled chlorins present in large excess (100 to 1) is efficiently transferred to the bacteriochlorin trap. If the covalent linkage is absent there is no energy transfer except when the two components are confined within liposomes. This is in accord with the Förster excitation energy transfer mechanism.

Very recently Balaban et al. could synthesize by different methods, some of them novel to porphyrin chemistry, the following porphyrin mimics of BChls which are able to self-assemble [193]:



A systematic variation was performed of the positions where the carbonyl group (either formyl or acetyl) and the hydroxy group (either as an achiral hydroxymethylene group or the chiral 1-hydroxyethyl group) are appended onto the porphyrin ring. The zinc metalated compounds ( $M = \text{Zn}$ ) self-assemble in nonpolar solvents and their optical properties can be fine tuned due to variations of the  $\pi$ - $\pi$  overlap. Furthermore, by separating the enantiomers of



the hydroxyethyl substituted compounds by means of chiral HPLC and then inducing these to self-assemble, chiral nanostructures are obtained which are enantiomorphic having mirror imaged CD spectra. Thus the chirality of the monomeric building block induces the chirality of the supramolecular assembly.

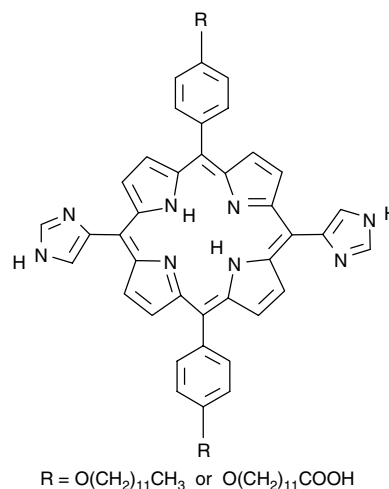
Another interesting example, where also crystallographic proof of the structure could be provided for the self-assembly combining Zn ligation with simultaneous hydrogen bonding and  $\pi$ - $\pi$  interactions, was provided by means of 2-aminopyrimidine groups which were appended in *meso*-porphyrinic positions [192]. For the first time a pyrimidine ligand was found to coordinate the central Zn atom of a porphyrin, thereby inducing the preferential formation of a closed tetramer (Fig. 32).

Inside the tetramer two 2-aminopyrimidine groups  $\pi$ -stack in an offset manner. The other two 2-aminopyrimidine groups pointing outward are involved in double hydrogen bonding (dotted lines) to neighboring tetramers which appear thus as beads on a hydrogen bonded string. Between the strands solvent molecules (cyclohexane) interact favorably with the bulky *t*-butyl groups.

If water molecules complex the central zinc atom within porphyrins, their ability to serve as hydrogen bond donors is enhanced. An interesting dimer could be crystallized from a 10,20-dioxoporphyrin having pendant ester groups whose carbonyl oxygens serve as the hydrogen bond acceptors [351].

**Assembly of Porphyrinic Nanostructures by Other Weak Interactions** In the absence of other stronger intermolecular interactions, even hydrophobic (or dispersive) forces can be used to assemble nanostructures which can perform light harvesting. An example was provided by Kobuke and co-workers who have prepared liposomes as small unilamellar vesicles of about 30 nm by sonicating dispersions in water of the following imidazolyl-substituted

porphyrins [311]:



It is also probable that  $\pi$ - $\pi$  interactions occur within these micellar assemblies which can include other fluorescent molecules such as pyranine. In polar media, in this case water, no imidazolyl-imidazolyl hydrogen bonding is expected to occur.

Porphyrin containing nanoparticles having average hydrodynamic radii in the 10–70 nm range were recently described and imaged by AFM [312]. In this case J-aggregates were formed, which are typical also for other chromophores. For some representative examples of J-aggregates see [313–317] and other references cited therein.

## 5. CONCLUSIONS: ARTIFICIAL PHOTOSYNTHESIS—PERSPECTIVES AND FUTURE GOALS

I have tried to give a broad overview of light-harvesting both in natural systems and in synthetic systems built by chemists. The vision is to engineer manmade compounds into devices capable of photosynthesis (i.e., to be able to use sunlight, even under low light illumination conditions, to produce useful energy). Plants and bacteria do this optimally due to evolution which has helped them optimize the quantum yields of each step involved so that the overall efficiency is stunning. In artificial photosynthesis the generated energy form maybe either direct photocurrent, as in photovoltaic devices, or producing reactive chemical species which thus store the light energy in a chemical form. Photocatalytic water splitting is a goal that is actively pursued by several research groups, both in academia and industry. The present state-of-the-art silicon based photovoltaic cells, although they represent a working technology, due to the high production cost and relatively low photocurrent efficiency (under 15%), have reached an evolutionary plateau

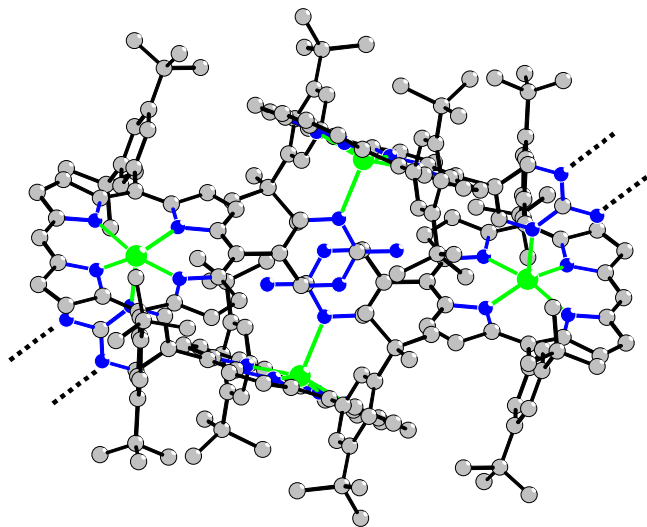


**Figure 32.** Self-assembled tetramer in the crystal. The dotted lines indicate hydrogen bonds to adjacent tetramers.

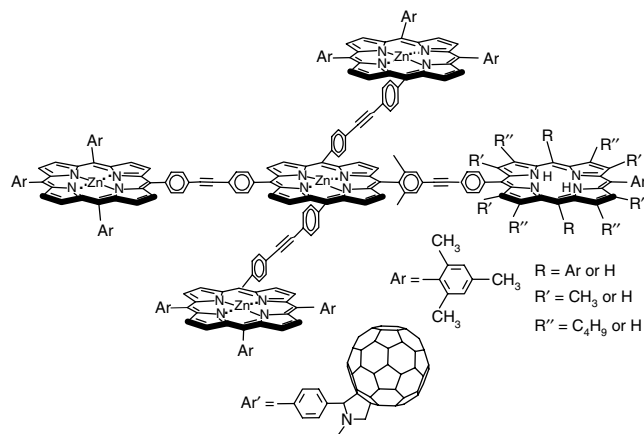
so that large scale applications are not yet envisageable. One of the most efficient nonsilicon based solar cell is the so-called “dry Grätzel cell” which uses nanotechnology to make an interpenetrating network of mesoporous nanocrystalline titanium dioxide. This wide band semiconductor cannot be directly excited by the solar spectrum but can be photosensitized with a chromophore, initially a ruthenium (II) bipyridine complex [318]. A hole transporting molecule, such as a spiro-bis-fluorene derivative, allows the hopping of electrons from a gold electrode to the dye which, after photoexcitation and charge separation, has injected an electron into the conduction band of the  $\text{TiO}_2$  semiconductor. Conversion of photons to current occurs with over 30% efficiency. The interested reader is referred to the excellent reviews by Grätzel et al. describing newer advances since the “wet Grätzel cell” which was based on electrolytes [319–321].

Several trials to improve with other light-harvesting chromophores the photosensitization of titanium dioxide have been undertaken. These include modified phthalocyanines [322], aggregated cyanines [323], porphyrins [324], or other ruthenium pyridyl complexes [325–327]. Sandwich-type structures were achieved by incorporating different dyes into zeolites, thus preventing the usual fluorescence quenching due to aggregation effects, and bidirectional cascade-type energy transfer could be observed [328]. An excellent review has been very recently published [352].

Newer technologies, based on organic solar cells, although the working principle has been proven, are still in their infancy with efficiencies around 3% [329–331]. In this case however, cheap production costs, as expected from the polymer industry, could be a trade-off for higher photocurrent yields. Addition of a polythiophene regioregular polymer as a hole conducting material gives enhanced photocurrents in organic solid-state cells employing Mg tetraphenylporphyrin or its free base [332]. Light-harvesting porphyrin-substituted polythiophenes which were electropolymerized were investigated for their performance in both photoelectrochemical cells and Schottky junction devices [333].

Highly efficient artificial models for the photosynthetic reaction center have been designed and synthesized, using amazing chemistry by Sauvage and co-workers. Very long charge separated states, entering the  $\mu\text{s}$  range, can be obtained with some porphyrinic systems which are mechanically interlocked into catenanes [334–336]. The principles for the construction of mechanical interlocked compounds where there are no bonds between electron donors and acceptors have been reviewed [337].

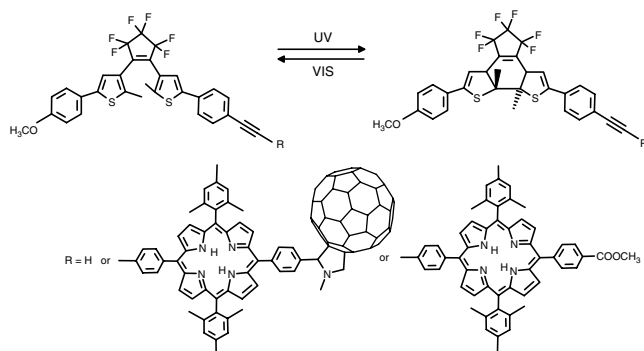
Finally, the recent achievements of the Arizona researchers led by Devens Gust together with Thomas and Anna Moore deserve special mention. An artificial reaction center formed from a tetrathiafulvalene–porphyrin–fullerene triad was shown to exhibit a very long-lived charge separated state (660 ns) [338]. In collaboration with the Lindsey group an efficient artificial photosynthetic antenna–reaction center covalent hybrid was synthesized and its photophysics were studied [339].



This hexad is formed from three peripheral antenna Zn porphyrins ( $\text{P}_{\text{ZP}})_3$ , a central Zn porphyrin ( $\text{P}_{\text{ZC}}$ ), a free base porphyrin (P) which acts as an energetic trap, and a fullerene ( $\text{C}_{60}$ ) as an electron acceptor. Depending on the substitution pattern of the free base porphyrin which influences the oxidation potentials and thus the driving force for generating a charge separated state, very different quantum yields and lifetimes could be determined. The best performing hexad has *meso*-mesityl-groups, being thus a tetraaryl free base porphyrin and not an octaalkyl one. Light is gathered by the peripheral Zn porphyrins and the energy is transferred to the central one generating its singlet excited state  $(\text{P}_{\text{ZP}})_3^{-1}\text{P}_{\text{ZC}}-\text{P}-\text{C}_{60}$  with a time constant of 50 ps. Part of this energy is then further trapped by the artificial reaction center part of the hexad generating the  $(\text{P}_{\text{ZP}})_3-\text{P}_{\text{ZC}}^{-1}\text{P}-\text{C}_{60}$  state with a time constant of 32 ps. The latter decays within 25 ps by means of a photoinduced electron transfer pathway to the fullerene forming thus the primary charge separated state  $(\text{P}_{\text{ZP}})_3-\text{P}_{\text{ZC}}-\text{P}^+-\text{C}_{60}^{\bullet-}$ . This state can also be accessed (with quantitative quantum yield) by exciting directly the free base porphyrin P. Secondary, long lived charge separated states,  $((\text{P}_{\text{ZP}})_3-\text{P}_{\text{ZC}})^{\bullet+}-\text{P}-\text{C}_{60}^{\bullet-}$  are subsequently formed with a rate constant of  $2.3 \times 10^9 \text{ s}^{-1}$  and an exceptional lifetime of 240 ns (for the mesityl-substituted P) and an extremely high quantum yield of 0.86. Almost every photon which is absorbed leads thus to charge separation and the long lifetime would in principle make such hexads suitable as components in solar cells or optoelectronic devices. The overall efficiency is, however, still lower than in natural photosynthesis which uses much larger antennas for each reaction center enabling them to harvest light in higher yields across the entire solar spectrum. Future improvements reside thus in increasing the size of the artificial antenna. We have recently presented a biomimetic approach of how this can be achieved by using synthetic porphyrins which have been equipped with the same groups that induce self-assembly as in the chlorosomal antenna [193, 194]. By using pigments other than porphyrins, with higher extinction coefficients, even better antennas are envisageable. A simple model exhibiting ultrafast energy transfer from a carotenoid to a covalently bound chlorin has already been described [340].

Another recent and interesting application consists of devising switches for energy and electron transfer. An initial

porphyrin–spiropyran dyad showed photoswitching ability of the energy transfer [341]. The spiro[indoline–benzopyran] moiety (Sp) can be present in a “closed” form which does not absorb light over 400 nm and upon irradiation in the near-UV valence tautomerizes to a “ring-opened” merocyanine form (Sp<sub>o</sub>) which absorbs strongly in the visible region (500–700 nm). Reclosure can occur either thermally (slowly with a time constant of 20 s) or more rapidly by irradiation into the 600 nm band. Excitation of the porphyrin present in the merocyanine form produces <sup>1</sup>P<sub>Zn</sub>–Sp<sub>o</sub> which decays to the P<sub>Zn</sub>–<sup>1</sup>Sp<sub>o</sub> within 130 ps with a quantum yield of 0.93 for the energy transfer. In the closed state, the porphyrins (either as free base or Zn-metalated) are unperturbed having much longer lifetimes. This provided light-activated control of the porphyrin excited states by means of gated energy transfer. A more recent photonic switch based on the Irie-type dithienylethene scaffold [342–344] allowed control of the photoinduced electron transfer from a porphyrin to a fullerene [345]:



Model compounds where R is H or a tetararylporphyrin were synthesized besides the active device which has the fullerene attached to the porphyrin. In the colorless, open form of the dithienylethene (DTE<sub>o</sub>), when the porphyrin is excited the charge separated state DTE<sub>o</sub>–P<sup>•+</sup>–C<sub>60</sub><sup>•-</sup> is generated with quantum yield of unity. In contrast, upon irradiation with UV light and conversion to the closed conjugated form (DTE<sub>c</sub>) the singlet excited state of the porphyrin (<sup>1</sup>P) is quenched by energy transfer to DTE<sub>c</sub> within ~2 ps thus inhibiting any electron transfer (quantum yield of the charge separated state < 0.09) to the fullerene. Irradiation with visible light returns the very stable perfluorocyclopentene DTE to its colorless open form DTE<sub>o</sub>. These two examples demonstrate that both energy and electron transfer processes can be photoswitched.

Definite proof that artificial photosynthesis is not only a dream has been brought forth by combining in a liposomal construct which mimics the natural photosynthetic membrane, an artificial reaction center assembled into a light driven proton pump which is used to drive an incorporated ATP-synthase to fabricate ATP [346]. For an excellent recent review on mimicking photosynthetic solar energy transduction see [347]. Very recently, transport of Ca<sup>2+</sup> ions against a thermodynamic gradient was demonstrated to be possible within a liposomal artificial photosynthetic membrane [348].

We hope that the present chapter might stimulate other researchers to enter this field and help the established

groups in finding solutions on improving artificial light harvesting and energy conversion. Paraphrasing Richard Feynmann with his famous phrase “there is plenty of room at the bottom,” which has forecasted the boom in nanoscience and nanotechnology, we can say that “there is plenty of room for perfecting artificial photosynthesis” from the current status to what Nature has achieved through evolution. Even imperfect solutions might become economically viable.

## GLOSSARY

**Antenna** A collection of natural or artificial molecules capable of absorption of electromagnetic radiation.

**Blueshift** Shift of the absorption maximum towards shorter wavelengths (i.e., to higher energy), also called *hypsochromic* shift.

**Catenane** Bi- or polycyclic molecular species which has mechanically interlocked parts, similarly to the rings within a chain.

**Chlorosome** Light-harvesting organelle of green photosynthetic bacteria *Chlorobiineae* and *Chloroflexaceae* appended on the inner side of the cytoplasmic membrane.

**Dendrimer** Monodisperse, usually highly branched, covalent molecular species formed by a repetitive sequence of chemical reactions which enable the transformation of one generation (G<sub>n</sub>) into the next one (G<sub>n+1</sub>).

**Electron transfer (eT)** A process by which an electron from a donor molecule is passed to an orbital of an acceptor molecule. If the process is activated by light one speaks of photoinduced eT.

**Energy trap** A pigment, or collection of pigment molecules (e.g. dimers) that can collect the energy from a light-harvesting apparatus, similarly to the focal point of a parabolic antenna or an optical lens. Usually, but not necessarily, the energetic traps are the most redshifted antenna pigments.

**Excitation energy transfer (EET)** A process by which the energy of a photon which brings one chromophore to its (usually singlet) excited state can be passed to another (usually adjacent) chromophore. Thereby the donor chromophore relaxes to the ground state while the acceptor chromophore becomes excited, becoming thus a potential new energy donor chromophore. The EET and can occur by different mechanisms: Förster (or dipolar) EET operates over a long range (1 to 8, or even 10 nm) between weakly coupled chromophores while the Dexter (or exchange) EET mechanism operates between strongly coupled chromophores, at short distances, and is actually a double electron transfer process.

**Exciton** An electron-hole pair which can be tightly coupled and residing in a confined portion of space (Frenkel exciton) or can be delocalized over larger regions (Wannier–Mott exciton).

**Nanostructure** Molecular, supramolecular, or ensemble of species with dimensions between 1 and 100 nm which has distinct properties as its components and which usually fulfills a specific function.

**Reaction center** Complex of molecules which after receiving the excitation energy from an energetic trap (which may

or not be part of the reaction center itself) is capable of charge separation (i.e., formation of an exciton) and of stabilizing it through subsequent electron transfer steps. If charge recombination is inhibited so that the exciton is sufficiently long-lived, it can be transformed into biochemical, electrochemical, or a photovoltaic potential.

**Redshift** Shift of the absorption maximum towards longer wavelengths (i.e. to lower energy), also called *bathochromic* shift.

**Recognition groups** Chemical groups, usually having complementary supramolecular binding sites, which decorate tectons in view of inducing self-assembly.

**Self-assembly** An enthalpy driven process, usually associated with an entropic loss, by which a supramolecular species is formed.

**Supramolecular species** A discrete ensemble of tectons which are held together by noncovalent interactions such as: ion pairing (or salt bridges), metal chelation, hydrogen bonding,  $\pi$ - $\pi$  interactions, hydrophobic or dispersive forces.

**Tecton** Molecular entity (or brick) programmed for self-assembly, i.e., which stores within its molecular architecture the information needed to construct supramolecular species.

## ACKNOWLEDGMENTS

Mihaela Carmen Balaban is thanked for help in preparation of the figures, retrieval of the PDB structural information, and reference database management, and for coping with the stress of the family related to writing reviews. Niels-Ulrik Frigaard is thanked for the design and elaboration of the chlorosome figure. Some of the work reviewed in this chapter from the author's laboratory was partially supported by the Center for Functional Nanostructures (CFN) of the Deutsche Forschungsgemeinschaft (DFG) within project C3.2.

## REFERENCES

- J. Disenhofer, O. Epp, K. Miki, R. Huber, and H. Michel, *Nature* 318, 618 (1985).
- U. Ermler, G. Fritsch, S. K. Buchanan, and H. Michel, *Structure* 2, 925 (1994).
- M. H. B. Stowell, T. M. McPhillips, C. D. Rees, S. M. Soltis, E. Abresch, and G. Feher, *Science* 276, 812 (1997).
- "The Photosynthetic Reaction Center" (J. Disenhofer and J. R. Norris, Eds.). Academic Press, San Diego, 1993.
- The Photosynthetic Bacterial Reaction Center—Structure and Dynamics" (J. Breton and H. Vermeglio, Eds.). Plenum Press, New York, 1988.
- D. Gust and T. A. Moore, *Science* 244, 35 (1989).
- D. Gust, T. A. Moore, and A. L. Moore, *Pure Appl. Chem.* 70, 2189 (1998).
- H. Kurreck and M. Huber, *Angew. Chem. Int. Ed. Engl.* 34, 849 (1995).
- A. Harriman and J.-P. Sauvage, *Chem. Soc. Rev.* 41 (1996).
- A. Zouni, H.-T. Witt, J. Kern, P. Fromme, N. Krauss, W. Saenger, and P. Orth, *Nature* 409, 739 (2001).
- P. Jordan, P. Fromme, H.-T. Witt, O. Klukas, W. Saenger, and N. Krauß, *Nature* 411, 909 (2001).
- R. E. Blankenship, Photosynthetic antennas and reaction centers: Current understanding and prospects for improvement, in "Research Opportunities in Photochemical Sciences" (A. J. Nozik, Ed.). NREL/CP-450-21097; DE96007867, 1996.
- T. Förster, *Ann. Phys. (Leipzig)* 2, 55 (1948).
- T. Förster, *Discuss Faraday Trans.* 27, 7 (1965).
- D. L. Dexter, *J. Chem. Phys.* 21, 836 (1953).
- R. A. Marcus and N. Sutin, *Biochim. Biophys. Acta* 811, 265 (1985).
- G. L. Closs and J. R. Miller, *Science* 244, 35 (1989).
- V. Balzani and F. Scandola, *J. Chem. Educ.* 60, 814 (1983).
- "Electron Transfer in Chemistry" (V. Balzani, Ed.), Vol. 1–5. VCH, Weinheim, 2001.
- R. Emerson and W. Arnold, *J. Gen. Physiol.* 16, 191 (1932).
- Cited in L. Stryer, "Biochemistry," 3rd ed., p. 520. Freeman, New York, 1988.
- R. van Grondelle, J. P. Dekker, T. Gillbro, and V. Sundstrom, *Biochim. Biophys. Acta* 1187, 1 (1994).
- H. van Amerongen and R. van Grondelle, *J. Phys. Chem. B* 105, 604 (2001).
- J.-M. Lehn, "Supramolecular Chemistry: Concepts and Perspectives." VCH, Weinheim, 1995.
- L. A. Staehelin, J. R. Golecki, R. C. Fuller, and G. Drews, *Arch. Microbiol.* 119, 269 (1978).
- L. A. Staehelin, J. R. Golecki, and G. Drews, *Biochim. Biophys. Acta* 589, 30 (1980).
- R. E. Blankenship, J. M. Olson, and M. Miller in "Anoxygenic Photosynthetic Bacteria" (R. E. Blankenship, M. T. Madigan, and C. E. Bauer, Eds.), pp. 399–435. Kluwer Academic, Dordrecht, 1995.
- R. E. Blankenship, D. C. Brune, and B. P. Wittmershaus, in "Light-Energy Transduction in Photosynthesis Higher Plant and Bacterial Models" (S. E. Stevens and D. A. Bryant, Eds.), pp 32–46. 1998.
- S. Chung and D. A. Bryant, *Photosynth. Res.* 50, 41 (1996).
- J. A. Eisen et al., *Proc. Natl. Acad. Sci. USA* 99, 9509 (2002).
- N.-U. Frigaard and D. A. Bryant, *Appl. Environ. Microbiol.* 67, 2538 (2001) and further work in progress.
- E. V. Vassilieva, V. L. Stirewalt, C. U. Jakobs, N.-U. Frigaard, K. Inoue-Sakamoto, M. A. Baker, A. Sotak, and D. A. Bryant, *Biochemistry* 41, 4358 (2002).
- N.-U. Frigaard, A. Gomez Maqueo Chew, H. Li, J. A. Maresca, and D. A. Bryant, *Photosynth. Res.* 78, 93 (2003).
- N.-U. Frigaard, S. Takaichi, M. Hirota, K. Shimada, and K. Matsuura, *Arch. Microbiol.* 167, 343 (1997).
- N.-U. Frigaard, K. Matsuura, M. Hirota, M. Miller, and R. P. Cox, *Photosynth. Res.* 58, 81 (1998).
- N.-U. Frigaard, S. Tokita, and K. Matsuura, *Biochim. Biophys. Acta* 1413, 108 (1999).
- S. Tokita, N.-U. Frigaard, M. Hirota, K. Shimada, and K. Matsuura, *Photochem. Photobiol.* 72, 345 (2000).
- N.-U. Frigaard and K. Matsuura, *Biochim. Biophys. Acta* 1412, 108 (1999).
- P. Hildebrandt, K. Griebenow, A. R. Holzwarth, and K. Schaffner, *Z. Naturforsch.* 46c, 228 (1991).
- P. Hildebrandt, H. Tamiaki, A. R. Holzwarth, and K. Schaffner, *J. Phys. Chem.* 98, 2192 (1994).
- H. Tamiaki, S. Takeuchi, R. Tanikaga, T. S. Balaban, A. R. Holzwarth, and K. Schaffner, *Chem. Lett.* 401 (1994).
- J. Chieffari, K. Griebenow, F. Fages, N. Griebenow, T. S. Balaban, A. R. Holzwarth, and K. Schaffner, *J. Phys. Chem.* 99, 1357 (1995).
- T. S. Balaban, A. R. Holzwarth, and K. Schaffner, *J. Mol. Struct.* 349, 183 (1995).
- T. S. Balaban, A. R. Holzwarth, K. Schaffner, G.-J. Boender, and H. J. M. de Groot, *Biochemistry*, 34, 15259 (1995).
- B. J. Van Rossum, G.-J. Boender, F. M. Mulder, J. Raap, T. S. Balaban, A. R. Holzwarth, K. Schaffner, S. Prytulla, H. Oschkinat, and H. J. M. de Groot, *Spectrochim. Acta A* 54, 1167 (1998).
- A. R. Holzwarth and K. Schaffner, *Photosynth. Res.* 41, 225 (1994).
- T. S. Balaban, J. Leitich, A. R. Holzwarth, and K. Schaffner, *J. Phys. Chem. B* 104, 1362 (2000).

48. N. Berova and K. Nakanishi, in "Circular Dichroism. Principles and Applications" (N. Berova, K. Nakanishi, and R. W. Woody, Eds.), 2nd ed., pp. 337–382. Wiley-VCH, New York, 2000.
49. B.-J. van Rossum, D. Stensgaard, F. M. Mulder, G.-J. Boender, K. Schaffner, A. R. Holzwarth, and H. J. M. de Groot, *Biochemistry* 40, 1587 (2001).
50. B. J. Van Rossum, B. Y. van Duyl, D. B. Steensgaard, T. S. Balaban, A. R. Holzwarth, K. Schaffner, and H. J. M. de Groot, in "Photosynthesis Mechanisms and Effects" (G. Garab, Ed.), Vol. I, p. 117. Kluwer Academic, Dordrecht, 1998.
51. M. I. Bystrova, I. N. Mal'gosheva, and A. A. Krasnovskii, *Mol. Biol.* 13, 440 (1979).
52. A. A. Krasnovskii and M. I. Bystrova, *BioSystems* 12, 181 (1980).
53. K. M. Smith, L. A. Kehres, and J. Fajer, *J. Am. Chem. Soc.* 105, 1387 (1983).
54. D. L. Worcester, T. J. Michalski, and J. J. Katz, *Proc. Natl. Acad. Sci. USA* 83, 3791 (1986).
55. D. L. Worcester, T. J. Michalski, M. K. Bowman, and J. J. Katz, *Mater. Res. Soc. Symp. Proc.* 174, 157 (1990).
56. T. P. Causgrove, D. C. Brune, R. E. Blankenship, and J. M. Olson, *Photosynth. Res.* 25, 1 (1990).
57. J. M. Olson and J. P. Pedersen, *Photosynth. Res.* 25, 25 (1990).
58. J. M. Olson, J. P. Pedersen, T. P. Causgrove, D. C. Brune, and R. E. Blankenship, in "Current Research in Photosynthesis" (M. Baltscheffsky, Ed.), p. 37. Kluwer Academic, Dordrecht, 1990.
59. J. M. Olson and R. P. Cox, *Photosynth. Res.* 30, 35 (1991).
60. J. M. Olson and J. P. Pedersen, in "Photosynthetic Light-Harvesting Systems," p. 365. de Gruyter, Berlin, 1991.
61. M. Hirota, T. Moriyama, K. Shimada, M. Miller, J. M. Olson, and K. Matsuura, *Biochim. Biophys. Acta* 1099, 271 (1992).
62. M. Miller, T. Gillbro, and J. M. Olson, *Photochem. Photobiol.* 57, 98 (1993).
63. K. Matsuura and J. M. Olson, *Biochim. Biophys. Acta* 1019, 233 (1990).
64. K. Matsuura, M. Hirota, K. Shimada, and M. Mimuro, *Photochem. Photobiol.* 57, 92 (1993).
65. M. Mimuro, Y. Nishimura, I. Yamazaki, M. Kobayashi, Z.-Y. Wang, T. Nozawa, K. Shimada, and K. Matsuura, *Photosynth. Res.* 48, 263 (1996).
66. Y. Zhu, B. L. Ramakrishna, P. I. van Noort, and R. E. Blankenship, *Biochim. Biophys. Acta* 1232, 197 (1995).
67. C. Bustamante, I. Tinoco, Jr., and M. F. Maestre, *Proc. Natl. Acad. Sci. USA* 80, 3568 (1983).
68. D. Keller and C. Bustamante, *J. Chem. Phys.* 84, 2972 (1986).
69. M.-H. Kim, L. Ulibarri, D. Keller, M. F. Maestre, and C. Bustamante, *J. Chem. Phys.* 84, 2981 (1986).
70. S. Savikhin, P. I. van Noort, R. E. Blankenship, and W. S. Struve, *Biophys. J.* 69, 1100 (1995).
71. S. Savikhin, P. I. van Noort, Y. Zhu, S. Lin, R. E. Blankenship, and W. S. Struve, *Chem. Phys.* 194, 245 (1995).
72. T. C. Causgrove, D. C. Brune, J. Wang, B. P. Wittmershaus, and R. E. Blankenship, *Photosynth. Res.* 26, 39 (1990).
73. T. C. Causgrove, D. C. Brune, and R. E. Blankenship, *Photochem. Photobiol. B* 15, 171 (1992).
74. M. Miller, T. Gillbro, and J. Olson, *Photochem. Photobiol.* 57, 98 (1993).
75. H. Tamiaki, T. Miyatake, R. Tanikaga, A. R. Holzwarth, and K. Schaffner, *Angew. Chem. Int. Ed. Engl.* 35, 772 (1996).
76. T. Miyatake, H. Tamiaki, A. R. Holzwarth, and K. Schaffner, *Helv. Chim. Acta* 82, 797 (1999).
77. T. Miyatake, H. Tamiaki, A. R. Holzwarth, and K. Schaffner, *Photochem. Photobiol.* 69, 448 (1999).
78. Y. Saga, T. Wazawa, T. Nakada, Y. Ishii, T. Yanagida, and H. Tamiaki, *J. Phys. Chem. B.* 106, 1430 (2002).
79. T. S. Balaban, P. Fromme, A. Holzwarth, N. Krauß, and V. I. Prokhorenko, *Biochim. Biophys. Acta* 1556, 1 (2002).
80. M. Byrdin, P. Jordan, N. Krauss, P. Fromme, D. Stehlik, and E. Schlodder, *Biophys. J.* 83, 433 (2002).
81. J. M. Olson, in "The Photosynthetic Bacteria" (R. K. Clayton and W. R. Sistrom, Eds.), p. 161. Plenum, New York, 1978; J. M. Olson, personal communication.
82. R. E. Fenna and B. W. Matthews, *Nature* 258, 573 (1975).
83. J. Deisenhofer, in "Chlorophylls" (H. Scheer, Ed.), Pergamon, Elmsford, NY, 1995.
84. R. M. Pearlstein, in "Chlorophylls" (H. Scheer, Ed.), p. 1048. Pergamon, Elmsford, NY, 1995.
85. Y.-F. Li, W. Zhou, R. E. Blankenship, and J. P. Allen, *J. Mol. Biol.* 271, 456 (1997).
86. D. Gülen, *J. Phys. Chem.* 100, 17683 (1996).
87. T. S. Balaban, *FEBS Lett.* 545, 97 (2003); *Erratum: ibid.* 547, 235 (2003).
88. T. Oba and H. Tamiaki, *Photosynth. Res.* 74, 1 (2002).
89. T. Oba and H. Tamiaki, *J. Photosci.* 9, 236 (2002).
90. M. Papiz, A. M. Hawthornthwaite, R. J. Cogdell, K. J. Wooley, L. A. Fergusson, and J. G. Lindsay, *J. Mol. Biol.* 209, 833 (1989).
91. G. McDermott, S. M. Prince, A. A. Freer, A. M. Hawthornthwaite-Lawless, M. Z. Papiz, R. J. Cogdell, and N. W. Isaacs, *Nature* 374, 517 (1995).
92. J. Koepke, X. Hu, C. Muenke, K. Schulten, and H. Michel, *Structure* 4, 581 (1996).
93. A. Freer, S. Prince, M. Papiz, A. Hawthornthwaite-Lawless, G. McDermott, R. J. Cogdell, and N. W. Isaacs, *Structure* 4, 449 (1996).
94. S. Hess, E. Åkesson, R. J. Cogdell, T. Pullerits, and V. Sundström, *Biophys. J.* 69, 2211 (1995).
95. T. Pulleritis and V. Sundstrom, *Acc. Chem. Res.* 29, 381 (1996).
96. R. J. Cogdell, M. F. Hipkins, W. MacDonald, and T. G. Truscott, *Biochim. Biophys. Acta* 634, 191 (1981).
97. X. Hu, T. Ritz, A. Damjanović, and K. Schulten, *J. Phys. Chem. B* 101, 3854 (1997).
98. X. Hu and K. Schulten, *Phys. Today* 50, 28 (1997).
99. T. Ritz, A. Damjanović, and K. Schulten, *Chem. Phys. Chem.* 3, 243 (2002).
100. W. Kühlbrandt, *Nature* 374, 497 (1995).
101. X. Hu, A. Damjanović, T. Ritz, and K. Schulten, *Proc. Natl. Acad. Sci. USA* 95, 5935 (1998).
102. J. L. Herek, W. Wohlleben, R. J. Cogdell, D. Zeidler, and M. Motzkus, *Nature* 417, 533 (2002).
103. K. McLuskey, S. M. Prince, R. J. Cogdell, and N. Isaacs, *Biochemistry* 40, 8783 (2001).
104. W. Jentzen, M. C. Simpson, J. D. Hobbs, X. Song, T. Ema, N. Y. Nelson, C. J. Medforth, K. M. Smith, M. Veyrat, M. Mazzanti, R. Ramasseul, J.-C. Marchon, T. Takeuchi, W. A. I. Goddard, and J. A. Shelnett, *J. Am. Chem. Soc.* 117, 11085 (1995).
105. X.-Z. Song, W. Jentzen, S.-L. Jia, L. Jaquinod, D. J. Nurco, C. J. Medforth, K. M. Smith, and J. A. Shelnett, *J. Am. Chem. Soc.* 118, 12975 (1996).
106. W. Jentzen, X.-Z. Song, and J. A. Shelnett, *J. Phys. Chem. B* 101, 1684 (1997).
107. C. M. Drain, S. Gentemann, J. A. Roberts, N. Y. Nelson, C. J. Medforth, S. Jia, M. C. Simpson, K. M. Smith, J. Fajer, J. A. Shelnett, and D. Holten, *J. Am. Chem. Soc.* 120, 3781 (1998).
108. R. E. Haddad, S. Gazeau, J. Pécaut, J.-C. Marchon, C. J. Medforth, and J. A. Shelnett, *J. Am. Chem. Soc.* 125, 1253 (2003).
109. S. Ollerich, M. Ketelaars, J.-M. Segura, G. Margis, W. de Ruijter, J. Köhler, J. Schmidt, and T. J. Aartsma, *Single. Mol.* 3, 319 (2002).
110. S. Karasch, P. A. Bullough, and R. Ghosh, *EMBO J.* 14, 631 (1995).
111. M. N. Paddon-Row, in "Stimulating Concepts in Chemistry" (F. Vögtle, J. Stoddart, and M. Shibasaki, Eds.), p. 267. Wiley-VCH, Weinheim, 2000.
112. E. Hofmann, P. M. Wrench, F. P. Sharples, R. G. Hiller, W. Welte, and K. Diederichs, *Science* 272, 1788 (1996).

113. W. Kühlbrandt, D. N. Wang, and Y. Fujiyoshi, *Nature* 367, 614 (1994).
114. R. Bassi, R. Croce, D. Cugini, and D. Sandonà, *Proc. Natl. Acad. Sci. USA* 96, 10056 (1999).
115. R. Croce, R. Remelli, C. Varotto, J. Breton, and R. Bassi, *FEBS Lett.* 456, 1 (1999).
116. R. Croce, S. Weiss, and R. Bassi, *J. Biol. Chem.* 274, 29613 (1999).
117. R. Croce, M. G. Müller, R. Bassi, and A. R. Holzwarth, *Biophys. J.* 80, 901 (2001).
118. J. P. Connelly, M. G. Müller, R. Bassi, R. Croce, and A. R. Holzwarth, *Biochemistry* 36, 281 (1997).
119. R. Simonetto, M. Crimi, D. Sandonà, R. Croce, G. Cinque, J. Breton, and R. Bassi, *Biochemistry* 38, 12974 (1999).
120. H. Wolf-Klein, C. Kohl, K. Müllen, and H. Paulsen, *Angew. Chem. Int. Ed.* 41, 3378 (2002).
121. S. Hobe, S. Prytulla, W. Kühlbrandt, and H. Paulsen, *EMBO J.* 13, 3423 (1994).
122. K. Kosemund, I. Geiger, and H. Paulsen, *Eur. J. Biochem.* 267, 1138 (2000).
123. U. Gerken, H. Wolf-Klein, C. Huschenbett, B. Götze, S. Schuler, F. Jelezko, J. Wrachtrup, and H. Paulsen, *Single. Mol.* 3, 183 (2002).
124. F. Vögtle, M. Frank, M. Nieger, P. Belser, A. von Zelewsky, V. Balzani, F. Barigelli, L. De Cola, and L. Flamigni, *Angew. Chem. Int. Ed. Engl.* 32, 1643 (1993).
125. M. G. H. Vicente, L. Jaquinod, and K. M. Smith, *Chem. Commun.* 1771 (1999).
126. A. K. Burrell, D. L. Officer, P. G. Plieger, and D. C. W. Reid, *Chem. Rev.* 101, 2751 (2001).
127. R. L. Brookfield, H. Ellul, A. Harriman, and G. Porter, *J. Chem. Soc., Faraday Trans. 2* 82, 219 (1986).
128. D. Gust, T. A. Moore, A. L. Moore, F. Gao, D. Luttrull, J. M. DeGraziano, X. C. Ma, L. R. Makings, S.-J. Lee, T. T. Trier, E. Bittersmann, G. R. Seely, S. Woodward, R. V. Bensasson, M. Rougée, F. C. De Schryver, and M. Van der Auweraer, *J. Am. Chem. Soc.* 113, 3638 (1991).
129. D. Gust, T. A. Moore, and A. L. Moore, *Acc. Chem. Res.* 26, 198 (1993).
130. J. Wendler and A. R. Holzwarth, *Biophys. J.* 52, 717 (1987).
131. R. A. Marcus, *J. Chem. Phys.* 24, 966 (1956).
132. R. W. Wagner, T. E. Johnson, and J. S. Lindsey, *J. Am. Chem. Soc.* 118, 11166 (1996).
133. J.-S. Hsiao, B. P. Krueger, R. W. Wagner, T. E. Johnson, J. K. Delaney, D. C. Mauzerall, G. R. Fleming, J. S. Lindsey, D. F. Bocian, and R. J. Donohoe, *J. Am. Chem. Soc.* 118, 11181 (1996).
134. J. Seth, V. Palaniappan, R. W. Wagner, T. E. Johnson, J. S. Lindsey, and D. F. Bocian, *J. Am. Chem. Soc.* 118, 11194 (1996).
135. F. Li, S. I. Yang, Y. Ciringh, J. Seth, C. H. Martin, III, D. L. Singh, D. Kim, R. R. Birge, D. F. Bocian, D. Holten, and J. S. Lindsey, *J. Am. Chem. Soc.* 120, 10001 (1998).
136. J. Li, A. Ambroise, S. I. Yang, J. R. Diers, J. Seth, C. R. Wack, D. F. Bocian, D. Holten, and J. S. Lindsey, *J. Am. Chem. Soc.* 121, 8927 (1999).
137. P. G. Van Patten, A. P. Shreve, J. L. Lindsey, and R. J. Donohoe, *J. Chem. Phys. B* 102, 4209 (1998).
138. D. Holten, D. F. Bocian, and J. L. Lindsey, *Acc. Chem. Res.* 35, 57 (2002).
139. J. L. Lindsey, H. C. Hsu, and I. C. Schreiman, *Tetrahedron Lett.* 27, 4969 (1986).
140. J. L. Lindsey, I. C. Schreiman, H. C. Hsu, P. C. Kearney, and A. M. Marguerettaz, *J. Org. Chem.* 52, 827 (1987).
141. J. L. Lindsey, S. Prathapan, T. E. Johnson, and R. W. Wagner, *Tetrahedron* 50, 8941 (1994).
142. C.-H. Lee and J. L. Lindsey, *Tetrahedron* 50, 11427 (1994).
143. B. J. Littler, M. A. Miller, C.-H. Hung, R. W. Wagner, D. F. O'Shea, P. D. Boyle, and J. S. Lindsey, *J. Org. Chem.* 64, 1391 (1999).
144. P. D. Rao, S. Dhanalekshmi, B. J. Littler, and J. S. Lindsey, *J. Org. Chem.* 65, 7323 (2000).
145. D. T. Gryko, C. Clausen, and J. S. Lindsey, *J. Org. Chem.* 64, 8635 (1999).
146. A. Osuka, N. Tanabe, S. Kawabata, I. Yamazaki, and Y. Nishimura, *J. Org. Chem.* 60, 7177 (1995).
147. A. Ambroise, J. Li, L. Yu, and J. S. Lindsey, *Org. Lett.* 2, 2563 (2000).
148. R. W. Wagner and J. S. Lindsey, *J. Am. Chem. Soc.* 116, 9759 (1994).
149. M. A. Miller, R. K. Lammi, S. Prathapan, D. Holten, and J. S. Lindsey, *J. Org. Chem.* 65, 6634 (2000).
150. J. Li, J. R. Diers, J. Seth, S. I. Yang, D. F. Bocian, D. Holten, and J. S. Lindsey, *J. Org. Chem.* 64, 9090 (1999).
151. O. Mongin, A. Schuwey, M.-A. Vallot, and A. Gossauer, *Tetrahedron Lett.* 40, 8347 (1999).
152. P. Brodard, S. Matzinger, E. Vauthey, O. Mongin, C. Papamicael, and A. Gossauer, *J. Phys. Chem. A* 103, 5858 (1999).
153. O. Mongin, N. Hoyler, and A. Gossauer, *Eur. J. Org. Chem.* 1193 (2000).
154. G. L. Closs, D. Piotrowak, J. MacInnis, and G. R. Fleming, *J. Am. Chem. Soc.* 110, 2652 (1998).
155. R. C. Jagessar and J. M. Tour, *Org. Lett.* 2, 111 (2000).
156. J. M. Tour, A. M. Rawlett, M. Kozaki, Y. Yao, R. C. Jagessar, S. M. Dirk, M. A. Reed, C.-W. Zhou, J. Chen, W. Wang, and I. Campbell, *Chem. Eur. J.* 7, 5118 (2001).
157. L. Giribabu, A. A. Kumar, V. Neeraja, and B. G. Maya, *Angew. Chem. Int. Ed.* 40, 3621 (2001).
158. A. Nakano, H. Shimidzu, and A. Osuka, *Tetrahedron Lett.* 39, 9489 (1998).
159. A. Nakano, A. Osuka, I. Yamazaki, T. Yamazaki, and Y. Nishimura, *Angew. Chem. Int. Ed.* 37, 3023 (1998).
160. N. Yoshida, N. Aratani, and A. Osuka, *Chem. Commun.* 197 (2000).
161. N. Aratani, A. Osuka, Y. H. Kim, D. H. Jeong, and D. Kim, *Angew. Chem. Int. Ed.* 39, 1458 (2000).
162. H. S. Cho, N. W. Song, Y. H. Kim, S. C. Jeoung, S. Hahn, D. Kim, S. Kim, N. Yoshida, and A. Osuka, *J. Phys. Chem. A* 104, 3287 (2000).
163. Y. H. Kim, D. H. Jeong, D. Kim, S. C. Jeoung, H. S. Cho, S. K. Kim, N. Aratani, and A. Osuka, *J. Am. Chem. Soc.* 123, 76 (2001).
164. A. Bhuiyan, J. Seth, N. Yoshida, A. Osuka, and D. F. Bocian, *J. Phys. Chem. B* 104, 10757 (2000).
165. M. Kasha, *Radiat. Res.* 20, 55 (1963).
166. M. Kasha, H. R. Rawls, and M. A. El-Bayoumi, *Pure Appl. Chem.* 11, 371 (1965).
167. R. M. Pearlstein, in "Photosynthesis: Energy Conversion by Plants and Bacteria" (Govindjee, Ed.), Vol. I, pp. 293-330. Academic Press, New York, 1982.
168. A. S. Davydov, "Theory of Molecular Excitons." Plenum, New York, 1971.
169. A. Tsuda and A. Osuka, *Science* 293, 79 (2001).
170. S. G. DiMagno, V. S. Y. Lin, and M. J. Therien, *J. Org. Chem.* 58, 5983 (1993).
171. V. S.-Y. Lin, S. G. DiMagno, and M. J. Therien, *Science* 264, 1105 (1994).
172. V. S.-Y. Lin and M. J. Therien, *Chem. Eur. J.* 1, 645 (1995).
173. J. T. Fletcher and M. J. Therien, *J. Am. Chem. Soc.* 124, 4298 (2002).
174. S. Anderson, H. L. Anderson, and J. K. M. Sanders, *J. Chem. Soc. Perkin Trans. 1* 2247 (1995).
175. G. S. Wilson and H. L. Anderson, *Synlett.* 1039 (1996).
176. P. N. Taylor, J. Huuskonen, G. Rumbles, R. T. Aplin, E. Williams, and H. L. Anderson, *Chem. Commun.* 909 (1998).
177. J. J. Piet, P. N. Taylor, H. L. Anderson, A. Osuka, and J. M. Warman, *J. Am. Chem. Soc.* 122, 1749 (2000).



178. J. J. Piet, P. N. Taylor, B. R. Wegewijs, H. L. Anderson, A. Osuka, and J. M. Warman, *J. Phys. Chem.* 105, 97 (2001).
179. T. E. O. Screen, I. M. Blake, L. H. rees, W. Clegg, S. J. Borwick, and H. L. Anderson, *J. Chem. Soc. Perkin Trans. 1* 320 (2002).
180. H. L. Anderson, *Chem. Commun.* 2323 (1999).
181. N. Bampos, C. N. Woodburn, M. E. Welland, and J. K. M. Sanders, *Angew. Chem. Int. Ed.* 38, 2780 (1999).
182. J. J. Piet, J. M. Warman, and H. L. Anderson, *Chem. Phys. Lett.* 266, 70 (1997).
183. J. Frenkel, *Phys. Rev.* 37, 1276 (1931).
184. G. H. Wannier, *Phys. Rev.* 52, 191 (1937).
185. N. F. Mott, *Trans. Faraday Soc.* 34, 500 (1938).
186. K. Okuyama, M. C. R. Cockett, and K. Kimura, *J. Chem. Phys.* 97, 1649 (1992).
187. M. J. Crossley and P. L. Burn, *J. Chem. Soc. Chem. Commun.* 39 (1987).
188. M. J. Crossley and P. L. Burn, *J. Chem. Soc. Chem. Commun.* 1569 (1991).
189. J. R. Reimers, T. X. Lü, M. J. Crossley, and N. S. Hush, *Nanotechnology* 7, 424 (1996).
190. T. A. Jung, R. R. Schlittler, and J. K. Gimzewski, *Nature* 386, 696 (1997).
191. J. K. Gimzewski and C. Joachim, *Science* 283, 1683 (1999).
192. T. S. Balaban, R. Goddard, M. Linke-Schaetzel, and J.-M. Lehn, *J. Am. Chem. Soc.* 125, 4233 (2003).
193. T. S. Balaban, A. Bhise, M. Linke-Schaetzel, C. Roussel, and N. Vanthuyne, *Angew. Chem. Int. Ed.* 42, 2140 (2003).
194. T. S. Balaban, M. Linke-Schaetzel, A. D. Bhise, N. Vanthuyne, and C. Roussel, submitted for publication.
195. T. S. Balaban, A. Eichhöfer, and J.-M. Lehn, *Eur. J. Org. Chem.* 4047 (2000).
196. H. L. Anderson, *Angew. Chem. Int. Ed.* 39, 2451 (2000).
197. K. Sugiura, H. Tanaka, T. Matsumoto, T. Kawai, and Y. Sakata, *Chem. Lett.* 1193 (1999).
198. K. Sugiura, Y. Fujimoto, and Y. Sakata, *Chem. Commun.* 1105 (2000).
199. G. Hungerford, M. Van der Auweraer, J.-C. Chambron, V. Heitz, J.-P. Sauvage, J.-L. Pierre, and D. Zurita, *Chem. Eur. J.* 5, 2089 (1999).
200. M. S. Vollmer, F. Würthner, F. Effenberger, P. Emele, D. U. Meyer, T. Stümpfig, H. Port, and H. C. Wolf, *Chem. Eur. J.* 4, 260 (1998).
201. K. Arnold, T. S. Balaban, M. N. Blom, O. T. Ehrler, S. Gilb, O. Hampe, J. E. van Lier, J. M. Weber, and M. M. Kappes, *J. Phys. Chem. A* 107, 794 (2003).
202. W. A. Nevin, W. Liu, S. Greenberg, M. R. Hemstead, S. M. Marcuccio, M. Melnik, C. C. Leznoff, and A. B. P. Lever, *Inorg. Chem.* 26, 891 (1987).
203. W. Liu, M. R. Hemstead, W. A. Nevin, M. Melnik, A. B. P. Lever, and C. C. Leznoff, *J. Chem. Soc. Dalton Trans.* 2511 (1987).
204. W. A. Nevin, M. R. Hemstead, W. Liu, C. C. Leznoff, and A. B. P. Lever, *Inorg. Chem.* 26, 570 (1987).
205. M. R. Hemstead, C. C. Leznoff, and A. B. P. Lever, *Can. J. Chem.* 65, 2677 (1987).
206. J. Li and J. S. Lindsey, *J. Org. Chem.* 64, 9101 (1999).
207. M. A. Miller, R. K. Lammi, S. Prathapan, D. Holten, and J. S. Lindsey, *J. Org. Chem.* 65, 6634 (2000).
208. E. M. Maya, P. Vázquez, and T. Torres, *Chem. Eur. J.* 5, 2004 (1999).
209. E. M. Maya, P. Vázquez, T. Torres, L. Gobbi, F. Diederich, S. Pyo, and L. Echegoyen, *J. Org. Chem.* 65, 823 (2000).
210. T.-H. Tran-Thi, *Coord. Chem. Rev.* 160, 53 (1997).
211. T. Norsten and N. Branda, *J. Chem. Soc. Chem. Commun.* 1257 (1998).
212. C. J. Hawker, K. L. Wooley, and J. M. J. Fréchet, *J. Am. Chem. Soc.* 115, 4375 (1993).
213. C. Devadoss, P. Bharathi, and J. S. Moore, *Angew. Chem. Int. Ed.* 36, 1633 (1997).
214. C. Devadoss, P. Bharathi, and J. S. Moore, *J. Am. Chem. Soc.* 118, 9635 (1996).
215. M. R. Shortreed, S. F. Swallen, Z.-Y. Shi, W. Tan, Z. Xu, C. Devadoss, J. S. Moore, and R. Kopelman, *J. Phys. Chem. B* 101, 6318 (1997).
216. J. S. Melinger, Y. Pan, V. D. Kleiman, Z. Peng, B. L. Davis, D. McMorro, and M. Lu, *J. Am. Chem. Soc.* 124, 12002 (2002).
217. P.-W. Wang, Y.-J. Liu, C. Devadoss, P. Bharathi, and J. S. Moore, *Adv. Mater.* 8, 237 (1996).
218. S. C. Koene, A. W. Freeman, K. A. Killeen, J. M. J. Fréchet, and M. E. Thompson, *Polym. Mater. Sci. Eng.* 80, 238 (1999).
219. A. W. Freeman, S. C. Koene, P. R. L. Malenfant, M. E. Thompson, and J. M. J. Fréchet, *J. Am. Chem. Soc.* 122, 12385 (2000).
220. D.-L. Jiang and T. Aida, *J. Am. Chem. Soc.* 120, 10895 (1998).
221. M. Kimura, T. Shiba, T. Muto, K. Hanabusa, and H. Shirai, *Macromolecules* 32, 8237 (1999).
222. D.-L. Jiang and T. Aida, *Nature* 388, 454 (1998).
223. R. Ballardini, B. Colonna, M. T. Gandolfi, S. A. Kalovidouris, L. Orzzel, F. M. Raymo, and J. F. Stoddart, *Eur. J. Org. Chem.* 288 (2003).
224. P. Bhyrappa, G. Vajayanthimala, and K. S. Suslick, *J. Am. Chem. Soc.* 121, 262 (1999).
225. P. J. Dandliker, F. Diederich, J.-P. Gisselbrecht, A. Louati, and M. Gross, *Angew. Chem. Int. Ed. Engl.* 34, 2725 (1995).
226. L. Merz, J. Hitz, U. Hubler, P. Weyermann, F. Diederich, P. Murer, D. Seebach, I. Widmer, M. Stöhr, H.-J. Güntherodt, and B. A. Hermann, *Single Mol.* 3, 295 (2002).
227. M. Kimura, Y. Sugihara, T. Muto, K. Hanabusa, H. Shirai, and N. Kobayashi, *Chem. Eur. J.* 5, 3495 (1999).
228. A. Adronov, S. L. Gilat, J. M. J. Fréchet, K. Ohta, F. V. R. Neuwahl, and G. R. Fleming, *J. Am. Chem. Soc.* 122, 1175 (2000).
229. A. Adronov and J. M. J. Fréchet, *Chem. Commun.* 1701 (2000).
230. S. Hecht and J. M. J. Fréchet, *Angew. Chem. Int. Ed.* 40, 74 (2001).
231. L. F. Lee, A. Adronov, R. D. Schaller, J. M. J. Fréchet, and R. J. Sakally, *J. Am. Chem. Soc.* 125, 536 (2003).
232. J. M. Serin, D. W. Brousmiche, and J. M. J. Fréchet, *J. Am. Chem. Soc.* 124, 11848 (2002).
233. L. A. J. Chrisstoffels, A. Adronov, and J. M. J. Fréchet, *Angew. Chem. Int. Ed.* 39, 2163 (2000).
234. S. Campagna, G. Denti, S. Serroni, A. Juris, M. Venturi, V. Ricevuto, and V. Balzani, *Chem. Eur. J.* 1, 211 (1995).
235. J. Issberner, F. Vögtle, L. De Cola, and V. Balzani, *Chem. Eur. J.* 3, 706 (1997).
236. F. Vögtle, M. Plevoets, M. Nieger, G. C. Azzellini, A. Credi, L. De Cola, V. De Marchis, M. Venturi, and V. Balzani, *J. Am. Chem. Soc.* 121, 6290 (1999).
237. U. Hahn, M. Gorka, F. Vögtle, V. Vicinelli, P. Ceroni, M. Maestri, and V. Balzani, *Angew. Chem. Int. Ed.* 41, 3595 (2002).
238. T. Gensch, J. Hofkens, A. Herrmann, K. Tsuda, W. Verheijen, T. Vosch, T. Christ, T. Basché, K. Müllen, and F. C. De Schryver, *Angew. Chem. Int. Ed.* 38, 3752 (1999).
239. J. Hofkens, M. Maus, T. Gensch, T. Vosch, M. Cotlet, F. Köhn, A. Herrmann, K. Müllen, and F. De Schryver, *J. Am. Chem. Soc.* 122, 9278 (2000).
240. M. A. Bopp, Y. W. Jia, L. Q. Li, R. J. Cogdell, and R. M. Hochstrasser, *Proc. Natl. Acad. Sci. USA* 94, 10630 (1997).
241. M. A. Bopp, A. Sytnik, T. D. Howard, R. J. Cogdell, and R. M. Hochstrasser, *Proc. Natl. Acad. Sci. USA* 96, 11271 (1999).
242. T. Weil, E. Reuther, and K. Müllen, *Angew. Chem. Int. Ed.* 41, 1900 (2002).
243. D. S. Lawrence, T. Jiang, and M. Levett, *Chem. Rev.* 95, 2229 (1995).
244. P. R. Ashton, R. A. Bissell, D. Philp, N. Spencer, and J. F. Stoddart, in "Supramolecular Chemistry" (V. Balzani and L. de Cola, Eds.), p. 1. Kluwer Academic, Dordrecht, 1992.

245. D. B. Amabilino and J. F. Stoddart, *Chem. Rev.* 95, 2725 (1995).
246. D. Philp and J. F. Stoddart, *Angew. Chem. Int. Ed. Engl.* 35, 1154 (1996).
247. R. E. Gillard, F. M. Raymo, and J. F. Stoddart, *Chem. Eur. J.* 3, 1933 (1997).
248. D. N. Reinhoudt, J. F. Stoddart, and R. Ungaro, *Chem. Eur. J.* 4, 1349 (1998).
249. M. D. Ward, *Chem. Soc. Rev.* 26, 365 (1997).
250. V. Balzani, M. Gómez-López, and J. F. Stoddart, *Acc. Chem. Res.* 31, 405 (1998).
251. V. Balzani, A. Credi, F. M. Raymo, and J. F. Stoddart, *Angew. Chem. Int. Ed.* 39, 3349 (2000).
252. G. Blondeel, A. Harriman, G. Porter, and A. Wilowska, *J. Chem. Soc. Faraday Trans. 2* 80, 867 (1984).
253. M. Gubelmann, A. Harriman, J.-M. Lehn, and J. Sessler, *J. Chem. Soc. Chem. Commun.* 77 (1988).
254. B. Valeur, "Molecular Fluorescence Principles and Applications." Wiley-VCH, Weinheim, 2002.
255. M. N. Berberan-Santos, J. Canceill, J.-C. Brochon, L. Jullien, J.-M. Lehn, J. Pouget, P. Tauc, and B. Valeur, *J. Am. Chem. Soc.* 114, 6427 (1992).
256. M. N. Berberan-Santos, J. Pouget, B. Valeur, J. Canceill, L. Jullien, and J.-M. Lehn, *J. Phys. Chem.* 97, 11376 (1993).
257. L. Jullien, J. Canceill, B. Valeur, E. Bardez, and J.-M. Lehn, *Angew. Chem. Int. Ed. Engl.* 33, 2438 (1994).
258. M. N. Berberan-Santos, J. Canceill, E. Gratton, L. Jullien, J.-M. Lehn, P. So, J. Sutin, and B. Valeur, *J. Chem. Phys.* 100, 15 (1996).
259. L. Jullien, J. Canceill, B. Valeur, E. Bardez, J.-P. Lefèvre, J.-M. Lehn, V. Marchi-Artzner, and R. Pansu, *J. Am. Chem. Soc.* 118, 5432 (1996).
260. "The Porphyrin Handbook" (K. M. Kadish, K. M. Smith, and R. Guillard, Eds.). Academic Press, New York, 2000.
261. A. K. Burrell, B. M. Jones, S. B. Hall, D. L. Officer, D. C. W. Reid, and K. Y. Wild, *J. Incl. Phenom. Macrocycl. Chem.* 35, 185 (1999).
262. C. M. Drain and J.-M. Lehn, *J. Chem. Soc. Chem. Commun.* 2313 (1994).
263. C. M. Drain, F. Nifatis, A. Vasenko, and J. D. Batteas, *Angew. Chem. Int. Ed. Engl.* 37, 2344 (1998).
264. J. Foekema, A. P. H. J. Schenning, D. M. Vriezema, F. B. G. Benneker, K. Norgaard, J. K. M. Kroon, T. Bjornholm, M. C. Feiters, A. E. Rowan, and R. J. M. Nolte, *J. Phys. Org. Chem.* 14, 501 (2001).
265. D.-J. Qian, C. Nakamura, and J. Miyake, *Chem. Commun.* 2312 (2001).
266. J. E. Redman, N. Feeder, S. J. Teat, and K. M. Sanders, *Inorg. Chem.* 40, 2486 (2001).
267. E. Iengo, B. Milani, E. Zangrando, S. Geremia, and E. Alessio, *Angew. Chem. Int. Ed. Engl.* 39, 1096 (2000).
268. A. Prodi, M. T. Indelli, C. J. Klverlaan, F. Scandola, E. Alessio, T. Gianferrara, and L. G. Marzilli, *Chem. Eur. J.* 5, 2668 (1999).
269. G. S. Wilson and H. L. Anderson, *Chem. Commun.* 1539 (1999).
270. S. Rucareanu, O. Mongin, A. Schuwey, N. Hoyler, and A. Gosauer, *J. Org. Chem.* 66, 4973 (2001).
271. L. Ulmer, J. Mattay, H. G. Torres-Garcia, and H. Luftmann, *Eur. J. Mass Spectrom.* 6 849 (2000).
272. C. A. Hunter and R. K. Hyde, *Angew. Chem. Int. Ed. Engl.* 35, 1936 (1996).
273. R. A. Haycock, A. Yartsev, U. Michelsen, V. Sundstrom, and C. A. Hunter, *Angew. Chem. Int. Ed.* 396, 3616 (2000).
274. C. A. Hunter and L. D. Sarson, *Angew. Chem. Int. Ed. Engl.* 34, 2424 (1995).
275. X. Chi, A. J. Guerin, R. A. Haycock, C. A. Hunter, and L. D. Sarson, *J. Chem. Soc. Chem. Commun.* 2567 (1995).
276. R. A. Haycock, C. A. Hunter, D. A. James, U. Michelsen, and L. R. Sutton, *Org. Lett.* 2, 2435 (2000).
277. J. Fan, J. A. Whiteford, B. Olenyuk, M. D. Levin, P. J. Stang, and E. B. Fleischer, *J. Am. Chem. Soc.* 121, 2741 (1999).
278. M. C. Lensen, M. Castriciano, R. G. E. Coumans, J. Foekema, A. E. Rowan, L. M. Scolaro, and R. J. M. Nolte, *Tetrahedron Lett.* 43, 9351 (2002).
279. R. F. Pasternack, C. Bustamante, P. J. Collings, A. Giannetto, and E. J. Gibbs, *J. Am. Chem. Soc.* 115, 5393 (1993).
280. R. F. Pasternack and P. J. Collings, *Science* 269, 935 (1995).
281. J. C. de Paula, J. H. Robblee, and R. F. Pasternack, *Biophys. J.* 68, 335 (1995).
282. P. J. Collings, E. J. Gibbs, T. E. Starr, O. Vafek, C. Yee, L. A. Pomerance, and R. F. Pasternack, *J. Chem. Phys. B* 103, 8474 (1999).
283. A. P. H. J. Schenning, F. B. G. Benneker, H. P. M. Geurts, X. Y. Liu, and R. J. M. Nolte, *J. Am. Chem. Soc.* 118, 8549 (1996).
284. H. A. M. Biemans, A. E. Rowan, A. Verhoeven, P. Vanoppen, L. Latterini, J. Foekema, A. Schenning, E. W. Meijer, F. C. de Schryver, and R. J. M. Nolte, *J. Am. Chem. Soc.* 120, 11054 (1998).
285. A. V. Chernook, U. Rempel, C. von Borczyskowski, A. M. Shulga, and E. I. Zenkevich, *Chem. Phys. Lett.* 254, 229 (1996).
286. E. I. Zenkevich, S. M. Bachilo, A. M. Shulga, U. Rempel, A. Willert, and C. von Borczyskowski, *Mol. Cryst. Liq. Cryst.* 324, 169 (1998).
287. E. I. Zenkevich, A. M. Shulga, U. Rempel, J. von Richthofen, and C. von Borczyskowski, *J. Lumin.* 76&77, 354 (1998).
288. A. Willert, S. Bachilo, U. Rempel, A. Shulga, E. Zenkevich, and C. von Borczyskowski, *J. Photochem. Photobiol. A* 126, 99 (1999).
289. E. I. Zenkevich and C. von Borczyskowski, in "Handbook of Polyelectrolytes and Their Applications" (S. K. Tripathy, J. Kumar, and S. Nalwa, Eds.). American Scientific, Los Angeles, 2002.
290. N. Fujita, K. Biradha, M. Fujita, S. Sakamoto, and K. Yamaguchi, *Angew. Chem. Int. Ed.* 40, 1718 (2001).
291. K. Ogawa and Y. Kobuke, *Angew. Chem. Int. Ed.* 39, 4071 (2000).
292. K. Ogawa, T. Zhang, K. Yoshihara, and Y. Kobuke, *J. Am. Chem. Soc.* 124, 22 (2002).
293. H. Shinmori, Y. Yasuda, and A. Osuka, *Eur. J. Org. Chem.* 1197 (2002).
294. M. Kondo, Y. Kimura, K. Wada, T. Mizutani, Y. Ito, and S. Kitagawa, *Chem. Lett.* 818 (2000).
295. Y. He, T. Ye, and E. Borguet, *J. Am. Chem. Soc.* 124, 11964 (2002).
296. A. Harriman, D. J. Magda, and J. L. Sessler, *J. Chem. Soc. Chem. Commun.* 345 (1991).
297. A. Harriman, D. J. Magda, and J. L. Sessler, *J. Phys. Chem.* 95, 1530 (1991).
298. C. M. Drain, R. Fischer, E. G. Nolen, and J.-M. Lehn, *J. Chem. Soc. Chem. Commun.* 243 (1993).
299. C. M. Drain, K. C. Russell, and J.-M. Lehn, *Chem. Commun.* 337 (1996).
300. X. Shi, K. M. Barkigia, J. Fajer, and C. M. Drain, *J. Org. Chem.* 66, 6513 (2001).
301. C. Fouquey, J.-M. Lehn, and A.-M. Levelut, *Adv. Mater.* 2, 254 (1990).
302. A. D. Bond, N. Feeder, J. E. Redman, S. J. Teat, and J. K. M. Sanders, *Cryst. Growth Design* 2, 27 (2002).
303. K. M. Barkigia, D. Melamed, R. M. Sweet, K. M. Smith, and J. Fajer, *Spectrochim. Acta A* 53A, 463 (1997).
304. A. Jesorka, T. S. Balaban, A. R. Holzwarth, and K. Schaffner, *Angew. Chem. Int. Ed. Engl.* 35, 2861 (1996).
305. T. S. Balaban, H. Tamiaki, A. R. Holzwarth, and K. Schaffner, *J. Phys. Chem. B* 101, 3424 (1997).
306. H. Tamiaki, T. Miyatake, and R. Tanikaga, *Tetrahedron Lett.* 38, 267 (1997).
307. H. Tamiaki, M. Kouraba, K. Takeda, S. Kondo, and R. Tanikaga, *Tetrahedron Asym.* 9, 2101 (1998).
308. S. Yagai and H. Tamiaki, *J. Chem. Soc. Perkin Trans. 1* 3135 (2001).

309. S. Yagai, T. Miyatake, Y. Shimono, and H. Tamiaki, *Photochem. Photobiol.* 73, 153 (2001).
310. S. Yagai, T. Miyatake, and H. Tamiaki, *J. Org. Chem.* 67, 49 (2002).
311. N. Nagata, S.-I. Kugimiya, and Y. Kobuke, *Chem. Commun.* 689 (2001).
312. X. Gong, T. Milic, C. Xu, J. D. Batteas, and C. M. Drain, *J. Am. Chem. Soc.* 124, 14290 (2002).
313. L. Dähne, *J. Am. Chem. Soc.* 117, 12855 (1995).
314. U. De Rossi, S. Dähne, C. J. Meskers, and P. J. M. Dekkers, *Angew. Chem. Int. Ed. Engl.* 35, 760 (1996).
315. M. Wang, G. L. Silva, and B. A. Armitage, *J. Am. Chem. Soc.* 122, 9977 (2000).
316. H. Yao, M. Omizo, and N. Kitamura, *Chem. Commun.* 739 (2000).
317. J. Hranisavljevic, N. M. Dimitrijevic, G. A. Wurtz, and G. P. Wiederrecht, *J. Am. Chem. Soc.* 124, 4536 (2002).
318. U. Bach, D. Lupo, P. Comte, J. E. Moser, F. Weissörtel, J. Salbeck, Spreitzer, and M. Grätzel, *Nature* 395, 583 (1998).
319. M. Grätzel and J. E. Moser, "Solar Energy Conversion in Electron Transfer in Chemistry" (V. Balzani, Ed.), Vol. 5, pp. 589–644. Wiley-VCH, Weinheim, 2001.
320. M. Grätzel, *Nature* 414, 338 (2001).
321. A. Hagfeldt and M. Grätzel, *Acc. Chem. Res.* 33, 269 (2000).
322. J. He, G. Benkö, F. Korodi, T. Polivka, R. Lomoth, B. Akermark, L. Sun, A. Hagfeldt, and V. Sundström, *J. Am. Chem. Soc.* 124, 4922 (2002).
323. A. Ehret, L. Stuhl, and M. T. Spitler, *J. Phys. Chem. B* 105, 9960 (2001).
324. Y. Tachibana, S. A. Haque, I. A. Mercer, J. R. Durrant, and D. R. Klug, *J. Phys. Chem. B* 104, 1198 (2000).
325. S. A. Haque, Y. Tachibana, R. L. Willis, J. E. Moser, M. Grätzel, J. R. Durrant, and D. R. Klug, *J. Phys. Chem. B* 104, 538 (2000).
326. S. G. Yan, J. S. Prieskorn, Y. Kim, and J. T. Hupp, *J. Phys. Chem. B* 104, 10871 (2000).
327. G. Benkö, P. Myllyperkiö, J. Pan, A. P. Yartsev, and V. Sundström, *J. Am. Chem. Soc.* 125, 1118 (2003).
328. M. Pauchard, A. Devaux, and G. Calzaferri, *Chem. Eur. J.* 6, 3456 (2000).
329. C. J. Brabec, S. N. Sariciftci, and J. C. Hummelen, *Adv. Funct. Mater.* 11, 15 (2001).
330. S. E. Shaheen, C. J. Brabec, N. S. Sariciftci, T. Fromherz, and J. C. Hummelen, *Appl. Phys. Lett.* 78, 841 (2001).
331. H. Frohne, S. E. Shaheen, C. J. Brabec, D. C. Müller, N. S. Sariciftci, and K. Meerholz, *Chem. Phys. Chem.* 795 (2002).
332. K. Takahashi, T. Iwanaga, T. Yamaguchi, T. Komura, and K. Murata, *Synth. Met.* 123, 91 (2001).
333. C. O. Too, G. G. Wallace, A. K. Burrell, G. E. Collis, D. L. Officer, E. W. Boge, S. G. Brodie, and E. J. Evans, *Synth. Met.* 123, 53 (2001).
334. M. Andersson, M. Linke, J.-C. Chambron, J. Davidsson, V. Heitz, J.-P. Sauvage, and L. Hammarström, *J. Am. Chem. Soc.* 122, 3526 (2000).
335. M. Linke, J.-C. Chambron, V. Heitz, J.-P. Sauvage, S. Encinas, F. Barigelletti, and L. Flamigni, *J. Am. Chem. Soc.* 122, 11834 (2000).
336. M. Andersson, M. Linke, J.-C. Chambron, J. Davidsson, V. Heitz, L. Hammarström, and J.-P. Sauvage, *J. Am. Chem. Soc.* 124, 4347 (2002).
337. J.-P. Sauvage, *Acc. Chem. Res.* 23, 327 (1990).
338. P. A. Liddell, G. Kodis, L. de la Garza, J. L. Bahr, A. L. Moore, T. A. Moore, and D. Gust, *Helv. Chim. Acta* 84, 2765 (2001).
339. G. Kodis, P. A. Liddell, L. de la Garza, P. C. Clausen, J. S. Lindsey, A. L. Moore, T. A. Moore, and D. Gust, *J. Phys. Chem. A* 106, 2036 (2002).
340. A. N. Macpherson, P. A. Liddell, D. Kuciauskas, D. Tatman, T. Gillbro, D. Gust, T. A. Moore, and A. L. Moore, *J. Phys. Chem. B* 106, 9424 (2002).
341. J. L. Bahr, G. Kodis, L. de la Garza, A. L. Moore, T. A. Moore, and D. Gust, *J. Am. Chem. Soc.* 123, 7124 (2001).
342. S. L. Gilat, S. H. Kawai, and J.-M. Lehn, *J. Chem. Soc. Chem. Commun.* 1034 (1993).
343. M. Irie, "Photoreactive Materials for Ultrahigh Density Optical Memory." Elsevier, New York, 1994.
344. A. Fernandez-Acebes and J.-M. Lehn, *Chem. Eur. J.* 5, 3285 (1999).
345. P. A. Liddell, G. Kodis, A. L. Moore, T. A. Moore, and D. Gust, *J. Am. Chem. Soc.* 124, 7668 (2002).
346. G. Steinberg-Yfrach, J.-L. Rigaud, E. N. Durantini, A. L. Moore, D. Gust, and T. A. Moore, *Nature* 392, 479 (1998).
347. D. Gust, T. A. Moore, and A. L. Moore, *Acc. Chem. Res.* 34, 40 (2001).
348. I. M. Bennett, H. M. V. Farfano, F. Bogani, A. Primak, P. A. Liddell, L. Otero, L. Sereno, J. J. Silber, A. L. Moore, T. A. Moore, and D. Gust, *Nature* 420, 398 (2002).
349. C. C. Mak, N. Bampos, and J. K. M. Sanders, *Angew. Chem. Int. Ed.* 37, 3020 (1998).
350. Y. Kim, M. F. Mayer, and S. C. Zimmermann, *Angew. Chem. Int. Ed.* 42, 1121 (2003).
351. A. D. Bond, N. Feeder, S. J. Teat, Z. Clyde-Watson, N. Bampos, and J. K. M. Sanders, *Acta Cryst.* E57, m454 (2001).
352. G. Calzaferri, S. Huber, H. Maas, and C. Minkowski, *Angew. Chem. Int. Ed.* 42, 3732 (2003).



# Light Scattering of Semiconducting Nanoparticles

G. Irmer, J. Monecke

*Freiberg University of Mining and Technology,  
Freiberg, Germany*

P. Verma

*Osaka University, Osaka, Japan*

## CONTENTS

1. Introduction
  2. Quantum Confinement in Semiconductors
  3. Electron–Phonon Coupling
  4. Acoustic Phonons
  5. Surface Phonons
  6. Optical Phonons
  7. New Instrumentation and Methods
- Glossary  
References

## 1. INTRODUCTION

The electronic and optical properties of semiconducting crystallites with a size of a few nanometers (often called nanocrystals or quantum dots) differ considerably from those of the corresponding bulk material. Systems with nanoparticles represent a new class of materials with promising properties due to their nonlinear optical, photoconductivity, photoemission, and electroluminescence behaviors. They have been thoroughly investigated during the last two decades for their promising practical applications, for instance, in solar energy conversion, optical processing devices, and photocatalytic processes.

The bulk crystalline structure is preserved in nanocrystals. However, due to quantum confinement nanocrystals have molecule-like discrete electronic states which exhibit strong size dependence. Semiconductor nanocrystal systems are often synthesized in oxide glass hosts or prepared in the form of dispersed colloids. Among numerous other methods that have been developed we mention the preparation of

nanocrystals in polymers, zeolites, and micelles. By electrochemical anodic oxidation of crystalline semiconductor substrates porous nanostructures or free standing columns can be produced.

Most of the light scattered by a particle is elastically scattered without an energy shift. A small part, a few orders weaker in intensity, is scattered inelastically. This inelastic scattering carries information about energetic levels of the particle. In a Raman scattering process with incident photon energy  $\hbar\omega_L$  the scattered photon  $\hbar\omega_S$  has lost (Stokes scattering) or gained (anti-Stokes scattering) the energy  $\hbar\omega$  of an elementary excitation (phonons, electronic transitions, etc.) of the particle:

$$\hbar\omega_S = \hbar\omega_L \mp \hbar\omega \quad (1)$$

The Raman scattering is sensitive for probing the local atomic arrangement. Crystalline and amorphous phases or the influence of strain can be detected in the Raman vibrational spectra. Light couples to phonons intermediate through electronic excitations by either the deformation potential interaction or the Fröhlich interaction. The deformation interaction is present in polar crystals such as the compound semiconductors as well as in nonpolar crystals such as Si and Ge. In polar crystals the electric fields induced by vibrations interact with electronic excitations via the Fröhlich mechanism. When the Raman scattering process involves real intermediate electronic states by excitation with energy near gaps of the electronic band structure, the scattering cross section may be resonantly enhanced [1]. The Raman scattering probes the electron–phonon interaction as well as the confinement of the phonons and contains information about the confined vibrational and electronic states.

The light-scattering process in an infinite crystal obeys the pseudo-momentum conservation relation

$$\hbar\vec{k}_S = \hbar\vec{k}_L \mp \hbar\vec{q} \quad (2)$$

where  $\vec{k}_s(\vec{k}_L)$  denote the wavevectors of the plane waves of the scattered (incident) light,  $\vec{q}$  is the wavevector transferred to the excitation. The energies of crystalline vibrations probed by Raman scattering are about  $<0.1$  eV and those of the exciting visible laserlight are about 2.5 eV (corresponding to the wavelength  $\lambda_L \approx 500$  nm). Therefore, from Eq. (1) we get  $\omega_s \approx \omega_L$  and the wavevector in a typical backscattering experiment will be on the order of  $|\vec{q}| \approx 4\pi n/\lambda_L$  and much smaller than the wavevector  $q = 2\pi/a$  at the boundary of the Brillouin zone,  $a$  is the lattice constant, and  $n$  denotes the refractive index of the sample. That means that only excitations near the center of the Brillouin zone ( $\Gamma$ -point) will contribute to the Raman scattering.

If the process of light scattering by excitations is limited to the finite space occupied by the nanoparticle, an uncertainty of the transferred wavevector  $\vec{q}$  occurs and excitations with wavevectors from the whole Brillouin zone contribute to the scattering. This effect will vary with size as well as with the eigenfrequencies of acoustic and optical phonons and the electron–phonon interaction in small particles. The vibrational Raman spectra of nanoparticles can therefore be used for size determinations. This is important because one of the major goals in the field of preparation is the synthesis of monodisperse nanocrystals with a narrow size distribution and with well-defined surfaces. Size effects will be discussed in Sections 3, 4, and 6.

In addition to acoustic and optical phonon modes, surface-related modes appearing in polar crystals will be discussed in Section 5. They are observable for particle sizes smaller than the wavelength of the exciting laser light inside the particle.

The pioneering work was the first observation of confined acoustic modes with low-frequency Raman scattering in nanocrystals embedded in glasses by Duval et al. [2] and the unambiguous observation of surface-related modes in semiconductor nanoparticles by Hayashi and Kanamori [3].

It is relatively easy to produce nanocrystals of II–VI compounds embedded in different media such as glasses, polymers, or solutions. Besides potential applications of such systems the possibility of growing isolated nanoparticles in glasses with desired size and narrow size distribution and nearly spherically shaped particles makes such systems interesting for light-scattering investigations in comparison with theoretical calculations.

The observation of strong visible photoluminescence at room temperature from porous Si [4] with the possibility of optoelectronic applications has initiated intensive research on nanostructured silicon (e.g., reviewed in [5]).

Intensive light emission from Ge nanocrystals has also been found.

Within the last few years there has also been progress in the fabrication of nanostructured compound semiconductors with desired structures, especially porous III–V semiconductors.

Nanostructuring provides important degrees of freedom for phonon engineering. It may change considerably the density of phonon states, induce surface-related vibrations, and spatially confine the bulk phonon modes.

Although not expected by use of the term “quantum dots” for nanoparticles, many properties of confined vibrations

and surface modes can be understood by applying classic physics developed about 100 years ago [6, 7].

Inelastic light scattering also has been very intensively investigated in two-dimensionally layered semiconductor structures exhibiting one-dimensional confinement in growth direction. Readers may refer to reviews in Refs. [8, 9].

## 2. QUANTUM CONFINEMENT IN SEMICONDUCTORS

Semiconductor crystals with sizes of a few nanometers typically contain several hundreds to several thousands of atoms; they are too small to have bulk electronic properties. Quantum confinement in such crystals arises due to the finite size of the crystal, which limits the motion of electrons, holes, and excitons. In a small nanocrystal with size comparable to the Bohr radius of the corresponding bulk material, spatial confinement effects on the electron–hole system become significant. At very small crystal sizes, the character of the exciton starts disappearing and the electrons and holes become individually confined, because the kinetic energies of the electrons and holes become dominant and the Coulomb interaction between electrons and holes starts losing its significance. Theoretical models predict [10] that the energy spectrum of such a material consists of a series of discrete lines, which change their positions with particle size, and a blueshift of the band gap with respect to the corresponding bulk material is observed. This blueshift gives a measure of the confinement, which can be observed, for example, in absorption [11] or photoluminescence (PL) [12] experiments.

For a bulk crystal, the electron wavelength can extend to infinity, facilitating  $\vec{k}$  to take all values including zero and, hence, the band structures are parabolic. Electrons (holes) can occupy any position on the parabolic conduction (valence) band. The band gap is defined as the energy difference between the conduction and the valence band at  $\vec{k} = 0$ . On the other hand, in the case of a nanocrystal, the electron wavelength is confined to the size of the crystal and, hence,  $\vec{k}$  takes only nonzero discrete values, depending on the particle size. The electrons and the holes with minimum energy can only take a position where  $\vec{k} \neq 0$ , and the band gap for a nanocrystal has to be defined as the energy difference between the conduction and the valence band at this nonzero value of  $\vec{k}$ , which is higher than the band gap of the corresponding bulk. This can be understood from the illustration presented in Figure 7 of Ref. [13]. The band gap for nanocrystals can be expressed as

$$E = E_g + \Delta E \quad (3)$$

where  $E_g$  is the bulk band gap. The energy difference  $\Delta E$  is referred as the confinement energy. The value of  $\Delta E$  depends on the crystal size and becomes zero for bulk. The confinement can be classified into two categories, depending upon the size of the crystal. If the Bohr radius of the exciton is  $a_B$  and  $R$  is the particle radius, then the system is said to have strong confinement if  $R \ll a_B$  and weak confinement if



$R \gg a_B$ . In the simplest approach, the confinement energy in the case of strong confinement is given by [10, 14–17]

$$\Delta E = \frac{\hbar^2 \chi^2}{2\mu R^2} \quad \text{with} \quad \frac{1}{\mu} = \frac{1}{m_e} + \frac{1}{m_h} \quad (4)$$

In the case of weak confinement the confinement energy is

$$\Delta E = \frac{\hbar^2 \chi^2}{2MR^2} \quad \text{with} \quad M = m_e + m_h \quad (5)$$

Here,  $m_e$  and  $m_h$  are the electron and the hole mass, respectively, and  $\chi$  are roots of the spherical Bessel functions; the first root for the lowest energy transition is  $\chi = \pi$ . The simple effective mass model was improved by empirical pseudopotential [18] and tight-binding [19, 20] methods with application to II–VI semiconductors. The first-principles pseudopotential method was also applied to silicon [21]. For more details see, for example, the review in Ref. [22].

The II–VI nanoparticles are the most investigated materials, and PL spectroscopy is widely used to measure the confined energy [12, 23]. A typical PL spectrum from nanoparticles contains a sharp structure corresponding to the band edge, and some broad structures related to shallow and deep traps. The structure corresponding to the band edge is usually asymmetrically broadened, partially due to the temperature and the shallow traps very close to the band edge. However, under careful experimental conditions, the luminescence at the band edge can still be used with sufficient accuracy to estimate the band gap of the material. As discussed above, the effective band gap of a nanoparticle system is increased due to confinement. This can be easily observed in PL spectra, in the form of a blueshift of the band-edge luminescence. Because this shift depends on particle size, and the samples usually have an asymmetric particle size distribution, the band-edge luminescence is also partially asymmetrically broadened due to the particle size distribution. It has been observed [13] that in some cases the peak position of the band-edge luminescence strongly depends on the probing laser power and, hence, it is important to measure the luminescence at very low probing power-density to avoid other causes, which may shift the luminescence peak. By measuring the peak position of this band-edge luminescence, one can estimate the effective band gap  $E = E_g + \Delta E$  of the material. By substituting the bulk band gap  $E_g$  and by using the above-mentioned equation for the confinement energies, one can estimate the particle size. Although the absolute particle size estimation using PL experiments alone may not give a very accurate value of the particle size, it gives a good estimation of the confinement energy, especially when one wants to compare the confinements due to changing particle sizes. A comparison with Raman scattering also shows satisfactory agreement for the particle size estimation.

### 3. ELECTRON–PHONON COUPLING

Electron–longitudinal optical (LO) phonon coupling, governed by the Fröhlich interaction, is very important in the electronic and optical properties of a nanoparticle system, and its investigation has attracted a lot of attention. The

coupling between free charge carriers and vibrational excitations plays a central role in determining the transport properties and the energy relaxation rates of the excited carriers. One of the interesting points is that the electron–phonon interaction in small nanoparticles can be investigated experimentally beyond the bulk approximations. In this system, the confinement effects influence not only the electronic and vibrational states, but also the coupling between them. Although the effect of size dependence on the electron–phonon coupling has inspired a lot of work, the initial studies have produced contradicting results. In the early work, Schmitt-Rink et al. [24] theoretically suggested that, if electron and hole charge distributions are identical, then exciton–LO phonon coupling should vanish in small nanoparticles. Klein et al. [25] predicted size-independent coupling, if the dimensions of the charge distribution scales as the particle size. However, other authors [26–28] suggested that electron–phonon coupling increases with decreasing particle size for small particles. Here, the electron–hole correlation, the valence band degeneracy, the conduction band nonparabolicity, and proper confined phonon wavefunctions were considered. Experimentally, absorption spectroscopy [29] and photoluminescence [30] measurements indicated that the electron–phonon coupling increases with decreasing particle size. On the other hand, in some resonant Raman scattering experiments, in which in principle the electron–phonon interaction can be directly probed, either a size-independent coupling [25] or a decrease of electron–phonon coupling with decreasing particle size was detected [31, 32]. Later, Scamarcio et al. [33] unambiguously demonstrated that the electron–LO phonon coupling increases with increasing confinement in the strong confinement region. This was experimentally demonstrated through the size dependence of the ratio between the two-phonon and the one-phonon Raman cross sections in the resonant Raman scattering of a prototype system. These experiments were done under improved conditions, with constant resonance conditioning being maintained for all the particle sizes investigated. It was experimentally shown that, as the nanoparticle size changes from about 3 to 2 nm, the electron–phonon interaction increases more than two times. They also suggested that the electron–phonon coupling governed by the Fröhlich interaction increases stronger than that governed by the deformation potential with decreasing particle size.

Resonant Raman scattering up to the third order was studied by Rodríguez-Suárez et al. [34]. The observed relative intensities of the overtones were found to be very sensitive to the particle size, in accordance with calculations considering the Fröhlich interaction between excitons and phonons.

For exciton–acoustic phonon interaction the deformation potential coupling mechanism was shown to predominate in semiconductor nanocrystals [35, 36].

## 4. ACOUSTIC PHONONS

### 4.1. Confinement

The finite size of nanoparticles restricts the motion of phonons inside a nanocrystal; hence the confinement effects on the phonons can be observed. For a bulk

crystal, the phonons can extend up to infinity, which allows  $\vec{q}$  to take any value in the reciprocal lattice, including zero. Owing to the scattering selection rules, phonons at the  $\Gamma$ -point ( $\vec{q} = 0$ ) are the only observable phonons in the first-order Raman scattering. Therefore, the acoustic phonons, with vanishing energy at the  $\Gamma$ -point, are not observed in the first-order Raman scattering of a bulk crystal. On the other hand, because of the uncertainty of momentum transfer for small particles, acoustic phonons in nanocrystals become observable in first-order Raman spectra. They are called “confined acoustic phonons.” The vibrational frequencies of these phonons are very close to zero. They appear in the low-frequency range of the Raman spectra, with frequencies inversely proportional to the diameter of the nanoparticles.

One way to understand these acoustic phonons is to consider the possible vibrations of the whole particle. To calculate these vibrations, the particle can be considered as an elastic sphere and elastic continuum theory can be used, along with the proper boundary conditions at the surface of the nanoparticle. More than 100 years ago, Lamb [6] discussed the vibrations of a homogeneous elastic body of spherical shape under stress-free boundary conditions. This model, which was extended later (see, e.g., Tamura et al. [37]), is valid if the wavelengths of the acoustic phonons sufficiently exceed those of the lattice constants. It has been proved to be useful as an approximation for the calculations of vibrational confinement in nanoparticles. The eigenfrequencies of the elastic body can be obtained by solving the differential equation

$$\partial^2 \vec{s} / \partial t^2 = v_t^2 \Delta \vec{s} + (v_l^2 - v_t^2) \text{grad div } \vec{s} \quad (6)$$

under the corresponding boundary conditions. Here,  $\vec{s}$  is the lattice displacement vector, and  $v_t$  and  $v_l$  are the transverse and the longitudinal sound velocities, respectively. By classifying the eigenfrequencies according to the symmetry group of the sphere, two types of vibrational modes can be obtained, spheroidal modes  $\omega^S$  and torsional modes  $\omega^T$ . The torsional modes are dilatation-free vibrations without a volume change of the sphere and the spheroidal modes are curl-free.

The eigenvalues are characterized by the angular quantum number  $\ell$  and by another quantum number  $p$ , which gives the order of the zeroth of the radial part of the wavefunction. The torsional mode is only defined for  $\ell \geq 1$  because the mode with  $\ell = 0$  has no displacement. The eigenvalues determine the quantized vibrational frequencies  $\omega_{\ell p}^S$  and  $\omega_{\ell p}^T$  for the particle with the radius  $R$  from the relations

$$\omega_{\ell p}^S = \frac{\xi_{\ell p}^S}{R} v_l \quad \omega_{\ell p}^T = \frac{\eta_{\ell p}^T}{R} v_t \quad (7)$$

where  $\xi$  and  $\eta$  are the eigenvalues of Eq. (6).

The “wavevectors” of acoustic phonons in nanoparticles are also quantized and are described by the two sets  $\xi_{\ell p}^S/R$  and  $\eta_{\ell p}^T/R$ . Figure 1a illustrates the deformations of the vibrating sphere for the eigenfrequencies with lowest indices. The total symmetric spheroidal mode or the “breathing” mode is denoted by  $\omega_{01}^S$ ,  $\omega_{21}^S$  indicates the quadrupolar symmetric spheroidal mode, and  $\omega_{21}^T$  is a torsional mode. Only the lowest modes  $\omega_{\ell p}^S$  with  $p = 1$  have large amplitudes

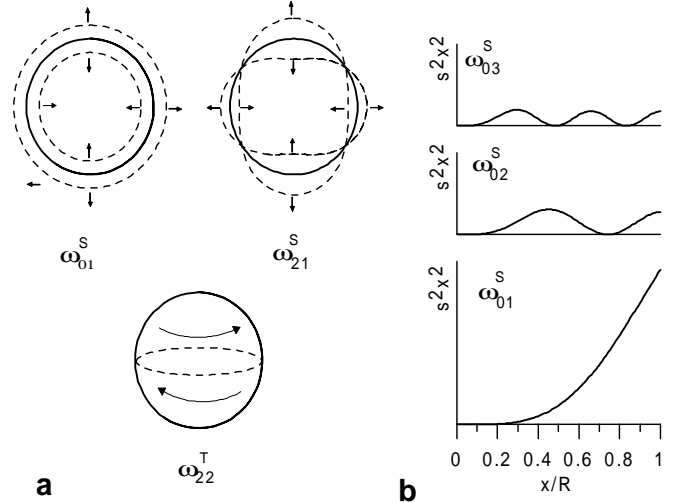


**Figure 1.** Some vibrational modes of an elastic isotropic sphere. (a) Spheroidal “breathing” mode  $\omega_{01}^S$  with  $\ell = 0$  and  $p = 1$ , spheroidal quadrupolar mode  $\omega_{21}^S$ , and torsional mode  $\omega_{21}^T$ . (b) Radial distribution of the energy density  $s^2 x^2$  of the spheroidal breathing mode  $\omega_{01}^S$  (surface mode) and the first two overtones  $\omega_{02}^S$  and  $\omega_{03}^S$  (inner modes) for spherical particles with free surface.

near the surface of the nanocrystals; the higher modes with  $p > 1$  correspond to inner modes. Figure 1b shows the radial distribution of the energy density  $s^2 R^2$  of the spheroidal breathing mode  $\omega_{01}^S$  (also called surface mode) and the first two overtones  $\omega_{02}^S$  and  $\omega_{03}^S$  (inner modes).

As shown by Duval [38], only the spheroidal modes with angular quantum numbers  $\ell = 0$  and  $\ell = 2$  are Raman active. The total symmetric mode  $\ell = 0$  is polarized, and the quadrupolar symmetric mode  $\ell = 2$  is depolarized. The simplest case  $\ell = 0$  with the eigenvalue equation

$$\sin(\xi) = 4\alpha^2 j_1(\xi) \quad (8)$$

can be analyzed easily. Here,  $j_1(x) = (\sin(x) - x \cos(x))/x^2$  is the spherical Bessel function of first order. Eigenvalue equations for higher quantum numbers are given, for example, in [37, 39, 40].

For a free particle, the parameter  $\alpha$  in Eq. (8) is given by the ratio of the transverse and longitudinal sound velocities  $v_t/v_l$ . In the case of an embedded particle, the relations for the continuity of the displacement and of the stress vectors at the spherical surface result in a generalized eigenvalue [41]. The parameter  $\alpha$  then additionally depends on the sound velocities in the matrix and on the ratio of the mass densities of the particle and the matrix. Further,  $\alpha$  is obtained as a complex number, sound emission into the matrix occurs, and therefore the particle vibrations are damped.

## 4.2. Raman Scattering

### 4.2.1. Scattering Efficiency

The Raman scattering is caused by fluctuations in the dielectric susceptibility due to the elastic waves. The Raman scattering efficiency can be expressed as a function of the

elasto-optic coefficients [1, 42]. The wavevector dependence of an acoustic mode is given by

$$d\sigma/d\Omega \sim (n(\omega) + 1)q \left[ \int_V \exp[-i(\vec{k}_L - \vec{k}_S - \vec{q}) \cdot \vec{r}] dV \right]^2 \quad (9)$$

where  $n(\omega) = (\exp(\hbar\omega/kT) - 1)^{-1}$  is the Bose-Einstein population factor. For bulk materials, corresponding to large dimensions of the scattering volume  $V$  in comparison with  $1/q$ , the integral in Eq. (9) can be replaced by the  $\delta$  function  $\delta(\vec{k}_L - \vec{k}_S - \vec{q})$ . This expresses the momentum conservation: The wavevectors of the scattered light  $\vec{k}_S$  and of the exciting light  $\vec{k}_L$  are very small. Therefore, only phonons near the center of the first Brillouin zone with wavevectors  $q = |\vec{k}_L - \vec{k}_S| \sim 0$  contribute to the light scattering which hinders the observation of Raman scattering by acoustic phonons in bulk material. By assuming nanoparticles to be spherically shaped with radius  $R$  and by integrating over the sphere volume, the Raman scattering efficiency results in

$$d\sigma/d\Omega \sim (n(\omega) + 1)qS(q, R) \quad (10)$$

with

$$S(q, R) = \left[ \frac{3j_1(qR)}{qR} \right]^2 \quad (11)$$

The scattering function  $S(q, R)$  replaces the  $\delta$  function. In this case, the wavevector selection rules are relaxed. Phonons with larger wavevectors contribute to the Raman scattering, and the observation of the confined acoustic phonons is allowed. For particles embedded in a matrix, the elastic excitations are exponentially damped due to complex eigenvalues. Therefore, we assume for the phonon modes  $\omega_{\ell p}^S$  Lorentzian bands  $L(\omega, \omega_{\ell p}, b_{\ell p}) \sim (1 + (2(\omega - \omega_{\ell p})/b_{\ell p})^2)^{-1}$  with the maximum at  $\omega_{\ell p}$  and half-width  $b_{\ell p}$  describing the damping. Further, we take into account the density of states  $\sim q^2$  and a size distribution  $c(R)$ . Then the Raman scattering intensity is obtained as

$$d\sigma/d\Omega \sim (n(\omega) + 1)\omega^3 \int S(q, R)c(R)V(R)L(\omega, \omega_{\ell p}^S, b_{\ell p})dR \quad (12)$$

with the wavevector  $q = \omega_{\ell p}^S/v_l$  and the particle volume  $V(R)$ .

The homogeneous line broadening due to the matrix effect is considerable and must be taken into account if one wants to deduce the particle size distribution from the Raman spectra [41].

#### 4.2.2. II–VI Semiconductors

Figure 2 represents as an example low-frequency Raman spectra of  $\text{CdS}_x\text{Se}_{1-x}$  nanoparticles with a mean radius of  $R = 3.1$  nm embedded in a silicate glass matrix. The spectra were excited with a Ti:sapphire laser operating at a wavelength far from resonance. The curves (a) and (b) correspond to polarized and depolarized configurations, respectively. For comparison, curve (c) shows an unpolarized spectrum of the base material, which contains no nanoparticles. The broad band with maximum at about  $50 \text{ cm}^{-1}$ , which

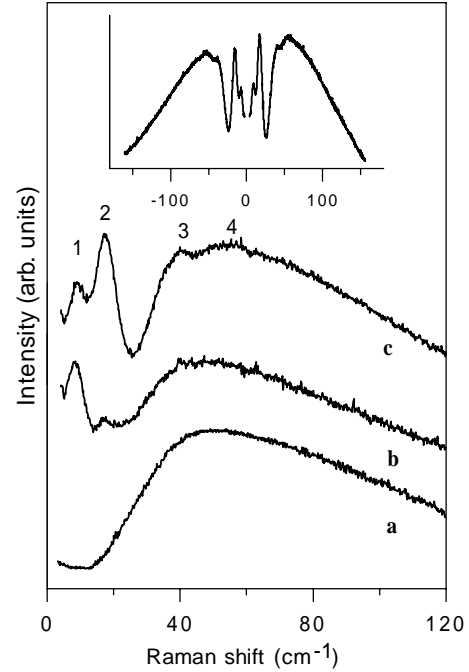


**Figure 2.** Low-frequency Raman scattering spectra of  $\text{CdS}_{0.67}\text{Se}_{0.33}$  nanocrystals embedded in borosilicate glass excited at the wavelength  $\lambda = 857$  nm below the absorption band. The mean particle radius is 3.1 nm. The quadrupolar mode is indicated by 1; the phonon modes 3 and 4 are overtones of the breathing mode 2. (a) Polarized spectrum; (b) depolarized spectrum; (c) base material of the sample. In the inset the polarized spectra in the anti-Stokes and in the Stokes regions are shown.

is typical for glass vibrations and is known as the Boson peak [43, 44], is also present in the spectra (a) and (b). Band 1 in curve (a) at  $8.5 \text{ cm}^{-1}$  corresponds to the depolarized spheroidal vibration with  $\ell = 2$  and  $p = 1$  and band 2 at  $17.5 \text{ cm}^{-1}$  corresponds to the polarized spheroidal vibration with  $\ell = 0$  and  $p = 1$ . Weaker bands 3 and 4 at about 40 and  $55 \text{ cm}^{-1}$  can be assigned to the inner modes with  $\ell = 0$  and  $p = 2$  and  $p = 3$ , respectively. The frequencies of the bands scale with  $1/R$ , as can be seen in Figure 3 where results for  $\text{CdS}_x\text{Se}_{1-x}$  nanoparticles with different sizes are shown. Such doped semiconductor glasses are used as sharp cutoff filters, the absorption edge being adjusted by changing the particle size. The value obtained experimentally agree well with calculations based on the continuum theory. The influence of the composition  $x$  is small as can be seen by the three curves for each phonon mode calculated for  $x = 0.8, 0.5$ , and  $0.2$ .

Nanocrystals of II–VI semiconductors are conventionally synthesized either in oxide glass hosts or by colloidal precipitation. The synthesis of quantum dots in polymer films has also been reported. For more information see, for example, Woggon [22], Herron [45], Kamat et al. [46], and references therein.

In the case of semiconductor-doped oxide glasses, precipitation of the semiconducting dots from the solid solution is obtained by annealing the glass after quenching. Silicate glasses containing  $\text{CdS}_x\text{Se}_{1-x}$  mixed crystals have been extensively investigated. Particle sizes have been obtained by Raman scattering of acoustic modes in

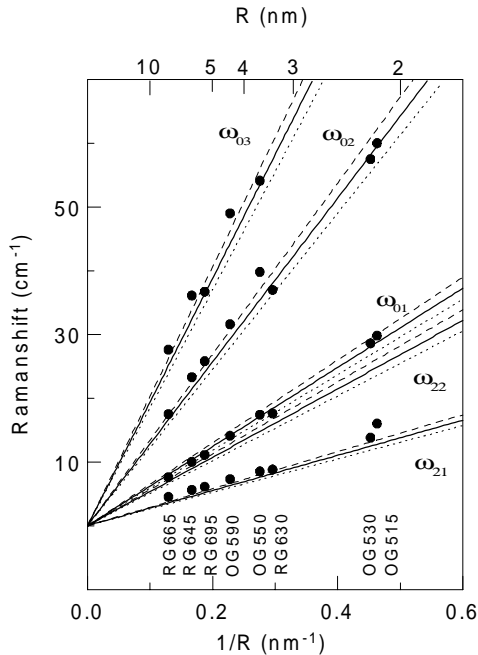


**Figure 3.** Measured low-frequency peaks in dependence on  $1/R$  for various filter glass samples.  $\omega_{ep}$  indicates various polarized modes, depolarized modes, and their overtones. The experimental values for the corresponding phonons are shown by full circles. The dashed, solid, and dotted lines correspond to the theoretical values calculated with  $x = 0.8, 0.5,$  and  $0.2,$  respectively. It can be seen that the influence of the composition  $x$  on the phonon frequencies is small. Reprinted with permission from [41], P. Verma et al. *Phys. Rev. B* 60, 5778 (1999). © 1999, American Physical Society.

$\text{CdS}_x\text{Se}_{1-x}$  [41, 47–52],  $\text{CdS}$  [49, 53, 54],  $\text{CdSe}$  [39, 55],  $\text{Zn}_x\text{Cd}_{1-x}\text{S}$  [49] crystals in silicate glass matrix,  $\text{CdS}$  [56], and  $\text{CdSe}$  [39] crystals in  $\text{GeO}_2$  glass matrix.

Other methods used to determine the particle sizes were transmission electron microscopy (TEM) [23, 47, 56–61], optical absorption [47, 49, 51, 59, 62], small angle scattering of neutrons (SANS) [63], small angle scattering of X-rays (SAXS) [13, 50, 53, 55, 64, 65], and photoluminescence [59, 66].

In addition to size-dependent shifts of the photoluminescence peaks, the discrete acoustic phonon modes could also be observed in photoluminescence spectra [67].

Saviot et al. [53, 54] observed size and excitation dependence of resonant low-frequency Raman scattering in  $\text{CdS}$  nanocrystals embedded in glass. They reported size-selective excitation, when the exciting laser wavelength was changed within the absorption band. With variation of the excitation within the absorption band, they observed dependence of the low-frequency band position and changes of its depolarization. The low-frequency band was 100% polarized for excitation below the absorption edge while it was depolarized when excited above the absorption.

#### 4.2.3. Si and Ge

Low-frequency Raman modes of nanometric Si crystallites were first observed in porous Si [65, 68]. Gregora et al. [68] found a well-defined peak at  $37 \text{ cm}^{-1}$  in the low-frequency spectra of porous silicon layers produced by electrochemical

etching in hydrofluoric acid solution of heavily boron-doped silicon wafers. With the assumption of spherical particles, on the basis of Eq. (7),  $2R = 6.5 \text{ nm}$  is obtained. However, due to the columnar morphology of the porous structure a model with particles of elongated nonspherical shapes is more realistic. For long cylinders this model yields  $2R \approx 4.1 \text{ nm}$ ,  $2R$  corresponds to the diameter of the columns. A similar value was deduced from the observed downshift and broadening of the  $520 \text{ cm}^{-1}$  one-phonon peak (see Section 6).

Liu et al. [65] succeeded in preparing Si clusters embedded in a porous Si skeleton. The Si clusters were produced by evaporation and inert gas condensation [69, 70], and the cluster size was controlled by adjusting the evaporation temperature, the Ar gas pressure, and the distance between the substrate and the W boat containing the Si powder. The cluster size was determined with TEM measurements. The strongest peaks in the low-frequency region of the Raman spectra were observed at  $29 \text{ cm}^{-1}$  (particle size  $3.8 \text{ nm}$ ) and at  $28 \text{ cm}^{-1}$  (particle size  $3.9 \text{ nm}$ ), respectively.

Raman scattering from acoustic phonons confined in Si nanocrystals which were dispersed in  $\text{SiO}_2$  thin films have been observed by Fujii et al. [71]. The samples were prepared by a radiofrequency cosputtering method [72, 73]. The sizes of the particles were determined from high-resolution electron microscopic observations. It was found that the Si nanocrystals are single crystals with good crystallinity. Raman spectra are shown in Figure 4. As the size decreases, the peaks shift to higher frequencies. The intensity ratio of the peaks in the polarized and depolarized spectra is about 0.25 for samples with  $d = 3.1$  and  $3.5 \text{ nm}$ ; for  $d = 5.5 \text{ nm}$  a distinct peak was not observed in the depolarized spectrum. However, the quantitative comparison between the experiment and the theory based on the continuum model is not successful. This will be discussed in Section 4.3.

Low-frequency Raman measurements on Ge microcrystals with sizes of  $5 \text{ nm}$  and greater embedded in a  $\text{GeO}_2$  glass matrix have been performed by Ovsyuk and Novikov [40, 74]. The crystals were grown using the reaction  $2\text{GeO}(\text{gas}) = \text{Ge} + \text{GeO}_2$  [74]. The low-frequency Raman scattering data

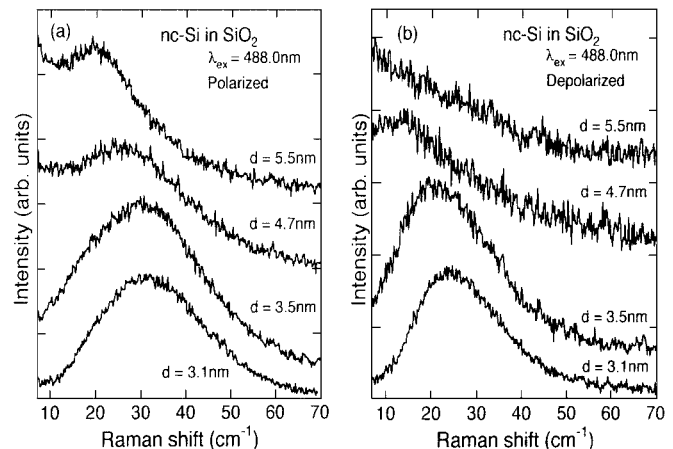


**Figure 4.** Low-frequency Raman scattering of Si nanocrystals embedded in  $\text{SiO}_2$  matrices. (a) Polarized spectra; (b) depolarized spectra. Reprinted with permission from [71], M. Fujii et al. *Phys. Rev. B* 54, R8373 (1996). © 1996, American Physical Society.

were used to show that the vibrations of the Ge nanocrystals differ considerably from those of free particles and that the influence of the matrix is considerable. Using the theory of Tamura et al. [37] the influence of the matrix on the spheroidal and torsional modes of nanocrystals was analyzed. It was found that surface vibrations were caused by the restoring force which limits the free rotation of microcrystals.

#### 4.2.4. Other Compounds

While in semiconducting nanoparticles the spheroidal breathing mode with  $\ell = 0$  and  $p = 1$  is the strongest in the Raman spectra, the scattering intensity of this mode is very low for metallic nanocrystals, for example, consisting of Ag or Au, and the light scattering of the quadrupolar mode dominates the Raman spectra. The reason is that in the latter case the inelastic light scattering is induced by the phonon-plasmon coupling. The electric dipole moment of the surface plasmon is modulated by the vibrational modes. As noted by Gersten et al. [75], the breathing mode ( $\ell = 0$ ) will produce no significant modulation; however, the quadrupolar vibrations ( $\ell = 2$ ) will be strongly coupled to the dipolar plasmon. A depolarization ratio of 0.75 was determined for the  $\ell = 2$  modes [76].

Light scattering is sensitive to the size and the shape of the nanoparticles. For ellipsoidally distorted shapes, the threefold degenerate dipolar plasmon splits into a lower-energy plasmon oscillating along the long axis of the ellipsoid and a twofold degenerate higher-energy plasmon oscillating perpendicular to this axis. Further, the fivefold degeneracy of the  $\ell = 2$  mode ( $m = 0, \pm 1, \pm 2$ ) is lifted. The observed large inhomogeneous width of the plasmon absorption of Ag clusters may be explained by ellipsoidal distortions because the plasmon energy very weakly depends on the size [77]. The shape of the clusters can even be selected by Raman scattering: Palpant et al. [78] investigated thin films consisting of small Ag clusters embedded in a porous alumina matrix. Most clusters were roughly spherical, but a noticeable amount of clusters, generally the larger ones, were found with a prolate ellipsoidal shape, as shown by TEM investigations. By excitation with the 457.9 nm Ar laser line close to the absorption maximum at 420 nm, the low-frequency peaks of spherical nanoclusters were observed with a depolarization ratio close to  $\frac{3}{4}$ . By shifting the excitation to the red region, the low-frequency peak was shifted to lower frequency with a depolarization ratio close to  $\frac{1}{3}$ . This can be explained by selective enhanced excitation of the nondegenerate plasmon along the long axis of the ellipsoidally distorted particles by excitation in the low-energy wing of the absorption band.

Silver nanocrystals embedded in  $\text{SiO}_2$  [79], alkali halide [76], and porous alumina matrix [78] were investigated too. It was shown that the observed low-frequency peaks agree fairly well with calculations based on Lamb's theory if the particle size is less than about 4 nm [79]. Courty et al. [80] performed low-frequency Raman measurements on silver nanocrystals self-organized on a hexagonal compact array on highly oriented pyrolytic graphite substrate. Besides the quadrupolar vibration mode, two weaker bands were observed at larger frequency shifts. They were attributed to

the spheroidal breathing modes  $\ell = 0$ , and  $p = 1, 2$ , and their observation was made possible by the high crystallinity and the narrow size distribution of the particles. Recently, low-frequency Raman measurements of Au particles supported on  $\text{CeO}_2$  and  $\text{Fe}_2\text{O}_3$  catalytic matrixes were performed [81, 82] with the aim of measuring their grain size. Supported by measurements of the depolarization ratio, it was concluded that the observed bands are due to the  $\ell = 0$  and  $\ell = 2$  spheroidal modes [82].

Confined acoustic phonons were investigated in Sn nanoparticles embedded in a  $\text{SiO}_x$  thin film, the inelastic scattered light was measured by a Sandercock interferometer [83]. The observed low-frequency modes scale with the inverse of the particle size in accordance with Lamb's theory. The vibrational modes of the smallest particles were overdamped. A similar result was obtained with femtosecond pump-and-probe spectroscopy measurements, where oscillations with comparable frequencies were detected for the big particles but not for the smaller ones. By increasing the temperature, clear effects of particle melting on the acoustic and the optical modes could be observed [84].

For  $\text{SnO}_2$  nanoparticles grain size and distribution deduced from Raman scattering were found in agreement with TEM measurements, especially for the smaller particles [85].

#### 4.3. Size Determination

In this section we will discuss other methods that are used for particle size determination and often correlated with Raman scattering measurements.

The average sizes calculated from the frequencies at the low-frequency peak maxima in the Raman spectra are overestimated if a size distribution is present because the scattering intensity is proportional to the particle volume. This is true for perfect lattice structure; however, lattice defects may reduce the scattering intensity due to spatial coherence effects as discussed by Duval et al. [86].

- (a) *Transmission electron microscopy.* TEM is often used to deduce a mean particle size and size distributions from a limited number of particle images. Preparation techniques are often pretentious and may affect the observation; the particle sizes are underestimated.

The lattice images of nanocrystals observed with high-resolution TEM are produced by interference of diffracted beams; different types of lattice images are found, depending on the orientation of the particle relative to the electron beam. They are visible when the crystal thickness exceeds a threshold value  $t_0$ . For the case of CdSe in glass, Champagnon et al. [47] estimated a threshold thickness of  $t_0 \approx 3$  nm. Therefore, the lattice is visible only in particles larger than the threshold thickness. Further, for larger particles the lattice image is produced from the central parts but may be invisible (below a threshold intensity) near the surface over a width  $w \approx t_0^2/4R$ , depending on the particle radius  $R$ . The deviation of the apparent size from the real size, therefore, is much more important at small sizes. This effect could be one possible reason for discrepancies in the observed sizes of very small

particles determined with different methods [47]; see Figures 6 and 7.

- (b) *Absorption, luminescence.* The energetically lowest optical transition can be used to determine the particle size. The corresponding absorption is often not a well-defined narrow peak. Some authors used the second derivative of the absorption spectrum [62] to locate the band edge; other authors took the energy at which the absorption appears to extrapolate to zero [87]. A clear inverse square size dependence in both the absorption edge and in the photoluminescence was observed in most cases, at least for II–VI compounds. Potter and Simmons [59] studied CdS crystals at sizes between 4 and 40 nm and obtained good agreement with the case of strong confinement [Eq. (4)]. The bulk Bohr radius in CdS is 2.8 nm. In general, the determination of size values from absorption and luminescence measurements depends on the model used and requires knowledge of parameters such as exciton masses.
- (c) *X-ray diffraction (XRD).* The finite crystallite size leads to a broadening of the peaks in the XRD spectra. This can be understood if one considers that in a finite crystal the number of rays reflected from successive lattice planes that add up in constructive or destructive interference is finite. Therefore, they do not reinforce or cancel out completely. The determination of the crystallite size from the XRD peaks is discussed in several books [88–90], mostly the Scherrer formula is used. The peak broadening gives a weighted average of the mean grain size, but the grain size may be considerably less than the particle size [91]. Variations in the lattice constant, for instance, from one crystallite to another and structural defects will also broaden the peaks. Several methods have been described to separate crystalline size- and distortion-induced broadenings. Further the XRD spectra can be influenced by particle shape effects. For prolate nanoparticles with more planes contributing to the diffraction in the direction of the prolate axis the corresponding XRD peaks can be increased in intensity and reduced in width as shown for CdSe nanocrystals [92] with sizes of about 8 nm and for Si nanocrystals [93] with sizes of about 50 nm. In the last case the peak-dependent linewidth broadening was used as evidence for pressure-induced diamond-to-hexagonal structure phase transition accompanied by shape changes from spherical to prolate.
- (d) *Small angle scattering (SAXS and SANS).* The size as well as the size distribution can be obtained with SAXS or SANS. We will discuss here as an example SAXS. The central scattering of X-rays due to the presence of nanoparticles having dimensions from several tens to several hundred times the X-ray wavelength  $\lambda$  is analogous to the well-known phenomenon of optical diffraction, where a halo is produced by the passage of a light ray in a powder with grain dimensions on the order of a hundred times the light wavelength. Let us consider a particle in a beam of X-rays; then all the electrons are sources of scattered

waves. The scattered waves are all in phase when the scattering direction is the same as that of the incident beam. As the scattering angle increases, the difference in phase between the various scattered waves also increases and the intensity of the resultant scattered wave decreases because of destructive interference. The intensity becomes zero when there are as many waves between 0 and  $\pi$  as between  $\pi$  and  $2\pi$ ; this will occur for a scattering angle of about  $2\vartheta \approx \lambda/L$ , where  $L$  is an average size of the particle. The scattering cross section for spherical particles with radius  $R$  and size distribution  $c(R)$  embedded in a matrix can be expressed as [94, 95]

$$\frac{d\sigma}{d\Omega}(q, E) \sim A(\Delta\rho(E)) \int S(q, R)c(R)V^2(R) dR \quad (13)$$

where  $q = (4\pi/\lambda) \sin(\vartheta)$  is the magnitude of the scattering vector,  $E$  is the X-ray energy, and the scattering function  $S(q, R)$  was defined in Eq. (11). The expression  $A$  depends on the electronic contrast  $\Delta\rho$  between the particle and the matrix. Figure 5 shows the scattering curve of a sample with  $\text{CdS}_{0.67}\text{Se}_{0.33}$  nanocrystals. The corresponding Raman spectrum is given in Figure 2. The solid line has been fitted by assuming spherically shaped particles with asymmetric size distribution as shown in the inset. The dashed line was calculated for a size distribution with a  $\delta$ -function-like profile.

From Eq. (13) it can be seen that particles with larger radius contribute much more to the scattering cross section than smaller ones. Therefore, average size values could be overestimated if Guinier plots and not a complete fit procedure are used.

In Figure 6 results of Raman measurements of nanocrystals in glass matrices are plotted against the inverse radius

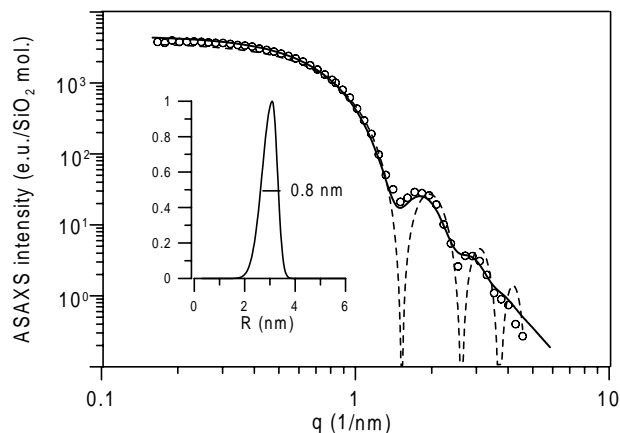


**Figure 5.** Small angle X-ray scattering curve of the sample with  $\text{CdS}_{0.67}\text{Se}_{0.33}$  nanocrystals described in Figure 2. The solid line has been fitted by assuming spherically shaped particles with asymmetric size distribution as shown in the inset. The dashed line was calculated for a size distribution with a  $\delta$ -function-like profile. Reprinted with permission from [95], G. Irmer et al. *J. Appl. Phys.* 88, 1873 (2000). © 2000, American Institute of Physics.



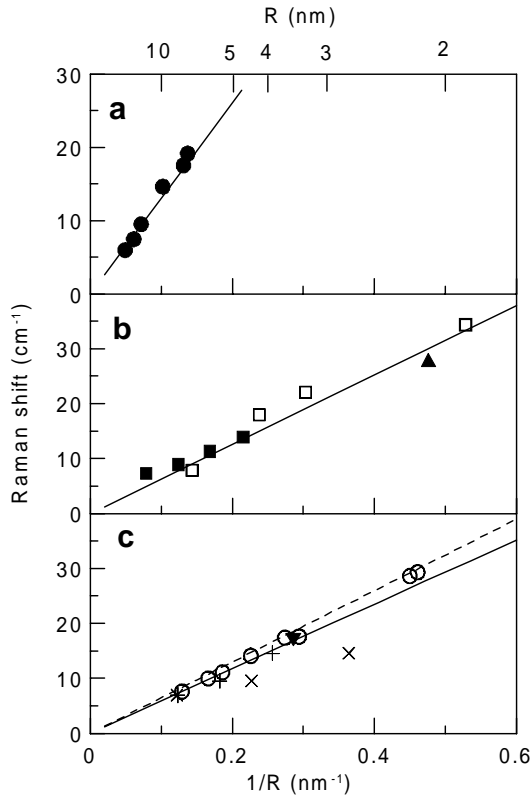


**Figure 6.** Position of the spheroidal mode  $\omega_{01}^s$  as a function of the inverse of the particle radius as observed by other scattering methods or TEM, respectively. (a) Nucleated cordierite glass: ●, SANS [2]. (b) CdS in glass matrix: □, SAXS [53]; ◇, [56]; ▲, [242]. (c) CdS<sub>x</sub>Se<sub>1-x</sub> in glass matrix: ○, anomalous SAXS [13]; ▼, SANS [62]; ×, SAXS [47]; +, TEM [47].

as determined by other scattering methods (SAXS, anomalous SAXS, or SANS) or TEM, respectively. The straight full lines are calculated with Lamb's theory for spheres with free surfaces, and the dotted line in Figure 6c takes into account the matrix effect. The agreement between various scattering methods is good; however, for smaller particles deviations from results of TEM measurements can be observed [47].

Large discrepancies between experimental results and the theory based on the continuum model were obtained for Si nanocrystals, as shown in Figure 7. Because the formulae in Section 4.1 are based on the isotropic elastic medium approximation, mean values for the sound velocities  $v_l$  and  $v_t$  were used for the calculation of the size dependence of the polarized spheroidal mode  $\omega_{01}$  and the depolarized spheroidal mode  $\omega_{21}$  of a free particle. The calculated values are much larger than those of the measured peaks, even if the large anisotropy of the elastic constants in Si is taken into account. The influence of the SiO<sub>2</sub> matrix [71] is discussed as one possible reason for the deviation between experiment and theory. However, quantitative estimations are still lacking and further theoretical studies are necessary. For instance, opposite predictions were made for the influence of SiO<sub>2</sub> matrices on Ag particles. Montagna and Dusi [96] predicted very small and negligible influences, while Ovsyuk and Novikov [40] reported that the phonon modes

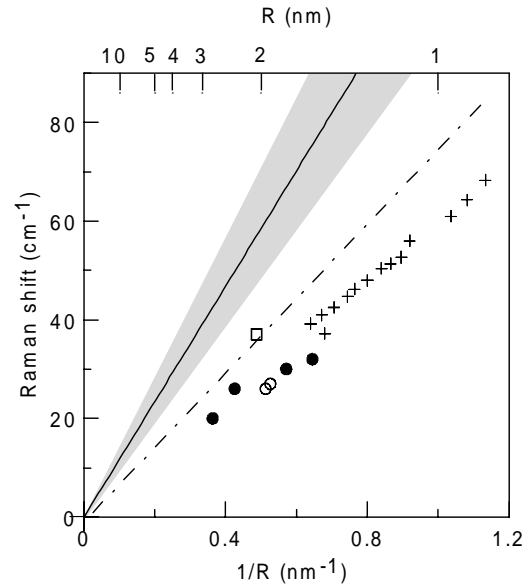


**Figure 7.** Position of the spheroidal mode  $\omega_{01}^s$  as a function of the inverse of the particle radius of Si nanocrystals. The radii were obtained by ●, TEM measurements [71]; ○, TEM measurements [65]; □, estimation of the size analyzing the shift and shape of the optical phonon band assuming a columnar structure (column radius  $R$ ) [68]. The straight lines were calculated based on Lamb's theory for particles with free surfaces: solid line, spheres; dotted line, columns, assuming isotropic elastic medium. The hatched region indicates the range of theoretical values when the elastic anisotropy of Si is taken into account. For comparison theoretical results (+) obtained with lattice dynamical calculations on Si clusters are included [170].

due to matrix effects shift to lower frequencies by considerable amounts.

## 5. SURFACE PHONONS

### 5.1. Surface Modes of Small Particles

The classical electromagnetic theory for the absorption and scattering of a sphere was given a century ago by Mie [7]. About 60 years later Mie's theory was applied to spherical ionic crystallites [99–102] characterized by the frequency-dependent dielectric function  $\varepsilon(\omega)$  which also describes the optical behavior of a polar semi-insulating cubic semiconductor in the infrared (IR) region:

$$\varepsilon(\omega) = \varepsilon_\infty \left[ \frac{\omega_{LO}^2 - \omega^2 - i\omega\gamma}{\omega_{TO}^2 - \omega^2 - i\omega\gamma} \right] \quad (14)$$

Here,  $\omega_{TO}$  and  $\omega_{LO}$  are the frequencies of the transverse and longitudinal optical bulk phonons, respectively,  $\varepsilon_\infty$  is the dielectric constant at high frequencies, and the constant  $\gamma$  takes damping into account. The bulk phonons in small particles have properties similar to those of the corresponding phonons in an infinite crystal; however their wavefunctions are adapted to the geometry of the small particle. For spherical geometry, for example, the phonon wavefunctions can be described by orthogonal eigenfunctions consisting of products of spherical Bessel functions  $j_\ell(q_{ln}r)$  with spherical harmonics  $Y_{\ell m}$ , classified by the quantum numbers

$\ell$ ,  $m$ , and  $n$ . The radial wavevectors  $q_{\ell n}$  are size-quantized due to the boundary conditions with  $q_{\ell n} = \nu_{\ell n}/R$ , where  $\nu_{\ell n}$  are the  $\ell$ th order spherical Bessel function roots [103].

In addition to the bulk phonons in small particles, there exist surface phonon modes, which have no counterpart in infinite crystals. Their frequencies  $\omega_\ell$  are intermediate between  $\omega_{\text{TO}}$  and  $\omega_{\text{LO}}$ . They can be obtained by solving the equation

$$\varepsilon(\omega) + \varepsilon_1 \cdot (\ell + 1)/\ell = 0, \quad \ell = 1, 2, 3, \dots \quad (15)$$

where  $\varepsilon_1$  is the dielectric constant of the embedding medium and  $\ell$  is an angular quantum number. Unlike bulk phonons, the surface phonons have nonvanishing electrical fields outside the particle; inside the electrical field changes with  $r^{\ell-1}$  radial dependence. The surface mode with the lowest index  $\ell = 1$  has a constant amplitude inside the sphere (therefore, the restriction of the notation ‘‘surface mode’’ to modes with  $\ell > 1$  is also in use). This mode of homogeneous polarization has a frequency  $\omega_F$  given by the solution of  $\varepsilon(\omega) + 2\varepsilon_1 = 0$  and is often called the Fröhlich mode [104]. With each surface mode a surface charge distribution is associated, which generates the polarization field inside the sphere. The Fröhlich mode with  $\ell = 1$  corresponds to a dipolar charge distribution, the mode with  $\ell = 2$  to a quadrupolar, and the inner modes with higher  $\ell$  to higher multipolar surface charge distributions. For particles that are small compared with the wavelength, the electrostatic approximation can be used and the mode with  $\ell = 1$  dominates [105].

Up to now we have considered a spherical particle. However, the shape has an important influence on the surface mode frequencies. As an example, we consider an ellipsoid of homogeneous polarization (Fröhlich mode). Three frequencies are obtained instead of one, given by the solutions of the equations

$$\varepsilon(\omega) + \varepsilon_1 \cdot (1/n_i - 1) = 0, \quad i = 1, 2, 3, \dots \quad (16)$$

where  $n_i$  are the so-called depolarization factors corresponding to the  $i$ th axis of the ellipsoid. The depolarization factors obey the relations  $0 \leq n_i \leq 1$  and  $n_1 + n_2 + n_3 = 1$ . The inverse of  $n_i$  is approximately proportional to the  $i$ th axis. Note, that for  $n_1 = n_2 = n_3 = \frac{1}{3}$  the case  $\varepsilon(\omega) + 2\varepsilon_1 = 0$  of the sphere is obtained; for an infinite long cylinder with  $n_1 = n_2 = \frac{1}{2}$ ,  $n_3 = 0$  the surface frequency is determined by  $\varepsilon(\omega) + \varepsilon_1 = 0$ . The electromagnetic theory was extended to cylindrical [106], cubic [107], and other nonspherical particles; reviews are given in Refs. [102, 105, 108].

Roca et al. [109] and Chamberlain et al. [110] extended the treatment of polar optical phonons in quantum dots by including mechanical boundary conditions. Phonon dispersion up to quadratic terms in the wavevector and the coupling between the mechanical displacement and the electrostatic potential were taken into account. Their model gives (1) uncoupled transverse optical (TO) modes with purely transverse character and (2) coupled modes with in general mixed LO–TO character.

$\ell = 0$ : The most important contribution to Raman scattering corresponds to the modes with  $\ell = 0$ . These LO modes

of longitudinal type are purely radial with the mechanical displacement vector

$$\vec{s}_{\ell=0,n} = A j_1(\nu_n r/R) \vec{e}_r \quad (17)$$

where  $\nu_n$  is the  $n$ th zero of the spherical Bessel function  $j_1$ . Assuming a quadratic negative bulk LO phonon dispersion, the eigenfrequencies of the modes with  $\ell = 0$  are given by

$$\omega_n^2 = \omega_{\text{LO}}^2 - \beta_L^2 (\nu_n/R)^2 \quad (18)$$

Here,  $\beta_L^2$  is a parameter describing the dispersion of the LO phonon in the bulk [109, 111]. For large  $R$ ,  $\omega_n \rightarrow \omega_{\text{LO}}$  is obtained. For example, for GaAs quantum dots embedded in AlAs, the  $n = 1$  mode was calculated to occur basically at the  $\omega_{\text{LO}}$  frequency of bulk GaAs for radii  $> 2.5$  nm.

$\ell \geq 1$ : The frequencies of these surface modes are more difficult to obtain [109]. However, for large  $R$  the frequencies are again solutions of Eq. (15), meaning that the effect of mechanical boundary conditions becomes important only for small  $R$ .

The theories mentioned above concern the optical response of an isolated particle embedded in a homogeneous medium characterized by a dielectric constant  $\varepsilon_1$ ; particle interactions are not included. However, in practice the particles are often not separated and light-scattering experiments have to be performed on collections of particles like powders or nanosized porous media. As mentioned above, the surface modes in polar semiconductors are accompanied by electrical fields. For instance, the Fröhlich mode of an particle with its dipole field will interact with those of other particles via dipole–dipole interaction. A theory that accounts approximately for the interactions is the effective medium theory.

## 5.2. Effective Medium Theory

For visible light interacting with semiconducting nanoparticles (characteristic size  $L$  and dielectric function  $\varepsilon_2$ ) distributed in a medium with the dielectric constant  $\varepsilon_1$  in the limit  $\lambda \gg L$  the heterogeneous composite can be treated as a homogeneous medium, and the so-called effective medium theory applies.

The effective dielectric function  $\varepsilon_{\text{eff}}$  is defined by

$$\langle \vec{D} \rangle = \varepsilon_{\text{eff}} \langle \vec{E} \rangle \quad (19)$$

where  $\langle \vec{D} \rangle$  and  $\langle \vec{E} \rangle$  denote spatial averages of the dielectric displacement and the electric field, respectively. For a composite of two materials with the dielectric functions  $\varepsilon_1$  and  $\varepsilon_2$  we get

$$(1-f)\varepsilon_1 \langle \vec{E} \rangle_1 + f\varepsilon_2 \langle \vec{E} \rangle_2 = \varepsilon_{\text{eff}} [(1-f)\langle \vec{E} \rangle_1 + f\langle \vec{E} \rangle_2] \quad (20)$$

where the averages are taken over the volumes occupied by the material with the dielectric function  $\varepsilon_1$  or  $\varepsilon_2$ , respectively. The parameter  $f$  is the relative volume  $V_2/V$  occupied by the material with  $\varepsilon_2$ . If the fields have the same directions in the two media (which has to be proved), the

dielectric function can be expressed as a function of the field ratio  $\beta = \langle E \rangle_2 / \langle E \rangle_1$ :

$$\varepsilon_{\text{eff}} = \frac{(1-f)\varepsilon_1 + f\varepsilon_2\beta}{(1-f) + f\beta} \quad (21)$$

The field ratio  $\beta$  can be obtained by solving the electrostatic equations  $\text{rot } \vec{E} = 0$  and  $\text{div } \vec{D} = 0$  under the appropriate boundary conditions. Exact solutions exist only in a few cases:

- (a) The medium consists of parallel slabs of both materials; the applied electrical field is parallel to the slabs (perpendicular to their common normal). Continuity of the tangential electric field components requires  $\beta = 1$  and we get from Eq. (21)

$$\varepsilon_{\text{eff}} = \varepsilon_{\text{upp}} = (1-f)\varepsilon_1 + f\varepsilon_2 \quad (22)$$

the so-called upper Wiener limit [112], because it can be proven to be the absolute upper limit for  $\varepsilon_{\text{eff}}$  for a two-material composite.

- (b) The medium consists of parallel slabs of both materials; the applied electrical field is perpendicular to the slabs (parallel to their common normal). Continuity of the normal displacement field components requires  $\beta = \varepsilon_1/\varepsilon_2$  and we get from Eq. (21) the so-called lower Wiener limit [112] as the absolute lowest limit for  $\varepsilon_{\text{eff}}$  for a two-material composite:

$$\frac{1}{\varepsilon_{\text{eff}}} = \frac{1}{\varepsilon_{\text{low}}} = \frac{(1-f)}{\varepsilon_1} + \frac{f}{\varepsilon_2} \quad (23)$$

- (c) An exact solution is also possible for the case of an external electrical field applied along an axis of an ellipsoid (e.g., dielectric function  $\varepsilon_2$ ) embedded into an infinite matrix (of dielectric function  $\varepsilon_1$ ); see, for example, Ref. [105]. Here, we restrict ourselves to the special case of a sphere. The field ratio is then  $\beta = 3\varepsilon_1/(\varepsilon_2 + 2\varepsilon_1)$ , often derived in textbooks of electrodynamics. From Eq. (21) we obtain the Maxwell–Garnett (MG) I result [113]; see Table 1,

three-dimensional case. The result is exact for the  $f \rightarrow 0$  limit (and for the trivial case  $f = 1$ ). Therefore, the application of the formula is justified if the matrix contains only a few well-separated spheres ( $f \rightarrow 0$ ), but often it is used as interpolation formula for all  $f$ . The formula, for example, describes the case of semiconducting spheres with concentration  $f$  and dielectric function  $\varepsilon_2 = \varepsilon(\omega)$  embedded in air ( $\varepsilon_1$ ). The replacements  $\varepsilon_1 \leftrightarrow \varepsilon_2$  and  $f \leftrightarrow 1-f$  result in the Maxwell–Garnett II formula  $\varepsilon_{\text{eff}} = \varepsilon_{\text{MGII}}$  (see Table 1) corresponding to the “swiss cheese” case of spherical air inclusions ( $\varepsilon_1$ ) in the semiconducting material with  $\varepsilon_2 = \varepsilon(\omega)$ . It can be shown that (if  $\varepsilon_1 < \varepsilon_2$ )  $\varepsilon_{\text{MGI}}$  and  $\varepsilon_{\text{MGII}}$  are the absolute lowest and the absolute upper limit, respectively, for the effective dielectric function  $\varepsilon_{\text{eff}}$  for isotropic or cubic two-material composites [114]:

$$\varepsilon_{\text{low}} < \varepsilon_{\text{MGI}} \leq \varepsilon_{\text{eff}} \leq \varepsilon_{\text{MGII}} < \varepsilon_{\text{upp}} \quad (24)$$

The replacements  $\varepsilon_1 \leftrightarrow \varepsilon_2$  and  $f \leftrightarrow 1-f$  do not result in  $\varepsilon_{\text{MGI}} = \varepsilon_{\text{MGII}}$ ; such a topology is called a matrix topology. If one of the phases is strongly diluted, the Maxwell–Garnett formulae are good approximations. Examples are semiconductor doped glasses with filling factors  $f$  of about 0.01 discussed in the next sections.

If phases 1 and 2 are equivalent, a so-called aggregate topology has to be described. An example is the Bruggeman expression [115] (see Table 1, first row). The solution  $\varepsilon_{\text{eff}}$  of the Bruggeman formula is invariant under the replacements  $\varepsilon_1 \leftrightarrow \varepsilon_2$  and  $f \leftrightarrow 1-f$ , characteristic of an aggregate topology. The Bruggeman formula can be derived by generalizing Eq. (21) for three materials, spherical inclusions  $\varepsilon_1$  and  $\varepsilon_2$  with volume fractions  $f_1 = V_1/V$  and  $f_2 = V_2/V$  embedded in a matrix  $\varepsilon_m$ :

$$\frac{\varepsilon_{\text{eff}} - \varepsilon_m}{2\varepsilon_m + \varepsilon_{\text{eff}}} = f_1 \frac{\varepsilon_1 - \varepsilon_m}{2\varepsilon_m + \varepsilon_1} + f_2 \frac{\varepsilon_2 - \varepsilon_m}{2\varepsilon_m + \varepsilon_2} \quad (25)$$

**Table 1.** Effective dielectric functions.

Topology	3D	2D
Matrix	Maxwell–Garnett I $\varepsilon_{\text{eff}} = \varepsilon_{\text{MGI}} = \varepsilon_1 \frac{2(1-f)\varepsilon_1 + (1+2f)\varepsilon_2}{(2+f)\varepsilon_1 + (1-f)\varepsilon_2}$	Maxwell–Garnett I $\varepsilon_{\text{eff}}^\perp = \varepsilon_1 \frac{(1-f)\varepsilon_1 + (1+f)\varepsilon_2}{(1+f)\varepsilon_1 + (1-f)\varepsilon_2}$
	Maxwell–Garnett II $\varepsilon_{\text{eff}} = \varepsilon_{\text{MGII}} = \varepsilon_2 \frac{(3-2f)\varepsilon_1 + 2f\varepsilon_2}{f\varepsilon_1 + (3-f)\varepsilon_2}$	Maxwell–Garnett II $\varepsilon_{\text{eff}}^\perp = \varepsilon_2 \frac{(2-f)\varepsilon_1 + f\varepsilon_2}{f\varepsilon_1 + (2-f)\varepsilon_2}$
Aggregate	Bruggeman $0 = (1-f) \frac{\varepsilon_1 - \varepsilon_{\text{eff}}}{2\varepsilon_{\text{eff}} + \varepsilon_1} + f \frac{\varepsilon_2 - \varepsilon_{\text{eff}}}{2\varepsilon_{\text{eff}} + \varepsilon_2}$	Bruggeman $0 = (1-f) \frac{\varepsilon_1 - \varepsilon_{\text{eff}}}{\varepsilon_{\text{eff}} + \varepsilon_1} + f \frac{\varepsilon_2 - \varepsilon_{\text{eff}}}{\varepsilon_{\text{eff}} + \varepsilon_2}$
	Monecke $\varepsilon_{\text{eff}} = \frac{\varepsilon_1 + 4f\varepsilon_1(\varepsilon_2 - \varepsilon_1)/(2\varepsilon_1 + \varepsilon_2)}{1 + f(\varepsilon_2 - \varepsilon_1)/(2\varepsilon_1 + \varepsilon_2)} + \frac{2f^2(\varepsilon_2 - \varepsilon_1)^2/(2\varepsilon_1 + \varepsilon_2)}{1 + f(\varepsilon_2 - \varepsilon_1)/(2\varepsilon_1 + \varepsilon_2)}$	

If, in a self-consistent way as the matrix material  $\varepsilon_m$  the effective medium  $\varepsilon_{\text{eff}}$  itself is chosen, with  $f_1 = (1 - f)$  and  $f_2 = f$ , the Bruggeman expression is obtained. It is often considered to be the best possible interpolation formula for an aggregate topology. It has, however, the following essential shortcoming. Let us consider a few semiconducting inclusions with the dielectric function  $\varepsilon_2(\omega)$  in a matrix of constant  $\varepsilon_1$ . In the IR region between the transverse and the longitudinal optical phonon,  $\varepsilon_2(\omega)$  is negative and  $2\varepsilon_1 + \varepsilon_2$  may become zero at the Fröhlich frequency  $\omega_F$ . For  $f \rightarrow 0$  the Maxwell–Garnett I formula is correct and results in a pole at  $2\varepsilon_1 + \varepsilon_2 = 0$ , giving rise to the Fröhlich mode [104]. This exact result is not reproduced for  $f \rightarrow 0$  by the Bruggeman formula. To overcome this deficiency, another interpolation formula for an aggregate topology has to be found. An isotropic aggregate topology is given, for example, by spherical  $\varepsilon_2$  inclusions in a matrix  $\varepsilon_1$  for  $f \rightarrow 0$  interpolated to spherical  $\varepsilon_1$  inclusions in a matrix  $\varepsilon_2$  for  $f \rightarrow 1$ . In both limits the field ratios are exactly known as  $\beta_{f \rightarrow 0} = 3\varepsilon_1 / (2\varepsilon_1 + \varepsilon_2)$  or  $\beta_{f \rightarrow 1} = [3\varepsilon_2 / (2\varepsilon_2 + \varepsilon_1)]^{-1}$ , respectively. The simplest interpolation for  $\beta$  is given by

$$\beta = \frac{3(1-f)\varepsilon_1 + f(2\varepsilon_2 + \varepsilon_1)}{3f\varepsilon_2 + (1-f)(2\varepsilon_1 + \varepsilon_2)} \quad (26)$$

By inserting  $\beta$  into Eq. (16), a new expression for  $\varepsilon_{\text{eff}}$  is obtained [116, 117]; see Table 1.

Often two-dimensional (2D) effective functions more adequately describe materials with nanosized structures. Examples are porous semiconductor structures produced by electrochemical etching with cylindrical pores, porous membranes with columnar semiconductor structures, and materials with quantum wires.

A typical porous polar semiconductor can be described as a heterogeneous material consisting of, for example, air-filled ( $\varepsilon_1 \approx 1$ ) cylindrical pores in the  $z$  direction, which are randomly distributed in the  $xy$  plane and embedded in the semiconducting matrix with  $\varepsilon_2 = \varepsilon(\omega)$ . The symmetry of the material is reduced. For a diatomic semiconductor with zincblende structure, the cubic point group  $T_d$  is changed to an uniaxial one [ $D_{2d}$  for a (100) surface and  $C_{3v}$  for a (111) surface]. In both cases the effective dielectric function becomes a tensor

$$\tilde{\varepsilon}_{\text{eff}} = \begin{pmatrix} \varepsilon_{\text{eff}}^{\perp} & 0 & 0 \\ 0 & \varepsilon_{\text{eff}}^{\perp} & 0 \\ 0 & 0 & \varepsilon_{\text{eff}}^{\parallel} \end{pmatrix} \quad (27)$$

For the electric field component parallel to the pores,  $\varepsilon_{\text{eff}}^{\parallel}$  is given exactly by the upper Wiener limit [Eq. (22)]. For  $\varepsilon_{\text{eff}}^{\perp}$  a two-dimensional variant of the Maxwell–Garnett model I can be used (see Table 1). The formula describes the morphology of the porous structure as an interpolation between two boundary cases: cylindrical voids in the semiconducting matrix (large material concentration) and a skeleton of intercrossing semiconductor plates (large void concentration). Being correct in both limits  $f \rightarrow 1$  and  $f \rightarrow 0$ , it can be used in the entire range  $f \in [0, 1]$ .

For columnar nanostructures it is more appropriate to use the two-dimensional equivalent of the Maxwell–Garnett

II formula. Single columns ( $f \rightarrow 0$ ) would then result in a Fröhlich mode given by  $\varepsilon(\omega_F) + \varepsilon_1 = 0$ .

Any dielectric function has to obey the Bergman spectral representation [118]. It can be shown that the effective dielectric functions given above fulfill the corresponding conditions. Additionally, in the two-dimensional case the Keller theorem [119] has to be fulfilled. This is the case for both Maxwell–Garnett formulae and for the Bruggeman expression.

The behavior of the effective dielectric function in the region of the optical phonons is illustrated in Figure 8. Parameters for GaP ( $\omega_{\text{TO}} = 366 \text{ cm}^{-1}$ ,  $\omega_{\text{LO}} = 402 \text{ cm}^{-1}$ ,  $\gamma = 1 \text{ cm}^{-1}$ ,  $\varepsilon_{\infty} = 8.5$ , and  $f = 0.7$ ) and the model interpolating between I and II were used. Phonons of transverse (longitudinal) character appear at the poles (zeros) of the real part  $\text{Re}(\varepsilon)$  of the effective dielectric function; see Figure 8c (the poles are smoothed due to the finite damping constant  $\gamma$  used). Between the pole corresponding to the TO phonon and the zero corresponding to the LO phonon an additional pole and an additional zero appear. They can be assigned to the Fröhlich mode. The unusual sequence, the longitudinal Fröhlich mode being below the transverse one, results from the fact that in any dielectric function poles should alternate with zeros in the sequence  $T \rightarrow L \rightarrow T \rightarrow L$ , etc., with increasing frequency. The Raman scattering efficiency is  $\propto \text{Im}(\varepsilon)$  for TO phonons and  $\propto \text{Im}(-1/\varepsilon)$  for LO phonons; the corresponding imaginary parts are plotted in Figure 8a and Figure 8b in arbitrary units. Although a strong Fröhlich mode phonon of longitudinal character can be seen, the transverse Fröhlich mode at  $\omega_{F-T}$  is very weak (not shown in Fig. 8b; its intensity is  $< 1\%$  of that of the TO

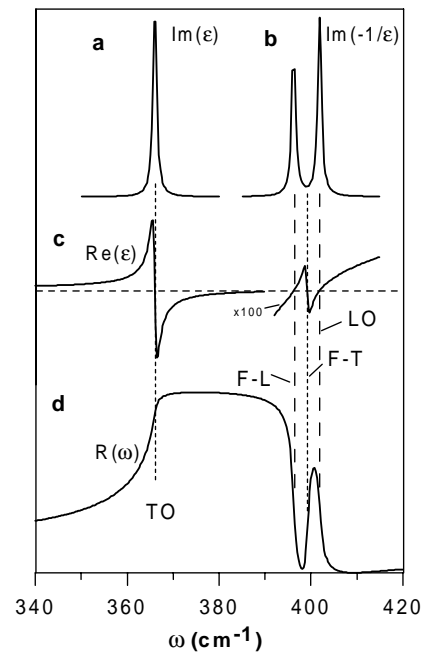


**Figure 8.** Effective dielectric function model: interpolation between three-dimensional (3D) MGI and 3D MGII [117]. Parameters:  $\omega_{\text{TO}} = 367 \text{ cm}^{-1}$ ,  $\omega_{\text{LO}} = 402 \text{ cm}^{-1}$ ,  $\gamma = 1 \text{ cm}^{-1}$ , and  $f = 0.74$  (closely packed spheres). (a) Imaginary part  $\text{Im}(\varepsilon)$ ; (b)  $\text{Im}(-1/\varepsilon)$ ; (c) real part  $\text{Re}(\varepsilon)$ ; (d) reflectivity  $R(\varepsilon)$ .

phonon) and should be not observable in the Raman spectra. However, the L–T splitting of the Fröhlich mode gives rise to a reflectivity minimum; see Figure 8d. The reflectivity is easy to calculate according to the standard formulae

$$R(\omega) = \frac{(n(\omega) - 1)^2 + \kappa(\omega)^2}{(n(\omega) + 1)^2 + \kappa(\omega)^2} \quad (28)$$

with  $n(\omega) = \sqrt{\sqrt{a^2 + b^2} + a}$ ,  $\kappa(\omega) = \sqrt{\sqrt{a^2 + b^2} - a}$ ,  $a = \text{Re}(\varepsilon_{\perp}(\omega))$ , and  $b = \text{Im}(\varepsilon_{\perp}(\omega))$ .

### 5.3. Raman Scattering

#### 5.3.1. III–V Semiconductors

Hayashi and Kanamori [3] were the first to observe Raman spectra by surface modes in polar semiconductors unambiguously. The GaP microcrystals they investigated were prepared by a gas evaporation technique. Figure 9 shows Raman spectra of samples with different particle sizes in the range between 51 and 430 nm. The surface peak can be clearly seen between the TO and the LO phonon peaks, when the microcrystals are about 1 order of magnitude smaller than the wavelength of the incident laser. For the samples used the surrounding medium was air. A frequency shift of the surface mode for different sizes was not reported. The frequency shifted to lower frequencies when the dielectric constant of the surrounding medium was increased.

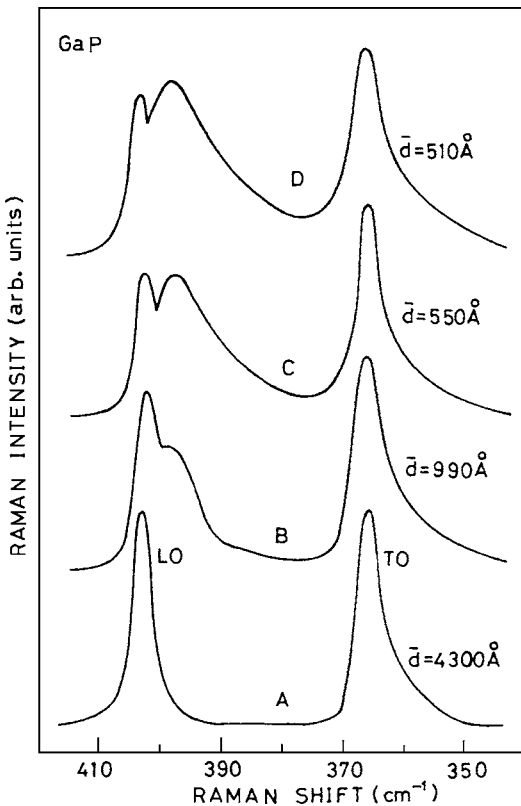


**Figure 9.** Light-scattering spectra of the surface mode of GaP nanoparticles.  $\bar{d}$  is the average particle size. Reprinted with permission from [3], S. Hayashi and H. Kanamori, *Phys. Rev. B* 26, 7079 (1982). © 1982, American Physical Society.

This was realized by embedding the microcrystals in the liquids nujol ( $\varepsilon_1 = 2.00$ ), aniline ( $\varepsilon_1 = 2.56$ ), and methylene iodide ( $\varepsilon_1 = 3.10$ ). The lineshape of the peaks attributed to an ellipsoidal particle shape was calculated using effective-medium theory [120]. It was observed that the intensity of the surface phonon peak increases as the average particle size decreases. An explanation was given based on calculations of Ruppin [103] for Raman scattering efficiencies of bulk and surface phonons in very small spherical crystals.

Watt et al. [121] investigated Raman spectra from arrays of GaAs cylinders fabricated by lithographic techniques with radii in the range of 30–100 nm and heights of 140–570 nm. Those with radius  $\leq 40$  nm showed a well-defined feature between the TO and LO phonons. The position of the additional peak was found to be in agreement with calculations based on the model developed by Ruppin and Englman [102] for the case of an infinite cylinder embedded in a dielectric medium. Wang et al. [122] reported Raman measurements of GaAs dots, fabricated by electron beam lithography and dry etching. It was found that the surface phonon intensity increased dramatically with decreasing dot sizes. da Silva et al. [123] observed the surface phonon at 287.6  $\text{cm}^{-1}$  in 6–10  $\mu\text{m}$  long wire-like crystals of GaAs with radii of 30 nm. The GaAs crystals were epitaxially grown on porous Si. They did not observe a dependence of the Raman intensity on the angle of the incident light, in contradiction to the observations of Watt et al. [121].

In recent years, in addition to porous silicon, increasing attention has been paid to porous III–V semiconductor materials [124–130] due to their potential applications in the field of electronics and photonics [131]. The nano-sized structures of such polar porous media (not in the case of the nonpolar Si) allow investigations of the surface modes. Their properties strongly depend on the morphology (i.e., symmetry, structural geometry, effective size, etc.) and on the constituents. The analysis of these modes helps to characterize the porous structure by the comparison of experimental results with theoretical calculations based on the effective-medium theory. Although for powders or nanocrystals embedded in homogeneous media 3D models of the effective-medium theory are successfully applied, 2D models are more appropriate to describe the morphology of porous semiconductors. The morphology of the porous structures fabricated by electrochemical etching of III–V materials depends mainly on the doping level of the bulk material, on the defect density on the surface and on the crystal orientation for given etching conditions [126, 127, 132–134]. A surface-related phonon mode in porous GaP at 397  $\text{cm}^{-1}$  observed by Tiginyanu et al. [135] was interpreted in terms of a Fröhlich mode on the basis of an effective medium approach [128]. It was shown that its frequency decreases with increasing anodization current. The fabrication of free-standing porous membranes, detached from the substrate, described in [136], enabled the investigation of the surface modes in porous membranes filled with liquids [137] and infrared reflectance measurements [134]. Figure 10 shows infrared reflectance spectra (a) and Raman scattering spectra (b) of a porous (111) GaP membrane. The pores of about 30 nm diameter exhibit a column-like shape, stretching into the sample perpendicularly to the initial crystal surface. The experimental spectra (upper row)

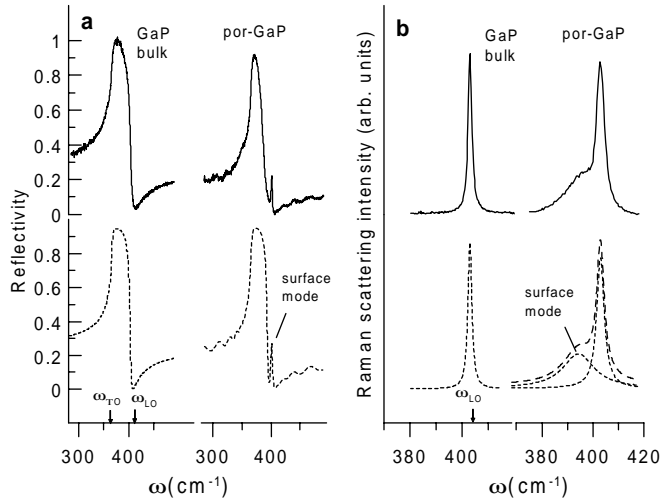


**Figure 10.** Surface modes in GaP with columnar nanosized pores. (a) Fourier transform infrared reflectivity spectra and (b) Raman spectra of porous and of bulk material. The lower row shows results of calculations based on the effective dielectric function corresponding to the 2D MGII model.

can be interpreted theoretically (lower row) using a two-dimensional effective dielectric function 2D MGII; see Table 1, which describes the morphology of the porous structures as an interpolation between two cases: cylindrical voids in the semiconducting matrix ( $f \rightarrow 1$ ) and a skeleton of intercrossing semiconductor plates ( $f \rightarrow 0$ ). The wave-like structures in the reflectance spectra of the porous membrane are interferences of light reflected at the membrane boundaries. The effect of hydrostatic pressure on the surface modes in porous GaP was investigated in [138] and the temperature influence in [139].

Sarua et al. [133, 134] studied the influence of free charge carrier in porous GaAs and porous InP on the surface phonons. It could be shown that the Fröhlich mode, like the LO phonon mode, couples to the plasmon modes induced by vibrations of the free carrier plasma of electrons. As the LO phonons, the Fröhlich modes were shifted to higher frequencies with increasing carrier density. In porous InP this effect could be observed both by light-scattering and by infrared reflectance measurements; in porous GaAs the F-T-F-L splitting is too small to be observed in the Fourier transform infrared experiment.

In GaN columnar nanostructures a new mode near  $716 \text{ cm}^{-1}$  was found by Raman scattering measurements [140]. The columnar structures with the thickness of about  $1.5 \mu\text{m}$  were fabricated by electrochemical dissolution of bulk material. Scanning electron microscope images proved that the columns with transverse dimensions of about 50 nm or less were oriented perpendicular to the initial surface. By Raman lineshape analysis based on the effective dielectric function for a composite of GaN columns in an air matrix (2D MGI; see Table 1) the new mode could be attributed to Fröhlich vibrational modes.

Electron–phonon coupling due to Fröhlich interaction has been considered by Efros et al. [26]. They investigated resonance Raman scattering of GaP nanocrystals embedded in glass. With laser excitation near the direct gap a strong LO

phonon and a surface mode approximately 10 times smaller in intensity were observed, in agreement with calculations based on the Fröhlich interaction and taking into account a degenerate valence band. Varying the excitation energy below the direct gap the LO phonon band decreases dramatically, whereas the intensity of the surface mode band is not much changed. This could be evidence that besides the Fröhlich interaction other scattering mechanisms like deformation potential scattering contribute to the surface mode scattering. However, up to now calculations on the electron–phonon interaction concentrated only upon the Fröhlich interaction.

### 5.3.2. II–VI Semiconductors

Surface modes in II–VI compounds were first observed by Scott and Damen [141] in cylindrical microcrystallites ( $\ll 1 \mu\text{m}$ ) of CdS in a polycrystalline film using Raman scattering. Pan et al. [142] studied Raman scattering of CdS nanocrystals (size  $< 30 \text{ nm}$ ) by surface modes in different organic media. Most Raman scattering experiments were performed with nanocrystals embedded in a glassy matrix: CdS [143], CdSe [25],  $\text{CdS}_x\text{Se}_{1-x}$  [34, 144–146], and ZnS [147]. As an example, we discuss here the case of  $\text{CdS}_x\text{Se}_{1-x}$  nanoparticles.

It is known that in the mixed crystal  $\text{CdS}_x\text{Se}_{1-x}$  the optical phonons show the so-called two-mode behavior, meaning that a CdS-like mode ( $\text{TO}_1$  and  $\text{LO}_1$ ) and a CdSe-like mode ( $\text{TO}_2$  and  $\text{LO}_2$ ) can be attributed to two oscillators which contribute with different oscillator strengths depending on the composition  $x$ .

The dielectric function of the mixed crystal can be described by

$$\varepsilon(\omega, x) = \varepsilon_\infty(x) \left( \frac{\omega_{\text{L}1}^2(x) - \omega^2 - i\gamma_1\omega}{\omega_{\text{T}1}^2(x) - \omega^2 - i\gamma_1\omega} \right) \times \left( \frac{\omega_{\text{L}2}^2(x) - \omega^2 - i\gamma_2\omega}{\omega_{\text{T}2}^2(x) - \omega^2 - i\gamma_2\omega} \right) \quad (29)$$

with  $\omega_{\text{L}1}(x) = 266 + 55x - 19x^2$ ,  $\omega_{\text{T}1}(x) = 266 - 28x$ ,  $\omega_{\text{L}2}(x) = 211 - 25x$ ,  $\omega_{\text{T}2}(x) = 168 + 17x$ , and  $\varepsilon_\infty(x) = 5.3x + 6.3(1 - x)$ . The parameters were taken from bulk measurements [148]. The phonon frequencies that depend on the composition  $x$  are plotted in Figure 11. The symbols correspond to measurements on  $\text{CdS}_x\text{Se}_{1-x}$  nanoparticles embedded in glass. Below both LO phonons additional modes can be observed (Fig. 12). In comparison with calculations on the basis of the effective dielectric function according to the 3D MGI model (dotted curve in Fig. 11), they can be attributed to Fröhlich modes.

To study the influence of the particle size on the optical phonons and the surface modes, a semiconductor doped glass slab was annealed in a furnace with an applied temperature gradient with temperatures between 850 and 1100 K. With increasing temperature the  $\text{CdS}_{0.6}\text{Se}_{0.4}$  particles grow to larger sizes. The composition  $x = 0.6$  was estimated from the position of the LO phonons [148]. The positions of the LO phonons and the surface mode were obtained by fitting with Lorentzian bands. The dotted lines in Figure 13a correspond to the calculated frequency of the Fröhlich modes



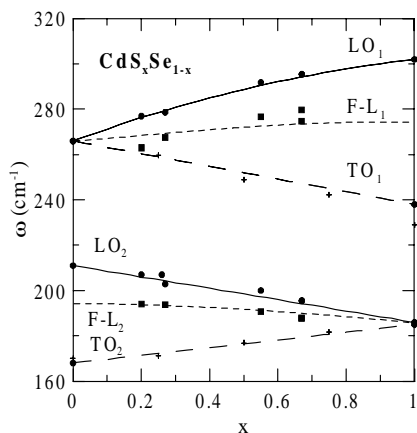


**Figure 11.** Dependence of the optical phonons and surface modes on the composition  $x$  of  $\text{CdS}_x\text{Se}_{1-x}$  nanoparticles embedded in borosilicate glass. The lines were calculated with the effective dielectric function of the 3D MGI model.

assuming spherical particles. Contrary to the acoustic vibrations (Fig. 13b), the optical phonons and the Fröhlich modes are nearly not size dependent. The effect of small shifts due to confinement effects for small particle sizes is discussed in Section 6.2.2.

The electron–phonon coupling in the case of the Fröhlich interaction between the field induced by the vibrational motion and the charge distribution was studied by several authors theoretically with different approximations and partly contradicting results (see Section 3). Klein et al. [25] observed surface modes in CdSe. Their calculations were based on a classical dielectric model. They concentrated their investigations on the  $1s-1s$  electronic transition and assumed that only the electron wavefunction is confined

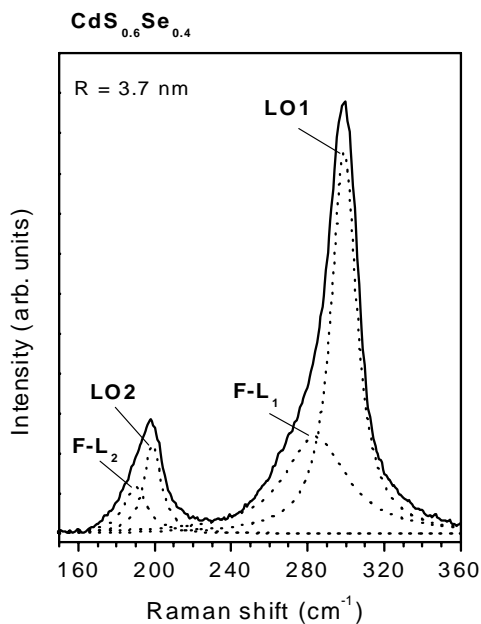


**Figure 12.** Surface modes in  $\text{CdS}_{0.6}\text{Se}_{0.4}$  nanoparticles embedded in borosilicate glass.

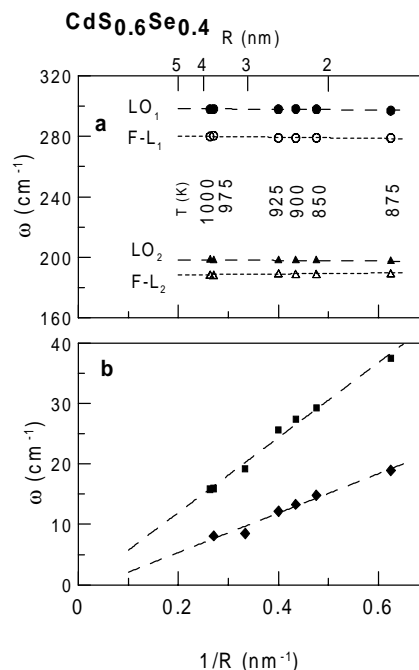


**Figure 13.** Size dependence of the (a) optical phonons and surface modes and (b) acoustic modes of  $\text{CdS}_{0.6}\text{Se}_{0.4}$  nanoparticles embedded in borosilicate glass.

whereas the hole resides near the center of the sphere. Their result is that the radial charge distribution in the spherical box does not couple to surface modes. As a possible reason for the observation of surface modes in the Raman spectra they assume deviations from the spherical particle shape. Efros et al. [26] included holes in a four-fold degenerate valence band in their calculation and showed that surface modes with  $\ell = 2$  are allowed due to a mixing of the valence bands even for perfectly spherical nanocrystals. Chamberlain et al. [110] considered the mechanical as well as the electrostatic boundary conditions in their model. In addition to the dipole approximation they considered the quadrupole contribution of the Fröhlich interaction, proportional to the wavevector. They showed that this term dominates for intersubband scattering and occurs only via  $\ell = 1$  phonons. Because they used a one-band effective mass model, the phonon modes are restricted to  $\ell = 0$  when the dipole approximation is used. The published calculations are based on the Fröhlich interaction, but other scattering mechanisms could contribute to the light scattering by surface modes, too. More detailed theoretical investigations are necessary and more experiments should be performed, analyzing the dependence on the excitation wavelength (near and far of resonance), on the polarization of the scattered light, and on the particle size to bring to light the properties of the surface modes.

The selection rules for Raman scattering of optical phonons in a homogeneous sphere are similar to those obtained for the acoustic vibrations discussed by Duval [38]. The vibrational modes must belong to the irreducible representations  $D_g^{(\ell)}$  and  $D_u^{(\ell)}$  of the three-dimensional rotation–inversion group  $O(3)$  ( $g$  and  $u$  mean even or odd upon inversion). The coupled optical (and the spheroidal acoustic)

modes transform according to  $D_g^{(0)}$ ,  $D_u^{(2)}$ , ... and the uncoupled optical (torsional) modes transform according to  $D_g^{(1)}$ ,  $D_u^{(2)}$ ,  $D_u^{(3)}$ , ... The Raman transition operator for dipole-allowed scattering is the polarizability tensor. Its components transform like  $D_g^{(0)}$  and  $D_g^{(2)}$ . The IR absorption is electric dipolar; the dipole operator transforms according to  $D_u^{(1)}$ . Therefore, the uncoupled transverse optical (torsional acoustic) modes are not expected to be optically active.

It should be noted that the considerations above do not reflect the crystal symmetry inside the sphere. For zincblende-type materials belonging to the point group  $T_d$  or wurtzite-type materials with point group  $C_{6v}$  the inversion symmetry is absent. For binary compounds such as GaAs, InP, and GaP, upon lowering of the symmetry from  $O(3)$  to  $T_d$  the representation  $D_g^{(0)}$  becomes  $\Gamma_1$  [109]. Scattering by optical phonons due to the so-called dipole forbidden Fröhlich interaction with diagonal Raman tensor belongs to this representation and will be visible. However, both representations  $D_g^{(2)}$  and  $D_u^{(1)}$  convert into  $\Gamma_{15}$ . The scattering by optical phonons due to deformation potential and electro-optic mechanisms belongs to this Raman activity and  $D_u^{(1)}$  surface modes are thus Raman active. The question of when, upon increasing  $R$ , the sphere will behave as a piece of bulk material, is discussed in more detail in [109], considering the coherence length of phonons.

### 5.3.3. Other Compounds

A reflectivity gap corresponding to surface modes in a polar porous semiconductor was first observed by Danishevskii et al. [149] in porous SiC and interpreted by McMillan et al. [150] on the basis of the effective medium theory. Sasaki et al. [50] measured Raman spectra from SiC fibers consisting of microcrystalline SiC about 50 nm in size embedded in amorphous SiC and carbon. They attributed features in the spectra between the TO and LO phonon frequencies to surface modes. The features observed were very weak and very broad, perhaps due to a high free carrier concentration and high plasmon damping of the SiC microcrystals and therefore difficult to interpret.

DiGregorio and Furtak [151] investigated commercially available 6H-SiC particles with an average size of about 3  $\mu\text{m}$ . The particles were irregular in shape with an average aspect ratio of about 2. They obtained a weak band in the Raman spectra below the LO phonon. However, scattering by surface modes is expected to be negligible in crystals that are larger than the wavelength of the exciting light. The appearance of weak surface modes was qualitatively explained as being caused by a decrease of the effective particle radius in irregularly shaped particles, enhancement of the intrinsic electric fields, and localization of surface modes near sharp corners and facets on the particles [152]. The observed mode frequencies 947  $\text{cm}^{-1}$  for the particles in air and 928  $\text{cm}^{-1}$  for particles embedded in KBr ( $\epsilon_1 = 2.33$ ) are near the solutions 932.3 and 948.8  $\text{cm}^{-1}$  of the equation  $\epsilon(\omega) + \epsilon_1 = 0$  for cylinder-like particles.

Raman scattering spectra in [50, 151] were obtained from SiC microcrystals of irregular shape and/or large size and, hence, weak surface phonon structures. This suggests the presentation here of Raman measurements of nanosized

particles nearly spherically shaped with an average diameter of about 30 nm as proved by XRD measurements. In the Raman spectra from these particles in air below the LO phonon a band at 937  $\text{cm}^{-1}$  was observed (Fig. 14c). Its position was found to be in agreement with calculations based on the effective medium theory. The observed half-width of the band is much larger than the half-width of the LO phonon. One reason could be local changes in the particle packing density. The theoretical curves (dotted lines in Fig. 14) were obtained with the 3D Mo model (Table 1), assuming a distribution of  $f$  values around  $f = 0.7$  with standard deviation  $\sigma = 0.3$ . The sensitivity of the surface mode to the environment of the particles was proved by embedding them into amorphous silica ( $\epsilon_1 \approx 2$ ). This was achieved by heating the powder in a laser beam. The temperature was controlled by measurement of the intensity ratio of the Stokes and anti-Stokes TO and LO phonons and by the frequency shift of the phonons. At about 1200 °C the oxidation of the SiC crystals starts, resulting in a  $\text{SiO}_2$  oxide layer around the particles [154, 155]. The  $\text{SiO}_2$  observed in the Raman spectra could be assigned to amorphous silica [156]. The corresponding peaks at about 500 and 600  $\text{cm}^{-1}$  are shown in Figure 14a. The small peak below the strong TO phonon is a weak phonon of TO character, indicating the 6H polytype of SiC.

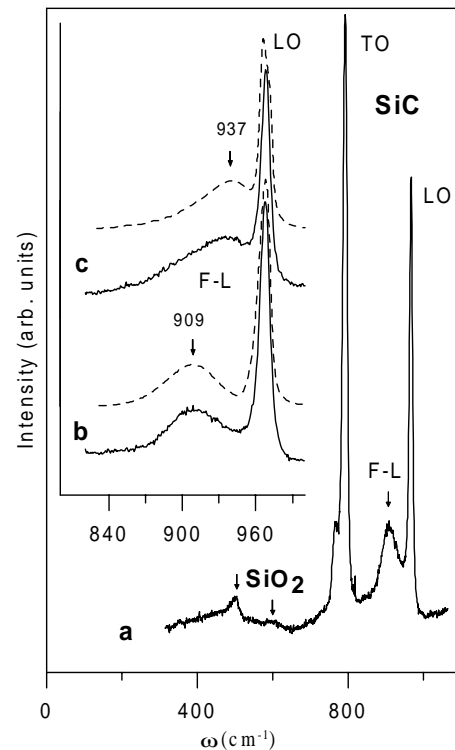


**Figure 14.** Influence of the embedding medium on the surface modes of SiC nanoparticles. (a) Raman spectrum of SiC nanoparticles embedded in an amorphous silica matrix. (b) Detail of spectrum (a) with surface mode F-L and phonon. (c) Raman spectrum of the SiC nanoparticles embedded in air. Calculations (dotted lines) were based on the effective dielectric function interpolated between 3D MGI and 3D MGII [153].

The surface mode is located at about  $909\text{ cm}^{-1}$  between the TO and LO phonons of SiC, shown in Figure 14a and in the inset (Fig. 14b). The theoretical curve in Figure 14b was calculated with  $f = 0.65$  and  $\sigma = 0.15$ .

In the optical phonon Raman spectra of SiC nanorods (diameters range from 3 to 30 nm; lengths are  $>1\ \mu\text{m}$ ) with a high density of defects, bands at 791, 864, and  $924\text{ cm}^{-1}$  were observed [157]. By comparison with calculations it was found that the Fröhlich enhanced effective density of states of the optical phonons, which becomes important because of the broken translation symmetry induced by defects, is responsible for the features in the Raman spectra.

Observations of surface phonon modes have also been reported for ZnO [158], SiO<sub>2</sub> [159], and Si [65].

## 6. OPTICAL PHONONS

### 6.1. Confinement Models

In the Raman spectra of nanocrystalline materials with particle sizes of a few nanometers, peak-position shifts, broadenings, and asymmetries of optical phonon bands appear. In most cases the Raman peak shifts to progressively lower energies and the lineshape gets progressively broader and asymmetric (on the low-energy side) as the particle size gets smaller. This effect can be used to determine the particle size. A typical Raman spectrum of the optical phonons of nanocrystals with about 3 nm diameter is shown in Figure 15,

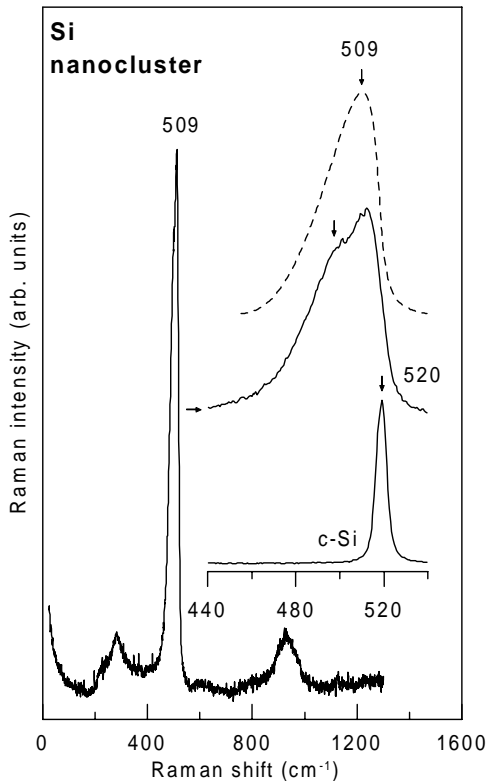


**Figure 15.** Raman scattering of confined optical phonons in nanocluster Si with crystals of about 3 nm size. The inset shows for comparison the Raman spectrum of an optical phonon in bulk Si. The dashed curve was calculated with the confinement model CM-II for spheres.

together with the Raman spectrum of a single crystal. The upper dashed curve in the inset shows a calculated profile. Different confinement models are in use to determine particle sizes and size distributions from the measured spectra.

### Confinement Model CM-I, Phenomenological Phonon Confinement Model

To characterize and interpret the observed bands, a phenomenological phonon-confinement model is very widely used; therefore, it is briefly outlined below. This model, originally proposed by Richter et al. [160], was later extended by Campbell et al. [161]. In a Stokes scattering process in an infinite crystal the wavevector difference  $\vec{k} = \vec{k}_L - \vec{k}_S$  is transferred to a phonon with wavevector  $\vec{q}_0$ . The wavefunction of a phonon with wavevector  $\vec{q}_0$  in an infinite crystal is

$$\Phi(\vec{q}_0, \vec{r}) = u(\vec{q}_0, \vec{r})e^{-i\vec{q}_0\vec{r}}, \quad (30)$$

where  $u(\vec{q}_0, \vec{r})$  has the periodicity of the lattice. The vibrational wavefunction of the nanocrystal is approximated by

$$\Psi(\vec{q}_0, \vec{r}) = W(\vec{r}, L)\Phi(\vec{q}_0, \vec{r}) = \Psi'(\vec{q}_0, \vec{r})u(\vec{q}_0, \vec{r}), \quad (31)$$

where the localization of the phonon in a microcrystal is taken into account by the weighting function  $W(\vec{r}, L)$ . A Gaussian weighting function  $W(r, R) \sim \exp(-\xi r^2/R^2)$ , introduced in [160] is mostly used in the traditional approach to bandshape analysis. The parameter  $\xi$  is fixed arbitrarily to get a small value at the sphere boundary  $R$ . Some other weighting functions were also applied [161–163].  $\Psi'(\vec{q}_0, \vec{r})$  can be expanded in a Fourier series, the Fourier coefficients being

$$C(\vec{q}_0, \vec{q}) = \frac{1}{2\pi^3} \int d^3r \Psi'(\vec{q}_0, \vec{r})e^{-i\vec{q}_0\vec{r}}. \quad (32)$$

The Raman scattering intensity is then described by a continuous superposition of Lorentzian curves with bandwidth  $\Gamma$  centered at the wavenumbers  $\omega(q)$  of the phonon dispersion curve and weighted by the  $|C(\vec{q}_0, \vec{q})|^2$  factor. By assuming a spherical Brillouin zone, isotropic dispersion curve, and  $\vec{q}_0 = \vec{k}_L - \vec{k}_S \approx 0$  for one-phonon scattering, the Raman intensity can be written as

$$I(\omega) \propto \int d^3q \frac{|C(\vec{q})|^2}{(\omega - \omega(q))^2 - (\Gamma/2)^2}. \quad (33)$$

The Fourier coefficients for the Gaussian weighting function are  $C(q) \sim \exp(-q^2L^2/4\xi)$ . This formula has been often used to fit Raman spectra to obtain mean particle sizes. However, there is no physical reason to use a Gaussian weighting function or in the assumption that the phonon wavefunction amplitude differs from zero at the crystalline boundary. For the fit parameter  $\xi$  the value  $\frac{1}{2}$  was originally used by Richter et al. [161]. Campbell et al. [160] found the best agreement with experiments setting  $\xi = 2\pi^2$ ; this value has been used by the most authors afterwards. With  $W^2(r, R) \sim \exp(-4\pi^2r^2/R^2)$  strong confinement of the phonons to the core is obtained:  $W^2(r, R)$  decreases from 100% at  $r = 0$  to 5% at  $r = 0.28R$  which means that the phonon energy is concentrated in only 2% of the sphere volume. Although the phonon confinement model is practicable to estimate particle sizes, it is theoretically not well founded.

**Confinement Model CM-II** This model uses the scattering function, which is well established in the analysis of SAXS experiments on small particles [164] (see Section 4.3). The application of similar expressions to light-scattering processes on small particles was also proposed in [48, 49, 96]. To derive the structure factor we follow Nemanich et al. [165], who presented an evaluation of the susceptibility function over a limited spatial extent. The results indicate that spectral changes are related to the phonon dispersion, and the photon wavevector uncertainty is accounted for.

The light-scattering cross section is proportional to the space-time Fourier transform of the correlation function of the fluctuations in the polarizability  $\delta\chi(\vec{r}, t)$  [42]:

$$I(\omega, \vec{k}) \propto \int d^3r \int d^3r' \int dt \langle \delta\chi^*(\vec{r}, t) \delta\chi(\vec{r}', 0) \rangle \times \exp(-i\vec{k} \cdot (\vec{r} - \vec{r}') - i\omega t) \quad (34)$$

The fluctuations  $\delta\chi(\vec{r}, t)$  can be expressed by the atomic displacements  $\delta\chi(\vec{r}, t) = \frac{\partial\chi}{\partial u} u(\vec{r}, t)$ .

In the absence of interaction between different phonon eigenmodes the displacements of modes with different  $\vec{q}$  are uncorrelated, and we obtain

$$\langle u^*(\vec{r}, t) u(\vec{r}', 0) \rangle = (1/V) \sum_{\vec{q}} \langle u^*(\vec{q}) u(\vec{q}) \rangle \times \exp(i\vec{q} \cdot (\vec{r} - \vec{r}') + i\omega_0 t) \quad (35)$$

where  $\omega_0(\vec{q})$  describes the dispersion of the phonon mode. The correlation function in Eq. (35) depends only on the difference  $\vec{r} - \vec{r}'$ . Therefore, the integrals can be factorized. Further, the displacement correlation function is expressed in terms of the Bose–Einstein factor  $n(\omega)$ , and Eq. (34) can be written

$$I(\omega, \vec{k}) \propto \frac{n(\omega) + 1}{\omega} \sum_{\vec{q}} A(\vec{q}, \omega) S(\vec{q}, \vec{k}) \delta(\omega - \omega_0(\vec{q})) \quad (36)$$

where the scattering function  $S$  is obtained by

$$S(\vec{q}, \vec{k}) = \left[ (1/V) \int_V d^3r \exp(i(\vec{q} - \vec{k}) \cdot \vec{r}) \right]^2 \quad (37)$$

The function  $S(\vec{q}, \vec{k})$  is a measure of the uncertainty of the wavevector  $\vec{q}$ . For an infinite transparent crystal with  $S(\vec{q}, \vec{k}) \sim \delta(\vec{q} - \vec{k})$  wavevector conservation is obtained. Before we discuss the scattering function for small particles, some remarks concerning absorption are needed. For a crystal that is opaque to light, the effective scattering volume is limited by the penetration depth, which is on the order of  $1/\alpha$ , where  $\alpha$  is the absorption coefficient. The effect of absorption can be described by assuming complex wavevectors  $\vec{k}_L = \vec{k}'_L + i\vec{k}''_L$  and  $\vec{k}_S = \vec{k}'_S + i\vec{k}''_S$ . By integration of Eq. (37) over the half-space  $z \leq 0$  we obtain a Lorentzian function  $S(\vec{q}) \propto ((q_z - (k'_L - k'_S))^2 + \alpha^2)^{-1}$ , where we have used  $\alpha \approx k''_L + k''_S$ . This means that the wavevector component  $q_z$  has a Lorentzian distribution centered at  $k = k'_L - k'_S$  with a half-width of  $2\alpha$ . Lorentzian distributions were successfully used to interpret Raman scattering of LO phonon–plasmon excitations [9] and Brillouin

scattering [10] in opaque semiconductors. However, because we have to deal with very small scattering volumes of particles with characteristic lengths  $L \ll 1/\alpha$ , the absorption can be neglected in general.

For finite scattering volumes the coupling of light to excitation modes with wavevectors  $\vec{q}$  in a range about  $\vec{k}$  is allowed and the function  $S(\vec{q}, \vec{k})$  describes the range of wavevectors that take part in the light-scattering process. For optical phonons we assume small frequency changes along the dispersion curves and we will use the approximation of a constant term  $A(\vec{q}, \omega)$ . The finite lifetime of the phonons is taken into account by replacing the  $\delta$ -function by a Lorentzian function and the sum is approximated by an integral over a spherical Brillouin zone. With  $\vec{k} = \vec{k}_L - \vec{k}_S \approx 0$  we obtain

$$I(\omega, \vec{k}) \propto \int d^3q \frac{S(\vec{q})}{(\omega - \omega(q))^2 - (\Gamma/2)^2} \quad (38)$$

an expression similar to Eq. (33) but with  $S(\vec{q})$  instead of  $|C(\vec{q})|^2$ . Table 2 presents the function  $S(q)$  for some differently shaped particles and for a layer. In Figure 16 these functions are shown in dependence on the dimensionless parameter  $\kappa$ :  $\kappa = q \cdot 2R$  for spheres with radius  $R$ ,  $\kappa = q_p \cdot 2R$  for long cylinders (length  $L \gg$  radius  $R$ ), and  $\kappa = q_x \cdot L$  for a cube (edge length  $L$ ). The function  $S(\kappa)$  describes the range of wavevectors that take part in the light-scattering process. For example, for spheres the curve  $S(q)$  diminishes from the value 1 at  $\kappa = 0$  ( $q = 0$ ) to a weight of  $\frac{1}{2}$  at about  $\kappa = 4$ , corresponding to a wavevector of  $q = 2/R$ ; wavevectors with less weight contribute up to about  $\kappa = 8$  corresponding to  $q = 4/R$ . The wavevector corresponds to a momentum  $p = \hbar q$ ; therefore, we can discuss these equations in terms of Heisenberg's uncertainty relation  $\Delta x \cdot \Delta p \geq \hbar/2$  correlating the uncertainties of the coordinate  $x$  and the momentum  $p$ . A Gaussian distribution of  $x$  values corresponds to a Gaussian distribution of  $p$  values. For Gaussian distributions only the lower limit  $\Delta p = \hbar/2\Delta x$  of Heisenberg's uncertainty relation is obtained [168]. In our case of  $x$  values strongly restricted to the particle volume the uncertainty is larger. Using the example of the sphere we estimate that  $\Delta p \approx 4\hbar/\Delta x$ , setting  $\Delta x = 2R$  and  $\Delta q \approx 2/R$ .

For comparison two Gaussian weighting functions used in the phonon confinement models CM-I are also shown ( $\xi = 1$

**Table 2.** Scattering functions  $S(q)$ .

Shape	$S(q)$	
Sphere	$9 \frac{j_1^2(qR)}{(qR)^2}$	$R$ : radius $j_1$ : spherical Bessel function
Cylinder	$\frac{4J_1^2(q_p R)}{(q_p R)^2} \cdot \frac{\sin^2(q_z L/2)}{(q_z L/2)^2}$	$R$ : radius $L$ : length in $z$ direction $J_1$ : Bessel function
Rhomboeder	$\prod_{i=x,y,z} \frac{\sin^2(L_i q_i/2)}{(L_i q_i/2)^2}$	$L_i$ : lengths of the edges
Layer	$\frac{\sin^2(L q_z/2)}{(L q_z/2)^2}$	$L$ : layer thickness in $z$ direction

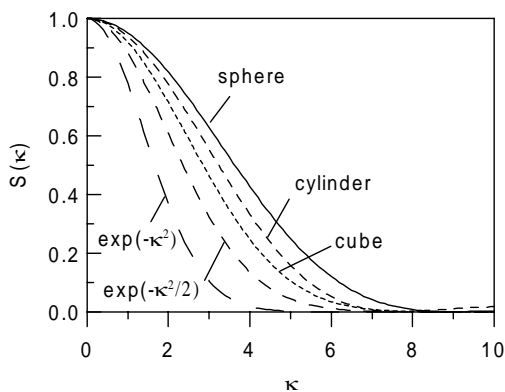


**Figure 16.** Scattering functions  $S(\kappa)$  for light scattering of differently shaped particles. The parameter  $\kappa$  is the dimensionless product of a characteristic length  $L$  ( $2R$  for spheres and cylinders; edge length for the cube) times the corresponding wavevector component.

and  $\xi = 1/4$ ). The two formulae [Eq. (33) and Eq. (38)] look similar, but their interpretations are different. It should be noted that the model CM-II does not involve arbitrary fitting parameters.

To take the phonon confinement into account, we should consider that the largest possible wavelength of the phonons in the particle is restricted by their size. For example, in a sphere the corresponding smallest wavevector is  $4.49/L$ , the wavevectors allowed are approximately  $4.49/L$ ,  $7.72/L$ , and  $10.90/L \dots 2\pi/a$ , where  $a$  is the lattice constant. For  $L \gg a$  the approximation of the sum over  $q$  values by an integral in Eq. (33) or (38) is justified.

The phonon dispersion curves often are approximated on the basis of a linear chain model by  $\omega(q) = -A + \sqrt{A^2 - B(1 - \cos(aq))}$ . The parameters  $A$  and  $B$  are chosen to fit neutron scattering data or theoretical calculations, and  $a$  is the lattice constant. Other approximation formulae are given in Ref. [109, 111, 145, 169].

**Other Confinement Models** Raman shifts of nanocrystals versus size were studied theoretically by a bond polarizability model [170]. In the first step the vibrational properties of clusters of some hundred atoms were calculated. The force constants and the atom positions were taken to be the same as those in the bulk. The force constants were considered up to the fifth order; a partial density approach [171] was adopted to calculate them. The vibrational eigenfrequencies and eigenfunctions were calculated for Si spheres and Si columns consisting of up to 657 atoms. Then the Raman spectra were calculated by a bond polarizability model [172, 173] as a sum of independent contributions from each bond. It was found that the Raman shifts due to the confinement effect could be described by  $\Delta\omega = \omega_0 - \omega(L) = A(a/L)^\gamma$ , where  $\omega(L)$  is the phonon frequency of the nanocrystal with size  $L$ ,  $\omega_0$  is the frequency of the optical phonon in bulk material at the Brillouin zone center, and  $a$  is the lattice constant. The fitted parameters were  $A = 47.41(20.92) \text{ cm}^{-1}$  and  $\gamma = 1.44(1.08)$  for spheres (cylinders), respectively.

A simple microscopic calculation using a one-dimensional linear chain model with bond polarizabilities to calculate the

Raman intensities was applied to different porous Si structures with connected or isolated Si structures [174]. Comparing the experimental spectra with those simulated by models the results were consistent with cylindrical nanocrystals of 3:1 length-to-diameter ratio and diameters of  $\sim 5 \text{ nm}$ , measured by TEM.

## 6.2. Size Determination by Raman Scattering

### 6.2.1. Si and Ge

The confinement of optical phonons has been investigated by Raman scattering in Si nanocrystals prepared by the plasma transport method [160, 175], the gas-evaporation technique [176], the reactive sputtering technique [177], molecular beam deposition [178], laser annealing of a-Si:H samples [179], plasma-enhanced chemical vapor deposition [180], and surface modification by implantation [181] and in porous Si layers [68, 162, 163, 174, 181–187]. From the observed phonon shifts the particle sizes have been estimated using the confinement model CM-I [Eq. (33)] with Gaussian weighting functions [169, 179, 180, 181, 185, 187] or with the weighting function  $W(r, L) = \sin(ar)/ar$ , by analogy with the ground state of an electron in a hard sphere [162, 163]. In some cases the particle sizes were determined independently by other methods. In Figure 17 observed frequency shifts and half-width broadenings are plotted versus the particle size determined by TEM [169] or XRD [177, 180]. For comparison calculated results were included, obtained with the phonon confinement model CM-I using

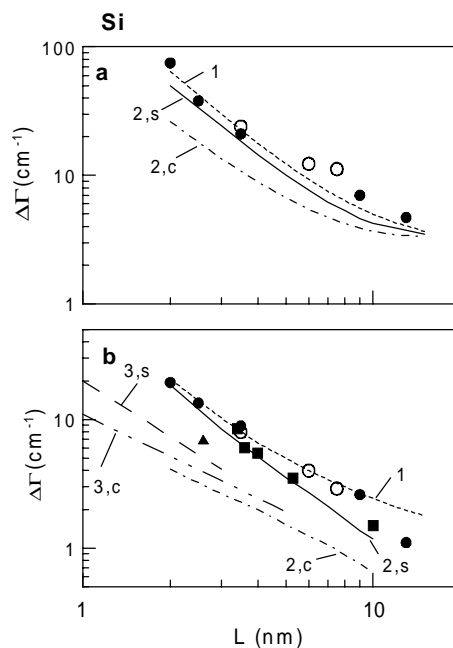


**Figure 17.** Observed frequency shifts and half-widths of the Raman bands of the optical phonon in nanocluster Si (○ [188], ▲ [177], ■ [180]) and porous Si (● [169]) depending on the particle size  $L$ . The curves are results of calculations: (1) confinement model CM-I, parameters taken from [169]; (2) confinement model CM-II; s, spheres; c, long cylinders; (3) microscopic calculations [170]; s: spheres; c: cylinders.

a Gaussian weighting function (parameters taken from Ref. [169]), with the model CM-II (spheres and cylinders), and results calculated with the bond polarizability model [170] (spheres and cylinders). For the following reasons the confinement models cannot be used without taking some care.

- (i) The particle shapes are often not well defined and the particles have a size distribution.  
A lineshape analysis of Raman spectra of porous Si by assuming that the crystallite sizes obey a log-normal distribution has been performed in [163], assuming two nanocrystalline components with Gaussian distributions in [187].
- (ii) Strain-induced changes in the phonon frequencies have to be taken into account [162, 180, 184]. It is known that in nanoporous Si the Raman peak can be shifted by strain to lower energies ( $\leq 2 \text{ cm}^{-1}$ ) [189, 190]. Stress inhomogeneities on a nanometer scale can be expected to broaden the Raman signal.
- (iii) The structure of the particles is not perfect crystalline.

In some cases spectral features were observed which consist of two or more bands [169, 176, 180, 187, 191–193]. Although a broad band at about  $475 \text{ cm}^{-1}$  can be assigned to amorphous Si, we supposed that the origin of two bands between this band and  $520 \text{ cm}^{-1}$  (bulk phonon frequency) is due to a splitting of the optical phonon (degenerate for  $q = 0$  in the Brillouin zone center) in TO and LO modes for larger  $q$  values [192] or to a combined contribution of two types of nanocrystallites [184, 187, 193, 194] or to a shell structure of the particles with modified vibrational contributions of the near-surface atoms. Xia et al. [180] observed one band for crystalline sizes  $L \leq 2.2 \text{ nm}$  and  $L \geq 5.3 \text{ nm}$  in hydrogenated nanocrystalline Si films. For samples with  $2.2 \text{ nm} \leq L \leq 5.3 \text{ nm}$  the Raman spectra were composed of two bands: one peaked at  $505\text{--}509 \text{ cm}^{-1}$  and the other at  $512\text{--}517 \text{ cm}^{-1}$ . A spherically shaped cluster with two shells was used to model the nanocrystals, and the observed Raman spectra were analyzed by combining the confinement model CM-I and strain effects. The size dependence of the relative intensity of the two bands corresponds to the ratio of the near-surface region and the crystalline core. It should be noted that a hexagonal phase of Si with Raman peak at about  $500 \text{ cm}^{-1}$  has also been found in pressure-treated Si [196] and in wear debris from dicing of silicon wafers [197].

For  $L \leq 1.5 \text{ nm}$  (corresponding to about 200 atoms) reported Raman spectra of Si clusters are to some extent similar to those of amorphous Si films. A new aspect is the observation of Raman bands around  $550 \text{ cm}^{-1}$  extending up to  $600 \text{ cm}^{-1}$ , well above the highest peaks of bulk Si in Si-rich  $\text{SiO}_2$  films with clusters [198]. The observed spectral shapes are in qualitative agreement with the density of states spectra calculated by Feldman et al. [199] for  $\text{Si}_{33}$  and  $\text{Si}_{45}$  clusters. Raman spectra of molecular clusters  $\text{Si}_4$ ,  $\text{Si}_6$ , and  $\text{Si}_7$  have been successfully measured by Honea et al. [200] by applying a technique of surface-enhanced Raman scattering. Si cluster ions were produced by laser vaporization, size-selected in a quadrupole mass spectrometer and co-deposited with an  $\text{N}_2$  matrix onto a liquid helium-cooled

substrate. By comparison of the observed very sharp vibrational lines with *ab initio* calculations they could determine the cluster structures.

In comparison with Si nanoparticles of the same size the observed frequency shifts and half-width broadenings in Ge nanoparticles are much smaller. A smaller shift is expected due to the position of the optical phonon in crystalline-Ge at the lower frequency of about  $300 \text{ cm}^{-1}$ , the main reason could be the smaller dispersion of the optical phonons, which was observed by neutron scattering for Ge [201] compared with measurements for Si [202–204]. Kanata et al. [205] investigated gas-evaporated Ge particles with sizes of 10–60 nm, as determined by Raman measurements and by XRD measurements. Good agreement was obtained by applying the CM-I model ( $\xi = 25/8$ ) and assuming spheres with a single-crystalline core and a coating amorphous shell. The confinement effect in Ge dots in the size range  $L = 2.6\text{--}13 \text{ nm}$  has been studied systematically by Bottani et al. [206] with Raman scattering, TEM, and absorption measurements. The samples were grown by an evaporation-condensation self-organization technique that allows obtaining nearly spherically shaped nanoparticles with a narrow size dispersion [207]. As the size decreases an inhomogeneous broadening, a redshift and a softening of the optical phonon peak were observed. The measurements were found to be in agreement with confinement model calculations (CM-I), taking into account the size distribution as measured by TEM. Sasaki and Horie [208] investigated gas-evaporated Ge nanocrystals in the size range 2.6–13 nm with resonant Raman scattering. They found that the size as deduced from the frequency shift and half-width broadening is about half of that obtained from the lowest electronic excitation energy measured in the resonant Raman scattering. Additional anharmonicity is assumed to be associated with a decay process including surface vibrational states. They used a confinement model with phonon waves confined to a cube and vanishing amplitudes at the surface.

Intensive photoluminescence around 2 eV has been observed by formation of Ge nanocrystals in  $\text{SiO}_2$  [209–211]. The phonon confinement measured by Raman scattering was used to show that the crystalline phase formed consists of Ge nanocrystals. If Si substrates are used, the analysis of the experimental results has to be done with extreme care, because an observed peak at about  $300 \text{ cm}^{-1}$  could originate from the two-phonon peak of the Si substrate and not from Ge ([211–213]; see also Fig. 15). To tackle this problem resonant Raman scattering with excitation laser energy at 2.4 eV and polarized Raman scattering can be used [214].

### 6.2.2. II–VI Semiconductors

In polar semiconductors the confinement effect of the optical phonons in particles of a few nanometers in size can be more difficult to observe due to the simultaneous appearance of surface modes between the LO and the TO phonons [145].

Small frequency shifts (up to about  $3 \text{ cm}^{-1}$ ) of the LO phonon of small quantum dots of II–VI compounds in comparison with the bulk value were observed for decreasing radii (down to  $\approx 2 \text{ nm}$ ) in glass matrices. Redshifts for CdSe dots [39, 54, 110, 146] blueshifts [61] as well as redshifts [52, 145] for  $\text{Cd}_x\text{Se}_{1-x}$  dots, and size-independent LO



phonon frequency for CdS dots [32] are reported. Obviously the shifts depend also on the glass matrix used [215]. To explain the observed phonon shifts and broadenings some authors, in addition to the confinement models, introduced lattice contraction caused by the mismatch of the thermal expansion between the quantum dots and their host material and surface tension increasing with decreasing dot size [61, 215]. Shiang et al. [32] estimated with a confinement model the observed asymmetric band shape, the increase in bandwidth, and the frequency downshift with decreasing size. They assumed that surface pressure effects nearly compensate for the confinement effect in such a way that no size dependence of the LO frequency results. For small CdSe nanoparticles embedded in glass, an asymmetrical broadening of the LO phonon band toward the low-frequency side for nanocrystals with  $R = 2.1$  and 1.8 nm and a decrease to lower frequencies was observed [111]. This was attributed to confinement of the LO phonons. The dispersion of the observed LO phonon frequencies was compared with *ab initio* calculations [111].

### 6.2.3. Other Compounds

Phonon confinement effects were also studied on self-assembled GaN quantum dots of 2–3 nm height [216], crystalline As precipitates in GaAs [217], in CeO<sub>2-y</sub> nanoparticles [218], diamond nanoparticles [219, 220] and in BN micro- and nanoparticles [165]. The latter case is interesting because an upward shift of the high frequency mode E<sub>2g</sub> was observed with decreasing particle size similar to that for small particles of graphite. Calculations were performed with the confinement model CM-II using phonon dispersion curves reported in [221].

Redshift or blueshift in dependence on the coating was observed in coated TiO<sub>2</sub> nanoparticles [222].

## 7. NEW INSTRUMENTATION AND METHODS

**High-Throughput Devices** Many applications of Raman spectroscopy benefit from developments to measure the usually weak signals more efficiently. For recording scattered light, charge-coupled devices (CCD) have become very widespread during the last 10 years and are now used in the most multichannel Raman spectrometers. They have a very high quantum efficiency over a broad spectral range and a very low dark count level when cooled. The separation of the Raman signals from the much stronger elastically scattered light has been achieved in the past by use of double or triple monochromators. Another technical solution, now used more and more, are Raman spectrometers consisting of a holographic notch filter for stray light suppression and a single grating spectrograph. Such spectrometers have up to 10 times larger optical throughput, are more compact with fewer optical components, and are less expensive than triple monochromators. The notch filters suppress the incident laser light by a factor of more than 10<sup>6</sup> while the rest of the spectrum is transmitted with a high efficiency of about 80%. The small edgewidth of less than 4 nm allows measurements of frequencies as low as 50 cm<sup>-1</sup>. The application of this new generation of Raman spectrometers is

attractive for measurements on nanoparticles with low signals, too. However, for low-frequency Raman measurements on acoustic modes closer to the laser line, better stray light rejection is required. This can be realized by application of a triple monochromator and a photomultiplier as detector or by using a double monochromator in the configuration as a cutoff filter followed by a single spectrograph and CCD as detector.

**Surface-Enhanced Raman Scattering** An enhancement of Raman scattering intensity was observed for molecules deposited on silver surfaces. A large increase in the local electric field intensity occurs when the wavevector of the surface plasmon mode of the silver film is matched to that of the incident laser [223–226]. Vibrational Raman spectra of small Si clusters, size-selected in a quadrupole mass spectrometer and co-deposited with an N<sub>2</sub> matrix onto a liquid helium-cooled silver film were measured with a signal enhancement of about 50 at the surface plasmon-polariton resonance [200].

The Raman scattering intensity of molecules can be enhanced in SERS processes by 5 to 6 orders of magnitude when they are adsorbed on a roughened silver surface.

Although all details of the origin of the signal enhancement are not yet understood, two main mechanisms are usually assumed to be responsible. The so-called electromagnetic effect is considered by most authors to be the major contributor to SERS. The electromagnetic effect was explained in terms of the excitation of localized surface plasmons in silver nanostructures (and nanostructures of a few other metals), which enhances the electromagnetic fields near the nanoparticle's surface. Resonance of the exciting/scattered fields with the surface plasmons is assumed. The second mechanism discussed, the so-called chemical enhancement effect, is attributed to resonant Raman processes involving charge transfer between the adsorbed molecule and the metal surface. Although the average enhancement factor has been normally measured to lie in the 10<sup>5</sup>–10<sup>6</sup> range, it has been shown recently that the enhancement is laterally highly inhomogeneous and concentrated at hot spots at the surface of the metallic nanostructures where the SERS enhancement can be as large as 10<sup>10</sup> [227, 228]. The lateral resolution is thus not determined by the diffraction limit, but by the spatial confinement of the local fields. Over the last 5 years it was shown that SERS can be observed even from single molecules [229–233]. The fact that enhancements large enough to allow single-molecule spectra to be detected have only been observed for some adsorbates (generally dye molecules) suggests that resonance processes are involved.

The target species are in local electromagnetic fields of high intensity and, in particular, also very strong field gradients. These effects could explain some observed results of SERS measurements on single carbon nanotubes, not seen with conventional Raman scattering, for example, exchange in scattering intensity between phonon modes and changes of the depolarization ratios [234, 235].

**Near-Field Optical Microscopy** In conventional Raman microscopy a pixel size no smaller than 1 μm is common. Resolutions of 100 nm or even substantially smaller can be realized by combining Raman scattering with the near-field

optical microscopy [236]. A laser beam is coupled into an optical fiber that is sharpened to a very small tip with conical shape at the end. The dimensions of the tip are much smaller than the wavelength of the exciting laser light. Initially, the major obstacles for obtaining Raman spectra were arising from the weak light intensity given by the excitation and the detection through small apertures and by the Raman scattering process. The principle of the method was demonstrated, for example, by the measurement of the phonon spectra of diamond with a fiber probe of 100 nm diameter [237]. In measurements of Raman spectra from liquid  $\text{CCl}_4$  the sampling volume of 70 nm diameter and 10 nm depth contained only about 250,000 molecules [238]. For applications with weaker scatterers a considerable improvement of the signals obtained is necessary. One way to enhance the Raman cross section is resonant excitation, which was already used in some cases. Another technique is the combination of near-field optical microscopy with SERS, with which strong enhancement of the Raman signals by many orders of magnitude was obtained [239, 240].

**Tip-Enhanced Near-Field Raman Spectroscopy** Tip-enhanced near-field Raman scattering is one of the forthcoming characterization techniques, which can be effectively used to understand the vibronic and electronic properties of a material at nanoscale. This technique can also be used even for a single molecule detection, because it allows for the detection of molecular vibration spectra with a resolution smaller than the diffraction limit of the light. It has recently been demonstrated [241] that the near-field detection of Raman scattering using a metallized tip achieves high spatial resolution beyond the known limits of surface-enhanced Raman scattering and reveals new weak vibrational modes, which cannot be seen in usual far-field measurements. It has been demonstrated that because of the local field enhancement, the Raman scattering is enhanced by a factor of 40 and the spectra could be measured at a spatial resolution of several tens of nanometers. By using this technique, single nanoparticle detection could be possible. Also, single molecule detection could be much more precise and accurate compared to SERS, where the spatial resolution is diffraction limited. For near-field detection, it is possible to observe the dynamics of a molecule with spatial resolution on a molecular scale. In these experiments, a metallic tip with a size of a few tens of nanometers is approached to the sample where the source light is tightly focused. The localized surface plasmon-polariton is excited at the tip apex. The area of the field localized at the tip corresponds to the diameter of the tip, which works as the near-field light source and attends the super-resolving capability. Molecules soaked in this localized field around the tip scatter inelastically through Raman scattering. The Raman spectra recorded contain useful information about molecular vibrations at the nanoscale level, which cannot be detected through other techniques. In this way, it is possible to understand the special behavior of molecules, excitons, and electron-phonon interaction inside a nanoparticle, which can reveal new understanding about the confinement and the effect of confinement on the electron-phonon system.

## GLOSSARY

**Effective medium theory** The properties (e.g., the dielectric function) of a composite are described by averaging over local inhomogeneities introducing suitable effective media models.

**Quantum confinement** In nanometer-sized structures (quantum wells, wires, and dots) the allowed energy states and the density of states are modified in comparison with the corresponding bulk material. Onset occurs when one or more dimensions of a structure become comparable to the characteristic length scale of an elementary excitation.

**Raman scattering process** Inelastic light scattering. The scattered photon has lost (Stokes process) or gained (anti-Stokes process) the energy of an elementary excitation (e.g., a phonon) compared with the energy of the incident photon.

**Rayleigh scattering process** Elastic light scattering. The scattered and the incident photon have the same energy.

**Small angle X-ray scattering (SAXS), small angle neutron scattering (SANS)** Scattering at small angles in the vicinity of the primary beam. The scattering features at these angles correspond to structures ranging from nanometers to submicrometers.

**X-ray diffraction (XRD)** Technique for characterizing crystalline materials. It provides information on structures, phases, average grain size, crystallinity, strain, crystal defects.

## ACKNOWLEDGMENTS

The authors acknowledge fruitful cooperation with Professor I. M. Tiginyanu (Technical University of Moldova), Dr. A. Sarua (University of Bristol), and Dr. W. Cordts (Technical University Bergakademie Freiberg) who contributed to many illustrative results presented in this chapter and express their gratitude to them for stimulating discussions.

## REFERENCES

1. M. Cardona, in "Light Scattering in Solids II" (M. Cardona and G. Güntherodt, Eds.), p. 19. Springer-Verlag, Berlin/Heidelberg/New York, 1982.
2. E. Duval, A. Boukenter, and B. Champagnon, *Phys. Rev. Lett.* 56, 2052 (1986).
3. S. Hayashi and H. Kanamori, *Phys. Rev. B* 26, 7079 (1982).
4. L. T. Canham, *Appl. Phys. Lett.* 57, 1046 (1990).
5. A. G. Cullis, L. T. Canham, and P. D. Calcott, *J. Appl. Phys.* 82, 909 (1997).
6. H. Lamb, *Proc. London Math.* 13, 189 (1882).
7. G. Mie, *Ann. Phys. (Leipzig)* 25, 377 (1908).
8. Jusserand and M. Cardona, in "Light Scattering in Solids V" (M. Cardona and G. Güntherodt, Eds.). Springer-Verlag, Berlin, 1982.
9. T. Ruf, "Phonon Raman Scattering in Semiconductors, Quantum Wells and Superlattices," Springer Tracts in Modern Physics, Vol. 142. Springer-Verlag, Berlin, 1998.
10. L. E. Brus, *J. Chem. Phys.* 80, 4403 (1984).
11. J. P. Zheng, L. Shi, F. S. Choa, P. L. Liu, and H. S. Kwok, *Appl. Phys. Lett.* 53, 643 (1988).
12. M. Kull and J. L. Coutaz, *J. Opt. Soc. Am.* B7, 1463 (1990).

13. P. Verma, G. Irmer, and J. Monecke, *J. Phys.: Condens. Matter* 12, 1097 (2000).
14. Al. L. Efros and A. L. Efros, *Fiz. Tekh. Poluprovodn.* 16, 1209 (1982); *Sov. Phys. Semicond.* 16, 772 (1982).
15. A. L. Efros and A. V. Rodina, *Solid State Commun.* 72, 645 (1989).
16. L. E. Brus, *J. Chem. Phys.* 79, 5566 (1983).
17. L. E. Brus, *J. Chem. Phys.* 90, 2555 (1986).
18. L.-W. Wang and A. Zunger, *Phys. Rev. B* 53, 9579 (1996).
19. G. T. Einevoll, *Phys. Rev. B* 45, 3410 (1992).
20. L. M. Ramaniah and S. V. Nair, *Phys. Rev. B* 47, 7132 (1993).
21. N. Hill and B. Whaley, *Phys. Rev. Lett.* 75, 1130 (1995).
22. U. Woggon, "Optical Properties of Semiconductor Quantum Dots," Springer Tracts in Modern Physics, Vol. 136. Springer-Verlag, Berlin, 1997.
23. N. F. Borrelli, D. Hall, H. Holland, and D. Smith, *J. Appl. Phys.* 61, 5399 (1987).
24. S. Schmitt-Rink, D. A. B. Miller, and D. S. Chemla, *Phys. Rev. B* 35, 8113 (1987).
25. M. C. Klein, F. Hache, D. Ricard, and C. Flytzanis, *Phys. Rev. B* 42, 11123 (1990).
26. A. L. Efros, A. I. Ekimov, F. Kozlowski, V. Petrova-Koch, H. Schmidbaur, and S. Shumilov, *Solid State Commun.* 78, 853 (1991).
27. J. C. Marini, B. Stebe, and E. Kartheuser, *Phys. Rev. B* 50, 14302 (1994).
28. S. Nomura and T. Kobayashi, *Phys. Rev. B* 45, 1305 (1992).
29. T. Itho, M. Nishijima, A. I. Ekimov, C. Gourdon, Al. L. Efros, and M. Rosen, *Phys. Rev. Lett.* 74, 1645 (1995).
30. L. Banyai, Y. Z. Hu, M. Lindberg, and S. W. Koch, *Phys. Rev. B* 38, 8142 (1988).
31. A. P. Alivisatos, T. D. Harris, P. T. Carrol, M. L. Steigerwald, and L. E. Brus, *J. Chem. Phys.* 90, 3463 (1990).
32. J. J. Shiang, S. H. Risbud, and A. P. Alivisatos, *J. Chem. Phys.* 98, 8432 (1993).
33. G. Scamarcio, V. Spagnolo, G. Ventruti, and M. Luga, *Phys. Rev. B* 53, R10489 (1996).
34. R. Rodríguez-Suárez, E. Menéndez-Proupin, C. Trallero-Giner, and M. Cardona, *Phys. Rev. B* 62, 11006 (2000).
35. T. Takagahara, *J. Lumin.* 70, 129 (1996).
36. S. V. Goupalov, A. I. Ekimov, O. G. Lublinskaya, and I. A. Merkulov, in "Optical Properties of Semiconductor Nanostructures" (M. L. Sadowski, M. Potemski, and M. Grynberg, Eds.), p. 421. Kluwer Academic, Dordrecht, 2000.
37. A. Tamura, K. Higata, and T. Ichinokawa, *J. Phys. C* 15, 4975 (1982).
38. E. Duval, *Phys. Rev. B* 46, 5795 (1992).
39. Tanaka, S. Onari, and T. Arai, *Phys. Rev. B* 45, 6587 (1992).
40. N. N. Ovsyuk and V. N. Novikov, *Phys. Rev. B* 53, 3113 (1996).
41. P. Verma, W. Cordts, G. Irmer, and J. Monecke, *Phys. Rev. B* 60, 5778 (1999).
42. A. Pinczuk and E. Burstein, in "Light Scattering in Solids I" (M. Cardona, Ed.), p. 23. Springer-Verlag, Berlin, 1983.
43. V. K. Malinovsky and A. P. Sokolov, *Solid State Commun.* 57, 757 (1986).
44. A. P. Sokolov, A. Kisliuk, D. Quitmann, and E. Duval, *Phys. Rev. B* 48, 7692 (1993).
45. N. Herron, in "Handbook of Nanophase Materials" (A. N. Goldstein, Ed.), p. 221. Marcel Dekker, New York, 1997.
46. P. V. Kamat, P. V. Kamat, K. Murakoshi, Y. Wada, and S. Yanagida, in "Nanostructured Materials and Nanotechnology" (H. S. Nalwa, Ed.), p. 130. Academic Press, San Diego, 2000.
47. B. Champagnon, B. Andrianasolo, A. Ramos, M. Gandais, M. Allais, and J.-P. Benoit, *J. Appl. Phys.* 73, 2775 (1993).
48. A. V. Baranov, Y. S. Bobovich, and V. I. Petrov, *Solid State Commun.* 83, 957 (1992).
49. A. V. Baranov, Y. S. Bobovich, and V. I. Petrov, *J. Raman Spectrosc.* 24, 767 (1993).
50. Y. Sasaki, Y. Nishina, M. Sato, and K. Okamura, *Phys. Rev. B* 40, 1762 (1989).
51. A. Roy and A. K. Sood, *Solid State Commun.* 97, 97 (1996).
52. M. Rajalakshmi, T. Sakuntala, and A. K. Arora, *J. Phys.: Condens. Matter* 9, 9745 (1997).
53. L. Saviot, B. Champagnon, E. Duval, and A. I. Ekimov, *Phys. Rev. B* 57, 341 (1998).
54. L. Saviot, B. Champagnon, E. Duval, and A. I. Ekimov, *J. Cryst. Growth* 184/185, 370 (1998).
55. L. Saviot, B. Champagnon, E. Duval, I. A. Kudriavtsev, and A. I. Ekimov, *J. Non-Cryst. Solids* 197, 238 (1996).
56. A. Tanaka, S. Onari, and T. Arai, *Phys. Rev. B* 47, 1237 (1993), erratum, *Phys. Rev. B* 56, 9977 (1997).
57. J. Warnock and D. D. Awschalom, *Phys. Rev. B* 32, 5529 (1985).
58. J. Warnock and D. D. Awschalom, *Appl. Phys. Lett.* 48, 425 (1986).
59. B. G. Potter, Jr. and J. H. Simmons, *Phys. Rev. B* 37, 10838 (1988).
60. L.-C. Liu and S. H. Risbud, *J. Appl. Phys.* 68, 28 (1990).
61. G. Scamarcio, M. Lugará, and D. Manno, *Phys. Rev. B* 45, 13792 (1992).
62. H. Yükselici, P. D. Persans, and T. M. Hayes, *Phys. Rev. B* 52, 11763 (1995).
63. T. Bischof, M. Ivanda, G. Lermann, A. Materny, and W. Kiefer, *J. Raman Spectrosc.* 27, 297 (1996).
64. U. Woggon, M. Müller, U. Lembke, I. Rückmann, and J. Cesnulevicius, *Superlattices Microstruct.* 9, 245 (1991).
65. F. Liu, L. Liao, G. Wang, G. Cheng, and X. Bao, *Phys. Rev. Lett.* 76, 604 (1996).
66. A. I. Ekimov, Al. L. Efros, and A. A. Onushenko, *Solid State Commun.* 56, 921 (1985).
67. U. Woggon, F. Gindele, O. Wind, and C. Klingshirn, *Phys. Rev. B* 54, 1506 (1996).
68. I. Gregora, B. Champagnon, and A. Halimaoui, *J. Appl. Phys.* 75, 3034 (1994).
69. G. H. Wang, H. Q. Zhang, M. Han, J. X. Ma, and Q. Wang, *Phys. Lett. A* 189, 218 (1994).
70. F. Q. Liu, M. Han, J. J. Zhao, X. S. Chen, Q. Wang, and G. H. Wang, *Appl. Phys. Lett.* 66, 523 (1995).
71. M. Fujii, Y. Kanzawa, S. Hayashi, and K. Yamamoto, *Phys. Rev. B* 54, R8373 (1996).
72. M. Fujii, S. Hayashi, and K. Yamamoto, *Phys. Rev. B* 44, 6243 (1991).
73. M. Fujii, S. Hayashi, and K. Yamamoto, *Jpn. J. Appl. Phys.* 30, 687 (1991).
74. N. N. Ovsyuk, L. M. Krivoputskaya, and A. P. Shebanin, *JETP Lett. (Engl. Transl.)* 48, 678 (1988).
75. J. I. Gersten, D. A. Weitz, T. J. Gramila, and A. Z. Genack, *Phys. Rev. B* 22, 4562 (1980).
76. G. Mariotto, M. Montagna, G. Viliani, E. Duval, S. Lefrant, E. Rzepka, and C. Mai, *Europhys. Lett.* 6, 239 (1988).
77. J. Lermé, B. Palpant, B. Prével, M. Pellarin, M. Treilleux, J. L. Vialle, A. Perez, and M. Broyer, *Phys. Rev. Lett.* 80, 5105 (1998).
78. B. Palpant, H. Portales, L. Saviot, J. Lermé, B. Prével, M. Pellarin, E. Duval, A. Perez, and M. Broyer, *Phys. Rev. B* 60, 17107 (1999).
79. M. Fujii, T. Nagareda, S. Hayashi, and K. Yamamoto, *Phys. Rev. B* 44, 6243 (1991).
80. A. Courty, I. Lisiecki, and M. P. Pileni, *J. Chem. Phys.* 116, 8074 (2002).
81. R. S. Cataliotti, G. Compagnini, C. Crisafulli, S. Minico, B. Pignataro, P. Sassi, and S. Scire, *Surf. Sci.* 494, 75 (2001).
82. R. S. Cataliotti, G. Compagnini, A. Morresi, M. Ombelli, and P. Sassi, *Phys. Chem. Chem. Phys.* 4, 2774 (2002).
83. A. Li Bassi, C. E. Bottani, A. Stella, P. Tognini, P. Cheyssac, and R. Kofman, *Mater. Sci. Eng. C15*, 21 (2001).
84. C. E. Bottani, A. Li Bassi, A. Stella, P. Cheyssac, and R. Kofman, *Europhys. Lett.* 56, 386 (2001).

85. A. Dieguez, A. Romano-Rodriguez, J. Ramon Morante, N. Barsan, U. Weimar, and W. Gopel, *Appl. Phys. Lett.* 71, 1957 (1997).
86. D. Duval, H. Portales, L. Saviot, M. Fujii, K. Sumitomo, and S. Hayashi, *Phys. Rev. B* 63, 075405 (2001).
87. V. Sukumar and R. H. Doremus, *Phys. Status Solidi B* 179, 307 (1993).
88. H. P. Klug and L. E. Alexander, "X-Ray Diffraction Procedures for Polycrystalline and Amorphous Materials," 2nd ed. Wiley, New York, 1974.
89. H. Lipson and H. Steeple, "Interpretation of X-Ray Powder Diffraction Patterns." St. Martin's Press, New York, 1970.
90. B. E. Warren, "X-Ray Diffraction." Addison-Wesley, Reading, MA, 1969.
91. P. D. Persans, A. Tu, Y.-J. Wu, and M. Lewis, *J. Opt. Soc. Am. B* 6, 818 (1988).
92. C. B. Murray, D. J. Norris, and M. G. Bawendi, *J. Am. Chem. Soc.* 115, 8706 (1993).
93. A. P. Alivisatos, *Mater. Res. Bull.* 8, 23 (1995).
94. G. Goerigk, H.-G. Haubold, C. Klingshirn, and A. Uhrig, *J. Appl. Crystallogr.* 27, 907 (1994).
95. G. Irmer, J. Monecke, P. Verma, G. Goerigk, and M. Herms, *J. Appl. Phys.* 88, 1873 (2000).
96. M. Montagna and R. Dusi, *Phys. Rev. B* 52, 10080 (1995).
97. J. Zi, K. Zhang, and X. Xie, *Phys. Rev. B* 58, 6712 (1998).
98. J. Zi, K. Zhang, and X. Xie, *Prog. Surf. Sci.* 54, 69 (1997).
99. R. Englman and R. Ruppim, *J. Phys. C* 1, 614 (1968).
100. R. Ruppim and R. Englman, in "Light Scattering Spectra of Solids" (G. B. Wright, Ed.), p. 157. Springer-Verlag, Berlin, 1969.
101. R. Fuchs and K. L. Kliewer, *J. Opt. Soc. Am.* 58, 319 (1968).
102. R. Ruppim and R. Englman, *Rep. Prog. Phys.* 33, 149 (1970).
103. R. Ruppim, *J. Phys. C* 8, 1969 (1975).
104. H. Fröhlich, "Theory of Dielectrics." Clarendon Press, Oxford, 1949.
105. C. F. Bohren and D. R. Huffman, "Absorption and Scattering of Light by Small Particles." Wiley, New York, 1983.
106. R. Englman and R. Ruppim, *J. Phys. C* 1, 1515 (1968).
107. R. Fuchs, *Phys. Rev. B* 11, 1732 (1975).
108. M. Kerker, "The Scattering of Light and Other Electromagnetic Radiation." Academic Press, San Diego, 1969.
109. E. Roca, C. Trallero-Giner, and M. Cardona, *Phys. Rev. B* 49, 13704 (1994).
110. M. P. Chamberlain, C. Trallero-Giner, and M. Cardona, *Phys. Rev. B* 51, 1680 (1995).
111. C. Trallero-Giner, A. Debernardi, M. Cardona, E. Menendez-Proupin, and A. I. Ekimov, *Phys. Rev. B* 57, 4664 (1998).
112. O. Wiener, *Abh. Math.-Phys. Kl. Königl. Sächs. Ges.* 32, 509 (1912).
113. J. C. Maxwell-Garnett, *Phil. Trans. R. Soc. A* 203, 385 (1904).
114. Z. Hashin and S. Shtrikman, *J. Appl. Phys.* 33, 3125 (1962).
115. D. A. G. Bruggeman, *Ann. Phys. (Leipzig)* 24, 636 (1935).
116. J. Monecke, *Phys. Status Solidi B* 154, 805 (1989).
117. J. Monecke, *J. Phys.: Condens. Matter* 6, 907 (1994).
118. D. J. Bergman, *Phys. Rep.* 43, 377 (1978).
119. J. B. Keller, *J. Math. Phys.* 5, 548 (1964).
120. S. Hayashi and R. Ruppim, *J. Phys. C* 18, 2583 (1985).
121. M. Watt, C. M. Sotomayor Torres, H. E. G. Arnot, and S. P. Beaumont, *Semicond. Sci. Technol.* 5, 285 (1990).
122. P. D. Wang, C. Cheng, C. M. Sotomayor Torres, and D. N. Batchelder, *J. Appl. Phys.* 74, 5907 (1993).
123. S. W. da Silva, J. C. Galazerani, D. I. Lubyshvand, and P. Basmaji, *J. Phys.: Condens. Matter* 10, 9687 (1998).
124. T. Takizawa, S. Arai, and M. Nakahara, *Jpn. J. Appl. Phys.* 33, 643 (1994).
125. A. Anedda, A. Serpi, V. A. Karavanskii, I. M. Tiginyanu, and V. M. Ichizli, *Appl. Phys. Lett.* 67, 3316 (1995).
126. P. Schmuki, J. Fraser, C. M. Vitus, M. S. Graham, and H. S. Isaacs, *J. Electrochem. Soc.* 143, 3316 (1996).
127. B. H. Erne, D. Vanmaekelbergh, and J. J. Kelly, *J. Electrochem. Soc.* 143, 1137 (1996).
128. I. M. Tiginyanu, G. Irmer, J. Monecke, and H. L. Hartnagel, *Phys. Rev. B* 55, 6739 (1997).
129. I. M. Tiginyanu, G. Irmer, J. Monecke, A. Vogt, and H. L. Hartnagel, *Semicond. Sci. Technol.* 12, 491 (1997).
130. D. J. Lockwood, P. Schmuki, H. J. Labbe, and J. Fraser, *Phys. E* 4, 102 (1999).
131. S. Bell, *Opto Laser Europe* 60, 31 (1999).
132. G. Oskam, A. Natarajan, P. C. Searson, and F. M. Ross, *Appl. Surf. Sci.* 119, 160 (1997).
133. A. Sarua, J. Monecke, G. Irmer, I. M. Tiginyanu, G. Gärtner, and H. L. Hartnagel, *J. Phys.: Condens. Matter* 13, 6687 (2001).
134. A. Sarua, G. Gärtner, G. Irmer, J. Monecke, I. M. Tiginyanu, and H. L. Hartnagel, *Phys. Status Solidi A* 182, 207 (2000).
135. I. M. Tiginyanu, V. V. Ursaki, V. A. Karavanskii, V. N. Sokolov, Y. S. Raptis, and E. Anastassakis, *Solid State Commun.* 97, 675 (1996).
136. J. Miao, I. M. Tiginyanu, H. L. Hartnagel, G. Irmer, J. Monecke, and B. L. Weiss, *Appl. Phys. Lett.* 70, 847 (1997).
137. A. Sarua, I. M. Tiginyanu, V. V. Ursaki, G. Irmer, J. Monecke, and H. L. Hartnagel, *Solid State Commun.* 112, 581 (1999).
138. I. M. Tiginyanu, G. Irmer, J. Monecke, H. L. Hartnagel, A. Vogt, C. Schwab, and I.-I. Grob, *Mater. Res. Soc. Symp. Proc.* 536, 99 (1999).
139. V. V. Ursaki, I. M. Tiginyanu, P. C. Ricci, A. Anedda, E. V. Foca, and N. N. Syrbu, *J. Phys.: Condens. Matter* 13, 4579 (2001).
140. I. M. Tiginyanu, A. Sarua, G. Irmer, J. Monecke, S. M. Hubbard, D. Pavlidis, and V. Valiaev, *Phys. Rev. B* 64, 233317 (2001).
141. J. F. Scott and T. C. Damen, *Opt. Commun.* 5, 410 (1972).
142. J. Pan, X. Xu, S. Dingand, and J. Pen, *J. Lumin.* 45, 45 (1990).
143. A. P. Alivisatos, A. L. Harris, N. J. Levinos, M. L. Steigerwald, and L. E. Bruns, *J. Chem. Phys.* 89, 4001 (1988).
144. F. Zhou, Y. Sun, and J. Pan, *J. Lumin.* 40/41, 739 (1988).
145. A. Roy and A. K. Sood, *Phys. Rev. B* 53, 12127 (1996).
146. F. Comas, C. Trallero-Giner, N. Studart, and G. E. Marques, *Phys. Rev. B* 65, 073303 (2002).
147. J. Xu, H. Mao, Y. Sun, and Y. Du, *J. Vac. Sci. Technol.* 15, 1465 (1997).
148. A. Tu and P. D. Persans, *Appl. Phys. Lett.* 58, 1506 (1991).
149. A. M. Danishevskii, V. B. Shuman, A. Yu. Rogachev, and P. A. Ivanov, *Semiconductors* 29, 1106 (1995) [Fiz. Tekh. Poluprovodn. 29, 2122 (1995)].
150. M. F. MacMillan, R. P. Devaty, W. J. Choyke, D. R. Goldstein, J. E. Spanier, and A. D. Kurtz, *J. Appl. Phys.* 80, 2412 (1996).
151. J. F. DiGregorio and T. E. Furtak, *Solid State Commun.* 89, 163 (1994).
152. P. A. Knipp and T. L. Reinecke, *Phys. Rev. B* 46, 10310 (1992).
153. J. Monecke, *Lithuanian J. Phys.* 42, 169 (2002).
154. J. Li, P. Eveno, and A. M. Huntz, *Werkstoffe Korrosion* 41, 716 (1990).
155. Z. Zheng, R. E. Tressler, and K. E. Spear, *J. Electrochem. Soc.* 137, 854 (1990).
156. G. Winterling, *Phys. Rev. B* 12, 2432 (1975).
157. S.-L. Zhang, B.-F. Zhu, F. Huang, Y. Yan, Er-yi Shang, S. Fan, and W. Han, *Solid State Commun.* 111, 647 (1999).
158. K. Yamamoto, C.-D. Tran, H. Shimizu, and K. Abe, *Jpn. J. Phys.* 42, 587 (1977).
159. Yu. D. Glinka and M. Jaroniec, *J. Appl. Phys.* 82, 3499 (1997).
160. H. Richter, Z. P. Wang, and L. Ley, *Solid State Commun.* 39, 625 (1981).
161. I. H. Campbell and P. M. Fauchet, *Solid State Commun.* 58, 739 (1986).
162. H. Münder, C. Andrzejak, M. G. Berger, U. Klemradt, H. Lüth, R. Herino, and M. Ligeon, *Thin Solid Films* 221, 27 (1992).

163. N. Brunetto and G. Amato, *Thin Solid Films* 297, 122 (1997).
164. A. Guinier and G. Fournet, "Small-Angle Scattering of X-Rays." Wiley, New York, 1955.
165. R. J. Nemanich, S. A. Solin, and R. M. Martin, *Phys. Rev. B* 23, 6348 (1981).
166. G. Abstreiter, R. Trommer, M. Cardona, and A. Pinczuk, *Solid State Commun.* 30, 703 (1979).
167. J. R. Sandercock, *Phys. Rev. Lett.* 28, 237 (1972).
168. M. V. Wickerhauser, "Adapted Wavelet Analysis from Theory to Software" (A. K. Peters, Ed.), p. 25. Wellesey, MA, 1994.
169. Y. Kanemitsu, H. Uto, Y. Masumoto, T. Matsumoto, T. Futagi, and H. Mimura, *Phys. Rev. B* 48, 2827 (1993).
170. J. Zi, H. Büscher, C. Falter, W. Ludwig, K. Zhang, and X. Xie, *Appl. Phys. Lett.* 69, 200 (1996).
171. C. Falter, *Phys. Rep.* 164, Nos. 1 and 2 (1988).
172. A. A. Maradudin and E. Burstein, *Phys. Rev.* 164, 1081 (1967).
173. S. Go, H. Bilz, and M. Cardona, *Phys. Rev. Lett.* 34, 580 (1975).
174. E. Ribeiro, F. Cerdeira, and O. Teschke, *Solid State Commun.* 101, 327 (1997).
175. S. Veprek, Z. Iqbal, H. R. Oswald, and A. P. Webb, *J. Phys. C* 14, 295 (1981).
176. T. Okada, T. Iwaki, K. Yamamoto, H. Kasahara, and K. Abe, *Solid State Commun.* 49, 809 (1984).
177. S. Furukawa and T. Miyasato, *Phys. Rev. B* 38, 5726 (1988).
178. J. Gonzalez-Hernandez, G. H. Azarbayejani, R. Tsu, and F. H. Pollak, *Appl. Phys. Lett.* 47, 1350 (1985).
179. P. Mishra and K. P. Jain, *Phys. Rev. B* 62, 14790 (2000).
180. H. Xia, Y. L. He, L. C. Wang, W. Zhang, X. N. Liu, X. K. Zhang, D. Feng, and H. E. Jackson, *J. Appl. Phys.* 78, 6705 (1995).
181. X. Huang, F. Ninio, L. J. Brown, and S. Praver, *J. Appl. Phys.* 77, 5910 (1995).
182. S. R. Goodes, T. E. Jenkins, M. I. J. Beale, J. D. Benjamin, and C. Pickering, *Semicond. Sci. Technol.* 3, 483 (1988).
183. J. C. Tsang, M. A. Tischler, and R. T. Collins, *Appl. Phys. Lett.* 60, 2279 (1992).
184. F. Kozlowski and W. Lang, *J. Appl. Phys.* 72, 5401 (1992).
185. X. Sui, P. P. Leong, I. P. Herman, G. S. Higashi, and H. Temkin, *Appl. Phys. Lett.* 60, 2086 (1992).
186. H. D. Fuchs, M. Stutzmann, M. S. Brandt, M. Rosenbauer, J. Weber, A. Breitschwerdt, P. Deákand, and M. Cardona, *Phys. Rev. B* 48, 8172 (1993).
187. M. N. Islam and S. Kumar, *Appl. Phys. Lett.* 78, 715 (2001).
188. Z. Iqbal and S. Veprek, *J. Phys. C* 15, 377 (1982).
189. Th. Englert, G. Abstreiter, and J. Pontcharra, *Solid-State Electron.* 23, 31 (1980).
190. Landoldt-Börnstein, New Series III, Vol. 17a. Springer-Verlag, Berlin, 1982.
191. D. J. Olego and H. Baumgart, *J. Appl. Phys.* 63, 2669 (1988).
192. R. Tsu, H. Shen, and M. Dutta, *Appl. Phys. Lett.* 60, 112 (1992).
193. S. Guha, G. Hendershot, D. Peebles, P. Steiner, F. Kozlowski, and W. Lang, *Appl. Phys. Lett.* 64, 613 (1994).
194. H.-P. Martin, G. Irmer, and E. Müller, *Eur. Ceram. Soc.* 18, 193 (1998).
195. J. Acker, K. Bohmhammel, E. Henneberg, G. Irmer, I. Röver, and G. Roewer, *Adv. Mater.* 12, 1605 (2000).
196. V. D. Blank and B. A. Kulnitskiy, *High Pressure Res.* 15, 31 (1996).
197. Y. Gogotsi, C. Baek, and F. Kirsch, *Semicond. Sci. Technol.* 14, 936 (1999).
198. Y. Kanzawa, S. Hayashi, and K. Yamamoto, *J. Phys.: Condens. Matter* 8, 4823 (1996).
199. J. L. Feldman, E. Kaxiras, and X.-P. Li, *Phys. Rev. B* 44, 8334 (1991).
200. E. C. Honea, A. Ogura, C. A. Murray, K. Raghavachari, W. O. Sprenger, M. F. Jarrold, and W. L. Brown, *Nature (London)* 366, 42 (1993).
201. R. E. Allen, G. P. Allredge, and F. W. de Wett, *Phys. Rev. B* 4, 1661 (1971).
202. J. Kulda, D. Strauch, P. Pavone, and Y. Ishii, *Phys. Rev. B* 50, 13347 (1994).
203. G. Dolling, in "Inelastic Scattering of Neutrons in Solids and Liquids," Vol. II, p. 37. IAEA, Vienna, 1963.
204. G. Nilsson and G. Nelin, *Phys. Rev. B* 6, 3777 (1972).
205. T. Kanata, H. Murai, and K. Kubota, *J. Appl. Phys.* 61, 969 (1986).
206. C. E. Bottani, C. Mantini, P. Milani, M. Manfredini, A. Stella, P. Tognini, P. Cheyssac, and R. Kofman, *Appl. Phys. Lett.* 69, 2409 (1996).
207. A. Stella, P. Cheyssac, and R. Kofman, "Science and Technology of Thin Films." World Scientific, Singapore, 1995.
208. Y. Sasaki and C. Horie, *Phys. Rev. B* 47, 3811 (1993).
209. S. Okada and Y. Kanemitsu, *Phys. Rev. B* 54, 16421 (1996).
210. Y. Maeda, *Phys. Rev. B* 51, 1658 (1995).
211. V. Craciun, C. Boulmer-Leborgne, E. J. Nicolls, and I. W. Boyd, *Appl. Phys. Lett.* 69, 1506 (1996).
212. X. L. Wu, T. Gao, X. M. Bao, F. Yan, S. S. Jiang, and D. Feng, *J. Appl. Phys.* 82, 2704 (1997).
213. T. Kobayashi, T. Endoh, H. Fukuda, S. Nomura, A. Sakai, and Y. Ueda, *Appl. Phys. Lett.* 71, 1195 (1997).
214. V. Kolobov, Y. Maeda, and K. Tanaka, *J. Appl. Phys.* 88, 3285 (2000).
215. Y.-N. Hwang, S. Shin, H. L. Park, S.-H. Park, U. Kim, H. S. Jeong, E. Shin, and D. Kim, *Phys. Rev. B* 54, 15120 (1996).
216. M. Kuball, J. Gleize, S. Tanaka, and Y. Aoyagi, *Appl. Phys. Lett.* 78, 987 (2001).
217. M. Herms, G. Irmer, G. Goerigk, E. Bedel, and A. Claverie, *Mater. Sci. Eng. B* 91-92, 466 (2002).
218. J. E. Spanier, R. D. Robinson, F. Zhang, S.-W. Chan, and I. P. Herman, *Phys. Rev. B: Condens. Matter* 64, 245407 (2001).
219. E. D. Obraztsova, V. L. Kuznetsov, E. N. Loubnin, S. M. Pimenov and V. G. Pereverzev, in "Nanoparticles in Solids and Solutions" (J. H. Fendler and I. Dékány, Eds.), p. 485. Kluwer Academic, Dordrecht, 1996.
220. Z. Wang, G. Yu, L. Yu, F. Zhu, D. Zhu, H. Xu, and M. Ruan, *J. Appl. Phys.* 91, 3480 (2002).
221. R. Nicklow, N. Wakabayashi, and H. G. Smith, *Phys. Rev. B* 5, 4951 (1972).
222. C. Y. Xu, P. X. Zhang, and L. Yan, *J. Raman Spectrosc.* 32, 862 (2001).
223. Y. J. Chen, W. P. Chen, and E. Burstein, *Phys. Rev. Lett.* 36, 1207 (1976).
224. K. Sakoda, K. Ohtaka, and E. Hanamura, *Solid State Commun.* 41, 393 (1982).
225. K. Kurosawa, R. M. Pierce, S. Ushioda, and J. C. Hemminger, *Phys. Rev. B* 33, 769 (1986).
226. H. Knobloch, H. Brunner, A. Leitner, F. Aussenegg, and W. Knoll, *J. Chem. Phys.* 98, 10093 (1993).
227. M. I. Stockman, *Phys. Rev. E* 56, 6494 (1997).
228. S. Grésillon, L. Aigouy, A. C. Boccara, J. C. Rivoal, X. Quelin, C. Desmarest, P. Gadenne, V. A. Shubin, A. K. Sarychev, and V. M. Shalaev, *Phys. Rev. Lett.* 82, 4520 (1999).
229. K. Kneipp, Y. Wang, H. Kneipp, L. T. Perelman, I. Itzkan, R. R. Dasari, and M. S. Feld, *Phys. Rev. Lett.* 78, 1667 (1997).
230. S. Nie and S. R. Emory, *Science (Washington, DC)* 275, 1102 (1997).
231. J. T. Krug, G. D. Wang, S. R. Emory, and S. M. Nie, *J. Am. Chem. Soc.* 121, 9208 (1999).
232. H. Xu, E. J. Bjerneld, M. Käll, and L. Börjesson, *Phys. Rev. Lett.* 83, 4357 (1999).

233. A. M. Michaels, M. Nirmal, and L. E. Brus, *J. Am. Chem. Soc.* 121, 9932 (1999).
234. K. Kneipp, A. Jorio, H. Kneipp, S. D. M. Brown, K. Shafer, J. Motz, R. Saito, G. Dresselhaus, and M. S. Dresselhaus, *Phys. Rev. B* 63, R81401 (2001).
235. K. Kneipp, A. S. Haka, H. Kneipp, K. Badizadegan, N. Yoshizawa, C. Boone, K. E. Shafer-Peltier, J. T. Motz, R. R. Dasari, and M. S. Feld, *Appl. Spectrosc.* 56, 150 (2002).
236. B. Hecht, B. Sick, U. P. Wild, V. Deckert, R. Zenobi, O. F. Martin, and D. W. Pohl, *J. Chem. Phys.* 112, 7761 (2000).
237. D. P. Tsai, A. Othonos, M. Moskovits, and D. Uttamchandani, *Appl. Phys. Lett.* 64, 1768 (1994).
238. J. Grausem, B. Humbert, A. Burneau, and J. Oswald, *Appl. Phys. Lett.* 70, 1671 (1997).
239. D. Zeisel, V. Deckert, R. Zenobi, and T. Vo-Dinh, *Chem. Phys. Lett.* 282, 381 (1998).
240. R. Stöckle, V. Deckert, C. Fokas, D. Zeisel, and R. Zenobi, *Vib. Spectrosc.* 682, 39 (1999).
241. N. Hayazawa, Y. Inouye, Z. Sekkat, and S. Kawata, *Chem. Phys. Lett.* 335, 369 (2001).
242. A. Othmani, Thesis, Université Lyon I, 1994.



# Localization and Interactions in Magnetic Nanostructures

F. G. Aliev

*Universidad Autonoma de Madrid, Cantoblanco, Madrid, Spain*

V. K. Dugaev

*Max-Planck-Institut für Mikrostrukturphysik, Halle, Germany*

J. Barnaś

*Adam Mickiewicz University, Poznań, Poland*

## CONTENTS

1. Introduction
  2. Early Experiments
  3. Effects of Magnetic Field on the Localization Corrections
  4. Electron–Electron Interaction in Spin Quantum Wells
  5. Role of Spin–Orbit Interaction
  6. Localization Corrections to the Anomalous Hall Effect
  7. Interplay Between Localization and Band Magnetism
  8. Localization Corrections Associated with Domain Walls
  9. Localization Corrections to Magnetic Interactions in Multilayers
  10. Localization Corrections to Spin Conductivity
  11. Localization Effects in Low-Carrier-Density Magnets
  12. Coulomb Interactions in Ferromagnetic Double Junctions
  13. Transport Through Quantum Dots with Electron Correlations
  14. Summary
- Glossary  
References

## 1. INTRODUCTION

One of the most spectacular phenomena discovered in recent years in magnetic artificially layered structures is the giant magnetoresistance (GMR) effect. The essence of the effect is the dependence of electrical resistance of a magnetic metallic multilayer on its magnetic configuration [1,2]. Such a configuration can be changed, for example, with an external magnetic field applied to the system. A typical structure in which the effect occurs is a multilayer with adjacent ferromagnetic films coupled antiferromagnetically across a nonmagnetic spacer [3,4] so that they have antiparallel magnetizations in the vanishing magnetic field. The magnetizations then rotate in an external field from the antiparallel configuration to the parallel one, and this rotation is accompanied by a decrease in the electrical resistance of the multilayer (an increase is also possible [5]). The effect exists for electric current flowing in the film plane [1,2,6], as well as for electric current flowing perpendicularly to the film plane [7–9]. The antiparallel alignment can also be obtained by other means. If, for instance, a multilayer consists of two types of ferromagnetic films (which have different coercive fields), then there is a range of magnetic fields during scan through the hysteresis loop where the magnetizations are antiparallel (being parallel above a certain saturation field) [6]. The GMR effect itself is a classical effect, and also exists at room temperature. Therefore, most of the experimental works on electronic transport in magnetic structures were done in this temperature range.

Whereas the transport properties of magnetic systems in the high-temperature regime are more interesting from

the application point of view, the low-temperature regime seems to be more interesting from the point of view of fundamental physics. This is because various quantum phenomena have peculiar contributions to transport characteristics, particularly in systems of reduced dimensionality. In such structures, usually one or more characteristic dimensions are in the nanometer range. When electrons propagate in a disordered system with the electron coherence length comparable to its (one or more) dimensions, the conductivity corrections due to quantum interference and electron–electron (e–e) interaction may play a significant role. Moreover, analysis of the phase-coherent effects in spin-polarized materials, particularly their dependence on the magnetic field and temperature, provides a sensitive way to investigate the degree and role of structural (morphological) and magnetic (domain walls) inhomogeneities. One may also expect that future spin electronics (spintronics) will take advantage of the phase-coherent transport in spin-polarized systems.

Localization effects in the transport properties of nonmagnetic metals and semiconductors were investigated very extensively during the last three decades, starting from the paper by Anderson [10]. The main results of these investigations have been summarized in several review articles [11–15]. The best developed seems to be the weak localization (WL) theory [11, 12], which gives a way to rigorously calculate localization corrections to the conductivity of disordered metals or degenerate semiconductors in the limit of  $\varepsilon_F \tau / \hbar \gg 1$ , where  $\varepsilon_F$  is the Fermi energy and  $\tau$  is the momentum relaxation time of electrons. These corrections turn out to be strongly dependent on the temperature and magnetic field, and therefore they have been clearly observed in many experiments (see [15] for a review). The interaction theory of disordered systems [13, 14], which accounts for the quantum corrections to conductivity due to e–e interaction, has been developed in the same spirit as WL. Even though these two theories are constructed as perturbation theories, and thus are restricted to relatively small quantum corrections to conductivity, they explained a great number of experiments on disordered metals, heavily doped semiconductors, and amorphous metallic films. One of the most surprising properties of disordered systems is the effect of dimensionality in films and wires, and in small metallic particles. The essential point is that disordered systems are characterized by two characteristic lengths—the electron mean-free path  $l$  and the phase coherence length  $L_\phi$  (or the Thouless length  $L_T$  in the interaction theory). The latter length scale corresponds to the distance at which the electron preserves its phase coherence, and this scale is associated with inelastic processes like scattering from phonons. When the geometrical size of a sample becomes smaller than  $L_\phi$ , its transport properties are drastically changed since the quantum corrections for systems of different effective dimensionality are significantly different too. When the sample size is smaller than  $L_\phi$ , the system is called *mesoscopic*. The origin of WL corrections to conductivity can be understood as a quantum effect due to the interference of electron waves propagating in a disorder potential [15, 16]. The quantum interference enhances the probability of an

electron to return back to the starting point, which results in a tendency of the electron to localize. The external magnetic field and inelastic scattering from phonons suppress the quantum interference, which effectively decreases the magnitude of localization corrections. A different response of WL and e–e interaction to the magnetic field usually allows us to distinguish between the localization and e–e contributions [17]. The relevant theoretical formalism makes use of *diffusons* (particle–hole propagator) and *cooperons* (particle–particle propagator) [11, 12]. They describe propagation in space and time of the electron density and of the fluctuations of superconductive density, respectively. The effects of temperature, magnetic field, and spin–orbit (SO) interaction can be accounted for theoretically by considering the corresponding influence on the diffusons and cooperons.

The quantum corrections to conductivity due to WL and e–e interactions are usually limited to low temperatures. However, e–e interaction can lead to other phenomena, which in certain systems also have a significant influence on electronic transport at high temperatures. An example of such systems are tunnel junctions. Broad interest in magnetic tunnel junctions was initiated by successful applications of the GMR effect in read/write heads and magnetic field sensors [18]. Indeed, an effect qualitatively similar to GMR was also observed in magnetic tunnel junctions. Now, the junction resistance varies when the magnetizations of the ferromagnetic electrodes rotate from an antiparallel to a parallel alignment. The effect is commonly known as the tunnel magnetoresistance (TMR) effect, and was first observed in Co/Ge/Fe junctions by Julliere [19]. It results from the spin-dependent electronic band structure of the ferromagnetic electrodes and spin-dependent tunneling rates. The effect occurs not only in simple planar junctions [20], but also in more complex ones, like double magnetic junctions with ferromagnetic outer electrodes and magnetic or nonmagnetic central ones. In the latter case, the TMR effect in the sequential tunneling regime results from spin accumulation in the central electrode, which in turn is a consequence of spin-dependent tunneling rates across the barriers [21]. However, it also may occur in the coherent tunneling regime, where an electron is in a coherent state of the whole double-barrier system, and therefore is sensitive to the magnetic configuration of the outer electrodes.

In the case of double-barrier planar junctions, the central electrode (called also an island in the following) is sufficiently large to neglect the effects due to electrostatic interaction of an electron tunneling to this electrode with other electrons already being there. When the island becomes small, the electrostatic interaction of the excess electrons with the other ones may play a crucial role in electronic transport, leading to Coulomb blockade phenomena [22]. In asymmetric junctions, transport characteristics then form the well-known Coulomb staircase. Interplay of the charging phenomena and ferromagnetism of the electrodes [23] are briefly reviewed too.

The review then summarizes the results of experimental and theoretical studies of localization in ferromagnets, magnetic layers, and multilayers, as well as in mesoscopic

magnetic structures. It also includes recent results on the e–e correction to conductivity in disordered ferromagnetic structures, and the results on electrostatic charging effects in double magnetic junctions.

## 2. EARLY EXPERIMENTS

The low-temperature anomaly in electrical conductivity of ferromagnetic metals and thin films was reported in several experimental works. These works clearly demonstrate that the localization and interaction corrections to conductivity occur not only in nonmagnetic systems, but also in ferromagnets. However, interpretation of the results was not quite certain because the corresponding theory was not developed at that time. Here, we review some of these early experimental works. Kobayashi et al. [24] studied the temperature and magnetic field dependence of the electrical conductivity of highly resistive thin Ni films (film thickness of 40 and 60 Å). The samples were prepared in the following way [25, 26]. First, vacuum deposition of ferromagnetic metal (Ni of an amount which corresponded to 1 nm) onto quartz substrate was carried out, followed by oxidation at  $6.5 \cdot 10^{-2}$  torr for a few minutes. At the next stage, this procedure was repeated two times with two more deposited Ni layers, each oxidized again. The resistance of the samples was controlled by changing the oxidation time. By analyzing electron micrographs, it was found that the film consisted of an ensemble of Ni nanoparticles with diameter of 1 nm (distribution of the size within  $\pm 5$  Å) dispersed on the substrate. The stack of three layers of the particles formed a well-connected two-dimensional network of particles having only little overlap in the direction normal to the substrate. The third layer was covered with 50 nm thick SiO for protection. Kobayashi et al. [24] observed that the sheet conductivity  $\Delta\sigma_{\square} \simeq [R_{\square}(T_0) - R_{\square}(T)]/R_{\square}^2(T_0)$  (here,  $R_{\square}(T)$  is the sheet resistance) as a function of temperature has the form  $\sigma_{\square} = \sigma_0 + A \ln T$ . They also found the parameter  $A$  to be close to  $e^2/(2\pi^2\hbar)$ , and to be almost independent of the film thickness below 60 Å. Magnetoconductivity was positive, independent of temperature, and as small as 0.1% at 10 kOe. These results are in agreement with the WL theory in the effectively 2-D case. Some conclusions about the importance of spin–orbit (SO) interaction in ferromagnets were also drawn there.

The magnetoresistance (MR) of thin  $\text{Pd}_{1-y}\text{Ni}_y\text{H}_x$  films of thickness 25, 50, and 100 Å was measured by Raffy et al. [27] between 1 and 5 K and in magnetic fields up to 1 T. With no hydrogen ( $x = 0$ ) and for  $y > 0.025$ , the alloys are ferromagnetic, and display localization behavior in a zero magnetic field. Hydrogenation suppresses ferromagnetism in these materials, and for ( $x \rightarrow 1$ ), the ground state is dominated by magnetic fluctuations. It was shown that MR for 25 Å  $\text{Pd}_{0.94}\text{Ni}_{0.06}\text{H}_x$  film could be fitted rather well by the 2-D form

$$\frac{\Delta R_{\square}}{R_{\square}^2} = \frac{e^2}{2\pi^2\hbar} (\beta - \alpha) Y\left(\frac{H}{H_0}\right) \quad (1)$$

where  $Y(x) = \ln x + \psi(1/2 + 1/x)$ , and  $\psi(x)$  is the digamma function, which has the property  $\psi(x) \simeq \ln(x)$  for  $x \gg 1$  [28]. This is the formula for quantum correction in nonmagnetic metals, where the coefficient  $\beta$  is due to the Maki–Thompson correction [29] and  $\alpha$  is due to the WL corrections, respectively, whereas  $H_0$  is the phase-breaking field determined by spin-flip scattering and inelastic processes. MR was positive, and therefore accounted for by the suppression of the antilocalization correction in a magnetic field. The antilocalization effect was attributed to strong SO scattering. It should be noted that Pd and Ni alloys are close to the ferromagnetic transition at low temperatures. Introducing hydrogen into ferromagnetic Pd turns it into the paramagnetic state, whereas a relatively small concentration of Ni atoms leads to the presence of large-moment localized magnetic impurities or small magnetic clusters. The fact that the system is close to the phase transition point makes the interpretation of experimental results much more complex.

The resistivity of thin Fe films (for thickness above 60 Å) grown epitaxially on GaAs was studied by Fuller et al. [30] and Rubinstein et al. [31]. The iron films were grown on GaAs substrates by the molecular beam epitaxy (MBE) method. The substrate face orientation was chosen to be (110) in order to obtain within the film plane the following three different crystalline axes: the magnetically easy [001], hard [111], and intermediate [110] ones. It is known that epitaxial few monolayer Fe films can be obtained on MgO [32] and GaAs substrates [33, 34] because the corresponding nearest neighbor distances are close (within less than 1%) to that of bcc iron. The deposition of Fe on GaAs is of special importance because magnetic films deposited on semiconductors are important for application in spintronics. However, in this particular experiment on weak localization phenomena in Fe, specially prepared highly insulating substrates were used to allow studying transport properties of the iron films. These specially doped with chromium ( $6 \cdot 10^{16}$  atoms  $\cdot$  cm $^{-3}$ ) and tin ( $2 \cdot 10^{16}$  atoms  $\cdot$  cm $^{-3}$ ) GaAs substrates remained highly insulating, even when heated to 625 °C in a vacuum for about 30 min. Several samples, grown with thicknesses from 60 to 200 Å, were photolithographically patterned to three conducting stripes, aligned along one of three different magnetic axes: easy, intermediate, and hard. The temperature dependence shows a shallow minimum at approximately 15 K, and at lower temperatures, obeyed the log law  $\sigma_{\square} = \sigma_0 + A \ln T$ , with the coefficient  $A$  very close to  $e^2/(2\pi^2\hbar)$  [30, 31]. It was shown that the anomalous temperature dependence did not vary with the current and sample orientation [31]. This temperature dependence was not affected by magnetic fields up to 600 G. A small negative MR was observed only at magnetic fields larger than 30 kG. No anomaly in the low-temperature conductivity was observed for films of thickness larger than 100 Å, which excludes the Kondo effect as a possible explanation of the experimental results. A comparison of the temperature dependence of the resistivity and of the normal Hall effect did not allow to distinguish between the interaction and WL corrections, mainly because of the experimental error. Finally, at 4.2 K, the high-field MR appeared to be negative, and varying linearly with the magnetic field between 30 and 130 kG. This is inconsistent

with the e-e interaction and WL theories, which predict the  $\ln H$  and  $-\ln H$  dependence in this regime, respectively.

Aprili et al. [35] measured the low-temperature conductivity of inhomogeneous Ni films near the percolation threshold. Homogeneous layers of thickness  $d = 6$  nm were first evaporated using electron guns in ultra high vacuum ( $10^{-9}$  torr). Percolating Ni films were prepared by controlled coalescence due to the annealing of homogeneous films at temperatures from 500 to 550 °C in ultrapure He vapor. The annealing process was controlled by resistance measurements, which provided an accurate method for following the evolution of the inhomogeneous state. Moreover, the annealing allowed a reduction of the amount of atomic size effects, leading to relatively large-scale topological disorder only. The metallic coverage ( $p$ ) was deduced by analyzing transmission electron microscopy images after annealing. A percolation coverage of about  $p_c = 0.56$  and a fractal dimensionality  $d_f = 1.8$  were found to be in good agreement with theoretical predictions [35]. Assuming the diffusion coefficient  $D = 5 \cdot 10^{-4} \text{ m}^2 \cdot \text{s}^{-1}$ , found in Ni-based percolation alloys [27], the authors estimated that, for temperatures below 30 K, the scale on which the phase coherence is preserved,  $L_T = \sqrt{D\hbar/k_B T}$ , should become larger than a typical film thickness, indicating possible two-dimensional quantum transport. Indeed, the  $\log T$  anomaly was found experimentally, which was well fitted with the formula  $\Delta\sigma_{\square} = (e^2/2\pi^2\hbar)[1 + 2(1 - F)]\log T - K_d T^\alpha/dR_{\square}$ , where the first two terms account for quantum transport (WL contributes to the coefficient 1 and e-e interaction to the factor  $2(1 - F)$ ,  $F$  being a screening factor). The second term reflects ordinary inelastic scattering with  $K_d$ , the coupling coefficient. It was also observed that the external magnetic field of 4 T did not affect  $\Delta\sigma_{\square}(T)$ , indicating that the quantum correction was mainly due to e-e interaction in 2-D. Moreover, from the  $\log T$  fit, one can obtain  $F = 0.55$ , which was close to the screening factor of 0.53 estimated theoretically. For percolating films, the logarithmic slope was found to be partially suppressed. Moreover, a signature of a modified dimensionality at  $T < 4$  K was reported, reflecting the transition to the regime, where the phase-coherent scale becomes close to the percolation length. Magnetoresistivity measurements performed by subtracting data obtained at 20 K (i.e., in the classical regime) showed that some contribution due to WL is also present. The dependence of a small additional (positive) contribution to the conductivity on the external magnetic field became logarithmic at high fields (above 3 T), and can be approximated by formula (1).

### 3. EFFECTS OF MAGNETIC FIELD ON THE LOCALIZATION CORRECTIONS

An analysis of the localization corrections in ferromagnetically ordered metals or semiconductors was carried out in [36–38], where the results were also compared to the corresponding ones derived for nonmagnetic materials [11, 12]. It was shown that there were two main sources which affect the localization corrections: the internal induction  $\mathbf{B}$  and the magnetization field  $\mathbf{M}$ . For theoretical analysis [36–38],

a model described by the following Hamiltonian

$$H = -\frac{\hbar^2}{2m} \left( \frac{\partial}{\partial \mathbf{r}} - \frac{i e \mathbf{A}}{\hbar c} \right)^2 - \mathbf{M} \cdot \boldsymbol{\sigma} \quad (2)$$

was used, where the vector potential  $\mathbf{A}$  is related to the magnetic induction  $\mathbf{B}$  by  $\mathbf{B} = \text{rot } \mathbf{A}$ ,  $\mathbf{M}$  has the dimensionality of energy, and  $\boldsymbol{\sigma}$  is the vector of Pauli matrices. The first term in Eq. (2) describes electrons moving in the magnetic field  $\mathbf{B}$ , whereas the second one takes into account the Zeeman splitting of spin-up and spin-down electron bands. Both factors in the Hamiltonian affect the localization corrections. It is known that the first term suppresses the cooperons, whereas the second one suppresses singlet cooperons and singlet diffusons [11, 12]. In good metallic ferromagnets, the magnitude of the spin-splitting  $M$  related to the second term of Eq. (2) is of the order of Fermi energy  $\varepsilon_F$ . On the other hand, there is a general condition,  $\varepsilon_F \tau / \hbar \gg 1$ , on which the WL theory is valid (i.e., when the localization corrections can be considered as small corrections). Therefore, one can assume that, in good ferromagnetic metals, the condition  $M\tau / \hbar \gg 1$  is also fulfilled. It can be shown [37] that when this condition is fulfilled, the contribution of singlet diffusons and cooperons can be neglected. Bearing this in mind, one can find the localization corrections to conductivity by direct generalization of the results derived for nonmagnetic metals [11, 12].

In the three-dimensional case, the localization correction to the conductivity, which includes only triplet cooperons and takes into account the magnetic induction  $B$ , can be written in the following form:

$$\begin{aligned} \Delta\sigma(B) = \Delta\sigma(0) - \frac{e^2}{16\pi^2\hbar l_B} \\ \times \sum_{n=0}^{\infty} \left[ \frac{1}{(n + 1/2 + \delta_{\uparrow})^{1/2}} - 2(n + 1 + \delta_{\uparrow})^{1/2} \right. \\ \left. + 2(n + \delta_{\uparrow})^{1/2} + \frac{1}{(n + 1/2 + \delta_{\downarrow})^{1/2}} \right. \\ \left. - 2(n + 1 + \delta_{\downarrow})^{1/2} + 2(n + \delta_{\downarrow})^{1/2} \right] \quad (3) \end{aligned}$$

where  $\sigma(0)$  does not include the effects due to magnetic induction, and is given by

$$\begin{aligned} \Delta\sigma(0) = C + \frac{e^2}{4\pi^2\hbar} \left[ \frac{1}{D_{\uparrow}^{1/2}} \left( \frac{1}{\tilde{\tau}_{\text{so}\uparrow}} + \frac{1}{\tau_{\varphi\uparrow}} \right)^{1/2} \right. \\ \left. + \frac{1}{D_{\downarrow}^{1/2}} \left( \frac{1}{\tilde{\tau}_{\text{so}\downarrow}} + \frac{1}{\tau_{\varphi\downarrow}} \right)^{1/2} \right] \quad (4) \end{aligned}$$

with the following notations introduced:

$$C \simeq -\frac{e^2}{2\pi^2\hbar l}, \quad \delta_{\uparrow(\downarrow)} = \frac{l_B^2}{4D_{\uparrow(\downarrow)}} \left( \frac{1}{\tilde{\tau}_{\text{so}\uparrow(\downarrow)}} + \frac{1}{\tau_{\varphi\uparrow(\downarrow)}} \right) \quad (5)$$

Here,  $D_{\uparrow(\downarrow)} = v_{F\uparrow(\downarrow)}^2 \tau_{\uparrow(\downarrow)} / 3$  are the diffusion coefficients, and  $v_{F\uparrow(\downarrow)}$  are the Fermi velocities for spin-up and spin-down electrons. Apart from this,  $l_B = (c\hbar/eB)^{1/2}$  is the magnetic length, and  $l$  is the electron mean-free path. Spin-orbit

interaction is included, and is described by the SO relaxation time of cooperons  $\tilde{\tau}_{\text{so}\uparrow(\downarrow)}$  and the phase relaxation time  $\tau_{\varphi\uparrow(\downarrow)}$ , related to the inelastic scattering of electrons from phonons. The dependence of  $\tau_{\varphi}$  on  $T$  results in the temperature dependence of conductivity at low  $T$ . Formula (3) was found by Kawabata's method [39], and is limited to weak magnetic induction, when  $l_B \gg l$ . The magnetoresistivity is found to be *negative* due to the suppression of the negative localization correction by magnetic induction  $\mathbf{B}$ . In the case of  $l_B < l$ , the localization correction vanishes, being completely suppressed by the magnetic induction. At  $\delta_{\uparrow}, \delta_{\downarrow} \ll 1$  (i.e., for low temperatures or strong magnetic induction), the sum in Eq. (3) is a constant  $C_2 = -0.13$  [39], which leads to the  $\sqrt{B}$  dependence of the localization correction on  $B$ . In the opposite limit of weak magnetic induction, one has  $\delta_{\uparrow}, \delta_{\downarrow} \gg 1$ , and the correction is proportional to  $B^2$ . The derived formulas describe the dependence on the total magnetic induction, which in turn depends on the external magnetic field.

In the effectively 2-D case, the localization correction has the form

$$\Delta\sigma(B) = -\frac{e^2}{4\pi^2\hbar} \left[ \psi\left(\frac{1}{2} + \frac{1}{\tau_{\uparrow}a_{\uparrow}}\right) - \psi\left(\frac{1}{2} + \frac{1}{\tilde{\tau}_{\text{so}\uparrow}a_{\uparrow}} + \frac{1}{\tau_{\varphi\uparrow}a_{\uparrow}}\right) + \psi\left(\frac{1}{2} + \frac{1}{\tau_{\downarrow}a_{\downarrow}}\right) - \psi\left(\frac{1}{2} + \frac{1}{\tilde{\tau}_{\text{so}\downarrow}a_{\downarrow}} + \frac{1}{\tau_{\varphi\downarrow}a_{\downarrow}}\right) \right] \quad (6)$$

where  $a_{\uparrow,\downarrow} = 4eBD_{\uparrow,\downarrow}/c\hbar$ . In the limit of  $B \rightarrow 0$ , the localization correction has a form similar to that in the nonmagnetic case:

$$\delta\sigma(0) = \frac{e^2}{4\pi^2\hbar} \ln \left[ \tau_{\uparrow}\tau_{\downarrow} \left( \frac{1}{\tilde{\tau}_{\text{so}\uparrow}} + \frac{1}{\tau_{\varphi\uparrow}} \right) \left( \frac{1}{\tilde{\tau}_{\text{so}\downarrow}} + \frac{1}{\tau_{\varphi\downarrow}} \right) \right] \quad (7)$$

In both effective 3-D and effective 2-D cases, the localization correction to conductivity is *negative*, and the magnitude of this correction decreases with increasing  $\mathbf{B}$ . The latter takes into account both the internal magnetic induction and the effect of the external magnetic field. Thus, the localization can be observed only in the case of a weak suppression of the localization correction by the internal induction.

The key question for quantum corrections is: how long is the phase coherence length? Tataru and Barbara [40] theoretically considered the Aharonov–Bohm effect in a disordered ferromagnetic ring. The Aharonov–Bohm effect is a macroscopic manifestation of the quantum interference of electron waves. It shows up as oscillations of electric current in a small metallic ring as a function of the external magnetic field. In the case of superconductors or pure nonmagnetic metals, the oscillation factor in the dependence of electric current on the magnetic field is known to be  $\cos(2\pi\phi/\phi_0)$ , where  $\phi$  is the magnetic flux penetrating through the ring, and  $\phi_0 = hc/e$  is the magnetic flux quantum. The corresponding theory for disordered normal metals was developed by Altshuler et al. [41], and it was shown that, in disordered metals, the corresponding factor should be  $\cos(4\pi\phi/\phi_0)$  instead of  $\cos(2\pi\phi/\phi_0)$ . This is because the cooperon contributing to the current in the ring carries the double electron charge  $2e$ , and therefore the effective magnetic quantum is half of the usual value  $hc/e$ . The theoretical prediction of [41] was later confirmed

in experiments with gold rings [42]. Due to the internal magnetization and internal induction in ferromagnets, the Aharonov–Bohm effect was shown [40] to be different from the analogous effect in nonmagnetic disordered metallic rings. The main difference is related to the influence of magnetization on the components of the cooperon. Each spin component contributes to the Aharonov–Bohm effect, with a damping factor depending on the scattering of electrons in each spin channel. Due to the possibility of a large difference in the mean-free paths of spin-up and spin-down electrons, only electrons of a specific spin orientation contribute to the effect. Thus, ferromagnetism does not suppress the Aharonov–Bohm effect, even if the difference in the spin-up and spin-down relaxation times is large (as, for example, in Fe).

Aliev et al. [43] measured MR of 17 nm thick Co wires with a width of 200 nm and a length of 1  $\mu\text{m}$  at temperatures from 4 K down to 100 mK, and in magnetic fields up to 15 T perpendicular to the structure. The polycrystalline wire structures were grown at room temperature by molecular beam epitaxy, followed by electron lithography patterning. Electric measurements were performed in a dilution He<sup>3</sup>–He<sup>4</sup> refrigerator by using the standard ac bridge technique (LR700), which assured low dissipation at low temperatures. The low-temperature resistivity (30  $\mu\Omega \cdot \text{cm}$ ) confirmed the polycrystalline structure of the sample, and indicated that the elastic mean-free path was slightly smaller than the strip cross-section dimensions. Figure 1 presents the data obtained at 100 mK at different values of electric currents between 10 and 1  $\mu\text{A}$ , and for magnetic fields well outside the region where the anisotropic MR (AMR) could affect the results. One can clearly see reproducible conductance fluctuations with an amplitude of the order of  $0.01e^2/h$  at the lowest currents and temperatures. Strong suppression of the resistance fluctuations with the current above 10  $\mu\text{A}$  and temperature  $T > 4$  K indicates that these anomalies are not induced by a reproducible rearrangement of the internal magnetic structure. These conductance fluctuations also indicate the phase-coherent transport.

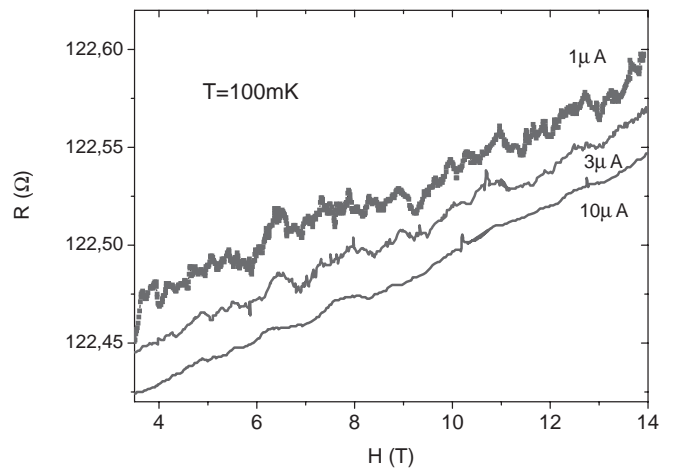


**Figure 1.** Reproducible magnetoresistance fluctuations in 17 nm thick Co line structures with width of 200 nm and length 1 of  $\mu\text{m}$  observed at ultralow temperatures (100 mK) at different electric currents from 10 to 1  $\mu\text{A}$ .

Recently, Kasai et al. [44] observed the Aharonov–Bohm effect in a ferromagnetic permalloy nanoring. The sample consisted of a nanoscale ring with leads made of permalloy ( $\text{Fe}_{19}\text{Ni}_{81}$ ) and patterned by using the lift-off technique and electron-beam lithography. First, a thin photoresist of 100 nm was spin coated onto a thermally oxidized Si substrate. The resist mask was then patterned with a 20 keV electron beam. After development, permalloy was deposited by an electron-beam evaporator with 0.5 nm/s. The sample was then obtained after the resist mask had been lifted off in solvent. A scanning electron microscope was used to image and determine the dimensions of the sample. For resistance measurement, Cu electrodes were attached to the leads. The distance between the two voltage electrodes was 2.5  $\mu\text{m}$ . The outer and inner diameters were, respectively, equal to 500 and 420 nm, whereas the thickness was 20 nm. The magnetoresistivity of the ring was measured from 30 mK to 4 K in a magnetic field perpendicular to the ring plane. For magnetic fields large enough to exclude AMR, the authors [44] observed aperiodic fluctuations and periodic resistance oscillations. The aperiodic fluctuations, similar to those found for Co line structures [43], have been identified as being due to the universal conductance fluctuations. By calculating the power spectrum from the Fourier transform of the MR data obtained in the range from 3 to 4 T, it was concluded that the Aharonov–Bohm oscillations had a period  $\Delta B = 0.0266$  T, which was consistent with the estimated range of  $0.0209T < \Delta B < 0.0299T$ , given by the inner and outer diameters of the ring. The oscillation period was found to be dependent on the magnetic field tilting angle. The amplitude of oscillations was estimated to be about  $0.001e^2/h$ , which was almost three orders of magnitude smaller than one might expect for the fully phase-coherent diffusive conductor. The reduced value of the conductance oscillations was explained by a small (as compared to paramagnetic metals) phase-coherence length (500 nm). In ferromagnets, the phase-coherence length is significantly reduced by spin-flip scattering.

#### 4. ELECTRON–ELECTRON INTERACTION IN SPIN QUANTUM WELLS

Contrary to WL, the e–e interaction corrections in ferromagnets are not suppressed by the internal magnetic induction. This is because the interaction corrections are described mainly by the diffusons, which are not affected by the magnetic induction. The main difference between nonmagnetic and ferromagnetic metals, as concerns the interaction corrections, is the suppression of the contribution due to singlet diffusons. Thus, taking into account only triplet diffusons, one finds the following form for the exchange term in the interaction correction [36, 38]:

$$\Delta\sigma_{ex} = \frac{e^2}{2\pi^2\hbar(\nu_{\uparrow} + \nu_{\downarrow})} \left[ \nu_{\uparrow} \ln\left(\frac{T\tau_{\uparrow}}{\hbar}\right) + \nu_{\downarrow} \ln\left(\frac{T\tau_{\downarrow}}{\hbar}\right) \right] \quad (8)$$

where  $\nu_{\uparrow(\downarrow)}$  is the density of states of spin-up (down) electrons at the Fermi level, and  $T$  is taken in the energy units.

The Hartree term in the correction, on the other hand, is given by the formula

$$\Delta\sigma_{Har} = -\frac{e^2}{4\pi^2\hbar} \left[ F_{\uparrow} \ln\left(\frac{T\tau_{\downarrow}}{\hbar}\right) + F_{\downarrow} \ln\left(\frac{T\tau_{\uparrow}}{\hbar}\right) \right] \quad (9)$$

The above expression contains the constants  $F_{\uparrow}$  and  $F_{\downarrow}$ , which are determined by the average ratio of the Coulomb interaction matrix elements with the momentum  $k$  to the matrix element with  $k = 0$  [13, 12]. Here,  $k$  is the momentum transferred due to e–e interaction for the electrons at the Fermi surface. The difference between  $F_{\uparrow}$  and  $F_{\downarrow}$  is due to the different Fermi surfaces of spin-up and spin-down electrons.

Experimentally, the interaction corrections to the conductivity were observed by Aliev et al. [45] in Co/(Cr/Ag)/Co multilayers. The multilayers were prepared on MgO(100) substrates in a molecular beam epitaxy (MBE) deposition system using electron-beam guns and a mass spectrometer control system to stabilize the growth rate. In order to vary the thickness systematically, the Cr and Ag films were grown in a wedge shape. Then the system was cut into long stripes. The following multilayer composition was studied: Co(45 Å)/Cr(0–15 Å)/Ag(0–20 Å)/Co(45 Å), covered by 20 Å of Ag as a protection layer. The sample surface and structure were studied in detail by atomic force microscopy (AFM), X-ray diffraction (XRD), and magnetic force microscopy (MFM) [45]. The AFM measurements on the thinnest part of the wedge gave an rms roughness of 0.4 nm over a  $2.5 \cdot 2.5 \mu\text{m}^2$  area, while for the thickest part of the wedge, an rms roughness of 1.5 nm was obtained for the same area. The average grain diameter observed using AFM images was 50 nm. Low-angle specular XRD spectra clearly showed a series of well-defined finite-size oscillations, again an indication of low film roughness. The temperature dependence of conductivity at  $T < 20$  K shows the logarithmic dependence on  $T$ , fitted by the formula  $\rho = A \log T + C$  (see Fig. 2). Possible reasons for the observed logarithmic increase of the resistivity at low temperatures could be: (1) the Kondo effect, (2) WL effects, (3) disorder-enhanced two-dimensional e–e interactions, or (4) the interaction of conduction electrons with two-level systems. The first two effects are sensitive to low magnetic fields, and give rise to negative MR. They can be distinguished from the other interactions by applying a sufficiently strong magnetic field. The estimated upper limit for the Kondo temperature was  $T_K = 7$  K, defined as the middle point of the temperature interval, where the resistivity grows logarithmically. Therefore, for the usual Kondo effect, the temperature dependence of the resistivity should be substantially changed by the field  $H = 110$  kG. Characteristic fields which suppress WL effects are usually lower than 1 kG. However, it was found [45] that even the magnetic field of 110 kG had almost no influence on the logarithmic slope. The lack of saturation of the resistivity down to ultralow temperatures, both for  $H = 0$  and in the magnetic field of 110 kG, implies that the logarithmic term in the resistivity is likely due to the 2-D type e–e interactions in the presence of disorder. However, the experimental data [45] do not allow to exclude some additional contribution to the resistivity due to scattering on two-level systems. The indication of such a possibility comes



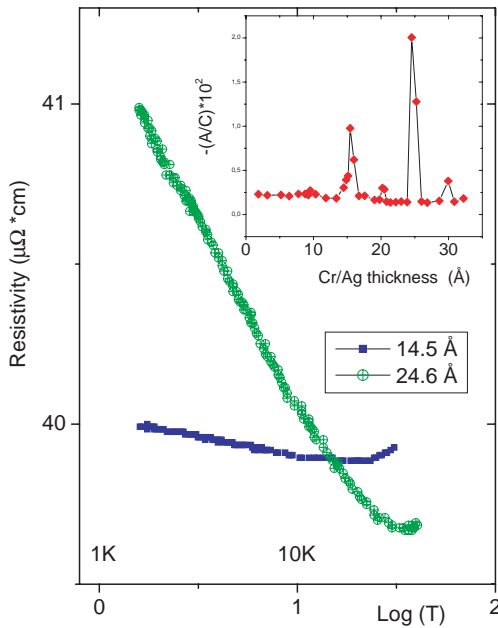


**Figure 2.** Logarithmic dependence of resistivity at  $T < 20$  K ( $\rho = A \cdot \log T + C$ ) for two Co (45 Å)/(Cr/Ag)/Co (45 Å) trilayers with different thicknesses of Cr/Ag spacer. Inset shows plot  $(-A/C)$  as a function of the Cr/Ag spacer thickness.

from the deviation from the  $\log$ - $T$  behavior in the resistivity at ultralow temperatures [46].

The thickness dependence of the observed normalized logarithmic term in the resistivity,  $A/C$ , was found to be rather unusual (see the inset in Fig. 2). For the elastic scattering times  $10^{-9}$ – $10^{-13}$  s within an accuracy of 0.01, the ratio  $A/C$  in the  $\log$ - $T$  fit is proportional to the product of the e–e interaction coefficient  $F$  and the residual resistivity [45]. For all studied strips, the coefficient  $F$  turned out to be strongly dependent on the thickness  $L$  of the (Cr/Ag) spacer layer. At some values of  $L$ , however, resonance-like peaks of  $F$  were observed. An explanation of this intriguing observation, given by Aliev et al. [45], was related to a change of disorder at the Cr/Ag interface with increasing thickness of the Cr/Ag spacer. The observed periodicity of 5 Å indeed corresponds roughly to 2.1 Å for Cr and 2.9 Å for Ag. An atomic monolayer of Cr in the preferential (110) direction is around 2.04 Å thick, which is in good agreement with the 2.1 Å estimated above. It is worth noting that interface-morphology-induced oscillations with a one monolayer periodicity also were observed in the magnetic properties and in the in-plane lattice spacing of cobalt [47–49] and gold ultrathin films [50].

Another possible explanation of this phenomenon is based on the screening effects in spin-separated quantum wells created by the multilayer structure [36]. In a simplified model, one may assume two different quantum wells, respectively for spin-up and spin-down electrons. Correspondingly, there are two different spin channels for the localization corrections. The coupling constant of e–e interaction is also associated with each of the spin channels. However, the screening of e–e interaction may include electrons with both spin orientations, provided that the corresponding matrix

elements obey certain selection rules. The resonance effect occurs when the ratio of the spin-up and spin-down quantum well widths is an integer. Physically, this corresponds to a commensurability of the wavefunctions of electrons with different spin orientations.

## 5. ROLE OF SPIN–ORBIT INTERACTION

The SO interaction plays an important role in the localization phenomena. It is well known that, in nonmagnetic metals, the presence of SO interaction can change the sign of the localization correction. As a result, the low-temperature conductivity of metals with strong SO interactions increases with decreasing temperature, what is known as the weak antilocalization effect. The change of the sign of localization correction is associated with the suppression of triplet cooperons by the SO interaction. In nonmagnetic metals, there are contributions from singlet and triplet cooperons, which have different signs and which enter with coefficients reflecting the multiplicity of the corresponding states: +1 for the singlet and  $-3$  for the triplet [13, 12]. Without SO interaction, this results in a negative correction since each component of the triplet gives the same contribution as one component of the singlet. By switching on a sufficiently strong SO interaction, one suppresses the triplet cooperon, and only the singlet cooperon is then relevant. This results in the sign reversal of the localization correction.

The situation is different in ferromagnetic metals, where the relatively strong internal magnetization completely excludes the singlet cooperons. Thus, the localization correction is negative, that is, there is no weak antilocalization. On the other hand, the SO interaction affects the triplet cooperons, decreasing the localization correction, making it smaller than in nonmagnetic metals. That is why the SO interaction is of main importance for the localization corrections in ferromagnets.

The SO interaction occurs as a relativistic effect in electron scattering from impurities and defects. It also occurs as the Rashba terms due to the interfaces [51], and the Dresselhaus terms [52] due to the higher order  $k$  terms in the electron Hamiltonian. The effects of SO interaction on the cooperons, related to the scattering from impurities and to the Rashba terms, have been studied theoretically in the case of bulk and effectively 2-D ferromagnets [37]. The most important result is that the SO interaction entering the cooperons turns out to be strongly dependent on the orientation of magnetization vector  $\mathbf{M}$  in 2-D structures. More precisely, the inverse SO relaxation time  $\tilde{\tau}_{so}^{-1}$  vanishes when the magnetization is in the plane of the layers.

It is worth noting that the SO interaction should be even more pronounced in the case of multilayered structures than in single films. As we pointed out before, the potential steps at the interfaces in combination with the relativistic terms in the Hamiltonian may produce strong SO scattering. The corresponding theory for the interface SO interaction was proposed by Bychkov and Rashba [51]. In the case of Fe/Cr multilayers, the potential steps are about 2.5 eV for the majority of electrons, and one can expect a significant SO scattering from the interface.

## 6. LOCALIZATION CORRECTIONS TO THE ANOMALOUS HALL EFFECT

Theoretical and experimental investigation of the anomalous (or extraordinary) Hall effect (AHE) in ferromagnets has a long history [53]. Recently, this effect has attracted much interest because it can be used to determine the magnitude and orientation of the magnetization in some magnetic materials, structures, and devices. AHE can be measured as a Hall voltage induced by an electric current flowing in the direction perpendicular to the magnetization  $\mathbf{M}$ . In contrast to the usual Hall effect, AHE does not require any external magnetic field. Two different mechanisms leading to AHE have been studied thoroughly: the so-called *side-jump* and *skew-scattering* mechanisms. They both essentially involve the SO interaction. The physical reason for AHE is a spin-dependent lateral displacement of the electron wave packet during the scattering from impurity (side jump) and a spin-dependent anisotropy of the scattering amplitude (skew scattering) [54].

The calculation of the off-diagonal conductivity  $\sigma_{xy}$  in a ferromagnet can be performed using the diagram technique. Considering a loop diagram with the SO correction to the vertex part (this is the side-jump mechanism), Crépieux and Bruno [54] found the following formula for  $\sigma_{xy}$ :

$$\sigma_{xy}^{(sj)} = \frac{e^2 \lambda_0^2}{6} (\nu_{\downarrow} k_{F\downarrow} v_{F\downarrow} - \nu_{\uparrow} k_{F\uparrow} v_{F\uparrow}) \quad (10)$$

where  $k_{F\uparrow, \downarrow}$ ,  $v_{F\uparrow, \downarrow}$ , and  $\nu_{\uparrow, \downarrow}$  are the electron momentum, electron velocity, and the density of states for spin-up and spin-down electrons at the Fermi surfaces. The constant  $\lambda_0$  measures the strength of the SO interaction. It has the dimensionality of length, and for nonrelativistic electrons in vacuum,  $\lambda_0 = \lambda_c/2\pi$ , where  $\lambda_c = 2\pi\hbar/m_0c$  is the Compton wavelength of electrons and  $m_0$  is the free electron mass. The magnitude of  $\lambda_0$  in crystals is changed due to crystalline fields.

Within the skew-scattering mechanism, one takes into account the loop diagrams with the third-order corrections due to scattering from impurities, keeping the first order in SO interaction [54]. The result of relevant calculation is

$$\sigma_{xy}^{(ss)} = \frac{\pi \langle V^3 \rangle \lambda_0^2 a_0^3}{6 \langle V^2 \rangle} [\sigma_{xx, \downarrow} k_{F\downarrow}^2 \nu_{\downarrow} - \sigma_{xx, \uparrow} k_{F\uparrow}^2 \nu_{\uparrow}] \quad (11)$$

where  $\sigma_{xx, \uparrow, \downarrow}$  are the diagonal conductivities in the spin-up and spin-down channels, and  $a_0$  is the lattice parameter. Here,  $V$  measures the amplitude of disorder, and the angle brackets mean averaging over disorder. The dimensionless ratio  $\langle V^3 \rangle / \langle V^2 \rangle^{3/2}$  depends only on the distribution  $P(V)$  of the random field  $V(\mathbf{r})$ , whereas  $\nu a_0^3 \langle V^2 \rangle^{1/2}$  characterizes the relative strength of the potential.

Localization correction to the anomalous Hall effect has been studied experimentally on several amorphous ferromagnetic Fe films with thickness from two to ten atomic layers [55]. The films were prepared *in-situ* by quenched condensation onto a crystalline quartz substrate held at helium temperature in a vacuum better than  $10^{-11}$  torr. Homogeneous amorphous iron films of less than two monolayers thickness could be obtained by this method if they were deposited on an insulating Sb buffer layer with a thickness of

ten monolayers. An additional indication on the amorphous structure of the films was the resistively detected irreversible transformation to the crystalline state for films of thickness of more than 18 monolayers, when they were heated to above 40 K. Details of the sample preparation are described in [56]. It has been found [55] that the quantum correction to the off-diagonal (Hall) conductance  $\Delta\sigma_{xy}$  is negligibly small in the low-temperature region, in which the correction to the conductance  $\Delta\sigma_{xx} \sim \log T$  is clearly seen. In other words, the quantum corrections due to localization and e-e interaction to the off-diagonal conductance vanish in ferromagnetic films. This result is in contrast to what is known of the localization corrections to the usual Hall effect [11, 12], for which the localization correction to the off-diagonal conductance is nonzero, and this exactly compensates the effect of localization correction in diagonal conductance for the Hall constant. As a result, the localization correction to the Hall constant is exactly zero, but the correction to  $\sigma_{xy}$  is not zero. The theoretical analysis for ferromagnets has been done in [57–60]. It was shown that the results are different for different mechanisms of AHE. Namely, the localization correction to  $\sigma_{xy}$  is nonzero for the skew scattering [57, 58], but it vanishes for the side-jump mechanism [58]. In the latter case, exact cancellation of the contributions from different diagrams takes place. In addition, the exchange interaction correction for the skew-scattering mechanism was shown to vanish too [57]. Thus, the experiment of Bergmann and Ye [55] can be interpreted either as the localization correction strongly suppressed by the SO interaction within the skew scattering [57], or as the localization correction within the side-jump mechanism [58]. The latter interpretation is better justified for an alloy-like type of disorder described by the Gaussian distribution of random fields. Such a type of disorder (alloys, amorphous systems) is in contrast to the impurity disorder (doped semiconductors).

## 7. INTERPLAY BETWEEN LOCALIZATION AND BAND MAGNETISM

The above discussion of the WL and e-e interaction corrections to conductivity applies to systems far from the critical point of ferromagnetic transition, where the magnetic fluctuations are very weak. An important issue is the influence of localization on the magnetic ordering in itinerant ferromagnets. This effect should be of key importance near the critical point, where the magnetic fluctuations are affected by the localization effects. In other words, magnetic fluctuations, cooperons, and diffusons should be considered at the same footing. This problem was studied in [61, 62]. Fukuyama [61] considered a ferromagnet in the framework of the Hubbard model and in the presence of random short-range impurities. He found that the Curie temperature  $T_c$  depends substantially on the disorder which leads to an increase in  $T_c$ . The reason for this is that the Coulomb interaction leading to ferromagnetism is effectively enhanced due to the diffusive motion of electrons.

A similar model, with two coupling constants describing the Hubbard interaction in a disordered electron system, was studied by Singh and Fradkin [62]. They found that the effect of enhancement of the e-e interaction by the localization can be so strong that the electrons can be localized, and

at the same time, the ferromagnetic ordering can persist. The authors called such a system the *ferromagnetic Anderson insulator*. The other important aspect of the self-consistent calculation in their work was *no suppression of the singlet cooperon* by the spontaneous magnetization. This resulted from an interplay of different types of fluctuations in the vicinity of the magnetic phase transition point.

Recently, Kim and Millis [63] predicted a singular renormalization of the amplitude of backscattering from impurities, when the correlation length near the ferromagnetic magnetic quantum critical point exceeds the mean-free path. In other words, long wavelength fluctuations may dramatically increase the backscattering by spinless impurities. This effect leads to an enhancement of the Altshuler–Aronov correction to conductivity from  $\log(1/T)$  to  $\log^2(1/T)$ . Besides, peculiar Friedel oscillations in the electron density near the impurities should occur for a magnetic-field-induced quantum-phase transition. Due to a nonzero magnetic field, the spin-up and spin-down Fermi surfaces are characterized by different wavevectors. Accordingly, two superimposed oscillations in the electron density may be expected near any impurity.

On the experimental side, localization effects due to the magnetically tuned quantum-phase transition were observed in synthetic antiferromagnet (Fe/Cr) [64] and natural quasi two-dimensional metal  $\text{Sr}_3\text{Ru}_2\text{O}_7$  [65]. The ruthenate  $\text{Sr}_3\text{Ru}_2\text{O}_7$  is the  $n = 2$  member of the series of layered perovskites  $\text{Sr}_{n+1}\text{Ru}_n\text{O}_{3n+1}$ . The end members of the series are the pseudocubic and itinerant ferromagnet  $\text{SrRuO}_3$  ( $n = \infty$ ) [66] and the strongly two-dimensional unconventional superconductor  $\text{Sr}_2\text{RuO}_4$  [67]. The high-quality single crystals were grown using methods described in [68]. It was found that critical fluctuations near the metamagnetic phase transition in quasi two-dimensional metal  $\text{Sr}_3\text{Ru}_2\text{O}_7$  strongly enhance the residual resistivity  $\rho_{\text{res}}$  as the temperature is lowered below a few kelvin [65]. The low-temperature resistivity, however, varies as  $\rho = \rho_{\text{res}} + AT^\alpha$ , with  $\alpha \simeq 1$ . Similar conclusions have been drawn from the study of the magnetic-field-tuned quantum-phase transition in antiferromagnetically coupled Fe/Cr multilayers (see the next section and [64] for details of the sample growth and characterization). The difference is that, in the latter case, the maximum in the residual resistivity is overshadowed by a strong magnetic-field-dependent resistance, that is, by the GMR effect.

## 8. LOCALIZATION CORRECTIONS ASSOCIATED WITH DOMAIN WALLS

It has been known for a long time that magnetic domain walls (DWs) contribute to MR (DWMR). Electron transport through a narrow DW is predominantly ballistic [69], whereas for thick DWs it is rather diffusive. In the latter case, the quantum corrections due to WL and e–e interaction in the presence of disorder can also play a significant role, leading to interesting MR phenomena [70–72]. Recent interest in the DW contribution to resistivity is stimulated by intriguing physics which underlies the DWMR effect [73–77], and also by possible applications. Indeed, DWs can have a significant influence on the electrical noise

and operation of magnetoelectronic devices [78]. Although the number of DWs was controlled and directly observed, for example, in Fe [77] and Co films [75] at room temperature, where DW formation is relatively well understood, no clear picture emerged which could allow an understanding of the results. AMR dominates the low-field MR, and complicates the extraction of the true DW contribution to the resistivity [79]. In order to minimize the AMR contribution, thin films with reduced magnetization and special DW configurations have been studied [80].

The localization corrections in the presence of DWs are affected by a specific perturbation, which can be described as an effective gauge field arising in the vicinity of DWs. This problem has been studied theoretically in several works [70–72]. Tataro and Fukuyama [70] showed that, using a local spin transformation, the problem of a smooth DW with a spatially varying magnetization  $\mathbf{M}(z)$  can be considered as a problem with constant magnetization, but with an additional spin-dependent gauge field. The effect of the gauge field on the cooperon is similar to that of the vector potential associated with a magnetic field, that is, the gauge field suppresses the cooperons. Thus, DWs cause suppression of the localization corrections, which leads to an increase in the conductivity in the presence of DWs. When the external magnetic field removes DWs, then the conductivity decreases, giving rise to positive magnetoresistivity. This effect should be observed in the low-temperature region, where the localization corrections are not negligible. Recently, Jonkers [81] predicted that, for a 2-D ferromagnetic wire with impurity scattering independent of the spin orientation, the suppression of WL by DWs increases with increasing impurity concentration and decreases with increasing width of the wall.

The theory described above [70, 71] was revised and further developed by Lyanda-Geller et al. [72]. They showed that, actually, the gauge field does not equivalently suppress all of the cooperon components. Strictly speaking, some components can be unaffected by this field, which means that the effect is smaller than that predicted in [70, 71].

One of the ways to quantify the effect of the domain walls on resistance of ferromagnetic films is to pattern high-quality thin (100 nm thick) epitaxially grown (110) oriented bcc Fe films [77]. These films, grown on sapphire substrates [82], display a large in-plane uniaxial magnetocrystalline anisotropy, with the easy axis parallel to the [001] direction. The films were patterned using projection optical lithography and ion milling to produce micron scale wires oriented perpendicular to the magnetic easy axis. The residual resistivity ratio of 30 and low residual resistance indicate the high crystalline quality of these films. The competition among magnetocrystalline, exchange, and magnetostatic interactions results in a pattern of regularly spaced stripe domains perpendicular to the wire axis. Variation of the wire width changes the ratio of these energies, and hence the domain size. The magnetic domain configurations were strongly affected by the magnetic history of the samples. Before imaging, the wires were magnetized to saturation with a magnetic field transverse or longitudinal to the wire axis. In the transverse case, the mean stripe domain length was 1.6  $\mu\text{m}$ —much larger than in the longitudinal case, where it was 0.4  $\mu\text{m}$ . The negative DW contribution to the

resistivity, which was extracted from the low-field MR of these epitaxial Fe films after taking into account the AMR contribution, was explained [77] as a possible indication for the localization corrections in the presence of DWs. However, the fact that the WL effect survived at elevated (77 K) temperatures is rather against such an explanation. A negative contribution to resistivity due to DWs was also reported by Hong and Giordano [83] in Ni wires at  $T < 20$  K. Very narrow strips were patterned from Ni films evaporated onto glass substrates. The patterning was accomplished using a step-edge method [84], with typical thicknesses and widths of 200–400 Å, and sample lengths of  $10 \mu\text{m} \cdot \text{km}$ . The elastic mean-free path, estimated from low-temperature resistivity (10–20  $\mu\Omega \cdot \text{cm}$ ) was comparable to, or slightly smaller than, the strip cross section. Further experimental details are given in [85]. These experiments [83], however, did not study the temperature dependence of the effect, and considered AMR as an alternative origin of the observation. In the following, we review recent experimental results on the localization corrections in antiferromagnetically coupled Fe/Cr multilayer structures in the presence of DWs [86, 87].

Antiferromagnetically (AF) coupled magnetic multilayers (MMLs) are systems of reduced magnetization, and therefore have strongly suppressed AMR. Weak pinning of DWs at high temperatures is expected to suppress the DWMR. For a fixed magnetic field, DWMR should occur at sufficiently low temperatures, where DWs become strongly pinned and their configuration is not affected by thermal fluctuations or electrical current. The GMR effect (see Section 1) in this system is dominated by realignment of the magnetization direction in adjacent magnetic layers [88]. The presence of DWs should result in a small additional in-plane MR [89]. While the GMR effect is known to saturate at low temperatures [90], the temperature dependence of DWMR is still a matter of controversy.

Epitaxial  $[\text{Fe}/\text{Cr}]_{10}$  multilayers with ten bilayers were prepared in an MBE system on MgO (100)-oriented substrates held at 50 °C and covered by a 12 Å thick Cr seed layer. *In-situ* high-energy electron diffraction and *ex-situ* X-ray diffraction measurements were used to control the structural quality of the multilayers. The thickness of the Cr layers was typically 12–13 Å, which corresponds to the first antiferromagnetic peak in the interlayer exchange coupling for the Fe/Cr system [91], and gives rise to maximum GMR, which is about 20% at 300 K and 100% at 4.2 K. The antiferromagnetic fraction exceeds 80%, and the bilinear AF coupling dominates the biquadratic exchange coupling [92]. A detailed description of the sample preparation and structural characterization is given in [93].

Typical magnetic images at  $T = 4.2$  K and room temperature [86, 87] reveal different irregularly shaped domains of micrometer size (which is a characteristic feature of strong AF coupling [88, 94]). The susceptibility data point toward a weak pinning of the DWs at room temperature and a strong pinning at low temperatures [87]. Figure 3a shows the temperature dependence of the electrical resistivity  $\rho$  for an  $[\text{Fe}(12 \text{ Å})/\text{Cr}]_{10}$  MML and for different magnetic fields ( $|H| \leq 300$  Oe). The magnetic field was applied in the plane of the film and parallel to the current flowing along the (110) axis. For  $|H| > 100$  Oe, the  $\rho(T)$  dependence reveals a

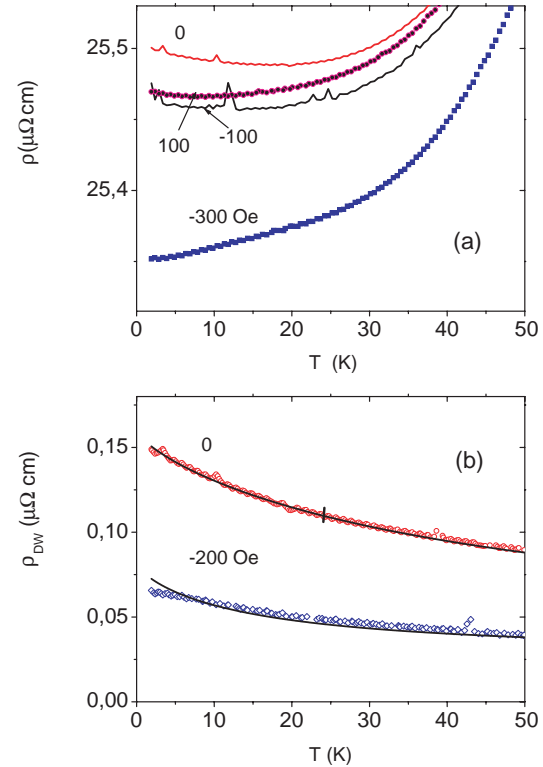


**Figure 3.** (a) Temperature dependence of the resistivity for  $[\text{Fe}(12 \text{ Å})/\text{Cr}]_{10}$  multilayer in different magnetic fields. Both the field and the current are along the (110) axis. (b) Temperature dependence of the DW contribution to the resistivity.  $\rho_{\text{DW}} = \rho(T, H) - \rho(T, H_S)$  determined from the data shown in (a) for  $H = 0$  and 200 Oe and  $H_S = -300$  Oe. The solid lines correspond to the fits which are described in the text. Vertical bar indicates maximum influence which could cause the GMR effect as on the estimated DW contribution.

metallic behavior, while for  $|H| \leq 100$  Oe, there is a shallow minimum in the  $\rho(T)$  curves.

In order to separate the DW contribution to magnetoresistivity from the GMR effect, the authors of [87] estimated the DW resistivity as  $\rho_{\text{DW}} = \rho(T, H) - \rho(T, H_S)$ , with  $|H_S| \leq 300$  Oe. Although this method may underestimate the magnetoresistivity due to DWs, because some of the domains may not be removed by the applied field  $H_S$ , it provides a possibility to determine the temperature dependence of the DW magnetoresistivity. Figure 3b shows  $\rho_{\text{DW}}(T, H)$  between 1.9 and 50 K for two magnetic fields (0 and –200 Oe) and zero field when  $H_S = -300$  Oe. In contrast to GMR, the DW magnetoresistivity is strongly temperature dependent at low temperatures, with no sign of saturation. The vertical bar indicates maximum influence, which could be caused by the GMR effect. This estimation was obtained from the temperature dependence of the magnetoresistivity measured for two different magnetic fields sufficiently large to remove all DWs. It is known from other measurements that, for Fe/Cr epitaxial multilayers, the GMR effect is weakly temperature dependent below 50 K; it saturates as  $T^2$ , and changes less than 7% [64]. The authors of [86, 87] also demonstrated that neither AMR (which depends on the relative orientation of the magnetization and the current  $I$ ) nor the ordinary magnetoresistivity caused by the Lorentz

force (which depends on the relative orientation of  $I$  and the magnetic induction  $B$ ) contributes to  $\rho_{\text{DW}}$ .

The ballistic approach to electron transport through DWs [69] requires that the mean-free path  $l$  in the epitaxial layers exceeds the DW width  $D$ , with  $20 < D < 200$  nm for Fe/Cr/Fe trilayers [95]. Therefore, the condition for ballistic transport may only be fulfilled at sufficiently low temperatures [93]. Although nonballistic effects have not yet been incorporated into the theory [69], it is clear that they cannot account for the strong variation of  $\rho_{\text{DW}}$  down to 1.9 K because the mean-free path is expected to saturate at low temperatures. Moreover, the strong pinning of DWs at low temperatures [87] implies that a distortion of the current lines by domain walls [73] or a change of the DW configuration cannot account for the observed strongly temperature-dependent low-field contribution to MR in antiferromagnetically coupled magnetic multilayers.

In order to explain the strong variation of the DW magnetoresistivity at low temperatures, one has to go beyond the classical approach [69]. A certain possibility is to link the observed phenomena either to standard, disorder-related, WL effects or to scattering by isolated spins. Experimental results [86, 87] are in conflict with both scenarios because the resistivity corrections with and without a magnetic field are different when a magnetic field is applied along the hard or easy axis. We note that both [70, 71] and [72] theoretical works predicted a destruction of WL by DWs, although the details of the destruction mechanism are different. Direct application of these models results in a sign of the DW magnetoresistivity, which is opposite that observed experimentally. However, the sign of the localization correction may be reversed due to strong spin-orbit scattering (antilocalization) [96]. The suppression of WL corrections by DWs, predicted in [70–72], is related to the associated effective gauge potential. In contrast to the electromagnetic vector potential corresponding to an external magnetic field, the gauge field depends on the electron spin giving rise to a different influence of DWs on the different components of the cooperon [72].

Measurements of Aliev et al. [86, 87] are consistent with the antilocalization effect in the absence of DWs ( $H > 300$  Oe) and its suppression in the presence of DWs ( $H = 0$ ). It is quite natural to assume the presence of a strong SO scattering in the vicinity of the interfaces of MMLs (Rashba term [97]). In the case of strong SO scattering, MR is caused by the destruction of the singlet cooperon by the gauge field associated with DWs.

When  $l \ll D$ , the system can be characterized in terms of the local conductivity, which is defined as an average over distances larger than  $l$ , but smaller than  $D$ . The localization correction for a particular DW is then determined by smaller diffusive trajectories with size  $L < D$ , as well as by large trajectories  $D < L < L_\varphi$ . The localization corrections associated with the small trajectories are suppressed by the gauge field since they are located within the DW. The contribution of large trajectories to localization is small, and for strong SO scattering, the local conductivity within a DW is

$$\sigma_{\text{DW}} \simeq \sigma_0 + \frac{e^2}{4\pi^2\hbar} \left[ \frac{1}{l} - \left( \frac{1}{L_{\text{DW}}^2} + \frac{1}{L_\varphi^2} \right)^{1/2} \right] \quad (12)$$

where  $L_{\text{DW}}$  is the characteristic length which is determined by the influence of the gauge potential  $A$ . Its magnitude can be estimated as  $A \sim 1/D$ , and consequently,  $L_{\text{DW}} \sim D$ .

Since the antilocalization correction without DW is

$$\sigma \simeq \sigma_0 + \frac{e^2}{4\pi^2\hbar} \left( \frac{1}{l} - \frac{1}{L_\varphi} \right) \quad (13)$$

one can estimate the difference in magnetoresistivity due to the DWs as

$$\sigma_{\text{DW}} - \sigma \simeq -\frac{e^2}{4\pi^2\hbar} \left[ \left( \frac{1}{L_{\text{DW}}^2} + \frac{1}{L_\varphi^2} \right)^{1/2} - \frac{1}{L_\varphi} \right] \quad (14)$$

The most important feature of this evaluation of the antilocalization effects is the fact that the correction to the local conductivity is determined by the gauge field inside DWs. If the current crosses a particular DW, the correction to the local conductivity, calculated for a narrow region inside the wall, shows up in the sample resistance.

One can also estimate the influence of an external magnetic field of 300 Oe and of the internal magnetization on the localization corrections. These effects are small when the magnetic length  $l_H \equiv \sqrt{\hbar c / (eH)} \gg l$ . For  $H = 300$  Oe,  $l_H \simeq 1.4 \cdot 10^{-5}$  cm. Assuming the internal magnetic induction  $B = 2$  T (a typical value for Fe), we obtain the corresponding length  $l_H \simeq 1.8 \times 10^{-6}$  cm. On the other hand, the mean-free path  $l \simeq 10^{-7}$  cm. Thus, both the external magnetic field and the magnetization are rather unable to effectively suppress the antilocalization corrections in these structures.

It is possible to fit the data [86, 87] to Eq. (14) by assuming that  $L_{\text{DW}}$  is independent of temperature, and that the phase-breaking length  $L_\varphi$  varies with temperature according to a power law  $L_\varphi \propto T^{-3/2}$  [12]. On the other hand, one has to introduce an additional (constant) shift of the data which takes into account the change of the resistance due to the variation of the angle between magnetic layers. It is important to note that the three different fits presented in Figure 3b correspond to the same fitting parameters, except for the parameter which describes the magnetic contrast ( $L_{\text{DW}}$ ). It is found that the effective DW width  $L_{\text{DW}}$  becomes about 2.5 times larger when the magnetic field is increased from 0 to 200 Oe. Thus, the detailed analysis shows that the experiments [86, 87] can be explained in terms of the suppression of antilocalization corrections by DWs.

As already mentioned, the dephasing effect may be induced, not only by the DWs, but also by the boundary magnetic field when a nonmagnetic conductor is sandwiched between two ferromagnetic layers. Tatara and Fukuyama [98] also found that spin mixing induced by SO interaction may suppress the antilocalization effect. This suppression is especially enhanced when the magnetizations of two layers are parallel.

## 9. LOCALIZATION CORRECTIONS TO MAGNETIC INTERACTIONS IN MULTILAYERS

The problem of magnetic interactions in magnetic multilayer structures is of high importance from the application point of view. It is closely related to the possibility of an

effective control of magnetization by an external magnetic field. Such a control is essential for the magnetoelectronic-device-based GMR effect [1,2]. During the last decade, the interlayer exchange coupling has been the subject of intensive study, both experimentally [3,4,99] and theoretically [100–104]. The main physics of the coupling is now well understood, and many experimental observations have been successfully explained by the existing theoretical models. There are several excellent review articles on the phenomenon [105–108].

The starting point of the analysis of magnetic coupling in the multilayer structures is the RKKY mechanism of *exchange interaction* between magnetic impurities in metals [109–111]. The indirect exchange interaction is mediated by itinerant electrons, which transfer the information about spin polarization from a particular impurity to another one. The key point of the RKKY mechanism is magnetic polarization of the electron gas by an impurity. Such a cloud of polarization couples to the spin of the other impurity. The effective exchange parameter varies with the distance  $R$  between magnetic impurities, and is proportional to  $\cos(2k_F R)/R^3$ , where  $k_F$  is the Fermi momentum of electrons in metal. Thus, the RKKY interaction changes sign with increasing  $R$ , and the corresponding oscillation period is  $\pi/k_F$ .

In contrast to the RKKY interaction between magnetic impurities, the magnetic interlayer coupling involves a collective interaction of a distributed magnetization within the magnetic layers. This makes the problem more complex for theoretical analysis because the application of perturbative methods is not well justified in this case. It also should be noted that both the homogeneity of the magnetization in the film plane and the finite layer thickness are of importance. This was shown in a number of works accounting for the oscillatory dependence of magnetic coupling on the layer thickness. The interlayer coupling generally depends on the spacer thickness as  $J = \sum_{\alpha} A_{\alpha} \sin(k_{\alpha} R)/R^2$ , where the index  $\alpha$  distinguishes different oscillatory components [108].

It turns out that the above-mentioned difference in the magnetic coupling between impurities and magnetic layers is crucial for the localization effects in the magnetic interaction. The problem concerns a range of the exchange interaction related to disorder. It was suggested in the past by de Gennes [112] that an inevitable disorder should impose a damping factor  $\exp(-R/l)$  on the exchange interaction between magnetic impurities, where  $l$  is the mean-free path of electrons in metal. However, a careful analysis of the interaction between magnetic impurities in disordered metals shows [113–115] that the exponential factor should be dropped in many cases. Namely, the result essentially depends on what physical quantity, determined by the interaction, is under averaging over possible realizations of the disorder.

Such a dependence is a manifestation of a nonself-averaging property of some physical quantities in the theory of disordered systems. A general rule is that we should average a physically observable quantity such as, for example, the magnitude of electric current (in many cases, it is the same as the averaging conductivity), depending on a specific realization of disorder. Correspondingly, to find the critical temperature  $T_c$  of a spin glass transition in a metallic system

with magnetic impurities, we should average the expression for the transition temperature, which contains  $J^2$ . The main result of [113,114] is that, without averaging over disorder (i.e., for any specific realization of disorder), the coupling between magnetic impurities does not contain any damping factor at all. Moreover, the averaged quantity  $\langle J^2 \rangle$  does not contain it either. The reason is that there is an exact compensation of the impurity contributions in diagrams describing the second power of coupling  $J$ .

However, the same approach to the theory of interlayer coupling [116] in magnetic structures with a disorder produced by nonmagnetic impurities and/or interface roughness shows that the effective interaction gains a damping factor  $\exp(-R/a)$ . However, the value of the interaction range  $a$  is not equal to  $l$ , and it can be considerably longer than the mean-free path of electrons in the spacer. In particular, the interfacial roughness does not change the damping factor, whereas it affects the electron mean-free path  $l$ . The nonvanishing damping factor in the interlayer coupling shows the self-averaging character of the magnetic interaction in magnetic structures, in contrast to the interaction between ions [116].

## 10. LOCALIZATION CORRECTIONS TO SPIN CONDUCTIVITY

The investigation of the transport properties of magnetic systems quite naturally invokes the problem of spin currents induced by some external fields (for instance, an electric field or the gradient of a magnetic field). A general theory of the spin-current response to external perturbations has been developed by Levy [117]. This approach distinguishes between the charge and spin currents, even though there is no real separation of spin and charge (both are related to the same particle). Nevertheless, in many cases, such an approach is better justified than the assumption of separated spin channels. In particular, the approach is justified for systems with large spin-orbit coupling, where a strong mixing of spin channels takes place, or for systems with strong Coulomb interaction which acts differently on the total charge and on the total spin (exchange interaction). The importance of the separation of charge and spin currents is also related to the conservation laws; there is a rigorous conservation law only for the total charge.

In the case of small perturbations, the corresponding linear response theory for the spin current can be easily developed. Such a linear response is described in terms of the spin conductivity. It can be shown that the spin conductivity and the spin diffusion coefficient obey Einstein's relation. The separation of spin and charge currents also allows us to separately study the localization effects on the spin and charge conductivities. Here, the spin conductivity is considered as a linear response of the system to an electric field. Physically, a nonvanishing spin current is possible in systems with some asymmetry in the transport properties of spin-up and spin-down electrons. The electric current in ferromagnets is usually associated with both the charge transfer and spin transfer.

The quantum corrections to spin conductivity can be derived using the same methods as in the case of corrections to charge conductivity. The localization correction to



the spin conductivity was analyzed in [118, 119], where it was shown that the correction vanishes in the absence of SO interaction. However, even if the SO interaction is present, the correction is rather small, which is due to cancellation of the contributions to spin conductivity from the spin-up and spin-down channels. It should be noted that this result is applicable to the disorder associated with localized impurity scatterers.

In the 3-D case (bulk ferromagnet), the correction to the spin conductivity has the following form:

$$\Delta\sigma_{\text{spin}}^{3\text{-D}} = \frac{e}{4\pi^2\hbar} \left[ \frac{1}{D_{\uparrow}^{1/2}} \left( \frac{1}{\tilde{\tau}_{\text{so}\uparrow}} + \frac{1}{\tau_{\varphi\uparrow}} \right)^{1/2} - \frac{1}{D_{\downarrow}^{1/2}} \left( \frac{1}{\tilde{\tau}_{\text{so}\downarrow}} + \frac{1}{\tau_{\varphi\downarrow}} \right)^{1/2} \right] \quad (15)$$

whereas in the effectively 2-D case, one finds

$$\Delta\sigma_{\text{spin}}^{2\text{-D}} = -\frac{e}{4\pi^2\hbar} \ln \left[ \frac{D_{\uparrow}(\tilde{\tau}_{\text{so}\downarrow}^{-1} + \tau_{\varphi\downarrow}^{-1})}{D_{\downarrow}(\tilde{\tau}_{\text{so}\uparrow}^{-1} + \tau_{\varphi\uparrow}^{-1})} \right] \quad (16)$$

The main contributions to the correction, originating from the shortest time  $\tau_{\sigma}$ , are exactly canceled. Thus, the correction to the spin conductivity is determined by the SO relaxation time and the phase relaxation rate.

## 11. LOCALIZATION EFFECTS IN LOW-CARRIER-DENSITY MAGNETS

The quantum corrections to low-temperature resistivity have been studied recently in perovskite-type manganites  $\text{La}_{1-x}\text{Pb}_x\text{MnO}_3$  [120] and bilayer manganites  $\text{La}_{1.2}\text{Sr}_{1.8}\text{Mn}_2\text{O}_7$  [121]. The interest in these compounds is mostly related to the colossal MR (CMR), which is usually attributed to the magnetic-field-controlled scattering from localized magnetic moments. The physics of manganites is very interesting and complex because of the interplay of magnetic effects, disorder, and strong electron–electron correlations leading to Mott-type phase transitions. This results in a complex character of the temperature dependence of resistivity, with a distinguished region of prevailing scattering from magnons. Single-crystalline  $\text{La}_{1.2}\text{Sr}_{1.8}\text{Mn}_2\text{O}_7$  manganites, used for studies of quantum interaction effects, were grown from sintered rods of the same nominal composition by the floating-zone method using a mirror furnace, described in detail in [122]. High-quality single crystals  $\text{La}_{1-x}\text{Pb}_x\text{MnO}_3$  were grown by the flux growth using the accelerated crucible rotation technique. The detailed preparation process and composition analysis are described in [123]. A temperature dependence for  $\text{La}_{1-x}\text{Pb}_x\text{MnO}_3$  perovskite manganites [120] clearly shows an increasing resistivity with decreasing temperature for  $T < 50$  K. This increase obeys the low  $T^{1/2}$  characteristic for quantum correction due to e–e interactions in 3-D metals or due to WL with the phase relaxation time  $\tau_{\varphi}$  depending on the temperature as  $\tau_{\varphi} \sim T^{-1/2}$  [12, 13]. The latter dependence is characteristic of the inelastic e–e scattering, which results in dephasing of the electrons. The key role of e–e interactions seems to be

quite natural for these compounds, which have typical characteristics of strongly correlated electron systems. MR was found to be positive and relatively large, up to 20% at 4.2 K. The positive sign of MR has been attributed to the e–e interaction in the presence of disorder [120]. The temperature dependence of the resistivity correction for  $\text{La}_{1.2}\text{Sr}_{1.8}\text{Mn}_2\text{O}_7$  was studied by Zhang et al. [121], who found the same  $T^{-1/2}$  dependence. The authors proposed the explanation in the framework of WL with the dephasing time  $\tau_{\varphi} \sim T^{-1/2}$ .

Another interesting example was the observation of quantum interference effects in  $\text{Fe}_{1-y}\text{Co}_y\text{Si}$  ferromagnets [124]. This system is peculiar because the two limiting compounds (for  $x = 0$  and  $x = 1$ ) are both nonmagnetic, whereas for almost all intermediate compositions, it is magnetic [125]. Polycrystalline pellets or small single crystals grown from Sb and Sn were produced from high-purity starting materials by arc melting in an argon atmosphere. Annealing of  $\text{Fe}_{1-y}\text{Co}_y\text{Si}$  ( $\text{Fe}_{1-x}\text{Mn}_x\text{Si}$ ) in evacuated quartz ampoules for 24 h at 1280 °C (four days at 1000 °C) improved the homogeneity of the samples. The linearity of the lattice constants with Co and Mn concentration indicates that Co or Mn successfully replaces Fe over the entire concentration range ( $0 < x < 1$ ;  $0 < y < 1$ ). Energy dispersive X-ray microanalysis confirmed the nominal concentrations. The Hall effect data established the sign and density of the carriers, and demonstrated a systematic increase in the carrier density ( $n$ ) proportional to the Co and Mn concentration at small  $x$  and  $y$  [124]. It was shown that  $n$  does not change when the Curie temperature is surpassed. Spontaneous magnetization determined from the saturated value of the magnetization at high magnetic fields corresponds to approximately  $1 \mu_B$  per Co atom. These materials are highly disordered low-carrier-density ferromagnets, where the same electrons are responsible for both the magnetic properties and the electric conduction. One should note, however, the rather low coercive magnetic field, as may be determined from the analysis of the magnetization hysteresis [124]. This implies either weak ferromagnetic crystalline anisotropy and/or weak domain wall pinning. A large positive and weakly temperature-dependent MR was observed at  $T < 35$  K (below the Curie temperature). Due to the similarity between the low-temperature magnetotransport for paramagnetic Al- and Mn-doped FeSi and  $\text{Fe}_{1-x}\text{Co}_x\text{Si}$ , the authors [124] concluded that the low-temperature MR in ferromagnetic  $\text{Fe}_{1-x}\text{Co}_x\text{Si}$  is due to e–e interaction enhanced by disorder. Indeed, the dependence of the correction on the magnetic field is in good agreement with the interaction theory of magnetoconductivity in nonmagnetic 3-D systems [12, 13], provided the magnetic field is substituted by an effective field  $H_{\text{eff}} = H + \alpha M$ , where  $\alpha$  is a constant and  $M$  is the internal magnetization. The temperature dependence of the correction to conductivity obeys the  $T^{-1/2}$  law. The temperature scaling  $(\sigma - \sigma_0)/T^{1/2}$  versus  $H_{\text{eff}}/T$  has been observed for temperatures up to 100 K in some alloys, which demonstrates the strong quantum interference effects at rather high temperatures. The experimental results of the above-described works are in rough agreement with our previous analysis. Indeed, in the case of strong ferromagnets, the magnetization completely suppresses the singlet cooperons and diffusons. The effect of an external magnetic field can be seen only on the triplet

cooperons, for which the magnetic field dependence appears as in the case of nonmagnetic metals with the magnetic field  $H$  replaced by the magnetic induction  $B$ . Finally, we note that the enhanced e–e interaction effects and WL were also reported in the conductivity of ferromagnetic glasses [126,127]. However, the presence of a minimum in resistivity at rather high temperatures (above 200 K) indicates the electron interaction with two-level systems as the most probable explanation of the effect [128].

## 12. COULOMB INTERACTIONS IN FERROMAGNETIC DOUBLE JUNCTIONS

When the central electrode (island) of a double-barrier junction is small, the addition of one extra electron may cost a significant amount of energy. This addition energy includes a contribution following from the quantization of the energy levels of the island, and also a term due to the electrostatic interaction of the extra electron with other electrons being on the island. These two contributions may be comparable. In a few-electron quantum dot, the discreteness is important. In metallic islands (grains) of nanometer size, on the other hand, the quantization of the energy levels is less important, and in that case, the energy related to the electrostatic interaction plays a dominant role. In the simplest case, one may approximate the electrostatic energy by a phenomenological charging energy  $E_c = e^2/2C$ , where  $C$  is the capacitance of the island. The charging energy defined in this way is independent of the distribution of electrons between different discrete levels. This phenomenological model describes the transport characteristics rather well for the energy relaxation time on the island smaller than the injection time (time between the following tunneling events). When the capacitance  $C$  is sufficiently small, one can then reach the regime where the charging energy  $E_c$  is larger than the thermal energy  $k_B T$ . If this is the case, discrete charging of the island with single electrons modifies the junction current–voltage characteristics, leading to a Coulomb blockade of the electric current below a certain threshold voltage and to characteristic Coulomb steps above the threshold [22]. When the system is in the blocked state, then the blockade can be removed by applying a gate voltage to the island. The system then acts like a transistor, in which, however, electrons are transmitted in a correlated way one by one, and therefore the device is called a single-electron transistor (SET).

There are two methods of magnetic control of the Coulomb blockade phenomena. First, one can apply a relatively strong magnetic field which, owing to the Zeeman splitting of the energy states and spin asymmetry in the density of electron states, induces a shift of the chemical potential in the ferromagnetic electrodes (external and/or central), and therefore effectively acts as a magnetic gate. This method, however, is limited to rather small charging energies and, consequently, to low temperatures (due to the small Zeeman energy) [23].

Another method of magnetic control of the Coulomb blockade effects follows from the sensitivity of the charging effects to the relative orientation of the magnetic moments of the grain (if it is magnetic) and external electrodes

[129,130]. This technique is not limited to low temperatures, and for realistic parameters, can also work at room temperatures. We will restrict our further considerations to this method and to a double junction, in which both external electrodes are ferromagnetic, while the island is nonmagnetic.

Generally, one can distinguish three relevant time scales in electronic transport through ferromagnetic (FM) or nonmagnetic (NM) double junctions: (1) spin-conserving energy relaxation time on the island  $\tau_\epsilon$ , (2) current injection time  $\tau_I$ , and (3) spin-flip relaxation time  $\tau_{sf}$ . In real systems,  $\tau_\epsilon$  is usually the shortest time scale,  $\tau_\epsilon < 10^{-9}$  s, whereas  $\tau_{sf}$  can be in the range  $10^{-9}$ – $10^{-6}$  s. On the other hand, for a current of 1 nA, the injection time is of the order of  $10^{-9}$  s. Thus, the slow spin relaxation limit is experimentally accessible. Accordingly, one may assume that the shortest time scale in many systems is the spin-conserving energy relaxation time. As concerns the other two time scales, we will distinguish two regimes. The first is the slow spin relaxation regime, where the longest time scale is the spin-flip relaxation time  $\tau_{sf} \gg \tau_I \gg \tau_\epsilon$ . In this regime, an electron tunneling to the island relaxes to the relevant Fermi level before the next tunneling processes occur. However, the electron can preserve its spin orientation for a time much longer than the time between successive tunneling events (injection time). This means that the electrons on the island in a steady state can be described by two Fermi levels corresponding to opposite spin orientations [131–133]. The second regime is the so-called fast spin relaxation regime, where  $\tau_{sf}$  becomes of the order of  $\tau_I$  or even shorter. In that case, there is a common Fermi level for different spin orientations [129,130]. In this limit, the two external electrodes become magnetically decoupled, and when the central electrode is nonmagnetic, the total current flowing through the system is independent of the magnetic configuration. In the following, we assume spin-conserving tunneling through the barriers, and define positive bias  $V$  as the one corresponding to current flowing from the left to the right (electrons flow in the opposite direction).

### 12.1. Limit of Continuous Density of States

Assume that the effects due to the quantization of energy levels on the island are negligible. Such an assumption is reasonable when the separation between discrete energy levels is much smaller than the charging energy, and also significantly smaller than the thermal energy  $k_B T$ . When the barrier resistances are larger than the quantum resistance  $R_q$  ( $R_q \approx 26$  k $\Omega$ ), one can use the “orthodox” tunneling theory to describe electronic transport. In the sequential tunneling regime, an electron tunnels to the island through one barrier, and later another electron leaves the island through the second barrier (or vice versa). These processes are suppressed below a certain threshold voltage, and therefore are dominant only above the first Coulomb step. The electric current  $I$  in the sequential tunneling regime can be calculated from the formula

$$\begin{aligned} I &= -e \sum_N P(N) \sum_\sigma \{ \Gamma_{l\sigma}^+(N) - \Gamma_{l\sigma}^-(N) \} \\ &= e \sum_N P(N) \sum_\sigma \{ \Gamma_{r\sigma}^+(N) - \Gamma_{r\sigma}^-(N) \} \end{aligned} \quad (17)$$

where  $e$  is the absolute value of electron charge ( $e > 0$ ),  $\Gamma_{\alpha\sigma}^{\pm}(N)$  ( $\alpha = l$  for the left junction and  $\alpha = r$  for the right junction) are the tunneling rates for electrons with spin  $\sigma$ , which tunnel to the island (+) from the lead  $\alpha$  or back (-), whereas  $P(N)$  is the probability of finding  $N$  excess electrons on the island.

The probability  $P(N)$  is usually calculated from the master equation

$$\begin{aligned} \partial P(N)/\partial t = 0 = & -\Gamma(N)P(N) + P(N-1) \sum_{\sigma} \Gamma_{\sigma}^{+}(N-1) \\ & + P(N+1) \sum_{\sigma} \Gamma_{\sigma}^{-}(N+1) \end{aligned} \quad (18)$$

where  $\Gamma_{\sigma}^{\pm}(N) = \Gamma_{l\sigma}^{\pm}(N) + \Gamma_{r\sigma}^{\pm}(N)$  and  $\Gamma(N) = \sum_{\sigma} \{\Gamma_{\sigma}^{+}(N) + \Gamma_{\sigma}^{-}(N)\}$ . From this follows that, in a steady state, the net transition rate between the states with  $N$  and  $N+1$  excess electrons on the island is equal to zero, which can be used to calculate the probability  $P(N)$  [134].

The transition rate  $\Gamma_{r\sigma}^{+}(N)$  is given by

$$\begin{aligned} \Gamma_{r\sigma}^{+}(N) = & \frac{2\pi}{\hbar} \int dE |T_{r\sigma}(E)|^2 D_{r\sigma}(E - E_F^{(r)}) D_{i\sigma}(E - E_{F\sigma}^{(i)}) \\ & \times f(E - E_F^{(r)}) [1 - f(E - E_{F\sigma}^{(i)})] \end{aligned} \quad (19)$$

where  $T_{r\sigma}(E)$  is an average transition matrix element for electronic states of energy  $E$ , while  $E_{F\sigma}^{(i)}$  and  $E_F^{(r)}$  are the Fermi levels, respectively, for the island and right electrode. Due to spin accumulation on the island in a general case, the Fermi level  $E_{F\sigma}^{(i)}$  is spin dependent. The difference between  $E_{F\sigma}^{(i)}$  and  $E_F^{(r)}$  depends on the applied voltage and the number of excess electrons on the grain, and can be written as  $E_{F\sigma}^{(i)} - E_F^{(r)} = E_c + \Delta E_{\sigma}^{(i)} - eV_r(N)$ . Here,  $E_c = e^2/2(C_l + C_r)$ , and  $V_r(N) = C_l V / (C_l + C_r) - Ne / (C_l + C_r)$ , with  $C_l$  and  $C_r$  the capacitances of the two junctions ( $C_l + C_r = C$ ). Apart from this,  $\Delta E_{\sigma}^{(i)}$  is a shift of the chemical potential of the grain for spin  $\sigma$ , which is caused by spin accumulation.

Generally, the spin dependence of the transition rates  $\Gamma_{\alpha\sigma}^{+}(N)$  and  $\Gamma_{\alpha\sigma}^{-}(N)$  ( $\alpha = 1, 2$ ) follows from the spin dependence of the matrix elements, the spin dependence of the density of electron states, and the spin dependence of the Fermi level. For constant (independent of energy) matrix elements and density of states in the electrodes, the transition rate  $\Gamma_{r\sigma}^{+}(N)$  can be written as

$$\Gamma_{r\sigma}^{+}(N) = \frac{1}{e^2 R_{r\sigma}} \frac{+eV_r(N) - E_c - \Delta E_{\sigma}^{(i)}}{1 - \exp\{[-eV_r(N) + E_c + \Delta E_{\sigma}^{(i)}]/kT\}} \quad (20)$$

where  $R_{r\sigma}$  is the resistance of the right junction for the spin channel  $\sigma$ . Formulas similar to Eq. (20) also can be written for  $\Gamma_{r\sigma}^{-}(N)$  and for the tunneling rates  $\Gamma_{l\sigma}^{+}(N)$  and  $\Gamma_{l\sigma}^{-}(N)$  through the left junction.

For arbitrary  $\tau_{sf}$ , the chemical potential shifts  $\Delta E_{\sigma}^{(i)}$  can be determined from the relevant balance equation which, for the case of a nonmagnetic island, takes the form

$$\frac{1}{e} (I_{\uparrow}^{(r)} - I_{\uparrow}^{(l)}) - \frac{2D}{\tau_{sf}} \Delta E_{\uparrow}^{(i)} = 0 \quad (21)$$

where  $I_{\uparrow}^{(\alpha)}$  ( $\alpha = l, r$ ) is the current of spin-up electrons through the  $\alpha$ th junction,  $D$  is the density of electron states in the island per spin, and the condition  $\Delta E_{\sigma}^{(i)} = -\Delta E_{-\sigma}^{(i)}$  was used (valid for nonmagnetic islands). The chemical potential shifts and electric current flowing through the junction have to be calculated self-consistently.

Typical transport characteristics of a double-barrier junction with a nonmagnetic island are shown in Figure 4 for both parallel and antiparallel magnetic configurations, and for the slow spin relaxation limit on the island. In both cases, the electric current is blocked below a certain threshold voltage, which is determined by the charging energy and the ratio of capacitances  $C_l/C_r$ . Current flows above the threshold voltage and a typical Coulomb staircase then can be observed. Each step corresponds to a new charge state of the island, and consequently, to a new channel for electron tunneling. The Coulomb steps are well resolved for an asymmetric junction, when the resistances of both barriers are significantly different. However, the steps of the Coulomb “staircase” above the threshold voltage are qualitatively different in the parallel and antiparallel configurations. This difference is due to spin accumulation and associated shifts of the chemical potentials. When the electrodes are of the same ferromagnetic material, there is no spin accumulation on the island in the parallel configuration, and consequently, no spin splitting of the chemical potential. Thus, the current–voltage curves in this configuration are similar to those for nonmagnetic junctions. In contrast, in the antiparallel configuration, the spin asymmetries for both junctions are different, and a nonequilibrium magnetic moment builds up on the island (spin accumulation) until the tunneling rates for a given spin orientation become equal for both junctions. The additional kinks on the  $I$ – $V$  curve for the antiparallel configuration correspond to the local maxima of spin accumulation. Since the  $I$ – $V$  characteristics are different in the parallel and antiparallel configurations, transition

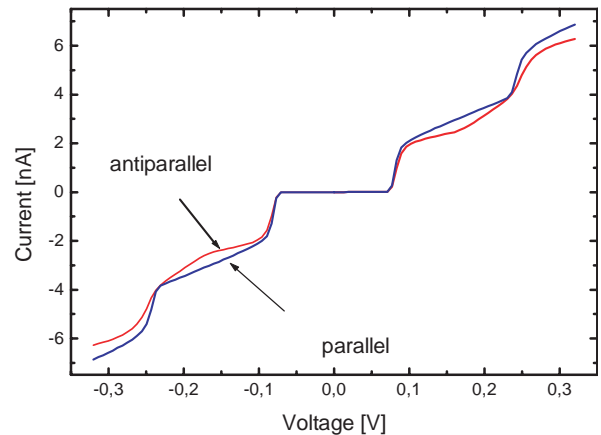


**Figure 4.** Typical current–voltage characteristics in the parallel and antiparallel configurations, calculated for the long spin-flip relaxation time limit. The junction consists of two identical ferromagnetic outer electrodes, two nonmagnetic barriers, and a nonmagnetic metallic central electrode. The parameters assumed are:  $E_c = 40$  meV,  $kT = 1$  meV,  $R_{1+} = 2$  M $\Omega$ ,  $R_{1-} = 0.5$  M $\Omega$ ,  $R_{2+} = 200$  M $\Omega$ ,  $R_{2-} = 50$  M $\Omega$ , and  $C_1/C_2 = 1$ . Here,  $\sigma = \pm$  corresponds to the majority (minority) electrons.

from one configuration to the other results in a nonvanishing TMR effect, which varies with the bias voltage reflecting the features in the corresponding  $I$ - $V$  curves.

When the spin-flip relaxation time for the island becomes shorter, the TMR effect decreases. In the case of a nonmagnetic island, no TMR appears in the fast spin relaxation limit. The transition from slow to fast spin relaxation was considered in [135], where it was shown that TMR drops relatively fast to almost zero when the spin relaxation time approaches the injection time.

Sequential tunneling processes are suppressed below the threshold voltage. However, there are still processes of higher order (cotunneling), which can transport charge between the source and drain electrodes [130]. In the cotunneling processes, two tunneling events are correlated in time, and are not blocked by the charging energy. Being of higher order, they are less effective, and therefore the electric current in the cotunneling regime is smaller than in the sequential one. Close to the threshold voltage, however, both currents may be comparable.

The cotunneling processes can be calculated perturbatively. The lowest order perturbation description is valid sufficiently well below the threshold voltage. However, a more general description has been worked out, which is also valid in the transition regime. Such a description was formulated in terms of closed-time path Green functions [136] for nonmagnetic SETs. This description was extended recently to magnetic systems [137]. It includes the double-barrier cotunneling processes directly contributing to electric current, and the single-barrier cotunneling processes which—although do not contribute directly to the flowing current—give an indirect contribution via modification of the magnetic state of the island. Other cotunneling processes lead to vertex and propagator renormalization. When the spin relaxation time on the island is long, the cotunneling processes—similarly as the sequential ones—lead to spin accumulation on the island.

## 12.2. Role of Discreteness

When  $kT \ll \Delta E$ , the size quantization of energy levels on the island must be taken into account [138–140]. To describe the transport properties, the “orthodox” tunneling theory [141] was generalized by taking into account the electron spin [140]. The electric current in a stationary state is now given by the formula [140]

$$I = -e \sum_{\sigma} \sum_{N_{\uparrow}, N_{\downarrow}} P(N_{\uparrow}, N_{\downarrow}) \{ \Gamma_{l\sigma}^{+}(N_{\uparrow}, N_{\downarrow}) - \Gamma_{l\sigma}^{-}(N_{\uparrow}, N_{\downarrow}) \} \\ = e \sum_{\sigma} \sum_{N_{\uparrow}, N_{\downarrow}} P(N_{\uparrow}, N_{\downarrow}) \{ \Gamma_{r\sigma}^{+}(N_{\uparrow}, N_{\downarrow}) - \Gamma_{r\sigma}^{-}(N_{\uparrow}, N_{\downarrow}) \} \quad (22)$$

where  $\Gamma_{\alpha\sigma}^{\pm}(N_{\uparrow}, N_{\downarrow})$  are the tunneling rates for electrons with spin  $\sigma$  tunneling to the island (+) from the lead  $\alpha = l, r$  or back (−), and  $P(N_{\uparrow}, N_{\downarrow})$  is the probability to find  $N_{\uparrow}$  and  $N_{\downarrow}$  excess electrons on the island with the spin  $\sigma = \uparrow$  and  $\sigma = \downarrow$ , respectively. The total number of excess electrons on the island is  $N = N_{\uparrow} + N_{\downarrow}$ , while its magnetic moment is determined by  $M = N_{\uparrow} - N_{\downarrow}$ . As before, only spin-conserving tunneling processes are taken into account in Ex. (22).

The probability  $P(N_{\uparrow}, N_{\downarrow})$  can be calculated from the following master equation [140]:

$$\partial P(N_{\uparrow}, N_{\downarrow}) / \partial t \\ = 0 = - [ \Gamma(N_{\uparrow}, N_{\downarrow}) + \Omega_{\uparrow, \downarrow}(N_{\uparrow}, N_{\downarrow}) + \Omega_{\downarrow, \uparrow}(N_{\uparrow}, N_{\downarrow}) ] \\ \times P(N_{\uparrow}, N_{\downarrow}) + \Gamma_{\uparrow}^{+}(N_{\uparrow} - 1, N_{\downarrow}) P(N_{\uparrow} - 1, N_{\downarrow}) \\ + \Gamma_{\downarrow}^{+}(N_{\uparrow}, N_{\downarrow} - 1) P(N_{\uparrow}, N_{\downarrow} - 1) + \Gamma_{\uparrow}^{-}(N_{\uparrow} + 1, N_{\downarrow}) \\ \times P(N_{\uparrow} + 1, N_{\downarrow}) + \Gamma_{\downarrow}^{-}(N_{\uparrow}, N_{\downarrow} + 1) P(N_{\uparrow}, N_{\downarrow} + 1) \\ + \Omega_{\uparrow, \downarrow}(N_{\uparrow} - 1, N_{\downarrow} + 1) P(N_{\uparrow} - 1, N_{\downarrow} + 1) \\ + \Omega_{\downarrow, \uparrow}(N_{\uparrow} + 1, N_{\downarrow} - 1) P(N_{\uparrow} + 1, N_{\downarrow} - 1) \quad (23)$$

where  $\Gamma_{\alpha\sigma}^{\pm}(N_{\uparrow}, N_{\downarrow}) = \sum_{\alpha=l,r} \Gamma_{\alpha\sigma}^{\pm}(N_{\uparrow}, N_{\downarrow})$  and  $\Gamma(N_{\uparrow}, N_{\downarrow}) = \sum_{\sigma} [ \Gamma_{\sigma}^{+}(N_{\uparrow}, N_{\downarrow}) + \Gamma_{\sigma}^{-}(N_{\uparrow}, N_{\downarrow}) ]$ . The tunneling rates  $\Gamma_{\alpha\sigma}^{\pm}(N_{\uparrow}, N_{\downarrow})$  include tunneling process between the lead  $\alpha$  and all discrete levels  $E_{n\sigma}$  of the island. The  $\Omega$  terms, on the other hand, take into account the spin-flip process on the island. For a nonmagnetic island, one may assume that the discrete energy levels  $E_{n\sigma}$  are independent of the spin orientation. One can also simplify the description further by assuming that the levels are equally separated, with the level spacing  $\Delta E$ . The tunneling rates  $\Gamma_{\alpha\sigma}^{\pm}(N_{\uparrow}, N_{\downarrow})$  can be then expressed in terms of the bare tunneling rates  $\gamma_{n\sigma}^{\alpha} = \Delta E / e^2 R_{\alpha\sigma}$  [141]. When the level separation  $\Delta E$  becomes of the order of  $k_B T$  or larger, but still smaller than  $E_c$ , the effects due to the discrete structure become visible in the transport characteristics as additional small steps [140].

## 13. TRANSPORT THROUGH QUANTUM DOTS WITH ELECTRON CORRELATIONS

Further features appear when  $E_c \leq \Delta E$ . A limiting case is when tunneling takes place through a single discrete level. The system consisting of a single-level nonmagnetic quantum dot coupled to two ferromagnetic leads can be described by the Hamiltonian  $H = H_l + H_r + H_d + H_t$ , where the first two terms,  $H_l$  and  $H_r$ , describe the left and right electrodes (in the noninteracting particle approximation, for simplicity), whereas the term  $H_d$  describes the dot, and can be taken in the Hubbard form  $H_d = \sum_{\sigma} \epsilon_d c_{\sigma}^{+} c_{\sigma} + U c_{\uparrow}^{+} c_{\uparrow} c_{\downarrow}^{+} c_{\downarrow}$ , in which  $\epsilon_d$  is the energy of the discrete level,  $U$  is the electron correlation parameter, and  $c_{\sigma}^{+}$  ( $c_{\sigma}$ ) are the creation (annihilation) operators for the dot. The energy level  $\epsilon_d$  includes the electrostatic part,  $\epsilon_d = \epsilon_d^0 + eU_e$ , where  $\epsilon_d^0$  is the level energy at zero bias, and  $U_e$  is the electrostatic potential of the dot. The last term,  $H_t$ , is the tunneling part of the Hamiltonian, where only spin-conserving tunneling processes are taken into account.

When the tunneling rates are small, the transport characteristics can be calculated within the master equation technique [142, 143]. In a more general situation, such a description is not sufficient since it does not properly take into account the electron correlations on the dot. It also breaks down in the strong tunneling regime and at low temperatures, where many body effects become important and lead to the Kondo effect. A more accurate description

is based on the nonequilibrium Green's functions (NGFs) [144, 145].

The tunneling current  $J_\sigma$  can be calculated from the formula [144–146]

$$J_\sigma = \frac{ie}{\hbar} \int \frac{d\epsilon}{2\pi} [f_l(\epsilon) - f_r(\epsilon)] \frac{\Gamma_\sigma^r(\epsilon)\Gamma_\sigma^l(\epsilon)}{\Gamma_\sigma^r(\epsilon) + \Gamma_\sigma^l(\epsilon)} \times [\langle\langle c_\sigma; c_\sigma^+ \rangle\rangle_\epsilon^r - \langle\langle c_\sigma; c_\sigma^+ \rangle\rangle_\epsilon^a] \quad (24)$$

where  $\langle\langle c_\sigma; c_\sigma^+ \rangle\rangle_\epsilon^r$  and  $\langle\langle c_\sigma; c_\sigma^+ \rangle\rangle_\epsilon^a$  are the retarded and advanced Green's functions,  $f_l(\epsilon)$  and  $f_r(\epsilon)$  are the Fermi distribution functions for the left and right electrodes, whereas  $\Gamma_\sigma^l(\epsilon)$  and  $\Gamma_\sigma^r(\epsilon)$  are the contributions to the half width of the discrete level due to electron tunneling to the left and right electrodes, respectively. The formula (26) is valid when  $\Gamma_\sigma^l(\epsilon)$  and  $\Gamma_\sigma^r(\epsilon)$  are proportional,  $\Gamma_\sigma^l(\epsilon) = \lambda\Gamma_\sigma^r(\epsilon)$ .

Equations of motion for the retarded and advanced Green's functions contain the occupation numbers  $n_\sigma = \langle c_\sigma^+ c_\sigma \rangle$ , which in turn are determined by the lesser Green's function  $\langle\langle c_\sigma; c_\sigma^+ \rangle\rangle_\epsilon^<$  via the formula,  $n_\sigma = \int (d\epsilon/2\pi) \times \text{Im}\langle\langle c_\sigma; c_\sigma^+ \rangle\rangle_\epsilon^<$ . Thus, to find the electric current, one needs to calculate self-consistently all of the Green's functions, occupation numbers, and the electrostatic potential. When the Kondo effect is irrelevant, the Green's functions can be calculated in the Hartree–Fock approximation.

When the temperature is sufficiently low, the Kondo resonance in the density of states is formed, which has a dramatic influence on transport through the dot. The Kondo effect occurs in quantum dots containing an odd number of electrons, and is related to screening of the dot spin by conduction electrons in the leads. This screening is a many-body effect which occurs due to exchange coupling between the electrons on the dot and in the leads. In the case of quantum dots connected to nonmagnetic leads, the Kondo effect was extensively studied in the past decade. However, some new interesting questions arise when the leads are ferromagnetic and the conduction electrons are spin polarized. Recent theoretical results show that the Kondo effect still persists in such systems, although its characteristics are significantly modified [147, 148].

## 14. SUMMARY

The localization and interaction corrections to electrical conductivity can be significant not only in nonmagnetic, but also in ferromagnetic disordered metals or nanoscopic structures. As ferromagnetism diminishes localization corrections (and generally suppresses the singlet cooperon leading to the absence of weak antilocalization), the interaction corrections are rather unaffected by the ferromagnetism, and therefore can be easily observed in ferromagnetic systems. The corrections are important only at relatively low temperatures. Generally, there are some experimental works which confirm the importance of the WL and e–e interaction corrections. These data were usually accounted for on the basis of the theoretical results obtained for nonmagnetic systems. Even though the physical origin of quantum corrections in ferromagnets is substantially the same as in nonmagnetic

systems, there is an important difference due to the presence of internal magnetization and magnetic induction in ferromagnets.

Electron–electron interaction also leads to significant effects in ferromagnetic mesoscopic double-barrier tunnel junctions, which are also observable at high temperatures. In the case of a sufficiently large central electrode, this interaction can be described by a phenomenological charging energy. This charging energy leads to a Coulomb blockade of electric current below a certain threshold voltage, and also to Coulomb steps at higher voltages. The interplay of ferromagnetism and charging effects leads to some new features in the transport characteristics. Some of these features result from nonequilibrium spin accumulation at the small central electrode. When the central electrode is a quantum dot, the Coulomb correlation on the dot can be described in terms of the Hubbard model. Electronic transport then takes place through a small number of discrete levels (or even through a single level), which leads to additional features.

Coherent transport in the low-temperature range as well as ferromagnetic tunnel junctions (also operating at high temperature) are of potential importance for applications in magnetoelectronics and spintronics devices. The ferromagnetic systems or ferromagnetic components of a more complex device can be either metallic or semiconducting. Recently, huge efforts have been undertaken to grow ferromagnetic semiconductors with room-temperature ferromagnetism. The phenomena described in this review apply to ferromagnetic semiconductors too.

## GLOSSARY

**Anisotropic magnetoresistance (AMR)** Magnetoresistance observed in ferromagnetic metals which depends on relative orientation of electric current and magnetization.

**Anomalous hall effect (AHE)** Transverse current induced by the electric field in ferromagnets in the absence of external magnetic field.

**Giant magnetoresistance (GMR)** Magnetoresistance in magnetic multilayer system related to the switch from antiferromagnetic to ferromagnetic ordering in magnetic layers by weak magnetic field.

**Magnetic multilayers (MMLs)** Alternating thin layers of magnetic and nonmagnetic metals.

**Magnetoresistance (MR)** Variation of the resistance of metals and semiconductors in magnetic field.

**Molecular beam epitaxy (MBE)** Technology of the epitaxial growth of thin films using molecular beams.

**Ruderman–Kittel–Kasuya–Yosida interaction (RRKY)** Magnetic interaction due to the exchange between magnetic impurities via free electron gas.

**Spin–orbit interaction (SO)** The interaction affecting the spin state of a particle due to its orbital motion.

**Tunneling magnetoresistance (TMR)** Magnetoresistance in tunneling systems with magnetic overlayers.

**Weak localization (WL)** Theory of weak corrections to conductivity in metals and heavily doped semiconductors induced by disorder.

## ACKNOWLEDGMENTS

V. K. Dugaev is grateful to P. Bruno for many stimulating discussions. F. G. Aliev thanks R. Villar for critical reading of the manuscript. This work was supported by the Polish Committee for Scientific Research under Grants 5 P03B 091 20 and PBZ/KBN/044/P03/2001, and also by Spanish MCyT (BFM2000-0016) and CM (07N/0050/2002).

## REFERENCES

1. M. N. Baibich, J. M. Broto, A. Fert, F. Nguyen van Dau, F. Petroff, P. Etienne, G. Creuzet, A. Friederich, and J. Chazelas, *Phys. Rev. Lett.* 61, 2472 (1988).
2. G. Binasch, P. Grünberg, F. Saurenbach, and W. Zinn, *Phys. Rev. B* 39, 4828 (1989).
3. P. Grünberg, R. Schreiber, Y. Pang, M. B. Brodsky, and H. Sowers, *Phys. Rev. Lett.* 57, 2442 (1986).
4. S. S. P. Parkin, N. More, and K. P. Roche, *Phys. Rev. Lett.* 64, 2304 (1990).
5. J. M. George, L. G. Pereira, A. Barthelemy, F. Petroff, L. Steren, J. L. Duval, A. Fert, R. Loloee, P. Holody, and P. A. Schroeder, *Phys. Rev. Lett.* 72, 408 (1994).
6. J. Barnaś, A. Fuss, R. E. Camley, P. Grünberg, and W. Zinn, *Phys. Rev. B* 42, 8110 (1990).
7. W. P. Pratt Jr., S. F. Lee, J. M. Slaughter, P. A. Schroeder, and J. Bass, *Phys. Rev. Lett.* 66, 3060 (1991).
8. M. A. M. Gijss, S. K. J. Lenczowski, and J. B. Giesbers, *Phys. Rev. Lett.* 70, 3343 (1993).
9. A. Blondel, J. P. Meier, B. Doudin, and J.-Ph. Ansermet, *Appl. Phys. Lett.* 65, 3019 (1994).
10. P. W. Anderson, *Phys. Rev.* 109, 1492 (1958).
11. B. L. Altshuler, A. G. Aronov, D. E. Khmel'nitskii, and A. I. Larkin, in "Quantum Theory of Solids" (I. M. Lifshits, Ed.), p. 130. Mir, Moscow, 1982.
12. P. A. Lee and T. V. Ramakrishnan, *Rev. Mod. Phys.* 57, 287 (1985).
13. B. L. Altshuler and A. G. Aronov, in "Electron-Electron Interaction in Disordered Systems" (A. L. Efros and M. Pollak, Eds.), p. 1. Elsevier, Amsterdam, 1985.
14. H. Fukuyama, in "Electron-Electron Interaction in Disordered Systems" (A. L. Efros and M. Pollak, Eds.), p. 155. Elsevier, Amsterdam, 1985.
15. G. Bergmann, *Phys. Rep.* 107, 1 (1984).
16. A. I. Larkin and D. E. Khmel'nitskii, *Usp. Fiz. Nauk* 182, 536 (1982).
17. C. Van Haesendonck, L. Van den dries, Y. Bruynseraede, and G. Deutercher, *Phys. Rev. B* 25, 5090 (1982).
18. G. A. Prinz, *J. Magn. Magn. Mater.* 200, 57 (1999).
19. M. Julliere, *Phys. Lett. A* 54, 225 (1975).
20. J. S. Moodera, L. R. Kinder, T. M. Wong, and R. Meservey, *Phys. Rev. Lett.* 74, 3273 (1995).
21. M. Wilczyński and J. Barnaś, *J. Magn. Magn. Mater.* 221, 373 (2000).
22. For a review, see: "Single Charge Tunneling" (H. Grabert and M. H. Devoret, Eds.), NATO ASI Series Vol. 294. Plenum, New York, 1992.
23. K. Ono, H. Shimada, S. Kobayashi, and Y. Ootuka, *J. Phys. Soc. Jpn.* 65, 3449 (1996); H. Shimada, K. Ono, and Y. Ootuka, *J. Phys. Soc. Jpn.* 67, 1359 (1998).
24. S. Kobayashi, Y. Ootuka, F. Komori, and W. Sasaki, *J. Phys. Soc. Jpn.* 51, 689 (1982).
25. S. Kobayashi, F. Komori, Y. Ootuka, and W. Sasaki, *J. Phys. Soc. Jpn.* 49, 1635 (1980).
26. F. Komori, S. Kobayashi, Y. Ootuka, and W. Sasaki, *J. Phys. Soc. Jpn.* 50, 1051 (1981).
27. H. Raffy, L. Dumoulin, and J. P. Burger, *Phys. Rev. B* 36, 2158 (1987).
28. "Handbook of Mathematical Functions" (M. Abramowitz and I. A. Stegun, Eds.), Natl. Bur. Stand. (U.S.) Appl. Math. Ser. GPO, New York, 1964.
29. A. I. Larkin, *JETP Lett.* 31, 220 (1980).
30. W. W. Fuller, M. Rubinstein, S. A. Wolf, and G. A. Prinz, "Proceedings of International Conference on Localization, Interaction, and Transport Phenomena in Impure Metals," Braunschweig, 1984, Vol. 135.
31. M. Rubinstein, F. J. Rachford, W. W. Fuller, and G. A. Prinz, *Phys. Rev. B* 37, 8689 (1988).
32. H. Jaffres, L. Ressler, J. P. Peyrade, A. R. Fert, P. Gogol, A. Thiaville, A. Schuchl, and F. Nguyen Van Dau, *J. Appl. Phys.* 84, 4375 (1998).
33. G. A. Prinz and J. J. Krebs, *Appl. Phys. Lett.* 39, 397 (1981).
34. G. A. Prinz, J. M. Ferrari, and M. Goldenberg, *Appl. Phys. Lett.* 40, 1551 (1982).
35. M. Aprili, J. Lesueur, L. Dumoulin, and P. Nédellec, *Solid State Commun.* 102, 41 (1997).
36. V. K. Dugaev and J. Barnaś, *Europhys. Lett.* 54, 105 (2001).
37. V. K. Dugaev, P. Bruno, and J. Barnaś, *Phys. Rev. B* 64, 144423 (2001).
38. V. K. Dugaev and J. Barnaś, *Physica E* 12, 391 (2002).
39. A. Kawabata, *Solid State Commun.* 34, 431 (1980).
40. G. Tataru and B. Barbara, *Phys. Rev.* 64, 172408 (2001).
41. B. L. Altshuler, A. G. Aronov, and B. Z. Spivak, *JETP Lett.* 33, 94 (1981).
42. A. G. Aronov and Yu. V. Sharvin, *Rev. Mod. Phys.* 59, 755 (1987).
43. F. G. Aliev, E. Senaev, and Ch. Van Haesendonck (unpublished).
44. S. Kasai, T. Niiyama, E. Saitoh, and H. Miyajima, *Appl. Phys. Lett.* 81, 316 (2002).
45. F. G. Aliev, E. Kunnen, K. Temst, K. Mae, G. Verbanck, J. Barnaś, V. V. Moshchalkov, and Y. Bruynseraede, *Phys. Rev. Lett.* 78, 134 (1997).
46. F. G. Aliev, V. V. Moshchalkov, and Y. Bruynseraede, *Phys. Rev. B* 58, 3625 (1998).
47. J. Fassbender, U. May, B. Schirmer, R. M. Jungblut, B. Hillebrands, and G. Güntherodt, *Phys. Rev. Lett.* 75, 4476 (1995).
48. W. Weber, C. H. Back, A. Bischof, Ch. Würsch, and R. Allenspach, *Phys. Rev. Lett.* 76, 1940 (1996).
49. J. Camarero, T. Graf, J. J. de Miguel, R. Miranda, W. Kuch, M. Zharnikov, A. Dittschar, C. M. Schneider, and J. Kirschner, *Phys. Rev. Lett.* 76, 4428 (1996).
50. M. Jalochowski and E. Bauer, *Phys. Rev. B* 37, 8622 (1988).
51. Yu. A. Bychkov and E. I. Rashba, *J. Phys. C* 17, 6093 (1984).
52. G. Dresselhaus, *Phys. Rev.* 100, 580 (1955).
53. "The Hall Effect and Its Applications" (C. L. Chien and C. R. Westgate, Eds.). Plenum, New York, 1980.
54. A. Crépieux and P. Bruno, *Phys. Rev. B* 64, 014416 (2001).
55. G. Bergmann and F. Ye, *Phys. Rev. Lett.* 67, 735 (1991).
56. G. Bergmann, *Phys. Rev. B* 7, 4850 (1973).
57. A. Langenfeld and P. Wölfle, *Phys. Rev. Lett.* 67, 739 (1991).
58. V. K. Dugaev, A. Crépieux, and P. Bruno, *Phys. Rev. B* 64, 104411 (2001).
59. A. Crépieux, J. Wunderlich, V. K. Dugaev, and P. Bruno, *J. Magn. Magn. Mater.* 242–245, 464 (2002).
60. V. K. Dugaev, A. Crépieux, and P. Bruno, *J. Magn. Magn. Mater.* 240, 159 (2002).
61. H. Fukuyama, *J. Phys. Soc. Jpn.* 54, 2092 (1985).
62. A. Singh and E. Fradkin, *Phys. Rev. B* 35, 6894 (1987).
63. Y. B. Kim and A. J. Millis, *Phys. Rev. B* 67, 085102 (2003).
64. F. G. Aliev, V. V. Moshchalkov, and Y. Bruynseraede, *Phys. Rev. Lett.* 81, 5884 (1998).
65. S. A. Grigera, R. S. Perry, A. J. Schofield, M. Chiao, S. R. Julian, G. G. Lonzarich, S. I. Ikeda, Y. Maeno, A. J. Millis, and A. P. Mackenzie, *Science* 294, 329 (2001).
66. P. B. Allen, H. Berger, O. Chauvet, L. Forro, T. Jarlborg, A. Junod, B. Revaz, and G. Santi, *Phys. Rev. B* 53, 4393 (1996).
67. K. Ishida, H. Mukuda, Y. Kitaoka, K. Asayama, Z. Q. Mao, Y. Mori, and Y. Maeno, *Nature* 396, 658 (1998).



68. R. S. Perry, L. M. Galvin, S. A. Grigera, L. Capogna, A. J. Schofield, A. P. Mackenzie, M. Chiao, S. R. Julian, S. I. Ikeda, S. Nakatsujii, Y. Maeno, and C. Pfeiderer, *Phys. Rev. Lett.* 86, 2661 (2001).
69. J. B. A. N. van Hoff, K. M. Schep, A. Braats, G. E. W. Bauer, and P. J. Kelly, *Phys. Rev. B* 59, 138 (1999).
70. G. Tatara and H. Fukuyama, *Phys. Rev. Lett.* 78, 3773 (1997).
71. G. Tatara, *Int. J. Mod. Phys. B* 15, 321 (2001).
72. Yu. Lyanda-Geller, I. L. Aleiner, and P. M. Goldbart, *Phys. Rev. Lett.* 81, 3215 (1998).
73. L. Berger, *J. Appl. Phys.* 49, 2156 (1978).
74. K. Hong and N. Giordano, *Phys. Rev. B* 51, 9855 (1995).
75. J. F. Gregg, W. Allen, K. Ounadjela, M. Viret, M. Hehn, S. M. Thompson, and J. M. D. Coey, *Phys. Rev. Lett.* 77, 1580 (1996).
76. P. M. Levy and S. Zhang, *Phys. Rev. Lett.* 79, 5110 (1997).
77. U. Ruediger, J. Yu, S. Zhang, A. D. Kent, and S. S. P. Parkin, *Phys. Rev. Lett.* 80, 5639 (1998).
78. S. Gider, B. U. Runge, A. C. Marley, and S. S. P. Parkin, *Science* 281, 797 (1998).
79. U. Ruediger, J. Yu, L. Thomas, S. S. P. Parkin, and A. D. Kent, *Phys. Rev. B* 59, 11914 (1999).
80. M. Viret, Y. Samson, P. Warin, A. Marty, F. Ott, E. Söndergård, O. Klein, and C. Fermon, *Phys. Rev. Lett.* 85, 3962 (2000).
81. P. A. E. Jonkers, *J. Magn. Magn. Mater.* 247, 178 (2002).
82. A. D. Kent, U. Ruediger, J. Yu, S. Zhang, P. M. Levy, and S. S. P. Parkin, *IEEE Trans. Magn.* 34, 900 (1998).
83. K. Hong and N. Giordano, *J. Phys.: Cond. Matter* 10, L401 (1998).
84. D. E. Pober, M. D. Feuer, and N. Giordano, *Appl. Phys. Lett.* 37, 94 (1980).
85. K. Hong and N. Giordano, *Phys. Rev. B* 51, 9855 (1995).
86. F. G. Aliev, R. Schad, Y. Bruynseraede, and R. Villar, *Physica B* 284–288, 1243 (2000).
87. F. G. Aliev, R. Schad, A. Volodin, K. Temst, C. Van Haesendonck, Y. Bruynseraede, I. Vavra, V. K. Dugaev, and R. Villar, *Europhys. Lett.* 63, 888 (2003).
88. A. Fert, P. Grünberg, A. Barthélémy, F. Petroff, and W. Zinn, *J. Magn. Magn. Mater.* 140–144, 1 (1995).
89. S. Zhang and P. M. Levy, *Phys. Rev. B* 50, 6089 (1994).
90. J. E. Mattson, M. E. Brubaker, C. H. Sowers, M. Conover, Z. Qiu, and S. D. Bader, *Phys. Rev. B* 44, 9378 (1991).
91. S. S. P. Parkin, *Phys. Rev. Lett.* 71, 1641 (1993).
92. J. C. Slonczewski, *Phys. Rev. Lett.* 67, 3172 (1991).
93. R. Schad, P. Beilen, G. Verbanck, V. V. Moshchalkov, Y. Bruynseraede, H. E. Fisher, S. Lefebvre, and M. Bessiere, *Phys. Rev. B* 59, 1240 (1999).
94. M. Rührig, R. Schäfer, A. Hubert, R. Mosler, J. A. Wolf, S. Demokritov, and P. Grünberg, *Phys. Status Solidi A* 125, 635 (1991).
95. C. M. Schmidt, D. E. Bürgler, D. M. Schaller, F. Meisinger, and H.-J. Güntherodt, *Phys. Rev. B* 60, 4158 (1999).
96. W. Knap, C. Skierbiszewski, A. Zduniak, E. Litwin-Staszewska, D. Bertho, F. Kobbi, J. L. Robert, G. E. Pikus, F. G. Pikus, S. V. Iordanskii, V. Mosser, K. Zekentes, and Yu. B. Lyanda-Geller, *Phys. Rev. B* 53, 3912 (1996).
97. Yu. A. Bychkov and E. I. Rashba, *J. Phys.* C17, 6093 (1984).
98. G. Tatara and H. Fukuyama, *J. Phys. Soc. Jpn.* 69, 2407 (2000).
99. S. S. P. Parkin, *Phys. Rev. Lett.* 67, 3598 (1991).
100. D. M. Edwards, J. Mathon, R. B. Muniz, and M. S. Phan, *Phys. Rev. Lett.* 67, 493 (1991).
101. P. Bruno and C. Chappert, *Phys. Rev. Lett.* 67, 1602 (1991); *Phys. Rev. Lett.* 67, 2592 (1991).
102. J. Barnaś, *J. Magn. Magn. Mater.* 111, L215 (1992).
103. M. D. Stiles, *Phys. Rev. B* 48, 7238 (1993).
104. P. Bruno, *Phys. Rev. B* 52, 411 (1995).
105. A. Fert and P. Bruno in “Ultrathin Magnetic Structures” (B. Heinrich and J. A. C. Bland, Eds.), Vol. 2, p. 82. Springer, Berlin, 1994.
106. P. Bruno, *J. Phys.: Cond. Matter* 11, 9403 (1999).
107. J. Kudrnovský, V. Drchal, I. Turek, P. Bruno, P. Dederichs, and P. Weinberger in “Electronic Structure and Physical Properties of Solids” (H. Dreyssé, Ed.), p. 313. Springer, Berlin, 2000.
108. P. Bruno, in “Magnetism: Molecules to Materials, III, Nanosized Magnetic Materials” (J. S. Miller and M. Drillon, Eds.). Wiley-VCH, Weinheim, 2002.
109. M. A. Ruderman and C. Kittel, *Phys. Rev.* 96, 99 (1954).
110. T. Kasuya, *Prog. Theor. Phys.* 16, 45 (1956).
111. K. Yosida, *Phys. Rev.* 106, 893 (1957).
112. P.-G. de Gennes, *J. Phys. Radium* 23, 630 (1962).
113. A. Yu. Zyuzin and B. Z. Spivak, *JETP Lett.* 43, 234 (1986).
114. L. N. Bulaeviski and S. V. Panyukov, *JETP Lett.* 43, 240 (1986).
115. A. Jagannathan, E. Abrahams, and M. J. Stephen, *Phys. Rev. B* 37, 436 (1988).
116. P. M. Levy, S. Maekawa, and P. Bruno, *Phys. Rev.* 58, 5588 (1998).
117. P. M. Levy, *Solid State Phys.* 47, 367 (1994).
118. V. K. Dugaev, P. Bruno, and J. Barnaś, *J. Magn. Magn. Mater.* 240, 200 (2002).
119. V. K. Dugaev, P. Bruno, and J. Barnaś, *J. Magn. Magn. Mater.* 242–245, 461 (2002).
120. P. Chen, D. Y. Xing, and Y. W. Du, *Phys. Rev. B* 64, 104402 (2001).
121. C. L. Zhang, X. J. Cheng, C. C. Almasan, J. S. Gardner, and J. L. Sarrao, *Phys. Rev. B* 65, 134439 (2002).
122. N. O. Moreno, P. G. Pagliuso, C. Rettori, J. S. Gardner, J. L. Sarrao, J. D. Thompson, D. L. Huber, J. F. Mitchell, J. J. Martinez, and S. B. Oseroff, *Phys. Rev. B* 63, 174413 (2001).
123. B. X. Gu, S. Y. Zhang, H. C. Zhang, and B. G. Shen, *J. Magn. Magn. Mater.* 204, 45 (1999).
124. N. Manyala, Y. Sidis, J. F. Di Tusa, G. Aeppli, D. P. Young, and Z. Fisk, *Nature* 404, 581 (2000).
125. J. E. Di Tusa et al., *Phys. Rev. Lett.* 78, 28431 (1997).
126. P. D. Babu, S. N. Kaul, L. F. Barquin, and J. C. Gomez Sal, *J. Magn. Magn. Mater.* 140–144, 295 (1995).
127. L. F. Barquin, J. C. Gomez Sal, P. D. Babu, and S. N. Kaul, *J. Magn. Magn. Mater.* 133, 82 (1994).
128. R. W. Cochrane, R. Harris, J. O. Ström-Olson, and M. J. Zuckermann, *Phys. Rev. Lett.* 35, 676 (1975).
129. J. Barnaś and A. Fert, *Phys. Rev. Lett.* 80, 1058 (1998).
130. S. Takahashi and S. Maekawa, *Phys. Rev. Lett.* 80, 1758 (1998).
131. J. Barnaś and A. Fert, *Europhys. Lett.* 44, 85 (1998).
132. A. Brataas, Yu. V. Nazarov, J. Inoue, and G. E. W. Bauer, *Phys. Rev. B* 59, 93 (1999).
133. A. N. Korotkov and V. I. Safarov, *Phys. Rev. B* 59, 89 (1999).
134. M. Amman, R. Wilkins, E. Ben-Jacob, P. D. Maker, and R. C. Jaklewic, *Phys. Rev. B* 43, 1146 (1991).
135. J. Barnaś and A. Fert, *J. Magn. Magn. Mater.* 192, L 391 (1999).
136. H. Schoeller and G. Schön, *Phys. Rev. B* 50, 18436 (1994).
137. J. Martinek, J. Barnaś, S. Maekawa, H. Schöller, and G. Schön, *Phys. Rev. B* 66, 014402 (2002).
138. D. C. Ralph, S. Gueron, C. T. Black, and M. Tinkham, *Physica B* 280, 420 (2000).
139. A. Brataas, Yu. V. Nazarov, J. Inoue, and G. E. W. Bauer, *Eur. Phys. J. B* 9, 421 (1999).
140. J. Barnaś, J. Martinek, G. Michałek, B. R. Bulka, and A. Fert, *Phys. Rev. B* 62, 12363 (2000).
141. C. W. J. Beenakker, *Phys. Rev. B* 44, 1646 (1991).
142. B. R. Bulka, *Phys. Rev. B* 62, 1186 (2000).
143. W. Rudziński and J. Barnaś, *Phys. Rev. B* 64, 085318 (2001).
144. A. P. Jauho, N. S. Wingreen, and Y. Meir, *Phys. Rev. B* 50, 5528 (1994).
145. C. Niu, L. Liu, and T. Lin, *Phys. Rev. B* 51, 5130 (1995).
146. R. Świrkwicz, J. Barnaś, and M. Wilczyński, *J. Phys.: Cond. Matter* 14, 2011 (2002).
147. N. Sergueev, Q. Sun, H. Guo, B. G. Wang, and J. Wang, *Phys. Rev. B* 65, 165303 (2002).
148. J. Martinek, Y. Utsumi, H. Imamura, J. Barnaś, S. Maekawa, J. König, and G. Schön, *Phys. Rev. Lett.* 91, 127203 (2003).



# Low-Dimensional Nanocrystals

Shu-Hong Yu, Jian Yang, Yi-Tai Qian

*University of Science and Technology of China, Hefei, Anhui, China*

## CONTENTS

1. Introduction
  2. Synthetic Routes for Low-Dimensional Nanocrystals
  3. Summary
- References

## 1. INTRODUCTION

Nanostructured semiconductors with a size range of 1–100 nm have been the focus of recent scientific research because of their important nonlinear optical properties [1], luminescent properties [2, 3], quantum size effects [4, 5], and other important physical and chemical properties [6]. In past decades, low-dimensional materials such as nanometer-size inorganic dots, tubes, and wires have exhibited a wide range of electronic and optical properties that depend sensitively on both size and shape, and are of both fundamental and technological interest [7, 8]. They are potentially ideal building blocks for nanoscale electronics and optoelectronics [9]. The ability to control the shapes of semiconductor nanocrystals affords an opportunity to further test theories of quantum confinement and yields samples with desirable optical characteristics from the point of view of application [10, 11].

The exciting emerging important applications of low-dimensional semiconductor nanocrystals include using QDs in biological assays [12–15], building blocks for assembly semiconductor nanodevices [16], hybrid nanorod-polymer solar cells that combine semiconducting polymers and nanoparticles in useful photovoltaic devices with relatively high conversion efficiencies [17], room-temperature ultraviolet lasing using ZnO nanowire (NW) arrays [18], light-emitting diodes (LEDs) [9], and nanosensors for biological and chemical species [19–21].

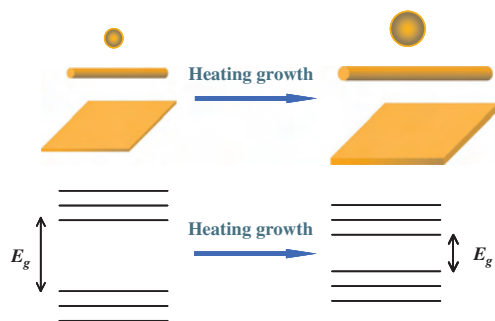
One of the current hottest issues in nanotechnology and nanoscience is how to control the size, shape, and dimensionality of nanocrystals because of their important applications in the design of new materials and devices in

various fields such as catalysis, electronics, medicine, ceramics, pigments, cosmetics, and biotechnology [11–22]. For example, shape control is of significant importance in the fabrication of semiconductor nanocrystals [11], metal nanocrystals [24], and other inorganic materials [25], which may add alternative variables in the tailoring of properties of nanomaterials and provide more possibilities in the fabrication of nanodevices. The key issue in the study and application of 1D materials is how to assemble individual atoms into 1D nanostructures in an effective and controllable way [23]. Scheme 1 shows a schematic illustration of ideal semiconductor nanocrystals with well-defined shapes and sizes, and the relationship of the band gap to nanoparticle size [26].

Considerable progress and a lot of effort have been made in the synthesis of technologically important semiconductors from the group II–VI, III–VI, and IV families of crystallites or nanocrystallines, which have been reviewed recently [27, 28]. However, all of these methods can only produce nanocrystallites with shapes never very far from spherical [23, 27–33]. Although several examples have been demonstrated, shape control has been more difficult to achieve. An intensive recent review by Yang et al. summarized the general strategies for the synthesis of various kinds of one-dimensional NWs or nanorods (NRs) [23]. In addition, a review by Nesper et al. [34] of the synthesis of oxide NR and nanotube (NT) materials appeared very recently.

This chapter will give a general overview of the state of the art for the variety of different synthesis routes of low-dimensional nanocrystals, with a focus on 1D NRs/NWs by solution pathways and emerging new approaches. Since the synthesis of NTs and oxide NWs/NRs has been reviewed very recently [23, 34], we will focus more on the synthesis of nonoxide low-dimensional nanocrystals by mild solution processes and introduce some promising new strategies for self-assembly of 1D, 2D nanocrystals and more complex structures.

The chapter is organized into the following parts: in the first part, a grand survey of research activities and progress



**Scheme 1.** Schematic illustration of the preparation of semiconductor nanocrystals with ideal shapes and sizes, and the relationship of the band gap to nanoparticle size. Reprinted with permission from [26], S. H. Yu, *J. Ceram. Soc. Jpn.* 109, S65 (2001). © 2001, Ceramic Society of Japan.

on the various low-dimensional nanocrystals was summarized in the form of tabulation.

The second part will discuss the main methodologies and emerging promising approaches for the synthesis of various important inorganic NWs/NRs, hierarchical nanostructures, and more complex superstructures with strong application potential. Generally, the synthetic strategies can be classified into two types, the “hard” and “soft” approaches, according to the preparation characteristics and reaction conditions. Among the “hard” approaches, usually foreign hard templates or drastic reaction conditions are needed; for example, the reaction medium is usually gas phase, and a high vacuum system and high temperature are applied. The main existing “hard” approaches for synthesis of 1D nanomaterials include four types: (i) The template-directed growth method, in which hard templates such as carbon nanotubes [7, 8, 35, 36] and porous aluminum template [37–40] are used. (ii) The vapor-liquid-solid (VLS) mechanism, which was previously proposed by Wagner in the 1960s [41]. This mechanism has been applied for the synthesis of various semiconductor NWs [42–47]. A laser ablation-based VLS catalytic growth process (LCG) makes it possible to synthesize semiconductor NWs with many different compositions [48]. (iii) The vapor-solid (VS) mechanism [49], in which NWs are generated directly from vapor condensation onto a substrate. Various metal oxides such as MgO, Al<sub>2</sub>O<sub>3</sub>, ZnO, and SnO<sub>2</sub> NWs or nanobelts (NBs) have been grown by either a carbon-thermal reduction process [50, 51] or direct thermal evaporation [52, 53]. (iv) The oxide-assisted NW growth route [54–59] was reported by Lee’s group for growing GaAs, GaN NWs and Si NWs with the advantages of not having to use a metal catalyst or a template.

In contrast, the “soft” approaches are based on solution reactions and do not need a foreign hard template. They do not involve the use of drastic conditions, and the reaction is usually initiated under mild conditions or under natural conditions. The emerging main approaches also include four types: (i) A solvothermal process, which has been emerging as a versatile solution route for the synthesis of various semiconductor nanocrystals with different sizes and shapes [26, 34, 60–65]. (ii) A solution-liquid-solid

(SLS) mechanism, which is used for growing III–V group nanofibers in hydrocarbon solvents at relatively low temperatures [60, 66–69] (group IV Ge, Si NWs can also be generated by a supercritical fluid solution-phase approach [70, 71]). (iii) Capping agent/surfactant-assisted synthesis [11, 25, 72–79]. Well-defined nanostructures can be obtained under hot conditions or natural/mild conditions. (iv) A bio-inspired approach for complex superstructures [73, 80–95]. In this approach, soft templates such as polymers, organic additives, or supramolecular templates are employed as crystal growth modifiers [88–90] and templates [94]. (v) An oriented attachment growth mechanism [96–103]. The spontaneous aggregation of smaller nanoparticles into well-structured nanocrystals has been reported in the case of TiO<sub>2</sub> [97–99], ZnO [100, 102], and CdTe [103]. These main strategies will be discussed in more detail with specific examples in the following parts after the general grand survey on the synthesis methodologies. Finally, we will give our own perspectives.

## 2. SYNTHETIC ROUTES FOR LOW-DIMENSIONAL NANOCRYSTALS

The intensive research and ongoing advances in the synthesis of various nanomaterials make it more and more difficult to keep up to date with all of the new achievements. However, in this section, we will try our best to briefly summarize various low-dimensional nanocrystals with strong application potentials synthesized by different routes in the past decade. We will focus more on the synthesis of 1D, 2D nanocrystals and more complex structures built up based on simple synthesis strategies, which we call “emerging and promising approaches” here.

Since intensive reviews on the synthesis of semiconductor nanodots (0D) have been published very recently [27, 28], we only focus on 1D and 2D nanomaterials such as NWs, NRs, NBs, nanoribbons, NTs, nanosheets (2D), and more complex structures. Table 1 is a general survey of various oxide NRs, NWs, NTs, and NBs or other novel/new nanostructures prepared by different strategies. Table 2 gives an intensive survey of nonoxide inorganic nanomaterials such as metal, semiconductor, and carbide- or nitride-based nanomaterials (NRs, NWs, NTs, nanoribbons, NBs, etc.).

### 2.1. Templated-Directed Growth Method

Template-based synthesis of low-dimensional nanomaterials has been widely employed in past decades. The characteristic of this method is the use of various templates to limited reactions to a confined nanoscale space such as channels or on a surface. Conventional templates include porous solid-state materials such as carbon NTs, anode aluminum oxide, zeolites, MCM-41 mesoporous silica, and porous polymers. Representative examples are given below to illustrate the application of these templates in the formation of various kinds of one-dimensional nanocrystals.

**Table 1.** Synthetic routes for oxide low-dimensional nanocrystals (published since 1995).

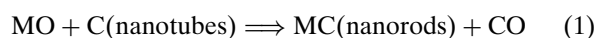
Nanomaterials	Synthetic method	Ref.
BaTiO <sub>3</sub> NRs	Solution-phase decomposition of bimetallic alkoxide precursors in the presence of coordinating ligands	[104]
SrTiO <sub>3</sub> NRs		[104]
BaSO <sub>4</sub> NWs and superstructures	Mineralization from aqueous solution in the presence of polymers	[88, 89]
BaCrO <sub>4</sub> NWs and chain structures	Reversed micelle templating method	[25, 75]
BaCrO <sub>4</sub> NWs and superstructures	Mineralization from aqueous solution in the presence of polymers	[89–91]
BaCO <sub>3</sub> NWs	A reverse micelle-based approach	[77]
BaWO <sub>4</sub> NRs	Reversed micelle templating method	[78]
BaWO <sub>4</sub> NWs	Cationic reverse micelles	[79]
BaWO <sub>4</sub> NWs arrays	Langmuir-Blodgett assembly of 1D nanostructures	[105, 106]
CaSO <sub>4</sub> NWs	A water-in-oil microemulsions route	[107]
CdO NBs	Evaporation of metal oxide powders at high temperatures, VS	[52]
CdWO <sub>4</sub> Nanosheets	Hydrothermal treatment in the presence of block copolymers	[92]
CdWO <sub>4</sub> NBs	Double jet reaction at room temperature	[92]
CdWO <sub>4</sub> NRs	Hydrothermal treatment of CdCl <sub>2</sub> and Na <sub>2</sub> WO <sub>4</sub>	[108]
Co <sub>3</sub> O <sub>4</sub> NRs	Template method with alumina membranes	[109]
Co <sub>3</sub> O <sub>4</sub> NRs	Calcination of precursor powders prepared in a novel inverse microemulsion	[110]
CuO NRs	Room-temperature reaction of CuCl <sub>2</sub> · 2H <sub>2</sub> O and NaOH with PEG 400	[111]
CuO NRs	Heating copper substrates in air	[112]
Eu <sub>2</sub> O <sub>3</sub> NRs	Sonication of an aqueous solution	[113]
Fe <sub>2</sub> O <sub>3</sub> NRs	Thin-film processing method	[114]
Fe <sub>2</sub> O <sub>3</sub> NRs	Grown onto a polycrystalline (or single-crystalline) substrate from an aqueous solution of ferric salts	[115]
Fe <sub>3</sub> O <sub>4</sub> NRs	Sonication of aqueous iron(II) acetate in the presence of β-cyclodextrin	[116]
Fe <sub>4</sub> [Fe(CN) <sub>6</sub> ] <sub>3</sub> · xH <sub>2</sub> O NWs	Electrodeposition with two-step anodizing anodic aluminum oxide films	[117]
Ga <sub>2</sub> O <sub>3</sub> NRs	Catalytic growth by arc discharge of GaN powders in Ar/O <sub>2</sub> mixture	[118]
Ga <sub>2</sub> O <sub>3</sub>	Gas reaction method starting from Ga and O <sub>2</sub>	[119]
Ga <sub>2</sub> O <sub>3</sub>	Physical evaporation at 300 °C from a bulk gallium target	[120]
Ga <sub>2</sub> O <sub>3</sub>	DC arc discharge (GaN, graphite, nickel powder)	[121]
Ga <sub>2</sub> O <sub>3</sub>	Electric arc discharge of GaN powders mixed with Ni and Co	[122]
Ga <sub>2</sub> O <sub>3</sub>	Heat treatment of Ga with SiO <sub>2</sub> powder and a Fe <sub>2</sub> O <sub>3</sub> catalyst	[123]
Ga <sub>2</sub> O <sub>3</sub> NTs, NWs Nano-paintbrushes	Molten gallium and microwave plasma containing a mixture of monatomic oxygen and hydrogen	[124]
Ga <sub>2</sub> O <sub>3</sub> NWs	Heating raw materials in N <sub>2</sub> or Ar without metal catalysts	[125]
GeO <sub>2</sub> NRs	Carbon-NT confined reaction of metallic Ge	[126]
GeO <sub>2</sub> NWs	Carbothermal reduction reaction between germanium dioxide and active carbons	[127]
GeO <sub>2</sub> NWs	Thermal oxidation of suboxide at high temperature	[128]
In <sub>2</sub> O <sub>3</sub> NBs	Evaporation of metal oxide powders at high temperatures, VS	[52]
In <sub>2</sub> O <sub>3</sub> NWs	A rapid heating process on Au-coated InP substrates in oxygen	[129]
IrO <sub>2</sub>	Templating against carbon NTs	[130]
K <sub>2</sub> Ti <sub>6</sub> O <sub>13</sub>	Calcination of KF and TiO <sub>2</sub>	[131]
LaPO <sub>4</sub> :Eu NWs	Hydrothermal synthesis	[132]
LaPO <sub>4</sub> :Ce NWs	Hydrothermal synthesis	[132]
MgO NRs	Vapor-solid growth process with <i>in-situ</i> generated Mg vapor	[51]
MgO NWs	Oxide-assisted catalytic growth method	[133]
MgO NWs	Vapor-phase method using MgB <sub>2</sub> as precursor	[134]
MgO NRs	Heating of MgCl <sub>2</sub> at 750 °C in mixture gas (Ar/H <sub>2</sub> )	[135]
Mg(OH) <sub>2</sub> NRs	Hydrothermal reaction of Mg, H <sub>2</sub> O, and ethylenediamine	[136]
MnO <sub>2</sub> NRs	Template method with alumina membranes by a sol-gel approach	[137]
MnO <sub>2</sub> NRs	Hydrothermal synthesis	[138]
Mn <sub>3</sub> O <sub>4</sub> NWs	Thermolysis of carbonates in NaCl flux and a surfactant NP9 at 850 °C	[139]
Mg <sub>2.11</sub> Mn <sub>5.46</sub> O <sub>12</sub> · xH <sub>2</sub> O nano-ribbons	A combination of techniques consisting of a sol-gel process for tetraethylammonium manganese oxide layered material, an ion-exchange method to a thin-film Mg-buserite precursor, and a hydrothermal reaction to transform the Mg-buserite to nanoribbonlike Mg-todorokite material	[140]
MoO <sub>3</sub> NRs	Template-directed reaction of molybdic acid and subsequent leaching process	[141]
MoO <sub>3</sub> NRs	Templating against carbon nanotubes	[130]
MoO <sub>2</sub> NRs	Templating against carbon NTs	[130]
Ni(OH) <sub>2</sub> NRs	Hydrothermal synthesis and deposition in a carbon-coated anodic alumina film	[142]

continued

Table 1. Continued

Nanomaterials	Synthetic method	Ref.
NiO NRs	Thermal decomposition of a precursor in NaCl flux	[143]
PbTiO <sub>3</sub> NWs	Sol-gel electrophoresis, deposition in polycarbonate membrane	[144]
RuO <sub>2</sub> NRs	Templating against carbon NTs	[130]
Sb <sub>2</sub> O <sub>3</sub> NRs	Microemulsion method for the system AOT-water-toluene	[145]
Sb <sub>2</sub> O <sub>3</sub> NRs	A vapor-solid route using Sb <sub>2</sub> S <sub>3</sub> nanopowders as raw material, VS	[146]
Sb <sub>2</sub> O <sub>3</sub> NRs	Templated against carbon NTs	[147]
Sb <sub>2</sub> O <sub>5</sub> NRs	Microemulsion method for the system AOT-water-toluene	[145]
SnO <sub>2</sub> NRs	Calcining precursors that are produced in inverse microemulsions	[148, 149]
SnO <sub>2</sub> NBs	Evaporation of metal oxide powders at high temperatures, VS	[52]
SnO <sub>2</sub> NWs, nanoribbons, NTs	Elevated temperature synthesis techniques using layered mixtures of Sn foil and SnO powder or simply SnO powder, VS	[150]
SnO <sub>2</sub> diskettes	Evaporating techniques using SnO or SnO <sub>2</sub> powders, VS	[151]
SnO nanoribbons	Evaporating SnO powders, VS	[152]
SiO <sub>2</sub> NWs	Helical mesostructured tubules from the Taylor vortex-assisted surfactant templates	[153]
SiO <sub>2</sub> NWs	Oxidation of Si wafer induced by molten gallium	[154]
SiO <sub>2</sub> NWs and bunches	Vapor-liquid-solid (VLS) process using molten gallium as a catalyst	[155]
SiO <sub>2</sub> NTs, NWs	Pyrolysis of mixed Si and SiO <sub>2</sub> powders	[156]
SiO <sub>2</sub> NWs	Using Au nanoparticle catalysts on a silicon substrate	[157]
SiC/SiO <sub>2</sub> helical core-shell NWs	Chemical vapor deposition technique	[158]
TiO <sub>2</sub> NWs	Electrochemically preparation using nanochannel alumina	[159]
TiO <sub>2</sub> NWs	Sol-gel template method employing alumina membranes	[160]
TiO <sub>2</sub> NWs	Electrochemically induced sol-gel preparation	[161]
TiO <sub>2</sub> NTs	Sol-gel-derived fine TiO <sub>2</sub> -based powders were treated with NaOH aqueous solution	[162]
TiO <sub>2</sub> NTs	Solution growth method by hydrolyzing TiF <sub>4</sub> under acidic condition	[163]
TiO <sub>2</sub> NTs	Sol-gel method and removing the polymer thermally	[164]
TiO <sub>2</sub> NTs	Calcination of an organic gelator prepared from supramolecular assemblies	[165]
VO <sub>x</sub> NTs	Hydrothermal using long-chain amine as templates	[166–168]
V <sub>2</sub> O <sub>5</sub> NRs	Vanadium pentoxide gels	[169]
V <sub>2</sub> O <sub>5</sub> NRs	Templating against carbon NTs	[130]
WO <sub>3</sub> NRs	Templating against carbon NTs	[130]
WO <sub>3</sub> NRs	Direct oxidation of tungsten metal	[170]
YBCO NRs	Laser ablation of a high T <sub>c</sub> superconductor YBa <sub>2</sub> Cu <sub>3</sub> O <sub>7</sub>	[171]
ZnO NRs	Gas reaction employing Zn and H <sub>2</sub> O	[172]
ZnO NWs	Heating Zn in N <sub>2</sub> or Ar without metal catalysts	[125]
ZnO NWs	Catalytic growth by vapor transport, VLS	[45, 173]
ZnO NBs	Evaporation of metal oxide powders at high temperatures, VS	[52]
ZnO NWs	Thermal evaporation, VS	[174]
ZnO NWs	Catalyzed epitaxial growth, VLS	[46]
ZnO NRs	Catalyst-free CVD method	[175]
ZnO NRs	Thermal decomposition of the precursor of ZnC <sub>2</sub> O <sub>4</sub> in the presence of surfactant nonyl phenyl ether and NaCl flux	[176]
ZnO NWs	Site-specific growth by catalysis-driven molecular beam epitaxy	[177]
ZnO NWs arrays	Electrodeposited in the pores of anodic alumina membranes	[178]
ZnO NWs on CNTs	Multiwall carbon NTs were treated with Zn	[179]
ZnO NRs	Oriented attachment growth from ZnO nanoparticles from solution	[102]
ZnO hierarchical nano-structures	Vapor transport and condensation process on In <sub>2</sub> O <sub>3</sub> core NWs	[53]
ZnO helical NRs	Biomimetic controlled nucleation and growth on ZnO NR arrays	[95]

Carbon NTs, which were discovered in 1991 [352], are a good candidate for template-induced growth. The first example using carbon NTs as templates came from the synthesis of metal carbide NRs [35]. In this approach, carbon NTs as a reactant were directly converted into MC<sub>x</sub> NRs by the reactions of volatile metal oxide species. Herein, MO should be a metal oxide or nonmetal oxide with a relatively high vapor pressure at the desired reaction temperature.



Similarly, GaN NRs were fabricated through the reaction of carbon NTs with MO (metal oxide) under an ammonia atmosphere [36]. Figure 1 shows typical TEM images of the original C NTs and GaN NRs templated from C NTs. Herein, MO should be a metal oxide or nonmetal oxide with a relatively high vapor pressure at the desired reaction temperature. The total reaction formula could be expressed as the following:

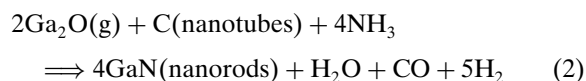




**Table 2.** Synthetic routes for nonoxide low-dimensional nanocrystals (published since 1995).

Nanomaterials	Synthetic method	Ref.
Ag ultrathin NWs	Grow inside the pores of self-assembled calyx [4] hydroquinone NTs by electro/photochemical redox reaction in an ambient aqueous phase	[180]
Ag NWs	Templated from the mesoporous silica	[181, 182]
Ag NWs	Metal NW formation using $\text{Mo}_3\text{Se}_3^-$ as reducing and sacrificing templates	[183]
Ag NRs and dendrites	Ultraviolet photoreduction technique at room temperature using poly(vinyl-alcohol) (PVA) as protection agent	[184]
Ag NRs, NWs	Seed-mediated growth in a rodlike micellar medium	[185]
Ag nanoprisms	A photoinduced method for converting large quantities of silver nanospheres into triangular nanoprisms	[186]
Ag NWs	Electron-beam-induced growth from zeolite crystallites	[187]
Ag NWs	Templated from AgBr nanocrystals	[188]
Ag nanoarrays	Formed inside micellar arrays of a template consisting of a (dendritic polyisobutylene)/polyisocyanide block copolymer reduced under the TEM electron beam	[189]
Ag NWs	Solid-liquid phase arc discharge method	[190]
Ag truncated triangular nanoplates	A solution phase method in the presence of cetyltrimethylammonium bromide micelles	[191]
Ag nanodisc	Mixing two reverse micellar solutions	[192]
Ag nanoprisms	Boiling $\text{AgNO}_3$ in <i>N,N</i> -dimethyl formamide, in the presence of poly(vinylpyrrolidone)	[193]
Ag NWs	Solvothermal reaction using Pt nanoparticles as seeds in ethylene glycol at 160 °C	[194]
2D Ag NWs arrays	Evaporating a drop of chloroform-dispersed dodecanethiol-capped prolate Ag nanocrystals on a carbon substrate, which were synthesized in the presence of tetraoctylammonium bromide	[195]
Au NRs	Electrochemical oxidation/reduction within a simple two-electrode-type cell in the presence of cationic surfactant $\text{C}_{16}\text{TAB}$	[196]
Au NWs	Templated from the mesoporous silica	[182]
Au NWs	Metal NW formation using $\text{Mo}_3\text{Se}_3^-$ as reducing and sacrificing templates	[183]
Au NRs	A solution seeding growth approach in the presence of an aqueous micellar template CTAB	[197, 198]
Au NRs	UV irradiation of $\text{HAuCl}_4$ solutions with 253.7-nm light in the presence of rodlike micelles of hexadecyltrimethylammonium chloride	[199]
Au NWs	DNA-directed assembly of gold NWs on complementary surfaces	[200]
2D Au NWs	Self-assembly of gold nanoparticles on water surfaces in the presence of surfactants	[201]
Au NWs	Ultrahigh vacuum TEM with the electron beam thinning technique	[202]
3D aggregates of Au NRs	DNA-driven self-assembly of gold NRs	[203]
$\text{Au}_{\text{core}}\text{Ag}_{\text{shell}}$ NRs	Reducing $\text{AgCl}_4^{3-}(\text{aq})$ with $\text{NH}_2\text{OH}$ selectively on the surface of gold NRs	[204]
Co NRs	The early stage of the thermal decomposition of $\text{Co}_2(\text{CO})_8$ in a mixture of oleic acid and trioctylphosphine oxide (TOPO)	[205]
Co NW array	Vertical arrays of Co NWs with high densities through direct current electrodeposition created by using ultra-high-density arrays of nanopore of diblock copolymer templates	[206]
Co NWs	The potentiostatic electrochemical template synthesis of NWs in polycarbonate track-etched membranes with nominal pore diameters	[207]
Cu NWs	The potentiostatic electrochemical template synthesis of NWs in polycarbonate track-etched membranes with nominal pore diameters	[207]
Fe NRs	Thermal decomposition of organometallic precursor ( $\text{Fe}(\text{CO})_5$ ) in the presence of a stabilizing surfactant TOPO at 340 °C under an argon atmosphere	[208]
In NWs	Room-temperature organometallic route using long-chain amines (hexadecylamine) as templates	[209]
$\text{In}_3\text{Sb}$ NWs	Room-temperature organometallic route using long-chain amines (hexadecylamine) as templates	[209]
Ni NRs	Surfactants hexadecylamine (HDA) or TOPO as capping agents in THF	[210]
Pb NWs	The NWs were embedded in tracked-etched polycarbonate membranes by electrodeposition	[211]
Pb NWs	Electrodeposition into anodic alumina membranes	[212]
Pd tetrahedras and octahedras	Reduction of metal ions in sodium dodecyl sulfate (SDS)/poly(acrylamide) gel by UV irradiation	[213]
Pd NWs	Using a mesoporous silica template via chemical vapor infiltration	[214]
Pd dendrites	Ultrasonically assisted synthesis using skeleton nickel as templates	[215]
Pt tetrahedra	Tetrahedral, cubic, irregular-prismatic, icosahedral, and cube-octahedral particle shapes were prepared with sodium polyacrylate as a capping agent	[216]
Mo NWs	A two-step process involving the electrodeposition of $\text{MoO}_2$ NWs on a highly oriented pyrolytic graphite (HOPG) surface followed by reduction	[217]

continued

Table 2. Continued

Nanomaterials	Synthetic method	Ref.
W NRs	Thermal decomposition of surfactant-inorganic mesostructures	[218]
B NWs	VLS growth of amorphous boron NWs	[219]
B NWs	Amorphous boron NWs by magnetron sputtering	[220]
B NWs	Chemical vapor deposition using a diborane-(B <sub>2</sub> H <sub>6</sub> )-in-Ar gas mixture	[221]
Bi NTs	Hydrothermal reaction	[222]
Ge NWs	Liquid solution synthesis, reduction of GeCl <sub>4</sub> and phenyl-GeCl <sub>3</sub> by sodium metal in an alkane solvent at elevated temperature and pressure	[70]
Ge NWs	Nucleation and growth seeded by organic monolayer-coated Au nanocrystals	[223]
Si NWs	Laser-assisted growth, VLS	[44]
Si NWs	Chemical vapor deposition of SiCl <sub>4</sub> , VLS	[43]
Si NWs	Vapor-liquid-solid (VLS) reaction using SiCl <sub>4</sub> as the Si source gas and Au as the mediating solvent	[224]
Si nanoribbons	Thermal evaporation of silicon monoxide (SiO) without templates or catalysts	[59]
Si NWs	Thermal evaporation	[225–227]
Si NWs	Laser ablation SiO	[228]
Si NWs	Supercritical fluid solution-phase growth, SLS	[71]
Si NW arrays	Electrochemistry approach by etching Si wafer in HF solution containing AgNO <sub>3</sub>	[229]
Si/SiGe Superlattice NWs	Block-by-block growth by hybrid pulsed laser ablation/chemical vapor deposition (PLA-CVD) process	[230]
Carbon-sheathed Sn-Pb NWs	Electrolytic formation of carbon-sheathed mixed Sn-Pb nanowires	[231]
Se NWs	Using cytochrome c <sub>3</sub> to make selenium NWs	[232]
Se NWs	Solution phase process	[233–234]
Te NTs	Reflexing a solution of orthotelluric acid in ethylene glycol at ~197 °C	[235]
Te nanobelts, NTs, nanohelices	Controlled hydrothermal route by reaction of sodium tellurite (Na <sub>2</sub> TeO <sub>3</sub> ) in aqueous ammonia solution at 180 °C	[236]
GaN NRs	Templating against carbon nanotubes	[32]
GaN NWs	Catalytic growth using Ga and NH <sub>3</sub> , VLS	[237–239]
GaN NWs	Catalytic synthesis using gallium acetylacetonate and NH <sub>3</sub> gas, VLS	[240]
GaN NBs	Thermal reaction of gallium, gallium nitride, and ammonia using iron and boron oxide as catalysts	[241]
GaN NWs	Laser-assisted catalytic growth, VLS	[48, 242]
GaN NWs	Oxide-assisted growth by laser ablating GaN mixed with gallium oxide	[56]
GaN NWs	Silica-assisted catalytic growth	[57]
GaN NWs	Hot-filament chemical vapor deposition	[243, 244]
GaN arrays of nanopillars	MOCVD using a single molecule precursor	[245]
GaN NRs	Pyrolysis of gallium dimethylamide and ferrocene under an NH <sub>3</sub> atmosphere	[246]
GaAs NWs	Laser-assisted catalytic growth, VLS	[48]
GaAs NWs	Oxide-assisted method	[55]
GaAs NWs	Solution-liquid-solid growth, SLS	[66, 69]
GaAs NWs	Molecular beam epitaxy, CVD	[247–249]
GaP NWs	Laser-assisted catalytic growth, VLS	[48, 250]
GaP NWs	Laser ablation of a powder mixture of GaP and Ga <sub>2</sub> O <sub>3</sub>	[251]
GaP NWs	Carbon NTs template against carbon NTs	[252]
GaP NWs	Hydride vapor phase epitaxy method	[253]
GaP NRs	Solution-liquid-solid growth, SLS	[66, 68]
GaP NRs	Thermal decomposition of Ga(P <sup>i</sup> Bu <sub>2</sub> ) <sub>3</sub> in trioctylamine (TOA), which was injected into a mixture of TOA and hexadecylamine (HDA) at 330 °C	[254]
Al <sub>x</sub> Ga <sub>1-x</sub> As NRs	Solution-liquid-solid growth, SLS	[69]
GaAs <sub>0.6</sub> P <sub>0.4</sub> NWs	Laser-assisted catalytic growth, VLS	[48]
InAs NRs	Solution-liquid-solid growth, SLS	[66]
InAs NRs	Molecular beam epitaxy and metal-organic vapor phase epitaxy	[249, 255]
InP NWs	Laser-assisted catalytic growth, VLS	[48]
InP NRs	Solution-liquid-solid growth, SLS	[66]
InAs <sub>0.6</sub> P <sub>0.5</sub> NWs	Laser-assisted catalytic growth, VLS	[48]
AlN NWs	Aluminum chloride-assisted nanowhisker growth	[256, 257]
AlN NRs	Templated against carbon nanotubes	[258]
AlN NWs	Silica assisted catalytic growth (same as GaN)	[57]
InN NWs	Catalyzed growth from azido-indium precursors, SLS	[259]
InN NWs	Thermal selective-area growth on gold-patterned Si substrates	[260]
BN NWs	Reaction of a mixture gas of N <sub>2</sub> and NH <sub>3</sub> over α-FeB particles	[261]
BN NTs	Catalytic growth of boron nitride NTs	[262]

continued

Table 2. Continued

Nanomaterials	Synthetic method	Ref.
BN NTs, nanobamboos, nanocables	Chemical vapor deposition method using B-N-O precursor	[263]
BN NWs	Magnetron sputtering for producing featherlike NWs	[264]
Si <sub>3</sub> N <sub>4</sub> NWs	Heating Si or (Si/SiO <sub>2</sub> ) in N <sub>2</sub> without catalyst	[125]
Si <sub>3</sub> N <sub>4</sub> NRs	From borosilicate glass	[265]
Si <sub>3</sub> N <sub>4</sub> NRs	Carbothermal reduction of SiO with amorphous activated C as a reductant	[266]
Si <sub>3</sub> N <sub>4</sub> NRs	Solvothermal reaction of SiCl <sub>4</sub> with NaN <sub>3</sub> at 670 °C	[267]
Ge <sub>3</sub> N <sub>4</sub> NBs	Thermal reduction Ge/SiO <sub>2</sub> in NH <sub>3</sub>	[268]
SiC NWs	Thermal evaporation	[269]
SiC NWs	Thermal evaporation of SiC powders using iron as a catalyst	[270]
SiC NWs	Laser ablation synthesis	[271]
SiC NRs	Template against carbon NTs	[35]
SiC nanocables	Reaction of SiO <sub>2</sub> with nanoscale C particles in Ar	[125]
SiC NWs	Reaction of arrays CTNs with SiO	[272]
SiC NWs	From the mixture of activated carbon and sol-gel-derived silica embedded with Fe nanoparticles	[273]
SiC NWs	Grown from SiO <sub>x</sub> thin films deposited on Si(100) substrate	[274]
SiC NWs	Reduction-carburization route	[275]
SiC NWs	Solvothermal reaction	[276]
B <sub>x</sub> C NRs	Template against carbon NTs	[35]
B <sub>x</sub> C nanosprings	Fe-catalyzed helical growth, VLS	[277]
AlC NWs	Lithium-assisted self-assembly	[278]
TiC NRs	Template against carbon NTs	[35]
TiC NWs	Reaction of TiO gas with methane in the presence of catalyst Fe, VLS	[279]
TiC NRs	Solvothermal reaction using C <sub>2</sub> Cl <sub>4</sub> , Ti, and N-containing nucleophilic solvents	[280]
MgB <sub>2</sub> NWs	Transport reaction using B NWs as template	[219]
MMo <sub>3</sub> Se <sub>3</sub> NWs	Cation exchange in organic solution (M = Li <sup>+</sup> , Na <sup>+</sup> , Rb <sup>+</sup> , Cs <sup>+</sup> , NMe <sub>4</sub> <sup>+</sup> )	[281]
ErSi <sub>2</sub> NWs	Epitaxial growth on silicon substrate	[282]
NiSi <sub>2</sub> /Si	Metal vapor vacuum arc implantation	[283]
CoSi <sub>2</sub> /Si	Metal vapor vacuum arc implantation	[283]
TiSi <sub>2</sub> NWs	Ti-catalyzed Si NWs by chemical vapor deposition	[284]
CdS NWs	Laser-assisted catalytic growth	[48]
CdS NWs	Electrodeposit in porous anodic aluminum oxide templates	[40, 285]
CdS NWs arrays	Sol-gel template synthesis with porous alumina template	[286]
CdS NRs	A single-source molecular precursor route to CdS nanorods	[287]
CdS NRs	Solvothermal reactions in ethylenediamine media	[61, 288]
CdS NRs	Solvothermal reaction in <i>n</i> -butylamine	[65]
CdS NRs, twinrod-, tetrapod-shaped	Solvothermal reaction in ethylenediamine media	[289]
CdS NWs	Polymer-controlled growth	[290]
Flat CdS triangle	Using Cd(AOT) <sub>2</sub> /isooctane/H <sub>2</sub> O	[291]
CdS, CdSe NRs	Arrested precipitation from inorganic ions in a CTAB micellar solution	[292]
CdS, CdSe NRs	Controlled synthesis of multi-armed architectures using monosurfactant hexadecylamine (HAD)	[293]
CdSe NWs	Laser-assisted catalytic growth, VLS	[48]
CdSe NWs arrays	Electrodeposit in porous anodic aluminum oxide templates	[294]
CdSe NRs and other shapes	Growth of nanoparticles in a mixture of hexylphosphonic acid and TOPO	[11, 72] [295]
CdSe NRs	Capping agent-driven solution reaction using CdO as precursor	[296]
CdSe NRs	Solvothermal reaction in ethylenediamine	[61, 297]
CdSe NRs	Solvothermal reaction in <i>n</i> -butylamine	[65]
CdSe NWs	PVA-assisted solvothermal synthesis	[298]
CdSe nanorods and dendrites	Hydrothermal method	[299]
CdS/ZnS shells on CdSe NRs	Epitaxial growth of graded CdS/ZnS shells on colloidal CdSe NRs	[300]
CdTe NWs	Electrodeposition in alumina membrane	[37]
CdTe NRs	Capping agent-driven solution reaction using CdO as precursor	[296]
CdTe NWs	Spontaneous oriented attachment from nanoparticles	[103]
CdTe NRs	Solvothermal reaction	[61]
CdTe NWs	PVA-assisted solvothermal synthesis	[298]
CdS <sub>x</sub> Se <sub>1-x</sub>	Solvothermal reaction	[301]
PbS NRs	Confined growth within the channels of mesoporous silica SBA-15	[302]

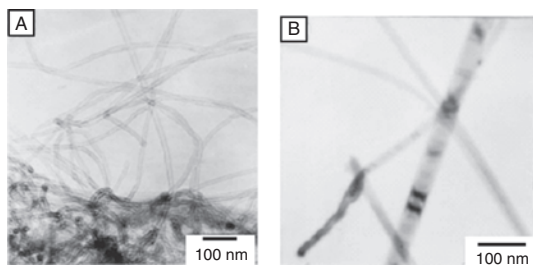
continued

Table 2. Continued

Nanomaterials	Synthetic method	Ref.
PbS NRs	Oriented growth in the presence of surfactant	[303]
Closed PbS NWs	Solvothermal reaction in the presence of poly[ <i>N</i> -(2-aminoethyl)acrylamide] in ethylenediamine/H <sub>2</sub> O (3:1, v/v) solvent	[304]
PbS NRs	Solvothermal interface reaction route	[305]
PbSe NWs	Solution reaction at room temperature	[306]
PbSe NWs arrays	Direct current electrodeposition within anodic alumina membrane	[307]
ZnS NWs	Laser-assisted catalytic growth, VLS	[48]
ZnS NWs	Synthesis in liquid crystal systems	[308]
ZnS NWs	Simultaneous formation in a liquid crystal template by gamma-irradiation	[309]
ZnS NWs	Micelle-template inducing synthesis	[310]
ZnS nanosheets	Templating from a sheet-like molecular precursor ZnS · (NH <sub>2</sub> CH <sub>2</sub> CH <sub>2</sub> NH <sub>2</sub> ) <sub>0.5</sub>	[64]
ZnSe NWs	Laser-assisted catalytic growth, VLS	[48]
ZnSe NRs	Solvothermal reaction in <i>n</i> -butylamine	[65]
ZnSe NWs	Solvothermal reaction in ethylenediamine	[297]
ZnSe NWs	Electrodeposition in a porous alumina film	[311]
ZnTe NRs	Thermal decomposition of a monomeric molecular precursor, [Zn(TePh) <sub>2</sub> ][TMEDA]	[312]
ZnTe NRs	Thermal decomposition of the precursor derived from a solvothermal reaction using Zn, Te, and N <sub>2</sub> H <sub>4</sub> ·H <sub>2</sub> O as reactants	[313]
Bi <sub>2</sub> S <sub>3</sub> NWs	Solvothermal decomposition process	[314, 315]
Bi <sub>2</sub> S <sub>3</sub> NRs	Hydrothermal ripening and crystallization	[316]
Bi <sub>2</sub> S <sub>3</sub> NWs arrays	Electrochemical deposition	[317]
Bi <sub>2</sub> Se <sub>3</sub> flakes	Solvothermal reaction	[318]
Bi(S, Se) NWs	Solvothermal reaction	[319]
Bi <sub>2</sub> Te <sub>3</sub> NWs	Electrodeposition into porous alumina membrane	[320, 321]
Arrays	Pulsed electrodeposition in anodic alumina membranes	[322]
Sb <sub>2</sub> S <sub>3</sub> NRs	Solvothermal decomposition process	[323]
	Electrodeposition within a porous polycarbonate membrane	[324]
Sb <sub>2</sub> Se <sub>3</sub> NWs	Solvothermal reaction of SbCl <sub>3</sub> and Se with Na <sub>2</sub> SO <sub>3</sub> in ethylene glycol	[325]
Ag <sub>2</sub> S NRs	Room-temperature solution-growth method with AgNO <sub>3</sub> , thiourea, and NaOH as the reagents	[326]
Ag <sub>2</sub> Se NWs	Template-directed synthesis using porous alumina	[327]
Ag <sub>2</sub> Se NWs	Solution reaction using Se NWs as templates	[328, 329]
Cu <sub>2</sub> S NWs	Oxide-assisted nucleation and growth	[330]
Cu <sub>2</sub> S NWs	Growth on copper surface at room temperature	[331]
Cu <sub>2</sub> S/Au core/sheath NWs	Redox deposition method	[332]
CuS NTs	Organic amine-assisted hydrothermal process	[333]
MnS NRs Cd <sub>1-x</sub> Mn <sub>x</sub> S NRs	Thermal decomposition of Mn(S <sub>2</sub> CNEt <sub>2</sub> ) <sub>2</sub> or Cd(S <sub>2</sub> CNEt <sub>2</sub> ) <sub>2</sub> in the presence of hexadecylamine	[334]
MoS <sub>2</sub> NWs	Solvothermal reaction	[335]
MoS <sub>2</sub> NTs	Heating trisulfide molybdenum complexes in a stream of H <sub>2</sub>	[336]
MoS <sub>2</sub> NTs	Catalyzed transport method using C <sub>60</sub> as a growth promoter, VS	[337]
MoS <sub>2</sub> NTs	Gas-solid reaction, VS	[338]
WS <sub>2</sub> NTs	After the heating of thin tungsten films in an atmosphere of H <sub>2</sub> S	[339]
WS <sub>2</sub> NTs	A two-step reaction using a tungsten oxide precursor	[340, 341]
WS <sub>2</sub> NTs bundles, foils	After the heating of WO <sub>3</sub> in mixed gas of H <sub>2</sub> S and H <sub>2</sub> /N <sub>2</sub>	[342]
NbS <sub>2</sub> -sheathed CNTs	Using carbon NT template-promoted growth	[343]
NbS <sub>2</sub> NTs	Employing carbon NT template-promoted growth	[344]
HfS <sub>2</sub> , ZrS <sub>2</sub> , TiS <sub>2</sub> NTs	Using carbon NT template-promoted growth	[343]
SnS <sub>2</sub> nanoflakes	Thermal decomposition of (CH <sub>2</sub> CH <sub>2</sub> CH <sub>2</sub> CH <sub>3</sub> ) <sub>4</sub> Sn	[345]
CdIn <sub>2</sub> S <sub>4</sub> NRs	Converting CdS NRs via the hydrothermal reaction	[346]
CuInS <sub>2</sub> NRs	Solvothermal reaction of In(S <sub>2</sub> CNEt <sub>2</sub> ) <sub>3</sub> and Cu(S <sub>2</sub> CNEt <sub>2</sub> ) <sub>2</sub> in ethylenediamine	[347]
AgInS <sub>2</sub> NRs	Solvothermal reaction of In(S <sub>2</sub> CNEt <sub>2</sub> ) <sub>3</sub> and Ag(S <sub>2</sub> CNEt <sub>2</sub> ) in ethylenediamine	[347]
AgBiS <sub>2</sub> NRs	Solvothermal process with AgCl, BiCl <sub>3</sub> , and K <sub>2</sub> S in ethylenediamine	[348]
Ag <sub>3</sub> CuS <sub>2</sub>	Hydrothermal reaction using AgCl and CuCl and thiourea as reactants	[349]
Cu <sub>3</sub> SnS <sub>4</sub> NRs	Solvothermal reaction using CuCl <sub>2</sub> · 2H <sub>2</sub> O, SnCl <sub>4</sub> · 5H <sub>2</sub> O, CH <sub>3</sub> CSNH <sub>2</sub> as reactants in absolute ethanol	[350]
PbSnS <sub>3</sub> NRs	An iodine transport hydrothermal route	[351]

The templating effect can be confirmed by a series of experiments. The mixture of Ga<sub>2</sub>O<sub>3</sub> and Ga was used to produce gaseous Ga<sub>2</sub>O, which is about 1 torr at 880 °C [353]. The powder mixture was separated from carbon NTs

by porous alumina membrane, which can ensure that only gaseous Ga<sub>2</sub>O flows up toward the side of carbon NTs to participate in the reaction. In such a reaction, carbon NTs act as templates to confine the reaction on NTs, which led



**Figure 1.** (A) TEM image of carbon nanotubes. (B) TEM image of GaN nanorods. Reprinted with permission from [36], W. Q. Han et al., *Science* 277, 1287 (1997). © 1997, American Association for the Advancement of Science.

to the formation of NRs. If carbon NTs are not present in this reaction, GaN powders still can be obtained by another reaction:



However, no GaN NRs were observed in this product [354]. On the other hand, carbon NTs did not change without Ga-Ga<sub>2</sub>O<sub>3</sub> mixtures, in spite of the presence of ammonia. The results confirmed the evidence that the formation of GaN NRs took place on the surface of carbon NTs according to Eq. (2).

Other examples include GaP NWs [252], AlN NRs [258], SiC NRs, and B<sub>x</sub>C NRs [35]. The carbon NT-templated oxide NRs include GeO<sub>2</sub> [126], IrO<sub>2</sub> [130], V<sub>2</sub>O<sub>5</sub>, WO<sub>3</sub> [130], MoO<sub>3</sub>, MoO<sub>2</sub> [130], Sb<sub>2</sub>O<sub>3</sub> [147], and ZnO [179].

Recently, the range of the compounds, which can be prepared by the use of carbon NTs as templates, has been extended widely [258, 355]. Now, not only ternary NRs/NWs such as CoFe<sub>2</sub>O<sub>4</sub> [355], but also disulfide NTs ReS<sub>2</sub> [356], NbS<sub>2</sub> [357], HfS<sub>2</sub>, ZrS<sub>2</sub>, and TiS<sub>2</sub> [343] can be fabricated with the use of carbon NTs as templates. However, in the case of the synthesis of disulfide NTs, carbon NTs do not participate in the reactions and just act as deposition substrates of disulfides.

In contrast to the above vapor-phase synthesis by hard template, another versatile methodology was solution-phase electrodeposition for the formation of various NWs with anode aluminum oxide (AAO) as a template. This methodology was first pioneered by Martin and Moskovits [37–40]. Since the electrodeposition is caused by electron transfer from the surface of the conducting material, the wires nucleate at the bottom of the channels of the AAO and grow continuously along the channels. Achieving continuous wires is a key advantage of electrodeposition, particularly for applications in which conductivity is important (e.g., thermoelectric devices, opto-electronic devices). On the other hand, porous alumina is a good choice for a template, because the pore diameters are easily adjusted (down to 9 nm) to sizes enabling quantum confinement. Moreover, the pore densities (10<sup>10</sup> pores/cm<sup>2</sup>) and aspect ratio (>100) are high, which is appropriate for the growth of NWs. Figure 2 shows that Bi<sub>2</sub>Te<sub>3</sub> NW arrays were electrodeposited in anode alumina oxide channels [320, 321]. A lot of inorganic NWs have been fabricated through this approach, such as Ag, Au, Pt,

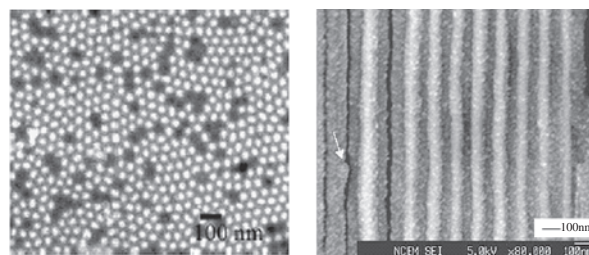


**Figure 2.** (Left) SEM image of a top view of Bi<sub>2</sub>Te<sub>3</sub> nanowires electrodeposited in AAO. Reprinted with permission from [321], A. L. Prieto et al., *J. Am. Chem. Soc.* 123, 7161 (2001). © 2001, American Chemical Society. (Right) SEM image of a side view of Bi<sub>2</sub>Te<sub>3</sub> nanowires in AAO. Reprinted with permission from [320], M. S. Sander et al., *Adv. Mater.* 14, 665 (2002). © 2002, Wiley-VCH.

TiO<sub>2</sub>, MnO<sub>2</sub>, ZnO, SnO<sub>2</sub>, CdS, and CdSe [358]. It should be pointed out that most of the wires are polycrystalline by the electrodeposition process, which could limit its applications in electronic transport study [23].

A report by Zhu et al. [229] shows that large-area silicon NW arrays can be fabricated on silicon wafers without the use of a template, but based on a so-called micro-electrochemical process that occurs at the surface of the silicon wafer in ionic metal (such as Ag<sup>+</sup>) HF solution. However, the applicability of this method must be further extended.

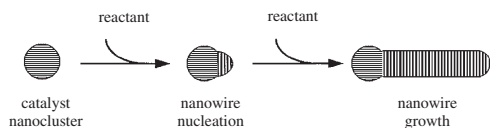
The above templates have to be removed by heating carbon NTs in air or by dissolving the anode aluminum oxide in a strong basic solution to get pure NWs. It is worth noting that such post-treatments will more or less affect the as-prepared NWs.

## 2.2. Vapor-Liquid-Solid Mechanism

Another extensive method is one-dimensional growth based on the VLS mechanism. Initially, the VLS mechanism was proposed by Wagner [41] to explain the growth of crystal whiskers. In 1992, Yazawa et al. demonstrated that high densities of InAs nanowhiskers with diameters of 20–30 nm can be epitaxially grown on InAs (111) substrates onto which one monolayer of Au atoms have been deposited [42]. They argued that the wirelike growth appears to be induced by ultrafine alloy droplets generated by the reactions between Au clusters and InAs substrates. Again, silicon NWs were grown on Si(111) via the VLS reaction, with silane as the Si source gas and Au as the mediating solvent [43].

Lieber's group [7, 8] proposed a general mechanism to illustrate the growth process of the nanowires. The main points of the mechanism are the orientation growth directed by the metal droplet on the tip of crystals. The metal droplet acts as an energetically favored site for absorption of gas-phase reactants. When the clusters dissolve in the metal droplet supersaturates, they will crystallize and grow one-dimensional nanowires. The process is illustrated in Scheme 2.

This group made a great contribution to the improvement of the application of this mechanism to the synthesis of various semiconductor NWs by employing the laser ablation technique to produce nanosized metal catalysts, which



**Scheme 2.** Schematic illustration on the catalytic growth based on the VLS mechanism, including three stages: alloying, nucleation, and axial growth. Reprinted with permission from [7], J. T. Hu et al., *Acc. Chem. Res.* 32, 435 (1999). © 1999, American Chemical Society.

defines the diameter of NWs grown by the VLS mechanism. A pulsed Nd-yttrium-aluminum-garnet laser (wavelength 532 nm) was used to bombard targets, which were composed of NWs and catalysts. The laser ablation on  $\text{Si}_{0.9}\text{Fe}_{0.1}$  generated NWs with a uniform diameter on the order of 10 nm and a length on the order of micrometers (Fig. 3A) [44]. Element analysis revealed that these NWs were Si cores coated by an amorphous  $\text{SiO}_2$  shell as shown in Figure 3B. All of the nanowires terminated at one end in metal nanoparticles, which have a slightly larger diameter than that of NWs. The appearance of these metal nanoparticles on the tips of NWs confirmed that the growth of NWs relies on the VLS mechanism. The authors proposed that the main composition of the catalyst solid should be  $\text{FeSi}_2$ , because  $\text{FeSi}_2$  is stable at the Si-rich region of the phase diagram. In addition, the NWs will stop growing when the temperature is below  $1207^\circ\text{C}$ , since there will be no liquid catalyst at such a low temperature. The agreement between experimental data and theoretical predictions indicates that it is possible to rationally design new catalysts and appropriate growth conditions for other NWs.



It should be noted that the metal selected as a catalyst has a certain solubility with reactants. Meanwhile, since the catalyst should become liquid at the desired reaction temperature, the melting point of the catalyst should be taken into account. The known phase diagrams of binary compounds will be helpful for the design of reactions and selection of catalysts; however, we still know little about the ternary phase diagrams.

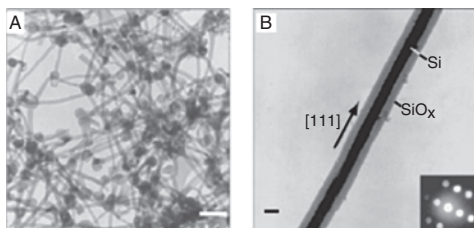


**Figure 3.** (A) TEM image of the nanowires produced following ablation of a  $\text{Si}_{0.9}\text{Fe}_{0.1}$  target. The white scale bar corresponds to 100 nm. (B) TEM image of a typical nanowire with crystalline Si core and an amorphous  $\text{SiO}_x$  sheath. The scale bar corresponds to 10 nm. Inset: Electron diffraction recorded along the [211] zone axis. Reprinted with permission from [44], A. M. Morales and C. M. Lieber, *Science* 279, 208 (1998). © 1998, American Association for the Advancement of Science.

This idea has been successfully implemented by the preparation of a broad range of binary NWs and ternary NWs such as III–V materials (GaAs, GaP, GaAsP, InAs, InP, InAsP), II–VI compounds (ZnS, ZnSe, CdS, CdSe), and SiGe alloys, with LCG, based on the VLS mechanism [48]. However, the mechanism also has its inherent weaknesses. First, to ensure that the catalyst remains liquid, the reaction temperature has to be relatively high ( $700\text{--}1200^\circ\text{C}$ ). This impedes the application of this approach with compounds that are unstable at high temperatures. Second, the products based this approach are not pure materials, because of the metal catalyst attached to the tip of the NWs. It is difficult to remove these catalysts from the as-prepared NWs. Third, the size distribution of these NWs is not ideal. Because the metal catalyst clusters tend to aggregate at high temperatures, this will lead to the decentralization of the size distribution of the NWs.

Yang et al. combined the conventional epitaxial crystal growth technique with the VLS mechanism to achieve precise orientation control during NW growth [46]. The result shows that this vapor-liquid-solid epitaxy (VLSE) is particularly powerful in controlling the synthesis of NW arrays. This group successfully epitaxially grew the highly oriented and well-aligned NW arrays on a patterned substrate by using a Au thin film as the catalyst for NW growth. Typical scanning electron microscopy (SEM) images of NW arrays grown on sapphire (110) substrates with patterned Au thin film fabricated by photolithography (Fig. 4) confirm that the ZnO NWs grow only in the Au-coated areas. The diameters of these wires range from 20 to 150 nm, whereas more than

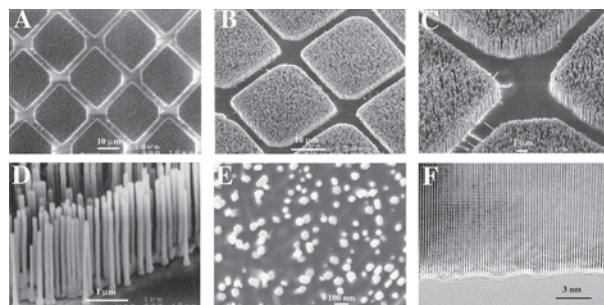


**Figure 4.** (A through E) SEM images of ZnO nanowire arrays grown on sapphire substrates. A top view of the well-faceted hexagonal nanowire tips is shown in (E). (F) High-resolution TEM image of an individual ZnO nanowire showing its  $\langle 0001 \rangle$  growth direction. For the nanowire growth, clean (110) sapphire substrates were coated with a 10- to  $35\text{-\AA}$ -thick layer of Au, with or without TEM grids as shadow masks (micro-contact printing of thiols on Au followed by selective etching has also been used to create the Au pattern). Equal amounts of ZnO powder and graphite powder were ground and transferred to an alumina boat. The Au-coated sapphire substrates were typically placed 0.5 to 2.5 cm from the center of the boat. The starting materials and the substrates were then heated to  $880^\circ$  to  $905^\circ\text{C}$  in an Ar flow. Zn vapor is generated by carbothermal reduction of ZnO and transported to the substrates where the ZnO nanowires grew. The growth generally took place within 2 to 10 min. Reprinted with permission from [46], M. Huang et al., *Science* 292, 1897 (2001). © 2001, American Association for the Advancement of Science.



95% of them have diameters of 70 to 100 nm. The room temperature ultraviolet lasing was successfully demonstrated within ZnO NW arrays [46]. More recently, Yang et al. [21] discovered that certain superstructures of ZnO NWs can readily be formed with Zn as vapor source. A large yield of comb-like structures made of ZnO NWs can be synthesized, in which the NWs are uniformly distributed on the side of the comb stem. Other interesting structures such as tetrapods and tapered NWs can also be synthesized by varying the vapor conditions [21].

This approach can also be extended to the synthesis of carbide materials such as TiC NWs [279] and  $B_xC$  nano-springs [277].

### 2.3. Vapor-Solid Mechanism

In fact, NWs can also be achieved in the absence of catalysts, with the classical VS mechanism [49]. Compared with the VLS mechanism, this route can avoid problems with the purity of products, because of the absence of catalysts. However, it is hard to find a strong and obvious driving force for the formation of NWs by this approach. So far, the researchers are inclined to assign the formation of NWs to the anisotropic growth rates of nanocrystals in different directions. However, these growth rates are related to many specific experimental conditions. The specific requirements for 1D crystal growth, such as the presence of a dislocation at the vapor-solid interface, are still controversial. One of the key factors is the control of supersaturation, the degree of which determines the prevailing growth morphology. The size of NWs can be controlled by supersaturation, nucleation sizes, and the growth process.

MgO,  $Al_2O_3$ , ZnO, and  $SnO_2$  NWs have been synthesized by a carbon-thermal reduction process by Yang's group [50, 51]. Recently, Wang's group has shown an elegant example of the application of the VS mechanism to the synthesis of semiconductor NWs and NBs [52]. In a typical experimental procedure, oxide powders were placed in an alumina tube. The products were collected by an alumina substrate at the downstream end of the tube. The pressure in the alumina tube, the reaction time, and the flow rate of Ar were kept at 300 torr, 2 h, and 50 sccm, respectively, for all of the experiments. The evaporation temperatures were determined by the melting points of individual oxides. The as-obtained hexagonal ZnO exhibits a unique belt-like shape as shown in Figure 5. The detailed structure characterization shows uniform structure, single crystals, and two different growth directions ( $[0001]$  and  $[0110]$ ). The subsequent success with  $SnO_2$ ,  $In_2O_3$ , and CdO NBs indicates that this method is not a minor approach to NBs. The crystal growth was governed by a vapor-solid process. Oxide vapor was generated by the oxide powders, was deposited on a substrate at a lower temperature zone, and grew into NBs.

More recently, Ren's group has shown that a variety of novel hierarchical ZnO nanostructures with 6-, 4-, and 2-fold symmetries can be grown by a vapor transport and condensation technique from a mixture of ZnO,  $In_2O_3$ , and graphite powders as raw materials, as shown in Figure 6 [53]. Since

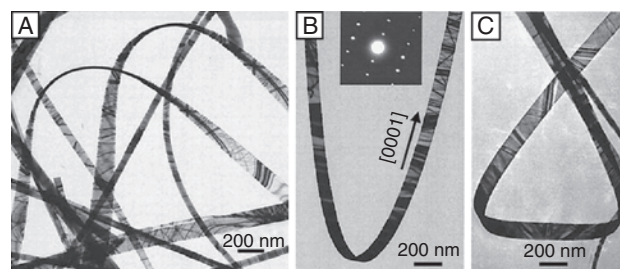


**Figure 5.** TEM and HRTEM images of ZnO nanobelts, showing their geometrical shape. (A to C) TEM images of several straight and twisted ZnO nanobelts, displaying the shape characteristics of the belts. Reprinted with permission from [52], Z. W. Pan et al., *Science* 291, 1947 (2001). © 2001, American Association for the Advancement of Science.

no catalyst is used in such a system, the  $In_2O_3$  NW growth should be based on the VL mechanism. It was found that the major core NWs are single-crystal  $In_2O_3$  with six, four, and two facets, and the secondary NRs are single-crystal hexagonal ZnO and grow either perpendicularly on or slanted to all of the facets of the core  $In_2O_3$  NWs (Fig. 4). The growth of ZnO NRs could also grow based on the VS mechanism because the  $In_2O_3$  core is covered by a ZnO layer that can be the basis for further ZnO NR growth. The high vapor pressure is necessary for the growth of the hierarchical structures compared with the aligned ZnO grown by the VLS mechanism [46]. The growth conditions, such as temperature, pressure, and source component ratios, are correlated to affect the supersaturation rate and the structure formed. This intriguing method could be extended for growing other oxide, carbide, and nitride materials with novel hierarchical nanostructures.

Based on the VS mechanism, various novel metal oxide nanostructures can also be synthesized, such as  $Sb_2O_3$  NRs [146],  $SnO_2$  NWs/nanoribbons/NTs [150],  $SnO_2$  nanodiskettes [151], SnO nanoribbons [152], and  $MoS_2$  NT bundles [337].

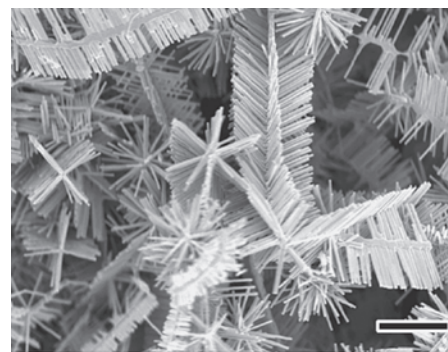
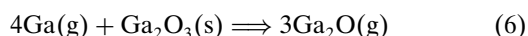
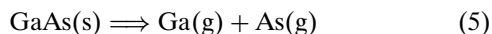


**Figure 6.** SEM image of ZnO nanostructures, showing the various structural symmetries. Three major basic symmetries of 6-, 4-, and 2-fold are clearly seen. Scale bar, 3  $\mu m$ . Reprinted with permission from [53], J. Y. Lao et al., *NanoLetters* 2, 1287 (2002). © 2002, American Chemical Society.

## 2.4. Oxide-Assisted Growth Route

The oxide-assisted growth mechanism of NWs was recently developed by Lee's group [54]. It is somewhat like the VLS mechanism, but with the metal droplets in VLS replaced by an oxide in this mechanism. Therefore, this process has an advantage of being free of a metal catalyst or a template compared with the VLS mechanism.

GaE (E = N, P, As) NWs were fabricated by laser ablation of the corresponding powders mixed with gallium oxide ( $\text{Ga}_2\text{O}_3$ ) under the flow of a carrier gas consisting of Ar and  $\text{H}_2$  [55–57]. The diameter of GaAs core wires and the thickness of the  $\text{GaO}_x$  sheath was in the range of 10–120 nm and 2–10 nm, respectively. The interface between the crystal core and amorphous sheath has an undulant contour. The following reactions were suggested during the growth process:



The results show that if a target made of pure GaAs powder without  $\text{Ga}_2\text{O}_3$  was used for laser ablation, no NWs were found in the products. This indicates that the presence of the oxide  $\text{Ga}_2\text{O}_3$  in the target is critical for the reaction in Eq. (6). Similar results were also observed in GaP, GaN NWs prepared by the same method, indicating that these NWs were grown by an oxide-assisted mechanism.

This mechanism can be further extended for the synthesis of Si NWs [58, 59]. Freestanding quasi-two-dimensional silicon nanoribbons have been realized in the present work with an oxide-assisted growth method (Fig. 7). Two kinds of morphology of the nanoribbons have been observed (Fig. 1A). Most of the ribbons have rippling edges (Fig. 1B), and a small portion of the ribbons has smooth edges (Fig. 1C). The thickness of the ribbons was estimated to be 10–20 nm. The rippling and curling features at the edge of most ribbons also further confirm that the nanoribbons are a quasi-two-dimensional structure and are distinctly different in shape from the one-dimensional silicon NWs with a smooth surface.

The oxide-assisted growth model is illustrated in Figure 8 with Si NWs as an example. Silicon oxide ( $\text{Si}_x\text{O}$ ) was deposited from the vapor phase and generated silicon nanoparticles on the surface (Fig. 8a). Because the surface melting temperatures of nanoparticles can be much lower than that of their bulk materials, this enhances atomic absorption, diffusion, and deposition in a growth process. At the same time, the  $\text{SiO}_2$  shell around silicon can effectively retard the radial growth of nanoparticles and impede the aggregation of nanoparticles. The structure defects at the tip of NWs provide favorable conditions for the faster axial growth of NWs (Fig. 8b). A detailed description of this mechanism and its application to Si NWs have been reported recently [58]. The characteristic of the product generated

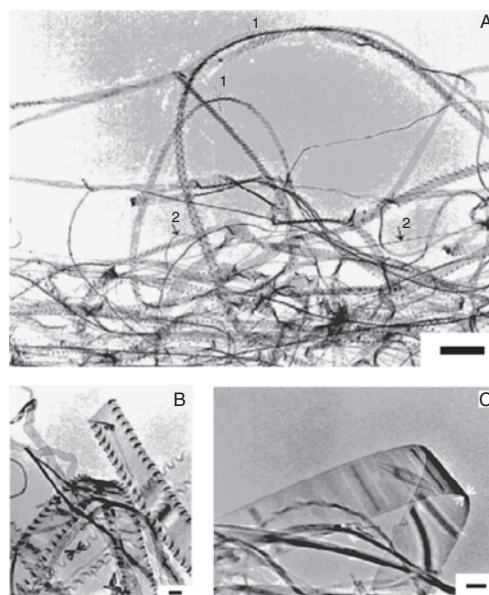


**Figure 7.** TEM images of (A) silicon nanoribbons collected from the substrate. Arrows 1 indicate the edge-on position, and arrows 2 indicate silicon nanowires grown together with nanoribbons. (B) Some rippling-edge ribbons. (C) A smooth-edge ribbon. The thicknesses of the ribbons estimated from the arrows indicating parts in B and C are 13 and 14 nm, respectively. Scale bars: 1  $\mu\text{m}$  in A and 100 nm in B and C. Reprinted with permission from [59], W. S. Shi et al., *J. Am. Chem. Soc.* 123, 11095 (2001). © 2001, American Chemical Society.

by this mechanism is that the desired NW materials were surrounded by an amorphous oxide sheath.

## 2.5. Solvothermal Process

A challenging trend in synthetic chemistry and materials science is determining how the traditional solid-state reaction can be conducted in round-bottom flasks (i.e., turning down the heat for the fabrication of crystals) [60, 67]. Recent developments in soft solution processing may provide an alternative, convenient, lower-temperature, and environmentally friendly pathway for the fabrication of advanced ceramic materials with desirable shapes and sizes [359]. As

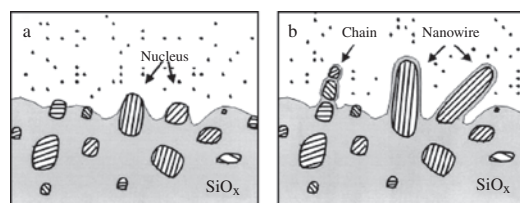


**Figure 8.** Schematic illustration of the oxide-assisted mechanism of nanowires. The parallel lines indicate the (112) orientation. (a) Si oxide vapor is deposited and forms the matrix within which the Si nanoparticles are precipitated. (b) Nanoparticles in a preferred orientation grow fast and form nanowires. Reprinted with permission from [58], S. T. Lee et al., *Mater. Sci. Eng., A* 286, 16 (2000). © 2000, Elsevier Science.

one kind of solution-based chemical process, the hydrothermal process has been widely used for the synthesis of a vast range of solid-state compounds such as oxides, sulfides, and halides [26, 34, 360–363] and molecular, zeolite, and other microporous phases [363], since the pioneering work from the 1960s to the 1980s.

Hydrothermal synthesis can be defined as the use of water as a solvent in a sealed reaction container when the temperature is raised above 100 °C. Under these conditions, the autogenous pressure (i.e., self-developing and not externally applied) is developed. The pressure within the sealed reaction container is found to increase dramatically with temperature, but it will also depend on other experimental factors, such as the percentage fill of the vessel and any dissolved salts. Figure 9 shows these data and demonstrates first the dramatic rise in pressure when a high percentage fill of the reaction vessel is used, and second how the pressure inside the reaction container can be controlled by choice of temperature and/or the volume of solvent used. Below the critical point of water, and even below 200 °C, a high percentage fill allows access to pressures of hundreds of atmospheres [365].

The use of hydrothermal conditions can exert significant effects on the reactivity of inorganic solids and the solubility of the compounds under conditions of elevated pressure and temperatures. The chemical reactivity of usually insoluble reagents can be much enhanced, and many sluggish solid-state reactions can be initiated under hydrothermal conditions. Usually hydrothermal synthesis occurs at higher temperatures (above 300 °C) and often takes place in the supercritical regime. However, even milder reaction conditions (temperature < 250 °C) can be applied not only to provide a convenient low-temperature route to materials with practical application, but also in the exploratory synthesis of new solids [364, 365].

The concepts embodied in the hydrothermal process have been extrapolated to nonaqueous system; therefore, its counterpart, the so-called solvothermal process, has

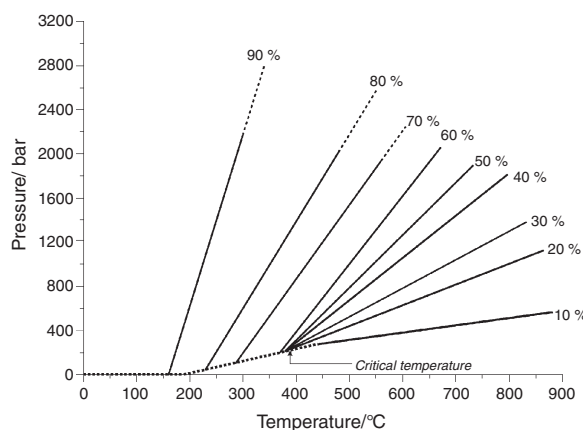


**Figure 9.** Pressure as a function of temperature and percentage fill of water in a sealed vessel. Reprinted with permission from [365], R. I. Walton, *Chem. Soc. Rev.* 31, 230 (2002). © 2002, Royal Society of Chemistry. Adapted from [361], A. Rabenau, *Angew. Chem., Int. Ed. Engl.* 24, 1026 (1985). © 1985, Wiley-VCH.

emerged, in which an organic solvent is used as the reaction medium instead of water, at an elevated temperature near its boiling point. As the counterpart of the hydrothermal process, the solvothermal process has emerged in recent years and has received great attention in synthetic chemistry and materials science.

Solvothermal reactions are usually performed in a Teflon-lined, stainless steel autoclave, as shown in Figure 10. The use of an autoclave is necessitated by the pressures developed in the solvothermal reactions, and the inert liner is used to protect the stainless steel outer shell from the corrosive reagents and solvents typically used in the synthesis. Such autoclaves can be used at up to 270 °C, and, depending on the engineering specifications of the steel walls, pressures of ~150 bar can be maintained [365]. The synthetic procedure is simple; however, the rational design of the reaction requires multidisciplinary and interdisciplinary knowledge.

There are several advantages of the solvothermal technique that distinguish it from the traditional solid-state reactions and hydrothermal process. First, many inorganic precursors can be solubilized in a suitable solvent similar to that in which reactants were solubilized in the molten flux of the solid-state reaction at high temperatures [366]. Second, the solvothermal technique removes diffusion control by the use of a suitable solvent under mild conditions [366]. Third, the conventional hydrothermal method is confined to the conditions that some reactants will decompose in the presence of water or the precursors are very sensitive to water, or some reactions will not happen in the presence of water, resulting in the failure of the synthesis of the desired compounds. By the substitution of nonaqueous solvents (both polar and apolar solvents) such as alcohols,  $C_6H_6$ , polyamines,  $NH_2NH_2$ , or liquid  $NH_3$  for water, solvothermal process allows many possibilities for the preparation of various nanocrystalline compounds and the initiation of some conventional solid-state reactions in organic media under mild conditions [26]. It can even be used to prepare carbonides, nitrides, phosphides, silicides, chalcogenides, and so on.

In the solvothermal process, one or several kinds of precursors are dissolved in nonaqueous solvents. The reactants are dispersed in solution and become more active. The reactions happen in the liquid phase or under supercritical status. The solvothermal process is relatively simple and easy

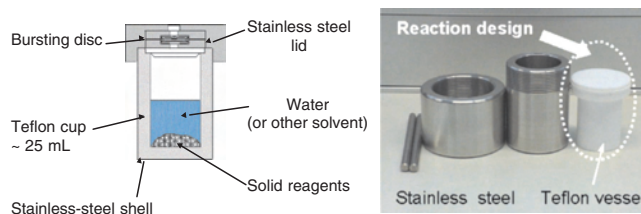


**Figure 10.** Left: A schematic of a Teflon-lined, stainless steel autoclave typically used in the laboratory to perform subcritical solvothermal synthesis. Reprinted with permission from [365], R. I. Walton, *Chem. Soc. Rev.* 31, 230 (2002). © 2002, Royal Society of Chemistry. Right: A set of autoclaves.



to control with several changeable parameters such as solvents, temperature, and reaction time. The sealed system can effectively prevent the contamination of the toxic and air-sensitive precursors. With the substitution of nonaqueous solvents such as polar and nonpolar solvents for water, the so-called solvothermal process can be widely extended to prepare various kinds of nonoxide nanocrystalline materials whose precursors are very sensitive to water.

In the past two decades, a trend toward very mild conditions (100–200 °C) has become increasingly apparent for inorganic synthesis chemistry and materials synthesis. The potential of this technique for preparative solid-state chemistry has been intensively reviewed [365–368]. Various oxide ceramic ultrafine powders were prepared by the solvothermal process [367]. Morris and Weigel [368] summarized some of the results of the recent works in the synthesis of molecular sieves from nonaqueous solvents.

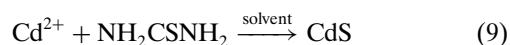
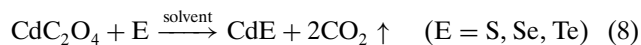
In recent years, rational solution routes to nanocrystals have been extensively explored [26, 34]. Various nonoxide compound nanocrystals such as metal chalcogenides [61–65, 310, 323, 369, 370, 372–379], phosphides [380], and metal nitrides can be synthesized [381–383]. The results showed that the physicochemical properties of the solvents have strong effects on the reactivity, shapes, sizes, and phases of the particles, since solvent properties such as polarity, viscosity, and softness will strongly influence the solubility and transport behavior of precursors under solvothermal conditions. Various kinds of inorganic NRs/NWs/NTs can be synthesized by solvothermal/hydrothermal processes as listed in Tables 1 and 2.

In the following sections, the latest development of the fabrication of nonoxide low-dimensional semiconductor nanocrystals with different shapes, sizes, and phases by mild solution routes will be reviewed with a focus on the emerging solvothermal processing of 1D NRs/NWs. Specific examples will be given to illustrate the reaction activity, the principle, and key parameters that dominated the synthesis process.

### 2.5.1. Fabrication of II–VI Group Low-Dimensional Nanocrystals

#### Shape, Size, and Phase Control of CdE Nanocrystals

Several solvothermal routes were designed for the synthesis of CdS nanoparticles with different shapes, sizes, and phases [61, 62, 369]:



The reaction was conducted in a Teflon-lined autoclave with a 40-ml capacity (as shown in Fig. 10), which was filled with a solvent up to 80% of the total volume. The autoclave was maintained at 80–180 °C for 3–12 h and air-cooled to room temperature. Different solvents were chosen to investigate the influence on the reactivity, crystal shape, size, and phase.

The shape, particle size, and phase of II–VI group semiconductor nanoparticles can be synthesized conveniently with high yield by the solvothermal process [61]. A CdS sample synthesized in ethylenediamine (en) via the reaction shown in Eq. (8) at 160 °C for 12 h can be indexed as the hexagonal phase of CdS (wurtzite structure) with cell constants  $a = 4.140 \text{ \AA}$ ,  $c = 6.72 \text{ \AA}$ , which are close to the reported data for CdS (JCPDS card file no. 41-1049). The TEM image in Figure 11A shows that the CdS crystallites synthesized in ethylenediamine are uniform NRs with diameters of 20–50 nm and lengths of 200–1300 nm. In addition, CdS crystallites synthesized in other polyamines such as diethylene triamine (dien) and triethylene tetraamine (trien) under the same experimental conditions display the same morphology. The CdS powders obtained in dien consist of uniform NRs with diameters of 30–60 nm and lengths of 200–4800 nm. Wurtzite CdSe NRs with diameters of 6–20 nm and lengths up to 100–500 nm can also be synthesized in en, dien, and trien. Similarly, CdTe NRs with a zinc-blende structure were obtained in en.

Solvent effects on the morphology of the products were investigated. Disc-like particles with a size of 40 nm were produced in pyridine (py) as shown in Figure 11B. A lower temperature is unfavorable for the growth of CdE NRs. The CdS particles formed in en at 120 °C for 12 h consist of both uniform spherical particles and shorter NRs. If the temperature is lower than 120 °C, the reaction is incomplete and may not even occur. These results suggest that relatively higher temperature and pressure in the system are necessary for the oriented growth of the NRs. The results indicate that the morphology of CdS, CdSe, and CdTe crystallites can be controlled by choosing different solvents.

Remarkable control over the shape, size, and phase of CdS can be readily realized with the choice of different solvents and reaction conditions and other modified solvothermal reactions as expressed in Eqs. (9) and (10) [62, 369]. The widths and sizes of CdS NRs can be varied by controlling the temperature and reaction time. The TEM image

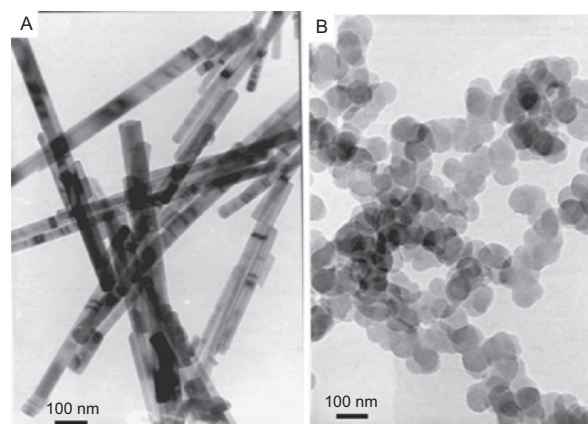


**Figure 11.** TEM images and ED patterns for the obtained CdS samples. (A) CdS synthesized in en at 160 °C for 12 h. (B) CdS nanoparticles synthesized in pyridine at 160 °C for 12 h. Reprinted with permission from [61], S. H. Yu et al., *Chem. Mater.* 10, 2309 (1998). © 1998, American Chemical Society.

in Figure 12a shows that the CdS powders obtained at 100 °C for 12 h consist of uniform NRs with diameters of 6–13 nm and lengths up to 140–480 nm. As the temperature approached 180 °C, the product was found to be uniform NRs with widths of 30–40 nm and lengths up to 280–900 nm (Fig. 12b). The CdS NRs show [001] preferential orientation as shown in a typical high-resolution transmission electron microscopy (HRTEM) image in Figure 12c, corresponding to a stronger and sharper (002) diffraction peak in the X-ray diffraction (XRD) pattern. The SEAD inserted in Figure 12c indicated the CdS NRs are polycrystalline with a wurtzite structure. Further results show that single-crystal CdS NRs can also be obtained at higher temperatures [63].

In addition to the shape control, both sizes and the phase of CdS nanocrystals can be controlled. A modified solvent thermal process as expressed in Eq. (10) was applied to prepare spherical CdS nanocrystals with different sizes via the reaction of CdSO<sub>4</sub> with Na<sub>2</sub>S<sub>3</sub> in benzene at 80–120 °C. It was found that solvent, temperature, and reactant have significant effects on the crystal structure and particle size of CdS nanocrystals. Increased temperature and use of a solvent with a low dielectric constant benefit the preparation of CdS nanocrystals with hexagonal structure. The water content in the system not only induces the presence of cubic phase CdS nanocrystals, but also leads to increasing particle size. Compared with the result from the solvothermal process, pure cubic CdS nanocrystals with an average size of 7 nm were obtained via the hydrothermal process at 100 °C for 12 h, with CdSO<sub>4</sub> · 8/3H<sub>2</sub>O and Na<sub>2</sub>S as reactants [369].

It is well known that the free energy difference between cubic and hexagonal structures for CdS is small [384, 385]. It is believed that solvents with a lower dielectric constant may minimize the free energy difference between the hexagonal and cubic phases and thus favor the formation of hexagonal phase CdS. In addition, the solvent has a significant effect on the shifting of the following equilibrium:

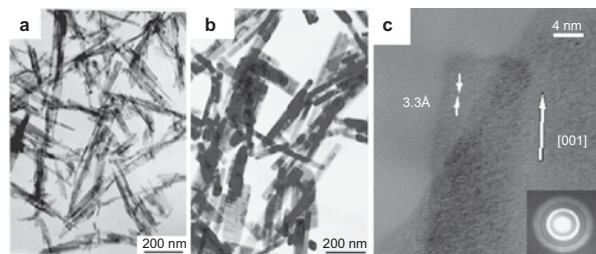
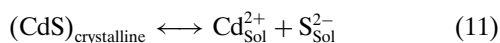


**Figure 12.** TEM and HRTEM images of CdS nanowires synthesized by a solvothermal reaction of Cd<sup>2+</sup> with thiourea in ethylenediamine (a) at 100 °C for 12 h. (b) 180 °C for 12 h. (c) HRTEM image indicating a typical CdS nanorod with a diameter of ~12 nm and well-resolved (002) lattice planes, which was obtained under condition (a). An inserted electron diffraction pattern (ED) shows that the CdS nanorods are of polycrystalline nature and can be indexed as the wurtzite structure. Reprinted with permission from [26], S. H. Yu, *J. Ceram. Soc. Jpn.* 109, S65 (2001). © 2001, Ceramic Society of Japan.

In this route, the presence of benzene, with a lower dielectric constant than water, will shift the equilibrium (11) to the left and slows the dissolution rate of CdS crystallites. Thus, it will lead to a difference in particle size of the final products. The effects of the solvent on crystal structures and particle size are also consistent with those reported by Ramsden et al. [386].

A modified solvothermal process produced CdTe crystals with different sizes, phase, and morphologies, with CdCO<sub>3</sub> reacting with Te in the presence of N<sub>2</sub>H<sub>4</sub> · H<sub>2</sub>O in the different solvents [370]. More interestingly, the meta-stable wurtzite CdTe phase and its conversion to the stable cubic CdTe phase under mild conditions were observed.

**Shape and Phase Control Synthesis of ZnS Nanocrystals** A rational design of the solvothermal reaction makes it possible to control both the dimensionality (dots, rods, and sheets) of ZnS nanocrystals and the phase. The solvothermal reaction of zinc salts such as Zn(CH<sub>3</sub>COO)<sub>2</sub> · 2H<sub>2</sub>O or ZnCl<sub>2</sub>, and with thiourea in en at 120–180 °C for 6–12 h, results in a white precipitate with the composition ZnS · (en)<sub>0.5</sub> [64].

The XRD pattern in Figure 13a shows that a new molecular precursor was obtained at 180 °C. It has been confirmed that either a solvothermal reaction of Zn<sup>2+</sup> with thiourea or a similar reaction between Zn (or Zn<sup>2+</sup>) and sulfur in en medium at 120–180 °C resulted in the same product. The SEM image in Figure 14a shows that all of the particles are sheet-like. EDX analysis of this lamellar precursor gave a Zn:S ratio of 1.00:0.98, indicating that this sulfide had the expected composition. In addition, both N and C signals were detected in the EDX spectrum. After removal of the en template, no N signal was detected in the EDX

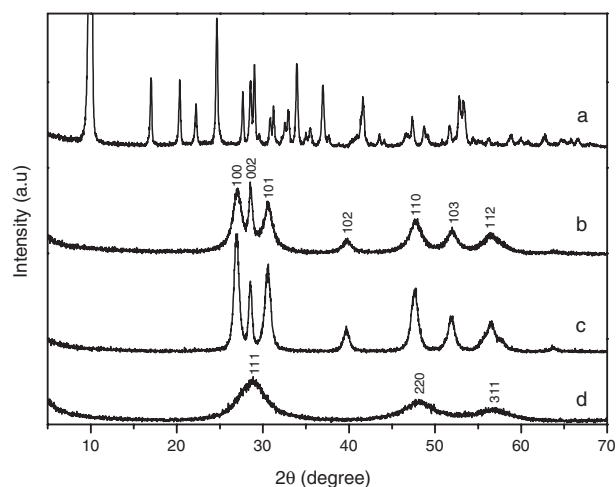


**Figure 13.** XRD patterns of the products. (a) A lamellar precursor ZnS · (en)<sub>0.5</sub> obtained by solvothermal reaction of Zn(CH<sub>3</sub>COO)<sub>2</sub> · 2H<sub>2</sub>O with thiourea in ethylenediamine (en) at 180 °C for 12 h. (b) and (c) Wurtzite ZnS nanoparticles obtained by thermal decomposition of lamellar ZnS · (en)<sub>0.5</sub> precursor at 250 °C, 500 °C for 0.5 h under vacuum, respectively. (d) Sphalerite ZnS (S) nanoparticles obtained by a similar solvothermal reaction in ethanol at 120 °C for 12 h. Reprinted with permission from [64], S. H. Yu and M. Yoshimura, *Adv. Mater.* 14, 296 (2002). © 2002, Wiley-VCH.

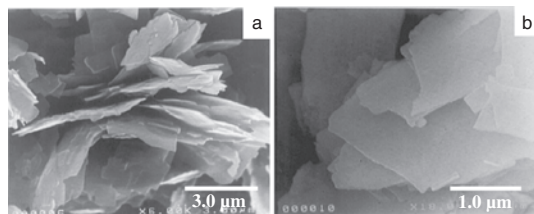


**Figure 14.** SEM images of (a) the lamellar precursor  $\text{ZnS} \cdot (\text{en})_{0.5}$  obtained by solvothermal reaction at 180 °C for 12 h and (b) ZnS nanosheets obtained by thermal decomposition of the precursor in vacuum at 250 °C for 0.5 h. Reprinted with permission from [64], S. H. Yu et al., *Adv. Mater.* 14, 296 (2002). © 2002, Wiley-VCH.

spectrum. TG-DTA analysis shows that the decomposition events of the precursor obtained at 120–180 °C happened at 362 °C, accompanying the weight loss of en. The net weight loss for the precursor obtained at 120 °C and 180 °C in this stage is 23.5%, which suggests a molecular precursor with a composition of  $\text{ZnS} \cdot (\text{en})_{0.5}$  (theory: 23.62%).

Pure wurtzite ZnS (W) was produced by removing the en by thermal decomposition at 250–500 °C under vacuum as confirmed by the XRD patterns in Figure 13c and d. The SEM image in Figure 14b and TEM images in Figure 15a show that ZnS nanoparticles are sheet-like with rectangle lateral dimensions in a range of 0.3–2 μm. The oxidation of the lamellar molecule in air produced wurtzite ZnO flake-like dendrites [64]. The nanosheets are well-crystallized single crystals with a growth direction along the *a* and *c* axes, as indicated by the SAED pattern in Figure 15a. The sharp nature of the (002) peak in Figure 13b and c suggests that the nanosheets grow along the *c* axis. The HRTEM image shows well-resolved (100) lattice planes with a lattice spacing of 3.3 Å, indicating that the preferred orientation is along the *a* axis (Fig. 15b). EDX analysis shows that the weight composition of Zn and S in the product is 67.24% and 32.76%, which is in good agreement with the stoichiometric composition of ZnS.

The synthetic method is both flexible and reproducible for controlling the phase, shape, and sizes of ZnS nanocrystals. By a similar solvothermal reaction at 120 °C, with

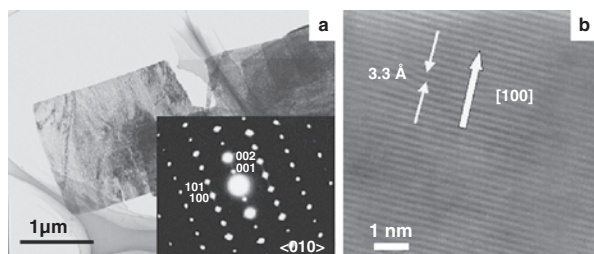


**Figure 15.** (a) TEM images and SAED patterns for wurtzite ZnS single-crystal nanosheets obtained by thermal decomposition of lamellar  $\text{ZnS} \cdot (\text{en})_{0.5}$  precursor at 500 °C for 0.5 h in vacuum. The inserted SAED pattern was recorded along the  $\langle 010 \rangle$  zone. (b) Well-resolved HRTEM image of the wurtzite ZnS single-crystal nanosheet. Reprinted with permission from [64], S. H. Yu and M. Yoshimura, *Adv. Mater.* 14, 296 (2002). © 2002, Wiley-VCH.

ethanol instead of en as a solvent, sphalerite ZnS (S) nanoparticles with a size of ~3 nm can easily be synthesized. Furthermore, wurtzite ZnS NRs can also be synthesized by using *n*-butylamine, a monodentate amine, as a solvent [65]. A typical TEM image is shown in Figure 16. In addition, the NRs could be aligned together to form bundle structures or arrays under limited experimental conditions. The further oxidation of ZnS NRs can generate ZnO wurtzite NRs. The general synthetic strategies for ZnS nanocrystals with different phases and shapes and ZnO dendrites are shown in Scheme 3. The results show that both shape and phase of the ZnS nanocrystals can be well controlled by choosing solvents.

These facile mild solution-based methods shed light on the possibility of controlling shape, dimensionality (0D, 1D, 2D), size, and phase. The unusual 1D, 2D wurtzite ZnS single-crystal NRs and nanosheets, flake-like ZnO dendrites, and ZnO NRs can easily be generated based on the solvothermal reactions. This synthetic strategy implies that other semiconductor nanocrystals could also be synthesized along the same line by using a suitable “shape controller” under solvothermal conditions that we will discuss in next section.

#### Formation Mechanism and General Synthesis of II–VI Nanorods

As stated above, only CdS nanocrystals prepared by the solvothermal reactions in en display a rod-like shape. If en were replaced by other organic molecules as solvents, CdS nanocrystals would be irregular or spherical. What dominates this process and results in the formation of NRs? If this mechanism is revealed, one can expect to make use of it to control the shape and size of nanocrystals. Moreover, this mechanism can be expanded to design a general and rational pathway to other 1D semiconductors. In this section, the detailed formation process of CdS NRs under solvothermal conditions was discussed at first. Then a general solvothermal synthesis of II–VI NRs was presented.

CdS nanocrystals were prepared with a previous synthetic method [62]. In a typical procedure, an appropriate amount of  $\text{Cd}(\text{NO}_3)_2 \cdot 4\text{H}_2\text{O}$  and  $\text{NH}_2\text{CSNH}_2$  (molar ratio 1:3) was added to a Teflon-lined stainless steel autoclave that had been filled with en to 80% of its capacity. Samples (a), (b), (c), and (d) were taken out of the autoclave after the reaction had been carried out at 120 °C for 1 h, 1.5 h, 2.5 h, and 3.5 h, respectively. Then the mixtures were cooled to room temperature immediately. The precipitates were filtered and

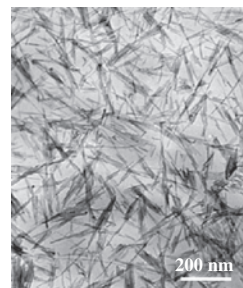
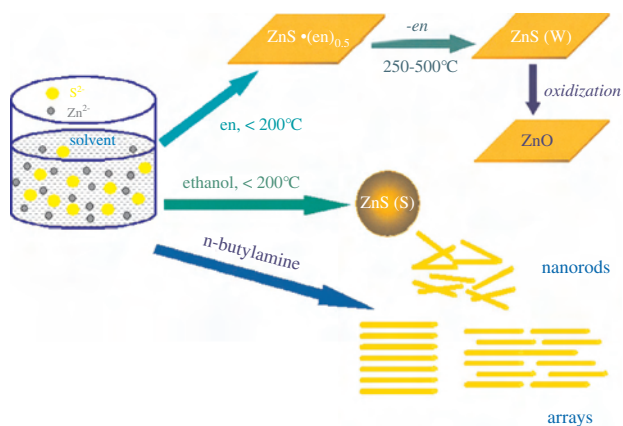


**Figure 16.** Wurtzite ZnS nanorods synthesized in *n*-butylamine at 250 °C for 12 h.





**Scheme 3.** Illustration of the controlled synthesis of ZnS nanocrystals with different dimensionalities and phases: ZnS dots, nanosheets, nanorods, and bundles. Partially adapted with permission from [64], S. H. Yu and M. Yoshimura, *Adv. Mater.* 14, 296 (2002). © 2002, Wiley-VCH.

washed repeatedly with distilled H<sub>2</sub>O and absolute ethanol to remove the excessive thiourea and other impurities. Finally the samples were dried in vacuum at 70 °C for 0.5 h.

The crystallinity of the samples is improved with the reaction time prolonged during the whole process, as shown in Figure 17. Furthermore, a preferential orientation and a rod-like shape were observed in the samples after a longer reaction time. TEM photographs show that there is an accordion-like folding process in the morphology evolution of the samples. The poorly crystallized sample (a) displayed a lamellar shape, as shown in Figure 18a, whereas the SAED pattern (inset of Fig. 18a) indicates that it was poorly crystallized, as confirmed by the XRD pattern in Figure 17a. A TEM photograph (Fig. 18b) of sample (b) reveals that the number of folds increased and these folds spontaneously agglomerated together. It seems that the shrinkage of the lamellae leads to both the increase and the agglomeration

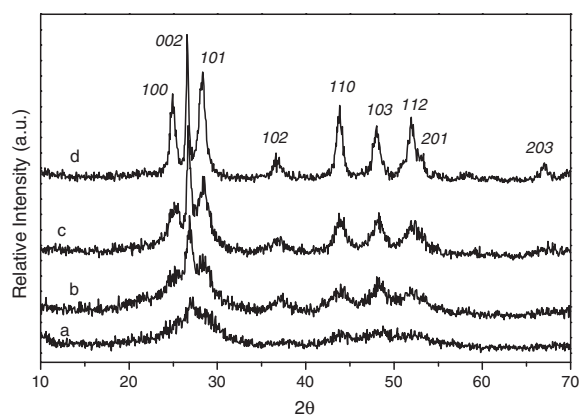


**Figure 17.** XRD patterns for the CdS samples obtained at 120 °C, en. (a)–(d) With time prolonged by 1, 1.5, 2.5, and 3.5 h, respectively. Reprinted with permission from [63], J. Yang et al., *Chem. Mater.* 12, 3259 (2000). © 2000, American Chemical Society.

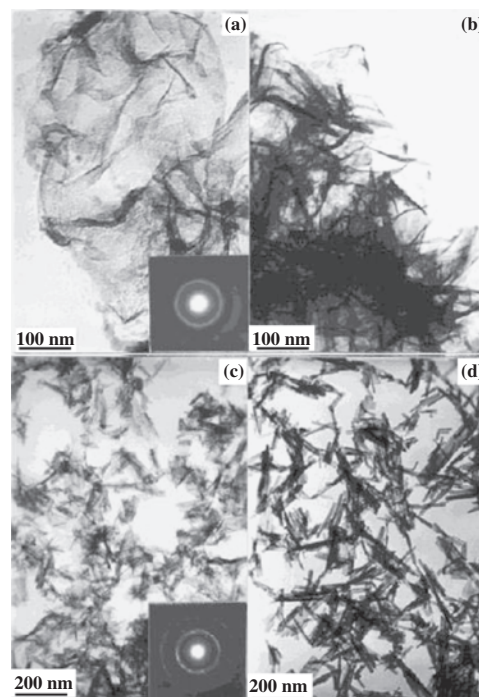


**Figure 18.** TEM images of the morphology evolution of CdS samples obtained at 120 °C in ethylenediamine. (a)–(d) With time prolonged by 1, 1.5, 2.5, and 3.5 h, respectively. Reprinted with permission from [63], J. Yang et al., *Chem. Mater.* 12, 3259 (2000). © 2000, American Chemical Society.

of the folds. Subsequently, there was an interesting shape change in the sample (c). The previously agglomerated folds broke into needle-like fragments as shown in Figure 18c, which is very critical in the formation process of CdS NRs. The SAED pattern shows a preferential orientation along (002), which coincides with the result from the XRD pattern. The sample (d) is composed of short NRs with widths of 12–17 nm and lengths of 40–160 nm.

According to these results, the formation of the obtained NRs can be divided into several steps. First cadmium nitrate and thiourea reacted to produce the lamellar CdS with many folds. After that, the folds on the lamellae agglomerated together. Then these folds broke into needle-like fragments. Finally these needles further grew into well-crystallized NRs. This transition process is interesting and is obviously different from the known 1D growth mechanisms. It is believed that en molecules adsorbed to the samples determined this morphology transition, and en molecules in the solution were not relevant to this transition process. If the sample (a) after filtering but without washing was put in a solvent such as absolute ethanol and solvothermally treated at 120 °C for 10 h, the products obtained were composed of CdS needles exclusively. However, if en molecules adsorbed to sample (a) were removed by washing several times with distilled H<sub>2</sub>O, most of the products prepared under the same conditions were uniform spherical particles. The results suggested that the transition process depends on en molecules adsorbed to the initial sample.

Although the close relationship between en molecules adsorbed to the surface and the formation of one-dimensional nanocrystals has been proved according to the above results, it is still not clear how en molecules control the formation of NRs. The IR spectrum of the starting solution was similar to that of  $[\text{Cd}(\text{en})_3]^{2+}$ , which is similar to the data reported in the literature [387]. This implies that the en molecule in the starting solution uses a *gauche* conformation to chelate with  $\text{Cd}^{2+}$  just like that in  $[\text{Cd}(\text{en})_3]^{2+}$  [388]. Although there is thiourea in the solution, the coordination capacity of thiourea is much smaller than that of the en molecule [389]. Therefore, a complex between thiourea and the  $\text{Cd}^{2+}$  ion was not observed in the IR spectra. The IR spectra of the CdS samples were close to that of  $\text{Cd}(\text{en})\text{Cl}_2$ , in which an en molecule uses a *trans* conformation to bridge an adjacent cadmium ion [391, 392]. This result indicates that the en molecule probably uses a *trans* conformation to coordinate with  $\text{Cd}^{2+}$  on the surface of CdS, which we assume to be due to the fact that sulfur bonded with  $\text{Cd}^{2+}$  impeded the formation of the chelate structure between the en molecule and  $\text{Cd}^{2+}$  on the surface of the CdS.

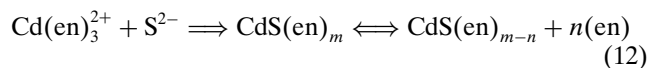
The *trans* conformation of the en molecule adsorbed to the surface of CdS is important for the formation of CdS NRs through this process. To certify this conclusion, *o*-phenanthroline was chosen as the solvent to prepare CdS powders by the same reaction at 210 °C for 36 h, since it merely forms the chelate structure with  $\text{Cd}^{2+}$  and its chelate ability is close to that of en [389]. Only irregularly shaped particles were observed in the product. This result demonstrates the importance of the conformation of the en molecule from the back. Reetz and co-workers also reported a nonchelating mode of coordination for  $\alpha$ -hydroxy carboxylates on the metal surface, which is likely to be the morphology-determining factor in the shape-selective preparation [393].

Although the IR spectra of the samples obtained at the different times were similar to each other, it was noted that the intensity of absorption peaks of the en molecules adsorbed to the surface of the CdS gradually decreased with regard to the adsorption peak of  $\text{NO}_3^-$  at  $1384.6\text{ cm}^{-1}$ . This indicates that the en molecule dissociates from the surface of CdS nanocrystallites during the morphology transition. The high temperature weakens the interaction between the en molecule and  $\text{Cd}^{2+}$  on the surface of CdS, which leads to the dissociation of en molecules from the CdS surface. When the obtained samples without post-treatment were heated in a vacuum at 70 °C for 1 h, the absorption peaks that belonged to the en molecule adsorbed to the surface of CdS greatly decreased in intensity. However, there was no shift in the position of the IR peaks, indicating that the interaction between the en molecule and  $\text{Cd}^{2+}$  on the surface of the CdS was destroyed.

If the dissociation of the en molecule adsorbed to the surface of CdS is restrained, the morphology transition will slow down and even stop. For example, when sample (a) without post-treatment was put into benzene at 120 °C for 10 h, the products kept almost their original morphology. This can be attributed to the fact that the low solubility of the en molecule in benzene limits the dissociation of the en molecule. The result confirmed that the dissociation of the en molecule adsorbed to the surface of CdS leads to the

morphology transition of CdS. This result also indicates that the dissociation of the en molecule in an apolar solvent is much slower than that in a polar solvent. In other words, the physicochemical properties of solvents have a great influence on the dissociation of the en molecule from CdS.

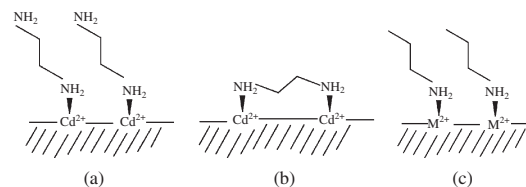
Based on all of these results, the whole forming process of CdS NRs can be expressed as follows:



First, the  $\text{Cd}^{2+}$  ion coordinated with the en molecule to form  $\text{Cd}(\text{en})_3^{2+}$  [387]. Thiourea decomposed to produce  $\text{S}^{2-}$  at low temperatures in the base environment. Then the reaction between  $\text{Cd}(\text{en})_3^{2+}$  and  $\text{S}^{2-}$  produced CdS powder with its surface-adsorbed en molecule. Meanwhile, the conformation of the en molecule coordinated with  $\text{Cd}^{2+}$  changed from the *gauche* conformation to the *trans* conformation. However, the interaction between the en molecule and  $\text{Cd}^{2+}$  on the surface of CdS was weak when the en molecule was used in the *trans* conformation. Therefore, this structure was destroyed at higher temperatures. This dissociation of the en molecule from the surface of CdS resulted in the evolution process of the morphology. In fact, the en molecule with the *trans* conformation acted as an intermediate.

There are still two questions to be resolved. One is to further ascertain the coordination mode between  $\text{Cd}^{2+}$  on the surface and the en molecules. Because it is difficult to judge whether the coordination mode between  $\text{Cd}^{2+}$  on the surface and the en molecules is monodentate (Scheme 4a) or bridging (Scheme 4b) based only on IR data, the en molecules in both cases are in the *trans* configuration. The other is to expand the controlling mechanism to the syntheses for other important one-dimensional semiconductors.

In as much as *n*-butylamine can act only as a monodentate ligand, the coordination between it and metal ions must be in a monodentate mode, as shown in Scheme 4c. Thus, it is employed as the solvent to answer the first question. CdS nanocrystals were chosen as the target to examine whether the same reaction in a monodentate ligand can produce NRs. In the IR spectrum of the as-prepared CdS nanocrystals, the characteristic absorption peak at  $1573.0\text{ cm}^{-1}$  can be undoubtedly assigned to the  $-\text{NH}_2$  bending vibration, which shifts to lower frequencies as compared with pure *n*-butylamine [394]. At the same time, the red shift of C-N bending vibration caused by this coordination is also observed in the IR spectrum [394]. These results indicate



**Scheme 4.** Illustration of the possible coordination mode on the surface (a) monodentate mode of en molecules, (b) polydentate mode of en molecules, (c) monodentate mode of *n*-butylamine. Reprinted with permission from [65], J. Yang et al., *Angew. Chem. Ed. Int.* 41, 4697 (2002). © 2002, Wiley-VCH.

that *n*-butylamine also uses the nitrogen atom to coordinate with metal ions on the surface of CdS nanocrystals in a monodentate mode.

As shown in Figure 19a, the XRD pattern of CdS obtained at 220 °C for 12 h can be identified as a hexagonal phase CdS (JCPDS card no. 41-1049). The crystal size, which can be roughly estimated by using the Scherrer equation, are 50 nm and 9 nm, based on the (002) and (110) diffraction peaks, respectively. The great difference between the coherence length in the [002] direction and that in the [110] direction implies the unusual shape of the products [394]. Short NRs 7–10 nm in width and 30–55 nm in length can be readily observed in Figure 19b. It is believed that plenty of (002) planes in NRs and the anisotropic shape of NRs result in a remarkable increase in the intensity and narrowing of the FWHM of the (002) diffraction.

That a number of rod-like CdS nanoparticles can be obtained in *n*-butylamine indicates that one anchor atom in a ligand is necessary and adequate to the formation of NRs, even though more anchor atoms may be present in a ligand. The close interaction between anchor atoms in ligands (Lewis base) and metal ions on the surface (Lewis acid) is another prerequisite for the formation of NRs, because the result of this weak interaction will be that ligand molecules will not impose effective influence on the nucleation and growth of nanoparticles [62]. Altering this kind of interaction strength between ligands and metal ions could control the shape and size of various chalcogenide nanocrystals, as demonstrated previously in the synthesis of CdS nanocrystals [62].

To verify whether a monodentate ligand can be used as a “shape controller” for the synthesis of other semiconductor NRs, a series of similar solvothermal reactions were performed in *n*-butylamine. A mixture of hexagonal phase CdSe and cubic phase CdSe was obtained at 160 °C for 12 h. The TEM image in Figure 20a shows that the CdSe nanocrystals are composed of NRs 12–16 nm in width and 200–400 nm in length. Similarly, wurtzite ZnSe nanoparticles can also be obtained at 220 °C for 12 h. The ZnSe nanocrystals are composed of NRs with diameters in the range of 25–50 nm and lengths up to 1000 nm. A well-crystallized single ZnSe NR with a growth direction along the *c* axis is presented in Figure 20b. Wurtzite ZnSe NRs were achieved for the first

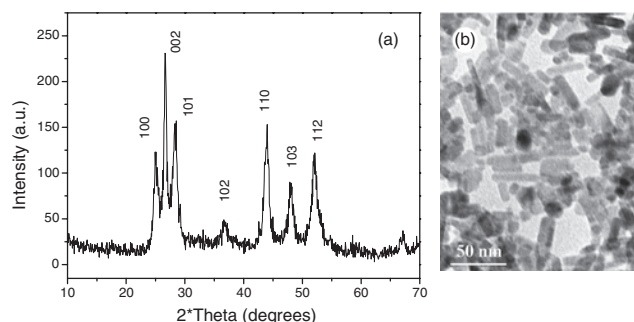


**Figure 19.** (a) XRD pattern and (b) TEM image of CdS nanocrystals obtained at 220 °C for 12 h. Reprinted with permission from [65], J. Yang et al., *Angew. Chem. Ed. Int.* 41, 4697 (2002). © 2002, Wiley-VCH.

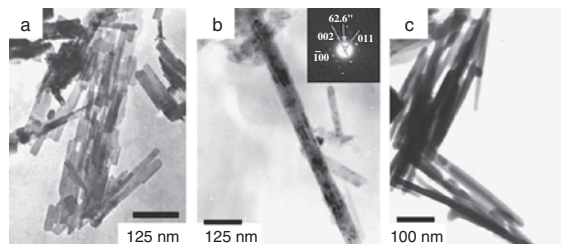


**Figure 20.** TEM images of (a) CdSe nanocrystals (160 °C, 12 h), (b) ZnSe nanocrystals (220 °C, 12 h), and (c) PbSe nanocrystals (80 °C, 12 h). Reprinted with permission from [65], J. Yang et al., *Angew. Chem. Ed. Int.* 41, 4697 (2002). © 2002, Wiley-VCH.

time in a solution system under mild conditions. Again, cubic PbSe NRs 12–20 nm in width and 200–450 nm in length as shown in Figure 20c can be obtained at 80 °C for 12 h. The growth direction of the NRs was along  $\langle 200 \rangle$ . These results indicate that selecting the proper experimental conditions is important for the formation of NRs, although NRs can be synthesized in *n*-butylamine.

This solvent-mediated controlling mechanism has been demonstrated to be successful in the synthesis of a variety of semiconductor NRs/NWs. In this mechanism, ligands control the shape of nanocrystals through the interaction between ligands and metal ions on the surface of nuclei. One anchor atom in a ligand such as *n*-butylamine is necessary and sufficient for the formation of 1D nanocrystals, even though more anchor atoms may be present in a ligand. The close interaction between anchor atoms in ligands and metal ions on the surface is another important prerequisite for NR formation. Furthermore, this route provides not only a possible general route to other chalcogenide NRs on a large scale but also a guide for further rational design of 1D chalcogenides.

### 2.5.2. Fabrication of Group V–VI Low-Dimensional Nanocrystals

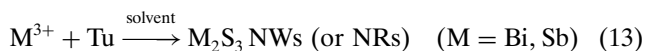
$A_2B_3^{VI}$  ( $A = \text{Sb, Bi, As}$  and  $B = \text{S, Se, Te}$ ) semiconductor compounds find applications in television cameras with photoconducting targets, thermoelectric devices, electronic and optoelectronic devices, and IR spectroscopy [395]. Bismuthinite ( $\text{Bi}_2\text{S}_3$ ) and stibnite ( $\text{Sb}_2\text{S}_3$ ) are direct band-gap materials that are useful for photodiode arrays or photovoltaics [396, 397].  $\text{Bi}_2\text{S}_3$  and  $\text{Sb}_2\text{S}_3$  also belong to a family of solid-state materials with applications in thermoelectric cooling technologies based on the Peltier effect [398]. These materials may be a starting material for the synthesis of semiconductors based on sulfo salts of bismuth and related compounds and sulfoantimonates of antimony and related compounds such as  $\text{M}(\text{NH}_3)_6\text{Cu}_8\text{Sb}_3\text{S}_{13}$  ( $M = \text{Mn, Fe, Ni}$ ) [399].

Conventionally,  $\text{Bi}_2\text{S}_3$  and  $\text{Sb}_2\text{S}_3$  can be prepared by direct reaction of elements and sulfur vapor in a quartz vessel at high temperature [395, 400]. The liquid solution syntheses of  $\text{Bi}_2\text{S}_3$  and  $\text{Sb}_2\text{S}_3$  generally yield products that are mostly amorphous, poorly crystallized, or colloidal particles [401]. Thermal degradation of metal complexes with sulfur-containing ligands seems to be an attractive method for the synthesis of metal sulfides [398, 402]; however,

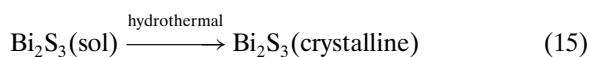
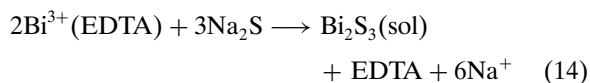


high temperature is required to decompose the complex. In contrast, chemical solution reaction methods that do not involve sophisticated vacuum systems and heating apparatus have some advantages for the preparation of  $\text{Bi}_2\text{S}_3$  and  $\text{Sb}_2\text{S}_3$ .

To avoid the hydrolysis of the bismuth and antimony salts in the presence of water, a so-called solvothermal decomposition process (SPD) was developed for the fabrication of  $\text{Bi}_2\text{S}_3$  and  $\text{Sb}_2\text{S}_3$  NWs (or NRs) [314–316], with  $\text{BiCl}_3$  or  $\text{SbCl}_3$  and thiourea (Tu) or thioacetamide (TAA) as starting reactants in polar solvents:



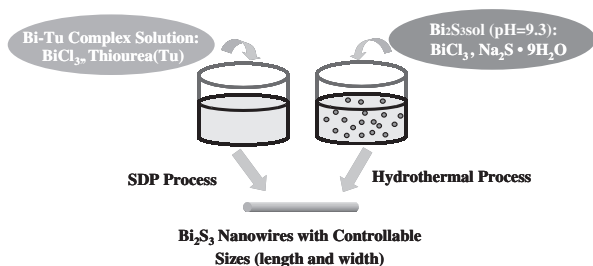
$\text{Bi}_2\text{S}_3$  nanoparticles can also be prepared by a hydrothermal crystallization method, by using ethylene diamine tetraacetic acid (EDTA) as a chelating agent to prevent the hydrolysis of  $\text{Bi}^{3+}$  in water:



The methods make it possible to produce  $\text{Bi}_2\text{S}_3$  and  $\text{Sb}_2\text{S}_3$  NRs/NWs conveniently with yields as high as 95%. The particle sizes can be well controlled through the choice of different solvents or different processes. The influence of solvents, reaction temperature, and reaction time on the formation of  $\text{Bi}_2\text{S}_3$  NWs was investigated. Since many metal ions can complex with thiourea or selenurea, the present technique is expected to synthesize other nanostructured metal chalcogenides.

The controllable synthesis of  $\text{Bi}_2\text{S}_3$  nanocrystals is illustrated in Scheme 5.  $\text{Bi}_2\text{S}_3$  NWs/NRs with controllable sizes can be selectively synthesized conveniently by the solvothermal decomposition process (SDP) and the hydrothermal process under suitable conditions, as shown in Figure 21.

Pure  $\text{Bi}_2\text{S}_3$  can be easily obtained in high yield in several polar solvents. The products can be indexed orthorhombic structure with cell constants  $a = 11.127$ ,  $b = 11.265$ ,  $c = 3.976$  Å, which are in agreement with the reported data (JCPDS card file 17-320). Different solvents were chosen for the investigation of the solvent effects on the



**Scheme 5.** Schematic illustration of the preparation of  $\text{Bi}_2\text{S}_3$  nanowires with controllable sizes. Reprinted with permission from [26], S. H. Yu, *J. Ceram. Soc. Jpn.* 109, S65 (2001). © 2001, Ceramic Society of Japan.

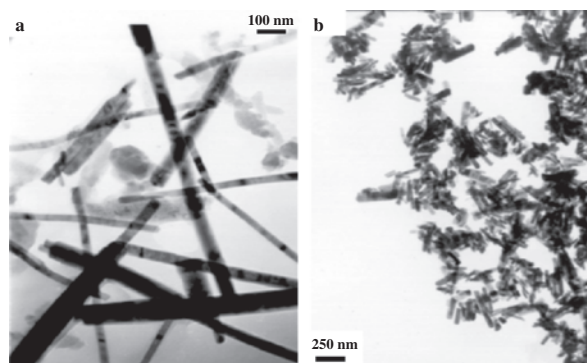


**Figure 21.** TEM images of (a)  $\text{Bi}_2\text{S}_3$  nanowires fabricated by the solvothermal decomposition process at 140 °C, 12 h, ethanol (eth) and (b) rod-like  $\text{Bi}_2\text{S}_3$  particles prepared by hydrothermal treatment of the sol (pH = 9.3) at 150 °C for 6 h. Reprinted with permission from [26], S. H. Yu, *J. Ceram. Soc. Jpn.* 109, S65 (2001). © 2001, Ceramic Society of Japan.

formation of  $\text{Bi}_2\text{S}_3$ . The solvents used included ethanol (eth), pyridine (py), ethylene glycol (EG), water, tetrahydrofuran (THF), en, 1,2-dimethoxyethane (DME), *N,N*-dimethylformamide (DMF), diethyl ether (DEE), benzene, and toluene. The effects of solvents on the synthesis of  $\text{Bi}_2\text{S}_3$  and their physicochemical properties are listed in Table 3. The results confirmed that the  $\text{Bi}_2\text{S}_3$  phase can be obtained in many polar solvents such as eth, py, EG,  $\text{H}_2\text{O}$ , DME, THF, en, and DMF. However, pure  $\text{Bi}_2\text{S}_3$  nanowires can only be obtained in eth, py, EG,  $\text{H}_2\text{O}$ , and DME. Some unidentified phases besides the  $\text{Bi}_2\text{S}_3$  phase in the products prepared in THF, en, and DMF were detected by XRD. In contrast, the Bi-Tu complex is difficult to form because of its poor solubility in apolar solvents such as DEE, benzene, and toluene due to the poor solubility of  $\text{BiCl}_3$  and thiourea in apolar solvents. Both  $\text{BiCl}_3$  and thiourea easily dissolve in polar solvents to form a yellow solution, which indicates the formation of Bi-Tu complexes.

The results confirmed that the polar solvents are more favorable for the formation of  $\text{Bi}_2\text{S}_3$  NWs. The difference in the width and length of the  $\text{Bi}_2\text{S}_3$  NWs may be related to the different physicochemical properties of the solvents. Solvent physicochemical properties such as polarity, viscosity, and softness will strongly influence the solubility and transport behavior of the precursors [366]. It has been reported that dielectric constants and dipole moments have been used in the quantitative characterization of solvent polarity [366]. These parameters are generally used to describe the overall solvation ability of a solvent. From Table 3, one can see that the dielectric constants are in the order  $\text{H}_2\text{O} > \text{EG} > \text{DMF} > \text{eth} > \text{en} > \text{py} > \text{THF}$ , whereas the dielectric constants for DEE, benzene, and toluene are much smaller than those polar solvents. The Bi-Tu complexes are more easily formed in polar solvents than in apolar solvents. It is believed that the difference in particle sizes (width and length) could be attributed to the influence of the solvents on the solubility of Bi-Tu complexes and the decomposition reaction rate of the Bi-Tu complexes.

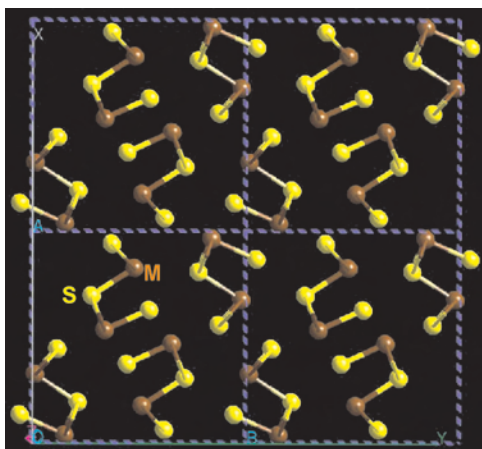
**Table 3.** Effect of solvents on the synthesis of  $\text{Bi}_2\text{S}_3$  and physical properties of solvents [403].

Solvent	Dielectric <sup>403</sup> constant	Boiling point <sup>403</sup> (°C)	Temperature (°C)	Time (h)	Product	Particle sizes
eth	24.55	78.3	140	12	$\text{Bi}_2\text{S}_3$	30 nm × 500 nm
py	12.3	115.2	140	12	$\text{Bi}_2\text{S}_3$	20–30 nm × 1–3 μm
EG	38.66	197.6	140	12	$\text{Bi}_2\text{S}_3$	130–200 nm × 3.5 μm
$\text{H}_2\text{O}$	80.1	100	140	12	$\text{Bi}_2\text{S}_3$	300 nm × 2.25 μm + short rods
$\text{H}_2\text{O}^a$	80.1	100	150	6	$\text{Bi}_2\text{S}_3$	40 nm × 150 nm
$\text{H}_2\text{O}^a$	80.1	100	100	6	$\text{Bi}_2\text{S}_3$	40 nm × 80 nm
DME	7.20	85.2	140	12	Bi-Tu	
THF	7.58	66	140	12	$\text{Bi}_2\text{S}_3$ + others	
en	14.2	117.3	140	12	$\text{Bi}_2\text{S}_3$ + others	
DMF	36.71	153	140	12	$\text{Bi}_2\text{S}_3$ + others	
DEE	4.335	34.6	140	12	No reaction	
Benzene	2.275	80.1	140	12	No reaction	
Toluene	2.568	110.8	140	12	No reaction	

<sup>a</sup> The  $\text{Bi}_2\text{S}_3$  powders were obtained by the hydrothermal treatment in [316].

The structural analysis shows that the infinite linear chains within the  $\text{M}_2\text{S}_3$  ( $\text{M} = \text{Sb, Bi}$ ) crystal structure will play a crucial role in the anisotropic growth characteristics as shown in Scheme 6. In fact, the one-dimensional growth of nanocrystals is actually the outside embodiment of inside crystal structures. However, the autogenous pressure in the solvothermal/hydrothermal process was found to play a key role in the orientation growth of the nanocrystals.

The reaction was conducted in a closed solution system, which may be similar to the sealed-tube pyrolysis reaction of  $\text{Bi}(\text{Sbn})_3$  ( $\text{Bn} = \text{CH}_2\text{C}_6\text{H}_5$ ) [398]. The solid-liquid interactions between the formed Bi-Tu complexes and the solvent and the decomposition of the complexes under sealed conditions could be responsible for the formation of the  $\text{Bi}_2\text{S}_3$  NWs. In addition, the solvent acts as both reaction medium and dispersion medium so that it will prevent the aggregation of the particles and favor the production of uniform  $\text{Bi}_2\text{S}_3$  powder with good dispersivity in the SDP.



**Scheme 6.** The  $XY$  projection of the structural view of  $\text{M}_2\text{S}_3$  ( $\text{M} = \text{Bi, Sb}$ ), showing the infinite chain structure. The modeling was done with the Cerius<sup>2</sup> software (Accelrys).

The  $\text{Bi}_2\text{S}_3$  NWs prepared by SDP are much longer than those obtained by the hydrothermal treatment of an alkaline sol ( $\text{pH} = 8.0\text{--}10.0$ ) from  $\text{BiCl}_3$  and  $\text{Na}_2\text{S} \cdot 9\text{H}_2\text{O}$ , with EDTA as a complexing agent, as shown in Figure 21. The direct mixing of  $\text{Bi}^{3+}$  with free  $\text{S}^{2-}$  with EDTA as complex in aqueous solution will result in spontaneous nucleation and produce a large number of nuclei. Then the nucleation is more accelerated than the growth. Therefore, only smaller particles can be produced. In contrast, the decomposition of the Bi-Tu complexes in the SDP will proceed slowly and produce a smaller number of nuclei in the solution than the direct ion-exchange reaction due to the position-resistance effect of the formed Bi-Tu complexes and its relatively stable property, which would be favorable for the oriented growth of the NWs. Therefore, the growth stage is more accelerated than the nucleation stage, since the system can finish the nucleation stage with a smaller number of nuclei.

$\text{Sb}_2\text{S}_3$  NRs can also be easily produced with high yield by the same procedure [315]. When anhydrous  $\text{SbCl}_3$  was added to the methanol solution of thiourea, the solution immediately turned yellow, which implies that the  $\text{Sb}^{3+}$ -thiourea complex is formed in the solution. The formation of such a complex was confirmed by the IR spectrum, UV-vis spectrum, and  $^1\text{H}$  NMR spectrum.

In the IR spectrum of the  $\text{Sb}^{3+}$ -thiourea complex (Fig. 22a), three characteristic absorption peaks at  $3370\text{ cm}^{-1}$ ,  $3290\text{ cm}^{-1}$ , and  $3184\text{ cm}^{-1}$  can undoubtedly be assigned to the  $\text{-NH}_2$  stretching vibration. The  $\text{-NH}_2$  bands did not shift to lower frequencies with regard to pure thiourea (Fig. 22b), which indicates that a bond from the nitrogen to the metal is not present [404]. Meanwhile, the frequency of the C-N stretching vibration of the complex blue shifted from  $1474\text{ cm}^{-1}$  in pure thiourea to  $1511\text{ cm}^{-1}$ , which approaches the value for a double bond. The blue shift of the C-N stretching vibration implies that thiourea uses the sulfur atom to coordinate with the metal ion in the complex [405]. The C=S stretching vibration of the complex at  $1413\text{ cm}^{-1}$  was split into two peaks because of the

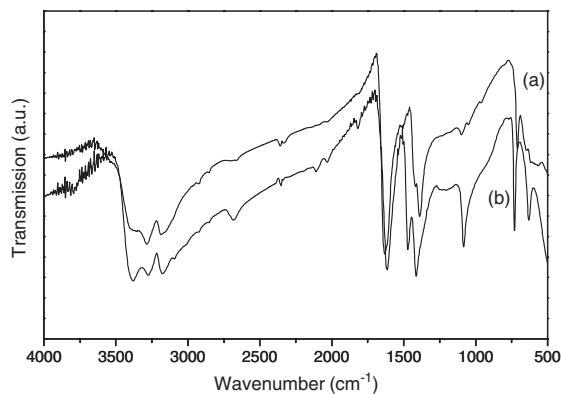


**Figure 22.** IR spectra of the as-prepared complex (a) and pure thiourea (b). Reprinted with permission from [323], J. Yang et al., *Chem. Mater.* 12, 2924 (2000). © 2000, American Chemical Society.

formation of a metal-sulfur bond [405]. Another very apparent difference in the IR spectrum between pure thiourea and the  $\text{Sb}^{3+}$ -thiourea complex appeared at approximately  $1100\text{ cm}^{-1}$ . The strong absorption peak of pure thiourea at  $1084\text{ cm}^{-1}$  was extremely weakened in the complex. In addition, another band associated with a  $\text{C}=\text{S}$  vibration of the complex was red shifted from  $729\text{ cm}^{-1}$  in pure thiourea to  $709\text{ cm}^{-1}$ . The red shift can be attributed to the reduced double-bond character of the  $\text{C}=\text{S}$  bond due to the sulfur bonding with the metal.  $^1\text{H}$  NMR spectrum presents one broad unresolved peak at 6.96 ppm that is shifted to the high field with regard to pure thiourea. It seems that the increase in electron density around the hydrogen atom is caused by the coordination of the ligand with the metal ion.

The crystallization process of the  $\text{Sb}_2\text{S}_3$  NRs from the complex was followed by the XRD technique. The results show that the crystallinity of stibnite has been improved greatly with the prolonged reaction time. Figure 23a shows that no diffraction peaks corresponding to the starting

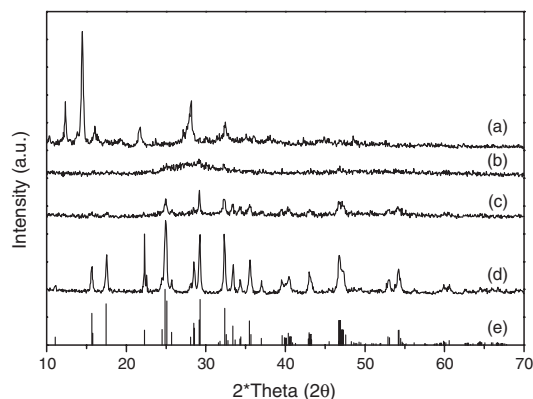


**Figure 23.** XRD patterns of the products obtained by solvothermal decomposition at different times at  $120\text{ }^\circ\text{C}$ . (a) The precursor. (b) 2 h. (c) 3 h. (d) 6 h. (e) The standard. Reprinted with permission from [323], J. Yang et al., *Chem. Mater.* 12, 2924 (2000). © 2000, American Chemical Society.

materials were observed. When the precursor was treated in an autoclave for 2 h at  $120\text{ }^\circ\text{C}$ , amorphous stibnite was obtained, as shown in Figure 23b. When the treatment time was prolonged to 3 h, the violet-red stibnite obtained was poorly crystallized, as shown in Figure 23c. Until the treatment time reached 6 h, the black-gray stibnite obtained was not well crystallized. The crystalline products (Fig. 23d) were identified as orthorhombic stibnite with cell constants  $a = 11.228\text{ \AA}$ ,  $b = 11.329\text{ \AA}$ ,  $c = 3.844\text{ \AA}$ , which are close to the values in the literature (JCPDS file no. 6-0474).

The time-dependent shape evolution of the nanocrystals during the crystallization was followed. When the reaction lasted for 2 h at  $120\text{ }^\circ\text{C}$ , the  $\text{Sb}_2\text{S}_3$  powders obtained were composed of amorphous nanoparticles with irregular shape and an average size of about 65 nm. When the reaction time was prolonged to 3 h, some NRs appeared in the poorly crystallized  $\text{Sb}_2\text{S}_3$  powders. After 6 h all of the initial irregular particles transformed into well-crystallized NRs with an average diameter of 60 nm that is close to the size of the initial amorphous nanoparticles. In this transformation process, many neck-like connections were observed among the adjacent nanoparticles. Meanwhile, in the head or edge of the NRs just formed, there were many obvious bulges formed by different nanoparticles. The results suggest that probably the initial adjacent nanoparticles self-assemble together to form the final  $\text{Sb}_2\text{S}_3$  NRs with the crystallinity improved.

The transformation from amorphous nanoparticles to crystallized NRs is much faster in a closed system than that in an open system. When the same solution was refluxed for 6 h in an oil bath, the products obtained were still irregular nanoparticles, as shown in Figure 24a. When the reflux time was prolonged to 10 h, some NRs did appear in the products, although the majority of the latter remained as irregular particles (Fig. 24b). When the initial amorphous nanoparticles were taken out and were washed to remove the adsorbed reactants and by-products, they were still transformed into NRs from the initial irregular nanoparticles as shown in Figure 24c, when they were treated in a closed autoclave for 10 h at  $120\text{ }^\circ\text{C}$ . With increasing reaction temperature, large  $\text{Sb}_2\text{S}_3$  single crystalline NRs with lengths of  $5\text{ }\mu\text{m}$  and 100 nm in diameter can be synthesized in

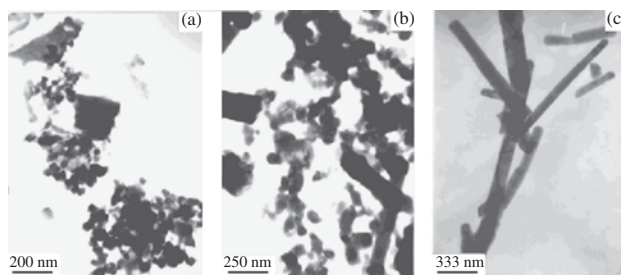


**Figure 24.** TEM photographs of the products obtained by (a) refluxing the methanol solution of the precursor for 6 h at  $120\text{ }^\circ\text{C}$  in a flask; (b) refluxing the methanol solution of the initial nanoparticles for 10 h in a flask at  $120\text{ }^\circ\text{C}$ ; (c) maintaining the methanol solution of the initial nanoparticles at  $120\text{ }^\circ\text{C}$  for 10 h in an autoclave. Reprinted with permission from [323], J. Yang et al., *Chem. Mater.* 12, 2924 (2000). © 2000, American Chemical Society.



methanol at 180 °C for 12 h. The Bi<sub>2</sub>S<sub>3</sub> and Sb<sub>2</sub>S<sub>3</sub> NWs/NRs with high aspect ratios may be useful for important applications. The time dependence of the shape evolution of the nanocrystals during the crystallization controlled by pressure can be illustrated as in Scheme 7.

The above solvothermal process can be rapidly extended for the synthesis of other chalcogenide nanomaterials through the choice of suitable reaction conditions and precursors. A recent report shows that Sb<sub>2</sub>Se<sub>3</sub> NWs with a diameter of 30 nm and lengths as long as 8 μm can be synthesized in diethylene (DEG) media at 120–140 °C by the solvothermal reaction, with SbCl<sub>3</sub>, ammonia, NaSO<sub>3</sub>, and Se as reactants [325]. The further optimization of the solvothermal reaction will make it possible to readily synthesize well-defined 1D III–IV nano-building blocks, which could be very useful for the synthesis of other 1D semiconductors based on sulfo salts of bismuth and related compounds and sulfoantimonates of antimony and related compounds.

### 2.5.3. Growth of Other Metal Chalcogenide Crystals

Both solvents and temperatures play important roles in the formation of different phases, their phase transformation, and morphologies of the products. It is possible to selectively synthesize metal chalcogenide nanostructured materials and grow large single crystals with perfect shapes and preferred sizes by choosing the suitable conditions. These materials with different phases and unusual shapes may have interesting catalytic, semiconducting, and magnetic properties. In this section, the influence of solvents on phase, shapes, and reactivity will be discussed with specific examples.

Various metal chalcogenide materials can be synthesized under mild conditions by the following solvothermal reaction [318, 372, 373]:

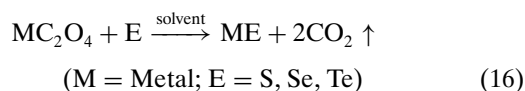
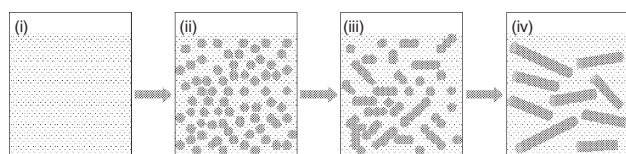


Table 4 lists experimental conditions for the synthesis of various metal chalcogenide materials and the characterization of the powders. As shown in Table 4, the solvothermal reactions in en proceed more completely than in other solvents such as py and THF, suggesting that the higher reactivity in en can be achieved compared with other solvents. Both solvent and temperature play key roles in the reaction, shapes, sizes, and phases. Solvent in particular has a significant effect on the morphology of the particles as shown in Table 4. The reaction of bismuth oxalate with selenium and tellurium proceeded in a manner similar to that of lead



**Scheme 7.** Pressure-controlled formation process of the Bi<sub>2</sub>S<sub>3</sub> and Sb<sub>2</sub>S<sub>3</sub> NRs.

oxalate. Bi<sub>2</sub>Se<sub>3</sub> particles with flake-like morphology are single crystal [318].

The influence of solvents on the phase transformation during the solvothermal reaction was well demonstrated by a Ni-S system [377]. A detailed study of the synthesis of various phases of nickel sulfide materials such as NiS, Ni<sub>3</sub>S<sub>2</sub>, NiS<sub>1.03</sub>, NiS<sub>2</sub>, metastable Ni<sub>3</sub>S<sub>4</sub>, and their phase transformation and the phase transformation under solvothermal conditions was recently reported to be studied with a liquid-solid interfacial reaction between nickel substrate and sulfur, and the reaction Ni<sup>2+</sup> ion with sulfur in different solvents such as en, water, ethanol, toluene, and py at lower temperatures (≤200 °C) [377]. When the nickel salt was used instead of metal Ni, the reaction proceeded more easily. The main results of the reaction between Ni<sup>2+</sup> and S in en at different temperatures are summarized in Scheme 8.

Through control of the reaction time, the phase transformation process from NiS (M) to NiS<sub>2</sub> (cubic) can be nicely captured. The SEM image in Figure 25a shows that NiS (M) whiskers, with diameters ranging from 1 μm and lengths up to several micrometers, and spherical NiS<sub>2</sub> particles with a size of 1.2 μm were found to coexist in the product obtained at 200 °C for 12 h. EDX analysis confirmed that the spherical particles and whiskers in Figure 25 are composed of exact compositions of NiS<sub>2</sub> and NiS (M) phases, respectively. The tips of the NiS whiskers tend to bend, “melt,” or dissolve further as shown in Figure 25b, indicating that the formation of the NiS<sub>2</sub> phase was at the expense of NiS (M) whiskers, and the transformation process from the NiS (M) phase to NiS<sub>2</sub> indeed exists during the reaction with the prolonging of the reaction time, which corresponds to the XRD results. Pure NiS<sub>2</sub> single crystals with well-defined dodecahedron crystals and uniform sizes of about 1.5–2.7 μm can be obtained by further prolonging the reaction time to 18 h at 200 °C as shown in Figure 25c. Figure 25d shows a typical NiS<sub>2</sub> single crystal with a well-developed dodecahedron {101} unit polytype shape and a size of 1.8 μm. Cubic NiSe<sub>2</sub> single crystals with a perfect octahedral shape and a size of 15 μm were obtained by a reaction of NiC<sub>2</sub>O<sub>4</sub> · 2H<sub>2</sub>O with Se in en [373]. FeSe<sub>2</sub>, CoSe<sub>2</sub> crystals can be synthesized by a modified solvothermal process [374].

Various ternary metal chalcogenide NRs such as CdIn<sub>2</sub>S<sub>4</sub> [346], CuInS<sub>2</sub>, AgInS<sub>2</sub> [347], AgBiS<sub>2</sub> [348], Ag<sub>3</sub>CuS<sub>2</sub> [349], Cu<sub>3</sub>SnS<sub>4</sub> [350], and PbSnS<sub>3</sub> [351] have been synthesized by solvothermal/hydrothermal approaches under mild conditions. Even though the mechanism of the reaction and the formation of 1D NRs are still not clear, solvothermal/hydrothermal processes have already shown powerful versatilities and capabilities in the controlled solution synthesis of nonoxide 1D nanocrystals, in contrast to previous high-temperature approaches.

### 2.5.4. Controlled Growth of 1D Chalcogen Nanocrystals with More Complexity

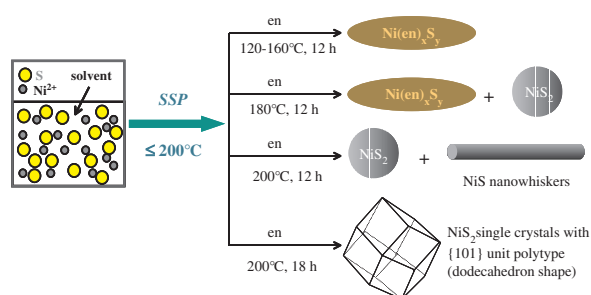
Chalcogens are a group of important elements with unique combinations of many interesting and useful properties [406], which are also important reactant sources for the generation of metal chalcogenides, such as for the synthesis of semiconductor materials.

**Table 4.** Summary of various metal chalcogenides synthesized by a solvothermal process, including experimental conditions such as reactants and mole ratio (M/E) (M = metal source, E = S, Se, Te), solvent, temperature, and time; the phases were detected by X-ray powder diffraction, symmetry, and the particle shape.

Reactants (M/E ratio)	Solvent	Reaction conditions	Phase	Symmetry	Shape
CdC <sub>2</sub> O <sub>4</sub> + S(2:1)	en	120–180 °C, 12 h	CdS	Hexagonal	Rod-like
CdC <sub>2</sub> O <sub>4</sub> + S(2:1)	py	160–180 °C, 12 h	CdS	Hexagonal	Spherical
CdC <sub>2</sub> O <sub>4</sub> + S(2:1)	EG	160–180 °C, 12 h	CdS	Hexagonal	Spherical
CdC <sub>2</sub> O <sub>4</sub> + Se(2:1)	en	140 °C, 12 h	CdSe	Hexagonal	Rod-like
CdC <sub>2</sub> O <sub>4</sub> + Se(2:1)	py	160 °C, 12 h	CdSe	Hexagonal	Spherical
CdC <sub>2</sub> O <sub>4</sub> + Se(2:1)	py	140 °C, 12 h	Se + CdSe <sup>a</sup>		
CdC <sub>2</sub> O <sub>4</sub> + Te(2:1)	en	180 °C, 12 h	CdTe	Cubic	Rod-like
PbC <sub>2</sub> O <sub>4</sub> + S(1:1)	en	120 °C, 12 h	PbS	Cubic	Square
PbC <sub>2</sub> O <sub>4</sub> + S(1:1)	py	120 °C, 12 h	PbS	Cubic	Square
PbC <sub>2</sub> O <sub>4</sub> + Se(1:1)	en	160 °C, 12 h	PbSe	Cubic	Square
PbC <sub>2</sub> O <sub>4</sub> + Se(1:1)	py	160 °C, 12 h	PbSe + Se <sup>a</sup>		
PbC <sub>2</sub> O <sub>4</sub> + Te(1:1)	en	160 °C, 12 h	PbTe	Cubic	Square
PbC <sub>2</sub> O <sub>4</sub> + Se(1:1)	py	160 °C, 12 h	PbTe + Te <sup>a</sup>		
SnC <sub>2</sub> O <sub>4</sub> + S(1:1.2)	en	240 °C, 8 h	SnS	Orthorhombic	Plate-like
SnC <sub>2</sub> O <sub>4</sub> + Se(1:1.2)	en	180 °C, 8 h	SnSe	Orthorhombic	Rod-like
SnC <sub>2</sub> O <sub>4</sub> + Te(1:1.2)	en	170 °C, 8 h	SnTe	Cubic	Spherical
Ag <sub>2</sub> C <sub>2</sub> O <sub>4</sub> + S(1:1)	en	140 °C, 12 h	Ag <sub>2</sub> S	Monoclinic	Spherical
Ag <sub>2</sub> C <sub>2</sub> O <sub>4</sub> + S(1:1)	py	140 °C, 12 h	Ag <sub>2</sub> S	Monoclinic	Spherical
Ag <sub>2</sub> C <sub>2</sub> O <sub>4</sub> + S(1:1)	THF	140 °C, 12 h	Ag <sub>2</sub> S	Monoclinic	Spherical
Ag <sub>2</sub> C <sub>2</sub> O <sub>4</sub> + Se(1:1)	en	140 °C, 12 h	Ag <sub>2</sub> Se	Orthorhombic	Plate-like
Ag <sub>2</sub> C <sub>2</sub> O <sub>4</sub> + Se(1:1)	py	140 °C, 12 h	Ag <sub>2</sub> Se + Se <sup>a</sup>		
Ag <sub>2</sub> C <sub>2</sub> O <sub>4</sub> + Se(1:1)	py	160 °C, 12 h	Ag <sub>2</sub> Se + Ag <sup>a</sup>		
Ag <sub>2</sub> C <sub>2</sub> O <sub>4</sub> + Se(1:1)	THF	140 °C, 12 h	Ag <sub>2</sub> Se + Se <sup>a</sup>		
Ag <sub>2</sub> C <sub>2</sub> O <sub>4</sub> + Te(1:1)	en	180 °C, 12 h	Ag <sub>2</sub> Te + Se <sup>a</sup>	Monoclinic	
Ag <sub>2</sub> C <sub>2</sub> O <sub>4</sub> + Te(1:1)	en	160 °C, 12 h	Ag + Ag <sub>2</sub> Te <sup>a</sup>		
Ag <sub>2</sub> C <sub>2</sub> O <sub>4</sub> + Te(1:1)	py	180 °C, 12 h	Ag + Ag <sub>2</sub> Te <sup>a</sup>		
Ag <sub>2</sub> C <sub>2</sub> O <sub>4</sub> + Te(1:1)	THF	180 °C, 12 h	Ag + Ag <sub>2</sub> Te <sup>a</sup>		
Bi <sub>2</sub> (C <sub>2</sub> O <sub>4</sub> ) <sub>3</sub> + Se(1:1)	en	140 °C, 12 h	Bi <sub>2</sub> Se <sub>3</sub>	Hexagonal	Plate-like
Bi <sub>2</sub> (C <sub>2</sub> O <sub>4</sub> ) <sub>3</sub> + Se(1:1)	py	140 °C, 12 h	Bi <sub>2</sub> Se <sub>3</sub> + Se <sup>a</sup>		
NiC <sub>2</sub> O <sub>4</sub> · 2H <sub>2</sub> O + Se(1:2.4)	en	170 °C, 8 h	NiSe <sub>2</sub>	Cubic	Octahedral
NiC <sub>2</sub> O <sub>4</sub> · 2H <sub>2</sub> O + Se(1:1)	en	200 °C, 8 h	Ni <sub>0.85</sub> Se	Hexagonal	Starfish-like
NiC <sub>2</sub> O <sub>4</sub> · 2H <sub>2</sub> O + Se(3:2)	en	220 °C, 8 h	Ni <sub>3</sub> Se <sub>2</sub>	Triclinic	Dendritic
NiC <sub>2</sub> O <sub>4</sub> · 2H <sub>2</sub> O + Se(1:1)	en	180 °C, 8 h	NiSe <sub>2</sub>	Cubic	Spherical
NiC <sub>2</sub> O <sub>4</sub> · 2H <sub>2</sub> O + Se(1:2.2)	py	180 °C, 8 h	NiSe <sub>2</sub>	Cubic	Octahedral
NiC <sub>2</sub> O <sub>4</sub> · 2H <sub>2</sub> O + Se(1:2.2)	THF	170 °C, 8 h	NiSe <sub>2</sub>	Cubic	Octahedral

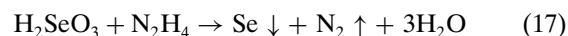
From [61, 318, 372, 373, 375].

<sup>a</sup> Dominant phase in the sample.



**Scheme 8.** Summary of the results of the reaction of Ni<sup>2+</sup> with S in ethylenediamine under different conditions. Reprinted with permission from [377], S. H. Yu and M. Yoshimura, *Adv. Funct. Mater.* 12, 277 (2002). © 2002, Wiley-VCH.

Trigonal selenium NWs with well-defined sizes and aspect ratios have been synthesized by a solution-phase approach [233, 234]. The first step of this approach involved the formation of amorphous  $\alpha$ -Se in an aqueous solution through the reduction of selenious acid with excess hydrazine by refluxing this reaction mixture at 100 °C:



When this solution was cooled to room temperature, the small amount of selenium dissolved in the solution precipitated out as nanocrystallites of trigonal *t*-Se. Cooling the solution to room temperature will produce a small amount of trigonal Se in the solution, which will act as seeds for the formation of a large amount of trigonal Se NWs during further aging of the solution in a dark place [233]. The 1D

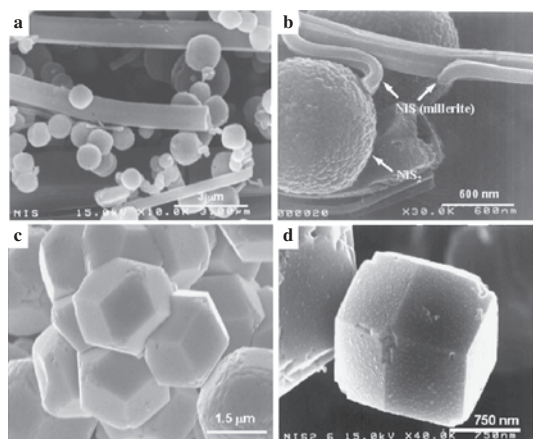


**Figure 25.** SEM images for products of the reaction of  $\text{Ni}(\text{NO}_3)_2 \cdot 6\text{H}_2\text{O}$  with S in ethylenediamine. (a) and (b) Coexistence of NiS nanowhiskers with uniform spherical  $\text{NiS}_2$  nanoparticles obtained at 200 °C, 12 h,  $[\text{Ni}^{2+}] = [\text{S}] = 0.005$  mol. (c) Uniform and well-developed  $\text{NiS}_2$  single crystals obtained at 200 °C for 18 h,  $[\text{Ni}^{2+}]:[\text{S}] = 1:3$ ,  $[\text{S}] = 0.005$  mol. (d) A typical  $\text{NiS}_2$  single crystal displayed well-developed  $\{101\}$  polytype with dodecahedron shape and a size of 1.2  $\mu\text{m}$ . Reprinted with permission from [377], S. H. Yu and M. Yoshimura, *Adv. Funct. Mater.* 12, 277 (2002). © 2002, Wiley-VCH.

morphology of the final product was determined by the linearity of infinite, helical chains of Se atoms contained in the trigonal phase.

A recent report by Xia et al. shows that single crystalline NWs of  $\text{Ag}_2\text{Se}$  can be synthesized by templating against the trigonal Se NWs [328, 329] at room temperature as shown in Figure 26.

In addition, trigonal tellurium NBs, NTs, and nanohelices can be synthesized [235, 236]. The tellurium NTs were synthesized by refluxing a solution of orthotelluric acid in ethylene glycol at  $\sim 197$  °C [235] as shown in Figure 27. The early stage shows that tubular structures grew from the cylindrical seeds as shown in Figure 27a.

A very simple controlled hydrothermal route has been developed for the synthesis of tellurium NBs, NTs, and nanohelices by reaction of sodium tellurite ( $\text{Na}_2\text{TeO}_3$ ) in aqueous ammonia solution at 180 °C [236]. The NBs have thicknesses of about 8 nm with widths of 30–500 nm and lengths up to several hundred micrometers, as shown in Figure 28a. The NBs tend to twist and form helices as shown in Figure 28b. When the NBs were further

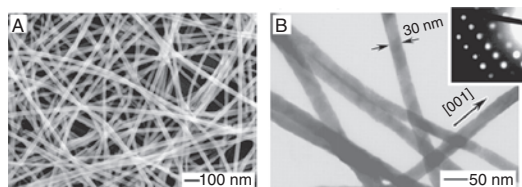


**Figure 26.** SEM (A) and TEM (B) images of uniform nanowires of  $\text{Ag}_2\text{Se}$  that were synthesized through a reaction between the 32-nm nanowires of *t*-Se and an aqueous solution of  $\text{AgNO}_3$  at room temperature. Reprinted with permission from [328], B. Gates et al., *J. Am. Chem. Soc.* 123, 11500 (2001). © 2001, American Chemical Society.

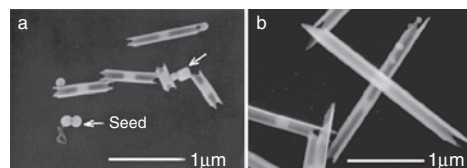


**Figure 27.** SEM images of the Te nanotubes synthesized by refluxing a solution of orthotelluric acid in ethylene glycol for (a) 4 min and (b) 6 min. The white arrow indicates the presence of seeds. Reprinted with permission from [235], B. Mayers and Y. N. Xia, *Adv. Mater.* 14, 279 (2002). © 2002, Wiley-VCH.

twisted and rolled, NTs formed. In addition, an interesting nanostructure, a “coaxed nanobelt within a nanotube,” was observed, as shown in Figure 28c. The template-roll-growth mechanism and template-twist-joint-growth mechanism were proposed to explain the formation of such special nanostructures [236]. However, the detailed mechanism still needs to be investigated further.

The above novel chalcogen nanostructures can be rapidly used as templates for the synthesis of other, more specialized and more complex 1D and 2D metal chalcogenide nanostructures, which could find interesting applications.

## 2.6. Solution-Liquid-Solid Mechanism

The solution-liquid-solid (SLS) growth mechanism, which is analogous to the well-known VLS mechanism, was first discovered by Buhro et al. [66]. This route is mainly for growing group III–V nanofibers (InP, InAs, GaAs,  $\text{Al}_x\text{Ga}_{1-x}\text{As}$ , InN) in hydrocarbon solvents at relatively low temperatures (less than or equal to 203 °C) [66–69]. More features about this route have been summarized in [67], as shown in Figure 29. The synthesis involved the methanolysis of  $\{t\text{-Bu}_2\text{In}[\mu\text{-P}(\text{SiMe}_3)_2]\}_2$  in aromatic solvents to produce polycrystalline InP fibers (dimensions 10–100 nm  $\times$  50–1000 nm) at 111–203 °C [68]. The chemical pathway consists of a molecular component, in which precursor substituents are eliminated, and a nonmolecular component, in which the InP crystal lattices are assembled. The two components working in concert comprise the SLS mechanism. The molecular component proceeds through a sequence of isolated and

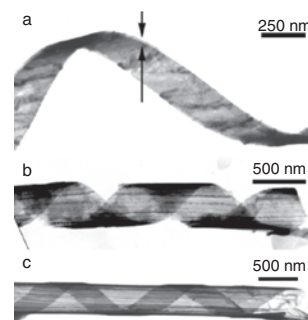


**Figure 28.** TEM images of (a) a typical tellurium nanobelt, (b) a helical nanobelt, (c) a typical helical nanobelt within a nanobelt-roll nanotube. Reprinted with permission from [236], M. S. Mo et al., *Adv. Mater.* 14, 1658 (2002). © 2002, Wiley-VCH.



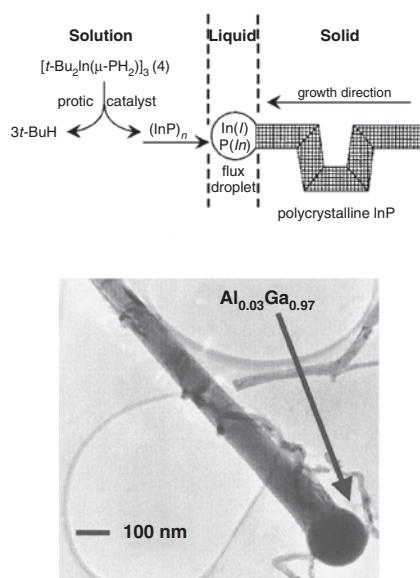


**Figure 29.** Solution-liquid-solid (SLS) mechanism and a representative  $\text{Al}_{0.1}\text{Ga}_{0.9}\text{As}$  nanowhisker grown by the SLS mechanism. Reprinted with permission from [68], T. J. Trentler et al., *J. Am. Chem. Soc.* 119, 2172 (1997), and [69], P. D. Markowitz et al., *J. Am. Chem. Soc.* 123, 4502 (2001). © 1997, 2001, American Chemical Society.

fully characterized intermediates to form the  $[\text{t-Bu}_2\text{In}(\mu\text{-PH}_2)_3]$  complex. The complex, which is alternatively prepared from  $\text{t-Bu}_3\text{In}$  and  $\text{PH}_3$ , undergoes alkane elimination catalyzed by the protic reagent  $\text{MeOH}$ ,  $\text{PhSH}$ ,  $\text{Et}_2\text{NH}$ , or  $\text{PhCO}_2\text{H}$ . In the subsequent nonmolecular component of the pathway, the resulting  $(\text{InP})_n$  fragments dissolve into a dispersion of molten In droplets and recrystallize as InP fibers [68].

This approach has been extended for the synthesis of InN NWs by solution-state thermolysis of the dialkyl(azido)indane precursor [259].

Group IV Si and Ge crystals can be generated by a supercritical fluid solution-phase approach [70]. Recently, Korgel et al. reported a supercritical fluid solution-phase self-assembly approach with a similar SLS mechanism for growing bulk quantities of defect-free Si NWs with diameters of about 4–5 nm and aspect ratios greater than 1000 by using alkanethiol-coated gold nanocrystals as uniform seeds to direct one-dimensional Si crystallization in supercritical hexane [71]. In this process, the sterically stabilized Au nanoparticles were dispersed in supercritical hexane together with diphenylsilane, which underwent decomposition at 500 °C and 270 bar. The phase diagram for Si and Au indicated that at temperatures above 363 °C, Si and Au will form an alloy in equilibrium with pure solid Si when the Si concentration with respect to Au is greater than 18.6%. Under this condition, the Si atoms dissolve into the sterically stabilized Au nanocrystals until the supersaturation is reached, at which point they are expelled from the particles as a thin nanometer-scale wire. The supercritical fluid medium with high temperature promotes Si crystallization. The Au nanocrystals will be maintained to seed NW growth under supercritical conditions.

## 2.7. Capping Agent/Surfactant-Assisted Synthesis

### 2.7.1. Self-Assembly under Hot Conditions

Capping agent/surfactant-assisted synthesis has been widely explored for the fabrication of NRs, NTs, and more complex structures. Recently, Alivisato's group synthesized the elongated CdSe nanocrystallites by injecting a solution of dimethylcadmium and selenium in tributylphosphine into a mixture of hexylphosphonic acid (HPA) and trioctylphosphine oxide (TOPO) at 340–360 °C [11, 72].

The surfactant molecules adsorb and desorb rapidly from the nanocrystal surface at the growth temperature, permitting the addition and removal of atoms from the crystallites, while aggregation is suppressed by the presence of (on average) one monolayer of surfactant at the crystallite surface. It is well known that the solubility of crystals increases as the size of the crystals decreases, according to the Gibbs-Thompson law. This law plays an important role in determining the growth kinetics of the nanocrystals. Peng et al. observed that if the monomer concentration in the solution is higher than the solubility of all existing nanocrystals, all nanocrystals in the solution grow and the size distribution narrows. The so-called focusing of size distribution can be exploited for the spontaneous formation of close to monodisperse colloidal nanocrystals and can form a three-dimensional orientation. The CdSe NRs with variable aspect ratios can be well achieved by kinetic control growth of the nanoparticles (Fig. 30).

The diverse range of observed shapes can be understood as arising from three basic effects: the nanocrystals will eventually tend toward nearly spherical shapes at slow growth rates; rods form at high growth rates by unidirectional growth of one face; and HPA accentuates the differences in the growth rates among various faces. A large injection

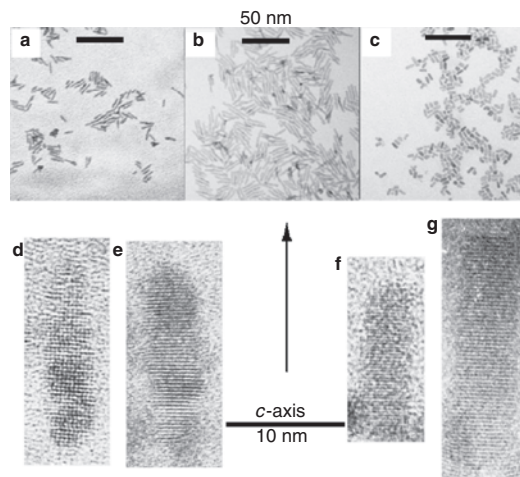


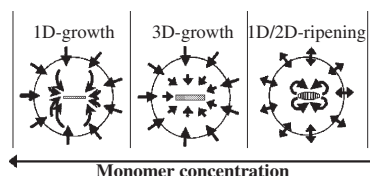
**Figure 30.** TEM images of different samples of quantum rods. (a–c) Low-resolution TEM images of three quantum-rod samples with different sizes and aspect ratios. (d–g) High-resolution TEM images of four representative quantum rods. (d) and (e) are from the sample shown in (a); (f) and (g) are from the sample shown in (c). Reprinted with permission from [11], X. G. Peng et al., *Nature* 402, 393 (1999). © 1999, Macmillan Magazines Ltd.

volume or a very high monomer concentration favors rod growth.

Recently, Peng et al. proposed a diffusion-controlled crystal growth model based on their careful observation of the shape evolution of CdSe NRs as shown in Scheme 9 [407]. They believed that a typical temporal shape evolution of CdSe quantum rods occurs in three distinguishable stages. When the Cd monomer concentration in the solution was between 1.4% and 2% of cadmium element by mass, all of the nanocrystals grew almost exclusively along their long axis, and both the aspect ratio and the volume of the crystals increased rapidly. This stage is called the “1D-growth stage.” The second stage, the “3D-growth stage,” occurred when the Cd monomer concentration dropped to between 0.5% and 1.4%. In this stage, crystals grew simultaneously in three dimensions [Fig. 31]. The aspect ratio remained constant, but the crystal volume increased. It should be mentioned that this stage was not observed before [11], probably because of the higher growth rates. The final stage, called “1D-to-2D ripening,” was identified when the Cd concentration was constant at 0.5%. The aspect ratio of the rods dropped noticeably, because the dimension of the crystals increased along the short axis and decreased along the long axis. Nanocrystal volumes and number remained constant, and there was no noticeable net growth or net dissolution of nanocrystals. This indicates that the monomers very likely moved on the surface of a crystal from one dimension ( $c$  axis) to the other two dimensions in an intraparticle manner.

The 1D-growth stage was confirmed by a reaction whose monomer concentration was maintained in the corresponding 1D-growth range for a longer time through the addition of more monomers to the reaction system at certain time intervals. The long axis of the quantum rods can be further extended from about 35 nm to over 100 nm by the secondary injections, but the short axis remained almost constant, at about 3–4 nm.

In this model, each crystal is surrounded by a diffusion sphere as shown in Scheme 9 [407]. The monomer concentration gradient between the bulk solution and the stagnant solution, as well as the diffusion coefficient of the monomers, determines the direction (out of or into the diffusion sphere) and the diffusion flux. The monomer concentration in the stagnant solution maintains the solubility of a given facet by the rapid growth onto or dissolution from the facet.



**Scheme 9.** A schematic diagram for the proposed mechanisms of the three stages of the shape evolution. The circle in each stage is the interface between the bulk solution and the diffusion sphere. Arrows indicate the diffusion directions of the monomers. The double-headed arrows represent the diffusion equilibrium in the 1D-to-2D ripening stage. Reprinted with permission from [407], Z. A. Peng and X. G. Peng, *J. Am. Chem. Soc.* 123, 1389 (2001). © 2001, American Chemical Society.

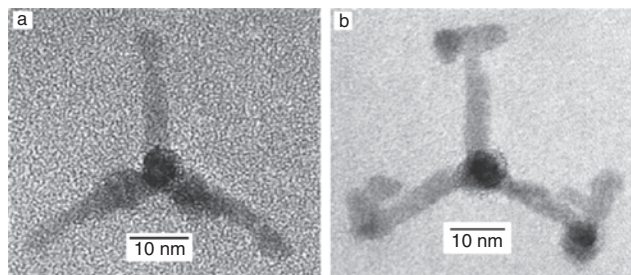
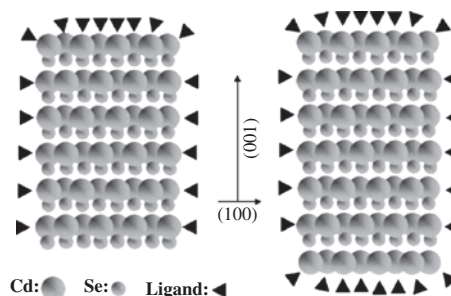


**Figure 31.** HRTEM image (a) of a typical tetrapod-shaped CdSe nanocrystal, looking down the  $[001]$  direction of one arm. Lattice spacings confirm that all four arms are of the wurtzite structure. In image (b), we see a tetrapod that has branches growing out of each arm. There are zinc blende layers near the ends of the original arms, and the branches are wurtzite with some stacking faults. Reprinted with permission from [72], L. Manna et al., *J. Am. Chem. Soc.* 122, 12700 (2000). © 2000, American Chemical Society.

The wurtzite structural characteristics are shown in Scheme 10, showing that all of the atoms on both facets perpendicular to the  $c$  axis (unique facets) have only one dangling bond without surface reconstruction [407]. The facets terminated by negatively charged Se atoms and positively charged Cd atoms are the  $(00\bar{1})$  facet and  $(001)$  facet, respectively. The negatively charged  $(00\bar{1})$  facet is more or less uncoated, because the ligands in the solution are all electron-donating ligands and should bind exclusively to cationic species. Additionally, without surface reconstructions, any surface Cd atom grown on the  $(00\bar{1})$  facet has to possess three dangling bonds, even if the surface Cd atoms reach a full monolayer. These unique structural features of the  $(00\bar{1})$  facet and the dipole moment along the  $c$  axis significantly increase the chemical potential of the unique facets, especially the  $(00\bar{1})$  facet, compared with the others [407].

The above surfactant-driven shape-controlled synthesis strategy was further extended for the synthesis of group III–VI semiconductor NRs for the first time by Cheon’s group



**Scheme 10.** Schematic structure of CdSe quantum rods in growth. The most stable form of a rod is shown on the left; its  $(00\bar{1})$  facet terminated by Se atoms does not have any ligands. After growing a monolayer of Cd atoms on the  $(00\bar{1})$  (right), this facet is still relatively active compared with the other facets, because the surface Cd atoms on this facet have three dangling bonds. See text for more details. Reprinted with permission from [407], Z. A. Peng and X. G. Peng, *J. Am. Chem. Soc.* 123, 1389 (2001). © 2001, American Chemical Society.

[254]. Gallium phosphide semiconductor nanocrystals can be synthesized by using thermal decomposition of a single molecular precursor, tris(di-*tert*-butylphosphino)gallane ( $\text{Ga}(\text{PtBu}_2)_3$ ), in a hot mixture of amine stabilizers. As in the case of CdSe, the shape of GaP nanocrystals can also be varied from nanospheres to rods with highly monodispersed size distributions by controlling the type and amount of stabilizing surfactants.

When only trioctylamine (TOA) was used as a stabilizer, spherical GaP nanoparticles with zinc blende structure were formed. Increasing the stabilizer ratio of HAD to TOA leads to the formation of NRs [254]. The addition of HDA to TOA leads to changes in the shape and crystalline phase of the GaP nanocrystals. Figure 32 shows that wurtzite GaP NRs with a diameter of 8 nm and a length of 45 nm were grown by thermal decomposition of the precursor in TOA solution, which was injected into a mixture of TOA and hexadecylamine (HDA) at 330 °C. A low HDA-to-TOA ratio seems to favor the formation of zinc blende nanospheres, but a high concentration of HDA leads to the formation of the wurtzite phase and induces anisotropic growth of the nanocrystals [254].

The steric effects of the stabilizers during crystal growth are illustrated in Scheme 11 [254]. The thermodynamically stable GaP zinc blende structure is a staggered conformation with  $\langle 111 \rangle$  directions, and the kinetically stable wurtzite structure is an eclipsed conformation with  $\langle 002 \rangle$  directions (Scheme 11). Kinetic stability of the wurtzite structure is induced by strong dipole interaction of incoming GaP monomers with surface GaP lattice atoms. The conformation of crystal structures is highly affected by changes in the stabilizer, since stabilizers can dynamically bind to the crystal surfaces during the GaP crystal growth. When the highly bulky tertiary amines (e.g., TOA) are used as stabilizers, a staggered conformation is favored, minimizing steric hindrance between these ligands and GaP lattices (Scheme 11, path A), and zinc blende GaP is preferred over wurtzite. In contrast, when an excess amount of less sterically hindered HDA is added to TOA, the rotational barrier between GaP-HDA complexes and GaP lattices is reduced. Therefore, the formation of the kinetically stable wurtzite GaP is now facilitated (Scheme 11, path B) under the kinetic growth regime induced by a high monomer concentration [254].

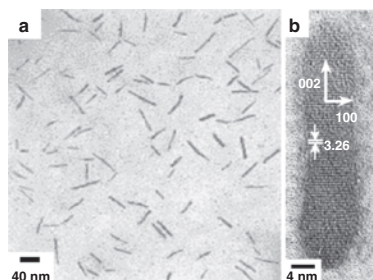
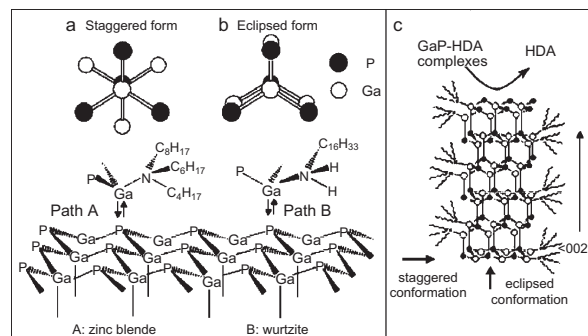


**Figure 32.** Large-area TEM image (a) and a HRTEM image (b) of GaP nanorods. Reprinted with permission from [254], Y.-H. Kim et al., *J. Am. Chem. Soc.* 124, 13656 (2002). © 2002, American Chemical Society.



**Scheme 11.** Proposed mechanism for surfactant-driven steric effects on the crystalline phases (a, b) and rod growth (c) of GaP nanocrystals. Reprinted with permission from [254], Y.-H. Kim et al., *J. Am. Chem. Soc.* 124, 13656 (2002). © 2002, American Chemical Society.

The steric difference between these two stabilizers seems to induce the anisotropic growth of the wurtzite GaP. It is likely that, when wurtzite seeds are formed, sterically bulky TOA selectively binds to the other faces (e.g., 100 and 110 faces) with staggered conformation rather than to 002 faces and blocks growth on these faces. On the other hand, GaP-HDA complexes continuously supply monomers on the 002 faces with high surface energy and therefore promote growth along the *c* axis (Scheme 11c). In addition, the thermolysis of a monomeric precursor  $[\text{Zn}(\text{TePh})_2][\text{TMEDA}]$  prepared from  $\text{Zn}(\text{TePh})_2$  and donor ligand TMEDA in a mixed surfactant trioctylamine-dimethylhexylamine produced ZnTe NRs [312], which could be templated from the rod-like micelles formed in the mixed-solvent system.

Currently, this approach has been successfully applied to the synthesis of transition metal NRs such as Co [205], Fe [208], and Ni [210], as well as perovskite  $\text{BaTiO}_3$ ,  $\text{SrTiO}_3$  NRs [104].

### 2.7.2. Self-Assembly under Natural/Mild Conditions

In contrast to the above capping agent/surfactant-driven synthesis of semiconductor NRs in hot solvent, self-assembly of nanofiber bundles, NTs, NWs, and their structure modulation under natural/mild conditions have emerged recently [25, 72–79]. The reverse micelle reaction medium usually consists of either the anionic surfactant AOT (sodium bis(2-ethylhexyl)sulfosuccinate) or nonionic surfactants. Various kinds of 1D inorganic NRs/NWs such as  $\text{BaCrO}_4$ , [25, 75],  $\text{BaSO}_4$  [74, 75],  $\text{BaCO}_3$  [77], and  $\text{BaWO}_4$  [78],  $\text{CaSO}_4$  [107],  $\text{CaCO}_3$  [408], CdS [292, 409], and Cu [410] have been synthesized in reverse micelle media or microemulsions. Other novel nanostructures, such as Ag nanodisc [192], flat CdS triangles [291], and CdS, CdSe NTs/NWs [76], can also be synthesized by this approach.

The strong binding interactions between surfactants and inorganic nuclei effectively inhibit the crystal growth and put the spontaneous structure reconstruction and self-organization of the primary nanoparticles under control. Micrometer-long twisted bundles of  $\text{BaSO}_4$  and  $\text{BaCrO}_4$  nanofilaments in water-in-oil microemulsions were prepared from the anionic surfactant AOT [25]. The reaction occurs at



room temperature in unstirred isoctane containing a mixture of  $\text{Ba}(\text{AOT})_2$  reverse micelles and  $\text{NaAOT}$  microemulsions with encapsulated sulfate (or chromate) anions. The reverse micelles are about 2 nm in diameter and consist of a spherical cluster of about 10  $\text{Ba}^{2+}$  ions strongly associated with the sulfonic acid headgroups of the surfactant, along with the water of hydration [25]. In contrast, the microemulsions are larger (4.5 nm across) because they contain bulk water (aqueous  $\text{Na}_2\text{SO}_4$  or  $\text{Na}_2\text{CrO}_4$ ) at a water-to-surfactant molar ratio of  $w = 10$ . When mixed together, the two reaction fields interact so that the constituents are slowly exchanged and  $\text{BaSO}_4$  or  $\text{BaCrO}_4$  nanoparticles nucleate and grow within the delineated space. With time, other filaments are formed parallel to the original thread to produce a small bundle of coaligned inorganic nanofilaments held together by surfactant bilayers. The locking in of new filaments by surfactant interdigitation generates a bending force in the nonattached segment of the longer primary thread. This results in the coiling of the bundle into a characteristic spiral-shaped structure several hundred nanometers in size that becomes self-terminating at one end because further addition of the primary nanoparticles is prevented by spatial closure.

The construction of higher-order structures from inorganic nanoparticle building blocks was successfully demonstrated by achieving sufficient informational content in the preformed inorganic surfaces to control long-range ordering through interactive self-assembly [25]. The NRs have flat surfaces with low curvature so that the hydrophobic driving force for assembly can be strengthened through intermolecular interaction, resulting in the formation of a bilayer between adjacent particles by the interdigitation of surfactant chains attached to nanoparticle surfaces. When the  $[\text{Ba}^{2+}]:[\text{SO}_4^{2-}]$  (or  $[\text{Ba}^{2+}]:[\text{CrO}_4^{2-}]$ ) molar ratio is equal to 1.0, remarkable linear chains of individual  $\text{BaSO}_4$  or  $\text{BaCrO}_4$  NRs are formed as shown in Figure 33.



**Figure 33.** TEM image showing ordered chains of prismatic  $\text{BaSO}_4$  nanoparticles prepared in AOT microemulsions at  $[\text{Ba}^{2+}]:[\text{SO}_4^{2-}]$  molar ratio = 1 and  $w = 10$ . Scale bar = 50 nm. Reprinted with permission from [25], M. Li et al., *Nature* 402, 393 (1999). © 1999, Macmillan Magazines Ltd.

Semiconductor NTs and NWs have recently been obtained with the use of nonionic surfactants such as *t*-octyl- $(\text{OCH}_2\text{CH}_2)_x\text{OH}$ ,  $x = 9, 10$  (Triton-X) and anionic surfactant AOT [76]. NWs of sulfides and selenides of Cu, Zn, and Cd with high aspect ratios can be prepared with Triton 100-X. The results show that it is possible to obtain both NTs and NWs of CdSe and CdS by this surfactant-assisted synthesis. For the synthesis of CdSe NTs, a suspension of cadmium oxide (10 mmol) was prepared in 20 ml of Triton 100-X (~24 mmol). A solution of  $\text{NaHSe}$  ( $\text{NaBH}_4/\text{Se}$  in 40 ml of water) was added dropwise under constant stirring to the suspension at 40 °C in an argon atmosphere. The resulting mixture was refluxed for 12 h and left overnight. The NTs are generally long, with lengths up to 5  $\mu\text{m}$ , as shown in Figure 34. The outer diameter of the NTs is in the 15–20-nm range, and the diameter of the central tubule is in the 10–15-nm range. The wall thickness is therefore around 5 nm. The formation mechanism of the NTs in the presence of surfactant is still not clear.

It should be pointed out that the poor crystallinity of the nanostructures obtained by this approach as well as the use of large excess surfactants could restrict the applicability of this approach.

## 2.8. Bio-Inspired Approach for Complex Superstructures

### 2.8.1. Polymer-Controlled Crystallization

Bio-inspired approaches to the synthesis of inorganic minerals have been a hot research subject [73, 80, 81]. Recently it was shown that so-called double-hydrophilic block copolymers (DHBCs) [81–94] can exert a strong influence on the external morphology and/or crystalline structure of inorganic particles such as calcium carbonate [82–85], calcium phosphate [86], barium sulfate [87, 88], barium chromate [89–91], cadmium tungstate [92], and zinc oxide [93].

Elegant nested calcium phosphate nanofibers were mineralized in the presence of DHBC poly(ethylene oxide)-*b*-alkylated poly(methacrylic acid) (PEO-*b*-PMAA- $\text{C}_{12}$ ), which was synthesized from PEO-*b*-PMAA by partial alkylation with dodecylamine [411]. Through the control of the pH of the  $\text{Ca}^{2+}$ -loaded polymer solution, delicate mesoskeletons of interconnected calcium phosphate nanofibers with star-like, neuron-like, and more complex nested forms can be obtained, as shown in Figure 35 [86].

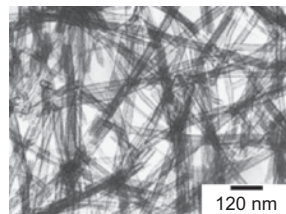


**Figure 34.** TEM image of CdSe nanotubes obtained with Triton 100-X as the surfactant. Reprinted with permission from [76], C. N. N. Rao et al., *Appl. Phys. Lett.* 78, 1853 (2001). © 2001, American Institute of Physics.

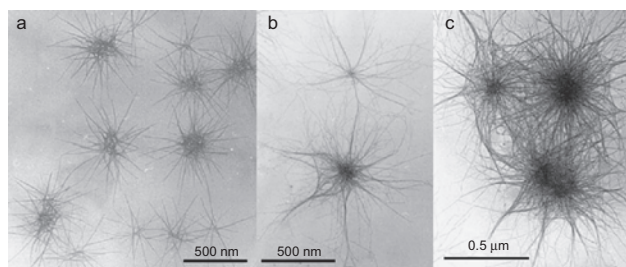


**Figure 35.** TEM images of calcium phosphate block copolymer nested colloids. (a) Star-like form at early stage at pH 3.5. (b) Later stage showing complex central core. (c) Neuron-like tangles produced at pH 5. Reprinted with permission from [86], M. Antonietti et al., *Chem. Eur. J.* 4, 2491 (1998). © 1998, Wiley-VCH.

Very long  $\text{BaSO}_4$  and  $\text{BaCrO}_4$  nanofibers and fiber bundles with remarkable similarity have been successfully fabricated by a polymer-controlled crystallization process at room temperature [88–90]. More complex morphologies of hashemite can be formed in the presence of partially phosphonated block copolymer poly(ethylene glycol)-*block*-poly(methacrylic acid) (PEG-*b*-PMAA- $\text{PO}_3\text{H}_2$ , PEG =  $3000 \text{ g mol}^{-1}$ , 68 monomer units; PMAA =  $700 \text{ g mol}^{-1}$ , 6 monomer units) [84]. Figure 36a and b shows SEM images of fibrous superstructures with sharp edges composed of densely packed, highly ordered, parallel nanofibers of  $\text{BaCrO}_4$ . The TEM micrograph with higher resolution in Figure 35c shows the self-organized nature of the superstructure. Whereas the majority of the fibers appear to be aligned in a parallel fashion, gaps between the single fibers can form but are also closed again. An electronic diffraction pattern taken from such an oriented planar bundle as shown in Figure 36d (right) confirmed that the whole structure

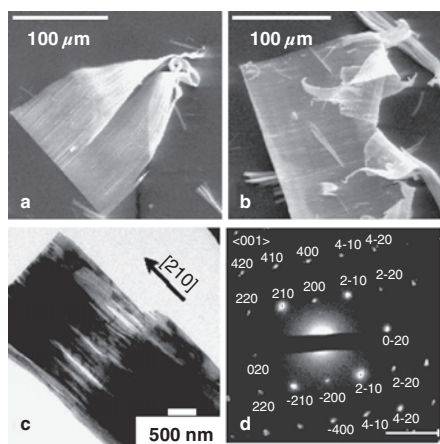


**Figure 36.** SEM and TEM images of highly ordered  $\text{BaCrO}_4$  nanofiber bundles obtained in the presence of PEG-*b*-PMAA- $\text{PO}_3\text{H}_2$  (21%, phosphonation degree) ( $1 \text{ g liter}^{-1}$ ) ( $[\text{BaCrO}_4] = 2 \text{ mM}$ ), pH 5. (a) Two fiber bundles with cone-like shape and length about  $150 \mu\text{m}$ . (b) Very thin fiber bundles. (c) TEM image of the thin part of the fiber bundles, inserted electronic diffraction pattern taken along the  $\langle 001 \rangle$  zone, showing the fiber bundles are well-crystallized single crystals and elongated along  $[210]$ . Reprinted with permission from [89], S. H. Yu et al., *Chem. Eur. J.* 8, 2937 (2002). © 2002, Wiley-VCH.

scatters as a well-crystallized single crystal where scattering is along the  $[001]$  direction and the fibers are elongated along  $[210]$ .

The initially formed nanoparticles stabilized by polymers are amorphous with sizes of up to 20 nm, which can aggregate to larger clusters. Evidently, this state of matter is the typical starting point for all types of highly inhibited reactions. The very low solubility product of barium chromate ( $K_{\text{sp}} = 1.17 \times 10^{-10}$ ) shows that the superstructures do not really grow from a supersaturated ion solution but by aggregation/transformation of the primary clusters formed [89].

All structures always grow from a single starting point, implying that the fibers grow against the glass wall or other substrates such as TEM grids, which obviously provide the necessary heterogeneous nucleation sites. The growth front of the fiber bundles is always very smooth, suggesting the homogeneous joint growth of all single nanofilaments with the ability to cure occurring defects, in line with the earlier findings for  $\text{BaSO}_4$  [88]. The opening angle of the cones is always rather similar, which seems to depend on temperature, degree of phosphonation of the polymer, and polymer concentration [89]. The control experiments show that the higher the temperature, the more linear the structures become. The superstructure developed more clearly, and to a much larger size, when the mineralization temperature was lowered to  $4^\circ\text{C}$ , as shown in Figure 37a. A rather lower phosphonation degree ( $\sim 1\%$ ) of a PEG-*b*-PMAA is already powerful enough to induce the formation of the fiber bundles and the superstructures, as shown in Figure 37b.

Interestingly, secondary cones can nucleate from either the rim or defects onto the cone, thus resulting in a tree-like structures (Fig. 37a). The fact that a cone stops growing once a second cone has nucleated at one spot on the rim shows that the growth presumably is slowing down with time, favoring the growth of the secondary cone. The cone-like superstructures tend to grow farther into a self-similar, multi-cone “tree” structure, which was observed before for barite mineralized in the presence of polyacrylates, but only under very limited experimental conditions [88]. From a structural viewpoint, the hashemite/barite crystals have a mirror plane perpendicular to the  $c$  axis, implying that a homogeneous nucleation will always result in crystals with identical charges of the opposite faces, and no dipole crystals can be formed. However, a dipole crystal may be favored

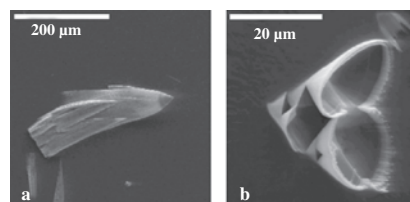


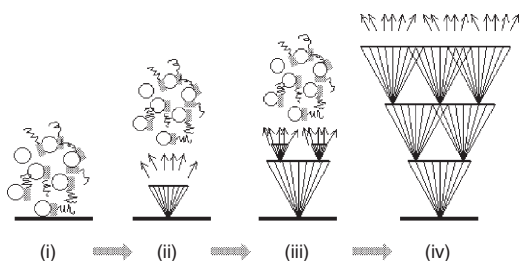
**Figure 37.** (a) A typical cone-like superstructure contains densely packed  $\text{BaCrO}_4$  nanofiber bundles in the presence of PEG-*b*-PMAA- $\text{PO}_3\text{H}_2$  (21%, phosphonation degree) ( $1 \text{ g liter}^{-1}$ ) ( $[\text{BaCrO}_4] = 2 \text{ mM}$ , pH 5), 2 days,  $4^\circ\text{C}$ ; (b) multi-funnel-like superstructures with remarkable self-similarity in the presence of PEG-*b*-PMAA- $\text{PO}_3\text{H}_2$  (1%, phosphonation degree) ( $1 \text{ g liter}^{-1}$ ) ( $[\text{BaCrO}_4] = 2 \text{ mM}$ , pH 5). Reprinted with permission from [89], S. H. Yu et al., *Chem. Eur. J.* 8, 2937 (2002). © 2002, Wiley-VCH.

for a heterogeneous nucleation as one end of the crystal is determined by the heterogeneous surface, the other by the solution/dispersion. The crystal has a dipole moment  $\mu = Q \cdot l$  ( $Q$  = charge and  $l$  = length of the crystal), which increases while the crystal is growing. This implies self-limiting growth so that a new heterogeneous nucleation event on the rim should become favorable after the dipole moment has reached a critical value due to energy minimization [89].

Based on the foregoing experimental observation and understanding, a self-limiting growth mechanism was proposed to explain the remarkable similarity of the superstructures [89] as shown in Scheme 12: (i) At the beginning, amorphous nanoparticles are formed, which are stabilized by the DHBCs (stage 1). (ii) Heterogeneous nucleation of fibers occurs on glass substrates, and the fibers grow under the control of a functional polymer, presumably by multipole field-directed aggregation of amorphous nanoparticles as proposed in [88]. (iii) The growth is continuously slowed down until secondary nucleation or overgrowth becomes more probable than the continuation of the primary growth. The secondary cone will grow as the first ones have done. (iv) The secondary heterogeneous nucleation event taking place on the rim can occur repeatedly, depending on the mass capacity of amorphous nanoparticles in the system.

A very recent observation shows that low-molecular-weight polyacrylic acid sodium salt serves as a very simple structure-directing agent for the room-temperature, large-scale synthesis of highly ordered cone-like crystals or very long, extended nanofibers made of  $\text{BaCrO}_4$  or  $\text{BaSO}_4$  with hierarchical and repetitive growth patterns as shown in Figure 38, where temperature and concentration variation permit control of the finer details of the architecture, namely length, axial ratio, opening angle, and mutual packing [90]. The formation of interesting hierarchical and repetitive superstructures is worth exploring further for other mineral systems.

Interestingly, single uniform  $\text{BaCrO}_4$  nanofibers can also be synthesized by a combination of polymer-controlled crystallization process and controlled nucleation by colloidal species producing locally a high supersaturation of both DHBCs and  $\text{Ba}^{2+}$ . The addition of a minor amount of a cationic colloidal structure such as PSS/PAH polyelectrolyte capsule (PSS/PAH: poly(styrene sulfonate, sodium salt)/polyallylamine hydrochloride) in the same reaction system can promote the independent growth of a number of



**Scheme 12.** Proposed mechanism for the formation of  $\text{BaCrO}_4$  complexity superstructure with self-similarity by polymer-controlled crystallization. Reprinted with permission from [89], S. H. Yu et al., *Chem. Eur. J.* 8, 2937 (2002). © 2002, Wiley-VCH.

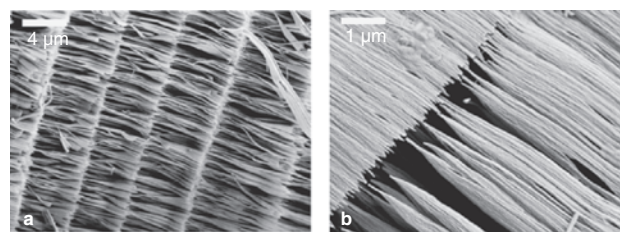


**Figure 38.** Complex forms of  $\text{BaSO}_4$  bundles and superstructures produced in the presence of 0.11 mM sodium polyacrylate ( $M_n = 5100$ ), at room temperature,  $[\text{BaSO}_4] = 2$  mM, pH = 5.3, 4 days. (a) Detailed superstructures with repetitive patterns. (b) Well-aligned bundles. Reprinted with permission from [90], S. H. Yu et al., *NanoLetters*, in press. © American Chemical Society.

fibers, thus leading to the dynamic discrimination of side nucleation and the resulting altered superstructures.

In addition to the formation of the mentioned superstructures under the control of block copolymers, DHBCs can also be used to fine-tune the nanostructural details of other inorganic crystals. Very thin 1D and 2D  $\text{CdWO}_4$  nanocrystals with controlled aspect ratios were conveniently fabricated at ambient temperature or by hydrothermal ripening under the control of DHBC [92]. The TEM image in Figure 40a shows very thin, uniform  $\text{CdWO}_4$  NRs/NBs with lengths in the range of 1 to 2  $\mu\text{m}$  and a uniform width of 70 nm along their entire length (aspect ratio of about 30). The thickness of the NBs is  $\sim 6\text{--}7$  nm. The slow and controlled reactant addition by the double-jet technique under stirring maintains the formation of intermediate amorphous nanoparticles at the jets [84] so that nanoparticles are the precursors for further particle growth rather than ionic species. Successive hydrothermal ripening after the double-jet reaction leads to a rearrangement of the rods into 2D lens-shaped, raft-like superstructures with a resulting lower aspect ratio, as shown in Figure 40b. In contrast, very thin and uniform nanofibers with a diameter of 2.5 nm, a length of 100–210 nm, and an aspect ratio of 40–85 as shown in Figure 40c

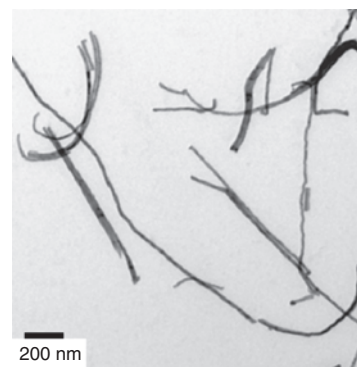


**Figure 39.** TEM images and electron diffraction pattern of the separated and very long  $\text{BaCrO}_4$  nanofibers with high aspect ratio obtained in the presence of a small amount of PSS/PAH capsules ( $20 \mu\text{l}$ ), PEG-*b*-PMAA- $\text{PO}_3\text{H}_2$ ,  $1 \text{ g liter}^{-1}$ ,  $[\text{BaCrO}_4] = 2$  mM, pH 5,  $25^\circ\text{C}$ . (a) A full view of the nanofibers. Reprinted with permission from [91], S. H. Yu et al., *Adv. Mater.*, in press. © Wiley-VCH.



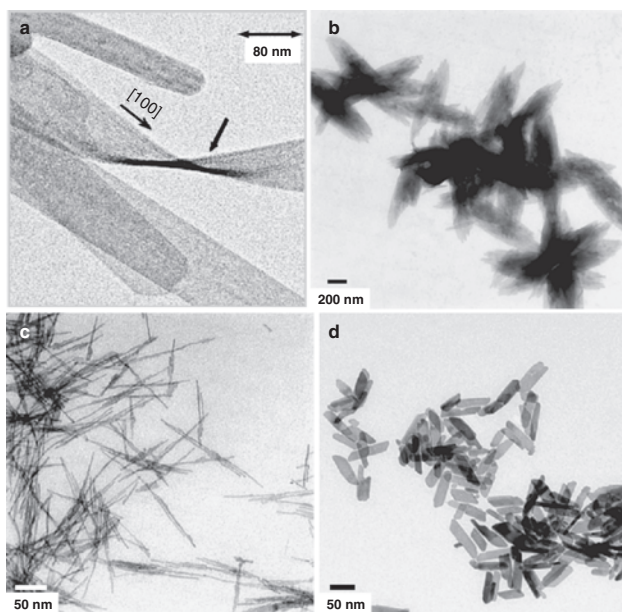


**Figure 40.** TEM images of the samples obtained under different conditions. (a) and (b) No additives: (a) pH = 5.3, double jet,  $[\text{Cd}^{2+}]:[\text{WO}_4^{2-}] = 8.3 \times 10^{-3}$  M (final solution), at room temperature; (b) pH = 5.3, double jet,  $[\text{Cd}^{2+}]:[\text{WO}_4^{2-}] = 8.3 \times 10^{-3}$  M (final solution), then hydrothermal crystallization: 80 °C, 6 h. (c) pH = 5.3, in the presence of PEG-*b*-PMAA (1 g liter<sup>-1</sup>), 20 ml, double jet,  $[\text{Cd}^{2+}]:[\text{WO}_4^{2-}] = 8.3 \times 10^{-3}$  M (final solution), then hydrothermal crystallization: 80 °C, 6 h. (d) Direct hydrothermal treatment of 20-ml solution containing equal molar  $[\text{Cd}^{2+}]:[\text{WO}_4^{2-}] = 8.3 \times 10^{-2}$  M, pH = 5.3, at 130 °C, 6 h, in the presence of 1 g liter<sup>-1</sup> PEG-*b*-PMAA-PO<sub>3</sub>H<sub>2</sub> (21%). Reprinted with permission from [92], S. H. Yu et al., *Angew. Chem. Int. Ed.* 41, 2356 (2002). © 2002, Wiley-VCH.

can readily be obtained when the DHBC PEG-*b*-PMAA is added to the solvent reservoir before the double-jet crystallization process, and the mixture is then hydrothermally ripened at 80 °C. When the partly phosphonated hydrophilic block copolymer PEG-*b*-PMAA-PO<sub>3</sub>H<sub>2</sub> (21%) (1 g liter<sup>-1</sup>) is added at an elevated temperature of 130 °C, even without the use of the double jets but at higher concentrations and coupled supersaturation, very thin platelet-like particles with a width of 17–28 nm, a length of 55–110 nm, and an aspect ratio of 2–4 are obtained by a direct hydrothermal process, as shown in Figure 40d. The nanoparticles display an interesting shape-dependent evolution of the luminescent properties, which may be of interest for applications.

Polymer-controlled crystallization in water at ambient temperature provides an alternative and promising tool for the morphogenesis of inorganic nanocrystals and superstructures that could be extended to various systems.

### 2.8.2. Supramolecular Self-Assembly

Supramolecular directed self-assembly of inorganic and inorganic/organic hybrid nanostructures has been emerging as an active area of recent research. The recent advance shows the remarkable feasibility of mimicking a natural mineralization system by a designed artificial organic template.

The supramolecular functional polymer can be directly employed for mineralization template of novel inorganic nanoarchitectures. CdS helices were successfully templated from supramolecular nanoribbons [94]. This novel inorganic nanostructure has a coiled morphology with a pitch of 40–60 nm, which can be rationalized in terms of the period of the twisted organic ribbons. A triblock architecture termed “dendron rodcoils” (DRC) can hydrogen bond in head-to-head fashion through dendron segments and self-assemble into nanoribbons [94]. The mineralization of the helical structures was done in both 2-ethylhexyl methacrylate (EHMA) and ethyl methacrylate (EMA). Figure 41 shows a typical CdS helix with a zigzag pattern and a pitch of 40–50 nm, which was isolated from a 1 wt% gel of the DRC in EHMA, to which a solution of cadmium nitrate in THF had been added prior to exposure to hydrogen sulfide gas [94]. HRTEM studies revealed that the polycrystalline zinc blende CdS is made up of small domains with grain sizes of about 4–8 nm. The results suggest that it is possible to achieve good control over the morphology of the templated product by using extremely uniform, stable, nonaggregated supramolecular objects as templates.

A peptide-amphiphile (PA) molecule was designed for the mineralization of PA nanofibers and hydroxyapatite (HAp) nanofibers [412]. This amphiphile molecule can assemble in water into cylindrical micelles because of the amphiphile’s overall conical shape, resulting in alkyl tails packed in the center of the micelle while the peptide segments are exposed to the aqueous environment [412]. The PA molecules were found to self-assemble at acidic pH but disassemble at neutral and basic pH. After self-assembly into nanofibers, the nanofibers were cross-linked by the oxidation of the cysteine thiol groups through treatment with 0.01 M I<sub>2</sub>. The cross-linked PA fibers contained intermolecular disulfide bonds, and intact fiber structures were still kept. These cross-linked fibers with negative charged surfaces are able to direct mineralization of HAp to form a composite material in which the crystallographic *c* axes of HAp are coaligned with the long axes of the fibers. The alignment of HAp nanofibers resembles the lowest level of hierarchical organization of bone [413].

In addition, supramolecular self-assembly using organogelators as template to transcribe inorganic nanostructures has been intensively studied. Organogelators are low-molecular-weight compounds that can gelate organic fluids at low

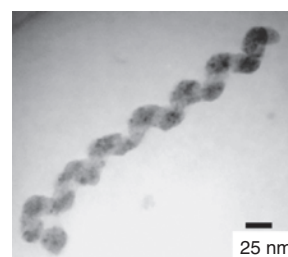


**Figure 41.** TEM micrograph of a typical CdS helix with a pitch of 40–50 nm precipitated in gels of the DRC in EHMA. Reprinted with permission from [94], E. D. Sone et al., *Angew. Chem. Int. Ed.* 41, 1705 (2002). © 2002, Wiley-VCH.

concentrations [414–419]. The gelators can gelate in organic solvents to form unique superstructures, which can transcribe inorganic nanostructures [420–429].

A helically structured silica has been successfully templated by a sol–gel transcription in chiral organogel systems [420–426]. The results show that certain cholesterol derivatives can gelate even tetraethoxysilane (TEOS), which can be used to produce silica by sol–gel polymerization [420]. Sol–gel polymerization of gelled TEOS solutions produces silica with a novel hollow fiber structure due to the template effect of the organogel fibers [420–426]. The formation of a three-dimensional network based on fibrous aggregates in organic fluids could be responsible for the formation of the gelling phenomenon.

This approach can be extended to the production of other metal oxide nanofibers or NTs with chiral structures.  $\text{TiO}_2$  fibers were fabricated with the use of an amphiphilic compound, *trans*-(1*R*,2*R*)-1,2-cyclohexanedi(11-aminocarbonylundecylpyridinium) hexafluorophosphate as template [427]. The amphiphilic compound containing cationic charge moieties is expected to electrostatically interact with anionic titania species under basic conditions in the sol–gel polymerization process of  $\text{Ti}[\text{OCH}(\text{CH}_3)_2]_4$ . Transition-metal (Ti, Ta, V) oxide fibers with chiral, helical, and nanotubular structures can be prepared by the sol–gel polymerization of metal alkoxides, with *trans*-(1*R*,2*R*)- or *trans*-(1*S*,2*S*)-1,2-di(undecylcarbonylamino)cyclohexane as structure-directing agents [428]. A recent report describes well-defined  $\text{TiO}_2$  helical ribbons and NTs obtained through sol–gel polymerization of titanium tetraisopropoxide  $[\text{Ti}(\text{O}_i\text{Pr})_4]$  in gels of a neutral dibenzo-30-crown-10-appended cholesterol gelator [429]. These chiral helical tubes could have various applications in electronics, optics, and photocatalysts.

### 2.8.3. Small Molecular Organic Species-Mediated Crystallization

In contrast to the previously mentioned polymer-controlled crystallization and supramolecular template synthesis, some small molecular organic species can also exert significant influence on crystal orientation growth.

A very recent report by Liu et al. describes unusually oriented and extended helical ZnO nanostructures grown from a synthetic ceramic method, which is surprisingly very similar to the growth morphology of nacreous calcium carbonate [95]. The helical ZnO nanostructures were grown on a glass substrate containing oriented ZnO NR arrays [430], which was placed in a solution containing  $\text{Zn}(\text{NO}_3)_2$ , hexamethylenetetramine, and sodium citrate and was reacted at 95 °C for 1 day. Figure 42 shows the similarity of SEM images of the helical ZnO nanocolumns (Fig. 42a and b) and the growth tip of a young abalone shell containing oriented columns of aragonite nanoplates (Fig. 42c). In the secondary growth on the helical NRs, aligned and well-defined nanoplates are formed, as in nacre. The side-width growth of the ZnO nanoplates leads to hexagonal ZnO plates that begin to overlap with one another.

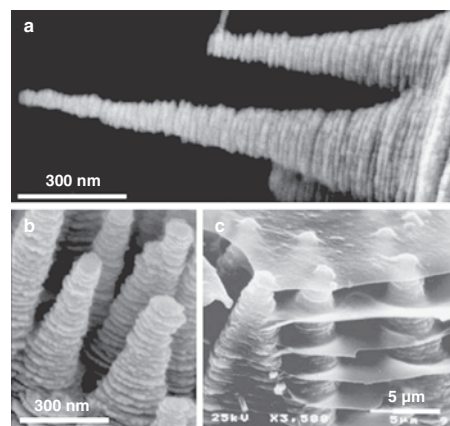


**Figure 42.** Comparison of ZnO helical structures with nacre. (a) and (b) High-magnification image of oriented ZnO helical columns. (c) Nacreous calcium carbonate columns and layers near the growth tip of a young abalone. Reprinted with permission from [95], Z. R. Tian et al., *J. Am. Chem. Soc.* 124, 12954 (2002). © 2002, American Chemical Society.

The organic species were reported to act as simple physical compartments or to control nucleation or to terminate crystal growth by surface poisoning in the biomineralization of nacre [431, 432]. The similarity of the biomimetic structures of helical ZnO rods to nacreous  $\text{CaCO}_3$  indicated that helical growth might play some role in the formation of organized nacreous calcium carbonate. However, the organic species citrate ion still plays critical roles in the formation of such structures since the citrate ion has a large tendency to inhibit the growth of the (002) surfaces, possibly through selective surface adsorption.

The discussed polymer controlled mineralization and small molecular organic species-mediated mineralization could shed new light on the morphology and orientation control of inorganic crystals.

### 2.9. Oriented Attachment Growth Mechanism

Traditionally, crystal growth can be described as an Ostwald ripening process. The formation of tiny crystalline nuclei in a supersaturated medium occurred first and then was followed by crystal growth. The larger particles will grow at the cost of the small ones because of the difference between large particles and the smaller particles of a higher solubility. Penn and Banfield [96–98] confirmed that both anatase and iron oxide nanoparticles with sizes of a few nanometers can coalesce under hydrothermal conditions in a way called “oriented attachment” (Fig. 43). The crystal lattice planes may be almost perfectly aligned, or dislocations at the contact areas between the adjacent particles lead to defects in the finally formed bulk crystals. The so-called oriented attachment was also proposed by other authors for the crystal growth of  $\text{TiO}_2$  [99] and for micrometer-sized ZnO particles during the formation of rod-like ZnO microcrystals [100]. However, until now, no direct evidence has been reported.

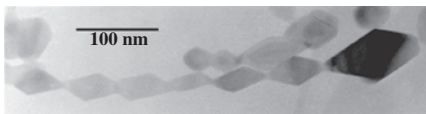


**Figure 43.** TEM micrograph of a single crystal of anatase that was hydrothermally coarsened in 0.001 M HCl, showing that the primary particles align, dock, and fuse to form oriented chain structures. Reprinted with permission from [98], R. L. Penn and J. F. Banfield, *Geochim. Cosmochim. Acta* 63, 1549 (1999). © 1999, Elsevier Science.

A very recent report by Weller et al. provided some strong evidence that ZnO NRs can be conveniently self-assembled from small ZnO quasi-spherical nanoparticles based on the oriented attachment mechanism by the evaporation and reflux of a solution containing 3–5-nm smaller nanoparticles [102]. Previously, self-assembly of nanoparticles capped by ligands was mainly driven by the interactions of the organic ligands rather than by the interaction of the particle cores.

ZnO sol with an average particle size of approximately 3 nm as shown in Figure 44a was easily prepared by adding dropwise a 0.03 M solution of KOH (65 ml) in methanol to a solution of zinc acetate dihydrate (0.01 M) in methanol (125 ml) under vigorous stirring at about 60 °C. Refluxing of the concentrated solution leads to the formation of rod-like nanoparticles. Prolonging the heating time mainly leads to an increase in the elongation of the particle along the *c* axis. After refluxing for 1 day, single crystalline NRs with average lengths of 100 nm and widths of approximately 15 nm were formed, as shown in Figure 44b. The authors argued that oxide nanoparticles are very favorable for oriented attachment for two reasons: first, organic ligands, which prevent intimate contact of crystal planes, are usually not needed for stabilization; and second, crystalline fusion of correctly attached particles leads to a gain not only in lattice-free energy but also in the free energy of polycondensation [102].

The spontaneous aggregation and self-assembly of the small nanoparticles into very elongated NRs/NWs was again observed in the case of CdTe when the protective shell of organic stabilizer on the surface of the initial CdTe nanoparticles was removed [103]. The presence of “pearl-necklace” agglomerates as intermediates of the

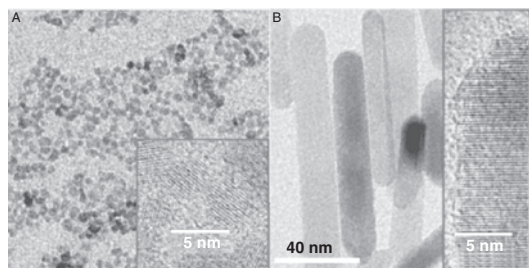


**Figure 44.** TEM images of ZnO. (A) Starting sol. (B) After 1 day of reflux of the concentrated sol. The insets show high-resolution TEM images of individual nanoparticles. Reprinted with permission from [102], C. Pacholski et al., *Angew. Chem. Int. Ed.* 41, 1188 (2002). © 2002, Wiley-VCH.

nanoparticle-NW transition suggested that the growth mechanism could be related to a special interaction/attraction between the nanoparticles. A dipole-dipole interaction was believed to be the driving force for such self-organization of the nanoparticles [103]. This approach provides a new pathway to high-quality luminescent CdTe NWs, even though the yield is still low.

Although there have been only few reports on the self-organization of nanoparticles, this new growth mechanism could offer an additional tool for the design of advanced materials with anisotropic material properties and could be used for the synthesis of more complex crystalline three-dimensional structures in which the branching sites could be added as individual nanoparticles, and could even lead to nearly perfect crystals [101, 102].

### 3. SUMMARY

In this chapter, the state of art of the synthesis of low-dimensional nanocrystals and more complex superstructures through the different approaches has been overviewed. The current advances in synthetic methodologies demonstrated that it is possible to rationally design 1D, 2D, and even more complex superstructures.

The “hard” approaches, such as template-directed growth method, the VLS mechanism, the VS mechanism, and oxide-assisted NW growth routes, have shown their powerful and straightforward pathways to the target 1D nanomaterials and their superstructures with high crystallinity, although they usually require either a carefully and costly predesigned template or rather strict reaction conditions.

The “soft” approaches show very promising alternative pathways for the synthesis of 1D nanocrystals. In addition to the strategies of solvent-mediated shape and structure modulation, the soft-hard interface between polymers/surfactants (or organic species) and inorganic crystals is also an area of great interest at present. The current progress indubitably emphasizes that all crystals will probably be amenable to morphosynthetic control by use of the appropriate templating molecules. The emerging new solution routes to 1D NRs/NWs and more complex superstructures, such as the solvothermal process, the SLS mechanism, capping agent/surfactant-assisted synthesis, bio-inspired approaches, and the oriented attachment growth mechanism, open alternative doorways to low-dimensional nanocrystals and more complex superstructures. Among these solution strategies, the solvothermal process shows possibilities and versatility for selective synthesis of various semiconductor nanocrystals with controllable shape, size, phase, and dimensionalities under mild conditions. The successful synthesis of various semiconductor NRs/NWs with the use of a suitable ligand solvent as a “shape controller” indicates that the solvothermal process is indicative of a fruitful and promising route to 1D and 2D semiconductor nanocrystals in the future.

The further understanding on the nucleation, crystallization, self-assembly, and growth mechanism of the nanocrystals in these solution strategies should open new rational pathways to prepare various kinds of highly crystalline nanowires/nanorods, nanotubes with well-defined monodispersed, sizes, and aspect ratios, and highly ordered/oriented



complex superstructures. Furthermore, it is no doubt needed to investigate the relationship between the structural specialties (shape, sizes, phases, dimensionality, and complexity etc.) of the low dimensional nanocrystals and their properties, which could shed light on their novel applications and fundamental properties as building blocks in nanoscience and nanotechnology.

## ACKNOWLEDGMENTS

S. H. Yu thanks the funding support from the “Hundreds of talent plan” of Chinese Academy of Sciences. We thank the financial support from National Natural Science Foundation of China.

## REFERENCES

1. M. G. Bawendi, M. L. Steigerwald, and L. E. Brus, *Annu. Rev. Phys. Chem.* 41, 477 (1990).
2. M. G. Bawendi, W. L. Wilson, L. Rothberg, P. J. Carrol, T. M. Jedju, M. L. Steigerwald, and L. E. Brus, *Phys. Rev. Lett.* 65, 1623 (1990).
3. W. Hoheisel, V. L. Colvin, C. S. Johnson, and A. P. Alivisatos, *J. Chem. Phys.* 101, 8455 (1994).
4. A. P. Alivisatos, *Science* 271, 933 (1996).
5. H. Weller, *Angew. Chem. Int. Ed. Engl.* 32, 41 (1993).
6. S. Mann, *Nature* 322, 119 (1988).
7. J. T. Hu, T. W. Odom, and C. M. Lieber, *Acc. Chem. Res.* 32, 435 (1999).
8. C. M. Lieber, *Solid State Commun.* 107, 607 (1998).
9. X. Duan, Y. Huang, Y. Cui, J. Wang, and C. M. Lieber, *Nature* 409, 66 (2001).
10. K. Leung, S. Pokrant, and K. B. Whaley, *Phys. Rev. B* 57, 12291 (1998).
11. X. G. Peng, L. Manna, W. D. Yang, J. Wickham, E. Scher, A. Kadavanich, and A. P. Alivisatos, *Nature* 404, 59 (2000).
12. G. P. Mitchell, C. A. Mirkin, and R. L. Letsinger, *J. Am. Chem. Soc.* 121, 8122 (1999).
13. M. J. Bruchez, M. Maronne, P. Gin, S. Weiss, and A. P. Alivisatos, *Science* 281, 2016 (1998).
14. W. C. W. Chan and S. M. Nie, *Science* 281, 2016 (1998).
15. M. Y. Han, X. H. Gao, J. Z. Su, and S. M. Nie, *Nat. Biol.* 19, 631 (2001).
16. Y. Cui and C. M. Lieber, *Science* 291, 851 (2001).
17. W. U. Huynh, J. J. Dittmer, and A. P. Alivisatos, *Science* 295, 2425 (2002).
18. P. Yang, in “Global Photonics Applications and Technology,” World Markets Series, Business Briefing, p. 42. 2002.
19. Y. Cui, Q. Q. Wei, H. K. Park, and C. M. Lieber, *Science* 293, 1289 (2001).
20. M. Law, H. Kind, B. Messer, F. Kim, and P. D. Yang, *Angew. Chem. Int. Ed.* 41, 2405 (2002).
21. P. D. Yang, H. Q. Yan, S. Mao, R. Russo, J. Hohnson, R. Saykally, N. Morris, J. Pham, R. R. He, and H. J. Choi, *Adv. Funct. Mater.* 12, 323 (2002).
22. E. Matijević, *Curr. Opin. Colloid Interface Sci.* 1, 176 (1996).
23. P. D. Yang, Y. Y. Wu, and R. Fan, *Int. J. Nanotechnol.* 1, 1 (2002).
24. T. S. Ahmadi, Z. L. Wang, T. C. Green, A. Henglein, and M. A. El-Sayed, *Science* 272, 1924 (1996).
25. M. Li, H. Schnablegger, and S. Mann, *Nature* 402, 393 (1999).
26. S. H. Yu, *J. Ceram. Soc. Jpn.* 109, S65 (2001).
27. T. Trindade, P. O'Brien, and N. L. Pickett, *Chem. Mater.* 13, 3843 (2001).
28. M. Green, *Curr. Opin. Solid State Mater. Sci.* 6, 355 (2002).
29. C. B. Murray, D. J. Norris, and M. G. Bawendi, *J. Am. Chem. Soc.* 115, 8706 (1993).
30. X. G. Peng, J. Wickham, and A. P. Alivisatos, *J. Am. Chem. Soc.* 120, 5343 (1998).
31. L. Spanhel, M. Haase, H. Weller, and A. Henglein, *J. Am. Chem. Soc.* 109, 5649 (1987).
32. J. E. B. Katari, V. L. Colvin, and A. P. Alivisatos, *J. Phys. Chem.* 98, 4109 (1994).
33. A. C. Jones, *Chem. Soc. Rev.* 101 (1997).
34. G. R. Patzke, F. Krumeich, and R. Nesper, *Angew. Chem. Int. Ed.* 41, 2447 (2002).
35. H. Dai, E. W. Wong, Y. Z. Lu, S. Fan, and C. Lieber, *Nature* 375, 769 (1995).
36. W. Q. Han, S. S. Fan, Q. Q. Li, and Y. D. Hu, *Science* 277, 1287 (1997).
37. J. D. Klein, R. D. Herrick, D. Palmer, M. J. Sailor, C. J. Brumlik, and C. R. Martin, *Chem. Mater.* 5, 902 (1993).
38. C. R. Martin, *Science* 266, 1961 (1994).
39. D. Almalawi, C. Z. Liu, and M. Motskovits, *J. Mater. Res.* 9, 1014 (1994).
40. D. Routkevitch, T. Bigioni, M. Moskovits, and J. M. Xu, *J. Phys. Chem.* 100, 14037 (1996).
41. R. S. Wagner and W. C. Elhs, *Appl. Phys. Lett.* 4, 89 (1964).
42. M. Yazawa, M. Koguchi, A. Muto, M. Ozawa, and K. Hiruma, *Appl. Phys. Lett.* 61, 2051 (1992).
43. J. Westwater, D. P. Gosain, S. Tomiya, S. Usui, and H. Ruda, *J. Vac. Sci. Technol., B* 15, 554 (1997).
44. A. M. Morales and C. M. Lieber, *Science* 279, 208 (1998).
45. M. H. Huang, Y. Wu, H. Feick, E. Webber, and P. Yang, *Adv. Mater.* 13, 113 (2000).
46. M. Huang, S. Mao, H. Feick, H. Yan, Y. Wu, H. Kind, E. Weber, R. Russo, and P. Yang, *Science* 292, 1897 (2001).
47. Y. Y. Wu, H. Q. Yan, M. Huang, B. Messer, J.-H. Song, and P. D. Yang, *Chem. Eur. J.* 8, 1260 (2002).
48. X. F. Duan and C. M. Lieber, *Adv. Mater.* 12, 298 (2000).
49. R. S. Wagner, in “Whisker Technology” (A. P. Levitt, Ed.), p. 47. Wiley, New York, 1970.
50. P. Yang and C. M. Lieber, *J. Mater. Res.* 12, 2981 (1997).
51. P. Yang and C. M. Lieber, *Science* 273, 1836 (1996).
52. Z. W. Pan, Z. R. Dai, and Z. L. Wang, *Science* 291, 1947 (2001).
53. J. Y. Lao, J. G. Wen, and Z. F. Ren, *NanoLetters* 2, 1287 (2002).
54. S. T. Lee, N. Wang, Y. F. Zhang, and Y. H. Tang, *MRS Bull.* 24, 1116 (2000).
55. W. S. Shi, Y. F. Zheng, N. Wang, C.-S. Lee, and S.-T. Lee, *Adv. Mater.* 13, 591 (2001).
56. W. S. Shi, Y. F. Zheng, N. Wang, C. S. Lee, and S. T. Lee, *Chem. Phys. Lett.* 345, 377 (2001).
57. C. C. Tang, S. S. Fan, H. Y. Dang, P. Li, and Y. M. Liu, *Appl. Phys. Lett.* 77, 1961 (2000).
58. S. T. Lee, N. Wang, and C. S. Lee, *Mater. Sci. Eng., A* 286, 16 (2000).
59. W. S. Shi, H. Y. Peng, N. Wang, C. P. Li, L. Xu, C. S. Lee, R. Kalish, and S. T. Lee, *J. Am. Chem. Soc.* 123, 11095 (2001).
60. A. Stein, S. W. Keller, and T. E. Mallouk, *Science* 259, 1558 (1993).
61. S. H. Yu, Y. S. Wu, J. Yang, Z. H. Han, Y. Xie, Y. T. Qian, and X. M. Liu, *Chem. Mater.* 10, 2309 (1998).
62. S. H. Yu, J. Yang, Z. H. Han, Yong Zhou, Ru-Yi Yang, Yi Xie, Yi-Tai Qian, and Yu-Heng Zhang, *J. Mater. Chem.* 9, 1283 (1999).
63. J. Yang, J. H. Zeng, S. H. Yu, L. Yang, G. E. Zhou, and Y. T. Qian, *Chem. Mater.* 12, 3259 (2000).
64. S. H. Yu and M. Yoshimura, *Adv. Mater.* 14, 296 (2002).

65. J. Yang, C. Xue, S. H. Yu, J. H. Zeng, and Y. T. Qian, *Angew. Chem. Ed. Int.* 41, 4697 (2002).
66. T. J. Trentler, K. M. Hickman, S. C. Goel, A. M. Viano, P. C. Gibbons, and W. E. Buhro, *Science* 270, 1791 (1995).
67. W. E. Buhro, K. M. Hickman, and T. J. Trentler, *Adv. Mater.* 8, 685 (1996).
68. T. J. Trentler, S. C. Goel, K. M. Hickman, A. M. Viano, M. Y. Chiang, A. M. Beatty, P. C. Gibbons, and W. E. Buhro, *J. Am. Chem. Soc.* 119, 2172 (1997).
69. P. D. Markowitz, M. P. Zach, P. C. Gibbons, R. M. Penner, and W. E. Buhro, *J. Am. Chem. Soc.* 123, 4502 (2001).
70. J. R. Heath and F. K. LeGoues, *Chem. Phys. Lett.* 208, 263 (1993).
71. J. D. Holmes, K. P. Johnston, R. C. Doty, and B. A. Korgel, *Science* 287, 1471 (2000).
72. L. Manna, E. C. Scher, and A. P. Alivisatos, *J. Am. Chem. Soc.* 122, 12700 (2000).
73. S. Mann, *Angew. Chem. Int. Ed.* 39, 3392 (2000).
74. J. D. Hopwood and S. Mann, *Chem. Mater.* 9, 1819 (1997).
75. M. Li and S. Mann, *Langmuir* 16, 7088 (2000).
76. C. N. N. Rao, A. Govindaraj, F. L. Deepak, and N. A. Gunari, *Appl. Phys. Lett.* 78, 1853 (2001).
77. L. Qi, J. Ma, H. Cheng, and Z. Zhao, *J. Phys. Chem. B* 101, 3460 (1997).
78. S. Kwan, F. Kim, J. Akana, and P. Yang, *Chem. Commun.* 447 (2001).
79. H. T. Shi, L. M. Qi, J. M. Ma, and H. M. Cheng, *Chem. Commun.* 1704 (2002).
80. E. Dujardin and S. Mann, *Adv. Mater.* 14, 775 (2002).
81. H. Cölfen, *Macromol. Rapid Commun.* 22, 219 (2001).
82. M. Sedlak, M. Antonietti, and H. Cölfen, *Macromol. Chem. Phys.* 199, 247 (1998).
83. M. Sedlak and H. Cölfen, *Macromol. Chem. Phys.* 202, 587 (2001).
84. H. Cölfen and M. Antonietti, *Langmuir* 14, 582 (1998).
85. S. H. Yu, H. Cölfen, J. Hartmann, and M. Antonietti, *Adv. Funct. Mater.* 12, 541 (2002).
86. M. Antonietti, M. Breulmann, C. G. Goltner, H. Cölfen, K. K. W. Wong, D. Walsh, and S. Mann, *Chem. Eur. J.* 4, 2491 (1998).
87. L. M. Qi, H. Cölfen, and M. Antonietti, *Angew. Chem. Int. Ed.* 39, 604 (2000).
88. L. M. Qi, H. Cölfen, M. Antonietti, M. Li, J. D. Hopwood, A. J. Ashley, and S. Mann, *Chem. Eur. J.* 7, 3526 (2001).
89. S. H. Yu, H. Cölfen, and M. Antonietti, *Chem. Eur. J.* 8, 2937 (2002).
90. S. H. Yu, M. Antonietti, and H. Cölfen, *NanoLetters* 3, 379 (2003).
91. S. H. Yu, H. Cölfen, and M. Antonietti, *Adv. Mater.* 15, 133 (2003).
92. S. H. Yu, M. Antonietti, H. Cölfen, and M. Giersig, *Angew. Chem. Int. Ed.* 41, 2356 (2002).
93. M. Öner, J. Norwig, W. H. Meyer, and G. Wegner, *Chem. Mater.* 10, 460 (1998).
94. E. D. Sone, E. R. Zubarev, and S. I. Stupp, *Angew. Chem. Int. Ed.* 41, 1705 (2002).
95. Z. R. Tian, J. A. Voigt, J. Liu, B. McKenzie, and M. J. Mcdermott, *J. Am. Chem. Soc.* 124, 12954 (2002).
96. F. Banfield, S. A. Welch, H. Zhang, T. T. Ebert, and R. L. Penn, *Science* 289, 751 (2000).
97. R. L. Penn and J. F. Banfield, *Science* 281, 969 (1998).
98. R. L. Penn and J. F. Banfield, *Geochim. Cosmochim. Acta* 63, 1549 (1999).
99. A. Chemseddine and T. Moritz, *Eur. J. Inorg. Chem.* 235 (1999).
100. M. A. Verges, A. Mifsud, and C. J. Serna, *J. Chem. Soc., Faraday Trans.* 86, 959 (1990).
101. A. P. Alivisatos, *Science* 289, 736 (2000).
102. C. Pacholski, A. Kornowski, and H. Weller, *Angew. Chem. Int. Ed.* 41, 1188 (2002).
103. Z. Y. Tang, N. A. Kotov, and M. Giersig, *Science* 297, 237 (2002).
104. J. J. Urban, W. S. Yun, Q. Gu, and H. Park, *J. Am. Chem. Soc.* 124, 1186 (2002).
105. P. Yang and F. Kim, *Chem. Phys. Chem.* 3, 503 (2002).
106. F. Kim, S. Kwan, J. Akana, and P. Yang, *J. Am. Chem. Soc.* 123, 4360 (2001).
107. G. D. Rees, R. Evans-Gowing, S. J. Hammond, and B. H. Robinson, *Langmuir* 15, 1993 (1999).
108. H.-W. Liao, Y.-F. Wang, X.-M. Liu, Y.-D. Li, and Y.-T. Qian, *Chem. Mater.* 12, 2819 (2000).
109. B. B. Lakshmi, C. J. Patrissi, and C. R. Martin, *Chem. Mater.* 9, 2544 (1997).
110. Y. K. Liu, G. H. Wang, C. K. Xu, and W. Z. Wang, *Chem. Commun.* 1486 (2002).
111. W. Wang, Y. Zhan, and G. Wang, *Chem. Commun.* 727 (2001).
112. X. Jiang, T. Herricks, and Y. Xia, *NanoLetters* 2, 1333 (2002).
113. V. G. Pol, O. Palchik, A. Gedanken, and I. Felner, *J. Phys. Chem. B* 106, 9737 (2002).
114. N. Beermann, L. Vayssieres, S.-E. Lindquist, and A. Hagfeldt, *J. Electrochem. Soc.* 147, 2456 (2000).
115. L. Vayssieres, N. Beermann, S.-E. Lindquist, and A. Hagfeldt, *Chem. Mater.* 13, 233 (2001).
116. R. Kumar, Y. Kolytyn, X. N. Xu, Y. Yeshurun, A. Gedanken, and I. Felner, *J. Appl. Phys.* 89, 6324 (2001).
117. P. Zhou, D. Xue, H. Luo, and X. Chen, *NanoLetters* 2, 845 (2002).
118. Y. C. Choi, W. S. Kim, Y. S. Park, S. M. Lee, D. J. Bae, Y. H. Lee, G.-S. Park, W. B. Choi, N. S. Lee, and J. M. Kim, *Adv. Mater.* 12, 746 (2000).
119. J. Y. Li, Z. Y. Qiao, X. L. Chen, L. Chen, Y. G. Cao, M. He, H. Li, Z. M. Cao, and Z. Zhang, *J. Alloys Compd.* 306, 300 (2000).
120. H. Z. Zhang, Y. C. Kong, Y. Z. Wang, X. Du, Z. G. Bai, J. J. Wang, D. P. Yu, Y. Ding, Q. L. Hang, and S. Q. Feng, *Solid State Commun.* 109, 677 (1999).
121. W. Q. Han, P. Kohler-Redlich, F. Ernst, and M. Rühle, *Solid State Commun.* 115, 527 (2000).
122. G.-S. Park, W.-B. Choi, J.-M. Kim, Y. C. Choi, Y. H. Lee, and C.-B. Lim, *J. Cryst. Growth* 220, 494 (2000).
123. C. C. Tang, S. S. Fan, de la Chapelle, and P. Li, *Chem. Phys. Lett.* 333, 12 (2000).
124. S. Sharma and M. K. Sunkara, *J. Am. Chem. Soc.* 124, 12288 (2002).
125. Y. Zhang, N. Wang, S. Gao, R. He, S. Miao, J. Liu, J. Zhu, and X. Zhang, *Chem. Mater.* 14, 3564 (2002).
126. Y. Zhang, J. Zhu, Q. Zhang, Y. Yan, N. Wang, and X. Zhang, *Chem. Phys. Lett.* 317, 504 (2000).
127. X. C. Wu, W. H. Song, B. Zhao, Y. P. Sun, and J. J. Du, *Chem. Phys. Lett.* 349, 210 (2001).
128. J. Q. Hu, Q. Li, X. M. Meng, C. S. Lee, and S. T. Lee, *Adv. Mater.* 14, 1396 (2002).
129. C. H. Liang, G. W. Meng, Y. Lei, F. Philipp, and L. D. Zhang, *Adv. Mater.* 13, 1330 (2001).
130. B. C. Satishkumar, A. Govindaraj, M. Nath, and C. N. R. Rao, *J. Mater. Chem.* 10, 2115 (2000).
131. G. L. Li, M. Liu, and G. H. Wang, *J. Mater. Res.* 16, 3614 (2001).
132. H. Meyssamy, K. Riwozki, A. Kornowski, S. Nased, and M. Haase, *Adv. Mater.* 11, 840 (1999).
133. C. Tang, Y. Bando, and T. Sato, *J. Phys. Chem. B* 106, 7449 (2002).
134. Y. Yin, G. Zhang, and Y. Xia, *Adv. Funct. Mater.* 12, 293 (2002).
135. Z. Cui, G. W. Meng, W. D. Huang, G. Z. Wang, and L. D. Zhang, *Mater. Res. Bull.* 35, 1653 (2000).
136. Y. Li, M. Sui, Y. Ding, G. Zhang, J. Zhuang, and C. Wang, *Adv. Mater.* 12, 818 (2000).
137. B. B. Lakshmi, C. J. Patrissi, and C. R. Martin, *Chem. Mater.* 9, 2544 (1997).
138. X. Wang and Y. Li, *J. Am. Chem. Soc.* 124, 2880 (2002).
139. W. Z. Wang, C. K. Xu, G. H. Wang, Y. K. Liu, and C. L. Zheng, *Adv. Mater.* 14, 837 (2002).
140. J. Liu, J. Cai, Y. C. Son, Q. M. Gao, S. L. Suib, and M. Aindow, *J. Phys. Chem. B* 106, 9761 (2002).

141. M. Niederberger, F. Krumeich, H.-J. Muhr, M. Müller, and R. Nesper, *J. Mater. Chem.* 11, 1941 (2001).
142. K. Matsui, T. Kyotani, and A. Tomita, *Adv. Mater.* 14, 1216 (2002).
143. W. Z. Wang, Y. K. Liu, C. K. Xu, C. L. Zheng, and G. H. Wang, *Chem. Phys. Lett.* 362, 119 (2002).
144. S. J. Limmer, S. Seraji, M. J. Forbess, Y. Wu, T. P. Chou, C. Nguyen, and G. Cao, *Adv. Mater.* 13, 1269 (2001).
145. L. Guo, Z. Wu, T. Liu, W. Wang, and H. Zhu, *Chem. Phys. Lett.* 318, 49 (2000).
146. C. H. Ye, G. W. Meng, L. D. Zhang, G. Z. Wang, and Y. H. Wang, *Chem. Phys. Lett.* 363, 34 (2002).
147. S. Friedrichs, R. R. Meyer, J. Sloan, A. I. Kirkland, J. L. Hutchison, and M. L. H. Green, *Chem. Commun.* 929 (2001).
148. Y. Liu, C. Zheng, W. Wang, C. Yin, and G. Wang, *Adv. Mater.* 13, 1883 (2001).
149. Y. Liu, C. Zheng, W. Wang, Y. Zhan, and G. Wang, *J. Cryst. Growth* 233, 8 (2001).
150. Z. R. Dai, J. L. Gole, J. D. Stout, and Z. L. Wang, *J. Phys. Chem. B* 106, 1274 (2002).
151. Z. R. Dai, Z. W. Pan, and Z. L. Wang, *J. Am. Chem. Soc.* 124, 8673 (2002).
152. Z. L. Wang and Z. W. Pan, *Adv. Mater.* 14, 1029 (2002).
153. S.-M. Yang and W.-J. Kim, *Adv. Mater.* 13, 1191 (2001).
154. B. Zheng, Y. Wu, P. Yang, and J. Liu, *Adv. Mater.* 14, 122 (2002).
155. Z. W. Pan, Z. R. Dai, C. Ma, and Z. L. Wang, *J. Am. Chem. Soc.* 124, 1817 (2002).
156. Z. L. Wang, R. P. Gao, J. L. Gole, and J. D. Stout, *Adv. Mater.* 12, 1938 (2000).
157. Z. Q. Liu, S. S. Xie, L. F. Sun, D. S. Tang, W. Y. Zhou, C. Y. Wang, W. Liu, Y. B. Li, X. P. Zou, and G. Wang, *J. Mater. Res.* 16, 683 (2001).
158. H.-F. Zhang, C.-M. Wang, and L.-S. Wang, *NanoLetters* 2, 941 (2002).
159. X. Y. Zhang, L. D. Zhang, W. Chen, G. W. Meng, M. J. Zheng, and L. X. Zhao, *Chem. Mater.* 13, 2511 (2001).
160. M. Zhang, Y. Bando, and K. Wada, *J. Mater. Sci. Lett.* 20, 167 (2001).
161. Z. Miao, D. Xu, J. Ouyang, G. Guo, X. Zhao, and Y. Tang, *NanoLetters* 2, 717 (2002).
162. T. Kasuga, M. Hiramatsu, A. Hoson, T. Sekino, and K. Niihara, *Langmuir* 14, 3160 (1998).
163. S. M. Liu, L. M. Gan, L. H. Liu, W. D. Zhang, and H. C. Zeng, *Chem. Mater.* 14, 1391 (2002).
164. R. A. Caruso, J. H. Schattka, and A. Greiner, *Adv. Mater.* 13, 1577 (2001).
165. S. Kobayashi, K. Hanabusa, N. Hamasaki, M. Kimura, and H. Shirai, *Chem. Mater.* 12, 1523 (2000).
166. M. E. Spahr, P. Bitterli, R. Nesper, M. Müller, F. Krumeich, and H.-U. Nissen, *Angew. Chem. Int. Ed.* 37, 1263 (1998).
167. F. Krumeich, H.-J. Muhr, M. Niederberger, F. Bieri, B. Schnyder, and R. Nesper, *J. Am. Chem. Soc.* 121, 8324 (1999).
168. H.-J. Muhr, F. Krumeich, U. P. Schönholzer, F. Bieri, M. Niederberger, L. J. Gauckler, and R. Nesper, *Adv. Mater.* 12, 231 (2000).
169. J. Livage, *Chem. Mater.* 3, 578 (1991).
170. G. Gu, B. Zheng, W. Q. Han, S. Roth, and J. Liu, *NanoLetters* 2, 849 (2002).
171. Y. F. Zhang, Y. H. Tang, X. F. Duan, Y. Zhang, C. S. Lee, N. Wang, I. Bello, and S. T. Lee, *Chem. Phys. Lett.* 323, 180 (2000).
172. J. Y. Li, X. L. Chen, H. Li, M. He, and Z. Y. Qiao, *J. Cryst. Growth* 233, 5 (2001).
173. P. D. Yang, H. Q. Yan, S. Mao, R. Russo, J. Johnson, R. Saykally, N. Morris, J. Pham, R. R. He, and H. J. Choi, *Adv. Funct. Mater.* 12, 323 (2002).
174. B. D. Yao, Y. F. Chan, and N. Wang, *Appl. Phys. Lett.* 81, 757 (2002).
175. J.-J. Wu and S.-C. Liu, *J. Phys. Chem. B* 106, 9546 (2002).
176. C. K. Xu, G. D. Xu, Y. K. Liu, and G. H. Wang, *Solid State Commun.* 122, 175 (2002).
177. Y. W. Heo, V. Varadarajan, M. Kaufman, K. Kim, D. P. Norton, F. Ren, and P. H. Fleming, *Appl. Phys. Lett.* 81, 3046 (2002).
178. Y. Li, G. S. Cheng, and L. D. Zhang, *J. Mater. Res.* 15, 2305 (2000).
179. H. Kim and W. Sigmund, *Appl. Phys. Lett.* 81, 2085 (2002).
180. B. H. Hong, S. C. Bae, C. W. Lee, S. Jeong, and K. S. Kim, *Science* 294, 348 (2001).
181. M. H. Huang, A. Choudrey, and P. D. Yang, *Chem. Commun.* 1063 (2000).
182. Y.-J. Han, J. M. Kim, and G. D. Stucky, *Chem. Mater.* 12, 2068 (2000).
183. J. H. Song, Y. Wu, B. Messer, H. Kind, and P. Yang, *J. Am. Chem. Soc.* 123, 10397 (2001).
184. Y. Zhou, S. H. Yu, C. Y. Wang, X. G. Li, Y. R. Zhu, and Z. Y. Chen, *Adv. Mater.* 11, 850 (1999).
185. N. R. Jana, L. Gearheart, and C. J. Murphy, *Chem. Commun.* 617 (2001).
186. R. C. Jin, Y. W. Cao, C. A. Mirkin, K. L. Kelly, G. C. Schatz, and J. G. Zheng, *Science* 294, 1901 (2001).
187. M. J. Edmondson, W. Zhou, S. A. Sieber, I. P. Jones, I. Gameson, P. A. Anderson, and P. P. Edwards, *Adv. Mater.* 13, 1608 (2002).
188. S. Liu, J. Yue, and A. Gedanken, *Adv. Mater.* 13, 656 (2001).
189. J. J. L. M. Cornelissen, R. van Heerbeek, P. C. J. Kamer, J. N. H. Reek, N. A. J. M. Sommerdijk, and R. J. M. Nolte, *Adv. Mater.* 14, 489 (2002).
190. Y. Zhou, S. H. Yu, X. P. Cui, C. Y. Wang, and Z. Y. Chen, *Chem. Mater.* 11, 545 (1999).
191. S. H. Chen and D. L. Carroll, *NanoLetters* 2, 1003 (2002).
192. M. Maillard, S. Giorgio, and M. P. Pileni, *Adv. Mater.* 14, 1084 (2002).
193. I. Pastoriza-Santos and L. M. Liz-Marzan, *NanoLetters* 2, 903 (2002).
194. Y. G. Sun, B. Gates, B. Mayers, and Y. Xia, *NanoLetters* 2, 165 (2002).
195. B. A. Korgel and D. Fitzmaurice, *Adv. Mater.* 10, 661 (1998).
196. Y. Yu, S. Chang, C. Lee, and C. R. C. Wang, *J. Phys. Chem. B* 101, 6661 (1997).
197. N. R. Jana, L. Gearheart, and C. J. Murphy, *J. Phys. Chem. B* 105, 4065 (2001).
198. C. J. Murphy and N. R. Jana, *Adv. Mater.* 14, 80 (2002).
199. K. Esumi, K. Matsuhisa, and K. Torigoe, *Langmuir* 11, 3285 (1995).
200. J. K. N. Mbindyo, B. D. Reiss, B. R. Martin, C. D. Keating, M. J. Natan, and T. E. Mallouk, *Adv. Mater.* 13, 249 (2001).
201. T. Hassenkam, K. Nørgaard, L. Iversen, C. J. Kiely, M. Brust, and T. Bjørnholm, *Adv. Mater.* 14, 1126 (2002).
202. Y. Kondo and K. Takayanagi, *Science* 289, 606 (2000).
203. E. Dujardin, L. B. Hsin, C. R. C. Wang, and S. Mann, *Chem. Commun.* 1264 (2001).
204. C. S. Ah, S. D. Hong, and D.-J. Jang, *J. Phys. Chem. B* 105, 7871 (2001).
205. V. F. Puntes, K. M. Krishnan, and A. P. Alivisatos, *Science* 291, 2115 (2001).
206. T. Thurn-Albrecht, J. Schotter, C. A. Kastle, N. Emley, T. Shibauchi, L. Krusin-Elbaum, K. Guarini, C. T. Black, M. T. Tuominen, and T. P. Russell, *Science* 290, 2126 (2000).
207. C. Schonenberger, B. M. I. van der Zande, L. G. J. Fokkink, M. Henny, C. Schmid, M. Kruger, A. Bachtold, R. Huber, H. Birk, and U. Staufer, *J. Phys. Chem. B* 101, 5497 (1997).
208. S.-J. Park, S. Kim, S. Lee, Z. G. Khim, K. Char, and T. Hyeon, *J. Am. Chem. Soc.* 122, 8581 (2000).
209. K. Soulantica, A. Maisonnat, F. Senocq, M.-C. Fromen, M.-J. Casanove, and B. Chaudret, *Angew. Chem., Int. Ed. Engl.* 40, 2983 (2001).
210. N. Cordente, M. Respaud, F. Senocq, M.-J. Casanove, C. Amiens, and B. Chaudret, *NanoLetters* 1, 565 (2001).

211. G. Yi and W. Schwarzacher, *Appl. Phys. Lett.* 74, 1746 (1999).
212. Y.-T. Pang, G.-W. Meng, L.-D. Zhang, Y. Qin, X.-Y. Gao, A.-W. Zhao, and Q. Fang, *Adv. Funct. Mater.* 12, 719 (2002).
213. K. Torigoe and K. Esumi, *Langmuir* 11, 4199 (1995).
214. K.-B. Lee, S.-M. Lee, and J. Cheon, *Adv. Mater.* 13, 517 (2001).
215. J. Xiao, Y. Xie, R. Tang, M. Chen, and X. Tian, *Adv. Mater.* 13, 1887 (2001).
216. T. S. Ahmadi, Z. L. Wang, T. C. Green, A. Henglein, and M. A. El-Sayed, *Science* 272, 1924 (1996).
217. M. P. Zach, K. Inazu, K. H. Ng, J. C. Hemminger, and R. M. Penner, *Chem. Mater.* 14, 3206 (2002).
218. Y. Li, X. Li, Z.-X. Deng, B. Zhou, S. Fan, J. Wang, and X. Sun, *Angew. Chem., Int. Ed. Engl.* 41, 335 (2002).
219. Y. Wu, B. Messer, and P. Yang, *Adv. Mater.* 13, 1487 (2001).
220. L. M. Cao, Z. Zhang, L. L. Sun, C. X. Gao, M. He, Y. Q. Wang, Y. C. Li, X. Y. Zhang, G. Li, J. Zhang, and W. K. Wang, *Adv. Mater.* 13, 1701 (2001).
221. C. J. Otten, O. R. Lourie, M. F. Yu, J. M. Cowley, M. J. Dyer, R. S. Ruoff, and W. E. Buhro, *J. Am. Chem. Soc.* 124, 4564 (2002).
222. Y. D. Li, J. W. Wang, Z. X. Deng, Y. Y. Wu, X. M. Sun, D. P. Yu, and P. D. Yang, *J. Am. Chem. Soc.* 123, 9904 (2001).
223. T. Hanrath and B. A. Korgel, *J. Am. Chem. Soc.* 124, 1424 (2002).
224. Y. J. Zhang, Q. Zhang, N. L. Wang, Y. J. Yan, H. H. Zhou, and J. Zhu, *J. Cryst. Growth* 226, 185 (2001).
225. J. L. Gole, J. D. Stout, W. L. Rauch, and Z. L. Wang, *Appl. Phys. Lett.* 76, 2346 (2000).
226. Q. Gu, H. Y. Dang, J. Cao, J. H. Zhao, and S. S. Fan, *Appl. Phys. Lett.* 76, 3020 (2000).
227. W. S. Shi, H. Y. Peng, Y. F. Zheng, N. Wang, N. G. Shang, Z. W. Pan, C. S. Lee, and S. T. Lee, *Adv. Mater.* 12, 1343 (2000).
228. Y. H. Tang, Y. F. Zhang, N. Wang, W. S. Shi, C. S. Lee, I. Bello, and S. T. Lee, *J. Vac. Sci. Technol., B* 19, 317 (2001).
229. K.-Q. Peng, Y.-J. Yan, S.-P. Gao, and J. Zhu, *Adv. Mater.* 14, 1164 (2002).
230. Y. Wu, R. Fan, and P. Yang, *NanoLetters* 2, 83 (2002).
231. W. K. Hsu, S. Trasobares, H. Terrones, M. Terrones, N. Grobert, Y. Q. Zhu, W. Z. Li, R. Escudero, J. P. Hare, H. W. Kroto, and D. R. M. Walton, *Chem. Mater.* 11, 1747 (1999).
232. A. Abdelouas, W. L. Gong, W. Lutze, J. A. Shelnett, R. Franco, and I. Moura, *Chem. Mater.* 12, 1510 (2000).
233. B. Gates, Y. D. Yin, and Y. N. Xia, *J. Am. Chem. Soc.* 122, 12582 (2000).
234. B. Gates, B. Mayers, B. Cattle, and Y. N. Xia, *Adv. Funct. Mater.* 12, 219 (2002).
235. B. Mayers and Y. N. Xia, *Adv. Mater.* 14, 279 (2002).
236. M. S. Mo, J. H. Zeng, X. M. Liu, W. C. Yu, S. Y. Zhang, and Y. T. Qian, *Adv. Mater.* 14, 1658 (2002).
237. C. C. Chen, C. C. Yeh, C. H. Chen, M. Y. Yu, H. L. Liu, J. J. Wu, K. H. Chen, L. C. Chen, J. Y. Peng, and Y. F. Chen, *J. Am. Chem. Soc.* 123, 2791 (2001).
238. C. C. Chen and C. C. Yeh, *Adv. Mater.* 12, 738 (2000).
239. J. Zhang, X. S. Peng, X. F. Wang, Y. W. Wang, and L. D. Zhang, *Chem. Phys. Lett.* 345, 372 (2001).
240. K. W. Chang and J. J. Wu, *J. Phys. Chem. B* 106, 7796 (2002).
241. S. Y. Bae, H. W. Seo, J. Park, H. Yang, J. C. Park, and S. Y. Lee, *Appl. Phys. Lett.* 81, 126 (2002).
242. X. Duan and C. M. Lieber, *J. Am. Chem. Soc.* 122, 188 (2000).
243. H. Y. Peng, X. T. Zhou, N. Wang, Y. F. Zheng, L. S. Liao, W. S. Shi, C. S. Lee, and S. T. Lee, *Chem. Phys. Lett.* 327, 263 (2000).
244. H. Y. Peng, N. Wang, X. T. Zhou, Y. F. Zheng, C. S. Lee, and S. T. Lee, *Chem. Phys. Lett.* 359, 241 (2002).
245. A. Wohlfart, A. Devi, E. Maile, and R. A. Fischer, *Chem. Commun.* 998 (2002).
246. W. Q. Han and A. Zettl, *Appl. Phys. Lett.* 80, 303 (2002).
247. K. Hiruma, M. Yazawa, T. Katsuyama, K. Ogawa, K. Haraguchi, M. Koguchi, and H. Kakibayashi, *J. Appl. Phys.* 77, 447 (1995).
248. K. Haraguchi, K. Hiruma, K. Hosomi, M. Shirai, and T. Katsuyama, *J. Vac. Sci. Technol., B* 15, 1685 (1997).
249. T. Shimada, K. Hiruma, M. Shirai, M. Yazawa, K. Haraguchi, T. Sato, M. Matsui, and T. Katsuyama, *Superlattices Microstruct.* 24, 453 (1998).
250. M. S. Gudixsen and C. M. Lieber, *J. Am. Chem. Soc.* 122, 8801 (2000).
251. W. S. Shi, Y. F. Zheng, N. Wang, C. S. Lee, and S. T. Lee, *J. Vac. Sci. Technol., B* 19, 1115 (2001).
252. C. Tang, S. Fan, M. Lamy de la Chapelle, H. Dang, and P. Li, *Adv. Mater.* 12, 1346 (2000).
253. H.-M. Kim, D. S. Kim, Y. S. Park, D. Y. Kim, T. W. Kang, and K. S. Chung, *Adv. Mater.* 14, 991 (2002).
254. Y.-H. Kim, Y.-W. Jun, B.-H. Jun, S.-M. Lee, and J. Cheon, *J. Am. Chem. Soc.* 124, 13656 (2002).
255. M. Yazawa, M. Koguchi, A. Muto, and K. Hiruma, *Adv. Mater.* 5, 577 (1993).
256. J. A. Haber, P. C. Gibbons, and W. E. Buhro, *J. Am. Chem. Soc.* 119, 5455 (1997).
257. J. A. Haber, P. C. Gibbons, and W. E. Buhro, *Chem. Mater.* 10, 4062 (1998).
258. Y. Zhang, J. Liu, R. He, Q. Zhang, X. Zhang, and J. Zhu, *Chem. Mater.* 13, 3899 (2001).
259. S. D. Dingman, N. P. Rath, P. D. Markowitz, P. C. Gibbons, and W. E. Buhro, *Angew. Chem., Int. Ed. Engl.* 39, 1470 (2000).
260. C. H. Liang, L. C. Chen, J. S. Hwang, K. H. Chen, Y. T. Hung, and Y. F. Chen, *Appl. Phys. Lett.* 81, 22 (2002).
261. K. F. Huo, Z. Hu, F. Chen, J. J. Fu, Y. Chen, B. H. Liu, J. Ding, Z. L. Dong, and T. White, *Appl. Phys. Lett.* 80, 3611 (2002).
262. C. C. Tang, Y. Bando, and T. Sato, *Chem. Phys. Lett.* 362, 185 (2002).
263. R. Ma, Y. Bando, and T. Sato, *Adv. Mater.* 14, 366 (2002).
264. L. M. Cao, K. Hahn, Y. Q. Wang, C. Scheu, Z. Zhang, C. X. Gao, Y. C. Li, X. Y. Zhang, L. L. Sun, W. K. Wang, and M. Rühle, *Adv. Mater.* 14, 1294 (2002).
265. C. C. Tang, X. X. Ding, X. T. Huang, Z. W. Gan, W. Liu, S. R. Qi, Y. X. Li, J. P. Ou, and L. Hu, *Jpn. J. Appl. Phys., Part 2* 41, L589 (2002).
266. Y. H. Gao, Y. Bando, K. Kurashima, and T. Sato, *Microsc. Microanal.* 8, 5 (2002).
267. K. Tang, J. Hu, Q. Lu, Y. Xie, J. Zhu, and Y. Qian, *Adv. Mater.* 11, 653 (1999).
268. Y. H. Gao, Y. Bando, and T. Sato, *Appl. Phys. Lett.* 79, 4565 (2001).
269. Z. L. Wang, Z. R. Dai, R. P. Gao, Z. G. Bai, and J. L. Gole, *Appl. Phys. Lett.* 77, 3349 (2000).
270. Z. S. Wu, S. Z. Deng, N. S. Xu, J. Chen, J. Zhou, and J. Chen, *Appl. Phys. Lett.* 80, 3829 (2002).
271. W. S. Shi, Y. F. Zheng, H. Y. Peng, N. Wang, C. S. Lee, and S. T. Lee, *J. Am. Ceram. Soc.* 83, 3228 (2000).
272. Z. W. Pan, H. L. Lai, F. C. K. Au, X. F. Duan, W. Y. Zhou, W. S. Shi, N. Wang, C. S. Lee, N. B. Wong, S. T. Lee, and S. S. Xie, *Adv. Mater.* 12, 1186 (2000).
273. C. H. Liang, G. W. Meng, L. D. Zhang, Y. C. Wu, and Z. Cui, *Chem. Phys. Lett.* 329, 323 (2000).
274. J. C. Li, C. S. Lee, and S. T. Lee, *Chem. Phys. Lett.* 355, 147 (2002).
275. J. Q. Hu, Q. Y. Lu, K. B. Tang, B. Deng, R. R. Jiang, Y. T. Qian, W. C. Yu, G. E. Zhou, X. M. Liu, and J. X. Wu, *J. Phys. Chem. B* 104, 5251 (2000).
276. Q. Y. Lu, J. Q. Hu, K. B. Tang, Y. T. Qian, G. Zhou, X. M. Liu, and J. S. Zhu, *Appl. Phys. Lett.* 75, 507 (1999).
277. D. N. McIlroy, D. Zhang, Y. Kranov, and M. G. Norton, *Appl. Phys. Lett.* 79, 1540 (2001).
278. H.-F. Zhang, A. C. Dohnalkova, C.-M. Wang, J. S. Young, E. C. Buck, and L.-S. Wang, *NanoLetters* 2, 105 (2002).
279. S. R. Qi, X. T. Huang, Z. W. Gan, X. X. Ding, and Y. Cheng, *J. Cryst. Growth* 219, 485 (2000).
280. X. Wang, J. Lu, P. Gou, and Y. Xie, *Chem. Lett.* 820 (2002).

281. J. H. Song, B. Messer, Y. Wu, H. Kind, and P. Yang, *J. Am. Chem. Soc.* 123, 9714 (2001).
282. Y. Chen, D. A. A. Ohlberg, G. Medeiros-Ribeiro, Y. A. Chang, and R. S. Williams, *Appl. Phys. Lett.* 76, 4004 (2000).
283. C. P. Li, N. Wang, S. P. Wong, C. S. Lee, and S. T. Lee, *Adv. Mater.* 14, 218 (2002).
284. T. I. Kamins, R. S. Williams, D. P. Basile, T. Hesjedal, and J. S. Harris, *J. Appl. Phys.* 89, 1008 (2001).
285. D. S. Xu, Y. J. Xu, D. P. Chen, G. L. Guo, L. L. Gui, and Y. Q. Tang, *Chem. Phys. Lett.* 325, 340 (2000).
286. H. Q. Cao, Y. Xu, J. M. Hong, H. B. Liu, G. Yin, B. L. Li, C. Y. Tie, and Z. Xu, *Adv. Mater.* 13, 1393 (2001).
287. P. S. Nair, T. Radhakrishnan, N. Revaprasadu, G. A. Kolawole, and P. O'Brien, *Chem. Commun.* 564 (2002).
288. Y. D. Li, H. W. Liao, Y. Ding, Y. T. Qian, L. Yang, and G. E. Zhou, *Chem. Mater.* 10, 2301 (1998).
289. M. Chen, M. Y. Xie, J. Lu, Y. J. Xiong, S. Y. Zhang, Y. T. Qian, and X. M. Liu, *J. Mater. Chem.* 12, 748 (2002).
290. J. H. Zhan, X. G. Yang, D. W. Wang, S. D. Li, Y. Xie, Y. Xia, and Y. T. Qian, *Adv. Mater.* 12, 1348 (2000).
291. N. Pinna, K. Weiss, J. Urban, and M. P. Pileni, *Adv. Mater.* 13, 261 (2001).
292. C.-C. Chen, C.-Y. Chao, and Z. H. Lang, *Chem. Mater.* 12, 1516 (2000).
293. Y.-W. Jun, S.-M. Lee, N.-J. Kang, and J. Cheon, *J. Am. Chem. Soc.* 123, 5150 (2001).
294. D. Xu, X. Shi, G. Guo, L. Gui, and Y. Tang, *J. Phys. Chem. B* 104, 5061 (2000).
295. Z. A. Peng and X. G. Peng, *J. Am. Chem. Soc.* 124, 3343 (2002).
296. Z. A. Peng and X. G. Peng, *J. Am. Chem. Soc.* 123, 183 (2001).
297. W. Z. Wang, Y. Geng, P. Yan, F. Y. Liu, Y. Xie, and Y. T. Qian, *Inorg. Chem. Commun.* 2, 83 (1999).
298. Q. Yang, K. Tang, C. Wang, Y. Qian, and S. Zhang, *J. Phys. Chem. B* 106, 9227 (2002).
299. Q. Peng, Y. J. Dong, Z. X. Deng, and Y. D. Li, *Inorg. Chem.* 41, 5249 (2002).
300. L. Manna, E. C. Scher, L.-S. Li, and A. P. Alivisatos, *J. Am. Chem. Soc.* 124, 7136 (2002).
301. S. H. Yu, J. Yang, Z. H. Han, R. Y. Yang, Y. T. Qian, and Y. H. Zhang, *J. Solid State Chem.* 147, 637 (1999).
302. F. Gao, Q. Y. Lu, X. Y. Liu, Y. S. Yan, and D. Y. Zhao, *NanoLetters* 1, 743 (2001).
303. S. H. Wang and S. H. Yang, *Langmuir* 16, 389 (2000).
304. D. B. Yu, D. B. Wang, Z. Y. Meng, J. Lu, and Y. T. Qian, *J. Mater. Chem.* 12, 403 (2002).
305. M. S. Mo, M. W. Shao, H. M. Hu, L. Yang, W. C. Yu, and Y. T. Qian, *J. Cryst. Growth* 244, 364 (2002).
306. W. Z. Wang, Y. Geng, Y. Qian, M. R. Ji, and X. M. Liu, *Adv. Mater.* 10, 1479 (1998).
307. X. S. Peng, G. W. Meng, J. Zhang, X. F. Wang, C. Z. Wang, X. Liu, and L. D. Zhang, *J. Mater. Res.* 17, 1283 (2002).
308. Y. Li, J. H. Wan, and Z. N. Gu, *Mol. Cryst. Liquid Cryst.* 337, 193 (1999).
309. X. Jiang, Y. Xie, J. Lu, L. Y. Zhu, W. He, and Y. T. Qian, *Chem. Mater.* 13, 1213 (2001).
310. Q. S. Wu, N. W. Zheng, Y. P. Ding, and Y. D. Li, *Inorg. Chem. Commun.* 5, 671 (2002).
311. N. Kouklin, L. Menon, A. Z. Wong, D. W. Thompson, J. A. Woollam, P. F. Williams, and S. Bandyopadhyay, *Appl. Phys. Lett.* 79, 4423 (2001).
312. Y. W. Jun, C. S. Choi, and J. Cheon, *Chem. Commun.* 101 (2001).
313. Y. D. Li, Y. Ding, and Z. Y. Wang, *Adv. Mater.* 11, 847 (2002).
314. S. H. Yu, Y. T. Qian, L. Shu, Y. Xie, L. Yang, and C. S. Wang, *Mater. Lett.* 35, 116 (1998).
315. S. H. Yu, L. Shu, J. Yang, Z. H. Han, Y. T. Qian, and Y. H. Zhang, *J. Mater. Res.* 14, 4157 (1999).
316. S. H. Yu, J. Yang, Y. S. Wu, Z. H. Han, Y. Xie, and Y. T. Qian, *Mater. Res. Bull.* 33, 1661 (1998).
317. X. S. Peng, G. W. Meng, J. Zhang, L. X. Zhao, X. F. Wang, Y. W. Wang, and L. D. Zhang, *J. Phys. D: Appl. Phys.* 34, 3224 (2001).
318. S. H. Yu, J. Yang, Y. S. Wu, Z. H. Han, J. Lu, Y. Xie, and Y. T. Qian, *J. Mater. Chem.* 8, 1949 (1998).
319. H. L. Su, Y. Xie, P. Gao, H. Lu, Y. J. Xiong, and Y. T. Qian, *Chem. Lett.* 790 (2000).
320. M. S. Sander, A. L. Prieto, R. Gronsky, T. Sands, and A. M. Stacy, *Adv. Mater.* 14, 665 (2002).
321. A. L. Prieto, M. S. Sander, M. S. Martin-Gonzalez, R. Gronsky, T. Sands, and A. M. Stacy, *J. Am. Chem. Soc.* 123, 7161 (2001).
322. Y. Zhang, G. H. Li, Y. C. Wu, B. Zhang, W. H. Song, and L. Zhang, *Adv. Mater.* 14, 1227 (2002).
323. J. Yang, J. H. Zeng, S. H. Yu, L. Yang, Y. H. Zhang, and Y. T. Qian, *Chem. Mater.* 12, 2924 (2000).
324. E. Roy, P. Fricoteaux, and K. Yu-Zhang, *J. Nanosci. Nanotechnol.* 1, 323 (2001).
325. D. Wang, D. Yu, M. Shao, W. Yu, and Y. Qian, *Chem. Lett.* 1056 (2002).
326. Q. Lu, F. Gao, and D. Zhao, *Angew. Chem., Int. Ed. Engl.* 41, 1932 (2002).
327. Y. J. Glanville, D. G. Narehood, P. E. Sokol, A. Amma, and T. Mallouk, *J. Mater. Chem.* 12, 2433 (2002).
328. B. Gates, Y. Y. Wu, Y. D. Yin, P. D. Yang, and Y. N. Xia, *J. Am. Chem. Soc.* 123, 11500 (2001).
329. B. Gates, B. Mayers, Y. Y. Wu, Y. G. Sun, B. Cattle, P. D. Yang, and Y. N. Xia, *Adv. Funct. Mater.* 12, 679 (2002).
330. N. Wang, K. K. Fung, S. Wang, and S. Yang, *J. Cryst. Growth* 233, 226 (2001).
331. S. H. Wang, S. H. Yang, Z. R. Dai, and Z. L. Wang, *Phys. Chem. Chem. Phys.* 3, 3750 (2001).
332. X. G. Wen and S. H. Yang, *NanoLetters* 2, 451 (2002).
333. Q. Y. Lu, F. Gao, and D. Y. Zhao, *NanoLetters* 2, 725 (2002).
334. Y.-W. Jun, Y.-Y. Jung, and J. Cheon, *J. Am. Chem. Soc.* 124, 615 (2002).
335. H. Liao, Y. Wang, S. Zhang, and Y. Qian, *Chem. Mater.* 13, 6 (2001).
336. M. Nath, A. Govindaraj, and C. N. R. Rao, *Adv. Mater.* 13, 283 (2001).
337. M. Remskar, A. Mrzel, Z. Skraba, A. Jesih, M. Ceh, J. Demsar, P. Stadelmann, F. Levy, and D. Mihailovic, *Science* 292, 479 (2001).
338. J. Chen, S. L. Li, Q. Xu, and K. Tanaka, *Chem. Commun.* 1722 (2002).
339. R. Tenne, L. Margulis, M. Genut, and G. Hodes, *Nature* 360, 444 (1992).
340. A. Rothschild, J. Sloan, and R. Tenne, *J. Am. Chem. Soc.* 122, 5169 (2000).
341. Y. Q. Zhu, W. K. Hsu, N. Grobert, B. H. Chang, M. Terrones, H. Terrones, H. W. Kroto, and D. R. M. Walton, *Chem. Mater.* 12, 1190 (2000).
342. R. Rosentsveig, A. Margolin, Y. Feldman, R. Popovitz-Biro, and R. Tenne, *Chem. Mater.* 14, 471 (2002).
343. M. Nath and C. N. R. Rao, *Angew. Chem., Int. Ed. Engl.* 41, 3451 (2002).
344. Y. Q. Zhu, W. K. Hsu, H. W. Kroto, and D. R. M. Walton, *J. Phys. Chem. B* 106, 7623 (2002).
345. Q. Yang, K. B. Tang, C. R. Wang, D. Y. Zhang, and Y. T. Qian, *J. Solid State Chem.* 164, 106 (2002).
346. J. Q. Hu, B. Deng, W. X. Zhang, K. B. Tang, and Y. T. Qian, *Inorg. Chem.* 40, 3130 (2001).
347. Y. Cui, J. Ren, G. Chen, Y. Qian, and Y. Xie, *Chem. Lett.* 236 (2001).
348. B. Xie, S. W. Yuan, Y. Jiang, J. Lu, Q. Li, Y. Wu, W. C. Yu, H. B. Zhang, and Y. T. Qian, *Chem. Lett.* 612 (2002).

349. J. Q. Hu, B. Deng, W. X. Zhang, K. B. Tang, and Y. T. Qian, *Int. J. Inorg. Mater.* 3, 639 (2001).
350. Y. Xiong, Y. Xie, G. Du, and H. Su, *Inorg. Chem.* 41, 2953 (2002).
351. C. R. Wang, K. B. Tang, Q. Yang, G. Z. Shen, B. Hai, C. H. An, J. Zuo, and Y. T. Qian, *J. Solid State Chem.* 160, 50 (2001).
352. S. Iijima, *Nature* 354, 56 (1999).
353. C. J. Frosch and C. D. Thurmond, *J. Phys. Chem.* 66, 877 (1962).
354. C. M. Balkas and R. E. Davis, *J. Am. Ceram. Soc.* 79, 2309 (1996).
355. C. Pham-Huu, N. Keller, C. Estournes, G. Ehret, and M. J. Ledoux, *Chem. Commun.* 1882 (2002).
356. M. Brorson, T. W. Hansen, and C. J. H. Jacobsen, *J. Am. Chem. Soc.* 124, 11582 (2002).
357. Y. Q. Zhu, W. K. Hsu, H. W. Kroto, and D. R. M. Walton, *Chem. Commun.* 2184 (2001).
358. A. Huczko, *Appl. Phys. A* 70, 365 (2000).
359. M. Yoshimura, W. Suchanek, and K. Byrappa, *MRS Bull.* 9, 17 (2000).
360. K. Byrappa and M. Yoshimura, Eds., "Handbook of Hydrothermal Technology." LLC/Noyes Publications, Park Ridge, NJ, 2000.
361. A. Rabenau, *Angew. Chem., Int. Ed. Engl.* 24, 1026 (1985).
362. J. P. Corbett, *Chem. Rev.* 85, 383 (1985).
363. H. Schafer, *Annu. Rev. Mater. Sci.* 15, 1 (1985).
364. S. Feng and R. Xu, *Acc. Chem. Res.* 34, 239 (2001).
365. R. I. Walton, *Chem. Soc. Rev.* 31, 230 (2002).
366. W. S. Sheldrick and M. Wachhold, *Angew. Chem., Int. Ed. Engl.* 36, 206 (1997).
367. G. Demazeau, *J. Mater. Chem.* 9, 15 (1999).
368. R. F. Morris and S. J. Weigel, *Chem. Soc. Rev.* 26, 309 (1997).
369. S. H. Yu, L. Shu, Y. S. Wu, K. B. Tang, Y. Xie, Y. T. Qian, and Y. H. Zhang, *Nanostruct. Mater.* 10, 1307 (1998).
370. J. Yang, X. L. Yang, S. H. Yu, X. M. Liu, and Y. T. Qian, *Mater. Res. Bull.* 35, 1509 (2000).
371. S. H. Yu, J. Yang, Y. T. Qian, and M. Yoshimura, *Chem. Phys. Lett.* 361, 362 (2002).
372. S. H. Yu, Z. H. Han, J. Yang, R. Y. Yang, Y. Xie, and Y. T. Qian, *Chem. Lett.* 1111 (1998).
373. Z. H. Han, S. H. Yu, Y. P. Li, H. Q. Zhao, F. Q. Li, Y. Xie, and Y. T. Qian, *Chem. Mater.* 11, 2302 (1999).
374. J. Yang, G. H. Cheng, J. H. Zeng, S. H. Yu, X. M. Liu, and Y. T. Qian, *Chem. Mater.* 13, 848 (2001).
375. Z. H. Han, Y. P. Li, S. H. Yu, C. Zhong, X. Y. Chen, H. Q. Zhao, and Y. T. Qian, *J. Cryst. Growth* 223, 1 (2001).
376. S. H. Yu, L. Shu, Y. S. Wu, Y. Xie, Y. T. Qian, and L. Yang, *J. Am. Ceram. Soc.* 82, 457 (1999).
377. S. H. Yu and M. Yoshimura, *Adv. Funct. Mater.* 12, 277 (2002).
378. J. Yang, S. H. Yu, X. L. Yang, and Y. T. Qian, *Chem. Lett.* 839 (1999).
379. J. Yang, S. H. Yu, Z. H. Han, Y. T. Qian, and Y. H. Zhang, *J. Solid State Chem.* 146, 387 (1999).
380. S. H. Yu, J. Yang, Y. S. Wu, Z. H. Han, L. Shu, Y. Xie, and Y. T. Qian, *J. Mater. Res.* 13, 3365 (1998).
381. Y. Xie, Y. T. Qian, W. Z. Wang, S. Y. Zhang, and Y. H. Zhang, *Science* 272, 1926 (1996).
382. J. Q. Hu, Q. Y. Lu, K. B. Tang, S. H. Yu, Y. T. Qian, G. E. Zhou, X. M. Liu, and J. X. Wu, *J. Am. Ceram. Soc.* 83, 430 (2000).
383. J. Q. Hu, Q. Y. Lu, K. B. Tang, S. H. Yu, Y. T. Qian, G. E. Zhou, X. M. Liu, and J. X. Wu, *J. Solid State Chem.* 148, 325 (1999).
384. R. Rossetti, R. Hull, J. M. Gibson, and L. E. Brus, *J. Chem. Phys.* 82, 552 (1995).
385. R. J. Bandaranayake, G. W. Wen, J. Y. Lin, H. X. Jiang, and C. M. Sorensen, *Appl. Phys. Lett.* 67, 831 (1995).
386. J. J. Ramsden, S. E. Webber, and M. Gratzel, *J. Phys. Chem.* 89, 2740 (1985).
387. K. Krishnan and R. A. Plane, *Inorg. Chem.* 5, 852 (1966).
388. K. Nakamoto, in "Infrared and Raman Spectra of Inorganic and Coordination Compounds," Chap. 3, 3rd ed. Wiley, New York, 1978.
389. J. A. Dean, in "Lange's Handbook," 12th ed. McGraw-Hill Book Company, New York, 1987.
390. A. Sabatini and S. Callfano, *Spectrochim. Acta* 16, 677 (1960).
391. G. Newman and D. B. Powell, *J. Chem. Soc.* 477 (1961).
392. T. Iwamoto and D. F. Shriver, *Inorg. Chem.* 10, 2428 (1971).
393. J. S. Bradley, B. Tesche, W. Busser, M. Maase, and M. T. Reetz, *J. Am. Chem. Soc.* 122, 4631 (2000).
394. X. Y. Jing, S. L. Chen, and S. Y. Yao, in "Practical Guide to Infrared Spectrum," Chap. 6. Tianjin Science and Technology Press, 1992.
395. D. Arivuoli, F. D. Gnanam, and P. Ramasamy, *J. Mater. Sci. Lett.* 7, 711 (1988).
396. L. J. Farrugia, F. J. Lawlor, and N. C. Norman, *Polyhedron* 14, 311 (1995).
397. B. B. Nayak, H. N. Acharya, G. B. Mitra, and B. K. Mathur, *Thin Solid Films* 105, 17 (1983).
398. P. Boudjouk, M. P. Remington, Jr., D. G. Grier, B. R. Jarabek, and G. J. McCarthy, *Inorg. Chem.* 37, 3538 (1998).
399. H. O. Stephan and M. G. Kanatzidis, *Inorg. Chem.* 36, 6050 (1997).
400. C. Kaito, Y. Saito, and K. Fujita, *J. Cryst. Growth* 94, 967 (1989).
401. B. F. Variano, D. M. Hwang, C. S. Sandroff, P. Wiltzius, T. W. Jing, and N. P. Ong, *J. Phys. Chem.* 91, 6455 (1987).
402. W. S. Rees and G. Kräuter, *J. Mater. Res.* 11, 3005 (1996).
403. J. A. Dean, in "Lange's Handbook of Chemistry," 13th ed. McGraw-Hill Book Company, New York.
404. G. F. Svatos, C. Curran, and J. V. Quagliano, *J. Am. Chem. Soc.* 77, 6159 (1955).
405. A. Yamaguchi, R. B. Penland, S. Mizushima, T. J. Lane, C. Curran, and J. V. Quagliano, *J. Am. Chem. Soc.* 80, 527 (1958).
406. L. I. Berger, Ed., "Semiconductor Materials," pp. 86–88. CRC Press, Boca Raton, FL, 1997.
407. Z. A. Peng and X. G. Peng, *J. Am. Chem. Soc.* 123, 1389 (2001).
408. D. Kuang, A. Xu, Y. Fang, H. Ou, and H. Liu, *J. Cryst. Growth* 244, 379 (2002).
409. B. A. Simmons, S. Li, V. T. John, G. L. McPherson, A. Bose, W. Zhou, and J. He, *NanoLetters* 2, 263 (2002).
410. M. P. Pileni, *Langmuir* 17, 7476 (2001).
411. M. Antonietti and M. Weissenberger, *Macromol. Chem. Rapid Commun.* 18, 295 (1997).
412. J. D. Hartgerink, E. Beniash, and S. I. Stupp, *Science* 294, 1684 (2001).
413. W. Traub and S. Weiner, *Proc. Natl. Acad. Sci. U.S.A.* 86, 9822 (1989).
414. P. Terech and R. G. Weiss, *Chem. Rev.* 97, 3133 (1997).
415. S. Shinkai and K. Murata, *J. Mater. Chem.* 8, 485 (1997).
416. O. Gronwald and S. Shinkai, *Chem. Eur. J.* 7, 4329 (2001).
417. K. Hanabusa, K. Hiratsuka, M. Kimura, and H. Shirai, *Chem. Mater.* 11, 649 (1999).
418. K. Hanabusa, M. Yamada, M. Kimura, and H. Shirai, *Angew. Chem., Int. Ed. Engl.* 35, 1949 (1996).
419. K. Murata, M. Aoki, T. Suzuki, T. Harada, H. Kawabata, T. Komori, F. Ohseto, K. Ueda, and S. Shinkai, *J. Am. Chem. Soc.* 116, 6664 (1994).
420. Y. Ono, K. Nakashima, M. Sano, Y. Kanekiyo, K. Inoue, J. Hojo, and S. Shinkai, *Chem. Commun.* 1477 (1998).
421. J. H. Jung, Y. Ono, and S. Shinkai, *J. Chem. Soc., Perkin Trans 2* 1289 (1999).



422. Y. Ono, K. Nakashima, M. Sano, J. Hojo, and S. Shinkai, *Chem. Lett.* 1119 (1999).
423. J. H. Jung, Y. Ono, and S. Shinkai, *Angew. Chem., Int. Ed. Engl.* 39, 1862 (2000).
424. J. H. Jung, Y. Ono, and S. Shinkai, *Chem. Eur. J.* 6, 4552 (2000).
425. J. H. Jung, Y. Ono, K. Hanabusa, and S. Shinkai, *J. Am. Chem. Soc.* 122, 5008 (2000).
426. Y. Ono, K. Nakashima, M. Sano, J. Hojo, and S. Shinkai, *J. Mater. Chem.* 11, 2412 (2001).
427. S. Kobayashi, K. Hanabusa, N. Hamasaki, M. Kimura, H. Shirai, and S. Shinkai, *Chem. Mater.* 12, 1523 (2000).
428. S. Kobayashi, N. Hamasaki, M. Suzuki, M. Kimura, H. Shirai, and K. Hanabusa, *J. Am. Chem. Soc.* 124, 6550 (2002).
429. J. H. Jung, H. Kobayashi, K. J. C. Bommel, S. Shinkai, and T. Shimizu, *Chem. Mater.* 14, 1445 (2002).
430. B. C. Bunker, P. C. Rieke, B. J. Tarasevich, A. A. Campbell, G. E. Fryxell, G. L. Graff, L. Song, J. Liu, and J. W. Virden, *Science* 264, 48 (1994).
431. G. Falini, S. Albeck, S. Weiner, and L. Addadi, *Science* 271, 67 (1996).
432. A. M. Belcher, X. H. Wu, P. K. Christensen, P. K. Hansma, G. D. Stucky, and D. E. Morse, *Nature* 381, 56 (1996).



# Low-Frequency Noise in Nanomaterials and Nanostructures

Mihai N. Mihaila

National Institute of Microtechnology, Bucharest, Romania

## CONTENTS

1. Introduction
  2. Small is Beautiful but Noisy
  3. There is Much Noise at the Bottom
  4. When the Electron is the Signal:  
Low-Frequency Noise in  
Single Electron Transistors
  5. Noise Engineering in Semiconductor  
Quantum Wires
  6. Noise in Point Contacts and  
Metallic Nanobridges
  7. Blinking Quantum Dots
- Glossary  
References

## 1. INTRODUCTION

Microscopic particles such as small pollen grains bounce erratically when immersed in water. The discovery of this phenomenon, systematically investigated by Brown [1] but observed long before, was the starting point in the study of fluctuations and noise. Almost eight decades were necessary for the scientists to understand that brownian motion is one of the most subtle macroscopic manifestation of the microscopic world. Fluctuations or noise proved to be very fine tools to access the microscopic world for they allowed the determination of the Avogadro number [2], Boltzmann constant [3, 4], the electron charge [5, 6], and, more recently, the fractional Laughlin charge,  $e/3$ , where  $e$  is the elementary charge [7].

Since Schottky's magistral work on the vacuum diode [8], it became clear that the performances of the electronic devices processing the signals are fundamentally limited by their intrinsic noise. Soon after Schottky's discovery, Johnson found that the brownian motion of the charged carriers generates thermal noise [3]. Both shot noise and thermal noise are unavoidable and act as fundamental limits,

especially in the high-frequency domain. During his experiments on thermal and shot noise, Johnson also found that at low frequency the noise spectrum in the vacuum diodes changes inversely to the frequency ( $1/f$  noise). For almost 80 years,  $1/f$  noise—as it is called today—proved to be a universal and one of the most difficult to explain phenomena.

Besides thermal, shot, and  $1/f$  noise, two other kinds of noise were found in semiconductors and the new solid-state devices: generation–recombination noise and a kind of noise which consists of random switching between two (or more) distinct levels. In large devices, it was called burst or popcorn noise, while in small dimensional structures it is known as random telegraph signal (RTS) noise. The unabated scaling of the device dimensions is systematically approaching the microscopic roots of these low-frequency noise phenomena. This inexorable trend requires the reduction of power supply voltages, which “amounts to reduction in the signal noise level” [9]. The top down approach in the contemporary nanotechnology will encounter some given thresholds where “the noise is the signal,” to quote Rolf Landauer [10] who used this syntagm in a different context, however. In nanoscaled solid-state devices, the signal to noise ratio is close to 1, thus leading us to the vicinity of the fundamental limits. As a consequence, finding where the noise comes from could be a *sine qua non* condition for the further evolution in the field. It is very interesting that the noise in nanostructures brings back to light some very old and unsolved problems regarding the controversial physical mechanisms of  $1/f$  noise.

In this context, the purpose of this contribution is twofold. On one hand, we will briefly review the status of the low-frequency noise research in nanomaterials and some nanostructures/nanodevices. On the other hand, we shall investigate whether the nanoscience could answer old, perennial questions, in the field of low-frequency noise. The very old yet hot problematics of the  $1/f$  noise will be discussed in the light of some new achievements in the nanoscience. It is shown that the very old question regarding the topology of the noise sources (surface or bulk origin) of this phenomenon is clarified, while its microscopic origin

cannot be unambiguously answered. Although present even in the quantum dots, the RTS noise as a fundamental component of the  $1/f$  spectrum seems to be a nonsequitur. The enhanced phonon density of states in nanomaterials seems to be a source of higher noise levels, while the surface anharmonicity is proposed as a possible ingredient in the generation of  $1/f$  noise in carbon nanotubes. The low-frequency noise appears to be a powerful tool to characterize nanomaterials and nanodevices.

## 2. SMALL IS BEAUTIFUL BUT NOISY

### 2.1. Infrared Catastrophe: From Vacuum Diode to Nanotriode and Carbon Nanotube

At high enough frequency, the noise of a vacuum diode is dominated by shot noise [8]. Below a given frequency, Johnson [3] observed that noise intensity starts to increase above shot noise. The noise continuously increases while the frequency decreases ( $1/f$ ). No tendency to roll off was found to date. Since its discovery, the phenomenon was found in an astonishing number of physical systems. In solid and solid-state devices,  $1/f$  noise is omnipresent. By analogy with the ultraviolet catastrophe in the theory of blackbody radiation,  $1/f$  noise was called infrared catastrophe.

Soon after its discovery,  $1/f$  and burst noise were found to dominate the low-frequency noise of bipolar transistors. In comparison with a vacuum triode, the bipolar transistor was very noisy [11], its performances being much worse than those of a vacuum diode. However, it was not due to the reduced dimensions of the new device but rather to the undeveloped technology. This is not the case for some microelectromechanical systems manufactured by advanced modern technology. For instance,  $1/f$  noise is the dominating noise mechanism in small piezoresistive ultrathin cantilevers [12]. Although a 100 nm thin cantilever features superior performances, its  $1/f$  noise is higher than in a 1  $\mu\text{m}$  thick cantilever [11]. Moreover, for the 100 nm thin cantilevers, the noise intensity increases while the volume decreases. The tendency for the noise is to decrease with the total number of the carriers in the cantilever, which is in agreement with the Hooge phenomenological formula [13],

$$\frac{S_V}{V^2} = \frac{\gamma}{Nf} \quad (1)$$

where  $S_V$  is noise spectral density, at a given frequency ( $f$ ), of a fluctuating voltage ( $V$ ) which develops across the terminals of a resistor when a current is injected in it;  $N$  is the total number of either electrons or atoms in the investigated sample (still in dispute). This fact clearly points out that the performances of reduced-dimensionality systems can be limited by noise. An illustrating example in this respect can also be the nanometer-scale electrometer whose ultimate performance at higher frequency is limited by thermal noise [14], whereas for frequencies lower than  $10^3$  Hz, the limits are imposed by  $1/f$  noise.

In fact, by reducing the dimensions we come closer to the limit imposed by the noise phenomena. Vacuum nanodiodes and nanotriodes have been recently fabricated and their

noise performances evaluated by Driskill-Smith et al. [15]. Nanopillars of 1 nm diameter or less and having heights up to 15 nm are formed on the cathode surface by a natural lithographic technique. In contrast to the classical vacuum diode, the electrons are emitted from the metallic cathode by the Fowler–Nordheim effect. The emission takes place at nanopillars, in a gas for nanodiodes and in vacuum in the case of the encapsulated nanotriodes. For both nanodiode and nanotriode, the turn-on voltage is about 8 V and does not depend on temperature. A fine structure in the field-emitted current (anode current) vs. gate voltage was observed from room temperature to 20 K. In the nanotriode, this structure does not depend on the time it has been registered or temperature, which suggests that it is an inherent property of the device. It is reminiscent of the universal conductance fluctuations observed in solid-state devices and is the fingerprint of the electron interference between cathode and anode.

As can be seen from Figure 1a, when a constant voltage is applied, the emission current shows time fluctuations. Bistable (burst or RTS) noise pulses were observed at room temperature, while at 20 K they disappeared. This behavior is in contrast to what happens in some other physical system such as, for instance, MOS transistors where the burst (RTS) noise becomes dominant at low temperature. When Fourier transformed, the  $1/f^\beta$  noise was found to dominate

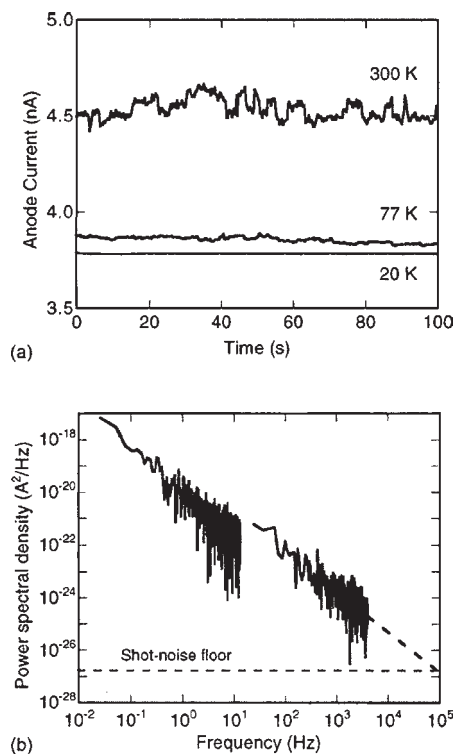


**Figure 1.** (a) Current stability of the nanotriode at 300, 77, and 20 K. RTS noise is observed at room temperature. (b)  $1/f$ -like noise spectrum in a nanotriode operating at 6 nA and at 300 K, in the frequency ranges 0.03–10 Hz and 10 Hz–4 kHz. Reprinted with permission from [15], A. G. Driskill-Smith et al., *J. Vac. Sci. Technol. B* 18, 3481 (2000). © 2000, American Vacuum Society.

the noise performance of the nanotriode below about  $10^4$  Hz (Fig. 1b). The frequency exponent  $\beta$  is about 1.3, but a closer look at the spectrum indicates that this is somehow larger, namely, 1.43. This is mainly due to the presence of the bistable noise at room temperature. The  $1/f$  spectrum crosses the shot noise floor at a corner frequency of about  $10^5$  Hz [15], while from the Johnson's data (from 1925!) [3] for classical triodes, most of the corner frequencies are far less than  $10^5$  Hz. Apparently, the nanotriode is much noisier than the classical triode.

However, one can compare quantitatively the noise performance of the two devices. For instance, in a vacuum triode (see Fig. 7 from Ref. [3]), at a frequency of about 1000 Hz, "the ratio of the apparent to the actual charge of the electron," in the terminology used by Johnson himself [3], is about 10. This is nothing but the ratio between  $1/f$  noise intensity and shot noise,  $2eI$ , where  $e$  is the electron charge and  $I = 5$  mA is the average current through the triode. With these data, one obtains  $S_{\text{shot}} = 2eI = 1.6 \times 10^{-21}$  A<sup>2</sup>/Hz and  $S_{1/f} = 10 \times S_{\text{shot}} = 1.6 \times 10^{-20}$  A<sup>2</sup>/Hz. From the noise data for nanotriode [15], we have  $S_{1/f} \approx 10^{-24}$  A<sup>2</sup>/Hz, at a frequency of 1000 Hz, for a current  $I = 6 \times 10^{-9}$  A. Assuming that noise intensity depends quadratically on current for both devices, one obtains the normalized noise intensity  $S_{1/f}/I^2 = 6.4 \times 10^{-16}$  Hz<sup>-1</sup> for the classical triode and  $S_{1/f}/I^2 = 2.7 \times 10^{-7}$  Hz<sup>-1</sup> for the nanotriode. Hence, in terms of normalized values, the nanotriode is apparently much noisier (eight orders of magnitude!) than the vacuum triode. However, this difference could be much smaller if the comparison is made between the  $1/f$  noise parameters,  $\gamma$ , because it depends on the total number of carrier ( $N$ ) in the sample. The simplest way out is to compare, as Johnson did [3], the Fano numbers, which is the ratio between the actual  $1/f$  noise and the shot noise intensity:  $S_{1/f}/S_{\text{shot}}$ . In this case, at the same frequency (1000 Hz),  $S_{1/f}/S_{\text{shot}} = 10$  for the vacuum triode and  $S_{1/f}/S_{\text{shot}} \approx 10^3$  for the nanotriode. Consequently, the very small nanotriode is two orders of magnitude noisier than its classical counterpart.

In the same line of argumentation, it came as a big surprise when, recently, Collins and co-workers [47] reported very high  $1/f$  noise levels in single-walled carbon nanotubes. The noise intensity was 4 to 10 orders of magnitude higher than in conventional systems. By conventional systems they meant carbon resistors which are well known for their very high noise levels. Usually, the recommendations are that for low-frequency noise circuitry these resistors should be avoided. In this context, the applicability of the carbon nanotubes for low-frequency noise applications is of great concern: "Unless the excess noise can be somehow suppressed, this certainly calls into question the applicability of SWNTs [single-walled carbon nanotubes] for many low-noise electronic applications," to cite Collins and co-workers [47]. Although the contacts are suspected to play a role in the noise measurement on carbon nanotube, there are some other groups that reported similar results.

Besides increased noise levels, in small dimensional structures unusual noise spectra can occur. If properly interpreted, they could be invaluable in the understanding of the noise mechanisms, some of them still in dispute.

## 2.2. "Forgotten" Spectra: The Case of the MOS Transistor

The case of MOS transistor is of particular interest not because this device is very noisy but merely for the fact that it is the most important constituent of the present and future ultralarge scale integrated circuits. In a sense, it can be considered as a paradigmatic example for the evolution of an electron device from microscopic scale to the nanoscale dimensions [16]. Its high noisiness is due to the specific surface conduction mechanism in the channel. McWhorter number fluctuation mechanism [17] due to the tunneling into interface/oxide states was for quite a long time used to explain the occurrence of  $1/f$  noise in this device. Tunneling into a single state generates a Debye-Lorentz spectrum. If the states are uniformly distributed in the oxide and the distribution of their relaxation time ( $\tau$ ) is proportional to  $1/\tau$ , a  $1/f$  spectrum is obtained by Lorentzian superposition.

The noise intensity scales inversely with the channel length ( $L$ ) [18, 19]. For channel length  $L < 0.6$   $\mu\text{m}$ , the McWhorter theory fails to explain experimental data [18]. However, a Lorentzian superposition is still used to generate the  $1/f$  noise spectrum. This approach is based on the observation that in small MOSFETs, the RTS is the dominant noise source. This is due to a carrier capture into a single trap located around the Fermi level. Experiments performed on very small devices [20–23], usually in the mesoscopic region, revealed that only Lorentzian spectra corresponding to RTS noise are present. The quite general belief is that  $1/f$  noise decomposes into its fundamental components, so in reducing the dimensions what we are seeing is the contribution of each fluctuator [20–24]. Ghibaudo et al. [25] observed that the noise intensity in MOS structures increases by orders of magnitude when the scaling factor increases. Of great concern is also the fact that the noise sample-to-sample dispersion strongly increases (three orders wide) with the scaling factor. At the same time, "a strong evolution of the noise spectra from  $1/f$  to Lorentzian like for devices with the channel lengths from 1 to 0.1  $\mu\text{m}$ " [24] was calculated.

Nevertheless, the observation of Lorentz spectra in very small devices does not have a unique interpretation. An alternative explanation would be that the mechanism generating  $1/f$  noise does not exist anymore or it is so weak that the RTS noise is dominant. Some examples given in this chapter seem to support this statement. In a very small MOSFET there is a good chance of having no trap in the channel. A related question would be: does  $1/f$  noise disappear when there is no trap in the channel? A partial answer to this question already exists, since the experiments performed by the Grenoble school [25] showed that the residual signal after the subtraction of the RTS noise exhibits a  $1/f$  spectrum. Similar results were obtained long ago by Strasilla and Strutt [26].

In some small MOSFETs,  $1/f$  noise is somewhat hidden. For instance, recently Bu et al. [27] performed noise measurements on nanometric MOSFETs with 100 nm channel length and 25 nm channel width. Although RTS noise was present in the time trace, Figure 2 shows that neither  $1/f$  nor Lorentzian spectra were observed but a  $1/f^3$  spectrum was found. Such spectra were long searched by van der Ziel's

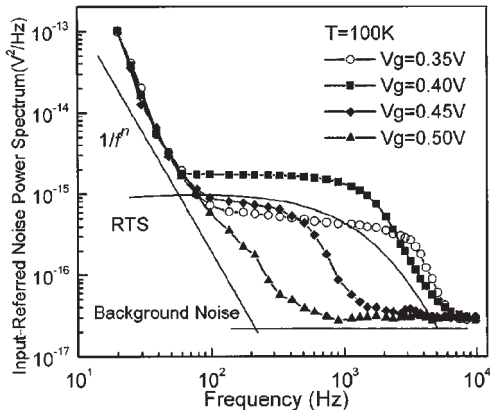


**Figure 2.**  $1/f^3$  input-referred noise spectra observed in a MOSFET with an ultranarrow channel at different gate voltages and  $T = 100$  K. Note that at frequencies lower than 100 Hz, the slope of the spectra is even higher. An RTS spectrum is presented for comparison. Reprinted with permission from [27], H. M. Bu et al., *Appl. Phys. Lett.* 76, 3250 (2000). © 2000, American Physical Society.

Minnesota school [28, 29] who predicted that such a spectrum could be described by the formula

$$S_I = \frac{A + B/f}{1 + (2\pi f)^2} \quad (2)$$

In this case,  $1/f$  noise and RTS noise go hand-in-hand, in the sense that one modulates the other. A spectrum of this form can be obtained only in the situation in which both phenomena have a common source. Such “forgotten” spectra are rarely discussed although they are not such a very *rara avis*. For, instance, a  $1/f^3$  spectrum was observed in a germanium filament by Mapple et al. [30] in 1955 and used by McWhorter himself in his famous paper (see Fig. 1 of Ref. [17]) to exemplify the existence of  $1/f$  noise. Apparently, these results do not support the RTS noise as the fundamental component of  $1/f$  noise. On the other hand, the fact that such a spectrum occurs in nanometer MOSFETs could be a chance to give an answer to this longstanding question.

Also, some experiments performed recently at Bell Labs [31] on deep submicron MOS transistors with 100 nm gate length and 40 nm gate oxide revealed that, in comparison with a  $0.5 \mu\text{m}$  gate length MOSFET, the  $1/f$  noise intensity increases by about two orders of magnitude and the spectrum spans over seven decades of frequency, with a corner frequency of about  $10^7$  Hz. To explain such an extension in the frequency, one needs more Lorentzians, therefore more traps. In direct connection with these results, one can come up with some questions such as: does the number of traps increases by decreasing the channel dimensions? This question has to be answered if credence is to be given to the idea that Lorentzian superposition is the source of the  $1/f$  noise. A possible answer to all these questions would be to look for other noise mechanisms in MOSFETs [32]. In essence, the new approach reveals the role of both surface and bulk phonons in the  $1/f$  noise generation in MOSFETs. Tunneling is not excluded but the noise is associated merely with the phonons which inelastically assist the carriers tunneling into surface states. The idea has also been

coined for some time in connection with the contribution of the RTS noise to the  $1/f$  noise [20, 33]. Recently, to check the role of the surface states, Kramer and Pease [34] proposed noise measurements on cylindrical surrounding-gate nanoscale MOS transistors. The dimension of the channel (few nanometers) could allow single or, possibly, “zero trap” behavior; hence, one can discriminate between different mechanisms of noise in MOSFETs. To date, we are not aware whether these measurements have been performed or not.

### 3. THERE IS MUCH NOISE AT THE BOTTOM [35]

#### 3.1. Low-Frequency Noise in Nanocrystalline and Nanoparticle Films

In the last half century, noise measurements have been performed on granular structures and discontinuous metal films. It is now well established that granularity and discontinuity are an important source of excess noise in these materials. In fact, it is considered that diffusion of the atoms at the grain boundaries or the tunneling between the metallic islands are the mechanisms responsible for the  $1/f$  noise generation in such systems. If in the case of some classical materials the granular structure was more or less accidental, this particular feature is a desired, intrinsic property of nanomaterials. The study of noise in granular, discontinuous, or grain-boundary-containing materials heralded what is going to happen in nanomaterials.

Specific to nanomaterials is the presence of the grain boundaries in a high concentration. Naturally, they strongly contribute to the scattering of conduction electrons, so they could be a source of excess noise. Performing noise measurements on gold nanocrystalline films, with grain diameters between 10 and 60 nm, Ochs et al. [36] found a  $1/f$  noise spectrum. Indeed, the noise intensity was about 5 times larger than in polycrystalline gold films. To our knowledge, this is the first noise measurement on a nanocrystalline film. Also, the grain boundary area per unit volume was found to be 5 times larger in nanomaterials than in the polycrystalline film. Consequently, the authors attributed the increased noise level to the presence of grain boundaries which “occupy a large volume fraction” [36] and, as such, large  $1/f$  noise is to be expected. According to Ochs et al. [36], noise measurement could be a novel tool to investigate the atomic motion at the grain boundaries between nanocrystallites.

Another way to understand why in nanocrystalline materials the  $1/f$  noise level is high would be to resort to the microscopic interpretation of the  $1/f$  noise parameter. As is well known, from Hooge’s [13] heuristic formula, the noisiness of a linear physical system can be evaluated by calculating the so-called  $1/f$  noise parameter,  $\gamma$ . Understanding the physical significance of this parameter has been a longstanding goal for the last three decades. In this respect, it has been recently proposed [37] that a connection between the  $1/f$  noise parameter ( $\gamma$ ) and the Eliashberg function,  $\alpha^2 F(\omega)$ , could exist,

$$\gamma \propto \alpha^2 F(\omega) \quad (3)$$



where  $F(\omega)$  is the phonon density of states,  $\alpha^2$  is the electron–phonon matrix element, and  $\omega$  is the atomic vibration frequency. The above equation predicts increased noise levels in systems with increased phonon density of states. Apparently, this is in contradiction with the role of the grain boundaries in generating excess  $1/f$  noise. However, recent results demonstrating that the atoms located at the grain boundaries are at the origin of enhanced phonon density of states in nanomaterials show that relation (3) is not incompatible with the role of the grain boundaries. For instance, it has been shown both theoretically [38, 39] and experimentally [40, 41] that in nanomaterials, at both low and high energy sides of the phonon spectrum, there is an enhancement in the phonon density of states. This enhancement is mainly “caused by the high number of grain-boundary atoms” [39], while the “atoms within grains do not noticeably contribute to the additional low-frequency modes” [41]. Moreover, the phonon density of states depends on the size and shape of the grains [41, 42]; namely,  $F(\omega)$  increases by decreasing grain size. This can explain, at least qualitatively, why in some physical systems the noise intensity increases with the particle size. All of these arguments support the idea that the increased noise levels observed by Ochs et al. [36] in nanocrystalline gold could be associated with an enhanced phonon density of states at grain boundaries.

Noise measurements have been used by Otten et al. [43] in order to investigate monocrystalline PbS nanoparticle films. The main goal was to look for an explanation of the “charge transport mechanisms in these structures” [43]. The samples were prepared by statistical deposition of 20 nm diameter PbS nanoparticles “until a nonhomogeneous film with a mean thickness of one monolayer is reached” [43]. As for the substrates, either GaAs or GaAs topped with a  $\text{SiN}_x$  layer for insulation was used. Prior to nanoparticle deposition, white noise has been detected on the  $\text{SiN}_x$  substrate. On GaAs samples, diffusion noise spectra have been found,  $1/f^\beta$ , with the slope  $\beta = 1/2$  and  $3/2$ . A problem here would be to explain where the factor  $1/2$  comes from, because it is specific to one-dimensional diffusion [44]. The weighted noise spectra exhibit maxima at frequencies which shift with the applied voltage. Assuming that the PbS nanoparticles create areas with different conductivity between the electrodes, it results that these areas “modulate the charge transport due to the interparticle potential barrier and the particle–substrate interface” [43]. The thermal agitation of the carrier between nanoparticles is influenced by the applied voltage through the interparticle potential. From the shift of the characteristic frequency, which is due to the different applied voltage [45], the diffusion coefficient can be calculated. Since the GaAs samples are three orders of magnitude more conductive than the  $\text{SiN}_x$ -type ones, the authors conclude “that the main charge transport takes place in the substrate and in the surface” [43]. Hence, the charge carriers located at the PbS nanoparticles randomly move between these and their movement is influenced by applied voltage through the interparticle potential. As is apparent from these results, the conduction phenomena in nanoparticle films could be quite complicated and the noise measurement offers a very fine tool to reveal as well as characterize them. This could prove very useful for device applications.

Tungsten trioxide ( $\text{WO}_3$ ) nanoparticle films have also been investigated by noise measurements by Hoel et al. [46]. The particles were deposited onto an indium tin oxide-coated glass substrate. Aluminum contacts were deposited on the nanoparticle film to create a capacitor. The authors found that thermal noise calculated from the ac impedance measurements is in very good agreement with the measured value, so the fluctuation–dissipation theorem is valid for this dielectric material.  $1/f$  noise has also been found, especially in the thinnest samples. It has been attributed to the penetrating columns of aluminum in the structure of the nanoparticles. All these results show “that noise measurements can be used for quality assessment of nanocrystalline insulating films” [46].

### 3.2. Low-Frequency Noise in Carbon Nanotubes: The End of an Old Controversy

The noise properties of carbon nanotubes are of great interest because they are perceived as the future building blocks for nanoelectronics and molecular electronics. The first noise measurements on carbon nanotubes have been performed by Collins et al. [47]. Excess  $1/f$  noise has been found in different configurations of SWNTs such as isolated individual tubes, two-dimensional (2D) films, and 3D materials. In a single SWNT, the noise power ( $S_V$ ) was found to depend quadratically on the dc biasing current. Therefore, as in many other solid-state physical systems,  $1/f$  noise in carbon nanotubes is due to genuine resistance fluctuations. A Hooge-type formula was used to characterize the absolute intensity of the voltage noise power for all 1D, 2D, or 3D morphologies:  $S_V = AV^2/f^\beta$ . Collins et al. found that the parameter  $A$  is a function of the sample resistance:  $A = 1.0 \times 10^{-11}R$ . For a sample with a resistance  $R = 100 \Omega$ , the noise amplitude is  $A = 10^{-9}$ . When compared with the conventional systems, such as high quality metal films or metal film containing grain boundaries, or damaged by electromigration or ion bombardment, carbon fibers or very noisy carbon composite resistors, the  $1/f$  noise in carbon nanotubes was found to be four to ten orders of magnitude larger! Carbon resistors are well known for their very high noise levels and usually, it is recommended to avoid their use for low-frequency noise circuitry. If so, the high noise level could strongly hinder the applicability of the carbon nanotubes in low-noise nanoelectronics.

When compared with the Hooge formula,  $A$  is simply connected with the  $1/f$  noise parameter ( $\gamma$ ) by the relation  $A = \gamma/N$ , where  $N$  is the total number of the carrier/atoms in the sample. For a SWNT with  $N = 10^4$  atoms  $\gamma \approx 0.2$ , which is two orders of magnitude larger than the value 0.002 postulated by Hooge [13]. The authors do not exclude the possible contact contribution to such large noise, although the measurements on 2D and 3D systems were done in a four-probe configuration. The authors suppose that the source of noise could be the electrical barriers at nanotube–nanotube junctions but this is not valid for single SWNTs. However, in this last case, the measurement was done in a two-probe configuration.

Recently, Roumiantsev et al. [48] have investigated noise on partially iron-filled, multiwalled carbon nanotubes

(MWNTs). Contacting the nanotube is a fundamental problem, in general, and in the noise measurements especially. In this experiment, the nanotubes were sprayed onto a SiO<sub>2</sub> surface and the individual nanotube, with optimal shape and most strategically placed in rapport to the previously deposited Cr/Au contacts, was contacted by focused ion beam (FIB) method. The noise measurements were done in the ohmic region of the  $I$ - $V$  characteristic. As in the case of Collins et al. [47],  $1/f^\beta$ -like noise spectra were found, with  $\beta$  close to unity. In contrast to the Collins et al. [47] results, Roumiantsev et al. [48] observed that the noise intensity is much smaller. Also, the current dependence of the  $1/f$  noise intensity was very different from the quadratic dependence found by Collins et al. [47]. In this case, the noise spectral density depends sublinearly on the injected current:  $S_V \sim I^\alpha$ , with  $\alpha$  between 1 and 1.5 for different samples. According to Roumiantsev and co-workers, “the noise could be generated by a small nonlinear contact resistance at the points of the contacts of FIB metal to the nanotube.” [48]. When measured in a simple FIB stripe, the noise showed a quadratic dependence on the current,  $S_I \sim I^2$ ; therefore the role of the contact is decisive in the noise measurements. It would be of interest to mention here that nonlinear effects in the  $1/f$  noise of a 2D electron gas have also been reported although the noise measurements were performed in the ohmic region of the  $I$ - $V$  characteristics [49]. The local deviations from the quadratic law have been attributed to the specific electron-phonon interaction in a 2D electron gas. Since the carbon nanotube is a quantum wire, one can expect nonlinear effects in its  $1/f$  noise even when the contact is perfect and this is due to the specific scattering mechanisms in a 1D electron gas. In addition, it is worth noting that the noise measurements of Collins et al. [47] were done at very small voltages (mV), while Roumiantsev et al. [48] measured at much higher voltages (volts). At these voltages, nonlinear effects can be very important.

$1/f$  noise has been very recently reported by Postma et al. [50] in individual metallic SWNTs. In equilibrium at room temperature, the thermal noise floor measured by Postma in a nanotube with a resistance  $R = 12.6$  k $\Omega$  was in excellent agreement with theory:  $S_V = 4k_B TR = 2.1 \times 10^{-16}$  V<sup>2</sup>/Hz, where the terms have their usual meaning. Under nonequilibrium conditions, when current is injected into the nanotube terminals, the noise spectrum of the voltage fluctuations is  $1/f$  and its intensity depends quadratically on voltage. For the resistance of 12.6 k $\Omega$ , a parameter  $A = \gamma/N = 1.8 \times 10^{-6}$  was found to fit the noise data. For a nanotube with a diameter of about 1.4 nm and a 0.5  $\mu$ m length [51], containing approximately 2000 conduction electrons, the  $1/f$  noise parameter is about  $\gamma = 3.6 \times 10^{-3}$ , very close to the value postulated by Hooge ( $2 \times 10^{-3}$ ). This value is at odds with the value calculated by Collins et al. [47], who found a two order of magnitude larger value. However, if it is to compare the noise data of Postma et al., for the nanotube with the resistance  $R = 12.6$  k $\Omega$ , with those of Collins et al., from the fitting relation  $A = 1.0 \times 10^{-11} R$  of Collins et al. [47], one finds  $A = 1.26 \times 10^{-7}$ , an order of magnitude smaller than the value obtained by Postma. In fact, the experimental values determined by Collins et al. (Fig. 3 from Ref. [47]) are of the order  $10^{-6}$ ; hence there is no discrepancy between the Postma et al. data and those

of Collins et al. in terms of parameter  $A$ . The discrepancies in the  $\gamma$  values come from the fact that Collins considers  $N = 10^4$  to be the total number of the atoms in the sample, while Postma considers  $N = 2000$  the total number of the conduction electrons in the sample.

Postma et al. also stated that “carbon nanotubes provide the right ingredients to study the origin of  $1/f$  noise in detail” [50]. Indeed, the temperature dependence of the  $1/f$  noise in carbon nanotube seems to be relevant for the physical mechanism of the  $1/f$  noise. It has been recently shown that the frequency exponent ( $\beta$ ) could be affected by the lattice anharmonicity (nonlinearity) [37]. The anharmonicity participation in the  $1/f$  noise can also be inferred from some simple analogies between the temperature dependence of  $1/f$  noise and the thermal conductivity of carbon nanotubes. In the first measurement on the temperature dependence of  $1/f$  noise in a SWNT, Postma et al. [50] reported that in a temperature range from 8 to 300 K, the  $1/f$  noise intensity ( $A$ ) increases by three orders of magnitude. In a temperature interval ranging from 4.2 to 290 K, Templeton and McDonald [52] found that  $1/f$  noise in conventional carbon resistors did not vary by more than an order of magnitude. The same situation was reported by Fleetwood et al. [53] between 77 and about 400 K.

The results of Postma et al. [50] are shown in Figure 3. Similar results were obtained on several samples, the sample-to-sample variation being roughly within one order of magnitude [51]. From Figure 3 one can speculate that there is a tendency in the noise to show a plateau or a maximum around 300 K. In the same temperature range, it has been experimentally demonstrated that the thermal conductivity of multiwalled carbon nanotubes increases by three orders of magnitude and exhibits a maximum at 320 K [54]. Also, Osman and Srivastava [55] calculated that the thermal conductivity of a nanotube with a diameter of 5 nm shows a maximum located at 300 K. It does not depend on chirality but on the diameter. This peak has been attributed to the participation of the phonon-phonon interaction, namely, to the Umklapp processes [54, 55]. If any, a maximum or a plateau in noise close to the temperature where the thermal conductivity is dominated by Umklapp processes would

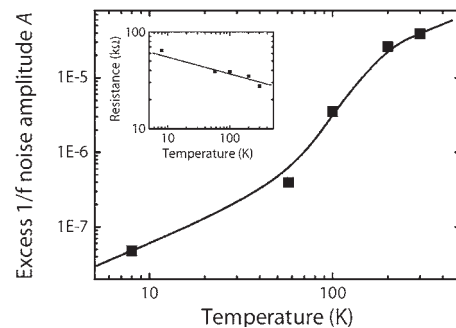


**Figure 3.** Temperature dependence of the parameter  $A = \gamma/N = fS_V/V^2$  for a single-wall carbon nanotube. The inset shows the temperature dependence of the nanotube resistance. The lines are guides to the eye. Reprinted with permission from [50], H. W. Ch. Postma et al., in “Electronic Correlations: From Meso- to Nanophysics” (T. Martin, G. Montanboux, and J. Trần Thanh Vân, Eds.) EDP Sciences, 2001, France. © 2001, EDP Sciences.

suggest that also Umklapp phonons are involved in the noise generation. Even more interesting, since the nanotube is nothing but a rolled surface, we are dealing with the surface anharmonicity which is stronger than bulk anharmonicity. However, it would be quite unusual for the surface anharmonicity to explain such a huge noise, 4 to 10 orders of magnitude more than in carbon resistors, as observed by Collins et al. [47].

Individual and two crossing multiwalled carbon nanotubes were investigated by noise measurements by Ouacha et al. [56]. The nanotube diameter was about 10 nm and the length from 1.5 to 3  $\mu\text{m}$ . At frequencies below  $10^3$  Hz, the noise intensity ( $S_V$ ) exceeded the thermal noise limit. In the individual nanotube, the spectrum is  $1/f^{1.02}$ , while in the crossed nanotubes the noise intensity is higher and the spectrum is  $1/f^{1.56}$ . A frequency exponent close to  $3/2$  would indicate a 1D diffusion noise in nanotube [44]. Such an exponent was never observed before in a carbon nanotube and, according to the authors, it “indicates a current dependent coupling mechanism to the measured voltage noise” [56]. In the individual nanotube, the noise intensity depends quadratically on the current,  $S_I \sim I^{1.98}$ , while a superlinear dependence has been observed in the crossed nanotubes. The authors consider that this unusual dependence can be assigned to the presence of a small resistance at the junction between the two nanotubes, or, possibly, to the metal–nanotube contacts. On the other hand, the quadratic dependence found in individual nanotubes is a clear indication that  $1/f$  noise comes from conductivity fluctuation. The ratio between the current noise ( $S_I$ ) and the shot noise ( $2eI$ ) was calculated, at a frequency  $f = 10^4$  Hz, and found to be about 2.47 for voltages higher than 50 mV. It shows that the noise intensity is quite close to shot noise “which suggests the presence of an electrical barrier at the nanotube–nanotube junction” [56].

In spite of some disputable problems regarding the noise measurement in such a very difficult to access physical system, the experiments on single wall carbon nanotubes are a beautiful demonstration of how nanoscience can clarify some very old disputes in the field of  $1/f$  noise. For instance, in the case of SWNT there is no bulk atom. “Every atom that constitutes the SWNT is a surface atom” [47]. Hence,  $1/f$  noise in a SWNT is a pure surface effect, a statement which is in glaring contradiction with Hooge’s idea that “ $1/f$  noise is no surface effect” [13]. It was the  $1/N$  dependence, where  $N$  is the total number of the carriers in the sample, which caused Hooge to state that  $1/f$  noise is a volume effect. It is also a matter of evidence that in carbon nanotubes McWhorter’s [17] number fluctuation model does not work at all. In this context, the surface atomic motion as a microscopic source of  $1/f$  noise comes to the fore, as experimentally demonstrated in very thin (8 nm) discontinuous platinum films [57, 58]. In this case, the role of the surface atomic motion proved to be fundamental. Excess phonon densities of states were found in carbon nanotubes in comparison with graphite [59]. According to the relation (3) between the  $1/f$  noise parameter and the phonon density of states, this could be a cause for the excess noise in nanotubes, although it is difficult to invoke for a quantitative justification. However, it turned out recently that lattice anharmonicity affects the frequency exponent [37]; thus one

could extend this observation and suppose that anharmonicity is involved in the  $1/f$  noise of carbon nanotubes, too. If this holds true, the role of the anharmonicity can be much more important in SWNT than in MWNT because the surface atoms feature stronger anharmonicity than bulk atoms. It can explain, at least in principle, the different noise levels between SWNT and MWNT. In this context, we propose surface lattice anharmonicity as a possible ingredient in the generation of  $1/f$  noise. This can be the result of some non-linear excitations in nanotubes.

#### 4. WHEN THE ELECTRON IS THE SIGNAL: LOW-FREQUENCY NOISE IN SINGLE ELECTRON TRANSISTORS

The single electron transistor (SET) or the Coulomb blockade electrometer [60] is considered to be the most probable candidate to replace the MOS transistor although it is very likely that the MOSFET will also be scaled down to the nanometer range [16]. However, as recently pointed out by Ahmed [61], if it is to work with 10 electrons in the channel, due to fluctuations in the number of electrons it would be impossible to distinguish between the two classical 0 and 1 levels. In this context, the advantage of working with a single electron becomes evident. The major obstacle in application of the SET transistor in the “single electronics” is the excess  $1/f$  noise observed in the fluctuating charge of the island. If these noise sources could be eliminated, what remains is the shot noise, which is due to the intrinsic conduction mechanism in SET.

Measurements performed by Zimmerli et al. [62] revealed that the shot-noise energy sensitivity of a SET “could approach  $\hbar$  (Planck constant) if the source of  $1/f$  noise were eliminated.” The energy sensitivity ( $E_N$ ) is defined as the ratio  $Q_N^2/2C_S$ , where  $Q_N$  is the charge noise and  $C_S$  is the island capacitance. According to Zimmerli et al. [62],  $1/f$  noise in SETs would be “probably associated with the presence of charge traps in the dielectric surrounding the island electrode.”

Using a multilayer fabrication process, Vissher et al. [63] obtained SET structures with better noise performance. Although they used amorphous SiO as dielectric layer, well known for its high density of traps and defects, the charge noise  $Q_N$  was found to be  $4 \times 10^{-4} e/\sqrt{\text{Hz}}$ , an order of magnitude lower than the result of Zimmerli et al. [62]. Verbrugh et al. [64] observed that charge noise intensity increases with the island size. They have also revealed that  $I$ – $V$  characteristics of different SET structures are well fitted by a model where the heat flow from the device is limited by the electron–phonon coupling in the island.

As for the origin of the  $1/f$  noise in SETs, it is still unclear but experiments performed to date [65, 66] indicate that this is due to fluctuating traps “distributed either in thin dielectric layers (including the barriers) adjacent to the island or, alternatively but more likely, in a volume of the substrate” [65]. According to Zimmerman et al. [66], a “significant modulation of the transistor island charge” could be induced by some noisy defects located outside the tunnel barriers. However, in aluminum single electron tunneling transistors, Tavkhelidze and Mygind [67] have observed the same noise

spectrum for fixed bias on both slopes of  $V(V_g)$ , where  $V$  is the dc voltage across the device terminals and  $V_g$  is the gate voltage. This is a hint that noise could be brought about by the trapping near or inside the junction which limits the tunnel current through the device.

Altogether, these results indicate that the substrate whereupon the island is placed is strongly contributing to the noise of the SET. Employing a stacked design which eliminates the effect of the substrate, Krupenin et al. [68] effectively reduced the substrate contribution to the background noise of metallic SET structures. They have also found evidence of a noise source due to the barrier conductance fluctuations but the mechanism producing these fluctuations remained obscure. Besides a gain dependent noise, excess noise has been reported in both Nb and Al SETs [69] but the noise intensity did not follow a quadratic dependence on the voltage; it excludes the association of this noise with the resistance fluctuations. This excess noise was tentatively attributed to the current which heats the SET. The influence of the temperature on the excess noise in SETs is crucial for the high-temperature applications. Kenyon et al. [70] investigated the temperature dependence of noise in metallic SETs between 85 mK and 4 K. They have found that above 1 K, the noise intensity increases quadratically with the temperature. An effect yet to be explained is that below about 0.5 K, the noise intensity does not tend to zero but saturates.

Single electron transistors have also been fabricated in crossed [71], freestanding [72], and buckled nanotubes [73]. The Coulomb blockade effect was observed in devices made from both SWNTs [71] and MWNTs. Ahlskog et al. [71] obtained a single electron transistor by crossing two MWNTs of 15 nm diameter. At low temperature, the lower tube is metallic while the upper one, playing the role of gate, is semiconducting. The Coulomb blockade in this device developed only at sub-Kelvin temperatures (150 mK). The authors investigated the transport and noise properties of the lower nanotube. The noise was measured over one period of the gate modulation curve. "The noise measured at the output of the SET had approximately a  $1/f$  power spectrum" [71] and the noise intensity featured an irregular dependence on the gate voltage ( $V_g$ ). When compared to the gain variation, it has been revealed that the noise intensity corresponding to the zero-gain point at a maximum of the current is rather shallow. This indicates the presence of some other noise sources in the nanotube SET, in addition to the charge fluctuations amplified by the SET. This could be a current dependent noise source for the noise measurement done outside the Coulomb blockade (room temperature) revealed that the noise power in MWNT is roughly equal to the high noise level observed by Collins et al. [47] in SWNTs. The input equivalent charge noise sensitivity at 10 Hz is about  $6 \times 10^{-4} e/\sqrt{\text{Hz}}$ , which compares very well with the typical values for metallic SETs.

Trapping centers of charge close to the island or in the tunneling barrier cause the  $1/f^\beta$  ( $\beta \sim 1 - 2$ ) in SET structures. To reduce noise intensity in SETs one has to avoid contact of the central island with the dielectric material. This solution has been selected by Roschier et al. [72] to realize an ultrasensitive electrometer using a freestanding carbon nanotube as island. A MWNT with a diameter of 14 nm

was manipulated by atomic force microscopy to move on top of two gold electrodes. A side gate was used to modulate the current. Noise measurement on this structure evidenced  $1/f^2$  spectra at both minimum and maximum gain. The charge noise of this freestanding carbon nanotube SET strongly improved. At a frequency of 45 Hz, a value of  $6 \times 10^{-6} e/\sqrt{\text{Hz}}$  has been found, which is comparable with the best metallic SETs.

Using the atomic force microscope, Postma et al. [73] created two buckles in a metallic nanotube. The nanotube segment between the two buckles featured Coulomb blockade effects when the nanotube potential was varied by a nearby gate [73]. When measured as a function of gate voltage, at a frequency of 10 Hz and a temperature of 60 K, the noise intensity clearly shaped the peaked  $I_{\text{DS}}$  vs. gate voltage characteristic, where  $I_{\text{DS}}$  is the drain-source current. The optimum value of the input equivalent charge noise is  $q = 2 \times 10^{-3} e/\sqrt{\text{Hz}}$ , which reasonably compares with the values for the conventional SET at very low temperature (mK).

## 5. NOISE ENGINEERING IN SEMICONDUCTOR QUANTUM WIRES

A quantum wire (QWR) has one unconfined direction and therefore it is a 1D conductor. As a consequence, the electronic density of states is highly localized and peaked [74], allowing for high electron mobility. This property is extremely useful to realize different nanostructures such as QWR field effect transistors, to give only an example. Progress in this field was somewhat hindered by the photolithographic accuracy. However, this disadvantage has been recently removed by the realization of a self-organized QWR structure, a technique successfully applied to obtain  $\text{In}_{0.15}\text{Ga}_{0.85}\text{As}/\text{GaAs}$  quantum-wire field effect transistors with very good performances [75]. To date, the noise performances of the semiconductor QWR-based nanodevices have not been evaluated. Also, the noise data for the quantum wire itself are scarce. However, Sugiyama et al. [76] measured noise in both V-groove and ridge  $\text{InGaAs}$  QWRs of 10 nm thickness, 100 nm width, and 2  $\mu\text{m}$  length. For both QWRs the noise spectrum was  $1/f$ -like. In the V-groove QWR, a bulge in the spectrum was found at around 10 kHz. The estimated  $1/f$  noise parameter at 1 Hz was  $2.1 \times 10^{-3}$  for the V-groove QWR, while for the ridge one calculations led to a value of  $6.4 \times 10^{-4}$ . The differences between the  $1/f$  noise parameter have been put down to different factors such as surface scattering, interface roughness scattering, and strain.

Due to the one-dimensional phonon confinement and the singular density of electronic states, the quantum wire is a system of particular interest to investigate the  $1/f$  noise mechanisms. The first theory of the  $1/f$  noise in semiconductor QWR has been introduced and elaborated by Balandin and co-workers [77]. Other contributions are due to Bandyopadhyay, Svizhenko, and others [78]. The theory naturally adopts the hypothesis of mobility fluctuation because the trapping–detrapping in such one-dimensional systems is very improbable. Momentum relaxation contributes significantly to mobility fluctuation  $1/f$  noise because it modifies the change in the velocity ( $\Delta v$ ) of an electron in the collision process. In such a 1D system, an electron can be scattered

directly forward or directly backward; thus no sideways scattering is possible. The first process does not considerably change  $\Delta v$ , so it contributes weakly to  $1/f$  noise. On the contrary, backscattering, which typically turns the electron around, consistently modifies  $\Delta v$ , so its contribution to  $1/f$  noise is important.

Quantitatively, the general idea of the theory is to calculate the change in the velocity,  $\Delta v$ , of an electron due to a collision process.  $(\Delta v)^2$  is then averaged in the wavevector space ( $k$ -space) over all final scattering states weighted by the scattering rate. The result,  $(\Delta v)^2(k)$ , is then averaged to obtain  $\langle(\Delta v)^2\rangle$  by ensemble averaging over the initial states assuming, in the case of Balandin et al. [77], that their occupation is described by a drifted Maxwellian distribution.  $\langle(\Delta v)^2\rangle$  can also be obtained directly by Monte Carlo simulation, as was done by Bandyopadhyay and Svizhenko [78]. Once  $\langle(\Delta v)^2\rangle$  is known, the  $1/f$  noise parameter can be calculated [79] from  $\gamma = 4\alpha/3\pi[\langle(\Delta v)^2\rangle/c^2]$ , where  $\alpha$  is the fine structure constant ( $\alpha = 1/137$ ) and  $c$  is the speed of light. The effect of the magnetic field on the  $1/f$  noise parameter was also taken into consideration. Balandin et al. [77] found that the theory gives  $\gamma$  values which are “less than or comparable to that found in three-dimensional mesoscopic samples” [77].

From the above considerations, it follows that to control the noise in a quantum wire one has to relax the energy without relaxing momentum. In the case of a bulk sample, if high energy phonons would be involved in the energy relaxation, the momentum would be relaxed too. This is due to the fact that such phonons have a high wavevector; therefore backward scattering is favored and naturally the momentum strongly relaxes. Hence, one has to look for phonons of high energy but small wavevector ( $k$ ), because they can relax energy without strongly affecting the momentum. In a quantum wire, phonon folding due to quantum confinement allows for the energy relaxation without relaxing the carrier momentum [74]. Consequently, although phonon folding increases the scattering rate, the  $1/f$  noise intensity goes down. It results that  $1/f$  noise suppression in QWR is possible and that phonon folding can be exploited in order to make quieter devices. To this purpose, bulk devices could be replaced with parallel arrays of QWR [78].

At the same time, in the presence of a magnetic field, the noise is strongly reduced especially at lower temperature and low electric field [78]. The explanation for  $1/f$  noise quenching is that magnetic field “suppresses the acoustic phonon mediated backscattering by spatially separating the wavefunctions of oppositely traveling states in a quantum wire” [77]. A disadvantage of the acoustic phonon confinement in a QWR is that it also degrades the mobility and, therefore, affects other parameters of the nanodevices. A solution could be the presence of a magnetic field. In appropriately designed QWRs or quantum wire-based nanodevices, high magnetic fields can be locally produced by inserting magnetic quantum dots of Fe, Ni, or Co [78].

## 6. NOISE IN POINT CONTACTS AND METALLIC NANOBRIDGES

Historically, the first noise measurement in mechanical point contacts (PC) was done by Hooge and Hoppenbrouwers [80, 81]. By using shear deformation in liquid helium,

Yanson et al. [82] later fabricated noble metal point contacts with the diameter ( $d$ ) smaller than the electron mean free path ( $\lambda$ ). These are much better than the “needle-anvil” pressure-type contact. Since  $d < \lambda$ , the contacts are satisfying the condition of ballistic transport regime for electrons. From the  $I$ - $V$  curve nonlinearities, the second derivatives  $d^2V/dI^2$  have been determined which, according to Yanson’s [83] point contact spectroscopy method, are the image of the Eliashberg function (phonon spectrum),  $\alpha^2F(\omega)$ . The noise spectra observed in all contacts were  $1/f$ -like. In the case of silver, no similarity was found between the Eliashberg function and the energy dependence of the noise intensity, while for copper there are some similarities but only for energies larger than the optical phonon energy (approx. 30 meV). However, in the case of the gold point contact, there is a good connection between the noise structure and the Eliashberg function, especially for longitudinal phonon peaks (see Fig. 1 of Ref. [82]).

The most interesting result found by Yanson and co-workers [82] is an oscillatory structure in the noise which is “approximately periodic in eV and independent of d.c. voltage polarity.” At higher temperature the oscillations are slightly smeared out, indicative of their spectroscopic origin. The authors assigned the structure to the coherent phonon emission, but it was also suggested that Umklapp processes, among others, could be important.

The role of Umklapp phonons was later clarified in a paper by Akimenko et al. [84]. To this purpose they have measured noise, at and below 4.2 K, in point contacts of metals with different Fermi surfaces. Point contacts with diameters between 10 and 30 nm have been prepared from Na, Cu, and Sn. For sodium contacts, the point contact phonon spectrum and the noise intensity were determined as a function of energy (eV) in all possible regimes: ballistic regime (both momentum and energy mean free path are much larger than the diameter), diffusion regime (the electrons are elastically scattered by impurities or defects), and the thermal regime (the PC properties are bulklike material). A very clear phonon spectrum was observed in the ballistic regime. At the same time, the noise featured a very well defined fine structure composed of maxima and minima. In the diffusion regime, the phonon spectrum is not essentially modified, while the noise structure is strongly smeared out. Both the phonon spectrum and the noise structure practically disappear in the thermal regime. The phonon spectrum is determined by the energy distribution function, which is the same in both ballistic and diffusion regimes. This feature explains why no differences occur between the phonon spectra in the two regimes. What is essentially different between the two regimes is the momentum distribution function. This is the reason behind the fact that strong differences exist between the noise structure in the two regimes. Therefore, the noise spectra in PC is determined “by the momentum distribution function of electrons and thus are more intimately connected with the electron-phonon scattering dynamics” [84].

By far, the most interesting phenomenon observed in the ballistic regime is the structure of minima and maxima in the noise vs.  $eV$ . No correlation between this structure and the differential resistance ( $dV/dI$ ) in all PCs has been determined; therefore the structure cannot be associated



with the resistance change. As before, the noise minima have been correlated with the phonons having wavevectors close to the Brillouin zone boundaries for the correlated emission can explain the deep noise. For sodium and copper, the noise maxima correlate well with the Umklapp phonons which assist the transitions between the Fermi surfaces in the adjacent Brillouin zones.

The noise measurements in nanometric point contacts evolved as a very fine tool to investigate the transport properties in materials. Moreover, the results of Akimenko et al. [84] show that the noise spectra are more sensitive to the crystallographic anisotropy than the PC phonon spectra because of the strong anisotropy of the nonequilibrium phonon distribution. This property can be exploited to properly design low noise nanostructures and nanodevices.

By the means of electron beam lithography and reactive ion etching, Ralls et al. [85–87] and Holweg et al. [88, 89] patterned a nanohole in a silicon nitride membrane. Evaporating metal onto both sides of the membrane, a nanobridge is formed between the two massive electrodes. A sketch of the nanobridge is presented in the inset of Figure 4. The metallic nanobridge is the microfabricated equivalent of the mechanical point contact but its mechanical and electrical stability is much better. At low temperature, the electron mean free path ( $\lambda$ ) is much larger than the diameter of the nanobridge, thus leading to ballistic transport. This is the situation that was probed by both groups of authors who found high quality point-contact phonon spectra (Eliashberg function) in investigated nanobridges. For a constriction with the radius  $a$ , the resistance  $R$  can be approximated with the relation [86]

$$R = \rho/2a + 4\rho\lambda/3\pi a^2 \quad (4)$$

where  $\rho$  is the resistivity. The first term (Maxwell) dominates the resistance in the diffusive regime, while the second one (Knudsen) is dominant in the ballistic regime ( $\lambda \geq a$ ).

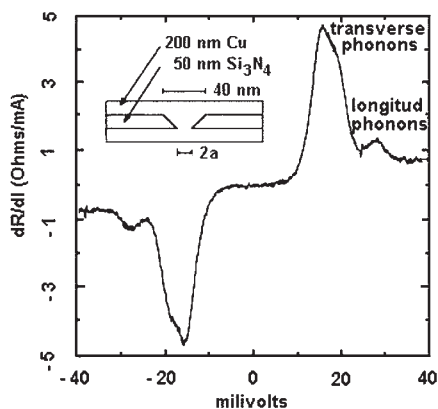


**Figure 4.** Eliashberg function (phonon spectrum) of a 15  $\Omega$  copper nanobridge, obtained by point-contact spectroscopy at 4.2 K. The spectrum is of high quality for the background signal is almost absent. The inset shows the schematic of the nanobridge, where  $a$  is the diameter of the nanoconstriction. Reprinted with permission from [85], K. S. Ralls and R. A. Buhrman, *Phys. Rev. Lett.* 60, 2434 (1988). © 1988, American Physical Society.

The last term depends only on the geometry of the constriction because  $\rho \sim 1/\lambda$ . According to the point-contact spectroscopy method [83], the derivative of  $R$  vs. applied voltage signal gives the phonon spectrum  $dR/dV \sim \alpha^2 F(\omega)$ , where the terms have their usual meaning. The phonon spectrum of a copper nanobridge, as determined by Ralls et al. [86], is shown in Figure 4. One observes that the background signal is very small and this is the proof that the nanoconstriction is of good quality.

Ralls et al. [86–88] performed detailed noise investigations on metallic nanobridges of copper, aluminum, and palladium with resistance ranging from 1 to 100  $\Omega$ , corresponding to the constriction diameter of (1.7–17) nm. The temperature dependence of the noise intensity differs from metal to metal. For instance, at temperatures below 150 K, sharp peaks in the noise were detected for copper and aluminum. They were assigned to “strategically placed defects” which give Lorentzian noise spectra. Below about 100 K, extremely rare two-level fluctuators (TLF) were observed in the Al nanobridge; therefore the noise was very small, impossible to measure. However, at about 100 K, the noise increases very sharply, one order of magnitude in about 20 K. In Pd, the metal with the highest melting point, the noise is almost temperature independent, although a close look at the data indicates some broad peaks in the noise, too. The different behavior of noise in the three metals is attributed to the “strong differences in the distribution of defect activation energies” [87]. Searching for the constituents, sometimes called fluctuators [90], of the  $1/f$  noise in metals, Ralls and Buhrman observed time trace noise signals in very small copper nanobridges at  $T < 150$  K. Usually, excess noise over the thermal noise was found only at some temperatures. The authors found that this excess noise is produced by resistance switching between two discrete levels. The amplitude of this random signal is independent of temperature and depends linearly on the applied bias, which points to the genuine resistance fluctuations. The average time ( $\tau$ ) spent in the low or high resistance state is thermally activated:  $\tau = \tau_0 \exp(E_0/kT)$ , where  $\tau_0$  is the so-called attempt time and  $E_0$  is the activation energy. For different fluctuators, the values of  $\tau_0$  were between  $10^{-11}$  and  $10^{-15}$  s, clustering around  $10^{-13}$  s, while the activation energies ranged from 30 to 300 meV. The attempt time value of  $10^{-13}$  s is characteristic for the atomic vibration in solid. From the amplitude of the resistance fluctuation  $\Delta R$ , the change in the cross section  $\Delta\sigma \sim \pi d^2(\Delta R/R)$ , where  $d$  is the constriction diameter, ranged from 0.28 to 3.6  $\text{\AA}^2$ , values of the order of atomic dimensions. Together with the values of the attempt time, the atomic dimensions of the cross scattering section point to “the individual atomic motion as the origin of this noise” [87]. Consequently, in the model elaborated by Ralls et al. TLF is generated by “reversible motion of a single defect in the constriction region between two metastable states” [87]. The above considerations show that low-frequency noise in nanobridges is not due to defect diffusion in nanoconstriction.

TLFs were also observed by Holweg et al. [89] in gold nanobridges. In both copper [86] and gold nanobridges [89], TLFs manifest at lower temperature and low bias voltages. At high voltages, many fluctuators are active and, at even higher voltages, net atomic motion (electromigration) occurs



in the sample. A consequence of the electromigration is that the average resistance changes. Different TLFs were observed in the time trace after such an event [86, 89]. The overall sample heating is excluded as a source of resistance fluctuation because of the small background signal observed in the phonon spectrum. Another reason is the asymmetry in the fluctuation rate as a function of the voltage polarity, an effect evidenced in both copper [86] and gold [89] nanobridges. A defect jumping back and forth in a double-well potential can be a source of two-level discrete resistance switching. Under the effect of the bias, the activation energy ( $E$ ) of the defect is modified,

$$E = E_0 - \zeta V \quad (5)$$

where  $\zeta$  is the electromigration parameter and  $V$  is the voltage. It was proved experimentally that for both bias polarities, the defect fluctuation rate increases, supposedly due to the fact that the temperature of the defect ( $T_d$ ) is higher than the lattice temperature ( $T$ ). Thus, one has to replace  $T$  with  $T_d$  in the expression of  $\tau$ :

$$\tau = \tau_0 [\exp(E_0 - \zeta V)/kT_d] \quad (6)$$

According to Holweg et al. [89], the local heating of the defect above lattice temperature is due to the inelastic scattering with the electrons. Under this assumption, a model, not presented here, was developed by Holweg et al. [89] which allowed for the calculation of  $T_d$ . With this expression, it was found that the relation (6) fits well the experimental dependence of the fluctuation rate in a gold nanobridge [89] in both lower and higher states of the resistance.

Ralls et al. [86] followed another way. First, from the experimental values of  $\tau_0$ ,  $E_0$ , and  $\zeta$  at low voltages  $V$ , the measured fluctuation time ( $\tau$ ) in an aluminum nanobridge was converted into an effective temperature of the defect ( $T_d$ ). Then, a model was elaborated which took into consideration the fact that the defect not only gains energy from the electrons but it can also lose energy to the lattice. They have found that the experimental data are well fitted by the theory for both bias polarities.

The effect of the lattice on the TLFs behavior in nanobridges, at large biases, was also investigated by Kozub and Rudin [91]. In this approach, the TLF is described with the help of the soft double-well potential model. Hence, the TLF behavior was investigated in terms of the interaction between the potential and the nonequilibrium phonons emitted by the ballistic (nonequilibrium) electrons. Calculating the probability for interlevel transition induced by both phonons ( $W_{ph}$ ) and the electrons ( $W_{el}$ ), they arrived at  $W_{ph} \geq W_{el}$ , which strongly supports the starting hypothesis. The analytical expression for the temperature of the defect (TLF) was finally found to fit well the bias dependence of the TLF relaxation time for aluminum, gold, and copper nanobridges. An important feature of the model is that it can explain the asymmetry of the TLF relaxation rate on bias polarity by the current flow direction-induced asymmetry in the spatial distribution of the nonequilibrium phonons. This asymmetry can be very different for normal phonons, in comparison with the Umklapp phonons.

In the theory of Kozub and Rudin [91], the role of nonequilibrium phonons is essential because they are

responsible for the activation of TLFs in nanobridges, hence for noise. Some other observations seem to further support this hypothesis. For instance, in a silver nanobridge, Holweg et al. [88] reported that the rms amplitude of the conductance starts to decrease at a bias voltage of 10 mV, which corresponds to the transverse-acoustic phonon peak in the point-contact phonon spectrum. This decreasing behavior was attributed to the phonon emission by electrons with excess energy  $eV$ . Another possible example is taken from Ralls and Buhrman [87]. They observed that noise in small resistance nanobridges—that is, “large” devices—is the same as in the bulk films deposited in the same manner. Large deviations occur for nanobridges of high resistance (small samples). To explain this, it was assumed that more active fluctuators exist in smaller samples and the cause could be the surface tension produced by the extremely small radius of curvature of the nanoconstriction. But a smaller radius can also lower the melting temperature and the activation energies for atomic motion in the nanobridge. As a consequence, they assumed that in small copper nanobridges one could get a maximum in the  $1/f$  noise intensity at a lower temperature than the one found (500 K) by Eberhard and Horn [92] for a bulk copper film. Indeed, as Figure 5 shows, for a  $7 \Omega$  ( $c \sim 6.4$  nm) nanobridge, a maximum exists at 350 K. Speculating about the origin of this peak, and in connection with the possible relationship (3) between the noise intensity and the Eliashberg function, we have tried to connect the maximum in noise with some specific phonon energies in copper [93]. In Figure 5, curve 1 represents the Eliashberg function for longitudinal phonons obtained by deconvolution of the point contact spectrum of Ralls and Buhrman (Fig. 1 from Ref. [87]) for a  $15 \Omega$  nanobridge. Its maximum at about 325 K is rather close to the noise maximum. In a better fit with the noise maximum is an Eliashberg function (curve 2 in Fig. 5) obtained by Yanson [83]

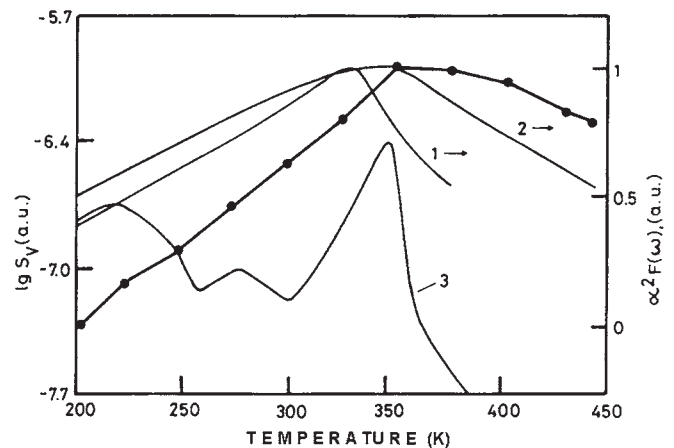


**Figure 5.** Comparison between the temperature dependence of the  $1/f$  noise spectral density ( $S_V$ ) in a  $7 \Omega$  copper nanobridge and the different Eliashberg functions: 1—from Ralls and Buhrman [85]; 2—from Yanson [83]. Curve 3 is the bulk phonon spectrum for copper calculated by Kurpick and Rahman [94]. Reprinted with permission from [93], M. Mihaila, in “Quantum  $1/f$  Noise and Other Low-Frequency Fluctuations in Electronic Devices” (P. H. Handel and A. L. Chung, Eds.), Am. Inst. Phys. Conf. Proc. Vol. 466, p. 48, American Institute of Physics, New York, 1999. © 1999, American Physical Society.

at 1.8 K for a Cu point contact of  $4 \Omega$ . It has a maximum at about 350 K, the better fit most probably due to the fact that the point-contact resistance is closer to the nanobridge resistance. Also shown in Figure 5 is the bulk phonon spectrum of Cu calculated in Ref. [94]. The highest peak, corresponding to the longitudinal phonons (30 meV), is located at the noise maximum.

As for the type of defect causing two-level resistance fluctuations, Ralls and Buhrman [87] did not get a definite answer. In any case, a single point defect is ruled out because there is no reason why interstitials, vacancies, or impurity atoms would jump between only two metastable positions. Complex time traces were found and analyzed by Ralls and Buhrman [85–87] in terms of the interactions between defects. In fact, they found that defect interaction dominates the fluctuation dynamics and it is the reason the system samples all times, which is essential for  $1/f$  noise. They conclude that there is actually no “independent defect even in crystalline films with elastic-scattering length of 200 nm” [87]. In this context, Ralls and Buhrman introduced the concept of “defect glass” as an entity composed of the defects involved, by their strong interaction, in the generation of  $1/f$  noise.

At room temperature, in both copper [87] and gold [89] nanobridges the resistance still switches but the noise spectrum changes from a Lorentzian, as it is at low temperature, to a  $1/f$ -like spectrum. Since the gold constriction is in the diffusion regime, Holweg et al. [89] calculated, from an estimation of the diffusive resistance, the  $1/f$  noise parameter ( $\gamma$ ). They obtained  $\gamma = 5.6 \times 10^{-3}$ , which is well within the domain found for other physical systems. The authors consider that this is an additional argument that  $1/f$  noise is due to the Lorentzian superposition. However, the frequency exponent of their spectrum is about 1.4, a value slightly outside the usual domain of the  $1/f$ -like frequency exponent ( $0.7 < \beta < 1.3$ ) and rather close to the specific diffusion noise exponent (3/2). A similar situation was presented by Ralls and Buhrman [87] for a copper nanobridge. In this case, the spectrum was also  $1/f$ -like, with  $\beta \approx 1.3$ . It seems that in the presence of TLFs at room temperature, the frequency exponent is always larger than 1 whereas, at low temperature, a pure TLF noise signal features a Lorentzian spectrum, as demonstrated by Holweg et al. [89]. This transition from a Lorentz spectrum to a  $1/f$ -like one is associated with the activation of many fluctuators. However, for the same physical system, the frequency exponent vs. temperature can be larger or smaller than 1, within the widely accepted values:  $0.7 \leq \beta \leq 1.3$ . At higher temperature, in the presence of TLFs, the frequency exponent tends to 1 but is consistently larger than 1. It would be interesting to see whether, in the presence of TLFs, the frequency exponent could be slightly lower than 1.

The first noise measurement in a quantum point contact (QPC) was done by Li et al. [95]. A 2D electron gas confined at the GaAs/AlGaAs heterointerface was constricted with two point-type gates (see the insert in Fig. 6). Figure 6 shows that the channel resistance ( $R$ ) has plateaus which are close (within 10%) to the theoretical quantized values ( $h/2eN$ , with  $N = 2, 3, 4$ , and 5). Below 1 kHz, the current noise spectrum  $S_I(f)$  has a  $1/f$  dependence and is described by the relation  $S_I(f) = A/f + S_{I0}$ , where  $S_{I0}$  is a white

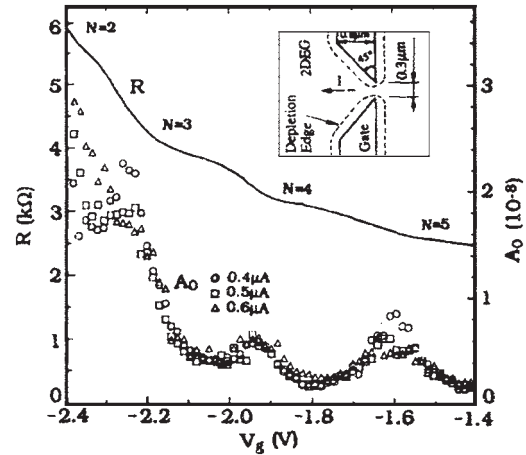


**Figure 6.** Dependence of the point contact resistance  $R$  vs.  $V_g$  and of the parameter  $A_0$  vs.  $V_g$ . The values of  $A_0$  were obtained at three currents ( $I = 0.4, 0.5$ , and  $0.6 \mu\text{A}$ ) from the fitting relation  $S_I(f) = A_0 I^2 / f + S_{I0}$ . The approximate plateaus in  $R$  are assigned to the quantized resistance  $h/2e^2 N$ , where  $N = 2, 3, 4$ , and 5. Device geometry is shown in the inset. Reprinted with permission from [95], Y. P. Li et al., *Appl. Phys. Lett.* 57, 774 (1990). © 1990, American Physical Society.

noise background. In general, when the gate voltage ( $V_g$ ) is fixed, the coefficient  $A \sim I^\alpha$ , with  $\alpha = 2 \pm 0.4$  for  $-2.4 \text{ V} < V_g < -1.4 \text{ V}$  and current  $I < 0.6 \mu\text{A}$ . A new coefficient  $A_0 = A/I^2$  was defined and represented in Figure 6 vs.  $V_g$ , for  $I = 0.4, 0.5$ , and  $0.6 \mu\text{A}$ . With some exceptions,  $A_0$  is independent of current, increases as the channel width goes down (by decreasing  $V_g$ ), and features peaks between the  $R$  plateaus. In this case, the  $1/f$  noise is correlated with the resistance quantization. The authors consider that  $1/f$  noise in the quantum point contact “may result from some processes which are related to the 1D density of states in the channel” [95]. The white noise component  $S_{I0}$  was attributed to the trapping and detrapping of the conduction electrons at the GaAs/AlGaAs interface, its intensity being, quite unexpectedly, below the full shot noise.

Low-frequency noise spectroscopy has been used to investigate the kinetics of charge transport in quantum point contacts [96, 97]. Dekker et al. [96] observed that low-frequency noise characteristics of quantum point contacts vary from device to device. For instance, in a QPC the noise spectrum was a Lorentzian, while in another one the spectrum was  $1/f$ -like and “weaker by many orders of magnitude” [96]. Although the spectra are very different, in both QPCs the normalized spectral density ( $S_V/V^2$ ), at low temperature (1.4 K), exhibits strong universal quantum size effects. Figure 7 shows that  $S_V/V^2$  vs.  $G$ , where  $G$  is the conductance in units of  $2e^2/h$ , features sharp minima at the quantized conductance plateaus, where the Fermi energy  $\epsilon_F$  is between the bottom energies  $E_n$  of two 1D subbands. The maxima in noise occur between the plateaus in  $G$ , where  $\epsilon_F = E_{n+1}$ . Attributing the quantum size effects in noise “to fluctuations in the transmission probability for the subband which is closest to cutoff,” Dekker and co-workers [97] found that  $S_V/V^2 = 1/G^2 [\partial G / \partial \epsilon_F]^2 S_{EF}$ , where  $S_{EF}$  is the spectral density of the fluctuations of Fermi energy.

The factor  $[\partial G / \partial \epsilon_F]^2 / G^2$  vs.  $G$  is shown at the bottom of Figure 7. It is evident that the universality of the

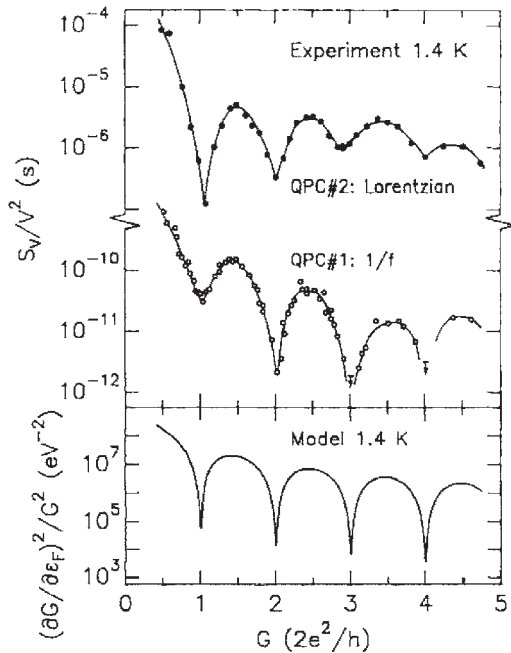


**Figure 7.** Relative noise spectral density  $S_V/V^2$  vs. conductance ( $G$ ), at 1.4 K, for two quantum point contacts: QPC1 with  $1/f$  noise spectrum (values measured at 100 Hz) and QPC2 with Lorentzian spectrum (values measured on the Lorentzian plateau). Arrows denote upper bounds. Bottom figure: calculated factor  $[\partial G/\partial \varepsilon_F]^2/G^2$  vs.  $G$ . Reprinted with permission from [96], C. Dekker et al., *Phys. Rev. Lett.* 66, 2148 (1991). © 1991, American Physical Society.

quantum size effect in noise comes from the dependence of  $S_V/V^2$  on the  $1/G^2[\partial G/\partial \varepsilon_F]^2$ . The difference between the two noise spectra resides in the fact that the discrete resistance switching (RTS noise) was observed in the QPC featuring a Lorentz noise spectrum. At high temperature ( $T > 15$  K), the RTS signal disappears and the noise spectrum changes its shape from a Lorentzian to a  $1/f$ -like one. Dekker et al. [96] explained the occurrence of the RTS noise by the presence of a single electron trap in the immediate vicinity of the point contact. Random filling and emptying of the trap modulate the electrostatic confining potential and thus the conductance of the QPC. In the presence of a strong external magnetic field, not only did the existing noise minima sharpen but additional minima were found [97]. It is an indication that a residual backscattering exists in the constriction. As in the case of QWRs, the magnetic field could be a possibility to engineer noise in QPC. The observation of Dekker et al. [96] that the disappearance of the RTS noise is accompanied by a transition from a Lorentz spectrum to a less intense  $1/f$ -like spectrum casts some doubt on the idea that RTS noise is the fundamental component of the  $1/f$  noise. The suppression of the RTS noise at the conductance plateaus has also been investigated by Timp et al. [98] and Cobden et al. [99, 100] in a one-dimensional wire (channel) using the same split-gate technique to constrict a highly conductive 2DEG. They found that the transition between two adjacent plateaus in the quantized conductance is accompanied by RTS noise. There is no RTS noise on the plateaus which signifies that “RTS is inhibited whenever an integral number of 1D subbands

are occupied” [98]. The absence of the noise on the conductance plateaus is due to the lack of scattering and this is the expression “of the insensitivity of the quantized resistance to the exact microscopic device parameters” [99]. Hence the quantum constriction “feels” the potential fluctuations induced by the presence of a defects only when the gate voltage value is between two consecutive plateaus. The defect can be located by modifying the gate voltage as done in Refs. [98, 100], but its nature is still not clear. Finally, we mention that some of the issues briefly reviewed here have also been discussed by Kogan [101].

## 7. BLINKING QUANTUM DOTS

Quantum dots (QDs) are the analogue of the real atoms because they have atomiclike energy levels. Often called “artificial atoms,” they stand as very attractive candidates for optical memories and high performance zero-dimensional devices such as optical switches, lasers, etc. At the same time the silicon single-electron quantum dot transistor operating at room temperature looks very promising for single-electron memory [102], while a quantum dot-based sensor was proposed to measure the magnetic fields at micron scale [103], to give just a few examples.

However, some of these possible applications could be affected by the fact that the luminescence of the quantum dots randomly switches between discrete levels. These are the so-called blinking quantum dots. The effect is the photoluminescence analog of the electrical RTS noise. This blinking phenomenon manifests in a variety of QDs realized from different materials [103–107]. To fully illustrate how a QD blinks, Figure 8 shows the time trace of the photoluminescence of an InP quantum dot as registered by Pistol et al. [113]. The photoluminescence switching between two or more states was attributed by Nirmal et al. [104] to QD photoionization.

Zhang et al. [106] reported the emission intermittences from II–IV ZnCdSe QDs with a diameter of about 120 Å, embedded in a ZnSe matrix. The intensity of the emission lines of the photoluminescence spectra, registered at 40 K and different time, featured sudden increases and decreases from run to run. These fluctuations qualified as “on” and,

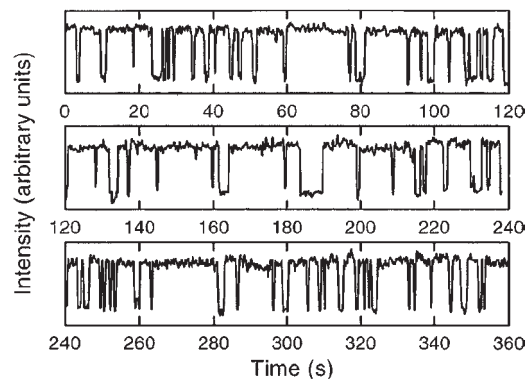


**Figure 8.** Discrete levels in the photoluminescence of an InP blinking quantum dot observed by Pistol et al. [112]. Reprinted with permission from [112], M.-E. Pistol et al., *Phys. Rev. B* 59, 10725 (1999). © 1999, American Physical Society.

respectively, “off” states “reflect the ionization and neutralization of the QDs” [106]. By decreasing the temperature the emission time became very long. This observation suggests an explanation in terms of the thermal ionization of QDs. Ionization, corresponding to the off state, can be produced either by thermal ionization or Auger scattering. In a thermal ionization process, the carriers in QDs are thermally excited over the confinement barrier into the matrix, while in an Auger process, the recombination energy of an electron–hole pair is transferred to a third particle which is ejected to the matrix. The reverse processes correspond to the “on” state. In the model proposed by Efros and Rosen [109], in the “off” state the luminescence is quenched by nonradiative Auger recombination, whereas “the durations of the off periods depends on the ionization rate of the dot via thermal or Auger autoionization” [109].

Temporal instabilities in both ground and first excited state luminescence have been observed by Bertram et al. [107] in a single strain-induced quantum dot realized in a GaAs/(AlGa)As material system. The photoluminescence spectra were extracted at 6.9 K. When registered at a given time, the ground state line was dominant, while after a few seconds, the spectral line of the first excited state took over. The effect was called two color blinking (TCB). The TCB appeared “as beating of the luminescence intensity between the ground and the excited state” [107]. No physical explanation was possible for this phenomenon. Aoki et al. [108] observed that macroscopic InGaAs clusters blink even at room temperature. The lifetimes spent by the blinking signal in both on and the off states superlinearly decreased when the excitation intensity went down. This is clear evidence that RTS noise is a many-carrier effect generated by a photoassisted process, not by a thermal one. It was suggested that the off state could be caused by nonradiative centers such as dislocations located in the InAlAs cluster. Only one from 100–1000 clusters shows RTS noise. Because the estimated average density of dislocations in a cluster was one, it resulted that not all dislocations generated RTS. Another possibility would be to have more than one dislocation in a cluster. It might be of some relevance for the above considerations to mention that burst noise, the equivalent of the RTS noise in larger devices, was quantitatively correlated with the presence of the dislocation clusters in the p–n junctions [110, 111].

Detailed investigations on the photoluminescence RTS noise in InP quantum dots were performed by Pistol et al. [112, 113]. The samples were grown on a InGaP barrier, which was lattice-matched to a GaAs substrate. The QDs were fully strained for they have been capped with a 300 nm InGaP layer. The dots were excited at 7 K with the 488 nm line of an Ar<sup>+</sup> laser or the 532 line of a YAG laser [112, 113]. Under these excitations, the QDs continuously emitted light. However, in some of them the intensity switches between two discrete levels [112] (see Fig. 8). One hundred of more than 100,000 dots exhibited RTS noise in the emission intensity. Quantum dot switching between three or even four levels have been found too [113]. Since no switching was observed at zero excitation power, it was concluded that the mechanism is induced by the excitation light. In the on state, the emission intensity vs. excitation power density is linear, while the switching rates scale superlinearly with

the power density. Hence, multiple particles are involved in the switching. For power excitation of about 50 W/cm<sup>2</sup>, the RTS disappears and the dot irreversibly remains in the on state even at reduced excitation power. The switching rates increase with both excitation power and temperature.

The results of Pistol et al. [112] for the emission spectra of a quantum dot in the on state and the off state, at different excitation power densities, are shown in Figure 9. As can be seen, the spectra are similar in both on and off state and there is no line energy shift. State filling is visible in the off state. Pistol et al. [112] observed that if the carriers are generated only in the dot and not in the barrier, RTS is still active; therefore the mechanism involved seems to be the modulation of the radiative recombination instead of the modulation of the carrier capture in the dot. Another interesting observation of Pistol [113] is that in the off state the emission lines are slightly “thiny” than in the on state, which is the signature of a lower electron concentration in the dot when in the off state. The most probable candidate to explain the effect is a competing nonradiative channel associated with a native defect in the neighborhood of the dot. The ways the dot “communicates” with the defect can be different. For instance, electric-field-assisted ionization of the dot due to a nearby charged defect is excluded because, under the influence of an electric field, no Stark shift was found in the case of a switching dot. The defect involved in the RTS noise has to be mobile; otherwise switching turn off under strong illumination conditions cannot be explained. A defect activated via phonon

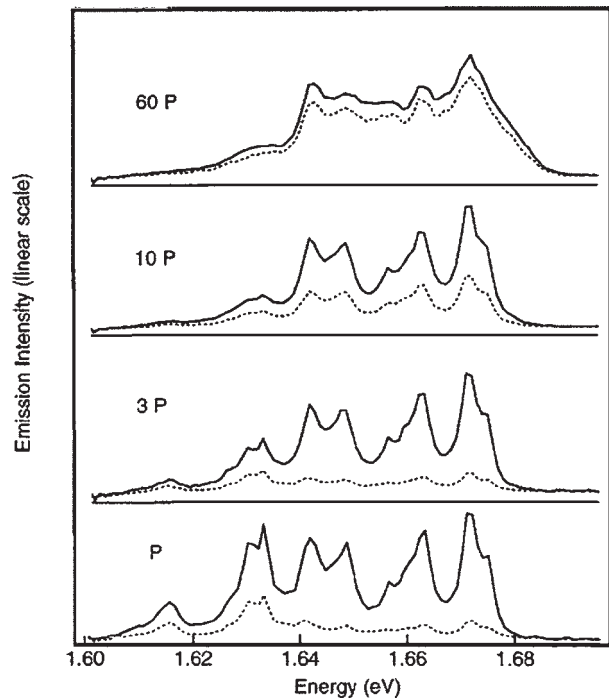


**Figure 9.** Photoluminescence spectra of a switching InP quantum dot registered by Pistol et al. [112] for different excitation power densities ( $P = 0.5 \text{ W/cm}^2$ ). Full lines correspond to the on state and dashed lines correspond to the off state. Reprinted with permission from [112], M.-E. Pistol et al., *Phys. Rev. B* 59, 10725 (1999). © 1999, American Physical Society.



emission (phonon-kick model) seems to fulfill this condition. Phonons could be generated by carrier relaxation in the dot [112]. Phonon-assisted recombination at the defect-induced deep levels would be another possibility [113]. Although the attempt of Pistol [113] to observe emitted infrared radiation failed, Sugisaki et al. [114] found that the blinking rate of a InP QD is sensitive to infrared radiation. In addition to a band-to-band excitation (Ar-ion laser), Sugisaki et al. [114] irradiated the dot with a near-infrared laser (Ti-sapphire) and observed that the switching rate is very sensitive to an infrared energy threshold of 1.5 eV. In addition, new blinking dots were triggered when the surface was intentionally scratched by a needle. They concluded that “deep defect levels with an excitation threshold energy of 1.5 eV” [114] are involved in the generation of InP QDs photoluminescence RTS noise. We mention that the phonon-activated defect model to explain RTS noise in QDs shows close resemblance to the model proposed by Kozub and Rudin [91] for the RTS noise in metallic nanobridges.

Also, fluorescence of 27 Å radius (ZnS overcoated) CdSe QDs fluctuates between two distinct levels [115]. Neither the quantum jump model nor the Auger ionization model are able to explain experimental facts [115]. Instead, an exponential distribution of traps within the semiconductor gap reasonably accounts for the probability distribution of the off state. However, for the on state this model fails to give an adequate answer. This is one of the reasons the “observed blinking kinetics is inconsistent with any static model and instead requires fluctuations in the QD environment” [115].

Genuine electrical RTS noise was observed by Peters et al. [116] in a silicon quantum dot of about 35 nm radius, placed in the channel of a deep submicron MOSFET. At liquid helium temperature and around the threshold, roughly equidistant peaks occurred in the conductance vs. gate voltage ( $V_g$ ) dependence. These Coulomb blockade oscillations are the signature of a quantum dot in the channel. Keeping the drain current constant and sweeping the gate voltage ( $V_g$ ), Peters et al. [116] observed that the drain voltage ( $V_D$ ) switches between two or more Coulomb oscillation curves. Maxima and minima were observed in the dependence of the amplitude of this RTS noise vs. gate voltage. The minima occur at the points where the two Coulomb curves cross each other. To provide an explanation for this result, the authors consider that the shift of the Coulomb curves is due to a single fluctuator which produces a fixed fluctuation,  $\Delta\Phi$ , of the dot potential  $\Phi$ , and, consequently, fluctuations  $\Delta G$  in the dot conductance  $G$ . Finally,  $\Delta G \sim \partial G / \partial V_G$ ; hence minima in  $\Delta G$  should occur where the conductance is zero. This is in good agreement with what has been experimentally found.

However, RTS noise manifested only in some “specific gate-voltage ranges.” Outside these voltage intervals, the noise was weaker and featured a  $1/f$ -like spectrum. In the ohmic region, it is a resistance fluctuation effect because its intensity has a quadratic dependence on drain current. The dependence of both normalized drain voltage noise  $fS_{VD}/V_D^2$  and  $V_D$  on gate voltage is shown in Figure 10a and b, respectively. The period of the noise variation is half that of the Coulomb oscillations. The noise is strongly suppressed at the conductance peaks and valleys. To explain this behavior, Peters et al. resorted again to the idea of

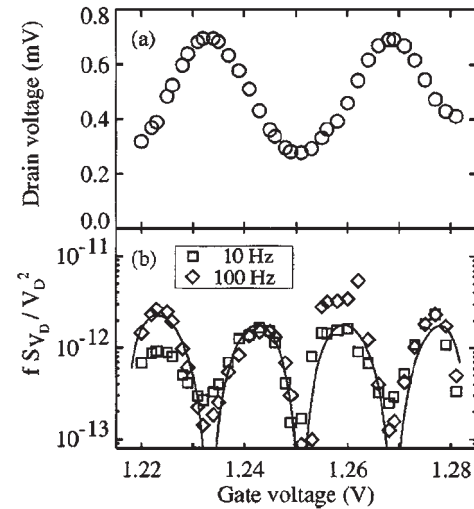


**Figure 10.** Coulomb oscillations in the drain voltage vs. gate voltage (a) and dependence of  $fS_{VD}/V_D^2$  vs. gate voltage (b) at two frequencies; the measurements were done at  $T = 1.9$  K and  $I_D = 6$  nA; the factor  $(1/V_D)^2(\partial V_D/\partial V_G)^2$  (times a constant) is presented with the full line. Reprinted with permission from [116], M. G. Peters et al., *J. Appl. Phys.* 86, 1523 (1999). © 1999, American Physical Society.

a “uniformly fluctuating potential created by a fixed distribution of fluctuators” [116]. Under this assumption, the drain spectrum  $S_{VD}$  is directly connected to the gate voltage fluctuation  $S_{Vg}$ :  $S_{VD} = (\partial V_D/\partial V_G)^2 S_{Vg}$ . Finally, the relative drain noise intensity  $fS_{VD}/V_D^2$  is described by the factor  $(1/V_D)^2(\partial V_D/\partial V_G)^2$ , which is determined from time-averaged characteristics (Fig. 10a). The authors concluded that if noise is considered “as a result of a complex superposition of an ensemble of fluctuators” its behavior can be described by a model which relies on time-averaged transport properties.

In summary, low-frequency noise phenomena in small dimensional systems such as nanotriodes, MOS transistors, single electron transistors, quantum wires, quantum dots, and nanomaterials such as nanocrystalline gold and carbon nanotubes were briefly presented.  $1/f$  noise and RTS noise are the dominating noise phenomena in nanodevices and nanomaterials. However, in nanostructures and nanodevices they could manifest in an unpredictable way, hence the difficulty to control. Small dimensional systems seem to be very noisy while, on the other hand, there is much information in the low-frequency noise. If properly interpreted, the noise can be an invaluable tool to investigate nanomaterials and nanoscaled solid-state devices. Low-frequency noise proves to be a noninvasive, inexpensive, very sensitive, subtle, and fundamental tool to characterize nanomaterials and nanostructures.

On the other side, some passages in this work brought some arguments that nanoscience could answer some longstanding questions in the field of low-frequency noise. Some of them such as topology of the  $1/f$  noise sources were in passing discussed in the light of the new phenomena observed in carbon nanotubes. Surface anharmonicity was proposed as a fundamental ingredient in the generation of  $1/f$  noise in carbon nanotubes. Through the noise measurements, the nanoscience and nanotechnology are already

paying a great tribute to the science from which they were born. And all these seem to be only the beginning. Much more is within reach.

## GLOSSARY

**Generation-recombination noise (g-r noise)** Fluctuations originating from the processes of generation and recombination in semiconductors.

**Noise spectrum** Frequency distribution function of a random signal.

**1/f noise** Fluctuations with a spectrum inversely proportional to the frequency ( $f$ ).

**Random telegraph signal (RTS) noise** Fluctuation mimicking telegraph signal and consisting of random transitions between two or more discrete levels.

**Shot noise** Fluctuations originating from the granular structure of the electrical charge.

**Thermal noise** Fluctuations originating from the random discontinuities in the motion (Brownian, m.n.) of the carriers due to their collisions with the atoms (R. E. Burgess, *British J. Appl. Phys.* 6, 185 (1955)).

## ACKNOWLEDGMENTS

The author is very grateful to Dr. Henk W. Ch. Postma for communicating some details about his noise measurement in carbon nanotubes. Many thanks are also due to Dr. Ioan Pavelescu and to Andrei-Petru Mihaila for invaluable help in preparing the manuscript.

## REFERENCES

1. R. Brown, *Philos. Mag.* 4, 161 (1928).
2. J. Perrin, "Les atoms." Paris, 1913.
3. J. B. Johnson, *Phys. Rev.* 26, 71 (1925).
4. H. D. Ellis and E. B. Moullin, *Proc. Cambridge Philos. Soc.* 28, 386 (1932).
5. C. A. Hartman, *Ann. Phys.* 65, 51 (1921).
6. A. W. Hull and N. H. Williams, *Phys. Rev.* 25, 147 (1925).
7. L. Saminadayar, D. C. Glatthi, Y. Jin, and B. Etienne, *Phys. Rev. Lett.* 79, 2596 (1997).
8. W. Schottky, *Ann. Phys.* 57, 541 (1918).
9. R. P. Jindal, in "Quantum  $1/f$  Noise and Other Low-Frequency Fluctuations in Electronic Devices" (P. H. Handel and A. L. Chung, Eds.), Vol. 282, pp. 1–7. Am. Inst. of Phys., New York, 1993.
10. R. Landauer, *Nature* 392, 658 (1998).
11. Ryder and Kirchner, *Bell Syst. Tech. J.* 28, 367 (1949).
12. J. A. Harley and T. W. Kenny, *J. Microelectromech. Syst.* 9, 226 (2000).
13. F. N. Hooge, *Phys. Lett. A* 29, 139 (1969).
14. A. Cleland and M. L. Roukes, *Nature* 392, 161 (1998).
15. A. G. Driskill-Smith, D. G. Hasko, and H. Ahmed, *J. Vac. Sci. Technol. B* 18, 3481 (2000).
16. H.-S. P. Wong, D. J. Frank, P. M. Solomon, C. H. J. Wann, and J. J. Welser, *Proc. IEEE* 87, 537 (1999).
17. A. L. McWhorter, in "Semiconductor Surface Physics" (R. H. Kingston, Ed.), p. 207. Univ. of Pennsylvania Press, Philadelphia, 1957.
18. Z.-C. Butler and P. Vasina, *Solid-State Electron.* 43, 1695 (1999).
19. E. Simoen and C. Claeys, *Solid-State Electron.* 43, 865 (1999).
20. K. S. Ralls, W. J. Skocpol, L. D. Jackel, R. E. Howard, L. A. Fetter, R. W. Epworth, and D. M. Tennant, *Phys. Rev. Lett.* 52, 228 (1984).
21. R. E. Howard, W. Skocpol, L. D. Jackel, P. M. Mankiewich, L. A. Fetter, D. M. Tennant, R. Epworth, and K. S. Ralls, *IEEE Trans. Electron Devices* ED-32, 1669 (1985).
22. M. J. Uren, D. J. Day, and M. J. Kirton, *Appl. Phys. Lett.* 47, 1195 (1985).
23. P. Restle, *Appl. Phys. Lett.* 53, 1862 (1988).
24. G. Ghibaudo, O. Roux-dit-Buisson, and J. Brini, *Phys. Status Solidi A* 132, 501 (1992).
25. J. Brini, G. Ghibaudo, G. Kamarinos, and O. Roux-dit-Boisson, in "Quantum  $1/f$  Noise and Other Low Frequency Fluctuations in Electronic Devices" (P. H. Handel and A. L. Chung, Eds.), American Institute of Physics Conference Proceedings, Vol. 282, p. 32. Am. Inst. of Physics, New York, 1993.
26. U. J. Strassilla and M. J. O Strutt, *Proc. IEEE* 62, 1711 (1988).
27. H. M. Bu, Y. Shi, X. L. Yuan, J. Wu, S. L. Gu, Y. D. Zheng, H. Majima, H. Ishikuro, and T. Hiramoto, *Appl. Phys. Lett.* 76, 3250 (2000).
28. A. van der Ziel, "Fluctuation Phenomena in Semiconductors." Butterworths Scientific, London, 1958.
29. X. L. Wu, A. van der Ziel, A. N. Birbas, and A. D. van Rheeunen, *Solid-State Electron.* 32, 1039 (1989).
30. T. G. Mapple, L. Bess, and H. A. Gebbie, *J. Appl. Phys.* 20, 490 (1955).
31. S. Martin, V. D. Archer III, D. M. Moulin, M. R. Frey, K. K. Ng, and R.-H. Yan, *Bell Labs Tech. J.* 30 (Summer 1997).
32. M. Mihaila, in "Noise in Physical Systems and  $1/f$  Fluctuations" (G. Bosman, Ed.), p. 169. World Scientific, Singapore, 2001.
33. J. H. Scofield, N. Borland, and D. M. Fleetwood, *Appl. Phys. Lett.* 76, 3248 (2000).
34. T. A. Kramer and R. F. W. Pease, <http://www.stanford.edu/~tkramer/ARLSymposium.pdf>.
35. A paraphrase of the famous and predictive R. P. Feynman's paper "There is plenty of room at the bottom," American Physical Society Meeting, Pasadena, CA, 29 December 1959; reprinted as R. P. Feynman, Infinitesimal machinery, *J. Microelectromech. Syst.* 2, 1 (1993).
36. E. Ochs, A. Seeger, H. Stoll, L. Kiss, and J. Soderlund, *Phys. Status Solidi A* 168, R9 (1998).
37. M. Mihaila, in "Noise in Oscillators and Algebraic Randomness" (M. Planat, Ed.), Lecture Notes in Physics, p. 216. Springer-Verlag, Berlin, 2000.
38. A. Kara and T. S. Rahman, *Phys. Rev. Lett.* 81, 1453 (1998).
39. P. M. Derlet, R. Meyer, L. J. Lewis, U. Stuhr, and H. Van Swygenhoven, *Phys. Rev. Lett.* 87, 205501 (2001).
40. B. Fultz, C. C. Ahn, E. E. Alp, W. Sturhahn, and T. S. Toellner, *Phys. Rev. Lett.* 79, 937 (1997).
41. U. Stuhr, H. Wipf, K. H. Andersen, and H. Hahn, *Phys. Rev. Lett.* 81, 1449 (1998).
42. B. Wassermann and K.-H. Rieder, *Phys. Rev. Lett.* 88, 045501 (2002).
43. F. Otten, L. B. Kish, C. G. Granquist, L. K. J. Vandamme, R. Vajtai, F. E. Kruis, and H. Fissan, *Appl. Phys. Lett.* 77, 3421 (2000).
44. A. van der Ziel, "Noise in Solid State Devices and Circuits." Wiley, New York, 1986.
45. L. B. Kish, F. Otten, L. K. J. Vandamme, R. Vajtai, C. G. Granquist, B. Marlow, E. Kruis, H. Fissan, J. Ederth, and P. Chaouang, *Phys. E* 11, 131 (2001).
46. A. Hoel, L. K. J. Vandamme, L. B. Kiss, E. Olsson, and Gy. Trefan, in "Noise in Physical Systems and  $1/f$  Fluctuations" (G. Bosman, Ed.), p. 755. World Scientific, Singapore, 2001.
47. Philip Collins, M. S. Fuhrer, and A. Zettl, *Appl. Phys. Lett.* 76, 894 (2000).



48. S. Roumiantsev, R. Vajtai, N. Pala, B. Q. Wey, M. S. Shur, L. B. Kiss, and P. M. Ajayan, in "Proceedings of the Ninth International Symposium on Nanostructure: Physics and Technology" (Z. Alferov, L. Esaki, and L. Solovyova, Eds.), St. Petersburg, 2001, p. 418.
49. M. Mihaila and A.-P. Mihaila, in "Noise in Physical Systems and  $1/f$  Noise" (C. Claeys and E. Simoen, Eds.), p. 51. World Scientific, Singapore, 1997.
50. H. W. Ch. Postma, T. F. Teepen, Z. Yao, and C. Dekker, in "Electronic Correlations: From Meso- to Nanophysics" (T. Martin, G. Montanboux, and J. Trần Thanh Vân, Eds.) EDP Sciences, 2001, France.
51. H. W. Ch. Postma, private communication, February 2002.
52. M. Templeton and D. K. C. MacDonald, *Proc. Phys. Soc. London Ser. B* 66, 680 (1953).
53. D. M. Fleetwood, T. Postel, and N. Giordano, *J. Appl. Phys.* 56, 3256 (1984).
54. P. Kim, L. Shi, A. Majumdar, and P. L. McEuen, *Phys. Rev. Lett.* 87, 215502-1 (2001).
55. M. Osman and D. Srivastava, *Nanotechnology* 12, 21 (2001).
56. H. Ouacha, M. Willander, H. Y. Yu, Y. W. Park, M. S. Kabir, S. H. Magnus Persson, L. B. Kish, and A. Ouacha, *Appl. Phys. Lett.* 80, 1055 (2002).
57. M. Mihaila, A. Stepanescu, and A. Masoero, in "Noise in Physical Systems and  $1/f$  Fluctuations" (V. Bareikis and R. Katilius, Eds.), p. 307. World Scientific, Singapore, 1995.
58. M. Mihaila and A.-P. Mihaila, in "Unsolved Problems of Noise" (Ch. Doering, L. B. Kiss, and M. F. Shlesinger, Eds.), p. 81. World Scientific, Singapore, 1997.
59. S. Rols, Z. Benes, E. Anglaret, J. L. Sauvajol, P. Papanek, J. E. Fisher, G. Coddens, H. Schober, and A. J. Dianoux, *Phys. Rev. Lett.* 85, 591 (1999).
60. K. K. Likharev, *Proc. IEEE* 87, 606 (1999).
61. H. Ahmed, *J. Vac. Sci. Technol. B* 15, 2101 (1997).
62. G. Zimmerli, T. M. Eiles, R. L. Kautz, and J. M. Martinis, *Appl. Phys. Lett.* 61, 237 (1992).
63. E. H. Visscher, S. M. Verbrugh, J. Lindeman, P. Hadley, and J. E. Mooij, *Appl. Phys. Lett.* 66, 305 (1995).
64. S. M. Verbrugh, M. L. Benhamadi, E. H. Visscher, and J. E. Mooij, *J. Appl. Phys.* 78, 2830 (1995).
65. A. B. Zorin, F.-J. Ahlers, J. Niemeyer, T. Weimann, H. Wolf, V. A. Krupenin, and S. V. Lotkhov, *Phys. Rev. B* 53, 13682 (1996-II).
66. N. M. Zimmerman, J. L. Cobb, and A. F. Clark, *Phys. Rev. B* 56, 7675 (1997-II).
67. A. N. Tavkhelidze and J. Mygind, *J. Appl. Phys.* 83, 310 (1998).
68. V. A. Krupenin, D. E. Presnov, H. Scherer, A. B. Zorin, and J. Niemeyer, *J. Appl. Phys.* 84, 3212 (1998).
69. A. Starmark, T. Henning, T. Claeson, P. Delsing, and A. N. Korotkov, *J. Appl. Phys.* 86, 2132 (1999).
70. M. Kenyon, C. J. Lobb, and F. C. Wellstood, *J. Appl. Phys.* 88, 6536 (2000).
71. M. Ahlskog, R. Tarkiainen, L. Roschier, and P. Hakonen, *Appl. Phys. Lett.* 77, 4037 (2000).
72. L. Roschier, R. Tarkiainen, M. Ahlskog, M. Paalanen, and P. Hakonen, *Appl. Phys. Lett.* 78, 3295 (2001).
73. H. W. Ch. Postma, T. Teepen, Z. Yao, M. Grifoni, and C. Dekker, *Science* 293, 20010 (2001).
74. B. K. Ridley, "Electrons and Phonons in Semiconductor Multilayers." Cambridge Univ. Press, Cambridge, UK, 1997.
75. F.-W. Yan, X.-J. Li, W.-J. Zhang, R.-G. Zhang, W.-J. Liu, J.-P. Ao, C.-G. Liang, and S.-Y. Liu, *Appl. Phys. Lett.* 78, 2793 (2001).
76. Y. Sugiyama, T. Sugaya, S. Kim, T. Nakagawa, M. Ogura, and M. Tacano, in "Noise in Physical Systems and  $1/f$  Fluctuations" (Ch. Surya, Ed.), p. 237. Bentham Press, London, 1999.
77. A. Balandin, K. L. Wang, A. Svizhenko, and S. Bandyopadhyay, *IEEE Trans. Electron Devices* ED-46, 1240 (1999).
78. S. Bandyopadhyay and A. Svizhenko, in "Eight A. van der Ziel Symposium on Quantum  $1/f$  Noise and Other Low-Frequency Fluctuations" (P. H. Handel and A. L. Chung, Eds.), American Institute of Physics Conference Proceedings, in press.
79. P. H. Handel, *IEEE Trans. Electron Devices* ED-41, 2023 (1994).
80. F. N. Hooge and A. M. H. Hoppenbrouwers, *Phys. Lett. A* 29, 642 (1969).
81. F. N. Hooge, *Phys. B/C* 83, 14 (1976).
82. K. Yanson, A. I. Akimenko, and A. B. Verkin, *Solid-State Comm.* 43, 765 (1982).
83. Y. K. Yanson, *Sov. Phys. JETP* 39, 506 (1974).
84. A. I. Akimenko, I. K. Yanson, and A. B. Verkin, *J. Low-Temp. Phys.* 54, 247 (1984).
85. K. S. Ralls and R. A. Buhrman, *Phys. Rev. Lett.* 60, 2434 (1988).
86. K. S. Ralls, D. C. Ralph, and R. A. Buhrman, *Phys. Rev. B* 40, 11561 (1989-I).
87. K. S. Ralls and R. A. Buhrman, *Phys. Rev. B* 44, 5800 (1991-I).
88. P. A. M. Holweg, J. A. Kokkedee, J. Caro, A. H. Verbruggen, S. Radelaar, A. G. M. Jansen, and P. Wyder, *Phys. Rev. Lett.* 67, 2549 (1991).
89. P. A. M. Holweg, J. Caro, A. H. Verbruggen, and S. Radelaar, *Phys. Rev. B* 45, 9311 (1992-II).
90. C. T. Rogers and R. A. Buhrman, *Phys. Rev. Lett.* 53, 1272 (1984).
91. V. I. Kozub and A. M. Rudin, *Phys. Rev. B* 47, 13737 (1993-II).
92. J. W. Eberhard and P. M. Horn, *Phys. Rev. B* 18, 6681 (1978).
93. M. Mihaila, in "Quantum  $1/f$  Noise and Other Low-Frequency Fluctuations in Electronic Devices" (P. H. Handel and A. L. Chung, Eds.), American Institute of Physics Conference Proceedings, Vol. 466, p. 48. Am. Inst. of Phys., New York, 1999.
94. U. Kurpick and T. R. Rahman, in "Surface Diffusion: Atomistic and Collective Processes" (M. Tringides, Ed.), NATO ASI Ser. B: Physics, Vol. 360, p. 389. Plenum, New York, 1997.
95. Y. P. Li, D. C. Tsui, J. J. Heremans, J. A. Simmons, and G. W. Weimann, *Appl. Phys. Lett.* 57, 774 (1990).
96. C. Dekker, A. J. Scholten, F. Liefink, R. Eppenga, H. van Houten, and C. T. Foxon, *Phys. Rev. Lett.* 66, 2148 (1991).
97. F. Liefink, A. J. Scholten, C. Dekker, R. Eppenga, H. van Houten, and C. T. Foxon, *Phys. B* 175, 273 (1991).
98. G. Timp, R. E. Behringer, and J. E. Cunningham, *Phys. Rev. B* 42, 9259 (1990).
99. A. H. Cobden, N. K. Patel, M. Pepper, D. A. Ritchie, J. E. F. Frost, and G. A. C. Jones, *Phys. Rev. B* 44, 1938 (1991-II).
100. A. H. Cobden, A. Savchenko, M. Pepper, N. K. Patel, D. A. Ritchie, J. E. F. Frost, and G. A. C. Jones, *Phys. Rev. Lett.* 69, 502 (1992).
101. Sh. Kogan, "Electronic Noise and Fluctuations in Solids." Cambridge Univ. Press, Cambridge, UK, 1996.
102. L. Zhuang, L. Guo, and S. Y. Chou, *Appl. Phys. Lett.* 72, 1205 (1998).
103. M. Switkes, A. G. Huibers, C. M. Marcus, K. Campman, and A. C. Gossard, *Appl. Phys. Lett.* 72, 471 (1998).
104. M. Nirmal, B. O. Dabbousi, M. G. Bawendi, J. J. Macklin, J. K. Trautman, T. D. Harris, and L. E. Brus, *Nature* 383, 802 (1996).
105. S. A. Empedocles, D. J. Norris, and M. G. Bawendi, *Phys. Rev. Lett.* 77, 3873 (1996).
106. B. P. Zhang, Y. Q. Li, T. Yasuda, W. X. Wang, Y. Segawa, K. Edamatsu, and T. Itoh, *Appl. Phys. Lett.* 73, 1266 (1998).
107. D. Bertram, M. C. Hanna, and A. J. Nozik, *Appl. Phys. Lett.* 74, 2666 (1999).
108. T. Aoky, Y. Nishikawa, and M. Kuwata-Gonokami, *Appl. Phys. Lett.* 78, 1065 (2001).

109. Al. L. Efros and M. Rosen, *Phys. Rev. Lett.* 78, 1110 (1997).
110. M. Mihaila, "Extended Abstracts of the Electrochemical Society Fall Meeting," Detroit, 1982, Abstract 239.
111. M. Mihaila, K. Amberiadis, and A. van der Ziel, *Solid-State Electron.* 27, 675 (1984).
112. M-E. Pistol, P. Castrillo, D. Hessman, J. A. Prieto, and L. Samuelson, *Phys. Rev. B* 59, 10725 (1999-II).
113. M.-E. Pistol, *Phys. Rev. B* 63, 113905 (2001).
114. M. Sugisaki, H.-W. Ren, S. V. Nair, J.-S. Lee, S. Sugou, T. Okuno, and Y. Masumoto, *J. Lumin.* 87-89, 40 (2000).
115. M. Kuno, D. P. Fromm, H. F. Hamann, A. Gallagher, and D. J. Nesbitt, *J. Chem. Phys.* 115, 1028 (2001).
116. M. G. Peters, J. I. Dijkhuis, and L. W. Molenkamp, *J. Appl. Phys.* 86, 1523 (1999).

# Low-Temperature Scanning Tunneling Microscopy

Wolf-Dieter Schneider

*Ecole Polytechnique Fédérale de Lausanne, Lausanne, Switzerland*

## CONTENTS

1. Introduction
  2. Experimental
  3. Magnetic Adatoms
  4. Surface States
  5. Supramolecular Self-Assembly
  6. Clusters
  7. Specific Nanostructures
  8. Conclusion
- Glossary  
References

## 1. INTRODUCTION

Nearly half a century ago, on December 29, 1959, Richard P. Feynman gave a visionary talk at the annual meeting of the American Physical Society, entitled *There is Plenty of Room at the Bottom* [1]. It was an invitation to enter a new field of physics, the problem of manipulating and controlling things on a very small scale, the nanoscale. Feynman was not afraid to consider the final question as to whether, ultimately—in the great future—we can arrange the atoms the way we want, the very atoms, all the way down! What would happen if we could arrange the atoms one by one the way we want them. . . The principles of physics do not speak against the possibility of maneuvering things atom by atom. It is not an attempt to violate any laws, it is something, in principle, that can be done, but, in practice, it has not been done because we are too big. . .

*When we get to the very, very small world—circuits of seven atoms—we have a lot of new things that would happen that represent completely new opportunities for design. Atoms on a small scale behave like nothing on a large scale, for they satisfy the laws of quantum mechanics. So, as we go down and fiddle around with the atoms down there, we are working with different laws, and we can expect to do different things. We can manufacture in different ways. We can use, not just circuits, but some system involving the quantized energy levels, or the*

*interactions of quantized spins, etc. . . At the atomic level, we have new kinds of forces and new kinds of possibilities, new kind of effects. . .*

*But it is interesting that it would be, in principle, possible for a physicist to synthesize any chemical substance that the chemist writes down. Give the orders and the physicist synthesizes it. How? Put the atoms down where the chemist says, and so you make the substance. The problems of chemistry and biology can be greatly helped if our ability to see what we are doing, and to do things on an atomic level, is ultimately developed—a development which cannot be avoided.*

In 1981 the vision of Feynman became closer to reality with the invention of the scanning tunneling microscope (STM) by G. Binnig, H. Rohrer, Ch. Gerber, and E. Weibel [2, 3]. They describe their invention as follows [3]. *The principle of the STM is straightforward. It consists essentially in scanning a metal tip over a the surface at constant tunnel current as shown in Figure 1. The displacements of the metal tip given by the voltages applied to the piezodrives then yield a topographic picture of the surface. The very high resolution of the STM rests on the exponential dependence of the tunnel current on the distance between the two tunnel electrodes, i.e., the metal tip and the scanned surface.*

Subsequently the STM and its numerous descendents have become the natural tool for investigations on the atomic scale. This instrument has allowed us to perceive individual atoms on surfaces and it was realized that the tip of the STM is a very versatile instrument, not only for imaging, but also for manipulation of individual atoms.

The first experiment to show a stunning realization of the atom-by-atom construction of artificial, man-made nanostructures in the spirit of Feynman was performed in 1990 by D. M. Eigler and E. K. Schweizer [4]. Using a scanning tunneling microscope operated at a temperature of 4 K, they were able to position Xe atoms on a single-crystal Ni surface with atomic-scale precision. This capability allowed the authors to fabricate structures of their own design, a linear cluster of 7 Xe atoms and the letters IBM consisting of 35 Xe atoms, atom by atom.

The last sentence in their publication *The prospect of atomic scale logic circuits is a little less remote* indicated the research direction which led to the realization of an

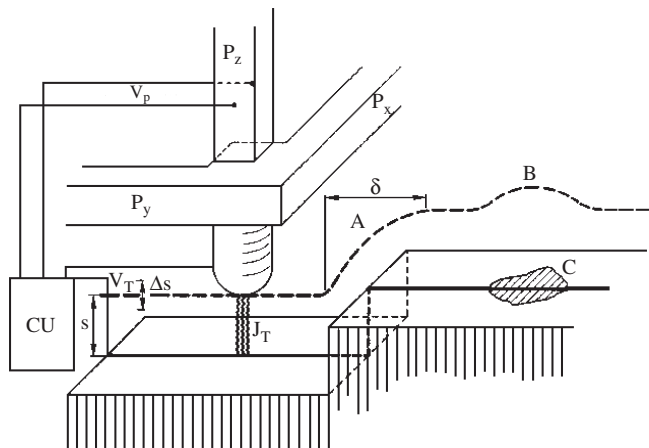


**Figure 1.** Principle of operation of the scanning tunneling microscope. (Schematic: distances and sizes are not to scale.) The piezodrives  $P_x$  and  $P_y$  scan the metal tip  $M$  over the surface. The control unit (CU) applies the appropriate voltage  $V_p$  to the piezodrive  $P_z$  for constant tunnel current  $J_T$  at constant tunnel voltage  $V_T$ . The broken line indicates the  $z$  displacement in a  $y$  scan at (A) a surface step and (B) a contamination spot, C, with lower work function. Reprinted with permission from [3], G. Binnig et al., *Phys. Rev. Lett.* 49, 57 (1982). ©1982, American Physical Society.

atomic switch realized with the STM [5] just one year later. The authors report the operation of a bistable switch which derives its function from the motion of a single Xe atom which is moved by applying a voltage pulse of the appropriate sign reversibly between two stable positions on the STM tip and on a Ni surface. The state of the switch was identified by measuring the conductance across the leads.

Most recently, A. J. Heinrich et al. [6] made a breakthrough in realizing atomic-scale circuits: nanometer-scale computation by cascades of molecular motion. They present a scheme in which all of the devices and interconnects required for the one-time computation of an arbitrary logic function are implemented by atomically precise arrangements of CO molecules bound to a Cu(111) surface. The motion of one molecule causes a nearby molecule to hop to a new site, which in turn moves another molecule in a cascade of motion similar to a row of toppling dominoes. They used a low-temperature STM to assemble and demonstrate a three-input sorter that uses several AND gates and OR gates. The most exciting feature of these molecular cascades is their size: a three-input sorter implemented in next generation CMOS technology requires an area of  $53 \mu\text{m}^2$ , while the cascade implementation uses only  $200 \text{nm}^2$ , an area 260,000 times smaller.

Feynman's dream of *put the atoms down where the chemist says, and so you make the substance* has also been realized very recently. Hla et al. [7] write in their abstract: *All elementary steps of a chemical reaction have been successfully induced on individual molecules with an STM in a controlled step-by-step manner utilizing a variety of manipulation techniques. The reaction steps involve the separation of iodine from iodobenzene by using tunneling electrons, bringing together two resultant phenyls mechanically by lateral manipulation and, finally, their chemical association to form a biphenyl molecule mediated by excitation with tunneling electrons. The procedures presented here constitute an important step towards the assembly*

*of individual molecules out of simple building blocks in-situ on the atomic scale.*

These few prominent examples from the nanoscale research laboratory set the scene for the present chapter. We have chosen to review recent advances in low-temperature scanning tunneling spectroscopy and microscopy of atoms, molecules, supermolecules, clusters, and islands on mostly metallic surfaces which have provided new opportunities for investigating locally and individually the geometric, electronic, optical, and magnetic properties of nanostructures on surfaces, created by manipulation with the STM tip (artificial nanostructures) or by self-assembly (diffusion and growth). The emphasis is on the discovery of new phenomena characteristic for the nano- and subnanometer scale. This choice was motivated by the fascination emerging from different aspects of local spectroscopies and microscopies documented by recent research highlights, the observation of, for example, light emission from single molecules and clusters [8–12], surface electron standing wave patterns at steps, quantum corrals, islands, and impurities [13–23], the Kondo effect of single magnetic adatoms and clusters [24–26], the quantum mirage [26], the observation of the Abrikosov flux lattice and the density of states near and inside a fluxoid [27–29], the local pair-breaking effects of magnetic impurities on superconductivity [30], the effect of individual impurity atoms on the superconductivity in a high-temperature superconductor [31], self-assembly phenomena of adsorbed molecules forming supramolecular structures [32–37], the formation of surface-supported supramolecular structures whose size and aggregation patterns are controlled by tuning the non-covalent interactions between individual adsorbed molecules [38], insulators at the ultrathin limit [39], spin-resolved tunneling determining magnetic properties of nanostructures [40–43], single-molecule vibrational spectroscopy [44], single-bond formation with an STM [45], chemical reactions on the nanoscale [7], manipulation of single atoms, molecules and clusters on surfaces including lateral movement, vertical transfer, and dissociation [4, 33, 46–57], nanometer-scale computation by cascades of molecular motion [6]. The cited examples clearly demonstrate that we are now able to construct, to image, to characterize, and, to some extent, to functionalize artificial man-made nanoscale objects.

These and related achievements with other scanning probe methods, for example, the atomic force microscope (AFM) [58], made it possible to give a definition for the emerging field of nanotechnology [59]. *Nanotechnology is the creation and utilization of materials, devices, and systems through control of matter on the nanometer-length scale, that is at the level of atoms, molecules, and supramolecular structures. The essence of nanotechnology is the ability to work at these levels to generate larger structures with fundamentally new molecular organizations. These nanostructures, made with building blocks understood from first principles are the smallest human-made objects, and they exhibit novel physical, chemical, and biological properties and phenomena. The aim of nanotechnology is to learn to exploit these properties and efficiently manufacture and employ the structures.*

As STM and STS have now become mature research tools for the nanoworld, there exist already a selection of books and review articles in the literature, treating both technical aspects and scientific subjects [60–70]. Especially

the proceedings of the series of *International Conferences on Scanning Tunneling Microscopy/Spectroscopy and Related Techniques*, which were organized in Santiago de Compostela (Spain) in 1986, Oxnard (USA) in 1987, Oxford (UK) in 1988, Oarai (Japan) in 1989, Baltimore (USA) in 1990, Interlaken (Switzerland) in 1991, Beijing (China) in 1993, Snow Mass Valley (USA) in 1995, Hamburg (Germany) in 1997, Seoul (South Korea) in 1999, Vancouver (Canada) in 2001 give an excellent account on the progress made in the field. The interested reader will find a wealth of valuable information in these publications which provide a good starting point to enter the field.

The present chapter is organized as follows. In Section 2, typical state-of-the-art setups of a low-temperature STM in ultrahigh vacuum and the different modes for scanning tunneling microscopy and spectroscopy including electrons and photons as probes are outlined. Subsequently, in Section 3, results on single, supported atoms concerning the Kondo effect are presented. In Section 4, the lifetime of surface state electrons is addressed and standing wave phenomena due to the scattering of surface state electrons at islands, steps, corrals, and other quantum well structures on the (111) surfaces of noble metals are reviewed. Section 5 deals with adsorbed molecules and two-dimensional supramolecular self-assembly. Section 6 summarizes the knowledge obtained on individual molecular and metal clusters. Section 7 discusses the dielectric and magnetic properties of nanostructures, with a brief account on vortices of magnetic flux lattices in classic and high-temperature superconductors. Finally, Section 8 presents a short summary and an outlook for the field.

## 2. EXPERIMENTAL

At low temperatures, due to the reduced broadening of the Fermi level of the STM tip and the sample, an energy resolution from the meV down to the  $\mu\text{eV}$  range in scanning tunneling spectroscopy (STS) is achievable. Moreover, the absence of surface diffusion together with the spatial resolution of the STM enables detailed studies of electronic states on and near single adsorbed atoms, molecules, clusters, and other nanoscale structures [69].

Typical low-temperature ultrahigh-vacuum (UHV) STMs [4, 25, 41, 71–86] operate at a pressure of  $10^{-11}$  mbar and employ temperatures down to 4 K and 1.3 K. In some of these low-temperature STMs, magnetic fields are applied in the tip-sample region [85–87] and, in addition, luminescence measurements are carried out [87]. More recently, a few new instrumental developments towards the millikelvin range using a dilution refrigerator [88] or a  $^3\text{He}$  refrigerator [6, 89, 90] with magnetic fields up to 7 and 11 Tesla in the tunnel junction have been reported. As STM tip material, usually, electrochemically etched W, Pt, or Ir tips were prepared in UHV by heating and rare-gas ion bombardment.

Information of the local density of states (LDOS) [91] is generally obtained by measuring the differential conductance  $dI/dV$  versus the sample bias voltage  $V$  performed under open feedback loop conditions with lock-in detection; see, for example, [13]. Constant-current topographs very close to the Fermi level have been shown to correspond to the LDOS of the sample surface [13]. Moreover,

simultaneously spectroscopic ( $dI/dV$ ) and constant-current images are acquired [26]. For recording spectra on, for example, semiconductors or ultrathin insulators, over wide voltage intervals, the tip-sample separation is varied continuously during the voltage sweep in different modes, (i) by a linear ramp [92], (ii) by keeping constant either the tunnel current or (iii) the tunnel resistance. In these modes, band onsets naturally appear as peaks [93, 94].

The tip-surface region of an STM emits light when the energy of the tunneling electrons is sufficient to excite luminescent processes [95]. Photons emitted from the tunneling gap are collected by a lens [8, 10] or a parabolic mirror [9] and transmitted through a sapphire viewport. Outside the vacuum chamber these photons are refocused onto an optical fiber leading to a cooled multi-alkali photomultiplier which is operated in a pulse counting mode. The count-rate is recorded by the STM electronics quasi-simultaneously with the acquisition of constant-current topographs for each image pixel [8, 11]. For spectroscopic measurements the light is focused outside the vacuum chamber onto the slit of a UV/visible-grating spectrograph and detected with a liquid nitrogen cooled CCD camera [9, 11, 96, 97].

## 3. MAGNETIC ADATOMS

The STM has been used to perform local spectroscopy with atomic-scale resolution in a study of Fe atoms on a clean Pt(111) surface [98]. Resonances of 0.5 eV width were found in the adatom local density of states above the Fermi level. Characteristic circular standing wave patterns around single adatoms have been detected in spatially resolved spectroscopic STM images [13, 14, 16, 18, 99]. Recently the local pair-breaking effects of a single magnetic adatom on a classical superconductor have been observed with scanning tunneling spectroscopy [30]. In what follows, the effects of magnetic and nonmagnetic adatoms on the LDOS of noble metal surfaces are reviewed. In particular, a depletion of the LDOS near the Fermi energy, which occurs for magnetic adatoms only, is interpreted in terms of Kondo scattering.

The interaction of a single magnetic impurity with the conduction electrons of its nonmagnetic metallic host gives rise to unconventional phenomena in magnetism, transport properties, and the specific heat. As the temperature approaches  $T = 0$  K, the local moment is gradually screened by the conduction electrons of the metal host and a many-body nonmagnetic singlet ground state is formed close to the Fermi energy. These low-energy excitations with a characteristic width of  $\delta = kT_K$  ( $T_K$  is the Kondo temperature and  $k$  the Boltzmann constant) are known as Abrikosov–Suhl [101, 102] or Kondo resonance [103–108]. High-resolution photoelectron spectroscopy (PES) provided direct experimental evidence of such a resonance [109–111]. However, a direct observation of the Kondo effect from a single magnetic impurity on an atomic length scale was achieved only recently in STM and STS experiments [24–26].

In the first experiment, magnetic Ce adatoms on a single-crystal Ag(111) surface were chosen to represent a typical Kondo system [24, 107, 110, 111]. Isolated Ce atoms and, for comparison, isolated Ag atoms on Ag(111) were deposited by evaporation from a tungsten filament onto the Ag substrate at  $T = 5$  K. The adatoms appear as protrusions with  $\approx 0.9$  Å and  $\approx 1.2$  Å height for Ag and Ce, respectively,

with typical widths of  $\approx 15 \text{ \AA}$  in constant-current topographs taken at a tunneling resistance of a few hundred  $M\Omega$ . Figure 2b displays a  $dI/dV$  tunneling spectrum measured on top of an isolated Ce adatom. A depression is observed in  $dI/dV$  around the Fermi energy. When the tip is moved laterally, the typical spectrum of the Ag(111) surface state onset (for Au(111) and Cu(111) see [13, 113, 114]) at  $E \cong -70 \text{ meV}$  reappears (Fig. 2e) [19, 115]. At intermediate distances (Fig. 2c,d) the surface state edge broadens reflecting a decreased hot-hole lifetime due to scattering of surface state electrons at the impurity [134]. The weak spectral features above the onset of the surface state are due to standing wave patterns caused by scattering at the adatoms [15, 19, 99]. These energy-resolved Friedel oscillations [114] are also visible in space [13–16] as weak circular waves around the adatoms (see Section 4).

The tunneling spectra of a single adsorbed Ag atom (Fig. 2a) are featureless throughout the range from  $-200 \text{ mV}$  to  $200 \text{ mV}$  which is attributed to quenching of the Ag(111) surface state [19]. These data indicate that the dip near the Fermi energy  $E_F$  is indeed characteristic of the magnetic Ce adatom.

The authors of [24] offered an explanation for the existence of an antiresonance in the tunneling spectra as opposed to the resonance predicted by theory [116] and measured by photoemission for similar systems [111, 117]. The probing of a localized state immersed in a continuum by the tunneling microscope resembles the spectroscopy of a discrete autoionized state, treated by Fano [118]. When the transition matrix element for the localized state approaches zero, the autoionization spectrum shows an antiresonance as a consequence of the interference effects at the site with the localized state. At the usual tip-surface distances, the STM is known to probe  $sp$  wave functions rather than the confined

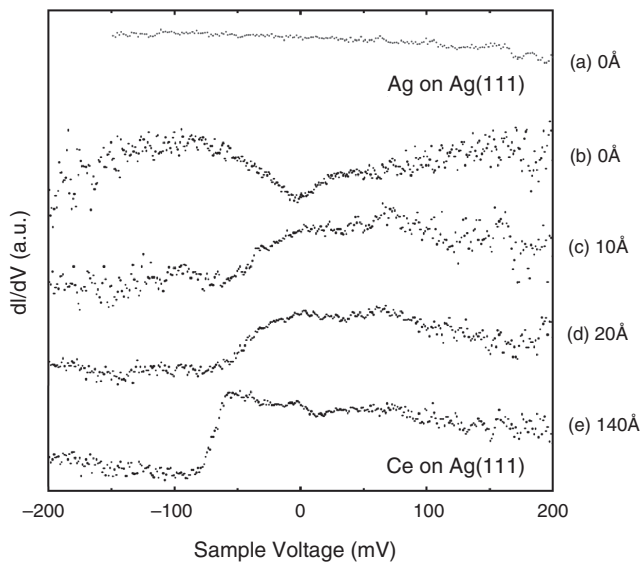


**Figure 2.**  $dI/dV$  spectra on (a) a single Ag adatom and (b)–(e) on and near a single Ce adatom at  $T = 5 \text{ K}$ . The lateral distance between the tip position and the center of the adatom is indicated. Before opening the feedback loop the tunnel parameters were  $V = 200 \text{ mV}$ ,  $I = 0.1 \text{ nA}$ . Reprinted with permission from [24], J. Li et al., *Phys. Rev. Lett.* 80, 2893 (1998). ©1998, American Physical Society.

$4f$  core-levels [119]. Thus, the  $dI/dV$  spectrum should show an antiresonance instead of a  $f$ -spectral peak as observed experimentally. By approximating the Fano dip shape by the inverse non-crossing-approximation (NCA) [117, 120] resonance [24], the lineshape in Figure 3 (solid curve) is obtained, in agreement with the experimental observations (dots). The width of the Kondo antiresonance obtained from the NCA calculation for the single isolated Ce impurity on Ag(111) (Fig. 3 (solid curve)) is  $\delta = kT_K = 25(5) \text{ meV}$  yielding a Kondo temperature of  $T_K = 290(50) \text{ K}$  which is considerably lower than the value of  $1000 \text{ K}$  found for bulk  $\alpha$ -Ce [107, 111]. This result is consistent with the expected decrease in hybridization with decreasing Ce coordination.

These findings and the interpretation within the Fano picture have been corroborated by related STS observations of Co atoms on Au(111) [25, 121] (see Figs. 4 and 5) and on Cu(111) [26]. Recent experiments [122] on Co adatoms on Cu(111) and Cu(100) have detected a scaling of the Kondo temperature with the host electron density at the magnetic impurity. Furthermore, a quantitative analysis of the tunneling spectra revealed that the Kondo resonance is dominated by the volume density of states. The same group observed the scattering phase shift of isolated Co impurities at the surfaces of Ag(111) [123].

A disappearance of the Kondo resonance for atomically fabricated Co dimers (i.e., by manipulation with the STM tip) on Au(111) has been reported and was explained as the result of reduced exchange coupling between Au conduction electrons and ferromagnetic cobalt dimers [124]. Recently, this group investigated the temperature-dependent electronic structure of isolated Ti atoms on Ag(100) [125]. They find that the Kondo resonance is strongly broadened when the temperature is increased, confirming the role of electron-electron scattering as the main thermal broadening mechanism.

The interaction of magnetic impurities with electrons confined in one dimension has been studied recently by spatially resolving the local electronic density of states of small Co

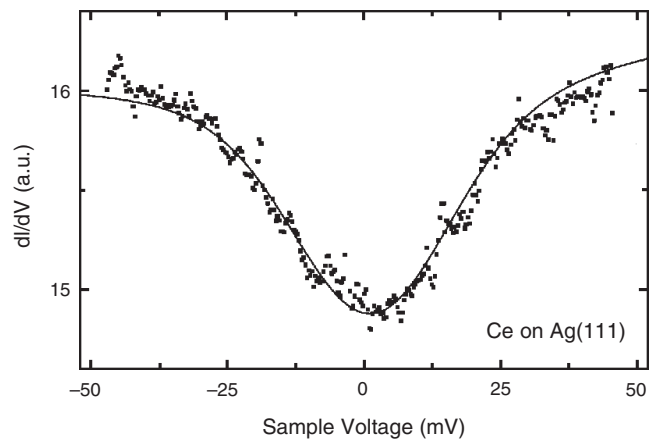


**Figure 3.**  $dI/dV$  spectra of a Ce impurity on Ag(111) for an energy range around the Fermi level. Squares: measurement ( $V = 100 \text{ mV}$ ,  $I = 0.1 \text{ nA}$  before opening the feedback loop). Solid line: calculation using the Anderson single impurity model (see text). Reprinted with permission from [24], J. Li et al., *Phys. Rev. Lett.* 80, 2893 (1998). ©1998, American Physical Society.



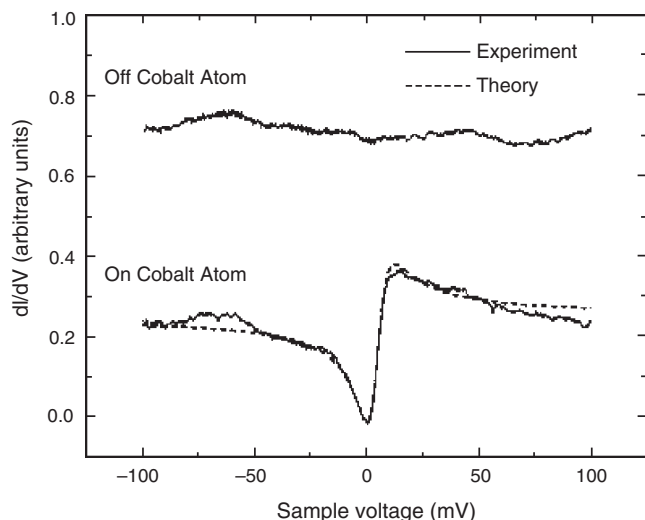


**Figure 4.**  $dI/dV$  of a Co impurity on Au(111) and over the nearby bare Au surface for an energy range around the Fermi level. Dashed line: fit to the data with a modified Fano theory. Reprinted with permission from [25], V. Madhavan et al., *Science* 280, 569 (1998). ©1998, American Association for the Advancement of Science.

clusters on metallic single-walled nanotubes. The spectroscopic measurements performed on and near these clusters exhibit a narrow peak near the Fermi level which had been identified as a Kondo resonance [126].

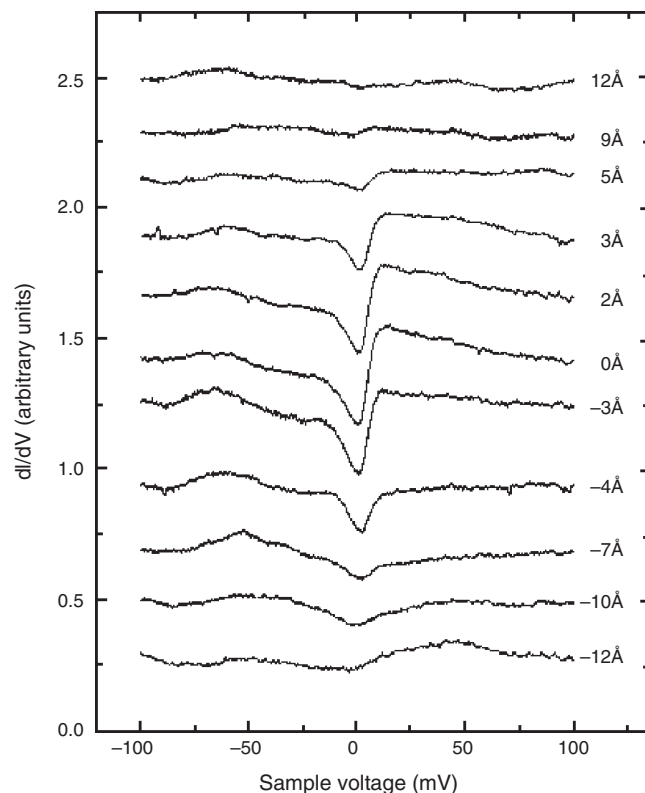


**Figure 5.** A series of  $dI/dV$  spectra with the tip held at various lateral spacings from the center of a single Co atom on Au(111). Reprinted with permission from [25], V. Madhavan et al., *Science* 280, 569 (1998). ©1998, American Association for the Advancement of Science.

Evidence for an orbital Kondo resonance on a transition-metal surface has been reported recently on an atomically clean Cr(001) surface. STS revealed a narrow resonance 26 meV above the Fermi level which was attributed to the manifestation of an orbital Kondo resonance formed by two degenerate  $d_{x,z}$ ,  $d_{y,z}$  surface states [127].

A Fano lineshape has been also obtained in recent theoretical treatments of the Kondo effect of a single magnetic adatom [128–131]. A beautiful experiment of a “quantum mirage” has been performed recently, where the Kondo resonance is seen in both foci of an elliptical quantum corral while the magnetic Co adatom is placed only at one focal position [26]. Evidently, detection and spectroscopy of individual magnetic adatoms open new perspectives for probing magnetic nanostructures.

The controlled modification of the electronic structure of a single Mn adsorbate placed within a geometrical array of adatoms on Ag(111) added a new aspect to the spectroscopy of single adatoms [22]. The spectral changes result from coupling between the adsorbate level and surface electronic states of the substrate. The surface state electrons are scattered coherently within the adatom array, influencing the local electronic structure of the single adatom within the array. The dimension and geometry of the adatom array provide a degree of control over the induced changes.

## 4. SURFACE STATES

### 4.1. Lifetimes

Noble-metal surface states have been the focus of substantial experimental and theoretical attention [13–16, 18, 19, 99, 114, 132, 135–143]. Accurate values are known for their binding energies, effective masses, and Fermi wavevectors, including the temperature dependence and their response to various changes in surface conditions [144]. Overall, there is good agreement of theoretical predictions with experimental results, mainly with angle-resolved photoemission spectroscopy (ARPES). However, measured values of the ARPES linewidth  $\Gamma$  of a surface state hole [145] which is linked to its lifetime  $\tau = h/\Gamma$ , despite prolonged investigation by ARPES [115, 146–148], deviated significantly from theoretical predictions. Surface imperfections have been invoked to explain the failure in observing theoretically predicted linewidths [144, 146, 148]. In the case of Ag(111), the experimental linewidth surpassed theoretical values by  $\sim 300\%$ .

STM with its ability to characterize surface topology and to identify minute amounts of contamination is ideally suited to address this issue. Defect-free surface areas can be selected for experimentation to avoid scattering from defects. Spectroscopy of the differential tunneling conductance  $dI/dV$  versus the sample voltage  $V$ , which is related to the local density of states above the surface [91, 119], can be used to probe the surface state on Ag(111). In typical conductance spectra ( $dI/dV$ ) measured at low temperatures, the surface state gives rise to a sharp rise in the conductance near  $-70$  meV which reflects the onset of tunneling from the surface state band. In the experiments, the overall slope of the spectra varies to some extent. The variations are presumably caused by differences in tip structure

or chemical composition. In more detailed measurements the width of the onset denoted  $\Delta$  is resolved. This width reflects the lifetime of the surface state hole left behind by a tunneling electron [134].

An alternative approach to measuring lifetimes, first indicated by Hasegawa and Avouris [14], is to analyze the spatial decay of electron standing wave patterns near defects [150].

An analytical relation between the experimental width  $\Delta$  and the ARPES linewidth  $\Gamma = 2\Sigma$ , where  $\Sigma$  is the imaginary part of the electron self-energy, is obtained, using approximations which have shown to be very acceptable in the context of surface state spectroscopy [13, 16, 18, 19, 99, 132]. The surface state is modeled by a two-dimensional electron gas with effective mass  $m^*$  and binding energy  $E_S$ . Lifetime effects are included via a constant self-energy  $\Sigma$ . The density of states at the surface,  $n(E)$ , then is [151]

$$n(E) = N_B + m^*[\pi - \phi(E - E_S)]/2\pi^2 \quad (1)$$

where

$$\cos \phi(E) = E/\sqrt{E^2 + \Sigma^2} \quad (2)$$

$N_B$  represents a constant background of bulk states at the surface.

A simple expression for the tunneling current can be used if the tip is electronically featureless, the coupling between the tip and the sample is weak, and the energy and momentum dependence of the tunneling matrix elements can be neglected. This yields

$$I(V) = C \int_{-\infty}^{\infty} n(\epsilon + V) [f(\epsilon) - f(\epsilon + V)] d\epsilon \quad (3)$$

where  $C$  is a constant and  $f$  the Fermi function. From Eq. (3), the differential conductance is

$$\frac{dI}{dV} = CN_B + \frac{Cm^*}{2\pi^2} \int_{-\infty}^{\infty} \frac{\Sigma}{E^2 + \Sigma^2} f(E - V + E_S) dE \quad (4)$$

Equation (4) describes a sharp increase near  $E_S$ , with a width determined by  $\Sigma$  as observed experimentally. A Sommerfeld expansion of Eq. (4)—which is reasonable since in the experiment at 5 K thermal broadening of the Fermi edge is small compared to  $\Sigma$ —yields

$$\Delta \simeq \pi\Sigma \left[1 + O(T/\Sigma)^2\right] \quad (5)$$

Equation (5) shows that the self-energy can be directly obtained from the experimental width of the onset  $\Delta$ . Thermal broadening can safely be neglected. More detailed calculations outlined below corroborate this result although the factor  $\pi$  is slightly modified to  $\simeq 0.9\pi$  in the case of Ag(111). This smaller value results from the part of the electronic wavefunction in the tunneling barrier region where  $\Sigma = 0$ .

For more realistic calculations of the conductance, multiple-scattering techniques were employed to obtain the sample Green function [152]. Lifetime effects were taken into account via an imaginary self-energy which is constant and restricted to the sample. For a tip modelled by a single atom, using a 4-eV optical potential to give a realistic spectral density [153], conductance spectra are obtained within

the many-body tunnelling theory of Zawadowski and Appelbaum and Brinkman [154].  $\Sigma$  affects the broadening of the onset of the surface state band. In addition, one observes that  $\Sigma$  also modifies the relative contribution of the surface state to the conductance above the onset. A comparison of low-temperature STM spectra with these calculations leads to an estimated imaginary self-energy of  $\Sigma \sim 5$  meV. For this value there is, in addition, an approximate agreement of the relative contribution of the surface state to the total conductance for voltages above the onset. The surface state doubles the total conductance in both experiment and calculation.

In ARPES, after eliminating experimental factors,  $\Sigma$  causes the full width at half maximum of the Lorentzian lineshape of the peak associated with the surface state  $\Gamma = 2\Sigma$ . McDougall et al. [147] have evaluated the temperature dependence of the width of the Cu(111) surface state. They observed  $\Gamma$  varying linearly between 75 meV at 625 K and 30 meV at 30 K and compared these data to a perturbative treatment of the electron-phonon coupling [155] with the Debye model and Fermi liquid theory for the electron-electron scattering [156]. Their model provides a quantitative explanation of the observed linear temperature dependence which is attributed to a dominant phonon contribution [147]. Nevertheless, the predicted absolute value  $\Gamma \sim 14$  meV at  $T = 30$  K lies well below the observations. Surface roughness has been invoked to explain this difference [147]. In agreement with this proposal, Theilmann et al. [148] observed a correlation between the photoemission linewidth and the width of LEED spots from the same surface. However, extrapolation to perfect surface order yields  $\Gamma = 43 \pm 5$  meV at room temperature, leaving a considerable gap to the theoretical estimate of  $\Gamma = 30$  meV.

For Ag(111), the situation was comparable. Using the ARPES data of Paniago et al. [115]— $\Gamma = 20$  meV at  $T = 56$  K—and repeating the calculations of [147] with an electron-phonon mass enhancement parameter of 0.13 [155] and Debye energy of 18 meV, one finds  $\Gamma = 5$  meV at  $T = 0$  K for states at the surface state binding energy. The phonon contribution increases  $\Gamma$  at  $T = 56$  K to  $\sim 6$  meV. Again, a sizeable difference exists to the ARPES value.

The value for  $\Sigma$  ( $=\Gamma/2$ ) of 5 meV represents a significantly lower experimental estimate of  $\Sigma$  than previously available. New experimental data obtained under improved experimental conditions by Kliewer et al. [157] indicate a yet smaller value of  $\Sigma \sim 3$  meV (see Fig. 6). Along with new, similar STM results for Au(111) and Cu(111), these data are explained by calculations which go beyond previous quasi-free electron gas models and take band-structure effects into account [157]. These calculations show that the contribution of electron-hole scattering for occupied surface states has previously been underestimated and remove the remaining discrepancy between experimental and calculated self-energies of noble-metal surface states.

On the other hand, new high-resolution photoemission data [158, 159] achieved now an instrumental resolution comparable to the one of STS, of  $\Gamma = 2\Sigma$  of 6 meV and 23 meV for the surface states on Ag(111) and on Cu(111), respectively. In view of the much larger surface area seen in photoemission, this is a bit surprising. In a recent STS investigation with still improved experimental conditions a

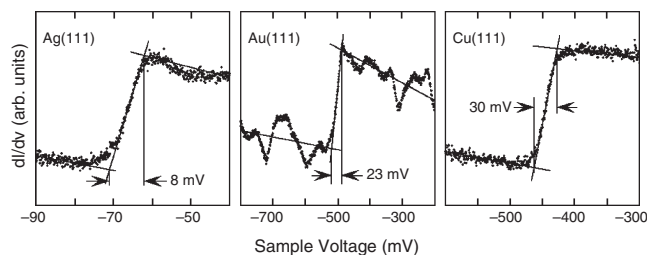


**Figure 6.**  $dI/dV$  spectra for Ag(111), Au(111), and Cu(111). All spectra were taken at least 200 Å away from impurities and are averages of different single spectra from varying sample locations and tips. Reprinted with permission from [157], J. Kliewer et al., *Science* 288, 1399 (2000). © 2000, American Association for the Advancement of Science.

value of  $\Gamma = 4.9 \pm 0.2$  meV has been obtained on Ag(111) which is in the direction of the above argument [160].

An interesting method to determine the energy dependence of surface state lifetimes has been developed recently. This method may be termed *lifetime engineering* [22, 23], as it is based again on the atom manipulation capabilities of the STM. Both groups arranged artificial arrays of atoms in the form of rectangles (Mn on Ag(111) [22]) or triangles (Ag on Ag(111) [23]). The scattering of the surface state electrons at these adatoms results in complex interference patterns (see next section) which were observed in spectroscopic images and local  $dI/dV$  spectroscopy. From a lineshape analysis of  $dI/dV$  spectra and multiple scattering calculations, quasiparticles lifetimes near the Fermi level were derived. The experimental results indicated that the electron lifetimes deviate from a  $(E - E_F)^{-2}$  dependence and reflect the electronic band structure at the surface as well as the local influence of the adatom array.

## 4.2. Standing Wave Phenomena

On the close-packed faces of the noble metals some electrons occupy surface states, quasi-two-dimensional states localized at the metal surface and which have nearly free-electron-like dispersion [161]. In recent years there has been a renaissance of interest in the physics of these electrons, which it is argued play an important role in a variety of physical processes, including epitaxial growth [162], in determining equilibrium crystal shapes [163], in surface catalysis [164], in molecular ordering [165], and in atom sticking [166]. This attention may be largely attributed to the advent of the scanning tunneling microscope (STM), which has enabled direct imaging in real space of electrons in surface states, and their interactions with single adsorbates [13, 17], steps [14, 16], and other structures [15, 16] (see Figs. 7 and 8).

Probably the most striking observation has been of the confinement of surface state electrons within artificial nanoscale structures [15], geometrical arrays of Fe atoms positioned with atomic-scale precision using the STM (see Fig. 9), and which have also received theoretical attention [167–171]. Scattering at natural structures such as steps has also been seen to result in lateral localization [16].

Confinement is important as it raises the energies of the surface state electrons, resulting in a depopulation of the

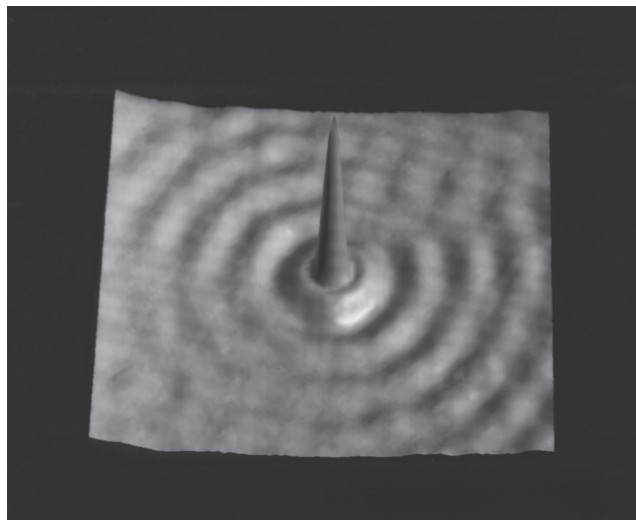


**Figure 7.** Constant current  $13 \times 13$  nm image of a single Fe adatom on the Cu(111) surface. The concentric rings surrounding the Fe atoms are standing waves due to the scattering of surface state electrons with the Fe adatom. Reprinted with permission from [15], M. F. Crommie et al., *Science* 262, 218 (1993). © 1993, American Association for the Advancement of Science.

surface state band and a concomitant modification of surface properties associated with the surface state electrons [162–164]. However, to date there has been little attention paid to the systematics of the confinement, especially in the limit of smaller-scale structures. Can one still talk of surface state electrons supported on a structure just three or four atoms wide? These structures are the ones most likely to result in significant depopulation, and exist naturally on surfaces especially during epitaxial growth. In contrast to the corral studies of [15], a recent angle-resolved photoemission study [172] on vicinal Cu(111) surfaces with monatomic

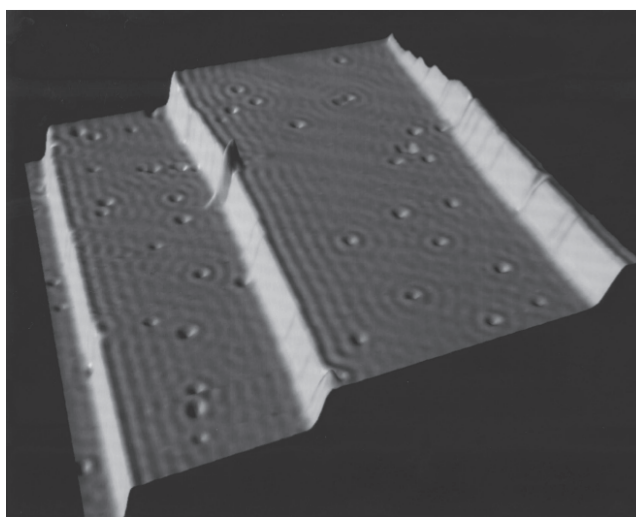


**Figure 8.** Constant current  $50 \times 50$  nm image of the Cu(111) surface at 5 K. Standing waves in the LDOS with a periodicity of  $\sim 1.5$  nm can be seen emanating from monatomic step edges. Reprinted with permission from [13], M. F. Crommie et al., *Nature* 363, 524 (1993). © 1993, Macmillan Magazines Ltd.

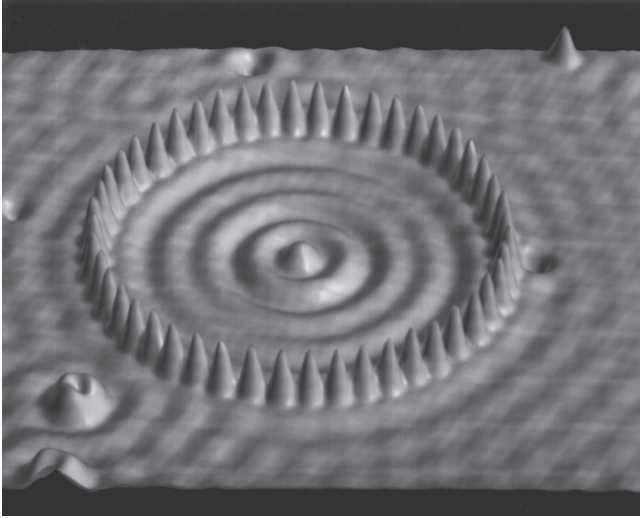


**Figure 9.** Circular quantum corral built from 48 Fe atoms on the Cu(111) surface. Average diameter of ring (atom center to atom center) is 14, 26 nm. An electronic interference pattern can be seen inside of the Fe ring. Reprinted with permission from [15, 168], M. F. Crommie et al., *Science* 262, 218 (1993). © 1993, American Association for the Advancement of Science, and M. F. Crommie et al., *Surf. Rev. Lett.* 2, 127 (1995). © 1995, World Scientific Publishing Company.

steps spaced  $\sim 1.5$  nm apart has found shifts in surface state energies only a fraction of those expected on the basis of ideal confinement, suggesting the step edges only act as weak and permeable barriers. Thus the validity of confinement as a mechanism of surface state depopulation seemed to be in question.

Standing waves on an Ag island at room temperature, identified as resulting from surface state confinement, have been first observed in [16]. Li et al. [19] report on a low-temperature study of surface state electrons confined to small Ag islands on Ag(111). In contrast to adatom corrals, these are stable structures even at elevated bias voltages in the STM, enabling the observation of standing waves over a wide range of voltages. Complementary electronic structure calculations enabled the authors to extend the investigation down to the smallest island sizes, quantifying the nature of surface state confinement.

Differential conductance maps taken above individual islands exhibit strongly voltage-dependent features. Figure 10 shows a typical series of scans taken above an island. For voltages around  $-65$  mV and lower (negative voltage corresponds to tunneling from the sample), the image of the interior of the island is featureless. At higher voltages standing wave patterns of increasing complexity are observed, beginning with a single peak near the center of the island and gradually evolving to multiple rings with sixfold azimuthal modulations, which are partially distorted by deviations of the island shape from hexagonal symmetry. STM measurements of  $dI/dV$  are related to the local density of states above the surface [91], and the standing waves may be identified as originating from surface state electrons, confined by the rapidly rising potential at the edges of the island. On the clean surface the surface state disperses upwards from  $E_0 = -67$  meV, with an effective mass  $m^* = 0.42$  [18, 115].

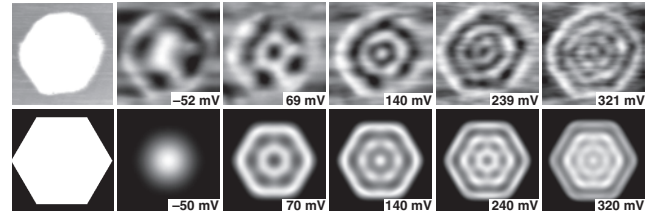


**Figure 10.** Upper row: topographic image of an approximately hexagonal Ag island on Ag(111) (area  $\sim 94$  nm<sup>2</sup>), and a series of  $dI/dV$  maps recorded at various bias voltages (at  $T = 50$  K). Lower: geometry of a hexagonal box confining a two-dimensional electron gas, and the resulting local density of states. Experimental values have been used for the surface state onset  $E_0$ , electron effective mass  $m^*$ , and the island size. The calculations include a self-energy of  $\Gamma = 0.2(E - E_0)$ . Reprinted with permission from [19], J. Li et al., *Phys. Rev. Lett.* 80, 3332 (1998). © 1998, American Physical Society.

Positioning the STM tip above the center of a particular island and recording  $dI/dV$  spectra, a series of peaks is observed, reminiscent of those measured at the center of adatom corrals [15]. The peaks correspond to energy levels of the confined surface state electrons, broadened into resonances by single-particle scattering processes [167, 169], many-body interactions [170], and instrumental effects such as thermal broadening. Electronic structure calculations on small Ag islands on Ag(111), using the multiple-scattering approach described in [170, 173], were performed to model the experimental observations [19]. The potentials were taken from *ab initio* calculations of the clean surface, which give the binding energy and effective mass of the surface state band as  $E_0 = -72$  meV and  $m^* = 0.37$ .

Regular hexagonal islands with sizes up to 631 atoms were considered. As the island size decreases, the calculated levels rise markedly, consistent with a high degree of confinement. To quantify the nature of the confinement the energy levels were analyzed in terms of two-dimensional “particle-in-a-box” eigenstates, corresponding to electrons with effective mass  $m^*$  confined within a hexagonal domain of potential  $E_0$  by infinitely high barriers [133].

The eigenvalues scale with the inverse of the area of the hexagon,  $\Omega$ . In atomic units ( $\hbar = m_e = e^2 = 1$ )

$$E_n = E_0 + \frac{\lambda_n}{m^* \Omega} \quad n = 1, 2, 3 \dots \quad (6)$$

Only eigenstates which transform according to the  $A_1$  representation of the group  $C_6$  (6 mm) of the hexagon [175] have a nonzero amplitude at the origin, and for these the lowest few are  $\lambda_1 = 9.296$ ,  $\lambda_4 = 48.70$ , and  $\lambda_{10} = 117.0$  [133]. In comparing with the experimental  $dI/dV$  data and/or the multiple-scattering calculations, it is not clear *a priori* what the relevant size of an island is. The confinement is effected by the rapid rise in the potential beyond the edges of the island. However, a sizeable fraction of the surface state extends into the first few layers of atoms and so will not be directly influenced by the island edge. The effective location of the boundary confining the surface state electrons is uncertain, relative to either the measured topological linescan of the island or the actual positions of the edge atoms. To circumvent this difficulty a *fit* of the results from the scattering calculations with the energies from Eq. (6)



was carried out, assuming the effective boundary lies a constant distance (independent of island size) beyond the positions of the edge atoms. This distance was the only fitting parameter. The scattering calculations were then used to simulate constant-current topographs by evaluating the integrated LDOS above the surface, enabling an identification *theoretically* of the effective boundary on the topographical cross section.

The location identified as the effective boundary of the surface state electrons lies close to the midpoint of the rise in the topological linescan,  $\sim 0.5$  nm beyond the edge atoms. The precise value depends upon the potential in the vicinity of the island edge, for which only an approximate description is available, but which always coincides closely with the midpoint of the rise in the simulated topological linescan. With this definition, remarkable agreement between the energies of the surface state electrons as derived from both experimental  $dI/dV$  spectra and the theoretical LDOS was found, compared to the scaling behavior expected of two-dimensional electrons. The smallest island contains just 19 atoms, and the smallest measured island is  $\Omega \sim 16$  nm<sup>2</sup> containing  $\sim 100$  atoms. These results indicate that as far as the energy levels are concerned, it is valid to talk of surface states confined to nanoscale islands, right down to the smallest island sizes. The confinement corresponds to an infinite barrier, and the area to which the electrons are confined corresponds to a boundary lying a fixed distance beyond the outermost atoms, independent of both energy and the island size.

There are deviations from this interpretation of the electron behavior, as witnessed by the finite width of the confined energy levels. The levels should be infinitely sharp for ideal confinement. The width of each energy level stripped of instrumental contributions,  $\Delta E_n$ , implies a finite lifetime for the confined electrons,  $\Delta t_n \simeq \hbar/\Delta E_n$ , dominated by scattering into other electron states at the island edges [167, 169, 170]. While these processes do not influence the energies of the levels, one potential consequence is that depopulation of the surface state only becomes significant for island sizes smaller than those derived from a two-dimensional analysis. Even at  $T = 0$  each energy level will have a finite width, resulting in partial occupation *after* the level has risen above the Fermi energy. Assuming a Lorentzian lineshape, the state will be 1/4 full when  $E_n$  lies  $\Delta E_n$  above the Fermi level. For an estimate of the significance of this effect, the experimental spectra yield

$$\Delta E_n \simeq 0.2 (E_n - E_0) \quad (7)$$

Using this relation, the island area at which the lowest level is 3/4 depopulated is 10% smaller than that which yields complete depopulation assuming perfect confinement. Hence the influence of the finite widths is marginal. A more detailed analysis of the level widths is given in [133, 134], incorporating them into the two-dimensional description as a self-energy provides a good model of the confined states. Allowing for the clear deviations in shape of the experimental island from the ideal hexagon assumed theoretically, which (alongside the finite resolution of the STM) results in the more rounded features, there is good agreement between the theoretical and experimental images. The

largest differences arise at the island edges, when experimental  $dI/dV$  data are influenced by tip-height variations [18] and because theoretically the background of bulk states is not included.

This quantitative study of electron confinement to nanoscale Ag islands on Ag(111) using low-temperature STM and electronic structure calculations confirmed the validity of the “particle-in-a-box” model for confined surface state electrons. The energies conform to the expected scaling behavior down to the smallest of island sizes, and the width of the confined levels has only a marginal effect on the surface state depopulation. For larger island sizes the island edges have the same atomic structure as low-energy steps oriented along  $\langle 1\bar{1}0 \rangle$  directions on the (111) surface, and so these conclusions should hold also for confinement to raised terraces and to finger-like structures characteristic of the dendritic formations which occur in the low-temperature growth of Ag/Ag(111) [176]. In addition, these conclusions should also hold for confinement on Cu(111) and Au(111) surfaces, due to the similarities in the band structures of the noble metals. The failure to observe these effects in angle-resolved photoemission [172], apart from limits in the instrumental resolution, most likely results from the presence of a sizeable distribution of terrace widths within the spot area of the incident radiation.

Subsequently, confinement of Ag(111) surface state electrons had been studied in symmetric and asymmetric resonators formed by two atomically parallel step edges. The local density of states in the resonator was measured by  $dI/dV$  spectroscopy and spectroscopic imaging and was analyzed within a simple Fabry–Pérot model. The energy-dependent reflection amplitudes and scattering phase shifts of the different step edges were determined [20].

A recent investigation of the surface state depopulation on such small Ag(111) terraces showed [177] that with decreasing terrace width, the electronic density in the occupied surface state shifts monotonically towards the Fermi level, leading to a depopulation at 3.2 nm terrace width in quantitative agreement with the above Fabry–Pérot model. These observations also confirm the earlier results obtained on small silver islands [19, 133].

It was shown later that a simple “particle-in-a-box” model is already sufficient to identify all major features in the observed  $dI/dV$  maps and in constant-current topographic images of a similar quantum box [160]. These authors obtained atomically resolved constant-current images of a Ag(111) single-crystal surface at a temperature of 5 K, which simultaneously display standing wave patterns arising from electron confinement of surface state electrons to nanoscale terraces. It was shown how the energy-dependent patterns develop from the superposition of allowed wavefunctions in the quantum box. This experiment constitutes a direct verification of the Tersoff–Hamann model for arbitrarily localized tip wavefunctions [160].

It has been predicted [178] and found recently that the standing waves mediate long-range oscillatory interactions between adatoms [179–181]. In the case of Cu on Cu(111), the interaction potential was determined by evaluating the distance distribution of two adatoms from a series of STM images taken at temperatures of 9–21 K [180]. The long-range interaction had a period of half the Fermi wavelength

and decayed for larger distances as  $1/d^2$ . A comparison of three adsorbate/substrate systems, Cu/Cu(111), Co/Cu(111), and Co/Ag(111), essentially confirmed the earlier observations and demonstrated that the long-range interactions depend crucially on the Fermi wavelength of the surface state electrons [181].

The realization of two-dimensional imaging of electronic wavefunctions in metallic single-walled carbon nanotubes represents another highlight in low-temperature STS [182]. The measurements reveal spatial patterns, which can be directly understood from the electronic structure of a single graphite sheet. The authors observed also energy-dependent interference patterns in the wavefunctions and exploit these to directly measure the linear electronic dispersion relation of the nanotube.

In the context of standing wave patterns, the observation of the development of one-dimensional band structure in artificial gold chains marks the beginning of manipulation and spectroscopy of local one-dimensional structures on surfaces [183]. The authors used the ability of the STM to manipulate single atoms to build well-defined gold chains on NiAl(110). The electronic properties of the one-dimensional chains are dominated by an unoccupied electron band, gradually developing from a single atomic orbital present in a gold atom. Spatially resolved conductance measurements along a 20-atom chain provided the dispersion relation, effective mass, and density of states of the free electron-like band.

## 5. SUPRAMOLECULAR SELF-ASSEMBLY

Self-assembly of regular arrays of thermodynamically stable nanostructures from appropriately functionalized molecules is a promising approach to future mass-fabrication of nanoscale structures [184, 185]. Molecules adsorbed on surfaces are particularly appealing because their arrangement is directly observable with the scanning tunneling microscope [186–190]. Understanding supramolecular aggregation starting from the basic interactions of the constituent molecules is a prerequisite to eventually control the self-assembly process.

The aromatic molecule 1-nitronaphthalene (NN, structure Fig. 11, inset) adsorbed on the reconstructed Au(111) surface [191] was chosen in a recent experiment as structural unit for self-assembly. The confinement of NN to two dimensions introduces a chirality not present in the gas phase. On the surface both enantiomers are present in equal amounts, thus forming a racemic mixture. The Au(111) sample was held at room temperature during the deposition and below 50 K during the measurements. In order to minimize tip-induced motion of the molecules at submonolayer coverages [192, 194, 195], small tunneling currents ( $I = 10$  pA) were used.

At coverages between 0.05 and 0.15 ML self-assembled quasi-0D clusters of distinct size and structure appear at the fcc elbows of the reconstruction (Fig. 11b). At slightly higher coverage (0.2 ML) identical clusters are observed within fcc domains (Fig. 11c) and, sporadically, within hcp domains and on domain walls. All decamers appear identical in the STM images, except for a mirror symmetry (clusters 1 and 2 in Fig. 11c). They consist of an 8-molecule ring surrounding

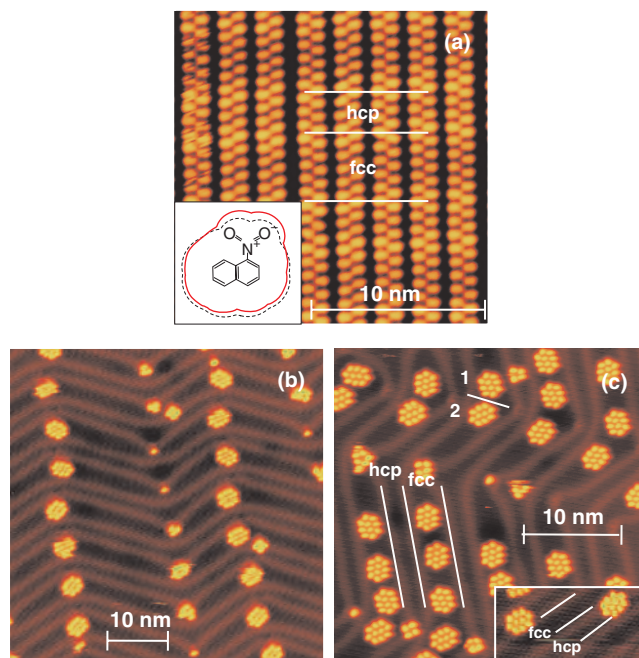


**Figure 11.** STM images at 50 K of a reconstructed Au(111) surface with adsorbed NN; (a) 0.7 ML NN. Inset: Structural formula of NN. The dashed line encloses the “exclusion” area resulting from steric repulsion. The distance of the full line from the dashed line indicates the strength of a negative electrostatic potential computed on the dashed line. (b) 0.1 ML NN at 65 K. (c) 0.2 ML NN at 50 K. Inset: 0.2 ML NN at 10 K. Reprinted with permission from [32], M. Böhlinger et al., *Phys. Rev. Lett.* 83, 324 (1999). © 1999, American Physical Society.

a 2-molecule core. Manipulation experiments at decreased tunneling resistance show that the decamers behave like stable “supermolecules” [33]. Therefore, the structure and stability of the decamers is determined by highly specific intermolecular forces while the interaction of these “supermolecules” with the reconstructed substrate and a mutual repulsion at small distances determine their lateral spacing.

At medium coverage (0.3–0.75 ML) the growth mode changes to the formation of 1D molecular double chains (Fig. 11a at 0.7 ML) guided by the reconstruction domains or by step edges. At full monolayer coverage 1D and 2D periodic molecular structures coexist on the surface [193].

At a tunneling voltage  $V = -2.3$  V, intramolecular structure is resolved and the contrast pattern shows the expected handedness [32]. The charge density calculated for the highest occupied molecular orbital (HOMO) of the free NN molecule closely resembles the observed submolecular structure [32]. At lower bias voltage hybridization with Au-substrate states results in a nearly symmetric appearance of the molecules [196] where the long axis of the ellipsoids coincides with the long axis of the naphthalene core.

Molecular-dynamics simulations rationalize the observed supramolecular arrangements [32]. Within each single strand the molecules are arranged in a “head-to-tail” configuration via hydrogen bonds between a negatively charged oxygen atom and the “backside” hydrogen atom at a carbon atom of a neighboring NN molecule. The second strand is rotated by  $180^\circ$  and shifted by half a period such that opposite charges are close to each other. The double chains are positively



charged outside and therefore mutually repel as observed experimentally. Straight, defect-free segments of the double chains consist of exclusively one NN enantiomer and thus represent a 1D conglomerate [32]. Below a critical density of molecules quasi-0D decamers are energetically more favorable than linear double chains with unsaturated hydrogen bonds at their ends [32]. In the decamers a homochiral molecular ring along the periphery is stabilized by a core composed of two molecules with opposite chirality.

STM observations and theoretical modeling led to a detailed understanding of the stability and the internal geometry of self-assembled supramolecular structures of the 2D chiral molecule 1-nitronaphthalene on Au(111). Recently, these tools were extended to obtain an understanding of the supramolecular self-assembly and selective step decoration of these molecules on the Au(111) surface [197]. Furthermore, a coverage-driven chiral phase transition from a conglomerate to a racemate was followed in real space [34, 198, 199].

Subsequently, other supramolecular nanostructures have been built by self-assembly on surfaces taking advantage of hydrogen bonding [35–37]. These range from one-dimensional supramolecular nanogratings on Ag(111) [35] made of chains of benzoic acid to the mesoscopic correlation of supramolecular chirality in one-dimensional hydrogen-bonded assemblies [36] (see Fig. 12). The stereochemical

effects in supramolecular self-assembly on surfaces, that is, the 1D versus 2D enantiomorphic ordering of these organic molecules, were reported in [37].

In the meantime, a promising new approach towards a controlled self-assembly had been developed for substituted porphyrin molecules adsorbed on a gold surface: the formation of surface-supported supramolecular structures whose size and aggregation pattern were rationally controlled by tuning the non-covalent interactions between individual adsorbed molecules [38].

## 6. CLUSTERS

### 6.1. Electronic Properties

Whereas the electronic structure of atoms, molecules, and extended solids is quite well explored from both an experimental and a theoretical viewpoint, very little is known about the systematic development of the electronic structure as single atoms are combined to form a solid. There are fundamental questions to be answered about the onset of metallic behavior in small metal clusters or the influence of quantum size effects on the electronic structure of small particles. Therefore, it is of primordial interest to study individually, that is, locally, these objects of “embryonic” condensed matter [200].

An ideal tool for this type of investigation is again offered by scanning probe methods which have been used in three pioneering studies of nanometer-size clusters of Au on GaAs(110) [201], Fe clusters on the same surface [202], and of size-selected  $\text{Si}_{10}$  clusters on a reconstructed Au(001) surface [203], which all have been published already in 1989. In the first investigation [201] a characteristic spectrum of bandgap states was observed for the Au particles grown on GaAs. Both donor and acceptor states have been observed and they have been identified with the first and second electron states of the Au-Ga bond, respectively. In the second study, the formation of a local Schottky barrier has been realized by deposition and growth of Fe clusters (9–127 atoms per cluster) on GaAs surfaces in ultrahigh vacuum. STS revealed the onset of the metallic character of the Fe clusters above about 35 atoms per cluster by the observation of a continuum of occupied cluster-induced states at the Fermi energy in the bandgap of the semiconductor [202]. The third experiment [203] represents the first STM/STS study of supported size-selected clusters on a solid surface. The Si clusters were generated by pulsed laser vaporization of a silicon rod in a continuous flow of He buffer gas. The quadrupole mass spectrometer was set to transmit only  $\text{Si}_{10}$  clusters and after mass analysis the ions were focused into a low-energy ion beam and deposited on the sample with an energy of approximately 5 eV, well below the threshold for cluster fragmentation. After cluster deposition the sample was transferred to the STM chamber. During deposition, transfer, and measurement, the sample was maintained under UHV conditions. The cluster images were found to depend on the sample bias voltage, and from STS measurements the clusters were found to have a bandgap of about 1 eV. A wide variety of cluster images were observed even though size-selected clusters were deposited. When only Si atoms were deposited on the surface flat islands

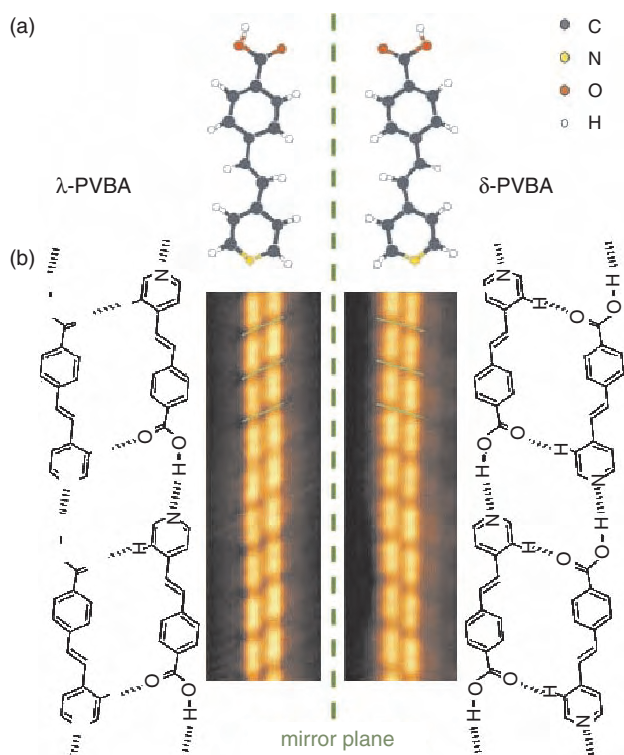


**Figure 12.** (a) Chirality of PVBA upon confinement to two dimensions. The mirror symmetry is reflected by a dashed line. (b) STM topographs of the two possible supramolecular chiral twin chains from self-assembly of PVBA on Ag(111) (image size  $4 \times 13.5$  nm). The corresponding models for the energetically favored configurations reveal the underlying chiral resolution (hydrogen bonds indicated by dashes). Reprinted with permission from [36], J. Weckesser et al., *Phys. Rev. Lett.* 87, 096101 (2001). © 2001, American Physical Society.

were formed. Surprisingly, in spite of these first promising results, up to the present time experiments on size-selected supported clusters with local probes have been scarce.

One interesting experiment used the fact that the tip-surface region of an STM emits light when the energy of the tunneling electrons is sufficient to excite luminescent processes [95]. These processes provide access to dynamic aspects of the local electronic structure that are not directly amenable to conventional STM experiments. In order to explore the lateral resolution obtainable in the photon signal, adsorbed  $C_{60}$  molecules on a reconstructed Au(110)( $1 \times 2$ ) surface were chosen [8]. At sub-monolayer coverage  $C_{60}$  islands with monomolecular height were observed. In the STM image of Figure 13a indi-

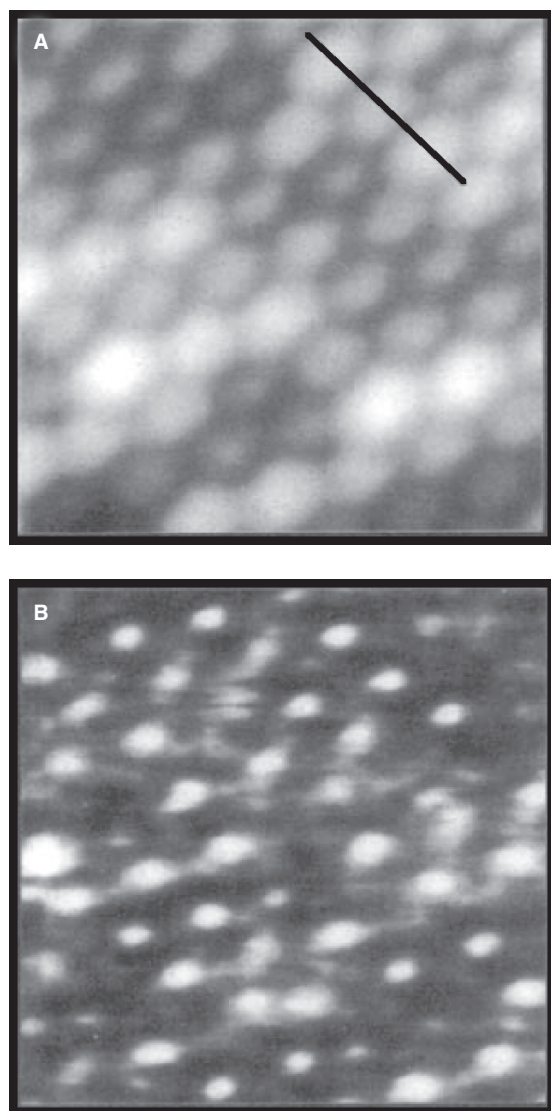


**Figure 13.** Au(110) surface covered with an annealed monolayer of  $C_{60}$ . Topograph (a) and photon map (b) are represented as gray-scale images. Area: 6.5 nm by 6.5 nm, tip voltage  $V_t = -2.8$  V, tunneling current  $I_t = 4.4$  nA, intensity scale: 800 cps, temperature of tip and sample: 50 K. Reprinted with permission [8], R. Berndt et al., *Science* 262, 1425 (1993). © 1993, American Association for the Advancement of Science.

vidual  $C_{60}$  molecules are resolved as protrusions. They form an approximately hexagonal array with a corrugation amplitude of 0.1 nm. A comparison of this STM image with the photon emission map measured simultaneously (Fig. 13b) shows that the individual  $C_{60}$  molecules give rise to bright spots in photon emission. The photon emission is maximal when the tip, acting as an electron source, is placed above a molecule. The emitted intensity from intermolecular regions is significantly lower. The lateral extent of the emission spots (0.4 nm full width at half maximum) is smaller than that of the topographic features (0.6 nm). For a few molecules no enhanced emission is observed, indicating that the photon emission channel contains some additional information on  $C_{60}$  not apparent in the topographic image. It was suggested [8] that the molecules interact strongly with the electromagnetic modes of the cavity between tip and sample. In analogy to the case of surface-enhanced Raman scattering (SERS) from molecules in pores of Ag films [100], such a confinement effect may also affect molecular photon emission.

The above experiment [8] was the first photon emission measurement where individual molecules self-assembled in nanometer separation were clearly resolved. This technique has again been used recently to measure photon emission spectra of individual alumina-supported silver clusters obtained by evaporation and growth [9]. The light emission was attributed to the excitation and the decay of local plasmon modes (Mie-plasmon resonances) in these particles [9]. As the cluster size decreases, the resonance shifts to higher energies and the linewidth increases. In the 1.5- to 12-nm size-range of the clusters studied, intrinsic size effects are proposed to be at the origin for the observed size dependence of the Mie resonance [9]. Similar investigations were carried out on Ag clusters on Si single-crystal surfaces, where the light emission enhancement was also ascribed to the excitation of plasmon modes [11]. Moreover, coupled plasmon modes were detected in an ordered hexagonal monolayer of silver nanospheres on Au(111) [10]. A very recent finding was the observation of luminescence from metallic quantum wells, a new phenomenon in STM-induced photon emission [96] from metal surfaces. Another recent highlight in STM-induced light emission was the observation of luminescence from individual supported molecules on an ultrathin alumina film [12].

The energy gap of pristine silicon clusters supported on HOPG has been studied recently by STM and STS [204]. The clusters have been obtained by magnetron sputtering of a Si target and deposition on HOPG at room temperature; that is, they were not size-selected but have been individually addressed by the tip of the STM. Clusters with sizes between 0.25 and 4 nm were studied and the size dependence of the bandgap was determined. For clusters below 1.5 nm, gaps up to 450 meV were found, while for larger particles no gaps were recorded. The results were explained in terms of a transformation from diamond to a compact structure occurring at 1.5 nm (about 44 atoms per cluster). For clusters with diamond structure the surface dangling bond density is high, leading to electronic states filling the energy gap. On the other hand, the compact arrangement of the smaller clusters tends to eliminate dangling bonds. Therefore, finite gap values are observed for clusters with less than 44 Si atoms [204]. Interesting STS results on individual non-size-selected

Pt and Ag clusters produced by a PACIS cluster source and deposited onto HOPG have been obtained recently [205]. The observed spectral structures for Pt have been interpreted in terms of a Fano resonance and those of Ag clusters in terms of three-dimensional electron confinement in analogy to recent spectroscopic findings and interpretations for Kondo systems (Ce atoms and Ce clusters on Ag(111) [24], Co atoms on Au(111) [25], and on Cu(111) [26]), and for two-dimensional electron confinement found in quantum corrals [15, 22, 26] and on islands [16, 19]. Effects of electron confinement have also been observed recently with STS for silver-islands grown in nanopits on HOPG [206].

Recently, STS and STM have been applied to study the onset of the catalytic activity of Au particles grown on titania [207], which appeared to be correlated with the layer thickness of the particles on the surface. In this context, the recent investigations of the catalytic activity of small supported Au clusters on MgO are interesting [208] where the challenge of local investigations with the STM still remains. While inert as bulk material, nanoscale gold particles dispersed on oxide supports exhibit a remarkable catalytic activity. Temperature-programmed reaction studies of the catalyzed combustion of CO on size-selected small monodispersed  $Au_n$  ( $n \leq 20$ ) clusters supported on magnesia, and first-principles calculations, reveal the microscopic origins of the observed unusual catalytic activity, with  $Au_8$  found to be the smallest catalytically active size. Partial electron transfer from the surface to the gold cluster and oxygen-vacancy F-center defects are shown to play an essential role in the activation of nanosize gold clusters as catalysts for the combustion reaction.

The above presentation of the spectroscopic results on deposited clusters clearly shows that valuable information on these nanosystems can now be obtained by the application of an arsenal of local and nonlocal surface science analysis methods. Therefore, in the near future a much more intense employment of scanning probe techniques such as STM, STS, AFM, and others will beyond any doubt improve considerably the assembly, characterization, and functionalization of size-selected clusters on solid surfaces.

## 6.2. Geometric Structure

The microscopic structure is of primordial interest as it influences most physical and chemical properties of the cluster. The determination of the exact microscopic arrangement of the atoms in a cluster on a surface is an enormous experimental challenge. Diffraction methods, which are perfectly adapted to obtain the positions of the atoms in a material, have been applied for the study of free clusters [209–212]. Two other experimental techniques were employed so far to obtain the geometric structure of clusters on surfaces, STM and infrared spectroscopy (IRS). In principle, STM is able to reveal the exact arrangement of all atoms in a planar cluster. For three-dimensional clusters the positions of the topmost layer of surface atoms can be imaged. In favorable cases, the atomic arrangement on the lateral facets was also obtained. In both cases a minimal cluster size seems to be necessary in order to obtain atomic resolution of the individual atoms of the cluster [213].

Infrared spectroscopy can in principle give a more complete picture if all the normal modes in the cluster are obtained. An example for measuring vibrational modes of ligand molecules in a nonlocal mode is given below [214]. When used on the local scale, inelastic electron tunneling spectroscopy (IETS) is especially promising [44].

First attempts for mapping metal clusters on surfaces with atomic resolution were performed in the late 1980s, summarized in [215]. Small two-dimensional platinum and aluminum clusters were imaged on highly oriented pyrolytic graphite (HOPG) with an STM at room temperature. The interpretation of this pioneering work is, however, unconfirmed, as pinning of clusters or contaminations on defects might have influenced the images. Mo et al. [216] showed in a beautiful measurement that the Stranski–Krastanov growth of Ge on Si(001) resulted in a metastable 3D phase consisting of small well-defined hut clusters. These were imaged with atomic resolution and shown to consist of prisms or four-sided pyramids with four [103] facets (see Fig. 14).

The group of Henry achieved a complete characterization of the morphology of a 27-atom palladium cluster supported on a cleaved  $MoS_2$  single crystal [217]. The three-dimensional shape, azimuthal orientation on the substrate, and arrangement of atoms on lateral facets were determined from atomically resolved images of a palladium cluster grown in UHV on the  $MoS_2$  (0001) facet. The resulting *in-situ* STM image is shown in Figure 15. The cluster clearly consists of two monolayers. The first layer is a regular hexagon with a three-atom wide side and an additional atom attached to the left hexagon side. This layer is composed of 20 atoms. The top layer has a regular hexagonal shape and the sides are composed of two atoms, resulting in a top layer of 7 atoms. This  $Pd_{27}$  cluster is schematically shown also in Figure 15. The observed atomic arrangement is identical to the structure of bulk palladium with a (111) basal plane. From this atomically resolved STM image, in particular from the two-dimensional representation, the relative orientation between cluster and the substrate is obtained in real space, showing that the azimuthal orientation of the particle dense-Pd-atom rows are parallel to the rows of sulfur atoms of the  $MoS_2$  surface. So far, this is the only experiment where the number of atoms is directly obtained from the STM image and it seems that the system was well chosen, as for

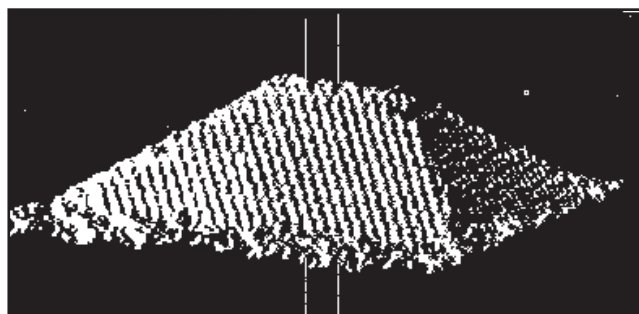


**Figure 14.** STM image of a single Ge hut cluster. Perspective plot: scan area  $40 \times 40$  nm. The height of the hut is 2.8 nm. Reprint with permission from [216], Y.-W. Mo et al., *Phys. Rev. Lett.* 65, 1020 (1990). © 1990, American Physical Society.



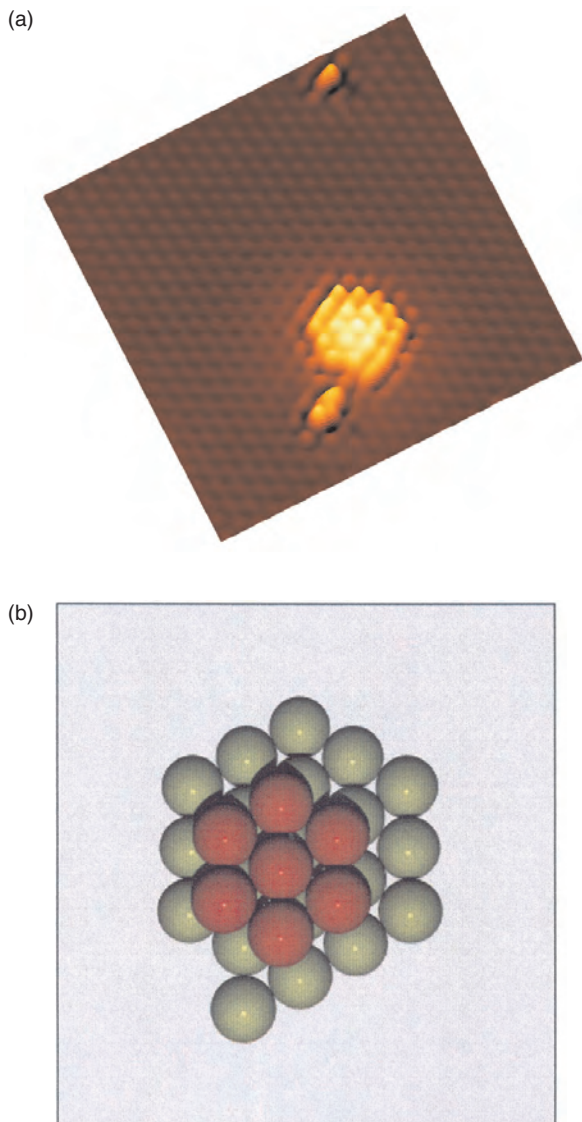


**Figure 15.** (a) STM image of an isolated Pd cluster of small size ( $\sim 1.5$  nm) supported on the (0001) surface of  $\text{MoS}_2$ . A single atom and a trimer are seen on the top and on the bottom of the figure, respectively. (b) Schematic representation of the cluster containing 27 atoms. Reprinted with permission from [217], A. Piednoir et al., *Surf. Sci.* 391, 19 (1997). © 1997, Elsevier Science B. V.

other systems atomic resolution of such small clusters was not obtained.

Imaging large particles on oxide surfaces with atomic resolution is less system-restricted. Hojrup Hansen et al. [213] reported atomic resolution on Pd particles hundreds to thousands of atoms large. The authors believe that obtaining atomic resolution is also possible for other systems as long as the particle diameter is larger than  $\sim 4$  nm and higher than about four layers ( $\geq 500$  atoms/particle). The Pd particles were grown on a 0.5-nm-thick  $\text{Al}_2\text{O}_3$  film. Figure 16 shows STM images of a Pd particle with atomic resolution. It reveals a (111) layer for the top facet. The measured nearest-neighbor distance is  $2.76 \pm 0.07$  Å, indicating the absence of any strain in the cluster ( $d = 2.75$  Å; for

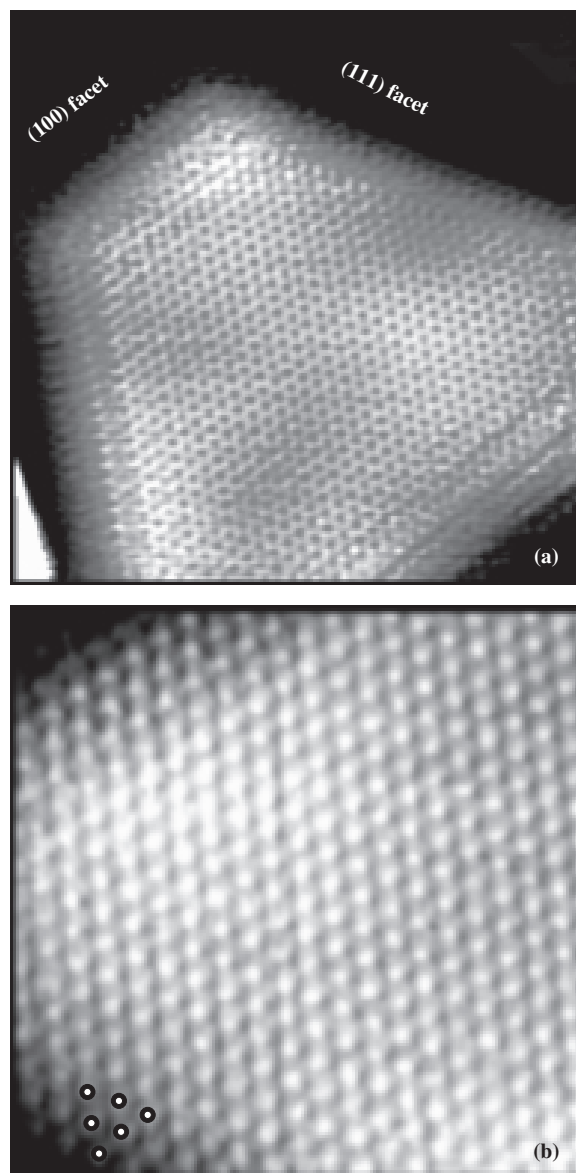


**Figure 16.** Atomic-resolution images of crystalline nanosize Pd clusters. (a)  $9.5 \times 9.5$  nm image size. The resolution is kept a few layers down the sides, allowing identification of the side facets. The dots in (b) indicate the atomic positions consistent with a (111) facet. Reprinted with permission from [213], K. Hojrup Hansen et al., *Phys. Rev. Lett.* 83, 4120 (1999). © 1999, American Physical Society.

Pd(111)). In addition, these results show that for such large particles supported on oxide surfaces it is possible to obtain atomic resolution across the entire cluster surface, although the tunneling conditions at the edge of the cluster change. As the tip-apex moves away from the top layer of the particle when approaching the edge, tunneling occurs between the top layer of the particle and the atoms on the side of the tip. In some cases the authors even report atomic resolution on the largest side facets of the particles and observed a (111) crystallographic orientation. In addition, the particle morphology was characterized by three parameters, which are the height of the particles, the width of the top facets, and the ratio between the side lengths of the top facets.

The smallest observed particle with a crystalline structure had a top facet of 2–3 nm widths and a height of 0.5–1 nm, corresponding to a thickness of 2–4 layers. Furthermore, these measurements revealed quantitative information on the work of adhesion. The observed shapes of the particles were compared with the ones resulting from a Wulff construction based on calculated surface energies. For Pd on  $\text{Al}_2\text{O}_3$  a value of  $W_{\text{adh}} = 2.8 \pm 0.2 \text{ J/m}^2$  was reported.

In another example [218] the same group synthesized on a Au(111) template single-layer  $\text{MoS}_2$  nanocrystals with a width of  $\sim 3 \text{ nm}$ . The  $\text{MoS}_2$  nanocrystals were obtained by first growing  $\sim 3\text{-nm}$ -wide Mo particles on the Au(111) template and by subsequent sulfidation in an  $\text{H}_2\text{S}$  atmosphere. Atom-resolved STM images reveal that the small nanocrystals exhibit triangular morphology in contrast to bulk  $\text{MoS}_2$ . Figure 17 depicts an atomically resolved STM image of such a triangular nanocrystal. The observed protrusions are arranged with hexagonal symmetry and an average interatomic spacing of  $3.15 \pm 0.05 \text{ \AA}$ . This is consistent with the interatomic spacing of S atoms in the (0001) basal plane of  $\text{MoS}_2$ . From the apparent height of only  $2.0 \pm 0.3 \text{ \AA}$  the authors conclude that the  $\text{MoS}_2$  nanocrystals are present as single layers on the Au surface. The triangular shape of the monolayer crystals is in contrast to the expected hexagonal morphology of multilayer  $\text{MoS}_2$ . This implies that one of the edge terminations is considerably more stable. To answer which edge structure is more stable, high-spatial-resolution images of the edge structures of the triangles were taken. These atomic-resolution images showed that the S atoms at

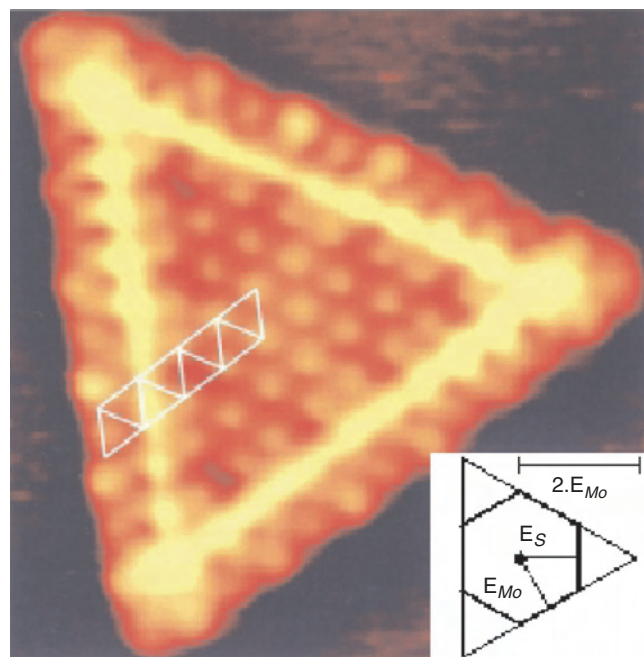


**Figure 17.** An atom-resolved STM image ( $4.1 \times 4.1 \text{ nm}$ ) of a  $\text{MoS}_2$  nanocrystal. The grids show the registry of the edge atoms relative to those in the basal plane of the  $\text{MoS}_2$  triangle. The yellow triangle is the manifestation of a one-dimensional electronic edge state. The inset shows a Wulff construction of the  $\text{MoS}_2$  crystal. Reprinted with permission from [218], S. Helveg et al., *Phys. Rev. Lett.* 84, 951 (2000). © 2000, American Physical Society.

the edges are out of registry with the S atoms in the hexagonal lattice of the basal plane and that they are shifted by half a lattice constant along the edge. A comparison with DFT calculations revealed that the observed edge structure is only obtained when the stoichiometry on the edges is changed; for example, only one S atom is bound to a Mo edge atom. Thus these atomic-resolution STM images provided insights into the morphology (shape) and edge structure of the  $\text{MoS}_2$  nanocrystals.

The same group observed directly by STM that a single layer of these  $\text{MoS}_2$  nanoparticles supports one-dimensional electronic edge states (see Fig. 17), which were viewed as one-dimensional conducting wires [219].

For small metal clusters composed of up to a few tens of atoms and supported on metal surfaces, no atomically resolved STM images exist; different cluster sizes can often be distinguished only by small variations in their heights and not by different contrasts in the measured electron density. An interesting method was introduced by Schaub et al. [220] where size-selected  $\text{Ag}_{19}$  clusters on a Pt(111) surface were decorated with rare-gas atoms. This leads to a pronounced corrugation in the rare-gas necklace around the cluster, making the rare-gas atoms a sensitive probe to determine cluster size. Figure 18 shows a high-resolution STM image and a linescan across the cluster of a gas phase deposited  $\text{Ag}_{19}$  cluster on Pt(111) surrounded by 12 Kr atoms. This situation can easily be obtained as the binding energy of Kr to step edges and around the cluster is enhanced. From the observed number of Kr atoms around the silver cluster and the shape of the ring, the cluster size is deduced. By assuming a silver atom diameter of  $2.77 \text{ \AA}$ , and knowing the Pt(111) lattice constant, and by determining the height of the cluster to be of only one monolayer, the authors showed that a regular hexagon containing 19 atoms fits perfectly the topographic image seen in

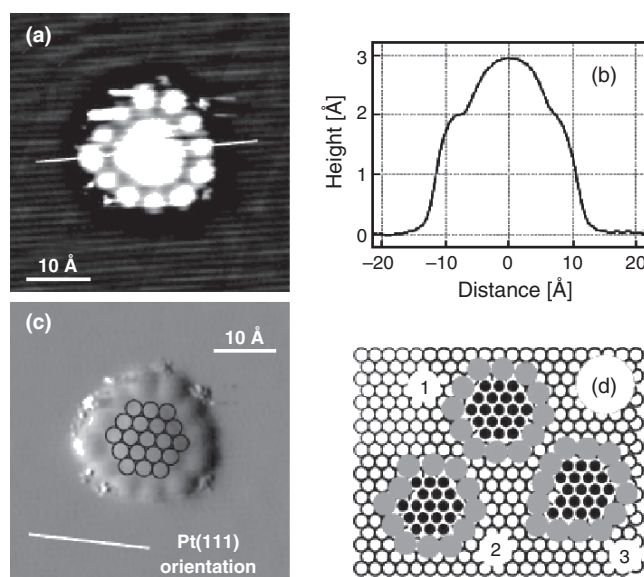


**Figure 18.**  $\text{Ag}_{19}$  cluster on Pd(111) surrounded by 12 Kr atoms. (a) The image has been filtered to increase the contrast. (b) Linescan across the cluster. (c) Model superimposed to the image. (d) Model. Reprinted with permission from [220], R. Schaub et al., *Phys. Rev. Lett.* 86, 3590 (2001). © 2001, American Physical Society.

Figure 18c. Figure 18d shows that the Kr necklace is sensitive to the form of the cluster and the exact number of silver atoms in the cluster. This is the first experiment where after cluster deposition a one-to-one correspondence between the cluster size in the beam and on the surface was obtained.

## 7. SPECIFIC NANOSTRUCTURES

### 7.1. Insulators

Metal oxides play a crucial role as insulators in many electronic and magnetic devices. As these devices become ever smaller, it becomes more and more important to understand the behavior of ultrathin insulating layers. Recently, the growth of ultrathin insulating NaCl layers on Al(111) [221] and of CoO and NiO layers on Ag(001) [222] has been studied by STM and atomic resolution has been obtained. From the change in image contrast a maximum thickness of three layers for successful imaging was inferred [221]. Based on image contrast as well as on tunneling current versus voltage curves taken on both NiO islands and Ag substrate, the existence of a bandgap has been deduced [222]. For nanostructures of CaF<sub>1</sub> and CaF<sub>2</sub> on Si(111), chemical imaging of insulators has been demonstrated using STS in combination with a simple model for tunneling across two barriers, the vacuum gap and the insulating film [94]. However, no atomic resolution has been obtained in this case and, for CaF<sub>2</sub>, it was only assumed that the full gap is already formed for the first CaF layer on Si(111) [94].

As model system for a metal oxide, Schintke et al. [39] have chosen MgO on silver. The films were grown on a Ag(001) substrate at 500 K by evaporating Mg in an O<sub>2</sub> partial pressure of  $1 \cdot 10^{-6}$  mbar [223]. After deposition of 0.3 ML MgO (Fig. 19a), two-dimensional square islands of 10–15 nm size have nucleated homogeneously on the Ag(001) surface. Some islands are embedded in the silver layer of the upper terrace, due to Ag adatom diffusion [224]. Two different island contrasts (i, ii) near a terrace step (Fig. 19a) are indicative of the position and orientation of the terrace step prior to nucleation. After deposition of about 2 ML MgO (Fig. 19d), the Ag surface is completely covered with MgO, forming terraces of typically 50 nm width and 3D pyramidal islands.

Figure 20a shows representative  $dI/dU$  spectra measured with the tip positioned above a 1-ML-thick MgO island. At negative sample bias (occupied sample states), the LDOS increases at  $-4$  V, whereas at positive sample bias (unoccupied states), two structures are detected around 1.7 V and 2.5 V. Between  $-4$  V and  $+1.7$  V, the tunnel current remains finite and the  $dI/dU$  spectrum is essentially flat. The intensity of the LDOS peak around 1.7 V observed in STS for 1 ML MgO diminishes for 2 ML and is no more detectable for a MgO film of 3 ML (Fig. 20b). This feature is attributed to MgO-Ag interface states [225]. In contrast, the high local density of unoccupied states around 2.5 eV does not decrease with film thickness and is identified with MgO states [226, 227]. Consequently the onset of the 2.5-eV peak observed in STS (Fig. 20a,b) corresponds to the onset of the MgO(001) empty surface state band [228–231].

Combining the local  $dI/dU$  observations of the occupied and unoccupied LDOS on the ultrathin MgO films (Fig. 20)

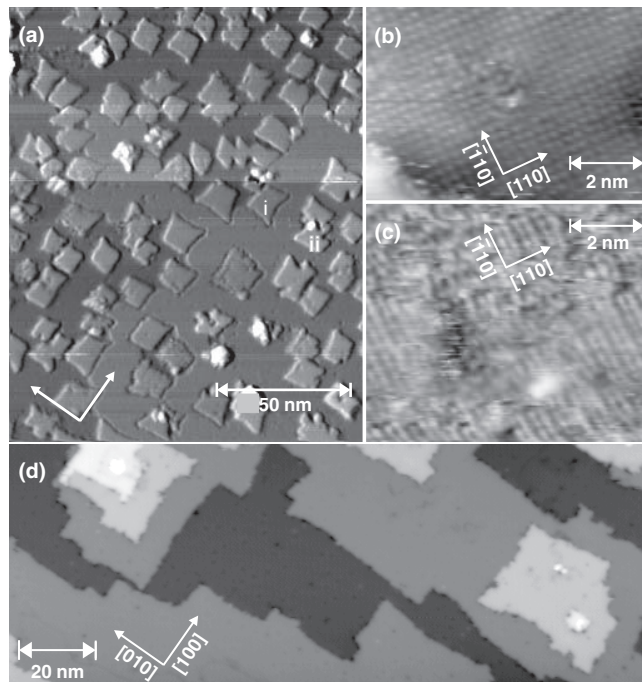


**Figure 19.** Morphology of MgO thin films: STM images at 50 K. (a) 0.3 ML MgO/Ag(001),  $U = 5.0$  V,  $I = 1.0$  nA; (b) Ag(001) atomic resolution through an MgO island,  $U = 30$  mV,  $I = 2$  pA (left bottom corner: bare Ag substrate); (c) atomic resolution of the MgO layer (one type of ion is resolved),  $U = 2.5$  V,  $I = 50$  pA; (d) 2.0 ML MgO/Ag(001),  $U = 3.0$  V,  $I = 1.0$  nA. Reprinted with permission from [39], S. Schintke et al., *Phys. Rev. Lett.* 87, 276801 (2001). © 2001, American Physical Society.

with the conventional surface science measurements on thick MgO films [232], implies that the electronic structure of a MgO(001) single-crystal surface develops already within the first three monolayers.

First-principles calculations based on DFT yielded the layer-resolved LDOS as a function of the number  $n$  of adsorbed MgO layers ( $0 \leq n \leq 3$ ) [39]. The states at  $\Gamma$  determine the minimum gap width, in agreement with the electronic structure of MgO [226, 231, 233]. In the gap, the average surface LDOS decays exponentially with the number of adsorbed MgO layers. Increasing the MgO film thickness up to three layers produces a surface bandgap corresponding to that of the five-layer pure MgO slab, which is representative for the MgO(001) surface.

Field resonance states influence the STM image contrast [234]. Their modified energetic positions when tunneling through the oxide are used to distinguish between the oxide and the metal. For STM images taken at, for example, 5 V (Fig. 19a), which corresponds to the energetic position of the second Ag(001) field resonance state when tunneling through 1 ML MgO [39], the 1 ML MgO islands appear higher than the Ag-Ag steps. At higher coverage, the apparent MgO-MgO step heights (e.g., Fig. 19d) are found to correspond to their geometric heights when tunneling into MgO states.

At a bias voltage of 2.5 V, atomic resolution of the MgO layer is obtained. (Fig. 19c). The observed surface lattice constant has twice the value of the one of MgO; thus only



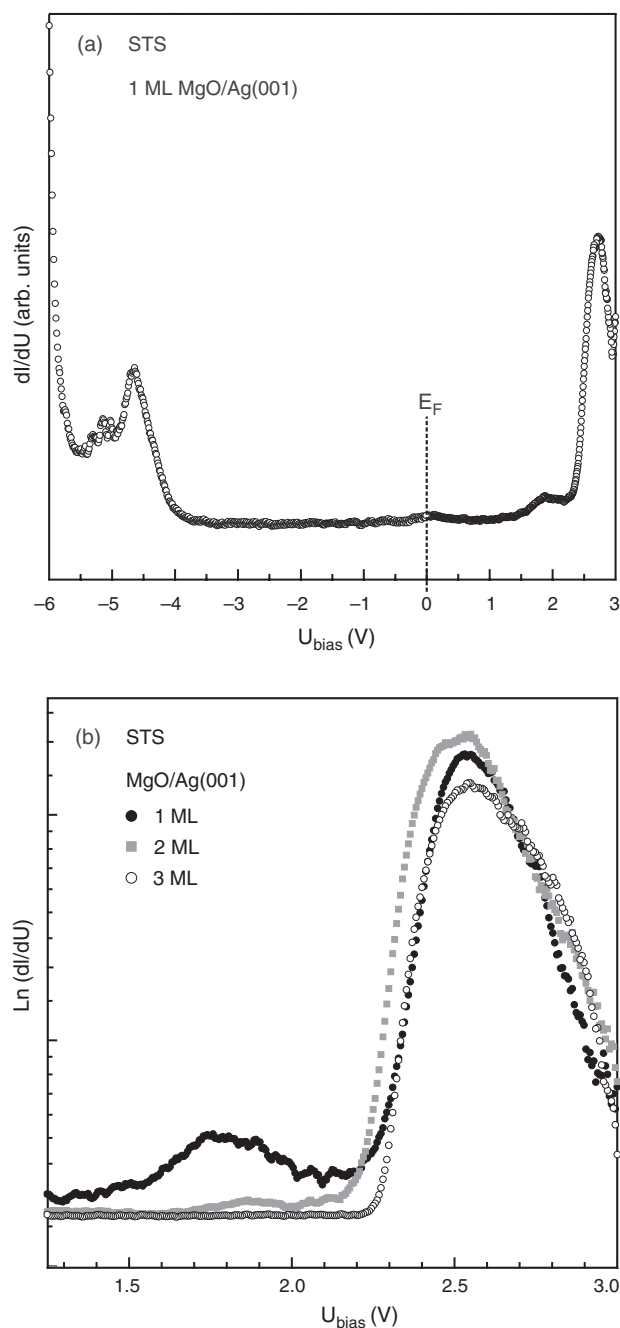


**Figure 20.** Electronic structure of ultrathin MgO/Ag(001) films as determined by STS- $dI/dU$  spectra on defect-free regions ( $U$ -sweep interval, tunneling parameters before opening the feedback loop, linear tip-sample distance variation): (a) tip placed above a 1 ML MgO island:  $-6.0$  to  $0$  V,  $U_0 = -6.0$  V,  $I_0 = 0.2$  nA,  $\frac{dz}{dU} = -0.12$  nm/V;  $3.0$  to  $0$  V,  $U_0 = 3.0$  V,  $I_0 = 0.2$  nA,  $\frac{dz}{dU} = -0.16$  nm/V; (b) film thickness dependent  $dI/dU$  spectra:  $3.0$  V to  $1.0$  V,  $U_0 = 3.0$  V,  $I_0 = 1.0$  nA,  $\frac{dz}{dU} = -0.25$  nm/V. Reprinted with permission from [39], S. Schintke et al., *Phys. Rev. Lett.* 87, 276801 (2001). © 2001, American Physical Society.

one type of ion is imaged. According to theory, the observed protrusions are due to accumulated charge density above the Mg atoms. Within the gap ( $-4$  V to  $+2.5$  V), MgO reduces exponentially the probability of tunneling into the substrate. The remaining finite density of Ag states within the gap leads to atomic resolution of the Ag(001) substrate imaged

through a 1 ML MgO island (Fig. 19b). For bias voltages outside the gap, the islands appear always with bright contrast.

Thus, within the first three atomic layers of MgO, a bandgap of about 6 eV develops corresponding to the value found for MgO(001) single crystals. These results do not just constrain the minimum usable thickness for layers of insulating MgO (and, by inference, other wide-bandgap materials). They also suggest that, by carefully controlling the number of dielectric monolayers deposited on a metal substrate, the electronic, magnetic, and chemical properties of the resulting surface could be tuned in a controlled manner. This opens new perspectives for the development of oxide heterostructure-based nanodevices [235].

## 7.2. Vortices

One of the more remarkable states of a superconductor, the Abrikosov flux lattice, is also accessible to STM. New insights into the nature of type-II superconductivity have been achieved by this local probe of the electronic density of states both inside and outside the flux cores [27–29].

The Abrikosov flux lattice was imaged in NbSe<sub>2</sub> by tunneling into the superconducting gap edge. The tunneling conductance into a single vortex core was found to be strongly peaked at the Fermi energy, suggesting the existence of core states or core excitations. Moving laterally away from the core, this peak evolves into a density of states which is consistent with a BCS superconducting gap [27]. Subsequent investigations of the same group [28] revealed a zero-bias peak in the superconducting-vortex-core spectra which splits within a coherence length of the core. Further away from the core these split peaks merge gradually with the gap edge and give a direct local measure of the superfluid velocity. Images of the vortex core states showed an anisotropy which was interpreted as a consequence of the crystalline band structure and the interaction with neighboring vortices of the Abrikosov flux lattice.

The local density of states of a superconducting vortex core has also been measured as a function of disorder in the alloy system Nb<sub>1-x</sub>Ta<sub>x</sub>Se<sub>2</sub> [29]. Here the peak observed in the zero-bias conductance at a vortex center was found to be very sensitive to disorder. The peak gradually disappeared with substitutional alloying and at  $x = 0.2$  the density in the vortex center was found to be equal to that in the normal state. It was suggested that the vortex-core spectra provide a sensitive measure of the quasi-particle scattering time.

## 7.3. Impurities and Superconductors

The competition between magnetism and superconductivity manifests itself in the dramatic reduction of the superconducting transition temperature when magnetic impurities are introduced into a superconductor [236]. Macroscopic planar tunnel junctions doped with magnetic impurities have shown sub-gap features in the density of states [237]. The first direct measurement on the structure of a magnetically induced quasi-particle excitation on the atomic length scale around a single magnetic impurity has only been achieved recently with a low-temperature STM [30].

Tunneling spectra obtained near magnetic adsorbates revealed the presence of excitations within the superconductor's energy gap which were detected over a few atomic

diameters around the impurity at the surface. The details of the local tunneling spectra were rationalized within a model calculation based on the Bogoliubov–de Gennes equations [30].

In the copper oxide high-temperature superconductors the superconductivity is believed to originate from strongly interacting electrons in the  $\text{CuO}_2$  planes. Substitution of a single impurity atom for a copper atom strongly perturbs the surrounding electronic environment and therefore was used to probe high-temperature superconductivity at the atomic scale.

In a very interesting recent experiment [31], a low-temperature STM had been employed to investigate the effects of individual zinc impurity atoms in the high-temperature superconductor  $\text{Bi}_2\text{Sr}_2\text{CaCu}_2\text{O}_{8+\delta}$ . Intense quasi-particle scattering resonances [238] were found at the Zn sites, coincident with a strong suppression of superconductivity within  $\sim 15\text{\AA}$  of the scattering sites. Imaging of the spatial dependence of the quasi-particle density of states in the vicinity of the impurity atoms revealed the long-sought fourfold symmetric quasi-particle cloud aligned with the nodes of the  $d$ -wave superconducting gap which is believed to characterize superconductivity in these materials.

#### 7.4. Nanoscale Magnetism

A long-standing challenge in magnetism was to correlate the structural and electronic properties on the local scale with the magnetic properties. Two different concepts have been used to achieve spin-polarized vacuum tunneling. (i) With magnetic STM probe tips the spin-valve effect [239] is exploited, which relies on the fact that the tunneling conductance between two ferromagnetic electrodes separated by an insulating barrier depends on whether the magnetic moments are directed parallel or antiparallel. This effect has been studied before in planar tunnel junctions [240–242] and has been applied in STM to probe the topological antiferromagnetic order of a  $\text{Cr}(001)$  surface with a  $\text{CrO}_2$  tip [243]. (ii) Optically pumped GaAs tips enable spin-polarized vacuum tunneling [244], a technique which had been applied to image the magnetic domain structure of thin Co films [245]. (Most recently, electron spin resonance techniques have been combined with STM to detect radio-frequency spin signals from clusters of a few organic molecules [250].)

These experiments were limited by the need to separate topographic, electronic, and magnetic information in the case of magnetic probe tips, and to eliminate thermal or film thickness induced effects in the case of semiconducting tips. These difficulties were overcome by tunneling into the surface state of  $\text{Gd}(0001)$  [40] which is exchange-split into a filled majority and an empty minority spin-contribution [246, 247]. In analogy to the low-temperature experiments performed with ferromagnet-insulator-superconductor planar tunneling junctions [248, 249], where the quasi-particle density of states of superconducting aluminum is split by a magnetic field into spin-up and spin-down part, Bode et al. [40] used two spin-polarized electronic states with opposite polarization to probe the magnetic orientation of the sample relative to the tip. The authors demonstrated spin-polarized tunneling by measuring the asymmetry of the differential tunneling conductance with magnetically (Fe) coated W-tips

at bias voltages corresponding to the energetic positions of the two spin-contributions of the exchange-split surface state in an external magnetic field. This method enabled the separation of the electronic and magnetic structure information. By mapping the spatial variation of the asymmetry parameter, they were able to observe the nanomagnetic domain structure of  $\text{Gd}(0001)$  ultrathin films with a spatial resolution below 20 nm [40].

This group achieved atomic resolution in spin-polarized STM at 16 K by imaging a two-dimensional antiferromagnetic structure within a pseudomorphic monolayer film of chemically identical Mn atoms on  $\text{W}(110)$  [41]. They show, with the aid of first-principles calculations, that the spin-polarized tunneling electrons give rise to an image corresponding to the magnetic superstructure and not to the chemical unit cell. Subsequently, this group observed a magnetic hysteresis on a nanometer scale in an ultrathin ferromagnetic film, consisting of an array of iron nanowires grown on a stepped  $\text{W}(110)$  substrate. The microscopic sources of hysteresis, domain wall motion, domain creation, and annihilation were observed with nanometer resolution [42].

Recently, Kubetzka et al. [43] performed low-temperature spin-polarized STM of two monolayers Fe on  $\text{W}(110)$  using tungsten tips coated with different magnetic materials. With Cr as a coating material, they recorded images with an antiferromagnetic tip. The advantage of its vanishing dipole field was most apparent in external fields. This approach appears to resolve the problem of the disturbing influence of a ferromagnetic tip in the investigation of soft magnetic materials and superparamagnetic particles.

## 8. CONCLUSION

In this review STM and STS experiments at the scale of atoms, molecules, supermolecules, clusters, and other nanostructures have been presented which reveal new and exciting physical and chemical phenomena. The common link is the characterization of the structural and electronic properties of supported nanostructures at atomic-scale spatial and meV-scale spectral resolution. The opportunities of this concept in the emerging field of nanotechnology, where size matters, are evident. For example, a reduction in size often provides an increase in speed for electronic or magnetic devices. Any further advancement towards a future nanotechnology will depend crucially on the precise control, characterization, and ultimately, functionalization, of matter at the atomic and molecular level. This prospect remains an inciting scientific and technological challenge. To cite again R. P. Feynman, *there is plenty of room at the bottom . . .*

## GLOSSARY

**Adatom** An atom adsorbed at the surface.

**Catalytic activity** The capacity of a substance to take part in a chemical reaction.

**Chemical imaging** The possibility to obtain a chemical (elemental) contrast in STM images.

**Cluster** Aggregate formed by atoms.

**Confined electronic state** An electronic state which is confined in one, two or three dimensions. The confinement gives rise to quantum size effects.

**Fano resonance** Interference between two competing electronic transitions leading to the same final state.

**Field resonance state** A two-dimensional unoccupied electronic state which is localized outside the surface.

**High-temperature superconductor** Superconductor with a high critical temperature, typically a ceramic.

**Impurity** An atom (or adatom) of a species different from the one of the medium.

**Kondo effect** Screening of the magnetic moment of an impurity by the conduction electrons of the medium.

**Lifetime** Laps of time during which an excited state exists, before it decays.

**Photon emission** Inelastic process in which photons are emitted during electron tunneling between tip and sample of an STM.

**Standing waves** Stationary electronic waves, due to constructive interference between waves travelling backward and forward.

**Superconductor** Material for which the following properties are verified below the critical temperature: it is perfect diamagnet, it has no measurable DC electrical resistivity, it presents a gap centered around the Fermi level.

**Supramolecular self-assembly** Self-organization of molecule, giving rise to molecular aggregates.

**Surface diffusion** The capacity of an adatom or a molecule to diffuse at surfaces. It depends on both, the adatom and the surface, as well as on the temperature.

**Surface state** Electronic state existing only at the surface, decaying exponentially into bulk and into vacuum.

**Ultrathin insulator** Insulator film grown on a substrate with a thickness of only few atomic layers.

**Vortices** In superconductors, regions of the material that remain in the normal state, through which the lines of the magnetic field pass.

## ACKNOWLEDGMENTS

It is a pleasure to acknowledge a very fruitful and stimulating collaboration with S. Abbet, A. Baldereschi, R. Berndt, M. Böhrringer, O. Bryant, R. Car, S. Crampin, B. Delley, A. De Vita, R. Gaisch, J. K. Gimzewski, U. Heiz, J. Li, L. Libioulle, F. Mauri, S. Messerli, K. Morgenstern, F. Patthey, M. Pivetta, B. Reihl, A. Sanchez, S. Schintke, R. R. Schlittler, F. Silly, M. Stengel, M. Tschudy, and M. Vladimirova. This work was supported by the Swiss National Science Foundation.

## REFERENCES

1. R. P. Feynman, *Eng. Sci.* 22 (February) (1960).
2. G. Binnig, H. Rohrer, Ch. Gerber, and E. Weibel, *Appl. Phys. Lett.* 40, 178 (1982).
3. G. Binnig, H. Rohrer, Ch. Gerber, and E. Weibel, *Phys. Rev. Lett.* 49, 57 (1982).
4. D. M. Eigler and E. K. Schweizer, *Nature* 344, 524 (1990).
5. D. M. Eigler, C. P. Lutz, and W. E. Rudge, *Nature* 352, 600 (1991).
6. A. J. Heinrich, C. P. Lutz, J. A. Gupta, and D. M. Eigler, *Science* 298, 1381 (2002).
7. S.-W. Hla, L. Bartels, G. Meyer, and K.-H. Rieder, *Phys. Rev. Lett.* 85, 2777 (2000).
8. R. Berndt, R. Gaisch, J. K. Gimzewski, B. Reihl, R. R. Schlittler, W.-D. Schneider, and M. Tschudy, *Science* 262, 1425 (1993).
9. N. Niliius, N. Ernst, and H.-J. Freund, *Phys. Rev. Lett.* 84, 3994 (2000).
10. F. Silly, A. O. Gusev, A. Taleb, F. Charra, and M.-P. Pileni, *Phys. Rev. Lett.* 84, 5840 (2000).
11. M. Sakurai and M. Aono, *Phys. Rev. B* 64, 045402 (2001).
12. X. H. Qiu, G. V. Nazin, and W. Ho, *Science* 299, 542 (2003).
13. M. F. Crommie, C. P. Lutz, and D. M. Eigler, *Nature* 363, 524 (1993).
14. Y. Hasegawa and Ph. Avouris, *Phys. Rev. Lett.* 71, 1071 (1993).
15. M. F. Crommie, C. P. Lutz, and D. M. Eigler, *Science* 262, 218 (1993).
16. Ph. Avouris and I. W. Lyo, *Science* 264, 942 (1994).
17. Ph. Avouris, I.-W. Lyo, and P. Molinàs-Mata, *Chem. Phys. Lett.* 240, 423 (1995).
18. J. Li, W.-D. Schneider, and R. Berndt, *Phys. Rev. B* 56, 7656 (1997).
19. J. Li, W.-D. Schneider, R. Berndt, and S. Crampin, *Phys. Rev. Lett.* 80, 3332 (1998).
20. L. Bürgi, O. Jeandupeux, A. Hirstein, H. Brune, and K. Kern, *Phys. Rev. Lett.* 81, 5370 (1998).
21. J. Kliewer, R. Berndt, and S. Crampin, *Phys. Rev. Lett.* 85, 4936 (2000).
22. J. Kliewer, R. Berndt, and S. Crampin, *New J. Phys.* 3, 22.1 (2001).
23. K.-F. Braun and K.-H. Rieder, *Phys. Rev. Lett.* 88, 096801 (2002).
24. J. Li, W.-D. Schneider, R. Berndt, and B. Delley, *Phys. Rev. Lett.* 80, 2893 (1998). See also: Errata, *Nature* 405, 752 (2000).
25. V. Madhavan, W. Chen, T. Jamneala, M. F. Crommie, and N. S. Wingreen, *Science* 280, 569 (1998).
26. H. C. Manoharan, C. P. Lutz, and D. M. Eigler, *Nature* 403, 512 (2000).
27. H.-F. Hess, R. B. Robinson, R. C. Dynes, J. M. Valles, Jr., and J. V. Waszcak, *Phys. Rev. Lett.* 62, 214 (1989).
28. H.-F. Hess, R. B. Robinson, and J. V. Waszcak, *Phys. Rev. Lett.* 64, 2711 (1990).
29. Ch. Renner, A. D. Kent, Ph. Niedermann, and Ø. Fischer, *Phys. Rev. Lett.* 67, 1650 (1991).
30. A. Yazdani, B. A. Jones, C. P. Lutz, M. F. Crommie, and D. M. Eigler, *Science* 275, 1767 (1997).
31. S. H. Pan, E. W. Hudson, K. M. Lang, H. Eisaki, S. Uchida, and J. C. Davis, *Nature* 403, 746 (2000).
32. M. Böhrringer, K. Morgenstern, W.-D. Schneider, R. Berndt, F. Mauri, A. De Vita, and R. Car, *Phys. Rev. Lett.* 83, 324 (1999).
33. M. Böhrringer, K. Morgenstern, W.-D. Schneider, and R. Berndt, *Angew. Chem.* 111, 832 (1999); *Angew. Chem. Int. Ed. Engl.* 38, 821 (1999).
34. M. Böhrringer, W.-D. Schneider, and R. Berndt, *Angew. Chem.* 112, 821 (2000); *Angew. Chem. Int. Ed. Engl.* 39, 792 (2000).
35. J. V. Barth, J. Weckesser, C. Cai, P. Günter, L. Bürgi, O. Jeandupeux, and K. Kern, *Angew. Chem. Int. Ed. Engl.* 39, 1230 (2000).
36. J. Weckesser, A. De Vita, J. V. Barth, C. Cai, and K. Kern, *Phys. Rev. Lett.* 87, 096101 (2001).
37. J. V. Barth, J. Weckesser, G. Trimarchi, M. Vladimirova, A. De Vita, C. Cai, H. Brune, P. Günter, and K. Kern, *J. Am. Chem. Soc.* 124, 7991 (2002).
38. T. Yokoyama, S. Yokoyama, T. Kamikado, Y. Okuno, and S. Mashiko, *Nature* 413, 619 (2001).
39. S. Schintke, S. Messerli, M. Pivetta, L. Libioulle, F. Patthey, M. Stengel, A. De Vita, and W.-D. Schneider, *Phys. Rev. Lett.* 87, 276801 (2001).

40. M. Bode, M. Getzlaff, and R. Wiesendanger, *Phys. Rev. Lett.* 81, 4256 (1998).
41. S. Heinze, M. Bode, O. Pietzsch, A. Kubetzka, X. Nie, S. Blügel, and R. Wiesendanger, *Science* 288, 1805 (2000).
42. O. Pietzsch, A. Kubetzka, M. Bode, and R. Wiesendanger, *Science* 292, 2053 (2001).
43. A. Kubetzka, M. Bode, O. Pietzsch, and R. Wiesendanger, *Phys. Rev. Lett.* 88, 057201 (2002).
44. B. C. Stipe, M. A. Rezaei, and W. Ho, *Science* 280, 1732 (1998).
45. H. J. Lee and W. Ho, *Science* 286, 1719 (1999).
46. G. Dujardin, R. E. Walkup, and P. Avouris, *Science* 255, 1232 (1992).
47. T.-C. Shen, C. Wang, G. C. Abeln, J. R. Tucker, J. W. Leyding, Ph. Avouris, and R. E. Walkup, *Science* 268, 1590 (1995).
48. T. A. Jung, R. R. Schlittler, J. K. Gimzewski, H. Tang, and C. Joachim, *Science* 271, 181 (1996).
49. J. Li, R. Berndt, and W.-D. Schneider, *Phys. Rev. Lett.* 76, 1888 (1996).
50. G. Meyer, L. Bartels, S. Zöphel, E. Henze, and K. H. Rieder, *Phys. Rev. Lett.* 78, 1512 (1997).
51. L. Bartels, G. Meyer, and K. H. Rieder, *Phys. Rev. Lett.* 79, 697 (1997).
52. B. C. Stipe, M. A. Rezaei, W. Ho, S. Gao, M. Persson, and B. I. Lundquist, *Phys. Rev. Lett.* 78, 4410 (1997).
53. L. Bartels, G. Meyer, K.-H. Rieder, D. Velic, E. Knoesel, A. Hotzel, M. Wolf, and G. Ertl, *Phys. Rev. Lett.* 80, 2004 (1998).
54. J. Li, W.-D. Schneider, and R. Berndt, *Appl. Phys. A* 66, S675 (1998).
55. J. K. Gimzewski and C. Joachim, *Science* 283, 1683 (1999).
56. S. Messerli, S. Schintke, K. Morgenstern, A. Sanchez, U. Heiz, and W.-D. Schneider, *Surf. Sci.* 465, 331 (2000).
57. L. J. Lauhon and W. Ho, *J. Phys. Chem. A* 104, 2463 (2000).
58. G. Binnig, C. F. Quate, and Ch. Gerber, *Phys. Rev. Lett.* 56, 930 (1986).
59. Nanotechnology Research Directions, M. C. Roco, R. S. Williams, and P. Alivisatos, Eds. Workshop Report, 1999. (<http://itri.loyola.edu/IWGN.Research.Directions/>).
60. P. K. Hansma and J. Tersoff, *J. Appl. Phys.* 61, R1 (1987).
61. R. M. Tromp, *J. Phys.: Condens. Matter* 1, 10211 (1989).
62. J. A. Stroscio and D. M. Eigler, *Science* 254, 1319 (1991).
63. R. Wiesendanger and H.-J. Güntherodt, Eds., "Scanning Tunneling Microscopy, Springer Series in Surface Science 28." Springer, Berlin, 1992.
64. C. J. Chen, "Introduction to Scanning Tunneling Microscopy." Oxford Univ. Press, London, 1993.
65. J. A. Stroscio and W. J. Kaiser, Eds., "Scanning Tunneling Microscopy, Methods of Experimental Physics," Vol. 27. Academic Press, New York, 1993.
66. R. M. Feenstra, *Surf. Sci.* 299/300, 965 (1994).
67. R. Wiesendanger, "Scanning Probe Microscopy and Spectroscopy, Method and Applications." Cambridge Univ. Press, 1994.
68. R. Wiesendanger, Ed., "Scanning Probe Microscopy—Analytical Methods, Nanoscience and Technology." Springer, Berlin, Heidelberg, 1998.
69. W.-D. Schneider, Ed., *J. Electron Spectrosc. Rel. Phen.* 109, 1 (2000).
70. S. Ushioda, *J. Electron Spectrosc. Rel. Phen.* 109, 169 (2000).
71. Ch. Renner, Ph. Niedermann, A. D. Kent, and O. Fischer, *Rev. Sci. Instrum.* 61, 965 (1990).
72. R. Gaisch, J. K. Gimzewski, B. Reihl, R. R. Schlittler, M. Tschudy, and W.-D. Schneider, *Ultramicroscopy* 42–44, 6844 (1992).
73. R. R. Schulz and C. Rossel, *Rev. Sci. Instrum.* 65, 1918 (1994).
74. S. H. Tessmer, D. J. van Harlingen, and J. W. Lyding, *Rev. Sci. Instrum.* 65, 2855 (1994).
75. G. Meyer, *Rev. Sci. Instrum.* 67, 2960 (1996).
76. S. Behler, M. K. Rose, J. C. Dunphy, D. F. Ogletree, M. Salmeron, and C. Chapelier, *Rev. Sci. Instrum.* 68, 2479 (1997).
77. H.-P. Rust, J. Buisset, E. K. Schweizer, and L. Cramer, *Rev. Sci. Instrum.* 68, 192 (1997).
78. C. Witneven, R. Dombrowski, S. H. Pan, and R. Wiesendanger, *Rev. Sci. Instrum.* 68, 3806 (1997).
79. J. H. Ferris, J. G. Kushmerick, J. A. Johnson, M. G. Yoshikawa Youngquist, R. B. Kessinger, H. W. Kingsbury, and P. S. Weiss, *Rev. Sci. Instrum.* 69, 2691 (1998).
80. L. E. Harrell and P. N. First, *Rev. Sci. Instrum.* 70, 125 (1999).
81. B. C. Stipe, M. A. Rezaei, and W. Ho, *Rev. Sci. Instrum.* 70, 137 (1999).
82. O. Pietzsch, A. Kubetzka, D. Hausde, M. Bode, and R. Wiesendanger, *Rev. Sci. Instrum.* 71, 424 (2000).
83. E. T. Foley, A. F. Kam, and J. W. Lyding, *Rev. Sci. Instrum.* 71, 3428 (2000).
84. P. T. Sprunger, E. Laegsgaard, I. Stensgaard, and F. Besenbacher, *Rev. Sci. Instrum.* 72, 1438 (2001).
85. T. H. Chang, C. H. Yang, M. J. Yang, and J. B. Dattelis, *Rev. Sci. Instrum.* 72, 2989 (2001).
86. Y. KoShibata, S. Chiba, M. Iwatsuki, and H. Tokumoto, *Rev. Sci. Instrum.* 72, 2977 (2001).
87. M. Kemering, J. W. Gerrisen, J. G. H. Hermsen, P. M. Koenrad, H. van Kempen, and J. H. Wolter, *Rev. Sci. Instrum.* 72, 132 (2001).
88. N. Moussy, H. Courtois, and B. Pannetier, *Rev. Sci. Instrum.* 72, 128 (2001).
89. S. H. Pan, E. W. Hudson, and J. C. Davis, *Rev. Sci. Instrum.* 70, 1459 (1999).
90. M. Kugler, Ch. Renner, V. Mikheev, G. Batey, and O. Fischer, *Rev. Sci. Instrum.* 71, 1475 (2000).
91. J. Tersoff and D. R. Hamann, *Phys. Rev. B* 31, 805 (1985).
92. R. M. Feenstra and P. Mårtensson, *Phys. Rev. Lett.* 61, 447 (1988); P. Mårtensson and R. M. Feenstra, *Phys. Rev. B* 39, 7744 (1989).
93. W. J. Kaiser and R. C. Jaklevic, *Surf. Sci.* 181, 55 (1987).
94. J. Viernow, D. Z. Petrovykh, A. Kirakosian, J.-L. Lin, F. M. Men, M. Henzler, and F. J. Himpsel, *Phys. Rev. B* 59, 10356 (1999).
95. J. K. Gimzewski, B. Reihl, J. H. Coombs, and R. R. Schlittler, *Z. Phys. B* 72, 497 (1988).
96. G. Hoffmann, J. Kliewer, and R. Berndt, *Phys. Rev. Lett.* 87, 176803 (2001).
97. G. Hoffmann, J. Kröger, and R. Berndt, *Rev. Sci. Instrum.* 73, 305 (2002).
98. M. F. Crommie, C. P. Lutz, and D. M. Eigler, *Phys. Rev. B* 48, 2851 (1993).
99. E. J. Heller, M. F. Crommie, C. P. Lutz, and D. M. Eigler, *Nature* 369, 464 (1994).
100. E. V. Albano, S. Daiser, R. Miranda, and K. Wandelt, *Surf. Sci.* 150, 386 (1985).
101. A. A. Abrikosov, *Physics* 2, 5, 61 (1965).
102. H. Suhl, in "Theory of Magnetism in Transition Metals" (W. Marshall, Ed.), pp. 116–205. Academic Press, London, 1967.
103. J. Kondo, *Progr. Theor. Phys.* 32, 37 (1964).
104. P. W. Anderson, *Phys. Rev.* 124, 41 (1961).
105. O. Gunnarsson and K. Schönhammer, in "Handbook on the Physics and Chemistry of Rare Earths, (K. A. Gschneidner, L. Eyring and S. Hüfner, Eds.), Vol. 10, p. 103. Elsevier, Amsterdam, 1987.
106. G. Gruner and A. Zawadowski, *Rep. Prog. Phys.* 37, 1479 (1974).
107. P. A. Lee, T. M. Rice, J. W. Serene, L. S. Sham, and J. W. Wilkins, *Comm. Condens. Matter Phys.* 12, 99 (1986).
108. A. C. Hewson, "The Kondo Problem to Heavy Fermions." Cambridge Univ. Press, 1993.
109. F. Patthey, J.-M. Imer, W.-D. Schneider, H. Beck, Y. Baer, and B. Delley, *Phys. Rev. B* 42, 8864 (1990).
110. D. Malterre, M. Grioni, and Y. Baer, *Adv. Phys.* 45, 299 (1996).
111. M. Garnier, K. Breuer, D. Purdie, M. Hengsberger, Y. Baer, and B. Delley, *Phys. Rev. Lett.* 78, 4127 (1997).
112. J. Li, Ph.D. Thesis, University of Lausanne, Switzerland, 1997.

113. M. P. Everson, R. C. Jaklevic, and W. Shen, *J. Vac. Sci. Technol. A* 8, 3662 (1990).
114. L. C. Davis, M. P. Everson, R. C. Jaklevic, and W. Shen, *Phys. Rev. B* 43, 3821 (1991).
115. R. Paniago, R. Matzdorf, G. Meister, and A. Goldmann, *Surf. Sci.* 336, 113 (1995).
116. S. Hershfield, J. H. Davies, and J. W. Wilkins, *Phys. Rev. Lett.* 67, 3720 (1991).
117. F. Patthey, W.-D. Schneider, Y. Baer, and B. Delley, *Phys. Rev. Lett.* 58, 2810 (1987).
118. U. Fano, *Phys. Rev.* 124, 1866 (1961).
119. N. D. Lang, *Phys. Rev. Lett.* 58, 45 (1987); *Phys. Rev. B* 34, 5947 (1986).
120. P. Coleman, *Phys. Rev. B* 29, 3035 (1984).
121. V. Madhavan, W. Chen, T. Jamneala, and M. F. Crommie, *Phys. Rev. B* 64, 165412 (2001).
122. N. Knorr, M. A. Schneider, L. Diekhöner, P. Wahl, and K. Kern, *Phys. Rev. Lett.* 88, 096804 (2002).
123. M. A. Schneider, L. Vitali, N. Knorr, and K. Kern, *Phys. Rev. B* 65, 1214065 (2002).
124. W. Chen, T. Jamneala, V. Madhavan, and M. F. Crommie, *Phys. Rev. B* 60, R8529 (1999).
125. K. Nagaoka, T. Jamneala, M. Grobis, and M. F. Crommie, *Phys. Rev. Lett.* 88, 077205 (2002).
126. T. W. Odom, J.-L. Huang, C. L. Cheung, and S. M. Lieber, *Science* 290, 1549 (2000).
127. O. Yu. Kolesnychenko, R. de Kort, M. I. Katsnelson, A. I. Lichtenstein, and H. van Kempen, *Nature* 415, 507 (2002).
128. A. Schiller and S. Hershfield, *Phys. Rev. B* 61, 9036 (2000).
129. O. Ujsaghi, J. Kroha, L. Szunyogh, and A. Zawadowski, *Phys. Rev. Lett.* 85, 2557 (2000).
130. M. Plihal and J. M. Gadzuk, *Phys. Rev. B* 63, 085404 (2001).
131. G. F. Fiete, J. S. Hersch, E. J. Heller, H. C. Manoharan, C. P. Lutz, and D. M. Eigler, *Phys. Rev. Lett.* 86, 2392 (2001).
132. Ph. Avouris, I.-W. Lyo, and R. E. Walkup, *J. Vac. Sci. Technol. B* 12, 1447 (1994).
133. J. Li, W.-D. Schneider, S. Crampin, and R. Berndt, *Surf. Sci.* 422, 95 (1999).
134. J. Li, W.-D. Schneider, R. Berndt, O. R. Bryant, and S. Crampin, *Phys. Rev. Lett.* 81, 4464 (1998).
135. D. Hoffmann, J. Y. Grand, R. Möller, A. Rettenberger, and K. Läufer, *Phys. Rev. B* 52, 13796 (1995).
136. W. Chen, V. Madhavan, T. Jamneala, and M. F. Crommie, *Phys. Rev. Lett.* 80, 1469 (1998).
137. M. A. Schneider, M. Wenderoth, K. J. Engel, M. A. Rosentreter, A. J. Heinrich, and R. G. Ulbrich, *Appl. Phys. A* 66, S161 (1998).
138. G. Hörmandinger and J. B. Pendry, *Phys. Rev. B* 50, 18607 (1994).
139. G. Hörmandinger, *Phys. Rev. Lett.* 73, 910 (1994).
140. S. Crampin, M. H. Boon, and J. E. Inglesfield, *Phys. Rev. Lett.* 73, 1015 (1994).
141. S. Crampin and O. R. Bryant, *Phys. Rev. B* 54, R17367 (1996).
142. H. K. Harbury and W. Porod, *Phys. Rev. B* 53, 15455 (1996).
143. Y. S. Chan and E. J. Heller, *Phys. Rev. Lett.* 78, 2570 (1997).
144. R. Matzdorf, *Surf. Sci. Rep.* 30, 153 (1997).
145. A. Goldmann, R. Matzdorf, and F. Theilmann, *Surf. Sci.* 414, L932 (1998).
146. S. D. Kevan, *Phys. Rev. Lett.* 50 526 (1983); J. Tersoff and S. D. Kevan *Phys. Rev. B* 28, 4267 (1983); S. D. Kevan and R. H. Gaylor, *Phys. Rev. B* 36, 5809 (1987).
147. B. A. McDougall, T. Balasubramanian, and E. Jensen, *Phys. Rev. B* 51, 13891 (1995).
148. F. Theilmann, R. Matzdorf, G. Meister, and A. Goldmann, *Phys. Rev. B* 56, 3632 (1997).
149. J. Tersoff and D. R. Hamann, *Phys. Rev. B* 31 (1985) 805; *Phys. Rev. B* 58, 45 (1987).
150. L. Bürgi, O. Jeandupeux, H. Brune, and K. Kern, *Phys. Rev. Lett.* 82, 4516 (1999).
151. E. N. Economou, "Green's Functions for Quantum Physics." Springer-Verlag, Berlin, 1983.
152. S. Crampin, *J. Phys. Condens. Matter* 5, 4647 (1993).
153. G. Hörmandinger, *Phys. Rev. B* 49, 13897 (1994).
154. A. Zawadowski, *Phys. Rev.* 163, 341 (1967); J. A. Appelbaum, and W. F. Brinkman, *Phys. Rev.* 186, 464 (1969).
155. G. Grimvall, "The Electron-Phonon Interaction in Metals." North-Holland, Amsterdam, New York, 1981.
156. D. Pines and P. Nozières, "The theory of quantum liquids." Benjamin, New York, 1969.
157. J. Klier, R. Berndt, E. V. Chulkov, V. M. Silkin, P. M. Echenique, and S. Crampin, *Science* 288, 1399 (2000).
158. F. Reinert, G. Nicolay, S. Schmidt, D. Ehm, and S. Hufner, *Phys. Rev. B* 63, 115415 (2001).
159. A. Eiguren, B. Hellsing, F. Reinert, G. Nicolay, E. V. Chulkov, V. M. Silkin, S. Hufner, and P. M. Echenique, *Phys. Rev. Lett.* 88, 066805 (2002).
160. M. Pivetta, F. Silly, F. Patthey, J. P. Pelz, and W.-D. Schneider, *Phys. Rev. B* 67, 193402 (2003).
161. E. Bertel and M. Donath, "Electronic Surface and Interface States on Metallic Systems." World Scientific, Singapore, 1995, and references therein.
162. N. Memmel and E. Bertel, *Phys. Rev. Lett.* 75, 485 (1995).
163. N. García and P. A. Serena, *Surf. Sci.* 330, L665 (1995).
164. E. Bertel, P. Roos, and J. Lehmann, *Phys. Rev. B* 52, R14384 (1995).
165. S. J. Stranick, M. M. Kamna, and P. S. Weiss, *Science* 266, 99 (1994).
166. E. Bertel, *Phys. Stat. Sol. A* 159, 235 (1997).
167. E. J. Heller, M. F. Crommie, C. P. Lutz, and D. M. Eigler, *Nature* 369, 464 (1994).
168. M. F. Crommie, C. P. Lutz, D. M. Eigler, and E. J. Heller, *Surf. Rev. Lett.* 2, 127 (1995).
169. S. Crampin, M. H. Boon, and J. E. Inglesfield, *Phys. Rev. Lett.* 73, 1015 (1994).
170. S. Crampin and O. R. Bryant, *Phys. Rev. B* 54, R17367 (1996).
171. H. K. Harbury and W. Porod, *Phys. Rev. B* 53, 15455 (1996); Y. S. Chan and E. J. Heller, *Phys. Rev. Lett.* 78, 2570 (1997).
172. O. Sánchez, J. M. García, P. Segovia, J. Alvarez, A. L. Vásquez de Parga, J. E. Ortega, M. Prietsch, and R. Miranda, *Phys. Rev. B* 52, 7894 (1995).
173. S. Crampin, *J. Phys.: Condens. Matter* 6, L613 (1994).
174. S. Crampin, M. Nekovee, and J. E. Inglesfield, *Phys. Rev. B* 51, 7318 (1995).
175. M. Tinkham, "Group Theory and Quantum Mechanics." McGraw-Hill, New York, 1964.
176. H. Röder, K. Bromann, H. Brune, and K. Kern, *Phys. Rev. Lett.* 74, 3217 (1995).
177. K. Morgenstern, K.-F. Braun, and K.-H. Rieder, *Phys. Rev. Lett.* 89, 226801 (2002).
178. K. H. Lau and W. Kohn, *Surf. Sci.* 75, 69 (1978).
179. E. Wahlström, I. Ekvall, H. Olin, and L. Wallden, *Appl. Phys. A* 66, S1107 (1998).
180. J. Repp, F. Moresco, G. Meyer, K.-H. Rieder, P. Hylgaard, and M. Persson, *Phys. Rev. Lett.* 85, 2981 (2000).
181. N. Knorr, H. Brune, M. Eppe, A. Hirstein, M. A. Schneider, and K. Kern, *Phys. Rev. B* 65, 115420 (2002).
182. S. G. Lemay, J. W. Janssen, M. van den Hout, M. Mooij, M. J. Bronikowski, P. A. Willis, R. E. Smalley, L. P. Kouwenhoven, and C. Dekker, *Nature* 412, 617 (2001).
183. N. Niluis, T. M. Wallis, and W. Ho, *Science* 297, 1853 (2002).
184. J. N. Randall, M. A. Reed, and G. A. Frazier, *J. Vac. Sci. Technol. B* 7, 1398 (1989).
185. G. M. Whitesides, J. P. Matthias, and C. T. Seto, *Science* 254, 1312 (1991).
186. H. Ohtani, R. J. Wilson, S. Chiang, and C. M. Mate, *Phys. Rev. Lett.* 60, 2398 (1988).

187. V. M. Hallmark, S. Chiang, J. K. Braun, and Ch. Wöll, *Phys. Rev. Lett.* 66, 48 (1991).
188. T. A. Jung, R. R. Schlittler, and J. K. Gimzewski, *Nature* 386, 696 (1997).
189. G. P. Lopinski, D. J. Moffatt, D. D. M. Wayner, and R. A. Wolkow, *Nature* 392, 909 (1998).
190. Kühnle, T. R. Linderoth, B. Hammer, and F. Besenbacher, *Nature* 415, 891 (2002).
191. J. V. Barth, H. Brune, G. Ertl, and R. J. Behm, *Phys. Rev. B* 42, 9307 (1990).
192. M. Böhringer, K. Morgenstern, W.-D. Schneider, and R. Berndt, *Surf. Sci.* 457, 37 (2000).
193. M. Böhringer, K. Morgenstern, W.-D. Schneider, M. Wühh, Ch. Wöll, and R. Berndt, *Surf. Sci.* 444, 199 (2000).
194. M. Böhringer, W.-D. Schneider, and R. Berndt, *Surf. Sci.* 57, 72 (1998).
195. M. Böhringer, W.-D. Schneider, R. Berndt, K. Glöckler, M. Sokolowski, and E. Umbach, *Phys. Rev. B* 57, 4081 (1998).
196. A. J. Fisher and P. E. Blöchl, *Phys. Rev. Lett.* 70, 3263 (1993).
197. M. Vladimirova, M. Stengel, A. De Vita, A. Baldereschi, M. Böhringer, K. Morgenstern, R. Berndt, and W.-D. Schneider, *Europhys. Lett.* 56, 254 (2001).
198. D. Andelman and P.-G. de Gennes, *C. R. Acad. Sci. (Paris)* 307, 233 (1988); D. Andelman, *J. Am. Chem. Soc.* 111, 6536 (1989).
199. L. Pérez-Garcia and D. B. Amabilino, *Chem. Soc. Rev.* 31, 342 (2002).
200. O. Bjornholm, *Contemp. Phys.* 31, 309 (1990).
201. R. M. Feenstra, *Phys. Rev. Lett.* 63, 1412 (1989).
202. P. N. First, J. A. Stroschio, R. A. Dragoset, T. D. Pierce, and J. R. Celotta, *Phys. Rev. Lett.* 63, 1416 (1989).
203. Y. Kuk, M. F. Jarrold, P. J. Silverman, J. E. Bower, and W. L. Brown, *Phys. Rev. B* 39, 11168 (1989).
204. B. Marsen, M. Lonfat, P. Scheier, and K. Sattler, *J. Electron Spectrosc. Rel. Phen.* 109, 157 (2000).
205. K.-H. Meiwes-Broer, in "Metal Clusters at Surfaces" (K.-H. Meiwes-Broer, Ed.), pp. 151 ff. Springer, Berlin, 2000.
206. H. Hövel, B. Grimm, M. Bödecker, K. Fieger, and B. Reihl, *Surf. Sci.* 465, 15 (2000).
207. M. Valden, X. Lai, and D. W. Goodman, *Science* 281, 1647 (1998).
208. A. Sanchez, S. Abbet, U. Heiz, W.-D. Schneider, H. Häkkinen, R. N. Barnett, and U. Landmann, *J. Phys. Chem. A* 103, 9573 (1999).
209. B. D. Hall, M. Flüeli, R. Monot, and J.-P. Borel, *Phys. Rev. B* 43, 3906 (1991).
210. B. D. Hall, M. Flüeli, D. Reinhard, J.-P. Borel, and R. Monot, *Rev. Sci. Instrum.* 62, 1481 (1991).
211. D. Reinhard, B. D. Hall, P. Berthoud, S. Valkealahti, and R. Monot, *Phys. Rev. Lett.* 79, 1459 (1997).
212. D. Reinhard, B. D. Hall, P. Berthoud, S. Valkealahti, and R. Monot, *Phys. Rev. B* 58, 4917 (1998).
213. K. Hojrup Hansen, T. Worren, S. Stempel, E. Laegsgaard, M. Bäumer, H.-J. Freund, F. Besenbacher, and I. Stensgaard, *Phys. Rev. Lett.* 83, 4120 (1999).
214. F. Vanolli, U. Heiz, and W.-D. Schneider, *Chem. Phys. Lett.* 277, 527 (1997).
215. K. Sattler, *Z. Phys. D* 19, 287 (1991).
216. Y.-W. Mo, D. E. Savage, B. S. Swartzentruber, and M. G. Lagally, *Phys. Rev. Lett.* 65, 1020 (1990).
217. A. Piednoir, E. Perrot, S. Granjeaud, A. Humbert C. Chapon, and C. R. Henry, *Surf. Sci.* 391, 19 (1997).
218. S. Helveg, J. V. Lauritsen, E. Laegsgaard, I. Stensgaard, J. K. Nørskov, B. S. Clausen, H. Topsoe, and F. Besenbacher, *Phys. Rev. Lett.* 84, 951 (2000).
219. M. V. Bollinger, J. V. Lauritzen, K. W. Jacobsen, J. K. Nørskov, S. Helveg, and F. Besenbacher, *Phys. Rev. Lett.* 87, 196803 (2001).
220. R. Schaub, H. Jödicke, F. Brunet, R. Monot, J. Buttet, and W. Harbich, *Phys. Rev. Lett.* 86, 3590 (2001).
221. W. Hebenstreit, J. Redinger, Z. Horozova, M. Schmid, R. Podloucky, and P. Varga *Surf. Sci.* 424, L321 (1999).
222. I. Sebastian, T. Betrams, K. Meinel, and H. Neddermeyer, *Faraday Discuss.* 144, 129 (1999).
223. J. Wollschläger, S. Viernow, T. Tegenkamp, D. Erdös, K. M. Schröder, and H. Pfnür, *Appl. Surf. Sci.* 142, 129 (1999).
224. J. Li, R. Berndt, and W.-D. Schneider, *Phys. Rev. Lett.* 76, 1888 (1996).
225. S. Altieri, L. H. Tjeng, and G. A. Sawatzky, *Phys. Rev. B* 61, 16948 (2000).
226. V. E. Henrich and P. A. Cox, "The Surface Science of Metal Oxides." Cambridge Univ. Press, 1994.
227. A. L. Shluger, P. V. Sushko, and L. N. Kantorovich, *Phys. Rev. B* 59, 2417 (1999).
228. V. E. Henrich, G. Dresselhaus, and H. J. Zeiger, *Phys. Rev. B* 22, 4764, (1980).
229. P. A. Cox and A. A. Williams, *Surf. Sci.* 175, L782 (1986).
230. M.-C. Wu, J. S. Corneille, J.-W. He, C. A. Estrada, and D. W. Goodman, *J. Vac. Sci. Technol. A* 10, 1467 (1992).
231. U. Schönberger and F. Aryasetiawan, *Phys. Rev. B* 52, 8788 (1995).
232. L. H. Tjeng, A. R. Vos, and G. A. Sawatzky, *Surf. Sci.* 235, 269 (1990).
233. J. P. LaFemina and C. B. Duke, *J. Vac. Sci. Technol. A* 9, 1847 (1991).
234. T. Jung, Y. W. Mo, and F. J. Himpsel, *Phys. Rev. Lett.* 74, 1641 (1995).
235. R. Chau et al., "Proceedings of IEEE International Electron Devices Meeting IEDM," 2000. (<http://www.intel.com/research/silicon/ieee/ieee6.htm>)
236. M. B. Maple, in: "Magnetism," (H. Suhl, Ed.), Vol. V, pp. 289–325. Academic Press, New York, 1973.
237. M. A. Woolf and F. Reif, *Phys. Rev.* 137, A557 (1965).
238. E. W. Hudson, S. H. Pan, A. K. Gupta, K.-W. Ng, and J. C. Davis, *Science* 285, 88 (1999).
239. J. C. Slonczewski, *Phys. Rev. B* 39, 6995 (1989).
240. M. Julliere, *Phys. Lett. A* 54, 225 (1975).
241. S. Maekawa and U. Gäfert, *IEEE Trans. Magn.* 18, 707 (1982).
242. J. S. Moodera, L. R. Kinder, T. M. Wong, and R. Meservey, *Phys. Rev. Lett.* 74, 3273 (1995).
243. R. Wiesendanger, H.-J. Güntherodt, G. Güntherodt, R. J. Gambino, and R. Ruf, *Phys. Rev. Lett.* 65, 247 (1990).
244. S. F. Alvarado and P. Renaud, *Phys. Rev. Lett.* 68, 1387 (1992); S. F. Alvarado, *Phys. Rev. Lett.* 75, 513 (1995).
245. Y. Suzuki, W. Naghan, and K. Tanaka, *Appl. Phys. Lett.* 71, 3153 (1997).
246. D. Li, J. Pearsson, S. D. Bader, D. N. McIlroy, C. Waldfried, and P. A. Dowben, *Phys. Rev. B* 51, 13895 (1995).
247. M. Donath, B. Gubanka, and F. Passek, *Phys. Rev. Lett.* 77, 5138 (1996).
248. P. M. Tedrow, R. Meservey, and P. Fulde, *Phys. Rev. Lett.* 25, 1270 (1970).
249. P. M. Tedrow and R. Meservey, *Phys. Rev. B* 7, 318 (1973).
250. C. Durkan and M. Welland, *Appl. Phys. Lett.* 80, 458 (2002).



# Luminescence of Semiconductor Nanoparticles

Wei Chen

*Nomadics, Inc., Stillwater, Oklahoma, USA*

Alan G. Joly

*Pacific Northwest National Laboratory, Richland, Washington, USA*

Shaopeng Wang

*Nomadics, Inc., Stillwater, Oklahoma, USA*

## CONTENTS

1. Introduction
  2. Fluorescence of Semiconductor Nanoparticles
  3. Luminescence Dynamics
  4. Photoluminescence of Doped Semiconductor Nanoparticles
  5. Electroluminescence of Nanoparticle Light Emitting Diodes
  6. Thermoluminescence
  7. Cathodoluminescence
  8. Magnetoluminescence
  9. Upconversion Luminescence and Anti-Stokes Luminescence
  10. Photostimulated Luminescence and Medical Imaging of Nanoparticles
  11. X-Ray Excited Optical Luminescence
  12. Biological Labels and Markers
  13. Fluorescence Energy Transfer and Biological/Chemical Sensors
  14. Luminescence Temperature Dependence and Temperature Sensors
  15. Luminescence Pressure Dependence
  16. Luminescent Nanoparticles for Optical Storage
  17. Summary
- Glossary  
References

## 1. INTRODUCTION

### 1.1. Quantum Size Confinement

There has been much recent interest in low dimensional systems such as quantum wells, quantum wires, and quantum dots. The interest of this subject stems from two main desires. The first is the desire to understand the transition from molecular to bulk electronic properties, while the other is the prospect of practical application of these materials to optoelectronic devices, photocatalysts, and chemical sensors. Perhaps the most striking property of nanoscale semiconductors is the massive change in optical properties as a function of size due to quantum confinement. This is most readily manifest as a blueshift in the absorption spectra with the decrease of the particle size. The variation of the energy gap in semiconductors with size may also result in different emission wavelengths for different sizes of nanoparticles. One example is shown in Figure 1 [1] for ZnS-capped CdSe nanoparticles with different sizes which display a fluorescence rainbow of blue–green–orange–yellow–red with the emission maxima at 443, 473, 481, 500, 518, 543, 565, 587, 610, and 655 nm, respectively.

The exciton Bohr radius is a useful parameter in quantifying the quantum confinement effects in semiconductor physics. The Bohr radius ( $a_B$ ) of an exciton in semiconductors may be calculated by [2]

$$a_B = \frac{\hbar^2 \varepsilon}{e^2} \left[ \frac{1}{m_e} + \frac{1}{m_h} \right] \quad (1)$$

where  $\varepsilon$  is the dielectric constant,  $\hbar$  is the Planck constant, and  $m_e$  and  $m_h$  are the electron and hole effective mass respectively. As the particle size is reduced to approach



**Figure 1.** Ten different emission colors of different size ZnS-coated CdSe nanoparticles excited with a near-UV lamp. From left to right (blue to red), the emission maxima are 443, 473, 481, 500, 518, 543, 565, 587, 610, and 655 nm, respectively. Reprinted with permission from [1], M. Y. Han et al., *Nature Biotechnol.* 19, 631 (2001). © 2001, Macmillan Magazines Ltd.

the exciton Bohr radius, there are drastic changes in the electronic structure and physical properties. These changes include shifts of the energy levels to higher energy, the development of discrete features in the spectra, and the concentration of the oscillator strength into just a few transitions (Fig. 2) [2].

A straightforward theoretical model based on the effective-mass approximation [2] can be applied to explain most observations. This model has established two limiting regimes: the weak and the strong confinement regimes. The weak confinement regime occurs when the particle radius is larger than the exciton radius. In this regime, the exciton translational motion is confined and the size dependence of the energy of the exciton can be expressed as

$$E_{nl} = E_g - \frac{R_y^*}{n^2} + \frac{\hbar^2 \chi_{nl}^2}{2MR^2} \quad (2)$$

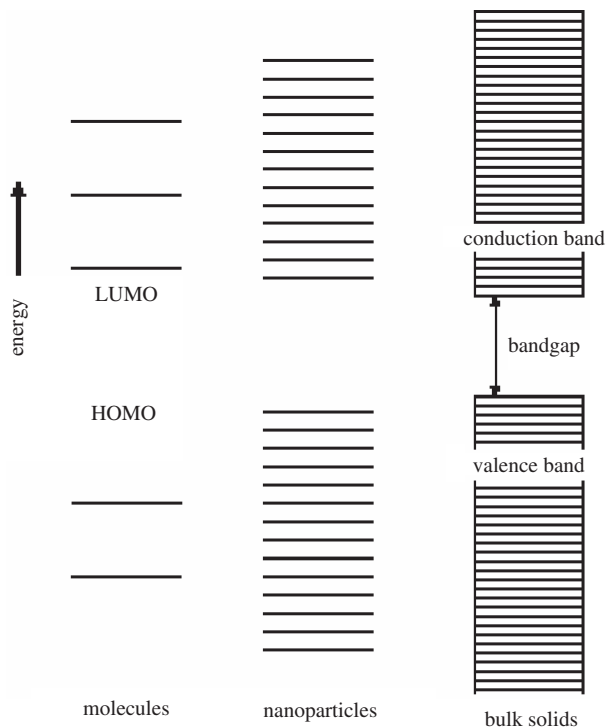


**Figure 2.** A schematic model for the energy structures of bulk solids, nanoparticles, and isolated molecules.

where  $E_g$  is the bulk bandgap,  $R_y^*$  is the exciton Rydberg energy,  $\hbar$  is the Planck constant,  $R$  is the particle size,  $M = m_e + m_h$ , and  $m_e$  and  $m_h$  are the effective mass of the electron and hole respectively.  $X_{nl}$  are the roots of Bessel functions describing the energy states with  $n$  being the number of the root and  $l$  being the order of the function ( $\varphi_{1S} = 3.14$ ,  $\varphi_{1P} = 4.49$ , and  $\varphi_{1D} = 5.76$ ) [2]. The strong confinement regime occurs when the particle radius is smaller than the exciton radius. In this regime, the individual motions of electrons and holes are independently quantized. In this case, the size dependence of the exciton energy can be expressed by

$$E_{nl} = E_g + \frac{\hbar^2}{2\mu R^2} \chi_{nl}^2 \quad (3)$$

where  $\mu$  is the reduced mass of the electron and hole pair,  $1/\mu = 1/m_e + 1/m_h$ .

In both regimes the main experimental effects of confinement are the appearance of a structured absorption spectrum due to the presence of discrete energy levels and the blueshift of the absorption edge, which is roughly proportional to the inverse of the square of the particle radius. However, some electronic properties such as electron–hole interactions are expected to be modified only in the strong confinement regime. This is due to the increase of the spatial overlap of the electron and hole wavefunctions with decreasing size. As a consequence, the splitting between the radiative and nonradiative exciton states is enhanced largely in the strong confinement regime.

Quantum confinement not only causes an increase of the energy gap (blueshift of the absorption edge) and the splitting of the electronic states but also changes the density of states (DOS). Many novel physical properties and potential applications of low-dimensional semiconductors and many of the differences between the electronic behavior of the bulk and of quantum-confined low-dimensional semiconductors are due to their differences in the density of states [3]. Figure 3 shows the variation of the DOS with dimensionality [3]. The dimensionality of the system describes the number of dimensions of free transport of an electron gas; thus boxes are two-dimensional structures, quantum wires are one-dimensional, and quantum dots are considered zero-dimensional because electrons are confined in all spatial dimensions. Passing from three dimensions to two dimensions the density of states  $N(E)$  changes from a continuous dependence, where  $N(E) \sim E^{1/2}$ , to a steplike dependence. Thus the optical absorption features are different for the bulk and for the quantum well structure. The optical absorption edge for a quantum well is at higher photon energy than for the bulk semiconductor and, above the absorption edge, the spectrum is stepped rather than smooth, the steps corresponding to allowed transitions between valence-band states and conduction-band states. In addition, at each step sharp peaks appear corresponding to confined electron–hole (exciton) pair states. In the case of lower dimensional systems (quantum dots, nanocrystallites, clusters, nanoparticles, colloids, etc.), the DOS becomes more discrete as the dimensionality decreases, and large optical absorption coefficients are observed [4]. The low-dimensional structure has proven to be very promising in applications to semiconductor lasers, due mainly to the quantum confinement of the

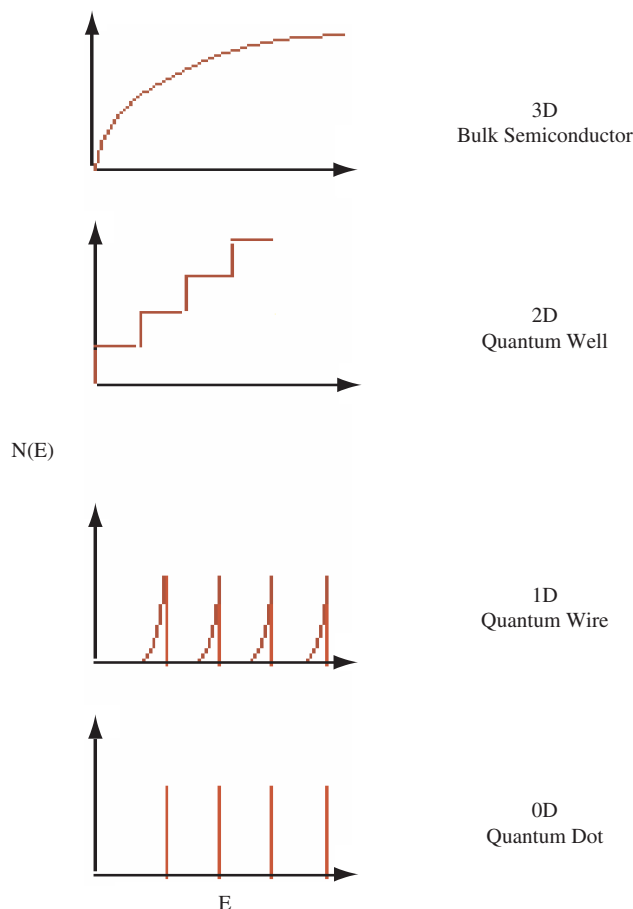


**Figure 3.** Profiles of the density of states of three-dimensional bulk semiconductors, a two-dimensional quantum well, a one-dimensional quantum wire, and zero-dimensional quantum dots. Reprinted with permission from [3], A. P. Alivisatos, *J. Phys. Chem.* 100, 13226 (1996). ©1996, American Chemical Society.

carriers and the variation of the density of states with dimensionality [5]. The changes in the DOS lead to a change in the gain profile, a reduction of threshold current density, and a reduction of the temperature dependence of the threshold current. Owing to the steplike density of states, high gain with a lower spontaneous emission rate has been realized in a GaAs/AlGaAs GRIN-SCH SQW laser [6]. Thus low-dimensional structured materials are interesting, for both basic research and practical applications.

### 1.2. Quantum Size Confinement and Quantum Efficiency of Nanoparticles

From these arguments, it is clear that nanoparticles may have tunable absorption and emission spectra. In addition, luminescent nanoparticles may have higher quantum efficiency than conventional phosphors, making it possible to design and fabricate more sensitive sensors or more efficient devices. The oscillator strength,  $f$ , is an important optical parameter that underlies the absorption cross-section,

recombination rate, luminescence efficiency, and the radiative lifetime in materials. The oscillator strength of the free exciton is given by [7]:

$$f_{\text{ex}} = \frac{2m}{\hbar} \Delta E |\mu|^2 |U(0)|^2 \quad (4)$$

where  $m$  is the electron mass,  $\Delta E$  is the transition energy,  $\mu$  is the transition dipole moment, and  $|U(0)|^2$  represents the probability of finding the electron and hole at the same site (the overlap factor). In nanostructured materials, the electron-hole overlap factor increases largely due to quantum size confinement, thus yielding an increase in the oscillator strength. The oscillator strength is also related to the electron-hole exchange interaction that plays a key role in determining the exciton recombination rate. In bulk semiconductors, due to the extreme dislocation of the electron or hole, the electron-hole exchange interaction term is very small, while in molecular-size nanoparticles, due to confinement, the exchange term should be very large. Therefore, there may be a large enhancement of the oscillator strength from bulk to nanostructured materials. The radiative decay lifetime ( $\tau$ ) is closely related to the oscillator strength of a transition by [8]

$$\tau = 4.5(\lambda_A^2/nf) \quad (5)$$

where  $n$  is the refractive index and  $\lambda_A$  is the emission wavelength. Thus, the lifetime may be shortened with decreasing size due to the increase of the oscillator strength,  $f$ . Higher efficiencies with concomitant shorter decay times thereby make nanoparticles a promising new type of luminescent material.

## 2. FLUORESCENCE OF SEMICONDUCTOR NANOPARTICLES

Typical absorption and fluorescence spectra of CdS nanoparticles are shown in Figure 4 [9]. The sizes of the two samples estimated from the absorption edge are 3.4 nm

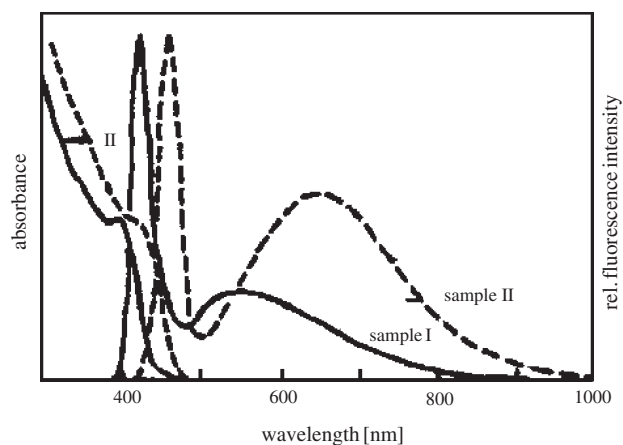


**Figure 4.** Absorption and emission spectra of CdS nanoparticles. Sample I is 3.4 nm in size and sample II is 4.3 nm. Reprinted with permission from [9], A. Hasselbarth et al., *Phys. Lett.* 203, 271 (1993). © 1993, Elsevier Science.

(sample I) and 4.3 nm (sample II) respectively. Both of the samples exhibit a sharp excitonic fluorescence band (at 435 nm for the 3.4 nm sample and 480 nm for the 4.3 nm sample), as well as a broad fluorescence band at longer wavelengths arising from the recombination of trapped charge carriers at surface or defect states.

Optical excitation of semiconductor nanoparticles often leads to both band-edge and deep trap luminescence. The size dependence of the excitonic or band edge fluorescence has been studied extensively and can be reasonably explained by the effective-mass approximation. The fluorescence process in semiconductor nanoparticles is very complex and most nanoparticles exhibit broad and Stokes-shifted luminescence arising from the deep traps of surface states [10]. Only clusters with good surface passivation show high band-edge emission. The absence of band-edge emission has been previously attributed to the large nonradiative decay rate of the free electrons trapped in these deep-trapped states. As the particles become smaller, the surface/volume ratio and hence the number of surface states increases rapidly, reducing the excitonic emission [11]. Thus, surface states often determine the physical properties, especially the optical properties, of nanoparticles. Often, however, little is known about the physical properties of the surface states.

For particles in such a small size regime, a large percentage of the atoms are on or near the surface. Surface states near the bandgap can mix with interior levels to a substantial degree, and these effects may also influence the spacing of the energy levels. Thus, in many cases it is the surface of the particles rather than the particle size that determines the properties. It is, therefore, a major goal to characterize the surface states and to control them through chemical modification. For example, 99% of the atoms are on the surface for a 1 nm sized Si particle [3]. The existence of this vast interface between the nanoparticles and the surrounding medium can have a profound effect on the particle properties. The imperfect surface of the nanoparticles may act as electron and/or hole traps following optical excitation. Thus the presence of trapped electrons and holes can in turn modify the optical properties of the particles.

Although there are many reports on the luminescence of nanoparticles, only a small number are dedicated to the size dependence of the fluorescence from surface states. By examining the size dependence of the two main emission features (i.e., the excitonic and the trapped emissions), it is possible to determine to what extent the carriers are confined in the emitting state. If the luminescence and the absorption of the surface states are dependent on size, it indicates that not only the excitons but also the trapped carriers at the surface states are confined by the quantum size effect. If the luminescence of the surface states is not dependent on size, then the trapped carriers are not likely confined by the quantum size effect. Thus knowledge of the surface and defect states response to quantum confinement may be important when attempting to adjust the energy levels of the surface states relative to the intrinsic levels through quantum confinement.

The emission spectra of ZnS nanoparticles of different sizes are shown in Figure 5 [12]. No excitonic emission is observed in the ZnS nanoparticles. The luminescence clearly arises from trap states, indicating that the surfaces of the

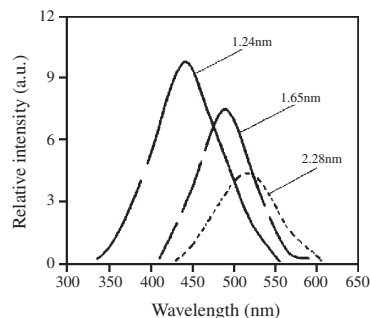


**Figure 5.** Luminescence spectra of ZnS nanoparticles with average sizes of 1.24, 1.65, and 2.28 nm, respectively. The luminescence exhibits almost exclusively trap state emission, likely because of poor surface passivation. Reprinted with permission from [12], W. Chen et al., *J. Appl. Phys.* 82, 3111 (1997). © 1997, American Institute of Physics.

particles are not well passivated. The luminescence intensity increases as the size decreases, as the increase in the trapped states results in more luminescence. The trap state emission also shifts to the blue as the size decreases demonstrating that the trap states exhibit quantum confinement behavior. Similarly, the results reported by Hoheisel et al. [13] show that both the excitonic and the trap state emission peaks shift in energy as a function of size in CdSe nanoparticles (Fig. 6), demonstrating that the emission energy of the surface states in these particles is also correlated to the quantum-size effects.

### 3. LUMINESCENCE DYNAMICS

Absorption of a photon places an atom or molecule in a naturally meta-stable excited state. This meta-stable state must ultimately re-emit the energy in one or more of three possible relaxation pathways. The first is radiative, via either fluorescence or phosphorescence. The second pathway is through nonradiative processes such as internal conversion

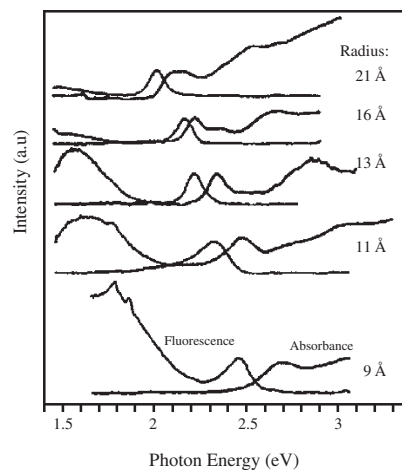


**Figure 6.** Absorption and emission spectra of CdSe nanoparticles with average sizes of 9, 11, 13, 16, and 21 Å. Quantum confinement results in both the excitonic and trap state emissions clear blueshift with decreasing particle size. Reprinted with permission from [13], V. Hoheisel et al., *J. Chem. Phys.* 101, 8455 (1994). © 1994, American Institute of Physics.

or energy transfer. The third possibility is chemical change, such as the breaking of bonds to form a new chemical species.

In a typical experiment, a photon is absorbed taking the atom or molecule from the ground state to an excited state, where the excited state may be a rotationally and/or vibrationally excited molecule in the electronic excited state. Internal conversion is the process where ro-vibrational energy is lost to the surroundings as the molecule cascades down the ro-vibrational ladder. In solids, promotion of an electron from the valence band to the conduction band produces an excited state which may then relax by phonon relaxation to the conduction band edge. This energy is ultimately lost as heat to the surroundings. Internal conversion in excited states is very rapid relative to radiative rates and therefore the system may be assumed to radiate from the lowest energy level of the lowest excited state of like multiplicity. This is known as “Kasha’s rule” and is obeyed a majority of the time [14].

Once in the lowest excited state, there are many possible forms of relaxation, both radiative and nonradiative. The total rate of relaxation is the sum of all rates. In this chapter we will assume that there is no chemical change and that all luminescence originates from the lowest excited state (Kasha’s rule) [14]. Therefore the total relaxation rate ( $k_t$ ) out of the lowest excited state is given by

$$k_t = k_{\text{rad}} + k_{\text{non}} \quad (6)$$

where  $k_{\text{rad}}$  and  $k_{\text{non}}$  are the radiative and nonradiative rates respectively. The observed luminescence therefore decays exponentially with time,

$$I(t) = I(0) \exp(-t/\tau_{\text{obs}}) \quad (7)$$

with the observed lifetime  $\tau_{\text{obs}}$  proportional to  $1/k_t$ . Thus, in a purely radiative system such as an isolated atom, the observed lifetime is proportional to the inverse of the radiative rate. In this case, the lifetime is termed the natural radiative lifetime. The natural lifetime may be related to the absorption strength or oscillator strength  $f$  by Eq. (5). Thus, a strong transition has a large radiative rate and therefore a short natural lifetime.

Most photochemical systems are not purely radiative; therefore the influence of nonradiative transitions must be taken into account. Nonradiative transitions in general serve to deplete the excited state, thus increasing  $k_t$ . This results in a shortened observed lifetime  $t_{\text{obs}}$ , which is shorter than the natural radiative lifetime. In some cases, nonradiative energy transfer from a nearby excited molecule or atom results in promotion of a ground state atom or molecule to its excited state. If the energy transfer is fast relative to the spontaneous luminescence rate, the luminescence does not display a single exponential decay but exhibits a rise followed by a decay as the population of the excited level initially increases due to the energy transfer. The rise time of the luminescence may then be related to the energy transfer rate, while the fall time can be related to  $k_t$  in a straightforward manner.

It is important to realize that in the absence of this energy transfer, all excited state luminescence from a single species should display a single exponential decay. In practice, often

biexponential or higher order lifetime decays are observed. The existence of a biexponential decay does not, however, imply two different rate processes for a single species but rather the existence of two distinct subsets of species, each with its own unique lifetime. Higher order, multiexponential decays then represent larger numbers of distinct species and often can be modeled as a distribution of species, each with its own decay constant.

It is clear that the longer the natural lifetime, the higher the probability for nonradiative processes to deplete the excited state. Nonradiative processes also result in a shortened lifetime; however, the luminescence efficiency similarly decreases. Thus, the goal in luminescent systems is to increase the luminescence efficiency either through increasing the radiative rate (decreasing the natural lifetime) or decreasing the nonradiative rate (increasing the observed lifetime). Nanoparticles may have an increased natural radiative rate and thus enhanced quantum efficiency due to the effects of quantum confinement on the electron-phonon coupling and DOS. However, in nanoparticles, perhaps the single most important contribution to the nonradiative rate is trapping to surface states. Trapping to surface states usually occurs on the subnanosecond timescale [15]. Figure 7 shows luminescence decays from  $\text{Eu}_2\text{O}_3$  nanoparticles encapsulated in the porous host MCM-41 [16]. The existence of multiple time regimes is apparent as subnanosecond to millisecond timescale decays are represented. The subnanosecond decays shown in the inset of Figure 7 have been attributed to either species exhibiting surface state trapping of carriers or else to energy transfer to defect states within the MCM-41. Passivation of surface states is therefore a key requirement in increasing the luminescence efficiencies of nanoparticles relative to bulk materials [16].

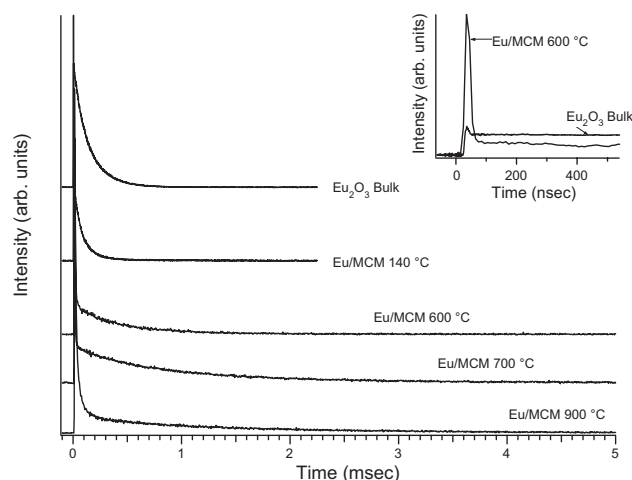


**Figure 7.** Lifetime decay curves of the  ${}^5D_0 \rightarrow {}^7F_2$  emission following excitation at 525 nm of  $\text{Eu}_2\text{O}_3$  bulk powder, an  $\text{Eu}_2\text{O}_3/\text{MCM-41}$  mixture, and  $\text{Eu}_2\text{O}_3$  particles in MCM-41 prepared by heat treatment at 140, 600, 700, and 900 °C. The inset shows an expanded view of the short-time (<1 microsecond) time regime for the bulk powder and the sample prepared at 600 °C. Reprinted with permission from [16], W. Chen et al., *J. Phys. Chem. B* 106, 7034 (2002). © 2002, American Chemical Society.



#### 4. PHOTOLUMINESCENCE OF DOPED SEMICONDUCTOR NANOPARTICLES

Semiconductor nanoparticles may also be doped with impurities that have a strong luminescence of their own. Quantum size confinement affects not only the excitonic emission in the host but also the luminescence from the dopants. Figure 8 shows the luminescence spectra of both nanocrystalline and bulk ZnS:Eu<sup>2+</sup> at different temperatures [17, 18]. Two differences can be observed between the bulk and the nanoparticles. One is that the emission of the nanoparticles is shifted to shorter wavelengths; the second is that strong luminescence is observed from the nanoparticles, while the luminescence from bulk ZnS:Eu<sup>2+</sup> is only observed at low temperature [18]. In order to understand the emission shift, the energy structure of the ZnS:Eu<sup>2+</sup> system must be considered. The ground state of Eu<sup>2+</sup> is 2.25 eV below the edge of the conduction band, and its first excited state is ~0.35 eV above the edge of the conduction band in bulk ZnS [18]. The excited states of Eu<sup>2+</sup> are degenerate with the continuum of the conduction band (CB). Photoionization occurs very easily, and no intraion transition is observed, because the intraion excitation process requires a larger energy than that for the photoionization transition. In order to observe the intraion transition of Eu<sup>2+</sup> in the ZnS:Eu<sup>2+</sup> system, the edge of the CB needs to be raised above the first excited state of Eu<sup>2+</sup>. This may be realized via quantum size confinement. If the diameter of ZnS:Eu<sup>2+</sup> nanoparticles is smaller than 3.5 nm, the edge of the ZnS conduction band moves to higher energy than the first excited state level of Eu<sup>2+</sup> and thus enables the intraion transition of Eu<sup>2+</sup> ions (see Fig. 9) [17].

The Eu<sup>2+</sup>-bound exciton luminescence in bulk ZnS decreases rapidly with increasing temperature from 4.2 to 80 K and is barely visible at 200 K [18]. However, in ZnS:Eu<sup>2+</sup> nanoparticles, the Eu<sup>2+</sup> bound exciton luminescence is observed at room temperature. This indicates that the bound exciton in nanostructured semiconductors may be more stable with respect to multiphonon relaxation, and its luminescence efficiency is higher compared to that of the bulk. This is attributed to quantum size confinement.

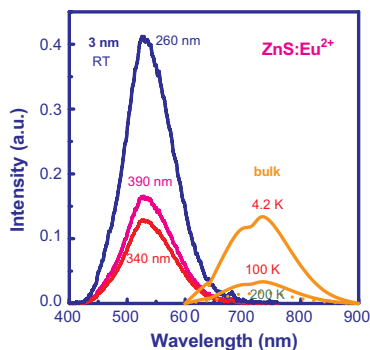


**Figure 8.** The traces on the left are the emission spectra of the 3 nm sized ZnS:Eu<sup>2+</sup> nanoparticle at room temperature excited at 260, 340, and 390 nm, respectively [17], and the traces on the right are the 488 nm excited emission spectra of bulk ZnS:Eu<sup>2+</sup> at 4.2, 100, and 200 K. Reprinted with permission from [18], W. Chen et al., *Phys. Rev. B* 61, 11021 (2000). © 2000, American Physical Society.

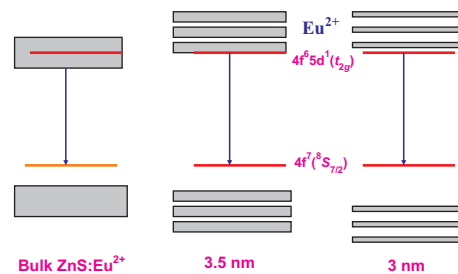


**Figure 9.** Energy levels of bulk ZnS:Eu<sup>2+</sup> and ZnS:Eu<sup>2+</sup> nanoparticles. The energy levels of Eu<sup>2+</sup> are in black, while the energy levels of the ZnS host are in gray. In bulk ZnS:Eu<sup>2+</sup>, the lowest excited state of Eu<sup>2+</sup> is within the conduction band of ZnS; no emission is observed from the intraion transition of Eu<sup>2+</sup>. In nanoparticles, due to the increase of the energy gap of ZnS, the lowest excited state of Eu<sup>2+</sup> is moved into the energy gap, and therefore strong luminescence from the intraion transition of Eu<sup>2+</sup> is observed at room temperature. Reprinted with permission from [18], W. Chen et al., *Phys. Rev. B* 61, 11021 (2000). © 2000, American Physical Society.

Quantum confinement increases the exciton binding energy and recombination rate, due to the increase of the overlap between electron and hole wavefunctions. In doped semiconductors, the excitons are bound to impurity centers. Thus, the oscillator strength is given by [19]

$$f = f_{\text{ex}} \left| \int dx F(x) \right|^2 / \Omega_{\text{mol}} \quad (8)$$

where  $f_{\text{ex}}$  is the oscillator strength of the free exciton,  $\Omega_{\text{mol}}$  is the volume of one molecule, and  $F(X)$  is the envelope function. The oscillator strength of a bound exciton is actually given by  $f$  multiplied by the number of molecules covered by the overlap of the electron and hole wavefunctions. The absorbance and luminescence efficiency are proportional to the exciton oscillator strength; therefore, they can be enhanced via quantum size confinement. Strong evidence for this theory comes from our observations of ZnS:Mn<sup>2+</sup> [20] and EuS [21] nanoparticles, since the luminescence intensity of the 1 nm sized ZnS:Mn<sup>2+</sup> nanoparticles in zeolite-Y is much stronger than other sizes of ZnS nanoparticles [20]. More interesting is that bulk EuS at room temperature is not luminescent but strong luminescence is observed when EuS nanoparticles are formed in zeolites [21].

#### 5. ELECTROLUMINESCENCE OF NANOPARTICLE LIGHT EMITTING DIODES

Light-emitting diodes (LEDs) from organic polymers and II–VI semiconductor nanocrystals have attracted considerable attention because polymer nanoparticle composites combine key properties required for flat-panel displays (FPDs) including low weight, low power, low voltage, and compact size [22]. FPDs are gradually replacing many of the traditional cathode ray tube (CRT) displays in military applications and in civilian technologies, such as information processing. However, FPDs do have limitations that prevent their wholesale adoption. Most notably they lack the



brightness and resolution of CRTs. This restricts their overall readability, particularly in bright light. Flat-panel displays also face area limitations because the complexity increases with size.

Technology based on highly luminescent semiconductors holds the potential to overcome these shortcomings. Nanoparticle LEDs (NLEDs) can provide improved brightness and multicolor capabilities compared to many of the existing flat-panel technologies. In addition, the extremely small size of nanoparticles creates the prospect of displays with unprecedented resolution. Besides their low cost and color availability, thin-film displays made from NLEDs offer additional competitive advantages over other display technologies. Importantly, NLEDs display turn-on voltages ( $E_{on}$ ) in the range of 5–10 V [22–24] which are significantly lower than in liquid crystal FPDs. One of the most appealing advantages is that a thin film formed either by spin coating or by layer-by-layer (LBL) assembly can be laid over virtually any solid substrate and will contour to the shape of the substrate.

Formation of a LBL assembled LED may be performed as follows: For deposition of poly(*p*-phenylenevinylene) (PPV) hole transport layers, indium tin oxide (ITO) glass is immersed in a poly-acrylic acid solution (1%, pH = 8) for 15 minutes then the ITO glass is rinsed with deionized water and immersed in a *p*-PPV solution for 15 minutes and rinsed with water. This step is repeated nine times, so that 10 bilayers of PPV with a total thickness of ~70 nm are deposited on the ITO slide.

Next, the nanoparticle emitting layers of CdTe/polydiallyldimethylammonium (PDDA) are deposited on the PPV-coated ITO slide. In order to accomplish this, the PPV-coated ITO is immersed in PDDA solution (1%, pH = 8–9) for 30 minutes, rinsed with deionized water, immersed in a CdTe nanoparticle solution for 30 minutes, and then rinsed again with deionized water. These steps are repeated to obtain a desired thickness, though the immersion time for subsequent cycles may be reduced to as short as 5 minutes.

Next, a cathode (Al) of about 0.97 cm<sup>2</sup> is deposited on the nanoparticle side by a thermal evaporator and contact leads are attached to the anode (ITO) and cathode (Al) for electroluminescence and current-voltage measurements. The structure of the nanoparticle LED is schematically shown in Figure 10. By applying voltage, electroluminescence (EL) is observed from the LED. Figure 11 shows electroluminescence spectra of a CdTe/PPV nanoparticle LED at different

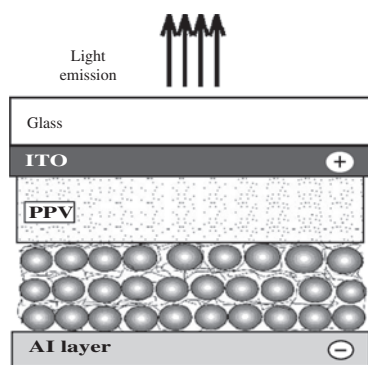


**Figure 10.** A schematic model for the structure of a semiconductor nanoparticle light-emitting diode.

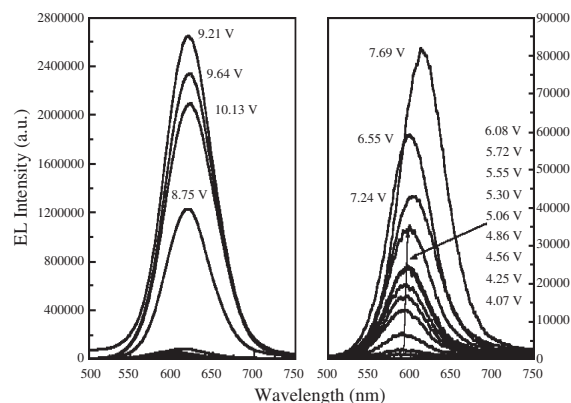


**Figure 11.** Electroluminescence spectra of a CdTe nanoparticle light-emitting diode at different applied voltages. Reprinted with permission from [24], W. Chen et al., *J. Nanosci. Nanotechnol.* 1, 47 (2002). © 2002, American Scientific Publishers.

applied voltages [24]. The electroluminescence of the LED is visible to the naked eye. At 4 V, the electroluminescence is detectable, and its intensity increases with applied voltage up to 9.21 V. At voltages greater than 9.21 V, the EL decreases in intensity. The color (emission wavelength) also changes at different voltages. At higher voltages, the emission wavelength shifts toward the red.

Figure 12 shows the absorption, photoluminescence, and electroluminescence spectra of the LED, CdTe nanoparticles, and *p*PPP/PPV solution [24]. The absorption of the *p*PPP/PPV solution occurs between 300 and 400 nm, while the absorption of CdTe nanoparticles is at around 550 nm. The fluorescence bands of *p*PPP/PPV are at 460

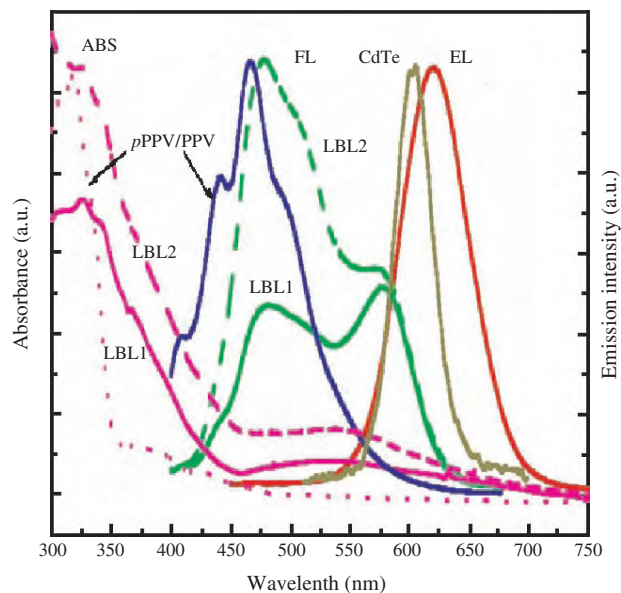


**Figure 12.** Absorption (ABS) and fluorescence (FL) of a *p*PPP/PPV solution (*p*PPP/PPV), a CdTe nanoparticle solution (CdTe), and CdTe/*p*PPP layer-by-layer thin film before (LBL1) and after (LBL2) curing. EL is the electroluminescence of the CdTe/*p*PPP device. Reprinted with permission from [24], W. Chen et al., *J. Nanosci. Nanotechnol.* 1, 47 (2002). © 2002, American Scientific Publishers.

and 510 nm, while the CdTe nanoparticles have emission at 600 nm. After curing, the absorption and luminescence of *p*PPV/PPV and CdTe particles both increase in intensity, and the luminescence emission of *p*PPV/PPV is stronger than that of CdTe nanoparticles. However, in the EL spectra, only the emission of CdTe nanoparticles is observed, due to the confinement of carriers (electrons and holes) in the particle layers. In addition, the EL emission spectrum is shifted to longer wavelengths compared to the PL spectra of the thin film and of the particle solution.

The redshift of EL from photoluminescence (PL) is a common phenomenon observed in nanoparticle light-emitting diodes [25]. This redshift has been attributed to the effect of reabsorption of a portion of the EL within the nanoparticle layer or to the Förster energy transfer from small to large nanoparticles [25]. However, these two processes cannot reasonably explain the redshift of the EL from PL, because reabsorption or Förster energy transfer from small to large particles occurs in both EL and PL, provided the emission of the small particles overlaps partially with the absorption of the larger particles.

This redshift may also be the result of size selection due to charge injection. For smaller nanoparticles, the carrier injection barriers are larger due to stronger quantum confinement (with larger energy gaps). Thus, at lower applied voltages, carrier injection occurs preferentially in larger particles while at higher voltages, injection occurs in both large and small particles. If this is the case, the EL should shift to the blue (shorter wavelengths) from low to high applied voltages. However, no shift has been observed in CdSe(CdS) nanoparticle LEDs reported in [25]. On the contrary, it has been observed here that the EL shifts to the red (longer wavelengths) at higher applied voltages. Thus, size selection does not reasonably explain the observed redshift of the EL from PL.

Heating and oxidation of the nanoparticles may cause a redshift of the emission energy. However, based on our observations, heating is not likely a major problem. If the device undergoes significant heating, spot lines longer than 700 nm should be observed, and the device should lose its emission quickly. The device continues working at 28 V and no spot line is detected until the device stops working, indicating little heating. On the other hand, oxidation cannot be avoided when the device operates in air. Oxidation may create some defects in the energy gap of the nanoparticles and may shift the emission to longer wavelengths [26].

In nanoparticles or clusters, most of the atoms or ions at the surface are not coordinatively saturated. Excited electrons or holes may be trapped at surface states located in the forbidden gaps. Thus in nanoparticles both excitonic and surface emissions are usually observed. It is known that the exciton luminescence from nanoparticles involves some contribution from the surface carriers, and this can shift the excitonic emission to lower energies. This may provide another explanation for the redshift of electroluminescence compared to photoluminescence. The excitation energy for electroluminescence is much less than the energy gap of the emitting materials. When the excitation energy is comparable to or higher than the barrier energy, which is 1 to 2 eV, carrier injection occurs and electroluminescence follows. Excitation at such low energies cannot produce a

transition from the ground state to the excited states as in photoluminescence; however, it can excite the surface trap states in the nanoparticles, which have energy depths of 0.5 to 2 eV [12, 27, 28, 31]. Similar ideas are used to explain the anti-Stokes luminescence of CdTe nanoparticles.

The quantum confined Stark effect (Franz-Keldysh effect) [26] is another factor that may lead to a redshift of the electroluminescence from the photoluminescence. The electric field may push electrons and holes in opposite directions making the energy separations smaller, inducing a redshift. If the redshift is induced by only the quantum confined Stark effect, the shift should be linear or monotonic to the red upon increasing applied voltage. However, this is not the case as observed in Figure 11. Therefore other factors such as the involvement of surface states must be considered in order to explain the observations.

## 6. THERMOLUMINESCENCE

Thermoluminescence (TL) is luminescence generated following excitation with heat instead of visible or near-infrared photons. Obviously the TL process is different from the PL process, as the energy of thermostimulation is not sufficiently high to excite the electrons from their ground states to their excited states. Thus, TL arises from defect or trap states within the bandgap. The energy corresponding to the peak of the TL spectrum, called a glow curve, is equal to the trap depth. In TL, trapped carriers may be formed during sample processing, because the small particles have large numbers of ions at the surface, and most ions at the surface are not coordinatively saturated. Carriers trapped at the surface states or defect sites may be released by heating to recombine to give thermoluminescence. Since trapping is a very fast process [15], spontaneous luminescence cannot effectively compete with it. Therefore, TL is a good method for studying the trapped carriers and the surface states.

Figure 13 shows the glow curves of capped ZnS nanoparticles recorded without prior irradiation. Equal amounts of sample were used for each measurement. The sizes of the particles are 1.24, 1.65, and 2.28 nm, respectively [12]. An obvious glow peak around 380 K is exhibited from the nanoparticles. All three samples show the glow peaks at almost the same position and the TL intensity increases as the particle size decreases. The intensity change of the TL is consistent with that of surface luminescence. The glow peaks in Figure 13 are caused by the trapped carriers which are produced during sample processing, because these samples had not been previously exposed to radiation. TL from semiconductor nanoparticles without any prior irradiation has been observed in CdS [30] and ZnS nanoparticles as well [12, 31]. Preexisting carriers or occupation of localized states has been proposed by Chenstnoy et al. [32] to explain the very weak dependence of the fluorescence decay lifetime upon CdS cluster size and by Klimov et al. [33] to explain the extremely fast buildup dynamics of the low-energy emission bands of CdS nanocrystals.

According to the theories of thermoluminescence [34], the TL intensity of clusters is given by

$$I = -\frac{dm}{dt} = mnA \quad (9)$$

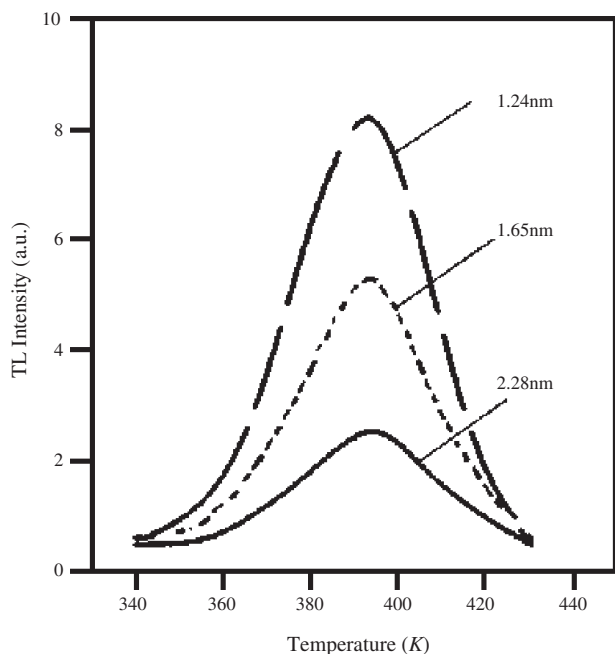


**Figure 13.** Thermoluminescence glow curves of ZnS nanoparticles with average sizes of 1.24, 1.65, and 2.28 nm, respectively. Reprinted with permission from [12], W. Chen et al., *J. Appl. Phys.* 82, 3111 (1997). © 1997, American Institute of Physics.

where  $m$  and  $n$  represent the density of holes and electrons for recombination, and  $A$  is the carrier recombination probability. Decreases in the particle size may enhance the surface ions and states rapidly. As the content of the surface states increases, the particles may provide more accessible carriers (holes and electrons) for the TL recombination [i.e.,  $m$  and  $n$  in Eq. (9) are proportional to the surface states]. Furthermore, in nanoparticles the overlap of the electron and hole wavefunctions is stronger, which may result in the increase of their recombination probability or rate ( $A$ ). These two effects may make the TL of small particles much stronger than that of the bulk and increase the intensity of the luminescence as the size decreases.

## 7. CATHODOLUMINESCENCE

Cathodoluminescence is luminescence excited by an electron beam such as that observed in traditional cathode ray technologies. The excitation mechanism under electron beam excitation consists of electron transitions from the valence to conduction band of the lattice followed by transfer of the electron-hole (e-h) recombination energy to luminescent ions that may be doped into the phosphor. The efficiency of the process ( $\eta_{cr}$ ) can be written as [35]

$$\eta_{cr} = (1 - r_b)(h\nu_m/\varepsilon)\eta_l\eta \quad (10)$$

where  $r_b$  is the primary backscattering coefficient,  $h\nu_m$  is the mean energy of the luminescent photons,  $\varepsilon$  is the average energy required to generate one e-h pair,  $\eta_l$  is the efficiency for transfer of the e-h recombination energy to luminescent ions, and  $\eta$  is the quantum efficiency of the activator

emission. In general,  $r_b$  increases with the average atomic number of the material atoms [35].

Within the material the incident electron loses its energy either by generating e-h pairs or by creation of optical phonons. The energy required to create e-h pairs ( $\varepsilon$ ) increases with increasing bandgap. For high efficiency the bandgap must be slightly larger than the energy of the photons emitted; therefore ZnS with a bandgap of 3.8 eV is an appropriate material for emission in the visible range.  $\varepsilon$  also increases with the phonon energy; thus sulfides are more favorable than oxides regarding this characteristic because sulfides in general have lower energy phonon spectra relative to their oxide counterparts. The highest efficiency cathodoluminescence materials include ZnS:Cu, Al, ZnS:Ag, Cl, CaS:Pb, and CaS:Ce, with energy efficiencies between 15 and 20%. Other materials such as Y<sub>2</sub>O<sub>2</sub>S:Eu, Gd<sub>2</sub>O<sub>2</sub>S:Tb, and LaOBr:Tb have efficiencies between 8 and 14%, while Y<sub>2</sub>O<sub>3</sub>:Eu, Y<sub>3</sub>(Al, Ga)<sub>5</sub>O<sub>12</sub>:Tb, YVO<sub>4</sub>:Eu, Zn<sub>2</sub>SiO<sub>4</sub>:Mn, and Y<sub>2</sub>Si<sub>2</sub>O<sub>7</sub>:Ce show relatively low 4–7% efficiencies [35].

The development of flat-panel field-emitting displays requires phosphors with high cathodoluminescence efficiency at electron acceleration voltages near 1 kV, and high-definition displays require submicrometer particle sizes to maximize screen resolution and screen efficiency [36, 37]. Semiconductor nanoparticles, particularly Mn-doped ZnS nanoparticles, have been shown to have the required cathodoluminescence properties and suitable size range [37, 38].

Recent studies have shown that the cathodoluminescence spectra of annealed ZnS:Mn/ZnO nanoparticles resemble the spectra of the bulk phosphor (Fig. 14) [38]. The inorganic ZnO cap layer is essential for bright cathodoluminescence, which is 4 times brighter than MgO capped nanoparticles. The annealed nanoparticles are about 200 times brighter than the unannealed particles and 40% as

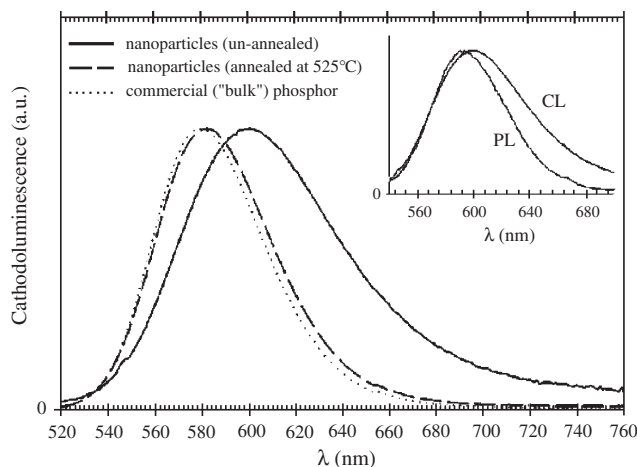


**Figure 14.** Cathodoluminescence spectra of ZnS:Mn/ZnO samples. The unannealed nanoparticles (solid curve), annealed nanoparticles (dashed curve), and the Sarnoff phosphor (dotted curve) are shown. The electron acceleration voltage was 650 V and the current was 24  $\mu$ A (120  $\mu$ A/cm<sup>2</sup>). Inset: comparison of the photoluminescence (PL) and cathodoluminescence (CL) spectra of the unannealed nanoparticles. Reprinted with permission from [38], A. D. Dinsmore et al., *J. Appl. Phys.* 88, 4985 (2000). © 2000, American Institute of Physics.

bright as the bulk material. In addition, the annealed nanoparticles exhibit 50% less saturation with increasing electron-beam current. Furthermore, the nanoparticle annealing temperature (535 °C) is much lower than the firing temperatures used in commercial bulk ZnS:Mn processes [37, 38].

In addition, the Mn doping concentration in ZnS:Mn material also affects the cathodoluminescence efficiency as for photoluminescence, and it has been found that ~2 wt% is the optimal concentration for bulk material [36] and may be similar in nanoparticles [38]. In short, small size, high quantum efficiency, reduced current saturation, and lower processing temperature make nanoparticles attractive for use in new high-resolution display technologies.

## 8. MAGNETOLUMINESCENCE

Recent advances in producing zero-dimensional semiconductor quantum well structures such as InGaAs/GaAs [39–41], InAs/GaAs [42–44], CdMnTe [45–48], CdSe/ZnSe [49, 50], and CdTe [47, 51] by use of epitaxial or other growth techniques has allowed the study of both excitonic structure and dilute magnetic systems (DMS) by using magnetoluminescence (ML). The quantum dots are prepared such that the vertical confinement is provided by the well potential and the lateral confinement is usually provided by a strain field due to lattice mismatch during growth. Thus quantum dots represent a zero-dimensional structure with few carriers within the well potential. The shallow well depth of the potential means that with magnetic fields of a few tens of Tesla, the cyclotron energy can be made larger than the binding energy, thus allowing the study of the transition from bound well states to bulklike Landau levels.

In a typical magnetoluminescence experiment in a semiconductor, the luminescence from either exciton recombination or dilute magnetic spin dopants such as  $Mn^{2+}$  is recorded as a function of an applied external magnetic field. One traditional problem with ML experiments is that the luminescence spectra from quantum dots (QDs) is often quite broad due to size and shape dispersion. The broad peaks tend to limit the shifts and splitting observed in a ML experiment. While the inhomogeneous nature of the luminescence usually results in broad lineshapes, early work on InGaAs/GaAs self-organized quantum wells was able to resolve the discrete states that exist in these unique structures [39]. Since then, most magnetoluminescence experiments have utilized various techniques to limit the luminescence viewing area to single or small numbers of QDs, in order to observe the underlying sharp excitonic structure in the inhomogeneously broadened spectra. Techniques such as near-field microscopy [52] and the use of small apertures or masks [46, 47, 49–51, 53] have allowed the observation of single or near single QDs with narrow emission linewidths.

Recently much work has been focused on the magnetoluminescence from semiconductor quantum dots, mostly using GaAs and InPGaAs structures. The magnetic length, given by  $(\hbar/eB)^{1/2}$ , of commonly used magnetic fields is on the order of 10 nm, making ML a good way to study interactions in small quantum dot systems. The application of a magnetic field has two effects on QDs. First it induces a

Zeeman splitting of the magnetic sublevels within an angular momentum state. Second, it induces a diamagnetic shift of the levels which, under high fields, resort to traditional bulklike Landau levels.

Most work has centered on excitonic luminescence in these systems. Due to the axial symmetry resulting from the strain field, the exciton in many QD systems may be characterized by a radial quantum number and an angular momentum quantum number  $m$ . In zero field, the  $m$  states are degenerate and form a single level. In an applied field, states with  $m \neq 0$  split linearly with the field strength, analogous to the Zeeman effect in molecular spectroscopy. Information about the exciton state may be obtained as  $S$ -like orbital states with  $m = 0$  do not split while  $p$ -like states split into two components and  $d$ -like orbitals split into 3. There is an additional shift of the energy levels, called the diamagnetic shift, which is proportional to the square of the applied field although it saturates to linear at high fields. Figure 15 displays the ML spectrum from QDs composed of self-organized InP islands atop an InGaAs/GaAs quantum well with the magnetic field oriented parallel (Fig. 15a) and perpendicular (Fig. 15b) to the growth direction [39]. No aperture was used to collect this spectrum so the luminescence bands are relatively broad. The dashed lines serve to connect the transitions split by the interaction with the magnetic field. The lowest energy transition clearly shows no splitting while the next higher lying transitions split into two and three states respectively (Fig. 15a).

Early ML work on InGaAs/GaAs QDs observed a splitting of the electronic levels of upper excited states due to the Zeeman effect while the ground state for which  $m = 0$  showed no Zeeman splitting and only a weak diamagnetic shift [39]. These effects were quantitatively modeled using a potential that consisted of a vertical quantum well and lateral, parabolic confinement due to strain [39]. Similar work distinguished three bound electron and hole states in 20–40 nm dots at zero magnetic field [40]. From the magnetic field dependences, the angular momentum quantum number of the states could be assigned and the states were seen to converge toward Landau levels at higher field strengths, consistent with calculations [40]. More recently, ML experiments utilizing high spatial resolution have been used to study biexcitons in CdSe/ZnSe QDs [49], to determine the effective mass of confined carriers [43, 44], and to study the effects of defects on excitonic states [53]. ML experiments on CdTe/ZnTe nanostructures have observed a doublet at zero field attributed to the splitting of excitonic states split by local asymmetries in the potential [51]. Increasing the magnetic field strength allows mixing of bright and dark exciton states and allows an estimate of the electron and hole  $g$ -factors and isotropic exchange energy [51].

While there have been ample studies of excitonic structure in zero-dimensional quantum dots using ML, there have also been numerous magnetoluminescence studies of dilute magnetic systems. II–VI semiconductor systems lend themselves to the incorporation of transition metals as dopants, particularly  $Mn^{2+}$ . The incorporation of Mn spins in the system gives rise to an  $sp$ – $d$  exchange interaction determined by the overlap of the Mn spins with the spins of charge carriers. Quantum confinement is expected to be smaller in

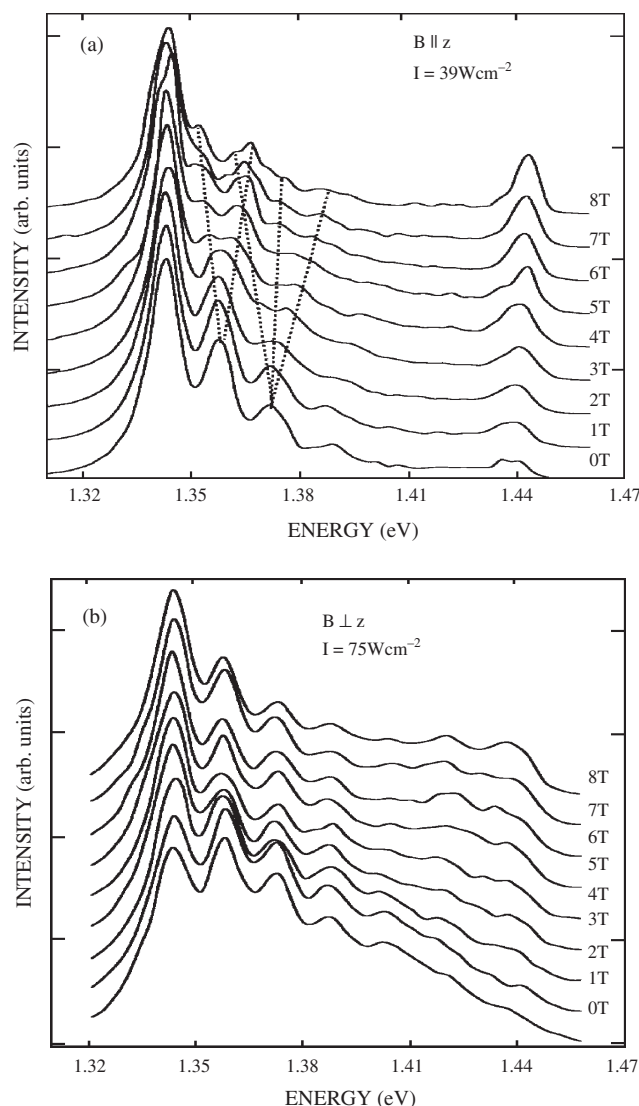


**Figure 15.** Magnetoluminescence spectra of InGaAs/GaAs quantum dots with the magnetic field oriented parallel (a) and perpendicular (b) to the growth axis. The dashed lines connect transitions split by the magnetic field. Reprinted with permission from [39], R. Rinaldi et al., *Phys. Rev. Lett.* 77, 342 (1996). © 1996, American Physical Society.

DMS of small sizes [54, 55] and has been confirmed experimentally [48, 55]. As carrier wavefunctions overlap more strongly with the  $Mn^{2+}$  spins, the effective g-factor becomes larger. For instance, g-factors of between 6 and 7 have been observed in II–IV magnetic quantum dots [50].

Recent experiments comparing semimagnetic  $Cd_{0.93}Mn_{0.07} \cdot Te/Cd_{0.60}Mg_{0.40}Te$  quantum dots with the nonmagnetic  $Cd_{0.93}Mg_{0.07}Te/Cd_{0.60}Mg_{0.40}Te$  counterpart show increased line broadening in the semimagnetic QDs due to this exchange interaction [46]. At higher magnetic fields, however, this broadening decreases significantly, becoming comparable to the nonmagnetic counterpart. This decrease has been explained by the suppression of magnetic fluctuations and the destruction of exciton magnetic polarons at high fields [46]. Other experiments on CdMnTe quantum dots also show increased broadening of the emission lines but the

linewidths did not decrease in width at higher fields presumably due to the relatively small size of the quantum dots used in that study [47].

## 9. UPCONVERSION LUMINESCENCE AND ANTI-STOKES LUMINESCENCE

Upconversion luminescence is a phenomenon in which the excitation energy (wavelength) is lower (longer) than the emission energy (wavelength). The mechanism responsible for upconversion is a popular issue that has attracted much attention. Sequential two-photon absorption can lead to upconversion excitation with a first photon populating an intermediate state and a second photon, which in the most general case would be of different energy, causing a transition from this intermediate state to a higher level. As an alternative, energy transfer between excited ions can result in efficient upconversion when a sufficiently large number of ions have been excited to an intermediate state [56].

A third type of efficient upconversion excitation is the photon avalanche process that involves excited state absorption of the pump light as well as interionic cross-relaxation. In addition, two-photon absorption and cooperative sensitization of luminescence [57] are two other channels for upconversion. Two-photon absorption processes via virtual states usually occur only at high excitation densities ( $\geq 10^3 \text{ W cm}^{-2}$ ) [58].

Cooperative luminescence is a special energy transfer process with energy transfer from one excited ion to another excited ion [56] resulting in one ground state ion and another “doubly excited” ion. Upconversion by cooperative energy transfer has the important advantage of requiring a single pump wavelength, obviating the problems related to beam alignment and pump efficiency that are associated with sequential two-photon absorption using two different pump lasers [56]. This is very favorable for practical applications like displays, infrared detection, optical storage, and communications.

In our recent research, we have investigated II–VI semiconductor nanoparticles doped or co-doped with transition or rare earth ions as a new type of upconversion material. The most common upconversion mechanisms for these systems are via two-photon absorption and energy transfer. For sequential two-photon absorption upconversion, the efficiency is mainly determined by the excited state absorbance and the emission efficiency, while for upconversion via energy transfer, the energy transfer rate and the intermediate state lifetime are the key parameters determining upconversion efficiency. A few basic principles serve to show how the quantum size effect can lead to improved upconversion efficiency.

First of all, quantum size confinement may enhance absorbance and luminescence efficiency and shorten decay lifetime, as discussed in Section 1.2. Second, for upconversion luminescence other than two-photon absorption, the energy transfer mechanism is very important. Many ions that demonstrate efficient sequential two-photon absorption upconversion pumping also exhibit cooperative energy transfer. In some ions the cooperative process is substantially more efficient than sequential two-photon absorption



upconversion. Thus, the enhancement of the energy transfer rate is very important.

For electric multipolar interactions the energy transfer probability [ $P_{SA}(R)$ ] can be generally written as [59]

$$P_{SA}(R) = \frac{(R_0/R)^s}{\tau_s} \quad (11)$$

where  $\tau_s$  is the actual lifetime of the donor excited state,  $R_0$  is the critical transfer distance for which excitation transfer and spontaneous deactivation of the donor have equal probability, and  $R$  is the separation between the donor and the acceptor.  $S$  is a positive integer taking the following values:

- $s = 6$  for dipole–dipole interactions
- $s = 8$  for dipole–quadrupole interactions
- $s = 6$  for quadrupole–quadrupole interactions

Equation (11) indicates that donor–acceptor separation is a key parameter in determining the energy transfer rate. The separation between ions is affected by dopant concentrations. The separation is smaller when the concentration is higher, which is favorable for energy transfer. The energy transfer rate and luminescence efficiency can also be enhanced by encapsulating nanoparticles in small cavities such as cavities in zeolite-Y [20, 21] and MCM-41 [16]; however, the enhancement mechanism is not yet clear.

The excited state luminescence may suffer quenching due to relaxation by phonons serving to decrease the upconversion yield. In bulk materials, the phonon density of states forms a continuous band that near the zone center can be described by the Debye model. Energy relaxation from high levels to low levels occurs by cascade emission of LO phonons and this process is controlled by the energy gap law [60]. The dependence of the multiphonon relaxation rate constant ( $K_{mp}$ ) across an energy gap ( $\Delta E$ ) on the phonon energy is well described by [60]

$$K_{mp} = C e^{-p\beta} \quad (12)$$

where  $C$  and  $\beta$  are positive constants characteristic of the material.  $p$  is defined as [60]

$$p = \frac{\Delta E}{\hbar\omega_{\max}} \quad (13)$$

such that  $p$  is the number of highest energy phonon quanta required to bridge the energy gap and  $\hbar\omega_{\max}$  is the highest lattice phonon energy. As a rule of thumb for multiphonon relaxation processes, the relaxation rate is smaller if  $p$  is larger. In other words, the lower the highest lattice phonon energy, the smaller the relaxation rate and the higher the upconversion efficiency. Similarly, the electron–phonon coupling determines the efficiency of energy transfer from the excited state to the phonons. The electron–phonon coupling strength in nanoparticles is determined by both the quantum confinement and the surface characteristics [61]. First, in nanocrystalline materials, the density of states is modified due to the size effect and, for an isolated nanoparticle, both the electronic energy and the phonon spectra become discrete. Thus, both the density of electron energy

and phonon energy levels decrease with decreasing size, which is likely to result in a weaker electron–phonon coupling. Similarly, the increased overlap between the electron and hole wavefunctions also decreases the electron–phonon coupling [61]. However, the overlap between the electron and hole wavefunctions may decrease due to the trapping of electrons or holes to the surface states. These factors indicate that electron–phonon interactions can be weaker in nanoparticles with good surface passivation.

Generally, it is not necessary to consider the host energy structure in order to understand multiphonon relaxation in insulating phosphors such as  $\text{BaF}_2:\text{Eu}^{3+}$  and  $\text{BaTiO}_3:\text{Er}^{3+}$  because the host energy gap is large ( $>8$  eV) [62] and the energy levels of the dopant are contained within the energy gap of the host. However, for semiconductor phosphors such as  $\text{ZnS}:\text{Tb}^{3+}$  or  $\text{CdS}:\text{Eu}^{3+}$ , the host energy structure must be considered because the host energy gap is less than 5 eV and the dopant energy levels intercept the host energy levels. Thus the energy relaxation from an excited state to a lower state of the dopant is possible via energy levels of the semiconductor host. This is particularly true for nanoparticles in which the energy levels are split. It is well known that the energy splitting between two levels increases with decreasing size [2]. According to Eq. (13),  $p$  increases with decreasing size. Therefore multiphonon relaxation from higher levels to lower levels may decrease in nanoparticles. This is actually the famous “photon bottleneck” [63]. According to the energy gap law, this is quite favorable for improving the upconversion efficiency.

Summarizing these arguments, in nanoparticles, due to size confinement, the increase of electron–hole wavefunction overlap may enhance the absorbance and luminescence efficiency as well as shorten the emitting state lifetime. Due to the decrease of both the phonon and electric state densities, the electron–phonon interaction is weaker. These are strong reasons to consider doped nanoparticles as a new type of upconversion material with good efficiency and faster response, whether the upconversion is due to energy transfer or two-photon absorption. For these reasons, upconversion luminescence of nanoparticles is becoming a topic under much investigation.

The study of nanoparticle upconversion luminescence is relatively new and not much work has been reported; yet strong upconversion luminescence of  $\text{Mn}^{2+}$  in  $\text{ZnS}:\text{Mn}^{2+}$  nanoparticles has been observed [64]. The upconversion emission band excited at 767 nm is redshifted from the photoluminescence emission excited at 300 nm (Fig. 16) [64]. In the nanoparticles, the decay lifetimes of the upconversion emission excited at 767 nm are shorter than the 300 nm excited luminescence lifetimes, while in bulk the two decays are almost identical. When the photoluminescence is obtained by excitation at 383.5 nm, which is the sum energy of two photons at 767 nm, the emission spectra and the lifetimes of the two types of luminescence are almost identical [64]. The power dependence of the photoluminescence is linear, while that of the upconversion emission is quadratic [64]. Based on these observations, two-photon excitation has been identified as the excitation mechanism responsible for the upconversion luminescence of  $\text{Mn}^{2+}$  in  $\text{ZnS}:\text{Mn}^{2+}$  nanoparticles.



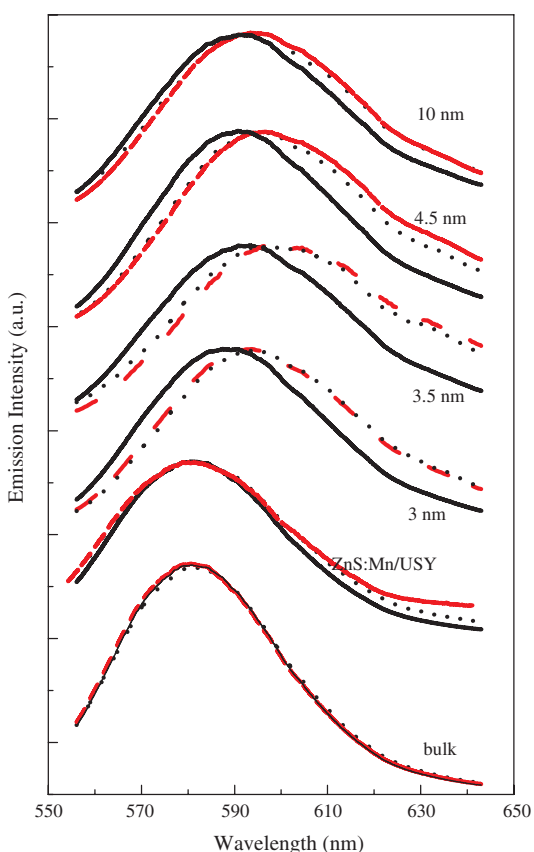


**Figure 16.** The photoluminescence spectra after excitation at 300 nm (solid), at 383.5 nm (dash), and the upconversion luminescence spectra resulting from 767 nm excitation (dot) of ZnS:Mn<sup>2+</sup> bulk and nanoparticles. Reprinted with permission from [64], W. Chen et al., *Phys. Rev. B* 64, 041202(R) (2001). © 2001, American Physical Society.

Upconversion luminescence is visible to the naked eye in these systems. This reveals that upconversion luminescence of ZnS:Mn<sup>2+</sup> can be realized at relatively low power densities. Our recent tests demonstrate that an 808-nm semiconductor quantum well laser module with 40 microwatts (power density of 1 mW/cm<sup>2</sup>) can stimulate upconversion luminescence of ZnS:Mn<sup>2+</sup> nanoparticles visible to the unaided eye. Similar upconversion luminescence is observed in ZnS:Mn<sup>2+</sup>, Eu<sup>3+</sup> nanoparticles. Emissions of both Mn<sup>2+</sup> and Eu<sup>3+</sup> are observed in the upconversion emission spectra and the upconversion is due to two-photon absorption of Mn<sup>2+</sup> and the emission of Eu<sup>3+</sup> is due to energy transfer from Mn<sup>2+</sup> [65].

Upconversion luminescence has also been reported in undoped semiconductor nanoparticles such as CdS and CdTe nanoparticles [66]. The term anti-Stokes luminescence is frequently used to describe the upconversion luminescence in undoped semiconductor nanoparticles. In general, any luminescence that occurs at frequencies larger than that of the excitation frequency is called anti-Stokes luminescence. Therefore, in this case, upconversion is just one variety of anti-Stokes luminescence. Figure 17a displays the optical absorption spectra of three CdTe nanoparticle samples [67]. The absorption edges of these nanoparticles are blueshifted from the 827 nm bulk CdTe bandgap as

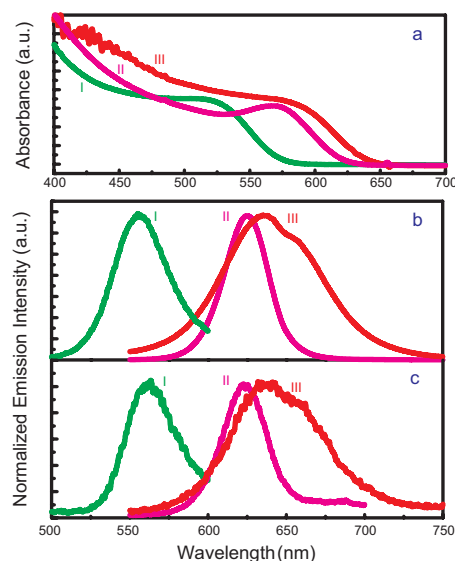


**Figure 17.** The absorption spectra (a), the photoluminescence emission spectra (b, excited at 350 nm), and the anti-Stokes luminescence spectra (c, excited at 750 nm) of CdTe nanoparticles with average sizes of 3 (I), 5 (II), and 6 nm (III), respectively [67].

a consequence of quantum size confinement. According to the shift and based on the effective-mass approximation [2], the estimated particle sizes are around 3, 5, and 6 nm, respectively. Their photoluminescence spectra are shown in Figure 17b. The nanoparticles show a pronounced excitonic luminescence band, which shifts to higher energies for smaller sizes. Strong anti-Stokes luminescence is observed from these nanoparticles as shown in Figure 17c with excitation at 750 nm. As in the photoluminescence, the anti-Stokes luminescence is also size dependent, shifting to higher energies for smaller nanoparticles. These results may be reasonably explained by a two-step absorption process via surface states [24, 67], which is actually upconversion luminescence through a two-step absorption.

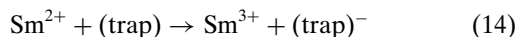
## 10. PHOTOSTIMULATED LUMINESCENCE AND MEDICAL IMAGING OF NANOPARTICLES

Photostimulated luminescence (PSL) describes the phenomenon in which phosphors release trapped charge carriers when stimulated by infrared or visible light [68]. The trapped carriers recombine with luminescent centers to generate the PSL. Thus, in photostimulated luminescence the stimulation (excitation) wavelength is longer than the emission wavelength in contrast to photoluminescence. Because photostimulable phosphors have the ability to store energy, they are also called storage phosphors. X-ray storage phosphors such as BaFBr:Eu<sup>2+</sup> have been widely discussed [68]. The PSL mechanism of BaFBr:Eu<sup>2+</sup> involving X-ray irradiation proposed by Takahashi et al. [69] assumes that during X-ray irradiation, the Eu<sup>2+</sup> ions are partly ionized into their trivalent charge state (Eu<sup>3+</sup>) and the liberated electrons drift via the conduction band to form F centers. Upon subsequent photostimulation, the electrons are released from the

F centers into the conduction band and they recombine with  $\text{Eu}^{3+}$  ions to produce the photostimulated luminescence of  $\text{Eu}^{2+}$  at 390 nm (Fig. 18) [69]. Other recent results indicate that tunneling may be the mechanism of recombination in  $\text{BaFBr:Eu}^{2+}$  phosphors [70].

In nanoparticles, the energy scheme can be modified via quantum size confinement. This offers a new way of designing PSL phosphors. When electrons and holes are produced in nanoparticles by photoexcitation, the electrons and holes may de-excite or relax to the lowest excited states and recombine to give luminescence. They also may be trapped by electron or hole traps at the surfaces, interfaces, and/or in a surrounding host. The electrons or holes at traps are in a metastable state. When stimulated by light or by heat, some may be released and recombine to give luminescence (i.e., photostimulated luminescence or thermoluminescence).

Controlled charge separation and trapping in nanoparticles are key to the processes of erasable optical storage, sensors, and digital imaging. The PSL of nanoparticles requires not only charge separation and trapping but also the return of the carriers to the nanoparticles. Evidence for charge separation, trapping, and subsequent return has been obtained from pump-probe measurements and photon-gated hole burning (PHB) of nanoparticles [71]. For example, in  $\text{BaFCl:Sm}^{2+}$ , the hole-burning process can be described as the photoionization reaction



If the electrons release from the traps and return to the  $\text{Sm}^{2+}$ , the hole will be erased, a process termed hole filling [72]. The hole burning corresponds to the photoionization process in PSL and the hole filling is similar to the photostimulation. Thus, the occurrence of PHB in a system is an indication of PSL, and vice versa.

In most systems, hole burning is only observable and stable at low temperatures. Only in a few materials is hole burning at room temperature possible. However, PSL is not as dependent on temperature. For example, in a

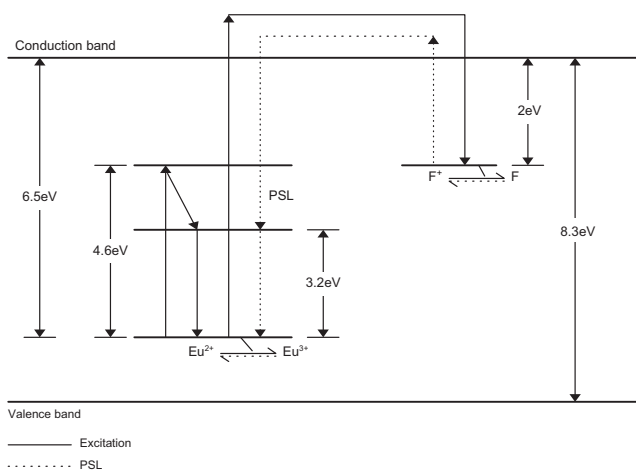


**Figure 18.** A schematic model for excitation and photostimulated luminescence processes in a  $\text{BaFBr:Eu}^{2+}$  phosphor. Reprinted with permission from [69], K. Takahashi et al., *J. Lumin.* 31–32, 266 (1984). © 1984, Elsevier Science.

$\text{BaFCl}_x\text{Br}_{1-x}:\text{Sm}^{2+}$  system, low temperature is necessary to observe PHB, while strong PSL is observed at room temperature [72]. The hole-burning efficiency or the storage density increases by a factor of  $\Gamma_I/\Gamma_H$ , where  $\Gamma_I$  is the inhomogeneous linewidth and  $\Gamma_H$  is the homogeneous linewidth. This ratio is highly temperature dependent. Phonon-broadening causes  $\Gamma_H$  to increase with temperature and makes hole burning difficult at high temperature. Phonon broadening has little effect in the PSL process; thus it is unnecessary to work at low temperature. This is one of the advantages of PSL and forms the basic premise for the construction of a doped nanoparticle that exhibits PSL for use in storage devices, sensors, and optical image display systems.

Two new and intriguing upconversion materials are Ag and AgI nanoclusters encapsulated in zeolite-Y (Ag/Y and AgI/Y). AgI nanoclusters encapsulated in zeolite-Y show strong luminescence and photostimulated luminescence at room temperature. Figure 19a shows the PL spectra of AgI/Y following excitation at 305 nm [73]. The broad emission band actually consists of two subbands. The first band results from AgI nanoparticle emission peaking at 474 nm and appears as a small but discernible shoulder on the blue energy edge of the broad emission peak in Figure 19a. The second band results from Ag nanocluster emission centered at 510 nm. Ag is known to coexist with AgI nanoparticles and efficient energy transfer is known to occur among them. The luminescence decreases in intensity when the sample is irradiated by ultraviolet light at 254 nm (Figure 19b). This decrease can be partially recovered by exposing the sample to visible light (Figure 19c).

After ultraviolet (UV) irradiation for a few minutes, strong PSL can be detected from AgI nanoparticles in zeolite-Y as shown in Figure 20 [73]. PSL excitation is easily stimulated using near-infrared wavelengths. Figure 20 shows that the emission consists almost exclusively of Ag nanoclusters resulting in a narrower band than the PL emission band [48]. Similarly, Ag nanoclusters in zeolite-Y (Ag/Y) are photosensitive and exhibit strong photostimulated luminescence. Similar to AgI/Y, Ag/Y particles show a marked decrease in PL after UV irradiation. This decrease

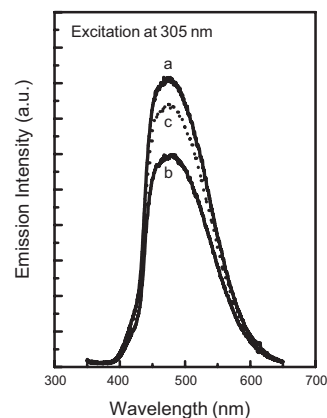


**Figure 19.** Photoluminescence spectra of AgI/Y before (a) and after (b) UV irradiation at 254 nm for 5 minutes. After exposure to a visible lamp for 5 minutes (c). Reprinted with permission from [73], W. Chen et al., *Phys. Rev. B* 65, 24554041 (2002). © 2002, American Physical Society.

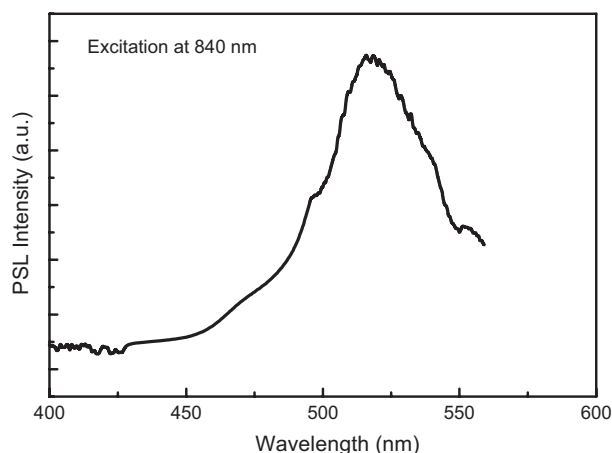


**Figure 20.** Photostimulated luminescence spectrum of AgI/Y after UV irradiation at 254 nm for 10 minutes. Excited at 840 nm. Reprinted with permission from [73], W. Chen et al., *Phys. Rev. B* 65, 24554041 (2002). © 2002, American Physical Society.

is almost completely reversible following irradiation by photons between 650 and 900 nm. Thus both materials may be considered for use as reusable image or digital storage media.

Figure 21a displays the PL lifetime decays at 500 nm from AgI/Y following excitation at 305 nm [73]. The inset shows the existence of a short (<15 nanosecond) component present in addition to the microsecond decays. The longest PL lifetime of Ag/Y particles at 500 nm is about 65 microseconds compared to AgI/Y particles which show about a 185 microsecond decay. In contrast to the PL decays, PSL measurements show only the fast (<15 nanosecond) component. Figure 21b shows PSL lifetime decays from both samples on a picosecond timescale following excitation at 800 nm. At 500 nm, the PSL decay from AgI/Y particles is 125 ps, which

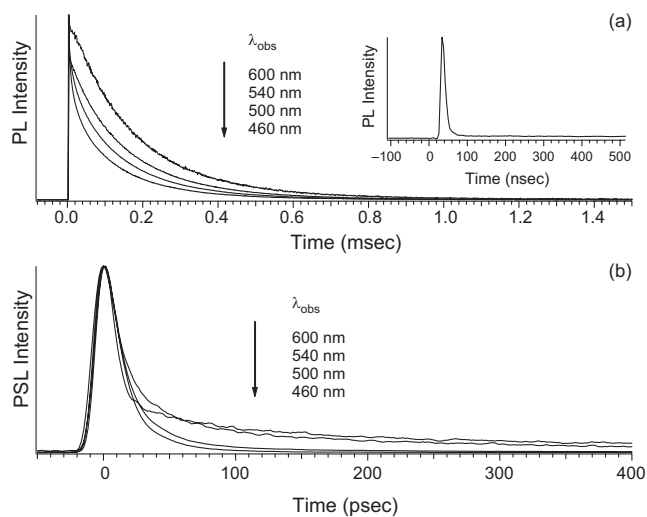


**Figure 21.** Lifetime decays of (a) photoluminescence (excitation at 305 nm) and (b) photostimulated luminescence (excitation at 800 nm) in AgI/Y nanoparticles. The inset in (a) displays the PL lifetime at higher time resolution showing the fast (<15 ns) time component. Reprinted with permission from [73], W. Chen et al., *Phys. Rev. B* 65, 24554041 (2002). © 2002, American Physical Society.

is almost a factor of 3 faster than the PSL decay from Ag/Y particles [73]. Even though in both cases the PSL derives from the silver particles, there is a noticeable difference in the PL and PSL lifetimes. This may reflect the differences in energetics between the two samples, given that Ag is metallic while AgI is a direct bandgap semiconductor.

In either sample, excitation by UV photons likely ionizes Ag to  $\text{Ag}^+$  leading to both a luminescent center,  $\text{Ag}^+$ , and a source of electrons. The electrons are then trapped in the zeolite framework, most likely at regions with a missing oxygen link, which serve as Lewis acid sites. Upon near-infrared (IR) excitation, this trapped electron is released and transfers to the nearby  $\text{Ag}^+$  site which is on the surface of the nanoparticles and at the zeolite–nanoparticle interface. This results in the characteristic emission of Ag as



where  $e$  represents an electron released from the color center,  $\text{Ag}^{0*}$  is the excited state of Ag, and  $\text{Ag}^0$  is the ground electronic state after emitting a photon,  $h\nu$ . This model explains the decrease in PL intensity following UV irradiation as the  $\text{Ag}^0$  is ionized and the electron becomes trapped in the zeolite. Following near-IR excitation, the electron is transferred to the nearby  $\text{Ag}^+$ . Therefore, the PSL is dominated by interfacial Ag clusters leading to exclusively Ag luminescence. The interfacial nature allows access to trap sites both at the surface and in the zeolite framework leading to extremely short lifetimes. The short lifetimes and strong PSL make these materials good candidates for new phosphor screens or digital storage applications.

The photostimulable phosphor used in commercial X-ray imaging system is  $\text{BaFBr:Eu}^{2+}$ ; yet the  $\text{BaFBr:Eu}^{2+}$  system suffers from poor resolution due to the long decay lifetime of  $\text{Eu}^{2+}$  emission (0.8  $\mu\text{s}$ ) as well as scattering of the stimulating laser light from the platelike polycrystals. In addition, the hygroscopic nature of this phosphor limits the stability of the system. Thus, a new type of PSL phosphor with improved characteristics is desirable and the subject of extensive investigation.

Most light detection systems suffer from low resolution due to the scattering of both the reading laser light and the emission light. The light scattering is due to the phosphor grain size, shape, and the grain boundary, as well as surface roughness [74]. Raleigh's approximation describing the interaction of light with matter indicates that for particles that are isotropic, the intensity of scattered light is approximately equal to the particle diameter to the sixth power [75]. Therefore, a 50-nm particle will scatter one million times more light than a 5-nm particle. Therefore, compared to the scattering in traditional micrometer-sized phosphors, the scattering of light in nanoparticles is negligible. This suggests that much higher resolution is possible using upconversion in nanoparticles and nanothin films for infrared detection and imaging.

Quantum size confinement of nanoparticles overcomes some of these problems. The higher luminescence efficiency, faster decay, and lower light-scattering for smaller particles results in higher spatial resolution and faster response. Nanosized  $\text{BaFBr:Eu}^{2+}$  phosphors show strong PSL [76]. The PSL from  $\text{BaFBr:Eu}^{2+}$  nanoparticles decays with a lifetime of 390 ns and provides a good example demonstrating

that the PSL imaging performance and temporal resolution may be improved via quantum size confinement.

Figure 22 shows the emission spectra of BaFBr:Eu<sup>2+</sup> nanoparticles having an average size of ~40 nm, as measured by X-ray diffraction [76]. The emission band is due to the  $4f^6 5d^1 (t_{2g}) \rightarrow 4f^7$  transition of Eu<sup>2+</sup>. In BaFBr:Eu<sup>2+</sup> nanoparticles, the emission band of Eu<sup>2+</sup> is at 407 nm, which is ~17 nm redshifted compared to that in bulk BaFBr:Eu<sup>2+</sup> at 390 nm. This is due to the change in crystal field or site symmetry of the nanoparticles.

The fluorescence of BaFBr:Eu<sup>2+</sup> nanoparticles is very sensitive to light. Under UV irradiation, the luminescence of Eu<sup>2+</sup> decreases in intensity. The luminescence is recovered by exposure to red light at approximately 600 nm (Fig. 22). Strong PSL is observed following stimulation at 600 nm, which is shown in Figure 23 [76]. The PSL spectrum is consistent with the PL spectrum. This indicates that the PSL is from the recombination of electrons with Eu<sup>2+</sup> centers as in bulk BaFBr:Eu<sup>2+</sup> phosphors.

Figure 24 shows the PL and PSL decays of BaFBr:Eu<sup>2+</sup> nanoparticles [76]. The results demonstrate that the PL decay lifetime of BaFBr:Eu<sup>2+</sup> nanoparticles is almost the same as that of bulk BaFBr:Eu<sup>2+</sup>, around 800 ns. However, the PSL decay lifetime of BaFBr:Eu<sup>2+</sup> nanoparticles is much shorter than that of bulk BaFBr:Eu<sup>2+</sup>. The PSL decay of BaFBr:Eu<sup>2+</sup> nanoparticles has two components. One is

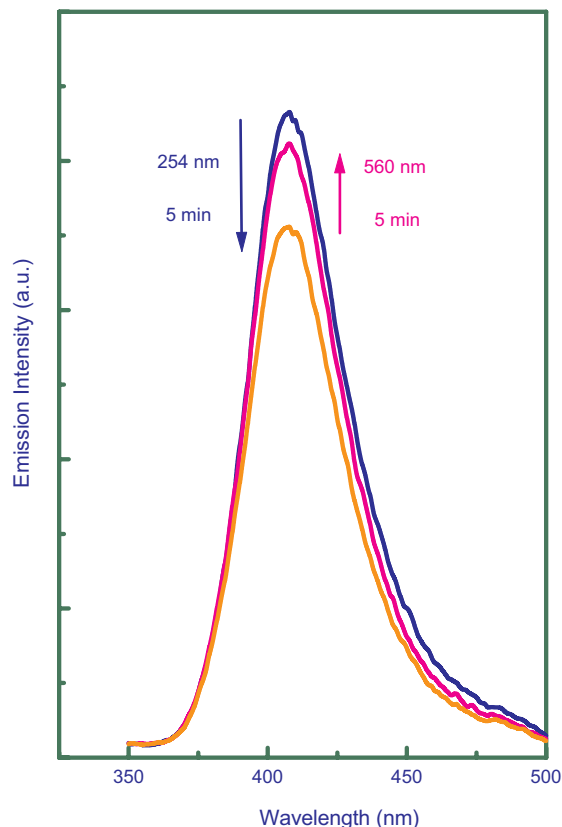


**Figure 22.** Emission spectra of BaFBr:Eu<sup>2+</sup> nanoparticles before (blue) and after UV irradiation at 254 nm for 5 min (orange), and then photostimulation at 560 nm for 5 min (magenta), respectively (excitation at 304 nm) [76].

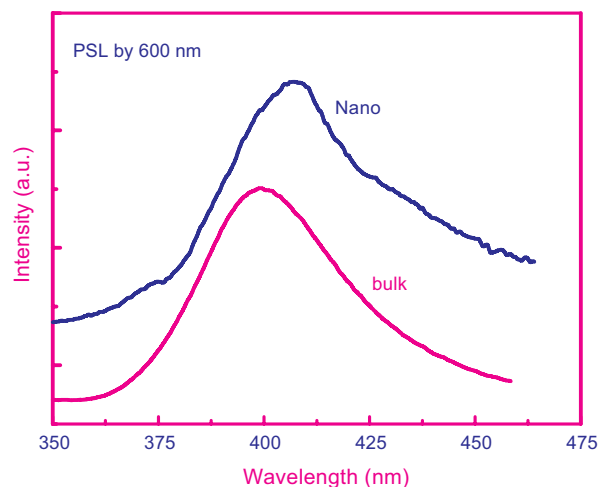


**Figure 23.** Photostimulated luminescence spectra (excited at 600 nm) of BaFBr:Eu<sup>2+</sup> nanoparticles and bulk after UV irradiation for 10 minutes.

shorter than 20 ns; the other is 340 ns. The short decay of less than 20 ns is likely due to surface states and the shortened decay of 340 ns is likely due to quantum confinement. The difference in the PSL decay behavior of the nanoparticles and the bulk material indicates that the PSL energetics in the bulk and the nanoparticles are different. The faster decay in the nanoparticles demonstrates that it is possible to improve the storage and imaging performance by the size effect.

Biological and biomedical applications of nanoparticles represent a new direction in nanoscience and nanotechnology [1, 77, 78]. This includes biological labeling, biomedical imaging, and diagnostics. The nanoparticle photostimulable phosphors described may be used in medical imaging devices such as a computerized radiography system.

One of the most important parts of the computerized radiography system is the imaging plate (IP) with its layer

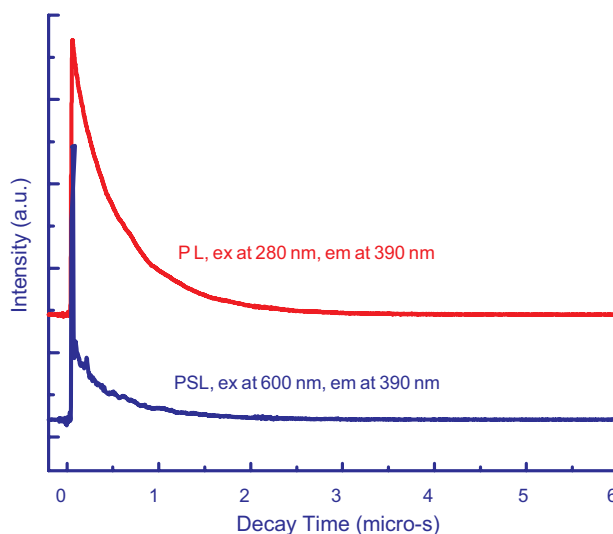


**Figure 24.** Photoluminescence (PL) and photostimulated luminescence (PSL) lifetime decays of BaFBr:Eu<sup>2+</sup> nanoparticles.

of photostimulable phosphor. During X-ray exposure, part of the energy of the absorbed X-rays is stored in the phosphors as trapped electrons and holes. The stored energy is released by a focused He–Ne laser which empties the traps by optical stimulation to give luminescence due to electron–hole recombination [68, 69]. The photostimulated luminescence intensity, which is proportional to the X-ray dose, is measured for each spot on the imaging plate, using a photomultiplier tube, and stored in a computer. It has been demonstrated in the laboratory that using this PSL system the X-ray dosage can be reduced to one-tenth of the conventional screen-film method while the radiograph remains of the same quality. This indicates that the photostimulable phosphor IP is an excellent detector for digital radiography, which may replace some of the conventional screen-film methods. When the IP is placed in a cassette, it can be used with conventional machines, and the digital imaging radiographs can be shared among hospitals through the Internet. In addition, large area IPs are conveniently produced, are reusable, have linear response over a wide range of X-ray dosage, and are erased simply by exposure to a uniform stimulating light or by thermal clearance. Thus, as compared to the conventional radiation image sensors, the IP method not only visualizes the latent radiation image with a high sensitivity through the digital process of conventional radiation image sensors but also makes it possible to quantify the position and intensity of the radiation image [68, 69].

Nanoparticles exhibit strong photostimulated luminescence, and therefore nanoparticle thin films display excellent potential for medical imaging applications. The advantages of using nanoparticle thin films for medical imaging may be summarized as follows:

- (1) high emission quantum efficiency resulting in higher sensitivity
- (2) low scattering resulting in better resolution
- (3) shortened decay lifetime leading to faster response
- (4) particles with desired size and shape
- (5) thin films with desired uniformity, area, thickness, and flexibility

These advantages may make nanoparticles a potentially more cost effective alternative to traditional medical imaging technologies.

## 11. X-RAY EXCITED OPTICAL LUMINESCENCE

X-ray excited optical luminescence (XEOL) refers to the measurement of the optical luminescence spectrum following excitation with X-ray photons. XEOL involves energy transfer from the initially absorbed X-ray photons and may be represented as the sequence of the following steps [79]:

- (1) absorption of the ionizing radiation (X-ray photons) and creation of primary electrons and holes
- (2) relaxation of primary electrons and holes which may produce secondary electrons, holes, photons, plasmons, and other electronic excitations
- (3) thermalization of the low-energy secondary electrons (holes) resulting in a number of electron–hole pairs (excitons) with energy roughly equal to the bandgap energy  $E_g$

- (4) energy transfer from the electron–hole pairs to the luminescence centers thereby inducing their excitation
- (5) emission from the luminescence centers

XEOL uses tunable soft X-ray sources such as synchrotron radiation and therefore can achieve state and site selective excitation [80], and thus XEOL is closely related to X-ray absorption near edge structures (XANES). XANES may be measured in terms of total electron yield (TEY), fluorescence yield (FLY), and photoluminescence yield (PLY) [80–82]. Generally, there is no obvious distinction made between “fluorescence” and “photoluminescence” yields. However, here the distinction is made that photoluminescence yield refers to the emission of optical photons and fluorescence yield typically refers to the emission of X-ray fluorescence photons. Thus, PLY typically deals with emission photons of the order of a few eV whereas FLY deals with emission photons that could be as much as several keV. The TEY measurement is sensitive to the surface and near-surface regions of the sample, while FLY is more sensitive to the bulk, and PLY is sensitive only to the sites where the photoluminescence originates [80–82]. By tuning the excitation photon to energies of a specific absorption band (valence region) or edge (core levels) of an element or its compounds, one can achieve some degree of site selectivity [80]. Table 1 lists the attenuation length of the incident photons for the four regions of interest for both silicon and SiO<sub>2</sub> [80]. Table 1 demonstrates that the incoming photons are completely absorbed within a couple of micrometers from the surface with the photons below the Si *K*-edge as an exception. Thus, tuning the photon energy from just below to just above the edge allows for a sudden increase of the absorption of the incident photons (energy) into a select excitation channel [80]. By using a combination of XEOL, TEY, FLY, and PLY information on the emitting states, the chemical environment, sites, coordination number, chemical bond length, and the sampling depth may be obtained. Recently, XEOL technology has successfully been applied to investigate the luminescence mechanism of porous silicon [83] and CdS nanoparticles [84].

**Table 1.** Attenuation length (one absorption) of incident photons in Si and SiO<sub>2</sub> below and above the relevant edge.

	Photon energy (eV)	Attenuation length ( $\mu\text{m}$ )	
		Si	SiO <sub>2</sub>
Inner valence	20–40	0.23–0.26	0.020–0.026
Si <i>L</i> <sub>3,2</sub> -edge	below 100 (Si), 105 (SiO <sub>2</sub> ) above 100 (Si), 105 (SiO <sub>2</sub> )	0.122	0.113
O <i>K</i> -edge	below 538 above 538	0.51	1.04
Si <i>K</i> -edge	below 1840 (Si), 1847 (SiO <sub>2</sub> ) above 1840 (Si), 1847 (SiO <sub>2</sub> )	14	7.4
		1.26	2.2

Source: Reprinted with permission from [80], S. J. Naftel et al., *Phys. Stat. Sol. A* 182, 373 (2000). © 2000, Wiley-VCH.



The discovery of luminescence from nanostructured porous silicon in 1990 is a breakthrough event in silicon optoelectronics [85]. However, there has been some debate as to the origin of the luminescence. Different models have been proposed to explain the luminescence from porous silicon, such as the quantum size confinement model [85], formation of siloxene [86], and the production of hydrogenated amorphous silicon [87]. Using XEOL, Sham et al. [83] have shown that porous silicon is essentially crystalline silicon locally, the surface silicon oxide components are not responsible for the luminescence, and, more importantly, the luminescence does not originate from siloxene. This result strongly supports the model of quantum size confinement [85].

The argument and controversy over the luminescence mechanism from porous silicon are due to the fact that porous silicon is very complex. Silicon oxides, siloxene, oxygen- and hydrogen-related defects, and surface states may exist in porous silicon produced by HF chemical etching [85]. In most cases, porous silicon is covered with a layer of amorphous SiO<sub>2</sub> which may contain defects that also exhibit luminescence. To distinguish these two luminescence mechanisms, the XEOL excited at and above the L<sub>3,2</sub> edge of Si and SiO<sub>2</sub>, respectively, are shown in Figure 25. The attenuation length of photons at the Si L<sub>3,2</sub> edge (~100 eV) is ~60 nm, which is significantly less than the thickness of porous silicon. An intense peak at around 650 nm and two satellites at 480 and 380 nm are observed in the XEOL spectrum [81]. The 650 nm peak is the most intense at 100 eV excitation; however, upon excitation into the SiO<sub>2</sub> absorption edge, the intensity decreases greatly while the two satellites increase in intensity. In addition, the two satellite peaks disappear upon HF treatment (a' in Figure 25) which removes the SiO<sub>2</sub> overlayer. These results strongly

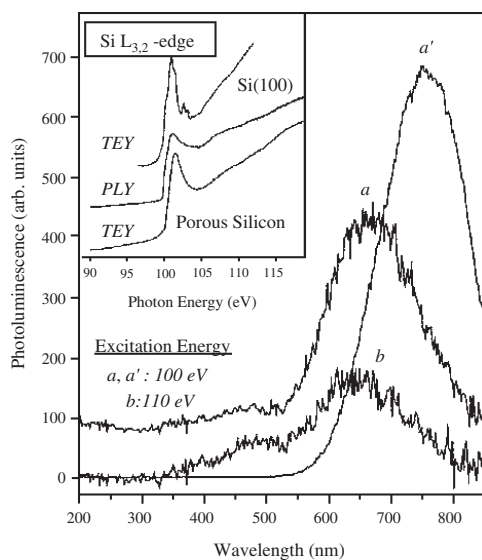


**Figure 25.** XEOL spectra excited at (a) 100 and (b) 110 eV from an as-prepared porous silicon sample. Luminescence of the HF treated sample excited at 100 eV is shown as (a'). XANES of the HF refreshed sample in TEY and PLY and of the Si(100) in TEY are shown in the inset. Reprinted with permission from [81], Y. F. Hu et al., *Rev. Sci. Instr.* 73, 1379 (2002). © 2002, American Institute of Physics.

imply that the emission at 650 nm is from the nanocrystalline silicon and that the two satellite peaks are from the surface oxide [80–82].

The particle size and porosity in porous silicon are determined by the preparation conditions which include the wafer resistance, HF concentration, current density, and etching time [4, 88]. Therefore, the luminescence energy (wavelength) and efficiency are determined by the preparation conditions [82]. One example is shown in Figure 26 for the XEOL of porous silicon samples prepared from *c*-Si wafers with two different resistances, 10 (a, b) and 16–20 Ω cm (A, B), at different current densities but the same HF concentration [88]. Figure 27 displays the XANES, recorded in TEY and PLY modes at the Si K edge of a typical porous silicon sample before (top) and after HF treatment [88]. The XANES spectra recorded by TEY and PLY for an aged sample (top) are very different in the region just above the edge, while they are nearly identical for the fresh sample (bottom). The peak at 1847 eV present in the TEY spectrum of the aged sample is a consequence of Si–O bonding due to the presence of SiO<sub>2</sub> on the surface. Because the TEY spectrum is surface sensitive, this peak is greatly enhanced relative to the PLY spectrum. This peak disappears after HF treatment

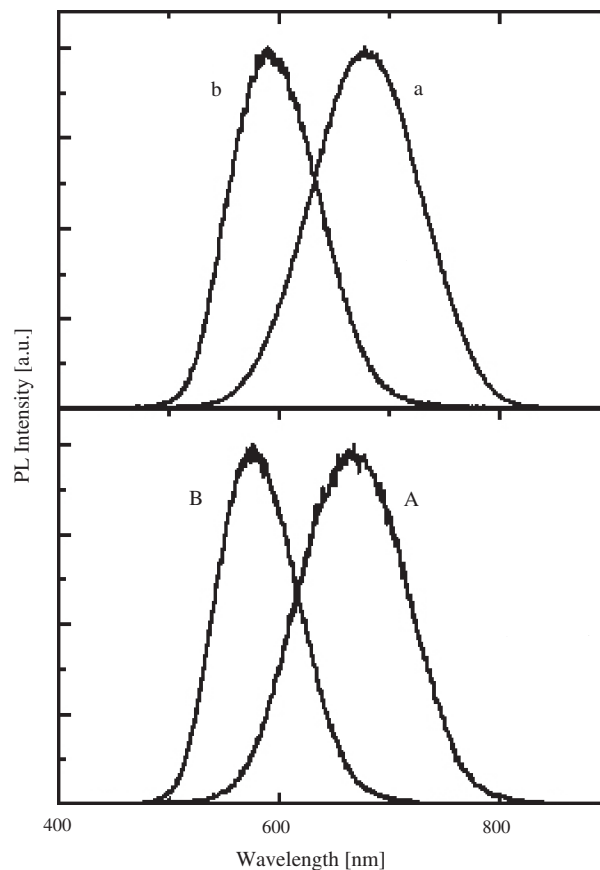


**Figure 26.** X-ray excited optical luminescence of a porous silicon fresh sample with wafer resistance of 10 (top) and 16–20 Ω m (bottom) at different current densities (A—28, B—65, a—40, b—90 mA/cm<sup>2</sup>) but the same HF concentration. Reprinted with permission from [88], G. Dalba et al., *J. Non-Crystal. Solids* 232–234, 370 (1998). © 1998, Elsevier Science.



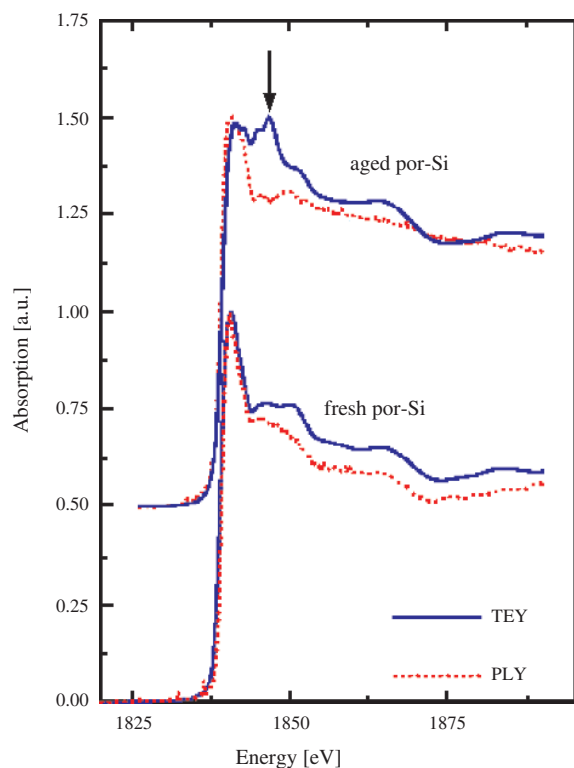


**Figure 27.** XANES spectra recorded in TEY and PLY modes at the Si  $K$  edge of a typical porous silicon sample before (top) and after HF treatment (bottom). Reprinted with permission from [88], G. Dalba et al., *J. Non-Crystal. Solids* 232–234, 370 (1998). © 1998, Elsevier Science.

as the  $\text{SiO}_2$  layer is etched away and the spectrum resembles the PLY spectrum. Therefore, the PLY signal does not depend on the Si–O bonds but is related only to the Si nanoclusters. These results further confirm that the luminescence does not originate from silicon oxide regions consistent with the results by Sham et al. [83].

Due to the availability of synchrotron radiation, XEOL is getting more and more popular. XEOL is being applied to investigate scintillation materials [79], organic thin films [89], and luminescent nanoparticles [84]. Figure 28 shows the XEOL spectra of 2 nm sized CdS nanoparticles stabilized in a dendrimer [81]. Spectra (a), (b), and (c) were excited with selected photon energies across the S  $K$  edge marked with vertical bars in the XANES (Fig. 28, inset), collected in both TEY and PLY. The PLY spectrum shows one strong resonance at 2474 eV due to the S ( $1S$ ) transition to the unoccupied orbitals in CdS. The TEY spectrum shows an additional peak at 2480 eV due to the S( $1S$ ) to  $\text{SO}_4^{2-}$  transition present because the surface of the dendrimers are oxidized to sulfate groups. The luminescence intensity increases greatly from (a), below the S  $K$  edge to (b), at the CdS S  $K$  edge. The luminescence decreases when excited at (c), corresponding to the surface sulfate groups and the strongest peak in the TEY spectrum. Since comparison of the CdS nanoparticle PLY XANES with the TEY of bulk CdS shows that they are identical, the luminescence originates mainly from CdS nanoparticles and not from the surface sulfate groups [81, 84].

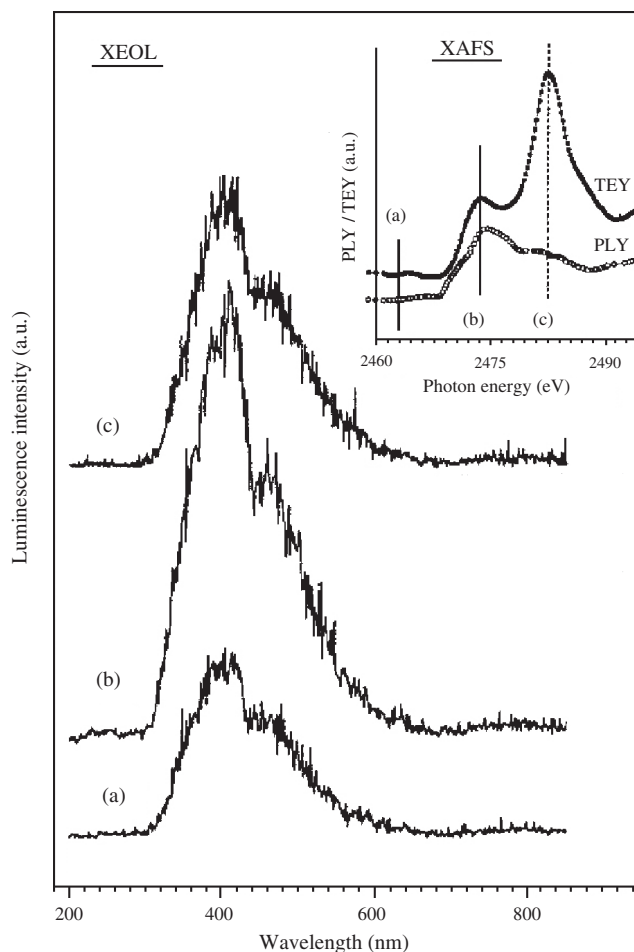


**Figure 28.** XEOL spectra of 2 nm sized CdS nanoparticles stabilized in dendrimer with various X-ray energies across the S  $K$  edge. The inset shows the XANES in TEY and PLY and the corresponding excitation photon energies (vertical bars) for (a), (b), and (c). Reprinted with permission from [81], Y. F. Hu et al., *Rev. Sci. Instr.* 73, 1379 (2002). © 2002, American Institute of Physics.

## 12. BIOLOGICAL LABELS AND MARKERS

Over the past 20 years, organic chemistry has developed a wide array of molecular probes, usually organic dyes, for a variety of applications in cellular imaging, biomolecular analysis, sensing, and biophysics. However, the current selection of organic dyes leaves much to be desired. Broad spectral overlap, photobleaching, difficult conjugation chemistry, poor water solubility, and expense are frequently cited as limitations of commercially available organic and organometallic probes. Recent research into the physical and chemical properties of nanoparticles suggests that the photophysical behavior of these tiny particles may be more finely tunable than that of dyes and, thus, may offer a promising way to solve some vexing problems with biological labeling. The crucial development in the application of nanoparticles to biological assays and imaging has been the creation of simple, reliable synthetic routes for a variety of nanostructures. The chemical synthesis of nanoparticles is typically achieved with just one reaction, involving a

chemical transformation of a precursor source of inorganic material followed by a nanocrystallization process in the same vessel. Desired and novel properties of nanoparticles can be obtained by fine control over the synthetic conditions to determine size, size distribution, emission wavelength, and surface characteristics. Thus, nanoparticle biological probes are easier to make and are potentially less expensive than organic dyes. More importantly, the specific photochemical reactions that cause organic dyes to photobleach or to cross-link nonspecifically with biological samples are far less common for inorganic nanoparticles. In comparison with conjugates formed with organic dyes such as rhodamine, this new class of luminescent probes is 20 times as bright, 100 times as stable against photobleaching, and 1/3 as wide in spectral linewidth [90]. Therefore, inorganic nanoparticle probes may have tremendous applications in biomedicine and biology even though there are still some problems that need to be solved, such as the blinking emission of some nanoparticles, the possible toxicity, and the biocompatibility with inorganic nanoparticles. However, these limitations may be overcome by the purposeful design and fabrication of nanostructures.

Another important advantage of luminescence nanoparticles for biological labeling is the recent discovery of upconversion (anti-Stokes) luminescence [64, 65]. Since the excitation wavelength is longer than the emission wavelength, there is very little background noise, which drastically reduces the detection limit. In regular Stokes fluorescence detection, the noise is primarily associated with the autofluorescence of biological tissues, which is nearly eliminated in the case of anti-Stokes emission (Fig. 29). In addition to the improvement of resolution and sensitivity, anti-Stokes luminescence allows the use of IR/NIR light sources, which are preferred for biological labeling and long-term sensing over UV light sources because the photoinduced damage done by IR quanta to biolabels and organisms is much lower. However, species with pronounced anti-Stokes luminescence are quite rare, and there are only a few phosphors that afford labeling and observation of the targets with anti-Stokes luminescence [91]. They are based exclusively on rare-earth metals and the biolabeling is achieved with fairly large particles of about 1 micrometer in diameter [92]. The large size of these micrometer-sized colloids,

strong scattering associated with it, and lower penetration ability are the major limiting factors for many applications. With transition to nanoscale materials, parasitic scattering is drastically reduced, and the diffusion rate increases, and therefore, the response time of the sensors is also enhanced. In addition, it is possible to significantly increase the quantum yield of upconversion by proper surface modification of the nanoparticles.

The broad range selection of the shell (stabilizer) structure of semiconductor nanoparticles makes biological labeling possible in many ways, from exchange reactions with stronger binding ligands to covalent conjugation with different linking reactions [93], as well as noncovalent labeling techniques such as electrostatic attractions to labeling proteins [77]. It has been demonstrated that nanoparticle bioconjugates selectively bind to cell components, DNA, or blood proteins and can be detected by strong luminescence tunable by the particle size [1, 78]. By using narrow band tunable color or luminescence nanoparticles, polymeric microbeads (1.2  $\mu\text{m}$ ) have been tagged by different colored nanoparticles to create multiplexed coding [1]. By controlling both the size and number of nanoparticles attached to the microbeads, 5–6 colors and 6 intensity levels yield 10,000 to 40,000 distinguishable codes under excitation with a single wavelength excitation source. These tagged microbeads can be used to label DNA and protein sequences and therefore have enormous potential in genomics and proteomics research areas.

The most commonly used covalent coupling method to conjugate nanoparticles to proteins is the sulfo-NHS (*N*-hydroxysulfo-succinimide) and EDC [1-ethyl-3-(3-dimethylaminopropyl) carbodiimide hydrochloride] reaction (Scheme 1). NHS-conjugated proteins have the highest bioactivity among other conjugates as established by several comparative studies [78, 93]. The carboxylic acid group of thioglycolic acid stabilized nanoparticles can form amide bonds with the primary amine groups of the protein, or the carboxylic acid groups of the protein can form amide bonds with the primary amine groups of cysteine stabilized nanoparticles. When using this method, the pH, concentration of reagents, and reaction time vary for each particular reaction. Possible aggregation due to multiple conjugations can be avoided by carefully choosing the reaction conditions.

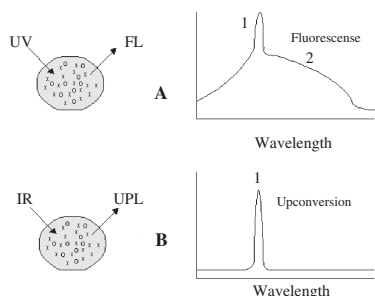
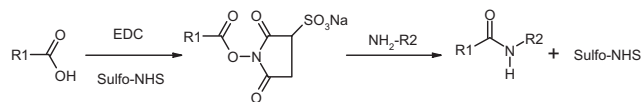


**Figure 29.** A schematic illustration for using fluorescence (top) and upconversion luminescence (bottom) in biological probing. Under ultraviolet excitation in the case of fluorescence, strong autofluorescence is observed along with the fluorescence. In upconversion luminescence, this autofluorescence can be avoided because the excitation energy is in the infrared. Thus, better resolution is possible using upconversion luminescence.

### 13. FLUORESCENCE ENERGY TRANSFER AND BIOLOGICAL/CHEMICAL SENSORS

Fluorescence resonance energy transfer (FRET) refers to transfer of the excited-state energy between two different luminescent molecules (or nanoparticles), from the initially excited donor (D) to an acceptor (A). FRET can occur when the donor molecules emit at wavelengths that overlap with



**Scheme 1.** Reprinted with permission from [93], S. Wang et al., *Nano Lett.* 2, 817 (2002). © 2002, American Chemical Society.

the absorption spectrum of the acceptor. Energy transfer occurs without the appearance of a photon and is the result of long-range dipole–dipole interactions between the donor and acceptor. An important characteristic of FRET is that the transfer rate is highly dependent on the distance between the donor and receptor. The distance at which FRET is 50% efficient, called the Förster distance, is typically 20–60 Å [59]. The relationship between the transfer efficiency  $E$  and the donor-to-acceptor (DA) distance  $r$  is given by

$$E = \frac{R_0^6}{R_0^6 + r^6} \quad (16)$$

where  $R_0$  is the Förster distance. This equation shows that the transfer efficiency is strongly dependent on distance when the DA distance is near  $R_0$ . FRET is widely used as a sensing mechanism for molecular level distance and binding event detection [94]. The detection limits of analytical processes based on FRET can be as low as 10 ppt with a linear dynamic range from 0.1 to 1000 ppb, while the utilization of antibodies enables the selective detection of substrates which may differ by only a few atoms. Luminescent semiconductor nanoparticles open new possibilities in this field of applications. The stability of nanoparticles under UV and visible light makes possible not only high-contrast multiplexed imaging but also a long-term monitoring of the environment, for instance for biological warfare agents or natural pathogenic organisms such as cholera and *E. coli*, which represent a critical problem for countries with limited water treatment capabilities. This task implies that no sample labeling/staining should be involved, which can be accomplished by taking advantage of the competitive inhibition of FRET in antigen–antibody immunocomplexes, as demonstrated in a recent report [93] founded on a FRET based immunological sensor using luminescent CdTe nanoparticles.

In this study, two different thioglycolic-acid-stabilized CdTe nanoparticles were used, one with a luminescence peak at 555 nm and the other one with the peak at 611 nm. Nanoparticle-conjugated BSA (bovine serum albumin) and anti-BSA IgG (immunoglobulin G) were prepared by the sulfo-NHS and EDC reaction (Scheme 1). The conjugations were purified with centrifuge and/or dialysis. The formation of conjugation was verified with electrophoresis, luminescence spectra, and high pressure liquid chromatography (HPLC). A one-to-one conjugation between nanoparticle and protein was confirmed by HPLC results. The biological structure and activity of the conjugates were retained as verified by circular dichroism spectra and ELISA (enzyme-linked immunosorbent assay).

When nanoparticle-IgG (anti-BSA) with green luminescence is combined with nanoparticle-labeled BSA with red luminescence, the nanoparticle-IgG/BSA-nanoparticle immunocomplex formed. As expected, a significant enhancement of the nanoparticle-BSA red emission at 611 nm and the corresponding quenching of the green emission of nanoparticle-IgG at 555 nm are observed after the self-assembly of the labeled biospecific ligands in the immunocomplex (Fig. 30, trace 2) [93]. The mutual affinity of the antigen and antibody brings the nanoparticles close

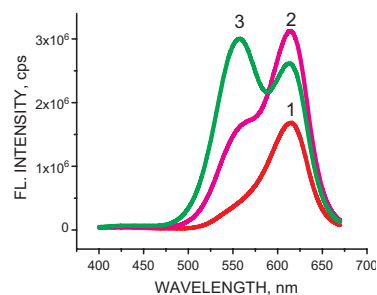


**Figure 30.** Fluorescence resonance energy transfer based detection of BSA in solution. (1) CdTe nanoparticle-1-BSA; (2) CdTe nanoparticle-BSA + CdTe-nanoparticle-2-IgG; (3) BSA + nanoparticle-1-BSA + nanoparticle-2-IgG. Concentrations: nanoparticle-BSA  $5 \times 10^{-7}$  M, nanoparticle-IgG  $5 \times 10^{-7}$  M, BSA  $2 \times 10^{-6}$  M. Reprinted with permission from [93], S. Wang et al., *Nano Lett.* 2, 817 (2002). © 2002, American Chemical Society.

enough together to allow the resonance dipole–dipole coupling required for FRET to occur. Thus, the energy of the excitonic state in the green-emitting nanoparticles is transferred to the similar state of the red-emitting nanoparticles. FRET efficiency is particularly high for green/red nanoparticle pairs because of the strong overlap of their emission and absorption spectra. Importantly, when unlabeled BSA is added to the immunocomplex, it competitively binds to nanoparticle-IgG, thereby replacing it in the immunocomplex with nanoparticle-BSA and inhibiting the FRET process. Therefore, the green emission peak of nanoparticle-IgG at 555 nm can be observed again, while the red emission peak at 610 nm shows decreased intensity (Fig. 30, trace 3). Alternatively, adding a high concentration of egg albumin, which does not bind to anti-BSA IgG, shows no influence on FRET efficiency between nanoparticle-IgG and nanoparticle-BSA. Unlike ELISA, the described detection process does not require multiple binding and washing steps. Following this approach, a detection limit of  $10^{-8}$  M BSA has been reported [93].

## 14. LUMINESCENCE TEMPERATURE DEPENDENCE AND TEMPERATURE SENSORS

Variation of temperature and pressure has proven to be a powerful probe for understanding electronic and optical phenomena in condensed phases [95]. Variations in temperature change the highest energy phonon population as well as the interatomic spacing. Thus, temperature dependences of luminescence may provide useful information on the electronic states of emitters, crystal field strength, energy transfer, electron–phonon coupling, and the interactions between the luminescence centers and their hosts [95]. One system under study is  $\text{Mn}^{2+}$  doped ZnS nanoparticles. Following excitation of the ZnS host, ZnS: $\text{Mn}^{2+}$  nanoparticles display both  $\text{Mn}^{2+}$  emission as well as a blue, defect-related emission. The  $\text{Mn}^{2+}$  emission is the result of energy transfer from the ZnS exciton to the  $\text{Mn}^{2+}$  impurity center. The temperature dependence of both the  $\text{Mn}^{2+}$  emission and defect-related blue emission in ZnS: $\text{Mn}^{2+}$  nanoparticles has been investigated [96–98].

The temperature dependences of both the  $\text{Mn}^{2+}$  emission and the blue donor–acceptor emission following excitation at 300 nm are displayed in Figure 31 [99]. The intensity of  $\text{Mn}^{2+}$  emission is weakly dependent on temperature (Fig. 31b). The blue DA emission intensity, however, shows a much more pronounced decrease with decreasing temperature. Figure 31c shows the changes in emission energy as a

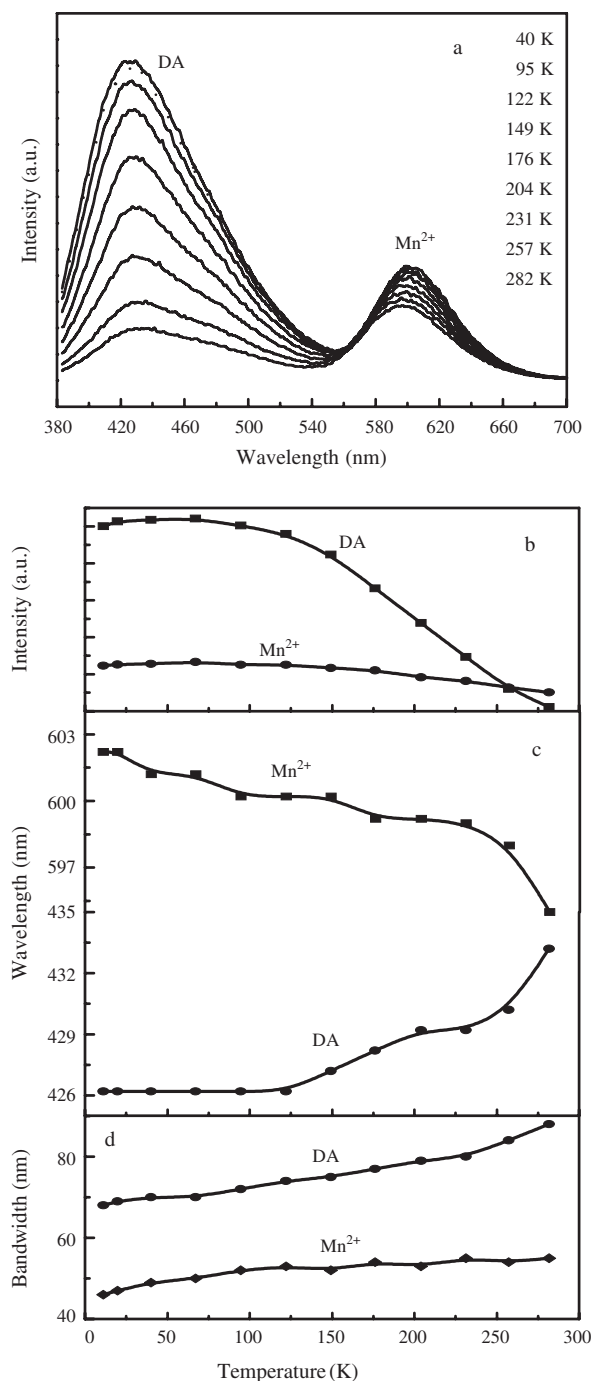


**Figure 31.** Temperature dependence of emission spectra (a), emission intensity (b), wavelength (c), and bandwidth (d) of the defect-related blue (DA) and  $\text{Mn}^{2+}$  emissions in ZnS:Mn nanoparticles. Reprinted with permission from [99], W. Chen et al., *J. Appl. Phys.* 92, 1950 (2002). © 2002, American Institute of Physics.

function of temperature. As the temperature decreases, the  $\text{Mn}^{2+}$  emission shifts to longer wavelengths. On the contrary, the blue DA emission shifts to shorter wavelengths with decreasing temperature. Figure 31d displays the changes in the full-width at half-maximum bandwidth of both emissions as a function of temperature. The bandwidths of both emissions show weak temperature dependences with slight decreases as the temperature is lowered.

In order to explain the temperature results, the nature of both the orange and blue luminescence from ZnS: $\text{Mn}^{2+}$  nanoparticles must be considered. The orange luminescence arises from the  ${}^4T_1-{}^6A_1$  transition of  $\text{Mn}^{2+}$ . The blue defect-related emission in ZnS has been investigated in detail by Oda and Kukimoto [100] and is considered to be a radiative recombination of a delocalized charge carrier (electron) with a trapped charge carrier (hole) at a sulfur vacancy. Oda and Kukimoto point out that the defect-related emission is a transition within the self-activated (SA) luminescence center with an appreciable Stokes shift [100]. The SA emission in ZnS is from the donor (isolated coactivator)–acceptor pair transition.

Based on the theory of thermal quenching, the temperature dependence of the emission intensity,  $I(T)$ , can be described by [101]

$$I(T) = \frac{I_0}{1 + ae^{-E_b/KT}} \quad (17)$$

where  $E_b$  is the activation energy (thermal quenching energy),  $K$  is the Boltzmann constant,  $a$  is a constant related to the ratio of the nonradiative rate to the radiative rate, and  $I_0$  is the emission intensity at 0 K. The solid lines in Figure 31b represent a simulation of the intensities using this theory. The parameters used to obtain these simulations are shown in Table 2 along with the data of bulk ZnS: $\text{Mn}^{2+}$  for comparison. Excellent agreement between theory and experiment suggests that the intensity decrease of the two emissions is mainly due to thermal quenching.

The  $a$  value for the DA pairs is larger than that for  $\text{Mn}^{2+}$ , indicating the nonradiative rate for DA pairs is greater than that for  $\text{Mn}^{2+}$ . It is generally accepted that the major non-radiative or energy relaxation channel in semiconductors is due to phonon quenching [102]. If the phonon coupling is stronger, the nonradiative rate is higher and the luminescence is more sensitive to temperature change [102]. Therefore, the simulated results show that the phonon coupling for the DA pairs is stronger than that for  $\text{Mn}^{2+}$  emitters. It is noted that the value of the  $a$  parameter from  $\text{Mn}^{2+}$  emission in nanoparticles (9.83) is smaller than in bulk (Tab. 2) [99]. This indicates that the radiative rate of  $\text{Mn}^{2+}$  in ZnS: $\text{Mn}^{2+}$  nanoparticles is larger than in bulk, providing for a higher luminescence efficiency.

The thermal quenching energy is related to the bound exciton binding energy [97]. For bulk ZnS: $\text{Mn}^{2+}$  the exciton binding energy is about 60 meV [97]. This value is very close to the thermal quenching energy (57 meV) as estimated from the temperature dependence of  $\text{Mn}^{2+}$  luminescence in bulk ZnS: $\text{Mn}^{2+}$  [97]. In the nanoparticles, the value for the quenching energy is  $\sim 70$  meV, which is larger than the exciton binding energy in the bulk (Tab. 2) [99]. This increase in exciton binding energy is likely due to the increase in the

**Table 2.** Simulated parameters for the temperature dependence of DA and Mn<sup>2+</sup> emissions in bulk and ZnS:Mn<sup>2+</sup> nanoparticles.

	Nanoparticle		Bulk	Bulk
Emitter	Mn <sup>2+</sup>	DA	Mn <sup>2+</sup>	Mn <sup>2+</sup>
$I_0$ (a.u.)	$(4.34 \pm 0.03) \times 10^3$	$(1.19 \pm 0.01) \times 10^6$	$(1.19 \pm 0.02) \times 10^8$	$(1.30 \pm 0.02) \times 10^8$
$a$ (a.u.)	$9.83 \pm 2$	$180 \pm 50$	$20 \pm 5$	$17 \pm 7$
$E$ (meV)	$70 \pm 6$	$93 \pm 6$	$23 \pm 2$	$45 \pm 7$

Source: Reprinted with permission from [99], W. Chen et al., *J. Appl. Phys.* 92, 1950 (2002). © 2002, American Institute of Physics.

overlap of the electron and hole wavefunctions as a result of quantum size confinement. The thermal quenching energy for the DA pairs is larger than that for Mn<sup>2+</sup> indicating that excitons bind more strongly to the DA centers compared to Mn<sup>2+</sup> ions.

As in bulk ZnS:Mn<sup>2+</sup>, the emission energy shifts of the Mn<sup>2+</sup> emission with temperature can be described by crystal field theory. The blueshift of the Mn<sup>2+</sup> emission wavelength with decreasing temperature is due to the enhancement of the crystal field strength at lower temperatures resulting from crystal lattice contraction. As a consequence, the emitting state, <sup>4</sup>T<sub>1</sub>(G) of Mn<sup>2+</sup>, shifts to lower energies with decreasing temperature, shifting the emission to longer wavelengths.

It is reasonable to treat the blue DA emission as a result of donor–acceptor recombination in which the donor is a trapped electron and the acceptor is a trapped hole. The emission energy may then be described by [99]

$$h\nu = E_{\text{gap}} - (E_A + E_D) + e^2/\varepsilon R \quad (18)$$

where  $E_{\text{gap}}$  is the energy gap of the host,  $E_A$  and  $E_D$  are ionization energies of the acceptor and the donor, while  $\varepsilon$  is the optical dielectric constant, and  $R$  is the distance between the donor and acceptor. Based on Eq. (18) the temperature dependence of the DA emission intensity can be explained. As temperature decreases the energy gap increases and the distance between the donor and the acceptor decreases due to crystal lattice contraction. As a consequence, the DA emission shifts to higher energy, as is observed experimentally.

From Figure 31d, it is clear that the bandwidth of both the DA and Mn<sup>2+</sup> emission decreases with temperature. Electron–phonon coupling is usually considered to be the major contribution for the variation of the emission bandwidth with temperature [101, 102]. Both emission bandwidths decrease slowly with decreasing temperature indicating that the electron–phonon coupling is only weakly dependent on temperature. The Huang–Rhys factor is a useful parameter for evaluation of the electron–phonon coupling strength [103, 104]. The emission bandwidth ( $W$ ) at half intensity can be related to the Huang–Rhys factor ( $S$ ) by [102]

$$W = 4(\ln 2)^{1/2}(KT S \hbar \omega_{\text{LO}})^{1/2} \quad (19)$$

where  $K$  is the Boltzmann constant,  $\omega_{\text{LO}}$  is the LO-phonon frequency,  $T$  is the temperature, and  $\hbar$  is Planck's constant. For bulk ZnS:Mn,  $\hbar \omega_{\text{LO}} = 350 \text{ cm}^{-1}$  [103], and for 3.6 nm nanoparticles,  $\hbar \omega_{\text{LO}} = 423 \text{ cm}^{-1}$  [96]. Using Eq. (19), the average Huang–Rhys factor for the DA emission center ( $\sim 8.4$ ) is larger than that for Mn<sup>2+</sup> ( $\sim 4.2$ ) indicating

that the electron–phonon coupling between the DA center and the lattice is stronger than that between the Mn<sup>2+</sup> ion and the lattice. This is consistent with the results from the intensity variation with temperature. The average  $S$  value for Mn<sup>2+</sup> obtained from the emission bandwidths is larger than that obtained from the Stokes shift of Mn<sup>2+</sup> nanoparticle emission from the lowest excited state ( $\sim 2.88$ ) [104] and larger than the  $S$  value ( $\sim 3.0$ ) of bulk ZnS:Mn<sup>2+</sup> obtained by measuring the zero phonon line at low temperature [105]. This is possibly a result of other broadening mechanisms in addition to the electron–phonon interaction. This additional broadening may result from either a distribution of particle sizes or a distribution of Mn<sup>2+</sup> environments [20].

The principle of luminescence temperature dependence at temperatures above room temperature is the same as described previously. Based on the temperature dependences of semiconductor nanoparticle luminescence properties, a new concept of using luminescent nanoparticles for thermometry applications has been recently described [106]. Temperature is a fundamental property of matter, and its measurement is often required for both scientific research and industrial applications. For industrial manufacturing, real-time temperature monitoring can be used to optimize processing, minimizing waste production and energy consumption. Spatially resolved temperature monitoring can establish regions of an integrated circuit in which heat builds up and suggest improvements in design of the circuit or its cooling system. Monitoring the temperature of high-speed moving parts, such as turbine blades, can identify changes that signify a weakness in the part.

In bioengineering and biochemistry, temperature changes of even a few degrees can mean the difference between life and death for a cell. Real-time, precise *in vivo* monitoring of temperature is of paramount importance in many biomedical diagnostic and treatment processes. Traditional methods of temperature measurement can be divided into two categories: contact methods, including thermocouples, thermistors, and resistance temperature detectors (RTDs), and noncontact methods such as measurement of emitted infrared light.

Fluorescence thermometry, using the fluorescence from luminescent materials to determine temperature, is a non-contact thermometry that has many advantages over other thermometry methods [107]. As the temperature of the phosphor changes, the intensity of the fluorescence, the decay lifetime of the fluorescence, the excitation spectra of the fluorescence, and the wavelength (energy) of the fluorescence may all change. Because the fluorescence can be both excited and measured optically, fluorescence-based temperature sensors are advantageous compared to contact temperature sensors (such as thermocouples, thermistors, and



RTDs) in applications where electromagnetic noise is strong or it is physically difficult to connect a wire (such as for spinning centrifuges or turbines or in wind tunnels). Emissivity does not affect the fluorescence signal, and wavelengths for fluorescence can be found for which glass and water are relatively transparent.

Conventional phosphors are made from crystalline semiconductor materials and typically have grain sizes of micrometers [107]. For noncontact thermometry, these grains are generally mixed with a binder material and coated on the surface of a part whose temperature is to be measured. The grain size limits resolution by scattering both the excitation light and emitted light. It also imposes a minimum thickness phosphor coating of several micrometers on the sample. Thick coatings are disadvantageous because the phosphor coating may act as an insulating layer on the part's surface, giving results for temperature that cannot be applied to similar uncoated parts. However, these problems can be solved by using much smaller nanoparticles [106].

As mentioned in Section 10, the light scattering is due to the phosphor grain size, the shape and the grain boundary, as well as surface roughness. According to Rayleigh's approximation [75], a 100-nm particle will scatter one million times more light than a 10-nm particle. This suggests that much higher spatial resolution is possible by using nanoparticles for fluorescence thermometry or thermal imaging. Thin films of nanoparticles could be coated or sprayed on samples. Small size and ultrathin films should enable a faster equilibration time with an underlying sample and high sensitivity, accuracy, and spatial resolution. Nanoparticles are also suited for incorporation into coatings that may already be applied to a part, such as corrosion protection, making a "smart" material. In addition, high efficiency with short decay times makes nanoparticles very good candidates for luminescence-based temperature sensors for high speed monitoring.

Another important application area of nanoparticle thermometry is in biological or biomedical applications for localized *in vivo* temperature probing, such as temperature monitoring during hyperthermia treatment. The small size, bioconjugation capability, and resistance to photobleaching make nanoparticle thermometry appealing compared to other methods.

To demonstrate the concepts of luminescent nanoparticle thermometry, the temperature response of several luminescent nanoparticle samples has been measured at temperatures above room temperature. The fluorescence peak intensity of CdTe nanoparticles is linearly and reversibly proportional to the temperature in the 30–60 °C range (Fig. 32), with a large response slope of 1.1% per °C. The signal-to-noise ratio of the fluorescence spectrometer is approximately 5000:1. Therefore, the resolution could be as good as 0.02 °C in principle. Both CdTe and ZnS:Mn<sup>2+</sup> nanoparticles could be suitable candidates for biomedical applications (*in vivo* and *in vitro* thermometry) due to their large and linear intensity shift over the physiological and hyperthermia temperature range. The –COOH group of the thioglycolic acid stabilized CdTe nanoparticle can be used to easily conjugate to the amine group of biological molecules (e.g., antibodies), such as by the widely used EDC/NHS reaction [93].

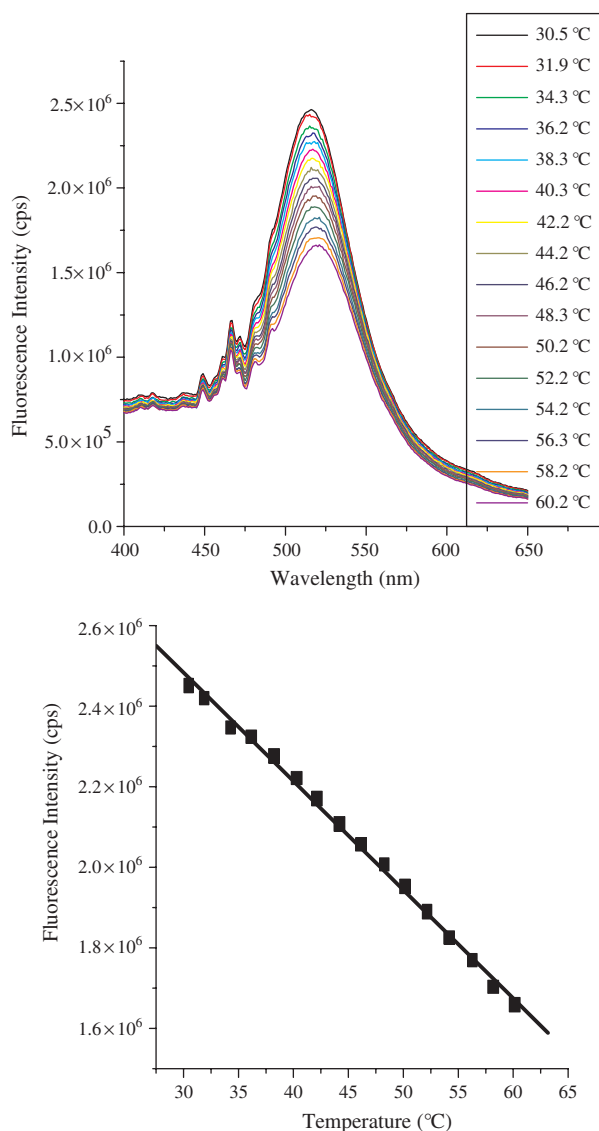


**Figure 32.** Fluorescence spectra of CdTe nanoparticles at different temperatures, from top to bottom: 30–60 °C with excitation wavelength at 350 nm (left). At right is the fluorescence peak intensity (518 nm) of CdTe nanoparticles as a function of temperature. Reprinted with permission from [106], S. Wang et al., *J. Phys. Chem. B* 106, 11203 (2002). © 2002, American Chemical Society.

Double-doped nanoparticles of ZnS:Mn<sup>2+</sup>,Eu<sup>3+</sup> show a different temperature response for each dopant; the ratio of their intensities provides a robust temperature measurement approach [106].

Other fluorescence characteristics such as the fluorescence lifetime should also respond to temperature change, as for conventional fluorophores. It may also be possible to synthesize structures in which fluorescence resonance energy transfer occurs between two different dopants in a nanoparticle or between two nanoparticles of different sizes or compositions. The FRET rate is inversely dependent on the distance between the donor and emitter to the sixth power. Therefore, if the distance between the dopants or nanoparticles is changed slightly due to thermal expansion of the



material, the energy transfer rate will be changed greatly. This may provide a useful method for temperature or pressure sensing [106].

Another potential approach to nanoparticle fluorescence thermometry is the use of upconversion luminescence in which the excitation wavelength is longer than the emission wavelength. The upconversion luminescence intensity of ZnS:Mn<sup>2+</sup> nanoparticles is highly temperature dependent [64, 65]. A close-to-linear temperature dependence of the upconversion intensity has been observed in ZnS:Mn<sup>2+</sup> nanoparticles formed in zeolite-Y [98]. One advantage of upconversion for temperature sensing or imaging, compared with fluorescence, is that the emission background from the surroundings that occurs with fluorescence can be avoided in upconversion. This is particularly interesting in biological or biomedical applications, because many biological components such as cells and tissues have strong autofluorescence upon excitation with UV light.

## 15. LUMINESCENCE PRESSURE DEPENDENCE

Similar to temperature behavior, variation of pressure has been used to understand electronic and optical phenomena in condensed phases. Increases in pressure decrease the interatomic distance and therefore increase the overlap among adjacent electronic orbitals. While pressure studies of luminescence properties in bulk materials are fairly common, there are fewer such investigations in nanoparticles. Recently Meulenberg and Strouse have measured optical properties of CdSe quantum dots in the low pressure regime [108]. These results show a size dependence roughly corresponding to the strong and weak confinement regimes for the exciton in CdSe [108]. Other results from Chen et al. on ZnS:Mn<sup>2+</sup> nanoparticles display a slightly increased pressure coefficient relative to the bulk value [109]. The increase has been attributed to an enhancement in the electron-phonon interaction in nanoparticles relative to their bulk counterparts.

Figure 33 displays the emission spectra under different pressures at room temperature (Fig. 33a) and the pressure dependences of the emission energies (Fig. 33b) of the Mn<sup>2+</sup> and the DA luminescence in ZnS:Mn<sup>2+</sup> nanoparticles [99]. The Mn<sup>2+</sup> emission shifts to lower energies with increasing pressure, while the blue emission peak changes little with pressure. The solid line in Figure 33b represents the result of the least-squares fit to the experimental data using a linear relation. The obtained pressure coefficient for Mn<sup>2+</sup> luminescence in ZnS:Mn<sup>2+</sup> nanoparticles is approximately -34.3 meV/GPa. The pressure coefficient of Mn<sup>2+</sup> emission in bulk ZnS:Mn<sup>2+</sup> is -31 meV/GPa [110]. Comparing these results, the pressure coefficient for the Mn<sup>2+</sup> luminescence in the 3.5 nm ZnS:Mn<sup>2+</sup> nanoparticles is about 10% larger than that of the bulk value, and the result from the 3.5 nm particles is also slightly larger than that for 4.5 nm particles (-33.3 meV/GPa) measured previously [109].

The pressure dependence of the luminescence energy reflects the interactions between the relevant electronic states of the center and its surrounding lattice ions. The absolute value of the pressure coefficient is related to the

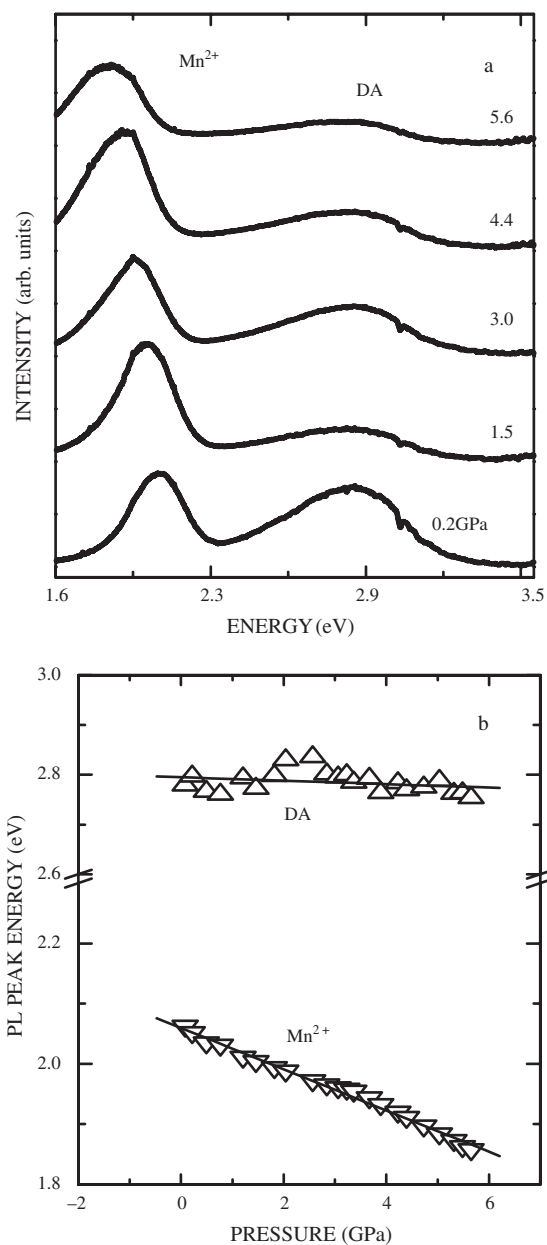


**Figure 33.** Pressure dependence of the emission spectra (a) and emission energy (b), of the blue (DA) and Mn<sup>2+</sup> emissions in ZnS:Mn<sup>2+</sup> nanoparticles. Reprinted with permission from [99], W. Chen et al., *J. Appl. Phys.* 92, 1950 (2002). © 2002, American Institute of Physics.

strength of the interaction between the emitter and the host or the strength of the crystal field on the emitter [111]. A large pressure coefficient normally indicates a stronger interaction between the emitter and the host.

The pressure dependence of Mn<sup>2+</sup> emission in ZnS:Mn<sup>2+</sup> can be calculated by using crystal field theory. The pressure induced change in the energy ( $E$ ) of the Mn<sup>2+</sup> emission band of ZnS:Mn<sup>2+</sup> is a function of the crystal field strength  $D_q$  and the Racah parameter  $B$  only, assuming that the Racah parameter ratio  $C/B$  is independent of pressure [112]

$$\frac{dE}{dP} = \delta \frac{d(D_q)}{dP} + (E - D_q \delta) \frac{1}{B} \frac{dB}{dP} \quad (20)$$

where  $\delta = d(E/B)/d(D_q/B)$ . For the  $\text{Mn}^{2+}$  ion,  $\delta$  is  $-10$ .  $D_q$ ,  $B$ , and  $C$  are the crystal field parameters. For the 3.5 nm  $\text{ZnS:Mn}^{2+}$  nanoparticles,  $B$ ,  $C$ , and  $D_q$  are 490, 3357, and  $586 \text{ cm}^{-1}$ , respectively [104]. For bulk  $\text{ZnS:Mn}$ ,  $dB/dP$  and  $d(D_q)/dP$  are  $-3.48$  and  $18.2 \text{ cm}^{-1}/\text{GPa}$ , respectively [113]. From Eq. (20),  $dE/dP \approx -34.6 \text{ meV/GPa}$ , which is in excellent agreement with the experimental value ( $-34.3 \text{ GPa}$ ). The fact that bulk values used for  $dB/dP$  and  $d(D_q)/dP$  accurately reproduce the data suggests that these parameters are not significantly different in nanoparticles relative to bulk  $\text{ZnS:Mn}^{2+}$  [109].

The pressure coefficient for the blue emission is  $-3.2 \text{ meV/GPa}$ . The pressure coefficients of the blue emission reported for bulk  $\text{ZnS}$  are  $+90$  [114] and  $+125 \text{ meV/GPa}$  [115]. In comparison, the pressure coefficient value in nanoparticles is much smaller and the pressure change of the emission energy is in the opposite direction.

This surprising value for the pressure coefficient of the DA emission may be explained by considering the increased binding energies and the effects of surface states in nanoparticles. In bulk  $\text{ZnS:Mn}^{2+}$ , the DA emission shifts to higher energy with increasing pressure due to a combination of effects. The bandgap increases with pressure while the dielectric constant and distance between donor and acceptor decrease. From Eq. (18) we would expect a rapid change in the emission energy with increasing pressure. However, House and Drickamer [114] have observed that the DA emission shift in the bulk material is not as dramatic as that expected from the increase in the bandgap. This is due to the fact that the binding energies of both the donor and acceptor also increase with pressure. This serves to offset the changes due to the bandgap, distance, and dielectric coefficients.

In nanoparticles, both the energy gap and binding energy increase with decreasing size. In the small nanoparticles under investigation, increases in the bandgap and Coulomb term [ $e^2/\epsilon R$  in Eq. (18)] with pressure are apparently offset with the changes in the ionization energies with pressure. The carrier binding energy of the donor or the acceptor is increased relative to bulk due to size confinement. This increase in the binding energy leads to the increase in  $E_D$  and  $E_A$  in Eq. (18). This serves to mitigate the effects of the other parameters leading to the overall weak pressure dependence.

In addition to the increases in binding energies, the influence of surface states must be considered. Due to the size effect, defects in nanoparticles often are localized at the surface sites [116]. Once the donor-acceptor pairs are localized at the surface states, the electron wavefunctions are more atomlike, less sensitive to their nearest neighbor bond lengths [117], and thereby not as sensitive to pressure increases compared to the bulk.

## 16. LUMINESCENT NANOPARTICLES FOR OPTICAL STORAGE

In recent years, a demand for improved data storage has accompanied the dramatic advances in computing and communication technology. The requirement for high capacity optical memory has led to much research in optical materials, medium structures, and system concepts. Using nanoparticles or QDs as a storage medium offers tremendous

potential. Enhanced, cost-effective storage of information requires ultrahigh packing densities as well as inexpensive self-assembling techniques and fast methods for writing and retrieving the information. Semiconductor quantum dots, which involve a few thousand atoms, may offer an attractive path toward achieving these goals. Single-electron storage has been suggested as a possibility with quantum dots [118]. Charge storage devices based on the resistivity change of a two-dimensional electron gas located near a layer of self-assembled QDs have been demonstrated at low temperature [119]. A memory cell based on field-effect tunable lateral potential modulation in the plane of a semiconductor quantum well [120] and acoustically driven storage in a quantum well [6] have been proposed and demonstrated. The shortcoming of these approaches is that they are limited to short durations (several hundred microseconds to several seconds) and function only at low temperature.

The fluorescence of  $\text{Eu}^{3+}$ -doped nanoparticles is very sensitive to light. The emission of  $\text{Eu}^{3+}$  can be quenched by UV irradiation, and this quenching can be recovered by visible light stimulation. This is a reversible optical process that can be potentially applied for optical storage. The emission spectra following excitation at 395 nm of  $\text{BaFBr:Eu}^{3+}$  are displayed in Figure 34 [121]. The three emission bands are from the transitions of  ${}^5D_0 \rightarrow {}^7F_0$ ,  ${}^5D_0 \rightarrow {}^7F_1$ ,  ${}^5D_0 \rightarrow {}^7F_2$ , and  ${}^5D_0 \rightarrow {}^7F_3$  of  $\text{Eu}^{3+}$ . Figure 34 shows that under UV irradiation at 225 nm the  $\text{Eu}^{3+}$  emission decreases in intensity. This luminescence quenching can be recovered slightly by exposure to a red light at 600 nm, and it can be recovered very quickly by exposure to a visible light (500 to 800 nm). Similar results have also been observed in  $\text{Eu}_2\text{O}_3$  nanoparticles encapsulated in zeolite-Y,  $\text{Eu}^{3+}$  nanoclusters in zeolite, and  $\text{Eu}^{3+}$ -doped  $\text{Y}_2\text{O}_3$  nanoparticles [121]. One example is shown in Figure 35 for  $\text{Eu}^{3+}$  clusters in zeolite-Y. Under UV irradiation at 254 nm, the emission of  $\text{Eu}^{3+}$

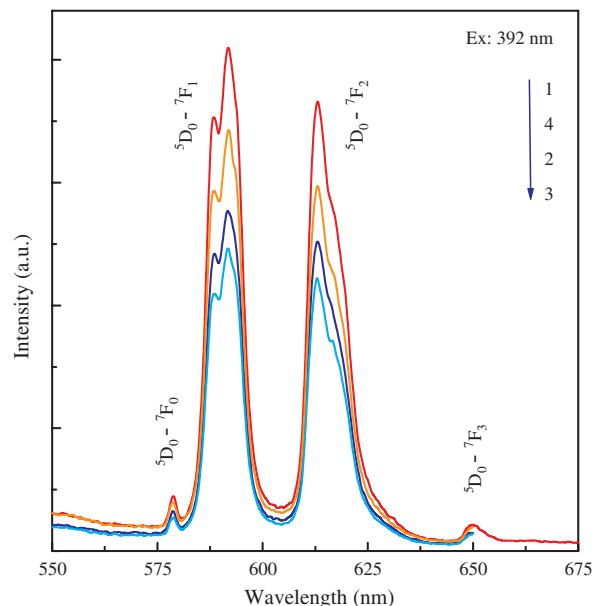


**Figure 34.** The emission spectra of  $\text{BaFBr:Eu}^{3+}$  nanoparticles before (1) and after UV irradiation at 225 nm for 10 (2) and 15 min (3) and then exposed to a visible lamp for 15 min (4), respectively [121].

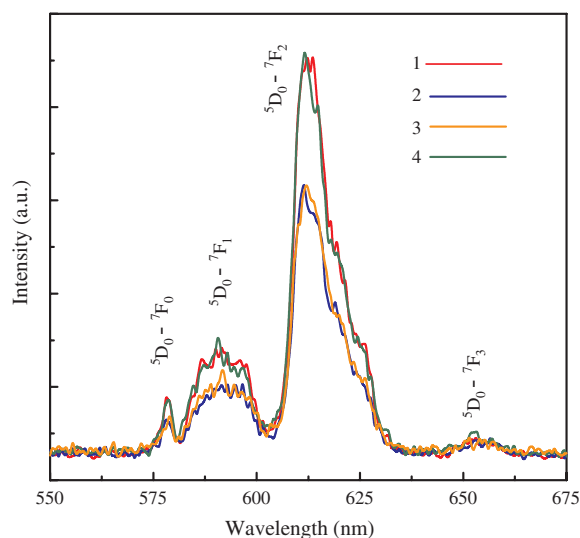


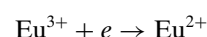
**Figure 35.** The emission spectra of  $\text{Eu}^{3+}$ -zeolite-Y before (1) and after (2) UV irradiation at 254 nm for 5 min, then photostimulation at 840 nm for 5 min (3), and then to a visible lamp for 10 min (4), respectively [121].

decreases. Under stimulation at 840 nm, very little recovery is observed. However, after stimulation from a visible lamp (500 to 800 nm), the fluorescence is recovered to almost 100% of its original value.

The emission spectral patterns of  $\text{Eu}^{3+}$  in  $\text{BaFBr}:\text{Eu}^{3+}$  and  $\text{Eu}^{3+}$ -zeolite-Y are noticeably different. In  $\text{BaFBr}:\text{Eu}^{3+}$ , the  ${}^5D_0 \rightarrow {}^7F_1$  emission band is more intense than the  ${}^5D_0 \rightarrow {}^7F_2$  emission band while in  $\text{Eu}^{3+}$ -zeolite-Y, the  ${}^5D_0 \rightarrow {}^7F_2$  band is much stronger than the  ${}^5D_0 \rightarrow {}^7F_1$  emission. This is due to the surrounding environments of  $\text{Eu}^{3+}$  which in the two materials are different. The  ${}^5D_0 \rightarrow {}^7F_1$  and  ${}^5D_0 \rightarrow {}^7F_2$  transitions are termed hypersensitive luminescence [16] because the luminescence is highly sensitive to

structure change and environmental effects. As a result, the intensity ratio of the  ${}^5D_0 \rightarrow {}^7F_1$  transition to the  ${}^5D_0 \rightarrow {}^7F_2$  transition can give much information about the site symmetry and structure of the materials.

The physical mechanism for the optical reversible process in  $\text{Eu}^{3+}$  doped nanoparticles is not yet clear. The most likely process is the reversible charge transfer between  $\text{Eu}^{3+}$  and  $\text{Eu}^{2+}$  ions. Charge transfer between  $\text{Eu}^{3+}$  and  $\text{Eu}^{2+}$  has been reported in several systems [122]. It has been reported that under high energy radiation, rare earth (RE) ions can be oxidized or reduced [122]. This is determined by the oxidation or reduction potentials of the ions. Nugent [123] has investigated extensively the oxidation states of RE ions. According to this investigation, the oxidation of  $\text{RE}^{3+}$  to  $\text{RE}^{4+}$  ions is possible if the optical electronegativity [ $\chi(\text{RE}^{4+})$ ] is less than or equal to 3.03, and the standard reduction potential [ $E_{\text{RE}}^0(\text{RE}^{4+} \rightarrow \text{RE}^{3+})$ ] is less than or equal to 5.2 V. For example,  $\chi(\text{Tb}^{4+})$  is 2.55 V and the  $E_{\text{RE}}^0(\text{Tb}^{4+} \rightarrow \text{Tb}^{3+})$  is 3.30 V [123], favoring the appearance of  $\text{Tb}^{4+}$  ions. For  $\text{Eu}^{3+}$  ions, oxidation to  $\text{Eu}^{4+}$  is unlikely because the  $\chi(\text{Eu}^{4+})$  (3.40) is larger than 3.03 and the  $E_{\text{RE}}^0(\text{Eu}^{4+} \rightarrow \text{Eu}^{3+})$  (6.4 V) is larger than 5.2 V [123]. This indicates the reduction of  $\text{Eu}^{3+}$  to  $\text{Eu}^{2+}$  is more favorable. In addition,  $\text{Eu}^{2+}$  is a half-filled configuration of  $4f^7$ ; thus energetically,  $\text{Eu}^{2+}$  is more stable than  $\text{Eu}^{3+}$ . Therefore, under UV irradiation at 254 nm, electrons and holes may be produced in the nanoparticles, and some  $\text{Eu}^{3+}$  ions are reduced to  $\text{Eu}^{2+}$  ions by recombination with electrons:



The UV generated holes may be trapped in the surface states of the nanoparticles or in the defects of the host materials like zeolites to form hole centers. Under visible or IR stimulation, holes can be released from their traps and recombine with  $\text{Eu}^{2+}$  to form  $\text{Eu}^{3+}$ ,

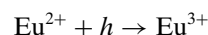


**Table 3.** A summary of the luminescence characteristics of some popular semiconductor nanoparticles.

Particles	FL	EL	TL	CL	ML	UPL	PSL	XEOL	Ref.
ZnS	*								[12, 31]
CdS	*	*	*			*	*	*	[9, 15, 30, 66, 84]
CdSe	*	*							[3, 23, 25, 49, 50]
CdTe	*	*				*			[24, 26, 47, 51, 66, 67]
PbSe	*								[124, 125]
PbS	*								[124, 125]
ZnS:Mn <sup>2+</sup>	*	*		*				*	[20, 37, 38]
CdS:Mn <sup>2+</sup>	*								[126]
ZnS:Eu <sup>2+</sup>	*								[17]
AgI	*						*		[28, 73, 127]
CuCl	*						*		[128, 129]
Si	*	*	*			*		*	[80–83, 85, 130–135]
InAs/GaAs	*				*				[39–44, 136–138]
ZnO	*			*					[37, 38, 139]
Y <sub>2</sub> O <sub>3</sub> :Eu <sup>3+</sup>	*								[140]
Eu <sub>2</sub> O <sub>3</sub>	*								[16, 141]

*Note:* This table is meant only as an overview of the many different types of luminescence from semiconductor nanoparticles. As new materials are made and new experiments performed, there will be countless additions to this rich field.

FL—fluorescence, EL—electroluminescence, TL—thermoluminescence, CL—cathodoluminescence, ML—magnetoluminescence, UPL—upconversion luminescence, PSL—photostimulated luminescence, XEOL—X-ray excited optical luminescence.

resulting in near complete recovery of the  $\text{Eu}^{3+}$  luminescence following visible or IR stimulation.

## 17. SUMMARY

Luminescent devices may benefit greatly from increased luminescence efficiencies, reduced size, and tunable wavelength selection. In this chapter, we have reviewed the luminescence of semiconductor nanoparticles which may serve to fill these needs. Quantum size confinement and the large surface-to-volume ratios of nanoparticles have profound influences on the luminescence efficiency and emission wavelength. Usually, semiconductor nanoparticles exhibit two kinds of emissions from the band-band (exciton) and surface states, respectively, and both emissions can be modified by size and surface modification. Thus, emission colors of nanoparticles can be easily adjustable by size, while the emission efficiency is highly determined by surface characteristics. Doped nanoparticles represent a new type of phosphor with promising potential applications. Their luminescence processes, decay dynamics, and temperature and pressure dependences make them ideal for many applications, such as light-emitting diodes based on electroluminescence, and temperature and pressure sensors based on the temperature and pressure dependences of nanoparticle luminescence. In addition, medical imaging, optical storage, radiation detection, and dosimetry based on photostimulated luminescence, thermoluminescence, and a newly reported reversible optical process in  $\text{Eu}^{3+}$  nanoparticles doped in zeolite-Y may benefit from nanosized materials. Sensors based on the energy transfer process have tremendous applications in chemical or biological sensors, temperature or pressure measurements, radiation detection and dosage control, medical imaging, diagnostics, and optical storage and communications.

## GLOSSARY

**Cathodoluminescence** Type of luminescence following excitation by an electron beam such as that observed in traditional cathode ray technologies.

**Electroluminescence** The emission of light from nonincandescent materials following direct (non-thermal) excitation by an electric current.

**Fluorescence** The emission of light from an excited state of like multiplicity as the lower state (usually a singlet state) and the lifetimes are typically nanoseconds or less.

**Fluorescence resonance energy transfer** A nonradiative transfer of excitation energy from one fluorescent molecule to another. Energy transfer quenches the fluorescence of the originally excited molecule and elicits the fluorescence of the absorbing molecule.

**Luminescence** The emission of light by a substance immediately after the absorption of energy from light of usually higher energy. It is formally divided into two categories, fluorescence and phosphorescence, depending on the nature of the excited state and the decay lifetime.

**Magnetoluminescence** Refers to luminescence observed under magnetic fields. Magnetoluminescence is used to study both excitonic structure and dilute magnetic systems.

**Nanoparticle** Refers to a particle with a size less than 100 nm. Also called nanocrystal, particle, nanocluster, or quantum dot.

**Phosphorescence** The emission of light from an excited state of different multiplicity and the lifetimes are usually in the millisecond to second range.

**Photostimulated luminescence** The phenomenon in which phosphors release trapped charge carriers when stimulated by infrared or visible light. The trapped carriers recombine with luminescent centers to generate the photostimulated luminescence. Thus in contrast to photoluminescence, in photostimulated luminescence the stimulation (excitation) wavelength is longer than the emission wavelength.

**Quantum size confinement** Refers to the changes in the electronic structure and physical properties as the particle size is reduced to approach the exciton Bohr radius. These changes include an increase of the energy gap, shifts of the absorption edge and emission peaks to higher energies with decreasing size, development of discrete features in the spectra, and concentration of the oscillator strength into just a few transitions.

**Semiconductor** A material with an electrical resistivity in the range of  $10^{-2}$ – $10^9$   $\Omega\text{cm}$ , or a material whose energy gap lies between zero and about 4 eV.

**Thermoluminescence** Luminescence generated following excitation with heat instead of visible or near-infrared photons.

**Upconversion luminescence** A phenomenon in which the excitation energy (wavelength) is lower (longer) than the emission energy (wavelength).

**X-ray excited optical luminescence** The measurement of the optical luminescence spectrum following excitation with X-ray photons.

## ACKNOWLEDGMENTS

The authors thank Nomadics, Inc., the National Science Foundation (NSF), the National Institute of Health (NIH), and the Oklahoma Center for Advanced Science and Technology (OCAST) for financial support of our research projects. The reviewed work here was partially supported by the President Foundation of the Chinese Academy of Sciences and the National Natural Science Foundation of China. Part of the research described in this chapter was performed at the W. R. Wiley Environmental Molecular Sciences Laboratory, a national scientific user facility sponsored by the Department of Energy's Office of Biological and Environmental Research and located at the Pacific Northwest National Laboratory (PNNL). PNNL is operated by Battelle for the U.S. Department of Energy under contract DE-AC06-76RLO1830. We thank Kim Falk at Nomadics, Inc. for her help in the reprinting of the literature figures.

## REFERENCES

1. M. Y. Han, X. Gao, J. Z. Su, and S. M. Nie, *Nature Biotechnol.* 19, 631 (2001).
2. Y. Wang, in "Advances in Photochemistry" (D. C. Neckers, D. H. Volman, and G. von Bunau, Eds.), Vol. 19, p. 179.

- Wiley, New York, 1995; A. I. Ekimov, A. L. Efros, and A. A. Onuschenko, *Solids State Commun.* 56, 921 (1985).
3. P. Alivisatos, *J. Phys. Chem.* 100, 13226 (1996).
  4. D. M. Mittleman, R. W. Schoenlein, J. J. Shiang, V. L. Colvin, A. P. Alivisatos, and C. V. Shank, *Phys. Rev. B* 49, 14435 (1994).
  5. Y. Arakawa and H. Sakaki, *Appl. Phys. Lett.* 40, 939 (1982).
  6. T. Fujii, S. Yamakoshi, K. Nabu, O. Wada, and S. Hiyamiza, *J. Vac. Sci. Technol.* 2, 259 (1984).
  7. R. S. Knox, "Theory of Excitons," Solid State Physics Supplements. Academic Press, New York, 1963.
  8. J. D. Curthbert and D. G. Thomas, *Phys. Rev.* 154, 763 (1967).
  9. A. Hasselbarth, E. Eychmuller, and H. Well, *Chem. Phys. Lett.* 203, 271 (1993).
  10. M. Tomita and M. Matsuoka, *J. Opt. Soc. Am. B* 7, 1198 (1990).
  11. Y. Wang and N. Herron, *J. Phys. Chem.* 95, 525 (1991).
  12. W. Chen, Z. G. Wang, Z. J. Lin, and L. Y. Lin, *J. Appl. Phys.* 82, 3111 (1997).
  13. W. Hoheisel, V. L. Colvin, C. S. Johnson, and A. P. Alivisatos, *J. Chem. Phys.* 101, 8455 (1994).
  14. M. Kasha, *Disc. Faraday Soc.* 9, 14 (1950).
  15. N. P. Ernsting, M. Kaschke, H. Weller, and L. Katsikas, *J. Opt. Soc. Am. B* 7, 1630 (1990).
  16. W. Chen, A. G. Joly, C. M. Kowalchuk, J.-O. Malm, Y. Huang, and J.-O. Bovin, *J. Phys. Chem. B* 106, 7034 (2002).
  17. W. Chen, J.-O. Malm, V. Zwiller, Y. Huang, S. M. Liu, R. Wallenberg, J.-O. Bovin, and L. Samuelson, *Phys. Rev. B* 61, 11021 (2000).
  18. K. Swiatek, M. Godlewski, and D. Hommel, *Phys. Rev. B* 42, 3628 (1990).
  19. E. I. Rashba and G. E. Gurgenishvili, *Soviet Phys.-Solid State* 4, 759 (1962); C. H. Henry and K. Nassau, *J. Lumin.* 1&2, 299 (1970).
  20. W. Chen, R. Sammynaiken, and Y. Huang, *J. Appl. Phys.* 88, 5188 (2000).
  21. W. Chen, X. H. Zhang, and Y. Huang, *Appl. Phys. Lett.* 76, 2328 (2000).
  22. T. P. Cassagneau, B. Sweryda-Krawiec, and J. H. Fendler, *Mater. Res. Soc. Bull.* 25, 40 (2000).
  23. V. L. Colvin, M. C. Schlamp, and A. P. Alivisatos, *Nature (London)* 370, 354 (1994).
  24. W. Chen, D. Grouquist, and J. Roark, *J. Nanosci. Nanotechnol.* 1, 47 (2002).
  25. M. C. Schlamp, X. Peng, and A. P. Alivisatos, *J. Appl. Phys.* 82, 5837 (1997).
  26. L. Rogach, L. Katsikas, A. Kornowski, D. Su, A. Eychmuller, and H. Weller, *Ber. Bunsenges. Phys. Chem.* 100, 1772 (1996).
  27. W. Chen, Z. Wang, Z. Lin, and L. Lin, *Phys. Lett. A* 232, 391 (1997).
  28. W. Chen, Z. Wang, Z. Lin, L. Lin, K. Fang, Y. Xu, M. Su, and J. Lin, *J. Appl. Phys.* 83, 3811 (1998).
  29. D. A. Miller, "Confined Excitons and Photons," p. 675. Plenum, New York, 1995.
  30. W. Chen, Z. G. Wang, and L. Y. Lin, *J. Lumin.* 71, 151 (1997).
  31. W. Chen, Z. G. Wang, Z. J. Lin, and L. Y. Lin, *Appl. Phys. Lett.* 70, 1465 (1997).
  32. N. Chenstnoy, T. D. Harris, R. Hull, and L. E. Brus, *J. Phys. Chem.* 90, 3393 (1986).
  33. V. Klimov, P. Haring Bolivar, and H. Kurz, *Phys. Rev. B* 53, 1463 (1996).
  34. R. Chen and Y. Kirsh, "Analysis of Thermally Stimulated Processes." Pergamon Press, Oxford, 1981.
  35. C. Fouassier, Luminescence, in "Encyclopedia of Inorganic Chemistry" (R. B. King, Ed.), Vol. 4, 1984.
  36. M. D. Bhise and M. Katiya, *J. Appl. Phys.* 67, 1492 (1990).
  37. A. D. Dinsmore, D. S. Hsu, H. F. Gray, S. B. Qadri, Y. Tian, and B. R. Ratna, *Appl. Phys. Lett.* 75, 802 (1999).
  38. A. D. Dinsmore, D. S. Hsu, S. B. Qadri, J. O. Cross, T. A. Kennedy, H. F. Gray, and B. R. Ratna, *J. Appl. Phys.* 88, 4985 (2000).
  39. R. Rinaldi, P. V. Giugno, R. Cingolani, H. Lipsanen, M. Sopanen, J. Tulkki, and J. Ahopelto, *Phys. Rev. Lett.* 77, 342 (1996).
  40. M. Bayer, A. Schmidt, A. Forchel, F. Faller, T. L. Reinecke, P. A. Knipp, A. A. Dremin, and V. D. Kulakovskii, *Phys. Rev. Lett.* 74, 3439 (1995).
  41. R. Cingolani, M. De Giorgi, R. Rinaldi, H. Lipsanen, M. Sopanen, R. Virkkala, K. Majjala, J. Tulkki, J. Ahopelto, K. Uchida, N. Miura, and Y. Arakawa, *Physica E* 7, 346 (2000).
  42. M. von Ortenberg, K. Uchida, N. Miura, F. Heinrichsdorff, and D. Bimberg, *Physica B* 246-247, 88 (1998).
  43. J. Oswald, K. Kuldova, J. Zeman, E. Hulicius, S. Jullian, and M. Potemski, *Mater. Sci. Eng. B* 69-70, 318 (2000).
  44. K. Kuldova, J. Oswald, J. Zeman, E. Hulicius, J. Pangrac, K. Melichar, and T. Simecek, *Mater. Sci. Eng. B* 88, 247 (2002).
  45. G. Prechtel, W. Heiss, S. Mackowski, and E. Janik, *Appl. Phys. Lett.* 78, 2140 (2001).
  46. G. Bacher, A. A. Maksimov, A. McDonald, H. Schomig, M. K. Welsch, V. D. Kulakovskii, A. Forchel, C. R. Becker, L. W. Molenkamp, and G. Landwehr, *Phys. Status Solidi B* 224, 573 (2001).
  47. S. Mackowski, J. Wrobel, K. Fronc, J. Kossut, F. Pulizzi, P. C. M. Christianen, J. C. Maan, and G. Karczewski, *Phys. Status Solidi B* 229, 493 (2002).
  48. G. Mackh, W. Ossau, A. Waag, and G. Landwehr, *Phys. Rev. B* 54, R5227 (1996).
  49. V. D. Kulakovskii, G. Bacher, R. Weigand, T. Kummell, A. Forchel, E. Borovitskaya, K. Leonardi, and D. Hommel, *Phys. Rev. Lett.* 82, 1780 (1999).
  50. P. A. Crowell, V. Nikitin, J. A. Gupta, D. D. Awschalom, F. Flack, and N. Samarth, *Physica E* 2, 854 (1998).
  51. L. Besombes, L. Marsal, K. Kheng, T. Charvolin, L. S. Dang, A. Wasiela, and H. Mariette, *J. Cryst. Growth* 214/215, 742 (2000).
  52. G. Eytan, Y. Yayon, I. Bar-Joseph, and M. L. Rappaport, *Ultramicroscopy* 83, 25 (2000).
  53. J. G. Tischler, D. Gammon, and A. S. Bracker, *Phys. Status Solidi B* 230, 315 (2002).
  54. A. K. Bhattacharjee, *Phys. Rev. B* 58, 15660 (1998).
  55. I. A. Merkulov, D. R. Yakovlev, A. Keller, W. Ossau, J. Geurts, A. Waag, G. Landwehr, G. Karczewski, T. Wojtowicz, and J. Kossut, *Phys. Rev. Lett.* 83, 1431 (1999).
  56. R. Scheps, *Progr. Quant. Electron.* 20, 27 (1996).
  57. E. Downing, L. Hesselink, J. Ralston, and R. M. Macfarlane, *Science* 273, 1185 (1996).
  58. P. P. Feofilov and V. V. Ovsyankin, *Appl. Opt.* 6, 1828 (1967).
  59. D. L. Dexter, *J. Chem. Phys.* 21, 836 (1953).
  60. J. M. F. van Dijk and M. F. H. Schuurmans, *J. Chem. Phys.* 78, 5317 (1983).
  61. J. Z. Zhang, *Acc. Chem. Res.* 30, 423 (1997).
  62. L. H. Brixner, *Mater. Chem. Phys.* 16, 253 (1987).
  63. H. Benisty, C. M. Sotomayor-Torres, and C. Weisbuch, *Phys. Rev. B* 44, 10945 (1991).
  64. W. Chen, A. G. Joly, and J. Z. Zhang, *Phys. Rev. B* 64, 041202 (R) (2001).
  65. W. Chen et al., to be published.
  66. E. Poles, D. C. Selmarten, O. I. Micc, and A. J. Nozik, *Appl. Phys. Lett.* 75, 971 (1999).
  67. W. Chen et al., unpublished result.
  68. K. Kato, Photostimulable phosphor radiography design considerations, in "Specification, Acceptance Testing and Quality Control of Diagnostic X-ray Imaging Equipment" (J. A. Seibert, G. T. Barnes, and R. G. Gould, Eds.), pp. 731-769, Am. Inst. of Phys., Woodbury, NY, 1994.
  69. M. Sonda, M. Takano, J. Miyahara, and H. Kato, *Radiology* 148, 833 (1983); K. Takahashi, K. Kohda, J. Miyahara, Y. Kanemitsu, K. Amitani, and S. Shionoya, *J. Lumin.* 31-32, 266 (1984).
  70. H. V. Seggern, T. Voigt, W. Knupfer, and G. Lange, *J. Appl. Phys.* 64, 1405 (1988).

71. Y. Masumoto, *J. Lumin.* 70, 386 (1996).
72. W. Chen and M. Z. Su, *J. Phys. Chem. Solids* 60, 371 (1999).
73. W. Chen, A. G. Joly, and J. Roark, *Phys. Rev. B* 65, 2454041 (2002).
74. M. Thoms, *Appl. Opt.* 35, 3702 (1996).
75. M. Kaszuba, *J. Nanopart. Res.* 1, 405 (1999).
76. W. Chen et al., unpublished result.
77. H. Mattoussi, J. M. Mauro, E. R. Goldman, T. M. Green, G. P. Anderson, V. C. Sundar, and M. G. Bawendi, *Phys. Status Solidi B* 224, 277 (2001).
78. W. Chan, D. J. Maxwell, X. Gao, R. Bailey, M. Y. Han, and S. M. Nie, *Current Opinion Biotechnol.* 13, 40 (2002).
79. P. A. Rodnyi, "Physical Processes in Inorganic Scintillators." CRC Press, New York, 1997.
80. S. J. Naftel, I. Coulthard, D. T. Jiang, T. K. Sham, B. W. Yates, and K. H. Tan, *Phys. Status Solidi A* 182, 373 (2000).
81. Y. F. Hu, K. H. Tan, P. S. Kim, P. Zhang, S. J. Nadtel, T. K. Sham, I. Coulthard, and B. W. Yates, *Rev. Sci. Instrum.* 73, 1379 (2002).
82. I. Coulthard, D. T. Jiang, Y. J. Zhu, and T. K. Sham, *J. Porous Mater.* 7, 165 (2000).
83. T. K. Sham, D. J. Jiang, I. Coulthard, J. W. Lorimer, X. H. Feng, K. H. Tan, S. P. Frigo, R. A. Rosenberg, D. C. Houghton, and B. Bryskiewicz, *Nature* 363, 331 (1993).
84. P. Zhang, S. J. Naftel, and T. K. Sham, *J. Appl. Phys.* 90, 2755 (2001).
85. L. T. Canham, *Appl. Phys. Lett.* 57, 1046 (1990).
86. P. Deak, M. Rosenbauer, M. Stutzmann, J. Weber, and M. S. Brandt, *Phys. Rev. Lett.* 69, 2531 (1992).
87. R. W. Fathauer, T. George, and A. Ksendzov, *Appl. Phys. Lett.* 60, 995 (1992).
88. G. Dalba, N. Daldosso, P. Fornasini, R. Graziola, R. Grisenti, and F. Rocca, *J. Non-Cryst. Solids* 232–234, 370 (1998).
89. T. K. Sham, R. Sammynaiken, Y. J. Zhu, P. Zhang, I. Coulthard, and S. J. Naftel, *Thin Solid Films* 363, 318 (2000).
90. W. C. Chan and S. M. Nie, *Science* 281, 2016 (1998).
91. P. V. dos Santos, M. T. de Araujo, A. S. Gouveia-Neto, J. A. Madeiros Neto, and A. S. B. Sombra, *IEEE J. Quantum Electron.* 35, 395 (1999).
92. H. Zijlmans, J. Bonnet, J. Burton, K. Kardos, T. Vail, R. S. Niedbala, and H. J. Tanke, *Anal. Biochem.* 267, 30 (1999).
93. S. Wang, N. Mamedova, N. A. Kotov, W. Chen, and J. Studer, *Nano Lett.* 2, 817 (2002).
94. J. R. Lakowicz, "Principles of Fluorescence Spectroscopy," 2nd ed., Klumer Academic/Plenum, New York, 1999.
95. T. Suski and W. Paul, "High Pressure in Semiconductor Physics, Semiconductors and Semimetals," Vol. 54. Academic Press, San Diego, 1998.
96. J. Q. Yu, H. M. Liu, Y. Y. Wang, F. E. Fernandez, and W. Y. Jia, *J. Lumin.* 76&77, 252 (1998).
97. M. Tanaka and Y. Masumoto, *Chem. Phys. Lett.* 324, 249 (2000).
98. A. G. Joly, W. Chen, J. Roark, and J. Z. Zhang, *J. Nanosci. Nanotechnol.* 1, 295 (2001).
99. W. Chen, F. Su, G. H. Li, A. G. Joly, J-O Malm, and J-O Bovin, *J. Appl. Phys.* 92, 1950 (2002).
100. S. Oda and H. Kukimoto, *J. Lumin.* 18/19, 829 (1979).
101. F. Seitz, *Trans. Faraday Soc.* 35, 79 (1939).
102. K. Huang and A. Rhy, *Proc. Roy. Soc. London A* 204, 406 (1950).
103. Anastassiadou, E. Liarokapis, and E. Anastassakis, *Solid State Commun.* 69, 137 (1988).
104. W. Chen, R. Sammynaiken, Y. Huang, J-O Malm, R. Wallenberg, J-O Bovin, V. Zwiller, and N. A. Kotov, *J. Appl. Phys.* 89, 1120 (2001).
105. C. Benecke and H.-E. Gumlich, in "Semiconductors and Semimetals" (J. K. Furdyna and J. Kossut, Eds.), Vol. 25, pp. 85–115. Academic Press, New York, 1988.
106. S. Wang, S. L. Westcott, and W. Chen, *J. Phys. Chem. B* 106, 11203 (2002).
107. S. W. Allison and G. T. Gillies, *Rev. Sci. Instrum.* 68, 2615 (1997).
108. R. W. Meulenberg and G. F. Strouse, *Phys. Rev. B* 66, 035317 (2002).
109. W. Chen, G. H. Li, J-O Malm, Y. Huang, H. Han, Z. Wang, and J-O Bovin, *J. Lumin.* 91, 139 (2000).
110. A. Anastassiadou, E. Liarokapis, S. Stoyanov, E. Anastassakis, and W. Giriat, *Solid State Commun.* 67, 633 (1988).
111. K. L. Bray, *Topics Current Chem.* 213, 1, (2001).
112. G. L. House and H. G. Drickamer, *J. Chem. Phys.* 67, 3230 (1977).
113. T. Koda and S. Shionoya, *Phys. Rev. A* 136, 541 (1964).
114. G. L. House and H. G. Drickamer, *J. Chem. Phys.* 67, 3221 (1977).
115. P. Jaszczyn\_kopec, J. P. Pinceaux, M. Zigone, J. M. Kenedy, and A. Stadtmuller, *Solid State Commun.* 32, 473 (1979).
116. R. K. Cavin III, D. J. C. Herr, and V. V. Zhirnov, *J. Nanoparticle Res.* 2, 213 (2000).
117. I-H. Choi and P. Y. Yu, *Phys. Status Solidi B* 211, 143 (1999).
118. S. Tiwari, F. Rana, H. Hanafi, A. Hartstein, E. F. Crabbe, and K. Chan, *Appl. Phys. Lett.* 68, 1377 (1996).
119. J. J. Finley et al., *Appl. Phys. Lett.* 73, 2618 (1998).
120. C. Rocke, S. Zimmermann, A. Wixforth, and J. P. Kotthaus, *Phys. Rev. Lett.* 78, 4099 (1997).
121. W. Chen et al., unpublished result.
122. W. Chen, R. Sammynaiken, and Y. Huang, *J. Appl. Phys.* 88, 1424 (2000).
123. L. J. Nugent, in "Lanthanides and Actinides" (K. W. Bagnall, Ed.), MIT Int. Rev. Sci. Inorg. Chem., Ser. Two, Vol. 7, p. 195. Butterworths, London, 1975.
124. F. W. Wise, *Acc. Chem. Res.* 33, 773 (2002).
125. F. Qu, R. S. Silva, and N. O. Dantas, *Phys. Status Solidi B* 232, 95 (2002).
126. L. Levy, N. Feltin, D. Ingert, and M. P. Pileni, *J. Phys. Chem. B* 101, 9153 (1997); L. Levy, N. Feltin, D. Ingert, and M. P. Pileni, *Langmuir* 15, 3386 (1999).
127. H. Vogelsang, O. Husberg, and W. von der Osten, *J. Lumin.* 86, 87 (2000).
128. T. Itoh, Y. Iwabuchi, and M. Kataoka, *Phys. Status Solidi B* 145, 567 (1988).
129. Y. Masumoto and S. Ogasawara, *Jpn. J. Appl. Phys.* 38, L623 (1999); *J. Lumin.* 87–89, 360 (2000).
130. S. A. Nepijko, D. N. Ievlev, D. B. Danko, R. D. Fedorovich, W. Schulze, and G. Ertl, *Physica B* 299, 32 (2001).
131. E. Savir, J. Jedrzejewski, A. Many, Y. Goldstein, S. Z. Weisz, M. Gomez, L. F. Fonseca, and O. Resto, *Mater. Sci. Eng.* 72, 138 (2000).
132. W. Theib, *Surf. Sci. Rep.* 29, 91 (1997).
133. A. Biesg and J. C. Vial, *J. Lumin.* 70, 310 (1996).
134. I. V. Blonskyy, M. S. Brodyn, A. Yu, Vakhnin, V. M. Kadan, and A. K. Kadashchuk, *Phys. Lett. A* 279, 391 (2001).
135. J. Diener, D. Kovalev, H. Heckler, G. Polisski, N. Kunzner, F. Koch, A. L. Efros, and M. Rosen, *Opt. Mater.* 17, 135 (2001).
136. B. Salem, J. Olivares, J. Brault, C. Mpnat, M. Gendry, G. Hollinger, H. Maaref, G. Guillot, and G. Bremond, *Microelectron. J.* 33, 579 (2002).
137. M. Hjiri, F. Hassen, and H. Maaref, *Mater. Sci. Eng.* 2–3, 255 (2002).
138. N. Tessler, V. Medvedev, M. Kazes, S. Kan, and U. Banin, *Science* 259, 1506 (2002).
139. J. Zhang, L. Sun, J. Yin, H. Su, C. Liao, and C. Yang, *Chem. Mater.* (2002).
140. Y. Tao, G. Zhao, W. Zhang, and S. Xia, *Mater. Res. Bull.* 32, 502 (1997).
141. G. Wakefield, H. A. Keron, P. J. Dobson, and J. H. Hutchison, *J. Colloids Interface Sci.* 215, 179 (1999).



# Luminescent Organic–Inorganic Nanohybrids

R. A. Sá Ferreira, L. D. Carlos

*Universidade de Aveiro, Aveiro, Portugal*

V. de Zea Bermudez

*Universidade de Trás-os-Montes e Alto Douro, Vila Real Codex, Portugal*

## CONTENTS

1. Introduction
  2. Synthesis of Rare-Earth-Doped Nanohybrids
  3. Local Structure
  4. Photoluminescence Spectroscopy
  5. Color Coordinates
  6. Absolute Emission Quantum Yields
  7. Energy-Transfer Mechanisms
  8.  $\text{Eu}^{3+}$  Local Coordination
  9. Luminescent Undoped Nanohybrids
  10. Summary
- Glossary  
References

## 1. INTRODUCTION

The concept of “hybrid organic–inorganic” materials emerged only very recently with the birth of “soft” inorganic chemistry processes (“chimie douce”) [1–6]. The unique low-temperature processing characteristics of the sol–gel process allow the chemical design of organic–inorganic hybrid materials through the incorporation of low-molecular-weight organic molecules with appropriate functionalities into inorganic moieties at temperatures for which the organics are not destroyed [1–39]. These materials are generally produced using various methodologies of “soft” inorganic chemistry in liquid or sol–gel media, and combine the most important properties of their constituents, such as low processing temperatures (polymer-like), high transparency, and sufficient thermal stability (glass-like). The characteristics of the sol–gel process, such as, for instance, the unique

availability of the respective precursors (commercially available metal alkoxides and organoalkoxysilanes, as well as nanoparticles), low processing temperatures, and the processing versatility of the colloidal state allow the combination of organic and inorganic components at the nanometric dimension, in virtually any ratio, leading to the so-called hybrid organic–inorganic nanocomposites [1–44]. The hybrid concept has made accessible an immense new area of materials science with extraordinary implications for the development of multifunctional materials. The combination of the appropriate processing conditions with the adequate choice of the organic and inorganic components dictates the morphology, molecular structure, and properties of the hybrids. Moreover, frequently, the combination of components provides an additional dimension to their properties in becoming part of the hybrid compound. Promising applications are therefore expected in many fields, including optics, electronics, optoelectronics, ionics, mechanics, membranes, protective coatings, catalysis, sensors, biology, and others [1–50].

Although no commercial products are available yet, there is widespread agreement within the sol–gel scientific community that active optical applications of multifunctional nanoscale organic–inorganic frameworks with tunable design and suitable features might present one of the most attractive fields to realize applications for the 21st century. We can refer to, for instance, optical switching and data storage hybrid devices [17, 51, 52]; photoelectrochemical cells and coatings for solar energy conversion [53–55]; and hybrid materials having excellent laser efficiencies and good photostability [56], fast photochromic responses [57], high and stable second-order nonlinear optical responses [58–62], or which can be used as fiber-optic sensors [63–65], photopattern waveguiding structures for integrated optics [66–74], and electroluminescent diodes [75, 76]. Further details concerning the photonic applications of siloxane-based organic–inorganic hybrid and nanocomposites throughout

the past decade may be found in various recent reviews [15, 17, 33, 36, 38, 40, 46–50].

The outgrowth of new full-color displays cheaper and less aggressive to the global environment is one of the main challenging tasks for the next generation of flat panel display systems and lighting technology. Different applications require different demands on emitted light; in some cases, pure colors are needed, whereas in other cases, a bright white light source is necessary, especially for backlight applications in large panel liquid-crystal displays. Efficient organic white light-emitting diodes (OLEDs) are currently considered as low-cost alternatives for applications in flat panel display systems and lighting technology due to the variety of attainable emission colors, the easiness of their production, and the high achievable electroluminescence quantum efficiency at relatively low operating voltages ( $\approx 4\%$ ) [77–82]. Since the first consideration of organic electroluminescent (EL) devices more than 30 years ago [83], OLEDs have been widely pursued, and near-commercial dot-matrix displays have recently been demonstrated [84]. Luminous efficiencies in excess of 30 lm/W and operating voltages as low as 4 V have been reported [85, 86]. To obtain white-light emission from OLEDs excitation, more than one molecular species is necessary since the luminescence of a single organic molecule typically does not span the entire visible spectrum. Several approaches have been established in recent years, allowing the achievement of white-light emission from OLEDs. We can emphasize, for instance, the use of multilayers in which the recombination zones are spatially controlled by the application of hole-blocking layers [87, 88], the spectral filtering of a large broad emission [89], the superposition of red, green, and blue OLEDs [90], the use of homogeneous polymer blends [80], the concept of exciplex emission [81], and the combination in a unique structure of InGaN and conjugated polymers [82]. However, obtaining pure emission colors (red, green, and blue) from conjugated polymers or small organic molecules is difficult because their emission spectra are broad, typically with full width at half maximum (FWHM) of 50–200 nm [91]. Moreover, mixing of red, green, and blue OLEDs in a single system brings forth difficulties in the integration of individual materials and electrical requirements [92]. These technical issues in the fabrication and manufacturing of light-emitting diodes (LEDs) also remain to be resolved, even if we consider the integration of different inorganic semiconductors, such as GaN, InGaN, AlInGaP, and InGaAlN [93]. In contrast to organic and semiconductor-based LEDs, very sharp emissions (FWHM  $< 4$  nm [94]) can be obtained using LEDs incorporating rare-earth (RE) ions. Moreover, the proper selection of red ( $\text{Eu}^{3+}$ ,  $\text{Pr}^{3+}$ ,  $\text{Sm}^{3+}$ ), green ( $\text{Tb}^{3+}$ ,  $\text{Er}^{3+}$ ), and blue ( $\text{Tm}^{3+}$ ,  $\text{Ce}^{3+}$ ) emitting RE ions as dopants in a common host material could simplify the LED structure, and hence, the fabrication processes, reducing the cost and resolving some of the critical integration problems. This is the case of the RE-based GaN LEDs reported recently [95–102]. On the other hand, due to the spectral sensitivity of the human eye, pure red-emitting LEDs based on  $\text{Eu}^{3+}$  are easily processed and more efficient than the corresponding ones based on polymers or organic chromophores. In fact, the main  $\text{Eu}^{3+}$  emission (610–620 nm) is still red, and appears brighter than red emission at longer wavelengths

[91, 96]. Pure red emission has been achieved recently in OLEDs by transferring energy from blue-emitting conjugated polymers to  $\text{Eu}^{3+}$ - $\beta$ -diketonate complexes [91]. Furthermore, RE-doped materials are of great interest for a wide range of other photonic applications such as tunable lasers (both in the ultraviolet (UV) and visible (Vis) ranges), low-energy scintillators, amplifiers for optical communications, and optical storage [94].

Despite the very efficient light emission under UV excitation characteristic of RE complexes of  $\beta$ -diketonates (some of them exhibit laser action in solution [103–105]), aromatic carboxylic acids, and heterocyclic ligands, such as 2,2'-bipyridine (bpy) and 1,10-phenanthroline (Phen), they have been excluded so far from practical use as tunable solid-state lasers or phosphor devices due essentially to their poor thermal stability and mechanical properties. Another drawback that derives from the use of RE  $\beta$ -diketonates lies in the difficulty in obtaining them in the anhydrous form. In general, the  $\beta$ -diketonate chelates are produced as hydrates in which two or three water molecules are attached to the central ion. The presence of water molecules in the RE first coordination shell quenches the emission, due to the activation of nonradiative decay paths. The substitution of the water molecules by other chemical species, such as heterocyclic ligands (e.g., bpy and Phen), substituted sulphoxides and phosphine oxides, aromatic carboxylic acids, among many others, has been extensively employed in order to improve the light-emission properties of RE  $\beta$ -diketonate chelates [106]. Crystalline mixed compounds, in the powder form and displaying unusually high emission quantum efficiencies (70–80%), have resulted from this concept [103–108]. Moreover, the RE  $\beta$ -diketonates are undoubtedly extremely promising for efficient light conversion molecular devices (LCMDs). Recently, these LCMDs have found a series of important applications, such as luminescent labels in fluoroimmunoassays, light concentrators for photovoltaic devices, antennas in photosensitive bioinorganic compounds, and high-technology optics [106]. One of the strategies adopted in the last few years to simultaneously improve the thermal stability, the mechanical properties, and the light-emission properties of RE complexes is to incorporate them into polymeric matrices [109–129]. However, low photostability and poor thermal stability still limit their applicability.

Taking into account the processing advantages of sol-gel matrices, such as low-temperature processing and shaping, high sample homogeneity and purity, availability of innumerable precursors, and the opportunity to prepare nanocomposites, much research has been focused recently on the possibility of using RE-based hybrid frameworks as matrices for RE photoluminescence (PL) [15, 17, 33, 36, 38, 46–50]. The luminescence efficiency of RE ions in conventional sol-gel-derived matrices is currently limited by hydroxyl quenching [130–132] originating from residual water, silanol groups, and dopant clustering [133–135]. To circumvent these drawbacks, various strategies of synthesis and chemical design of innovative sol-gel-derived hybrids have been developed recently [17, 36, 38]. A significant part of this research involves the encapsulation of RE organic complexes with  $\beta$ -diketonates, aromatic carboxylic acids, and heterocyclic ligands in sol-gel-derived matrices (in

particular, siloxane-based ones) through the simple embedding of the complexes within the sol–gel matrix [53, 55, 136–152], or through the use of complexing ligands covalently grafted to the framework [153–161]. In general, the embedding of the complexes within the sol–gel matrix gives rise to Class I nanocomposite hybrid materials [11], that is, hybrid systems where one of the components is entrapped within a network of the other component. In this case, weak interactions (van der Waals contacts, hydrogen bonding, or electrostatic interactions) between the host network and the entrapped species will be established. The sol–gel synthesis of hybrid nanostructural RE complexes *in-situ* leads instead to Class II hybrid materials [11], in which at least a proportion of the organic and inorganic components are typically grafted together by means of strong chemical interactions (covalent or ionocovalent bonds). All of these sol–gel-derived organic–inorganic hybrid photonic materials exhibit notably improved luminescence properties with respect to the simple incorporation of metal ions in silica. Indeed, such organic complexes increase the concentration of lanthanide salts in the inorganic matrix, the ligands protect the central RE ions from silanol groups present in the silica matrix, thus diminishing nonradiative decay pathways of the RE ions, and finally, RE ions encapsulated by absorbing ligands can give rise to intramolecular energy transfer from the coordinating ligands to the central lanthanide ions, which in turn undergo the corresponding radiative emitting process (the so-called “antenna effect”).

The hybrid concept has also been employed recently to synthesize stable and efficient Class II RE-doped amine or amide functionalized hybrids [153–190]. Among these functionalized nanohybrids reported, mention must be made of those which comprise polyether-based chains of variable length grafted to both ends to a siliceous backbone through urea or urethane cross linkages, termed *di-ureasils* and *di-urethanesils*, respectively [162–187]. Small-angle X-ray scattering (SAXS) data of the undoped hybrid matrices showed the presence of a well-defined peak attributed to the existence of a liquid-like spatial correlation of siloxane-rich domains embedded in the polymer matrix and located at the ends of the organic segments [178–183]. For the undoped di-ureasils, the siloxane particle radius and the average interparticle distance increase from 5 to 7 Å (error within 10%) and from  $25 \pm 2$  to  $40 \pm 2$  Å, respectively, as the average polymer molecular weight increases from 600 to 2000 g·mol<sup>-1</sup> [181]. Values slightly smaller, 3 and 15 Å (error within 10%), respectively, were found for undoped di-urethanesils with an average polymer molecular weight of 300 g·mol<sup>-1</sup> [183]. The incorporation of RE ions (particularly Eu<sup>3+</sup>) into the di-ureasil and di-urethanesils nanohybrid hosts promotes the formation of a two-level structure in which the primary level is composed of rather close-packed siloxane nanoparticles with radius between 3–10 Å (errors within 5%), depending on the matrix and on the Eu<sup>3+</sup> concentration. Clusters of these particles form the second level [181, 183].

Moreover, these diurea and diurethane cross-linked xerogels, which are easily produced as thin, elastomeric, and highly transparent monoliths, may withstand the presence of large amounts of guest dopant compound. The di-ureasils, for instance, when doped with Nd<sup>3+</sup>, Eu<sup>3+</sup>, Tb<sup>3+</sup>, Er<sup>3+</sup>,

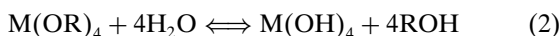
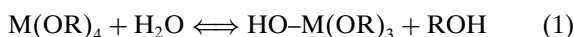
and Tm<sup>3+</sup> ions, display remarkable emission properties. Besides a broad long-lived emission associated with the hybrid host [191–196], the di-ureasils exhibit the typical intra-4f monochromatic emission in the green (Tb<sup>3+</sup>) [172, 185], red (Eu<sup>3+</sup>) [162–164, 166, 168, 170–172, 177, 180, 184, 186, 187], and even in the infrared (Nd<sup>3+</sup> [169, 173, 174, 176], Er<sup>3+</sup> [173, 174], and Tm<sup>3+</sup> [172]), thus opening challenging new prospects for their applications. In addition, the color emitted by the Eu<sup>3+</sup>-doped di-ureasils may be readily tuned across the CIE (Commission Internationale d'Éclairage) chromaticity diagram by varying either the salt concentration or the excitation wavelength [166, 168, 170, 171]. In spite of these properties, energy transfer from the hybrid's emitting centers (the NH groups of the urea linkages and the siliceous nanodomains [191–196]) to the Eu<sup>3+</sup> ions is quite inefficient, and high multiphonon decay rates are observed for the Eu<sup>3+</sup>-excited states. Calculated quantum efficiencies around 8% are obtained for emission from the Eu<sup>3+</sup> <sup>5</sup>D<sub>0</sub> excited state within the entire range of compositions studied up to now [170]. Moreover, the activation of the energy transfer mechanism depends noticeably on the ion local coordination. For the high-molecular-weight di-ureasils, energy transfer occurs as the Eu<sup>3+</sup> coordination involves the carbonyl-type oxygen atoms of the urea bridges, which are located near the hybrid's host emitting centers. On the contrary, in the low-molecular polyether-based di-ureasils, the Eu<sup>3+</sup> ions are coordinated to the polymer chains, and therefore, the distance between the hybrids emitting centers and the metal ions is large enough to allow efficient energy transfer mechanisms [170].

This review attempts to cover the most recent advances of photoluminescent Class II siloxane-based organic–inorganic hybrids incorporating RE complexes. Emphasis is essentially given to sol–gel-derived hybrids in which: (1) an organic molecule—which is part of the hybrid framework itself—is able to complex RE ions, and (2) RE salts or complexes are encapsulated within cross-linked Class II matrices. The synthesis, the PL features, and a description of the recombination mechanisms of photoluminescent Class II siloxane-based organic–inorganic hybrids lacking activating centers are reviewed. Furthermore, some results of Class I siloxane-based photoluminescent hybrid materials incorporating RE ions are also included. This review does not, therefore, focus on Class I hybrids incorporating RE ions derived from non-siloxane precursors. The reader will be invited to travel from the description of the materials synthesis and structure features to the photoluminescent results that stress the potential application of these materials as innovative photonic hybrids. Particular attention will be given to the determination of the emission color coordinates and absolute emission quantum yields, and to the description of the host-to-metal ion energy transfer mechanisms intrinsically associated with the ion local coordination. We have tried to make this review as comprehensive as possible, and we apologize in the event that we were not successful in this regard.

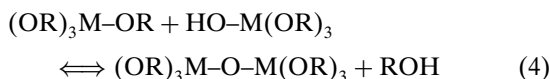
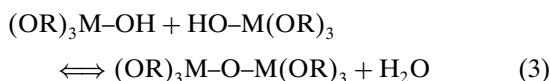
## 2. SYNTHESIS OF RARE-EARTH-DOPED NANOHYBRIDS

The sol–gel process is a chemical synthetic procedure known for many years, which is based on inorganic polymerization reactions that lead to the production of dispersed

inorganic materials in solvents, through the growth of metal-oxo polymers [6]. Because of their high reactivity with water, metal alkoxides, in particular tetraethoxyortosilane [TEOS,  $\text{Si}(\text{OCH}_2\text{CH}_3)_4$ ], are the most widely used precursors in the sol–gel method. Upon *hydrolysis*, hydroxyl groups become attached to the metal ion of such compounds, and an alcohol is formed concomitantly. Depending on the amount of water and catalyst added, the hydrolysis may yield to partially hydrolyzed species,  $\text{M}(\text{OR})_{4-n}(\text{OH})_n$  (where M and R represent the metal atom and an alkyl group, respectively) [Eq. (1)] or go to completion [Eq. (2)]



Through a *condensation* reaction, two partially hydrolyzed molecules (or one partially hydrolyzed molecule and a non-reacted one) bond to each other, and a small molecule, such as water [Eq. (3)] (or alcohol [Eq. (4)]), is produced:



These reactions proceed, giving rise to large metal-based molecules, respectively. The substance will be called a *gel* when the molecule reaches macroscopic dimensions and extends throughout the solution. The *gel point* is the time at which the last bond is formed that completes this giant molecule. *Gelation* may occur after the sol (or colloidal suspension of solid particles in a liquid) is cast into a mold, allowing objects of a required shape to be made.

Bond formation does not stop at the gel point. *Aging* is the process of change in structure and properties that takes place after gelation. Aging may involve further condensation, dissolution, and reprecipitation of monomers and oligomers, or phase transformations within the solid and liquid phases [6]. *Drying* under normal conditions is accompanied by shrinkage of the gel network. The resulting dried gel, usually called *xerogel*, is reduced in volume by a factor of 5–10 compared to the original wet gel. This shrinkage process involves deformation of the network and the transport of the liquid through the pores. If the wet gel is dried under supercritical conditions, the shrinkage will be minimum, and the resulting product will be called *aerogel*. When the smallest dimension of the gel is greater than a few millimeters, the material is usually classified as a *monolith*. If, however, gelation occurs through rapid evaporation of the solvent, films and fibers are obtained.

The wide range of structures, microstructures, and compositions that can be achieved by the sol–gel method through a careful control of the several process parameters, such as the  $\text{H}_2\text{O}/\text{M}$  ratio, the nature and concentration of the catalyst, and the type of solvent, open many possibilities for practical applications.

In the remainder of this section, we will describe some particular aspects of the synthetic procedure of the most cited sol–gel-derived hybrids discussed in the present review.

It is well known that the structure, degree of order, and general features of these nanosized systems depend not only

on the chemical features of the organic and inorganic components, but also on the interactions which are established between them. Thus, the most important factors that govern the design of hybrid materials are the nature, extent, and accessibility of the inner interfaces [11, 15, 40]. On the basis of the type of interactions occurring between both components, it is possible to divide the large class of hybrid materials into two distinct subclasses, usually designated as Class I and Class II [11].

Class I includes all of those hybrid systems in which both components are linked only through weak interactions, such as van der Waals contacts, hydrogen bonding, or electrostatic forces. In contrast, in Class II, at least a proportion of the organic and inorganic components of the hybrids are grafted together by means of strong chemical bonds (covalent, ionocovalent, or acid-base bonds). Thus, the synthesis of Class II hybrids strongly depends on the relative chemical stability of the chemical bonds that associate the various components. It implies the use of precursor molecules with at least two different functionalities: alkoxy groups, which undergo hydrolysis–condensation reactions in the presence of water and yield the oxo-polymer framework, and metal-carbon bonds, which are stable with respect to hydrolysis.

## 2.1. Class I Hybrids

A significant number of promising Class I organic–inorganic frameworks based on silica ( $\text{SiO}_2$ ) alumina ( $\text{Al}_2\text{O}_3$ ) or mixtures of  $\text{SiO}_2$  and titania ( $\text{SiO}_2/\text{TiO}_2$ ) or  $\text{SiO}_2$  and zirconia ( $\text{SiO}_2/\text{ZrO}_2$ ) have been proposed in the last few years as adequate host structures for luminescent dopants, in particular RE salts and complexes [53, 55, 135–152].

Although the description of the synthetic procedure of all of the Class I systems investigated to date is beyond the scope of the present review, it is of interest to briefly mention some of the most recent works reported in this domain, and to stress the great diversity of systems proposed by the numerous researchers devoted to the investigation of the Class I hybrids.

Li et al. [148] developed attractive  $\text{Eu}^{3+}$ - and  $\text{Tb}^{3+}$ -doped complexes composed of  $\text{SiO}_2$ -based matrices. The preparation of such composites involved the addition of a metal alkoxide  $\text{M}(\text{OR})_2$  (where  $\text{M} = \text{Zr}$  and  $\text{Ta}$ ) to a mixture of TEOS, water ( $\text{H}_2\text{O}$ ), and ethanol ( $\text{CH}_3\text{CH}_2\text{OH}$ ) (molar ratio 1:10:1) and a few drops of diluted hydrochloric acid ( $\text{HCl}$ ) solution, which acted as a catalyst. The emitting centers (bis-1,10-phenanthroline europium(III) chloride ( $[\text{Eu}(\text{phen})_2]\text{Cl}_3$ ) and terbium bis-2,2'-bipyridine terbium(III) chloride ( $[\text{Tb}(\text{bpy})_2]\text{Cl}_3$ ) were dissolved in  $\text{H}_2\text{O}$  and  $\text{N,N}$ -dimethylformamide (DMF), and added to the precursor solution (molar ratio of  $(\text{Si} + \text{M})$ :complex:  $\text{H}_2\text{O}$ :DMF = 1:y:4:1, where  $y = 0.01$ –0.2). Solid composite samples were obtained after stirring and casting the above mixture and aging it at moderate temperature for several days.

The light yellow monoliths obtained by Ji et al. [145] were produced by first dissolving  $\text{Eu}(\text{TTA})_3\text{phen}$  (where TTA is trifluorothenoxyacetate) or  $\text{Tb}(\text{Sal})_3$  (where Sal represents salicylate), hydroethyl methacrylate (HEMA), and benzoyl peroxide (BPO) in DMF and then mixing them with TEOS. The latter compound was hydrolyzed and polycondensed

under acidic conditions at 40–45 °C. When the reaction reached the gel point, the container was placed in a desiccator for removal of H<sub>2</sub>O and solvents. A heat treatment at 70–100 °C was necessary for two days to initiate the polymerization of HEMA.

It is also worth referring to the Class I hybrids developed by Li et al. [146], which were synthesized in a slightly different manner. TEOS and vinyltrimethoxysilane (VTMOS) were first mixed with HCl in H<sub>2</sub>O (molar ratio TEOS:VTMOS:H<sub>2</sub>O = 1:1:4). Appropriate amounts of the Eu(TTA)<sub>3</sub>phen complex were dissolved in DMF, and this solution was added to the above one. The final mixture was stirred, and methylmethacrylate (MMA) monomer was added (molar ratio VTMOS:MMA = 1:1). BPO (10 wt% of MMA) was used as the initiator of the polymerization reaction. The sol was transferred into cuvettes, and thermal curing was performed at 70 °C until the sample solidified.

In some hybrid Class I frameworks, the organic component is a polymer segment instead of a complex. The Eu<sup>3+</sup>-containing siloxane/poly(ethylene glycol) (PEG) composites prepared by Molina et al. [150] represent a good example of this particular architecture. These authors mixed TEOS and a dilute aqueous solution of HCl under ultrasound. PEG600 (where 600 is the average molecular weight of PEG) was then added to this silica sol under ultrasound. The Eu<sup>3+</sup> ions, introduced as europium perchlorate (Eu(ClO<sub>4</sub>)<sub>3</sub>), were added to the previous solution after dissolving the salt in CH<sub>3</sub>CH<sub>2</sub>OH. Gels were obtained by pH increasing with the addition of ammonium hydroxide (NH<sub>4</sub>OH). Xerogels were obtained by submitting the casted sols to heat treatment at 50 °C for 24 h.

Cordoncillo et al. [152] synthesized two nanocomposite matrices. One was obtained through hydrolysis/condensation of the diethoxymethylsilane (MDES) and methyltriethoxysilane (MTEOS) precursors in the presence of a europium(III) salt and zirconium tetrapropoxide (ZrP). MDES and MTEOS were first hydrolyzed with neutral H<sub>2</sub>O in CH<sub>3</sub>CH<sub>2</sub>OH. The molar ratio MDES:MTEOS:H<sub>2</sub>O:CH<sub>3</sub>CH<sub>2</sub>OH was 1:1:2:2. An ethanolic solution of ZrP and europium trichloride (EuCl<sub>3</sub>) in the presence of acetylacetone was then added to the siloxane-based sol. The final molar ratio Zr:Eu:Si was 1:0.01:9. The other sol–gel-derived matrix was prepared by first cohydrolyzing EuCl<sub>3</sub> with MDES and triethoxysilane (TREOS) (molar ratio MDES:TREOS:Eu:H<sub>2</sub>O:CH<sub>3</sub>CH<sub>2</sub>OH = 1.4:0.6:0.02:2:1). This siloxane-based sol was then added to a solution of ZrP in propanol (molar ratio Zr:Si = 2:10). In both systems, the mixing of the ZrP solution and the siloxane sol leads to the evolution of hydrogen gas, which was used as a reducing agent to decrease the valence of the europium cations from III to II. The resulting clear sols were magnetically stirred for 30 min in an argon atmosphere, and then poured into plastic cuvettes or deposited onto previously cleaned glass sheets. Transparent monolithic gels and coating a few microns thin were thus obtained.

## 2.2. Class II Hybrids

In this section, we will discuss in detail the synthesis process of several examples of the two types of Class II hybrid structures that have been mentioned for the complexation

of RE emitting centers, for examples (1) hybrid frameworks in which an organic molecule—which is part of the hybrid structure itself—is able to complex RE ions, and (2) cross-linked hybrid matrices in which RE salts or complexes are encapsulated.

### 2.2.1. Complexation via an Organic Molecule

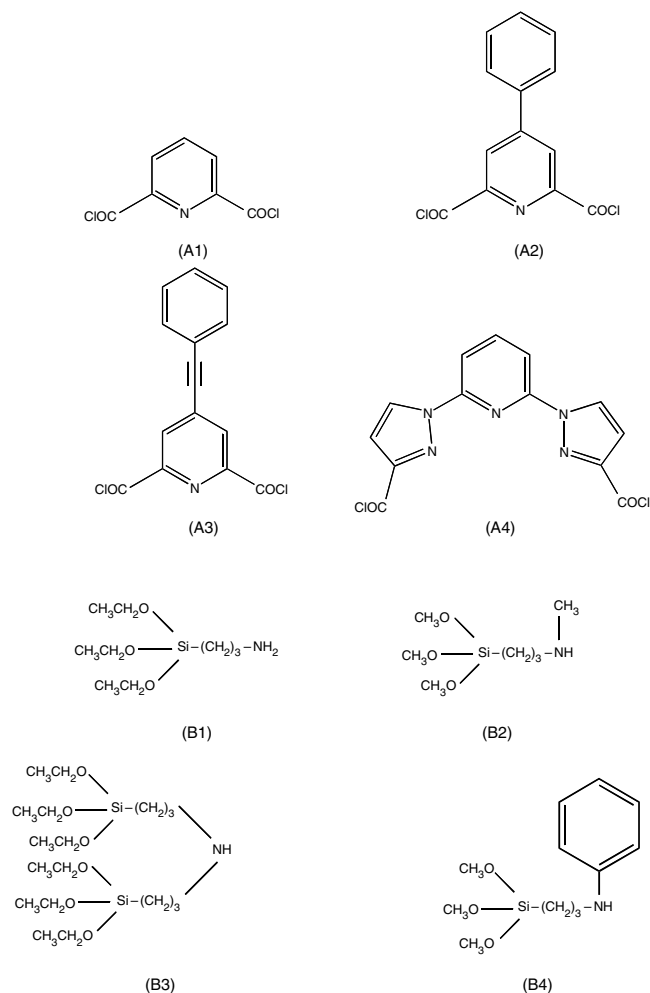
The first stage of the synthesis of the RE-activated organic–inorganic hybrid materials proposed by Franville et al. [153] involves two major types of amidation coupling reactions.

1. Reaction of the acid chloride functions of a dicarboxylic acid chloride [2,6-pyridinedicarboxylic acid chloride (A1), 4-phenyl-2,6-pyridinedicarboxylic acid chloride (A2), 4-(phenylethynyl)-2,6-pyridine acid chloride (A3), or 2,6-bis-(3-carboxy-1-pyrazolyl)pyridine acid chloride (A4)] with the primary amine group of 3-aminopropyltriethoxysilane (APTES) (B1) (Schemes 1 and 2) [155].
2. Reaction of the acid chloride functions of the dicarboxylic acid chloride A1 with the primary or secondary amine group of an aminoalkylalkoxysilane [B1], [3-(methylamino)propyl]trimethoxysilane (B2), bis[3-(triethoxysilyl)propyl]amine (B3), or N-[3-(triethoxysilyl)propyl]aniline (B4)] (Schemes 1 and 3) [153, 154].

The reactions were carried out in diethyl ether and in the presence of pyridine. The resulting solutions were stirred under argon at room temperature (RT) to prevent hydrolysis of the alkoxy groups. The nonhydrolyzed hybrid precursors were recovered by filtration of the precipitated pyridinium chloride, followed by removal of the solvents, and were then dried on a vacuum line.

The sol–gel reaction was performed in an ethanolic or methanolic medium. The RE ions (Eu<sup>3+</sup> and gadolinium, Gd<sup>3+</sup>) were introduced as hexahydrate nitrate salts (Eu(NO<sub>3</sub>)<sub>3</sub> · 6H<sub>2</sub>O and Gd(NO<sub>3</sub>)<sub>3</sub> · 6H<sub>2</sub>O, respectively). A negligible amount of HCl, used as an acid catalyst, was incorporated. The H<sub>2</sub>O/Si and Ln<sup>3+</sup>/(nonhydrolyzed hybrid precursor) molar ratios were, respectively, 1:1 and 1:3. In a typical sol–gel preparation, the hybrid precursor was dissolved in absolute alcohol, and appropriate amounts of the RE salt were then added. Water was added only in the case of the synthetic procedure involving the use of B3, to ensure that the H<sub>2</sub>O/Si molar ratio was 1:1. The mixture was vigorously stirred for about 1 h before introducing HCl to foster the hydrolysis (pH = 2). The solution was stirred for 30 additional min, and the resulting sol was aged in covered Teflon beakers at RT until the onset of gelation, which occurred within four–seven days (reaction (1) [154]) or eight–ten days (reaction (2) [153]). The gels were obtained as monolithic bulks.

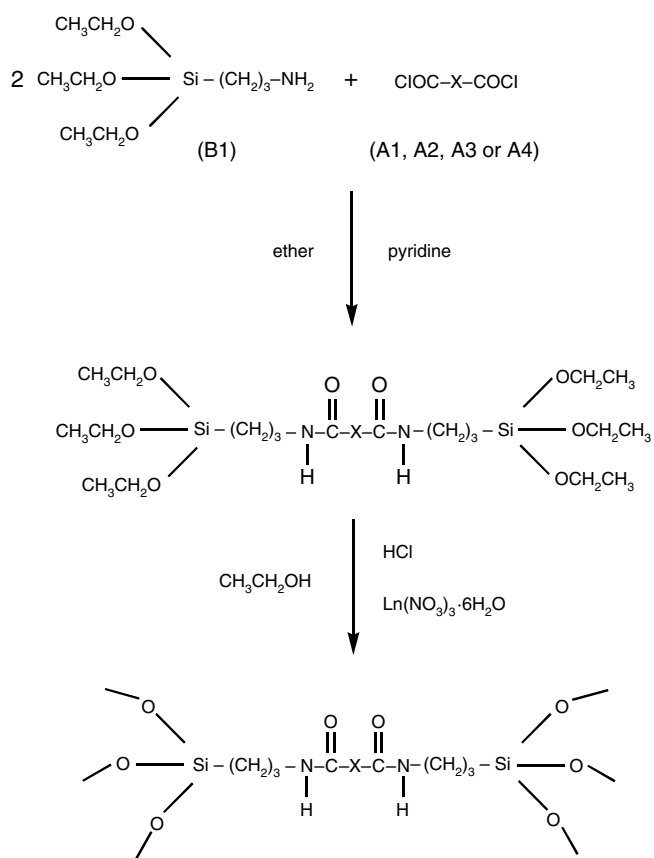
Dong et al. [156] developed two series of novel transparent and crack-free nanostructured hybrid Eu<sup>3+</sup>- and Tb<sup>3+</sup>-based complex films. The precursor material, classified as TAT, was synthesized from trimellitic anhydride and APTES (Scheme 4). In a typical procedure for the preparation of the hybrid films, a Eu<sup>3+</sup> solution of DMF and deionized H<sub>2</sub>O (acidified with HCl) was added to a TAT solution of DMF.



**Scheme 1.** Adapted with permission from [154], A.-C. Franville et al., *Chem. Mater.* 12, 428 (2000), Scheme 1. © 2000, American Chemical Society.

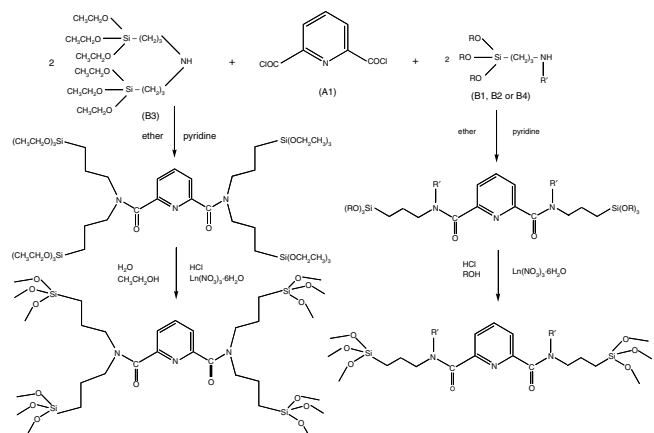
The mixture was stirred, immediately forming a homogeneous solution. After being kept in air at room temperature for two days, the solution was spin coated onto a quartz substrate to yield a wet gel film. After aging the wet gel at 60 °C during a week, a transparent film was obtained. The molar ratio of H<sub>2</sub>O:TAT was 1.5:1. It was concluded that the lanthanide ion concentration did not exert any effect on the transparency of the films. After the complete removal of the solvent, crack-free films were obtained.

Embert et al. [157] prepared a series of highly luminescent europium(III)-containing nanostructured hybrids. These materials were obtained through the hydrolysis and condensation via the sol–gel method of isolated Eu complex monomers. The authors described in detail in their paper the synthesis of five different phosphine oxides, five phosphine oxide–europium salt complexes, and one phosphine oxide–gadolinium salt complex (Schemes 5 and 6). All of the europium salts were dehydrated by a chemical reaction between the hydrated salt and ethyl orthoformate. The europium-based complexes 6–10 (Scheme 6) were obtained in the following way: a boiling ethanolic solution of europium salt (50 mmol/L) was treated with 3 equiv of



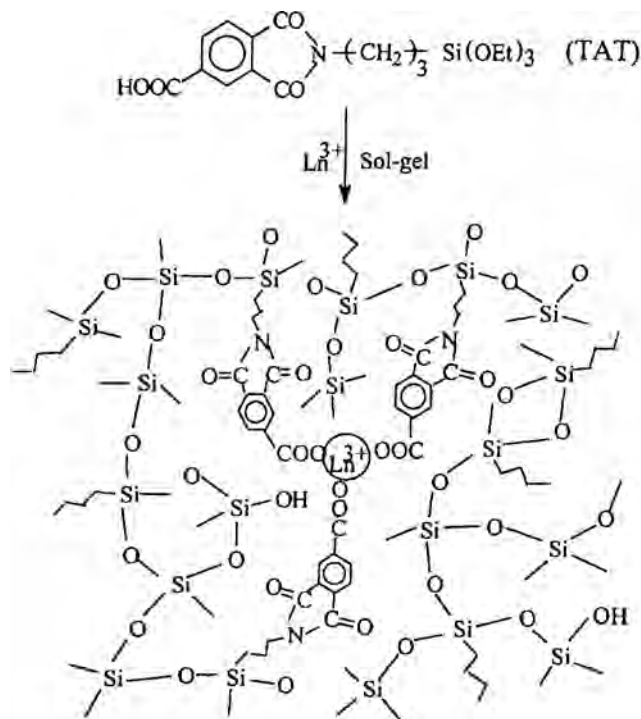
**Scheme 2.** Adapted with permission from [154], A.-C. Franville et al., *Chem. Mater.* 12, 428 (2000), Scheme 2, Ref. [49b]. © 2000, American Chemical Society.

phosphine oxide in boiling ethanol (solution 0.2 M). The formation of a white precipitate occurred immediately. The preparation of the representative compound X<sub>A</sub>10a (where X indicates the xerogel and A specifies that 10% of HCl was used as a gelification catalyst) will be described as follows as an example. A solution of complex 10a (1.50 g) (Scheme 7)



**Scheme 3.** Adapted with permission from [154], A.-C. Franville et al., *Chem. Mater.* 12, 428 (2000), Scheme 3. © 2000, American Chemical Society.

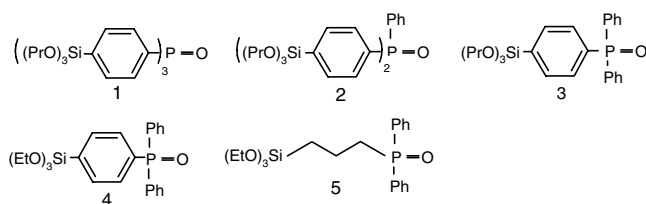




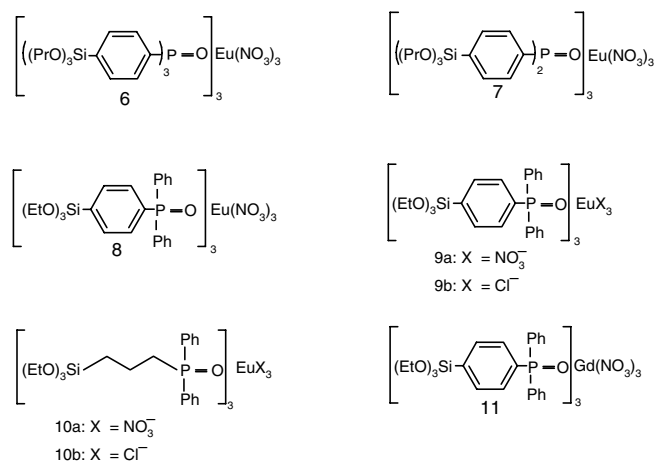
**Scheme 4.** Adapted with permission from [156], D. Dong et al., *Adv. Mater.* 12, 646 (2000), Scheme 1. © 2000, Wiley–VCH Verlag GmbH & Co.

in tetrahydrofuran (THF) (1.45 mL) was placed in a Pyrex test tube. A 0.96 mL sample of a THF solution, 4.5 M in H<sub>2</sub>O and 0.1 M HCl (10 mol%), was added dropwise at RT with a syringe. After 3 min of stirring, the solution was placed in a thermostated water bath at 30 °C without stirring. After 20 h, a gel was formed. The wet white opaque gel was allowed to age for five days at 30 °C. After this period, it was powdered and washed with acetonitrile and ether. The gel was then repowdered and dried under vacuum for 13 h at 120 °C, yielding 1.05 g of a white powder.

The hybrid proposed by Li et al. [158] consists of a europium 1,10-phenanthroline complex covalently attached to a silica-based network denoted as Phen-Si (Scheme 7). This hybrid precursor was prepared according to the synthetic procedure indicated in Scheme 7, using 5-amino-1,10-phenanthroline (Phen-NH<sub>2</sub>) as the starting reagent. Phen-NH<sub>2</sub> was dissolved in 20 mL of chloroform (CHCl<sub>3</sub>) in a round bottom flask. This solution was stirred as 2 mL of 3-isocyanatopropyltriethoxysilane (ICPTES) was added



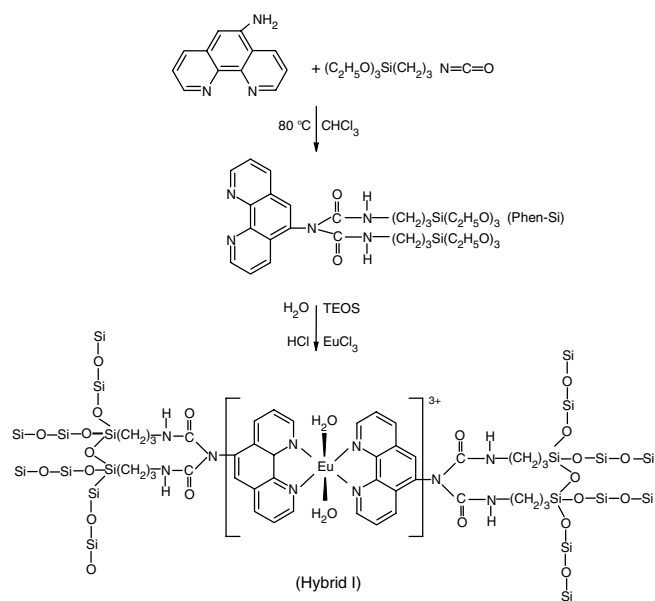
**Scheme 5.** Adapted with permission from [157], F. Embert et al., *Chem. Mater.* 13, 4542 (2001), Scheme 2. © 2001, American Chemical Society.



**Scheme 6.** Adapted with permission from [157], F. Embert et al., *Chem. Mater.* 13, 4542 (2001), Scheme 1. © 2001, American Chemical Society.

dropwise. CHCl<sub>3</sub> was evaporated at atmospheric pressure, and the resulting mixture was heated at 80 °C in a covered flask for 12 h. Cold hexane was then added to precipitate the white powder. The latter powder was collected by filtration, purified in methanol, and dried in vacuum.

The sol-gel-derived lanthanide-doped Hybrid I was prepared through the dissolution of Phen-Si in methanol and the subsequent addition of TEOS and H<sub>2</sub>O (pH = 2) under stirring. An appropriate amount of EuCl<sub>3</sub> mixed with 2 mL of DMF was added to the resulting solution. This mixture was agitated magnetically to achieve a single phase, and then transferred into a cuvette. Thermal curing was carried out at 60 °C, and continued until the sample became a solid. The molar ratio of Phen-Si:TEOS:H<sub>2</sub>O:Eu<sup>3+</sup> was 1:1:4:0.5.

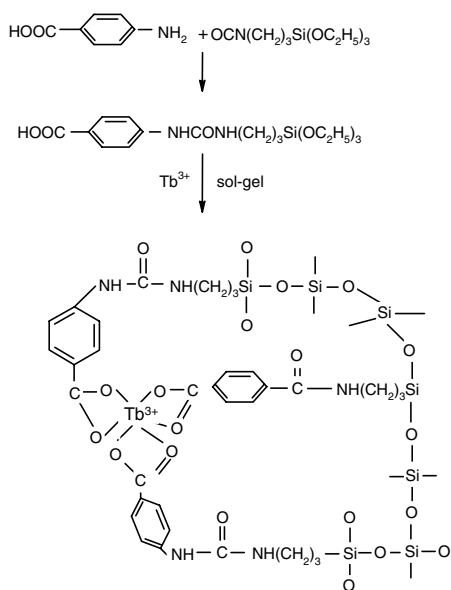


**Scheme 7.** Adapted with permission from [158], H. R. Li et al., *Chem. Mater.* 14, 3651 (2002), Scheme 1. © 2002, American Chemical Society.

Liu et al. [160] developed a series of sol–gel-derived luminescent films composed of terbium-complex-bridged polysilsesquioxanes using the dip-coating process. In these materials, the new bridging organic component of the silica precursor used (DPS) includes the ligand that complexes the  $Tb^{3+}$  species. DPS was obtained by reacting 10 mmol of ICPTES with 5 mmol of 2,6-diaminopyridine previously dissolved in 10 mL of dry  $CHCl_3$ . The resulting solution was refluxed for 5 h. A volume of petroleum ether (60 mL) was then added to this solution, and the white precipitate formed was filtered off and washed with petroleum ether. In a typical procedure of a doped hybrid film, a solution of  $Tb^{3+}$  in DMF and deionized  $H_2O$  acidified to 0.2 M HCl were added to a solution of DPS in DMF (molar ratio DPS:  $Tb^{3+}$  = 1). The mixture was vigorously stirred at room temperature for 8 h, and then allowed to stand for four days. The solution was dip coated onto freshly cleaned quartz substrate at 10 cm/min to give a wet film. A transparent film was obtained after the wet gel was kept at 55 °C for one week.

With the goal of developing materials well adapted for photonics, Liu et al. [161] introduced a series of Class II  $Tb^{3+}$ - and  $Gd^{3+}$ -activated hybrid thin films where: (1) the leaching of the dopants is prevented, (2) the dopant concentration limit does not exist, and (3) the aggregation of the active species is avoided. The preparation of these xerogels involved the synthesis of a urea cross-linked sol–gel precursor, classified as PABI (N-(4-benzoic acid-yl),N'-(propyltriethoxysilyl)urea) (Scheme 8).

In a typical experiment, 5 mmol of p-aminobenzoic acid were dissolved in 15 mL of dry THF. To this solution, 7.5 mmol of ICPTES were added. The resulting solution was stirred for 8 h. The white precipitate produced was filtered off and washed with 50 mL of petroleum ether to remove the

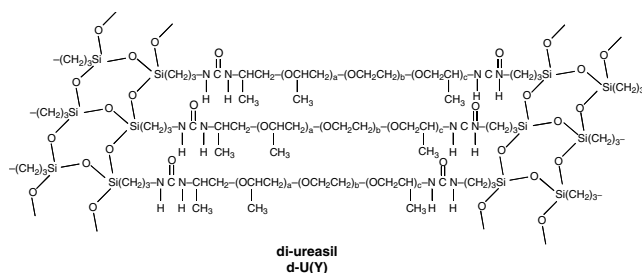


**Scheme 8.** Adapted with permission from [161], F. Liu et al., *Thin Solid Films* 419, 178 (2002), Scheme 1. © 2002, Elsevier Science.

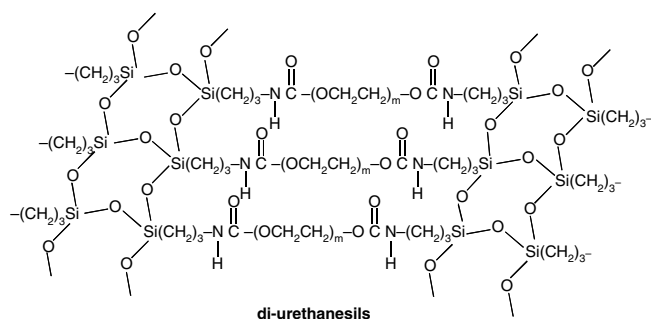
excess of ICPTES. The precipitate was finally dried on a vacuum line to get 1.8 g of PABI at 95% yield. The  $Tb^{3+}$ -doped samples were obtained through the addition of a DMF solution of terbium oxide,  $Tb_4O_7$ , and deionized  $H_2O$  (acidified to 0.2 M HCl) to a solution of PABI in DMF (Scheme 8). This mixture was vigorously stirred at RT for 12 h, and then allowed to stand for three days. The solution was then dip coated onto quartz substrates at 5 cm/min to give a wet gel film. A transparent, crack-free film 2.5  $\mu m$  thick was obtained after aging the gel at 50 °C for two weeks. Molar ratios  $Tb^{3+}$ /PABI of 1.5, 1:20, 1:50, 1:100, and 1:200 were employed, whereas the molar ratio  $H_2O$ /PABI was 1.5:1 in all of the cases. The  $Gd^{3+}$ -based compounds were prepared by adding under stirring a solution of 1 mmol of gadolinium chloride,  $GdCl_3$ , in  $CH_3CH_2OH$  to a THF solution containing 3 mmol of PABI. The white precipitate produced was filtered off, washed with  $CH_3CH_2OH$  and THF, and dried on a vacuum line.

## 2.2.2. Complexation via the Cross Linkages

The preparation of the *di-ureasils* and of the *di-urethanesils* proposed by our group [162–176, 181–183] can be summarized in two main steps (Schemes 9 and 10). Step 1 corresponds to the formation in THF of urea linkages between the terminal amine groups of double functional diamines (chemically  $\alpha,\omega$ -diaminepoly(oxyethylene-co-oxypropylene) or O,O'-bis(2-aminopropyl)polyethylene glycol) and the isocyanate group of an alkoxy silane precursor (ICPTES) (Scheme 9). The reaction of ICPTES with the terminal hydroxyl groups of PEG induces the formation of urethane bridges (Scheme 10). The two diamines used are commercially designated as Jeffamine ED-2001® (with  $a + c = 2.5$  and  $b = 40.5$ ) (Jeffamine ED-900® (with  $a + c = 2.5$  and  $b = 15.5$ ), and Jeffamine ED-600® (with  $a + c = 2.5$  and  $b = 8.5$ ), and have average molecular weights of 2000 and 600  $mol \cdot g^{-1}$ , respectively (Scheme 9). The PEG used has an average molecular weight of 300  $mol \cdot g^{-1}$  (Scheme 10). The grafting step leads to a urea and a urethane cross-linked organic–inorganic nonhydrolyzed hybrid precursor—so-called ureapropyltriethoxysilane (d-UPTES(Y), where Y = 2000, 900, and 600 are related to the Jeffamine molecular weight, and correspond to 40.5, 15.5, and 8.5 polymer repeat units, respectively) and urethanepropyltriethoxysilane [d-UtPTES(Y'), where Y' = 2000 and 300 represents the average molecular weight of the PEG, and corresponds to approximately 45 and 6 oxyethylene repeat units]. In the second stage of the synthesis, the addition of a mixture of  $H_2O$



**Scheme 9.** Molecular structure of the di-ureasils.



**Scheme 10.** Molecular structure of the di-urethanesils.

and  $\text{CH}_3\text{CH}_2\text{OH}$  to the d-UPTES and d-UtPTES solutions (Schemes 9 and 10) promotes the hydrolysis and condensation reactions transforming the precursor into the final xerogels. Europium, gadolinium, neodymium, and erbium trifluoromethanesulphonates ( $\text{Eu}(\text{CF}_3\text{SO}_3)_3$ ,  $\text{Gd}(\text{CF}_3\text{SO}_3)_3$ ,  $\text{Nd}(\text{CF}_3\text{SO}_3)_3$ , and  $\text{Er}(\text{CF}_3\text{SO}_3)_3$ , respectively) were incorporated in this step, by dissolving them in the  $\text{H}_2\text{O}$  and  $\text{CH}_3\text{CH}_2\text{OH}$  mixture (molar ratio  $\text{ICPTES}:\text{CH}_3\text{CH}_2\text{OH}:\text{H}_2\text{O} = 1:4:1.5$ ). The nanohybrids were identified by the designation d-U( $Y$ ) $_n\text{Ln}(\text{CF}_3\text{SO}_3)_3$ —di-ureasils—and d-Ut( $Y'$ ) $_n\text{Ln}(\text{CF}_3\text{SO}_3)_3$ —di-urethanesils, where U and Ut denote the urea and urethane groups, Ln stands for Eu, Gd, Nd, or Er, and  $Y' = 300$  and  $2000 \text{ g}\cdot\text{mol}^{-1}$ , corresponding to 45 and 6  $\text{OCH}_2\text{CH}_2$  repeat units) and  $n = [\text{O}]/[\text{Eu}]$ , so-called composition, represents the number of ether-type oxygen atoms of poly(oxyethylene) (POE) per  $\text{Ln}^{3+}$  cation.  $\text{U}(600)_n\text{Ln}(\text{CF}_3\text{SO}_3)_3$  and  $\text{U}(2000)_n\text{Ln}(\text{CF}_3\text{SO}_3)_3$  ( $\text{Ln} = \text{Eu}, \text{Nd}, \text{Er}$ ) were synthesized with compositions  $20 \leq n \leq 400$ , which correspond to a variation of the  $\text{Ln}^{3+}$  content versus the total mass between 4.96 and 0.58%. Two  $\text{U}(Y)_{80}\text{Gd}(\text{CF}_3\text{SO}_3)_3$ ,  $Y = 2000$  and  $600$ , di-ureasils were also prepared.

Ribeiro et al. [177] proposed a slightly different synthetic procedure to obtain the di-ureasils. These authors prepared the molecular precursor through the stoichiometric reaction of ICPTES and O,O'-bis(2-aminopropyl)polyethylene glycol with an average molecular weight of approximately  $800 \text{ g}\cdot\text{mol}^{-1}$ . THF was used as a solvent, and the reaction was carried out under reflux at  $80^\circ\text{C}$  for 6 h. The hybrid precursor was isolated after evaporation of the THF, and ammonium fluoride ( $\text{NH}_4\text{F}$ ) dissolved in  $\text{CH}_3\text{CH}_2\text{OH}$  was added, to work as catalyst for the hydrolysis reaction of the precursor (molar ratio  $\text{NH}_4\text{F}/\text{Si} = 0.005$ ). A volume of 0.2 mL of an aqueous solution of  $\text{Eu}(\text{ClO}_4)_3$  was then added by stirring, allowing the formation of a clear monolithic wet gel in 4 h.  $\text{CH}_3\text{CH}_2\text{OH}$  and  $\text{H}_2\text{O}$  were removed at  $50^\circ\text{C}$  to yield a rubbery and good optical quality transparent body. Samples with  $n = 4, 8, 15, 100$ , and  $355$  were prepared.

The first stage of the preparation of the  $\text{Tb}^{3+}$ -doped urea cross-linked xerogels proposed by Bekiari et al. [185] involved mixing stoichiometric amounts of ICPTES and O,O'-bis(2-aminopropyl)polyethylene glycol with an average molecular weight of approximately  $800 \text{ g}\cdot\text{mol}^{-1}$ . The solution was stirred in refluxing THF for 6 h. The THF was evaporated to yield the hybrid precursor. The second stage

of the synthesis of the polyether-based xerogels implied the addition of  $\text{H}_2\text{O}$  and a catalyst ( $\text{NH}_4\text{F}$ ) (molar ratio  $\text{H}_2\text{O}:\text{NH}_4\text{F}:\text{Si} = 5:0.01:1$ ). The condensation of the silicon atoms led to the formation of a rubbery material within 8 h. The incorporation of the  $\text{Tb}^{3+}$  ions was achieved through the introduction of the latter material in a 20 mM  $\text{CH}_3\text{CH}_2\text{OH}$  solution of terbium nitrate,  $\text{Tb}(\text{NO}_3)_3$ . This procedure lasted a week. The terbium-enriched sample was then immersed in a  $\text{CH}_3\text{CH}_2\text{OH}$  solution of 0.1 M bpy for two days.

In another work, Bekiari et al. [186] synthesized a series of POE- and poly(oxypropylene) (POP)-based hybrid materials, and doped them with europium, terbium, neodymium, and cerium nitrates. The precursors were obtained by reacting the O,O'-bis(2-aminopropyl)polypropylene glycol (molecular weights, MW, equal to 4000, 2000, and 230) and O,O'-bis(2-aminopropyl)polyethylene glycol (MW = 1900, 800, and 500) with ICPTES in THF under reflux ( $64^\circ\text{C}$ ) for 6 h. Urea-connecting groups were thus formed. After evaporation of the THF under vacuum, a viscous hybrid precursor resulted. The chemical structure of the POE- and POP-containing precursors is illustrated in Scheme 9. The sol-gel stage involved dissolution of 4.5 g of the hybrid precursor in 15 mL of  $\text{CH}_3\text{OH}$ . The solution was stirred for 5 mn, and 0.5 mL HCl was then added. An additional stirring period of 30 mn followed. In the case of the weak-base catalyzed hydrolysis, 0.04 M  $\text{NH}_4\text{F}$  was used instead of HCl. After stirring, the sols were poured into uncovered PMMA cuvettes, and were allowed to dry in air for one week. The dopant salts were introduced by previous solubilization in  $\text{CH}_3\text{OH}$ .

Moleski et al. [187] synthesized a series of sol-gel-derived hybrid matrices incorporating organolanthanide complexes. The hybrid frameworks were obtained by mixing O,O'-bis(2-aminopropyl)polypropylene glycol (MW = 4000) in ICPTES (molar ratio 1:2) in THF under reflux ( $64^\circ\text{C}$ ) for 6 h. The reaction that took place involved the isocyanate groups of the organoalkoxysilane and the amino groups of the diamine producing urea-connecting groups between the polymer units and the inorganic part. After evaporation of the THF under vacuum, a viscous precursor, which was stable for several months, was obtained (Scheme 9). The sol-gel step was performed using the acetic acid solvolysis method that is carried out in the absence of  $\text{H}_2\text{O}$ . 0.5 g of the nonhydrolyzed hybrid precursor was first dissolved in 2 mL of  $\text{CH}_3\text{CH}_2\text{OH}$ . Acetic acid (0.4 mL) was then added to this solution under stirring. After 1/2 h, the latter solution became a gel. In the case of the synthesis of the doped materials, 20 mM of europium nitrate, 60 mM of TTA, and 20 mM of bpy were added in this order to the precursor ethanolic solution. The films were obtained by spin coating the sol on glass slides at 4000 rpm.

The  $\text{Eu}^{3+}$ -based hybrids proposed by Li et al. [188] were prepared by first synthesizing pure, crystalline  $[\text{Eu}(\text{phen})_2]\text{Cl}_3$ . An appropriate amount of this complex was dissolved in DMF and added to a mixed solution of  $\text{H}_2\text{O}$ ,  $\text{CH}_3\text{CH}_2\text{OH}$ , TEOS, and 3-(trimethoxysilyl)propyl methacrylate, TMSPM (molar ratio  $[\text{Eu}(\text{phen})_2]\text{Cl}_3:\text{H}_2\text{O}:\text{CH}_3\text{CH}_2\text{OH}:\text{TMSPM} = 12:12:3:1$ ). Dilute HCl at pH = 1 was then added to this mixture. The solution was stirred for two days, and then coated on the substrate by means of the

spin-coating process. The substrate was placed on a spin-coating machine and spun at 1000–3000 rev/min. The coated film was treated at different temperatures. The resulting dried xerogel was kept in a Petri dish at room temperature.

The synthesis of hybrid composite phosphors doped with terbium carboxyl complexes *in-situ* by the sol–gel route was reported by Li et al. [189]. Carboxyl was first dissolved in a mixture of absolute  $\text{CH}_3\text{CH}_2\text{OH}$  and DMF under stirring. TEOS, TMPSPM, and a certain amount of  $\text{Tb}(\text{NO}_3)_3$ . Carboxyl acids [benzoic acid (BA), *o*-aminobenzoic acid (*o*-ABA), *m*-aminobenzoic acid (*m*-ABA), and *p*-aminobenzoic acid (*p*-ABA)] (molar ratio 1:3) were added to the above mixture. HCl-acidified  $\text{H}_2\text{O}$  (pH = 2) was also added to the resulting solution to foster the hydrolysis and condensation reactions of the TEOS and TMPSPM precursors. The molar ratio TEOS:TMPSPM: $\text{CH}_3\text{CH}_2\text{OH}$ : $\text{H}_2\text{O}$  was 3:1:12:12. The solution was stirred at room temperature for several hours, and the resulting transparent sols were subsequently cast into plastic cups and cured at 50 °C for a month to accomplish their gelation. Additional heat treatments were carried out at various temperatures (100–200 °C) in air.

### 3. LOCAL STRUCTURE

The local structure of RE-based organic–inorganic hybrids has been intensively analyzed using different techniques, such as X-ray diffraction (XRD), SAXS, extended X-ray absorption fine structure (EXAFS),  $^{29}\text{Si}$  and  $^{13}\text{C}$  magic-angle spinning nuclear magnetic resonance ( $^{29}\text{Si}$  and  $^{13}\text{C}$  MAS NMR), and Fourier transform infrared (FTIR) measurements.

To illustrate the work performed for the characterization of the local structure of lanthanide-based Class I hybrids, we will refer to SAXS results of the  $\text{Eu}^{3+}$ -containing siloxane/PEG composites prepared by Molina et al. [150]. These data show that the nanocomposites with a low  $\text{Eu}^{3+}$  content consist of a mixture of siloxane aggregates with a fractal structure embedded in a nearly homogeneous PEG matrix. Increasing the amount of incorporated  $\text{Eu}^{3+}$  leads to a decrease in the interparticle repulsion interactions and the subsequent formation of larger aggregates. An additional aggregation process promoting the formation of very large secondary aggregates is observed for highly concentrated hybrids. The structural changes deduced from SAXS are in accordance with the observed increase in mechanical strength and glass transition temperature for increasing  $\text{Eu}^{3+}$  content [150].

In the case of the Class II materials reviewed here in which an organic molecule that complexes RE ions is anchored in the hybrid framework [153–159], a very small fraction of work was devoted to the detailed characterization of their local structure. In the next paragraphs, we will briefly refer to some structural results concerning this class of hybrids.

Apart from the typical bands due to the organic component, the FTIR spectra of the RE-activated organic–inorganic hybrid precursors prepared by Franville et al. [153–155] exhibit the characteristic absorption bands of the trialkoxysilyl groups, that is, those arising from the stretching vibration of the Si–C, Si–OEt (or Si–OMe)

groups. The sharp band situated at 1680–1640  $\text{cm}^{-1}$  confirmed the formation of the amide groups. The absence of the bands due to carboxylic acid chloride and carboxylic functions in the 1760–1720  $\text{cm}^{-1}$  range was considered as clear evidence of the completion of the reaction. The FTIR spectra of the corresponding hybrid xerogels were characterized by a band located between 1193 and 1188  $\text{cm}^{-1}$  due to the Si–C stretching vibration, a proof that the Si–C bonds remained intact during the hydrolysis/condensation reactions. The formation of the siloxane bonds was confirmed by the occurrence of a broad band around 1120–1000  $\text{cm}^{-1}$ . The presence of residual silanol groups was indicated by the band found at about 900  $\text{cm}^{-1}$ , demonstrating that the condensation process had not been complete. The complexation of the metal ions by the oxygen atoms of the carbonyl groups was accompanied by a shift of the C=O stretching band to lower wavenumbers. Some of these hybrids [155] were examined by means of  $^{13}\text{C}$  and  $^{29}\text{Si}$  CPMAS NMR spectroscopies. The  $^{13}\text{C}$  CPMAS NMR spectra displayed peaks located near 43, 23, and 11 ppm, which were associated with the  $\text{CH}_2$  aliphatic chains. The signal due to the C=O groups was clearly evidenced at 164 ppm, whereas the remaining signals in the spectra were ascribed to the aromatic carbons. The absence of new signals in the  $^{13}\text{C}$  CPMAS NMR spectra with respect to those of the hybrid precursor was considered as a solid piece of evidence that proves that the organic component was not modified under the conditions used for the sol–gel process. The broad signal found between –80 and –40 ppm in the  $^{29}\text{Si}$  CPMAS NMR spectra was attributed to trifunctional– $\text{CSiO}_3$  groups [155]. No indications of the presence of tetrafunctional groups were found, proving that the organic moieties remained covalently attached to the siloxane network via Si–C bonds. The silicon sites are labeled according to the conventional  $T_n$  notation, where  $n$  ( $n = 1, 2, 3$ ) is the number of Si-bridging oxygen atoms. Peaks due to  $T_1$ ,  $T_2$ , and  $T_3$  sites could be distinguished. The relative proportions of the different silicon species and the condensation rates were calculated. These data supported that the main species were the  $T_2$  ones, and that the condensation rates ranged from 75 to 80%.

Infrared spectroscopy allowed Dong et al. [156] to conclude that the bands occurring at 1774, 1718, 1370, and 730  $\text{cm}^{-1}$  in the spectrum of the TAT hybrid precursor (Scheme 4) could be assigned to the symmetric carbonyl stretching, asymmetric carbonyl stretching, C–N stretching, and ring carbonyl deformation vibrations, respectively. It was noted that the spectrum of the lanthanide-doped xerogel was different, as the characteristic carboxylic band around 2700–2300  $\text{cm}^{-1}$  disappeared, whereas several new features appeared at 1652 and 1385  $\text{cm}^{-1}$ , assigned to the asymmetric and symmetric stretching vibrations of the  $\text{COO}^-$  group, respectively. According to the authors, the latter findings indicate the formation of coordinated bonds between the carboxylic groups and the lanthanide ion. The proposed local structure is depicted in Scheme 4.

The phosphine oxide-based complexes proposed by Embert et al. [157] were characterized by  $^{13}\text{C}$  and  $^{29}\text{Si}$  and  $^{31}\text{P}$  CPMAS NMR spectroscopy. The resulting data allowed these authors to conclude the following.

1. While about 81% of the P=O groups remained complexed in the hybrids originating from ligands 3 and 4,

in the case of the xerogels obtained from the more flexible ligand 5, approximately 91% of the P=O moieties were found to be complexed.

2. The absence of signals in the  $^{29}\text{Si}$  CPMAS NMR spectra between  $-90$  and  $-110$  ppm was interpreted as an indication that the Si–C bonds were not cleaved during the sol–gel process.
3. No evidences of the presence of remaining ethoxy or isopropoxy groups were detected in the  $^{13}\text{C}$  CPMAS NMR spectra, suggesting the complete hydrolysis of the compounds.

The Raman spectra of the materials incorporating europium nitrate provided conclusive evidence that the contact ion pairs  $\text{Eu}^{3+}\text{NO}_3^-$  observed in the salt, which gave rise to the band situated at  $1037.5\text{ cm}^{-1}$ , persisted in the xerogels. The absence of the  $1047.4\text{ cm}^{-1}$  feature was correlated with the absence of hydrogen bonding between the nitrate ions and either water molecules or OH vibrators. The presence in the infrared spectra of the sol–gel-derived compounds of the  $741$  and  $815\text{ cm}^{-1}$  events were considered as additional proofs of the formation of contact ion pairs and the absence of hydrogen bonding around the anions.

Li et al. [158] used infrared spectroscopy to monitor the grafting reaction that yielded the Phen–Si compound. The growth of the bands located at  $1653$  and  $1645\text{ cm}^{-1}$  was attributed to the formation of the  $-\text{CONH}-$  amide group. Other spectral changes observed in the spectrum of the Hybrid I material were correlated with the hydrolysis/condensation of TEOS and Phen–Si, and with the formation of a complex between the latter compound and the  $\text{Eu}^{3+}$  ions. The presence of the organic groups in Hybrid I was further confirmed by means of  $^{13}\text{C}$  CPMAS NMR spectroscopy [158]. Peaks detected at  $43$ ,  $26$ , and  $13$  ppm were ascribed to the  $(\text{CH}_2)$ -based chains, whereas the signals seen between  $110$  and  $150$  ppm were ascribed to aromatic carbons, and the characteristic peak of the carbonyl group was found at  $161$  ppm [158]. The local structure of Hybrid I was also investigated by photoluminescence spectroscopy. The details of such a study will be reviewed in Section 4.1.

The local structure of RE-doped di-ureasils and di-urethanesils was described using XRD [162, 163, 165], SAXS [178, 179, 181–183], EXAFS [166, 180, 184], and FTIR [164, 165, 171, 181] results. The SAXS technique is particularly adequate for studying the structure of hybrid materials because of their disordered nature and the contrast of electronic densities between the organic and inorganic phases [178, 179, 181–183, 197]. The XRD patterns of the di-ureasils and di-urethanesils present a broad band, Gaussian in shape, centered around  $20$ – $22^\circ$ , and associated with the amorphous siliceous domains [165]. The polymer chains are, essentially, in a disordered regime for all of the hybrids, except in the RE-based high-molecular-weight di-ureasils and di-urethanesils (i.e.,  $\text{U}(2000)$  and  $\text{Ut}(2000)$ , respectively). In the latter case, the XRD diffractograms revealed the presence of well-defined Bragg peaks associated with the diffraction of crystalline oxyethylene units,  $\text{OCH}_2\text{CH}_2$  [163, 165]. In low-salt concentration hybrids (e.g.,  $80 \leq n \leq 400$ ), the two main peaks characteristic of the crystalline polyether chains are clearly observed at  $19.15$ – $19.3^\circ$  and  $23.45$ – $23.50^\circ$  [165]. This indicates that the incorporation of the europium

salt does not destroy the crystalline order of the polyether chains. Moreover, it strongly suggests that the  $\text{Eu}^{3+}$  ions are not coordinated to the ether oxygens of the short polyether chains present in the materials, contradicting what has been observed for analogous POE-based electrolytes. This is consistent with the thermal analysis, particularly with the differential scanning calorimetry (DSC) results discussed elsewhere [165], and is explicitly confirmed by SAXS, FTIR, and PL results [181]. For the high-molecular-weight di-ureasils and di-urethanesils, the oxyethylene moieties merely play the role of plastifying agents.

The SAXS data of  $\text{Eu}^{3+}$ -doped di-ureasils and di-urethanesils were modeled with an isotropic structure model consisting of a dense set of spherical colloidal particles of approximately the same size with short-range spatial correlation—the siloxane domains—embedded in a homogeneous matrix—the polymer chains [181–183]. A similar multiple-scale structure model based on identical spherical particles embedded in a homogeneous matrix has been successfully applied by Beaucage et al. to experimental SAXS data of similar siloxane–polymer nanocomposites [197]. The results indicate the formation of a two-level hierarchical local structure in which the primary level is constituted by strongly spatially correlated siloxane nanodomains of radius between  $3$  and  $10\text{ \AA}$ , and errors within  $5\%$ . Large clusters of these regions, with a radius between  $80$  and  $100\text{ \AA}$  (errors within  $10\%$ ), form the second level [181].

The nature of the  $\text{Eu}^{3+}$ -first coordination shell varies with the salt concentration and with the polymer molecular weight. In di-ureasils containing long organic segments,  $\text{U}(2000)_n\text{Eu}(\text{CF}_3\text{SO}_3)_3$  ( $40 \leq n \leq 400$ ), the  $\text{Eu}^{3+}$  ions interact mainly with the carbonyl-type oxygens of the urea cross links located at the organic–inorganic interface. On the contrary, in  $\text{U}(600)_n\text{Eu}(\text{CF}_3\text{SO}_3)_3$  ( $n \geq 60$ ), as the  $\text{Eu}^{3+}$  ions are unable to disrupt the strong and ordered hydrogen-bonded urea–urea structures [198], the preferential coordination sites are the ether-type oxygens of the polymer chains. However, for high-salt concentration hybrids,  $n \leq 40$ , besides the coordination to the polymer ether oxygens, a distinct cation local site environment involving the interaction with the urea carbonyl oxygens atoms at the siloxane–POE interface is detected. At  $n = 10$ , the hydrogen-bonded urea–urea structures of the  $\text{U}(600)$  network are probably destroyed by the larger amount of salt present, and therefore, the carbonyl oxygens of the urea cross links are the only active coordinating groups. We must stress that, in these hybrids, only at compositions lower than approximately  $4$ , there is one urea group per each incorporated  $\text{Eu}^{3+}$  ion. This ability to tune the  $\text{Eu}^{3+}$  coordination between the carbonyl oxygens of the urea groups and the ether oxygen atoms of the poly(oxyethylene) chains—controlling both the salt concentration and the polymer molecular weight—illustrates one of the most interesting features of these materials, and opens new prospects into their potential fields of application.

The first  $\text{Eu}^{3+}$  coordination shell was further characterized by fitting filtered EXAFS spectra, using phase and amplitude functions obtained from the standard  $\text{Eu}_2\text{O}_3$  spectrum [166]. Good fits were obtained for all samples. The EXAFS results suggested a decrease in the coordination number with the increase in the relative  $\text{Eu}^{3+}$  concentration, from  $13 \pm 1$  ( $n = 200$ ) to  $10 \pm 1$  ( $n = 40$ ). The average Eu–O

distance remains constant, 2.48 Å, in the salt concentration range investigated, and the decrease of the Debye–Waller disorder factor in that range indicates the tendency of the dispersion of the Eu–O distances to decrease [166].

The FTIR spectra of the Eu<sup>3+</sup>-doped di-ureasils with  $n \geq 5$  were examined in detail to determine the nature of the species involved in the coordination of the lanthanide ions [165]. Several features observed in the spectrum of the U(2000)<sub>5</sub>Eu(CF<sub>3</sub>SO<sub>3</sub>)<sub>3</sub> compound clearly demonstrated the coordination between the ether oxygens of the polyether segments of the hybrid matrix and the lanthanide ions, and substantiated the formation of a crystalline complex. One of the most significant spectral evidences of this complexation effect was the absence of the strong band attributed to the CO stretching vibration of noncoordinated polyether chains from the spectrum of U(2000)<sub>5</sub>Eu(CF<sub>3</sub>SO<sub>3</sub>)<sub>3</sub>. This band, found at 1110 cm<sup>-1</sup> in the spectrum of U(2000)<sub>20</sub>Eu(CF<sub>3</sub>SO<sub>3</sub>)<sub>3</sub>, was replaced by a strong band at 1056 cm<sup>-1</sup> and a shoulder at 1069 cm<sup>-1</sup>. The downshift observed was associated with a change in the environment of the ether oxygens, probably produced by the coordination to metal ions. No evidences of changes in the environment of the ether oxygens, which would result from the dissolution of Eu(CF<sub>3</sub>SO<sub>3</sub>)<sub>3</sub>, were, however, found in the spectra of a series of doped di-ureasils with  $n \geq 20$  [164, 165]. These findings were interpreted as clear proof that all of the ether oxygens were coordinated to the Eu<sup>3+</sup> ions at  $n = 5$ . The spectra of the di-ureasils also exhibited dramatic differences in the 1000–800 cm<sup>-1</sup> spectral region, which includes absorption bands produced by a mixture of skeletal stretching and CH<sub>2</sub> rocking vibrational modes, and is known to be extremely sensitive to coordination effects arising from interactions between ether oxygens of the polyether chains and metal cations. While the dominating features in the spectrum of U(2000)<sub>20</sub>Eu(CF<sub>3</sub>SO<sub>3</sub>)<sub>3</sub> were a medium intensity band located at 954 cm<sup>-1</sup>, due to the coupled vibration of CC stretching and CH<sub>2</sub> rocking modes, and a weak band found at 846 cm<sup>-1</sup>, attributed to the coupled vibration of CO stretching and CH<sub>2</sub> rocking modes, in the spectrum of U(2000)<sub>5</sub>Eu(CF<sub>3</sub>SO<sub>3</sub>)<sub>3</sub>, the strongest band detected was a weak new absorption situated at 937 cm<sup>-1</sup>. Another new band, also weak, was observed at 892 cm<sup>-1</sup> in the latter spectrum. This pair of bands was associated with the presence of a crystalline complex. Another relevant result was retrieved from the analysis of the spectral region due to the symmetric deformation of the CF<sub>3</sub> group [ $\delta_s(\text{CF}_3)$ ], which allows us to evaluate the extent of ionic association in systems doped with triflate salts. In the spectrum of U(2000)<sub>20</sub>Eu(CF<sub>3</sub>SO<sub>3</sub>)<sub>3</sub>, a very weak band at 755 cm<sup>-1</sup> and an even weaker shoulder at about 763 cm<sup>-1</sup> were observed in this range of wavenumbers, whereas that of U(2000)<sub>5</sub>Eu(CF<sub>3</sub>SO<sub>3</sub>)<sub>3</sub> displayed three bands: (1) the shoulder at 763 cm<sup>-1</sup> grew in intensity, and became the dominating feature of this spectral region; (2) the intensity of the absorption at 755 cm<sup>-1</sup> was drastically reduced, and the band was transformed into an almost insignificant shoulder located at 757 cm<sup>-1</sup>; (3) an additional shoulder, stronger than the latter one, appeared at 774 cm<sup>-1</sup>. The band at 764 cm<sup>-1</sup> and the shoulder at 774 cm<sup>-1</sup> were assigned to the presence of the crystalline complex. The ordered local structure of U(2000)<sub>5</sub>Eu(CF<sub>3</sub>SO<sub>3</sub>)<sub>3</sub> was further confirmed

by the breadth of its characteristic absorption bands which were markedly narrower than those of the spectrum of U(2000)<sub>5</sub>Eu(CF<sub>3</sub>SO<sub>3</sub>)<sub>3</sub>, a fact that confirmed the crystalline character of the di-ureasil with  $n = 5$ .

The local structure of the di-ureasils doped with Eu(ClO<sub>4</sub>)<sub>3</sub> reported by Ribeiro et al. has been described in detail combining SAXS, EXAFS, thermomechanical analysis (TMA), and PL [177, 180]. The experimental SAXS curves show a single peak attributed to an interference effect in the X-ray scattering amplitude produced by the existence of a spatial correlation between siloxane clusters to which polymer chain ends are grafted [180]. The average radius of the siloxane nanodomains and the average distance between them, 4–5 and 25–27 Å, respectively, are similar to the values found for the di-ureasils doped with Eu(CF<sub>3</sub>SO<sub>3</sub>)<sub>3</sub>. The slight decrease in the siloxane intercluster spacing for increasing Eu<sup>3+</sup> content is interpreted as a contraction of the polymer structure due to the increase in the number of O–Eu<sup>3+</sup>–O cross linkages between polymeric chains induced by the Eu<sup>3+</sup> coordination to the PEO ether-type oxygens. This interpretation was confirmed by TMA measurements [180] and FTIR results [171]. The glass transition temperature of the samples increases for increasing europium doping level, in accordance with the already mentioned interaction between the Eu<sup>3+</sup> ions and the polymer ether-type oxygens [180]. The first coordination shell of Eu<sup>3+</sup> was further characterized by fitting filtered EXAFS spectra (recorded at the XAFS beamline at LNLS, Campinas, S.P., Brazil) using phase and amplitude functions obtained from a standard solution (Eu<sup>3+</sup> 0.2 M aqueous solution) [180]. The results indicate a decrease in the coordination number at increasing Eu<sup>3+</sup> concentration, from 10 ± 1 ( $n = 80$ ) to 8 ± 1 ( $n = 8$ ). Furthermore, in this salt concentration range, the Eu–O average distance and the Debye–Waller disorder factor remain approximately constant, 2.41–2.42 Å and 0.090–0.093, respectively. All of these results are in accordance with the those obtained for similar hybrids incorporating Eu(CF<sub>3</sub>SO<sub>3</sub>)<sub>3</sub> [166].

The local environment of the Eu<sup>3+</sup> ions in the luminescent sol–gel-derived materials proposed by Ribeiro et al. [177] was studied in depth by FTIR and PL spectroscopies. The combination of the information retrieved from the analysis of characteristic bands of the FTIR spectra—the perchlorate and the Amide I/Amide II features—with that obtained from the PL data demonstrated that, at compositions  $n = 232$  and 62, the anions are free, whereas the Eu<sup>3+</sup> ions were complexed by the heteroatoms of the polyether chains. At higher salt concentration, the cations are coordinated, not only to the perchlorate ions, but also to the ether oxygen atoms of the organic segments and to the carbonyl oxygen atoms of the urea linkages. The dual behavior of the hybrid matrix with respect to cation coordination was attributed to the presence in this nanohybrid of strong hydrogen-bonded urea–urea structures which, at low salt content, cannot be disrupted, thus inhibiting the formation of Eu<sup>3+</sup>⋯O=C(urea) contacts, and promoting the interaction between the lanthanide ions and the (OCH<sub>2</sub>CH<sub>2</sub>) moieties. This Eu<sup>3+</sup> local coordination is entirely in accordance with the results aforementioned for the same matrix, U(600), incorporated Eu(CF<sub>3</sub>SO<sub>3</sub>)<sub>3</sub> in a concentration  $n \geq 60$ . These studies enabled the authors to



conclude that the activation of the coordinating sites of the hybrid di-ureasil-type framework can be tuned by varying either the guest salt concentration at constant chain length or the length of the organic segments at constant salt concentration, an extremely relevant property that opens challenging new prospects into the fields of application of this class of hybrids.

Liu et al. [160] recorded the FTIR spectra of the  $\text{Tb}^{3+}$ -containing and nondoped DPS-derived films. The presence of the bands associated with the stretching modes of the Si–C and Si–OEt groups, located at 1194 and 1080  $\text{cm}^{-1}$ , respectively, in the spectrum of DPS led these authors to the conclusion that the Si–C bonds and the ethoxy (OEt) groups had not been affected by the grafting reaction performed between ICPTES and the diamine used. The features observed at 1682, 1652, and 1562  $\text{cm}^{-1}$ , produced by the urea cross links, were interpreted as a confirmation of the success of the grafting process. In the spectra of the  $\text{Tb}^{3+}$ -based hybrids, Liu et al. [160] observed a significant downshift (20  $\text{cm}^{-1}$ ) of the carbonyl stretching band upon doping.

The bands found at 1652, 1565, and 1592  $\text{cm}^{-1}$  in the FTIR spectrum of the nondoped PABI hybrid introduced by Liu et al. [161] allowed these authors to conclude that ICPTES had been successfully grafted to p-aminobenzoic acid. The feature observed at 1689  $\text{cm}^{-1}$  was assigned to the stretching mode ( $\nu\text{C}=\text{O}$ ) of the carboxylic acid function. The events discerned around 1193 and 1080  $\text{cm}^{-1}$  were attributed to the stretching vibration of the Si–C and Si– $\text{OCH}_2\text{CH}_3$  moieties, respectively. In the spectra of the corresponding  $\text{Tb}^{3+}$ -doped materials, it was observed that, while the  $\nu\text{C}=\text{O}$  mode of the carboxylic function had disappeared, new bands associated with the asymmetric and symmetric stretching modes of the  $\text{COO}^-$  species emerged at 1556 and 1417  $\text{cm}^{-1}$ , respectively. These findings were interpreted as proof of the interaction between the  $\text{Tb}^{3+}$  ion and the carboxylic group.

## 4. PHOTOLUMINESCENCE SPECTROSCOPY

### 4.1. Emission and Time-Resolved Spectra

Figure 1A shows the RT emission spectra obtained for the di-ureasils  $\text{U}(\text{Y})_{40}\text{Eu}(\text{CF}_3\text{SO}_3)_3$ ,  $\text{Y} = 600$  and 2000. Both spectra are composed of the  $\text{Eu}^{3+}$  characteristic intra- $4f^6$  transitions,  $^5\text{D}_0 \rightarrow ^7\text{F}_{0-4}$ , overlaying a large broad between 350 and 580 nm [162–164, 166, 168, 170, 171, 173, 174, 176, 177, 181]. This large broad band is red shifted toward the greenish–blue spectral region relative to that observed in the undoped di-ureasils, Section 9, and was assigned to the convolution of donor–acceptor pair recombinations occurring in the siliceous nanodomains and in the NH groups of the urea linkages [191, 193–196]. The PL spectra of the remaining di-ureasils resemble those presented in Figure 1A.

Ribeiro et al. also reported a similar result for a set of short polymer chain di-ureasil hybrids modified by  $\text{Eu}(\text{ClO}_4)_3$ , as shown in Figure 2A [177].

Bekiarı et al. recorded the luminescence spectra of a U(600) type di-ureasil modified by  $\text{Tb}^{3+}$  ions in an ethanolic solution (see curve 1 in Fig. 3), where a large broad band in

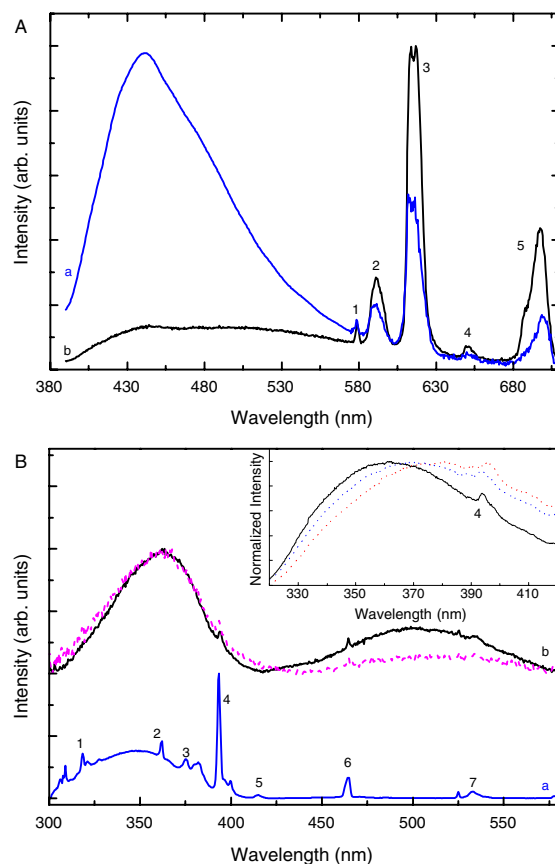


**Figure 1.** (A) RT PL spectra excited at 375 nm for  $\text{U}(\text{Y})_{40}\text{Eu}(\text{CF}_3\text{SO}_3)_3$ , (a)  $\text{Y} = 600$  and (b)  $\text{Y} = 2000$ . (1), (2), (3), (4), and (5) denote the intra- $4f^6$  transitions:  $^5\text{D}_0 \rightarrow ^7\text{F}_{0-4}$ , respectively. (B) RT PLE spectra for the  $\text{U}(\text{Y})_{80}\text{Eu}(\text{CF}_3\text{SO}_3)_3$ , (a)  $\text{Y} = 600$  and (b)  $\text{Y} = 2000$ , monitored around 614 nm. The dashed spectra correspond to the RT PLE spectrum of the  $\text{U}(2000)_{80}\text{Eu}(\text{CF}_3\text{SO}_3)_3$  di-ureasil detected around 700 nm. (1), (2), (3), (4), (5), (6), and (7) denote the intra- $4f^6$  transitions:  $^7\text{F}_0 \rightarrow ^5\text{H}_4$ ,  $^5\text{D}_4$ ,  $^5\text{G}_1$ ,  $^5\text{L}_6$ ,  $^5\text{D}_3$ ,  $^5\text{D}_2$ , and  $^5\text{D}_1$ , respectively. The inset shows the 14 K PLE spectra of the  $\text{U}(2000)_n\text{Eu}(\text{CF}_3\text{SO}_3)_3$ , solid line  $n = 40$ , dashed line  $n = 60$ , and dotted line  $n = 80$ .

the same spectral region (350–380 nm) is observed together with a series of intra- $4f^8$   $\text{Tb}^{3+}$  lines assigned to the transitions  $^5\text{D}_4 \rightarrow ^7\text{F}_{6-3}$  [185].

Time-resolved measurements performed on the di-ureasils modified by  $\text{Eu}(\text{CF}_3\text{SO}_3)_3$  unequivocally demonstrated that the large broad band results from the overlap of two distinct emissions whose recombination mechanisms occur in unlike time scales, as previously reported for the undoped hosts [194, 195]. Figure 4A presents the time-resolved spectra for  $\text{U}(2000)_{80}\text{Eu}(\text{CF}_3\text{SO}_3)_3$  and  $\text{U}(600)_{200}\text{Eu}(\text{CF}_3\text{SO}_3)_3$  nanohybrids detected at a start delay (SD) time of 0.08 ms, clearly establishing the presence of two emission bands. Increasing the SD, only one band remains (inset of Fig. 4A). The respective lifetimes, measured at 14 K, although smaller than the ones measured for the undoped hosts [194, 195], are of the same magnitude, being around 100 and 1 ms (errors within 5%) for the lower and higher energy bands, respectively [181]. Besides the different recombination time scales, these two emission components also behave differently when the excitation wavelength

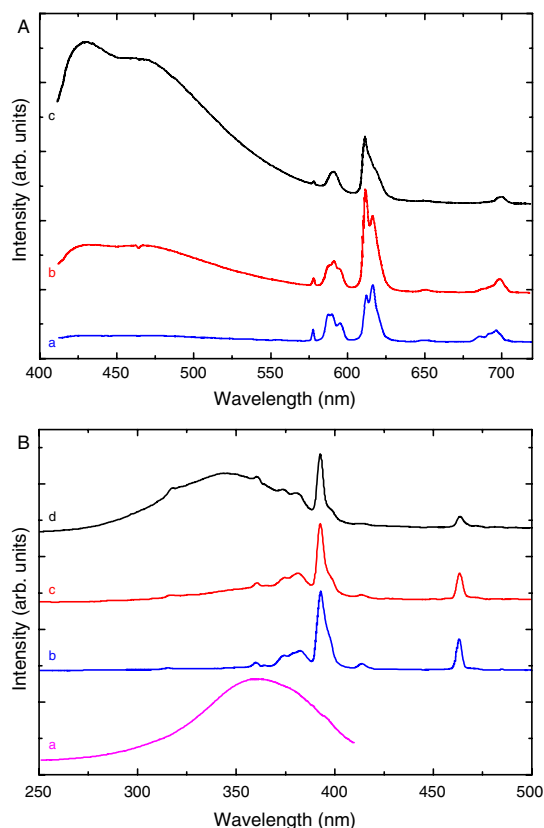


**Figure 2.** (A) RT PL spectra obtained under 394 nm for the  $U(600)_n \cdot Eu(CF_3SO_3)_3$ , (a)  $n = 4$ , (b)  $n = 15$ , and (c)  $n = 100$ . (B) RT PLE spectra for the  $U(600)_n Eu(ClO_4)_3$ . (a)  $n = 100$ , monitored around 430 nm, (b)  $n = 4$ , (c)  $n = 15$ , and (d)  $n = 100$ , monitored around 611 nm. Reprinted with permission from [177], S. J. L. Ribeiro et al., *J. Sol-Gel Sci. Technol.* 13, 427 (1998). © 1998, Kluwer Academic.

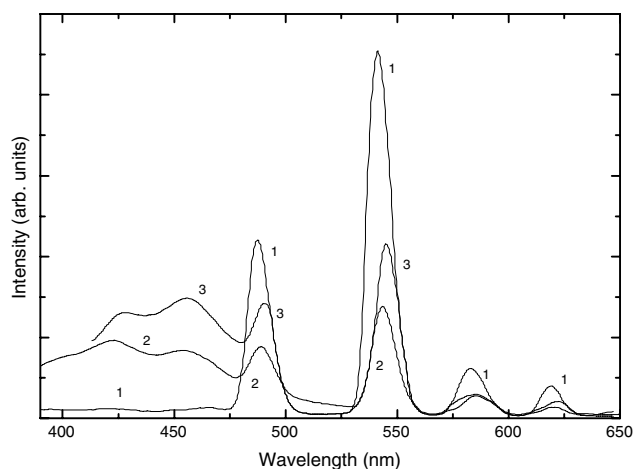


**Figure 3.** RT PL spectra: (1)  $Tb^{3+}$  and 2,2-byp absorbed by a silica/POE hybrid gel from ethanolic solutions obtained under 318 nm; (2) same sample under 365 nm excitation; and (3) a similar sample without 2,2-bipyridine under 365 nm. Reprinted with permission from [185], V. Bekiari et al., *Chem. Phys. Lett.* 307, 310 (1999). © 1999, Elsevier Science.

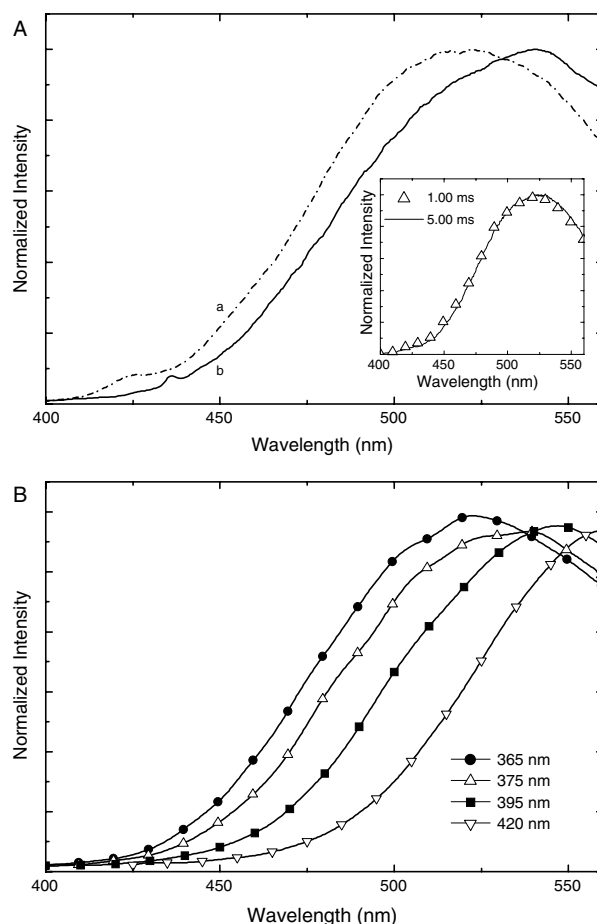


**Figure 4.** 14 K time-resolved emission spectra obtained at delay times of (A) 0.08 ms for (a)  $U(600)_{200}Eu(CF_3SO_3)_3$  and (b)  $U(2000)_{80}Eu(CF_3SO_3)_3$ , excited at 365 and 375 nm, respectively; (B) 0.08 ms for  $U(2000)_{80}Eu(CF_3SO_3)_3$  for excitation wavelengths between 365 and 420 nm. The inset of (A) shows the time-resolved spectra for the  $U(600)_{200}Eu(CF_3SO_3)_3$  di-ureasil, excited at 365 nm, obtained at delay times of 1.00 and 5.00 ms.

is varied (Fig. 4B). Similarly to what was observed for the undoped di-ureasils, Section 9, only the lower energy band shifts to the red as the excitation wavelength decreases, while the peak energy of the other band remains approximately constant [191, 193–196].

To summarize the analyses of the steady-state emission of the  $Eu^{3+}$ -based di-ureasils (Figs. 1A and 2A), it may be said that the relative energy of the host band with respect to the intra- $4f^6$  lines strongly depends on the amount of  $Eu^{3+}$  incorporated. In all of the hybrids, the broad band intensity is greater for the lower concentrated hybrid, while as the concentration increases, the reverse situation occurs both for the di-ureasils incorporating  $Eu(CF_3SO_3)_3$  [162–164, 166, 168, 170, 173, 181] and  $Eu(ClO_4)_3$  [171, 177]. In the particular case of the  $U(600)_nEu(CF_3SO_3)_3$  di-ureasils, the hybrids' host emission overlaps with greater intensity the cation lines for the di-ureasils with  $n = 60$  and  $n = 200$  since, for these hybrids, the broad band is red-shifted with respect to the remaining samples [170].

The variation of the excitation wavelength is another factor that changes the relative intensity between the hybrid host emission band and the  $\text{Eu}^{3+}$  lines, as Figure 5 exemplifies for the  $\text{U}(600)_{200}\text{Eu}(\text{CF}_3\text{SO}_3)_3$  di-ureasil. It is also possible to observe that increasing the excitation wavelength results in a red shift of the hybrids' host emission. The ion lines dependence on the excitation wavelength will be discussed in the next paragraphs.

In an attempt to further characterize the host emission, a deconvolution fitting procedure was applied to the emission spectra of all of the samples for the excitation wavelength range between 330 and 420 nm (3.76 and 2.95 eV) [181], adopting the same fitting procedure applied to the undoped matrix [191, 193–196]. First, the spectra measured under the higher excitation wavelength (465 nm) were fitted by a single Gaussian-type function. Since the FWHM is determined primarily by carrier–phonons interaction, its value should not depend on the excitation wavelength [199]. Therefore, the FWHM was kept as a fixed parameter, whereas the intensity and peak position were free to vary within the excitation wavelength interval used. For the U(600)-based hybrids, the deconvolution fitting procedure revealed the presence of two Gaussian bands in the green and blue spectral regions for excitation wavelengths between 330 and 395 nm (3.76 and 3.14 eV). For excitation wavelengths higher than 395 nm (3.76 eV), the emission spectra were fitted only to the green Gaussian component. For the high-molecular-weight di-ureasils, the fitting procedure always revealed the presence of two bands within the referred excitation wavelength interval. Resembling the deconvolution performed on the di-ureasil hybrid host emission spectra [191, 193–196], Section 9, the lower and higher Gaussian components were assigned to the emission arising from electron–hole recombination occurring in the NH groups of the urea linkages (green band) and in the siliceous nanodomains (blue band), respectively. The energy of the NH-related emission varies between 2.4 and 2.6 eV for both di-ureasil series, whereas the band associated with the siliceous nanodomains varies between 2.5 and 3.0 eV for the

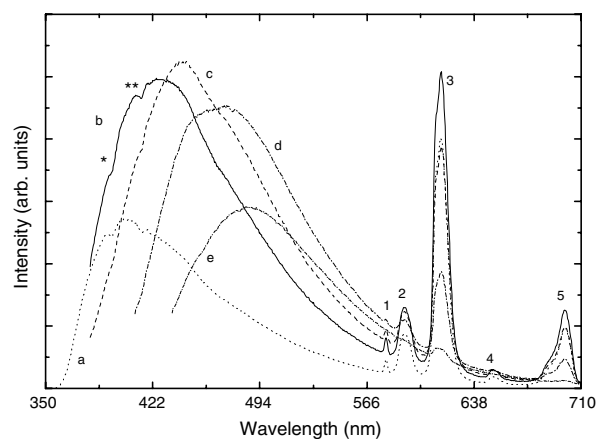


**Figure 5.** RT emission spectra for the  $\text{U}(600)_{200}\text{Eu}(\text{CF}_3\text{SO}_3)_3$  di-ureasil measured at different excitation wavelengths: (a) 330 nm, (b) 350 nm, (c) 365 nm, (d) 395 nm, and (e) 420 nm. (\*) and (\*\*) denote intra- $4f^6$  self-absorptions:  ${}^7\text{F}_0 \rightarrow {}^5\text{D}_4$ ,  ${}^5\text{L}_6$ , respectively. (1), (2), (3), (4), and (5) correspond to intra- $4f^6$  transitions:  ${}^5\text{D}_0 \rightarrow {}^7\text{F}_{0-4}$ , respectively.

$\text{U}(2000)_n\text{Eu}(\text{CF}_3\text{SO}_3)_3$  hybrids and between 2.8 and 3.1 eV for the  $\text{U}(600)_n\text{Eu}(\text{CF}_3\text{SO}_3)_3$  di-ureasils. For each di-ureasil sample, the energy of the green band does not depend on the excitation wavelength, whereas the blue band, associated with the presence of the siliceous nanodomains, shifts to the red as the excitation wavelength increases. For each excitation wavelength used, while the energy of the green band is almost independent of the amount of  $\text{Eu}^{3+}$  incorporated, the variation of the energy of the emission related to the siliceous nanodomains with the  $\text{Eu}^{3+}$  content presents the same behavior as the one displayed in Figure 6 for the 365 nm (3.30 eV) excitation wavelength [181]. The energy of the undoped host ( $n = \infty$ ) is also plotted in the same figure. Figure 6 evidences the opposite behavior expressed by the two di-ureasils series: when an increase in the emission energy with the concentration increase is observed in one series, the other hybrid types present a decrease in the respective emission (and vice versa). This behavior can be related to the respective nanodomain size. In fact, it is well known that, in silicon-based nanostructured materials, the dimensional hierarchy of the backbone determines the emission energy in such a way that an increase in the dimensional network dimension results in a decrease of the corresponding energy gap [181, 200–203]. Accordingly, the emission energy of the siliceous nanodomains can be related to the SAXS-determined siloxane particle radius (Section 3).

Upon lowering the temperature down to 14 K, the overall RT luminescence features described remain the same, apart from a small blue shift of the hybrids' host emission.

The ensuing paragraphs will focus on the  $\text{Eu}^{3+}$  emission. For both di-ureasil series, the number of components measured for the  ${}^7\text{F}_{0,1,2}$  levels is one, three, and five, respectively, although the lower energy component of the  ${}^7\text{F}_2$  level is not clearly distinguished. The lines related to the  ${}^5\text{D}_0 \rightarrow {}^7\text{F}_{3,4}$  transitions are hard to identify due to the low intensity of some components, in particular the  ${}^5\text{D}_0 \rightarrow {}^7\text{F}_3$  transition. The number of components of each manifold and the relative intensity between the  ${}^5\text{D}_0 \rightarrow {}^7\text{F}_{0-4}$  transitions are not affected by changing the  $\text{Eu}^{3+}$  content or the polymer chain

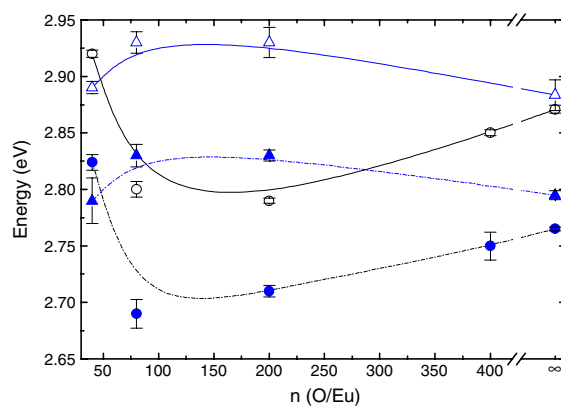


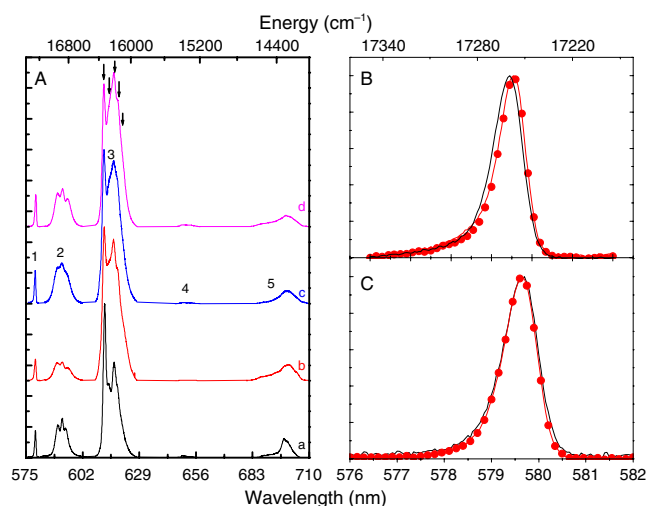
**Figure 6.** Fitted energy of the siloxane-nanodomain-connected blue/purplish-blue emission excited at 3.14 eV (● and ▲) and 3.40 eV (○ and △) for the  $\text{U}(600)_n\text{Eu}(\text{CF}_3\text{SO}_3)_3$  and  $\text{U}(2000)_n\text{Eu}(\text{CF}_3\text{SO}_3)_3$  di-ureasils, respectively. The lines are drawn as guides to the eyes. Reprinted with permission from [181], K. Dahmouche et al., *J. Mater. Chem.* 11, 3249 (2001). © 2001, Royal Society of Chemistry.

length. Figure 7A shows in detail the intra- $4f^6$  lines for the  $U(600)_nEu(CF_3SO_3)_3$ ,  $200 \leq n \leq 60$ , di-ureasils.

For the di-ureasils  $U(2000)_nEu(CF_3SO_3)_3$ ,  $400 \leq n \leq 40$ , and  $U(600)_nEu(CF_3SO_3)_3$ ,  $200 \leq n \leq 60$ , the  $Eu^{3+}$  emission lines do not depend on the excitation wavelength. On the contrary, for the most concentrated hybrids of the latter di-ureasils series ( $n = 40$  and  $20$ ), changes in the emission spectra were observed, namely, in the energy of the  ${}^5D_0 \rightarrow {}^7F_0$  transition, as Figure 7B and C point out. This transition occurs between two nondegenerated levels, so changes detected in the energy of such a transition induced by variations on the excitation wavelength strongly suggest a structured profile for such a transition, meaning the existence of more than one local  $Eu^{3+}$  site. The presence of two distinct coordination local environments was also observed for the di-ureasils with a shorter polymer chain modified by  $Eu(ClO_4)_3$  [171]. In that particular case, the existence of two  $Eu^{3+}$  local environments was observed for concentration around  $n = 62$  [171]. Section 8 will focus on the cation local coordination as the  $Eu^{3+}$  content and the polymeric chain length vary.

Although salts and complexes based in the  $Eu^{3+}$  ion are the most reported ones [162–168, 170–173, 177, 180–187], other rare-earth ions have also been incorporated in the di-ureasils, namely,  $Nd^{3+}$  [169, 173, 176],  $Gd^{3+}$  [170],  $Tb^{3+}$  [172, 185],  $Er^{3+}$  [173, 174], and  $Tm^{3+}$  [172].

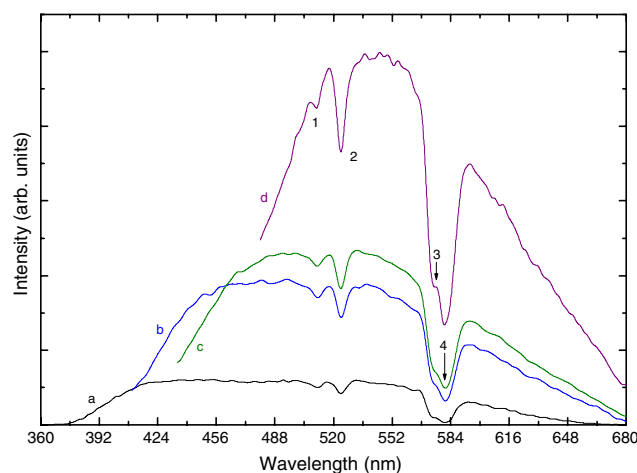
The di-ureasils modified by  $Nd^{3+}$  and  $Er^{3+}$  combine the white-light emission associated with the hybrid host skeleton with intra- $4f$  straight lines in the infrared spectral region characteristic of the RE ions [169, 173, 174, 176]. Figure 8 shows the emission for the  $U(2000)_{60}Nd(CF_3SO_3)_3$  detected in the visible spectral range. It is possible to discern the typical large broad band of the hybrid host, which occurs in the same spectral region observed for the  $Eu^{3+}$ -based hybrid



**Figure 7.** (A) 14 K  $Eu^{3+}$  emission lines, excited at 395 nm, for the  $U(600)_nEu(CF_3SO_3)_3$  hybrids: (a), (b), (c), and (d) denote  $n = 20, 40, 60$ , and  $200$ , respectively. (1), (2), (3), (4), and (5) correspond to intra- $4f^6$  transitions:  ${}^5D_0 \rightarrow {}^7F_{0-4}$ , respectively.  ${}^5D_0 \rightarrow {}^7F_0$  transition measured at 14 K for the  $U(600)_nEu(CF_3SO_3)_3$  di-ureasils, (B)  $n = 40$ , and (C)  $n = 200$ , excited at 350 nm (—●—) and 395 nm (—○—). Reprinted with permission from [181], K. Dahmouche et al., *J. Mater. Chem.* 11, 3249 (2001). © 2001, Royal Society of Chemistry.

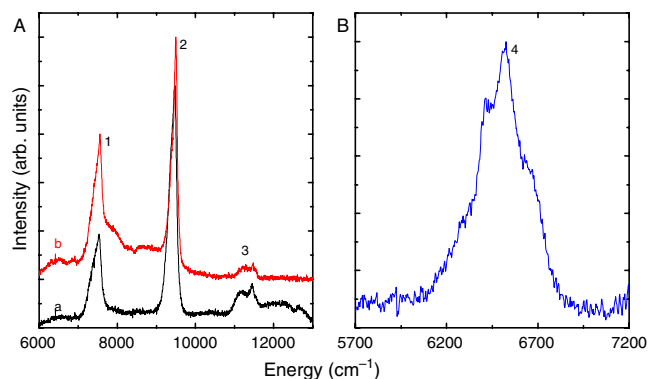
(Fig. 1A). Although no visible emission arising from the  $Nd^{3+}$  levels is detected, it is possible to observe a series of intra- $4f^3$  self-absorptions, overlapping the hybrid host emission. The presence of such self-absorptions indicates that visible light emitted by the di-ureasil's emitting centers is absorbed by the cations, and then probably converted into near-infrared emission. Increasing the excitation wavelength causes a red shift of the maximum intensity energetic position, similarly to what was reported for the xerogels modified by  $Eu^{3+}$  (Fig. 5). The RT lifetime measured for the two hybrids' host emitting centers is of the same magnitude as the respective lifetimes measured for the undoped host [176]. Indeed, a smaller diminution of the lifetimes in the presence of  $Nd^{3+}$  with respect to the incorporation of  $Eu^{3+}$  was detected. This fact allowed the experimental detection of the lifetime associated with the luminescence arising from the siliceous nanodomains  $\tau_{Si}$ , and originated in the NH groups of the urea linkages  $\tau_{NH}$ , except for the more concentrated sample ( $n = 10$ ), whose lifetimes are smaller than the lower experimental detection limit of the experimental setup used ( $10^{-5}$  s) [176].

Figure 9A and B displays the infrared luminescence component of the  $Nd^{3+}$  and  $Er^{3+}$  di-ureasils, respectively [169, 173, 174, 176]. The emission lines are assigned to the intra- $4f^3$ ,  ${}^4F_{3/2} \rightarrow {}^4I_{13/2-9/2}$ , and to the intra- $4f^{11}$ ,  ${}^4I_{13/2} \rightarrow {}^4I_{15/2}$ , transitions of  $Nd^{3+}$  and  $Er^{3+}$ , respectively. Variations of salt concentration do not lead to changes in the IR spectra, namely, in the energy and shape of the observed transitions. Moreover, concentration-quenching effects on the reported IR luminescence seem to be insignificant in the di-ureasils, as the experimental detection conditions were approximately the same in the whole range of  $Nd^{3+}$  and  $Er^{3+}$  concentration reported [169, 173, 174, 176]. It is quite unusual to observe RT radiative emission from sol-gel-derived  $Nd^{3+}$ - and  $Er^{3+}$ -based hybrids, due to the numerous organic groups, particularly hydroxyl, present in classical sol-gel-derived materials



**Figure 8.** Visible emission spectra detected at 14 K for the  $U(2000)_{60}Nd(CF_3SO_3)_3$  di-ureasil, measured at different excitation wavelengths: (a) 350 nm, (b) 375 nm, (c) 420 nm, and (d) 460 nm. The  ${}^4I_{9/2} \rightarrow {}^4G_{5/2}, {}^4G_{7/2}$  (500–540 nm) and the  ${}^4I_{9/2} \rightarrow {}^4G_{7/2}, {}^2K_{13/2}, {}^4G_{9/2}$  (570–590 nm) intra- $4f^3$  self-absorptions are indicated by arrows. Reprinted with permission from [169], L. D. Carlos et al., *Electrochim. Acta* 45, 1555 (2000). © 2000, Elsevier Science.





**Figure 9.** (A) RT infrared emission excited under 514.5 nm of (a)  $\text{U}(900)_{60}\text{Nd}(\text{CF}_3\text{SO}_3)_3$  and (b)  $\text{U}(2000)_{100}\text{Nd}(\text{CF}_3\text{SO}_3)_3$ ; (1), (2), and (3) correspond to the intra- $4f^3$  transitions:  ${}^4F_{3/2} \rightarrow {}^4I_{13/2,11/2,9/2}$ . (B) RT infrared emission of  $\text{U}(600)_3\text{Er}(\text{CF}_3\text{SO}_3)_3$  recorded under the excitation 488 nm; (4) corresponds to the intra- $4f^{11}$  transition:  ${}^4I_{13/2} \rightarrow {}^4I_{15/2}$ .

that prevent any RT  $\text{Nd}^{3+}$  and  $\text{Er}^{3+}$  radiative emission [169, 173, 174, 176]. However, in the di-ureasil hybrids, the  $\text{Nd}^{3+}$  and  $\text{Er}^{3+}$  ions are active at RT, indicating that the di-ureasil hybrid framework efficiently protects the RE ions from nonradiative deactivations induced essentially by hydroxyl groups [169, 173, 174, 176].

The substitution of rare-earth salts by rare-earth complexes intends to increase the efficiency of the absorption and energy transfers processes, namely, the antenna effect, and consequently, to achieve greater emission intensity. In the following paragraphs, we will present some examples that illustrate this concept.

Bekiari et al. compared the luminescence intensity, excited at 365 nm, of a hybrid sample containing  $\text{Tb}^{3+}$  ions before and after the incorporation of the bpy ligand [185]. Through the analyses of Figure 3, the authors suggested that the presence of this ligand contributed to an enhancement of the PL intensity. From that figure, it is also possible to infer that the hybrid host is also transferring energy to the  $\text{Tb}^{3+}$  ions since, by changing the excitation wavelength to 318 nm, the intensity of the hybrid host broad band intensity is approximately zero [185].

$\beta$ -diketonate complexes of  $\text{Eu}^{3+}$ ,  $\text{Tm}^{3+}$ , and  $\text{Tb}^{3+}$  ions were incorporated in the  $\text{U}(2000)$  hybrid host [172]. The emission properties of such a hybrid revealed themselves as strongly dependent on the temperature, as plotted in Figure 10. For temperatures lower than 200 K, the emission features are similar, and the green  $\text{Tb}^{3+}$  transition,  ${}^5D_4 \rightarrow {}^7F_2$ , dominates the spectra, as the  $\text{Eu}^{3+}$  transitions, namely,  ${}^5D_0 \rightarrow {}^7F_2$ , have a lower intensity. No sign of visible  $\text{Tm}^{3+}$  luminescence could be detected [172]. For temperatures between 200 and 300 K, the green  $\text{Tb}^{3+}$  luminescence decreases, and we observe an increase of the red  $\text{Eu}^{3+}$  emission [172]. The  $\text{Tm}^{3+}$  emission was only observed in the infrared spectral region [172]. For direct excitation into the  ${}^5D_2$   $\text{Eu}^{3+}$  level (465 nm), the  ${}^5D_0 \rightarrow {}^7F_6$  transition was also observed [172]. The typical hybrid host luminescence band could only be detected for an excitation wavelength around 420 nm, which corresponds to the direct excitation of the hybrids host emitting centers [194–196].

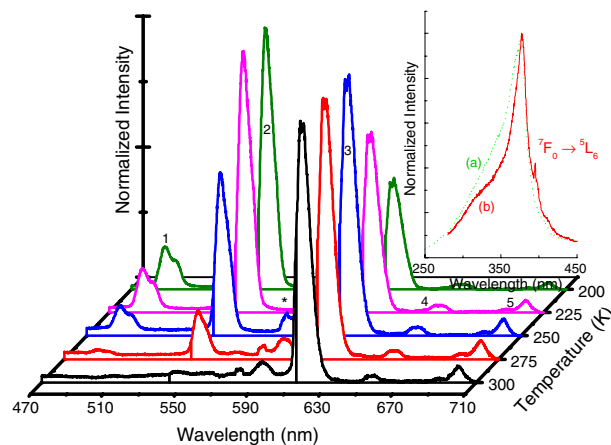


**Figure 10.** PL spectra of  $\text{U}(2000)_{80}(\text{Eu}_{0.05}\text{Tb}_{0.15}\text{Tm}_{0.80})(\text{BTFA})_3 \cdot 2\text{H}_2\text{O}$  recorded at temperatures between 200 and 300 K (excitation wavelengths used: 377 nm at 200–225 K, and 382 nm at 250–300 K). (1), (2), (3), (4), and (5) correspond to the intra- $4f^6$ ,  ${}^5D_4 \rightarrow {}^7F_{6,7}$  ( $\text{Tb}^{3+}$ ), and intra- $4f^6$  transitions,  ${}^5D_0 \rightarrow {}^7F_{2-4}$  ( $\text{Eu}^{3+}$ ), respectively. In the area marked with an asterisk, there is an overlap between the  ${}^5D_0 \rightarrow {}^7F_{0,1}$  ( $\text{Eu}^{3+}$ ) and  ${}^5D_4 \rightarrow {}^7F_4$  ( $\text{Tb}^{3+}$ ) transitions. The inset shows the PLE spectra monitored within the  $\text{Tb}^{3+}$  (dashed line) and  $\text{Eu}^{3+}$  (solid line) emissions. Reprinted with permission from [172], L. D. Carlos et al., *Adv. Funct. Mater.* 12, 819 (2002). © 2002, Wiley–VCH Verlag GmbH & Co.

The lifetimes of the  $\text{Tb}^{3+}$  and  $\text{Eu}^{3+}$  cations excited states  ${}^5D_4$  and  ${}^5D_0$ , respectively, were measured as a function of the temperature [172]. The  ${}^5D_0$  lifetime is independent of the temperature, being around 0.6 ms between 14 and 300 K. The  ${}^5D_4$  lifetime is around 0.7 ms for the temperature range between 14 and 150–170 K, decreasing six–seven times as the temperature is increased until the RT [172]. This behavior indicates a thermally activated mechanism that will be focused on in detail in Section 7.

Zhang groups' reported the PL features of a series of organically modified silicate (*ormosils*) hybrids doped with  $\text{Eu}[(\text{phen})_2]\text{Cl}_3$  complexes. The relative emission quantum yield and the lifetime of the  ${}^5D_0$   $\text{Eu}^{3+}$  excited level were compared with those of conventional silica films synthesized under the same conditions as used for the hybrids [188]. The hybrids and the silica films were identified as  $\text{SiO}_2/\text{SPM}:\text{Eu}[(\text{phen})_2]^{3+}$  and  $\text{SiO}_2:\text{Eu}[(\text{phen})_2]^{3+}$ , respectively. The corresponding PL spectra excited under UV excitation are plotted in Figure 11 [188]. All of the spectra present the typical  $\text{Eu}^{3+}$  red emission corresponding to transitions between the  ${}^5D_0$  level and the  ${}^7F_{0-4}$  manifolds. Although the  ${}^5D_0 \rightarrow {}^7F_2$  dominates in both spectra, the number of observed components for all of the transitions is different. The higher number of Stark components observed for the  ${}^5D_0 \rightarrow {}^7F_{1-4}$  transitions in  $\text{SiO}_2/\text{SPM}:\text{Eu}[(\text{phen})_2]^{3+}$  indicates a lower local-symmetry site for the  $\text{Eu}^{3+}$  ions relative to the  $\text{SiO}_2:\text{Eu}[(\text{phen})_2]^{3+}$  samples.

Zhang et al. compared the relative quantum efficiency of the  $\text{Eu}^{3+}$  emission in the hybrid matrix and in the silica host, and concluded that, for the same amount of  $\text{Eu}[(\text{phen})_2]\text{Cl}_3$  incorporated (0.5%), the relative quantum efficiency of the  $\text{SiO}_2:\text{Eu}[(\text{phen})_2]^{3+}$  is 0.08 with respect to the efficiency observed in the  $\text{SiO}_2/\text{SPM}:\text{Eu}[(\text{phen})_2]^{3+}$  hybrid [188]. The hybrid host behaved as an efficient  $\text{Eu}^{3+}$  host, contributing to an increase of its emission intensity.

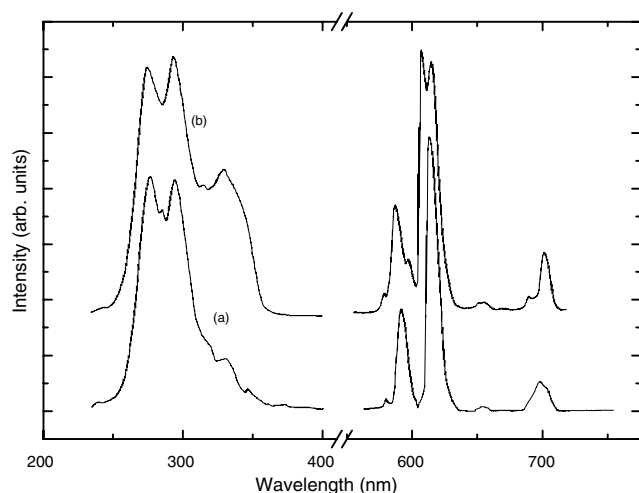


**Figure 11.** PL and PLE spectra of the  $\text{SiO}_2\text{:}[\text{Eu}(\text{phen})_2]^{3+}$  (a) and  $\text{SiO}_2/\text{SPM:}[\text{Eu}(\text{phen})_2]^{3+}$  (b) materials in air. Reprinted with permission from [188], Y. Li et al., *Thin Solid Films* 385, 205 (2002). © 2002, Elsevier Science.

The lifetime of the  $^5\text{D}_0$   $\text{Eu}^{3+}$  level measured for both samples was well fitted by a double exponential, indicating inhomogeneities in the  $\text{Eu}^{3+}$  local environment. The  $^5\text{D}_0$  lifetime values are  $1.404 \pm 0.350$ ,  $4.152 \pm 0.600$  ms and  $0.889 \pm 0.090$ ,  $0.060 \pm 0.006$  ms for  $\text{SiO}_2/\text{SPM:Eu}[(\text{phen})_2]^{3+}$  and  $\text{SiO}_2\text{:Eu}[(\text{phen})_2]^{3+}$ , respectively [188]. The lower values found for the lifetime of the  $^5\text{D}_0$  level in the  $\text{SiO}_2\text{:Eu}[(\text{phen})_2]^{3+}$  film were interpreted on the basis that the ormosil matrix prevents ligand vibrations around the  $\text{Eu}^{3+}$  cation, contributing to a decrease in the nonradiative channels [188].

Li et al. also reported the luminescence properties of a series of composite phosphors modified by terbium carbonyl complexes, identified as  $\text{SiO}_2/\text{SPM:Tb-}o\text{-ABA}$ ,  $\text{SiO}_2/\text{SPM:Tb-}p\text{-ABA}$ ,  $\text{SiO}_2/\text{SPM:Tb-BA}$  and  $\text{SiO}_2/\text{SPM:Tb-}m\text{-ABA}$  [189]. The emission spectra of all of the hybrids are displayed in Figure 12. The spectra are composed of a large broad band between 350 and 480 nm superimposed by a series of straight lines in the green spectral region assigned to the intra- $4f^8$  transitions:  $^5\text{D}_4 \rightarrow ^7\text{F}_{6-3}$ . The large broad band was related to the presence of carboxyl radicals in the hybrids [189]. The authors of this work analyzed the temperature influence on the luminescence intensity of all four hybrids. The luminescence intensity was measured as the heat treatment temperature increased from 50 to 150 °C, and a decrease of the emission intensity with increasing temperature was detected for all of the composites [189]. To explain this result, the authors noted that, as the heat temperature increases, a greater quantity of solvents ( $\text{H}_2\text{O}$ ,  $\text{CH}_3\text{COOH}$ , acid) escapes from the sample, so that carbonyl may exist in the form of a negative ion, meaning that its lowest triplet excited state transforms  $\pi\pi^*$  into  $n\pi^*$ . It is more unlikely that the singlet  $n\pi^*$  state transmits to the triple state  $\pi\pi^*$  and, consequently, the energy transfer processes from the ligands to the  $\text{Tb}^{3+}$  cations become more inefficient [189].

The lifetimes of the  $^5\text{D}_4$  level were measured at RT under 335 nm excitation wavelength within the  $^5\text{D}_4 \rightarrow ^7\text{F}_5$  transition [189]. The experimental data were well adjusted by a sin-

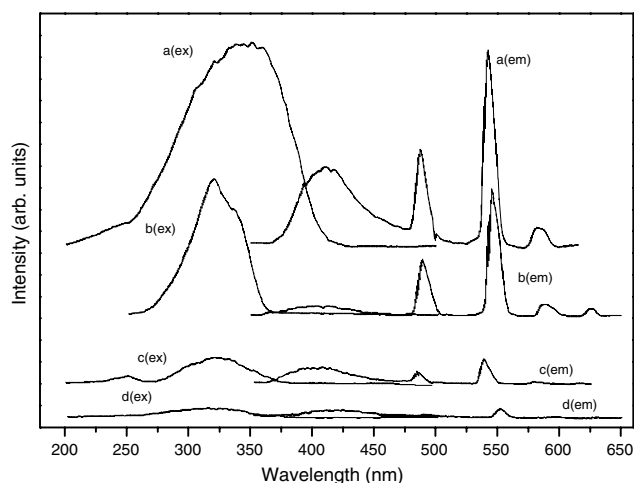


**Figure 12.** PL and PLE spectra of the  $\text{SiO}_2/\text{SPM}$ -terbium carbonyl complexes. (a)  $\text{SiO}_2/\text{SPM:Tb-}o\text{-ABA}$ . (b)  $\text{SiO}_2/\text{SPM:Tb-}p\text{-ABA}$ . (c)  $\text{SiO}_2/\text{SPM:Tb-BA}$ . (d)  $\text{SiO}_2/\text{SPM:Tb-}m\text{-ABA}$ . Reprinted with permission from [189], Y. Li et al., *Mater. Lett.* 56, 597 (2002). © 2002, Elsevier Science.

gle exponential function indicating lifetime values between  $1.200 \pm 0.015$  and  $0.600 \pm 0.016$  ms for the  $\text{SiO}_2/\text{SPM:Tb-}o\text{-ABA}$  and  $\text{SiO}_2/\text{SPM:Tb-}m\text{-ABA}$ , respectively. The higher lifetime value found for the  $\text{SiO}_2/\text{SPM:Tb-}o\text{-ABA}$  composite was attributed to the stability of the  $\text{Tb-}o\text{-ABA}$  complex that might contribute to a decrease of the ligand vibrations around the  $\text{Tb}^{3+}$  ions, enhancing, in turn, the experimental lifetime [189].

Recently, Corriu et al. reported a comparative study of the PL properties of hybrid organic–inorganic materials obtained from a mixture of  $\text{Ph}_2\text{P}(\text{CH}_2)_3\text{Si}(\text{OMe})_3$  and  $n'$  equiv of  $\text{Si}(\text{OEt})_4$  ( $n' = 4, 7, 9, 12, 14, 19$ , and 35) doped with  $\text{Eu}^{3+}$  in the presence and absence of a surfactant,  $n$ -hexadecylamine [190]. Note that, in order to avoid confusion with the  $n$  ratio, the nomenclature proposed by Corriu et al. was replaced here by  $n'$ . Accordingly, the materials will be identified as  $\text{A}_{n'}$  and  $\text{B}_{n'}$ , respectively. As an example, we show the emission spectra of the  $\text{EuA}_0$  and  $\text{EuB}_7$  hybrids recorded at 2 K under laser excitation at 325 nm [190]. As Figure 13 shows, the entire PL spectra are composed of the typical  $^5\text{D}_0 \rightarrow ^7\text{F}_{0-4}$  transitions. In both types of materials,  $\text{A}_{n'}$  and  $\text{B}_{n'}$ , the  $^5\text{D}_0 \rightarrow ^7\text{F}_0$  transition displays only one line peaking around the same energy value, indicating only one similar  $\text{Eu}^{3+}$  local environment in the two hybrid materials [190].

In spite of the similar PL properties and  $\text{Eu}^{3+}$  local coordination site in both  $\text{A}_{n'}$  and  $\text{B}_{n'}$  hybrids, they behave differently regarding the  $\text{Eu}^{3+}$  complexation. Due to the presence of  $\text{P}=\text{O}$  groups within the porous part of the  $\text{A}_{n'}$  materials, rather than their uncontrolled distribution in the  $\text{B}_{n'}$  hybrids, Corriu et al. concluded that the former system is more adequate for  $\text{Eu}^{3+}$  coordination [190]. This fact indicated that the  $\text{Eu}^{3+}$  coordination requires not only three  $\text{P}=\text{O}$  coordinating groups, but also a certain favorable geometry, as suggested by  $^{31}\text{P}$  NMR results and elemental analysis (see Section 3) [190]. This observation was also sustained by the analyses of the complexation degree with the increasing  $\text{Eu}^{3+}$  content as  $n'$  varied between 4 and 35. The



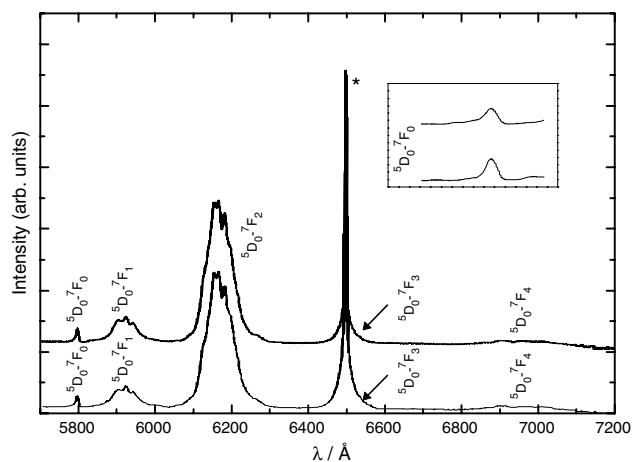


**Figure 13.** PL spectra of  $\text{EuA}_9[\text{O}]$  (upper) and  $\text{EuB}_7[\text{O}]$  (lower) recorded under laser excitation at 325 nm at 2 K. \* Corresponds to the second-order-scattered laser beam. The inset shows the  $^5\text{D}_0 \rightarrow ^7\text{F}_0$  emission. Reprinted with permission from [190], R. J. P. Corriu et al., *Chem. Commun.* 1116 (2001). © 2001, Royal Society of Chemistry.

optimum complexation degree (80%) occurred around  $n' = 9$  for the  $\text{A}_{n'}$  hybrids. For  $n' < 9$ , in spite of the greater proximity between the  $\text{P}=\text{O}$  groups, the complexation degree decreases, and for the more diluted samples, namely,  $n' > 14$ , there is no  $\text{Eu}^{3+}$  complexation in  $\text{A}_{n'}$  and  $\text{B}_{n'}$  materials [190]. With this work, Corriu et al. demonstrated that the complexation of  $\text{Eu}^{3+}$  in hybrid materials containing phosphine oxide groups within the porous part is favored.

The most exhaustive studies concerning the PL properties of hybrid materials in which the RE organic ligands are covalently grafted to the hybrid framework regard  $\text{Eu}^{3+}$  and  $\text{Tb}^{3+}$  ions. The typical lanthanide ligands incorporated in these sol–gel-derived organic–inorganic nanostructured hybrids include  $\beta$ -diketonate complexes [153–159, 172, 184, 185, 187], phenanthroline [53, 143, 158], and bipyridine [53, 143, 187].

Figure 14A shows the low-temperature emission properties of  $\text{Eu}^{3+}$ -activated organic–inorganic hybrids materials with four different dicarboxylic acids, denoted as  $\text{EuH}_1$ ,  $\text{EuH}_2$ ,  $\text{EuH}_3$ , and  $\text{EuH}_4$ , directly excited within the organic absorption band (337.1 nm) [155]. All of the spectra are similar, presenting the  $^5\text{D}_0 \rightarrow ^7\text{F}_{0-4}$  intra- $4f^6$  transitions. The large and unresolved profile of the spectra evidences the amorphous nature of these materials. Moreover, these hybrids display a relatively high PL intensity, in particular,  $\text{EuH}_2$  and  $\text{EuH}_3$ , in which the organic complex retains 85% of the luminescence intensity [155].

A comparative study was performed involving the 1,10-phenanthroline complex covalently bonded to the silica backbone in the presence of the  $\text{Eu}^{3+}$  ions (Hybrid I) with a simple mixture of the silica gel,  $\text{Eu}^{3+}$ , and  $\text{Phen-NH}_2$  (Hybrid II) [158]. The respective PL spectra are plotted in Figure 15A and B, respectively. The Hybrid I emission is characterized by the typical  $\text{Eu}^{3+}$  lines, and no emission arising from the ligands levels could be detected. In contrast, in the Hybrid II, a large broad band resulting from the ligand levels superimposes the  $\text{Eu}^{3+}$  emission. This states that the energy transfer processes from the  $\text{Phen-Si}$  ligands are more efficient in the Hybrid I case, showing the effective

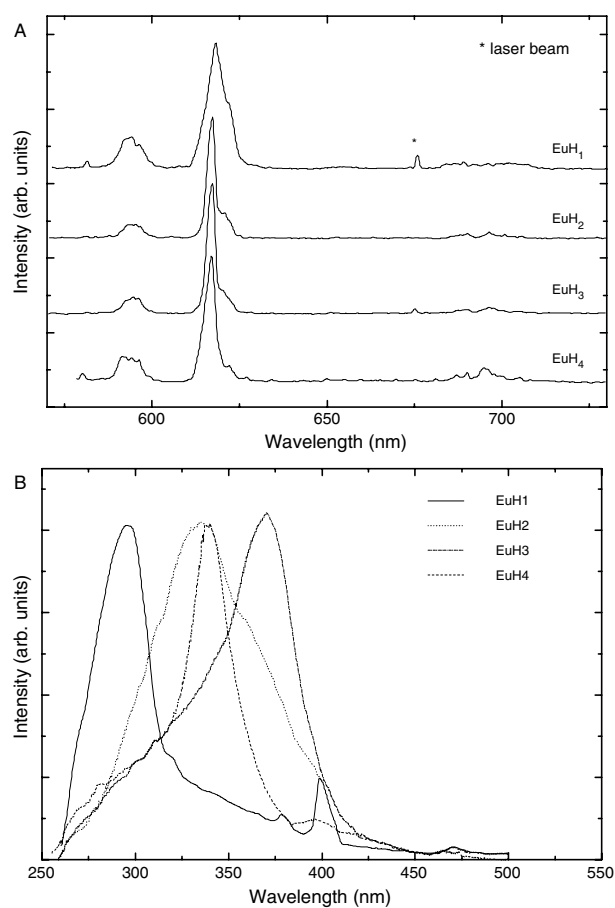


**Figure 14.** (A) Low-temperature (15 K) PL spectra excited under 337.1 nm. (B) RT PLE spectra monitored around 616.0 nm for the  $\text{EuH}_i$  ( $i = 1-4$ ) hybrid materials. Reprinted with permission from [155], A.-C. Franville et al., *Solid State Sci.* 3, 221 (2001). © 2001, Elsevier Science.

importance of the covalent graft between the organic and inorganic components [158]. The decrease in the emission intensity in the spectrum of the Hybrid II, regarding that of Hybrid I (clearly demonstrated by the noisy spectrum of Fig. 15B), was attributed to the presence of  $\text{NH}$  oscillators of the  $\text{NH}_2$  groups that act as nonradiative channels for the  $\text{Eu}^{3+}$  ion [158].

In the RT PL spectra of 2-pyridinecarboxylic acid europium(III),  $\text{Eu}(\text{PA})_3$ , complexes prepared by the chemically synthesized method [159] (Fig. 16), it is possible to discern only the lanthanide ion emission. A similar result was reported for a series of phosphine oxides coordinated to one, two, or three  $\text{Si}(\text{OR})_3$  groups treated with anhydrous europium salts (see Fig. 17) [157].

The hybrids incorporating  $\text{Tb}^{3+}$  ions that we will discuss in the following paragraphs present, in all cases, the typical green emission resulting from radiative transitions between the  $^5\text{D}_4$  and the  $^7\text{F}_{3-6}$  levels [156, 160, 161].

Zhang et al. reported the synthesis and photoluminescent properties of two  $\text{Tb}^{3+}$ -complex bridged hybrids involving the DPS and PAIB monomers [160, 161]. In their former work [160], the luminescence properties of the hybrid film and pure  $\text{Tb-DPS}$  complex were analyzed. Figure 18 shows

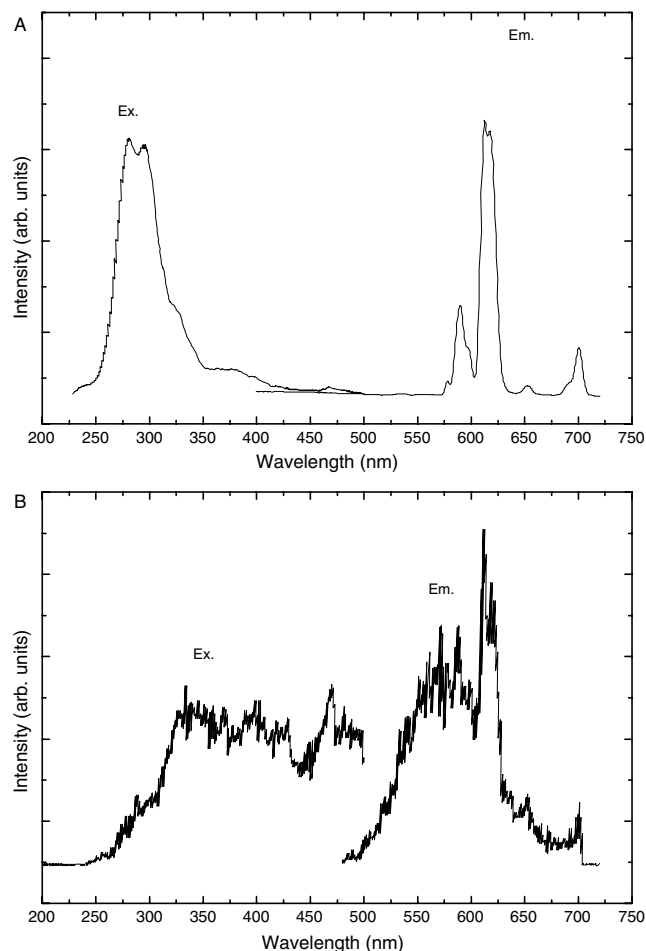


**Figure 15.** PLE and PL spectra of (A) Hybrid I, and (B) Hybrid II. Reprinted with permission from [158], H. R. Li et al., *Chem. Mater.* 14, 3651 (2002). © 2002, American Chemical Society.

the PL spectra of the Tb–DPS complex and of the corresponding hybrid film [160]. The spectra look similar, indicating that the  $\text{Tb}^{3+}$  ions are coordinated to the ligand within the hybrid material. The emission properties of the Tb–PABI hybrid were discussed as a function of the variation of the molar ratio  $\text{Tb}^{3+}$  ion/PABI from 1:5 to 1:200 [161]. All of the spectra present the typical  $\text{Tb}^{3+}$   $^5\text{D}_4 \rightarrow ^7\text{F}_{3-6}$  transitions, whose intensity increases with increasing complex content [161]. The  $^5\text{D}_4$  lifetime was measured for the Tb–PABI hybrid samples and for the hybrid involving the Tb–DPS complex. In all cases, the experimental decay curve was well reproduced by a single exponential function, suggesting that the  $\text{Tb}^{3+}$  ions lie in the same average chemical environment. The resulting lifetimes were 1.2 and 0.35 ms for the hybrids with Tb–PABI and Tb–DPS complexes, respectively [160, 161]. A decrease of the lifetime of the  $^5\text{D}_4$  level both in the Tb–DPS and Tb–PABI hybrid films with respect to the value found in the pure complexes was observed. Zhang et al. attributed such a decrease to a possible quenching by silanol groups in the hybrid case [160, 161].

In the following paragraphs, we will refer briefly, to some PL results concerning the Class I hybrids whose synthesis was described in Section 2.1.

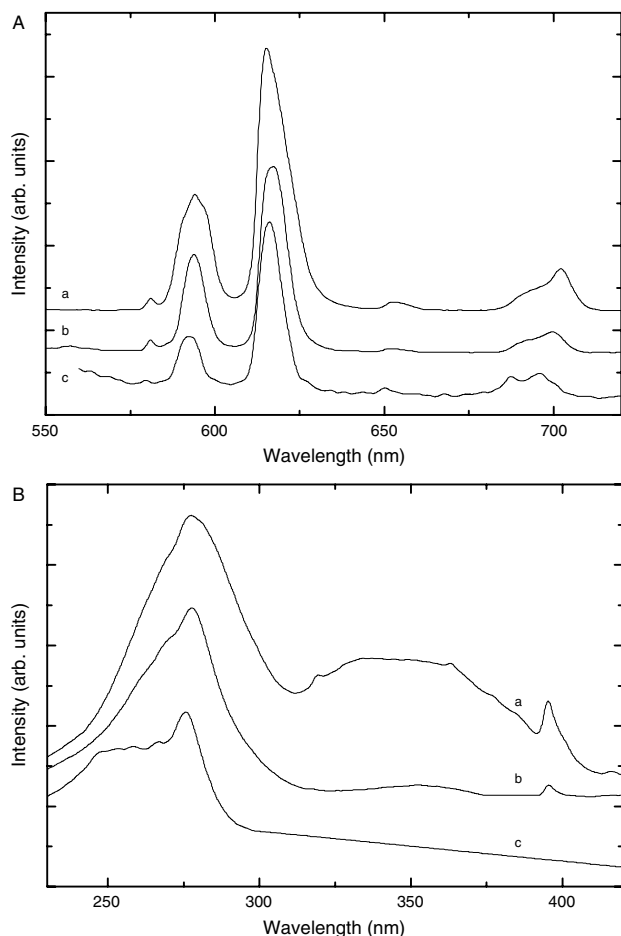


**Figure 16.** (A) RT PL and (B) PLE spectra of the (a)  $\text{Eu}(\text{PA})_3$  complex powders which were prepared by chemical synthesized method (b) of the 1%  $\text{EuCl}_3$  and 3% PA codoped gel which was heat treated for 1 h at 90 °C, (c) and of the HAC solution in which the  $\text{Eu}(\text{PA})_3$  complex powders were dissolved. Reprinted with permission from [159], X. Fan et al., *Chem. Phys. Lett.* 358, 115 (2002). © 2002, Elsevier Science.

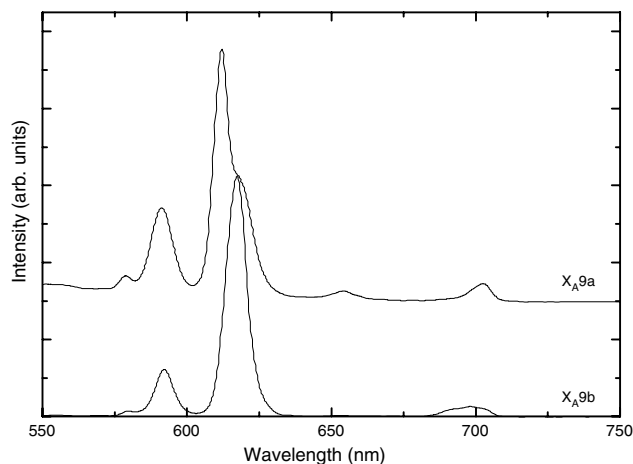


**Figure 17.** RT PL spectra recorded under laser excitation at 345 and 395 nm of the xerogels  $X_{A9a}$  and  $X_{A9b}$ , respectively. Reprinted with permission from [157], F. Embert et al., *Chem. Mater.* 13, 4542 (2001). © 2001, Elsevier Science.

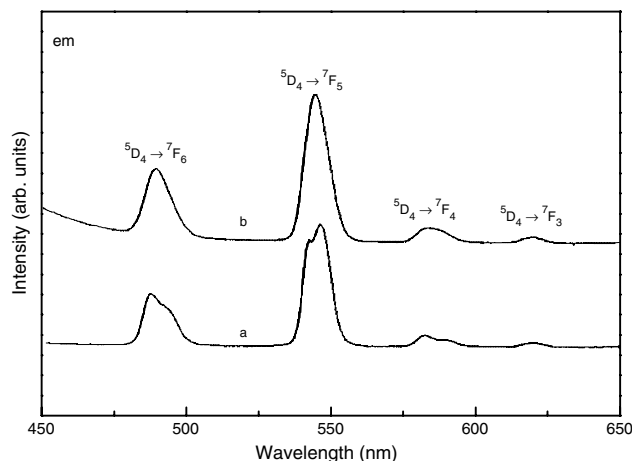


**Figure 18.** PL spectra of (a) the hybrid film and (b) the pure Tb–DPS complex in DMF (excited at 269 nm). Reprinted with permission from [160], F. Liu et al., *New J. Chem.* (in press). © 2003, Royal Society of Chemistry.

Molina et al. reported the luminescence study of a family of siloxane/PEG Class I hybrids modified by  $\text{Eu}(\text{ClO}_4)_3$ , with the  $\text{Eu}^{3+}$  content ranging from  $n = 300$  to  $n = 8$  [150]. The emission spectra display the typical  $\text{Eu}^{3+}$  intra- $4f^6$  transitions,  $^5\text{D}_0 \rightarrow ^7\text{F}_{0-4}$ , that overlap a large broad band, whose origin was not discussed in detail [150]. The most intense transition is the magnetic dipolar one,  $^5\text{D}_0 \rightarrow ^7\text{F}_1$ , an indication that the  $\text{Eu}^{3+}$ -coordination sites have an inversion center. The authors suggested that this observation reflects the presence of  $\text{H}_2\text{O}$  molecules in the  $\text{Eu}^{3+}$  first coordination shell [150]. The presence of OH oscillators surrounding the cations, which act as nonradiative routes for the lanthanide ions, demonstrates that these Class I hybrids are not efficient hosts to encapsulate the  $\text{Eu}^{3+}$  ions. This fact can be overcome either by choosing an  $\text{Eu}^{3+}$  complex instead of  $\text{Eu}(\text{ClO}_4)_3$  or by synthesizing Class II hybrids.

The use of lanthanide-based complexes in Class I materials was reported, for instance, by Li et al., who incorporated europium  $\beta$ -diketonate complexes into such types of systems [143]. Among the  $\text{Eu}^{3+}$ -based complexes studied, the  $\text{Eu}(\text{TTA})_3\text{phen}$  is the one that emits with highest intensity. The authors stated that the hybrid contributes to the stabilization of the  $\text{Eu}(\text{TTA})_3\text{phen}$  complex, due to the substitution of  $-\text{OH}$  groups by  $-\text{OSi}(\text{CH}_3)_3$  groups of the hybrid host [143]. Other  $\text{Eu}^{3+}$  and  $\text{Tb}^{3+}$  complexes, such as  $[\text{Tb}(\text{byp})_2]\text{Cl}_2$  and  $[\text{Eu}(\text{phen})_2]\text{Cl}_3$ , were introduced in Class I hybrids by Adachi's group [140, 148]. The emission spectra of these materials are composed of the green and red emissions associated with the  $\text{Eu}^{3+}$  and  $\text{Tb}^{3+}$  transitions,  $^5\text{D}_4 \rightarrow ^7\text{F}_{6-3}$  and  $^5\text{D}_0 \rightarrow ^7\text{F}_{0-4}$ , respectively [140, 148]. Similarly to the previous case, the authors report that the Class I ormosil matrices contribute to reduce the water absorption of the  $\text{Eu}^{3+}$  and  $\text{Tb}^{3+}$  complexes, so that these hybrids can be used as phosphors for practical uses [140, 148].

Cordoncillo et al. [152] and Zaiton et al. [149] reported the synthesis of  $\text{Eu}^{2+}$ -doped Class I hybrid materials. A large band in the blue spectral region assigned to the  $4f^65d^1 \rightarrow 4f^7$  transition characterizes the  $\text{Eu}^{2+}$  emission [94]. While the lanthanide ion trivalent state is energetically favorable, in

certain chemical environments, the divalent state can be stabilized [94]. Cordoncillo et al. used the cleavage of the Si–H groups from the alkoxide precursors as an *in-situ* reducing agent [152]. In order to determine the best synthesis conditions that contribute to reduce  $\text{Eu}^{3+}$  to  $\text{Eu}^{2+}$  during the sol–gel reaction, Lin et al. studied the influence of the preparation conditions, namely, the pH of the sols, counterions, chelating agents, and solvent type, in the creation of electron–hole defects in the Class I host matrix [149]. In both studies, it was possible to observe the RT intrinsic  $\text{Eu}^{2+}$  blue emission.

## 4.2. Excitation Spectra

The excitation spectra of  $\text{Tb}^{3+}$ - [185] and  $\text{Eu}^{3+}$ -based hybrids [166, 170, 177] were measured. In all cases, the excitation spectra were found to be strongly dependent on the detection wavelength. To clearly identify the components present in the excitation spectra, we will discuss separately the excitation spectra monitored around the RE emission lines and along the hybrid host emission band. We will start by presenting the excitation spectra detected around the hybrid host emission band of the  $\text{Eu}^{3+}$ -based di-ureasils [170].

Figure 19 reproduces the RT PLE spectra for the di-ureasil  $\text{U}(600)_{200}\text{Eu}(\text{CF}_3\text{SO}_3)_3$  monitored at detection wavelengths between 410 and 550 nm, in order to cover the hybrids' host emitting region. All of the spectra are composed of a large broad band between 300 and 520 nm [170].

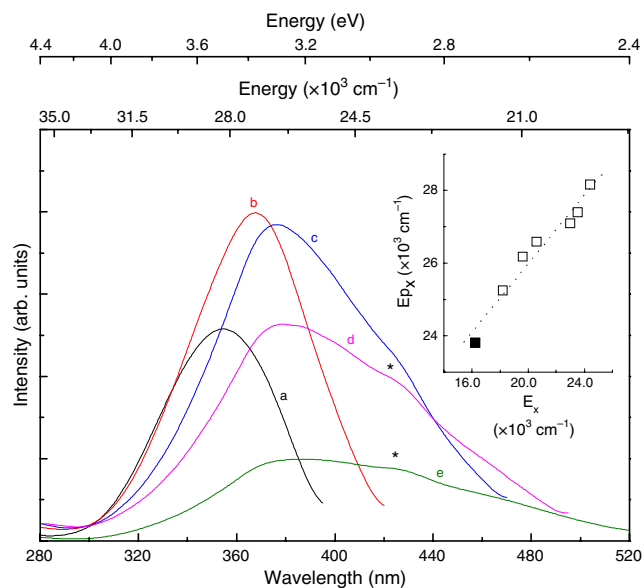


**Figure 19.** RT PLE spectra for the di-ureasil  $\text{U}(600)_{200}\text{Eu}(\text{CF}_3\text{SO}_3)_3$  monitored at different detection wavelengths: (a) 410 nm, (b) 435 nm, (c) 485 nm, (d) 510 nm, and (e) 550 nm. The inset shows the excitation maximum intensity position versus the respective detection energy along the hybrid host emission band for the  $\text{U}(600)_{200}\text{Eu}(\text{CF}_3\text{SO}_3)_3$  di-ureasil. The solid square represents the excitation of the hybrid's backbone detected around the strongest  $^7\text{F}_2$  line, 616 nm. The solid line corresponds to the data linear fit ( $r > 0.99$ ). Reprinted with permission from [170], R. A. Sá Ferreira et al., *Chem. Mater.* 13, 2991 (2001). © 2001, Elsevier Science.

Ribeiro et al. reported a analogous PLE spectrum detected around 435 nm for similar U(600)-based hybrids modified by  $\text{Eu}(\text{ClO}_4)_3$ , as shown in Figure 2B, whose maximum intensity position occurs at 355 nm [177]. Bekiari et al. also observed a large broad band in the same spectral region, peaking around 360 nm, in the PLE spectra of  $\text{Tb}^{3+}$ -based U(600) di-ureasils [185].

As Figure 19 demonstrates, with the increase of the detection wavelength, the maximum intensity energetic position shifts toward the red, and its FWHM increases from 3000 to 6000  $\text{cm}^{-1}$  [170]. When the detection wavelength is greater than 435 nm, a second band, peaking around 420 nm, is also discerned (marked with an asterisk in Fig. 19). As the detection wavelength increases, its relative intensity with respect to the spectra maximum intensity increases, and its peak position remains approximately independent of the monitoring wavelength, contrary to what was observed for the maximum intensity energetic position. The inset of Figure 19 displays the PLE spectra peak position,  $E_{p_x}$  as the monitoring energy increases,  $E_x$  [170]. This behavior is maintained until the detection wavelength reaches 610–615 nm, as we will discuss later. These results clearly establish the presence of two distinct emitting components, in accordance with the PL results aforementioned similarly in Section 4.1. Moreover, this was also observed for the nondoped hosts (Section 9) [191–196]. As we will see in this section, the less energetic band can be assigned to the preferential excitation of the NH groups' D–A pairs, and the more energetic one can be attributed to the preferential excitation of the siliceous nanodomains [191–196].

Figure 1B represents the RT PLE spectra for the di-ureasils  $\text{U}(\text{Y})_{80}\text{Eu}(\text{CF}_3\text{SO}_3)_3$ ,  $\text{Y} = 600$  and 2000, monitored around the  ${}^5\text{D}_0 \rightarrow {}^7\text{F}_{2,4}$   $\text{Eu}^{3+}$  lines. The spectra are composed of a Gaussian-like band centered around 340 and 365 nm, and a less intense band in the low energetic side of the spectra. These two bands are overlapped by a series of straight lines assigned to the excitation of the intra- $4f^6$  levels. The band in the lower wavelength side of the spectra has a greater contribution for the PLE spectra of the high-molecular-weight di-ureasils. Its peak position follows the same linear relation found for the variation of the maximum intensity position with the increasing monitoring energy (inset of Fig. 19). This finding allows us to infer that this band is associated with the excitation of the hybrid host emitting centers detected in the red spectral region. In fact, as the hybrid host emission is still visible in that spectral region, despite its lower intensity, the PLE spectra monitored in that region have a contribution to the hybrid host emitting centers [170].

The most intense band is blue shifted with respect to the PLE spectra monitored around the large broad band, suggesting that a possible origin in the hybrid host emitting centers can be readily excluded. This conclusion could only be achieved owing to the fact that the PLE spectra of the  $\text{Eu}^{3+}$ -based hybrids were monitored along the large broad band and at the cation lines; otherwise, the lack of information regarding the features of the PLE spectra detected along the band of the hybrid host emitting centers could lead to uncorrected conclusions. Therefore, this band was assigned to LMCT states, resulting from the interaction between the

lanthanide ion and the first ligands [166, 170]. Two experimental results confirmed this suggestion: the measurement of PLE spectrum (1) monitored around the  ${}^5\text{D}_0 \rightarrow {}^7\text{F}_4$  transition (700 nm), and (2) of two di-ureasils modified by  $\text{Gd}^{3+}$ , under the same experimental conditions used for the detection of the PLE spectra of  $\text{Eu}^{3+}$ -based hybrids. The  $\text{Gd}^{3+}$  excitation spectrum is a useful spectroscopic tool since the energetic difference between the first excited state and the fundamental level is too high to allow the detection of a charge-transfer state in the UV/Vis range. By measuring such spectra, we may expect to detect only the PLE components that are not related to the charge-transfer processes. The excitation spectra monitored around 700 nm are plotted in Figure 1B, overlapping the one detected around 612 nm, for an easier comparative analysis. No changes were observed in the main band, namely, in its peak position and FWHM, while the intensity of the lower energetic band is approximately half reduced. In the  $\text{Gd}^{3+}$ -based di-ureasils, the presence of the LMCT states was not detected, and only the less intense band could be observed. This fact clearly assigned the latter band to the excitation of the hybrid host emitting centers, and excluded it from any connection with charge-transfer mechanisms. In addition, the observed decrease of the relative intensity with respect to the LMCT band in the PLE spectra monitored around 700 nm should not occur if the nature of both bands is the same.

The  $\text{U}(600)_n\text{Eu}(\text{CF}_3\text{SO}_3)_3$  di-ureasils always present a higher energetic LMCT band when compared to the  $\text{U}(2000)_n\text{Eu}(\text{CF}_3\text{SO}_3)_3$  hybrids within the concentration range studied here. The energy of the LMCT states depends on the number and type of the lanthanide ion first neighbors. The following equation relates the energy of such states,  $E_{\text{LMCT}}$ , to the ionization potential of the cation,  $I_{\text{RE}}$ , and to the ionization potential of the ligands,  $I_L$  [204]:

$$E_{\text{BTC}} = I_L - I_{\text{RE}} + \alpha \quad (5)$$

where  $\alpha$  is a constant associated with the local geometry around the cation [166, 204]. According to Eq. (5), a blue shift of the energy of the LMCT states is related to an increase in the effective charge of the lanthanide cation. This behavior might be induced by: (1) an increase in the cations' first ligand distances, and/or (2) a reduction of the number of ligands and/or a decrease in the effective charge of the ligands. Therefore, it was suggested that the  $\text{Eu}^{3+}$  cations experience a more covalent environment in the  $\text{U}(2000)_n\text{Eu}(\text{CF}_3\text{SO}_3)_3$  hybrids than in the  $\text{U}(600)_n\text{Eu}(\text{CF}_3\text{SO}_3)_3$  di-ureasils. This fact is mainly induced by changes in the nature of the first ligands. In the high-molecular-weight hybrids, the  $\text{Eu}^{3+}$  cations interact mainly with the carbonyl oxygen atoms of the urea bridges, for  $40 \leq n \leq 400$ , and in the shorter polymer chain di-ureasils, the rare-earth ions are coordinated to the ether-type oxygen atoms, for  $40 \leq n \leq 200$ , and only for higher concentrations,  $n < 40$ , was the coordination to the oxygen atoms of the carbonyl groups observed together with the presence of  $\text{Eu}^{3+}$  cations in the polymer chains [170]. As the carbonyl oxygen atoms have a greater tendency to establish covalent bonds than the ether-type oxygen atoms [205], a more energetic LMCT state is expected in the latter case. Besides changes in the type of first ligands, changes in the number of first

neighbors also influence the covalency degree of the cation first coordination shell.

Upon decreasing the temperature from 300 to 14 K, we observe an increase of around 40% of the PLE intensity, whereas the other PLE features described at RT remain constant. This explains why the energy of the LMCT states was analyzed at 14 K. The inset in Figure 1B shows the low-temperature PLE spectra for the U(2000) di-ureasils, evidencing the energy dependence of the LMCT states, with the increase of the salt concentration between  $n = 200$  and  $n = 20$ . While for concentrations  $200 \geq n \geq 40$  and for  $40 \geq n \geq 20$  the energy of the LMCT states shifts to lower energies, for concentrations in the range  $80 \geq n \geq 40$ , the energy of the LMCT states moves to higher energies. According to Eq. (5), this behavior suggests a decrease in the covalency nature of the  $\text{Eu}^{3+}$  first coordination shell as the concentration decreases between  $n = 40$  and  $n = 80$ . As the mean radius of the first shell coordination is, approximately, constant in the entire concentration interval studied (as suggested by EXAFS measurements; see Section 3), changes in the energy of the LMCT states (and consequently, in the covalency degree of the first coordination shell) must be related to changes in the type of the first ligand atoms. In fact, upon increasing the concentration from  $n = 80$  to  $n = 40$ , the number of available oxygen atoms of the carbonyl groups of the urea linkages per incorporated ion decreases from 4 to 2. As the total number of first ligands does not depend on the concentration, it was demonstrated that the carbonyl–oxygen-type atoms are replaced by  $\text{H}_2\text{O}$  molecules that are known to have a lower tendency to establish covalent bonds with  $\text{Eu}^{3+}$  [166, 168, 170, 205]. In that series of hybrids, the covalency degree of the first coordination shell depends on the salt content, in contrast to the situation observed for the  $\text{U}(600)_n\text{Eu}(\text{CF}_3\text{SO}_3)_3$  di-ureasils, where the energy of the LMCT states is approximately constant within the concentration range presented. We will return to this point in Section 8.

When the RE salt incorporated in the di-ureasils is replaced by RE-based complexes, namely  $\beta$ -diketonate [172, 184] and *byp* [185], or when the lanthanide ions are surrounded by organic ligands that are covalently grafted to the hybrid framework [53, 143, 153–159], the respective PLE spectra monitored around the cation emission lines are mainly composed of a large broad band in the UV/Vis region. As an example, we can refer the PLE spectra of the U(2000) di-ureasil codoped with  $\text{Eu}^{3+}$ ,  $\text{Tb}^{3+}$ , and  $\text{Tm}^{3+}$ , monitored around the  $^5\text{D}_4 \rightarrow ^7\text{F}_4$  ( $\text{Tb}^{3+}$ ) and  $^5\text{D}_0 \rightarrow ^7\text{F}_2$  ( $\text{Eu}^{3+}$ ) transition [172], plotted in the inset of Figure 10. Besides the respective intra-4f transitions, a large broad band peaking around 382 nm, assigned to the ligand excitation, composes each PLE spectrum. The low relative intensity of the intra-4f transitions regarding this band indicates an effective ligand-to-metal energy transfer mechanism.

Evidence of energy transfer mechanisms between the ligands and the RE ion is also found in the PLE spectra of  $\text{SiO}_2/\text{SPM}:\text{Eu}[(\text{phen})_2]^{3+}$  and  $\text{SiO}_2:\text{Eu}[(\text{phen})_2]^{3+}$  [188]. In both PLE spectra, it is possible to discern the presence of three main absorption bands around 280, 300, and 325 nm [188], which were ascribed to the matrix, to the Eu-based complex, and to the  $\pi\pi^*$  band of the phen ligands [188]. The

similarity between the  $\text{SiO}_2/\text{SPM}:\text{Eu}[(\text{phen})_2]^{3+}$  and  $\text{SiO}_2:\text{Eu}[(\text{phen})_2]^{3+}$  PLE spectra shows that the  $[\text{Eu}(\text{phen})_2]^{3+}$  complex cations exist in both samples [188].

Figure 12 shows the PLE spectra of all of the  $\text{SiO}_2/\text{SPM}$ -terbium complexes monitored within the main  $\text{Tb}^{3+}$  line [189]. The large broad band present in the spectra of all of the hybrids corresponds to an efficient  $\pi\pi^*$  transition based on the conjugated double bonds of the carboxyl ligands [189], unequivocally establishing the importance of the ligands in the excitation of the cations levels.

The Class II hybrid frameworks incorporating an organic molecule which is able to covalently complex RE ions also show efficient ligands-to-metal ions energy transfer mechanisms. Let us briefly discuss some examples.

Franville et al. studied the PLE spectra of four  $\text{Eu}^{3+}$ -based hybrids monitored around the cation's most intense transition (see Fig. 14B) [153]. All of the spectra are mainly composed of a large broad band in the UV spectral region, 294–370 nm, resulting from an  $\text{S}_0 \rightarrow \text{S}_1$  absorption within the chromophore ligand [153]. The authors interpreted the presence of this band as a clear indication of efficient sensitization of the luminescent centers by the organic ligands.

Fan et al. reached the same conclusion with respect to the PLE spectra of three complexes of 2-pyridinecarboxylic acid europium (III) (see Fig. 16B) [159]. In spite of the presence of intra-4f<sup>6</sup> transitions, all of the spectra are dominated by a band, resulting from the existence of energy transfer between the ligands and the lanthanide ions.

Li et al. established the importance of the covalent bond between the organic complex and the hybrid's backbone by comparing the PLE results of the Hybrid I and Hybrid II samples, shown in Figure 15B [158]. While the spectrum of Hybrid I is composed of only a band centered around 282 nm, which is characteristic of the efficient transition based on the conjugated double bonds of the heterocyclic ligand, the Hybrid II spectrum displays a noisy band in the same spectral region superimposed by the  $^7\text{F}_0 \rightarrow ^5\text{L}_6$  and  $^5\text{D}_2$  transitions [158].

The PLE spectrum of the  $\text{Tb}$ -PABI hybrid film monitored around the  $\text{Tb}^{3+}$  emission is formed by a large broad band peaking around 292 nm, which was ascribed to the ligands' absorptions, indicating effective energy transfer to the  $\text{Tb}^{3+}$  ions [161].

## 5. COLOR COORDINATES

The di-ureasil hybrid's emission appears to be white to the naked eye, due to the convolution of the  $\text{Eu}^{3+}$  intrinsic luminescence with the emission associated with the hybrid host emitting centers, namely, the electron–hole recombinations that occur in the NH groups of the urea linkages and in the siliceous nanodomains. This is well illustrated by a set of real time frames, extracted from a video film that recorded the light emitted, during UV exposure and after the excitation source was turned off, of the  $\text{U}(2000)_{80}\text{Eu}(\text{CF}_3\text{SO}_3)_3$  di-ureasil (Fig. 20). Under UV excitation, the cation orange–red emission dominates. Since this emission is characterized by a shorter lifetime, regarding the one typical of the hybrid host emitting centers, when the UV excitation is turned off, the sample displays only the green–blue color typical of the matrix [166].

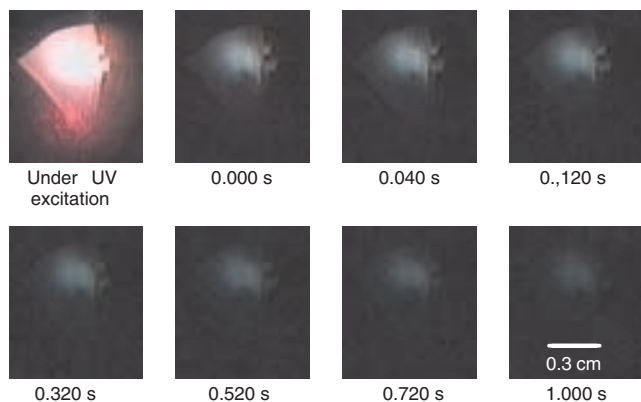


**Figure 20.** Set of real-time frames illustrating the white-light emission of  $U(2000)_{80}Eu(CF_3SO_3)_3$  at 14 K and UV excitation (331.1 and 351.4 nm) and during 1 s after the laser beam (100 mW) was turned off. Reprinted with permission from [166], L. D. Carlos et al., *Phys. Rev. B* 60, 10042 (1999). © 1999, American Physical Society.

It should be noted that the di-ureasil's white light is achieved by a different process than the one usually associated with the emission of multiwavelength phosphors based in LEDs [80, 82, 87]. The greenish–blue component is not totally absorbed by the  $Eu^{3+}$  metallic ions, and thus, the overall emission is a sum of both contributions. This fact is a critical advantage, as recently suggested for the hybrids LEDs made of InGaN and conjugated polymers [82].

In order to quantify and compare the emission of the hybrid organic–inorganic materials discussed in this review with regard to color, it is important to employ a universal quantitative way to infer this information. The color coordinates are usually calculated using the system of the Commission International de L'Éclairage created in 1931 [195, 206–208]. This procedure is based on the human eye's response to the visible light. The human eye possesses three cone cells responsible for the color distinction. Each cone cell presents a different sensibility, designated as  $\bar{x}_\lambda$ ,  $\bar{y}_\lambda$ , and  $\bar{z}_\lambda$ , with maximum value at ca. 419, 531, and 558 nm, respectively. The sum of the three cone sensitivity functions is called the *photonic response*, and displays a maximum sensibility centered at 555 nm, in the green spectral region. The  $\bar{x}_\lambda$ ,  $\bar{y}_\lambda$ , and  $\bar{z}_\lambda$  are called the CIE color-matching functions, and characterize the 2° standard observer recommended by CIE in 1931. In addition, the CIE defined three new primaries colors  $X$ ,  $Y$ , and  $Z$ , needed to match any specific color. These quantities,  $X$ ,  $Y$ , and  $Z$ , are known as tristimulus values. These primary colors established by the CIE have a large advantage when compared with other color systems since the color-matching functions do not display negative parts. The  $\bar{x}_\lambda$ ,  $\bar{y}_\lambda$ , and  $\bar{z}_\lambda$  can be used as weighting functions of the luminescence data, in order to determinate the  $X$ ,  $Y$ , and  $Z$  that characterize a given emission spectra. The corresponding  $X$ ,  $Y$ , and  $Z$  are obtained by adding all emission wavelengths' tristimulus values through the following equations set [195, 206–208]:

$$\begin{cases} X = \int_i \bar{x}_i \cdot E_i d\lambda \\ Y = \int_i \bar{y}_i \cdot E_i d\lambda \\ Z = \int_i \bar{z}_i \cdot E_i d\lambda \end{cases} \quad (6)$$

where  $E$  stands for the emission spectra intensity and  $i$  represents the emission wavelengths. To simplify the calculus, the spectra can be divided into small wavelength intervals  $\Delta\lambda$  (usually  $\Delta\lambda = 5$  or 10 nm), and Eq. (7) can be rewritten as

$$\begin{cases} X = \sum_{\lambda=380}^{720} \bar{x}_\lambda \cdot E_\lambda \Delta\lambda \\ Y = \sum_{\lambda=380}^{720} \bar{y}_\lambda \cdot E_\lambda \Delta\lambda \\ Z = \sum_{\lambda=380}^{720} \bar{z}_\lambda \cdot E_\lambda \Delta\lambda \end{cases} \quad (7)$$

To make the color perception easier, the tristimulus are converted into a two-dimensional system through a linear transformation. The tristimulus are transformed into chromaticity coordinates  $(x, y)$  that are plotted in a two-dimensional chromaticity diagram. The chromaticity coordinates are related to  $X$ ,  $Y$ , and  $Z$  by [195, 206–208]

$$\begin{cases} x = \frac{X}{X + Y + Z} \\ y = \frac{Y}{X + Y + Z} \end{cases} \quad (8)$$

The chromaticity diagram has particular characteristics, namely: (1) the center of the diagram is taken as the white point (0.33,0.33); (2) the curve is made of the pure colors from the blue to the red, covering the entire spectral visible range (380–730 nm), being denoted as the *spectral locus*; and (3) the straight line that connects the two extremes of the *spectral locus* is denoted as a purple boundary. The colors represented by the purple boundary are not pure colors, as they include a mixture of pure red and blue. The area circumscribed by the diagram, spectral locus, and purple boundary encloses the domain of all colors. The CIE tristimulus  $X$ ,  $Y$ , and  $Z$  do not belong to the spectral locus, and therefore they do not represent real colors. This is a direct consequence of the postulate that states that any visible color can be obtained by adding only positive quantities of  $X$ ,  $Y$ , and  $Z$  [195, 206–208].

Depending on the application's demands, pure colors or white-light-emitting materials might be requested. A white phosphor material should have color coordinates closer to the center of the CIE diagram (0.33;0.33), while the emission of a potential pure color-emitting material must be specified by pure (saturated) color coordinates, situated along the spectral locus. The CIE system enables us to specify such a color characteristic through the determination of the hue and saturation or purity [206–208]. The hue corresponds to the dominant wavelength, which can be determined by connecting with a straight line the color coordinates of the emission under analysis with the center of the diagram  $(x_w, y_w) = (0.33, 0.33)$ . Then, the line is prolonged until it intercepts the spectral locus. The intercepting point defines the dominant wavelength. The color purity indicates how close an emission color is from that dominant wavelength, that is, how close is a given emission color from the desired pure color. The color purity  $p$  can be quantitatively inferred by

$$p = \frac{y_c - y_w}{y_{\text{dom}} - y_w} \quad (9)$$



or

$$p = \frac{x_c - x_w}{x_{\text{dom}} - x_w} \quad (10)$$

where  $(x_{\text{dom}}, y_{\text{dom}})$ , and  $(x_c, y_c)$  are the chromaticity coordinates of the pure color and of the emission of the sample in analysis [206–208].

The chromaticity color coordinates  $(x, y)$  were calculated for all of the hybrid organic–inorganic materials discussed here, through the data available in the References. The following results include all of the hybrids from which it was possible to access the respective PL spectra in all of the visible range (380–720 nm).

The color emission arising from organic–inorganic hybrids modified by lanthanide ions can be easily tuned across the CIE diagram, either by changing chemical parameters—molecular weight of the organic precursors, type, and amount of the lanthanide-based salt or complexes, synthesis conditions ( $\text{H}_2\text{O}/\text{Si}$  ratio, nature and concentration of the catalyst, and type of solvent)—and physical parameters—excitation wavelength and temperature. Figure 21 exhibits the CIE diagram where the color coordinates represent the RT emission for the di-ureasils incorporating  $\text{Eu}(\text{CF}_3\text{SO}_3)_3$  [166], the U(600)-based di-ureasils doped with  $\text{Eu}(\text{ClO}_4)_3$  [177], and for ethanolic solutions of the U(600) hybrid with  $\text{Tb}(\text{NO}_3)_3$  and with a mixture of  $\text{Tb}(\text{NO}_3)_3$  and 2,2-byp [185]. For the hybrids modified with  $\text{Eu}^{3+}$  ions, the emission color chromaticity is easily tuned from the blue to the orange–red spectral region, crossing the white color spectral area (Table 1). The emission color of the ethanolic solutions of the  $\text{Tb}^{3+}$ -based U(600) hybrids, under 365 nm excitation, is also closer to the center of the diagram. Exciting the  $\text{Tb}^{3+}$ -based U(600) hybrid with 2,2-byp around the wavelength that maximizes the lanthanide ion PL intensity, the respective CIE color coordinates are within the green spectral region, (0.27, 0.55) (Table 1).

The emission arising from the  $\text{SiO}_2/\text{SPM}:\text{Tb}$  complexes reported by Li et al. is also characterized by  $(x, y)$  color coordinates close to the center of the diagram, due to the overlap between the emission of carboxyl radicals in the hybrid host with that originating from the  $\text{Tb}^{3+}$  ions [189]. The CIE color coordinates vary from (0.28, 0.33) to (0.32, 0.35) for the  $\text{SiO}_2/\text{SPM}:\text{Tb}-o\text{-ABA}$  and  $\text{SiO}_2/\text{SPM}:\text{Tb}-p\text{-ABA}$ , respectively. The  $\text{SiO}_2/\text{SPM}:\text{Tb}-\text{BA}$  and  $\text{SiO}_2/\text{SPM}:\text{Tb}-m\text{-ABA}$  hybrid complexes have similar  $(x, y)$  color coordinates: (0.30, 0.33) and (0.30, 0.30), respectively (Table 2).

The color coordinates of the ormosils-type hybrids doped with  $\text{Eu}[(\text{phen})_2\text{Cl}_3]$  complexes and of the silica films proposed by Li et al., identified as  $\text{SiO}_2/\text{SPM}:\text{Eu}[(\text{phen})_2]^{3+}$  and  $\text{SiO}_2:\text{Eu}[(\text{phen})_2]^{3+}$ , respectively [188], are pure colors within the red spectral region. This is a direct consequence of the fact that only the red intra- $4f^6$  lines could be detected in their PL spectra. The emission color of the  $\text{SiO}_2:\text{Eu}[(\text{phen})_2]^{3+}$  and  $\text{SiO}_2/\text{SPM}:\text{Eu}[(\text{phen})_2]^{3+}$  is described by  $(x, y)$  coordinates of (0.65, 0.35) and (0.60, 0.40), respectively, as shown in the inset of Figure 21 and in Table 2.

Similarly to the preceding case, the color coordinates of the hybrid materials in which the RE organic ligands are covalently grafted to the hybrid framework diverge from the center of the diagram, representing in most of the cases pure colors, namely, red ( $\text{Eu}^{3+}$ ) and green ( $\text{Tb}^{3+}$ ), as shown in

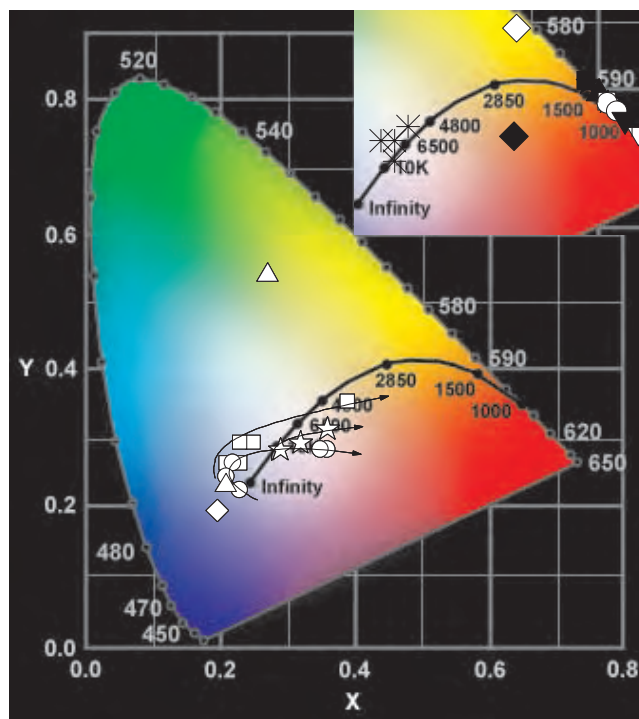


**Figure 21.** CIE chromaticity diagram showing the  $(x, y)$  emission color coordinates (calculated for the 2° standard observer) for the di-ureasils incorporating  $\text{Eu}(\text{CF}_3\text{SO}_3)_3$ , (□)  $\text{U}(2000)_n\text{Eu}(\text{CF}_3\text{SO}_3)_3$ ,  $40 \leq n \leq 400$ , and (○)  $\text{U}(600)_n\text{Eu}(\text{CF}_3\text{SO}_3)_3$ ,  $20 \leq n \leq 200$ , for the (★) U(600)-based di-ureasil doped with  $\text{Eu}(\text{ClO}_4)_3$ , and for ethanolic solutions of the U(600) hybrid with (◆)  $\text{Tb}(\text{NO}_3)_3$ , and with (▲) a mixture of  $\text{Tb}(\text{NO}_3)_3$  and 2,2-byp. The inset shows the CIE color coordinates for the (★)  $\text{Eu}(\text{PA})_3$  complexes, (◆) Hybrid I and (◇) Hybrid II,  $\text{Eu}^{3+}$ -activated organic–inorganic hybrid materials with four different dicarboxylic acids [(☆)  $\text{EuH}_1$ , (□)  $\text{EuH}_2$ , (○)  $\text{EuH}_3$ , and (△)  $\text{EuH}_4$ ], phosphine oxides bonded to  $\text{Si}(\text{OR})_3$  groups treated with anhydrous europium salts [(♣)  $\text{X}_A9a$  and (♠)  $\text{X}_A9b$ ], (\*),  $\text{SiO}_2/\text{SPM}:\text{terbium carbonyl complexes}$ , and (+)  $\text{SiO}_2/\text{SPM}:\text{Eu}[(\text{phen})_2]^{3+}$  and  $\text{SiO}_2:\text{Eu}[(\text{phen})_2]^{3+}$ .

the inset of Figure 21. This derives directly from the efficient intramolecular energy conversion from the ligands to the lanthanide ion that disables the emission arising from the hybrid host and/or the ligands. Consequently, the emission color is dominated by the cation PL, contrary to the di-ureasils modified by  $\text{Eu}(\text{CF}_3\text{SO}_3)_3$  and  $\text{Eu}(\text{ClO}_4)_3$ , whose overall emission appears white to the naked eye, due to the contribution of the hybrid host emitting centers to the PL spectra (see Section 4.1). The CIE color coordinates of these hybrid materials in which the RE organic ligands are covalently grafted to the hybrid skeleton are indicated in Table 3.

For the  $\text{Eu}^{3+}$ -based di-ureasil hybrids, it is possible to achieve a wide tuning of the emission color by changing the excitation wavelength from 330 to 465 nm, as the CIE diagram in Figure 22 shows. For instance, the color coordinates of two di-ureasil hybrids,  $\text{U}(600)_n\text{Eu}(\text{CF}_3\text{SO}_3)_3$ ,  $n = 20$  and 200, change from (0.27, 0.19) to (0.33, 0.56) and from (0.41, 0.26) to (0.42, 0.54), respectively (Table 4).

The calculation of the emission color coordinates regarding the emission properties of the  $\text{U}(2000)_{80} \cdot (\text{Eu}_{0.05}\text{Tb}_{0.15}\text{Tm}_{0.80})(\text{BTEFA})_3 \cdot 2\text{H}_2\text{O}$  hybrid as a function of

**Table 1.** CIE ( $x, y$ ) chromaticity color coordinates (calculated for the 2° standard observer) of the emission of the di-ureasils incorporating  $\text{Eu}(\text{CF}_3\text{SO}_3)_3$ ,  $\text{U}(2000)_n\text{Eu}(\text{CF}_3\text{SO}_3)_3$ ,  $40 \leq n \leq 400$ , and  $\text{U}(600)_n\text{Eu}(\text{CF}_3\text{SO}_3)_3$ ,  $20 \leq n \leq 200$ ,  $\text{U}(600)$ -based di-ureasil doped with  $\text{Eu}(\text{ClO}_4)_3$ , and ethanolic solutions of the  $\text{U}(600)$  hybrid with (◆)  $\text{Tb}(\text{NO}_3)_3$  and with (▲) a mixture of  $\text{Tb}(\text{NO}_3)_3$  and 2,2-byp. The excitation wavelength used is also presented,  $\lambda_x$ .

$\lambda_x$ (nm)	$\text{U}(600)_n\text{Eu}(\text{CF}_3\text{SO}_3)_3$						$\text{U}(2000)_n\text{Eu}(\text{CF}_3\text{SO}_3)_3$						$\text{U}(600)_n\text{Eu}(\text{ClO}_4)_3$ [177]			$\text{U}(600)$ ethanolic solution with [185] $\text{Tb}(\text{NO}_3)_3$ and 2,2-byp		
	$n = 200$	$n = 80$	$n = 60$	$n = 40$	$n = 20$	$n = 400$	$n = 200$	$n = 80$	$n = 60$	$n = 40$	$n = 100$	$n = 15$	$n = 4$	$\text{Tb}(\text{NO}_3)_3$	$\text{Tb}(\text{NO}_3)_3$	$\text{Tb}(\text{NO}_3)_3$	and 2,2-byp	
$x$	0.36	0.23	0.22	0.35	0.21	0.21	0.23	0.25	0.23	0.39	0.29	0.32	0.36	0.20	0.21	0.27		
$y$	0.29	0.23	0.27	0.29	0.25	0.27	0.30	0.30	0.27	0.36	0.29	0.30	0.32	0.20	0.24	0.55		

the temperature (see Section 4.1) nicely illustrates the relative variation of the  $\text{Eu}^{3+}$  and  $\text{Tb}^{3+}$  characteristic luminescence. In fact, by changing the temperature between 200 and 300 K, it is possible to tune the emission color from the green (0.32, 0.58) to the red (0.47, 0.32) spectral regions [172], as Figure 23 illustrates (see also Table 5).

Although the above description of the hybrid's emission features reveals that they may be considered innovative and versatile white-light phosphors, an accurate evaluation of the potential technological impact of these materials as competitive new hybrid multiwavelength phosphors requires knowledge of their external emission quantum yields.

## 6. ABSOLUTE EMISSION QUANTUM YIELDS

There are few reports dealing with the determination of the absolute emission quantum yields in siloxane-based organic–inorganic hybrids modified by RE ions [170, 209]. For  $\text{Ce}^{3+}$ -based hybrids, Isakawi et al. [209] reported external quantum yield values similar to those determined for di-ureasil hybrids incorporating  $\text{Eu}(\text{CF}_3\text{SO}_3)_3$ , 4.6–11.0% [170]. Higher quantum yields, 17.0–27.0%, were found for distinct organic–inorganic hybrids formed by incorporating the  $\text{Eu}^{3+}$   $\beta$ -diketonate complexes in semiconducting polymers [91].

The absolute emission quantum yields  $\phi$ , defined as the ratio between the number of emitted photons and the number of absorbed ones, were measured for the di-ureasils incorporating  $\text{Eu}(\text{CF}_3\text{SO}_3)_3$  by the experimental technique for powdered samples described by Wrighton et al. [210], and were calculated using the following expression:

$$\phi = \frac{A}{R_S - R_H} \quad (11)$$

where  $A$  is the area under the sample's emission spectrum, and  $R_S$  and  $R_H$  are the diffuse reflectance of the reflecting standard (designated as white standard) and of the samples, respectively. Both the reflectance diffuse and the emission spectra were detected with a 24.5° angle with respect to the incident light. The excitation monochromator slits were set in such a way that only the sample was illuminated. These experimental conditions were kept constant for all of the di-ureasil and di-urethanesil hybrids. The experimental errors in the quantum yield values associated with this technique were estimated within 25% [210].

There are several compounds that can be used as white standards, the more common ones being KCl, MgO,  $\text{Na}_2\text{SO}_4$ , and KBr [210]. In our case, we used the high-purity KBr that was maintained in an oven prior to use due to its hygroscopic nature. We chose KBr because its powder size and packing fraction are similar to the size and packing fraction of the hybrid's powder, which is a crucial factor since the intensity of the diffuse reflectance depends on it. To ensure a similar powder size and packing fraction, we chose a wavelength  $\lambda_i$  that corresponded to an energy that was not absorbed by the hybrids, and the diffuse reflectance around  $\lambda_i$  was measured for the standard  $R_S$  and for the hybrids  $R_H$  ( $\lambda_i$  was set equal to 720 nm). The powder samples were grounded until  $R_S$  overlapped  $R_H$ , indicating that we had achieved the same powder size and packing fraction. Figure 24A shows  $R_S$  overlapping  $R_H$  for the  $\text{U}(600)_{80}(\text{EuCF}_3\text{SO}_3)_3$  di-ureasil. Then, both the standard diffuse reflectance and the emission were measured with respect to different excitation wavelengths, corresponding to: (1) the maximum intensity of the hybrid's backbone excitation spectra, (2) around the maximum intensity of the LMCT band, and (3) three wavelengths related with direct excitation of  $\text{Eu}^{3+}$  levels, namely, 395 nm ( ${}^5\text{L}_6$ ),

**Table 2.** CIE ( $x, y$ ) chromaticity color coordinates (calculated for the 2° standard observer) of the emission of the  $\text{SiO}_2/\text{SPM}$ : terbium carbonyl complexes,  $\text{SiO}_2/\text{SPM}:\text{Tb-}o\text{-ABA}$ ,  $\text{SiO}_2/\text{SPM}:\text{Tb-}p\text{-ABA}$ ,  $\text{SiO}_2/\text{SPM}:\text{Tb-BA}$ , and  $\text{SiO}_2/\text{SPM}:\text{Tb-}m\text{-ABA}$  and of the ormosils-type hybrids and silica films,  $\text{SiO}_2/\text{SPM}:\text{Eu}[(\text{phen})_2]^{3+}$  and  $\text{SiO}_2:\text{Eu}[(\text{phen})_2]^{3+}$ , respectively. The excitation wavelength used is also presented,  $\lambda_x$ .

$\lambda_x$ (nm)	$\text{SiO}_2/\text{SPM}$ : terbium carbonyl complexes [189]				Ormosils-type hybrids and silica films [188]	
	$\text{Tb-}o\text{-ABA}$	$\text{Tb-}p\text{-ABA}$	$\text{Tb-BA}$	$\text{Tb-}m\text{-ABA}$	$\text{SiO}_2/\text{SPM}:\text{Eu}[(\text{phen})_2]^{3+}$	$\text{SiO}_2:\text{Eu}[(\text{phen})_2]^{3+}$
$x$	0.28	0.32	0.30	0.30	0.60	0.65
$y$	0.33	0.35	0.33	0.30	0.40	0.35

**Table 3.** CIE ( $x, y$ ) chromaticity color coordinates (calculated for the 2° standard observer) of the emission of the  $\text{Eu}(\text{PA})_3$  complexes, 2-pyridinecarboxylic acid europium (III) complexes, Hybrid I and Hybrid II,  $\text{Eu}^{3+}$ -activated organic–inorganic hybrids materials with four different dicarboxylic acids,  $\text{EuH}_i$ ,  $i = 1, 2, 3, 4$ , and phosphine oxides bonded  $\text{Si}(\text{OR})_3$  groups treated with anhydrous europium salts,  $\text{X}_A9a$  and  $\text{X}_A9b$ . The excitation wavelength used is also presented,  $\lambda_x$ .

	Eu(PA) <sub>3</sub> -based hybrids [159]			1,10-phenanthroline-based hybrids [158]		Dicarboxylic acids-based hybrids [155]				Phosphine oxides-based hybrids [157]	
	(a)	(b)	(c)	Hybrid I	Hybrid II	EuH <sub>1</sub>	EuH <sub>2</sub>	EuH <sub>3</sub>	EuH <sub>4</sub>	X <sub>A</sub> 9 <sub>a</sub>	X <sub>A</sub> 9 <sub>b</sub>
$\lambda_x$ (nm)	275	275	275	282	394	377.1	377.1	377.1	377.1	325	325
$x$	0.35	0.35	0.37	0.48	0.24	0.39	0.38	0.38	0.41	0.42	0.46
$y$	0.55	0.55	0.55	0.34	0.56	0.54	0.54	0.54	0.54	0.54	0.53

420 nm ( $^5\text{D}_3$ ), and 465 nm ( $^5\text{D}_2$ ). Figure 24B–D shows the diffuse reflectance curves for the standard and the  $\text{U}(600)_{80}(\text{EuCF}_3\text{SO}_3)_3$  di-ureasil for three different excitation wavelengths. The number of absorbed photons  $R_S - R_H$  corresponds to the shadowed area in Figure 24B–D.

For both di-ureasil series, and independently of the  $\text{Eu}^{3+}$  concentration,  $\phi$  presents the same trend, that is, when the excitation wavelength varies between 340 and 500 nm, a maximum value is measured around 395 nm. This wavelength maximizes the emission quantum yield because it corresponds to the greater overlap between the excitation spectra of the two hybrid's emitting centres (see Fig. 25A). Figure 25B shows the PL quantum yield values for the two series of di-ureasils for that excitation wavelength (395 nm). In the high-molecular-weight di-ureasils,

the quantum yield values undergo a decrease from 13.0 ( $n = 400$ ) to 1.4% ( $n = 40$ ) [170]. In these hybrids, excluding the less doped sample ( $n = 400$ ), lower quantum yield values were measured when compared to the undoped hybrid that presents  $\phi \approx 9.0\%$  [194, 195]. The quantum yield values for  $\text{U}(600)_n\text{Eu}(\text{CF}_3\text{SO}_3)_3$  ( $n \geq 40$ ) are similar to the one found for the undoped  $\text{U}(600)$  di-ureasil, 7.0% [194, 195], within the experimental error. However, the more concentrated sample ( $n = 20$ ) presents a lower quantum yield value of  $\approx 2.6\%$  [170]. The decrease in the emission quantum yield observed for the two di-ureasil series (Fig. 25B) as the  $\text{Eu}^{3+}$  amount incorporated in the hybrid host increases is clearly evidence of energy transfer between the emitting centers of the matrix (donors) and the metal ions (acceptors) [170, 212]. We will return to this point in the next section.

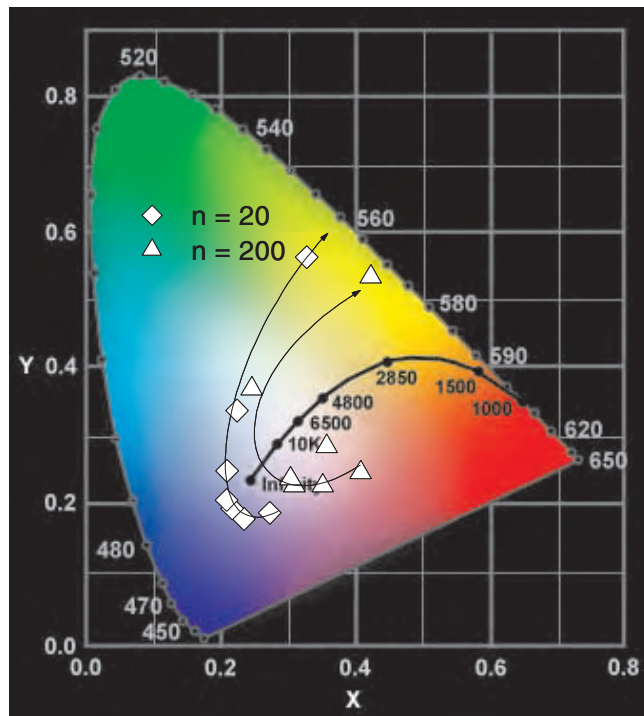


**Figure 22.** CIE chromaticity diagram showing the ( $x, y$ ) emission color coordinates (calculated for the 2° standard observer) for the  $\text{U}(600)_n\text{Eu}(\text{CF}_3\text{SO}_3)_3$ , ( $\Delta$ )  $n = 20$  and ( $\blacklozenge$ )  $n = 200$ . The arrows indicate the variation of the excitation wavelength between 330 and 465 nm. Reprinted with permission from [170], R. A. Sá Ferreira et al., *Chem. Mater.* 13, 2991 (2001). © 2001, Elsevier Science.

## 7. ENERGY-TRANSFER MECHANISMS

One of the most important features regarding hybrid-host-to-metal ion energy-transfer processes in the di-ureasils is that the efficiency of such processes depends noticeably on the ion local coordination site. According to the work of Reinsfeld and Jørgensen on oxide, phosphate, and fluoride glasses containing RE elements [212], the efficiency of the energy transfer between two species can be evaluated from different experimental data, namely, the donor measured lifetime and absolute emission quantum yield, in the presence and absence of the acceptor, and by the emission of the acceptor ion excited at the donor absorption band, together with the emission excited via the acceptor (see [212, p. 61]). In the  $\text{Nd}^{3+}$ - and  $\text{Eu}^{3+}$ -based di-ureasil cases, it was possible to determine the energy-transfer efficiency through the donor measured lifetime and absolute emission quantum yield, in the presence and absence of the acceptor, respectively, by the related following equations [212]:

$$\eta = \left[ 1 - \frac{\tau_D}{\tau_0^D} \right] \quad (12)$$

and

$$\eta = \left[ 1 - \frac{\phi_D}{\phi_0^D} \right] \quad (13)$$

where  $\tau_0$ ,  $\phi_0$ ,  $\tau_0^D$ , and  $\phi_0^D$  represent the donor measured lifetime and absolute emission quantum yield in the presence and absence of the acceptor, respectively [212].

**Table 4.** CIE ( $x$ ,  $y$ ) chromaticity color coordinates (calculated for the 2° standard observer) of the emission of the  $U(600)_nEu(CF_3SO_3)_3$ ,  $n = 20, 200$  at different excitation wavelengths  $\lambda_x$ .

$\lambda_x$ (nm)	U(600) <sub>20</sub> Eu(CF <sub>3</sub> SO <sub>3</sub> ) <sub>3</sub> [170]							U(600) <sub>200</sub> Eu(CF <sub>3</sub> SO <sub>3</sub> ) <sub>3</sub> [170]						
	330	350	365	375	395	420	465	330	350	365	375	395	420	465
$x$	0.41	0.35	0.31	0.30	0.36	0.25	0.42	0.27	0.24	0.22	0.21	0.21	0.23	0.33
$y$	0.25	0.23	0.23	0.24	0.28	0.37	0.54	0.19	0.18	0.20	0.21	0.25	0.34	0.56

It is important to note that, in the case of the  $Eu^{3+}$ -based di-ureasils, we could achieve only a mean value for the efficiency of the energy transfer  $\eta$  using Eq. (13) since we do not know the relative contribution of each host-emitting center. However, as in the  $Nd^{3+}$ -based hybrids, it was possible to measure the lifetime of the NH groups and siliceous nanodomain emitting levels independently; we could separately evaluate the respective contribution for the energy-transfer mechanisms through Eq. (12) [173, 176].

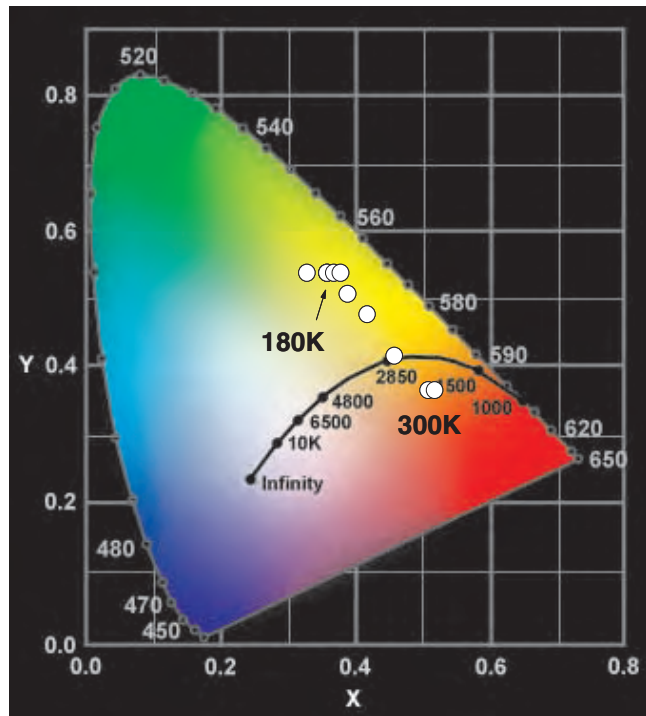
We estimated the efficiency of the energy transfer for all of the nanohybrids of both  $Eu^{3+}$ -based di-ureasil series where a decrease of the quantum yield value was observed with respect to the value measured for the corresponding undoped xerogels. Thus, whereas for the  $U(2000)_nEu(CF_3SO_3)_3$  series the  $n = 400$  sample is the only one where energy-transfer processes seem to be unimportant (as clearly expressed by the increase of the emission quantum yield with respect to that of the undoped hybrid), for the  $U(600)_nEu(CF_3SO_3)_3$  hybrids, the energy-transfer

mechanisms are activated only at  $n = 20$  (Fig. 25B). For the  $U(2000)_nEu(CF_3SO_3)_3$  di-ureasils, the efficiency of the energy transfer increases from 27 to 84% with the increase in the europium content from  $n = 200$  to 40. The value found for the  $U(600)_{20}Eu(CF_3SO_3)_3$  nanocomposite is 63%. These values were calculated for an excitation wavelength of 395 nm, and are independent of the excitation wavelength used [170]. The energy-transfer efficiency in the di-ureasils modified by  $Nd^{3+}$  ions was calculated for all of the di-ureasils with concentrations lower than  $n \geq 40$  since, for higher concentrations, it was not possible to detect the experimental lifetimes of the NH and siliceous nanodomain emitting levels (see Section 4.1). For the  $Nd^{3+}$ -based  $U(900)$  and  $U(2000)$  di-ureasils, the energy-transfer efficiency values from the NH groups  $\eta_{NH}$  and siliceous nanodomains  $\eta_{Si}$  to the  $Nd^{3+}$  ions ranges from 0.16 to 0.83 and 0.05 to 0.86, respectively [176, Table 1].

As noted for the  $Eu^{3+}$ -based hybrids, the cation local coordination site controls the activation of the energy transfer mechanisms. Thus, it is easy to explain why the energy-transfer mechanisms are active in both  $Nd^{3+}$ -based di-ureasils and for the whole concentration range studied since the cations are coordinated to the oxygen atoms of the carbonyl groups of the urea linkages [169, 176]. In both series, the energy-transfer efficiency increases with the increase of the  $Nd^{3+}$  concentration, as more cations are located near the hybrid host emitting centers [176]. We should stress that, although the concentration range expressed in terms of  $n$  is equal for both the  $U(900)$ - and  $U(2000)$ -based hybrids, the  $Nd^{3+}$  content is greater in the latter materials.

In order to verify if the energy transfer occurring between the hybrid host and the  $Nd^{3+}$  cations effectively contributes to an enhancement of the  $Nd^{3+}$  infrared luminescence, the spectra were detected under different excitation wavelengths: (1) 514.5 nm, direct excitation into the intra- $4f^3$  levels, ( $^5G_{9/2}$ ), and (2) 475.9 nm, which corresponds to the preferential excitation of the hybrid host emitting centers, and thus, nonresonant with any one of the lanthanide ion levels [176]. Regardless of the excitation wavelength used, the infrared spectra are similar to the ones displayed in Figure 9A. In order to allow a qualitative comparison between the integrated intensity of each spectrum measured under different excitation wavelengths, all of the spectra were measured consecutively, and the experimental conditions were kept constant. As Figure 26 shows, the emission-integrated intensity depends on the excitation wavelength used, in such a way that the excitation via the di-ureasil host contributes to increase the  $Nd^{3+}$  infrared emission [176].

The possible energy-transfer paths between the cation ( $Eu^{3+}$  and  $Nd^{3+}$ ), the hybrid host emitting centers, and

**Figure 23.** CIE chromaticity diagram showing the ( $x$ ,  $y$ ) emission color coordinates (calculated for the 2° standard observer) for the  $U(2000)_{80}(Eu_{0.05}Tb_{0.15}Tm_{0.80})(BTEFA)_3 \cdot 2H_2O$  hybrid as the temperature varies from 14 to 300 K. Reprinted with permission from [172], L. D. Carlos et al., *Adv. Funct. Mater.* 12, (2002). © 2002, Wiley-VCH Verlag GmbH & Co.



**Table 5.** CIE ( $x, y$ ) chromaticity color coordinates (calculated for the 2° standard observer) of the emission of the  $U(2000)_{80}(Eu_{0.05}Tb_{0.15}Tm_{0.80}) \cdot (BTFA)_3 \cdot 2H_2O$  hybrid at 377 nm excitation wavelength within the temperature range 14–300 K.

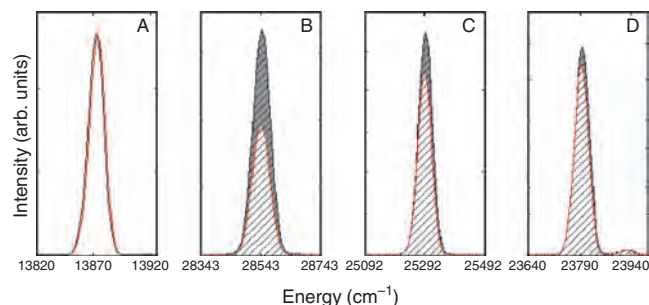
$T$ (K)	$U(2000)_{80}(Eu_{0.05}Tb_{0.15}Tm_{0.80})(BTFA)_3 \cdot 2H_2O$ [172]									
	14	50	100	150	180	200	225	250	275	300
$x$	0.36	0.33	0.36	0.37	0.38	0.39	0.42	0.46	0.51	0.52
$y$	0.54	0.54	0.54	0.54	0.54	0.51	0.48	0.42	0.37	0.37

the LMCT states observed in the case of the  $Eu^{3+}$ -based di-ureasils is illustrated in Figure 27 for the latter hybrids. Figure 27 shows a schematic illustration of the LMCT states, hybrid's host emitting centers, and  $Eu^{3+}$  levels for  $U(2000)_n \cdot Eu(CF_3SO_3)_3$  (Fig. 27A) and  $U(600)_n \cdot Eu(CF_3SO_3)_3$  (Fig. 27B) di-ureasils. For the LMCT band and the hybrid's host emitting levels, the diagram depicts the lowest and the highest energy limits obtained for the different excitation wavelengths (300–420 nm) and for the  $Eu^{3+}$  content for which energy transfer between the hybrid host and the cations occurs.

The involvement of the di-ureasil emitting centers in the luminescent properties of the  $U(2000)$  hybrid codoped with  $Tb^{3+}$ ,  $Eu^{3+}$ , and  $Tm^{3+}$ , namely, the energy transfer from the host to the lanthanide ions, was also demonstrated [172]. The  $Tb^{3+} \ ^5D_4$  lifetime dependence with the variation of the temperature was described by a thermally activated nonradiative mechanism. In the case of the lanthanide ions, this mechanism is usually related to the LMCT states, but for  $U(2000)$  codoped with  $Tb^{3+}$ ,  $Eu^{3+}$ , and  $Tm^{3+}$ , the deexcitation occurs via the hybrid host emitting levels [172, 213]. The Mott–Seitz model approximately described the probability of nonradiative deexcitation of the  $^5D_4$  excited level with the temperature variation through the following expression:

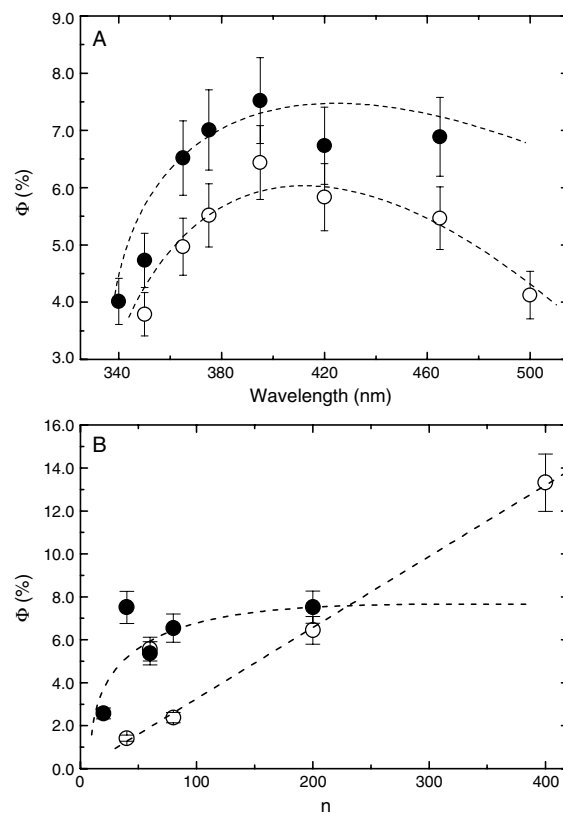
$$\tau^{-1} = \tau_0^{-1} + k \exp(-\Delta E/k_B T) \quad (14)$$

where  $\tau$  is the experimental lifetime,  $\tau_0$  is the lifetime at 0 K,  $k$  is the migration energy rate,  $\Delta E$  is the energy gap between the  $^5D_4$  level and the deexcitation levels, and  $k_B$  is the Boltzmann constant. The obtained activation energy is  $1365.5 \text{ cm}^{-1}$ , which is in agreement with the hypothesis that the energy levels involved in the nonradiative thermally activated deexcitation are the hybrid host emitting levels (siliceous nanodomains and NH groups) [172]. In fact, for

**Figure 24.** Room-temperature diffuse reflectance for the  $U(600)_{80} \cdot (EuCF_3SO_3)_3$  di-ureasil (solid line and solid circles) and KBr (solid line) for: (A) 720 nm, (B) 355 nm, (C) 395 nm, and (D) 420 nm excitation wavelengths.

the excitation wavelength that favors the excitation of the di-ureasil emitting centers (420 nm), the PL spectrum is composed of not only the intra- $4f^6$  lines, but also of the hybrid host characteristic band (400–600 nm) [172]. In spite of the fact that the value determined through Eq. (14) for the activation energy is underestimated, the Mott–Seitz model can be generally applied to describe the  $^5D_4 \rightarrow ^7F_6$  quenching for temperatures between 180 and 300 K [172].

For hybrid materials in which the RE organic ligands are covalently grafted to the hybrid framework, the energy-transfer mechanisms involve predominantly energy transfer from the ligand excited states to the energy levels of the lanthanide ions. This evidence is clearly demonstrated by the presence of a large broad band in the UV/Vis spectral region in the PLE spectra of such hybrids. As noted in

**Figure 25.** RT absolute emission quantum yields values for (a)  $U(600)_{200}(EuCF_3SO_3)_3$  (●) and  $U(2000)_{200}(EuCF_3SO_3)_3$  (○) di-ureasils, excitation wavelenths between 340 and 500 nm, and (b) the  $U(2000)_n(EuCF_3SO_3)_3$  (○) and  $U(600)_n(EuCF_3SO_3)_3$  (●) di-ureasils. Reprinted from [170], R. A. Sá Ferreira et al., *Chem. Mater.* 13, 2991 (2001). © 2001, American Chemical Society.

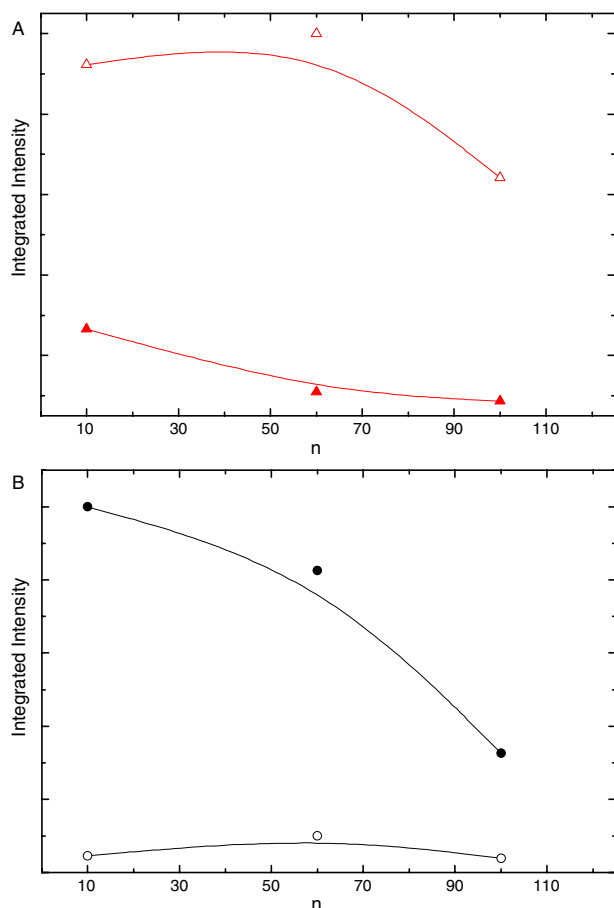


**Figure 26.** Infrared emission integrated intensity recorded under excitation of 514.5 and 457.9 nm for the (a)  $U(900)_nEu(CF_3SO_3)_3$ ,  $n = 10, 40$ , and 100,  $\Delta$  and  $\blacktriangle$ , respectively, and (b)  $U(2000)_nEu(CF_3SO_3)_3$ ,  $n = 10, 40$ , and 100,  $\circ$  and  $\bullet$ , respectively. The lines are guides to the eyes.

Section 4.2, the band in the PLE spectra monitored around the cations lines (essentially,  $Eu^{3+}$ ) (Figs. 14B, 15B, and 16B) was assigned to a transition occurring within the ligand levels. The efficiency of energy transfer in this hybrid type was demonstrated both by the lack of emission arising from the ligands/host in the PL spectra and by the lower intensity of the intra- $4f^6$  transitions, relative to the ligand excitation band, in the PLE spectra monitored around the  $Eu^{3+}$  emission lines.

Franville et al. compared the luminescence intensity of the  $EuH_i$  ( $i = 1-4$ ) hybrids, and found the following decreasing order:  $EuH_2 > EuH_3 > EuH_1 > EuH_4$  [155]. The main factor considered to be responsible for this result was attributed to the efficiency of the energy-transfer mechanisms between the ligand and the  $Eu^{3+}$  cation, which depend on the relative positions between the intra- $4f^6$  levels and the excited states of the ligands, namely, the singlet ( $S_1$ ) and triplet ( $T_1$ ) states [155]. The  $S_1$  and  $T_1$  energies were determined by measuring the absorption/emission spectra of the corresponding  $GdH_i$  ( $i = 1-4$ ) materials (see Fig. 28). The emission intensity differences were attributed to the resonant condition between the  $Eu^{3+}$   $^5D_1$  level and the ligand excited state  $T_1$  since it is known that the most efficient energy transfer occurs from the ligands to the intra- $4f^6$  level [155]. As Figure 28 shows,

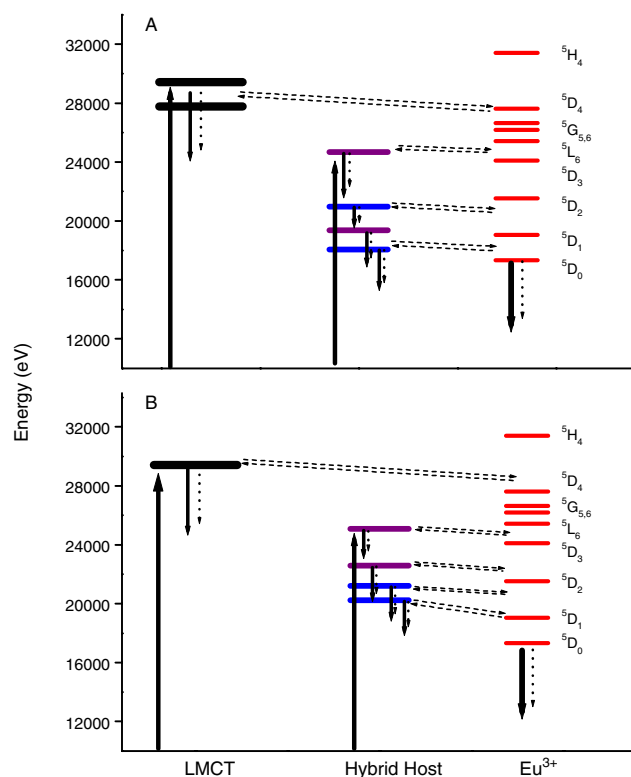


**Figure 27.** Schematic illustration of the energy diagram for (a)  $U(2000)_nEu(CF_3SO_3)_3$ ,  $40 \leq n \leq 200$ , and (b)  $U(2000)_{20}Eu(CF_3SO_3)_3$ . For the hybrid levels, the black and gray lines correspond to the siliceous nanodomain and NH group emitting levels, respectively. The solid and dotted lines indicate radiative and nonradiative processes, respectively. The dashed lines exemplify possible energy-transfer paths between the host and the  $Eu^{3+}$  ions and between the LMCT states and the intra- $4f^6$  levels. Reprinted with permission from [170], R. A. Sá Ferreira et al., *Chem. Mater.* 13, 2991 (2001). © 2001, Elsevier Science.

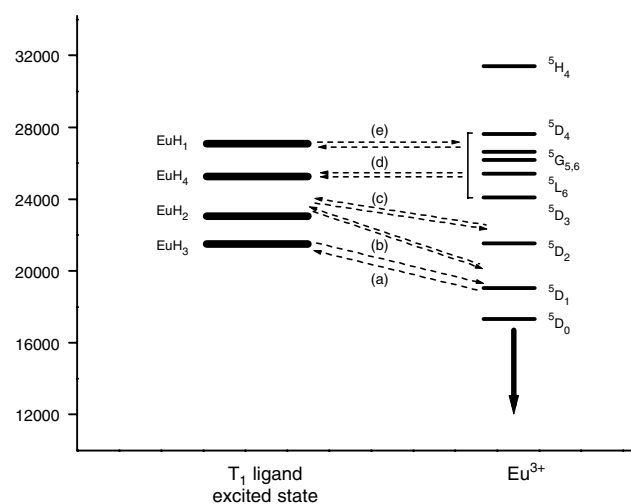


**Figure 28.** Schematic illustration of the energy diagram for the  $EuH_i$  ( $i = 1, 2, 3, 4$ ) hybrids reported in [155]. The possible energy-transfer paths between the ligands excited triplet state and the  $Eu^{3+}$  levels are illustrated. Reprinted with permission from [155], A.-C. Franville et al., *Solid State Sci.* 3, 221 (2001). © 2001, Elsevier Science.



the state  $T_1$  is closer to the  $^5D_1$  level for the  $\text{EuH}_2$  and  $\text{EuH}_3$  hybrids, contributing to a more efficient energy transfer (a); the low intensity of the  $\text{EuH}_2$  regarding that of the  $\text{EuH}_3$  was attributed to the possible back transfer from the  $^5D_2$  level to the ligand excited level (b). For the remaining samples, two major factors were considered as responsible for their low relative emission intensity: (1) the higher energetic  $T_1$  triplet state, and (2) back transfer from intra- $4f^6$  levels (c) and (d), namely,  $^5L_6$  and  $^5D_3$  [155].

## 8. $\text{Eu}^{3+}$ LOCAL COORDINATION

The  $\text{Eu}^{3+}$  local coordination was investigated in great detail for the di-ureasils,  $\text{U}(\text{Y})_n\text{Eu}(\text{CF}_3\text{SO}_3)_3$ ,  $\text{Y} = 600$  and  $2000$ , and  $\text{U}(600)_n\text{Eu}(\text{Cl}_4\text{O})_3$ , [166, 170, 171, 177, 180, 181], and for the  $\text{Eu}^{3+}$ -activated hybrids with four different dicarboxylic acids, designated as  $\text{EuH}_i$  ( $i = 1-4$ ) [153, 155].

The typical  $\text{Eu}^{3+}$  emission lines for the di-ureasil hybrids were already presented in Figure 7. The number of components clearly identified for the  $^7F_{0-2}$  levels is one, three, and five, respectively. While for the  $^7F_1$  level it is possible to discern unequivocally the three components, in the  $^7F_2$  level, there is some uncertainty in the assignment of the lower energetic component [166]. The  $\text{Eu}^{3+}$  luminescence features, namely, the number of Stark components and respective energy, do not vary either with the excitation wavelength or the ion content, except in the case of highly concentrated  $\text{U}(600)_n\text{Eu}(\text{Cl}_4\text{O})_3$  ( $n > 62$ ) and  $\text{U}(600)_n\text{Eu}(\text{CF}_3\text{SO}_3)_3$  ( $n > 40$ ) [170, 171, 181]. For these samples, a variation of the energetic position of the emission lines with the variation of the excitation wavelength was observed, namely, in the energy of the nondegenerated  $^5D_0 \rightarrow ^7F_0$  transition (see Fig. 7B and C). The number of local-field splitting  $^7F_{1,2}$  Stark components detected and the presence of the  $^5D_0 \rightarrow ^7F_{0,3}$  transitions indicate a low-symmetry environment for the  $\text{Eu}^{3+}$  ions in the di-ureasil's host. Generally, the  $\text{Eu}^{3+}$  ions are accommodated in a continuous distribution of closely similar network sites in the di-ureasils, excluding the  $\text{U}(600)_n\text{Eu}(\text{Cl}_4\text{O})_3$  ( $n > 62$ ) and  $\text{U}(600)_n\text{Eu}(\text{CF}_3\text{SO}_3)_3$  ( $n > 40$ ) hybrids, where two different local environments were discerned. This is also suggested by the high values found for the FWHM of the  $^5D_0 \rightarrow ^7F_0$  transition, between 17 and  $31 \text{ cm}^{-1}$  [166].

The chemical nature of the  $\text{Eu}^{3+}$  local sites can be discussed in greater detail through the analysis of the energy of the  $^5D_0 \rightarrow ^7F_0$  transition in a given sample  $E_{\text{complex}}$  relative to the value calculated for gaseous  $\text{Eu}^{3+}$  ions ( $E_{\text{gaseous}} = 17374 \text{ cm}^{-1}$  [166, 168, 205]). This shift  $\Delta E$  was related to the nature of the  $\text{Eu}^{3+}$  first coordination shell through the following phenomenological equation [166, 168, 205]:

$$\Delta E = E_{\text{complex}} - E_{\text{gaseous}} = C_N [n_1 \delta_1 + \dots + n_j \delta_j] \quad (15)$$

where  $C_N$  is a nephelauxetic parameter adjustment related to the total number of first-ligand atoms,  $n_j$  is the number of atoms of type  $j$  in the first coordination shell, and  $\delta_j$  is an adjusted parameter that measures the tendency of a particular atom to bond covalently to the  $\text{Eu}^{3+}$  ion [166, 168, 205]. Frey et al. gathered the energy of the  $^5D_0 \rightarrow ^7F_0$  transition of several  $\text{Eu}^{3+}$ -based materials whose local structures were known, and determined the typical  $\delta_j$  parameters for

several ligands, ordering the ligand types in terms of their tendency to produce the *nephelauxetic* effect [205]:  $\text{Cl} > \text{OT} > \text{O} > \text{O}\beta > \text{ON} > \text{NT} > \text{OH} > \text{OE} > \text{OW}$ , where OT, O,  $\text{O}\beta$ , ON, NT, OH, OE, and OW represent oxygen atoms that belong to charged carboxylate, amide carbonyl,  $\beta$ -diketonate, nitrate, hydroxyl, ether groups, and  $\text{H}_2\text{O}$  molecules, respectively [205]. This ordination suggests that the oxygen atoms that belong to the polyether chain (OE) have a lower tendency to establish covalent bonds to  $\text{Eu}^{3+}$  than the oxygen atoms of the carbonyl groups (OT) of the urea cross linkages.

An ordinal scale of covalency for lanthanide compounds based on the overlap polarizability of a chemical bond was recently proposed by Malta et al. [214], showing a good correlation with the *nephelauxetic* effect, observed from the red shift of the  $^5D_0 \rightarrow ^7F_0$  transition in the  $\text{Eu}^{3+}$  complexes, relatively to the value reported for free ion. This corroborates the conclusion reached in [205] and [215] stressing the importance of covalency in the mechanism that governs the red shift in the energy of certain transitions when the ions are incorporated into solid structures, relatively to the value found for free ions.

Considering the structural information supplied by EXAFS and FTIR (see Section 3), Eq. (15) was used to simulate the first coordination shell of the  $\text{U}(2000)_n \cdot \text{Eu}(\text{CF}_3\text{SO}_3)_3$ ,  $n = 40, 60$ , and  $80$ , di-ureasils. An 11-fold coordination was considered in all cases. FTIR results suggested that one of the three-triflate anions does not belong to the first coordination shell. Therefore, five (or four) oxygen atoms of the  $\text{SO}_3$  end groups of the remaining triflate anions establish a tri- and a bidentate (monodentate) coordination to the  $\text{Eu}^{3+}$  [164, 166, 168]. If the  $\text{Eu}^{3+}$  concentration is expressed in terms of the number of available oxygen atoms of the carbonyl group per  $\text{Eu}^{3+}$  cation, then there are four, three, and two oxygen atoms of that type for the di-ureasils with  $n = 80, 60$ , and  $40$ , respectively. The 11-fold coordination is thus completed with two, three, and four  $\text{H}_2\text{O}$  molecules, respectively. As expressed in Table 6, the predicted energy shift  $\Delta E$  agrees well (within the correlation uncertainty reported for the  $C_N$  and  $\delta_j$  coefficients,  $\pm 3 \text{ cm}^{-1}$ ) with the experimental values  $\Delta E_{\text{exp}}$ . These calculations were performed using the  $C_N$  and  $\delta_j$  coefficients present in [205, Table 2]. Note that, since the  $\delta_j$  coefficient was not reported for the  $\text{SO}_3$  group, the value proposed for the nitrate group was used. We should stress that this assumption seems to be correct, as the predicted and

**Table 6.** Energy of the  $^5D_0 \rightarrow ^7F_0$  transition for the  $\text{U}(2000)_n \cdot \text{Eu}(\text{CF}_3\text{SO}_3)_3$ ,  $n = 40, 60$ , and  $80$ ,  $E_{\text{complex}}$ . The experimental ( $\Delta E_{\text{exp}}$ ) and simulated ( $\Delta E$ ) energetic shifts and the type and number of  $\text{Eu}^{3+}$  first ligands, denoted according to the notation of [205], are also presented.

	$\text{U}(2000)_n\text{Eu}(\text{CF}_3\text{SO}_3)_3$		
	$n = 40$	$n = 60$	$n = 80$
$E_{\text{complex}} \text{ (cm}^{-1}\text{)}$	17496.2	17494.7	17488.1
$\Delta E_{\text{exp}} \text{ (cm}^{-1}\text{)}$	-122.2	-120.7	-114.1
$\Delta E \text{ (cm}^{-1}\text{)}$	-120.6	-117.4	-114.8
Local environment	4 $\text{SO}_3$ , 2OT, 1OW	4 $\text{SO}_3$ , 3OT, 2OW	4 $\text{SO}_3$ , 4OT, 3OW

experimental values coincide, within the referred correlation uncertainty.

The decrease of  $\Delta E$  when increasing the  $\text{Eu}^{3+}$  content suggests that the covalence degree of the lanthanide first coordination shell decreases with the increase in the amount of incorporated  $\text{Eu}^{3+}$ . This occurs due to the replacement of oxygen atoms of the carbonyl group by  $\text{H}_2\text{O}$  molecules in the  $\text{Eu}^{3+}$  first ligands, whose  $\delta_j$  coefficient is inferior to that of the oxygen atoms of the carbonyl groups [166, 168].

As already noted in Section 3, the local coordination of the  $\text{Eu}^{3+}$  ion depends on the length of the polymer chain. In fact, for the U(2000)-based hybrids ( $40 \leq n \leq 400$ ), the lanthanide ions are mainly coordinated to the oxygen atoms of the carbonyl group of the urea linkages, whereas for the U(600)-based di-ureasils ( $n \geq 60$ ), the preferential coordination sites are the ether-type oxygens of the polymer chains. As ether-oxygen atoms are characterized by a lower  $\delta_j$  coefficient than that of the oxygen atoms of the carbonyl groups, it is expected that the  $\text{Eu}^{3+}$  first coordination shell in the latter case presents a lower degree of covalence.

In fact, the PLE spectra monitored around the  $\text{Eu}^{3+}$  emission lines (Section 4.2) confirm this suggestion. The LMCT states are more energetic in the U(600)-based hybrids than in the U(2000)-based di-ureasils. As the energy of these states is related to the covalence degree of the  $\text{Eu}^{3+}$  local environment in such a way that a decrease in the LMCT state's energy is related to an increase in the covalence of the  $\text{Eu}^{3+}$  coordination shell [see Eq. (5)], the PL data are in perfect agreement with the different local coordination sites suggested by the structural results.

The covalency and polarizability degree of the  $\text{Eu}^{3+}$  first coordination shell may also be inferred from the calculus of the intensity parameters,  $\Omega_\lambda$  ( $\lambda = 2, 4, 6$ ) [129, 168, 170, 216, 217]. The  $\Omega_{2,4,6}$  parameters are determined from the RT emission spectra by expressing the emission intensity of the  ${}^5\text{D}_0 \rightarrow {}^7\text{F}_{0-6}$  transitions  $I_{i \rightarrow j}$  in terms of the surface of their emission curves  $S_{i \rightarrow j}$ :

$$I_{i \rightarrow j} = \hbar\omega_{i \rightarrow j} A_{i \rightarrow j} N_i \equiv S_{i \rightarrow j} \quad (16)$$

where  $i$  and  $j$  represent the initial ( ${}^5\text{D}_0$ ) and final ( ${}^7\text{F}_{0-6}$ ) levels, respectively,  $\hbar\omega_{i \rightarrow j}$  is the transition energy,  $A_{i \rightarrow j}$  is the corresponding Einstein's coefficient of spontaneous emission, and  $N_i$  is the population of the emitting level ( ${}^5\text{D}_0$ ) [106–108, 129, 158, 168, 170, 216, 217]. The radiative transition probability  $k_{\text{rad}}$  from the  ${}^5\text{D}_0$  to the  ${}^7\text{F}_{0-6}$  levels may be expressed from the Einstein's spontaneous emission probability between levels  $i$  and  $j$ :

$$A_{i \rightarrow j} = k_{\text{rad}} = \sum_{j=0}^6 A_{0 \rightarrow j} \quad (17)$$

Usually, the  $\Omega_\lambda$  intensity parameters are obtained from absorption data. However, for the  $\text{Eu}^{3+}$  ion, the pure magnetic dipole character of the  ${}^5\text{D}_0 \rightarrow {}^7\text{F}_1$  transition enables the determination of such parameters from the emission spectra. Since this transition does not depend on the local ligand field seen by the  $\text{Eu}^{3+}$  cations, it may be used as a reference for the entire spectrum,  $A({}^5\text{D}_0 \rightarrow {}^7\text{F}_1) \approx 50 \text{ s}^{-1}$

[218]. In that way, it is possible to express the radiative transition probability  $k_{\text{rad}}$  between the first excited state  ${}^5\text{D}_0$  and the  ${}^7\text{F}_{0-6}$  levels as

$$k_{\text{rad}} = \frac{A_{0 \rightarrow 1} \hbar\omega_{0 \rightarrow 1}}{S_{0 \rightarrow 1}} \times \sum_{j=0}^6 \frac{S_{0 \rightarrow j}}{\hbar\omega_j} \quad (18)$$

Moreover, the electric dipolar  ${}^5\text{D}_0 \rightarrow {}^7\text{F}_{2,4,6}$  transitions depend only on the  $U^{(2)}$ ,  $U^{(4)}$ , and  $U^{(6)}$  reduced matrix elements, respectively, which allows the evaluation of the  $\Omega_\lambda$  intensity parameters directly from the RT emission spectra. It is important to note that theoretical calculations indicate the contribution to the values of the  $\Omega_\lambda$  intensity parameters of two different mechanisms: forced electric dipole and dynamic coupling [216, 217, 219]. Jørgensen and Judd first reported the dynamic coupling mechanism in 1945 [220]. In a simple way, the dynamic coupling mechanism can be described assuming that the electric field of the incident radiation induced the formation of oscillating dipoles on the atoms in the neighborhood of the  $\text{Eu}^{3+}$  cations, producing an additional oscillating electric field. An interesting aspect of two such mechanisms, forced electric dipole and dynamic coupling, is that they contribute with opposite signs to the value of the  $\Omega_\lambda$  intensity parameters, so that when such parameters are phenomenologically evaluated, it is not possible to individually identify each contribution. Nevertheless, there are some empirical evidences that make relevant the phenomenological evaluation of the  $\Omega_\lambda$  intensity parameters. The major contribution to the  $\Omega_2$  intensity parameter comes from the hypersensitivity electric dipole  ${}^5\text{D}_0 \rightarrow {}^7\text{F}_2$  transition. It was empirically observed that, in complexes where a higher degree of covalence in the  $\text{Eu}^{3+}$  first coordination shell should be expected, a higher value for the respective  $\Omega_2$  intensity parameter was also observed [212]. Another correlation was reported between the  $\Omega_{4,6}$  intensity parameters and the local vibrational modes involving the  $\text{Eu}^{3+}$  ions, suggesting that a greater rigidity of the material is observed at higher values of such intensity parameters [212]. The  $\Omega_6$  intensity parameter is not usually calculated due to the low relative intensity of the  ${}^5\text{D}_0 \rightarrow {}^7\text{F}_6$  transition, regarding the remaining intra- $4f^6$  transitions.

Summarizing, the expressions used in the calculus of the Einstein spontaneous emission coefficients  $A_{0 \rightarrow 2}$  and  $A_{0 \rightarrow 4}$  are, respectively,

$$\frac{\hbar\omega_{0 \rightarrow 2} A_{0 \rightarrow 2}}{\hbar\omega_{0 \rightarrow 1} A_{0 \rightarrow 1}} = \frac{S_{0 \rightarrow 2}}{S_{0 \rightarrow 1}} \quad (19)$$

and

$$\frac{\hbar\omega_{0 \rightarrow 4} A_{0 \rightarrow 4}}{\hbar\omega_{0 \rightarrow 1} A_{0 \rightarrow 1}} = \frac{S_{0 \rightarrow 4}}{S_{0 \rightarrow 1}} \quad (20)$$

where  $\hbar\omega_{0 \rightarrow j}$  and  $S_{0 \rightarrow j}$  ( $j = 1, 2,$  and  $4$ ) are the energies of the center of gravity and the integrated intensities of the emission curves of the  ${}^5\text{D}_0 \rightarrow {}^7\text{F}_{1,2,4}$  transitions, respectively. Finally, the expressions used for the calculus of the  $\Omega_{2,4}$  intensity parameters are

$$A_{0 \rightarrow 2} = \frac{4e^2}{3\hbar^4 c^3} (\hbar\omega_{0 \rightarrow 2})^3 \frac{n_0(n_0^2 + 2)}{9} \Omega_2 \left( {}^5\text{D}_0 \| U^{(2)} \| {}^7\text{F}_2 \right)^2 \quad (21)$$

and

$$A_{0 \rightarrow 4} = \frac{4e^2}{3\hbar^4 c^3} (\hbar\omega_{0 \rightarrow 4})^3 \frac{n_0(n_0+2)}{9} \Omega_4 \left\langle {}^5D_0 \parallel U^{(4)} \parallel {}^7F_4 \right\rangle^2 \quad (22)$$

where  $e$  is the electron charge (in these equations, an undimensional number equal to  $1.16140 \times 10^{-3}$ ),  $\hbar$  is the Planck constant (units  $\text{cm}^{-1} \cdot \text{s}$ ),  $c$  is the velocity of the light (in  $\text{cm} \cdot \text{s}^{-1}$ ),  $n_0$  is the refractive index of the medium, and  $U^{(2)}$  and  $U^{(4)}$  are reduced matrix elements (values of 0.0032 and 0.0023, respectively [221]). In the case of the di-ureasils,  $n_0$  was set to 1.5, a value very close to that measured for similar organic–inorganic hybrids [55, 72, 74].

The  $\Omega_{2,4}$  intensity parameters calculated for the  $\text{U}(2000)_n\text{Eu}(\text{CF}_3\text{SO}_3)_3$ ,  $400 \geq n \geq 20$  [168] and  $\text{U}(2000)_n \cdot \text{Eu}(\text{CF}_3\text{SO}_3)_3$ ,  $200 \geq n \geq 40$  di-ureasils are listed in Table 7. The  $\Omega_2$  and  $\Omega_4$  intensity parameters found for the precursor salt  $\text{Eu}(\text{CF}_3\text{SO}_3)_3$  were 0.6 and 5.8, respectively [168]. The high-molecular-weight di-ureasils exhibit higher values for the  $\Omega_{2,4}$  intensity parameters than those of the  $\text{U}(600)$ -based hybrids within the entire  $\text{Eu}^{3+}$  concentration range examined. This result unequivocally states that the  $\text{Eu}^{3+}$  experiences a more covalent first coordination shell in the former hybrids. This is exactly the same conclusion already derived from the analysis of the energy observed for the LMCT states detected in the PLE spectra monitored around the  $\text{Eu}^{3+}$  lines.

The relatively high values found for the  $\Omega_2$  intensity parameters indicate that the local environment around the  $\text{Eu}^{3+}$  cations is highly polarizable, suggesting an improvement of the di-ureasil luminescence when compared with that of the  $\text{Eu}(\text{CF}_3\text{SO}_3)_3$  [168]. Increasing the concentration in the  $\text{U}(2000)$ -based series results in a decrease of the  $\Omega_2$  values, except for the  $\text{U}(2000)_{80}\text{Eu}(\text{CF}_3\text{SO}_3)_3$  hybrid, which presents the highest value of the  $\Omega_2$  intensity parameter, indicating a higher degree of covalence for the  $\text{Eu}^{3+}$  first coordination shell. This conclusion was independently suggested by the lower energy observed for the LMCT states of the remaining  $\text{Eu}^{3+}$  concentrations, and is in perfect agreement with the suggestion of the maximum number (four) of carbonyl-type oxygen atoms in the  $\text{Eu}^{3+}$  first coordination shell [168, 170]. For the  $\text{U}(600)_n\text{Eu}(\text{CF}_3\text{SO}_3)_3$  di-ureasils, the variation of the  $\Omega_{2,4}$  intensity parameters with the increase of the concentration from  $n = 200$  to  $n = 80$  does not present the same trend observed for the high-molecular-weight hybrids. In fact, the values of the  $\Omega_{2,4}$  intensity parameters oscillate between 5.6 ( $n = 60$ ) and 7.6 ( $n = 40$ ). A detailed interpretation of these results is hard to realize since, as no EXAFS measurements were performed in these di-ureasils, we do not know how the number of  $\text{Eu}^{3+}$  first neighbors changes with the increase

of the  $\text{Eu}^{3+}$  content. However, the slight variation of the  $\Omega_{2,4}$  intensity parameters between  $n = 200$  and  $n = 40$  suggests that possible changes in the  $\text{Eu}^{3+}$  coordination shell are not as noteworthy as in the case of the  $\text{U}(2000)$ -based hybrids.

Franville et al. carried out a detailed study of the  ${}^5D_0 \rightarrow {}^7F_0$   $\text{Eu}^{3+}$  excitation spectra for the  $\text{EuH}_i$  ( $i = 1-4$ ) organic–inorganic hybrids [155]. These spectra were recorded at 15 K by monitoring the  ${}^5D_0 \rightarrow {}^7F_2$  transition of the four hybrids. For all of the samples, the measured excitation spectra revealed the presence of two contributions in the profile of the  ${}^5D_0 \rightarrow {}^7F_0$  transition [155]. This observation clearly established the presence of two distinct local  $\text{Eu}^{3+}$  coordination sites as this transition occurs between nondegenerated levels. Assuming a sum of two Gaussian functions, the spectra of the  ${}^5D_0 \rightarrow {}^7F_0$  transition were fitted, and the peak energy, FWHM, and relative intensity between the two contributions were estimated [155]. The low and high energetic  ${}^5D_0 \rightarrow {}^7F_0$  transitions were related to two local  $\text{Eu}^{3+}$  environments, designated as *A* and *B*, respectively. For the  $\text{EuH}_i$  ( $i = 1-3$ ) hybrids, the  ${}^5D_0 \rightarrow {}^7F_0$  energy of the two contributions *A* and *B* was detected around 17212–17218 and 17238–17240  $\text{cm}^{-1}$ , and present an FWHM of 11.1–12.4 and 21.2–22.1  $\text{cm}^{-1}$ , respectively. For the  $\text{EuH}_4$  hybrid, a blue shift of both *A* and *B*  ${}^5D_0 \rightarrow {}^7F_0$  transitions (17248 and 17262  $\text{cm}^{-1}$ ) and an increase in the respective FWHM values (13.5 and 24.3  $\text{cm}^{-1}$ ) were observed [155].

Taking into account that the energy of the  ${}^5D_0 \rightarrow {}^7F_0$  transition can be correlated with the number and type of the  $\text{Eu}^{3+}$  first neighbors [Eq. (15)] [205], Franville et al. related the aforementioned results with the structural data known for each hybrid. The  $\text{EuH}_i$  ( $i = 1-3$ ) materials presented a similar coordination mode for the lanthanide ion involving a ninefold coordination, while the  $\text{EuH}_4$  sample exhibited a fivefold coordination that was completed by nitrogen atoms. The blue shift observed for the  ${}^5D_0 \rightarrow {}^7F_0$  transition of the latter hybrid was attributed to the presence of N atoms, from  $\text{NO}_3$  groups, that are known to have a lower tendency to establish covalent bonds with  $\text{Eu}^{3+}$  compared with carbonyl-type oxygen atoms [155, 205].

The presence of two singular  $\text{Eu}^{3+}$  environments was further demonstrated by recording the  ${}^5D_0 \rightarrow {}^7F_0$  excitation spectra at selective monitoring wavelengths that correspond to each contribution (*A* and *B*) and under different delay times after the laser pulse. Although no change was observed in the shape of the spectra, the fitting procedure revealed changes in the intensity ratio of the *A/B*  $\text{Eu}^{3+}$  distributions [155].

**Table 7.**  $\Omega_2$  and  $\Omega_4$  intensity parameters [ $10^{-20} \text{ cm}^2$ ] for the  $\text{U}(Y)_n\text{Eu}(\text{CF}_3\text{SO}_3)_3$ ,  $Y = 2000$ ,  $400 \leq n \leq 40$  and  $Y = 600$ ,  $200 \leq n \leq 40$ .

	$\text{U}(600)_n\text{Eu}(\text{CF}_3\text{SO}_3)_3$				$\text{U}(2000)_n\text{Eu}(\text{CF}_3\text{SO}_3)_3$				
	$n = 200$	$n = 80$	$n = 60$	$n = 40$	$n = 400$	$n = 200$	$n = 80$	$n = 60$	$n = 40$
$\Omega_2$	6.5	7.1	5.6	7.6	10.9	10.4	11.8	9.6	8.1
$\Omega_4$	4.6	6.6	4.1	4.3	8.6	8.4	12.2	9.7	8.4

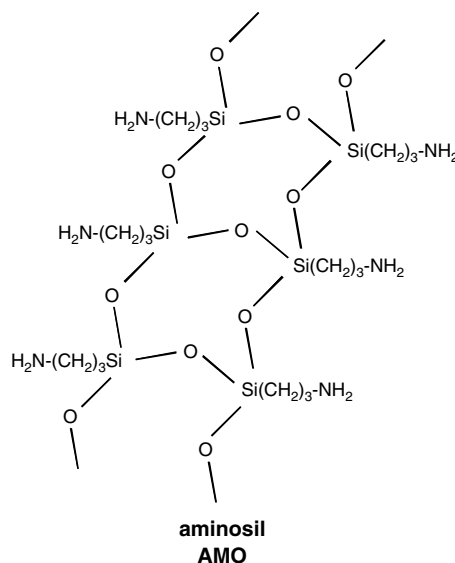
## 9. LUMINESCENT UNDOPED NANOHYBRIDS

The hybrid concept also has been employed to synthesize stable and efficient white-light photoluminescent amine-functionalized hybrids lacking metal activator ions, such as these obtained from APTES and 3-glycidoxypropyltrimethoxysilane (GPTES) with carboxylic acids, and from urea and urethane precursors (di-ureasils and di-urethanesils; Schemes 9 and 10) [163, 177, 186, 191–195, 198, 222–230]. The APTES–formic acid hybrid is one of the most efficient phosphors known among those lacking activator metal ions as it exhibits an external PL quantum yield of  $0.35 \pm 0.01$  [222]. For APTES–acetic acid phosphors, lower limits of 0.21 and 0.12 were estimated for the quantum yields of the two distinct emissions reported [223, 224]. Similar values were found for the di-ureasils and di-urethanesils [194].

Comparing the PL efficiencies of these amine-functionalized cross-linked hybrids with the characteristic values of other materials used in solid-state luminescent displays (e.g., amorphous porous silicon, *p*-Si, and conjugated conducting polymers), we note that the RT quantum yield for these amine-based hybrids is higher than that reported for *p*-Si [231], and similar to the typical values of the most efficient conjugated polymers [232]. Nevertheless, the PL features of the latter materials present substantial intensity degradation under laboratory ambient conditions, with the consequent drastic decrease in the quantum yield.

In spite of the potential technological relevance of the amine-functionalized hybrids, the origin of their efficient white-light intrinsic PL is not completely clarified [194–196, 228–230]. The identification of the nature of the emitting centers and the characterization of the recombination mechanisms subjacent to the intrinsic emission of these amine-functionalized cross-linked hybrids will certainly open new directions for developing other siloxane-based hybrids with similar or even greater light emission efficiency. Moreover, as we have described in the previous sections, most of the research on organic–inorganic frameworks has been focused on the PL features of lanthanide-based hybrid matrices, seeking essentially to take advantage of the high chromaticity and long excited lifetime characteristic of the metal ions, and of the improvement in the emission features and mechanical stability of the samples (compared to those of conventional silica gel hosts).

This section reviews the synthesis and the PL features of sol-gel-derived APTES-based hybrids (classed as aminosils; Scheme 11) and urea and urethane cross-linked organic–inorganic xerogels (Schemes 9 and 10). The nature of the white-light emission and the characterization of the recombination mechanisms subjacent to this intrinsic emission are also discussed. A detailed review on this subject was recently published [195]. The conclusions may be easily generalized to the di-ureasil precursor compounds (e.g., the diamines) and to other amine-functionalized hybrids, such as those based on GPTES and APTES incorporating carboxylic acids such as formic (HCOOH), lactic (CH<sub>3</sub>CHOHCOOH), acetic (CH<sub>3</sub>COOH), and valeric (CH<sub>3</sub>(CH<sub>2</sub>)<sub>3</sub>COOH) [222–224, 228–230].



**Scheme 11.** Molecular structure of the aminosils.

### 9.1. Synthesis

The synthetic procedure of the white-light phosphors proposed by Green et al. [222], which involves the reaction of the TEOS and tetramethoxyortosilane (TMOS) precursors with an excess of an organic carboxylic acid (formic, lactic, acetic, trifluoroacetic, cyclopropanoic, malonic, citric, tartaric, glyoxylic, or oxalic acids) at RT and under nitrogen atmosphere, leads to the formation of gels at times ranging from a few minutes to several days [222]. Solid acids were dissolved in a minimum of anhydrous methanol, whereas most acids were used as neat liquids. Thermal treatment performed in air between 200 and 500 °C gave rise to white or yellowish solid materials that underwent PL. The reaction of APTES with some of the carboxylic acids listed above (performed also by other groups all over the world [223, 224, 229, 230]) yielded a clear water-soluble material that could be drawn into fibers from a melt or cast into films or monolithic structures without any shrinking or cracking [222, 223, 229, 230].

The nondoped di-ureasil d-U(Y) and di-urethanesil d-Ut(Y') hybrids were synthesized using the procedure described in Section 2.2.2, dealing with the detailed description of the synthesis of Class II RE-doped hybrids. The three diamines used were Jeffamine ED-2001® (with  $a + c = 2.5$  and  $b = 40.5$ ), Jeffamine ED-900® (with  $a + c = 2.5$  and  $b = 15.5$ ), and Jeffamine ED-600® (with  $a + c = 2.5$  and  $b = 8.5$ ) (Scheme 9). The PEGs employed have average molecular weights of 300 and 2000 g/mol (PEG(300) and PEG(2000)), with  $m = 6$  and 45, respectively; Scheme 10). A slightly different synthesis procedure was proposed for the di-ureasil hybrids using HCl or NH<sub>4</sub>F for acid- or base-catalyzed hydrolysis, respectively [177, 186, 233]. Recently, the synthesis of di-ureasil hybrids by a completely distinct method involving acetic acid solvolysis in the absence of water was introduced [230].

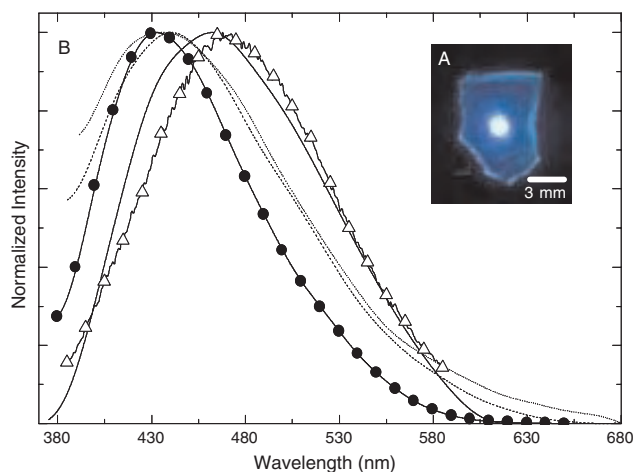
The aminosil hybrids discussed here (Scheme 11) were prepared using the same procedure employed by Rousseau et al. [234]. APTES was mixed, at RT, with H<sub>2</sub>O and

methanol (molar ratio 1 Si:9.6 CH<sub>3</sub>CH<sub>2</sub>OH:1.5 H<sub>2</sub>O). This procedure is substantially different from that reported previously for similar hybrids in which APTES reacts with carboxylic acids [222–224, 229, 230].

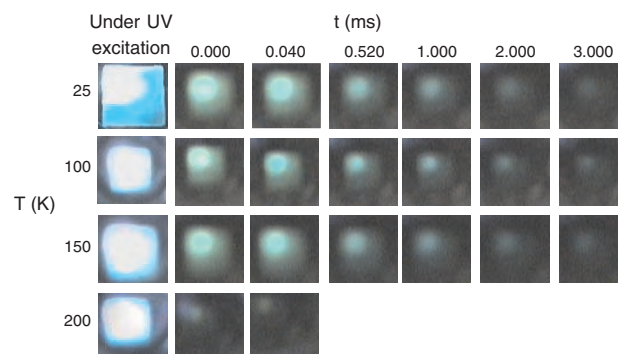
## 9.2. Photoluminescence

Figure 29 displays the PL spectra of representative amine-based functionalities, the nonhydrolyzed precursors, and the di-ureasil, di-urethanesil, and aminosil hybrids. Apart from minor shifts in energy and in relative intensities, the emission of the other two diamines (Jeffamine-ED-900® and Jeffamine-ED-600®), nonhydrolyzed precursors, di-ureasils, and di-urethanesils are quite similar. The spectra also resemble those reported for APTES-derived hybrids with HCOOH, CH<sub>3</sub>CHOHCOOH, and CH<sub>3</sub>COOH carboxylic acids [222–224, 226, 230]. Furthermore, both the di-ureasils prepared with HCl or NH<sub>4</sub>F catalysts [177, 186] and by means of acetic acid solvolysis (a procedure carried out in the absence of water) [230] show identical PL features. The hypothesis that these PLs might arise from any contaminant present in the starting commercial products used in the synthesis was readily discarded [194–196]. Moreover, based on the molecular structure of ICPTES and APTES and on the fact that pure PEG (the organic precursor of the di-urethanesils) is not luminescent, a suggestion relating that emission with the lone pair of electrons of the NH-related groups existent in all of these amine-functionalized materials was previously pointed out in several works dealing with the PL features of amine-based hybrids [191–196, 222, 223, 230].

The PL features of a series of solutions of Jeffamine ED-2001®, using H<sub>2</sub>O and THF as solvents, provides other



**Figure 29.** (A) Photograph showing the white-light emission of U(2000) at 298 K under UV excitation (Ar ion laser). The diameter of the emitting area is  $\approx 3$  mm<sup>2</sup>. (B) PL spectra (360–365 nm excitation at 298 K) of representative amine-based functionalities, precursors, and di-ureasil and di-urethanesil hybrids: Jeffamine ED-2001® (dashed curve), nonhydrolyzed U(2000) precursor (dotted curve), U(2000) (solid curve), Ut(2000) (solid curve with circles), and aminosil (solid curve with triangles). Reprinted with permission from [195], L. D. Carlos et al., in “Handbook of Organic-Inorganic Hybrid Materials and Nanocomposites” (H. S. Nalwa, Ed.), Vol. 1, p. 353. American Scientific Publishers, Morth Lewis Way, CA, (2003). © 2003, American Scientific Publishers.



**Figure 30.** Set of frames showing the real-time dependence (14–220 K) of the di-urethanesil Ut(300) white-light emission during 3 s after the Ar ion laser beam was turned off. Note that the emission color is slightly distorted by the video camera. The real color is more “whitish-blue.” Reprinted with permission from [172], L. D. Carlos et al., *Adv. Funct. Mater.* 2, 111 (2001). © 2001, Wiley–VCH.

experimental evidence indicating that the NH-related groups must be involved in the PL features of these materials [195, 196]. The supralinear decrease of the PL intensity with the decrease of the diamine concentration in the solutions was related to the increase of the average distance between NH<sub>2</sub> groups (belonging to different chains) induced by the dilution. A similar suggestion was recently pointed out, stressing that the emission properties of amine-functionalized hybrids are connected to the existence of clusters involving both the organic and inorganic components [186, 230]. In di-ureasils and di-urethanesils, SAXS data [178, 181–183] and fluorescence probing [225, 227] were used to study these clusters.

The difference between the PL features of the hybrids and those of their respective precursors was well established by time-resolved spectroscopy [194–196]. As previously reported for di-ureasils and di-urethanesils, for SDs between  $0.08 \times 10^{-3}$  and  $5.00 \times 10^{-3}$  s, two components are clearly observed in the hybrids’ spectra, namely, in the blue ( $\approx 2.50$  eV) and in the purplish–blue ( $\approx 2.92$  eV) spectral regions. In contrast, the diamines’ time-resolved spectra display only one component, peaking at  $\approx 2.50$  eV [194]. Upon increasing the time delay beyond  $5.00 \times 10^{-3}$  s, the time-resolved emissions of the hybrids and the related diamines became similar, as the more energetic purplish–blue emission in the hybrids’ spectra disappeared, and only the longer lived component remained [194]. Besides having dissimilar recombination time scales, the two bands also behaved differently when the excitation wavelength was varied from 330 to 420 nm (2.95 to 3.76 eV). While the blue band was visible in the entire excitation range, the purplish–blue component could only be detected within the interval between 350 and 375 nm (3.31 and 3.54 eV) [194]. Furthermore, the less energetic band energy strongly depended on the excitation wavelength, displaying a red shift as the excitation wavelength increased, contrary to the purplish–blue emission that presented no significant variation of its energetic position [194, 195].

These results showed that another emission component appeared after gelation, establishing the unequivocal presence of two distinct emissions in the bulk organic–inorganic

hybrids. These two emissions bands should arise from different chemical–physical origins since the recombination mechanisms subjacent to each one occur in distinct time scales [191, 194, 195] and present different behaviors when the excitation wavelength changes.

The PL decay profiles of each di-ureasil emission component and of Jeffamine ED-2001® emission could be described by an exponential behavior, and were detected at the maximum intensity position of each emission band under an excitation of 365 nm (3.40 eV). The 14 K di-ureasil's lifetimes were 160.0 and 3.5 ms (errors within 3–5%) for the blue and purplish–blue emissions, respectively [194, 195]. Raising the temperature up to 220 K led to no changes in the lifetime of the longer lived emission, whereas the purplish–blue band displayed a typical Arrhenius behavior [194, 195]. Above approximately 220 K, an abrupt decrease of both lifetimes was observed. This was well illustrated by a set of real time frames, extracted from a video film that recorded the white-light emission after the excitation source was turned off (Fig. 31). For temperatures higher than 220 K, the lifetimes were in a time scale smaller than  $10^{-5}$  s, being ca.  $10^{-8}$  s at RT [223], disabling the chance to record the emission with the aforementioned experimental setup.

The 14 K lifetime of the diamine emission was  $\approx 120.0$  ms, and thus of the same order of magnitude as the U(2000) blue band lifetime. Upon raising the temperature, the Jeffamine ED-2001® lifetime remained constant until 200 K, and for temperatures higher than 220 K, the value belonged to a time scale smaller than  $10^{-5}$  s, thus resembling the characteristic behavior of the hybrid's less energetic band [194].

The PL characterization of the Jeffamines®, non-hydrolyzed precursors, di-ureasils, di-urethanesils, and APTES-based hybrids supported persuasive arguments that the full color emission (namely, the blue band) might involve the NH groups of the cross linkages [186, 191, 194–196, 222, 227, 230]. For instance, the white-light emission of the APTES hybrids with a variety of organic carboxylic acids

was explicitly related to the presence of amide functionalities [222]. Furthermore, in di-ureasils and di-urethanesils, the grafting of  $\text{NH}_2$  or OH to the isocyanate group—with the subsequent formation of urea or urethane groups, respectively—did not significantly alter the emission properties of the diamines [191, 194, 195]. Nevertheless, a new band with completely distinct features was detected after polycondensation and building up of the inorganic network [191, 194, 195]. According to SAXS results, the di-ureasil and di-urethanesil morphology has a diphasic structure made of spatially correlated siliceous nanoclusters dispersed and located at the ends of the organic chains [178–183, 191]. Consequently, the purplish–blue component present in the emission spectra of the final xerogels must be related to the existence of these siliceous nanodomains. This was further confirmed by altering the conditions at which the hydrolysis and condensation reactions occurred, thus modifying the local structures of those siliceous nanoregions. A new U(600) di-ureasil sample was synthesized using a different ICPTES: ethanol: water ratio, which altered both the condensation degree and the relative proportions between the two local Si surroundings, as confirmed by  $^{29}\text{Si}$  MAS NMR results. The 14 K time-resolved spectra for that hybrid displayed a long-lived blue band similar to the one observed in all of the other samples. However, a new short-lived band, centered at  $\approx 450$  nm, was detected in the purplish–blue region, supporting the suggested influence of the siliceous nanoclusters on the full color emission detected, particularly in the purplish–blue band [194, 195].

The emission of these classes of amine-functionalized hybrids depended noticeably on the excitation wavelength [186, 191–195, 222–224, 227]. Figure 31 exemplifies the situation found for the RT emission of the aminosil, the U(2000) di-ureasil and the Ut(2000) di-urethanesil. When the excitation wavelength increases, the maximum intensity of the spectra moves to lower energies. The emission tuning by choosing an appropriate excitation wavelength was also observed for the sol–gel-derived APTES– $\text{CH}_3\text{COOH}$  phosphors, both in fresh samples and in the gels aged for 30–60 days at 50 °C [223, 224]. The excitation wavelengths were varied between 340 and 470 nm, and the corresponding emission spectra were detected from the blue to the orange–red spectral ranges. This is also reported for di-ureasils obtained by carboxylic acid solvolysis [230].

In order to quantify the energy of those two distinct emissions, a deconvolution fitting procedure was applied to the emission spectra [191, 192, 194]. The procedure used to fit the experimental emission spectra to the Gaussian parameters (peak energy, integrated intensity, and FWHM) was described previously for the  $\text{Eu}^{3+}$ -based samples (Section 4.1).

For excitation wavelengths between 300 and 400 nm (3.10–4.00 eV), the curve-fitting method revealed the presence of two Gaussian bands in the blue ( $\approx 2.50$ – $2.60$  eV) and in the purplish–blue (2.80–3.10 eV) spectral regions [191–196]. Only the former component could be accounted for in the 400–420 nm excitation wavelength range (2.95–3.10 eV). The FWHM reached approximately 0.40 and 0.35 eV for the blue and purplish–blue bands, respectively. The Gaussian peak energies resulting from the fitting procedure clearly show that it is the purplish–blue

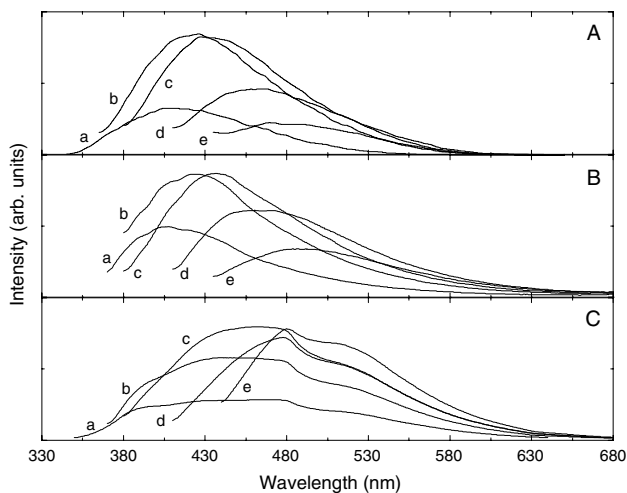


**Figure 31.** RT PL spectra of (A) the Ut(2000) di-urethanesil, (B) the U(2000) di-ureasil, and (C) the aminosil under different excitation wavelengths, (a) 330 nm, (b) 350 nm, (c) 375 nm, (d) 395 nm, and (e) 420 nm.



component that originates the shift of the emission spectra as the excitation wavelength is varied. In the range of excitation wavelengths used, the luminescence position of the blue band remains approximately constant, around 2.50 eV. The purplish–blue band shifts linearly as the excitation wavelength increases from 350 to 400 nm (3.54–3.10 eV). For excitation wavelengths between 330 and 300 nm (3.76 and 4.13 eV), the emission is invariably peaked between 415 and 400 nm (3.00 and 3.10 eV) [191–195].

This strong dependence of the emission energy the excitation wavelength is characteristic of all of the materials under analysis (diamines, nonhydrolyzed precursors and final di-ureasil, di-urethanesil, and APTES-based xerogels), providing strong evidence of disorder-related processes generally associated with transitions occurring within localized states in noncrystalline structures (e.g., *p*-Si [235], hydrogenated amorphous Si, *a*-Si:H [236], and As<sub>2</sub>Se<sub>3</sub> glasses [237]). An identical dependence was also reported for a nonhydrolyzed di-ureasil precursor [186] and for APTES-based hybrids with carboxylic acids [230].

Although no significant changes were detected in the energy of the blue component, the energy of the purplish–blue band depends on the sample. In fact, in silicon-based nanostructured materials, the dimensional hierarchy of the backbone determines the energy in such a way that an increase in the siliceous network corresponds to a decrease in the respective energy gap [238–241]. Figure 32 shows the dependence of the di-ureasil emission energy on the respective domain sizes determined by SAXS [178, 181, 182] and by XRD [191], designated as  $R_p$  and  $L_p$ , respectively. We notice that the energy range of the emitting siliceous nanodomains depends on the polymer chain length in such a way that an increase in the domain size results in a decrease of the corresponding energy gap. For each excitation wavelength used, the emission energy follows approximately the same trend presented in Figure 32. The different values found for  $R_p$  and  $L_p$  are due to the fact that these parameters were calculated from different experimental data and different structural models. However, the crucial point is

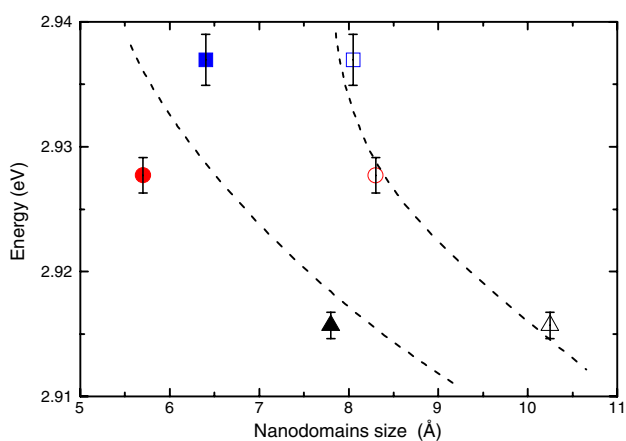


**Figure 32.** Relation between the emission energy, excited at 365 nm, of the di-ureasils, ( $\blacktriangle$ ,  $\triangle$ ) U(600), ( $\bullet$ ,  $\circ$ ) U(900), and ( $\blacksquare$ ,  $\square$ ) U(2000), and the respective size domain determined by SAXS (solid symbols) and XRD (open symbols) measurements. The dashed lines are a guide to the eyes.

that, independently of the absolute value found for  $R_p$  and  $L_p$ , we observe that greater nanodomain sizes correspond to smaller emission energies. A similar behavior was reported for other materials like, for example, nanocrystals of oxidized silicon [242] and hydrogenated silicon clusters [243]. There are also other reports referring to the theoretical calculation of the emission energy as a function of the nanodomain size [238, 240, 242, 243].

### 9.3. Recombination Mechanisms

In order to enlighten the nature of the white-light emission detected in amine-functionalized hybrids, our following discussion will be based on the recombination mechanisms known for crystalline semiconductors, *c*-SC, with relevance to amorphous materials. In *c*-SC, there are two types of transitions, recognized as near band-edge and deep transitions [199, 244, 245]. The former type involves either intrinsic states or donor–acceptor levels, whereas the latter type is related to defects or deep impurities, usually oxygen or metal transitions. The near band-edge transitions can be divided into four main classes: (1) free exciton, (2) bound exciton, (3) free carrier to neutral acceptor–donor, and (4) donor–acceptor, *D*–*A*, pairs. The distinction between the various near band-edge transitions can be made through the analysis of the behavior of the emission intensity as the excitation power is varied [244, 246]. The emission intensity  $I$  depends on the excitation power  $L$  according to the power law  $I \propto L^k$ . When  $1 < k < 2$ , we are in the presence of exciton-like transitions;  $k \leq 1$  is characteristic of free-to-bound and donor–acceptor pairs [244, 246]. Deviations from this behavior were observed either when  $L$  was varied more than two orders of magnitude or when the selected excitation energy was resonant with the semiconductor band gap [244].

Figure 33 represents the integrated intensity of the U(2000) di-ureasil steady-state emission calculated for different magnitudes of the excitation power [196]. A curve-fitting

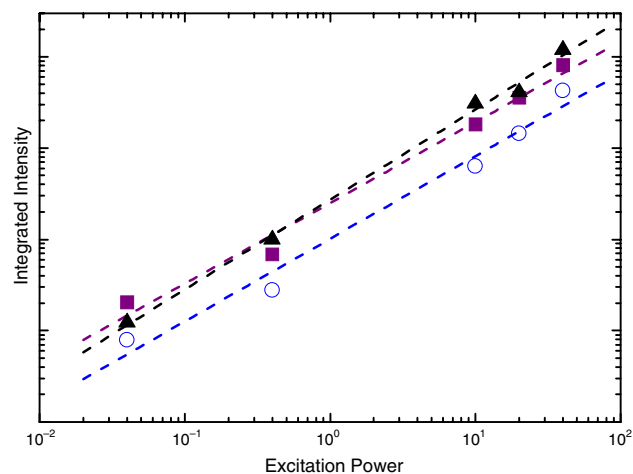


**Figure 33.** RT integrated intensity of the di-ureasil U(2000) emission components, ( $\circ$ ) blue and ( $\blacksquare$ ) purplish–blue and of the ( $\blacktriangle$ ) Jeffamine ED-2001® excited with an He–Cd laser (325 nm) at different power excitations. The lines correspond to the data linear fit ( $r > 0.99$ ).

procedure was applied to all of the emission spectra in order to access the energy and integrated intensity values of both components independently [191]. The integrated intensity depends sublinearly on the power excitation, with a  $k$  value of  $0.91 \pm 0.07$  and  $0.89 \pm 0.06$  for the blue and purplish–blue components, respectively (Fig. 33). This is a clear indication that both emissions revealed a recombination mechanism typical of  $D$ – $A$  pairs, mediated by some localized centers [244, 246]. Similar dependence on the power excitation  $k = 0.98 \pm 0.03$  was detected for the integrated emission intensity of Jeffamine ED-2001® (Fig. 33).

Relevant additional experimental evidence allowing the identification of  $D$ – $A$  transitions can be obtained from time-resolved spectroscopy [247, 248]. For longer delay times, a red shift is expected in the spectrum because distant pairs have a smaller recombination probability. The respective energy levels therefore have larger lifetimes, a situation that is favored with the increasing delay time. As a consequence, the recombination takes place at lower energies [199, 245–248].

The results obtained for the energetic shift ( $\Delta E$ ) between the energy of the maximum intensity of the time-resolved spectra, measured for SD between  $8 \times 10^{-5}$  and  $10^{-1}$  s, and the corresponding value measured under continuous excitation for the two components of the di-ureasil emission are consistent with  $D$ – $A$  pair recombination [195, 196].

The paragraphs that follow deal with several comments regarding the possible chemical nature and the recombination mechanisms that induce the blue and the purplish–blue  $D$ – $A$  pair-related emissions. Let us start with the discussion of the former component.

It has been clearly evidenced that the existence of oppositely charged defects in  $c$ – $SC$  [248], amorphous semiconductors  $a$ – $SC$ , [246, 249], and organic compounds [250–252] provides a good method for radiative electron–hole recombinations. In the 1970s, it was reported that urea [ $OC(NH_2)_2$ ] and thiourea [ $SC(NH_2)_2$ ] crystals exhibited luminescence in the blue and green spectral regions (400–500 nm), induced by X-ray radiation [250, 251]. It was proposed that the defects responsible for the emission were related to the rupture of intermolecular hydrogen bonds established between packed urea molecules. The oxygen atom of each urea molecule binds four hydrogen atoms of two adjacent molecules, forming weak hydrogen-type bonds ( $N-H \cdots O=C$ ). When the urea crystals were irradiated, proton transfer was induced, and two defects with opposite charges,  $NH_3^+$  and  $NH^-$ , were formed. These two defects can act as electron and hole traps, respectively, recombine radiatively, and account for the observed emission. Photoinduced proton transfer has been also reported in many other materials, for example, organic systems involving amine groups [252], semiconducting polymers [253], and microporous zeolites [254–256].

We have proposed the same type of defects as the chemical species responsible for the PL blue component of diamines, aminosils, di-ureasils, and di-urethanesils, that is,  $NH_3^+/NH^-$ , for the diamines and aminosils, and  $NH_2^+/N^-$  for the urea and urethane-based hybrids [195, 196]. Furthermore, similar defects could also be responsible for the PL of GPTES- and APTES-based hybrids with carboxylic acids, that is,  $NH_3^+$  and  $RCOO^-$ ,  $R = H, CH_3, CH_3CHOH$ , or  $CH_3(CH_2)_3$  for  $HCOOH, CH_3CHOHCOOH, CH_3COOH,$

and  $CH_3(CH_2)_3COOH$ , respectively. It is interesting to note that the presence of  $NH_3^+/CH_3COO^-$  defects was recently proposed in xerogels formed by reactions of APTES, TEOS, and  $CH_3COOH$  [229].

The above suggestion is consistent with the observed behavior of the emission intensity of Jeffamine ED-2001® solutions in  $H_2O$  and THF. The two solvents differ in the polarity of their molecules. The  $H_2O$  molecules are more polar than those of the THF. Therefore,  $H_2O$  behaves as a more efficient vehicle for proton transport than THF, thus contributing to a more efficient luminescent mechanism. As a consequence, the PL intensity of the aqueous solutions is higher than that of the THF solutions [195, 196]. Moreover, the observed red shift of the PL spectra of the aqueous solutions, with respect to those of THF (characteristic of emission-size-dependent) [195, 196] may also be explained on the basis of the differences in the polarity between the molecules of the two solvents. Considering the photoinduced proton-transfer model,  $D$ – $A$  pairs are formed in distinct  $NH_2$  groups, and the distance between them determines the emission energy in such a way that distant pairs emit at longer wavelengths. For the aqueous solutions, the emission arising from more distant  $NH_2$  groups is then favored due to the presence of a much more efficient proton transfer vehicle (greater polarity), resulting in a spectra blue shift with respect to the emission measured for the THF solutions. Another experimental result that supports the previous suggestion is the variation of the emission quantum yield of the blue component with the length of the polymeric chain [196]. For the di-ureasil with shorter polymer chains, U(600), strong hydrogen bonds are formed [198] that localize the proton and render difficult the induced proton transfer between  $NH$  groups, leading to the corresponding decrease of the quantum yield. For di-ureasils containing longer polymer chains, U(900) and U(2000), there is no evidence of interactions via hydrogen bonds [198]. Therefore, in spite of the larger distance between the  $NH$  groups, the protons have a greater degree of mobility, a situation that favors higher quantum yields.

The existence of mobile (free) protons in the hybrids and in the diamines is further demonstrated by complex impedance measurements. At RT, the ionic conductivity of U(2000), U(900), U(600), and Jeffamine ED-2001® is about  $3.4 \times 10^{-8}$ ,  $5.0 \times 10^{-9}$ ,  $9.2 \times 10^{-10}$ , and  $3.9 \times 10^{-9}$  S/cm, respectively. These results show that the mobility of the protons decreases from U(2000) to U(600), confirming the conclusions drawn from quantum yield analysis.

The explanation of the siliceous nanodomain-related emission is less straightforward since, for silicon-based materials, several mechanisms and chemical origins have been proposed as responsible for the luminescence features [242, 257–263].

One hypothesis for the observed RT emission invokes the presence of Si nanoparticles or Si quantum wires that, due to quantum confinement effects, are responsible for the visible emission [258]. The quantum confinement of the carriers in the Si nanowires leads to a significant widening of the band gap and to an enhancement of the oscillator strength, thereby inducing efficient radiative recombination. An alternative mechanism suggested for the emission of amorphous or disordered silicon-based structures is the existence of

delocalized states induced by the lack of long-range order or by the presence of impurities or defects [235–237]. It is known that the radiative recombination arising from localized states depends on the excitation wavelength [235–237], and also that it is a thermally activated process.

Although the energy of the purplish–blue emission depends on the nanodomain size, the red shift observed in the emission spectra as the excitation wavelength decreases [191–194] and the typical Arrhenius behavior displayed by the respective lifetime [194] as the temperature increases from 14 to 300 K strongly suggest the presence of localized states probably created either by the amorphous properties of the siliceous domains or by the presence of defects.

In parallel with the discussion concerning the physical mechanisms under visible emission of silicon-based materials, several hypotheses concerning the chemical nature of the luminescent species were proposed, namely: (1) surface contamination due to luminescent organic solvents [257]; (2) the presence of an amorphous silicon, *a*-Si, phase [235]; (3) the existence of silicon-based structures, like siloxene ( $\text{Si}_6\text{O}_3\text{H}_6$ ) and siloxene derivatives, hydrides, and polysilane chains  $[(\text{SiH})_n]$  [249] and the silanone bond ( $\text{Si}=\text{O}$ ) [261]; and (4) oxygen-related defects [261].

The possible influence of oxygen defects in the emission features of APTES-based hybrids containing carboxylic acids [229] and TEOS- and MTEOS-based hybrids containing acetylacetonate (acac) and zirconium propoxide [228] was previously suggested. In the APTES-based hybrids case, it was observed that the luminescence intensity of such organic–inorganic hybrids increases with the increase of the heat treatment temperature between 20 and 200 °C. Furthermore, the luminescence intensity is greater in the xerogels treated under vacuum than in the hybrids treated in air [229]. This finding was interpreted as an indication that higher temperatures and vacuum conditions favor the creation of oxygen-related defects [229]. The TEOS- and MTEOS-based hybrids with doped with acac and zirconium propoxide [229] were studied by the electron paramagnetic resonance (EPR) technique, which demonstrated the existence of oxygen-related defects and silicon dangling bonds.

Another defect type associated with carbon impurities was proposed as being in the origin of the luminescence of sol–gel-derived silica gels based on TEOS and TMOS incorporating a variety of carboxylic acids [222]. Under adequate heat treatments, above 520 K, at least, a carbon impurity is created in the  $-\text{O}-\text{Si}-\text{O}-$  network forming  $-\text{O}-\text{C}-\text{O}-$  and/or  $-\text{Si}-\text{C}-$  bonds [222]. However, the carbon-related defects are only luminescently active after a heat treatment [222]. This situation contrasts with that found with oxygen-related defects, as the luminescent centers are active prior to any thermal treatment.

Since the di-ureasils and di-urethanesils discussed here are RT efficient emitters, without needing a prior heat treatment, we can rule out carbon-defect impurities as being responsible for the siliceous nanodomain emission features.

The PL results on amine-based hybrids related to the siliceous nanodomains undoubtedly show recombination mechanisms associated with disordered structures mediated by localized states, namely, the emission energy dependence on the excitation wavelength and the Arrhenius behavior characteristic of the respective lifetime. However, a detailed

description of the chemical–physical nature of such emission remains unsolved because, so far, we have not obtained experimental evidence that enables us to unequivocally identify the chemical nature of the *D*–*A* pairs responsible for the luminescent features described. However, we note that preliminary RT EPR studies performed on the di-ureasils demonstrated the existence of paramagnetic signals. This experimental evidence is in agreement with the possible existence of *D*–*A* pairs arising from nitrogen-, silicon-, and oxygen-related defects.

## 10. SUMMARY

The interest in organic–inorganic hybrids is basically associated with the extraordinary implications resulting from the tailoring of novel multifunctional advanced materials induced by the mixture in a single material and at the nanosize level of organic, inorganic, and even biological components. The synergy of that combination and the particular role of the inner interfaces open up exciting directions in materials science research and related technologies for the processing of novel multiuse advanced materials with innovative and unparalleled performances. Moreover, these hybrids present preeminent advantages in assisting the integration, miniaturization, and multifunctionalization of the devices, opening, therefore, a series of new opportunities for many applications.

The synthesis of such hybrids requires “soft” chemistry methods. The sol–gel process is probably the preeminent “soft” process allowing a “bottom-up” nanotechnology approach in the chemical design of organic–inorganic structures as an assembly of nano-building blocks. Furthermore, the sol–gel method clearly offers the flexibility necessary for implementing the chemical design strategies that are the basis of photonic hybrid materials, which are perhaps one of the first systems to take real advantage of the hybrid materials approach.

The PL features of the RE-based hybrid frameworks reviewed here illustrate nicely the impact on photonics that could result from the encapsulating of RE complexes in siloxane-based matrices through the simple embedding of the complexes within the sol–gel-derived matrix (generally Class I hybrid materials), or by using complexing ligands covalently grafted to the framework (Class II hybrid materials).

## GLOSSARY

**CIE color coordinates** Two chromaticity coordinates (*x*, *y*) that map the color with respect to hue and saturation on the two-dimensional CIE chromaticity diagram.

**CIE color system** Characterization of colors based on the spectral power distribution of the light emitted from a colored object and factored by sensitivity curves that have been measured for the human eye.

**Class I hybrid materials** Hybrids in which the organic and inorganic components are linked through weak interactions (van der Waals contacts, hydrogen bonding or electrostatic forces).

**Class II hybrid materials** Hybrids in which the organic and inorganic components are linked through strong chemical bonds (covalent, ionocovalent or acid-base bonds).

**Electroluminescence** Emission of radiation obtained by electric excitation.

**Electroluminescence external quantum efficiency** Fraction of generated photons that leave the light-emitting diode.

**Emission quantum yields** The ratio of photons absorbed to photons emitted through emission of radiation. The quantum yield gives, therefore, the probability of an excited state being deactivated by emission rather than by non-radiative mechanisms.

**Glass transition temperature** The glass transition temperature is the temperature at which the amorphous domains of a polymer take on the characteristic properties of the glassy state—brittleness, stiffness, and rigidity.

**Hydroxyl quenching** The luminescence efficiency of RE ions is quenched by nonradiative multiphonon relaxation of OH oscillators.

**Ligand-to-metal charge transfer transition** An electronic transition of a metal complex that corresponds to excitation populating an electronic state in which considerable electron transfer from a ligand to a metal center has occurred.

**Nephelauxetic effect (“could expanding” in Greek)** A slight shift of peak positions of f-f transitions depending on the matrix, relatively to the values found for the free ion. Electron–electron repulsion and spin-orbit coupling primarily determine the excited levels of transition bands. For covalent compounds the apparent values of the inter-electronic repulsion parameters are smaller than those in aqueous solutions, inducing a shift of the peak positions toward lower energy with increasing covalency of the surrounding media.

**Organic light-emitting diodes (OLEDs)** OLEDs are made from plastic compounds or small organic molecules that glow when a voltage is applied.

**Organic/inorganic hybrids** Materials combining organic and inorganic components at the nanosize level.

**Photoluminescence** Emission of radiation (usually in the visible or in the infrared regions of the electromagnetic spectrum) obtained by photon excitation (often in the ultraviolet).

**Quantum efficiency of emission** Ratio between the radiative transition probability and the experimental transition probability (sum of the radiative and non-radiative transition probabilities). The inverse of the experimental transition probability is the lifetime of the state.

**Recombination mechanisms** Recombination of electrons and holes is a process by which both carriers annihilate each other. The electrons occupy—through one or multiple steps—the empty state associated with a hole and both carriers eventually disappear in the process. The energy difference between the initial and final state of the electron is released in the process.

**Sol-gel method** Versatile “soft” chemical synthetic process that involves the hydrolysis and condensation of precursor molecules (often metal alkoxides) to yield gels with tunable shape and properties.

**Stark Effect** Splitting of a free ion electronic level in a series of Stark components due to the local charge distribution around a rare earth ion.

**White light emission** Emission of polychromatic radiation.

## ACKNOWLEDGMENTS

Financial support from FEDER and Fundação para a Ciência e Tecnologia, POCTI Program (POCTI/CTM/33653/99 and SFRH/BPD/11480/02) is gratefully acknowledged.

## REFERENCES

1. H. Schmidt, A. Kaiser, H. Patzelt, and H. Sholze, *J. Phys. Colloq. C9*, 275 (1982).
2. D. Avnir, D. Levy, and R. Reisfeld, *J. Phys. Chem.* 88, 5956 (1984).
3. G. L. Wilkes, B. Orler, and H. Huang, *Polym. Prep.* 26, 300 (1985).
4. H. Schmidt, *J. Non-Cryst. Solids* 73, 681 (1985).
5. J. Livage, M. Henry, and C. Sanchez, *Prog. Solid State Chem.* 18, 259 (1988).
6. C. J. Brinker and G. W. Scherer, “Sol-Gel Science, The Physics and Chemistry of Sol-Gel Processing.” Academic, San Diego, 1990.
7. A. Morikawa, Y. Iyoku, M. Kakimoto, and Y. Imai, *J. Mater. Chem.* 2, 679 (1992).
8. Y. Chujo and T. Saegusa, *Adv. Polym. Sci.* 100, 11 (1992).
9. B. Novak, *Adv. Mater.* 5, 422 (1993).
10. C. Sanchez and F. Ribot, Eds., “Proceedings of the 1st European Workshop on Hybrid Organic–Inorganic Materials,” Special issue of *New J. Chem.* 18 (1994).
11. C. Sanchez and F. Ribot, *New J. Chem.* 18, 1007 (1994).
12. U. Schubert, N. Hüsing, and A. Lorenz, *Chem. Mater.* 7, 2010 (1995).
13. D. A. Loy and K. J. Shea, *Chem. Rev.* 95, 1431 (1995).
14. J. Wen and G. L. Wilkes, *Chem. Mater.* 8, 1667 (1996).
15. P. Judeinstein and C. Sanchez, *J. Mater. Chem.* 6, 511 (1996).
16. R. J. P. Corriu and D. Leclercq, *Angew. Chem., Int. Ed. Engl.* 35, 1420 (1996).
17. C. Sanchez, F. Ribot, and B. Lebeau, *J. Mater. Chem.* 9, 35 (1999).
18. S. I. Stupp and P. V. Braun, *Science* 277, 1242 (1999).
19. P. V. Braun, P. Osenar, V. Tohver, S. B. Kennedy, and S. I. Stupp, *J. Am. Chem. Soc.* 121, 7302 (1999).
20. A. K. Cheetham, C. J. Brinker, M. L. Macartney, C. Sanchez, D. W. Schaefer, and G. L. Wilkes, Eds., “Better Ceramics Through Chemistry VI,” Vol. 346. Materials Research Society, Pittsburgh, 1994.
21. B. K. Coltrain, C. Sanchez, D. W. Schaefer, and G. L. Wilkes, Eds., “Better Ceramics Through Chemistry VII: Organic/Inorganic Hybrid Materials,” Vol. 435. Materials Research Society, Pittsburgh, 1996.
22. R. Laine, C. Sanchez, C. J. Brinker, and E. Gianellis, Eds., “Hybrid Materials,” Vol. 519. Materials Research Society, Pittsburgh, 1998.
23. L. C. Klein, L. F. Francis, M. R. De Guire, and J. E. Mark, Eds., “Organic/Inorganic Hybrid Materials II,” Vol. 576. Materials Research Society, Pittsburgh, 1999.
24. R. M. Laine, C. Sanchez, C. J. Brinker, and E. Gianellis, Eds., “Organic/Inorganic Hybrid Materials—2000,” Vol. 628. Materials Research Society, Pittsburgh, 2000.
25. J. D. Mackenzie and D. R. Ulrich, Eds., “Sol-Gel Optics I,” Vol. 1328. SPIE—International Society of Optical Engineering Series, Bellingham, WA, 1990.
26. J. D. Mackenzie, Ed., “Sol-Gel Optics II,” Vol. 1758. SPIE—International Society of Optical Engineering Series, Bellingham, WA, 1992.

27. J. D. Mackenzie, Ed., "Sol-Gel Optics III," Vol. 2288. SPIE—International Society of Optical Engineering Series, Bellingham, WA, 1994.
28. J. D. Mackenzie, Ed., "Sol-Gel Optics IV," Vol. 3136. SPIE—International Society of Optical Engineering Series, Bellingham, WA, 1997.
29. "7th International Workshop on Glasses and Ceramics from Gels," Special issue of *J. Sol-Gel Sci. Technol.* 2 (1994).
30. D. Avnir, S. Braun, O. Lev, D. Levy, and M. Ottolenghi, in "Sol-Gel Optics, Processing and Applications" (L. Klein, Ed.), p. 539. Kluwer Academic, Dordrecht, The Netherlands, 1994.
31. L. L. Klein and C. Sanchez, Eds., "Hybrid Organic-Inorganic Materials," Special issue of *J. Sol-Gel Sci. Technol.* 5 (1995).
32. J. E. Mark, Ed., "Hybrid Organic-Inorganic Composites," Vol. 585. ACS Series, Washington, DC, 1995.
33. D. Avnir, *Acc. Chem. Res.* 28, 328 (1995).
34. L. Hubert and S. I. Najafi, Eds., "Organic-Inorganic Hybrids for Photonics," Vol. 3469. SPIE—International Society of Optical Engineering Series, Bellingham, WA, 1998.
35. K. Moller and T. Bein, *Chem. Mater.* 10, 2950 (1998).
36. B. Lebeau and C. Sanchez, *Curr. Opin. Solid State Mater. Sci.* 4, 11 (1999).
37. B. S. Dunn, E. J. A. Pope, H. K. Schmidt, and M. Yamane, Eds., "Sol-Gel Optics V," Vol. 3943. SPIE—International Society of Optical Engineering Series, Bellingham, WA, 2000.
38. C. Sanchez and B. Lebeau, in "Hybrid Organic-Inorganic Materials" (D. A. Loy, Ed.), *Mater. Res. Soc. Bull.* 26, 377 (2001).
39. P. Gomez-Romero, *Adv. Mater.* 13, 163 (2001).
40. C. Sanchez, G. J. de A. A. Soler-Illia, F. Ribot, T. Lalot, C. R. Mayer, and V. Cabuil, *Chem. Mater.* 13, 3061 (2001).
41. B. J. Scott, G. Wirnsberger, and G. D. Stucky, *Chem. Mater.* 13, 3140 (2001).
42. T. Keeling-Tucker and J. D. Brennan, *Chem. Mater.* 13, 3331 (2001).
43. B. Arkles, *Mater. Res. Soc. Bull.* 26, 402 (2001).
44. G. Schottner, *Chem. Mater.* 13, 3422 (2001).
45. E. Jeong Cho and F. V. Bright, *Anal. Chem.* 74, 1462 (2002).
46. B. Dunn and J. I. Zink, *J. Mater. Chem.* 1, 903 (1991).
47. M. P. Andrews, in "Integrated Optics Devices: Potential for Commercialization" (S. I. Najafi and M. N. Armenise, Eds.), Vol. 2997, p. 48. SPIE—International Society of Optical Engineering Series, Bellingham, WA, 1997.
48. A. B. Seddon, in "Sol-Gel and Polymer Photonic Devices; Critical Review of Optical Science and Technology Series," Vol. CR68, p. 143. SPIE—International Society of Optical Engineering Series, Bellingham, WA, 1997.
49. A. B. Seddon, *Proc. IEE, Circuits Devices Syst.* 145, 369 (1998).
50. H. Schmidt, G. Jonschker, S. Goedicke, and M. Mennig, *J. Sol-Gel Sci. Technol.* 19, 39 (2000).
51. V. Ptatschek, B. Schreder, K. Herz, U. Hilbert, W. Ossau, G. Schottner, O. Rahaüser, T. Bischof, G. Lermann, A. Materny, W. Kiefer, G. Bacher, A. Forchel, D. Su, M. Giersig, G. Müller, and L. Spanhel, *J. Phys. Chem. B* 101, 44 (1997).
52. G. Schottner, W. Grond, L. Kümmerl, and D. Haarer, *J. Sol-Gel Sci. Technol.* 2, 657 (1994).
53. T. Jin, S. Inoue, K. Machida, and G. Adachi, *J. Electrochem. Soc.* 144, 4054 (1997).
54. S. D. Burnside, V. Shklover, C. A. Barbe, K. Brooks, P. Comte, F. Arendse-Durieux, M. Jirousek, and M. Graetzel, in "Hybrid Materials" (R. Laine, C. Sanchez, C. J. Brinker, and E. Gianellis, Eds.), Vol. 519, p. 59. Materials Research Society, Pittsburgh, 1998.
55. H. Li, S. Inoue, D. Ueda, K. Machida, and G. Adachi, *Electrochem. Solid State Lett.* 2, 354 (1999).
56. M. Faloss, M. Canva, P. Georges, A. Brun, F. Chaput, and J.-P. Boilot, *Appl. Opt.* 36, 6760 (1997).
57. B. Schaudel, C. Guermeur, C. Sanchez, K. Nakatani, and J. Delaire, *J. Mater. Chem.* 7, 61 (1997).
58. C. Sanchez and B. Lebeau, *Pure Appl. Opt.* 5, 689 (1996).
59. B. Lebeau, C. Sanchez, S. Brasselet, and J. Zyss, *Chem. Mater.* 9, 1012 (1997).
60. M. Canva, B. Darracq, F. Chaput, K. Lahlil, F. Bentivegna, M. Brunel, M. Falloss, P. Georges, A. Brun, J.-P. Boilot, and Y. Lévy, in "Organic-Inorganic Hybrids for Photonics" (L. Hubert and S. I. Najafi, Eds.), Vol. 3469, p. 164. SPIE—International Society of Optical Engineering Series, Bellingham, WA, 1998.
61. H. K. Kim, S.-J. Kang, S.-K. Choi, Y.-H. Min, and C.-S. Yoon, *Chem. Mater.* 11, 779 (1999).
62. F. Chaumel, H. W. Jiang, and A. Kakkar, *Chem. Mater.* 13, 3389 (2001).
63. C. M. McDonagh, A. M. Shields, A. K. McEvoy, B. D. MacCraith, and J. F. Gouin, *J. Sol-Gel Sci. Technol.* 13, 207 (1998).
64. P. Lavin, C. M. McDonagh, and B. D. MacCraith, *J. Sol-Gel Sci. Technol.* 13, 641 (1998).
65. K. Rose, V. MatĚjec, M. Hayer, and M. Pospíšilová, *J. Sol-Gel Sci. Technol.* 13, 729 (1998).
66. S. Motakef, J. M. Boulton, and D. R. Uhlmann, *Opt. Lett.* 19, 1125 (1994).
67. C. Roscher, R. Buestrich, P. Dannberg, O. Rösch, and M. Popall, in "Hybrid Materials" (R. Laine, C. Sanchez, C. J. Brinker, and E. Gianellis, Eds.), Vol. 519, p. 239. Materials Research Society Series, Pittsburgh, 1998.
68. K. K. Li, E. J. Salley, P. Salley, M. J. Tabasky, J. Zhao, and C.-Y. Li, in "Organic-Inorganic Hybrids for Photonics" (L. Hubert and S. I. Najafi, Eds.), Vol. 3469, p. 58. SPIE—International Society of Optical Engineering Series, Bellingham, WA, 1998.
69. A. B. Seddon and A. Adamjee, in "Organic-Inorganic Hybrids for Photonics" (L. Hubert and S. I. Najafi, Eds.), Vol. 3469, p. 108. SPIE—International Society of Optical Engineering Series, Bellingham, WA, 1998.
70. S. I. Najafi, T. Touam, R. Sara, M. P. Andrews, and M. A. Fardad, *J. Lightwave Technol.* 16, 1640 (1998).
71. R. Buestrich, F. Kahlenberg, M. Popall, P. Dannberg, R.-M. Fiedler, and O. Rösch, *J. Sol-Gel Sci. Technol.* 20, 181 (2001).
72. R. R. Gonçalves, G. Carturan, L. Zampedri, M. Ferrari, M. Montagna, A. Chiasera, G. C. Righini, S. Pelli, S. J. L. Ribeiro, and Y. Messaddeq, *Appl. Phys. Lett.* 81, 28 (2002).
73. R. R. Gonçalves, M. Ferrari, A. Chiasera, M. Montagna, E. A. Morais, L. V. A. Scalvi, C. V. Santilli, Y. Messaddeq, and S. J. L. Ribeiro, *Mater. Sci. Forum* 403, 107 (2002).
74. E. J. Nassar, R. R. Gonçalves, M. Ferrari, Y. Messaddeq, and S. J. L. Ribeiro *J. Alloys Comp.* 344, 221 (2002).
75. T. Dantas de Moraes, F. Chaput, J.-P. Boilot, K. Lahlil, B. Darracq, and Y. Lévy, *Adv. Mater.* 11, 107 (1999).
76. D. B. Mitzi, K. Chondroudis, and C. R. Kagan, *IBM J. Res. Dev.* 45, 29 (2001).
77. C. I. Chao and S. A. Chen, *Appl. Phys. Lett.* 73, 426 (1998).
78. Y. Cao, I. D. Parker, G. Yu, C. Zhang, and A. J. Heeger, *Nature* 397, 414 (1999).
79. R. H. Friend, R. W. Gymer, A. B. Holmes, J. H. Burroughes, R. N. Marks, C. Taliani, D. D. C. Bradley, D. A. Dos Santos, J. L. Bredas, M. Logdlund, and W. R. Salaneck, *Nature* 397, 121 (1999).
80. S. Tasch, E. J. W. List, O. Ekström, W. Graupner, G. Leising, P. Schlichting, U. Rohr, Y. Geerts, U. Scherf, and K. Müllen, *Appl. Phys. Lett.* 71, 2883 (1997).
81. J. Feng, F. Li, W. Gao, S. Liu, Y. Liu, and Y. Wang, *Appl. Phys. Lett.* 78, 3947 (2001).
82. F. Hide, P. Kozody, S. P. DenBaars, and A. J. Heeger, *Appl. Phys. Lett.* 70, 2664 (1997).
83. J. Dresner, *RCA Rev.* 30, 322 (1969).
84. T. Wakimoto, H. Ochi, S. Kawami, H. Ohata, K. Nagayama, R. Murayama, Y. Okuda, H. Nakada, T. Tohma, T. Naito, and H. Abiko, *J. Soc. Info. Display* 5, 235 (1997).

85. S. E. Shaheen, G. E. Jabbour, B. Kippelen, N. Peyghambarian, J. D. Anderson, S. R. Marder, N. R. Armstrong, E. Bellmann, and R. H. Grubbs, *Appl. Phys. Lett.* 74, 3212 (1999).
86. M. A. Baldo, S. Lamansky, P. E. Burrows, M. E. Thompson, and S. R. Forrest, *Appl. Phys. Lett.* 75, 4 (1999).
87. J. Kido, M. Kaimura, and K. Nagai, *Science* 267, 1332 (1995).
88. M. Berggren, O. Inganäs, G. Gustafsson, J. Rasmusson, M. R. Andersson, T. Hjertberg, and O. Wennerström, *Nature* 372, 444 (1994).
89. R. H. Jordan, A. Dodabalapur, M. Strukelj, and T. M. Miller, *Appl. Phys. Lett.* 68, 1192 (1996).
90. S. Tasch, C. Brandstätter, F. Meghdadi, G. Leising, L. Athouel, and G. Froyer, *Adv. Mater.* 9, 33 (1997).
91. M. D. McGehee, T. Bergstedt, C. Zhang, A. P. Saab, M. B. O'Regan, G. C. Bazan, V. I. Srdanov, and A. J. Heeger, *Adv. Mater.* 11, 1349 (1999).
92. M. Meyer, *Comp. Semicond.* (Special Issue) 49 (1997).
93. R. Birkhahn, M. Garter, and A. J. Steckl, *Appl. Phys. Lett.* 74, 2161 (1999).
94. G. Blasse and B. C. Grabmaier, "Luminescent Materials." Springer-Verlag, Berlin, 1994.
95. A. J. Steckl, M. Garter, R. Birkhahn, and J. D. Scofield, *Appl. Phys. Lett.* 73, 2450 (1998).
96. J. Heikenfeld, M. Garter, D. S. Lee, R. Birkhahn, and A. J. Steckl, *Appl. Phys. Lett.* 75, 1189 (1999).
97. R. Birkhahn, M. Garter, and A. J. Steckl, *Appl. Phys. Lett.* 73, 2161 (1999).
98. A. J. Steckl, M. Garter, D. S. Lee, J. Heikenfeld, and R. Birkhahn, *Appl. Phys. Lett.* 75, 2184 (1999).
99. D. S. Lee, J. Heikenfeld, R. Birkhahn, M. Garter, B. K. Lee, and A. J. Steckl, *Appl. Phys. Lett.* 76, 1525 (2000).
100. D. S. Lee, J. Heikenfeld, A. J. Steckl, U. Hommerich, J. T. Seo, A. Braud, U. Hömmerich, J. T. Seo, A. Braud, and J. M. Zavada, *Appl. Phys. Lett.* 79, 719 (2001).
101. D. S. Lee, J. Heikenfeld, and A. J. Steckl, *Appl. Phys. Lett.* 80, 344 (2002).
102. E. E. Nyein, U. Hömmerich, J. Heikenfeld, D. S. Lee, A. J. Steckl, and J. M. Zavada, *Appl. Phys. Lett.* 79, 719 (2001).
103. H. Samelson, A. Lempicki, C. Brecher, and V. A. Brophy, *Appl. Phys. Lett.* 5, 173 (1964).
104. S. Bjorklund, G. Kellermeyer, C. R. Hurt, N. McAvoy, and N. Filipescu, *Nature* 10, 16 (1967).
105. B. Whittaker, *Nature* 228, 157 (1970).
106. G. F. de Sá, O. L. Malta, C. De Mello Donegá, A. M. Simas, R. L. Longo, P. A. Santa-Cruz, and E. F. da Silva, Jr., *Coord. Chem. Rev.* 196, 165 (2000).
107. H. F. Brito, O. L. Malta, C. H. A. de Carvalho, J. F. S. Menezes, L. R. Souza, and R. Ferraz, *J. Alloys Comp.* 277, 254 (1998).
108. L. D. Carlos, C. De Mello Donegá, R. Q. Albuquerque, S. Alves, Jr., J. F. S. Menezes, and O. L. Malta, *Mol. Phys.* 101, 1037 (2003).
109. E. Banks, Y. Okamoto, and Y. Ueda, *J. Appl. Polym. Sci.* 25, 359 (1980).
110. W. M. Azevedo, P. N. M. dos Anjos, O. L. Malta, and G. F. de Sá, *J. Alloys Comp.* 180, 125 (1992).
111. L. D. Carlos and A. L. L. Videira, *Phys. Rev. B* 49, 11771 (1994).
112. A. Brodin, B. Mattsson, and L. Torell, *J. Chem. Phys.* 101, 4621 (1994).
113. L. D. Carlos and A. L. L. Videira, *J. Chem. Phys.* 101, 8827 (1994).
114. L. D. Carlos, M. Assunção, and L. Alcácer, *J. Mater. Res.* 10, 202 (1995).
115. H. Ohno and H. Yoshihara, *Solid State Ionics* 80, 251 (1995).
116. L. D. Carlos and A. L. L. Videira, *J. Chem. Phys.* 105, 8878 (1996).
117. L. D. Carlos, *Solid State Ionics* 85, 181 (1996).
118. L. D. Carlos and A. L. L. Videira, *Chem. Phys. Lett.* 57, 264 (1997).
119. V. Di Noto, M. Bettinelli, M. Furlani, S. Lavina, and M. Vidali, *Macromol. Chem. Phys.* 197, 375 (1996).
120. A. Ferry, M. Furlani, A. Franke, P. Jacobsson, and B.-E. Mellander, *J. Chem. Phys.* 109, 2921 (1998).
121. M. Makiigawa and H. Ohno, *J. Electroanal. Chem.* 452, 141 (1998).
122. V. Bekiari, G. Pistolis, and P. Lianos, *J. Non-Cryst. Solids* 226, 200 (1998).
123. V. Bekiari and P. Lianos, *Adv. Mater.* 10, 1455 (1998).
124. V. Bekiari, G. Pistolis, and P. Lianos, *Chem. Mater.* 11, 3189 (1999).
125. V. de Zea Bermudez, L. D. Carlos, M. M. Silva, and M. J. Smith, *J. Chem. Phys.* 112, 3293 (2000).
126. V. Bekiari and P. Lianos, *Adv. Mater.* 12, 1603 (2000).
127. L.-H. Wang, W. Wang, W.-G. Zhang, E.-T. Kang, and W. Hang, *Chem. Mater.* 12, 2212 (2000).
128. G. Yu, Y. Liu, X. Wu, D. Zhu, H. Li, L. Jin, and M. Wang, *Chem. Mater.* 12, 2537 (2000).
129. F. P. Duclerc, H. F. Brito, J. R. Matos, and L. D. Carlos, *J. Appl. Polym. Sci.* 83, 2716 (2002).
130. E. J. A. Pope and J. D. Mackenzie, *J. Non-Cryst. Solids* 106, 236 (1988).
131. S. Chakrabarti, J. Sahu, M. Chakraborti, and H. N. Acharya, *J. Non-Cryst. Solids* 180, 96 (1994).
132. B. Viana, N. Koslova, P. Ashehoug, and C. Sanchez, *J. Mater. Chem.* 5, 719 (1995).
133. M. J. Lochhead and K. L. Bray, *Chem. Mater.* 7, 572 (1995).
134. V. C. Costa, M. J. Lochhead, and K. L. Bray, *Chem. Mater.* 8, 783 (1996).
135. Y. Kurokawa, T. Ishizaka, T. Ikoma, and S. Tero-Kwbot, *Chem. Phys. Lett.* 287, 737 (1998).
136. L. R. Matthews and E. T. Knobbe, *Chem. Mater.* 5, 1697 (1993).
137. L. R. Matthews, X.-J. Wang, and E. T. Knobbe, *J. Non-Cryst. Solids* 178, 44 (1994).
138. O. A. Serra, E. J. Nassar, G. Zapparolli, and I. L. V. Rosa, *J. Alloys Comp.* 207/208, 454 (1994).
139. O. A. Serra, E. J. Nassar, and I. L. V. Rosa, *J. Lumin.* 72–74, 263 (1997).
140. T. Jin, S. Inoue, S. Tsutsumi, K. Machida, and G. Adachi, *J. Non-Cryst. Solids* 223, 123 (1998).
141. B. Yan, H. J. Zhang, and J. Z. Ni, *J. Mater. Sci. Eng.* B52, 123 (1998).
142. M. A. Zaiton, T. Kim, and C. T. Lin, *J. Phys. Chem. B* 102, 1122 (1998).
143. H. Li, S. Inoue, K. Machida, and G. Adachi, *Chem. Mater.* 11, 3171 (1999).
144. P. A. Tanner, B. Yan, and H. J. Zhang, *J. Mater. Sci.* 35, 4325 (2000).
145. X. Ji, B. Li, S. Jiang, D. Dong, H. Zhang, X. B. Jing, and B. Z. Jiang, *J. Non-Cryst. Solids* 275, 52 (2000).
146. H. R. Li, H. J. Zhang, J. Lin, S. B. Wang, and K. Y. Yang, *J. Non-Cryst. Solids* 278, 218 (2000).
147. G. Qian and M. Wang, *J. Am. Ceram. Soc.* 83, 703 (2000).
148. H. Li, S. Inoue, K. Machida, and G. Adachi, *J. Lumin.* 87–89, 1069 (2000).
149. M. A. Zaiton, D. M. Goken, L. S. Bailey, T. Kim, and C. T. Lin, *J. Phys. Chem. B* 104, 189 (2000).
150. C. Molina, K. Dahmouche, C. V. Santilli, A. F. Craievich, and S. J. L. Ribeiro, *Chem. Mater.* 13, 2818 (2001).
151. T. Ishizaka, R. Nozaki, and Y. Kurokawa, *J. Phys. Chem. Solids* 63, 613 (2002).
152. E. Cordoncillo, B. Viana, P. Escribano, and C. Sanchez, *J. Mater. Chem.* 8, 507 (1998).
153. A. C. Franville, D. Zambon, R. Mahiou, S. Chou, Y. Troin, and J. C. Cousseins, *J. Alloys Comp.* 275–277, 831 (1998).
154. A.-C. Franville, D. Zambon, R. Mahiou, and Y. Troin, *Chem. Mater.* 12, 428 (2000).
155. A.-C. Franville, R. Mahiou, D. Zambon, and J.-C. Cousseins, *Solid State Sci.* 3, 221 (2001).
156. D. Dong, S. Jiang, Y. Men, X. Ji, and B. Jiang, *Adv. Mater.* 12, 646 (2000).



157. F. Embert, A. Mehdi, C. Rey , and R. J. P. Corriu, *Chem. Mater.* 13, 4542 (2001).
158. H. R. Li, J. Lin, H. J. Zhang, L. S. Fu, Q. G. Meng, and S. B. Wang, *Chem. Mater.* 14, 3651 (2002).
159. X. Fan, Z. Wang, and M. Wang, *Chem. Phys. Lett.* 358, 115 (2002).
160. F. Liu, L. Fu, J. Wang, Q. Meng, H. Li, J. Guo, and H. Zhang, *New J. Chem.* (in press).
161. F. Liu, L. Fu, J. Wang, Z. Liu, H. Li, and H. Zhang, *Thin Solid Films* 419, 178 (2002).
162. L. D. Carlos, V. de Zea Bermudez, M. C. Duarte, M. M. Silva, C. J. Silva, M. J. Smith, M. Assun o, and L. Alc cer, in "Physics and Chemistry of Luminescent Materials VI," (C. Ronda and T. Welker, Eds.), Vol. 97-29, p. 352. Electrochemical Society Proceedings, San Francisco, 1998.
163. V. de Zea Bermudez, L. D. Carlos, M. C. Duarte, M. M. Silva, C. J. Silva, M. J. Smith, M. Assun o, and L. Alc cer, *J. Alloys Comp.* 275–277, 21 (1998).
164. L. D. Carlos, V. de Zea Bermudez, and R. A. S  Ferreira, *J. Non-Cryst. Solids* 247, 203 (1999).
165. M. M. Silva, V. de Zea Bermudez, L. D. Carlos, A. P. Passos de Almeida, and M. J. Smith, *J. Mater. Chem.* 9, 1735 (1999).
166. L. D. Carlos, R. A. S  Ferreira, V. de Zea Bermudez, C. Molina, L. A. Bueno, and S. J. L. Ribeiro, *Phys. Rev. B* 60, 10042 (1999).
167. V. Zea Bermudez, L. Alc cer, J. L. Acosta, and E. Morales, *Solid State Ionics* 116, 197 (1999).
168. L. D. Carlos, Y. Messaddeq, H. F. Brito, R. A. S  Ferreira, V. de Zea Bermudez, and S. J. L. Ribeiro, *Adv. Mater.* 12, 594 (2000).
169. L. D. Carlos, R. A. S  Ferreira, and V. de Zea Bermudez, *Electrochim. Acta* 45, 1555 (2000).
170. R. A. S  Ferreira, L. D. Carlos, R. R. Gon alves, S. J. L. Ribeiro, and V. de Zea Bermudez, *Chem. Mater.* 13, 2991 (2001).
171. V. de Zea Bermudez, R. A. S  Ferreira, L. D. Carlos, C. Molina, and S. J. L. Ribeiro, *J. Phys. Chem. B* 105, 3378 (2001).
172. L. D. Carlos, R. A. S  Ferreira, J. P. Rainho, and V. de Zea Bermudez, *Adv. Funct. Mater.* 12, 819 (2002).
173. L. D. Carlos, R. A. S  Ferreira, and V. de Zea Bermudez, in "Organic-Inorganic Hybrids II, Proceedings of the International Conference on Organic-Inorganic Hybrids II," Paint Research Association, Teddington, 2002, paper 35.
174. S. M. Gomes Correia, V. de Zea Bermudez, R. A. S  Ferreira, L. D. Carlos, M. M. Silva, S. Barros, and M. J. Smith, *Ionics* 8, 73 (2002).
175. M. C. Gon alves, V. de Zea Bermudez, D. Ostrovskii, and L. D. Carlos, *Ionics* 8, 62 (2002).
176. R. A. S  Ferreira, L. D. Carlos, V. de Zea Bermudez, C. Molina, K. Dahmouche, Y. Messaddeq, and S. J. L. Ribeiro, *J. Sol-Gel Sci. Technol.* 26, 315 (2003).
177. S. J. L. Ribeiro, K. Dahmouche, C. A. Ribeiro, C. V. Santilli, and S. H. Pulcinelli, *J. Sol-Gel Sci. Technol.* 13, 427 (1998).
178. K. Dahmouche, C. V. Santilli, S. H. Pulcinelli, and A. F. Craievich, *J. Phys. Chem. B* 103, 4937 (1999).
179. K. Dahmouche, C. V. Santilli, M. da Silva, C. A. Ribeiro, S. H. Pulcinelli, and A. F. Craievich, *J. Non-Cryst. Solids* 247, 108 (1999).
180. C. Molina, S. J. L. Ribeiro, K. Dahmouche, C. V. Santilli, and A. F. Craievich, *J. Sol-Gel Sci. Technol.* 19, 615 (2000).
181. K. Dahmouche, L. D. Carlos, V. de Zea Bermudez, R. A. S  Ferreira, A. P. Passos de Almeida, C. V. Santilli, and A. F. Craievich, *J. Mater. Chem.* 11, 3249 (2001).
182. K. Dahmouche, L. D. Carlos, C. V. Santilli, V. de Zea Bermudez, and A. F. Craievich, *J. Phys. Chem. B* 106, 4377 (2002).
183. K. Dahmouche, M. C. Gon alves, C. V. Santilli, V. de Zea Bermudez, L. D. Carlos, and A. F. Craievich, *Nucl. Instrum. Meth., Phys. Res. B* 199, 117 (2003).
184. C. Molina, K. Dahmouche, Y. Messaddeq, S. J. L. Ribeiro, M. A. P. Silva, V. de Zea Bermudez, and L. D. Carlos, *J. Lumin.* 104, 93 (2003).
185. V. Bekiari, P. Lianos, and P. Judeinstein, *Chem. Phys. Lett.* 307, 310 (1999).
186. V. Bekiari, E. Stathatos, P. Lianos, U. L. Stangar, B. Orel, and P. Judeinstein, *Chem. Mater.* 12, 3095 (2000).
187. R. Moleski, E. Stathatos, V. Bekiari, and P. Lianos, *Thin Solid Films* 416, 279 (2002).
188. Y. Li, H. Zhang, S. B. Wang, Q. Meng, H. R. Li, and X. H. Chuai, *Thin Solid Films* 385, 205 (2002).
189. Y. Li, H. Zhang, H. Li, J. Lin, Y. Yu, and Q. Meng, *Mater. Lett.* 56, 597 (2002).
190. R. J. P. Corriu, F. Embert, Y. Guari, A. Mehdi, and C. Rey , *Chem. Commun.* 1116 (2001).
191. L. D. Carlos, V. de Zea Bermudez, R. A. S  Ferreira, L. Marques, and M. Assun o, *Chem. Mater.* 11, 581 (1999).
192. R. A. S  Ferreira, L. D. Carlos, and V. de Zea Bermudez, *Thin Solid Films* 470, 343 (1999).
193. L. D. Carlos, R. A. S  Ferreira, I. Orion, V. de Zea Bermudez, and J. Rocha, *J. Lumin.* 87–89, 702 (2000).
194. L. D. Carlos, R. A. S  Ferreira, V. de Zea Bermudez, and S. J. L. Ribeiro, *Adv. Funct. Mater.* 2, 111 (2001).
195. L. D. Carlos, R. A. S  Ferreira, and V. de Zea Bermudez, in "Handbook of Organic-Inorganic Hybrid Materials and Nanocomposites" (H. S. Nalwa, Ed.), Vol. 1., Chap. 9, pp. 353–380, American Scientific Publishers, Morth Lewis Way, California, 2003.
196. L. D. Carlos, R. A. S  Ferreira, M. Assun o, and V. de Zea Bermudez, unpublished results.
197. G. Beaucage, T. A. Ulibarri, E. P. Black, and D. W. Schaefer, in "Hybrid Organic-Inorganic Composites" (J. E. Mark, C. Y.-C. Lee, and P. A. Bianconi, Eds.), Vol. 585, p. 97. American Chemical Society Symposia Proceedings, Washington, 1995.
198. V. de Zea Bermudez, L. D. Carlos, and L. Alc cer, *Chem. Mater.* 569, 11 (1999).
199. R. A. Street, *Adv. Phys.* 30, 593 (1981).
200. T. Takagahara and K. Takeda, *Phys. Rev. B* 46, 15578 (1992).
201. G. Allan, C. Delerue, and M. Lannoo, *Phys. Rev. B* 48, 7951 (1993).
202. Y. Kanemitsu, K. Susuki, S. Kyushin, and H. Matsumoto, *Phys. Rev. B* 51, 13103 (1995).
203. A. O. Konstantinov, A. Henry, C. I. Harry, and E. Janz n, *Appl. Phys. Lett.* 66, 2250 (1995).
204. V. V. Ovsyankin, in "Spectroscopy of Solids Containing Rare-Earth Ions" (A. A. Kaplianskii and R. M. MacFarlane, Eds.), p. 371. Elsevier Science, Amsterdam, 1987.
205. S. T. Frey and W. De Horrocks, Jr., *Inorg. Chim. Acta* 229, 383 (1995).
206. R. W. Hunt, "Measuring Colour." Ellis Horwood Series in Applied Science and Industrial Technology, Wiley, New York, 1987.
207. D. B. Judd and G. Wyszecski, "Color in Business, Science and Industry." Wiley, New York, 1963.
208. K. Narisada and S. Kanaya in "Phosphor Handbook" (S. Shionoya and W. M. Yen, Eds.), p. 799. CRC Press, Boca Raton, 1999.
209. M. Isakawi, J. Kuraki, and S. Ito, *J. Sol-Gel Sci. Technol.* 13, 587 (1998).
210. M. S. Wrighton, D. S. Gingley, and D. L. Morse, *J. Phys. Chem.* 78, 2229 (1974).
211. O. L. Malta, H. F. Brito, J. F. S. Menezes, F. R. Gon alves e Silva, C. De Mello Doneg , and S. Alves, Jr., *Chem. Phys. Lett.* 282, 233 (1998).
212. R. Reisfeld and C. K. J rgenson, in "Handbook on the Physics and Chemistry of Rare Earths" (K. A. Gschneider, Jr. and L. Eyring, Eds.), Vol. 9, p. 61. Elsevier Science, Amsterdam, 1987.
213. B. Canny and D. Curie, in "Advances in Non-Radiative Processes in Solids" (B. DiBartolo, Ed.), p. 1. Plenum, New York, 1991.
214. O. L. Malta, H. J. Batista, and L. D. Carlos, *Chem. Phys.* 282, 21 (2002).
215. F. Gao and S. Zhang, *J. Phys. Chem. Solids* 58, 1991 (1997).

216. O. L. Malta, M. A. Couto dos Santos, L. C. Thompson, and N. K. Ito, *J. Lumin.* 69, 77 (1996).
217. O. L. Malta, H. F. Brito, J. F. S. Menezes, F. R. Gonçalves e Silva, S. Alves, Jr., F. S. Farias, Jr., and A. V. M. Andrade, *J. Lumin.* 75, 255 (1996).
218. M. F. Hazenkamp and G. Blasse, *Chem. Mater.* 2, 105 (1990).
219. O. L. Malta, S. J. L. Ribeiro, M. Faucher, and P. Porcher, *J. Phys. Chem. Solids* 52, 587 (1991).
220. C. K. Jørgensen and B. R. Judd, *Mol. Phys.* 8, 281 (1945).
221. W. T. Carnall, H. Crosswhite, and H. M. Crosswhite, in “Energy Structure and Transitions Probabilities of the Trivalent Lanthanides in LaF<sub>3</sub>,” Argonne National Laboratory Report, 1977.
222. W. H. Green, K. P. Le, J. Grey, T. T. Au, and M. J. Sailor, *Science* 276, 1826 (1997).
223. V. Bekiari and P. Lianos, *Langmuir* 14, 3459 (1998).
224. V. Bekiari and P. Lianos, *Chem. Mater.* 10, 3777 (1998).
225. E. Stathatos, P. Lianos, U. L. Stangar, B. Orel, and P. Judeinstein, *Langmuir* 16, 8672 (2000).
226. Y. Uchida, Y.-I. Nobu, I. Momiji, and K. Matsui, *J. Sol-Gel Sci. Technol.* 19, 705 (2000).
227. V. Bekiari, E. Stathatos, P. Lianos, U. L. Stangar, B. Orel, and P. Judeinstein, *Monatsh. Chem.* 132, 97 (2001).
228. E. Cordoncillo, F. J. Guaita, P. Escribano, C. Philippe, B. Viana, and C. Sanchez, *Opt. Mater.* 18, 309 (2001).
229. Y. Han, J. Lin, and H. Zhang, *Mater. Lett.* 54, 389 (2002).
230. T. Brankova, V. Bekiari, and P. Lianos, *Chem. Mater.* 15, 1855 (2003).
231. L. Pavesi, L. Dal Negro, C. Mazzoleni, G. Franzó, and F. Priolo, *Nature* 408, 440 (2000).
232. N. C. Greenham, I. D. W. Samuel, G. R. Hayes, R. T. Philips, Y. A. R. R. Kessenger, S. C. Moratti, A. B. Holmes, and R. H. Friend, *Chem. Phys. Lett.* 241, 89 (1995).
233. K. Dahmouche, M. Atik, N. C. Mello, T. J. Bonagamba, H. Panepucci, M. A. Aegerter, and P. Judeinstein, *J. Sol-Gel Sci. Technol.* 8, 711 (1997).
234. F. Rousseau, C. Poinsignon, J. Garcia, and M. Popall, *Chem. Mater.* 7, 828 (1995).
235. S. Sinha, S. Banerjee, and B. M. Arora, *Phys. Rev. B* 49, 5706 (1994).
236. J. Shah, A. Pinczuk, and F. B. Alexander, *Solid State Commun.* 42, 717 (1982).
237. J. Shah and P. M. Bridenbaugh, *Solid State Commun.* 34, 101 (1980).
238. T. Takagahara and K. Takeda, *Phys. Rev. B* 46, 15578 (1992).
239. G. Allan, C. Delerue, and M. Lannoo, *Phys. Rev. B* 48, 7951 (1993).
240. Y. Kanemitsu, K. Susuki, S. Kyushin, and H. Matsumoto, *Phys. Rev. B* 51, 13103 (1995).
241. A. O. Konstantinov, A. Henry, C. I. Harry, and E. Janczén, *Appl. Phys. Lett.* 66, 2250 (1995).
242. Y. Kanemitsu, S. Okamoto, M. Otake, and S. Oda, *Phys. Rev. B* 55, 7375 (1997).
243. J. Chelikowsky, *Mater. Res. Soc. Bull.* 27, 951 (2002).
244. T. Schmidt, K. Lischka, and W. Zulehner, *Phys. Rev. B* 45, 8989 (1992).
245. J. I. Pankove, “Optical Processes in Semiconductors.” Dover, New York, 1990.
246. K. S. Zhuravlev, A. M. Gilinsky, and A. Y. Kobitsky, *Appl. Phys. Lett.* 73, 2965 (1998).
247. K. Maeda, *Phys. Chem. Solids* 26, 595 (1964).
248. H. Koyama, T. Ozaki, and N. Koshida, *Phys. Rev. B* 52, R11561 (1995).
249. S. M. Strokes, O. J. Glembocki, V. M. Bermudez, R. Kaplan, L. E. Friedersdorf, and P. C. Searson, *Phys. Rev. B* 45, 13788 (1992).
250. A. Serpi and P. M. Serpi, *J. Lumin.* 8, 261 (1974).
251. P. M. Serpi, A. Rucci, and A. Serpi, *J. Lumin.* 9, 488 (1975).
252. P.-T. Chou, G. R. Wu, C. Y. Wei, C. C. Cheng, C. P. Chang, and F. T. Hung, *J. Phys. Chem. B* 104, 7818 (2000).
253. R. M. Tarkka, X. Zhang, and S. A. Jenekhe, *J. Am. Chem. Soc.* 118, 9438 (1996).
254. L. W. Beck, T. Xu, J. B. Nicholas, and J. F. Haw, *J. Am. Chem. Soc.* 117, 11594 (1995).
255. J. Haw, T. Xu, J. B. Nicholas, and P. W. Goguen, *Nature* 389, 832 (1997).
256. I. S. Afanasyev, N. K. Moroz, and I. A. Belitsky, *J. Phys. Chem. B* 104, 6804 (2000).
257. B. A. Wilson, *Phys. Rev. B* 23, 3102 (1981).
258. L. T. Canham, *Appl. Phys. Lett.* 57, 1046 (1990).
259. L. Brus, *J. Phys. Chem. B* 98, 3575 (1994).
260. S. M. Prokes, *Appl. Phys. Lett.* 62, 3244 (1995).
261. F. Zhou and J. D. Head, *J. Phys. Chem. B* 104, 9981 (2000).
262. I. S. Altman, D. Lee, J. D. Chung, J. Song, and M. Choi, *Phys. Rev. B* 63, 161402 (2000).
263. J. H. Stathis and M. A. Kastner, *Phys. Rev. B* 35, 2972 (1982).

# Macroscopically Aligned Carbon Nanotubes

Pascale Launois

*Université Paris, Orsay Cédex, France*

Philippe Poulin

*Université Bordeaux I, Pessac, France*

## CONTENTS

1. Introduction
  2. Processing Materials of Aligned Nanotubes
  3. Direct Synthesis of Macroscopically Aligned Nanotubes by Chemical Vapor Deposition
  4. Conclusion
- Glossary  
References

## 1. INTRODUCTION

Single-wall and multi-wall carbon nanotubes (SWNT, MWNT) have unique physical properties associated to their one-dimensional nanostructures. They are considered very promising materials for various applications [1–3]. For instance, thanks to their structure-dependent conducting or semi-conducting character, nano components such as diodes and transistors have already been made with nanotubes [4, 5]. Patterning nanotubes at the nanoscopic scale is thus a challenge for what might be the electronics of the future. But in this article, we focus rather on another challenge—obtaining nanotube materials with interesting macroscopic properties. For instance, nanotubes have remarkable mechanical properties, with Young modulus of the order of 1 TPa [6–9], and one may hope to obtain very strong materials with them. More precisely, in this article, we do not consider composite materials that include only a small fraction of nanotubes, generally embedded in polymeric matrices; rather we focus on materials comprised mostly of nanotubes. The physical properties of these one-dimensional objects being strongly anisotropic, aligned nanotubes materials are of particular interest. The topic is in strong development, as is illustrated in Figure 1 by the “exponential-type” of increase of the number of related

publications during the last few years. To obtain aligned nanotube materials, two different approaches are followed: (i) processing nanotubes, starting from an isotropic soot, and (ii) the direct synthesis of aligned nanotubes. The processing methods developed up to now are reviewed in Section 2. The degree of alignment of the nanotubes and the related properties of materials are also discussed. Section 3 is the counterpart of Section 2 for chemical vapor deposition, which is the most widely used method for synthesizing aligned nanotubes.

## 2. PROCESSING MATERIALS OF ALIGNED NANOTUBES

After the discovery of nanotubes in 1991 [10], an important step was the production of nanotubes in macroscopic quantities, in 1996 and 1997, using laser ablation [11] and electric arc [12] methods. As produced, nanotubes are under the form of a fragile and isotropic soot. This soot is rather difficult to use. Processing nanotubes on macroscopic scales to obtain materials of more practical use was, and is still now, a major challenge. In most cases, the nanotubes are initially dispersed in liquid media. Dispersing nanotubes is also widely used for filtrations and purifications of raw materials [13]. To be dispersed in a given medium, carbon nanotubes generally have to be either chemically modified [14, 15] or coated by adsorbed amphiphilic molecules [16]. Detailed discussion of the phase behavior of these suspensions is beyond the scope of this article, but we want to emphasize that it is of critical importance.

In this introduction, we briefly discuss the methods used to quantify the degree of alignment of nanotubes. For single-wall nanotubes, it can be deduced from electron and X-ray scattering or from polarized Raman spectroscopy. Single-wall nanotubes are usually assembled in bundles, forming a two-dimensional hexagonal array perpendicular to

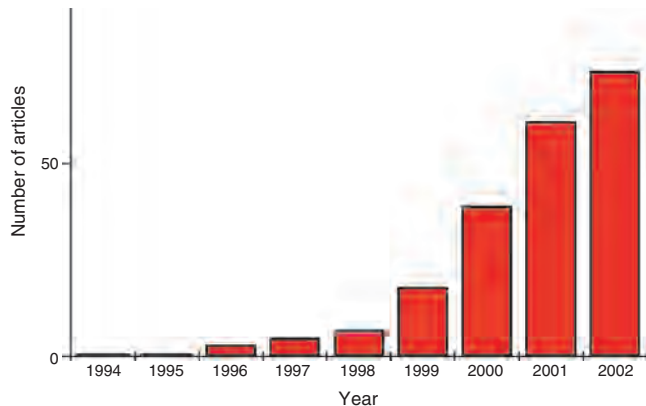


**Figure 1.** Evolution of the number of articles with “align” and “nano-tube” in the title, after ISI web of science

the bundle axis. The crystalline nature of the bundles has been used to quantitatively probe their degree of alignment using electron and X-ray diffraction. Mosaic distributions are obtained from the angular intensity distributions of the first diffraction peak of their hexagonal lattice (Fig. 2). In most cases, it can be fitted by a Gaussian function with a full width at half maximum (FWHM) related to the angular distribution of nanotube axes in direct space. The smaller it is, the better the nanotube alignment. For a two-dimensional distribution of nanotube orientations within a plane, the width of the intensity distribution directly gives that of the distribution of orientations in direct space. For a given FWHM, 76% of the nanotubes long axes lie within  $\pm\text{FWHM}/2^\circ$  from the mean direction of alignment. For a three-dimensional distribution around an axis, the width of the distribution in direct space is equal to that in reciprocal space for  $\text{FWHM} < 40^\circ$ , and then becomes slightly smaller: it is for instance equal to  $70^\circ$  for  $75^\circ$  in reciprocal

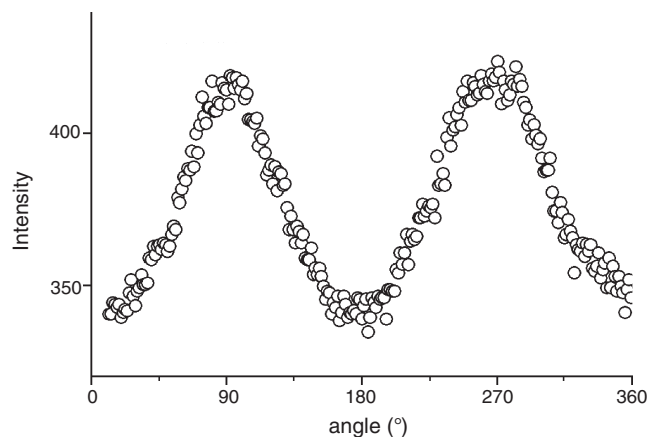


**Figure 2.** X-ray scattering study [18] of the orientation of the nanotubes along the axis of a fiber obtained by the spinning process described in [16]. The angular distribution of the scattered intensity from a nanotube fiber at constant Q value of  $0.4 \text{ \AA}^{-1}$ , which corresponds to the (1, 0) peak position of nanotube hexagonal array, is reported. The orientation of the nanotubes with respect to the fiber axis can be deduced from the width of this angular distribution.

space [17]. For  $\text{FWHM} = 30^\circ$  ( $75^\circ$ ),  $\sim 50\%$  of the nanotube axes lie inside a cone of angle  $15^\circ$  ( $35^\circ$ ). In this article, we will refer to widths in reciprocal space, as was done in quoted publications. A “two-phase” model can be considered with partially aligned nanotubes, characterized by the Gaussian distribution, plus a fraction of nonaligned nanotubes [18, 19]. The nonaligned fraction may be sample dependent for a given method [20] and is not always discussed in quoted references. Some information about tubes not assembled, or poorly crystallized in bundles, may be obtained from the analysis of the diffuse intensity distribution outside of the Bragg peaks [19]. The nanotube alignment can also be deduced from polarized Raman measurements. Indeed, Raman line intensities depend on the angles made by the polarization of the laser excitation and that of the scattered light with the nanotubes long axes (Fig. 3). This is explained within a resonant model for highly anisotropic tube absorption. All nanotubes assembled in bundles or not, are probed in the same way with this method. An advantage of the X-ray scattering method, with respect to electron scattering or Raman spectroscopy, is that the volume investigated is much larger. Moreover, the interpretation of X-ray scattering experiments is more direct than that of Raman experiments. On the other hand, Raman spectroscopy probes all nanotubes, and not preferentially those organized in crystalline bundles. Finally, for multi-wall nanotubes, the method used to study their orientation is X-ray (or electron) diffraction, the analysis of

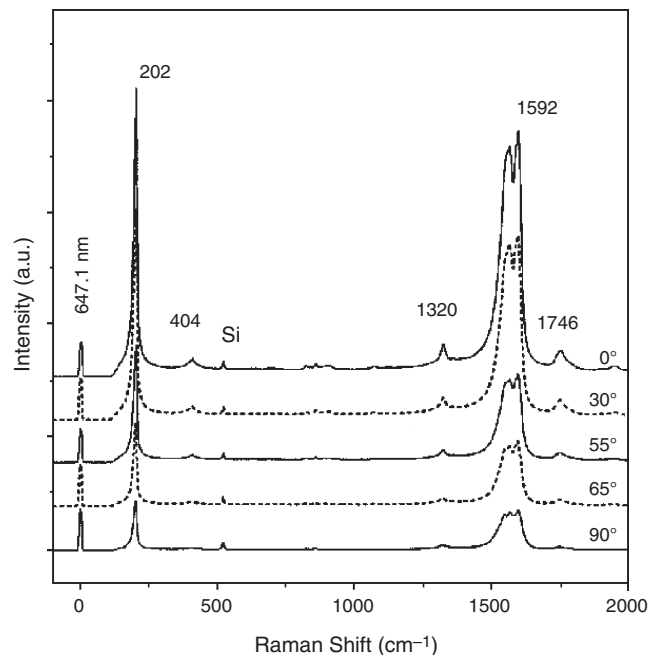


**Figure 3.** Raman scattering spectra (excitation wave-length = 647.1 nm) of a SWNT fiber obtained by electrophoresis (H. H. Gommans et al.). The analyzer polarization direction is parallel to the incident polarization. The angle between the fiber axis and the excitation polarization—indicated at the right of the curves—varies from  $0^\circ$  to  $90^\circ$  direction. The intensity of the nanotube lines decreases with increasing angle. Reprinted with permission from [36], H. H. Gommans et al., *J Appl. Phys.* 88, 2509 (2000). © 2000, American Institute of Physics.

the intensity distribution being made on the diffraction peak corresponding to the interwalls distance ( $\sim 3.4$  Å). Other methods are also reported in the literature, but they are not quantitative. Under a scanning electron microscope (SEM), the nanotubes can be visualized and thereby their alignment roughly estimated. However, it is a rather local and only two-dimensional probe. If the material is sufficiently transparent (not too thick), it can be placed between crossed vertical and horizontal polarizers: due to nanotube birefringence, a bright transmitted light is seen when the nanotubes axes make an angle of  $45^\circ$  with respect to the polarizers axes.

A variety of different methods have been developed during the last few years to achieve films or fibers of nanotubes with a marked preferential orientation, as shown in the following (first results have been reviewed in [21]).

## 2.1. Films of Magnetically Aligned Nanotubes

Classical films of buckypaper [13] are made by deposition from suspensions of single-wall carbon nanotubes onto a membrane filter. The nanotubes lie preferentially in the plane of the film but they are randomly oriented within this plane. Moreover, the in-plane orientation is far from being perfect: the upper limit for the FWHM of the Gaussian distribution of nanotubes orientations with respect to the plane of the paper is  $56^\circ$ , as deduced from X-ray scattering experiments [19, 22]. One may notice that much better in-plane orientation (FWHM  $\approx 4^\circ$ ) has been obtained very recently by pressing a raw nanotube powder up to a pressure of 10 kbars [23]. Despite their relatively poor two-dimensional alignment, buckypapers obtained by deposition already present interesting properties. Indeed, electromechanical actuators based on such papers were shown to generate higher stresses than natural muscles and higher strains than high-modulus ferroelectrics [24]. As a reference for measurements on aligned nanotubes materials, we also give here the Young modulus of buckypaper  $Y \sim 1.2$  GPa [24].

By filtering the nanotube suspension in a strong magnetic field Walters et al. [25] have achieved a preferential orientation of the nanotubes in the plane of the film, as schematically drawn in Figure 4(b). The film thickness typically ranges between 1 and 5  $\mu\text{m}$ . The obtained materials are denser than classical films of buckypaper because of the higher compactness of oriented nanotubes. According to Smith et al. [22], the empty volume in magnetically aligned nanotubes is about 30%, whereas it is between 70% and 90% in ordinary buckypaper, and of about 95% as produced materials. The films cleave along a direction in parallel to that of the applied magnetic field  $H$ , which indicates anisotropic strength of the film, maximal along the  $H$ -direction (Fig. 5(a)). The degree of alignment within the plane of the film has been measured using electron and X-ray scattering [19, 22, 26], and with polarized Raman experiments [19]. The FWHM deduced from Gaussian fits typically ranges between  $25^\circ$  and  $45^\circ$ . The first results were obtained under high magnetic field (26 T) at the National High Magnetic Field Laboratory in Florida. But it was shown recently that similar values of FWHM  $\approx 35^\circ$  are obtained with  $H = 7$  T [19]. This last result is very

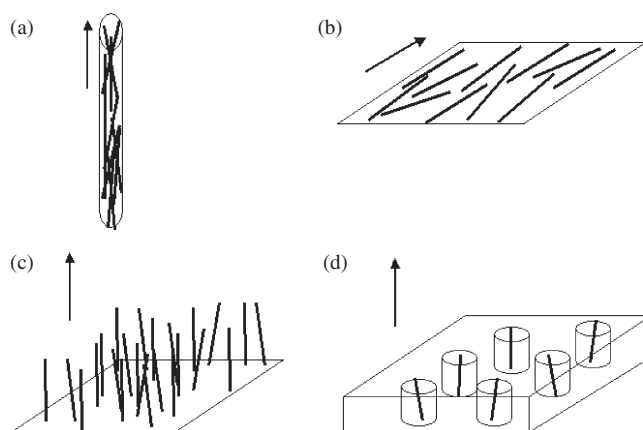


**Figure 4.** Schematic representation of the real materials of aligned nanotubes obtained up till now. Nanotubes are represented by the thick sticks; their direction of preferential orientation is indicated by an arrow. (a) A fiber where the nanotubes are preferentially oriented along the fiber axis, (b) a film where nanotubes have a preferential orientation along a direction within the film, (c) array of nanotubes perpendicular to a surface, and (d) nanotubes inside meso or nanoporous materials.

interesting because seven Tesla fields can be reached in many laboratories using superconducting solenoids. It also allows the authors to conclude that further enhancements in anisotropic properties of the films may require optimizing the filter deposition process rather than large magnetic fields. The degree of alignment of nanotubes with respect to the plane of the film should be higher than within the plane, due to conjugated deposition and magnetic field effects. However, no value for it has been given yet.

Hone et al. [27] have reported quantitative measurements of the anisotropic electrical and thermal transport properties of magnetically aligned nanotubes. Both electrical and thermal conductivities are found to be higher in the  $H$ -alignment axis. The ratios between the parallel and perpendicular components of the conductivity vary between 6 and 24 for different samples, the highest value corresponding to the best nanotube alignment. Good correlation between resistivity and texture parameters is found within a simple geometrical model [19]. For annealed samples, where electronic “doping” effects are minimized, the order of magnitude of resistivity is  $\sim 10^{-5}$   $\Omega\text{m}$  in the  $H$ -direction at room temperature, to be compared with  $\sim 10^{-6}$   $\Omega\text{m}$  for a single bundle [28] and to  $\sim 1.7 \cdot 10^{-5}$   $\Omega\text{m}$  for buckypaper [13]. Thermal transport properties have been shown to be different in aligned and nonaligned materials. At room temperature, the conductivity is about 230 W/mK in aligned materials along the applied field axis and about 30 W/mK in nonaligned materials. We note that the thermal conductivity of aligned materials is within an order of magnitude of that of graphite, parallel to the layers. Liu et al. [26] have performed momentum-dependent electron energy-loss studies, taking advantage of the macroscopic alignment of the nanotubes. They have shown that the  $\pi$  plasmon is strongly anisotropic, confirming experimentally its previously postulated polarization dependent momentum dependence.



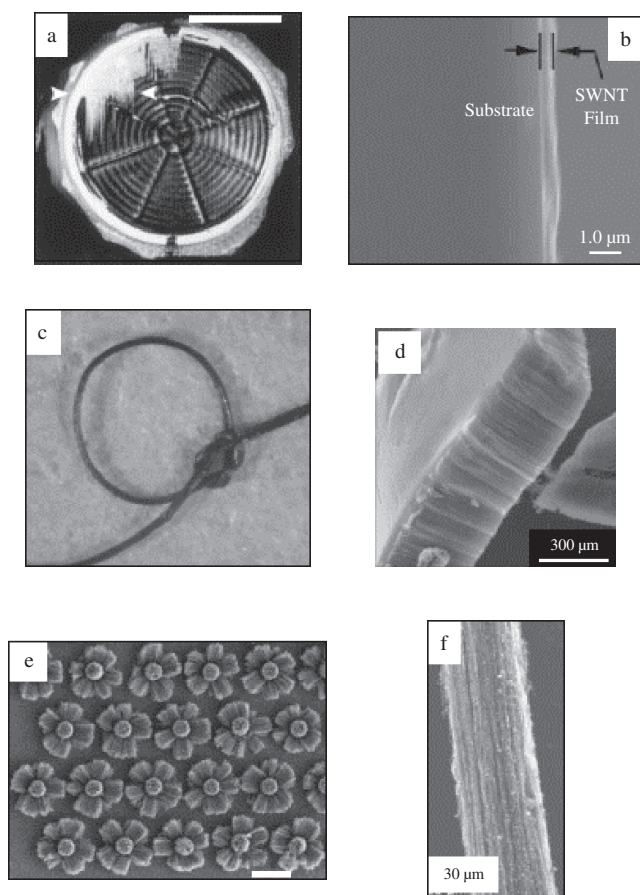


**Figure 5.** Examples of oriented assemblies of nanotubes from the literature. (a) In plane-aligned assembly of SWNTs, obtained by filtration, under a magnetic field (reprinted with permission from [25], D. A. Walters et al., *Chem. Phys. Lett.* 338, 14 (2001). © 2001, Elsevier Science). Scale bar = 1 cm. The membrane was partially removed from the filter: cleavage is found to occur parallel to the field axis. (b) Membrane of self-organized SWNTs on a Si substrate: an edge-on SEM image (reprinted with permission from [30], H. Shimoda et al., *Adv. Mat.* 14, 899 (2002). © 2002, Wiley-VCH). The nanotubes have a preferred orientation within the membrane plane. (c) Optical micrograph of a SWNT fiber obtained after a spinning process (typical fibers diameters: 10–100  $\mu\text{m}$  [16]). The nanotubes are preferentially aligned along the fiber axis. The knot reveals the high flexibility of the fiber. (d) Flake of aligned MWNTs collected on quartz tube walls, after pyrolysis of homogeneously dispersed, toluene-ferrocene aerosols (from Martine Mayne-L’Hermite, DSM/DRECAM/SPAM/LFP, URA-CNRS 2453, CEA-Saclay and Luc Belin, DEN/DMN/SEMI, CEA-Saclay; image credit: CEA-Saclay). (e) Repeating patterns containing mutually orthogonal MWNTs arrays obtained by CVD on 5- $\mu\text{m}$  deep silica cylinders machined on silicon substrates (reprinted with permission from [79], B. Q. Wei et al., *Nature* 416, 495 (2002). © 2002, Nature). Scale bar-50  $\mu\text{m}$ . (f) SEM image of a long SWNT fiber obtained by CVD (reprinted with permission from [80], H. W. Zhu et al., *Science* 296, 884 (2002). © 2002, American Association for Advancement of Science). The nanotubes are preferentially aligned along the fiber axis.

In summary, the thermal and electrical properties of magnetically aligned nanotubes are strongly anisotropic and significantly improved when compared to that of traditional buckypaper. Moreover, alignment of nanotubes at a macroscopic scale has made possible the experimental study of some electronic properties of nanotubes.

## 2.2. Films of Mechanically Aligned Nanotubes

As was said in the introduction, we do not consider in this article composite materials that include only a small fraction of nanotubes. However, let us mention the work of Jin et al. [29], which will allow us to illustrate the effect of mechanical stretching at still relatively high nanotube weight fraction. Multi-wall nanotubes are mixed with a thermoplastic polymer (polyhydroxyaminoether), and in this case, the amount of nanotubes is rather large (50 wt % of raw carbon nanotube materials incorporated). The obtained composite films are uniaxially stretched at 100° C and are found to remain elongated after removal of the load at room temperature (final length  $L$  greater than initial length  $L_0$ ). For  $L/L_0 = 330\%$ , 58% of the nanotubes are partially aligned along the stress direction, this alignment being characterized by a FWHM = 46°, showing the efficiency of the process.

## 2.3. Films of Self-Assembled Nanotubes

Self-assembly of preformed single-wall carbon nanotubes was reported in 2002 by Shimoda et al. [30]. Nanotubes lengths were reduced to  $\sim 1 \mu\text{m}$  by chemical etching. A homogeneous suspension of such nanotubes could be obtained in deionized water, probably because of the presence of sidewall defects terminated by polar groups due to chemical etching. A hydrophilic glass slide was immersed in the solution. When the water gradually evaporated, a continuous nanotubes film is formed at the surface of the glass (Fig. 5(b)). The process invoked for the film formation is heterogeneous nucleation. The film thickness ranges between 0.1 and 1  $\mu\text{m}$ , depending on the nanotube concentration in the suspension. Shimoda et al. also demonstrated that they could obtain a great variety of two-dimensional structures by using hydrophobic surfaces patterned with hydrophilic regions. The above-mentioned sidewall defects on nanotubes can finally be removed after annealing at 400 °C in  $10^{-6}$  torr vacuum. Transmission electron microscopy (TEM), polarized Raman spectroscopy, and optical measurements between crossed polarizers revealed that the nanotubes exhibit a preferential orientation within the film (Fig. 4(b)). The ordering may be attributed to the interactions between nanotubes and to surface tension effects at the interface between water and the hydrophilic surface. These promising results are very recent: quantitative studies of nanotube alignment or of the film properties are much awaited.

## 2.4. Ribbons of Self-Assembled Nanotubes

Li et al. [31] reported in 2002 the self-organization of aligned multi-wall nanotubes in ribbons. After adequate treatment, in particular with concentrated nitric acid and hydrofluoric acid, the nanotubes are put in solution in deionized water. While the solution is annealed at 373 K in vacuum for 12 h, long ribbons form on the wall of the container. The ribbons are about 50–100  $\mu\text{m}$  wide, 4–12  $\mu\text{m}$  thick, and 100 mm long, with a very clear rectangular cross-section. Scanning electron microscopy shows that the nanotubes are preferentially aligned along the long axis of the ribbon. The oxidation with acid has introduced many functional groups at



the surface of the nanotubes, which play a major role in the self-organization phenomenon (no ribbons form when nanotubes are not refluxed with acid). It is suggested that polycondensation may take place through the functional groups [32].

The Young modulus of as-grown ribbon is  $Y \sim 24$  GPa. However, this is much below the Young modulus value of a single nanotube [6–8], which can be attributed to too weak interactions between the nanotubes. After thermal treatment at 2200 °C under argon atmosphere, the Young modulus of ribbons increases to 60 GPa (Fig. 6(a)) [32]. This is attributed to graphitization between nanotubes, which would lead to stronger intertube cohesion.

## 2.5. Langmuir–Blodgett Films of Nanotubes

The Langmuir–Blodgett (LB) technique has been developed for depositing molecularly ordered ultra-thin films with controlled thickness and orientation [33]. In the case of nanotubes, a main impediment with respect to this method was their poor dispersibility in aqueous solutions. In 2002, Guo et al. [34, 35] reported the elaboration of homogeneous films of single-wall carbon nanotubes with preferential orientation within the film by this method. The nanotubes are chemically modified: solubility of nanotubes in chloroform is brought by the attachment of octadecylamine groups to the tubes. They are then mixed with an amphiphilic polymer matrix

of poly(N-dodecylacrylamide) (PDDA). The SWNT/PDDA mixtures are deposited on the water surface and condensed mixed films are obtained, as in the case of pure PDDA. They can thus be transferred vertically on glass, quartz, and silicon substrates. Multilayer LB films have been successfully realized. Their homogeneity is controlled by light absorption and mass measurements. Scanning electron microscopy and polarized Raman spectroscopy show that the nanotubes are preferentially aligned along the dipping direction of the substrate (but the extent to which they are aligned has not been quantified yet). Guo et al. underline that the realization of these thin films of oriented SWNTs with controlled thickness and optical transparency may be a useful tool for a better understanding of some electronic and optoelectronic properties of nanotubes.

## 2.6. Fibers Made By an Electrophoretic Method

In 2000 Gommans et al. [36] have developed a method for making fibers of SWNTs possessing substantial alignment along the fiber axis (cf. the schematic drawing in Fig. 4(a)). The first step of the method consists of dispersing nanotubes in N,N-dimethylformamide. A commercially available carbon fiber is attached to a conducting wire coupled to a motor-driven translation stage. The carbon fiber is translated along its axis down in the nanotube suspension to a depth of few mm. The set-up is designed so that a voltage can be applied between the carbon fiber and the suspension. When a voltage is applied with the carbon fiber as the positive electrode, the nanotubes are attracted and form a cloud around the carbon fiber. Then the carbon fiber is slowly withdrawn from the suspension. As it pulls out of the liquid, another fiber attached to its end, forms spontaneously from the nanotube cloud. The formation of SWNTs cloud around a positive electrode indicates that nanotubes are negatively charged when dispersed in N,N-dimethylformamide; they migrate electrophoretically towards the positively charged carbon fiber. The fibers are several centimeters long and their diameters typically range between 2 and 10 microns depending on the preparation conditions. Selected area electron diffraction has been used to characterize the structure of the fibers. The results qualitatively evidence a substantial alignment of the nanotubes along the fiber axis. However, this probe was restricted to the side of the fibers to allow transmission of the electron beam. More detailed analysis has been achieved using polarized Raman spectroscopy by Gommans et al. and Hwang et al. [36, 37]. This study was the first of this type. The authors have developed a model to interpret the change of the Raman intensities depending on polarization (Fig. 3) by considering that absorption phenomena induce an angle-dependent resonance enhancement. The intensities have been fitted within a Lorentzian model for the distribution of nanotubes orientations. The FWHM of the distribution was found to be 23°, showing a rather good alignment of nanotubes. Since the above-mentioned publications [36, 37] in 2000, no new result has been published on these fibers. Their mechanical, electrical, and thermal properties are still to be analyzed.

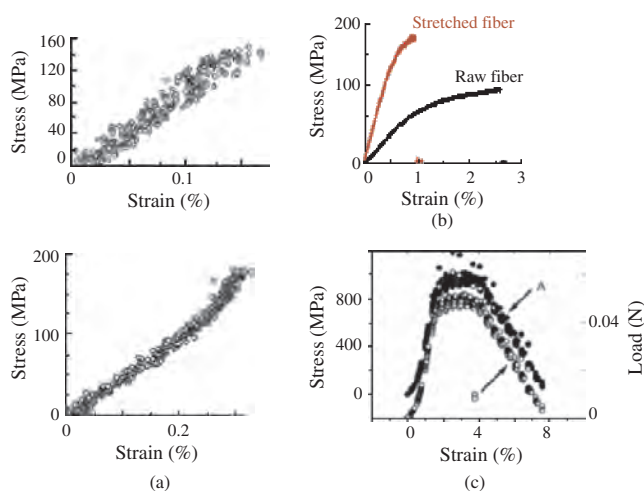


**Figure 6.** The Young modulus ( $Y$ ) is deduced from the slope of stress versus strain curve at the origin. Stress-strain measurements: (a) For an as-grown, self-organized ribbon of MWNTs (upper curve)— $Y \approx 24$  GPa—and for a graphitized ribbon (lower curve)— $Y \approx 60$  GPa (reprinted with permission from [32], Y.-H. Li et al., *Chem. Phys. Lett.* 365, 95 (2002). © 2002, Elsevier), (b) For a raw SWNT fiber obtained by a spinning process— $Y \approx 10$  GPa—and for a fiber stretched by 145% in water— $Y \approx 40$  GPa (reprinted with permission from [20], B. Vigolo et al., *Appl. Phys. Lett.* 81, 1210 (2002). © 2002, American Institute of Physics); (c) For a SWNT fiber synthesized by CVD— $Y \approx 77$  GPa (reprinted with permission from [80], H. W. Zhu et al., *Science* 296, 884 (2002). © 2002, American Association for Advancement of Science). The authors have plotted true stress versus strain curve (A) and the load versus engineering strain curve (B) because of the possible variation of the diameter of the fiber during deformation. They present almost the same slope.

## 2.7. Ribbons and Fibers made by a Spinning Process

Vigolo et al. [16] reported in 2000 a simple method to assemble single-wall carbon nanotubes into long ribbons and fibers. Their process is reminiscent of the flow-induced alignment processes already used for rigid polymers [38] or anisotropic colloids [39]. The nanotube bundles are dispersed in water with the help of a commercially available surfactant molecule—sodium dodecyl sulfate (SDS). A detailed study of the phase diagram of the surfactant stabilized nanotube dispersions has been performed, to determine the optimized concentrations in surfactant and nanotubes. The aim was to obtain a homogeneous suspension with a relatively large concentration in nanotubes (an optimum was found for 0.35 wt % of SWNTs and 1 wt % of SDS). The SWNTs dispersion was injected in the co-flowing stream of a polymer solution that contains between 2 and 6 wt % of polyvinylalcohol (PVA), an amphiphilic polymer. The PVA adsorbs onto the tubes and provides a strong bridging attraction [40] between the bundles. This process leads to the formation of long ribbons that remain stable in the absence of flow. In [16], the nanotubes used were single-wall nanotubes obtained by the electric arc method [12]. Since then, the same process was successfully applied to single-wall nanotubes obtained from the laser vaporization method [11] or by using the more recent HiPCO process [41], and to multi-wall nanotubes [42]. The alignment of nanotubes in the ribbons has been studied by SEM and by optical observations between crossed polarizers [16]. The nanotubes have a clear preferential orientation along the long axis of the ribbons. However, no quantitative measurements of this orientation have been published yet.

In order to make systems that are more compact, rinsed ribbons are vertically drawn out of water [16]. Capillary forces, water drainage, and evaporation cause the ribbon to collapse into a dense fiber (density  $\sim (1.4 \pm 0.3) \text{ g/cm}^3$  for electric arc raw material) with a diameter ranging from a few micrometers to 100 micrometers when dry. This simple method leads to several tens of centimeter long fibers. Such a fiber is shown in Figure 5(c). A knot was intentionally made with it, to reveal its high flexibility. The amount of nanotubes with respect to that of PVA is about 60% as determined by thermogravimetric experiments [43]. Moreover, PVA can be completely removed by annealing the fibers at high temperature [18]. Nanotube alignment in electric arc nanotube fibers has been studied using X-ray scattering [18] and polarized Raman spectroscopy [44]. The FWHM within a Gaussian model is found to be  $\sim 75 \pm 5^\circ$  using X-ray scattering (Fig. 2). It remains the same if PVA is burnt. Surprisingly, Raman measurements indicate much better alignment; this apparent discrepancy is under study. The value of FWHM, as determined by X-ray scattering, is strongly dependent on the raw material used. FWHMs  $\sim 45^\circ$  are found for fibers made from HiPCO single-wall nanotubes [45]. Different hypotheses can be put forward to account for the better nanotube alignment in HiPCO nanotube fibers. The lower amount of impurities in the as-produced material is one of them: HiPCO samples contain less amorphous carbon [41]. Others include the shorter length of HiPCO nanotubes and the fact that HiPCO nanotubes may be less entangled.

A procedure has been recently developed to improve nanotube alignment in the fibers [20]. The fibers are rewetted, swollen in a solvent of the polymer, and redried vertically under tensile load with a weight attached to their end. Even in a solvent in which the polymer is highly soluble, they do not disassemble (this amazing result is attributed to the fact that the networks of nanotubes and adsorbed polymers form cross-linked assemblies). The reader can refer to [20] for a more detailed discussion on the role of the fibers wetting agent. The fibers can be stretched up to  $\sim 160\%$ , the improvement of the nanotube alignment being significant: FWHMs, determined by X-ray scattering [20], are reduced by 40%, that is, to about  $45^\circ$  for arc discharge nanotubes. Full width at half maximum as low as  $30^\circ$  are reached for stretched fibers of HiPCO nanotubes [45].

Let us emphasize that the spinning process, as well as the post-synthesis one developed to improve the nanotube alignment, are very simple and could be easily scaled up for industrial developments.

Mechanical measurements show that the mixed nanotube-PVA fibers exhibit an elastic behavior followed by a plastic one before they break (when PVA is removed, the plastic region disappears and the Young's modulus is slightly reduced). The Young's modulus of nonannealed fibers, deduced from the slope of the curve stress versus strain in the elastic region, varies between 10 and 20 GPa for arc discharge nanotubes raw fibers [16]. It is one order of magnitude greater than the modulus of high-quality buckypaper [24]. After fiber stretching, Young moduli of  $\sim 40$  GPa can be found (Fig. 6(b)) [20]. Globally, the Young modulus increases when the nanotube alignment gets better. A similar trend was found for fibers made of HiPCO single-wall nanotubes or of multi-wall nanotubes. One should notice that the mechanical properties of nanotube fibers are still far away from those of individual nanotube bundles [9], or from those of carbon fibers (mechanical properties of carbon fibers are summarized in [2]). This is probably to be attributed to too weak intertube interactions, as was already discussed in Section 2.4. Further improvements are expected if strong covalent bonding between nanotubes could be established by functionalization, for instance. The study of the electrical and thermal properties of the fibers is in progress [46]. For such studies, insulating PVA is removed by annealing. Room temperature electrical resistivities as low as  $6 \cdot 10^{-5} \Omega\text{m}$  could be obtained for purified HiPCO nanotube fibers. Finally, the fibers can be used as electromechanical actuators (Fig. 7) [47]. Stress generation and work per cycle are higher than that of buckypaper.



**Figure 7.** Electromechanical actuation of a HiPCO SWNT spun fiber in an electrolyte solution (NaCl 1 M) when an alternative voltage of 1 V is applied at a frequency of 1 Hz. It exhibits a periodic motion as shown in the pictures.

At the end of this section about nanotube processing, it is interesting to compare the main results. They are also summarized in Table 1.

Processing of SWNTs or MWNTs can be performed after solubilization of the raw soot obtained by usual synthesis methods. Films, ribbons, and fibers have been successfully realized, using very different processes: alignment of nanotubes under magnetic field, in the flow of a polymer solution, by electrophoretic migration, or because of their (self-) interactions. It is even possible to obtain two-dimensional patterned arrays of these aligned nanotubes, or to precisely control the film deposit width by the LB technique. In fibers, the nanotubes are preferentially aligned along the fibers long axes, as is schematically drawn in Figure 4(a). In films and ribbons, the nanotubes are preferentially aligned within the plane of the film or of the ribbon (Fig. 4(b)), with possibly some additional out-of-plane misalignment. Typical FWHMs, characteristic of the degree of alignment of nanotubes in fibers or films, are about  $30^\circ$ .

The mechanical properties of aligned nanotube assemblies are better than those of buckypapers with Young moduli up to 60 GPa to be compared to  $\sim 1$  GPa. The Young modulus increases with the nanotube alignment. Further improvement, to approach properties of individual tubes or of carbon fibers, would need stronger interactions between nanotubes inside the materials. Anisotropic electrical, thermal, and optical properties are measured and found to be correlated with the degree of alignment of nanotubes. Moreover, electrical resistivities of  $\sim 10^{-5}$ – $5 \cdot 10^{-5}$   $\Omega\text{m}$ , to be compared with  $10^{-6}$   $\Omega\text{m}$  for individual SWNTs bundles, indicate rather good contacts between nanotubes.

### 3. DIRECT SYNTHESIS OF MACROSCOPICALLY ALIGNED NANOTUBES BY CHEMICAL VAPOR DEPOSITION

Primary synthesis methods for producing carbon nanotubes include arc-discharge [10, 12], laser ablation [11, 13], and chemical vapor deposition (CVD) from hydrocarbons [48–51]. These methods classically lead to the production of entangled and disoriented nanotubes, and for CVD, to nanotubes whose structure is often not perfectly graphitic, as noted by Dai in his review article on nanotube growth [2]. However, improved CVD methods have allowed one to synthesize large arrays of aligned nanotubes with controlled diameters and lengths (as an exception, let us cite Liu et al. [52], who reported the synthesis of macroscopically long ropes of well-aligned, single-walled carbon nanotubes along plasma flow direction using an electric arc technique). In this article, we focus on CVD results. First, we briefly review the main approaches developed to make arrays and films of aligned nanotubes (the literature on the subject is very abundant; our aim here is only to give an overview of the different realizations via a few examples). Then, we discuss more recent works showing the direct synthesis of long macroscopic nanotube fibers by CVD methods. These fibers are reminiscent of the ones described in Section 2.7. However, the fibers described in this section result from a direct or quasi-direct synthesis instead of being produced by post-synthesis spinning process.

**Table 1.** Illustrates the variety of materials formed with aligned, single-wall nanotubes (SWNTs) and multi-wall nanotubes (MWNTs). FWHM is a measure of nanotube alignment, as explained in the text. Given here are the smallest FWHMs reported for different methods used to obtain aligned nanotubes materials, corresponding to the best alignments.

Geometry	Sort of nanotubes	Nanotube alignment	Method used	Some properties
One-dimensional fibers	SWNTs	FWHM $\sim 30^\circ$ [45]	Processing (spinning [16], electrophoretic process [36]) and CVD [80]	Young modulus increases with the degree of alignment [20]; electromechanical actuation [47]
	MWNTs		Processing from a powder: spinning [16]; spinning from a CVD film [81]	
Two-dimensional films (or ribbons): nanotubes preferred orientation within the plane of the film	SWNTs	FWHM $\sim 25$ – $35^\circ$ (magnetic field [22])	Processing (spinning [16], magnetic field [25], self-organization [30], LB method [34])	Anisotropic strength [25], anisotropy of electrical and thermal conductivities [27], anisotropic optical properties [30], $\pi$ plasmon anisotropy [26]
	MWNTs		Processing (mechanical constraint [29], self-organization [31])	
Two dimensional films: nanotubes preferred orientation perpendicular to the plane of the film	MWNTs	FWHM $\sim 16^\circ$ [73]	CVD [63, 65, 66, 71–73]. (Elaborated patterns such as pillows of aligned nanotubes: [77, 79])	Field emission [66], ultrahydrophobic materials [78]
Nanotubes inside meso or nanoporous materials	MWNTs	FWHM $\sim 34^\circ$ [56]	CVD [53, 55, 57]	Membranes for lithium-ion batteries [54]
	SWNTs	FWHM $< 1^\circ$ [60]	CVD [58]	Superconductivity [62]

### 3.1. Growth Inside Templates

Nanotubes can be obtained by CVD of different precursors inside nanoporous materials (Fig. 4(d)). The main advantage of the method is that the orientation and diameter of nanotubes may be controlled by the pores inside which they grow.

As an example, we mention here the results obtained by Che et al. [53, 54] inside alumina template membranes (200 nm diameter pores, 60  $\mu\text{m}$  thick). Ethylene or pyrene were used as precursors and heated to 900 °C. Nanotubes formed inside alumina pores. Their outer diameter was the same as that of the pores, and they formed a highly ordered assembly [53]. After further removal of the template, the authors obtained freestanding nanoporous carbon membranes. The tubes being electrochemically active for intercalation of lithium ion, they suggested possible applications of the membranes for lithium-ion batteries [54]. The use of templates to grow nanotubes can also allow one to obtain more elaborate nanotube assemblies than parallel nanotubes with the same outer diameter. For instance, Suh et al. have recently made brushes of linearly joined nanotubes of 60- and 30-nm diameter, respectively [55]. The location and shapes of the junctions are controlled by a multistep anodization and pore-widening process of alumina membranes. Acetylene was used as a precursor and decomposed at 700 °C. Only a few quantitative measurements of the degree of nanotube alignment inside templates are reported in the literature. We mention here the X-ray scattering experiments of Dore et al. [56] on multi-wall nanotubes obtained by CVD in microporous alumina [57]: the angular intensity distribution is characterized by a FWHM  $\approx 34^\circ$ .

The synthesis of aligned single-wall nanotubes by CVD methods is much less developed than that of aligned MWNTs. However, a few examples are shown in this article: aligned SWNTs suspended between electrodes (Section 3.2), SWNTs fibers (Section 3.3), and SWNTs inside zeolite crystals. In this last case, the use of templates has allowed the synthesis of one of the smallest diameter single-wall carbon nanotubes observed so far. The template is single crystal zeolite  $\text{AlPO}_4\text{-5}$ , with very narrow parallel pores. In 1998, Tang et al. [58] reported the formation of parallel-aligned single-wall carbon nanotubes in the channels of single-crystal zeolite by pyrolysis of tripropylamine. The nanotube diameter, as determined for instance by X-ray scattering [59], is about 4 Å. Their orientation is nearly perfect (FWHM  $< 1^\circ$ ) [60]. The above-mentioned nanoporous materials were amorphous, while zeolite is crystalline. Thus one might hope that interactions with the zeolite during nanotube formation could have led to the selection of only one helicity, but recent Raman results [61] contradict this hypothesis. However, a very interesting effect could be observed on these 4 Å diameter nanotubes: they exhibit superconducting behavior below 20 K [62]. Evidence for anisotropic Meissner effect was made possible thanks to the nanotubes alignment.

### 3.2. Growth on Substrates

Chemical vapor deposition techniques have been developed to grow controlled arrays of aligned nanotubes at the surface of a template. In 1996, Li et al. [63] achieved the large-scale

synthesis of aligned carbon nanotubes by a CVD method, with iron nanoparticles embedded in mesoporous silica. The nanotubes, obtained from decomposition of acetylene at 700 °C, are multi-walled with their inner diameter at about 4 nm and their outer diameter at about 30 nm. They are on average perpendicular to the surface of the substrate and the spacing between the tubes is about 100 nm. The alignment may be attributed to the constraint of the vertically aligned pores from which the nanotubes grow out. In 1997 Terrones et al. [64] obtained arrays of MWNTs aligned with nanotracks of cobalt particles deposited on a silica substrate by laser etching, by pyrolysis of 2-amino-4,6-dichloro-*s*-triazine. The method allowed the control of the length, up to 50 microns, and a diameter between 30 and 50 nm of the tubes. In 1998, Ren et al. [65] proposed a plasma-enhanced, hot filament CVD method that allowed them to work below the strain point of glass ( $\sim 650^\circ\text{C}$ ), which is of interest for display device fabrication. Acetylene gas was used as the carbon source and aligned MWNTs were grown on nickel-coated glass. Their external diameters range from 20 to 400 nanometers, depending on the nickel layer thickness. Lengths from 0.1 to 50  $\mu\text{m}$  are obtained. In 1999, Fan et al. [66] obtained similar MWNTs arrays, but on silicone substrates, with the promising possibility to develop nanotube devices integrated into the existing semiconductor technology. Multi-wall carbon nanotubes form after catalytic decomposition of acetylene on iron oxide particles. Their alignment, perpendicular to the silicon film, is attributed to van der Waals interactions between their outermost walls. Their length, from  $\sim 35$  to 240  $\mu\text{m}$ , can be controlled by tuning the CVD reaction time. The sample properties with respect to field emission appear interesting, with low-operating voltage and high-current stability. For a review on “carbon films as electron field emitters,” the reader can refer to [67]. The ideal cathode would be formed of well-spaced nanotubes aligned in the electrical field direction. However, no better results have yet been obtained for aligned nanotube materials with respect to nonaligned ones [68]. One has to improve in particular the nanotube crystallinity and to control the spacing between them.

We have listed above some of the earliest contributions dealing with the synthesis of arrays of nanotubes using CVD methods. These methods have been largely developed and improved by several other groups in the last few years. Among the improvements we emphasize, through several examples, the recently shown possibilities to grow aligned nanotubes in high yields, as well as very long nanotubes, and to achieve a higher degree of control using external fields.

After Rao et al. showed that aligned nanotube bundles can be obtained in copious quantities from ferrocene pyrolysis [69], progress was made toward important production through catalytic decomposition of a ferrocene-xylene mixture [70]. In 2001 Mayne et al. [71] synthesized aligned MWNTs by pyrolyzing aerosols generated from benzene/ferrocene mixtures at 800° or 950 °C. Syntheses from toluene/ferrocene mixtures are also currently performed (Fig. 5(d)). The nanotubes form on quartz tube walls and show good alignment. They are 10–200 nm outer diameter and are partially filled with metal [71]. The method opens up new avenues in carbon nanotube synthesis using liquid hydrocarbon and catalyst precursor. Due to the continuous

feeding of the reactor, high yields of nanotubes can be produced. The nanowires inside tubes could also be of strong interest. Furthermore, in 2002, Zhang et al. [72] have grown arrays of very long MWNTs by catalytic decomposition of a ferrocene-xylene mixture at 850 °C on a quartz substrate. The nanotubes grow perpendicularly to the quartz surface at a very high rate of 50  $\mu\text{m}/\text{min}$  and reach 1.5 mm length in about 30 mm. Their outer diameter ranges from 30 to 60 nm. They are also partially filled with iron.

Controlled structures have been even achieved by CVD of acetylene on contoured surfaces, instead of flat films, using a plasma-induced alignment method [73]. Bower et al. have grown uniform nanotube films on substrates of different geometries. The MWNTs always grow perpendicular to the local substrate surface. The alignment is primarily induced by the electric self-bias field imposed on the surface from the plasma environment. For flat silicon surfaces, FWHM  $\sim 16^\circ$  has been deduced from X-ray diffraction studies, regardless of the substrate orientation in the growth chamber. Radially grown nanotubes could even be obtained on the highly curved surface of a 125- $\mu\text{m}$  diameter optical fiber. Moreover, the growth rate in these experiments is rather high ( $\sim 6 \mu\text{m}/\text{min}$ ). The influence of an electrical field on the nanotube synthesis was also expertly illustrated by Zhang et al. [74] who have shown electric field-directed CVD growth of single-wall nanotubes. They were able to grow aligned, suspended SWNTs between silicon electrodes, by applying an electric field during CVD of methane mixed with hydrogen at 900 °C. These results appear promising for directed growth of ordered molecular-wire architectures and networks on surfaces.

Finally, attempts to obtain elaborated assemblies of aligned nanotube patterns have been recently reported. The growth of a single crystal of single-walled nanotubes formed by self-assembly, using thermolysis of nano-patterned precursors, was reported in 2001 [75]. However, it was shown recently that the majority of the structures formed are compounds of molybdenum, carbon, and oxygen [76]. Wang et al. [77] have synthesized pillars of bamboo-like MWNTs by pyrolysis of iron(II) phthalocyanine. The growth mechanism of these patterns is yet to be clarified. Recent results indicate that such nanotube arrays are good candidates for ultra-hydrophobic materials [78]. Wei et al. [79] were able to grow aligned MWNTs in several directions at once in a single process: the pyrolysis of xylene-ferrocene at 800 °C over lithographically machined substrates of silica over silicon. Indeed, nanotubes grow selectively on and normal to silica surfaces. A beautiful pattern of “nanotube flowers” obtained by the authors is shown in Figure 5(e).

In brief, MWNTs can be grown by CVD at the surface of porous templates and of plain plates of quartz, silicon, silica, glass, etc. In most cases, nanotubes are aligned perpendicularly to substrates [63, 65, 66, 71, 72], as drawn in Figure 4(c). The precursors are hydrocarbons or metal-organic compounds. With hydrocarbons as precursors, metal catalysts (Fe, Ni, Co, etc.) should be added on the surface. Aligned MWNTs and SWNTs can also be obtained on highly curved surfaces [73] or between electrodes [74], under the action of an electric field along which nanotubes grow. More elaborated patterns, such as pillows or flowers of aligned MWNTs, have also been recently made [77, 79].

Chemical vapor deposition methods are now rather well controlled (Table 1). Their versatility makes them promising processes for a variety of future applications ranging from field emission devices to nanoelectronics through more specific domains such as biomimetic ultra-hydrophobic surfaces.

### 3.3. Direct or Quasi-Direct Synthesis of Fibers by CVD Methods

The synthesis of films and arrays by CVD methods is not particularly suitable for the production of macroscopic 3-dimensional materials containing aligned nanotubes. The limitation of being attached to a template or a patterned substrate has been recently overcome with two examples of synthesis of nanotube fibers [80, 81]. Unlike previous methods that are reviewed in Section 2, the fibers are directly grown or spun from nanotubes synthesized by CVD. The first method consists in the direct growth by a CVD method in a vertical furnace [80]. The second one consists in drawing out nanotube yarns from aligned arrays of nanotubes [81]. We describe in the next section the main features of these two methods and of the obtained fibers.

#### 3.3.1. Direct Synthesis of Single-Wall Nanotube Strands

Zhu et al. [80] have optimized a floating catalyst method in a vertical furnace, where *n*-hexane is catalytically pyrolyzed. The *n*-hexane solution, which contains some amount of ferrocene and thiophene, was introduced into the reactor at a rate of 0.5 ml/min with hydrogen as the carrier gas flowing at a rate of 250 ml/min. Single-wall nanotubes formed during this continuous process with yields of  $\sim 0.5 \text{ g/h}$ . The formation of very long SWNT strands is a unique characteristic of this vertical floating process.

The obtained strands generally have a diameter of  $\sim 0.3 \text{ mm}$ . Scanning electron microscopy images showed the preferential alignment of the tubes (Fig. 5(f)). Raman spectroscopy measurements suggest that both metallic and semiconducting single-wall nanotubes coexist with a wide distribution of diameters, ranging from 1.1 to 1.7 nm with a dominant diameter of 1.1 nm. Additional structural characterizations were achieved using X-ray diffraction [82]: the angular distribution is characterized by FWHM  $\sim 44^\circ$ . This value is of the same order as that measured on raw HiPCO nanotube fibers obtained by a spinning process, but it is larger than that of  $\sim 30^\circ$  obtained after fiber stretching [45].

The SWNT strands exhibit a metallic behavior above 90 K, with an electrical resistivity of about  $7 \times 10^{-6} \Omega \text{ m}$  at room temperature. Such a low value of the resistivity suggests that there are macroscopic lengths of continuous conducting paths in the strands. Young's modulus was measured and found to range from 49 to 77 GPa (Fig. 6(c)). This is far from Young's modulus of individual nanotubes, but among the best present results for fibers or ribbons of aligned nanotubes.

The synthesis of nanotube strands by this improved CVD method leads to promising materials with high electrical conductivity and reasonable mechanical strength.



### 3.3.2. Spinning From Nanotube Films

Jiang et al. [81] have shown that carbon nanotubes can be self-assembled into yarns of up to 30 cm in length, simply by being drawn out from aligned arrays of carbon nanotubes. While pulling out carbon nanotubes from an array several hundred micrometers high and grown on a silicon substrate, the authors obtained a continuous yarn of pure nanotubes. They estimate that an array of about 1 cm<sup>2</sup> can generate about 10 m of yarn. The authors could make optical polarizers by parallel alignment of their nanotube yarns. When a beam of light passes through the nanotube polarizer, photons having a polarization direction parallel to the axis of the tubes are absorbed, whereas those that are perpendicularly polarized pass through it. The authors have also submitted their fibers to a strong voltage under vacuum. After 3 h at 70 V, the conductivity of the filament slightly increases and the tensile strength changes from 1 mN to 6.4 mN. These results indicate that some welding effect may be occurring at the weak connection points, because these points have a higher resistivity and, as a result, a higher temperature when a current is applied. Therefore it seems that the properties of the fibers can be improved using this method. Nevertheless, the comparison with the properties of other materials remains difficult because the data reported by Jiang et al. are not normalized with respect to the mass or section of the fibers.

In summary, the CVD synthesis of nanotubes aligned perpendicularly to a substrate (Fig. 4(c)), or inside a mesoporous template (Fig. 4(d)), has been the subject of numerous studies during the last few years. Within this method, mostly MWNTs are synthesized. Possible applications of these materials as field emitter screens, as membranes for batteries or as ultra-hydrophobic surfaces are evoked. Moreover, fibers of SWNTs have been recently synthesized by CVD. The first results reported on these fibers appear very promising: the Young modulus is slightly higher than that of the fibers obtained by spinning, and electrical conductivity is low. Nanotube alignment is given by FWHM  $\sim 45^\circ$ , to be compared to  $30^\circ$  for the best-aligned fibers obtained by spinning and stretching.

## 4. CONCLUSION

For a few years, great progresses have been made in the elaboration of aligned nanotube-based macroscopic assemblies. Substantial alignments can now be obtained (with typically FWHM  $\approx 30^\circ$ ). It concerns both single-wall and multi-walls nanotubes. Nanotubes can be aligned (i) within fibers by post-synthesis processing or CVD methods, (ii) parallel to two-dimensional planes via processing, or (ii) perpendicular to two-dimensional films, and within meso- or nano-porous materials, by CVD (Fig. 4, Table 1). Nanotube processing can be realized by different methods: under the action of a magnetic field, using a spinning process, by an electrophoretic method, by a LB technique; or nanotubes can even self-assemble under appropriate conditions. Via CVD methods, one can vary the precursor, the catalyst, and the substrate, and even control the alignment by applying an electrical field.

The obtained materials present anisotropic optical, mechanical, electrical, and thermal properties. Their field

emission properties or their electrochemical activity are also particularly exciting. Fiber mechanical properties still have to be improved but are progressing (Young modulus multiplied by 3–4 within the last year). Aligned nanotube materials may thus find industrial applications in the future. In this respect, let us underline that spinning processes and CVD methods developed to produce nanotube fibers could be scaled-up for large-scale production.

In this article, we have mentioned examples of fundamental studies on electronic properties of nanotubes, by electron energy loss spectroscopy on films of magnetically aligned nanotubes, or on superconductivity and Meissner effect for nanotubes inside zeolite crystals. We emphasize that the alignment of nanotubes on a macroscopic scale is also of critical importance for the understanding of their fundamental properties.

## GLOSSARY

**Carbon multi-wall nanotube (MWNT)** Nanotube formed of concentric single-wall nanotubes.

**Carbon single-wall nanotube (SWNT)** Cylinder at the surface of which carbon atoms are organized in a honeycomb lattice.

**Chemical vapor deposition (CVD) method** A method to deposit solid films via chemical reaction of gases.

**Nanotube (NT)** Tube with a very small diameter (less than 10 nm).

**Process** A series of actions that bring about a particular result (in this article, the result is the alignment of nanotubes).

**Self-assembly** Spontaneous organization (in this article: spontaneous organization of nanotubes).

## REFERENCES

1. R. Saito, G. Dresselhaus, and M. S. Dresselhaus, "Physical Properties of Carbon Nanotubes." Imperial College Press, 1998.
2. M. Dresselhaus, G. Dresselhaus, and Ph. Avouris (Eds.), "Carbon Nanotubes: Synthesis, Structure, Properties and Applications." Springer-Verlag, Berlin, 2001.
3. P. G. Collins and P. Avouris, *Scientific American* 283, 62 (2000).
4. Z. Yao, H. W. Ch. Postma, L. Balents, and C. Dekker, *Nature* 402, 273 (1999).
5. P. G. Collins, S. M. Arnold, and P. Avouris, *Science* 292, 706 (2001).
6. M. M. J. Treacy, T. W. Ebbesen, and J. M. Gibson, *Nature* 381, 678 (1996).
7. E. W. Wong, P. E. Sheehan, and C. M. Lieber, *Science* 277, 1971 (1997).
8. P. Poncharal, Z. L. Wang, D. Ugarte, and W. A. de Heer, *Science* 283, 1513 (1999).
9. J. P. Salvetat, G. A. D. Briggs, J. M. Bonard, R. R. Bacsa, A. J. Kulik, T. Schöckli, N. A. Burnham, and L. Forró, *Phys. Rev. Lett.* 82, 944 (1999).
10. S. Iijima, *Nature* 354, 56 (1991).
11. A. Thess, R. Lee, P. Nikolaev, H. Dai, P. Petit, J. Robert, X. Chui, H. L. Young, K. G. Seong, A. G. Rinzler, D. T. Colbert, G. E. Scuseria, D. Tomaneck, J. E. Fisher, and R. E. Smalley, *Science* 273, 483 (1996).
12. C. Journet, W. K. Maser, P. Bernier, A. Loiseau, M. Lamy de la Chapelle, S. Lefrant, P. Deniard, R. Lee, and J. E. Fisher, *Nature* 388, 756 (1997).



13. A. G. Rinzler, J. Liu, H. Dai, P. Nikolaev, C. B. Huffman, F. J. Rodriguez-Macias, P. J. Boul, A. H. Lu, D. Heymann, D. T. Colbert, R. S. Lee, J. E. Fisher, A. M. Rao, P. C. Eklund, and R. E. Smalley, *Appl. Phys. A* 67, 29 (1998).
14. J. Chen, A. M. Hamon, H. Hu, Y. Chen, A. M. Rao, P. C. Eklund, and R. C. Haddon, *Science* 282, 95 (1998).
15. V. Georgakilas, K. Kordatos, M. Prato, D. M. Guldi, M. Holzinger, and A. Hirsch, *J. Am. Chem. Soc.* 124, 760 (2002).
16. B. Vigolo, A. Pénicaud, C. Coulon, C. Sauder, R. Pailler, C. Journet, P. Bernier, and P. Poulin, *Science* 290, 1331 (2000).
17. P. Launois, unpublished calculations.
18. P. Launois, A. Marucci, B. Vigolo, P. Bernier, A. Derré, and P. Poulin, *J. Nanosci. Nanotech.* 1, 125 (2001).
19. J. E. Fisher, W. Zhou, J. Vavro, M. C. Llaguno, C. Guthy, R. Haggemueller, M. J. Casavant, D. E. Walters, and R. E. Smalley, *J. Appl. Phys.* 93, 2157 (2003).
20. B. Vigolo, P. Poulin, M. Lucas, P. Launois, and P. Bernier, *Appl. Phys. Lett.* 81, 1210 (2002).
21. P. Poulin, B. Vigolo, and P. Launois, *Carbon* 40, 1741 (2002).
22. B. W. Smith, Z. Benes, D. E. Luzzi, J. E. Fisher, D. A. Walters, M. J. Casavant, J. Schmidt, and R. E. Smalley, *Appl. Phys. Lett.* 77, 663 (2000).
23. N. Bendiab, R. Almairac, J. L. Sauvajol, S. Rols, and E. Elkaim, *J. Appl. Phys.* 93, 1769 (2003).
24. R. H. Baughman, C. Cui, A. A. Zakhidov, Z. Iqbal, J. N. Barisci, G. M. Spinks, G. G. Wallace, A. Mazzoldi, D. De Rossi, A. G. Rinzler, O. Jaszinski, S. Roth, and M. Kertesz, *Science* 284, 1340 (1999).
25. D. A. Walters, M. J. Casavant, X. C. Qin, C. B. Huffman, P. J. Boul, L. M. Ericson, E. H. Haroz, M. J. O'Connell, K. Smith, D. T. Colbert, and R. E. Smalley, *Chem. Phys. Lett.* 338, 14 (2001).
26. X. Liu, T. Pichler, M. Knupfer, M. S. Golden, J. Fink, D. A. Walters, M. J. Casavant, J. Schmidt, and R. E. Smalley, *Synthetic Metals* 121, 1183 (2001).
27. J. Hone, M. C. Llaguno, N. M. Nemes, A. T. Johnson, J. E. Fisher, D. A. Walters, M. J. Casavant, J. Schmidt, and R. E. Smalley, *Appl. Phys. Lett.* 77, 666 (2000).
28. J. Fisher, H. Dai, A. Thess, R. Lee, N. M. Hanjani, D. L. Dehaas, and R. E. Smalley, *Phys. Rev. B* 55, R4921 (1997).
29. L. Jin, C. Bower, and O. Zhou, *Appl. Phys. Lett.* 73, 1197 (1998).
30. H. Shimoda, S. J. Oh, H. Z. Geng, R. J. Walker, X. B. Zhang, L. E. McNeil, and O. Zhou, *Adv. Mater.* 14, 899 (2002).
31. Y.-H. Li, C. Xu, B. Wei, X. Zhang, M. Zheng, D. Wu, and P. M. Ajayan, *Chem. Mater.* 14, 483 (2002).
32. Y.-H. Li, J. Wei, X. Zhang, C. Xu, D. Wu, L. Lu, and B. Wei, *Chem. Phys. Lett.* 365, 95 (2002).
33. G. L. Gaines, "Insoluble Monolayers at Liquid-Gas Interfaces." Interscience, New York, 1966.
34. Y. Guo, J. Wu, and Y. Zhang, *Chem. Phys. Lett.* 362, 314 (2002).
35. Y. Guo, N. Minami, S. Kazaoui, J. Peng, M. Yoshida, and T. Miyashita, *Physica B* 323, 235 (2002).
36. H. H. Gommans, J. W. Alldredge, H. Tashiro, J. Park, J. Magnusson, and A. G. Rinzler, *J. Appl. Phys.* 88, 2509 (2000).
37. J. Hwang, H. H. Gommans, A. Ugawa, H. Tashiro, R. Haggemueller, K. I. Winey, J. E. Fisher, D. B. Tanner, and A. G. Rinzler, *Phys. Rev. B* 62, R13310 (2000).
38. M. Doi and S. F. Edwards, "The Theory of Polymer Dynamics." Oxford University Press, New York, 1986.
39. S. M. Clarke, A. R. Rennie, and P. Convert, *Europhys. Lett.* 35, 233 (1996).
40. D. H. Everett, "Basic Principles of Colloid Science," pp. 138–139, 191–201. Royal Society of Chemistry, London, 1988.
41. P. Nikolaev, M. J. Bronikowski, R. K. Bradley, F. Rohmund, D. T. Colbert, K. A. Smith, and R. E. Smalley, *Chem. Phys. Lett.* 313, 91 (1999).
42. S. Delpoux, K. Szostak, E. Frackowiak, S. Bonnamy, and F. Béguin, *J. Nanosci. Nanotechnol.* 2, 481 (2002).
43. A. Derré and S. Badaire, private communication.
44. E. Anglaret, A. Righi, J. L. Sauvajol, P. Bernier, B. Vigolo, and P. Poulin, *Phys. Rev. B* 65, 165426 (2002).
45. M. Lucas, B. Vigolo, S. Badaire, D. Le Bolloc'h, A. Marucci, D. Durand, M. Hamilton, C. Zakri, P. Poulin, and P. Launois, *AIP Conf. Proc.* 633 (H. Kuzmany, J. Fink, M. Mehring, and S. Roth, Eds.), 579 (2002).
46. S. Badaire, C. Zakri, P. Poulin, and J. Fisher, unpublished results.
47. B. Vigolo, P. Launois, M. Lucas, S. Badaire, P. Bernier, and P. Poulin, *Mater. Res. Soc. Symp. Proc.* 706, Z1.4.2 (2002).
48. M. Endo, K. Takeuchi, S. Igarashi, K. Kobori, M. Shiraiishi, and H. W. Kroto, *J. Phys. Chem. Solids* 54, 1841 (1993).
49. M. Ge and K. Sattler, *Appl. Phys. Lett.* 64, 710 (1994).
50. V. Ivanov, J. B. Nagy, Ph. Lambin, A. Lucas, X. B. Zhang, X. F. Zhang, D. Bernaerts, G. Van Tendeloo, S. Amelinckx, and J. Van Landuyt, *Chem. Phys. Lett.* 223, 329 (1994).
51. M. Endo, K. Takeuchi, K. Kobori, K. Takahashi, H. W. Kroto, and A. Sarkar, *Carbon* 33, 873 (1995).
52. C. Liu, H. M. Cheng, H. T. Cong, F. Li, G. Su, B. L. Zhou, and M. S. Dresselhaus, *Adv. Mater.* 12, 1190 (2000).
53. G. Che, B. B. Lakshmi, C. R. Martin, E. R. Fisher, and R. S. Ruoff, *Chem. Mater.* 10, 260 (1998).
54. G. Che, B. B. Lakshmi, E. R. Fisher, and C. R. Martin, *Nature* 393, 346 (1998).
55. J. S. Suh, J. S. Lee, and H. Kim, *Synthetic Metals* 123, 381 (2001).
56. J. C. Dore, A. Burian, T. Kyotani, and V. Honkimaki, *ESRF Highlights* 23 (2001).
57. T. Kyotani, L. Tsai, and A. Tomita, *Chem. Mater.* 8, 2109 (1996).
58. Z. K. Tang, H. D. Sun, J. Wang, J. Chen, and G. Li, *Appl. Phys. Lett.* 73, 2287 (1998).
59. P. Launois, R. Moret, D. Le Bolloc'h, P. A. Albouy, Z. K. Tang, G. Li, and J. Chen, *Solid State Comm.* 116, 99 (2000).
60. P. Launois et al., unpublished results.
61. A. Jorio, A. G. Souza Filho, G. Dresselhaus, M. S. Dresselhaus, A. Righi, F. M. Matinaga, M. S. S. Dantas, M. A. Pimenta, J. Mendes Filho, Z. M. Li, Z. K. Tang, and R. Saito, *Chem. Phys. Lett.* 351, 27 (2002).
62. Z. K. Tang, L. Zhang, N. Wang, X. X. Zhang, G. H. Wen, G. D. Li, J. N. Wang, C. T. Chan, and P. Sheng, *Science* 292, 2462 (2001).
63. W. Z. Li, S. S. Lie, L. X. Qian, B. H. Chang, B. S. Zou, W. Y. Zhou, R. A. Zhao, and G. Wang, *Science* 274, 1701 (1996).
64. M. Terrones, N. Grobert, J. Olivares, J. P. Zhang, H. Terrones, K. Kordatos, W. K. Hsu, J. P. Hare, P. D. Townsend, K. Prassides, A. K. Cheetham, H. W. Kroto, and D. R. M. Walton, *Nature* 388, 52 (1997).
65. Z. F. Ren, Z. P. Huang, J. W. Xu, J. H. Wang, P. Bush, M. P. Siegal, and P. N. Provencio, *Science* 282, 1105 (1998).
66. S. Fan, M. G. Chapline, N. R. Franklin, T. W. Tomblor, A. M. Cassell, and H. Dai, *Science* 283, 512 (1999).
67. J. M. Bonard, M. Croci, C. Klinke, R. Kurt, O. Noury, and N. Weiss, *Carbon* 40, 1715 (2002).
68. O. Zhou, H. Shimoda, B. Gao, S. Oh, L. Fleming, and G. Yue, *Acc. Chem. Res.* 35, 1045 (2002).
69. C. N. R. Rao, R. Sen, B. C. Satishkumar, and A. Govindaraj, *Chem. Commun.* 1525 (1998).
70. R. Andrews, D. Jacques, A. M. Rao, F. Debyshire, D. Qian, X. Fan, E. C. Dickey, and J. Chen, *Chem. Phys. Lett.* 303, 467 (1999).
71. M. Mayne, N. Grobert, M. Terrones, R. Kamalakaran, M. Rühle, H. W. Kroto, and D. R. M. Walton, *Chem. Phys. Lett.* 338, 101 (2001).
72. X. Zhang, A. Cao, B. Wei, Y. Li, J. Wei, C. Xu, and D. Wu, *Chem. Phys. Lett.* 362, 285 (2002).
73. C. Bower, W. Zhu, S. Jin, and O. Zhou, *Appl. Phys. Lett.* 77, 830 (2000).

74. Y. Zhang, A. Chang, J. Cao, Q. Wang, W. Kim, Y. Li, N. Morris, E. Yenilmez, J. Yong, and H. Dai, *Appl. Phys. Lett.* 79, 3155 (2001).
75. R. R. Schlittler, J. W. Seo, J. K. Gimzewski, C. Durkan, M. S. M. Saifullah, and M. E. Welland, *Science* 292, 1136 (2001).
76. C. Durkan, A. Ilie, M. S. M. Saifullah, and M. E. Welland, *Appl. Phys. Lett.* 80, 4244 (2002).
77. X. Wang, Y. Liu, and D. Zhu, *Chem. Comm.* 751 (2001).
78. X. Wang, Y. Liu, and D. Zhu, *Adv. Mater.* 14, 165 (2002).
79. B. Q. Wei, R. Vajtai, Y. Jung, J. Ward, R. Zhang, G. Ramanath, and P. M. Ajayan, *Nature* 416, 495 (2002).
80. H. W. Zhu, C. L. Xu, D. H. Wu, B. Q. Wei, R. Vajtai, and P. M. Ajayan, *Science* 296, 884 (2002).
81. K. Jiang, Q. Li, and S. Fan, *Nature* 419, 801 (2002).
82. B. Wei, R. Vajtai, Y. Y. Choi, P. M. Ajayan, H. Zhu, C. Xu, and D. Wu, *Nanoletters* 2, 1105 (2002).

# Magnesium-Nickel Nanocrystalline and Amorphous Alloys for Batteries

H. K. Liu

*University of Wollongong, Wollongong, Australia*

## CONTENTS

1. Introduction
2. Magnesium–Nickel Alloys for Hydrogen Storage
3. Magnesium–Nickel Alloys Electrodes for Ni-MH Batteries
4. Conclusions  
Glossary  
References

## 1. INTRODUCTION

Rechargeable batteries are used in modern communications, computers, and electric vehicles. The Ni-MH battery is one of the key competitors in the rechargeable battery market, especially for commercial electric powered vehicles, which constitute a rapidly expanding market. Rechargeable batteries made from nickel–metal hydride are a better choice for rechargeable batteries than those made from nickel–cadmium in terms of environmental benefits and performance.

For most commercial Ni-MH batteries, their negative electrodes are of rare-earth system alloys, which have low theoretical discharge capacities (LaNi<sub>5</sub> alloy has a theoretical discharge capacity of 370 mAh/g). The capacities of the negative alloy electrodes restrict the further improvement of the capacities of nickel–metal hydride batteries. In order to increase the energy density of the Ni-MH battery, it is necessary to improve the negative (metal hydride) electrode properties.

Mg and Mg-based hydrogen storage alloys are promising energy conversion and storage materials because they possess very high theoretical hydrogen storage capacities; for example, the theoretical discharge capacity of Mg<sub>2</sub>Ni alloy is 999 mAh/g [1]. Magnesium is also abundant in nature, light in weight, and relatively low in cost. However, the absorption and desorption of hydrogen in Mg-based hydrogen storage alloys require high temperatures (over 250 °C for Mg<sub>2</sub>Ni) at

around atmospheric pressure [2], and therefore many efforts have been made to lower the hydrogen-absorbing temperature of Mg alloys for practical application in Ni-MH batteries [3–5].

A large number of investigations have shown that amorphous and nanocrystalline metals and alloys have the features of new alloy compositions and new atomic configurations, which are different from those of crystalline alloys. There also appear to be some possibilities of achieving high discharge capacities with amorphous and nanocrystalline Mg-based alloys.

### 1.1. Amorphous Alloys

The distinctive feature of the amorphous state for a single-phase solid alloy is that it has no crystal lattice, no grain boundaries, and no dislocations. However, it does have a structure that is dependent on the way its atoms are arranged, and this structure is important in determining the properties described in some metallic glass structural models, such as the dense random-packed hard sphere model [6], local-coordination model [7], and so on.

#### 1.1.1. Methods for Achieving Amorphous Alloys

Amorphous metals and alloys can be made using rapid quenching from the liquid and the vapor phase [8], mechanical alloying [9], mechanical milling [9], evaporation deposition [10], sputtering deposition [11], ion-implantation [12], and electrodeposition [13]. The amorphous metals and alloys prepared by rapid solidification processing have features that enable various kinds of characteristics to be achieved, such as excellent mechanical properties, useful physical properties, and unique chemical properties, which have not been obtained for conventional crystalline alloys [14]. Solid-state amorphization by mechanical alloying (MA) and mechanical milling (MM) has become the most effective method for obtaining amorphous alloys [9].

### 1.1.2. Rapid Quenching (RQ) from Melt

This is one of the most commonly used methods in preparing amorphous alloys. Amorphous alloys formed by RQ are also named metallic glasses because they are formed when liquids are cooled but fail to crystallize and instead continuously and uniformly congeal into solids [8]. The basic principle of obtaining amorphous alloys by RQ from the melt is that the liquid must be converted very rapidly from a droplet or jet into a thin layer or wire in contact with a highly thermally conductive metal to produce thin plates, ribbons, or wires.

### 1.1.3. Mechanical Alloying (MA) and Mechanical Milling (MM)

For a large-scale production of amorphous alloys, MA/MM is the most commonly used method. Mechanical alloying/milling is usually carried out in high-energy mills such as vibratory mills, planetary mills, and attrition mills. The energy transfer to the powder particles in these mills takes place by a shearing action or impact of the high-velocity balls with the powder. In addition to the above mills, several other types of mills such as the rod mill, modified rod mill, and other specially designed mills have been used for mechanical alloying/milling.

During MA/MM processes, the kinetics of alloying and other phase transformations depend on the energy transferred to the powder from the balls. The energy transfer is governed by many parameters such as the type of mill, milling speed, type and size of the balls, ball/powder weight ratio, choice of dry or wet milling, atmosphere in the mill, and the duration of milling.

The ball-milling sequence consists primarily of collision, shearing, wearing, and cold-welding. The formation of amorphous phase by MA/MM is a very complicated process, which not only depends on the alloy system but is also affected by many ball-milling parameters. The MA process synthesizes amorphous alloy powders by reacting elemental crystalline powders through solid-state chemical diffusion, being often accompanied by a negative heat of formation. In the MM process, however, crystalline alloy or compound powders are transformed into amorphous solid powders by destroying the periodic long-range order of atomic arrangement without any changes of chemical composition due to long-distance solid-state diffusion.

MA is a chemical reaction of  $mA$  (crystal) +  $nB$  (crystal)  $\rightarrow A_mB_n$  (amorphous) proceeding from a higher free-energy state to a lower one, providing a continuous evolution in the local chemical composition through long-range solid-state chemical diffusion.

MM is a phase transformation of  $A_mB_n$  (crystal)  $\rightarrow A_mB_n$  (amorphous) going from the ground state to an excited state caused by destroying the long-range order of atomic arrangement, without any changes of chemical composition [15].

## 1.2. Nanocrystalline Materials

A novel way of transforming a material to a metastable state is to reduce its grain size to very small values of a few nanometers where the proportion of atoms lying on grain

boundaries is equivalent to or higher than that of those in the interior of the grains. Materials with such small grain sizes are referred to as nanocrystalline materials, which are defined as single or multiphase polycrystals, with a crystal size typically within the range 1–100 nm. Because of their ultrafine grain sizes, nanocrystalline materials exhibit a variety of properties that are different from and often considerably better than those of conventional coarse-grained polycrystalline materials [16]. These include higher catalytic activity [17], more uniform corrosion [18] and superior localized corrosion resistance [19], improved strength/hardness [20], enhanced diffusivity [21], higher electrical resistivity [22], increased specific heat [23], higher thermal expansion coefficient [24], and better magnetic properties [25] compared with conventional coarser-grained materials.

### 1.2.1. Structure of Nanocrystalline Materials

The structures of nanocrystalline materials are dominated by their ultrafine grain sizes and their large number of grain boundaries. Much research has been done to determine the structure of nanocrystalline materials. Most of the results have been interpreted according to a two-components microstructure: perfect long-range ordered atomic arrangement within the grains and a random interfacial atomic arrangement [16, 24, 26, 27]. Because of their ultrafine grain size, nanocrystalline materials have a significant fraction of their atoms in grain boundary environments, where they occupy positions relaxed from their normal lattice sites. For conventional high-angle grain boundaries, these relaxations extend over about two atomic planes on either side of the boundary, with the greatest relaxation occurring in the first plane [28, 29]. The percentage of atoms in grain boundaries (including grain boundary junctions) of a nanocrystalline material is a function of grain diameter [30], assuming that the average grain boundary thickness ranges from 0.5 to 1.0 nm, about 2 to 4 atomic planes. Assuming that grains are spherical, the volume fraction of nanocrystalline materials associated with the boundaries can be calculated [31].

### 1.2.2. Synthesis and Processing of Nanocrystalline Materials

In principle, any method capable of producing very fine grain size polycrystalline materials can be used to produce nanocrystalline materials. If a phase transformation is involved, for example, liquid to solid or vapor to solid, then steps have to be taken to increase the nucleation rate and decrease the growth rate during formation of the product phase. The methods include inert gas condensation [32], mechanical milling [33], chemical vapor deposition [34], sputtering [35], spray conversion processing [36], electrodeposition [37], sol–gel processing [38], spark erosion [39], plasma processing [40], and quenching a melt under high pressure [41]. Among these, gas condensation and mechanical milling methods are the most commonly used. A typical apparatus [16, 42] for gas condensation is widely used for synthesis of nanocrystalline materials by the *in-situ* consolidation of gas-condensed clusters.

Mechanical milling (MM) is a popular method for making nanocrystalline materials because of its simplicity,

the relatively inexpensive equipment needed, and the applicability to essentially all classes of materials. MM produces nanostructures not by cluster assembly but by the structural decomposition of coarser-grained structures as the result of severe plastic deformation. The major advantage often quoted is the possibility for easily scaling up to tonnage quantities of material for various applications [43]. This process consists of repeated welding, fracturing, and rewelding of powder particles in a dry high-energy ball mill. In this process, a metal, an alloy, or mixtures of elemental or pre-alloyed powder are subjected to grinding under a protective atmosphere in equipment such as attrition mills, vibrating ball mills, and shaker mills. A majority of the work on nano-crystalline materials has been carried out in highly energetic small shaker mills, and it has been shown that nanometer-sized grains can be obtained for almost any material after sufficient milling time. The grain sizes were found to decrease with milling time down to a minimum value, which appeared to scale inversely with the melting temperature. Further, mechanical alloying of immiscible metals can be achieved with very large metastable solid solutions, presumably related to solute segregation at the nanocrystalline grain boundaries [33].

## 2. MAGNESIUM–NICKEL ALLOYS FOR HYDROGEN STORAGE

In the early 1970s, the interest in metal hydrides and the development of their applications started with the discovery of hydrogen absorption by  $\text{LaNi}_5$  [44] at Philips Research Laboratories in Holland and  $\text{FeTi}$  [45] at the Brookhaven National Laboratory in the United States. Since then, many metals, intermetallics, and alloys that react reversibly with hydrogen to form hydrides have been observed. In the 1970s and 1980s, the practical applications for these new materials included hydrogen storage, hydrogen compression and purification, heat pumping, refrigeration, and thermal storage [46]. Later in the 1980s, utilizing hydrogen storage alloys instead of cadmium as an anode material in alkaline rechargeable batteries had brought about a revolution in power sources. By 1990, the first Ni-MH batteries reached the marketing stage [47]. In late 1997, a hybrid electric vehicle power-assisted by a high-power Ni-MH battery was commercialized in Japan by Toyota [48]. More recently, attention has been paid to the investigation and development of various new hydrogen storage alloys with high hydrogen absorption capacities and low costs.

### 2.1. Types of Hydrogen Storage Alloys

The hydrogen storage alloys in common use are classified in terms of their stoichiometric composition into four categories:  $\text{AB}_5$ ,  $\text{AB}_2$ ,  $\text{AB}$ , and  $\text{A}_2\text{B}$  types [49]. Here are some examples of hydrogen storage alloys studied by researchers around the world:

- $\text{AB}_5$ -type ( $\text{LaNi}_5$ ; La is often replaced by mischmetal (Mm), which is a commercial mixture of rare earths, predominated by Ce, La, Nd, and Pr. Ni is partially substituted by Al, Si, Fe, Mn, Sn, etc.)

- $\text{AB}_2$ -type ( $\text{MgNi}_2$ ,  $\text{ZrV}_2$ ,  $\text{ZrCr}_2$ ,  $\text{TiV}_2$ ,  $\text{TiMn}_2$ ,  $\text{TiCr}_2$ ,  $\text{ZrNi}_2$ ,  $\text{ZrMn}_2$ , etc.)
- $\text{AB}$ -type ( $\text{TiNi}$ ,  $\text{MgNi}$ ,  $\text{CaNi}$ ,  $\text{TiFe}$ , etc.)
- $\text{A}_2\text{B}$ -type ( $\text{Ti}_2\text{Ni}$ ,  $\text{Mg}_2\text{Ni}$ ,  $\text{Mg}_2\text{Cu}$ , etc.)

In these alloys, it is the A component which forms the stable hydride. The B component performs several functions [50]: (i) playing a catalytic role in enhancing the hydriding/dehydriding characteristics; (ii) altering the equilibrium pressures for the hydrogen absorption/desorption and raising it or lowering it to a desired level, and (iii) stabilizing the alloys. The last function is important because some of the A components can be readily oxidized. The hydriding/dehydriding characteristics of these alloys can be altered by a partial substitution or a small addition of other elements. Anani and co-workers [50] summarized the roles of some substitutes or additives as follows: (i) to increase or decrease the crystal lattice constants, thereby changing the equilibrium pressure for hydrogen absorption/desorption; (ii) to decrease the hysteresis during hydrogen absorption/desorption; (iii) to catalyze hydriding/dehydriding reactions; and (iv) to improve the stability of these alloys, thus preventing oxide formation on one or more of the components.

### 2.2. Magnesium-Based Alloys for Hydrogen Storage

Magnesium is the lightest of the commercial structural materials and is the sixth most abundant element on the earth. Magnesium can also reversibly store about 7.65 wt.% hydrogen according to the reaction ( $\text{Mg} + \text{H}_2 \rightarrow \text{MgH}_2$ ).  $\text{MgH}_2$  contains much more hydrogen than other metal hydrides. Unfortunately, the reaction is generally difficult to nucleate because the surface is usually contaminated by magnesium oxide ( $\text{MgO}$ ), or magnesium hydroxide ( $\text{Mg}(\text{OH})_2$ ) which either inhibits the dissociative adsorption of hydrogen or the transfer of hydrogen from the surface to bulk.

In order to eliminate the limitations of using Mg alone, studies of numerous metal additions to Mg (binary, ternary, and multicomponent) were carried out in order to find the optimum alloy for hydrogen storage. Reilly and Wiswall [51, 52] reported a fairly rapid reaction of  $\text{Mg}_2\text{Ni}$  and  $\text{Mg}_2\text{Cu}$  with hydrogen at about 300 °C. They concluded that the presence of Ni or Cu has a catalytic effect on the hydrogenation of Mg. The catalytic effect of these elements is probably due to the formation of oxide-free penetration sites on the surface of Mg particles, as reported for the Mg- $\text{Mg}_2\text{Cu}$  system [53–55].

### 2.3. Mg–Ni Based Alloys for Hydrogen Storage

It is known that in the phase diagram of the Mg-Ni system, two intermetallic compounds are formed:  $\text{Mg}_2\text{Ni}$  and  $\text{MgNi}_2$ . The latter does not react with hydrogen at pressures up to 540 atm in the temperature range –196 to 300 °C. However,  $\text{Mg}_2\text{Ni}$  reacts with hydrogen to form a ternary hydride  $\text{Mg}_2\text{NiH}_4$  even at room temperature, and it will react rapidly at 200 °C and a pressure of 14 atm [51]. The hydrogen content in  $\text{Mg}_2\text{NiH}_4$  is about 3.6 wt.%, which is

still a very good value compared to other hydrogen storage materials, but it is less than one-half the amount of hydrogen in  $\text{MgH}_2$  (7.65 wt%).

Substitution is one of the most widely used methods to control or improve the hydrogenation properties of the hydrogen storage alloys. Many substituted  $\text{Mg}_2\text{Ni}$  alloys have been investigated with a view to improving their hydrogenation properties. In the early 1980s, Oesterricher et al. [56] suggested that the partial substitution of Mg in  $\text{Mg}_2\text{Ni}$  by an element with a more exothermic heat of hydride formation, such as Ca, Sc, or Y, might result in a rise of equilibrium pressure for the substituted  $\text{Mg}_2\text{Ni}$ . This would bring  $\text{Mg}_2\text{Ni}$  into the range of reversible room temperature hydrogen sorption. Yvon et al. [57] suggested that the maximum hydrogen concentration of this compound is mainly limited by electronic factors and that structurally related compounds having more than four hydrogen atoms per formula unit could possibly be stabilized by partially replacing Ni with a transition metal of lower valence, or Mg by a non-transition metal of higher valence.

The compounds prepared by partially replacing Ni by 3d elements [58–62], and Mg by non-transition elements [61], in the binary phase of  $\text{Mg}_2\text{Ni}$  show that the alloys prepared could not form to hydrides having more than four H atoms per formula unit. On the other hand, they show some interesting properties with respect to hydriding and dehydriding kinetics as well as the dissociation temperature of the hydride. It was also reported [63–65] that the partial substitution of Mg by 3d metals on Mg-rich, rare-earth intermetallic compounds resulted in improved dehydriding kinetics.

In order to achieve partial substitution of Ni atoms in  $\text{Mg}_2\text{Ni}$  by iron or cobalt, some experiments were performed by Mintz et al. [58]. However, no significant amount of substitution occurred in the  $\text{Mg}_2\text{Ni}_{1-x}\text{M}_x$  ( $\text{M} = \text{Fe}$  or  $\text{Co}$ ) systems. The highest substituent concentrations of about 2 at.% were obtained for Co. The effects of these low-concentration additives on the stability of the corresponding hydrides were negligible. The same observation was reported by Darnaudery et al. [60] for the addition of Mn or Ti, but they did observe the substitution of other elements such as V, Cr, Fe, Co, Cu, and Zn. On the contrary, Lupu et al. [62] reported that there was no substitution of Ni by Fe in  $\text{Mg}_2\text{Ni}_{1-x}\text{Fe}_x$  ( $x \leq 0.37$ ) alloys. This was explained on the basis of Extended X-ray Absorption Fine Structure (EXAFS) measurements with Mössbauer spectral results. In this range of composition multiphase alloys were obtained containing  $\text{Mg}_2\text{Ni}$ , Mg, and more or less finely dispersed Fe in the form of isolated atoms or small clusters as proved by the EXAFS technique and Mössbauer spectroscopy. Thus they confirmed that there is no significant substitution of Ni by Fe atoms in the  $\text{Mg}_2\text{Ni}$  lattice, which is in agreement with the observation of Mintz et al. [58].

A study of the action of hydrogen on  $\text{Mg}_2\text{Ni}_{1-x}\text{M}_x$  ( $\text{M} = \text{V}$ , Cr, Fe, Co, Cu, or Zn;  $x = 0.25$ ) alloys has been carried out [60]. Hydriding of the alloys resulted in the formation of quaternary hydrides. The hydriding process leads to ternary alloys, except in the case of the Cu-containing alloy. This behavior of  $\text{Mg}_2\text{Ni}_{0.75}\text{Cu}_{0.25}$  seems to be similar to that of  $\text{Mg}_2\text{Cu}$  due to the decomposition of the alloy during the hydriding reaction [52]. The thermal stabilities of these

compounds are close to that of  $\text{Mg}_2\text{NiH}_4$ . In each case the hydrogen/alloy mole ratio is lower than for  $\text{Mg}_2\text{NiH}_4$ .

The replacement of Ni in  $\text{Mg}_2\text{Ni}$  by the 3d elements alters the dissociation temperature markedly. For example, the dissociation temperature in 1 atm pressure for the Cu-containing alloy drops significantly from 250 °C to 227 °C, whereas for the Co-containing alloy this temperature increases to 267 °C. The absorption and desorption rates for  $\text{Mg}_2\text{Ni}_{1-x}\text{M}_x$  alloys are close to those obtained with  $\text{Mg}_2\text{Ni}$  except for the Co-containing alloy. Because of the encouraging results obtained with the  $\text{Mg}_2\text{Ni}_{1-x}\text{Cu}_x$  system, Darnaudery et al. [66] continued their work on the same system by varying the  $x$  values from 0 to 0.85 in order to optimize the composition. The absorption and desorption rates for these alloys are close to those obtained with  $\text{Mg}_2\text{Ni}$ .

Au and co-workers [67] have investigated the hydrogen storage properties of multi-component Mg-based alloys and found that  $\text{Mg}_{0.833}\text{Ni}_{0.066}\text{Cu}_{0.095}\text{Ml}_{0.006}$  (Ml stands for La-rich mischmetal) has good hydriding/dehydriding properties. It can absorb 4.75 wt.% hydrogen at 330 °C under 0.1 MPa pressure in 0.5 h. The alloying elements Ni, Cu, and Re (rare-earth metal) are identified as having positive effects on the kinetic properties of Mg-based alloys. The intermetallic compound of Mg with Ni, Cu (and Re), namely  $\text{Mg}_2(\text{Cu}, \text{Ni})$ , plays the key role in improving the kinetic properties of the multicomponent Mg-based alloy.

Iwakura et al. [68] investigated the effect of partial substitution of Mg in MgNi with both Ti and V and found that subsequent surface modification with graphite greatly enhanced the hydrogen desorbability of the MgNi alloy compared with either the partial substitution or the surface modification.

## 2.4. Hydrogenation Properties of Nanocrystalline and Amorphous MgNi Alloys

As Mg and Mg-based alloys are some of the most promising hydrogen storage alloys, there has been extensive work on Mg-based hydrogen storage alloys for more than three decades, from both fundamental and applications points of view. In recent years, it has been found that ball milling is a highly effective method of improving the hydriding/dehydriding kinetics and hydrogenation characteristics of Mg-based alloys. In the late 1980s, Khrussanova et al. reported that ball milling a 90 wt.% Mg and 10 wt.%  $\text{TiO}_2$  mixture in a planetary mill results in improvement of the absorption and desorption characteristics of magnesium [69] and that ball milling is favorable to the appearance of a clean Mg surface without the usual thin oxide film [70]. Ball-milled 90 wt.% Mg and 10 wt.%  $\text{V}_2\text{O}_5$  mixture is activated quickly and has a high hydrogen capacity which is preserved after prolonged cycling. It also has good desorption characteristics [71]. Ball milling can also greatly improve the hydrogen absorption rate of  $\text{Mg}_2\text{Ni}$  intermetallic compound [72]. Song [73–75] investigated the hydriding and dehydriding characteristics of mechanically milled Mg and mechanically alloyed mixtures with the compositions Mg- $x$  wt.% Ni ( $x = 5, 10, 25$ , and 55) using a planetary mill. The results indicated that the Mg- $x$  wt.% Ni and Mg-25 wt.%



Ni mixtures are easily activated with the activation accelerated within 5 min, and also show much larger hydrogen storage capacities and much higher hydriding rates, and higher dehydriding rates, than other magnesium-based alloys or mixtures. Mechanically milled Mg-based composites, Mg-G (graphite) and Mg-Pd-G (graphite), were extremely active with respect to hydrogen absorption even at 27 °C and showed good reversibility for hydriding/dehydriding [76–79]. The ball-milled MgNi alloy with graphite can also absorb hydrogen at 30 °C in much larger quantities than that prepared by induction melting [80]. Considerable work has also been done on ball milling ternary hydrogen storage alloys, such as  $Mg_2Ni_{1-x}Zr_x$  ( $0 < x \leq 0.3$ ) [81], and Mg-based composite [82–85], which has led to better hydriding/dehydriding kinetics and/or larger hydrogen absorption abilities of the materials.

Ball milling is the most effective and simplest method to manufacture nanocrystalline and amorphous MgNi alloys. The activation of nanocrystalline  $Mg_2Ni$  is much easier, or even unnecessary. At high temperatures (about 300 °C), the hydrogen absorption rate is very high, even for as-made nanocrystalline samples. The absorption rate can be further improved by applying one hydrogenation cycle as a pretreatment. Nanocrystalline  $Mg_2Ni$  also exhibits hydrogen absorption at lower temperatures (for instance at 200 °C, i.e., below the temperature of structural transformation of the  $Mg_2NiH_4$  hydride) without any activation [86]. Tanaka et al. investigated the hydrogen absorbing rates and pressure–composition isotherms ( $P$ - $C$ - $T$ ) of nanocrystalline MgNi and MgNi-Re (Re = La, Nd) alloys prepared by a melt-spinning and crystallization method. These nanocrystallized alloys, particularly of the MgNi-Re systems, exhibit excellent hydrogen absorbing kinetics and  $P$ - $C$ - $T$  characteristics in comparison with those of the corresponding as-cast alloys with coarse eutectic structure [87].

Orimo et al. investigated the hydrogenation properties of amorphous MgNi alloys prepared by ball milling under a hydrogen atmosphere [88, 89]. The hydrogen pressure–composition isotherms in dehydriding processes of amorphous MgNi alloy show that the dehydriding reaction proceeds below 0.1 MPa even at 160°C. The pressure dependence of the hydrogen content is small, compared to the other amorphous alloys with a broad site energy distribution for hydrogen atoms, such as the FeTi system [90, 91]. This suggests that the energy distribution is narrower in amorphous MgNi alloy. Funaki et al. [92] synthesized amorphous  $MgNiC_x$  ( $x = 0$ –1.31) by mechanical alloying of amorphous MgNi and graphite as starting materials. Upon hydrogenation of  $MgNiC_x$ , the atomic ratio of hydrogen plus carbon to metal ( $(H + C)/M$ ) remained at a constant value of about 0.9.

Tsushio and co-workers investigated the effect of elemental substitutions on the hydrogenation properties of amorphous  $Mg_2Ni_{0.86}M_{0.03}$  ( $M = Cr, Fe, Co, Mn$ ) alloys prepared by ball milling [93]. Most of the  $P$ - $C$ - $T$  curves were completely different from those of the crystalline  $Mg_2Ni-H_2$ ,  $Mg-H_2$  systems, and even amorphous MgNi alloy [89]. They show a monotonic increase of hydrogen content with the logarithm of applied pressure with no plateau. The synthesis and hydriding/dehydriding properties of  $Mg_2Ni_{1.9}M_{0.1}$  ( $M =$  none, Ni, Ca, La, Y, Al, Si, Cu, and Mn) alloys mechanically alloyed from  $Mg_2Ni_{1.9}M_{0.1}$  and Ni powder were also

reported [94]. The pressure–composition isotherms of amorphous  $Mg_2Ni_{1.9}M_{0.1}$  ( $M =$  none, Ca, and Cu) indicate that elemental substitutions of amorphous MgNi alloys can effectively change their hydriding/dehydriding properties [94]. The formation of amorphous or nanocrystalline Mg-based hydrogen storage alloys produced by ball milling results in dramatic changes in hydrogen sorption properties, especially by elimination of the need for activation and improvement of hydriding/dehydriding kinetics. Yang et al. have successfully synthesized  $Mg_2Ni_{0.75}M_{0.25}$  ( $M = Ti, Cr, Mn, Fe, Co, Ni, Cu,$  and  $Zn$ ) alloys by the ball-milling diffusion method [95]. Results show that the alloys after treatment have the best performance: the hydrogen desorption capacity reaches the highest value after only two adsorption/desorption cycles. The ratio of H/M is about 1.18 (approx. 3.3 wt.%) under the STP conditions for each alloy. After substitution for Ni in  $Mg_2Ni$  (Fig. 1), there are three results: Cr, Mn, and Co all lower the decomposition plateau pressure of  $Mg_2Ni$ ; Ti and Cu have the opposite effect on  $Mg_2Ni$  from Cr, Mn, and Co; Fe and Zn have little effect. The preparation and hydrogen absorption/desorption capacities of the alloys reported by various researchers are shown in Table 1.

### 3. MAGNESIUM–NICKEL ALLOYS ELECTRODES FOR Ni-MH BATTERIES

After the invention of the Pb-acid battery in 1859 and the Ni-Cd battery in 1899, no successful rechargeable battery appeared for 90 years. The Ni-MH battery is the third practical secondary battery and is now a key component not only for advanced information and telecommunication systems, but also for the next generation of vehicles in which energy can be used efficiently with low emissions to the environment. The key materials for this high-tech battery are the hydrogen storage alloys [48].

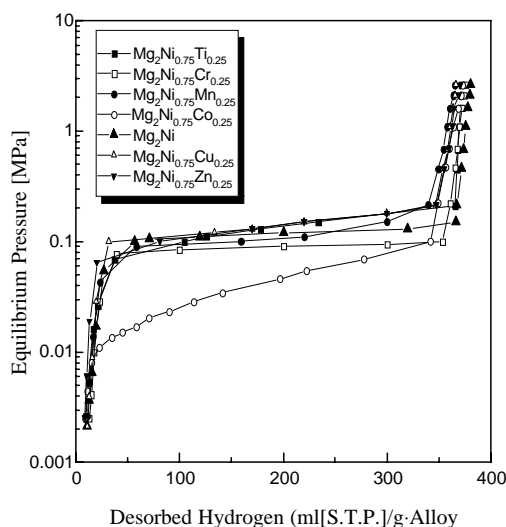


**Figure 1.**  $P$ - $C$  desorption isotherms of the ternary  $Mg_2Ni_{0.75}M_{0.25}$  alloys. Reprinted with permission from [95], H. B. Yang et al., *J. Alloys Comp.* 330, 640 (2002). © 2002, Elsevier Science.

**Table 1.** Preparation method and hydrogen absorption/desorption capacity of the alloys reported by various researchers.

Alloys	Preparation	Hydrogen absorption/desorption capacity of the alloy	Ref.
MgNi MgNi <sub>1.5</sub> MgNi <sub>2</sub>	MgNi <sub>x</sub> alloys were prepared by ball milling mixtures of metallic Mg and Ni	2.0 wt.% 1.1 wt.% 0.7 wt.%	[130]
MgNi	MgNi alloy was prepared from Mg and Ni mixed powders by mechanical alloying under Ar for seven days	An amount of absorbed hydrogen saturated at H/M ratios of ca. 1.0 and 0.58 for the alloys prepared by MA and induction melting respectively	[80]
Mg <sub>2</sub> Ni <sub>0.75</sub> M <sub>0.25</sub> (M = Ti, Cr, Mn, Fe, Co, Ni, Cu and Zn)	Mg, Ni, and M powders were mixed, ball-milled under Ar for 2 h, pressed to pellets, and sintered in Ar	H/M = 1.3, ≈3.3 wt.%	[95]
Mg <sub>2</sub> Ni Mg <sub>2</sub> Ni <sub>0.9</sub> Cu <sub>0.1</sub>	Mixing of Mg and Ni powders, then mechanical alloying 120 h Mechanical alloying 120 h	At 200 °C, 2.6 wt.% (abs.) at 5 MPa At 300 °C, 3.75 wt.% (abs.) at 5 MPa At 200 °C, 3. wt.% (abs.) at 0.01 MPa	[128]
Mg <sub>2-x</sub> Ni (x = 0) Mg <sub>2-x</sub> Ni (x = 0.25) Mg <sub>2-x</sub> Ni (x = 0.5) (Nanostructured)	Mg flakes and Ni powders were premixed and poured into a die cavity. The mixture of powders was repeatedly extruded and compressed using a high-speed forging machine	H/M = 0.11 H/M = 0.23 H/M = 0.26  Alloys were immersed in 6 M KOH solution for 44 h	[117]
Mg <sub>2</sub> Ni Mg <sub>2</sub> Ni <sub>1-x</sub> Zr <sub>x</sub>	Mg, Ni, and Zr powders were mixed, ball-milled under Ar for 2 h, pressed to pellets, and sintered in Ar	3.3 wt.% for Mg <sub>2</sub> Ni <sub>0.7</sub> Zr <sub>0.3</sub> , which is a little higher than that of Mg <sub>2</sub> Ni	[131]
Mg <sub>2</sub> Ni + Ni Mg <sub>1.9</sub> Mn <sub>0.1</sub> Ni (M = Al, Mn)	Alloys were prepared in an induction furnace under inert gas, pulverized, then mechanically ground (MG) for 100 h	H/M = 0.1 for Mg <sub>1.9</sub> Al <sub>0.1</sub> Ni (80 °C), Mg <sub>1.9</sub> Mn <sub>0.1</sub> Ni (125 °C), and Mg <sub>2</sub> Ni (150 °C)	[110]
MG-Mg <sub>2</sub> Ni + Ni		H/M = 1.2 (80 °C)	
Mg <sub>2</sub> Ni-Ni composite Crystalline Mg <sub>2</sub> Ni	Ingot of Mg <sub>2</sub> Ni alloy was prepared by induction melting, pulverized, mixed with Ni powder	H/M = 1.02, ≈4.0 wt.% for Mg <sub>2</sub> Ni and 2.4 wt.% for Mg <sub>2</sub> Ni-Ni  Theoretical value 3.6 wt.% on basis of Mg <sub>2</sub> NiH <sub>4</sub>	[132]
Mg <sub>1.8</sub> Ag <sub>0.2</sub> Ni	Pure Mg, Ni, and Ag metal powders were mixed, ground, and ball-milled under Ar; pressed into pellets under Ar and heated for 4 h	Hydriding and dehydriding process can take place at 150 °C. Hydrogen storage capacity reached 2.2 wt.% at 150 °C	[139]

In 1969, Zijlstra and Westendorp accidentally found during research on rare-earth magnets (SmCo<sub>5</sub>) that rare-earth intermetallic compounds absorbed large amounts of hydrogen [96], opening a new scientific and technical field—hydrogen storage alloys. Soon after the discovery of hydrogen storage alloys, intermetallic compounds were applied as “hydrogen storage alloy electrodes,” for instance, TiNi-Ti<sub>2</sub>Ni [96], LaNi<sub>5</sub> [97, 98], and LaNi<sub>5-x</sub>M<sub>x</sub> (M = Al, Cr, Cu, Mn) [99–101]. Markin et al. constructed and evaluated the rechargeable nickel–metal hydride (Ni-MH) batteries composed of nickel hydroxide positive electrodes and metal hydride negative electrodes using LaNi<sub>5</sub> [102, 103].

Since 1985, a tremendous research and development effort has been conducted on MH electrodes and the Ni-MH

battery, leading to outstanding progress in every area of performance. The good combination of both metal hydride technology and Ni-Cd technology resulted in the rapid commercialization of the sealed Ni-MH battery by the end of 1990 [104]. The hydrogen storage alloys used for the negative electrode materials of Ni-MH batteries must satisfy the following requirements [7, 105, 106]:

- Large electrochemical hydrogen storage capacity.
- High electrochemical catalytic activity.
- High durability against oxidation in concentrated alkaline solution.
- Good electrochemical hydriding-dehydriding kinetics.
- Low cost.

**Table 2.** Capacity of MgNi-based alloy electrodes.

Alloy	Discharge current density (mA/g)	Discharge capacity (mAh/g)	Ref.
Mg <sub>2</sub> Ni-Ni composite		1090 (theo.)	[112]
Mg <sub>2</sub> Ni	50	very low	
Ball-milled Mg <sub>2</sub> Ni		440	
Mg <sub>2</sub> Ni-Ni composite (Homogeneous amorphous) (Ball milling)		1082 mAh/g(Mg <sub>2</sub> Ni)	
Mg <sub>2</sub> Ni-Ni composite (Homogeneous amorphous) (Ball-milling)	50	870 mAh/g(Mg <sub>2</sub> Ni)	[111]
MG-Mg <sub>2</sub> Ni + Ni	20	750 mAh/g(Mg <sub>2</sub> Ni)	[109]
MG-Mg <sub>1.9</sub> Al <sub>0.1</sub> Ni (All are amorphous) (Mechanical grinding)		690 mAh/g(alloy)	[110]
Mg <sub>50</sub> Ni <sub>50</sub>	100	387.2	[126]
Mg <sub>50</sub> Ni <sub>45</sub> Ti <sub>5</sub>		400	
Mg <sub>50</sub> Ni <sub>45</sub> Zn <sub>5</sub>		388.3	
Mg <sub>50</sub> Ni <sub>45</sub> Mn <sub>5</sub>		345	
Mg <sub>50</sub> Ni <sub>45</sub> Cu <sub>5</sub>		343.3	
Mg <sub>50</sub> Ni <sub>45</sub> Fe <sub>5</sub>		273.3	
Mg <sub>50</sub> Ni <sub>45</sub> Co <sub>5</sub>		247.5	
Mg <sub>50</sub> Ni <sub>45</sub> Zr <sub>5</sub>		239.2	
Mg <sub>50</sub> Ni <sub>45</sub> W <sub>5</sub>		226.7	
Mg <sub>50</sub> Ni <sub>45</sub> Cr <sub>5</sub>		204.2	
Mg <sub>50</sub> Ni <sub>45</sub> Se <sub>5</sub>		93.3	
Mg <sub>50</sub> Ni <sub>45</sub> Sb <sub>5</sub>		28.3	
Mg <sub>50</sub> Ni <sub>45</sub> C <sub>5</sub> (All are amorphous) (Mechanical alloying)		13.3 mAh/g(alloy)	
Mg <sub>0.9</sub> Ti <sub>0.06</sub> V <sub>0.04</sub> Ni	50	510	[124]
Mg <sub>0.9</sub> Ti <sub>0.1</sub> Ni		490	
Mg <sub>0.9</sub> V <sub>0.1</sub> Ni		480	
MgNi (All are amorphous) (Mechanical alloying)		520 mAh/g(alloy)	
MgNi	50	490	[113]
MgNi <sub>1.5</sub>		370	
MgNi <sub>2</sub> (All are amorphous) (Mechanical alloying)		200 mAh/g(alloy)	
Amorphous MgNi (Ball milling)	20	522 mAh/g(alloy)	[140]
Mg <sub>2</sub> Ni (Surface fluorination) (Mechanical alloying)	100	120	[141]
Mg <sub>2</sub> Ni (without fluorination)		130	
Mg <sub>50</sub> Ni <sub>50</sub> (12 h)	20	15	[127]
(24 h)		365	
(60 h)		500	
Mg <sub>50</sub> Ni <sub>50</sub> (12 h)	100	7.5	
(24 h)		255	
(60 h)		405	

continued

Table 2. Continued

Alloy	Discharge current density (mA/g)	Discharge capacity (mAh/g)	Ref.
Mg <sub>50</sub> Ni <sub>50</sub> (as-cast)	20	50	
Mg <sub>50</sub> Ni <sub>40</sub> Co <sub>10</sub>		450	
Mg <sub>50</sub> Ni <sub>45</sub> Si <sub>5</sub>		422	
Mg <sub>50</sub> Ni <sub>45</sub> Al <sub>5</sub>		285	
Mg <sub>50</sub> Ni <sub>22.5</sub> Co <sub>22.5</sub> Si <sub>5</sub>		158	
Mg <sub>50</sub> Ni <sub>40</sub> Co <sub>10</sub>	100	324	
Mg <sub>50</sub> Ni <sub>45</sub> Si <sub>5</sub>		181	
Mg <sub>50</sub> Ni <sub>45</sub> Al <sub>5</sub>		110	
Mg <sub>50</sub> Ni <sub>22.5</sub> Co <sub>22.5</sub> Si <sub>5</sub>		106	
(All are amorphous)		mAh/g(alloy)	
(Mechanical alloying)			
Mg <sub>2</sub> Ni (120 h-milled)	10	170	[128]
Mg <sub>2</sub> Ni <sub>0.9</sub> Cu <sub>0.1</sub> (120 h-milled)		350	
Mg <sub>2</sub> Ni <sub>0.9</sub> Mn <sub>0.1</sub> (120 h-milled)		130	
Mg <sub>2</sub> Ni <sub>0.9</sub> Co <sub>0.1</sub> (120 h-milled)		40	
(Nanocrystalline)		mAh/g(alloy)	
(Mechanical alloying)			
MgNi-Pd	50	110–410	[142]
MgNi-La		27–34	
MgNi-Ca		30–120	
(amorphous)		mAh/g(alloy)	
MgNi by ball milling Mg <sub>2</sub> Ni (amorphous)	250	30	[143]
	80	149	
	40	255	
	20	388	
	10	435	
	5	496	
		mAh/g(alloy)	
MgNiC <sub>x</sub> (x = 0)	20	522	[144]
MgNiC <sub>x</sub> (x = 3.5 wt.%)		332	
(Mechanical alloying)		mAh/g(alloy)	
Mg <sub>2</sub> Ni (Ni-mixed) (Polycrystalline)	50	95 mAh/g(Mg <sub>2</sub> Ni)	[129], [123]
Mg <sub>2</sub> Ni (Ni-ball-milled) (Amorphous)	50	680 mAh/g(Mg <sub>2</sub> Ni)	
	100	538 mAh/g(Mg <sub>2</sub> Ni)	
	200	390 mAh/g(Mg <sub>2</sub> Ni)	
Mg <sub>2</sub> Ni (Ni-coated) (Amorphous)	50	756 mAh/g(Mg <sub>2</sub> Ni)	
	100	612 mAh/g(Mg <sub>2</sub> Ni)	
	200	440 mAh/g(Mg <sub>2</sub> Ni)	
Mg <sub>2</sub> Ni (ball-milled with Co powder)	50	476 mAh/g(Mg <sub>2</sub> Ni)	
	100	440 mAh/g(Mg <sub>2</sub> Ni)	
	200	390 mAh/g(Mg <sub>2</sub> Ni)	
Mg <sub>2</sub> Ni <sub>0.9</sub> Mn <sub>0.1</sub>	50	118 mAh/g(alloy)	
	100	5 mAh/g(alloy)	
Mg <sub>2</sub> Ni <sub>0.9</sub> Mn <sub>0.1</sub> (ball-milled)	50	672 mAh/g(alloy)	
	100	437 mAh/g(alloy)	
	200	140 mAh/g(alloy)	
Mg <sub>2</sub> Ni <sub>0.9</sub> Mn <sub>0.1</sub> (Ni-coated)	50	780 mAh/g(alloy)	
	100	546 mAh/g(alloy)	
	200	190 mAh/g(alloy)	
Mg <sub>1.85</sub> Ti <sub>0.15</sub> Ni <sub>0.9</sub> Co <sub>0.1</sub> (Amorphous)	50	778 mAh/g(alloy)	
	400	560 mAh/g(alloy)	

continued

Table 2. Continued

Alloy	Discharge current density (mA/g)	Discharge capacity (mAh/g)	Ref.
Mg <sub>1.9</sub> Al <sub>0.1</sub> Ni <sub>0.8</sub> Co <sub>0.1</sub> Mn <sub>0.1</sub> (Ball-milled with Ni for 50 h, alloy is amorphous)	50	630 mAh/g(alloy)	[121]
Mg <sub>1.9</sub> Al <sub>0.1</sub> Ni <sub>0.8</sub> Co <sub>0.1</sub> Mn <sub>0.1</sub> (Ball-milled with Ni for 120 h, alloy is amorphous)	50	510 mAh/g(alloy)	
Mg <sub>2-x</sub> Ni ( $x = 0$ )	17	414	[117]
Mg <sub>2-x</sub> Ni ( $x = 0.25$ )	17	445	
Mg <sub>2-x</sub> Ni ( $x = 0.5$ ) (After forging and compression cycles, implying amorphous for $x = 0.25$ and $0.5$ )	17	534	

### 3.1. Capacities of Mg-Ni-Based Alloy Electrodes

In recent years, some research has shown that the MgNi-type alloys are promising materials for increasing the negative electrode capacity of Ni-MH batteries.

By sintering Mg and Ni powders in their required proportions under an argon atmosphere, crystalline Mg<sub>2</sub>Ni alloys can be prepared. The sintered crystalline Mg<sub>2</sub>Ni alloys have extremely low discharge capacities of only 15 or 18 mAh/g at a discharge current density of 50 mA/g, which is negligibly small in comparison with their theoretical discharge capacity. Thus, common crystalline Mg<sub>2</sub>Ni alloy is not suitable for use as a rechargeable anode material in an alkaline solution at room temperature.

Orimo and Fujii [107] reported that by ball milling Mg<sub>2</sub>Ni with Ni powder, the resulting MgNi alloy absorbed hydrogen more easily than the initial crystalline Mg<sub>2</sub>Ni alloy. Iwakura et al. [108] have also improved the discharge capacity of MA Mg-based alloy with graphite surface modification by ball milling (BM). Kohno et al. reported that by mechanical grinding of Mg<sub>2</sub>Ni alloys with Ni powders, a discharge capacity of 750 mAh/g (Mg<sub>2</sub>Ni) was obtained at a discharge current density of 20 mA/g [109, 110]. Iwakura et al. reported that the calculated discharge capacity of the Mg<sub>2</sub>Ni-Ni composite is ~1090 mAh/g(Mg<sub>2</sub>Ni) [112], while a Mg<sub>2</sub>Ni-70 wt.% Ni (Mg<sub>2</sub>Ni/Ni = 1/1.28 in mole ratio) composite had a homogeneous amorphous structure and exhibited a maximum discharge capacity of ca. 1082 mAh/g(Mg<sub>2</sub>Ni) (636 mAh/g(Mg<sub>2</sub>Ni + Ni)) at 30 °C [111, 112]. However, the capacity decay of the Mg-based alloy electrode is still serious, which makes it difficult to use as an electrode material in practice.

Table 2 lists the capacity of MgNi-based alloy electrodes reported by various researchers. It is seen from Table 2 that the addition of other elements can increase the discharge capacities of Mg<sub>2</sub>Ni electrodes. Cui and co-workers reported a discharge capacity of 150 mAh/g for Mg<sub>1.9</sub>Al<sub>0.1</sub>Ni<sub>0.9</sub>Y<sub>0.1</sub> alloy [114, 115] and 90 mAh/g for Mg<sub>1.8</sub>Ti<sub>0.2</sub>Ni<sub>0.75</sub>Fe<sub>0.25</sub> alloy [116] compared with only 8 mAh/g for Mg<sub>2</sub>Ni alloy at a discharge current density of 5 mA/g.

### 3.2. Cycle Lives of Mg-Ni-Based Alloy Electrodes

When Mg is immersed in an alkaline solution, hydrogen gas generation and Mg(OH)<sub>2</sub> formation take place, but these reactions terminate soon after immersion because the Mg surface is coated with Mg(OH)<sub>2</sub>. Mg(OH)<sub>2</sub> could thus also form on the Mg<sub>2-x</sub>Ni alloy surfaces. Kuji et al. found that during the first charging–discharging cycle, the alloys were severely corroded. Especially during the discharging process, the alloys were anodically polarized, so that the maximum hydrogen concentration obtained by the second charging process was markedly reduced and as a result only a small discharge capacity was obtained [117].

Microencapsulation of Mg<sub>2</sub>Ni-type alloys by metal and alloy coatings can improve the electrode performance. Luo and Cui [118] increased the discharge capacity of Mg<sub>1.9</sub>Al<sub>0.1</sub>Ni<sub>0.9</sub>Y<sub>0.1</sub> alloy to about 175, 200, and 230 mAh/g at a current density of 10 mA/g by microencapsulation with Ni-B, Ni-P, and Ni-Pd-P, respectively. The discharge capacity of the bare Mg<sub>1.9</sub>Al<sub>0.1</sub>Ni<sub>0.9</sub>Y<sub>0.1</sub> alloy was only 140 mAh/g at the same discharge current density. Lei et al. prepared MgNi alloy by mechanical alloying (MA) and demonstrated discharge capacities of around 500 mAh/g at a current density of 20 mA/g [119, 120]. Mg<sub>1.9</sub>Al<sub>0.1</sub>Ni<sub>0.8</sub>Co<sub>0.1</sub>Mn<sub>0.1</sub> alloy fabricated by ball milling with Ni powder for 50 h showed good discharge capacity at a discharge current density of 50 mA/g [121].

Zhang et al. [113] reported that the cycle performance of MgNi<sub>x</sub> alloys can be significantly enhanced by increasing the  $x$  value. The X-ray patterns of the MgNi<sub>x</sub> alloys show that only broad peaks at around 40–45° were observed, indicating that amorphous MgNi<sub>x</sub> phases were formed for the MgNi, MgNi<sub>1.5</sub>, and MgNi<sub>2.0</sub> alloys shown in Figure 2. The charge–discharge capacities of MgNi<sub>x</sub> alloys as a function of the cycle number are shown in Figure 3.

The electrode containing the nickel ball-milled Mg<sub>1.8</sub>Ti<sub>0.2</sub>Ni alloy gave a discharge capacity of 720 mAh/g at a discharge current density of 50 mA/g and over 42 cycles to a specific capacity of 100 mAh/g [122]. A discharge capacity of 780 mAh/g was achieved at a discharge current

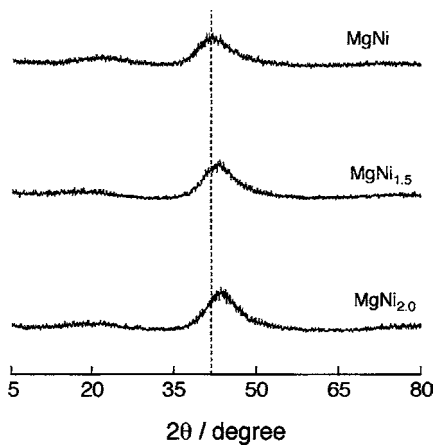


**Figure 2.** X-ray diffraction patterns of  $\text{MgNi}_x$  alloys ( $x = 1, 1.5$  and  $2.0$ ). Reprinted with permission from [113], S. G. Zhang et al., *J. Alloys Comp.* 293–295, 552 (1999). © 1999, Elsevier Science.

density of 50 mAh/g for Ni-coated  $\text{Mg}_2\text{Ni}_{0.9}\text{Mn}_{0.1}$  electrodes [123]. Figure 4 shows the discharge capacities of the bare, nickel ball-milled, and nickel coated  $\text{Mg}_2\text{Ni}_{0.9}\text{Mn}_{0.1}$  alloy electrodes as a function of cycle number. Figure 5 shows the discharge capacity as a function of the cycle number for  $\text{Mg}_2\text{Ni}$  alloy, ball-milled  $\text{Mg}_2\text{Ni}$  alloy, and  $\text{Mg}_2\text{Ni}$ -Ni composite. The  $\text{Mg}_2\text{Ni}$ -Ni composite exhibited a longer cycle life than the ball-milled  $\text{Mg}_2\text{Ni}$  alloy and  $\text{Mg}_2\text{Ni}$  alloy.

$\text{Mg}_{0.9}\text{Ti}_{0.06}\text{V}_{0.04}\text{Ni}$  alloy prepared by mechanical alloying showed better performance than either  $\text{Mg}_{0.9}\text{Ti}_{0.1}\text{Ni}$  or  $\text{Mg}_{0.9}\text{V}_{0.1}\text{Ni}$  alloy [124]. Figure 6 shows that the discharge capacity of  $\text{MgNi}$  alloy decreases greatly with increasing discharge current density, which may be due to the low electrochemical reactivity of the alloy surface and poor diffusivity of hydrogen into the alloy bulk [68]. In charge-discharge cycle tests, the partial substitution of Mg with Ti and V or surface modification with graphite suppressed the decay of discharge capacity with increasing cycle number.  $\text{Mg}_{0.9}\text{Ti}_{0.06}\text{V}_{0.04}\text{Ni}$  alloy modified with graphite exhibited further improved cycle performance as compared with either unmodified  $\text{Mg}_{0.9}\text{Ti}_{0.06}\text{V}_{0.04}\text{Ni}$  or  $\text{MgNi}$  alloy modified

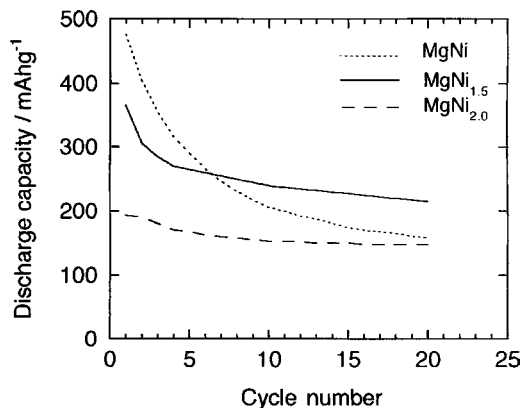


**Figure 3.** Discharge capacity as a function of the cycle number for the  $\text{MgNi}_x$  alloys ( $x = 1, 1.5$ , and  $2.0$ ). Reprinted with permission from [113], S. G. Zhang et al., *J. Alloys Comp.* 293–295, 552 (1999). © 1999, Elsevier Science.

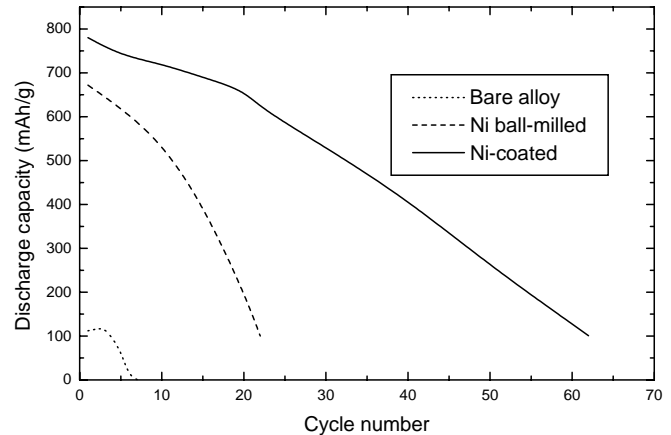


**Figure 4.** The discharge capacities of the bare, nickel ball-milled, and nickel-coated alloy  $\text{Mg}_2\text{Ni}_{0.9}\text{Mn}_{0.1}$  electrodes as a function of cycle number. Reprinted with permission from [129], H. K. Liu et al., *Materials Science Forum* 315–317, 545 (1999). © 1999, Trans Tech Publications Ltd.

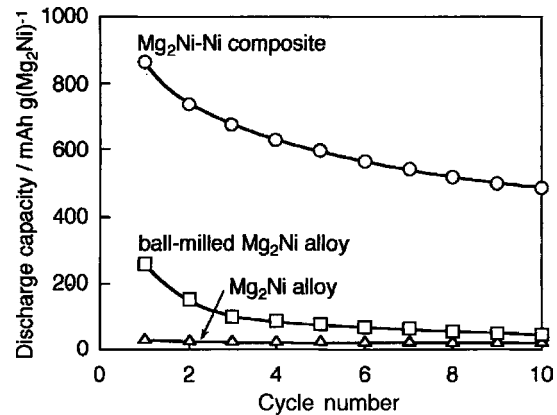


**Figure 5.** Discharge capacity ( $30^\circ\text{C}$ ) as a function of the cycle number for the  $\text{Mg}_2\text{Ni}$  alloy, ball-milled  $\text{Mg}_2\text{Ni}$  alloy, and  $\text{Mg}_2\text{Ni}$ -Ni composite electrodes. Reprinted with permission from [111], S. Nohara et al., *J. Alloys Comp.* 267, 76 (1998). © 1998, Elsevier Science.

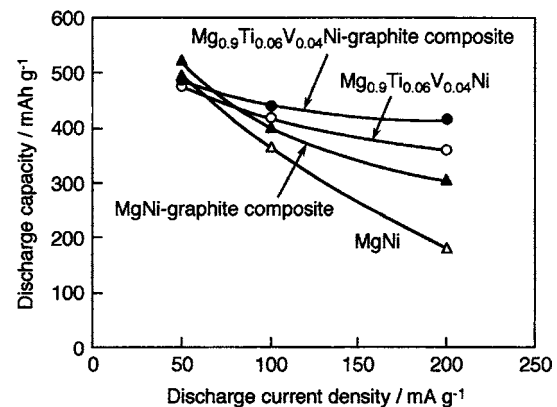


**Figure 6.** Discharge capacities at  $30^\circ\text{C}$  as a function of discharge current density for  $\text{MgNi}$ ,  $\text{Mg}_{0.9}\text{Ti}_{0.06}\text{V}_{0.04}\text{Ni}$ ,  $\text{MgNi}$ -graphite composite, and  $\text{Mg}_{0.9}\text{Ti}_{0.06}\text{V}_{0.04}\text{Ni}$ -graphite composite electrodes. Reprinted with permission from [68], C. Iwakura et al., *J. Solid State Ionics* 148, 499 (2002). © 2002, Elsevier Science.



**Table 3.** Discharge capacity and cycle life of the Mg-based alloy electrodes reported by various researchers.

Alloy composition	Capacity (mAh/g)	Cycle life to capacity (mAh/g)	Ref.		
Mg <sub>2</sub> Ni + Ni	750	20	(250 mAh/g)	[110]	
Mg <sub>1.9</sub> Al <sub>0.1</sub> Ni + Ni (Mechanical grinding)	690	20	(400 mAh/g)		
Mg <sub>2</sub> Ni	95	8	(0 mAh/g)	[129]	
Mg <sub>2</sub> Ni (ball-milled)	680	18	(100 mAh/g)		
Mg <sub>2</sub> Ni (Ni-coated)	756	56	(100 mAh/g)		
Mg <sub>2</sub> Ni <sub>0.9</sub> Mn <sub>0.1</sub>	118	7	(0 mAh/g)		
Mg <sub>2</sub> Ni <sub>0.9</sub> Mn <sub>0.1</sub> (ball-milled)	672	20	(100 mAh/g)		
Mg <sub>2</sub> Ni <sub>0.9</sub> Mn <sub>0.1</sub> (Ni-coated)	780	62	(100 mAh/g)		
BM- Mg <sub>2</sub> Ni	420	12	(100 mAh/g)	[123]	
BM-Ni-Mg <sub>2</sub> Ni	680	28	(100 mAh/g)		
BM- Mg <sub>1.8</sub> Ti <sub>0.2</sub> Ni	490	20	(100 mAh/g)		
BM-Ni-Mg <sub>1.8</sub> Ti <sub>0.2</sub> Ni	720	42	(100 mAh/g)		
BM-Mg <sub>1.8</sub> Ce <sub>0.2</sub> Ni	414	17	(100 mAh/g)		
BM-Ni-Mg <sub>1.8</sub> Ce <sub>0.2</sub> Ni	658	31	(100 mAh/g)		
BM-Mg <sub>1.8</sub> Mn <sub>0.2</sub> Ni	580	15	(100 mAh/g)		
BM-Ni-Mg <sub>1.8</sub> Mn <sub>0.2</sub> Ni	560	32	(100 mAh/g)		
BM-Mg <sub>1.8</sub> Co <sub>0.2</sub> Ni	470	16	(100 mAh/g)		
BM-Mg <sub>1.8</sub> Co <sub>0.2</sub> Ni	710	38	(100 mAh/g)		
Mg <sub>2</sub> Ni	55	7	(0 mAh/g)		
Mg <sub>1.9</sub> Ti <sub>0.1</sub> Ni	88	16	(0 mAh/g)		
Mg <sub>1.8</sub> Ti <sub>0.2</sub> Ni	90	19	(0 mAh/g)		
Mg <sub>1.9</sub> Ce <sub>0.1</sub> Ni	83	14	(0 mAh/g)		
Mg <sub>1.8</sub> Ce <sub>0.2</sub> Ni	85	17	(0 mAh/g)		
Mg <sub>2</sub> Ni <sub>0.9</sub> Mn <sub>0.1</sub>	78	8	(0 mAh/g)		
Mg <sub>2</sub> Ni <sub>0.8</sub> Mn <sub>0.2</sub>	74	7	(0 mAh/g)		
Mg <sub>2</sub> Ni <sub>0.9</sub> Co <sub>0.1</sub>	76	9	(0 mAh/g)		
Mg <sub>2</sub> Ni <sub>0.8</sub> Co <sub>0.2</sub>	70	10	(0 mAh/g)		
Mg <sub>1.9</sub> Al <sub>0.1</sub> Ni <sub>0.8</sub> Co <sub>0.1</sub> Mn <sub>0.1</sub> (ball-milled for 50 h)	630	22	(243 mAh/g)		[121]
Mg <sub>1.9</sub> Al <sub>0.1</sub> Ni <sub>0.8</sub> Co <sub>0.1</sub> Mn <sub>0.1</sub> (ball-milled for 120 h)	510	22	(280 mAh/g)		
MgNi	490	20	(150 mAh/g)		[113]
MgNi <sub>1.5</sub>	370	20	(210 mAh/g)		
MgNi <sub>2</sub> (Mechanical alloying)	200	20	(~150 mAh/g)		
Mg <sub>0.9</sub> Ti <sub>0.06</sub> V <sub>0.04</sub> Ni	510	20	(360 mAh/g)	[124]	
Mg <sub>0.9</sub> Ti <sub>0.1</sub> Ni	500	20	(275 mAh/g)		
Mg <sub>0.9</sub> V <sub>0.1</sub> Ni	480	20	(275 mAh/g)		
MgNi (Mechanical alloying)	520	20	(200 mAh/g)		

with graphite [125]. The partial substitution of Ti for Ni in Mg<sub>50</sub>Ni<sub>50</sub> increases both the discharge capacity and the degradation rate. The substitution of Zn for Ni shows no effect on the discharge capacity but increases the deterioration rate. The substitution of Fe, W, Cu, Al, or C for Ni decreases both the deterioration rate and the discharge capacity, while the substitution of Se, Sb, Co, or Si decreases both the discharge capacity and the cycle life [126, 127]. Woo and Lee reported that the discharge capacity of a nanostructured Mg<sub>2</sub>Ni electrode is much higher than that of a polycrystalline one, while the partial substitution of Cu for Ni increased the hydrogen desorption of the nanostructured Mg<sub>2</sub>Ni electrode at 30 °C [128]. All the investigation suggests that the amorphous Mg-based alloys differ greatly

in nature from the crystalline ones, and Ni may play an extremely important role in facilitating the absorption and desorption of hydrogen.

Table 3 lists the discharge capacity and cycle life of the Mg-based alloy electrodes at different discharge current densities. The best performance in discharge capacity and cycle life is found with Ti-containing alloys. It is clearly seen that the discharge capacity, high-rate discharge capability, and cycle life of these Mg-based alloy electrodes were greatly improved by the ball-milling and nickel-coating processes. For example, the discharge capacities of the bare Mg<sub>2</sub>Ni<sub>0.9</sub>Mn<sub>0.1</sub> alloy electrode at 50 mA/g and 100 mA/g were only 118 mAh/g and 5 mAh/g, respectively, and the corresponding discharge capacities of the nickel-coated

**Table 4.** Comparison of LaNi<sub>5</sub>, ZrV<sub>2</sub>, and Mg<sub>2</sub>Ni hydrogen storage alloys as the negative electrode of Ni-MH batteries.

Type of alloys	AB <sub>5</sub>	AB <sub>2</sub>	A <sub>2</sub> B
Example of alloys	LaNi <sub>5</sub> MmNi <sub>3.55</sub> Co <sub>0.75</sub> Mn <sub>0.4</sub> Al <sub>0.3</sub>	ZrV <sub>2</sub> Cubic or hexagonal [137] C15, Zr <sub>3</sub> V <sub>3</sub> O, BCC [138]	Mg <sub>2</sub> Ni Hexagonal
Structure type	Mm (mischmetal including La, Ce, Pr, Nd) Hexagonal [137]		Amorphous-like state [110]
Example of hydrides	LaNi <sub>5</sub> H <sub>6</sub>	ZrV <sub>2</sub> H <sub>5.3</sub> [137]	Mg <sub>2</sub> NiH <sub>4</sub>
Hydrogen content wt.%	1.4 [138]	2.2, BCC [138]	3.6
Theoretical capacity (mAh/g)	372	763	999
Practical capacity (mAh/g)	300	400	750 [110, 129] 780 [111] 870 [111] 1082 [112]
Mg <sub>2</sub> Ni-Ni composite			
Alloy density (g/cm <sup>3</sup> )	7.8	5.4	2.5
Electrical activation (cycles at 0.2C rate)	5	10	1
High-rate discharge	0.2C to 5C	0.2C to 1C	0.2C to 0.4C
Capacity decay (0.2C rate)	10% (500 cycles)	8% (1000 cycles)	10% (50 cycles)
Self-discharge	high	low	high
Discharge plate potential (mV vs Hg/HgO)	−810	−810	−830
Commercial price (\$/Kg)	15	22.5	7.5
Advantages	Environment acceptable Higher specific energy Higher charge-rate capability compared with Ni/Cd batteries	Environment acceptable Higher specific energy Higher charge-rate capability compared with Ni/Cd batteries	High capacity Light weight Relative abundance Lower cost
Disadvantages	Low capacity Expensive Poisonous element Co Deterioration and disintegration of electrodes	Low capacity Expensive Poisonous element V Slow electrode activation Poor high rate discharge Low charging efficiency	Serious capacity decay  Poor hydriding/dihydriding kinetics
Present use	MmNi <sub>3.55</sub> Co <sub>0.75</sub> Mn <sub>0.4</sub> Al <sub>0.3</sub> is commercialized and mostly used in Ni-MH battery.	Used by several companies	Under development

Mg<sub>2</sub>Ni<sub>0.9</sub>Mn<sub>0.1</sub> electrodes at 50 mA/g and 100 mA/g were 780 mAh/g and 546 mAh/g.

The reasons for the short cycle life of MgNi-based alloy electrode are that (1) magnesium oxide easily forms on the alloy surface exposed to air and the MgO layer prevents hydrogen molecules from penetrating into the bulk; (2) Mg on the surface of MgNi-based alloy is easily corroded to Mg(OH)<sub>2</sub> in alkaline solutions, and the insoluble Mg(OH)<sub>2</sub> layer may prevent the diffusion of hydrogen into the alloy bulk to form the hydride. So for improving

the anticorrosion properties and overcoming the kinetic limitations of MgNi-based alloys, it is necessary to suppress the oxidation of the alloys. Yang et al. [133] reported that the electrochemical properties of the ternary alloys Mg<sub>2-x</sub>Mm<sub>x</sub>Ni ( $x < 0.2$ ) show that the substitution of Mm for Mg reduces the reaction resistances and improves the absorption/desorption properties. Zhang et al. reported that the loss of the active hydrogen-absorbing element Mg is definitely the main cause for cycling capacity deterioration [134]. Han et al. have reported that Ni and graphite can

protect the Mg from oxidation in nanocrystalline and amorphous Mg<sub>2</sub>Ni-based alloys for Ni-MH batteries: after 50 cycles, the degradation of the bare electrode was 94% of maximum capacity, but that of coated electrode with Ni and graphite was 45 and 76% of maximum capacity [135]. Han et al. reported from electrochemical impedance spectroscopy analysis that the charge transfer resistance between the Mg<sub>0.7</sub>Ti<sub>0.3</sub>Ni alloy and the electrolyte does not increase during charge–discharge cycles. They also reported from auger electron spectroscopy that the thickness of the surface oxide layer on the Mg<sub>0.7</sub>Ti<sub>0.3</sub>Ni alloy is thinner than that of the oxide layer on the MgNi alloy and from X-ray photoelectron spectroscopy that the magnesium in the Mg<sub>0.7</sub>Ti<sub>0.3</sub>Ni alloy exists in a metallic state while the titanium forms an oxide layer, indicating that the titanium oxide layer not only prevents further oxidation of magnesium, but also induces a nickel-enriched layer on the alloy surface [136].

Table 4 is the basic information on comparison of the magnesium–nickel hydride alloys with two current battery materials. It is clear that the practical capacity is nearly double the current one while the cost is about one-half to one-third of the current cost. The capacity has been reached 750–780 mAh/g (Mg<sub>2</sub>Ni), the remarkable value for Mg-based hydrogen storage alloys [109–112, 123]. The capacity decay of the nickel-coated alloy electrode was 10% after 50 cycles [123] at high-rate charge–discharge (50 mA/g). This breakthrough has a real commercial potential.

#### 4. CONCLUSIONS

The MgNi-based alloys are promising hydrogen storage materials because of their high storage capacities and the abundance of the constituent elements in nature. However, they are inadequate for practical use in hydrogen storage applications because of their poor hydriding and dehydriding properties at ambient temperature and easy corrosion in alkaline solutions. The kinetics of the hydriding/dehydriding reactions of Mg-based alloy electrodes can be greatly improved by the processes of ball milling with Ni (or graphite) and chemical coating. The amorphous Mg-based alloys differ greatly from the crystalline ones, and Ni (or graphite) may play an extremely important role in facilitating the absorption and desorption of hydrogen. A surface modification to protect MgNi alloys from corrosion is very effective in improving hydrogen desorbability and charge–discharge cycle performance of the alloys for practical applications. From the encouraging results, it is expected that Mg-based alloys will be excellent negative electrode materials of the third generation for nickel–metal hydride batteries.

#### GLOSSARY

**Amorphous alloy** For a single-phase solid alloy at amorphous state, it has no crystal lattice, no grain boundaries, and no dislocations.

**C rate** The discharge or charge current, in milliamperes (mA), expressed as a multiple of the rated capacity in milliampere-hours (mAh).

**Capacity** The total number of milliampere-hours that can be withdrawn from a fully charged battery under specified conditions of discharge.

**Cycle** Set of charge and discharge steps for a secondary battery.

**Cycle life** The number of cycles that can be delivered by a secondary battery before it fails to meet specified performance criteria.

**Electrode** The conductor and associated active materials at which an electrochemical reaction occurs.

**Nanocrystalline alloys** They are defined as single- or multiphase polycrystals with a crystal size typically within the range 1–100 nm.

**Ni-MH battery** It is composed of nickel hydroxide positive electrodes and metal hydride negative electrodes using LaNi<sub>5</sub>.

**Rechargeable battery** A cell which may be restored to a fully charged state by passage of an electric current through the cell (opposite direction to that used in discharging the cell.)

**Specific capacity or capacity density** Ah/kg (ampere hour per kilogram) or mAh/g (milliampere per gram).

#### ACKNOWLEDGMENTS

Financial support by the Australian Research Council/Department of Education, Training and Youth Affairs, the Strategic Partnerships with Industry–Research and Training (SPIRT) Scheme Grant (File Number: C00001879) is gratefully acknowledged. Thanks are given to Drs. B. Luan, N. Cui, J. Chen, and L. Sun for their valuable research work during their time at the University of Wollongong. The author also thanks Dr. T. Silver for valuable suggestions for improving the manuscript.

#### REFERENCES

1. J. J. Reilly and R. H. Wiswall, *Inorg. Chem.* 6, 2220 (1967).
2. J. F. Stempfer, C. E. Holley, and F. F. Suttle, *J. Am. Chem. Soc.* 82, 3504 (1960).
3. C. Iwakura, S. Hazui, and H. Inoue, *Electrochimica Acta* 41, 471 (1996).
4. S. Orimo, K. Ikeda, H. Fujii, Y. Kitano, and K. Yamamoto, *Acta Mater.* 45, 2271 (1997).
5. L. B. Wang, Y. J. Wang, and H. T. Yuan, *J. Mater. Sci. Tech.* 17, 590 (2001).
6. J. D. Bernal, *Nature* 185, 68 (1960).
7. P. H. Gaskell, *Nature* 276, 484 (1978).
8. W. Klement, Jr., R. H. Willems, and P. Duwez, *Nature* 187, 869 (1960).
9. C. C. Koch, O. B. Cavin, C. G. Mckamey, and J. O. Scorbrough, *Appl. Phys. Lett.* 43, 1017 (1983).
10. D. Turnbull, *Metall. Trans.* A12, 695 (1981).
11. S. D. Dahlgren, "Proceedings of the 3<sup>rd</sup> International Conference on Rapidly Quenched Metals," Vol. 2, p. 36.
12. J. A. Borders, *Annu. Rev. Mater. Sci.* 9, 313 (1979).
13. S. Hoshino, H. A. Laitinen, and G. B. Hoflund, *J. Electrochem. Soc.* 133, 681 (1986).
14. H. S. Chen, *Rep. Prog. Phys.* 43, 353 (1980).
15. J. Eckert, L. Schultz, E. Hellstern, and K. Urban, *J. Appl. Phys.* 64, 3224 (1988).

16. H. Gleiter, *Prog. Mater. Sci.* 33, 223 (1989).
17. L. Sun, H. K. Liu, and S. X. Dou, *Mater. Lett.* 33, 79 (1997).
18. R. Rofagha, R. Langer, A. M. El-sherik, U. Erb, G. Palumbo, and K. T. Aust, *Scr. Metall. Mater.* 25, 2867 (1991).
19. R. B. Inturi and Z. Szklavska-Smialowska, *Corrosion* 48, 298 (1992).
20. J. S. C. Jang and C. C. Koch, *Scr. Metall.* 22, 677 (1988).
21. J. Harvath, R. Birringer, and H. Gleiter, *Solid State Commun.* 62, 319 (1987).
22. X. D. Liu, J. T. Wang, and B. Z. Ding, *Scr. Metall. Mater.* 28, 59 (1993).
23. J. Rupp and R. Birringer, *Phys. Rev. B* 36, 7888 (1987).
24. R. Birringer, *Mater. Sci. Eng.* A117, 33 (1989).
25. G. Herzer, *Mater. Sci. Eng.* A133, 1 (1991).
26. H. E. Schaefer, R. Wurschum, R. Birringer, and H. Gleiter, *J. Less-Common Met.* 140, 161 (1988).
27. H. Ouyang, B. Fultz, and H. Kuwano, in “Nanophases and Nanocrystalline Structures” (R. D. Shell and J. M. Sanchez, Eds.), p. 95. TMS, Warrendale, PA, 1993.
28. D. Wolf and F. F. Lutsko, *Phys. Rev. Lett.* 60, 1170 (1988).
29. D. Wolf and F. F. Lutsko, *J. Mater. Res.* 4, 1427 (1989).
30. R. W. Siegel, *Ann. Rev. Mater. Sci.* 21, 559 (1991).
31. T. Mutschele and R. Kirchheim, *Scr. Metall.* 21, 1101 (1987).
32. R. Birringer, H. Gleiter, H. P. Klein, and P. Marquart, *Phys. Lett.* 102A, 365 (1984).
33. C. C. Koch, *Nanostructured Mater.* 2, 109 (1993).
34. W. Chang, G. Skandan, S. C. Danforth, and B. H. Kear, *Nanostructured Mater.* 4, 507 (1994).
35. H. Chang, C. J. Alstetter, and R. S. Averback, *J. Mater. Res.* 7, 2962 (1992).
36. B. H. Kear and L. E. Mccandlish, *Nanostructured Mater.* 3, 19 (1993).
37. G. Palumbo, S. J. Thorpe, and K. T. Aust, *Scr. Metall. Mater.* 24, 1437 (1990).
38. R. A. Roy and R. Roy, *Mater. Res. Bull.* 19, 169 (1984).
39. A. E. Berkowitz and J. L. Walter, *J. Mater. Res.* 2, 277 (1987).
40. C. H. Chou and J. Phillips, *J. Mater. Res.* 7, 2107 (1992).
41. D. J. Li, B. Z. Ding, B. Yao, Z. Q. Hu, A. M. Wang, S. L. Li, and W. D. Wei, *Nanostructured Mater.* 4, 323 (1994).
42. R. W. Siegel, *MRS Bull.* 15, 60 (1990).
43. C. C. Koch, *Nanostructured Mater.* 9, 13 (1997).
44. J. Van-Vucht, F. A. Kuijpers, and H. Bruning, *Philips Res. Rept.* 25, 133 (1990).
45. J. J. Reilly and R. H. Wiswall, Jr., *Inorg. Chem.* 13, 218 (1974).
46. F. E. Lynch, *J. Less-Common Met.* 172–174, 943 (1991).
47. I. Uehara, T. Sakai, and H. Ishikawa, *J. Alloys Comp.* 253/254, 635 (1997).
48. T. Sakai, I. Uehara, and H. Ishikawa, *J. Alloys Comp.* 293–295, 762 (1999).
49. G. Sandrock, *J. Alloys Comp.* 293–295, 877 (1999).
50. A. Anani, A. Visintin, K. Petrov, S. Srinivasan, J. J. Reilly, J. R. Johnson, R. B. Schwarz, and P. B. Desch, *J. Power Sources* 47, 261 (1994).
51. J. J. Reilly and R. H. Wiswall, Jr., *Inorg. Chem.* 7, 2254 (1968).
52. J. J. Reilly and R. H. Wiswall, Jr., *Inorg. Chem.* 6, 2220 (1967).
53. Z. Luz, J. Genossar, and P. S. Rudman, *Scr. Metall.* 14, 275 (1980).
54. Z. Luz, J. Genossar, and P. S. Rudman, *J. Less-Common Met.* 73, 113 (1980).
55. A. Karty, J. Genossar, and P. S. Rudman, *J. Appl. Phys.* 50, 7200 (1979).
56. H. Oesterricher, K. Ensslen, A. Kerlin, and E. Bucher, *Mater. Res. Bull.* 15, 275 (1980).
57. K. Yvon, J. Schefer, and F. Stucki, *Inorg. Chem.* 20, 2776 (1981).
58. M. H. Mintz, Z. Gavra, G. Kimmel, and Z. Hadari, *J. Less-Common Met.* 74, 263 (1980).
59. D. Lupu, A. Biris, and E. Indrea, *Int. J. Hydrogen Energy* 7, 783 (1982).
60. J. P. Darnaudery, B. Darriet, and M. Pezat, *Int. J. Hydrogen Energy* 8, 705 (1983).
61. T. Hirata, T. Matsumoto, M. Amano, and Y. Sasaki, *J. Less-Common Met.* 89, 85 (1983).
62. D. Lupu, A. Biri, E. Indera, N. Alden, R. V. Bucur, and M. Morariu, *Int. J. Hydrogen Energy* 8, 797 (1983).
63. B. Darriet, A. Hbika, and M. Pezat, *J. Less-Common Met.* 75, 43 (1980).
64. M. Pezat, A. Hbika, and B. Darriet, *Mater. Res. Bull.* 15, 139 (1980).
65. M. Pezat, B. Darriet, and P. Hagemuller, *J. Less-Common Met.* 74, 427 (1980).
66. J. P. Darnaudery, M. Pezat, and B. Darriet, *J. Less-Common Met.* 92, 199 (1983).
67. M. Au, J. Wu, and Q. D. Wang, *Int. J. Hydrogen Energy* 20, 141 (1995).
68. C. Iwakura, S. Nohara, and H. Inoue, *Solid State Ionics* 148, 499 (2002).
69. M. Khrussanova, M. Terzieva, P. Peshev, and E. Y. Ivanov, *Mater. Res. Bull.* 22, 405 (1987).
70. P. Peshev, M. Khrussanova, D. Chakarov, and E. Y. Ivanov, *Mater. Res. Bull.* 24, 207 (1989).
71. M. Khrusanova, M. Terzieva, and P. Peshev, *Int. J. Hydrogen Energy* 15, 799 (1990).
72. K. Aoki, H. Aoyagi, A. Memezawa, and T. Masumoto, *J. Alloys Comp.* 203, L7 (1994).
73. M. Y. Song, *J. Mater. Sci.* 30, 1343 (1995).
74. M. Y. Song, *Int. J. Hydrogen Energy* 20, 221 (1995).
75. M. Y. Song, J. Manaud, and B. Darriet, *J. Alloys Comp.* 282, 243 (1999).
76. H. Imamura and N. Sakasai, *J. Alloys Comp.* 231, 810 (1995).
77. H. Imamura, N. Sakasai, and Y. Kajii, *J. Alloys Comp.* 232, 218 (1996).
78. H. Imamura, N. Sakasai, and T. Fujinaga, *J. Alloys Comp.* 253/254, 34 (1997).
79. H. Imamura, Y. Takesue, T. Akimoto, and S. Tabata, *J. Alloys Comp.* 293–295, 564 (1999).
80. S. Nohara, H. Inoue, Y. Fukumoto, and C. Iwakura, *J. Alloys Comp.* 252, L16 (1997).
81. Y. Zang, H. Yang, H. Yuan, Z. Zhou, and D. Song, *J. Alloys Comp.* 269, 278 (1998).
82. M. Terzieva, M. Khrussanova, P. Peshev, and D. Radev, *Int. J. Hydrogen Energy* 20, 53 (1995).
83. K. J. Gross, P. Spatz, A. Zuttel, and L. Schlapbach, *J. Alloys Comp.* 240, 206 (1996).
84. K. J. Gross, P. Spatz, A. Zuttel, and L. Schlapbach, *J. Alloys Comp.* 261, 276 (1997).
85. M. Terzieva, M. Khrussanova, and P. Peshev, *J. Alloys Comp.* 267, 235 (1998).
86. L. Zaluski, A. Zaluska, and J. O. Strom-Olsen, *J. Alloys Comp.* 217, 245 (1995).
87. K. Tanaka, Y. Kanda, M. Furuhashi, K. Saito, K. Kuroda, and H. Saka, *J. Alloys Comp.* 293–295, 521 (1999).
88. S. Orimo, K. Ikeda, H. Fujii, Y. Fujikawa, Y. Kitano, and K. Yamamoto, *Acta Mater.* 45, 2271 (1997).
89. S. Orimo, H. Fujii, K. Ikeda, Y. Fujikawa, and Y. Kitano, *J. Alloys Comp.* 253/254, 94 (1997).
90. L. Zaluski, S. Hosatte, T. Tessier, D. H. Ryan, J. O. Strom-Olsen, M. L. Trudeau, and R. Schulz, *Z. Phys. Chem.* 183, 1067 (1994).
91. L. Zaluski, P. Tessier, D. H. Ryan, C. B. Doner, A. Zaluska, J. O. Strom-Olsen, M. L. Trudeau, and R. Schulz, *J. Mater. Res.* 8, 3059 (1993).
92. K. Funaki, S. Orimo, H. Fujii, and H. Sumida, *J. Alloys Comp.* 270, 160 (1998).
93. Y. Tsushio, H. Enoki, and E. Akiba, *J. Alloys Comp.* 281, 301 (1998).

94. N. Terashita, M. Takahashi, K. Kobayashi, T. Sasai, and E. Akiba, *J. Alloys Comp.* 293–295, 541 (1999).
95. H. B. Yang, H. T. Yuan, J. T. Ji, H. Sun, Z. X. Zhou, and Y. S. Zhang, *J. Alloys Comp.* 330, 640 (2002).
96. H. Zijlstra and F. F. Westendorp, *Solid State Commun.* 7, 857 (1969).
97. E. W. Justi, H. H. Ewe, A. W. Kalberlah, N. M. Saridakis, and M. H. Schaefer, *Energy Convers.* 10, 183 (1970).
98. H. H. Ewe, E. W. Justi, and K. Stephan, *Energy Convers.* 13, 109 (1973).
99. G. Bronoel, J. Sarradin, A. Percheron-Guegan, J. C. Achard, and L. Schlapbach, *Int. J. Hydrogen Energy* 1, 251 (1976).
100. G. Bronoel, J. Sarradin, A. Percheron-Guegan, and J. C. Achard, *Mater. Res. Bull.* 13, 1265 (1978).
101. M. H. J. Van Rijswijk, in “Hydrides for Energy Storage” (A. F. Andresen and A. J. Maeland, Eds.), p. 126. Pergamon Press, Oxford, 1978.
102. T. L. Markin and R. M. Dell, *J. Electroanal. Chem.* 118, 217 (1981).
103. T. L. Markin, R. Bennett, N. J. Bridger, and R. M. Dell, in “Power Sources” (J. Thompson, Ed.), Vol. 8, p. 445. Academic Press, London, 1981.
104. T. Sakai, M. Matuoka, and C. Iwakura, in “Handbook on the Physics and Chemistry of Rare Earths” (K. A. Gschneidner, Jr. and L. Eyring, Eds.), Vol. 21, p. 133. Elsevier Science, New York Amsterdam, 1995.
105. S. R. Ovshinsky, M. A. Fetcenko, and J. Ross, *Science* 260, 176 (1993).
106. C. Iwakura and M. Matuoka, *Prog. Batteries & Battery Materials* 10, 81 (1991).
107. S. Orimo and H. Fujii, *J. Alloys Comp.* 232, L16 (1997).
108. C. Iwakura, S. Nohara, H. Inoue, and Y. Fukumoto, *J. Chem. Soc. Chem. Commun.* 1831 (1996).
109. T. Kohno, S. Tsuruta, and M. Kanda, *J. Electrochem. Soc.* 143, L198 (1996).
110. T. Kohno and M. Kanda, *J. Electrochem. Soc.* 144, 2384 (1997).
111. S. Nohara, N. Fujita, S. G. Zhang, H. Inoue, and C. Iwakura, *J. Alloys Comp.* 267, 76 (1998).
112. C. Iwakura, H. Inoue, S. G. Zhang, and S. Nohara, *J. Alloys Comp.* 270, 142 (1998).
113. S. G. Zhang, Y. Hara, T. Morikawa, H. Inoue, and C. Iwakura, *J. Alloys Comp.* 293–295, 552 (1999).
114. N. Cui, B. Luan, H. K. Liu, and S. X. Dou, *J. Power Sources* 63, 209 (1996).
115. N. Cui, B. Luan, H. J. Zhao, H. K. Liu, and S. X. Dou, *J. Alloys Comp.* 233, 236 (1996).
116. N. Cui, B. Luan, H. K. Liu, H. J. Zhao, and S. X. Dou, *J. Power Sources* 55, 263 (1995).
117. T. Kuji, H. Nakano, and T. Aizawa, *J. Alloys Comp.* 330–336, 590 (2002).
118. J. L. Luo and N. Cui, *J. Alloys Comp.* 264, 299 (1998).
119. Y. Q. Lei, Y. M. Wu, Q. M. Yang, J. Wu, and Q. D. Wang, *Z. Phys. Chem.* 183, 379 (1994).
120. D. L. Sun, Y. Q. Lei, W. H. Liu, J. J. Jiang, J. Wu, and Q. D. Wang, *J. Alloys Comp.* 231, 621 (1995).
121. L. Sun, H. K. Liu, D. H. Bradhurst, and S. X. Dou, *Electrochem. Solid-State Lett.* 2, 121 (1999).
122. J. Chen, P. Yao, D. H. Bradhurst, S. X. Dou, and H. K. Liu, *J. Alloys Comp.* 293–295, 675 (1999).
123. J. Chen, D. H. Bradhurst, S. X. Dou, and H. K. Liu, “Proceedings of IMEA Conference,” 1998, pp. 615–620.
124. C. Iwakura, R. Shin-ya, K. Miyanoara, S. Nohara, and H. Inoue, *Electrochimica Acta* 46, 2781 (2001).
125. C. Iwakura, H. Inoue, S. Nohara, R. Shin-ya, S. Kurosaka, and K. Miyanoara, *J. Alloys Comp.* 330, 636 (2002).
126. W. H. Liu, H. Q. Wu, Y. Q. Lei, Q. D. Wang, and J. Wu, *J. Alloys Comp.* 261, 289 (1997).
127. Y. Q. Lei, Y. M. Wu, Q. M. Yang, J. Wu, and Q. D. Wang, *Zeitschrift für Physikalische Chemie* Bd. 183, S. 379, 1419 (1994).
128. J. H. Woo and K. S. Lee, *J. Electrochem. Soc.* 146, 819 (1999).
129. H. K. Liu, J. Chen, L. Sun, D. H. Bradhurst, and S. X. Dou, *Materials Science Forum* 315–317, 545 (1999).
130. S. G. Zhang, Y. Hara, S. Suda, T. Morikawa, H. Inoue, and C. Iwakura, *J. Solid State Electrochem.* 5, 23 (2001).
131. Y. S. Zhang, H. B. Yang, H. T. Yuan, E. D. Yang, Z. X. Zhou, and D. Y. Song, *J. Alloys Comp.* 269, 278 (1998).
132. C. Iwakura, S. Nohara, S. G. Zhang, and H. Inoue, *J. Alloys Comp.* 285, 246 (1999).
133. H. B. Yang, H. Sun, E. D. Yang, F. Gao, H. T. Yuan, Z. X. Zhou, and S. H. Guo, *J. Electrochem. Soc.* 149, A543 (2002).
134. Y. Zhang, S. Q. Li, L. X. Chen, Y. Q. Lei, and D. Q. Wang, *Transactions of Nonferrous Metals Society of China* 12, 238 (2002).
135. S. S. Han, H. Y. Lee, N. H. Goo, W. T. Jeong, and K. S. Lee, *J. Alloys Comp.* 330, 841 (2002).
136. S. C. Han, P. S. Lee, J. Y. Lee, A. Zuttel, and L. Schlapbach, *J. Alloys Comp.* 306, 219 (2000).
137. G. G. Libowitz, *Electrochemical Society Proceedings* 92-5, 3 (1993).
138. E. Akiba and H. Iba, *Intermetallics* 6, 461 (1998).
139. L. Wang, Y. Tang, Y. Wang, Q. Li, H. Song, and H. Yang, *J. Alloys Comp.* 337, 297 (2002).
140. S. Ruggeri, C. Lenain, L. Roue, G. Liang, J. Huot, and R. Schulz, *J. Alloys Comp.* 339, 195 (2002).
141. J. S. Kim, C. R. Lee, J. W. Choi, and S. G. Kang, *J. Power Sources* 104, 201 (2002).
142. S. Yamaura, H. Kim, H. Kimura, A. Inoue, and Y. Arata, *J. Alloys Comp.* 339, 230 (2002).
143. D. Mu, Y. Hatano, T. Abe, and K. Watanabe, *J. Alloys Comp.* 334, 232 (2002).
144. S. Ruggeri, L. Roue, G. Liang, J. Huot, and R. Schulz, *J. Alloys Comp.* 343, 170 (2002).





# Magnetic Field Effects in Nanostructures

R. Riera, J. L. Marín, H. León

*Universidad de Sonora, Hermosillo, Sonora, México*

R. Rosas

*Universidad de Sonora, Hermosillo, Sonora, México*

## CONTENTS

1. Introduction
  2. Effect of Static External Magnetic Field on the Quasi-Particle Energy Levels in the Low Dimensional Structures
- Glossary  
References

## 1. INTRODUCTION

In recent years, there has been renewed interest in the problem of motion of charge carriers in nanostructured systems, perturbed by external magnetic fields. The principal tool for their study has been the so-called “effective mass approximation” or “envelope function approximation,” which replaces the effect of the periodic field by a mass tensor, the elements of which are determined by the unperturbed band structures.

We can consider the crystal as a quantum system formed by two subsystems, a gas of electrons and a gas of phonons. All the phenomena or elementary excitations that take place in a solid are given by one of these two subsystems or by their interaction, which is known as electron–phonon coupling, or also for the answer that each one of them separately, or together, gives to an external perturbation, which can be represented by a impurity potential, an electric field, a wave of light or acoustics, a thermal source, a barrier potential, or finally a magnetic field.

Between the elementary excitations and quasi-particles more well known in the solids we can mention the following: excitons, polarons, plasmons, polaritons, magnons, Cooper pairs, etc. The definition of a solid as a mixture of electrons and phonons is implicit to the consideration of the electron as a quasi-particle and of the phonon as an elementary excitation.

When a crystal undergoes to the presence of a magnetic field, a series of phenomena can occur that involves the electron as much as the phonon and their interaction or coupling. We can distinguish four types of phenomena or fundamental effects, such as:

- (i) The interaction of the orbital angular moment of the electron with the magnetic field. In the semiconductors and the metals this phenomenon gives rise to Landau levels.
- (ii) The interaction of the angular moment of spin of the electron with the magnetic field. In the semiconductors this phenomenon gives rise to splitting of each Landau level in two.
- (iii) The interaction of the orbital angular moment of the electron with the phonon and both with the magnetic field. This is known as the electron–magnetophonon resonance phenomenon.
- (iv) The interaction of the angular moment of spin of the electron with the phonon and both with the magnetic field. This is known as the spin–magnetophonon resonance phenomenon.

These four phenomena are shown in Figure 1.

The polar semiconductors are artificially created compounds, uniting two or three elements of the periodic table. The binary polar semiconductors generally are formed by III–V, II–V, and III–VII chemical elements, although the most abundant and exploited in the technological applications are the first two. The ternary compounds are semiconductors binary doped with a metal. When this metal is of magnetic origin such as Mn, Fe, Zn, and Ni, then they are called diluted magnetic semiconductors.

One of the most significant movements in semiconductor physics has been the progressive miniaturization of devices. On the one hand, this led to explosive growth in computer technology; on the other hand, the opportunity to fabricate devices with characteristic dimensions significantly below

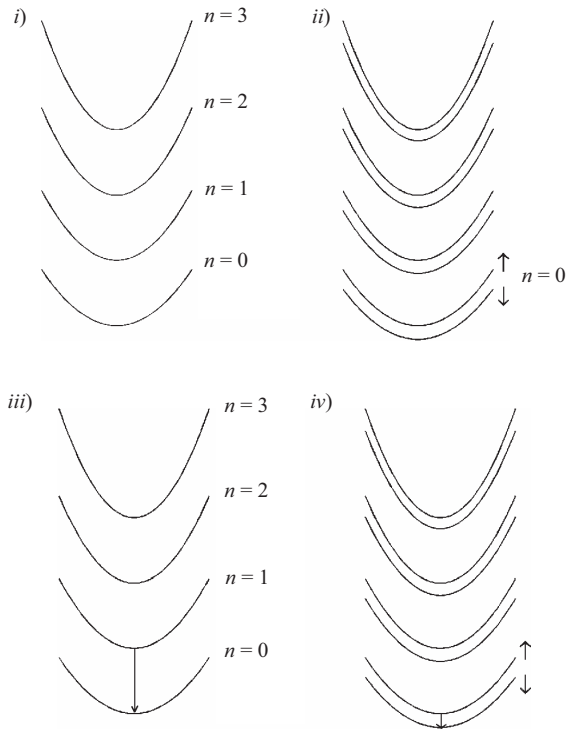


**Figure 1.** Schematic view of the magnetic field effect on the energy bands of semiconductors.

1  $\mu\text{m}$  led to the investigation of a whole range of novel physical phenomena. In turn, these new physical phenomena promise to give rise to new generations of devices working on completely different physical principles than their predecessors.

The nanostructured systems are real solids built artificially with polar semiconductors, binary and ternary. In this way the quasi-particles and elementary excitations in them feel a potential barrier that limits their movement to a determined space of mesoscopic dimensions, giving rise to a set of energy discrete states, which it makes these solids very attractive systems for their novel properties.

In the past three decades, nanostructured semiconductors have been studied extensively both theoretically and experimentally and applied to various electronic and photonic devices. The interest in the quantum size effects present in the low dimensional structures has been primarily motivated by the fact that the optical and electronic properties of these structures are modified and improved by the reduction of dimensionality. It is expected that the same properties will be further improved by the reduction of dimensionality. The fabrication of quantum structures by methods such as molecular-beam epitaxy, metal-organic chemical vapor deposition, lithography and others allows one to obtain high-quality samples which are required in investigations with experimental techniques, including optical studies such as photoluminescence spectroscopy and photoluminescence excitation spectroscopy [1–6]. In addition, theoretical properties have been reported [7–14], such as electronic structure [15–26], impurity levels [27–42] and excitonic states [43–52].

Experiments in magnetic fields are of particular interest in order to understand the basic physical properties of

nanostructures, because the magnetic confinement potentials compete with the geometric confinement potentials depending on the strength and orientation of magnetic field. The magnetic length can be varied from values which are larger than the typical lateral dimensions of quantum wires and quantum dots to values that are smaller than these dimensions. This information about the geometric confinement potentials can be obtained in a very direct way by magnetic field studies.

A number of magneto-optical studies on interband transitions in GaAs based quantum wires and dots have been performed previously [53–59]. An anisotropy of the photoluminescence of GaAs wires for different orientations of the magnetic field relative to the wire axis was observed [57]. For  $\text{In}_{0.13}\text{Ga}_{0.87}\text{As}/\text{GaAs}$  wires [58] and  $\text{GaAs}/\text{Al}_{0.36}\text{Ga}_{0.64}\text{As}$  wires [59] a transformation from quasi-one-dimensional quantum wire states to quasi-zero-dimensional, fully quantized states was observed with increasing magnetic field normal to the wire axis. However, all these studies were performed on wire patterns that contained only wires of one fixed lateral width. Other work on the magnetic field effect in nanostructures can be found in [60–76].

## 2. EFFECT OF STATIC EXTERNAL MAGNETIC FIELD ON THE QUASI-PARTICLE ENERGY LEVELS IN THE LOW DIMENSIONAL STRUCTURES

### 2.1. Magnetic Field Effect in the Quasi-Two-Dimensional System

The study of the magnetic field effects (Landau quantization) gives access to fine characterization methods of conducting in the quasi-two-dimensional structures through cyclotron resonance or Shubnikov–de Haas experiments [79]. At the same time, they prove to be difficult to understand. As we shall see, a magnetic field  $\vec{B}$  completely reorganizes the energy spectrum of quasi-two-dimensional electrons by splitting the continuum of the low dimensional structure density of states ( $B = 0$ ) into highly degenerate levels which are separated by finite bandgaps ( $B \neq 0$ ). Thus, what was a metallic system at  $B = 0$  is now either metallic or insulating at finite  $B$  depending on whether the Fermi level sits in the gaps or in the levels. The existence of finite bandgaps is responsible for the quantization of the Hall conductivity into multiples of the fundamental constant  $e^2/\hbar$ . The quantized Hall effect has become one of the most spectacular experimental effects discovered in solid state physics these last three decades.

In the following discussions band structure effects are ignored. The carriers are characterized by an isotropic effective mass, which is assumed to be position independent.

In this topic we consider the motion of a quasi-two-dimensional electron under the action of a static and uniform magnetic field  $\vec{B}$ , which forms an angle  $\theta$  with respect to the growth  $z$  axis of the structure (see Fig. 2). Thus  $\vec{B}$  is given by

$$\vec{B} = (0, B \sin \theta, B \cos \theta) \quad (1)$$

It can be shown that the Lorentz force  $(q/c)\vec{v} \times \vec{B}$  acting on a particle of charge  $q$  can be derived using the Hamilton equations

$$\frac{d\vec{r}}{dt} = \frac{\partial H}{\partial \vec{p}} \quad \frac{d\vec{p}}{dt} = -\frac{\partial H}{\partial \vec{r}} \quad (2)$$

provided the particle momentum  $\vec{p}$  is replaced by  $\Pi$  in the classical Hamiltonian. The vector  $\Pi$  is equal to

$$\Pi = \vec{p} - \frac{q}{c}\vec{A} \quad (3)$$

where  $\vec{A}$  is the vector potential of the magnetic field  $\vec{B}$  which is related as

$$\vec{B} = \nabla \times \vec{A} \quad (4)$$

and  $q$  is the algebraic charge of the carrier ( $q = -e$  for electrons). Unfortunately  $\vec{A}$  is only a mathematical tool which is in fact not very convenient since, if  $\vec{A}$  is replaced by  $\vec{A}' = \vec{A} + \nabla f$  where  $f$  is an arbitrary differentiable scalar function, the magnetic field  $\vec{B}' = \nabla \times \vec{A}'$  coincides with  $\vec{B}$ . Thus, there is a large ambiguity in the choice of the vector potential which corresponds to a given field  $\vec{B}$ . Since only  $\vec{B}$  retains a physical significance, the results should only depend on  $\vec{B}$  and not on the precise choice of  $\vec{A}$  (i.e., should be gauge invariant). In the following we will use

$$\vec{A} = (Bz \sin \theta, Bx \cos \theta, 0) \quad (5)$$

as well as the notations

$$B \sin \theta = B_{\perp} \quad B \cos \theta = B_{\parallel} \quad (6)$$

$$\omega_{c\perp} = \frac{eB_{\perp}}{m_e^*c} \quad \omega_{c\parallel} = \frac{eB_{\parallel}}{m_e^*c} \quad (7)$$

The electron spin  $\sigma$  interacts with the field adding to the particle energy the quantity

$$g^* \mu_B \sigma \cdot \vec{B} \quad (8)$$

where  $\mu_B = e\hbar/2m_0c$  is the Bohr magneton and  $g^*$  is the effective Landé  $g$  factor of the quasi-particle ( $g^* = 2$  for electrons in the vacuum,  $g^* > 0$  or  $g^* < 0$  in the semiconductors). The operator  $\sigma$  has the eigenvalues  $\pm 1/2$ . The electron Hamiltonian is expressed by

$$\begin{aligned} \hat{H} = & \frac{1}{2m_e^*} \left( -i\hbar \frac{\partial}{\partial x} + \frac{e}{c} B_{\perp} z \right)^2 + \frac{1}{2m_e^*} \left( -i\hbar \frac{\partial}{\partial y} + \frac{e}{c} B_{\parallel} x \right)^2 \\ & + \frac{\hat{p}_z^2}{2m_e^*} + V_b(z) + g^* \mu_B \sigma \cdot \vec{B} \end{aligned} \quad (9)$$

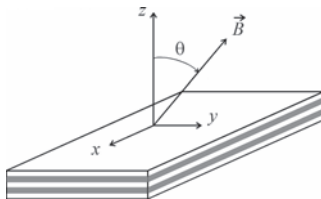


Figure 2.

Thus, the envelope wave function for  $\hat{H}$  can be written as a product of functions depending on separated orbital and spin variables

$$f(\vec{r}, \sigma) = f(\vec{r})\alpha(\sigma) \quad (10)$$

Suppose  $\sigma$  is quantized along  $\vec{B}$ . Let us denote by  $|\uparrow\rangle$  and  $|\downarrow\rangle$  the two eigenvectors of  $\sigma_z$  and by  $|\nu\rangle$  the eigenstates of the orbital part of  $\hat{H}$ , associated with the eigenvalues  $\varepsilon_{\nu}$ . The eigenstates and eigenenergies of Eq. (9) are obtained in the following form:

$$f(\vec{r}, \sigma) = \langle \vec{r} | \nu \rangle \otimes |\uparrow\rangle \quad \varepsilon_{\nu} + \frac{1}{2} g^* \mu_B B \quad (11)$$

$$f(\vec{r}, \sigma) = \langle \vec{r} | \nu \rangle \otimes |\downarrow\rangle \quad \varepsilon_{\nu} - \frac{1}{2} g^* \mu_B B \quad (12)$$

The spin term is rotationally invariant. Therefore, if  $\sigma$  is quantized along a fixed direction (say  $z$ ), which is not necessarily colinear to  $\vec{B}$ , we will obtain (after diagonalizing  $g^* \mu_B \sigma \cdot \vec{B}$ ) the same spin eigenvalues  $\pm(1/2)g^* \mu_B B$ . Thus the spin splitting  $g^* \mu_B B$  depends on the modulus of  $\vec{B}$ , not on its direction.

Since the spin effects are now well known, let us put our attention on the search for the eigenvalues  $\varepsilon_{\nu}$ . The spin effects, however, will have to be taken into account when evaluating the carrier density of states.

The enveloped wave function for the orbital part of  $\hat{H}$ , considering that the motion in  $y$  is independent, can be written as

$$f_{\nu}(\vec{r}) = \frac{1}{\sqrt{L_y}} \exp(ik_y y) \varphi_{\mu}(x, z) \quad (13)$$

Generally [ $\theta \neq 0$ ,  $V_b(z)$  arbitrary],  $x$  and  $z$  variables cannot be separated. However, except when  $\theta$  is close to  $\pi/2$ , the separability between  $x$  and  $z$  motions appears to be a good zero order approximation. In fact, let us rewrite  $\hat{H}$  in the form

$$\hat{H} = \hat{H}_{\parallel} + \hat{H}_{\perp} + \delta\hat{H} \quad (14)$$

where

$$\hat{H}_{\parallel} = \frac{\hat{p}_z^2}{2m_e^*} + V_b(z) \quad (15)$$

$$\hat{H}_{\perp} = \frac{\hat{p}_x^2}{2m_e^*} + \frac{1}{2m_e^*} \left( \hbar k_y + \frac{e}{c} B_{\parallel} x \right)^2 \quad (16)$$

$$\delta\hat{H} = \delta\hat{H}_1 + \delta\hat{H}_2 = \frac{1}{2m_e^*c^2} e^2 B_{\perp}^2 z^2 + \hat{p}_x z \frac{eB_{\perp}}{m_e^*c} \quad (17)$$

and where Eq. (13) was used. If the splitting of our original Hamiltonian proves to be correct, the zero order energies (i.e., those of  $\hat{H}_{\parallel} + \hat{H}_{\perp}$ ) will only depend on  $B_{\parallel}$  and not on  $B_{\perp}$ . This means that, in contrast to the spin term, the eigenvalues  $\varepsilon_{\nu}$  will depend on the component of  $\vec{B}$  parallel to the growth axis.

An immediate experimental check of this property for a given heterostructure is to rotate the sample with respect to

$B$  and to see whether the physical property (of orbital origin) which is under study depends on  $B_{\parallel}$  (i.e., on the angle  $\theta$ ). For a three-dimensional isotropic system with vanishing  $V_b(z)$ , it is very easy to show that the eigenvalues of  $\hat{H}$  only depend on the modulus of  $\vec{B}$  and not on its direction. Thus, provided the decoupling of  $\hat{H}$  into a main separable term and a small nonseparable one is valid, a clear proof of the existence of quasi-two-dimensional electron gas in a given heterostructure is obtained by studying the angular dependence of magnetic field dependent properties.

Let us then examine the validity of the decoupling procedure. First we investigate the eigenstates of  $\hat{H}_{\parallel} + \hat{H}_{\perp}$ . The wave functions  $\varphi_{\mu}(x, z)$  factorize into

$$\varphi_{\mu}(x, z) = \chi_m(z)\varphi_n(x) \quad (18)$$

where

$$\hat{H}_{\parallel}\chi_m(z) = \xi_m\chi_m(z) \quad (19)$$

and

$$\begin{aligned} \hat{H}_{\perp}\varphi_n(x) &= \left\{ \frac{\hat{p}_x^2}{2m_e^*} + \frac{1}{2m_e^*} \left( \hbar k_y + \frac{eB_{\parallel}}{c} x \right)^2 \right\} \varphi_n(x) \\ &= \varepsilon_n \varphi_n(x) \end{aligned} \quad (20)$$

$\chi_m(z)$  are the wave functions for the  $z$  motion, which correspond to the  $m$ th state (bound or unbound) of energy  $\xi_m$  for the heterostructure Hamiltonian at zero magnetic field. The functions  $\varphi_n(x)$  are the eigensolutions of a harmonic oscillator problem (frequency  $\omega_q$ ) centered at

$$x_0 = -\frac{\lambda^2 k_y}{\cos \theta} \quad (21)$$

where  $\lambda$  is the magnetic length

$$\lambda = \sqrt{\frac{\hbar c}{eB}} \quad (22)$$

The eigenvalues of Eq. (20) are  $k_y$  independent and evenly spaced in  $\hbar\omega_q$ . They are the celebrated Landau levels:

$$\varepsilon_n(k_y) = \left( n + \frac{1}{2} \right) \hbar\omega_q \quad n = 0, 1, 2, \dots \quad (23)$$

The eigenfunctions of Eq. (15) which correspond to the eigenvalue  $(n + 1/2)\hbar\omega_q$  can be expressed in terms of the Hermite polynomials

$$\begin{aligned} \varphi_n(x) &= \frac{\cos \theta^{1/4}}{\sqrt{\lambda}} \frac{1}{\sqrt{2^n n! \sqrt{\pi}}} \exp \left[ -\frac{\cos \theta}{2\lambda^2} (x - x_0)^2 \right] \\ &\times H_n \left[ \left( \frac{x - x_0}{\lambda} \right) \sqrt{\cos \theta} \right] \end{aligned} \quad (24)$$

where

$$H_n(x) = (-1)^n \exp(x^2) \frac{d^n}{dx^n} \exp(-x^2) \quad (25)$$

It can be verified that

$$\langle n-1|x|n \rangle = \int_{-\infty}^{\infty} \varphi_{n-1}(x)x\varphi_n(x) dx = \frac{\lambda}{\sqrt{\cos \theta}} \sqrt{\frac{n}{2}} \quad (26)$$

$$\langle n|x|n \rangle = x_0 \quad (27)$$

$$\left\langle n-1 \left| \frac{\partial}{\partial x} \right| n \right\rangle = \frac{\sqrt{\cos \theta}}{\lambda} \sqrt{\frac{n}{2}} \quad (28)$$

We have thus succeeded in classifying the eigenstates of  $\hat{H}_{\parallel} + \hat{H}_{\perp}$ . These eigenstates consist of Landau level ladders, which are attached to each of the zero field heterostructures bound (or unbound) states. Each of the levels is degenerate with respect to  $k_y$  or to  $x_0$ , the center of the  $n$ th harmonic oscillator function. Thus, apart from the spin quantum number we may write

$$|\nu\rangle = |m, n, k_y\rangle \quad (29)$$

which corresponds to the energy

$$\varepsilon_{\nu} = \xi_m + \left( n + \frac{1}{2} \right) \hbar\omega_{c\parallel} \quad (30)$$

The remarkable point is that the carrier motion is entirely quantized;  $V_b(z)$  has quantized the  $z$  component of the carrier motion, while the  $B_{\parallel}$  component, which is parallel to the growth axis, has quantized the in plane motion.

Each of the eigenvalues  $\varepsilon_{\nu}$  is, however, enormously degenerate. This orbital degeneracy  $g_{\text{orb}}$  can be calculated as follows: the center of the harmonic oscillator function has to be in the crystal. Thus

$$-\frac{L_x}{2} < x_0 < \frac{L_x}{2} \quad (31)$$

where the dimension  $L_x$  is so large that the crystal boundaries were justifiably ignored in Eqs. (14)–(17).

The allowed  $k_y$  values are uniformly distributed and separated by the interval  $2\pi/L_y$  (periodic boundary condition applied to the  $y$  axis). Thus, the degeneracy of the eigenvalue  $\varepsilon_{\nu}$  is equal to

$$g_{\text{orb}} = \frac{L_x L_y}{2\pi\lambda^2} \cos \theta \quad (32)$$

Notice that  $g_{\text{orb}}$  is exact at  $\theta = 0$  ( $\delta\hat{H}_1 = \delta\hat{H}_2 = 0$  in this case) but only approximate at  $\theta \neq 0$  since the effects of  $\delta\hat{H}_1$ ,  $\delta\hat{H}_2$  have not yet been evaluated.

We now have to investigate the effects of  $\delta\hat{H}$  on the zeroth order eigenstates  $|m, n, k_y\rangle$ . The first term  $\delta\hat{H}_1$  does not affect the separability between  $x$  and  $z$  (as a matter of fact  $\delta\hat{H}_1$  could have been included into  $\hat{H}_{\parallel}$ ). The only effect is that the different quantum states of the  $z$  motion are admixed. For a state  $|m\rangle$ , which is sufficiently energy separated from the others (e.g., the ground state),  $\delta\hat{H}_1$  can be treated by first order perturbation calculus. Thus  $\xi_m$  is changed by  $\delta\xi_m$  where

$$\delta\xi_m = \frac{e^2}{2m_e^*c^2} B_{\perp}^2 \langle \chi_m | z^2 | \chi_m \rangle \quad (33)$$

To ensure the convergence of our perturbative scheme  $\langle \chi_n | \delta \hat{H}_1 | \chi_m \rangle$  should remain much smaller than the level spacing  $\xi_n - \xi_m$ . For the states of a confined particle by a potential well of range  $\approx L$ ,  $\xi_n \approx \hbar^2 \pi^2 n^2 / 2m_e^* L^2$  whereas  $\langle \chi_n | z^2 | \chi_m \rangle \approx L^2$ . Thus,  $\langle \chi_1 | \delta \hat{H}_1 | \chi_2 \rangle / (\xi_2 - \xi_1) \approx L^4 \sin^2 \theta / 3\pi^2 \lambda^4$  and the perturbative approach will be justified for the ground state if the Landau quantization along the  $z$  direction remains much smaller than the size quantization arising from  $V_b(z)$ .

Suppose, for instance, that the heterostructure consists of a quantum well of thickness  $L$ , clad between impenetrable barriers. For the ground state we obtain

$$\delta \xi_1 = \frac{e^2 B^2}{4m_e^* c^2} \sin^2 \theta L^2 \left( \frac{1}{6} - \frac{1}{\pi^2} \right) \quad (34)$$

If  $B = 10$  T,  $\theta = \pi/4$ ,  $L = 100$  Å,  $m_e^* = 0.067m_0$ , we obtain  $\delta \xi_1 \approx 0.2$  meV, which is much smaller than  $\xi_2 - \xi_1 \approx 168$  meV. Note, however, that  $\delta \xi_1 \approx \xi_2 - \xi_1$  if  $L \geq 500$  Å. In the latter situation, the first order perturbation becomes insufficient. A better approach would have been to include  $\delta \hat{H}_1$  into  $\hat{H}_\parallel$  from the very beginning. However, the failure of the perturbative approach indicates that the whole decoupling procedure underlying Eqs. (14) and (15) becomes dubious. This is what happens when the system is weakly two-dimensional, either because the bound states supported by  $V_b(z)$  are too dense or [when  $V_b(z)$  is finite] too close to the continuum. A better zero order Hamiltonian is the whole magnetic field dependent term (bulklike). The perturbation becomes  $V_b(z)$  and, if  $B$  is large enough, the effects associated with  $V_b(z)$  can be treated within the subspace which is spanned by all the states of a given  $n$ . For more complete treatments of tilted magnetic effects in superlattices, see [80, 81].

The second kind of perturbing term,  $\delta \hat{H}_2$ , can be rewritten as  $z \hat{p}_x \omega_{c\perp}$ .  $\delta \hat{H}_2$  has no nonvanishing diagonal elements in the  $|m, n, k_y\rangle$  basis since  $\langle n | \hat{p}_z | n \rangle = 0$ . To the second order of perturbation theory we obtain

$$\delta(\xi_m + \varepsilon_n) = \sum_{m', n' \neq m, n} \frac{\omega_{c\perp}^2 |\langle \chi_m | z | \chi_{m'} \rangle|^2 |\langle \varphi_n | \hat{p}_x | \varphi_{n'} \rangle|^2}{\xi_m - \xi_{m'} + (n - n') \hbar \omega_q} \quad (35)$$

Thus,  $\delta \hat{H}_2$  couples Landau levels of different subbands whose indexes  $n'$ ,  $n$  differ by one. In addition, if  $V_b(z)$  is even in  $z$ , only subbands of opposite parities are coupled by  $\delta \hat{H}_2$ . Note that  $\delta[\xi_m + \varepsilon_n]$  can become very large (but cannot be described by means of perturbative treatments) when the energy denominators in Eq. (35) vanish. Practically, this means that two consecutive Landau levels, which belong to two adjacent subbands, intersect. For the sake of definiteness, let us assume that the involved levels and subbands are  $n = 0$ ,  $n = 1$ , and  $m = 1$ ,  $m = 2$  respectively. Notice that at  $\theta = 0$  the two levels  $|1, 1, k_y\rangle$  and  $|2, 0, k_y\rangle$  can cross since  $\delta \hat{H}_2$  vanishes. Let us denote by  $B_c$  the crossing fields at  $\theta = 0$ :  $B_c = (\xi_2 - \xi_1) m_e^* c / \hbar e$ . At finite  $\theta$ , the crossing field would take place at  $B_c / \cos \theta$ . However, the  $\delta \hat{H}_2$  matrix element which connects the two levels is now nonvanishing and increases with  $\theta$ . Thus, the crossing is suppressed and

replaced by an anticrossing (see Fig. 3). Retaining the dominant  $\delta \hat{H}_2$  contributions and neglecting  $\delta \hat{H}_1$ , we can write

$$|f\rangle \approx \alpha |1, 1, k_y\rangle + \beta |2, 0, k_y\rangle \quad B \approx B_c / \cos \theta \quad (36)$$

The eigenvalues are the solutions of

$$\begin{vmatrix} \xi_1 + \frac{3}{2} \hbar \omega_q - \varepsilon & \langle 2, 0, k_y | \delta \hat{H}_2 | 1, 1, k_y \rangle \\ \langle 1, 1, k_y | \delta \hat{H}_2 | 2, 0, k_y \rangle & \xi_2 + \frac{1}{2} \hbar \omega_q - \varepsilon \end{vmatrix} = 0 \quad (37)$$

or

$$\varepsilon_{\pm} = \frac{\xi_1 + \xi_2}{2} + \hbar \omega_q \pm \sqrt{\left( \frac{\xi_2 - \xi_1 - \hbar \omega_q}{2} \right)^2 + |\langle 2, 0, k_y | \delta \hat{H}_2 | 1, 1, k_y \rangle|^2} \quad (38)$$

The magnitude of the anticrossing (which is the energy difference  $\delta \varepsilon = \varepsilon_+ - \varepsilon_-$  evaluated at  $B = B_c / \cos \theta$ ) is

$$|\delta \varepsilon| = \frac{1}{\lambda(B_c)} \langle \chi_1 | z | \chi_2 \rangle \frac{\hbar e B_c}{m_e^* c} \tan \theta \sqrt{2} \quad (39)$$

which varies like  $B_c^{3/2}$ . At the anticrossing the mixing between the two interacting levels is complete:  $|\alpha| = |\beta| = 1/\sqrt{2}$ . Note finally the close formal analogy between this type of anticrossing and those that arise when the cyclotron energy  $\hbar \omega_q$  becomes equal to the energy of the longitudinal optical phonon energy  $\hbar \omega_{LO}$  (magnetopolaron [82]).

### 2.1.1. Magnetic Field Density of States

Since the effects of  $\delta \hat{H}_1$  are only approximately known, our attention in this section will be restricted to the case of  $\theta = 0$ , taking into account the spin splitting effect. As the  $z$  and  $(x, y)$  motions are separable, we can decompose the

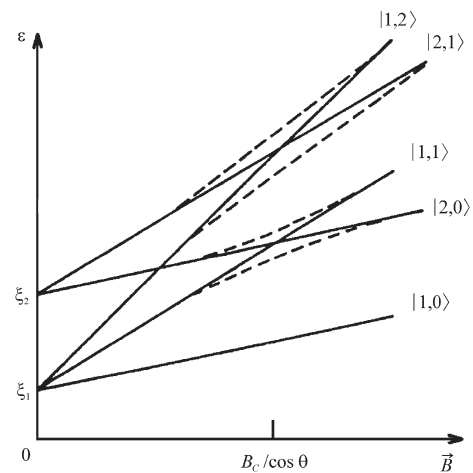


**Figure 3.** Schematic fan charts of Landau levels attached to two subbands 1 and 2 with confinement energies  $\xi_1$  and  $\xi_2$  respectively. The dashed lines represent the effect of the anticrossing induced by  $\delta \hat{H}_2$ . Reprinted with permission from [186], J. L. Marín et al., "Handbook of Advanced Electronic and Photonic Materials and Devices" (H. S. Nalwa, Ed.). Academic Press, San Diego, 2001. © 2001, Academic Press.

total density of states into contributions which arise from different subbands  $m$ ,

$$\rho(\varepsilon) = \sum_m \rho_m(\varepsilon) \quad (40)$$

where

$$\rho_m(\varepsilon) = \sum_{\sigma_z, k_y, n} \delta \left\{ \varepsilon - \xi_m - \left( n + \frac{1}{2} \right) \hbar \omega_q - g^* \mu_B \sigma_z \right\} \quad (41)$$

$$\sigma_z = \pm \frac{1}{2}$$

Since the eigenenergies are  $k_y$  independent, the summation over  $k_y$  can immediately be performed. This results in the appearance of the orbital degeneracy factor  $g_{\text{orb}}$ . Thus

$$\rho_m(\varepsilon) = \frac{S}{2\pi\lambda^2} \sum_{n, \sigma_z} \delta \left\{ \varepsilon - \xi_m - \left( n + \frac{1}{2} \right) \hbar \omega_q - g^* \mu_B B \sigma_z \right\} \quad (42)$$

As the carrier motion is entirely quantized, the density of states is zero except at the discrete energies

$$\varepsilon_{m\sigma_z} = \xi_m + \left( n + \frac{1}{2} \right) \hbar \omega_q + g^* \mu_B B \sigma_z \quad (43)$$

where it is infinite. The results of Eqs. (41)–(43) are quite remarkable when compared with the zero field situation:

$$\rho_{m\sigma_z}^{B=0}(\varepsilon) = \frac{m_e^* S}{2\pi \hbar^2} Y(\varepsilon - \xi_m) \quad (44)$$

At zero field the quasi-two-dimensional electron gas is metallic, with a gapless density of states for  $\varepsilon > \xi_1$ . A finite magnetic field dramatically alters this situation, replacing the continuum Eq. (44) by pointlike singularities [Eq. (42)] separated by gaps. Thus, depending on the respective locations of the characteristic electron energy  $\eta$  (the Fermi energy for a degenerate electron gas at  $T = 0$  K) and  $\varepsilon_{m\sigma_z}$ , the electron gas will behave either like an insulator ( $\eta \neq \varepsilon_{m\sigma_z}$ ) or a metal ( $\eta = \varepsilon_{m\sigma_z}$ ). Notice that similar effects cannot be found in bulk materials: the carrier-free motion along the field prevents the density of states from vanishing at any energy larger than  $\hbar \omega_c / 2 - |g_c^*| \mu_B B / 2$ .

Of course, we know that imperfections (impurities, interface defects, etc.) will alter the deltalike singularities of  $\rho_m(\varepsilon)$ , rounding off the peaks, adding states into the gaps. However, it remains generally accepted that, if  $B$  is large enough (i.e.,  $B \geq$  few Teslas in good GaAs–Ga<sub>1-x</sub>Al<sub>x</sub>As heterostructures at low temperature), the previous conclusions retain their validity, at least for the following meaning: for energies belonging to a certain bandwidth of finite (yet undefined) extension, the density of states is large and corresponds to conducting states, whereas for other energy segments, the states are localized (i.e., at  $T = 0$  K are unable to contribute to the electrical conduction at vanishingly small electric fields).

Some words have to be added concerning the broadening effects. The present state of the art is far from being satisfactory. First, there is, to the authors' knowledge, no general consensus on the microscopic origin of these effects.

Most likely it is sample dependent: in some samples, charged impurities play a dominant part. In others, interface roughness or alloy scattering (if it exists) may dominate. Second, even if we assume that the disorder potential has a simple algebraic form (e.g., uncorrelated deltalike scatterers), it proves difficult, if not impossible, to obtain precise information on  $\rho_m(\varepsilon)$  by any method other than by numerical simulation. The complications are twofold:

- The unperturbed density of states is highly singular. This precludes the use of non-self-consistent perturbative treatments of the disorder potential.
- When the required self-consistency is included, calculations are performed up to a finite order in the perturbation approach. By doing so, the nature of the states which occur in the tails of the broadened delta function are ill-treated: a localized level requires an inclusion of the electron disorder potential to an infinite order.

## 2.2. Magnetic Effect in Quasi-One-Dimensional Systems

The energy spectrum of a particle confined within a circle in the presence of an external magnetic field perpendicular to the plane of confinement is studied both exactly and approximately by the quasi-classical formalism (WKB). For pure spatial confinement (without magnetic field) the energy spectrum for states other than the ground state is twofold degenerate, while in the case of pure magnetic confinement the spectrum shows infinite-fold degeneration, typical of Landau states. For both types of confinement, the latter infinite-fold degeneration is lifted due to spatial confinement. Interestingly enough, for a given ratio between spatial and magnetic confining lengths, the magnetic flux is quantized. The conditions for the quantization of the flux are established; the nature and peculiarity of the energy spectrum are also discussed.

Basically, the physical properties are implicitly contained in the wavefunction; it is clear that this function is modified whenever the system is restricted on its available space either by its size (spatial confinement) or by an external perturbation (field confinement).

In this context, the first attempt at the study of these kind of systems will be the solution of the Schrödinger equation in which the corresponding Hamiltonian addresses in one way or another some of the characteristics of the spatial restrictions [83].

If the boundary which encloses the system is impenetrable, its energy increases as the confinement region decreases in agreement with the uncertainty principle; that is, more localization in space means an increase in the moment and consequently in the energy. If the latter boundary is penetrable then there is a probability of the system to escape and thus if the surroundings possess available states the system can occupy those which will be consistent with its energy and selection rules.

One of the simplest systems of this kind is a single particle confined by impenetrable boundaries and perturbed by an external magnetic field. This system was first studied by Stransky [52] to show how the energy spectrum transforms



smoothly to that of a free particle spectrum as the magnetic field strength goes to zero.

In this context we shall study a similar system but we further analyze the situations raised whenever the typical length introduced by both types of confinement are far apart or nearly equal.

### 2.2.1. Spatial Confinement

Let us consider the two-dimensional confinement of a particle within a circle of radius  $r_0$  and  $k_z = 0$ . The Hamiltonian in this case can be written as

$$\hat{H}_0 = \frac{\hat{p}^2}{2m^*} + V_b(r) \quad (45)$$

where the confining potential is given by

$$V_b(r) = \begin{cases} 0 & 0 \leq r \leq r_0 \\ \infty & r > r_0 \end{cases} \quad (46)$$

In polar coordinates  $(r, \varphi)$ , the corresponding Schrödinger equation for  $\hat{H}_0$  is given by

$$\left\{ \frac{1}{r} \frac{\partial}{\partial r} \left( r \frac{\partial}{\partial r} \right) + \frac{1}{r^2} \frac{\partial^2}{\partial \varphi^2} + \frac{2m^*}{\hbar^2} [\varepsilon_0 - V_b(r)] \right\} f_0(r, \varphi) = 0 \quad (47)$$

where  $\varepsilon_0$  is the energy of the particle and  $f_0(r, \varphi)$  is its envelope wavefunction that must satisfy

$$f_0(r_0, \varphi) = 0 \quad (48)$$

due to the form of the confining potential  $V_b$ . The solutions of Eq. (47) have already been studied previously; thus, considering the condition for the wavefunction given by Eq. (48) the energy spectrum is obtained as

$$\varepsilon_0^{n, |m|} = \frac{\hbar^2 \alpha_{n, |m|}^2}{2m^* r_0^2} \quad (49)$$

Here,  $\alpha_{n, |m|}$  denotes the  $n$ th zero of  $J_{|m|}$ .

Note that for  $m \neq 0$ , the energy levels are twofold degenerate with eigenfunctions

$$f_0^{n, m} = \frac{1}{\sqrt{2\pi}} A_{n, |m|} J_{|m|} \exp(im\varphi) \quad (50)$$

and

$$f_0^{n, -m} = \frac{1}{\sqrt{2\pi}} A_{n, |m|} J_{|m|} \exp(-im\varphi) = (f_0^{n, m})^* \quad (51)$$

Due to the properties of the zeroes of  $J_{|m|}$ , the energy levels satisfy

$$\varepsilon_0^{1, |m|} < \varepsilon_0^{1, |m|+1} < \varepsilon_0^{2, |m|} < \varepsilon_0^{2, |m|+1} < \varepsilon_0^{3, |m|} \dots \quad (52)$$

The dependence of the lowest energy levels on the confinement radius  $r_0$  is displayed in Figure 4.

Two main features emerge from this figure: (i) as the confinement radius decreases the energy of each level increases. This fact is consistent with the uncertainty principle (i.e., more localization of the particle implies an increase

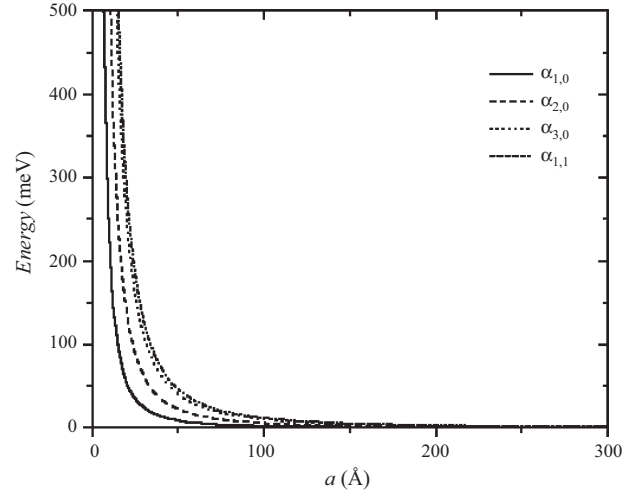


**Figure 4.** Energy  $\varepsilon_0^{n, |m|}$  as a function of confinement radius  $r_0$ . From bottom to top, the states with  $(n, |m|) = (1,0), (1,1), (1,2),$  and  $(1,3)$  are displayed. Reprinted with permission from [186], J. L. Marin et al., “Handbook of Advanced Electronic and Photonic Materials and Devices” (H. S. Nalwa, Ed.). Academic Press, San Diego, 2001. © 2001, Academic Press.

of its momentum and consequently a greater energy). (ii) As the confinement radius is increased, the energy level separation decreases and they coalesce smoothly into a single one, the free particle spectrum. The latter is consistent with the results of Rensink [52], as expected.

### 2.2.2. Magnetic Confinement

Let us now consider the case of a charged particle moving in the plane  $(x, y)$  in the presence of a homogeneous magnetic field  $\vec{B} = B_0 \hat{e}_z$ , without spatial confinement [i.e.,  $V_b(r) = 0$ ]. The Hamiltonian for this system can be written as

$$\hat{H} = \frac{\hat{P}^2}{2m^*} \quad (53)$$

where

$$\hat{P}^2 = \left( \hat{p} - \frac{q}{c} \vec{A} \right)^2 = \hat{p}^2 - \frac{q}{c} \hat{p} \cdot \vec{A} - \frac{q}{c} \vec{A} \cdot \hat{p} + \frac{q^2}{c^2} \vec{A}^2 \quad (54)$$

Now, for any state vector  $\Phi$

$$\begin{aligned} (\hat{p} \cdot \vec{A})\Phi &= -i\hbar \nabla \cdot (\vec{A}\Phi) = -i\hbar [(\nabla \cdot \vec{A})\Phi + \vec{A} \cdot (\nabla\Phi)] \\ &= [-i\hbar(\nabla \cdot \vec{A}) + \vec{A} \cdot \hat{p}]\Phi \end{aligned} \quad (55)$$

Then, when the gauge  $\nabla \cdot \vec{A} = 0$  is chosen,  $\hat{p} \cdot \vec{A} = \vec{A} \cdot \hat{p}$ ; that is,  $\vec{A}$  and  $\hat{p}$  commute and  $\hat{H}$  can be written as

$$\hat{H} = \frac{\hat{p}^2}{2m^*} - \frac{q}{m^*c} \vec{A} \cdot \hat{p} + \frac{q^2}{2m^*c^2} \vec{A}^2 \quad (56)$$

As a consequence of the symmetric gauge  $\nabla \cdot \vec{A} = 0$ ,  $\vec{A}$  is of the form

$$\vec{A} = \frac{1}{2} \vec{B} \times \vec{r} = \frac{1}{2} B_0 (-\hat{e}_x y + \hat{e}_y x) = \frac{1}{2} B_0 r \hat{e}_\varphi \quad (57)$$

This choice leads to

$$\vec{A} \cdot \hat{p} = -\frac{1}{2}i\hbar B_0 \left( x \frac{\partial}{\partial y} - y \frac{\partial}{\partial x} \right) = -\frac{1}{2}i\hbar B_0 \frac{\partial}{\partial \varphi} = \frac{1}{2}B_0 \hat{L}_z \quad (58)$$

where  $\hat{L}_z$  is the z-component of the angular momentum  $\vec{L}$ . If we define the cyclotron frequency  $\omega_c = -qB_0/m^*c$ ,  $\hat{H}$  is now given by

$$\hat{H} = -\frac{\hbar^2}{2m^*} \nabla^2 + \frac{1}{2}\omega_c \hat{L}_z + \frac{1}{8}m^* \omega_c^2 r^2 \quad (59)$$

This Hamiltonian can be envisioned as that of a two-dimensional oscillator (first and third terms in  $\hat{H}$ ) with oscillating frequency  $\omega = \omega_c/2$ , perturbed by the “potential”  $\omega_c \hat{L}_z/2 = \omega \hat{L}_z$ . That is,

$$\hat{H} = \hat{H}_{\text{osc}} + \hat{H}' \quad (60)$$

with  $\hat{H}_{\text{osc}} = -(\hbar^2/2m^*)\nabla^2 + (1/2)m^*\omega^2 r^2$  and  $\hat{H}' = \omega \hat{L}_z$ .

Moreover, it can be easily shown that  $[\hat{H}, \hat{H}'] = [\hat{H}_{\text{osc}}, \hat{H}']$ , a property that allows one to establish that  $\hat{H}$ ,  $\hat{H}_{\text{osc}}$ , and  $\hat{H}'$  possess common eigenfunctions. In view of the latter, if  $f_{lm}(r, \varphi)$  is the complete set of eigenfunctions of  $\hat{H}$ , then

$$\hat{H}_{\text{osc}} f_{lm}(r, \varphi) = \varepsilon_{\text{osc}} f_{lm}(r, \varphi) \quad (61)$$

and

$$\hat{H}' f_{lm}(r, \varphi) = \varepsilon' f_{lm}(r, \varphi) = \hbar \omega m f_{lm}(r, \varphi) \quad (62)$$

Here  $\varepsilon_{\text{osc}}$  is the energy of a two-dimensional isotropic harmonic oscillator, which can be found by separating the corresponding Schrödinger equation in polar coordinates, to give

$$\varepsilon_{\text{osc}} = \hbar \omega (2l + |m| + 1) \quad l = 0, 1, 2, \dots \quad (63)$$

The total energy for this system is then given by

$$\begin{aligned} \varepsilon_{lm} &= \varepsilon_{\text{osc}} + \varepsilon' = \hbar \omega (2l + |m| + m + 1) \\ &= \frac{1}{2} \hbar \omega_c (2l + |m| + m + 1) \end{aligned} \quad (64)$$

and the wavefunctions

$$\begin{aligned} f_{lm}(r, \varphi) &= \frac{N_{lm}}{\sqrt{2\pi}} r^{|m|} \exp\left(-\frac{1}{2}\alpha r^2\right) \\ &\times F(-l, |m| + 1, \alpha r^2) \exp(im\varphi) \end{aligned} \quad (65)$$

where  $\alpha = m^* \omega_c / 2\hbar$ ,  $N_{lm}$  is a normalization constant, and  $F$  is the confluent hypergeometric function [52, 78]. As can be immediately seen, the energy levels for a given  $l$  and  $m$  negative or zero are infinitely degenerate since  $|m| + m = 0$  in such a case. The levels given by Eq. (64) are the well-known Landau levels [84].

Moreover, as  $\omega_c \rightarrow 0$  (i.e., when the field is vanishingly small), the levels coalesce into a single level corresponding to the free particle, analogous to the previous section. Figure 5 shows the behavior of the energy levels as a function of the strength of the magnetic field  $B_0$ .

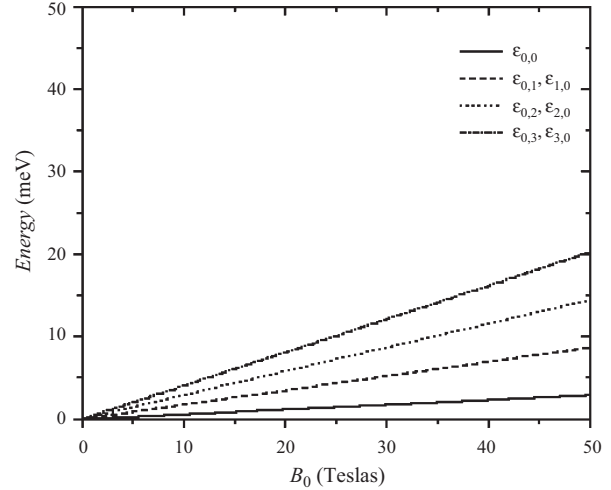


**Figure 5.** Energy  $\varepsilon_0^{n,|m|}$  as a function of magnetic field strength  $B_0$ . From bottom to top, the states with  $(l, m) = (0,0)$ ,  $(0,1)$ ,  $(0,2)$ , and  $(0,3)$  are displayed. Note that the states  $(l, 0) = (l, m)$  with  $m = 0$  or negative are infinitely degenerate, while the states  $(l, 0) = (0, m)$  with  $m$  positive are twofold degenerate. Reprinted with permission from [186], J. L. Marín et al., “Handbook of Advanced Electronic and Photonic Materials and Devices” (H. S. Nalwa, Ed.). Academic Press, San Diego, 2001. © 2001, Academic Press.

### 2.2.3. Spatial and Magnetic Confinement

In this context we shall study the case of a charged particle with both types of confinement considered in the previous cases. In this context, the Hamiltonian can be written as

$$\hat{H}_{bc} = -\frac{\hbar^2}{2m^*} \nabla^2 + \frac{1}{2}\omega_c \hat{L}_z + \frac{1}{8}m^* \omega_c^2 r^2 + V_b(r) \quad (66)$$

As can be seen, the inclusion of the term  $V_b(r)$  requires that the wavefunction satisfy the boundary condition given by Eq. (48) and this fact prevents  $l$  [Eq. (63)] from being a good quantum number as in the previous section. Instead, the boundary condition is now satisfied if [see Eq. (65)]

$$F(-\beta_{nm}, |m| + 1, \alpha r^2) = 0 \quad (67)$$

where now  $\beta_{nm}$  represents the  $n$ th zero of  $F$ . Then the energy for the system can be written as

$$\varepsilon_{nm} = \frac{1}{2} \hbar \omega_c (2\beta_{nm} + |m| + m + 1) \quad (68)$$

an expression similar to Eq. (64), but the infinite degeneracy of the levels for a given  $n$  and  $m$  negative is lifted by the spatial confinement because, in spite of the fact that  $m$  is still a good quantum number, the zeroes of  $F$  depend on its value, in contrast with the case of the preceding section. Hence, the problem can be solved if we find the zeroes of  $F$  as a function of  $r_0$  for a given value  $m$  and  $\omega_c$ .

Alternatively, it is interesting to note that  $\hat{L}_z$  commutes with all operators appearing in Eq. (66) and then the states of the new situation have a definite value of  $m$ . The latter

property allows one to construct the total wavefunction as the expansion

$$\begin{aligned} f_{bc}^m(r, \varphi) &= \sum_{n=0}^{\infty} a_n f_0^{n,m}(r, \varphi) \\ &= \frac{1}{\sqrt{2\pi}} \exp(im\varphi) \sum_{n=0}^{\infty} a_n J_{|m|} \left( \frac{\alpha_{n,|m|} r}{r_0} \right) \\ &= \sum_{n=0}^{\infty} a_n |nm\rangle \end{aligned} \quad (69)$$

Here we have exploited the fact that radial functions found in Section 2.2.1 represent a complete set of orthogonal functions satisfying the proper boundary condition. Of course this is not the only basis in which the total wavefunction can be expanded, but it would represent an alternative representation of  $F$  in terms of  $J_{|m|}(\alpha_{n,|m|} r/r_0)$  to that of [78].

As can be noted, in the Dirac notation,

$$\langle nm|n'm'\rangle = \delta_{nn'} \delta_{mm'} \quad (70)$$

Hence, to find the energy levels for a given value of  $m$ , we must diagonalize the matrix with elements

$$A_{nn'} = \left[ \varepsilon_0^{n,|m|} + \frac{1}{2} \hbar m \omega_c \right] \delta_{nn'} + \frac{1}{8} m^* \omega_c^2 \langle n|r^2|n'\rangle \quad (71)$$

Strictly speaking, the involved matrix is infinite, but in practice we can use one large enough, but finite, depending on the precision required to find the eigenvalues. In the present case we have used a (256,256) matrix, a choice that leads to a precision of about six decimal places.

The diagonalization procedure will render the eigenvalues as well as the eigenvectors  $\{a_n\}$  and thus we have the complete solution of this problem. In Figure 6, the energy of the lowest states is displayed as a function of the strength of

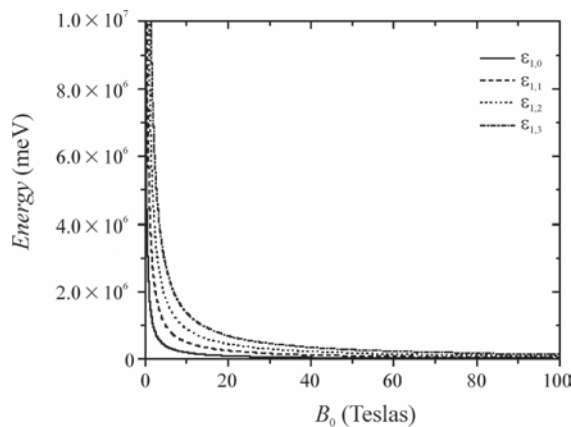


**Figure 6.** Energy of the lowest states for a particle confined within a circle of radius  $r_0 = 2.0$  Bohrs, as a function of magnetic field strength. From bottom to top, the states with  $(n, m) = (1, 0)$ ,  $(1, 1)$ ,  $(1, 2)$ , and  $(1, 3)$  are displayed. Note the energy scales introduced by the selected confinement regime. Reprinted with permission from [186], J. L. Marín et al., “Handbook of Advanced Electronic and Photonic Materials and Devices” (H. S. Nalwa, Ed.). Academic Press, San Diego, 2001. © 2001, Academic Press.

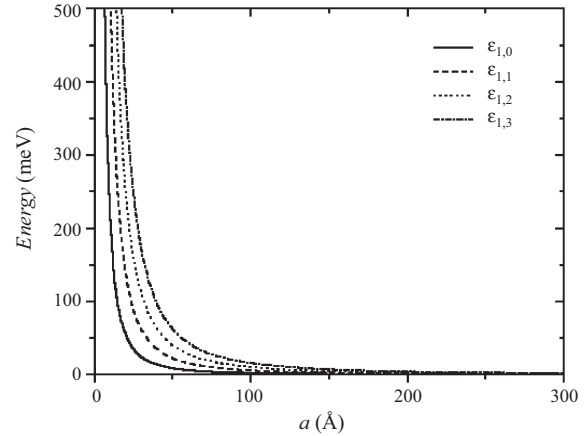


**Figure 7.** Energy of the lowest states for a particle confined within a magnetic field  $B_0 = 1$  Tesla, as a function of confining radius  $r_0$ . From bottom to top, the states with  $(n, m) = (1, 0)$ ,  $(1, 1)$ ,  $(1, 2)$ , and  $(1, 3)$  are displayed. Reprinted with permission from [186], J. L. Marín et al., “Handbook of Advanced Electronic and Photonic Materials and Devices” (H. S. Nalwa, Ed.). Academic Press, San Diego, 2001. © 2001, Academic Press.

the field for  $r_0 = 2.0$  Bohrs, while Figure 7 shows the same levels as a function of  $r_0$  for  $B_0 = 1$  Tesla.

Before closing this case we can mention three main points: (i) the spatial confinement lifts the degeneracy on the Landau levels (see Fig. 6). (ii) The magnetic confinement lifts the degeneracy of levels with positive and negative values of  $m$  (see Fig. 7). (iii) Each kind of confinement introduces a typical length; namely, the spatial confinement length is of the order of  $r_0$  while the magnetic confinement length is of the order of  $l_m \approx \sqrt{\hbar c/|q|B_0} \cong 484.52 B_0^{-1/2}$  (Bohrs), when  $|q| = |e|$  and  $B_0$  is given in Teslas.

In this sense, we can talk about a competition between the two kinds of confinement depending on the ratio of  $r_0/l_m$ , a fact that will be discussed in the next section.

## 2.2.4. WKB Approximation for Energy Levels

Now we shall study approximately a variety of situations raised depending on the relative size of confining region  $a$  and the characteristic length introduced by the magnetic field  $l_m$ . To do the latter we shall follow the WKB formalism as developed in the book of Morse and Feshbach [85]. In the first place, we note that the extension of one-dimensional WKB formalism to the two- or three-dimensional radial Schrödinger equation is accompanied by the change

$$\begin{aligned} m^2 - \frac{1}{4} &\rightarrow m^2 \quad (\text{two-dimensional}) \quad \text{or} \\ l(l+1) &\rightarrow \left(l + \frac{1}{2}\right)^2 \quad (\text{three-dimensional}) \end{aligned} \quad (72)$$

in the centrifugal barrier. Once the latter is recognized, the formalism can be applied in exactly the same way as in the one-dimensional case.

The effective potential in our case is of the form

$$V_{\text{eff}}(r) = \beta^2 r^2 + \frac{m^2}{r^2} \quad (73)$$

For illustrative purposes, this potential is displayed in Figure 8 from which two different situations merge, depending on the size of spatial confinement as compared with magnetic confinement, namely, when the energy is smaller or greater than  $V_{\text{eff}}(a) = \beta^2 r_0^2 + m^2/r_0^2$ . This fact is important since we are interested in analyzing approximately the solution of this problem, say by the quasi-classical method or more precisely by the WKB method.

Notice that when the energy is smaller than  $V_{\text{eff}}(r_0)$  there are two classical turning points whereas when it is greater there is only one, and hence the application of the WKB approximation is different for each case.

When only one turning point exists, the approximate wavefunction can be written as

$$F(r) \approx A \cos\left(\int_{r_1}^r q_r dr - \frac{1}{4}\right) \quad (74)$$

where  $A$  is a normalization constant and  $r_1$  is the turning point (lowest zero of  $q_r$ ), where

$$q_r = \sqrt{\alpha^2 - V_{\text{eff}}} \quad (75)$$

and

$$\alpha^2 = \frac{2m^* \varepsilon}{\hbar^2} - \frac{m^* \omega_c}{\hbar} m \quad (76)$$

Additionally, the boundary condition demands that  $F(r_0) = 0$ , which implies that

$$\int_{r_1}^a q_r dr - \frac{1}{4}\pi = \left(N + \frac{1}{2}\right)\pi \quad (77)$$

or

$$\int_{r_1}^a q_r dr = \left(N + \frac{3}{4}\right)\pi \quad (78)$$

which represents the quantization condition as a function of  $r_0$  and the magnetic field through  $r_1$  (lowest zero of  $q_r$ ).

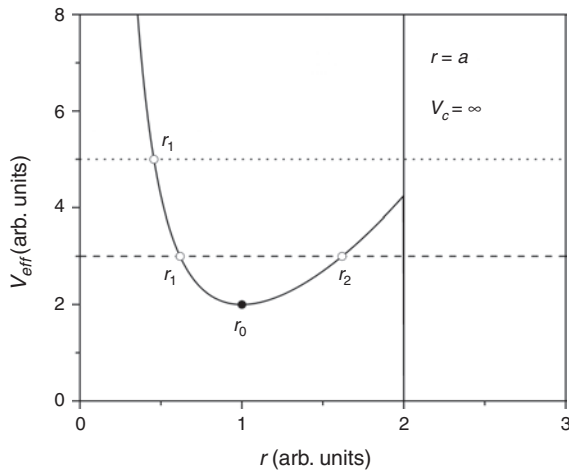


**Figure 8.** Qualitative drawing of  $V_{\text{eff}}(r)$  used to illustrate its turning points and minimum.

Performing the integral of  $q_r$ , the eigenvalues satisfy the following transcendental equation:

$$\sqrt{\alpha^2 r_0^2 - \beta^2 r_0^4 - m^2} + \left(\frac{\alpha^2}{2\beta}\right) \left(\frac{\pi}{2} - \arcsin\left[\frac{\alpha^2 - 2\beta^2 r_0^2}{\sqrt{\alpha^4 - 4m^2\beta^2}}\right]\right) - |m| \left(\frac{\pi}{2} + \arcsin\left[\frac{\alpha^2 r_0^2 - 2m^2}{r_0^2 \sqrt{\alpha^4 - 4m^2\beta^2}}\right]\right) = 2\pi \left(N + \frac{3}{4}\right) \quad (79)$$

In the case when  $r_0 \cong r_2$  (greatest zero of  $q_r$ ) it can be easily shown that

$$\varepsilon_{Nm} \cong \frac{1}{2} \hbar \omega_c \left(2N + |m| + m + \frac{3}{2}\right) \quad (80)$$

an expression which is similar to that of the Landau levels [see Eq. (64)], except that the level spacing is slightly different because of the boundary condition on the wavefunction at  $r = r_0 \cong r_2$ . Thus in the case when the greatest turning point is equal to the radius of the confining region, the corresponding spectrum is Landau-like and represents an extreme situation because in this case

$$r_0 \cong r_2 = \frac{\alpha}{\sqrt{2\beta}} \left(1 + \sqrt{1 - \frac{4m^2\beta^2}{\alpha^4}}\right)^{\frac{1}{2}} \quad (81)$$

from which one can see that

$$\alpha^2 = \beta^2 r_0^2 + \frac{m^2}{r_0^2} = V_{\text{eff}}(r_0) \quad (82)$$

Then when  $\alpha^2 \geq V_{\text{eff}}(r_0)$ , only one turning point can exist and the energy spectrum of the system is of Landau type. However, when  $\alpha^2 \leq V_{\text{eff}}(r_0)$  two turning points merge and the quantization rule, in the standard WKB approximation, would be

$$\int_{r_1}^a q_r dr = \left(N + \frac{1}{2}\right)\pi \quad (83)$$

but this result will only be valid for  $r_2 \ll r_0$  because the corresponding WKB function in the region  $r_2 < r < r_0$  is exponentially decaying and does not satisfy the boundary condition at  $r = r_0$ . Hence only when  $r_2 \ll r_0$  will the latter function approximately be consistent with this boundary condition and will the energy spectrum of the system behave Landau-like [i.e., as that given by Eq. (80)]. Whenever the condition  $r_2 \ll r_0$  is not fulfilled, the standard WKB approximation cannot be used.

Another interesting situation corresponds to the case when there is only one turning point but  $r_0 \cong a$  (see Fig. 8). At this point  $V_{\text{eff}}$  has a minimum when  $a = \sqrt{|m|/\beta}$ . Then inserting this value into Eq. (79), we obtain

$$\sqrt{V^-} r_0 + \frac{\pi V^-}{4\beta} - \frac{V^+}{2\beta} \arcsin\left(\frac{\sqrt{V^-}}{\sqrt{V^+}}\right) = 2\pi \left(N + \frac{3}{4}\right) \quad (84)$$

where

$$V^- = \alpha^2 - 2|m|\beta \quad (85)$$

and

$$V^+ = \alpha^2 + 2|m|\beta \quad (86)$$

Moreover, when  $\alpha^2 \gg 2|m|\beta$ ,

$$\frac{\sqrt{V^-}}{\sqrt{V^+}} \cong 1 - \frac{2|m|\beta}{\alpha^2} \quad (87)$$

and the approximation

$$\arcsin(1-z) \cong \frac{\pi}{2} - (2z)^{1/2} \quad z \ll 1 \quad (88)$$

can be used to obtain

$$\varepsilon_{Nm} = \frac{\hbar^2 \pi^2 [N + \frac{1}{2}(|m| + \frac{3}{2})]^2}{2m_0 r_0^2} + \frac{1}{2} m \hbar \omega_c \quad (89)$$

which clearly resembles the energy of a particle in a box “perturbed” by a term related with the eigenvalues of  $\widehat{L}_z$ . Since the minimum of  $V_{\text{eff}}$  depends on  $m$  and the strength of the field, we note also that the infinite degeneration is removed for the level whose value of  $m$  is “tuned” by the field strength to satisfy  $r_0 = \sqrt{|m|/\beta}$ . The latter property could not be applied to the ground state since in such a case  $r_0 = 0$  and the system would behave as a confined oscillator whose energy levels would be similar to those studied in [86]. Interestingly enough, if we analyze more closely the situation when  $r_0 = a = \sqrt{|m|/\beta}$  it can be seen that

$$r_0^2 = \frac{|m|}{\beta} = |m| \frac{2\hbar}{m^* \omega_c} = 2|m| \frac{\hbar c}{|e| B_0} \quad (90)$$

or

$$B_0 \pi r_0^2 = |m| \frac{hc}{|e|} \quad (91)$$

The term of the left is just the magnetic flux across the confining circle while the term of the right represents an integer number of times  $|m|$  the quantum flux  $\hbar c/|e|$ . The latter means that in this situation the magnetic flux is quantized; thus by changing the field strength, the system can be tuned into states in which the magnetic flux is quantized. It also must be noted that when  $r_0 = a$ ,  $r_0 = \sqrt{2}|m|l_m$ , where  $l_m$  is the magnetic length defined in the previous case.

The results obtained in Sections 2.2.1, 2.2.2, and 2.2.3, which are summarized in Figures 4–7, show the same trends as those obtained by Rensink [52]; that is, when the spatial confining radius is much greater than the magnetic length the spectrum approaches smoothly the free particle spectrum, while when it is much less the energy spectrum is a sort of Landau-like spectrum. In between, the spectrum is very rich because the typical infinite-folded degeneration of the Landau-like spectrum is lifted by the spatial confinement.

Special attention is necessary for the energy spectrum for which the spatial confining radius coincides with the minimum of the effective potential, since in this case three main features merge:

- (i) The magnetic flux is quantized for field strengths which are an integer multiple of the inverse of the cross-sectional area of spatial confining [see Eq. (91)].

- (ii) The nature of these states is quite different from those of Landau-like or pure spatial confining-like states, since they can only be observed when the spatial confining length is an integer multiple of the magnetic length. In this sense, they may be called “surface states.”

- (iii) These special or “surface states” are nondegenerate [see Eq. (89)] and their energies are greater than those of the “bulk” states [87] [compare Eq. (68) and (89)].

The aforementioned properties make this system attractive for further study and characterization. It would be interesting to study its energy spectrum and/or some important physical properties when, for instance, the confining potential is finite. The latter would also motivate new experiments, which would lead to some insight on the overall physical properties of these kinds of systems.

### 2.3. Two-Dimensional Quantum Dot in an External Magnetic Field

In the last few years the properties of the fundamental quantum systems, quantum dots, defined in two-dimensional electron gases in semiconductor heterostructures, have become the subject of intensive research because these systems are widely used in many fields of modern technology [88]. In this connection, the problem of creation of quantum computers [89–91], memory devices and electronics (see [92] and references therein), new types of lasers [93–95], and other problems connected with the ultrafast switching and quantum information processing should be mentioned. Quantum dots are the most promising candidates for this kind of technology because they have a discrete atomiclike density of states, due to the strong quantum confinement. Many important results on quantum dot can be found in a great number of review articles (see for example [96, 97]).

For all the applications mentioned, the feature of bigger importance is the flexibility of the electronic structure of quantum dot, which is controlled by magnetic and electric external fields, so it is of particular interest to investigate the structure of the states in more detail for different external conditions.

Here we discuss the one-electron energy spectra in a two-dimensional quantum dot with magnetic confinement. The spectra are calculated under the assumption of two different types of the boundary conditions. In the first case, there is only the spatial confinement due to a nonmagnetic finite potential barrier (we will call spatial confinement); in the second case the spatial confinement is combined with the magnetic spatial confinement.

#### 2.3.1. Equations

The Hamiltonian for an electron confined by the finite potential  $V(\vec{r})$  within a magnetic field  $\vec{B}$  in a two-dimensional quantum dot is given by

$$H = -\frac{\hbar^2}{2m^*} \nabla^2 + \frac{\omega_c}{2} L_z + \frac{1}{8} m^* \omega_c^2 r^2 + V(\vec{r}) \quad (92)$$

where  $r$  and  $\nabla$  are defined in the plane. We have used the same symmetric gauge as that used by Rosas et al. [83].

In this work we begin with a more realistic shape of the potential  $V(\vec{r})$  instead of that used in [83]. Namely, let the potential be described by the following expression:

$$V(\vec{r}) = \begin{cases} 0 & 0 \leq r \leq a \\ V_c & r > a \end{cases} \quad (93)$$

In this case the Schrödinger equation can be rewritten in polar coordinates,

$$\left\{ \frac{\hbar^2}{2m^*} \left[ \frac{1}{r} \frac{\partial}{\partial r} \left( r \frac{\partial}{\partial r} \right) + \frac{1}{r^2} \frac{\partial^2}{\partial \varphi^2} \right] + i\hbar\omega \frac{\partial}{\partial \varphi} - \frac{m^*}{2} \omega^2 r^2 + E - V_c \right\} \Psi = 0 \quad (94)$$

where the frequency  $\omega = \omega_c/2$  was introduced.

### 2.3.2. Quantum Dot without Magnetic Field

If the magnetic field is not included, Eq. (94) can be rewritten as

$$\frac{\hbar^2}{2m^*} \left( \frac{1}{r} \frac{\partial}{\partial r} \left( r \frac{\partial}{\partial r} \right) \right) \psi + \frac{\hbar^2}{2m^*} \frac{1}{r^2} \frac{\partial^2}{\partial \varphi^2} \psi + (E - V_c) \Psi = 0 \quad (95)$$

In this equation  $E$  is the energy of the particle and the wave function  $\psi$  must satisfy the boundary condition at  $r = a$ :

$$\frac{\psi'_-(r, \varphi)}{\psi_-(r, \varphi)} = \frac{\psi'_+(r, \varphi)}{\psi_+(r, \varphi)} \quad (96)$$

Here  $\psi_-$  is the solution of Eq. (95) for the region  $0 \leq r \leq a$  and  $\psi_+$  for  $r > a$  and the derivatives are taken with respect to  $r$ . However, for the region  $0 \leq r \leq a$  we should take the solution of the Schrödinger equation with the magnetic field instead of  $\psi_-$ . Let us consider Eq. (95) in the region  $r > a$ . In this case the variables are separable and the substitution  $\psi = R(r)\Phi(\varphi)$  yields the set of well-known equations

$$r(rR)' - (r^2|k|^2 + m^2)R = 0 \quad (97)$$

$$\Phi'' + m^2\Phi = 0 \quad (98)$$

where  $m$  is a separation constant and

$$|k|^2 = \frac{2m^*}{\hbar^2} (E - V) < 0 \quad \text{for } r > a$$

The solution of this equation set is

$$\Psi_+ = AK_m(kr)e^{im\varphi} \quad (99)$$

where  $K_m$  is the modified Bessel functions (or Macdonald functions), and  $A$  is a constant.

The solution of Eq. (95) in the region  $0 \leq r \leq a$  as well as the energy spectrum have been discussed earlier [83]. For this reason we do not need consider it here again (in this region of  $r$  we are interested in the wavefunction that corresponds to the case with magnetic field).

### 2.3.3. Quantum Dot with Magnetic Confinement

The case of a charged particle moving in the homogeneous magnetic field  $B_0$  without a spatial confinement was discussed in a previous work [83]. Here we would only like to mention that in this case the Schrödinger equation for a particle of mass  $m^*$  is

$$\left\{ \frac{\hbar^2}{2m^*} \left[ \frac{1}{r} \frac{\partial}{\partial r} \left( r \frac{\partial}{\partial r} \right) + \frac{1}{r^2} \frac{\partial^2}{\partial \varphi^2} \right] + i\hbar\omega \frac{\partial}{\partial \varphi} - \frac{m^*}{2} \omega^2 r^2 + E \right\} \psi = 0 \quad (100)$$

which has the solution

$$\psi_m = Ae^{im\varphi} e^{-\frac{x}{2}} x^{\frac{|m|}{2}} F \left( -\frac{\varepsilon - m - |m| - 1}{2}, |m| + 1; x \right) \quad (101)$$

where

$$\begin{aligned} x &= \frac{r^2}{2l_m^2} & l_m^2 &= \frac{\hbar}{m^* \omega_c} = \frac{c\hbar}{eB_0} \\ \omega &= \frac{\omega_c}{2} & \varepsilon &= \frac{E}{\hbar\omega} \end{aligned} \quad (102)$$

In the case when we need to take in consideration the spin of the electron we should change the energy  $E$  by  $(E + \mu_s \frac{\omega_c}{s} B_0)$  in the last expression, and the corresponding degeneracy will be lifted.

The energy levels that can be obtained with the boundary condition at  $r = a$  for the wavefunctions corresponding to the regions  $0 \leq r \leq a$  and  $r > a$  are [see Eq. (96)]

$$\frac{1}{m^*} \frac{\Psi'_m(r^2)}{\Psi_m(r^2)} = \frac{1}{m^*} \frac{K'_m(r)}{K_m(r)} \quad (103)$$

where  $\Psi_m(r^2)$  is the solution of Eq. (101) in the region  $0 \leq r \leq a$ ,  $r^2 = 2xl_m^2$ , and  $K_m(r)$  is the Macdonald function which is the solution of Eq. (100) for the region  $r > a$ .

### 2.3.4. A More Realistic Potential

It is clear that the energy levels obtained from condition (103) are approximations. More strictly speaking, we should substitute in this equation the solution of Eq. (100) for the region  $r > a$  with an additional constant  $-V$ , the height of the potential barrier, instead of the function  $K_m(r)$  [the potential in this case becomes  $((m^*/2)\omega^2 r^2 + V)$ ]. In this case Eq. (100) takes the form

$$\psi'' + \frac{1}{x} \Psi' - \frac{m^2}{4x^2} \Psi + \frac{\varepsilon - V - m}{2x} \Psi + \frac{1}{4} \psi = 0 \quad (104)$$

and its solutions can be written as

$$\Psi_m^{(+)} = Ae^{im\varphi} e^{-\frac{x}{2}} x_1^{\frac{|m|}{2}} F_1 \left( -\frac{\varepsilon - V - m - |m| - 1}{2}, |m| + 1; x \right) \quad (105)$$



for the region  $r > a$  (in this case we have the relation  $E - V < 0$ ), and for the internal region the solution is equal to (101),

$$\Psi_m^{(-)} = A e^{im\varphi} e^{-\frac{x}{2}} x_1^{\frac{|m|}{2}} F_1\left(-\frac{\varepsilon - m - |m| - 1}{2}, |m| + 1; x\right) \quad (106)$$

where all variables are the same as in Eq. (105), and  $\varepsilon = (E + \mu_s \frac{\sigma}{s} B) \frac{1}{\hbar\omega}$ . In this case the boundary condition is

$$\frac{\Psi_m'(-)}{\Psi_m(-)} = \frac{\Psi_m'(+) }{\Psi_m(+)} \quad (107)$$

which leads to the transcendental equation for energy:

$$\begin{aligned} & (\alpha - V)_1 F_1\left(-\alpha + \frac{V}{2} + 1, |m| + 2; x\right)_1 F_1(-\alpha, |m| + 1; x) \\ & - \alpha_1 F_1(-\alpha + 1, |m| + 2; x)_1 \\ & \times F_1\left(-\alpha + \frac{V}{2}, |m| + 1; x\right) = 0 \end{aligned} \quad (108)$$

The results of calculations of the energy spectra that correspond to the boundary conditions of Eq. (107) are presented in Figure 9. The energies are plotted as functions of the parameters of the problem—the magnetic field and the height of the rectangular potential barriers—and all values are shown in relative units. In this figure it can also be observed that for the size of the potential barrier ( $V_c/\hbar\omega = 1$ ) there are no energy states when the spatial confinement and magnetic confinement are almost the same. The energy states exist when  $a > l_m$ , and for the case when  $a < l_m$  the intensity of the magnetic field is such that the electron energy levels are located above the potential barrier and electrons escape from the interior of the quantum dot. Under these conditions the magnetic field can be used in order to tune the electronic states inside the quantum

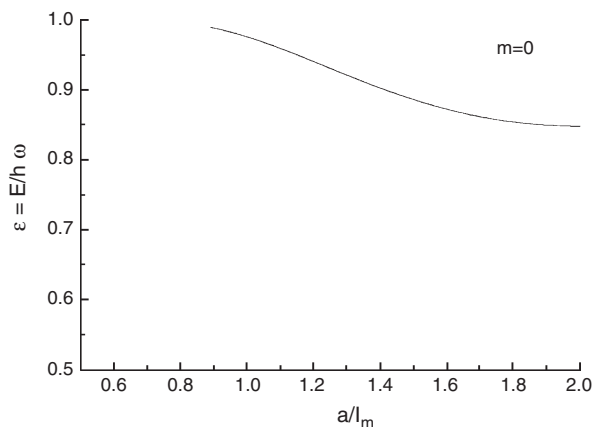


**Figure 9.** The one-electron energy spectrum for a QD, with the magnetic field only in the inner part of the QD where the confinement potential is  $V(r)$ . The energy is calculated under assumption of boundary condition (107) as a function of the width of the confinement potential  $a/l_m$  for constant value  $V_c/\hbar\omega = 1$ . Reprinted with permission from [88], A. Lipovka et al., *Phys. Low-Dim. Struct.* 9/10, 97 (2002). © 2002, VSV.

dot. As should be expected, these results are similar to those calculated in [83], but our results are thought to be more realistic ones.

In Figure 10 one can see a more detailed comparison of the one-electron energy spectra for the two cases which correspond to different potentials [boundary conditions (103) and (107)]. The corresponding one-electron energy spectra are presented as functions of external magnetic field. It also is observed that for a potential barrier bigger than the potential barrier of Figure 9 there only exist energy states with  $a < l_m$  for  $m = 0$  since the state with  $m = 1$  only exists with  $a > l_m$ ; this only happens for magnetic fields inside the quantum dot. However, with the magnetic fields inside or outside the quantum dot the energy level with  $m = 0$  extends to  $a/l_m = 1.7$  approximately (i.e., from the region with  $a < l_m$  to the region  $a > l_m$ ). Thus, with a magnetic field in the exterior of the quantum dot the energy states inside the quantum dot can be manipulated. We can also conclude that the choice of a diamagnetic or paramagnetic material in the exterior of the quantum dot can be used to manipulate or tune the electronic states in the quantum dot for a fixed  $a$  and  $B$ .

In Figures 11, 12, and 13 the variation of state with  $m = 0$  with respect to the potential barrier  $V(r)$  for several values of  $a/l_m$ , which characterize the relation between the spatial and the magnetic confinements, is shown. In Figure 11,  $a = 0.5l_m$ , in Figure 12  $a = l_m$ , and in Figure 13  $a = 2l_m$ . The variation of the curves means that when the spatial confinement increases the energy states due to magnetic confinement appear for a lower potential barrier  $V(r)$ ; on the other hand, if the magnetic confinement decreases the energy states tend to disappear, as one can expect. Also plotted in Figure 13 is the state with  $m = 1$  and we can observe that for barriers lower than that of Figure 11 this state goes out to the exterior of the quantum dot because

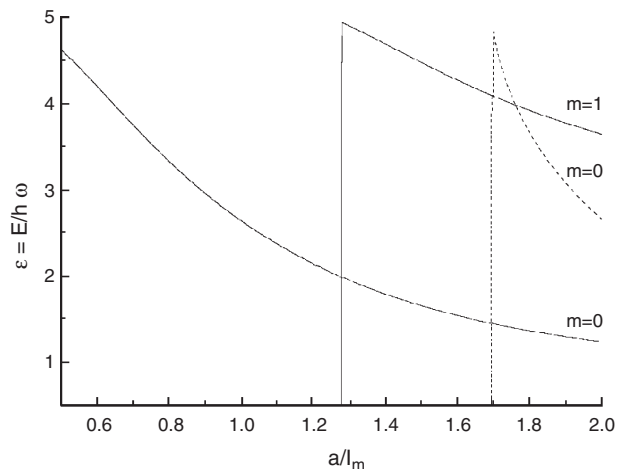


**Figure 10.** Solid lines are the same as in Figure 9, but for  $V_c/\hbar\omega = 5$ . Dashed line is the one-electron energy spectrum for the QD, with the magnetic field inside and outside the QD where the confinement potential is  $V(r)$ . The energy is calculated under the assumption of boundary condition (107) as a function of the width of the confinement potential  $a/l_m$  for constant value  $V_c/\hbar\omega = 5$ . Reprinted with permission from [88], A. Lipovka et al., *Phys. Low-Dim. Struct.* 9/10, 97 (2002). © 2002, VSV.

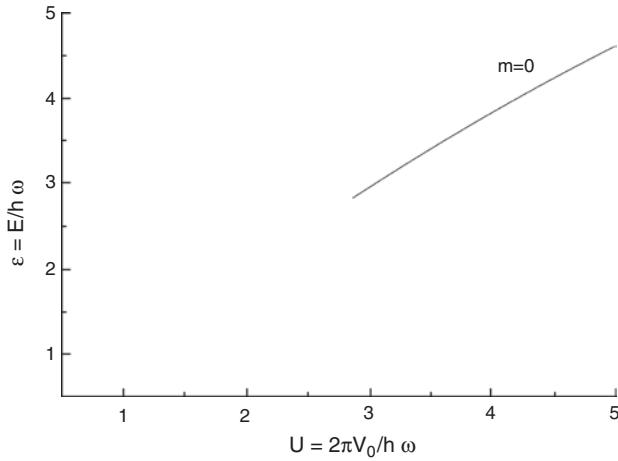


**Figure 11.** The one-electron energy spectrum in the QD with the magnetic field only in the inner part of the QD with the confinement potential given by  $V(r)$ . The energy is calculated under the assumption of boundary condition (107) as a function of the depth of the confinement potential  $V_c/\hbar\omega$  for a constant value  $a/l_m = 0.5$ . Reprinted with permission from [88], A. Lipovka et al., *Phys. Low-Dim. Struct.* 9/10, 97 (2002). © 2002, VSV.

it has a larger energy than for  $m = 0$ . Thus, the existence of this energy state inside the quantum dot requires bigger potential barriers  $V(r)$ .

#### 2.4. Exciton Binding Energy in a Quantum Wire in the Presence of a Magnetic Field

A calculation of the ground state energy of an exciton confined in a cylindrical quantum wire in the presence of a uniform magnetic field as a function of wire radius is made using a variational approach. It is assumed that the magnetic field is applied parallel to the axis of the wire. The calculations have been performed using a suitable variational wavefunction taken as a product of the appropriate confining confluent hypergeometric functions and a hydrogenic

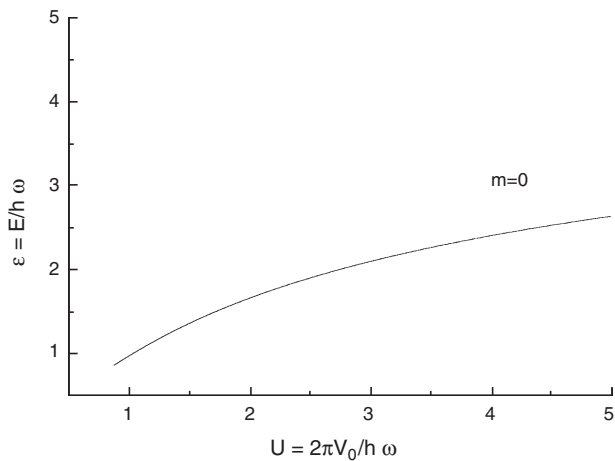


**Figure 12.** The same as in Figure 11 but for  $a/l_m = 1$ . Reprinted with permission from [88], A. Lipovka et al., *Phys. Low-Dim. Struct.* 9/10, 97 (2002). © 2002, VSV.

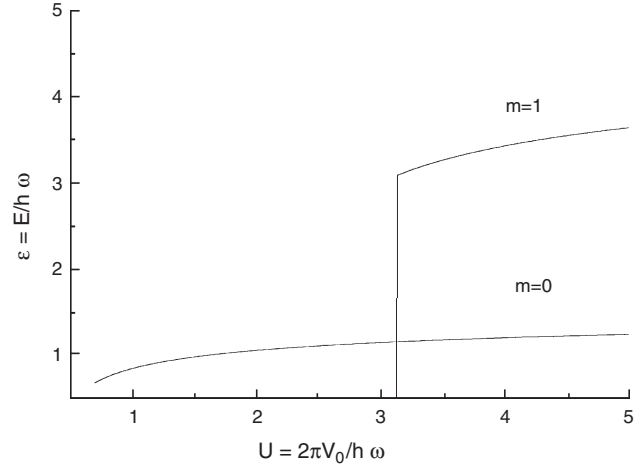


**Figure 13.** The same as in Figure 11 but for  $a/l_m = 2$ . Reprinted with permission from [88], A. Lipovka et al., *Phys. Low-Dim. Struct.* 9/10, 97 (2002). © 2002, VSV.

function for infinite and finite confining potentials [98]. For a given value of the magnetic field, the binding energy is found to be larger than the zero field case. This behavior is explained in terms of an average electron–hole separation, which depends on the wire radius and the magnetic field strength.

##### 2.4.1. Infinite Potential Barrier Case

The Hamiltonian for the interacting electron–hole pair inside a cylindrical wire of radius  $r_0$ , with infinite potential barrier at the surface, in the presence of a magnetic field applied parallel to wire axis, is given by

$$\hat{H} = \frac{1}{2m_e^*} \left( \hat{p}_e + \frac{e}{c} \vec{A}_e \right)^2 + \frac{1}{2m_h^*} \left( \hat{p}_h - \frac{e}{c} \vec{A}_h \right)^2 - \frac{e^2}{\kappa |\vec{r}_e - \vec{r}_h|} + V_e(\rho_e, \phi_e) + V_h(\rho_h, \phi_h) \quad (109)$$

where

$$|\vec{r}_e - \vec{r}_h| = [\rho_e^2 + \rho_h^2 - 2\rho_e\rho_h \cos(\phi_e - \phi_h) + z^2]^{1/2} \quad (110)$$

and

$$V_{e(h)}(\rho_{e(h)}, \phi_{e(h)}) = \begin{cases} 0 & 0 \leq \rho_e \text{ and } \rho_h \leq r_0 \\ \infty & \rho_e \text{ or } \rho_h > r_0 \end{cases} \quad (111)$$

For a uniform magnetic field we can write

$$\vec{A}_{e(h)}(\vec{r}_{e(h)}) = \frac{\vec{B} \times \vec{r}_{e(h)}}{2} \quad (112)$$

where  $\vec{B} = B\vec{e}_z$ . In cylindrical coordinates the magnetic field potential becomes  $A_\rho = A_z = 0$ ,  $A_\phi[e(h)] = B\rho_{e(h)}/2$ . The inclusion of the Coulombic potential leads to a nonseparable differential equation which cannot be solved analytically. Therefore, it is necessary to use a variational approach to calculate the eigenfunctions and eigenvalues of the Hamiltonian.

Following Brown and Spector [46] we take into account the cylindrical confining symmetry, the presence of the magnetic field, and the electron-hole Coulombic potential, by choosing a trial wavefunction for the ground state, which can be written as product of a hydrogenic part and the radial solutions of an electron and a hole in a cylindrical wire in the presence of magnetic field, applied parallel to the wire axis:

$$f(\vec{r}) = \begin{cases} N \exp\left[-\frac{(\xi_e + \xi_h)}{2}\right] F(-a_{01e}, 1; \xi_e) \\ \quad \times F(-a_{01h}, 1; \xi_h) \exp[-\lambda|\vec{r}_e - \vec{r}_h|] & 0 \leq \rho_e \text{ and } \rho_h \leq r_0 \\ 0 & \rho_e \text{ or } \rho_h > r_0 \end{cases} \quad (113)$$

In Eq. (113) the variable

$$\xi_{e(h)} = \frac{\rho_{e(h)}^2}{2\alpha_{c[e(h)]}^2} = \frac{eB\rho_{e(h)}^2}{2\hbar c} \quad \alpha_{c[e(h)]} = \left( \frac{\hbar}{m_{e(h)}^* \omega_{c[e(h)]}} \right) \quad (114)$$

is the cyclotron radius,  $\omega_{c[e(h)]} = eB/m_{e(h)}^*c$  is the cyclotron frequency,  $N$  is the normalization constant, and  $\lambda$  is a variational parameter. Equation (113) satisfies the boundary condition that  $f(\rho_{e(h)} = r_0) = 0$ , while  $a_{01[e(h)]}$  is the eigenvalue for the electron (hole) in a wire in a magnetic field, calculated numerically from the boundary condition eigenvalue equation.  $N$  is given by

$$N^{-2} = -2\pi \frac{dG}{d\lambda} \quad (115)$$

with

$$G = \int_0^{r_0} \rho_e d\rho_e \int_0^{r_0} \rho_h d\rho_h \exp\left(-\frac{\rho_e^2}{2\alpha_{c(e)}^2}\right) \\ \times F^2\left(-a_{01(e)}, 1; \frac{\rho_e^2}{2\alpha_{c(e)}^2}\right) \exp\left(-\frac{\rho_h^2}{2\alpha_{c(h)}^2}\right) \\ \times F^2\left(-a_{01(h)}, 1; \frac{\rho_h^2}{2\alpha_{c(h)}^2}\right) I_0(2\lambda\rho_{<}) K_0(2\lambda\rho_{>}) \quad (116)$$

where  $\rho_{<}(\rho_{>})$  is the lesser (greater) of  $\rho_e$  and  $\rho_h$ ; the particular values for  $\rho_{<}$  and  $\rho_{>}$  are determined by electron and hole locations and the integration limits. In Eq. (116),  $I_0$  and  $K_0$  are the modified Bessel functions of the second kind of order zero.

The binding energy  $\varepsilon_b(r_0, B)$  for the exciton is defined as the ground state energy of a system without Coulombic interaction, minus the ground state energy  $\varepsilon_0(r_0, B) = \langle \hat{H}(r_0, B) \rangle$  in the presence of electron-hole interaction. That is,

$$\varepsilon_b(r_0, B) = \hbar\omega_{c(e)}\left(a_{01(e)} + \frac{1}{2}\right) + \hbar\omega_{c(h)}\left(a_{01(h)} + \frac{1}{2}\right) \\ - \varepsilon_0(r_0, B) \quad (117)$$

The binding energy defined in this way is a positive quantity.

The ground state energy  $\langle \hat{H}(r_0, B) \rangle = \langle T \rangle + \langle V \rangle$  is found after tedious algebra,

$$\langle T \rangle = \hbar\omega_{c(e)}\left(a_{01(e)} + \frac{1}{2}\right) + \hbar\omega_{c(h)}\left(a_{01(h)} + \frac{1}{2}\right) + \frac{\hbar^2}{2\mu^*}\lambda^2 \quad (118)$$

where  $\mu^*$  is the effective reduced mass and

$$\langle V \rangle = -\frac{4\pi e^2}{\kappa} N^2 G \quad (119)$$

Therefore,

$$\varepsilon_b(r_0, B) = -\frac{\hbar^2}{2\mu^*}\lambda^2 - \frac{2e^2}{\kappa} \frac{G}{dG/d\lambda} \quad (120)$$

For computational purposes, we normalize the expression for the binding energy  $\varepsilon_b(r_0, B)$  [Eq. (120)] in Rydberg units and define  $\gamma_{e(h)} = \hbar\omega_{c[e(h)]}/2R_{y, \text{exc}}^*$ . In addition, we transform the integral for  $G$  in a dimensionless form by letting  $\rho = tr_0$ ; the expressions for  $\langle \hat{H}(r_0, B) \rangle$  and  $\varepsilon_b(r_0, B)$  are then written as

$$\langle \hat{H}(r_0, B) \rangle = \gamma_e(1 + 2a_{01(e)}) + \gamma_h(1 + 2a_{01(h)}) \\ + (\lambda a_B^*)^2 + 4a_B^* \frac{G_1}{dG_1/d\lambda} \quad (121)$$

$$\varepsilon_b(r_0, B) = -(\lambda a_B^*)^2 - 2a_B^* \frac{G_1}{dG_1/d\lambda} \quad (122)$$

where

$$G_1 = \int_0^1 t_e dt_e \int_0^1 t_h dt_h \exp(-t_e^2 \xi_{r_0(e)}) F^2(-a_{01(e)}, 1; t_e^2 \xi_{r_0(e)}) \\ \times \exp(-t_h^2 \xi_{r_0(h)}) F^2(-a_{01(h)}, 1; t_h^2 \xi_{r_0(h)}) \\ \times I_0(2\lambda r_0 t_{<}) K_0(2\lambda r_0 t_{>}) \quad (123)$$

and  $\xi_{r_0[e(h)]} = r_0^2/2\alpha_{c[e(h)]}^2$ .

In order to find the minimum of  $\langle \hat{H}(r_0, B) \rangle$  with respect to  $\lambda$  and thus to obtain a lower bound to the ground state the variational method is used. The radial double integration in  $G_1$  is performed numerically since there is no analytical method to evaluate it.

#### 2.4.2. Finite Potential Barrier Case

For the finite potential barrier case, the potential in the Hamiltonian [Eq. (109)] is taken as zero for  $\rho_{e(h)} < r_0$  and  $V_0$  for  $\rho_{e(h)} > r_0$ . All the other assumptions remain the same. Furthermore, we assume that the electron and hole masses are constant (at their values in GaAs) across the barrier. Again, following Brown and Spector [46] we take into account the cylindrical confining symmetry, the presence of the magnetic field, and the Coulomb potential by choosing a trial wavefunction for the ground state, which can be written as a product of a hydrogenic part and the radial solutions of

an electron and a hole in a cylindrical wire in the presence of a magnetic field, parallel to the wire axis,

$$f(\vec{r}_e, \vec{r}_h) = \begin{cases} N \exp\left(-\frac{\xi_e + \xi_h}{2}\right) F(-a_{01(e)}, 1; \xi_e) \\ \times F(-a_{01(h)}, 1; \xi_h) \exp(-\lambda|\vec{r}_e - \vec{r}_h|) & 0 \leq \rho_e \text{ and } \rho_h \leq r_0 \\ N \frac{F(-a_{01(e)}, 1; \xi_{r_0e})}{U(-a'_{01(e)}, 1; \xi_{r_0e})} \exp\left(-\frac{\xi_e + \xi_h}{2}\right) \\ \times U(-a'_{01(e)}, 1; \xi_e) F(-a_{01(h)}, 1; \xi_h) \\ \times \exp(-\lambda|\vec{r}_e - \vec{r}_h|) & \rho_e > r_0 \text{ and } \rho_h \leq r_0 \\ N \frac{F(-a_{01(h)}, 1; \xi_{r_0h})}{U(-a'_{01(h)}, 1; \xi_{r_0h})} \exp\left(-\frac{\xi_e + \xi_h}{2}\right) \\ \times F(-a_{01(e)}, 1; \xi_e) U(-a'_{01(h)}, 1; \xi_h) \\ \times \exp(-\lambda|\vec{r}_e - \vec{r}_h|) & \rho_e \leq r_0 \text{ and } \rho_h > r_0 \\ N \frac{F(-a_{01(e)}, 1; \xi_{r_0e})}{U(-a'_{01(e)}, 1; \xi_{r_0e})} \frac{F(-a_{01(h)}, 1; \xi_{r_0h})}{U(-a'_{01(h)}, 1; \xi_{r_0h})} \\ \times \exp\left(-\frac{\xi_e + \xi_h}{2}\right) U(-a'_{01(e)}, 1; \xi_e) \\ \times U(-a'_{01(h)}, 1; \xi_h) \exp(-\lambda|\vec{r}_e - \vec{r}_h|) & \rho_e \text{ and } \rho_h > r_0 \end{cases} \quad (124)$$

where  $\xi_{e(h)} = \rho_{e(h)}^2 / 2\alpha_{e(h)}^2$ . Equation (124) satisfies the boundary condition

$$\frac{1}{m_i^*} \frac{\partial f_i}{\partial \rho_{e(h)}} = \frac{1}{m_o^*} \frac{\partial f_o}{\partial \rho_{e(h)}} \quad \text{at } \rho_{e(h)} = r_0 \quad (125)$$

while  $a_{01e(h)}$  and  $a'_{01e(h)}$  are the eigenvalues for the ground state of the problem inside and outside the wire for an electron and a hole, respectively.  $N$  is given by

$$N^{-2} = -4\pi^2 \frac{d}{d\lambda} (I_K + I_L + I_M + I_N) \quad (126)$$

with

$$I_K = \int_0^{r_0} \rho_e d\rho_e \int_0^{r_0} \rho_h d\rho_h \exp[-(\xi_e + \xi_h)] F^2(-a_{01(e)}, 1; \xi_e) \\ \times F^2(-a_{01(h)}, 1; \xi_h) I_0(2\lambda\rho_<) K_0(2\lambda\rho_>) \quad (127)$$

$$I_L = \frac{F^2(-a_{01(e)}, 1; \xi_{r_0e})}{U^2(-a'_{01(e)}, 1; \xi_{r_0e})} \int_0^\infty \rho_e d\rho_e \exp(-\xi_e) \\ \times U^2(-a'_{01(e)}, 1; \xi_e) K_0(2\lambda\rho_e) \int_0^{r_0} \rho_h d\rho_h \exp(-\xi_h) \\ \times F^2(-a_{01(h)}, 1; \xi_h) I_0(2\lambda\rho_h) \quad (128)$$

$$I_M = \frac{F^2(-a_{01(h)}, 1; \xi_{r_0h})}{U^2(-a'_{01(h)}, 1; \xi_{r_0h})} \int_0^{r_0} \rho_e d\rho_e \exp(-\xi_e) \\ \times F^2(-a_{01(e)}, 1; \xi_e) I_0(2\lambda\rho_e) \int_{r_0}^\infty \rho_h d\rho_h \exp(-\xi_h) \\ \times U^2(-a'_{01(h)}, 1; \xi_h) K_0(2\lambda\rho_h) \quad (129)$$

and

$$I_N = \frac{F^2(-a_{01(e)}, 1; \xi_{r_0e})}{U^2(-a'_{01(e)}, 1; \xi_{r_0e})} \frac{F^2(-a_{01(h)}, 1; \xi_{r_0h})}{U^2(-a'_{01(h)}, 1; \xi_{r_0h})} \\ \times \int_{r_0}^\infty \rho_e d\rho_e \int_{r_0}^\infty \rho_h d\rho_h \exp[-(\xi_e + \xi_h)] \\ \times U^2(-a'_{01(e)}, 1; \xi_e) U^2(-a'_{01(h)}, 1; \xi_h) \\ \times I_0(2r_0 t_<) K_0(2\lambda r_0 t_>) \quad (130)$$

The binding energy  $\varepsilon_b(r_0, B)$  is calculated as in the infinite potential barrier case, leading to the following expression:

$$\varepsilon_b(r_0, B) = -\frac{\hbar^2}{2\mu^*} \lambda^2 - \frac{2e^2}{\kappa} \frac{(I_K + I_L + I_M + I_N)}{d(I_K + I_L + I_M + I_N)/d\lambda} \quad (131)$$

We normalize the expression for the binding energy  $\varepsilon_b(r_0, B)$ , in units of exciton Rydberg  $R_{y, \text{exc}}^*$ ,

$$\varepsilon_b(r_0, B) = -(\lambda a_B^*)^2 - 4a_B^* \frac{(I_{KK} + I_{LL} + I_{MM} + I_{NN})}{d(I_{KK} + I_{LL} + I_{MM} + I_{NN})/d\lambda} \quad (132)$$

where

$$I_{KK} = \int_0^1 t_e dt_e \int_0^1 t_h dt_h \exp(-t_e^2 \xi_{r_0e}) \\ \times F^2(-a_{01(e)}, 1; t_e^2 \xi_{r_0e}) \exp(-t_h^2 \xi_{r_0h}) \\ \times F^2(-a_{01(h)}, 1; t_h^2 \xi_{r_0h}) I_0(2\lambda r_0 t_<) K_0(2\lambda r_0 t_>) \quad (133)$$

$$I_{LL} = \frac{F^2(-a_{01(e)}, 1; \xi_{r_0e})}{U^2(-a'_{01(e)}, 1; \xi_{r_0e})} \int_1^\infty t_e dt_e \exp(-t_e^2 \xi_{r_0e}) \\ \times U^2(-a'_{01(e)}, 1; t_e^2 \xi_{r_0e}) K_0(2\lambda r_0 t_e) \int_0^1 t_h dt_h \\ \times \exp(-t_h^2 \xi_{r_0h}) F^2(-a_{01(h)}, 1; t_h^2 \xi_{r_0h}) I_0(2\lambda r_0 t_h) \quad (134)$$

$$I_{MM} = \frac{F^2(-a_{01(h)}, 1; \xi_{r_0h})}{U^2(-a'_{01(h)}, 1; \xi_{r_0h})} \int_0^1 t_e dt_e \exp(-t_e^2 \xi_{r_0e}) \\ \times F^2(-a_{01(e)}, 1; t_e^2 \xi_{r_0e}) I_0(2\lambda r_0 t_e) \\ \times \int_1^\infty t_h dt_h \exp(-t_h^2 \xi_{r_0h}) U^2(-a'_{01(h)}, 1; t_h^2 \xi_{r_0h}) \\ \times K_0(2\lambda r_0 t_h) \quad (135)$$

and

$$I_{NN} = \frac{F^2(-a_{01(e)}, 1; \xi_{r_0e})}{U^2(-a'_{01(e)}, 1; \xi_{r_0e})} \frac{F^2(-a_{01(h)}, 1; \xi_{r_0h})}{U^2(-a'_{01(h)}, 1; \xi_{r_0h})} \\ \times \int_1^\infty t_e dt_e \int_1^\infty t_h dt_h \exp[-(t_e^2 \xi_{r_0e} + t_h^2 \xi_{r_0h})] \\ \times U^2(-a'_{01(e)}, 1; t_e^2 \xi_{r_0e}) U^2(-a'_{01(h)}, 1; t_h^2 \xi_{r_0h}) \\ \times I_0(2\lambda r_0 t_<) K_0(2\lambda r_0 t_>) \quad (136)$$

The values of the physical parameters pertaining to the material GaAs used in the calculations are given in Table 1 [77].

**Table 1.** Physical parameters pertaining to the material GaAs.

	$m_e^*$	$\kappa$	$\gamma_1$	$\gamma_2$	$m_{hh}^*(x, y)$	$m_{hh}^*(z)$	$m_h^*(x, y)$	$m_h^*(z)$
GaAs	$0.067m_0$	12.5	7.36	2.57	$0.10m_0$	$0.45m_0$	$0.21m_0$	$0.08m_0$

For mathematical convenience and without any loss of physical insight, isotropic hole mass is assumed and, therefore, we can write an expression for an isotropic hole mass:

$$(m_h^*)^{-1} = \frac{2}{3}(m_h^*(x, y))^{-1} + \frac{1}{3}(m_h^*(z))^{-1} \quad (137)$$

The reduced mass for the heavy hole exciton is  $0.0447m_0$  and that for the light hole exciton is  $0.0449m_0$ . Since both heavy and light hole exciton masses are close to each other, for the rest of the topic we present results for the heavy exciton.

In Figure 14 the variation of the exciton binding energy  $\varepsilon_b$  as a function of wire radius  $r_0$  for several values of the magnetic field in the infinite potential barrier case is shown. For a given value of the magnetic field the binding energy increases as the wire radius is reduced and diverges as  $r_0 \rightarrow 0$ . For small values of the wire radii ( $r_0 \leq a_B$ ) and for values of the magnetic field considered in this work, the exciton binding energy is relatively insensitive to the variation of the magnetic field, since the confinement effect due to the potential barrier is more significant than that due to the application of the magnetic field. For large values of the wire radii ( $r_0 \geq 3a_B^*$ ) the binding energy for  $B = 0$  approaches its value in the bulk GaAs (i.e., the exciton Rydberg) and

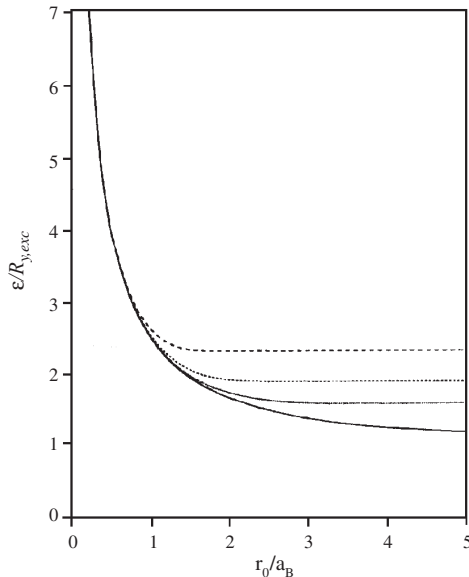


**Figure 14.** Variations of the binding energy of a heavy hole exciton  $\varepsilon_b$ , expressed in terms of an exciton Rydberg  $R_{y,exc}^*$  in GaAs ( $\approx 3.9$  meV) as a function of the radius of the wire  $r_0$  expressed in terms of Bohr radius  $a_B$  in GaAs ( $\approx 148$  Å) for  $B_0 = 0$  kG (solid line), 50 kG (dotted line), 100 kG (short dashed line), and 200 kG (long dashed line). Reprinted with permission from [186], J. L. Marín et al., “Handbook of Advanced Electronic and Photonic Materials and Devices” (H. S. Nalwa, Ed.). Academic Press, San Diego, 2001. © 2001, Academic Press.

varies with the magnetic field essentially in the same fashion as calculated by Aldrich and Greene [99].

In Figure 15 the variation of the exciton binding energy  $\varepsilon_b$  as a function of magnetic field for several values of the wire radii in the infinite potential barrier case is plotted. Again, for small values of the wire radii ( $r_0 \leq a_B^*$ ) the binding energy is relatively insensitive to the variations of the magnetic field; however, for large values of the wire radii ( $r_0 \geq 3a_B^*$ ) the variation of  $\varepsilon_b$  with magnetic field is much more pronounced due to the strong confinement effect of the magnetic field.

In Figure 16 the variation of the exciton binding energy  $\varepsilon_b$  as a function of the radius of the wire for several values of the magnetic field for a finite potential barrier is plotted. The Al concentration in the barrier material is assumed to be  $x = 0.3$ . For a given value of the magnetic field the binding energy increases from its bulk value in GaAs as the wire radius is reduced, reaches a maximum value, and then drops to the bulk value characteristic of the barrier material as the wire radius goes to zero. This is due to the fact that as the wire radius is decreased the electron wavefunction is compressed thus leading to the enhancement of the binding energy. However, below a certain value of  $r_0$  the leakage of the wavefunction into the barrier region becomes more important and, thus, the binding energy starts decreasing until it reaches a value that is characteristic of the barrier material as  $r_0 \rightarrow 0$ . For a given value of  $r_0$  the binding energy increases as a function of the magnetic field due to the increasing compression of the wavefunction with magnetic field.

In Figure 17 the variation of the exciton binding energy as a function of the magnetic field for several values of the wire radius is shown. It is found that for small values of  $r_0/a_B^*$  ( $< 1$ ) the change in the binding energy with magnetic

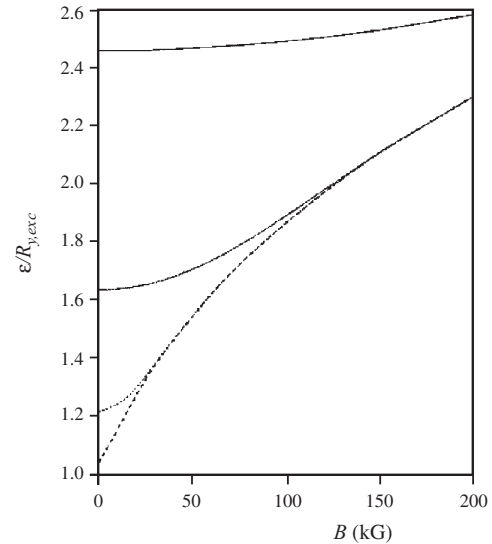


**Figure 15.** Variations of the binding energy of a heavy hole exciton  $\varepsilon_b$ , as a function of the magnetic field  $B$  for  $r_0 = 0a_B^*$  (solid line),  $2a_B^*$  (dotted line),  $4a_B^*$  (short dashed line), and  $10a_B^*$  (long dashed line). Reprinted with permission from [186], J. L. Marín et al., “Handbook of Advanced Electronic and Photonic Materials and Devices” (H. S. Nalwa, Ed.). Academic Press, San Diego, 2001. © 2001, Academic Press.

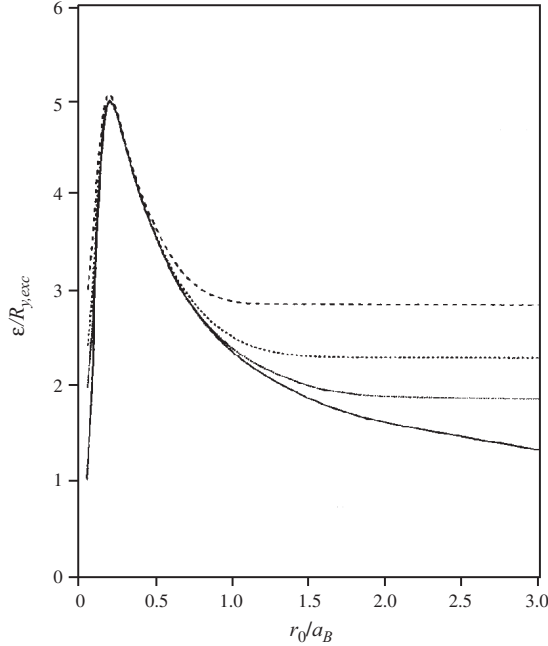


**Figure 16.** Variations of the binding energy of a heavy hole exciton  $\epsilon_b$ , as a function of the radius of the wire  $r_0$ .  $B_0 = 0$  kG (solid line), 100 kG (dotted line), 200 kG (short dashed line), and 400 kG (long dashed line). Reprinted with permission from [186], J. L. Marín et al., “Handbook of Advanced Electronic and Photonic Materials and Devices” (H. S. Nalwa, Ed.). Academic Press, San Diego, 2001. © 2001, Academic Press.

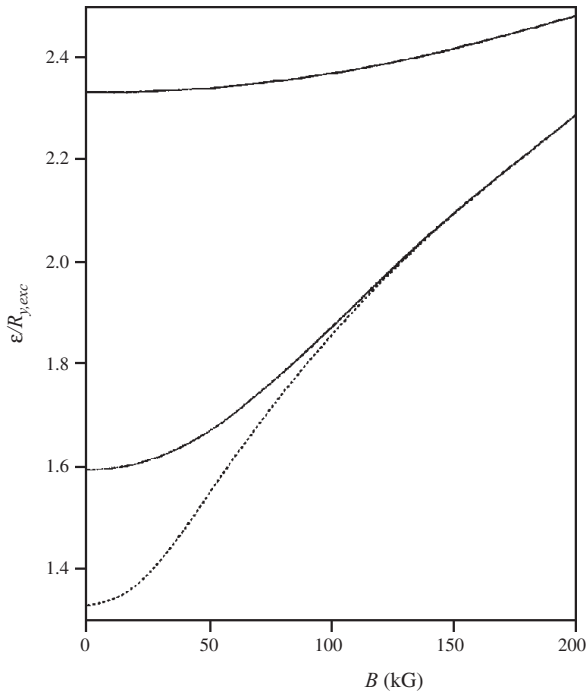


**Figure 17.** Variations of the binding energy of a heavy hole exciton  $\epsilon_b$ , as a function of the magnetic field  $B$  for  $r_0 = a_B^*$  (upper line),  $2a_B^*$  (medium line), and  $3a_B^*$  (lower line). Reprinted with permission from [186], J. L. Marín et al., “Handbook of Advanced Electronic and Photonic Materials and Devices” (H. S. Nalwa, Ed.). Academic Press, San Diego, 2001. © 2001, Academic Press.

field is similar to that in the case of bulk GaAs, since most of the wavefunction resides in the barrier. For intermediate values of  $r_0/a_B^*$  ( $\approx 1.0$ ) the variation of the binding energy with magnetic field is considerably smaller since the electron wavefunction is highly confined by the barrier potential. For larger values of  $r_0/a_B^*$  ( $\geq 3.0$ ) the exciton binding energy varies with magnetic field essentially the same way as it does in bulk GaAs.

## 2.5. Magnetoconductivity of a Quasi-Two-Dimensional Electron Gas

### 2.5.1. Macroscopic Derivation

Let us consider a quasi-two-dimensional electron gas subjected to a strong magnetic field. We are interested in its linear response to a weak static electric field  $\vec{E} \perp \hat{e}_z$  (i.e., applied in the layer plane of the heterostructure). The electron gas responds to this external disturbance with an electrical current which, since  $E$  is assumed to be small, will be proportional to  $\vec{E}$ . Thus, we may write that the  $x, y$  components of the areal current density  $\vec{J}$  are related to  $\vec{E}$  by

$$J_x = \sigma_{xx}E_x + \sigma_{xy}E_y \quad J_y = \sigma_{yx}E_x + \sigma_{yy}E_y \quad (138)$$

As we are dealing with cubic host materials  $\sigma_{xx} = \sigma_{yy}$  and the Onsager relationships [101, 102] show that

$$\sigma_{xy} = -\sigma_{yx} \quad (139)$$

The conductivity tensor  $\vec{\sigma}$  is the quantity that is most naturally calculated. Practically, however, the resistivity tensor

$$\vec{\rho} = \vec{\sigma}^{-1} \quad (140)$$

is the most accessible to the experiments. If we invert Eq. (138), we obtain

$$\rho_{xx} = \rho_{yy} = \frac{\sigma_{xx}}{\sigma_{xx}^2 + \sigma_{xy}^2} \quad \rho_{yx} = -\rho_{xy} = \frac{\sigma_{xy}}{\sigma_{xx}^2 + \sigma_{xy}^2} \quad (141)$$

Let us consider a sample with “spider” geometry. It consists of a long bar ( $L_x \gg L_y$ ) with side contacts (see Fig. 18). The voltage  $V_x$  is imposed via a battery and the voltage  $V_H$  is measured across the small dimension of the bar. Since  $J_y$  vanishes we have

$$E_x = \rho_{xx}J_x \quad E_y = \rho_{yx}J_x \quad (142)$$

If one assumes that the current densities  $J_x, J_y$  are uniform in the sample (the spatial variation of  $\vec{J}$  is still a matter of controversy) we may write

$$J_x = \frac{I_x}{L_y} \quad V_H = E_y L_y \quad V_x = E_x L_x \quad (143)$$

Thus

$$V_x = \frac{\rho_{xx}}{L_y} L_x I_x = R_{xx} I_x \quad V_H = \rho_{yx} I_x = R_{yx} I_x \quad (144)$$



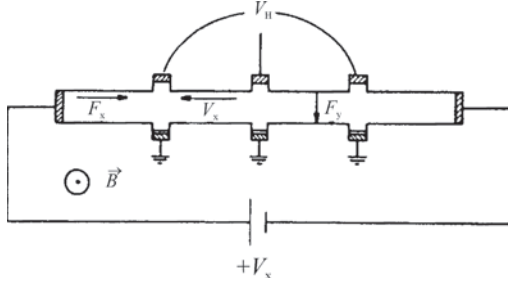


**Figure 18.** Sample geometry used to measure the resistivity tensor  $\vec{\rho}(B)$ . Reprinted with permission from [186], J. L. Marín et al., “Handbook of Advanced Electronic and Photonic Materials and Devices” (H. S. Nalwa, Ed.). Academic Press, San Diego, 2001. © 2001, Academic Press.

where  $V_z, V_H$  are expressed in volts,  $I_x$  in amperes, and  $R_{xx}, R_{yx}$  in ohms. Finally

$$R_{xx} = \frac{L_x}{L_y} \frac{\sigma_{xx}}{\sigma_{xx}^2 + \sigma_{yy}^2} \quad R_{yx} = \frac{\sigma_{xy}}{\sigma_{xx}^2 + \sigma_{yy}^2} \quad (145)$$

The resistance  $R_{xx}$  involves the geometrical factor  $L_x/L_y$  and thus is sample dependent. In literature, people often get rid of this inconvenience by quoting the resistance which would be measured in samples with a square shape but which are otherwise identical to their investigated samples. Thus, to recall this feature,  $R_{xx}$  measurements are given in units of square ohms ( $\Omega_0$ ).

On the other hand, the Hall resistance  $R_{yx}$  is independent of the sample shape. This explains why several Bureaux of Standards, in the hope of defining a new resistance standard, are interested in accurate  $R_{yx}$  data [103]. The former will be independent of sample size and thus free of dilata-tion effects, which often plague the usual ohm standards, which are presently based on resistance of platinum rods. Finally let us stress once more that both  $R_{xx}, R_{yx}$  as well as  $\rho_{xx}, \rho_{xy}$  are expressed in ohms. Nothing is wrong with the latter property. Only the resistivities  $\rho_{xx}, \rho_{xy}$  are two-dimensional resistivities. We know that in the dimension equation

$$\rho = \frac{m_e^*}{\eta_e e^2 \tau} \quad (146)$$

As in bulk materials  $\tau$  has the dimension of a relaxation time. However, in Eq. (146)  $\eta_e$  is an areal electron concentration instead of a volumetric concentration as usually found in bulk materials.

### 2.5.2. Microscopic Discussion

The linear response theory, originally derived by Kubo et al., has been used to evaluate the components  $\sigma_{xx}$  and  $\sigma_{yx}$  of the static magnetoconductivity tensor in the independent electron approximation [104]. We found that at  $T = 0$  K

$$\sigma_{xx} = \frac{\pi \hbar e^2}{(m_e^*)^2 S} \text{Trace} \left\{ \delta(\varepsilon_F - \hat{H}) \Pi_x \delta(\varepsilon_F - \hat{H}) \Pi_x \right\} \quad (147)$$

$$\sigma_{yx} = \frac{-ie^2 \hbar}{(m_e^*)^2 S} \int_{-\infty}^{+\infty} f(\varepsilon) d\varepsilon \times \text{Trace} \left\{ \delta(\varepsilon - \hat{H}) \left[ \Pi_y \frac{1}{(\varepsilon - \hat{H})^2} \Pi_x - \Pi_x \frac{1}{(\varepsilon - \hat{H})^2} \Pi_y \right] \right\} \quad (148)$$

where  $f(\varepsilon)$  is the Fermi–Dirac distribution function which, at zero temperature, is a step function of the argument  $\varepsilon_F - \varepsilon$  where  $\varepsilon_F$  is the Fermi level. In Eqs. (147) and (148)  $\Pi$  is  $\hat{p} + (e/c)\vec{A}$  and  $\hat{H}$  is the quasi-two-dimensional Hamiltonian which includes disorder,

$$\begin{aligned} \hat{H} &= \frac{\hat{p}_x^2}{2m_e^*} + \frac{1}{2m_e^*} \left( \hat{p}_y + \frac{e}{c} Bx \right)^2 \\ &\quad + \varepsilon_1 + g^* \mu_B B \sigma_z + V_{\text{disorder}}(\vec{\rho}) \\ \hat{H} &= \hat{H}_0 + V_{\text{disorder}}(\vec{\rho}) \end{aligned} \quad (149)$$

where

$$V_{\text{disorder}}(\vec{\rho}) = \int dz \chi_1^2(z) V_{\text{disorder}}(\vec{r}) \quad (150)$$

and  $\varepsilon_1$  is the confinement energy of the ground subband (wavefunction  $\chi_1$ ) which arises from the size quantization along the growth axis of the heterostructures. In Eqs. (149) and (150)  $\vec{\rho}(x, y), \vec{r} = (x, y, z)$ . To make sense, Eq. (149) requires a pronounced two-dimensionality of the electron gas; that is, the excited subbands  $\varepsilon_2, \dots$  must be far enough away from  $\varepsilon_1$  to allow a factorization of the carrier wavefunction  $\psi(\vec{r})$  in  $\chi_1(z)\varphi(\vec{\rho})$ . The assumed strong two-dimensionality also allows us to treat the case of the tilted magnetic fields with respect to the growth axis. Only the magnetic field  $B$ , which appears in Eq. (149), has to be understood as the projection of  $B$  along the  $z$  axis. The matrix elements of  $\Pi_x, \Pi_y$  on the Landau level basis (eigenstates of  $\hat{H}_0$ ) are

$$\begin{aligned} \langle n, k_y, \sigma_z | \Pi_x | n', k'_y, \sigma'_z \rangle &= \frac{i\hbar}{\lambda\sqrt{2}} [\sqrt{n}\delta_{n', n-1} - \sqrt{n+1}\delta_{n', n+1}] \\ &\quad \times \delta_{k'_y, k_y} \delta_{\sigma'_z, \sigma_z} \end{aligned} \quad (151)$$

$$\begin{aligned} \langle n, k_y, \sigma_z | \Pi_y | n', k'_y, \sigma'_z \rangle &= \frac{\hbar}{\lambda\sqrt{2}} [\sqrt{n}\delta_{n', n-1} + \sqrt{n+1}\delta_{n', n+1}] \\ &\quad \times \delta_{k'_y, k_y} \delta_{\sigma'_z, \sigma_z} \end{aligned} \quad (152)$$

In a perfect heterostructure  $V_{\text{disorder}}(\vec{\rho})$  vanishes. Thus the states  $|n, k_y, \sigma_z\rangle$  are eigenstates of  $\hat{H}$ . Consequently the matrix elements

$$\langle n, k_y, \sigma_z | \delta(\varepsilon - \hat{H}) | n', k'_y, \sigma'_z \rangle \quad (153)$$

are equal to

$$\begin{aligned} \langle n, k_y, \sigma_z | \delta(\varepsilon - \hat{H}) | n', k'_y, \sigma'_z \rangle \\ = \delta(\varepsilon - \varepsilon_{n\sigma_z}) \delta_{nn'} \delta_{k'_y, k_y} \delta_{\sigma'_z, \sigma_z} \end{aligned} \quad (154)$$

Equations (152)–(154) immediately lead to

$$\sigma_{xx} = 0 \quad \sigma_{yx} = \frac{\eta_e e^2}{m_e^* \omega_c} \quad (155)$$

Thus, for a perfect system the microscopic evaluation of the conductivity tensor leads to the same result as the classical Drude type of calculations.

Equation (155) is not surprising but merely serves as a reminder that, in the absence of scattering, a carrier subjected to crossed electric and magnetic fields actually drifts along a direction perpendicular to these two fields. The electrical transport along the electric field is entirely due to collisions, that is, to a nonvanishing  $V_{\text{disorder}}(\vec{\rho})$ .

We have already stated that very little is known about the exact shape of  $V_{\text{disorder}}(\vec{\rho})$ . Its spatial average over a macroscopic area should, however, vanish. Thus, in the  $(x, y)$  plane,  $V_{\text{disorder}}(\vec{\rho})$  shows uncorrelated fluctuations, which are either repulsive or attractive for electrons. (Notice that for very large magnetic fields both kinds of fluctuations, when considered as isolated, are capable of supporting bound states.) Taking the randomness of the disorder potential into account implies that Eqs. (147) and (148) should be completed by a spatial average over  $V_{\text{disorder}}(\vec{\rho})$ , and by taking the limit  $S \rightarrow \infty$ . If  $V_{\text{disorder}}(\vec{\rho})$  can be written as the sum of one-defect potentials centered at  $\vec{\rho}_i$

$$V_{\text{disorder}}(\vec{\rho}) = \sum_{\rho_i} W(\vec{\rho} - \vec{\rho}_i) \quad (156)$$

The spatial average signifies an average over the positions  $\vec{\rho}_i$  of the defects, which are assumed to be uncorrelated.

**Magnetic Field Dependence of  $\sigma_{xx}$  (Shubnikov–de Haas Effect)** Let us evaluate  $\sigma_{xx}$  by taking the eigenstates  $|\nu\rangle$  of  $\hat{H}$  as the basis vectors:

$$\sigma_{xx} = \frac{\pi e^2 \hbar}{(m_e^*)^2 S} \sum_{\mu, \nu} \delta(\varepsilon_F - \varepsilon_\mu) \delta(\varepsilon_F - \varepsilon_\nu) |\langle \nu | \Pi_x | \mu \rangle|^2 \quad (157)$$

Equation (157) shows that the zero temperature conductivity  $\sigma_{xx}$  is proportional to the number of pairs of states which have exactly the Fermi energy ( $\varepsilon_F = \varepsilon_\mu = \varepsilon_\nu$ ), weighted by the square of the  $\Pi_x$  matrix element between them.

Let us now suppose that we adopt the scheme of broadened Landau levels whose tail states are localized. Then, if the Fermi energy stays within the tail states, the matrix element  $\langle \nu | \Pi_x | \mu \rangle$  will decay (say exponentially) with  $|\vec{\rho}_\mu - \vec{\rho}_\nu|$  which is the distance separating the two localized states  $|\mu\rangle, |\nu\rangle$ . In addition, due to the randomness of  $V_{\text{disorder}}(\vec{\rho})$  the number of states with exactly the same energy  $\varepsilon_\mu = \varepsilon_\nu$  is extremely small. All these facts lead us to the conclusion that  $\sigma_{xx}$  is a very small at  $T = 0$  K. More sophisticated analysis [105] shows that  $\sigma_{xx}$  does indeed vanish when the limit of infinite  $S$  is taken. The previous argument does not hold for extended states of the broadened Landau levels at least because  $\langle \nu | \Pi_x | \mu \rangle \approx 1/\lambda$  for those states. Thus, when the magnetic field is swept and the Fermi energy passes through the consecutive Landau levels,  $\sigma_{xx}$  undergoes oscillations and is zero when  $\varepsilon_F$  is in the localized levels (or in a region where the density of states vanishes) and positive when  $\varepsilon_F$  coincides with the extended states of the spectrum.

Such behavior is analytically derived within the framework of the self-consistent Born approximation. In such a model, one obtains [106]

$$\sigma_{xx} = 0 \quad \text{if} \quad \left| \varepsilon_F - \left( n + \frac{1}{2} \right) \hbar \omega_c - \varepsilon_1 - g^* \mu_B B \sigma_z \right| > \Gamma_n \quad (158)$$

$$\sigma_{xx} = \frac{e^2}{\pi^2 \hbar} \left( n + \frac{1}{2} \right) \times \left\{ 1 - \left[ \frac{\varepsilon_F - \left( n + \frac{1}{2} \right) \hbar \omega_c - \varepsilon_1 - g^* \mu_B B \sigma_z}{\Gamma_n} \right]^2 \right\} \quad (159)$$

elsewhere. Here  $2\Gamma_n$  is the width of the  $n$ th broadened Landau level whose density of states is given by Eq. (42). Despite the incorrect treatment of the tail states, the formula [Eq. (159)] is very helpful in explicitly showing the oscillatory behavior of  $\sigma_{xx}$  upon  $B$ .

These oscillations are well known (Shubnikov–de Haas effect) [79, 104] and have been observed in a variety of bulk materials and heterostructures. They are of quantum origin (being absent in a Drude-type analysis of the magnetoconductivity tensor) and evidence the magnetic field-induced singularities of the density of states.

The  $\sigma_{xx}$  maxima [or equivalently the  $\rho_{xx}$  maxima since  $\sigma_{xx} \ll \sigma_{xy}$  in the first of Eq. (141)] are evenly spaced in  $1/B$ . The fields  $B_{n\sigma_z}$  where  $\sigma_{xx}$  is maximum are such that

$$\varepsilon_F - \varepsilon_1 = \left[ n + \frac{1}{2} + \frac{g^* \mu_B \sigma_z m_e^*}{\hbar e} \right] \frac{\hbar e}{m_e^*} B_{n\sigma_z} \quad (160)$$

This means that a plot of  $B_{n\sigma_z}^{-1}$  versus integer  $n$  should be a straight line (Fig. 19) whose slope  $S_B$  yields direct

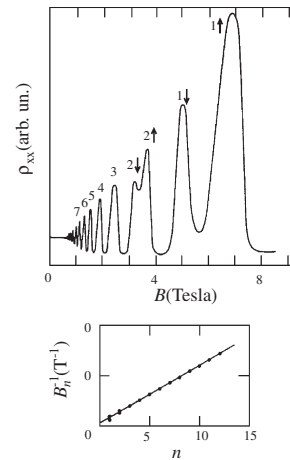


**Figure 19.** Oscillatory behavior displayed by  $\rho_{xx}(B)$  upon  $B$  (Shubnikov–de Haas effect) in a GaAs–Ga<sub>0.7</sub>Al<sub>0.3</sub>As heterojunction at  $T = 2$  K (upper panel). The inverses of the magnetic fields  $1/B_n$  corresponding to maxima of  $\rho_{xx}(B)$  are plotted versus consecutive integers  $n$  (lower panel). The slope of the straight line  $B_n^{-1}$  versus  $n$  directly yields the areal concentration of quasi-two-dimensional electrons  $n_c$ .  $\vec{B} \parallel \hat{e}_z$ ,  $\eta = 3.93 \times 10^{11} \text{ cm}^{-2}$ . Reprinted with permission from [186], J. L. Marín et al., “Handbook of Advanced Electronic and Photonic Materials and Devices” (H. S. Nalwa, Ed.). Academic Press, San Diego, 2001. © 2001, Academic Press.

information on  $\varepsilon_F - \varepsilon_1$  or, equivalently, on the areal carrier concentration  $\eta_c$ , which is present in the heterostructure:

$$\eta_c = \frac{m_e^*}{\pi \hbar^2} (\varepsilon_F - \varepsilon_1) \quad (161)$$

$$S_B = \frac{\hbar e}{m_e^* (\varepsilon_F - \varepsilon_1)} = \frac{e}{\pi \hbar \eta_c} \quad (162)$$

The determinations of  $\eta_c$  by means of the Shubnikov–de Hass effect are very accurate. In addition they do not require any information concerning the sample geometrical details (shape, distance between contacts, etc.).

## 2.6. Magnetic Field Dependence of $\sigma_{xy}$ : The Quantized Hall Effect

In the self-consistent Born approximation, there should exist corrections to the perfect Hall effect ( $\sigma_{xy} = -\eta_c e^2 / m_e^* \omega_c$ ). However, it is not very interesting to discuss these corrections insofar as the most spectacular effects are completely missed by any theory, which neglects the localized states in the tails of the Landau levels.

What was experimentally observed is the appearance of plateaus in the  $\rho_{xy}$  curves versus  $B$  (Fig. 20) at low temperatures ( $T \leq 4.2$  K). The  $\rho_{xy}$  plateaus are exactly (within at least one part per million) quantized, being subharmonics of  $\hbar/e^2$ . The so-called quantized Hall effect, discovered by von Klitzing et al. [107] in Si-MOSFETs, can be termed a universal effect. It has also been observed in other two-dimensional systems:  $\text{Ga}_{1-x}\text{Al}_x\text{As-GaAs}$  [108],  $\text{InP-Ga}_{0.47}\text{In}_{0.53}\text{As}$  [109],  $\text{AlSb-InAs}$  [110],  $\text{GaSb-InAs}$  [111]. Its occurrence is independent of the band structure of the host materials: the quantized Hall effect can be observed when the carriers are electrons belonging to a single conduction band ( $\text{Ga}_{1-x}\text{Al}_x\text{As-GaAs}$ ) [108] or to a multivalley conduction band (Si-MOSFET) [107]. It is also observed when the carriers are holes belonging to a degenerate valence band ( $\text{Ga}_{1-x}\text{Al}_x\text{As-GaAs}$ ) [112] and even when there is a mixed conduction ( $\text{GaSb-InAs}$ ) [111].

The width  $\Delta B$  of a given  $\rho_{xy}$  plateau increases as the temperature decreases, reaching an amplitude which is close to the maximum one at very low  $T$  (milli-Kelvin range) [113]. It appears established that  $\rho_{xy}$  develops plateaus when the Fermi level coincides with the localized states of the broadened Landau levels. In fact, in the plateau regimes for  $\rho_{xy}$ ,  $\rho_{xx}$  (and  $\sigma_{xx}$ ) are almost zero. The deviation from the zero resistance state exponentially decreases as temperature decreases. Such a feature evidences a hopping type of transport along the electric field. The details of the hopping processes remain uncertain: the hopping laws

$$\sigma_{xx}(T) \approx \exp \left[ - \left( \frac{T_0}{T} \right)^\alpha \right] \quad (163)$$

fit the data reasonably well but the exponent  $\alpha$  is sample dependent [111, 114, 115]. Perhaps the disorder potential responsible for the existence of localized states is markedly different in different types of heterostructures.

That  $\sigma_{xy}$  could be exactly quantized in units of a fundamental constant  $e^2/h$  irrespective of the band structure, defects, etc. clearly called for a theoretical explanation

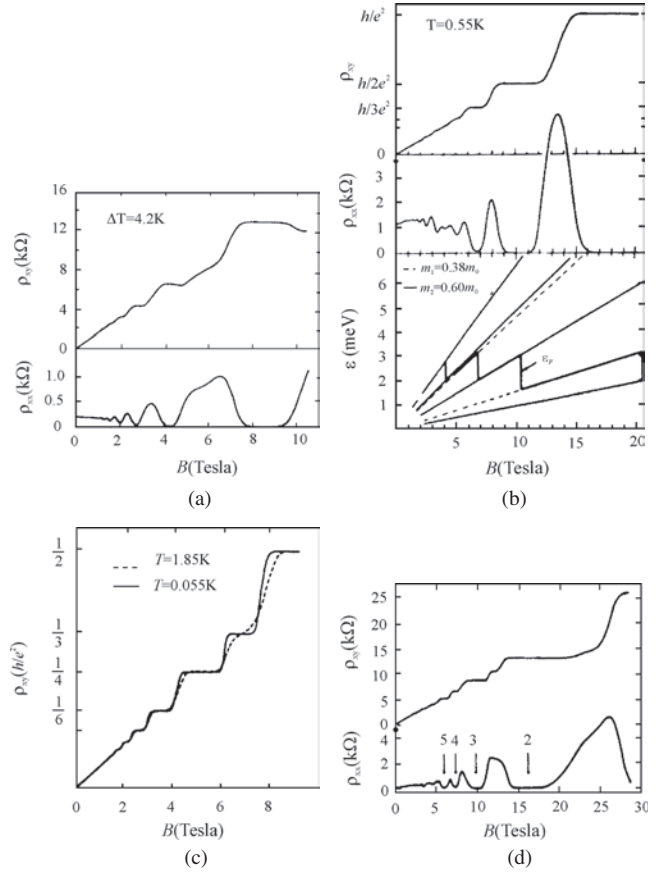


**Figure 20.** The quantized Hall effect in III-V heterostructures. The  $\rho_{xy}$  curves plotted versus  $B$  are shown for: (a)  $n\text{-Ga}_{1-x}\text{Al}_x\text{As-GaAs}$ , (b)  $p\text{-Ga}_{1-x}\text{Al}_x\text{As-GaAs}$ , (c)  $p\text{-Ga}_{1-x}\text{Al}_x\text{As-GaAs}$ , and  $n\text{-GaSb-InAs-GaSb}$ . Reprinted with permission from [186], J. L. Marín et al., “Handbook of Advanced Electronic and Photonic Materials and Devices” (H. S. Nalwa, Ed.). Academic Press, San Diego, 2001. © 2001, Academic Press.

which would go beyond the usual perturbative approaches of the magnetoconductivity tensor and which would exploit the genuine characteristic of two-dimensional magnetotransport, which is the existence of nonconducting states separating conducting ones.

It was Aoki and Ando [116] and Prange [117] who first pointed out that localized levels do not contribute to  $\sigma_{xy}$  and that, moreover, delocalized states, in the presence of localized ones, conduct more efficiently, thus ensuring the pinning of  $\sigma_{xy}$  to a multiple of  $e^2/h$ . The theoretical breakthrough was made by Laughlin [118] who showed that the gauge invariance of the electromagnetism implies the quantization of  $\sigma_{xy}$ , at  $T = 0$  K, provided that the Fermi level sits in the localized levels ( $\sigma_{xx} = 0$ ). For a detailed discussion of the theoretical aspects of the quantized Hall effect, see [119].

There is no available theory of the quantized Hall effect at finite temperature. Such a theory is, however, very desirable in order to ascertain the magnitude and temperature dependence of the corrections to the  $T = 0$  K value, and thus the accuracy of new resistance standards based on the quantized Hall effect.

### 2.6.1. Fractionally Quantized Hall Effect

When the Fermi level has passed the  $0^-$  Landau level, nothing is expected to occur. A wealth of extra features was in fact detected for fractional occupancies of the remaining  $0^+$  sublevel (Fig. 21) [120, 121]. These features are only seen in samples with very high zero-field mobilities. Like the “normal” quantized Hall effect, the fractionally quantized Hall effect does not depend on the band structure of the host materials. It has been observed in both electrons [120–122] and holes [123] in quasi-two-dimensional systems. Of the fractional  $p/q$  defined by

$$\rho_{xy} = \frac{q}{p} \frac{h}{e^2} \quad (164)$$

only those with odd denominators have been unambiguously observed. The fractionally quantized Hall effect has been explained by Laughlin [124, 125] in terms of a condensation of the electron (or hole) system into a microscopic collective ground state due to electron–electron (or hole–hole) interaction. This ground state is separated from the excited one by  $\approx 0.03e^2/\lambda$ , where  $\lambda$  is the magnetic length defined in Eq. (22). That a repulsive interaction between carriers may give rise to a condensation is intimately linked to the quasi-two-dimensionality of the electron motion. In a bulk material two such electrons can never form a bound state, whereas the two-dimensional motion prevents the escape of the two electrons at infinite distance from each other. Laughlin’s wavefunction of the condensed ground state has been generalized by Halperin [126]. The exact microscopic nature of the ground state is still disputed [127].

### 2.6.2. Cyclotron Resonance

As can be shown, the frequency-dependent magnetoconductivity tensor  $\sigma_{\alpha\beta}(\omega)$  (which describes the linear response of the electron gas to a periodically varying electric field)

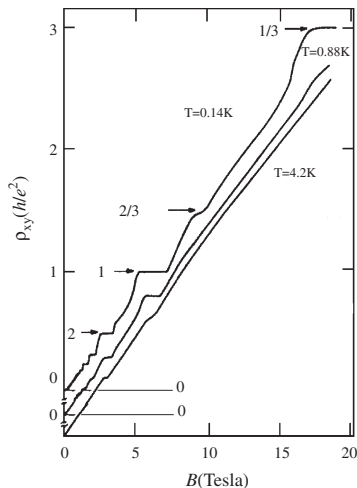


**Figure 21.** Fractionally quantized Hall effect in a  $n\text{-Ga}_{1-x}\text{Al}_x\text{As-GaAs}$  single heterojunction. The plateaus labeled  $2/3$  and  $1/3$  take place when the fractional occupation of the last ( $0^+$ ) Landau level is equal to  $2/3$  and  $1/3$  respectively.  $\eta = 1.48 \times 10^{11} \text{ cm}^{-2}$ . Reprinted with permission from [186], J. L. Marín et al., “Handbook of Advanced Electronic and Photonic Materials and Devices” (H. S. Nalwa, Ed.). Academic Press, San Diego, 2001. © 2001, Academic Press.

exhibits singularities at  $\omega = \omega_c$ . Let us work in the Drude model (classical description) and assume that

$$\vec{E}(\vec{r}, t) = E \hat{e}_x \cos \omega t \quad (165)$$

The equation of motion of the complex velocity

$$\xi = v_x + i v_y \quad (166)$$

is

$$\frac{d\xi}{dt} = -\frac{\xi}{\tau} + i \omega_c \xi - \frac{eE}{m_e^*} \cos \omega t \quad (167)$$

where a viscous friction force  $-m_e^* v/\tau$  accounts for the scattering mechanisms. In the permanent regime,  $\xi$  oscillates at the frequency  $\omega$  and the  $\hat{e}_x$  component of the areal current density  $\vec{j} = -\eta_e e \vec{v}$  is found to behave like

$$j_x = \frac{\eta_e e^2 \tau}{2m_e^*} E \left\{ \frac{\cos \omega t + \tau(\omega - \omega_c) \sin \omega t}{1 + (\omega - \omega_c)^2 \tau^2} + \frac{\cos \omega t + \tau(\omega + \omega_c) \sin \omega t}{1 + (\omega + \omega_c)^2 \tau^2} \right\} \quad (168)$$

Over a period  $2\pi/\omega$ , the average power taken to the electric field is

$$\langle P \rangle = \frac{\omega}{2\pi} \int_0^{2\pi/\omega} j_x E \cos \omega t dt \quad (169)$$

or

$$\langle P \rangle = \frac{\eta_e e^2 \tau}{4m_e^*} E^2 \left\{ \frac{1}{1 + (\omega - \omega_c)^2 \tau^2} + \frac{1}{1 + (\omega + \omega_c)^2 \tau^2} \right\} \quad (170)$$

There are two contributions to  $\langle P \rangle$ . The first one presents a resonance at  $\omega = \omega_c$ , while the second one is a decreasing function of  $\omega_c$  or  $\omega$ . The resonant term arises from the  $\exp(+i\omega t)/2$  part of the electric field. Indeed, the linear vibration [Eq. (165)] can be rewritten as the sum of two clockwise and counterclockwise circular vibrations:

$$E(t) = \begin{cases} E \cos \omega t \\ 0 \end{cases} = \begin{cases} \frac{1}{2} E \cos \omega t \\ \frac{1}{2} E \sin \omega t \end{cases} + \begin{cases} \frac{1}{2} E \cos(-\omega) t \\ \frac{1}{2} E \sin(-\omega) t \end{cases} \quad (171)$$

The first kind of circular vibration is, for  $\omega = \omega_c$ , constantly in phase with the electron motion. As a result, it transfers a finite amount of energy to the electron during a cyclotron period. On the other hand, the second type of circular vibration partly accelerates and partly decelerates the electron and, on average, does not transfer energy to the electron. Note that, ultimately, the carrier does not store the electromagnetic energy. Instead, this energy is given up to the lattice via the viscous friction force. In the limit  $\tau \rightarrow \infty$ ,  $\langle P \rangle$  would be zero unless  $\omega = \omega_c$ . Figure 22 shows a plot of  $\langle P \rangle$  versus  $\omega_c/\omega$  for three values of  $\omega\tau$ . Two features are remarkable:

- (i)  $\langle P \rangle$  displays an asymmetric lineshape at low  $\omega\tau$  and a rather symmetric one at large  $\omega\tau$ .
- (ii)  $\langle P \rangle$  gets narrower for larger  $\omega\tau$ .



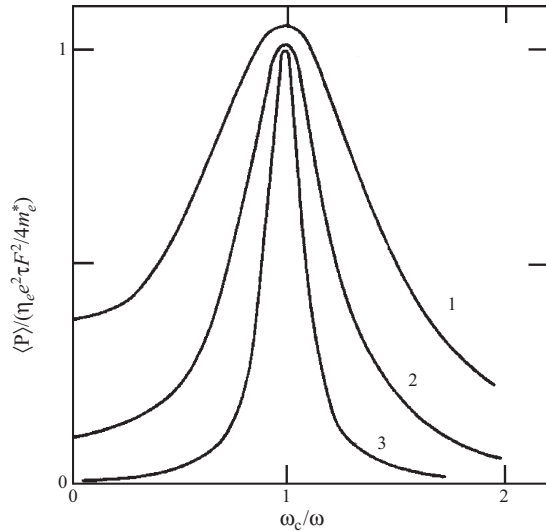


**Figure 22.** The power absorbed by a classical electron gas from an electromagnetic wave (angular frequency  $\omega$ ), averaged over a period of the cyclotron motion, is plotted versus the dimensionless ratio  $\omega_c/\omega$  for  $\omega\tau = 2.1$  (1), 4.1 (2), 10.1 (3), respectively. Reprinted with permission from [186], J. L. Marín et al., “Handbook of Advanced Electronic and Photonic Materials and Devices” (H. S. Nalwa, Ed.). Academic Press, San Diego, 2001. © 2001, Academic Press.

Suppose we consider a heterostructure with a dc mobility of  $10^4$  cm<sup>2</sup>/V s. The condition  $\omega_c\tau \geq 1$ , which ensures that the electron has completed a revolution around  $\vec{B}$  without being scattered, is fulfilled as soon as  $B \geq 1$  Tesla. The cyclotron resonance absorption  $\omega = \omega_c$  is observed in the far infrared or millimeter parts of the electromagnetic spectrum for the actual masses of III–V heterostructures. Two experimental techniques are used: either sweep the magnetic field while keeping  $\omega$  fixed or work at fixed  $B$  by sweeping the frequency  $\omega$ . The first technique requires the use of far-infrared lasers or carcinotrons as monochromatic sources and a magnet to produce the field. It is more practical than the second one, which requires the use of Fourier interferometers combined with a magnet. By reporting the photon energies  $\hbar\omega_n$  versus the observed resonance fields  $B_n$  on a  $(B, \hbar\omega)$  diagram one gets a straight line (for parabolic band structures) whose slope  $\hbar e/m_e^*$  yields a very precise determination of the carrier effective mass  $m_e^*$ .

It is clear that the Drude model cannot describe very accurately all the experimental observations in quasi-two-dimensional electron gases. In particular, the quantity  $\tau$ , which accounts for the scattering effects, has, in practice, no reason to be  $\omega$ - and  $B$ -independent as postulated in the Drude model.

A better model of the cyclotron resonance absorption has been derived by Ando and is based on the microscopic calculation of  $\sigma_{\alpha\beta}(\omega)$  within the framework of the self-consistent Born approximation [128]. This model predicts resonance absorptions of the electromagnetic wave, not only at  $\omega = \omega_c$  but also at the harmonics  $\omega = n\omega_c$ . In addition, when the width  $\Delta B$  at half maximum of the main cyclotron resonance line ( $\langle P \rangle$  versus  $B$  at fixed  $\omega$ ) is large enough (i.e., when the dc mobility is not too high) to allow the Fermi level to be crossed by several Landau levels (i.e., when  $\eta_e$

is large enough), the cyclotron resonance lineshape is calculated to exhibit extra oscillations which are  $\omega$ -independent. These Ando oscillations are of the Shubnikov–de Hass type. They have been observed in Si-MOS structures [129], as well as in modulation-doped Ga<sub>1-x</sub>Al<sub>x</sub>As–GaAs heterostructures [130].

Apart from the Si-MOSFET’s the most complete study of the cyclotron absorption has been performed in Ga<sub>1-x</sub>Al<sub>x</sub>As–GaAs heterostructures [130–133]. The first output of these studies is the effective mass of the carrier in the GaAs channel. It has been found that this mass is slightly enhanced over the band edge conduction mass of bulk GaAs ( $0.067m_0$ ). The mass enhancement is, however, modest (few percent) and is in general attributed to the weak nonparabolicity of the GaAs conduction band. It has not yet been proved that part of the enhancement does not originate from the matching conditions for the wavefunction and its derivative at the interface between GaAs and Ga<sub>1-x</sub>Al<sub>x</sub>As.

The most striking results of cyclotron resonance experiments pertain to the cyclotron resonance linewidth and lineshape. If interference effects are carefully excluded from the experiments, the lineshape of the cyclotron absorption is rather symmetric in Ga<sub>1-x</sub>Al<sub>x</sub>As–GaAs heterostructures. For heterostructures with modest mobilities ( $\leq 10^5$  cm<sup>2</sup>/V s) the width at half maximum of the absorption curves follows the predictions of Ando’s model [128]. In high mobility heterostructures it has been shown [133] that the cyclotron resonance linewidth  $\Delta B$  plotted versus the resonance field displays oscillations, whereas Ando’s model (at least with pointlike scatterers) would rather predict a smooth increase of  $\Delta B$ . The carriers have tentatively correlated such oscillations with the oscillations of the screening of the scattering potentials.

In fact, if the resonance field corresponds to a situation where the Fermi level stays in the localized levels of a broadened Landau level or in the gap separating two such levels, the screening is inefficient, since the heterostructure is, for that particular field, an insulator. If, on the other hand, the resonance field is such that the Fermi level coincides with the extended states of a Landau level, the screening effects are very pronounced due to the large polarizability of the electron gas for that particular configuration. When the screening effects are weak, both the damping effects and the cyclotron resonance linewidth are large and vice versa.

When the host materials of the heterostructure are markedly nonparabolic (e.g., GaSb–InAs [134], InSb MOS structures [135]) many subbands are often populated (both effects arise from the smallness of the effective mass). These subbands have different cyclotron resonance effective masses and the ground subband displays the heavier mass. Thus, the cyclotron resonance absorption shows structures which can be associated with the cyclotron resonance absorption of each individual subband.

## 2.7. Magnetoconductivity of Quantum Wires with Elastic and Inelastic Scattering

In this section a Boltzmann equation is used to determine the magnetoconductivity of quantum wires, following Bruus et al. [136]. The presence of a confining potential in addition

to the magnetic field removes the degeneracy of the Landau levels and allows one to associate a group velocity with each single particle state. The distribution function describing the occupation of these single particle states satisfies a Boltzmann equation, which may be solved exactly in the case of impurity scattering. In the case where the electrons scatter against both phonons and impurities the integral equation for the distribution function is solved numerically, and in certain limits analytically, and is determined by the conductivity as a function of temperature and magnetic field. The magnetoconductivity exhibits a maximum at a temperature which depends on the relative strength of the impurity and electron–phonon scattering and shows oscillations when the Fermi energy or the magnetic field is varied.

The suppression of scattering between edge states, due to the presence of the magnetic field, was discussed by several authors [137–140]. The effects of impurity and boundary scattering on the Hall effect in quantum wires were treated by Akera and Ando [141] starting from a Boltzmann equation. The Kubo method [142] has been used for considering the effect of the coupling to optical phonons [143, 144] and the influence of impurity scattering [145] on the magnetotransport through quantum wires. Momentum and energy balance equations have been derived [146, 147] for a quasi-one-dimensional gas of electrons in a magnetic field. Other authors [148] have used the Keldysh method to discuss magnetotransport in the presence of impurity scattering, while the formalism due to Landauer [149] and Büttiker [150] was employed in [151] to treat the influence of disorder on the Hall effect in quantum wires.

Transport in strong magnetic fields has traditionally been treated within the Kubo formalism, since this allows one to fully take into account the quantization of the motion of an electron in a magnetic field. The resulting diagrammatic expansion of the conductivity requires the consideration of both self-energy effects and vertex corrections. It was demonstrated in [145] that it is essential to include vertex corrections in order to determine the effect of impurity scattering on the magnetoconductivity of a quantum wire. The physical reason for this is that only backscattering from the impurities contributes to the resistivity.

In this section a Boltzmann equation to determine the transport properties of quantum wires formed by additional confinement of the two-dimensional electron gas of, for example, a GaAs–GaAlAs heterojunction, is used. The presence of a confining potential in addition to the magnetic field removes the degeneracy of the Landau levels and allows one to associate a group velocity with each single particle state. The distribution function describing the occupation of these single particle states satisfies a Boltzmann equation, which we solve exactly in the case of impurity scattering. The resulting magnetoconductivity agrees with that obtained in [145] within the Kubo approach. In the case of electron–phonon scattering we solve numerically—and in certain cases analytically—the integral equation for the distribution function. The conductivity is determined as a function of temperature and magnetic field in the case when both impurities and phonons contribute to the scattering of the electrons.

Apart from its simplicity, the use of the Boltzmann equation has the additional advantage that it allows one to go

beyond linear response theory in a straightforward manner. Although this section treats in detail only the regime of linear response, the approach may readily be generalized to take nonlinear effects into account.

Since conduction in a quantum wire involves current transport in one dimension it is necessary to consider the role of localization. This was done in [152], where it was shown that weak localization in quantum wires is destroyed in a magnetic field greater than a critical value  $B_c$  where the critical magnetic field  $B_c$  apart from numerical factors is given by  $B_c \approx h\ell/eL_\phi W^2$ . Here  $\ell$  is the elastic scattering length,  $W$  is the width of the quantum wire, while  $L_\phi$  is the phase coherence length. In what follows we shall assume that the magnetic field is sufficiently strong that localization effects are always negligible. The transport properties of the quantum wires may then be obtained from a Boltzmann equation, in which the quantizing effect of the magnetic field is incorporated in the manner described. We shall also disregard Coulomb-blockade effects, which have been shown to be of importance in some systems [153].

### 2.7.1. Single Particle Energy Spectrum

We consider an electron moving in the  $xy$  plane under the influence of a constant magnetic field in the  $z$  direction. In addition a parabolic confinement potential limits its motion in the  $y$  direction whereby a wire is formed in the  $x$  direction. The Hamiltonian for such an electron is

$$\hat{H} = \frac{1}{2m^*} (\hat{p} + e\vec{A})^2 + \frac{1}{2}Ky^2 \quad (172)$$

with  $m^*$  being the effective (band) mass of the electron. For simplicity we have neglected the Zeeman splitting, since we shall be mainly concerned with quantum wires in GaAs based structures, where the Zeeman energy is a few percent of the cyclotron energy  $\hbar\omega_c$  to be defined. The electron spin therefore only enters as a factor of 2 in the expression for the current density. In the  $x$  direction we impose periodic boundary conditions, and for the vector potential  $\vec{A}$  we use the Landau gauge  $\vec{A} = B(-y, 0, 0)$ . Consequently the eigenfunctions of the Hamiltonian are products of plane waves and harmonic-oscillator functions involving Hermite polynomials  $H_n$ ,

$$\begin{aligned} \psi_{nk} = & \frac{1}{\sqrt{L}} \exp(ikx) \frac{1}{(\sqrt{\pi}2^n n! \ell_h)^{1/2}} H_n \left( \frac{y - y_k}{\ell_h} \right) \\ & \times \exp \left( -\frac{(y - y_k)^2}{2\ell_h^2} \right) \end{aligned} \quad (173)$$

with  $L$  being the length of the quantum wire. The center coordinate  $y_k$  and the characteristic length  $\ell_h$  of the harmonic oscillator are specified below. The wavefunction in the  $z$  direction is taken to be a  $\delta$  function.

In the case where  $K$  is zero and only the magnetic field is present the natural system of units is based on the cyclotron frequency  $\omega_c$  and the magnetic length  $\ell_c$ , given by

$$\omega_c = \frac{eB}{m^*} \quad \ell_c^2 = \frac{\hbar}{eB} \quad (174)$$



When  $K$  is different from zero, we define the quantity  $\gamma$ , which describes the relative strength of the confinement potential, by

$$\gamma \equiv \frac{K}{m_e^* \omega_c^2} \quad (175)$$

and the natural units are now based on the hybrid frequency  $\omega_h$  and the hybrid characteristic length  $\ell_h$  given by

$$\omega_h = (1 + \gamma)^{1/2} \omega_c \quad \ell_h = (1 + \gamma)^{-1/4} \ell_c \quad (176)$$

By inserting the function (173) in the Schrödinger equation

$$\hat{H} \psi_{n\bar{k}} = \varepsilon_{n\bar{k}} \psi_{n\bar{k}} \quad (177)$$

one finds that (177) is satisfied, provided that

$$\varepsilon_{n\bar{k}} = \hbar \omega_h \left( n + \frac{1}{2} \right) + \frac{\hbar^2 k^2}{2m^*} \quad n = 0, 1, 2, \dots \quad (178)$$

where  $m^*$  is a renormalized mass defined by

$$m^* = \frac{1 + \gamma}{\gamma} m_e^* \quad (179)$$

The center of the harmonic oscillator wavefunctions is given by

$$y_k = \frac{\omega_c \hbar k}{m_e^* \omega_h^2} = (1 + \gamma)^{-1/2} k \ell_h^2 \quad (180)$$

The confinement potential  $Ky^2/2$  removes the degeneracy of the Landau levels through the  $k$  dependence exhibited in Eq. (178). Note that the dispersion relation is that of a free particle with a renormalized mass  $m^*$ . When the strength of the confinement potential goes to zero, the renormalized mass  $m^*$  becomes infinite (corresponding to degenerate Landau levels), while in the opposite limit ( $\gamma \rightarrow \infty$ ), the renormalized mass becomes equal to the effective mass  $m_e^*$ .

In the following we shall describe conduction through the quantum wire on the basis of the Boltzmann equation for the distribution function of the excitations with energy  $\varepsilon_{nk}$ . The group velocity  $v$  of the excitations is seen to be

$$v_{nk} = \frac{1}{\hbar} \frac{\partial \varepsilon_{nk}}{\partial k} = \frac{\hbar k}{m} \quad (181)$$

If the confinement potential is not simply parabolic, the relation between  $v_{nk}$  and  $k$  becomes more complicated than Eq. (181), but the method described in the following is still applicable, provided one modifies the group velocity accordingly and incorporates the new wavefunctions into the matrix elements appearing in the collision probability.

## 2.7.2. Boltzmann Equation

We consider the distribution function  $f_{nk}$  for the excitations specified by the energy  $\varepsilon_{nk}$ , with group velocity  $v_{nk} = \hbar k/m$ . Unlike the usual semiclassical description of transport in a magnetic field, the magnetic field has here been taken into account from the very beginning, in defining the excitations with dispersion relation (178). The effect of an electric field  $E_x$  in the  $x$  direction is, however, included in the usual manner through the acceleration equation

$$\hbar \dot{k} = -eE_x \quad (182)$$

The Boltzmann equation [154] is

$$\frac{\partial f_{nk}}{\partial t} + \dot{k} \frac{\partial f_{nk}}{\partial k} = \left( \frac{\partial f_{nk}}{\partial t} \right)_{\text{coll}} \quad (183)$$

where the right-hand side of the equation contains the collision term. Since we are interested in the linear response to a static electric field, the time derivative  $\partial f/\partial t$  is equal to zero, while  $f_{nk}$  in the second term on the left-hand side may be replaced by the equilibrium function  $f_{nk}^0$ . Using Eq. (182) the Boltzmann equation then becomes an inhomogeneous integral equation of the form

$$\frac{eE_x}{k_B T} v_{nk} f_{nk}^0 (1 - f_{nk}^0) = \left( \frac{\partial f_{nk}}{\partial t} \right)_{\text{coll}} \quad (184)$$

with the integral term on the right-hand side the collision term to be specified.

Before we consider specific scattering mechanisms, let us write the conductivity  $\sigma$  in terms of the distribution function. We define  $\sigma$  as  $\sigma \equiv j_x/E_x$ ,  $j_x$  being the current density in the  $x$  direction. In terms of the two-dimensional resistivity tensors  $\rho$  we get  $\sigma = 1/\rho_{xx}$  because  $j_y = 0$ . However, in the presence of the magnetic field a current in the  $x$  direction will also induce an electric field in the  $y$  direction. For  $j_x$  we have

$$j_x = -2e \sum_n \int_{-\infty}^{\infty} \frac{dk}{2\pi} v_{nk} f_{nk} \quad (185)$$

We shall introduce the deviation function  $\psi_{nk}$  by the definition

$$f_{nk} \equiv f_{nk}^0 + f_{nk}^0 (1 - f_{nk}^0) \psi_{nk} \quad (186)$$

Then the current density becomes

$$j_x = -2e \sum_n \int_{-\infty}^{\infty} \frac{dk}{2\pi} v_{nk} f_{nk}^0 (1 - f_{nk}^0) \psi_{nk} \quad (187)$$

Since we shall be dealing with distribution functions that change sign upon  $k \rightarrow -k$ , we may restrict  $k$  to positive values and work instead with the distribution function as a function of energy:  $\psi_n(\varepsilon)$ . In this notation  $k$  is then a function of energy, and we denote the  $k$  value, which solves  $\varepsilon = \varepsilon_{nk}$  by  $k_n(\varepsilon)$ . Furthermore, by introducing the function  $\phi_n$  defined by

$$\phi_n \equiv \frac{k_B T}{eE_x} \psi_n \quad (188)$$

we may express the conductivity as

$$\sigma \equiv \frac{j_x}{E_x} = \frac{2e^2}{h} 2 \sum_n \int_0^\infty d\varepsilon \left( -\frac{\partial f^0(\varepsilon)}{\partial \varepsilon} \right) \phi_n(\varepsilon) \quad (189)$$

since  $dk = d\varepsilon/\hbar v$ . Note that  $\phi$  has dimension of length. The chemical potential entering the equilibrium distribution function  $f^0$  will be assumed to be independent of temperature, equal to  $\varepsilon_F$  since the quantum wire under typical experimental conditions is in contact with a large reservoir of electrons.

The Boltzmann equation considered in this section is an inhomogeneous integral equation of the form

$$X_{nk} = H\psi_{nk} \quad (190)$$

where

$$X_{nk} = -\frac{eE_x}{k_B T} v_{nk} f_{nk}^0 (1 - f_{nk}^0) \quad (191)$$

while the integral operator  $H$  is defined by

$$\left( \frac{\partial f_{nk}}{\partial t} \right)_{\text{coll}} = -H\psi_{nk} \quad (192)$$

with

$$H\psi_{nk} = \sum_{n'} \int_{-\infty}^\infty \frac{L}{2\pi} dk' K_{nn'}(k, k') (\psi_{nk} - \psi_{n'k'}) \quad (193)$$

Here  $K$  is an integral kernel specified in the previous section.

By introducing the scalar product  $(A, B)$  through the definition

$$(A, B) = \sum_n \int_{-\infty}^\infty \frac{dk}{2\pi} A_{nk} B_{nk} \quad (194)$$

the conductivity may be written as

$$\sigma = \frac{2k_B T}{E_x^2} (X, \psi) \quad (195)$$

In cases where we cannot solve explicitly for  $\psi$ , it is useful to employ a variational principle which yields a lower bound on  $\sigma$  by virtue of the Schwarz inequality

$$(\psi, H\psi)(U, HU) \geq (U, H\psi)^2 \quad (196)$$

where  $U$  is an arbitrary trial function. Since  $H\psi = X$ , this gives a lower bound on the conductivity

$$\sigma \geq \frac{2k_B T}{E_x^2} \frac{(X, U)^2}{(U, HU)} \quad (197)$$

This lower bound will be used to determine the low-temperature conductivity when the scattering is due to acoustic phonons, both with and without impurities, and the resulting analytic expressions are compared to the results of the numerical solution of the integral equation.

We shall always write our calculated values of the conductivity, as limited by the various scattering mechanisms to be considered in subsequent sections, in the form

$$\sigma = \frac{2e^2}{h} l \quad (198)$$

where  $l$  has the dimension of a length. As may be expected, in the presence of impurity scattering  $l$  tends to a finite value as  $T$  tends to zero, while it increases exponentially in the absence of impurity scattering, when the electrons are scattered only by phonons.

### 2.7.3. Impurity Scattering

In this section we consider the case of elastic impurity scattering. The collision integral is

$$\left( \frac{\partial f_{nk}}{\partial t} \right)_{\text{coll}} = -\sum_{n'} \int_{-\infty}^\infty \frac{L}{2\pi} dk' W_{nn'}(k, k') (f_{nk} - f_{n'k'}) \quad (199)$$

since the scattering is elastic. According to the golden rule we have

$$W_{nn'}(k, k') = \frac{2\pi}{\hbar} |\langle nk|V|n'k' \rangle|^2 \delta(\varepsilon_{nk} - \varepsilon_{n'k'}) \quad (200)$$

The square of the matrix element  $\langle nk|V|n'k' \rangle$  for scattering from impurities may be written as

$$|\langle nk|V|n'k' \rangle|^2 = \int d^2r \int d^2r' V(\vec{r})V(\vec{r}') \langle nk|\vec{r} \rangle \langle \vec{r}|n'k' \rangle \times \langle n'k'|\vec{r}' \rangle \langle \vec{r}'|nk \rangle \quad (201)$$

We shall perform an ensemble average over the distribution of impurities, corresponding to the replacement

$$V(\vec{r})V(\vec{r}') \rightarrow \langle V(\vec{r})V(\vec{r}') \rangle = F(\vec{r}, \vec{r}') \quad (202)$$

When the impurity potential may be approximated by a  $\delta$  function in space, the function  $F$  is proportional to the  $\delta$  function  $\delta(\vec{r} - \vec{r}')$ , corresponding to a “white-noise” model

$$F(\vec{r}, \vec{r}') = A^2 n_{\text{imp}} \delta(\vec{r} - \vec{r}') \quad (203)$$

Here we have introduced the number or impurities per unit area  $n_{\text{imp}}$  together with the constant  $A$ , which denotes the magnitude of the matrix element for scattering from a single impurity. The dimension of  $A$  is that of energy times area.

In order to distinguish between states of equal energy but opposite sign of  $k$ , we introduce the “branch index”  $s = \pm 1$ ,

$$k_{ns}(\varepsilon) \equiv sk_n(\varepsilon) = s \sqrt{\frac{2m}{\hbar^2} \left[ \varepsilon - \left( n + \frac{1}{2} \right) \hbar \omega_h \right]} \quad (204)$$

provided

$$\left( n + \frac{1}{2} \right) \hbar \omega_h \leq \varepsilon \quad (205)$$

The density of states at the Fermi energy  $\varepsilon_F$  is inversely proportional to the  $s$ -independent Fermi velocity  $v_n(\varepsilon_F) = \hbar k_n(\varepsilon)/m$ . Finally, since  $\phi_{ns}$  is odd in  $k$  and hence changes

sign with  $s$ , we may write  $\phi_{ns} = s\phi_n$ . The problem then becomes that of solving the matrix equation

$$s = \sum_{n's'} B_{ns}^{n's'} (s\phi_n - s'\phi_{n'}) \quad (206)$$

and calculating the conductivity according to Eq. (189). The matrix  $B_{ns}^{n's'}$  is positive and symmetric with respect to interchange of  $ns$  with  $n's'$ . Its elements are

$$B_{ns}^{n's'} = \frac{1}{\hbar^2} A^2 n_{\text{imp}} \frac{1}{v_n v_{n'}} \frac{1}{\ell_h \sqrt{2\pi}} F_{ns}^{n's'} \quad (207)$$

Here we have defined the following dimensionless quantities:

$$F_{ns}^{n's'} = \sqrt{2\pi} \ell_h \int_{-\infty}^{\infty} dy |u_n(y - y_{k_{ns}})|^2 |u_{n'}(y - y_{k_{n's'}})|^2 \quad (208)$$

where  $u_n(y)$  is the normalized  $y$ -dependent part of the wavefunction (173). The overlap integral  $F_{ns}^{n's'}$  has the form  $P_{ns}^{n's'}(z) \exp(-z)$ , where  $P_{ns}^{n's'}(z)$  is a polynomial in  $z$ , and where  $z = (y_{k_{ns}} - y_{k_{n's'}})^2 / 2l_h^2$ .

In Figure 23 we show the result of solving the matrix Eq. (206) and calculating the conductivity according to Eq. (189) as a function of the Fermi energy  $\varepsilon_F$ , for different choices of the parameter  $\gamma$  determining the strength of the confining potential. As can be seen in the figure the conductivity rises quickly as the Fermi level increases above

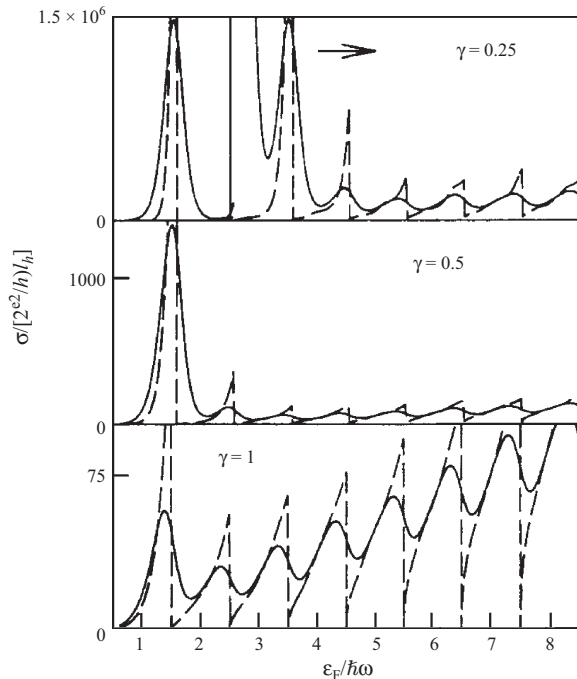


**Figure 23.** The conductivity for a quantum well wire with impurity scattering plotted versus the Fermi level for three different choices of the confinement potential corresponding to  $\gamma = 1, 0.5$  and  $0.25$ . The dashed line is the  $T = 0$  result and the solid lines correspond to  $k_B T = 0.05 \hbar \omega_h$ . The magnetic field is 9 T. Reprinted with permission from [186], J. L. Marín et al., “Handbook of Advanced Electronic and Photonic Materials and Devices” (H. S. Nalwa, Ed.). Academic Press, San Diego, 2001. © 2001, Academic Press.

$\hbar \omega_h / 2$ . This is due to the increasing separation between the two edge states, expressed by the overlap integral  $F_{0-}^{0+}$  of Eq. (208) which leads to the exponential factor in Eq. (209) below. When  $\varepsilon_F$  hits the next Landau level, the conductivity starts to decrease because a channel for backscattering is opened (i.e., the  $n = 0$  edge state can scatter to the opposite edge through the  $n = 1$  edge states). However, when the  $n = 1$  edge states become decoupled, the conductivity starts to increase again. This qualitative behavior is repeated each time a new Landau level crosses the Fermi level. The height of the conductance peak at  $3\hbar \omega_h / 2$  increases strongly with increasing channel width. At finite temperature these features are somewhat smeared, as evidenced by the figure, but still clearly visible.

Our calculation is relevant for the case where the scattering between different channels is so strong that the Boltzmann picture is valid; in other words, the calculated mean free path must be considerably shorter than the length of the wire. In the high magnetic field limit this means that the wire may not be so broad that the edge states become decoupled. Thus in practice we are dealing with wires only a few times  $l_h$  wide.

When  $\hbar \omega_h / 2 \leq \varepsilon_F \leq 3\hbar \omega_h / 2$  only the lowest Landau level is involved, corresponding to  $n = n' = 0$  in Eq. (206). Then the solution becomes particularly simple,  $\phi_0 = 1/2 B_{0+}^{0-}$ . By means of the Sommerfeld expansion we obtain the low-temperature expression for the conductivity  $\sigma = 2e^2/h B_{0+}^{0-}$ ,

$$\sigma = \frac{2e^2}{h} l_h \sqrt{2\pi} \frac{\hbar^2}{A^2 n_{\text{imp}}} \frac{\hbar^2 k_F^2}{m^{*2}} \exp\left(\frac{2k_F^2 l_h^2}{1 + \gamma}\right) \times \left\{ 1 + \frac{8\pi^2}{3\gamma^2} \left(1 + \frac{1 + \gamma}{k_F^2 l_h^2}\right) \left(\frac{k_B T}{\hbar \omega_h}\right)^2 \right\} \quad (209)$$

where  $k_F = k_{0+}(\varepsilon_F)$  is the Fermi momentum. The conductivity increases with temperature because electrons are excited into states, which have a smaller overlap with the states at the opposite branch. Consequently the electrons have a smaller backscattering probability. The result (209) is valid only to lowest order in  $k_B T / \hbar \omega_h$ . In obtaining our numerical results we do not use the Sommerfeld expansion but calculate directly the integral over energy according to expression (189).

As an illustration of the matrix inversion involved in the solution of the Boltzmann equation we shall also give the expression for the zero-temperature conductivity in the case when  $3\hbar \omega_h / 2 \leq \varepsilon_F \leq 5\hbar \omega_h / 2$ . By utilizing the symmetry  $\phi_{n+} = -\phi_{n-}$  the  $4 \times 4$  matrix equation becomes a  $2 \times 2$  equation which may readily be solved for  $\phi_{0+}$  and  $\phi_{1+}$ . The resulting conductivity  $\sigma = (2e^2/h) 2(\phi_{0+} + \phi_{1+})$  is at  $T = 0$  K given by

$$\sigma = \frac{2e^2}{h} \frac{2(2B_{0+}^{1+} + B_{1+}^{1-} + B_{0+}^{0-})}{2(B_{0+}^{1+} B_{0+}^{1-} + B_{0+}^{0-} B_{1+}^{1-}) + (B_{0+}^{1+} + B_{0+}^{0-})(B_{0+}^{0-} + B_{1+}^{1-})} \quad (210)$$

The result (210) yields the conductivity at zero temperature, when the Fermi energy  $\varepsilon_F$  satisfies the condition  $3\hbar \omega_h / 2 \leq \varepsilon_F \leq 5\hbar \omega_h / 2$ . The generalization to more Landau levels is straightforward. The  $B$  matrix in Eq. (206) is in general a

$2(n_0 + 1) \times (2n_0 + 1)$  matrix given by Eq. (207), where  $n_0$  is the quantum number associated with the highest occupied Landau level at  $T = 0$  K.

It is convenient to relate the conductivity calculated in the following two sections to the zero-temperature conductivity  $\sigma_{2D}$  associated with motion in two dimensions in the absence of a magnetic field and a confinement potential. The latter is given by

$$\sigma_{2D} = \frac{e^2 n_{2D}}{m_e^*} \tau_{\text{imp}} = e n_{2D} \mu_{\text{imp}} \quad (211)$$

where  $n_{2D}$  is the electron sheet density and  $\mu_{\text{imp}}$  is the zero-field, zero-temperature mobility,

$$\mu_{\text{imp}} = \frac{e \tau_{\text{imp}}}{m_e^*} \quad (212)$$

with

$$\frac{1}{\tau_{\text{imp}}} = \frac{m_e^* A^2 n_{\text{imp}}}{\hbar^3} \quad (213)$$

We shall thus express the calculated conductivity in units of  $(2e^2/h)l_{\text{imp}}$ , where

$$l_{\text{imp}} = \tau_{\text{imp}} \omega_c l_c \quad (214)$$

is a characteristic length which depends on the impurity content as well as the magnetic field.

#### 2.7.4. Electron–Phonon Scattering

Next we turn to the consideration of inelastic processes. The present section treats the case where the electrons are scattered by acoustical phonons due to the combined deformation potential and piezoelectric coupling, while the following section discusses the coupling of electrons to optical phonons.

Before specializing to a particular model let us write the contribution to the collision operator from the scattering against phonons. The phonons are assumed to be in thermal equilibrium. Then the integral operator  $\hat{H}$  is given by the following expression:

$$\begin{aligned} \hat{H} \psi_{nk} &= \frac{2\pi}{\hbar} \sum_{n'} \sum_{k'} \sum_{\vec{q}} |g_{\vec{q}}|^2 f^0(\varepsilon_{nk}) \\ &\times [1 - f^0(\varepsilon_{n'k'})] \delta_{k, k'+q_z} (\psi_{nk} - \psi_{n'k'}) \\ &\times \{ \delta(\varepsilon_{n'k'} - \varepsilon_{nk} + \hbar\omega_q) [1 + N^0(\omega_q)] \\ &+ \delta(\varepsilon_{n'k'} - \varepsilon_{nk} - \hbar\omega_q) N^0(\omega_q) \} \quad (215) \end{aligned}$$

Here  $g_{\vec{q}}$  is the electron–phonon coupling parameter, which will be specified, while  $N^0(\omega_q)$  is the equilibrium phonon distribution. For simplicity we have assumed that the phonon frequencies only depend on the magnitude of  $\vec{q}$ . In Eq. (215) we have explicitly written the factor  $\delta_{k, k'+q_z}$  discussed in Section 2.7.6.

Utilizing the relationship

$$\begin{aligned} f(\varepsilon) [1 - f(\varepsilon \pm \hbar\omega_q)] \\ = [f(\varepsilon) - f(\varepsilon \pm \hbar\omega_q)] [1 + N^0(\pm\omega_q)] \quad (216) \end{aligned}$$

the collision integral (215) can be written as

$$\begin{aligned} \hat{H} \psi_{nk} &= \frac{2\pi}{\hbar} \sum_{n' \vec{q} \sigma} |g_{\vec{q}}|^2 \frac{|f^0(\varepsilon_{nk}) - f^0(\varepsilon_{nk} + \sigma \hbar\omega_q)|}{4 \sinh^2(\hbar\omega_q/2k_B T)} \\ &\times (\psi_{nk} - \psi_{n'k-q_z}) \delta(\varepsilon_{n'k-q_z} - \varepsilon_{nk} - \sigma \hbar\omega_q) \quad (217) \end{aligned}$$

with  $\sigma$  assuming the two values  $+1$  and  $-1$  corresponding to phonon absorption and emission, respectively.

The calculations of  $g_{\vec{q}}$  are based on the standard electron–phonon interaction Hamiltonian, which disregarding umklapp processes takes the form

$$\hat{H}_{ep} = \sqrt{\frac{\hbar}{2V\rho\omega_q}} \sum_{\lambda, \vec{q}} M_{\lambda}(\vec{q}) \hat{\rho}(\vec{q}) (\hat{b}_{\vec{q}} + \hat{b}_{-\vec{q}}^+) \quad (218)$$

where  $\rho$  is the ion mass density,  $V$  is the normalization volume,  $\hat{\rho}(\vec{q})$  is the Fourier component of the electron density operator,  $\hat{b}_{-\vec{q}}^+$  is a phonon creation operator, and  $\lambda$  is the polarization index. The coupling function  $M$  is given by

$$M_{\lambda}(\vec{q}) = -V(\vec{q}) \vec{q} \cdot \vec{e}_{\lambda} \quad (219)$$

$V(\vec{q})$  being the electron–ion potential and  $\vec{e}_{\lambda}$  a unit vector describing the polarization  $\lambda$ . For a detailed treatment of electron–phonon coupling in semiconductors see, for example, [155]. The values of the GaAs parameters used in these calculations are listed in Table 2.

**Coupling to Acoustical Phonons** In GaAs heterostructures at low temperatures the electron–phonon scattering is mainly due to the combined piezoelectric coupling and the deformation potential coupling [100, 156–158]. We briefly sketch how these couplings are derived.

The deformation potential coupling only involves the longitudinal acoustical phonons. The coupling to the transverse acoustical phonons is suppressed by the square of the ratio between the speed of sound and the speed of light. In the long wavelength limit the coupling function  $M^{df}$  for the deformation potential coupling is written as

$$M^{df} = \Xi_{\vec{q}} \quad (220)$$

where  $\Xi$ , known as the deformation potential, is the zero wavevector limit of  $V(\vec{q})$ .

**Table 2.** The GaAs constants used in this section.

Parameter	Symbol	Value
Ion mass density	$\rho$	$5.3 \times 10^3 \text{ kg m}^{-3}$
Longitudinal sound velocity	$c$	$5.2 \times 10^3 \text{ m s}^{-1}$
Transverse sound velocity	$xc$	$3.0 \times 10^3 \text{ m s}^{-1}$
Sound velocity ratio	$x$	0.58
Static dielectric constant	$\kappa_0$	12.8
High-frequency dielectric constant	$\kappa_{\infty}$	10.6
Piezoelectric constant	$h_{14}$	$1.38 \times 10^9 \text{ V m}^{-1}$
Piezoelectric potential	$P$	$5.4 \times 10^{-20} \text{ J}^2 \text{ m}^{-2}$
Deformation potential	$\Xi$	$2.2 \times 10^{-18} \text{ J}$
Effective electron mass	$m_e^*$	$0.067 m_0$
Optical–phonon energy	$\hbar\omega_0$	36 meV

The electron-ion potential  $V$  for the piezoelectric coupling is found from the basic piezoelectric equations [155]. For GaAs (zinc blende structure) the only nonvanishing independent piezoelectric constant is  $h_{14}$  (reduced notation), and the coupling function  $M_\lambda^{pz}$  in this case becomes

$$M_\lambda^{pz} = i2eh_{14}(\hat{q}_x\hat{q}_y\hat{e}_{\lambda,z} + \hat{q}_y\hat{q}_z\hat{e}_{\lambda,x} + \hat{q}_z\hat{q}_x\hat{e}_{\lambda,y}) \quad (221)$$

where  $\hat{q}_i = (\vec{q}/q)_i$ . In the piezoelectric case  $\lambda$  is retained.

It is noted that  $M^{df}$  is real while  $M^{pz}$  is imaginary; thus to second order the two terms do not interfere, and the absolute square of the total coupling function  $M^{ac}$  is given by

$$|M^{ac}|^2 = |M^{df}|^2 + |M^{pz}|^2 \quad (222)$$

To obtain a more tractable form of the piezoelectric coupling we perform angular averages for the longitudinal and the (two) transverse modes separately and then add the terms [155, 159]. While this represents an approximation compared to retaining the full  $\vec{q}$  dependence of the coupling in the collision integral, we expect it to involve only minor quantitative differences. In adding the transverse and longitudinal contribution we must remember the different average sound velocities associated with each of the terms, originating in the factor  $1/\sqrt{\omega_q} = 1/\sqrt{cq}$  in Eq. (218). Expressing the transverse sound velocity as  $x$  times the longitudinal sound velocity we obtain the angular average of the absolute square of the piezoelectric coupling function  $M^{pz}$ ,

$$|M^{pz}|^2 = (eh_{14})^2 \left( \frac{12}{35} + \frac{1}{x} \frac{16}{35} \right) \equiv P \quad (223)$$

where we have introduced the constant  $P$ , and where it is understood that the only sound velocity appearing in the following is the longitudinal one.

The electron-phonon coupling parameter  $g_{\vec{q}}$  introduced in Eq. (215) now becomes

$$|g_{ac}(q)|^2 = \frac{\hbar}{2\rho Vc} \frac{1}{q} (\Xi^2 q^2 + P) |\langle nk | \exp(i\vec{q} \cdot \vec{r}) | n'k' \rangle|^2 \quad (224)$$

The matrix element appearing in this expression is treated in detail in the Section 2.7.6. In writing Eq. (224) we have taken the phonon frequency  $\omega_q$  to be given by

$$\omega_q = cq \quad (225)$$

**Coupling to Acoustical Phonons in the Low-Temperature Limit** In an analytical study of the low-temperature limit we use the variational principle discussed in Section 2.7.2 and choose a trial function given by

$$U = U_{nk} = \text{sgn}(k) \quad (226)$$

Thus  $U$  is 1 on the branches corresponding to  $k$  being positive, while it is  $-1$  on the branches corresponding to  $k$  being negative. This choice will lead to an expression for the conductivity which in the case of a single occupied Landau level and in the limit of low temperature agrees with a numerical solution of the integral equation. This suggests that the trial function is in fact the exact one under these conditions.

First we evaluate the scalar product  $(U, X)$  appearing in the general expression (197) for the lower bound on the conductivity. By changing the integration variable to the energy  $\varepsilon_{nk}$  we get

$$(X, U) = \frac{eE_x}{\hbar\pi} \sum_n f^0(\varepsilon_{n0}) \quad (227)$$

where  $\varepsilon_{n0}$  is the  $k = 0$  value of  $\varepsilon_{nk}$ . Because of the symmetry of the integral operator  $\hat{H}$  given in Eq. (217) the denominator occurring in Eq. (197) becomes

$$(U, HU) = \sum_n \int_{-\infty}^{\infty} \frac{dk}{2\pi} \int_{-\infty}^{\infty} \frac{dk'}{2\pi} \sum_{n'} K_{nn'}(k, k') \times \frac{1}{2} [1 - \text{sgn}(k)\text{sgn}(k')]^2 \quad (228)$$

As was discussed in Section 2.7.6  $k' = k - q_x$ . The occurrence of the factor  $[1 - \text{sgn}(k)\text{sgn}(k - q_x)]$  in the integrand of Eq. (228) implies that the summation over  $q_x$  becomes restricted by  $q_x > k$  for  $k > 0$ , while  $q_x < k$  for  $k < 0$ . Using the symmetry with respect to reversal of all momentum variables we may thus restrict the  $k$  integral to the interval 0 to  $\infty$ , which limits  $q_x$  to the region  $q_x > k$ . If  $\theta$  denotes the angle between  $\vec{q}$  and the  $x$  axis, the integration over  $\theta$  is therefore restricted by

$$\cos \theta > \frac{k}{q} \quad 0 < q < \infty \quad (229)$$

Thus we have to carry out three integrations (over  $q$ ,  $k$ , and  $\cos \theta$ ) as well as two sums (over  $n$  and  $n'$ ).

Let us consider the simplest case, in which  $n = n' = 0$ . If the sound velocity is much less than the Fermi velocity then the energy-conserving  $\delta$  functions are

$$\delta(\varepsilon_{n'k'} - \varepsilon_{nk} \pm \hbar\omega_q) \cong \delta\left(\frac{\hbar^2}{2m^*} (q^2 \cos^2 \theta - 2kq \cos \theta)\right) \quad (230)$$

The  $q$  integral is now restricted to the interval  $q > 2k$ , while  $k/q < \cos \theta < 1$ . This yields, after performing the  $\phi$  integral as shown in Section 2.7.6,

$$(U, \hat{H}U) = \frac{1}{4\pi^3 \hbar^2 c \rho} \int_0^\infty \frac{d\varepsilon}{v^2(\varepsilon)} \int_{2k}^\infty dq (\Xi^2 q^2 + P) \times I_{0,0} \left( q, 2\frac{k}{q} \right) \frac{|f^0(\varepsilon_{nk}) - f^0(\varepsilon_{nk} + \sigma \hbar\omega_q)|}{4 \sinh^2(\hbar\omega_q/2k_B T)} \quad (231)$$

where  $I_{0,0}(q, 2k/q)$  is given by Eq. (255) of Section 2.7.6. We may carry out the final integration over energy by expanding the difference of the Fermi functions in powers of  $\omega_q$ . Since the contribution due to terms involving higher order derivatives of the Fermi function is seen to vanish by the use of partial integration, we obtain

$$(U, \hat{H}U) = \frac{1}{2\pi^3 \hbar^2 c \rho} \int_0^\infty \frac{d\varepsilon}{v^2(\varepsilon)} \left( -\frac{\partial f^0}{\partial \varepsilon} \right) \int_{2k}^\infty dq \times \frac{(\Xi^2 q^2 + P) I_{0,0}(q, 2k/q) \hbar\omega_q}{4 \sinh^2(\hbar\omega_q/2k_B T)} \quad (232)$$

The remaining steps are standard. We assume that the temperature is much less than the Fermi temperature, so that the integral over  $\varepsilon$  yields  $1/v_F^2$ , while  $k$  may be replaced by the Fermi momentum  $k_F$ . Furthermore, we assume that the temperature is small compared to the characteristic temperature  $\Theta$  defined by

$$k_B \Theta = \hbar k_F c \quad (233)$$

Then we obtain

$$(U, \hat{H}U) = \frac{8}{\pi^2} \frac{m^{*2} k_F k_B T}{\rho c \hbar^4} \left( \Xi^2 + \frac{P}{4k_F^2} \right) \times \exp[-2k_F^2 \ell_h^2 / (1 + \gamma)] \exp(-2\Theta/T) \quad (234)$$

This results in the final conductivity expression

$$\sigma = \frac{2e^2}{h} l_\sigma \quad (235)$$

where the length  $l_\sigma$  is given by

$$l_\sigma = \frac{\pi c \hbar^3 \rho k_F}{m^{*2} (4k_F^2 \Xi^2 + P)} \exp[2k_F^2 \ell_h^2 / (1 + \gamma)] \exp(2\Theta/T) \quad (236)$$

At low temperatures the conductivity thus increases exponentially, in agreement with the result of the numerical calculation (see Fig. 24). In the presence of impurities, as we shall see in next section, the scattering against phonons yields a contribution to the inverse conductivity which is proportional to  $T^3$  rather than  $\exp(-2\Theta/T)$ , provided the temperature is sufficiently low that the impurities dominate the scattering.

### Scattering from Acoustical Phonons and Impurities

When the impurity scattering dominates we may use the variational principle with a trial function, which is proportional to the solution for impurity scattering alone. We shall consider the case where only the lowest Landau level  $n = 0$  is important. The trial function is thus chosen to be proportional to  $1/B_{0+}^0$ , as given by Eq. (207):

$$U(k) = k^2 \exp[2k^2 \ell_h^2 / (1 + \gamma)] \quad (237)$$

Since we have chosen the exact solution to the impurity problem as our trial function, the calculated upper bound on the contribution from electron-phonon scattering  $1/\sigma$  is exact, to lowest order in the magnitude of the electron-phonon coupling. At low temperatures we may make the approximation

$$[U(k) - U(k')]^2 \cong \left( \frac{dU(k)}{dk} \right)^2 (k - k')^2 \quad (238)$$

which is justified, since  $k - k' = q_x$  and the restriction to low temperatures implies that the phonon momentum is small. Furthermore, we may neglect the deformation potential coupling since the piezoelectric coupling dominates for small

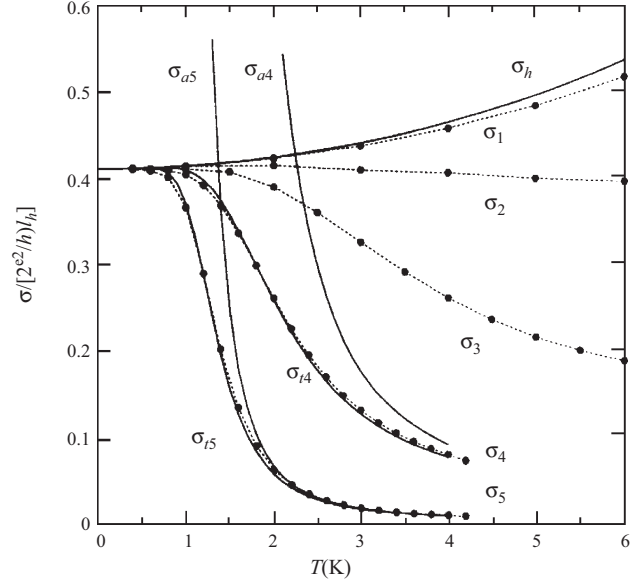


**Figure 24.** Normalized conductivity in GaAs as a function of temperature for  $B = 9$  T,  $\gamma = 0.5$ ,  $\varepsilon_F = 0.6\hbar\omega_h$ . Dotted lines are used as reference ( $\sigma_1, \sigma_2, \sigma_3, \sigma_4, \sigma_5$ ),  $T = 0$  K,  $B = 0$  T,  $\mu_{\text{imp}}^0 = 7.5, 75, \mu_{\text{imp}}^0 = 7.5, 300, 3000, \text{ and } 30000$  m<sup>2</sup>/(V s). Full lines: ( $\sigma_{a4}, \sigma_{a5}$ ), only acoustical phonon scattering was considered (normalized to  $\sigma_4, \sigma_5$ ). ( $\sigma_i$ ), only impurity scattering was considered. ( $\sigma_{i4}, \sigma_{i5}$ ), assuming that the inverse conductivities for both mechanisms are additive. Reprinted with permission from [186], J. L. Marín et al., “Handbook of Advanced Electronic and Photonic Materials and Devices” (H. S. Nalwa, Ed.). Academic Press, San Diego, 2001. © 2001, Academic Press.

$q$  according to Eq. (224), and we also set the matrix element appearing in Eq. (224) equal to unity. By inserting  $U$  in Eq. (197) and carrying out the integrals we obtain

$$\sigma_{\text{ph}}^{-1} = \frac{h}{2e^2} l_{\text{ph}}^{-1} \frac{3s(3)}{8\pi} \frac{1 + \gamma}{\gamma \tilde{\varepsilon}_F^3} \left( 1 + \frac{4\tilde{\varepsilon}_F}{\gamma} \right)^2 \left( \frac{k_B T}{\hbar\omega_h} \right)^3 \quad (239)$$

where  $\tilde{\varepsilon}_F = \varepsilon_F / \hbar\omega_h$ , and

$$l_{\text{ph}}^{-1} = \frac{P m_e^*}{\rho c^2 \hbar^2} \quad (240)$$

This  $T^3$  behavior agrees well with our numerical calculations in the parameter range where it is expected to apply. In Figures 24 and 25 is shown the calculated conductivity, obtained by numerical solution of the integral equation, for samples with different amounts of impurities.

### 2.7.5. Scattering from Optical Phonons

Next we investigate the combined effects of scattering by longitudinal optical phonons [145] and impurities. The chief differences from the preceding section involve the  $q$  dependence of the electron-phonon matrix element and the absence of dispersion in the phonon frequencies. The conductivity is obtained by solving the Boltzmann equation in the limit where the temperature is much less than  $\hbar\omega_0/k_B$ .



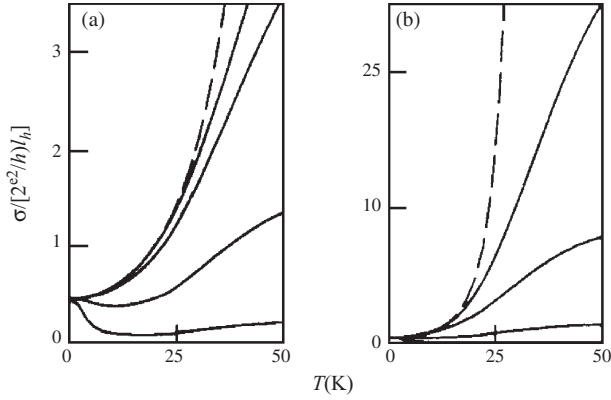


**Figure 25.** Plots of the normalized conductivity versus temperature for a GaAs quantum well wire at the magnetic field  $B = 9$  T and the Fermi level  $\varepsilon_F = 0.6\hbar\omega_h$ . The confinement parameter in panel (a) is  $\gamma = 1.0$  and in (b) is  $\gamma = 0.5$ . The dashed curve in each panel is the case where only impurity scattering is taken into account. The four full curves in each panel are the result of combining impurity and acoustical-phonon scattering for each of the following values of the zero-field, zero-temperature mobility  $\mu_{\text{imp}} = 0.9, 9, 90,$  and  $900$   $\text{m}^2/(\text{V s})$ . Reprinted with permission from [186], J. L. Marín et al., “Handbook of Advanced Electronic and Photonic Materials and Devices” (H. S. Nalwa, Ed.). Academic Press, San Diego, 2001. © 2001, Academic Press.

**Coupling to Optical Phonons** We shall use the simple model where the phonon frequency is independent of momentum,

$$\omega_q \cong \omega_0 \quad (241)$$

The electron-phonon matrix element [155] is given by

$$|g(nn', \vec{q})|^2 = \frac{1}{q^2} \frac{M_0^2}{V} M_n^{n'}(u) \quad (242)$$

where  $V$  is the normalization volume and where

$$M_0^2 = 2\pi \frac{e^2 \hbar \omega_0}{\varepsilon_0} \left( \frac{1}{\kappa_\infty} - \frac{1}{\kappa_0} \right) \quad (243)$$

The function  $M$  is given by

$$M_n^{n'}(u) = |\langle nk | \exp(i\vec{q} \cdot \vec{r}) | n' k' \rangle|^2 \quad (244)$$

which is calculated in Section 2.7.6, where also  $u$  is defined.

The approximation in Eq. (241) allows us to integrate over the  $y$  and  $z$  components of the phonon momentum. Using a  $\delta$  function for the wavefunction in the  $z$  direction, we get

$$\sum_{q_y, q_z} |g(nn', \vec{q})|^2 = \frac{M_0^2}{(2\pi)^2 L} K_n^{n'}(q_x) \quad (245)$$

where

$$K_n^{n'}(q_x) = \int_{-\infty}^{\infty} \frac{dq_y}{\sqrt{q_x^2 + q_y^2}} M_n^{n'}[u(q_x, q_y)] \quad (246)$$

**Scattering from Optical Phonons and Impurities** We now consider the case of impurity and optical-phonon scattering. The Boltzmann equation in this case reads

$$\frac{eE_x}{k_B T} v_{nk} f_{nk}^0 (1 - f_{nk}^0) = \left( \frac{\partial f_{nk}}{\partial t} \right)_{\text{coll}}^{\text{imp}} + \left( \frac{\partial f_{nk}}{\partial t} \right)_{\text{coll}}^{\text{op}} \quad (247)$$

The collision integral for the phonon scattering given in Eq. (217) simplifies in the case of optical phonons to

$$\begin{aligned} \left( \frac{\partial f_{nk}}{\partial t} \right)_{\text{coll}}^{\text{op}} &= -\frac{M_0^2}{\hbar 2\pi L} \frac{1}{4 \sinh^2(\hbar\omega_0/2k_B T)} \sum_{n'q_x} \sum_{\sigma} K_n^{n'}(q_x) \\ &\times |f^0(\varepsilon_{nk}) - f^0(\varepsilon_{nk} + \sigma\hbar\omega_0)| (\psi_{nk} - \psi_{n'k-q_x}) \\ &\times \delta(\varepsilon_{n'k-q_x} - \varepsilon_{nk} - \sigma\hbar\omega_0) \end{aligned} \quad (248)$$

with  $K_n^{n'}(q_x)$  given in Eq. (246). The argument of the energy-conserving  $\delta$  function is zero for

$$q_x = k \left[ 1 - s \sqrt{1 + \frac{\hbar\omega_h(n-n') + \sigma\hbar\omega_0}{\hbar^2 k^2 / 2m^*}} \right] \quad (249)$$

for each value of  $nk$ , provided the square root is real. The branch index  $s$  assumes the values  $+1$  and  $-1$  corresponding to forward and backward scattering. The Boltzmann equation now simplifies to

$$\begin{aligned} 1 &= \sum_{n's'} B_{n+}^{n's'}(\varepsilon) [\phi_n(\varepsilon) - s' \phi_{n'}(\varepsilon)] + \sum_{n's'} C_{n+}^{n's'}(\varepsilon, \sigma) \\ &\times [\phi_n(\varepsilon) - s' \phi_{n'}(\varepsilon + \sigma\hbar\omega_0)] \end{aligned} \quad (250)$$

where the matrix  $B$  is given by Eq. (207). The optical-phonon scattering gives rise to the matrix  $C$ , which is given by

$$\begin{aligned} C_{ns}^{n's'}(\varepsilon, \sigma) &= \frac{1}{f^0(\varepsilon)[1-f^0(\varepsilon)]} \frac{M_0^2}{\hbar^2 (2\pi)^2} \frac{1}{4 \sinh^2(\hbar\omega_0/2k_B T)} \\ &\times \sum_{\sigma} |f^0(\varepsilon) - f^0(\varepsilon + \sigma\hbar\omega_0)| \\ &\times \frac{K_n^{n'}[sk_n(\varepsilon) - s'k_{n'}(\varepsilon + \sigma\hbar\omega_0)]}{v_n(\varepsilon)v_{n'}(\varepsilon + \sigma\hbar\omega_0)} \end{aligned} \quad (251)$$

In GaAs the typical optical-phonon energies are about 36 meV. Furthermore, since the cyclotron energy  $\hbar\omega_c$  in GaAs is 1.5 meV  $B/T$ , the typical situation will be that the energy spacing between the Landau levels as modified by the confinement potential  $\hbar\omega_h$  is much smaller than the phonon energies  $\hbar\omega_0 \gg \hbar\omega_h$ . Since we are interested in temperatures that are small or comparable in magnitude to the energy spacing  $\hbar\omega_h$ , we are therefore always in a situation where  $k_B T$  is much less than  $\hbar\omega_0$ . Under these circumstances it is possible to simplify the Boltzmann equation for electrical transport by considering it to be a coupled system of equations for the functions  $\phi(\varepsilon \pm n\hbar\omega_0)$  with  $n$  integers. Since the current is mainly determined by the distribution of electrons  $\phi(\varepsilon)$  within a thermal layer of thickness comparable to  $k_B T$ , it is sufficiently accurate to neglect the contributions from  $\phi(\varepsilon \pm n\hbar\omega_0)$ , when  $n$  is different from zero. The collision integral may therefore be approximated by the

“scattering-out” term, corresponding to the neglect of vertex corrections in the Kubo approach.

In calculating the conductivity from Eq. (205) we thus neglect the “scattering-in” terms involving  $\phi_{n'}(\varepsilon + \sigma\hbar\omega_0)$  while retaining the full collision matrix for the impurities. We have then evaluated the solution of Eq. (250) numerically and inserted the solution in the conductivity formula, Eq. (189). Results are shown in Figure 26. The low-temperature behavior is dominated by the impurities, which give rise to an initial increase of the conductivity, in accordance with Eq. (209). The optical phonons come in at higher temperatures, yielding a maximum of the conductivity as a function of temperature. The position of the maximum is roughly proportional to the logarithm of the strength of the impurity scattering, since the phonon contribution depends exponentially on temperature. Note, however, that the acoustical phonons have reduced the conductivity for the high mobility cases rather strongly at the temperature range shown here; see Figure 25. The dashed line represents the conductivity without optical-phonon scattering.

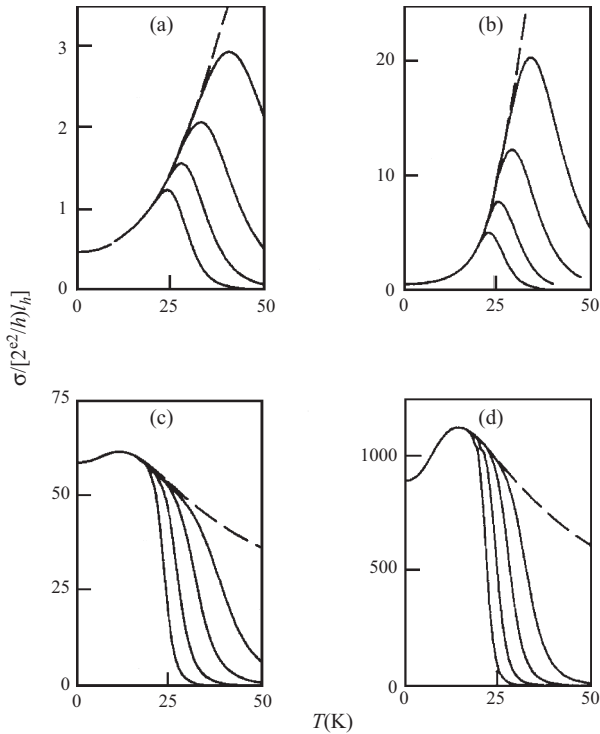


**Figure 26.** The conductivity with combined impurity and optical-phonon scattering for a GaAs quantum well wire. The normalized conductivity is plotted versus temperature for different choices of confinement potential strengths, Fermi energies, and mobilities. The magnetic field is  $B = 9$  T. The confinement parameter is  $\gamma = 1.0$  for panels (a) and (c) and  $\gamma = 0.5$  for (b) and (d); the Fermi level is  $\varepsilon_F = 0.6\hbar\omega_h$  (i.e., close to the bottom of the first band) for (a) and (b), and panels (c) and (d) have  $\varepsilon_F = 1.3\hbar\omega_h$ . The conductivity is shown for each of the following values of the zero-field, zero-temperature mobility:  $\mu_{\text{imp}} = 0.9, 9, 90,$  and  $900$   $\text{m}^2/(\text{Vs})$ . The dashed curve in each panel is the case where only impurity scattering is taken into account. Reprinted with permission from [186], J. L. Marín et al., “Handbook of Advanced Electronic and Photonic Materials and Devices” (H. S. Nalwa, Ed.). Academic Press, San Diego, 2001. © 2001, Academic Press.

In comparing the curves in Figures 24–26 we observe that the optical-phonon scattering in clean systems tends to dominate the total scattering already at fairly low temperatures, around 50 K. This is in contrast to the situation in typical GaAs-based two-dimensional electron [100] gases, where the optical-phonon scattering begins to dominate around 100 K. This effect originates in the increased phase space for scattering in one dimension, caused by the fact that only the  $x$  component of the momentum is conserved in the scattering process, while Eq. (246) includes contributions from all perpendicular components  $q_y$ .

We have shown that the magnetoconductivity of quantum wires may be discussed in a simple and unified fashion within the framework of a Boltzmann equation, by taking into account the influence of the magnetic field on the electron group velocity and the matrix elements governing the transition probability. By treating in detail the scattering from acoustical as well as optical phonons in the presence of impurity scattering, we have determined the temperature dependence of the magnetoconductivity for realistic choices of parameters in GaAs-based structures. In particular, we have found that the magnetoconductivity exhibits a maximum as a function of temperature, depending on the relative strength of the impurity and electron-phonon scattering. The calculated magnetoconductivity oscillates when the Fermi energy or the magnetic field is varied. Our detailed calculations show that the scattering against optical phonons in quantum wires is significant at temperatures somewhat smaller than the corresponding temperatures for the two-dimensional case.

We have found that the inverse of the sum of the inverse conductivities (the Matthiessen conductivity) in general is not a good approximation to the total conductivity. If impurity scattering dominates, the temperature dependence of the electron-phonon contribution is changed from exponential to power law behavior; cf. Eqs. (236) and (239). If the different scattering contributions are of comparable magnitude the Matthiessen conductivity overestimates the total conductivity up to a factor of 2 dependent on parameter values. This overestimation is in accordance with the general resistivity theorem [154] for the Boltzmann equation:  $\rho_{\text{tot}} \geq \rho_1 + \rho_2$ . Only in the case where the phonon scattering dominates do we find a good agreement between the Matthiessen conductivity and the total conductivity; cf. Figure 24.

### 2.7.6. Matrix Element in Electron-Phonon Coupling Parameter

In this section we study the square of the matrix element  $\langle nk | \exp(i\vec{q} \cdot \vec{r}) | n'k' \rangle$ . Using the single-electron wavefunctions in Eq. (173) and performing the  $x$  and  $y$  integrals one obtains

$$\begin{aligned} & |\langle nk | \exp(i\vec{q} \cdot \vec{r}) | n'k' \rangle|^2 \\ &= \delta_{k, k'+q_x} \frac{n_{\min}!}{n_{\max}!} u^{|n-n'|} [L_{n_{\min}}^{|n-n'|}(u)]^2 \exp(-u) \end{aligned} \quad (252)$$

where  $n_{\min} = \min(n, n')$  and  $n_{\max} = \max(n, n')$ ;  $L_n^m(u)$  are the Laguerre polynomials while  $u$  is given by

$$u = \frac{1}{1+\gamma} \frac{1}{2} (q_x \ell_h)^2 + \frac{1}{2} (q_y \ell_h)^2 \quad (253)$$

The Kronecker  $\delta$  function appearing in Eq. (252), and which is written explicitly in the expression for the integral operator  $\hat{H}$  in Eq. (215), is a consequence of the translational invariance along the  $x$  direction.

In calculations involving acoustical phonons it is natural to use the polar coordinates  $(q, \theta, \varphi)$  with the  $x$  axis as the polar axis so that  $q_x = q \cos \theta$ ,  $q_y = q \sin \theta \cos \varphi$ , and  $q_z = q \sin \theta \sin \varphi$ . According to Eqs. (215) and (224) the only  $\varphi$  dependence is through  $u$  defined previously. It is therefore of interest to calculate the integral

$$I_{n,n'}(q, \cos \theta) \equiv \int_0^{2\pi} d\varphi u^{|n-n'|} [L_{n_{\min}}^{|n-n'|}(u)]^2 \exp(-u) \quad (254)$$

From Eq. (253) it follows that the  $\varphi$  dependence of  $u$  is of the form  $u = \beta + \alpha \cos^2 \varphi$ , so the integrand of  $I_{n,n'}$  therefore takes the form of a polynomial in  $\cos^2 \varphi$  times  $\exp(-\alpha \cos^2 \varphi)$ . The integral over  $\varphi$  may then be carried out explicitly in terms of the beta function and Gauss's hypergeometric function.

In the case where we consider only the lowest Landau level we just need to calculate  $I_{0,0}$ . Using the results quoted previously we find

$$I_{0,0}(q, q_x/q) = 2\pi \exp\left[-\frac{1}{2}(q_x \ell_h)^2 \frac{1}{1+\gamma} - \frac{1}{4}\ell_h^2(q^2 - q_x^2)\right] \times I_0\left(\frac{1}{4}\ell_h^2(q^2 - q_x^2)\right) \quad (255)$$

where  $I_0(x)$  is the modified Bessel function of order zero.

## 2.8. Hydrogenic Impurities in a Spherical Quantum Dot in the Presence of a Magnetic Field

The ground state and binding energies for a hydrogenic impurity in a spherical quantum dot in the presence of a uniform magnetic field are calculated by a variational method within the effective mass approximation [160]. The simple hydrogenic trial wavefunctions used in this calculation are flexible enough to treat on-center, off-center, and edge states of impurities in a quantum dot. Overall results are in reasonable agreement when compared to other calculations. Interestingly enough, in the case of an off-center impurity, a critical point from which bulk states change their nature (edge states) is also found.

Semiconductors composed of III-V materials usually have small effective masses, which means that the Bohr radius associated with the impurity is large compared to achievable quantum dot sizes. The binding energy of the impurity increases as the size of the confining region becomes of the order of Bohr radius, which makes possible, for instance, the fabrication of a low-threshold laser diode [161].

In this section a variational study about the effect of a magnetic field on the ground state and binding energies of a hydrogenic impurity within spherical quantum dot is made. The impurity can be located on (off) the center of symmetry to get a symmetric (asymmetric) situation, or near the boundary of quantum dot to get surfacelike states (edge states) of this system.

### 2.8.1. Theory and Model

Within the framework of the effective mass approximation, the Hamiltonian of a hydrogenic impurity located at the center of symmetry of a spherical quantum dots of radius  $r_0$ , in the presence of magnetic field, can be written as

$$\hat{H} = \frac{1}{2m_e^*} \left( \hat{p} - \frac{e}{c} \vec{A} \right)^2 - \frac{e^2}{\kappa r} + V_b(\vec{r}) \quad (256)$$

where  $\kappa$  is the dielectric constant of material inside the quantum dot,  $m_e^*$  is the electron effective mass,  $\vec{A}$  is the vector potential, and  $V_b(\vec{r})$  is the confining potential defined by

$$V_b(\vec{r}) = \begin{cases} 0 & 0 \leq r \leq r_0 \\ \infty & r > r_0 \end{cases} \quad (257)$$

For a uniform magnetic field,  $\vec{A}(\vec{r}) = \vec{B} \times \vec{r}/2$  if the Coulomb gauge  $\nabla \cdot \vec{A} = 0$  is chosen. In spherical coordinates, if the magnetic field is along the  $z$  direction,  $\vec{B} = B\hat{e}_z$ , the Hamiltonian can be expressed as

$$\hat{H} = -\frac{1}{2m_e^*} \nabla^2 - \frac{e^2}{\kappa r} - \frac{e}{2m_e^* c} B \hat{L}_z + \frac{e^2}{8m_e^* c^2} B^2 r^2 \sin^2 \theta \quad (258)$$

Here,  $\hat{L}_z$  is the  $z$  component of the angular momentum operator;  $\theta$  is the usual polar angle in these coordinates. The magnetic field preserves the azimuthal symmetry (i.e.,  $m$  is still a "good" quantum number). As only the ground state is studied, the value  $m = 0$  is required; thus the Hamiltonian [Eq. (258)] will retain the quadratic dependence on  $B$  only.

Because of confinement, the solution of Schrödinger equation associated with Eq. (258) must satisfy

$$\psi(r = r_0, \theta, \varphi) = 0 \quad (259)$$

In order to use the variational method, the trial wavefunction for the calculation of the ground state energy is chosen as

$$\begin{aligned} \psi(r) &= N \exp(-\alpha r) \exp\left(-\frac{1}{8} B r^2 \sin^2 \theta\right) (r_0 - r) \\ &= N \exp(-\alpha r) \exp\left(-\frac{1}{12} B r^2\right) (r_0 - r) \end{aligned} \quad (260)$$

where  $N$  is the normalization constant and  $\alpha$  is a variational parameter to be determined. The last term has been obtained considering that in absence of  $\vec{A}$  the system holds spherical symmetry. A similar choice of the trial wavefunction to calculate the ground state energy has widely been used in the case of hydrogenic impurities within spherical quantum dots [162] and cylindrical quantum wires [163] without magnetic field.

In the case of a hydrogenic impurity displaced a constant distance  $a$  from the center of symmetry of a quantum dot, the Hamiltonian of Eq. (256) is modified as

$$\hat{H} = \frac{1}{2m_e^*} \left( \hat{p} - \frac{e}{c} \vec{A} \right)^2 - \frac{e^2}{\kappa |\vec{r} - a\hat{e}_z|} + V_b(\vec{r}) \quad (261)$$

where the confining potential,  $V_b(\vec{r})$ , is still given by Eq. (257), and  $\hat{e}_z$  is a unit vector on  $z$  axis. Hence, the corresponding Hamiltonian and trial wavefunction, Eqs. (258) and (260), are given by

$$\hat{H} = -\frac{1}{2m_e^*} \nabla^2 - \frac{e^2}{\kappa|\vec{r} - a\hat{e}_z|} - \frac{e}{2m_e^*c} B \hat{L}_z + \frac{e^2}{8m_e^*c^2} B^2 r^2 \sin^2 \theta \quad (262)$$

and

$$\psi(r) = N \exp(-\alpha|\vec{r} - a\hat{e}_z|) \exp\left(-\frac{1}{8} B r^2 \sin^2 \theta\right) (r_0 - r) \quad (263)$$

respectively.

Notice that the wavefunction [Eq. (263)] satisfies the boundary condition imposed by Eq. (259). Again, since  $m = 0$  is chosen, the Hamiltonian [Eq. (262)] will not have linear dependence on magnetic field  $B$ , just like the symmetric case studied before.

As we shall see, the trial wavefunction [Eq. (263)] is flexible enough to describe the case when the radius of the confining sphere becomes infinite and the hydrogenic impurity is close to its boundary. The latter would correspond to the case of a hydrogenic impurity close a plane, which allows us to investigate the ground state edge level of the spherical quantum dot.

The binding energy ( $\varepsilon_b$ ) for the hydrogenic impurity is defined as the ground state energy of the system without Coulombic interaction ( $\varepsilon_w$ ) minus the ground state energy including the presence of the electron–nucleus interaction ( $\varepsilon_0$ ); that is,

$$\varepsilon_b = \varepsilon_w - \varepsilon_0 \quad (264)$$

The binding energy defined before is a positive quantity. The  $\varepsilon_w$  term of Eq. (264) is the ground state energy of an electron confined inside a spherical quantum dot of radius  $r_0$ ; that is

$$\varepsilon_w = \frac{\pi^2 \hbar^2}{2m_e^* r_0^2} \quad (265)$$

The values of the physical parameters pertaining to a GaAs quantum dot used in these calculations, for the sake of comparison, are  $m_e^* = 0.067m_0$  and  $\kappa = 12.5$ ; thus  $a_B^* = 98.7 \text{ \AA}$  and  $R_y^* = 5.83 \text{ meV}$ . Moreover, the linear dependence term on  $B$ , in Eq. (258), can be scaled down to

$$\gamma m = \frac{e\hbar}{2m_e^* c R_y^*} B m = \frac{m_0}{m_e^* R_y^*} \mu_0 B m \quad (266)$$

where  $\mu_0 = 5.78838263 \times 10^{-2} \text{ meV T}^{-1}$  is the Bohr magneton; then the value  $B = 6.75 \text{ T}$  corresponds to an effective Rydberg ( $\gamma = 1$ ).

The results for the symmetric case (on-center impurity) are displayed in Figure 27, in which the binding energy of the hydrogenic impurity is plotted as a function of the quantum dot radius for different magnetic field strengths. The qualitative and quantitative behavior of the results is in good agreement with those of Xiao et al. [164], and Branis et al.

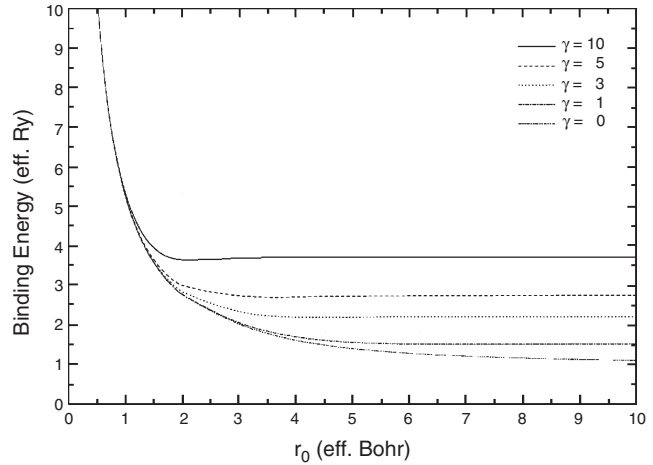


**Figure 27.** The binding energy of an on-center hydrogenic impurity as a function of the quantum dot radius for different magnetic fields. Reprinted with permission from [186], J. L. Marín et al., “Handbook of Advanced Electronic and Photonic Materials and Devices” (H. S. Nalwa, Ed.), Academic Press, San Diego, 2001. © 2001, Academic Press.

[42], who studied the magnetic field dependence over the binding energies of hydrogenic impurities in quantum dots and quantum well wires, respectively. In the strong spatial confinement case ( $r_0 < a_B^*$ ), the binding energy is relatively insensitive to the magnetic field and diverges as the dot radius  $r_0 \rightarrow 0$ , as in the case of zero magnetic field. The latter reflects that the main contribution to the binding energy is due to electron spatial confinement, which prevails over magnetic field confinement. The latter can be estimated through the magnetic length defined as

$$l_B = \sqrt{\frac{\hbar c}{eB}} = 484.82 \times B^{-1/2} \quad (267)$$

where  $l_B$  is expressed in effective Bohrs, and  $B$  is given in Teslas. For dot radius  $r_0 \cong a_B^*$ , the different magnetic field curves deviate from each other reaching steady values as the dot radius increases. For weak spatial confinement ( $r_0 \gg a_B^*$ ), the binding energy converges asymptotically to the corresponding bulk values. In the limit of large dot radius, the binding energy for  $B = 0$  approaches its bulk value,  $\varepsilon_b = 1R_y^*$ , as expected. An increase of the field strength decreases the magnetic length as compared with the dot radius; thus in this case the binding energy increases due to magnetic confinement that compels the electron to move “closer” to the on-center impurity.

Figure 28 shows the behavior of binding energy as a function of field strength for different dot radii of an on-center impurity. The variation of binding energy as the field increases is less sensitive as dot radius decreases, thus enforcing the previous comment regarding Figure 27.

The results for the asymmetric case (off-center impurity) are plotted in Figures 29 and 30 with zero magnetic field. Figure 29 shows the ground state energy for different sizes of quantum dot versus the relative position of the off-center impurity ( $a/r_0$ ). The ground state energy increases from its on-center impurity value ( $a/r_0 = 0$ ) as the impurity is shifted off the center; this is a general behavior. For larger radii

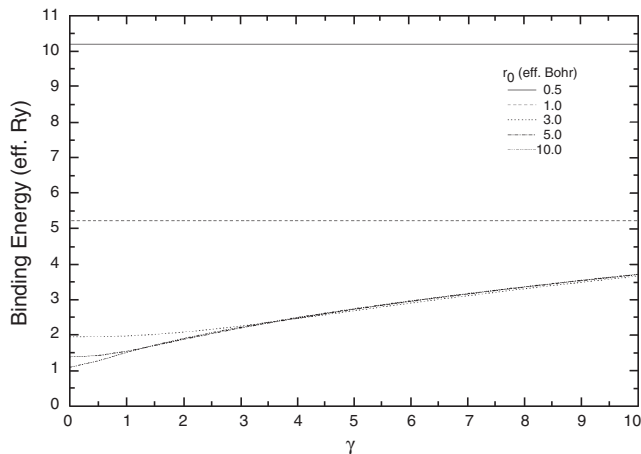


**Figure 28.** The binding energy of an on-center hydrogenic impurity as a function of the magnetic field for different dot radii. Reprinted with permission from [186], J. L. Marín et al., “Handbook of Advanced Electronic and Photonic Materials and Devices” (H. S. Nalwa, Ed.). Academic Press, San Diego, 2001. © 2001, Academic Press.

the ground state energy becomes lower, and then, for closer distances to the wall, evolves from the  $1s$  “free” hydrogen ground state ( $-1/2$ -Hartree) to the  $2p_z$  “free” hydrogen first excited state ( $-1/8$ -Hartree). These results are in good agreement with those of Brownstein [165], Gorecki and Byers Brown [166], and Marín et al. [162]. It is clear now that the trial wavefunction as chosen is flexible enough to describe the case when the size of the quantum dot becomes infinite and the nucleus is close to the surface. The latter corresponds to the case of a hydrogenic impurity close to a plane. This situation will be discussed later when the effect of a magnetic field on the ground state of a hydrogenic impurity near the semiconductor surface will be considered.

In Figure 30, the binding energy for different sizes of quantum dot versus the relative position of the off-center

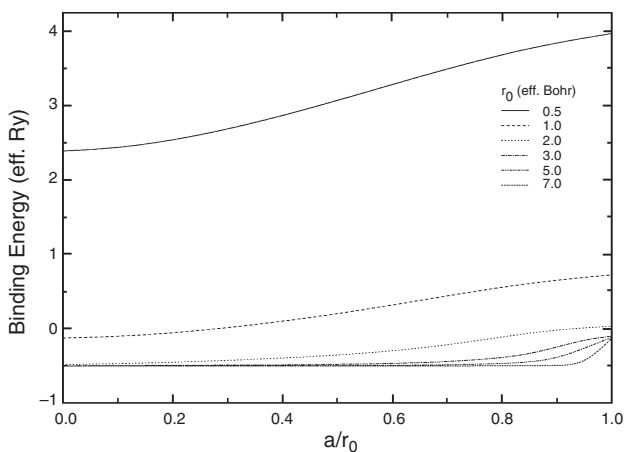


**Figure 29.** The ground state energy of an off-center hydrogenic impurity as a function of the relative position of the impurity for different dot radii. Reprinted with permission from [186], J. L. Marín et al., “Handbook of Advanced Electronic and Photonic Materials and Devices” (H. S. Nalwa, Ed.). Academic Press, San Diego, 2001. © 2001, Academic Press.

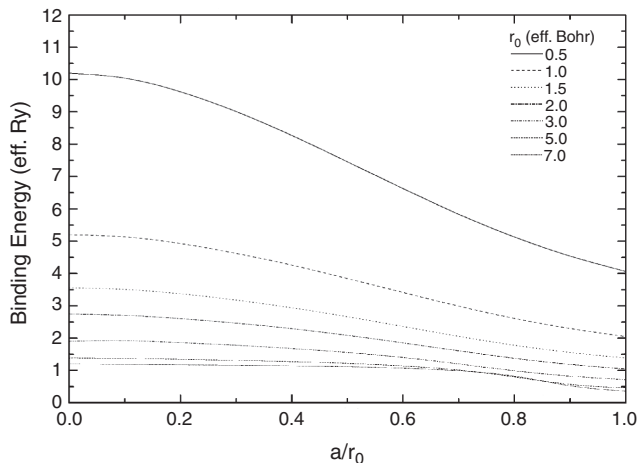


**Figure 30.** The binding state energy of an off-center hydrogenic impurity as a function of the relative position of the impurity for different dot radii. Reprinted with permission from [186], J. L. Marín et al., “Handbook of Advanced Electronic and Photonic Materials and Devices” (H. S. Nalwa, Ed.). Academic Press, San Diego, 2001. © 2001, Academic Press.

impurity ( $a/r_0$ ) has been plotted. The binding energy decreases as the impurity approaches to the boundary of the quantum dot. This behavior is due to the fact that wavefunctions vanish at the boundaries and thus their contributions to the binding energy of a quantum dot with an off-center impurity are smaller than a quantum dot with an on-center impurity. The results are similar to the case of a hydrogenic impurity placed in rectangular [167] or circular [163] cross-section quantum well wires, and in a spherical quantum dot [164].

The problem of a hydrogenic impurity near a crystal surface as a limit case of a hydrogenic impurity in a spherical quantum dot of very large radius will be considered next. In Figure 31, the ground state energy for different radii of quantum dot versus the relative position of the off-center impurity ( $a/r_0$ ) is shown. For very large quantum dot radii the Levine ground state energy of an atom located precisely on the surface of a semi-infinite medium is obtained; that is, the ground state energy changes gradually from its bulk value ( $-1$  Rydberg) into the Levine state ( $-1/4$  Rydberg) as the impurity reaches the surface.

In Figure 32, the ground state binding energy for different radii of quantum dot versus the relative position of the off-center impurity ( $a/r_0$ ) has been plotted. For the too large quantum dot radii considered here, binding energy curves cross one another and define a point from which the edge states begin to appear. This critical point corresponds to a hydrogenic impurity placed at the relative distance  $a/r_0 = 0.68$  from the center of the quantum dot. The associated binding energy with the quantum dot of largest radius ( $r_0 = 100$  effective Bohr) decreases from  $1R_y^*$  (effective Rydberg) for an impurity located far from a quantum dot surface to  $1/4R_y^*$  for an impurity located exactly at the surface of a quantum dot. The binding energy behavior is in reasonable agreement with that of Chen [168], who studied the problem of hydrogenic donors near semiconductor surfaces. Furthermore, starting from the critical point (near the quantum dot



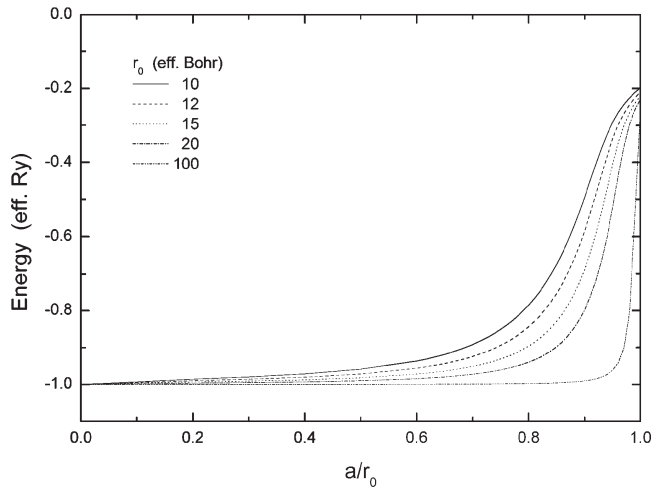


**Figure 31.** The ground state energy of a hydrogenic impurity in a spherical quantum dot of very large radius. Note that the ground state changes gradually from its bulk value ( $-1R_0^*$ ) to the Levine state ( $-1/4R_0^*$ ). Reprinted with permission from [186], J. L. Marín et al., “Handbook of Advanced Electronic and Photonic Materials and Devices” (H. S. Nalwa, Ed.). Academic Press, San Diego, 2001. © 2001, Academic Press.

surface), there is an inversion of binding energy for quantum dots of different radii. This occurs due to the fact that the boundary has a greater effect on binding energy when the quantum dot size increases, as a result of the strong spatial limitation due to the closeness of the impurity to the surface. When a magnetic field is applied, the critical point is removed and the binding energy curves cross one another at only one point. Moreover, crossing points are shifted away from the boundary as the magnetic field is increased; finally a moderate field strength causes them to vanish.

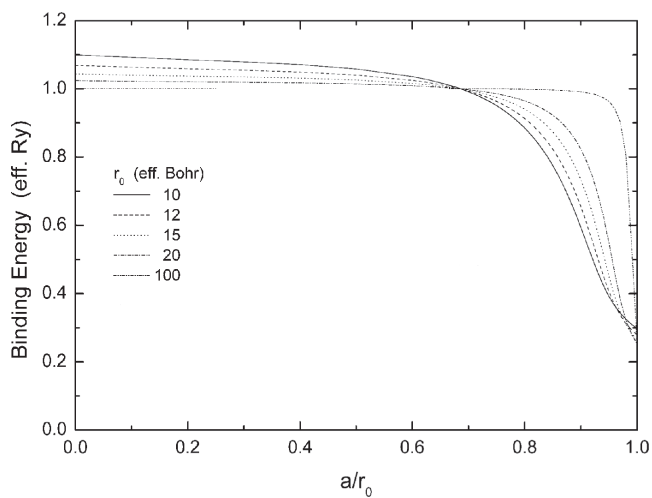


**Figure 32.** The binding state energy of a hydrogenic impurity as a function of the relative position of the impurity for large dot radii. Note that there is a point from which the edge states start to appear. Reprinted with permission from [186], J. L. Marín et al., “Handbook of Advanced Electronic and Photonic Materials and Devices” (H. S. Nalwa, Ed.). Academic Press, San Diego, 2001. © 2001, Academic Press.

## 2.9. Energy States of Two Electrons in a Parabolic Quantum Dot in Magnetic Field

The energy spectra of two interacting electrons in a quantum dot confined by a parabolic potential in an applied magnetic field of arbitrary strength are obtained in this section. The shifted  $1/N$  expansion method is used to solve the effective mass Hamiltonian [68]. The influence of the electron–electron interaction on the ground state energy and its significant effect on the energy level crossings in states with different angular momenta are shown. The dependence of the ground state energy on the magnetic field strength for various confinement energies is presented.

The magnetic field dependence plays a useful role in identifying the absorption features. The effects of the magnetic field on the state of the impurity [169] and excitons [170–174] confined in quantum dot have been extensively studied. Kumar et al. [175] have self-consistently solved the Poisson and Schrödinger equations and obtained the electron states in GaAs–GaAlAs for both cases: in zero and for magnetic fields applied perpendicular to the heterojunctions. The results of their work [175] indicated that the confinement potential can be approximated by a simple one-parameter adjustable parabolic potential. Merkt et al. [176] have presented a study of quantum dots in which both the magnetic field and the electron–electron interaction terms were taken into account. Pfannkuche and Gerhardt [177] have devoted a theoretical study to the magneto-optical response to far-infrared radiation (FIR) of quantum dot helium, accounting for deviations from the parabolic confinement. More recently, De Groote et al. [178] have investigated the thermodynamic properties of quantum dots taking into consideration the spin effect, in addition to the electron–electron interaction and magnetic field terms. The purpose of this section is to show the effect of the electron–electron interaction on the spectra of the quantum dot states with nonvanishing azimuthal quantum numbers and the transitions in the ground state of the system as the magnetic field strength increases.

Here we shall use the shifted  $1/N$  expansion method to obtain an energy expression for the spectra of two confined electrons in a quantum dot by solving the effective mass Hamiltonian including the following terms: the electron–electron interaction, applied field, and the parabolic confinement potential.

### 2.9.1. Theory and Model

Within the effective mass approximation, the Hamiltonian for an interacting pair of electrons confined in a quantum dot by parabolic potential of the form  $m_e^* \omega_0 r^2 / 2$  in a magnetic field applied parallel to the  $z$ -axis (and perpendicular to the plane where the electrons are restricted to move) in the symmetric gauge is written as

$$\hat{H} = \sum_{i=1}^2 \left\{ -\frac{\hbar^2 \nabla_i^2}{2m_e^*} + \frac{1}{2} m_e^* \omega_0^2 r_i^2 + \frac{\hbar \omega_c}{2} L_i^z \right\} + \frac{e^2}{\kappa |\vec{r}_1 - \vec{r}_2|} \quad (268)$$

where the two-dimensional vectors  $\vec{r}_1$  and  $\vec{r}_2$  describe the positions of the first and the second electron in the  $(x, y)$



plane, respectively.  $L_i^z$  stands for the  $z$ -component of the orbital angular momentum for each electron and  $\omega_c = eB/m_e^*c$ ,  $m_e^*$ , and  $\kappa$  are the cyclotron frequency, effective mass, and dielectric constant of the medium, respectively. The frequency  $\omega$  depends on both the magnetic field  $B$  and the confinement frequency  $\omega_0$  and is given by

$$\omega = \left( \omega_0^2 + \frac{\omega_c^2}{4} \right)^{1/2} \quad (269)$$

The natural units of length and energy to be used are the effective Bohr radius  $a_b^* = \kappa \hbar^2 / m_e^* e^2$  and effective Rydberg  $R_y^* = \hbar^2 / 2m_e^* a_b^{*2}$ . The dimensionless constant  $\gamma = \hbar \omega_c / 2R_y^*$  plays the role of an effective magnetic field strength.

Upon introducing the center of mass  $\vec{R} = (\vec{r}_1 + \vec{r}_2) / \sqrt{2}$  and the relative coordinates  $\vec{r} = (\vec{r}_1 - \vec{r}_2) / \sqrt{2}$ , the Hamiltonian [178] in Eq. (268) can be written as a sum of two separable parts that represent the center of mass motion Hamiltonian,

$$\hat{H}_R = -\frac{\hbar^2}{2m_e^*} \nabla_R^2 + \frac{m_e^*}{2} \omega^2 R^2 + \frac{\hbar \omega_c}{2} L_z^R \quad (270)$$

and the relative motion Hamiltonian,

$$\hat{H}_r = -\frac{\hbar^2}{2m_e^*} \nabla_r^2 + \frac{m_e^*}{2} \omega^2 r^2 + \frac{\hbar \omega_c}{2} L_z^r + \frac{e^2}{r} \quad (271)$$

Equation (270) describes the Hamiltonian of the harmonic oscillator with the well-known eigenenergies

$$\varepsilon_{n_{cm}, m_{cm}} = (2n_{cm} + |m_{cm}| + 1) \hbar \omega + \frac{\hbar \omega_c}{2} m_{cm} \quad (272)$$

labeled by the radial ( $n_{cm} = 0, 1, 2, \dots$ ) and azimuthal ( $m_{cm} = 0, \pm 1, \pm 2, \pm 3, \dots$ ) quantum numbers. The problem is reduced to obtaining eigenenergies  $\varepsilon_{n_r, m}$  of the relative motion Hamiltonian. The energy states of the total Hamiltonian are labeled by  $CM$  and relative quantum numbers by  $|n_{cm} m_{cm}; n_r m\rangle$ . The coexistence of the electron-electron and the oscillator terms makes the exact analytic solution with the present special functions impossible.

### 2.9.2. Shifted $1/N$ Expansion Method

The shifted  $1/N$  expansion method,  $N$  being the spatial dimensions, is a pseudoperturbative technique in the sense that it proposes a perturbation parameter that is not directly related to the coupling constant [179–181]. The aspect of this method has been clearly stated by Imbo et al. [179, 180] who had displayed step-by-step calculations relevant to this method. Following, their work here is presented only by the analytic expressions, which are required to determine the energy states.

The method starts by writing the radial Schrödinger equation, for an arbitrary cylindrically symmetric potential, in a  $N$ -dimensional space as

$$\left\{ -\frac{d^2}{dr^2} + \frac{(k-1)(k-3)}{4r^2} + V(r) \right\} \psi(r) = \varepsilon_r \psi(r) \quad (273)$$

where  $k = N + 2m$ .

In order to get useful results from  $1/\bar{k}$  expansion, where  $\bar{k} = k - a$  and  $a$  is a suitable shift parameter, the large  $\bar{k}$ -limit of the potential must be suitably defined [182]. Since the angular momentum barrier term behaves like  $\bar{k}^2$  at large  $\bar{k}$ , so the potential should behave similarly. This will give rise to an effective potential which does not vary with  $\bar{k}$  at large values of  $\bar{k}$  resulting in a sensible zeroth order classical result. Hence, Eq. (273) in terms of the shift parameter becomes

$$\left\{ -\frac{d^2}{dr^2} + \frac{\bar{k}^2 [1 - (1-a)/\bar{k}] [1 - (3-a)/\bar{k}]}{4r^2} + \frac{V(r)}{Q} \right\} \psi(r) = \varepsilon_r \psi(r) \quad (274)$$

where

$$V(r) = \frac{2}{r} + \frac{1}{4} \omega^2 r^2 + m \frac{\omega_c}{2} \quad (275)$$

and  $Q$  is a scaling constant to be specified from Eq. (277). The shifted  $1/N$  expansion method consists in solving Eq. (274) systematically in terms of the expansion parameter  $1/\bar{k}$ . The leading contribution term to the energy comes from

$$\bar{k}^2 V_{\text{eff}}(r) = \frac{\bar{k}^2}{r_0^2} \left( \frac{1}{4} + \frac{r_0^2 V(r_0)}{Q} \right) \quad (276)$$

where  $r_0$  is the minimum of the effective potential, given by

$$2r_0^3 V'(r_0) = Q \quad (277)$$

It is convenient to shift the origin to  $r_0$  by the definition

$$x = \bar{k}^{1/2} (r - r_0) / r_0 \quad (278)$$

and expanding Eq. (274) about  $x = 0$  in powers of  $x$ . Comparing the coefficients of powers of  $x$  in the series with the corresponding ones of the same order in the Schrödinger equation for a one-dimensional anharmonic oscillator, we determine the anharmonic oscillator frequency, the energy eigenvalue, and the scaling constant in terms of  $\bar{k}$ ,  $Q$ ,  $r_0$ , and the potential derivatives. The anharmonic frequency parameter is

$$\bar{\omega} = \left[ 3 + \frac{V''(r_0)}{V'(r_0)} \right]^{1/2} \quad (279)$$

and the energy eigenvalues in powers of  $1/\bar{k}$  (up to third order) read

$$\varepsilon_{n_r, m} = V(r_0) + \frac{\bar{k}^2}{4r_0} + \frac{1}{r_0^3} \left[ \frac{(1-a)(3-a)}{4} + \gamma_1 \right] + \frac{\gamma_2}{\bar{k} r_0^2} \quad (280)$$

The explicit forms of  $\gamma_1$  and  $\gamma_2$  are given in Section 2.9.3. The shift parameter  $a$ , which introduces an additional

degree of freedom, is chosen so as to make the first term in the energy series of order  $\bar{k}$  to vanish, namely,

$$\frac{\bar{k}}{r_0^2} \left[ \left( n_r + \frac{1}{2} \right) \bar{\omega} - \frac{(2-a)}{2} \right] = 0 \quad (281)$$

by requiring an agreement between  $1/\bar{k}$  expansion and the exact analytic results for the harmonic and Coulomb potentials. From Eq. (281) we obtain

$$a = 2 - (2n_r + 1)\bar{\omega} \quad (282)$$

where  $n_r$  is the radial quantum number related to the principal  $n$  and magnetic  $m$  quantum numbers by the relation  $n_r = n - |m| - 1$ . Energies and lengths in Eqs. (273)–(282) are expressed in units of  $R_y^*$  and  $a_B^*$ , respectively.

For the two-dimensional case,  $N = 2$ , Eq. (277) takes the following form:

$$\sqrt{2r_0 V'(r_0)} = 2 + 2m - a = Q^{1/2} \quad (283)$$

Once  $r_0$  (for a particular quantum state and confining frequency) is determined, the task of computing the energy is relatively simple.

The results are presented in Figures 33–37 and Tables 3 and 4. The relative ground state energy  $|00\rangle$  of the relative motion, for the zero magnetic field case, against the confinement length is displayed in Figure 33. The present results (black dots) clearly show excellent agreement with the numerical results of [176] (dashed line). In Figure 34, the first low energy levels,  $|00\rangle$ ,  $|10\rangle$ , and  $|20\rangle$ , of the relative Hamiltonian are presented as a function of the effective confinement frequency  $\omega$ , using parameters appropriate to InSb, where the dielectric constant  $\kappa = 17.88$ , electron effective mass  $m_e^* = 0.014m_0$ , and confinement energy  $\hbar\omega_0 = 7.5$  meV [178]. The energy levels obviously show a linear dependence on the effective frequency. As the effective frequency  $\omega$  increases the confining energy term dominates the interaction energy term and thus the linear relationship

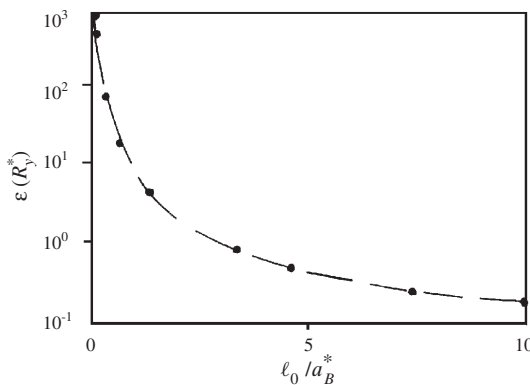


**Figure 33.** The relative ground state energy  $|00\rangle$  for the electrons in a quantum dot as a function of confinement length  $\ell_0 = (\hbar/m_e^* \omega_0)^{1/2}$  for zero magnetic field: this section’s calculations are given by closed circles; those of [175] are given by the solid line. Reprinted with permission from [186], J. L. Marín et al., “Handbook of Advanced Electronic and Photonic Materials and Devices” (H. S. Nalwa, Ed.). Academic Press, San Diego, 2001. © 2001, Academic Press.

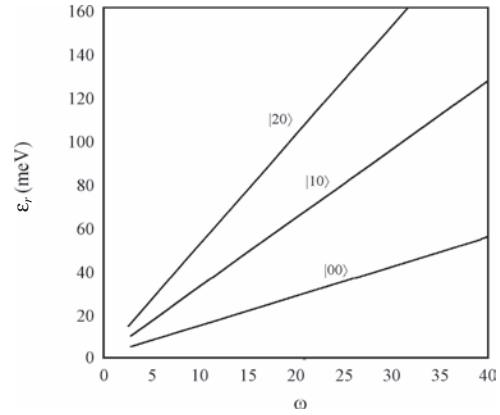


**Figure 34.** The low-lying relative states  $|00\rangle$ ,  $|10\rangle$ , and  $|20\rangle$  for two electrons in a quantum dot made of InSb as a function of confinement frequency  $\omega$ . Reprinted with permission from [186], J. L. Marín et al., “Handbook of Advanced Electronic and Photonic Materials and Devices” (H. S. Nalwa, Ed.). Academic Press, San Diego, 2001. © 2001, Academic Press.

between the energy and the frequency is maintained. This result is consistent with [178].

To investigate the effect of the electron–electron interaction on the energy spectra of the quantum dot, we have plotted in Figure 35 the total ground state energy  $|00; 00\rangle$  of the full Hamiltonian for independent (solid line) and interacting (dashed line) electrons as a function of the ratio  $\omega_c/\omega_0$ . The figure shows, as we expect, a significant energy enhancement when the electron–electron Coulombic interaction term is turned on. Furthermore, as the magnetic field increases, the electrons are further squeezed in the quantum dot, resulting in an increase of the repulsive electron–electron Coulombic energy and in effect the energy levels.

The energy level crossings are shown in Figure 36. We have displayed the eigenenergies of the states  $|00; 0m\rangle$ ;

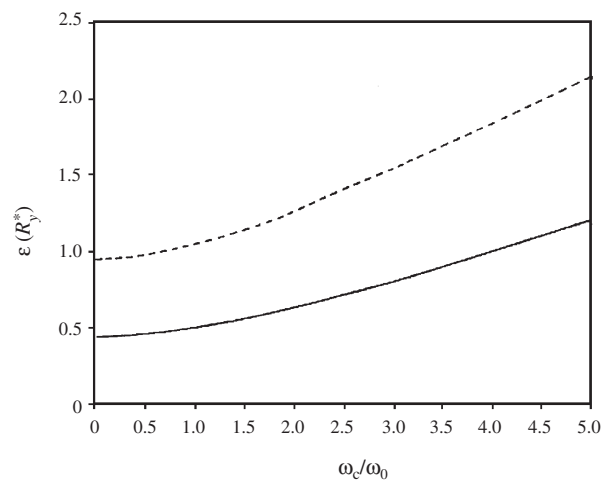


**Figure 35.** The total ground state energy  $|00; 00\rangle$  for two electrons in a quantum dot as a function of the ratio  $\omega_c/\omega_0$ . For independent (solid line) and interacting (dashed line) electrons. Reprinted with permission from [186], J. L. Marín et al., “Handbook of Advanced Electronic and Photonic Materials and Devices” (H. S. Nalwa, Ed.). Academic Press, San Diego, 2001. © 2001, Academic Press.

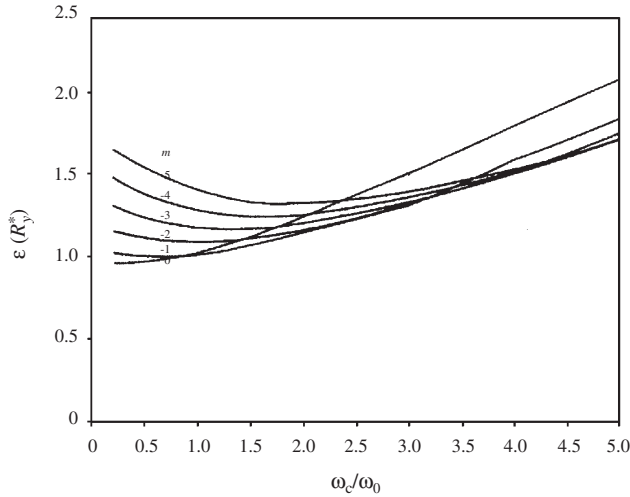


**Figure 36.** The total eigenenergies of the states  $|00; 0m\rangle$ ,  $m = 0, -1, -2, \dots, -5$ , for two interacting electrons parabolically confined in the quantum dot of size  $\ell_0 = 3a_B^*$  as a function of the ratio  $\omega_c/\omega_0$ . Reprinted with permission from [186], J. L. Marín et al., “Handbook of Advanced Electronic and Photonic Materials and Devices” (H. S. Nalwa, Ed.). Academic Press, San Diego, 2001. © 2001, Academic Press.

$m = 0, -1, -2, \dots, -5$ , for two interacting electrons parabolically confined in the quantum dot of size  $\ell_0 = 3a_B^*$  as a function of the ratio  $\omega_c/\omega_0$ . As the magnetic field strength increases the energy of the state  $m = 0$  increases while the energy of the states with nonvanishing quantum number  $m$  decreases, thus leading to a sequence of different ground states, as reported in [182]. In the interacting system, the interaction energy is the lower the higher the angular momentum of the relative motion. This is caused by the structure of the relative wavefunction: The larger the angular momentum the larger the spatial extent and therefore the larger the distance between the electrons [183].

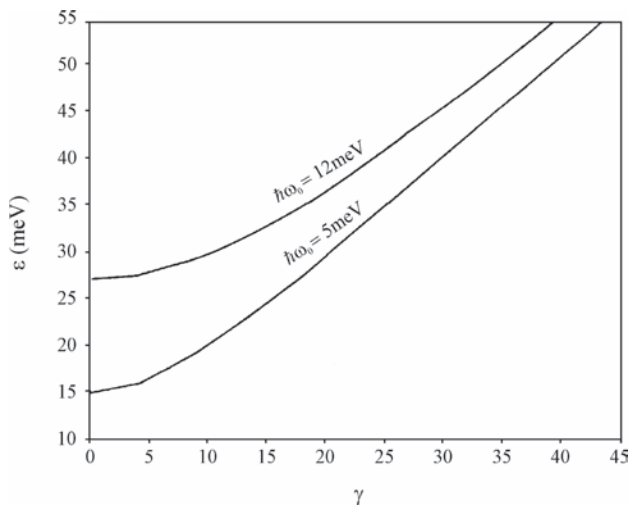


**Figure 37.** The relative ground state  $|00\rangle$  energy versus the magnetic field strength for two different confinement energies. Reprinted with permission from [186], J. L. Marín et al., “Handbook of Advanced Electronic and Photonic Materials and Devices” (H. S. Nalwa, Ed.). Academic Press, San Diego, 2001. © 2001, Academic Press.

**Table 3.** The roots  $r_0$  determined by Eq. (684) for quantum dot states with nonvanishing azimuthal quantum number ( $m$ ) against the ratio  $\omega_c/\omega_0$ .

$m$	$\omega_c/\omega_0$	0	-1	-2	-3	-4	-5
1		4.262	4.827	5.457	6.075	6.659	7.209
2		3.692	3.682	4.212	4.719	5.193	5.635
3		3.188	2.943	3.398	3.825	4.229	4.586

To confirm this numerically, we list in Table 3 the roots  $r_0$  of the potential for the interacting electrons in the quantum dot, for states with different angular momenta. At particular values of the ratio  $\omega_c/\omega_0$ , as the azimuthal quantum number  $|m|$  increases, the root  $r_0$  also increases and thus the electron–electron interaction  $V_{ee}(r) = 2/r_0$ , in the leading term of the energy series expression, decreases.

In Figure 37, we have shown the dependence of the ground state energy on the magnetic field strength for confinement energies:  $\hbar\omega_0 = 6$  and 12 meV, for a constant value of the magnetic field, the larger the confinement energy and the greater the energy of the interacting electrons in the quantum dot. The spin effect can be included in the Hamiltonian Eq. (268) added to the center of mass part as a space independent term, and Eq. (270) is still an analytically solvable harmonic oscillator Hamiltonian [178].

We have compared, in Table 4, the calculated results for the ground state energies  $|00\rangle$  of the relative Hamiltonian at different confining frequencies with the results of Taut [184]. In a very recent work, Taut has reported a particular analytical solution of the Schrödinger equation for two interacting electrons in an external harmonic potential. Table 4 shows that as  $1/\omega$  increases the difference between both results noticeably decreases until it becomes  $\approx 1.4 \times 10^{-3}$  at  $1/\omega = 1419.47$ .

Quantum dots with more than two electrons can also be studied. The Hamiltonian for  $n_e$ -interacting electrons, provided that the electron–electron interaction term depends only on the relative coordinates between electrons  $V(|r_i - r_j|) = e^2/k|r_{ij}|$ , and parabolically confined in the quantum dot, is separable into a  $CM$  and a relative Hamiltonian. The parabolic potential form  $V(r_i) = m_i\omega_0^2 r_i^2/2$ ,  $i = 1, 2, 3, \dots, n_e$  is the only potential which leads to a separable Hamiltonian. The  $CM$  motion part is described by the one-particle Hamiltonian [see Eq. (270)], with the electron mass replaced by the total mass  $M = n_e m_e^*$

**Table 4.** The ground state energies (in atomic units) of the relative Hamiltonian calculated by  $1/N$  expansion at different frequencies, compared with the results of Taut [278].

$1/\omega$	$1/N$ expansion	Taut
4	0.4220	0.6250
20	0.1305	0.1750
54.7386	0.0635	0.0822
115.299	0.0375	0.0477
523.102	0.0131	0.0162
1054.54	0.0081	0.0100
1419.47	0.0067	0.0081

and the electron charge replaced by the total charge  $Q = n_e e$ . The relative Hamiltonian part, which involves only the relative coordinates and momenta, has a cylindrically symmetric potential and can be handled by the  $1/N$ -expansion technique. When the confining potential is quadratic, FIR spectroscopy is insensitive to the interaction effects because of the  $CM$  and relative motions. If the radiation dipole operator  $\sum_i e_i \vec{r}_i = Q\vec{R}$ , being a pure  $CM$  variable, then it does not couple to  $\hat{H}_r$ , which contains all the electron–electron interactions. The dipole operator then induces transitions between the states of the  $CM$  but does not affect the states of the relative Hamiltonian. The eigenenergies for the  $CM$  Hamiltonian, Eq. (272), do not change because  $\omega_c$  in the energy expression remains the same; namely,  $QB/Mc = eB/m_e^* c$ . Consequently, the FIR absorption experiments see only the feature of the single-electron energies. There are only two allowed dipole transitions ( $\Delta m = \pm 1$ ) and the FIR resonance occurs at frequencies

$$\omega_{\pm} = \sqrt{\left(\frac{\omega_c}{2}\right)^2 + \omega_0^2} \pm \frac{\omega_c}{2} \quad (284)$$

Many different experiments on quantum dots have proved the validity of Kohn's theorem and that the observed resonance frequency of an electron system in a parabolic potential is independent of electron–electron interactions and thus the actual number of electrons in the well, as reported by Wixforth et al. in a very recent review article [185].

In conclusion we have obtained the energy spectra of two interacting electrons as a function of confinement energies and magnetic field strength. The method has shown good agreement with the numerical results of Merkt et al. [176], Taut [184], and Wagner et al. [182]. Our calculations have also shown the effect of the electron–electron interaction term on the ground state energy and its significance on the energy level crossings in states with different azimuthal quantum numbers. The shifted  $1/N$  expansion method yields quick results without putting restrictions on the Hamiltonian of the system.

### 2.9.3. Calculation of Parameters $\gamma_1$ and $\gamma_2$

The explicit forms of the parameters  $\gamma_1$  and  $\gamma_2$  are given in the following. Here  $R_y^*$  and  $a_B^*$  are used as units of energy and length, respectively

$$\gamma_1 = c_1 e_2 + 3c_2 e_4 - \bar{\omega}^{-1} [e_1^2 + 6c_1 e_1 e_3 + c_4 e_2^3] \quad (285)$$

and

$$\gamma_2 = T_7 + T_{12} + T_{16} \quad (286)$$

where

$$\begin{aligned} T_7 &= T_1 - \bar{\omega}^{-1} [T_2 + T_3 + T_4 + T_5 + T_6] \\ T_{12} &= \bar{\omega}^{-2} [T_8 + T_9 + T_{10} + T_{11}] \\ T_{16} &= \bar{\omega}^{-2} [T_{13} + T_{14} + T_{15}] \end{aligned} \quad (287)$$

with

$$\begin{aligned} T_1 &= c_1 d_2 + 3c_2 d_4 + c_3 d_6 & T_2 &= c_1 e_2^2 + 12c_2 e_2 e_4 \\ T_3 &= 2e_1 d_1 + 2c_5 e_4^2 & T_4 &= 6c_1 e_1 d_3 + 30c_2 e_1 d_5 \\ T_5 &= 6c_1 e_1 d_3 + 2c_4 e_3 d_3 & T_6 &= 10c_6 e_3 d_5 \\ T_8 &= 4e_1^2 e_2 + 36c_1 e_1 e_2 e_3 & T_9 &= 8c_4 e_2 e_3^2 \\ T_{10} &= 24c_1 e_1^2 e_4 + 8c_7 e_1 e_3 e_4 & T_{11} &= 12c_8 e_3^2 e_4 \\ T_{13} &= 8e_1 e_3 + 108c_1 e_1 e_3 & T_{14} &= 48c_4 e_1 e_3 \\ T_{15} &= 30c_9 e_3 \end{aligned} \quad (288)$$

where  $c$ 's,  $d$ 's, and  $e$ 's are parameters given as

$$\begin{aligned} c_1 &= 1 + 2n_r & c_4 &= 11 + 30n_r + 30n_r^2 \\ c_8 &= 57 + 189n_r + 225n_r^2 + 150n_r^3 \\ c_2 &= 1 + 2n_r + 2n_r^2 & c_5 &= 21 + 59n_r + 51n_r^2 + 34n_r^3 \\ c_3 &= 3 + 8n_r + 6n_r^2 + 4n_r^3 & c_6 &= 13 + 40n_r + 42n_r^2 + 28n_r^3 \\ c_9 &= 31 + 109n_r + 141n_r^2 + 94n_r^3 & c_7 &= 31 + 78n_r^2 + 78n_r^3 \\ e_j &= \kappa_j / \bar{\omega}^{-j/2} & d_i &= \delta_i / \bar{\omega}^{i/2} \end{aligned} \quad (289)$$

where  $j = 1, 2, 3, 4$  and  $i = 1, 2, 3, 4, 5, 6$ .

$$\begin{aligned} \kappa_1 &= (2 - a) & \kappa_2 &= -\frac{3(2 - a)}{2} \\ \kappa_3 &= -1 - \frac{2r_0}{Q} & \kappa_4 &= \frac{5}{4} + \frac{2r_0}{Q} \\ \delta_1 &= -\frac{(1 - a)(3 - a)}{2} & \delta_2 &= -\frac{3(1 - a)(3 - a)}{4} \\ \delta_3 &= 2(2 - a) & \delta_4 &= -\frac{5(2 - a)}{2} \\ \delta_5 &= -\frac{3}{2} - \frac{2r_0}{Q} & \delta_6 &= \frac{7}{4} + \frac{2r_0}{Q} \end{aligned} \quad (290)$$

## GLOSSARY

**Binding energy** Energy necessary to keep bound the electron-hole pair.

**Charged carrier** It is an electron or a hole.

**Conduction band** Energy band in a crystalline solid partially filled by electrons.

**Effective mass** The mass of a particle in a crystalline solid.

**Elastic scattering** A process in which the scattered particle has the same energy before and after event.

**Exciton** Electron-hole pair correlated by a coulomb-like interaction.

**Gap** Forbidden region for the electrons, which it is determined by the difference of energies between conduction and valence bands.

**Hole** Its the absence of an electron in the valence band.

**Impurity** An atom or molecule embedded in a different material.

**Inelastic scattering** A process in which the scattered particle has different energy before and after event.

**Magnetoconductivity** The conductivity of the charge carriers in presence of an external magnetic field.

**Quantum dot** A quantum system, in which the carriers are confined in all directions.

**Quantum Hall effect** The quantization of the Resistivity in a confined system due to the presence of a magnetic field.

**Quantum well wire** A quantum system, in which the carriers are confined in two directions, the other remains free.

**Quasi-dimensional system** A three-dimensional quantum system in which the movement of carriers is restricted in one, two or three directions of a few nanometers.

**Resistivity** Magnitude that characterizes the opposition to the movement of a charge carrier through a material.

**Valence band** Energy band in a crystalline solid completely filled by electrons.

## REFERENCES

- D. Gershoni, J. S. Weiner, S. N. G. Chu, G. A. Baraf, J. M. Vandenberg, L. N. Pfeiffer, K. West, R. A. Logan, and T. Tanbun-Ek, *Phys. Rev. Lett.* 65, 1631 (1990).
- H. Lage, D. Heitmann, R. Cingolani, P. Grambow, and K. Ploog, *Phys. Rev. B* 44, 6550 (1991).
- M. Walther, E. Kapon, D. M. Hwang, E. Colas, and L. Nunes, *Phys. Rev. B* 45, 6333 (1992).
- Ch. Gréus, R. Spiegel, P. A. Knipp, T. L. Reinecke, F. Faller, and A. Forchel, *Phys. Rev. B* 49, 5753 (1994).
- M. Bayer, A. Schmidt, A. Forchel, F. Faller, T. L. Reinecke, P. A. Knipp, A. A. Dremin, and V. D. Kulakovskii, *Phys. Rev. Lett.* 74, 3439 (1995).
- P. Ils, A. Forchel, K. H. Wang, Ph. Pagnod-Rossiaux, and L. Goldstein, *Phys. Rev. B* 50, 11746 (1994).
- J. Lee, *J. Appl. Phys.* 54, 5482 (1983).
- J. Lee and H. N. Spector, *J. Appl. Phys.* 57, 366 (1985).
- S. S. Kubakaddi and B. G. Mulimani, *J. Phys. C* 18, 6647 (1985).
- H. H. Hassan and H. N. Spector, *J. Vac. Sci. Technol. A* 3, 22 (1985).
- H. S. Cho and P. R. Prucnal, *Phys. Rev. B* 39, 11150 (1989).
- P. C. Sercel and K. J. Vahala, *Phys. Rev. B* 44, 5681 (1991).
- U. Bockelmann and G. Bastard, *Phys. Rev. B* 45, 1688 (1992); 45, 1700 (1992).
- R. Cingolani, M. Lepore, R. Tommasi, I. M. Catalano, H. Lage, D. Heitmann, K. Ploog, A. Shimizu, H. Sakaki, and T. Ogawa, *Phys. Rev. Lett.* 69, 1276 (1992).
- J. A. Brum, G. Bastard, L. L. Chang, and L. Esaki, *Superlatt. Microstruct.* 3, 47 (1987).
- K. B. Wong, M. Jaros, and J. P. Hagon, *Phys. Rev. B* 35, 2463 (1987).
- J. A. Brum and G. Bastard, *Superlatt. Microstruct.* 4, 443 (1988).
- M. Sweeny, J. Xu, and M. Shur, *Superlatt. Microstruct.* 4, 623 (1988).
- D. S. Citrin and Y. C. Chang, *Phys. Rev. B* 40, 5507 (1989).
- P. C. Sercel and K. J. Vahala, *Phys. Rev. B* 42, 3690 (1990).
- A. Baraff and D. Gershoni, *Phys. Rev. B* 43, 4011 (1991).
- Y. Arakawa, T. Yamauchi, and J. N. Schulman, *Phys. Rev. B* 43, 4732 (1991).
- U. Bockelmann and G. Bastard, *Europhys. Lett.* 15, 215 (1991).
- J. B. Xia, *Phys. Rev. B* 44, 3211 (1992).
- C. R. Poestro, *Phys. Rev. B* 45, 11911 (1992).
- H. Wu, D. W. L. Sprung, and J. Martorell, *Phys. Rev. B* 45, 11960 (1992); *J. Appl. Phys.* 72, 151 (1992).
- J. Lee and H. N. Spector, *J. Vac. Sci. Technol. B* 2, 16 (1984).
- G. W. Bryant, *Phys. Rev. B* 29, 6632 (1984); 31, 7812 (1985).
- J. A. Brum, *Solid State Commun.* 54, 179 (1985).
- J. W. Brown and H. N. Spector, *J. Appl. Phys.* 59, 1179 (1986).
- G. Weber, P. A. Schulz, and L. E. Oliveira, *Phys. Rev. B* 38, 2179 (1988).
- H. S. Cho and P. R. Prucnal, *J. Vac. Sci. Technol. B* 7, 1363 (1989).
- A. Ferreira da Silva, *Phys. Rev. B* 41, 1684 (1990).
- N. P. Montenegro, J. López-Gondar, and L. E. Oliveira, *Superlatt. Microstruct.* 9, 5 (1991).
- N. P. Montenegro, J. López-Gondar, and L. E. Oliveira, *Phys. Rev. B* 43, 1824 (1991).
- N. P. Montenegro, A. Latgé, and L. E. Oliveira, *J. Appl. Phys.* 70, 5555 (1991).
- S. I. Tsonchev and P. L. Goodfriend, *Phys. Rev. B* 44, 1329 (1991).
- D. B. T. Thoai, *Solid State Commun.* 81, 945 (1992).
- A. Latgé, N. P. Montenegro, and L. E. Oliveira, *Phys. Rev. B* 45, 9420 (1992).
- D. S. Chuu, C. M. Hsiao, and W. N. Mei, *Phys. Rev. B* 46, 3898 (1992).
- Z. Y. Deng, H. Sun, and S. W. Gu, *Phys. Lett. A* 169, 186 (1992).
- S. V. Branis, G. Li, and K. K. Bajaj, *Phys. Rev. B* 47, 1316 (1993).
- T. Kodama, Y. Osaka, and M. Yamanishi, *Jpn. J. Appl. Phys.* 24, 1370 (1985).
- T. Kodama and Y. Osaka, *Jpn. J. Appl. Phys.* 25, 1875 (1985).
- Y. C. Chang, L. L. Chang, and L. Esaki, *Appl. Phys. Lett.* 47, 1324 (1985).
- J. W. Brown and H. Spector, *Phys. Rev. B* 35, 3009 (1987).
- M. Degani and O. Hipólito, *Phys. Rev. B* 35, 9345 (1987).
- L. Báyai, I. Galbraith, C. Ell, and H. Haug, *Phys. Rev. B* 36, 6099 (1987).
- I. Suemune and L. A. Coldren, *IEEE J. Quantum Electron.* QE-24, 1778 (1988).
- Y. Chen, *Phys. Rev. B* 41, 10604 (1990).
- T. Ogawa and T. Tagagahara, *Phys. Rev. B* 44, 8138 (1992).
- M. E. Rensink, *Am. J. Phys.* 37, 900 (1969).
- R. Rinaldi, M. Ferrera, R. Cingolani, U. Marti, D. Marti, F. Morier-Gemoud, P. Ruterana, and F. K. Reinhart, *Phys. Rev. B* 50, 11795 (1994).
- M. Kohl, D. Heitmann, P. Grambow, and K. Ploog, *Phys. Rev. Lett.* 63, 2124 (1989).
- A. S. Plaut, H. Lage, P. Grambow, D. Heitmann, K. Von Klitzing, and K. Ploog, *Phys. Rev. Lett.* 67, 1642 (1991).
- L. V. Kukushkin, V. I. Fal'ko, K. von Klitzing, K. Ploog, and D. Heitmann, *Pis'ma Zh. Eksp. Teor. Fiz.* 53, 321 (1991); *JETP Lett.* 53, 335 (1991).
- Y. Nagamune, Y. Arakawa, S. Tsukamoto, M. Nishioka, S. Sasaki, and N. Miura, *Phys. Rev. Lett.* 69, 2963 (1992).
- M. Bayer, A. Forchel, I. E. Itskevich, T. L. Reinecke, P. A. Knipp, Ch. Gréus, R. Spiegel, and F. Faller, *Phys. Rev. B* 49, 14782 (1994).
- M. Oestreich, A. P. Heberle, W. W. Ruhle, H. Lage, D. Heitmann, and K. Ploog, *J. Lumin.* 60/61, 390 (1994).
- L. A. Falkovsky and S. Klama, *Phys. Lett. A* 190, 341 (1994).
- G. Li, S. V. Branis, and K. K. Bajaj, *J. Appl. Phys.* 77, 1097 (1995).
- C. S. Lent, *Phys. Rev. B* 43, 4179 (1991).
- M. Bayer, P. Ils, M. Michel, A. Forchel, T. L. Reinecke, and P. A. Knipp, *Phys. Rev. B* 53, 4668 (1996).
- W. Hansen, T. P. Smith, III, K. Y. Lee, J. A. Brum, C. M. Knoedler, J. M. Hong, and D. P. Kern, *Phys. Rev. Lett.* 62, 2168 (1989).
- A. Balandin and S. Bandyopadhyay, *Phys. Rev. B* 52, 8312 (1995).
- L. Solimany and B. Kramer, *Solid State Commun.* 96, 471 (1995).
- H.-S. Sim, K.-H. Ahn, and K. J. Chang, *Phys. Rev. Lett.* 80, 1501 (1998).
- M. El-Said, *J. Phys. I France* 5, 1027 (1995).
- M. Persson, J. Pettersson, B. Von Sydow, P. E. Lindelof, A. Kristensen, and K. F. Berggren, *Phys. Rev. B* 52, 8921 (1995).
- M. Dineykhon and R. G. Nazmitdinov, *Phys. Rev. B* 55, 13707 (1997).
- F. J. Ribeiro, A. Latgé, M. Pacheco, and Z. Barticevic, *J. Appl. Phys.* 82, 270 (1997).

72. D. Huang, Y. Zhu, and S. Zhou, *J. Phys. Condens. Matter* 2, 641 (1990).
73. G. Ihm, M. L. Falk, S. K. Noh, S. J. Lee, and T. W. Kim, *Phys. Rev. B* 46, 15270 (1992).
74. M. Robnik, *J. Phys. A* 19, 3619 (1986).
75. M. Bayer, O. Schilling, A. Forchel, T. L. Reinecke, P. A. Knipp, Ph. Pagnod-Rossiaux, and L. Goldstein, *Phys. Rev. B* 53, 15810 (1996).
76. F. Geerinckx, F. M. Peeters, and J. T. Devreese, *J. Appl. Phys.* 68, 3435 (1990).
77. R. L. Greene, K. K. Bajaj, and D. E. Phelps, *Phys. Rev. B* 29, 1807 (1984).
78. M. Abramowitz and I. A. Stegun, "Handbook of Mathematical Functions." Dover, New York, 1970.
79. P. N. Argyres and L. M. Roth, in "Physics of III-V Compounds" (R. K. Willardson and A. C. Beer, Eds.), Vol. 1. Academic Press, New York, 1966.
80. J. C. Maan, *Springer Ser. Solid States Sci.* 53, 183 (1984).
81. T. Ando, *J. Phys. Soc. Japan* 50, 2978 (1981).
82. S. Das Sarma, *Surf. Sci.* 142, 341 (1984).
83. R. Rosas, R. Riera, J. L. Marín, and H. León, *Am. J. Phys.* 68, 835 (2000).
84. L. D. Landau and E. M. Lifschitz, "Quantum Mechanics." Pergamon Press, New York, 1977.
85. P. M. Morse and H. Feshbach, "Methods of Theoretical Physics." McGraw-Hill, New York, 1953.
86. J. L. Marín and S. A. Cruz, *Am. J. Phys.* 56, 1134 (1988).
87. J. L. Marín and S. A. Cruz, *Am. J. Phys.* 59, 931 (1991).
88. A. Lipovka, J. L. Marín, R. Riera, and R. Rosas, *Phys. Low-Dim. Struct.* 9/10, 97 (2002).
89. D. Loss and D. P. Di Vincenzo, *Phys. Rev. A* 57, 120 (1998).
90. P. Zanardi and F. Rossi, *Phys. Rev. Lett.* 81, 4752 (1998).
91. L. Quiroga and N. F. Johnson, *Phys. Rev. Lett.* 83, 2270 (1999).
92. G. Burkard, H. A. Engel, and D. Loss, *Fortschr. Phys.* 48, 965 (2000).
93. M. Grundmann, *Physica E* 5, 167 (2000).
94. M. Grundmann, D. Blimberg, and N. N. Ledentsov, "Quantum Dot Heterostructures." Wiley, New York, 1998.
95. S. Fafard, K. Hinzler, S. Raymond, M. Dion, J. Mc. Caffrey, Y. Feng, and S. Charbonneau, *Science* 274, 1350 (1996).
96. L. P. Kouwenhoven, C. M. Marcus, P. L. McEuen, S. Tarucha, R. M. Westervelt, and N. S. Wingreen, in "Mesoscopic Electron Transport, Proceedings of a NATO Advanced Study Institute" (L. P. Kouwenhoven, G. Schön, and L. L. Sohn, Eds.). Kluwer, Dordrecht, 1997.
97. L. Jacak, P. Hawrylak, and A. Wojs, "Quantum Dotsss." Springer, Berlin, 1998.
98. G. Li, S. V. Branis, and K. K. Bajaj, *J. Appl. Phys.* 77, 1097 (1995).
99. C. Aldrich and R. L. Greene, *Phys. Status Solidi B* 93, 343 (1979).
100. W. Walukiewicz, H. E. Ruda, J. Lagowski, and H. C. Gatos, *Phys. Rev. B* 29, 4818 (1984).
101. L. Onsager, *Phys. Rev.* 37, 405 (1931).
102. L. Onsager, *Phys. Rev.* 38, 2265 (1931).
103. K. Von Klitzing, in "Festkörperprobleme Advances in Solid State Physics" (J. Treusch, Ed.). Vieweg, Branschweig, 1981.
104. R. Kubo, S. B. Miyake, and N. Hashitsume, *Solid State Phys.* 17, 269 (1965).
105. H. Aoki and T. Ando, *Phys. Rev. Lett.* 54, 831 (1985).
106. T. Ando and Y. Uemura, *J. Phys. Soc. Japan* 36, 959 (1974).
107. K. von Klitzing, G. Dorda, and M. Pepper, *Phys. Rev. Lett.* 45, 494 (1980).
108. D. C. Tsui and A. C. Gossard, *Appl. Phys. Lett.* 38, 550 (1981).
109. Y. Guldner, J. P. Hirtz, J. P. Vieren, P. Voisin, M. Voos, and M. Razeghi, *J. Phys. Lett. France* 43, L-613 (1982).
110. C. A. Chang, E. E. Mendez, L. L. Chang, and L. Esaki, *Surf. Sci.* 142, 598 (1984).
111. E. E. Mendez, L. L. Chang, C. A. Chang, L. F. Alexander, and L. Esaki, *Surf. Sci.* 142, 215 (1984).
112. H. L. Stormer, A. M. Chang, Z. Schlesinger, D. C. Tsui, A. C. Gossard, and W. Wiegmann, *Phys. Rev. Lett.* 51, 126 (1983).
113. M. A. Paalanen, D. C. Tsui, A. C. Gossard, and J. C. M. Hwang, *Solid State Commun.* 50, 841 (1984).
114. G. Ebert, K. Von Klitzing, C. Probst, E. Schuberth, K. Ploog, and G. Weimann, *Solid State Commun.* 45, 625 (1983).
115. M. A. Paalanen, D. C. Tsui, and A. C. Gossard, *Phys. Rev. B* 25, 5566 (1982).
116. H. Aoki and T. Ando, *Solid State Commun.* 38, 1079 (1981).
117. R. E. Prange, *Phys. Rev. B* 23, 4802 (1981).
118. R. Laughlin, *Phys. Rev. B* 23, 5632 (1981).
119. R. B. Laughlin, *Springer Ser. Solid State Sci.* 53, 272 (1984).
120. D. C. Tsui, H. L. Stormer, and A. C. Gossard, *Phys. Rev. Lett.* 48, 1559 (1982).
121. D. C. Tsui, H. L. Stormer, J. C. M. Hwang, J. S. Brooks, and M. J. Maughton, *Phys. Rev. B* 28, 2274 (1983).
122. E. E. Mendez, M. Heiblum, L. L. Chang, and L. Esaki, *Phys. Rev. B* 28, 4886 (1983).
123. H. L. Stormer, A. M. Chang, D. C. Tsui, J. C. M. Hwang, A. C. Gossard, and W. Wiegmann, *Phys. Rev. Lett.* 50, 1953 (1983).
124. R. B. Laughlin, *Phys. Rev. B* 27, 3383 (1983).
125. R. B. Laughlin, *Phys. Rev. Lett.* 50, 1395 (1983).
126. B. I. Halperin, *Helv. Phys. Acta* 56, 75 (1983).
127. R. Tao and D. J. Thouless, *Phys. Rev. B* 28, 1142 (1983).
128. T. Ando, *J. Phys. Soc. Japan* 38, 989 (1975).
129. G. Abstreiter, J. P. Kothaus, J. F. Koch, and G. Dorda, *Phys. Rev. B* 14, 2480 (1976).
130. P. Voisin, Y. Guldner, J. P. Vieren, M. Voos, J. C. Maan, P. Delescluse, and N. T. Linh, *Physica B* 117/118, 634 (1983).
131. H. L. Stormer, R. Dingle, A. C. Gossard, W. Wiegmann, and M. D. Sturge, *Solid State Commun.* 29, 705 (1979).
132. E. Gornik, W. Seidenbush, R. Lassnig, H. L. Stormer, A. C. Gossard, and W. Wiegmann, *Springer Ser. Solid States Sci.* 53, 183 (1984).
133. Th. Englert, J. C. Maan, Ch. Uihlein, D. C. Tsui, and A. C. Gossard, *Physica B* 117/118, 631 (1983).
134. Y. Guldner, J. P. Vieren, P. Voisin, M. Voos, J. C. Maan, L. L. Chang, and L. Esaki, *Solid State Commun.* 41, 755 (1982).
135. A. Darr, A. Huber, and J. P. Kotthaus, "Physics of Narrow Gap Semiconductors" (J. Rauluszkiwicz, M. Gorska, and E. Kaczmarek, Eds.). P. W. N.-Polish Scientific, Warsaw, 1978.
136. H. Bruus, K. Flensberg, and H. Smith, *Phys. Rev. B* 48, 11144 (1993).
137. T. Martin and S. Feng, *Phys. Rev. Lett.* 64, 1971 (1990).
138. T. Martin and S. Feng, *Phys. Rev. B* 44, 9084 (1991).
139. D. L. Maslov, Y. B. Levinson, and S. M. Badalian, *Phys. Rev. B* 46, 7002 (1992).
140. S. Komiyama, H. Hirai, M. Ohsawa, Y. Matsuda, S. Sasa, and T. Fujii, *Phys. Rev. B* 45, 11085 (1992).
141. H. Akera and T. Ando, *Phys. Rev. B* 41, 11967 (1990).
142. R. Kubo, *J. Phys. Soc. Jpn.* 12, 570 (1957).
143. P. Vasilopoulos, P. Warmenbol, F. M. Peeters, and J. T. Devreese, *Phys. Rev. B* 40, 1810 (1989).
144. N. Mori, H. Momose, and C. Hamaguchi, *Phys. Rev. B* 45, 4536 (1992).
145. H. Bruus and K. Flensberg, *J. Phys. Condens. Matter* 4, 9131 (1992).
146. H. C. Tso and P. Vasilopoulos, *Phys. Rev. B* 44, 12952 (1991).
147. I. I. Boiko, P. Vasilopoulos, and V. I. Sheka, *Phys. Rev. B* 46, 7794 (1992).
148. M. Wagner, *Phys. Rev. B* 45, 11606 (1992).
149. R. Landauer, *Philos. Mag.* 21, 768 (1986).
150. M. Büttiker, *Phys. Rev. Lett.* 57, 1761 (1986).
151. K. Shepard, *Phys. Rev. B* 44, 9088 (1991).
152. M. Suhrke and S. Wilke, *Phys. Rev. B* 46, 2400 (1992).



153. A. A. M. Staring, H. van Houten, C. W. J. Beenakker, and C. T. Foxon, *Phys. Rev. B* 45, 9222 (1992).
154. H. Smith and H. H. Jensen, "Transport Phenomena." Oxford Univ. Press, Oxford, 1989.
155. G. D. Mahan, in "Polarons in Ionic Crystals and Polar Semiconductors" (J. T. Devreese, Ed.). North-Holland/Elsevier, Amsterdam, 1972.
156. P. J. Price, *Surf. Sci.* 113, 119 (1982).
157. P. J. Price, *Surf. Sci.* 143, 145 (1982).
158. E. E. Mendez, P. J. Price, and M. Heiblum, *Appl. Phys. Lett.* 45, 294 (1984).
159. J. D. Zook, *Phys. Rev. A* 136, 869 (1964).
160. A. Corella-Madueño, R. A. Rosas, J. L. Marín, and R. Riera, *Int. J. Quantum Chem.* 77, 509 (2000).
161. P. Ramvall, S. Tanaka, S. Nomura, P. Riblet, and Y. Aoyagi, *Appl. Phys. Lett.* 73, 1104 (1998).
162. J. L. Marín, R. Rosas, and A. Uribe, *Am. J. Phys.* 63, 460 (1995).
163. A. Corella-Madueño, R. Rosas, J. L. Marín, and R. Riera, *Phys. Low-Dim. Struct.* 5/6, 75 (1999).
164. Z. Xiao, J. Zhu, and F. He, *J. Appl. Phys.* 79, 9181 (1996).
165. K. R. Brownstein, *Phys. Rev. Lett.* 71, 1427 (1993).
166. J. Gorecki and W. Byers Brown, *J. Phys. B* 22, 2659 (1989).
167. F. A. P. Osório, M. H. Degani, and O. Hipólito, *Phys. Rev. B* 37, 1402 (1988).
168. Y. Chen, *Phys. Lett. A* 143, 152 (1990).
169. K. D. Zhu and S. W. Gu, *Phys. Lett. A* 172, 296 (1993).
170. Y. Kayanuma, *Phys. Rev. B* 41, 10261 (1990).
171. G. T. Einevoll, *Phys. Rev. B* 45, 3410 (1992).
172. G. W. Bryant, *Phys. Rev. B* 37, 8763 (1988).
173. W. Que, *Phys. Rev. B* 45, 11036 (1992).
174. G. W. Bryant, *Phys. Rev. Lett.* 59, 1140 (1987).
175. A. Kumar, S. E. Laux, and F. Stern, *Phys. Rev. B* 42, 5166 (1990).
176. U. Merkt, J. Huser, and M. Wagner, *Phys. Rev. B* 43, 7320 (1991).
177. D. Pfannkuche and R. R. Gerhardt, *Phys. Rev. B* 44, 13132 (1991).
178. J. J. S. De Groote, J. E. M. Honos, and A. V. Chaplik, *Phys. Rev. B* 46, 12773 (1992).
179. T. Imbo, A. Pagnamento, and U. Sukhatme, *Phys. Rev. D* 29, 8763 (1984).
180. T. Imbo and U. Sukhatme, *Phys. Rev. D* 31, 2655 (1985).
181. R. Dutt, Mukherji, and Y. P. Varshni, *J. Phys. B* 19, 3411 (1986).
182. M. Wagner, U. Merkt, and A. V. Chaplik, *Phys. Rev. B* 45, 1951 (1992).
183. D. Pfannkuche and R. R. Gerhardt, *Physica B* 189, 6 (1994).
184. M. Taut, *Phys. Rev. A* 48, 3561 (1993).
185. A. Wixforth, M. Kaloudis, C. Rocke, K. Ensslin, M. Sundaram, J. H. English, and A. C. Gossard, *Semicond. Sci. Technol.* 9, 215 (1994).
186. J. L. Marín, R. Rieva, and R. A. Rosas, in "Handbook of Advanced Electronic and Photonic Materials and Devices" (H. S. Nalwa, Ed.). Academic Press, San Diego, 2001.



# Magnetic Semiconductor Nanostructures

Wolfram Heimbrodt, Peter J. Klar

*Philipps-University Marburg, Marburg, Germany*

## CONTENTS

1. Introduction
  2. Fundamental Properties of Bulk Magnetic and Diluted Magnetic Semiconductors
  3. Preparation of Magnetic Semiconductor Nanostructures
  4. Properties of Magnetic and Diluted Magnetic Semiconductor Nanostructures and Ultrafine Particles
  5. Concluding Remarks and Outlook
- Glossary  
References

## 1. INTRODUCTION

The majority of the elements in the periodic table are elements with partially filled inner *d*- or *f*-shells. Therefore there are a large number of solid-state materials that contain transition or rare-earth elements. For many decades these transition and rare-earth compounds have been investigated, mainly under the aspect of magnetism. The metals, on the one hand, and the rather insulating materials, such as ferrites or perovskites, on the other hand, dominated the field. Even the investigation of the metal–insulator transitions of the perovskites has a long-standing tradition. The magnetic semiconductors played a rather minor role for a long time because the physics of this subgroup of magnetic solid-state materials is obviously cross-disciplinary ground. Scientists working on magnetic phenomena in solids have widely ignored the semiconductors and their special properties, and, similarly, researchers in the field of semiconductors, in general, show only little interest in solid-state magnetism. A conventional semiconductor is described well in the rather simple one-electron approximation. This does not hold for a “magnetic” semiconductor, which contains localized magnetic moments, as “magnetism” requires many-particle interactions. Thus, the bridge in solid-state physics between magnetic and semiconducting phenomena

is hard to build without suitable introduction of electron–electron interactions, many-particle descriptions, and correlation effects.

The first excellent surveys of the field of magnetic semiconductors were given by Methfessel [1] as well as by Austin and Elwell [2] in 1970. The materials studied up to this time have been mainly insulating materials such as the perovskites or the Eu chalcogenides, which exhibit ferromagnetism with Curie temperatures from about 75 K for EuO or about 16 K for EuS, and the antiferromagnetic *3d* oxides like NiO, MnO, and CoO. In 1950 Jonker and van Santen [3, 4] discovered ferromagnetism up to room temperature in LaMnO<sub>3</sub> due to an insulator–metal transition caused by oxygen deficiency or by replacement of La<sup>3+</sup> by Sr<sup>2+</sup> or Cr<sup>2+</sup>. This led to an uncountable number of papers. In the 1970s the now classical semiconductors for electronics and optoelectronics (e.g., Si, Ge, GaAs, etc.) led a rather shadowy existence with respect to attempts to enhance their weak magnetic properties. On the one hand, it was not expected that their magnetic behavior could be enhanced such that applications in magnetic devices would become feasible; that is, there were always other materials. On the other hand, it was still early days for the semiconductor industry, and the quest for miniaturization was just at the beginning. Ideas for quantum computing and spin electronics were still utopian, which are currently the main driving forces for making classical semiconductors magnetic.

The situation changed after the first reports about giant enhancements of magneto-optical effects in a new group of semiconducting materials, the so-called diluted magnetic semiconductors (DMS) or semimagnetic semiconductors (SMS) by Komarov et al. [5], Galazka et al. [6, 7], Gaj [8], and Furdyna [9] at the beginning of the 1980s. The early papers reported about II–VI semiconductors, where a fraction of the cations was replaced at random by the transition metal Mn<sup>2+</sup>. An early review was given by Brandt and Moshalkov [10]. Later on, the investigations have been extended toward different magnetic ions as dopands in the II–VI host material, like Fe [11, 12], Co [13, 14], and Cr [15, 16]. Even the narrow gap IV–VI DMS became attractive, and various magnetic ions as dopands have been investigated (e.g., Mn [17], Eu [18], or Gd [19]). Rare-earth doped II–VI semiconductors, with a solubility

limit of about  $10^{18} \text{ cm}^{-3}$ , have never reached the concentration of solid solutions, but remained rather in the doping regime. The main interest in those materials was exploiting the luminescence properties of the internal transitions rather than the magnetic properties [20].

The real breakthrough for diluted magnetic semiconductors was achieved by the possibility of growing them by epitaxial methods like molecular beam epitaxy (MBE) or metal-organic vapor phase epitaxy (MOVPE). Now the way was open to prepare two-dimensional nanostructures. Early reviews of (II,Mn)VI-based semiconductor nanostructures were given by Furdyna [21] and Goede and Heimbrodt [22]. In 1989 Munekata et al. reported on MBE grown (In,Mn)As [23] as the first III-V-based magnetic semiconductor. Up to this time, manganese was considered only as an acceptor and p-dopant for III-V semiconductors. Later on further magnetic III-V semiconductors (e.g., (Ga,Mn)As [24], (Ga,Fe)As [25], (Ga,Mn)Sb [26], (Ga,Mn)N [27], (Ga,Mn)P [28], (Ga,Cr)As [29], (Ga,Fe)N [30], (Ga,Er)As [31]) as well as corresponding nanostructures were prepared.

Whether the very new (III,Mn)VI diluted magnetic semiconductors like (Ga,Mn)Se [32], (Ga,Mn)S [33] and (Ga,Fe)Se [34] will attract much attention is not yet clear. Very promising is however the first report on the group IV ferromagnetic semiconductor  $\text{Mn}_x\text{Ge}_{1-x}$  [35]. The obvious compatibility with present day semiconductor materials may be the beginning of a new era.

Modern information technology is based on highly sophisticated electronic and opto-electronic devices made of semiconductors. The charge of carriers is used to process information. Semiconductors are the appropriate materials because their conductivity can be controlled in the range of several orders of magnitude by changing the doping levels, and their bandgaps can be easily engineered by the material composition or preparation of desired heterostructures. Magnetic materials are also used to store information. The orientation of a localized magnetic moment or even of a single localized spin should be sufficient to present a bit or even a quantum bit in magnetic memories. The future aim is to combine the charge and the spin degree of freedom. This so-called magneto-electronics or spin electronics is an only recently emerging field where devices comprise small-scale magnetic elements and conventional semiconductor elements, to obtain completely new functionalities.

The beginning of this field was the discovery of the exchange coupling of Fe layers across the Cr interlayer by Grünberg et al. [36] and the subsequent observation of the giant magneto-resistance (GMR) in 1988 by Baibich et al. [37], with the current in the plane of the layers and 3 years later with the current perpendicular to the metal multilayers. The first applications are already commercially available, like magnetic field sensors in the read head of magnetic recording discs for computer information storage. These heads were a considerable improvement in size, weight, and cost. Magnetic random access memory (MRAM) cells, which will have the advantage of being nonvolatile, may replace direct random access memory (DRAM) soon. But all of the present applications are based solely on metallic multilayers. The exploitation of the spin degree of freedom in a real semiconductor electronics or optoelectronics is still ahead. Very promising candidates for key components in

devices of such a magneto- or spin electronics are the magnetic semiconductors. Understanding the electronic, optical, and magnetic properties of magnetic semiconductors with reduced dimension down to nanometer length scales (e.g., two-dimensional quantum wells, one-dimensional quantum wires, or zero-dimensional quantum dots) is, therefore, a central issue of the present magnetic semiconductor physics. This paper will give a survey of the present knowledge in this field.

We will restrict ourselves to those semiconductors which are subject to artificial structuring in one, two, or three dimensions. That means we will not consider the actually rich variety of materials which do exhibit naturally two-dimensional or one-dimensional magnetism, even not if they exhibit semiconducting properties. Although these natural low-dimensional semiconductors are most interesting from a physical point of view and are very often ideal model systems, they are unlikely to play an important role in electronic applications in the foreseeable future. The goal is to create magnetic materials which are compatible with the classical semiconductor materials and processing technology, making them attractive for integration into present-day or near-future electronics.

## 2. FUNDAMENTAL PROPERTIES OF BULK MAGNETIC AND DILUTED MAGNETIC SEMICONDUCTORS

Although this review is dedicated to nanostructured magnetic semiconductors, we will give in this chapter a short overview of the properties of the bulk crystals as far as they are necessary for the discussions of the properties of magnetic semiconductors with reduced dimensions in the following sections. For a more detailed discussion of the bulk magnetic semiconductors we refer the reader to some thorough reviews on II-VI [10, 21, 22, 38], III-V [39, 40], and IV-VI [41, 42] based materials.

### 2.1. Material Preparation and Crystal Structure

In the II-VI-based magnetic semiconductors a magnetic ion (transition metal or rare-earth metal) usually replaces a cation by contributing both the  $s^2$  electrons to the chemical bonding. All II-VI semiconductors have tetrahedral nearest-neighbor environments, and the bonding can be described well by  $sp^3$  hybrid orbitals. As the magnetic ions have the same outer electron configuration as the group II elements, the  $sp^3$  bonding is not affected by the substitution, and the local configuration of the magnetic ions is well defined. As the  $d$ - or  $f$ -shells of the magnetic ions do not contribute to the bonding in II-VI magnetic alloys, their electronic configuration is determined rather unambiguously by Hund's rule. Only at very high concentrations of the magnetic impurities might segregation effects occur, which lead to different crystallographic local environments of the magnetic ions due to the different crystal structure of the magnetic binary (e.g., ZnS:Mn has a wurtzite structure, whereas the stable phase of MnS is the rock salt structure). The situation is very different when a



with increasing  $x_{\text{Mn}}$  from zincblende to wurtzite) can be compared easily.

It is important for the following discussion of the optical and magnetic properties that the real microscopic bond lengths around the magnetic ions vary much less with increasing incorporation of magnetic ions than expected from Vegard's law. Extended X-ray absorption fine structure (EXAFS) measurements provide detailed information about the atomic environment of a given lattice site. It has been shown for (Cd,Mn)Te by Balzarotti et al. [62] that the mean Mn-Te and Cd-Te bond lengths remain practically constant throughout the entire range of composition between  $x_{\text{Mn}} = 0$  and  $x_{\text{Mn}} = 0.7$ . Only the weighted average of these bond lengths then leads to the  $d_c(x_{\text{Mn}})$  variation measured by X-ray diffraction and following Vegard's law.

The solubility of Eu in the II-VI or IV-VI semiconductor crystals is very low in the case of Bridgman techniques or chemical (e.g., iodine) transport methods. The maximum concentrations reported are less than 0.5% and in practice do not exceed the doping level. High concentrations of magnetic ions can be achieved in those cases exclusively by preparation methods away from the thermodynamical equilibrium (e.g., by MBE or MOVPE). They will be discussed in Section 3. In [63] (Pb,Eu)Te single-crystal films have been prepared by a modified hot wall technique with Eu concentrations of up to 5%.

The preparation of III-V-based diluted magnetic semiconductors in bulk form is also limited to very low Mn concentrations. Doping the III-V semiconductors with transition-metal impurities is, however, not a new issue in the III-V semiconductor technology. The solubility limits are generally about  $10^{17} \text{ cm}^{-3}$  (e.g., [64] and references therein). Beyond these limits surface segregation and phase separation effects may occur. Therefore, even for magnetic III-V semiconductors, a successful preparation of diluted magnetic semiconductors was reported only for preparation methods away from the thermodynamic equilibrium (e.g., low-temperature MBE and MOVPE). Details are also given in Section 3.

## 2.2. Bandgap and Optical Properties of Bulk Semiconductors

In this section the optical properties of the bulk crystals are reviewed only as far as necessary for the understanding of the optical properties of nanoscaled magnetic semiconductors.

The conventional optical properties of the alloys are known most precisely for the (II,Mn)VI semiconductors. All of these alloys are direct-gap semiconductors with the direct gap at the  $\Gamma$ -point of the Brillouin zone. The parent II-VI semiconductors exhibit either an open wurtzite or zincblende gap or a zero gap in the case of HgTe, HgSe, and HgS. The bandgaps of the zero-gap semiconductors open up with increasing Mn concentration. As can be seen from Figure 2, the energy gaps of all alloys except (Zn,Mn)S increase with increasing Mn concentration. (Zn,Mn)S exhibits the opposite behavior. The energy gaps of the (II,Mn)VI magnetic semiconductors are well known from the corresponding free Wannier-type A-exciton structures, which can be observed in low-temperature reflection, absorption, or photoluminescence spectra. In the case

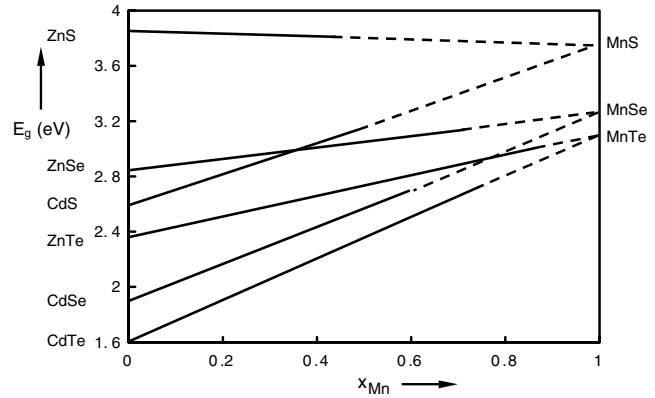


**Figure 2.** Bandgaps of (II,Mn)VI compounds as a function of the Mn concentration. Reprinted with permission from [22], O. Goede and W. Heimbrot, *Phys. Stat. Sol. B* 146, 11 (1988). © 1988, Wiley-VCH Verlag, Berlin.

of (Cd,Mn)Te [65], (Cd,Mn)Se [66], and the (HgMn)VI [21, 67, 68] alloys a nearly linear dependence of the energy gap on the Mn concentration was found, which can be described by the following relations ( $T \leq 4.2 \text{ K}$ ):

$$\begin{aligned} (\text{Cd,Mn)Te} \quad E_{A\text{-exc}}(x_{\text{Mn}}) &= 1.595 + 1.59 \cdot x_{\text{Mn}} \text{ (eV)} [65] \\ (\text{Cd,Mn)Se} \quad E_{A\text{-exc}}(x_{\text{Mn}}) &= 1.821 + 1.54 \cdot x_{\text{Mn}} \text{ (eV)} [66] \\ (\text{Hg,Mn)Te} \quad E_{A\text{-exc}}(x_{\text{Mn}}) &= -0.3 + 3.5 \cdot x_{\text{Mn}} \text{ (eV)} [67, 68] \\ (\text{Hg,Mn)Se} \quad E_{A\text{-exc}}(x_{\text{Mn}}) &= -0.27 + 3.57 \cdot x_{\text{Mn}} \text{ (eV)} [21] \end{aligned}$$

A unique behavior has been reported for the wider-gap systems. For (Zn,Mn)Te [69], (Zn,Mn)Se [70, 71], (Cd,Mn)S [72, 73], and, probably, (Zn,Mn)S [74] and (Zn,Mn)O [54], the measured  $E_g(x_{\text{Mn}})$  dependence can be approximated by a linear function for higher manganese concentrations, but at Mn concentrations  $x_{\text{Mn}} < 0.2$ , a nonlinear deviation from the linear behavior toward lower energies becomes apparent. This bowing is much stronger than the usual bandgap bowing in solid solutions due to alloy disorder. Two possible mechanisms that may be responsible for this bowing in the wide-gap (II,Mn)VI are discussed. First, it can be due to the  $p$ - $d$  hybridization of the valence band states and the  $d$ -states, which are known to lie 3–3.5 eV energetically below the valence band edge [70, 75]. The larger bandgap, as well as the smaller lattice constant, may enhance the resulting  $p$ - $d$  hybridization at the valence band edge. Tworzydło [76, 77] showed that not only the antiferromagnetic coupling as discussed by Bylsma et al. [69], but also the spin-dependent scattering, needs to be considered to explain the bowing effect theoretically. He was able to describe the bowing of (Cd,Mn)S very well, using an approach which goes beyond the virtual-crystal approximation (VCA) and the molecular-field approximation, explicitly taking into account the chemical and magnetic disorder due to substitutional Mn ions [76, 77]. Second, the effect can be the same as reported recently for the Ga(N,As) and (Ga,In)(N,As) [78, 79] or Zn(Te,S) and Zn(Te,Se) [80] solid solutions. In (Ga,In)(N,As), a level repulsion of a nitrogen-induced  $s$ -type band above the conduction band edge and the conduction band edge itself leads to a tremendous red shift of the bandgap energy. The reason for this is the strong perturbation of the lattice by the large difference in size and



the strong difference of the electronegativity between the N ions and the anions of the host. A similar mechanism could explain the bowing in the case of wide band gap (II,Mn)VI semiconductors. The larger the bandgap the closer are the Mn-induced *s*-states to the band edge. A conclusive answer cannot be given at the moment.

In Figure 3 the bandgap bowing of (Zn,Mn)Se is given as an example. In [81] the band offsets for a series of (Zn,Mn)Se/ZnSe quantum well structures have been determined carefully from the measured light hole (lh) and heavy hole (hh) exciton splitting, including the known strain state of the samples. In this way it was possible to determine independently the offset for the conduction band edge as well as of the valence band edge as a function of *x*. As can be seen from Figure 3, the bowing has been found to be solely at the conduction band edge. The pairs of thick and thin lines, respectively, are the upper and lower limits for the band edge shifts, determined by the authors. The difference is caused mainly by the uncertainty of the deformation potentials but does not change the bowing effect. The bowing of the conduction band is a strong indication that even in the wide-gap (II,Mn)VI semiconductors the level repulsion of the Mn *s*-states and the conduction band yields the strong bowing of the bandgap rather than the change in the hybridization between the *p*-states and the Mn *3d* states.

The linear extrapolation to  $x_{\text{Mn}} = 1$  through the miscibility gap for  $E_g(x_{\text{Mn}})$  of the ternaries always yields for the corresponding Mn chalcogenides the values in Figure 2, which are the energy gaps of the unstable zincblende (or wurtzite) structures. The following mean values are obtained:

$$E_g(\text{MnTe}) = 3.2 \text{ eV}, \quad E_g(\text{MnSe}) = 3.3 \text{ eV}, \\ E_g(\text{MnS}) = 3.7 \text{ eV}$$

The available experimentally determined  $E_g$  values are not very reliable, as no sharp bandgap exciton structures in the optical spectra were observed. The measured low-temperature energetic positions are consistent, however, with the values given above [49–53].

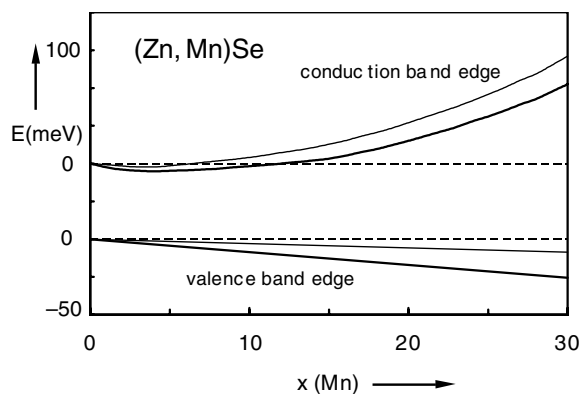


**Figure 3.** Valence band and conduction band shift of (Zn,Mn)Se as a function of the Mn concentration (the thin line indicates the upper limit and the thick line indicates the lower limit with respect to the experimental uncertainty). Reprinted with permission from [81], W. Heimbrodt et al., *J. Lumin.* 60–61, 344 (1994). © 1994, Elsevier Science.

The IV–VI parent structures of the (IV,Mn)VI or (IV,Eu)VI diluted magnetic semiconductor alloys also exhibit a direct band gap, but at the L-point of the Brillouin zone, and, therefore, are many-valley semiconductors. For the low concentrations of the magnetic ions,  $x < 10\%$  in the (IV,Mn)VI or (IV,Eu)VI, it is found that the bandgap remains at the L-point. The following linear relations for the bandgaps for  $x < 10\%$  [42, 82] have been reported ( $T = 4.2 \text{ K}$ ):

$$\begin{aligned} (\text{Pb,Mn})\text{Te} \quad E_g(x_{\text{Mn}}) &= 0.190 + 2.510 \cdot x_{\text{Mn}} \text{ (eV)} [42] \\ (\text{Pb,Mn})\text{Se} \quad E_g(x_{\text{Mn}}) &= 0.146 + 3.800 \cdot x_{\text{Mn}} \text{ (eV)} [82] \\ (\text{Pb,Eu})\text{Te} \quad E_g(x_{\text{Eu}}) &= 0.190 + 6.000 \cdot x_{\text{Eu}} \text{ (eV)} [42] \\ (\text{Pb,Eu})\text{Se} \quad E_g(x_{\text{Eu}}) &= 0.114 + 11.370 \cdot x_{\text{Eu}} \text{ (eV)} [42] \end{aligned}$$

Of course, the values of  $E_g(x)$  in the limit  $x \rightarrow 1$  cannot be compared with the bandgaps of the binary compounds. The corresponding MnVI magnetic compounds all have the bandgap at the  $\Gamma$ -point and not at the L-point of the Brillouin zone. The band structures and absorption spectra of the Eu-chalcogenides are very complicated and are still under discussion [83]. The *4f* and *5d* states modify the *p*- and *s*-bands tremendously and make a quantitative comparison between experimental results and calculated band structures difficult.

Little is known about the band gaps of (III,Mn)V compounds. The main reason for this is that the concentrations achievable in bulk material are in the doping regime. Quasi-bulk-like epitaxial layers, where  $x_{\text{Mn}}$  values of up to 14% have been obtained, are of rather poor optical quality for  $x_{\text{Mn}} > 1\%$ , probably because Mn is a deep acceptor in the III–V materials. A small red shift of the  $\text{Ga}_{1-x}\text{Mn}_x\text{As}$  band gap with increasing  $x_{\text{Mn}}$  was observed at low temperatures on epitaxial layers grown by MOVPE [84]. A Burstein–Moss shift of the bandgap due to the acceptor properties of Mn could be ruled out at the low temperatures used in the paper, suggesting that this shift is a genuine alloying effect. Such a red shift is also observed for the  $E_1$  gap.

The optical properties of the magnetic semiconductors are essentially modified by the *d*- or *f*-states of the magnetic ions, as already indicated in the discussion of the bandgap bowing of the wide-gap (II,Mn)VI materials. In addition, if the band gap is wide enough, the electronic transitions within the partially filled *d*- or *f*-shells become observable. The high degeneracy of the *d*- or *f*-configurations is partially removed by the intra-ionic electron–electron interaction and by the ligand–field interaction. The electron–electron interaction, already present in the free ions, lifts the L-degeneracy and can be described by two Racah parameters, *B* and *C*. *B* in particular is often somewhat reduced in comparison with the free ion *B*-value because of covalence effects. The  $T_d$  symmetric crystal field of the chalcogen ligands, on the other hand, splits a fivefold degenerate one-electron *d*-state into  $t_2$  and *e* states. The two interactions are of the same order of magnitude in the case of *d*-states and can be accounted for by the perturbation approach after Tanabe and Sugano [85], leading to the ground and excited states of the ions as a function of the ligand field parameter *Dq*. In Figure 4 the curves are depicted for the  $\text{Mn}^{2+} 3d^5$  ion. The states are classified by the irreducible representation of  $T_d$ . The dominating occupation numbers in

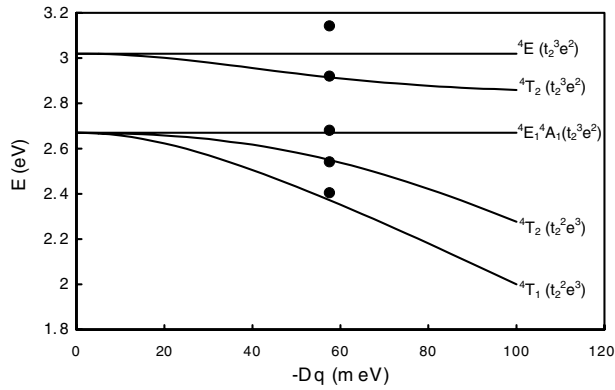


**Figure 4.** Energies of the lowest excited states of a  $\text{Mn}^{2+} 3d^5$  ion in a  $T_d$  symmetric ligand field as function of the Racah parameter  $Dq$  with  $B = 50$  meV and  $C = 434$  meV obtained for  $\text{MnS}_{\text{ZB}}$  with the Tanabe–Sugano matrices [85]. Experimental points with  $Dq = -57$  meV are for  $\text{MnS}_{\text{ZB}}$ . Reprinted with permission from [22], O. Goede and W. Heimbrodt, *Phys. Stat. Sol. B* 146, 11 (1988). © 1988, Wiley-VCH Verlag, Berlin.

the one-electron picture are given in parentheses. The optical dipole transitions between the ground and excited states are forbidden by spin and symmetry selection rules, which, however, are softened by spin–orbit interaction and mixing with electronic states of suitable symmetry, respectively. In the case of the transition metals the strong hybridization between the  $3d$ -states and the anion  $p$ -states are typical for the chalcogenides. The mixing of the states also yields, apart from the bandgap bowing already mentioned, a relaxation of the spin and symmetry selection rules and is the basic mechanism for the magnetic behavior, which will be discussed in the next section. The usually suggested softening of the symmetry-induced selection rules by electron–phonon interaction or other symmetry-reducing perturbations should be comparatively less important.

As shown in Figure 5, the  $d$ – $d$  transitions of the Mn ion are observable in various (II,Mn)VI alloys, if the bandgap

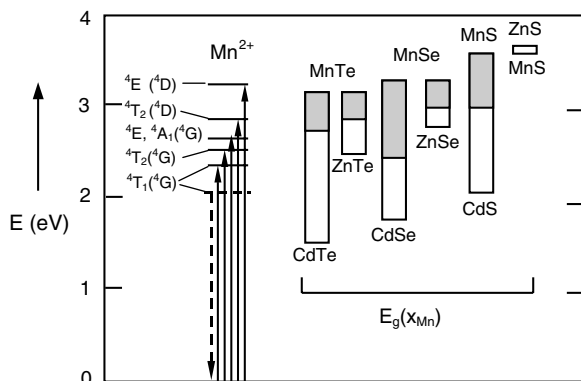


**Figure 5.** Internal transitions of the  $\text{Mn}^{2+} 3d^5$  shell of (Zn,Mn)S in comparison with realizable variations of the bandgap  $E_g(x_{\text{Mn}})$  for the (Zn,Mn) and (Cd,Mn) chalcogenides. The arrows (full line) represent the internal absorption transitions, and the dashed arrow represents the Franck–Condon shifted yellow emission. Reprinted with permission from [22], O. Goede and W. Heimbrodt, *Phys. Stat. Sol. B* 146, 11 (1988). © 1988, Wiley-VCH Verlag, Berlin.

as a function of the Mn concentration is wide enough. In (Zn,Mn)S, which has the widest bandgap of all (II,Mn)VI compounds, five  $d$ – $d$  transitions (indicated in Fig. 5) can be observed in the whole Mn concentration range. The peak positions are almost independent of temperature and Mn concentration. According to the point-ion model,  $Dq$  should vary proportionally to  $d_c^{-5}$ , where  $d_c$  is the Mn anion bond length. A variation according to Vegard’s law would result in a remarkable peak shift of about 100 meV to higher energies. The experimentally observed shift of less than 20 meV is in excellent agreement with the EXAFS results discussed above. Only if the bandgap window is sufficiently opened by a corresponding high Mn concentration is the detection of a set of distinct internal transitions within the  $\text{Mn}^{2+} 3d^5$  shell possible in all of the other solid solutions. In (Cd,Mn)S, for example,  $x_{\text{Mn}} > 0.1$  is required to observe the first absorption band ( ${}^6A_1 \rightarrow {}^4T_1$ ), whereas the corresponding yellow emission is already observable for the lowest Mn concentrations. The tremendous Stokes shift between the emission and absorption bands is caused by the strong electron–phonon coupling. In (Cd,Mn)Te the PL becomes observable for  $x_{\text{Mn}} > 0.4$ , but the  ${}^6A_1 \rightarrow {}^4T_1$  absorption is resolvable only for  $x_{\text{Mn}} > 0.6$ . In the case of the closed gap Hg-chalcogenides, only for (Hg,Mn)Te would the Mn solubility allow the observation of internal  $\text{Mn}^{2+} 3d^5$  transitions.

For changing anion ligands of the  $\text{Mn}^{2+}$  ion, a chemical trend is expected for the internal transitions within the series  $\text{S} \rightarrow \text{Se} \rightarrow \text{Te}$ . The observed shift for (Zn,Mn)Se compared with (Zn,Mn)S is, however, rather vanishing, and the corresponding shift of the (Cd,Mn)Te bands is smaller than expected. The reason for this is not clear, but the expected shift to lower energies might be compensated for by growing covalence effects.

## 2.3. Magnetic Properties of Bulk Semiconductors

Now we want to review the magnetic properties of magnetic and diluted magnetic semiconductors.

It is known that the magnetic dipole–dipole interaction of the magnetic moments cannot be the reason for the magnetic ordering and the spontaneous magnetization, as it is orders of magnitude too small. It is the exchange energy as part of the Coulomb interaction which results in the magnetic phenomena which will be discussed in this review article. Dirac showed that the energy operator of the exchange interaction between two particles can be written in the form

$$H_{\text{exchange}} = -2J_{12}(r_{12})S_1S_2 \quad (1)$$

where  $J_{12}$  is the exchange integral and  $S_1$  and  $S_2$  are the spin operators. The exchange integral decreases rapidly with increasing distance  $r_{12}$  between the particles. In magnetic semiconductors interacting magnetic moments are usually separated by such large distances that a direct exchange interaction cannot be responsible for the magnetic ordering. Different mechanisms of indirect exchange interaction are known. In ionic semiconductors, the exchange interaction of cation-magnetic moments mediated via the anions situated between them is the dominant mechanism. In highly doped semiconductors, similar to metals, the mediation of

the interaction via conduction band electrons or valence band holes can be of the greatest importance. In both cases, the Hamiltonian can be approximated by the Dirac formula in Eq. (1). A system of magnetic moments, localized on lattice sites and interacting with each other according to Eq. (1), is the so-called Heisenberg model of a magnetically ordered material. A more general model has to take into account the weaker magnetic dipole–dipole interaction of the magnetic moments and the Zeeman interaction with an applied magnetic field. Two main assumptions are made by the Heisenberg model: (i) the magnetic moments are assumed to be localized completely, and (ii) the orbital magnetic moments are neglected. The first assumption is satisfied for magnetic semiconductors. The second assumption is highly satisfied for most magnetic semiconductors with transition metals due to the quenching of the orbital momenta. When the quenching is not sufficiently strong, the weak influence of the orbital momenta can be taken into account in the framework of a generalized model. It can be assumed, first, that the  $g$ -value in the Zeeman term is modified. Second, a term describing the magnetic anisotropy, which is caused by the spin–orbit interaction, is added to the Hamiltonian. In magnetic semiconductors with rare-earth ions, for example, the quenching of the angular momenta is much weaker or does not take place at all. In those cases the spin orbital interaction, which combines spin and orbital momentum to the total angular momentum, is strong. Nevertheless, the Heisenberg model may be used for such semiconductors in most cases, but the spin angular momenta in Eq. (1) must then be replaced by the total angular momenta.

In the following, we want to assemble the basic knowledge necessary for understanding the behavior of magnetic semiconductors with reduced geometrical dimensions. Most magnetic semiconductors that are considered for applications are ternary alloys. Nevertheless, we will start with the binary magnetic compounds, which represent the limits approached when the magnetic ion content of the magnetic semiconductor alloys is increased to 100%. A thorough knowledge of these binary compounds is essential for a full understanding of the magnetic properties of the corresponding ternary magnetic semiconductor alloys.

All binary compounds with a rare-earth metal or transition metal on cation site are known to exhibit, at sufficiently low temperatures, a phase transition from the paramagnetic state into an ordered magnetic state, which is either ferromagnetic or antiferromagnetic. We want to start the survey with the most prominent class of materials, the Mn chalcogenides.

### 2.3.1. Mn Chalcogenides

All Mn chalcogenides are known to become antiferromagnetic below a Néel temperature  $T_N$ , which depends on the crystal structure. In the paramagnetic phase ( $T > T_N$ ) the  $\text{Mn}^{2+} 3d^5$  spins and the corresponding magnetic moments are distributed at random. In an external field the orientation of the magnetic moment with  $M_j = -5/2$  is energetically most favored. The temperature and magnetic-field dependence of the magnetization per mole in the paramagnetic phase is given by

$$M = N_A \mu_B \tilde{g} S \cdot B_{5/2}(\xi) \quad (2)$$

where  $\tilde{g} \approx 2$  is the effective Landé factor,  $S = 5/2$ ,  $N_A$  is Avogadro's number, and

$$\langle S_z \rangle_{\text{mol}} = N_A \langle S_z \rangle = -N_A S \cdot B_{5/2}(\xi) \quad (3)$$

is the mean molar spin density, where  $B_{5/2}$  is the Brillouin function,

$$B_{5/2}(\xi) = \frac{6}{5} \coth \frac{6\xi}{5} - \frac{1}{5} \coth \frac{\xi}{5}; \quad \xi = \frac{\tilde{g} \mu_B S H}{k_B (T + \Theta)} \quad (4)$$

For  $\xi \ll 1$  (low field case) the magnetization is proportional to the external field, and from Eq. (2) the usual Curie–Weiss law for the molar magnetic susceptibility  $\chi$  can be derived:

$$\chi = \frac{\partial M}{\partial H} = \frac{N_A S(S+1) \tilde{g}^2 \mu_B^2}{3k_B (T + \Theta)}; \quad T > T_N \quad (5)$$

The appearance of a Curie–Weiss temperature  $\Theta > 0$  is an immediate consequence of the antiferromagnetic exchange interaction between the  $\text{Mn}^{2+}$  ions and leads to a decrease in the magnetic susceptibility in comparison with an ideal paramagnetic behavior ( $\Theta = 0$ ) as both the thermal disorder ( $k_B T$ ) and the antiferromagnetic interaction ( $k_B \Theta$ ) oppose the paramagnetic ordering of the spins in a magnetic field.

Some typical values for  $T_N$  and  $\Theta$  from measurements (e.g., magnetic susceptibility, specific heat, thermal expansion, electron paramagnetic resonance (EPR), inelastic neutron scattering, and neutron diffraction) are given in Table 2. The mean values for  $T_N$ , being nearly the same for MnS and MnSe, are about 150 K and 100 K for the rock salt and zinblende structures, respectively. For MnTe with NiAs structure the Néel temperature is much higher,  $T_N > 300$  K. For the zinblende phase of MnTe a value  $T_N = 67$  K was reported. The effective Landé factor in the Mn chalcogenides is found to decrease only slightly in comparison with the free-ion value, and, therefore, the maximum  $z$ -component of the magnetic moment  $gS\mu_B$  approximately equals  $5\mu_B$ .

The antiferromagnetic interaction between the  $\text{Mn}^{2+} 3d^5$  ions can be described phenomenologically to a good approximation by a Heisenberg Hamiltonian,

$$H_H = - \sum_{\substack{i, j \in \\ \text{fcc sublattice}}} J(R_{ij}) \vec{S}_i \vec{S}_j = -J_{\text{nn}} \sum_{\substack{i, k \\ (i, k = \text{nn})}} \vec{S}_i \vec{S}_k - J_{\text{nnn}} \sum_{\substack{i, l \\ (i, l = \text{nnn})}} \vec{S}_i \vec{S}_l \quad (6)$$

taking into account only the isotropic nearest-neighbor (nn) and next-nearest neighbor (nnn) interactions.  $S_i$  is the total-spin operator acting on the Mn sublattice site  $i$ , and  $R_{ij}$  is the real space vector between the sites  $i$  and  $j$ . The corresponding exchange interaction parameters  $J_{\text{nn}}$  and  $J_{\text{nnn}}$  (which are also given in Table 2) can be determined experimentally by using their relation to  $T_N$  and  $\Theta$ . In the molecular field approximation one obtains from Eq. (6), for an fcc sublattice,

$$\Theta = - \frac{(24J_{\text{nn}} + 12J_{\text{nnn}})S(S+1)}{3k_B} \quad (7)$$

$$T_N^{\text{type II}} = - \frac{12J_{\text{nnn}}S(S+1)}{3k_B} \quad (8)$$

$$T_N^{\text{type III}} = - \frac{(8J_{\text{nn}} - 4J_{\text{nnn}}) \cdot S(S+1)}{3k_B} \quad (9)$$

**Table 2.** Magnetic parameters of Eu and Mn chalcogenides.

Compound	Crystal structure	Type	Transition temperature (K) [Ref.]	$\Theta$ (K) [Ref.]	$J_{nn}/k_B$ (K)		$J_{nnn}/k_B$ (K)	
					Exp.	Theor.	Exp.	Theor.
MnO	RS	af	$T_N = 116$ [86]		-7.2 [86]		-3.5 [86]	
MnS	RS	af	$T_N = 147$ [92, 84] 152 [95, 96]	465 [92,93]	-7.0 [101]	-5 [104]	-12.5 [101, 102]	-13.5 [104]
					-7.3 [102]		-4.5 [86]	
MnSe	ZB	af	100 [97]	900 [93]	-4.4 [86]	-10.2 [103]	-7.2 [86]	-0.02 [103]
					-10.5 [86]			
	RS	af	$T_N = 150$ [94] 147 [98] 153 [99] 119 [51]	500 [94] 370 [100]	-12.4 [103]		-12.8 [102]	
					-7.9 [102]			
MnTe	NiAs	af	$T_N = 323$ [114]	584 [114] 585 [115]				
EuO	RS	f	$T_C = 69.2$ [90] 77 [88]	80 [88]	-8.7 [108] <sup>a</sup>	-12 [105]		
					-9.9 [109] <sup>a</sup>	-17 [106]		
					-8.1 [110] <sup>a</sup>	-16 [107]		$J_1/J_2 = 4.5$ [105]
EuS	RS	f	$T_C = 16.6$ [90] 18K [88]	19 18 [88]	+0.606 [90]		+0.119 [90]	
EuSe	RS	f/af	$T_N = 4.7$ [87] $T_C = 2.8$ [87]		+0.24 [90] +0.2 [91]		-0.12 [90] -0.08 [91]	
EuTe	RS	af	$T_N = 9.6$ [89]	1 [89]	+0.1 [89]		-0.21 [89]	

Note: RS, rock salt; ZB, zincblende; af, antiferromagnetic; f, ferromagnetic;  $T_N$ , Néel temperature;  $T_C$ , Curie temperature.

<sup>a</sup>Obtained from measurements of (Zn,Mn) and (Cd,Mn) chalcogenide solid solutions, assuming that  $J_{nn}$  is independent of  $x_{Mn}$ ; see also Section 2.4.

where the superscripts type II and type III correspond to two different magnetic unit cells described below. More sophisticated relations were obtained on the basis of Eq. (6), using Green's function method [117], magnon theory, or high temperature expansion [102]. There is a surprisingly good agreement with the theoretical values for  $J_{nn}$  and  $J_{nnn}$  obtained from band structure calculations [103–105, 107, 119, 120]. Because of the strong localization of the Mn  $3d$ -states the direct Mn–Mn exchange interaction is negligible in the Mn chalcogenides, and the Anderson  $p$ – $d$  superexchange mechanism [121] dominates. A schematic picture of this anion-mediated interaction is given in Figure 6.

The negative values of  $J_{nn}$  and  $J_{nnn}$  mean that the antiparallel orientation of the spins for a considered pair of both nn and nnn is energetically favored. The resulting magnetic ordering has been studied by neutron diffraction measurements. In the case of the rock salt structure for MnS and MnSe, the so-called type II fcc antiferromagnetic ordering was found [122], which is characterized by parallel

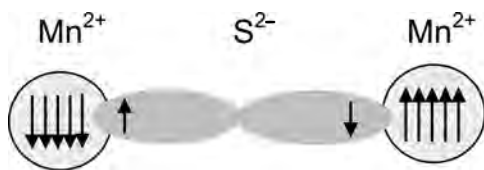


**Figure 6.** Schematic presentation of the anion-mediated superexchange mechanism, resulting in an antiferromagnetic coupling between two  $Mn^{2+}$  ions.

orientation of all  $Mn^{2+}$  spins in a (111) plane and antiparallel orientation of the spins in neighboring (111) planes (see Fig. 7). For the zincblende MnS, MnSe, and MnTe the somewhat more complicated type III fcc antiferromagnetic ordering is found. It should be noted, however, that the definite spin orientation with respect to the crystallographic directions is determined by anisotropic contributions to the exchange Hamiltonian, which are omitted in Eq. (6) for simplicity.

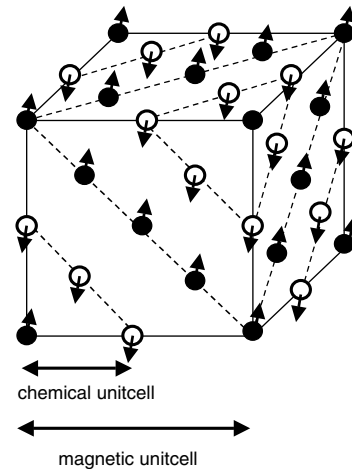


**Figure 7.** Schematic picture of the type II fcc antiferromagnetic ordering.

In Figure 8 the  $\text{Mn}^{2+}$  spin orientations in the elementary clusters of the rock salt and zincblende structures are shown for both types of antiferromagnetic ordering, which reduce the symmetry of a lattice site from  $O_h$  to  $D_{3d}$  and from  $T_d$  to  $C_{2v}$ , for the RS and ZB structures, respectively. In the case of type II the spins of six of the 12 nn and of all six nnn  $\text{Mn}^{2+}$  ions are antiparallel with respect to the spin of a considered  $\text{Mn}^{2+}$  ion. In type III, however, the spins of eight nn but only two nnn  $\text{Mn}^{2+}$  ions have the energetically favored antiparallel orientations. The spins of the remaining  $\text{Mn}^{2+}$  neighbors are parallel to the spin of the central  $\text{Mn}^{2+}$  ion. The type of the antiferromagnetic ordering is determined by the ratio  $J_{\text{nnn}}/J_{\text{nn}}$ .

### 2.3.2. Eu Chalcogenides

The bulk Eu chalcogenides crystallize in the rock salt structure. The magnetic properties were investigated in detail, as already mentioned, a long time ago [123]. EuO, EuS, and EuSe are typical ferromagnets of the Heisenberg type, which can be described by Eq. (6). As can be seen from Table 2, the exchange integrals  $J_{\text{nn}}$  are positive in sign, which consequently leads to a ferromagnetic ordering, as long as a negative  $J_{\text{nnn}}$  does not become dominant. It is noteworthy that it cannot be the indirect Anderson superexchange mechanism which leads to the ferromagnetic coupling, as such  $180^\circ f-p-f$  coupling inevitably leads to an antiferromagnetic coupling. The key point is the rock salt structure of the Eu-chalcogenides. The nearest-neighbor coupling is a  $90^\circ$  coupling, which is a very weak coupling in the case of  $p$ -orbitals. According to the so-called Goodenough–Kanamori–Anderson (GKA) rules [124], the  $90^\circ$  exchange is weak and ferromagnetic. The phenomenological idea of this rule is depicted in Figure 9. It can easily be seen that in the  $90^\circ$  configuration two different  $p$ -orbitals of the same anion overlap with the  $f$ -orbitals of the two Eu ions. Assuming that one electron of either  $p$ -orbital hops into the corresponding overlapping  $f$ -shell, the spins of the two electrons remaining in the  $p$ -orbitals of the anion must be parallel according to Hund's rule. Thus, the spins of the Eu ions should be parallel too.

Another, much more straightforward, explanation is also very likely. The cation radius of  $\text{Eu}^{2+}$  is rather large

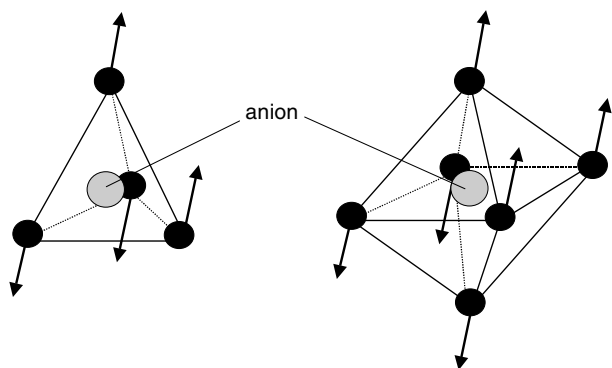


**Figure 8.**  $\text{Mn}^{2+}$  spin orientations in the elementary clusters of zincblende (left) and rock salt (right) structures in the case of an fcc type III (left) and fcc type II (right) antiferromagnetic ordering, respectively.

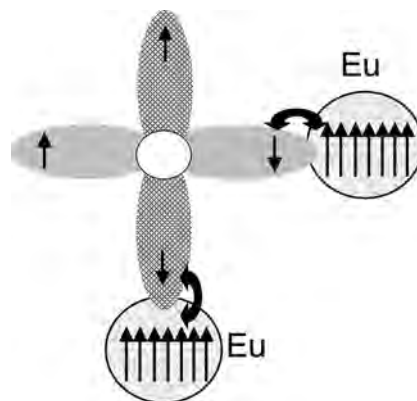


**Figure 9.** Schematic picture of the  $90^\circ$  superexchange interaction of the ferromagnetic coupled  $\text{Eu}^{2+}$  ions in the rock salt Eu-chalcogenides.

compared to e.g. the oxygen anion radius. Therefore the direct  $90^\circ$  overlap of the Eu ions may be the reason for the positive  $J_{\text{nn}}$ . The increasing radius from  $\text{O} \rightarrow \text{S} \rightarrow \text{Se} \rightarrow \text{Te}$  then decreases the direct exchange and therefore the ferromagnetic coupling compared to the antiferromagnetic coupling of the indirect  $180^\circ$  exchange interaction.

The  $180^\circ$  coupling via  $p$ -orbitals is as for Mn antiferromagnetic (see Fig. 6) and is much more effective. Therefore, it yields a stronger tendency for the  $J_{\text{nnn}}$  to be negative. The positive sign of  $J_{\text{nnn}}$  in the case of EuO may be caused again by a remaining contribution of the direct exchange due to the small lattice parameter. The decreasing Curie temperatures from about 70 K for EuO to about 2.8 K for EuSe are caused by a reduction of  $J_{\text{nn}}$  due to a decreasing wavefunction overlap of the localized  $f$ -orbitals of Eu with each other or with the  $p$ -orbitals of the anion as the lattice constant increases in the chalcogenides because of the increase in the anion radius from oxygen to selenium.

In a mean field approximation one derives, from Eq. (6),

$$T_C = \frac{(12J_{\text{nn}} + 6J_{\text{nnn}})2S(S+1)}{3k_B} \quad (10)$$

The increasing influence of the  $J_{\text{nnn}}$  leads to the antiferromagnetic ordering of EuTe in an fcc-type II antiferromagnetic structure with a Néel temperature  $T_N = 9.6$  K. Although  $J_{\text{nn}}$  is still positive, an antiferromagnetic phase transition occurs as  $J_{\text{nnn}} < 0$ . For EuSe an interesting and unique behavior is observable. A special antiferromagnetic structure was reported above  $T_C$  between  $T_N = 4.7$  K and  $T_C = 2.8$  K. All of the spins in two adjacent (111) planes are ferromagnetically ordered, whereas the subsequent two layers are antiferromagnetically arranged with respect to the former, yielding a NNSS antiferromagnetic order.

In the case of opposite signs of the exchange integrals, the state with the lowest energy, which can be either ferromagnetic or antiferromagnetic, will determine which spin structure is favored. Comparing Eq. (8) and Eq. (10), one obtains the condition  $|J_{\text{nnn}}| > |J_{\text{nn}}|$  for an antiferromagnetic ordering, which is defined by  $k_B T_N > k_B T_C$ . This is the case for EuTe. For EuS it holds that  $|J_{\text{nnn}}| < |J_{\text{nn}}|$ , yielding the ferromagnetic state, as it is now  $k_B T_N < k_B T_C$ . There are no reliable values for the nn and nnn exchange integrals of EuSe. Considering the exchange constants versus

the lattice parameters for the Eu-chalcogenides (Fig. 10), it can be estimated that  $|J_{\text{nnn}}| \cong |J_{\text{nn}}|$  for EuSe. This leads to the quasi-antiferromagnetic phase below 4.7 K as  $|J_{\text{nnn}}| \geq |J_{\text{nn}}|$ , yielding  $k_{\text{B}}T_{\text{N}} > k_{\text{B}}T_{\text{C}}$ . With decreasing temperature, because of the increasing overlap of the wavefunctions by reduction of the anion-anion distance, the exchange integrals are enhanced. This enhancement seems to be slightly stronger for  $J_{\text{nn}}$  compared with  $J_{\text{nnn}}$ . This might be the reason for the transition to the ferromagnetic state below 2.8 K with  $|J_{\text{nnn}}| \leq |J_{\text{nn}}|$ .

### 2.3.3. Mn-Pnictides

The Mn-pnictides are not semiconductors but show semimetallic behavior. Therefore, strictly speaking, they are not subject of this review. The recent interest in the growth of (III,Mn)V semiconductors has led, however, also to the fabrication of hybrid structures consisting of a diluted magnetic semiconductor matrix and Mn-pnictide clusters as a result of segregation processes. It was shown that Mn-V clusters can be prepared in a controlled manner during the MBE or MOVPE growth or by thermal annealing of the layers after a low temperature MBE growth (see also sections 3.1 and 3.3.2). A giant negative magnetoresistance has been observed for GaAs/MnAs [125, 126, 527] layered and granular hybrid structures which further provoked the interest. Therefore a brief review of the structural and magnetic properties of the Mn pnictides is essential for the understanding of the corresponding hybrid structures.

The bulk MnAs, MnSb and MnBi crystallize in the hexagonal NiAs structure with four atoms in the primitive unit cell. The favorable zincblende structure is thermodynamically not stable. The Mn ions are in the low spin state ( $3d^4 \text{ Mn}^{3+}$ ). The magnetic state is a ferromagnetically ordered state below the Curie temperature. It is worth noting, that the Curie temperature increases with increasing anion radius from MnAs ( $T_{\text{C}} = 318 \text{ K}$  [124] over MnSb ( $T_{\text{C}} = 587 \text{ K}$  [124]) to MnBi ( $T_{\text{C}} = 633 \text{ K}$  [124]). Above  $T_{\text{C}}$  they also undergo a structural change to the orthorhombic MnP-type structure. The MnP-type structure differs from the NiAs-type structure only by a distortion in the basal plane. It is well established (e.g. for the extensively studied MnAs) that this magnetic and structural phase transition takes place

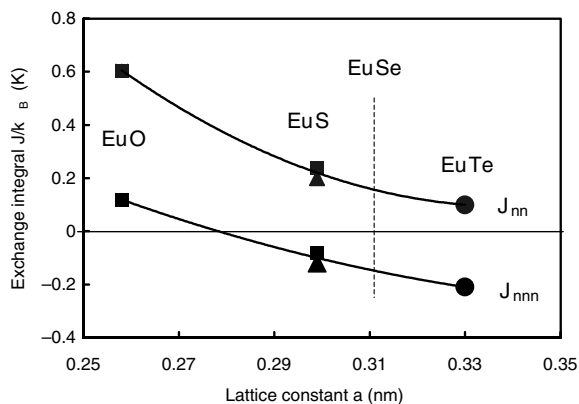


**Figure 10.** Exchange constant  $J_{\text{nn}}$  and  $J_{\text{nnn}}$  versus the lattice parameter for the Eu-chalcogenides. Experimental points: ■ [90], ▲ [91], ● [89]. The dashed line marks the position of the EuSe lattice parameter.

at different  $T_{\text{C}}$  on heating and on cooling. On heating the spontaneous magnetization of MnAs vanishes at  $T_{\text{C}} = 318 \text{ K}$ , but on cooling the respective  $T_{\text{C}}$  is only 306 K [see [127] and refs. therein]. Furthermore it must be taken into account, that  $T_{\text{C}}$  of MnAs films is obviously somewhat dependent on the preparation conditions. Tilsley et al. [128] were able to reduce  $T_{\text{C}}$  on heating from 320 K down to 312 K by changing the substrate temperature during growth from 400 °C to 600 °C.

The orthorhombic MnP ( $a > b > c$ ) itself is ferromagnetic between 47 K and 291 K. Below 47 K a screw phase has been observed in which the moments rotate in the  $bc$ -plane. MnN is known to have a NaCl-type structure at room temperature and has been reported to be antiferromagnetic with a Néel-temperature of 650 K [129]. Studying the diluted magnetic semiconductor  $\text{Ga}_{1-x}\text{Mn}_x\text{N}$  with  $x_{\text{Mn}} < 0.01$  which grows in a hexagonal phase, Zajac et al. [130] were able to determine the Mn-Mn nearest neighbor exchange integral which was clearly antiferromagnetic with  $J_{\text{nn}}/k_{\text{B}} \approx -1.9 \text{ K}$ . The most interesting phase of the Mn-nitrides is probably the  $\text{Mn}_4\text{N}$ -type compound [131] which exhibits a ferrimagnetic phase with a high resulting magnetic moment and a Néel-temperature of 745 K.

### 2.3.4. Diluted Magnetic Semiconductors

Decreasing the concentration  $x$  of magnetic ions in diluted magnetic II-VI or IV-VI alloys restricts the spin ordering effects to the lower temperature region. As an example, Figure 11 shows schematic magnetic phase diagrams for (Cd,Mn)Te and (Cd,Mn)S. The two phase diagrams are typical for all (II,Mn)VI alloy systems. The paramagnetic phase extends to lower temperatures with decreasing  $x_{\text{Mn}}$ . A (disordered) antiferromagnetic phase (af) occurs that has a long-range spin ordering below a critical temperature  $T_{\text{N}}(x_{\text{Mn}})$  for a sufficiently high Mn concentration  $x_{\text{Mn}} > 0.8$  (beyond the miscibility gap (mg)) for (Cd,Mn)S. The corresponding phase transition is characterized by peaks at  $T_{\text{N}}$  in both the magnetic susceptibility and the specific heat. For Mn concentrations below the miscibility gap a spin-glass

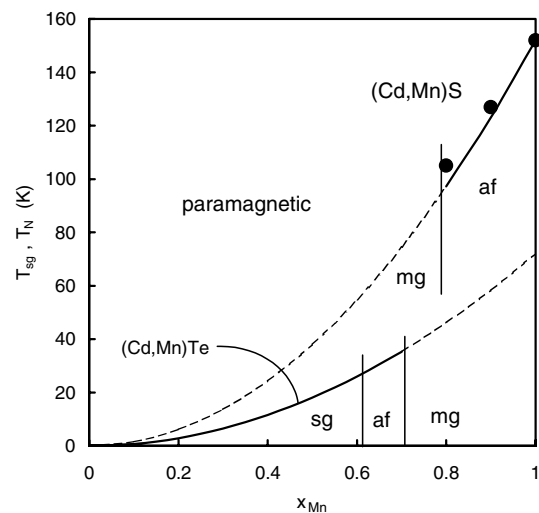


**Figure 11.** Magnetic phase diagrams of (Cd,Mn)Te and (Cd,Mn)S. Experimental points are from [482].



phase (sg) is observed for temperatures below  $T_{sg}(x_{Mn})$ . In the case of (Cd,Mn)Te even a transition to the antiferromagnetic phase has been reported for  $x_{Mn} = 0.7$  [132], which means that it is still below the miscibility gap. The spin-glass phase is characterized by an antiferromagnetic short-range ordering of the spins, as well as frustration effects. As an example, in Figure 12 a triangle is depicted, where the third spin can either be spin up or spin down, as both states are energetically degenerate. A quantum mechanical calculation reveals that the ground-state spin of such a closed triangle is not  $S_z = -5/2$ , but  $S_z = -1/2$  [133]. The somewhat diffuse phase transition from the paramagnetic into the spin-glass phase leads to a peak or kink at  $T_{sg}(x_{Mn})$  in the temperature dependence of the magnetic susceptibility, but no anomaly in the specific heat is observable. Neutron scattering experiments have shown that small antiferromagnetically ordered clusters already appear above  $T_{sg}$ , which grow in size with decreasing temperature. Another surprising fact is that a spin-glass phase is observable not only above the percolation limit ( $x_{Mn} \approx 0.2$ ), but also below. In the very low concentration range, a rather long-range interaction is necessary, in addition to the short-range superexchange interaction, to yield a spin-glass phase. The spin freezing temperatures below the percolation concentration are very small, for example, between 0.1 K and 1 K for  $x_{Mn} \approx 0.01$ . The dipole-dipole interaction between more distant  $Mn^{2+}$  ions is proposed to be the required long-range interaction responsible for this spin-ordering mechanism, despite the fact that the dipole-dipole interaction might be too weak to cause the ordering at finite temperatures [134].

A very striking feature of diluted magnetic semiconductors is the strong correlation of magnetism and doping. Figure 13 depicts various Mn-containing DMS arranged schematically according to their free carrier concentration and Mn concentration. It can be seen that in (II,Mn)VI and (III,Mn)V (top graph) as well as in the (IV,Mn)VI (bottom graph) semiconductors the coupling between the Mn ions changes from antiferromagnetic (AF) to ferromagnetic (F) with increasing free carrier concentration. The critical free-carrier concentration, where the transition between the two types of coupling occurs, is about  $10^{18} \text{ cm}^{-3}$  for the (II,Mn)VI and (III,Mn)V compounds and about  $10^{19} \text{ cm}^{-3}$  for the (IV,Mn)VI compounds. It should be pointed out that the (II,Mn)VI semiconductors usually have free-carrier concentrations below the critical concentrations [21, 22]. Only recently very high p-doping concentrations of  $10^{20} \text{ cm}^{-3}$  were achieved in  $Zn_{1-x}Mn_x\text{Te:N}$  with

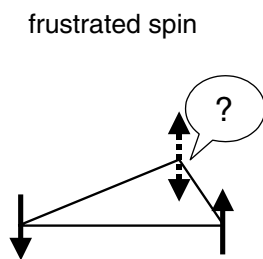


**Figure 12.** Degeneracy of the spin states in a closed triangle of  $Mn^{2+}$  ions.

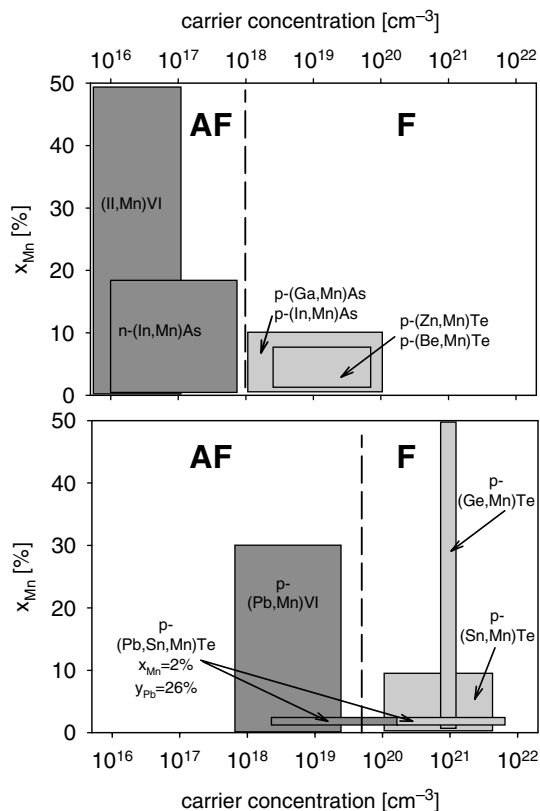


**Figure 13.** Correlation of the magnetism of the Mn subsystem and the doping of the host. Top graph: (II,Mn)VI and (III,Mn)V semiconductors. Bottom graph: (IV,Mn)VI semiconductors. AF and F denote antiferromagnetic and ferromagnetic coupling between Mn ions, respectively.

$x \approx 2\%$  [135, 136]. These samples show a ferromagnetic phase at low temperatures. Similar results have also been reported for (Zn,Mn)Te:N and (Be,Mn)Te:N with  $x$  ranging from 0.5% to 7% [137]. The (IV,Mn)VI materials can easily be prepared over a wide range of free-carrier concentrations; thus, they were the first class of DMS where samples exhibiting either antiferromagnetic or ferromagnetic coupling between the Mn ions were found [138]. The (III,Mn)V usually have very high free-carrier concentrations, as Mn acts as a dopant in these compounds. It is worth noting that Ohno et al. [139] demonstrated that it is possible to switch from ferromagnetic to antiferromagnetic coupling in one and the same (In,Mn)As layer by varying the free-carrier density with an external electric field. The structure used was a metal-insulator-semiconductor field-effect transistor with (In,Mn)As as the semiconductor material.

Because of the usually rather small carrier concentrations ( $<10^{18} \text{ cm}^{-3}$ ) in (II,Mn)VI alloys, even for the narrow gap materials, the indirect RKKY mechanism between the  $Mn^{2+}$  ions does not play a role. The magnetic ordering phenomena are determined by the Anderson superexchange as the dominant exchange mechanism.

Recently Saito et al. [140] reported the observation of ferromagnetism in  $Zn_{1-x}Cr_x\text{Te}$  layers on GaAs substrate. They found Curie temperatures of about 15 K for 3.5% chromium. As we will discuss in the next chapter the

$p$ - $d$  exchange integral (see Table 4) is actually positive e.g. ferromagnetic. It does however not necessarily mean that the  $d$ - $d$  coupling is ferromagnetic as well. The reason for the ferromagnetism of (Zn,Cr)Te is not clear to date. Shoren et al. [141] suggested a carrier-induced mechanism in case of an unintentionally doped sample. Blinowski et al. [142] discussed, however, on the basis of their theoretical calculation the opportunity of a ferromagnetic superexchange mechanism. It is known, that the  $180^\circ$  exchange interaction in case of  $3d^4$  cations (e.g.  $\text{Cr}^{2+}$ ,  $\text{Mn}^{3+}$ ,  $\text{Fe}^{4+}$ ) is ferromagnetic in most cases [124].

Dominating Anderson superexchange also seems to be valid for some of the (IV,Mn)VI alloys such as (Pb,Mn) $X$  ( $X = \text{S, Se, Te}$ ) [143, 144]. However, others (e.g., (Sn,Mn)Te [145, 146] or (Ge,Mn)Te [147, 148], which have typical free-carrier concentrations above  $10^{20} \text{ cm}^{-3}$ ) exhibit ferromagnetic interactions between the  $\text{Mn}^{2+}$  spins (i.e., the RKKY exchange mechanism dominates over the Anderson superexchange). With varying carrier concentration in the quaternary alloy  $\text{Pb}_{1-x-y}\text{Sn}_y\text{Mn}_x\text{Te}$ , either antiferromagnetic or ferromagnetic ordering is possible [149, 150]. The schematic phase diagram representative for ferromagnetic (IV,Mn)VI compounds is shown in Figure 14. An example for such compounds is  $p$ -type (Sn,Mn)Te [145].  $\text{Sn}_{1-x}\text{Mn}_x\text{Te}$  typically has a free-hole density of  $10^{20} \text{ cm}^{-3} < p < 5 \times 10^{20} \text{ cm}^{-3}$ , presumably because of Sn vacancies. At higher temperatures the system is paramagnetic (P). For concentrations  $x < 3\%$ , a spin-glass (SG) phase occurs below the spin freezing temperature, but at larger concentrations a ferromagnetic phase (F) is observed. This ferromagnetic phase is characterized by the existence of a spontaneous magnetization, in a definite range of temperatures, below the Curie temperature  $T_C$ . The ferromagnetic long-range ordering down to Mn concentrations as small as 3% is due to the RKKY indirect exchange mediated by the  $10^{20} \text{ cm}^{-3}$  holes present in the sample. At the lowest temperatures a reentrant spin-glass phase is observed. This reentrant spin-glass phase is a manifestation of the delicate interplay of the Mn concentration  $x$  and free carrier concentration  $p$ . The RKKY exchange

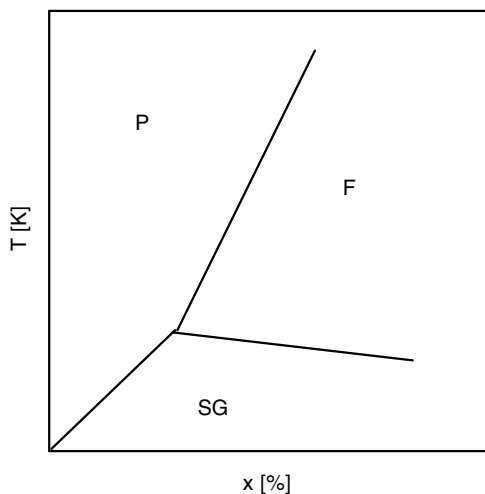


**Figure 14.** Schematic phase diagram of a ferromagnetic (IV,Mn)VI semiconductor.

constant  $J_{\text{RKKY}}$  is a rapidly oscillating function given by

$$J_{\text{RKKY}} \propto \frac{\sin(2k_F \cdot R_{ij}) - 2k_F \cdot R_{ij} \cdot \cos(2k_F \cdot R_{ij})}{(2k_F \cdot R_{ij})^4} \quad (11)$$

where  $k_F$  ( $\propto p^{1/3}$ ) is the Fermi wave vector and  $R_{ij}$  is the distance between the magnetic ions. For  $2 \cdot k_F R_{ij} \rightarrow 0$  the interaction is ferromagnetic. The relationship between the two characteristic lengths  $R_0$  and  $R_{\text{Mn-Mn}}$  determines the magnetism of the system.  $R_0$  is the distance at which the first change from ferromagnetic to antiferromagnetic interaction occurs. At a fixed  $x$ ,  $R_0$  is proportional to  $p^{-1/3}$ . The average distance  $R_{\text{Mn-Mn}}$  between  $\text{Mn}^{2+}$  ions is proportional to  $x^{-1/3}$ . If  $R_0 \ll R_{\text{Mn-Mn}}$  there is a competition between positive, ferromagnetic coupling and negative, antiferromagnetic coupling between  $\text{Mn}^{2+}$  spins, leading to the spin-glass phase [146]. This happens in (Sn,Mn)Te as the free carrier concentration  $p$  decreases with cooling.

The strong correlation of magnetism and doping effects is also manifested in the phase diagrams of the (III,Mn)V alloys. As an example, the phase diagram of  $\text{Ga}_{1-x}\text{Mn}_x\text{As}$  for  $x < 10\%$  is shown in Figure 15 with experimental points from [151–153]. First one should note that the  $\text{Ga}_{1-x}\text{Mn}_x\text{As}$  as a random alloy is a metastable phase and is grown far from the thermodynamical equilibrium, usually by low-temperature MBE. The upper limit of the Mn concentration is currently about 10%, where a random alloy was still grown successfully. Segregation always occurs at higher Mn contents. Similarly, annealing or raising the growth temperature always leads to the formation of MnAs clusters in a  $\text{Ga}_{1-x}\text{Mn}_x\text{As}$  matrix with a low  $x$  of about 0.1%. Also there is a competition between different sites of the Mn atom in the alloy. It can be incorporated as an acceptor on a Ga site or as donor-like centers such as small disordered sixfold-coordinated centers with As, known from closely related  $\text{In}_{1-x}\text{Mn}_x\text{As}$  [44]. At elevated temperatures the alloy is paramagnetic, but at low temperatures  $\text{Ga}_{1-x}\text{Mn}_x\text{As}$  becomes ferromagnetic. It can be seen in Figure 15 that

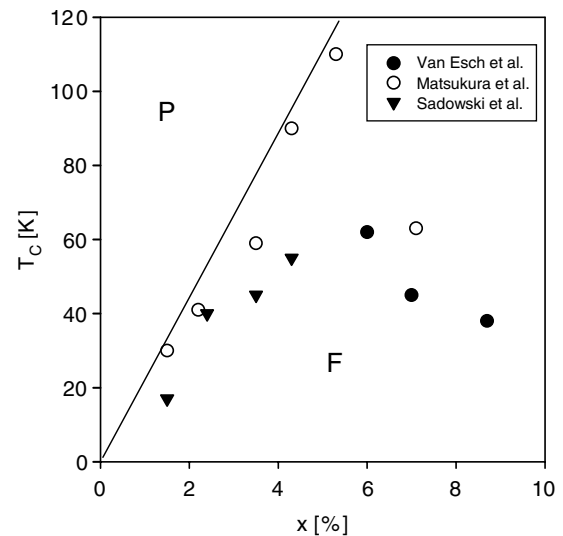


**Figure 15.** Phase diagram of (Ga,Mn)As. Experimental points: ○ [151], ▼ [152], ● [153].

the Curie temperature increases rather linearly with  $x$  up to  $T_C = 110$  K for  $x \approx 5\%$ . The Curie temperatures of samples with higher Mn concentrations deviate from the linear curve and are significantly lower. This drop in the Curie temperature is related to the self-compensation process in  $\text{Ga}_{1-x}\text{Mn}_x\text{As}$ . At high  $x$  the relative amount of Mn incorporated as donors instead of acceptors is increased. This correlation was shown nicely by Matsukura et al. [151], who observed, for a series of  $\text{Ga}_{1-x}\text{Mn}_x\text{As}$  of different  $x$ , that both the net hole concentration and the Curie temperature had their maximum values at about 5%. Similar results were reported for  $(\text{In},\text{Mn})\text{As}$  [154]. It is therefore very clear that the ferromagnetic coupling of the Mn ions in  $\text{Ga}_{1-x}\text{Mn}_x\text{As}$  with sufficiently high Mn content ( $x > 0.5\%$ ) results from interaction with holes [39, 155–157]. However, the details of the mechanism are still being discussed. It is worth noting that no signs of a spin-glass phase have been reported so far for this alloy system.

Room temperature ferromagnetism in  $(\text{Ga},\text{Mn})\text{N}$  has been reported by Reed et al. [27]. Sonoda et al. [158] reported for  $\text{Ga}_{1-x}\text{Mn}_x\text{N}$  films with  $x_{\text{Mn}} = 0.057$  a Curie-temperature  $T_C \approx 940$  K on the basis of SQUID measurements. This value is higher than the known Curie-temperatures of  $\text{Mn}_4\text{N}$  or  $\text{MnGa}$ . Therefore the authors suggested, that the ferromagnetism is mediated by the free holes, which are of the order between  $10^{19}$  and  $10^{20}$   $\text{cm}^{-3}$  at room temperature. The extremely high  $T_C$  could be explained then on the basis of the mean-field model of ferromagnetism mediated by holes in tetrahedrally coordinated semiconductors developed by Dietl et al. [156, 159]. According to this model the high hole mass of GaN would be the main reason for the high  $T_C$ .

However, Overberg et al. [160] reported a Curie-temperature of only 10 to 25 K for MBE grown  $(\text{Ga},\text{Mn})\text{N}$  alloys with a Mn content of about 7%. There is obviously no clear recipe for obtaining  $(\text{Ga},\text{Mn})\text{N}$  with high Curie temperatures.

As already mentioned in the discussion of the  $(\text{II},\text{Mn})\text{VI}$  phase diagrams, even in the paramagnetic phase (i.e., above  $T_{\text{sg}}$ ), cluster formation reduces the paramagnetic response. The dependence of the (molar) magnetization on the magnetic field, temperature, and concentration of the magnetic ions can be described by a relation introducing phenomenological parameters [161, 162],

$$M(x) = a(x) \cdot x \cdot M = \tilde{g} \mu_B \langle S_z \rangle_{\text{mol}} \quad (12)$$

In the alloy the mean molar spin density is, therefore,

$$\langle S_z \rangle_{\text{mol}} = N_A x \langle S_z \rangle = -a(x) \cdot N_A \cdot x \cdot S \cdot B_S(\xi) \quad (13)$$

with

$$\xi = \frac{\tilde{g} \cdot \mu_B \cdot S \cdot H}{k_B(T + \Theta(x))}$$

where  $S$  is the spin of the magnetic ions and  $B_S$  is the corresponding Brillouin function. The Curie–Weiss parameter  $\Theta(x)$  is considered an empirical  $x$ -dependent fitting parameter, and  $a(x)$  is a scaling factor. Both parameters account for the cluster effects. The scaling factor  $a(x)$  is always smaller than unity, with the limiting property  $a(x \rightarrow 0) \rightarrow 1$ .

The parameter  $\Theta(x)$  decreases superlinearly with decreasing  $x$ , and for sufficiently low Mn concentrations an ideal paramagnetic behavior is found as  $\Theta(x \rightarrow 0) \rightarrow 0$ .

With extension of the low-temperature measurements of the magnetization to very high magnetic fields ( $H \gg 10$  Tesla), distinct steps in the magnetization have been observed at  $H_n$  ( $n = 1, 2, \dots$ ) for  $(\text{Cd},\text{Mn})\text{S}$  [109, 163, 164],  $(\text{Cd},\text{Mn})\text{Se}$  [108, 165, 166, 167],  $(\text{Cd},\text{Mn})\text{Te}$  [162, 166–168],  $(\text{Zn},\text{Mn})\text{Se}$  [109, 163, 165, 167],  $(\text{Zn},\text{Mn})\text{Te}$  [102, 103, 167, 169, 170],  $(\text{Zn},\text{Mn})\text{S}$  [164],  $(\text{Hg},\text{Mn})\text{Se}$ , and  $(\text{Hg},\text{Mn})\text{Te}$  [171]. These steps are caused by a magnetic field-induced successive alignment of antiferromagnetically ordered nn pairs of  $\text{Mn}^{2+}$  ions. The saturation steps correspond to increasing total spin quantum numbers  $S_p = 0, 1, 2, \dots, 5$  of the pairs. For isolated pairs and sufficiently low temperatures ( $k_B T \ll 2|J_{\text{nn}}|$ ),  $H_n$  is simply determined by

$$H_n = -\frac{2nJ_{\text{nn}}}{\mu_B \tilde{g}} \quad n = 1, 2, \dots, 5 \quad (14)$$

The energy levels of a Mn pair and the respective steps in the magnetization are depicted schematically in Figure 16. Taking into account the influence of the more distant  $\text{Mn}^{2+}$  neighbors on a considered pair in a mean-field approximation, a more exact relation for  $H_n$  was developed [112, 113]. Lowering the temperature in the experiments further to 20 mK allows one to determine higher exchange constants up to fourth nearest neighbors, which are more than one order of magnitude smaller than  $J_{\text{nn}}$  [172, 173]. These smaller exchange constants have been the subject of theories and conjecture [120, 174–176]. However, up to now there has been no satisfactory agreement between theory and experiment.

The antiferromagnetic nn exchange constants  $J_{\text{nn}}$  have also been determined for various Mn-containing or Eu-containing IV–VI and II–VI compounds from magnetization

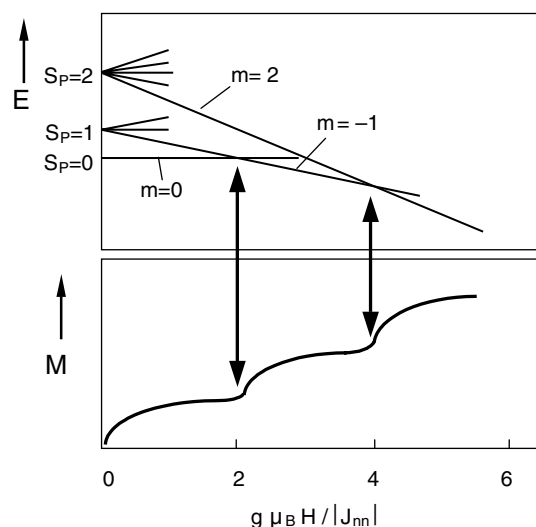


**Figure 16.** Lowest energy levels of a pair of Mn spins as a function of the magnetic field. The resulting magnetization steps are depicted schematically. Adapted from [162] with permission from the American Institute of Physics.

measurements or magnetic susceptibility measurements [177–179]. The exchange constants for the diluted magnetic IV–VI semiconductors are about an order of magnitude smaller than those of the corresponding II–VI compounds. Therefore, until about 1995, no distinct magnetization steps were observed in magnetization experiments on diluted magnetic IV–VI semiconductors because  $|J_{nn}| < 2 \cdot k_B T$  held in all experiments. However,  $J_{nn}$  could be extracted by fitting the magnetization data and adding a pair term  $M_p$  to Eq. (12) [178],

$$M_p = \frac{1}{2} \tilde{g} \mu_B x_p \times \frac{\sum_{s=0}^{S_p, \max} \exp[(J_{nn}/k_B T)s(s+1)] \cdot [\sinh((2s+1)/2s)\xi_p]}{\sum_{s=0}^{S_p, \max} \exp[(J_{nn}/k_B T)s(s+1)] \cdot [\sinh((2s+1)/2s)\xi_p]} \cdot s B_s(\xi_p) \quad (15)$$

with

$$\xi_p = (s \tilde{g} \mu_B H) / (k_B T)$$

where  $x_p \approx (1 - a(x))$  is the percentage of magnetic ions forming isolated pairs, and  $S_{p, \max} = 2 \cdot S$  is the total spin of an isolated pair.  $S = 5/2$  and  $S = 7/2$  for the Mn- and Eu-containing samples, respectively. Only recently, magnetization steps have been observed in (Pb,Eu) $X$  compounds with  $X = S, Se, Te$  [180–182], which allowed a more accurate determination of  $J_{nn}$ . For isolated Eu–Eu pairs the total spin quantum number  $S_p$  can take values 0, 1, 2, . . . , 7, and, correspondingly,  $n = 0, 1, 2, \dots, 7$  in Eq. (14). Table 3 lists ranges of  $J_{nn}$  values for some diluted magnetic II–VI and IV–VI compounds.

Some interesting trends can be observed in Table 3. First, the  $J_{nn}$  of the (II,Mn)VI DMS scale with the size of the anions and the cations. For example, the  $J_{nn}$  of the sulfides are bigger than those of the selenides, and these again are bigger than those of the tellurides. Moreover, the Cd compounds have smaller  $J_{nn}$  than the corresponding Zn compounds. Spalek et al. [183] were able to relate these trends to the variation of the bond angle between adjacent  $Mn^{2+}$  ions and the anion. Second, the exchange constants in the Mn-containing II–VI alloys are about an order of magnitude bigger than those in the Mn-containing IV–VI alloys.

**Table 3.** Nearest-neighbor exchange constants of various diluted magnetic semiconductors.

DMS	Crystal structure	$J_{nn}/k_B$ (K)
Zn <sub>1-x</sub> Mn <sub>x</sub> O	W	-15
Cd <sub>1-x</sub> Mn <sub>x</sub> S	W	-8.6 . . . -11.0
Zn <sub>1-x</sub> Mn <sub>x</sub> S	ZB	-16.9, -16.1
Cd <sub>1-x</sub> Mn <sub>x</sub> Se	W	-7.6 . . . -10.6
Zn <sub>1-x</sub> Mn <sub>x</sub> Se	ZB	-9.9 . . . -13.5
Cd <sub>1-x</sub> Mn <sub>x</sub> Te	ZB	-6.1 . . . -7.7
Zn <sub>1-x</sub> Mn <sub>x</sub> Te	ZB	-7.9 . . . -12.0
Pb <sub>1-x</sub> Mn <sub>x</sub> S	RS	-0.47 . . . -0.67
Pb <sub>1-x</sub> Mn <sub>x</sub> Se	RS	-0.93 . . . -1.95
Pb <sub>1-x</sub> Mn <sub>x</sub> Te	RS	-0.62 . . . -1.20
Pb <sub>1-x</sub> Eu <sub>x</sub> S	RS	-0.228 ± 0.007
Pb <sub>1-x</sub> Eu <sub>x</sub> Se	RS	-0.24 ± 0.03
Pb <sub>1-x</sub> Eu <sub>x</sub> Te	RS	-0.264 ± 0.018

Note: W, wurtzite; ZB, zinblend; RS, rock salt.

Anderson, Gorska, and co-workers [177, 178] ascribed the reduction of  $J_{nn}$  in the (IV,Mn)VI alloys compared with the (II,Mn)VI alloys primarily to the increased separation between the Mn ion and an adjacent anion. However, one should keep in mind that the bandgaps in the materials are at different points of the Brillouin zone, and, therefore, the wavefunctions involved are different. Third, the exchange constants of the Eu-containing IV–VI alloys are smaller than those of the corresponding Mn-containing alloys by a factor of 5–10. This is mainly caused by the stronger localization of the  $4f^7$  orbitals compared with the  $3d^5$  orbitals. More interesting is the fact that the exchange constants  $J_{nn}$  of the Eu-containing IV–VI alloys are very different from those of the corresponding binary Eu-chalcogenides given in Table 2. The former are negative (i.e., antiferromagnetic), whereas, for EuS, EuSe, and EuTe, the largest antiferromagnetic exchange constant is  $J_{nnn}$ , and  $J_{nn}$  itself is ferromagnetic. Despite the fact that they share the same RS crystal structure, the pure Eu-chalcogenides and the corresponding (IV,Eu)VI have again very different electronic band structures. The bandgaps of the former are at the  $\Gamma$ -point, whereas those of the latter are at the L-point; furthermore, the positions of the  $4f^7$  levels of the  $Eu^{2+}$  contribute differently to the band structure. In general, one can conclude that the trends of the exchange mechanisms in the pure Mn- or Eu-chalcogenides as well as in the corresponding diluted II–VI and IV–VI systems are fairly well understood in the case of bulk samples, despite the lack of a comprehensive theory.

## 2.4. Magneto-Optical Properties of Bulk Semiconductors

The changes in the magneto-optical effects connected with electron and hole band states are rather large in magnetic semiconductors compared with those in conventional semiconductors. These dramatic changes in the magneto-optical properties are some of the main reasons for the considerable and continuous physical and applicative interest in these materials. In diluted magnetic semiconductors, for example, the so-called giant Zeeman splitting of free excitons is observable, which for (II,Mn)VI and (IV,Mn)VI semiconductors is about two orders of magnitude larger than the usual Zeeman splitting. The usual Zeeman splitting of conduction and valence band states is amplified strongly by the  $s$ - $d$  and  $p$ - $d$  exchange interaction with the  $Mn^{2+}$   $3d$  electrons, which are paramagnetically oriented in an external magnetic field. All of the diluted magnetic semiconductors have the advantage, compared with magnetic semiconductors, that the strong antiferromagnetic ion intersite interaction can be partly suppressed and even controlled. In magnetic semiconductors very high magnetic fields are required to overcome the “internal” fields which are induced by the ion–ion interaction, as discussed in Section 2.3. In diluted magnetic semiconductors, it is possible to adjust the magnetic ion concentration such that it is high enough to give a strong enhancement of the external field but is still low enough not to induce strong intersite correlations between the magnetic ions for the majority of the spins.

When a diluted magnetic semiconductor contains localized magnetic moments, its band structure will be modified.

Such interaction is included in the Hamiltonian  $H$  by adding a Kondo-like exchange term  $H_{\text{exch}}$  to the Hamiltonian  $H_0$ :

$$H = H_0 + H_{\text{exch}} = H_0 - \sum_i J(\vec{r} - \vec{R}_i) \vec{S}_i \vec{\sigma} \quad (16)$$

For the zincblende (II,Mn)VI and (III,Mn)V alloys, the mean-field approximation leads to a lattice-periodic form,

$$H_{\text{exch}} = -x_{\text{Mn}} \sigma_z \langle S_z \rangle \sum_{R \in \text{fcc sublattice}} J(\vec{r} - \vec{R}) \quad (17)$$

As the extended conduction band states interact simultaneously with a sufficiently large number of  $\text{Mn}^{2+}$  ions, the spin operator can be replaced by its thermal mean value. Furthermore, in a virtual-crystal approximation  $J(r - R_i)$  is replaced by  $x_{\text{Mn}} J(r - R)$ , taking the summation over all cation-sublattice sites  $R$ .

The advantage of Eq. (17) is that in this form  $H_{\text{exch}}$  has the periodicity of the lattice. This allows one to use the same wave functions for solving Eq. (17), as those used for diagonalizing  $H_0$ . In the case of a zincblende crystal this is the set of basic functions introduced in the Pidgeon–Brown model:

$$\Gamma_6 \begin{cases} |S \uparrow\rangle = \Psi_{1/2, 1/2} \\ |iS \downarrow\rangle = \Psi_{1/2, -1/2} \end{cases} \quad (18)$$

$$\Gamma_8 \begin{cases} \frac{1}{\sqrt{2}} |(X + iY) \uparrow\rangle = \Psi_{3/2, 3/2} \\ i \frac{1}{\sqrt{2}} |(X - iY) \downarrow\rangle = \Psi_{3/2, -3/2} \\ \frac{1}{\sqrt{6}} |(X - iY) \uparrow + 2Z \downarrow\rangle = \Psi_{3/2, -1/2} \\ i \frac{1}{\sqrt{6}} |(X - iY) \downarrow + 2Z \uparrow\rangle = \Psi_{3/2, 1/2} \end{cases} \quad (19)$$

$$\Gamma_7 \begin{cases} i \frac{1}{\sqrt{3}} |-(X - iY) \uparrow + Z \downarrow\rangle = \Psi_{1/2, 1/2} \\ \frac{1}{\sqrt{3}} |(X + iY) \downarrow + Z \uparrow\rangle = \Psi_{1/2, -1/2} \end{cases} \quad (20)$$

Here  $S$ ,  $X$ ,  $Y$ , and  $Z$  are the Kohn–Luttinger amplitudes, with  $s$ ,  $p_x$ ,  $p_y$ , and  $p_z$  symmetry, respectively, and  $\uparrow$ ,  $\downarrow$  are the Pauli spinors.

$$E_{k\uparrow}^c = (l + \frac{1}{2}) \hbar \omega_c \pm \frac{1}{2} (g_c^* \mu_B H - N_0 \alpha x_{\text{Mn}} \langle S_z \rangle) \quad (21)$$

where  $\omega_c$  and  $g_c^*$  are the cyclotron frequency and the Landé factor of the conduction band electron, respectively.  $l = 0, 1, \dots$  is the Landau quantum number.  $\alpha = \langle S|J|S \rangle$  is the  $s$ - $d$  exchange interaction parameter, and  $N_0$  denotes the number of unit cells per  $\text{cm}^3$ . The upper and lower signs correspond to the  $\uparrow$  and  $\downarrow$  spin states. An effective  $g$ -factor can be defined:

$$g_{\text{eff}} = g_c^* - \frac{x_{\text{Mn}} N_0 \alpha \langle S_z \rangle}{\mu_B H} \quad (22)$$

The consequences for a  $\Gamma_6$  conduction band are illustrated schematically in Figure 17 for *narrow gap* semiconductors. Since the sign of  $N_0 \alpha$  is positive, the exchange term in

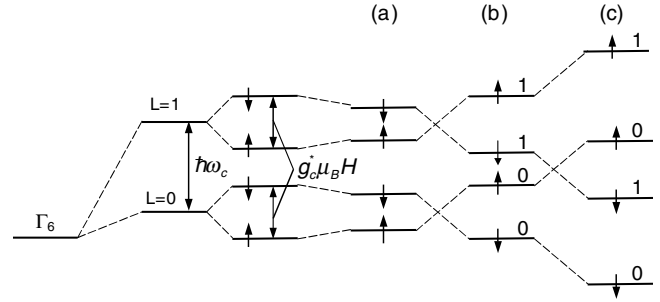


**Figure 17.** Conduction band states of a narrow gap semiconductor in a magnetic field. (a) Since the sign of  $N_0 \alpha$  is positive, its sign is opposite that of  $g_c^*$  and reduces the usual Zeeman splitting. (b) If  $g_{\text{eff}} > 0$  a reverse of the total Zeeman splitting occurs. (c) For large values of  $g_{\text{eff}}$  ( $|g_{\text{eff}} \mu_B H| > |\hbar \omega_c|$ ) a mixture of the Landau level sequence occurs.

Eq. (22) has a sign opposite that of  $g_c^*$  and reduces the usual Zeeman splitting (Fig. 17a). If  $g_{\text{eff}} > 0$ , a reverse of the total Zeeman splitting occurs (Fig. 17b), and for large values of  $g_{\text{eff}}$  ( $|g_{\text{eff}} \mu_B H| > |\hbar \omega_c|$ ) even a mixture of the Landau level sequence is possible (Fig. 17c). It must be taken into account, however, that the Brillouin function saturates at higher fields while the cyclotron splitting is continuously increasing.

In *zero gap* (II,Mn)VI materials like (Hg,Mn)Te with small Mn concentrations ( $x_{\text{Mn}} < 0.1$ ) the situation is even more complicated because of the degeneracy of the conduction and valence band at the  $\Gamma$ -point. The relevant exchange integral is now  $N_0 \beta$ , where  $\beta = \langle X|J|X \rangle$  is the corresponding  $p$ - $d$  exchange interaction parameter, which exhibits a negative sign. The negative exchange integral enhances the usual Zeeman splitting, as depicted in Figure 18a. But still a mixing of the Landau levels might occur (Fig. 18b) if the exchange interaction is strong enough. In the case of an open gap (Hg,Mn)Te ( $x_{\text{Mn}} > 0.2$ )  $N_0 \alpha$  becomes again a relevant exchange integral as the conduction band is now dominantly made of  $s$ -states.

The situation is considerably simpler in the case of *wide bandgap* (II,Mn)VI alloys. Here, the intrinsic spin splitting (usual Zeeman splitting) and the Landau-level splitting are much smaller than the exchange splittings. This is due to the rather heavy effective masses of the wide-gap semiconductors. In this approximation the magnetic splitting of the

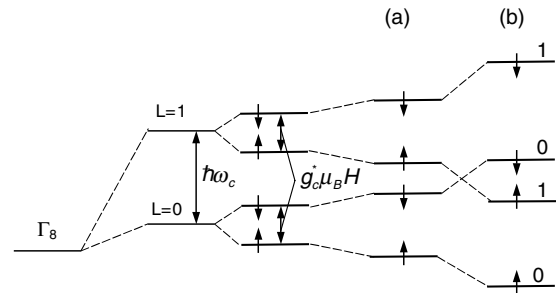


**Figure 18.** Possible  $\Gamma_8$  spin splitting of the first two Landau levels in zero-gap II–VI DMS in an applied magnetic field. The negative exchange integral  $N_0 \beta$  enhances the usual Zeeman splitting (a), but a mixing of the Landau levels might occur (b) if the exchange interaction is strong enough.

energy levels is entirely due to the exchange terms. Excitonic effects are primarily devoted to the bottom of the conduction band and to the top of the valence band at  $k = 0$ . One obtains for the  $\Gamma_6$  conduction band splitting and for the  $\Gamma_8$  valence band splitting, respectively,

$$\langle \Psi_{1/2} | H_{\text{exch}} | \Psi_{1/2} \rangle = \begin{vmatrix} a & 0 \\ 0 & -a \end{vmatrix} \quad (23)$$

and

$$\langle \Psi_{3/2} | H_{\text{exch}} | \Psi_{3/2} \rangle = \begin{vmatrix} b & 0 & 0 & 0 \\ 0 & \frac{1}{3}b & 0 & 0 \\ 0 & 0 & -\frac{1}{3}b & 0 \\ 0 & 0 & 0 & -b \end{vmatrix} \quad (24)$$

with

$$a = \frac{1}{2} N_0 \alpha x_{\text{Mn}} \langle S_z \rangle \quad (25a)$$

$$b = \frac{1}{2} N_0 \beta x_{\text{Mn}} \langle S_z \rangle \quad (25b)$$

The shift and splitting of the conduction band states are now

$$\Delta E_C = -x_{\text{Mn}} N_0 \alpha \langle S_z \rangle m_j, \quad m_j = \pm \frac{1}{2} \quad (26)$$

and the corresponding splitting of the valence band states

$$\Delta E_V = -\frac{1}{3} x_{\text{Mn}} N_0 \beta \langle S_z \rangle m_j, \quad m_j = \pm \frac{1}{2}, \pm \frac{3}{2}. \quad (27)$$

A schematic picture of the exchange interaction-induced spin splitting is depicted in Figure 19. The diagram also shows the electrical dipole allowed transitions for the circular polarizations rotating transverse to the applied field, designated by  $\sigma^+$  and  $\sigma^-$  for right and left circular polarization ( $\Delta m_j = \pm 1$ ), respectively, in Faraday configuration, with the propagation vector of the light parallel to the field direction. The linear  $\pi$  polarization ( $\Delta m_j = 0$ ) is observable in the Voigt configuration only, with the propagation

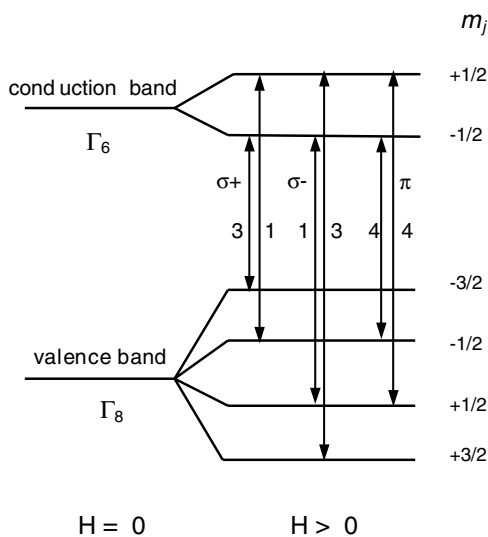


**Figure 19.** Giant Zeeman splitting of wide-gap II–VI DMS in an applied magnetic field. Reprinted with permission from [22], O. Goede and W. Heimbrodt, *Phys. Stat. Sol. B* 146, 11 (1988). © 1988, Wiley-VCH Verlag, Berlin.

vector perpendicular to the field direction. The numbers in Figure 19 give the relative transition probabilities. As a typical example, Figure 20 depicts the excitonic splitting of a thick epitaxial layer of (Zn,Mn)Se, with  $x_{\text{Mn}} = 0.16$ , grown by MBE. The zero field splitting of the light hole (lh) and heavy hole (hh) excitons is caused by the biaxial strain in the sample, due to epitaxial growth on a GaAs substrate. The strain influence in the case of epitaxial structures is discussed in Section 4.1.

Similar results of excitonic splitting in bulk samples have been reported for (Cd,Mn)Te [161, 168, 184–188], (Zn,Mn)Te [189–192], (Cd,Mn)Se [193–195], and (Cd,Mn)S [196–199]. Only for (Zn,Mn)S and (Zn,Mn)O are reliable results still not available. By evaluation of the splitting energies for all of the excitonic components,  $N_0\alpha$  and  $N_0\beta$  can be determined independently. Representative values are given in Table 4. It is found that in the case of (II,Mn)VI alloys  $N_0\alpha > 0$  and  $N_0\beta < 0$  always, which means that the conduction band electrons are coupled ferromagnetically to the Mn spins, whereas the valence band electrons are coupled antiferromagnetically to them. The positive sign of  $N_0\alpha$  results from the direct exchange of the conduction band states with the  $d$ -electrons of Mn (see, e.g., the paper by Kacman [221]). The negative sign of  $N_0\beta$  is due to a dominant role of the hybridization-mediated  $p$ - $d$  kinetic exchange. An essentially different situation was found for Cr-containing crystals. A ferromagnetic  $p$ - $d$  coupling  $N_0\beta > 0$  was observed. This sign can easily be understood by considering virtual jumps of the  $p$ -electrons to the  $d$ -states and back. In the case of half-filled  $d$ -shells ( $\text{Mn}^{2+}$ ), or even in the case of  $\text{Fe}^{2+}(3d^6)$  or  $\text{Co}^{2+}(3d^7)$ , the spin has to be aligned antiferromagnetically, as jumps are possible only into the unoccupied spin  $3d$  states. For ions with less than half-filled  $d$ -shells, like  $\text{Cr}^{2+}(3d^4)$ , a ferromagnetic coupling is possible, as the spin of the hopping electron should be aligned parallel to the others according to Hund's rule.

The situation is even more complicated in the case of (Ga,Mn)As, where for the smallest Mn concentrations a ferromagnetic  $p$ - $d$  coupling was found by Heimbrodt et al. [219]. This ferromagnetic coupling is compensated for by an antiferromagnetic coupling with increasing  $x_{\text{Mn}}$  along with the formation of MnAs clusters. The physical reason for

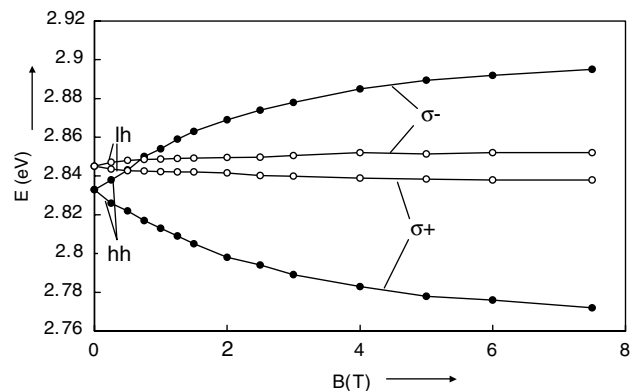


**Figure 20.** Excitonic giant Zeeman splitting of a strained (Zn,Mn)Se epitaxial layer. ●, heavy-hole exciton; ○, light-hole exciton.  $x_{\text{Mn}} = 0.16$ ,  $T = 1.8$  K.



**Table 4.** *s, p-d* exchange interaction parameters of various II–VI DMS and (Ga,Mn)As.

Alloy	$N_0\alpha$ (eV) [Ref.]	$N_0\beta$ (eV) [Ref.]
(Zn,Mn)Te	0.2 [190]	-1.1 [191]
	0.19 [192]	-1.14 [192]
(Cd,Mn)Te	0.22 [161]	-0.88 [161, 188]
	0.16 [188]	
	0.18 [200]	
(Hg,Mn)Te	0.4 [68]	-0.6 [68]
(Zn,Mn)Se	0.24 [201]	-1.22 [201]
	0.26 [202]	-1.31 [202]
	0.29 [195]	-1.4 [195]
(Cd,Mn)Se	0.26 [203]	
	0.23 [195]	-1.26 [195]
	0.24 [204]	-1.2 [204]
(Hg,Mn)Se	0.43 [68]	-0.74 [68]
(Cd,Mn)S	0.22 [205]	
	0.2 [195]	-2.7 [196]
		-1.8 [198]
	0.23 [199]	-1.7 [199]
(Zn,Cr)S	(0.22) [206]	+0.62 [206]
(Zn,Cr)Se	(0.22) [206]	+0.95 [206]
(Zn,Cr)Te	(0.22) [206]	+4.25 [206]
(Cd,Cr)S	0.22 [207]	
(Zn,Co)Te	0.31 [208]	-3.03 [208]
(Cd,Co)Te		-2.1 [213]
(Cd,Co)Se	0.279 [212]	-1.87 [212]
	0.27 [211]	-2.25 [211]
	0.274 [209]	-2.12 [209]
	0.32 [210]	
(Zn,Fe)Te		-1.6 [214]
(Zn,Fe)Se	0.22 [215]	-1.74 [215]
	0.25 [216]	-1.76 [216]
(Cd,Fe)Se	0.25 [217]	-1.45 [217]
	0.23 [215]	-1.9 [215]
(Cd,Fe)Te	0.3 [218]	-1.27 [218]
(Ga,Mn)As	0.023 [219]	+2.3 ( <i>p</i> -conductivity) [219]
	0.17 [220]	≈0...-1 ( <i>n</i> -conductivity) [219]

the sign reversal, however, is the same as that already discussed. Only recently the same authors [222] found that the sign of the exchange integral in (Ga,Mn)As is correlated with the type of conductivity. For *n*-type conductivity all of the Mn acceptors are compensated and  $A^-$  centers will be dominant. The coupling of the *p*-orbital to the half-filled  $3d^5$  with all of the spins aligned is now antiferromagnetic. For *p*-type conductivity a hole is bound to the Mn acceptor at low temperatures with a polarized spin and can therefore accommodate preferably valence band electrons with a spin parallel to the spins in the *d*-shell. Such an  $A^0$  center behaves, therefore, in a manner similar to that of the  $3d^4$  state, which couples ferromagnetically as discussed above.

From Eqs. (13), (26), and (27) it follows for the splitting of the hh excitons that

$$\Delta E_{\text{hh}} = x_{\text{Mn}} N_0 (\alpha - \beta) a(x_{\text{Mn}}) S B_{5/2} \left( \frac{\tilde{g} \mu_B S H}{k(T + \Theta)} \right) \quad (28)$$

The splitting of the hh depends strongly on the manganese concentration. In Figure 21 the hh splitting is depicted for a series of (Zn,Mn)Se epitaxial layers versus the magnetic

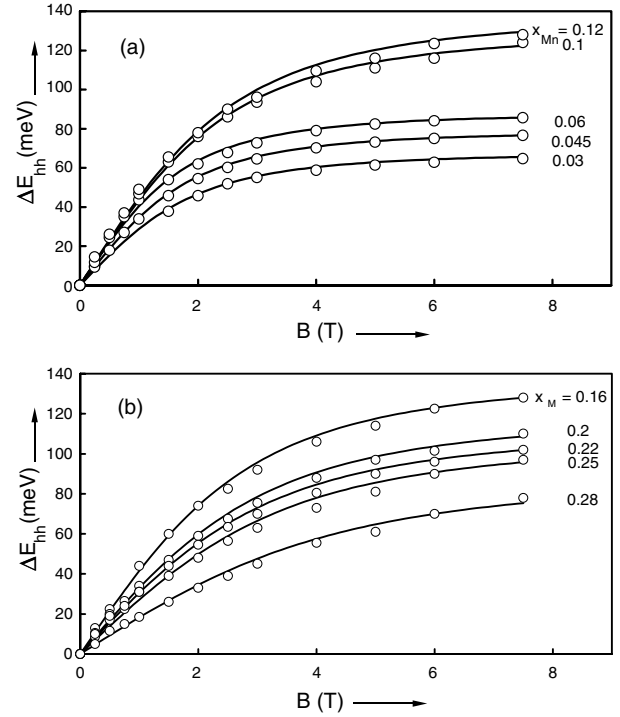


**Figure 21.** Heavy-hole excitonic giant Zeeman splitting for a series of  $\text{Zn}_{1-x}\text{Mn}_x\text{Se}$  epitaxial layers. (a) Increasing splitting up to  $x_{\text{Mn}} = 12\%$ . (b) Decreasing for  $x_{\text{Mn}} > 16\%$ .  $T = 1.8$  K. Curves are calculated with  $N_0\alpha = 0.26$  eV,  $N_0\beta = -1.31$  eV, and the parameters given in Table 5.

field strength. For small  $x_{\text{Mn}}$  (Fig. 21a) the splitting increases with increasing Mn concentration, whereas for higher  $x_{\text{Mn}}$  the hh splitting decreases again because of increasing cluster effects. At the saturation field strength of 7.5 Tesla the maximum hh splitting has been found at  $x_{\text{Mn}} \approx 0.15$ , as can be seen from Figure 22, where the saturation values are depicted versus the Mn concentration. The curves in Figure 21 have been calculated with Eq. 28. The resulting  $a(x_{\text{Mn}})$  and  $\Theta(x_{\text{Mn}})$ , obtained from the best fit to the experimental points, are given in Table 5.

At low Mn concentrations  $\Delta E_{\text{hh}}$  increases because of increasing mean spin density, whereas for larger  $x_{\text{Mn}}$  the Curie–Weiss parameter increases and the parameter  $a(x_{\text{Mn}})$

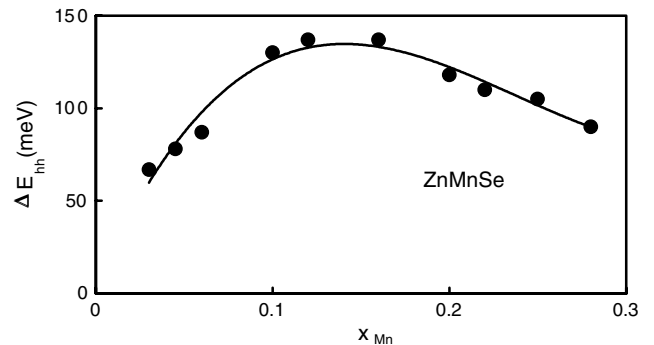


**Figure 22.** Saturation values  $\Delta E_{\text{hh}}$  (see also Table 5) of the heavy-hole excitonic giant Zeeman splitting of (Zn,Mn)Se layers as a function of the manganese concentration.  $B = 7.5$  T,  $T = 1.8$  K.

**Table 5.** Effective Mn concentration  $a(x_{\text{Mn}})$  and Curie-Weiss parameter  $\theta$  of (Zn,Mn)Se epitaxial layers.

$x_{\text{Mn}}$	$\Delta E_{\text{hh}}$ (meV)	$a(x_{\text{Mn}})$	$\Theta$ (K)
0.03	67	0.57	1.46
0.045	78	0.44	1.40
0.06	87	0.37	1.32
0.1	130	0.33	2.58
0.12	137	0.29	2.75
0.16	137	0.22	3.15
0.2	118	0.15	3.59
0.22	110	0.13	3.65
0.25	105	0.11	4.09
0.28	90	0.08	5.7

decreases strongly because of the antiferromagnetic coupling of pairs, triples, and higher clusters, which reduces the effective Mn concentrations and subsequently the mean spin density and  $\Delta E_{\text{hh}}$ . The values given in Table 5 are typical for MBE-grown thick epitaxial layers. To a certain extent these parameters depend on the real growth conditions, as, for example, segregation and clustering effects are completely different in crystals grown at thermodynamical equilibrium (when a random distribution of the magnetic ions is likely) compared with growth methods away from the thermodynamical equilibrium, like MBE or other thin-film technologies. These growth methods are discussed in Section 3. It was shown by Bednarski et al., Weston et al., and Harrison et al., using different theoretical approaches, that  $a(x_{\text{Mn}})$  and  $\Theta(x_{\text{Mn}})$  can vary dramatically if the distribution of the Mn ions is changed [223–226].

The description of the magneto-optical phenomena in diluted magnetic IV–VI semiconductors also uses Eq. (16) as a starting point. However, as the direct bandgap is situated at the L-point of the Brillouin zone, the situation is more complex. The conduction band minimum is associated with the point group representation  $L_6^-$  (odd parity,  $p$ -like) and the valence band maximum with  $L_6^+$  (even parity,  $s$ - and  $d$ -like). The constant energy surfaces are ellipsoids along the  $\langle 111 \rangle$  direction. The many-valley character of the IV–VI DMS, together with the rather small bandgaps, makes the description of the band structure and, in particular, of their magneto-optical properties rather difficult because of the different orientations of the ellipsoids with respect to the applied magnetic field. The  $k \cdot p$  treatment is described in detail in [41] and references therein.

We will outline briefly the main steps of the calculation. As there are slight differences in the conduction band structure of the various IV–VI, we will discuss as an example Eu- and Mn-containing PbTe. In the  $k \cdot p$  theoretical approach the lowest conduction bands and the highest valence bands are included exactly, while two higher conduction and two lower valence bands are taken into account in approximation to  $k^2$  terms. A set of four basis functions is used:

$$L_6^- \begin{cases} C^+ = -i \sin \theta^- Z \uparrow - \cos \theta^- X_+ \downarrow \\ C^- = i \sin \theta^- Z \downarrow - \cos \theta^- X_- \uparrow \end{cases} \quad (29)$$

$$L_6^+ \begin{cases} V^+ = i \cos \theta^+ R \uparrow + \sin \theta^+ S_+ \downarrow \\ V^- = i \cos \theta^+ R \downarrow + \sin \theta^+ S_- \uparrow \end{cases}$$

where  $C^\pm$  and  $V^\pm$  are, respectively, the lowest conduction band and highest valence band wave functions at the L-point. The pairs  $C^\pm$  and  $V^\pm$  are both Kramer's pairs. Because of the spin-orbit coupling, they do not correspond to pure spin states and are nondegenerate [227]. The spin functions  $\uparrow$  and  $\downarrow$  refer to the eigenstates of  $\sigma_z$  in the atomic coordinate system with  $z$  along the  $[120]$  axis of the valley,  $x$  along  $[-1-12]$ , and  $y$  along  $[1-10]$ . The spatial parts of the wave functions have the following transformation properties about the site of the metal nucleons:  $R$  is isotropic (atomic  $s$ -state), and  $X_\pm$  and  $Z$  transform like atomic  $p$ -states with  $m_z = \pm 1$  and  $m_z = 0$ , respectively.  $S_\pm$  transform like atomic  $d$ -functions with  $m_z = \pm 1$ . The spin-orbit mixing parameters  $\theta^\pm$  are obtained from band structure calculations [228].

Assuming that the magnetic field is in the  $xz$  plane, one obtains the  $k \cdot p$ -Hamiltonian

$$H = \begin{bmatrix} \widehat{V}^+ & \frac{1}{2}g_T^+ \mu_B H_x & \nu_L \hbar k_z & \sqrt{2}\nu_T \hbar k_- \\ \frac{1}{2}g_T^+ \mu_B H_x & \widehat{V}^- & \sqrt{2}\nu_T \hbar k_+ & -\nu_L \hbar k_z \\ \nu_L \hbar k_z & \sqrt{2}\nu_T \hbar k_- & \widehat{C}^+ & \frac{1}{2}g_T^- \mu_B H_x \\ \sqrt{2}\nu_T \hbar k_+ & -\nu_L \hbar k_z & \frac{1}{2}g_T^- \mu_B H_x & \widehat{C}^- \end{bmatrix} \quad (30)$$

where

$$[c]\widehat{V}^\pm = \frac{-E_g}{2} - \frac{\hbar^2 k_x^2 + \hbar^2 k_y^2}{2m_T^\pm} - \frac{\hbar^2 k_z^2}{2m_L^\pm} \pm \frac{1}{2}g_L^\pm \mu_B H_z$$

$$\widehat{C}^\pm = \frac{E_g}{2} - \frac{\hbar^2 k_x^2 + \hbar^2 k_y^2}{2m_T^\mp} - \frac{\hbar^2 k_z^2}{2m_L^\mp} \pm \frac{1}{2}g_L^\mp \mu_B H_z$$

$$\nu_L \hbar k_z = \frac{\hbar}{m_0} \langle V^+ | \hat{\pi} | C^+ \rangle \mathbf{k} = -\frac{\hbar}{m_0} \langle V^- | \hat{\pi} | C^- \rangle \mathbf{k} \quad (31)$$

$$\sqrt{2}\nu_T \hbar k_+ = \frac{\hbar}{m_0} \langle V^- | \hat{\pi} | C^+ \rangle \mathbf{k}$$

$$\sqrt{2}\nu_T \hbar k_- = \frac{\hbar}{m_0} \langle V^+ | \hat{\pi} | C^- \rangle \mathbf{k}$$

$$\hat{\pi} = \mathbf{p} + \frac{\hbar}{4m_0 c^2} (\hat{\sigma} \times \nabla V_0)$$

$m_L^\pm, m_T^\pm, g_L^\pm, g_T^\pm$  denote the effective masses and  $g$ -factors. The subscripts L and T refer to the longitudinal and transverse axes of the ellipsoids. The superscripts + and – refer traditionally to the valence and conduction bands, respectively.  $\hat{\pi}$  is the sum of momentum operator and spin-orbit interaction, where  $\hat{\sigma}$  presents the Pauli spin operators,  $V_0$  is the periodic crystal potential, and  $m_0$  is the free-electron mass.

The interaction between the extended band states and the magnetic ions is accounted for in a fashion similar to that for the (II,Mn)VI compounds. Equation (16) becomes

$$H_{\text{exch}} = x \langle S_0 \rangle \sum_{R \in \text{sublattice}} J(\vec{r} - \vec{R}) \cdot [\sin \varphi \cdot \sigma_x + \cos \varphi \cdot \sigma_z] \quad (32)$$

Again, it was assumed that the magnetic field is in the  $xz$  plane.  $\varphi$  is the angle between the magnetic field  $H$  and the  $z$  axis.  $\langle S_0 \rangle$  is the thermal mean value of the spin of the magnetic ions which is parallel to  $H$ . Evaluating the Hamiltonian

by using the basis function set given in Eq. (29) yields an exchange matrix of the form

$$H_{\text{exch}} = \frac{1}{2}x\langle S_0 \rangle \begin{pmatrix} A \cos \varphi & a_1 \sin \varphi & 0 & 0 \\ a_1 \sin \varphi & -A \cos \varphi & 0 & 0 \\ 0 & 0 & B \cos \varphi & -b_1 \sin \varphi \\ 0 & 0 & -b_1 \sin \varphi & -B \cos \varphi \end{pmatrix} \quad (33)$$

where the coefficients are combinations of exchange integrals and band structure parameters given by [229]

$$\begin{aligned} A &= \alpha \cos^2 \theta^+ - \delta \sin^2 \theta^+ & a_1 &= \alpha \cos^2 \theta^+ \\ B &= \beta_{\parallel} \sin^2 \theta^- - \beta_{\perp} \cos^2 \theta^- & b_1 &= \beta_{\parallel} \sin^2 \theta^- \end{aligned} \quad (34)$$

The exchange integrals are defined via the  $s$ ,  $d$ , and  $p$ -like wave function components,

$$\begin{aligned} \alpha &= \frac{1}{\Omega_0} \langle R|J|R \rangle & \delta &= \frac{1}{\Omega_0} \langle S_{\pm}|J|S_{\pm} \rangle \\ \beta_{\parallel} &= \frac{1}{\Omega_0} \langle X_{\pm}|J|X_{\pm} \rangle & \beta_{\perp} &= \frac{1}{\Omega_0} \langle Z|J|Z \rangle \end{aligned} \quad (35)$$

where  $\Omega_0$  is the volume of the unit cell. It is worth noting that the definition of the exchange integrals for the IV–VI diluted magnetic semiconductors in Eq. (35) differs slightly from that of the II–VI diluted magnetic semiconductors. The factor  $\Omega_0^{-1}$  corresponds to the  $N_0$  of Eqs. (21) and (25).

The major optical spectroscopic techniques employed to study the band structure of the IV–VI diluted magnetic semiconductors are magneto-reflectivity or magneto-absorption experiments examining the interband transitions and coherent anti-Stokes Raman scattering (CARS) and the spin-flip transitions in the conduction and valence bands. Usually a combination of the methods is needed to acquire a sufficiently large data set to compare experiment and theory. Applying a magnetic field lifts the degeneracy at the L-point, and signals arising from L-valleys with different orientations with respect to the magnetic field direction can be observed simultaneously. This is illustrated in Figure 23, where plots of the CARS intensity (at  $\omega + \Delta\omega$ ) versus magnetic field are shown for a  $\text{Pb}_{0.94}\text{Mn}_{0.06}\text{Te}$  sample at 1.8 K and 12 K, respectively [229]. For the chosen magnetic field orientation  $B \parallel [-110]$ , two valleys in the conduction and in the valence band are oriented with an angle  $\varphi = 90^\circ$  between their main axis and the applied field, and the other two valleys are oriented with an angle  $\varphi = 35.26^\circ$ . Four resonances are observed. These correspond to spin-flip transitions within the  $n = 0$  Landau states of holes (b:  $\varphi = 90^\circ$ ; d:  $\varphi = 35.26^\circ$ ) and electrons (a:  $\varphi = 90^\circ$ ; c:  $\varphi = 35.26^\circ$ ). Tuning the frequency difference  $\Delta\omega$  by using various combinations of  $\text{CO}_2$  laser frequencies allows one to obtain fan diagrams of the resonance positions versus magnetic field, as shown in Figure 24, which can be compared with theory. In most publications, only the parameters  $A$ ,  $B$ ,  $a_1$ , and  $b_1$  extracted from the magneto-optical data are given, and the  $s$ - $d$ ,  $p$ - $d$  and  $d$ - $d$  exchange integrals are not calculated explicitly. However, for the sake of comparison with the data for the II–VI diluted magnetic semiconductors, we have tabulated some average exchange integrals in Table 6.

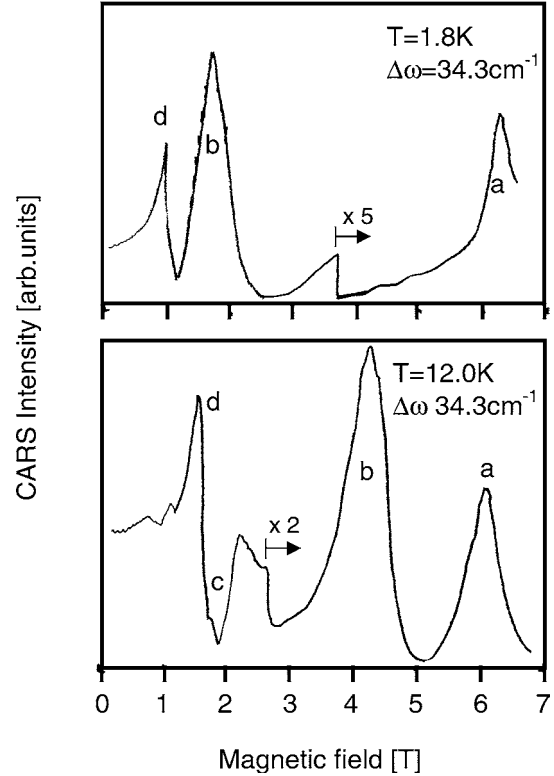


**Figure 23.** CARS intensity versus magnetic field for  $p$ -type  $\text{Pb}_{0.94}\text{Mn}_{0.06}\text{Te}$  at 1.8 K and 12 K. Reprinted with permission from [229], H. Pascher et al., *Phys. Rev. B* 36, 9395 (1987). © 1987, American Physical Society.

### 3. PREPARATION OF MAGNETIC SEMICONDUCTOR NANOSTRUCTURES

The growth of two-dimensional semiconductors in the form of heterostructures, quantum wells, or superlattices is a standard technology at present. The MBE is a favorable growth technique for magnetic semiconductor quantum wells (QWs), as it provides epitaxial layers and heterostructures

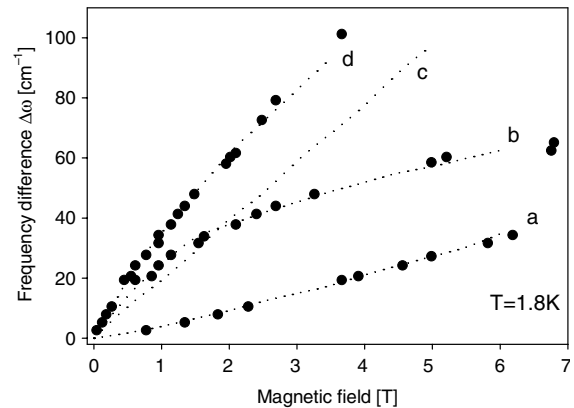


**Figure 24.** Plot of the resonance positions of electron and hole spin-flip transitions as a function of magnetic field for  $\text{Pb}_{0.94}\text{Mn}_{0.06}\text{Te}$ . Reprinted with permission from [229], H. Pascher et al., *Phys. Rev. B* 36, 9395 (1987). © 1987, American Physical Society.

**Table 6.**  $s, p-d$  exchange interaction parameters of some (IV,Mn)VI and (IV,Eu)VI alloys at  $T = 2$  K.

	$\alpha$ (eV)	$\beta_{\parallel}$ (eV)	$\beta_{\perp}$ (eV)	$\delta$ (eV)
Pb <sub>1-x</sub> Mn <sub>x</sub> Te [229]	-0.305	0.197	0.119	(-2.17)
Pb <sub>1-x</sub> Mn <sub>x</sub> Se [82]	-0.219	0.255	0.135	(0.58)
Pb <sub>1-x</sub> Eu <sub>x</sub> Te [230]	0.025	(-0.007)	(0.000)	(-0.048)
Pb <sub>1-x</sub> Eu <sub>x</sub> Se [230]	0.033	0.003	0.012	(-0.105)

of very high quality. An overview of two-dimensional structures is given in Section 3.1. Far less work has been carried out on magnetic one- and zero-dimensional semiconductor nanostructures. Again the methods are similar to those used for the fabrication of other semiconductor nanostructures. A clear distinction between methods for fabricating one- and zero-dimensional structures cannot be made. For example, the lithographic and etching techniques for obtaining quantum dots (QDs) and quantum wires (QWRs) from two-dimensional epitaxial structures are very similar. Nevertheless, we will address the fabrication of diluted magnetic QWs and QDs in two separate sections, 3.2 and 3.3, respectively. More general overviews of the fabrication of semiconductor nanostructures are given in the reviews of Gossard and Fafard [231], Bryant [232], Nötzel [233], Pileni [234], and Ekimov [235].

A high degree of order of QDs or QWRs can only be obtained so far by combining lithographic pattern definition with epitaxial semiconductor growth techniques, either by growing structures on patterned substrates or by post-growth patterning and etching of the epitaxial semiconductor layers. However, the smallest lateral sizes achievable by those techniques are still bigger than 10 nm. Other approaches, such as DMS clusters in silicate glass, DMS clusters in reverse micelles, or self-assembling by Stranski-Krastanov growth, yield cluster sizes below 10 nm but show a much smaller degree of order. The major challenge in the fabrication of magnetic nanostructures for most desired applications is to achieve simultaneously small lateral dimensions of the individual nanostructures and a high degree of order of the ensembles (e.g., size distribution, geometrical arrangement, high density of nanostructures). If this is achieved magnetic nanostructures will provide the link between magnetism on a microscopic atomic level and the macroscopic magnetic state, and the interesting properties can be successfully studied, which are expected as the geometrical dimensions of the clusters become comparable to the characteristic nanoscopic and mesoscopic length scales (e.g., magnetic exchange length, domain width).

### 3.1. Growth of Epitaxial Layers and Quantum Wells

The first successful preparation of magnetic semiconductor quantum well structures was reported in 1984 by Bicknell and co-workers [236] and Kolodziejski and co-workers [237]. They prepared CdTe/(Cd,Mn)Te by MBE. Up to now MBE is by far the dominating growth method for II-VI, IV-VI, and III-V based magnetic semiconductors, which will be considered first (Section 3.1.1). Only a few attempts at growing two-dimensional systems by MOVPE

have been reported, which will be discussed in Section 3.1.2. Other technologies, like liquid phase epitaxy (LPE), hot wall epitaxy (HWE), pulsed laser evaporation epitaxy (PLEE), electron beam evaporation (EBE), or atomic layer epitaxy (ALE), are of minor importance.

#### 3.1.1. Molecular Beam Epitaxy

**(II,Mn)VI Semiconductors** MBE has typically a low growth rate of about 1  $\mu\text{m/h}$  and relatively low growth temperatures for the (II,Mn)VI semiconductor layers. For CdTe/(Cd,Mn)Te superlattices the substrate temperatures are usually in the range of 200 to 325  $^{\circ}\text{C}$  [238–241]. Different substrates have been successfully used, for example, (100) or (111) GaAs covered with a thick CdTe buffer layer to avoid misfit dislocations in the superlattices [239, 241] or the better lattice matched (001) InSb [238, 240]. The growth temperatures of ZnSe-based diluted magnetic semiconductors are somewhat higher and were in the range of 300 to 450  $^{\circ}\text{C}$  [242, 243] and the substrate was always GaAs. For (Zn,Mn)Te-based systems, however, the better lattice matched GaSb was preferred [244, 245].

The ability of abrupt cessation or initiation of growth by mechanical shutters for each effusion source (Knudsen cell) is useful in preparing a smooth surface on an atomic scale. The atoms form a well-collimated beam, because the ultra-high-vacuum (UHV) environment (about  $10^{-11}$  torr) permits a ballistic transport on the way to the substrate. In principle it is difficult to control the crystal stoichiometry in MBE growth, but the UHV makes it possible to utilize electron or ion-based *in-situ* methods, like mass spectrometry, Auger electron spectroscopy (AES), low-energy electron diffraction (LEED), reflection high-energy electron diffraction (RHEED), and X-ray as well as ultraviolet photoemission spectroscopy (XPS and UPS). RHEED is, however, the standard analytical tool used *in-situ* during MBE growth. Usually the following information can be derived from RHEED: (i) The general appearance of the RHEED pattern provides information about the crystallinity and the surface reconstruction. (ii) Counting the number of RHEED intensity oscillation periods gives the number of monolayers grown. By these two standard methods, however, the potential of RHEED is not exhausted. Hoffmann et al. [246] used the so-called phase-locked epitaxy to grow ZnSe/(Zn,Mn)Se quantum well structures. Operating the shutter in different phases of RHEED intensity oscillations and comparing the layer thickness with the number of oscillation periods provides information about the relation between surface coverage and the RHEED intensity oscillation phase. Furthermore, they obtained information about the Mn concentration by comparing the oscillation periods observed when either ZnSe or (Zn,Mn)Se is grown. It has been found that the oscillation period varies with the composition  $x_{\text{Mn}}$  of the Zn<sub>1-x</sub>Mn<sub>x</sub>Se layers. The expected MnSe mole fraction can be determined from the RHEED oscillation period of ZnSe and Zn<sub>1-x</sub>Mn<sub>x</sub>Se by the empirical expression for  $0 \leq x_{\text{Mn}} \leq 0.3$  given in [246]:

$$x = -0.71 \ln \frac{t(\text{ZnMnSe})}{t(\text{ZnSe})} \quad (36)$$

where  $t(\text{ZnMnSe})$  and  $t(\text{ZnSe})$  are the oscillation times of the  $(\text{Zn,Mn})\text{Se}$  and  $\text{ZnSe}$ , respectively. The underlying physics for this expression is the high sticking coefficient of Mn and the resulting superlinear increase in the  $(\text{Zn,Mn})\text{Se}$  growth rate.

In the case of solid solutions like diluted magnetic semiconductors, it turned out, however, that a strong damping of the oscillation does not allow monitoring of the growth of thick epitaxial layers. The surface becomes rough under these circumstances because of growth fluctuations. Surfaces can be smoothed by a growth interruption. It was reported that the growth interruption was most effective under Se-rich conditions. Two processes contribute to the smoothing of the surface: a fast process acting within seconds and a slow process acting within minutes. Growth interruption must therefore last several minutes with the Se shutter open [247, 248]. The growth of magnetic semiconductor structures has therefore proceeded as follows. After the growth of a few lattice planes, a growth interruption of about 10 s took place, leading to a recovery of RHEED oscillations. In Figure 25a the RHEED oscillations are depicted as a typical example of the growth of a  $\text{ZnSe}/\text{Zn}_{0.8}\text{Mn}_{0.2}\text{Se}$  multiple quantum well structure with well widths of 16 monolayers and 85-nm barrier widths. The structure has been grown on a  $\text{ZnSe}$  buffer of 0.8- $\mu\text{m}$  thickness. The  $\text{ZnSe}$  wells have been grown in the phase-locked epitaxial mode, where the shutter was closed  $240^\circ$  after each fourth RHEED intensity maximum. A short break of 10 s after every growth cycle leads to complete recovery of the oscillations. In Figure 25b the RHEED pattern of the growth of a  $(\text{Zn,Mn})\text{Se}$  layer in the normal mode is shown for comparison.

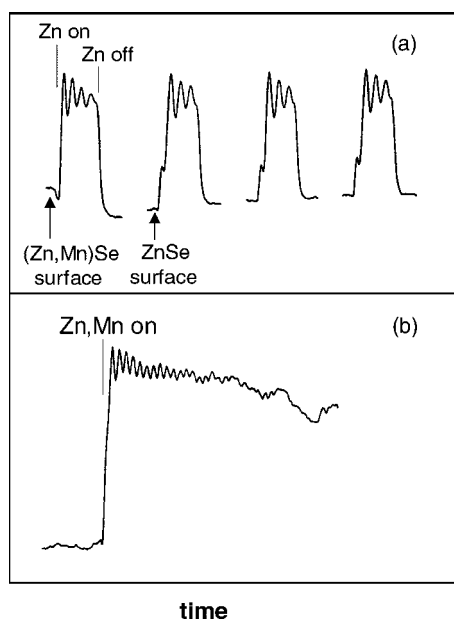


**Figure 25.** RHEED oscillations recorded (a) during the growth of a  $\text{ZnSe}/\text{Zn}_{0.8}\text{Mn}_{0.2}\text{Se}$  MQW with a well width of 16 monolayers and 85-nm-thick barriers in phase-locked epitaxial mode and (b) during the growth of a thick  $(\text{Zn,Mn})\text{Se}$  epitaxial layer in normal mode. Reprinted with permission from [246], N. Hoffmann et al., *J. Cryst. Growth* 146, 422 (1995). © 1995, Elsevier Science.

**(III,Mn)V Semiconductors** The first successful growth of a diluted magnetic III-V semiconductor was reported in 1989 by Munekata et al. [23]. This was  $(\text{In,Mn})\text{As}$  on  $(100)$   $\text{GaAs}$  substrates. The key parameters for the growth on  $(100)$   $\text{GaAs}$  substrates are the temperatures and the Mn concentration. For very low substrate temperatures ( $T_s = 200^\circ\text{C}$ ) the  $(\text{In,Mn})\text{As}$  layers have been  $n$ -type, and no indication of a segregation of  $\text{MnAs}$  has been found up to a Mn concentration of 24%. At higher substrate temperatures ( $T_s = 300^\circ\text{C}$ ) the layers are  $p$ -type, at least at low Mn concentrations. At higher concentrations the  $\text{MnAs}$  clusters start to form, and the layers become  $n$ -type again [40]. No epitaxy was observed at substrate temperatures above  $400^\circ\text{C}$ . Contrary to these results,  $p$ -type conductivity has been found for layers also grown at  $T_s = 200^\circ\text{C}$  but on thick buffer layers of  $\text{AlSb}$  or  $(\text{Al,Ga})\text{Sb}$ , which were grown on  $\text{GaAs}$  substrates before the growth of  $(\text{In,Mn})\text{As}$  [164, 249].

A systematic study of  $(\text{Ga,Mn})\text{As}$  growth has been made by Shen et al. [250]. The samples have also been prepared on  $\text{GaAs}$  substrates. For substrate temperatures below  $200^\circ\text{C}$  they found polycrystalline growth, whereas above  $350^\circ\text{C}$  the growth of  $\text{MnAs}$  clusters occurs. In the intermediate range  $p$ -type  $(\text{Ga,Mn})\text{As}$  layers can be formed with Mn concentrations up to 4%.

$(\text{Ga,Mn})\text{N}$  films have also been grown by MBE on  $(0001)$  sapphire substrates using either ammonia as nitrogen source [250] or a nitrogen plasma source [27, 30].

**(IV,Mn)VI and (IV,Eu)VI Semiconductors**  $\text{PbTe}/\text{Pb}_{1-x}\text{Mn}_x\text{Te}$  QWs with  $x < 4\%$  were grown by MBE on cleaved  $(111)$   $\text{BaF}_2$  substrates. The effusion cells of  $\text{PbTe}$ ,  $\text{Mn}$ , and  $\text{Te}$  were at temperatures of 800, 870–900, and  $350\text{--}400^\circ\text{C}$ , respectively. The substrate temperature was between 300 and  $400^\circ\text{C}$ . Typical growth rates were about  $4\ \mu\text{m}/\text{h}$ . After an initial three-dimensional nucleation of  $\text{PbTe}$  or  $\text{Pb}_{1-x}\text{Mn}_x\text{Te}$  on the  $\text{BaF}_2$  surface, a 2D growth mode is established after about 100 nm. This growth mode is kept stable during the deposition of the superlattice by opening and closing of the Mn shutter [252]. The growth was controlled by RHEED [253]. A serious problem in the growth of these superlattice structures is Mn diffusion [254]. Further details are given in [255].

$\text{PbSe}/\text{Pb}_{1-x}\text{Mn}_x\text{Se}$  with  $x < 3\%$  were also grown by MBE with effusion cells for  $\text{PbSe}$ ,  $\text{Mn}$ , and  $\text{Se}$ . A thick  $\text{PbSe}$  layer was deposited on the  $(111)$   $\text{BaF}_2$  substrate before the growth of the superlattice to ensure nearly complete strain relaxation. The lattice mismatch between the  $\text{PbSe}$  and the  $\text{Pb}_{1-x}\text{Mn}_x\text{Se}$  layers is comparatively small. Thus, the thicknesses of the  $\text{Pb}_{1-x}\text{Mn}_x\text{Se}$  layers ( $d < 20\ \text{nm}$ ) as well as that of the entire superlattice stack are well below the critical thickness. Therefore, the  $\text{Pb}_{1-x}\text{Mn}_x\text{Se}$  are under biaxial tensile strain, whereas the  $\text{PbSe}$  QWs are unstrained [256]. A detailed description of the growth is given in [255].

$\text{PbTe}/\text{Pb}_{1-x}\text{Eu}_x\text{Te}$  QWs with  $x < 4\%$  were grown by MBE on cleaved  $(111)$   $\text{BaF}_2$  substrates by a few groups [254, 258]. Typically, the beam flux rates from the  $\text{PbTe}$ ,  $\text{Eu}$ , and  $\text{Te}_2$  effusion cells were measured by an ion gauge beam flux monitor. *In-situ* RHEED was used to monitor the growth process. For low substrate temperatures a large number of RHEED intensity oscillations were observed, which could be used to determine the absolute growth rates [259].

These were close to 1  $\mu\text{m}/\text{h}$ . Detailed growth conditions are described elsewhere [258, 260].

**Mn-VI/II-VI and Eu-VI/IV-VI Multilayers** Although MBE is a nonequilibrium growth technique, the substrate temperatures required for good crystallinity are still fairly high, some 100 °C. As a consequence, it is, in most cases, very difficult to grow thick epitaxial layers of metastable magnetic binaries (such as MnSe, MnTe, EuTe, etc.) on the available substrates. Therefore, it is necessary to stabilize these metastable phases by inserting semiconductor spacer layers, that is, by growing superlattices. The preparation with this stabilizing method of structures consisting of more than 100 periods has been reported. Because of the excellent control of the thickness of all of the layers, such MBE-grown multilayered structures, consisting of ferromagnetic or antiferromagnetic layers separated by diamagnetic semiconducting spacer layers, are ideal model systems for studying magnetic phenomena (such as magnetic interlayer coupling and 2D breakdown of magnetic order).

MnSe/ZnSe is a type I heterosystem with ZnSe acting as the quantum well and MnSe as the barrier. It was the first of a large variety of magnetic binary-containing superlattices realized up to now. Ultrathin MnSe layers in the zincblende structure separated by ZnSe spacer layers on GaAs substrates were grown first by Kolodziejski et al. [53]. The superlattice structure consisted of 100 periods of  $8 \pm 1$  Å MnSe separated by 45 Å ZnSe on a 2- $\mu\text{m}$  ZnSe buffer, which was deposited on  $n^+$  Si-doped GaAs (100) substrates. The structures were grown in a Perkin-Elmer model 400 MBE system. The substrate temperature was 400 °C. The oven temperatures of the separate effusion cells for Zn, Mn, and Se were 296, 860, and 190 °C, respectively. The growth rates were 0.5–1.5 Å  $\text{s}^{-1}$ . The sharp interfaces and the high degree of periodicity of the superlattice structure were controlled by *in-situ* RHEED monitoring and later confirmed by TEM studies. Klosowski et al. grew MnSe/ZnSe as well as MnSe/ZnTe superlattice structures with thick ZnSe and ZnTe buffer layers on (100) GaAs substrates [261, 262]. This allows a variation of the biaxial strain in the magnetic layers from compressive to tensile and, thus, changes the ratio of the  $J_{\text{nn}}$  coupling parameters for perpendicular and parallel to the growth direction. The samples were grown with a Riber MBE 32 R&D system equipped with effusion cells for Zn, Te, Se, and Mn. Heimbrodt et al. grew MnSe/ZnSe superlattices on (100) GaAs substrates at substrate temperatures of 300 °C. Above a critical thickness of 5 nm per MnSe sublayer, a partial phase transformation into the stable rock salt structure was found [51], even in the stabilized multilayered heterosystem.

MnTe-containing superlattice structures, with either CdTe or ZnTe as spacer materials, were also studied. It is worth noting that the growth of thick epitaxial layers of zincblende MnTe has been achieved up to 0.5  $\mu\text{m}$ , in contrast to the few nanometers of MnSe. This was possible because CdTe was available as a suitable substrate [240]. Durbin et al. were also the first to grow MnTe/CdTe SQW structures of different well widths, which confirm that this system has also a type I band alignment. Superlattices of MnTe/ZnTe on (100) GaAs have been grown by Giebultowicz et al. [116]. Recently, studies of Cl-doped MnTe/ZnTe superlattices on

(100) GaAs have been reported [263]. The doping levels were nominally between  $10^{17}$  and  $10^{18}$   $\text{cm}^{-3}$ . Doping of these structures is of interest, as it is expected that an increased carrier density modifies the interlayer coupling. MnTe/CdTe superlattices can also be prepared by ALE [264–266]. In this technique a “self-regulatory” growth mode allows a precise thickness control of the CdTe layers ( $\geq 2$  monolayers). For this system the lattice mismatch of 2.2% is considerably less than that of the Mn-VI/Zn-VI system. Another important aspect of this material combination is that, because of the excellent thickness control of the nonmagnetic layers, superlattices with very thin CdTe layers can be grown, where interlayer spin-spin correlations become observable.

Superlattice structures consisting of EuTe and PbTe are also thoroughly studied. Rock salt EuTe is also antiferromagnetic, as are the zincblende Mn-VI compounds, but exhibits a type II antiferromagnetic order instead of the more complex type III antiferromagnetic order of the Mn-VI compounds with zincblende structure. Thus, EuTe layers of the superlattice structures with a (111) growth plane consist of ferromagnetic sheets of  $\text{Eu}^{2+}$  spins which are antiferromagnetically coupled to the adjacent  $\text{Eu}^{2+}$  sheets [266]. In the case of an odd number of  $\text{Eu}^{2+}$  sheets per EuTe layer, a net magnetization per layer can be obtained (i.e., the layers are ferrimagnetic), giving rise to a very significant interlayer coupling.  $[(\text{EuTe})_{\xi}(\text{PbTe})_{\eta}]_n$  superlattices of various compositions ( $\xi = 2\text{--}14$ ,  $\eta = 6\text{--}25$ , and  $n = 300\text{--}600$ ) were fabricated by MBE at the Johannes Kepler University in Linz. The Riber MBE system was equipped with effusion cells for PbTe, Eu, and  $\text{Te}_2$ . The substrate material was (111)  $\text{BaF}_2$ . A 2000–4000-nm PbTe buffer layer was grown on top of the substrate at a temperature of 350 °C. This ensures a complete strain relaxation of the PbTe buffer. For the growth of the actual superlattice structure the substrate temperature was lowered to 250–280 °C. At this temperature, EuTe can only be deposited with the use of separate effusion cells for Eu and  $\text{Te}_2$ . Detailed descriptions of the growth can be found elsewhere [267–272]. The superlattices are of very high quality and have abrupt interfaces between the EuTe and PbTe layers showing very little interdiffusion [273, 274]. The interface roughness is on the order of a single monolayer [275]. All of the Mn-VI/II-VI and Eu-VI/IV-VI multilayers discussed so far consist of antiferromagnetic layers separated by nonmagnetic semiconducting layers. EuS/PbS superlattices represent a ferromagnetic/nonmagnetic semiconductor-based system [276]. The epitaxial EuS/PbS multilayers were grown by thermal evaporation of PbS from a tungsten boat and by electron beam evaporation of EuS in oil-free vacuum ( $10^{-6}$  to  $10^{-7}$  torr) and their sequential condensation on (100) KCl or (111)  $\text{BaF}_2$  substrates at 250 °C. Before the growth of the actual superstructure a 20–70-nm-thick PbS layer was grown to accommodate the lattice mismatch between the superlattice and the substrate. Typically, X-ray diffraction rocking curves of the multilayers show full widths at half maximum of 300 arcsec and diffraction patterns with satellite peaks of second and third order. Wosnitza et al. studied EuS/SrS ferromagnetic/nonmagnetic multilayers [277]. The samples were grown by MBE on (111) Si substrates. EuS and SrS were used as starting materials and alternatively evaporated onto the substrate by two electron guns. The substrate



temperature was between 600 and 1000 °C. The growth rate was about 0.4 μm/h.

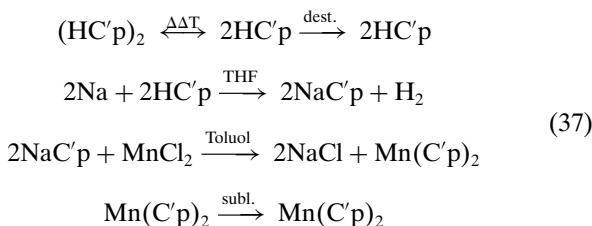
Another class of ferromagnetic/nonmagnetic semiconductor-based multilayer systems that may be of interest in the future is Mn-V/III-V systems. Great progress has been made in the MBE growth of MnAs films on (100) GaAs [278–281] and of MnSb on (100) GaAs and (0001) sapphire [282]. First ferromagnetic/ferromagnetic MnAs/MnSb multilayers on (100) GaAs [283] as well as ferromagnetic/antiferromagnetic MnSb/MnTe heterostructures [284] have been reported.

### 3.1.2. Metal-Organic Vapor Phase Epitaxy

There have been only a few attempts to grow magnetic semiconductors by MOVPE [84, 219, 285–287]. The relatively high growth temperatures, which used to be necessary to obtain high-quality layers of nonmagnetic semiconductors, impede the achievement of a high concentration of magnetic ions in the semiconducting host material.

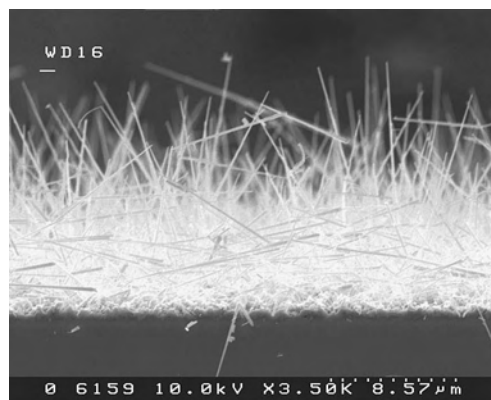
Lusson et al. [285] reported the preparation of CdTe/(Cd,Mn)Te quantum wells on GaAs substrates. A horizontal commercial reactor (MR Semicon Quantax 226) containing an IR-heated graphite susceptor was used. The samples were grown at a substrate temperature of 365 °C, with diisopropyltelluride (DIPTe), dimethylcadmium (DMCd), and methylpentacarbonylmanganese (PCMMn) as precursors. The carrier gas was hydrogen. Before the growth of the quantum wells a buffer layer of about 1.5 μm was always prepared. The low pyrolysis temperature of PCMMn molecules of about 100 °C, which is much less than the decomposition temperature of DIPTe and DMCd, actually raises enormous problems in achieving homogeneous layers. With a total flow rate increased to 8 L/min and rotation of the substrate, high-quality heterostructures have been obtained.

The successful growth of Ga<sub>1-x</sub>Mn<sub>x</sub>As layers on (100) GaAs substrates by means of MOVPE has been reported by Hartmann et al. [84] and Heimbrodt et al. [219]. Bis(methylcyclopentadienyl) manganese ((MeCp)<sub>2</sub>Mn) has been selected to be the source compound because of its thermal decomposition characteristics, which are appropriate for the MOVPE of the Ga<sub>1-x</sub>Mn<sub>x</sub>As material system. At room temperature, (MeCp)<sub>2</sub>Mn is in the solid phase with an estimated vapor pressure of about 10<sup>-2</sup> hPa. The following chemical synthesis of the compound has been chosen:

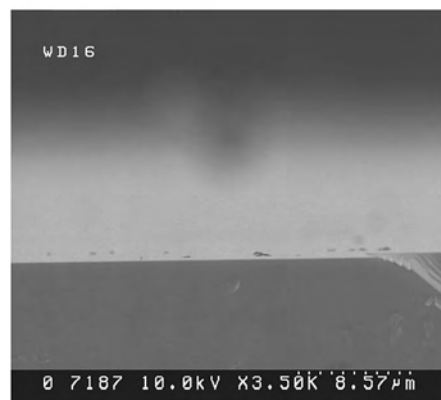


where C'p is CH<sub>3</sub>-C<sub>5</sub>-H<sub>4</sub>. The chemical identity of the product of this synthesis was confirmed by gas chromatography combined with mass spectrometry. The yield of this synthesis was between 70% and 90%. MOVPE growth has been performed in a horizontal reactor system (Aix 200-GFR; Aixtron Corporation) at a reduced reactor pressure of 50 mbar with 6.8 L/min of H<sub>2</sub> carrier gas. Triethylgallium (TEGa)

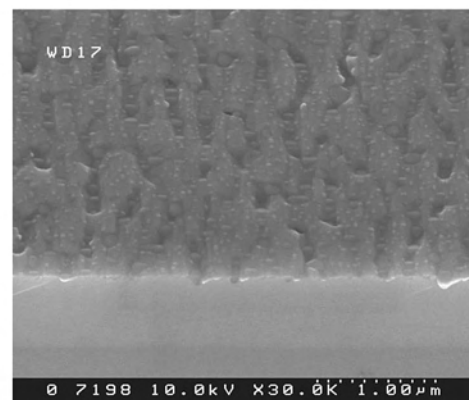
and tertiarybutylarsine (TBAs) have been used as efficient source compounds. A strong dependence of the layer constitution on the growth temperature range has been found. For substrate temperatures below 450 °C a whisker growth can be seen, as depicted in the scanning electron micrograph (SEM) in Figure 26a. For higher temperatures up to about 600 °C (Ga,Mn)As layers of high structural quality can be



(a)



(b)



(c)

**Figure 26.** SEM images of MOVPE (Ga,Mn)As phases. (a) Whisker growth at substrate temperatures below 450 °C. (b) Layers of high structural quality can be grown at substrate temperatures up to about 600 °C. (c) At higher (MeCp)<sub>2</sub>Mn partial pressure the formation of Mn(Ga)As clusters takes place.

grown, but the manganese concentration is limited to less than 1%. The smooth surface is clearly seen in Figure 26b. With increasing  $(\text{MeCp})_2\text{Mn}$  partial pressure the formation of  $\text{Mn}(\text{Ga})\text{As}$  clusters takes place as depicted in Figure 26c. Details of the formation process are reported in [528]. For the application of these clusters it is important to realize that they are embedded in the  $(\text{Ga},\text{Mn})\text{As}$  matrix, almost lattice matched and without any indication of dislocations, as can be seen in the TEM images in Figure 27. In addition, their crystallographic orientation is well defined; that is, the  $c$  axis of the hexagonal  $\text{MnAs}$  is parallel to the (111) directions of the zincblende  $\text{Ga}_{1-x}\text{Mn}_x\text{As}$  host.

The successful preparation of  $(\text{Ga},\text{Mn})\text{N}$  by MOVPE was also reported. Reed et al. [287] prepared 40 nm buffer layers on (0001) sapphire at a low temperature of about 500 °C. The growth was followed by a high temperature annealing to achieve a recrystallization. 2  $\mu\text{m}$  GaN epitaxial layers were deposited on top of the buffer layer at about 1000 °C. Afterwards Mn was deposited by a laser technique on the

nitride sample. The background vacuum during deposition was about  $10^{-8}$  torr. The Mn thickness ranged from 10 to 100 nm. Mn doping was achieved by deposition and annealing at different temperatures ranging from 250–800 °C. The film quality of the  $(\text{Ga},\text{Mn})\text{N}$  layers during deposition and after annealing was checked by RHEED, X-ray diffraction and TEM. By SIMS measurements the authors verify the diffusion of Mn into the hexagonal GaN layer, forming a concentration gradient that levels out at about 1% of Mn.

Using  $(\text{DPM})_3$  as Er source Morinaga et al. [31] reported the successful preparation of a rare-earth based diluted magnetic semiconductor by MOVPE. Er concentrations up to  $2 \times 10^{20} \text{ cm}^{-3}$  have been reported in GaAs films grown in the temperature range from 530 °C to 630 °C.

### 3.2. Growth and Preparation of Quantum Wires

Different ways of preparing one-dimensional nanostructures have been reported. The easiest way is to start with two-dimensional quantum wells and to use a subsequent etching procedure. This method will be described in Section 3.2.1. Another elegant and successful method is the epitaxial overgrowth of substrates patterned by selective etching procedures discussed in Section 3.2.2. In Section 3.2.3 a rather novel approach is introduced where  $(\text{II},\text{Mn})\text{VI}$  semiconductors are incorporated into mesoporous  $\text{SiO}_2$  matrices with a highly homogeneous and well-ordered pore structure via an intrapore formation process from solution.

#### 3.2.1. Lateral Patterning by Lithographic Methods Followed by Etching

The most commonly used lithographic technique for the fabrication of QWRs based on diluted magnetic semiconductors is electron beam lithography (EBL), as it allows the writing of patterns with very high accuracy (down to a few nanometers in width) together with a flexibility of choice of pattern (e.g., wire width, distances between wires, etc.) [289–292]. However, other lithographic patterning techniques can also be used; for example, Darhuber et al. [293] used laser holographic patterning to write wire structures with a width of about 100 nm. The major obstacle in nanostructure fabrication starting from epitaxial two-dimensional structures is, however, pattern transfer into the semiconductor by etching. Different etching processes have been developed, that is, wet-chemical etching methods [290–292], dry etching techniques such as reactive ion etching (RIE) [293] or ion-beam etching (IBE), or combinations of dry and wet etching steps [289]. All etching techniques have their advantages and disadvantages. For example, wet-chemical etching is usually fairly isotropic, making it difficult to obtain an accurate pattern transfer into the semiconductor because of the underetching of the etch masks. IBE allows high aspect ratios but causes a damaged layer of poor optical quality close to the surface of the nanostructures. RIE is probably the best technique, as fairly high aspect ratios and steep sidewalls of the nanostructures can be obtained.

Oka et al. fabricated  $\text{Cd}_{1-x}\text{Mn}_x\text{Se}/\text{Zn}_{1-y}\text{Cd}_y\text{Se}$  QWRs of different widths ranging from 26 to 300 nm, starting from MBE-grown  $\text{Cd}_{1-x}\text{Mn}_x\text{Se}/\text{Zn}_{1-y}\text{Cd}_y\text{Se}$  QW samples with  $x_{\text{Mn}} = 8\%$  and  $y_{\text{Cd}} = 30\%$  on (100) GaAs [290–292].

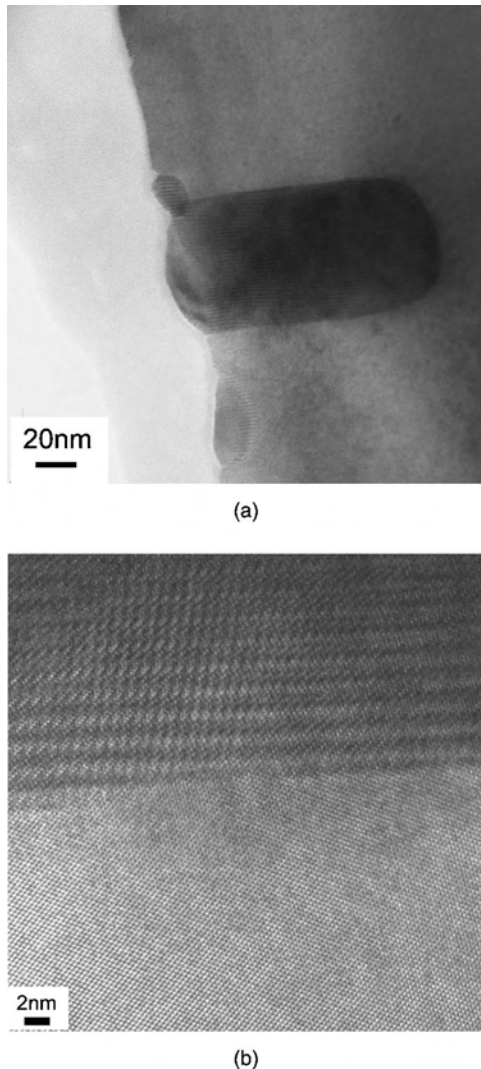


**Figure 27.** TEM images of  $\text{Mn}(\text{Ga})\text{As}$  clusters in a  $\text{Ga}_{1-x}\text{Mn}_x\text{As}$  host matrix of low  $x_{\text{Mn}}$ . (a) Bright-field TEM image. (b) High-resolution image of a cluster–matrix interface.

After spin-coating of the QW samples with ZEP-520 resist and prebaking, homogeneous wire-array patterns of  $0.5 \times 0.5 \text{ mm}^2$  were defined by EBL (Elionics ERA-8000 FE) on the two-dimensional structure. After a postbaking step and a developing step of the resist, the pattern was transferred by wet-chemical etching with a solution of  $\text{K}_2\text{Cr}_2\text{O}_7:\text{HBr}:\text{H}_2\text{O}$  to a depth of 100 nm.

Klar et al. obtained  $\text{ZnSe}/(\text{Zn,Mn})\text{Se}$  QWRs and  $(\text{Zn,Cd,Mn})\text{Se}/\text{ZnSe}$  QWRs of different widths ranging from 50 to 500 nm from the corresponding MBE-grown quantum well structures by an EBL pattern definition followed by a combination of IBE and wet-chemical etching. Figure 28 depicts the end of a single  $\text{ZnSe}/(\text{Zn,Mn})\text{Se}$  QWR after IBE and wet-chemical etching before removal of the Ti-etch mask [289]. The nanofabrication process consists of nine steps and is similar to that employed for the fabrication of QD samples, which is described in detail in Section 3.3.1.

One-hundred-nanometer-wide  $\text{CdTe}/\text{MnTe}$  multiple QWRs were realized by holographic lithography (Ar ion laser operating at 457.8 nm) and subsequent RIE with a mixture of  $\text{CH}_4$  and  $\text{H}_2$  [293]. The two-dimensional structure was an MBE-grown superlattice consisting of 20 periods of 17 nm  $\text{CdTe}$  and 2 nm  $\text{MnTe}$ . The ionization of the molecules was done with a 13.56-MHz radio frequency source in a parallel-plate reactor (Oxford 80 Plus). The supplied power was 180 W, and the total pressure during operation was 10 mTorr. The etch rate of the  $\text{CdTe}/\text{MnTe}$  layers was determined to be 15 nm/min, and the total etch time was 30 min. Very high aspect ratios and very steep sidewalls were obtained, as can be seen in Figure 29.

### 3.2.2. Epitaxial Growth on Patterned Substrates

In addition to the direct patterning of two-dimensional layers to obtain QWRs, the epitaxial growth on patterned substrates is an important technology for the fabrication of one-dimensional semiconductor nanostructures by both MOVPE [294] and MBE [295]. The ALE of GaAs QWRs was successfully demonstrated by Isshiki et al. [296]. Basically the growth on patterned substrates is a selective growth method, which provides control of the lateral dimensions of semiconductors. In contrast to the lateral structuring

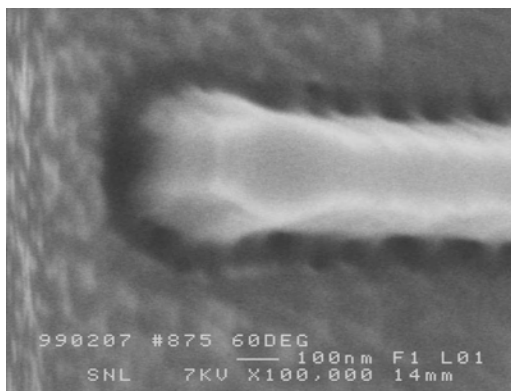


**Figure 28.** SEM image of the end of a single  $\text{ZnSe}/(\text{Zn,Mn})\text{Se}$  QWR after IBE and wet-chemical etching before the removal of the Ti-etch mask.

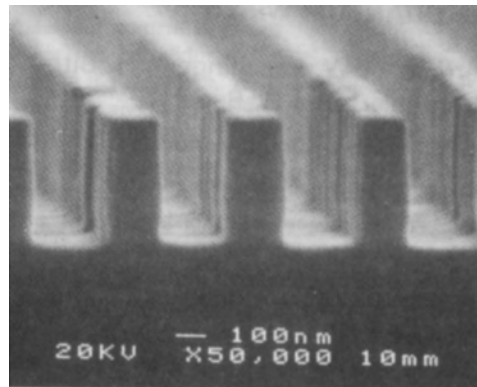


**Figure 29.** SEM image of  $\text{CdTe}/\text{MnTe}$  QWR structures obtained by RIE. Reprinted with permission from [293], A. A. Darhuber et al., *Mater. Sci. Forum* 182–184, 423 (1995). © 1995, Trans Tech Publications.

discussed in Section 3.2.1, this technique does not generate additional chemical or mechanical defects in the wires.

Although the selective epitaxial growth on patterned substrates is well established for nonmagnetic semiconductors, this technique has hardly been used for growing magnetic semiconductor nanostructures. Parthier and co-workers [297] reported the successful growth of  $\text{ZnSe}/(\text{Zn,Mn})\text{Se}$  and Chen et al. [298] the growth of  $(\text{Cd,Mn})\text{Te}/(\text{Cd,Mg})\text{Te}$  QWRs by MBE on patterned GaAs substrates. The preparation method for the  $\text{ZnSe}/(\text{Zn,Mn})\text{Se}$  QWRs was described in detail in [295, 297]. The (001)-oriented GaAs substrates were structured by photolithography or EBL followed by wet-chemical etching. The orientation of the masks (stripes of about 1–2  $\mu\text{m}$ ) were along the [110] or [1–10] directions. To prepare grooves with  $\{111\}_A$  sidewalls an etching solution,  $\text{H}_3\text{PO}_4/\text{H}_2\text{O}_2/\text{H}_2\text{O}$  or  $\text{KBrO}_3/\text{H}_2\text{O}_2/\text{H}_2\text{O}$ , was used. Nearly V-shaped grooves could be grown in the [1–10] direction, and trapezoid-shaped grooves could be grown in the [110] direction. Grooves with  $\{111\}_B$  sidewalls were obtained by etching with  $\text{KHCO}_3/\text{H}_2\text{O}_2/\text{H}_2\text{O}$  solution. The resulting shape of the grooves is complementary to  $\{111\}_A$ . The reported dissolution rates of the (001) surface at room temperature were about 0.8  $\mu\text{m}/\text{min}$  for  $\text{H}_3\text{PO}_4$ , about 0.72  $\mu\text{m}/\text{min}$  for  $\text{KBrO}_3$ , and about 0.17  $\mu\text{m}/\text{min}$  for  $\text{KHCO}_3$  etchant, respectively. Patterned GaAs substrates with structures with a strip width on top of the etched wires between 1 and 0.1  $\mu\text{m}$  were obtained. Figure 30 shows SEM pictures of a cleaved  $\{110\}$  cross section of selectively grown ZnSe on A-anisotropically etched (001) GaAs with top stripes oriented along the [1–10] direction. The huge difference in strip width for the structures depicted in Figure 30 was realized by means of different etching solutions. With the use of a mask with 2- $\mu\text{m}$  stripes, the  $\text{H}_3\text{PO}_4$  etchant yields a 0.15- $\mu\text{m}$  width (Fig. 30a), whereas  $\text{KBrO}_3$  etchant leads to stripes with a width of 1.4  $\mu\text{m}$  on the top (see Fig. 30b). Different growth rates  $R$  on the individual surfaces  $R_{\{111\}_A} < R_{(001)}$  can be used to prepare QWRs. Parthier et al. [297] reported a growth rate ratio  $R_{\{111\}_A}/R_{(001)} = 0.36$ . An overgrowth of the patterned substrate leads to a strong narrowing of the top stripes. This is clearly seen in Figure 30b. The GaAs substrate (grayish dark) has been overgrown by MBE with a ZnSe-layer (grayish-bright). The plateau becomes smaller with increasing MBE overgrowth. This effect has been

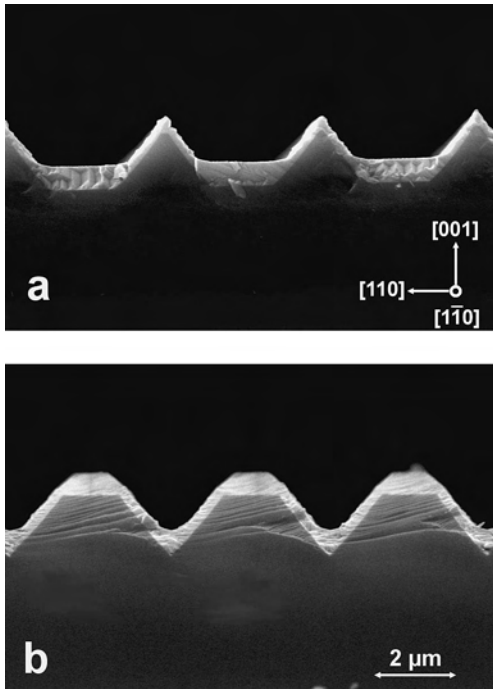


**Figure 30.** SEM image of cleaved  $\{110\}$  cross sections of selectively grown ZnSe on A-anisotropically etched (001) GaAs for different etching conditions (a–b). Reprinted with permission from [295], L. Parthier et al., *J. Cryst. Growth* 159, 99 (1996). © 1996, Elsevier Science.

used to prepare ZnSe quantum wires between magnetic (Zn,Mn)Se barriers. In Figure 31 a SEM picture is seen, with the cross section perpendicular to the wire direction. A 55-nm ZnSe buffer layer has been grown on the patterned GaAs substrate. Afterward a (Zn,Mn)Se/ZnSe superlattice structure consisting of five periods of 13-nm  $\text{Zn}_{0.78}\text{Mn}_{0.22}\text{Se}$  and 11-nm ZnSe has been grown on top to reduce the strain. The superlattice structure is well resolved in the grooves of the structure. After another 40-nm (Zn,Mn)Se barrier, a 4-nm ZnSe quantum well has been grown, which is still resolvable in the groove but is hardly to be seen on top of the stripes. From geometrical considerations, the lateral extension of the wire is expected to be less than 1 nm.

Morishita et al. reported the growth of MnAs wire-like structures by MBE on (111)A facets of V-grooved GaAs substrates [297]. The V-grooves with (111)A sidewalls were prepared by conventional chemical etching of the (100) GaAs substrates. Afterward an undoped GaAs buffer layer was grown at  $T_S = 600^\circ\text{C}$ . With  $T_S$  lowered to about  $250^\circ\text{C}$  and

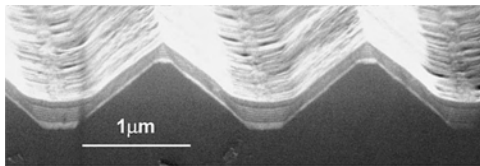


**Figure 31.** SEM image of the cleaved  $\{110\}$  cross section of a 4-nm ZnSe QWR within 40-nm (Zn,Mn)Se barriers grown on a ZnSe(11 nm)/(Zn,Mn)Se(13 nm) MQW buffer with five periods and 50 nm ZnSe (ZnSe is bright). Reprinted with permission from [297], L. Parthier et al., *J. Cryst. Growth* 184–185, 339 (1998). © 1998, Elsevier Science.

adjustment of the direction of the Mn flux, MnAs grew only the (111)A facets of the V-grooves that faced the Mn flux.

One can state that overall, the overgrowth of patterned substrates is an excellent technique for preparing high-quality QWRs with dimensions in the real quantum limit.

### 3.2.3. Template-Directed Growth of Ordered Arrays of Nanostructures

The organic-template-directed synthesis of mesoporous silica in 1992 by Mobil Oil Company opened new pathways in material design [300, 301]. Depending on the synthesis conditions, highly ordered organic-template/SiO<sub>2</sub> superstructures can be prepared. The superstructures of these so-called M41S materials are either of hexagonal (MCM-41; MCM = Mobil Composition of Matter), cubic (MCM-48), or lamellar (MCM-50) symmetry. Removal of the organic template of the three-dimensional superstructures (i.e., MCM-41 and MCM-48) in a calcination process leaves a highly ordered mesoporous SiO<sub>2</sub> matrix with regular wire-like pores. Figure 32 is a high-resolution TEM image of a grain of a MCM-48 SiO<sub>2</sub> matrix. The pore diameters as well as the distances between neighboring pores are only a few nanometers and can be accurately adjusted during the synthesis process [302]. These mesoporous SiO<sub>2</sub> materials are well suited as host materials for semiconductors and even magnetic semiconductors because of their high degree of order as well as the large bandgap of the SiO<sub>2</sub> (which serves as barrier material). The first successful incorporation of the semimagnetic semiconductor  $\text{Cd}_{1-x}\text{Mn}_x\text{S}$  into MCM-41 SiO<sub>2</sub> was reported in [303–305]. It is a very interesting way of creating highly ordered arrays of magnetic QWRs for possible applications in magneto and spin-electronics.

The preparation procedure was as follows. A gel mixture of 1 SiO<sub>2</sub>:0.25 CTABr:0.2 TMAOH:35 H<sub>2</sub>O was used for the synthesis of the MCM-41 SiO<sub>2</sub> matrix. The gel mixture was stirred at  $60^\circ\text{C}$  for 30 min. It was poured into a Teflon-lined steel autoclave and kept there at room temperature for 24 h. Afterward it was synthesized for 24 h at  $150^\circ\text{C}$  under autogeneous pressure. The product was washed with water several times and calcined at  $550^\circ\text{C}$ . The pore size and the wall thickness were determined to be  $3.1 \pm 0.1$  nm and about 2 nm, respectively. The  $\text{Cd}_{1-x}\text{Mn}_x\text{S}$  was implanted in a MCM-41 SiO<sub>2</sub> matrix as follows: 0.5 g calcined MCM-41 silica was suspended in a 0.5 M solution of cadmium

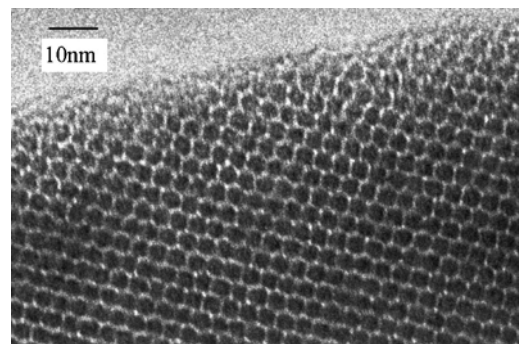


**Figure 32.** High-resolution TEM image of a grain of MCM-48 SiO<sub>2</sub> matrix.

acetate and manganese acetate in water with different ratios of Cd/Mn and stirred for 10 min. The precipitate was centrifuged and vacuum dried. The acetates were converted into the sulfide by thermal treatment in a  $\text{H}_2\text{S}$  atmosphere. Samples with Mn contents of  $0 \leq x \leq 30\%$  and  $80\% \leq x \leq 100\%$  were synthesized. Figure 33 depicts a TEM image of a  $\text{SiO}_2$  MCM-41 host after incorporation of  $\text{Cd}_{1-x}\text{Mn}_x\text{S}$ . The lattice has a regular hexagonal structure with wirelike filled pores 3.5 nm in diameter. The Mn concentrations  $x$  were determined by chemical analysis. (Cd,Mn)Se and (Zn,Mn)S QWRs have recently been synthesized in a similar fashion [306, 529]. It is also possible to vary the wire diameter (i.e., 3 nm, 6 nm, and 9 nm were realized) by using different organic templates in the synthesis process [529].

### 3.3. Growth and Preparation of Quantum Dots

There are two completely different approaches for obtaining quasi-zero-dimensional nanostructures. The first approach is based on epitaxial growth techniques, such as those introduced in Sections 3.1 and 3.2. The second approach is the direct growth of nanocrystals in an organic or inorganic matrix. With two-dimensional epitaxial growth on a substrate as the starting point, two principal ways of realizing quantum dots (QDs) can be distinguished. One is the subsequent etching procedure, which will be discussed in Section 3.3.1, and the other is the exploitation of the self-organized (often called self-assembled) growth of island-like dots from a wetting layer by the so-called Stranski–Krastanov method, which is discussed in Section 3.3.2. The other fundamental approach is the growth of QDs in a matrix, which also has to be considered a self-activated growth. In particular, growth in inorganic glass matrices is a diffusion-controlled process which exhibits some analogies to the self-activated growth from a wetting layer and is also described in Section 3.3.2. Currently, an effort is being made to grow magnetic binary QDs in ternary semimagnetic semiconductors by the control of segregation effects. These structures are possible candidates for ferromagnetic semiconductor hybrids, which can be

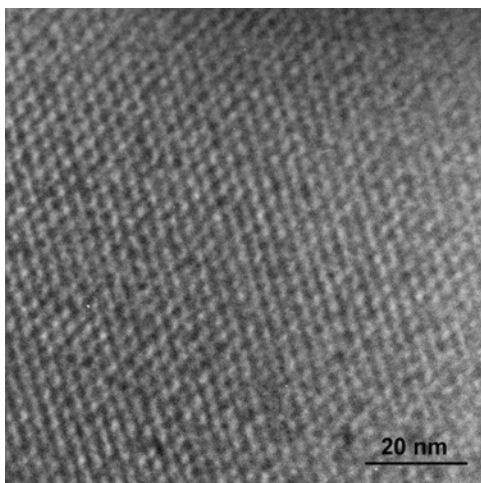


**Figure 33.** TEM image of a grain of a MCM-41  $\text{SiO}_2$  matrix after intrapore formation of (Cd,Mn)S.

combined with conventional semiconductors for magneto-electronics and spin-electronics at room temperature. Some of these magnetic semiconductor hybrids are also discussed in Section 3.3.2. The growth of nanocrystals in liquid or micelle media as well as in polymers is also controlled by, in addition to the diffusion-limited mechanism, chemical reactions and is therefore discussed in an extra Section, 3.3.3.

#### 3.3.1. Lateral Patterning by Lithographic Methods

The techniques employed for the fabrication of QDs by lithographic methods are very similar to those introduced in Section 3.2.1 for the fabrication of QWRs. Again the main lithographic technique is EBL followed by one or several etching steps for transferring the pattern into the semiconductor [307–311]. There is an alternative lithographic approach, which combines lithography and pattern transfer. This is the so-called focused ion beam lithography, where dots are fabricated by controlled intermixing of quantum well and barrier materials due to a bombardment with 100-keV  $\text{Ga}^+$  ions [312, 313].

Ribayrol et al. fabricated QD samples from CdTe/(Cd,Mn)Te QW samples grown by MBE on (100) InSb as well as on (100) (Cd,Zn)Te substrates [307]. Various patterns of  $400 \mu\text{m} \times 400 \mu\text{m}$  consisting of dots of the same diameter were defined on the QW samples with EBL. After the resist was developed, 30 nm of Ti was evaporated onto the sample, and the resist was removed in a lift-off process. The titanium served as an etching mask in the RIE process. The pattern was transferred by RIE to a depth of about 400 nm with the use of a plasma of  $\text{CH}_4:\text{H}_2:\text{O}_2$ . Steep sidewalls were obtained with the use of 1:8  $\text{CH}_4:\text{H}_2$  and a small amount of  $\text{O}_2$  at a RF power density of 0.44–0.66  $\text{W cm}^{-2}$ . Details of control of the dot profile in the described RIE process can be found elsewhere [314, 315].

Klar et al. fabricated QD samples in various wide-gap (II, Mn)VI systems (i.e., CdTe/(Cd,Mn)Te [309], ZnTe/(Zn,Mn)Te [308], ZnSe/(Zn,Mn)Se [310], and (Zn,Cd,Mn)Se/ZnSe [311]). The nanofabrication started from MBE-grown quantum well structures and consisted of nine steps. First, the specimen was cleaned with acetone in an ultrasonic bath and rinsed with isopropanol. In the second step, it was spin-coated with a two-layer resist consisting of a 140-nm bottom layer of copolymer P(MMA-MAA) and a 50-nm top layer of 950k PMMA. Afterward, the EBL was carried out with a JEOL JBX 5DII system with a  $\text{LaB}_6$  cathode and an acceleration voltage of 50 kV, a final aperture of  $60 \mu\text{m}$ , a working distance of 14 nm, and a beam current of 1 nA. Typically a patterned area covered  $3.2 \times 3.2 \text{ mm}^2$  on the specimen. Squares of  $200 \times 200 \text{ nm}^2$  were exposed with a nominally homogeneous dose (typical values are  $220 \mu\text{C cm}^{-2}$  for Te-based dots and  $200 \mu\text{C cm}^{-2}$  for Se-based dots). These squares were arranged on a lattice with a lattice constant of 400 nm. The diameter of the beam and the proximity effect result in a circular exposure profile under these conditions. In the fourth step, the exposed sample was developed in a solution of 20 ml of isopropanol and 2 ml of distilled water for 60 s. Afterward, a 30-nm Ti film was deposited on the resist mask, and after subsequent lift-off in warm acetone, a pattern of circular Ti dots with a

diameter of about 200–220 nm was obtained. This pattern was transferred onto the semiconductor to the desired depth with the use of  $\text{Ar}^+$  IBE under normal incidence with a relatively low acceleration voltage of 200 V and a current density of  $0.16 \text{ mA cm}^{-2}$ . The etch rate varied for the different semiconductors (e.g., about  $18 \text{ nm min}^{-1}$  for the tellurides and about  $8 \text{ nm min}^{-1}$  for the selenides). An additional optional wet-etching step can be introduced to reduce the lateral dimensions of the QDs further. This has been done in the case of the Se-based QDs [310, 311]. For the wet-etching step either a solution of  $\text{Br}_2 : \text{HOCH}_2\text{CH}_2\text{OH}$  at 2:1000 or a solution of  $\text{HBr} : \text{K}_2\text{Cr}_2\text{O}_7 : \text{H}_2\text{O}$  at 1:195:250 has been used. Typical etching times were 30 s. In the final step, the Ti etch mask was removed with hydrofluoric acid. As typical examples for specimens obtained by employing solely  $\text{Ar}^+$  IBE in the etching step, SEM images of 200-nm and 100-nm QDs fabricated from a  $\text{CdTe}/(\text{Cd},\text{Mn})\text{Te}$  MQW structure are depicted in Figure 34a and b, respectively. To allow a better view of the individual QDs, the SEM images were taken at defects or at the edge of the QD arrays and with the specimens tilted by  $30^\circ$ . The arrays of QDs were very homogeneous over the whole area of  $3.2 \times 3.2 \text{ mm}^2$ , with only a few macroscopic defects. It can be seen in the figures that the top of the 200-nm QDs is still flat in contrast to the tiplike shape of the 100-nm QDs. This indicates that damage of the QWs closest to the surface of the MQW structure has occurred in the 100-nm QDs, whereas for the 200-nm sample the core of the QDs is undamaged by the nanofabrication process. The sidewalls of the QDs are inclined, as is typical for  $\text{Ar}^+$  ion etched specimens [316]; similar inclinations

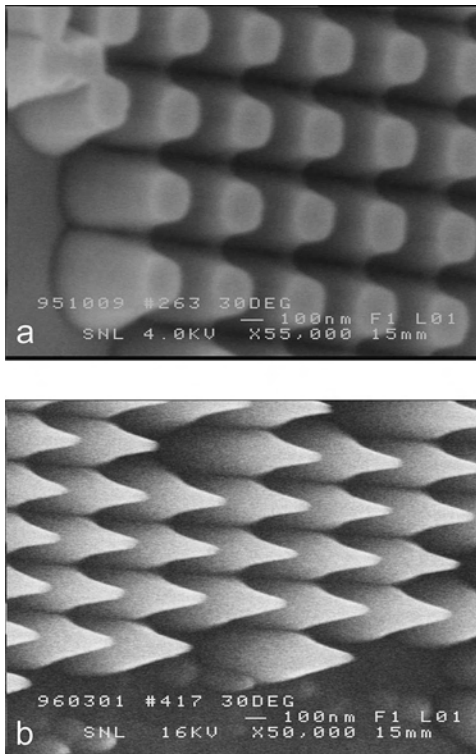


**Figure 34.** SEM images of 200-nm and 100-nm  $\text{CdTe}/(\text{Cd},\text{Mn})\text{Te}$  QDs obtained by IBE.

were observed by other groups in II–VI materials with the use of similar acceleration voltages [317, 318]. Figure 35 shows an SEM image of a  $\text{ZnSe}/(\text{Zn},\text{Mn})\text{Se}$  QD sample prepared with a combination of  $\text{Ar}^+$  IBE and wet-chemical etching to transfer the dot pattern into the semiconductor. The specimen is tilted by  $40^\circ$ , and the Ti etch mask is not removed. An underetching of the Ti mask is observed, which is typical for the rather isotropic wet etching.

Bacher et al. [312, 313] prepared buried  $\text{CdTe}$  QD samples from MBE-grown  $\text{CdTe}/\text{Cd}_{0.76}\text{Mn}_{0.24}\text{Te}$  on (100)  $\text{Cd}_{0.96}\text{Zn}_{0.04}\text{Te}$  substrates by focused ion beam lithography. A single 6-nm  $\text{CdTe}$  QW is embedded between a  $\text{Cd}_{0.76}\text{Mn}_{0.24}\text{Te}$  buffer and a 40-nm  $\text{Cd}_{0.76}\text{Mn}_{0.24}\text{Te}$  capping layer. The ion implantation for creating the dots was carried out with an EIKO 100 focused ion beam system with a  $\text{Ga}^+$  source. The beam diameter is about 30 nm, the ion energy is 70 keV, and the implantation doses varied between  $6 \times 10^{12}$  and  $5 \times 10^{13} \text{ cm}^{-3}$ . To create single dots small mesas with lateral dimensions of  $20 \mu\text{m} \times 20 \mu\text{m}$  were implanted homogeneously, except for a circle with a diameter of  $2 \mu\text{m}$  in the center of the mesas. The ion bombardment already leads to an intermixing of the barrier and well material. This intermixing can be further enhanced by a rapid thermal annealing step after the implantation. The annealing temperature was varied between 330 and  $500^\circ\text{C}$ . The ion dose and the annealing temperature allow one to reduce the effective dot size and to control the effective confining potential of the dots, which corresponds to an inverted Gaussian profile. It should be noted that the effective extension of the ground-state excitonic wavefunction of the dot is only about 50 nm.

### 3.3.2. Self-Organized Growth

The term “self-organized growth” is misleading, as, strictly speaking, any growth process is self-organized. From a physical point of view the processes that are called self-organized are those which go through a transformation from a thermodynamically unstable state (e.g., prepared by a low-temperature growth) into a thermodynamically stable state with a reduced overall energy. Two very different methods, which make use of self-organization, have been used to prepare QDs on the basis of magnetic semiconductors. First, we shall consider the so-called Stranski–Krastanov method.

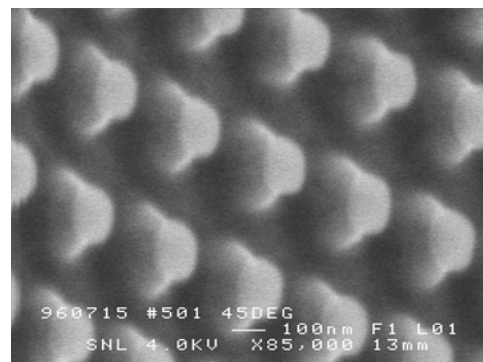


**Figure 35.** SEM image of a  $\text{ZnSe}/(\text{Zn},\text{Mn})\text{Se}$  QD sample prepared by a combination of  $\text{Ar}^+$  IBE and wet-chemical etching. Reprinted with permission from [310], P. J. Klar et al., *Phys. Rev. B* 57, 7114 (1998). © 1998, American Physical Society.



The driving force of this growth process is a strain misfit between the layer materials of a quantum well heterostructure. The strain has to exceed a critical value, leading to a transition from 2D growth to 3D growth. Second, we shall discuss the preparation procedure of dots in a glass matrix. The diffusion permits the formation of energetically favored clusters. The cluster size is determined by the minimum of the free energy.

**Stranski–Krastanov Growth** Kuroda et al. [319, 320] reported the successful growth of self-organized QDs of zincblende MnTe on CdTe layers on a (100) GaAs substrate by MBE. The CdTe layer thickness varied from about 0.5  $\mu\text{m}$  to 2  $\mu\text{m}$  to permit lattice relaxation. The deposition of MnTe was performed by two different methods. (i) The Mn and Te fluxes were supplied simultaneously, which is the conventional MBE. The Mn/Te ratio was about 1:10, and the growth rate was about 0.1 monolayer per second. (ii) Both fluxes were supplied subsequently. This technique is comparable to ALE. For both methods the substrate temperature was about 300–325 °C. Self-organized cone-shaped dots were formed after the deposition of about 10–13 monolayers. The QDs obtained by method (i) were (70  $\pm$  10) nm in height and (140  $\pm$  10) nm in diameter, whereas those obtained by method (ii) were only (8  $\pm$  1) nm in height and had diameters of (60  $\pm$  5) nm.

In a similar fashion the same authors grew  $\text{Cd}_{1-x}\text{Mn}_x\text{Te}$  QDs with  $x = 0$ –18% on a (100) ZnTe buffer layer of 0.6–1.0  $\mu\text{m}$  deposited on (100) GaAs [321, 322]. Typically these dots had diameters of about 20 nm and were about 2 nm in height. The dot density was about  $10^{11} \text{ cm}^{-2}$  for  $x = 3\%$ , but decreased significantly with increasing Mn concentration of the QDs. Mackowski et al. [323] grew  $\text{Cd}_{1-x}\text{Mn}_x\text{Te}$  QDs in ZnTe in a similar fashion. Some details about the growth can be found in a publication on a related system, CdTe QDs in ZnTe [324].

Takahashi et al. prepared  $\text{Cd}_{1-x}\text{Mn}_x\text{Se}$  QDs on (100) ZnSe in a Stranski–Krastanov growth mode by MBE [292]. A smooth wetting layer for the dot system was realized by the growth of two monolayers of CdSe. Subsequently, a five-monolayer-thick  $\text{Cd}_{1-x}\text{Mn}_x\text{Se}$  layer was grown at a temperature of 280 °C with the use of vapor fluxes of Cd, Se, and Mn. Self-organization was initiated by raising the substrate temperature to 310 °C. After the formation process, the dots were covered with a ZnSe capping layer. The effective dot size was about 5 nm and  $x \approx 3\%$ . (Cd,Mn)Se QD samples in a ZnSe matrix were also grown by Mackowski et al. [323].

Xin et al. [325] prepared CdSe QDs in  $\text{Zn}_{1-x}\text{Mn}_x\text{Se}$  matrices with  $x = 0, 5,$  and 10% by MBE from elemental sources. Before the growth of the CdSe QDs a  $\text{Zn}_{1-x}\text{Mn}_x\text{Se}$  buffer of about 2  $\mu\text{m}$  was deposited on a (100) GaAs substrate at 300 °C. For the growth of the CdSe QDs, the substrate temperature was raised to 350 °C. A typical effective growth rate for the QD layer was 0.4 monolayers per second. The best results were obtained for a thickness of 2.5 monolayers. At the beginning of the CdSe deposition, a clear transformation of the RHEED pattern from streaky to spotty, indicative of the onset of Stranski–Krastanov growth, was observed. Uncapped and capped samples for AFM and optical studies, respectively, were prepared. In the latter case, the capping layer was about 500 Å. Examination of the

uncapped samples within 1 h after the growth revealed a typical dot density of 25 dots/ $\mu\text{m}^2$ , a uniform dot diameter of (40  $\pm$  5) nm, and an average height of (10  $\pm$  3) nm for the samples with  $x = 0\%$ . The Mn-containing samples show higher QD densities and reduced QD sizes. A possible reason for this might be the smaller lattice mismatch between (Zn,Mn)Se and CdSe compared with that between ZnSe and CdSe. However, other effects due to the presence of Mn cannot be ruled out.

Zhou et al. prepared Mn-including InAs dots embedded in GaAs by MOMBE in a Stranski–Krastanov growth mode [326].

Vertically aligned quasi-regular arrays of QDs have been prepared by MBE in the IV–VI system  $\text{PbSe/Pb}_{1-x}\text{Eu}_x\text{Te}$  [327–330]. The samples were grown by MBE on thick PbTe buffer layers predeposited on (111)  $\text{BaF}_2$  substrates. The substrate temperature was 360 °C. The growth rates were 0.08 ML/s and 0.96 ML/s for PbSe and  $\text{Pb}_{1-x}\text{Eu}_x\text{Te}$ , respectively. The superlattices consist of up to 100 periods of five monolayers of PbSe, alternating with diluted magnetic  $\text{Pb}_{1-x}\text{Eu}_x\text{Te}$  spacer layers with thicknesses ranging from 200 to 1000 Å. Because of the  $-5.4\%$  lattice mismatch with respect to the PbTe, PbSe grows in Stranski–Krastanov mode, with the formation of 3D islands once the critical coverage of 1.5 ML is exceeded [331]. During the overgrowth a rapid replanarization takes place such that, after 200 Å, a smooth 2D surface is regained [327]. The only difference in the samples was the thickness and composition of the ternary  $\text{Pb}_{1-x}\text{Eu}_x\text{Te}$  layers, where  $x$  was adjusted to achieve a complete strain symmetrization of the superlattice stack (e.g.,  $x = 7\%$  for 470-Å spacers) with respect to the PbTe buffer layer [327]. The possibility of simultaneously achieving in-plane ordering and vertical stacking in the dot superlattices as the spacer thickness is varied is very interesting. Three regimes are observed as shown in the TEM images of Figure 36: (i) for thin spacers vertically aligned dot columns are obtained, but with a changing dot shape along the growth direction (Fig. 36a); (ii) for intermediate spacer thicknesses an fcc-stacking ABCABC of adjacent dot layers

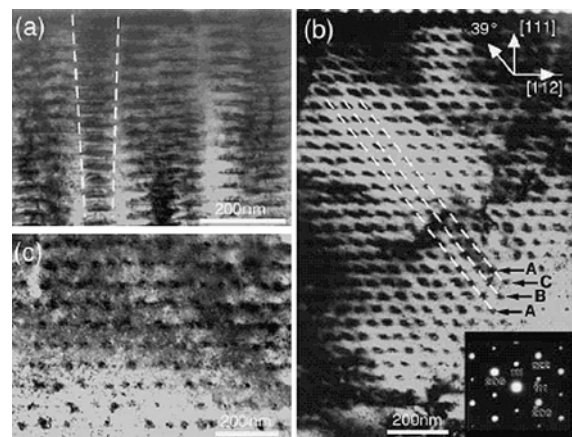


**Figure 36.** TEM images of vertically stacked PbSe QDs in a (Pb,Eu)Te matrix for different (Pb,Eu)Te spacer thicknesses. Reprinted with permission from [330], G. Springholz et al., *Phys. Rev. Lett.* 84, 4669 (2000). © 2000, American Physical Society.

is observed, with constant dot spacing and dot size throughout the superlattice stack (Fig. 36b); and (iii) for the thickest spacers the vertical correlation disappears again (Fig. 36c). The scaling behavior of the lateral dot separation  $L$  versus the vertical superlattice period  $D$  for the PbSe/Pb<sub>1-x</sub>Eu<sub>x</sub>Te dot stacks is shown in Figure 37. The three regimes also show different in-plane ordering, as can be seen in the three AFM images of Figure 38. The insets are fast Fourier transformation (FFT) power spectra of the AFM images. For samples of regime (i), although the dots seem to nucleate at random positions, six broad satellite peaks are visible in the FFT spectrum, indicating a preferred hexagonal arrangement (Fig. 38a). In regime (ii) the degree of in-plane order is even higher (Fig. 38b). The FFT spectrum shows a sixfold symmetry and a large number of higher order peaks, indicating the existence of large hexagonally ordered dot domains. In regime (iii) no in-plane ordering is observed, indicated by the diffuse ring in the FFT spectrum (Fig. 38c). The magnetic properties of these superlattice structures have not yet been studied; however, interesting effects can be expected, considering the enhanced magnetic properties of (Pb,Eu)Te.

**Quantum Dots in Glass Matrices** The range of semiconductor materials used for the preparation of QDs in glass matrices covers almost all kinds of known substances. Well-elaborated preparation methods and theories are known which give detailed information about the diffusion-controlled growth process and the correlation between annealing temperature and annealing time on one hand and the mean dot sizes and size distribution on the other. For a detailed review see, for example, the book by Woggon [332]. There are, however, only a few papers concerning magnetic nanocrystals in glass matrices prepared by RF sputtering [333–337] or by sol–gel processes [338–341]. In particular, in the latter case the preparation procedures can vary considerably.

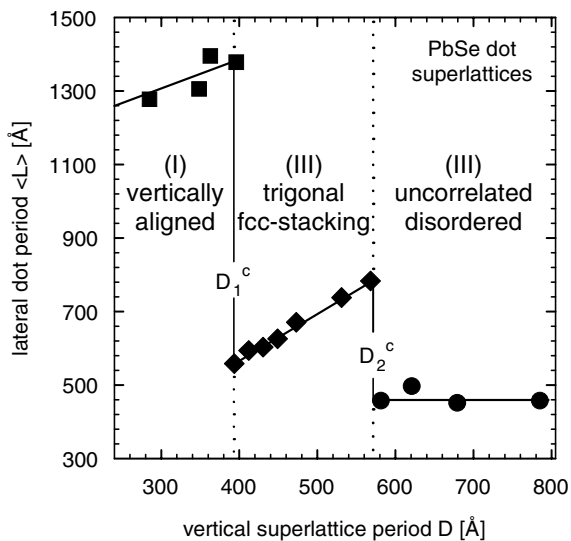


**Figure 37.** Scaling behavior of the lateral PbSe dot separation versus vertical PbSe/Pb<sub>1-x</sub>Eu<sub>x</sub>Te SL period. Reprinted with permission from [330], G. Springholz et al., *Phys. Rev. Lett.* 84, 4669 (2000). © 2000, American Physical Society.

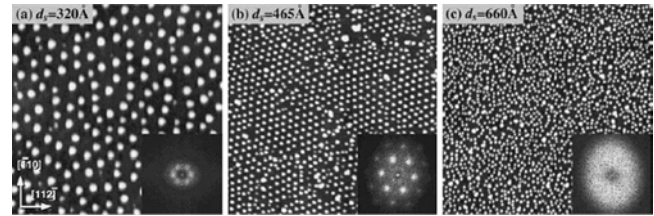


**Figure 38.** AFM images of the in-plane ordering in the three regimes (see text for details). Reprinted with permission from [330], G. Springholz et al., *Phys. Rev. Lett.* 84, 4669 (2000). © 2000, American Physical Society.

Nanocrystals of (Cd,Mn)Te and (Cd,Mn)Se were prepared by RF sputtering with a composite target which consisted of small pieces of (Cd,Mn)Te or (Cd,Mn)Se crystals on a SiO<sub>2</sub> disk [333–337]. By simultaneous sputtering of the magnetic semiconductor and SiO<sub>2</sub> thin films of about 1- $\mu$ m thickness were obtained. The films were heat treated at 300–600 °C for several hours. During this thermal treatment QDs of (Cd,Mn)Te or (Cd,Mn)Se were formed. The diameters of the QDs can vary from 1 to 50 nm.

Wang et al. were the first to report the preparation of (Zn,Mn)S clusters in glass matrices by a sol–gel method [338]. The fabrication process is described in detail in their paper. In summary, two solutions were prepared. The first solution consisted of tetramethylorthosilicate in methanol. The second solution was a mixture of manganese and zinc nitrate (the ratio of Zn/Mn nitrates determined the doping level in the QDs) in diluted nitric acid. The two solutions were added together, vigorously stirred for a few minutes, and then transferred into polypropylene vials. When the vials are left at room temperature overnight a rigid gel is formed. The gel was then dried and calcinated at elevated temperatures to obtain a dried porous glass. To generate Zn<sub>1-x</sub>Mn<sub>x</sub>S clusters, the porous glass, which already contains Zn<sup>2+</sup> and Mn<sup>2+</sup> ions, was exposed to H<sub>2</sub>S at 200 °C. The glass containing the Zn<sub>1-x</sub>Mn<sub>x</sub>S clusters was impregnated with methylmethacrylate in a final step. The resulting composite is strong enough to allow cutting and polishing of thin disks.

Morita et al. prepared sol–gel ZrO<sub>2</sub> films with CdS : Mn<sup>2+</sup> (or Eu<sup>3+</sup>) QDS by a dipping method [340]. Small quartz slides were dipped successively in mother solutions of *n*-propanol which contained the following reagents: zirconia tetrapropoxide, cadmium acetate, manganese acetate (or europium nitrate), and sodium thiocyanate. After dip coating the samples were dried at room temperature for a day and afterward heated in an electric oven at 350 °C for another 24 h to form the QDs. The whole process can be repeated several times to obtain thick samples.

Artemyev et al. [341] and Chamarro et al. [339] used approaches where Cd<sub>1-x</sub>Mn<sub>x</sub>S QDs were first synthesized by a precipitation process (see Section 3.3.3) and then dispersed in a sol–gel matrix for stabilization.

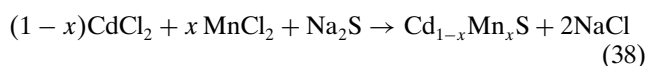
**Formation of Binary Ferromagnetic Quantum Dots by Controlled Segregation Effects** As mentioned in Sections 3.1.1 and 3.1.2, a segregation of ferromagnetic MnAs clusters can occur under certain conditions in the MBE and MOVPE growth of (Ga,Mn)As epitaxial layers.

An alternative approach to obtaining MnAs clusters in GaAs is Mn<sup>+</sup> ion implantation and subsequent annealing [342, 343]. The formation of MnAs has also been observed in the MBE growth of (Ga,In,Mn)As [344]. Ferromagnetic MnSb clusters have also been prepared on S-passivated (100) GaAs surfaces [345], and MnSb clusters occur in the MBE growth of (Ga,Mn)Sb [346]. Thus, this segregation of binary ferromagnetic Mn-V can be considered a general feature of all Mn-containing III-V. It is worth noting that at present this is not simply considered an undesired effect. On the contrary, there are now serious efforts to control the formation (e.g., size, position in the structure, etc.) of such ferromagnetic clusters in semiconductor structures. De Boeck et al. [347, 348] clearly demonstrated that size control and positioning of MnAs clusters within GaAs layers in annealed (Ga,Mn)As/AlAs and (Ga,Mn)As/(Ga,In)As superlattices is possible. First the whole superlattice structure is grown under growth conditions where no MnAs segregation occurs. In a subsequent annealing step, clusters with a small size distribution will be formed within the (Ga,Mn)As layer. The cluster formation is restricted to these layers, and the cluster size can be increased by choosing a higher annealing temperature. At this time, this is the only way of achieving quasi-ferromagnetic semiconductor material with Curie temperatures above room temperature.

### 3.3.3. Preparation by Liquid Solution Precipitation

A very common method of preparation of nanocrystals is based on chemical reactions and precipitation in aqueous solution or organic solvents (see, e.g., [234, 348, 350]). The dilemma of these chemical preparation methods is that, on the one hand, high synthesis temperatures (>300 °C) are required to obtain good quality material (as known from the binary QDs of CdSe, CdS, etc. [351]), whereas, on the other hand, doping with Mn works best at low temperatures. The reason for this is that, because in a QD any embedded Mn<sup>2+</sup> ion is always close to the surface (within a few lattice constants), the thermal energy at higher synthesis temperatures is in general sufficient to anneal out the Mn<sup>2+</sup> ions [352]. Thus the same thermal effect which drives out unwanted defects leads to an elimination of Mn from the QD.

**Cd<sub>1-x</sub>Mn<sub>x</sub>S** Cd<sub>1-x</sub>Mn<sub>x</sub>S quantum dots with a size distribution in the range 2–100 nm and 0 ≤ x ≤ 0.5 have been synthesized by Bandaranayake et al. [353] on the basis of a reaction in aqueous solution of Na<sub>2</sub>S with a mixture of MnCl<sub>2</sub> and CdCl<sub>2</sub>. The water used in the preparation has to be distilled, deionized, and deoxygenated. The latter can be accomplished by bubbling the solution with argon gas. The desired Cd/Mn ratio was prepared with appropriate volumes of manganese and cadmium chlorides. The pH of the solution has to be adjusted to 1.5–2.0 by the addition of HCl to avoid the formation of Mn hydroxide after the addition of Na<sub>2</sub>S. Na<sub>2</sub>S was added to reach a stoichiometry of the reaction.



The precipitate has to be dried afterward. The as-grown particles have a cubic, zincblende structure and a mean

crystallite size of about 2.5 nm. By a subsequent annealing procedure in argon gas, a phase transformation into the stable hexagonal, wurtzite structure occurs. The phase transformation temperature was found to be about 300 °C. In [353] it was reported that the mean particle size increases during the annealing process, depending on the annealing temperature. The particle size can reach about 100 nm for an annealing temperature of about 500 °C.

A different way to prepare Cd<sub>1-x</sub>Mn<sub>x</sub>S was reported by Levy et al. [354, 355]. The syntheses of the QDs were performed in reverse micelles. A coprecipitation takes place with the mixing two micellar solutions: one is sodium di(ethyl-2-hexyl) sulfosuccinate (Na-(AOT)), and the other is a mixed micellar solution of Cd(AOT)<sub>2</sub>, Mn(AOT)<sub>2</sub>, and Na(AOT)<sub>2</sub>. A selective surface reaction occurs between the derivate and the cadmium and manganese ions at the interface. The solvent can be removed simply by evaporation. This allows the extraction of the particles. The coated dots have to be washed in ethanol to remove the surfactants. The very narrow size distribution of the Cd<sub>1-x</sub>Mn<sub>x</sub>S dots can be changed somewhat from an average size of about 1.8 nm to about 3.2 nm by varying the water content. The reported manganese concentration was 0 ≤ x ≤ 0.23.

**Zn<sub>1-x</sub>Mn<sub>x</sub>S** The first preparation of Mn-doped ZnS nanocrystals by a precipitation approach was reported by Bhargava et al. [356]. The QDs with sizes varying from 3.5 to 7.5 nm were precipitated by a reaction of diethylzinc with hydrogen sulfide in toluene to form ZnS. To dope the dots of ZnS, manganese chloride was reacted with ethylmagnesium chloride to form diethylmanganese in a tetrahydrofuran solvent and added to the reaction. The separation of the dots is maintained by coating with the surfactant methacrylic acid.

Bol and Meijerink [357, 358] prepared (Zn,Mn)S by an organometallic and an inorganic synthesis method. In the organometallic procedure Zn(C<sub>2</sub>H<sub>5</sub>)<sub>2</sub> and manganese cyclohexabutyrates were dissolved in toluene, and a methacrylic acid (stabilizer) was added. After the addition of a saturated solution of H<sub>2</sub>S in toluene, a white suspension appeared instantaneously. The inorganic procedure is similar to the standard method of nanocrystalline II-VI semiconductors. The synthesis was done in aqueous solution. Zn(CH<sub>3</sub>COO)<sub>2</sub>, Mn(CH<sub>3</sub>COO)<sub>2</sub>, and Na(PO<sub>3</sub>)<sub>n</sub> (stabilizer) were used. Again after the addition of Na<sub>2</sub>S solution a white fluid is obtained. In both methods the particles can be separated from the solution by centrifuging and must be rinsed with distilled water and dried. The X-ray diffraction pattern reveals a zincblende modification of the QDs. The size distribution was analyzed by transmission electron microscopy and was found to range from 3 to 5 nm; the majority of the particles were about 4 nm.

**Zn<sub>1-x</sub>Mn<sub>x</sub>Se** Norris et al. [359] prepared Zn<sub>1-x</sub>Mn<sub>x</sub>Se QDs with low x < 1% by adapting the high-temperature, organometallic synthesis of ZnSe reported by Hines and Guyot-Sionnest [360]. Dimethylmanganese (MnMe<sub>2</sub>) was used as organometallic Mn source. It was freshly prepared in a helium glovebox by reacting 0.5 ml of a 0.2 M MnCl<sub>2</sub> slurry in anhydrous tetrahydrofuran (THF) with 0.2 ml of 3 M methylmagnesium chloride in THF. The resulting clear golden solution was then diluted in 1.8 ml of anhydrous toluene. Subsequently, 0.5 ml of this 0.04 M MnMe<sub>2</sub> solution

was added to a syringe containing 4 ml of troctylphosphine (TOP), 1 ml of 1 M Se in TOP, and 82  $\mu\text{l}$  of diethylzinc. The syringe was removed from the glovebox and was used to inject the solution into a vigorously stirred reaction vessel with 15 ml of distilled hexadecylamine at 310°C under dry nitrogen.  $\text{Zn}_{1-x}\text{Mn}_x\text{Se}$  nanocrystals were then grown at 240–300 °C. The QDs were isolated from the growth solution by standard filtering techniques. The Mn concentration was adjusted by changing the amount of  $\text{MnMe}_2$  added to the reaction. Despite relatively high Mn:Zn ratios of the precursors, only a fraction of Mn (1–5% of the available Mn) was actually incorporated into the nanocrystals. Therefore, the reported Mn concentrations  $x_{\text{Mn}}$  are only in the range of 0.025–0.125%.

#### 4. PROPERTIES OF MAGNETIC AND DILUTED MAGNETIC SEMICONDUCTOR NANOSTRUCTURES AND ULTRAFINE PARTICLES

The presence of magnetic ions in nanostructures does not necessarily lead to completely new physics compared with nonmagnetic semiconductors. This holds in particular for diluted magnetic semiconductor nanostructures. In a zero magnetic field, the electronic and optical properties of these nanostructures can be described theoretically as being very similar to those of other semiconductor nanostructures. Quantum confinement effects and strain effects are dealt with in the same fashion as in nonmagnetic structures. For example, in  $\text{CdTe}/(\text{Cd},\text{Mn})\text{Te}$  or  $\text{ZnSe}/(\text{Zn},\text{Mn})\text{Se}$  multiple quantum wells, it is possible to treat the electronic states of the wells in the framework of the envelope function approximation by using the respective parameters (e.g., effective masses, dielectric constants, deformation potentials, etc.) of bulk  $\text{CdTe}$ ,  $\text{ZnSe}$ ,  $(\text{Cd},\text{Mn})\text{Te}$ , and  $(\text{Zn},\text{Mn})\text{Se}$ , respectively. In Section 4.1, we give an overview of these “nonmagnetic” effects due to the reduction of dimensions, as the knowledge of these effects is of fundamental importance for understanding their interplay with the modified magnetic properties. This will be discussed, in detail, for the diluted magnetic semiconductor nanostructures in Section 4.2. As there have been numerous publications over the last decade concerning two-dimensional diluted magnetic semiconductor structures such as quantum wells and superlattices, the corresponding sections about two-dimensional systems cannot be fully comprehensive. The major aim of the first two sections is to highlight the fact that today’s understanding of diluted magnetic semiconductor nanostructures is such that these structures have the potential to serve as good model systems in semiconductor technology. This offers interesting research possibilities for the future, for example, by making contributions to the development and improvement of growth and nanofabrication processes. Special heterostructures and nanostructures can be designed to address specific questions that can only be answered by using the magnetic properties of DMS. In addition, there are still many fundamental physical questions for which DMS heterostructures and nanostructures can offer novel ways of providing answers. Section 4.3 addresses semiconductor nanostructures which

exhibit spontaneous magnetization phenomena. We will discuss the effect of reduced dimensions on magnetic phase transitions as well as coupling phenomena between magnetic nanostructures.

### 4.1. Optical and Electronic Properties of Magnetic Semiconductor Nanostructures

#### 4.1.1. Quantum Wells and Superlattices

Conventionally the band structure of a heterostructure is represented only by the band lineup of the conduction band minimum and the valence band maximum as a function of the spatial coordinate  $z$  in the growth direction. Three possible band lineups can be imagined between a layer of material A and a layer of material B. These are depicted in Figure 39 as the “straddling” lineup, the “staggered” lineup, and the “broken gap” lineup. A priori it is not obvious if the band lineup is an intrinsic property of two materials A and B or mainly results from the growth conditions. Several theories have been developed over the last four decades, and many experiments have been performed to answer this question (for reviews see [361, 362]). The tuning of such interface discontinuities has now become a major tool in bandgap engineering [363, 364].

The band lineups with respect to the vacuum level of some wide-bandgap II–VI compounds, including Mn–VI and Mg–VI, are depicted in Figure 40. Data for zincblende  $\text{MnTe}$  and  $\text{MnSe}$  are deduced from the calculations of Wei and Zunger [365]; the data for the other compounds are from Faschinger et al. [366]. For the wide-bandgap compounds the band lineups are either “staggered” or “straddling” lineups. In this context a characteristic parameter, the chemical valence band offset (VBO), can be defined as the difference in the absolute energy positions of the valence band maxima of the two isolated materials:

$$\Delta E_v(A/B) = E_v(B) - E_v(A) \quad (39)$$

A linear change in the chemical VBO as a function of composition following the linear composition dependence of the bandgap is observed for the chemical VBO in heterosystems where material A is a ternary alloy and material B is one of the parent binary compounds, such as  $\text{Al}_{1-x}\text{Ga}_x\text{As}/\text{GaAs}$  or  $\text{Cd}_{1-x}\text{Mn}_x\text{Te}/\text{CdTe}$  [367, 368]. It is therefore meaningful to describe alloy systems by a chemical VBO ratio defined as chemical VBO per total bandgap difference (e.g., 35% for  $\text{Al}_{1-x}\text{Ga}_x\text{As}/\text{GaAs}$  and 35% for  $\text{Cd}_{1-x}\text{Mn}_x\text{Te}/\text{CdTe}$ ). Only a

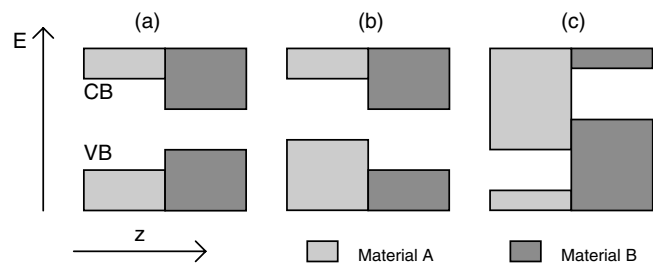


**Figure 39.** Possible band lineup between two semiconductors A and B. (a) Straddling. (b) Staggered. (c) Broken gap.

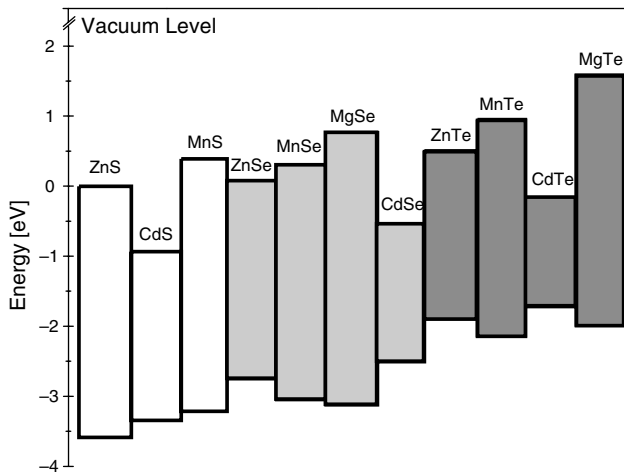


**Figure 40.** Band lineups with respect to the vacuum level for various wide-gap II-VI compounds, Mn-VI, and Mg-VI compounds.

few chemical VBO investigations have been carried out for the two systems  $\text{Zn}_{1-x}\text{Mn}_x\text{Te}/\text{ZnTe}$  and  $\text{Zn}_{1-x}\text{Mn}_x\text{Se}/\text{ZnSe}$ , which both show a nonlinear compositional dependence of the alloy bandgap. The results of Heimbrodt et al. [81] suggest that this leads to a nonlinear compositional behavior of the chemical VBO ratio. Optical experiments on electronic and excitonic states in quantum well structures offer a variety of possibilities for determining the chemical VBO. Two types of quantum well structures can be derived from the staggered or straddling band lineups. These are denoted as type I and type II, with electrons and holes spatially confined either in the same layer or in different layers. The two situations are depicted in Figure 41.

In the case of pseudomorphic growth the successive layers in the heterostructures are alternately subjected to biaxial tensile or compressive stresses, because of the different lattice parameters of the quantum well and the barrier material, respectively. Such biaxial stress fields can be considered as a sum of a hydrostatic and a uniaxial stress parallel to the growth direction. The influence of both stress fields on the bandgap energies of the individual layers of a heterostructure is well known. Strain effects contribute strongly to the net VBO.

Most II-VI and III-V DMS are grown on (100) substrates. The only relevant stress tensor elements in this case are

$$\sigma_{xx} = \sigma_{yy} = \sigma \neq 0 \quad (40)$$

$$\sigma_{zz} = 0 \quad (41)$$

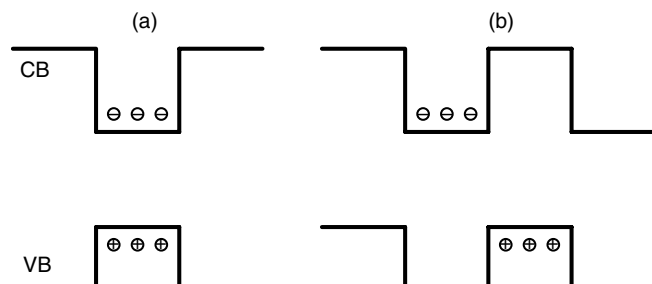


**Figure 41.** Type I and type II band alignments in QW structures.

It follows for the strain that

$$\varepsilon_{xx} = \varepsilon_{yy} = \frac{C_{11}}{(C_{11} - C_{12})(C_{11} + 2C_{12})} \cdot \sigma = \varepsilon \quad (42)$$

$$\varepsilon_{zz} = \frac{-2C_{12}}{(C_{11} - C_{12})(C_{11} + 2C_{12})} \cdot \sigma \quad (43)$$

$$\varepsilon_{xy} = \varepsilon_{xz} = \varepsilon_{yz} = 0 \quad (44)$$

The corresponding shifts of the energy bands and the valence band splitting can be calculated on the basis of the Bir-Pikus theory [369],

$$\Delta E_c = 2a_c \frac{C_{11} - C_{12}}{C_{11}} \cdot \varepsilon$$

$$\Delta E_{hh} = \left[ 2a_v \frac{C_{11} - C_{12}}{C_{11}} + b \frac{C_{11} + 2C_{12}}{C_{11}} \right] \cdot \varepsilon \quad (45)$$

$$\Delta E_{lh} = \left[ 2a_v \frac{C_{11} - C_{12}}{C_{11}} - b \frac{C_{11} + 2C_{12}}{C_{11}} \right] \cdot \varepsilon$$

where  $a_c$ ,  $a_v$ , and  $b$  are the deformation potentials and  $C_{11}$ ,  $C_{12}$  are the elastic constants.

In Figure 42 the strain dependence of the band structure is shown schematically for a zincblende-type semiconductor in the case of a biaxial strain. The valence band degeneracy at the  $\Gamma$ -point, caused by the cubic symmetry, is lifted. Schematic band diagrams for  $\text{CdTe}/(\text{Cd},\text{Mn})\text{Te}$  and  $\text{ZnSe}/(\text{Zn},\text{Mn})\text{Se}$  assuming a type I band alignment are depicted in Figure 43. For the  $\text{CdTe}$  wells the heavy hole (hh) is above the light hole (lh) band because of compressive strain in the well, whereas for the  $\text{ZnSe}$  wells the lh band is above the hh, because of the tensile strain.

Most IV-VI DMS are grown on (111) substrates. In this case, it is convenient to describe the stress tensor in the coordinate system  $(x', y', z')$ , where  $x' \parallel [1-10]$ ,  $y' \parallel [11-2]$ , and  $z' \parallel [111]$ . The stress tensor element  $\sigma_{z'z'}$  along the growth direction is zero, whereas the stresses in plane  $\sigma_{x'x'}$  and  $\sigma_{y'y'}$  are nonzero and no torsion occurs. Again the stress

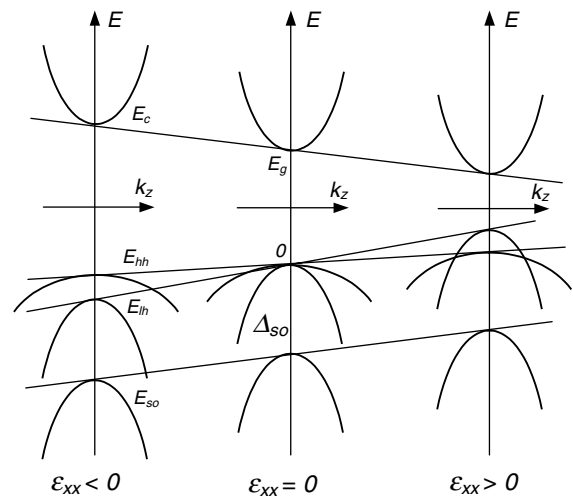


**Figure 42.** Band structure at the  $\Gamma$ -point for a zincblende-type semiconductor under biaxial compressive ( $\varepsilon_{xx} < 0$ ), zero ( $\varepsilon_{xx} = 0$ ), and tensile ( $\varepsilon_{xx} > 0$ ) strain.

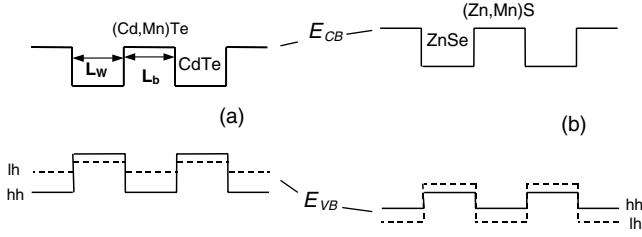


**Figure 43.** Schematic diagrams for the  $\Gamma$ -point band structure in (a) compressively strained CdTe QWs with (Cd,Mn)Te barriers under tensile strain and (b) tensilely strained ZnSe QWs with (Zn,Mn)Se barriers under compressive strain, assuming a free-standing superlattice.

tensor is related to the strain tensor elements  $\varepsilon_{x'x'}$ ,  $\varepsilon_{y'y'}$ , and  $\varepsilon_{z'z'}$ , where  $\varepsilon_{x'x'} = \varepsilon_{y'y'} = \varepsilon$ . The in-plane strain is usually determined by x-ray diffraction. The following relationship holds [258]:

$$\varepsilon_{z'z'} = -2 \frac{C_{11} + 2C_{12} - 2C_{44}}{C_{11} + 2C_{12} + 4C_{44}} \varepsilon \quad (46)$$

where  $C_{11}$ ,  $C_{12}$ , and  $C_{44}$  are elastic constants given in the crystallographic  $(x, y, z)$  coordinate system. The strain leads to energy shifts only of the conduction band and valence band states at the L-point, which are already nondegenerate because of the spin-orbit splitting [370]. However, because of the reduction of the symmetry the valleys in the conduction and valence band at the L-point are no longer equivalent. Different energy shifts arise for the [111] and the three equivalent, oblique (i.e., [11-1], [1-11], and [-111]) valleys of constant energy [371]:

$$\begin{aligned} \Delta E_{c,v}^{[111]} &= D_d^{c,v} (2\varepsilon_{x'x'} + \varepsilon_{z'z'}) + D_u^{c,v} \varepsilon_{z'z'} \\ \Delta E_{c,v}^{\text{oblique}} &= D_d^{c,v} (2\varepsilon_{x'x'} + \varepsilon_{z'z'}) + D_u^{c,v} \left( \frac{8}{9} \varepsilon_{x'x'} + \frac{1}{9} \varepsilon_{z'z'} \right) \end{aligned} \quad (47)$$

where  $D_d^{c,v}$  and  $D_u^{c,v}$  are the deformation potentials of the conduction (c) and valence (v) band states. The corresponding strain Hamiltonians are diagonal in the basis Bloch function sets used for the  $k \cdot p$  description of the  $\Gamma$ -point of III-V and II-VI DMS (Eqs. (18–20)) and of the L-point of the IV-VI DMS (Eq. (29)), respectively.

In Figure 44 the interplay of confinement and strain effects is seen on the lowest lh and hh excitons of ZnSe/(Zn,Mn)Se quantum wells with varying well width and  $x_{\text{Mn}} = 0.25$  in the barriers of same widths. The higher energy, in spite of the bigger hole mass of the hh exciton in the  $z$  direction, is due to the overcompensation of the confinement effect by tensile strain. The stronger confinement effect of the lh exciton with decreasing well width is due to the lighter effective mass in the  $z$  direction. The envelope function approximation is the most commonly used empirical approach to describing theoretically electronic states in heterostructures, taking into account band alignment, strain, and quantum confinement. There are several other methods, either other empirical ones such as tight-binding methods and pseudo-potential methods, or “first principal” ones such as local density functional methods and self-energy calculations in the local density approximation (for a review see [372]). The band lineup in a heterostructure consisting of layers of different semiconductors with abrupt interfaces

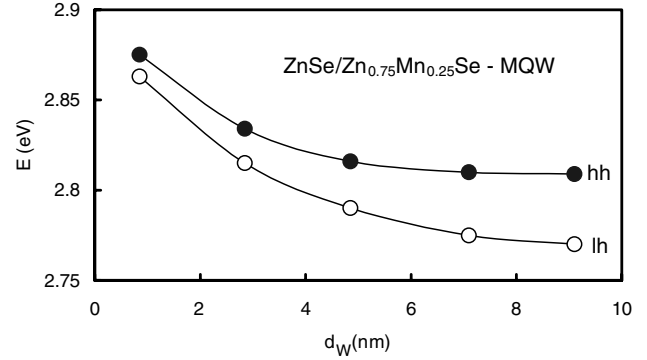


**Figure 44.** Exciton energies of ZnSe/(Zn,Mn)Se MQWs measured by reflection spectroscopy (five wells, barrier width  $L_b = 85$  nm,  $x_{\text{Mn}} = 0.25$ ). Reprinted with permission from [81], W. Heimbrodt et al., *J. Lumin.* 60–61, 344 (1994). © 1994, Elsevier Science.

acts on the band electrons as a slowly varying potential along the growth direction  $z$  in addition to the fast varying lattice-periodic crystal potential in each layer. Assuming that the valence and conduction bands in each layer can be described by the corresponding Hamiltonians in the framework of the Kane model and that the set of basis Bloch functions used is the same for all layers allows a separation ansatz for the wavefunction. The Hamiltonian splits into a bulk-like contribution in the layer ( $xy$  plane) and a contribution along the  $z$  direction, which can be interpreted as a Hamiltonian of an electron of band effective mass in a confining potential given by the band lineup. In its solution the envelope function has to fulfil boundary conditions at the interfaces between adjacent layers, leading to energy quantization in the  $z$  direction. The two assumptions restrict the applicability of the envelope function approximation to heterostructures with a conduction band minimum and valence band maximum, respectively, at the same points of the Brillouin zone. They also imply that no mixing between bands takes place at the interface. Both of these implications are reasonably fulfilled for almost all DMS heterostructures.

The Hamiltonian in the vicinity of the conduction band minimum and the valence band maximum can be written, respectively, as sums of  $k \cdot p$  contribution, strain contribution, and magnetic field contribution, for each layer. The matrix elements  $H_{ij}^{\text{tot}}$  of the respective total Hamiltonians in the representation of the corresponding set of basis functions are [373, 374]

$$\begin{aligned} H_{\text{tot}}^{ij} &= H_k^{ij} + H_{\text{strain}}^{ij} + H_{\text{mag}}^{ij} \quad i, j \in \{1, \dots, N\} \\ &= \sum_{\alpha, \beta} \{ D_{ij}^{\alpha\beta} k_\alpha k_\beta + P_{ij}^\alpha k_\alpha + E_{ij} \} \quad \alpha, \beta \in \{x, y, z\} \end{aligned} \quad (48)$$

To account for the band lineup, the constants on the diagonal of the  $k \cdot p$  Hamiltonian representing the band energy positions for  $k = 0$  must be given with respect to the vacuum level. Magnetic field and strain are  $k$ -independent quantities, so that the coefficients  $D_{ij}^{\alpha\beta}$  and  $P_{ij}^\alpha$  originate solely from the  $k \cdot p$  contribution, whereas the  $E_{ij}$  are sums of the band energy positions at  $k = 0$  and the strain and magnetic field contributions. The crystal periodicity in the layer plane is conserved in the heterostructure, so that  $k_x$  and  $k_y$



(the in-plane components of the momentum) remain good quantum numbers, whereas  $k_z$  is no longer a good quantum number because the periodicity along the  $z$  direction is disturbed by the additional potential originating from the band lineup across the heterostructure. To account for this,  $k_z$  is replaced by  $-i\frac{\partial}{\partial z}$  in Eq. (48). The following ansatz for the wavefunction in each layer can be made:

$$\begin{aligned}\psi^A(r) &= \sum_{j=1}^N F_j^A(r) u_{j0}^A(r) \\ F_j^A(r) &= \exp(ik_x x + ik_y y) \chi_j^A(z) \quad \forall j \in \{1, \dots, N\}\end{aligned}\quad (49)$$

The  $F_j^A$  are the coefficients of the wavefunction in the representation of the basis set ( $u_j^A$ ) in layer A. Combining Eqs. (48) and (49) gives a Schrödinger-like matrix equation for the envelope functions  $\chi_j^A$  for each layer A, with  $k_x$  and  $k_y$  acting as parameters:

$$\sum_{i=1}^N H_{ji}^A \chi_i^A(z) = E \chi_j^A(z) \quad \forall j \in \{1, \dots, N\} \quad (50)$$

where the operators  $H_{ij}^A$  are quadratic forms in  $-i\frac{\partial}{\partial z}$ . This is a system of  $N$  coupled second-order linear differential equations which can be solved for any value of  $E$  for each layer. The boundary conditions at the interface between layers of different materials A and B define the eigenvalues  $E$  of the heterostructure.

Usually continuity of the total wavefunction  $\psi(r)$  and a continuity condition for its derivative based on the conservation of particle current are demanded. Assuming the sets of basis functions in layers A and B are similar,

$$u_{j0}^A(r) = u_{j0}^B(r) \quad \forall j \in \{1, \dots, N\} \quad (51)$$

which is reasonable, given that the structural and chemical similarities between the host materials and their magnetic alloys (this has been shown for III–V materials [375–377] and can be shown in a similar way for the IV–VI and II–VI materials) allow the continuity conditions to be transferred to the envelope functions. The following  $2N$  conditions are obtained at the interface [374]:

$$\begin{aligned}\chi_j^A(z=0^-) &= \chi_j^B(z=0^+) \\ &\times \sum_{l=1}^N \left[ (D_{jl}^{zx} + D_{jl}^{xz}) k_y - 2i D_{jl}^{zz} \frac{\partial}{\partial z} \right]^A \chi_l^A(z=0^-) \\ &= \sum_{l=1}^N \left[ (D_{jl}^{zx} + D_{jl}^{xz}) k_y - 2i D_{jl}^{zz} \frac{\partial}{\partial z} \right]^B \\ &\times \chi_l^B(z=0^+) \quad \forall j \in \{1, \dots, N\}\end{aligned}\quad (52)$$

The second boundary condition for the derivative reduces in the  $N = 1$  case, assuming that  $D^{\alpha\beta}$  is diagonal in  $\alpha$  and  $\beta$ , to

$$\frac{1}{m_A^*} \frac{\partial}{\partial z} \chi^A(z=0^-) = \frac{1}{m_B^*} \frac{\partial}{\partial z} \chi^B(z=0^+) \quad (53)$$

as derived by other authors [378–380].

Solving Eq. (51) for all of the layers of the heterostructure and matching the envelope functions at each interface

according to Eq. (52) allows one to calculate the energy quantization in the  $z$  direction. Calculating for different parameters  $k_x$  and  $k_y$  gives the energy dispersions within these subbands.

This treatment of the heterostructure assumes ideal interfaces with no changes in the lattice periodicity of the basis functions and no additional potentials in the interface monolayer. It is shown in several papers that interface effects modify the boundary conditions given in Eq. (52). Zhu and Kroemer [381, 382] and Ando et al. [383, 384] have investigated the effects of discontinuity potentials at the interface monolayer. Trzeciakowski has investigated the effects of different symmetries of the basis functions and different lattice periodicity in the adjacent layers [385, 386]. All of these investigations show as well that the modifications of the boundary conditions are negligible in the case of a type I quantum well structure with bands of similar symmetry in the quantum well and the barrier, and structurally similar well and barrier materials.

The resulting set of  $N$  linear second-order differential equations is usually solved by a transfer matrix approach. In most cases the electronic states of the II–VI and III–V DMS can be calculated by a simple one-dimensional transfer matrix method [387–389]. This also holds in magnetic fields (as discussed in Section 4.2) as long as the quantization directions due to magnetic field, strain, and confinement are the same. If this is not the case (for example, magnetic field experiments in Voigt geometry) the Hamiltonian in the valence band has nonzero off-diagonal elements due to the magnetic field coupling of light and heavy holes, and a higher-dimensional transfer matrix method needs to be applied [390–394] (see also Section 4.2.3). Also for the IV–VI DMS, a higher-dimensional transfer matrix method is needed [395].

Another important aspect which needs to be considered in a theoretical treatment of semiconductor structures is excitonic effects. In several optical experiments an electron is excited from a state in the fully occupied valence band into a state in the unoccupied conduction band, leaving an unoccupied state in the valence band behind. This state, commonly denoted as a hole, can be treated as a positively charged particle of the valence band effective mass. The Coulomb interaction binds electron and hole together into an electron–hole pair called an exciton [396]. In the effective mass approximation the exciton energy levels can be described by a hydrogenic energy level scheme given for 3D and 2D excitons by [397]

$$E_{3D} = E_g - \frac{\mu}{m_0} \frac{1}{\varepsilon^2} R_y \frac{1}{n^2}, \quad E_{2D} = E_g - \frac{\mu}{m_0} \frac{1}{\varepsilon^2} R_y \frac{1}{(n-1/2)^2} \quad (54)$$

where  $R_y = 13.6$  eV is the Rydberg constant,  $\mu$  is the reduced mass of the electron–hole pair, and  $\varepsilon$  is the dielectric constant of the semiconductor material. Typical parameters are  $\varepsilon \approx 10$  and  $\mu \approx 0.1m_0$ , giving 3D exciton binding energies on the order of 10 meV. The Bohr radii, defined by analogy with the hydrogen atom, are on the order of 100 Å, which justifies the use of a macroscopic dielectric constant. The dimensionality of the system has a major impact on the magnitude of the exciton binding energy. The 2D binding

energy in the lowest excitonic state  $n = 1(1s)$  representing a QW of zero width and with infinitely high barriers is already four times larger than the respective binding energy in the 3D case. QWs in semiconductor heterostructures have finite widths and finite barrier heights. Models used to calculate  $1s$  exciton binding energies in heterostructures have to account for the dimensionality aspect and should, therefore, give binding energies somewhere between the 3D and 2D limits.

Various approaches to calculation of the exciton binding energies have been reported in the literature. As examples, we want to discuss three approaches. One is a simple analytical approach applicable to calculation of the exciton binding energy between the lowest electron and the lowest hole state in type I quantum structures. This approach accounts for the dimensionality effect by introducing a fractional dimension  $\alpha$  with values between 2 and 3 [398–400]. The other two methods are variational approaches solving the Schrödinger equation for an electron and a hole in the conduction band and valence band lineup plus a Coulomb interaction term. In one of the methods the Coulomb interaction is treated as a perturbation, assuming that the confining potentials in the conduction and the valence band are bigger than the exciton binding energy [401, 402]. The second variational method is applicable in the case where the confinement potential in the conduction band is bigger than the exciton binding energy but the confinement energy in the valence band can be of the same magnitude or even smaller than the exciton binding energy [403]. This method has to be used in the calculation of excitonic transitions in the vicinity of a magnetic field-induced type I–type II transition. Many more sophisticated calculations of excitonic energies have been carried out in recent years, taking into account refinements such as valence band mixing [404], Coulomb coupling with continuum states, nonparabolicity of the conduction band, and the effective mass and dielectric constant mismatch [405] for systems where better knowledge of the material parameters is available (e.g., the  $\text{Ga}_{1-x}\text{Al}_x\text{As}/\text{GaAs}$  system).

A full knowledge of the band structure of DMS heterostructures in a zero magnetic field is essential for studying the magneto-optical properties of these systems. Because of the strong influence of strain and band alignment on the band states, these parameters also influence the interplay of the band states with the subsystem of the localized magnetic ions (e.g., the giant Zeeman splitting, etc.). In general, strain state and band alignment of semiconductor heterostructures can be determined by careful experimental studies of the optical transitions in these structures and then comparing the experimental values with model calculations, as described above. For example, the splitting between the lowest hh exciton and the lowest lh exciton as a function of QW width is very sensitive to the VBO in many structures. This has also been used to determine the VBO for several DMS systems such as  $\text{CdTe}/(\text{Cd},\text{Mn})\text{Te}$  [368]. In other systems, where the strain splitting is comparable to the band gap difference, such as  $\text{ZnTe}/\text{Zn}_{1-x}\text{Mn}_x\text{Te}$  [398] with  $x < 10\%$  or  $\text{ZnSe}/\text{Zn}_{1-x}\text{Mn}_x\text{Se}$  with  $x \approx 20\%$  [406], this measurement is not a good probe of the VBO. This is shown in Figure 45 for  $\text{ZnTe}/\text{Zn}_{0.93}\text{Mn}_{0.07}\text{Te}$  QWs. The lh-hh splitting  $\Delta$  as a function of well width is not a sensitive probe of the

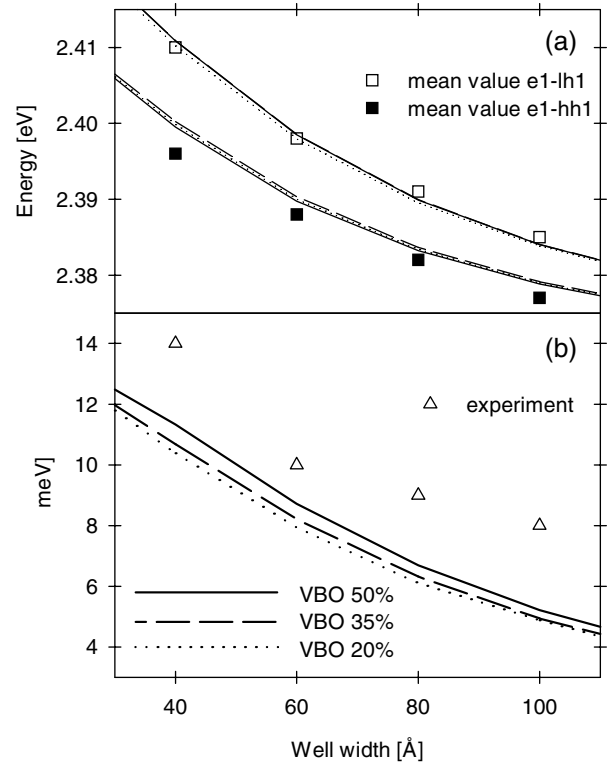


**Figure 45.** Splitting between hh exciton and lh exciton as a function of well width for  $\text{ZnTe}/\text{Zn}_{0.93}\text{Mn}_{0.07}\text{Te}$  QWs. See text for details. Experimental points are from [398], with permission from Institute of Physics Publishing.

VBO. In the case of DMS heterostructures, it is also possible to determine the VBO by approaches which are based on the unusual magneto-optical properties of DMS, and, thus, to explore the strong dependence of the giant Zeeman splitting on overlap of the band states with the localized magnetic ions. These approaches comprise studies of the magnetic-field-induced type I–type II transition [407–410], spin-flip Raman scattering studies of the electrons confined in the QWs [406, 411], as well as studies of the giant Zeeman splittings between  $\sigma^+$  and  $\sigma^-$  QW excitons [406], or even specially designed structures [412]. However, these DMS-specific approaches also yield some difficulties; in particular, one needs to account for the modified magnetic properties of the magnetic ions in heterostructures compared with bulk material. Some of these aspects are discussed in more detail in Section 4.2. Most of the work dealing with the band alignment of II–VI DMS heterostructures has been carried out on  $(\text{Cd},\text{Mn})\text{Te}/\text{CdTe}$ . A nearly complete list of references concerning the VBO of this system can be found in [412]. In the case of IV–VI DMS a combination of zero-field and magnetic field experiments is usually required to determine the band alignment accurately, as the band structure is more complex in this class of DMS than in the case of the II–VI DMS [256, 413, 418]. Table 7 gives an overview of the band alignments of various heterostructures containing DMS. In particular for IV–VI structures, strong temperature dependences of the VBO were reported for some material systems (e.g., Heinrich et al. observed a type I–type II transition for  $\text{PbSe}/(\text{Pb},\text{Eu})\text{Se}$  with decreasing temperature [428]).

**Table 7.** VBO for various DMS quantum well structures.

Semiconductor A	Semiconductor B	$x$ (%)	$y$ (%)	$z$ (%)	$T$ (K)	VBO ratio (%)	Type [Ref.]
PbTe	$\text{Pb}_{1-x}\text{Mn}_x\text{Te}$	$\leq 3$			2	0	I [413]
PbTe	$\text{Pb}_{1-x}\text{Eu}_x\text{Te}$	5			300	50	I [414]
		$\approx 3$			5, 77	$45 \pm 20$	I [415]
PbTe	$\text{Pb}_{1-x}\text{Eu}_x\text{Te}_{1-y}\text{Se}_y$	$\leq 3$			2–5	$50 \pm 30$	I [416]
PbSe	$\text{Pb}_{1-x}\text{Mn}_x\text{Se}$	10	11		4	80	I [417]
		$\approx 1$			$< 20$	–50	II [418]
		$< 2$			2	–60	II [307]
ZnSe	$\text{Zn}_{1-x}\text{Mn}_x\text{Se}$	$\approx 20$			2	$20 \pm 10$	I [406]
		27			2	5–10	I [419]
		5			2		Flat band [420]
$\text{Zn}_{1-x}\text{Mn}_x\text{Se}$	$\text{Zn}_{1-y-z}\text{Be}_y\text{Mg}_z\text{Se}$	5	8	16	2	$22 \pm 4$	I [421]
		9	2.8	0	2		Flat band [421]
$\text{Zn}_{1-y}\text{Cd}_y\text{Se}$	$\text{Zn}_{1-y}\text{Mn}_y\text{Se}$	16	15		2	$13 \pm 2$	I [422]
ZnSe	$\text{Zn}_{1-x}\text{Fe}_x\text{Se}$	10			4	5	I [423]
		1			4		Flat band [424]
ZnTe	$\text{Zn}_{1-x}\text{Mn}_x\text{Te}$	7			4	$28 \pm 4$	I [409]
		7			2	$30 \pm 10$	I [407]
$\text{Cd}_{1-x}\text{Mn}_x\text{Se}$	$\text{Zn}_{1-y}\text{Mn}_y\text{Te}$	25	0		2	–150	II [425]
		0	6, 10		2	$\approx -90$	II [426]
CdTe	$\text{Cd}_{1-x}\text{Mn}_x\text{Te}$	$\leq 3$			2	$35 \pm 5$	I [408]
		$\approx 7$			2	$45 \pm 5$	I [411]
		20–30			2	$25 \pm 7$	I [412]
		12, 27			2	$30 \pm 6$	I [427]

#### 4.1.2. Quantum Wires and Quantum Dots

There are not many papers about optical and electronic properties of diluted magnetic QWRs, but there are numerous papers about QDs made of magnetic and diluted magnetic semiconductors. Therefore, we will discuss results on both types of nanostructures together if possible.

**Enhanced Bowing of the Band Gap with Mn Concentration** The bandgap variation with increasing Mn concentration was measured for (Cd,Mn)S and (Cd,Mn)Se QWRs by Brieler et al. [305] and Chen et al. [306]. Figure 46 shows a comparison of the energy positions of the band gaps of bulk  $\text{Cd}_{1-x}\text{Mn}_x\text{S}$  and  $\text{Cd}_{1-x}\text{Mn}_x\text{S}$  wires. Because of the quantum confinement of the excitons in the wires

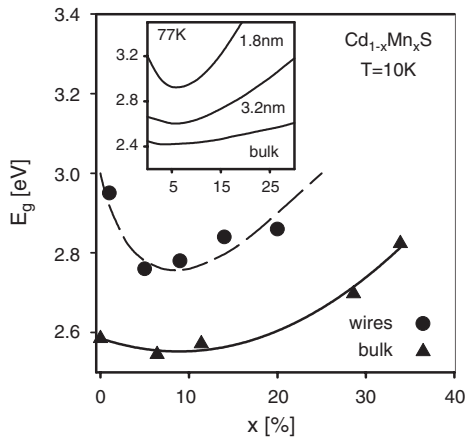


**Figure 46.** Bandgap variation for  $\text{Cd}_{1-x}\text{Mn}_x\text{S}$  QWRs as a function of  $x$ . Inset: Bandgap variation as a function of  $x_{\text{Mn}}$  of  $\text{Cd}_{1-x}\text{Mn}_x\text{S}$  QDs of two different sizes.

an increase in the direct bandgap of about 200 meV was observed for (Cd,Mn)S. Similar results were found for  $\text{Cd}_{1-x}\text{Mn}_x\text{Se}$  bulk and wires. The quantum confinement effect in this system is about 350 meV. The larger blue shift for (Cd,Mn)Se is due to the larger exciton Bohr radius. An interesting result is that both wire systems exhibit a larger bowing of the bandgap depending on the manganese concentration than do the corresponding bulk samples. This agrees with results reported for (Cd,Mn)S QDs [355] by Levy et al., who were able to show that the exchange interaction-induced bandgap bowing becomes stronger with decreasing dot diameter (see schematic inset of Fig. 46). As already discussed in Section 2.2, such a bowing is known for bulk (II,Mn)VI. In bulk, as a rule of thumb, the bowing is stronger when the bandgap is wider (i.e., bulk (Cd,Mn)S shows a band gap bowing, but (Cd,Mn)Se bulk does not).

The present interpretation of this effect, based on the discussion in Section 2.2, is twofold: (i) a change in the exchange integrals and in the  $p$ - $d$  hybridization may cause this enhanced bowing or (ii) the  $s$ -level repulsion model may explain the effect. It should be mentioned at this point that the magneto-optical measurements, which are discussed in Section 4.2.2, will give further indications that an enhancement of the  $p$ - $d$  exchange integrals takes place. Albe et al. [429] determined the effects of the inclusion of manganese in small ZnS dots in the framework of a tight-binding model with renormalized parameters. The main result was that Mn doping enhances the energy gap in addition to the confinement. However, in the calculation hardly any shift of the valence band compared with undoped ZnS is observed, and the main shift occurs in the conduction band. The effect is stronger when the dots are smaller. This result somewhat contradicts the above interpretation. However, only a single

Mn impurity in the center of the ZnS cluster was assumed in the calculation (corresponding to  $x \approx 0.5\%$  for a spherical cluster with a 3-nm diameter), and no explicit concentration dependence was calculated. We address the possible effects of reduced dimensions on the  $p$ - $d$  hybridization again in Section 4.2 in the context of the magneto-optical properties.

### Energy Transfer from the Band States into the Mn Subsystem

In 1994 Bhargava et al. [356] reported that Mn-doped ZnS nanocrystals can yield both high luminescent efficiencies and lifetime shortening of the  $\text{Mn}^{2+}$  transitions. They studied Mn-doped ZnS nanocrystals with sizes varying from 3.5 to 7 nm. The measured external quantum efficiency was about 18% and increased with decreasing particle size. The luminescence decay was at least five orders of magnitude faster than the corresponding  $\text{Mn}^{2+}$  transitions in bulk crystals. The explanation given by Bhargava et al. was twofold: first, there was an enhanced energy transfer to the Mn states, because of the strong localization of the free carriers in the dots, and second, there was a faster decay of the Mn transition because of an enhanced  $s$ ,  $p$ - $d$  mixing. In a theoretical paper, Yan et al. [430] presented a possible mechanism to explain the results of Bhargava et al. Yan et al. considered the exchange Coulomb interaction between the  $d$  electrons of the manganese and the electrons of the host lattice of the dot. The authors could demonstrate, assuming that the spin of the ground state of the dot is not zero and that the exchange interaction causes a mixing between the excited  ${}^4T_1(3d)$  state of the manganese ions and a certain excited state of the dot, that the spin forbidden transition could almost be allowed. Furthermore, it was shown that the degree of mixing increases with decreasing particle size. A completely different explanation was given by Bol and Meijerink [358]. They showed that the normal decay time of the  $\text{Mn}^{2+}$  internal transition is not really changed and is still about 2 ms, as known from the bulk material, but a fast component is observable, which has to be attributed to processes of transfer into defect related bands, which differ for various preparation methods. Tanaka et al. [431] studied the energy levels of the  $3d^5$  multiplet in  $\text{ZnS}:\text{Mn}^{2+}$  and concluded that the degree of mixing of the  $s$  and  $p$  states with the  $3d$  orbitals does not change significantly in the dots with a reduction of the diameter down to a few nanometers.

There are other reports of the introduction of  $\text{Mn}^{2+}$  ions into samples with self-activated growth of dots (e.g., by the Stranski-Krastanov method). It is assumed that the influence of different surface states of such dots is reduced compared with dots in glassy or liquid matrices or even as powder samples. It was reported that by introducing only a small amount of Mn either into the QDs [432, 433] or into the matrix with undoped QDs [433, 434], the excitonic luminescence is drastically reduced compared with that of undoped samples. In particular, by the application of an external magnetic field, the excitonic luminescence can be strongly enhanced. The reason for this is a very effective energy transfer from the excitonic states into the  $3d$  shell. This effect is also observable in bulk samples if the bandgap is wide enough to excite and observe the internal  $\text{Mn}^{2+}(3d^5)$  states. The crucial point is the spin selection rule for the overall system of the excited band state and the  $3d$  shell.

The transfer channel can be suppressed because of the Zeeman spin splitting. This energy transfer, however, is not a special property of nanostructures made of diluted magnetic semiconductors. Therefore, it will not be further discussed here. The reader may refer to papers that are particularly devoted to this subject (e.g., [435, 436, 530]).

### Changes of Band Alignment Due to Nanofabrication

In Section 4.1.1 we discussed in detail the interplay of strain and quantum confinement effects on the electronic and excitonic band structures of 2D semiconductor heterostructures. In what follows we show that this interplay is also of importance in lower dimensional structures. In particular, we show that changes in the strain state in QWRs and QDs prepared by combinations of lithography and etching from MBE- or MOVPE-grown parent structures already occur at length scales much bigger than those where additional quantum confinement effects become relevant. This feature is again common to all semiconductor nanostructures prepared in this fashion. However, we still want to discuss this point, as this zero-field effect has a considerable impact on the magneto-optical properties of the samples. As an example, Figure 47 shows photomodulated reflectance spectra of a  $\text{ZnTe}/\text{Zn}_{0.93}\text{Mn}_{0.07}\text{Te}$  QD sample and its parent MQW structure [308]. The dot diameter is 200 nm. For these lateral dimensions no additional quantum confinement effects are expected. Nevertheless, the energy positions of the excitonic features shift dramatically, as indicated by the arrows in the figure. This effect can be fully explained by a change in the strain state of MQW region of the sample due to

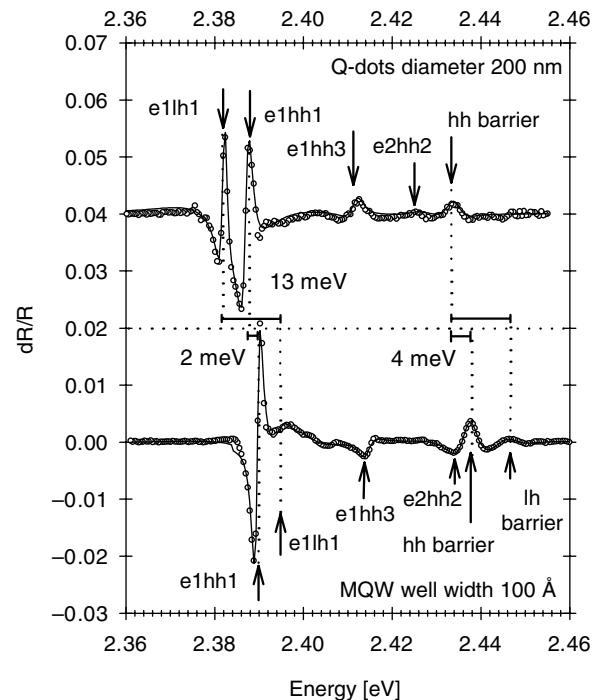


**Figure 47.** Photomodulated reflectance spectra of a  $\text{ZnTe}/\text{Zn}_{0.93}\text{Mn}_{0.07}\text{Te}$  quantum disc sample and its parent MQW structure. Reprinted with permission from [308], P. J. Klar et al., *Semicond. Sci. Technol.* 11, 1863 (1996). © 1996, Institute of Physics Publishing.

the nanofabrication process. The MQW layers of the parent structure were pseudomorphically strained to the ZnTe buffer layer (giving rise to a splitting of the  $\text{Zn}_{0.93}\text{Mn}_{0.07}\text{Te}$  barrier states in the corresponding spectrum). The more or less freestanding dot pillars show a strain relaxation and are strained, to good approximation, to an intermediate value of the ZnTe and the  $\text{Zn}_{0.93}\text{Mn}_{0.07}\text{Te}$  lattice constant weighted by the overall thickness of the corresponding layers in the dot pillar. This effect leads to a reversal of the order of light hole and heavy hole states such that the lowest excitonic state in the QD sample is the  $e1lh1$  exciton, whereas the lowest state in the MQW parent sample is the  $e1hh1$  exciton. This leads to very different magneto-optical properties of the two samples, as shown by magneto-PL [437]. Strain changes have also been observed in  $\text{ZnSe}/(\text{Zn,Mn})\text{Se}$  QD pillar structures of similar lateral dimensions (see also Fig. 48) [310].

#### Improving the Sample Quality by Nanofabrication

Again this is an aspect peculiar to QWRs and QDs prepared by combinations of lithography and etching with lateral dimensions where no additional confinement effects are expected ( $100 \text{ nm} < d < 500 \text{ nm}$ ), but those lateral sizes are comparable to length scales concerned with doping and dislocations. Figure 48 depicts photoluminescence spectra of two QD samples with diameters of 200 nm and 100 nm, respectively, and the corresponding parent  $\text{ZnSe}/\text{Zn}_{0.72}\text{Mn}_{0.28}\text{Se}$  SQW structure [310].  $D^0X$  and  $X_{e1lh1}$  denote the donor-bound and the free exciton emission bands, respectively, from the QW layer in each specimen. There are several interesting changes in the PL from the ZnSe well. The shifts of the  $D^0X$  and the  $X_{e1lh1}$  lines toward lower energy in the two disc samples are due to changes in a strain relaxation in the QD pillars as discussed above. Here, we focus on two other noticeable features: (i) the

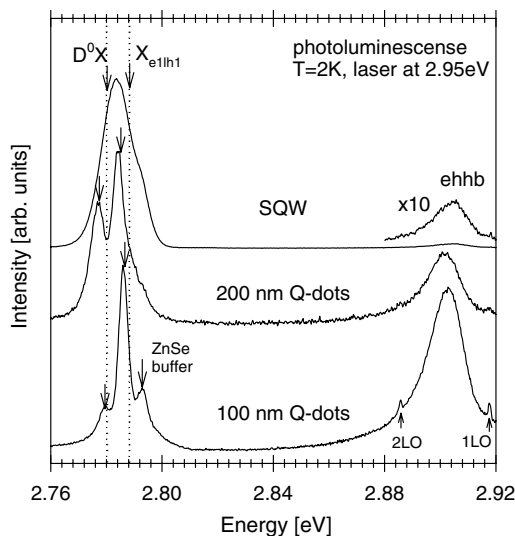


**Figure 48.** Photoluminescence spectra of two QD samples with diameters of 200 nm and 100 nm, respectively, and the corresponding parent  $\text{ZnSe}/\text{Zn}_{0.72}\text{Mn}_{0.28}\text{Se}$  SQW structure.  $D^0X$  and  $X_{e1lh1}$  denote the donor-bound and the free exciton emission bands, respectively, from the QW layer in each specimen. Reprinted with permission from [310], P. J. Klar et al., *Phys. Rev. B* 57, 7114 (1998). © 1998, American Physical Society.

sharpening of the two emission lines in the QD samples compared with the parent SQW which is also observed in the PLE excitation spectra and (ii) the decrease in intensity of the  $D^0X$  emission relative to the  $X_{e1lh1}$  emission. The former can be explained as follows. The linewidth in the original SQW is determined mainly by the inhomogeneous strain fields associated with dislocations. Assuming a typical value of  $10^7 \text{ cm}^{-2}$  for the dislocation density implies a mean separation of 3000 nm between dislocations. The strain fields of the dislocations overlap and lead to a non-uniform perturbation of the excitonic potential, resulting in an inhomogeneous broadening of the emission lines. This perturbation is obviously switched off in the QD pillars which do not contain a dislocation; thus the emission of such a QD pillar is much sharper. With decreasing dot size the relative number of dot pillars without dislocations increases. Point (ii) is related to the doping. The samples were unintentionally doped  $n$ -type. An upper limit is about  $10^{16} \text{ cm}^{-3}$ . A simple estimate shows that this corresponds on average to about two donors in the ZnSe well region per pillar of the 200-nm QD sample and to about 0.5 donors in the ZnSe well region per pillar of the 100-nm QD sample. Statistically the number of QDs without donor ions in the well increases with decreasing QD diameter. For this argument to hold, one has to assume that the cross-sectional area for exciton capture by a donor is bigger than the lateral dimension of the QD. However, this is a reasonable assumption, as discussed in [310].

Of course, other effects come into play when the dot size is decreased further in the fabrication of nanostructures by combined lithography and etching techniques. These are surface damage, interdiffusion, etc. caused by etching, which can cause the sample quality to seriously deteriorate. We discuss some of these aspects in the next section and show how the degree of interdiffusion between the well region and the DMS barrier due to IBE etching can be accessed in  $\text{CdTe}/\text{Cd}_{1-x}\text{Mn}_x\text{Te}$  QDs by magneto-optical experiments. However, in the dot size regime between 500 and 100 nm, nanofabrication allows one to improve the sample quality considerably without altering the 2D character of the samples. Such samples can prove very useful in the study of magneto-optical phenomena in DMS [311, 438].

## 4.2. Diluted Magnetic Semiconductor Nanostructures in an External Magnetic Field

As has been remarked previously, most interesting magnetic phenomena observed in diluted magnetic semiconductors are based on the  $s,p-d$  exchange interaction between the extended band states and the localized magnetic ions. As a consequence the electronic and excitonic states experience giant Zeeman splittings when a magnetic field is applied. Interesting phenomena arise in nanostructures consisting of alternating layers of magnetic and nonmagnetic semiconductors, since the band edges of the magnetic semiconductor experience large shifts and splittings, whereas the corresponding splittings in the nonmagnetic layers are negligible. The conduction and valence band offsets can be tuned simply by applying a magnetic field. It is possible, for example, to convert a type I band alignment into a type II and

vice versa [423, 439, 440]. Furthermore, the tuning is spin selective. Spin-up and spin-down electrons experience different band shifts and therefore different band offsets. This can be used to separate spins with different spin orientations into different layers. Such spin superlattices were first suggested by von Ortenberg [441] and have been realized on the basis of the ZnSe/(Zn,Mn)Se heterosystem by various authors [420, 424, 442]. Furthermore, the field dependence can be used to control the coupling between wells which are separated by a barrier of a diluted magnetic semiconductor. Tunneling processes in particular can be studied in great detail [443–445].

We emphasize that a huge number of papers have been published concerning these interesting phenomena, which cannot be reviewed here. But it is interesting to note that most of the effects are rather universal and are not properties specific to diluted magnetic semiconductor nanostructures. The diluted magnetic semiconductor nanostructures are, however, an excellent tool for the study of those phenomena in one and the same sample. In the case of nonmagnetic semiconductor nanostructures, the preparation of series of samples would be necessary to obtain a comparable amount of information. Thus, the value of such information is often restricted by the limited reproducibility of the preparation parameters in series of nanostructures.

In the following we want to focus on properties and effects which are rather unique for the magnetic nanostructures. These are the magnetic properties, with special emphasis on their dependence on the restricted geometries (e.g., reduced dimensions).

#### 4.2.1. *s,p-d Exchange Interaction: Influence of the Interface*

The giant Zeeman splitting caused by the *s,p-d* exchange interaction is reduced in quasi-two-dimensional layers of heterostructures consisting of alternating DMS and non-DMS layers. This is valid for DMS QWs between nonmagnetic barriers as well as for nonmagnetic QWs between DMS barriers because of the reduced interaction of the carrier wavefunctions with the manganese ions. A part of the probability density experiences a layer without magnetic ions in both cases. The reduction of the giant Zeeman splitting is determined by the penetration of the barriers by the wavefunctions. Let us consider, for example, the type I CdTe/(Cd,Mn)Te heterosystem, where (Cd,Mn)Te is the barrier. The CdTe QW states in the magnetic field can be calculated in the framework of the envelope function approximation simply by using the known bulk values for the splittings of the conduction band and valence band states of (Cd,Mn)Te as a function of the magnetic field to define at each field confining potentials for the different spin orientations. The splitting of the barrier potential results then in a respective field-dependent splitting of the QW excitonic states. At first sight it seems that no additional new physics needs to be introduced, as the applied magnetic field can be considered simply as a parameter. The calculation is basically a calculation of QW states for different barrier heights (see Section 4.1.1). It has been found, however, that doing so leads to poor agreement with the experimental results [442, 446, 447]. The reduced effective Mn concentration  $x_{\text{eff}} = a(x_{\text{Mn}}) \cdot x_{\text{Mn}}$  introduced in Eq. (12) is due to the cluster

formation as result of the statistical distribution of the Mn<sup>2+</sup> ions on the cation lattice, as already mentioned in Section 2.4, which yields a reduced mean molar spin density. Mn-Mn pairs on nn cation sites couple antiferromagnetically and do not contribute to the magnetization, as they do not respond to magnetic fields of moderate strengths. The ground state of three Mn<sup>2+</sup> ions on nn sites depends on whether they are an open triple or a closed triangle. Nagata et al. [133] determined the ground-state spin of an open triangle to be  $S_{\text{OT}} = 5/2$ , and the ground state of the closed triple to be  $S_{\text{CT}} = 1/2$ . At a surface or interface of a diluted magnetic semiconductor the number of clusters is drastically reduced, yielding an enhanced paramagnetism at the surface compared with the bulk value for the same concentration  $x$ . This effect is further enhanced by the fact that a real interface is never an abrupt interface. The interface roughness can be considered an extra dilution with corresponding enhanced paramagnetism.

Most theoretical work on the behavior of the Mn<sup>2+</sup> ions at the interface [446, 448] is based on the work of Behringer on the formation of single, double, and triple clusters in a lattice occupied by two different atomic species [449]. Grieshaber et al. and Ossau and Kuhn-Heinrich were able to explain qualitatively the intrinsic magnetic properties of an interface such as the increase in the scaling parameters  $a$  and the decrease in the Curie–Weiss-like parameter  $\theta$  in Eq. (13) by modifying the expressions derived in [449] for the cluster formation probabilities in bulk material for the case of an ideal interface. There are two theoretical approaches in the literature that include extrinsic interface effects. Both approaches neglect the effects of Mn clusters formed by three and more Mn<sup>2+</sup> ions. The first model of Grieshaber et al. [448] is applicable to arbitrary interface profiles. A local average Mn<sup>2+</sup> spin  $S_{\text{local}}(x_{\text{NN}}(z), B, T)$  of the Mn<sup>2+</sup> ions is assigned to each monolayer in the growth direction, where  $x_{\text{NN}}$  is the average of the actual Mn contents in the monolayer at  $z$  and the two adjacent layers. Using a known empirical dependence of the bulk average Mn<sup>2+</sup> spin  $S_{\text{bulk}}(x, B, T)$  given in Eq. (13), the following relation is assumed:

$$S_{\text{local}}(x(z), B, T) = S_{\text{bulk}}(x_{\text{NN}}(z), B, T) \frac{x(z)}{x_{\text{NN}}(z)} \quad (55)$$

With the use of this model the effects of interface roughness and diffusion [447, 451], interface profiles, and segregation [452, 453] have been investigated for asymmetric Cd<sub>1-x</sub>Mn<sub>x</sub>Te/CdTe/ Cd<sub>1-y</sub>Zn<sub>y</sub>Te QW structures. The interface yields an important contribution to the enhanced Zeeman splitting of the QW states [450, 452, 454]. Cibert et al. [447] and Gaj et al. [452] were able to show that the roughness of a CdTe/(Cd,Mn)Te interface is very different from that of a (Cd,Mn)Te/CdTe interface and can be clearly distinguished by their difference in Zeeman splitting, because of the different paramagnetic response. The QW excitons in heterostructures with DMS barriers (such as CdTe/(Cd,Mn)Te, ZnSe/(Zn,Mn)Se, etc.) are extremely sensitive to the interface, as the probability density at the interface (i.e., the first few monolayers) is high compared with the bulk of the barrier due to the exponential decay of the wavefunction. These results are summarized in the



publication by Grieshaber et al. [448]. Recently, Syed et al. added a thorough study of the dependence of the optical properties of (Zn,Mn)Se/ZnSe small-offset superlattices on the magnetic-nonmagnetic interface structure [531].

The second model by Fatah et al. [450] simulates a bulk effective Mn concentration  $x_{\text{eff}}$  numerically as the number of Mn singlets per total number of cation sites in a cube lattice consisting of  $2 \times 10^5$  atoms. Analyzing the two monolayers at the surface of the cube allows one to determine the enhanced effective Mn concentration at an ideal interface. The results have been compared with experimental results on bulk II–VI DMS materials, and good agreement was obtained, although the formation of higher clusters was neglected. The results are independent to a first approximation of the II–VI host material. The model has been extended to investigate extrinsic effects in four-monolayer-wide steplike interfaces as displayed in Figure 49. The height of the step is characterized by the roughness parameter  $\chi$  [454, 455]. The effective Mn concentrations calculated for the monolayers *a* to *f* are depicted for two values of  $\chi$  in Figure 50. In agreement with the other studies, it can be seen that interface effects are of considerable importance for Mn concentrations  $x > 10\%$  and can be ignored for lower Mn concentrations.

It has been shown by Klar et al. for the ZnSe/(Zn,Mn)Se [406] and ZnTe/(Zn,Mn)Te [407] heterosystems that a careful consideration of both effects, the interface roughness and the enhanced paramagnetism at the interface, is needed to get accurate values of the conduction and valence band offsets of paramagnetic–diamagnetic interfaces. This is illustrated in Figures 51 and 52. For a fixed depth of the zero-field potential of a particular single particle, an enhanced paramagnetism leads to an increase in the magnetic-field splitting between the two spin components of the single particle. Neglect of the enhanced paramagnetism of the interface region in the calculation of such a splitting would have to be compensated for by a decreased potential depth compared with the real potential depth. The authors performed two types of experiments: (i) spin-flip Raman scattering on donor-bound QW electrons to determine the saturation Raman shift  $S_{\text{sat}}$  (i.e., probing the Zeeman splitting in the conduction band only) and (ii) magneto-optical experiments to probe the giant Zeeman splitting  $\Delta_{\text{hh}}$  of the e1hh1 QW states (i.e., probing a combination of conduction band and valence band splitting). Neglecting the paramagnetism in the analysis of the  $S_{\text{sat}}$  data would lead to an underestimation of the chemical conduction band offset which is equivalent

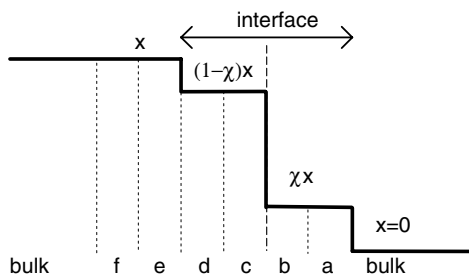


**Figure 49.** Step-like interface profile as proposed by Stirner et al. [454]. The parameter  $\chi$  is a measure for the step height.  $\chi = 0$  corresponds to an ideal interface. The interface is four monolayers wide (*a*, *b*, *c*, *d*).

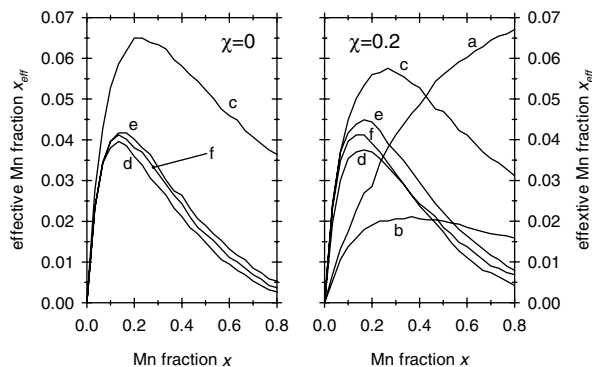


**Figure 50.** Calculated effective Mn concentrations as a function of bulk barrier Mn content  $x$  for the monolayers *a* to *f* depicted in Figure 49.

to an overestimation of the VBO. Because of a magnetic field splitting between the two heavy hole components in the barrier that is five times bigger than the magnetic splitting between the two electron components in the barrier,  $\Delta_{\text{hh}}$  will be dominated by the contribution from the valence band. Thus, neglect of the enhanced paramagnetism would lead to an underestimation of the VBO in the calculation of  $\Delta_{\text{hh}}$ . A combined analysis of  $\Delta_{\text{hh}}$  and  $S_{\text{sat}}$  allows the elimination of interface roughness effects in the determination of the VBO and, furthermore, should allow a determination of the interface parameter  $\chi$ . In this case the combined analysis yields a value of 20% for the VBO and an interface roughness described by  $\chi = 0.1$ .

As a second example we will show how knowledge of the interplay of band states (in this case conduction band states only, probed by spin-flip Raman scattering) and enhanced paramagnetism of the  $\text{Mn}^{2+}$  ions at interfaces and interdiffused layers can be used to access damage in DMS nanostructures due to the fabrication process. This highlights again the usefulness of DMS structures as model systems in semiconductor technology. Figure 53 depicts series of spin-flip Raman (SFR) spectra of a QD sample with a dot diameter of 100 nm and the corresponding parent CdTe/Cd<sub>0.93</sub>Mn<sub>0.07</sub>Te MQW. The QD sample was prepared by EBL followed by Ar<sup>+</sup> IBE, as described in Section 3.

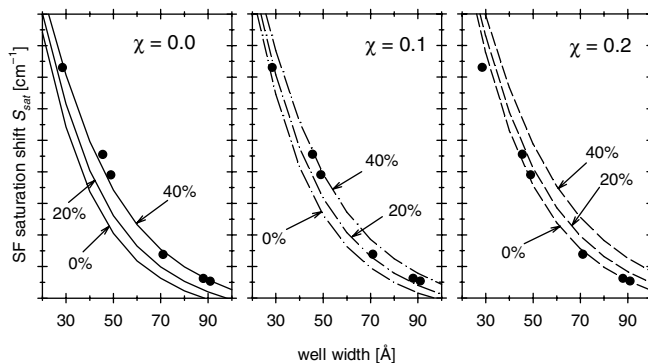


**Figure 51.** Calculated dependences of the spin-flip saturation shift  $S_{\text{sat}}$  on well width and different VBOs for three different interface parameters  $\chi = 0.0$  (left),  $\chi = 0.1$  (center), and  $\chi = 0.2$  (right) together with the experimental data obtained by fitting spin-flip Raman scattering spectra. Reprinted with permission from [406], P. J. Klar et al., *Phys. Rev. B* 57, 7103 (1998). © 1998, American Physical Society.

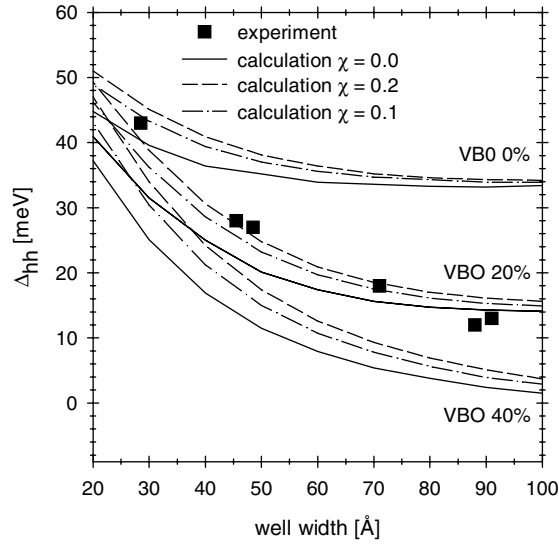


**Figure 52.** Calculated dependences of the splitting between the  $\sigma^+$  and the  $\sigma^-$  components of the  $e1hh1$  exciton for different pairs of ( $\chi$ , VBO), together with the experimental values obtained from the photoluminescence excitation spectra at 3 T. Reprinted with permission from [406], P. J. Klar et al., *Phys. Rev. B* 57, 7103 (1998). © 1998, American Physical Society.

An SEM image of the QD sample is shown in Figure 54. In Figure 53 the left graph depicts the series of SFR spectra of the MQW and the right graph the SFR spectra of the 100-nm QDs. The two displayed series cover the same range of excitation energies, 1.615–1.625 eV. The spectra of the MQW show two bands, SF1 and SF2, which have previously been assigned to SFR signals of electrons bound, respectively, to donors in the QW and to donors near the well–barrier interface [411, 456]. The arrows in the figure

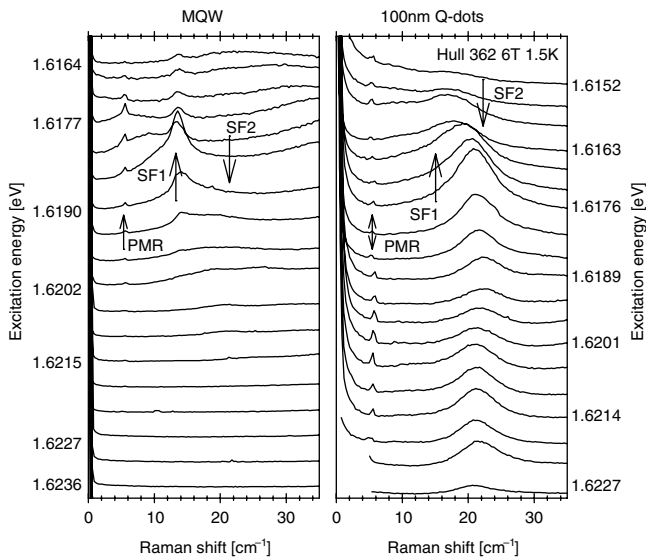


**Figure 53.** Spin-flip Raman scattering spectra for  $\text{Cd}_{1-x}\text{Mn}_x\text{Te}/\text{CdTe}$  QD and MQW samples ( $T = 1.5$  K,  $B = 6$  T) for excitation energies ranging approximately from 1.615 eV to 1.625 eV. The spectra are displaced vertically for clarity. The QD sample was prepared by EBL followed by  $\text{Ar}^+$  IBE (see Fig. 54).

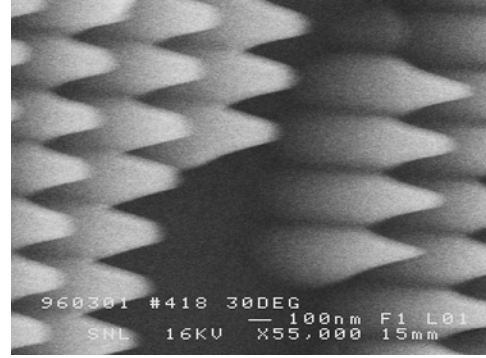


**Figure 54.** SEM image of 100-nm  $\text{CdTe}/\text{Cd}_{1-x}\text{Mn}_x\text{Te}$  QD sample prepared by EBL followed by  $\text{Ar}^+$  IBE.

mark the positions of the signals SF1 and SF2. The SF1 signal (which is the stronger signal in the MQW) is much reduced for the 100-nm QD sample and can hardly be distinguished from SF2 by eye. This can be interpreted in terms of increased interdiffusion with Mn in the sidewalls of the QDs and a destruction or interdiffusion with Mn of the top QWs, both of which increase the number of donor positions where the bound electrons have a large overlap with  $\text{Mn}^{2+}$  ions. Thus, SF2 is enhanced and SF1 is reduced. This shows that the damage due to the  $\text{Ar}^+$  etching during the nanofabrication process is quite considerable in this sample. This becomes clear when we look again at the SEM image of this QD sample in Figure 54. The QDs have a pointed top, indicating that the Ti protection mask was already destroyed before the IBE process had ended, leading to an exposure of the original sample surface to the  $\text{Ar}^+$  ions for the remaining time of the etch process. The depth of such a damaged layer in  $\text{Cd}_{1-x}\text{Zn}_x\text{Te}/\text{CdTe}$  QD samples etched under comparable conditions has been estimated by Gourgon et al. [457] and Mariette et al. [458] to be approximately 30 nm. An interesting point to note in Figure 53 is the Raman signal at  $5.5\text{ cm}^{-1}$ , which is the PMR (i.e., a spin-flip of an  $e^-$  in the  $3d$  orbital of a  $\text{Mn}^{2+}$  ion). The PMR signal, like the spin-flip signal of the QW electrons, is strongly enhanced in resonance with the QW transitions [459], and its resonance width is an indication of the range of energies of the respective excitonic transitions. The sharp resonance of the SF1 signal in the MQW sample is associated with a sharp resonance of the PMR signal; the width of the resonance is in both cases about 4 meV. A different behavior is observed for the PMR signal in the series of spectra of the 100-nm QDs. It shows a much wider resonance from 1.615–1.622 eV. This is associated with an enhanced SF2 signal for the higher excitation energies in the spectra of the QDs compared with the MQW, where neither a SF signal nor a PMR signal is visible. The Raman shift of the SF2 signal of the QDs hardly changes in this range. This can be explained by assuming that the SF2 signal in this range originates from the QWs on top of the QDs, which are probably totally interdiffused with Mn and therefore have SF signals with a larger Raman shift and excitonic transitions with a magnetic field behavior different from that of lower QWs which are still intact.

### 4.2.2. *s,p-d* Exchange Interaction: Influence of the Dimensional Crossover

In addition to the relevance of the interface in the discussion of magneto-optical effects in DMS nanostructures, another important aspect needs to be considered: whether the *s-d* and *p-d* exchange integrals themselves show a dimensional dependence. As already shown in Section 4.1.2, the bowing of the bandgap energy increases tremendously with enhanced quantum confinement. It is known that in the series (Cd,Mn)Te–(Cd,Mn)Se–(Cd,Mn)S, as a chemical trend, the *p-d* and *d-d* exchange interactions increase. The value of the exchange integrals is determined by the anion-derived upper valence band, as discussed in detail by Larson et al. [120]. In the case of bulk material, the difference between the *d*-states and the valence band edge, however, is almost constant ( $E_v - E_{3d} \approx 3 \dots 3.5$  eV). This rather surprising result is caused by the fact that the shift of the valence band edge is compensated for by a corresponding shift of the *d*-level energy to lower energies because of the larger Mn-to-anion charge transfer. The reason for the increasing exchange integrals of the bulk series is the enhanced hybridization due to the reduced anion–cation distance. The situation is different in the case of quantum confinement, as discussed in Section 4.1.2 for nanowires and nanodots. Now the decreasing  $E_v - E_{3d}$ , apart from possible strain effects, should be the dominant reason for the enhanced bowing. Decreasing  $E_v - E_{3d}$  will lead to an increased exchange interaction integral. A direct experimental determination of the dimensional dependence would be desirable. Because of the interface effects, which have been discussed above, an unambiguous deduction of the pure exchange integrals, however, is not an easy task.

Magneto-optical studies have been performed by Heimbrodt et al. [442, 460], with special emphasis on the dimensional dependence of the *s,p-d* exchange interaction in (Zn,Mn)Se layers. A series of layers with  $x_{Mn} = 0.04$  and layer thicknesses between 500 nm and five monolayers have been studied. It is known that because of the exchange-induced bowing of the bandgap of the (Zn,Mn)Se alloys, ZnSe/Zn<sub>0.96</sub>Mn<sub>0.04</sub>Se forms a so-called spin superlattice [441]. In a zero magnetic field no band offsets between the ZnSe layers and the (Zn,Mn)Se layers occur. Applying an external field the giant Zeeman splitting of the magnetic (Zn,Mn)Se layers modifies the band structure, as depicted schematically in Figure 55. For one spin component of the conduction band and the valence band, the (Zn,Mn)Se layer

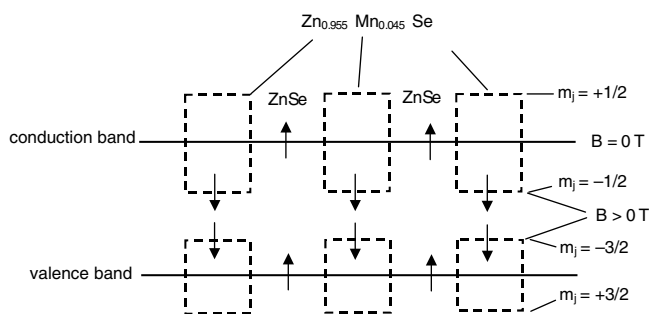


**Figure 55.** Schematic band alignment of a ZnSe/ZnMnSe superlattice with  $x_{Mn} = 0.045$ . - - - -  $B > 0$  T; ———,  $B = 0$  T.

forms a QW, and the corresponding spin bands of ZnSe act as barriers. For the other spin states the situation is reversed (i.e., the (Zn,Mn)Se is a barrier and the ZnSe acts as the QW). In that way it was ensured in [442] that the excitonic oscillator strength of the  $\sigma^+$  component of the (Zn,Mn)Se excitons was sufficient to be measured, even for samples with only a few monolayers of (Zn,Mn)Se. In Figure 56a the energy positions are given for various (Zn,Mn)Se layers, depending on the magnetic field. In many publications such curves were simply fitted by Brillouin functions, and reduced exchange integrals  $N_0\alpha$  and  $N_0\beta$  were claimed. The main reason for the strong effective decrease in the exchange integral, however, is the tremendous penetration of the excitonic wavefunction into the barriers where no  $Mn^{2+}$  ions are located and not a genuine 3D  $\rightarrow$  2D crossover effect. To take into account the different amounts of penetration of the excitonic wavefunctions, Heimbrodt et al. [442] determined the corresponding shifts of the (Zn,Mn)Se well bottom energies by eliminating the confinement effects. The genuine Zeeman shift of (Zn,Mn)Se and its dependence on the field and well widths are given in Figure 56b. It has been shown in the paper that, with decreasing layer width, a strong increase in  $a(x_{Mn})$  and a strong decrease in the Curie–Weiss parameter  $\Theta$  in Eq. (13) were necessary to fit the experimental curves with a modified Brillouin function. The experimental values are given as full squares for  $a(x_{Mn})$  and full circles for  $\Theta$  versus the well

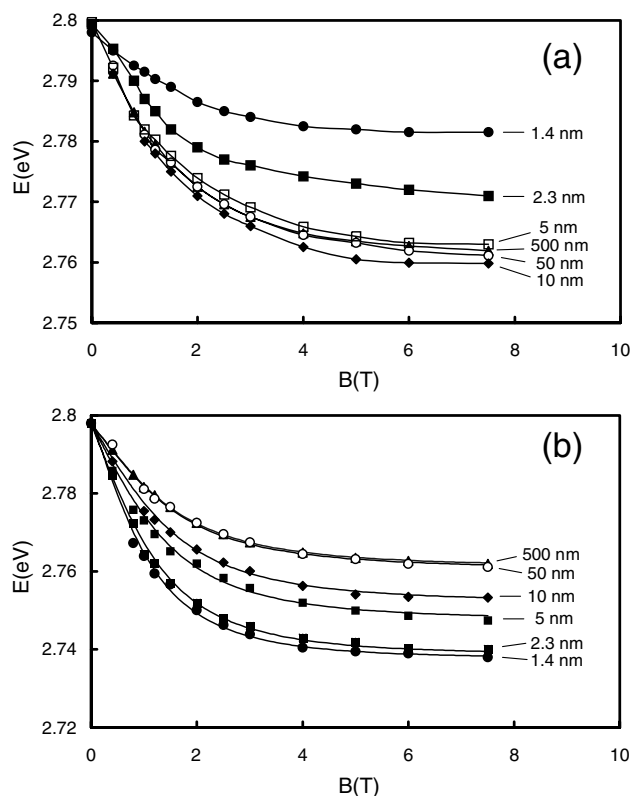


**Figure 56.** (a) Experimental determined energies of the  $\sigma^+$  excitonic states of (Zn,Mn)Se QWs of different thicknesses ( $x_{Mn} = 0.045$ ). (b) Calculated QW bottom energies of QWs of (a) (see text for details). Reprinted with permission from [442], W. Heimbrodt et al., *Mat. Sci. For.* 182–184, 755 (1995). © 1995, Trans Tech Publications.

width in Figure 57, respectively. The full line, including the enhanced paramagnetism at the interface, was calculated. As discussed in [442], even a realistic interdiffusion profile of three or four monolayers is not sufficient to explain the strong enhancement of the experimental  $a(x_{\text{Mn}})$  with decreasing well width. In a subsequent paper the authors gave further indications that interface effects alone cannot account for the enhanced paramagnetism. Using a series of (Zn,Mn)Se/ZnSe QW samples with  $x_{\text{Mn}} = 0.12$ , one can transform the type I heterosystem into a type II system [460] by applying a magnetic field. The electrons remain in the ZnSe wells, whereas the holes will move into the (Zn,Mn)Se layers. The resulting spatially indirect excitons are an extremely sensitive probe of the interface behavior, as they are constrained to stay at the interface because of the Coulomb interaction. It has been shown that even in this case, where excitons are strongly localized near the interface, a tremendous enhancement of  $a(x_{\text{Mn}})$  with decreasing thickness of the magnetic layer is necessary to explain the observed Zeeman splitting. It could be concluded convincingly that this is not due to an increasing influence of the interface with its interdiffusion profile (which, of course, becomes more important with decreasing layer width compared with the volume effect), but rather to a change in the paramagnetic response itself. The authors concluded that an extra dimensional dependence of the paramagnetic response is very likely.

What are the possible physical reasons for a dimensional dependence of the paramagnetic response? There are basically two explanations: (i) An enhanced exchange integral  $N_0(\alpha - \beta)$  could explain the experimental findings. This would be in agreement with the enhanced bandgap bowing, discussed above. (ii) The existence of a long-range  $d-d$  exchange interaction could give rise to a smaller  $a(x_{\text{Mn}})$  than calculated by assuming nearest-neighbor interaction only. Such long-range  $d-d$  interaction would then lead vice versa to a quasi-enhanced paramagnetism in the case of a  $3\text{D} \rightarrow 2\text{D}$  transition, because a strong dimensional dependence is expected. Such a long-range effect could be the magnetic dipole-dipole interaction. A dipole-dipole interaction would also explain the fact that a spin glass transition

is observable in the diluted magnetic semiconductors, even below the percolation limit, as discussed in Section 2.3.

Let us start with some remarks about the second explanation. Some measures of the rather long-range interaction are the Curie-Weiss parameter  $\Theta_{(\text{B})}$  in the modified Brillouin function and the Curie-Weiss temperature  $\Theta$ . The high temperature susceptibility  $\chi$  shows a Curie-Weiss behavior,

$$\chi = C/(T - \Theta) \quad (56)$$

It must be considered that the Curie-Weiss parameter  $\Theta_{(\text{B})}$  and the Curie-Weiss temperature  $\Theta$  are not necessarily identical, as the former is usually determined at low fields and low temperatures. In the low-field and low-temperature case, nn pairs do not contribute to the paramagnetic response. Therefore only more distant pairs lead to a finite  $\Theta_{(\text{B})}$  in the case of diluted magnetic semiconductors. As shown by Spalek et al. [183], the Curie-Weiss temperature can be calculated in the high-temperature limit:

$$\Theta(x_{\text{Mn}}) = -\frac{2}{3}x_{\text{Mn}}S(S+1)\sum_p J_p z_p / k_B \quad (57)$$

In this expression  $J_p$  is the exchange integral for a pair of the  $p$ th neighbor shell, and  $z_p$  is the number of cations on the  $p$ th sphere around a given cation. In the case of the Curie-Weiss temperature  $\Theta$  the sum runs from  $p = 1$  to infinity, but in the case of the Curie-Weiss parameter  $\Theta_{(\text{B})}$  the sum runs in the simplest approximation from  $p = 2$  to infinity. The Curie-Weiss temperature  $\Theta$  probes the sum of all interactions, whereas the low-temperature Curie-Weiss parameter  $\Theta_{(\text{B})}$  mainly probes the long-ranged tail of the interaction. Evidence for the correctness of these statements is obtained from the steplike behavior of the magnetization as discussed in Section 2. Apart from other higher order corrections, which are necessary at low temperatures, it is evident from Eq. (57) that a  $3\text{D} \rightarrow 2\text{D}$  crossover will reduce the Curie-Weiss parameter simply by reducing the number of cations on all neighbor shells. Theory predicts that the exchange integral  $J_p$  should decrease rapidly with increasing distance of the neighbor shell, since the physical origin is the exchange interaction with an exponential decay. It has been found by various authors, however, on the basis of experimental data on thermodynamic properties like specific heat, magnetization, susceptibility, and the paramagnetic spin glass phase transition, that a phenomenological power law describes the experimental findings much better. A detailed discussion of the experimental results and interpretation has been given by de Jonge and Swagten [138]. The determined exchange interaction parameters behave like

$$J_p(R) \propto R^{-n} \quad (58)$$

where  $R$  is the distance of the  $p$ th neighbor shell. The parameter  $n$  varies in the range of  $n \approx 7.6$  for (Zn,Mn)S and 6.8 for all of the (Cd,Mn)-chalcogenides, (Zn,Mn)Se, and (Zn,Mn)Te. For the narrow gap diluted magnetic semiconductors (Hg,Mn)Te and (Hg,Mn)Se a somewhat smaller value of  $n \approx 5$  has been found. Recent magnetization experiments on (II,Mn)VI performed at 20 mK revealed magnetization steps which allowed a determination of higher

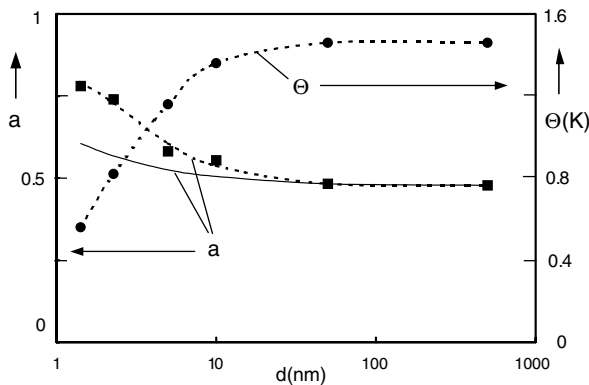


**Figure 57.** Experimental values of  $a(x_{\text{Mn}})$  and of the Curie-Weiss parameter  $\Theta(x_{\text{Mn}})$  as a function of the (Zn,Mn)Se QW width ( $x_{\text{Mn}} = 0.04$ ). The full line is calculated (see text for details). Reprinted with permission from [442], W. Heimbrodt et al., *Mat. Sci. For.* 182–184, 755 (1995). © 1995, Trans Tech Publications.

exchange constants, that is,  $J_1(=J_{nn})$ ,  $J_2(=J_{nnn})$  to  $J_4$ . It was found that the exchange constants do not decrease monotonically with increasing distance. In particular, it was always  $|J_4| > |J_2|$  [172, 173].

The important point for our discussion is that the increasing number of cations in the  $p$ th shell leads to remarkable contributions of the pair interactions in the case of bulk 3D diluted magnetic semiconductors. The strong decrease in  $\Theta$  with decreasing well width (see Fig. 57) is a clear hint that this might be the underlying effect. Those long-range interactions must then consequently have an effect on the overall value  $a(x_{Mn})$ , and a 3D  $\rightarrow$  2D transition would eventually result in an increasing parameter  $a(x_{Mn})$ , as was observed in the experiment.

Let us now come back to the first explanation. As already mentioned, it is very likely that the enhanced  $p$ - $d$  exchange integral may contribute to the enhanced paramagnetism. This has been suggested already in [460]. The quantum confinement effect shifts the  $p$ -states to lower energies, and the better energetic overlap between the  $p$ -states and the  $d$ -states leads to the increasing  $p$ - $d$  hybridization. This is in good agreement with the semiempirical tight-binding calculations of Larson et al. [120], where the valence band exchange integral has been determined to be

$$N_0\beta = -32V_{pd}^2[(E_{3d} + U_{\text{eff}} - E_v)^{-1} + (E_v - E_{3d})^{-1}] \quad (59)$$

where  $V_{pd}$  is the hybridization parameter and  $U_{\text{eff}}$  is the electron-electron interaction term of the Hubbard form. As a rather intra-atomic property of manganese,  $U_{\text{eff}}$  is not expected to change appreciably. So it is obvious from Eq. (59) that the hybridization parameter  $V_{pd}$  (mainly dependent on the Mn-anion distance) and the energy separation of the valence band edge and the  $3d$  levels  $E_v - E_{3d}$  determine the exchange integral  $N_0\beta$ . In our opinion, it is not clear currently which effect is the dominant one. It is very likely, however, that each plays a role.

It must be mentioned that there are more experimental results which seem to be in contradiction to the second effect and make the whole situation even more puzzling. In a very recent paper Yasuhira et al. [461] made a similar analysis of the photoluminescence Zeeman shift of magnetic (Cd,Mn)Te QWs between (Cd,Mg)Te barriers. They described the Zeeman shift by a reduction factor which accounts for the penetration into the nonmagnetic barriers of the electrons and holes, respectively. This description is physically equivalent to the calculation done in [442]. Nevertheless, Yasuhira et al. [461] needed a second reduction factor which accounts for the dimensionality effect. This reduction factor varies from about 0.95 for 114-nm QWs down to about 0.75 for 2.8-nm QWs. In contrast to this, the exchange integral  $J_{nn}$ , which was estimated from the magnetization steps, did not show any well width dependence. The authors ascribed this discrepancy to the fact that  $J_{nn}$  is based on a rather local interaction, and a larger range of  $k$  values may influence the exchange integral, whereas for  $N_0\beta$  a rather limited  $k$  range comes into play. This explanation is based on a theoretical calculation of Bhattacharjee [462], who studied the Zeeman splitting at reduced dimensions in the framework of an effective mass approximation for the confined states and the wave vector dependence of

the  $s,p$ - $d$  exchange interaction parameters in bulk diluted magnetic semiconductors. Bhattacharjee could show that the wave vector dependence of the  $s,p$ - $d$  exchange interaction parameters leads to a dimensionality effect. Mackh et al. [463] studied QWs of (Cd,Mn)Te/(Cd,Mn,Mg)Te with a substantial band offset but only a small discontinuity in the fractional Mn concentration across the interfaces. The assumption was that there is no discontinuity in the  $s,p$ - $d$  or  $d$ - $d$  exchange interactions. The giant Zeeman splitting of the heavy hole excitons was found, however, to be reduced with respect to the bulk by a factor which depends on the (Cd,Mn)Te well width. A minimum of about 0.9 at a well width of 4.5 nm was reported. In the aforementioned paper, Bhattacharjee calculated an effect which was much smaller than these experimental findings, but the minimum could be shown to be in qualitative agreement with the experimental data. In a recent paper Merkulov et al. [464] studied a sample similar to that used by Mackh et al. [463] by spin-flip Raman scattering and found a strong reduction of the  $s$ - $d$  exchange integral by 25%. As a responsible mechanism they suggested again the kinetic exchange term of the conduction band electrons with finite momentum. They could achieve a quantitative agreement between the experimental data and the calculations.

There are not many experimental results on samples with further reduced dimensions, (e.g., QWRs or QDs). Recently Chen et al. [298] studied the magneto-photoluminescence of mesa-shaped (Cd,Mn)Te/(Cd,Mg)Te QWRs. The Zeeman shift of the excitonic photoluminescence from the mesas in a magnetic field was significantly decreased compared with a similar QW. The wire width, however, was about 70 nm, and therefore no lateral confinement effect was observed. Because of the relaxation of the (Cd,Mn)Te well inside the wire compared with the compressive strained QW, a red shift was seen. The relaxation is accompanied by an increase of the Mn-anion distance, and, therefore, as has been mentioned, the  $p$ - $d$  exchange parameter in Eq. (59) should be reduced, which inevitably explains the reduced Zeeman shift.

Feltn et al. [465, 466] reported recently on the magnetic properties of (Cd,Mn)S nanoparticles of diameters in the range 1.8–4 nm and various concentrations in the range  $0 < x_{Mn} < 0.25$ . The authors fitted the Zeeman shifts with a modified Brillouin function and found that the effective spin  $S_{\text{eff}}$  (which is based on the nomenclature used in this review,  $S_{\text{eff}} = a(x_{Mn}) \cdot S$ ) is smaller in the nanoparticles than in bulk samples. The authors concluded that the number of spin-correlated clusters is higher in the nanocrystals, which should be due to a stronger  $Mn^{2+}$ - $Mn^{2+}$  interaction in the dots compared with bulk. The stronger interaction was directly derived from increasing ESR linewidth with decreasing cluster size, at the same Mn concentration. It was not discussed, however, how much the ESR linewidth is broadened because of the increasing fluctuation of the Mn concentration with decreasing dot sizes. Furthermore, the authors did not take into account that an increasing  $d$ - $d$  interaction, which is the basis for a stronger coupling, is based on or is, at least, correlated with an increase in the  $p$ - $d$  exchange interaction, which was assumed to be constant. On the basis of the above-mentioned semiempirical

tight-binding calculations of Larson et al. [120], the  $d$ - $d$  exchange integral has been determined to be

$$J_{dd}(R_{ij}) \propto -2V_{pd}^4 [U_{\text{eff}}^{-1}(E_v - E_{3d} - U_{\text{eff}})^{-2} - (E_v - E_{3d} - U_{\text{eff}})^{-3}] \quad (60)$$

In a comparison of Eqs. (59) and (60), the correlation between the superexchange interaction and the  $p$ - $d$  exchange integral is obvious. This would partly relax, however, the interpretation of the authors where an unchanged  $p$ - $d$  exchange integral  $N_0\beta$  was used. The Zeeman shift and splitting (see Eqs. (26) and (27)) are determined, however, by the product of  $N_0\beta$  and  $S_{\text{eff}}$ , as  $\Delta E \propto a(x_{\text{Mn}}) \cdot S \cdot x_{\text{Mn}} \cdot N_0(\alpha - \beta)$ . Thus, a different interpretation might be possible, which is based on a reduced  $s$ , $p$ - $d$  exchange interaction integral similar to the results discussed above. But even a second effect must be taken into account. All of the interpretations are based on the assumption of a random distribution of the Mn ions. A deviation of the random distribution (e.g., a higher probability to form clusters) would immediately lead to a similar reduction of the effective spin. As already mentioned, there have been several reports of the correlation of preparation parameters and the probability of an enhanced segregation or enhanced clustering. This actually opens up a Pandora's box, and an interpretation is impossible without exact knowledge of the real distribution of the magnetic ions.

Summarizing all of the present information, it is not easy to find the way out of this apparently puzzling situation. Further experimental work is needed to definitely determine whether the  $s$ - $d$  and  $p$ - $d$  exchange integrals exhibit a dimensional dependence.

### 4.2.3. Magneto-Optical Anisotropy

A particular problem one faces in semiconductor nanostructures is the change of symmetry due to the reduced dimensions. The symmetry reduction of QW layers is caused by the two-dimensional character of the layer or by the lattice mismatch induced strain. For example, for zincblende structures the symmetry is reduced from  $O_h$  for bulk (neglecting the lack of inversion symmetry) to  $D_{2d}$  for a [001] QW. As a consequence of the reduced symmetry, the zone center heavy hole and light hole valence band states split. In most II-VI and IV-VI DMS heterostructures, in contrast to most nonmagnetic heterostructures, the zero-field splitting between light and heavy holes (which is on the order of tens of meV) is comparable to the giant Zeeman splittings. As both perturbations of the band structure (induced by the reduced dimensions or strain and by the magnetic field) are of the same order of magnitude and may have different quantization directions, a competition between the two occurs. This leads to a mixing of the valence band states, and, hence, a magneto-optical anisotropy of the excitonic transition energies occurs, which has been reported by various authors [394, 467–470, 511]. It is worth noting that a magneto-optical anisotropy is also observed in hexagonal bulk DMS, in which the  $c$  axis is the symmetry axis. This was demonstrated for (Cd,Mn)Se [194], (Cd,Fe)Se [215], and (Cd,Mn)S [215]. The energies and transition probabilities for wurtzite DMS have been calculated by Gubarev [471].

In the case of two-dimensional nanostructures, made of DMS of cubic symmetry in the bulk, different Zeeman splittings can be observed for orientations of the magnetic field either parallel or perpendicular to the symmetry axis of the heterostructure. In Figure 58 a typical splitting pattern is depicted, which was obtained by reflection spectroscopy of the excitons of a (Cd,Mn)Te layer constrained to the lattice constant of CdTe. Because of the tensile strain the lh exciton is lower in energy than the hh state. It is interesting to note that the hh splitting, which is strongest in the Faraday configuration with the magnetic field parallel to the observation direction, is almost zero at very low magnetic field strengths in the Voigt configuration with the field in the plane of the sample and perpendicular to the observation direction. The splitting of the lh is enhanced, however, in the Voigt configuration compared with the Faraday configuration. Another important feature is the anticrossing behavior of the states in the Voigt configuration. From the latter fact we can conclude that a coupling of the states should explain this surprising effect.

Peyla et al. [468] explained the splitting pattern in the Voigt configuration by the anisotropy of the band structure, which causes a coupling of lh and hh states of finite momentum. A theoretical approach was given by Suisky et al. [394] and Stirner et al. [393], where the lh-hh coupling is mediated by the magnetic field itself. This effect is common for all zincblende semiconductors with reduced symmetry but is strongly enhanced in diluted magnetic semiconductors by the  $s$ , $p$ - $d$  exchange interaction. Whereas the Zeeman splitting of the conduction band is isotropic and independent of the field orientation, the valence band splitting can be calculated by the matrix

$$H_{\text{mag}}^v = \begin{pmatrix} \frac{3}{2}\delta & \gamma & 0 & 0 \\ \gamma^* & \frac{1}{2}\delta & \lambda & 0 \\ 0 & \lambda^* & -\frac{1}{2}\delta & \gamma \\ 0 & 0 & \gamma^* & -\frac{3}{2}\delta \end{pmatrix} \quad (61)$$

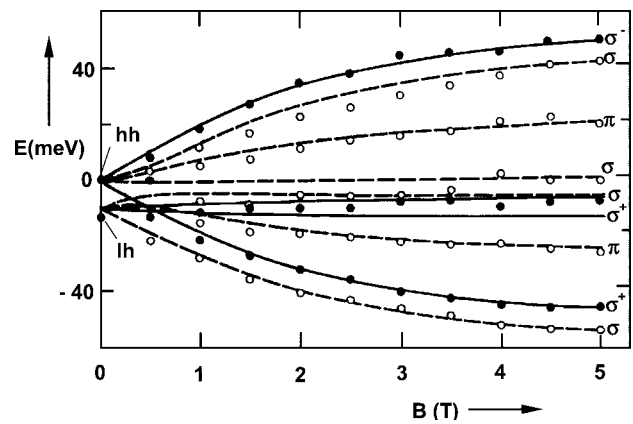


**Figure 58.** Magneto-optical anisotropy in a strained (Cd,Mn)Te layer observed by reflection spectroscopy ( $x_{\text{Mn}} = 0.21$ ,  $T = 2$  K). Experimental points: ●, Faraday configuration; ○, Voigt configuration.  $\sigma_{\pm}$ ,  $\sigma$ , and  $\pi$  indicate the polarization of the light with respect to the magnetic field direction. Reprinted with permission from [511], O. Goede et al., *Phys. Stat. Sol. B* 166, 531 (1991). © 1991, Wiley-VCH Verlag, Berlin.



with

$$\lambda = i(G_x^v + G_y^v), \quad \gamma = i\frac{\sqrt{3}}{2}\lambda, \quad \delta = G_z^v \quad (62)$$

and

$$(G_x^v, G_y^v, G_z^v) = a \cdot x \cdot B_{5/2} \cdot \frac{\vec{B}}{|\vec{B}|} \quad (63)$$

As has been shown in [394], the formalism enables the calculation for all of the orientations of the magnetic field and is not restricted to the preferential Faraday and Voigt configurations. Using the transfer matrix method in the framework of the envelope function approximation, the authors were even able to calculate the magneto-optical anisotropy of any QW structure. Recently, Klar et al. [438, 530] demonstrated that there is a magneto-optical anisotropy not only of the transition energies, but also of the linewidth of excitonic transitions and the energy transfer from the excitonic states into the Mn-subsystem in (Zn,Cd,Mn)Se samples.

### 4.3. Spontaneous Magnetization of Magnetic Semiconductor Nanostructures

In a paper by Mermin and Wagner [472] in 1966 it was shown mathematically that in one- and two-dimensional magnetic systems of the Heisenberg type no spontaneous phase transition into a magnetically ordered ferromagnetic or antiferromagnetic state is possible. This theorem can be proved even for different models like the Hubbard model, the sf model, or the XY model. It is noteworthy, however, that the theorem is not proved for  $T = 0$  K. According to the spin-wave theory for the Heisenberg model, the number of excited spin waves at finite temperatures diverges in one- and two-dimensional systems. This implies that a phase transition from the paramagnetic state to the ordered state does not occur. The Mermin–Wagner theorem is strictly based, however, on an isotropic system. Any anisotropy may break this strong theorem, and a transition to a magnetically ordered state becomes possible.

Relativistic corrections which break the rotational invariance with respect to the spin quantization axis are the dipole–dipole interaction and the spin–orbit coupling. In a bulk crystal this will result in a shape anisotropy (entirely based on dipole–dipole interaction) and in magnetocrystalline anisotropy (based on spin–orbit coupling). As was pointed out by Néel in 1954 [473], atoms near an interface have a different environment compared with bulk atoms, and this gives additional contributions to the magnetic anisotropy, which may be especially relevant for nanostructures with large interfaces or surfaces. Another source of anisotropy is the strain of epitaxially grown layers. Unfortunately less is known about the influence of the two-dimensional strain on spin–orbit coupling as the source for magnetic anisotropy. This may differ considerably for the various systems. Two remarks are important. First, all of the anisotropy terms are orders of magnitude smaller than the exchange interaction terms, as the former arise from relativistic corrections. Second, the anisotropy terms are effective mainly in the case of ferromagnetic samples. In the case of antiferromagnetic samples, which is the majority of magnetic semiconductors, the relevance is not obvious. The shape anisotropy, for example, is negligible anyway.

In the following we survey the present knowledge of the magnetic behavior of magnetic semiconductors, which are known to be a good approximation of Heisenberg-type systems as bulk samples. We consider the magnetic properties by the reduction of geometrical extensions of the magnetic semiconductors toward two-dimensional systems (Section 4.3.1) and one- or zero-dimensional systems (Section 4.3.3). In Section 4.3.2 we focus on a subject of very recent interest, namely the interlayer coupling of magnetic semiconductors across diamagnetic semiconductors. Whereas in metallic systems, where free carriers are always present, the coupling between ferromagnetic layers across diamagnetic metals can be explained either by the RKKY model or by the quantum state model, a respective explanation for semiconductor systems is not yet given. We shall concentrate mainly on the present experimental knowledge.

#### 4.3.1. Two-Dimensional Systems

There are several crystals which have naturally two-dimensional ferromagnetic and antiferromagnetic layers (e.g.,  $K_2CuF_4$ ,  $CrBr_3$ ,  $Rb_2MnF_4$ , etc.). These are nonartificial magnetic nanostructures and thus are not a subject of this review, but why they show spontaneous magnetization is, of course, an interesting question. The answer is: A strong anisotropy is responsible for the magnetic phase transition taking place in these quasi-2D systems. The situation is not clear in the case of material systems, which are highly isotropic in the 3D case, like the zincblende magnetic semiconductors. Those systems can be well described by an isotropic Heisenberg Hamiltonian. There are some reports of the absence of a phase transition from a paramagnetic state to an ordered magnetic state or to a spin-glass state for thin layers of magnetic semiconductors [51, 53, 474–476]. In the following we want to address the paramagnetic–antiferromagnetic, the paramagnetic–spin-glass, and the paramagnetic–ferromagnetic phase transitions. Finally, carrier-induced ferromagnetism in (II,Mn)VI QWs, a somewhat related phenomenon, is discussed.

#### Paramagnetic–Antiferromagnetic Phase Transition

Let us consider antiferromagnetic MnSe as an example. Bulk MnSe is thermodynamically stable in the octahedral coordination (rock salt) and exhibits an fcc-type II antiferromagnet phase transition with a Néel temperature of about 120 K (see Section 2, Table 2). Zincblende MnSe could be prepared as thin polycrystalline films by thermal evaporation on glass or quartz substrates with substrate temperatures  $T_s < 50$  K. The Néel temperature of those unstable tetrahedrally coordinated zincblende (fcc-type III) MnSe films was found to be about 70 K [51]. However, highly crystalline material can only be obtained by a stabilized MBE growth method (described in Section 3.1.1) as layers of only a few monolayers in ZnSe/MnSe superlattices. Such ultrathin zincblende MnSe layers seem to exhibit paramagnetic behavior down to the lowest temperatures. This has been shown, for example, by Kolodziejski et al. [53, 474] by means of Zeeman measurements of such MnSe/ZnSe QW structures. The authors reported no shift of the ZnSe excitonic photoluminescence for  $d_{MnSe} > 3$  nm. This was interpreted as evidence that the MnSe layers are in the antiferromagnetic state. For ultrathin MnSe layers

with  $d_{\text{MnSe}} \leq 1$  nm, however, a peak shift based on the  $s, p-d$  exchange interaction between the ZnSe band states and the magnetic moments of the MnSe layers was found, which is clear evidence of the paramagnetic giant Zeeman effect.

From neutron diffraction studies of zinc-blende MnSe/ZnSe superlattices, Klosowski et al. [261] reported an antiferromagnetic phase transition at 70 K even for 3 monolayers only of MnSe. The reported phase transition temperature of thicker layers of MnSe was  $T_N = (107 \pm 5)$  K. The high Néel-temperature is however an indication for fractional phase transitions into the stable rocksalt structure with  $T_N = 120$  K.

Precht et al. performed a similar magneto-PLE experiment on a CdTe/(Cd,Mg)Te QW structure grown on a (001) Cd<sub>0.96</sub>Zn<sub>0.04</sub>Te substrate with a single monolayer of MnTe in the center of the CdTe layer to study the paramagnetic-antiferromagnetic phase transition of the MnTe layer [477, 532]. In the temperature dependences of the inverse Zeeman splitting as well as the linewidth of the PLE bands, the authors observed a kink and a peak, respectively, at a temperature of 50 K. This temperature value is assigned to the Néel temperature. In a later publication, the same group presented results on fractional MnTe monolayers embedded in nonmagnetic QWs. For half of a MnTe monolayer and for a quarter of a MnTe monolayer of MnTe they found critical temperatures of 34 K and 13 K, respectively [478]. In particular, in the case of the fractional layers it is not clear whether the observed effect really is an indication of a paramagnetic-antiferromagnetic phase transition or rather of a paramagnetic-spin-glass transition.

An alternative but very sensitive optical method for the study of the magnetic phase transition from the paramagnetic to the antiferromagnetic state is the detection of energy shifts of the internal Mn<sup>2+</sup> transitions below the Néel temperature. This method can only be applied for wide bandgap semiconductors, where the internal Mn<sup>2+</sup> ( $3d^5$ ) transitions are observable. Those shifts of the internal transitions below the Néel temperature have been reported earlier for bulk samples of MnS, (Cd,Mn)S [479, 480], and MnO [481]. It was reported in [51] that with this method MnSe-MBE layers of up to 3 nm did not show clear hints of a phase transition down to a temperature of 1.6 K. In Figure 59 are depicted the energy positions of the Mn<sup>2+</sup> ( $3d^5$ ) internal transitions ( ${}^6A_1 \rightarrow {}^4A_1$ ,  ${}^4E$ ,  ${}^6A_1 \rightarrow {}^4T_2$ ) in bulk MnSe, measured by photoluminescence excitation spectroscopy. The photoluminescence was detected on the yellow manganese luminescence band ( ${}^4T_1 \rightarrow {}^6A_1$ ). An almost steplike shift is seen, which occurs just below the indicated Néel temperatures of about 120 K for the MnSe<sub>oct</sub> in the rock salt structure and about 70 K for the polycrystalline MnSe<sub>tet</sub> thin film of about 5  $\mu\text{m}$  in the zincblende modification. The Néel temperatures for these bulk samples have been measured by EPR. The determination of  $T_N$  by EPR is very accurate. The method is based on the linewidth divergence of the Mn<sup>2+</sup> EPR line due to the corresponding decrease in the spin-spin relaxation time [482], which is correlated with the divergence of the correlation length.

The successive spin-ordering below the spin freezing temperature leads to an energy relaxation of the various internal Mn<sup>2+</sup> ( $3d^5$ ) states and subsequently to the shift of the

excitation bands, which is depicted in Figure 59. No such steplike behavior was found for MBE layers with thicknesses up to 4 nm. In Figure 59 the measured Mn<sup>2+</sup> ( $3d^5$ ) internal transitions ( ${}^4A_1$ ,  ${}^4E \rightarrow {}^6A_1$ ,  ${}^4T_2 \rightarrow {}^6A_1$ ) for a MnSe/ZnSe superlattice with a MnSe layer thickness of 6 nm are also shown. Again no clear evidence for a magnetic phase transition down to the lowest temperatures is seen. However, it should be mentioned that a partially structural phase transition has been observed in samples in which the MnSe layers exceed a critical thickness of about 5 nm. From absorption measurements it has been concluded that about 60% of the MnSe layer exhibits the zincblende structure, whereas about 40% changes into the stable rock salt phase. It was not clear whether a grainlike separation took place or rather complete monolayers transform. In summary, it can be stated that zincblende MnSe layers with thicknesses of  $\leq 4$  nm do not show any clear and convincing indications of a magnetic phase transition.

In the following we want to examine briefly the physical reason for the energy shift of the excitation bands below the Néel temperature. The energy relaxation of the various states can be estimated again in the framework of an isotropic Heisenberg Hamiltonian describing the  $d-p-d$  superexchange interaction in zincblende MnSe (see also Section 2.3),

$$H = - \sum_{i,j} J_{ij} S_i S_j \quad (64)$$

Including only the nearest neighbor (nn) and next nearest neighbor (nnn) interaction by  $J_{nn}$  and  $J_{nnn}$ , respectively ( $J_{nn}, J_{nnn} < 0$ ), the exchange interaction induced relaxation

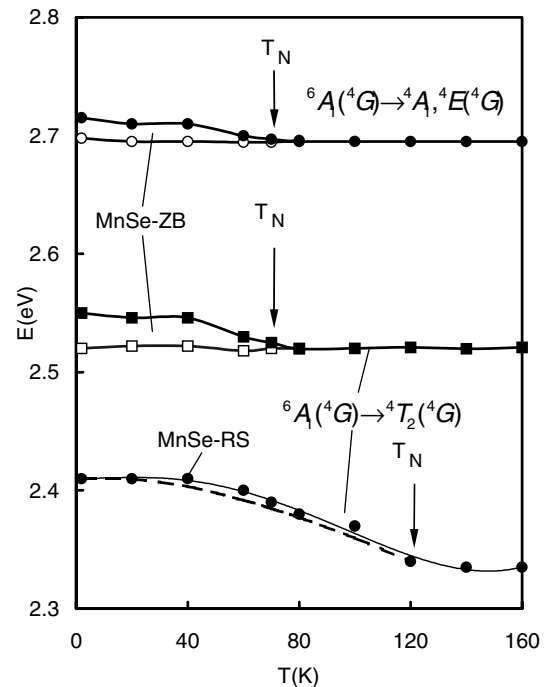


**Figure 59.** Energy positions of the Mn<sup>2+</sup> ( $3d^5$ ) internal transitions in bulk MnSe and in MnSe/ZnSe superlattices as a function of temperature. For quasi-bulk-like structures a shift to higher energies below the Néel temperature is observable, which disappears for quasi-2D layers.

$E(T)$  per  $\text{Mn}^{2+}$  ion is then obtained in a mean-field approximation (MFA),

$$\begin{aligned} E(T) &= \langle H_{i=1} \rangle = - \sum_j J_{1j} \langle S_1^z \rangle \langle S_j^z \rangle \\ &= - \langle S_1^z \rangle \left[ J_{\text{nn}} \sum_{\text{nn}} \langle S_j^z \rangle + J_{\text{nnn}} \sum_{\text{nnn}} \langle S_j^z \rangle \right] \end{aligned} \quad (65)$$

As fluctuation effects are neglected in the MFA one obtains  $E(T \geq T_N) = 0$  and a complete antiferromagnetic spin ordering at  $T = 0$ , corresponding to an fcc-type II and an fcc-type III spin superlattice in the cases of RS and ZB, respectively. To apply Eq. (65) to the zincblende and rock salt MnSe of Figure 59, one has to sum over the given spin-up and spin-down states of the nearest neighbor and next nearest neighbor shells. For a  $\text{Mn}^{2+}$  ion in the ground state ( $S = 5/2$ ) this leads to

$$E_g(0) = \begin{cases} 6J_{\text{nnn}}S^2 & \text{for MnSe}_{\text{RS}} \\ (4J_{\text{nn}} - 2J_{\text{nnn}})S^2 & \text{for MnSe}_{\text{ZB}} \end{cases} \quad (S = 5/2) \quad (66a)$$

$$(66b)$$

At sufficiently low excitation densities an excited (single)  $\text{Mn}^{2+}$  ion can be assumed to be placed in an unchanged mean spin field of neighboring  $\text{Mn}^{2+}$  ions. For the spin-ordering-induced energy relaxation  $E_{\text{ex}}(0)$  of such an excited  $\text{Mn}^{2+}$  ion in one of the lowest energy (quartet) states ( $S' = 3/2$ ) one derives

$$\begin{aligned} E_{\text{ex}}(0) &= \begin{cases} 6J_{\text{nnn}}^{\text{ex}}SS' & \text{for MnSe}_{\text{RS}} \\ (4J_{\text{nn}}^{\text{ex}} - 2J_{\text{nnn}}^{\text{ex}})SS' & \text{for MnSe}_{\text{ZB}} \end{cases} \quad (S=5/2, S'=3/2) \end{aligned} \quad (67a)$$

$$(67b)$$

where  $J_{\text{nn}}^{\text{ex}}, J_{\text{nnn}}^{\text{ex}}$  denote the various exchange interaction parameters between the considered excited  $\text{Mn}^{2+}$  ion and an nn or nnn  $\text{Mn}^{2+}$  ion in the ground state. The measured total spin-ordering-induced shift of the various excitation peaks,  $\Delta E(0) = (E_{\text{ex}} - E_g)_{T=0} - (E_{\text{ex}} - E_g)_{T_N}$ , is then given by

$$\Delta E(0) = E_{\text{ex}}(0) - E_g(0) \quad (68)$$

The otherwise hardly accessible exchange parameters for the excited  $\text{Mn}^{2+}$  states can now be obtained from Eq. (68). For the  $\text{Mn}^{2+}$  ground state we use the exchange parameter of  $\text{MnSe}_{\text{RS}}$ ,  $J_{\text{nnn}}/k_B = -12.8$  K [22]. For the zincblende modification the value for the exchange integral  $J_{\text{nn}}/k_B$  varies between  $-8.1$  and  $-9.9$  K [22]. Using a mean value for  $\text{MnSe}_{\text{ZB}}$ ,  $J_{\text{nn}}/k_B \approx -9$  K, and assuming  $|J_{\text{nnn}}| \ll |J_{\text{nn}}|$  (which is a good approximation for the zincblende antiferromagnets), one can deduce from Eqs. (66) and (67) that  $J_{\text{nnn}}^{\text{ex}}/k_B = +14.8$  K for the  ${}^4T_2$  state of the octahedrally coordinated MnSe. For zincblende MnSe one obtains  $J_{\text{nn}}^{\text{ex}}/k_B = +4.3$  K for the  ${}^4T_2$  and  $J_{\text{nn}}^{\text{ex}}/k_B = +1.8$  K for the  ${}^4A_1, {}^4E$  state. It is an important result that the exchange integrals of the excited states show a significant trend toward a ferromagnetic coupling. The same tendency was already reported for MnS [479]. The excited state for the spin-flipped electron is a rather delocalized state. The remaining localized core is then rather a  $S = 4/2$  state, which now explains the tendency to show a ferromagnetic  $p$ - $d$  coupling, as already explained

in more detail in Section 2.4, and, consequently, a ferromagnetic superexchange coupling to the nearest neighbor  $\text{Mn}^{2+}$  ions in the ground state with  $S = 5/2$ . It is important to note that even in the case of an ideal two-dimensional layer a shift of the internal transition is expected. For a (001) plane of the zincblende lattice with  $|J_{\text{nnn}}| < |J_{\text{nn}}|$  the magnetic ordering is a two-dimensional cubic lattice with antiferromagnetic ordering of type I. This means that all four nn ions are aligned antiparallel, but the four nnn ions are aligned parallel. Proceeding in the same fashion as for bulk (see Eqs. (66), (67), and (68)), one obtains the following nonzero energy shift of the internal  $3d$  transitions at the paramagnetic–antiferromagnetic phase transition for the 2D case:

$$\Delta E(0) = E_{\text{ex}}(0) - E_g(0) = 4(J_{\text{nn}}^{\text{ex}} - J_{\text{nnn}}^{\text{ex}})SS' - 4(J_{\text{nn}} - J_{\text{nnn}})S^2 \quad (69)$$

The high quantum efficiency of the internal transitions permits a measurement down to the smallest sample sizes, which is a big advantage over other methods like neutron diffraction or magnetic susceptibility measurements. Finally we want to discuss the temperature dependence of the peak shift, which exhibits a typical Brillouin-like behavior. The temperature dependence of the spin-ordering-induced peak shifts can be described again in MFA. This will be shown for  $\text{MnSe}_{\text{RS}}$  as an example. In the case of fcc-type II antiferromagnetic spin-ordering it is

$$\langle S_1^z \rangle = S_1 B_{S_1} \left( \frac{12S_1 J_{\text{nnn}} \langle S_{\text{nnn}}^z \rangle}{k_B T} \right) \quad (70)$$

$B_{S_1}$  is the Brillouin function. For the central  $\text{Mn}^{2+}$  ion in the ground state ( $S_1 = 5/2$ ) it is

$$\langle S_1^z \rangle_g = - \langle S_{\text{nnn}}^z \rangle_g = S \cdot m(T) > 0 \quad (71)$$

Here  $m(T)$  is the spin-ordering parameter. According to Eq. (70)  $m(T)$  is implicitly given by the self-consistency condition

$$m(T) = B_S \left( \frac{3S}{S+1} \frac{T_N}{T} m(T) \right) \quad (72)$$

where the MFA expression for the Néel temperature  $k_B T_N = 4|J_{\text{nnn}}|S(S+1)$  is used. According to Eq. (65) it follows that

$$E_g(T) = 6J_{\text{nnn}}S^2 m^2(T) \quad (73)$$

For the central ion considered it follows for the excited (quartet) state that

$$E_{\text{ex}}(T) = 6J_{\text{nnn}}^{\text{ex}}S^2 m(T) \langle S_1^z \rangle_{\text{ex}} \quad (74)$$

with

$$\langle S_1^z \rangle_{\text{ex}} = S' B_{S'} \left( \frac{3S'}{S+1} \frac{J_{\text{nnn}}^{\text{ex}} T_N}{J_{\text{nnn}} T} m(T) \right) \quad (75)$$

The calculated curve  $\Delta E = E_{\text{ex}}(T) - E_g(T)$  is represented by the dashed line in Figure 59. It is seen that the temperature dependence can be well described by Eq. (75).

**Paramagnetic–Spin-Glass Phase Transition** For spin-glass systems based on metallic alloys, it is known that the spin-glass (sg) freezing temperature decreases with decreasing layer thickness, but the sg phase survived down to mono-layer thicknesses [483–485].

Awschalom et al. [475, 476] studied the sg transition in (111)-oriented  $\text{Cd}_{0.8}\text{Mn}_{0.2}\text{Te}$  layers of different thicknesses grown by MBE. They reported that no sg phase was observable down to the lowest temperatures for layers with thicknesses of 2 nm and smaller. This rather surprising result was drawn from ac magnetic susceptibility measurements versus temperature. A distinct kink was observable for  $d = 8.6$  nm at about 3.8 K. Even for a layer thickness of 4 nm a sg freezing temperature of about 3.8 K was found, which equals the value of an 8.6-nm sample and is almost the sg transition temperature known from the bulk  $\text{Cd}_{0.8}\text{Mn}_{0.2}\text{Te}$ . For a 2-nm sample no distinct kink, but a hysteresis effect of the ac susceptibility versus temperature was seen.

Sawicki et al. [117] carried out similar studies on (100) oriented  $\text{Cd}_{0.5}\text{Mn}_{0.5}\text{Te}/\text{CdTe}$  superlattices, where the thickness of the CdTe layer was 5.2 nm for all samples and the thickness of the  $\text{Cd}_{0.5}\text{Mn}_{0.5}\text{Te}$  layer was varied between 1.6 and 6.4 nm. The sg freezing temperature was determined very accurately with thermoremanent magnetization experiments. A sg transition was observed in all specimens. The freezing temperature seems to depend linearly on the layer thickness in the range of thicknesses studied. Thus, there are no signs of a discontinuity below a thickness of 5 nm. The following values for  $T_{\text{sg}}$  were obtained: 6, 11, 14, and 17.5 K for layer thicknesses of 1.6, 3.2, 4.8, and 6.4 nm, respectively. The value of the 6.2-nm sample was close to the corresponding bulk value.

**Paramagnetic–Ferromagnetic Phase Transition** A series of multilayer structures of ferromagnetic EuS with varying layer thicknesses and diamagnetic PbS spacer layers was grown by Stachow-Wójcik [276] by electron beam evaporation. In addition to the interesting result of an antiferromagnetic interlayer coupling, which is discussed in the next section, they investigated the dependence of the transition from the paramagnetic to the ferromagnetic phase. The Curie temperature  $T_C$  was determined from magnetization measurements versus temperature. They determined a decreasing  $T_C$  with decreasing EuS layer thickness. The measured Curie temperatures were somewhat different for different orientations and substrates. In the case of KCl substrates with (100) orientation a quasi-bulk value (200 monolayers) of  $T_C \approx 17.3$  K was determined. On (111)  $\text{BaF}_2$  substrates the quasi-bulk value was found to be  $T_C \approx 13.6$  K. The discrepancy between these quasi-bulk values and the known bulk value of EuS should be caused by strain effects in the EuS layers due to the substrate. For thin layers ( $d_{\text{EuS}} < 10$  monolayers) a systematic reduction of  $T_C$  with decreasing layer thickness was measured. Even for a thickness of just two monolayers a  $T_C = 10$  K for EuS on (100) KCl and  $T_C = 9$  K for EuS on (111)  $\text{BaF}_2$  were found. From the angle dependence of the ferromagnetic resonances a strong anisotropy effect could be deduced. The reason for the surprisingly strong anisotropy may be the strain or the shape anisotropy, which is especially important for ferromagnetic layers but only plays a minor

role for antiferromagnetic samples. Therefore, one can conclude that for ferromagnetic semiconductors (even if they are, as bulk crystals, rather Heisenberg-type ferromagnets) anisotropy effects (most likely shape anisotropy) lead to a 3D  $\rightarrow$  2D transition with decreasing but still relatively high Curie temperatures down to almost 2D layers.

In conclusion, there is no consistent picture concerning the behavior of the magnetic phase transition in case of the 3D  $\rightarrow$  2D crossover. This is not really surprising, however. Although the magnetic semiconductor systems discussed in this section are considered to be rather isotropic Heisenberg-type ferro- or antiferromagnets, the amount of anisotropy is not really known, but most likely is never really zero. In particular, the influence of two-dimensional strain on spin–orbit coupling as one of the most important sources for magnetic anisotropy is not known and may differ considerably for the various systems.

**Carrier-Induced Ferromagnetism** As already discussed in Section 2.3, it is known from IV–VI DMS materials that it is possible to overcome antiferromagnetic superexchange coupling by RKKY interaction via free carriers. Use of this effect in the case of II–VI nanostructures was motivated by a theoretical paper of Dietl et al. [486], who predicted a paramagnetic–ferromagnetic phase transition for highly  $p$ -doped (II,Mn)VI bulk ( $p \approx 10^{19}$  to  $10^{20}$   $\text{cm}^{-3}$ ) and modulation-doped heterostructures ( $p \approx 10^{11}$  to  $10^{12}$   $\text{cm}^{-2}$ ) when the RKKY exchange mechanism dominates over the Anderson superexchange. Corresponding experiments were carried out with the use of modulation-doped heterostructures consisting of an 8-nm  $\text{Cd}_{1-x}\text{Mn}_x\text{Te}$  QW with  $x$  varying between 2 and 4% embedded between  $\text{Cd}_{0.66}\text{Mg}_{0.27}\text{Zn}_{0.07}\text{Te}$  barriers [487–490]. The barriers were  $\delta$ -doped with nitrogen. The doped region in the front barrier is located close to the QW (spacer thickness 10–20 nm). In addition, both barriers had doped layers 100 nm from the QW. The doping was such that sheet densities in the QW of  $1\text{--}3 \times 10^{11}$   $\text{cm}^{-2}$  could be obtained. The authors employed magneto-optical spectroscopy to study the phase transition and its dependence on Mn concentration and hole sheet density. The findings were as follows: (i) In the absence of an external magnetic field  $H$  and below a characteristic temperature  $T_C$ , the luminescence of the QW (excited in energy below the  $\text{Cd}_{0.66}\text{Mg}_{0.27}\text{Zn}_{0.07}\text{Te}$  barrier) exhibits a splitting into two bands and a slight red shift. In addition, the PL decay time increases significantly. These bands are assigned to the spontaneous spin-splitting of the band states due to the ferromagnetism. (ii) As  $T_C$  is approached from above, the magnetic susceptibility  $\chi(T)$  diverges at  $T_C$ .  $\chi$  can be determined at each temperature in the paramagnetic regime from the low-field limit of the giant Zeeman splitting  $\Delta E$  between the  $\sigma^+$  and  $\sigma^-$  components of the heavy-hole QW exciton, with the use of

$$\chi = \lim_{H \rightarrow 0} \frac{g\mu_B N_0}{|N_0\alpha - N_0\beta|} \left( \frac{\partial(\Delta E)}{\partial H} \right) \quad (76)$$

where  $g = 2$  is the  $g$ -factor of the  $\text{Mn}^{2+}$  ions, and  $N_0\alpha$  and  $N_0\beta$  are the  $s$ - $d$  and  $p$ - $d$  exchange integrals, respectively. (iii) The behavior described in (i) and (ii) is observed neither in an undoped sample nor in the modulation-doped samples under illumination with light in energy above the barriers. The latter strongly decreases the free hole density in the QW

by trapping photo-excited holes in the barrier and by partly neutralizing the remaining holes by photo-excited electrons from the barriers. The authors interpret these results as evidence of a paramagnetic–ferromagnetic phase transition in these modulation-doped  $p$ -(Cd,Mn)Te/(Cd,Mg,Zn)Te QWs. The dependence of the Curie temperature on the Mn concentration and sheet doping density is in agreement with the predictions of the mean-field model developed in [486]. The Curie temperatures reported are about 2 K. Further confirmation that carrier-induced ferromagnetism is possible in heavily doped wide-gap (II,Mn)VI systems was given recently by the experiments on  $p$ -type (Zn,Mn)Te (see also Section 2.3) [135–137].

### 4.3.2. Interlayer Coupling

It is a very interesting effect that an interlayer coupling of magnetic semiconductors has been observed in a variety of systems with nonmagnetic spacers [263, 491–494]. In metallic superlattices consisting of ferromagnetic and diamagnetic layers carrier-assisted mechanisms were discussed as possible explanations for the ferro- or antiferromagnetic coupling between the ferromagnetic layers, depending on the thickness of the intermediate layers. In the case of semiconducting or insulating layers the situation seems to be much more difficult, as the density of carriers is several orders of magnitude lower than in metals. Although not all results from semiconductor systems are clearly understood, the experimental facts provide strong evidence that there are specific mechanisms capable of transferring magnetic information across thick nonmagnetic layers without the assistance of mobile carriers.

Two classes of magnetic superlattices with an interlayer coupling have been studied. One is made of the antiferromagnetic layers EuTe and MnTe, and the other is made of the ferromagnetic layers EuS and (Ga,Mn)As. The appropriate research tool for detecting the correlations between the layers is neutron diffraction. This method, especially the way to distinguish the ferromagnetic and antiferromagnetic coupling of the layers, has been described in detail by Giebultowicz et al. [495]. Pronounced coupling effects have been reported for the zincblende MnTe across CdTe or ZnTe layers [263, 491, 492], but the systems behave very differently. The MnTe layers in CdTe/MnTe superlattices with a [001] growth axis are under tensile strain. It was reported by Giebultowicz et al. [496] that a transition from the commensurate type III antiferromagnetic ordering to a new phase with a helical structure was observed. The axis of the spin helix is in-plane, and the helix pitch is incommensurate with the lattice parameter. Neutron diffraction studies of samples with different CdTe spacer layers show that the pitch of the helix gradually increases with increasing spacer thickness from 2 to 14 monolayers, which can be explained only by assuming a correlation between adjacent layers. In contrast to CdTe/MnTe superlattices, the MnTe layers are under compressive strain in the ZnTe/MnTe superlattices. Lin et al. [492] performed measurements on ZnTe/MnTe samples with different spacer thicknesses. They found that the spins in adjacent MnTe layers couple in an in-phase antiferromagnetic structure with identical spin orientations in all MnTe layers. With increasing temperature the ordering

transforms into an antiphase coupling in which the alternate MnTe layers have reversed spin directions. For increasing ZnTe layer thickness, a systematic reduction in the magnetic correlation range was observed. It was shown by Stumpe et al. [263] that by Cl doping of ZnTe the correlation range could be extended from about 22.5 nm (five bilayers) for the undoped samples to about 45 nm for the Cl-doped samples at low temperatures ( $T \approx 15$  K). The individual spacer thicknesses were up to 2 nm and have been somewhat shorter than in CdTe/MnTe.

The largest spacer thicknesses with interlayer interaction have been reported for the EuTe/PbTe superlattices, where the interaction could be measured for spacers as thick as 7 nm. The samples have been grown in the [111] direction. EuTe is an antiferromagnet with an fcc type II ordering. The spins are aligned in (111) planes, and the planes are antiferromagnetically coupled to one another. An antiferromagnetic coupling between ferromagnetic layers has also been observed for (001) EuS/PbS all-semiconductor superlattices [495]. As mentioned in Section 2.4, EuS is a ferromagnet with a Curie temperature  $T_C = 16.6$  K. The maximum spacer thickness for which coupling was observed was 2 nm.

For the (Ga,Mn)As/(Al,Ga)As/(Ga,Mn)As trilayer system a magnetic interaction between the ferromagnetic (Ga,Mn)As layers has been reported for spacer thicknesses of 10 monolayers (about 3 nm) by Ohno [497]. It is interesting to note that the coupling disappeared when the Al content of the spacer was as high as 29%. Although the conclusion of Ohno concerning this result was that the RKKY interaction may play a role in the interlayer coupling of those trilayer systems, one has to state that the physical origin of the interlayer interaction is still an open question. It is quite clear that the number of free carriers in most of the presented systems is orders of magnitude too small to be the reason for a coupling.

There have been some attempts to present a theoretical approach to the problem. Rusin [498] proposed a model using “hydrogenic centers,” which might be formed by electrons bound to impurities or defects. Those centers may have Bohr radii of several nanometers. These centers may polarize  $Mn^{2+}$  ions at the interface or may couple the polarization between adjacent interfaces, which eventually may couple the layer polarizations themselves. Blinowski and Kacman [499] studied the coupling in a three-dimensional tight-binding model, accounting for the band and magnetic structure of the constituent superlattice components. They calculated the spin-dependent part of the total electronic energy and found for EuS/PbS superlattices as well as for EuTe/PbTe that the antiferromagnetic coupling is energetically favored. Only recently there were first results of calculations reported which predict the possibility to obtain an antiferromagnetic coupling of ferromagnetic layers via virtual conduction band states with self-polarization effects [500].

### 4.3.3. One- and Zero-Dimensional Systems

There has not been much work reported to date concerning the question of magnetic phase transitions in magnetic semiconductor QWRs and QDs. We discuss the present results in the next two paragraphs. In the third paragraph we briefly mention the hybrid system consisting

of a paramagnetic (Ga,Mn)As matrix and ferromagnetic Mn(Ga)As dots. A somewhat different aspect, namely the formation of magnetic polarons in QDs, is discussed in the fourth paragraph.

### Paramagnetic–Antiferromagnetic Phase Transition

Brieler et al. [305] and Chen et al. reported MnS and MnSe QWRs with diameters of  $<3$  nm in silica matrices [306]. Template-directed growth is described in Section 3.2.3. Bulk samples of zincblende MnS and MnSe are known to be antiferromagnets of the fcc type III with Néel temperatures of 100 K and 70 K, respectively (see Table 2). Even the stable rock salt modification exhibits antiferromagnetism with Néel temperatures of about 150 K. Brieler and co-workers [305] and Chen and co-workers [306] used EPR measurements to study the phase transition of QWRs. In bulk samples, the linewidth  $\Delta H$  of the EPR signal diverges at the Néel temperature when approaching it from higher temperatures, as can be seen in the top graph of Figure 60. In contrast,  $\Delta H$  of the EPR signal of the corresponding wire samples does not diverge down to the lowest achievable temperatures of about 1.6 K, as shown in the bottom graph of Figure 60. Thus, no phase transition was observed, for either MnS or MnSe wire samples. It is worth noting that

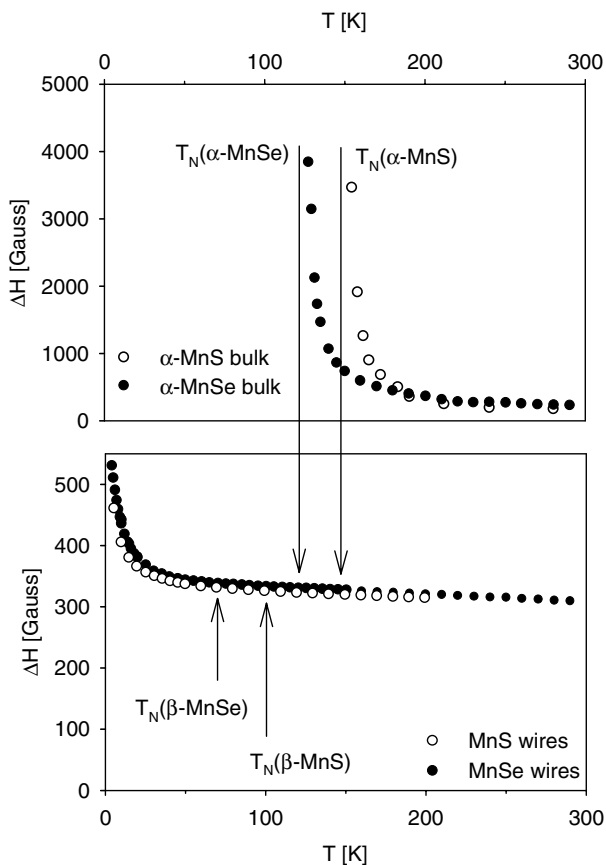


**Figure 60.** EPR linewidth as a function of temperature for MnSe and MnS bulk samples (top graph) and MnSe and MnS quantum wires (bottom graph). A suppression of the paramagnetic–antiferromagnetic phase transition in MnSe and MnS wires with diameters of about  $d = 3$  nm is seen.

both the linewidth  $\Delta H$ , as well as the Curie–Weiss parameters  $\theta$  derived from inverse plots of the EPR intensity as a function of temperature, is about one order of magnitude smaller in the wires compared with bulk. This indicates that the antiferromagnetic coupling between the  $\text{Mn}^{2+}$  spins in the samples is strongly suppressed because of the reduced dimensions of the nanowires.

**Paramagnetic–Spin-Glass Phase Transition** He et al. studied the magnetic properties of rf-sputtered  $\text{Cd}_{1-x}\text{Mn}_x$ Te with  $x = 0.5$  and  $0.6$  and with grain sizes ranging from 80 to 100 nm [501, 502]. They deduced Curie–Weiss parameters  $\theta = 11$  and  $13$  K from plots of the inverse susceptibility  $\chi(T)^{-1} \propto (T + \theta)$  for  $x = 0.5$  and  $0.6$ , respectively. The  $\theta$  values are considerably reduced compared with bulk (e.g., Oseroff et al. reported  $\theta$  values of 310 K and 350 K for bulk  $\text{Cd}_{0.47}\text{Mn}_{0.53}\text{Te}$  and  $\text{Cd}_{0.4}\text{Mn}_{0.6}\text{Te}$  [503]). Nevertheless, a paramagnetic–spin-glass transition was still observable for these relatively large clusters. It manifested itself as a cusp in the susceptibility when the samples were zero-field cooled. Surprisingly, the values  $T_{\text{sg}} = 14$  K and  $17$  K observed for the nanoclusters with  $x = 0.5$  and  $0.6$ , respectively, are approximately the same as the corresponding bulk values (see, for example, [132, 504]).

Bandaranayake et al. [353] reported SQUID measurements of (Cd,Mn)S ultrafine particles. They reported a size and field dependence of the spin-glass transition. The susceptibility was measured versus temperature for  $\text{Cd}_{0.5}\text{Mn}_{0.5}\text{S}$  particles of different size. They found a decreasing freezing temperature  $T_{\text{sg}}$  with decreasing particle size. The measured bulk value was  $T_{\text{sg}} = 18$  K, but  $T_{\text{sg}} = 15.5$  K and  $T_{\text{sg}} = 14$  K were found for mean dot diameters of  $d = 50$  nm and  $d = 16$  nm, respectively. The important observation was, however, the absence of a cusp for small particles with a mean size of  $d < 3$  nm.

Chen et al. [306] studied  $\text{Cd}_{1-x}\text{Mn}_x\text{S}$  QWR samples with  $x \leq 0.2$  and  $\text{Cd}_{1-x}\text{Mn}_x\text{Se}$  with  $x \leq 0.3$  and with lateral dimensions smaller than 3 nm by EPR and SQUID measurements. The samples showed no sign of a paramagnetic–spin-glass phase transition in the temperature range studied, that is, down to 1.8 K in the case of the (Cd,Mn)S QWRs and down to 4 K in the case of the (Cd,Mn)Se QWRs. The  $\theta$  values obtained by analyzing the SQUID and EPR data increase with increasing Mn content. Again, the  $\theta$  values are more than an order of magnitude smaller than for corresponding bulk samples. The results lead to the conclusion that the antiferromagnetic coupling between the  $\text{Mn}^{2+}$  spins in the samples is strongly suppressed because of the reduced dimensions of the nanowires.

**Ferromagnetic Mn(Ga)As dots** Hybrid ferromagnet–semiconductor structures have received considerable attention because they may provide various spin-dependent applications. An interesting subclass are ferromagnetic dots embedded in a semiconducting matrix. As already mentioned in section 3.1.2 the Mn(Ga)As dots fit almost perfectly into the (Ga,Mn)As matrix with their  $c$ -axes along the GaAs [111] direction. The Curie temperature reported for the clusters is 330 K [84, 219, 343]. From energy dispersive X-ray analysis (EDX) it is known that there is a certain amount of Ga in the MnAs dots. From



high-resolution TEM we know that all the Ga-ions which are present in our MnAs-dots are on lattice site. The reason for the higher Curie-temperature is the tensile strain inside the MnAs dots, which are not entirely lattice-matched to the (Ga,Mn)As matrix. The pressure coefficient of  $T_C$  has been found to be negative for MnAs with NiAs-structure [506]. At room temperature the  $c$ -axes of MnAs is 0.571 nm. The basal plane distance  $d = 0.2855$  nm is therefore much smaller, than the distance  $d_{\text{GaAs}} = 0.3262$  nm of the (111) planes of GaAs at room temperature. The incorporation of Mn into the GaAs matrix might even enhance this difference. Consequently it means that the tensile strain, which enhances  $T_C$ , dominates over the size effects, which alone should reduce  $T_C$ . If the size of the dots is as low as about 6 nm they show superparamagnetic behavior with a blocking temperature of about 200 K [125]. With increasing dot size the blocking temperature increases further and was about 270 K for 13 nm diameters of the MnAs nanoclusters. Hartmann et al. [507] performed ferromagnetic resonance studies of Mn(Ga)As dots with diameters varying between 50 and 100 nm in a semiconducting (Ga,Mn)As matrix. The authors observed an abrupt reduction of the ferromagnetic resonance field at about 290 K. The Curie temperature of the dots was again 330 K. The abrupt change of the resonance field might be ascribed to the blocking temperature for larger dots.

Using annealing temperatures of 750 K to cause MnAs precipitation in low temperature grown (Ga,Mn)As, hybrid material with Curie temperatures up to 360 K was obtained by Wellmann et al. [343]. These Curie temperatures are well above that of  $T_C = 318$  K of bulk MnAs. It is known, however, that  $T_C$  of MnGa precipitations in GaAs is about 400 K. Thus, the very high  $T_C$  found by Wellmann et al. [343] is most likely due to additional MnGa precipitations. For metallic particles it is established, that the Curie temperature is strongly size dependent, but decreases as the particle volume is reduced. The reduction is an obvious consequence of finite size and surface effects [505].

Other hybrid structures consisting of ferromagnetic inclusions in a semiconducting matrix are currently under study. Park et al. [508] reported about nanoscale  $\text{Mn}_{11}\text{Ge}_8$  ferromagnetic clusters in a  $\text{Mn}_x\text{Ge}_{1-x}$  dilute magnetic matrix and Theodoropoulou et al. [509] studied ferromagnetic (Ga,Mn)N platelets in GaN:Mn.

**Magnetic Polarons in Quantum Dots** The formation of magnetic polarons is basically not a special issue of nanostructures. There is, however, an interesting fact which makes the magnetic polarons in QDs of diluted magnetic semiconductors interesting and may open up new device applications. For ZnSe:Mn dots [359] and CdS:Mn dots [510] it was reported that there is a zero-field splitting which is caused by the presence of  $\text{Mn}^{2+}$  ions in the nanocrystals. The splitting is caused by the polaron effect, with the unique situation of just one polaron per dot. Unfortunately, the splitting cannot be observed on an ensemble of nanocrystals at zero field since the dot spins are randomly oriented. Nevertheless, at a modest external magnetic field this splitting can be revealed, as the dots align like micromagnets in an external field. The method of investigation is, therefore, single-dot spectroscopy as used by Maksimov et al. [512] on

(Cd,Mn)Te dots in a (Cd,Mg)Te matrix and Bacher et al. on CdSe dots in a (Zn,Mn)Se matrix [513]. They could show that the alignment of the spins inside the magnetic polaron volume leads to a strong line narrowing.

The interesting aspect concerning the DMS dots is the opportunity to align the Mn spins inside a dot by optical excitation via the polaron effect, without applying an external magnetic field. It is likely that even after the annihilation of the electron hole pair this alignment may persist, since the Mn spin relaxation time is much longer. This means that the dot carries information on a time scale much longer than the carrier lifetime and could be read out by a probe beam even after a delay. This is essentially the basic principle of a magneto-optical memory on a semiconductor basis.

## 5. CONCLUDING REMARKS AND OUTLOOK

In this review, we have addressed fundamental properties of diluted magnetic and magnetic semiconductor nanostructures. The emphasis was on the magnetic properties and phenomena specific to these structures (which do not occur in “non-magnetic” semiconductor nanostructures) rather than on applications. We intended to compile the current knowledge in the field. During this process it became obvious that the properties of two-dimensional structures are currently much better understood than those of one- and zero-dimensional structures. On the one hand, this is due to the high quality of state-of-the-art layered structures obtained by MOVPE and MBE, which can be grown with monolayer precision. So far, there is no fabrication technique for QWRs and QDs which may yield samples of comparable quality. On the other hand, it has to be noted that geometric and statistical aspects become more and more important with decreasing dimensionality of the magnetic semiconductor nanostructures. For example, in QDs the surface-to-volume ratio increases dramatically with decreasing diameter. This will strongly modify the magnetic properties compared with bulk. Moreover, the number of magnetic ions in DMS QDs as well as their location with respect to the surface will vary strongly, even in dots consisting of the same number of atoms due to ion statistics. Therefore, most of the studies of ensembles of diluted magnetic QDs are rather unsatisfactory because the “real” physics of the low dimensions is hidden by statistics. To overcome this problem studies of single nanostructures will become increasingly important. The first studies of this kind have been reported [312, 512–519]. In addition, it will be necessary to characterize the single nanostructure under study on the atomic level. For the extraction of the physics of the low dimensions, it will be essential to know the lattice sites of each magnetic ion, which, of course, poses severe experimental challenges. The difficulties in studying these one-dimensional and zero-dimensional magnetic semiconductor nanostructures experimentally also explains the small amount of theoretical work published, particularly that concerning the modification of magnetic properties by reduction of the dimensions. Therefore, there is currently no full consistent picture of the properties of magnetic semiconductor nanostructures and their modification with reduced dimensionality.

Our review presents a snapshot of the knowledge at the beginning of a new millennium—a new millennium not only in the calendrical sense, but also from the viewpoint of application. The current drive toward “spin electronics” (i.e., of introducing the quantum mechanical entity spin into semiconductor electronics and optoelectronics) has strongly enhanced the interest in magnetic semiconductor structures which may act as key components, such as spin filters and spin aligners of future spin electronic devices [515–517]. Apart from aspects of manipulation of single spins (such as optical spin polarization, spin transport, and spin conversion into a photon) in semiconductors in general, the aspect of miniaturization of magnetic semiconductors (mainly for magnetic spin polarization) in particular will be of major importance. The dimensional dependence of the magnetism of magnetic semiconductor nanostructures, magnetic coupling phenomena between magnetic and nonmagnetic semiconductor nanostructures, etc., which are all aspects addressed in this review, will need to be further understood and developed. A further understanding of these phenomena will immediately yield new device ideas as fundamental physics and application go hand in hand. It is beyond the scope of this chapter to determine whether spin electronics and spin optoelectronics based on magnetic semiconductors are feasible in the near future. The ideas for devices containing magnetic semiconductors are manifold, ranging from electrical devices such as the spin transistor suggested by Datta and Das [518], active opto-electronic devices such as polarization-switchable lasers [519–522], and passive opto-electronic devices such as Faraday rotators and optical isolators [523, 524], to spin quantum computers [515]. It is very likely that an all-semiconductor spin electronics at low temperatures can be realized in the very near future [520, 521, 525, 526]. However, a major breakthrough of all-semiconductor spin electronics will depend strongly on whether ferromagnetic semiconductor nanostructures with Curie temperatures sufficiently above room temperature can be realized.

## GLOSSARY

**Anderson superexchange** Exchange interaction between magnetic ions on adjacent cation sites mediated via the  $p$ -orbital of the anion between them in diluted magnetic semiconductors such as (II,Mn)VI and magnetic oxides such as MnO. The Anderson superexchange leads to an antiferromagnetic coupling of the Mn-spins.

**Diluted magnetic semiconductor** Class of semiconductors where a fraction  $x$  of the cations is replaced by magnetic ions such as rare earths or transition metals. Large subgroups are the  $\text{II}_{1-x}\text{Mn}_x\text{VI}$ ,  $\text{III}_{1-x}\text{Mn}_x\text{V}$  and  $\text{IV}_{1-x}\text{Mn}_x\text{VI}$  alloys.

**Energy transfer** Between the semiconductor band states and the localized  $d$ - or  $f$ -shells of the incorporated magnetic ions. These energy transfer processes in wide-gap diluted magnetic semiconductors such as ZnS:Mn can lead to a quenching of the bandgap-related emission in favor of  $d$ - or  $f$ -shell internal emission.

**Europium chalcogenides** Binary compounds AB formed by Eu and group VI elements, i.e. ferromagnetic EuO, EuS, EuSe, and antiferromagnetic EuTe.

**Giant Zeeman effect** Strong enhancement of the Zeeman splitting of the conduction band states ( $s = 1/2$ ,  $s_z = \pm 1/2$ ) and of the valence band states ( $j = 3/2$ ,  $j_z = \pm 3/2, \pm 1/2$ ) in diluted magnetic semiconductors due to the  $s,p-d$  exchange interaction with the localized magnetic moments of the magnetic ions.

**Internal transitions** Transitions between excited states and the lowest state of an inner  $d$ - or  $f$ -shell of a transition-metal or rare-earth ion incorporated in a wide-gap diluted magnetic semiconductor such as ZnS:Mn or ZnS:Eu or a magnetic semiconductor such as MnS. The transition energies depend strongly on the crystal at the site of the magnetic ion. The energies are usually described in the framework of Tanabe-Sugano diagrams.

**Magnetic interlayer coupling** Coupling between magnetic layers separated by a layer of nonmagnetic (diamagnetic) material often leading to a ferromagnetic or antiferromagnetic coupling.

**Magnetic polarons** A local stable state formed by Mn-ions and a free carrier or exciton via the  $s,p-d$  exchange interaction. The free carrier or exciton locally aligns the spins of the magnetic ions leading to a reduction of its energy and to a self localization.

**Magnetic semiconductor hybrid structure** Layered or granular structures consisting of a semiconductor and a ferromagnetic material (often a metal or semimetal). Examples are GaAs/MnAs hybrids or Ge/Mn<sub>11</sub>Ge<sub>8</sub> hybrids.

**Magnetic semiconductor nanostructure** Nanostructured dilute magnetic or magnetic semiconductor exhibiting modified electronic, vibronic or magnetic properties due to reduced lateral dimensions.

**Magnetic semiconductor** Term often used for semiconductors exhibiting spontaneous magnetization i.e. antiferromagnetism or ferromagnetism such as ferromagnetic (III,Mn)V or the manganese chalcogenides and europium chalcogenides.

**Magneto-electronic** Metal-based electronics making use of the magnetic properties of layered magnetic structures such as the giant magnetoresistance (GMR) effect or the tunneling magnetoresistance (TMR) effect.

**Magneto-optical anisotropy** Anisotropy of the Giant Zeeman splitting arising due to a competition of the quantization direction of the electronic states due to crystal structure (or strain) and the quantization direction induced by the magnetic field.

**Manganese chalcogenides** Antiferromagnetic binary compounds AB formed by Mn and group VI elements, i.e. antiferromagnetic MnO, MnS, MnSe, MnTe.

**Manganese pnictides** Binary compounds AB formed by Mn and group V elements, i.e., antiferromagnetic MnN and ferromagnetic MnP, MnAs, MnSb, MnBi.

**Mermin–Wagner theorem** Mathematical theorem stating that in one- and two-dimensional magnetic systems of the Heisenberg-type (i.e. isotropic magnetic interactions) no spontaneous phase transition into a magnetically ordered ferromagnetic or antiferromagnetic state is possible.

**Modified Brillouin function** The Brillouin function describing the magnetic field response of an ensemble of non-interacting localised spins is modified to account for a weak

antiferromagnetic coupling between the spins in paramagnetic  $\text{II}_{1-x}\text{Mn}_x\text{VI}$  diluted magnetic semiconductors. This is done by introducing two parameters, a prefactor  $a$  ( $0 \leq a \leq 1$ ) which describes an effective reduction of the Mn-concentration  $x$  and a Curie-Weiss parameter  $\Theta$  which accounts for the effective increase of the temperature due to the antiferromagnetic coupling.

**Quantum dot** Semiconductor nanostructure exhibiting quantum confinement along all three lateral dimensions.

**Quantum well** Layered (two-dimensional) semiconductor nanostructure consisting of a thin (typically a few nanometers) layer of semiconductor A embedded between two layers of semiconductor B. Usually the band gap of A is smaller than that of B leading to confinement of the carriers in the conduction and/or valence band of A perpendicular to the layer plane.

**Quantum wire** Semiconductor nanostructure exhibiting quantum confinement along two lateral dimensions.

#### Rudermann-Kittel-Kasuya-Yosida interaction (RKKY)

Mechanism to explain long-range coupling between magnetic ions. The coupling is mediated via the magnetic polarization of a free carrier gas. The RKKY mechanism is the basis for current theories of the ferromagnetism in (III,Mn)V semiconductors.

**$s,p$ - $d$  exchange interaction** Exchange interaction between the pseudo-spins of the free carriers in the  $s$ -like conduction band (or  $p$ -like valence band) and the localized  $S = 5/2$  spins of the Mn-ions in Mn-based diluted magnetic semiconductors.

**Semimagnetic semiconductor** Synonym for diluted magnetic semiconductor.

**Spin-optoelectronics** Semiconductor-based optoelectronics where the spin-selectivity of the optical selection rules is explored.

**Spintronics** Short for spinelectronics, semiconductor-based magnetoelectronics.

## REFERENCES

1. S. Methfessel, *IBM J. Res. Dev.* 14, 207 (1970).
2. I. G. Austin and D. Elwell, *Contemp. Phys.* 11, 455 (1970).
3. G. H. Jonker and J. H. van Santen, *Physica* 16, 337 (1950).
4. G. H. Jonker and J. H. van Santen, *Physica* 16, 559 (1950).
5. A. V. Komarov, S. M. Ryabchenko, O. V. Terletskij, I. I. Zheru, and R. D. Ivanchuk, *Zh. eksp. teor. fiz.* 73, 608 (1977).
6. R. R. Galazka, in "Physics of Semiconductors" (B. L. Wilson, Ed.), p. 133. Institute of Physics, London, 1982.
7. R. R. Galazka, *Lect. Notes Phys.* 152, 294 (1982).
8. J. A. Gaj, *J. Phys. Soc. Jpn.* 49 (Suppl. A), 747 (1980).
9. J. K. Furdyna, *J. Appl. Phys.* 53, 7637 (1982).
10. N. B. Brandt and V. V. Moshchalkov, *Adv. Phys.* 33, 193 (1984).
11. A. Mycielsky, *J. Appl. Phys.* 19, 3279 (1988).
12. A. Twardowski, in "Diluted Magnetic Semiconductors" (M. Jain, Ed.), p. 276. World Scientific, Singapore, 1991.
13. A. Lewicki, A. I. Schindler, J. K. Furdyna, and W. Giriat, *Phys. Rev. B* 40, 2379 (1989).
14. F. Hamdani, J. P. Lascaray, D. Coquillat, A. K. Bhattacharjee, M. Nawrocki, and Z. Golacki, *Phys. Rev. B* 45, 13298 (1992).
15. W. Mac, N. T. Khoi, A. Twardowski, J. A. Gaj, and M. Demianiuk, *Phys. Rev. Lett.* 71, 2327 (1993).
16. T. M. Pekarek, J. E. Luning, I. Miotkowski, and B. C. Crooker, *Phys. Rev.* 50, 16914 (1994).
17. G. Bauer, *Matter. Res. Soc. Proc.* 89, 107 (1987).
18. A. Lambrecht, N. Herres, B. Spanger, S. Kuhn, H. Bottner, M. Tacke, and J. Evers, *J. Cryst. Growth* 108, 301 (1991).
19. A. Bruno, J. P. Lascaray, M. Averous, G. Fillion, and J. F. Dumas, *Phys. Rev.* 37, 1186 (1988).
20. R. Boyn, *Phys. Status Solidi B* 148, 11 (1988).
21. J. K. Furdyna, *J. Appl. Phys.* 64, R29 (1988).
22. O. Goede and W. Heimbrodt, *Phys. Status Solidi B* 146, 11 (1988).
23. H. Munekata, H. Ohno, S. von Molnar, A. Segmüller, L. L. Chang, and L. Esaki, *Phys. Rev. Lett.* 63, 1849 (1989).
24. H. Ohno, A. Shen, F. Matsukura, A. Oiwa, A. Endo, S. Katsumoto, and Y. Iye, *Appl. Phys. Lett.* 69, 363 (1996).
25. S. Haneda, M. Yamaura, Y. Takatani, K. Hara, S. Harigae, and H. Munekata, *Jpn. J. Appl. Phys.* 39, L9 (2000).
26. T. Adhikari and S. Basu, *J. Magn. Magn. Mater.* 161, 282 (1996).
27. M. L. Reed, N. A. El-Masry, H. H. Stadelmaier, M. K. Ritums, M. J. Reed, C. A. Parker, J. C. Roberts, and S. M. Bedair, *Appl. Phys. Lett.* 79, 3473 (2001).
28. M. E. Overberg, B. P. Gila, C. R. Abernathy, S. J. Pearton, N. A. Theodoropoulou, K. T. McCarthy, S. B. Arnason, and A. F. Hebard, *Appl. Phys. Lett.* 79, 3128 (2001).
29. H. Saito, W. Zaets, R. Akimoto, K. Ando, Y. Mishima, and M. Tanaka, *J. Appl. Phys.* 89, 7392 (2001).
30. S. Kuwabara, K. Ishii, S. Haneda, T. Kondo, and H. Munekata, *Physica E* 10, 233 (2001).
31. Y. Morinaga, T. Edahiro, N. Fujimura, T. Ito, T. Koide, Y. Fujiwara, and Y. Takeda, *Physica E* 10, 391 (2001).
32. T. M. Pekarek, B. C. Crooker, I. Miotkowski, and A. K. Ramdas, *J. Appl. Phys.* 83, 6557 (1998).
33. T. M. Pekarek, C. Maymi, J. Garner, D. Hall, I. Miotkowski, and A. K. Ramdas, *J. Appl. Phys.* 91, 7496 (2002).
34. T. M. Pekarek, C. L. Fuller, J. Garner, B. C. Crooker, I. Miotkowski, and A. K. Ramdas, *J. Appl. Phys.* 89, 7030 (2001).
35. Y. D. Park, A. T. Hanbicki, S. C. Erwin, C. S. Hellerg, J. M. Sullivan, J. E. Mattson, T. F. Ambrose, A. Wilson, G. Spanos, and B. T. Jonker, *Science* 295, 651 (2002).
36. P. Grünberg, R. Schreiber, Y. Pang, M. B. Brodsky, and H. Sowers, *Phys. Rev. Lett.* 57, 2442 (1986).
37. M. Baibich, J. Broto, A. Fert, F. Nguyen van Dau, F. Petroff, P. Etienne, G. Creuzet, A. Friederich, and J. Chazelas, *Phys. Rev. Lett.* 61, 2472 (1988).
38. J. K. Furdyna and J. Kossut, Eds., "Diluted Magnetic Semiconductors," Semiconductors and Semimetals (R. K. Willardson and A. C. Beer, Eds.), Vol. 25. Academic Press, San Diego, 1988.
39. H. Ohno and F. Matsukura, *Solid State Commun.* 117, 179 (2001).
40. H. Ohno, *Mater. Sci. Forum* 182–184, 443 (1995).
41. G. Bauer, H. Pascher, and W. Zawadzki, *Semicond. Sci. Technol.* 7, 703 (1992).
42. G. Bauer and H. Pascher, in "Diluted Magnetic Semiconductors" (M. Jain, Ed.), p. 340. World Scientific, Singapore, 1991.
43. A. M. Hennel, in "Emis Data Review Series: Properties of Gallium Arsenide" (M. R. Brozel and G. E. Stillman, Eds.), Vol. 16, p. 248. INSPEC, London, 1996.
44. A. Krol, Y. L. Soo, S. Huang, Z. H. Ming, Y. H. Kao, H. Munekata, and L. L. Chang, *Phys. Rev.* 47, 7187 (1993).
45. X. C. Liu, D. Heiman, J. Hao, and K. C. Hsieh, *Mater. Sci. Forum* 182–184, 627 (1995).
46. J. Schneider, U. Kaufmann, W. Wilkening, M. Bäumlner, and F. Köhl, *Phys. Rev. Lett.* 59, 240 (1987).
47. A. Twardowski, *Mater. Sci. Engin.*, B 63, 96 (1999).
48. J. Szczytko, A. Twardowski, K. Swiatek, M. Palczewska, M. Tanaka, T. Hayashi, and K. Ando, *Phys. Rev.* 60, 8304 (1999).
49. O. Goede, W. Heimbrodt, and V. Weinhold, *Phys. Status Solidi B* 136, K49 (1986).
50. O. Goede, W. Heimbrodt, V. Weinhold, E. Schnürer, and H. G. Eberle, *Phys. Status Solidi B* 143, 511 (1987).

51. W. Heimbrodt, O. Goede, I. Tschentscher, V. Weinhold, A. Klimakow, U. Pohl, K. Jacobs, and N. Hoffmann, *Physica B* 185, 357 (1993).
52. P. Klosowski, T. M. Giebultowicz, J. J. Rhyne, N. Samarth, H. Luo, and J. K. Furdyna, *J. Appl. Phys.* 70, 6221 (1991).
53. L. A. Kolodziejski, R. L. Gunshor, N. Otsuka, B. P. Gu, Y. Hefetz, and A. V. Nurmikko, *Appl. Phys. Lett.* 48, 1482 (1986).
54. T. Fukumura, Z. Jin, A. Ohthoma, H. Koinuma, and M. Kawasaki, *Appl. Phys. Lett.* 75, 3366 (1999).
55. D. R. Joder-Short, M. Debska, and J. K. Furdyna, *J. Appl. Phys.* 58, 4056 (1985).
56. J. K. Furdyna, W. Giriat, D. F. Mitchell, and G. I. Sproule, *J. Solid State Chem.* 46, 349 (1983).
57. H. Wiedemeier and A. Khan, *Trans. Metal. Soc. AIME* 242, 1969 (1968).
58. N. Bottka, J. Stankiewicz, and W. Giriat, *J. Appl. Phys.* 52, 4189 (1981).
59. A. Pajczkowska and A. Rabenau, *J. Solid State Chem.* 21, 43 (1977).
60. A. Pajczkowska and A. Rabenau, *Mater. Res. Bull.* 12, 183 (1977).
61. R. T. Delves and B. Lewis, *J. Phys. Chem. Solids* 24, 549 (1963).
62. A. Balzarotti, U. Czyzyk, A. Kisiel, N. Motta, M. Podgorny, and M. Zimnal-Starnawska, *Phys. Rev.* 30, 2295 (1984).
63. A. Krost, B. Harbecke, R. Faymanville, H. Schlegel, E. J. Fantner, K. E. Ambrasch, and G. Bauer, *J. Phys. C: Solid State Phys.* 18, 2119 (1985).
64. A. Zunger, in "Solid State Physics" (H. Ehrenreich and D. Turnbull, Eds.), Vol. 39, p. 276. Academic Press, Orlando, 1986.
65. Y. R. Lee and A. K. Ramdas, *Solid State Commun.* 51, 861 (1984).
66. P. Wisniewski and M. Nawrocki, *Phys. Status Solidi B* 117, K43 (1983).
67. M. Jacyznski, J. Kossut, and R. R. Galazka, *Phys. Status Solidi B* 88, 73 (1978).
68. M. Dobrowolska, W. Dobrowolski, M. Otto, T. Dietl, and R. R. Galazka, *J. Phys. Soc. Jpn.* 49 (Suppl. A), 815 (1980).
69. A. Twardowski, P. Swiderski, M. von Ortenberg, and R. Pauthenet, *Solid State Commun.* 50, 509 (1984).
70. R. B. Bylisma, W. M. Becker, J. Kossut, and U. Debska, *Phys. Rev.* 33, 8207 (1986).
71. A. Twardowski, T. Dietl, and M. Demianiuk, *Solid State Commun.* 48, 845 (1983).
72. C. T. Tsai, S. H. Chen, D. S. Chuu, and W. C. Chou, *Phys. Rev.* 33, 8207 (1996).
73. M. Ikeda, K. Itoh, and H. Sato, *J. Phys. Soc. Jpn.* 25, 455 (1968).
74. D. Theis, *Phys. Lett. A* 59, 154 (1976).
75. M. Takahashi, *Phys. Rev.* 60, 15858 (1999).
76. J. Tworzdylo, *Phys. Rev.* 50, 14591 (1994).
77. J. Tworzdylo, *Solid State Commun.* 94, 821 (1995).
78. W. Shan, W. Walukiewicz, J. M. Ager, III, E. E. Haller, J. F. Geisz, D. J. Friedman, J. M. Olson, and S. R. Kurtz, *Phys. Rev. Lett.* 82, 1221 (1999).
79. J. D. Perkins, A. Mascarenhas, Y. Zhang, J. F. Geisz, D. J. Friedman, J. M. Olson, and S. R. Kurtz, *Phys. Rev. Lett.* 82, 3312 (1999).
80. W. Walukiewicz, W. Shan, K. M. Yu, J. W. Ager, III, E. E. Haller, I. Miotkowski, M. J. Seong, H. Alawadhi, and A. K. Ramdas, *Phys. Rev. Lett.* 85, 1552 (2000).
81. W. Heimbrodt, O. Goede, V. Weinhold, K. Hieke, M. Happ, N. Hoffmann, J. Griesche, and K. Jacobs, *J. Lumin.* 60–61, 344 (1994).
82. F. Geist, H. Pascher, N. Frank, and G. Bauer, *Phys. Rev.* 53, 3820 (1996).
83. T. Kasuya, *J. Magn. Magn. Mater.* 195, 141 (1999).
84. Th. Hartmann, M. Lampalzer, W. Stolz, K. Megges, J. Lorberth, P. J. Klar, and W. Heimbrodt, *Thin Solid Films* 364, 209 (2000).
85. Y. Tanabe and S. Sugano, *J. Phys. Soc. Jpn.* 9, 753 (1954).
86. J. S. Smart, in "Magnetism" (G. Rado and H. Shul, Eds.), p. 3, Table 7. Academic Press, New York and London, 1963.
87. H. W. White, D. C. McCollum, and J. Callaway, *Phys. Lett.* 25A, 388 (1967).
88. T. R. McGuire, B. E. Argyle, M. W. Shafer, and J. S. Smart, *Appl. Phys. Lett.* 1, 17 (1962).
89. N. F. Oliveira, S. Foner, and Y. Shapira, *Phys. Rev.* 5, 2634 (1972).
90. L. Passell, O. W. Dietrich, and J. Als-Nielsen, *Phys. Rev.* 14, 4897 (1976).
91. S. H. Charap and E. L. Boyd, *Phys. Rev.* 133, A811 (1964).
92. M. E. Lines and E. D. Jones, *Phys. Rev.* 141, 525 (1966).
93. L. Corliss, N. Elliot, and J. Hastings, *Phys. Rev.* 104, 924 (1956).
94. E. D. Jones, *Phys. Rev.* 151, 315 (1966).
95. J. W. Battles, *J. Appl. Phys.* 42, 1286 (1971).
96. D. R. Huffman and R. L. Wild, *Phys. Rev.* 148, 526 (1966).
97. W. S. Carter and K. W. H. Stevens, *Proc. Phys. Soc. B* 69, 1006 (1956).
98. G. Kerimov and T. A. Madov, *Fiz. Met. Metalloved.* 28, 188 (1968).
99. R. Lindsay, *Phys. Rev.* 84, 569 (1951).
100. R. MacLaren Murray, B. C. Forbes, and R. D. Heyding, *Canad. J. Chem.* 50, 4059 (1972).
101. L. C. Bartel, *Solid State Commun.* 11, 55 (1972).
102. R. Shanker and R. A. Singh, *Indian J. Pure Appl. Phys.* 12, 589 (1974).
103. L. Jansen, R. Ridler, and E. Lombardi, *Physica* 71, 425 (1974).
104. T. Oguchi, K. Terakura, and A. R. Williams, *Phys. Rev.* 28, 6443 (1983).
105. B. E. Larson, K. C. Hass, H. Ehrenreich, and A. E. Carlson, *Solid State Commun.* 56, 347 (1985).
106. K. C. Hass and H. Ehrenreich, *J. Vac. Sci. Technol., A* 1, 1678 (1983).
107. S.-H. Wei and A. Zunger, *Phys. Rev.* 35, 2340 (1987).
108. R. L. Aggarwal, S. N. Jasperson, Y. Shapira, S. Foner, T. Skakibara, T. Goto, N. Miura, D. Dwight, and A. Wold, in "Proceedings of the 17th International Conference on the Physics of Semiconductors" (J. D. Chadi and W. A. Harrison, Eds.), p. 1419. Springer-Verlag, New York, 1985.
109. J. P. Lascaray, M. Nawrocki, J. M. Broto, M. Rakoto, and M. Demianiuk, *Solid State Commun.* 61, 401 (1987).
110. D. M. Bartholomew, E. K. Suh, S. Rodriguez, A. K. Ramdas, and R. L. Aggarwal, *Solid State Commun.* 62, 235 (1987).
111. T. M. Giebultowicz, J. J. Rhyne, W. L. Ching, and D. L. Huber, *J. Appl. Phys.* 57, 3415 (1985).
112. J. P. Lascaray, A. Bruno, M. Nawrocki, J. M. Broto, J. C. Ousset, S. Askenazy, and R. Triboulet, *Phys. Rev.* 35, 6860 (1987).
113. G. Barilero, C. Rigaux, Nguyen Hy Hau, J. C. Picoche, and W. Giriat, *Solid State Commun.* 62, 345 (1987).
114. J. J. Banicz, R. F. Heidelberg, and A. H. Luxem, *J. Phys. Chem.* 65, 615 (1961).
115. T. Komatsubara, M. Murakami, and E. Hirahara, *J. Phys. Soc. Jpn.* 18, 356 (1963).
116. T. M. Giebultowicz, P. Klosowski, N. Samarth, H. Luo, J. K. Furdyna, and J. J. Rhyne, *Phys. Rev.* 48, 12817 (1993).
117. M. Sawicki, S. Kolesnik, T. Wojtowicz, G. Karczewski, E. Janik, M. Kutrowski, A. Zakrzewski, T. Dietl, and J. Kossut, *Superlattices Microstruct.* 15, 475 (1994).
118. M. E. Lines, *Phys. Rev.* 135, A1336 (1964).
119. S.-H. Wei and A. Zunger, *Phys. Rev.* 48, 6111 (1993).

120. B. E. Larson, K. C. Hass, H. Ehrenreich, and A. E. Carlson, *Phys. Rev. B* 37, 4137 (1988).
121. P. W. Anderson, in "Solid State Physics" (F. Seitz and D. Turnbull, Eds.), Vol. 14, p. 99. Academic Press, New York, 1963.
122. H. van der Heide, C. F. van Bruggen, G. A. Wiegers, and C. Haas, *J. Phys. C: Solid State Phys.* 16, 855 (1983).
123. P. Wachter, in "Handbook on the Physics and Chemistry of Rare Earths" (K. A. Gschneiderner and L. Eyring, Eds.). North-Holland, Amsterdam, 1979.
124. J. B. Goodenough, "Magnetism and the Chemical Bond" Interscience, New York and London, 1963.
125. H. Akinaga, J. De Boeck, G. Borghs, S. Miyanshi, A. Asamitsu, W. Van Roy, Y. Tomioka, and L. H. Kuo, *Appl. Phys. Lett.* 72, 3368 (1998).
126. P. J. Wellmann, J. M. Garcia, J.-L. Feng, and P. M. Petroff, *Appl. Phys. Lett.* 73, 3291 (1998).
127. L. Pytlík and A. Zieba, *J. Magn. Magn. Mater.* 51, 199 (1985).
128. M. E. G. Tilsley, N. A. Smith, B. Cockayne, I. R. Harris, P. A. Lane, P. E. Oliver, and P. J. Wright, *J. Alloys & Compounds*, 248, 125 (1997).
129. M. Tabuchi, M. Takahashi, and F. Kanamura, *J. Alloys & Compounds*. 210, 143 (1994).
130. M. Zajac, J. Gosk, M. Kaminska, A. Twardowski, T. Szyszko, and S. Podsladło, *Appl. Phys. Lett.* 79, 2432 (2001).
131. W. J. Takei, R. R. Heikes, and G. Shirane, *Phys. Rev.* 125, 1893 (1962).
132. R. R. Galazka, S. Nagata, and P. H. Keesom, *Phys. Rev.* 22, 3344 (1980).
133. S. Nagata, R. R. Galazka, D. P. Mullin, H. Akbarzadeh, G. D. Khattak, J. K. Furdyna, and P. H. Keesom, *Phys. Rev.* 22, 3313 (1980).
134. M. A. Novak, O. G. Symko, D. J. Zheng, and S. Oseroff, *Phys. Rev.* 33, 6391 (1986).
135. D. Ferrand, J. Cibert, C. Bourgognon, S. Tatarenko, A. Wasiela, G. Fishman, A. Bonanni, H. Sitter, S. Kolesnik, J. Jaroszynski, A. Barcz, and T. Dietl, *J. Cryst. Growth* 214–215, 387 (2000).
136. D. Ferrand, J. Cibert, A. Wasiela, C. Bourgognon, S. Tatarenko, G. Fishman, T. Andrearczyk, J. Jaroszynski, S. Kolesnik, T. Dietl, B. Barbara, and D. Dufeu, *Phys. Rev.* 63, 85201 (2000).
137. M. Sawicki, Le Van Khoi, L. Hansen, D. Ferrand, L. W. Molenkamp, A. Waag, and T. Dietl, *Phys. Status Solidi B* 223, 717 (2002).
138. W. J. M. de Jonge and H. J. M. Swagten, *J. Magn. Magn. Mater.* 100, 322 (1991).
139. H. Ohno, D. Chiba, F. Matsukura, T. Omla, E. Abe, T. Dietl, Y. Ohno, and K. Ohtani, *Nature* 408, 944 (2000).
140. H. Saito, V. Zayets, S. Yamagata, and K. Ando, *Phys. Rev. B* 66, 081201(R) (2002).
141. H. Shoren, F. Ikemoto, K. Yoshida, N. Tanaka, and K. Motizuki, *Physica E* 10, 242 (2001).
142. J. Blinowski, P. Kacman, and J. A. Majewski, *Phys. Rev. B* 53, 9524 (1996).
143. M. Escorne, A. Mauger, J. L. Tholence, and R. Triboulet, *Phys. Rev.* 29, 6306 (1984).
144. G. Karczewski and M. von Ortenberg, *Solid State Commun.* 55, 249 (1985).
145. A. Mauger and M. Escorne, *Phys. Rev.* 35, 1902 (1987).
146. C. W. H. M. Vennix, E. Frikkee, P. J. T. Eggenkamp, H. J. M. Swagten, K. Kopinga, and W. J. M. de Jonge, *Phys. Rev.* 48, 3770 (1993).
147. R. W. Cochrane, M. Plischke, and J. O. Ström-Olsen, *Phys. Rev.* 9, 3013 (1974).
148. T. Hamasaki, *Solid State Commun.* 32, 1069 (1979).
149. T. Story, R. R. Galazka, R. B. Frankel, and P. A. Wolff, *Phys. Rev. Lett.* 56, 777 (1986).
150. T. Story, P. J. T. Eggenkamp, C. H. W. Swüste, H. J. M. Swagten, W. J. M. de Jonge, and A. Szczerbakow, *Phys. Rev.* 47, 227 (1993).
151. F. Matsukura, H. Ohno, A. Shen, and Y. Sugawara, *Phys. Rev.* 57, R2037 (1998).
152. J. Sadowski, J. Z. Domagala, J. Bak-Misiuk, S. Kolesnik, M. Sawicki, K. Swiatek, J. Kanski, L. Ilver, and V. Ström, *J. Vac. Sci. Technol., B* 18, 1697 (2000).
153. A. Van Esch, L. Van Bockstal, J. De Boeck, G. Verbanck, A. S. van Steenberghe, P. J. Wellmann, B. Grietens, R. Bogaerts, F. Herlach, and G. Borghs, *Phys. Rev.* 56, 13103 (1997).
154. H. Ohno, H. Munekata, S. von Molnar, and L. L. Chang, *J. Appl. Phys.* 69, 6103 (1991).
155. B. Beschoten, P. A. Crowell, I. Malajovich, D. D. Awschalom, F. Matsukura, A. Shen, and H. Ohno, *Phys. Rev. Lett.* 83, 3073 (1999).
156. T. Dietl, H. Ohno, F. Matsukura, J. Cibert, and D. Ferrand, *Science* 287, 1019 (2000).
157. J. König, H.-H. Lin, and A. H. MacDonald, *Phys. Rev. Lett.* 84, 5628 (2000).
158. S. Sonoda, S. Shimizu, T. Sasaki, Y. Yamamoto, and H. Hori, *J. Cryst. Growth* 237–239, 1358 (2002).
159. T. Dietl, H. Ohno, and F. Matsukura, *Phys. Rev. B* 63, 195205 (2001).
160. M. E. Overberg, C. R. Abenathy, and S. J. Pearton, *Appl. Phys. Lett.* 79, 1312 (2001).
161. J. A. Gaj, R. Planel, and G. Fishman, *Solid State Commun.* 29, 435 (1979).
162. J. K. Furdyna and N. Samarth, *J. Appl. Phys.* 61, 3526 (1987).
163. Y. Shapira and N. F. Oliveira, *Phys. Rev.* 35, 6888 (1987).
164. Y. Shapira, S. Foner, D. Heiman, P. A. Wolff, and C. R. McIntyre, *Solid State Commun.* 71, 355 (1989).
165. Y. Shapira, S. Foner, D. H. Ridgley, K. Dwight, and A. Wold, *Phys. Rev.* 30, 4021 (1984).
166. E. D. Isaacs, D. Heiman, P. Becla, Y. Shapira, R. Kershaw, K. Dwight, and A. Wold, *Phys. Rev.* 38, 8412 (1988).
167. S. Foner, Y. Shapira, D. Heiman, P. Becla, R. Kershaw, K. Dwight, and A. Wold, *Phys. Rev.* 39, 11793 (1989).
168. R. L. Aggarwal, S. N. Jasperson, P. Becla, and R. R. Galazka, *Phys. Rev.* 32, 5132 (1985).
169. Y. Shapira, S. Foner, P. Becla, D. M. Domingues, M. J. Naughton, and J. S. Brooks, *Phys. Rev.* 33, 356 (1986).
170. R. L. Aggarwal, S. N. Jasperson, P. Becla, and J. K. Furdyna, *Phys. Rev.* 34, 5894 (1986).
171. R. R. Galazka, W. Dobrowolski, J. P. Lascaray, M. Nawrocki, A. Bruno, J. M. Broto, and J. C. Ousset, *J. Magn. Magn. Mater.* 72, 174 (1988).
172. V. Bindilatti, E. ter Haar, N. F. Oliveira, Jr., Y. Shapira, and M. T. Liu, *Phys. Rev. Lett.* 80, 5425 (1998).
173. V. Bindilatti, E. ter Haar, N. F. Oliveira, Jr., Y. Shapira, and M. T. Liu, *J. Appl. Phys.* 85, 5950 (1999).
174. T. M. Rusin, *Phys. Rev.* 53, 12577 (1996).
175. A. Bruno and J. P. Lascaray, *Phys. Rev.* 38, 9168 (1988).
176. A. Twardowski, H. J. M. Swagten, W. J. M. de Jonge, and M. Demianiuk, *Phys. Rev.* 36, 7013 (1987).
177. M. Gorska and J. R. Anderson, *Phys. Rev.* 38, 9120 (1988).
178. J. R. Anderson, G. Kido, Y. Nishina, M. Gorska, L. Kowalczyk, and Z. Golacki, *Phys. Rev.* 41, 1014 (1990).
179. T. Fukumura, Z. Jin, M. Kawasaki, T. Shono, T. Hasegawa, S. Koshihara, and H. Koinuma, *Appl. Phys. Lett.* 78, 958 (2001).
180. V. Bindilatti, N. F. Oliveira, Jr., Y. Shapira, G. H. McCabe, M. T. Liu, S. Isber, S. Charar, M. Averous, E. J. McNiff, Jr., and Z. Golacki, *Phys. Rev.* 53, 5472 (1996).
181. E. ter Haar, V. Bindilatti, N. F. Oliveira, Jr., G. H. McCabe, Y. Shapira, Z. Golacki, S. Charar, M. Averous, and E. J. McNiff, Jr., *Phys. Rev.* 56, 8912 (1997).
182. V. Bindilatti, E. ter Haar, N. F. Oliveira, Jr., M. T. Liu, Y. Shapira, X. Gratens, S. Charar, S. Isber, P. Masri, M. Averous, Z. Golacki, and E. J. McNiff, Jr., *Phys. Rev.* 57, 7854 (1998).

183. J. Spalek, A. Lewicki, Z. Tarnawski, J. K. Furdyna, R. R. Galazka, and Z. Obuszko, *Phys. Rev.* 33, 3407 (1986).
184. A. Twardowski, M. Nawrocki, and J. Ginter, *Phys. Status Solidi B* 96, 497 (1979).
185. J. A. Gaj, R. R. Galazka, and M. Nawrocki, *Solid State Commun.* 25, 193 (1978).
186. J. A. Gaj, J. Ginter, and R. R. Galazka, *Phys. Status Solidi B* 89, 655 (1978).
187. S. M. Ryabchenko, Yu. G. Semenov, and O. V. Terletsii, *Sov. Phys. JETP* 55, 557 (1982).
188. A. V. Komarov, S. M. Ryabchenko, O. V. Terletsii, I. I. Zheru, and R. D. Ivanchuk, *Zh. Eksp. Teor. Fiz.* 73, 608 (1977).
189. A. Twardowski, *Phys. Lett. A* 94, 103 (1983).
190. J. P. Lascaray, M. C. D. Deruelle, and J. Coquillat, *Phys. Rev. B* 35, 675 (1987).
191. Y. R. Lee, A. K. Ramdas, and R. C. Aggarwal, *Phys. Rev. B* 33, 7383 (1986).
192. A. V. Komarov, S. M. Ryabchenko, and N. I. Vitrikhovskij, *Zh. Eksp. Teor. Fiz.* 27, 441 (1978).
193. L. Bryja, M. Arciszewska, and J. A. Gaj, *Acta Phys. Pol., A* 69, 1051 (1986).
194. R. L. Aggarwal, S. N. Jaspersen, J. Stankiewicz, Y. Shapira, S. Foner, B. Khazai, and A. Wold, *Phys. Rev.* 28, 6907 (1983).
195. L. A. Kolodziejski, R. L. Gunshor, R. Venkatasubramanian, T. C. Bonsett, R. Frohne, S. Datta, N. Otsuka, R. B. Bylisma, W. M. Becker, and A. V. Nurmikko, *J. Vac. Sci. Technol., B* 4, 583 (1986).
196. V. G. Abramishvili, S. I. Gubarev, A. V. Komarov, and S. M. Ryabchenko, *Fiz. Tverd. Tela* 26, 1095 (1984).
197. S. I. Gubarev, *Zh. Eksp. Teor. Fiz.* 80, 1175 (1981).
198. M. Nawrocki, J. P. Lascaray, D. Coquillat, and M. Demianiuk, *Mater. Res. Soc. Symp. Proc.* 89, 65 (1987).
199. Yu. G. Semenov, V. G. Abramishvili, A. V. Komarov, and S. M. Ryabchenko, *Phys. Rev.* 56, 1868 (1997).
200. D. L. Peterson, A. Petrou, M. Dutta, A. K. Ramdas, and S. Rodriguez, *Solid State Commun.* 43, 667 (1982).
201. D. Heiman, Y. Shapira, and S. Foner, *Solid State Commun.* 51, 849 (1984).
202. A. Twardowski, M. von Ortenberg, M. Demianiuk, and R. Pauthenet, *Solid State Commun.* 51, 849 (1984).
203. Y. Shapira, D. Heiman, and S. Foner, *Solid State Commun.* 44, 1243 (1982).
204. A. V. Komarov, S. M. Ryabchenko, and Yu. G. Semenov, *Zh. Eksp. Teor. Fiz.* 79, 1554 (1980).
205. D. Heiman, Y. Shapira, and S. Foner, *Solid State Commun.* 45, 899 (1983).
206. W. Mac, A. Twardowski, and M. Demianiuk, *Phys. Rev.* 54, 5528 (1996).
207. A. Twardowski, D. Heiman, M. T. Liu, Y. Shapira, and M. Demianiuk, *Phys. Rev.* 53, 10728 (1996).
208. M. Zielinski, C. Rigaux, A. Lemaitre, A. Mycielski, and J. Deportes, *Phys. Rev.* 53, 674 (1996).
209. U. Gennser, X. C. Liu, D. Heiman, T. Fries, Y. Shapira, M. Demianiuk, and A. Twardowski, *Phys. Rev.* 51, 9606 (1995).
210. D. U. Bartholomew, E.-K. Suh, A. K. Ramdas, S. Rodriguez, U. Debska, and J. K. Furdyna, *Phys. Rev.* 39, 5865 (1989).
211. N. Adachi, M. Inoue, I. Mogi, and G. Kido, *J. Phys. Soc. Jpn.* 64, 1378 (1995).
212. M. Nawrocki, F. Hamdani, J. P. Lascaray, Z. Golacki, and J. Deportes, *Solid State Commun.* 77, 111 (1991).
213. V. G. Abramishvili, A. V. Komarov, S. M. Ryabchenko, A. I. Savchuk, and Yu. G. Semenov, *Solid State Commun.* 100, 397 (1997).
214. W. Mac, M. Herbich, N. T. Khoi, and A. Twardowski, *Acta Phys. Pol., A* 88, 845 (1995).
215. A. Twardowski, K. Pakula, I. Perez, P. Wise, and J. E. Crow, *Phys. Rev.* 42, 7567 (1990).
216. A. Twardowski, P. Glod, P. Pernambuco-Wise, J. E. Crow, and M. Demianiuk, *Phys. Rev.* 46, 7537 (1992).
217. O. W. Shih, R. L. Aggarwal, Y. Shapira, S. H. Bloom, V. Bindilatti, R. Kershaw, K. Dwight, and A. Wold, *Solid State Commun.* 74, 455 (1990).
218. C. Testelin, C. Rigaux, A. Mycielski, M. Menant, and M. Guillot, *Solid State Commun.* 78, 659 (1991).
219. W. Heimbrod, Th. Hartmann, P. J. Klar, M. Lampalzer, W. Stolz, K. Volz, A. Schaper, W. Treutmann, H. A. Krug von Nidda, A. Loidl, T. Ruf, and V. F. Sapega, *Physica E* 10, 175 (2001).
220. V. F. Sapega, T. Ruf, and M. Cardona, *Phys. Status Solidi B* 226, 339 (2001).
221. P. Kacman, *Semicond. Sci. Technol.* 16, R25 (2001).
222. Th. Hartmann, S. Ye, T. Henning, P. J. Klar, M. Lampalzer, W. Stolz, and W. Heimbrod, to be published in *J. Superconductivity Incorporating Novel Magnetism* 16, 423 (2003).
223. H. Bednarski, J. Cisowski, and J. C. Portal, *Phys. Rev.* 55, 15762 (1997).
224. H. Bednarski, J. Cisowski, W. Heimbrod, and J. C. Portal, *Solid State Commun.* 113, 419 (2000).
225. S. J. Weston, M. O'Neill, J. E. Nicholls, J. Miao, W. E. Hagston, and T. Stirner, *Phys. Rev.* 58, 7040 (1998).
226. P. Harrison, J. M. Fatah, T. Stirner, and W. E. Hagston, *J. Appl. Phys.* 79, 1684 (1996).
227. D. L. Mitchell and R. F. Wallis, *Phys. Rev.* 151, 581 (1966).
228. R. L. Bernick and L. Kleinman, *Solid State Commun.* 8, 569 (1970).
229. H. Pascher, P. Röhlein, G. Bauer, and L. Palmethofer, *Phys. Rev.* 36, 9395 (1987).
230. F. Geist, W. Herbst, C. Mejia-Garcia, H. Pascher, R. Rupprecht, Y. Ueta, G. Springholz, G. Bauer, and M. Tacke, *Phys. Rev.* 56, 13042 (1997).
231. A. C. Gossard and S. Fafard, *Solid State Commun.* 92, 63 (1994).
232. G. W. Bryant, *J. Lumin.* 70, 108 (1996).
233. R. Nötzel, *Semicond. Sci. Technol.* 11, 1365 (1996).
234. M. P. Pileni, *Cryst. Res. Technol.* 33, 1155 (1998).
235. A. Ekimov, *J. Lumin.* 70, 1 (1996).
236. R. N. Bicknell, R. W. Yanka, N. C. Giles-Taylor, D. U. Blanks, E. L. Buckland, and J. F. Schetzina, *Appl. Phys. Lett.* 45, 92 (1984).
237. L. A. Kolodziejski, T. C. Bonsett, R. L. Gunshor, S. Datta, R. B. Bylisma, W. M. Becker, and N. Otsuka, *Appl. Phys. Lett.* 45, 440 (1984).
238. D. E. Ashenford, B. Lunn, J. J. Davies, J. H. C. Hogg, J. E. Nicholls, C. G. Scott, D. Shaw, H. H. Sutherland, C. P. Hilton, T. J. Gregory, D. Johnston, B. C. Cavenett, G. R. Johnson, and M. Haines, *J. Cryst. Growth* 95, 557 (1989).
239. S. Datta, J. K. Furdyna, and R. L. Gunshor, *Superlattices Microstruct.* 1, 327 (1985).
240. S. M. Durbin, J. H. Sungki, O. M. Kobayashi, D. R. Menke, R. L. Gunshor, Q. Fu, N. Pelekanos, A. V. Nurmikko, D. Li, J. Gon-salves, and N. Otsuka, *Appl. Phys. Lett.* 55, 2087 (1989).
241. J. Warnock, A. Petrou, R. N. Bicknell, N. C. Giles-Taylor, D. K. Blanks, and J. F. Schetzina, *Phys. Rev.* 32, 8116 (1985).
242. N. Hoffmann, J. Griesche, W. Heimbrod, O. Goede, and K. Jacobs, *J. Cryst. Growth* 127, 347 (1993).
243. L. A. Kolodziejski, R. L. Gunshor, N. Otsuka, S. Datta, W. M. Becker, and A. V. Nurmikko, *IEEE J. Quantum Electron.* QE-22, 1666 (1986).
244. N. J. Duddles, J. E. Nicholls, T. J. Gregory, W. E. Hagston, B. Lunn, and D. E. Ashenford, *J. Vac. Sci. Technol., B* 10, 912 (1992).
245. N. Pelekanos, Q. Fu, A. V. Nurmikko, S. Durbin, J. H. Sungki, O. D. Menke, M. Kobayashi, and R. L. Gunshor, *J. Cryst. Growth* 101, 628 (1990).
246. N. Hoffmann, J. Griesche, W. Heimbrod, V. Weinhold, and K. Jacobs, *J. Cryst. Growth* 146, 422 (1995).
247. J. Griesche, N. Hoffmann, M. Rabe, and K. Jacobs, *Appl. Surf. Sci.* 75, 64 (1994).



248. J. Griesche, N. Hoffmann, and K. Jacobs, *J. Cryst. Growth* 138, 55 (1994).
249. H. Munekata, T. Penney, and L. L. Chang, *Surf. Sci.* 267, 342 (1992).
250. A. Shen, F. Matsukura, S. P. Guo, Y. Sugawara, H. Ohno, M. Tani, H. Abe, and H. C. Liu, *J. Cryst. Growth* 201–202, 679 (1999).
251. T. Sasaki, S. Sonoda, Y. Yamamoto, K. Suga, S. Shimizu, K. Kindo, and H. Hori, *J. Appl. Phys.* 91, 7911 (2002).
252. H. Clemens, H. Krenn, P. C. Weilguni, U. Stromberger, and G. Bauer, *Surf. Sci.* 228, 236 (1990).
253. H. Clemens, P. C. Weilguni, U. Stromberger, and G. Bauer, *J. Vac. Sci. Technol., A* 7, 3197 (1989).
254. H. Krenn, E. Koppensteiner, A. Holzinger, A. Voiticek, G. Bauer, and H. Clemens, *J. Appl. Phys.* 72, 97 (1992).
255. N. Frank, A. Voiticek, H. Clemens, A. Holzinger, and G. Bauer, *J. Cryst. Growth* 126, 293 (1993).
256. F. Geist, H. Pascher, M. Kriechbaum, N. Frank, and G. Bauer, *Phys. Rev.* 54, 4820 (1996).
257. S. Yuan, H. Krenn, G. Springholz, Y. Ueta, G. Bauer, and P. J. McCann, *Phys. Rev.* 55, 4607 (1997).
258. E. Abramof, P. H. O. Rappl, A. Y. Ueta, and P. Motisuke, *J. Appl. Phys.* 88, 725 (2000).
259. G. Springholz and G. Bauer, *Appl. Phys. Lett.* 60, 1600 (1992).
260. G. Springholz, G. Bauer, and G. Ihninger, *J. Cryst. Growth* 127, 302 (1993).
261. P. Klosowski, T. M. Giebultowicz, J. J. Rhyne, N. Samarth, H. Luo, and J. K. Furdyna, *J. Appl. Phys.* 69, 6109 (1991).
262. T. M. Giebultowicz, P. Klosowski, J. J. Rhyne, N. Samarth, H. Luo, and J. K. Furdyna, *Physica B* 180–181, 485 (1992).
263. L. E. Stumpe, J. J. Rhyne, H. Kaiser, S. Lee, U. Bindley, and J. K. Furdyna, *J. Appl. Phys.* 87, 6460 (2000).
264. W. Faschinger and H. Sitter, *J. Cryst. Growth* 99, 566 (1990).
265. V. Nunez, T. M. Giebultowicz, W. Faschinger, G. Bauer, H. Sitter, and J. K. Furdyna, *J. Magn. Magn. Mater.* 140–144, 633 (1995).
266. T. M. Giebultowicz, H. Luo, N. Samarth, J. K. Furdyna, V. Nunez, J. J. Rhyne, W. Faschinger, G. Springholz, G. Bauer, and H. Sitter, *Physica B* 198, 163 (1998).
267. G. Springholz and G. Bauer, *Phys. Rev.* 48, 10998 (1993).
268. G. Springholz and G. Bauer, *Appl. Phys. Lett.* 62, 2399 (1993).
269. E. Koppensteiner, G. Springholz, P. Hamberger, and G. Bauer, *J. Appl. Phys.* 74, 6062 (1993).
270. G. Springholz, N. Frank, and G. Bauer, *Appl. Phys. Lett.* 64, 2970 (1994).
271. G. Springholz and G. Bauer, *J. Appl. Phys.* 77, 540 (1995).
272. G. Springholz, *Mater. Sci. Forum* 182–184, 573 (1995).
273. J. J. Chen, G. Dresselhaus, M. S. Dresselhaus, G. Springholz, C. Pichler, and G. Bauer, *Phys. Rev.* 54, 402 (1996).
274. Z. Wilamowski, W. Jantsch, and G. Springholz, *Mater. Sci. Forum* 182–184, 669 (1995).
275. N. Frank, G. Springholz, and G. Bauer, *Phys. Rev. Lett.* 73, 2236 (1994).
276. A. Stachow-Wójcik, T. Story, W. Dobrowolski, M. Arciszewska, R. R. Galazka, M. W. Kreijveld, C. H. W. Swüste, H. J. M. Swagten, W. J. M. de Jonge, A. Twardowski, and A. Y. Sipatov, *Phys. Rev.* 60, 15220 (1999).
277. J. Wosnitzer, H. v. Löhneysen, U. Walz, and W. Zinn, *Z. Phys. B: Condens. Matter* 77, 25 (1989).
278. M. Tanaka, *Mater. Sci. Eng., B* 31, 117 (1995).
279. Y. Morishita, K. Iida, A. Tsuboi, H. Taniguchi, and K. Sato, *J. Cryst. Growth* 187, 228 (1998).
280. F. Schippan, A. Trampert, L. Däweritz, K. H. Ploog, B. Dennis, K. U. Neumann, and K. R. A. Ziebeck, *J. Cryst. Growth* 201–202, 674 (1999).
281. S. Huang, Z. H. Ming, Y. L. Soo, Y. H. Kao, M. Tanaka, and H. Munekata, *J. Appl. Phys.* 79, 1435 (1996).
282. H. Akinaga, K. Tanaka, K. Ando, and T. Katayama, *J. Cryst. Growth* 150, 1144 (1995).
283. K. Ono, T. Uragami, M. Mizuguchi, H. Fujioka, M. Oshima, M. Tanaka, and H. Akinaga, *J. Cryst. Growth* 209, 556 (2000).
284. H. Akinaga, S. Miyanishi, Y. Suzuki, K. Tanaka, T. Katayama, and K. Ando, *J. Cryst. Growth* 159, 1022 (1996).
285. A. Lussion, V. Sallet, R. Druilhe, Y. Marfaing, and R. Triboulet, *Mater. Sci. Forum* 182–184, 411 (1995).
286. G. N. Pain, N. Bharatula, G. I. Christiansz, M. H. Kibel, M. S. Kwietniak, C. Sandford, T. Warminski, R. S. Dickson, R. S. Rowe, K. McGregor, G. B. Deacon, B. O. West, S. R. Glanville, D. G. Hay, C. J. Rossouw, and A. W. Stevenson, *J. Cryst. Growth* 101, 208 (1990).
287. M. Migita, O. Kanehisa, M. Shiiki, and H. Yamamoto, *J. Cryst. Growth* 93, 686 (1988).
288. M. L. Reed, M. K. Ritums, H. H. Stadelmaier, M. J. Reed, C. A. Parker, S. M. Bedair, and N. A. El-Masry, *Mater. Lett.* 51, 500 (2001).
289. P. J. Klar, W. Heimbrot, and T. Henning, unpublished observations.
290. Y. Oka, J. X. Shen, K. Takabayashi, N. Takahashi, H. Mitsu, I. Souma, and R. Pittini, *J. Lumin.* 83–84, 83 (1999).
291. K. Takabayashi, N. Takahashi, I. Yagi, K. Yui, I. Souma, J. X. Shen, and Y. Oka, *J. Lumin.* 87–89, 347 (2000).
292. N. Takahashi, K. Takabayashi, I. Souma, J. Shen, and Y. Oka, *J. Appl. Phys.* 87, 6469 (2000).
293. A. A. Darhuber, H. Straub, S. O. Ferreira, W. Faschinger, H. Sitter, E. Koppensteiner, G. Brunthaler, and G. Bauer, *Mater. Sci. Forum* 182–184, 423 (1995).
294. J. A. Lebens, C. S. Tsai, K. J. Vahala, and T. F. Kuech, *Appl. Phys. Lett.* 56, 2642 (1990).
295. L. Parthier, H. Wissmann, and M. von Ortenberg, *J. Cryst. Growth* 159, 99 (1996).
296. H. Isshiki, Y. Aoyagi, T. Sugano, S. Iwai, and T. Meguro, *Appl. Phys. Lett.* 63, 1528 (1993).
297. L. Parthier, S. Luther, O. Portugall, M. von Ortenberg, K. Uchida, H. Kanimatsu, and N. Miura, *J. Cryst. Growth* 184–185, 339 (1998).
298. Z. H. Chen, M. C. Debnath, K. Shibata, T. Saitou, T. Sato, and Y. Oka, *J. Appl. Phys.* 89, 6701 (2001).
299. Y. Morishita, Y. Sugawara, M. Itoh, and K. Sato, *J. Cryst. Growth* 209, 599 (2000).
300. C. T. Kresge, M. E. Leonowicz, W. J. Roth, J. C. Vartuli, and J. S. Beck, *Nature (London)* 359, 710 (1992).
301. Q. Huo, D. I. Margolese, U. Ciesla, P. Feng, T. E. Gier, P. Sieger, R. Leon, P. M. Petroff, F. Schüth, and G. D. Stucky, *Nature (London)* 368, 317 (1994).
302. M. Thommes, R. Köhn, and M. Fröba, *J. Phys. Chem. B* 104, 7932 (2000).
303. L. Chen, P. J. Klar, W. Heimbrot, F. Brieler, and M. Fröba, *Appl. Phys. Lett.* 76, 3531 (2000).
304. L. Chen, P. J. Klar, W. Heimbrot, F. Brieler, M. Fröba, H.-A. von Nidda, and A. Loidl, *Physica E* 10, 369 (2001).
305. F. J. Brieler, M. Fröba, L. Chen, P. J. Klar, W. Heimbrot, H.-A. Krug von Nidda, and A. Loidl, *Chem. Eur. J.* 8, 185 (2002).
306. L. Chen, H. Falk, P. J. Klar, W. Heimbrot, F. Brieler, M. Fröba, H.-A. Krug von Nidda, A. Loidl, Z. Chen, and Y. Oka, *Phys. Status Solidi B* 229, 31 (2002).
307. A. Ribayrol, Y. S. Tang, H. P. Zhou, D. Coquillat, C. M. Sotomayor Torres, J. P. Lascaray, B. Lunn, D. E. Ashenford, G. Feuillet, and J. Cibert, *J. Cryst. Growth* 159, 434 (1996).
308. P. J. Klar, D. Wolverson, D. E. Ashenford, B. Lunn, and T. Henning, *Semicond. Sci. Technol.* 11, 1863 (1996).
309. P. J. Klar, D. Wolverson, J. J. Davies, B. Lunn, D. E. Ashenford, and T. Henning, in “Proceedings of the 23rd International Conference on the Physics of Semiconductors” (M. Scheffler and R. Zimmermann, Eds.), Vol. 2, p. 1485. World Scientific, Singapore, 1996.

310. P. J. Klar, D. Wolverson, J. J. Davies, W. Heimbrodt, M. Happ, and T. Henning, *Phys. Rev.* 57, 7114 (1998).
311. W. Heimbrodt, H. Falk, and P. J. Klar, *J. Lumin.* 87–89, 344 (2000).
312. G. Bacher, T. Kümmell, D. Eisert, A. Forchel, B. König, W. Ossau, C. R. Becker, and G. Landwehr, *Appl. Phys. Lett.* 75, 956 (1999).
313. G. Bacher, M. K. Welsch, A. McDonald, T. Kümmell, A. Forchel, B. König, C. Becker, W. Ossau, and G. Landwehr, *Phys. Status Solidi A* 178, 359 (2000).
314. M. A. Foad, C. D. W. Wilkinson, C. Dunscomb, and R. H. Williams, *Appl. Phys. Lett.* 60, 2531 (1992).
315. K. Tsutsui, E. L. Hu, and C. D. W. Wilkinson, *Jpn. J. Appl. Phys.* 32, 6233 (1993).
316. S. Somekh and H. C. Casey, Jr., *Appl. Opt.* 16, 126 (1977).
317. L. S. Dang, C. Gourgon, N. Magnea, H. Mariette, and C. Vieu, *Semicond. Sci. Technol.* 9, 1953 (1994).
318. G. Bacher, M. Illing, A. Forchel, A. Waag, T. Litz, and G. Landwehr, *Phys. Status Solidi B* 187, 371 (1995).
319. S. Kuroda, Y. Terai, K. Takita, T. Okuno, and Y. Masumoto, *J. Cryst. Growth* 184–185, 971 (1998).
320. S. Kuroda, Y. Terai, K. Takita, T. Okuno, and Y. Masumoto, *J. Cryst. Growth* 184–185, 274 (1998).
321. Y. Terai, S. Kuroda, and K. Takita, *Appl. Phys. Lett.* 76, 2400 (2000).
322. Y. Terai, S. Kuroda, K. Takita, T. Takamasu, and G. Kido, *J. Lumin.* 87–89, 396 (2000).
323. S. Mackowski, S. Lee, J. K. Furdyna, M. Dobrowolska, G. Prechtel, W. Heiss, J. Kossut, and G. Karczewski, *Phys. Status Solidi B* 229, 469 (2002).
324. G. Karczewski, S. Mackowski, M. Kutrowski, T. Wojtowicz, and J. Kossut, *Appl. Phys. Lett.* 74, 3011 (1999).
325. S. H. Xin, P. D. Wang, A. Yin, C. Kim, M. Dobrowolska, J. L. Merz, and J. K. Furdyna, *Appl. Phys. Lett.* 69, 3884 (1996).
326. Y. K. Zhou, H. Asahi, J. Asakura, S. Okumura, K. Asami, and S. Gonda, *J. Cryst. Growth* 221, 605 (2000).
327. M. Pinczolits, G. Springholz, and G. Bauer, *Phys. Rev.* 60, 11524 (1999).
328. G. Springholz, M. Pinczolits, V. Holy, P. Mayer, K. Wiesauer, T. Roch, and G. Bauer, *Surf. Sci.* 454–456, 657 (2000).
329. G. Springholz, J. Stangl, M. Pinczolits, V. Holy, P. Mikulík, P. Mayer, K. Wiesauer, G. Bauer, D. Smilgies, H. H. Kang, and L. Salamanca-Riba, *Physica E* 7, 870 (2000).
330. G. Springholz, M. Pinczolits, P. Mayer, V. Holy, G. Bauer, H. H. Kang, and L. Salamanca-Riba, *Phys. Rev. Lett.* 84, 4669 (2000).
331. M. Pinczolits, G. Springholz, and G. Bauer, *Appl. Phys. Lett.* 73, 250 (1998).
332. U. Woggon, “Optical properties of Semiconductor Quantum Dots,” Springer Tracts in Modern Physics, Vol. 136. Springer-Verlag, Berlin, Heidelberg, and New York, 1997.
333. K. Suzuki, M. Nakamura, I. Souma, K. Yanata, Y. Oka, H. Fujiyasa, and H. Noma, *J. Cryst. Growth* 117, 881 (1992).
334. K. Yanata, K. Suzuki, and Y. Oka, *J. Appl. Phys.* 73, 4596 (1993).
335. K. Yanata and Y. Oka, *Superlattices Microstruct.* 15, 233 (1994).
336. K. Yanata and Y. Oka, *Jpn. J. Appl. Phys.* 34, 164 (1995).
337. Y. Oka and K. Yanata, *J. Lumin.* 70, 35 (1996).
338. Y. Wang, N. Herron, K. Moller, and T. Bein, *Solid State Commun.* 77, 33 (1991).
339. M. A. Chamarro, V. Voliotis, R. Grousson, P. Lavallard, T. Gacoin, G. Counio, J. P. Boilot, and R. Cases, *J. Cryst. Growth* 159, 853 (1996).
340. M. Morita, D. Rau, H. Fujii, Y. Minami, S. Murakami, M. Baba, M. Yoshita, and H. Akiyama, *J. Lumin.* 87–89, 478 (2000).
341. M. V. Artemyev, L. I. Gurinovich, A. P. Stupak, and S. V. Gaponenko, *Phys. Status Solidi B* 224, 191 (2001).
342. K. Ando, A. Chiba, and H. Tanoue, *Appl. Phys. Lett.* 73, 387 (1998).
343. P. J. Wellmann, J. M. Garcia, J.-L. Feng, and P. M. Petroff, *Appl. Phys. Lett.* 71, 2532 (1997).
344. A. Van Esch, W. Van Roy, J. De Boeck, I. Francois, H. Bender, G. Borghs, L. Van Bockstal, R. Bogaerts, and F. Herlach, *Mater. Sci. Forum* 182–184, 623 (1995).
345. M. Mizuguchi, H. Akinaga, K. Ono, and M. Oshima, *J. Cryst. Growth* 209, 552 (2000).
346. E. Abe, F. Matsukura, H. Yasuda, Y. Ohno, and H. Ohno, *Physica E* 7, 981 (2000).
347. J. De Boeck, R. Oesterholt, H. Bender, A. Van Esch, C. Bruynseraede, C. Van Hoof, and G. Borghs, *J. Magn. Magn. Mater.* 156, 148 (1996).
348. J. De Boeck, A. Akinaga, C. Bruynseraede, H. Bender, and G. Borghs, *IEEE Trans. Magn.* 34, 891 (1998).
349. A. Henglein, *Ber. Bunsen-Ges. Phys. Chem.* 101, 1592 (1997).
350. C. Laungdilok and D. Meisel, *Isr. J. Chem.* 33, 53 (1993).
351. C. B. Murray, D. J. Norris, and M. G. Bawendi, *J. Am. Chem. Soc.* 115, 8706 (1993).
352. F. V. Mikulec, M. Kuno, M. Bennati, D. A. Hall, R. G. Griffin, and M. G. Bawendi, *J. Am. Chem. Soc.* 122, 2532 (2000).
353. R. J. Bandaranayake, J. Y. Lin, H. X. Jiang, and C. M. Sorensen, *J. Magn. Magn. Mater.* 169, 289 (1997).
354. L. Levy, J. F. Hochepeid, and M. P. Pileni, *J. Phys. Chem.* 100, 18322 (1996).
355. L. Levy, N. Feltin, D. Ingert, and M. P. Pileni, *J. Phys. Chem. B* 101, 9153 (1997).
356. R. N. Bhargava, D. Gallagher, X. Hong, and A. V. Nurmikko, *Phys. Rev. Lett.* 72, 416 (1994).
357. A. A. Bol and A. Meijerink, *Phys. Rev.* 58, R15997 (1998).
358. A. A. Bol and A. Meijerink, *J. Lumin.* 87–89, 315 (2000).
359. D. J. Norris, Nan Yao, F. T. Charnock, and T. A. Kennedy, *Nanotechnology* 1, 3 (2001).
360. M. A. Hines and P. Guyot-Sionnest, *J. Phys. Chem. B* 102, 3655 (1998).
361. H. Kroemer, *J. Vac. Sci. Technol., B* 2, 433 (1984).
362. G. Margaritondo, *J. Vac. Sci. Technol., B* 11, 1362 (1993).
363. F. Capasso and A. Y. Cho, *Surf. Sci.* 299–300, 878 (1994).
364. F. Capasso, *Thin Solid Films* 216, 59 (1992).
365. S. H. Wei and A. Zunger, *Phys. Rev.* 53, R10457 (1996).
366. W. Faschinger, S. Ferreira, H. Sitter, R. Krump, and G. Brunthaler, *Mater. Sci. Forum* 182–184, 29 (1995).
367. W. Mönch, *Appl. Phys. Lett.* 67, 2209 (1995).
368. W. Ossau, B. Kuhn-Heinrich, A. Waag, T. Litz, and G. Landwehr, *Superlattices Microstruct.* 15, 503 (1994).
369. G. L. Bir and G. E. Pikus, “Symmetry and Deformation Effects in Semiconductors.” Wiley, New York, 1974.
370. L. G. Ferreira, *Phys. Rev.* 137, A1601 (1965).
371. M. Kriechbaum, K. E. Ambrosch, E. J. Fantner, H. Clemens, and G. Bauer, *Phys. Rev.* 30, 3394 (1984).
372. L. J. Sham and Y. T. Lu, *J. Lumin.* 44, 207 (1989).
373. M. Altarelli, *J. Lumin.* 30, 472 (1985).
374. M. Altarelli, *Phys. Rev.* 28, 842 (1983).
375. P. Y. Yu and M. Cardona, “Fundamentals of Semiconductors.” Springer-Verlag, Berlin 1996.
376. G. Bastard, “Wave Mechanics Applied to Semiconductor Heterostructures,” les éditions de physique. Les Ulis Cedex 1990.
377. R. J. White and L. J. Sham, *Phys. Rev. Lett.* 47, 879 (1981).
378. G. Bastard, *Phys. Rev.* 24, 5693 (1981).
379. G. Bastard, *Phys. Rev.* 25, 7584 (1982).
380. D. J. BenDaniel and C. B. Duke, *Phys. Rev.* 152, 683 (1966).
381. Q. G. Zhu and H. Kroemer, *Phys. Rev.* 27, 3519 (1983).
382. H. Kroemer and Q. G. Zhu, *J. Vac. Sci. Technol.* 21, 551 (1982).
383. T. Ando, S. Wakahara, and H. Akera, *Phys. Rev.* 40, 11609 (1989).
384. T. Ando, *Inst. Phys. Conf. Ser.* 145, 1203 (1996).
385. W. Trzeciakowski, *Phys. Rev.* 38, 4322 (1988).
386. W. Trzeciakowski, *Phys. Rev.* 38, 12493 (1988).
387. R. Tsu and L. Esaki, *Appl. Phys. Lett.* 22, 562 (1973).
388. M. O. Vassell, Johnson Lee, and H. F. Lockwood, *J. Appl. Phys.* 54, 5206 (1983).

389. P. F. Yuh and K. L. Wang, *Phys. Rev.* 38, 13307 (1988).
390. L. H. Ram-Mohan, K. H. Yoo, and R. L. Aggarwal, *Phys. Rev.* 38, 6151 (1988).
391. B. Chen, M. Lazzouni, and L. H. Ram-Mohan, *Phys. Rev.* 45, 1204 (1992).
392. D. Suisky, F. Neugebauer, J. Röseler, and S. Rex, *Acta Phys. Pol., A* 82, 861 (1992).
393. T. Stirner, S. Ahmed, and W. E. Hagston, *J. Cryst. Growth* 159, 1027 (1996).
394. D. Suisky, W. Heimbrot, C. Santos, F. Neugebauer, M. Happ, B. Lunn, J. E. Nicholls, and D. E. Ashenford, *Phys. Rev.* 58, 3969 (1998).
395. M. Kriechbaum, P. Kocevar, H. Pascher, and G. Bauer, *IEEE J. Quantum Electron.* 24, 1727 (1988).
396. G. H. Wannier, *Phys. Rev.* 52, 191 (1937).
397. M. Shinada and S. Sugano, *J. Phys. Soc. Jpn.* 21, 1936 (1966).
398. P. J. Klar, C. M. Townsley, D. Wolverson, J. J. Davies, D. E. Ashenford, and B. Lunn, *Semicond. Sci. Technol.* 10, 1568 (1995).
399. H. Mathieu, P. Lefebvre, and P. Christol, *J. Appl. Phys.* 72, 300 (1992).
400. H. Mathieu, P. Lefebvre, and P. Christol, *Phys. Rev.* 46, 4092 (1992).
401. C. P. Hilton, J. Goodwin, P. Harrison, and W. E. Hagston, *J. Phys. A: Math. Gen.* 25, 5365 (1992).
402. C. P. Hilton, W. E. Hagston, and J. E. Nicholls, *J. Phys. A: Math. Gen.* 25, 2395 (1992).
403. P. Peyla, Y. Merle d'Aubigné, A. Wasiela, R. Romestain, H. Mariette, M. D. Sturge, N. Magnea, and H. Tuffigo, *Phys. Rev.* 46, 1557 (1992).
404. G. W. Bauer and T. Ando, *Phys. Rev.* 38, 6015 (1988).
405. L. C. Andreani and A. Pasquarello, *Phys. Rev.* 42, 8928 (1990).
406. P. J. Klar, D. Wolverson, J. J. Davies, W. Heimbrot, and M. Happ, *Phys. Rev.* 57, 7103 (1998).
407. P. J. Klar, J. R. Watling, D. Wolverson, J. J. Davies, D. E. Ashenford, and B. Lunn, *Semicond. Sci. Technol.* 12, 1240 (1997).
408. P. Chen, J. E. Nicholls, J. H. C. Hogg, T. Stirner, W. Hagston, B. Lunn, and D. E. Ashenford, *Phys. Rev.* 50, 4732 (1995).
409. H. H. Cheng, R. J. Nicholas, M. J. Lawless, D. E. Ashenford, and B. Lunn, *Phys. Rev.* 52, 5269 (1995).
410. S. Kuroda, K. Kojima, K. Takita, K. Uchiba, and N. Miura, *J. Cryst. Growth* 159, 967 (1996).
411. M. P. Halsall, S. V. Railson, D. Wolverson, J. J. Davies, B. Lunn, and D. E. Ashenford, *Phys. Rev.* 50, 11755 (1994).
412. T. Lebihen, E. Deleporte, and C. Delalande, *Phys. Rev.* 55, 1724 (1997).
413. H. Pascher, P. Röhlein, M. Kriechbaum, N. Frank, and G. Bauer, *Superlattices Microstruct.* 8, 69 (1990).
414. A. Ishida, S. Matsuura, M. Mizuno, and H. Fujiyasu, *Appl. Phys. Lett.* 51, 478 (1987).
415. S. Yuan, G. Springholz, G. Bauer, and M. Kriechbaum, *Phys. Rev.* 49, 5476 (1994).
416. G. Springholz, M. Kriechbaum, W. Hofmann, F. Geist, H. Pascher, S. Yuan, H. Krenn, and G. Bauer, *Superlattices Microstruct.* 13, 25 (1993).
417. L. S. Kim, H. D. Drew, R. E. Doezema, J. P. Heremans, and D. L. Partin, *Phys. Rev.* 35, 2521 (1987).
418. F. Geist, H. Pascher, N. Frank, G. Bauer, and M. Kriechbaum, *Semicond. Sci. Technol.* 8, S147 (1993).
419. E. Deleporte, T. Lebihen, B. Ohnesorge, P. Roussignol, C. Delalande, S. Guha, and H. Munkata, *Phys. Rev.* 50, 4514 (1994).
420. N. Dai, H. Luo, F. Zhang, N. Samarth, M. Dobrowolska, and J. K. Furdyna, *Phys. Rev. Lett.* 67, 3824 (1991).
421. B. König, D. R. Yakovlev, W. Ossau, T. Gerhard, M. Keim, A. Waag, and G. Landwehr, *Phys. Rev.* 60, 2653 (1999).
422. W. J. Walecki, A. V. Nurmikko, N. Samarth, H. Luo, J. K. Furdyna, and N. Otsuka, *Appl. Phys. Lett.* 57, 466 (1990).
423. X. Liu, A. Petrou, J. Warnock, B. T. Jonker, G. A. Prinz, and J. J. Krebs, *Phys. Rev. Lett.* 63, 2280 (1989).
424. W. C. Chou, A. Petrou, J. Warnock, and B. T. Jonker, *Phys. Rev. Lett.* 67, 3820 (1991).
425. H. Luo, W. C. Chou, N. Samarth, A. Petrou, and J. K. Furdyna, *Solid State Commun.* 85, 691 (1993).
426. F. C. Zhang, H. Luo, N. Dai, N. Samarth, M. Dobrowolska, and J. K. Furdyna, *Phys. Rev.* 47, 3806 (1993).
427. B. Kuhn-Heinrich, W. Ossau, T. Litz, A. Waag, and G. Landwehr, *J. Appl. Phys.* 75, 8046 (1994).
428. H. Heinrich, C. Panhuber, A. Eisenbeiss, H. Preier, and Z. Feit, *Superlattices Microstruct.* 5, 175 (1989).
429. V. Albe, C. Jounin, and D. Bertho, *Phys. Rev.* 57, 8778 (1998).
430. K. Yan, C. Duan, Y. Ma, S. Xia, and J.-C. Krupa, *Phys. Rev.* 58, 13585 (1998).
431. M. Tanaka, J. Qi, and Y. Masumoto, *J. Lumin.* 87–89, 472 (2000).
432. Y. Wu, K. Arai, N. Kuroda, T. Yao, A. Yamamoto, M.-Y. Shen, and T. Goto, *Jpn. J. Appl. Phys.* 36, L1648 (1997).
433. K. Shibata, K. Takabayashi, I. Souma, J. Shen, K. Yanata, and Y. Oka, *Physica E* 10, 358 (2001).
434. C. S. Kim, M. Kim, S. Lee, J. K. Furdyna, and M. Dobrowolska, *J. Cryst. Growth* 214–215, 395 (2000).
435. H. Falk, W. Heimbrot, P. J. Klar, J. Hübner, M. Oestreich, and W. W. Rühle, *Phys. Status Solidi B* 229, 781 (2002).
436. M. Nawrocki, Y. G. Rubo, J. P. Lascaray, and D. Coquillat, *Phys. Rev.* 52, R2241 (1995).
437. I. J. Griffin, P. J. Klar, D. Wolverson, J. J. Davies, B. Lunn, D. E. Ashenford, and T. Henning, *J. Cryst. Growth* 184–185, 325 (1998).
438. P. J. Klar, H. Falk, and W. Heimbrot, *Solid State Commun.* 116, 125 (2000).
439. W. Heimbrot, O. Goede, V. Weinhold, M. Happ, R. Knoch, K. Hieke, N. Hoffmann, J. Griesche, K. Jacobs, F. Neugebauer, D. Suisky, and J. Röseler, *J. Cryst. Growth* 138, 601 (1994).
440. E. Deleporte, J. M. Barroir, G. Bastard, C. Delalande, J. M. Hong, and L. L. Chang, *Phys. Rev.* 42, 5891 (1990).
441. M. von Ortenberg, *Phys. Rev. Lett.* 49, 1041 (1982).
442. W. Heimbrot, V. Weinhold, N. Hoffmann, and J. Griesche, *Mater. Sci. Forum* 182–184, 755 (1995).
443. K. Hieke, W. Heimbrot, W. W. Rühle, Th. Pier, H.-E. Gumlich, D. E. Ashenford, and B. Lunn, *Solid State Commun.* 93, 257 (1995).
444. K. Hieke, W. Heimbrot, Th. Pier, H.-E. Gumlich, W. W. Rühle, J. E. Nicholls, and B. Lunn, *J. Cryst. Growth* 159, 1014 (1996).
445. W. Heimbrot, L. Gridneva, M. Happ, N. Hoffmann, M. Rabe, and F. Henneberger, *Phys. Rev.* 58, 1162 (1998).
446. W. J. Ossau and B. Kuhn-Heinrich, *Physica B* 184, 422 (1993).
447. J. Cibert, W. Grieshaber, J. A. Gaj, Y. Merle d'Aubigné, and A. Wasiela, *Mater. Sci. Forum* 182–184, 567 (1995).
448. W. Grieshaber, A. Haury, J. Cibert, Y. Merle d'Aubigné, A. Wasiela, and J. A. Gaj, *Phys. Rev.* 53, 4891 (1996).
449. R. E. Behringer, *J. Chem. Phys.* 29, 537 (1958).
450. J. M. Fatah, T. Piorek, P. Harrison, T. Stirner, and W. E. Hagston, *Phys. Rev.* 49, 10341 (1994).
451. W. Grieshaber, C. Bodin, J. Cibert, J. A. Gaj, Y. Merle d'Aubigné, A. Wasiela, and G. Feuillet, *Appl. Phys. Lett.* 65, 1287 (1994).
452. J. A. Gaj, W. Grieshaber, C. Bodin-Deshayes, J. Cibert, G. Feuillet, Y. Merle d'Aubigné, and A. Wasiela, *Phys. Rev.* 50, 5512 (1994).
453. W. Grieshaber, J. Cibert, J. A. Gaj, Y. Merle d'Aubigné, and A. Wasiela, *Phys. Rev.* 50, 2011 (1994).
454. T. Stirner, J. M. Fatah, R. G. Roberts, T. Piorek, W. E. Hagston, and P. Harrison, *Superlattices Microstruct.* 16, 11 (1994).
455. P. Harrison, T. Stirner, S. R. Bardorff, W. E. Hagston, S. Jackson, K. A. Dhese, J. H. C. Hogg, V. Hower, J. E. Nicholls, and M. O'Neill, *Superlattices Microstruct.* 13, 431 (1993).
456. D. Wolverson, S. V. Railson, M. P. Halsall, J. J. Davies, D. E. Ashenford, and B. Lunn, *Semicond. Sci. Technol.* 10, 1475 (1995).

457. C. Gourgon, L. S. Dang, H. Mariette, C. Vieu, and F. Muller, *Appl. Phys. Lett.* 66, 1635 (1995).
458. H. Mariette, C. Gourgon, L. S. Dang, C. Vieu, N. Pelekanos, and W. W. Rühle, *Mater. Sci. Forum* 182–184, 99 (1995).
459. J. Stühler, M. Hirsch, G. Schaack, and A. Waag, *Phys. Rev.* 49, 7345 (1994).
460. W. Heimbrod, L. Gridneva, M. Happ, F. Neugebauer, D. Suisky, N. Hoffmann, and J. Griesche, *J. Cryst. Growth* 159, 1005 (1996).
461. T. Yasuhira, K. Uchida, Y. H. Matsuda, N. Miura, S. Kuroda, and K. Takita, *Physica E* 13, 568 (2002).
462. A. K. Bhattacharjee, *Phys. Rev.* 58, 15660 (1998).
463. G. Mackh, W. Ossau, A. Waag, and G. Landwehr, *Phys. Rev.* 54, R5227 (1996).
464. I. A. Merkulov, D. R. Yakovlev, A. Keller, W. Ossau, J. Geurts, A. Waag, G. Landwehr, G. Karczewski, T. Wojtowicz, and J. Kosut, *Phys. Rev. Lett.* 83, 1431 (1999).
465. N. Feltn, L. Levy, D. Inger, and M. P. Pileni, *J. Phys. Chem. B* 103, 4 (1999).
466. N. Feltn, L. Levy, D. Inger, E. Vincent, and M. P. Pileni, *J. Appl. Phys.* 87, 1415 (2000).
467. O. Goede, W. Heimbrod, Th. Koepf, H.-E. Gumlich, and B. Lunn, *J. Cryst. Growth* 117, 886 (1992).
468. P. Peyla, A. Wasiela, and Y. Merle d'Aubigné, *Phys. Rev.* 47, 3783 (1993).
469. B. Kuhn-Heinrich, W. Ossau, E. Bangert, A. Waag, and G. Landwehr, *Solid State Commun.* 91, 11 (1994).
470. W. Y. Yu, A. Twardowski, L. P. Fu, A. Petrou, and B. T. Jonker, *Phys. Rev.* 51, 9722 (1995).
471. S. I. Gubarev, *Phys. Status Solidi B* 134, 211 (1986).
472. N. D. Mermin and H. Wagner, *Phys. Rev. Lett.* 17, 1133 (1966).
473. L. Néel, *J. Phys. Rad.* 15, 225 (1954).
474. L. A. Kolodziejski, R. L. Gunshor, N. Otsuka, B. P. Gu, Y. Hefetz, and A. V. Nurmikko, *J. Cryst. Growth* 81, 491 (1987).
475. J. M. Hong, D. D. Awschalom, L. L. Chang, and A. Segmuller, *J. Appl. Phys.* 63, 3285 (1988).
476. D. D. Awschalom, J. M. Hong, L. L. Chang, and G. Grinstein, *Phys. Rev. Lett.* 59, 1733 (1987).
477. G. Precht, W. Heiss, A. Bonanni, H. Sitter, W. Jantsch, S. Mackowski, and G. Karczewski, *Physica E* 7, 1006 (2000).
478. G. Precht, W. Heiss, S. Mackowski, A. Bonanni, E. Janik, H. Sitter, and W. Jantsch, in "Proceedings of the 25th International Conference on the Physics of Semiconductors" (N. Miura and T. Ando, Eds.), Springer Proceedings in Physics, Vol. 87, Pt. 1, p. 216. Springer-Verlag, Berlin, 2001.
479. W. Heimbrod, C. Benecke, O. Goede, and H.-E. Gumlich, *Phys. Status Solidi B* 154, 405 (1989).
480. W. Heimbrod, C. Benecke, O. Goede, and H.-E. Gumlich, *J. Cryst. Growth* 101, 911 (1990).
481. M. S. Seehra and R. D. Groves, *J. Phys. C: Solid State Phys.* 16, L411 (1983).
482. O. Goede, D. Backs, W. Heimbrod, and M. Kanis, *Phys. Status Solidi B* 151, 311 (1989).
483. L. Hoines, R. Stubi, R. Loloee, J. A. Cowen, and J. Bass, *Phys. Rev. Lett.* 66, 1224 (1991).
484. A. Gavrin, J. R. Childress, C. L. Chien, B. Martinez, and M. B. Salamon, *Phys. Rev. Lett.* 64, 2438 (1990).
485. G. G. Kenning, J. M. Slaughter, and J. A. Cowen, *Phys. Rev. Lett.* 59, 2596 (1987).
486. T. Dietl, A. Haury, and Y. Merle d'Aubigné, *Phys. Rev.* 55, R3347 (1997).
487. A. Haury, A. Wasiela, A. Arnoult, J. Cibert, S. Tatarenko, T. Dietl, and Y. Merle d'Aubigné, *Phys. Rev. Lett.* 79, 511 (1997).
488. Y. Merle d'Aubigné, A. Arnoult, J. Cibert, T. Dietl, A. Haury, P. Kossacki, S. Tatarenko, and A. Wasiela, *Physica E* 3, 169 (1998).
489. J. Cibert, P. Kossacki, A. Haury, A. Wasiela, Y. Merle d'Aubigné, T. Dietl, A. Arnoult, and S. Tatarenko, *J. Cryst. Growth* 184–185, 898 (1998).
490. P. Kossacki, D. Ferrand, A. Arnoult, J. Cibert, S. Tatarenko, A. Wasiela, Y. Merle d'Aubigné, J.-L. Staehli, J.-D. Ganiere, W. Bardyszewski, K. Swiatek, M. Sawicki, J. Wrobel, and T. Dietl, *Physica E* 6, 709 (2000).
491. V. Nunez, T. M. Giebultowicz, W. Faschinger, G. Bauer, H. Sitter, and J. K. Furdyna, *Mater. Res. Soc. Symp. Proc.* 376, 589 (1995).
492. J. Lin, J. J. Rhyne, J. K. Furdyna, and T. M. Giebultowicz, *J. Appl. Phys.* 83, 6554 (1998).
493. H. Kepa, K. I. Goldman, T. M. Giebultowicz, C. F. Majkrzak, G. Springholz, H. Krenn, S. Holl, F. Schinagl, and G. Bauer, *Physica E* 2, 399 (1998).
494. H. Kepa, J. Kutna-Pielaszek, A. Twardowski, C. F. Majkrzak, J. Sadowski, T. Story, and T. M. Giebultowicz, *Phys. Rev.* 64, 121302 (R) (2001).
495. T. M. Giebultowicz, H. Kepa, J. Blinowski, and P. Kacman, *Physica E* 10, 411 (2001).
496. T. M. Giebultowicz, N. Samarth, H. Luo, J. K. Furdyna, P. Klosowski, and J. J. Rhyne, *Phys. Rev.* 46, 12076 (1992).
497. H. Ohno, *Science* 281, 951 (1998).
498. T. M. Rusin, *Phys. Rev.* 58, 2107 (1998).
499. J. Blinowski and P. Kacman, *Phys. Rev.* 64, 45302 (2001).
500. S. Schwieger and W. Nolting, *Phys. Rev. B* 65, 205210 (2002).
501. X. F. He, A. Kotlicki, P. Donsanjh, B. G. Turrell, J. F. Carolan, S. Jimenez-Sandoval, and P. Lozano-Tovar, *Superlattices Microstruct.* 14, 261 (1993).
502. X. F. He, A. Kotlicki, P. Donsanjh, B. G. Turrell, J. F. Carolan, S. Jimenez-Sandoval, and P. Lozano-Tovar, *J. Electron. Mater.* 26, 73 (1997).
503. S. B. Oseroff, R. Calvo, W. Giriat, and Z. Fisk, *Solid State Commun.* 35, 539 (1980).
504. S. B. Oseroff, *Phys. Rev.* 25, 6584 (1982).
505. X. Batlle and A. Labarta, *J. Phys. D* 35, R15 (2002).
506. N. Menyuk, J. A. Kafalas, K. Dwight, and J. B. Goodenough, *Phys. Rev.* 177, 942 (1969).
507. Th. Hartmann, M. Lampalzer, P. J. Klar, W. Stolz, W. Heimbrod, H.-A. Krug von Nidda, A. Loidl, and L. Svistov, *Physica E* 13, 572 (2002).
508. Y. D. Park, A. Wilson, A. T. Hanbicki, J. E. Mattson, T. Ambrose, G. Spanos, and B. T. Jonker, *Appl. Phys. Lett.* 78, 2739 (2001).
509. N. Theodoropoulou, A. F. Hebard, M. E. Overberg, C. R. Abernathy, S. J. Pearton, S. N. G. Chu, and R. G. Wilson, *Appl. Phys. Lett.* 78, 3475 (2001).
510. D. M. Hoffmann, B. K. Meyer, A. I. Ekimov, I. A. Merkulov, A. L. Efros, M. Rosen, G. Couino, T. Gacoin, and J. P. Boilot, *Solid State Commun.* 114, 547 (2000).
511. O. Goede, W. Heimbrod, Th. Köpp, H.-E. Gumlich, B. Lunn, and D. E. Ashenford, *Phys. Status Sol. B* 166, 531 (1991).
512. A. A. Maksimov, G. Bacher, A. McDonald, V. D. Kulakovskij, A. Forchel, C. R. Becker, G. Landwehr, and L. W. Molenkamp, *Phys. Rev.* 62, R7767 (2000).
513. G. Bacher, H. Schömig, M. K. Welsch, S. Zaitsev, V. D. Kulakovskij, A. Forchel, S. Lee, M. Dobrowolska, J. K. Furdyna, B. König, and W. Ossau, *Appl. Phys. Lett.* 79, 524 (2001).
514. S. Mackowski, J. Wrobel, K. Fronc, J. Kosut, F. Pulizzi, P. C. M. Christianen, J. C. Maan, and G. Karczewski, *Phys. Status Solidi B* 229, 493 (2002).
515. S. Das Sarma, J. Fabian, X. Hu, and I. Zutic, *Solid State Commun.* 119, 207 (2001).
516. P. Ball, *Nature (London)* 404, 918 (2000).
517. G. A. Prinz, *Science* 282, 1660 (1998).
518. S. Datta and B. Das, *Appl. Phys. Lett.* 56, 665 (1990).
519. Y. Ohno, D. K. Young, B. Beschoten, F. Matsukura, H. Ohno, and D. D. Awschalom, *Nature (London)* 402, 790 (1999).

520. R. Fiederling, M. Kelm, G. Reuscher, W. Ossau, G. Schmidt, A. Waag, and L. W. Molenkamp, *Nature (London)* 402, 787 (1999).
521. B. T. Jonker, Y. D. Park, B. R. Bennett, H. D. Cheong, G. Kioseoglou, and A. Petrou, *Phys. Rev.* 62, 8180 (2000).
522. M. Oestreich, J. Hübner, D. Hägele, M. Bender, N. Gerhardt, M. Hofmann, W. W. Rühle, H. Kalt, Th. Hartmann, P. J. Klar, W. Heimbrod, and W. Stolz, *Adv. Solid State Phys.* 41, 173 (2001).
523. H. Akinaga, S. Miyanishi, K. Tanaka, W. Van Roy, and K. Onodera, *Appl. Phys. Lett.* 76, 97 (2000).
524. H. Shimizu, M. Miyamura, and M. Tanaka, *J. Vac. Sci. Technol., B* 18, 2063 (2000).
525. M. Oestreich, J. Hübner, D. Hägele, P. J. Klar, W. Heimbrod, W. W. Rühle, D. E. Ashenford, and B. Lunn, *Appl. Phys. Lett.* 74, 1251 (1999).
526. J. C. Egues, *Phys. Rev. Lett.* 80, 4578 (1998).
527. S. Ye, P. J. Klar, Th. Hartmann, W. Heimbrod, M. Lampalzer, S. Nau, T. Torunski, W. Stolz, T. Kurz, H.-A. Krug von Nidda, and A. Loidl, *Appl. Phys. Lett.* 83, 3927 (2003).
528. M. Lampalzer, K. Volz, W. Treutmann, S. Nau, T. Torunski, K. Megges, J. Lorberth, and W. Stolz, *J. Cryst. Growth* 248, 474 (2003).
529. L. Chen, P. J. Klar, W. Heimbrod, F. J. Brieler, M. Fröba, H.-A. Krug von Nidda, T. Kurz, and A. Loidl, *J. Appl. Phys.* 93, 1326 (2003).
530. H. Falk, J. Hübner, P. J. Klar, and W. Heimbrod, *Phys. Rev. B* 68, 165203 (2003).
531. M. Syed, G. L. Yang, J. K. Furdyna, M. Dobrowolska, S. Lee, and L. R. Ram-Moham, *Phys. Rev. B* 66, 075213 (2002).
532. G. Precht, W. Heiss, A. Bonanni, W. Jantsch, S. Mackowski, and E. Janik, *Phys. Rev. B* 68, 165313 (2003).





# Magnetism in Nanoclusters

C. Binns

*University of Leicester, Leicester, United Kingdom*

## CONTENTS

1. Introduction
  2. Production of Size-Selected Nanoclusters
  3. Magnetic Measurements on Clusters
  4. Morphology and Structure of Clusters and Cluster-Assembled Films
  5. Magnetism in Free Clusters
  6. Magnetism in Exposed Clusters Adsorbed on Surfaces
  7. Magnetism in Embedded Clusters
  8. Applications of Cluster-Assembled Films
  9. Conclusion
- Glossary  
References

## 1. INTRODUCTION

Over the last few years there has been an explosion of interest in the magnetic behavior of nanostructures from a wide range of scientific disciplines. Mesoscopic magnetism is not as well understood as in either the atomic or bulk regimes and there is a fascination by physicists and chemists to obtain a better fundamental grasp of the consequences of restricting the magnetic electrons within systems only a few atomic spacings in dimension. This increase in interest has been coupled with the development of technologies that can manufacture tightly controlled magnetic nanostructures including quantum dots, monolayers, self-organized islands, quantum wires, and deposited nanoclusters. Undoubtedly much of the enthusiasm comes from a growing realization of the enormous potential of magnetic nanostructures in the formation of high performance magnetic materials and devices.

In addition there is a growing interest in natural magnetic nanostructures that are to be found in a diverse variety of environments. An example is the MV-1 bacterium that manufactures nanoparticles of magnetite arranged in chains to

maintain alignment with the earth's magnetic field [1]. Similar magnetite chains discovered in meteorites from Mars are considered to be the strongest evidence for the previous existence of extraterrestrial bacteria [2]. It has also been suggested that magnetic nanoparticles play a crucial role in seeding the condensation of the interstellar medium to form free-floating planets [3].

This chapter will review the recent research on magnetic nanostructures produced by forming clusters in the gas phase and depositing them on surfaces. Just over two decades ago, based on earlier work at Karlsruhe on cryogenic free jet expansions [4], the technology to produce beams of gas-phase, size-selected metal nanoclusters was developed [5]. In the case of magnetic clusters this afforded the wonderful opportunity to study how the magnetism in matter develops as a substance is built atom by atom from the monomer. Magnetism is well understood at the limiting scales of atoms and the bulk but in mesoscopic systems containing a few to a few thousand atoms (1–5 nm), magnetic behavior depends on size and can change significantly with the addition or removal of a single atom.

Nanoclusters are single-domain particles (i.e., systems in which it is energetically unfavorable to form a domain boundary). These have held enormous fascination since the classic work of Stoner and Wohlfarth [6] and Néel [7] over half a century ago. The particles, notwithstanding complications such as canted spins at the surface [8], can be considered as giant moments of ferromagnetically coupled atomic spins. At temperatures much lower than those required to perturb the internal magnetic alignment, the particle moment as a whole can fluctuate over the anisotropy barrier separating different spin directions at time scales varying from nanoseconds to eons. At low temperatures, there is interest in the possibility of the tunneling of the magnetization vector through the barrier—one of the few examples of macroscopic quantum tunneling [9–11].

At  $T = 0$  K, reversing the direction of the cluster magnetization requires an external field to drive the magnetization vector across the anisotropy boundary  $KV$  separating different magnetic alignments, where  $K$  is the anisotropy constant and  $V$  is the particle volume. At elevated temperatures when  $kT \gg KV$  the anisotropy barrier becomes

unimportant but the external field must compete with thermal fluctuations of the moment. In general, when a saturating field is removed from a particle (or an assembly) at temperature,  $T$ , the magnetization decays with a relaxation rate,  $\tau$ , that can be approximated by the Arrhenius relationship

$$\frac{1}{\tau} = f_0 \exp\left(\frac{-KV}{k_B T}\right) \quad (1)$$

where  $f_0$  is the natural gyromagnetic frequency of the particle. For volumes typical in deposited transition metal clusters, observations must be done at cryogenic temperatures ( $\leq 5$  K) for the magnetic relaxation to be slower than typical measurement times. At room temperature, the thermal energy  $k_B T$  is much greater than the anisotropy energy of each particle so that all magnetization directions are almost energetically equal. The magnetization is then described by the classical Langevin function

$$M = N\mu_{\text{cluster}} \left[ \coth\left(\frac{\mu_{\text{cluster}} H}{k_B T}\right) - \frac{k_B T}{\mu_{\text{cluster}} H} \right] \quad (2)$$

where  $\mu_{\text{cluster}}$  is the magnetic moment of each cluster. This can be several hundred atomic spins and so, unlike isolated atoms where very low temperatures or very high fields are required to achieve saturation, assemblies of clusters can be saturated easily. The temperature at which half the cluster moments have relaxed during the time of a measurement is known as the blocking temperature,  $T_B$ , and only a narrow temperature region around  $T_B$  separates, essentially, permanently frozen moments from superparamagnetic behavior. The quest to find deposited clusters smaller than 5 nm in which  $T_B$  is above room temperature is an important challenge for future generations of magnetic recording technology (see Section 8).

For particles smaller than about 5 nm, either as free clusters or supported on a surface, the fundamental spin and orbital moments per atom can be substantially increased over the bulk value [12–18]. This was originally discovered by magnetic deflection experiments using gradient magnetic fields applied to free clusters in flight [12] but it is now known that isolated clusters maintain significant enhancements after they have been deposited on a surface [15, 16] or embedded in a matrix [18].

As the flux from cluster sources has steadily improved [19], the field has evolved to consider not just isolated clusters but films up to several  $\mu\text{m}$  thick built out of the preformed clusters. These can be deposited in conjunction with a vapor of another material to form a granular material of the particles embedded in a matrix. This affords independent control over the grain size and volume fraction and it is even possible to effect some control over the cluster shape by adjusting the impact energy on the surface [20]. In addition it has been shown that the clusters maintain their identity in a matrix of a material that alloys with that of the particles [21] enabling the production of nanoscale *granular* mixtures of *miscible* materials. This is not possible by any other fabrication technique. This degree of control over the nanostructure has generated great interest in

cluster deposition as a technique for producing high performance magnetic materials. Examples include high saturation moment films [22] and giant magnetoresistance sensors [23].

In all such industrial applications, the required cluster volume fraction is high—at or near the percolation threshold—so there are strong interactions between the clusters. Understanding the detailed nature of the cluster interactions has therefore become increasingly important. Interparticle interactions produce a rich variety of magnetic configurations resulting from competing energy terms. The dipolar interaction introduces frustration as it is impossible to obtain an optimum alignment for every particle. In addition there is frustration resulting from the competition between the interparticle dipolar and exchange terms and the intraparticle anisotropy energy (magnetocrystalline, shape, magnetoelastic etc.) that requires the magnetization vector to be aligned along specific axes in each particle.

In the next two sections the experimental methods used to produce clusters and measure their magnetic properties will be described. This is followed in Section 4 by a brief description of the morphology and atomic structure expected in transition metal clusters. Sections 5–7 will review the magnetic behavior of clusters in three different environments, that is, as free particles, as exposed clusters adsorbed on a surface in ultrahigh vacuum (UHV), and as embedded clusters in a matrix. Section 7 will also discuss the effect of interparticle interactions in dense interacting assemblies. In the last section some technological applications of cluster-assembled films will be described.

## 2. PRODUCTION OF SIZE-SELECTED NANOCCLUSERS

### 2.1. Cluster Sources

Sources capable of producing free beams of nanoscale metal clusters with a wide range of sizes were first reported more than 20 years ago [5, 24]. The technology continues to develop rapidly, however, as beam intensities are pushed ever higher and new capabilities are introduced such as UHV compatibility [25, 26], the production of binary metal clusters [27], new mass-selection techniques, etc. At the heart of most cluster sources is a region in which a supersaturated vapor of the material to be studied is generated by ejecting a gas-phase metal plume into a flow of a cooled inert gas. The metal vapor can be generated by laser ablation [24], sputtering [28], a pulsed [29] or continuous [30] arc, or thermally [5].

Monte Carlo simulations [31] show that the dominant cooling mechanism for the growing clusters is by evaporation of atoms. This is approximately balanced by the heating due to the adsorption of new atoms (latent heat) and the cooling by the gas, although inefficient, provides the *extra* cooling required to allow the clusters to grow. The simulation also revealed that the initial formation of dimers is a critical bottleneck to the clustering process. The growth of clusters is complete after a dwell time in the source of the

order of 10 ms after which the cluster size is described by a log-normal distribution [32]

$$F(n) = \frac{1}{\sqrt{2\pi} \ln \sigma} \exp - \left( \frac{\ln n - \ln \bar{n}}{\sqrt{2} \ln \sigma} \right)^2 \quad (3)$$

where  $n$  is the number of atoms per cluster and  $\sigma$  is the variance.

The region in which the metal vapor initially mixes with the rare gas is typically at a pressure of a few mbar to a few bar and at the end of this region there is an aperture with a diameter of a few  $\mu\text{m}$  to a few mm. In some sources clustering continues in the region just after the aperture in the free jet expansion. This expansion accelerates the clusters and in the limit of high pressure differential between the two regions separated by the aperture, the clusters can acquire the full thermal distribution of the bath gas atom velocities. In weaker expansions there is a velocity slip between the carrier gas and the metal clusters.

Brief descriptions of the operation of various sources based on gas condensation are given next (see Fig. 1). For more comprehensive descriptions of these and other types the reader is referred to existing reviews [19, 34].

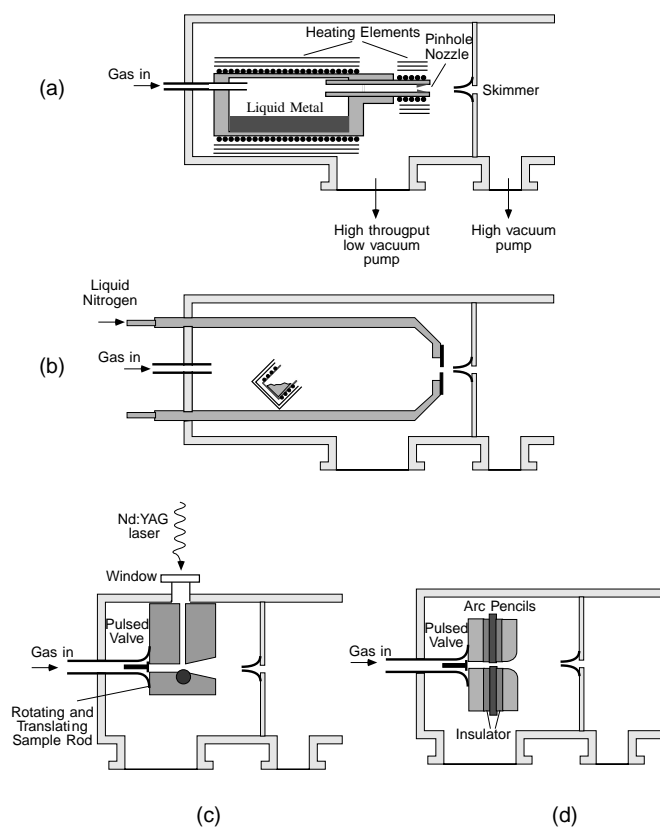


**Figure 1.** Basic layout of sources using rare gases to produce super-saturated vapors. (a) Seeded supersonic nozzle source. (b) Gas aggregation source. (c) Laser evaporation source. (d) Pulsed arc cluster ion source. Reprinted with permission from [33], C. Binns, *Surf. Rev. Lett.* 44, 1 (2001). © 2001, Elsevier Science.

### 2.1.1. Seeded Supersonic Nozzle Source

These are designed to produce very high fluxes of low melting point (usually alkali) metals (Fig. 1a). The furnace containing the melt is heated to a sufficiently high temperature to yield a metal vapor pressure in the region of 10–100 mbar and this vapor is mixed with (seeded into) a rare gas introduced at a pressure of several atmospheres. The hot mixture expands adiabatically into vacuum through a small aperture and the rapid cooling occurring close to the nozzle condenses the metal into clusters. The clustering continues until the mean free path becomes too long to allow significant interactions between the condensed particles. The technical difficulty of the containment of the melt in a relatively large furnace has restricted the temperatures achievable to below 1600 K. The source is thus confined to the study of high vapor pressure materials. It is, however, capable of producing a flux in excess of  $10^{18}$  atoms/sec of clustered material. The very high rate of consumption has encouraged the development of *in-situ* refilling devices [35].

### 2.1.2. Gas Aggregation Source

This was the first type of metal cluster source reported [5] and a common design is illustrated in Figure 1b. Improvements since 1980 include the *in-situ* positioning of the crucible assembly within the gas flow to optimize the output and an adjustable gap between the first aperture and the skimmer [25]. Generally there is a larger aperture to the high vacuum region and the free jet expansion is weaker than in the seeded supersonic nozzle source (SSNS). Since only the crucible is heated, with a careful design, materials can be contained at temperatures above 2000 K and thermal sources have been built that are capable of producing beams of magnetic transition metal clusters [25]. As with the SSNS, with careful outgassing, the source is particularly suited to producing very clean cluster beams and to UHV-compatible operation [25, 36]. The inert gas pressure within the clustering region in a typical gas aggregation source (GAS) is compatible with magnetron sputtering and the thermal source can be replaced by a sputtered target [28]. This brings several advantages including the ability to produce clusters of the most refractory materials and, with a hollow cathode target geometry, very high fluxes can be attained [37]. Clustering is highly efficient as the sputtered vapor is rich in dimers overcoming the initial bottleneck for condensation. In addition, the emerging cluster beam is highly ionized with a greater proportion of ions than achievable with a conventional ionizer. This is an important factor if the clusters are to be mass-selected since most mass analyzers filter charged particles.

### 2.1.3. Laser Evaporation Source

Light pulses from a Nd-YAG laser focused onto a suitable target can vaporize even refractory materials and if the laser pulse coincides with a gas burst across the target produced by a pulsed valve, suitable conditions for clustering can be achieved (Fig. 1c). The first report of this type of source [24] was quickly followed by improvements including a mechanism for driving the target rod in a screw motion so that a fresh region is exposed to each laser pulse [38]. Clustering occurs within the nozzle as the metal vapor encounters the

rare gas and continues in the strong expansion as the mixture is ejected. There is a strong adiabatic cooling despite the relatively large nozzle diameters since the instantaneous carrier gas pressure is very high—up to several atmospheres. The processes are thus a combination of those found in the SSNS and the GAS and, as in the former type, clustering is complete within a nozzle diameter of the aperture. Despite the short duty cycle of the laser, the peak output is so high that the average flux from the source easily competes with the other types previously described. A useful variable is the phase of the laser pulse relative to the valve opening that can be used to control the size distribution of clusters by altering the average gas pressure during the pulse [39]. Phasing becomes particularly powerful in sources employing two targets to produce binary clusters [27, 40] since it can be used to control the distribution of elements within the cluster. The pulsed output couples efficiently to time-of-flight analyzers (see following section).

#### 2.1.4. Pulsed Arc Cluster Ion Source

This is closely related to the laser evaporation source (Fig. 1d) but in this case the evaporated plume is produced by a pulsed arc coinciding with the gas burst [29]. The clustering process is very similar to that found in the laser evaporation source (LES). As with the GAS employing sputtering, the cluster output contains a high proportion of ions (~10%) and is particularly suited to charged-particle mass analyzers.

## 2.2. Mass Selection

Due to the relatively low rate of deposition produced by most sources, the mass resolution used for studies of deposited particles is normally less than in the case of free clusters where individual particles are counted. In fact much of the work reported so far has been on assemblies of clusters where no postaggregation filtering has been carried out. In this case there is still some degree of control over the size distribution by changing the source parameters such as the gas temperature or pressure in the aggregation region. Some sources employ two mass filters: a high resolution instrument such as a time-of-flight analyzer to measure the mass-spectrum in the free beam and a lower resolution high-throughput device to narrow the native mass distribution prior to deposition [39]. Most mass separators require the clusters to be charged and, with the exception of sources that rely on sputtering to produce the metal plume, which inherently produce a large proportion of charged clusters, ionization is inefficient so that the majority of clusters are discarded.

In general a mass separator for charged particles must be able to determine the mass independently of the initial ion velocity. In the case of a hard free jet expansion in the source in which the clusters all have the same velocity distribution irrespective of mass, filtering can be achieved by a simple parallel-plate electrostatic deflector. If this is not the case a more sophisticated device is required and various charged-particle mass separators that can operate without assuming an initial velocity distribution are described below as well as schemes for mass selection of neutral clusters.

### 2.2.1. Radio Frequency Quadrupole

This instrument, illustrated in Figure 2a, operates using electric fields only and was first described by Paul et al. [41, 42]. Four cylindrical poles in the geometry shown have a radio frequency (rf) modulation on a dc offset ( $U + V \cos \omega t$ ) applied to one pair of opposite poles and the negative of the same potential to the other pair. In order to be transmitted by the filter, the oscillatory motion of an ion as it moves along the poles must have a stable amplitude and this can only occur, irrespective of its mass, if the ratio  $U/V$  is less than 0.168. For ratios lower than this the instrument passes specific masses given by the absolute value of  $V$ . For a quadrupole operating at the stability limit, the range of masses passed depends on the energy of the ions entering the filter, the frequency,  $\omega$ , and the length of the poles. Operating with  $U/V$  ratios below the stability limit produces a band pass filter with a top hat amplitude function. One of the attractive features of the instrument is that a simple electronic adjustment of  $U/V$  allows a trade-off between flux and resolution. Other advantages are that the filter is light and compact, and it operates axially, which is convenient in a deposition source. Technically the maximum resolving power

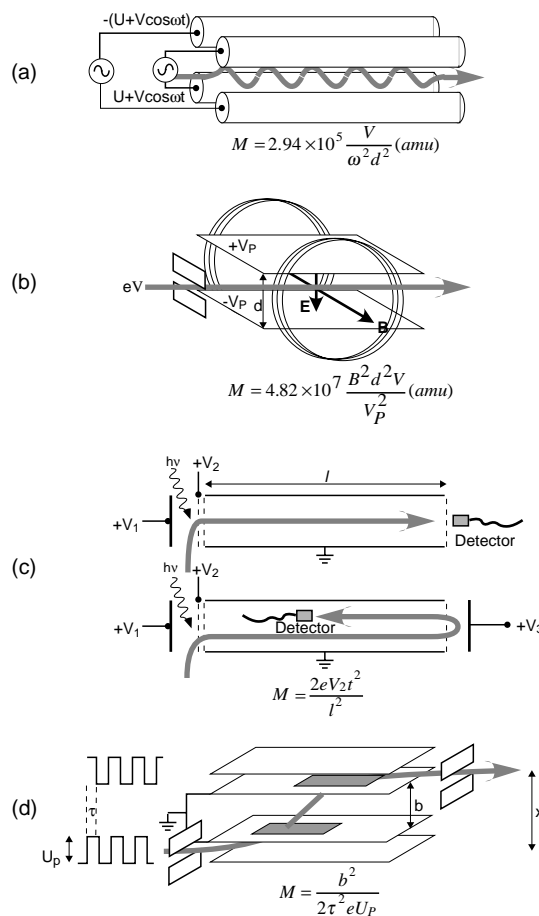


**Figure 2.** Mass separators for charged clusters. (a) Rf quadrupole. (b) Wien filter. (c) Time-of-flight mass spectrometer with direct and reflectron configurations. (d) Pulsed field mass selector. Reprinted with permission from [33], C. Binns, *Surf. Rev. Lett.* 44, 1 (2001). © 2001, Elsevier Science.

$(M/\Delta M)$  obtainable from this type of mass spectrometer is about 4000 and so for a resolution of 1 amu or better the mass range is restricted to clusters smaller than about 100 atoms. If the single amu resolution requirement is relaxed and the instrument is treated as a band pass filter with a variable bandwidth, it is possible to pass arbitrarily large masses. For a quadrupole operating at the stability (high resolution) limit the central mass passed is

$$7.45 \times 10^7 \frac{V}{f^2 d^2} \quad (\text{amu}) \quad (4)$$

and the resolution is

$$\Delta M = 3.92 \times 10^9 \frac{E_z}{f^2 L^2} \quad (\text{amu}) \quad (5)$$

where  $E_z$  is the ion energy entering the filter (in V),  $f$  is the rf frequency ( $=\omega/2\pi$ ),  $d$  is the diameter, and  $L$  is the length of the rods. The maximum mass range reported for a quadrupole filter [25] is 60,000 amu with a resolution of about 200 amu (resolving power = 300). In the case of Fe for example, this corresponds to clusters containing  $1000 \pm 4$  atoms, or in terms of size, particles with a diameter of  $2.82 \pm 0.008$  nm.

### 2.3. Wien Filter

This type of mass filter, illustrated in Figure 2b, applies orthogonal electric and magnetic fields to a charged particle with velocity  $v$ . The antiparallel forces on the ion balance when

$$v = \frac{2V_p}{Bd} \quad (\text{ms}^{-1}) \quad (6)$$

where  $2V_p$  is the voltage applied across the electrostatic plates and  $d$  is the plate spacing. The device is really a velocity filter and it is operated as a mass filter by initially accelerating the ions through a fixed potential  $V$  so each mass has a different velocity. The mass passed by the filter is then given by

$$4.82 \times 10^7 \frac{B^2 d^2 V}{V_p^2} \quad (\text{amu}) \quad (7)$$

The resolution is determined by the collimating slits and the velocity spread in the ion beam prior to acceleration. The effect of the latter can be minimized by using a high accelerating potential but this puts a heavy demand on the magnetic field strength required to operate up to a high mass. A thorough analysis of the performance of a commercial Wien filter for the mass separation of clusters emerging from a pulsed arc cluster ion source (PACIS) was carried out by Wrenger and Meiwes-Broer [43]. They showed that the instrument was capable of distinguishing clusters with specific numbers of atoms,  $N$ , up to about  $N = 20$ . With a constant magnetic field there was good agreement between the calculated and actual voltage settings to pass a given mass for the small clusters and so the calculated values could be used to set up a band pass filter for unresolved masses up to  $N \approx 1000$ .

### 2.4. Time-of-Flight Mass Spectrometers

In this scheme (Fig. 2c) a well defined pulse of ions is created, usually by a pulsed ultraviolet laser or electron gun. The packet of ions is accelerated into a field-free drift tube and the arrival time at the end of the tube is recorded by an ion detector. The resolution of the simple instrument is limited mainly by the timing accuracy and the preionization spread in position and velocity. These latter two effects can be minimized by the reflectron scheme [44–46] shown in the figure that uses a simple diode reflector at the end of the drift tube. Slower ions of a given mass take a shorter path in the reflector than faster ones so ions of the same mass will be bunched closer together on reflection. With this system resolving powers of  $10^5$  have been achieved.

The analyzer can be used as a filter by adding an electrostatic kicker mechanism that pulses a set of steering plates a set time after each ionizing pulse to expel ions of a given mass from the drift tube. A potential problem with this scheme is harmonics (i.e., simultaneously selecting slow heavy ions from a previous pulse and lighter ions from the present pulse). This type of mass analyzer is most efficiently matched to a pulsed cluster source such as the PACIS or LES types that typically operate at around 100 Hz. The ionizing laser in the case of a LES is operated at the same frequency as the evaporation laser so the ion packets are separated by around 10 ms while typical flight times are of the order of 0.1 ms so harmonics are unlikely to be a problem with the typical time structures presently used.

### 2.5. Pulsed Field Mass Selector

Recently a simple and ingenious mass filter was reported [47] that uses an electric field pulse to displace an ion beam sideways into a field-free region (Fig. 2d). For a given strength and timing of the pulse the lateral velocity of the ions in the field-free region depends on their mass. A given time later a second decelerating pulse deflects the ions onto a path parallel to the original one and through an aperture. The timing between the accelerating and decelerating pulses determines the selected mass. The instrument can filter masses up to an arbitrarily high limit with a transmission greater than 50%, and with a mass resolution given by

$$\frac{M}{\Delta M} = \frac{x}{\Delta x} \quad (8)$$

where  $x$  is the ion beam lateral displacement and  $\Delta x$  is the exit slit width. In practice this is in the range 20–50 (i.e., not as high as the other filters but sufficient for most studies of deposited clusters). As stated earlier, in real deposition experiments, if a mass filter is used, it is normally detuned to pass an adequate cluster flux.

### 2.6. Mass Separation of Neutral Clusters

Mass selecting neutral particles has always been a highly prized goal since most ionizers are inefficient and even in sputter sources that produce a high proportion of ions, the majority of the emitted clusters are uncharged. Most attempts to mass-select neutral particles to date are based on the size-dependent velocity slip between the carrier gas and the clusters during the free jet expansion [48]. Roux

et al. [49] used a velocity selector made from a pair of rotating slotted wheels based on the design by Hostettler and Bernstein [50]. The filter was able to shift the peak of the mass distribution of the neutral clusters but due to its low resolution was not found to significantly affect the width.

Mechanical velocity selectors can also be used to mass select in conjunction with sources that naturally produce a pulsed output such as the pulsed arc or laser ablation types. At typical repetition rates of about 100 Hz the bunches of clusters are about a meter apart and well separated. Each packet will have an expanding cylindrical envelope due to the different velocities of the clusters within it and, because of the size dependence of the velocity slip in the free jet expansion, the leading edge will become increasingly rich in small clusters and the trailing edge will accumulate the larger clusters. Thus a mechanical chopper operating at the same frequency as the source but phased to be transparent to only a portion of the cluster bunches will size-select with 100% transparency irrespective of the resolution setting. This scheme has yet to be tested.

Recently a new scheme has been suggested by Di Fonzo et al. [51] and Tafreshi et al. [52] that exploits “aerodynamic focusing” [53]. This is produced by a series of orifices that induce several expansions and contractions of the gas flow with the result that at each stage the particles become more collimated within the gas flow. Deposited features with linewidths of 50  $\mu\text{m}$  were demonstrated without the use of micronozzles. The cluster beam collimation is size-dependent and by careful design of the lenses it should be possible to spatially separate particles with different sizes. This remains to be demonstrated.

### 3. MAGNETIC MEASUREMENTS ON CLUSTERS

#### 3.1. Free Clusters

##### 3.1.1. Gradient Field Deflection

The founding experiments on cluster magnetism were carried out on free particles and determined the magnitude of the magnetic moment as a function of cluster size [12, 13, 54–56]. The first setup capable of this measurement was reported by Cox et al. [54] and is based on the classic Stern–Gerlach experiment that first detected the electron spin [57]. Figure 3a shows, schematically, a typical arrangement. A collimated cluster beam generated by a pulsed laser evaporation source with a variable temperature nozzle is guided into a magnetic field gradient  $dB/dz$  that will deflect vertically any particle with a magnetic moment  $\mu$  by an amount

$$d = \mu \frac{dB}{dz} L^2 \frac{(1 + 2D/L)}{2Mv_x^2} \quad (9)$$

where  $L$  is the length of the magnet,  $D$  is the distance from the end of the magnet to the detector,  $M$  is the cluster mass, and  $v_x$  is its velocity when it enters the magnet. A pulsed ionizing laser probes the beam profile after the magnet and is the source for a time-of-flight mass filter. Thus it is possible to measure the deflection of a given mass and determine its magnetic moment as long as  $v_x$  is known. This can be defined by a controlled delay between the evaporation laser

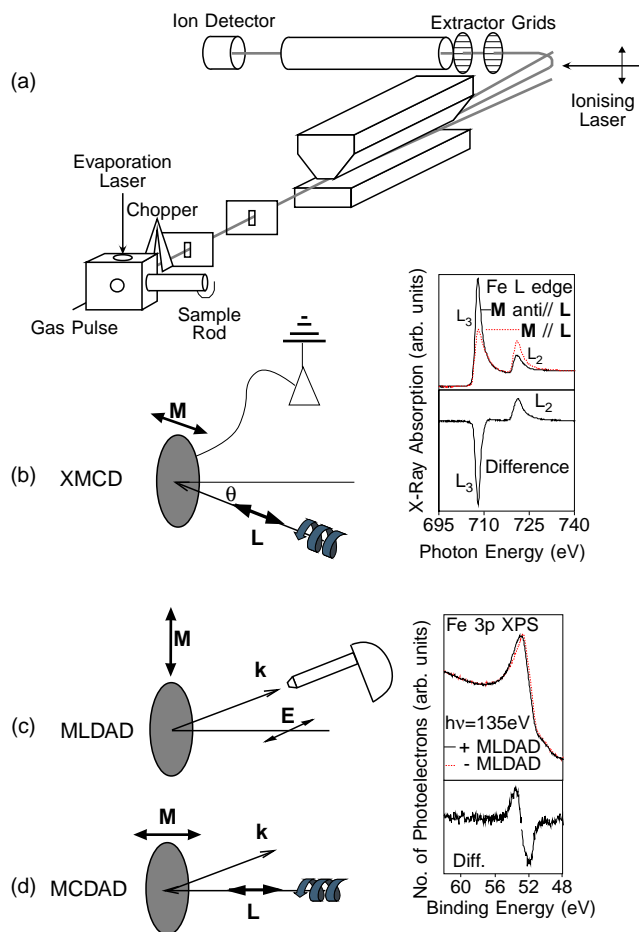


**Figure 3.** (a) Schematic of experiment to measure the magnetic moment of free clusters. (b) X-ray magnetic circular dichroism (XMCD) measures the difference in  $L$ -edge absorption between parallel and antiparallel alignment of the magnetization vector and photon spin. The magnetic field is applied along the direction of the photon beam and at a variable angle,  $\theta$ , relative to the sample normal. (c) Magnetic linear dichroism in the angular distribution (MLDAD) measures the difference in the Fe  $3p$  photoemission spectra taken with linearly polarized extended ultra-violet (XUV) light on reversing the magnetization in the sample plane and perpendicular to the photon polarization vector. (d) Magnetic circular dichroism in the angular distribution (MCDAD) measures the difference in the Fe  $3p$  photoemission spectra taken with circularly polarized XUV light on reversing the magnetization along the direction of the photon spin. All data shown were obtained from Fe nanoclusters on highly oriented pyrolytic graphite (HOPG) [15, 61]. Reprinted with permission from [62], C. Binns, *J. Nanosci. Nanotechnol.* 1, 243 (2001). © 2001, American Scientific Publishers.

and the ionizing laser. Since the duration of the pulse of clusters can be several ms wide, a mechanical chopper in front of the source (also shown in Fig. 3a) is used to better define the pulse start time. The chopper can be phased with the vaporizing laser to define clusters emerging from the nozzle at a specific time relative to the vaporizing pulse, a feature that was found to be important in order to define the cluster temperature.

Interpreting the data from clusters provided by the instrument is, however, not straightforward and requires a careful consideration of the detailed operation of the source. The problem is in accurately defining the cluster vibrational



temperature,  $T_{\text{vib}}$ . It is found for transition metals that they always deflect toward the direction of highest field, which is indicative of superparamagnetism. That is, clusters enter the magnet with a rapidly fluctuating moment and within the field become magnetized to a degree depending on the temperature and the field, as described by Eq. (2). Since the residence time in the magnet ( $\sim$ ms) is orders of magnitude longer than the time scale of the magnetic fluctuation ( $\sim$ ns), clusters of a given size will attain the same mean magnetization and deflect by the same amount.

During the initial experiments on free cluster magnetism, significant deviations from the predictions of the superparamagnetic model were found for small residence times of the clusters in the source. The original proposal to explain this [58] was that for short times ( $<1$  ms) after the laser pulse, the gas pressure within the source is still high and the clusters are cooled well below the nozzle temperature by the adiabatic expansion. This was based on the observation that Ar added to the He bath gas was adsorbed onto the surface of the clusters indicating that they were much colder than the temperature within the source. The nonequilibrium conditions can create a situation where the rotational temperature ( $T_{\text{rot}}$ ) is less than the vibrational temperature ( $T_{\text{vib}}$ ) and may be of the same order of magnitude as the magnetic precessional frequency in the applied field, which can lead to a resonant spin rotation coupling that reduces the magnetization [12, 59]. In order for the clusters to be thermalized with the nozzle temperature, the chopper must select clusters produced after delays that are sufficient for the gas pressure to drop below the values where significant cooling occurs in the free jet expansion. The cluster temperature is then the nozzle temperature and the cluster magnetization is superparamagnetic in the case of Fe, Co, and Ni clusters. An alternative mechanism proposed by Douglass et al. [13] is that at short residence times the metal vapor is still hot and requires time to thermalize with the carrier gas. They found no significant supercooling in their free jet expansion and were unable to produce the rare gas adsorption results obtained by Milani and de Heer [58]. In either case, for sufficiently long residence times, the clusters attain the nozzle temperature, which can be controlled, and then all results for the transition metals are consistent with the superparamagnetic model. A more subtle consideration is whether a nanocluster containing a few tens of atoms has a sufficient density of states to constitute a heat bath so that thermodynamically based laws are valid. This is assumed to be the case based on the success of the superparamagnetic model in describing the results after the above technical considerations are addressed [60].

In rare earth clusters, rotational effects can again become important since the spin-orbit interaction can be sufficiently strong to lock the cluster magnetic moment to its atomic lattice. Douglass et al. [13] showed that whether Gd clusters display superparamagnetic or locked-moment behavior is a sensitive function of their size. The results are discussed in detail in Section 5.

### 3.2. Exposed Clusters on a Surface

The gradient-field deflection technique is the only one that can determine the magnetic moments in free clusters. Next are described several experiments that can be used to study

magnetism *in-situ* in clusters deposited on a surface and exposed in ultrahigh vacuum.

#### 3.2.1. X-Ray Magnetic Circular Dichroism

This is a powerful technique for studying magnetic behavior at surfaces and in nanostructures. In the case of transition metals, it involves the measurement of the difference in  $L$ -edge X-ray absorption spectra obtained using circularly polarized X-rays with their angular momentum parallel or antiparallel to the sample magnetization. The orbital ( $m_L$ ) and spin ( $m_S$ ) contributions to the total magnetic moment can be determined independently and (in heterogenous systems) for each element by applying magneto-optical sum rules to the absorption spectra [63, 64]. The experimental geometry and an  $L$ -edge absorption spectrum taken from Fe clusters deposited on graphite [15] are shown in Figure 3b.

More precisely, the technique measures the quantities  $\langle L_z \rangle$  and  $\langle S_z + 7T_z \rangle$  per valence band hole,  $n_h$ , where  $\langle L_z \rangle$  and  $\langle S_z \rangle$  are the expectation values of the  $z$  (static) components of the orbital and spin angular momenta of the atoms, and  $\langle T_z \rangle$  is the expectation value of the magnetic dipole operator given by

$$T = \frac{1}{2}[\mathbf{S} - 3\hat{\mathbf{r}}(\hat{\mathbf{r}} \cdot \mathbf{S})] \quad (10)$$

This averages to zero over all directions and does not appear in conventional magnetic measurements but since the X-rays sample a directional cut through the atomic electron density, the term must be included in the sum rule. It can be eliminated, yielding the pure spin moment, by averaging measurements over all X-ray incidence angles, making a single measurement on a polycrystalline sample or, for samples with rotational symmetry about the substrate normal, making a single measurement at the “magic” angle [65, 66]. The number of valence band holes can be determined by measuring the integrated (white line)  $L$ -edge absorption strength, which is proportional to  $n_h$ , of a thick film of the same material *in-situ* and comparing it to that of the clusters. One of the powerful attributes of XMCD is that, since it is derived from an X-ray absorption edge, it is element-specific. Thus it can determine, separately, the orbital and spin moments localized in different magnetic elements in heterogenous systems.

The only sources that emit a sufficiently high flux of circularly polarized X-rays to study nanostructures by XMCD are synchrotron storage rings. These produce circularly polarized radiation of either helicity above and below the orbit plane of the electrons and also from insertion devices such as helical undulators [67].

#### 3.2.2. Dichroism in Photoelectron Spectroscopy

A dichroism is also observed in the  $3p$  angle-resolved photoemission spectra of the transition metals taken with linearly or circularly polarized light with the geometries shown in Figure 3c and d. The techniques measure the difference in the spectra in response to reversing the alignment between the in-plane sample magnetization and the linear polarization of the XUV light (MLDAD [68]) or between the

out-of-plane sample magnetization and angular momentum of circularly polarized light (MCDAD [69]). Since angle-resolved photoemission spectra must be collected in zero field, the techniques are, in general, restricted to measuring remanence but they are surface sensitive and capable of measuring submonolayer quantities of material. Schemes using magnetic substrates that expose the clusters to fields  $\sim 1$  T but still allow photoemission measurements have also been developed [70]. As with XMCD, a synchrotron source must be used to provide the polarized XUV radiation and endstations at which light of variable polarization is available can be fitted with movable magnetizing coils allowing both geometries to be combined in a single experiment. This enables the comparison of in-plane and out-of-plane remanent magnetization.

### 3.2.3. Surface Magneto-Optical Kerr Effect

In a surface magneto-optical Kerr effect experiment, the rotation of the polarization of a light beam when it is reflected from a magnetic surface is measured [71]. The rotation is by the same process as Faraday rotation in transmission. It is a popular method for measuring magnetism in surfaces and ultra-thin films since it is relatively inexpensive to set up and is easily made compatible with UHV since the light source, usually a He-Ne laser, and all the polarization detection equipment are external to the vacuum system with the incident and reflected beams transmitted through windows. The optical penetration depth of visible light is of the order of 20 nm in metals and the signal from a deposited monolayer is a small fraction of the total signal so the rotation of the polarization vector is a fraction of a degree. With careful design and good quality optics it is possible to measure hysteresis loops in magnetic monolayers. Three geometries are used: polar, longitudinal, and transverse. The maximum signal is obtained when the  $\varepsilon$  vector of the light is perpendicular to the sample magnetization [72].

### 3.2.4. UHV Vibrating Sample Magnetometry

Vibrating sample magnetometry is a standard technique for measuring the magnetic moment in materials that was originally described by Foner [73] over 40 years ago. The magnetic moment of a sample is determined by vibrating it between conducting coils and measuring the alternating voltage developed at the same frequency. The sensitivity of the technique has steadily improved and modern instruments can measure moments as low as  $10^{-7}$  A m<sup>2</sup>, corresponding to  $\sim 10^{16}$  Fe atoms. Recently, a system that allows *in-situ* measurements on exposed clusters in UHV has been demonstrated [74]. A deposited cluster layer is deposited onto a substrate and then sealed, in its UHV environment, within an ampoule that can be withdrawn and inserted into the magnetometer without exposing the sample to atmosphere.

The technique is not sensitive enough to measure significantly less than a single cluster layer so it cannot be used to study isolated particles. The ability to measure exposed layers is, however, important since, as will be shown in Section 7, even thick cluster films show a marked change in magnetic behavior when coated with a protective nonmagnetic capping layer to allow removal from the vacuum for *ex-situ* measurements.

## 3.4. Isolated Embedded Clusters

In the case of embedded clusters, it is unnecessary to make *in-situ* measurements as the samples can be taken into air without contaminating the magnetic clusters and so the whole range of magnetic measurements becomes possible. The two techniques presented below are sufficiently sensitive to measure the magnetization in a *single* embedded nanocluster.

### 3.4.1. Micro-SQUID Measurements

Superconducting quantum interference devices (SQUIDS) are the most sensitive magnetic detectors known and recent developments in lithographed devices of  $\mu\text{m}$  dimension have enabled the measurement of the switching field of individual nanoclusters [75]. The technique involves making the loop and Josephson junctions out of a cluster-assembled film consisting of nanoclusters embedded in a superconducting matrix. The film is deposited over a whole substrate that is then patterned using lithography into superconducting loops with weak links. Although every loop contains clusters over its entire surface, there is only significant flux coupling from those that are embedded within the bridge. In the devices reported the junction regions have an area  $30 \times 50$  nm<sup>2</sup> and the clusters are embedded in a 20 nm thick Nb film. Thus if clusters with a volume  $\sim 20$  nm<sup>3</sup> are embedded with a volume fraction  $\sim 0.1\%$ , there will be on average 1 cluster per bridge region. One then makes measurements from a number of SQUIDS on the sample and it is clear from the switching field distribution which ones are detecting a single particle.

### 3.4.2. Micro-Hall Probes

Using conventional photolithography and wet chemistry it is possible to produce submicrometer size III-V semiconductor Hall bars in which the conducting layer is an ultrathin two-dimensional electron gas (2DEG) localized at the surface [76, 77]. A magnetic particle deposited onto the central bar produces an intense local magnetic field that penetrates the 2DEG and generates a significant Hall voltage. Wirth and von Molnár [77] have shown how matching the size of the particle array to the active area of the Hall bar produces the optimum sensitivity and recently, Li et al. [78] measured the magnetization curve at temperatures up to 75 K, of a single Fe nanoparticle with a diameter of 5 nm. At present the technique does not quite match the sensitivity of the micro-SQUID but it is much more versatile since it can measure over a much wider temperature range ( $\leq 100$  K) and is not restricted to particles embedded in superconducting materials.

## 4. MORPHOLOGY AND STRUCTURE OF CLUSTERS AND CLUSTER-ASSEMBLED FILMS

### 4.2. Morphology

The high proportion of surface atoms in nanoclusters magnifies the importance of the surface energy and it is the competition between this and the local bonding forces that

determines their morphology. Simple metal clusters with highly isotropic bonding are at one extreme and are pulled into spheres with the system behaving very much like a liquid drop. In fact the abundance spectra show “magic numbers” that correspond to especially stable electronic configurations within a spherical jellium model [79, 80]. In the case of the transition metals the magic numbers always correspond to stable atomic geometries rather than filled electronic shells. For example the body-centered cubic (bcc) metals Fe, Nb, and Ta show magic numbers at  $n = 7, 13,$  and  $15$  that correspond to a pentagonal pyramid, an icosahedron, and a double icosahedron respectively [81]. In this situation, in larger clusters, faceting becomes thermodynamically stabilized and in the case of metals with close-packed cubic crystal structures, the clusters tend to form truncated octahedrons [23, 82]. Generally the growth in the gas phase occurs in shells with the successive filling of layers of the cuboctahedral structure [83–85]. From a given stable configuration, reaching the next larger size begins by growth at a (111) face and switches to an adjacent (111) or (100) face when the first is full.

The morphology can change when the clusters land on a substrate, either by direct damage from the impact or due to subsequent diffusion and aggregation of clusters. These latter effects dominate the morphology of simple metal clusters deposited on graphite surfaces and they tend to form large fractal structures in which the original cluster morphology is lost [86]. This is not the case with transition metal clusters which, for landing energies less than  $\sim 0.5$  eV/atom, maintain their free cluster shape. Diffusion is also limited so that films build up by a random positioning of clusters. This type of structure is seen in Figure 4, which shows deposits of Fe clusters on Si(111) surfaces [87]. There is no tendency for the clusters to line up along atomic steps or to coalesce when they come into contact but remain as distinct grains. This remains the case even in very dense assemblies in which there is more than one layer of clusters. Closer inspection (Fig. 4b) reveals faceting of the clusters and that they tend to align along the facets when they come into contact. As shown in Figure 5, the faceted morphology is also preserved in nanoclusters embedded in matrices [74].

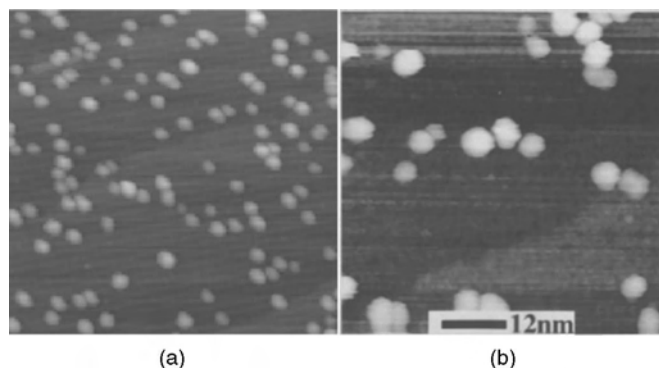


**Figure 4.** Morphology of exposed Fe clusters on Si(111). (a) Scanning tunneling microscopy (STM) images ( $100 \times 100$  nm) of unfiltered cluster deposition. (b) High magnification image ( $40 \times 40$  nm) of deposition shown in (a). Reprinted with permission from [131], C. Binns and M. J. Maher, *New J. Phys.* 4, 85.1 (2002). © 2002, IOP Publishing.

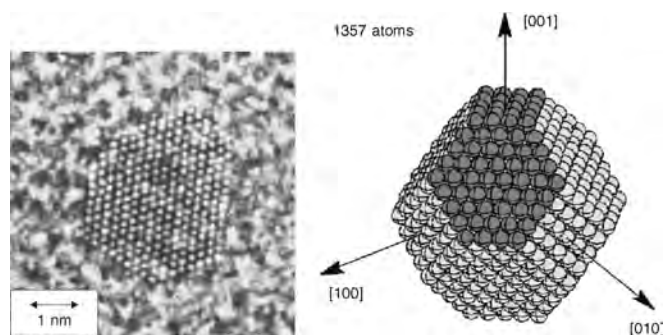


**Figure 5.** TEM image of a single 3 nm Co cluster embedded in amorphous carbon showing a cuboctahedral morphology and a fcc atomic structure. Reprinted with permission from [75], M. Jamet et al., *Phys. Rev. Lett.* 86, 4676 (2001). © 2001, American Physical Society.

### 4.3. Structure

The atomic structure of a transition metal nanocluster is a size-dependent property and for metals with close packed cubic structures in the bulk, very small clusters are generally predicted to have icosahedral structures. Above some critical size the structure changes to a cubic close packed though this may be a face-centered cubic (fcc) structure in metals that are hexagonal close packed in the bulk. An example is Co and Figure 5 shows a transmission electron microscopy (TEM) image of a single cuboctahedral Co cluster embedded in amorphous carbon with a fcc structure [75]. In the case of metals with a bulk bcc structure, one expects an intermediate fcc phase between the icosahedral and bcc structures. There is evidence for this transition in Fe clusters from the free cluster magnetization measurements by Billas et al. [12] that indicate a change in the magnetic behavior at sizes of about 100 atoms. From specific heat measurements by Gerion et al. [90] of free Fe clusters containing about 270 atoms there is also evidence for a phase transition at about 600 K.

## 5. MAGNETISM IN FREE CLUSTERS

Studying mass-selected magnetic clusters as free particles enables one to address fundamental questions regarding the development of magnetism in materials as they are built atom by atom from the monomer. Various novel behaviors have been observed in free clusters including enhanced magnetic moments in ferromagnetic metals [12], magnetism in metals that are nonmagnetic in the bulk [56], ferrimagnetism in antiferromagnetic metals [88], canted spin arrangements in ferromagnetic rare earths [13, 89], and lowered [12, 90] or increased [91] Curie temperatures. Theoretical models have been developed that explain many of these phenomena. Ab initio methods and total energy calculations can be used to determine the cluster structure as well as their magnetic properties but are restricted to small clusters containing up to about 10 atoms. Hartree–Fock based methods can be used to calculate the magnetic behavior of much larger clusters but an atomic structure must be assumed. It is found in all cases that the atomic structure and the nearest neighbor distance are critical to determining the magnetic properties in clusters. Experimentally this information is sparsely

available at present and has been determined in a limited number of cases by indirect methods such as the observation of magic numbers in the mass spectra of the clusters [81]. The situation is complicated by the existence in some cases of several isomers of clusters of a give size.

The magnetic measurements are restricted to the gradient-field experiment described in Section 3 that measures the deflection and the modification of the beam profile of a beam of clusters by an inhomogenous magnetic field. In principle this can measure the total magnetic moment of a mass-selected cluster as a function of the field magnitude and the cluster temperature. As discussed earlier, initial controversies regarding the interpretation of data have been resolved. It is generally accepted that in transition metal clusters with their low magnetocrystalline anisotropy, at typical temperatures encountered in cluster sources the moment is decoupled from the atomic lattice and the magnetization obeys the superparamagnetic model. The magnetization of rare-earth clusters on the other hand is described by the superparamagnetic model only at some cluster sizes. Clusters with different sizes show locked-moment behavior. A review of results on free clusters of various types is presented below. For measurements on superparamagnetic clusters, the magnetization measured at finite temperatures is used to extract the intrinsic value of  $\mu_{\text{cluster}}$  (usually expressed in  $\mu_B/\text{atom}$ ) using Eq. (2).

### 5.1. Ferromagnetic 3d Transition Metals

Figure 6 shows a compilation of the total moments in free  $\text{Fe}_N$ ,  $\text{Co}_N$ , and  $\text{Ni}_N$  clusters for  $N = 10\text{--}740$  atoms, measured by Billas et al. [92], Apsel et al. [93], and Knickelbein [94, 95] using the gradient-field deflection technique. The step in the Ni data reported by Apsel et al. [93] at  $N = 200$  arises from a change in the measurement temperature and a resulting change in the systematic error. The total moment is enhanced relative to the bulk in all three metals but there is a convergence to the bulk value for cluster sizes greater than  $\sim 600$  atoms. The convergence is not monotonic, however, as gentle ripples in the moment are observed above the noise level throughout the size spectrum. It has recently been suggested that these weak variations may be due to an oscillation of the magnetic anisotropy energy and thus the systematic error with size, rather than changes in the magnetic moment [96].

For clusters smaller than about 20 atoms, dramatic changes occur. The most prominent is observed in Fe clusters in which going from  $\text{Fe}_{12}$  to  $\text{Fe}_{13}$  changes the moment per atom from nearly the atomic limit to close to the bulk value. The detailed changes in small  $\text{Fe}_N$  and  $\text{Ni}_N$  clusters for  $N < 100$  are shown in Figure 7. It is observed that  $\text{Fe}_{12}$  has a moment ( $5.4\mu_B/\text{atom}$ ), which is close to the atomic limit of  $\mu_z = 6\mu_B$ , assuming a  $d^6$  configuration of the valence shell, as in the case of atomic Fe [97]. In order to achieve this the atoms in the cluster must have most of the atomic spin moment ( $3\mu_B$ ) and most of the atomic orbital moment ( $3\mu_B$ ). The addition of a single atom, however, reduces the moment by almost  $3\mu_B$  to  $2.44\mu_B$  observed in  $\text{Fe}_{13}$ . Independent measurements by Knickelbein [94] and Apsel et al. [93] also demonstrate an especially low moment in  $\text{Ni}_{13}$ . Mass spectra of several types of metal cluster including Fe, Ti, Zr,

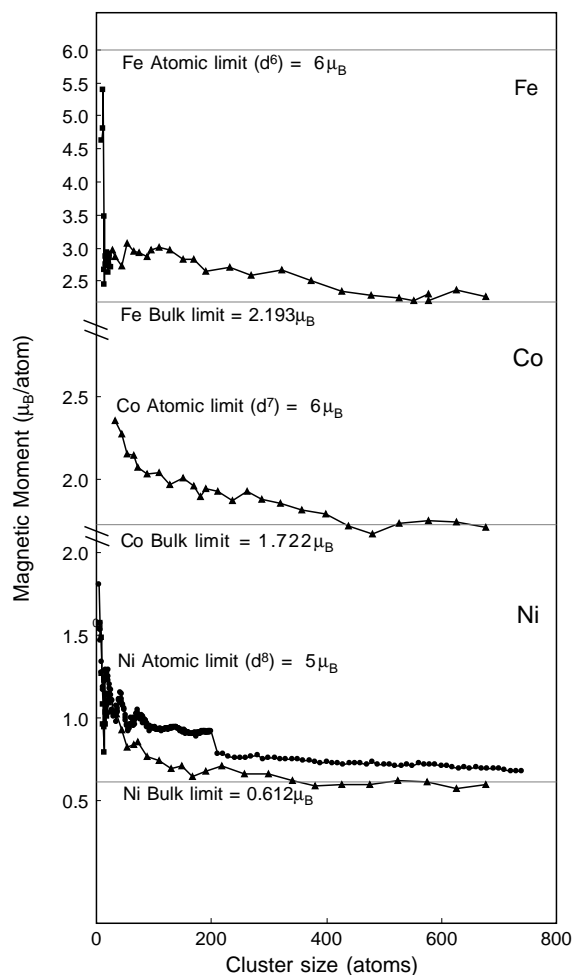


**Figure 6.** Total moments (in  $\mu_B/\text{atom}$ ) observed in free Fe, Co, and Ni clusters as a function of size measured by Knickelbein [94, 95] (squares), Billas et al. [92] (triangles), and Apsel et al. [93] (circles).

Nb, and Ta [81] have identified  $N = 13$  as a magic number and the structure is assumed to be the densely packed icosahedron shown in the figure.

The results of some calculations are also shown in Figure 7. In all cases the calculation of the magnetic moment is restricted to the spin component; that is, the orbital contribution is neglected and this leads to a general underestimation of the magnetic moment. The tight binding molecular dynamics calculation by Andriotis and Menon [98] of the moment in free  $\text{Fe}_N$  clusters in the range  $N = 1\text{--}169$  shows good agreement with the measured values for  $N > 13$  atoms. In the smallest clusters, however, it continues to predict a moment of about the same size as the larger clusters while the experimental data show the large step up to close to the atomic limit for  $N = 12$ . This discrepancy is interesting as it implies that the step is due to the appearance of the orbital moment at close to its atomic value. It seems therefore that the formation of the close-packed icosahedron at  $N = 13$  almost completely quenches the orbital moment and it does not reappear at larger cluster sizes. For  $N > 13$  the moment is mostly due to spin but is still enhanced significantly relative to the bulk value. Fujima [101] predicted that  $\text{Fe}_7$  clusters with a pentagonal bipyramidal structure have a

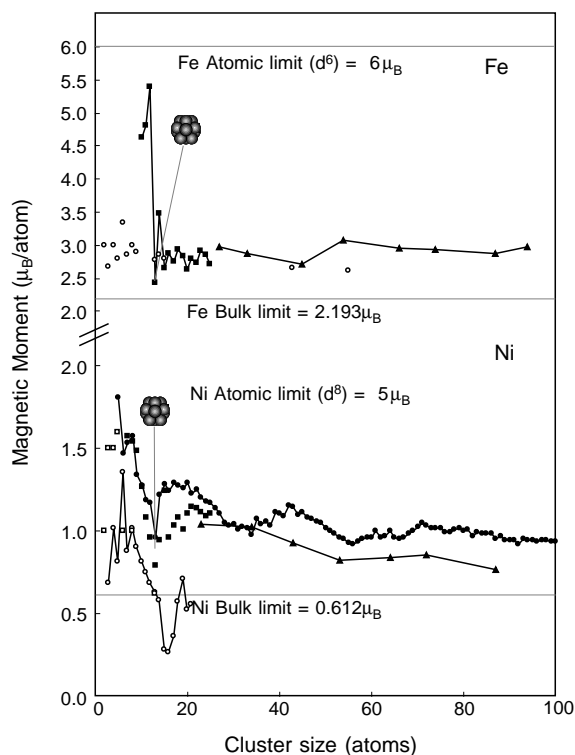


**Figure 7.** Total moments (in  $\mu_B/\text{atom}$ ) in free  $\text{Fe}_N$  and  $\text{Ni}_N$  clusters as a function of  $N$  for  $N < 100$  measured by Knickelbein [94, 95] (squares), Billas et al. [92] (triangles), and Apsel et al. [93] (circles). The measured values are compared with calculations by Andriotis and Menon [98] (open circles), Reddy et al. [99] (open circles plus line), and Reuse and Khanna [100] (open squares).

spin moment of  $2.86\mu_B/\text{atom}$  for the bulk interatomic spacing but a slight contraction results in a coplanar (i.e., not collinear) arrangement of the moments.

The calculations for  $\text{Ni}_N$  clusters by Reddy et al. [99] shows a minimum in the moment for  $N = 16$  rather than  $N = 13$  as observed. This is probably due to omission of the orbital moment as in the case of Fe implying again that formation of the icosahedron at  $N = 13$  quenches the orbital moment in Ni clusters though the effect is not as big as in Fe clusters. Reuse and Khanna [100] calculated moments in free Ni clusters for sizes up to  $N = 13$  and found a low moment at this size as well as predicting the icosahedral structure. They did not continue the calculation to larger sizes, however, so the minimum moment predicted by the model may not be at  $N = 13$ .

## 5.2. Antiferromagnetic 3d Transition Metals

The small number of atoms in nanoclusters of metals that are antiferromagnetic in the bulk leads to the possibility of an imbalance of the spin sublattices and frustration. Thus a ferrimagnetic or even ferromagnetic ground state may be expected. An initial experimental study of Cr clusters by Douglass et al. [102] using the gradient field deflection technique showed that  $\text{Cr}_N$  did not have a detectable net magnetic moment for  $N$  in the range 9–31 atoms. The sensitivity of the apparatus led them to conclude that the upper bounds for any net moment varied from  $0.77\mu_B/\text{atom}$

for  $\text{Cr}_9$  to  $0.42\mu_B/\text{atom}$  for  $\text{Cr}_{31}$ . This result was in contrast to many early calculations that predicted large and easily measurable net moments for  $\text{Cr}_N$  clusters for  $N$  up to 51 [103–105], though the expected moments were shown to be highly sensitive to the structure [105]. Lee and Callaway [106] calculated the magnetic moment in  $\text{Cr}_9$  and  $\text{Cr}_{15}$  clusters in a bcc structure as a function of lattice spacing and observed the disappearance of a net moment below a critical value. They found that at the bulk Cr spacing the magnetic moment for both  $\text{Cr}_9$  and  $\text{Cr}_{15}$  clusters was below the detectable threshold of the experiment. A structure-optimized calculation by Cheng and Wang [107] showed a unique growth by dimers up to  $\text{Cr}_{11}$  after which the bcc structure is stabilized. They found that the clusters were always antiferromagnetic with a size-dependent atomic moment. Subsequent calculations have investigated the stability of noncollinear moments resulting from frustration [101, 108]. Kohl and Bertsch [108] found that  $\text{Cr}_N$  clusters for  $N \leq 13$  strongly favor noncollinear configurations and Fujima [101] found that with decreasing interatomic spacing in  $\text{Cr}_7$  clusters, with a pentagonal bipyramid structure, the spin configuration changes from collinear (antiparallel) to coplanar.

Recently the field gradient deflection experiment on Cr clusters was repeated by Bloomfield et al. [109] using a more sensitive apparatus and it was found that all clusters studied in the size range  $N = 8$ –156 atoms showed a net magnetic moment that varied from almost zero to  $1.87\mu_B/\text{atom}$ . Even more interesting was the discovery that at a given cluster size there were always two isomers with different moments. The null result of the earlier experiment was due to the fact that the isomers with the largest moments had a low abundance. For example  $\text{Cr}_9$  has an abundant isomer with a moment of  $0.65\mu_B/\text{atom}$  and a rare one with a moment of  $1.87\mu_B/\text{atom}$ . In this latter case, for a collinear alignment of the moments even if the localized atomic moment was close to the free atom value of  $5\mu_B$  ( $d^5$  configuration), at least six of the nine spins must be parallel. The finding of multiple moments at a given cluster size, however, is not necessarily due to isomers with a different atomic structure. An earlier calculation by Lee and Callaway [110] revealed that  $\text{Cr}_9$  clusters with a bcc structure could exist in several magnetic states with different moments simultaneously. They found that for some atomic spacings four or five states could coexist. The data of Bloomfield et al. [109] may well be an experimental confirmation of this prediction.

Figure 8 shows the magnetic moments in free  $\text{Mn}_N$  clusters for  $N = 11$ –99 measured by Knickelbein [88]. He observed a moment across the size range that attains a maximum value of  $1.5\mu_B/\text{atom}$  for  $N = 15$ . Deep minima were also observed for  $N = 13$  and  $N = 19$  suggesting an icosahedral and double icosahedral structure at these cluster sizes. Calculations are not available for Mn clusters in this size range but density functional calculations for  $\text{Mn}_2$ – $\text{Mn}_5$  [111] find compact and symmetrical equilibrium geometries but also the existence of isomers whose binding energy is only slightly higher than the ground state structure. In all cases magnetic moments of  $5\mu_B$  were found; that is, the spin configuration is ferromagnetic and the spin moment has the atomic value. The conditions required for noncollinear

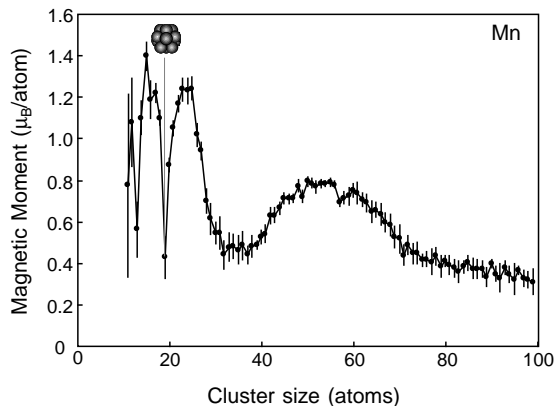


**Figure 8.** Total moments (in  $\mu_B/\text{atom}$ ) in free  $\text{Mn}_N$  clusters as a function of  $N$  for  $N = 1-99$ . Reprinted with permission from [88], M. B. Knickelbein, *Phys. Rev. Lett.* 86, 5255 (2001). © 2001, American Physical Society.

alignment of the moments in  $\text{Mn}_7$  clusters with a pentagonal bipyramidal structure were examined by Fujima [101]. He found that as the interatomic spacing relative to the bulk value varies between 0.8 and 1 the spin configuration changes from collinear (antiparallel) to disordered to coplanar.

### 5.3. Nonmagnetic 3d and 4d Metals

The Stoner criterion for itinerant magnetism [112] is  $D(E_F)I > 1$  where  $D(E_F)$  is the density of states at the Fermi level and  $I$  is the exchange integral

$$I = \int \gamma^2(\mathbf{r})K(\mathbf{r}) d\mathbf{r} \quad (11)$$

in which  $K(\mathbf{r})$  is the exchange-correlation enhancement of the applied field and  $\gamma(\mathbf{r})$  is proportional to the charge density at the Fermi level. Both  $D(E_F)$  and  $I$  are modified at interfaces and in nanostructures leading to the possibility of stabilizing magnetism in small clusters of elements that are paramagnetic in the bulk. Despite several theoretical predictions for permanent magnetic moments in V clusters [103, 113, 114] none have been detected [102].

There is a general decrease in  $I$  with increasing atomic number [115] so that magnetism is less favored in 4d and 5d elements and is not found in any bulk elements from these series. Although many 4d and 5d metals have been predicted to show magnetism as monolayers [116] there are only two experimentally proven examples of 4d magnetism, that is, Ru monolayers on graphite [117] and free Rh nanoclusters [56].

The magnetic moment per atom as a function of Rh cluster size is shown in Figure 9 and compared with the unrestricted Hartree–Fock calculations by Villaseñor-Gonzalez et al. [118]. The calculation optimized the structure at each size by determining the optimum bond length for icosahedral, fcc, and bcc atomic arrangement and then observing which of these had the highest cohesive energy. The predicted structure at each point is shown in Figure 9 and it is seen that the most stable arrangement alternates between all three structures. The calculations of the magnetic moment

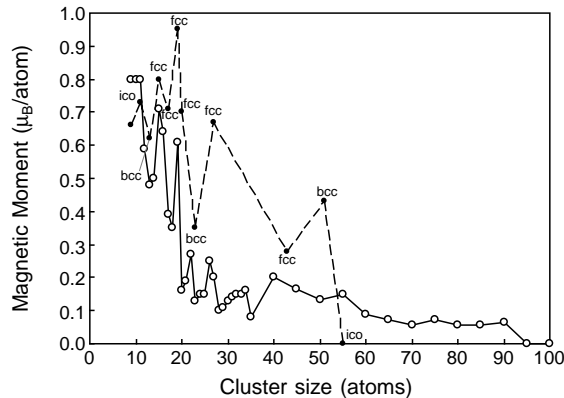


**Figure 9.** Total moments (in  $\mu_B/\text{atom}$ ) in free  $\text{Rh}_N$  clusters for  $N < 100$  measured by Cox et al. [56] (open circles). The measured values are compared with calculations by Villaseñor-Gonzalez et al. [118] (filled circles). The most stable structure, for which the calculation was performed, is shown at each cluster size. Reprinted with permission from [118], P. Villaseñor-Gonzalez et al., *Phys. Rev. B* 55, 15084 (1997). © 1997, American Physical Society.

of the most stable structures at each cluster size reproduce the data reasonably well and in particular reproduce the minima at  $N = 13$ ,  $N = 17$ , and the maximum at  $N = 19$ . Interestingly the most stable structure at  $N = 13$  is found to be bcc-like instead of the icosahedra assumed in the case of the 3d transition metals. A 13-atom icosahedral Rh cluster is found to show a magnetization maximum in contrast to the data. The double icosahedron at  $N = 19$  also shows a maximum in agreement with the measurements. The variations in the magnetic moment per atom derive not only from changes in magnitude of the individual atomic moments but also from spin alignments that are sometimes antiferromagnetic. The neglect of the orbital contribution in this type of calculation may, however, change the agreement with the experiment, in which the total (orbital + spin) moment is measured. Cox et al. [56] also attempted to detect magnetism in Pd and Ru clusters in the size range 10–115 atoms but found no measurable moment and set upper limits of  $0.32\mu_B/\text{atom}$  for  $\text{Ru}_{10}$  clusters and  $0.4\mu_B/\text{atom}$  for  $\text{Pd}_{13}$  clusters. A tight binding calculation including  $s$ ,  $p$  and  $d$ -orbitals of  $\text{Pd}_N$  and  $\text{Rh}_N$  clusters up to  $N = 19$  showed either small or zero moments for Pd clusters and larger values for Rh clusters [119].

### 5.4. Rare Earths

The character of magnetism in rare earths is very different from that of transition metals because the 4f orbitals, which produce most of the magnetic moment, are screened from the environment by the 6s electrons. The localization of the 4f electrons within screening orbitals generally results in both the orbital and spin moments maintaining their full atomic values in the bulk. The large orbital moment and spin–orbit coupling is responsible for the very high values of the magnetic anisotropy energy observed in rare earths.

Magnetic deflection experiments on free Gd clusters [13, 91, 120] at temperatures around 100 K have revealed two types of behavior depending on the number of atoms in the cluster. At some cluster sizes, the deflection profiles show that the cluster magnetization scales with  $B/T$  and these



are assumed to be superparamagnetic as in the case of transition metal clusters. At other sizes the cluster moment, measured from the deflection profile, does not scale with  $B/T$  and in this regime the behavior is ascribed to the moments being blocked so that they are locked to the crystal lattice and undergo the same rotation as the cluster. The simplest interpretation of these observations is that the magnetic anisotropy, which is higher in the rare earths than the transition metals, varies with the number of atoms in the cluster producing a consequent variation in the cluster blocking temperature  $T_B$ . For example Gerion et al. [91] found that  $T_B$  is between 45 and 75 K for  $Gd_{13}$  and  $Gd_{21}$  but around 180 K for  $Gd_{22}$ .

The different experiments disagree, however, on the cluster sizes that show the different behaviors. Douglass et al. [120] found that all cluster sizes in the range  $Gd_{11}$ – $Gd_{26}$  displayed locked-moment behavior with the exception of  $Gd_{22}$ , which was superparamagnetic. In contrast, Gerion et al. [91] showed that  $Gd_{13}$  and  $Gd_{21}$  were superparamagnetic while  $Gd_{22}$  was blocked. Tb also shows the locked-moment or superparamagnetic behaviors described above depending on the cluster size [121].

For the superparamagnetic clusters it is possible to extract the total moment per atom from the magnetization vs  $B/T$  using Eq. (2) as with the transition metals and in all cases moments/atom significantly lower than the bulk value were found. For example  $Gd_{13}$  and  $Gd_{21}$  clusters have moments of 5.4 and  $5\mu_B$ /atom respectively compared with a bulk value of  $7.55\mu_B$ /atom. This has been explained by a theoretical model that takes into account an Ruderman, Kittel, Kasuya and Yosida (RKKY)-type interaction between the atoms in which the exchange force between nearest neighbors is ferromagnetic but switches to antiferromagnetic between second nearest neighbors [89]. The clusters are found to adopt a hexagonal structure and within a range of the ratio of the ferromagnetic to antiferromagnetic coupling strengths, canting of individual atomic spins away from perfect ferromagnetic alignment is predicted. Thus the moment per atom measured along the applied field will be reduced. The reduction in moment relative to the bulk is also observed in Tb clusters [121], presumably for the same reason.

### 5.5. Magnetic Ordering Temperature

The thermal behavior of the moment has so far been discussed in terms of superparamagnetism where the cluster supermoment is excited over the cluster anisotropy barrier. At sufficiently high temperatures the internal spin alignment will be disrupted leading eventually to normal paramagnetism. Gerion et al. [90] measured the specific heat of free  $Fe_{250-290}$ ,  $Co_{200-240}$ , and  $Ni_{200-240}$  clusters in the temperature range 80–900 K. The method involves using an experimental setup similar to that used in measuring the magnetic moments and the perturbation of the beam profile in response to a heating laser is used to determine the specific heat. The clearest results are for  $Ni_{200-240}$  which shows a broad peak centered at 340 K on top of a nearly constant baseline of 6 cal/(mol K)—the classical Dulong and Petite value for bulk Ni. The peak is interpreted as due to the ferromagnetic to paramagnetic phase transition in the clusters

and its width is well described by the mean-field approximation. The temperature of the transition is significantly reduced relative to the bulk value of 627 K. The specific heat for the  $Co_{200-240}$  clusters shows a monotonic rise from 5.5 cal/(mol K) at 300 K to 15 cal/(mol K) at 900 K implying that the phase transition is not reachable in the temperature range of the experiment. The behavior of  $Fe_{250-290}$  clusters is more enigmatic showing specific heat values significantly lower than the Dulong and Petite values. A peak at around  $T = 600$  K does occur but is poorly described by mean-field theory. One possibility discussed in the paper is that Fe clusters undergo a magnetic transition between a high-moment and low-moment state with different lattice parameters.

Billas et al. [12] observed the magnetic ordering temperatures in  $Fe_N$  and  $Ni_N$  clusters directly by measuring the magnetic moment as a function of temperature up to over 900 K. In all cases they found the magnetic moment was constant above some critical temperature  $T_C(N)$ , which was interpreted as the transition temperature for paramagnetism. The magnetization in this state,  $\mu_{para}$ , should attain a value  $\mu_{T=0}/\sqrt{N}$  corresponding to  $N$  randomly aligned atomic moments so that in a cluster where  $N \sim 100$ ,  $\mu_{para}$  is significantly above zero. In fact it was found that  $\mu_{para}$  was higher than  $\mu_{T=0}/\sqrt{N}$ . This was later explained by Pastor and Dorantes-Dávila [122] as due to short-range magnetic order (SRMO) above the transition temperature, which is also observed in bulk magnetic materials. The effect of this is to increase the paramagnetic moment to  $\mu_{T=0}\sqrt{\nu/N}$  where  $\nu$  is the average number of atoms in a SRMO domain.

The high temperature behavior of rare-earth clusters contrasts with that of the transition metals. The measured ordering temperatures (420 K for  $Gd_{21}$  and over 500 K for  $Gd_{13}$ ) are significantly higher than the bulk value of 293 K. In addition the moment above the ordering temperature tends asymptotically to  $\mu_{T=0}/\sqrt{N}$  [91] indicating that there is no SRMO above the ordering temperature and the disorder is on the atomic scale. The decay in magnetic moment per atom with temperature found for  $Gd_{13}$  clusters is consistent with the canted spin model [91, 123].

## 6. MAGNETISM IN EXPOSED CLUSTERS ADSORBED ON SURFACES

In this section, the behavior of magnetic clusters deposited on a surface and left exposed to vacuum will be considered. Working in this regime requires that the cluster deposition must be done *in-situ* and the measurements performed in very good UHV conditions ( $\sim 10^{-11}$  mbar) to avoid contamination of the clusters. In the case of free clusters, some gas adsorption on the clusters can be tolerated as the mass separation can distinguish the clean clusters from those with gas molecules attached. In deposited samples, most *in-situ* magnetic measurements have been done with spatially averaged techniques that measure the entire cluster assembly and are unable to discriminate between the behavior of clean and contaminated clusters. There are, however, several experimental advantages in studying adsorbed clusters; for example, it is possible to exert accurate control over the cluster temperature down to low cryogenic values allowing the blocked state to be observed. In addition structural

techniques such as X-ray diffraction, STM, and TEM can be used as well as more powerful magnetic probes such as XMCD, which is able to determine the spin and orbital components of the total moment. Finally, the interactions between the clusters can be studied by accumulating a sufficient density on the surface.

### 6.1. Magnetism in Isolated Adsorbed Clusters

A natural starting point in describing adsorbed clusters is to review measurements carried out at very low coverages to determine the behavior of the isolated particles. An important question to address is whether the enhanced magnetic moments observed in free transition metal clusters are retained if the cluster is adsorbed on a surface. The earliest reported studies of isolated and exposed magnetic clusters deposited from the gas phase onto surfaces in UHV were of size-selected 2.5 nm (700-atom) Mn clusters at very low coverages on HOPG substrates [124, 125]. Photoelectron spectroscopy using synchrotron radiation was used to probe shallow core levels and showed changes in the lineshape of the Mn 3s photoemission spectra that were consistent with an increased magnetic moment of the atoms in the cluster estimated at about 20% larger than the bulk value. The experiment was insensitive to the spin configuration.

More recently the powerful XMCD technique has been utilized in deposited cluster experiments and as well as addressing the magnitude of the moment it is possible to obtain information on the separate contributions of the spin and orbital components. To gain some understanding of the effect of the interaction with the substrate it is useful to consider results from isolated atoms of Fe, Co, and Ni adsorbed on K and Na films obtained by Gambardella et al. [126]. They studied films with coverages as low as 0.2% of a monolayer and used the most accurately measured quantity obtainable by the XMCD technique, that is, the ratio (see Section 3)

$$R = \frac{\langle L_z \rangle}{2\langle S_z \rangle + 7\langle T_z \rangle} \quad (12)$$

to determine how “atomic-like” the adsorbed atoms were. The valence state of each element was determined by modelling the shape of the  $L_{2,3}$  absorption edge and was found to be  $d^7$  for Fe,  $d^8$  for Co, and  $d^9$  for Ni. Knowing this the quantities in Eq. (12) can be obtained by Hund’s rules and the atomic value of  $R$  ( $R_{\text{atom}}$ ) compared with the measured one ( $R_{\text{exp}}$ ). The ratio  $R_{\text{exp}}/R_{\text{atom}}$  was found to be 100%, 89%, and 63% for Ni, Co, and Fe respectively; that is, Ni has the same moments as in a free atom with the same valence while Co and Fe show a 10% and a 37% decrease respectively. The reductions are due to a partial quenching of the orbital moment but even in the case of Fe the quenching is much less than in isolated Fe impurities embedded in a bulk host.

Mass-selected  $\text{Fe}_N$  clusters with sizes  $N = 2-9$  adsorbed, at the dilute limit, on Ni thin film substrates have been studied by Lau et al. [127]. For such small clusters it is important to ensure a soft landing and this was achieved by depositing the clusters, decelerated to 2 eV/atom onto Ar multilayers that were physisorbed at 15 K on the substrate. These

were then removed by flash-heating to 100 K. Substantial increases in the orbital to spin ratio and the spin and orbital moments per valence band hole relative to the bulk were observed but uncertainty in  $n_h$  and the  $\langle T_z \rangle$  term meant that absolute values were not given. Larger clusters in the size range 180–690 atoms deposited at low coverage on graphite were studied using XMCD by Baker et al. [128]. In this study the value of  $n_h$  was obtained by comparing the total Fe  $L_{2,3}$  absorption cross section of the clusters with that of a thick conventional film deposited *in-situ* and was found to be the same within experimental uncertainty. Thus  $n_h$  could be taken as the bulk value of 3.39 [129]. In addition the  $\langle T_z \rangle$  term was obtained by measuring the dichroism as a function of the incident angle of the X-rays so absolute values of the magnetic moments were obtained and the total moment was found to be about 10% greater than the bulk value with about half of this enhancement coming from an increased orbital contribution.

The different datasets for adsorbed Fe atoms [126], small  $\text{Fe}_N$  ( $N = 1-9$ ) clusters [127], and large Fe clusters [128] can be compared directly by plotting the orbital ( $\langle L_z \rangle$ ) and spin ( $\langle S_z \rangle$ ) angular momenta per valence band hole,  $n_h$ , as is done in Figure 10. For the adsorbed Fe atoms on K, the valence state was identified as  $d^7$  so  $n_h = 3$  [126]. The orbital and spin moments for the isolated atoms shown in Figure 10 were derived from the published  $R$  value, assuming that most of the reduction in  $R$  is due to a partial quenching of the orbital moment. For the small clusters the published data for the orbital component,  $\langle L_z \rangle/n_h$ , can be entered directly on the plot. The spin term is given as  $\langle S_z \rangle + 7/2\langle T_z \rangle$  and the pure spin component has been extracted assum-

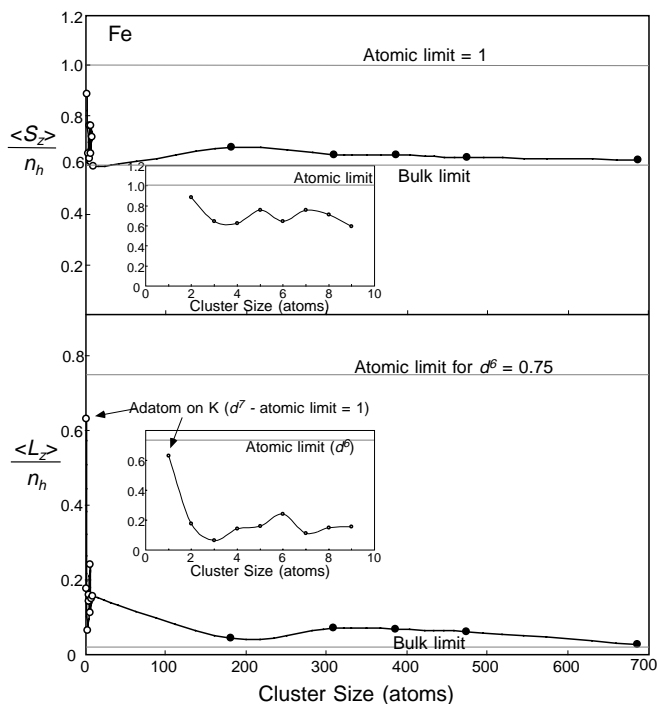


**Figure 10.** Angular momentum values  $\langle S_z \rangle$  and  $\langle L_z \rangle$  measured by XMCD for Fe clusters adsorbed on surfaces.  $\text{Fe}_1/\text{K}$  data from Gambardella et al. [126],  $\text{Fe}_1\text{--}\text{Fe}_9/\text{Ni}$  data from Lau et al. [127], and  $\text{Fe}_{180}\text{--}\text{Fe}_{690}/\text{HOPG}$  data from Baker et al. [128].

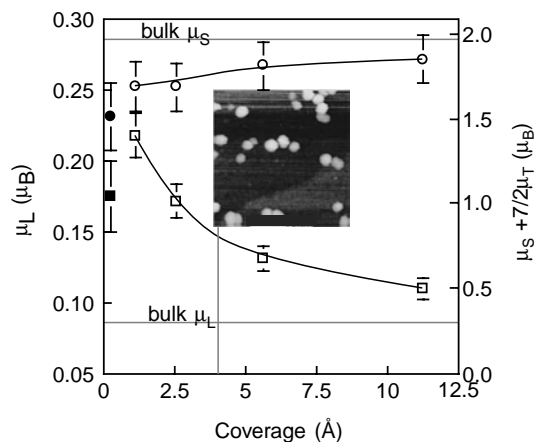
ing that  $\langle T_z \rangle$  is the average of the value in isolated atoms ( $-1/7$ ) and that in the larger deposited clusters ( $-0.11/7$ ) [128]. The  $\langle L_z \rangle/n_h$  and  $\langle S_z \rangle/n_h$  values for the larger clusters were obtained from the published orbital and spin magnetic moments and dividing by the value of  $n_h$  (3.39) measured during the experiment. Whatever the inaccuracies in the assumptions made in the comparison of the different datasets and notwithstanding the different substrates used in the experiments some general conclusions can be drawn from Figure 10 about the size-dependent magnetic behavior of supported Fe nanoclusters. Both the orbital and spin components decrease rapidly with cluster size and with only three atoms/cluster values close to the bulk value are found for both  $\langle L_z \rangle/n_h$  and  $\langle S_z \rangle/n_h$ . This is different from the behavior of free Fe clusters in which moments close to the atomic limit were found up to  $N = 12$ . There is evidence for short and long period oscillations in both moments as a function of size. Over a wide size range the total magnetic moment is about 10% larger than the bulk with about half of the enhancement coming from the orbital moment. The adsorbed cluster moments converge with the bulk values for  $N \geq 700$ , as observed in free clusters.

Ab initio calculations of the spin moment in small  $4d$  metal clusters with different geometries on Ag(100) were carried out by Wildbererger et al. [130]. While they found a permanent moment in dimers for elements between Mo and Rh in the periodic table, magnetism was less favored as the cluster size increased. In the case of the largest clusters studied (i.e., nine-atom flat islands), only Ru and Rh had stable moments. The Rh moment was  $0.6\mu_B$ , which compares with  $0.8\mu_B$  measured in nine-atom free Rh clusters [56].

## 6.2. Effect of Cluster-Cluster Interactions

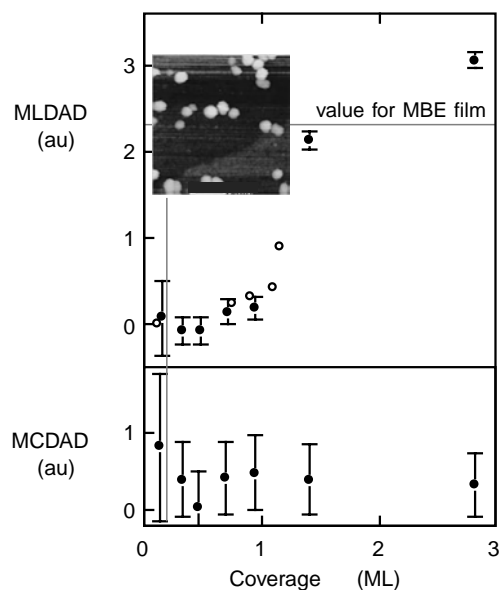
All the results presented are at the dilute limit when the clusters can be assumed to be noninteracting. As the density on a surface is increased the effect of the interaction between the clusters can be observed. Figure 11 shows how the orbital and spin moments, measured by XMCD, vary with coverage for unfiltered Fe clusters with a mean size of 600 atoms deposited on HOPG [14]. The coverage is expressed as the equivalent film thickness in  $\text{\AA}$  so for clusters of this size a complete monolayer corresponds to  $\sim 20 \text{\AA}$ . Also shown on the diagram (filled symbols) are the measured moments for a mass-selected deposit with the filter set to the mean value of the unfiltered distribution. It is evident that the orbital and spin values at low coverage in the filtered and unfiltered deposits are similar. With increasing coverage the orbital moment drops toward the bulk value as the clusters come into contact. The spin term increases but this is due to a decreasing contribution from the (negative)  $\mu_T$  (dipole) component as the film becomes more bulklike.

Figure 12 shows the development with cluster density of the remanence at 40 K of films produced by depositing unfiltered Fe clusters with a mean size of  $\sim 450$  atoms on Cu and HOPG substrates [61]. The data were obtained using magnetic linear and circular dichroism in the angular distribution of Fe  $3p$  photoelectrons (MLDAD and MCDAD) that measure, respectively, the in-plane and out-of-plane



**Figure 11.** Orbital (unfilled squares) and spin (unfilled circles) moments for unfiltered Fe clusters (mean size 600 atoms) deposited on HOPG as a function of cluster coverage expressed as the equivalent film thickness. The filled symbols are the values for a mass-filtered deposit with the filter central mass set to 600 atoms. An STM image at a coverage of approximately 0.2 cluster monolayers ( $4 \text{\AA}$ ) is shown. Reprinted with permission from [14], K. W. Edmonds et al., *Phys. Rev. B* 60, 472 (1999). © 1999, American Physical Society.

remanent magnetization. At this temperature, isolated clusters are superparamagnetic and will have zero remanence. The behavior is independent of substrate and for coverages below half a cluster monolayer, the MLDAD signal is zero within experimental error. A small but finite MLDAD signal



**Figure 12.** MCDAD (out-of-plane remanent magnetization) and MLDAD (in-plane remanent magnetization) signals as a function of coverage for unfiltered Fe clusters with an average size  $\sim 450$  atoms deposited on graphite (open circles) and Cu (filled circles). All measurements were at 40 K. The dense film shows an in-plane anisotropy with a remanence higher than a molecular beam epitaxy-grown film deposited *in-situ*. An STM image at a coverage of approximately 0.2 cluster monolayers is shown. Reprinted with permission from [61], K. W. Edmonds et al., *J. Appl. Phys.* 88, 3414 (2000). © 2000, American Institute of Physics.

is observed between 0.5 and 1 ML thickness, followed by a steep rise between 1 and 1.4 ML. No MCDAD signal is visible at 40 K at any coverage above the noise level.

As the coverage increases, the interactions between the clusters lead to a stabilization of the magnetization at 40 K. This, however, produces strong out-of-plane demagnetizing fields, and so the remanent magnetization of the sample is in-plane due to the coherent shape anisotropy of the film. At the highest coverage the remanence exceeds that of an Fe film of the same thickness grown *in-situ* with a conventional evaporator.

## 7. MAGNETISM IN EMBEDDED CLUSTERS

Co-depositing clusters and vapor from a conventional deposition source enables one to embed clusters with a known size distribution and a controlled volume fraction in a matrix of another material. The removal of the requirement to work *in-situ* allows a wide range of measurement techniques to be applied including conventional magnetometry.

### 7.1. Isolated Clusters—The Dilute Limit

A comprehensive magnetometry study of Fe and Co clusters deposited from the gas phase and embedded in co-deposited Ag films at very low volume fraction was carried out by Binns and Maher [131]. Magnetic isotherms measured in the plane of the surface, at temperatures 50–300 K, of unfiltered Fe clusters embedded with a 1% volume fraction in Ag are shown in Figure 13a (symbols). Each was fitted by a set of Langevin functions [Eq. (2)] with different moment values where the amplitude of each Langevin function was a fitting variable. Ten size bins were used in the range 0.5–8 nm and the average amplitude as a function of particle size (moment) after fitting all data sets is shown in the inset in Figure 13a. The calculated curves are displayed as lines and the fit is excellent in every case. The size distribution is the usual asymmetric shape and fitting it to a log-normal distribution (inset) gives a most probable cluster size of 2.57 nm with a standard deviation of 1.95 giving a median diameter of 3.0 nm. This distribution is similar to those obtained by direct STM imaging of deposited cluster films. It was pointed out by Allia et al. [132], however, that this procedure is hazardous. In an interacting system it is possible to obtain an excellent Langevin fit with an “apparent size” that is different from the real size and varies with temperature. Three conditions must be met to confirm ideal superparamagnetism with no interactions between the clusters:

- The isotherms should display no hysteresis.
- The isotherms should scale with  $H/T$ .
- The fitted size distribution should be independent of temperature.

The lack of hysteresis is evident and the other two conditions are demonstrated in Figure 13b, which is the data in Figure 13a replotted against  $H/T$  and an inset that shows the invariance with temperature of the median size obtained from the Langevin fits. This sample thus displays perfect superparamagnetism above 50 K.

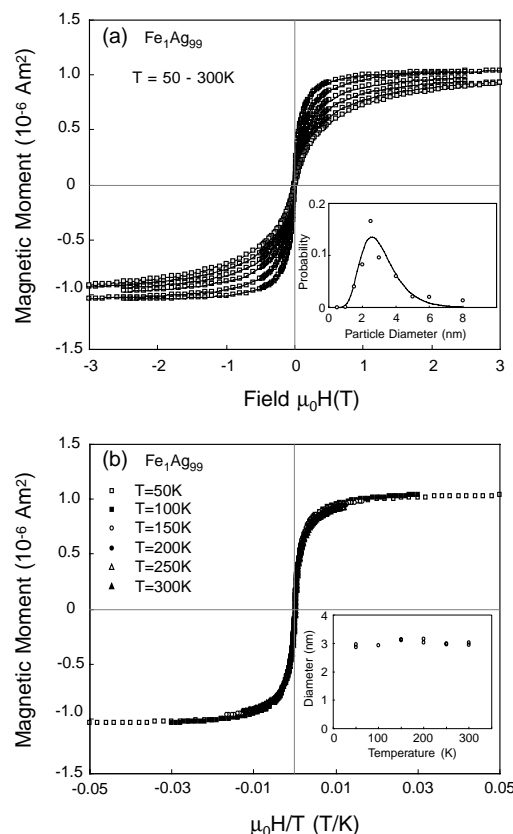


**Figure 13.** (a) Magnetization isotherms in the range 50–300 K of  $\text{Fe}_1\text{Ag}_{99}$  (open squares) compared to fits by Langevin functions (lines) with a size distribution represented by 10 size bins in the range 0.5–8 nm. The inset shows the average probability of each bin for the optimum fit to curves at temperatures  $> 50$  K ( $\circ$ ) and the corresponding log-normal distribution (line) with  $d_{\text{max}} = 2.57$  nm and  $\sigma = 1.95$ . (b) The same data plotted against  $H/T$  showing the scaling predicted by the Langevin functions. The inset shows the median size from the distributions as a function of temperature and demonstrates the invariance of the fitted size vs  $T$  required for an ideal superparamagnetic system. Reprinted with permission from [131], C. Binns and M. J. Maher, *New J. Phys.* 4, 85.1 (2002). © 2002, IOP Publishing.

The magnetic isotherms measured in the plane of the surface at temperatures 50–300 K of unfiltered Co clusters embedded with a 2% volume fraction in Ag [131] are shown in Figure 14a (symbols) along with the Langevin fits using the procedure already described (lines). In this case the fitted median size displayed in the inset in Figure 14b is temperature-dependent below about 150 K. This could either be due to weak dipolar interactions at the slightly higher volume fraction [132] or to the higher anisotropy of the Co clusters relative to Fe requiring a higher temperature to reach the superparamagnetic limit. In either case the superparamagnetic limit is reached at a temperature  $\sim 150$  K. This is also demonstrated in Figure 14b in which the same data are plotted against  $H/T$  and only the 100 and 50 K curves are visibly separated from the rest. The size distribution obtained by Langevin fits as described above to the curves taken at 150 K and above along with the fitted log-normal distribution is shown in the inset in Figure 14a.

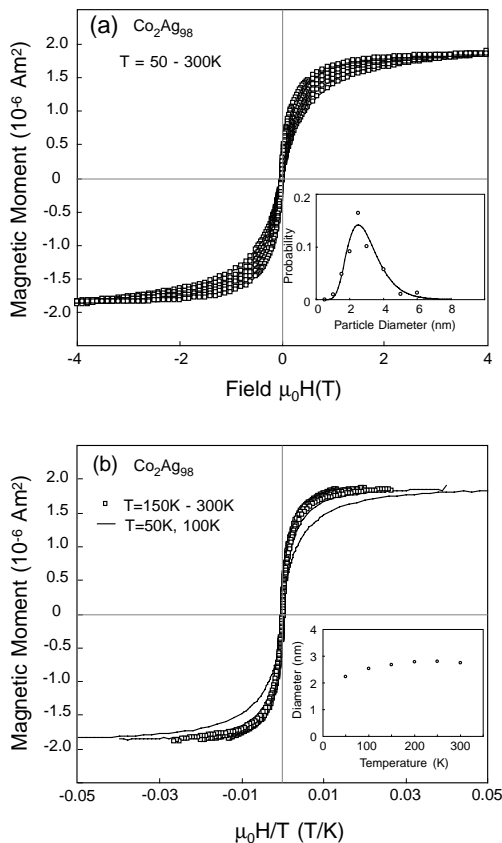


**Figure 14.** (a) Magnetization isotherms in the range 50–300 K of  $\text{Co}_2\text{Ag}_{98}$  (open squares) compared to fits by Langevin functions (lines) with a size distribution represented by 10 size bins in the range 0.5–8 nm. The inset shows the average probability of each bin for the optimum fit to curves at temperatures >150 K (○) and the corresponding log-normal distribution (line) with  $d_{\text{max}} = 2.45$  nm and  $\sigma = 1.81$ . (b) The same data plotted against  $H/T$  showing the scaling predicted by the Langevin functions for data in the range 150–300 K (open squares). The data at 100 and 50 K (line) show a departure from the scaling law. The inset shows the fitted median size as a function of temperature and demonstrates that the apparent size becomes temperature-invariant (the true size) above 150 K. Reprinted with permission from [131], C. Binns and M. J. Maher, *New J. Phys.* 4, 85.1 (2002). © 2002, IOP Publishing.

For the Co clusters the most probable size is 2.45 nm with a standard deviation of 1.81 giving a median diameter of 2.8 nm.

At 2 K most of the clusters in the  $\text{Fe}_1\text{Ag}_{99}$  sample discussed above are below the blocking temperature and as shown in Figure 15a the magnetic isotherm develops hysteresis [131]. The remanence,  $M_r$ , of an assembly of blocked particles reveals the symmetry of the anisotropy axes and their distribution in space. For example uniaxial anisotropy axes randomly distributed over three dimensions give  $M_r/M_s = 0.5$  but if they are distributed over two dimensions (2D) in the plane of the applied field,  $M_r/M_s = 0.71$ . The equivalent values for cubic anisotropy axes are 0.82 distributed over 3D and 0.91 distributed over 2D. The measured remanence is  $\approx 0.4$  and is thus closest to the case for uniaxial anisotropy axes randomly distributed over 3D. In this case the magnetization between saturation and

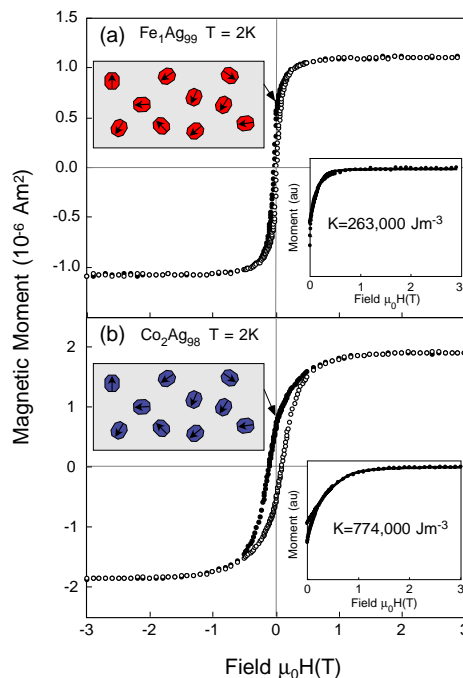


**Figure 15.** (a) Magnetization isotherms at 2 K of  $\text{Fe}_1\text{Ag}_{99}$  sample: (●) field sweeping down, (○) field sweeping up. The inset shows the decay from saturation (●) compared to a calculation (line) assuming a random distribution of uniaxial anisotropy axes [Eq. (13)]. The best fit anisotropy constant is displayed in the inset. (b) As (a) but for  $\text{Co}_2\text{Ag}_{98}$ . Reprinted with permission from [132], C. Binns and M. J. Maher, *New J. Phys.* 4, 85.1 (2002). © 2002, IOP Publishing.

remanence is obtained at each field value by minimizing over all alignments of the anisotropy axes the intraparticle energies

$$E_\phi = KV \sin^2(\phi - \theta) - \mu_B \cos \phi \quad (13)$$

where  $K$  is the anisotropy constant,  $V$  is the particle volume, and  $\theta$  and  $\phi$  are the angles between the applied field and the anisotropy axis and particle magnetization vector respectively. The inset in Figure 15a compares the curve calculated thus with the data and it is evident that this simple model reproduces the data accurately. So in zero field the system is a collection of static, randomly aligned cluster giant moments each pointing along the local anisotropy axis. The anisotropy constant is a parameter of the fit and optimizes at  $K = 2.63 \times 10^5 \text{ J m}^{-3}$ , which is in reasonable agreement with the value of  $K = 2.3 \times 10^5 \text{ J m}^{-3}$  obtained by a SQUID measurement of a similar sample [133] and is about 5 times the bulk value. As discussed next a more detailed study of cluster anisotropy by Jamet et al. [75] showed that the magnetocrystalline term is a small component of the total measured value. A uniaxial anisotropy of the individual clusters is expected as it will be produced by any incomplete atomic shell. Only clusters containing magic numbers of atoms are expected to have a cubic anisotropy but even in this case it is likely to be lost due to other processes during deposition such as collision with the substrate.

The blocking temperature,  $T_b$ , of a cluster with a volume  $V$  and anisotropy constant  $K$  is given by

$$T_b = \frac{KV}{k_B \ln(\tau_{\text{exp}}/\tau_0)} \quad (14)$$

where  $\tau_{\text{exp}}$  is the measurement time ( $\sim 100$  sec for dc magnetometry) and  $\tau_0$  is the lifetime due to the natural gyro-magnetic frequency of the particles. A measurement of Fe nanocluster with a similar size distribution embedded in Ag yielded  $\tau_0 = 10^{-8}$  s [133] so for the Fe particles having the median size (3 nm) in the  $\text{Fe}_{10}\text{Ag}_{90}$  sample, with the anisotropy constant shown in Figure 15a, a value of  $T_b = 8.5$  K is obtained. At 2 K clusters with a diameter less than 1.4 nm, or about 5% of the distribution shown in the inset in Figure 13a, are unblocked explaining in part the observation of a remanence less than 0.5.

The magnetic isotherms were found to be almost isotropic but a slightly higher anisotropy constant was found by fitting Eq. (13) to the out-of-plane data. This was interpreted as a slight shape or stress anisotropy resulting from the deposition onto the surface. The coherent in-plane anisotropy of the cluster film was estimated to be  $\sim 9 \times 10^3 \text{ J m}^{-3}$  [131].

The isotherms at 2 K of the dilute Co cluster sample are shown in Figure 15b. Again the remanence is slightly less than 50% and assuming the clusters are randomly oriented over 3D and have a uniaxial anisotropy the approach to saturation can be modelled using Eq. (13). This is compared to the data in the inset in Figure 15b and the anisotropy constant obtained is over three times larger than that found in the Fe cluster assembly giving a blocking temperature of  $\sim 20$  K. The larger blocking temperature will require a higher temperature than Fe clusters to obtain superparamagnetism as already observed.

Jamet et al. [75] provided yet more detail on the isolated properties of embedded nanoparticles by using the  $\mu$ -SQUID technique (Section 3) to determine the three-dimensional switching field distribution of a single Co nanoparticle containing about 1000 atoms embedded in Nb. The data could be fitted by the Stoner–Wohlfarth model [6] with the anisotropy constants:  $K_1 = 2.2 \times 10^5 \text{ J m}^{-3}$  along the easy direction,  $K_2 = 0.9 \times 10^5 \text{ J m}^{-3}$  along the hard direction and a fourth order term, and  $K_4 = 0.1 \times 10^5 \text{ J m}^{-3}$ . By estimating the contributions from shape and magnetoelastic terms they concluded that the main source of anisotropy in the particle was the surface anisotropy term described by Néel [134] with the fourth order term corresponding to the magnetocrystalline anisotropy.

An XMCD study of Co clusters assembled at low volume fraction in Cu matrices was carried out by Eastham and Kirkman [18] who measured an orbital magnetic moment 2.2 times larger than the bulk value—a similar enhancement to that found in exposed Fe clusters (Section 5). By a careful analysis of the orbital to spin ratio as a function of the applied field, they were able to show that the atomic spin direction is determined only by the external field and the surface anisotropy, which again highlights the importance of this term in determining the cluster magnetization.

As pointed out earlier, one of the most important advantages of cluster assembly is the ability to prepare granular films of miscible materials and thus magnetic grains can be

studied in a magnetic matrix. Baker et al. [128] used MXCD to measure the orbital and spin moments in mass-selected Fe clusters coated with Co. As discussed in Section 3 XMCD can focus on the orbital and spin values within specific elements and they found that the Co coating increases the total magnetic moment within the Fe particles to a value similar to that found in free Fe clusters. This was due to a large increase in the spin moment as also observed in Fe–Co alloys and within a rigid band model is ascribed to an increase in the majority spin band population by electrons from the Co [135]. In the case of the cluster-assembled film there is not a well mixed alloy although there may be alloying at the interface [16]. In addition, no significant change was observed in the total Fe  $L$ -edge X-ray absorption (“white line”) intensity indicating that there is no significant change in the number of Fermi level  $d$ -band holes in the Fe. The increase in the spin moment was attributed to an increase in the Fe valence band exchange splitting produced by the interaction with the Co.

## 7.2. Interacting Cluster Films

Developing a detailed understanding of the effect of interactions between clusters embedded at higher volume fractions is important not only to satisfy scientific curiosity but also in order to fully exploit such systems in the development of high performance magnetic materials, for example high-moment films (see next section). In such applications the required volume fraction of nanoparticles is close to or above the percolation threshold and is well into the strong interaction regime. When the interparticle interactions become significant the system displays a rich variety of magnetic configurations resulting from competing energy terms. The dipolar interaction introduces frustration as it is impossible to produce an optimum alignment for every particle. In addition there is frustration resulting from the competition between the interparticle dipolar and exchange terms and the intraparticle anisotropy energy (magnetocrystalline, shape, magnetoelastic, etc.) that requires the magnetization vector to be aligned along specific axes in each particle.

A thorough investigation of Fe clusters assembled in Ag matrices at volume fractions from the dilute limit to pure cluster films with no matrix was carried out by Binns et al. [74]. Below the percolation threshold (volume fraction  $< 30\%$ ) a Curie–Weiss-like extension to superparamagnetism developed by Allia et al. [132] was used to analyze the magnetic isotherms. It was found that the films could be described in terms of cluster aggregates, in which the individual nanoclusters were exchange-coupled. For example in a film with a 10% volume fraction of Fe clusters, a typical aggregate would consist of 6–7 of the deposited nanoclusters. These aggregates would behave as a single particle and would interact with each other by dipolar forces.

With a further increase in volume fraction up to the pure cluster limit, the magnetic configuration in the film at 300 K becomes a correlated superspin glass [74, 131]. This state is illustrated in Figure 16c and results from the random anisotropy whose length scale is that of a single nanocluster. The exchange coupling between adjacent clusters tries to align their moments but perfect alignment is prevented



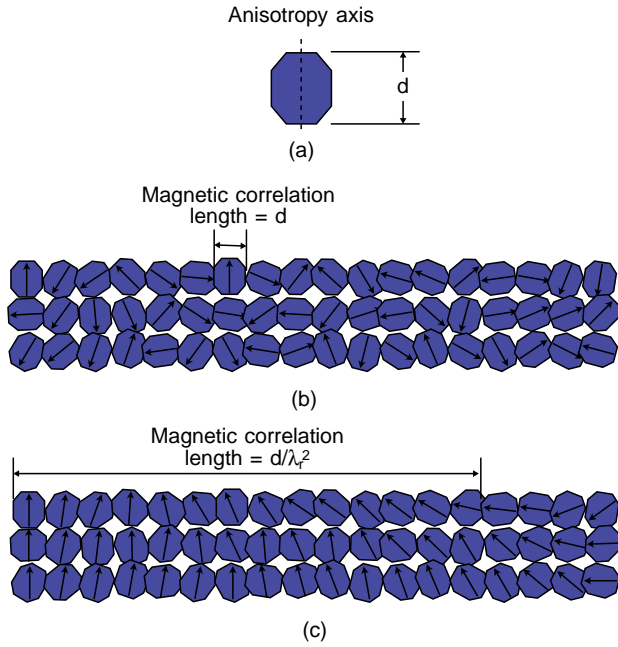


**Figure 16.** (a) Schematic representation of a magnetic nanoparticle with a uniaxial anisotropy axis (represented by a slight elongation). (b) and (c) A stack of particles with randomly oriented anisotropy axes. In (b)  $\lambda_r \geq 1$  and the magnetization vector points along the local anisotropy axis so the magnetic correlation length is a single particle diameter. In (c)  $\lambda_r < 1$  and the magnetic vectors are nearly aligned. The random perturbation from perfect alignment results in a finite magnetic correlation length that is a factor  $1/\lambda_r^2$  larger than a single particle. Reprinted with permission from [131], C. Binns and M. J. Maher, *New J. Phys.* 4, 85.1 (2002). © 2002, IOP Publishing.

by the random direction of the anisotropy axes of neighboring clusters. This produces a small randomized canting of adjacent spins resulting in a loss of magnetic order after a sufficient number of clusters. Thus there is a mesoscopic magnetic correlation length that is much greater than a single cluster diameter. At high volume fractions the magnetic isotherms were analyzed using a random anisotropy (RA) model developed by several authors in the last two decades [136–139]. In the RA formalism, the magnetic ground state in a granular film is determined by the relative strength of a random anisotropy field

$$H_r = \frac{2K_r}{M_s} \quad (15)$$

and an exchange field

$$H_{\text{ex}} = \frac{2A}{M_s R_a^2} \quad (16)$$

where  $K_r$  is the (randomly oriented) anisotropy of the grains,  $M_s$  is their saturation magnetization,  $A$  is the exchange constant for the interaction between the grains, and  $R_a$  is the nanometer sized region over which the local anisotropy axis is correlated (i.e., the characteristic grain

size). Their relative strength is given by the dimensionless parameter

$$\lambda_r = \frac{H_r}{H_{\text{ex}}} = \frac{K_r R_a^2}{A} \quad (17)$$

The model was developed to describe amorphous films in which a local, randomly oriented anisotropy is due to local atomic order. It is even better suited to providing a description of the magnetization in cluster-assembled films in which the distance  $R_a$  over which an anisotropy axis is correlated is well defined (i.e., the particle diameter). In addition, as pointed out by Löffler et al. [140], the exchange interaction at the boundaries between particles is weaker than the intraparticle atomic exchange further reinforcing the image of separate but interacting particles.

For  $\lambda_r > 1$  the magnetic correlation length at zero field is  $R_a$ , and the magnetic vector in each particle points along the local intraparticle anisotropy axis. Note that in an arrow representation this state would be identical to that in isolated noninteracting particles at absolute zero. This regime is illustrated in Figure 16b. With increasing interparticle exchange (or decreasing intraparticle anisotropy) the configuration becomes a correlated superspin glass (CSSG) in which the magnetization vector in neighboring particles is nearly aligned but the random deviation of the moments from perfect alignment produces a smooth rotation of the magnetization throughout the system with a magnetic correlation length that is a factor  $1/\lambda_r^2$  larger than the particle diameter. This regime is illustrated in Figure 16c. The disordered CSSG state is fragile and application of a small field produces a “ferromagnet with wandering axes” [137] with an approach to saturation that follows a  $1/\sqrt{H}$  dependence in three dimensions [137] and a  $1/H$  dependence in two dimensions [136]. These both change to a  $1/H^2$  dependence above a crossover field [139]  $H_{\text{co}} = 2A/M_s R_a^2$ .

Other studies of pure Fe and Ni cluster-assembled films have used the RA model to analyze magnetization data from cluster-assembled films [140–142]. The magnetic configuration could be described as a CSSG in all cases. This is an important find for technological applications as it shows that dense interacting cluster assemblies are magnetically soft.

Binns et al. [131] found that at 300 K, films with an Fe volume fraction  $>70\%$  formed CSSGs but at 2 K, for all volume fractions, Fe cluster assemblies coated with Ag were in the random magnetization state depicted in Figure 16b. Thus at a sufficiently low temperature the anisotropy dominates the exchange coupling and the magnetization at zero field in each nanocluster is forced to lie along the local anisotropy axis. This is the state predicted by the RA model for  $\lambda_r > 1$ . The increase in anisotropy at low temperature was ascribed to magnetoelastic stress induced by the different expansion coefficients of the Fe cluster film and the Ag capping layer. This analysis was supported by the observation that uncapped pure cluster samples transferred into the magnetometer in UHV, as described in Section 3, did not undergo the transition to the random cluster magnetization at low temperature and remained in the CSSG state all the way down to 2 K [74, 131]. A summary of the behavior of Fe cluster assemblies embedded in Ag is provided by the phase diagram shown in Figure 17 [74].

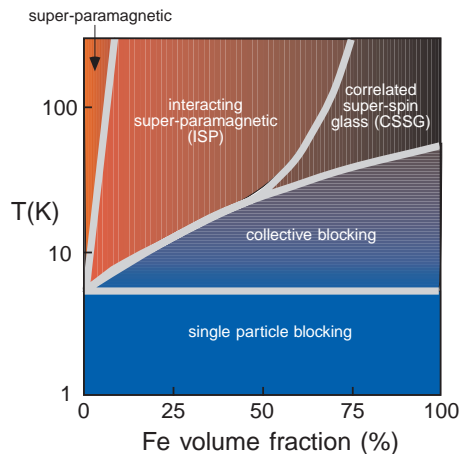


**Figure 17.** Magnetic phase diagram of Ag-capped Fe nanoclusters (3 nm diameter) assembled in Ag matrices.

## 8. APPLICATIONS OF CLUSTER-ASSEMBLED FILMS

In this section examples of technological applications that exploit the flexibility in the control of magnetic properties afforded by assembling films from nanoclusters will be described.

### 8.1. High-Saturation-Moment Materials

One of the important advantages of the cluster deposition technique in the creation of artificial materials is its ability to make granular mixtures of even the most miscible metals. For example a study using extended X-ray absorption fine structure (EXAFS) has shown [21] that for Co clusters embedded in Pt, alloying is limited to a single atomic layer at the interface leaving a pure core of Co within the grains. The same result was found for Co clusters embedded in a Nb matrix [143]. For Fe clusters embedded in a Co film, XMCD data show that the number of Fe 3d holes per atom is indistinguishable from the bulk demonstrating that the grains consist mainly of pure Fe with intermixing confined to the particle surfaces [16]. Creating granular mixtures of miscible materials is important for the creation of new magnetic materials.

A prized discovery would be a substance that had a saturation magnetization density greater than conventional  $\text{Fe}_{70}\text{Co}_{30}$  alloy (permendur)—the most magnetic material available today. This would be an important find for a wide range of technologies and most immediately for the magnetic recording industry. The conventional alloy has a magnetic moment per atom of  $2.45\mu_B$ , which is 10% greater than bulk Fe. Free Fe nanoparticles can have magnetic moments up to  $5.4\mu_B$  per atom in the case of  $\text{Fe}_{12}$  (see Fig. 7) but these reduce significantly when the clusters are deposited on a surface (see Fig. 10) and drop further toward the bulk value when the particles are brought into contact to make a film [14]. On the other hand it has been shown that coating the supported Fe nanoclusters with Co restores the magnetic moment back to the free cluster value [128]. The results are displayed in Figure 18, which shows the spin moment

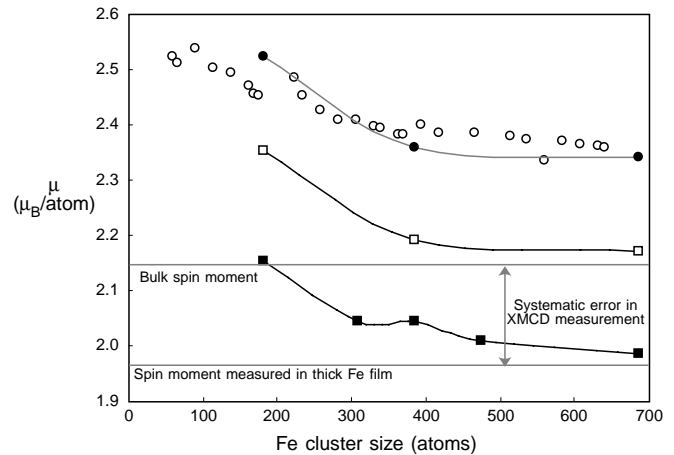


**Figure 18.** Variation of the spin moment with cluster size in exposed Fe clusters on HOPG (filled squares), Co-coated Fe clusters on HOPG (open squares), and the calculated spin moments for free Fe clusters coated with Co [144]. Also shown is the spin moment measured by XMCD in a conventional Fe film deposited *in-situ* and the accepted spin moment for bulk Fe. Correcting the measured spin moments in the Co-coated clusters by the discrepancy gives the values shown by the filled circles.

in  $\mu_B/\text{atom}$  of exposed (filled squares) and Co-coated (open squares) Fe clusters on HOPG as a function of size. The data reveal that the enhanced spin moments measured in the exposed clusters relative to that in a conventional Fe film deposited *in-situ* are increased further by about 10% after coating with Co. Also shown in Figure 18 are the values of the spin moments in  $\text{Fe}_n\text{Co}_{1021-n}$  clusters, composed of a pure Fe core coated with Co, as a function of  $n$  calculated by Xie and Blackman [144] (open circles). These are higher than the measured values but as discussed in Section 6, even after accounting for the  $\langle T_z \rangle$  term, XMCD measurements of spin moments have systematic errors due to uncertainties in the number of valence band holes,  $n_h$ , and inaccuracies in applying the magneto-optical sum rules [63, 64] to solid state systems. In addition XMCD is insensitive to any spin polarization of the  $s$ - $p$  electrons, which is included in the calculation. An estimate of the systematic error in this particular experiment can be obtained by comparing the spin moment measured in a conventional Fe film under the same experimental conditions to the accepted bulk Fe spin moment. Shifting the measured values for the Co-coated Fe clusters by this difference yields the values shown by the filled circles, which agree well with the calculation. This procedure is, however, insecure since all the sources of error (e.g.,  $n_h$ ,  $s$ - $p$  spin polarization, etc.) are different in the clusters to the bulk. Clearly however, XMCD underestimates the spin moment and coating the Fe clusters with Co substantially increases their spin moment. The orbital moment averages  $0.16\mu_B$  over the size range shown [128] and adding this to the data gives a total magnetic moment of  $2.7\mu_B/\text{atom}$  in 100-atom Fe clusters coated with Co.

Thus embedded Fe cluster assemblies in Co matrices hold real promise for creating a new material with a record magnetization density. This depends to some extent on the value of the Co moment but with a high volume fraction of the Fe grains, the Co matrix itself will be in the form of

nanoscale grains in which moments as high as  $2.3\mu_B$  have been observed [145]. Interestingly the calculation by Xie and Blackman [144] revealed a further increase in the spin moment if a degree of Fe–Co intermixing at the interface was included. This suggests that a moderate heat treatment of the cluster-assembled Fe–Co films could yield higher moments. As pointed out in the previous section, dense interacting cluster assemblies are magnetically soft and thus would be valuable in applications such as write heads where a strong local controllable field is required.

## 8.2. High Anisotropy Binary Clusters

The ultimate limit of magnetic recording is defined by storage on individual single-domain particles. For example if these were 5 nm particles separated in both directions by 10 nm, the density would be 1000 Gbits/cm<sup>2</sup>, or about 1000 × the storage density in modern hard disk drives. Leaving aside the technical problem of making organized arrays of the particles over macroscopic areas or exactly how to read and write there is the more fundamental problem that transition metal particles of this size are superparamagnetic at room temperature. In order to realize this next level of technology it is necessary to create nanoparticles with a sufficiently high anisotropy to be blocked at room temperature. A promising avenue is the use of transition metal/rare-earth mixtures as reported by Negrier et al. [146] who made SmCo clusters by using a SmCo<sub>5</sub> target in their laser evaporation source. Measurements using X-ray photoelectron spectroscopy (XPS) of the deposited films showed that although the stoichiometry of the target was preserved, the Sm was in the form of Sm<sub>2</sub>O<sub>3</sub> while the Co was pure. The most likely arrangement is that the Sm oxide forms a skin around a pure Co core. Despite the lack of elemental mixing within the clusters, a significant increase in the coercivity was observed relative to pure Co clusters in a Ag matrix with a corresponding increase in the blocking temperature from 25 to 45 K. Further increases can be expected with improved control of the mixing within the cluster by, for example, using sources with two targets.

Any recording application using clusters requires that the clusters be organized into regular arrays over macroscopic length scales. Large-scale self-organization remains one of the holy grails of nanotechnology and several promising techniques have been demonstrated in the case of atomic deposition. Recently Perez et al. [147] demonstrated the formation of organized arrays using deposited Au nanoclusters on functionalized graphite substrates that had been patterned using a focused ion beam. A careful study of all the growth parameters showed that it was possible to obtain conditions where every cluster was at a defect site with none in between. Although it is impossible to obtain a condition where every defect contains a single cluster it is possible to have every defect site contain a small group of clusters. If these were magnetic they would be exchange coupled and act as a storage bit.

## 9. CONCLUSION

This chapter has tried to demonstrate the enormous benefit of studying magnetic nanoclusters in understanding the fundamental magnetic behavior of matter. Addressing this

borderland between the atom and the bulk requires the development of a deep understanding of the electronic and magnetic properties of materials and how they are influenced by atomic structure. It is also clear that films made from deposited clusters will form an important class of materials in future technologies.

## GLOSSARY

**Amorphous material** A solid material in which the atoms are not arranged on a crystal lattice but are distributed randomly, as in a snapshot of a liquid structure.

**Anisotropy boundary (or barrier)** The energy barrier separating two different alignments of the magnetization in a solid.

**Anisotropy energy** The energy associated with a specific alignment of the magnetization.

**Antiferromagnetic material** A material containing magnetically ordered atoms in which there are equal numbers of atoms with their magnetizations pointing in opposite directions so the material presents no external magnetic field.

**Atomic number** The number of protons in an atom of the element showing its position in the periodic table.

**bcc lattice** Body-centered cubic lattice. A crystal lattice consisting geometrically of a stack of cubes in which the atoms are arranged in the corners of the cubes with an additional atom at the center of each cube.

**Blocking temperature** The temperature below which a nanocluster has a static non-fluctuating magnetization.

**Bond length** The distance between atoms in a solid.

**Cohesive energy** The difference in energy between N atoms as isolated atoms and the same atoms bound in a cluster.

**Correlated super-spin glass (CSSG)** A magnetic configuration in a solid built out of nanoclusters in which the magnetization of neighboring clusters is approximately aligned but over a larger distance becomes uncorrelated.

**Curie temperature** The temperature above which the atoms in a ferromagnetic material become magnetically disordered.

**Density of states** The number of allowed (electron) states per unit energy interval.

**Dimer** Two atoms bonded into a pair.

**Dipolar interaction** The classical long-range interaction between magnetic dipoles (*see also* exchange interaction).

**Domain boundary** The boundary between two magnetic domains in a magnetic material.

**Electronic shell** The allowed electron states contained within a specific pair of allowed values of the principal ( $n$ ) and angular momentum ( $l$ ) quantum numbers. The number of electrons in a shell is determined by the number of allowed values of the remaining magnetic ( $m_l$ ) and spin ( $m_s$ ) quantum numbers within the specific ( $n, l$ ) pair.

**Extended X-ray absorption fine structure (EXAFS)** The ripples in X-ray absorption strength for photon energies greater than an X-ray absorption edge (*see* X-ray absorption edge) resulting from inter-atomic X-ray scattering.

**Exchange interaction** A short range (atomic scale) magnetic interaction between two atomic electrons arising from the difference in energy produced by reversing the spin quantum number of one of the electrons. The interaction has no classical analogue and at the range of atomic separations is much more powerful than the classical dipolar energy.

**fcc lattice** Face centered cubic lattice. A crystal lattice consisting geometrically of a stack of cubes in which the atoms are arranged in the corners of the cubes with additional atoms at the center of each of the faces of the cubes.

**Fermi level** The energy of the highest filled electron state in a solid.

**Ferrimagnetic material** Magnetic material containing magnetically ordered atoms with their magnetic moments pointing in different directions but in which there is a net imbalance of the magnetization in one direction.

**Ferromagnetic material** Magnetic material containing magnetically ordered atoms in which the magnetic moments of all the atoms within a magnetic domain are aligned.

**Fractal** Object with a structure that repeats on smaller and smaller scales and which can be defined to have a non-integer dimensionality.

**Giant magnetoresistance (GMR)** Anomalously large variation in electrical resistance as a function of applied magnetic field found in nanostructured magnetic materials.

**Hall Probe** An instrument using the Hall effect, i.e. the voltage developed across a current-carrying conductor on application of a magnetic field, to measure the magnetization of a material.

**Hartree-Fock (also tight binding)** A scheme for calculating electronic states by summing over atomic orbital basis sets.

**hcp** A crystal structure consisting geometrically of a stack of planes in which each has atoms ordered in a hexagonal structure.

**Helical undulators** An insertion device in an electron storage ring which induces a helical distortion in the electron orbit to produce circularly polarized synchrotron radiation.

**Hysteresis** Process in magnetic materials whereby the magnetization depends not only on the existing applied field but also on the magnetization history of the sample.

**Icosahedron** Twenty-sided body. Particularly stable structure often found in small atomic clusters.

**Inert (or rare) gas** One of the gases He, Ne, Ar, Kr, Xe, Rn containing only filled electronic shells making them particularly unreactive.

**Isomer** Alternative structure containing the same number of atoms.

**Laser ablation** Process where material is evaporated from a target by an incident high power laser.

**Macroscopic quantum tunneling** The process of quantum tunneling, i.e., the transition of a quantum particle through an energy barrier that is forbidden in a classical system, in objects that are much larger than a single atom.

**Magic number** A number of atoms in a cluster that forms a particularly stable structure.

**Magnetic anisotropy** The tendency of the magnetization in a magnetic material to be aligned along specific directions as a result of a minimum in the anisotropy energy.

**Magnetic correlation length** The distance over which the direction of magnetization in a magnetic material is aligned.

**Magnetic domain** Mesoscopic region in a magnetic material over which the atomic magnetic moments are aligned. A magnetic material tends to form domains since this produces a lower energy configuration than having all atoms in the sample magnetized in the same direction.

**Magnetic isotherms** The magnetization versus applied field curve for a magnetic material obtained at a specific temperature.

**Magnetic precession** The rotation of a magnetic moment in response to an applied magnetic field.

**Magnetocrystalline anisotropy** The magnetic anisotropy due to the crystal structure of a magnetic material producing a minimum in the anisotropy energy along certain crystallographic directions.

**Magnetoelastic etc anisotropy** The magnetic anisotropy arising from strain along a particular direction in the material.

**Magnetic circular dichroism in the angular distribution (MCDAD)** The variation in the intensity of photoemission along a particular direction arising from a change in the relative alignment of the sample magnetization and the angular momentum of the incident radiation.

**Mesoscopic** A length scale that is large compared to atomic dimensions but small compared to macroscopic sizes. A typical mesoscopic size is of the order of 1  $\mu\text{m}$ .

**Magnetic linear dichroism in the angular distribution (MLDAD)** The variation in the intensity of photoemission along a particular direction arising from a change in the relative alignment of the sample magnetization and the linear polarization of the incident radiation.

**Monolayer** A single layer of atoms adsorbed on a surface.

**Monomer** A single isolated atom.

**Monte Carlo simulation** A calculation scheme for systems of large numbers of particles where the evolution of the system is followed by allowing random steps of the particles and determining the lowest energy configuration at each step.

**Nanocluster (or cluster)** A small cluster of atoms typically containing 10–1000 atoms (1–3 nm diameter).

**Nanostructure** A generic name for a structure that is a few nm across. Includes nanoclusters, islands formed by depositing atoms on surfaces, monolayers, etc.

**Neel temperature** The temperature above which the magnetic moment of the atoms in an antiferromagnetic material become disordered.

**Orbital moment** The magnetic moment in an atom arising from the orbital motion of the atoms around the atomic nucleus.

**Paramagnetic material** Material displaying no magnetic order of its constituent atoms but which acquires a magnetization in the same direction as an applied magnetic field.

**Percolation threshold** The volume fraction of grains in a granular material at which there is at least one continuous

pathway through touching particles from one side of the sample to the other.

**Photoemission (or photoelectron spectroscopy)** The emission of electrons from a surface resulting from the application of ultra-violet light with a photon energy greater than the electron work function.

**Photon spin** The angular momentum of circularly polarized light.

**Quantum dots** Nanostructure whose dimensions are of the same order as the electron wavelength in all three directions. In such devices the electrons are bound to the structure as a whole with corresponding energy levels.

**Quantum wires** A very narrow strip whose width is of the same order as the electron wavelength in two dimensions but is macroscopic in the third dimension.

**Remanence** The magnetization remaining after a magnetic field has been applied to a ferromagnetic material and then removed.

**Rotational temperature** The temperature associated with the rotation of a nanocluster.

**Saturating (or saturation) field** The magnetic field required to produce magnetic saturation in a ferromagnetic material.

**Saturation** A state in a ferromagnetic material in which all the atomic magnetic moments are pointing in the same direction.

**Shape anisotropy** Magnetic Anisotropy produced resulting from any non-spherical shape of a sample.

**Single-domain particles** A piece of magnetic material that is too small (typically <100 nm) for the formation of domains to be energetically favorable. In such a particle the atomic magnetic moments are all aligned so there is magnetic saturation without an applied magnetic field. The particle magnetic moment direction in nanoclusters however may be fluctuating except at very low temperatures.

**Spin moment (or spin)** The magnetic moment in an atom arising from the intrinsic angular momentum (spin) of the electrons.

**Spin sublattice** The crystal lattice in an antiferromagnetic material containing atoms whose spin is in the same direction.

**Sputtering** Process where atoms are ejected from the surface of a solid as a result of bombardment by energetic ions.

**Superconducting quantum interference device (SQUID)** A device that measures the magnetization in a sample by measuring oscillation in the current flowing through a bridge of normal material between two superconductors. The device is the most sensitive magnetometer available.

**Scanning tunneling microscopy (or microscopy) (STM)** Device or process in which nanostructures on a surface are imaged by measuring the variation in a tunneling current between the surface and an atomically sharp tip brought to within a few atomic dimensions of the surface.

**Superparamagnetism** The magnetic behavior of a collection of single-domain particles above the blocking temperature of the individual particles. The magnetization of each particle fluctuates as a whole but the assembly can be magnetized in the same direction by an applied magnetic field.

**Synchrotron storage ring** Machine in which a high energy electron beam is constrained to move in an orbit. The electrons emit synchrotron radiation in the process that covers wavelengths from the infra-red to X-rays. The machines are used as source of intense radiation for experiments.

**Ultra-high vacuum (UHV)** A vacuum of the order of 10<sup>-10</sup> m bar or better that is required in order for a surface to remain atomically clean during an experiment.

**Valence shell** The most energetic electronic shell in an atom.

**Vibrational temperature** Temperature associated with the atomic vibration in a nanoparticle (see also rotational temperature).

**X-ray magnetic circular dichroism (XMCD)** The change in the spectral intensity of an X-ray absorption edge in response to changing the relative alignment between the sample magnetization and the photon spin of the incident X-rays.

**X-ray absorption edge** The vast change in X-ray absorption strength as the photon energy of X-rays incident on a sample is tuned through the energy difference between a core electron binding energy and the Fermi level.

## REFERENCES

1. R. E. Dunin-Borkowski, M. R. McCartney, M. Posfai, R. B. Frankel, D. A. Bazylinski, and P. R. Buseck, *Eur. J. Mineral.* 13, 671 (2001).
2. K. L. Thomas-Keprta, C. J. Clemett, D. A. Bazylinski, J. L. Kirschvink, D. S. McKay, S. J. Wentworth, H. Vali, E. K. Gibson, M. F. McKay, and C. S. Romanek, *Proc. Nat. Acad. Sci. USA* 98, 2164 (2001).
3. R. F. Jameson, C. Binns, and P. Dobbie, submitted for publication.
4. J. Gspann, *Surf. Sci.* 106, 219 (1981).
5. K. Sattler, J. Mühlback, and E. Recknagel, *Phys. Rev. Lett.* 45, 821 (1980).
6. E. C. Stoner and E. P. Wohlfarth, *Philos. Trans. Roy. Soc. London A* 240, 599 (1948).
7. L. Néel, *Ann. Geophys.* 5, 99 (1949).
8. M. Respaud, *J. Appl. Phys.* 86, 556 (1999).
9. E. M. Chudnovsky and J. R. Friedman, *Phys. Rev. Lett.* 85, 5206 (2000).
10. B. Barbara, I. Chiorescu, R. Giraud, A. G. M. Jansen, and A. Caneschi, *J. Phys. Soc. Japan* 69, 383 (2000).
11. B. Barbara, L. Thomas, F. Lioni, I. Chiorescu, and A. Sulpice, *J. Magn. Magn. Mater.* 200, 167 (1999).
12. I. M. L. Billas, J. A. Becker, A. Châtelain, and W. A. de Heer, *Phys. Rev. Lett.* 71, 4067 (1993).
13. D. C. Douglass, A. J. Cox, J. P. Bucher, and L. A. Bloomfield, *Phys. Rev. B* 47, 12874 (1993).
14. K. W. Edmonds, C. Binns, S. H. Baker, S. C. Thornton, C. Norris, J. B. Goedkoop, M. Finazzi, and N. B. Brookes, *Phys. Rev. B* 60, 472 (1999).
15. K. W. Edmonds, C. Binns, S. H. Baker, M. J. Maher, S. C. Thornton, O. Tjernberg, and N. B. Brookes, *J. Magn. Magn. Mater.* 231, 113 (2001).
16. K. W. Edmonds, C. Binns, S. H. Baker, M. J. Maher, S. C. Thornton, O. Tjernberg, and N. B. Brookes, *J. Magn. Magn. Mater.* 220, 25 (2000).
17. H. A. Dürr, S. S. Dhesi, E. Dudzik, D. Knabben, G. van der Laan, J. B. Goedkoop, and F. U. Hillebrecht, *Phys. Rev. B* 59, 701 (1999).
18. D. A. Eastham and I. W. Kirkman, *J. Phys.: Condens. Matter* 12, L525 (2000).

19. P. Milani and S. Iannotta, "Cluster Beam Synthesis of Nanostructured Materials." Springer, Berlin, 1999.
20. H. Haberland, Z. Insepov, and M. Moseler, *Phys. Rev. B* 51, 11061 (1995).
21. M. Negriér, Ph.D. Thesis, Université Claude Bernard Lyon, 2000.
22. C. Binns, S. Louch, S. H. Baker, K. W. Edmonds, M. J. Maher, and S. C. Thornton, *IEEE Trans. Magn.* 38, 141 (2002).
23. F. Parent, J. Tuillon, L. B. Stern, V. Dupuis, B. Prevel, A. Perez, P. Melinon, G. Guiraud, R. Morel, A. Barthelemy, and A. Fert, *Phys. Rev. B* 55, 3683 (1997).
24. T. G. Dietz, M. A. Duncan, D. E. Powers, and R. E. Smalley, *J. Chem. Phys.* 74, 6511 (1981).
25. S. H. Baker, S. C. Thornton, K. W. Edmonds, M. J. Maher, C. Norris, and C. Binns, *Rev. Sci. Instrum.* 71, 3178 (2000).
26. E. Barborini, F. Siviero, S. Vinati, C. Lenardi, P. Piseri, and P. Milani, *Rev. Sci. Instrum.* 75, 2060 (2002).
27. W. Bouwen, P. Thoen, F. Vanhoutte, S. Bouckaert, F. Despa, H. Weidele, R. E. Silverans, and P. Lievens, *Rev. Sci. Instrum.* 71, 54 (2000).
28. H. Haberland, M. Karrais, M. Mall, and Y. Thurner, *J. Vac. Sci. Technol. A* 10, 3266 (1992).
29. H. R. Siekmann, Ch. Luder, J. Faehrmann, H. O. Lutz, and K. H. Meiwes-Broer, *Z. Phys. D* 20, 417 (1991).
30. R. P. Methling, V. Senz, D. Klinkenberg, T. Diederich, J. Tiggesbaumker, G. Holzhuter, J. Bansmann, and K. H. Meiwes-Broer, *Eur. Phys. J. D* 16, 173 (2001).
31. B. Briehl and H. M. Urbassek, *J. Vac. Sci. Technol. A* 17, 256 (1999).
32. C. G. Granqvist and R. A. Buhrman, *J. Appl. Phys.* 47, 2200 (1976).
33. C. Binns, *Surf. Rev. Lett.* 44, 1 (2001).
34. W. A. de Heer, *Rev. Mod. Phys.* 65, 611 (1993).
35. L. Bewig, U. Buck, Ch. Mehlmann, and M. Winter, *Rev. Sci. Instrum.* 63, 3936 (1992).
36. I. M. Goldby, B. von Issendorf, L. Kuipers, and R. E. Palmer, *Rev. Sci. Instrum.* 68, 3327 (1997).
37. K. Ishii, K. Amano, and H. Hamakake, *J. Vac. Sci. Technol. A* 17, 310 (1999).
38. P. Milani and W. A. de Heer, *Rev. Sci. Instrum.* 61, 1835 (1990).
39. R. T. Laaksonen, D. A. Goetsch, D. W. Owens, D. M. Poirer, F. Stepniak, and J. H. Weaver, *Rev. Sci. Instrum.* 65, 2267 (1994).
40. A. Nakajima, K. Hoshino, T. Naganuma, Y. Sone, and K. Kaya, *J. Chem. Phys.* 95, 7061 (1991).
41. W. Paul and H. Steinwedel, *Z. Naturforsch.* 8a, 448 (1953).
42. W. Paul, H. P. Reinhard, and U. von Zahn, *Z. Phys.* 152, 143 (1958).
43. Bu. Wrenger and K. H. Meiwes-Broer, *Rev. Sci. Instrum.* 68, 2027 (1997).
44. V. I. Karataev, B. A. Mamyurin, Y. I. Gaziev, A. D. Melnik, and G. I. Petrenko, *J. Anal. Chem. USSR* 42, 214 (1987).
45. T. Bergmann and T. P. Martin, *Rev. Sci. Instrum.* 60, 347 (1989).
46. T. Bergmann and T. P. Martin, *Rev. Sci. Instrum.* 60, 792 (1989).
47. B. von Issendorf and R. E. Palmer, *Rev. Sci. Instrum.* 70, 4497 (1999).
48. M. Broyer, B. Cabaud, A. Hoareau, P. Mélinon, D. Rayane, and B. Tribollet, *Mol. Phys.* 62, 559 (1987).
49. J. F. Roux, B. Cabaud, G. Fuchs, D. Guillot, A. Hoareau, and P. Mélinon, *Appl. Phys. Lett.* 64, 1212 (1994).
50. H. U. Hostettler and R. B. Bernstein, *Rev. Sci. Instrum.* 37, 872 (1960).
51. F. Di Fonzo, A. Gidwani, M. H. Fan, D. Neumann, D. I. Iordanoglou, J. V. R. Heberlein, P. H. McMurry, and S. L. Girshick, *Appl. Phys. Lett.* 77, 910 (2000).
52. H. V. Tafreshi, G. Benedek, P. Piseri, S. Vinati, E. Barborini, and P. Milani, *Aerosol. Sci. Technol.* 35, 593 (2002).
53. P. Liu, P. J. Ziemann, D. B. Kittelson, and P. H. McMurry, *Aerosol. Sci. Technol.* 22, 293 (1995).
54. D. M. Cox, D. J. Trevor, R. L. Whetton, E. A. Roling, and A. Kaldor, *Phys. Rev. B* 32, 7290 (1985).
55. W. A. de Heer, P. Milani, and A. Châtelain, *Phys. Rev. Lett.* 65, 488 (1990).
56. A. J. Cox, J. G. Louderback, S. E. Apsel, and L. A. Bloomfield, *Phys. Rev. B* 49, 12295 (1994).
57. W. Gerlach and O. Stern, *Z. Phys.* 8, 110 (1922).
58. P. Milani and W. A. de Heer, *Phys. Rev. B* 44, 8346 (1991).
59. I. M. L. Billas, J. A. Becker, and W. A. de Heer, *Z. Phys. D* 26, 325 (1993).
60. S. N. Khanna and S. Linderroth, *Phys. Rev. Lett.* 67, 742 (1991).
61. K. W. Edmonds, C. Binns, S. H. Baker, S. C. Thornton, and P. Finetti, *J. Appl. Phys.* 88, 3414 (2000).
62. C. Binns, *J. Nanosci. Nanotechnol.* 1, 243 (2001).
63. B. T. Thole, P. Carra, F. Sette, and G. van der Laan, *Phys. Rev.* 68, 1943 (1992).
64. P. Carra, B. T. Thole, M. Altarelli, and X. Wang, *Phys. Rev. Lett.* 70, 694 (1993).
65. J. Stöhr and H. Knig, *Phys. Rev. Lett.* 75, 3748 (1995).
66. G. van der Laan, *Phys. Rev. B* 57, 5250 (1998).
67. P. Elleaume, *J. Synchr. Rad.* 1, 19 (1994).
68. G. Panaccione, F. Sirotti, and G. Rossi, *Solid State Commun.* 113, 373 (2000).
69. G. van der Laan, *Phys. Rev. B* 51, 240 (1995).
70. F. Sirotti, S. Girlando, P. Prieto, L. Floreano, G. Panaccione, and G. Rossi, *Phys. Rev. B* 61, R9221 (2000).
71. S. D. Bader, *Proc. Inst. Elect. Electron. Eng.* 78, 909 (1990).
72. L. M. Falicov and J. Braz, *J. Phys.* 23, 233 (1993).
73. S. Foner, *Rev. Sci. Instrum.* 30, 548 (1959).
74. C. Binns, M. J. Maher, Q. A. Pankhurst, D. Kechrakos, and K. N. Trohidou, *Phys. Rev. B* 66, 184413 (2002).
75. M. Jamet, W. Wernsdorfer, C. Thirion, D. Mailly, V. Dupuis, P. Mélinon, and A. Perez, *Phys. Rev. Lett.* 86, 4676 (2001).
76. A. D. Kent, S. von Molnár, S. Gider, and D. D. Awschalom, *J. Appl. Phys.* 76, 6656 (1994).
77. S. Wirth and S. von Molnár, *Appl. Phys. Lett.* 76, 3282 (2000).
78. Y. Li, P. Xiong, S. von Molnár, S. Wirth, Y. Ohno, and H. Ohno, *Appl. Phys. Lett.* 80, 4644 (2002).
79. W. D. Knight, K. Clemenger, W. A. de Heer, W. A. Saunders, M. Y. Chou, and M. L. Cohen, *Phys. Rev. Lett.* 52, 2141 (1984).
80. J. Pedersen, S. Bjørnholm, J. Borggreen, K. Hansen, T. P. Martin, and H. D. Rasmussen, *Nature* 353, 733 (1991).
81. M. Sakurai, K. Watanabe, K. Sumiyama, and K. Suzuki, *J. Chem. Phys.* 111, 235 (1999).
82. J. Tuillon et al., *Philos. Mag. A* 76, 493 (1997).
83. M. Pellarin et al., *Chem. Phys. Lett.* 217, 349 (1994).
84. T. P. Martin, U. Nher, and H. Schaber, *Chem. Phys. Lett.* 199, 470 (1992).
85. S. Valkealahti and M. Manninen, *Phys. Rev. B* 57, 15533 (1998).
86. B. Yoon, V. M. Akulin, Ph. Cahuzac, F. Carlier, M. de Frutos, A. Masson, C. Mory, C. Colliex, and C. Bréchnignac, *Surf. Sci.* 443, 76 (1999).
87. M. D. Upward, B. N. Cotier, P. Moriarty, P. H. Beton, S. H. Baker, C. Binns, and K. W. Edmonds, *J. Vac. Sci. Technol. B* 18, 2646 (2000).
88. M. B. Knickelbein, *Phys. Rev. Lett.* 86, 5255 (2001).
89. D. P. Pappas, A. P. Popov, A. N. Anisimov, B. V. Reddy, and S. N. Khanna, *Phys. Rev. Lett.* 76, 4332 (1996).
90. D. Gerion, A. Hirt, I. M. L. Billas, A. Catelain, and W. A. de Heer, *Phys. Rev. B* 62, 7491 (2000).
91. D. Gerion, A. Hirt, and A. Chatelain, *Phys. Rev. Lett.* 83, 532 (1999).
92. I. M. L. Billas, A. Châtelain, and W. A. de Heer, *Science* 265, 1682 (1993).



93. S. E. Apsel, J. W. Emmert, J. Deng, and L. A. Bloomfield, *Phys. Rev. Lett.* 76, 1441 (1996).
94. M. B. Knickelbein, *J. Chem. Phys.* 116, 9703 (2002).
95. M. B. Knickelbein, *Chem. Phys. Lett.* 353, 221 (2002).
96. Y. Xie and J. A. Blackman, submitted for publication.
97. H. E. White, "Introduction to Atomic Spectra," McGraw-Hill, New York, 1934.
98. A. N. Andriotis and M. Menon, *Phys. Rev. B* 57, 10069 (1998).
99. B. V. Reddy, S. K. Nayak, S. N. Khanna, B. K. Rao, and P. Jena, *J. Chem. Phys. A* 102, 1748 (1998).
100. F. A. Reuse and S. N. Khanna, *Chem. Phys. Lett.* 234, 77 (1995).
101. N. Fujima, *Eur. Phys. J. D* 16, 185 (2001).
102. D. C. Douglass, J. P. Bucher, and L. A. Bloomfield, *Phys. Rev. B* 45, 6341 (1992).
103. D. R. Salahub and R. P. Messmer, *Surf. Sci.* 106, 415 (1981).
104. V. L. Moruzzi, *Phys. Rev. Lett.* 57, 2211 (1986).
105. G. M. Pastor, J. Dorantes-Dávila, and K. H. Bennemann, *Phys. Rev. B* 40, 7642 (1989).
106. K. Lee and J. Callaway, *Phys. Rev. B* 48, 15358 (1993).
107. H. Cheng and L.-S. Wang, *Phys. Rev. Lett.* 77, 51 (1996).
108. C. Kohl and G. F. Bertsch, *Phys. Rev. B* 60, 4205 (1999).
109. L. A. Bloomfield, J. Deng, H. Zhang, and J. W. Emmert, in "Clusters and Nanostructure Interfaces" (P. Jena, S. N. Khanna, and B. K. Rao, Eds.), p. 213. World Scientific, Singapore, 2000.
110. K. Lee and J. Callaway, *Phys. Rev. B* 49, 13906 (1994).
111. S. K. Nayak, B. K. Rao, and P. Jena, *J. Phys.: Condens. Matter* 10, 10863 (1998).
112. E. C. Stoner, *Proc. Roy. Soc. London. Ser. A* 235, 372 (1938).
113. C. Rau, B. Xing, and M. Robert, *J. Vac. Sci. Technol. A* 6, 579 (1988).
114. F. Liu, S. N. Khanna, and P. Jena, *Phys. Rev. B* 43, 8179 (1991).
115. J. F. Janak, *Phys. Rev. B* 16, 25 (1977).
116. S. Blügel, *Phys. Rev. Lett.* 68, 851 (1992).
117. R. Pfandzelter, G. Steierl, and C. Rau, *Phys. Rev. Lett.* 74, 3467 (1995).
118. P. Villaseñor-Gonzalez, J. Dorantes-Dávila, H. Dreysse, and G. M. Pastor, *Phys. Rev. B* 55, 15084 (1997).
119. C. Barreateau, R. Guirado-López, D. Spanjaard, M. C. Desjonquères, and A. M. Oleś, *Phys. Rev. B* 61, 7781 (2000).
120. D. C. Douglass, J. P. Bucher, and L. A. Bloomfield, *Phys. Rev. Lett.* 68, 1442 (1992).
121. D. C. Douglass, J. P. Bucher, D. B. Haynes, and L. A. Bloomfield, in "Physics and Chemistry of Finite Systems: From Clusters to Crystals" (P. Jena, S. N. Khanna, and B. K. Rao, Eds.), NATO-ASI Series, p. 759. Kluwer, Dordrecht, 1992.
122. G. M. Pastor and J. Dorantes-Dávila, *Phys. Rev. B* 52, 13799 (1995).
123. V. Z. Cerovski, S. D. Mahanti, and S. N. Khanna, *Eur. Phys. J. D* 10, 119 (2000).
124. C. Binns, S. H. Baker, A. M. Keen, C. Norris, and S. N. Mozley, *Solid State Commun.* 99, 353 (1996).
125. A. M. Keen, C. Binns, S. H. Baker, S. Mozley, C. Norris, and S. C. Thornton, *Surf. Sci.* 352-354, 715 (1996).
126. P. Gambardella, S. S. Dhesi, S. Gardonio, C. Grazioli, P. Ohresser, and C. Carbone, *Phys. Rev. Lett.* 88, 047202 (2002).
127. J. T. Lau, A. Frölich, R. Nietubyc, M. Reif, and W. Wurth, *Phys. Rev. Lett.* 89, 057201 (2002).
128. S. H. Baker, C. Binns, K. W. Edmonds, M. J. Maher, S. C. Thornton, S. Louch, and S. S. Dhesi, *J. Magn. Magn. Mater.* 247, 19 (2002).
129. C. T. Chen, Y. U. Idzerda, H.-J. Lin, N. V. Smith, G. Meigs, E. Chaban, G. H. Ho, E. Pellegrin, and F. Sette, *Phys. Rev. Lett.* 75, 152 (1995).
130. K. Wildberger, V. S. Stepanyuk, P. Lang, R. Zeller, and P. H. Dederichs, *Phys. Rev. Lett.* 75, 509 (1995).
131. C. Binns and M. J. Maher, *New J. Phys.* 4, 85.1 (2002).
132. P. Allia, M. Coisson, P. Tiberto, F. Vinai, M. Knobel, M. A. Novak, and W. C. Nunes, *Phys. Rev. B* 64, 144420 (2001).
133. T. J. Jackson, C. Binns, E. M. Forgan, E. Morenzoni, Ch. Niedermayer, H. Glückler, A. Hofer, H. Luetkens, T. Prokscha, T. M. Riseman, A. Schatz, M. Birke, J. Litterst, G. Schatz, and H. P. Weber, *J. Phys.: Condens. Matter* 12, 1399 (2000).
134. L. Néel, *J. Phys. Radium* 15, 225 (1954).
135. P. Söderlind, O. Eriksson, B. Johansson, R. C. Albers, and A. M. Boring, *Phys. Rev. B* 45, 12911 (1992).
136. E. M. Chudnovsky, *J. Magn. Magn. Mater.* 40, 21 (1983).
137. E. M. Chudnovsky, W. M. Saslow, and R. A. Serota, *Phys. Rev. B* 33, 251 (1986).
138. W. M. Saslow, *Phys. Rev. B* 35, 3454 (1987).
139. E. M. Chudnovsky, *J. Appl. Phys.* 64, 5770 (1988).
140. J. F. Löffler, H.-B. Braun, and W. Wagner, *Phys. Rev. Lett.* 85, 1990 (2000).
141. L. Thomas, J. Tuaille, J. P. Perez, V. Dupuis, A. Perez, and B. Barbara, *J. Magn. Magn. Mater.* 140, 437 (1995).
142. J. P. Perez, V. Dupuis, J. Tuaille, A. Perez, V. Paillard, P. Melinon, M. Treilleux, L. Thomas, B. Barbara, and B. Bouchet-Fabre, *J. Magn. Magn. Mater.* 145, 74 (1995).
143. M. Jamet, V. Dupuis, P. Mélinon, G. Guiraud, A. Pérez, W. Wernsdorfer, A. Traverse, and B. Baguenard, *Phys. Rev. B* 62, 493 (2000).
144. Y. Xie and J. A. Blackman, *Phys. Rev. B* 66, 085410 (2002).
145. J. P. Chen, C. M. Sorensen, K. J. Klabunde, and G. C. Hadjipanayis, *Phys. Rev. B* 51, 11527 (1995).
146. M. Négrier, J. Tuaille, V. Dupuis, C. Tonon, and A. Perez, *Nanostruct. Mater.* 12, 303 (1999).
147. A. Perez, L. Bardotti, B. Prevel, P. Jensen, M. Treilleux, P. Mélinon, J. Gierak, G. Faini, and D. Mailly, *New J. Phys.* 4, 76.1 (2002).



# Magnetism in Rare Earth/Transition Metal Multilayers

V. O. Vas'kovskiy, A. V. Svalov

*Ural State University, Ekaterinburg, Russia*

G. V. Kurlyandskaya

*Universidad de Oviedo, Calvo Sotelo, Oviedo, Asturias, Spain*

## CONTENTS

1. Introduction
  2. Preparation and Characteristics of R/T Multilayers
  3. Magnetism of R/T Multilayers
  4. Magnetic Anisotropy
  5. Attendant Properties
  6. Conclusions
- Glossary  
References

## 1. INTRODUCTION

Nearly 40 years ago, heterogeneous films containing rare earth (R) and 3d transition metal components (T) first attracted the attention of the scientific community [1]. The current method of artificially creating complex magnetic systems came about as techniques for the preparation of R/T structures were developed. The presence of exchange interactions through adjacent surfaces of two magnetic substances with very dissimilar characteristics was neatly demonstrated in these structures. However, not all questions about the physics of new magnetic objects have been resolved because of limited technical capacity. In particular, the relationship between the thickness and structure of individual layers and the magnetic properties of R/T multilayered films has not been clarified nor has the role of interfaces. The application range of these materials has not been described.

Interest in R/T multilayered structures reappeared in the 1980s [2–4] and continues to increase to this day. This can be explained by the development of ion sputtering and

molecular beam epitaxy as thin films preparation methods, with a correspondingly high level of parameter control [5]. The research techniques have also been refined. Together with high-resolution electron microscopy [6], neutronography [7], and Mössbauer spectrometry, X-ray synchrotron radiation [8–12] and field ion microscopy [13] are usually used nowadays. Finally, multilayered R/T films have been used successfully in practice to increase the energy of hard magnetic materials [14], to reduce the magnetic saturation field in giant magnetostrictive materials [15], and to create the new materials for high-density magneto-optical data storage applications [16, 17].

This chapter is devoted to problems of R/T films such as layers and interfaces, atomic structure, magnetic structure, and the way magnetic structure changes under external magnetic field application or with changes in temperature. We also discuss the mechanism of the interlayer exchange interaction and perpendicular magnetic anisotropy. In addition, some data on hysteresis, magneto-optic, magnetotransport, and magnetostrictive properties are included; that is, we review the basic knowledge needed to understand possible technological applications for R/T films.

## 2. PREPARATION AND CHARACTERISTICS OF R/T MULTILAYERS

The atomic structure and fundamental magnetic characteristics of low-dimensional nanoscale subjects like R/T multilayers, such as spontaneous magnetization, Curie temperature, and crystalline magnetic anisotropy, are highly dependent on preparation conditions and geometry. This is the reason for both scientific and practical interest in R/T multilayers and

for the special attention given to the problem of parameter control in film technology.

## 2.1. Fabrication Technology

For scientific purposes, there are two R/T films preparation methods: ion sputtering and vacuum thermal evaporation of initial materials. Ion sputtering is the expulsion of the atoms from the target surface by inert gas ion bombardment. The target can be of either R or T composition. The formation and acceleration of inert gas ions, Ar as a rule, might take place in a direct electric field (DC sputtering) [4, 18] or in a radiofrequency electric field (rf sputtering) [19, 20]. It can be done in the presence of an additional magnetic field, which stimulates increasing electrical discharge, that is, magnetron sputtering [21, 22]. Comparatively high deposition rates (0.1–0.5 nm/s), high density, adhesion, and uniform thickness for large sample areas are the advantages of this method.

Vacuum thermal evaporation [23, 24] involves strong local heating, usually by a high-energy electron beam created by an electron beam gun. The film preparation occurs at ultrahigh vacuum of  $10^{-8}$ – $10^{-10}$  torr, called ultrahigh thermal evaporation or molecular beam epitaxy. However, the latter is not true for R/T multilayers; the epitaxial building of structure does not take place in alternating deposition of R and T layers, because of the great differences in atomic and structural parameters of rare earth and 3d transition metals. A comparatively low evaporation rate and minimal value of impurities in the deposited films are specific features of this method. Thermal evaporation allows us to achieve very low deposition rates (of 0.2–0.5 Å/s) and minimal contamination of the samples.

The two methods described above include a certain number of important technological parameters. Quantitatively the influence of these parameters on the quality of the nanoscale multilayers has been learned from experience in R–T thin films preparation. The possibility of direct transference of the parameters of thin film preparation to the case of multilayers is different for each experimental setup and, so far, there is no systematic study of the problem in the literature; one of the few examples is the analysis of the influence of the substrate electrical bias on the structural state of the Fe layer in Gd/Fe magnetron sputtered multilayers [25].

The technology of deposition very often depends on the purpose of R/T multilayer preparation. For basic study, especially in structural studies, the method of thermal evaporation seems more appropriate because it has the advantage of low contamination of the samples. For studies in the material science field, the ion sputtering process is more reasonable because it can be more easily adapted to industrial conditions. Apart from R and T targets, the vacuum systems for multilayer preparation usually offer additional possibilities for depositing other layers such as buffers of Cu [26], Mo [27], nonmagnetic spacers of Cu, Y [28, 29], Cu, Si [30], Pt, or Cr [31], or protecting layers of Si [32], Al [33], V [18], or Ag [34] to avoid oxidation. The last point is very important for R layers, which have a very high oxidation rate.

Substrates play an important role in thin film microstructure and property formation. At the same time, for nonepitaxially grown multilayers, like R/T structures, the substrate

material is less important. This is a consequence of the relatively high ( $\geq 100$  nm) total thickness of the samples and of the repeated alternation of different layers. In practice, monocrystalline Si or glass (for example, Corning glass) substrates of appropriate quality are utilized.

## 2.2. Structure of a R/T System in a View of Preparation Conditions and Thickness: Interfaces

The structural state is a key parameter for the formation of many physical properties of thin films as well as the magnetic properties between them [35, 36]. The type of atomic structure can be determined by the presence/absence of order in the positions of the atoms at precise distances compared with the atomic size. The presence of larger ordered formations is called microstructure. The components of the microstructure are the amorphous matrix part, crystalline grains, boundaries between the grains, space, and compositional defects. If the thickness of the film is relatively high ( $L > 10$  nm), the structural state first of all depends on the temperature regime of the deposition. However, in very thin films the thickness plays a key structural role. This is true both for uniform films and multilayers. For the latter, the characteristic size parameter is the thickness of each individual layer.

Transmission electron microscopy and X-ray diffraction are the most widespread methods for studying the structure of all kinds of thin films. Figure 1 shows the electron diffraction pattern and the microstructure images in a dark-field regime for a rf-sputtered Si/[Gd(7.5)/Co(3)]<sub>4</sub>/Si sample. This formula contains all the important information about the general structure of the multilayered film. It says that this sample has buffer and covered Si layers and Gd layers of thickness  $L_{\text{Gd}} = 7.5$  nm alternated with Co layers of thickness  $L_{\text{Co}} = 3$  nm. The structure  $L_{\text{Gd}} + L_{\text{Co}} = L_p$  is repeated four times, where  $L_p$  is a period of the structure.

The main feature of this electron diffraction pattern is two very diffused rings, corresponding to the Gd and Co components. The diffused state of the reflections testifies to the amorphous state of these metals. At the same time, one can define the most probable distances between the atoms (0.3 and 0.2 nm, respectively). Dark-field observation enables us to separate the images corresponding to different diffraction maxima, that is, related to mainly Gd or Co (Fig. 1a and 1b).

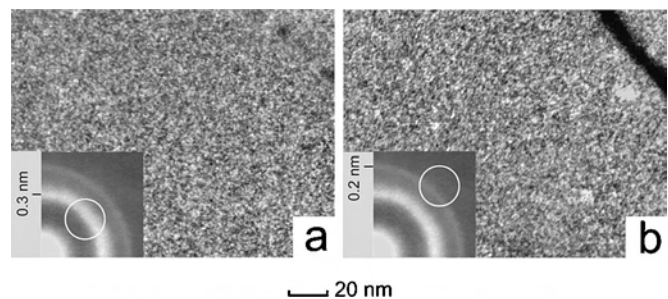


**Figure 1.** Electron diffraction patterns and dark-field microstructure images corresponding to different diffraction maximums for an Si/[Gd(7.5)/Co(3)]<sub>4</sub>/Si sample. The systematic interatomic distances are 0.3 and 0.2 nm.

The common feature for such different metals is the very small size (<2 nm) of the volumes of coherent dispersion, which look like bright points in the photographs.

Amorphization of the rare earth and 3d metals, which occurs as the thickness of the layers decreases, has been reported in many cases both for thermal evaporation [23, 32, 37–40] and ion sputtering methods [4, 21, 25, 41]. The details of the transformation from the amorphous to the nanocrystalline state of Gd/Fe, Tb/Fe, and Dy/Fe systems are shown below (Table 1). The amorphous state of these metals is observed for very small and slightly different layer thickness:  $L_R < 1.1$  nm and  $L_{Fe} < 0.8$  nm. Real transitions from one structure to another do not show up as jumps but take place in some interval of the layer thickness; thus the data shown above are only an estimate. There is a long transition zone between the crystalline and amorphous states. See, for example, [42] in which Mössbauer spectrometry was used to get information about structure of the [Tb/Fe]<sub>20</sub> multilayer through the analysis of the hyperfine field of the iron isotope <sup>57</sup>Fe. The percentage of crystalline body-centered cubic (bcc) phase in comparison with total Fe volume decreases with the decrease in the thickness of the layers. The features of this phase transition depend on the substrate temperature. At a thickness of about 2 nm complete amorphization takes place.

In nanoscale R/T multilayers, the decrease in layer thickness results in the transition from a crystalline to an amorphous state. The quantitative parameters of this transition depend to some extent on the preparation conditions, but the average thicknesses are 1.5–2 nm for R = Gd, Dy, and Tb and 1.5–2.5 nm for T = Fe and Co.

**Table 1.** R/T multilayer studies.

R element	$L_R < 2$ nm	$L_R > 2$ nm
Tb	10, 35, 37, 41, 42–81	7, 10, 35, 39, 43, 48, 56, 57, 59, 76, 81–86
Dy	37, 48, 54, 56, 87, 88	37, 54, 56, 85, 87
Gd	12, 18, 28, 31, 37, 38, 48, 56, 90–92	6, 11, 24, 26, 27, 28, 32, 35, 36, 38, 40, 48, 56, 89–123, 132
Pr	38, 48, 56	38, 48, 56
Nd	19, 38, 48, 56, 87	19, 38, 48, 56, 85, 87, 124
Sm	48, 56, 125–127	48, 56, 127
Y	48, 56, 129	48, 56, 129
La	48, 56	48, 56
Ce	48, 56	48, 56
Eu	48, 56	48, 56
Ho	48, 56	48, 56
Er	48, 56	48, 56
Tm	48, 56	48, 56
Yb	48, 56	48, 56
Lu	48, 56	48, 56

*Note:* Publications reporting R/T multilayer studies are listed in this table, taking into account the type of rare earth layer (R) (first column) and the structural state of the R layer. It is known that R thickness is an important parameter. In each particular case there is a certain thickness ( $L_T$ ) corresponding to the transition from the amorphous to the crystalline state.  $L_T$  depends on composition and fabrication conditions but usually it is about 2 nm. Therefore, we have divided all references into two large groups with respect to this parameter. It is clear from the table that this approach has an internal logic: group one ( $L_R < 2$  nm) has collected the data about R/T structures with thin Tb layers and perpendicular anisotropy interesting with respect to magnetic recording; group two ( $L_R > 2$  nm) has collected data with relatively thick Gd for model study.

The interfaces, zones between different layers, play a very important role in influencing macroscopic magnetic properties. Although there is great scientific interest in studying the interface problem, many questions about their structure and chemical state are still unanswered. The main point of discussion is the level of mixing of the different layers.

Low-angle X-ray diffraction is a powerful method for study of interface. This method provides the opportunity to work in a framework of Woolf–Bragg conditions for reflecting atomic planes, which are situated relatively far apart. In multilayers, the surfaces of the layers act as reflecting surfaces. Therefore, the appearance and position of the diffraction maximum of low-angle X-ray dispersion helps to define the presence of the periodic structure and its period. At the same time, the profile of the low-angle diffraction contains even more profound information about the state of the reflecting surfaces. Extracting this information usually includes a modeling process and the comparison of the calculated diffractogram with the experimental results [27].

Figure 2 shows an example of low-angle X-ray diffraction in Cu–K $\alpha$  radiation for the Cu/[Gd(7.5)/Co(3)]<sub>20</sub>/Cu. One can see up to five diffraction peaks; these confirm to the very high localization level of the layers. At the same time the total diffraction profile depends not only on the perfection of the interfaces but also on their relative volume in the total volume of the material. Because of this fact, there is a tendency for the number of maxima to be reduced as the period of the multilayered structure gets smaller [2, 130]. Nevertheless, the authors of [4] found, for the rf sputtered R/Fe multilayers (R = Gd, Tb, and Dy), that the presence of the layered structure was maintained up to the layer thickness of the atomic size scale, thus providing the experimental basis for their conclusion about the possibility of preventing mixing in the materials of the type mentioned above. The same conclusion was reached in [24], on the basis of numerical analysis of the low-angle X-ray diffraction profiles of thermal deposited Tb/Fe multilayers. These researchers found a good match between the experimental and the calculated curves, assuming wave-shaped interfaces and no mixing. However, many other publications reported significant diffusion between R and T layers on the basis of Auger electron spectroscopy measurements [23, 27, 43–46, 82, 94, 131]. This method allows definition of

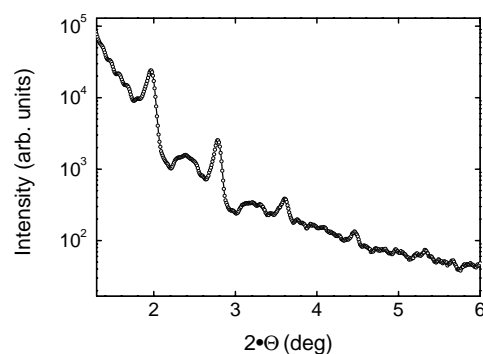


**Figure 2.** Low-angle X-ray diffraction for the Cu/[Gd(7.5)/Co(3)]<sub>20</sub>/Cu film prepared by rf sputtering. Reprinted with permission from [93], V. O. Vas'kovskiy et al., *Phys. Met. Metall.* 86, 140 (1998). © 1998, MAIK “Nanka/Interperiodica.”

the element composition of the surfaces. In combination with the method of ion etching, it makes it possible to construct the composition profiles of the film samples. Figure 3, in accordance with [94], shows the example of such a profile of a two-layer Gd(50)/Co(21) film prepared by ion sputtering. The transition region between the Gd and Co layers is not sharp and has a thickness of about 10 nm as a consequence of interlayer diffusion. Two points have to be mentioned regarding this last example: first, the Auger electrons give information not only about the surface but also about the narrow zone near the surface; and second, the ion etching process very often results in formation of a different surface relief. Both the first and the second processes may imitate the mixing effect.

Another interesting fact is that there is asymmetry in the variation of the concentration changes related to the thickness of Gd and Co bilayers (Fig. 3). This can be explained, to some extent, by taking into account the higher oxygen concentration in the Gd layer. Another, and it seems more important, reason is the difference in the mobility of Gd and Co atoms. As a result of this, Co usually diffuses better than Gd into the neighbor layer (up to 3 nm). The same conclusion is reached in [131] and [27]. In the last case the low-angle diffraction data were taken using synchrotron radiation.

An even more detailed interface study was made using Mössbauer spectrometry [47]. These researchers investigated the state of Fe layers in Tb/Fe multilayers by introducing the isotope  $^{57}\text{Fe}$  as an additional 0.5 nm sublayer. If one deposits Fe on the Tb surface, mixing takes place. For Tb deposition onto the Fe surface there is a clear boundary between well-separated layers. Similar conclusions were drawn for the Gd/Co [27] and CoNi/Gd [132] systems. Theoretical analysis of low-angle diffraction shows higher levels of interface imperfection for Co deposited onto Gd than for Gd deposited onto Co.

Certain information about interfaces can be gathered by analyzing variations in the deposition parameters and by subsequent heat treatments of the multilayers. Many efforts have been made with the objective of fabricating multilayers with interfaces that are as narrow and as sharp as possible by, for example, utilization of the appropriate substrate temperature,  $T_s$ . In the majority of studies researchers were dealing with films deposited on a cooled substrate at temperatures  $T_s = 80$  K [130],  $T_s = 90$  K [32],  $T_s = 190$  K [133],

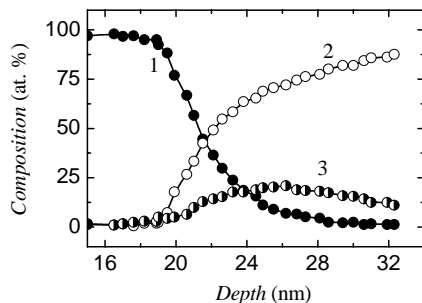


**Figure 3.** Composition depth profile taken by Auger spectroscopy of the Gd(50)/Co(21) bilayer: (1) Co; (2) Gd; (3) O. Film was deposited onto a glass substrate by ion sputtering. From [94] J. P. Andres et al., *J. Appl. Phys.* 87, 2483 (2000). © 2000, American Institute of Physics.

$T_s = 200$  K [2],  $T_s = 220$  K [48], and  $T_s = 240$  K [134]. There are data for room temperature deposition regimes [82, 135] and even deposition at elevated temperatures of  $T_s = 310$ – $370$  K [27] and  $T_s = 390$  K [46]. These experimental results are very difficult to compare because they are not systematic and the types of deposition equipment are very different with many additional parameters involved. There are interesting exceptions [42, 47] for which comparative studies of the samples were made for two deposition temperatures of 150 and 300 K. The result seems trivial; the higher the deposition temperature, the less separated the layers are. However, there is another study [136] in which the temperature  $T_s = 410$  K is declared to be optimal when one is trying to achieve smooth interfaces. The results of [49], based on the Tb/Fe multilayer study after heat treatments, are in accord with those of [136]. The authors found localization of the magnetic layers in an amorphous structure of a very thin layered system at the beginning of the heat treatments for annealing temperatures  $t_a < 370$  K. In other words, a process opposite to mixing took place. A similar conclusion was drawn in [137]. Interlayer diffusion takes place only at more elevated temperatures and results in the formation of an amorphous Tb–Fe unhomogeneous composition interface. In its amorphous state, a layered system is generally rather thermostable. It changes only at  $t_a > 520$  K and the crystallization of Tb, Fe, and Tb–Fe and as a result destruction of the multilayered structure take place at  $t_a \geq 770$  K [49].

Other methods of influencing the interfaces include the use of different substrates and buffer layers, electrical bias of the substrates, and implantation. The structural characteristics of Gd/Co films [27, 95] prepared by molecular beam epitaxy deposition onto an  $\text{Al}_2\text{O}_3$  substrate with a Mo buffer layer were compared with those deposited onto a Si substrate and a Si substrate with a SiN buffer layer. Low-angle X-ray diffraction analysis shows the maximum mobility of Co into Gd for the  $\text{Al}_2\text{O}_3$  substrate, resulting effectively in a reduction of the thickness of the pure Co layer by more than 50%. A difference in the diffusion level was observed for multilayers deposited onto Si substrate: it is higher in the presence of the buffer layer. The influence of the substrate on the properties of the multilayered films is achieved through substrate relief and formation of a special thermal regime during the deposition. In our view, this last factor could play the key role in the above experiment.

The influence of the voltage applied to the substrate (electric substrate bias) during the rf sputtering deposition [138] has also been studied by means of low-angle X-ray diffraction of Gd/Fe films. It was shown that the presence of a negative bias of  $-30$  V causes smoother interfaces and smaller crystalline grains. Possibly these two effects have a reciprocal relationship and the interface smoothing is the result of the increased microstructure dispersion.

Different effects were reported for the ion implantation treatment [50, 137, 139]. The simplest consists of layer mixing as a result of irradiation, for example, in a Gd/Co sample by Ar ions with energy of 150–300 keV (a dose of  $10^{16}$   $\text{cm}^{-2}$ ) [131]. It was found that in multilayered structures with small periods ( $< 10$  nm), such treatment can lead to complete layer mixing and amorphization of the nanosized layer structure. For samples with structure periods greater than 20 nm the



mixing and amorphization processes take place only partially. Clear structural changes do not appear after the use of lower energy/dose radiation for the Tb/Fe samples, but one can see measurable differences in magnetic properties before and after irradiation [51].

Rather delicate changes in the interface structure of Tb/Fe multilayers were observed after irradiation by different hard ions like Kr, Xe, Pb, and U [52, 53, 140]. Mössbauer spectroscopy was used to get information about structure. Two steps of structural change were reported [52, 140]. At the beginning of the treatment, if the ion beam power is low, there is an increase in the thickness of the iron layers, known as de-mixing, that is, the opposite process to the layer mixing described earlier. Let us remember that the same effect appears [49] at low temperature heat treatment of multilayers. The cause of changes in properties during low-energy ion bombardment may be a trivial heating of the material. In the second step, when the ion flow power increases, interlayer diffusion dominates, and the layered structure disappears. The differences between the structures of Tb on Fe compared with those of Fe on Tb interface increase as well [53].

All these results demonstrate the great variety of structural states of the multilayers and, especially, interfaces in R/T multilayers, which clearly depend on composition and method of preparation. One can develop a model that is appropriate for the experimental methods to be used in any specific study, but we emphasize the need for special analysis for each particular case.

### 3. MAGNETISM OF R/T MULTILAYERS

Multilayered R/T films have unique combinations of magnetic properties, corresponding to the different elements of their structure, because they are formed from very dissimilar magnetic materials. First are magnetoactive 3d transition metals, known as band magnets. The main carriers of magnetism in these magnets are 3d electrons, which are collectivized to a great extent and not related to a particular atom of crystalline lattice. In this case, magnetic ordering is short range and is achieved through direct exchange interaction. As a rule, these metals have ferromagnetic ordering, high Curie temperature, and high spontaneous magnetization.

Second, in rare earth metals, magnetism is caused by 4f electrons located in internal electron shells. This leads to localization of magnetic moments on atoms and to the absence of direct exchange interaction in the 4f electron system. Magnetic ordering occurs because of indirect exchange through the conduction electrons. This interaction is oscillating and acts over a long range. It causes low values of magnetic ordering temperatures and aids the formation of complex magnetic structures.

The third category of materials, namely alloys of rare earth and 3d elements, may easily appear in R/T structures because of interlayer mixing during preparation, after annealing [49] or ion irradiation [51]. In their crystalline state, R–T alloys do not form continuous solid solutions, because of differences in ion radii and occur as stable intermetallic compounds. High magnetic anisotropy and magnetostriction are distinctive features of some of them. As was

shown in Section 2, the actual R/T multilayers tend to amorphization. It might be supposed, therefore, that interfaces with fluctuating composition, if they appear, are amorphous.

Amorphous R–T alloys are well known. It is not very difficult to get them in an amorphous state in thin film geometry using special preparation technology, because of the differences in ion radii. Amorphous Gd–Co, Gd–Fe, and Tb–Fe films have been well investigated [141]. They were the starting point of interest in corresponding multilayered structures. High structural stability, the presence of magnetic ordering over a large range of temperatures, and monotonous change of the main magnetic characteristics according to composition are the important features of amorphous R–T films.

Thus, the magnetism and nonmagnetic properties which, in R/T multilayered systems, depend on the presence of magnetic order, connect with the combination and superposition of properties of R and T metals and their alloys. Another important feature is specific interlayer interactions. This section is devoted to the magnetism of R/T multilayers.

#### 3.1. Magnetic Properties of Nanocomponents

Research interest in R/T multilayered films is determined by practical needs. Therefore, layered structures containing strong magnetic components, namely metals in which magnetic ordering occurs at high temperatures, are of special interest. These are Fe and Co from the group of 3d metals and Gd, Tb [125], and Dy from the group of rare earth elements. As exceptions, it is possible to mention experiments using Ni [82], Sm [125–127], Nd [124], and R = any rare earth element [48, 56] (Table 1).

Fe and Co are the most widely used ferromagnetic materials and their properties are well known. However, in the thin film state some peculiar features may appear [29, 142, 143]. This is true, first of all, for atomic structure. As mentioned in Section 2, sufficiently thin films have a tendency to amorphization. It is known that the transition to the amorphous state has a relatively weak influence on Co magnetism. Cobalt retains high spontaneous magnetization and high Curie temperature,  $T_c$ . A different process takes place for iron. At amorphization the iron atomic magnetic moment decreases greatly and  $T_c$  drops. What is the reason for this phenomenon? In the amorphous state the average number of nearest neighbors is restricted to about 12 for any selected atom. It corresponds to the number of nearest neighbors in the bcc crystalline lattice. Thus, from the point of view of atomic structure, the amorphous structure is similar to that corresponding to the low-spin state of crystalline iron,  $\gamma$ -Fe.

Corresponding experimental data for layered structures were obtained by investigation of the samples containing only one sort of magnetic layer separated by nonmagnetic spacers, for example, Fe/Y multilayers [129, 144–147]. Yttrium does not have a magnetic moment, but its structural–chemical properties are similar to those of rare earth metals. Typical dependence of the average Fe atomic magnetic moment,  $\mu_{Fe}$ , on Fe layer thickness is shown in Figure 4a (curve 1). It was measured at room temperature in  $[\text{Fe}(L_{Fe})/\text{Y}(7.8)]_n$  multilayers prepared by molecular beam

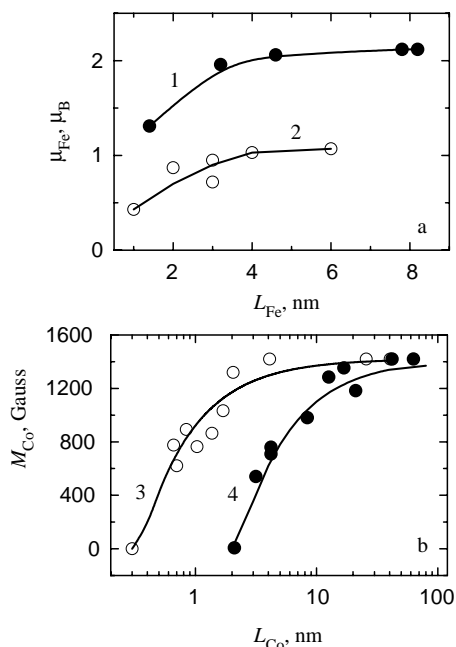


**Figure 4.** Dependence of Fe average magnetic moment (a) and Co spontaneous magnetization (b) on magnetic layer thickness at room temperature for different structures: (1)  $[Fe(L_{Fe})/Y(7.8)]_n$ . Reprinted with permission from [129], Z. S. Zhang, et al., *Phys. Stat. Sol. A* 179, 237 (2000). © 2000, Wiley-VCH. (2)  $[Fe(L_{Fe})/Ti(1)]_n$ . Reprinted with permission from [156], A. Fnidiki et al., *J. Appl. Phys.* 84, 3311 (1998). © 1998, American Institute of Physics. (3)  $[Co(L_{Co})/Cu(2.5)]_{20}$ . (4)  $[Co(L_{Co})/Si(2)]_{20}$ .

epitaxy [129]. It is seen that a significant decrease in  $\mu_{Fe}$  takes place at  $L_{Fe} < 4$  nm. Naturally one might associate this tendency with amorphization of the magnetic layers and the increase in the low-magnetic Fe phase fraction. However, the authors of [129] point to another potential reason for  $\mu_{Fe}$  change, namely the elements of superparamagnetic behavior of Fe/Y multilayers at  $L_{Fe} < 1.4$  nm. It means that Fe layers have lost continuity. Thermal fluctuations of the magnetic moments of ultrathin particles, formed as a result of discontinuity, lead to a decrease in the average magnetization of the macroscopic sample from which the atomic magnetic moment is experimentally determined. Ultrathin particles, formed as a result of discontinuity, that is, granular ferromagnetic thin Fe films deposited on  $Al_2O_3$  substrates in ultrahigh vacuum, and low temperature ferromagnetic quenching effects in Fe(110) contacting nanoscale islands, were observed and studied in [142].

Although the Fe/Cr system is not a R/T system, we feel that it should be mentioned because of its enormous contribution in stimulating research. In the same way that exchange interaction between ferromagnetic films across nonmagnetic metallic Y spacers was considered for Gd [143, 148, 149] and Dy [150], this was also done for the Fe/Cr structures [151–153]. Interest in the basic physics of the exchange-coupled multilayers and especially in Fe/Cr multilayers was enhanced by the discovery of giant magnetoresistance in the antiferromagnetically coupled Fe/Cr system [154] (see Section 5.2). Although multilayered R/R systems were carefully studied as well, they are

less adaptable for technological applications. The interested reader may find all information about this system reviewed in [155].

In thin-layered films the reciprocal influence of layers plays an important role. The presence of adjacent layers may effect structural transformation in iron or influence magnetic properties in a specific way. The  $\mu_{Fe}(L_{Fe})$  dependence for  $[Fe(L_{Fe})/Ti(1)]_n$  is shown in Figure 4a (curve 2) as a typical example [156]. It can be seen that the dependence is far lower than that for  $[Fe(L_{Fe})/Y(7.8)]_n$  multilayers (curve 1), because it is connected with interlayer mixing and formation of an amorphous Fe–Ti alloy or intermetallic compounds like  $TiFe_2$  with reduced magnetization. At the same time, significant interlayer diffusion may be caused by peculiarities of the preparation method (rf ion sputtering or molecular beam epitaxy) and/or by properties of contiguous materials.

There are few data in the literature about the individual characteristics of Co when it forms part of a R/T structure. To a certain degree these are determined by the weak correlation, already discussed, between the atomic structure and magnetic properties of cobalt. However, this ferromagnetic material combines resistance to structural transition and sensitivity to the influence of the adjacent layers. It follows from the analysis of the properties of multilayered films containing both Co layers and nonmagnetic spacers. Figure 4b shows the dependence of the Co layer spontaneous magnetization,  $M_{Co}$ , on the thickness of the Co layer as a part of  $[Co(L_{Co})/Cu(2.5)]_{20}$  (curve 3) and  $[Co(L_{Co})/Si(2)]_{20}$  (curve 4) structures. In both cases, the decrease in the magnetic layer thickness leads to  $M_{Co}$  decay but it appears at different intervals of  $L_{Co}$ .

For Cu spacers, appreciable changes of magnetization occur at  $L_{Co} < 2$  nm whereas in nonmonocrystalline multilayers the disturbance of continuity (or granulation) plays a dominant role. It leads to a decrease in the magnetic ordering temperature and an increase in superparamagnetism [157]. In films with Si spacers the decrease of magnetization begins at higher thicknesses ( $L_{Co} \leq 20$  nm) and therefore at  $L_{Co} < 2$  nm layers are nonmagnetic. X-ray and electron diffractions do not detect the presence of Si compounds, which may cancel out the magnetically ordered state of Co. In connection with this process, the change of the electron structure of Co by electrons of Si spacers (charge transfer effect) is the most probable reason for the  $M_{Co}$  decrease. Perhaps this phenomenon takes place at the contact of Co and Si. The thickness of the transition region with changed electron structure may reach 1.5 nm. This phenomenon can also be observed in homogeneous, amorphous Co–Si films [158].

Let us now turn to rare earth metals. From the R elements mentioned above, gadolinium has a maximum Curie temperature of 293 K, and it is the only collinear ferromagnet at all temperature intervals below  $T_c$ . Tb and Dy display ferromagnetic ordering up to 215 and 85 K, respectively. Tb and Dy have helical magnetic structures over the temperature intervals of 215–230 and 85–179 K, respectively. This structure does not produce total magnetization. In addition, these metals have very different magnetic anisotropy. The spherical shape of the electron shell of Gd ions causes low crystalline magnetic anisotropy, but anisotropic Tb and Dy ions form high single-ion anisotropy. This peculiarity

is a reason for the practical interest in R/T multilayered films, with  $R = \text{Tb}$  as a medium, for perpendicular magnetic recording. However, Gd is more suitable for the analysis of magnetism of rare earth metals in the thin film state.

The majority of studies devoted to Gd thin layers have been carried out on single crystal (epitaxial) samples, both homogeneous Gd films [159, 160] and layered structures composed of Gd layers and nonmagnetic spacers [89, 90, 96, 143, 148, 149, 161–164]. The results of these investigations do not always agree. For example, an oscillation of the Gd magnetic moment with  $W$  thickness was detected for Gd/W multilayers in [161], with  $Y$  thickness in [143, 148], and it was not detected in [162]. It was shown [148, 149] that the sign of the exchange interaction between two Gd layers in a Gd/ $Y$  structure may oscillate, being positive or negative as a function of the thickness of the  $Y$  layer. The oscillation period is a function of the number of  $Y$  spacers in this case. Some properties, including the dependence of Curie temperature on Gd thickness, were measured reliably enough. Corresponding experimental data for multilayered films can be found in [162]; here the decrease of  $T_c$  with the reduction of  $L_{\text{Gd}}$  takes place. The study devoted to Dy thin layers in a Dy/ $Y$  system have been carried out in [150].

We should also mention the sensitivity of spontaneous magnetization to heat treatments. According to [160] annealing at temperatures up to 620 K increases the slope of  $M_s(T)$  dependence and the  $T_c$  rises substantially, by up to 15°. The authors of [160] connect this change in magnetic properties with the relaxation of microstrains of structural defects and macrostrains caused by the difference of crystalline lattice parameters in the film–substrate system. Thus, the fundamental characteristics of magnetic ordering in Gd films exhibit sensitivity to structural conditions. This unusual phenomenon is probably associated with the peculiarities of exchange interaction in rare earth metals, namely long-range and distance oscillation.

In multilayered R/T structures the epitaxial growth of the layers is impossible because of large differences in the parameters of the crystalline lattices of R and T metals. Moreover, both thin rare earth and 3d metal layers tend to amorphization (see Section 2.2). Naturally, one might suppose that the changes in the magnetic state are a consequence of the structural transformation of gadolinium. The corresponding experimental data for rf-sputtered Gd/Cu and Gd/Si films [97, 98] are shown in Figure 5: the dependence of a specific torque mechanical moment  $P$  on the temperature for the bulk sample (curve 1), for a single-layered Gd film of 720 nm (curve 2), and for a multilayered  $[\text{Gd}(L_{\text{Gd}})/\text{Cu}(1)]_n$  with different thicknesses of magnetic layers (curves 3 and 4). Let us keep in mind that  $P(H)$  dependency reflects the spontaneous magnetization behavior in the absence of structural anisotropy.

The comparison of  $P(H)$  curves provides the basis for concluding that even a very thick uniform film has a lower Curie temperature (of about 250 K) and smoother magnetization changes than the bulk sample. The transition into the thin film state by introduction of Cu sublayers is accompanied by an additional decrease of the Curie temperature and the appearance of a fold point in the 160 K zone. This behavior of the mechanical moment indicates the multiphase magnetic state of Gd layers and its dependence on

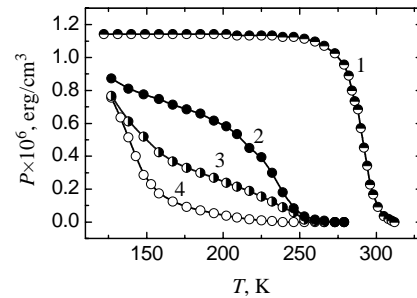


**Figure 5.** Temperature dependence of torque of a Gd bulk sample (1) and  $[\text{Gd}(L_{\text{Gd}})/\text{Cu}(1)]_n$  films with different magnetic layer thicknesses: (2) 780 nm; (3) 22.5 nm; and (4) 7.5 nm. Reprinted with permission from [98], V. O. Vas'kovskiy et al., *Physica B* 315, 143 (2002). © 2002, Elsevier Science.

Gd layer thickness,  $L_{\text{Gd}}$ . Very similar results were reported for  $[\text{Gd}(L_{\text{Gd}})/\text{Si}(1)]_n$  showing clear differences between Co and Gd. The properties of the latter are not very sensitive to the properties of adjacent magnetic layers.

Figure 6 shows the microstructure and diffractogram for  $[\text{Gd}(L_{\text{Gd}})/\text{Si}(1)]_n$  structures with various thicknesses of Gd layers. The absence of sharp lines (Fig. 6a) is a typical indication of the amorphous state of a thin Gd layer. The state of the samples with  $L_{\text{Gd}} = 15$  nm (Fig. 6b) is intermediate; there are both amorphous and crystalline parts as well as for the samples with  $L_{\text{Gd}} = 40$  nm (Fig. 6c). However, in the last case the crystalline  $\alpha$ -Gd phase is better separated and quantitatively dominates.

The results of the study of layered Gd films show a direct connection between the structure and effectiveness of the

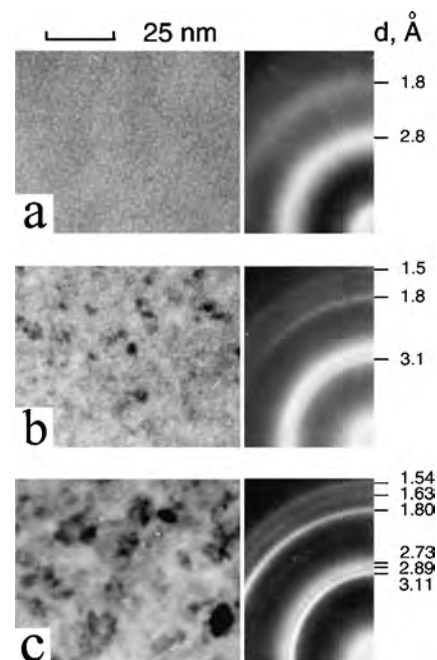


**Figure 6.** Electron diffraction patterns and microstructure for  $[\text{Gd}(L_{\text{Gd}})/\text{Si}(1)]_n$  films with different magnetic layer thicknesses: (a) 7.5 nm; (b) 15 nm; and (c) 40 nm. The numbers indicate the interplanar distances  $d$  corresponding to the different lines under study.

exchange in the rare earth metals. Curie temperature decay and spin system frustration occur as consequences of the degradation of the crystalline structure. Space amorphization of the rare earth metals takes place over a wide interval of layer thicknesses by the mechanism of microdeformation accumulation. The coexistence of crystalline, amorphous, and a number of intermediate phases leads to multiphase magnetic states of rare earth layers.

Interlayer interfaces may play an important role in R/T magnetism. In Section 2 we described the discussion related to the role of interfaces. Once the idea of the existence of interfaces is accepted, it is logical to suppose that they have a structure of amorphous R–T alloys with a varied composition depending on the thickness. Amorphous R–T systems, especially Gd–Co, are well known in the physics of magnetically ordered materials. The key property of all systems with heavy rare earth ions is collinear ferrimagnetism. Moreover, in contrast with crystalline ferrimagnetic materials, the amorphous alloys show continuous change of the value of sublattice magnetizations as a function of composition.

Typical dependencies on temperature for spontaneous magnetization of amorphous  $Gd_xCo_{100-x}$  films were reported in [165]. The special selection of the composition helps to show the most interesting feature of magnetization behavior, that is, nonmonotonous changes of  $M_s(T)$ . The difference in temperature dependencies of magnetization of sublattices of gadolinium ( $M_{Gd}$ ) and cobalt ( $M_{Co}$ ) condition this behavior. At a certain point near the compensation temperature,  $T_{comp}$ , the magnetization absolute values are equalized ( $M_{Gd} = M_{Co}$ ) and a minimum of  $M_s(T)$  appears. The compensation temperature of amorphous ferrimagnetic materials is a monotonous function of composition.

Experimental values were compared with those calculated by the mean field theory of magnetization for  $Gd_{21}Co_{79}$  and  $Gd_{18}Co_{82}$  films [166]. Although, the theoretical description matches the experimental data well enough, it is necessary to make the correct allowances for a large number of parameters, for example, Co spin. Cobalt spin is sensitive to composition and decreases abruptly as the gadolinium concentration increases [167]. Co does not have a magnetic moment at Gd concentrations above 50 atomic %. It occurs because of the charge transfer effect described above. In this case the Co electron structure changes by Gd one. This feature, together with the charge transfer in Co/Si layers, suggests a high probability of charge transfer in Gd/Co multilayers.

### 3.2. Spontaneous Magnetization

In the earliest publications about R/T multilayered films, exchange interactions between layers were identified [2, 3, 136]. The character of the exchange interactions in R/T systems is very similar to that of homogeneous R–T materials between R and T subsystems. The magnetic moments of the Fe and Co layers are parallel to the magnetic moments of the light R element layers and antiparallel to the magnetic moments of the heavy rare earth element layers. This last case is most interesting because it corresponds in some way to a ferrimagnetic structure, where the magnetic moments of R and T layers play the role which,

in a classic ferrimagnet, would be played by the magnetic moments of the sublattices.

The spontaneous magnetizations  $M_s(T)$  of different ferrimagnetic multilayers, such as homogeneous R–T ferrimagnetic materials, have very different temperature dependencies [4, 38, 41, 91, 54]. For example, nonmonotonous dependencies of  $M_s(T)$  may either increase or decrease at different layer thicknesses, as a result of the behavior of partial R and T layer magnetizations and variations in their contributions to  $M_s$ . The minimum can be identified as a magnetic compensation state where the magnetic moments of the R and T subsystems are equal. However, in contrast with homogeneous R–T ferrimagnets,  $M_s(T)$  is significantly higher than zero for R/T multilayers. To explain this difference, one might suggest the higher level of volume heterogeneity of the R/T system due to the surface relief, for example.

The changes of layer thickness in ferrimagnetically ordered multilayers correspond to changes of the composition in homogeneous RT ferrimagnets. At the same time it is not the only factor influencing R/T spontaneous magnetization. If the layered structure contains iron, as mentioned in Section 3.1, amorphization and decreases of the atom magnetic moment may occur as a result of the reduction in the thickness of the layers. Some quantitative data on this subject are reported for  $[Gd/Fe]_n$  multilayers with equal thickness of the iron and gadolinium layers  $L_{Fe}$  and  $L_{Gd}$ , with a different period of the structure  $L_p = L_{Fe} + L_{Gd}$  [130]. The sharp decline in the magnetic moment  $\mu_{Fe}(L_p)$  appears for  $L_p < 15$  nm. The decrease in the contribution of the Fe layer to the spontaneous magnetization of the whole structure should result in the growth of the compensation temperature with an  $L_p$  decrease. The same tendency was observed for  $[Gd/Fe]_n$  films. The  $\mu_{Fe}(L_p)$  value [130] was calculated on the basis of spontaneous magnetization measurements made at temperature  $T = 4.2$  K, assuming independence from the thickness of the layers for the Gd magnetic moment on. It is a logical assumption, but there is a probability that Gd amorphization, which takes place with the reduction of the Gd layer thickness, is accompanied by noncollinear magnetic structure formation. The consequences of this transition are decreases in the level of the contribution of Gd subsystem and in the accuracy of the  $\mu_{Fe}$  definition. Another point to discuss is the exchange interaction feature. The temperature dependence of the spontaneous magnetization of Gd is a function of the exchange parameters: it has an “internal” Gd–Gd component and an “external” Gd–Fe exchange part. The exchange interaction between the layers, Gd–Fe, depends on the distance: it is at a maximum level near the interface and decays toward the center of the Gd layer. Therefore, the effectiveness of the exchange in Gd increases with the  $L_{Gd}$  decrease. As a result, in multilayers with thinner layers, magnetization declines less abruptly with temperature and  $T_{comp}$  is higher. The above-described mechanism and the  $\mu_{Fe}(L_p)$  dependence have similar tendencies of  $T_{comp}(L_p)$  change; therefore, their separation is not an easy task and has to be supported by additional theoretical analysis.

Let us now examine the role of exchange interaction between layers in multilayered structures using  $[Gd/Co]_n$

as a model. This system shows nonmonotonous temperature dependence of spontaneous magnetization at certain intervals of the layer thickness. Figure 7 shows compensation temperature dependencies on the value of the period of layered structure at a fixed ratio of  $L_{\text{Gd}}/L_{\text{Co}}$  [99, 100]. In both cases the compensation temperature increases as the period of the multilayered structure decreases. Because spontaneous magnetization of Co is not very sensitive to amorphization, the main reason for the increase in compensation temperature is probably an increase of the magnetic order in Gd due to growing exchange influence of Co. Here again additional comments are needed. The structural transitions of Gd may influence its contribution to the spontaneous magnetization and consequently the compensation temperature. The charge transfer may play a certain role as well. We mentioned in Section 3.1 that the charge transfer effect results in a decrease of the Co atomic magnetic moment. The charge is carried through the interface; therefore, its influence should become less important toward the center of the layer. To summarize, the magnetization of the Co layer can be nonuniform over the layer thickness. When the  $L_{\text{Co}}$  gets smaller, the relative role of the interfaces, where the magnetization is smaller, increases, and average magnetization corresponding to all parts of the Co component decays. The consequence of these peculiarities is that spontaneous magnetization depends on the structural state of the films or the preparation technology. The discrepancy between the experimental results reported in [99] and [100] can be explained by taking into account the fact that the authors used multilayers with very different thickness ratios,  $L_{\text{Gd}}/L_{\text{Co}}$  being 2.5 and 1.2, respectively.

Additional information about spontaneous magnetization can be derived from the study of structures with relatively thin layers. For example, the dependence of the specific magnetization,  $\sigma$ , of the systems  $[\text{Tb}(0.45)/\text{Fe}(L_{\text{Fe}})]$  and  $[\text{Dy}(0.5)/\text{Fe}(L_{\text{Fe}})]$  on the Fe layer thickness was reported in [168]. The shape of the  $\sigma(L_{\text{Fe}})$  curves is rather complicated. The measurements were performed at room temperature, that is, the state when Tb and Dy are not magnetically ordered. Apart from this, thin Fe layers are in an amorphous state and can be nonferromagnetic as well. Therefore, in the  $L_{\text{Fe}} < 0.7$  nm region, we observe the presence of detectable magnetization connected with formation of the amorphous Tb-Fe and Dy-Fe alloys due to mixing of the adjacent layers. The magnetization changes for thin Fe layers depend on the variations in composition of the mixed interfaces.

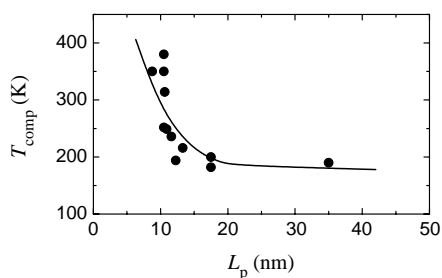


**Figure 7.** The dependence of compensation temperature on the period of  $[\text{Gd}/\text{Co}]_n$  films. Reprinted with permission from [99], A. V. Svalov et al., *J. Alloys Compd.* 327, 5 (2001). © 2001, Elsevier Science.

Changes in the  $\sigma$  sign values mean changes in the relative magnetizations of each sublattice in the ferrimagnetic R-Fe structure. In the  $L_{\text{Fe}} \sim 1$  nm region two curves have a fold and plateau, these being the manifestation of the appearance of Fe amorphous layers with minimum magnetization and increasing thickness. Consequently, we conclude that the thickness of the interface of the variable composition from the Fe side can be up to 0.5 nm. The sharp growth of magnetization immediately after the plateau is the consequence of the Fe crystallization and its transition into a high-spin state. The critical thickness of high-spin state transition depends on the composition adjacent to the iron layers.

Together with the magnetic layer thickness, nonmagnetic spacers introduced between R and T metals can be considered as an effective instrument for influencing spontaneous magnetization of the R/T structures. It is clear that nonmagnetic spacers should decrease the interlayer exchange and transform the  $M_s(T)$  dependence. The following publications on the use of nonmagnetic spacers are of interest: [28, 143, 148] for Y and Cu, [30] for Si and Cu, and [31] for Cr and Pt with Gd/Co as a model structure. The Gd/Co system is characterized by having the strongest interlayer interactions. The compensation temperature was found to be very sensitive to the state of the interface quantitative parameter. Figure 8 shows examples of the  $T_{\text{comp}}$  dependencies on the thickness of Cu and Si spacers. One may compare these data taken for  $[\text{Gd}(7.5)/\text{X}/\text{Co}(3)/\text{X}]_{20}$  films with very interesting results for  $[\text{Gd}(3)/\text{X}/\text{Co}(3)/\text{X}]_n$  multilayers for Y and Cu spacers [28]. We observed a decrease in the compensation temperature as the thickness of spacers  $L_s$  increased as a result of the weakening of the ordering exchange influence of Co on Gd and the decrease in the gadolinium magnetization.

This general tendency for change in the compensation temperature can also be accompanied by a significant quantitative difference of the  $T_{\text{comp}}(L_s)$  behavior for spacers of different composition. The spacer can work as a passive element, simply changing the distance between magnetic layers, but most probably the increase in thickness of nonmagnetic spacers plays an active role at the interval of 0 to 1 nm. The active parts of nonmagnetic spacers have an island structure and the  $L_s$  increase actually corresponds to a decrease in the area of direct contact between magnetic layers. Thus, the particular morphology and relief of each component of the multilayer may be important parameters. The

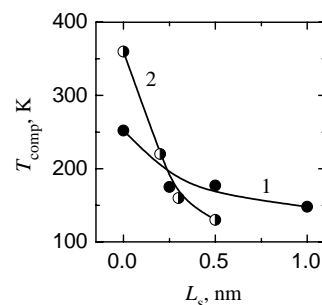


**Figure 8.** The dependence of compensation temperature on X spacer thickness for  $[\text{Gd}(7.5)/\text{X}/\text{Co}(3)/\text{X}]_{20}$  films: (1) Cu; (2) Si; experimental data, circles; result of calculation, lines.

effectiveness of the interlayer exchange interaction, which is achieved most probably by an indirect mechanism, should depend on the conductivity of nonmagnetic spacers. Neither the direct nor the indirect mechanism has yet been systematically studied.

Nonmagnetic spacers may play an active role and influence the adjacent layers. For example, the authors of [28] associated the tendency for rapid reduction of the compensation temperature in multilayered structures with the introduction of additional Cu layers and the consequent formation of a nonmagnetic part of the Gd–Cu alloy. The effective thickness of nonmagnetic layers is increased compared with the calculated Cu layer thickness. However, such an abrupt compensation temperature decline (Fig. 8, curve 1) was not observed in another study. Even more curious, one might think that the heat treatment ought to result in the Gd and Cu mixing and a decrease in the compensation temperature, but the data of [101] show an increase in  $T_{\text{comp}}$  in the case under consideration. The results of the Si spacer introduction are less uncertain (Fig. 8, curve 2). The high Si effectiveness may be attributed to the phenomenon of charge transfer from Si to Co. Silicon brings down the magnetization of Co in the area near the surface and weakens the exchange interaction more than would be the case if it were just simply increasing the distance between interacting layers.

In concluding this section, we can say that spontaneous magnetization of R/T multilayers with heavy rare earth elements acts in accord with the general principles of ferrimagnetism, but localization of the negative exchange interaction in the contact zone results in spontaneous magnetization being highly sensitive to the geometrical, structural, and compositional characteristics of the multilayered films.

### 3.3. Magnetic Structure of R/T Multilayers in a Magnetic Field

The general features of R/T multilayer magnetism are determined by the exchange interactions between R and T magnetic systems forming pseudo-ferrimagnetic structures. One effective way of getting information about these exchange interactions is to study their magnetization processes. This study is especially attractive in the case of R/T films because it is possible to modify the properties in relatively low fields. The magnetic phase transitions induced by the external magnetic field is one of the important indications of collinear ferrimagnetism. The transitions from the collinear to the noncollinear phase [102–107] were found in different R/T multilayers by magnetometry [169], magnetoresistance measurements [170], magneto-optic effects [108], Mössbauer spectroscopy [171], and resonant X-ray magnetic scattering [109].

The distinctive feature of a magnetic phase transition is a change in the slope of the magnetization curve or hysteresis loop  $M(H)$  (see example for  $[\text{Gd}(10)/\text{Co}(10)]_{50}$  in Fig. 9 [110]). One may see break points, which correspond to the appearance of noncollinear structures in both the positive and negative fields. Even more pronounced transformations are seen on the magnetoresistive curve  $\Delta R(H)$  (Fig. 9). The measurements of the magnetoresistance were done in parallel geometry, that is, with the current flowing parallel to the direction of the applied magnetic field.

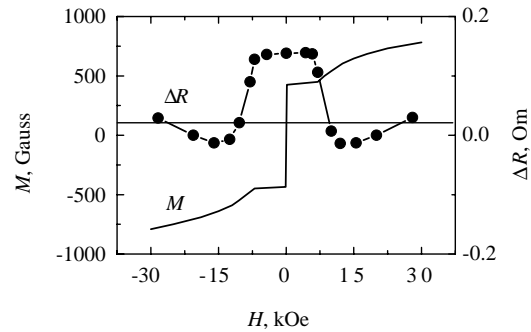


**Figure 9.** The dependence of magnetization  $M$  and longitudinal magnetoresistance  $\Delta R$  on the magnetic field for  $[\text{Gd}(10)/\text{Co}(10)]_{50}$  films at 5 K. Reprinted with permission from [110], H. Nagura et al., *J. Magn. Mater.* 240, 183 (2002). © 2002, Elsevier Science.

The break points of the magnetization curves can only be easily detected in a low temperature region ( $\sim 4.2$  K). At higher temperatures the paraprocess in gadolinium plays a “masking” role. Figure 10 shows the hysteresis loop of  $[\text{Gd}(7.5)/\text{Si}(0.5)/\text{Co}(3)/\text{Si}(0.5)]_{20}$ , measured at 97 K [111]. Against the background of the monotonous magnetization changes, the break points of the  $M(H)$  curve, which are related to the noncollinear structure formation, are almost invisible. In this case the magnetoresistance and magneto-optical effects are more helpful as indicators of the phase transitions. The difference between the magnetic hysteresis loop  $M(H)$  and the magneto-optical  $F(H)$  loop (Fig. 10) confirms this conclusion. The higher sensitivity of the  $\Delta R(H)$  and  $F(H)$  curves in the break point visualization is due to the fact that the magnetoresistance anisotropy and the plane of the light polarization rotation (Kerr effect) are much higher for 3d than for rare earth metals. Therefore, as the paraprocess takes place mainly in the R subsystem it makes only a very small contribution to the  $\Delta R$  and  $F$  values.

Mössbauer spectroscopy is usually associated with the introduction of the  $^{57}\text{Fe}$  isotope into the system being studied. It is very productive, therefore, for the R/Fe multilayers and gives information about the state of Fe layers [32, 42, 171] such as the  $T$ - $H$  phase diagram for Gd/Fe systems with various layer thicknesses [32]. In the coordinate plane of “temperature–magnetic field strength,” it represents the areas where the different magnetic phases exist in

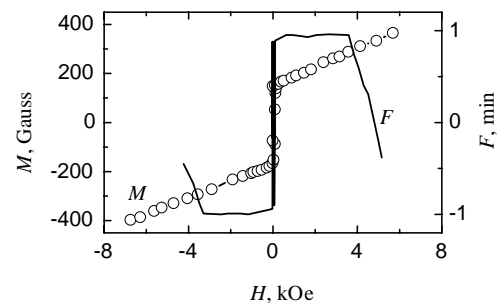


**Figure 10.** Field dependence of the magnetization  $M$  and Kerr rotation  $F$  for  $[\text{Gd}(7.5)/\text{Si}(0.5)/\text{Co}(3)/\text{Si}(0.5)]_{20}$  at  $T = 97$  K. Reprinted with permission from [111], D. N. Merenkov et al., *Low Temp. Phys.* 27, 137 (2001). © 2001, Fizika Nizkih Temperature.



the structure with a compensation temperature of  $\sim 200$  K. These areas are separated by the curve that defines the critical field of the phase transition for each temperature. The areas corresponding to the collinear structures are situated below this curve, where the magnetic moment of Gd layers is parallel to the field for  $T < T_{\text{comp}}$ , and for  $T > T_{\text{comp}}$  the external field direction and the magnetic moment of Fe are also parallel. Above the critical field curve lies the area of the angular phase, this phase is described as *twisted*.

The term *twisted magnetic phase* was not introduced by accident, but specifically to emphasize a special feature of noncollinear magnetic structure in layered materials. In contrast to uniform ferrimagnets, in multilayers the negative exchange interaction between magnetic elements is spread nonuniformly through the multilayer volume: the highest value corresponds to the interfaces and it decays very fast toward the center of the magnetic layer. As a result there is a spatial nonuniformity in noncollinear structures, in which the angle between the local magnetization and an external field decreases from the separating interface toward the center of the layer. Very weak self-exchange interaction and the dependence of the magnetization of R layers on the thickness produce additional complications. The latter is conditioned by the magnetic action of the 3d layer in the area near the interface on the Gd in this area. As a result, the twisted magnetic structure is formed basically in R layers and is characterized by the angular and amplitude dependence of the magnetization. This model was first developed theoretically [172] and then confirmed by resonance X-ray magnetic dispersion [24, 109].

Magnetic phase transitions can be stimulated not only by magnetic field variation but also in a fixed field by temperature variation (see as an example the measured and calculated  $T$ - $H$  diagram for  $[\text{Gd}(8.4)/\text{Fe}(4.2)]_n$  in [32]). The temperature dependencies of R/T multilayers magnetization are peculiar in this case. Figure 11 shows  $M(T)$  dependencies

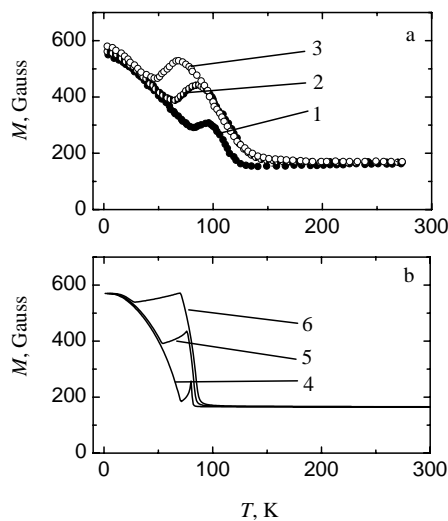


**Figure 11.** Experimental (a) and calculated (b) temperature dependencies of the magnetization of  $[\text{Gd}(7.5)/\text{Si}(1)/\text{Co}(3)/\text{Si}(1)]_{20}$ . The curves are recorded in the fields  $H = (1)$  and  $(4)$  200 Oe,  $(2)$  and  $(5)$  500 Oe,  $(3)$  1000 Oe, and  $(6)$  750 Oe. Reprinted with permission from [112], G. S. Patrin et al., *JETP Lett.* 75, 159 (2002). © 2002, IAPC “Nauka/Interperiodica.”

for a  $[\text{Gd}(7.5)/\text{Si}(1)/\text{Co}(3)/\text{Si}(1)]_{20}$  multilayered structure, with in-plane measurements made for the magnetic field of 200–1000 Oe [112]. All curves have local maxima. Their origin seems to be associated with the existence of a noncollinear magnetic structure and the increase of the magnetization within its frame. The low values of critical fields are related to weak interlayer exchange in the R/T structure because of the presence of the nonmagnetic Si spacer. The increase in the magnetic field strength results in the extension of the temperature interval where the anomalous critical points appear basically by extension in the low temperature region. On the high temperature side, the positions of the anomalous critical points are limited by the Gd transition to the paramagnetic state.

R/T multilayers show the disturbance of the collinear structure in the magnetic field, that is, the most general property of all low anisotropy ferrimagnets. Special features of multilayered structures are the low field of the magnetic phase transitions and space nonuniformity of the twisted magnetic phase.

### 3.4. Phenomenological Models

Although results of many experiments on the magnetic properties of R/T multilayers have been published recently, their microscopic theory remains to be developed. The situation is easy to understand, because of the influence of factors such as their complicated structural/chemical state and the strong role of technological factors when it comes to the repetition and comparison of experimental data. Meanwhile phenomenological models of interlayer exchange based on mean field theory have been developed.

The simplest model supposes nonuniform layer mixing; for Co/Dy see, for example, [37]. According to this model there is a sine-shaped modulation of the composition over the thickness from pure Co to pure Dy. To calculate spontaneous magnetization, the film has to be sectioned into thin sublayers of corresponding composition of amorphous Dy–Co for each one. The calculation corresponding to all layers enables us to calculate the temperature dependencies of the spontaneous magnetization  $M_s(T)$  for different periods of the layered structure. Using the Co/Dy system as a model, Shan et al. [37] demonstrated the nonmonotonous behavior of the calculated dependencies and achieved reasonable agreement with experiments. But, at the same time, this approach should be considered as something of a simplification, because it does not allow adequate description of the field behavior of the magnetic structure.

Mixing of the layers is the key assumption of a more complicated theory [173] where the R/T layered structure is treated on the base of a cubic lattice with partial mixing of the different types of atoms in the interface area. In a Heisenberg model framework, using Monte Carlo simulations, it was shown that the temperature dependence of spontaneous magnetization, compensation, and Curie temperatures may depend on the layer thickness and the interface state. The theoretical and experimental results for Tb/Fe structures are in satisfactory agreement, when one takes into consideration the concentration dependencies of the atomic exchange parameters and variation of the Tb atomic magnetic moment.

In contrast, the well-defined layers approach is used in [174] with the iteration method to find the equilibrium magnetization distribution with temperature and applied field as parameters. The film structure is divided into thin sublayers with uniform magnetization in each one as oriented in the plane of the sublayer. The transfer from one sublayer to the next is characterized by changes to the value and orientation of magnetization in a discrete way. Both the first and second sublayers depend on the kind of atoms under consideration (R or T) and the presence of an effective field in each sublayer. In the absence of magnetic anisotropy and self-demagnetization, the effective field in each sublayer consists of the sum of the external field and the exchange fields of the adjacent sublayers. The exchange fields between layers of the same composition are positive and those of different compositions are negative. The aim is to construct the configuration of the magnetic moments to minimize the energy in the external field and the exchange energy of the system.

The search for equilibrium magnetic configuration is carried out by the iteration method. In the initial state there is random orientation of the magnetic moments of all layers. The first iteration consists of fixing of the magnetic moment of a randomly selected sublayer parallel to the effective field and calculation of its value at a certain temperature. The temperature dependence of the magnetization is described by the Brillouin function. Then the whole procedure is repeated for the fixed moment of the first sublayer and repeated until we have achieved parallel orientation of the magnetic moments and local effective fields in all sublayers and their corresponding values at the temperature under consideration. This state corresponds to the minimum of free energy.

In the localized layer model [44, 172, 175] efforts have been made to use an analytical approach to describe R/T structures according to molecular field theory. The spontaneous magnetization at  $T = 4.2$  K and temperature dependence of the  $M_s$  were calculated for Gd/Fe multilayers with different periods of the layered structure. The agreement with experimental data is close enough, given the condition of a sharp decay of the magnetic moment of Fe atoms in the films with less than a 15 nm period. This condition seems to be related to the Fe transition to the amorphous state.

Among the studies based on the sharp interface approach, we have listed a theoretical study [176]. Here the exchange interaction is assumed not only to be effective at the interface but also to be spread through the volume by exponential decay. Therefore, the authors use an additional model parameter, the characteristic length of the exchange interaction ( $l_{ex}$ ). Temperature dependencies of the spontaneous magnetization for Tb/Co multilayers with different layer thickness and different compensation temperatures have been calculated according to mean field theory. The best agreement of the theory with an experiment was found at  $l_{ex} = 0.5$  nm.

In another nonuniform interlayer exchange model [30, 93, 99, 113], assumptions are made about exponential law for the exchange interaction and the iteration method is used for definition of the equilibrium magnetic structure. Figure 12 (curve 1) shows the temperature dependence of spontaneous magnetization for the  $[Gd(7.5)/Co(3)]_{20}$  structure calculated by this method. The result of  $M_s(T)$

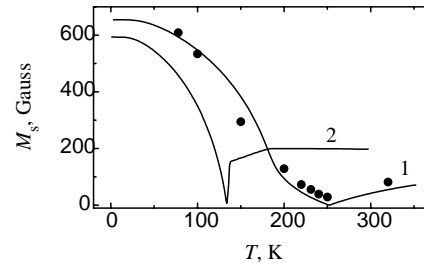


**Figure 12.** Temperature dependence of the magnetization for a  $[Gd(7.5)/Co(3)]_{20}$  film: circles, experimental results; (1) calculated by the model of nonuniform exchange interaction between layers; and (2) by the model of partial mixing layers. Reprinted with permission from [113], A. V. Gorbunov et al., *Phys. Met. Metall.* 91, 560 (2001). © 2001, IAPC “Nauka/Inteperiodica.”

calculations for the mixed layers model, but without taking interlayer exchange into account, is shown in Figure 12 (curve 2) for comparison. The first model describes the experimental data (points) better. The studies [30, 93, 99, 113] take into account the influence of different neighbors on magnetic properties of the R and T layers. As a result changes in the compensation temperature of the Gd/Co films with nonmagnetic spacers were calculated (Fig. 10) and anomalies in the temperature dependencies of the magnetization were explained (Fig. 11b).

In summary, there are several phenomenological models of R/T magnetism. The majority of them give a satisfactory description of the temperature dependence of spontaneous magnetization and magnetization behavior in the magnetic field. It is difficult to say which one is the best, because all of them operate by adjusting some theoretical parameters, but we can state the general principle, which helps achieve adequate description of the magnetic properties of R/T multilayers, namely, the presence of long range, nonuniform exchange between R and T layers and the reciprocal dependence of the atomic and electronic structures of the adjacent layers.

#### 4. MAGNETIC ANISOTROPY

Why do R/T multilayers attract so much attention in the scientific community? The answer is simple: because they may have perpendicular magnetic anisotropy (PMA) [2]. PMA is uniaxial magnetic anisotropy with an easy magnetization axis perpendicular to the plane of the film; that is, the orientation of the magnetization vector is perpendicular to the plane of the layered structure, even without application of an external magnetic field. Because of this property R/T multilayers are considered as a potentially interesting medium for perpendicular recording, including magneto-optical perpendicular recording [177]. Other interesting magnetic anisotropy features of these materials are very high PMA value [41], localization of most anisotropy parts in areas near to the surface of the magnetic layers [62], and the characteristics of the shape anisotropy of R/T multilayered structures [115].

#### 4.1. Structural Origins of Perpendicular Magnetic Anisotropy

Macroscopic magnetic anisotropy is the manifestation of structural anisotropy, which appears in one way or another in all magnetically ordered systems. The main kinds of structural anisotropy, which may drive magnetic anisotropy are crystalline lattice, preferred orientation of the axes of like-atom pairs, anisotropy elastic deformation, nonuniform distribution of the defects over the grain boundaries, ordered distribution of microscopic structural formations possessing shape anisotropy, and shape anisotropy of the macroscopic objects.

All of the structural features mentioned above can appear in thin films. However, such small subjects have an additional very specific feature, namely, surface anisotropy. This occurs when atoms located near the surface are in a specific position. The surface atoms have asymmetrically arranged nearest neighbors. The volume fraction of these atoms and role of the surface anisotropy increase with a decrease in the thickness of the layer. In multilayered systems, the atoms near the interfaces are in the same situation. Therefore, in the majority of publications related to the study of R/T anisotropy, the most attention has been devoted to the structure of the interfaces.

We discussed the size parameters of interfaces in Section 1, but more detailed data on the atomic structure of the interfaces are needed to understand the nature of their magnetic anisotropy. One of the sources of such information is the method of extended X-ray absorption fine structure (EXAFS). On the basis of data collected by the EXAFS method for Tb/Fe, the atomic distribution anisotropy in the interfaces can be quantified [178–180]. The main effect is interlayer diffusion with a preference direction perpendicular to the interface plane. As a result there is asymmetry for nearest neighbors around any selected atom: on the side of the terbium layer there are more Tb atoms among the nearest neighbors and there are more iron atoms on the Fe side.

Structural anisotropy is connected with a gradient of chemical components, oriented perpendicular to the multilayer plane. By analogy with perpendicular magnetic anisotropy, this is called perpendicular structural anisotropy (PSA). The PSA unit,  $K_{\text{psa}}$ , is the relative difference of probabilities for two atoms of the same kind to be nearest neighbors in the directions parallel and perpendicular to the film plane [180].

Figure 13 shows the experimental and calculated  $K_{\text{psa}}$  dependencies for iron atoms on the period,  $L_p$ , of the Tb/Fe layered structure if the thickness of the iron and terbium layers is the same,  $L_{\text{Tb}} \approx L_{\text{Fe}}$ . This dependence is non-monotonous with a maximum corresponding to the period value of 1–2 nm. This result is confirmed by experimental study of PMA. For example, one can compare the dependencies for the anisotropy constant,  $K_u$ , on the thickness of 3d layers in R/T structures of various compositions [37]. All  $K_u(L_T)$  dependencies have a maximum. Their position is variable on the  $L_T$  axis depending on the components, but always in the interval from 0.4 to 1 nm, the same as the position of the structural anisotropy maximum. At the same time linear decay of  $K_u$  was reported [57] for Tb/Fe structure in the interval of  $L_p$  from 0.6 to 5 nm. Although the

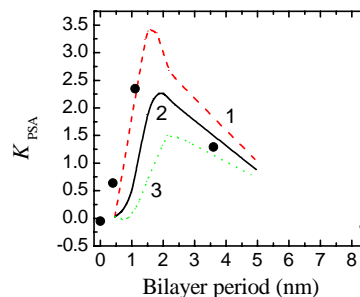


**Figure 13.** Comparison of experimental (circles) and calculated (lines) perpendicular structural anisotropy obtained from Fe EXAFS and simulation, respectively. Different curves corresponds to different diffusion degree. Reprinted with permission from [180], Y. Fujiwara et al., *J. Magn. Magn. Mater.* 177–181, 1173 (1998). © 1998, Elsevier Science.

relationship between PSA and PMA is not contested, PSA is mentioned in other studies [4, 39, 55, 181, 182]. The PMA value was also found to be almost independent of the substrate; that is, mechanical tensions which sometimes arise on the substrate–film boundary have very little effect [181].

#### 4.2. Mechanisms of Magnetic Anisotropy

The fact that perpendicular magnetic anisotropy in R/T multilayers depends on the structural magnetic anisotropy does not define the mechanism of magnetic anisotropy. The atomic structure of the interlayer interfaces described above has given rise to two different explanations of the principal governing PMA mechanisms. The first is two-ion anisotropy as a result of different dipole interactions of neighbor atoms (the Neel–Taniguchi and Yamamoto model). The second is single-ion anisotropy, which may occur because of spin–orbital interaction in metals that have anisotropic electron shells. Most research tends to favor the second theory. One of the arguments supporting the second point of view is easy to accept: strong PMA appears only in multilayers that contain anisotropic electron shell ions [58, 83, 84, 183]. The data on the anisotropy of Dy/Fe, Dy/Co, Tb/Co, Gd/Fe, and Gd/Co systems can be found in [37]. In multilayers with anisotropic Dy and Tb ions the perpendicular anisotropy constant is 1 order of magnitude higher than that corresponding to the spherical Gd ion. The authors of the Nd/Fe, Pr/Fe, and Gd/Fe study [38] came to the same conclusion.

However, nonspherical electron shell shape, that is, a nonzero orbital ion moment, is not in itself a sufficient condition for the formation of PMA. For instance, the comparative study of Fe/Nd and Fe/Tm multilayers [136] resulted in the fact that PMA was found only in the Fe/Nd multilayer although Tm is also a nonspherical ion.. The complete analysis of all R/Fe spectrum multilayers (R = Y, La, Ce, Pr, Nd, Sm, Eu, Gd, Tb, Dy, Ho, Er, Tm, Yb, or Lu) can be found in [56]. Only nonmagnetic Y, La, Yb, Lu, and Gd with zero orbital moment do not lead to single ion anisotropy formation. For other elements there is no prohibition, but PMA was found only in multilayers containing Pr, Nd, Tb, and Dy. Finally, not only is anisotropy of the electron shell important, but also the configuration of the crystalline field of the neighbor ions is important. Perhaps the atomic structure of the interfaces forming the crystalline field depends

slightly on the kind of rare earth atoms, but these variations are small and difficult to detect.

An even more surprising conclusion was drawn recently [69] on the basis of X-ray magnetic dichroism analysis of Tb/Fe multilayers where transformation of the Tb electronic structure was observed as a consequence of a decrease in the layer thickness. It consists of the loss of orbital moment by Tb ions automatically prohibiting their taking part in single ion anisotropy formation. In the Dy/Co study [181], the anisotropy dipole interaction of the atomic magnetic moments approach is used to describe PMA, in the same way as for Gd–Co amorphous films [184, 185]. However, in the multilayered structures the anisotropy carriers are localized in the interfaces, which leads to an almost incredibly high value of the parameter that defines the pair distribution anisotropy.

### 4.3. Influence of Various Factors on the Magnetic Anisotropy

To clarify the nature of the magnetic anisotropy in R/T multilayers, continued detailed investigation of the atomic structure of both magnetic layers and interfaces is needed. The lack of direct experimental data has stimulated many indirect studies of the influence of different factors on the PMA.

As a result of the temperature dependence of the Dy/Co multilayer magnetic anisotropy study [54], the PMA value at  $T = 4.2$  K was found to be many times stronger than that for  $T = 300$  K. The  $K_u$  temperature dependence correlates with  $M_{Dy}^2$  temperature behavior. This seems to support the single-ion theory of the PMA mechanism. Many attempts have been made to clarify the connection between different characteristics of interfaces and PMA, but it is not easy to make a comparative analysis of different authors' data because of differences in preparation and experimental methods.

The Mössbauer effect has been very useful for obtaining information about the magnetic anisotropy of R/T multilayers. In particular, it was shown that in Nd/Fe multilayers, magnetic anisotropy increases as the interface thickness decreases [186]. The decrease of PMA due to interface roughness was described in [68, 187]. In addition, the conclusion connecting PMA with a very wide mixed interface in the Tb/Fe system was reached [188]. In Dy/Co multilayers, the maximum PMA value was found at 0.6 nm for both Dy and Co layers. In this condition, the ratio of the interface size and the total volume is maximum [54, 87, 189].

It must be kept in mind that the interface structure may depend on the deposition order of the layers. The delicate experiments for the magnetic anisotropy study for two-layered Tb/Fe and three-layered Tb/Fe/Ag films [59–61, 190, 191] were carried out in this context. The interface was considered to be the major source of PMA for Tb deposition onto the Fe layer. The interfaces are sharp and, in this case, Fe has a crystalline structure. Fe deposition onto the Tb layer creates rough interfaces and initiates the amorphization of the layers [92]. The influence of different interfaces on PMA was investigated in the [Tb/Fe/Y]<sub>10</sub>, [Y/Fe/Tb]<sub>10</sub>, and [Tb/Fe]<sub>10</sub> systems [62]. The Y layer was introduced to exclude the Tb on Fe and Fe on Tb boundaries. All systems had more or less pronounced PMA. At temperatures below 100 K, stronger anisotropy was detected for Tb on Fe than

for Fe on Tb. In the 250 to 300 K temperature range, Fe on Tb related anisotropy was higher. A possible explanation might include the differences in magnetism for the two types of boundaries. At low temperatures strong single ion Tb anisotropy corresponding to the sharp interface dominates. At temperatures higher than that of Tb magnetic ordering (219 K) it decreases, but weaker anisotropy related to mixed boundaries starts to be important. The mixed boundary actually consists of a ferrimagnetic alloy of Tb–Fe with high Neel temperature. The length of this boundary results in low PSA and correspondingly small PMA. Comparison of PMA values at room temperature revealed the lowest  $K_u$  value for Tb on Fe, an intermediate value for Fe on Tb, and the highest for the two types of boundaries together because, apart from the one-ion anisotropy in Tb/Fe samples, dipole interaction between Fe layers through the Tb layer may take place. This mechanism was suggested as an explanation for the CeH<sub>2</sub>/Fe system anisotropy [193].

The magnetic layers themselves may play a certain role in the formation of magnetic anisotropy. The main point here is the influence of the thickness on the magnetic properties of each layer in multilayered structures. For example, the increase of magnetization and consequently of the demagnetizing field is the result of increased layer thickness in Tb/Fe multilayers [41] together with a decrease in PMA [67]. At the same time, amorphization of the relatively thin layers appears. At room temperature both Fe and Tb lose their magnetic order whereas a decrease in magnetic phase volume leads to a corresponding decrease in the PMA value. Similar ideas were considered for R/Fe (R = Pr, Nd, and Tb) system analysis [48].

There are data about the presence of PMA only in those Tb/Fe structures that do not have pure terbium [43, 44, 194]. When pure Tb layers have been included in a multilayered structure, PMA has been detected at temperatures below 220 K, that is, after the Tb transition in the ferromagnetic state. It is on this basis that the conclusion about PMA induction in the interfaces in the presence of the exchange interaction between Fe layers through the Tb layers has been reached. A similar result has been reported in a study by transmission electron microscopy of pure Tb segregation with Tb layer thickness of more than 1 nm [64]. The occurrence of segregation coincides with PMA disappearance at room temperature. However, there are also data about the presence of PMA in Tb/Fe multilayers with  $L_{Tb} = 2$  nm [65].

One interesting feature of the structural transition taking place in R/T structures as the layer thickness changes is the iron crystallization and, as a consequence, an increase in PMA, which is caused by the formation of a sharp interface between the layers [42]. Comparing the multilayer properties formed at two different substrate temperatures of 150 and 300 K, these authors found that iron crystallization took place at 300 K with thinner layers and it was precisely these samples, with a minimum thickness of crystalline Fe, which had the maximum PMA value. The increase of the perpendicular magnetic anisotropy value after heat treatments of Tb/Fe has been explained in other research by the very sharp interface formation [49, 63]. The temperatures and thickness of the layers related to structural changes of multilayers vary from one publication to another because of dependence on varying preparation methods.

Let us now return to the results of the R/T study at different temperatures. We have discussed the possibility of a significant increase in PMA values at low temperatures, but this is true only for structures with relatively thin layers, where the interfaces play the main role. At greater thicknesses the temperature decrease may cause an opposite effect, even so far as to change the magnetization orientation to the film plane from perpendicular into parallel. Such a reorientation of the spins is brought about by a change in the correlation between the induced perpendicular anisotropy and shape anisotropy. The existence of the reorientation itself and the reorientation temperature both depend on the average chemical composition of the multilayer (correlation of the thickness of the layers) and period of the layered structure [41]. The dependence on the multilayer period to a certain extent can be explained by changes of the interlayer exchange interaction whose role increases with a decrease of the period of the layered structure. Similar results were reported in [195], although in [63, 196] the authors found no dependence of the magnetization orientation on the thickness of the Fe and Tb layers at low temperatures.

An additional important factor influencing PMA is the number of periods,  $n$ , in multilayer structure [55, 66]. For  $[\text{Tb}(0.42)/\text{Fe}(0.75)]_n$  magnetization is oriented in the plane of the layered structure if  $n$  varies from 1 to 30. Increasing the number of layers ( $n$ ) up to 35 causes PMA to occur, but its value shows only very small changes for further increase in  $n$ . For the  $[\text{Tb}(0.95)/\text{Fe}(1.15)]_n$  structure, PMA appears at  $n \geq 5$ , but the authors do not discuss the possible origin of these variations [55, 66]. We might suppose that the temperature regime of deposition plays an important role because it may vary over the extended period of total deposition time needed for structures with high  $n$  value.

#### 4.4. Enhanced Magnetostatic Effect

The majority of the results discussed are related to R/T multilayers with perpendicular magnetic anisotropy. The most important condition of PMA formation is the presence of layers with anisotropic rare earth ions in a multilayered structure. Gd is irrelevant in this case. It makes Gd/T multilayers less attractive for magnetic recording applications. However, due to high Curie temperature and collinear ferromagnetism, Gd/T can be very useful as a model system for studying R/T structures [93, 114, 174, 197, 198]. Specifically, study of the magnetic anisotropy of a layered ferrimagnetic  $[\text{Gd}(7.5)/\text{Co}(3)]_{20}$  structure was undertaken in a magnetic compensation region of 200 to 300 K including the compensation temperature ( $T_{\text{comp}} \approx 240$  K) and no perpendicular anisotropy was detected [115]. In accordance with shape anisotropy, the magnetization was oriented in the plane of the films, but the actual shape anisotropy constant was much higher than  $2\pi M_s^2$ , where  $M_s$  is the spontaneous magnetization of the ferrimagnetic structure. Figure 14 shows  $K(T)$  and  $2\pi M_s^2(T)$  dependencies in the magnetic compensation region. This discrepancy disappears if we take into account an additional contribution in magnetostatic energy related to the rising of the magnetic charges in the interface areas. Because of a negative exchange interaction between Co and Gd, the surface density of these charges is defined as a sum

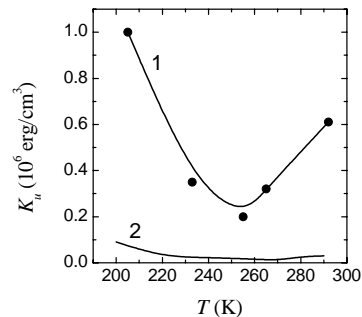


**Figure 14.** Temperature dependencies of magnetic anisotropy constants measured by a torquemeter (1) and calculated as  $K_s = 2\pi M_s^2$  (2), respectively. Reprinted with permission from [115], V. O. Vas'kovskiy et al., *J. Magn. Magn. Mater.* 203, 295 (1999). © 1999, Elsevier Science.

of the normal components of the magnetizations of the layers, but not as a normal component of total magnetization of the ferrimagnetic Gd/Co structure. A similar enhanced magnetostatic effect was also observed in  $\text{Gd}_{15}\text{Fe}_{85}/\text{Gd}_{40}\text{Co}_{60}$  amorphous multilayers [199].

## 5. ATTENDANT PROPERTIES

Magnetoordered substances possess a number of physical properties that are not directly related to the set of inherent magnetic properties, but become available because of the existence of spontaneous magnetization. Usually, they are revealed during magnetization and consist of changes in size (magnetostriction) or electrical resistance (magnetoresistance effect) of the samples or of changes in the characteristics of the refracted or reflected light (magneto-optical effects), the absorption of the electromagnetic field energy (magnetic resonance), etc. Thus, generally there is a possibility of driving the nonmagnetic parameters of these materials and of products made from them using a magnetic field. Very often properties that are precisely attendant on magnetism define the importance of the material for technological applications. The values of the effects described above, as well as those of spontaneous magnetization, are defined to a considerable extent by the chemical composition but may also reflect the structural state. Furthermore, many features of nonmagnetic properties depend on the type of magnetic structure and on features of their magnetic anisotropy. In this section we review very briefly these related phenomena in R/T multilayers.

### 5.1. Magnetostriction

The elastic deformation, which, in the presence of magnetic ordering, occurs in a crystal lattice or in an amorphous structure of a solid-state body, reflects the existence of the exchange and the magnetic interactions between elemental carriers of magnetism. As a result the volume and shape of macroscopic subjects are changed. We say that volume and, accordingly, linear magnetostrictions take place. Linear spontaneous magnetostriction is important for applications, because the elongation or shortening of the magnetic sample

in a certain direction depends on the spontaneous magnetization orientation. The magnetization process takes place by rotation of the magnetization vector in the whole sample or only in part of it, and this causes a rotation of the total or local deformation axis resulting in changes in the sample size in the direction of the applied field. Deformation caused in this way is defined as magnetostriction. Magnetostriction is an even effect; that is the deformation does not depend on the sign of the magnetization.

Very high, giant magnetostriction is a characteristic feature of many rare earth magnets. As for single-ion magnetic anisotropy, it is caused by rare earth ions. The magnetization rotation caused by spin-orbital interaction is accompanied by a change in the orientation of the electron orbits of these ions in an intercrystalline field and deformation of the atomic structure and of the sample as a whole. Among the crystalline magnets with giant magnetostriction, a  $\text{TbFe}_2$  crystalline intermetallic compound is well known. In the thin film state it is usually amorphous but shows relatively high magnetostriction. The main disadvantage in terms of practical applications for this material and for materials of similar composition is their low magnetic susceptibility. Many efforts have been made to decrease magnetic anisotropy while keeping the high magnetostriction of R-based materials. Among other possibilities is that of creating multilayered thin film structures with optimal magnetoelastic properties, for instance, trying to improve the magnetic susceptibility of a Tb-Fe film by introducing soft magnetic material sublayers with high magnetization (like Fe) [200]. The best results were achieved in a  $[\text{Tb}_{0.4}\text{Fe}_{0.6}(4.5)/\text{Fe}(6.5)]_n$  system with strong exchange interactions between the elements of the layered structure. After heat treatment at 550 K the magnetostriction in the low field of 200 Oe is 1 order of magnitude higher than that corresponding to single-layer films of the same composition, and this sounds very promising.

A similar effect of introducing Fe sublayers has been reported for  $\text{Tb}_{34.2}\text{Fe}_{65.8}$  films [201]. Figure 15 shows the dependence of magnetostriction,  $\lambda$ , on the strength of the magnetic field  $H$  for single-layer Tb-Fe films and for  $[\text{Tb}_{34.22}\text{Fe}_{65.8}(L_{\text{Tb}})/\text{Fe}(10)]_n$  with different thicknesses of Tb-Fe layers. The authors believe that creation of the layered structure results in a decrease in the strong perpendicular anisotropy, which is typical of single-layer films of this composition and as a consequence facilitates the in-plane magnetization process. The authors have also pointed out that the multilayers have a ferrimagnetic structure that transits in a noncollinear phase in the field of about 1 kOe. The magnetostriction curves  $\lambda(H)$  reflect in some way the magnetization process, opening the possibility of using it as a tool for the R/T multilayer study. The same opinion is expressed in relation to the Gd/Fe ferromagnetic resonance study [116], in which the magnetoelastic deformations were found to depend on the deposition methods. Specifically multilayers prepared by DC sputtering have higher magnetostriction than those prepared by rf sputtering. This can be explained by the presence of sharp interfaces in the first type of films.

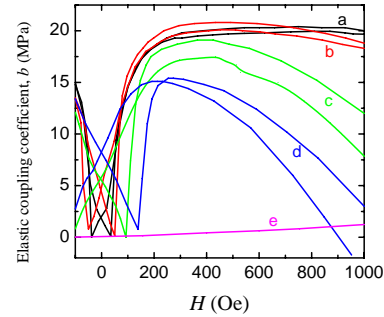


**Figure 15.** Elastic coupling coefficients (magnetostriction) of  $[\text{Tb-Fe}(X \text{ nm})/\text{Fe}(10 \text{ nm})]_n$  multilayers with various Tb-Fe thicknesses: (a)  $X = 15$ , (b) 20, (c) 25, and (d) 30 nm and (e) a Tb-Fe single layer film measured in the longitudinal direction of the magnetic field. Reprinted with permission from [201], T. Shima et al., *J. Magn. Magn. Mater.*, 239, 573 (2002). © 2002, Elsevier Science.

## 5.2. Magnetoresistance

Magnetoresistance is the change in electric resistance,  $R$ , of a ferromagnetic conductor caused by a magnetic field. This is a galvanomagnetic effect. In magnetically ordered materials it reflects a magnetic contribution to the conductive electron scattering, which depends on the value and orientation of the spontaneous magnetization. Therefore, one may separate the two components. In uniform magnets only the component related to the magnetization orientation is of practical interest, that is, anisotropic magnetoresistance. The magnetic field causes magnetization rotation and changes the electrical resistance of the sample, and thus the effect of the anisotropy of the magnetoresistance takes place. As for magnetostriction, magnetoresistance is an even effect.

Some time ago, a new type of magnetoresistive effect, *giant magnetoresistance* (GMR), was discovered in multilayered and granular magnetic structures [154, 202]. It consists of the change in electrical resistance at a variation of mutual orientation of magnetizations in heterogeneous magnetic structures with ultrathin elements. Let us emphasize that for both magnetoresistance and giant magnetoresistance we are dealing with direct current flowing over the ferromagnetic conductor. The discovery of GMR in Fe/Cr systems was preceded by the discovery and study of exchange coupling between magnetic layers across a nonmagnetic metallic layer [151, 153, 202] (see Section 3.1). The GMR effect occurs in a Fe/Cr system at a certain Cr thickness when antiferromagnetic coupling takes place and adjacent Fe layers have the opposite orientation to the spontaneous magnetization. When an external magnetic field aligns magnetizations in parallel configuration, the multilayer resistance decreases. Although GMR of Fe/Cr is induced by antiferromagnetic coupling, it was shown that antiferromagnetic coupling is not a necessary condition of GMR which can be caused, for example, by hysteresis effects [203, 204]. GMR is due to propagation of spin-polarized conductive electrons through the ferromagnetic films, divided by sublayer or spin-dependent scattering at the interfaces.

In R/T multilayers both the first effect, magnetoresistance, and the second, giant magnetoresistance, take place. R and T layers are not identical in terms of anisotropic magnetoresistance [91, 130, 170] because, compared with



rare earth metals, 3d metals have much higher anisotropic magnetoresistance. Because of the high specific resistance in R layers, the electric current flowing in a multilayer is pushed out from the R to the T layers as well. Therefore, the magnetoresistance of a R/T system reflects mainly the magnetoresistance of its T layers. It was shown in Section 3.3 that this feature is successfully used for registration and study of the magnetic phase transitions induced by a magnetic field [100, 110, 117]. Moreover, magnetoresistance analysis may yield certain information about the atomic structure [118].

The word *giant* is not very appropriate for describing the spin-dependent resistance of R/T multilayers because the value of the effect is small, even compared with ordinary anisotropic magnetoresistance. The small value of the effect makes it difficult to study when the geometry of the experiment determines that the electric current and the applied field are parallel to the plane of the film (CIP geometry). If the electric current flows perpendicular to the plane of the film (CPP geometry) and an external field is applied in the plane of the multilayered structure [202] and, therefore, magnetization occurs in the plane of the sample, the GMR is easier to measure because anisotropic magnetoresistance is absent. It is absent because magnetization and the electric current are perpendicular all the time. There is an opinion that resistance changes in the field take place because of deformations of the ferrimagnetic structure caused by the magnetic moments of R and T layers [110]. Figure 16 shows an example of  $R(H)$  dependence for a Gd/Co structure. High fields used in this, as in many other similar studies, cause a paraprocess in the gadolinium subsystem. Changes of the spontaneous magnetization of Gd should influence the  $R(H)$  behavior.

The low value of magnetoresistance is a great disadvantage for R/T multilayers in technological applications and makes them noncompetitive with many other magnetoresistive materials. At the same time, it is possible to use R/T structures as a part of more complicated systems showing GMR. Figure 17 shows the magnetometrical and magnetoresistive hysteresis loops for a  $[\text{Tb}(1)/\text{Co}(1)]_{16}/\text{Co}(5)/\text{Cu}(2.5)/\text{Co}(5)$  sample [70]. Here the multilayered  $[\text{Tb}(1)/\text{Co}(1)]_{16}$  element with in-plane magnetic anisotropy and a high coercive field acts as a pinning layer. The  $[\text{Tb}(1)/\text{Co}(1)]_{16}$  structure and the adjacent Co layer are

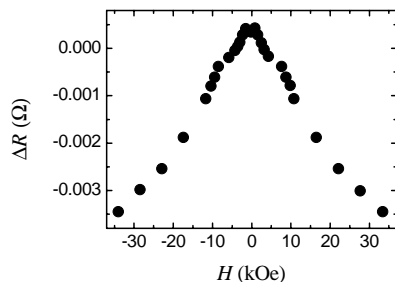


**Figure 16.** Resistance changes  $\Delta R$  in CPP geometry for a  $[\text{Co}(10) \text{ nm}/\text{Gd}(10 \text{ nm})]_{50}$  multilayer as a function of the applied magnetic field measured at 4.2 K. The initial resistance before applying the magnetic field is defined as  $\Delta R = 0$ . Reprinted with permission from [110], H. Nagura et al., *J. Magn. Magn. Mater.* 240, 183 (2002). © 2002, Elsevier Science.

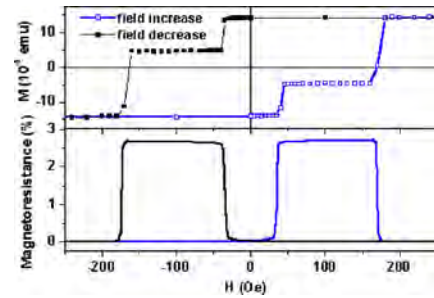


**Figure 17.** Magnetometrical (a) and magnetoresistive (b) hysteresis loops for the  $[\text{Tb}(1)/\text{Co}(1)]_{16}/\text{Co}(5)/\text{Cu}(2.5)/\text{Co}(5)$  spin-valve structure.

connected to each other by exchange interaction and the multilayered structure provides the stability of the Co layer in the external field. At the same time, another Co layer, separated from the first by a Cu spacer, has the possibility of remagnetization in a small magnetic field. As a result, mutual magnetization of the cobalt layers may be changed by an external magnetic field, that is, GMR, which, in this particular case, could be better described as the *spin-valve* effect, occurs. The term spin-valve relates to a case where the possibility of separate remagnetization of the layers is caused not by the negative exchange interaction between the layers, but by the difference in the magnetic anisotropy or the coercive field of the layers [203, 205].

### 5.3. Magneto-optical Kerr Effect

Magneto-optical effects are certain changes of optical properties of a medium caused by application of the external magnetic field. In magnetically ordered materials they have special peculiarities due to the existence of spontaneous magnetization. From both basic and practical points of view, the most interesting are the Faraday and Kerr effects. They consist of the rotation of plane polarization at light refraction through (Faraday) or reflection from (Kerr) the magnet. In metals, the light penetration depth is limited by a skin effect and does not exceed 100 nm. Therefore, for multilayers only the magneto-optical Kerr effect (MOKE) is really interesting. The suitably smooth surface of multilayers is an advantage in this case. Different effects are produced depending on the direction and angle of the light incidence. The polar effect corresponds to geometry when magnetization points along the surface; a normal effect results in the rotation of the plane of polarization as a function of the perpendicular component of the magnetization. The longitudinal effect describes the plane polarization rotation for the light inclination onto the surface of the sample when the position of the magnetization is in the plane of the sample. The longitudinal effect can also be used for perpendicular polarization. It is proportional to the magnetization component in the plane of the light incidence. The transverse orientation effect in which the magnetization is perpendicular to the plane of incidence produces little contrast in a visible image [206].

There are a number of reasons for interest in the Kerr effect as observed in R/T multilayers [16, 20, 71, 72, 88, 92, 119, 178, 206–212]. The first is the comparison of the optical properties of multilayers with single-layer analogues

material. The authors of [207] have studied the Kerr rotation spectra for uniform amorphous and multilayered Gd/Fe films. The value of the effect is similar in both samples, but the layered structure opens the way for an additional technological possibility of controlling the magnetic and magneto-optical properties [190] useful for applications such as magnetic recording. Both high anisotropic Tb/Fe and low anisotropic Gd/Co films are interesting for the technique of super high resolution [16, 73] (see Section 5.4) as well as for other applications. The second line of interest is based on the Kerr effect using the magnetization process study method [88, 178]. The magneto-optical effect, in contrast to magnetostriction and magnetoresistance, is an odd effect; that is, it contains information about the sign of magnetization. As we mentioned in Section 3.3, the magneto-optical hysteresis loops are more informative than magnetometric loops for studying phase transitions. One may explain this finding by taking into account the fact that T metals have higher plane polarization rotation values than R metals. Figure 10 shows an example of a magneto-optical hysteresis loop observed via the longitudinal Kerr effect for perpendicular polarization. Direct domain structure observation is possible through the Kerr effect, although the number of publications related to R/T multilayers is small [66, 74, 92, 213]. Structural investigations can also be undertaken via the Kerr effect [20, 119]. Elegant, quick, and appropriate ways of detecting different types of coupling in layered magnetic structures by means of the MOKE were presented as the basis for the magnetic domain study [204, 214].

#### 5.4. R/T Structures and Magneto-optical Recording

Can you imagine our community without audio and video recorders, CD-ROMs, etc.? They are part of our lives. The two basic methods of recording are magnetic and optical. Here we describe very briefly the general principles of magneto-optical recording and the role of R/T materials.

The principle behind any recording is representation of numbers by the state of a bistable physical system; therefore, in the recording process we are dealing with binary numbers. Any number in a binary system can be written as a specific sequence of the elements equivalent to "1" or "0." In the magneto-optical recording medium we have a rather complicated multilayer structure of different layers, not all of which are magnetic. At the beginning, the homogeneously magnetized medium stores no information. We can then write onto it the required sequence of digits by a process of thermomagnetic writing, that is, cooling in or without a local magnetic field after local heating by a short laser pulse to a temperature close to the Curie temperature. Any zone with initial magnetization direction may represent the information unit "1." If a field biased in the opposite orientation is present during cooling, a magnetic domain is formed with opposite magnetization orientation to the initial magnetization. This represents the information unit "0." The size of the domain is determined by the temperature and by the profile of the temperature-dependent coercivity, that is, the magnetic properties of the magnetic film used. The stability of this information unit depends on the type

of the domain wall between the homogeneous part of the disc and the information unit, on the magnetization, and on the anisotropy energy. The reading process is performed by using the magneto-optical Kerr effect at typical wavelengths of 780 and 820 nm. To obtain the maximum signal, the magnetization should be perpendicular to the film plane (perpendicular recording) [212].

The quality and stability of the writing and subsequent reading depend strongly on the material properties of the magneto-optical films. PMA is required to keep the magnetization of the domains normal to the plane of the film/disc. Therefore, the energy of the demagnetizing field must be compensated for by the energy of the perpendicular anisotropy. This condition can be fulfilled when the magnetization is sufficiently small. It is achieved in modern devices by use of amorphous thin films consisting of R and T metals, coupled antiferromagnetically. The film thickness is on the order of 50 to 100 nm.  $Tb_{25}Fe_{75}$  is the most usual composition. In closely related compounds Tb and Fe are partially substituted for by other R metals (Dy and Gd) and T metals (Co and Ni), respectively. As mentioned in Section 3.1, different temperature dependencies of the magnetic T and R sublattices of the films normally have a compensation point, where the magnetizations of R and T cancel each other out, and the total magnetization is zero. The compensation point can be chosen close to room temperature by appropriate composition selection. As a consequence of a very small magnetization, the coercivity becomes very large at the compensation temperature and a very high field would be required for changes of the magnetic moments. As a result, a domain structure written at a temperature of about 500 K, close to Curie temperature, is very stable against external fields at room temperatures.

In addition to the magnetic layer for magneto-optical processing, the recording disc incorporates a nonmagnetic antireflecting coating, which reduces the polarization component of directly reflected light. To increase the signal-to-noise ratio a magneto-optical double layer ( $Tb_{11}Fe_{64}Co_{25}/Tb_{24}Fe_{65}Co_{11}$ ) [215] or trilayers or quadrilayers with an additional reflecting layer [216] can be used. To increase data access time, the erasing process can be incorporated into a so-called direct overwrite cycle [217]. One solution applies exchange-coupled double layers (ECDLs) as storage media [218]. These ECDLs can be used for magnetic super-resolution [16, 73], where one of the layers works as a magneto-optical mask for the super-resolution. It allows an increase in the density of information recording.

One may see from our very short description that a magneto-optical recording medium contains a number of different magnetic and nonmagnetic layers. From this point of view they are similar to R/T multilayers. The composition of magnetic layers in a magneto-optical structure includes R and T elements. R/T multilayers may have suitable magneto-optical and magnetic properties for them to be used in real devices. The basic principles of magneto-optical recording have many points in common with the physics of R/T multilayers. We can say, therefore, that R/T systems could be considered as a model structure or potential candidates for magneto-optical recording.

## 5.5. Magnetic Resonance

Magnetic resonance consists of the intensive absorption of high-frequency field energy by a magnet when the frequency of the oscillations of the external field and oscillations of the magnetic moment of the magnet are equal. In magnetically ordered materials this resonance frequency is defined by the effective field, which reflects all interactions related to magnetization. The components of the effective field are the demagnetizing field, the anisotropy field, and exchange (including interlayer) interactions. This explains a potential interest in ferromagnetic resonance as a method to study R/T magnetism.

There are just a few publications on R/T structures. Let us mention the ferrimagnetic Tb/Fe [59], Gd/Fe [116], and Gd/Co [99, 120, 121] multilayers. Interesting results were reported for a  $[\text{Gd}(7.5)/\text{Si}(L_{\text{Si}})/\text{Co}(3)/\text{Si}(L_{\text{Si}})]$  study at various temperatures. The magnetic compensation appeared in this structure in the range of 100 to 300 K. The compensation temperature depends on the thickness of the Si sublayer  $L_{\text{Si}}$ . To describe ferromagnetic resonance in uniform two-sublattice ferrimagnets, the effective magnetomechanic ratio,  $\gamma_{\text{eff}}$ , is used. This is defined as the difference between magnetizations of the sublattices divided by the difference of the specific mechanical moments of these sublattices. In practice, it is more convenient to use its normalized value, known as the effective  $g$ -factor,  $g_{\text{eff}}$ , instead of using  $\gamma_{\text{eff}}$ . Figure 18 shows the temperature dependencies of  $g_{\text{eff}}$  calculated on the basis of experimental resonance field data for the samples with  $L_{\text{Si}} = 0.3$  nm (curve 1) and  $L_{\text{Si}} = 0.5$  nm (curve 2). Dashed vertical lines mark  $T_{\text{comp}}$ . The character of the  $g_{\text{eff}}(T)$  changes near the compensation temperature and is different at high and low temperatures. There is a break point in the curve corresponding to  $T_{\text{comp}}$ . This can be interpreted in terms of sequential changes in the states of compensation of the magnetic moments and mechanical moments of the Gd and Co layers as the temperature increases. Therefore, there is a general possibility of using phenomenological ferromagnetic resonance theory to interpret the resonance properties of layered ferrimagnetic structures.

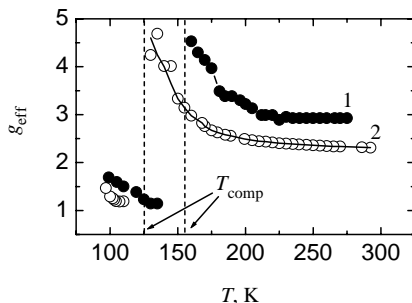


**Figure 18.** Temperature dependence of an effective  $g$ -factor for  $[\text{Gd}(7.5)/\text{Si}/\text{Co}(3)/\text{Si}]_{20}$  films with different Si spacer thickness: (1) 0.3 nm; (2) 0.5 nm. Dashed lines indicate the compensation temperatures of the films.

## 6. CONCLUSIONS

Multilayered structures consisting of rare earth and 3d metal layers have been intensively studied for the last 15 years. Different technologies for their preparation such as ultrahigh vacuum thermal evaporation and ion sputtering have been developed. Independently of the preparation method, these subjects may be described as a system of magnetic layers connected by exchange interaction. It is precisely this type of interaction, together with the individual properties of the different layers, that defines the R/T system magnetism.

Rare earth (Tb, Gd, and Dy) and 3d (Fe and Co) metals are those used most frequently for the sublayers that define the negative exchange interaction and ferrimagnetic ordering in a system of magnetic layers. The characteristic feature of the temperature dependence of spontaneous magnetization is the existence of magnetic compensation. The quantitative characteristics of the spontaneous magnetization and compensation temperature depend on many parameters, including the sublayer thickness ratio, period of the layered structure, structural state, and the presence of nonmagnetic spacers. The main structural features of R/T multilayers are amorphization, which appears at a relatively low thickness of layers, and the existence of interface areas. The morphology of the interfaces depends on the preparation technology, order of the layer deposition, and subsequent treatments.

R/T multilayers with anisotropic Tb or Dy ions show strong perpendicular anisotropy, which has a single ion nature and is caused by anisotropy of the atomic structure of the interfaces. An enhanced self-demagnetization effect takes place in all ferrimagnetic multilayers. It occurs because of formation of demagnetizing fields in the interfaces. The characteristic feature of the magnetization process of R/T structures is a magnetic phase transition and a twisted structure.

A number of phenomenological models were developed to describe R/T spontaneous magnetization and changes of the spontaneous magnetization in the external magnetic field. It seems that the most suitable is the model of nonuniform interlayer exchange with reciprocal influence of the sublayers, and charge transfer.

Some nonmagnetic properties such as magnetostriction, magnetoresistance, the magneto-optic Kerr effect, and magnetic resonance have been studied with the objective of using R/T multilayers in the future both as a tool for magnetization process research and as a basis for technological applications.

We have a relatively clear picture of the nature of magnetism in R/T multilayers today. Major progress in this field of modern physics depends very much on progress in the technology of preparation, but meanwhile valuable work can be done by extending the range of magnetic and nonmagnetic components in layered structures, by precise study of the properties attendant on magnetic ordering, by increasing the reproduction level, and by special study of the compatibility of these materials with the aim of increasing their technological applications and improving miniaturization.

## GLOSSARY

**Atomic structure** The presence/absence of order in the positions of the atoms at precise distances compared with the atomic size.

**Interfaces** Zones between different layers of multilayered structures.

**Ion sputtering** The expulsion of the atoms from the target surface by inert gas ions bombardment.

**Magnetism in rare earth metals** Caused by 4f electrons located in internal electron shells. This leads to localization of magnetic moments on atoms and to the absence of direct exchange interaction in the 4f electron system. Magnetic ordering occurs because of indirect exchange through the conduction electrons. This interaction is oscillating and acts over a long range. It causes low values of magnetic ordering temperatures and aids in the formation of complex magnetic structures.

**Nanoscale rare earth/transition metal (R/T) multilayers**  $NM/[R(a)T(b)]_n/NM$  samples. This formula contains all the important information about the general structure of the multilayered film. It says that this film has buffer and covered nonmagnetic (NM) layers and rare earth (R) layers of thickness  $L_R = a$  nm alternated with transition layers (T) of thickness  $L_T = b$  nm. The structure  $L_R + L_T = L_p$  is repeated  $n$  times, where  $L_p$  is a period of the structure.

**R/T ferrimagnetic structure** The magnetic moments of R and T layers play the role which, in a classic ferrimagnet, would be played by R and T, the magnetic moments of the sublattices.

**Twisted magnetic phases** Special feature of a noncollinear magnetic structure in layered materials. In contrast to uniform ferrimagnets, in multilayers the negative exchange interaction between magnetic elements is spread nonuniformly through the multilayer volume. As a result there is a spatial nonuniformity in noncollinear structures, in which the angle between the local magnetization and an external field changes from the separating interface toward the center of the layer.

**Ultrahigh vacuum thermal evaporation or molecular beam epitaxy (MBE)** Film preparation at ultrahigh vacuum of  $10^{-8}$ – $10^{-10}$  torr, involving strong local heating of the target, as a rule by a high-energy electron beam created by an electron beam gun.

## ACKNOWLEDGMENTS

We gratefully thank Jane Kalim for her help with the manuscript and Professor Blanca Hernando for the encouragement to write this chapter. This work was partially supported by Award Rec-005 of USA Civilian Research & Development Foundation for the Independent States of the Former Soviet Union (CRDF), MCyT and Universidad de Oviedo in the framework of the “Ramon y Cajal” program, and by the Spanish CICYT under Grants MAT2000-1047 and MAT2001-0082-C04-01. The authors would like to express their gratitude for all authors (J. Teillet, A. Fnidiki, D. García, A. Hernando, M. Vázquez, A. V. Gorbunov, J. P. Andrés, J. L. Sacedon, J. Colino, J. M. Riveiro, Z. S. Zhang, Y. T. Wang, F. Pan,

N. H. Duo, T. M. Danh, M. Kaabouchi, C. Sella, N. N. Schegoleva, S. M. Zadvorin, J. M. Barandiarán, N. G. Bebenin, L. Lezama, J. Gutiérrez, D. Schmool, H. Nagura, K. Takanashi, S. Mitani, K. Saito, T. Shima, D. N. Merenkov, A. B. Chizhik, S. I. Gnatchenko, M. Baran, R. Szymchak, G. S. Patrin, D. A. Velikanov, Y. Fujiwara, T. Masaki, X. Y. Yu, S. Tsunashima, S. Iwata, H. Fujimori, and P. A. Savin) and publishers (International Academic Publishing Company MAIK “Nauka/Interperiodica,” American Institute of Physics, Wiley-VCH Verlag GmbH, Elsevier Science, and B. Verkin Institute for Low Temperature Physics and Engineering) for their permission to reproduce the figures from publications.

## REFERENCES

1. A. Yelon, in “Physics of Thin Films” (M. H. Francombe and R. W. Hoffman, Eds.), Vol. VI, p. 228. Academic Press, New York, 1971.
2. T. Morishita, Y. Togami, and K. Tsushima, *J. Phys. Soc. Jpn.* 49, 37 (1985).
3. H. Okuno, Y. Sakaki, and Y. Sakurai, *J. Phys. D: Appl. Phys.* 19, 873 (1986).
4. N. Sato and K. Habu, *J. Appl. Phys.* 61, 4287 (1987).
5. R. F. C. Farrow, C. H. Lee, and S. S. P. Parkin, *IBM J. Res. Dev.* 34, 903 (1990).
6. A. K. Petford-Long, *Thin Solid Films* 275, 35 (1996).
7. J. Tappert, F. Klose, Ch. Rehm, W. S. Kim, R. A. Brand, H. Maletta, and W. Keune, *J. Magn. Mater.* 156, 58 (1996).
8. S. G. Ovchinnikov, *Uspekhi Fiz. Nauk* 169, 869 (1999).
9. J. Kortright, D. D. Awschalom, J. Stohr, S. D. Bader, Y. U. Idzherda, S. S. P. Parkin, I. K. Schuller, and H.-C. Siegmann, *J. Magn. Mater.* 207, 7 (1999).
10. T. Ruckert, W. Keune, W. Sturhahn, and E. E. Alp, *J. Magn. Mater.* 240, 562 (2002).
11. D. R. Lee, Y. J. Park, S. H. Park, Y. H. Jeong, K.-B. Lee, N. Ishimatsu, H. Hashizume, and N. Hosoito, *Physica B* 248, 146 (1998).
12. E. Meltchakov, H.-Ch. Mertins, W. Jark, and F. Schäfers, *Nucl. Instrum. Methods Phys. Res., Sect. A* 467–468, 1411 (2001).
13. L. Veiller, F. Danoix, and J. Taillet, *J. Appl. Phys.* 87, 1379 (2000).
14. D. Givord, J. Betz, K. Mackay, J. C. Toussaint, J. Voiron, and S. Wuchner, *J. Magn. Mater.* 159, 71 (1996).
15. E. Quandt, A. Ludwig, J. Betz, D. Givord, and K. Mackay, *J. Appl. Phys.* 81, 5420 (1997).
16. S. Tsunashima, *J. Magn. Mater.* 156, 283 (1996).
17. D. J. Sellmyer, M. Yu, and R. D. Kirby, *Nanostruct. Mater.* 12, 1021 (1999).
18. E. Meltchakov, H.-Ch. Mertins, M. Scheer, S. Di Fonzo, W. Jark, and F. Schafers, *J. Magn. Mater.* 240, 550 (2002).
19. D. J. Sellmyer, Z. R. Zhao, Z. S. Shen, and S. Nafis, *J. Appl. Phys.* 61, 4323 (1987).
20. J. A. Gonzalez, J. P. Andres, M. A. L. Lopez de la Torre, and J. M. Riveiro, *J. Magn. Mater.* 242–245, 547 (2002).
21. H. Okuno, Y. Sakaki, and Y. Sakurai, *J. Phys. D: Appl. Phys.* 19, 873 (1986).
22. A. Koizumi, M. Takagaki, M. Suzuki, N. Kawamura, and N. Sakai, *Phys. Rev. B* 61, 14909 (2000).
23. T. Morishita, Y. Togami, and K. Tsushima, *J. Phys. Soc. Jpn.* 49, 37 (1985).
24. N. Hosoito, H. Hashizume, and Ishimatsu, *J. Phys.: Condens. Matter* 14, 5289 (2002).
25. M. Nawate, K. Doi, and S. Honda, *J. Magn. Mater.* 126, 279 (1993).
26. G. S. Bains, A. Yoshibara, K. Takanashi, and H. Fujimori, *J. Magn. Mater.* 126, 329 (1993).

27. J. B. Pelka, W. Paszkowicz, A. Wawro, L. T. Baczewski, and O. Seeck, *J. Alloys Comp.* 328, 253 (2001).
28. K. Takahashi, H. Fujimori, and H. Kurokawa, *J. Magn. Magn. Mater.* 126, 242 (1993).
29. I. M. L. Billas, J. A. Becker, A. Chatelain, and W. A. de Heer, *Phys. Rev. Lett.* 71, 4061 (1993).
30. A. V. Gorbunov, V. O. Vas'kovskiy, and A. V. Svalov, in "The Problems of Nanocrystalline Materials" (V. V. Ustinov and N. I. Noskova, Eds.), p. 493. UD RAS, Ekaterinburg, 2002.
31. G. Suci, J. C. Toussaint, and J. Voiron, *J. Magn. Magn. Mater.* 240, 229 (2002).
32. M. Sajjeddine, Ph. Bauer, K. Cherifi, C. Dufour, G. Marchal, and R. E. Camley, *Phys. Rev. B* 49, 8815 (1994).
33. K. O'Grady, T. Thompson, and S. J. Greaves, *J. Appl. Phys.* 75, 6849 (1994).
34. T. Katsuyoshi, F. Miki, K. Satoru, S. Hiroshi, and I. Fumitake, *J. Magn. Magn. Mater.* 240, 565 (2002).
35. M. J. O'Shea and P. Perera, *J. Magn. Magn. Mater.* 156, 141 (1996).
36. D. J. Webb, R. G. Walmsley, K. Parvin, P. H. Dickinson, T. H. Geballe, and R. M. White, *Phys. Rev. B* 32, 4667 (1985).
37. Z. Shan, D. J. Sellmyer, S. S. Jaswal, Y. J. Wang, and J. X. Shen, *Phys. Rev. Lett.* 63, 449 (1989).
38. S. Honda, M. Nawate, and I. Sacamoto, *J. Appl. Phys.* 79, 365 (1996).
39. F. Yang and F. Pan, *J. Magn. Magn. Mater.* 246, 22 (2002).
40. J. Landes, Ch. Sauer, B. Kabius, and W. Zinn, *Phys. Rev. B* 44, 8342 (1991).
41. F. Richomme, J. Teillet, A. Fnidiki, P. Auric, and Ph. Houdy, *Phys. Rev. B* 54, 416 (1996).
42. F. Richomme, J. Teillet, A. Fnidiki, and W. Keune, *Phys. Rev. B* 64, 094415 (2001).
43. A. E. Freitag and A. R. Chowdhury, *J. Appl. Phys.* 85, 5756 (1999).
44. A. E. Freitag and A. R. Chowdhury, *J. Appl. Phys.* 85, 4696 (1999).
45. F. Yang and F. Pan, *Physica B* 315, 227 (2002).
46. F. Yang, T. He, J. B. Chen, and F. Pan, *J. Appl. Phys.* 91, 3114 (2002).
47. F. Richomme, B. Scholz, R. A. Brand, W. Keune, and J. Teillet, *J. Magn. Magn. Mater.* 156, 195 (1996).
48. K. Mibu, N. Hosoito, and T. Shinjo, *J. Magn. Magn. Mater.* 126, 343 (1993).
49. A. Fnidiki, J. Juraszek, J. Teillet, F. Richomme, and J. P. Lebertois, *J. Magn. Magn. Mater.* 165, 405 (1997).
50. J. Juraszek, A. Fnidiki, J. Teillet, M. Toulemonde, A. Michel, and W. Keune, *Phys. Rev. B* 61, 12 (2000).
51. C. Tosello, L. M. Grattton, G. Principi, A. Gupta, and Gupta, *Surf. Coat. Technol.* 84, 338 (1996).
52. F. Richomme, A. Fnidiki, J. Teillet, and M. Toulemonde, *Nucl. Instrum. Methods Phys. Res., Sect. B* 107, 374 (1996).
53. J. Juraszek, A. Fnidiki, and M. Toulemonde, *Solid State Commun.* 106, 83 (1998).
54. Z. Shan and D. J. Sellmyer, *Phys. Rev. B* 42, 10433 (1990).
55. N. Sato, *J. Appl. Phys.* 59, 2514 (1986).
56. K. Mibu and T. Shinjo, *Hyperfine Interact.* 113, 287 (1998).
57. Y. J. Wang and W. Kleemann, *Phys. Rev. B* 44, 5132 (1991).
58. M. Trhlik, P. De Moor, N. Severijns, A. Van Geert, L. Vanneste, K. Mibu, and T. Shinjo, *J. Magn. Magn. Mater.* 165, 408 (1997).
59. E. V. Shypil, A. M. Pogorily, D. I. Podyalovski, and Y. A. Pogoryelov, *Low Temp. Phys.* 27, 879 (2001).
60. E. Shypil, A. Pogorily, Ye. Pogoryelov, T. H. Kim, G. Berera, and J. Moodera, *J. Magn. Magn. Mater.* 242–245, 532 (2002).
61. W. S. Kim, W. Kleemann, J. Tappert, and W. Keune, *J. Appl. Phys.* 84, 4384 (1998).
62. W.-S. Kim, W. Andrä, and W. Kleemann, *Phys. Rev. B* 58, 6346 (1998).
63. J. Juraszek, A. Fnidiki, and J. Teillet, *J. Appl. Phys.* 84, 379 (1998).
64. F. Yang and F. Pan, *Physica B* 315, 227 (2002).
65. T. Thomson, K. O'Grady, and G. Bayreuther, *J. Phys. D: Appl. Phys.* 30, 1577 (1997).
66. J. Pommier, J. P. Jamet, J. Ferré, P. Houdy, P. Boher, and F. Pierre, *J. Magn. Magn. Mater.* 136, 251 (1994).
67. B. Lanchava and H. Hoffmann, *J. Magn. Magn. Mater.* 192, 403 (1999).
68. A. Paul, *J. Magn. Magn. Mater.* 240, 497 (2002).
69. K. Takano, M. Furuhashi, S. Kobayashi, H. Sakurai, and F. Itoh, *J. Magn. Magn. Mater.* 240, 565 (2002).
70. A. V. Svalov, P. A. Savin, G. V. Kurlyandskaya, J. Gutiérrez, and V. O. Vas'kovskiy, *Tech. Phys.* 47, 987 (2002).
71. L.-Y. Chen, P. He, S. Nafis, W. A. McGahan, J. A. Woollam, and D. J. Sellmyer, *J. Appl. Phys.* 69, 5989 (1991).
72. M. Nývlt, J. Ferré, J. P. Jamet, P. Houdy, P. Boher, Š. Višňovský, R. Urban, and R. Lopusník, *J. Magn. Magn. Mater.* 156, 175 (1996).
73. S. Becker, T. Lucinski, H. Rohrmann, F. Stobiecki, and K. Röhl, *J. Magn. Magn. Mater.* 140–144, 521 (1995).
74. P. Meyer, J. P. Jamet, V. Grolier, F. Ott, P. Houdy, and P. Boher, *J. Magn. Magn. Mater.* 148, 361 (1995).
75. G. Garreau, E. Beaurepaire, K. Ounadjela, and M. Farle, *Phys. Rev. B* 53, 1083 (1996).
76. J. Tappert, C. Fermon, and R. A. Brand, *Physica B* 213–214, 239 (1995).
77. W. S. Kim, W. Kleemann, S. Neumann, J. Tappert, B. Sholz, and W. Keune, *J. Magn. Magn. Mater.* 156, 191 (1996).
78. G. N. Phillips, K. O'Grady, and R. W. Chantrell, *J. Magn. Magn. Mater.* 155, 364 (1996).
79. F. Richomme, J. Teillet, A. Fnidiki, J. P. Lebertois, P. Auric, and P. Veillet, *J. Magn. Magn. Mater.* 156, 181 (1996).
80. F. Richomme, J. Teillet, P. Auric, P. Veillet, A. Fnidiki, Ph. Houdy, and P. Boher, *J. Magn. Magn. Mater.* 140–144, 627 (1995).
81. O. Kuzmak, A. Pogorily, and V. Shevchenko, *J. Magn. Magn. Mater.* 148, 36 (1995).
82. T. Schmidt and H. Hoffmann, *J. Magn. Magn. Mater.* 248, 181 (2002).
83. M. Trhlik, K. Mibu, P. De Moor, P. P. Pari, M. Rotter, N. Severijns, T. Shinjo, A. Van Geert, and L. Vanneste, *J. Phys.: Condens. Matter* 8, 8907 (1996).
84. M. Sajjeddine, Ph. Bauer, A. Bruson, and G. Marchal, *Solid State Commun.* 99, 965 (1996).
85. P. Perera and M. J. O'Shea, *Phys. Rev. B* 53, 3381 (1996).
86. J. Tappert, F. Klose, Ch. Rehm, W. S. Kim, R. A. Brand, H. Maletta, and W. Keune, *J. Magn. Magn. Mater.* 157–158, 317 (1996).
87. Z. S. Shan, S. Nafis, K. D. Aylesworth, and D. J. Sellmyer, *J. Appl. Phys.* 63, 3218 (1988).
88. Z. S. Shan, J. X. Shen, R. D. Kirby, S. H. Liou, and D. J. Sellmyer, *J. Appl. Phys.* 70, 6203 (1991).
89. Y. Li, C. Polaczyk, J. Kapoor, and D. Riegel, *J. Magn. Magn. Mater.* 165, 165 (1997).
90. Y. Li, C. Polaczyk, and D. Riegel, *Surf. Sci.* 402–404, 386 (1998).
91. H. Fujimori, Y. Kamiguchi, and Y. Hayakawa, *J. Appl. Phys.* 67, 5716 (1990).
92. G. Choe and R. M. Walser, *J. Appl. Phys.* 79, 6306 (1996).
93. V. O. Vas'kovskiy, D. Garcia, A. V. Svalov, A. Hernando, M. Vazquez, G. V. Kurlyandskaya, and A. V. Gorbunov, *Phys. Met. Metall.* 86, 140 (1998).
94. J. P. Andres, J. L. Sacedon, J. Colino, and J. M. Riveiro, *J. Appl. Phys.* 87, 2483 (2000).
95. J. B. Pelka, W. Paszkowicz, P. Dłuzewski, E. Dynowska, A. Wawro, L. T. Baczewski, M. Kozłowski, A. Wisniewski, O. Seeck, S. Mes-soloras, and H. Gamari-Seale, *J. Phys. D: Appl. Phys.* 34, A208 (2001).
96. P. Donovan and J. V. Harkins, *J. Magn. Magn. Mater.* 156, 224 (1996).
97. V. O. Vas'kovskiy, A. V. Svalov, A. V. Gorbunov, N. N. Schegoleva, and S. M. Zadvorkin, *Phys. Solid State* 43, 672 (2001).

98. V. O. Vas'kovskiy, A. V. Svalov, A. V. Gorbunov, N. N. Schegoleva, and S. M. Zadvorkin, *Physica B* 315, 143 (2002).
99. A. V. Svalov, V. O. Vas'kovskiy, J. M. Barandiarán, N. G. Bebenin, G. V. Kurlyandskaya, A. V. Gorbunov, L. Lezama, J. Gutiérrez, and D. Schmool, *J. Alloys Compd.* 327, 5 (2001).
100. J. Colino, J. P. Andres, J. M. Riveiro, J. L. Martínez, C. Prieto, and J. L. Sacedon, *Phys. Rev. B* 60, 6678 (1999).
101. V. O. Vas'kovskiy, A. V. Svalov, A. N. Sorokin, P. V. Krapivin, and A. V. Zinin, *J. Alloys Compd.* 285, 238 (1999).
102. C. Dufor, K. Cherifi, G. Marchal, Ph. Mangin, and M. Hennion, *Phys. Rev. B* 47, 14572 (1993).
103. C. Fermon, O. F. K. McGrath, and D. Givord, *Physica B* 214–215, 236 (1995).
104. O. F. K. McGrath, N. Ryzhanova, C. Lacroix, D. Givord, C. Fermon, C. Miramond, G. Saux, S. Young, and A. Vedyayev, *Phys. Rev. B* 54, 6088 (1996).
105. H. Hashizume, N. Ishimatsu, O. Sakata, T. Iizuka, N. Hosoito, K. Namikawa, T. Iwazumi, G. Srajer, C. T. Venkataraman, J. C. Lang, C. S. Nelson, and L. E. Berman, *Physica B* 248, 133 (1998).
106. K. Cherifi, C. Dufour, Ph. Bauer, G. Marchal, and Ph. Mangin, *Phys. Rev. B* 44, 7733 (1991).
107. W. Hahn, M. Loewenhaupt, Y. Y. Huang, G. P. Felcher, and S. S. P. Parkin, *Phys. Rev. B* 52, 16041 (1995).
108. S. L. Gnatchenko, A. B. Chizhik, D. N. Merenkov, V. V. Ere- menko, H. Szymczak, R. Szymczak, K. Fronc, and R. Zuberek, *J. Magn. Magn. Mater.* 186, 139 (1998).
109. N. Ishimatsu, H. Hashizume, S. Hamada, N. Hosoito, C. S. Nelson, C. T. Venkataraman, G. Srejer, and J. C. Lang, *Phys. Rev. B* 60, 9596 (1999).
110. H. Nagura, K. Takanashi, S. Mitani, K. Saito, and T. Shima, *J. Magn. Magn. Mater.* 240, 183 (2002).
111. D. N. Merenkov, A. B. Chizhik, S. I. Gnatchenko, M. Baran, R. Szymczak, V. O. Vas'kovskiy, and A. V. Svalov, *Low Temp. Phys.* 27, 137 (2001).
112. G. S. Patrin, V. O. Vas'kovskiy, D. A. Velikanov, and A. V. Svalov, *JETP Lett.* 75, 159 (2002).
113. A. V. Gorbunov, V. O. Vas'kovskiy, and A. V. Svalov, *Phys. Met. Metall.* 91, S60 (2001).
114. L. T. Baczewski, R. Kalinowski, and A. Wawro, *J. Magn. Magn. Mater.* 177–181, 1305 (1998).
115. V. O. Vas'kovskiy, A. V. Svalov, M. Vazquez, A. Hernando, G. V. Kurlyandskaya, D. Garcia, and A. V. Gorbunov, *J. Magn. Magn. Mater.* 203, 295 (1999).
116. R. Zuberek, K. Fronc, H. Szymczak, A. Nabialek, T. Stobiecki, and J. Sokulski, *J. Magn. Magn. Mater.* 139, 157 (1995).
117. M. Vaezzadeh, B. George, and G. Marchal, *Phys. Rev. B* 50, 6113 (1994).
118. T. Stobiecki, M. Czapkiewicz, and M. Kopcewicz, *J. Magn. Magn. Mater.* 140–144, 535 (1995).
119. J. M. Riveiro, J. P. Andrés, and J. Colino, *J. Magn. Magn. Mater.* 198–199, 428 (1999).
120. A. V. Svalov, J. M. Barandiarán, V. O. Vas'kovskiy, G. V. Kurlyandskaya, L. Lezama, N. G. Bebenin, J. Gutiérrez, and D. Schmool, *Chin. Phys. Lett.* 18, 973 (2001).
121. G. S. Patrin, V. O. Vas'kovskii, A. V. Svalov, D. A. Velikanov, N. V. Volkov, E. V. Eremin, and M. A. Panova, "Moscow International Symposium on Magnetism (MISM-02)," Book of Abstracts, p. 260, 2002.
122. D. Haskel, G. Srajer, J. C. Lang, J. Pollmann, C. S. Nelson, J. S. Jiang, and S. D. Bader, *Phys. Rev. Lett.* 87, 207201 (2001).
123. Y. Li, C. Polaczyk, F. Mezei, and D. Riegel, *Physica B* 234–236, 489 (1997).
124. L. T. Baczewski, K. Mibu, T. Nagahama, S. Hamada, and T. Shinjo, *J. Phys. D: Appl. Phys.* 35, 2479 (2002).
125. X. X. Zhang, L. Balcells, J. M. Ruiz, J. L. Tholence, B. Barbara, and J. Tejada, *J. Phys.: Condens. Matter.* 4, L163 (1992).
126. J. M. Ruiz, X. X. Zhang, C. Ferrater, and J. Tejada, *Phys. Rev. B* 52, 1022 (1995).
127. J. M. Riveiro, J. P. Andres, and J. Rivas, *J. Magn. Magn. Mater.* 156, 243 (1996).
128. Z. S. Zhang, M. Zhang, and F. Pan, *J. Magn. Magn. Mater.* 192, 53 (1999).
129. Z. S. Zhang, Y. T. Wang, and F. Pan, *Phys. Status Solidi A* 179, 237 (2000).
130. K. Takanashi, Y. Kamiguchi, H. Fujimori, and M. Motokawa, *J. Phys. Soc. Jpn.* 61, 3721 (1992).
131. G. Choe and R. M. Walser, *J. Appl. Phys.* 79, 6306 (1996).
132. B. Altuncevahir and A. R. Koymen, *J. Appl. Phys.* 90, 2939 (2001).
133. J. Tappert, W. Keune, R. A. Brand, P. Vulliet, J.-P. Sanchez, and T. Shinjo, *J. Appl. Phys.* 80, 4503 (1996).
134. G. Garreau, E. Beaurepaire, M. Farle, and K. Ounadjela, *Phys. Rev. B* 53, 1083 (1996).
135. A. Sanz-Medel, J. E. Sanchez Uria, M. Tejedor, and A. Fernandez Suarez, *J. Anal. At. Spectrosc.* 1, 100 (1986).
136. L. T. Baczewski, M. Piecuch, J. Durand, G. Marchal, and P. Dele- croix, *Phys. Rev. B* 40, 11237 (1989).
137. A. Paul and A. Gupta, *J. Alloys Compd.* 326, 246 (2001).
138. M. Nawate, K. Doi, and S. Honda, *J. Magn. Magn. Mater.* 126, 279 (1993).
139. F. Richomme, J. Teillet, A. Fnidiki, and M. Toulemonde, *Nucl. Instrum. Methods Phys. Res., Sect. B* 122, 507 (1997).
140. J. Juraszek, A. Fnidiki, J. Teillet, F. Richomme, M. Toulemonde, and W. Keune, *Nucl. Instrum. Methods Phys. Res., Sect. B* 146, 244 (1998).
141. N. Heiman, A. Onton, D. F. Kyser, K. Lee, and C. R. Guarnieri, *J. Magn. Magn. Mater.* 24, 573 (1975).
142. Z. Sefroiuoui, J. L. Menéndez, E. Navarro, A. Cebollada, F. Briones, P. Crespo, and A. Hernando, *Phys. Rev. B* 64, 224431 (2001).
143. A. Hernando and J. M. Rojo, "Física de los Materiales Magnéticos," Editorial Síntesis, 2001, p. 216.
144. F. Badia, C. Ferrater, and B. Martínez, *J. Magn. Magn. Mater.* 93, 429 (1991).
145. X. Y. Zhang, R. Zquiak, and J. M. Ruiz, *J. Magn. Magn. Mater.* 118, 70 (1993).
146. S. Handschuh, J. Landes, and U. Kobler, *J. Magn. Magn. Mater.* 119, 254 (1993).
147. S. Honda and M. Nawate, *J. Magn. Magn. Mater.* 136, 163 (1994).
148. C. F. Majkrzak, J. W. Kabe, J. Kwo, M. Hong, D. B. McWhan, Y. Yafet, J. W. Waszczak, and C. Vettier, *Phys. Rev. Lett.* 56, 2700 (1986).
149. J. Kwo, M. Hong, J. Di Salvo, J. V. Waszczak, and C. F. Majkrzak, *Phys. Rev. B* 35, 7295 (1987).
150. M. B. Salamon, S. Sinha, J. J. Rhine, J. E. Cunningham, R. W. Erwin, and C. P. Flynn, *Phys. Rev. Lett.* 56, 259 (1986).
151. P. Grünberg, R. Schreiber, Y. Pang, M. B. Brodsky, and H. Sowers, *Phys. Rev. Lett.* 57, 2442 (1986).
152. S. S. P. Parkin, N. More, and K. P. Roche, *Phys. Rev. Lett.* 64, 2304 (1990).
153. P. Grünberg, in "Magnetic Multilayers and Giant Magnetoresistance. Fundamentals and Industrial Applications" (U. Hartmann, Ed.), p. 49. Springer-Verlag, Berlin, 2000.
154. M. N. Baibich, J. M. Broto, A. Fert, F. Ngyuen Van Dau, P. Etienne, G. Creuzet, A. Friederich, and J. Chazelas, *Phys. Rev. Lett.* 61, 2472 (1988).
155. J. J. Rhine and R. W. Erwin, in "Handbook of Magnetic Materials" (K. H. J. Buschow, Ed.), Vol. 8, p. 1. North-Holland, Elsevier, Amsterdam, 1995.
156. A. Fnidiki, J. Juraszek, J. Teillet, N. H. Duo, T. M. Danh, M. Kaabouchi, and C. Sella, *J. Appl. Phys.* 84, 3311 (1998).
157. V. O. Vas'kovskiy, A. A. Yuvenchenko, V. N. Lepalovskii, N. N. Shchegoleva, and A. V. Svalov, *Phys. Met. Metall.* 93, 43 (2002).



158. I. M. Fallon, C. A. Faunce, and P. J. Grundy, *J. Phys. Condens. Matter* 12, 4075 (2000).
159. M. Farle, *Rep. Prog. Phys.* 61, 755 (1998).
160. M. Farle and W. A. Lewis, *J. Appl. Phys.* 75, 5604 (1994).
161. A. Heys and P. E. Donovan, *J. Magn. Magn. Mater.* 126, 326 (1993).
162. J. Samuel Jiang and C. L. Chien, *J. Appl. Phys.* 79, 5615 (1996).
163. A. K. Petford-Long, R. C. Doole, and P. E. Donovan, *J. Magn. Magn. Mater.* 126, 41 (1993).
164. Y. Li, C. Polaczyk, J. Kapoor, F. Klöse, F. Mezei, and D. Riegel, *Physica B* 234–236, 492 (1997).
165. A. Gangulee and N. J. Kobliska, *J. Appl. Phys.* 49, 4169 (1978).
166. R. Hasegawa, *J. Appl. Phys.* 45, 3109 (1974).
167. R. C. Taylor and A. Gangulee, *J. Appl. Phys.* 47, 4666 (1976).
168. Z. Shan and D. J. Sellmyer, in “Handbook on the Physics and Chemistry of Rare Earths” (K. A. Gschneidner, Jr. and L. Eyring, Eds.), Vol. 22, p. 81. Elsevier North-Holland, Amsterdam, 1996.
169. H. Dohnomae and T. Shinjo, *J. Jpn. ICR* 14, 331 (1990).
170. Y. Kamiguchi, H. Fujimori, Y. Hayakawa, and K. Takanashi, *J. Jpn. ICR* 14, 355 (1990).
171. T. Shinjo, K. Yoden, N. Horoito, J.-P. Sanchez, and J.-M. Freidt, *J. Phys. Soc. Jpn.* 58, 4255 (1989).
172. H. Dohnomae, T. Shinjo, and M. Motokawa, *J. Magn. Magn. Mater.* 90–91, 88 (1990).
173. L. Veiller, D. Ledue, and J. Teillet, *J. Appl. Phys.* 87, 432 (2000).
174. R. E. Camley and D. R. Tilley, *Phys. Rev. B* 37, 3413 (1988).
175. M. Motokawa and H. Dohnomae, *J. Phys. Soc. Jpn.* 60, 1355 (1991).
176. J. Smakov, S. Lapinskas, E. E. Tornau, and A. Rosengren, *J. Magn. Magn. Mater.* 190, 157 (1998).
177. M. Tanaka, H. Yuzurihara, and T. Tokita, *IEEE Trans. Magn. MAG-23*, 2955 (1987).
178. S. Tsunashima, T. Ohtani, X. Y. Yu, S. Iwata, and S. Uchiyama, *J. Magn. Magn. Mater.* 104–107, 1021 (1992).
179. Y. Fujiwara, X. Y. Yu, S. Tsunashima, S. Iwata, M. Sakurai, and K. Suzuki, *J. Appl. Phys.* 79, 6270 (1996).
180. Y. Fujiwara, T. Masaki, X. Y. Yu, S. Tsunashima, and S. Iwata, *J. Magn. Magn. Mater.* 177–181, 1173 (1998).
181. Z. S. Shan, D. J. Sellmyer, S. S. Jaswal, Y. J. Wang, and J. X. Shen, *Phys. Rev. B* 42, 10446 (1990).
182. F. Badía, M. A. Badry, X. X. Zhang, J. Tejada, R. A. Brand, B. Scholz, and W. Keune, *J. Appl. Phys.* 70, 6209 (1991).
183. Y. J. Wang, C. P. Luo, W. Kleemann, B. Scholz, R. A. Brand, and W. Keune, *J. Appl. Phys.* 73, 6907 (1993).
184. G. S. Cargill III and T. Mizoguchi, *J. Appl. Phys.* 49, 1753 (1978).
185. T. Mizoguchi and G. S. Cargill III, *J. Appl. Phys.* 50, 3570 (1979).
186. K. Mibu, N. Hosoi, and T. Shinjo, *Hyperfine Interact.* 68, 341 (1991).
187. A. Gupta, A. Paul, R. Gupta, D. K. Avasthi, and G. Principi, *J. Phys.: Condens. Matter* 10, 9669 (1998).
188. C. Dufour, K. Cherifi, A. Brusson, G. Marchal, and Ph. Mangin, *Phys. Status Solid A* 125, 561 (1991).
189. Z. S. Shan and D. J. Sellmyer, *J. Appl. Phys.* 64, 5745 (1988).
190. B. Scholz, R. A. Brand, and W. Keune, *Phys. Rev. B* 50, 2537 (1994).
191. C. Rau and G. Xing, *J. Vac. Sci. Technol.*, A 7, 1889 (1989).
192. J. Tappert, J. Jungermann, B. Scholz, R. A. Brand, and W. Keune, *J. Appl. Phys.* 76, 6293 (1994).
193. O. Schulte, F. Klöse, and W. Felsch, *Phys. Rev. B* 52, 6480 (1995).
194. A. E. Freitag and A. R. Chowdhury, *J. Appl. Phys.* 82, 5039 (1997).
195. M. Sajjeddine, Ph. Bauer, C. Dufour, K. Cherifi, G. Marchal, and Ph. Mangin, *J. Magn. Magn. Mater.* 113, 243 (1992).
196. B. Scholz, R. A. Brand, and W. Keune, *J. Magn. Magn. Mater.* 104–107, 1889 (1992).
197. R. E. Camley, *Phys. Rev. B* 39, 12316 (1989).
198. J. P. Andrés, L. Chico, J. Colino, and J. M. Riveiro, *Phys. Rev. B* 66, 094424 (2002).
199. N. C. Koon, K. D. Aylesworth, V. G. Harris, and B. N. Das, *J. Alloys Compd.* 181, 409 (1992).
200. E. Quandt, A. Ludwig, J. Mencik, and E. Nold, *J. Alloys Compd.* 258, 133 (1997).
201. T. Shima, K. Takanashi, and H. Fujimori, *J. Magn. Magn. Mater.* 239, 573 (2002).
202. A. Barthélémy, A. Fert, and F. Petroff, in “Handbook of Magnetic Materials” (K. H. J. Buschow, Ed.), Vol. 12, p. 1. Elsevier, North-Holland, Amsterdam, 1999.
203. R. Coehoorn, in “Magnetic Multilayers and Giant Magnetoresistance. Fundamentals and Industrial Applications” (U. Hartmann, Ed.), p. 320. Springer-Verlag, Berlin, 2000.
204. J. Barnas, A. Fuss, R. E. Camley, P. Grünberg, and W. Zinn, *Phys. Rev. B* 42, 8110 (1990).
205. P. P. Freitas, J. L. Leal, T. S. Plaskett, L. V. Melo, and J. C. Soares, *J. Appl. Phys.* 75, 6480 (1994).
206. A. Hubert and R. Schäfer, “Magnetic Domains: The Analysis of Magnetic Microstructures.” Springer-Verlag, Berlin, 1998.
207. S. Uchiyama, X. Y. Yu, and S. Tsunashima, *J. Phys. Chem. Solids* 56, 1557 (1995).
208. X. Y. Yu, A. Sugie, Y. Fujiwara, S. Iwata, and S. Tsunashima, *J. Magn. Magn. Mater.* 177–181, 1203 (1998).
209. E. Stavrou, R. Sbiaa, and T. Suzuki, *J. Appl. Phys.* 87, 6899 (2000).
210. M. Tejedor, A. Fernandez Suarez, M. A. Cerderia, *Rev. Sci. Instrum.* 69, 4000 (1998).
211. M. Tejedor, A. Fernandez Suarez, and B. Hernando, *IEEE Trans. Magn.* 24, 1995 (1988).
212. K. Röhl, in “Magnetic Multilayers and Giant Magnetoresistance. Fundamentals and Industrial Applications” (U. Hartmann, Ed.), p. 13. Springer-Verlag, Berlin, 2000.
213. G. N. Phillips, K. O’Grady, and M. El-Hilo, *J. Magn. Magn. Mater.* 248, 418 (2002).
214. M. Rührig, R. Schäfer, A. Hubert, R. Mosler, J. A. Wolf, S. Demokritov, and P. Grünberg, *Phys. Status Solidi* 125, 635 (1991).
215. H. Sughara, K. Tsutsumi, K. Hashima, T. Tokunaga, and Y. Fuji, *IEEE Trans. Magn. MAG* 24, 2455 (1988).
216. Y. Itoh and T. Takase, *IEEE Trans. Magn. MAG* 27, 3756 (1991).
217. K. Tsutsumi and T. Fukami, *J. Magn. Magn. Mater.* 118, 231 (1993).
218. J. Saito, M. Sato, H. Matsumoto, and H. Akasaka, *Jpn. J. Appl. Phys.* 26, 155 (1987).



# Magnetoimpedance in Nanocrystalline Alloys

B. Hernando, P. Gorria, M. L. Sánchez, V. M. Prida, G. V. Kurlyandskaya  
*Universidad de Oviedo, Calvo Sotelo, Oviedo, Spain*

## CONTENTS

1. Impedance
  2. Magnetoimpedance
  3. Soft Magnetic Nanocrystalline Alloys
  4. Magnetoimpedance Effect in Nanocrystalline Alloys
- Glossary  
References

## 1. IMPEDANCE

Our interest in impedance is due to the change of this magnitude in a magnetic material under the application of some external parameters like stress, torsion, magnetic fields, and so on. Impedance is not only sensitive to the magnetic properties of a material, but also to its structure. Therefore, it is a good parameter that allows the study of the properties of nanostructured magnetic materials.

Our magnetic nanostructured sample is submitted to an ac drive current passing through it. The drive current frequency is  $f$ . The sample is now part of an ac circuit, and according to the well-known Ohm's law, a voltage is induced between the ends of the sample with the same frequency of the drive current, and its value is proportional to the drive current. The proportionality is established by using the complex impedance  $Z$ .

$$V_{ac} = I_{ac}Z \quad (1)$$

The induced voltage can be measured by an oscilloscope.

The impedance  $Z$  depends on the drive current frequency, and can be separated into its real and imaginary components ( $Z = Z' + jZ''$ ).

Let us consider the current distribution in the sample's section. When the drive current frequency increases, the current will be mainly concentrated close to the surface of the sample [1] due to the skin effect. The exact solution to the problem generally depends on the shape of the conducting sample and the drive current. To obtain the solution, the Maxwell equations have to be applied.

The Maxwell equations can be easily solved for the case of a sample with cylindrical symmetry. Our wire-shaped sample has a conductivity  $\sigma$  and circular permeability  $\mu_\phi$ . The magnetic field induced by the drive current is circular,  $B_\phi = \mu_\phi H_\phi$ . The impedance can then be derived in this case by solving Maxwell equations [2]:

$$Z = \frac{1}{2}R_{dc}ka \left[ \frac{J_0(ka)}{J_1(ka)} \right] \quad (2)$$

with  $k = (1 + j)(a/\delta)$  and  $\delta = (c/2\pi)(\sigma\mu_\phi f)^{-1/2}$ , where  $j = \sqrt{-1}$ , and  $J_0$  and  $J_1$  are Bessel functions of the first and second kind,  $R_{dc}$  is the resistance of the wire at  $f = 0$ , and  $\delta$  is the skin penetration depth.

The impedance depends on the properties of the material through the skin penetration depth, where  $\sigma$  and  $\mu_\phi$  appear. The magnetic and structural properties of the material are characterized by these parameters. The action of other external properties, such as a magnetic field, would change these parameters through the change of the magnetic domain configuration or structure. The ac frequency also affects the skin effect: the higher the frequency, the smaller  $\delta$  is, and the narrower the outer shell of the sample is, through which the current flows.

In the case of a sample with no circular cross section, the resolution of the Maxwell equations is difficult, although the impedance shows the same dependence on the skin penetration depth, and the behavior of the impedance can be explained qualitatively through the interaction of all of the involved parameters.

## 2. MAGNETOIMPEDANCE

In the last ten years, there has been a considerable interest in transport phenomena due to their possibilities for use in technological applications, such as magnetic recording and magnetic sensors. One of them is the magnetoimpedance (MI) effect concerning large variations in the impedance (both real and imaginary components) of a soft ferromagnetic conductor when submitted to a static magnetic field, with a high-frequency drive current flowing through it. This

effect was discovered in FeCoSiB amorphous wires [3–6] and ribbons [7]. The MI effect has been observed in other different Co-rich amorphous ribbons, microwires, and thin films [8–26], and also in nanocrystalline Fe-rich wires, ribbons, and thin films [17, 26–56].

As mentioned above, the MI effect has a classical electromagnetic origin, and can be explained by solving the Maxwell equations and Landau–Lifshitz equation of motion [1] for a magnetic conductor when a high-frequency driving current flows along it. The MI effect is a consequence of the impedance  $Z$ , dependence on the applied bias field  $H$ , and the drive frequency  $f$  due to the skin effect.  $Z$  can be expressed in terms of real (resistive) and imaginary (reactive) components as  $Z(f, H) = Z'(f, H) + jZ''(f, H)$ .

In the MI measurements, an ac drive current flows through the sample. The current amplitude is kept constant during the measurements. An axial magnetic field is applied in the axial direction by a pair of Helmholtz coils. The ac current induces a voltage between the ends of the sample that is measured by a digital oscilloscope and that is proportional to the impedance.

The magnetoimpedance ratio is obtained with respect to a maximum field  $H_{\max}$  at which the sample is saturated. A 45 Oe field is high enough to saturate a 10 cm long sample.

$$\Delta Z/Z(\%) = 100 \times \frac{Z(H) - Z(H_{\max})}{Z(H_{\max})} \quad (3)$$

The MI rate behavior depends on the drive current amplitude and frequency, and on other parameters, such as magnetic permeability, magnetostriction, induced anisotropy, and so on. When the axial field is applied, the transversal permeability which appears on the skin penetration depth  $\delta$  decreases, making  $\delta$  increase, and changing the current distribution in the sample section. This produces a change in impedance [57].

The MI depends on several parameters, and can also give information about them, as will be explained in the following sections. The magnetostriction coefficient seems to play an important role since the highest values are obtained at an almost negligible magnetostriction. This is related to the magnetic softness of the sample, as well as to a high permeability value.

The magnetoimpedance phenomenon appears at a frequency at which the  $\delta$  is on the order of the sample thickness, at about  $10^4$  Hz in the case of 130  $\mu\text{m}$  diameter wires, and at a somewhat higher frequency for 20  $\mu\text{m}$  thick ribbons. The MI spectrum shows a maximum at a certain frequency, and then decreases, for all type of samples.

### 3. SOFT MAGNETIC NANOCRYSTALLINE ALLOYS

This section is subdivided into four parts, and constitutes a general introduction to the nanocrystalline soft ferromagnetic alloys. The most remarkable aspects related to the preparation methods used to synthesize these compounds, the different treatments applied in order to improve their magnetic response, as well as some generalities concerning the structural and magnetic evolution during the nanocrystallization process are explained.

### 3.1. Introduction

The term “soft magnetic nanocrystalline alloy” is commonly applied to a singular type of material that exhibits a superb soft magnetic response due to its ultralow values of the magnetic anisotropy (excellent research reviews on this topic are, for example, those by Herzer [58] and McHenry et al. [59]). These kinds of alloys are usually obtained by devitrification of Fe-rich metallic glasses, and in the last decade, they have been the subject of an enormous research effort due to their promising applications in a large variety of technological devices.

On the other hand, these materials have also opened new and unexplored fields of basic research in magnetism, as well as in solid-state physics in general because the competition between two or more magnetic phases, amorphous and nanocrystalline, coexisting in the same system, gives rise to a very rich scenario for the study of complex magnetic interactions [60].

During the last three decades, nanostructured materials have attracted huge attention, not only because of their unusual structural, electrical, magnetic, and optical properties, different from corresponding noncrystalline precursor alloys, but because they have conditions and techniques of preparation different from the bulk materials as well. Fine-grain structures can be obtained by heat treating an amorphous alloy precursor with a noncrystalline structure. Amorphous alloys inherently have a uniform distribution of constituent elements. The last is a condition suitable for the formation of nanostructured materials, making the glassy alloys promising precursors for controlling the nanoscale structure because of the high degree of freedom for a topological and chemical structure that persists in these amorphous materials [61]. Currently, minority elements are added in a glass-forming amorphous alloy to promote massive nucleation through the addition of insoluble atoms such as Cu, and to inhibit grain growth by adding refractory and stable species such as Nb, Ta, and so on. The addition of these elements has a key effect on the improvement of material properties, such as mechanical strength or corrosion resistance [62].

In the late 1980s and early 1990s, Yoshizawa et al. [63], Herzer [64], and Suzuki et al. [65] obtained, for the first time, these kinds of alloys in a nanocrystalline state, and published their unique soft magnetic behavior results. The interest in these alloys, as already mentioned, lies in the very soft magnetic properties shown, especially in the low-frequency range (megahertz), surpassing the magnetic response shown by their precursor alloys in the amorphous state. These properties include high saturation magnetic polarization (up to 2–2.1 T), quasivanishing macroscopical anisotropy, nearly zero saturation magnetostriction ( $\lambda_s \approx 10^{-7}$ ), and therefore, high magnetic permeability ( $\mu \approx 10^5$ ). All of these features combined with the reduction of magnetic losses, in the low-frequency range, originating by an appreciable decrease of the electrical resistivity and coercive field ( $H_c < 1$  A/m) values, shown in the nanocrystalline state, make them good candidates for technological applications such as power transformers, common-mode choke coils, flux-gate magnetometers, or magnetoelastic microsensors and transducers [59].

The composition of these nanocrystalline soft magnetic compounds is based on the Fe–*M* metallic glasses (where *M* is a metalloid such as B, Si, Al, P, or Ge), largely studied in the 1970s and 1980s, but with the addition of a small amount (less than 15at%) of transition metals (TM) such as Zr, Nb, Cu, Hf, V, Ta, and so on [58, 59, 63–67]. There are four families of such alloys.

1. Fe–TM–Cu–Si–B alloys: TM is Nb, Ta, V, and so on, the percentage of metalloid atoms is around 20–25at%, the amount of TM is rather low (around 3at%), and the percentage of Fe is not higher of 75at%. These alloys show the lowest values for the coercive field (less than 1 A/m), but due to the high amount of metalloids, and the fact that the magnetic nanocrystalline phase is FeSi, the saturation magnetic polarization  $J_s$  never exceeds 1.3–1.4 T. The better magnetic response is obtained with TM = Nb, the so-called FINEMET alloys.
2. Fe–TM–B–(Cu) alloys: In this case, TM is Zr, Hf, or Nb, the percentage of metalloids is lower than in the previous group (2–10at%), and the amount of Fe is over 85at%. The nanocrystalline phase is now nearly pure  $\alpha$ -Fe, giving rise to high values of  $J_s$  (up to 1.7 T), but the coercivity is about one order of magnitude higher than in group 1) above, reaching values of several amperes per meter, due to the slightly higher saturation magnetostriction. The most studied compounds of this group are FeZrB(Cu) alloys, commonly known as NANOPERM alloys.
3. Fe–Co–TM–B–(Cu) alloys: The composition of these alloys is similar to those of group 2), but Fe atoms are substituted for Co ones in several concentrations, reaching values of  $J_s$  above 2 T, as for an Fe<sub>44</sub>Co<sub>44</sub>Zr<sub>7</sub>B<sub>4</sub>Cu<sub>1</sub> alloy. However, the coercivity never decreases below 20 A/m because the ferromagnetic nanocrystalline phase, actually FeCo, has larger anisotropy values due to the presence of Co atoms. These alloys are called HITPERM.
4. Other alloys: There is a huge number of ferromagnetic nanocrystalline alloys in which other metalloids, such as Al, P, or Ge, substitute B and/or Si or, also, Ni is included in the composition, substituting Fe and/or Co atoms, but up to now, none of these has shown better soft magnetic properties than the compounds included in the previous three groups.

If the so-called nanocrystalline regime is pursued, these alloys have to be submitted to appropriate heat treatments in order to provide enough thermal energy to favor the structural transition from a disordered metastable glassy structure to a stable and more ordered crystalline one. In other words, the crystallization of the initial amorphous state takes place when the alloy is annealed. The crystallization process takes place in two differentiated steps [68, 69]. In the first step, the ferromagnetic Fe or FeSi crystalline phase, with an average grain size of about 10–15 nm, is formed. At this moment, the system is composed of a mixed structure of Fe(Si) nanograins embedded in a remaining amorphous matrix or intergranular region, which becomes more and more inhomogeneous as this first crystallization step continues. Once the first crystallization process has finished,

the second step leads to the crystallization of the remaining amorphous matrix, enriched in B and TM, into Fe–B or FeTM(B) phases (with much higher values for the magnetic anisotropy), and the growing of the Fe(Si) nanograins above 20 nm. These two processes overlap in most cases, when Fe–metalloid alloys are submitted to heat treatments [70], and occur for temperatures above 400 °C; hence, the nanocrystalline state is never reached, and the soft magnetic properties shown in an amorphous state do not improve during the crystallization process. However, the addition of a small amount of Cu, which acts as a nucleation center for crystallites, accelerates the first step, and takes place at lower temperatures (below 500 °C). On the other hand, the effect of the addition of other transition metals, such as those mentioned above, retards the second crystallization step up to temperatures above 700 °C, and prevents grain growth. In between both steps, the structure of these materials consists of a large amount of Fe or FeSi nanosized grains (around 70–80% of the sample) surrounded by the remaining amorphous ferromagnetic matrix (less than 30%) [71]. The origin of the excellent soft magnetic properties displayed in this state lies in the nanometer grain size of the Fe(Si) phase, which is lower than the exchange correlation length. As is well known, this critical dimension plays a definite role in magnetic interactions. This behavior has been largely explained in the framework of the random anisotropy model [72] by Herzer [58, 64]. Another reason contributes to this magnetic softening: say, some of these systems, especially those of group 1), exhibit near-zero average magnetostriction due to the opposite sign of this parameter for the Fe(Si) nanocrystals and for the amorphous matrix, so no macroscopic magnetoelastic anisotropy is present in the samples.

### 3.2. Preparation: Composition and Geometry (Thin Films, Ribbons, Wires, and Microwires)

As mentioned above, the magnetoimpedance phenomenon consists of the change of total impedance of a ferromagnetic conductor under the application of a magnetic field [7–14]. Therefore, by definition, the MI effect is expected in the sample only under the conditions of the ferromagnetic state, that is, below the Curie temperature, and if it is large enough to show the ferromagnetic behavior. What is large enough? Some time ago, we could answer the question about critical size of the ferromagnetic sample only on the basis of theoretical predictions. But new experimental methods like the micro SQUID setup [73] are available now to study the magnetization behavior of an individual magnetic cluster, for instance, of 1000 atoms, which is about 3 nm in size in the case of cobalt [74]. Magnetic nanostructures are subjects of special interest due to many possible potential applications. One may distinguish between tiny separate nanosized elements showing interesting properties and macroscopic objects having nanosize structural units. The nanosize clusters [73, 74], polycrystalline materials with grains of nanosize [26, 28, 37, 44, 49, 51, 53, 56, 63, 64, 75–78], or multilayers with layers of nanoscale thickness [16, 48, 79–82] are examples of such new structures.

Although the term “as small as possible” seems most popular for modern applications, there are theoretical and

technological limits on the size of the elements involved in the functionality for each particular case. Here, we wish to show that, for an MI element, the size limit of the ferromagnetic state lies far below the critical size for the appearance of a strong MI effect.

As mentioned in the Introduction, the MI effect in a uniform ferromagnetic conductor is based on the impedance dependence on the classic skin penetration depth  $\delta = (\rho\pi f\mu)^{1/2}$  for the flowing ac current of angular frequency  $\omega = 2\pi f$ .

The impedance of a ferromagnetic sheet of thickness  $d$ , width  $b$ , and length  $L$  under the condition  $b \gg d \gg \delta$  can be written as [12]

$$Z \approx L(1 + j) \frac{(4\pi\rho f\mu)^{1/2}}{4b} \quad (4)$$

where  $\rho (= 1/\sigma)$  is the electrical resistivity, and  $\mu$  is the low-frequency transverse magnetic permeability. Figure 1 shows the frequency dependence of the skin depth and the impedance for different values of the transverse magnetic permeability. The geometrical parameters of the sheets were:  $L = 10$  cm,  $b = 0.8$  mm,  $d = 20$   $\mu\text{m}$ , that is, the  $b \gg d$  condition was satisfied. We are interested in comparing the results of the MI measurements for a nanocrystalline sample (FINEMET ribbons, for example), with an approximation taken in the framework of the classical model (Eq. (2) [1]) for samples of the same geometry. The same parameters for approximation were taken as for experimental samples. The resistivity  $\rho = 1.5$   $\mu\Omega \cdot \text{m}$  was measured using the four-point method for a dc current of 10 mA. One may see that an increase of the exciting current frequency

results in a decrease of the calculated penetration depth and an increase of the total impedance. But there is a strong dependence of  $\delta$  and  $Z$  values on the magnetic state of the sample: the higher the effective magnetic permeability, the less, for the same frequency, the penetration depth and the higher the impedance variation are. The inset in Figure 1a shows the impedance dependence on the exciting frequency for selected values of the permeability. The calculated data are compared with the results of MI measurements for FINEMET nanocrystalline ribbons of the same geometry; they are in the reasonable agreement.

The second condition,  $d \gg \delta$ , for the frequency range under consideration can be satisfied only for the sheets with very high transverse permeability ( $\mu = 1000$  in Fig. 1b). The dashed line  $\delta = 20$   $\mu\text{m}$  corresponds to the thickness of our nanocrystalline ribbon. When do the skin effect, and consequently the MI effect, appear? When  $\delta$  is less than half the thickness of the sample. Therefore, if we are interested in a small size of the sample, the size condition of the skin effect results in a strong increase of the operating frequency. This is, of course, an undesired complication. Let us illustrate these ideas for the sample with a very high, but realistic effective permeability of  $\mu = 1000$ . Figure 1b shows that, for the 20  $\mu\text{m}$  thick element, the skin/MI effect appears at  $f \cong 0.8$  MHz, but for the 2  $\mu\text{m}$  element, the operating frequency is about 110 MHz. Two “stars” in Figure 1b prompt this question: “size or frequency?” A high operating frequency on the order of 100 MHz required another level of the electronic part of the device (higher price, complicated circuit, etc.). Therefore, one has to decide up to which size the complication of the sensing process and price of the device can be compensated by the miniaturization. Another important point to mention is that the higher the effective permeability of the magnetic material is, the lower the operating frequency we need for the same size of sensitive element.

The size of the sensitive element based on the ribbon geometry material is not acceptable for many applications. Therefore, there were many theoretical and experimental studies of the MI effect in thin-film geometries [1, 12, 16, 79, 80, 82]. But just a few results were reported for nanocrystalline thin films on the strong dependence of the properties on the technology of preparation [48]. Nie et al. [83] reported that MI of the Mumetal sheets depends very much on the thickness of the samples, being maximum for a thickness of 1 mm and negligible for a 12.5  $\mu\text{m}$  thick sheet. This means that, for nanocrystalline materials, apart from the usual dependence of the MI on the geometry of the sample, there are many additional parameters related to nanocrystallization and induced anisotropy features in thin samples.

The nanocrystalline materials can be obtained from a metallic glass with the shape of ribbons, wires, or microwires, as described below. Metallic glasses are obtained using a rapid solidification technique. The composition is first chosen and mixed. Afterwards, it is pressed and sintered in an  $\text{H}_2$  atmosphere, in order to eliminate oxygen and avoid oxidation during the melting process. The next step is to melt the alloy in an induction furnace at 1500  $^\circ\text{C}$ . The alloys will be used to produce metallic glasses with different shapes. All rapidly quenching techniques are based on a melted alloy falling over a moving surface, and cooling down at about  $10^6$  K/s.

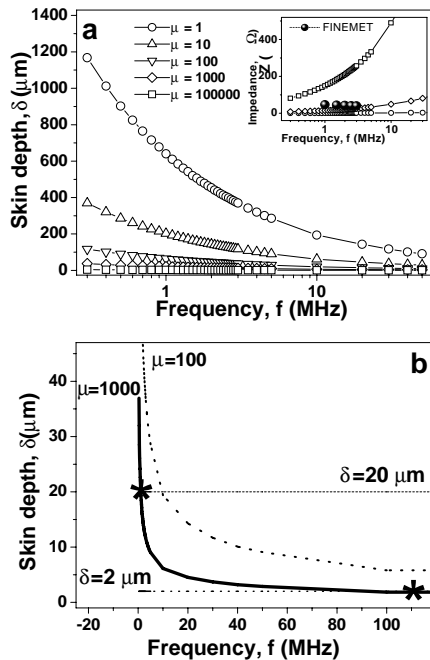


**Figure 1.** Calculated frequency dependencies of classic penetration depth and the impedance of a conductive sheet with different values of the effective permeability. The measurements of a nanocrystalline FINEMET  $\text{Fe}_{73.5}\text{Cu}_1\text{Nb}_3\text{Si}_{13.5}\text{B}_9$  ribbon (inset) are in agreement with the model estimation.



### 3.2.1. Ribbons

The technique employed first by Duwez [84] is used to obtain ribbon-shaped samples. The melt-spinning technique consists of the injection of the melted alloy over a Cu wheel, which is spinning at a high speed. The Cu is a good thermal conductor, and produces cooling of the alloy at a rate of about  $10^6$  K/s.

The prepared solid alloy, by using this method, is introduced in the quartz melting pot, which has a hole of about tenths of a millimeter at the bottom. The alloy is molten with an induction furnace at 1300 °C and in an Ar atmosphere. The furnace works at 2500 kHz. As the sample contains 80% of metals, the Foucault currents produce the heating and melting of the sample. A higher Ar pressure is applied to produce the expelling of the alloy over the spinning wheel. The thickness, width, and characteristics of the ribbon depend on the speed of the wheel, the Ar pressure, the orifice diameter of the melting pot, its distance and inclination with respect to the wheel, and the alloy temperature at the expelling time. The ribbons obtained with this technique have a thickness on the order of several tenths of microns, and widths between 1 and 3 mm.

### 3.2.2. Wires

Samples with a circular section can be obtained by the melt-spinning technique. The production technique was initially developed by Masumoto et al. [85]. The molten alloy is obtained in the same way as explained above. The method consists of injecting the melting alloy in a flow of water, which is turning at a high speed. The water is introduced in a hollow toroid that is spinning, making the water turn and keeping it inside due to the centrifugal force. A rapid transfer of heat freezes the atoms when the metal hits the water, obtaining an amorphous solid. The cooling speed is about  $10^6$  K/s. The cooling of the alloy takes place from the outer surface of the alloy, which acquires a cylindrical shape when it falls into the water. Wires with diameters between 100 and 150  $\mu\text{m}$  can be obtained by this procedure.

### 3.2.3. Microwires

The microwires have a ferromagnetic nucleus and a glass cover. They are obtained by the Taylor–Ulitsky technique, which has been modified in the last 40 years [86]. The alloy is introduced in a Pyrex tube, that will be melted with the alloy [87]. The alloy is melted by the furnace as explained above in the other techniques, and the Pyrex is melted due to the contact with the molten alloy. The molten alloy with a glass layer is cooled when it passes a flow of cooling material (water, oil, etc.), and it is collected in a coil that produces an axial stress on the microwire. The microwire diameter varies with the following parameters: furnace potency, distance of the alloy to the furnace, and speed of the coil collecting the sample. The diameters of the nuclei vary from 1 to 25  $\mu\text{m}$ , and the glass coat has a thickness between 1 and 10  $\mu\text{m}$ . The internal stresses are much stronger than the conventional amorphous wires as a consequence of the presence of the glass coating which, coupled with the magnetostriction, can give rise to strong magnetoelastic anisotropy which determines the magnetization process. Amorphous and nanocrystalline microwires may show a magnetoimpedance effect in a very

high range of the frequency from kilohertz up to hundreds of megahertz [88, 89].

Nanocrystalline materials have been obtained from an amorphous alloy. Nanocrystals of sizes ranging from 5 to 10 nm and compositions of AlRu, SiRu, NiTi, or CuEr have been obtained in this way. Amorphous alloys of FeB also have been produced using this technique, in order to induce crystals with sizes in the 10 nm range after a suitable annealing technique.

Nanocrystals have been obtained in the Fe<sub>73.5</sub>Si<sub>13.5</sub>B<sub>9</sub>Cu<sub>1</sub>Nb<sub>3</sub> alloy by Yoshizawa et al. [63]. This alloy is produced as an amorphous ribbon, obtaining a nanocrystallized state after an additional treatment above the crystallization temperature. Ultrafine grains of the  $\alpha$ -FeSi phase and sizes between 10–20 nm are obtained after a suitable treatment. The interest of this composition lies in the high magnetic permeability and soft magnetic properties when the grain size is about 10–20 nm [64]. The magnetic softness is a dramatic function of the grain size.

In order to determine the nanocrystalline structure of the material obtained with any geometry, an additional annealing treatment is needed [90]. This annealing can be performed in a conventional furnace, heating the sample above the crystallization temperature. The annealing has also been successfully performed by using the current annealing technique, which consists of the application of a dc current across the sample. The temperature increases in the sample due to the Joule effect, reaching the desired temperature in a very quick way, although a dc magnetic field is induced, and is not homogeneous inside the sample.

### 3.2.4. Thin Films and Multilayers

Magnetic materials in a thin-film shape can be prepared by different methods, such as thermal deposition on a cold substrate, electrodeposition, laser ablation, or sputtering. Sputtering can be provided using alternating or direct current in the inert gas atmosphere (Ar or Kr). The ions of the inert gas move from the substrate (anode) to the target (cathode). As a result of the ion bombardment, some atoms of the target are set free, and then are deposited onto the substrate. If the rate of deposition is high enough (on the order of 0.1 nm/s) and cooling of the substrate is used (by water, liquid nitrogen, or even liquid helium), the deposited film shows an amorphous structure. Apart from the composition of the target, the deposition rate, and the temperature/type of the substrate, the thickness of the film can be a critical parameter in order to obtain an amorphous or nanocrystalline state in as-deposited films. The same as for nanocrystalline ribbons, it is much easier to prepare thin films in a nanocrystalline state using sputtering deposition, followed by conventional or field annealing for nanocrystallization [48]. The thickest single-layer samples usually do not exceed the 5  $\mu\text{m}$  limit, even if deposited onto Si because of the separation of the sample on the substrate.

In any sputtering system, it is very important to ensure the homogeneity of the deposited samples from the point of view of the composition and thickness. There are many methods to control these parameters and to avoid strong deviations [91–94]. Homogeneity can even be a more critical parameter in the case of the MI thin-film element because it

includes not only the magnetic film itself, but also the electrical contacts and other parts of the imprinted circuit. Up to now, we have been addressing a single-layer MI thin-film element. A very sensitive magnetoimpedance recently has been reported to appear in multilayered structures of two very soft magnetic layers separated by a highly conductive layer [12, 48, 82, 95–97]. In such a complicated structure, the homogeneity of the sample properties is very important in order to avoid critical stresses in a three-dimensional structure. The sensitivity of the magnetoimpedance in single-layer Co-rich thin films typically does not exceed 10%/Oe [98], but it can be on the order of 30%/Oe in the case of a Co-based sandwich with a Cu conductive lead, where a large impedance change appears at lower frequencies. The condition of a strong skin effect is not required in “soft ferromagnetic/conductor/soft ferromagnetic” sandwiches. For a sufficiently large width of the MI sandwich, the contribution of the outer magnetic layers to the total impedance is defined by the external inductance. In this case, the impedance shows linear variation with effective magnetic permeability and frequency. Although there have been many optimistic discussions with respect to the potential of the MI sandwiches to be employed in developing magnetic heads for high-density magnetic recording, finally it seems that they are better suited sensor applications as very sensitive detectors of a small magnetic field. An additional advantage of a thin-film MI structure consists of the possibility to use the thin-plate permanent magnet attached to the substrate to generate the bias magnetic field to achieve a better response.

The MI sandwich is composed of an inner conductive lead of a nonmagnetic material (Cu, Ag, Au) and two outer layers of amorphous or nanocrystalline very soft magnetic material. In order to enhance the value of the effect, two magnetic layers and a conductive layer are deposited in the shape of a closed-loop structure. The unidirectional magnetic anisotropy in each magnetic layer of the MI sandwich is formed in the transverse direction, that is, perpendicular to the conductive lead, but in the plane of the magnetic films. It can be done by application of a constant magnetic field, usually on the order of 100 Oe, during the deposition. The MI effect in MI sandwiches is much stronger compared with that in a single-layered thin film of the same thickness. This can be explained taking into account the very weak influence of stray fields in an MI closed-loop structure, being actually part of the more general fact that all mechanisms involved in the magnetization process contribute to the magnetoimpedance effect [99].

The new types of magnetic sensors on the basis of the MI effect in sandwiched thin-film structures were developed recently to be employed as direction, revolution, and position sensors [100]. They show no hysteresis, good linearity, reasonable temperature stability, and very high sensitivity with a detection resolution of  $10^{-3}$  Oe, that is, higher than any other type of thin-film sensor like an element based on magnetoresistance or the Hall effect. A self-oscillation circuit technology is very useful for construction of the MI-element-based sensor in order to avoid parasitic displacement currents and reflected signals. In oscillation circuits like the Colpitts oscillator, the MI element is employed as inductance, and the MI effect is amplified in a resonant circuit due to a simultaneous change of

both the impedance and the current amplitude [101, 102]. Another example of possible technological applications of the impedance sandwiches is strain sensor, which detects the change in impedance with applied strain in magnetostrictive thin films [103, 104]. Reported in this case are gauge factors ten times larger than those of semiconductor strain gauges.

### 3.3. Postpreparation Treatments

Once the samples are prepared in any of the geometries mentioned in the previous section, two kind of heat treatments, with different main objectives, are used, with the aim of reaching the optimal magnetic state of the particular alloy: first, to nanocrystallize the samples, and second, to obtain a particular anisotropy distribution combining heat treatments with the application of a magnetic field, tensile, and or torsional stresses. These two aspects are explained in the following paragraphs.

- **Nanocrystallization treatments:** The nanocrystalline state is obtained when the as-prepared amorphous samples are conveniently annealed. Conventional heat treatments are performed using a furnace under controlled atmosphere (Ar, He, or vacuum) to prevent oxidation of the samples. The range of the annealing temperatures is in between 450 and 600 °C, and time periods on the order of several minutes or hours [58, 59]. There is another way to heat the samples that consists of passing an electrical current along the sample, particularly used in the case of ribbon or wire geometries. This method, called flash annealing, current annealing, or Joule heating, is based on the Joule effect [105], and allows us to obtain the sample in a nanocrystalline state in a quicker way (10–100 s) [106, 107].
- **Induction of anisotropies:** Magnetic anisotropy in nanocrystalline soft magnetic materials for MI applications can be induced by traditional methods like annealing in a magnetic dc or ac field [78] or stress annealing [75, 76]. Many parameters play an important role in the magnetic anisotropy, and consequently, MI response formation. For example, for FeCuNbSiB ribbons, the Si content could be critical for the field annealing, leading to a decrease or increase of the magnetoimpedance ratio [100]. All treatments below the Curie point usually need to be provided in a magnetic field higher than the saturation one. The temperature, time of exposure, rate of heating and cooling, and specific stress for stress annealing are the important parameters. Both the stress and field annealing can be done in two different ways: annealing of as-cast samples under field or stress, or using previously nanocrystallized samples, and then submitting them to a stress or field annealing. Since the magnetoimpedance depends on the permeability, there are many possibilities for modifying the GMI responses. Apart from the objective of nanocrystallization in order to achieve extra soft magnetic material, one may take into account the value of the transverse induced magnetic anisotropy [44, 80]; the anisotropy distribution [44] and thermal or time stability may be the parameters of interest both for the

study of technological applications and magnetization processes. Magnetic anisotropy in nanocrystalline soft magnetic materials for MI applications can be induced by traditional methods like annealing in a magnetic field [44, 75, 76]. Usually, it is a dc field applied in the direction of the ribbon or wire axis or in a perpendicular direction [37]. There were attempts to use low- and high-frequency ac [77] fields as well. It is known that ac field annealing leads to a magnetic structure formation with no stabilization of the domain walls, which is a very favorable feature for the MI conditions of the magnetization. Stress annealing is another effective method of anisotropy formation. It was found that, not only can simple uniaxial magnetic anisotropy be formed as a result of stress annealing, but also, a very complicated high-order anisotropy, which results in interesting and unwanted hysteresis of the MI. As mentioned, many parameters play an important role in magnetic anisotropy formation. For example, for FeCuNbSiB ribbons, the Si content could be critical for field annealing to decrease or increase the MI ratio, as well as the cooling conditions [77, 78]. All treatments below the Curie point usually need to be provided in a magnetic field higher than the saturation one, and kept at room temperature during the cooling process. The temperature, time of exposure, specific stress for stress annealing, and rate of heating and cooling are very important, not only as each parameter itself, but also, they have a mutual influence, and should be checked together in many cases. Both stress and field annealing could be done in two different ways: annealing of as-cast samples under field or stress, or using previously nanocrystallized samples, and then submitting them to stress or field annealing [37].

### 3.4. Structural Evolution

The conditions that allow the formation of these nanostructured materials depend on the crystallization temperatures, the thermodynamic quantities such as the crystal-interfacial energy and the free-energy driving force for homogeneous versus heterogeneous crystal nucleation, the small or large crystal nucleation frequency at sufficiently low growth rates, and the volume change during the crystallization.

It was mentioned previously that the crystallization of these materials takes place in two differentiated steps, which are clearly separated. Figure 2 constitutes a schematic approach to the crystallization process of these kinds of alloys. In the upper plot, two different curves are shown, a differential thermal analysis (DTA) scan, together with a resistivity versus temperature  $\rho(T)$  curve for a typical FINEMET alloy. Three different pictures representing the internal structure of the alloys in three characteristic structural situations (amorphous, nanocrystalline, and fully crystallized states) are included as insets, in order to clarify the whole picture. Among this, and in the lower part of Figure 2, the X-ray diffraction patterns and hysteresis loops that correspond to the three different structural are also presented. The two exothermic peaks of the DTA curve and the two minima of the  $\rho(T)$  curve situated around 550 and 700 °C

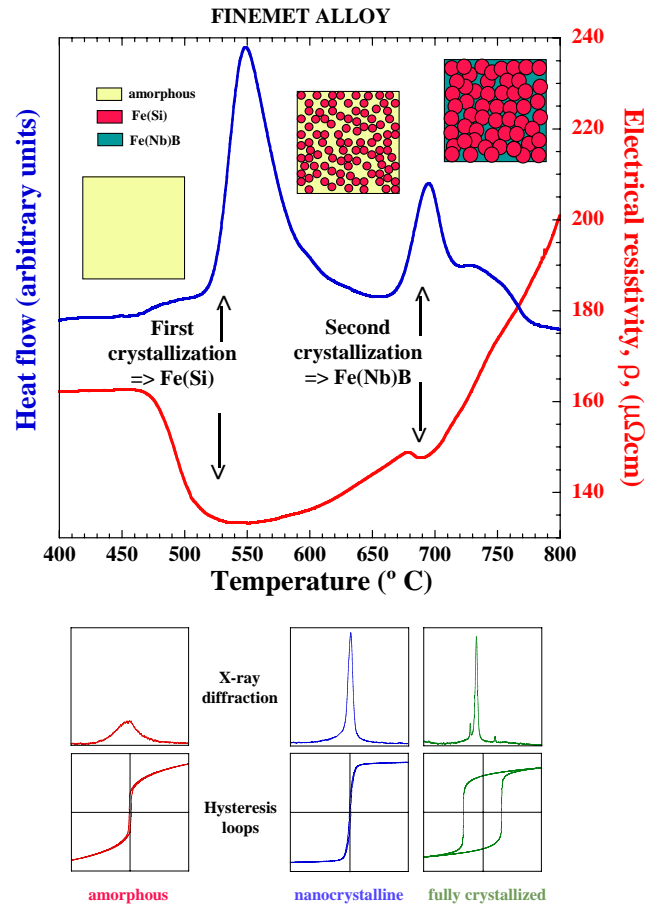


**Figure 2.** Schematic view of the crystallization process for a typical FINEMET alloy, showing the thermal evolution of the electrical resistivity, a DTA curve, as well as X-ray diffraction patterns and hysteresis loops at three characteristic structural stages.

correspond to the beginning of both crystallization steps. In between both peaks, the system is in a nanocrystalline state, that is, a mixture of small grains, of a few nanometers in average size, embedded in the remaining amorphous matrix. The most common experimental technique used to evaluate the degree of crystallization in a given material is obviously X-ray powder diffraction [69] because it is available in most of the research laboratories. This technique allows us to confirm the amorphous state of the as-prepared sample (only broad haloes are present in the diffraction patterns, instead of the characteristic sharp peaks corresponding to the Bragg reflections), as well as the evolution of the structure during the heat treatments. In this way, the values of the most important structural parameters, such as lattice constant and average grain size, can be obtained from the position of the peaks and their widths, respectively. Also, neutron diffraction is a valuable technique that gives information on the whole sample (not only from the surface, as is the case for X-rays), and also permits *in situ* structural studies of the nanocrystallization kinetics [108]. But these diffraction techniques are not the unique ones that help in the structural evolution study, Mössbauer spectroscopy give detailed and quantitative information on the amount of Fe atoms in each different environment, as well as details of the hyperfine magnetic parameters [69, 109, 110]. Also, electron

microscopies give information about the average grain sizes of the nanocrystallites, and their distribution along the sample surface [62]. Finally, it is worth noting that a relatively new technique, atomic force microscopy, allows us to obtain high-resolution topographic 3-D images of the alloy surface [111], as can be seen in Figure 3a and b for a FINEMET-type alloy in an amorphous and a nanocrystalline state, respectively.

The crystallization process of this kind of material can be summarized as follows. In the first step, the soft magnetic Fe or FeSi crystalline phase, with an average grain size around 10–15 nm, is formed, leading to a mixed structure of nanograins embedded in the remaining amorphous matrix or intergranular region, which is becoming more and more inhomogeneous when first crystallization occurs. The composition and structure of the nanograins depend on the alloy composition as well.

- For FINEMET alloys, the structure of the nanograins is a BCC–FeSi solid solution (when the amount of Si is less than 12at%) or a  $\text{DO}_3$ –FeSi (for percentages of Si above 12at%).
- For NANOPERM alloys, the structure is BCC–Fe.
- For HITPERM alloys, the structure varies, depending on the percentage of Co, and can be a BCC–FeCo ordered ( $\alpha$ ) for a nearly equal content of Fe and Co (Co atoms occupy fixed Fe positions) or a disordered ( $\alpha'$ ) solid solution for a low Co content (Co atoms occupy Fe atoms randomly).

Once the first step is finished, the second step leads to the crystallization of the remaining amorphous matrix into Fe–B or FeMT(B) phases (with high values for the magnetic anisotropy; see the evolution of the hysteresis loops in Fig. 2), and the growing of the Fe(Si) phase. These two processes overlap in most cases, when FeSiB alloys are submitted to heat treatments, and occur for temperatures above 400 °C; thus, the nanocrystalline state is never reached, and the soft magnetic properties shown in an amorphous state do not improve during the crystallization process. However, the addition of a small amount of Cu, which acts as a nucleation center for crystallites, accelerates the first step, and it takes place at lower temperatures (below 500 °C); meanwhile, the addition of other transition metals, such as those mentioned above, retards the second crystallization step up to temperatures above 700 °C, and prevents grain growth. In between both steps, the structure of these materials consists of a large amount of Fe or FeSi nanosized grains (around 70–80% of the sample), surrounded by the remaining amorphous ferromagnetic matrix (less than 30%).

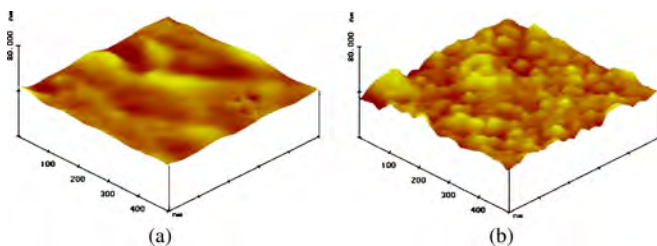


**Figure 3.** Atomic force microscopy 3-D images of a FINEMET alloy, a: in an amorphous (as-prepared) and b in a nanocrystalline state.

### 3.5. Magnetic Behavior

As shown above, nanocrystalline alloys consist of particles or grains with sizes ranging in the nanometer scale up to 20–30 nm embedded in the amorphous matrix-forming nanocomposite. The precipitation of these nanocrystalline particles from the amorphous matrix improves the tensile strength and ductility of the alloy due to the strong reduction of the anisotropy induced by residual internal stresses and, as a consequence of that, the softening of the magnetic properties in the nanostructured state.

Metallic Fe–TM–metalloid-based amorphous and nanostructured materials produced by rapid solidification of the melt are the most important ones from a commercial point of view because their soft magnetic properties make these nanocrystalline materials very suitable for use as high-frequency electronic components in magnetic devices or magnetic sensors [9, 62, 112–115].

Fe-based amorphous ferromagnetic metallic glasses show a larger magnetization than those based on Co, and much larger than those containing Ni. However, iron-rich amorphous alloys generally have fairly high magnetostriction ( $\lambda_s \approx 20 \times 10^{-6}$ ), limiting their magnetic permeability. The formation of a nanocrystalline Fe-rich alloy can lead to a drastic reduction in magnetostriction and coercivity due to the well-coupled Fe nanocrystallites by exchange interaction, thus favoring easy magnetization and, simultaneously, high permeability. These nanocrystalline alloys are composed primarily of crystalline Fe grains, having at least one dimension on the order of a few nanometers, that are embedded in a residual amorphous matrix. Thus, such materials provide an excellent context in which to study the principles of magnetism in nanometer structures [112, 113].

In particular, the so-called soft ferromagnetic alloys (characterized by high values of saturation polarization and low values for the coercive force and core losses) have been the most widely studied, and the typical composition in atomic percent is about 70–80% of Fe and 20–30% of metalloid atoms, such as B, Si, P, and so on [62, 113, 114]. The origin of the soft magnetic properties lies in the weak magnetic anisotropy presented by these materials in the amorphous state. When the alloys are submitted to temperatures above 450–600 °C, crystallization of the system takes place, leading to magnetic hardening of the material due to the appearance of different crystalline phases with high values of the magnetocrystalline anisotropy.

However, the addition of a small amount (5–10at%) of transition metals such as Nb, Zr, Cu, Ta, and so on drastically changes the crystallization kinetics. First, the crystallization temperature increases slightly, and second, there is a large interval of temperatures (up to 200 °C) in which the average grain size of the principal crystalline phase remains below 15–20 nm lower than the typical exchange correlation length for these systems, which is about  $l \approx 35$  nm. The magnetic response of the nanostructured material is, at this point, even better than in an amorphous state [61, 71, 116] and nowadays, typical compositions of prototype Fe-rich nanocrystalline alloys such as  $\text{Fe}_{73.5}(\text{SiB})_{22.5}\text{Cu}_1\text{Nb}_3$  (FINEMET alloys) or  $\text{Fe}_{100-x}(\text{ZrB})_x$  (NANOPERM alloys) are the softest magnetic materials known, with attractive soft magnetic properties, including



values of the coercive force  $H_C$  below  $1 \text{ A} \cdot \text{m}^{-1}$ , vanishing magnetostriction ( $\lambda_s \approx 10^{-7}$ ) due to the balancing between the opposite contribution of this parameter from the Fe(Si) nanocrystals and from the residual amorphous matrix, magnetic permeability  $\mu$  higher than  $10^5$ , and polarization saturation values  $J_s$  over  $1 \text{ T}$  [63, 117, 118].

The change in the surface magnetic domain structure from the as-cast state to the nanocrystalline one, during the annealing of the ferromagnetic samples, can be investigated by using the Bitter technique, where the colloidal ferrofluid is attracted by the Bloch wall's gradient field, thus revealing the intersection of every Bloch wall with the sample surface [19]. Photographs a)–c) in Figure 4 show the evolution of the magnetic domain structure for the  $\text{Fe}_{73.5}\text{Si}_{16.5}\text{B}_6\text{Cu}_1\text{Nb}_3$  ribbons from the as-cast state a) to the different annealed states. In all photographs, the longitudinal ribbon axis lies along the horizontal direction. Hence, photograph 4a) reveals an island domain structure on the bright surface of the as-cast sample. The observed islands domain in a) correspond to closure domains resulting from compressive internal stresses, in which the anisotropy direction lies perpendicular to the ribbon plane, and whose narrow laminar widths are between  $4.1\text{--}5.8 \mu\text{m}$ . These experimental measured values are in good agreement with the theoretical one, around  $4.3 \mu\text{m}$ , calculated for the corresponding Landau–Lifshitz domain width [120].

When the annealing temperature is increased up to  $425\text{--}475 \text{ }^\circ\text{C}$ , the internal stresses are nearly removed, and nanocrystallization begins to take place, with a mean grain diameter around  $12 \text{ nm}$ . It can be observed that a stripe domain structure appears in these annealed samples, with a measured domain width around  $5.5\text{--}6.8 \mu\text{m}$  for the ribbon annealed at  $425 \text{ }^\circ\text{C}$  [Fig. 4b)], which exhibits a magnetic hardening, and which diminishes to  $2.7 \mu\text{m}$  for the ribbon annealed at  $475 \text{ }^\circ\text{C}$  [Fig. 4c)], when the nanocrystallization begins. The latest domain width value measured is in very good agreement with that calculated from the random anisotropy model ( $2.8 \mu\text{m}$ ) [72]. In this late state, all of the

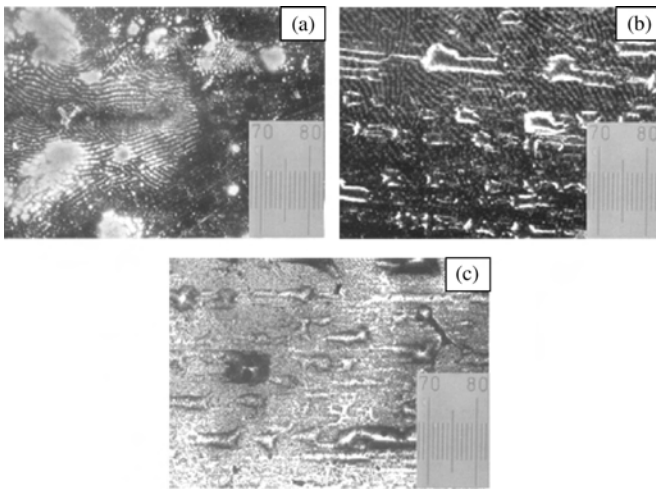


**Figure 4.** Pattern domain of  $\text{Fe}_{73.5}\text{Cu}_1\text{Nb}_3\text{Si}_{16.5}\text{B}_6$  amorphous and nanocrystalline ribbons. a) As-cast sample. b), c) Annealed at  $425$  and  $475 \text{ }^\circ\text{C}$ , respectively. The scale shows a  $0.1 \text{ mm}$  division. Reprinted with permission from [54], M. Tejedor et al., *J. Non-Cryst. Solids* 287, 396 (2001). © 2001, Elsevier Science.

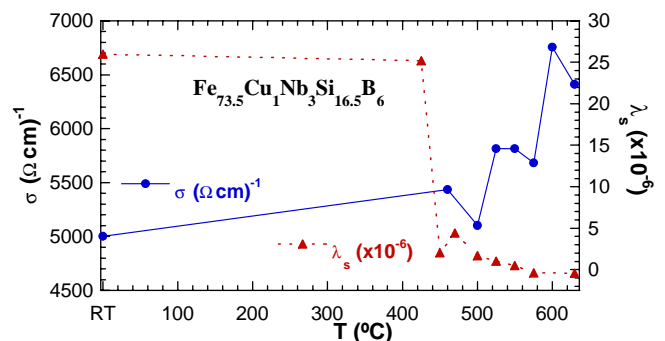
anisotropies start to vanish, and the magnetization vector tends to align parallel to the ribbon plane, increasing the transversal magnetic permeability, and therefore improving the magnetic properties of the sample. At higher annealing temperatures, the pattern domain exhibits a much more fine stripe structure, where the easy axis of magnetization may lie between the longitudinal and transverse directions, as can be observed through other techniques [81, 38]. The transverse-induced anisotropy in a nanocrystalline FeSiB–CuNb alloy could mainly be due to the magnetoelastic anisotropy exerted through annealing, by the FeSi nanocrystallites, that induces a transverse anisotropy via magnetoelastic interaction with tensile back stresses created by the inelastically deformed residual amorphous matrix [37, 44, 54, 121, 122]. If this transverse anisotropy is sufficiently large, the domains will orient themselves along the anisotropy axis. Hence, this uniaxial anisotropy can control the magnetization in the ribbon domains, and therefore the high-frequency response of these soft nanocrystalline materials.

Figure 5 shows the variation of both magnetostriction and conductivity with the annealing temperature for the  $\text{Fe}_{73.5}\text{Si}_{16.5}\text{B}_6\text{Cu}_1\text{Nb}_3$  [FINEMET (B6)] ribbons. It is important to note that near-zero magnetostriction can be achieved in Fe-rich alloys by nanostructuring. In nanocrystalline alloys, the sum of the volume-weighted magnetostrictions of the nanocrystalline grain phase and of the amorphous grain boundary phase can result in a net vanishing magnetostriction, even when the precursor amorphous alloy shows strong magnetostriction. In FINEMET nanocrystalline systems, the positive magnetostriction of the residual amorphous phase ( $\lambda_s \text{ amorph} = 20 \times 10^{-6}$ ) is balanced by the negative magnetostriction of the growing  $\alpha\text{-Fe(Si)}$  nanocrystalline phase ( $\lambda_s \text{ FeSi} = -6 \times 10^{-6}$ ) [62, 64, 113, 123].

In our particular composition, FINEMET (B6), a compensated or zero magnetostriction value is obtained after heating at a temperature of about  $565 \text{ }^\circ\text{C}$ , measured by the small angle magnetization rotation technique [124].

Heating at higher temperatures gives rise to slightly negative values of magnetostriction, which also lead to the modification of the domain structure that, in this case, results in the appearance of transversal domains [54].

On the other hand, it is clear that the conductivity can also influence the impedance and magnetic permeability



**Figure 5.** Evolution of conductivity  $\sigma$  and saturation magnetostriction  $\lambda_s$  with annealing temperature for  $\text{Fe}_{73.5}\text{Nb}_3\text{Cu}_1\text{Si}_{16.5}\text{B}_6$  ribbons. Lines are guides for the eye.

of the sample, and therefore its high-frequency response [125, 126]. As can be observed in Figure 5, not only is  $\lambda_s$  modified during the successive annealing, but also  $\sigma$ , where  $\sigma$  increased from about 5000 ( $\Omega \cdot \text{cm}$ )<sup>-1</sup> in the as-quenched state to about 6800 ( $\Omega \cdot \text{cm}$ )<sup>-1</sup> at the higher annealing temperature of about 575–580 °C.

This strong increase in the conductivity of the nanocrystalline ribbons ( $\sigma_{\text{nanocryst}}$  is on the order of 15% higher than  $\sigma_{\text{amorph}}$ ) reduces the skin depth, which contributes to an increase of the impedance of the sample, because this fact favors the appearance of both macroscopic eddy currents as well as the microscopic-induced currents due to the free transverse domain wall displacements [125, 127, 128].

#### 4. MAGNETOIMPEDANCE EFFECT IN NANOCRYSTALLINE ALLOYS

Another interesting feature, recently discovered in these kinds of nanostructured materials in the form of FeCuNb-SiB ribbons, wires, microwires, and films, or similar compositions, is the so-called magnetoimpedance effect, which consists of a strong decrease of the electrical impedance  $Z$  of the ferromagnetic sample when submitted to an external static magnetic field, as was mentioned above [11, 21, 26–39, 41–44, 48–56, 129–136].

In the case of FINEMET materials, and using the classical eddy-current theory, it was found that large MI was associated with the reduction in resistivity during the crystallization of the samples, together with a vanishing magnetostriction [11, 28–34, 39]. The first fact can be explained by taking into account that a decrease in the electrical resistivity implies an increase of the eddy-current losses, and hence the MI maximum. Moreover, if we consider the approach of the existence in the material of current lines distorted and dragged by magnetic domain walls oriented perpendicular to the current direction, we may take into account the effects of microeddy currents generated by the free displacement of the domain walls on the effective magnetic permeability for these soft ferromagnetic nanocrystalline materials. Therefore, we cannot neglect the influence of microeddy currents on the MI effect [11].

There is a clear relationship among the reduction of the resistivity of the samples, the vanishing of the residual anisotropies accompanied by the strong reduction of the saturation magnetostriction, and the maximum of the magnetic permeability and MI effect response as the crystallization process advances. In fact, and as shown in Figure 6, the maximum MI value is obtained for the ribbon annealed at 575 °C when the value of  $\rho$  is 15% lower than the corresponding one for the amorphous precursor, and the transverse magnetic permeability is maximum [39, 41]. Similar results are found in samples with other geometries and compositions [21, 28, 37, 48, 77].

These results are in agreement with the evolution of the surface magnetic domain structure of the annealed samples and the behavior of the electrical conductivity and magnetostriction shown above. The ribbon of FINEMET (B6) annealed at 575 °C, which exhibits the maximum MI effect, is the one that presents the smallest magnetostriction value ( $\lambda_s \approx -3.6 \times 10^{-7}$ ), which involves vanishing residual anisotropies, and the appearance of a transverse anisotropy

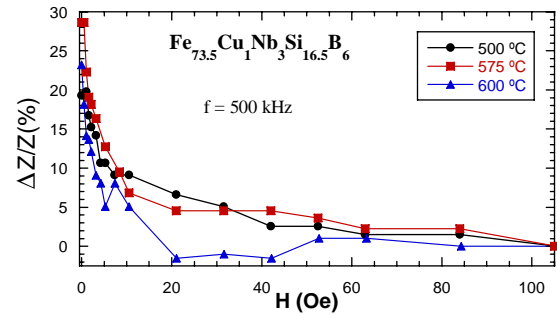


**Figure 6.** Field dependence of the magnetoimpedance ratio for some annealed Fe<sub>73.5</sub>Cu<sub>1</sub>Nb<sub>3</sub>Si<sub>16.5</sub>B<sub>6</sub> ferromagnetic ribbons at a frequency of 500 kHz.

induced by the magnetoelastic interaction between the FeSi nanocrystallites formed with tensile stresses of the residual amorphous matrix, resulting in a transversal magnetic permeability maximum.

All that, accompanied by a strong reduction in the resistivity of about 15% with respect to the as-cast state, which favors the appearance of both macroscopic eddy currents and the microscopic ones due to the free transverse domain wall displacements, gives rise to a drastic increase of the MI effect at low frequencies of the passing current across these nanostructured materials.

#### 4.1. Research Tool

The magnetoimpedance effect can be employed as a research tool to study magnetic properties of amorphous and nanocrystalline materials. It is not only important for the development of new technological applications, but also in the field of basic research in order to provide information about other interesting magnetic parameters of the materials. Due to its dependence on several soft magnetic properties, like anisotropy field, magnetostriction, and magnetization processes, the behavior of these properties can be inferred from the magnetoimpedance dependence on frequency and magnetic field and its value.

##### 4.1.1. Magnetostriction Coefficient

The MI effect shows a characteristic behavior with the applied magnetic field. In the case of as-quenched or annealed samples, the magnetoimpedance rate shows a monotonous decrease from a maximum value at  $H = 0$  Oe, as in the case of nanocrystalline samples that have been annealed at a certain temperature in order to obtain their softest magnetic properties. When the sample has a transverse-induced anisotropy, the impedance curve versus the applied field shows a peak at a field on the order of the anisotropy field of the sample [137]. This fact can be used to determine the anisotropy field of the samples, which can provide us with valuable information, for example, to determine magnetostriction coefficients, as explained in the next paragraph.

Figure 7 shows the behavior of magnetoimpedance as a function of the applied magnetic field, together with the hysteresis loop for a stress-annealed amorphous ribbon. The behavior of nanocrystalline-annealed samples, with an



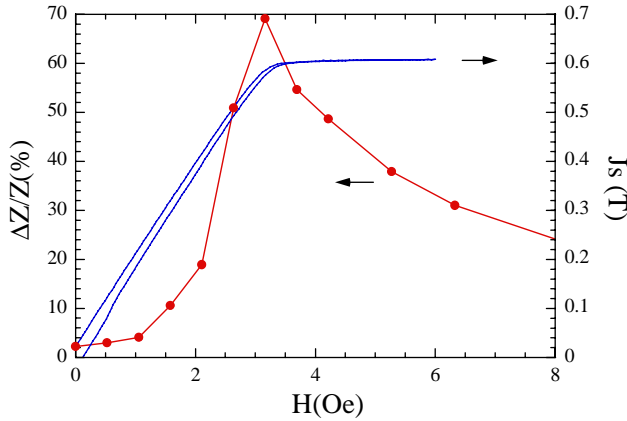


**Figure 7.** Magnetoimpedance ratio at 1 MHz versus the applied magnetic field and hysteresis loop obtained at 50 Hz of a  $\text{Co}_{66.5}\text{Fe}_{3.5}\text{Si}_{12}\text{B}_{18}$  amorphous ribbon subjected to an annealing treatment of 340 °C, followed by a stress annealing at 340 °C with a 300 MPa applied tensile stress.

induced transverse anisotropy, is exactly the same. It can be seen how the anisotropy field can be obtained by the maximum of magnetoimpedance.

One of the properties that can be deduced from the MI behavior is the saturation magnetostriction coefficient. The magnetostriction can be obtained from the MI effect due to the MI dependence on the applied stress.  $\lambda_s$  has a linear dependence on applied stress [138]

$$\lambda_s = \lambda_s(0) - k\sigma \quad (5)$$

The impedance behavior as a function of the applied bias field depends on the anisotropy field, which can be changed by the application of tensile stresses. A peak of MI appears at the anisotropy field, and its position can be determined.

Let us consider the case of a soft magnetic sample with a negative magnetostriction and no induced anisotropy. In the unstressed state of the sample, the impedance drops continuously with the increasing bias field. The application of tensile stresses on this sample would increase the magnetoelastic anisotropy field, and the MI peak would appear at a higher field. This would be the case for nanocrystallized samples, which have a negative saturation magnetostriction coefficient that usually occurs when the sample has been annealed above around 550 °C, depending on the composition.

When the saturation magnetostriction coefficient is positive, the behavior of the magnetic sample is somewhat different. The value of the anisotropy field could not be determined because the MI effect would have a maximum at  $H = 0$ . But if the positive magnetostriction sample has an induced anisotropy, it will have a peak at  $H_k$  in the unstressed state, and further application of tensile stresses, which would decrease the anisotropy field, would lead to a smaller value of the anisotropy field, which can be determined [139].

The anisotropy field does not vary linearly with stress, but it can be fitted as a second-order polynomial of the form

$$H_k = a\sigma^2 + b\sigma + c \quad (6)$$

where  $a$ ,  $b$ , and  $c$  are constants. There is a relationship between the magnetostriction and the anisotropy field:

$$\lambda_s = \frac{\mu_0 M_s}{3} \left( \frac{dH_k}{d\sigma} \right) \quad (7)$$

It can be easily verified that the saturation magnetostriction is a linear function of stress, as shown in Eq. (5). From Eqs. (7) and (5), we can obtain

$$\lambda_s(0) = \frac{\mu_0 M_s b}{3} \quad (8)$$

which is the unstressed value of the saturation magnetostriction coefficient, and

$$k = \frac{d\lambda_s}{d\sigma} = \frac{2\mu_0 M_s a}{3} \quad (9)$$

which is the measured slope.

Using this procedure, we can find the  $\lambda_s(0)$  values of all types of samples, with positive and negative magnetostriction, with an accuracy similar to the well-known SAMR (small angle magnetization rotation) method [124, 140]. This method can be applied to all types of samples, but in the case of nanocrystallized samples, the application of stresses might produce the breaking of the sample due to its fragility.

Although this method is accurate, some specific problems can be found. The  $\Delta Z/Z - H$  curves may be broad and not symmetric, it being difficult to correctly estimate the position of the impedance peak.

#### 4.1.2. Nanocrystalline State

The MI effect shows a great variation in its value due to structural changes in the magnetic nanocrystalline samples. A correlation between magnetoimpedance and microstructure as a function of the average grain size can be established. The average grain size of the FeSi crystallites in these samples is about 10–15 nm in the studied range of annealing temperatures. Other materials with similar compositions have similar values of grain sizes [141]. The grain size increases strongly after annealing at temperatures of 600 °C, approximately, when new crystalline phases nucleate as well.

Figure 8 shows the dependence of the MI ratio as a function of the annealing temperature in  $\text{Fe}_{73.5}\text{Cu}_1\text{Nb}_3\text{Si}_{16.5}\text{B}_6$  ribbons. The highest value of the MI ratio, close to 60%, is reached for an annealing temperature of 575 °C, which corresponds to the softest behavior of this material due to the grain size.

The MI temperature dependence allows us to investigate the nanocrystalline state of annealed samples by measuring the magnetoimpedance. This behavior has been seen in ribbon- and wire-shaped nanocrystalline materials [27], showing that the MI rate response depends on the sample structure, and the sample shape influence is not as important. The highest MI rate is obtained when the nanocrystalline sample reaches its softest magnetic behavior, that is, when the FeSi crystallites have grain sizes of about 10 nm.

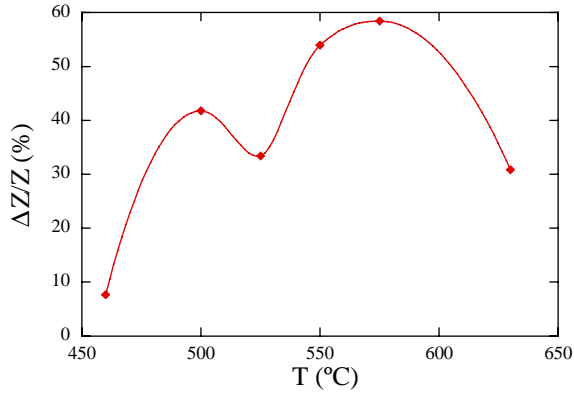


**Figure 8.** Magnetoimpedance ratio as a function of the annealing temperature of the nanocrystalline  $\text{Fe}_{73.5}\text{Cu}_1\text{Nb}_3\text{Si}_{16.5}\text{B}_6$  ribbons.

#### 4.1.3. Permeability Measurement

The real and imaginary components of impedance can be obtained by using a lock-in amplifier, which separates the out-of-phase components. The magnetoimpedance ratio and sensitivities for both components of impedance can be calculated in the same way, as  $\Delta Z'/Z'(\%)$  and  $\Delta Z''/Z''(\%)$  for the resistance, and reactance, respectively. The total impedance would be written as  $Z^* = Z' + jZ''$ , where  $j = (-1)^{1/2}$ .

When dealing with a magnetic system, it is often advantageous to use the complex inductance formalism, and deal with  $L^*$  instead of  $Z^*$  since it is directly related to the value of permeability. The transformation from impedance to permeability (through inductance) can be simply written as

$$\mu^* = kL^* = -\left(\frac{kj}{\omega}\right)Z^* \quad (10)$$

where  $\omega = 2\pi f$  is the angular frequency.

Note that, due to the form of this transformation, the real component of permeability  $\mu'$  depends on the imaginary part of impedance, and conversely, the imaginary part of permeability  $\mu''$  is obtained from the real part of impedance. The geometrical constant  $k$  can be evaluated in the case of a wire-shaped sample by assuming, as a first approximation, a wire homogeneously magnetized in the circumferential direction. By defining the induction  $L$  as the ratio of magnetic flux  $\Phi$  to the current intensity  $i$ ,  $L = \partial\Phi/\partial i$  [142].

Figure 9 shows the case of a wire with composition  $\text{Fe}_{73.5}\text{Cu}_1\text{Nb}_3\text{Si}_{16.5}\text{B}_6$  that has been annealed at different temperatures in the range 400–640 °C during 1 h in an Ar atmosphere. The wires have a length of 8.5 cm and a diameter of 120  $\mu\text{m}$ . The figure shows the behavior of permeability, evaluated as explained above, versus the applied axial magnetic field. The magnetic softening of the sample can be inferred from the permeability behavior. At low annealing temperatures, up to around 500 °C, the permeability shows low values, but the largest permeability at  $H = 0$  Oe is obtained at 550 °C. The annealing at higher temperatures leads to a further magnetic hardening of the sample. The softest magnetic properties, including the lowest coercive force, are achieved for annealing temperatures close to 550 °C, where the nanostructured FeSi phase precipitates.

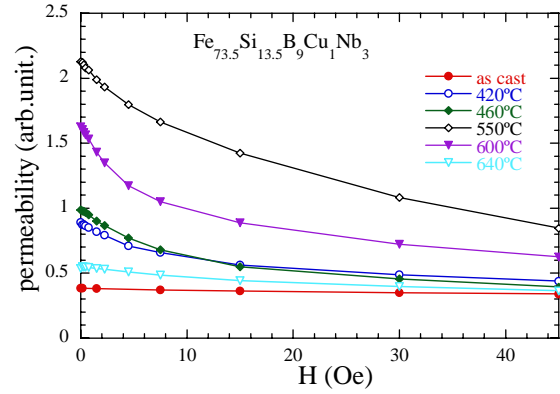


**Figure 9.** Permeability obtained from the impedance measurements in nanocrystallized wires versus the applied magnetic field.

This phase has a mean grain size of about 10 nm. Finally, an important magnetic hardening occurs for temperatures above 600 °C, mainly as a consequence of the precipitation of new Fe–B phases [141]. As the applied magnetic field is increased, the transverse permeability decreases, due to the magnetization of the sample in the axial direction.

The behavior of permeability as a function of frequency and other parameters can then be obtained from Eq. (10) for all types of samples, without taking into account the geometrical constant  $k$ . Figure 10 collects the permeabilities of nanocrystallized ribbons in arbitrary units as a function of the drive current frequency. For low frequencies (up to  $10^4$  Hz), the permeabilities for all of the samples have the same value. For higher frequencies, the nanostructure of the ribbons influences the permeabilities, making them change. The 460 °C annealed ribbon has the lowest permeability in all of the studied frequency range. When the annealing temperature is increased, the permeability increases. Up to  $4 \times 10^4$  Hz, the 575 °C annealed sample has the largest permeability. For higher frequencies up to  $10^5$  Hz, the highest value corresponds to the 550 °C annealed ribbon. A further increase of the annealing temperature leads to a hardening of the magnetic behavior of nanocrystalline samples, and to a decrease in permeability, as can be observed in the above-mentioned figure.

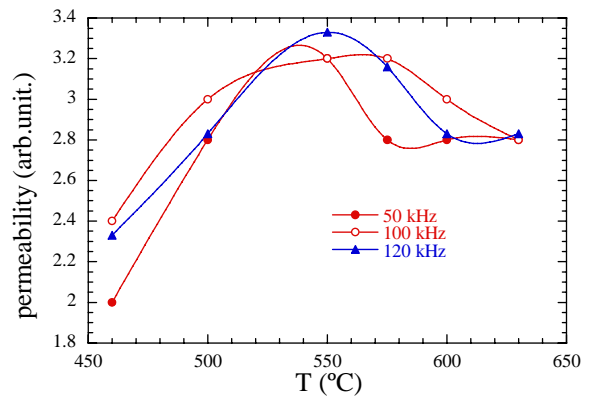


**Figure 10.** Permeability obtained from magnetoimpedance measurements for annealed  $\text{Fe}_{73.5}\text{Cu}_1\text{Nb}_3\text{Si}_{16.5}\text{B}_6$  ribbons as a function of the annealing temperature for three selected drive current frequencies.

#### 4.1.4. Magnetization Processes

The MI effect behavior depends on the magnetization processes that take place in the sample when the ac current is flowing through it, and is subjected to external influences that modify its magnetization. The magnetoimpedance rate spectra give us information about the magnetization processes that take place at different frequencies. The different domain structures of as-quenched and nanocrystalline samples are responsible for their distinguishable MI effects [38]. At low frequencies, the magnetization processes take place by domain wall displacements, but at higher frequencies, the domain walls are not able to follow the ac magnetic field, and the magnetization processes are due to moment rotations. The relaxation frequency  $f_x$  is the frequency which separates the two main areas of different magnetization processes. The MI spectrum shows a maximum in this area, and  $f_x$  can be easily obtained.

The value of  $f_x$  has been recently seen to be dependent on the magnetostriction coefficient [143]. This matter is still undergoing research, but could show in the future why the MI effect has larger values when the saturation magnetostriction coefficient is small and negative. The relaxation frequency decreases with an increase of the magnetostriction coefficient for all types of samples, both nanocrystalline and amorphous ones. Figure 11 shows this dependence for a nanocrystalline sample, and a comparison to an amorphous one. The high magnetostriction value and low permeability of the FeCuNbSiB ribbon in the as-quenched state explain that the MI effect is not observed until partial devitrification and a softer magnetic behavior are achieved by annealing. Although all treatments for the amorphous ribbon resulted in a decrease of the relaxation frequency as a function of the magnetostriction coefficient (see arrows in the curves), the opposite tendency is observed for the nanocrystalline ribbons: the relaxation frequency becomes higher after the treatments. And the representation of the relaxation frequency as a function of the magnetostriction coefficient shows the same behavior in all of the samples: it is a monotonous decay. The same behavior has been previously observed in other amorphous ribbons [143].

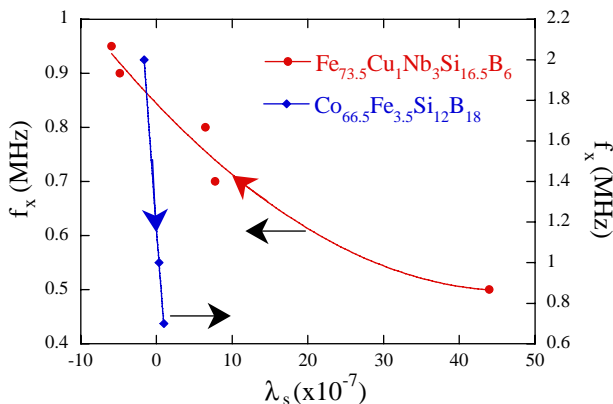


**Figure 11.** Relaxation frequency  $f_x$  relationship with the magnetostriction coefficient of nanocrystalline ribbons, and comparison to amorphous ribbons. The arrows guide the eye and indicate the scales.

#### 4.2. Technological Applications

The earliest work on applications based on the MI effect was devoted to a magnetic field sensor employing amorphous ribbons [144–147]. Active research recently has been done on the development of miniaturized sensors based in MI [12]. The special advantage of the MI effect as detected in amorphous wires in comparison with other magnetic phenomena is that even small fields (below  $100 \text{ A} \cdot \text{m}^{-1}$ ) can produce a strong impedance variation. In fact, they look very competitive in comparison with magnetic field sensors based on magnetoresistance or the Hall effect. The main applications are related to the influence of the magnetic field. In particular, current sensors and proximity sensors are actually sensor devices measuring the magnetic field.

The MI effect strongly depends on the magnetic softness of the sample, including both higher induction and permeability, and for special environmental conditions, materials capable of operating at higher temperatures. As previously mentioned, large circular (wire shape) or transversal (ribbon shape) permeability and a small resistivity and magnetostrictive coefficient are required to observe the MI effect. The magnetic permeability is determined by the chemical composition, crystal structure, microstructure, and shape of the sample. Alloys with small magnetocrystalline anisotropies and magnetostrictions give rise to particularly soft magnetic materials. Amorphous and nanocrystalline magnetic materials are now competitive with SiFe bulk alloys and Fe–Co alloys, and their soft magnetic properties exceed those of the bulk alloys based on Fe, Co, and Fe–Co [59].

The first MI measurements in nanostructured materials were performed in FeSiBCuNb wires devitrified from an amorphous precursor by annealing at different temperatures [28, 148]. Optimum soft magnetic behavior was achieved after annealing at about  $550 \text{ }^\circ\text{C}$ . Meanwhile, the maximum impedance variation appears for the softest nanocrystalline wire; a larger MI ratio is observed after annealing at a higher temperature (near  $600 \text{ }^\circ\text{C}$ ), where the resistivity clearly decreases as a consequence of crystallization [13]. We should also remark that the MI effect in nanocrystalline materials (wire or ribbon morphology) [28, 39] does not reach values as large as for amorphous Co-rich alloys. This must be associated with the smaller values of the circular or transversal permeability in that nanocrystalline material. It could be possible that the nanocrystalline sample is softer when it is axially magnetized, but what is required in the MI effect is a very large circular or transversal permeability, which involves a circular or transversal and very weak magnetic anisotropy.

#### 4.3. Unique Properties of Nanocrystalline Alloys for Special Applications

Giant magnetoimpedance has attracted significant attention in the last years due to possible technological applications in position sensors, rotary encoders, and direction sensors for navigation, current sensors, biomedical and environmental controllers, nondestructive control sensors, and reading heads [7, 12, 44, 48, 80, 101, 135, 145–153]. It is possible to modify and adapt the magnetoimpedance responses of appropriate material for each particular application performing specific treatments. Although many of the proposed

applications can be realized using very different materials for the same type of application, there are a few of them where amorphous materials are useless due to particular conditions.

Recently, high-temperature magnetic measurements were reported, opening the possibility to study both the basic problems of the exchange-coupling process in nanocrystalline materials and the conditions of possible high-temperature applications of the magnetic materials [154, 155]. Why do we need sensors for high-temperature applications? It is easy to answer this question by reference to the everyday needs of our life surrounded by modern technology: it would be much easier to control the space and aircraft engines and other technical blocks, nuclear and power station functionality, metallurgical production, and many other potentially dangerous processes in order to avoid a catastrophe or simply little controlled actions. The high-temperature sensing has different basic problems. The first one is the temperature dependence of the saturation magnetization and the Curie point existence [156, 157]. It is very difficult to find a magnetic material at elevated temperatures, which can be used at the same time for sensing processes. We say that temperatures from 0 to 180 °C correspond, in most general estimations, to the normal functionality interval. There are many amorphous materials with a measurable MI response at room temperature in which MI effect totally disappears at 180 °C because of a low Curie temperature (for example, in  $\text{Fe}_3\text{Co}_{64}\text{Cr}_3\text{Si}_{15}\text{B}_{12}$  ribbons with a Curie temperature of 160 °C and a crystallization temperature of 570 °C [158, 159]). Another problem is structural stability. The amorphous state is a metastable one. The closer we are to the crystallization temperature (around 500 °C for many amorphous materials), the less stable are the structural features of the amorphous sensitive element. Especially important, if we take into account those facts, is the presence of *proper induced magnetic anisotropy*, which shows even faster temperature degradation compared with the changes of structural parameters [160, 161].

A high-temperature giant magnetoimpedance effect was reported for  $\text{Fe}_{73.0}\text{Cu}_{1.0}\text{Nb}_{2.5}\text{V}_{1.0}\text{Si}_{13.5}\text{B}_{9.0}$  nanocrystalline ribbons with measuring temperatures up to 550 °C [135]. A maximum relative change of the impedance of about 60% of the MI ratio with a sensitivity of about 20%/Oe in a small field appears at about 320 °C. Let us emphasize that the maximum sensitivity of magnetic sensors based on a giant magnetoresistance effect does not exceed 2%/Oe in CoCu multilayers at room temperature. The MI effect of  $\text{Fe}_{73.0}\text{Cu}_{1.0}\text{Nb}_{2.5}\text{V}_{1.0}\text{Si}_{13.5}\text{B}_{9.0}$  nanocrystalline ribbons still exists at 500 °C (being 5%). The authors explain these outstanding properties by the thermal evolution of the magnetic softness and magnetic anisotropy of the nanocrystalline sample: as the temperature rises, a combination of stress release and magnetocrystalline anisotropy decrease in the amorphous phase further softens the ribbon magnetically, increasing its MI. There were additional attempts to study the MI effect in amorphous and nanocrystalline thin films and MI sandwiches of similar composition ( $\text{Fe}_{71.5}\text{Cu}_1\text{Cr}_{2.5}\text{V}_4\text{Si}_{12}\text{B}_9$ ) [150, 154]. The MI ratio reaches its maximum of about 140% at a very low characteristic frequency of 4 MHz in FeCu-CrVSiB/Ag/FeCuCrVSiB, but the temperature measurements for nanocrystalline films are missing at the moment.

#### 4.4. Recent Progress of the Magnetoimpedance Effect in Nanocrystalline Materials

In this section, an updated overview covering the very recent works based in the MI effect in nanocrystalline alloys is given.

The principles of remote-interrogated stress sensors based on high-frequency magnetic materials showing the inverse magnetostrictive or magnetoimpedance effects has been reported by Ludwig et al. [162].  $\text{Fe}_{50}\text{Co}_{50}/\text{Co}_{80}\text{B}_{20}$  amorphous/nanocrystalline multilayers have been prepared, showing ferromagnetic resonance frequencies up to 5 GHz and good magnetoelastic properties in the gigahertz range. The high-frequency remote interrogation allows the reduction of the sensor antenna size and measurements using high bandwidths.

The MI effect in powder samples of Fe-based nanocrystalline  $\text{Fe}_{73}\text{Cu}_1\text{Nb}_{1.5}\text{V}_2\text{Si}_{13.5}\text{B}_9$  has been reported for the first time [163]. The magnetic permeability of the powder materials may not be as high as that of thin films or ribbons and the coercivity may not be as small, but they can be conveniently pressed into different shapes such as cylinders and rings, offering less brittleness than nanocrystalline ribbons and wires, and many possible high-frequency applications.

A systematic study of the high-temperature MI effect in nanocrystalline  $\text{Fe}_{73.5}\text{Cu}_1\text{Nb}_3\text{Si}_{13.5}\text{B}_9$  ribbons with different annealing temperatures has been presented [164]. The discussion is given on the basis of a random anisotropy model [165], to explain the relationship between the thermal dependence of the MI and the magnetic coupling between grains.

A small GMI effect was found in nanocrystalline  $\text{Fe}_{79.5}\text{P}_{12}\text{C}_6\text{Mo}_{0.5}\text{Cu}_{0.5}\text{Si}_{1.5}$  ribbons obtained by annealing the precursor amorphous at temperatures ranging from 350 to 500 °C [166].

A review of the amorphous alloy preparation, measurement system, and various annealing techniques used in the MI enhancement can be found in [167].

The effects of Cr substitution, the type of thermal treatments (in a conventional furnace and by current annealing), and the sample length in MI have been reported in  $\text{Fe}_{73.5-x}\text{Cr}_x\text{Cu}_1\text{Nb}_3\text{Si}_{13.5}\text{B}_9$  ( $x = 0$  and 10) nanocrystalline wires [168], and a similar study of the MI effect with annealing temperature was done in glass-covered CoB-SiMn microwires [169]. The domain structure and induced anisotropy influences on the MI are both discussed.

Two other recent works contribute to the study of the evolution of the MI effect in some nanocrystalline ribbons, previously submitted to different annealing treatments in an as-cast state: stress annealing on  $\text{Fe}_{88.02}\text{Zr}_{4.69}\text{Nb}_{2.31}\text{B}_{4.98}$  ribbons [170], and current annealing on  $\text{Fe}_{73.5}\text{Cu}_1\text{Nb}_3\text{V}_2\text{Si}_{15.5}\text{B}_7$  [171]. The MI behavior is explained in both papers by taking into account the role of the induced magnetic anisotropy, saturation magnetostriction coefficient, and the microstructural changes developed with the thermal treatments.

A correlation among the structural, electrical, and magnetic properties, together with the MI effect response in some heat-treated FINEMET types of different composition and FeZrB ribbons, is given in [172]. High values of the MI ratio up to 130% have been achieved, at a drive frequency of 5 MHz, by subjecting FeZrB ribbons to a current annealing treatment.

Table 1 displays a brief summary of some of the investigations mentioned through this chapter, indicating the studied material composition and its main properties related to the MI effect, with the respective references.

Finally, we can conclude that these compounds could be excellent candidates for the design and development of new magnetic sensors and high-frequency devices based on nanocrystalline alloys.

**Table 1.** MI Effect in Nanostructured Medium.

Composition	Properties/remarks	Ref.
$\text{Fe}_{4.3}\text{Co}_{68.2}\text{Si}_{12.5}\text{B}_{15}$ $\text{Co}_{68.15}\text{Fe}_{4.35}\text{Si}_{12.55}\text{B}_{15}$	Low magnetostriction alloys. Induced anisotropy. MI and magnetoinductive effects.	[4, 12, 17]
FeCoSiB, HyMu <sup>®</sup> alloy, $\text{Fe}_{77.5}\text{Si}_{7.5}\text{B}_{15}$ , $\text{Co}_{68.5}\text{Mn}_{6.5}\text{Si}_{10}\text{B}_{15}$ ; CoP, $\text{Fe}_{73.5}\text{Cu}_1\text{Nb}_3\text{Si}_{13.5}\text{B}_9$ , NiFe, CoFeB	Overview of the MI effect in magnetic materials with different geometries (wires, ribbons, tubes, and thin films is given), including materials with a nanocrystalline structure. Sensitive field and frequency-dependent impedance.	[7, 8, 17]
$\text{Fe}_{73.5}\text{Cu}_1\text{Nb}_3\text{Si}_x\text{B}_{22.5-x}$ ( $x = 9, 16$ )	Magnetic anisotropy distribution and giant magnetoeimpedance. Domain wall motion influence on MI.	[53, 128]
FeNiCrSiB, FeNiCrSiB/Cu/FeNiCrSiB, FeCuNbSiB, FeCuNbSiB/Cu/FeCuNbSiB, Fe/Cr nanoscale structures, FeNi/Cu/FeNi and FeNi/Si/Cu/Si/FeNi, FeNi based multilayers	GMI effect in sputtered films and sandwiches at relatively low frequencies, and under the effect of an antisymmetric transverse bias field. Domain structure. Giant magnetoresistance in multilayers.	[16, 20, 48, 57, 79, 82, 93, 94, 97]
$\text{Fe}_{73.5}\text{Cu}_1\text{Nb}_3\text{Si}_{13.5}\text{B}_9$	The correlation between GMI and magnetic anisotropy has been studied in field and stress one- and two-step annealed ribbons. Stress-annealed ribbons with nonuniform induced anisotropy. Hysteretic behavior of MI. Magnetic anisotropy in as-quenched and stress-annealed nanocrystalline alloys: creep-induced and magnetoelastic components.	[37, 44, 75, 76, 160, 161]
$\text{Fe}_{73.5}\text{Cu}_1\text{Nb}_3\text{Si}_{16.5}\text{B}_6$	High saturation polarization and magnetostriction in as-cast state.  High magnetic permeability, low coercive field, and vanishing magnetostriction in nanocrystalline state. Influence of nanocrystallization on evolution of domains and MI effect.	[49, 54, 77, 78, 122, 143, 157, 167, 172]
$\text{Fe}_{84}\text{Zr}_7\text{B}_6\text{Cu}_1\text{Al}_2$	dc and ac field-induced magnetic anisotropy. Ultrasoft magnetic properties such as large MI, incremental permeability, nearly zero coercivity, zero magnetostriction.	[50]
$\text{Fe}_{81}\text{B}_{11}\text{Nb}_7\text{Cu}_1$	Ultrasoft magnetic properties of nanocrystalline alloy.	[51]
FeCoNi tubes	Nonlinear magnetoeimpedance.	[52, 151]
Permalloy/Ag nanoscale multilayers	MI effect in homogeneous permalloy films and multilayers.	[80]
$\text{Ni}_{77}\text{Fe}_{14}\text{Cu}_5\text{Mo}_4$	MI in commercial Mumetal for different thicknesses.	[83]
FeNiCu	MI of glass-coated microwires up to 200 MHz.	[88]
$\text{Co}_{68.25}\text{Fe}_{4.5}\text{Si}_{12.25}\text{B}_{15}$	Influence of current annealing on magnetic properties and giant magnetoeimpedance in glass-covered microwires.	[89]
$\text{Fe}_{73.5}\text{Cu}_1\text{Nb}_3\text{Si}_{13.5}\text{B}_9/\text{SiO}_2/$ $\text{Ti}/\text{Cu}/\text{Ti}/\text{SiO}_2/\text{Fe}_{73.5}\text{Cu}_1\text{Nb}_3\text{Si}_{13.5}\text{B}_9$	Giant magnetoeimpedance in amorphous and nanocrystalline multilayers: experiment and theory.	[95]
(CoFe) <sub>80</sub> B <sub>20</sub> FeCoSiB	MI in sputtered films for Colpitts oscillator-type field sensor.	[98, 102]
FeCoSiB/Cu/FeCoSiB, CoSiB/Cu/CoSiB	Thin-film magnetic field sensor utilizing MI effect. MI effect in magnetostrictive sandwiches.	[100, 104]
$\text{Fe}_{73}\text{Cu}_1\text{Nb}_{1.5}\text{V}_2\text{Si}_{13.5}\text{B}_9$ $\text{Fe}_{73}\text{Cu}_1\text{Nb}_{2.5}\text{V}_1\text{Si}_{13.5}\text{B}_9$	High-frequency longitudinally driven GMI effect in stress-annealed nanocrystalline ribbons.	[45, 134, 135]
$\text{Fe}_{92-x-y}\text{Zr}_7\text{B}_x\text{Cu}_1\text{Al}_y$ ( $x = 2, 4, 6, 8,$ $y = 0, 0.5, 1, 1.5$ )	MI effect in the nanocrystalline alloy system.	[136]
FeCuCrVSiB	Magnetic properties and GMI in RF-sputtered films, followed by annealing treatment.	[149, 152]
$\text{Ni}_{77}\text{Fe}_{14}\text{Mo}_5\text{Cu}_4$	Angular dependence of the MI in RF magnetron-sputtered films.	[150]
$\text{Fe}_{77.5}\text{Si}_{7.5}\text{B}_9$ , $\text{Co}_{67}\text{Fe}_3\text{Cr}_3\text{Si}_{15}\text{B}_{12}$	Comparative study of the anisotropy, magnetic properties, and domain structure and MI.	[158–159]
$\text{Fe}_{79.5}\text{P}_{12}\text{C}_6\text{Mo}_{0.5}\text{Cu}_{0.5}\text{Si}_{1.5}$	MI in nanocrystalline ribbons.	[168]
$\text{Fe}_{88.02}\text{Zr}_{4.69}\text{Nb}_{2.31}\text{B}_{4.98}$	MI in stress-annealed nanocrystalline ribbons.	[170]
$\text{Fe}_{91}\text{Zr}_7\text{B}_2$	MI in current-annealed nanocrystalline ribbons	[172]

## GLOSSARY

**Amorphous alloy** Alloy with no long range atomic order.

**Magnetic anisotropy** The magnetic properties depend on the direction in which they are measured.

**Magnetic domain** Volume of material in which all atomic magnetic moments are aligned in the same direction.

**Magnetic permeability** The ability of a material to support a magnetic flux density.

**Magnetoimpedance** Impedance change in a ferromagnetic sample when submitted to a magnetic field.

**Magnetostriction** Deformation of a magnetic substance due to its magnetic state.

**Nanocrystalline alloy** Alloy containing crystalline nanograins embeded in an amorphous matrix.

## REFERENCES

1. L. D. Landau and E. M. Lifschitz, "Electrodynamics of Continuous Media," 2nd ed. Pergamon, New York, 1984.
2. R. S. Beach and A. E. Berkowitz, *Appl. Phys. Lett.* 64, 3652 (1994).
3. K. Mohri, T. Kohzawa, K. Kawashima, H. Yoshida, and L. V. Panina, *IEEE Trans. Magn.* 28, 3150 (1992).
4. L. V. Panina, K. Mohri, K. Bushida, and M. Noda, *J. Appl. Phys.* 76, 6198 (1994).
5. L. V. Panina and K. Mohri, *Appl. Phys. Lett.* 65, 1189 (1994).
6. K. V. Rao, F. B. Humphrey, and J. L. Costa-Krämer, *J. Appl. Phys.* 76, 6204 (1994).
7. R. S. Beach and A. E. Berkowitz, *J. Appl. Phys.* 76, 6209 (1994).
8. F. L. A. Machado, C. S. Martins, and S. M. Rezende, *Phys. Rev. B* 51, 3926 (1995).
9. R. L. Sommer, C. L. Chien, and R. Hasegawa, *J. Appl. Phys.* 79, 6117 (1996).
10. M. L. Sartorelli, M. Knobel, J. Schoenmaker, J. Gutierrez, and J. M. Barandiarán, *Appl. Phys. Lett.* 71, 2208 (1997).
11. W. Ku, F. Ge, and J. Zhu, *J. Appl. Phys.* 82, 5050 (1997).
12. K. Mohri, T. Uchiyama, and L. V. Panina, *Sensors Actuators A* 59, 1 (1997).
13. M. Vázquez, M. Knobel, M. L. Sánchez, R. Valenzuela, and A. P. Zhukov, *Sensors Actuators A* 59, 20 (1997).
14. D.-X. Chen, J. L. Muñoz, A. Hernando, and M. Vázquez, *Phys. Rev. B* 57, 10699 (1998).
15. N. A. Usov, A. S. Antonov, and A. N. Lagar'kov, *J. Magn. Magn. Mater.* 185, 159 (1998).
16. D. P. Makhnovskiy, A. S. Antonov, A. N. Lagar'kov, and L. V. Panina, *J. Appl. Phys.* 84, 5698 (1998).
17. M. Vázquez, J. P. Sinnecker, and G. V. Kurylyanskaya, *Mater. Sci. Forum* 30, 209 (1999).
18. M. Britel, D. Menard, P. Ciureanu, A. Yelon, M. Rouabhi, and R. W. Cochrane, *J. Appl. Phys.* 85, 5456 (1999).
19. H. B. Nie, X. X. Zhang, A. B. Pakhomov, Z. Xie, X. Yan, A. Zhukov, and M. Vázquez, *J. Appl. Phys.* 85, 4445 (1999).
20. S. Q. Xiao, Y. I. Liu, Y. Y. Dai, L. Zhang, S. X. Zhou, and G. D. Liu, *J. Appl. Phys.* 85, 4127 (1999).
21. M. Vázquez, J. M. García Beneytez, J. M. García, J. P. Sinnecker, and A. P. Zhukov, *J. Appl. Phys.* 88, 6501 (2000).
22. K. Mandal, S. Puerta, M. Vázquez, and A. Hernando, *Phys. Rev. B* 62, 6598 (2000).
23. M. Tejedor, B. Hernando, M. L. Sánchez, V. M. Prida, and M. Vázquez, *Sensors Actuators A* 81, 98 (2000).
24. P. Aragonese, A. P. Zhukov, J. González, J. M. Blanco, and L. Dominguez, *Sensors Actuators A* 81, 86 (2000).
25. J. M. Blanco, A. Zhukov, and J. González, *J. Appl. Phys.* 87, 4813 (2000).
26. B. Hernando, M. L. Sanchez, V. M. Prida, M. Tejedor, and M. Vázquez, *J. Appl. Phys.* 90, 4783 (2001).
27. M. Knobel, M. L. Sánchez, P. Marín, C. Gómez-Polo, M. Vázquez, and A. Hernando, *IEEE Trans. Magn.* 31, 4009 (1995).
28. M. Knobel, M. L. Sánchez, C. Gómez-Polo, P. Marín, M. Vázquez, and A. Hernando, *J. Appl. Phys.* 79, 1646 (1996).
29. C. Chen, K. Z. Luan, Y. H. Liu, L. M. Mei, H. Q. Guo, B. G. Shen, and J. G. Zhao, *Phys. Rev. B* 54, 6092 (1996).
30. C. Chen, T. Y. Zhao, H. Q. Guo, L. M. Mei, Y. H. Liu, B. G. Shen, and J. G. Zhao, *J. Phys.: Condens. Matter* 9, 1951 (1997).
31. C. Chen, L. M. Mei, H. Q. Guo, K. Z. Luan, Y. H. Liu, B. G. Shen, and J. G. Zhao, *J. Phys.: Condens. Matter* 9, 7269 (1997).
32. W. Ku, F. Ge, and J. Zhu, *J. Phys. D: Appl. Phys.* 30, 1842 (1997).
33. Y. Ueda, S. Ikeda, and W. Takura, *J. Appl. Phys.* 81, 5787 (1997).
34. M. Knobel, J. Schoenmaker, J. P. Sinnecker, R. Sato-Turtelli, R. Grössinger, W. Hofstetter, and H. Sassik, *Mater. Sci. Eng. A* 226, 546 (1997).
35. H. Q. Guo, C. Chen, M. Li, T. Y. Zhao, K. Z. Luan, B. G. Shen, Y. H. Liu, J. G. Zhao, L. M. Mei, and H. Kronmüller, *Mater. Sci. Eng. A* 226, 551 (1997).
36. X. L. Yang, J. X. Yang, G. Chen, G. T. Shen, B. Y. Hu, and K. Y. Jiang, *J. Magn. Magn. Mater.* 175, 285 (1997).
37. G. V. Kurylyanskaya, J. M. García-Beneytez, M. Vázquez, J. P. Sinnecker, V. A. Lukshina, and A. P. Potatov, *J. Appl. Phys.* 83, 6581 (1998).
38. H. Q. Guo, H. Kronmüller, T. Dragon, C. Chen, and B. G. Shen, *J. Appl. Phys.* 84, 5673 (1998).
39. M. Tejedor, B. Hernando, M. L. Sánchez, V. M. Prida, J. M. García-Beneytez, M. Vázquez, and G. Herzer, *J. Magn. Magn. Mater.* 185, 61 (1998).
40. P. Aragonese, D. Holzer, H. Sassik, A. Zhukov, R. Grössinger, and J. González, *J. Magn. Magn. Mater.* 203, 292 (1999).
41. M. Tejedor, B. Hernando, M. L. Sánchez, and V. M. Prida, *J. Magn. Magn. Mater.* 203, 114 (1999).
42. J. He, H. Q. Guo, B. G. Shen, K. Y. He, and H. Kronmüller, *J. Appl. Phys.* 86, 3873 (1999).
43. J. A. Moya, B. Arcondo, H. Sirkin, M. L. Sartorelli, M. Knobel, and M. Vázquez, *J. Magn. Magn. Mater.* 203, 117 (1999).
44. M. Vázquez, G. V. Kurylyanskaya, J. M. García-Beneytez, J. P. Sinnecker, J. M. Barandiarán, V. A. Lukshina, and A. P. Potatov, *IEEE Trans. Magn.* 35, 3358 (1999).
45. L. Zeng, G. Chen, F. F. Gong, Z. C. Wang, J. X. Yang, and X. L. Yang, *J. Magn. Magn. Mater.* 208, 74 (2000).
46. P. Allia, M. Coisson, P. Tiberto, F. Vinai, and L. Lanotte, *J. Magn. Magn. Mater.* 215–216, 346 (2000).
47. H. Lee, Y.-K. Kimb, T.-K. Kimb, and S.-C. Yuc, *J. Magn. Magn. Mater.* 215–216, 307 (2000).
48. S. Q. Xiao, Y. H. Liu, S. S. Yan, Y. Y. Dai, L. Zhang, and L. M. Mei, *Phys. Rev. B* 61, 5734 (2000).
49. H. Q. Guo, H. Kronmüller, T. Dragon, Z. H. Chen, and B. G. Shen, *J. Appl. Phys.* 89, 514 (2001).
50. H. S. Kwon, H. Lee, K. Kim, S. C. Yu, and Y. K. Kim, *J. Alloys Compounds* 326, 309 (2001).
51. H. Lee, K. J. Lee, Y. K. Kim, K. Kim, and S. C. Yu, *J. Alloys Compounds* 326, 313 (2001).
52. G. V. Kurylyanskaya, H. P. Yakabchuk, E. Kisker, N. G. Bebenin, H. García-Miquel, M. Vázquez, and V. O. Vaskovskiy, *J. Appl. Phys.* 90, 6280 (2001).
53. V. Franco and A. Conde, *Mater. Lett.* 49, 256 (2001).
54. M. Tejedor, B. Hernando, M. L. Sánchez, V. M. Prida, and P. Gorria, *J. Non-Cryst. Sol.* 287, 396 (2001).
55. C. Appino, C. Beatrice, M. Coisson, P. Tiberto, and F. Vinai, *J. Magn. Magn. Mater.* 226–230, 1476 (2001).
56. P. Gorria, V. M. Prida, M. Tejedor, B. Hernando, and M. L. Sánchez, *Physica B* 299, 215 (2001).
57. L. V. Panina and K. Mohri, *J. Magn. Magn. Mater.* 157–158, 137 (1996).



58. G. Herzer, in "Handbook of Magnetic Materials" (K. H. J. Buschow, Ed.), Vol. 10, p. 415. Elsevier Science, Amsterdam, 1997.
59. M. E. McHenry, M. A. Willard, and D. E. Laughlin, *Progr. Mater. Sci.* 44, 291 (1999).
60. A. Hernando, *J. Phys.: Condens. Matter* 11, 9455 (1999).
61. K. Suzuki, *J. Non-Cryst. Sol.* 192–193, 1 (1995).
62. R. C. O'Handley, "Modern Magnetic Materials. Principles and Applications," Chap. 12. Wiley, New York, 2000.
63. Y. Yoshizawa, S. Oguma, and K. Yamauchi, *J. Appl. Phys.* 64, 6044 (1988).
64. G. Herzer, *IEEE Trans. Magn.* 25, 3327 (1989).
65. K. Suzuki, A. Makino, A. Inoue, and T. Masumoto, *J. Appl. Phys.* 70, 6232 (1991).
66. K. Suzuki, A. Inoue, A. Makino, and T. Masumoto, *J. Appl. Phys.* 74, 3316 (1993).
67. J. González, N. Murillo, J. M. Blanco, J. M. González, and T. Kulik, *J. Appl. Phys.* 76, 1131 (1994).
68. G. Herzer and H. Warlimont, *Nanostruct. Mater.* 1, 263 (1992).
69. J. M. Barandiarán, L. Fernández Barquín, J. C. Gómez Sal, P. Gorria, and A. Hernando, *Solid State Commun.* 8, 75 (1993).
70. C. Issro, P. Winotai, and I. M. Tang, *Solid State Commun.* 108, 775 (1998).
71. P. Gorria, J. S. Garitaonandia, and J. M. Barandiarán, *J. Phys.: Condens. Matter* 8, 5925 (1996).
72. R. Alben, J. J. Becker, and M. C. Chi, *J. Appl. Phys.* 49, 1653 (1978).
73. W. Wensdorfer, D. Mailly, and A. Benoit, *J. Appl. Phys.* 87, 5094 (2000).
74. M. Jamet, W. Wensdorfer, C. Thirion, D. Mailly, V. Dupuis, P. Mélinon, and A. Pérez, *Phys. Rev. Lett.* 86, 4676 (2001).
75. B. Hoffmann and H. J. Kronmüller, *J. Magn. Magn. Mater.* 152, 91 (1996).
76. V. A. Lukshina, N. V. Dmitrieva, and A. P. Potapov, *Phys. Met. Metall.* 4, 376 (1996).
77. G. V. Kurylanskaya, M. Vázquez, E. H. C. P. Sinnecker, A. P. Zhukov, J. P. Sinnecker, A. Hernando, and M. El Ghannami, "Proceedings of the 5th International Workshop on Non-Crystalline Solids" (J. Rivas and M. A. López-Quintela, Eds.), Non-Crystalline and Nanoscale Materials, World Scientific, 1998, p. 190.
78. G. V. Kurylanskaya, M. Vázquez, E. H. C. P. Sinnecker, A. P. Zhukov, J. P. Sinnecker, A. Hernando, and M. El Ghannami, *Text. Microstruct.* 32, 269 (1999).
79. M. N. Baibich, J. M. Broto, A. Fert, F. Nguen Van Dau, F. Petroff, P. Eitanne, G. Creuzet, A. Friedreich, and J. Chazelas, *Phys. Rev. Lett.* 61, 2472 (1988).
80. R. L. Sommer, A. Gündel, and C. L. Chien, *J. Appl. Phys.* 86, 1057 (1996).
81. A. V. Svalov, V. O. Vas'kovskiy, J. M. Barandiarán, N. G. Bebenin, G. V. Kurylanskaya, A. V. Gorbunov, L. Lezama, J. Gutiérrez, and D. Schmool, *J. Alloys Compounds* 327, 5 (2001).
82. G. V. Kurylanskaya, J. L. Muñoz, J. M. Barandiarán, A. García-Arribas, A. V. Svalov, and V. O. Vas'kovskiy, *J. Magn. Magn. Mater.* 242–245, 291 (2002).
83. H. B. Nie, A. B. Pakhomov, X. Yan, X. X. Zhang, and M. Knobel, *Solid State Commun.* 112, 285 (1999).
84. P. Duwez, *Trans. Am. Soc. Metals* 60, 607 (1967).
85. T. Masumoto, I. Ohnaka, A. Inoue, and M. Hagiwara, *Scripta Metall.* 15, 293 (1981).
86. G. F. Taylor, *Phys. Rev.* 23, 655 (1924).
87. A. Antonov, A. Granovskiy, A. Lagar'kov, N. Perov, N. Usov, and T. Furmanova, *Physica A* 241, 420 (1997).
88. J. Wiggins, H. Srikanth, K.-Y. Wang, L. Spinu, and J. Tang, *J. Appl. Phys.* 87, 4810 (2000).
89. K. R. Pirota, L. Kraus, H. Chiriac, and M. Knobel, *J. Magn. Magn. Mater.* 221, L243 (2000).
90. M. Vázquez and A. P. Zhukov, *J. Magn. Magn. Mater.* 160, 223 (1996).
91. K. Handrich and S. Kobe, "Amorphe Ferro- und Ferrimagnetika" Akademie-Verlag, Berlin, 1980.
92. A. N. Sorokin and A. V. Svalov, *Vacuum* 46, 113 (1995).
93. A. V. Svalov, V. O. Vas'kovskiy, and Yu. M. Yarmoshenko, *Phys. Met. Metall.* 79, 53 (1995).
94. U. Hartmann, "Magnetic Multilayers and Giant Magnetoresistance: Fundamentals and Industrial Applications." Springer-Verlag, Heidelberg, 2000.
95. A. S. Antonov, S. N. Gadetskiy, L. B. Granovskiy, A. L. Diachkov, V. P. Paramonov, N. C. Perov, A. F. Prokoshin, N. A. Usov, and A. N. Lagar'kov, *Phys. Met. Metall.* 83, 60 (1997).
96. T. Morikawa, Y. Nishibe, H. Yamadera, Y. Nonomura, M. Takeuchi, J. Sakata, and Y. Taga, *IEEE Trans. Magn.* 32, 4367 (1997).
97. D. P. Makhnovskiy and L. V. Panina, *Sensors Actuators* 81, 91 (2000).
98. T. Uchiyama, K. Mohri, L. V. Panina, and K. Furuno, *IEEE Trans. Magn.* 31, 3182 (1995).
99. J. M. Barandiarán, A. García-Arribas, J. L. Muñoz, G. V. Kurylanskaya, and R. Valenzuela, *J. Appl. Phys.* 91, 7451 (2002).
100. Y. Nishibe, H. Yamadera, N. Ohta, K. Tsukada, and Y. Nonomura, *Sensors Actuators A* 82, 155 (2000).
101. M. Katoh, T. Sone, and K. Mohri, *J. Magn. Soc. Jpn.* 19, 621 (1995).
102. K. Bushida, K. Mori, and T. Uchiyama, *IEEE Trans. Magn.* 31, 3134 (1995).
103. K. H. Shin, M. Inoue, and K. Arai, *J. Appl. Phys.* 85, 5465 (1999).
104. H. Yamadera and Y. Nishibe, *J. Appl. Phys.* 87, 5356 (2000).
105. T. Jagielinski, *IEEE Trans. Magn.* MAG-26, 1925 (1983).
106. P. Gorria, I. Orue, F. Plazaola, and J. M. Barandiarán, *J. Appl. Phys.* 73, 6600 (1993).
107. P. Gorria, L. Fernández Barquín, V. M. Prida, and W. S. Howells, *J. Magn. Magn. Mater.* 254–255, 504 (2003).
108. L. Fernández Barquín, J. C. Gómez Sal, P. Gorria, J. S. Garitaonandia, and J. M. Barandiarán, *J. Phys.: Condens. Matter* 10, 5027 (1997).
109. G. Rixecker, P. Schaaf, and U. Gonser, *J. Phys.: Condens. Matter* 4, 10295 (1992).
110. M. Kopcewicz, A. Grabias, P. Nowicki, and D. L. Williamson, *J. Appl. Phys.* 79, 993 (1996).
111. P. Gorria, V. M. Prida, J. I. Paredes, and B. Hernando, *J. Magn. Magn. Mater.* 258–259, 526 (2003).
112. G. Herzer, in "Encyclopedia of Materials: Science and Technology" (K. H. J. Buschow, Ed.), p. 149. Elsevier, Amsterdam, 2001.
113. G. Herzer, in "Encyclopedia of Materials: Science and Technology" (K. H. J. Buschow, Ed.), p. 5897. Elsevier, Amsterdam, 2001.
114. T. Aihara, E. Akiyama, K. Aoki, M. Sherif El-Eskandarany, H. Habazaki, K. Hashimoto, A. Kawashima, M. Naka, Y. Ogino, K. Sumiyama, K. Suzuki, and T. Yamasaki, in "Amorphous and Nanocrystalline Materials, Preparation, Properties, and Applications" (A. Inoue and K. Hashimoto, Eds.), Advances in Materials Research, Chap. 4. Springer-Verlag, Berlin, 2001.
115. D. V. Louzguine and A. Inoue, in "Amorphous and Nanocrystalline Materials, Preparation, Properties, and Applications" (A. Inoue and K. Hashimoto, Eds.), Advances in Materials Research, Chap. 5. Springer-Verlag, Berlin, 2001.
116. K. Suzuki and J. M. Cadogan, *Phys. Rev. B* 58, 2730 (1998).
117. N. Kataoka, T. Shima, and H. Fujimori, *J. Appl. Phys.* 70, 6238 (1991).
118. S. Ikeda, M. Nagai, and Y. Ueda, *Jpn. J. Appl. Phys.* 34, 6046 (1995).
119. P. Schönhuber, H. Pfützner, G. Harasko, T. Klinger, and K. Futschik, *J. Magn. Magn. Mater.* 112, 349 (1992).
120. H. Kronmüller, R. Schäfer, and G. Schroeder, *J. Magn. Magn. Mater.* 6, 61 (1977).

121. E. Van de Riet, W. Klaassens, and F. Roozeboom, *J. Appl. Phys.* 81, 806 (1997).
122. H. Q. Guo, H. Kronmüller, T. Dragon, Z. H. Chen, and B. G. Shen, *Phys. Rev. B* 62, 5760 (2000).
123. N. Murillo, J. González, J. M. Blanco, and M. Vázquez, *J. Appl. Phys.* 74, 3323 (1993).
124. K. Narita, J. Yamasaki, and H. Fukunaga, *IEEE Trans. Magn.* MAG-16, 435 (1980).
125. R. P. del Real, C. Prados, E. Pulido, and A. Hernando, *J. Appl. Phys.* 73, 6618 (1993).
126. P. Allia, M. Baricco, P. Tiberto, and F. Vinai, *J. Non-Cryst. Sol.* 156–158, 585 (1993).
127. M. Vázquez, P. Marín, H. A. Davies, and A. O. Olofinjana, *Appl. Phys. Lett.* 64, 3184 (1994).
128. J. Gutierrez, D. Atkinson, P. T. Squire, and J. M. Barandiarán, *J. Magn. Magn. Mater.* 196–197, 169 (1999).
129. M. Knobel, *J. Phys. IV* 8, 213 (1998).
130. H. Chiriac, T.-A. Óvari, and C. S. Marinescu, *J. Appl. Phys.* 83, 6584 (1998).
131. H. Chiriac, T.-A. Óvari, and C. S. Marinescu, *Nanostruct. Mater.* 12, 775 (1999).
132. J. He, H. Q. Guo, B. G. Shen, K. Y. He, and J. F. Hu, *J. Phys.: Condens. Matter* 11, 4251 (1999).
133. V. Zhukova, A. F. Cobeño, A. Zhukov, J. M. Blanco, V. Larin, and J. González, *Nanostruct. Mater.* 11, 1319 (1999).
134. C. Wang, F. F. Gong, X. L. Yang, L. Zeng, G. Chen, J. X. Chang, S. M. Qian, and D. P. Yang, *J. Appl. Phys.* 87, 4819 (2000).
135. G. Chen, X. L. Yang, L. Zeng, J. X. Yang, F. F. Gong, D. P. Yang, and Z. C. Wang, *J. Appl. Phys.* 87, 5263 (2000).
136. H. Lee, K.-J. Lee, Y.-K. Kim, T.-K. Kim, C.-O. Kim, and S.-C. Yu, *J. Appl. Phys.* 87, 5269 (2000).
137. M. Tejedor, B. Hernando, M. L. Sánchez, and A. García-Arribas, *J. Magn. Magn. Mater.* 157, 141 (1996).
138. M. Knobel, C. Gómez-Polo, and M. Vázquez, *J. Magn. Magn. Mater.* 160, 243 (1996).
139. M. Knobel, M. Vázquez, M. L. Sánchez, and A. Hernando, *J. Magn. Magn. Mater.* 160, 89 (1997).
140. M. Tejedor, B. Hernando, M. L. Sánchez, V. M. Prida, and M. Vázquez, *J. Phys. D: Appl. Phys.* 31, 2431 (1998).
141. R. Grössinger and R. Sato Turtelli, *IEEE Trans. Magn.* 30, 6044 (1994).
142. M. L. Sánchez, R. Valenzuela, M. Vázquez, and A. Hernando, *J. Mater. Res.* 11, 2486 (1996).
143. M. L. Sánchez, V. M. Prida, B. Hernando, G. V. Kurlyandskaya, J. D. Santos, M. Tejedor, and M. Vázquez, *Chin. Phys. Lett.* 19, 1870 (2002).
144. V. E. Makhotkin, B. P. Shurukhin, V. A. Lopatin, P. Yu. Marchakov, and Yu. K. Levin, *Sensors Actuators A* 25–27, 759 (1991).
145. A. Makino, T. Hatanai, A. Inoue, and T. Masumoto, *Mater. Sci. Eng. A* 226–228, 594 (1999).
146. P. Marín and A. Hernando, *J. Magn. Magn. Mater.* 215–216, 729 (2000).
147. H. Hauser, L. Kraus, and P. Ripka, *IEEE Instrum. Meas. Mag.* 28 (2001).
148. C. Gómez-Polo, A. O. Olofinjana, P. Marín, M. Vázquez, and H. A. Davies, *IEEE Trans. Magn.* 29, 2673 (1993).
149. Y. Y. Dai, Y.-H. Liu, S.-Q. Xiao, L. Zhang, L.-Q. Yue, H.-Z. Wu, and Y.-Z. Zhang, *Phys. Status Solidi (a)* 181, 413 (2000).
150. W.-S. Cho, H. Lee, and C.-O. Kim, *Thin Solid Films* 375, 51 (2000).
151. G. V. Kurlyandskaya, H. P. Yakabchuk, E. Kisker, N. G. Bebenin, H. García-Miquel, M. Vázquez, and V. O. Vas'kovskiy, *Chin. Phys. Lett.* 18, 1268 (2001).
152. Y. Y. Dai, S.-Q. Xiao, Y.-H. Liu, L. Zhang, H.-Z. Wu, and Y.-Z. Zhang, *Chin. Phys. Lett.* 18, 272 (2001).
153. P. Marín, M. López, P. Agudo, M. Vázquez, and A. Hernando, *Sensors Actuators A* 91, 218 (2001).
154. A. Hernando, P. Marín, M. Vázquez, J. M. Barandiarán, and G. Herzer, *Phys. Rev. B* 58, 366 (1998).
155. X. L. Yang, J. X. Yang, K. Y. Liang, G. Chen, H. J. Lin, and Y. Z. Zhang, *J. Appl. Phys.* 85, 5124 (1999).
156. P. Weiss, *J. de Phys. Rad.* 6, 661 (1907).
157. A. Hubert and R. Schäfer, "Magnetic Domains." Springer-Verlag, 1998.
158. J. P. Sinnecker, P. Tiberto, G. V. Kurlyandskaya, M. Vázquez, E. H. C. P. Sinnecker, and A. Hernando, *J. Appl. Phys.* 84, 5814 (1999).
159. G. V. Kurlyandskaya, M. Vázquez, J. McCord, J. L. Muñoz, D. García, and A. P. Potapov, *Phys. Met. Metall.* 90, 549 (2000).
160. N. V. Dmitrieva, V. A. Lukshina, G. V. Kurlyandskaya, and A. P. Potapov, *Text. Microstruct.* 32, 280 (1999).
161. L. Kraus, K. Záveta, O. Heczko, P. Duhaj, G. Vlasák, and J. Schneider, *J. Magn. Magn. Mater.* 112, 275 (1992).
162. A. Ludwig, M. Tewes, S. Glasmachers, M. Löhndorf, and E. Quandt, *J. Magn. Magn. Mater.* 242–245, 1126 (2002).
163. Z. J. Zhao, F. Bendjaballah, X. L. Yang, and D. P. Yang, *J. Magn. Magn. Mater.* 246, 62 (2002).
164. L. Zeng, Z. J. Zhao, X. L. Yang, J. Z. Ruan, and G. Chen, *J. Magn. Magn. Mater.* 246, 422, (2002).
165. G. Herzer, *IEEE Trans. Magn.* 26, 1397 (1990).
166. J. Hu, H. Qin, S. Zhou, Y. Wang, and Z. Wang, *Mater. Sci. Eng. B* 83, 24 (2001).
167. Md. Kamruzzaman, I. Z. Rahman, and M. A. Rahman, *J. Mater. Process. Tech.* 119, 312 (2001).
168. Y.-F. Li, M. Vázquez, and D.-X. Chen, *J. Magn. Magn. Mater.* 249, 342 (2002).
169. S. N. Kane, M. Vázquez, S. Puerta, and A. Hernando, *J. Magn. Magn. Mater.* 249, 333 (2002).
170. M. N. Gona, S. Yanase, S. Hashi, and Y. Okazaki, *J. Magn. Magn. Mater.* 254–255, 466 (2003).
171. C. Miguel, A. P. Zhukov, and J. González, *J. Magn. Magn. Mater.* 254–255, 463 (2003).
172. V. M. Prida, P. Gorriá, G. V. Kurlyandskaya, M. L. Sánchez, B. Hernando, and M. Tejedor, *Nanotechnol.* 14, 231 (2003).